Project Title: Effect of H_2S and CO_2 in HPHT Wells on Tubulars and Cement

Report Type: Monthly Report

Report #: 01

Reporting Period: September 22 to October 21, 2011

Authors:

Ramadan Ahmed

Subhash Shah

Samuel Osisanya

Prepared under BOEMRE Project # M11PC00030

by

THE UNIVERSITY OF OKLAHOMA

October 21, 2011

1. Summary of Work Accomplished

This report presents the progress made during the first month (Sept. 22 – Oct. 21, 2011) of the project. During this period, the research team focused on: i) laboratory space selection for high-pressure experimental setups involving sour gases; ii) safety training needed to successfully accomplish the proposed research; iii) development of final design for the setups; and iv) literature review on cement degradation. In addition, as required by the contract, we have prepared the agenda and summary for the kick-off meeting, which was held on October 12, 2011.

As most of the cement aging and corrosion experiments will be performed under high-pressure high-temperature sour gas environments, obtaining a laboratory space that fulfills all the safety requirements is challenging. After considering different options including indoor and outdoor laboratory spaces, we have identified a suitable laboratory that was used previously as a mobile rock property lab. The lab has all the required utilities such as ventilation and air conditioning, power supply, water and compressed air lines.

To assure safe operation of the planned test facilities, our research equipment specialist, Joe Flenniken, has taken a special course on safely handling hydrogen sulfide and sour gases. The course is aimed to develop a training program for the project. Faculty, staff and research assistants involved in the project will be routinely trained.

As outlined in the project schedule, the design and development of experimental setups (Task 2.1 and Task 3.1a) and literature review (Task 1.1a) have been initiated. At this stage of the project, the literature survey is focusing on gathering information needed for finalizing the designs of the experimental facilities and analyzing available data from previous studies to investigate the sensitivity of measurements to the test parameters. This facilitates the development of a test matrix for preliminary experiments as required by the Design of Experiments (DoE) method.

Preparations of the final designs for cement-degradation test setups (cement specimen aging cell and confined compressive/tensile strength measuring facilities) have been started after the approval of the project. The final design presents every detail of the facilities, including equipment and piping designs, instrumentation, and control circuits. Purchase orders for the components of these setups will be placed once the design is completed.

2. Overall Project Progress

2.1 Theoretical Studies (Task 1)

This task is primarily aimed at establishing a theoretical basis for degradation and leaching processes of cement, and corrosion of tubulars. Limited studies have been conducted in the past to understand the degradation of well cement and tubulars under elevated temperature and pressure conditions. In addition, corrosion performance of different steels and steel alloys under sour gas environments has been investigated. Even though most of these studies are performed under low-pressure conditions, they still provide useful input for our planned research. A research assistant is assigned to carry out literature survey, compile, and analyze published data, which is in the public domain. The survey focuses on the degradation of cement exposed to sour gas environments. As outlined by the DoE method, the outcome of the analysis is expected to provide the necessary information to develop a preliminary test matrix for the experimental investigation. Details of the literature survey will be presented in the subsequent reports.

2.2 Experimental Studies on Degradation of Cement (Task 2)

This task includes development of experimental setups for cement durability studies and testing the performance of conventional and new cement formulations. The primary subtask planned for the first six months is the development of the experimental facilities. Upon approval of the award, more effort has been put into developing the facilities. The first task that the project team undertook was selecting an appropriate lab space for the experimental setups. Different locations were considered, including indoor and outdoor laboratory spaces. After careful consideration of project safety and performance issues, it was decided to set up the experimental facility in a mobile lab (**Fig. 1**) that was originally designed to perform field core analysis and rock property measurements. The lab is furnished with (**Fig. 2**) an air conditioning system, power supply, and utilities (compressed air and water). It has not been used for the last couple of years and needs cleanup and minor repair.

Safe operation of the test facilities is critical for the success and timely completion of the project. To assure the planned experiments are preformed safely and according to federal and state regulatory standards, our research equipment specialist has completed the required course at the OSHA Training Institute, which is a member of The Texas A&M University System. The course (Hydrogen Sulfide Instructor Development): i) explains the hazards associated with H_2S; ii) describes the federal and state H_2S regulatory standards; iii) presents the methods to reduce

the potential of exposure and risks involved with H_2S; and iv) helps to develop an effective training program for specific sites. The specialist will develop a training program for the project. All personnel involved in the project are required to participate in the routine training, which will be provided every six months.

Fig. 1 Mobile rock property lab

(a) **(b)**

Fig. 2 Inside view of the rock property lab

Significant progress has been made on improving the design of injection cylinders during this reporting period. The injection cylinder is used to regulate sour gas composition and boost the supply gas pressure. The original design (**Fig. 3**) requires a floating piston with a rod, which is connected to a displacement sensor. This configuration requires a high-pressure seal, which

requires routine repair and replacement. In addition, the seal may allow gas leakage during the experiment. Therefore, the improvement was necessary. The new design avoids the use of the piston rod; instead, the position of the piston is determined based on the amount of liquid pumped to the cylinder (i.e. based on volumetric balance). This approach is safer and has the same level of measurement reliability.

The design of the cement specimen aging setup will be finalized next. Purchase orders for custom-made components of the setup, such as the aging cell and injection cylinder, will be placed once the final design is completed and price quotations are finalized.

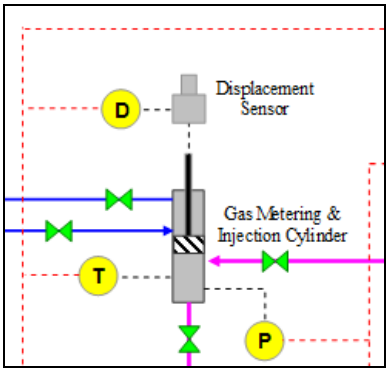

Fig. 3 Injection cylinder

2.3 Experimental Studies on Corrosion of Tubulars (Task 3)

Although tubular corrosion studies are planned for Years 2 and 3, the design of the test setup for these studies will be completed in the first year of the project. As the design of the facility is more complicated than the cement aging setup, it is expected to take a longer time to complete. Some components require customization to suit the planned experimental needs. During this reporting period, we have contacted suppliers of major components to provide detailed technical specifications of their products and discussed their customization options.

3. Meetings and Contacts

As outlined by the contract agreement, a web-based kick-off conference was held on October 12, 2011. The principal investigators from the University of Oklahoma and the Contracting Officer's Representative (COR) of the project and other experts from BOEMRE participated in the meeting. A number of technical and managerial issues were discussed and directions were given by the COR regarding TAB meeting presentation approval process and consideration of the Board's technical suggestions and recommendations. The details of this meeting are presented in the kick-off meeting summary. A draft copy of the summary has been submitted to the COR for review and approval. The final copy will be submitted next week.

Technical Advisory Board (TAB) meetings (conferences) are expected to be held every six months. The first TAB meeting is scheduled for November 9, 2011 in Norman, Oklahoma. All TAB members from the industry (Halliburton, Schlumberger, Det norske and Baker Hughes)

have confirmed their participation. In addition, the Contracting Officer's Representative will be attending the meeting. One of the TAB members from the University of Stavanger will not be able to attend the meeting in person. Arrangements will be made for him to be able to participate in the conference online. The outcome of the conference will be presented in the next monthly report.

4. Planned Activities

- Completion of the design of cement specimen aging setup.
- Begin ordering custom-made components of the experimental setups and standard items with a long lead-time.
- Continue literature survey on cement degradation.
- Repair and prepare the laboratory spaces needed for test facilities.
- Technical advisory board meeting.

Project Title: Effect of H_2S and CO_2 in HPHT Wells on Tubulars and Cement

Report Type: Monthly Report

Report #: 02

Reporting Period: Oct. 22nd to Nov. 21st, 2011

Authors:

Ramadan Ahmed

Subhash Shah

Samuel Osisanya

Prepared under BOEMRE Project # M11PC00030

by

THE UNIVERSITY OF OKLAHOMA

November 22, 2011

1. Summary of Work Accomplished

This report presents the progress made during the second month (Oct. 22 – Nov. 21, 2011) of the project. The research team spent most of the time on preparing laboratory space for high-pressure experimental setup, developing the final design for the cement aging setup, and reviewing literature on cement degradation. In addition, the Technical Advisory Board (TAB) meeting was held on November 9th, 2011. As required by the contract, the minutes of the meeting are presented in the appendix.

As reported last month, we have identified a suitable laboratory for setting up the proposed test facilities. The lab consists of three 13 ft x 7 ft containers that are longitudinally connected to each other, end to end. During this reporting period, the labs have been cleaned and repaired. Even though the lab is furnished with ventilation and air conditioning, power supply, water and compressed air lines, some of these utilities are not in compliance with explosive operating environment regulations. Hence, new power lines which are compatible with said regulations will be installed, and the ventilation system will be upgraded to meet the explosion proof standard.

The final designs for cement-degradation test setups (cement specimen aging cell and confined compressive/tensile strength measuring facilities) have been completed. The final design presents every detail of the facilities including equipment and piping designs, instrumentations, and control circuits. A purchase order (P.O.) has been completed to acquire long lead-time items such as the aging cell and injection cylinder. Once the P.O. is approved, our Purchasing Department will place the order for these items.

Currently, a graduate research assistant is working on literature and theoretical studies on cement degradation. During this reporting period, the focus is on studying different cement formulations, and properties and performance in sour gas environment. The outcomes of the survey will enable us to develop a test matrix for the preliminary experiments as required by the Design of Experiments (DoE) method.

2. Overall Project Progress

2.1 Theoretical Studies (Task 1)

The principal objective of this task is to establish a theoretical basis for degradation and leaching processes of cement, and corrosion of tubulars. Limited studies have been conducted in the past to understand the degradation of well cement and tubulars under elevated temperature and pressure conditions with the presence of sour gases. During this reporting period, the literature survey has been focused on components of Portland cement, cement testing techniques and procedures, and cement additives. The information obtained from the survey will enable us to develop a preliminary test matrix for the experimental investigation. Details of the literature survey will be presented in subsequent reports.

2.2 Experimental Studies on Degradation of Cement (Task 2)

This task includes development of experimental setups for cement durability studies and testing the performance of conventional and new cement formulations. The primary subtask planned for the first six months of Year 1 is development of the experimental facilities. As reported previously, a mobile lab will be used to carry out the proposed experiments. The lab has been cleaned and repaired (**Fig. 1**). However, some improvement is necessary to meet the experimental requirements. Existing power lines and lighting and ventilation systems are not compatible with explosive environments. The power lines, lighting, and ventilation systems will be upgraded to meet the explosion proof standard.

(a) **(b)**

Fig. 1 Inside view of the mobile lab after repair and clean-up

The design of the cement specimen aging setup has been finalized (**Fig. 2**). The new design allows venting of the system using different exhaust lines. The additional exhaust line enables us to depressurize the system when the main venting line plugs off. Air combined with natural gas can create explosive mixtures. To avoid this, nitrogen will be used to purge the air from the system before injecting flammable gases. Aging cell bottom and top inlet/outlet piping are cooled to maintain ambient temperature conditions in the other parts of the setup. This will minimize piping and fittings leaks and wear resulting from high temperature conditions. Two relief systems (relief valve and rapture disk) will be installed on the aging cell setup to prevent over-pressurization of the system resulting from over-heating or excessive injection pressure. The vented gas will be accumulated in a low-pressure waste gas accumulator.

After completing the design, price quotations are also finalized for custom-made components of the setup such as the aging cell and injection cylinder. Purchase requests for these items have been completed.

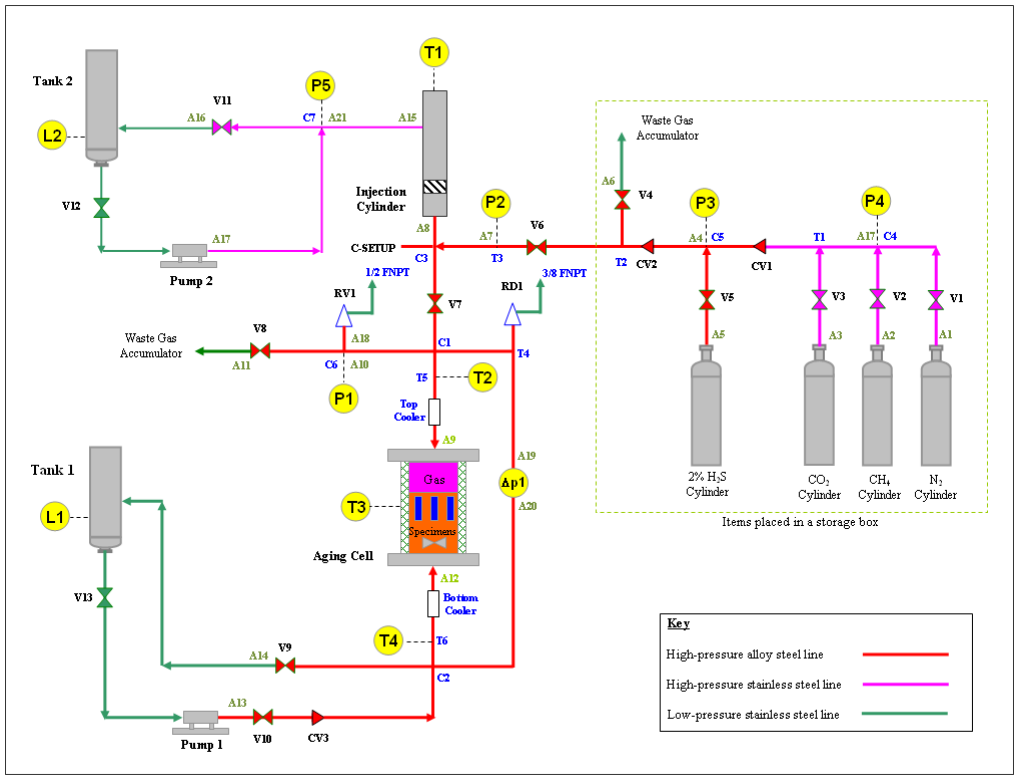

Fig. 2 Revised schematic of the aging cell setup

2.3 Experimental Studies on Corrosion of Tubulars (Task 3)

Although tubular corrosion studies are planned for Years 2 and 3, the design of the test setup for these studies will be completed in the first year of the project. As the design of the facility is more complicated than the cement aging setup, it is expected to take more time to complete. Some components require customization to suit the planned experimental needs. During this reporting period, we have contacted special sensor manufacturers and obtained a quote for high-pressure, high-temperature conductivity sensors. The sensors will be installed on the corrosion setup to monitor in-situ electrical conductivity of the liquid, which is in contact with the test specimen. The measurement is useful to study the corrosion of tubulars resulting from dissolved CO_2 and H_2S. Moreover, the measurements may be used to predict the pH of the liquid in the aging cell in cement degradation experiments. We are investigating the method of obtaining pH from conductivity measurements.

3. Meetings and Contacts

The first Technical Advisory Board (TAB) meeting (conference) was held on November 9th, 2011 in Norman. All TAB members from the industry (Halliburton, Schlumberger, Det norske and Baker Hughes) and the Contracting Officer's Representative attended the meeting. One of the TAB members from the University of Stavanger was unable to participate due to schedule conflict. The details of this conference are presented in the meeting minutes attached to this report.

4. Planned Activities

- Continue ordering components of the experimental setups.
- Prepare the final design of the corrosion setup.
- Continue literature survey on cement degradation.
- Upgrade the laboratory spaces needed for test facilities.

5. Project Expenditures

This section presents the project expenses during the month of October and the cumulative expenditures.

Table 1 Monthly and cumulative expenditure

No.	Budget Categories	Current Expenses	Cumulative Expenses
1	Salaries & Wages	$ -	$ -
2	Fringe Benefits	$ -	$ -
3	Project Materials	$ 670	$ 670
4	Travel	$ -	$ -
5	Conference Expenses	$ -	$ -
6	Other Direct Costs	$ -	$ -
7	Equipment	$ -	$ -
8	Space Rental	$ -	$ -
9	Indirect Cost	$ 335	$ 335
10	**Total**	**$ 1,005**	**$ 1,005**

APPENDIX

Minutes

Technical Advisory Board Meeting

BOEMRE Project # M11PC00030

Project Title: Effect of H_2S and CO_2 in HPHT Wells on Tubulars and Cement

Meeting Date: November 9, 2011

Time: 10:30 a.m. to 3:30 p.m.

Meeting Location: Sarkeys Energy Center, Room # 350, 100 E. Boyd St., Norman, OK 73019-1003

Attendees:

Timothy Steffek, BOEMRE, COR

Andreas Brandl, Baker Hughes

Arild Saasen, Det Norske

Ashok Santra, Halliburton

Gunnar DeBruijn, Schlumberger

Ramadan Ahmed, OU, PI

Subhash Shah, OU, Co-PI

Joseph Flenniken, OU

Majed Enfis, OU

The first Technical Advisory Board (TAB) meeting for the Project # M11PC00030 titled "Effects of Hydrogen Sulfide (H_2S) and Carbon Dioxide (CO_2) in HPHT Wells on Tubulars and Cement." was held at 10:30 a.m. on Wednesday, November 9, 2011. Dr. Ahmed gave a warm welcome to all attendees and was pleased to have the first technical advisory board meeting at the early stage of the project. He introduced the agenda for

the meeting and invited the meeting attendees to introduce themselves. After a brief introduction period, the project overview was presented by Dr. Subhash Shah. He presented the project objectives, expected outcomes, scope and methodology, task descriptions, and reporting and progress evaluation. Some questions were raised from the TAB members during the presentation concerning specimen aging duration, types of cement formulation, and applicability of laboratory measurements for field applications. The limitations of laboratory tests in terms of time and use of extremely harsh conditions were discussed. TAB members suggested the use of gas compositions that are more common in the field. However, some of the participants stressed that actual field concentrations may result in slow degradation that requires extremely long experimental duration.

During the discussion about cement degradation studies, TAB members expressed their willingness to provide test material for the studies. The investigators welcomed the TAB members' initiative and indicated that the research team will be working closely with the industry members to acquire generic cement formulations with known compositions.

After lunch break, Dr. Ahmed made technical presentations on degradation of cement and corrosion of tubulars. He presented the scope and methodology of the research, experimental setups and procedure, test equipment and materials, sample preparation procedures and techniques, and proposed theoretical and modeling studies.

Questions were raised about the specifications of conventional cement (baseline cement). At present, different conventional cement formulations are being used in the field. Mr. Steffek, the contracting officer representative (COR), stated Class H API cement is the most widely used cement in the Gulf of Mexico and as the contract requirement; the project should be using this cement as the baseline formulation. The research team will work closely with BOEMRE experts and TAB members in specifying the baseline formulation. For temperature greater than 230°F, silica will be added to the neat cement. The cement formulation screening study will include different sulfate

resistant cements (medium and high sulfate-resistant cements). The project will also consider other formulations suggested by TAB members for testing as long as their compositions are disclosed. TAB members expressed that any newly formulated cement must have acceptable properties such as rheology, fluid loss and other required cement properties for successful application. The properties of potential cement formulations will be tested rigorously before considering them for the degradation experiments.

Participants discussed manufacturer and batch-wise variability of the same grade cement, and cement property change with time due to environmental exposure and aging. It was mentioned that these variations can have the potential to substantially affecting the key measurements. The need for periodic quality control was discussed. The properties of stored cement will be routinely tested and monitored to ensure cement quality. For baseline cement, the project will be using the single source of cement, possibly one batch. All cement powders and additives used in the project will be kept in an appropriate storage area which will eliminate on-site and environmental exposure and minimize property change that occurs with time.

Regarding cement specimen curing, TAB members indicated that in-situ condition is the best but difficult to perform. They recommended following the standard API procedure to prepare the specimens. The specimens will be prepared under ambient conditions and after curing, they will be placed in the aging cell. TAB members also asked about the specimen casting procedure. PIs described the casting procedure and the application of grease on the wall of the casting mold to lubricate the sample. Participants discussed the potential effects of the grease on the measurements and coring the specimens. Some TAB members suggested coring the specimens instead of casting. During the preliminary testing phase, the project will consider comparing these two methods of specimen preparation techniques and their effects on measurements.

Furthermore, TAB members mentioned the poor reproducibility of shear bonding measurements. The PIs shared their previous experience with these types of

measurements and indicated that if necessary repeated tests will be carried out to determine average values and reduce data scattering.

Dr. Ahmed presented the compressive strength measurement procedure and stated that the project will be using a standard device, which is available in the lab. TAB members asked about the confining pressure for these tests. The PIs replied that the confining pressure will be the same as the aging pressure. In addition, Dr. Ahmed discussed different measurements taken during and after cement specimen aging including pH measurement. One of the TAB members asked how the pH measurements will be conducted. The PI described the measurement procedures. Accordingly, pH measurements will be carried out under atmospheric conditions when the aging cell is depressurized. These measurements do not represent the pH value under the aging condition but may be used for comparison purposes between different tests or predicting the actual pH using models. The project will also explore the possibility of measuring pH under high pressure and temperature conditions.

Some TAB members who conducted similar research indicated the potential fluid leak at high pressure and temperature conditions. Also, the issue of safety was raised and discussed during the meeting. Questions were asked by the TAB members regarding safety and emergency plans. The PIs described the safety plan including the routine safety-training plan for students and personnel involved in the project. In addition, the project will develop an emergency plan.

During the meeting, the need for additional TAB members was also discussed. TAB members suggested inviting Chevron and Total to participate in the project. The PIs pointed out the need for industrial experts in the area of tubular corrosion research.

Dr. Ahmed presented corrosion mechanisms involved with H_2S and CO_2 environment. He discussed experimental setups and test plans. TAB members raised questions regarding the conventional casing material. Participants indicated the application of

different tubular materials in the field. The tubular material for baseline tests will be selected in consultation with TAB members and BOEMRE experts. In addition, some TAB members suggested testing of other tubular materials such as Aluminum and Titanium. These materials may be considered in the tubular screening tests, if they are approved by the COR.

Finally, the meeting was adjourned at 3:30 p.m.

Project Title: Effect of H_2S and CO_2 in HPHT Wells on Tubulars and Cement

Report Type: Monthly Report

Report #: 03

Reporting Period: Nov. 22nd to Dec. 21st, 2011

Authors:

Ramadan Ahmed

Subhash Shah

Samuel Osisanya

Prepared under BOEMRE Project # M11PC00030

by

THE UNIVERSITY OF OKLAHOMA

December 23, 2011

1. Summary of Accomplishments

This monthly report presents the progress made during the project period Nov. 22 – Dec. 21, 2011. Efforts were continued to prepare laboratory space for test facilities, develop experimental setups for testing the cement and tubular specimens, and review literature on cement degradation under harsh downhole conditions.

As previously reported, the laboratory utilities will be upgraded to meet the explosion proof standards. We have identified the necessary items for the upgrade and improvement of the lab space. The upgrade and improvement of the lab will be continued in the coming weeks.

The final designs for cement-degradation test setups were completed during the last month. Based on the design, a number of purchase orders were completed to acquire custom-made and long lead-time items such as the aging cell and injection cylinder. Our Purchasing Department has processed and issued purchase orders to vendors supplying these items. Designs of the aging cell and injection cylinder have been completed. According to the manufacturer, these items will be delivered in February.

Literature review and theoretical studies are underway on cement degradation. The primary focus is to better understand the effects of cement additives on the performance under sour gas environment. The results of the studies will enable to develop a test matrix for the preliminary experiments. After submitting the previous month report along with the TAB meeting minutes, we received feedback from the contracting officer representative (COR) regarding the baseline cement. Based on the COR's recommendation, we communicated with the Technical Advisory Board (TAB) members to receive their final recommendations on the specifications of the baseline cement formulation. The members unanimously recommended the use of Class H cement as the baseline formulation or conventional cement in Task 2.2. They also recommended special cement formulations that will be considered in the cement formulation screening studies (Task 2.3).

2. Overall Project Progress

2.1 Theoretical Studies (Task 1)

One of the objectives of this project is to investigate the degradation and leaching processes of cement under harsh downhole environment. Literature review and theoretical studies on cement deterioration are in progress to better understand the degradation of oil well cement under high-temperature and high-pressure conditions in presence of sour gases. The literature survey is focused on components of Portland cement, cement testing techniques and procedures, and cement additives. The deterioration of cementitious materials exposed to acid attack is being theoretically investigated. Currently two research assistants are involved in this task. The outcome of these studies will enable us to develop a preliminary test matrix for the experimental investigation. Details of the literature survey will be presented in subsequent reports.

2.2 Experimental Studies on Degradation of Cement (Task 2)

This task includes development of experimental setups for cement durability studies and testing the performance of conventional and new cement formulations. The primary subtask planned for the first six months of Year 1 is development of the experimental facilities. During this reporting period, purchase orders have been issued to vendors supplying custom-made and long lead-time components including: i) cement specimen aging cell; ii) injection cylinder; iii) remote control valves; iv) pressure, temperature and conductivity sensors; v) cement consistometer; and vi) electro-pneumatic converters and data acquisition systems. Designs of the aging cell (**Fig. 1**) and injection cylinder (**Fig. 2**) have been completed. The manufacturer requires 6 to 8 weeks lead time afterapproval of the designs.

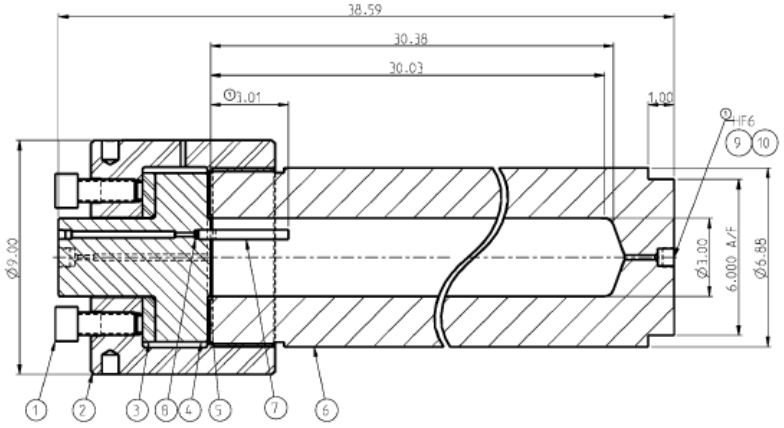

All dimensions are in inches

Fig. 1 Design of cement specimen aging cell

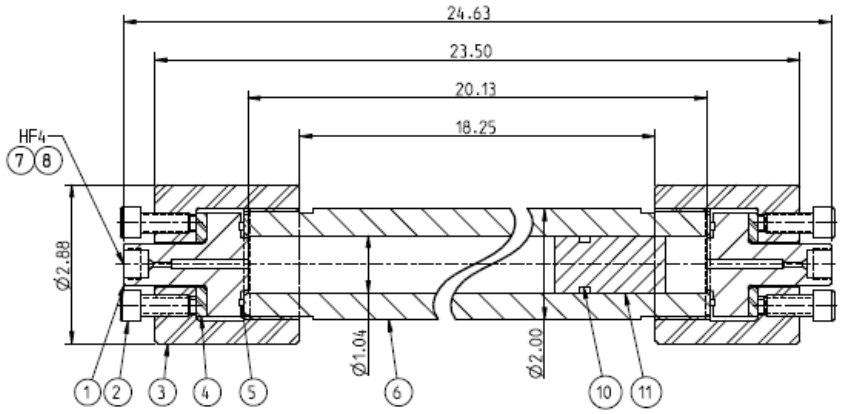

All dimensions are in inches

Fig. 2 Design of injection cylinder

The research team is also working on the improvement of the laboratory space. The laboratory power and instrumentation lines will be upgraded to meet the explosion proof standards (Class I, Division 2, and Group C & D). We have identified switches, lighting fixtures, motor starters, motors, generators, outlets, control panels, and electrical components that meet our specific requirements. The items will be ordered and installed in the coming weeks.

2.3 Experimental Studies on Corrosion of Tubulars (Task 3)

Although tubular corrosion studies are planned for Years 2 and 3, the design of the test setup for these studies will be completed in the first year of the project. During this reporting period, we begin to finalize the designs of test facilities required for these studies. Starting from January 2012, two research assistants will be assigned to conduct literature survey and theoretical studies on corrosion of tubulars.

3. Meetings and Contacts

After receiving feedback from the COR regarding the baseline cement formulation, we contacted TAB members (Halliburton, Schlumberger and Baker Hughes) to obtian their final recommendation on the specifications of the baseline cement formulation. The members recommended the use of Class H cement as the baseline formulation or conventional cement in Task 2.2. In addition, TAB members recommended adding sufficient amount of silica to neat cement (i.e. 35%-40% by weight of cement with the goal to reduce the formal molar ratio of CaO/SiO_2 to around 1 in the final cement recipe) for high temperature tests (i.e. temperature above 230ºF) to prevent deterioration of mechanical properties of the cement. They also suggested the following special cement formulations to be considered in the cement-formulation screening studies in Task 2.3:

a) Plain Class H + water + free water preventive additive at slurry density of 16.4 lbm/gal.
b) Class H + Fly Ash (Class F) (50:50) + water + free water preventive additive at density 16.4 lb/gal
c) Same as in (a) and (b) above; however, with Class G cement instead to examine the particle size effects. Class G cement is finer than Class H.
d) Class H at slurry density less than 16.4 lbm/gal.
e) Class H + Fly Ash (Class F) 50:50 at lower density.

TAB members invited our research team to visit their experimental facilities to share their experience in laboratory testing of cement specimens under elevated pressure conditions. The PIs will be visiting the testing facilities in Houston early next year.

4. Problems Encountered

At present, we are in the process of ordering tubing for cement testing setup. The manufacturer notified that the alloy tubing (3/8-in. high-pressure C-276 tubing) we specified is out of stock. Therefore, to avoid delay in the project, the design of the experimental setups will be revised to match the tubing sizes currently available.

5. Planned Activities

- Revise the design of cement setup and complete purchase order for tubing and fittings.
- Continue ordering components of the experimental setups.
- Prepare the final design of the corrosion setup.
- Continue literature survey and theoretical studies on cement and tubular degradation.
- Upgrade the laboratory spaces needed for test facilities.

6. Project Expenditures

The update on the project expenses during the month of November will be presented in the next monthly report.

Project Title: Effect of H_2S and CO_2 in HPHT Wells on Tubulars and Cement

Report Type: Monthly Report

Report #: 04

Reporting Period: Dec. 22nd, 2011 to Jan. 21st, 2012

Authors:

Ramadan Ahmed, Principal Investigator

Subhash Shah, Co-Principal Investigator

Samuel Osisanya, Co-Principal Investigator

Majed Enfis, Research Assistant

Himanshu Maheshwari, Research Assistant

Prepared under BOEMRE Project # M11PC00030

by

THE UNIVERSITY OF OKLAHOMA

December 30, 2011

1. Summary of Accomplishments

This monthly report summarizes the progress made during the project period Dec. 22, 2012 – Jan. 21, 2012. During this reporting period, the preparation of laboratory space was continued. Progress was made in the development of experimental setups for testing cement and tubular specimens. In addition, literature survey was conducted on cement degradation resulting from high-temperature and sour gas exposure.

Purchase orders have been completed for items needed to improve the laboratory utilities. In the coming weeks, an exhaust fan and lighting, and power systems will be installed. As reported previously, some piping elements required for cement degradation testing facility were out of stock. The test setup design has been revised to utilize currently available elements. Subsequently, the purchase orders for the remaining items have been completed.

Literature review and theoretical studies on cement and tubular degradation were conducted. The research team was focused on the effects of high-temperature and harsh environment. According to recent studies, the effect of temperature on cement properties strongly depends on the calcium to silica ratio. High-temperature retrogression of cement can be prevented by adding more silica to the cement to stabilize the tobermorite or transform it into xonotlite and/or gyrolite. Deterioration resulting from aggressive fluids increases porosity and permeability and diminishes the sealing and isolation performance of the cement. Filler materials such as silica fume and fly ash have a negative impact on the carbonation process and help control degradation caused by CO_2 containing fluids.

The deterioration process of cement involves a number of complex processes. As a result, theoretical analysis of this process is very challenging. However, recent modeling studies show the potential of the theoretical approach in understanding the mechanisms of degradation and predicting the effects of cement additives, composition and properties of the fluid in contact with the cement, temperature, and other down-hole parameters.

2. Overall Project Progress

2.1 Theoretical Studies (Task 1)

Literature review and theoretical studies on cement deterioration are in progress to better understand the degradation of oil well cement under high-temperature and high-pressure conditions in presence of sour gases. The literature survey presented in Appendix A shows that the effect of temperature on the cement properties depends on the calcium to silica ratio. At high temperature (greater than 110°C) and high calcium to silica ratio, the tobermorite (C-S-H) phase transforms into more stable α-C_2SH phase, resulting in increased permeability and low compressive strength. This can be prevented by adding more silica to the cement and allowing more stable tobermorite to form. At higher temperatures (greater than 150°C), the tobermorite converts into xonotlite and/or gyrolite. This conversion improves the cement properties and its performance.

Deterioration of cement in aggressive environment leads to increased porosity and permeability that drastically affects the sealing and isolation performance of the cement. The increase in porosity and permeability further intensifies the degradation process by allowing more aggressive fluid to penetrate into the cement and reach the uncarbonated zone. The depth of CO_2 penetration depends upon two factors, namely, permeability and the amount of $Ca(OH)_2$ in the cement system. To lower the depth of penetration, we need to lower the amount of $Ca(OH)_2$ by increasing the amount of filler materials such as silica fume and fly ash. Since there is less amount of the substance which reacts with CO_2, there will be less carbonation. More detail is presented in Appendix B.

Cement deterioration involves a number of complex physico-chemical phenomena, which affect the chemical, mechanical and flow properties of the cement. Due to its complexity, phenomenological approaches are often preferred to study the degradation process. However, for the past two decades, theoretical analysis and modeling of cement degradation have been gaining momentum. Studies presented in Appendix C have been conducted applying different levels of theoretical modeling including: diffusion-based approach; reactive transport model; and multi-ionic transport model.

2.2 Experimental Studies on Degradation of Cement (Task 2)

This task includes the development of experimental setups for cement durability studies and testing the performance of conventional and new cement formulations. The primary subtask planned for the first six months of Year 1 is development of the experimental facilities. As indicated in the last report, the alloy tubing we specified was out of stock. Therefore, to avoid delay in the project, the design of the experimental setup was revised to match the tubing sizes currently available. Subsequently, purchase orders have been issued to vendors supplying high pressure tubing, tube fittings, sensors and measuring instruments. At present, we are receiving previously ordered items. Atmospheric cement consistmeter and data acquisition systems have been delivered.

The research team is also working on the improvement of the laboratory space. The laboratory power and instrumentation lines will be upgraded to meet the explosion proof standards (Class I, Division 2, and Group C & D). Purchase orders for previously identified items such switches, lighting fixtures, exhaust and circulation fans, window shutters, and H_2S and CH_4 detectors have been completed.

2.3 Experimental Studies on Corrosion of Tubulars (Task 3)

During the past month, designs of the corrosion test facilities have been revised. Additional improvements are still needed to complete the design. Some required items such as a high-pressure recirculation pump are not available in the market. We are continuing our search for a pump that fits the desired specifications. Currently, two research assistants are conducting literature survey and theoretical studies on corrosion of tubulars. Details of the literature survey will be presented in subsequent reports.

3. Meetings and Contacts

We have received a review comment[†] on our previous report from the COR. The review was conducted by Candi Hudson. A summary of our response is presented here:

Task 2.1 - Theoretical Studies & Literature Review

How is "the deterioration of cementitious materials exposed to acid attack being theoretically investigated?"

Response: The deterioration of cementitious materials such as tobermorite gel ($3CaO.2SiO_2.3H_2O$) will be theoretically studied considering both thermodynamic and kinetic aspects of the tobermorite calcification process. Understanding the diffusion process of the reactants and products is also very critical as the overall process rate may be determined by this phenomenon.

What specifically is being conducted theoretically?

Response: Study on tobermorite calcification process and diffusion of the reactants and products in porous cement is underway.

What type of models are being performed?

Response: Currently, we are looking at different models that are presented in the Appendix C.

What are the parameters, governing equations, boundary conditions of the mathematical models? Example not related e.g. Raoults Law? Stirling approximation?

Response:
Parameters: Cement and fluid compositions and properties, temperature, and pressure.
Governing equations: conservation of mass and energy, thermodynamic laws, diffusion equation, equations describing the kinetics of the reactions involved, models describing

[†] Review comments are displayed in italic font.

behavior of mixtures (Raoults and Henery's Laws, dissociation/ionization of carbonic acid (H_2CO_3) and hydrosulfuric acid (H_2S (aq)).

Boundary conditions: Depend on specific problem and application. Boundary conditions for laboratory experiments may be different from the conditions used for field applications.

Are the models of theoretical studies strictly based on literature review in which the experimental cement degradation tests will be developed? Or new models derived?

Response: The models will be based on the existing ones. However, we will adopt them for oil field applications.

Cement Studies – General Comments

Wouldn't it also be beneficial to examine the particle size effects of Class H cement as well as Class G? Recognizing that Class G has more finer particle size than Class H.

Response: We may be able to conduct limited tests with Class G cement to examine the size effect.

Excellent – Class H, cement formulation and addition of silica for high temperature test conditions

4. Planned Activities

- Continue ordering components of the experimental setups.
- Continue preparing the final design of the corrosion setup.
- Upgrade the laboratory spaces needed for test facilities.
- Continue literature survey and theoretical studies on cement and tubular degradation.
- Develop cement core preparation procedure.

5. Project Expenditures

This section presents the project expenses during the months of November (Table 1) and December (Table 2), and the cumulative expenditures.

Table 1 Monthly and cumulative expenditure, November 30, 2011

No.	Budget Categories	Current Expenses	Cumulative Expenses
1	Salaries & Wages	$1,500.00	$1,500.00
2	Fringe Benefits	$82.50	$82.50
3	Project Materials	$1,077.21	$1,747.16
4	Travel	$0.00	$0.00
5	Conference Expenses	$0.00	$0.00
6	Other Direct Costs	$0.00	$0.00
7	Equipment	$0.00	$0.00
8	Space Rental	$0.00	$0.00
9	Indirect Cost	$1,329.86	$1,664.84
10	**Total**	**$3,989.57**	**$4,994.50**

Table 2 Monthly and cumulative expenditure, December 31, 2011

No.	Budget Categories	Current Expenses	Cumulative Expenses
1	Salaries & Wages	$1,500.00	$3,000.00
2	Fringe Benefits	$82.50	$165.00
3	Project Materials	$2,234.58	$3,981.74
4	Travel	$919.59	$919.59
5	Conference Expenses	$0.00	$0.00
6	Other Direct Costs	$0.00	$0.00
7	Equipment	$8,690.00	$8,690.00
8	Space Rental		$0.00
9	Indirect Cost	$2,368.34	$4,033.18
10	**Total**	**$15,795.01**	**$20,789.51**

Appendix A: Effects of CO_2 and H_2S on Mechanical Properties of Cement

Introduction

Cementing operations are critical to the success of drilling and completion operations of a well. The function of cement is to i) protect and support the casing, ii) prevent fluid migration and channeling behind the casing, iii) isolate the vugular and fractured formations from the fluid movements, iv) close an abandoned portion of the well, and v) provide zonal isolation necessary to drill further or control production. During the life of the well, the cement sheath integrity is affected by the high-pressure and high-temperature (HPHT) downhole conditions, which result in the deterioration of the cement. Furthermore, cement degradation occurs due to chemical attacks under downhole conditions.

Mineralogy of Portland Cement

Portland cement, in accordance with the American Petroleum Institute (API), is specified into four crystalline compounds in the clinker that hydrate to form a rigid structure. These compounds are:

Tricalcium Silicate: $3CaO.SiO_2$ (C_3S, main contributor to the cement strength)
Dicalcium Silicate: $2CaO.SiO_2$ (C_2S, provides long term strength)
Tricalcium Aluminate: $3CaO.Al_2O_3$ (C_3A, promote rapid hydration of cement)
Tetracalcium Aluminoferrite: $4CaO.Al_2O_3.Fe_2O_3$ (C_4AF)

Different classes (A to H) of Portland cement are used in the field. API has classified three standard types of cement for use in wells: i) Ordinary type (O); ii) Moderate sulfate-resistant (MSR), and iii) High sulfate-resistant (HSR).

Cement Hydration

During cement hydration, the main reaction products (Fig. A-1) formed are tobermorite gel ($3CaO.2SiO_2.3H_2O$), which is known as C-S-H phase and the portlandite ($Ca(OH)_2$). The tobermorite gel is the main binding material. Reaction equations for hydration of C_3S and C_2S are written as:

$$2(3CaO.SiO_2) + 6H_2O \rightarrow 3CaO.2SiO_2.3H_2O + 3Ca(OH)_2 \quad \text{(1)}$$

$2(2CaO.SiO_2) + 4H_2O \rightarrow 3CaO.2SiO_2.3H_2O + Ca(OH)_2$ (slow reaction) …… (2)

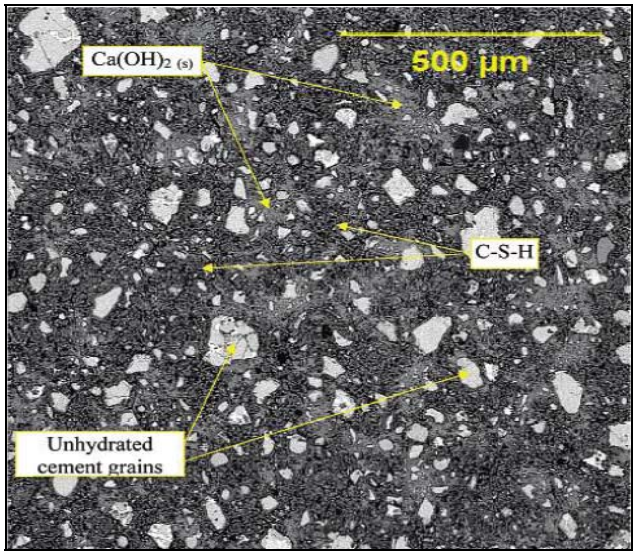

Fig. A-1 SEM-BSE image of cement cured for 28 days at 22°C and 0.1 MPa (Kutchko et al., 2007)

The C_3A also hydrates very rapidly and produces most of the heat of hydration observed during the first few days. To control this rapid hydration, gypsum is added to the clinker. The C_3A is attacked very fast with the water containing sulfates.

$3CaO.Al_2O_3 + 12H_2O + Ca(OH)_2 \rightarrow 3CaO.Al_2O_3.Ca(OH)_2.12H_2O$ (fast reaction) ……..... (3)

$3CaO.Al_2O_3 + 10H_2O + CaSO_4.2H_2O \rightarrow 3CaO.Al_2O_3.CaSO_4.12H_2O$ ……..……..……..... (4)

C_4AF is hydrated in presence of portlandite and it has only minor effects on the physical properties of the cement.

$4CaO.Al_2O_3.Fe_2O_3 + 10H_2O + 2CaO.H_2O \rightarrow 6CaO.Al_2O_3.Fe_2O_3.12H_2O$ (slow) ……..…..…… (5)

Cement Degradation due to High Temperature

Temperature can strongly affect the properties of oil well cement. The effects of temperature on cement properties depend on its composition. Adding 30 to 40% silica (by weight of cement: BWOC) on neat cement prevents the strength retrogression phenomena, which takes place at temperatures above 230°F (110°C) as the tobermorite (C-S-H) phase transforms into a more stable α-C_2SH phase. This transformation leads to increased permeability and loss of

compressive strength of the cement set (Brandl et al., 2010). By adding SiO_2 to the cement, the calcium to silica ratio decreases, and the C-S-H phase can be stabilized, preserving its high permeability and compressive strength. As the temperature exceeds 302°F (150°C), the tobermorite converts to xonotlite ($Ca_6Si_6O_{17}(OH)_2$) and/or gyrolite ($NaCa_{16}Si_{23}AlO_{60}(OH)_8.64(H_2O)$). These two phases result in decreased permeability and improved compressive strength (Brandl et al., 2010).

Noik and Rivereau (1999) presented compressive strength (Fig. A-2) and permeability (Fig. A-3) measurements obtained from experiments conducted using silica-containing Class G cement. Tests were carried out at different temperatures (120, 140, and 180°C) and for periods of up to 2 years. Figure A-2 presents variations in compressive strength of the cement specimens as a function of time at three different temperatures. Data points are highly scattered. However, they apparently indicate the trend of the compressive strength. The results show mixed trends. For lower temperature tests (120 and 140°C), the compressive strength decreased with aging time as some of the C-S-H phase converted to more stable phase (α-C_2SH). For specimens aged at 180°C, the compressive strengths slightly increased indicating the transformation of tobermorite into xonotlite phase, which was confirmed by X-Ray Diffraction and Nuclear Magnetic Resonance (NMR) analysis.

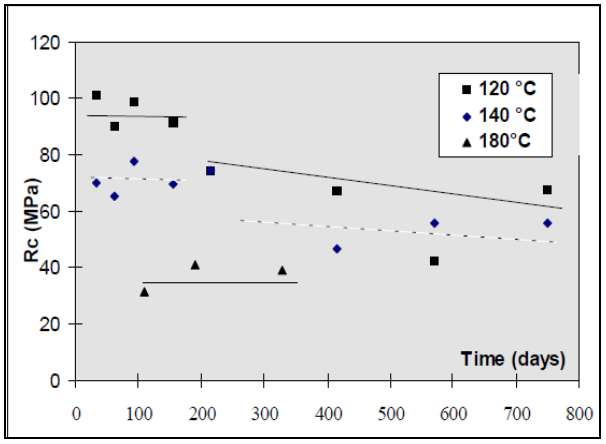

Fig. A-2 Compressive strength variation with temperature (Noik and Rivereau, 1999)

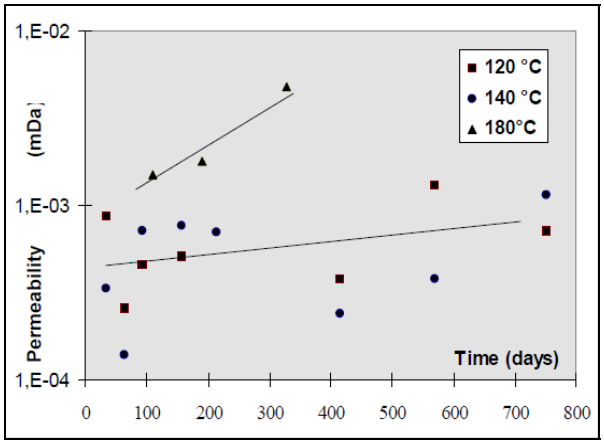

Fig. A-3 Permeability variation with temperature (Noik and Rivereau, 1999)

Figure A-3 shows that the permeability change occurred during high temperature aging. Like the compressive strength measurements, data points display high scattering. Lower temperature aging tests (120 and 140°C) showed slight increases in permeability. At 180°C, a substantial increase in permeability was observed, even though high temperature favors the formation of

xonotlite phase. This contradicts the presumptions of other investigators (Brandl et al., 2010) that the formation of xonotlite phase enhances the sealing property of cement by reducing the cement permeability.

Short-term compressive strength of cement, aged in deionized water, was studied by Dubois et al. (1999). Cement slurry formulations were prepared by adding 20 to 40% crushed sand and 10 to 30% silica fume to the neat cement. The results showed (Fig. A-4) that the compressive strength slightly decreased as temperature was increased from 90 to 120°C, which is believed to be due to C-S-H phase transformation into a more stable α-C_2SH phase. However, at higher temperature (140°C), the compressive strength slightly increased with the aging time indicating the conversion of the tobermorite into xonotlite and/or gyrolite. Similar results (Fig. A-5) have also been reported by Johnson and Garvin (1972). Cement aged at increased temperature showed a reduction in compressive strength. Additives such as bentonite have substantial influence on the temperature sensitivity of the cement. At temperature above 160°C, the compressive strength trend changes. This could be due to the conversion of tobermorite to xonotlite that dominates the transformation of tobermorite to α-C_2SH phase at higher temperatures (T > 160°C).

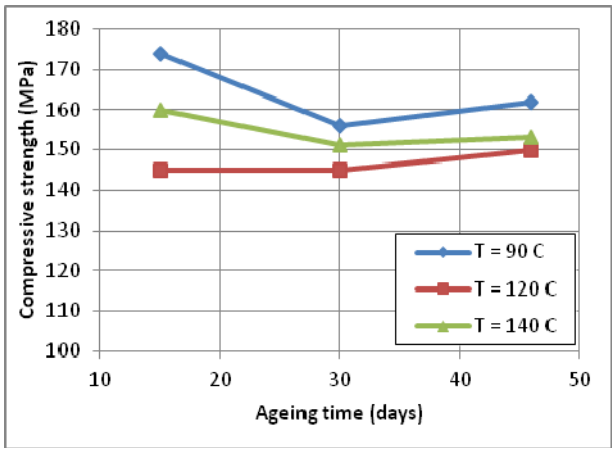

Fig. A-4 Compressive strength vs. aging time at different temperatures (Dubois et al., 1999)

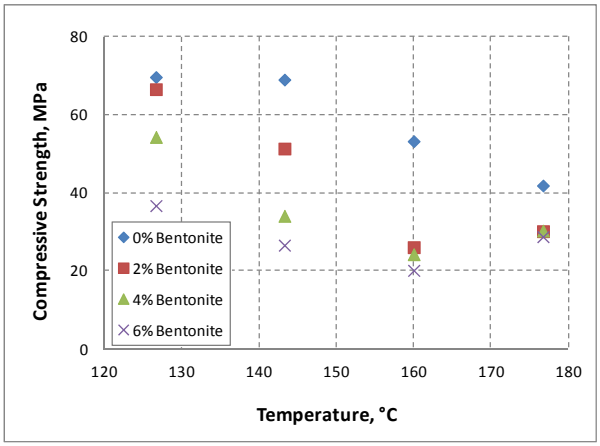

Fig. A-5 Compressive strength vs. temperature after 28 days of aging (Garvin, 1972)

Cement Degradation due to Chemical Attack

Due to the complexity of cement chemistry, the mechanisms of chemical attack on cement are complicated. The chemical changes occurring within the hydrated cement matrix lead to the degradation of the cement. The types of chemical change (attack) can be different, such as

sulfate attack, acid attack, and magnesium attack. The sulfate attack is known as an expansive attack because it penetrates into the cement pores and forms voluminous water-insoluble products. As the size of the crystal is expanded, the pressure inside the cement pores will increase resulting in cracks, fractures, and fragments. The American Society of Testing and Material (ASTM) defines the sulfate attack as the chemical or physical reaction, or both, occurring between the sulfate and the calcium aluminate hydrates, which leads to deterioration of the cement. Morales et al. (2003) presented that the reaction between the C_3A and gypsum, which is commonly added to the clinker to regulate the rate of the hydration that occurs during the first 24 hrs of hydration forming a primary ettringite ($Ca_6Al_2(SO_4)_3(OH)_{12}{\cdot}26(H2O)$).

Temperature plays an important role on the cement sulfate attack. A decrease in the degree of sulfate attack was reported (Morales et al., 2003) with an increase in temperature, which has been supported by many authors. The reason of this observation is that the solubility of the etrringite increases with the increase in the temperature until it becomes completely soluble above 150°F (~ 65°C). However, below 150°F, the cement pastes should be improved to reduce the effect of the sulfate attack. It was reported (Morales et al., 2003) that the effect of sulfate attack can be reduced by decreasing the permeability using pore blocking additives such as latex, sodium silicate, or microsilica.

Effects of CO_2 on Cement Degradation

Carbon dioxide dissolves in water forming acidic solution (water + carbonic acid). This reaction reduces the local pH. Temperature, partial pressure of CO_2 and other ions present in water, such as salts, determine the pH of the solution. The produced carbonic acid penetrates into the cement matrix and attacks the main hydration products or binding materials. The reaction (i.e. carbonation reaction) produces calcium carbonate ($CaCO_3$), amorphous silica (silica gel, $SiO_2.H_2O$) and water as:

$$H_2CO_3 + Ca(OH)_2 \rightarrow CaCO_3 + 2H_2O \quad \text{..... (6)}$$

$$C\text{-}S\text{-}H + H_2CO_3 \rightarrow CaCO_3 + \text{amorphous silica} + H_2O \quad \text{..... (7)}$$

The first reaction (Eq. 6) is considered faster than the second one (Eq. 7). These reactions cause densification, which increases the cement hardness and decreases its permeability, resulting in reduced CO_2 diffusion and expansion up to 6% in volume that can create micro to

macro cracks in the cement matrix (Santra et al., 2009). The produced $CaCO_3$ is leached out by the carbonic acid as:

$$CaCO_3 + H_2CO_3 \rightarrow Ca(HCO_3)_2 \quad \text{..... (8)}$$

The leaching or dissolution of $CaCO_3$ occurs when the cement is surrounded by liquid water containing dissolved CO_2. The dissolution tends to increase porosity and permeability, and degrade mechanical properties of the cement. However, if the above reaction stops after the carbonation of the calcium hydroxide, the $CaCO_3$ formed would cause an increase in compressive strength and a decrease in permeability (Fakhreldin et al., 2010).

Cement specimens aged in the aqueous phase under high-pressure conditions showed an altered region containing distinct zones (Figs. A-6 and A-7) situated in a radial pattern in cylindrical samples (Kutchko et al., 2007). Microscopic examination showed the presence of:

- Unaltered central zone.
- Zone 1 with slightly increased porosity and decreased in $Ca(OH)_2$.
- Zone 2 with decreased porosity and increased calcium content.
- Zone 3 with low calcium content and increased porosity as a result of dissolution.

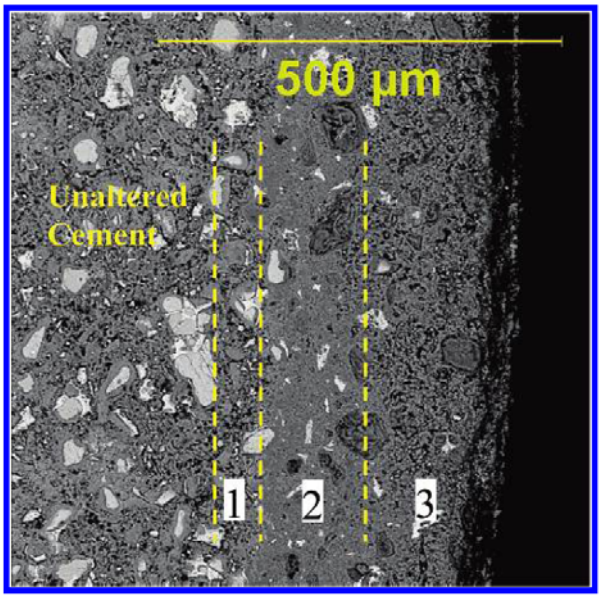

Fig. A-6 Microscopic image of sectioned-cement core after CO_2 exposure (Kutchko et al., 2007)

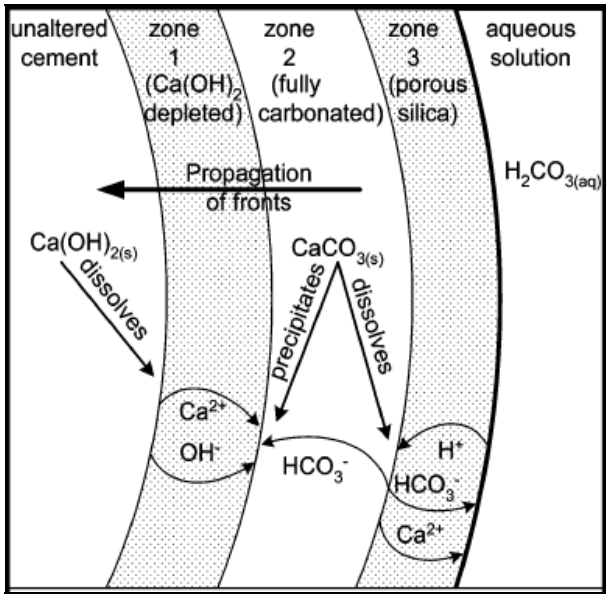

Fig. A-7 Formation of distinct zones in the degraded cement specimen (Kutchko et al., 2007)

These changes taking place in the cement matrix are due to the interaction between the components of the cement and CO_2-saturated brine resulting in the carbonation and bicarbonation of the C-S-H and $Ca(OH)_2$. These distinct zones are formed as a result of the balance between dissolution reaction and species transport in the porous cement. More recently, a similar study (Rimmele et al., 2008) was conducted to investigate the effects of wet supercritical CO_2 and CO_2-saturated water on cement degradation. Results (Fig. A-8) demonstrated surface carbonation of the cement sample after two days of exposure to wet supercritical CO_2 and CO_2-saturated water at 180°C and 280 bars. After 3 months of exposure, the carbonation became clear as the samples showed a thick white layer on their surface, which indicate the formation of calcium carbonate. The carbonation is commonly accompanied by the development of cracks. After 6 months of aging, the carbonated rim on the surface of the samples was flaked out as the carbonation layer became very thick. The pH of water used for aging the cement cores reduced from 13 to 6.5 after the exposure.

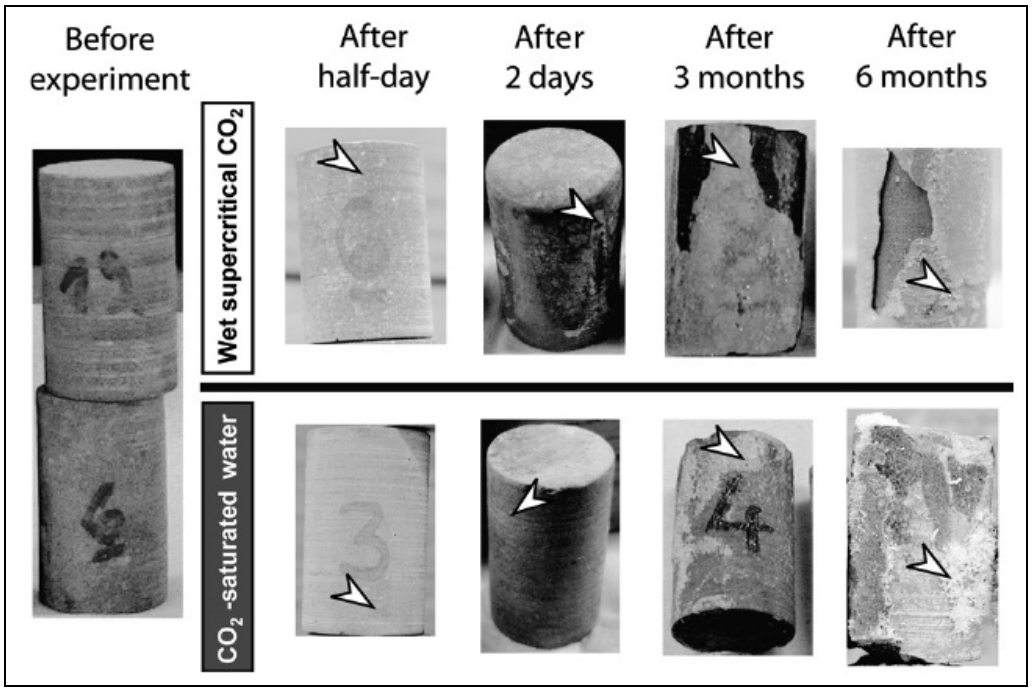

Fig. A-8 Portland cement samples before and after CO_2 exposure at 90 °C and 280 bars (Rimmele et al., 2008)

Cement failure often occurs at the interface between the cement sheath and casing. The shear and hydraulic bonding characteristics of oil well cement are very critical for the performance of the cement. These properties are affected by the exposure of the cement to reactive fluids such as water saturated with CO_2 and/or H_2S. The shear bonding is defined as the force required to break the bonding between the casing and cement sheath per unit contact area. The hydraulic

bond strength is a measure of the hydraulic pressure required to initiate leakage of fluid between the plug and casing. Condor and Asghari (2009) measured these two mechanical properties for cement samples that were exposed to a mixture of brine and CO_2 for 2 months. Results show that the shear bonding were reduced from its initial value of 1240 psi to 30 psi while the hydraulic bond strength reduced from 315 psi to 40 psi after the exposure. It was pointed out that the reduction could be due to shrinkage of the cement in the casing, which creates cracks and micro channels for CO_2 to pass through the clearance between the cement sheath and casing.

Summary

The effects of high-temperature and chemical attack on the mechanical properties and integrity of the cement have been summarized. The literature survey shows that the effects of temperature on the cement properties strongly depend on the calcium to silica ratio. At high temperature (greater than 110°C) and high calcium to silica ratio, the C-S-H phase will transform into more stable α-C_2SH phase that leads to increased permeability and loss of compressive strength of the cement sheath. This can be prevented by adding more silica to the cement to stabilize the tobermorite phase. At temperature greater than 150°C, the tobermorite converts into xonotlite and/or gyrolite. This improves the cement properties. The cement exposed to CO_2 environment may shrink, which creates a pathway between the cement and casing resulting in fluid leakage.

Appendix B: Effects of H_2S and CO_2 on Porosity and Permeability of Cement

Introduction

It is estimated that 40% of the world's remaining gas reservoirs contain more than 2% CO_2 and more than 100 ppm H_2S, (Lecolier et al., 2006). Processes like CO_2 sequestration or CO_2 capture and storage (CCS) demand high quality cement to have zonal isolation. Hence, better understanding of cement degradation is needed for successful well planning and cementing applications. There is limited data for the CO_2 associated cement degradation but data for cement deterioration resulting from H_2S exposure is scarce. This study will investigate the effects of both the CO_2 and H_2S related degradations on the cement porosity and permeability.

It is important to have a long-term cement integrity and zonal isolation for CCS technology (Santra and Sweatman, 2011). In the CCS process, CO_2 is stored by displacing the hydrocarbons from the reservoir pores and trapping CO_2 in reservoir porosity. The carbonation of Portland cement causes an increase in porosity and permeability. This opens a pathway for the stored CO_2 to again escape into the atmosphere. Moderate carbonation can be beneficial for cement porosity and permeability, since it forms $CaCO_3$ that plugs the pores of the cement. However extensive carbonation can result in the loss of structural integrity (Carey et al., 2007). The basic chemistry describing this process carbonation is presented in Appendix A.

When H_2S reacts with water, it forms a weak acid and lowers the pH. Portland cement degrades when it comes in contact with acidic fluids. It is important to understand the interactions of the acid and components of the cement that can react with H_2S (because of higher affinity towards H_2S than Portland cement) and the mechanisms of species transport in the porous cement thereby preventing the cement from severe degradation.

The degradation rate of the cementitious material in the presence of acidic fluid depends upon the acid concentration, pH of the solution and also the type and amount of hydrated phases present in the reaction. For instance, the dissolution of Fe^{3+} and Al^{3+} is slower and occurs at a lower pH value. So when the pH lowers, portlandite ($Ca(OH)_2$) and Tobermorite gel (C-S-H) initially dissolve and then calcium aluminate and ferrite hydrates dissolve. When pH is between 4 and 6, calcium hydrates dissolve leaving behind aluminate and ferrite hydrate. However, at

low pH values (pH ≈ 2), only silica gel is left after the alteration process of the cementitious material (Lecolier et al., 2008).

Experimental Studies

Incorporating filters (silica fumes and fly ash) chemically reduces $Ca(OH)_2$ and C-S-H composition in cement (Table B-1) thereby reducing the formation of calcium carbonate which forms water soluble calcium bicarbonate (Santra et al., 2009).

Table B-1 Comparing the effects of using two different filter materials in cement (Santra et al., 2009)

Filler	Silica Fumes	Fly Ash
Filler material content	35%	98%
Particle size	Finer	Coarser
Porosity & permeability (ϕ and k)	Less	More
Water-solid Ratio	High	Low
$Ca(OH)_2$	Low	High
Depth of penetration	1) Low due to reduction of $Ca(OH)_2$ content 2) Low due to ϕ and k 3) High due to W/S Ratio	1) Low due to reduction of $Ca(OH)_2$ content 2) High due to ϕ and k 3) Low due to W/S Ratio

Depth of CO_2 penetration depends upon the following two factors: i) permeability of the original rock (before carbonation) that controls rate of CO_2 penetration in the rock; and ii) amount of $Ca(OH)_2$ in the system that facilitates the conversion of CO_2 thereby producing more $CaCO_3$, which plugs the pores and results in decreased porosity and penetration depth. Therefore, to lower the depth of penetration, the amount of $Ca(OH)_2$ needs to be lowered by increasing the amount of filler materials such as silica fume and fly ash. To study the effects of filler materials on the carbonation process, Santra et al. (2009) conducted experiments using 11 samples (Table B-2). After aging for 15 days at 2000 psi and 200ºF in the presence of fresh water saturated with CO_2, the samples were cut in half to examine the degree of penetration. Penetration depth was determined by examining different colors formed on carbonated and uncarbonated portions of the sample. The images of the samples presented in Fig. B-1 shows that Samples 5 and 6 were full-penetrated due to extensive CO_2 invasion, which was confirmed by TGA (Thermo-

Table B-2 Slurry compositions (Santra et al., 2009)

Sample, No.	Cement, %	Silica Fume, %	Fly Ash, %
1	100	0	0
2	83.3	16.7	0
3	71.4	28.6	0
4	62.5	37.5	0
5	55.6	44.4	0
6	50	50	0
7	83.3	0	16.7
8	71.4	0	28.6
9	62.5	0	37.5
10	55.6	0	44.4
11	50	0	50

Gravimetric Analysis) and XRD (Santra et al., 2009). Figure B-2 compares the measured depth of penetrations using different filler materials and shows the effect of concentration of the fillers.

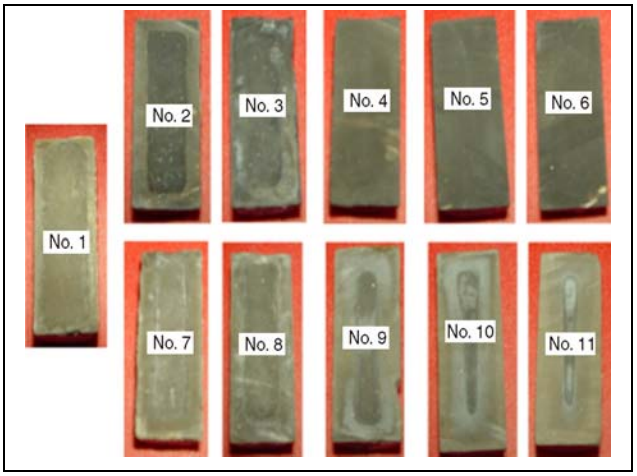

Fig. B-1 Cement core samples after 15-day of aging in water saturated with CO2 (Santra et al., 2009)

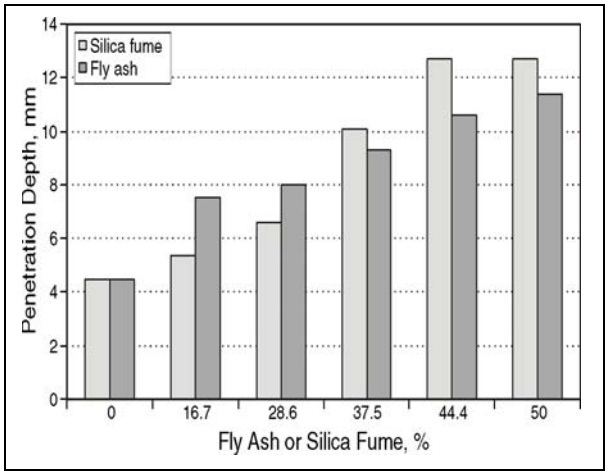

Fig. B-2 Measured penetration depth (Santra et al., 2009)

Recently, Santra and Sweatman (2011) reported the analysis of two different cement samples before and after the CO_2 treatment (i.e. water + supercritical CO_2). The two samples were:

I. Cement sample A – CO_2 resistant formulation
II. Neat Portland cement – Class G cement at 15.8 ppg density

They used the TGA method as a characterization tool. The TGA method is a type of testing performed on samples to determine the change in sample weight in relation to the temperature. Figure B-3a shows the TGA results of the neat cement and System A before the CO_2 treatment. The peaks represent the initial amounts of portlandite. The portlandite amount is significantly less in system A than in the neat cement. Figure B-3b shows the TGA results after the CO_2 treatment. The peak represents the amount of $CaCO_3$ formed. This shows that cement system A is a better option because it has less amount of the substance (portlandite i.e. $Ca(OH)_2$) which can react with CO_2 to form $CaCO_3$.

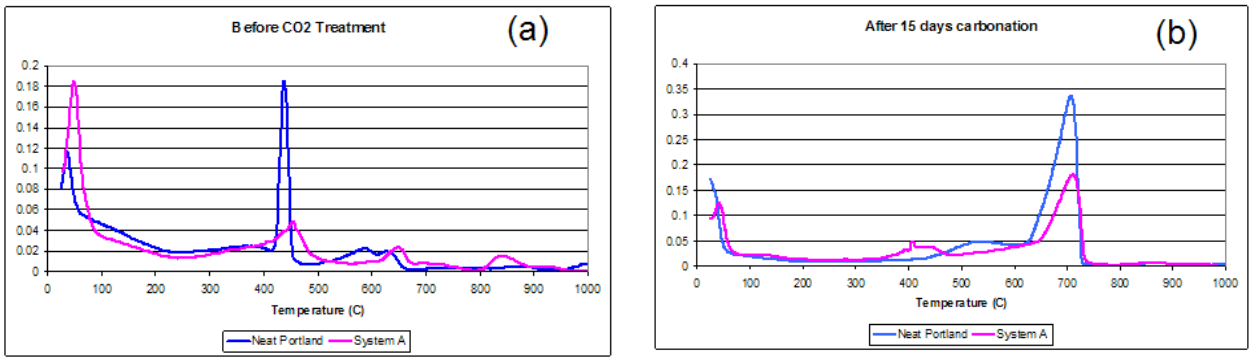

Fig. B-3 Thermo-Gravimetric Analysis: a) before CO_2 treatment; and b) after CO_2 treatment (Santra & Sweatman, 2011)

Temperature Effect

Long-term permeability, shrinkage and compressive strength of different cement core samples exposed to high temperature and high pressure environment were experimentally investigated (Jennings, 2005). Three types of cement samples that are shown below were considered in the investigation.

- **72 PCF:** 71-lbm/ft^3 – hollow ceramic spheres (HCS) blend + 0.15% by weight of blend (BWOB) fluid loss additives + 0.06 gallon/sack dispersant + 0.025 gallon/sack retarder + 0.15% BWOB anti-settling + 2 pt/10 bbls defoamer at 8.80 gallon/sack total mixing fluid.
- **101 PCF:** 101 lbm/ft^3 – Class G (HSR) + 1.9 % BWOC Bentonite (pre-hydrated) + 35% BWOC (silica flour) + 0.60% BWOC fluid loss additives + 0.05 gallon/sack dispersant + 0.025 gal/sack retarder + 2 pt/10 bbls defoamer at 11.47 gal/sack total mixing fluid.
- **118 PCF:** 118 lbm/ft3 – Class G (HSR) + 35% BWOC silica flour + 0.60% BWOC fluid loss additives + 0.10 gal/sack dispersant + 0.03 gal/sack retarder + 1 pt/10 bbls defoamer at 6.26 gal/sack total mixing fluid.

Result show substantial increase in the permeability of samples (72 PCF and 101 PCF) that were made without adding silica flour (Table B-3). The retrogression appears to take place gradually with time (Fig. B-4). The 118 PCF cement exhibited minimum permeability that decreased with aging. This observation is consistent with other similar studies (Brandl et al., 2010) conducted to examine high temperature degradation/retrogression of cement.

Table B-3 Permeability change before and after aging the sample (Jennings, 2005)

Cement Sample	Temp.	Pressure	Permeability (mD)	
			Before	After
72 PCF	300°F	3000 psi	0.10	0.77
101 PCF	300°F	3000 psi	0.60	1.07
118 PCF	300°F	3000 psi	0.02	0.01

Barlet-Gouédard et al. (2006) presented the results of a comprehensive study on the degradation of cement in simulating the interaction of the set cement with injected supercritical CO_2 and water-saturated with CO_2. The study compared (Table B-4) the conventional cement with new CO_2-resistant cement (17 ppg density, which contains a reduced amount of Portland cement).

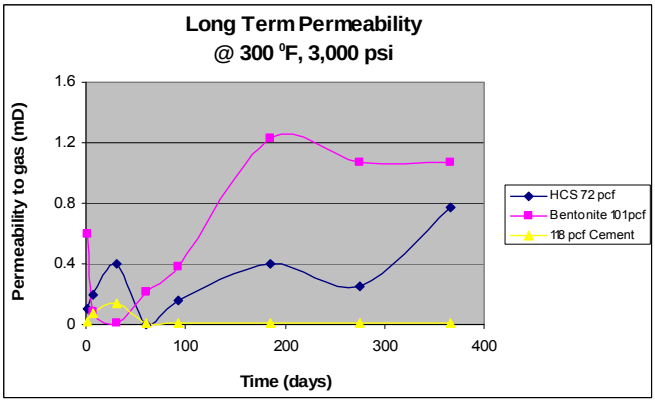

Fig. B-4 Permeability of three different cement cores (Jennings, 2005)

Table B-4 Comparison of conventional and CO2 resistant cement (Barlet-Gouédard et al., 2006)

Cement Sample	Temperature	Pressure	Porosity	Sample Size
Conventional Portland cement (class G, 1.89 g/cm^3, water/cement ratio equal to 0.44)	90°C [194°F]	28 MPa [4061 psi]	In wet supercritical CO_2, the porosity continuously decreases, from initially 33% to 15% after 6 weeks. It rapidly decreases (from 33% to 27%) in the first two days, before the decrease slows down over the next 6 weeks In water-saturated with CO_2, the porosity changes in two distinct phases. During the first phase of approximately three weeks, the porosity rapidly decreases from 33% to 9%. At this stage, the carbonation front has quite completely entered the cores. During the second phase after three weeks, the porosity in-creases from 9% to 21% up to 6 weeks.	0.5-inch-diameter x 1-inch (1.27-cm OD x 2.54-cm) and 1- inch-diameter x 2-inch (2.54-cm OD x 5.08-cm).
A new CO2-resistant material	90°C [194°F]	28 MPa [4061 psi]	CO_2-resistant material remains stable from the first two days to a longer duration.	

After aging, the core samples were cut in half and examined using a microscope (Fig. B-5). The aged cement cores displayed a particular geometry with concentric zones at different test durations on back-scattered electron images. From the core towards the rim of samples, the cement sample consisted of: i) uncarbonated zone; ii) dissolution front; iii) carbonation front; and iv) dissolution back-front. The uncarbonated zone is the inner part of the core, surrounded by the dissolution front. The dissolution front is a highly porosity zone where C-S-H progressively dissolves. The carbonation front is a 50 to 100 µm-large zone of very low porosity. The dissolution back-front is located at the rear of the carbonation front. In this zone, neo-formed carbonates are dissolved, increasing the porosity and resulting in severe degradation of the cement. In contrast, a homogeneous pattern with a limited carbonation threshold is observed with the CO_2-resistant material, which has good mechanical behavior over a wide density range. This material remains comparably inert in both wet supercritical CO_2 and water-saturated with CO_2. Weight, density, compressive strength, microstructural characterizations and Hg porosity measurements confirm good CO_2-resistance of the new cement.

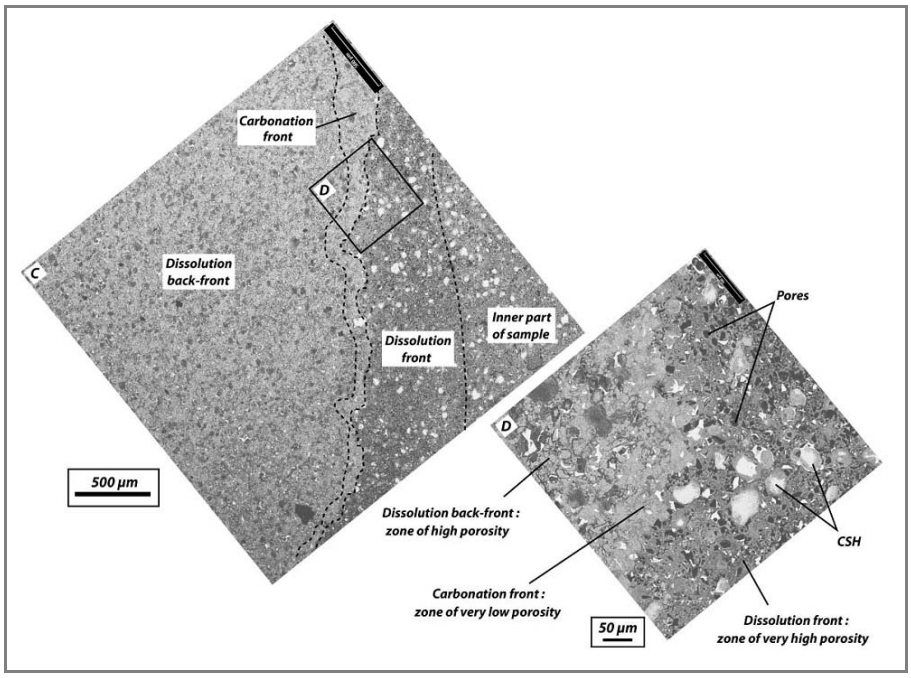

Fig. B-5 Microscopic image of half-core sample after 88 hr aging in CO_2 in wet supercritical CO_2 fluid (Barlet-Gouédard et al., 2006)

Another similar study (Lécolier et al., 2006) considered different cement samples (silica containing cements, conventional cement, and mortar) and two types of aging fluids, namely: reservoir fluid and H_2S saturated brine. The permeability of cement samples containing silica

decreased while the conventional cement showed a substantial increase in permeability. The reason for the increase in permeability is due to excessive calcium leaching (dissolution of portlandite and decalcification of C-S-H).

Effects of Additives

Cement additives may not have direct effect on the nature of the cementitious material, but at the same time they can prevent it from acidic degradation. The two minerals proposed by Lecolier et al. (2008) that have a high affinity for H_2S are:

- Fe_2O_3 (Hematite)
- Mn_3O_4 (Hausmanite)

Conclusions

- Depth of CO_2 penetration depends upon different factors including porosity, permeability and amount of Ca(OH)2.
- The depth of the penetration can be reduced, by lowering the amount of Ca(OH)2 and/or increasing the amount of filler material i.e. silica fume or fly ash. Since there is less amount of the substance which reacts with CO_2, there will be less carbonation.

Appendix C: Theoretical Analysis and Modeling of Cement Degradation

Understanding the degradation mechanisms of cement is essential to develop a theoretical model that can reasonably describe the process. The degradation is a complex phenomenon, which influences the chemical, mechanical and diffusive properties of the cement. As a result, phenomenological methods are often preferred to investigate the degradation process. Nonetheless, for the past two decades, cement degradation modeling has been developing and applying different approaches to formulate models that can predict the change occurring in chemical, mechanical and flow properties of the cement (composition, compressive strength, permeability and porosity) as a function of time after exposure to sour gas containing environments. Depending on their approach, some models are less complex than others. Complex models, compared to simplified models, provide more accurate and detailed descriptions of the process and the influence of different parameters.

Earlier studies (Carde et al., 1996); Carde and Frarqois, 1999) presented a simplified cement degradation model that predicts the increase in porosity and loss of compressive strength. The model is formulated on two basic assumptions: i) linearly varying decalcification of the C-S-H phase in relation to the depth; and ii) the change in compressive strength is similar to the change in calcium content during cement degradation. In its present form, the model does not require a cumbersome numerical procedure to make predictions. The model successfully reproduced experimentally measured porosity (Fig. C-1) and compressive strength variations (Fig. C-2) occurred after aging the sample in ammonium nitrate solution.

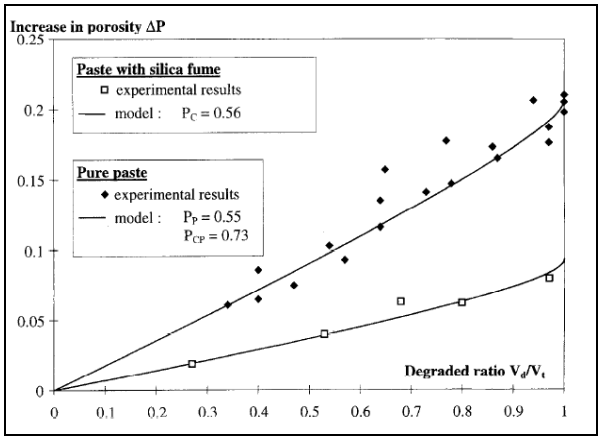

Fig. C-1 Increase in porosity as a function of degradation ratio (Carde and and Frarqois, 1999)

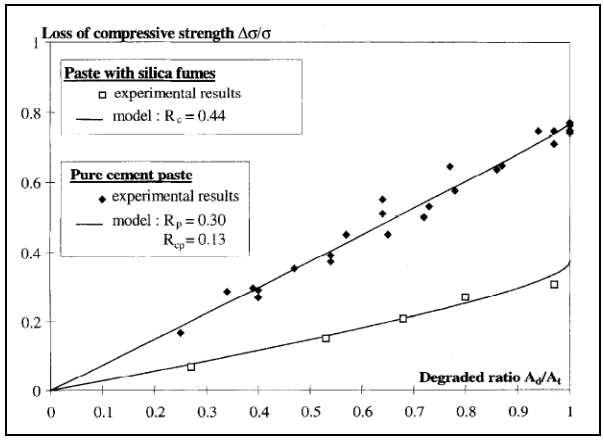

Fig. C-2 Loss of compressive strength as a function of degradation ratio (Carde and and Frarqois, 1999)

Diffusion-based approach is one of the methods frequently used in modeling cement degradation. Buil and Revertegat (1992) presented a model for pure water and lime solutions to predict long-term cement degradation. The deterioration of cement is modeled by ionic diffusion in the cement pore coupled with mass exchange between the solid and the aqueous phases. The model only considers portlandite and C-S-H as the solid phases. It assumes: i) an exchange of matter between the aqueous interstitial solution and the solid phases (dissolution and precipitation); and ii) transport of the species in solution through the pores of the cement. The model predicted the existence of an undamaged core, portlandite dissolution front and a progressive C-S-H decalcification zone. The model predictions and degradation measurements showed a satisfactory agreement (Fig. C-3). The model requires measurable input parameters such as porosity, calcium and portlandite contents, and diffusion coefficient.

Reactive transport modeling approach has the potential to provide reasonable predictions of cement degradation. Different reactive transport models have been presented recently. Casey and Lichtner (2007) developed a model that incorporates solid solutions into equations describing reactive transport in porous material to express cement degradation. In order to complete the model, a thermodynamic module for C-S-H was developed from experimental measurements. The model is used to predict decalcification of C-S-H and carbonation mechanisms. The model successfully predicted the degradation of wellbore cement.

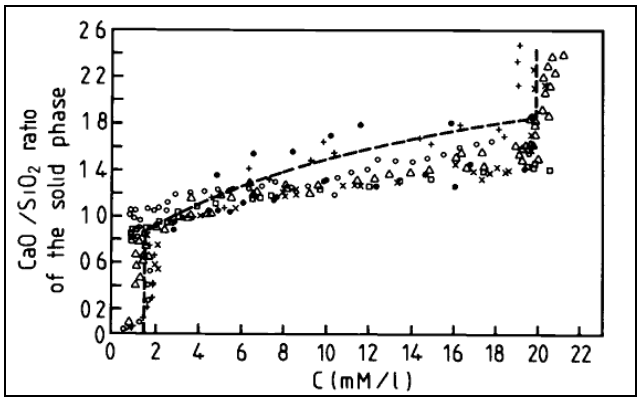

Fig. C-3 CaO/SiO2 ratio vs. calcium concentration

Samson and Marchand (2007) presented a multi-ionic transport model to describe the degradation of cement exposed to aggressive environments. The model uses a two step procedure to obtain numerical solutions. First, the model solves the transport equations ignoring the effects of the chemical reactions. The concentration profile of each ionic species is determined considering diffusion, electrical coupling between the ions, chemical activity effects and advection caused by a capillary suction flow. Then, the effects of the chemical reactions are incorporated to satisfy the equilibrium conditions between the pore solution and reactive cement components.

More recently, a multi-scale homogenization model (Stora et al., 2010) has been developed to predict change in cement composition, flow and mechanical properties inside a concrete material subjected to degradation and leaching. Simulation results obtained using the model provided more insight into the understanding of the interactions between damage and chemical deteriorations.

Nomenclature

API = American Petroleum Institute
bbls = Barrels
BHCT = Bottom hole circulating temperature
BWOB = by weight of blend
BWOC = by weight of cement
HCS = hollow ceramic spheres
HGS = hollow glass spheres
HSR = High sulfate resistant
NMR = Nuclear Magnetic Resonance
MSR = Medium sulfate resistant
PCF = Pounds per cubic foot
TGA = Thermo-Gravimetric Analysis
XRD = X-ray Diffraction

References

Barlet-Gouédard, V., Rimmelé, G., Goffé, B., and Porcherie O. 2006. Mitigation Strategies for the Risk of CO2 Migration Through Wellbores. Paper IADC/SPE 98924 presented at the IADC/SPE Drilling Conference held in Miami, Florida, U.S.A., February 21–23.

Brandl, A., Cutler, J., Seholm, A., Sansil, M., and Braun, G. 2010. Cementing Solutions for Corrosive Well Environments, paper SPE-132228-MS-P presented at the CPS/SPE International Oil & Gas Conference and Exhibition in China held in Beijing. Jun 8-10.

Buil, M. and Revertegat, E. 1992. Model of the attack of pure water or undersaturated lime solutions on cement: Stabilization and Solidification of Hazardous, Radioactive, and Mixed Wastes, Astm Special Technical Publication, Edited by T. Michael Gilliam and Carlton C. Wiles, 227-241.

Condor, J. and Asghari, K. 2009. Experimental Study of Stability and Integrity of Cement in Wellbores Used for CO2 Storage, Energy Procedia, 1, 3633-3640.

Carde, C., Francois, R. and Torrenti, J M. 1996. Leaching of both calcium hydroxide and C-S-H from cement paste: Modeling the mechanical behavior, Cement and Concrete Research, Volume: 26, Issue: 8, Pages: 1257-1268.

Carde, C. and Frarqois, R. 1999. Modelling the loss of strength and porosity increase due to the leaching of cement pastes, Cement & Concrete Composites, 21, 181-188.

Casey, J.W. and Lichtner, P.C. 2007. Calcium silicate hydrate (C-S-H) solid solution model applied to cement degradation using the continuum reactive transport model flowtran, Transport Properties and Concrete Quality: Materials Science of Concrete, Editors: Barzin Mobasher and Jan P. Skalny, 73-104.

Dubois, N., Bouygues, Noik, Ch., Rivereau, A. 1999. Improvement of low-permeable cement for zonal isolation at high-temperature Conditions, paper SPE 50782, presnted at the SPE International Symposium on Oilfield Chemistry held in Houston, Texas, February 16–19.

Fakhreldin, Y., Al-Sharji, H., Ruwehy, A. M., Saadi, K., Taoutaou, S., Al-Kalbani, S. 2010, Advanced Cement System for Acid Gas Injection Wells, paper SPE-132345-MS-P, presented at the SPE Asia Pacific Oil & Gas Conference and Exhibition held in Brisbane, Queensland, Australia, October 18-20.

Jennings S.S., 2005. Long-Term High-Temperature Laboratory Cement Data Aid in the Selection of Optimized Cements, paper SPE 95816 presented at the 2005 SPE Annual Technical Conference and Exhibition held in Dallas, Texas, U.S.A., 9 – 12 October 2005.

Johnson, R, M., and Garvin, T, R. 1972. Cementing Practices, SPE AIME-MMIJ Meeting, May 25-27, Tokyo, Japan.

Kutchko, B. G.; Strazisar, B. R.; Dzombak, D. A.; Lowry, G. V.;Thaulow, N. 2007. Degradation of Well Cement by CO2 under Geologic Sequestration Conditions, Environ. Sci. Technol., 41 (12), 4787–4792.

Lécolier E., Rivereau A., Ferrer N., Audibert A. and Longaygue X., 2006. Durability of Oilwell Cement Formulations Aged in H2S-Containing Fluids, paper SPE 99105 presented at the IADC/SPE Drilling Conference, Miami, Florida, February 21–23.

Morales, M., Morris, W., Criado, M. A., Robles, J., Bianchi, G. 2003. Improving the Sulfate Resistance Performance of API Cement Class A upon Appropriate Slurry Design, paper SPE 81000, presented at the SPE Latin American and Caribbean Petroleum Engineering Conference held in Port-of-Spain, Trinidad, West Indies, April 27-30.

Noik, Ch., and Rivereau, A. 1999. Oil well Cement Durability, paper SPE 56538, presented at the SPE Annual Technical Conference and Exhibition held in Houston, Texas, October 3–6.

Rimmelé, G., Barlet-Gouedard, V., Porcherie, O., Goffe, B., Brunet, F. 2008, Heterogeneous Porosity Distribution in Portland Cement Exposed to CO2-Rich Fluids, Cement and Concrete Research, 38, 1038-1048.

Samson, E. and Marchand, J. 2007. Modeling the transport of ions in unsaturated cement-based materials, Computers and Structures, 85, 1740–1756.

Santra, A. and Sweatman, R. 2011. Understanding the Long-Term Chemical and Mechanical Integrity of Cement in a CCS Environment, Energy Procedia, 4, 5243–5250.

Santra, A., Reddy, B. R., Liang, F., and Fitzgerald, R. 2009. Reaction of CO2 with Portland Cement at Downhole Conditions and the Role of Pozzolanic Supplements, paper SPE 121103, presented at the SPE International Symposium on Oilfield Chemistry held in The Woodlands, Texas, USA, April 20–22.

Stora, E., Bary, B., He, Q.C., Deville, E. and Montarnal, P. 2010. Modelling and simulations of the chemo-mechanical behaviour of leached cement-based materials: Interactions between damage and leaching, Cement and Concrete Research, Volume 40, Issue 8, Pages 1226–1236.

Project Title: Effect of H_2S and CO_2 in HPHT Wells on Tubulars and Cement

Report Type: Monthly Report

Report #: 05

Reporting Period: Jan. 22nd, 2012 to Feb. 21st, 2012

Authors:

Ramadan Ahmed, Principal Investigator

Subhash Shah, Co-Principal Investigator

Samuel Osisanya, Co-Principal Investigator

Majed Enfis, Research Assistant

Rida Elgaddafi, Research Assistant

Himanshu Maheshwari, Research Assistant

Adarsh Naidu, Research Assistant

Prepared under BOEMRE Project # M11PC00030

by

THE UNIVERSITY OF OKLAHOMA

March 1, 2012

1. Summary of Accomplishments

This monthly report presents the progress made during the project period Jan. 22, 2012 – Feb. 21, 2012. During this reporting period, the development of experimental setups for testing cement and tubular specimens was continued. Progress was made in the preparation of laboratory space. In addition, literature survey and theoretical studies were conducted on cement and tubular degradation resulting from sour gas exposure under high-pressure high-temperature (HPHT) conditions.

In the coming weeks, we will begin building the experimental setup for cement corrosion. Major components for the experimental setup, such as the aging cell and gas injection cylinder, control values, and aging cell depressurization system have been delivered. All items for the cement setup have been order, with the exception of the aging cell heating system. We are considering two different heating systems: electrical heaters and high temperature circulating fluid. A decision will be made after reviewing quotations obtained from vendors and manufacturers.

Cement specimens are often prepared by coring from a larger piece or casting in a mold. As indicated in the previous report, we are testing these two methods of cement specimen preparation procedures. Special mold-coating grease/oil, which is applied on the casting mold surface, is required to prepare casted specimens. Casting molds are manufactured to compare the methods.

In the actual field conditions, cement hydration occurs under the borehole environment. The hydration process is affected by many variables, including chemical composition, water-cement ratio and temperature. Hydration kinetics is strongly influenced by the temperature. We are considering curing the cores at elevated temperature to simulate field conditions.

Theoretical and modeling studies on cement and tubular degradation were continued. The changes in mechanical properties of well cement due to the effects of degradation were investigated. Results showed a linear relationship between the degradation depth and square root of exposure time. The trend follows the prediction based on the Fickian second law of diffusion. In addition, studies indicated that the bonding between cement and casing or cement and formation may be more prone to the CO_2 attack than cement matrix.

Furthermore, literature review and theoretical studies on corrosion of tubulars were carried out during this reporting period. Studies showed that corrosion rate of carbon steel in CO_2 saturated brine is influenced by many factors, including fluid composition, temperature, pressure and pH.

2. Overall Project Progress

2.1 Theoretical Studies (Task 1)

Literature review and theoretical studies on cement degradation and tubular corrosion were continued to better understand the deterioration of these materials and develop mechanistic model that predicts the level of degradation occurring under borehole conditions. During this reporting period, more focus is given to examine the effect of acid attack on physical properties of the cement. When cement is exposed to CO_2 environment, carbonation occurs as the first stage of degradation process. The depth of carbonation is strongly dependent on the type of cement, composition of the surrounding fluid, temperature and pressure. Temperature tends to facilitate the carbonation process. Some studies show significant increase in carbonation depth with the increase in temperature (Fig. 1).

The relationship between the carbonation depth and the square root of exposure time can be approximated by a straight line that represents the Fickian second law of diffusion. In some cases, the Fickian type linear plots were not observed, especially for cement cores exposed to CO_2 saturated brine, indicating that the cement carbonation process is more complicated than simple diffusion. During the carbonation process, the calcium carbonate formed in the pore space creates a high-density and low-permeability region in the cement. As a result, experimental data may deviate from the Fickian straight line. In this case, other models such as the Elovich equation (Fig. 2) presented by Kutchko et al. (2008) can be applied. The carbonation process eventually results in deterioration of cement and degradation of its physical properties and mechanical strength.

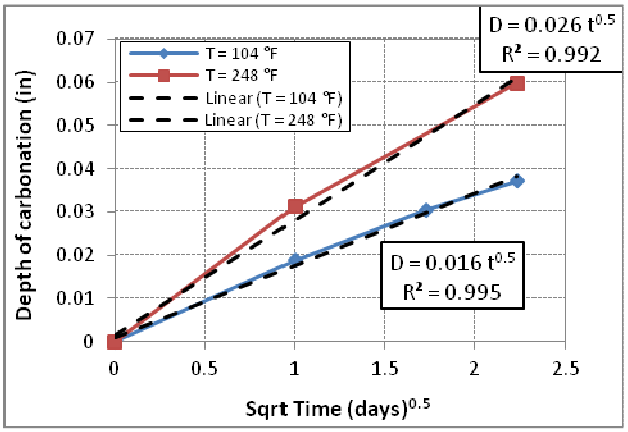

Fig. 1 Carbonation depth vs. square root of time for cement exposed to CO_2 environment (Sauki and Irawan, 2010)

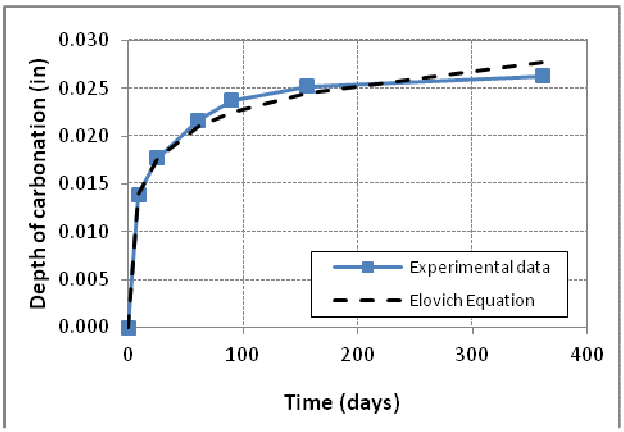

Fig. 2 Carbonation depth vs. time for cement exposed to CO_2-saturated brine (Kutchko et al., 2008)

Bonding behavior of cement is critical to achieve the desired zonal isolation. Crow et al., (2009) emphasized the fact that the migration path of CO_2 cannot necessarily follow the cement matrix. They performed a hydraulic isolation test to determine the presence of fluid migration through the cement-casing interface (micro channeling) due to poor bonding. The cement-casing interface was found to be more prone to acid attack than the cement matrix. Hence, the degradation of the bond is of great concern.

Carefully designed cement formulations can provide good resistance to sour gas attack. Lécolier et al., (2008) described the behavior of cement formulations, which incorporate mineral admixtures such as Fe_2O_3 (hematite) and Mn_3O_4 (hausmanite). These mineral admixtures have been chosen because of their high chemical affinity with hydrogen sulfide. Incorporating hematite resulted in strong matrix damage due to acid reaction, leading to total loss of mechanical strength. Whereas incorporating Mn_3O_4 showed promising results. A recent study (Benge, 2009) considered different approaches to improve the sealing capability of cement including:

i. Modified Portland cement
ii. Non-Portland cement
    - Calcium sulfoaluminate-based cements (One of the most resistant systems is 'calcium aluminate cement' that does not react at all with CO_2)
    - Geopolymeric cements (alkali aluminosilicates),
    - Magnesium oxide cements and
    - Hydrocarbon-based cements
iii. Swell Technology - Swelling technologies have been very promising in recent years. Special cementing materials that have swelling property can change their volume with a change in wellbore conditions. When these materials encounter the fluid present in the wellbore, they expand thereby giving a tighter seal to the annulus.
    - Self-healing cements – these cements have an additive that reacts with the fluids and the products thus generated inhibit the flow of these fluids
    - Swell packers – similar to the self-healing cement, these packers expand when in contact with a wellbore fluid.
iv. Stress modeling – predicting:
    - Failure at the cement-formation and cement-casing interfaces
    - Tensile failure of the cement sheath

Literature survey and theoretical studies on corrosion of tubulars have been conducted during this reporting period. Under a CO_2-containing environment, tubular corrosion rate is influenced by: i) electrochemistry of CO_2 corrosion; ii) CO_2 water chemistry including formation of protective scales and scales; iii) effects of temperature, CO_2 partial pressure, and pH. Corrosion products can be insoluble or soluble materials. Insoluble solids precipitate on the corroded surface. As a result, tubular corrosion is often accompanied by the formation of scales such as iron carbonate ($FeCO_3$). The scales can be protective or non-protective depending on their physiochemical characteristics. The most common type of protective scale formed during CO_2 corrosion is iron carbonate (Nešić, 2007). The scale covers the corroded surface and prevents the diffusion of species involved in the corrosion process. There are many factors that influence the formation of iron carbonate scale including water chemistry and temperature. Both water chemistry and temperature affect the solubility of iron carbonate. High temperature favors the rapid precipitation of iron carbonate and the formation of impermeable protective film. However, at low temperatures (less than 60℃), precipitation occurs slowly resulting in the formation of non-protective film on the corroded surface.

The major corrosion problem in the oil and gas industry is associated with gases containing H_2S. To better understand the corrosion mechanisms, the solubility of hydrogen sulfide in brine and the dissociation of hydrosulfuric acid have been investigated for the past two decades. The thermodynamic and kinetics of these processes are also very critical to develop models for sour gas corrosion. A number of correlations have been presented to predict solubility and dissociation constants at different pressure and temperature conditions.

Adding trace amount of H_2S into brine saturated with CO_2 tends to accelerate or inhibit the corrosion process. Ramirez and Ruiz (1998) determine the critical H_2S concentration that maximizes the corrosion rate. Corrosion rate experiments were conducted using A-516 steel in aqueous solution containing 5% NaCl. Test temperature and H_2S concentration were varied from 50℃ to 200℃ and 0 to 40 ppm, respectively. The maximum corrosion rate was observed at approximately 10 ppm (Fig. 3), regardless of the test temperature. The corrosion rate reduction at higher H_2S concentration is related to the formation protective film (Kvarekval and Videm, 1995) the maximum corrosion

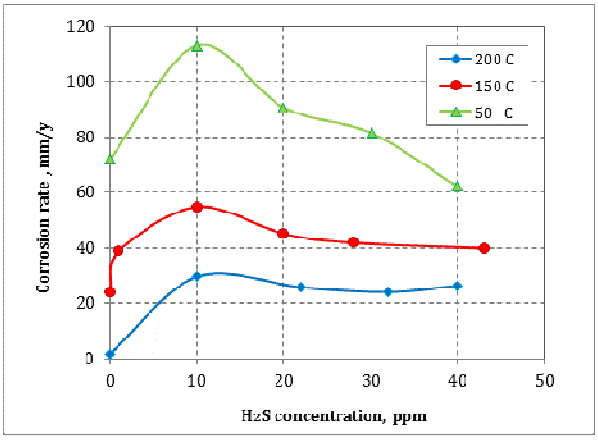

Fig. 3 Corrosion rate vs. H_2S concentrations in CO_2 saturated brine (5% NaCl) (Ramirez and Ruiz, 1998)

rate is independent of the temperature. Temperature reduces the solubility of H_2S; as a result, corrosion rate decreases with an increase in temperature. The influence of temperature on the corrosion rate is more pronounced than that of the H_2S concentration. The impact of temperature on the corrosion process is more complicated as it affects gas solubility, acid dissociation and other physical and electrochemical reactions.

2.2 Experimental Studies on Degradation of Cement (Task 2)

This task is aimed to develop an experimental facility for testing cement degradation. The plan for the first six months of the project is to develop the facility. We have received major components of this facility including aging cell, gas injection cylinder, control valves, and waste gas accumulator (i.e. gas expansion tank). The remaining components are: aging cell heating system, static pressure sensors, and high pressure pipe fittings. Except the heating system, other items are expected to arrive in the coming weeks. We are considering two different heating systems: i) electrical band heaters; and ii) high temperature fluid circulation system. Potential vendors have been identified to provide electrical band heaters (Fig. 4) and a high temperature circulating bath. We are waiting for the heater manufacturer to provide custom-made explosion proof heaters. The other alternative is to use an expensive fluid circulating bath that requires installing a heating jacket on the aging cell (Fig. 5) for circulating the heat transfer-medium. A decision on this will be made once the quotations are received.

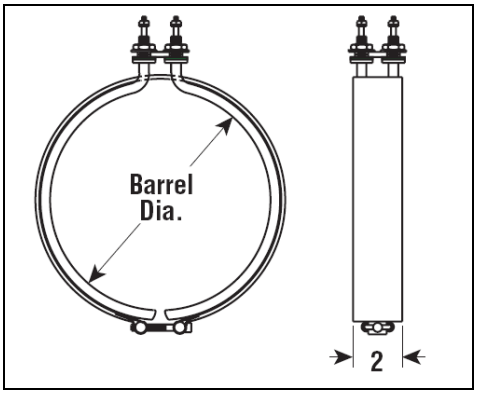

Fig. 4 Aging cell band heaters

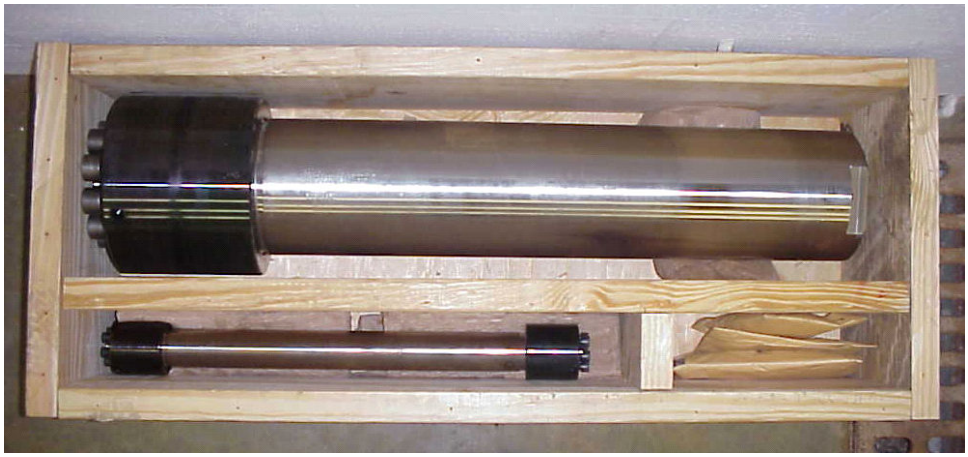

Fig. 5 Aging cell and injection cylinder

During the experimental investigation, the cement slurry will be prepared in accordance with API specifications. On occasion, special additives will be included in the slurry in order to improve degradation resistance of the cement. Sample coring must be carried out slowly to minimize micro cracking and overheating the specimens. We will be using our variable speed coring machine shown in Fig. 6. For the planned laboratory testing, cement specimens are either cored or casted in a special mold. In both cases, the specimens are first casted in a mold and cured for a period of time in sealed curing chambers (Fig. 7) containing water under elevated temperature and pressure conditions. The chambers are placed in an oven to maintain high temperature curing condition. When the curing process is completed, the casted samples are recovered from the mold and washed to remove the mold release coating (grease/oil) from their surfaces. Five cylindrical molds (L = 2" and ID = 1") presented in Fig. 8, have been manufactured to produce casted specimens. Cored samples are needed to compare these two specimen preparation techniques. To create cored specimens, the cement slurry will be casted and cured in a cylindrical mold (Fig. 9) that has a diameter greater than the outer diameter of the coring bit. The specimens will then be cored from the casted cement that has completed the curing process. Before aging the specimens, initial physical and mechanical properties will be measured.

Fig. 6 Variable speed coring machine with direct cooling system

Fig. 7 Curing chamber

Fig. 8 Cylindrical cement casting molds (2" X 1") and a plunger needed for recovering the cement specimens

Fig. 9 Cylindrical cement casting molds (3" X 2") used for preparing cored specimens

2.3 Experimental Studies on Corrosion of Tubulars (Task 3)

As previously reported, high-pressure recirculation pumps are not commonly available in industry. The search for the pump will continue. We are considering different options including using an injection cylinder as a pump or acquiring a custom-made pump that meets the desired specifications. After selecting the pump and knowing its specifications, we will be able to finalize the design of the corrosion setup and begin ordering items necessary for developing the facility.

3. Meetings and Contacts

As mentioned in the last report, TAB members invited our research team to visit their experimental facilities to share their experience in laboratory testing of cement specimens under elevated pressure and temperature conditions. The PI visited the Schlumberger cement testing facility located in Houston on January 26, 2012.

Furthermore, we are in communication with the TAB members to get the materials needed for the test. Texas Lehigh Cement Co LP has donated 2,000 lb of Class H cement for the project. Currently, we are using the cement for preliminary testing.

4. Planned Activities

- Build cement aging test setup on a moving chart.
- Continue ordering components of the experimental setups.
- Continue preparing the final design of the aging cell heating system.
- Upgrade the laboratory spaces needed for test facilities.
- Continue literature survey and theoretical studies on cement and tubular degradation.
- Develop cement core preparation procedure.

5. Project Expenditures

This section presents the project expenses during the months of January (Table 1) and the cumulative expenditures.

Table 1 Monthly and cumulative expenditure, January 30, 2011

No.	Budget Categories	Current Expenses	Cumulative Expenses
1	Salaries & Wages	$3,000.00	$6,000.00
2	Fringe Benefits	$165.00	$330.00
3	Project Materials	$10,366.66	$14,348.40
4	Travel	$0.00	$919.59
5	Conference Expenses	$0.00	$0.00
6	Other Direct Costs	$0.00	$0.00
7	Equipment	$0.00	$8,690.00
8	Space Rental	$0.00	$0.00
9	Indirect Cost	$6,765.83	$10,799.01
10	**Total**	**$20,297.49**	**$41,087.00**

References

Benge G., (2009) Improving Wellbore Seal Integrity in CO2 Injection Wells. GHGT-9, Energy Procedia 1 (2009) 3523-3529.

Crow W., Williams D. B., Carey J. W., Celia M., Gasda S., (2009) Wellbore integrity analysis of a natural CO2 producer. GHGT-9, Energy Procedia 1 (2009) 3561-3569.

Kutchko, B. G.; Strazisar, B. R.; Lowry, G. V.; Dzombak, D. A.; Thaulow, N. 2008. Rate of CO2 Attack on Hydrated Class H Well Cement under Geologic Sequestration Conditions. Environ. Sci. Technol. 42: 6237–6242.

Kvarekval. J. and Videm, K., 1995. Corrosion of Carbon Steel in Carbon Dioxide-Saturated Solutions Containing Small Amounts of Hydrogen Sulfide. NACE international, April.

Lécolier E., Rivereau A., Ferrer N., Audibert A., Longaygue X., (2008) Study of New Solutions for Acid-Resistant Cements. SPE 116066, Annual Technical Conference and Exhibition, Denver, Colorado, USA, 21-24 September 2008.

Nešić, S. 2007. Key issues related to modelling of internal corrosion of oil and gas pipelines, Corrosion Science, Vol. 49, Issue 12, December 2007, Pages 4308–4338.

Ramirez, M. and Ruiz, A.,1998. The Effect of Small Amounts of H2S on CO2 Corrosion of a Carbon Steel. NACE international.

Sauki, A, B. and Irawan, S. 2010. Effects of Pressure and Temperature on Well Cement Degradation by Supercritical CO2. International Journal of Engineering and Technology 10: 53-61.

Project Title: Effect of H_2S and CO_2 in HPHT Wells on Tubulars and Cement

Report Type: Monthly Report

Report #: 06

Reporting Period: Feb. 22nd, 2012 to March 21st, 2012

Authors:

Ramadan Ahmed, Principal Investigator

Subhash Shah, Co-Principal Investigator

Samuel Osisanya, Co-Principal Investigator

Majed Enfis, Research Assistant

Rida Elgaddafi, Research Assistant

Himanshu Maheshwari, Research Assistant

Adarsh Naidu, Research Assistant

Prepared under BOEMRE Project # M11PC00030

by

THE UNIVERSITY OF OKLAHOMA

April 3, 2012

1. Summary of Accomplishments

This monthly report presents the progress made during the project period Feb. 22, 2012 – March 21, 2012. The development of experimental setups for testing cement degradation was continued during this reporting period. Major items of cement degradation testing setup have been installed. The aging-cell heating system was redesigned and purchase orders for items needed to build the system have been completed. The items will be delivered in the coming weeks. In addition, progress was made in the development of compressive strength testing equipment. Furthermore, theoretical and modeling studies were continued on cement and tubular degradation resulting from sour gas exposure under high-pressure high-temperature (HPHT) conditions.

As indicated in the last report, we have continued our effort to develop cement specimen preparation procedure. During this period, different procedures were tested including coring and casting. A variety of mold release materials (light mineral oil, non-stick cooking spray, and silicone-based mold release spray) were used for casting. Specimens made by casting showed less geometric irregularities and surface roughness. Cement specimens prepared using mineral oil and non-stick cooking spray as mold release, were covered with oil film that may influence the degradation measurements. Specimens prepared using silicone-based spray show acceptable quality. They were free of oil film, because the silicone spray quickly dries when it is applied creating very smooth and non-sticking surface.

Theoretical and modeling studies on cement and tubular degradation were continued. The leaching process of cement in water and carbon dioxide containing environment was investigated using a shrinking core model. The model expresses the cumulative amount of leached calcium per exposed surface area as a function of effective diffusion coefficient, initial calcium carbonate concentration, calcium ion mobility factor, concentration of hydrogen ions (pH) in the pore fluid, acid neutralization capacity and exposure time. In addition, literature review and theoretical studies on corrosion of tubulars were continued. Accurate prediction of downhole pH is essential to estimate corrosion rate of tubulars. The pH of a solution in contact with acidic gas is directly related to gas solubility and the level of acid dissociation, which are functions of temperature, pressure and ionic strength. Model based parametric study shows mixed H_2S solubility trend with temperature.

Our plan for the coming weeks is to finalize the development of cement degradation setup and prepare the system for preliminary testing. We will continue our theoretical and modeling studies on cement degradation and tubular corrosion.

2. Overall Project Progress

2.1 Theoretical Studies (Task 1)

Literature review and theoretical studies on cement degradation and tubular corrosion were continued to better understand the degradation behavior of these materials and develop a model that can predict the level of deterioration occurring under harsh borehole conditions. During this reporting period, more focus was given to examine the leaching process of cement in water and carbon dioxide containing environment. When cement is exposed to CO_2 saturated water, carbonation occurs as the first stage of degradation process. Studies (Santra et al., 2009) showed that leaching of the binding component of the cement causes deterioration of mechanical and sealing properties. When cement is exposed to water saturated with carbon dioxide, the gas dissolves in water forming carbonic acid. The acid penetrates into the cement matrix and reacts with the main cement hydration products or binding materials. The reaction produces calcium carbonate that can be leached out by the carbonic acid as the insoluble calcium carbonate reacts with the acid forming soluble calcium bicarbonate. The leaching tends to increase porosity and permeability, and degrade mechanical properties of the cement.

Van Eijk et al. (1998) presented a shrinking core model used to describe the leaching phenomenon occurring in cement due to acid attack. The model expresses the cumulative amount of leached calcium per exposed surface area as a function of effective diffusion coefficient, initial calcium carbonate concentration, calcium ion mobility factor, concentration of hydrogen ions (pH) in the pore fluid, acid neutralization capacity and exposure time. The pH of the pore fluid has great impact on leaching rate. Based on experimental results, Oddo et al. (1982) presented the following correlation to estimate the pH of pore fluid.

$$pH = -\left(log_{10}\frac{p_{CO_2}}{C_{HCO_3^-}}\right) + 8.68 + 4.05 * 10^{-3}T + 4.58 * 10^{-7}T^2 - 3.07 * 10^{-5}P - 0.4771I^{0.5} + 0.193I$$

where

p_{CO_2}= Partial Pressure of CO_2, psi

$C_{HCO_3^-}$ = Concentration of bicarbonate ion, M

T = Temperature, °F

P = Total pressure, psi

I = Ionic strength of water, M

Parametric study conducted using this model shows that the pH slightly decreases as the partial pressure of CO_2 increases (Fig. 1). However, maintaining other parameters constant and increasing the temperature tends to increase the pH (Fig. 2).

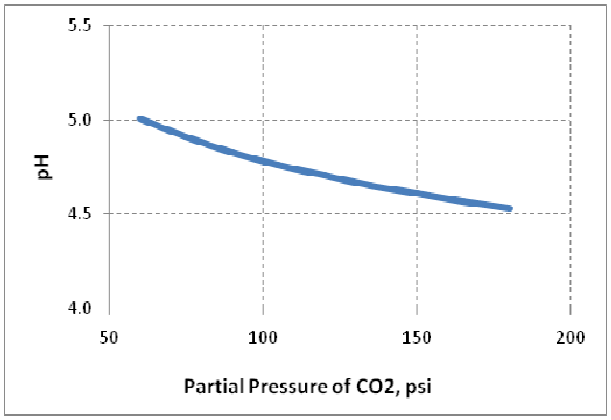

Fig. 1 pH vs. partial pressure of CO2

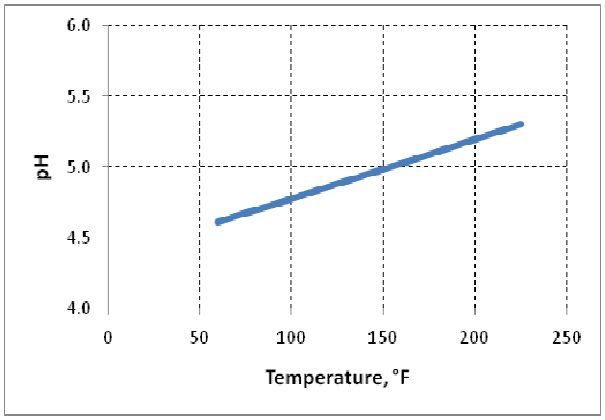

Fig. 2 pH vs. temperature

Literature survey and theoretical studies on corrosion of tubulars were continued during the reporting period. A number of studies found that corrosion in tubulars is substantially affected by the pH of the surrounding liquid. Gas solubility is one of the key parameters, which determines the pH of solutions that are in contact with acidic gases. Accurate prediction of gas solubility over a wide range of pressure, temperature and ionic strength is essential to determine the pH of formation fluid that is saturated with sour gases. Downhole parameters such as pressure and temperature have strong impact on gas solubility and subsequently the pH. As a result, these parameters often determine the corrosion mechanisms and rate.

The pH of a solution in contact with acidic gas is directly related to the level of acid dissociation. The solubility and dissociation of hydrogen sulfide and carbon dioxide are influenced by temperature, pressure and ionic strength of the solution. Daun and Sun (2007) presented a widely accepted thermodynamic model to predict the solubility of hydrogen sulfide in water and brine. The model is based on the specific particle interaction theory and the equation of state. It is valid for wide range of pressure, temperature and ionic strength conditions (pressure: 0 to 2900 psi, temperature: 30 to 440°F and ionic strength: 0 to 6 M). The model validation performed at pressures less than 100 bar (1500 psi) showed good agreement between measurements and predictions. Parametric study using the model shows (Fig. 3) reversed solubility trend at high pressures (above 100 bar). At low pressures, H_2S solubility decrease with the increase in temperature. However, this trend changes at high pressures and the gas becomes more soluble as the temperature increases.

Furthermore, the liquid phase tends to saturate with the gas at low temperatures (86 and 140°F). At high temperatures (410 and 464°F), saturation phenomenon does not occur. The salinity reduces the solubility of the gas regardless of the pressure and temperature of the system.

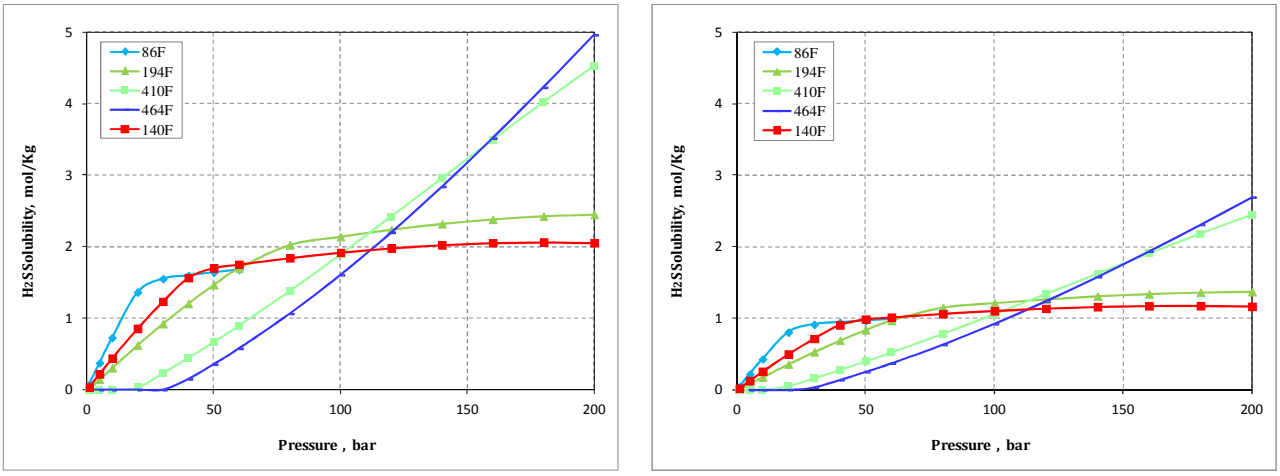

(a) (b)

Fig. 3 Solubility of H2S in brine solutions as a function of pressure at different temperatures: a) 1 M solution; and b) 4 M solution

The pH of a solution in contact with acidic gas is estimated using solubility and dissociation constants. The following steps show the method of calculating the pH of pure solution:

I. Determining the concentrations of CO_2 and H_2S in the liquid phase using the solubility model;

II. Estimating the first (K_{a1}) and the second (K_{a2}) dissociation constants of hydrogen sulfide and carbon dioxide in the solution. The second dissociation constant of H_2S can be neglected (i.e. K_{a1} is much greater than K_{a2}).

III. Determining the hydrogen ion concentration applying the dissociation equation and material balance.

Figure 4 presents results of a parametric study conducted to investigate the effects of temperature and pressure on the pH of brine solutions in contact with H_2S. The predictions show a mixed trend. As the temperature increase from 140°F, first slight decrease in pH is expected. This trend changes at high temperatures (i.e. above 300°F) and the pH moderately increases with the temperature.

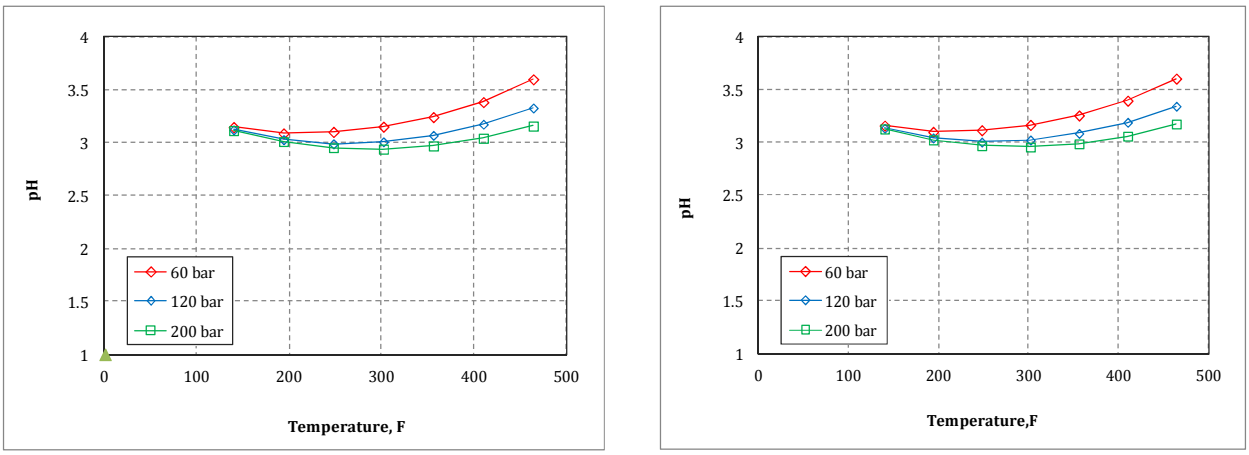

Fig. 4 pH of brine solutions vs. temperature at different pressures: a) 4 M NaCl; and b) 6 M NaCL

2.2 Experimental Studies on Degradation of Cement (Task 2)

This task is aimed to develop an experimental facility for testing cement degradation. The plan for the first six months of the project is to develop the facility. Major items of this facility have been assembled on a mobile cart (Fig. 5). As indicated in the previous report, two types of heating systems (electrical and heating bath systems) were considered to maintain the aging-cell temperature at the desired level. The potential vendor for the electrical heaters was unable to provide explosion proof heating clamps. Therefore, we decided to use a high-temperature circulating bath to maintain the cell temperature. A heating jacket will be installed on the cell to circulate the heating medium (silicone oil). The design (Fig. 6) of the jacket was prepared and provided to a local machining shop for manufacturing. Purchase orders have been completed to acquire silicone oil and the heating bath. We expect the items to arrive in the coming weeks.

Fig. 5 Experimental facility for aging cement specimens

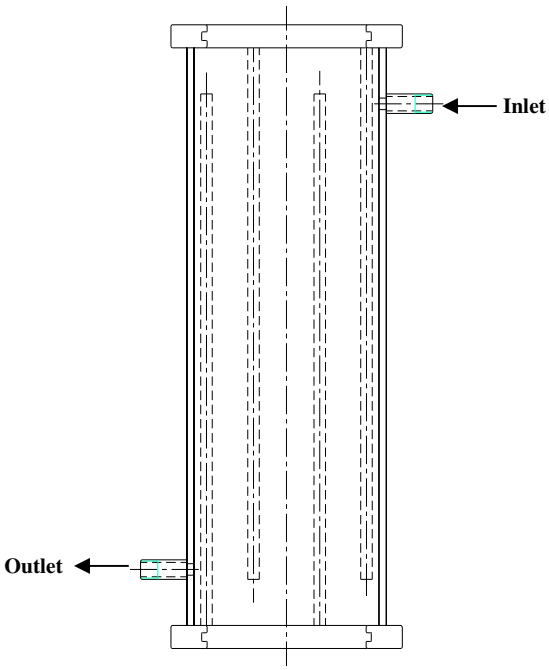

Fig. 6 Heating jacket

For the planned laboratory testing, both cored and casted cement specimens have been considered. We are developing cement specimen preparation procedure. Different procedures involving coring and casting were tested. Casted specimens were prepared with and without mold release agents. All cement slurries were prepared by mixing neat cement class H with tap water for 35 minutes to produce a cement paste with water to cement ratio of 38%. The slurries were casted using 1-inch and 2-inch diameter cylindrical molds. The 1-inch molds were coated with different materials (mineral oil, non-stick cooking spray, and silicone-based mold release spray) to ease the release of cement specimens. After coating the molds with mold release, the cement slurry was prepared and poured slowly into the molds while gently mixing the slurry to bubble out trapped air and maintain homogeneity. Then, the slurry was left inside the molds for 24 hours to harden. The hardened specimens were place in water for 5 days to cure. The cured specimens (Fig. 7) were recovered from the molds using a plunger mounted on a hydraulic jack. Specimens casted (Fig. 8) in the 2-inch mold were cored using a 1-inch coring bit and then trimmed on both sides to have a length of 1.5 inches. Then, the specimens made by coring were compared with those made by casting. Normally, cement specimens prepared by casting showed very smooth surface and minor geometric irregularities. However, casted specimens prepared using mineral oil and non-stick cooking spray were covered with thin oil film that may have some effect on degradation measurements. Specimens prepared using silicone-based spray were very clean and free of film coating. After application, silicone spray quickly dried on

the surface of the mold creating very smooth surface that prevents the formation strong bond between the cement and mold. Specimens prepared without mold release showed small cracks on their surfaces. Generally, silicone-based spray provides best result and therefore, it will be used in future experiments.

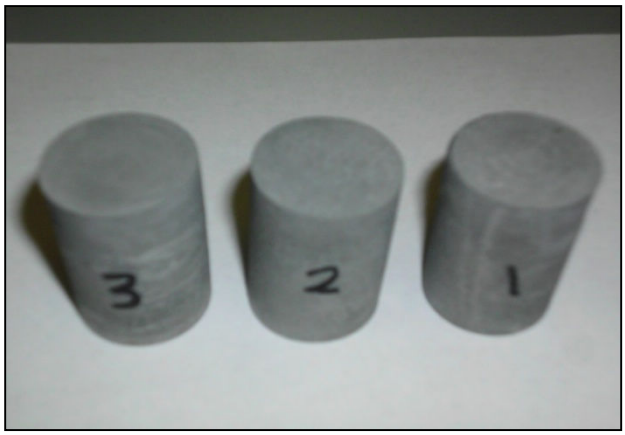

Fig. 7 Cored samples

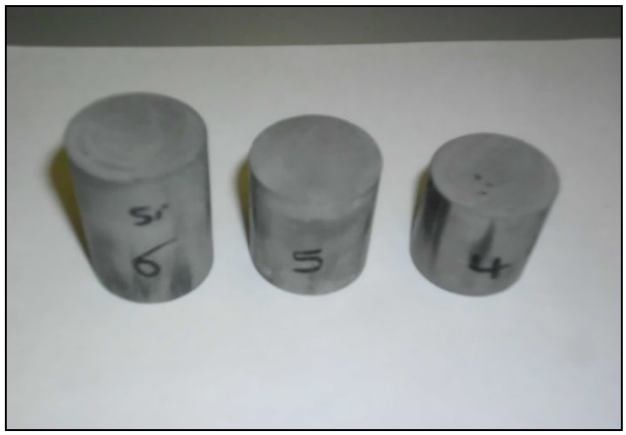

Fig. 8 Casted samples

In order to measure the permeability and porosity, the casted specimens were sanded from both sides (bottom and top) and washed with water. Then, the specimens were placed in an oven for 24 hours to dry at 110°F. Porosity and permeability of the dried specimens were measured using a fully automated Porosimeter-Permeameter (CSI Model AP-608). The equipment (Fig. 9) was calibrated and leak-tested to obtain reliable and accurate measurements. The apparatus uses unsteady state method to determine the permeability. It provides both gas and klinkenberg corrected liquid permeabilities. Two different gases (helium and nitrogen) were used for these measurements. Nitrogen was used for measuring permeability. Porosity measurements were conducted using helium. In these experiments, the confining pressure was maintained at 2000 psi. The results of the experiment (Table 1) show good repeatability of measurements. However, data obtained from Specimen # 9 showed significant difference due to the formation of micro-cracks during sample preparation. Similar tests will be carried out to verify reproducibility of measurements among different batches of cement slurries.

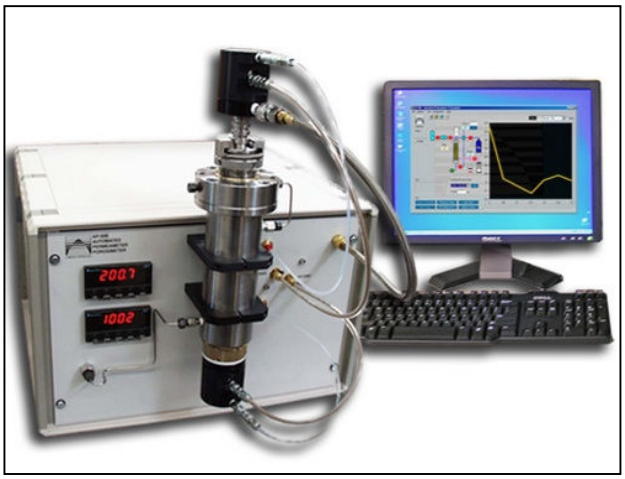

Fig. 9 Automated Porosimeter-Permeameter (AP-608)

Table 1 Porosity and permeability of the cement specimens

No.	Core Type	Core dimensions			Porosity				Permeability	
		Diameter	Length	Weight	V_b	V_g	V_p	Porosity	K_{air}	K_{klink}
		in	in	lbm	in^3	in^3	in^3	%	md	md
8	Cast / sealed	1	1.04	0.053	0.815	0.590	0.226	27.7	0.27	0.19
9	Cast / sealed	1	1.02	0.050	0.796	0.552	0.244	30.7	0.39	0.29
10	Cast / sealed	1	1.23	0.063	0.961	0.707	0.255	26.5	0.26	0.18
11	Cast / sealed	1	1.16	0.059	0.906	0.669	0.236	26.1	0.22	0.15

In addition to porosity and permeability, the degradation of cement is often qualitatively evaluated measuring compressive strength of aged specimens. In this project, an experimental setup will be developed to measure confined compressive of strength cement specimens. The initial design of the compressive strength testing setup is slightly modified. With the current design, the setup (Fig. 10) includes: i) confining cell that; ii) power cylinder to apply the compression force; iii) oil pump to develop the confining pressure; iv) electric-driven high-pressure syringe pump to supply hydraulic power to the cylinder; and v) instrumentation and data acquisition (DAQ) systems. The design of the confining cylinder (Fig. 11) was completed and provided to a manufacturer. The cylinder will be delivered in the coming weeks. During the test, the specimen will be placed in a Hassler sleeve (core holder). Then, the cell pressure (confining pressure) is increased gradually. Subsequently, the syringe pump pressure is increased at a constant rate using the DAQ system. The pressure developed by the pump is carefully controlled using a variable speed motor. The test ends when the syringe pump pressure abruptly drops indicating a compressive failure.

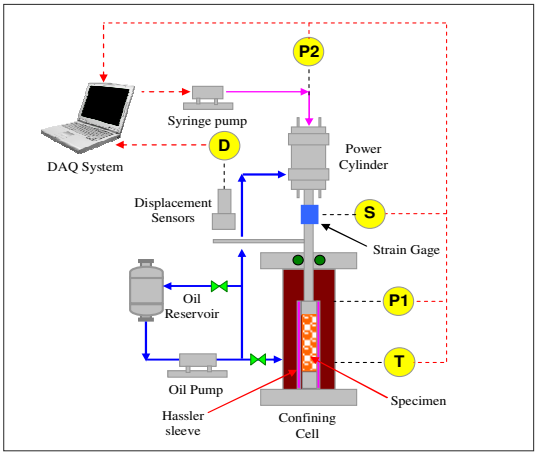

Fig. 10 Schematic of compressive strength measuring setup

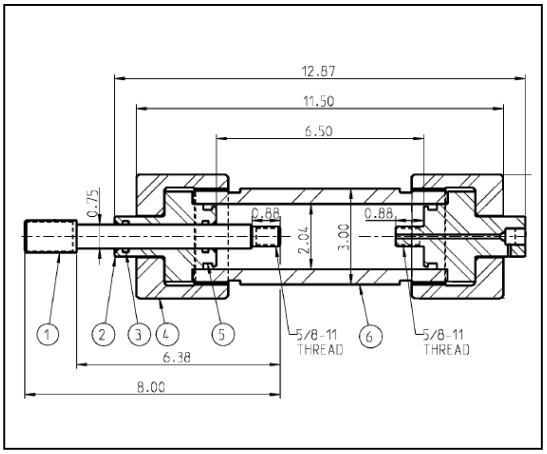

Fig. 11 Design of confining cell

2.3 Experimental Studies on Corrosion of Tubulars (Task 3)

Searching for high-pressure recirculation pumps was continued. We are considering different options including using an injection cylinder as a pump, acquiring a custom-made pump or syringe type pump that meets the desired specifications. The design of the corrosion setup will be finalized after specifying the pump.

3. Meetings and Contacts

The second Technical Advisory Board (TAB) meeting is scheduled for May 16, 2012. The meeting will be held in Norman. All TAB members from the industry (members from Halliburton, Schlumberger, Det norske and Baker Hughes) have confirmed their participation. In addition, the Contracting Officer's Representative (COR) will be attending the meeting. One of the TAB members from the University of Stavanger has notified us that he will not be attending the meeting in person. We will make the necessary arrangements for him to attend the meeting online. In consultation with the COR, we have invited Vallourec & Mannesmann to join the advisory board. Vallourec & Mannesmann is one of the leading manufacturers of casing and tubular products. It has several steel manufacturing and processing plants in the US.

4. Planned Activities

- Installing aging-cell heating system.
- Testing and calibration of cement specimen-aging setup.
- Continue literature survey and theoretical studies on cement and tubular degradation.
- Continue evaluating cement core preparation procedure.
- Assembling compressive strength measuring setup.

5. Project Expenditures

This section presents the project expenses during the months of February and March (Table 2) and the cumulative expenditures.

Table 2 Current and cumulative expenditures, February and March, 2012

No.	Budget Categories	Current Expenses	Cumulative Expenses
1	Salaries & Wages	$6,000.00	$12,000.00
2	Fringe Benefits	$330.00	$660.00
3	Project Materials	$16,320.31	$30,668.71
4	Travel	$18.32	$937.91
5	Conference Expenses	$0.00	$0.00
6	Other Direct Costs	$0.00	$0.00
7	Equipment	$43,824.32	$52,514.32
8	Space Rental	$0.00	$0.00
9	Indirect Cost	$11,637.89	$22,436.90
10	**Total**	**$78,130.84**	**$119,217.84**

References

Duan, Z., Sun, R. and Zhu, C., 2007, Accurate Thermodynamic Model for the Calculation of H_2S Solubility in Pure Water and Brines, Energy Fuels, 2007, 21 (4), pp 2056–2065.

Oddo J. E., Thomson M. B., 1982, Simplified calculations of CaCO3 saturation at high temperatures and pressures in brine solutions, Journal of Petroleum Technology, July, 1583-1590, 1982.

Santra, A., Reddy, B. R., Liang, F., and Fitzgerald, R. 2009. Reaction of CO2 with Portland Cement at Downhole Conditions and the Role of Pozzolanic Supplements, paper SPE 121103, presented at the SPE International Symposium on Oilfield Chemistry held in The Woodlands, Texas, USA, April 20–22.

Van Eijk R.J., Brouwers H.J.H., 1998. Study of the Relation between Hydrated Portland cement Composition and Leaching Resistance. Cement and Concrete Research, Vol. 28, No. 6, pp. 815–828, 1998.

Project Title: Effect of H_2S and CO_2 in HPHT Wells on Tubulars and Cement

Report Type: Monthly Report

Report #: 07

Reporting Period: March 22nd, 2012 to April 21st, 2012

Authors:

Ramadan Ahmed, Principal Investigator

Subhash Shah, Co-Principal Investigator

Samuel Osisanya, Co-Principal Investigator

Majed Enfis, Research Assistant

Rida Elgaddafi, Research Assistant

Himanshu Maheshwari, Research Assistant

Adarsh Naidu, Research Assistant

Prepared under BOEMRE Project # M11PC00030

by

THE UNIVERSITY OF OKLAHOMA

May 8, 2012

1. Summary of Accomplishments

This monthly report presents the progress made during the project period March 22, 2012 – April 21, 2012. The development of experimental setups for testing cement degradation (Task 2.1) was continued during this reporting period. A heating jacket was installed on the aging-cell and tested for leak tightness with compressed air. Then, the cell was fully insulated using high-temperature resistant micro-porous material. As previously reported, the cell and its accessories were assembled on a cart. After testing the jacket, the cart is placed in a mobile lab where actual aging tests will be carried out. Control valves and measuring instruments are connected to the power supply and control lines. Gases (nitrogen, sour gas, and carbon dioxide) that are needed for the aging process have been housed in a separate box outside the lab. The gas delivery system is fully automated to control remotely the injection of these gases. In spite of these achievements, the completion of this task (Task 2.1) has been delayed by two months due to delays in delivery of critical items needed to complete the development of the setup. The delay may not affect the overall project schedule. However, it can shift the completion dates of the experimental studies on cement degradation (i.e. all subtasks that are included in Task 2) by two months.

Furthermore, the development of confined compressive strength measuring setup was continued. Major items of the setup have been assembled. The delivery of the confining cylinder has been delayed. We expect the item to arrive within days. The system will be calibrated before running the actual compressive strength measurements.

Literature review conducted on cement degradation has been completed. Published experimental data gathered during the review has been summarized in Appendix A. Theoretical and modeling studies on cement degradation (carbonation and leaching) were continued. A theoretical model developed for analyzing the leaching process of cement in water containing dissolved (ionized) materials has been investigated. Results show that the concentration of saturated calcium ion (CSCI) is strongly affected by temperature and sodium chloride concentration in the solution. The CSCI increases with the increase in NaCl concentration and decreases with the increase in temperature.

Our effort to develop cement specimen preparation procedure was continued. During this period, more focus was given to examine the impact of curing temperature on porosity and permeability of cement specimens. The temperature slightly increased the permeability and porosity of the specimens cured at elevated temperature.

Our plan for the coming weeks is to finalize the development of cement degradation and compressive strength measuring setups and prepare them for preliminary testing. We will continue our theoretical and modeling studies on cement degradation and tubular corrosion.

2. Overall Project Progress

2.1 Theoretical Studies (Task 1)

Extensive literature review was carried out on cement degradation resulting from acid attack. However, under high-pressure and high-temperature sour gas environment, very limited experimental investigations were conducted on cement deterioration. A summary of published laboratory measurements is presented in the Appendix. In addition to experimental studies, theoretical investigations and modeling techniques were thoroughly reviewed.

Theoretical and modeling studies on cement carbonation and leaching were continued to better understand the mechanisms of the deterioration process. During this reporting period, more focus was given to model the leaching process of cement in water containing dissolved materials. Calcium leaching is one of the major stages in cement degradation. When a cement-based material is in contact with pure or acidic water, ionic transfers occur between the external water and the pore solution, which is strongly a basic solution. Due to the interaction between pore fluid and cement matrix, some of cement hydration products dissolve, thus increasing the porosity and permeability of the cement and decreasing its mechanical strength. During the dissolution process, portlandite ($Ca(OH)_2$) is the first mineral to be dissolved, then the calcium silicate hydrates (C–S–Hs) are decalcified. The degradation is characterized by several dissolution–precipitation fronts delimiting zones with different physicochemical and mechanical characteristics (Kamali et al., 2008).

Mainguy and Coussy (2000) presented a theoretical model that predicts the amount of leached calcium ion resulting from exposure of cement to an aggressive environment. The analytical solution of the model is presented in dimensionless form. To relate the calcium ion concentration in the liquid phase to that in the solid phase, Nakarai et al. (2006) studied the solid-liquid calcium ion concentration-equilibrium using a chemo-physical coupled model. The model predicts the calcium concentration in the solid-phase that corresponding to given concentration in the liquid-phase by considering the dissolution of the calcium hydroxide and calcification of C-S-H gel. According to Mainguy and Coussy (2000), the dimensionless concentration for the solute (C_{ion}) can be calculated as:

$$\overline{C_{ion}} = \begin{cases} \frac{C_{ion}}{C_{satu}} = \frac{erf(\xi)}{erf(\xi_d)} & 0 \le \xi \le \xi_d \\ 1 & \xi_d \le \xi \end{cases} \quad \text{..... (1)}$$

where:

$\overline{C_{ion}}$ is the dimensionless calcium ion concentration.

C_{ion} is the calcium ion concentration in mmol/l.

ξ is the dimensionless distance from the outer surface of the sample.

ξ_d is the dimensionless distance from the edge of the sample to the degradation depth.

C_{satu} is the concentration of saturated calcium ions (CSCI) in mmol/l.

As proposed by Nakarai et al. (2006), the concentration of saturated calcium ions is estimated as:

$$C_{satu} = \frac{1}{2}\sqrt[3]{2K_{sp}} \quad \text{..... (2)}$$

The solubility product of calcium hydroxide (K_{sp}) must be corrected to include the effects of sodium chloride and temperature. Thus:

$$K_{sp} = K_{sp}^{T} + K_{sp}^{Cl} \quad \text{..... (3)}$$

where K_{sp}^{T} and K_{sp}^{Cl} are the solubility products that account for temperature and salinity variations, respectively. The K_{sp}^{T} is a function of absolute temperature (T).

$$K_{sp}^{T} = 0.0125 \times 10^{9}.e^{-0.019T} \quad \text{..... (4)}$$

And, the K_{sp}^{Cl} is estimated as:

$$K_{sp}^{Cl} = A'.(5 \times 10^{4}.\sqrt[3]{Cl}) \quad \text{..... (5)}$$

$$A' = \begin{cases} -2Cl^{3} + 3Cl^{2} & (0.0 \le Cl \le 1.0) \\ 1 & (1.0 < Cl) \end{cases} \quad \text{..... (6)}$$

where Cl is the concentration (mass fraction) of the sodium chloride in the pore solution. The solubility products (K_{sp}^{T} and K_{sp}^{Cl}) have the same unit of $mmol^3/l^3$. The effects of temperature and salinity on concentration of saturated calcium ions (CSCI) are presented in Fig. 1. The CSCI increases with the increase in the NaCl content and decreases with the increase in temperature resulting from the change in the solubility product.

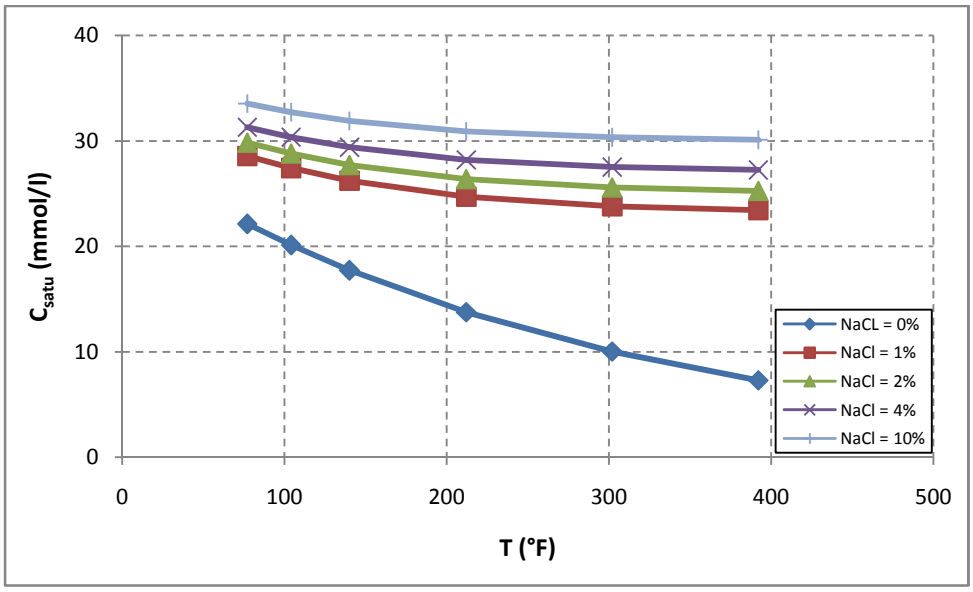

Fig. 1 Effects of temperature and salt content on the concentration of saturated calcium ions

Nakarai et al. (2006) developed a theoretical model for the dimensionless degradation distance (depth) presented in Eq. (1). The model relates the dimensionless degradation distance with porosity and diffusion coefficient.

$$\varepsilon \exp\left(-\xi_d^2\right) = \sqrt{\pi}\, \xi_d \operatorname{erf}\left(\xi_d\right) \quad \text{..... (7)}$$

Dimensionless quantities in Eq. (7) are defined as:

$$\xi = \frac{x}{2\sqrt{Dt}} \quad \text{..... (8)}$$

$$\varepsilon = \frac{\emptyset\, C_{satu}}{C_{total}} \quad \text{..... (9)}$$

where $\emptyset$ is the cement porosity. C_{total} is the total concentration of the calcium in solid form, which is defined as the sum of the amount of calcium in the solid phases of the C-S-H gel and

calcium hydroxide in mmol/l. The diffusion rate of calcium can be calculated as a function of porosity (Tognazzi, 1998).

$$D\ (m^2/s) = 2.35 \exp(9.95\ \emptyset) \quad \text{..... (10)}$$

where D is the diffusion coefficient. In Figs. 2 and 3, the calcium concentration profiles are presented in dimensionless and dimensional forms, respectively. The leaching depth is calculated from the dimensionless distance obtained from Eq. (7) as:

$$x_d = 2\xi_d\sqrt{Dt} \quad \text{..... (11)}$$

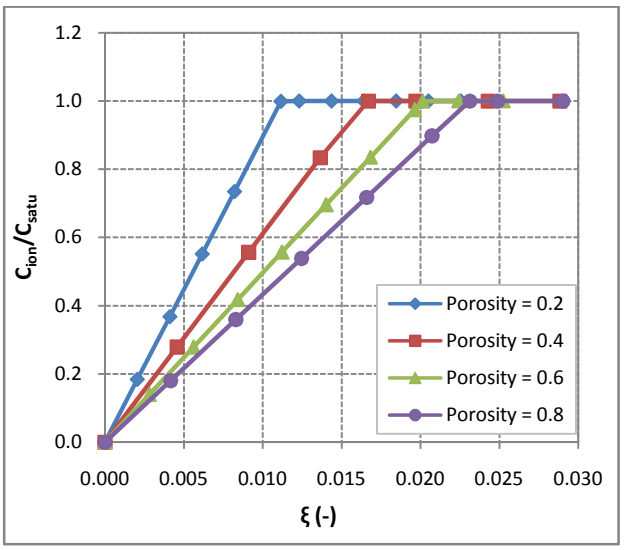

Fig. 2 Dimensionless calcium ions distribution vs. dimensionless distance (t =30 days, C_{satu} = 19.9 mmol/l and C_{total} = 15000 mmol/l)

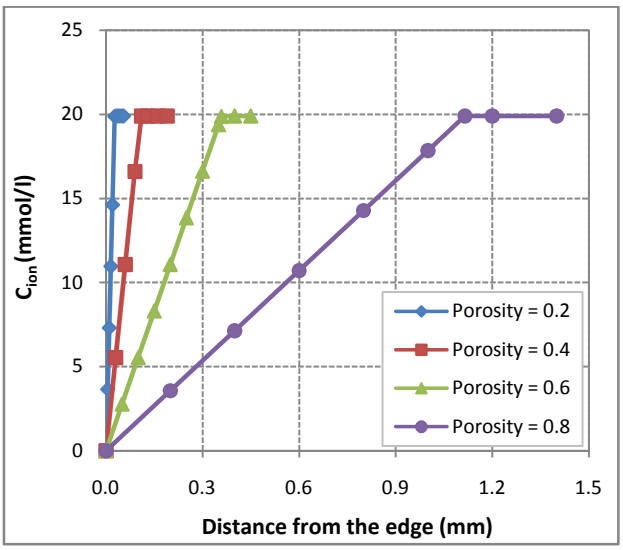

Fig. 3 Calcium ions distribution vs. distance from the outer surface at different porosities (t =30 days, C_{satu} = 19.9 mmol/l C_{total} = 15000 mmol/l)

To study the time effect on the calcium ion concentration-profile, results were obtained varying the exposure time (Figs. 4 and 5). As expected, results show increased leaching depth as the time of exposure increases. Moreover, increased porosity and saturated calcium concentration facilitate the leaching process.

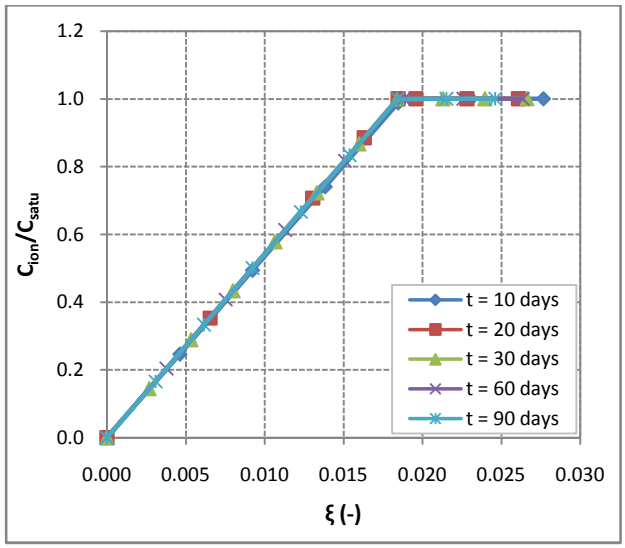

Fig. 4 Dimensionless calcium ions distribution vs. dimensionless distance at different exposure times (Ø =0.5, C_{satu} = 19.9 mmol/l and C_{total} = 15000 mmol/l)

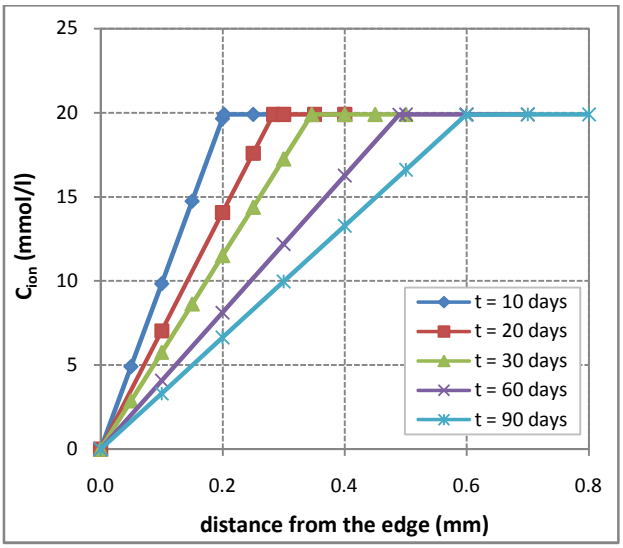

Fig. 5 Calcium ions distribution vs. distance from the outer surface at different exposure times (Ø =0.5, C_{satu} = 19.9 mmol/l C_{total} = 15000 mmol/l)

As previously mentioned, the C_{satu} is affected by the solubility product of the calcium hydroxide, which is in turn affected by temperature and sodium chloride concentration. As temperature increases or sodium chloride concentration decreases, the saturated calcium ion concentration decreases (Fig. 1). Additionally, the increase in the C_{satu} causes an increase in the leaching depth at constant porosity and total calcium concentration in the solid phase (Figs. 6 and 7).

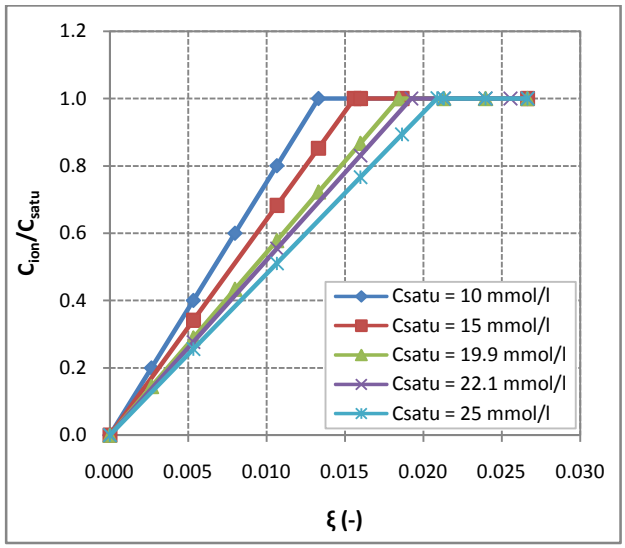

Fig. 6 Dimensionless calcium ions distribution vs. dimensionless distance at different C_{satu} (Ø =0.5, t = 30 days and C_{total} = 15000 mmol/l)

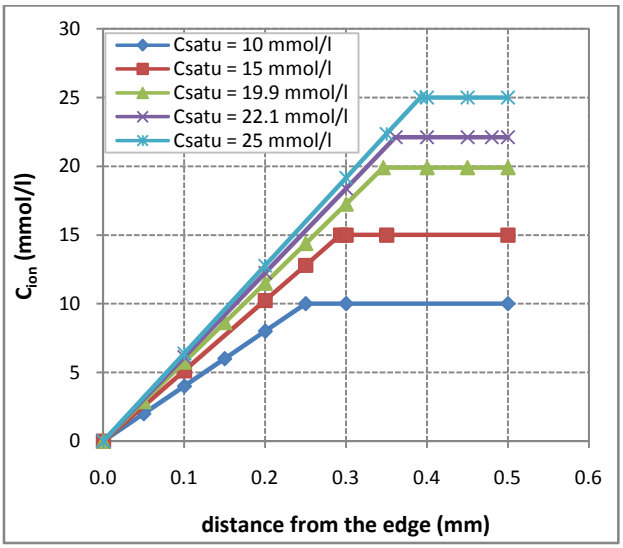

Fig. 7 Calcium ions distribution vs. distance from the outer surface at different C_{satu} (Ø =0.5, t = 30 days and C_{total} = 15000 mmol/l)

Furthermore, Nakarai et al. (2006) developed the following set of equations to determine the calcium concentration in solid phase as a function of the calcium ion concentration in the surrounding liquid (Fig. 8).

$$C_{solid} = f(C_{ion}) = A.\left\{C_{CSH}.\left(\frac{C_{ion}}{C_{satu}}\right)^{1/3}\right\} + B \quad \text{..... (12)}$$

$$A = \begin{cases} -\frac{2}{x_1^3}C_{ion}^3 + \frac{3}{x_1^2}C_{ion}^2 & (0.0 \le C_{ion} \le x_1) \\ 1 & (x_1 < C_{ion}) \end{cases} \quad \text{..... (13)}$$

$$B = \begin{cases} 0 & (0.0 \le C_{ion} \le x_2) \\ \frac{C_{CH}}{(C_{satu}-x_2)^3}(C_{ion}-x_2)^3 & (x_2 < C_{ion}) \end{cases} \quad \text{..... (14)}$$

where:

C_{solid} is the calcium concentration in solid phase in mmol/l.

C_{CH} is the concentration of calcium in the solid phase of the calcium hydroxide (mmol/l).

C_{CSH} is the amount of calcium in the solid form of the C-S-H gel (mmol/l)

x_1 is the liquid phase calcium ion concentration when the rapid transition of C-S-H gel into silica gel begins (mmol/l)

x_2 is the liquid phase calcium ion concentration when the calcium hydroxide has completely dissolved and the dissolution of C-S-H gel begins (mmol/l).

Equations (12) through (14) have been applied using input parameters presented in a published study (Gerard et al., 2002). In Fig. 9, the calcium concentration in solid phase is plotted as a function of calcium ions in the liquid.

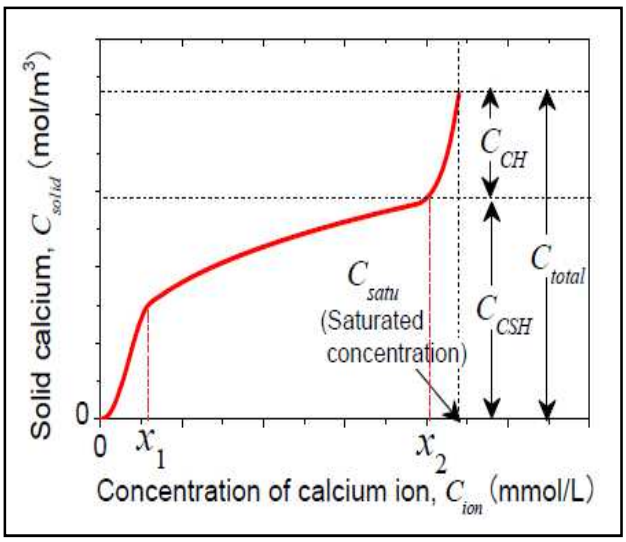

Fig. 8 Solid-liquid equilibrium distribution for calcium (Nakarai et al., 2006)

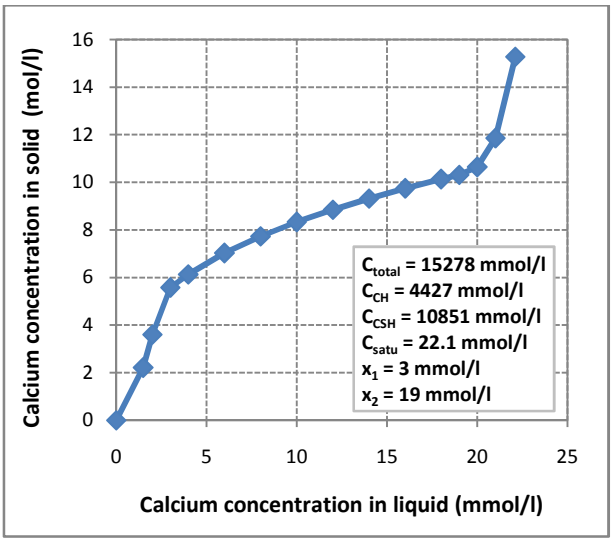

Fig. 9 Solid-liquid equilibrium distribution for calcium using input data from Gerard et al. (2002)

2.2 Experimental Studies on Degradation of Cement (Task 2)

The objectives of this task are to develop experimental facilities and conduct the proposed experimental studies on cement degradation. The plan for the first six months of the project is to develop aging cell setup (Task 2.1). This task is delayed by two months due to delays in delivery of critical items needed to complete the assembly process. Nonetheless, the apparatus has been assembled and placed in the lab (Fig. 10) where the specimen aging will be carried out. As indicated in the previous report, a high-temperature circulating bath heating system was selected to heat or cool the aging cell. A heating jacket was manufactured and installed on the cell to circulate the heating medium (silicone oil). After testing for leakage, the jacket was fully insulated using micro-porous insulation material compatible with high temperature application. Gases (nitrogen, sour gas, and carbon dioxide) required for the aging process have been placed in a separate box (Fig. 11) outside the lab. Actuating valves and measuring instruments are installed in the box to control remotely the injection of these gases.

Fig. 10 Aging cell setup in the lab

Fig. 11 Gas storage box

In addition to the aging cell, an experimental setup will be developed to measure confined compressive of strength cement specimens. Except the confining cylinder, major items of the setup have been assembled (Fig. 12). The delivery of this item has been delayed. We expect it will be delivered in the coming days. The system will be calibrated before running the actual compressive strength measurements.

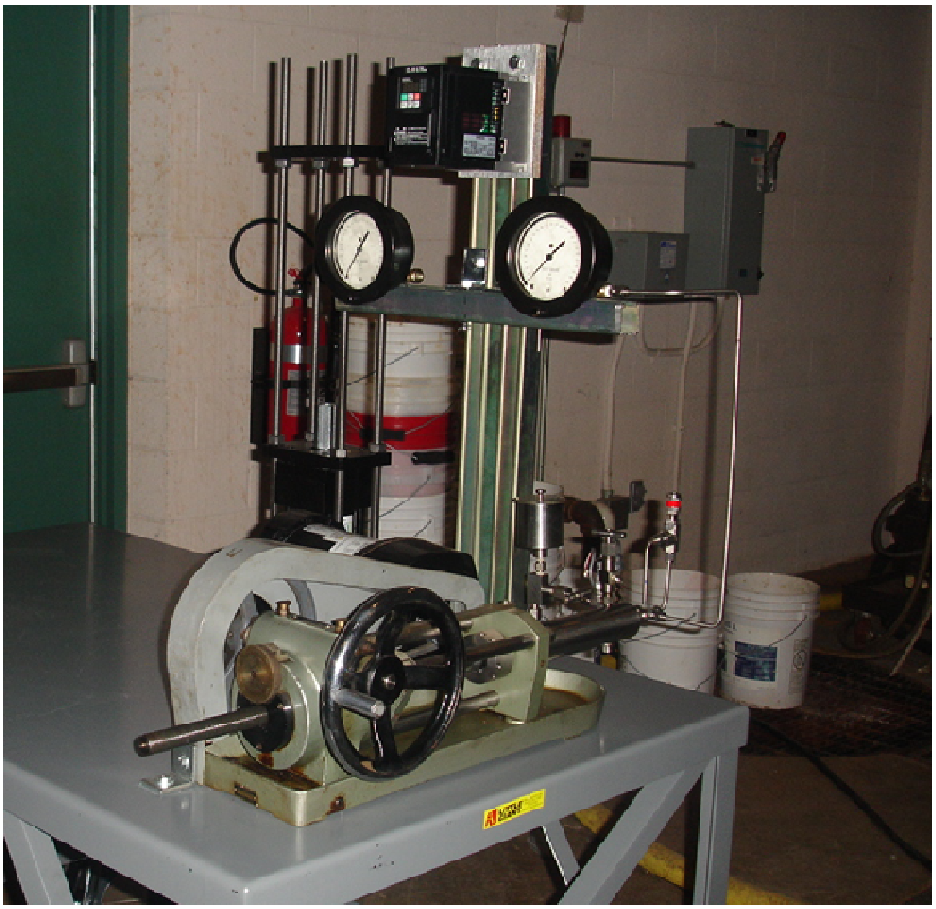

Fig. 12 Compressive strength measuring setup

The development of an established specimen preparation procedure was continued. Cement slurries with water to cement ratio of 38% were prepared by adding 1.896 lbm of neat Class H cement to 0.721 lbm of tap water while mixing. Then, the cement slurry was poured into moulds (1" Diameter x 2" Length) which were sprayed with silicon release. The slurry was left in the moulds for 24 hours to harden and develop the initial strength under ambient conditions. Subsequently, the specimens were cured at 200°F in tap water for 5 days and recovered from the moulds using a hydraulic plunger. After recovering, the specimens were dried in an oven at 110°F to a constant weight (Table 1) and their porosity and permeability were measured. Specimen dimensions, weight, and measured parameters are shown in Table 2. These measurements are compared with porosity and permeability of specimens that were cured at ambient conditions (Figs. 13 and 14). Results show that the porosity and permeability of the cement slightly increase with the increase in curing temperature.

Table 1 Specimen weight during drying to a constant weight

Drying Time (hrs)	Weight (lbm)		
	Specimen # 17	Specimen # 18	Specimen # 19
0	0.061	0.061	0.058
6	0.057	0.057	0.054
20	0.056	0.056	0.053
21	0.056	0.056	0.053
26	0.056	0.056	0.053

Table 2 Specimen dimension, weight, porosity, and permeability

	Specimen dimension			Porosity				Permeability	
Specimen #	Diameter	Length	Weight	V_b	V_g	V_p	Porosity	K_{air}	K_{klink}
	in	in	lbm	in^3	in^3	in^3	%	md	md
17	0.99	1.18	0.056	0.90	0.60	0.30	33.2	0.501	0.370
18	0.98	1.17	0.056	0.88	0.61	0.27	31.0	0.589	0.445
19	1.00	1.13	0.053	0.89	0.59	0.31	34.2	0.721	0.555

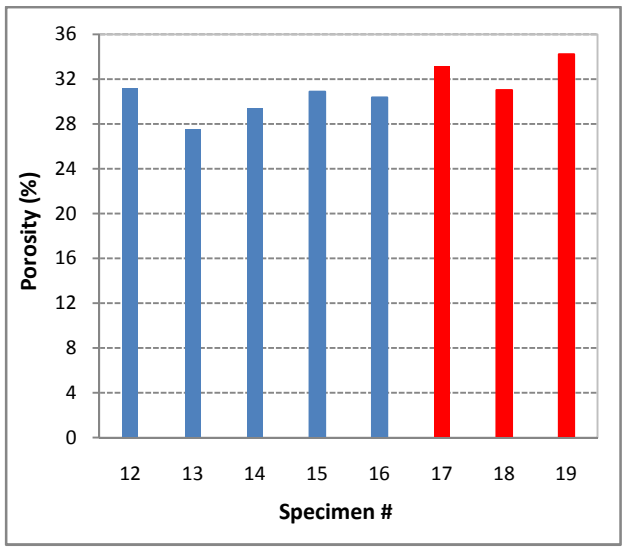

Fig. 13 Porosities of specimens cured at ambient conditions (blue) and 200°F (red)

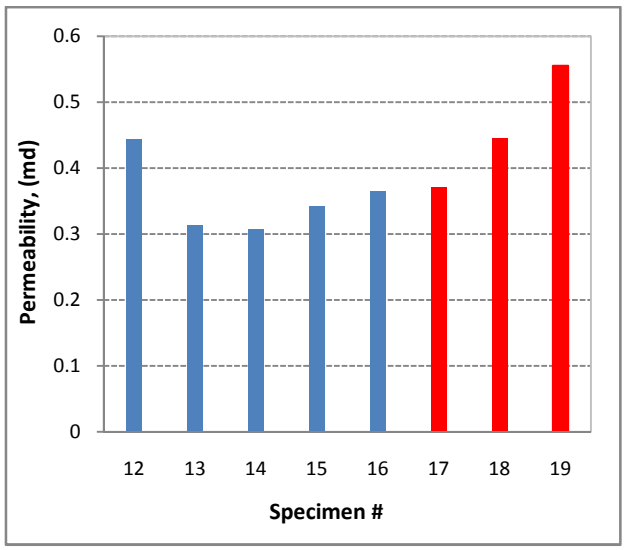

Fig. 14 Permeabilities of specimens cured at ambient conditions (blue) and 200°F (red)

2.3 Experimental Studies on Corrosion of Tubulars (Task 3)

Searching for high-pressure recirculation pumps was continued. We are considering different options including using an injection cylinder as a pump, acquiring a custom-made pump or syringe type pump that meets the desired specifications. The design of the corrosion setup will be finalized after specifying the pump.

3. Problems Encountered

One of the major problems during this reporting period was delay in delivery of items needed to complete the development experimental facilities. The deliveries the following items have been delayed by more than two weeks:

1. Circulation bath for the heating system
2. Confining vessel for compressive strength measuring setup
3. Tools needed to prepare high-pressure tube fittings

To avoid significant delay in the project, an existing heating bath with a lower heating capacity will be used until we receive the new. According to the vendor, the confining vessel will delivered in the coming days. To facilitate the assembling of the aging cell setup, existing worn-out tools were used to prepare high-pressure tube lines. As a result, some of these lines may have gas leaks and need repairs using the new tools that we have received this week.

In addition to the delivery delays, unavailability of a qualified applicant for the post-doc position has been a main problem to the project. The post-doc position is a full time position with several duties and responsibilities. Even though the position was advertised in November 2011, we were not able to find an applicant with the required qualifications and experiences. After waiting for more than six months, recently we have found a PhD candidate from the University of Tulsa who will be graduating this May, receiving a doctorate degree in Mechanical Engineering with dissertation title "*Characterization and Prediction of Inhibited Erosion-Corrosion in CO2-Saturated Systems*". The candidate is well published in the area of corrosion studies including CO_2 corrosion modeling and measurements. His resume is presented in Appendix B.

4. Planned Activities

- Completing the installation of the aging-cell heating system.
- Testing and calibration of cement specimen-aging setup.
- Continue theoretical and modeling studies on cement and tubular degradation.
- Continue evaluating cement core preparation procedure.
- Testing and calibration of compressive strength measuring setup.

5. Project Expenditures

This section presents the project expenses during the months of April (Table 3) and the cumulative expenditures.

Table 3 Current and cumulative expenditures, April, 2012

No.	Budget Categories	Current Expenses	Cumulative Expenses
1	Salaries & Wages	$3,000.00	$15,000.00
2	Fringe Benefits	$165.00	$825.00
3	Project Materials	$2,055.96	$32,724.67
4	Travel	$0.00	$937.91
5	Conference Expenses	$0.00	$0.00
6	Other Direct Costs	$0.00	$202.38
7	Equipment	$26,096.38	$78,611.19
8	Space Rental	$0.00	$0.00
9	Indirect Cost	$2,610.48	$24,845.00
10	**Total**	**$33,927.82**	**$153,146.15**

References

Barlet-Gouédard, V., Rimmelé, G., Goffé,B. and Porcherie,O. 2006. Mitigation Strategies for The Risk of CO2 Migration Through Wellbores, paper IADC/SPE 98924, presented at the IADC/SPE Drilling Conference, 21-23 February 2006, Miami, Florida, USA.

Brandl, A., Cutler, J., Seholm, A., Sansil, M., and Braun, G. 2010. Cementing Solutions for Corrosive Well Environments, paper SPE-132228-MS-P, presented at the CPS/SPE International Oil & Gas Conference and Exhibition in China held in Beijing. Jun 8-10.

Garnier, A., Laudet, G., Neuville, N., et al. 2010. CO2-Induced Changes In Oil Well Cements under Downhole Conditions First Experimental Results, paper SPE 134473, presented at the SPE Annual Technical Conference and Exhibition, 19-22 September 2010, Florence, Italy.Mainguy, M, Tognazzi, C., Torrenti, J., Adenot, F. 2000. Modelling of Leaching in Pure Cement Paste and Mortar. Cement and Concrete Research, 30. 83-90.

Gérard, B., Le Bellego, C., and Bernard, O., 2002. Simplified modeling of calcium leaching of concrete in various environments, Materials and Structures, 35: 632-640.

Kutchko, B., Strazisar, B., Lowry, G., Dzombak, D., and Thaulow, N. 2008. Rate of CO2 Attack on Hydrated Class H Well Cement under Geologic Sequestration Conditions, Environ. Sci. Technol Mainguy, M. and Coussy, O. 2000. Propagation Fronts During Calcium Leaching and Chloride Penetration. Journal of Engineering Mechanics.

Lécolier E., Rivereau A., Ferrer N., Audibert A. and Longaygue X., 2006. Durability of Oilwell Cement Formulations Aged in H2S-Containing Fluids, paper SPE 99105 presented at the IADC/SPE Drilling Conference, Miami, Florida, February 21–23.

Lécolier, E., Rivereau, A., Le Saoût G. and Audibert-Hayet, A. 2007. Durability of Hardened Portland Cement Paste used for Oil well Cementing, Oil & gas science and technology, Rev. IFP, Vol. 62 (2007), No. 3, pp. 335-345.Nakarai, K. Usui, T. and Ishida, T. 2007. Numerical Evaluation of Calcium Leaching from Cementitious Materials in contact with Bentonite, The International Symposium on Social Management Systems (ISMS2007), Yichang, China.

Nakarai, K., Ishida, T. and Maekawa, K. 2006. Modeling of Calcium Leaching from Cement Hydrates Coupled with Micro-Pore Formation, Journal of Advanced Concrete Technology, 4: (3), pp.395-407.

Noik, Ch., and Rivereau, A. 1999. Oil well Cement Durability, paper SPE 56538, presented at the SPE Annual Technical Conference and Exhibition held in Houston, Texas, October 3–6.

Sauki, A. and Irawan, S. 2010. Effects of Pressure and Temperature on Well Cement Degradation by Supercritical CO2, International Journal of Engineering and Technology, IJET-IJENS Vol: 10 No: 04.

Appendix A: Summary of Published Data

Table A-1 Available experimental data on degradation of oil well cement

Reference	Cement Specimen		Curing Information				Aging Information			Measured Data				
	Cement Type	Size	Temp. °F	Pressure Psi	Condition	Curing Time Days	Temp. °F	Press. Psi	Fluid	Aging Time Days	Degradation Depth in	Perm. md	Porosity %	Comp. Strength Psi
Garnier et al. (2010)	Portland Class G	Cylindrical (0.787 in diameter x 1.574 in length)	194	14.7	Lime-saturated water	28	194	1160	Supercritical CO_2 above water	0	0.000			
										7	0.035			
										36	0.118			
										65	0.157			
	Portland Class G + 35% silica flour		284	3000		10	284	1160		0	0			
										4	0.037			
										12	0.120			
										21	0.154			
										31	0.256			
										55	0.445			
										88	0.787			
Barlet-Gouedard et al. (2006)	Portland Class G	Cylindrical (0.5 in diameter x 1 in length), (1 in diameter x 2 in length)	194	3000	Water	3	194	4061	Wet supercritical CO_2	0	0			
										2	0.079			
										4	0.098			
										8	0.138			
										22	0.236			
										42	0.335			
										85	0.472			
									CO_2-saturated water	0	0.000			
										2	0.039			

										4	0.079			
										8	0.118			
										22	0.197			
										42	0.276			
										85	0.315			
Sauki and Irawan (2010)	Portland Class G	For curing: Cube (2 in height x 2 in length) For testing: Cylindrical (1.5 in diameter x 2 in length)	104 248	1522.89 2030.5	Unclear	1/3	104	1522.89	Wet supercritical CO2	0	0.0000			
										1	0.0305			
										3	0.0409			
										5	0.0496			
									CO2-saturated brine	0	0.0000			
										1	0.0131			
										3	0.0171			
										5	0.0250			
							104	2030.5	Wet supercritical CO2	0	0.0000			
										1	0.0189			
										3	0.0305			
										5	0.0372			
									CO2-saturated brine	0	0.0000			
										1	0.0079			
										3	0.0151			
										5	0.0213			
							248	2030.5	Wet supercritical CO2	0	0.0000			
										1	0.0313			
										3	0.0374			
										5	0.0598			
									CO2-saturated brine	0	0.0000			
										1	0.0124			
										3	0.0218			
										5	0.0307			
Kutchko et al. (2008)	Portland Class H		122	4394.6	1% NaCl (brine) solution	28	122	4394.6	Supercritical CO2	0	0.0000			
										9	0.0027			
										25	0.0045			

										61	0.0065			
										90	0.0056			
										156	0.0066			
										361	0.0119			
									CO2-saturated brine	0	0.0000			
										9	0.0139			
										25	0.0177			
										61	0.0216			
										90	0.0237			
										156	0.0252			
										361	0.0263			
Lecolier et al. (2006)	Cement I (Special cement)	Bar 0.787 x 0.787 x 6.3 in Bar 1.57 x 1.57 x 6.3 in disk 2.36 in diameter disk 1.5 in diameter	176	1015.26	Unclear		248	1015.26	Reservoir fluids	0				24656.4
										30				28427.4
										90				29587.7
										212				29297.6
										365				29007.5
	Mortar									0				13372.5
										30				11632.0
										90				10790.8
										212				12444.2
										365				14126.7
	Cement II (Special cement)	Cylindrical 1 in diameter x 2 in length					248	2175.56	H2S-saturated brine	0				196
										21				22
	Conventional Portland Cement									0				47
										21				2
Brandl et al. (2010)	Portland Class G + silica flour + Pozzolan + sea water	1 in diameter x 2 in length	300	3000	Unclear	4	300	3000	CO2 environment	0		2.02E-04		5840
										30		4.50E-03		5890
										90		5.99E-03		5910
										180		2.78E-03		5820
	Portland Class G + 35% silica flour +									0		2.97E-04		5910
										30		3.37E-03		5890
										90		2.53E-03		5910

										180		4.35E-03		5910
Lecolier et al. (2007)	Portland Class G	Cylindrical (1 in diameter x 2 in height) and bar (0.787 x 0.787 in cross section and 6.3 in length)	176	1015.26	Water	30	176	1015.26	Water with no renewed	0				9427.5
										30				8557.2
										110				8484.7
										170				8557.2
										355				7687.0
									Brine with monthly renewed	0				8992.3
										30				8122.1
										90				8702.3
										160				6816.8
										350				4525.2
									Crude oil	0		8.11E-04	29	7977.1
										30		6.59E-04	25	7251.9
										90		7.09E-04	27	8267.1
										170		7.30E-04	25	8847.3
Noik and Rivereau, (1999)	Portland Class G	Cylindrical (1 in diameter x 2 in height)	356	1015.26	Water		356	1015.26	Deionised water	90				797.7
										180				748.4
										250				751.3
										380				758.5
	Portland Class G + (35%-40%) silica sand						248			30		8.70E-04		14648.8
										60		2.60E-04		13053.4
										90		4.60E-04		14503.8
										150		5.00E-04		13343.5
										210		3.80E-04		10732.8
										420		1.30E-03		9717.5
										570		7.23E-04		6091.6
										750				9862.6
							284			30		3.40E-04		10152.6
										60		1.40E-04		9427.5
										90		7.23E-04		11312.9
										150		7.70E-04		10152.6
										210		7.10E-04		6816.8
										420		2.40E-04		7977.1

										570		3.80E-04		8122.1
										750		1.15E-03		
							356			110		1.45E-03		4496.2
										190		1.74E-03		5946.5
										330		4.76E-03		5511.4
	Portland Class G + (35%-40%) silica sand + Additives						356			100				6932.8
										165				5903.0
										270				6526.7
										400				4351.1
										600				4061.1
	RPC (Portland Class G + silica sand + silica fume)						248		Deionised water	15				16824.4
										30				18564.8
										90				13198.4
										180				20015.2
										360				22916.0
									Sea water	15				19435.1
										30				21755.7
										90				17114.4
										180				24076.3
										360				26686.9
									Sea water + H_2S	15				14503.8
										30				21755.7
										90				16099.2
										180				23786.2
										360				26541.9
									Sea water + gas oil	15				22045.7
										30				20450.3
										180				23786.2
										360				26396.9
							284		Deionised water	0				20450.3
										30				28572.4
										60				24656.4
										90				27586.2

									180					27571.7
							356		Deionised water	0				21900.7
										30				21610.6
										90				18419.8
										180				16969.4
	Portland Class G + silica sand + Additives + MnO						356		Deionised water	90				6004.6
										200				3379.4
										290				3408.4
										390				3190.8
	Portland Class G + silica sand + Additives + Fe_2O_3						356		Deionised water	90				9137.4
										200				5830.5
										290				5874.0
										390				5801.5
Barlet-Gouedard et al. (2007)	Portland Class G	Cylindrical (0.5 in diameter x 1 in length), (1 in diameter x 2 in length)	194	3000	Water	3	194	4061.06	Wet supercritical CO2	0			32.5	
										0.5			27	
										2			23.5	
										8			19	
										22			18.2	
										42			13.8	
										83			26.5	
									CO2-saturated water	0			33	
										0.5			27	
										2			23.5	
										8			19	
										22			9.5	
										42			20.5	
										83			28.5	
	CO_2-resistant material cement	Cylindrical (0.5 in diameter x 1 in length)							Wet supercritical CO2	0.0			14	
										0.5			16	
										1.3			20	
										7.3			21.4	
										41.5			19	

										84.8			21.3	
									CO2-saturated water	0.0			14	
										0.5			18	
										1.3			20.6	
										7.3			20	
										21.6			24	
										41.5			23.6	
										84.8			23.3	
Mueller et al. (1991)	Portland Class H + 35% silica flour + 50% H_2O		350	3000	Unclear	90	350	3000	Unclear	1				5440
										7				4800
										29				3850
										90				4737
	Portland Class H + 35% silica flour + 0.2% citric acid + 111% H_2O									1				2150
										7				2300
										29				1425
										90				1495
Santra and Sweatman (2011)	Cement sample A with a CO2-resistant formulation	Cylindrical (1 in diameter x 2.5 in length)	140	2000	Water	28	140	2000	Supercritical CO2 + fresh water	0				5594
										15				7951
										30				7958
										180				7002
										365				8866
Sauki et al. (2010)	Portland cement Class G	Cylindrical (1.5 in diameter x 2 in length)	104	1522.89	Unclear	1/3	104	1522.89	CO2 dissolved in brine (1.754 M)	0	0			
										1	0.269			
										3	0.466			
										5	0.533			
			104	2030.5			104	2030.5	CO2 dissolved in brine (2.1 M)	0	0			
										1	0.384			
										3	0.523			
										5	0.624			
			248	1522.89			248	1522.89	CO2 dissolved in brine (0.446 M)	0	0			
										1	0.172			
										3	0.25			

										5	0.269				
			248	2030.5			248	2030.5	CO2 dissolved in brine (0.569 M)	0	0				
										1	0.243				
										3	0.35				
										5	0.442				

Appendix B: Resume of Postdoctoral Research Associate

SHOKROLLAH HASSANI
(918) 853-6143 or shokrollah-hassani@utulsa.edu

Objective | Research Interests

To work in the field of Corrosion and Electrochemistry, CO_2 and H_2S Corrosion, Material Characterization and Selection, Erosion-Corrosion in Oil and Gas Pipeline, and Surface Coating and Engineering

Education

- ✓ **PhD candidate in Mechanical Engineering**, Department of Mechanical Engineering, The University of Tulsa (TU), Oklahoma, USA, Expected Graduation: May 2012
  Thesis: "***Characterization and Prediction of Inhibited Erosion-Corrosion in CO_2-Saturated Systems***", under supervision of Prof. M. A. Golozar and Dr. K. Raiessi.
  GPA: 3.9/4
- ✓ **M.Sc. in Metallurgy Engineering (Corrosion and Protection of Materials).** Department of Materials Engineering, Isfahan University of Technology (IUT), Isfahan, Iran, May 2008
  Thesis: "***Creation of Electrodeposited Microcrystalline and Nanocrystalline Nickel/Cobalt Alloy Coatings and Evaluation of Corrosion Behavior and Coating Electrodeposition Mechanism***", under supervision of Prof. M. A. Golozar and Dr. K. Raiessi.
  GPA: 17.23/20
- ✓ **B.Sc. in Department of Materials Engineering**, Semnan University, Semnan, Iran, May 2005
  Thesis: **"*Creation and Comparative Study of Tribological Behavior of Bronze-Graphite Composite and Bronze-Lead Alloy*"**, under supervision of Dr. A. Habibollahzadeh and Dr. M. Tajalli.
  GPA: 16.16/20

Work Experience

- ✓ For the past three years I have been working as an assistant researcher at the Erosion-Corrosion Research Center at the University of Tulsa on a project for PETROBRAS Company on different corrosion subjects including;
  - CO_2 Corrosion, Sand Erosion
  - Erosion-Corrosion, Chemical Inhibition of CO_2 corrosion
  - Effect of Oil on CO_2 Corrosion and Effect of Chloride on CO_2 Corrosion
  - CO_2 Corrosion Modeling and erosion-corrosion modeling
  - Effect of Sand Erosion on Chemical inhibition
- ✓ I have previously worked as an assistant researcher at the Isfahan University of technology on several corrosion projects for Iranian national Oil and Gas Company including:
  - Long term corrosion measurement in HCl solution
  - Cathodic protection by zinc rich paints
  - Cadmium coatings corrosion and abrasion behavior

Journal Publication

1. Sh. Hassani, J. R. Shadley, S. A. Shirazi, E. F. Rybicki, K. P. Roberts, , C. Joia, "Flow Loop Study of NaCl Concentration Effect on Erosion, Corrosion, and Erosion-Corrosion of Carbon Steel in CO_2-Saturated Systems", *Corrosion Journal, Volume 68, Issue 2, February 2012*
2. Sh. Hassani, J. R. Shadley, S. A. Shirazi, E. F. Rybicki, K. P. Roberts, , C. Joia, "Characterization and Prediction of Chemical Inhibition Performance for Erosion-Corrosion Conditions in Sweet Oil and Gas Production", Accepted for *CORROSION Journal January 2012*
3. Sh. Hassani, k. Raissei, M. A. Golozar, "Electrochemical Study of Saccharin and Overpotential Effects on Electrodeposited Ni-Co Nanocrystalline Coating", *Journal of Applied Electrochemistry, Springer Netherlands, vol. 38, no. 5, pp. 689-694, 2008 (Cited 12 times)*
4. Sh. Hassani, K. Raeissi, M. Azzi, D. Li, M.A. Golozar, J.A. Szpunar, "Improving the corrosion and tribocorrosion resistance of Ni–Co nanocrystalline coatings in NaOH solution", *Corrosion Science*, *Volume 51, Issue 10*, *October 2009*, *Pages 2371-2379 (Cited 5 times)*
5. Sh. Hassani, J. R. Shadley, S. A. Shirazi, E. F. Rybicki, K. P. Roberts, C. Joia, "A new approach for studying inhibited erosion-corrosion in CO_2 saturated systems", Under revision for SPE Journal

Conference Publication

1. Sh. Hassani, J. R. Shadley, S. A. Shirazi, E. F. Rybicki, K. P. Roberts, "Flow Loop Study of Chloride Concentration Effect on Erosion, Corrosion and Erosion-Corrosion of carbon Steel in CO_2 Saturated Systems", CORROSION 2011, Houston, Paper No. 11237 *(in English)*.
2. Sh. Hassani, J. R. Shadley, S. A. Shirazi, E. F. Rybicki, K. P. Roberts, C. Joia, "Characterization and Prediction of Chemical Inhibition Performance for Erosion-Corrosion Conditions in Sweet Oil and Gas Production", CORROSION 2012, Salt Lake City, UT *(in English)* paper accepted.
3. Sh. Hassani, J. R. Shadley, S. A. Shirazi, E. F. Rybicki, K. P. Roberts, C. Joia, "A new approach for studying inhibited erosion-corrosion in CO_2 saturated systems", SPE CORROSION 2012, Aberdeen, UK *(in English)* Abstract accepted.
4. Sh. Hassani, k. Raissei, M. A. Golozar, "Saccharin effects in Ni/Co nanocrystalline electrodeposits coatings", *10^{th} International congress of corrosion*, Tehran, Iran, 2007 *(in English)*.

5. A. Azizi, Sh. Hassani, A. Habibollahzadeh, M. Tajjali, "Creation and Comparative Study of Tribological Behavior of Bronze-Graphite Composite and Bronze-Lead Alloy", *7th National Congress of Surface Science and Engineering,* Isfahan, Iran, 2005 *(in Persian)*.
6. Sh. Hassani, k. Raissei, M. A. Golozar, "Effect of Saccharin and Current Density on Grain Size of Nanocrystalline Ni/Co Electrodeposited Coating", *National Symposium of Steel,* Isfahan, Iran, 2006 *(in Persian)*.
7. Sh. Hassani, K. Raissei, M. A. Golozar, "The Study of Texture and Morphology of Electrodeposited Ni/Co Nanocrystalline Coating", *2th National Congress of Nano Technology,* Kashan, Iran, 2007 *(in Persian)*.
8. Sh. Hassani, k. Raissei, M. A. Golozar, "The Study on Corrosion Behavior of Nanocrystalline Ni/Co Electrodeposit in 3.5%wt NaCl", *11th congress of Iranian Metallurgical Society,* Isfahan, Iran, 2007 *(in Persian)*.
9. A. Mostaed, k. Raissei, Sh. Hassani, M. A. Golozar, "Corrosion of Steel in Reinforcement Concrete at 3.5%wt NaCl Aquatic Solution", *11th congress of Iranian Metallurgical Society,* Isfahan, Iran, 2007 *(in Persian)*.
10. Sh. Hassani, k. Raissei, M. A. Golozar, "The Study of the Effect of Saccharin on Tribo-Corrosion Behavior of Nanocrystalline Ni/Co Electrodeposited Coating in 10%wt NaOH", *9th National Congress of Surface Science and Engineering*, Tehran, Iran, 2008 *(in Persian)*.
11. Sh. Hassani, J. R. Shadley, S. A. Shirazi, E. F. Rybicki, K. P. Roberts, "Erosion-Corrosion in CO_2 Saturated Systems with Sand and in High Concentration of Salt", CORROSION 2010, San-Antonio, Student Poster Session *(in English)*.
12. Sh. Hassani, J. R. Shadley, S. A. Shirazi, E. F. Rybicki, K. P. Roberts, "Erosion-Corrosion of Carbon Steels in CO2-Saturated Systems in Presence of Sand, Oil, High Chloride Concentration, and Inhibitor", CORROSION 2011, Houston, Student Poster Session *(in English)*.
13. Sh. Hassani, J. R. Shadley, S. A. Shirazi, E. F. Rybicki, K. P. Roberts, "Flow Loop Study of Oil Cut Effect on CO_2 Corrosion and Inhibitor Performance", CORROSION 2012, Salt Lake City, Student Poster Session *(in English).*
14. Sh. Hassani, J. R. Shadley, S. A. Shirazi, E. F. Rybicki, K. P. Roberts, "Erosion-Corrosion of Carbon Steels in CO_2-Saturated Systems in Presence of Sand, Oil, High Chloride Concentration, and Inhibitor", Research Curriculum, Spring 2011, The University of Tulsa – University of Oklahoma, Poster Session *(in English)*.
15. Sh. Hassani, J. R. Shadley, S. A. Shirazi, E. F. Rybicki, K. P. Roberts, "Flow Loop Study of Oil Cut Effect on CO_2 Corrosion and Inhibitor Performance", The fifteenth annual student research colloquium held jointly with the 86th annual meeting of the American association for the advancement of science – southwestern & rocky mountain region, Spring 2012, The University of Tulsa, (in English).

Reviewed Paper

- ✓ M. Jones and R.J. Llewellyn, "erosion-corrosion, erosion, corrosion resistance, carbides, nickel and alloys", *CORROSION Journal*

Awards

- ✓ Allen Chapmen Distinguished PhD Student Award, The University of Tulsa, 2009-10, 2010-11, and 2011-12
- ✓ NACE Foundation Book Scholarship Award, 2011

Computer Software

- ✓ Fluent and Gambit
- ✓ Mathematica
- ✓ VBA programming

Laboratory Techniques

- ✓ Potentiostat/Galvanostat Instrument (EIS, LPR, PDYN, Cyclic Voltametery, EFM)
- ✓ Frequency Response Analyzer Instrument
- ✓ Electrical Resistance Probe Technique
- ✓ Flow loop pipeline study

Memberships

- ✓ Member of Erosion-Corrosion Research Center, The University of Tulsa
- ✓ Member of NACE since 2009
- ✓ Member of SPE since 2009
- ✓ Member of ASTM since 2009

References

Available upon request

Project Title: Effect of H_2S and CO_2 in HPHT Wells on Tubulars and Cement

Report Type: Monthly Report

Report #: 08

Reporting Period: April 22nd, 2012 to May 21st, 2012

Authors:

Ramadan Ahmed, Principal Investigator

Subhash Shah, Co-Principal Investigator

Samuel Osisanya, Co-Principal Investigator

Shokrallah Hassani, Postdoctoral Research Associate

Majed Enfis, Research Assistant

Rida Elgaddafi, Research Assistant

Himanshu Maheshwari, Research Assistant

Adarsh Naidu, Research Assistant

Prepared under BSEE Project # E12PC00035

by

THE UNIVERSITY OF OKLAHOMA

June 15, 2012

1. Summary of Accomplishments

This monthly report presents the progress made during the project period April 22, 2012 – May 21, 2012. The development of experimental setups for testing cement degradation has been completed. The aging cell and compressive strength measuring setup have been tested. Preliminary specimen aging will begin in the coming days. Moreover, literature review, and theoretical and modeling studies on cement degradation have been completed. A report summarizing the results of these studies is presented in Appendix A. Published experimental data gathered during the review has been summarized and presented in Appendix B.

A theoretical model developed for analyzing the leaching process of cement in brine solutions has been improved to account for the presence of acidic gas in the surrounding fluid system. Model predictions show that cement degradation can be strongly affected by temperature, salt concentration and pH of the surrounding liquid, total pressure of the system, and partial pressure of acidic gas. Reduction in temperature or salt concentration exacerbates the degradation.

Our effort to develop cement specimen preparation procedure was continued. During this reporting period, the effect of salinity on porosity and permeability of cement specimens were examined. The effect of salinity on porosity and permeability of the specimens were found to be minimal.

Cement specimens cured in a small-sized oven showed thermal degradation resulting from direct heating (i.e. placing the specimens in a heating chamber that has the heating element inside). To avoid the overheating, curing was carried out in a large-sized oven, which has the heating element in a separate chamber. It is possible to produce undamaged specimens using the large oven.

Theoretical and modeling studies on tubular degradation were continued. Different CO_2 corrosion modeling techniques were investigated. The models relates the corrosion rate to the composition and pH of the surrounding liquid, CO2 content of the gas phase, temperature, pressure, and fluid movement . Moreover, literature review and theoretical studies on corrosion of tubulars were continued. Accurate pH prediction is essential to estimate corrosion rate of tubulars. The solubility and pH of aqueous solutions saturated with H_2S-contianing natural gas were investigated using existing models.

The second Technical Advisory Board (TAB) meeting was held on May 16, 2012. The minutes of the meeting are presented in Appendix C.

Our plan for the coming weeks is to begin the preliminary aging experiments. We will continue our theoretical and modeling studies on tubular corrosion.

2. Overall Project Progress

2.1 Theoretical Studies (Task 1)

Theoretical and modeling studies on cement degradation have been completed. During this reporting period, more focus was given to develop a leaching model for cement in brine saturated with acidic gas. The model assumes calcium leaching as the main mechanism for cement degradation. When cement is in contact with acidic salt solution, ionic transfers occur between the solution and pore fluid, which is strong alkaline. Due to the interaction between pore fluid and cement matrix, cement hydration products (portlandite and calcium silicate hydrates) dissolve, thus increasing the porosity and permeability of the cement and decreasing its mechanical strength.

The leaching model predicts the amount of leached calcium ion resulting from exposure to acidic solutions. It relates the calcium ion concentration in the liquid phase to that in the solid phase. The change in the concentration profile of calcium ion in the solid phase indicates the level of cement deterioration in terms porosity and permeability variations, and depth of degradation. Then, mechanical properties of the cement can be predicted by knowing the degradation depth and calcium ion concentration profile in the solid phase. Details of theoretical and modeling studies on cement degradation are presented in Appendix A.

Theoretical and modeling studies on corrosion of tubulars were continued. There are numerous CO_2 and H_2S corrosion models available in the literature to predict corrosion rate and protective film thickness and properties. CO_2 corrosion models can be divided into three main categories: i) empirical models (de Waard and Milliam, 1975; de Waard et al. 1991), ii) Semi-empirical models (dewaard et al., 1995), and iii) mechanistic models (Dayalan et al, 1995; Pots, 1995; Nesic et al., 1996; Zhang et al. 1997; Dayalan et al, 1998; Anderko and Young, 1999; High et al., 2000; Nordsveen et al. 2003; Nesic et al. 2003; Sun et al., 2008). There are also some models available for H_2S corrosion modeling available in the literature (Smith and Pacheco, 2002; Ramachandran et al., 2002; Hoffmeister, 2005; Hoffmeister, 2007; Sun and Nesic, 2007; Nesic et al., 2008; Sun and Nesic, 2009; Nesic et al., 2009).

Most of the available CO_2 and H_2S corrosion models are developed for low temperature and low pressure applications whereas validity of these models at high temperature and pressure conditions has not been fully tested. Synergistic effects between CO_2 corrosion and H_2S corrosion is also an important area of consideration for corrosion modeling in oil and gas applications. In this project, first, the available CO_2/H_2S corrosion models will be reviewed and then the available models will be modified for high-temperature high-pressure applications and also synergistic effects between CO_2 and H_2S corrosion will be considered in the modeling

process. Nyberg (2010) summarized the characteristics of fourteen CO_2/H_2S corrosion models used in the oil and gas industry and discussed the abilities and limitations of these models.

2.2 Experimental Studies on Degradation of Cement (Task 2)

The objectives of this task are to develop experimental facilities and conduct the proposed experimental studies on cement degradation. The plan for the first six months of the project is to develop aging cell setup (Task 2.1). As reported previously, this task was delayed by two months due to delays in delivery of critical items (such as the heating system) needed to complete the assembly process of the aging cell (**Fig. 1**). High-temperature circulating bath heating system has been selected to control the aging cell temperature. The circulating bath is installed (**Fig. 2**) in a separate box outside of the lab because it is not rated for hazardous environment.

Fig. 1 Aging cell setup in the lab

Fig. 2 Circulating bath system

During this month, we have received all undelivered items needed to make the aging cell operational. We have completed the installation and testing of the components of the aging cell and compressive strength testing apparatus. All key components of the setup are functioning.

Items that failed during the test were returned to the manufactures for replacement or repair. The development of experimental setups for testing cement degradation has been completed. Specimen aging and compressive strength testing will be started in the coming days.

The development of an established specimen preparation procedure was continued. Cement slurries with water to cement ratio of 38% were prepared by adding 1.9 lbm of neat Class H cement to 0.72 lbm of tap water (fresh water). The slurry was mixed for 35 seconds using a standard laboratory agitator. However, API procedure requires using special high speed mixers (4,000 and 12,000 rpm preset speeds) to prepare cement slurries. Thus, a new cement mixer is purchased and will be delivered in the coming weeks. After preparing the cement slurry, the paste was poured into five identical stainless steel moulds (1" Diameter x 2" Length) which were sprayed with silicon release. It was left for 24 hours to harden in the moulds and develop the initial strength under ambient conditions. Then, the specimens (cores) were cured in tap water for 5 days. Three of the specimens were cured at elevated temperature (200ºF) using small-sized laboratory oven. The remaining cores were cured at ambient conditions. All the specimens were recovered from the moulds using a hydraulic plunger. Two of the specimens that were cured at elevated temperature showed surface damage resulting from localized overheating which occurred on one side of the specimen facing the heating element. The damaged specimens were discarded. Then, another batch of specimens were prepared and cured in 3% brine solution for 5 days. To avoid localized heating a large-sized oven was used for curing. The oven uses indirect heating method in which air is first heated to the desired temperature in a separate chamber and supplied to the oven. After curing, the cores were recovered from the moulds and dried to a constant weight. Then, their porosity and permeability were measured. Specimen dimensions, weight, and measured parameters are shown in **Table 1**. Results presented in **Figs. 3 and 4** show that the porosity and permeability of the cement slightly increase with the increase in curing temperature. The effect of salinity on the porosity and permeability is minimal. No apparent difference between samples cured in fresh water and brine solution.

Table 1 Porosity-permeability data for different neat cement specimens/cores

Core #	Core dimensions			Porosity				Permeability		Remarks		
	Diameter	Length	Weight	V_b	V_g	V_p	Porosity	K_{air}	K_{klink}			
	mm	mm	g	c.c	c.c	c.c	%	md	md			
20	24.90	27.85	23.96	13.56	9.41	4.15	30.60	0.261	0.180	Fresh water curing in Small Oven	Cured at 200°F	Mixing Time is 35 seconds
21	24.98	28.83	25.75	14.13	10.34	3.79	26.82	0.201	0.135		Cured at ambient conditions	
22	25.31	29.73	26.91	14.96	10.94	4.02	26.87	0.153	0.098			
23	25.09	31.49	27.02	15.57	10.64	4.93	31.7	0.203	0.136	Cured with 3% brine under 200°F in Large Oven		Mixing Time is 35 seconds
24	25.08	30.92	26.34	15.28	10.51	4.77	31.2	0.239	0.162			
25	25.38	28.88	25.18	14.61	9.85	4.76	32.58	0.180	0.118			
26	24.73	30.42	25.71	14.61	10.1	4.51	30.87	0.219	0.147			
27	24.82	31.51	26.52	15.25	10.38	4.87	31.93	0.135	0.083			

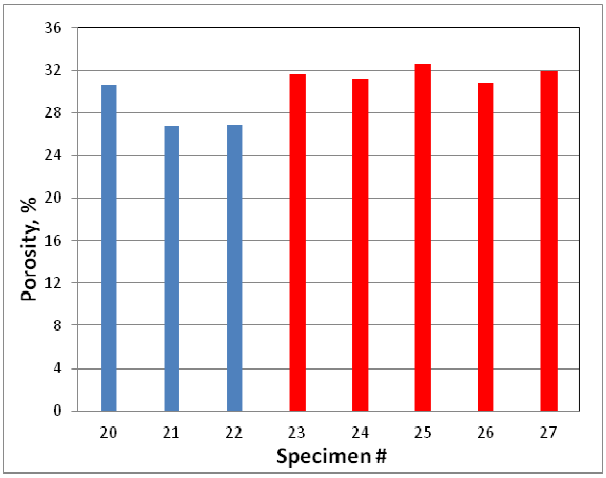

Fig. 3 Porosities of specimens cured in fresh water (blue) and 3% brine (red)

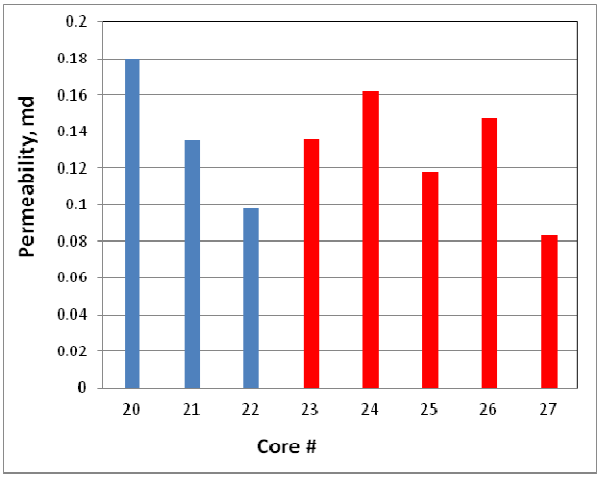

Fig. 4 Permeability of specimens cured fresh water (blue) and 3% brine (red)

2.3 Experimental Studies on Corrosion of Tubulars (Task 3)

Searching for high-pressure recirculation pumps was continued. We are considering different options including using an injection cylinder as a pump, acquiring a custom-made pump or syringe type pump that meets the desired specifications. The design of the corrosion setup will be finalized after specifying the pump.

3. Meetings and Contacts

The second Technical Advisory Board (TAB) meeting (conference) was held on May 16, 2012 in Norman. TAB members from Schlumberger, Det norske and Baker Hughes attended the meeting. However, TAB members from Halliburton and the University of Stavanger were unable to participate due to schedule conflict. The Contracting Officer's Representative and an expert from BSEE attended the meeting. The minutes of the meeting are attached (Appendix C).

4. Planned Activities

- Preliminary aging experiments.
- Continue theoretical and modeling studies on cement and tubular degradation.
- Continue evaluating cement core preparation procedure.

5. Project Expenditures

This section presents the project expenses during the months of May (Table 2) and the cumulative expenditures.

Table 2 Current and cumulative expenditures, May, 2012

No.	Budget Categories	Current Expenses	Cumulative Expenses
1	Salaries & Wages	$11,571.38	$26,571.38
2	Fringe Benefits	$2,725.88	$3,550.88
3	Project Materials	$1,334.47	$34,059.14
4	Travel	$0.00	$937.91
5	Conference Expenses	$0.00	$0.00
6	Other Direct Costs	$103.00	$305.38
7	Equipment	$19,102.13	$97,713.32
8	Space Rental	$0.00	$0.00
9	Indirect Cost	$7,867.37	$32,712.37
10	**Total**	**$42,704.23**	**$195,850.38**

References

Abtahi, M., Kaada, B., Vindstad, J. E., and Østvold, T. (1996). Calcium carbonate precipitation and pH variations in oil field waters. A comparison between experimental data and model calculations. Acta Chem. Scand. 50:114–121.

Adams, C.D., Garber, J.D. and Singh, R.K. 1996. Computer Modeling to Predict Corrosion Rates in Gas Condensate Wells Containing CO_2, Paper No. 31, presented at the NACE CORROSION conference, Houston, TX.

Adsani, E., Shirazi, S.A. Shadley, J.R., Rybicki, E.F. 2006. Validation of Mass Transfer Coefficient Models used in Predicting CO_2 Corrosion in Vertical Two-Phase Flow in the Oil and Gas Production, Paper 06573, presented at the NACE Corrosion conference, Houston, TX.

Anderko, A. and Young, R. D. 1999. Simulation of CO_2/H_2S Corrosion Using Thermodynamic and Electrochemical Models, Paper No. 31, presented at the NACE CORROSION conference, Houston, TX.

Anderko, A. 2000. Simulation of $FeCO_3/FeS$ Scale Formation Using Thermodynamic and Electrochemical Models, Paper No. 102, presented at the NACE CORROSION conference, Houston, TX.

Barlet-Gouédard, V., Rimmelé, G., Goffé, B., and Porcherie O. 2006. Mitigation Strategies for the Risk of CO_2 Migration Through Wellbores. Paper IADC/SPE 98924 presented at the IADC/SPE Drilling Conference held in Miami, Florida, U.S.A., February 21–23.

Benge G. 2009. Improving Wellbore Seal Integrity in CO_2 Injection Wells. GHGT-9, Energy Procedia 1, 3523-3529.

Bentz, D.P. and Garboczi, E.J. 1992. Modeling the leaching of calcium hydroxide from cement paste: effects on pore space percolation and diffusivity, Materials and Structures, Volume 25, Number 9, 523-533, DOI: 10.1007/BF02472448.

Bonis, M. R. and Crolet, J. L. 1989. Basics of the Prediction of the Risks of CO_2 Corrosion in Oil and Gas Wells. Paper No. 466, presented at the NACE CORROSION conference, Houston, TX.

Brandl, A., Cutler, J., Seholm, A., Sansil, M., and Braun, G. 2010. Cementing Solutions for Corrosive Well Environments, Paper SPE-132228-MS-P presented at the CPS/SPE International Oil & Gas Conference and Exhibition in China held in Beijing. Jun 8-10.

Breysse, D., and Gerard, B., 1997, Modeling Of Permeability In Cement-Based Materials: Part L-Uncracked Medium, *Cement and Concrete Research*, Vol. 27. No. 5, pp. 761-775.

Buil, M. and Revertegat, E. 1992. Model of the attack of pure water or under saturated lime solutions on cement: Stabilization and Solidification of Hazardous, Radioactive, and Mixed Wastes, ASTM Special Technical Publication, Edited by T. Michael Gilliam and Carlton C. Wiles, 227-241.

Carde, C., Francois, R. and Torrenti, J M. 1996. Leaching of both calcium hydroxide and C-S-H from cement paste: Modeling the mechanical behavior, Cement and Concrete Research, Volume: 26, Issue: 8, Pages: 1257-1268.

Carde, C. and Frarqois, R. 1999. Modeling the loss of strength and porosity increase due to the leaching of cement pastes, Cement & Concrete Composites, 21, 181-188.

Carey, J.W. and Lichtner, P.C. 2007. Calcium silicate hydrate (C-S-H) solid solution model applied to cement degradation using the continuum reactive transport model FLOTRAN, Transport Properties and Concrete Quality: Materials Science of Concrete, Editors: Barzin Mobasher and Jan P. Skalny, 73-104.

Condor, J. and Asghari, K. 2009. Experimental Study of Stability and Integrity of Cement in Wellbores Used for CO_2 Storage, Energy Procedia, 1, 3633-3640.

Crolet, J. L., Bonis, M. R., 1991. Prediction of the Risks of CO2 Corrosion in Oil and Gas Well.SPE Production Engineering, Vol. 6, No. 4, p. 449.

Crolet, J.-L. and Bonis, M.R. 1991. Prediction of the Risks of CO2 Corrosion in Oil and Gas Well, SPE Prod. Eng. 6, p. 449.

Crow W., Williams D. B., Carey J. W., Celia M. and Gasda S. 2009. Wellbore integrity analysis of a natural CO2 producer. GHGT-9, Energy Procedia 1, 3561-3569.

Danyushevsky , V.S. and Djabarov, K.A. 1973. RILEM Int. Symp. on Pore Structure and Properties of Materials, Prague, D97-DI 14

Dayalan, E., Vani, G., Shadley, J.R., Shirazi, S.A. and Rybicki, E.F. 1995. Modeling CO_2 corrosion of carbon steel in pipe flow, Paper No. 118, presented at the NACE corrosion conference.

Dayalan, E., de Moraes, F.D., Shadley, J.R., Shirazi, S.A., Rybicki, E.F., 1998. CO2 Corrosion Prediction in Pipe Flow Under $FeCO_3$ Scale-Forming Conditions, Paper no. 51, presented at the NACE CORROSION conference, Houston, TX.

de Waard, C.and Milliams, D.E., Corrosion 31 (1975): p. 131.

de Waard, C, Lotz, U., Milliams, D.E., Corrosion 47 (1991): p. 976.

de Waard, C, Lotz, U. and Dugstad, A. 1995. Influence of Liquid Flow Velocity on CO_2 Corrosion: A Semi-Empirical Model, Paper No. 128, presented at the NACE CORROSION conference, Houston, TX.

de Waard, C., Smith, L. and Craig, B.D. 2003. The Influence of Crude Oil on Well Tubing Corrosion Rates, Paper No. 03629, presented at the NACE CORROSION conference, Houston, TX.

Dickey, P. A., Collins, A. G. and Fajardo, M. I. 1972. Chemical composition of deep formation waters in southwestern Louisiana: AAPG Bulletin, v. 56, p. 1530-1570.

Duan, Z., Sun, R. and Zhu, C., 2007, Accurate Thermodynamic Model for the Calculation of H_2S Solubility in Pure Water and Brines, Energy Fuels, 2007, 21 (4), pp 2056–2065.

Dubois, N., Bouygues, Noik, Ch. and Rivereau, A. 1999. Improvement of low-permeable cement for zonal isolation at high-temperature Conditions, Paper SPE 50782, presnted at the SPE International Symposium on Oilfield Chemistry held in Houston, Texas, February 16–19.

Dugstad, A., Lunde, L. and Videm, K. 1994. Parametric Study of CO_2 Corrosion of Carbon Steel, Paper No. 14, presented at the NACE CORROSION conference, Houston, TX.

Fakhreldin, Y., Al-Sharji, H., Ruwehy, A. M., Saadi, K., Taoutaou, S. and Al-Kalbani, S. 2010. Advanced Cement System for Acid Gas Injection Wells, Paper SPE-132345-MS-P, presented at the SPE Asia Pacific Oil & Gas Conference and Exhibition held in Brisbane, Queensland, Australia, October 18-20.

Fertl, W. H. 1976. Abnormal formation pressures, in Developments in petroleum science: New York, Elsevier, v. 2, 382 p.

Garber, J.D., Polaki, V., Adams, C. and Varanasi, N.R. 1998. Modeling Corrosion Rates in Non-Annular Gas Condensate Wells Containing CO_2, Paper No. 53, presented at the NACE CORROSION conference, Houston, TX.

Gartland, P.O. and Salomonsen, J. E. 1999. A Pipeline Integrity Management Strategy Based on Multiphase Fluid Flow and Corrosion Modelling, Paper No. 622, prestned at CORROSION conference, Houston, TX.

Gartland, P.O., Johnsen, R. and Øvstetun, I., 2003. Application of Internal Corrosion Modeling in the Risk Assessment of Pipelines, Paper No. 03179, presented at the NACE CORROSION conference, Houston, TX.

John, R.C., Jordan, K. G., Young, A. L., Kapusta, S. D. and Thompson, W. T. 1998. SweetCor: An Information System for the Analysis of Corrosion of Steels by Water and Carbon Dioxide, Paper No. 20, presented at the NACE CORROSION conference, Houston, TX.

Ghabezloo, S., Sulem, J. and Saint-Marc, J. 2009. Evaluation of a permeability-porosity relationship in a low permeability creeping material using a single transient test, Int J Rock Mech Min Sci 46 (4), 761-76.

Garnier, A., Laudet, J., Neuville, N., Guen, Y., Fourmaintraux, L., Rafai, N., and Burlion, N. 2010. CO_2-Induced Changes in Oil well Cements Under Downhole Conditions: First Experimental Results, Paper SPE-134473-MS, presented at the SPE Annual Technical Conference and Exhibition, 19-22 September, Florence, Italy.

Gérard, B., Le Bellego, C., and Bernard, O., 2002. Simplified modeling of calcium leaching of concrete in various environments, *Materials and Structures*, 35: 632-640.

Gunaltun, Y. M., 1996. Combining research and field data for corrosion rate prediction. Paper No. 27, presented at the NACE CORROSION conference, Houston, TX.

Halvorsen, A.M.K., Søntvedt, T., 1999. CO_2 Corrosion Model for Carbon Steel Including a Wall Shear Stress Model for Multiphase Flow and Limits for Production Rate to Avoid Mesa Attack, Paper No. 42, presented at the NACE CORROSION conference, Houston, TX.

Hanor, J. S. 1994. Physical and chemical controls on the composition of waters in sedimentary basins, Marine and Petroleum Geology, Volume 11 Number 1.

Hedges, B. Chapman, R., Harrop, D., Mohammed, I., Sun, Y., 2005. A Prophetic CO_2 Corrosion Tool - But When is it to be Believed?, Paper No. 05552, presented at the NACE CORROSION conference, Houston, TX, April 3 - 7.

High, M.S., Wagner, J. and Natarajan, S. 2000. Mechanistic Modeling of Mass Transfer in the Laminar Sublayer in Downhole Systems, Paper No. 62, presented at the NACE CORROSION conference, Houston, TX.

Hoffmeister, 2005. Modeling of H_2S Corrosion by Coupling of Phase and Polarization Behavior, Paper No. 5476, presented at the NACE CORROSION conference, Houston, TX, April 3 - 7.

Hoffmeister, 2007, Modeling The Effect of Chloride Content on H_2S Corrosion by Coupling of Phase and Polarization Behavior, Paper No. 7501, presented at the NACE CORROSION conference, Nashville, TN, March 11 – 15.

Jacquemet,J., Pironon, J., Lagneau, V., Saint-Marc, J., 2012. Armouring of well cement in H_2S–CO_2-saturated brine by calcite coating–Experiments and numerical modeling. Applied Geochemistry 27. 782–795

Jennings S.S. 2005. Long-Term High-Temperature Laboratory Cement Data Aid in the Selection of Optimized Cements, paper SPE 95816 presented at the 2005 SPE Annual Technical Conference and Exhibition held in Dallas, Texas, U.S.A., 9 – 12 October 2005.

Jepson, W.P., Kang, C., Gopal, M. and Stitzel, S. 1997. Model for Sweet Corrosion in Horizontal Multiphase Slug Flow, Paper No. 11, presented at the NACE CORROSION conference, Houston, TX.

Johnson, R, M., and Garvin, T, R. 1972. Cementing Practices, SPE AIME-MMIJ Meeting, May 25-27, Tokyo, Japan.

Jones, P. H., 1975, Geothermal and hydrocarbon regimes, northern Gulf of Mexico basin: Proceedings, First Geopressured-Geothermal Energy Conference, Center for Energy Studies, University of Texas, Austin, Texas, p. 15-89.

Kamali, S., Moranville, M., & Leclerco, S. (2008). Material and environmental parameter effects on the leaching of cement pastes: experiments and modelling. Cement and Concrete Research, 38, 575–585.

Kutchko, B. G.; Strazisar, B. R.; Dzombak, D. A.; Lowry, G. V.;Thaulow, N. 2007. Degradation of Well Cement by CO_2 under Geologic Sequestration Conditions, Environ. Sci. Technol., 41 (12), 4787–4792.

Kutchko, B. G.; Strazisar, B. R.; Lowry, G. V.; Dzombak, D. A.; Thaulow, N. 2008. Rate of CO_2 Attack on Hydrated Class H Well Cement under Geologic Sequestration Conditions. Environ. Sci. Technol. 42: 6237–6242.

Kutchko, B.G., Strazisar, B.R., Hawthorne, S.B., Lopano, C.L., Miller, D.J., Hakala, J.A., and Guthrie, J.D., 2011, H_2S–CO_2 reaction with hydrated Class H well cement: Acid-gas injection and CO_2 Co-sequestration, International Journal of Greenhouse Gas Control5 880–888

Kvarekval. J. and Videm, K., 1995. Corrosion of Carbon Steel in Carbon Dioxide-Saturated Solutions Containing Small Amounts of Hydrogen Sulfide. NACE international, April.

Lécolier E., Rivereau A., Ferrer N., Audibert A., Longaygue X., (2008) Study of New Solutions for Acid-Resistant Cements. SPE 116066, Annual Technical Conference and Exhibition, Denver, Colorado, USA, 21-24 September 2008.

Lécolier E., Rivereau A., Ferrer N., Audibert A. and Longaygue X., 2006. Durability of Oilwell Cement Formulations Aged in H2S-Containing Fluids, paper SPE 99105 presented at the IADC/SPE Drilling Conference, Miami, Florida, February 21–23.

Lerch, W. Ford, C.L., 1948. Long-term study of cement performance in concrete: chapter 3. Chemical and physical tests of the cements, ACI Journal 19 (8) 745–795.

Lin, F., Meyer, C., 2009. Hydration kinetics modeling of Portland cement considering the effects of curing temperature and applied pressure, Cement and Concrete Research 39, 255–265.

Mainguy, M., Tognazzi, C., Torrenti, J., Adenot, F. 2000. Modelling of Leaching in Pure Cement Paste and Mortar. *Cement and Concrete Research*, 30. 83-90.

Mainguy, M., and Coussy, O. 2000. Propagation Fronts During Calcium Leaching and Chloride Penetration. Journal of Engineering Mechanics.

Matteo, E. N., Scherer, G. W., Huet, B., and Pel, L. 2011. Understanding Boundary Condition Effects on the CorrosionKinetics of Class H Well Cement. *Energy Procedia 4. 5370–5376*

Mehta, P.K., Manmohan, D., 1980, 7th Int. Cong. Chemistry of Cement, Paris, III, l-5

McMahon, A.J., Paisley, D.M.E., 1997. Corrosion Prediction Modelling—A Guide to the Use of Corrosion Prediction Models for Risk Assessment in Oil and Gas Production and Transportation Facilities, Report no. ESR.96.ER.066 (Sunbury: BP International)

Millero, F., Huang, F., Graham, T., Pierrot, D., 2007, The dissociation of carbonic acid in NaCl solutions as a function of concentration and temperature, *Geochimica et Cosmochimica Acta* 71 pp. 46-55

Morales, M., Morris, W., Criado, M. A., Robles, J., Bianchi, G. 2003. Improving the Sulfate Resistance Performance of API Cement Class A upon Appropriate Slurry Design, paper SPE 81000, presented at the SPE Latin American and Caribbean Petroleum Engineering Conference held in Port-of-Spain, Trinidad, West Indies, April 27-30.

Moran, K. 2003. Formation Waters In The Upper Wilcox Of Southeastern Texas, MS Thesis Submitted to the Louisiana State University, Baton Rouge, Louisiana.

Morton, R. A. And Land, L. S. 1987. Regional Variations in Formation Water Chemistry, Frio Formation (Oligocene), Texas Gulf Coast, The American Association of Petroleum Geologists Bulletin, V. 71, No. 2, P. 191-206.

Mueller, D.T. and Dillenbeck, R.L. 1991 The Versatility of Silica Fume as an Oilwell Cement Admixture. SPE 21688

Nakarai, K., Ishida, T. and Maekawa, K. 2006. Modeling of Calcium Leaching from Cement Hydrates Coupled with Micro-Pore Formation, *Journal of Advanced Concrete Technology*, 4: (3), pp.395-407.

Nesic, S., Postlethwaite, J., Olsen, S., 1996. An Electrochemical Model for Prediction of Corrosion of Mild Steel in Aqueous Carbon Dioxide Solutions. Corrosion, Vol. 52, No. 4, p. 280.

Nesic, S., Nordsveen, M., Nyborg, R., Stangeland, A., 2003. A Mechanistic Model for CO_2 Corrosion with Protective Iron Carbonate Films - Part 2: A Numerical Experiment. Corrosion, Vol. 59, No. 6, pp. 489-497.

Nesic, S., Li, H., Huang, J., Sormaz, D., 2009. An Open Source Mechanistic Model for CO_2 / H_2S Corrosion of Carbon Steel, NACE corrosion conference, Paper No. 9572

Nešić, S. 2007. Key issues related to modeling of internal corrosion of oil and gas pipelines, Corrosion Science, Vol. 49, Issue 12, December 2007, Pages 4308–4338.

Noik, Ch., and Rivereau, A. 1999. Oil well Cement Durability, paper SPE 56538, presented at the SPE Annual Technical Conference and Exhibition held in Houston, Texas, October 3–6.

Nordsveen, M., Nesic, S., Nyborg, R., Stangeland, A., 2003. A Mechanistic Model for CO_2 Corrosion with Protective Iron Carbonate Films - Part 1: Theory and Verification. Corrosion, Vol. 59, No. 5, pp. 443-456.

NORSOK Standard no. M-506. 1998. CO2 Corrosion Rate Calculation Model. Norwegian Technology Standards Institution, http://www.nts.no/norsok

Nyborg, R. Dugstad, A., 2003. Understanding and Prediction of Mesa Corrosion Attack, Paper No. 3642, presented at the NACE CORROSION conference, San Diego CA, March.

Nyborg, R., 2006. Field Data Collection, Evaluation and Use for Corrosivity Prediction and Validation of Models, Part II: Evaluation of Field Data and Comparison of Prediction Models, Paper no. 06118, NACE CORROSION conference, Houston, TX.

Nyborg, R., 2009. Guidelines for prediction of CO2 corrosion in oil and gas production systems, Material Technology, IFE, Kjeller, ISBN 978-82-7017-791-2.

Nyborg, R. 2010. CO2 Corrosion Models for Oil and Gas Production Systems, Paper No 10371, presented at the NACE corrosion conference, March 14 - 18, San Antonio, TX.

Oddo J. E. and Thomson M. B., 1982, Simplified calculations of CaCO3 saturation at high temperatures and pressures in brine solutions, Journal of Petroleum Technology, July, 1583-1590, 1982.

Overton, H. L. and Timko, D. J. 1969. The salinity principle: a tectonic stress indicator in marine sands: Oil and Gas Jour., v. 67, no. 40, p. 115-124.

Perkins, R.S., Fang, C.S., Garber, J. D., Singh, R. K., 1996. Predicting Tubing Life in Annular-Flow Gas Condensate Wells Containing Carbon Dioxide, Corrosion, Vol. 52, No. 10, p. 801.

Pots, B.F.M., 1995. Mechanistic Models for the Prediction of CO_2 Corrosion Rates under Multi-Phase Flow Conditions, Paper No. 137, NACE CORROSION conference, Houston, TX.

Pots, B.F.M., John, R.C., Rippon, I.J., Thomas, J.S., Kapusta, S. D., Girgis, M. M. and Whitham, T. 2002. Improvements on de Waard - Milliams Corrosion Prediction and Applications to Corrosion Management, Paper No. 02235, presented at the NACE CORROSION conference, Houston, TX.

Pots, B.F.M. and Kapusta, S. D., 2005. Prediction of Corrosion Rates of the Main Corrosion Mechanisms in Upstream applications, Paper No. 05550, presented at the NACE CORROSION conference, Houston, TX.

Ramachandran, S., Ward M. B., and Bartrip, K. A., 2002. Molecular Modeling of Corrosion of Iron in H2S Environments, Paper No. 2240, presented at the NACE corrosion conference, April 7 - 11, Denver, CO.

Ramirez, M. and Ruiz, A.,1998. The Effect of Small Amounts of H_2S on CO_2 Corrosion of a Carbon Steel. NACE international.

Renpu, W. 2011. Advanced Well Completion Engineering, Gulf Professional Publishing; 3rd Edition, Gulf Professional Publishing.

Rimmelé, G., Barlet-Gouedard, V., Porcherie, O., Goffe, B. and Brunet, F. 2008, Heterogeneous Porosity Distribution in Portland Cement Exposed to CO2-Rich Fluids, Cement and Concrete Research, 38, 1038-1048.

Samson, E. and Marchand, J. 2007. Modeling the transport of ions in unsaturated cement-based materials, Computers and Structures, 85, 1740–1756.

Sangita, K. A. and Srinivasan, S., 2000. An Analytical Model to Experimentally Emulate Flow Effects in Multiphase CO2/H2S Systems. Paper No. 58, presented at the NACE CORROSION conference, Houston, TX.

Santra, A. and Sweatman, R. 2011. Understanding the Long-Term Chemical and Mechanical Integrity of Cement in a CCS Environment, Energy Procedia, 4, 5243–5250.

Santra, A., Reddy, B. R., Liang, F., and Fitzgerald, R. 2009. Reaction of CO_2 with Portland Cement at Downhole Conditions and the Role of Pozzolanic Supplements, paper SPE 121103, presented at the SPE International Symposium on Oilfield Chemistry held in The Woodlands, Texas, USA, April 20–22.

Sauki, A, B. and Irawan, S. 2010. Effects of Pressure and Temperature on Well Cement Degradation by Supercritical CO_2. International Journal of Engineering and Technology 10: 53-61.

Schmidt, G. W. 1973. Interstitial water composition and geochemistry of deep Gulf Coast shales and sandstones: AAPG Bulletin, v. 57, p. 321-337.

Smith S. N., Pacheco, J.L., 2002, Prediction of Corrosion in Slightly Sour Environment, Paper No. 2241, presented at the NACE International corrosion conference, Houston TX.

Smith, L. and de Waard, C. 2005. Corrosion Prediction and Materials Selection for Oil and Gas Producing Environments, Paper No. 05648, presented at the NACE CORROSION conference, Houston, TX.

Srinivasan, S. and Kane, R. D., 1996. Prediction of Corrosivity of CO_2 / H_2S Production environments. Paper No. 11, presented at the NACE CORROSION conference, Houston, TX.

Srinivasan S. and Kane, R. D. 2003. Critical Issues in the Application and Evaluation of a Corrosion Prediction Model for Oil and Gas Systems. Paper No. 03640, presented at the NACE CORROSION conference, Houston, TX.

Srinivasan, S., Kane, R.D., 1996. Prediction of Corrosivity of CO_2/H_2S Production Environments, Paper No. 11, presented at the NACE CORROSION conference, Houston, TX.

Stora, E., Bary, B., He, Q.C., Deville, E. and Montarnal, P. 2010. Modeling and simulations of the chemo-mechanical behavior of leached cement-based materials: Interactions between damage and leaching, Cement and Concrete Research, Volume 40, Issue 8, Pages 1226–1236.

Sugma, T. 2006. Advanced Cements for Geothermal Wells, Technical Report , Brookhaven National Laboratory, BNL-77901-2007-IR.

Sun, W., Nesic, S. 2007. A Mechanistic Model of H2S Corrosion of Mild Steel, Paper No. 7655, presented at the NACE corrosion conference, March 11 - 15, Nashville, TN.

Sun, W., Nesic, S. 2008. A Mechanistic Model of Uniform Hydrogen Sulfide/ Carbon Dioxide Corrosion of Mild Steel, Corrosion Journal, Vol. 65. No, 5.

Sundaram, M., Raman, V., High, M.S., Tree, D.A. and Wagner, J. 1996. Deterministic Modeling of Corrosion in Downhole Environments, Paper No. 30, presented at the CORROSION/96, Houston, TX.

Wallace, R. H., Taylor, R. E. and Wesselman, J.B. 1977. Use of hydrogeologic mapping techniques in identifying potential geopressured-geothermal reservoirs in the lower Rio Grande embayment, Texas: Proceedings, Third Geopressured-Geothermal Energy Conference, v. 2, p. GII-GI88.

Van Eijk R.J. and Brouwers H.J.H. 1998. Study of the Relation between Hydrated Portland cement Composition and Leaching Resistance. Cement and Concrete Research, Vol. 28, No. 6, pp. 815–828, 1998.

Zhang, R., Gopal, M. and Jepson, W.P. 1997. Development of a Mechanistic Model for Predicting Corrosion Rate in Multiphase Oil/Water/Gas Flows, Paper No. 601, presented at the NACE CORROSION conference, Houston, TX.

Appendix A

Report on Literature Review, Theoretical and Experimental Studies on Cement Degradation

Summary

The effects of high-temperature and chemical attack on the mechanical properties and integrity of the cement have been summarized. The literature survey shows that the effects of temperature on the cement properties strongly depend on the calcium to silica ratio. At high temperature (greater than 110℃) and high calcium to silica ratio, the C-S-H phase will transform into more stable α-C_2SH phase that leads to increased permeability and loss of compressive strength of the cement sheath. This can be prevented by adding more silica to the cement to stabilize the tobermorite phase. At temperature greater than 150℃, the tobermorite converts into xonotlite and/or gyrolite. This improves the cement properties.

Deterioration of cement in aggressive environment leads to increased porosity and permeability that drastically affects the sealing and isolation performance of the cement. The increase in porosity and permeability further intensifies the degradation process by allowing more aggressive fluid to penetrate into the cement and reaches the undamaged zone. The depth of penetration depends upon several factors, namely, permeability, porosity, the calcium content of the cement system, and composition the surrounding fluid. To lower the degraded zone depth (i.e. depth of penetration), The calcium content in the cement should be lowered by increasing the amount of filler materials such as silica fume and fly ash.

A model has been developed to predict degradation depth, compressive strength, porosity, and permeability of the well cement in brine solution saturated with acidic gases. The model assumes the leaching of calcium ion from the set cement as the dominant cement degradation mechanism. Input variables for this model are water/cement ratio, temperature, partial pressure of acid gas, NaCl concentration, size of the specimen, and pH of surrounding liquid. The pH can be either an input variable or it can be also predicted as a function of temperature, partial pressure of acid gas, and NaCl concentration. Proposed model was validated using some experimental data available in the literature. Results show satisfactory agreement between measurements and predictions. Subsequently, the model is used to simulate degradation of cement under proposed experimental conditions. Degradation depth was predicted at different temperatures, CO_2 partial pressures, and salt concentrations. Specimen diameter of 7/8 inches and specimen length of 2 inches were assumed. According to the model, degradation depth for cement under the proposed experimental conditions after 25

days of aging is expected to in the range of 0.1 - 0.2 mm. Results show that raising temperature or NaCl concentration decreases the degradation depth.

A.1. Introduction

It is estimated that a substantial amount of the world's remaining gas reservoirs contain more than 2% CO_2 and more than 100 ppm H_2S, (Lecolier et al., 2006). Processes like CO_2 sequestration or CO_2 capture and storage demand high quality cement to have zonal isolation. Hence, better understanding of cement degradation is needed for successful well planning and cementing applications. There is limited data for the CO_2associated cement degradation but data for cement deterioration resulting from H_2S exposure is scarce. In addition, studies are more focused on degradation occurring under ambient and elevated pressure and elevated temperature conditions. This study will investigate the effects of both the CO_2 and H_2S related degradations on the cement performance under high-pressure high-temperature (HPHT) conditions.

Cementing operations are critical to the success of drilling and completion operations of a well. The function of cement is to: i) protect and support the casing, ii) prevent fluid migration and channeling behind the casing, iii) isolate the vugular and fractured formations from the fluid movements, iv) close an abandoned portion of the well, and v) provide zonal isolation necessary to drill further or control production. During the life of the well, the cement sheath integrity is affected by the high-pressure and high-temperature (HPHT) downhole conditions, which result in the deterioration of the cement. Furthermore, cement degradation such as carbonation occurs due to chemical attacks under downhole conditions. The carbonation and leaching of Portland cement cause an increase in porosity and permeability, and open a pathway for the stored CO_2 to escape into the atmosphere. Moderate carbonation can be beneficial for cement porosity and permeability, since it forms $CaCO_3$ that plugs the pores of the cement. However, extensive carbonation can result in the loss of structural integrity (Carey et al., 2007). The basic chemistry describing this process carbonation is presented in Appendix A.

A.2. Mineralogy of Portland Cement

Portland cement, in accordance with the American Petroleum Institute (API), is specified into four crystalline compounds in the clinker that hydrate to form a rigid structure. These compounds are:

- Tricalcium Silicate: $3CaO.SiO_2$ (C_3S, main contributor to the cement strength)
- Dicalcium Silicate: $2CaO.SiO_2$ (C_2S, provides long term strength)
- Tricalcium Aluminate: $3CaO.Al_2O_3$ (C_3A, promote rapid hydration of cement)

- Tetracalcium Aluminoferrite: $4CaO.Al_2O_3.Fe_2O_3$ (C_4AF)

Different classes (A to H) of Portland cement are used in the field. API has classified three standard types of cement for use in wells: i) Ordinary type (O); ii) Moderate sulfate-resistant (MSR), and iii) High sulfate-resistant (HSR).

A.3. Cement Hydration

During cement hydration, the main reaction products (Fig. A.3.1) formed are tobermorite gel ($3CaO.2SiO_2.3H_2O$), which is known as C-S-H phase and the portlandite ($Ca(OH)_2$). The tobermorite gel is the main binding material. Reaction equations for hydration of C_3S and $C_2S$are written as:

$$2(3CaO.SiO_2) + 6H_2O \rightarrow 3CaO.2SiO_2.3H_2O + 3Ca(OH)_2 \quad \text{..... (3.1)}$$

$$2(2CaO.SiO_2) + 4H_2O \rightarrow 3CaO.2SiO_2.3H_2O + Ca(OH)_2 \text{ (slow reaction) ..... (3.2)}$$

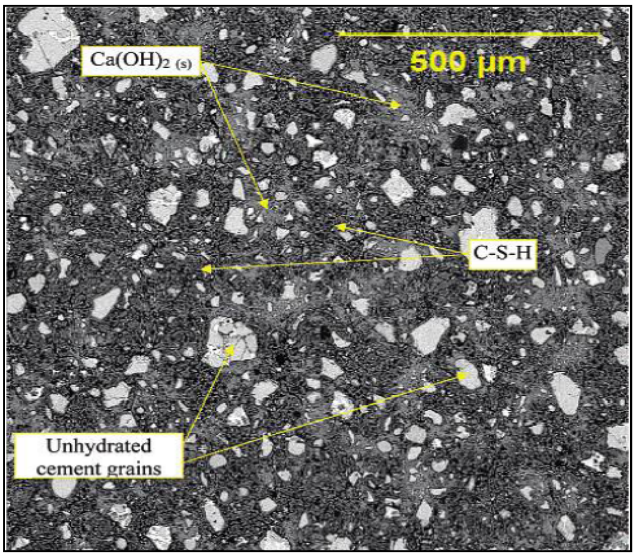

Fig. A.3.1 SEM-BSE image of cement cured for 28 days at 22℃ and 0.1 MPa (Kutchko et al., 2007)

The C_3A also hydrates very rapidly and produces most of the heat of hydration observed during the first few days. To control this rapid hydration, gypsum is added to the clinker. The C_3A is attacked very fast with the water containing sulfates.

$$3CaO.Al_2O_3 + 12H_2O + Ca(OH)_2 \rightarrow 3CaO.Al_2O_3.Ca(OH)_2.12H_2O \text{ (fast reaction) ..... (3.3)}$$

$$3CaO.Al_2O_3 + 10H_2O + CaSO_4.2H_2O \rightarrow 3CaO.Al_2O_3.CaSO_4.12H_2O \quad \text{..... (3.4)}$$

C_4AF is hydrated in presence of portlandite and it has only minor effects on the physical properties of the cement.

$$4CaO.Al_2O_3.Fe_2O_3 + 10H_2O + 2CaO.H_2O \rightarrow 6CaO.Al_2O_3.Fe_2O_3.12H_2O \text{ (slow)} \quad \ldots\ldots \quad (3.5)$$

A.4. Cement Degradation Mechanisms

The degradation of cement occurring under downhole conditions involves a number of chemical and physical processes including: i) ionic transport in porous material; ii) chemical reaction between cement hydration products and dissolved acid gases (carbonation, calcification, and sulfidation); and iii) dissolution and leaching of carbonation and calcification products from the matrix.

A.4.1. Cement Degradation under CO_2 Exposure

Carbon dioxide is water-soluble gas. It dissolves in water or aqueous solutions quickly forming acidic solution. The reaction reduces the pH of the solution. Temperature, partial pressure of CO_2 and other ions present in water, such as salts, influence the pH. The produced carbonic acid penetrates into the cement matrix and attacks the main hydration products or binding materials (portlandite and C-S-H). The reaction (i.e. carbonation and calcification reactions) produces calcium carbonate ($CaCO_3$), amorphous silica (silica gel, $SiO_2.H_2O$) and water as:

$$H_2CO_3 + Ca(OH)_2 \rightarrow CaCO_3 + 2H_2O \quad \ldots\ldots \quad (4.1)$$

$$C\text{-}S\text{-}H + H_2CO_3 \rightarrow CaCO_3 + \text{amorphous silica} + H_2O \quad \ldots\ldots \quad (4.2)$$

The first reaction (Eq. 4.1) is considered faster than the second one (Eq. 4.2).These reactions cause densification, which increases the cement hardness and decreases its permeability, resulting in reduced CO_2 diffusion and expansion up to 6% in volume that can create micro to macro cracks in the cement matrix (Santra et al., 2009). The produced $CaCO_3$ is leached out by the carbonic acid as:

$$CaCO_3 + H_2CO_3 \rightarrow Ca(HCO_3)_2 \quad \ldots\ldots \quad (4.3)$$

The leaching or dissolution of $CaCO_3$ occurs when the cement is surrounded by carbonated aqueous solution. The dissolution tends to increase porosity and permeability, and degrade mechanical properties of the cement. However, if the above reaction stops after the carbonation

of the calcium hydroxide, the $CaCO_3$ formed would cause an increase in compressive strength and a decrease in permeability (Fakhreldin et al., 2010).

Cement specimens aged in the aqueous phase under high-pressure conditions showed an altered region containing distinct zones (Figs. A.4.1 and A.4.2) situated in a radial pattern in cylindrical samples (Kutchko et al., 2007). Microscopic examination showed the presence of:

- Unaltered central zone.
- Zone 1 with slightly increased porosity and decreased in $Ca(OH)_2$.
- Zone 2 with decreased porosity and increased calcium content.
- Zone 3 with low calcium content and increased porosity as a result of dissolution.

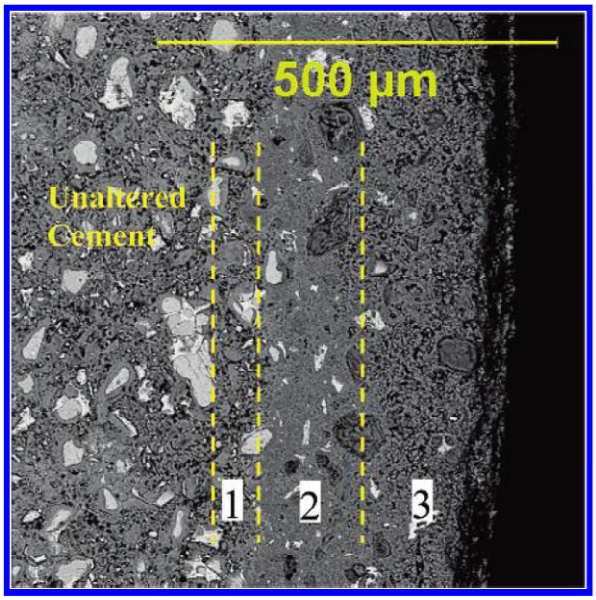

Fig. A.4.1 Microscopic image of sectioned-cement core after CO_2 exposure (Kutchko et al., 2007)

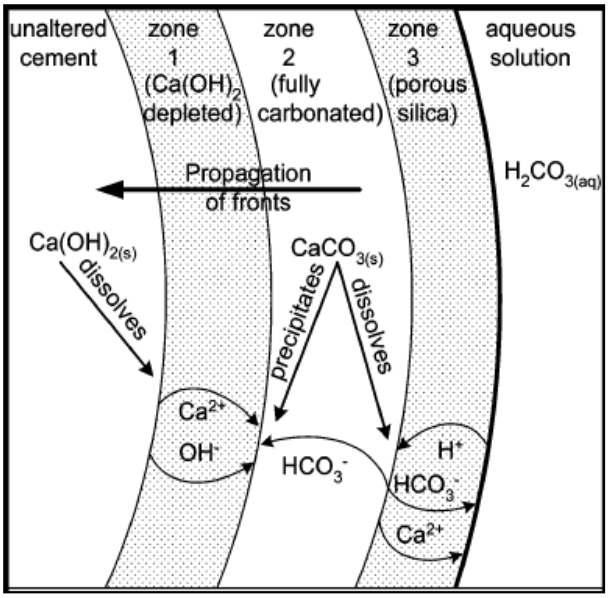

Fig. A.4.2 Formation of distinct zones in the degraded cement specimen (Kutchko et al., 2007)

These changes taking place in the cement matrix are due to the interaction between the components of the cement and CO_2-saturated brine resulting in the carbonation and bicarbonation of the C-S-H and $Ca(OH)_2$. These distinct zones are formed as a result of the balance between dissolution reaction and species transport in the porous cement. More recently, a similar study (Rimmele et al., 2008) was conducted to investigate the effects of wet supercritical CO_2 and CO_2-saturated water on cement degradation. Results (Fig. A.4.3) demonstrated surface carbonation of the cement sample after two days of exposure to wet supercritical $CO_2$and CO_2-saturated water at 180°C and 280 bars. After 3 months of exposure, the carbonation became clear as the samples showed a thick white layer on their surface, which

indicate the formation of calcium carbonate. The carbonation is commonly accompanied by the development of cracks. After 6 months of aging, the carbonated rim on the surface of the samples was flaked out as the carbonation layer became very thick. The pH of water used for aging the cement cores reduced from 13 to 6.5 after the exposure.

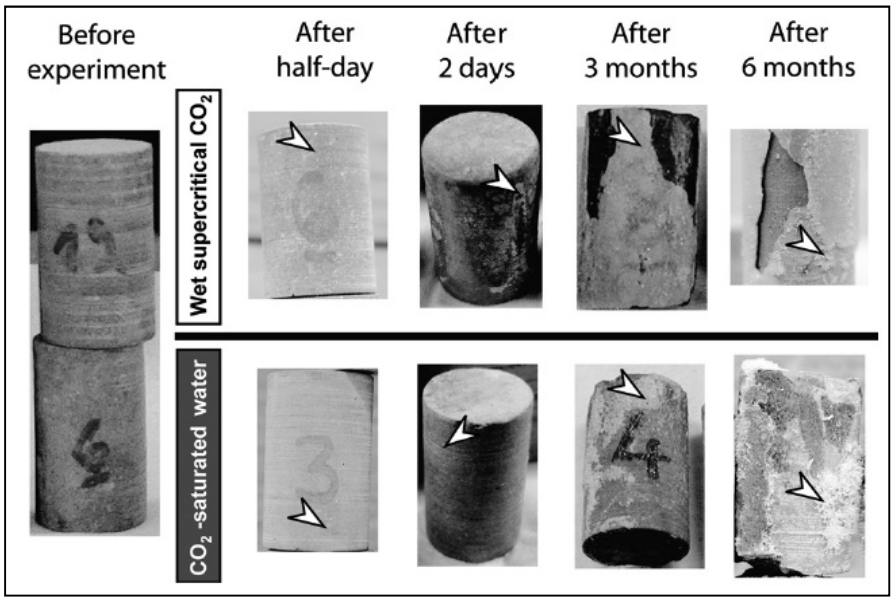

Fig. A.4.3 Portland cement samples before and after CO_2 exposure at 90 ℃ and 280 bars (Rimmele et al., 2008)

A.4.2. Cement Degradation under H_2S Exposure

Like carbon dioxide, H_2S dissolves in aqueous liquids and form weak acid solution. The acid attacks some of the components of set cement resulting in the formation of CaS, FeS, and $Ca(HS)_2$, CaS and Al_2S_3 when H_2S concentration is high (Renpu, 2011). The H_2S attack depends strongly on the pH of the acid solution and composition of the cement. Intuitively, the impact of H_2S degradation on cement is expected to be limited as it predominately attacks minor components of cement (ferrites) by sulfidation (Fakhreldin et al., 2010). Moreover, portlandite and hydrated calcium aluminate (C_3A) in set cement may react with the acid causing cement failure due to the formation of expansive reaction products. The C_3A content of the cement needs to be reduced by adding tetra calcium alumino-ferrite (C_4AF) to minimize the expansion ratio. The portlandite content can be controlled by introducing activated SiO_2-rich materials such as silica flour or volcanic ash. These materials can react with the portlandite and generate C-S-H phase which is less reactive than portlandite.

Furthermore, as the H_2S reduces the pH of the solution, it facilitates the dissolution and leaching of hydration products that diminishes the mechanical strength of the cement (Kutchko

et al., 2011). The presence of methane gas in the system may also promote the degradation of cement in H_2S containing environment (Renpu, 2011).

Due to the complexity of cement chemistry, the mechanisms of chemical attack on cement are complicated. During H_2S exposure, the chemical changes occurring within the hydrated cement matrix lead to the degradation of the cement, resulting from sulfate attack, which is identified as expansive attack because the acid penetrates into the cement pores and forms voluminous water-insoluble products (crystals). As the size of the crystals grows, the pressure inside the cement pores will increase resulting in cracks, fractures, and fragments. The American Society of Testing and Material (ASTM) defines the sulfate attack as the chemical or physical reaction, or both, occurring between the sulfate and calcium aluminate hydrates, which leads to deterioration of the cement. Morales et al. (2003) presented the chemical reaction between the C_3A and gypsum, which is commonly added to the clinker to regulate the rate of the hydration that occurs during the first 24 hrs of hydration forming a primary ettringite ($Ca_6Al_2(SO_4)_3(OH)_{12}{\cdot}26(H2O)$).

Morales et al. (2003) proposed a mechanism for sulfate attack of cement including the following three steps:

Step 1: During first 24 hrs of hydration

$$3(CaO.Al_2O_3)+3(CaSO_4.2H_2O)\rightarrow Ca_6[Al(OH)_6]_2(SO_4)_3.26H_2O \quad (4.4)$$

Step 2: As cement hydration takes place, gypsum concentration reduces and therefore ettringite is transformed into calcium mono-sulfo-aluminate hydrate

$$Ca_6[Al(OH)_6]_2(SO_4)_3.26H_2O+2(CaO.Al_2O_3)+4H_2O \rightarrow 3(CaO.Al_2O_3.CaSO_4.12H_2O) \quad (4.5)$$

Step 3: When hydrated cement is placed in an environment containing high sulfate concentrations, as could be the case of many formations, the calcium mono-sulfo-aluminate hydrate and the calcium hydroxide present in the cement paste will react with the sulfate ions coming from the environment to form what is known as secondary or delayed ettringite

$$3(CaO.Al_2O_3.CaSO_4.12H_2O) +2(CaSO_4.2H_2O) +16\ H_2O\rightarrow 3(CaO.Al_2O_3.3CaSO_4.32H_2O) \quad (4.6)$$

The product of the final reaction, represented by Eq. (4.6), is ettringite, which is a crystal compound that contains 32 water molecules. Therefore, the formation of ettringite results in considerable expansion and volume growth. As the reaction takes place, the expansive products (mainly ettringite) begin filling the cement pores and under confined conditions generate internal pressure that causes cement cracking and strength loss (Fig. A.4.4).

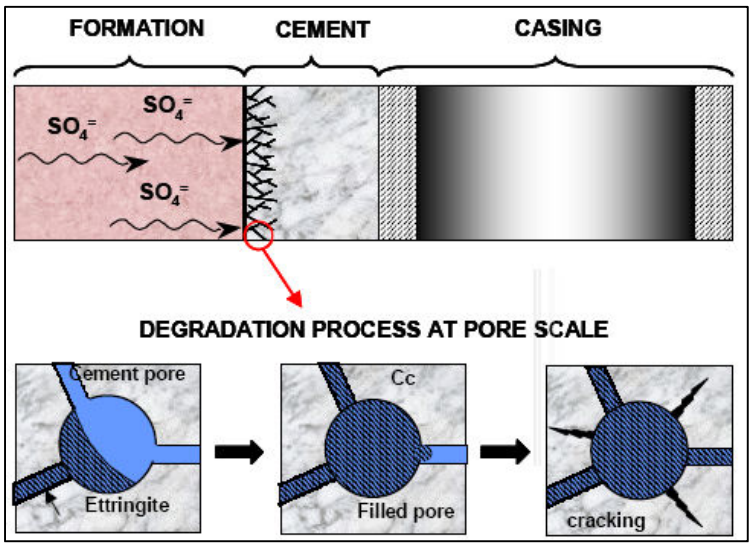

Fig. A.4.4 Mechanism of sulfate attack of cement (Morales et al., 2003)

Kutchko et al. (2011) also proposed a two-step mechanism for sulfate attack shown below:

Step 1: Sulfur migrates into the cement and reacts with species of the cement pore solution to form sulfate via:

$$8Fe(OH)_{3(am)} + HS^- \leftrightarrow 8Fe^{2+} + SO_4^{2-} + 5H_2O + 15OH^- \quad \text{.....(4.7)}$$

Step 2: The stability of ettringite is governed by the temperature, pH, and the activity of calcium. Although formulas for ettringite formation vary depending on the reaction pathway and species, an approximation is as follows:

$$6Ca^{2+} + 2Al(OH)_4^- + 4OH^- + 3SO_4^{2-} + 26H_2O \leftrightarrow Ca_6[Al(OH)_6]2.(SO_4)_2.26H_2O \quad \text{.....(4.8)}$$

Morales et al (2003) used Eq. (4.9) to predict the degradation depth of sulfate attack. The sulfate effective diffusion coefficient (D_{ef}) can be determined by curve fitting the

experimental results to the analytical solution of Fick's second law of diffusion. A semi-infinite diffusion process with a constant surface concentration (C_s) can be assumed. C_o is the bulk sulfate concentration.

$$C(X,t) = C_s - (C_s - C_o).erf\left(\frac{X}{2\sqrt{Def.t}}\right) \quad \text{.....(4.9)}$$

A.4.3. Cement Degradation in Mixed H_2S and CO_2 System

The mechanism of cement degradation in a system containing a mixture of H_2S and CO_2 is different from those occurring in pure gas systems. In pure H_2S system, the primary source of sulfate attack resulting from ettringite formation is the H_2S. However, in a mixed H_2S and CO_2 system, as the CO_2 follows H_2S penetration into the cement, the pH is lowered as carbonation progresses (pH < 12). Once the pH decreases approximately below10.5, the ettringite will dissolve. Thus, as expected, ettringite is not observed in the carbonated zone as it is not stable due to the lower pH (<~10.5) of the cement pore fluid. In addition, ettringite is unstable at T > 90ºC and therefore was not observed in published high-temperature experiments.

A laboratory study (Kutchko et al., 2011), conducted on cement exposed to pure CO_2 and mixed gas systems, showed the formation of the typical carbonation rim when cement was exposed to pure CO_2 system (Fig. A.4.5a). In mixed gas system, a similar carbonation rim was formed (Fig. A.4.5b). However, the samples displayed additional sequence of oxidation–reduction and sulfidation reactions. Ettringite and pyrite were formed in the interior region and carbonated rim of the samples, respectively. The pore water pH buffering is believed to have great impact on the mineralogical change occurring in the samples.

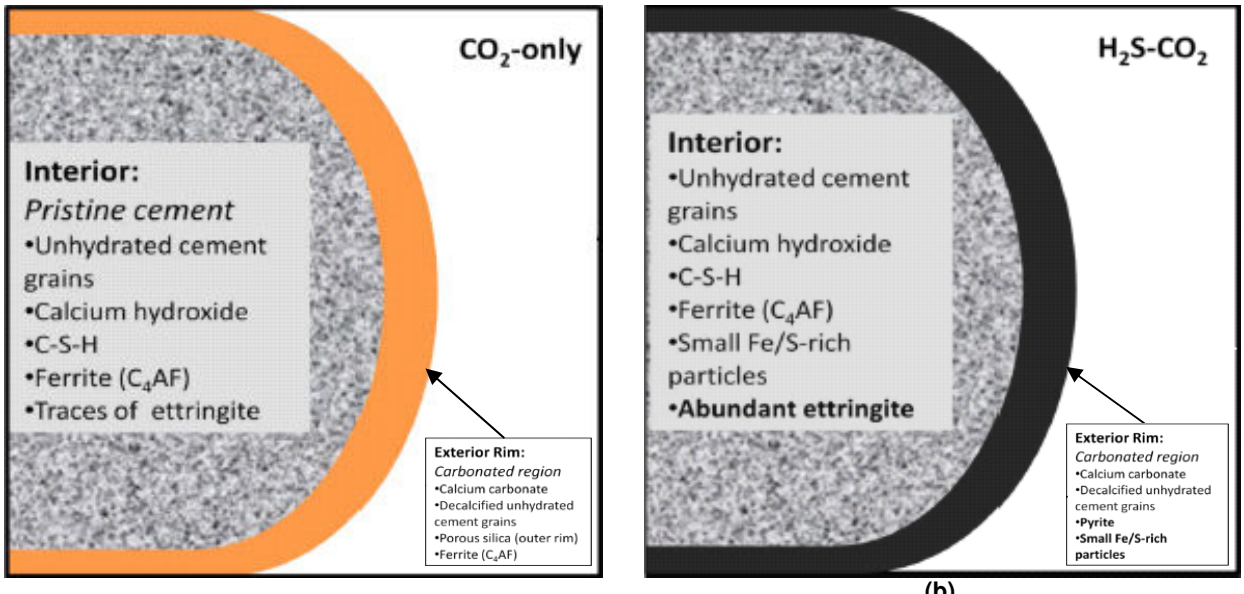

Fig. A.4.5 Cement samples aged in: a) pure CO_2; and b) H_2S-CO_2 system (Kutchko et al., 2011)

Temperature plays an important role on the cement sulfate attack. A decrease in the degree of sulfate attack was reported (Morales et al., 2003) with an increase in temperature, which has been supported by many authors. The reason of this observation is that the solubility of the ettringite increases with the increase in the temperature until it becomes completely soluble above 150℉ (~ 65℃). However, below 150℉, the cement pastes should be improved to reduce the effect of the sulfate attack. It was reported(Morales et al., 2003) that the effect of sulfate attack can be reduced by decreasing the permeability using pore blocking additives such as latex, sodium silicate, or microsilica.

A.4.4. Thermal Retrogression of Cement

The effect of temperature on the cement properties depends on the calcium to silica ratio. At high temperature (greater than230℉) and high calcium to silica ratio, the tobermorite (C-S-H) phase transforms into more stable α-C_2SH phase, resulting in increased permeability and low compressive strength. This can be prevented by adding more silica to the cement and allowing more stable tobermorite to form. At higher temperatures (greater than 302℉), the tobermorite converts into xonotlite and/or gyrolite. This conversion improves the cement properties and its performance. The following equations summarize possible C-S-H high temperature transformations. At high calcium-to-silica ratios and temperature greater than 230℉:

$$\text{C-S-H} \rightarrow \alpha\text{-}C_2\text{-S-H} \quad \text{(4.10)}$$

At low calcium-to-silica ratios (i.e. cement containing more than 35% silica)and temperature between 230℉and 302℉:

$$\text{C-S-H} \rightarrow \text{Tobermorite } (C_5\text{-}S_6\text{-}H_5) \quad \text{(4.11)}$$

At low calcium-to-silica ratios and temperature above 302℉:

$$\text{Tobermorite } (C_5\text{-}S_6\text{-}H_5) \rightarrow \text{Xonotlite } (C_6\text{-}S_6\text{-H}) \quad \text{(4.12)}$$

Temperature can strongly affect the properties of oil well cement. The impacts of temperature on cement properties mainly depend on its composition and the surrounding fluid. Adding30 to 40% silica (by weight of cement: BWOC)on neat cement prevents the strength retrogression phenomena, which takes place at temperatures above 230℉ as the tobermorite (C-S-H) phase transforms into a more stable α-C_2SH phase. This transformation leads to

increased permeability and loss of compressive strength of set cement (Brandl et al., 2010). By adding SiO_2 to the cement, the calcium to silica ratio can be decreased, and the C-S-H phase can be stabilized, preserving its high permeability and compressive strength. As the temperature exceeds 302°F, the tobermorite converts to xonotlite ($Ca_6Si_6O_{17}(OH)_2$) and/or gyrolite ($NaCa_{16}Si_{23}AlO_{60}(OH)_8.64(H_2O)$). The formation of these two phases results in decreased permeability and improved compressive strength (Brandl et al., 2010).

Noik and Rivereau (1999) presented compressive strength (Fig. A.4.6) and permeability (Fig. A.4.7) measurements obtained from experiments conducted using silica-containing Class G cement. Tests were carried out at different temperatures (120, 140, and 180°C) and for periods of up to 2 years. Fig. A.4.6 presents variations in compressive strength of the cement specimens as a function of time at three different temperatures. Data points are highly scattered. However, they apparently indicate the trend of the compressive strength. The results show mixed trends. For lower temperature tests (120 and 140°C), the compressive strength decreased with aging time as some of the C-S-H phase converted to more stable phase (α-C_2SH). For specimens a aged at 180°C, the compressive strengths slightly increased indicating the transformation of tobermorite into xonotlite phase, which was confirmed by X-Ray Diffraction (XRD) and Nuclear Magnetic Resonance (NMR) methods.

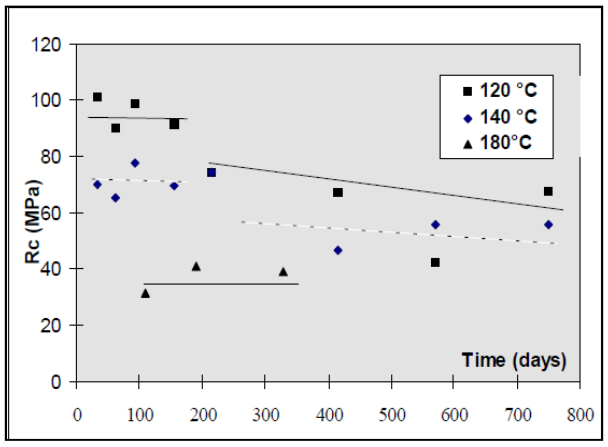

Fig. A.4.6 Compressive strength variation with temperature(Noik and Rivereau, 1999)

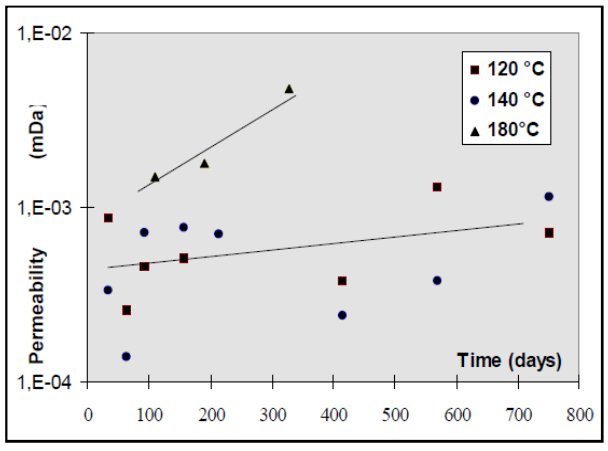

Fig. A.4.7 Permeability variation with temperature (Noik and Rivereau, 1999)

Fig. A.4.7 shows that the permeability change occurred during high temperature aging. Like the compressive strength measurements, permeability data points display high scattering. Lower temperature aging tests (120 and 140°C) showed slight increases in permeability. At 180°C, a substantial increase in permeability was observed, even though high temperature favors the formation of xonotlite phase. This contradicts the presumptions of other investigators

(Brandl et al., 2010) that the formation of xonotlite phase enhances the sealing property of cement by reducing the cement permeability.

Compressive strength of cement can be affected by temperature and aging time. Short-term compressive strength of cement, aged in deionized water, was studied by Dubois et al. (1999). Cement slurry formulations were prepared by adding 20 to 40% crushed sand and 10 to 30% silica fume to the neat cement. The results showed (Fig. A.4.8) that the compressive strength slightly decreased as temperature was increased from 90 to 120℃, which is believed to be due to C-S-H phase transformation into a more stable α-C_2SH phase. However, at higher temperature (140℃), the compressive strength slightly increased with the aging time indicating the conversion of the tobermorite into xonotlite and/or gyrolite. Similar results (Fig. A.4.9) have also been reported by Johnson and Garvin (1972). Cement aged at increased temperature showed a reduction in compressive strength. Additives such as bentonite have substantial influence on the temperature sensitivity of the cement. At temperature above 160℃, the compressive strength trend changes. This could be due to the conversion of tobermorite to xonotlite that dominates the transformation of tobermorite to α-C_2SH phase at higher temperatures (T > 160℃).

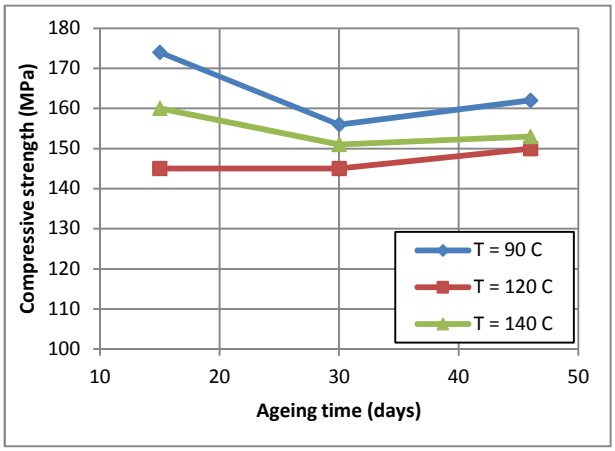

Fig. A.4.8 Compressive strength vs. aging time at different temperatures (Dubois et al., 1999)

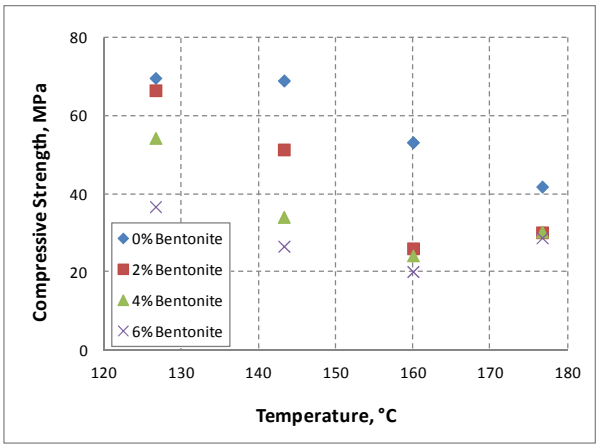

Fig. A.4.9 Compressive strength vs. temperature after 28 days of aging (Johnson and Garvin, 1972)

Thermal retrogression of cement greatly depends on its composition. Jennings (2005) experimentally investigated long-term permeability, shrinkage and compressive strength of different cement core samples exposed to high temperature and high pressure environment. Three types of cement samples that are shown below were considered in the investigation.

- **72 PCF:** 71-lbm/ft^3–hollow ceramic spheres (HCS) blend + fluid loss additives (0.15% by weight of blend: BWOB) + dispersant (0.06 gallon/sack) + retarder (0.025 gallon/sack) +

anti-settling (0.15% BWOB) + defoamer (2 pt/10 bbls) and total mixing fluid at 8.80 gallon/sack.

- **101 PCF:** 101 lbm/ft^3 – Class G (HSR) + pre-hydrated Bentonite (1.9% BWOC) + silica flour (35% BWOC) + fluid loss additives (0.60% BWOC) + dispersant (0.05 gallon/sack) + retarder (0.025 gal/sack) + defoamer (2 pt/10 bbls) at total mixing fluid of 11.47 gal/sack.
- **118 PCF:** 118 lbm/ft3 – Class G (HSR) + silica flour(35% BWOC) + fluid loss additives(0.60% BWOC) + dispersant(0.10 gal/sack) + retarder(0.03 gal/sack) + defoamer (1 pt/10 bbls) and total mixing fluid at 6.26 gal/sack.

Results show substantial increase in the permeability of samples (72 PCF and 101 PCF) that were made without adding silica flour (Table A.4.1). The thermal retrogression appears to take place gradually with time (Fig. A.4.10). The 118 PCF cement exhibited minimum permeability that decreased with aging. This observation is consistent with other similar studies (Brandl et al., 2010) conducted to examine high temperature degradation/retrogression of cement.

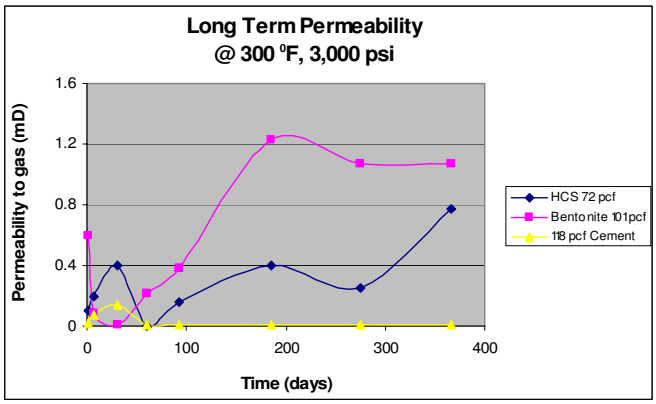

Fig. A.4.10 Permeability of three different cement cores (Jennings, 2005)

Table A.4.1 Permeability change before and after aging the sample (Jennings, 2005)

Cement Sample	Temp.	Pressure	Permeability (mD)	
			Before	After
72 PCF	300 °F	3000 psi	0.10	0.77
101 PCF	300 °F	3000 psi	0.60	1.07
118 PCF	300 °F	3000 psi	0.02	0.01

A.4.5. Leaching of Cement

Calcium leaching is one of the major stages in cement degradation. When a cement-based material is in contact with pure or acidic water, ionic transfers occur between the external water and the pore solution, which is strongly a basic solution. Due to the interaction between pore fluid and cement matrix some of cement hydration products dissolve; thus, increasing the porosity and permeability of the cement and decreasing its mechanical properties. During the dissolution process, portlandite ($Ca(OH)_2$) is the first mineral to be dissolved then calcium silicate hydrates (C–S–Hs) are decalcified. The degradation is characterized by several

dissolution–precipitation fronts delimiting zones with different physicochemical and mechanical characteristics (Kamali et al., 2008).

Mainguy and Coussy (2000) presented a theoretical model that predicts the amount of leached calcium ion resulting from exposure of cement to an aggressive environment. The analytical solution of the model is presented in dimensionless form. To relate the calcium ion concentration in the liquid phase to that in the solid phase, Nakarai et al. (2006) studied the solid-liquid calcium ion concentration-equilibrium using a chemo-physical coupled model. The model predicts the calcium concentration in the solid-phase that corresponding to given concentration in the liquid-phase by considering the dissolution of the calcium hydroxide and calcification of C-S-H gel.

A.4.6. Cement Degradation and Surrounding Fluid pH and Composition

The degradation rate of the cementitious material in the presence of acidic fluid depends upon the composition of the surrounding liquid (salinity), acid concentration, pH of the solution and also the type and amount of hydrated phases present in the reaction. For instance, the dissolution of Fe^{3+} and Al^{3+} is slower and occurs at a lower pH value. Thus, when the pH is lowered, portlandite ($Ca(OH)_2$) and Tobermorite gel (C-S-H) initially dissolve and then calcium aluminate and ferrite hydrates dissolve. When pH is between 4 and 6, calcium hydrates dissolve leaving behind aluminate and ferrite hydrate. However, at low pH values (pH ≈ 2), only silica gel is left after the alteration process of the cementitious material (Lecolier et al., 2008).

A.7.2.1. pH of Pore Fluid Saturated with CO_2

The pH of the pore fluid has great impact on leaching rate. Based on experimental results, Oddo et al. (1982) presented a simplified correlation to estimate the pH of aqueous pore fluid saturated with CO_2.

$$pH = -\left(log_{10}\frac{p_{CO_2}}{C_{HCO_3^-}}\right) + 8.68 + 4.05 * 10^{-3}T + 4.58 * 10^{-7}T^2 - 3.07 * 10^{-5}P - 0.4771I^{0.5} + 0.193I \quad \text{...(4.13)}$$

where

p_{CO_2}= Partial Pressure of CO_2, psi

$C_{HCO_3^-}$ = Concentration of bicarbonate ion, M

T = Temperature, °F

P = Total pressure, psi

I = Ionic strength of water, M

Parametric study conducted using this model shows that the pH slightly decreases as the partial pressure of CO_2 increases (Fig. A.4.11). However, maintaining other parameters constant and increasing the temperature tends to increase the pH (Fig. A.4.12). Parameters that are kept constant during the parametric study are given in Table A.4.2.

Table A.4.2 Constant Parameters

Pco2 (psi)	C(Bi) (Molar)	T (°F)	P (psi)	I (Molar)
150	0.01	60	3000	0.01

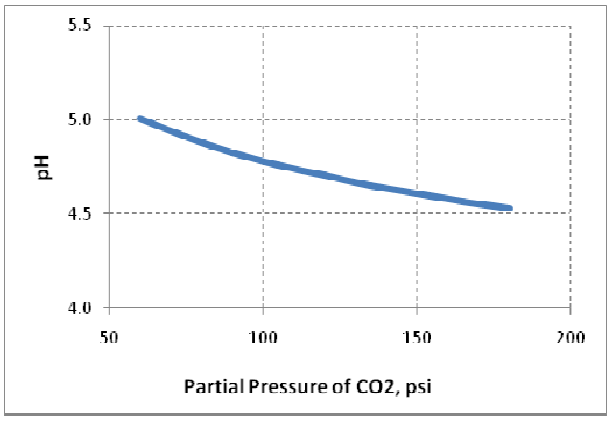

Fig. A.4.11 pH vs. partial pressure of CO_2

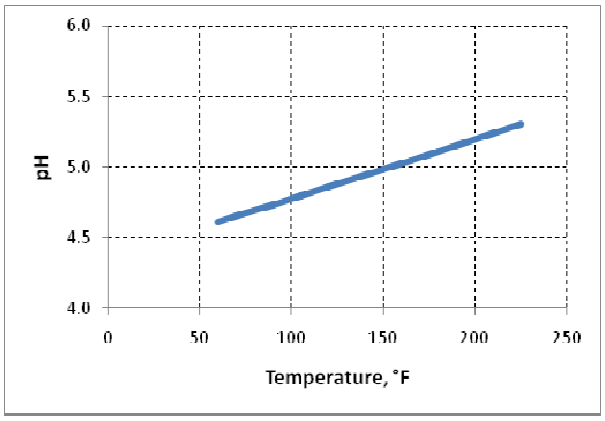

Fig. A.4.12 pH vs. temperature

More advanced and accurate pH model has been developed in this investigation. The model determines the amount of CO_2 soluble in the brine solution at different pressures and temperatures as (Duan et al., 2007):

$$\ln\frac{y_{CO2}P}{m_{CO2}} = \frac{\mu_{CO2}^{l(0)}}{RT} - \ln\phi_{CO2} + \sum_c 2\lambda_{CO2-Na}m_{Na} + \sum_a 2\lambda_{CO2-Cl}m_{Cl} + \sum_c\sum_a \xi_{CO2-Na-Cl}m_{Na}m_{Cl} \quad .(4.14)$$

The model can be modified by expressing the total pressure as: $P = p_{CO2} + p_{H2O} + p_{CH4}$. The fugacity of CO_2 in system (ϕ_{CO2}) is determined according to the model developed by Duan and Sun (2003).In the above equation, λ, ξ and the dimensionless standard chemical potential $\frac{\mu_{CO2}^{l(0)}}{RT}$ are the interaction parameters (Par) that depend on temperature and pressure. These parameters can be estimated from the following generalized equation:

$$Par(T,P) = C_1 + C_2T + C_3/T + C_4T^2 + C_5/(630-T) + C_6P + C_7P\ln T + C_8P/T + C_9P/(630-T) + C_{10}P^2/(630-T)^2 + C_{11}T\ln P \quad (4.15)$$

Table A.4.3 Constants for interaction parameters (Duan et al., 2007)

$T-P$ coefficient	$\mu^{l(0)}_{CO_2}/RT$	λ_{CO_2-Na}	$\xi_{CO_2-Na-Cl}$
c_1	28.9447706	−0.411370585	3.36389723e−4
c_2	−0.0354581768	6.07632013e−4	−1.98298980e−5
c_3	−4770.67077	97.5347708	
c_4	1.02782768e−5		
c_5	33.8126098		
c_6	9.04037140e−3		
c_7	−1.14934031e−3		
c_8	−0.307405726	−0.0237622469	2.12220830e−3
c_9	−0.0907301486	0.0170656236	−5.24873303e−3
c_{10}	9.32713393e−4		
c_{11}		1.41335834e−5	

The partial pressure of water vapor, p_{H2O}, is considered to be the saturated pressure at a given temperature:

$$P_{H2O} = (P_CT/T_C)\left[1 + C_1(-t)^{1.9} + C_2t + C_3t^2 + C_4t^3 + C_5t^4\right] \quad \text{.....(4.16)}$$

where T is temperature in K, $t = (T - T_C)/T_C$ and T_C and P_C are the critical temperature and pressure of water, respectively. The values of constants C_1 to C_5 are given in Table A.4.4.

Table A.4.4 Values of constants C_1 to C_5

c_1	−38.640844
c_2	5.8948420
c_3	59.876516
c_4	26.654627
c_5	10.637097

The first and the second dissociation constants of the carbon dioxide in the pK form (i.e. pK_i = -log (K_i)) are estimated using correlation presented by Millero et al. (2007). The model is valid for temperature up to 482°F and NaCl concentration up to 6 m.

$$pK_i^* - pK_i = A_i + B_i/T + C_i\ln T \quad \text{.....(4.17)}$$

where pK_i is corresponding to pure water and parameters A_i, B_i, C_i are a function of molality. T is absolute temperature in Kelvin.

$$pK_1 = -402.56788 + 11656.46/T + 72.173\ln T - 0.161325T + 7.5526\times10^{-5}T^2 \quad \text{.....(4.18)}$$

$$pK_2 = -122.4994 + 5811.18/T + 20.5263\ln T - 0.0120897T \quad \text{.....(4.19)}$$

A_1, A_2, B_1, B_2, C_1, C_2 can be calculated using the following correlations

$$A_1 = 31.3616m^{0.5} + 0.86644m - 0.33611m^{1.5} + 0.05888m^2$$
$$B_1 = -1422.25317m^{0.5}$$
$$C_1 = -4.84141m^{0.5}$$
$$A_2 = 36.88545m^{0.5} + 1.66599m - 0.68730m^{1.5} + 0.12070m^2$$
$$B_2 = -1669.55918m^{0.5}$$
$$C_2 = -5.83555m^{0.5} \quad \text{.....(4.20)}$$

In order to find hydrogen concentration, the first and second dissociation steps can be combined in the form of:

$$H_2O + CO_2 \Leftrightarrow 2H^+ + CO_3^{2-} \quad \text{.....(4.21)}$$

The overall dissociation constant for the above equation can be expressed as:

$$K_{overall} = K_1(CO_2)\times K_2(CO_2) = \frac{[H^+]^2.[CO_3^{2-}]}{[CO_2]} \quad \text{.....(4.22)}$$

Then, the overall dissociation constant can be used to determine the hydrogen concentration.

$$[H^+] = \sqrt{\frac{K_{overall}[CO_2]}{[CO_3^{2-}]}} \quad \text{.....(4.23)}$$

Finally, the pH of the solution is calculated from the hydrogen concentration.

$$pH = -\log[H^+] \quad \text{.....(4.24)}$$

In Fig. A.4.13, model predictions are compared with the experimental data presented by Abtahi et al. (1996).The comparison shows acceptable agreement.

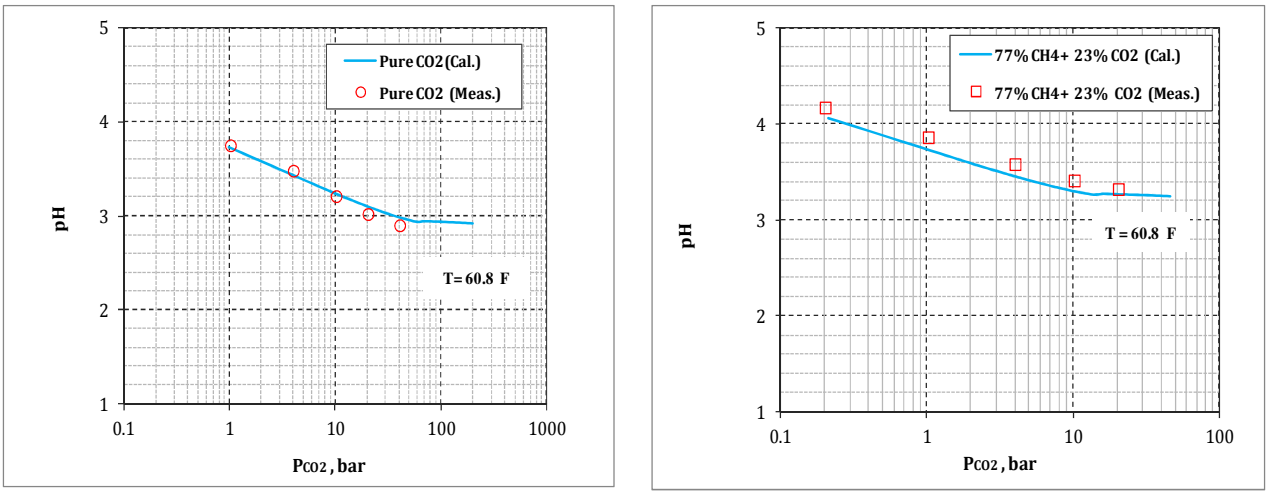

(a) (b)

Fig. A.4.13 Comparison of model prediction with measurements by Abtahi et al. (1996): a) pure CO_2; and b) 23% CO_2 + 77% CH_4

A.7.2.2. pH of Pore Fluid Saturated with H_2S

The pH of a solution in contact with acidic gas is directly related to the level of acid dissociation. The solubility and dissociation of hydrogen sulfide and carbon dioxide are influenced by temperature, pressure and ionic strength of the solution. Duan et al. (2007) presented a widely accepted thermodynamic model to predict the solubility of hydrogen sulfide in water and brine. The model is based on the specific particle interaction theory and the equation of state. It is valid for a wide range of pressure, temperature and ionic strength conditions (pressure: 0 to 2900 psi, temperature: 30 to 440°F and ionic strength: 0 to 6 M). The model validation performed at pressures less than 100 bar (1500 psi) showed good agreement between measurements and predictions. Parametric study using the model shows (Fig. A.4.14) reversed solubility trend at high pressures (above 100 bar). At low pressures, H_2S solubility decrease with the increase in temperature. However, this trend changes at high pressures and the gas becomes more soluble as the temperature increases.

Furthermore, the liquid phase tends to saturate with the gas at low temperatures (86 and 140°F). At high temperatures (410 and 464°F), saturation phenomenon does not occur. The salinity reduces the solubility of the gas regardless of the pressure and temperature of the system.

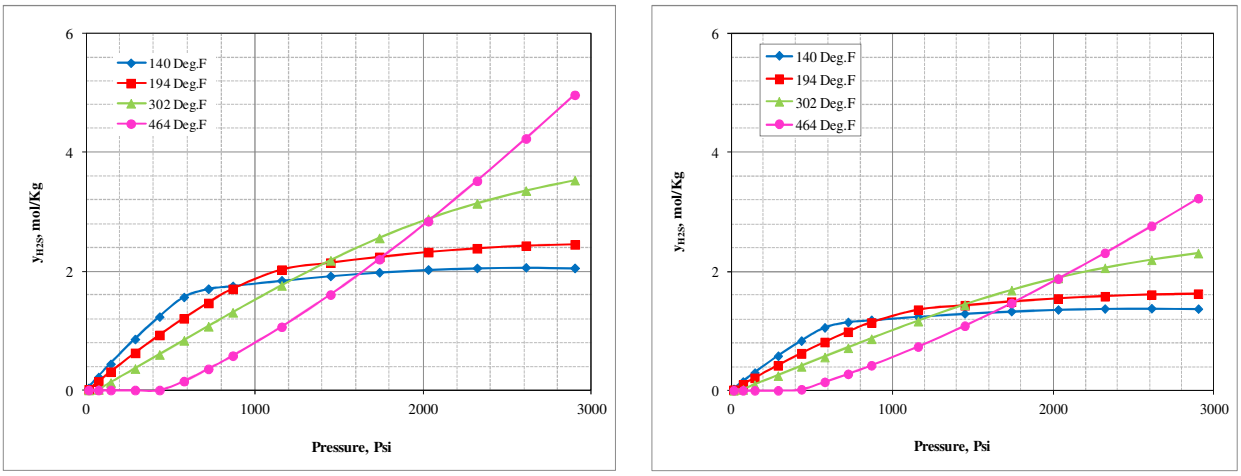

(a) **(b)**

Fig. A.4.14 Solubility of H_2S in brine solutions as a function of pressure at different temperatures: a) 1 M solution (5.2% NaCl); and b) 4 M solution (15.8% NaCl)

The pH of a solution in contact with acidic gas is estimated using solubility and dissociation constants. The following steps show the method of calculating the pH of pure solution:

I. Determining the concentrations of CO_2 and H_2S in the liquid phase using the solubility model.

II. Estimating the first (K_{a1}) and the second (K_{a2}) dissociation constants of hydrogen sulfide and carbon dioxide in the solution. The second dissociation constant of H_2S can be neglected (i.e. K_{a1} is much greater than K_{a2}).

III. Determining the hydrogen ion concentration applying the dissociation equation and material balance.

Duan et al. (2007) presented thermodynamic model to predict the solubility of hydrogen sulfide in pure water and in aqueous NaCl solutions. The model was validated using published experimental data obtained at high-pressure and high-temperature (Pressure: 0-2900 psi and Temperature: 32–440ºF) conditions. The model utilizes the particle interaction theory and the equation state. It expresses the solubility of H_2S as a function of interaction parameters:

$$\ln\frac{y_{H2S}P}{m_{H2S}} = \frac{\mu^{l(0)}_{H2S}}{RT} - \ln\phi_{H2S} + \sum_{Na} 2\lambda_{H2S-Na} m_{Na} + \sum_{Cl} 2\lambda_{H2S-Cl} m_{Cl} + \sum_{Na}\sum_{Cl} \xi_{H2S-Na-Cl} m_{Na} m_{Cl}$$

…….. (4.25)

where m_{H2S}, m_{Na} and m_{Cl} are molalities of H_2S, sodium ion, and chloride ion, respectively. ϕ_{H2S} is fugacity coefficient. In the above equation, λ, ξ and the dimensionless standard chemical potential $\frac{\mu_{H2S}^{l(0)}}{RT}$ are the interaction parameters (Par), which depend on the temperature and pressure according to a generalized equation given below:

$$Par(T,P) = C_1 + C_2 T + \frac{C_3}{T} + C_4 T^2 + \frac{C_5}{(680-T)} + C_6 P + \frac{PC_7}{(680-T)} + \frac{C_8 P^2}{T} \quad \ldots\ldots (4.26)$$

where T is temperature in Kelvin and P is pressure in bar. The forth term in the right hand side of Eq. (4.25) is zero (Duan et al., 2007). The values of the constants in Eq. (4.26) are provided in Table A.4.5.Partial pressures of H_2S and CH_4 are calculated based on the composition of the gas phase. In addition, the partial pressure of water vapor in the gas phase is calculated from the water saturation pressure.

Table A.4.5 Constants for interaction parameters (Duan et al., 2007)

$T-P$ coefficient	$\mu_{H_2S}^{l(0)}/RT$	λ_{H_2S-Na}	$\zeta_{H_2S-Na-Cl}$
c_1	42.564957	8.5004999E−2	−1.0832589E−2
c_2	−8.6260377E−2	3.5330378E−5	
c_3	−6084.3775	−1.5882605	
c_4	6.8714437E−5		
c_5	−102.76849		
c_6	8.4482895E−4	1.1894926E−5	
c_7	−1.0590768		
c_8	3.5665902E−3		

$$p_{H2O} = (P_C T / T_C)\left[1 + C_1(-t)^{1.9} + C_2 t + C_3 t^2 + C_4 t^3 + C_5 t^4\right] \quad \ldots\ldots\ldots\ldots\ldots\ldots (4.27)$$

where T is temperature in Kelvin. T_C and P_C are the critical temperature and pressure of water(T_C = 647.3K and P_C = 220.9 bar), respectively. The values of the parameters listed in Eq. (4.27) are: c_1 = -38.64, c_2 = 5.89, c_3 = 59.88, c_4 = 26.65 and c_5 = 10.64. The parameter t is defined as: $t = (T - T_C)/T_C$.

Ionic concentrations in the solution must be determined to predict the pH of the solution. The procedure requires estimating first and second dissociation constants (K_1 and K_2) of the hydrogen sulfide using a correlation (Hershey, 1988), which is valid for temperature up to 572°F and salt concentration of 6 M. The pK1 of H_2S (i.e. pK_1 = -Log (K_1)) in pure water can be estimated as:

$$pK_1 = 32.55 + 1519.44/T - 15.67 \log T + 0.027T \quad \ldots\ldots\ldots\ldots\ldots\ldots (4.28)$$

where T is temperature in K. The pK_1 calculated from the above equation needs to be corrected for salinity. Thus:

$$pK_1^* = pK_1 - 0.78708\, I^{0.5} + 0.50475\, I - 0.05134713\, I^{1.5} \quad \text{.....(4.29)}$$

where I is molar concentration of the salt.

The second dissociation constant of H_2S is negligible. Hence, the equilibrium equation of H_2S dissociation can be written as: $H_2S_{(aq)} \Leftrightarrow H^+ + HS^-$. Then, the dissociation constant is used to determine the concentration of H^+, and subsequently the pH of the solution. Fig. A.4.15 presents results of a parametric study conducted to investigate the effects of temperature and pressure on the pH of brine solutions in contact with H_2S. The predictions show a mixed trend. As the temperature increase from 140°F, the pH slightly decreased. This is expected because the increase in temperature tends to reduce solubility of the gas. At high temperatures (i.e. above 300°F), this trend changes due to other factors such as variation in dissociation constant as temperature increases. As a result, the pH moderately increases with increasing the temperature.

Formation water salinity of varies substantially from one location to another. It is also dependent on the depth of the formation. Although the effect of salinity on the pH of the solution is minimal (Fig. A.4.15), its influence on cement degradation can be substantial.

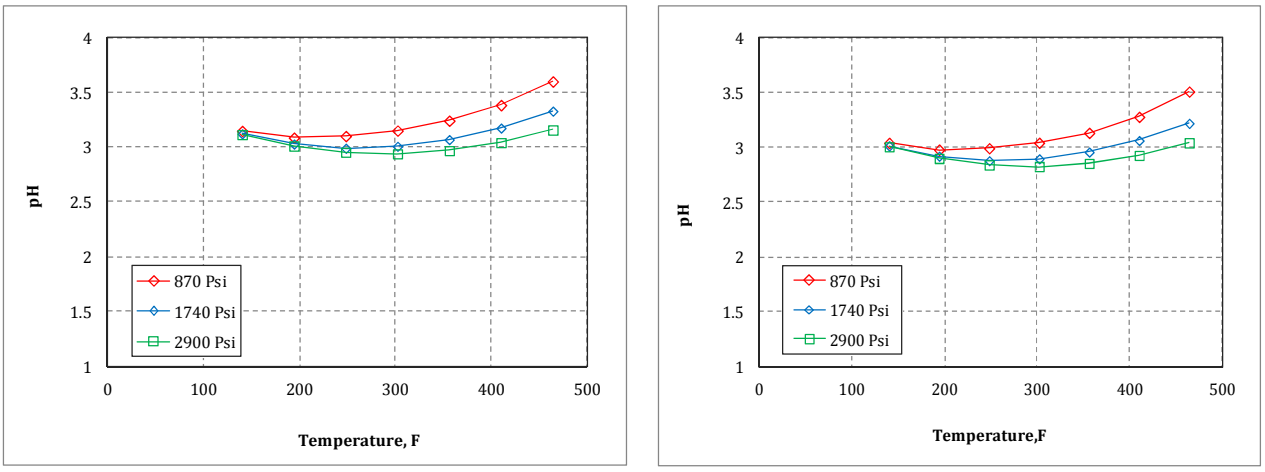

(a) (b)

Fig. A.4.15 pH of brine solutions vs. temperature at different pressures: a) 1 M solution (5.2% NaCl); and b) 4 M NaCl (15.8%)

A.7.2.3. Composition of Formation Water

The composition of aqueous fluids in sedimentary basins is determined by diagenetic reactions and physical processes that generate fluid and ion movements such as fluid convection, hydrodynamic dispersion, and ionic diffusion (Hanor, 1994). In the Gulf of Mexico sedimentary

basin, formation waters exhibit a wide range of composition variation depending on the depth and geographical location of the formation. Abnormal pressure conditions in the formation may also affect the composition of formation fluid (Overton and Timko, 1969; Dickey et al, 1972; Schmidt, 1973; Jones, 1975; Fertl, 1976; Wallace et al., 1977). As reported by Moran (2003), in some Gulf of Mexico formations, the total dissolved solid (Fig. A.4.16) and chloride contents (Fig. A.4.16) of the pore fluid linearly vary with depth (Hanor, 1979). As the depth increases the chloride concentration increases.

.

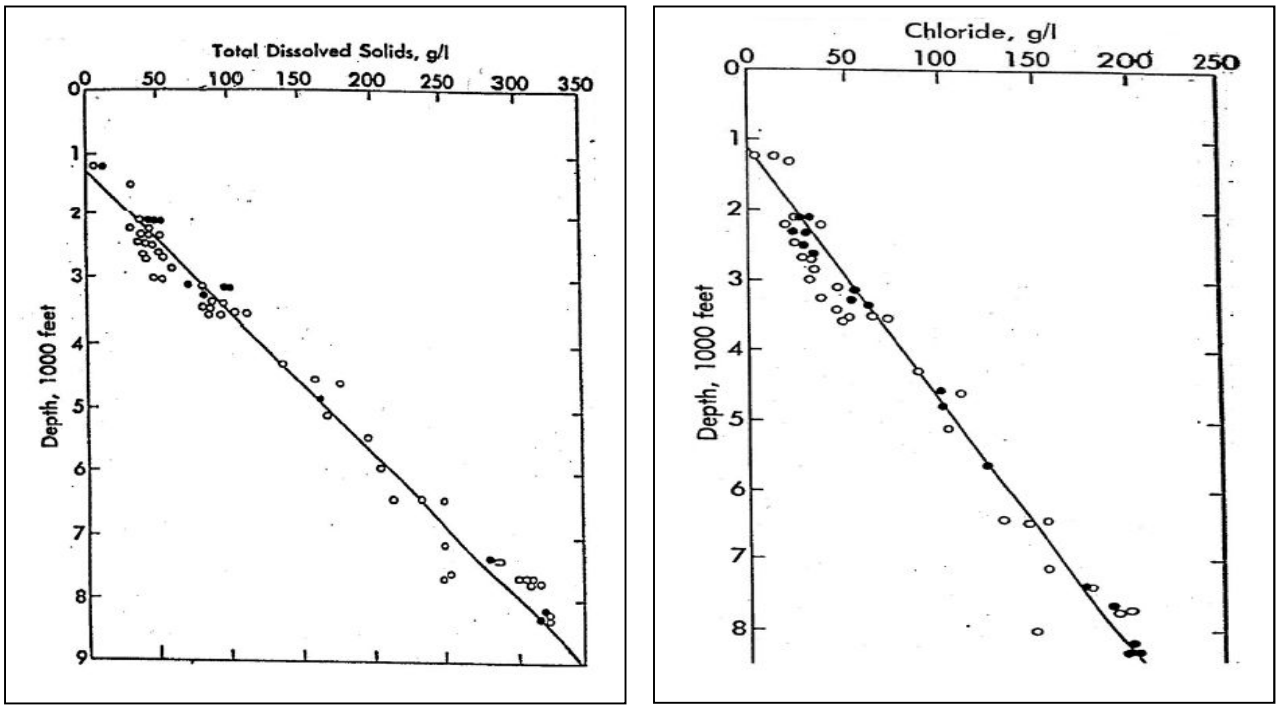

(a) **(b)**

Fig. A.4.16 Variation of solids and chloride contents with depth in southern Arkansas and northern Louisiana: a) total dissolved solids; and b) chloride content (Hanor, 1979)

Morten and Land (1987) studied regional compositional variations information water encountered in the Frio formations in Texas coastal plain. The formation water shows a wide range of variation in sodium ion content (Table A.4.6). Samples taken from different fields (Alta Loma, Portland and Candelaria) in Frio Formation showed substantial compositional variations (Fig. A.4.17). Alta Loma field formation water contains high level of sodium salt (Na^+ concentration of 29.8 g/L). Water sample from Candelaria field showed the highest concentration of $CaCl_2$ (Ca^+ concentration of 22.3 g/L).

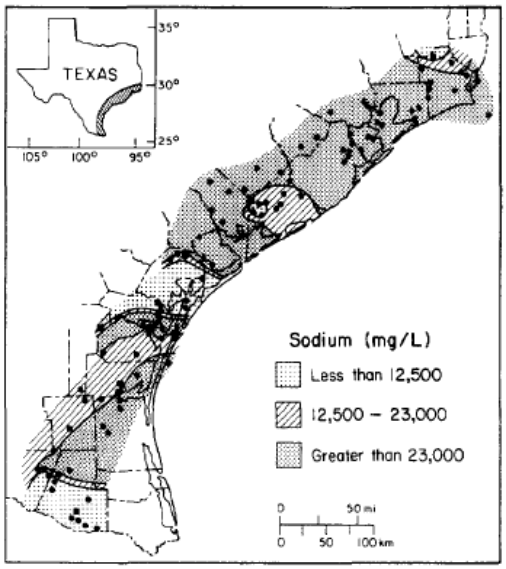

Fig. A.4.17 Sodium ion content in Frio formations (Morten and Land, 1987)

Table A.4.6 Composition of reservoir water from Frio Formation (Robert and Land, 1987)

Subregion	1	2	3
Field	Alta Loma, West	Portland	Candelaria
Well	Hunt 1 Tacquard	Fort Worth O&G D1L Portland Gas Unit	Exxon 57D C. M. Armstrong
Water type	NaCl	Acetate	Ca-rich
Na*	29,800	7,330	17,870
K*	230	40	140
Mg*	151	8	117
Ca*	1,490	48	22,260
Sr*	272	6	1,220
B*	54	57	47
SiO_2*	84	111	144
Alkalinity*	536	2,760	61
Cl*	46,300	8,900	65,400
Br*	57	40	299
SO_4*	18	37	2
Temperature (°C)	129	110	113
Depth (m)	3,741	2,963	2,890
$\delta^{18}O$ (SMOW)	4.3	6.9	5.5
$^{87}Sr/^{86}Sr$	0.7099	0.7086	0.7102
Density (in situ)	1.016	0.980	1.024

*Concentrations expressed in milligrams/liter.

A.5. Special Cements for Acidic Environment

Laboratory measurements and field data analysis showed that several factors are responsible for the rapid degradation of cement under harsh downhole conditions (Brandl et al., 2010). Chemical composition and physical properties of the cement are the key factors in determining the resistance of the cement against acid attack. The hydration of standard API cement mainly produces Calcium-Silicate-Hydrate (C-S-H), which is the major binding material and portlandite ($Ca(OH)_2$), which is very susceptible for acidic attack. One of the methods used to control acid attack is to add pozzolanic materials to reduce the concentration of portlandite. This will minimize the reaction between the acid and the portlandite base. In addition, lowering the water

content in the cement system can reduce the porosity and permeability of the cement hinders the diffusion of the acidic solution in the porous cement and degradation process. Moreover, synthetic and epoxy-based cement binding additives provide greater chemical resistance and good mechanical performance.

Another approach to tackle the problem of cement degradation is to replace the Portland based cement with a non-Portland system such as calcium sulfoaluminate-based cements, geopolymeric cements (alkali aluminosilicates), magnesium oxide cements and hydrocarbon-based cements (Benge, 2009). However, non-Portland systems are not readily available and conventional additives may or may not work in this cement. In addition, rapid setting of non-Portland systems can occur due to contamination with Portland cement. As a result, these types of cements are not commonly used (Santra and Sweatman 2011).

A.7.1. Carbon Dioxide Resistant Cements

Recently, Brookhaven National Laboratory (BNL) developed two cement formulations for CO_2-contianing environments (Sugama, 2006). The formulations are: i) calcium aluminate phosphate (CaP) cement containing four basic components, calcium aluminate cement (CaO-Al_2O_3-P_2O_5-H_2O), sodium polyphosphate (Na_2O-CaO-Al_2O_3-SiO_2-P_2O_5-H_2O), Class F fly ash, and water; and ii) sodium silicate-activated slag (SSAS) cement consisting of Na_2O-CaO-SiO_2-MgO-H_2O and Na_2O-CaO-Al_2O_3-SiO_2-MgO-H_2O systems, Class F fly ash, and water. Long-term exposure of these cements to an environment containing acidic fluids resulted in shrinkage and expansion of test specimens caused by the in-situ phase transformation and the excess growth of crystalline reaction products. The phenomena developed internal stresses that initiation cracks. The bonding durability of cement-casing interface is strongly affected by the magnitude of the stresses. In addition, factors such as thermal and mechanical properties of the cement and the casing influence the development of internal stress.

As previously mentioned, incorporating pozzolanic fillers such as silica fumes and fly ash effectively decreases portlandite and C-S-H contents of the cement (Table A.5.1) thereby reducing the formation of calcium carbonate, which further reacts with the acid to form water soluble calcium bicarbonate that can be easily leached out (Santra et al., 2009).

Table A.5.1 Comparing the effects of using two different filter materials in cement (Santra et al., 2009)

Filler	Silica Fumes	Fly Ash
Filler material content	35%	98%
Particle size	Finer	Coarser
Porosity & permeability (ϕ and k)	Less	More
Water-solid Ratio	High	Low
$Ca(OH)_2$	Low	High
Depth of penetration	1) Low due to reduction of $Ca(OH)_2$ content 2) Low due to ϕ and k 3) High due to W/S Ratio	1) Low due to reduction of $Ca(OH)_2$ content 2) High due to ϕ and k 3) Low due to W/S Ratio

Table A.5.2 Slurry compositions (Santra et al., 2009)

Sample, No.	Cement, %	Silica Fume, %	Fly Ash, %
1	100	0	0
2	83.3	16.7	0
3	71.4	28.6	0
4	62.5	37.5	0
5	55.6	44.4	0
6	50	50	0
7	83.3	0	16.7
8	71.4	0	28.6
9	62.5	0	37.5
10	55.6	0	44.4
11	50	0	50

To study the effects of filler materials on the carbonation process, Santra et al. (2009) conducted experiments using 11 samples-containing different quantities of silica and fly ash (Table A.5.2). After aging for 15 days at 2000 psi and 200ºF in the presence of fresh water saturated with CO_2, the samples were cut in half to examine visually the degree of penetration. The penetration depth was determined by examining different colors formed on carbonated and uncarbonated portions of the sample when phenolphthalein indicator was applied. The images of the samples presented in Fig. A.5.1 shows that Samples 5 and 6 were fully penetrated due to extensive CO_2 invasion, which was confirmed by TGA (Thermo-Gravimetric Analysis) and XRD (X-ray diffraction) tests (Santra et al., 2009). Fig. A.5.2 compares the measured depth of penetration of samples containing different concentrations of filler materials. Depth of CO_2 penetration depends upon the following two factors: i) permeability of the original rock (before carbonation) that controls rate of CO_2penetration in the rock; and ii) amount of $Ca(OH)_2$ in the system that facilitates the conversion of CO_2 thereby producing more $CaCO_3$, which plugs the pores and results in decreased porosity and penetration depth. Therefore, to lower the depth of penetration, the amount of $Ca(OH)_2$ needs to be lowered by increasing the amount of filler materials such as silica fume and fly ash.

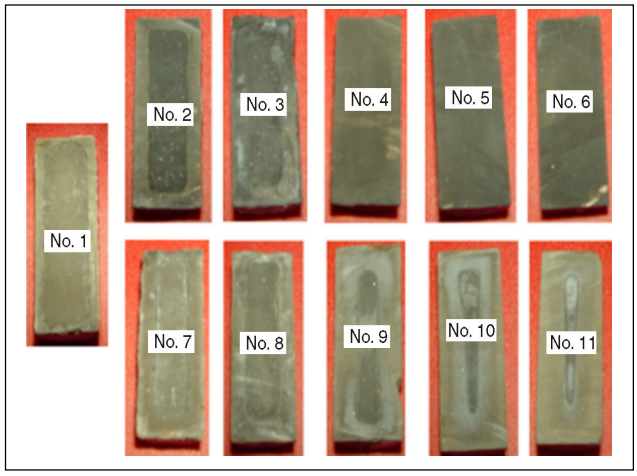

Fig. A.5.1 Cement core samples after 15-day of aging in water saturated with CO2 (Santra et al., 2009)

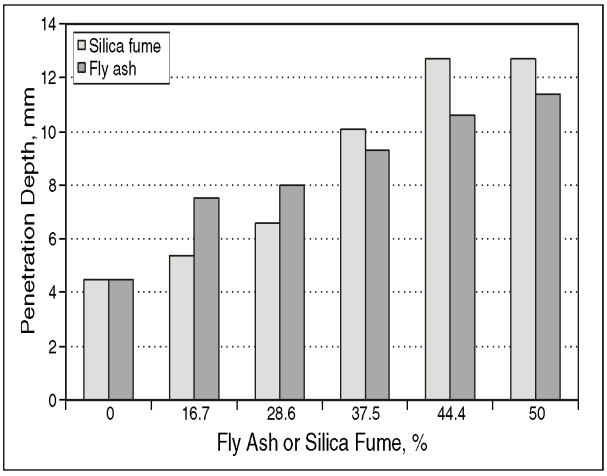

Fig. A.5.2 Measured penetration depth (Santra et al., 2009)

Distinct zones with different degradation processes form when acid attacks cement. Barlet-Gouédard et al. (2006) presented results of a comprehensive study on the degradation of cement in simulating the interaction of the set cement with injected supercritical CO_2 and water-saturated with CO_2. The study compared (Table A.5.3) the conventional cement with new CO_2-resistant cement formulation that contains a reduced amount of Portland cement.

Table A.5.3 Comparison of conventional and CO_2 resistant cement (Barlet-Gouédard et al., 2006)

Cement Sample	Temperature	Pressure	Porosity	Sample Size D X L
Conventional Portland cement (class G, 1.89 g/cm^3, water/cement ratio equal to 0.44)	90°C [194°F]	28 MPa [4061 psi]	In wet supercritical CO_2, the porosity continuously decreased, from 33% to 15% after 6 weeks. It rapidly decreased from 33% to 27% in the first two days, and then decreased slowly down 15%. In water-saturated with CO_2, the porosity changes in two distinct phases. During the first phase of approximately three weeks, the porosity rapidly decreased from 33% to 9%. During the second phase after three weeks, the porosity in- creased from 9% to 21% up to 6 weeks.	0.5" X 1.0" and 1.0" X 2.0"
A new CO_2-resistant material	90°C [194°F]	28 MPa [4061 psi]	CO_2-resistant material remains stable from the first two days to a longer duration.	

After aging in aggressive environment, the core samples were cut in half and examined using a microscope (Fig. A.5.3). The aged cement cores displayed a particular geometry with concentric zones at different test durations on back-scattered electron images. From the core towards the rim of samples, the cement sample consisted of: i) uncarbonated zone; ii) dissolution front; iii) carbonation front; and iv) dissolution back-front. The uncarbonated zone is the inner part of the core, surrounded by the dissolution front. The dissolution front is a highly porous zone where C-S-H progressively dissolves. The carbonation front is a 50 to 100 µm-large zone of very low porosity. The dissolution back-front is located at the rear of the carbonation front. In this zone, neo-formed carbonates are dissolved, increasing the porosity and resulting in severe degradation of the cement. In contrast, a homogeneous pattern with a limited carbonation threshold is observed with the CO_2-resistant material, which has good mechanical behavior over a wide density range. This material remains comparably inert in both wet supercritical CO_2 and water-saturated with CO_2. Weight, density, compressive strength, micro structural characterizations and Hg porosity measurements confirm good CO_2-resistanceof the new cement.

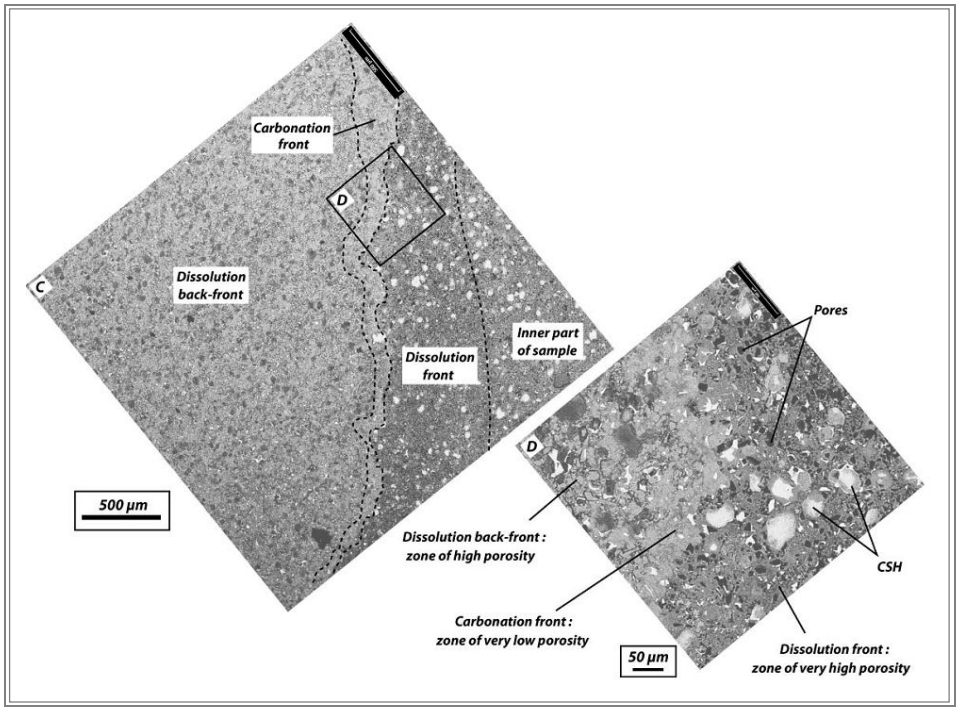

Fig. A.5.3 Microscopic image of half-core sample after 88 hr aging in CO_2 in wet supercritical CO_2 fluid (Barlet-Gouédard et al., 2006)

Recently, Santra and Sweatman (2011) reported experimental results of two different cement samples (CO_2 resistant cement and Class G cement) before and after the CO_2 treatment

(i.e. water + supercritical CO_2). The two samples were analyzed using the TGA method. System A cement showed better resistant to CO_2 attack than Class G cement.

A.7.2. Hydrogen Sulfide Resistant Cements

When H_2S reacts with water, it forms a weak acid and lowers the pH. Portland cement reactive to acidic solutions and as a result it degrades when exposed to acidic fluids. It is important to understand the interactions of the acid and components of set cement that react with H_2S and the mechanisms of species transport in the porous cement thereby preventing the deterioration of cement.

In brine saturated with H_2S, the acid attack occurs when the H_3O^+ ions penetrate into the cement matrix and react with hydration products. Lécolier et al. (2006) studied durability of different cementing materials (silica containing cements, conventional cement, and mortar) in reservoir fluid and H_2S saturated brine containing 12.6% NaCl and 0.42% Na_2SO_4. All samples were cured at 80ºC and 7 MPa. Aging was performed at 120ºC and 15 MPa in non-agitated cell. Cement specimens (D = 1" and L = 2") were fully immersed in the brine solution. The ratio between the aging fluid and sample volume was approximately 2. System pressure quickly reduced during the first hours when the H_2S gas dissolved in the liquid. The permeability of silica-containing samples decreased while the conventional cement showed a substantial increase in permeability. The reason for the permeability increase is attributed to excessive calcium leaching (dissolution of portlandite and decalcification of C-S-H).

Cement additives may not have direct effect on the nature of the cementitious material, but at the same time, they can prevent it from acidic degradation. The two metallic oxides proposed by Lecolier et al. (2008) that have a high affinity for H_2S are:

- Fe_2O_3 (Hematite)
- Mn_3O_4 (Hausmanite)

Cement specimens containing these additives were tested by aging in H_2S-saturated saline water. Incorporating hematite leads to strong damaging of cement matrix due to acid reaction, resulting in total destruction (Fig. A.5.4a); however, adding Mn_3O_4 showed encouraging results (Fig. A.5.4b).

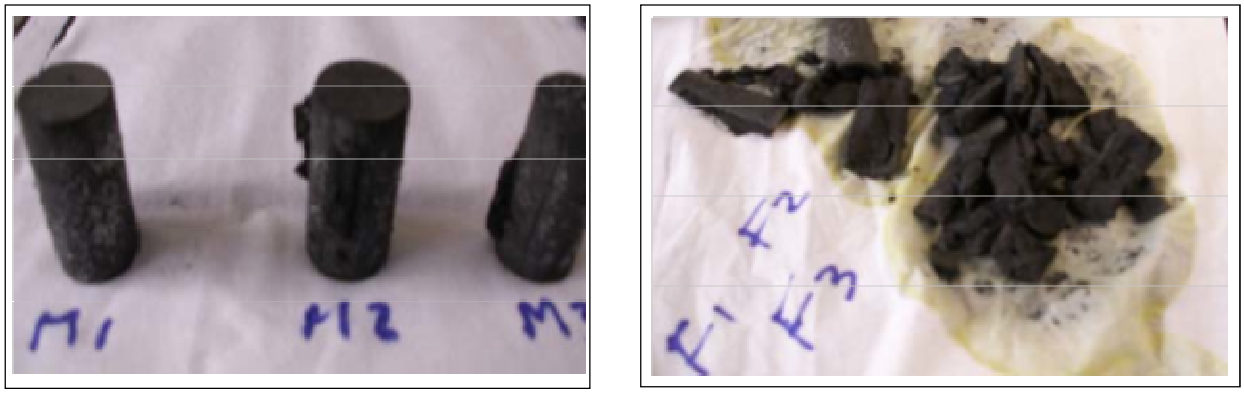

(a) (b)

Fig. A.5.4 Cement specimens after one-week aging in H_2S-saturated saline water :a) 15% Mn_3O_4-Cement system; and ii) 30% Fe_2O_3-Cement (Lécolier et al 2008)

The reaction of cement with H_2S in some cases results in production of expanding products that can generate micro-cracks in the system. These micro-cracks increase the porosity and permeability of the affected cement. However, in case of Mn_3O_4based cement, there was no significant expansion noticed. Introducing Mn_3O_4 substantially reduced the adverse effect of H_2S but it could not 'completely' eliminate the degradation. In spite of these observations, another study (Jacquemet et al., 2007) conducted on crushed cement using mixture of H_2S and CO_2 showed the dominating effect of CO_2 on cement degradation. The mineralogy of aged and un-aged cement samples were analyzed using XRD method. The analysis showed reduction in tobermorite and ferrite contents. The residual gas analysis showed traces of H_2 and COS. The initial gas mixture composition was 66% H_2S and 34 mol% CO_2.The gases were consumed during the aging process and the initial concentration changed. The amount of consumed H_2S and CO_2 ranged from 1 to 15 mol% and 65 to 75 mol%, respectively. The H_2S attack was limited since the H_2S reactivity is only responsible for the sulfidation of ferrites (Ca_2AlFeO_5 or C_4AF) into pyrite (FeS).

A.6. Cement and Casing Bond Failure

Cement failure often occurs at the interface between the cement sheath and casing. The shear and hydraulic bonding characteristics of oil well cement are very critical for the performance of the cement. These properties are affected by the exposure of the cement to reactive fluids such as water saturated with CO_2 and/or H_2S. The shear bonding is defined as the force required to break the bonding between the casing and cement sheath per unit contact area. The hydraulic bond strength is a measure of the hydraulic pressure required to initiate leakage of fluid between the plug and casing. Condor and Asghari (2009) measured these two mechanical properties for cement samples that were exposed to a mixture of brine and CO_2 for 2 months.

Results show that the shear bonding were reduced from its initial value of 1240 psi to 30 psi while the hydraulic bond strength reduced from 315 psi to 40 psi after the exposure. It was pointed out that the reduction could be due to shrinkage of the cement in the casing, which creates cracks and micro channels for CO_2 to pass through the clearance between the cement sheath and casing.

A.7. Modeling Cement Degradation

A.7.1. Introduction

Understanding the degradation mechanisms of cement is essential to develop a theoretical model that can reasonably describe the process. The degradation is a complex phenomenon, which influences the chemical, mechanical and diffusive properties of the cement. As a result, phenomenological methods are often preferred to investigate the degradation process. Nonetheless, for the past two decades, cement degradation modeling has been developing and applying different approaches to formulate models that can predict the change occurring in chemical, mechanical and flow properties of the cement (composition, compressive strength, permeability and porosity) as a function of time after exposure to sour gas containing environments. Depending on their approach, some models are less complex than others. Complex models, compared to simplified models, provide more accurate and detailed descriptions of the process and the influence of different parameters.

Earlier studies (Carde et al., 1996; Carde and Frarqois, 1999) presented a simplified cement degradation model that predicts the increase in porosity and loss of compressive strength. The model is formulated on two basic assumptions: i) linearly varying decalcification of the C-S-H phase in relation to the depth; and ii) the change in compressive strength is similar to the change in calcium content during cement degradation. In its present form, the model does not require a cumbersome numerical procedure to make predictions. The model successfully reproduced experimentally measured porosity (Fig. A.7.1) and compressive strength variations (Fig. A.7.2) occurred after aging the sample in ammonium nitrate solution.

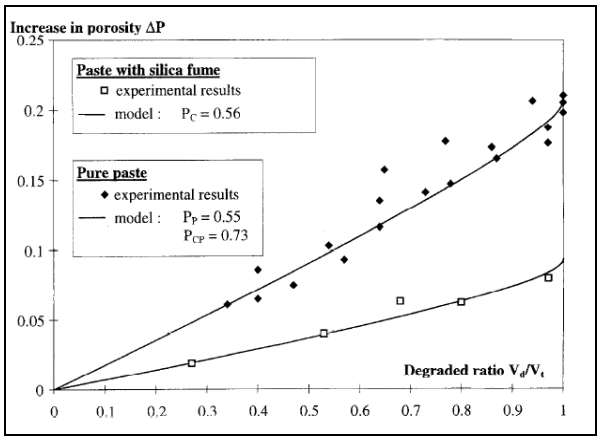

Fig. A.7.1 Increase in porosity as a function of degradation ratio (Carde and and Frarqois, 1999)

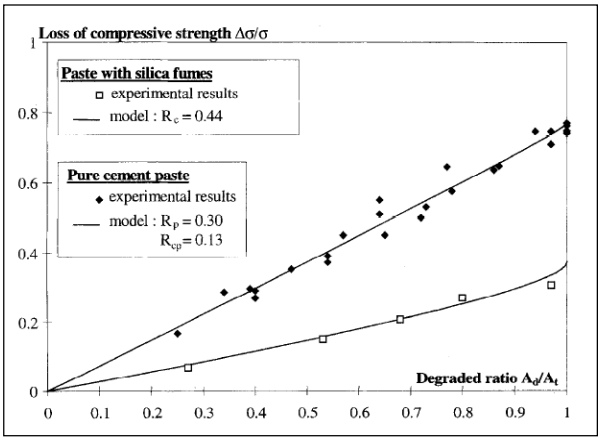

Fig. A.7.2 Loss of compressive strength as a function of degradation ratio (Carde and and Frarqois, 1999)

Diffusion-based approach is one of the methods frequently used in modeling cement degradation. Buil and Revertegat (1992) presented a model for pure water and lime solutions to predict long-term cement degradation. The deterioration of cement is modeled by ionic diffusion in the cement pore coupled with mass exchange between the solid and the aqueous phases. The model only considers portlandite and C-S-H as the solid phases. It assumes: i) an exchange of matter between the aqueous interstitial solution and the solid phases (dissolution and precipitation); and ii) transport of the species in solution through the pores of the cement. The model predicts the existence of an undamaged core, portlandite dissolution front and a progressive C-S-H decalcification zone. The model predictions and degradation measurements shows a satisfactory agreement (Fig. A.7.3). The model requires measurable input parameters such as porosity, calcium and portlandite contents, and diffusion coefficient.

Reactive transport modeling approach has the potential to provide reasonable predictions of cement degradation. Different reactive transport models have been presented recently. Carey and Lichtner (2007) developed a model that incorporates solid solutions into equations describing reactive transport in porous material to express cement degradation. In order to complete the model, a thermodynamic module for C-S-H was developed from experimental measurements. The model is used to predict decalcification of C-S-H and carbonation mechanisms. The model successfully predicted the degradation of wellbore cement.

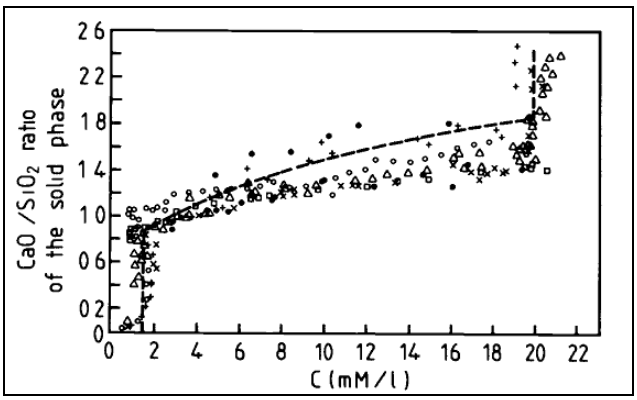

Fig. A.7.3 CaO/SiO_2 ratio vs. calcium concentration (Buil and Revertegat, 1992)

Samson and Marchand (2007) presented a multi-ionic transport model to describe the degradation of cement exposed to aggressive environments. The model uses a two steps procedure to obtain numerical solutions. First, the model solves the transport equations ignoring the effects of the chemical reactions. The concentration profile of each ionic species is determined considering diffusion, electrical coupling between the ions, chemical activity effects and advection caused by a capillary suction flow. Then, the effects of the chemical reactions are incorporated to satisfy the equilibrium conditions between the pore solution and reactive cement components.

More recently, a multi-scale homogenization model (Stora et al., 2010) has been developed to predict change in cement composition, flow and mechanical properties inside a concrete material subjected to degradation and leaching. Simulation results obtained using the model provided more insight into the understanding of the interactions between damage and chemical deteriorations.

Leaching can be one of the degradation mechanisms that control the rate of deterioration of cement. A number of leaching-based cement degradation models (Bentz and Garboczi, 1992: Mainguy and Coussy 2000: Nakarai et al. 2006: Mainguy et al. 2000) have been developed to predict the change in chemical and mechanical properties occurring after exposure to harsh environment. Leaching occurs under any condition of temperature and pressure and with or without the presence of acidic gases. As a result, leaching models are applied to predict the life of cement in different industrial applications.

A.7.2. Cement Leaching Model

Leaching-based models generally represent the dissolution process of portlandite ($Ca(OH)_2$) and decalcification of calcium silicate hydrates (C–S–Hs). They incorporate: i) ionic transfer occurring between the external water and pore solution; ii) the interaction between pore fluid and cement matrix; iii) chemical species transport in the cement pores; and iv) models that relates the variation in mechanical properties of cement to the change in physical and chemical properties occurring due to degradation.

This report presents a new cement leaching model developed to predict the degradation depth, relative compressive strength, porosity, and permeability of well cement as a function of time, temperature, CO_2 pressure, pH, corrosive solution chemistry (i.e. NaCl concentration), water/cement ratio, paste diameter, and cement class. Fig. A.7.4 shows the formulation and numerical algorithm of the model.

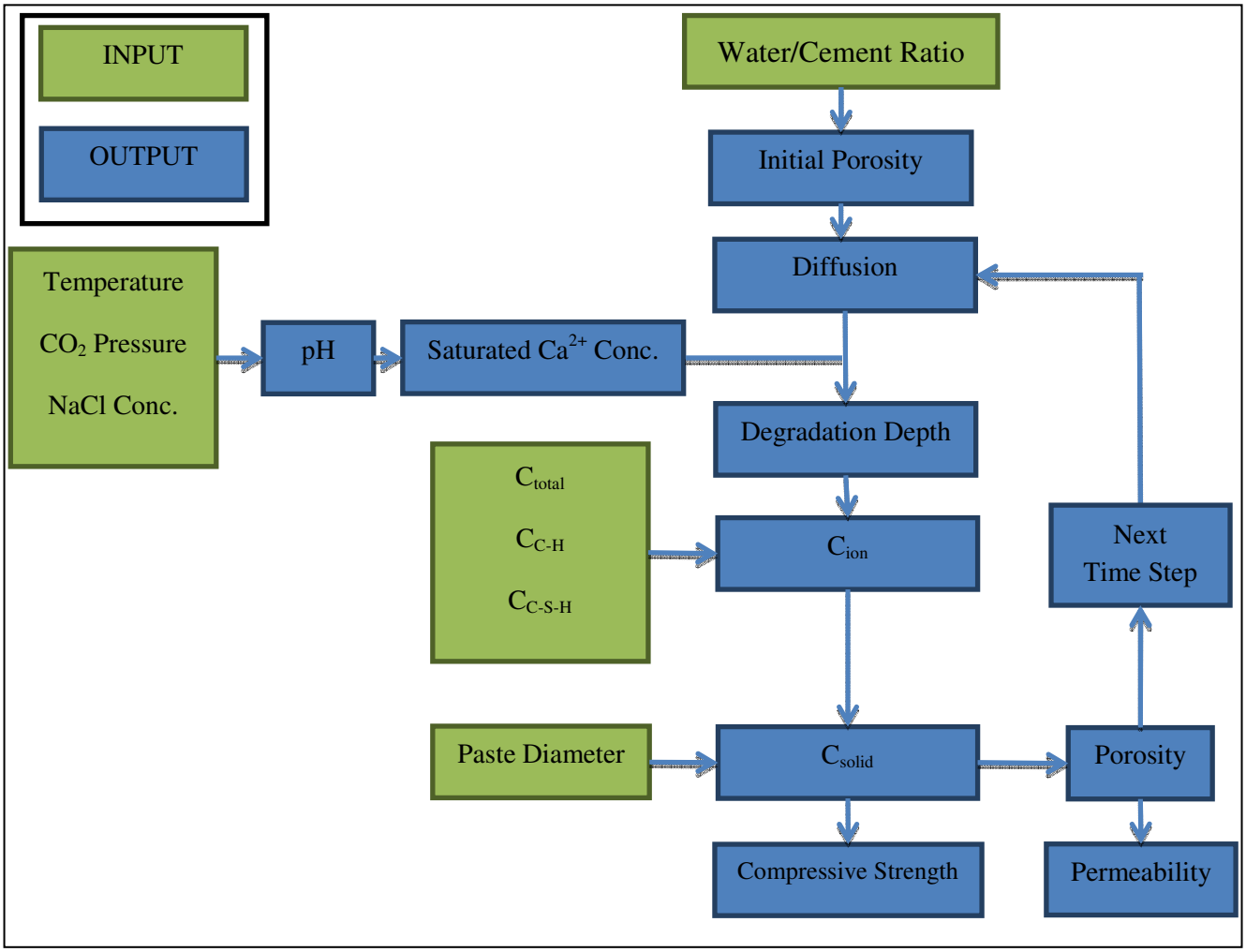

Fig. A.7.4 Algorithm of cement leaching model

In order to formulate a general cement leaching model, first, a simplified model, which is valid for brine solutions has been develop following the method established by Mainguy and Coussy (2000). Then, the model is improved to predict the leaching process in CO_2 saturated brine systems.

A.7.2.1. Leaching Model for Cement in Salt Solutions

Using the cement leaching model, mechanical properties of cement can be predicted by knowing the degradation thickness and calcium ion concentration profile in the solid phase of cement. Therefore, degradation depth of cement has to be predicted first. Degradation depth of cement can be determined using Eq. (7) which is the analytical solution of the governing equation presented by Mainguy and Coussy (2000). Accordingly, the solution for the cement degradation depth for 1D diffusion-dissolution problem can be obtained by solving the mass balance equation, diffusion equation (Transport law of the solute through the porous medium),

equilibrium equation (Law governing the kinetics of dissolution), and jump condition (i.e. initial condition at the time of exposure).

$$\varepsilon\, exp\left(-\xi_d^2\right) = \sqrt{\pi}\xi_d erf\ (\xi_d) \quad (7.1)$$

where dimensionless quantities in the previous equations are defined as:

$$\xi = \frac{\mathrm{x}}{2\sqrt{\mathrm{Dt}}} \quad (7.2)$$

$$\varepsilon = \frac{\emptyset C_{satu}}{\mathrm{C_{total}}} \quad (7.3)$$

where $\emptyset$ is porosity at any time and location. $\mathrm{C_{total}}$ is the total concentration of the calcium in solid form which is defined as a summation of the amount of calcium in the solid phase of the C-S-H gel (mmol/l) and the amount of calcium in the solid phase of calcium hydroxide (mmol/l). The porosity at any time and position is given by the following expression (Lund and Fogler, 1976):

$$\emptyset = \emptyset_o + (1 - \emptyset_o)(W_o - W)\frac{M_F}{\rho_s} \quad (7.4)$$

where $\emptyset_o$ and $W_o$are initial porosity and calcium concentration (mol/L), respectively. W is calcium concentration at any time and location (mol/L). M_F is average molecular weight of calcium (40.0 g/mol), and ρ_s is cement density. The initial porosity can be calculated using Eq. (7.5) as a function of water to cement ratio applying the correlation developed by Haga et al. (2005):

$$\emptyset_o = 40.18 \times Ln\left(\frac{w}{c}\right) + 59.15 \quad (7.5)$$

where w/c is the water/cement ratio.

Initial calcium concentration is the total calcium concentration from two difference sources: calcium hydroxide (CH) and calcium silicate hydrate (CSH). The initial concentrations of CH and CSH can be predicted using a cement hydration model such as the model developed by Lin and Meyer (2009), which is presented in section A.8 of this report. Calculation of calcium concentration at any time, any location will be explained later by equations 7.29 through 7.31. Calcium concentration in the solid phase decreases with time. Therefore, according to Eq.

(7.4), porosity increases with time. Fig. A.7.5 shows the porosity profile as a function of time at two different locations (close to the outer surface and close to the degradation depth) on the set cement. Low porosities are expected in areas close to the degradation depth and high porosity is expected on the outer surface of the cement.

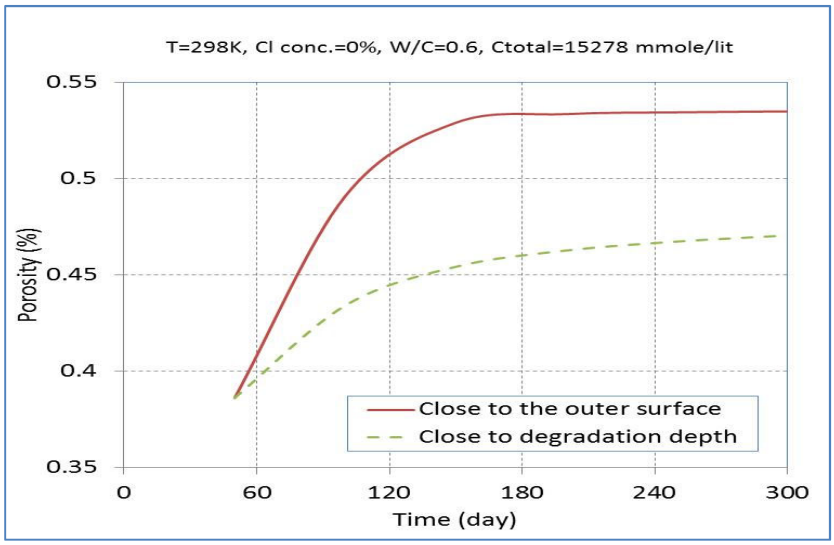

Fig. A.7.5 Porosity as a function of time for two different locations on the cement specimen: Close to the surface and close to the degradation depth

The diffusion rate of calcium ion in porous cement can be calculated as:

$$\mathrm{D}\ (\mathrm{m}^2/\mathrm{s}) = 2.35 \times 10^{-13} \exp(9.95\ \emptyset) \quad \text{(7.6)}$$

where D is the diffusion coefficient. The leaching depth is calculated from the dimensionless distance obtained from Eq. (7.7) as:

$$x_d = 2\xi_d\sqrt{Dt} \quad \text{(7.7)}$$

Unknowns in Eq.7.7 are porosity, C_{satu}, and C_{total}. However, C_{satu} can be predicted as a function of temperature and chloride concentration based on the correlation suggested by Nakarai et al. (2006).

$$C_{satu} = \frac{1}{2}\sqrt[3]{2K_{sp}} \quad \text{(7.8)}$$

The solubility product of the cement, K_{sp}, is a function of chloride ion concentration and temperature. Thus, the solubility product is expressed as the sum of two functions.

$$K_{sp} = K_{sp}^{T} + K_{sp}^{Cl} \quad \text{(7.9)}$$

where K_{sp}^{T} is the solubility product of calcium hydroxide considering the effect of temperature ($mmol^3/L^3$) andK_{sp}^{Cl} is the solubility product of $Ca(OH)_2$ considering the effect of sodium chloride. For temperature effect, the solubility is calculated as:

$$K_{sp}^{T} = 0.0125 \times 10^{9}.e^{-0.019T} \quad \text{(7.10)}$$

where T is the absolute temperature (K). The solubility product due to sodium chloride effect is predicted as:

$$K_{sp}^{Cl} = A^{'}.(5 \times 10^{4}.\sqrt[3]{Cl}) \quad \text{(7.11)}$$

$$A^{'} = \begin{cases} -2Cl^3 + 3Cl^2 (0.0 \le Cl \le 1.0) \\ 1 \qquad\qquad\qquad (1.0 < Cl) \end{cases} \quad \text{(7.12)}$$

Nakarai et al. (2006) compared the predictions of the above method with experimental data. Results showed a good agreement (Fig. A.7.6).

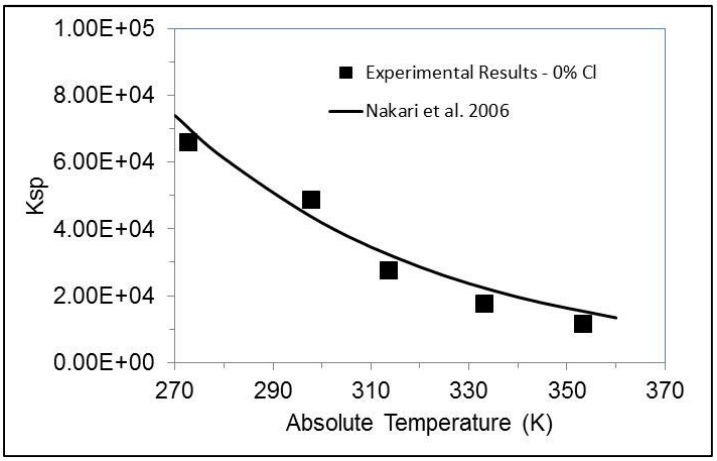

Fig. A.7.6 Ksp calculation and experimental measurement were compared with the graph presented in a paper by Nakarai et al. (2006)

Applying the leaching model, the effects of chloride concentration and temperature on the degradation depth was investigated. C_{total} was assumed to be 15278 mmol/L based on the available literature data (Gerard et al. 2002) and degradation depths were calculated as a function of time for different temperature and NaCl concentrations (Fig. A.7.7). Degradation depth calculated using this technique for brine solution without CO_2 is shown in Fig. A.7.7.

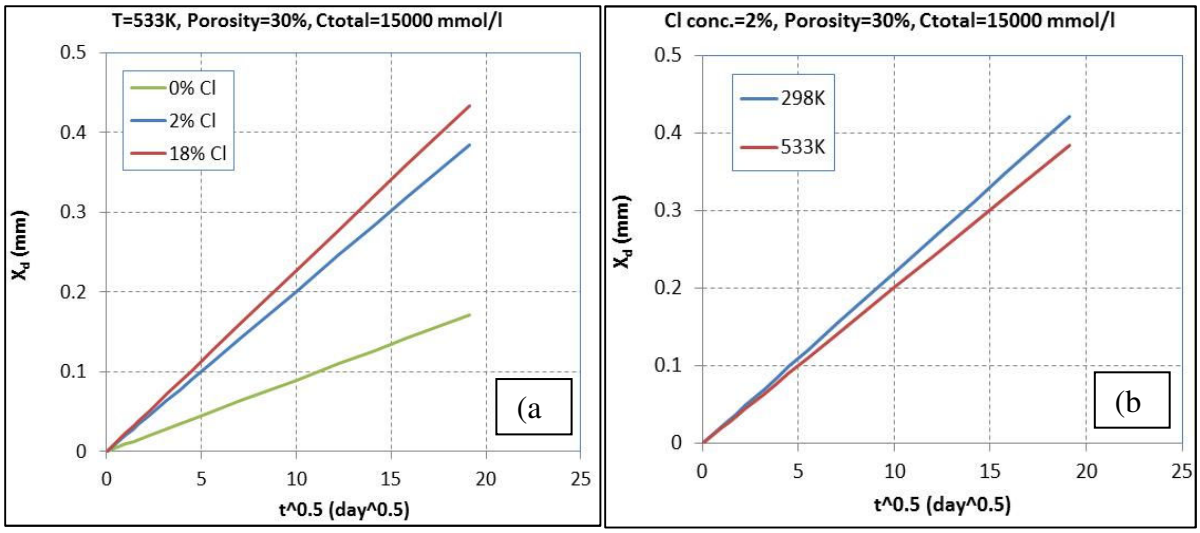

Fig. A.7.7 Degradation depth vs. square root of time at different: a) chloride concentrations; b) temperatures

Increasing the temperature and also decreasing the chloride concentration reduces the degradation rate by decreasing the solubility product (K_{sp}). Corrosive gases (H_2S and CO_2) can be also accelerating the leaching process and increase the degradation rate by increasing the solubility of calcium to the liquid phase. Mainguy and Coussy (2000) used ammonium nitrate to accelerate the leaching process. Ammonium nitrate accelerates the leaching process by increasing the equilibrium calcium saturation concentration (C_{satu}) in the liquid phase (Fig. A.7.8). Higher equilibrium calcium saturation concentration means more calcium can be dissolved in the liquid phase and therefore calcium leaching process will be faster.

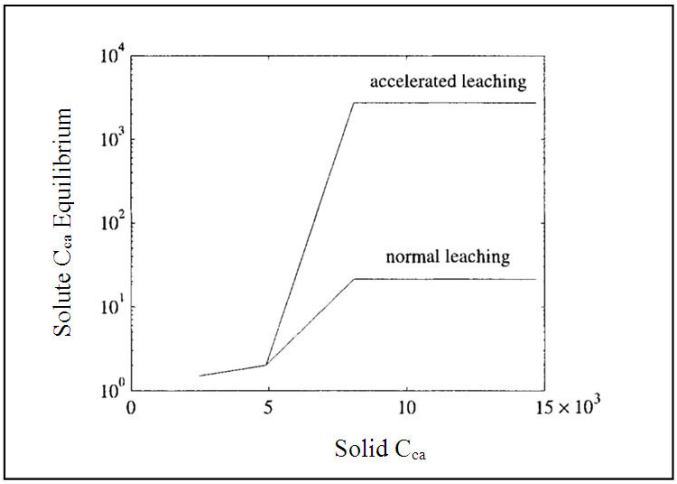

Fig. A.7.8 Solid calcium concentration versus solute calcium concentration at equilibrium

In general, leaching in CO_2 saturated solutions has three main steps: i) dissolution of calcium ion from the solid phase to the liquid phase in porosity; ii) porous media diffusion of calcium ion from liquid phase in porosity to the bulk solution; and iii) porous media diffusion of CO_2 from the bulk solution to the liquid phase of porosity.

Dissolution rate of calcium ion from solid phase to the liquid phase in porous material is a function of solubility product (K_{sp}) of calcium ion in the pore fluid/solution. K_{sp} is also a function of chemistry of the pore solution and temperature. Increasing the chloride concentration and decreasing the temperature increases the K_{sp} and consequently increases the solubility of calcium ion. Therefore, degradation rate of the cement increases by increasing the chloride concentration and decreasing the temperature and consequently mechanical properties and permeability of the cement decreases.

The second step in leaching process is the diffusion of calcium ion from the pore space to the bulk solution. The transport process is diffusion in porous media; and hence, diffusivity coefficient valid for porous media has to be applied in the modeling. The diffusion and dissolution processes occur in series (Fig. A.7.9) and the slower process controls the leaching rate. Therefore, the rate of diffusion of calcium ion from porosity to the bulk solution, rate of diffusion of CO_2 from bulk solution to the porosity or dissolution rate of calcium can be the controlling step in the leaching process.

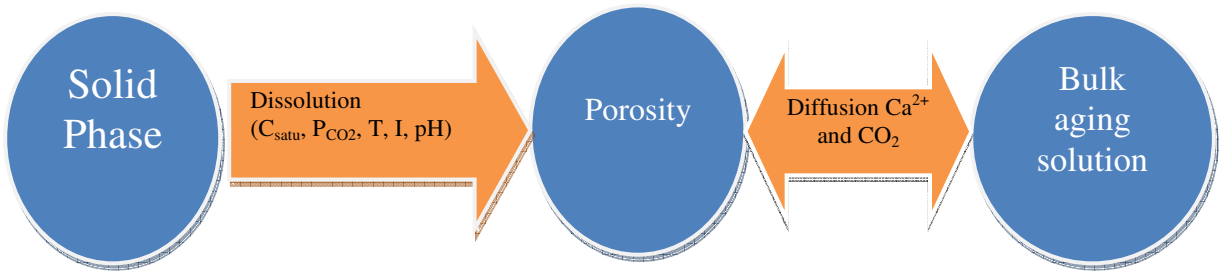

Fig. A.7.9 Reactions controlling the leaching process

Before exposing the cement to the aggressive environment, concentration of calcium ions in the solid phase is C_{total} and the pore fluid is saturated with calcium ions because if it was not saturated, calcium would dissolve to the pore fluid. After exposure, leaching starts and calcium concentration in pore fluid decreases because some of the calcium diffuses from the pore to the bulk solution. At the same time, concentration of calcium in the solid phases decreases because calcium concentration in pore fluid is less than saturation and this results in dissolution of calcium.

A.7.2.2. Leaching Model for Cement Exposed to Brine Saturated with CO_2 gas

Adding CO_2 to the system affects the leaching process by changing the calcium saturation concentration in the liquid phase of cement. All the chemical reactions during CO_2 attack have to be included in the calculation of calcium ion saturation concentration. The following is a

systematic approach to calculate the solubility of calcium carbonate and calcium saturation concentration.

I. Dissociation and Dissolution Reactions Involved:

$$CaCO_{3(s)} \overset{K_{sp}}{\leftrightarrow} Ca^{2+} + CO_3^{2-} \Rightarrow K_{sp}^{*} = \frac{[Ca^{2+}].[CO_3^{2-}]}{1} \quad \text{.....(7.13)}$$

$$CO_{2(g)} \overset{K_H}{\leftrightarrow} CO_{2(aq)} \Rightarrow K_H = \frac{[CO_{2(aq)}]}{P_{CO_{2(g)}}} \quad \text{.....(7.14)}$$

$$CO_{2(aq)} + H_2O \overset{K_h}{\leftrightarrow} H_2CO_3 \Rightarrow K_h = \frac{[H_2CO_3]}{[CO_{2(aq)}]} \quad \text{.....(7.15)}$$

$$H_2CO_3 \overset{K_1}{\leftrightarrow} H^+ + HCO_3^- \Rightarrow K_1 = \frac{[H^+].[HCO_3^-]}{[H_2CO_3]} \quad \text{.....(7.16)}$$

$$HCO_3^- \overset{K_2}{\leftrightarrow} H^+ + CO_3^{2-} \Rightarrow K_2 = \frac{[H^+].[CO_3^{2-}]}{[HCO_3^-]} \quad \text{.....(7.17)}$$

$$H_2O \overset{K_w}{\leftrightarrow} H^+ + OH^- \Rightarrow K_w = \frac{[H^+].[OH^-]}{1} \quad \text{.....(7.18)}$$

II. Charge Balance

$$\sum_{i=1}^{n} Z_i C_i \Rightarrow \qquad 2[Ca^{2+}] + 3[H^+] - 4[CO_3^{2-}] - [OH^-] = 0 \quad \text{.....(7.19)}$$

The overall process can be describes as:

$$CaCO_3(s) + CO_2(g) + H_2O \leftrightarrow Ca^{2+}(aq) + HCO_3^-(aq) \quad \text{.....(7.20)}$$

By solving Eqs. (7.13) to (7.19), seven equations for seven unknowns, $[Ca^{2+}]$ at equilibrium can be determined. The equilibrium concentration (saturation concentration of calcium) represents the maximum quantity of calcium carbonate soluble in pore fluid:

$$C_{Satu} = [Ca^{2+}]_{max} = \frac{K_{sp}^{*} K_H}{K_h K_1 K_2} \frac{[H^+]^2}{P_{CO_2}} \quad \text{.....(7.21)}$$

where:

$$[H^+] = 10^{-pH} \quad \text{.....(7.22)}$$

Dissolution constant of calcium carbonate is determined as:

$$K_{sp}^{*} = \frac{[Ca^{2+}].[CO_3^{2-}]}{1} = 6 \times 10^{-9} \ldots\ldots\ldots\

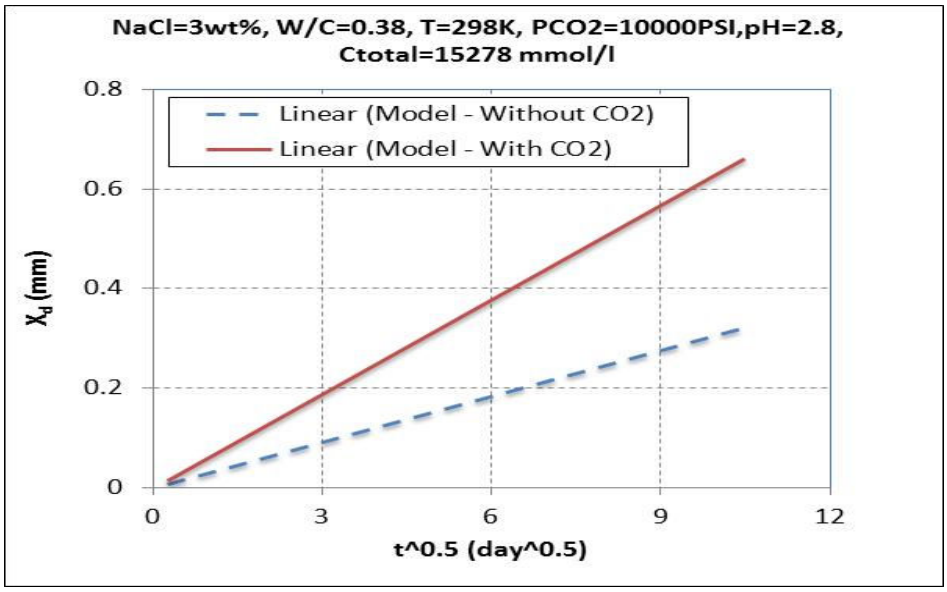

Fig. A.7.10 Degradation depth vs. time with and without of the presence of CO_2

In addition to the partial pressure of CO_2, the pH of the surrounding liquid can affect the degradation depth of cement. Fig. A.7.11a shows that increasing the CO_2 pressure at a constant pH reduces the degradation depth of cement by reducing the saturation concentration of calcium ion. However, in real downhole conditions, the pressure increase can affect the pH of the liquid phase (as presented in Section 4.6.1) resulting in increased degradation depth. The pH of the liquid has considerably effect on the degradation rate of the cement (Fig. A.7.11b). Decreasing the pH of the solution (i.e. more acidic environment) increases the saturation concentration of calcium ion and consequently increases the degradation depth.

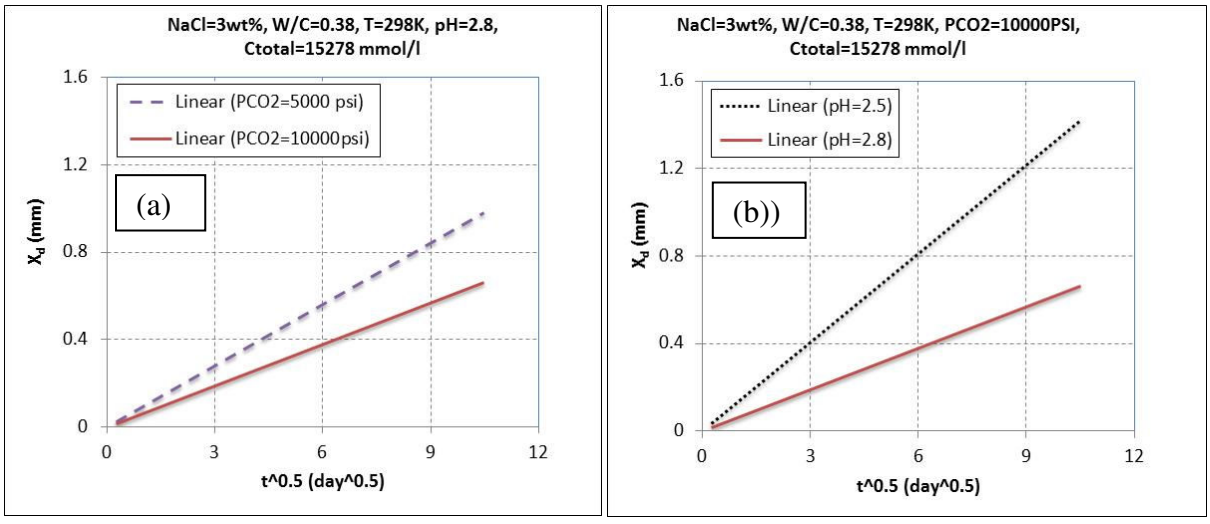

Fig. A.7.11 Degradation depth vs. square root of time at different: a) CO_2 pressures; and b) pH of the surrounding liquid

As it mentioned earlier, mechanical properties of cement can be predicted by knowing the calcium ion concentration profile in the solid phase of cement. Calcium ion concentration in liquid phase of cement has to be predicted first in order to predict the calcium concentration profile in the solid phase. Calcium ion concentration profile in the liquid phase can be calculated using Eq (7.28).

$$\overline{C_{ion}} = \begin{cases} \frac{C_{ion}}{C_{satu}} = \frac{\mathrm{erf}(\xi)}{\mathrm{erf}(\xi_d)} & 0 \le \xi \le \xi_d \\ 1 & \xi_d \le \xi \end{cases} \quad \text{..... (7.28)}$$

Fig. A.7.12 shows the effect of temperature and chloride concentration on calcium ion concentration in the surrounding liquid. The degradation depth and calcium ion concentration in the liquid phase increase when salt is added to the aging solution. However, increasing the temperature decreases the degradation depth of the cement and also calcium ion concentration in the liquid phase.

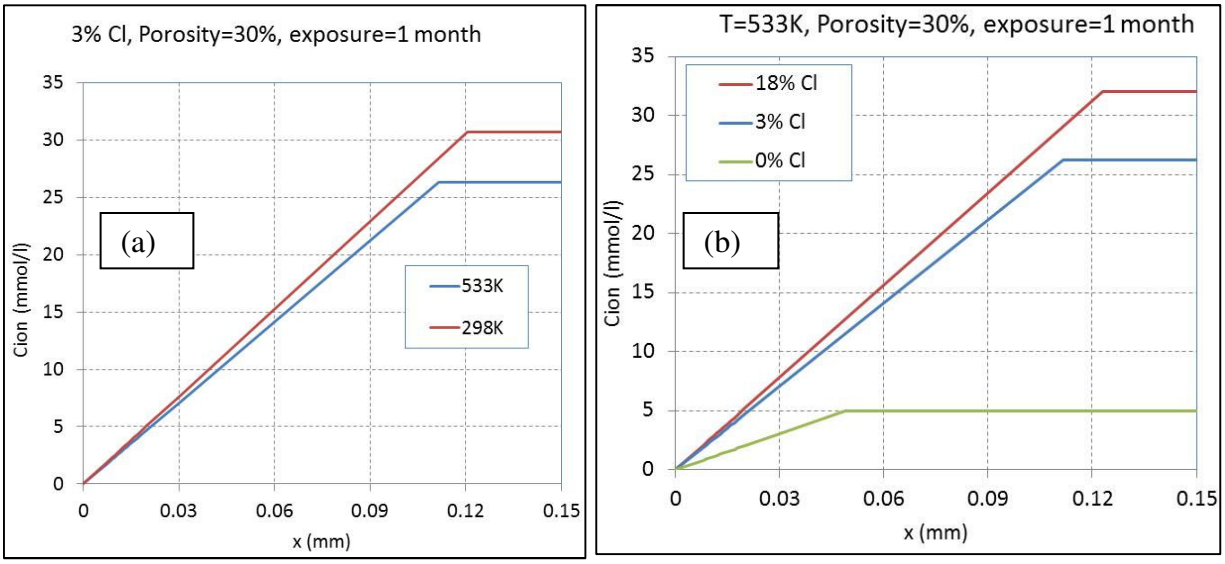

Fig. A.7.12 Calcium ion concentration profiles in degraded cement at different: a) temperatures; and b) chloride concentrations

Equilibrium calcium concentration in the solid phase (Fig. A.7.13) of the cement can be calculated using solid-liquid equilibrium model (Eq.7.29) developed by Nakarai et al. (2006). Calcium ion concentration profile in the liquid phase should be predicted first to determine the equilibrium concentration in the solid phase.

$$C_{solid} = f(C_{ion}) = A.\left\{C_{CSH}.\left(\frac{C_{ion}}{C_{satu}}\right)^{1/3}\right\} + B \quad \text{..... (7.29)}$$

$$A = \begin{cases} -\frac{2}{x_1^3} C_{ion}^3 + \frac{3}{x_1^2} C_{ion}^2 (0.0 \leq C_{ion} \leq x_1) \\ 1 \qquad\qquad (x_1 < C_{ion}) \end{cases} \quad \text{..... (7.30)}$$

$$B = \begin{cases} 0 \qquad\qquad (0.0 \leq C_{ion} \leq x_2) \\ \frac{C_{CH}}{(C_{satu} - x_2)^3} (C_{ion} - x_2)^3 \qquad (x_2 < C_{ion}) \end{cases} \quad \text{..... (7.31)}$$

where C_{solid} is the total calcium concentration in solid phase in mmol/L. C_{CH} is the amount of calcium present in the solid phase in the form of calcium hydroxide (mmol/L). C_{CSH} is the amount of calcium present in the solid phase in the form of C-S-H gel (mmol/L). X_1 is the liquid phase calcium ion concentration when the rapid transition of C-S-H gel into silica gel begins (mmol/L) and X_2 is the liquid phase calcium ion concentration when the calcium hydroxide has completely dissolved and the dissolution of C-S-H gel begins (mmol/L). C_{CSH} and C_{CH} obtained from available data by Gerard et al. (2002). Two different sets of X_1 and X_2 were obtained from the literature (Table A.7.1)

Table A.7.1 Published valuesX_1 and X_2

	Gerard et al. (2002)	Nakarai et al. (2006)
X_1	3	2
X_2	19	C_{satu}-2.99

Eqs (7.29) through (7.31) have been applied using input parameters presented in Gerard et al. (2002). In Fig. A.7.14, the calcium concentration in solid phase is plotted as a function of calcium ions in the liquid.

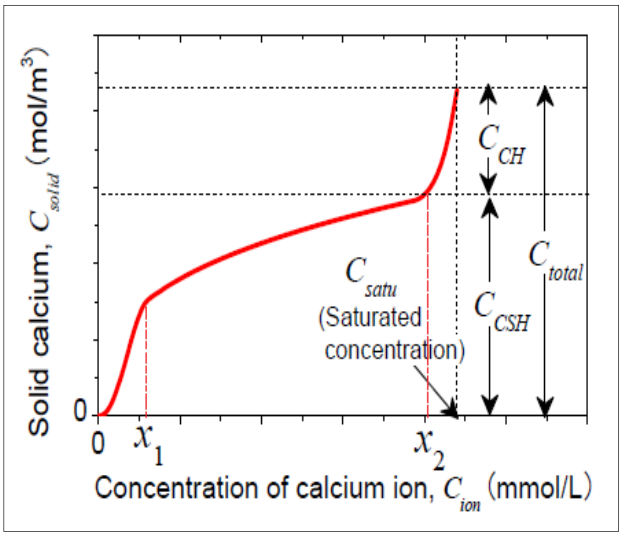

Fig. A.7.13 Solid-liquid equilibrium distribution for calcium (Nakarai et al., 2006)

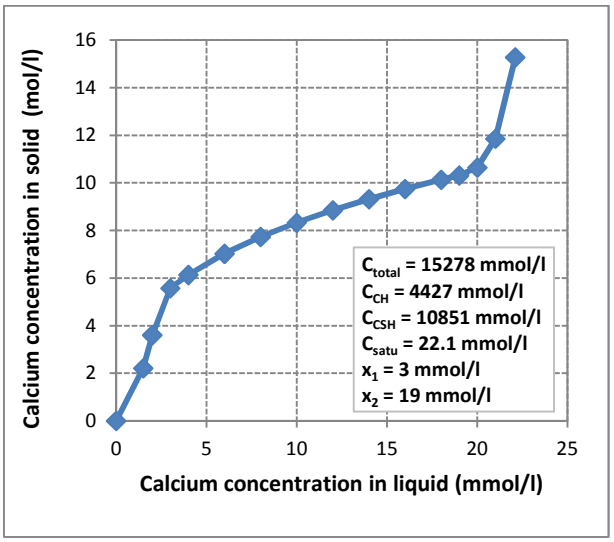

Fig. A.7.14 Solid-liquid equilibrium distribution for calcium using input data from Gerard et al. (2002)

Prediction of calcium concentration profile in the solid phase of cement as a function of chloride concentration in the bulk fluid using two different sets of X_1 and X_2 are shown in Figs A.7.15 and A.7.16. Fig. A.7.15 which is based on X_1 and X_2 values proposed by the Gerard et al. (2002) shows that at chloride concentrations lower than 1%, calcium concentration in the sound (undegraded) zone is equal to the calcium concentration in CSH which means that CH is leached out completely in the sound zone. Therefore, X_2 assumption is wrong. However, when we apply the X_1 and X_2 values proposed by Nakarai et al. (2006) the result (Fig. A.7.16) show that calcium concentration in the sound zone for all the chloride concentrations is equal to total calcium concentration. The model predictions show that the X_1 and X_2 values proposed by Nakarai et al. (2006) are more realistic. It is also important to note that the impact of chloride concentration on the degradation depth considerable when the chloride concentration is less than 1%. Increasing the chloride concentration more than 1% slightly increases the degradation depth.

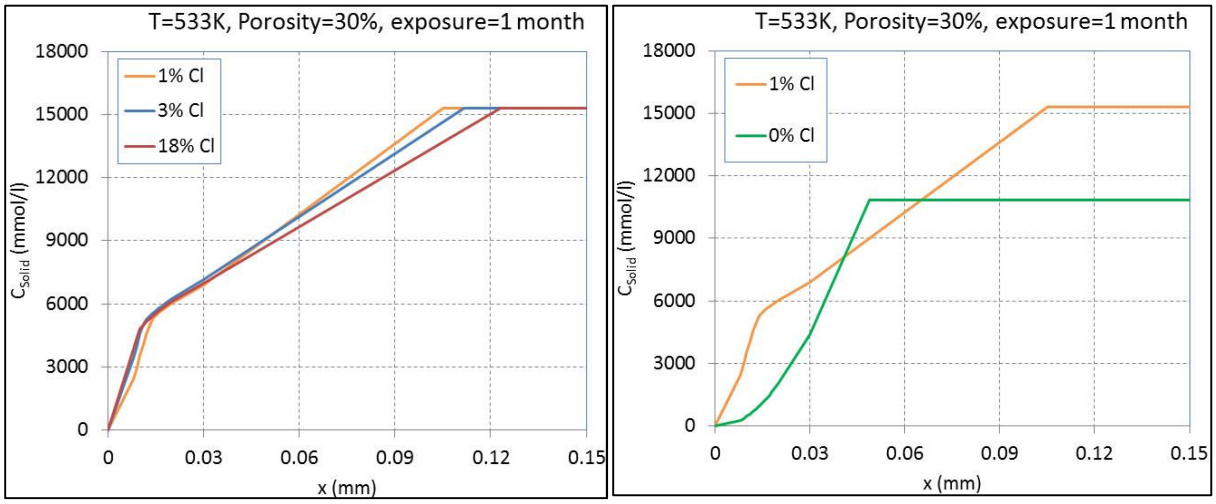

Fig. A.7.15 Calcium concentration in the solid phase of cement as a function of chloride concentration using X_1=3 and X_2=19

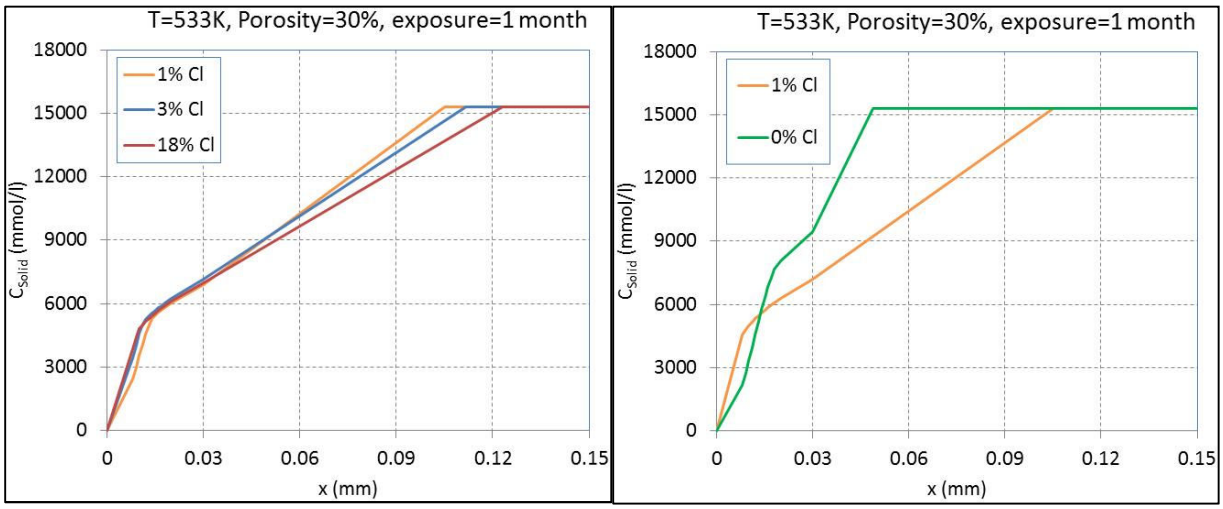

Fig. A.7.16 Calcium concentration in the solid phase of cement as a function of chloride concentration using X_1=2 and X_2=C_{satu}-2.99

A.7.2.3. Modeling the Mechanical Properties of Cement

In order to model the mechanical properties of the cement, first the leaching process and acid attack have to be modeled. Carde et al. (1996) showed that relative loss of average strength can be calculated using Eq. (7.32).

$$\frac{\Delta F}{F} = \frac{F_T - F_d}{F_T} = 1 - \frac{1}{r^2}\left[\left(\frac{1-R_c}{3}\right).x_d^2 + r.(R_c - 1)x_d + r^2\right] \quad \text{(7.32)}$$

where r is the radius of specimen, X_d is the degradation depth, and R_c is a constant which was calculated by Carde et al. (1996) by fitting the model to the experimental data (R_c=0.44). R_c is defined by Eq (7.33) and Fig. A.7.17.

$$R_C = \frac{\sigma_{T-C}}{\sigma_T} \quad \text{(7.33)}$$

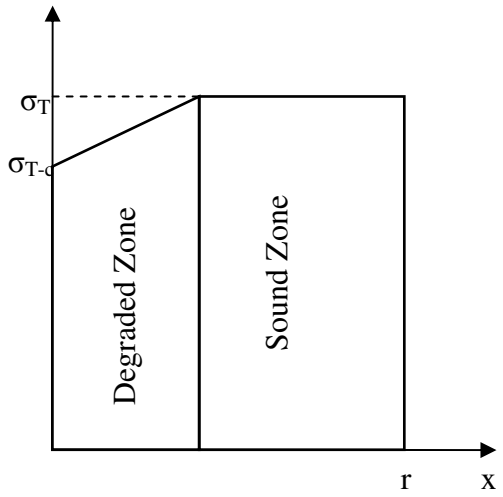

Fig. A.7.17 Compressive strength profile of aged cement specimen

The proposed approach in this research is calculating R_c using calcium concentration profile in the solid phase of the cement since calcium leaching represent the loss in mechanical properties. Therefore, calcium in the solid phase was used to calculate the R_c using Eq. 7.34 and Fig. A.7.18. For example, R_c in different Cl^- concentration solution using Fig. A.7.17 is about 0.3. In this case, compressive strength profile of the cement can be calculated in this case using Eq. (40).

$$R_C = \frac{C_{Surface}}{C_{Total}} \quad \text{(7.34)}$$

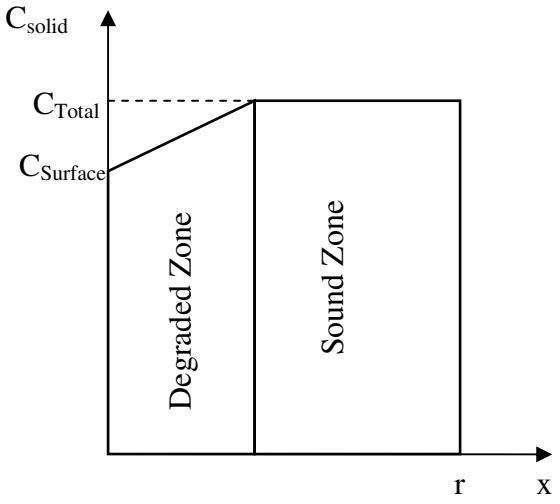

Fig. A.7.18 Calcium concentration profile in the solid phase of aged cement specimen

The following procedure is applied to predict the strength loss as a function of level of degradation:

Step 1: Use mass balance equation to calculate the calcium concentration in the liquid phase and degradation depth:

i. Calcium saturation concentration in pore fluid has to be determined
ii. Solubility product of $Ca(OH)_2$, K_{sp}, needs to be computed.

Step 2: Apply the solid/liquid equilibrium to calculate the calcium concentration in the solid phase.

Step 3: Utilize the mechanical behavior model to predict the compressive strength loss.

Some sample mechanical properties predictions using this approach are shown in model validation part of this report.

A model for prediction of porosity is presented in Section 7.2.1. Accordingly, the change in porosity during the aging process is a function of initial porosity, total calcium concentration, calcium concentration profile as a function of time during leaching process, and cement matrix density. Initial porosity is only a function of water to cement ratio. Therefore, cement porosity can be predicted as a function of exposure time. Cement porosity model is imbedded in the cement leaching model and explained in previous section because leaching increases the porosity and porosity also increasing the leaching rate as a function of exposure time.

As reviewed by Breysse and Gerard (1997), different approaches have been suggested in the literature for relating porosity and permeability. Phenomenological models relate the permeability to other parameters based on physical concept and observations obtained from

experiments and/or numerical simulations. The following phenomenological models have been presented in the literature:

I. Danyushevsky and Djabarov, (1973) suggested this simple correlation for calculating the permeability.

$$\text{Permeability}=(\text{Porosity})^{4.75} \quad \text{..... (7.35)}$$

II. Metha and Manmohan (1980) suggested the following correlation for predicting the permeability.

$$K = \exp\left(3.84V_1 + 0.2V_2 + 0.56 \times 10^{-6}TD + 8.09MTP - 2.53\right) \quad \text{..... (7.36)}$$

where K is permeability constant, V_1 and V_2 are volumes of two classes of pores, TD is threshold diameter, and MTP is modified total porosity.

III. Breysse and Gerard, (1997) also suggested that the porosity can be correlated to the experimental permeability by assuming a power function under the form $K_{exp}=a.\Phi^b$, a linear relation can be established in a log-log diagram. The following relation was suggested for cement paste:

$$Ln\left(K_{exp}\right) = -5.39 + 14.73\left(\frac{w}{c}\right) \qquad (r^2 = 0.79) \quad \text{.....(7.37)}$$

IV. Ghabezloo et al. (2009)

$$K = 1.20 \times 10^{-19}\left(\frac{\emptyset_F}{0.26}\right)^{11} \quad \text{.....(7.38)}$$

where K is permeability coefficient (m^2), and Φ_F is porosity filled by fluid.

In this investigation, Ghabezloo et al. (2009) empirical correlation is used to predict the cement permeability.

A.7.2.4. Validation of Model Predictions

Model presented in Section 7.2.2 is able to predict the degradation depth, mechanical properties, porosity, and permeability of cement exposed to harsh downhole conditions. This

model accounts for different variables including: temperature, pressure, acidic gas content, NaCl concentration, water-cement ratio, and initial porosity, permeability, and compressive strength. The model is able to predict the pH of the aging fluid as a function of acidic gas content, pressure, temperature, and ionic strength. Initial porosity of the cement paste is estimated using the water-cement ratio. Figure A.7.19 compares model predicted and measured cement degradation depths as a function of square root of time for cement aged in CO_2 saturated brine. In spite of some discrepancies, predicted degradation depth shows good agreement with the general trend of experimental data points. Therefore, test durations for aging experiments in CO_2 saturated brine solution can be determined using the model.

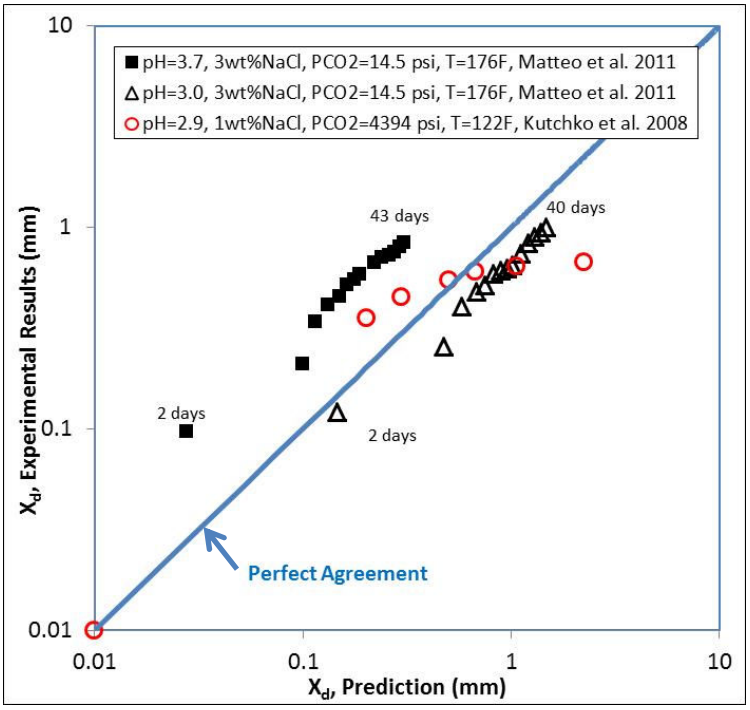

Fig. A.7.19 Comparison between degradation depth experimental data and model prediction for class H cement exposed to CO_2 environment at different pH, CO_2 pressures and temperatures

Prediction of mechanical properties of oil well cement is an important area of concern in the industry. Calcium concentration profile in solid phase predicted by leaching model was used to predict the reduction of compressive strength of the cement because of exposure to harsh condition. The mechanical properties prediction model, developed by Carde and Frarqois (1999), has been improved by calculating the constant R_c based on calcium concentration profile in the solid phase. The improved model is implemented into the leaching model proposed in this research. Prediction of mechanical properties using the improved model showed good agreement with experimental data by Carde and Frarqois, 1999 (Fig. A.7.20).

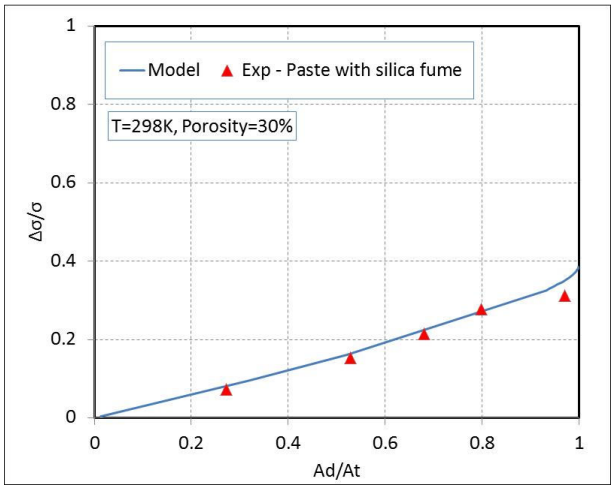

Fig. A.7.20 Comparison between prediction and experimental results for strength loss as a function of degraded area at T=298K and 30% porosity

Proposed model was used to predict the degradation depth of the cement and prepare a test matrix for future laboratory experiments. Degradation depth was predicted at two different temperatures (200°F and 400°F), total pressure of 10,000 psi, CO_2 partial pressure of 1000, and 3000 psi, and two different brine solution containing 5 and 15% NaCl by weight. Specimen diameter of 7/8 inches and specimen length of 2 inches were also considered for initial condition of prediction.

Cement degradation is strongly influenced by the composition of the surrounding fluid (both liquid and gas phases). Carbon dioxide content of the gas phase can be critically affected the degradation behavior of well cement. Fig. A.7.21 shows the prediction of well cement degradation depth as a function of square root of time at total pressure of 10,000 psi, 5% (by weight) NaCl, temperature of 200°F, water to cement ratio of 0.38, and two different CO_2 pressure of 1000 and 3000 psi. pH of the aging solution was predicted using the pH prediction model presented in Section 4.6.1. The pHs of the aging solution at CO_2 pressure of 1000 and 3000 psi were estimated to be about 3.18 and 2.98, respectively. Therefore, increasing the CO_2

pressure decreases the pH of the solution and makes it more acidic. Increasing either CO_2 pressure or pH of the aging solution decreases the calcium saturation concentration (Eq. 7.21) and consequently decreases the leaching rate and degradation depth; however, at the same time increasing the CO_2 pressure decreases the pH of the solution. In general, at a constant pH, increasing the CO_2 pressure decreases the degradation depth and at a constant CO_2 pressure, decreasing the pH increases the degradation depth. As shown in Fig. A.7.21, effect of increasing the CO_2 pressure for 1000 to 3000 psi is stronger than decreasing the pH from 3.18 to 2.98. Therefore, the general trend for the combination of these two effects is decreasing the degradation depth. The predicted degradation depth for cement under these conditions after 25 days is about 0.1 - 0.2 mm (Fig. A.7.21).

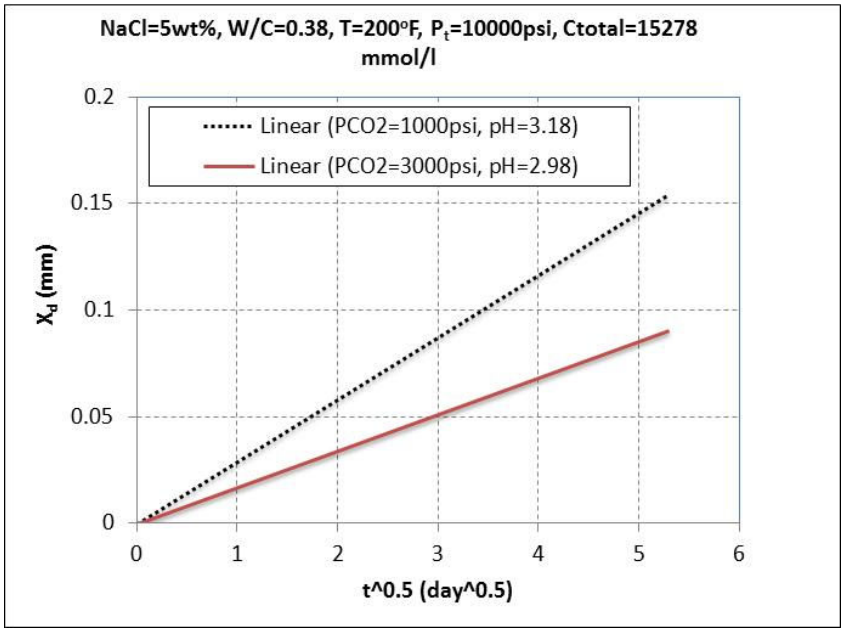

Fig. A.7.21 Predicted degradation depth a function of square root of time for two different CO_2 partial pressures

Borehole temperature has tremendous effect on the life of well cement. In addition to thermal retrogression, it can affect the gas solubility, pH of the aging fluid and degradation rate of the cement. Fig. A.7.22 shows the prediction of well cement degradation depth as a function of square root of time at total pressure of 10,000 psi, 5% NaCl by weight, CO_2 pressure of 1000 psi, water to cement ratio of 0.38, and two different temperatures (200 and 400°F). First, pHs of the aging solution were predicted at different temperatures (200°F and 400°F). Increasing the temperature increases the pH of the solution and makes the fluid less acidic. The effect of increasing the temperature in the range of 200 to 400°F on the first and second dissociation constants of carbonic acid (Eq. 7.24 and Eq. 7.25) is in the order of 10^{-16} and therefore negligible. Therefore, the major effect of raising temperature is increasing the pH of the aging

solution and consequently decreasing the calcium saturation concentration and degradation depth (Fig. A.7.22).

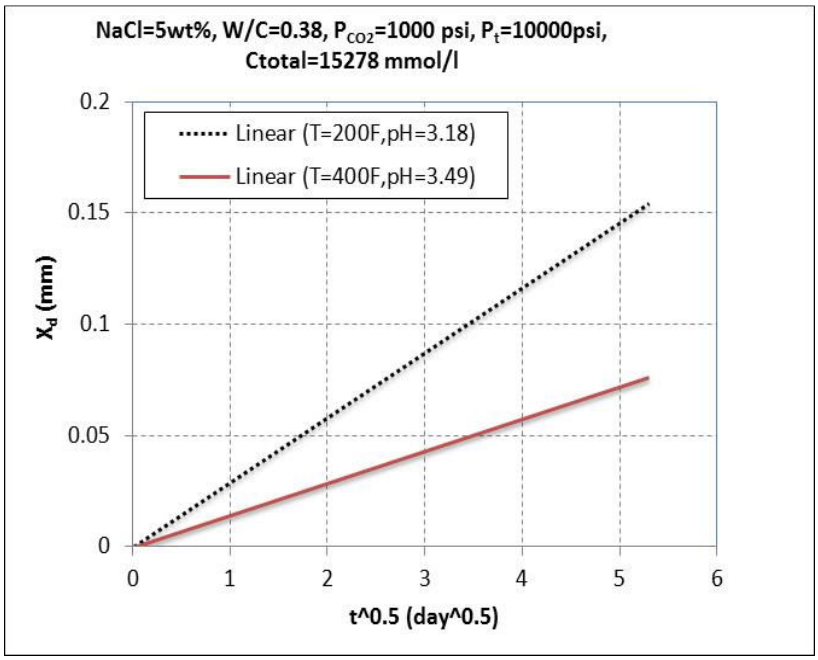

Fig. A.7.22 Predicted degradation depth as a function of square root of time for two different temperatures

In addition to temperature and particle pressure of CO_2, the salinity of the aging liquid has substantial effect on the depth of cement degradation. Fig. A.7.23 shows predicted degradation depth as a function of square root of time for two different NaCl concentrations (5 and 15% by weight). The pH of the aging solution is expected to vary slightly with salinity because of variations in gas solubility. Therefore, increasing the NaCl concentration shows the similar effect as temperature and increases the pH of the solution and makes it less acidic. Effect of NaCl concentration on CO_2 dissociation is also minor. Therefore, the predominate effect of increasing the NaCl concentration is change in solubility of CO_2 gas and consequently decreasing the calcium saturation concentration and degradation depth (Fig. A.7.23). Expected degradation depth for cement specimen under these conditions after 25 days is also about 0.1-0.15 mm (Fig. A.7.23).

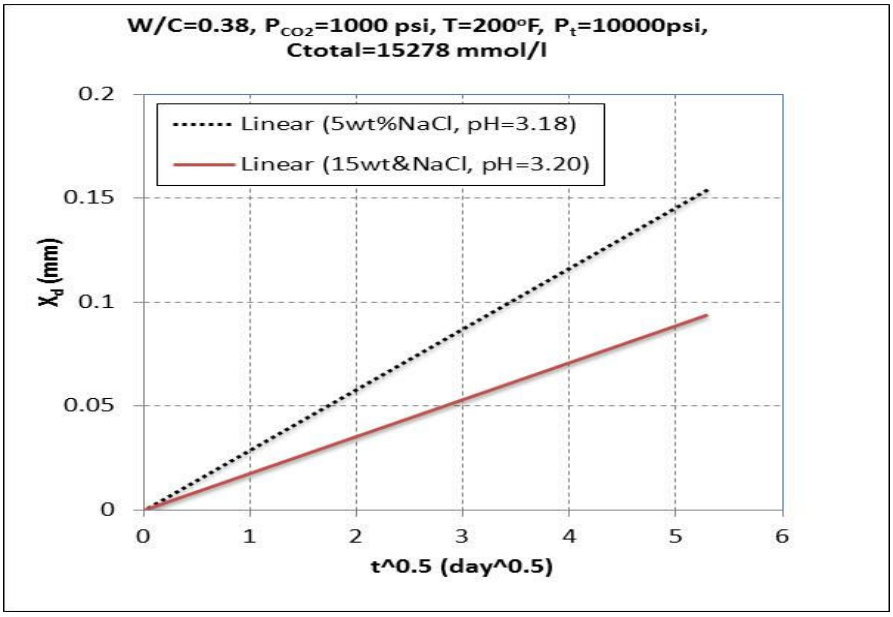

Fig. A.7.23 Predicted degradation depth as a function of square root of time for two different NaCl concentrations

A.8 Cement Hydration Model

As it mentioned earlier, the initial CH and CSH concentrations in cement are need for predicting the leaching rate, degradation depth, porosity, permeability, and mechanical properties of well cement. The degree of hydration of cement must be known in order to calculate the initial CH and CSH concentrations in cement. In this investigation, a model developed by Lin and Meyer (2009) was used to predict the hydration rate. The model predicts the degree hydration as a function of chemical composition of cement (i.e. C_3S, C_2S, C_3A, and C_4AF weight fraction), temperature, water-to-cement ratio, pressure, and fineness of cement. In Fig. A.8.1, model prediction results are compared with experimental results (Lerch and Ford, 1948).

Lin and Meyer, 2009 also discussed the effect of different parameter on hydration rate. Based on experimental data and model predictions, increasing the water-cement ratio also leads to a higher hydration rate after middle period of hydration, but only has a small effect on the hydration rate at early stages (Fig. A.8.2). A fine cement, or cement with a large surface area, provides a large contact area with water and hence causes a higher hydration rate (Fig. A.8.2). The effects of curing temperature on hydration kinetics have been shown to be twofold. On the one hand, the degree of hydration α increases with the increase in temperature (Fig. A.8.3). On the other hand, the density of hydration products at higher temperature is higher, which slows down the infiltration of free water through the hydration products. Therefore, during the late period, the hydration rate is lower at elevated temperature and the ultimate degree of hydration may thus be lower. The composition of cement is the most important factor of all.

Experimental results show that the four major clinker phases of cement (i.e. C_3S, C_2S, C_3A and C_4AF) have different reaction rates with water. It is well known that C_3A reaction is the fastest, followed by that of C_3S and the other two. However, whether the individual constituent phases hydrate independently from one another or at equal fraction rates is still not resolved. Because of different reaction rates of the clinker phases and their interactions, it is generally accepted that the so-called degree of hydration of cement is just an overall and approximate measure.

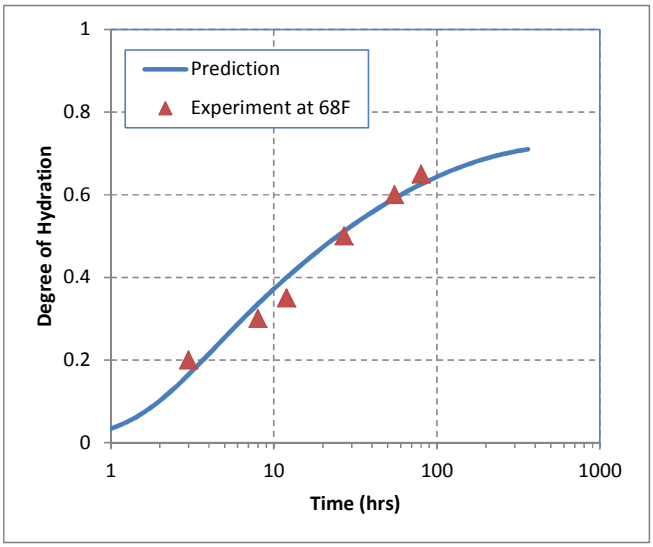

Fig. A.8.1 Degree of hydration as a function of time

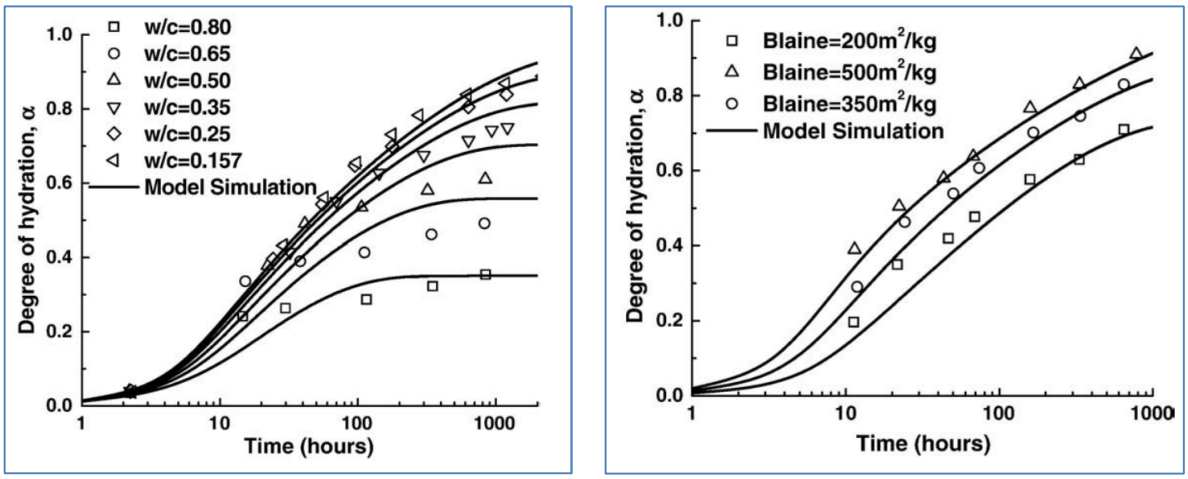

Fig. A.8.2 Effect of water-cement ratio and cement finenss on hydration rate (Lin and Meyer, 2009)

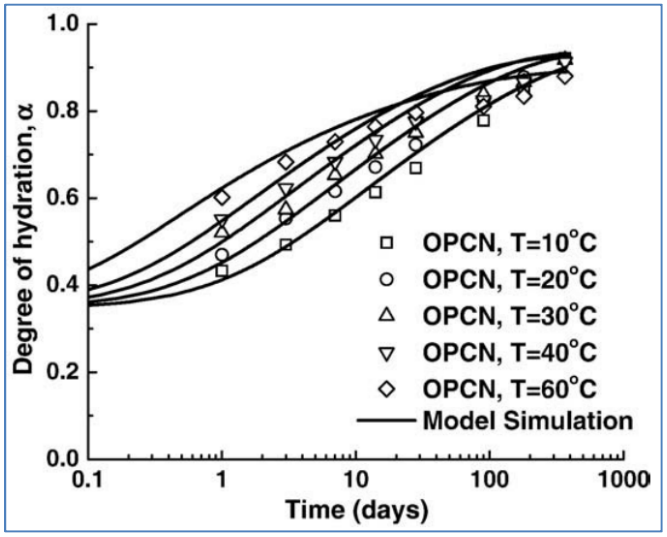

Fig. A.8.3 Effect of temperature on hydration rate (Lin and Meyer, 2009)

Appendix B: Summary of Published Data

Table B.1 Published measurements on cement degradation depth

Ref.	Cement Samples Information		Curing Information				Test Information			Ageing Time, Days	Degradation Depth, in
	Cement Type	Core Dimensions, in	Curing Temperature, °F	Curing Pressure, Psi	Curing Environment	Curing Time, Days	Test Temperature, °F	Test Pressure, Psi	Ageing Fluid		
Garnier et al. 2010	Portland Class G	Cylindrical (0.787 in diameter x 1.574 in length)	194	14.7	Lime-saturated water	28	194	1160	Supercritical CO_2 above water	0	0.000
										7	0.035
										36	0.118
										65	0.157
	Portland Class G + 35% silica flour		284	3000		10	284	1160		0	0.000
										4	0.037
										12	0.120
										21	0.154
										31	0.256
										55	0.445
										88	0.787
Barlet-Gouedard et al. 2006	Portland Class G	Cylindrical (0.5 in diameter x 1 in length), (1 in diameter x 2 in length)	194	3000	Water	3	194	4061	Wet supercritical CO_2	0	0.000
										2	0.079
										4	0.098
										8	0.138
										22	0.236
										42	0.335
										85	0.472
									CO_2-saturated water	0	0.000
										2	0.039
										4	0.079
										8	0.118
										22	0.197
										42	0.276
										85	0.315
Sauki and Irawan	Portland Class G	For curing: Cube	104 248	1522.89 2030.5	Unclear	1/3	104	1522.89	Wet supercritical	0	0.000

2010		(2 in height x 2 in length) For testing: Cylindrical (1.5 in diameter x 2 in length)							CO2	1	0.031
										3	0.041
										5	0.050
									CO2-saturated brine	0	0.000
										1	0.013
										3	0.017
										5	0.025
							104	2030.5	Wet supercritical CO2	0	0.000
										1	0.019
										3	0.031
										5	0.037
									CO2-saturated brine	0	0.000
										1	0.008
										3	0.015
										5	0.021
							248	2030.5	Wet supercritical CO2	0	0.000
										1	0.031
										3	0.037
										5	0.060
									CO2-saturated brine	0	0.000
										1	0.012
										3	0.022
										5	0.031
Kutchko et al. 2008	Portland Class H		122	4394.6	1% NaCl (brine) solution	28	122	4394.6	Supercritical CO2	0	0.000
										9	0.003
										25	0.005
										61	0.007
										90	0.006
										156	0.007
										361	0.012
									CO2-saturated brine	0	0.000
										9	0.014

										25	0.018
										61	0.022
										90	0.024
										156	0.025
										361	0.026
Sauki et al. 2010	Portland cement Class G	Cylindrical (1.5 in diameter x 2 in length)	104	1522.89	Unclear	1/3	104	1522.89	CO2 dissolved in brine (1.754 M)	0	0.000
										1	0.269
										3	0.466
										5	0.533
			104	2030.5			104	2030.5	CO2 dissolved in brine (2.1 M)	0	0.000
										1	0.384
										3	0.523
										5	0.624
			248	1522.89			248	1522.89	CO2 dissolved in brine (0.446 M)	0	0.000
										1	0.172
										3	0.250
										5	0.269
			248	2030.5			248	2030.5	CO2 dissolved in brine (0.569 M)	0	0.000
										1	0.243
										3	0.350
										5	0.442

Table B.2 Published measurements on permeability, porosity and compressive strength

Ref.	Cement Samples Information		Curing Information				Test Information			Permeability			Porosity			Compressive Strength		
	Cement Type	Core S	Curing Temp., °F	Curing Pressure Psi	Curing Fluid	Curing Time Days	Test Temperature °F	Test Pressure Psi	Ageing Fluid	Test Type	Ageing Time Days	K, md	Test Type	Ageing Time Days	ϕ, %	Test Type	Ageing Time, Days	σ_c, Psi
Lecolier et al. 2006	Cement I (Special cement)	Bar 0.787 x 0.787 x 6.3 in Bar 1.57 x 1.57 x 6.3 in disk 2.36 in diameter disk 1.5 in diameter	176	1015.26	Unclear		248	1015.26	Reservoir fluids	Water	0	0.003				Uniaxial	0	24656.4
											90	3.00E-06					30	28427.4
											365	1.00E-08					90	29587.7
																	212	29297.6
																	365	29007.5
	Mortar									Water	0	0.01				Uniaxial	0	13372.5
											90	0.0003					30	11632
											365	0.02					90	10790.8
																	212	12444.2
																	365	14126.7
	Cement II (Special cement)	Cylindrical 1 in diameter x 2 in length					248	2175.56	H2S-saturated brine (14% NaCl & 0.4% NaSO4)	Water	0	6.50E-06				Uniaxial	0	196
											21	0.01					21	22
	Conventional Portland Cement									Water	0	0.00046				Uniaxial	0	47
											21	0.044					21	2
Brandl et al. 2010	Portland Class G + silica flour + Pozzolan + sea water	1 in diameter x 2 in length	300	3000	Unclear	4	300	3000	CO2 environment	Water (Confining Pressure = 4500 psi)	0	2.02E-04				Uniaxial and Triaxial (Confining Pressure = 1000 Psi)	0	5840
											30	4.50E-03					30	5890
											90	5.99E-03					90	5910
											180	2.78E-03					180	5820
	Portland Class G + 35% silica flour +									Water (Confining Pressure = 4500 psi)	0	2.97E-04				Uniaxial and Triaxial (Confining Pressure = 1000 Psi)	0	5910
											30	3.37E-03					30	5890
											90	2.53E-03					90	5910
											180	4.35E-03					180	5910
Lecolier et al. 2007	Portland Class G	Cylindrical (1 in diameter x 2 in height) and bar (0.787 x	176	1015.26	Water	30	176	1015.26	Water with no renewed							Uniaxial	0	9427.5
																	30	8557.2
																	110	8484.7
																	170	8557.2

		0.787 in cross section and 6.3 in length)															355	7687
									Brine with monthly renewed							Uniaxial	0	8992.3
																	30	8122.1
																	90	8702.3
																	160	6816.8
																	350	4525.2
									Crude oil	Water (Confining Pressure = 580.15 psi and 1160.3 psi)	0	8.11E-04	Mercury	0	29	Uniaxial	0	7977.1
											30	6.59E-04		30	25		30	7251.9
											90	7.09E-04		90	27		90	8267.1
											170	7.30E-04		170	25		170	8847.3
Noik and Rivereau, 1999	Portland Class G	Cylindrical (1 in diameter x 2 in height)	356	1015.26	Water		356	1015.26	Deionized water							Unclear	90	797.7
																	180	748.4
																	250	751.3
																	380	758.5
	Portland Class G + (35%-40%) silica sand						248			Water	30	8.70E-04				Unclear	30	14648.8
											60	2.60E-04					60	13053.4
											90	4.60E-04					90	14503.8
											150	5.00E-04					150	13343.5
											420	3.80E-04					210	10732.8
											570	1.30E-03					420	9717.5
											750	7.23E-04					570	6091.6
																	750	9862.6
							284			Water	30	3.40E-04				Unclear	30	10152.6
											60	1.40E-04					60	9427.5
											90	7.23E-04					90	11312.9
											150	7.70E-04					150	10152.6
											210	7.10E-04					420	6816.8
											420	2.40E-04					570	7977.1
											570	3.80E-04					750	8122.1
											750	1.15E-03						
							356			Water	110	1.45E-03				Unclear	110	4496.2
											190	1.74E-03					190	5946.5

										330	4.76E-03					330	5511.4
	Portland Class G + (35%-40%) silica sand + Additives						356								Unclear	100	6932.8
																165	5903
																270	6526.7
																400	4351.1
																600	4061.1
	RPC (Portland Class G + silica sand + silica fume)						248		Deionized water						Unclear	15	16824.4
																30	18564.8
																90	13198.4
																180	20015.2
																360	22916
									Sea water						Unclear	15	19435.1
																30	21755.7
																90	17114.4
																180	24076.3
																360	26686.9
									Sea water + H_2S						Unclear	15	14503.8
																30	21755.7
																90	16099.2
																180	23786.2
																360	26541.9
									Sea water + gas oil						Unclear	15	22045.7
																30	20450.3
																180	23786.2
																360	26396.9
							284		Deionized water						Unclear	0	20450.3
																30	28572.4
																60	24656.4
																90	27586.2
																180	27571.7
							356		Deionized water						Unclear	0	21900.7
																30	21610.6
																90	18419.8

																	180	16969.4
	Portland Class G + silica sand + Additives + MnO					356		Deionized water							Unclear		90	6004.6
																	200	3379.4
																	290	3408.4
																	390	3190.8
	Portland Class G + silica sand + Additives + Fe_2O_3					356		Deionized water							Unclear		90	9137.4
																	200	5830.5
																	290	5874
																	390	5801.5
Barlet-Gouedard et al. 2007	Portland Class G	Cylindrical (0.5 in diameter x 1 in length), (1 in diameter x 2 in length)	194	3000	Water	3	194	4061.06	Wet supercritical CO2				Mercury	0	32.5			
														0.5	27			
														2	23.5			
														8	19			
														22	18.2			
														42	13.8			
														83	26.5			
									CO2-saturated water				Mercury	0	33			
														0.5	27			
														2	23.5			
														8	19			
														22	9.5			
														42	20.5			
														83	28.5			
	CO_2-resistant material cement	Cylindrical (0.5 in diameter x 1 in length)							Wet supercritical CO2				Mercury	0	14			
														0.5	16			
														1.3	20			
														7.3	21.4			
														41.5	19			
														84.8	21.3			
									CO2-saturated water				Mercury	0	14			
														0.5	18			
														1.3	20.6			
														7.3	20			

														21.6	24			
														41.5	23.6			
														84.8	23.3			
Mueller and Dillenbeck 1991	Portland Class H + 35% silica flour + 50% H_2O		350	3000	Unclear	90	350	3000	Unclear							Ultrasonic Technique	1	5440
																	7	4800
																	29	3850
																	90	4737
	Portland Class H + 35% silica flour + 0.2% citric acid + 111% H_2O															Ultrasonic Technique	1	2150
																	7	2300
																	29	1425
																	90	1495
Santra and Sweatman 2011	Cement sample A with a CO2-resistant formulation	Cylindrical (1 in diameter x 2.5 in length)	140	2000	Water	28	140	2000	Supercritical CO2 + fresh water							Unclear	0	5594
																	15	7951
																	30	7958
																	180	7002
																	365	8866

Appendix C

MINUTES

2st Technical Advisory Board Meeting

Project Title: Effect of H_2S and CO_2 in HPHT Wells on Tubulars and Cement

Meeting Date: Wednesday May 16th, 2012
Time: 10:00 AM – 3:30 PM Central Time
Meeting Location: OU Norman Campus, Norman, OK & http://petroluem.webex.com

Attendees:
Timothy Steffek (BSEE)
Arild Saasen (DET NORSKE)
Sturla Wold (DET NORSKE)
Marco May (VALLOUREC)
Ramadan Ahmed (OU)
Subhash Shah (OU)
Samuel Osisanya (OU)
Shokrallah Hassani OU)
Joe Flennken OU)
Majed Enfis (OU)
Rida Mohamed (OU)
Himanshu Maheshwari (OU)
Adarsh Naidu (OU)

Online Attendees:
Candi Hudson (BSEE)
Andreas Brandl (Baker Hughes)

This was the 2nd Technical Advisory Board (TAB) Meeting of the BSEE Project # E12PC00035 titled "Effects of Hydrogen Sulfide (H_2S) and Carbon Dioxide (CO_2) in HPHT Wells on Tubulars and Cement."

Dr. Ahmed started the meeting at 10:00 AM on Wednesday May 16, 2012 by welcoming the meeting participants. He then made a presentation on the overall project overview to date. He discussed the project objectives, scope, schedule, deliverables, and challenges. The project work is divided into three main tasks: one theoretical and two experimental tasks. The theoretical task deals with understanding of the degradation of tubulars and cement in the presence of sour gases (H_2S and CO_2) under HPHT conditions. The first experimental work is to investigate the degradation of cement in the presence of sour gases under HPHT conditions. The second experimental work is investigating the degradation of tubulars in the presence of sour gases under HPHT conditions.

Following Dr. Ahmed's project overview, five more presentations were made which addressed the objectives and tasks stated in the contract. Two presentations were made during the morning session on the effects of sour gases on porosity, permeability, and mechanical properties of cement. During the afternoon session, three. presentations were made on corrosion of tubulars in sour gas environment. Below are the details of the various presentations.

Morning Session

First Presentation

Dr. Ahmed presented the status of the project as at this time. He disused the project accomplishments and the challenges faced in achieving the objectives. Major challenges during this first eight months were: i) unavailability of required instruments and equipment due to testing conditions of HPHT; ii) delay in delivery of items used for test setup; and iii) unavailability of a qualified applicant for the post-doctoral position. This last challenge of post-doctoral position has just been solved by the coming on board of Dr. Shokrollah Hassani who has just completed his PhD on subject very related to this project.

Finally, Dr. Ahmed went through the development of the test facilities located on the North Campus Research Facilities of University of Oklahoma. He talked extensively about gas venting system, preparation of the laboratory space, designs of the aging cell and injection cylinder, assembling of the cell on the moveable cart, considerations of the heating systems, aging cell setup in the laboratory, and gas storage boxes. Throughout the presentation on the

development of the test facilities and during the visit later in the day, Dr. Ahmed emphasized SAFETY and the ENVIRONMENT.

2nd Presentation by Himanshu Maheshwari (MS Graduate Student)

He presented the results of theoretical studies of the effects of sour gases exposure on the permeability and porosity of oil well cement. Cement degradation is due to a process called carbonation during which major binding components of the hydrated cement (Calcium-Silicate-Hydrate and Portlandite) react with the acid forming calcium carbonate. The studies showed that the major parameters affecting cement degradation are cement composition, temperature, pressure, pH, and the composition of the surrounding fluids. Decreasing the amount of Calcium-Silicate-Hydrate and Portlandite as well as porosity and permeability reduces carbonation. Also, the incorporation of metal oxides helps reduce H_2S attack of cement. The pH model was used to evaluate the effects of temperature and pressure on the degradation of cement resulting from CO_2 exposure.

3rd Presentation by Majed Enfis (PhD Graduate Student)

His presentation was on mechanical properties of oil well cement in sour gases environment. He reported the theoretical findings of the effects of sour gases on well cements. Again literature review showed the following: carbonation is the main cause of cement degradation. The depth of carbonation increases with temperature and porosity, and varies with the type of fluid exposed to. The compressive strength of cement decreases with temperature and varies with the composition of the surrounding fluid. There was a significant decrease in the shear bonding strength of cement exposed to sodium sulfate solution for 60 days. Finally, porosity and permeability data on various cement specimens cured under atmospheric conditions and 200°F were presented. The basic idea here is to establish the procedure for preparing consistent samples. Results obtained from cast cement specimens (1" x 2") sprayed with silicon showed consistent porosity and permeability at ambient and 200°F curing temperatures. TAB members discussed the effect of specimen drying on the mechanical properties of the cement. They recommended not to dry the specimens used for compressive strength measurements.

Visit to Test Facilities Located at OU Norman Campus Research Center

After lunch break, the meeting participants were taken on a tour of the test facilities for this project. The setup and the various equipment, sensors, and computer/data gathering systems

were seen firsthand. Again, SAFETY and ENVIRONMENT were emphasized throughout the tour.

Afternoon Session

4th Presentation by Adarish Naidu (Graduate Student)

This presentation focused on corrosion of tubulars exposed to CO_2 containing fluids. Simulation results obtained using an existing CO_2 corrosion model (NORSOK model) were presented on the effect of different parameters (temperature, total pressure, and mass flow rate) on corrosion of tubulars. The results clearly showed that corrosion rate increases with temperature up to a temperature of about 175°F. However, above 175°F the corrosion rate decreases with increase in temperature. The reason was the formation of protective film that prevents further corrosion. Finally, different corrosion measuring techniques were presented: weight loss, linear polarization resistance (LPR), and electrochemical noise (ECN) methods. The three methods were compared and contrasted. It was recommended that a combination of LPR and ECN methods will give better results than using them individually.

5th Presentation by Dr. Shokrollah Hassani (Post-Doctoral Fellow)

Dr. Hassani presented the fundamentals of corrosion of carbon steel. He talked about corrosion mechanisms such as uniform corrosion, pitting corrosion, and hydrogen sulfide stress cracking corrosion. He then listed the effects of different parameters to be studied theoretically and experimentally as related to CO_2/H_2S corrosion of tubulars at HPHT conditions: pH, temperature, pressure, and water chemistry.

6th Presentation by Rida Elgaddafi (PhD Graduate Student)

The presentation here also focused on corrosion behavior of tubulars under sour gases environment. Literature reviews of several papers were presented. One paper showed the formation of Fes and FeCO3 as byproducts of corrosion of iron. However, the effect of H_2S concentration on CO_2 corrosion of tubulars is not fully understood at the moment due to the effect of other environmental factors. Solution pH is considered a key factor in the corrosion of tubulars. In general corrosion rate of tubulars is high at low pH. It was also discovered that corrosion rate is influenced more by temperature than H_2S concentration. Moreover, the formation of protective film has great impact on corrosion rate. The composition and structure of the film depend mainly on CO_2 and H_2S partial pressure and temperature.

In summary, the theoretical and modeling studies so far on the effects of sour gases in HPHT wells on tubulars and cement will help in determining the parameters to focus on in the planned experimental studies.

Date for the Next Technical Advisory Board (TAB) Meeting

The time for next TAB meeting is set for Friday, November 2, 2012. The meeting will be held in Houston.

Finally, the meeting was adjourned at 3:30 p.m.

Project Title: Effect of H_2S and CO_2 in HPHT Wells on Tubulars and Cement

Report Type: Monthly Report

Report #: 09

Reporting Period: May 22nd, 2012 to June 21st, 2012

Authors:

Ramadan Ahmed, Principal Investigator

Subhash Shah, Co-Principal Investigator

Samuel Osisanya, Co-Principal Investigator

Shokrollah Hassani, Postdoctoral Research Associate

Majed Enfis, Research Assistant

Rida Elgaddafi, Research Assistant

Himanshu Maheshwari, Research Assistant

Adarsh Naidu, Research Assistant

Prepared under BSEE Project # E12PC00035

by

THE UNIVERSITY OF OKLAHOMA

July 18, 2012

1. Summary of Accomplishments

This monthly report presents the progress made during the project period May 22, 2012 – June 21, 2012. The development of experimental setups for testing cement degradation has been completed. Testing of the aging cell and compressive strength measuring setup has been completed. Cored specimens have been prepared to carry out the aging experiments that will begin in the coming days. Literature review, and theoretical and modeling studies on tubular degradation is in progress. Moreover, in order to predict the amount of calcium present in the cement (initial calcium concentration) after curing, cement hydration models were investigated. The initial calcium concentration is necessary to predict the degradation depth, mechanical properties, and permeability of the cement. A report summarizing the results of these studies is presented in Appendix A and B.

Our effort to develop cement specimen preparation procedure was continued. During this reporting period, cement specimens were prepared using fresh water and the effects of sample preparation techniques (i.e. casting and coring) on porosity and permeability of cement specimens were examined. The sample preparation techniques have little effect on porosity and permeability of the specimens. Cored specimens were prepared using more advanced coring machine that has minimal bit vibration and irregularities. Using the new coring machine, uniform samples were prepared. The cored specimens had better quality and geometric uniformity than the casted ones. Beside this, microscopic examination of casted specimens showed the presence of micro cracks.

Porosity predictions were made for the specimens based on free water in cement system after curing using the cement hydration model. Porosity measurements and predictions showed a good agreement. Two different porosity measurement techniques were used for dry and wet specimens. Experimental porosity measurement results were the same for the dry and wet specimens.

Scanning Electron Microscopy (SEM), X-Ray Fluorescence (XRF), and Fourier Transform Infrared Spectroscopy (FTIR) were used to analyze the cement specimen. SEM was used to study different phases in cement including CH, CSH, and unhydrated cement. XRF were used to study different elements and phases in the cement. FTIR measurements taken before and after cement hydration do not show significant differences. We are exploring the possibility of using X-ray Diffraction (XRD) technique to analyze the cement specimens.

Investigation on tubular corrosion is one of the key components of this project. A number of CO_2 and H_2S corrosion models have been reviewed during the past month. Different

empirical, semi-empirical, and mechanistic models are available for CO_2 and H_2S corrosion prediction. Most of the models available in the literature are limited to low-temperature low-pressure conditions. Research is in progress to develop a new mechanistic model for CO_2 and H_2S corrosion rate prediction under high-temperature and high-pressure conditions.

Our plan for the coming weeks is to perform aging experiments. We will continue our theoretical and modeling studies on tubular corrosion as well.

2. Overall Project Progress

2.1 Theoretical Studies (Task 1)

Initial porosity of the cement is an important factor in predicting the leaching rate of the cement and consequently mechanical properties and permeability of the cement. The initial porosity of cement is a function of water-to-cement ratio and degree of hydration. In order to predict the initial porosity of cured specimens, cement hydration model developed by Lin and Meyer (2009) was applied for Classes H and G cements at different temperatures. Predicted porosity measurements show a good agreement with measurements. The degree of hydration versus time plot for different temperatures can be used to determine the appropriate curing time needed to get maximum hydration. Furthermore, the model was used to predict the maximum calcium concentration in classes H and G cements.

Theoretical and modeling studies on corrosion of tubulars were continued. Most commonly used CO_2/H_2S corrosion models were reviewed. There are numerous CO_2 and H_2S corrosion models available in the literature to predict corrosion rate and protective film thickness and properties. However, most of these models are developed for low-temperature and low-pressure applications. The validity of these models at high temperature and pressure conditions has not been verified. Improvements have been proposed to one of the available CO_2 corrosion models (Dayalan et al., 1995). Proposed modifications change some of the basic hypotheses of the model including temperature and pressure limitations. In the coming months, a model will be developed for H_2S corrosion. The Synergistic effect of CO_2 corrosion and H_2S corrosion is also an important area of consideration for combining the two models. Details of theoretical and modeling studies on tubular CO_2 and H_2S corrosion are presented in Appendix B.

2.2 Experimental Studies on Degradation of Cement (Task 2)

The objective of this task is to test the performance of conventional cement under different test conditions. Cement specimen setup and test condition for first set of aging experiment are shown in Fig. 1. Two different classes of cement G and H will be aged under high-pressure

high-temperature conditions (9000 psi and 350^{o}F). Silica is added to the cement to improve the high temperature resistance. Effect of fly ash will be studied for the first set of aging experiment. Fly ash as a cement additive reduces the cost of cement, reduces the slurry density, increases the strength of cement, increases the thickening time, and also reacts with calcium hydroxide and form calcium silicates. Fly ash class F is used in this research because it has lower sulfate content. Amount of fly ash added to the cement is 100% by weight. Two aged cement samples will be used for porosity and permeability testing; they can also be use for FTIR, SEM, and cross sectioning and studying the degradation depth. Three samples will be used for compressive strength testing. First batch of the samples will be removed after 15 days and the second batch will be removed after 30 days. Sample coding is based on the batch number, shelf number, and order number as shown in Fig. 1.

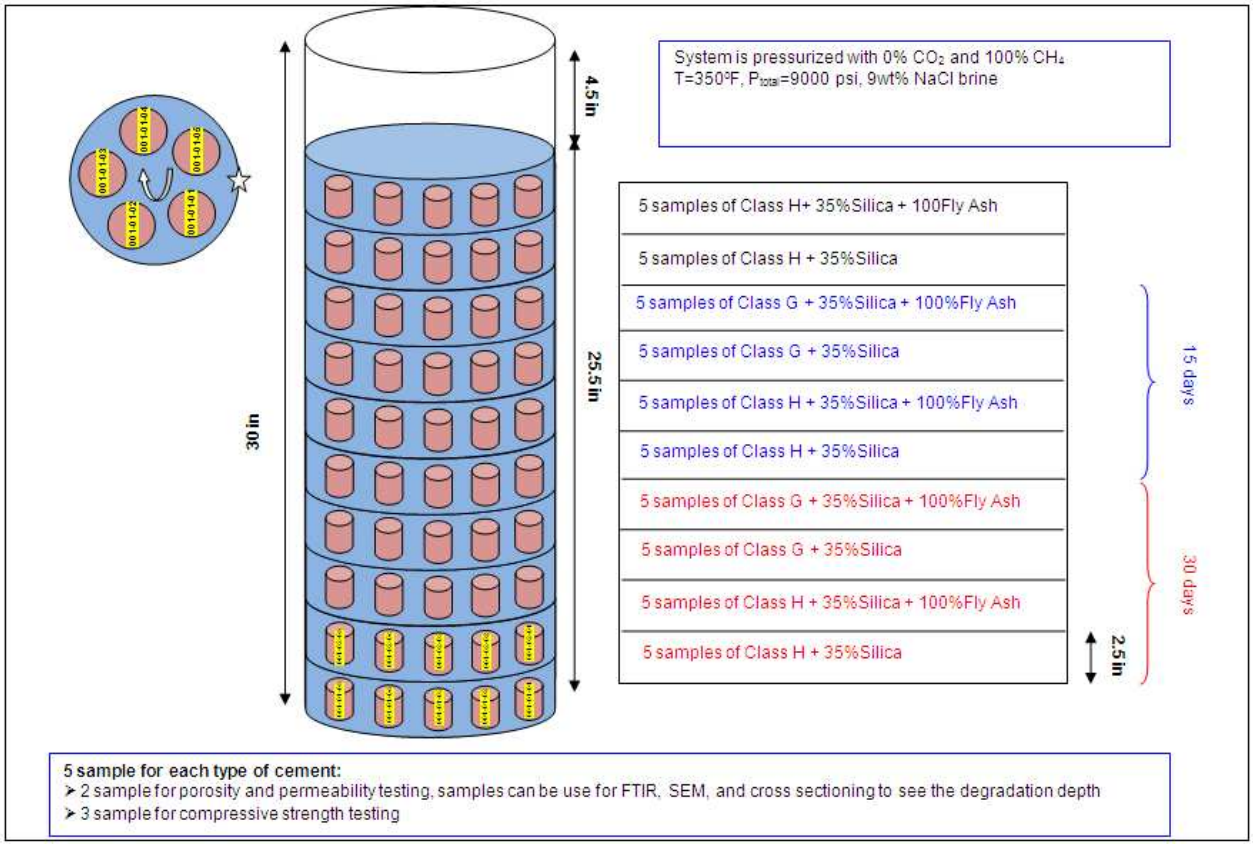

Fig. 1 Cement specimen setup and test condition for first set of aging experiment

The development of an established specimen preparation procedure was continued. Cement slurries with water to cement ratio of 38% were prepared by adding 1.9 lbm of neat Class H cement to 0.72 lbm of tap water (fresh water). The slurry was mixed for 35 seconds

using a standard laboratory agitator. However, API procedure requires using special high speed mixers (4,000 and 12,000 rpm preset speeds) to prepare cement slurries. Thus, a new cement mixer has been purchased to be used during slurry preparation. After preparing the cement slurry, the paste was poured into five identical stainless steel molds (1" Diameter x 2" Length) which were sprayed with silicon release. The paste was also poured in a bigger beaker for preparing the core specimens. Poured paste was left for 24 hours to harden in the moulds and develop the initial strength under ambient conditions. Then, the specimens (cores) were cured in tap water for 5 days at temperature of 200ºF using a large-sized laboratory oven. After curing, the cores were recovered from the moulds and dried to a constant weight. Then, their porosity and permeability were measured. Specimen dimensions, weight, and measured porosity and permeability are shown in Table 1. Results presented in Figs. 2 and 3 show that the effect of sample preparation techniques (i.e. casting or coring) on porosity and permeability of the cement is very minimal. However, coring was selected as the best method for sample preparation because cored specimens were more uniform than the cast ones. In addition, the casted specimens had micro cracks as shown in SEM images. The micro cracks could be as a result of high plunger force needed for taking out the sample out of mold.

Table 1 Porosity-permeability data for different neat cement specimens/cores

	Core dimensions				Porosity				Permeability		Remarks	
Core #	Diameter	Length	Weight (g)		V_b	V_g	V_p	Porosity	K_{air}	K_{klink}		
	mm	mm	Wet	Dry	c.c	c.c	c.c	%	md	md		
20	24.90	27.85		23.96	13.56	9.41	4.15	30.60	0.261	0.180	Cured under 200°F	Mixing Time is 35 seconds
21	24.98	28.83		25.75	14.13	10.34	3.79	26.82	0.201	0.135	Cured under ambient temp.	
22	25.31	29.73		26.91	14.96	10.94	4.02	26.87	0.153	0.098		
23	25.09	31.49		27.02	15.57	10.64	4.93	31.7	0.203	0.136	Cured under 200°F	Mixing Time is 35 seconds
24	25.08	30.92		26.34	15.28	10.51	4.77	31.2	0.239	0.162		
25	25.38	28.88		25.18	14.61	9.85	4.76	32.58	0.180	0.118		
26	24.73	30.42		25.71	14.61	10.1	4.51	30.87	0.219	0.147		
27	24.82	31.51		26.52	15.25	10.38	4.87	31.93	0.135	0.083		
28	24.76	30.30	30.71	26.52	14.59	10.47	4.12	28.24	0.106	0.064	Cured with 3% brine under 200°F, Cement slurry prepared in 3% brine, 2:30 min.	
29	25.15	30.25	30.33	25.57	15.03	10.05	4.98	33.13	0.313	0.220		
30	25.40	30.76	30.98	26.10	15.59	10.52	5.07	32.52	0.208	0.139		
31	25.40	26.46	26.77	22.35	13.41	8.9	4.51	33.63	0.253	0.174		
32	24.65	30.92	29.27	27.99	14.76	11.19	3.57	24.19	0.054	0.03	Slurry in fresh water, cured in 9% brine at 200°F, 2:30 min. (**CASTING**)	
33	25.01	30.14	28.11	26.54	14.81	10.47	4.34	29.30	0.299	0.211		
34	24.68	28.60	26.49	24.96	13.68	9.62	4.06	29.68	0.388	0.282		
35	24.75	28.30	26.11	24.72	13.62	9.68	3.94	28.93	-	-		
36	24.88	28.53	26.34	24.84	13.87	9.99	3.88	27.97	0.287	0.202		
37	25.23	27.03	26.28	23.73	13.51	9.62	3.89	28.79	0.273	0.188	Slurry in fresh water, cured in 9% brine at ambient conditions, 2:30 min. (**CORING**)	
38	25.23	28.29	25.81	24.31	14.14	9.82	4.32	30.55	0.336	0.238		
39	25.26	27.73	26.24	24.01	13.9	9.67	4.23	30.43	0.322	0.227		
40	25.24	29.46	26.99	25.13	14.74	10.12	4.62	31.34	0.372	0.266		
41	25.26	26.83	25.58	23.13	13.45	9.32	4.13	30.71	0.309	0.217		
42	25.25	29.67	27.43	25.73	14.86	10.32	4.54	30.55	0.318	0.223		
43	25.27	30.45	28.53	26.45	15.27	10.61	4.66	30.52	0.292	0.202		
44	25.23	25.95	24.61	22.41	12.97	8.99	3.98	30.69	0.356	0.255		
45	25.24	62.39	57.76	54.18	31.22	21.5	9.72	31.13	0.412	0.287		

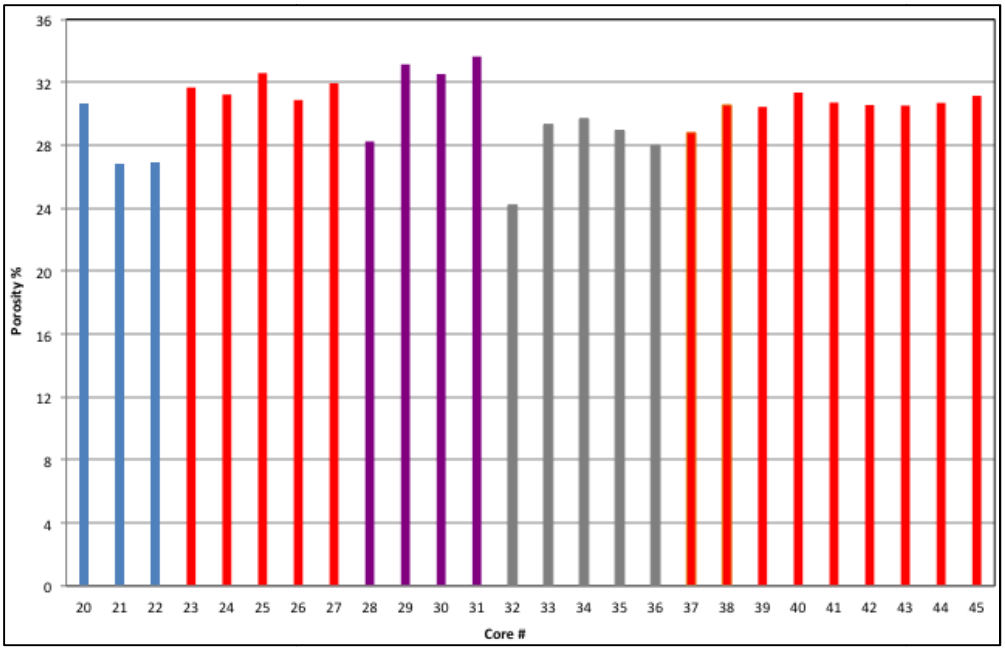

Fig. 2 Porosity measurements

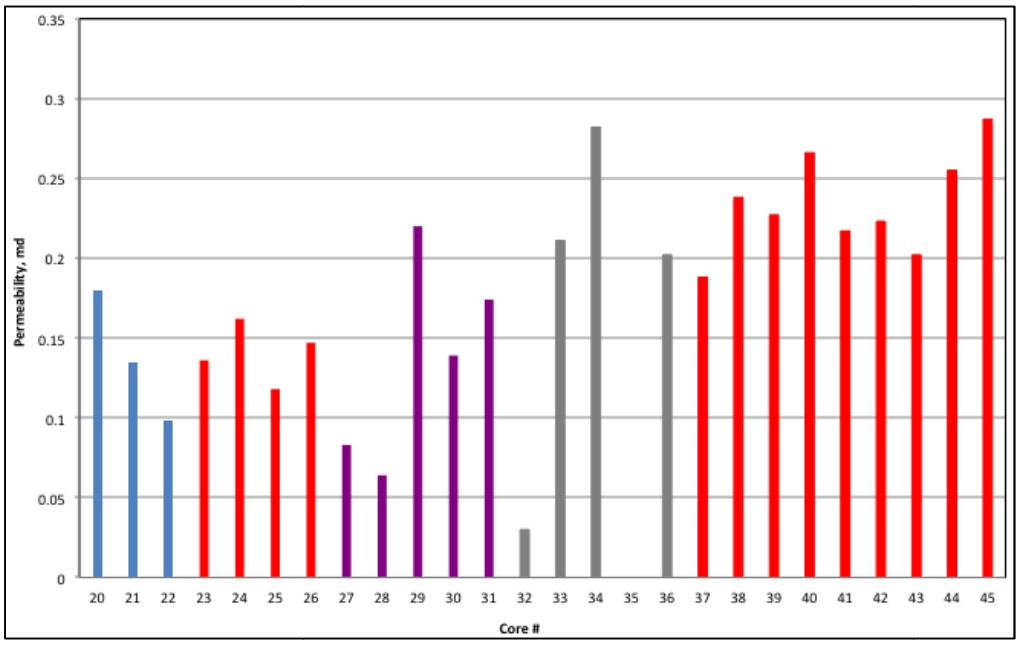

Fig. 3 Permeability measurements

Nuclear magnetic resonance (NMR) and gas porosimeters were used to measure the porosity of wet and dry samples, respectively. Results are shown in Table 2 and Fig. 4. NMR makes use of the Gibbs-Thomson effect, which is based on the assumption that small crystals of a liquid in the pores melt at a lower temperature than the bulk liquid. As a result, the melting point depression is inversely proportional to the pore size. The technique is closely related to

that of the use of gas adsorption to measure pore sizes (Kelvin equation). This technique is particular case of the Gibbs equations (Josiah Willard Gibbs); the Kelvin equation is the constant temperature case, and the Gibbs-Thomson equation is the constant pressure case. To make a NMR measurement, a liquid is imbibed into the porous sample, the sample cooled until all the liquid is frozen, and then warmed slowly while measuring the quantity of the liquid melted. Thus, it is similar to DSC thermoporosimetry, but has higher resolution, as the signal detection does not rely on transient heat flows, and the measurement can be made arbitrarily slowly. It is suitable for measuring pore diameters in the range 2 nm–2 μm. Experimental results showed that the wet and dry porosity of the cement samples measured using these two different techniques are almost the same.

Table 2 Comparison of wet porosity with dry porosity

Core #	Wet Porosity (NMR)	Dry Porosity (air)
32	24.78%	24.19%
33	29.19%	29.30%
34	28.81%	29.68%
35	28.20%	28.93%
36	28.67%	27.97%

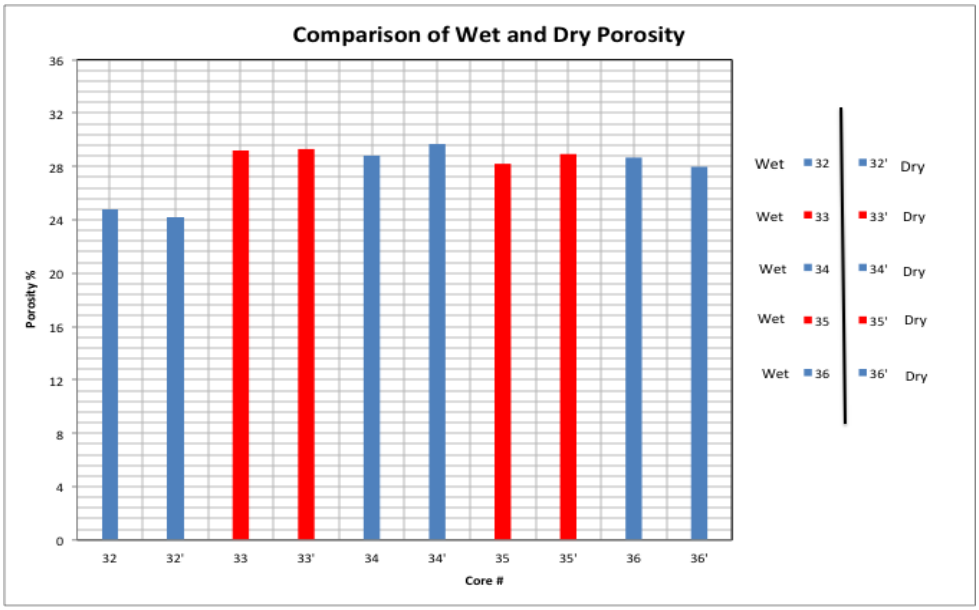

Fig. 4 Comparison of wet porosity with dry porosity

Total porosity of the cement samples were also measured using the low pressure pycnometer (LPP) technique. LPP is based on measuring the grain volume of finely crushed samples after removing free water. Once the bulk volume is determined the sample is ground into powder; it is carefully dried to remove free moisture and the volume of the powder (grains) is accurately determined. The difference between the bulk volume and grain volume is the measure of pore volume. Porosity measured using LPP technique (31.16%) was almost similar to porosity measured using AP608 technique (28.24%). This means that the total porosity of cement specimens is almost the same as connected porosity. In other words, most of the pores in the cement specimens are connected to each other.

SEM was used to study the different phases in the cement. Fig. 5 shows the back scattered SEM image of the cement surface at two different magnifications of 200X and 1000X. In these figures, white phase shows the unhydrated cement, light gray shows the CH phase, and dark gray shows the CSH phase. Prediction of molar concentration of CH and CSH of class H cement (Section A.1.6) shows that CH molar concentration is almost twice as CSH which shows good agreement with SEM experimental results. Light gray (i.e. CH) is approximately as twice as dark gray (i.e. CSH) in the SEM image.

A micro crack was observed in the SEM image. Therefore, it is preferred to use the coring technique for sample preparation. SEM image also shows the amount of unhydrated cement (white area in Fig 5). Prediction of maximum degree of hydration for class H cement (Section A.1.5) shows that the maximum hydration is about 60% which shows almost a good agreement with the amount of hydrated and unhydrated cement observed in SEM image in magnification of 1000X.

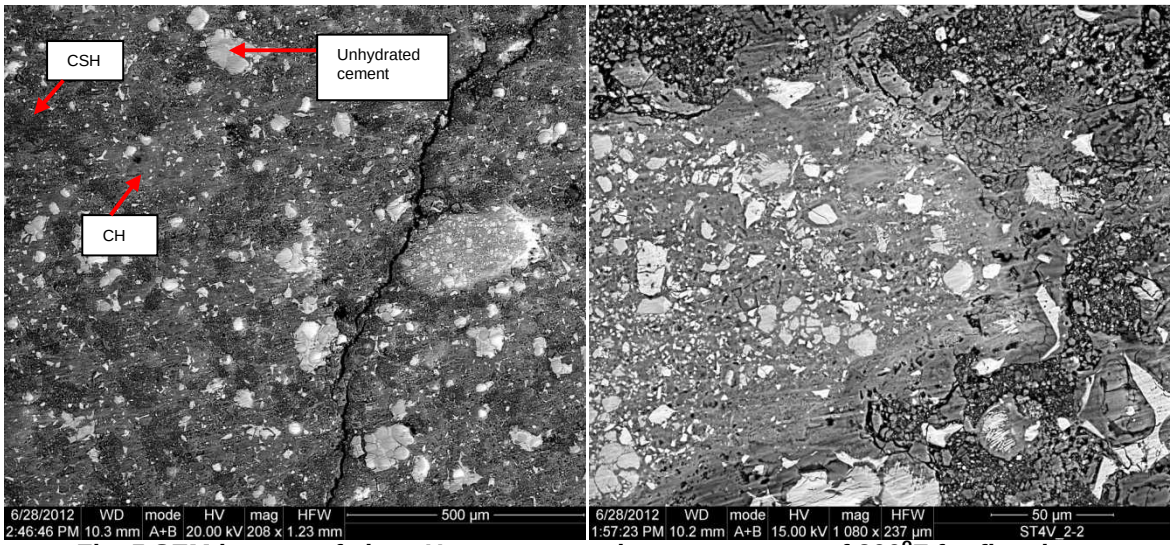

Fig. 5 SEM images of class H cement cured at temperature of 200^{o}F for five days

During SEM imaging, XRF was also applied to analyze the amount of different elements in different phases observed in the SEM image (Figs. 6 through 8). XRF analysis results show that calcium is the dominant element in the cement. Different elements including Fe, Si, Mg, Na, O and Al can also be observed in the XRD pattern. Si is the second dominant element in the cement, which presents in CSH and unhydrated cement.

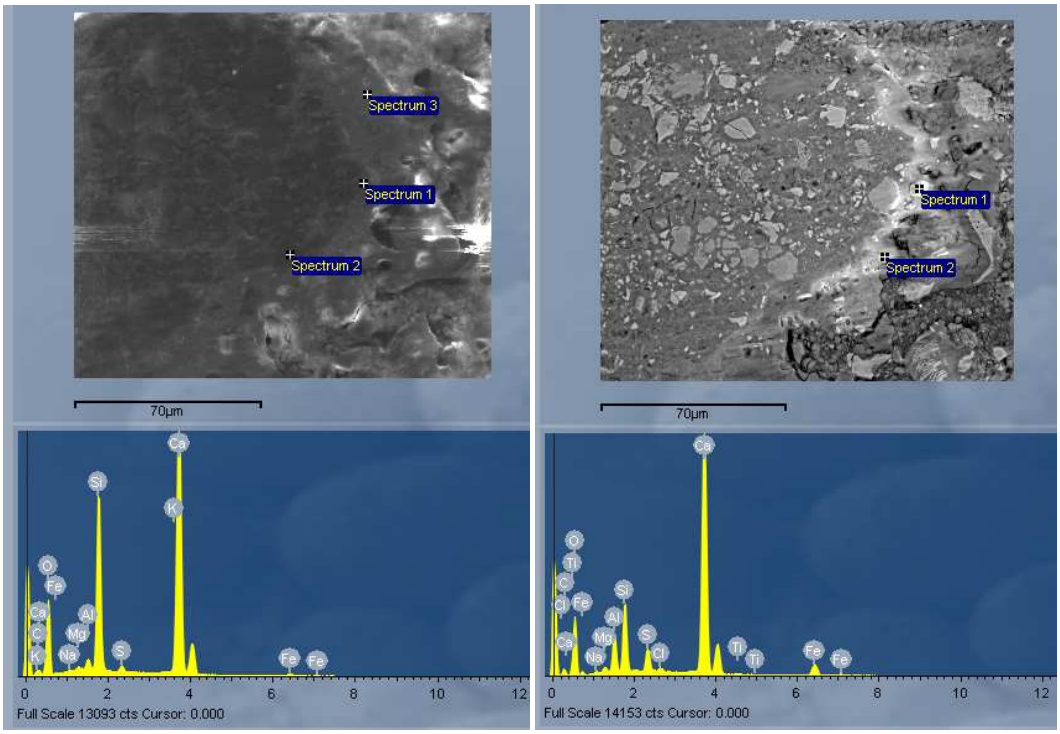

Fig. 6 XRF analysis of Core 28 (Left: spectrum 1, Right: spectrum 2)

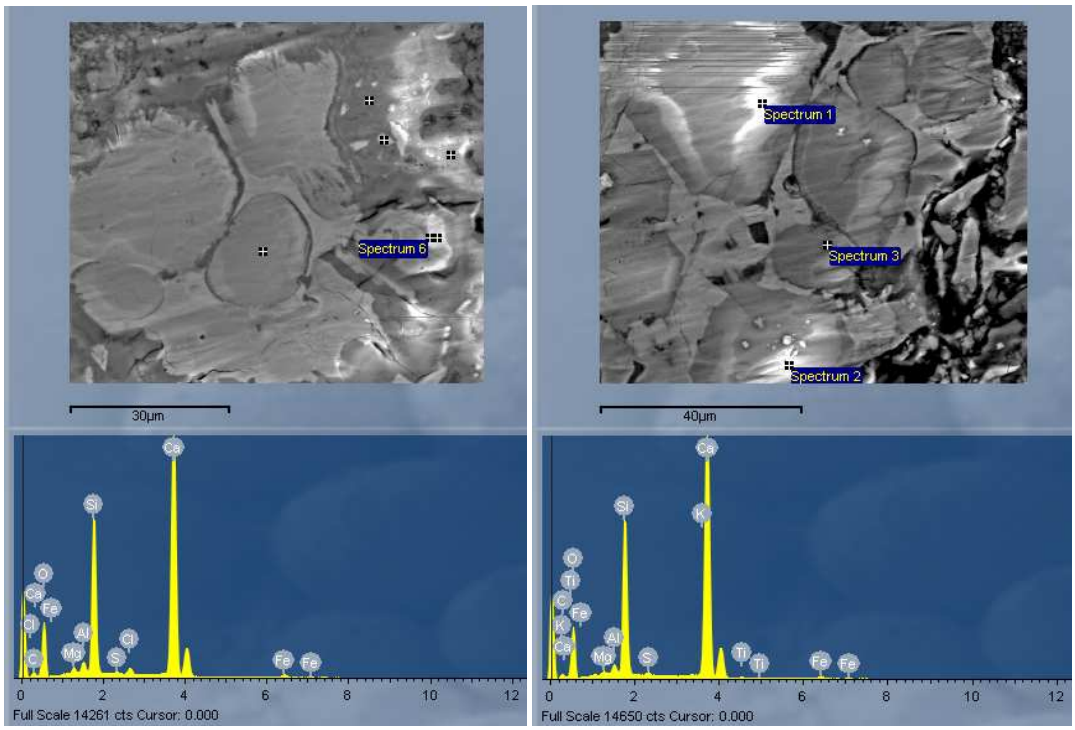

Fig.7 XRF analysis of Core 28 (Left: spectrum 6, Right: spectrum 3)

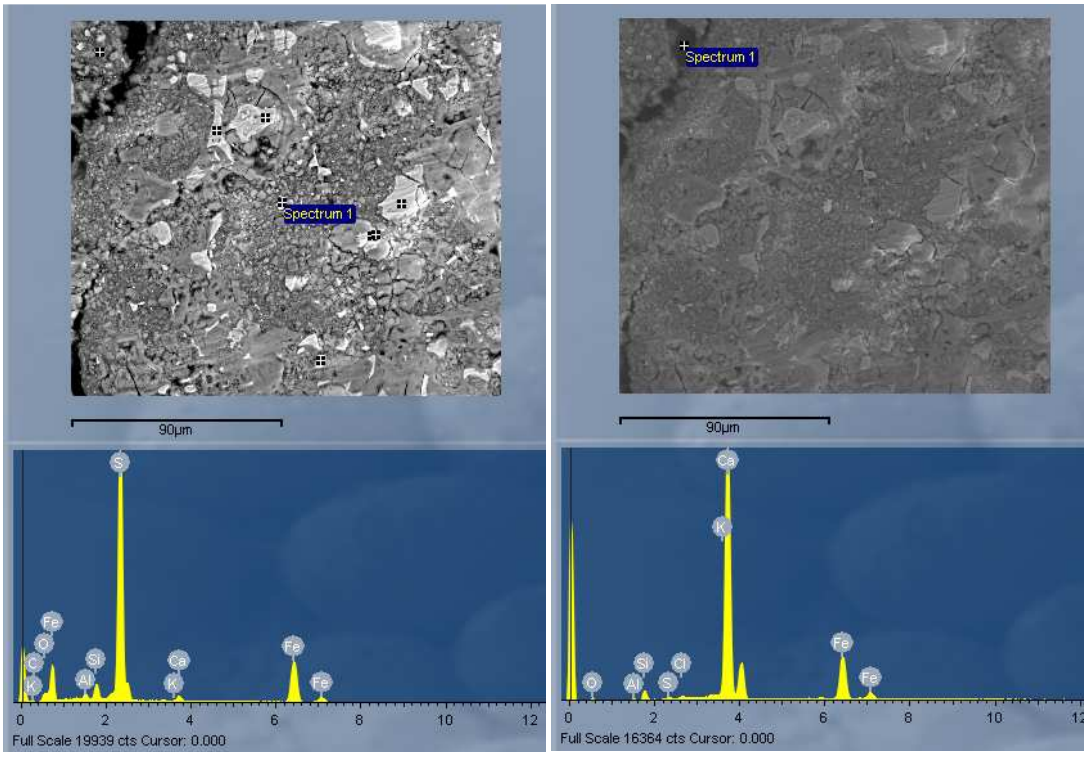

Fig.8 XRF analysis of Core 28 (Left: spectrum 1, Right: spectrum 1)

Fourier Transform Infra-Red (FTIR) spectroscopy was also used to study the applicability of this technique for studying the hydration process and also to qualitative and

quantitative detection of different phases in cement (Figs. 9 through 11). Three different samples were used for FTIR test as follow:

i. Hydrated cement with ashing (i.e. the powdered sample is kept where all the present organic content is removed and hence FTIR measurements)
ii. Hydrated cement without ashing
iii. Unhydrated cement sample (Class H cement powder before mixing with water)

FTIR spectrums of hydrated cement with and without ashing (Fig. 9 and 10 respectively) were almost similar to each other. FTIR spectrum of unhydrated cement (Fig. 11) was slightly different from the hydrated one. Experimental FTIR spectrums were compared with FTIR spectrum of well debris, $CaCO_3$ (Fig. 12), unexposed cement, and aged cement (Fig. 13). In general, the FTIR spectrums were less helpful for quantitative and qualitative analysis of cement. Therefore, the feasibility of other techniques such as XRD will be explored in future to fulfill the need of phase analysis.

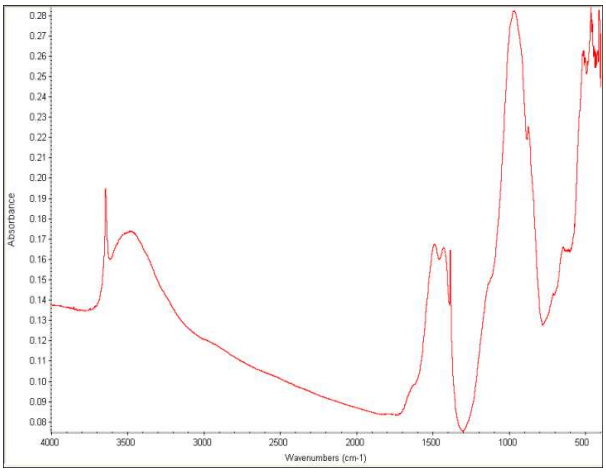

Fig. 9 FTIR spectra for hydrated cement sample with ashing

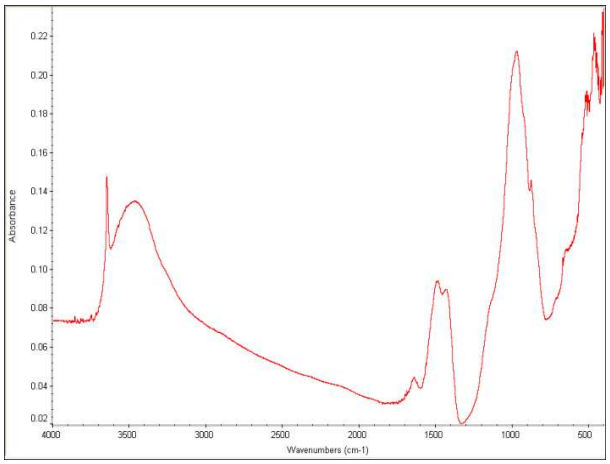

Fig. 10 FTIR spectra for hydrated cement sample without ashing

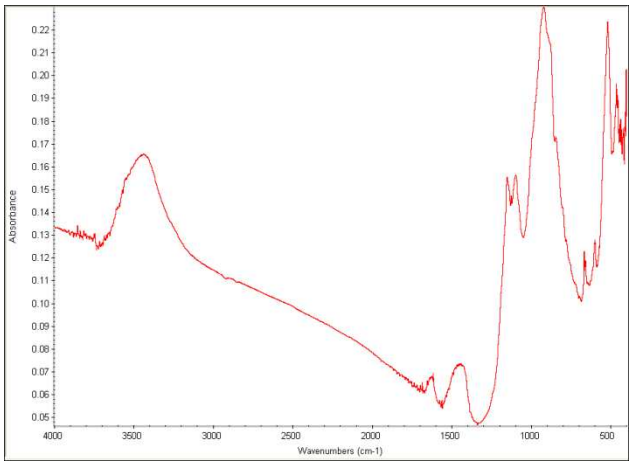

Fig. 11 FTIR spectra for unhydrated cement sample

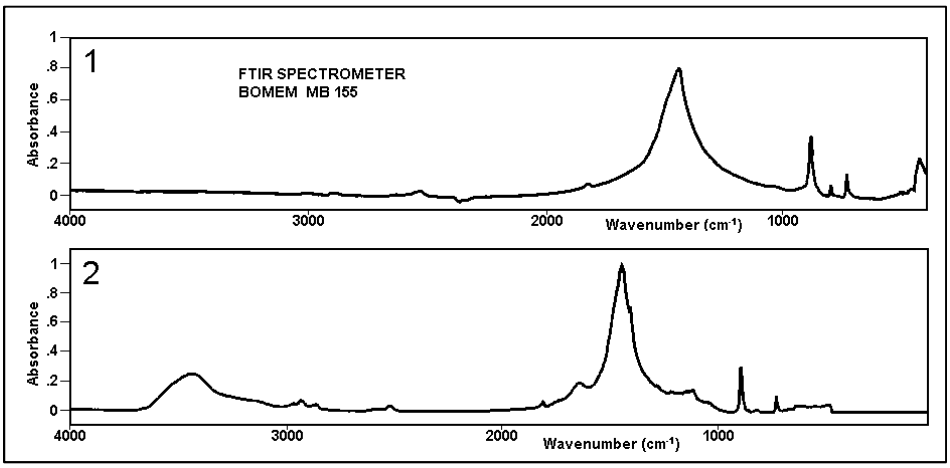

Fig. 12 FTIR spectra: 1) for well debris; and 2) for $CaCO_3$ (Krilov et al., 2000)

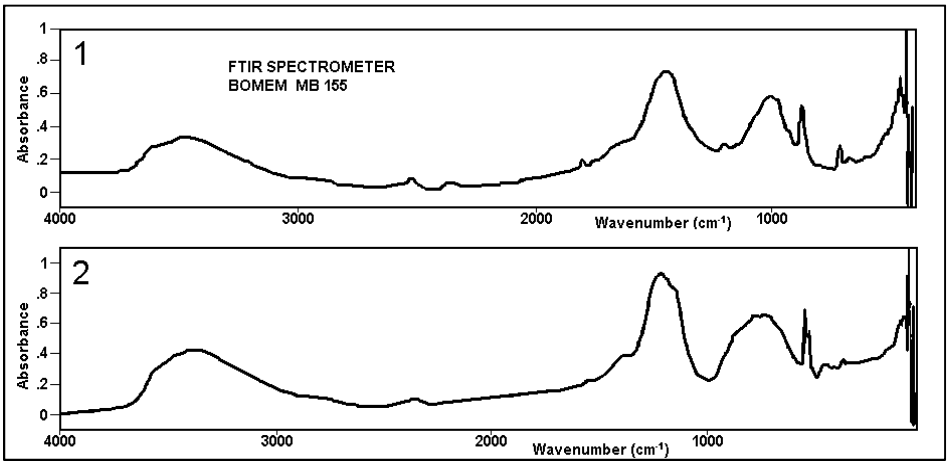

Fig. 13 FTIR spectra of cement: 1) before aging; and 2) after aging (Krilov et al., 2000)

In addition to the compositional analysis, unconfined compressive strength of four cement cores (Sample # 40, 42, 43, and 45) were measured. Compressive strength test results (Fig. 14a) for were fairly consistent for 1-inch long cores (Core # 40, 42 and 43). However, for 2-inch long core (Core # 45), measured compressive strength is slightly higher. Stress-strain graph of Core # 45 is shown in Fig. 14b. The stress-strain relationship is approximately linear. Elastic module of the core is found to be 500,000 psi.

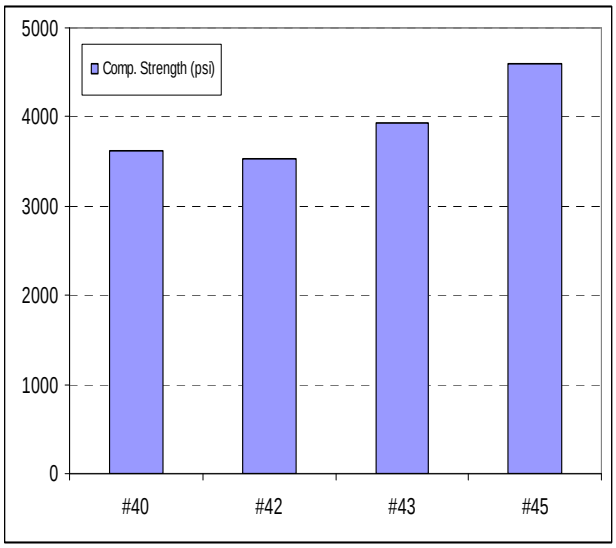

Fig. 14a Compressive strength cement cores

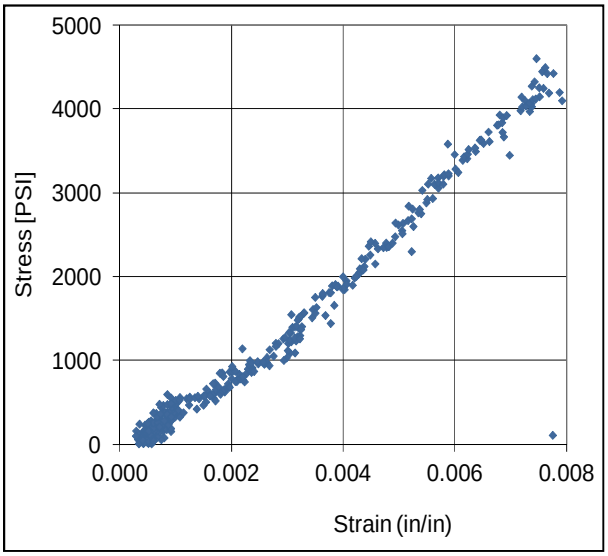

Fig. 14b Measured stress vs. strain for core #45

2.3 Experimental Studies on Corrosion of Tubulars (Task 3)

Searching for high-pressure recirculation pumps was continued. We are considering different options including using an injection cylinder as a pump, acquiring a custom-made pump or syringe type pump that meets the desired specifications. The design of the corrosion setup will be finalized after specifying the pump.

3. Planned Activities

- Aging experiments.
- Continue theoretical and modeling studies on cement and tubular degradation.
- Continue evaluating cement core preparation procedure.
- Designing of test setups to conduct tubular corrosion experiments.

4. Meeting and contacts

During this reporting period, we have made contacts with TAB members, Mr. Gunnar DeBruijn and Dr. Ashok Santra to discuss in detail cement slurry mixing procedure and formulations. Members recommend the use of API cement mixer for preparing the slurry. After the consultations, the following (Tables 2 through 5) cement slurries have been prepared using the API mixer to carry out the first aging experiments. In addition, TAB members pointed out the need of slow depressurization of the aging cell after aging the cement specimens. This is to minimize the development of micro cracks in the specimens because of quick expansion of the pore fluid.

Table 2 Cement Class H plus 35%silica and 100%fly ash

Material	Percent	Mass (g)	Specific Gravity	Volume (cc)
HEC	0.1% of water of filler	0.45	-	-
Cement	100%	860	3.14	273.9
Silica Fume	35% of cement	301	2.63	114.4
Fly Ash	100% of cement	860	2.63	327.0
Water for cement	38% cement	327	1.00	326.8
Water for Silica	38.5% silica	116	1.00	115.8
Water for Fly ash	38.5% fly ash	331	1.00	330.9
Total		**2795**		**1488.9**
Density (g/cc)	**1.88**			
Density (lbm/gal)	**15.66**			

Table 3 Cement Class H plus 35%silica

Material	Percent	Mass (g)	Specific Gravity	Volume (cc)
HEC	0.1% of water of filler	0.12	-	-
Cement	100%	860	3.14	273.9
Silica Fume	35% of cement	301	2.63	114.4
Fly Ash	100% of cement	0	2.63	0.0
Water for cement	38% cement	327	1.00	326.8
Water for Silica	38.5% silica	116	1.00	115.8
Water for Fly ash	38.5% fly ash	0	1.00	0.0
Total		**1604**		**831.0**
Density (g/cc)	**1.93**			
Density (lbm/gal)	**16.11**			

Table 4 Cement Class G+35%silica +100%fly ash

Material	Percent	Mass (g)	Specific Gravity	Volume (cc)
HEC	0.1% of water of filler	0.45	-	-
Cement	100%	860	3.14	273.9
Silica Fume	35% of cement	301	2.63	114.4
Fly Ash	100% of cement	860	2.63	327.0
Water for cement	44% cement	378	1.00	378.4
Water for Silica	38.5% silica	116	1.00	115.8
Water for Fly ash	38.5% fly ash	331	1.00	330.9
Total		**2846**		**1540.5**
Density (g/cc)	**1.85**			
Density (lbm/gal)	**15.42**			

Table 5 Cement Class G+35%silica

Material	Percent	Mass (g)	Specific Gravity	Volume (cc)
HEC	0.1% of water of filler	0.12	-	-
Cement	100%	860	3.14	273.9
Silica Fume	35% of cement	301	2.63	114.4
Fly Ash	100% of cement	0	2.63	0.0
Water for cement	44% cement	378	1.00	378.4
Water for Silica	38.5% silica	116	1.00	115.8
Water for Fly ash	38.5% fly ash	0	1.00	0.0
Total		**1655**		**882.6**
Density (g/cc)	**1.88**			
Density (lbm/gal)	**15.65**			

We also contacted Dr. Daniel Resasco from our Chemical Engineering department and Dr. Cornell from the University of Tulsa to explore the possibility of running XRD tests. Using XRD measurements, the compositional change occurring in the cement as a result of acid attack can be determined.

5. Project Expenditures

This section presents the project expenses during the months of June (Table 3) and the cumulative expenditures.

Table 3 Current and cumulative expenditures, June, 2012

No.	Budget Categories	Current Expenses	Cumulative Expenses
1	Salaries & Wages	$33,014.61	$59,585.99
2	Fringe Benefits	$11,494.95	$15,045.83
3	Project Materials	$604.60	$34,663.74
4	Travel	$139.31	$1,077.22
5	Conference Expenses	$0.00	$0.00
6	Other Direct Costs	$0.00	$305.38
7	Equipment	$4,818.44	$102,531.76
8	Space Rental	$0.00	$0.00
9	Indirect Cost	$22,626.74	$55,339.11
10	**Total**	**$72,698.65**	**$268,549.03**

Nomenclature

$\dot{\alpha}$	Normalized hydration rate
A_α	Chemical affinity
η_α	Permeability of the hydration products around the anhydrous cement
E_a	Apparent activation energy
R	Universal gas constant
T	Absolute temperature
α_u	Ultimate degree of hydration
α	Degree of hydration
Blaine	Fineness of cement particles
s(α, p)	Effect of applied hydrostatic pressure p
p	Hydrostatic pressure
R_p	Polarization Resistance
i_{corr}	Corrosion Current
B	Empirical polarization resistance constant
*Y**	Admittance representation
K_{mt}	Mass transfer coefficient
$[Fe^{2+}]_s$	Iron ion concentration on the metal surface
$[Fe^{2+}]_b$	Iron ion in the bulk solution
F	Faraday constant
K_{Fe}	Electrochemical reaction rate constant of iron ions
B	Transfer coefficient (the value of B is 0.5 for most of the reactions),
E_{corr}	Corrosion potential
E^o_{Fe}	Standard potential of iron at temperature T
K_1	First dissociation constant of Carbonic Acid
K_2	Second dissociation constant of Carbonic Acid
h	Plank's constant
ϑ	Frequency of vibration of complex
K	Boltzman's constant.
R_x	Reaction rate constant
$\Delta G^{\#}$	Gibbs free energy
i_o	Exchange current density
E_o	Equilibrium open circuit potential

References

Adsani, E., Shirazi, S.A. Shadley, J.R., Rybicki, E.F. 2006. Validation of Mass Transfer Coefficient Models used in Predicting CO_2 Corrosion in Vertical Two-Phase Flow in the Oil and Gas Production, Paper 06573, presented at the NACE Corrosion conference, Houston, TX.

Anderko, A. and Young, R. D. 1999. Simulation of CO_2/H_2S Corrosion Using Thermodynamic and Electrochemical Models, Paper No. 31, presented at the NACE CORROSION conference, Houston, TX.

Anderko, A. 2000. Simulation of $FeCO_3$/FeS Scale Formation Using Thermodynamic and Electrochemical Models, Paper No. 102, presented at the NACE CORROSION conference, Houston, TX.

Bentz, D.P. and Garboczi, E.J. 1992. Modeling the leaching of calcium hydroxide from cement paste: effects on pore space percolation and diffusivity, Materials and Structures, Volume 25, Number 9, 523-533, DOI: 10.1007/BF02472448.

Bentz, D.P., Garboczi, E.J., 1989. A digitized simulation model for microstructural development, in: S. Mindess (Ed.), Advances in Cementitious Materials, American Ceramic Society, Westville, Ohio, USA, pp. 211–226.

Bogue, R.H., 1947. The Chemistry of Portland Cement, Reinhold Publishing Corp., New York, USA.

Bonis, M. R. and Crolet, J. L. 1989. Basics of the Prediction of the Risks of CO_2 Corrosion in Oil and Gas Wells. Paper No. 466, presented at the NACE CORROSION conference, Houston, TX.

Chokshi, K., W. Sun, S. Nešić, 2005. Iron carbonate film growth and the effect of inhibition in CO_2 corrosion of mild steel, NACE International corrosion conference: Houston, TX.

Crolet, J. L., Bonis, M. R., 1991. Prediction of the Risks of CO2 Corrosion in Oil and Gas Well.SPE Production Engineering, Vol. 6, No. 4, p. 449.

Crolet, J.-L. and Bonis, M.R. 1991. Prediction of the Risks of CO2 Corrosion in Oil and Gas Well, SPE Prod. Eng. 6, p. 449.

Danielson, U., 1962. Heat of hydration of cement as affected by water–cement ratio, Paper IV-S7, Proceedings of the 4th International Symposium on the Chemistry of Cement, Washington DC, USA, pp. 519–526.

Dayalan, E., Vani, G., Shadley, J.R., Shirazi, S.A. and Rybicki, E.F. 1995. Modeling CO_2 corrosion of carbon steel in pipe flow, Paper No. 118, presented at the NACE corrosion conference.

Dayalan, E., de Moraes, F.D., Shadley, J.R., Shirazi, S.A., Rybicki, E.F., 1998. CO2 Corrosion Prediction in Pipe Flow Under $FeCO_3$ Scale-Forming Conditions, Paper no. 51, presented at the NACE CORROSION conference, Houston, TX.

de Waard, C.and Milliams, D.E., Corrosion 31 (1975): p. 131.

de Waard, C, Lotz, U., Milliams, D.E., Corrosion 47 (1991): p. 976.

de Waard, C, Lotz, U. and Dugstad, A. 1995. Influence of Liquid Flow Velocity on CO_2 Corrosion: A Semi-Empirical Model, Paper No. 128, presented at the NACE CORROSION conference, Houston, TX.

de Waard, C., Smith, L. and Craig, B.D. 2003. The Influence of Crude Oil on Well Tubing Corrosion Rates, Paper No. 03629, presented at the NACE CORROSION conference, Houston, TX.

Dugstad, A., Lunde, L. and Videm, K. 1994. Parametric Study of CO_2 Corrosion of Carbon Steel, Paper No. 14, presented at the NACE CORROSION conference, Houston, TX.

Epelboin, I., M. Keddam, and H. Takenouti, 1972. Use of impedance measurements for the determination of the instant rate of metal corrosion Journal of Applied Electrochemistry, 2: p. 71-79.

Fang, H., B. Brown, and S. Nešić, High salt, 2010. concentration effects on CO_2 corrosion and H_2S corrosion. NACE Intrnational corrosion conference, San Antonio, TX.

Fosbøl, P.L., Thomsen, K., Stenby, E. H., 2009. Improving mechanistic CO_2 corrosion Models.

Garber, J.D., Polaki, V., Adams, C. and Varanasi, N.R. 1998. Modeling Corrosion Rates in Non-Annular Gas Condensate Wells Containing CO_2, Paper No. 53, presented at the NACE CORROSION conference, Houston, TX.

Gartland, P.O. and Salomonsen, J. E. 1999. A Pipeline Integrity Management Strategy Based on Multiphase Fluid Flow and Corrosion Modelling, Paper No. 622, prestned at CORROSION conference, Houston, TX.

Gartland, P.O., Johnsen, R. and Øvstetun, I., 2003. Application of Internal Corrosion Modeling in the Risk Assessment of Pipelines, Paper No. 03179, presented at the NACE CORROSION conference, Houston, TX.

Gray, L.G.S., B.G. Anderson, M.J. Danysh, P.G. Tremaine, 1989. Mechanism of carbon steel corrosion in brines containing dissolved carbon dioxide at pH 4, NACE International corrosion conference: Houston, TX.

Gunaltun, Y. M., 1996. Combining research and field data for corrosion rate prediction. Paper No. 27, presented at the NACE CORROSION conference, Houston, TX.

Halvorsen, A.M.K., Søntvedt, T., 1999. CO_2 Corrosion Model for Carbon Steel Including a Wall Shear Stress Model for Multiphase Flow and Limits for Production Rate to Avoid Mesa Attack, Paper No. 42, presented at the NACE CORROSION conference, Houston, TX.

Hassani, S., Roberts K.P., Shirazi S.A., Shadley J.R., Rybicki E.F., Joia C., 2011. Flow Loop Study of Chloride Concentration Effect on Erosion, Corrosion and Erosion-Corrosion of carbon Steel in CO_2 Saturated Systems, NACE International corrosion conference, Houston, TX.

Hedges, B. Chapman, R., Harrop, D., Mohammed, I., Sun, Y., 2005. A Prophetic CO_2 Corrosion Tool - But When is it to be Believed?, Paper No. 05552, presented at the NACE CORROSION conference, Houston, TX, April 3 - 7.

Heidersbach, R., 2011. Metallurgy and Corrosion Control in Oil and Gas Production. Hoboken, NJ: Wiley.

High, M.S., Wagner, J. and Natarajan, S. 2000. Mechanistic Modeling of Mass Transfer in the Laminar Sublayer in Downhole Systems, Paper No. 62, presented at the NACE CORROSION conference, Houston, TX.

Hoffmeister, 2005. Modeling of H_2S Corrosion by Coupling of Phase and Polarization Behavior, Paper No. 5476, presented at the NACE CORROSION conference, Houston, TX, April 3 - 7.

Hoffmeister, 2007, Modeling the Effect of Chloride Content on H_2S Corrosion by Coupling of Phase and Polarization Behavior, Paper No. 7501, presented at the NACE CORROSION conference, Nashville, TN, March 11 – 15.

Hudak, P.F. and D.J. Wachal, 2001. Effects of brine injection wells, dry holes, and plugged oil/gas wells on chloride, bromide, and barium concentrations in the Gulf Coast Aquifer, southeast Texas, USA. Environment International, 26(7-8): p. 497-503.

Jacquemet,J., Pironon, J., Lagneau, V., Saint-Marc, J., 2012. Armouring of well cement in H_2S–CO_2-saturated brine by calcite coating–Experiments and numerical modeling. Applied Geochemistry 27. 782–795

Jepson, W.P., Kang, C., Gopal, M. and Stitzel, S. 1997. Model for Sweet Corrosion in Horizontal Multiphase Slug Flow, Paper No. 11, presented at the NACE CORROSION conference, Houston, TX.

John, R.C., Jordan, K. G., Young, A. L., Kapusta, S. D. and Thompson, W. T. 1998. SweetCor: An Information System for the Analysis of Corrosion of Steels by Water and Carbon Dioxide, Paper No. 20, presented at the NACE CORROSION conference, Houston, TX.

Keienburg, R.R., 1976. Particle Size Distribution and Normal Strength of Portland Cement, PhD Thesis, Karlsruhe University, Germany.

Kvarekval. J. and Videm, K., 1995. Corrosion of Carbon Steel in Carbon Dioxide-Saturated Solutions Containing Small Amounts of Hydrogen Sulfide. NACE international, April.

Lerch, W. Ford, C.L., 1948. Long-term study of cement performance in concrete: chapter 3. Chemical and physical tests of the cements, ACI Journal 19 (8) 745–795.

Lin, F., Meyer, C., 2009. Hydration kinetics modeling of Portland cement considering the effects of curing temperature and applied pressure, Cement and Concrete Research 39, 255–265.

McMahon, A.J., Paisley, D.M.E., 1997. Corrosion Prediction Modelling—A Guide to the Use of Corrosion Prediction Models for Risk Assessment in Oil and Gas Production and Transportation Facilities, Report no. ESR.96.ER.066 (Sunbury: BP International)

Millero, F., Huang, F., Graham, T., Pierrot, D., 2007, The dissociation of carbonic acid in NaCl solutions as a function of concentration and temperature, *Geochimica et Cosmochimica Acta* 71 pp. 46-55

Nesic, S., Postlethwaite, J., Olsen, S., 1996. An Electrochemical Model for Prediction of Corrosion of Mild Steel in Aqueous Carbon Dioxide Solutions. Corrosion, Vol. 52, No. 4, p. 280.

Nesic, S., Nordsveen, M., Nyborg, R., Stangeland, A., 2003. A Mechanistic Model for CO_2 Corrosion with Protective Iron Carbonate Films - Part 2: A Numerical Experiment. Corrosion, Vol. 59, No. 6, pp. 489-497.

Nesic, S., Li, H., Huang, J., Sormaz, D., 2009. An Open Source Mechanistic Model for CO_2 / H_2S Corrosion of Carbon Steel, NACE corrosion conference, Paper No. 9572

Nešić, S. 2007. Key issues related to modeling of internal corrosion of oil and gas pipelines, Corrosion Science, Vol. 49, Issue 12, December 2007, Pages 4308–4338.

Nordsveen, M., Nesic, S., Nyborg, R., Stangeland, A., 2003. A Mechanistic Model for CO_2 Corrosion with Protective Iron Carbonate Films - Part 1: Theory and Verification. Corrosion, Vol. 59, No. 5, pp. 443-456.

NORSOK Standard no. M-506. 1998. CO2 Corrosion Rate Calculation Model. Norwegian Technology Standards Institution, http://www.nts.no/norsok

Nyborg, R. Dugstad, A., 2003. Understanding and Prediction of Mesa Corrosion Attack, Paper No. 3642, presented at the NACE CORROSION conference, San Diego CA, March.

Nyborg, R., 2006. Field Data Collection, Evaluation and Use for Corrosivity Prediction and Validation of Models, Part II: Evaluation of Field Data and Comparison of Prediction Models, Paper no. 06118, NACE CORROSION conference, Houston, TX.

Nyborg, R., 2009. Guidelines for prediction of CO2 corrosion in oil and gas production systems, Material Technology, IFE, Kjeller, ISBN 978-82-7017-791-2.

Nyborg, R. 2010. CO2 Corrosion Models for Oil and Gas Production Systems, Paper No 10371, presented at the NACE corrosion conference, March 14 - 18, San Antonio, TX.

Perkins, R.S., Fang, C.S., Garber, J. D., Singh, R. K., 1996. Predicting Tubing Life in Annular-Flow Gas Condensate Wells Containing Carbon Dioxide, Corrosion, Vol. 52, No. 10, p. 801.

Pots, B.F.M., 1995. Mechanistic Models for the Prediction of CO_2 Corrosion Rates under Multi-Phase Flow Conditions, Paper No. 137, NACE CORROSION conference, Houston, TX.

Pots, B.F.M., John, R.C., Rippon, I.J., Thomas, J.S., Kapusta, S. D., Girgis, M. M. and Whitham, T. 2002. Improvements on de Waard - Milliams Corrosion Prediction and Applications to Corrosion Management, Paper No. 02235, presented at the NACE CORROSION conference, Houston, TX.

Pots, B.F.M. and Kapusta, S. D., 2005. Prediction of Corrosion Rates of the Main Corrosion Mechanisms in Upstream applications, Paper No. 05550, presented at the NACE CORROSION conference, Houston, TX.

Ramachandran, S., Ward M. B., and Bartrip, K. A., 2002. Molecular Modeling of Corrosion of Iron in H2S Environments, Paper No. 2240, presented at the NACE corrosion conference, April 7 - 11, Denver, CO.

Ramirez, M. and Ruiz, A.,1998. The Effect of Small Amounts of H_2S on CO_2 Corrosion of a Carbon Steel. NACE international.

Roberge, P.R., 1999. Handbook of Corrosion Engineering. New York: McGrow-Hill.

Ropital, F., 2010. Corrosion and degradation of metallic materials: Understanding of the phenomena and applications in petroleum and process industries.

Sangita, K. A. and Srinivasan, S., 2000. An Analytical Model to Experimentally Emulate Flow Effects in Multiphase CO2/H2S Systems. Paper No. 58, presented at the NACE CORROSION conference, Houston, TX.

Silva, C.A.R., X. Liu, and F.J. Millero, 2002. Solubility of Siderite in NaCl Solutions. Journal of Solution Chemistry, 31(2): p. 97-108.

Smith S. N., Pacheco, J.L., 2002, Prediction of Corrosion in Slightly Sour Environment, Paper No. 2241, presented at the NACE International corrosion conference, Houston TX.

Smith, L. and de Waard, C. 2005. Corrosion Prediction and Materials Selection for Oil and Gas Producing Environments, Paper No. 05648, presented at the NACE CORROSION conference, Houston, TX.

Srinivasan, S. and Kane, R. D., 1996. Prediction of Corrosivity of CO_2/H_2S Production environments. Paper No. 11, presented at the NACE CORROSION conference, Houston, TX.

Srinivasan S. and Kane, R. D. 2003. Critical Issues in the Application and Evaluation of a Corrosion Prediction Model for Oil and Gas Systems. Paper No. 03640, presented at the NACE CORROSION conference, Houston, TX.

Srinivasan, S., Kane, R.D., 1996. Prediction of Corrosivity of CO_2/H_2S Production Environments, Paper No. 11, presented at the NACE CORROSION conference, Houston, TX.

Sun, W., Nesic, S. 2007. A Mechanistic Model of H_2S Corrosion of Mild Steel, Paper No. 7655, presented at the NACE corrosion conference, March 11 - 15, Nashville, TN.

Sun, W., Nesic, S. 2008. A Mechanistic Model of Uniform Hydrogen Sulfide/Carbon Dioxide Corrosion of Mild Steel, Corrosion Journal, Vol. 65. No, 5.

Sun, W., S. Nesic, and R.C. Woollam, 2009. The effect of temperature and ionic strength on iron carbonate ($FeCO_3$) solubility limit. Corrosion Science, 51(6): p. 1273-1276.

Schmitt, G. and B. Rothmann, 1977. Corrosion Mechanism of Unalloyed Steel in Oxygen-Free Carbon Dioxide Solutions - 1. Untersuchungen Zum Korrosionsmechanismus Von Unlegiertem Stahl In Sauerstoffreinen Kohlensaeureloesungen - 1. Kinetik Der Wasserstoffabscheidung., 28(12): p. 816-822.

Shoesmith, D.W., Taylor, P., Bailey, M.G., Owen, D.G., 1980. The formation of ferrous monosulfide polymorphs during the corrosion of iron by aqueous hydrogen sulfide at 21 C, J. Electrochem. Soc. 127, 1007–1015.

Taplin, J.H., 1969. A method for following hydration reaction in Portland cement paste, Australian Journal of Applied Sciences 10 329–345.

Uhlig, H.H.a.R.W.R., 1985. Corrosion and corrosion control: An introduction to corrosion science and engineering. 4th ed. Hoboken, NJ: John Wiley & Sons.

Wang, S., K. George, S. Nešić, 2004. High pressure CO_2 corrosion electrochemistry and the effect of acetic acid, NACE International corrosion conference: Houston, TX.

Zhang, G.A. and Y.F. Cheng, 2009. Electrochemical corrosion of X65 pipe steel in oil/water emulsion. Corrosion Science, 51(4): p. 901-907.

Zhang, R., Gopal, M. and Jepson, W.P. 1997. Development of a Mechanistic Model for Predicting Corrosion Rate in Multiphase Oil/Water/Gas Flows, Paper No. 601, presented at the NACE CORROSION conference, Houston, TX.

Zhou, Q., Beaudoin, J.J., 2003. Effect of applied hydrostatic stress on the hydration of Portland cement and C_3S, Advances in Cement Research 15 (1) 9–16

Appendix A

Cement Hydration Modeling

Summary

Cement hydration modeling is essential to predict the amount of calcium presents in the CH and CSH phase of cement after curing and before aging. Calcium concentration in the solid phase (matrix) is necessary to predict the degradation depth, mechanical properties, and permeability of the cement using degradation models.

The rate and degree of cement hydration depends on cement composition, water-cement ratio, temperature, pressure, and cement fineness. Results obtained from a recent hydration model proposed by Lin and Meyer 2009 showed a good agreement with experimental data for seven different types of cement. The model is applied to predict the hydration degree of cement class H and G used in this project at two different temperatures. Maximum degree of hydration for class H and G is about 60%, which happens after 100 hours of curing in temperature of 200^{o}F. Therefore, sample curing for more than 4 days at temperature of 200^{o}F is sufficient to get the maximum possible hydration.

During this investigation, samples will be cured for 5 days at temperature of 200ºF. The hydration model provides the free (unhydrated) water remained after hydration, which is needed to predict the cement porosity after curing. Porosity prediction for cement class H cured for five days at temperature of 200^{o}F is approximately 26% which showed a good agreement with experimental data (25-30%). Porosity prediction for cement class G cured for five days at temperature of 200^{o}F was about 31%. Higher porosity for class G in comparison with class H is related to the higher water-cement ratio of class G cement. Porosity of sample after curing and before aging is used in leaching model to predict the degradation depth, mechanical properties, and permeability of the cement.

Adding silica fume to the cement affects the amount of CH and CSH in cement. Silica reacts with about 25% of free CH and produces CSH. Therefore, silica decreases the amount of CH and increases the amount of CSH.

A.1. Cement Hydration Modeling

Portland cement contains four crystalline compounds that hydrate to form a rigid structure. These compounds are: i) Tricalcium Silicate: $3CaO.SiO_2$ (C_3S, main contributor to the cement strength); ii) Dicalcium Silicate: $2CaO.SiO_2$ (C_2S, provides long term strength); iiI) Tricalcium Aluminate: $3CaO.Al_2O_3$ (C_3A, promote rapid hydration of cement); iv) Tetracalcium

Aluminoferrite: $4CaO.Al_2O_3.Fe_2O_3$ (C_4AF). During cement hydration, the main reaction products formed are tobermorite gel ($3CaO.2SiO_2.3H_2O$), which is known as calcium silicate hydrate (CSH) phase and the portlandite/calcium hydroxide (CH).

$$2(3CaO.SiO_2) + 6H_2O \rightarrow 3CaO.2SiO_2.3H_2O + 3Ca(OH)_2 \quad \text{(A.1)}$$

$$2(2CaO.SiO_2) + 4H_2O \rightarrow 3CaO.2SiO_2.3H_2O + Ca(OH)_2 \text{ (slow reaction)} \quad \text{(A.2)}$$

$$3CaO.Al_2O_3 + 12H_2O + Ca(OH)_2 \rightarrow 3CaO.Al_2O_3.Ca(OH)_2.12H_2O \text{ (fast reaction)} \quad \text{(A.3)}$$

$$3CaO.Al_2O_3 + 10H_2O + CaSO_4.2H_2O \rightarrow 3CaO.Al_2O_3.CaSO_4.12H_2O \quad \text{(A.4)}$$

$$4CaO.Al_2O_3.Fe_2O_3 + 10H_2O + 2CaO.H_2O \rightarrow 6CaO.Al_2O_3.Fe_2O_3.12H_2O \text{ (slow)} \quad \text{(A.5)}$$

The hydration of cement causes heat generation, strength development and shrinkage. A thorough understanding of chemical, physical and mechanical processes is important for cement hydration modeling.

Lin and Meyer (2009) developed a hydration kinetics model for Portland cement which is applicable for elevated temperatures and high pressure conditions. The model is based on thermodynamics analysis of multiphase porous media which was first proposed by Ulm and Coussy (1995). This model considers the effects of chemical composition and fineness of cement, water–cement ratio, curing temperature, and applied pressure the analysis. The model was calibrated using the experimental data obtained from eight different Portland cements. In addition, correlations were developed to relate model parameters and cement composition.

CH and CSH concentration in cement is needed for predicting the leaching rate, degradation depth, porosity, permeability, and mechanical properties of well cement. Degree of hydration has to be predicted in order to calculate the CH and CSH concentrations in cement. In this project, the model developed by Lin and Meyer (2009) is used to predict the hydration level in cement specimens. Applying the model, degree of hydration can be predicted as a function of influential parameters such as chemical composition of cement (i.e. C_3S, C_2S, C_3A, and C_4AF weight fraction), temperature, water-cement ratio, pressure, and fineness of cement. In this study, the effects of different influential parameters on the degree of hydration are investigated.

A.1.1 Effects of Influential Parameters on Hydration Rate

A.1.1.1 Chemical Composition of Cement

The composition of cement is one of the most important influential parameters that affects degree of cement hydration. Because of different reaction rates of the clinker phases (i.e. C_3S, C_2S, C_3A, and C_4AF) and their interactions, it is generally accepted that the so-called degree of hydration of cement is just an overall and approximate measure.

A.1.1.2 Water-Cement Ratio

Experimental results have shown that a higher water–cement ratio leads to a higher hydration rate after the middle period of hydration, but only has a small effect on the hydration rate in the early stage. The water–cement ratio also determines the ultimate degree of hydration (α_u). Theoretically, a water–cement ratio of about 0.4 is sufficient for the complete hydration of cement (i.e. α_u=1.0). The hydration products around the anhydrous cement particles prevent further hydration if there is insufficient amount of free water in the macro-pores.

A.1.1.3 Fineness

The finer cement particles lead to the higher α_u, and consequently the higher the hydration rate. Bentz and Haecker (1989) also found that at low water–cement ratios, the influence of cement fineness on α_u diminishes. A finer cement, or cement with a larger surface area, provides a larger contact area with water and hence causes a higher hydration rate. Also, at the same degree of hydration, a larger surface area corresponds to a smaller thickness of hydration products around the anhydrous cement particles, which increases the ultimate degree of hydration. Apart from fineness, the particle size distribution of cement influences the hydration rate.

A.1.1.4 Curing Temperature

The effects of curing temperature on hydration kinetics have been shown to be twofold. On the one hand, the reaction rate $\dot{\alpha}$ increases with the increase in temperature. On the other hand, the density of hydration products at higher temperature is higher, which slows down the permeation of free water through the hydration products. Therefore, during the late period, the hydration rate is lower at elevated temperature and the ultimate degree of hydration may thus also be lower.

A.1.1.5 Pressure

Zhou and Beaudoin (2003) found that applied hydrostatic pressure increases the hydration rate of Portland cement; however, it has only a negligible effect on the pore structure of hydration products when different cement pastes at similar degrees of hydration are compared. This finding is important since it implies that the density of the hydration products is not considerably affected by the applied hydrostatic pressure, at least not up to 6.8 MPa, which is the pressure they used in the investigation.

A.1.2 Cement Hydration Mechanism

Van Breugel (1991) suggested three main stages (early, middle and late periods) of cement hydration. The early stage includes a short period of rapid chemical dissolution, termed as the pre-induction period, which is followed by a dormant stage, which lasts for several hours. After that, cement hydration enters the middle stage that can last for 24 to 48 hours, in which ions transport to and from the surfaces of anhydrous cement particles through gradually growing layers of hydration products. During the late stage, which is the longest and dominant one, the reaction is totally diffusion-controlled. The free water in macro-pores diffuses through the hydration products formed around the anhydrous cement core, making further reactions possible. It was reported that cement hydration follows two different mechanisms (phase boundary and diffusion controlled mechanisms) at different stages. During the early and middle periods, the phase boundary mechanism prevails, while in the late period, the diffusion-controlled reaction dominates. However, it is very difficult to define a clear or definite boundary between the two mechanisms.

The hydration model presented by Lin and Meyer (2009) is a unified model. It considers the phase boundary mechanism as a special case of the diffusion-controlled reaction when the layers of hydration products around the anhydrous cement cores are very thin. The mechanisms of cement hydration are then unified to be the diffusion-controlled one. Cement hydration is interpreted as a chemical reaction in which the free water in the macro-pores combines as a reactant phase with the anhydrous cement and becomes the chemically bound water as a product phase, and the dominant mechanism of the reaction kinetics is the diffusion of free water through layers of hydration products.

A.1.3 Cement Hydration Model Formulation

The normalized hydration rate $\dot{\alpha}$ can be written as:

$$\dot{\alpha} = A_\alpha \eta_\alpha \exp\left(-\frac{E_a}{RT}\right) \exp\left(-\frac{E_a}{293R}\right) \quad \text{(A.6)}$$

where A_α is chemical affinity, η_α represents the permeability of the hydration products around the anhydrous cement and can be calculated using Eqs. (A.17) through (A.22), E_a is the apparent activation energy (Eq. A.23), R is the universal gas constant, and T is the absolute temperature. The normalization in Eq. (A.6) ensures that the material constants of the model can be obtained from experimental results at room temperature and will not vary considerably for different values of activation energy.

The chemical affinity A_α is expressed as:

$$A_\alpha\left(\alpha, \frac{W}{C}, Blaine, P\right) = k\left(\frac{A_o}{k\alpha_u} + \alpha\right).(\alpha_u - \alpha).S(\alpha, P) \quad \text{(A.7)}$$

where the constants k can be represented by a nonlinear function (Eq. A.8) of mass fractions of C_3S, C_2S, and C_3A (Bogue, 1947). A_o can be calculated using Eqs. (A.9) and (A.10). α_u is ultimate degree of hydration which can be calculated using Eq.(A.11) through (A.14). α is degree of hydration. Blaine represents the fineness of cement particles. The function s(α, p) represents the effect of applied hydrostatic pressure p which can be calculated using Eq. (A.16).

$$k = 0.56\left(P_{C_3S}\right)^{-0.206}\left(P_{C_2S}\right)^{-0.128}\left(P_{C_3A}\right)^{0.161} \quad \text{(A.8)}$$

$$A_o = \frac{\acute{A}_o \times Blaine}{350} \quad \text{(A.9)}$$

$$\acute{A}_o = -0.0767 P_{C_4AF} + 0.0184 \quad \text{(A.10)}$$

$$\alpha_u = \alpha_{u,293} exp[-0.00003(T - 293)^2 . SGN(T - 293)] \quad \text{(A.11)}$$

$$\alpha_{u,293} = \frac{\beta_1(Blaine) \times \frac{W}{C}}{\beta_2(Blaine) + \frac{W}{C}} \leq 1.0 \quad \text{(A.12)}$$

$$\beta_1(Blaine) = \frac{1}{9.33\left(\frac{Blaine}{100}\right)^{-2.82} + 0.38} \quad \text{(A.13)}$$

$$\beta_2(Blaine) = \frac{Blaine-220}{147.78+1.656(Blaine-220)} \quad \text{(A.14)}$$

Equations (A.13) and (A.14) are valid for Blaine ≥ 270 m^2/kg. When Blaine < 270 m^2/kg, β_1 and β_2 are assumed to be constant.

$$SGN(T-293) = \begin{cases} 1, when\ T \geq 293K \\ -1, when\ T < 293K \end{cases} \quad \text{(A.15)}$$

$$S(\alpha, P) = exp\left\{0.02\left(\frac{P}{P_{atm}}-1\right)^{0.07}\left[\frac{\alpha}{\alpha_u}-1.5\left(\frac{\alpha}{\alpha_u}\right)^2+0.4\right]\right\} \quad \text{(A.16)}$$

Free water permeability can be written as the following correlation.

$$\eta_\alpha = exp(-n\alpha) \quad \text{(A.17)}$$

In which "n" is a parameter that depends on curing temperature, degree of hydration, and fineness of cement. The value of "n" can be determined using Equations (A.18) through (A.22).

$$n = n_o f_1(Blaine, \alpha).f_2(T, \alpha) \quad \text{(A.18)}$$

$$n_o = 10.945\left(P_{C_3S}\right) + 11.25\left(P_{C_2S}\right) - 4.1\left(P_{C_3A}\right) - 0.892 \quad \text{(A.19)}$$

$$f_1(Blaine, \alpha) = 1 + (1-\alpha)^2.Ln\left(\frac{350}{Blaine}\right) \quad \text{(A.20)}$$

$$f_2(T, \alpha) = \left(\frac{V_{293}}{V(T)}\right)^{10(\alpha)^4} \quad \text{(A.21)}$$

$$\frac{V_{293}}{V(T)} = exp(28 \times 10^{-6}(T-293)^2) \quad \text{(A.22)}$$

Apparent activation energy (E_a) can be calculated using the Eq. (A.23) as a function of C_3A, and C_4AF weight fractions and Blaine fineness of cement.

$$E_a = 22100 \times \left(P_{C_3A}\right)^{0.3}\left(P_{C_4AF}\right)^{0.25}(Blaine)^{0.35} \quad \text{(A.23)}$$

In general, hydration degree can be written as a function of chemical composition of cement (i.e. C_3S, C_2S, C_3A, and C_4AF weight fraction), temperature, water-cement ratio, pressure, and fineness of cement (Eq. A.24).

$$\frac{d\alpha}{dt} = \dot{\alpha} = A_\alpha \eta_\alpha \exp\left(-\frac{E_a}{RT}\right)\exp\left(-\frac{E_a}{293R}\right)$$

$$= 0.56\left(P_{C_3S}\right)^{-0.206}\left(P_{C_2S}\right)^{-0.128}\left(P_{C_3A}\right)^{0.161}\left(\frac{A_o}{0.56\left(P_{C_3S}\right)^{-0.206}\left(P_{C_2S}\right)^{-0.128}\left(P_{C_3A}\right)^{0.161}\frac{\frac{1}{9.33\left(\frac{Blaine}{100}\right)^{-2.82}+0.38}\times\frac{W}{C}}{\frac{Blaine-220}{147.78+1.656(Blaine-220)}+\frac{W}{C}}\times exp[-0.00003(T-293)^2]}\right.$$

$$\left.+\alpha\right).\left(\frac{\frac{1}{9.33\left(\frac{Blaine}{100}\right)^{-2.82}+0.38}\times\frac{W}{C}}{\frac{Blaine-220}{147.78+1.656(Blaine-220)}+\frac{W}{C}}\times exp[-0.00003(T-293)^2]\right.$$

$$\left.-\alpha\right).exp\left\{0.02\left(\frac{P}{P_{atm}}-1\right)^{0.07}\left[\frac{\alpha}{\frac{1}{9.33\left(\frac{Blaine}{100}\right)^{-2.82}+0.38}\times\frac{W}{C}}{\frac{Blaine-220}{147.78+1.656(Blaine-220)}+\frac{W}{C}}\times exp[-0.00003(T-293)^2]}-1.5\left(\frac{\alpha}{\frac{1}{9.33\left(\frac{Blaine}{100}\right)^{-2.82}+0.38}\times\frac{W}{C}}{\frac{Blaine-220}{147.78+1.656(Blaine-220)}+\frac{W}{C}}\times exp[-0.00003(T-293)^2]}\right)^2\right]\right.$$

$$\left.+0.4\right\}exp\left(-\left[\left\{10.945\left(P_{C_3S}\right)+11.25\left(P_{C_2S}\right)-4.1\left(P_{C_3A}\right)-0.892\right\}\left\{1\right.\right.\right.$$

$$\left.\left.\left.+(1-\alpha)^2.Ln\left(\frac{350}{Blaine}\right)\right\}.\left(exp(28\times10^{-6}(T-293)^2)\right)^{10(\alpha)^4}\right]\alpha\right)exp\left(-\frac{22100\times\left(P_{C_3A}\right)^{0.3}\left(P_{C_4AF}\right)^{0.25}(Blaine)^{0.35}}{RT}\right)\exp\left(-\frac{22100\times\left(P_{C_3A}\right)^{0.3}\left(P_{C_4AF}\right)^{0.25}(Blaine)^{0.35}}{293R}\right)$$

……..…(A.24)

A.1.4 Model Validation

Figures A.1 through A.4 compare model predictions with published experimental measurements (Lerch and Ford 1948, Keienburg, 1976, Danielson, 1962, Taplin, 1969). Seven different cements shown in Table A.1 are used to validate the model. A satisfactory agreement is found between the model and experimental measurements.

Table A.1 Cement composition and the corresponding material constants

	Bogue Composition				
Cement ID#	C_3S	C_2S	C_3A	C_4AF	Blaine Fineness (m^2/kg)
#A (Lerch and Ford 1948)	0.514	0.226	0.111	0.079	372
#B (Lerch and Ford 1948)	0.416	0.344	0.054	0.132	314
#C (Lerch and Ford 1948)	0.600	0.135	0.089	0.081	564
#D (Lerch and Ford 1948)	0.240	0.515	0.049	0.116	360
#E (Keienburg, 1976)	0.717	0.059	0.090	0.100	350
#F (Danielson, 1962)	0.567	0.172	0.067	0.079	312
#H (Taplin, 1969)	0.414	0.340	0.098	0.075	312

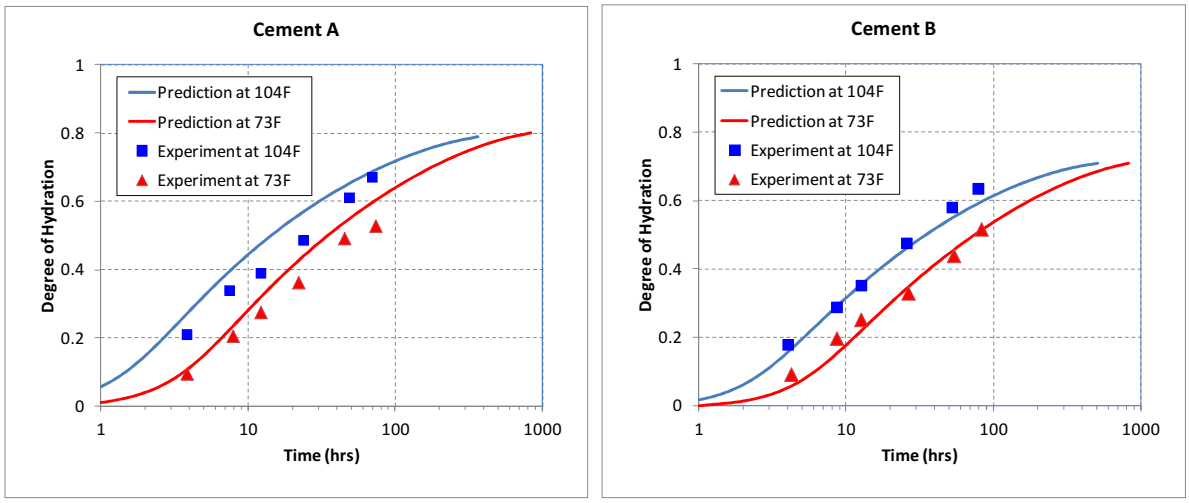

Fig. A.1 Comparison between experimental data and model predictions for cement #A and #B at different temperatures

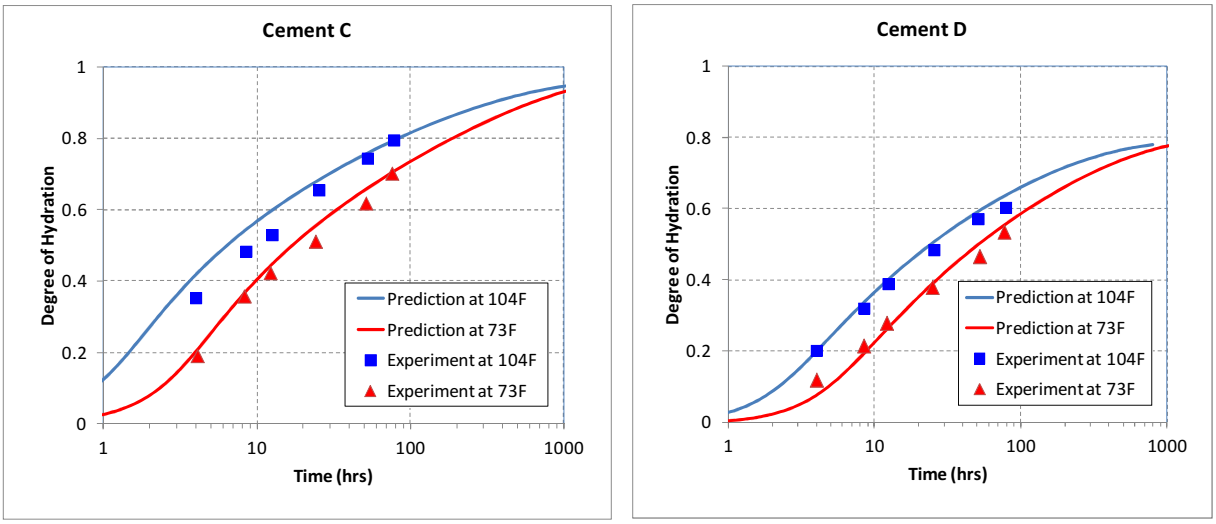

Fig. A.2 Comparison between experimental data and model predictions for cement #C and #D at different temperatures

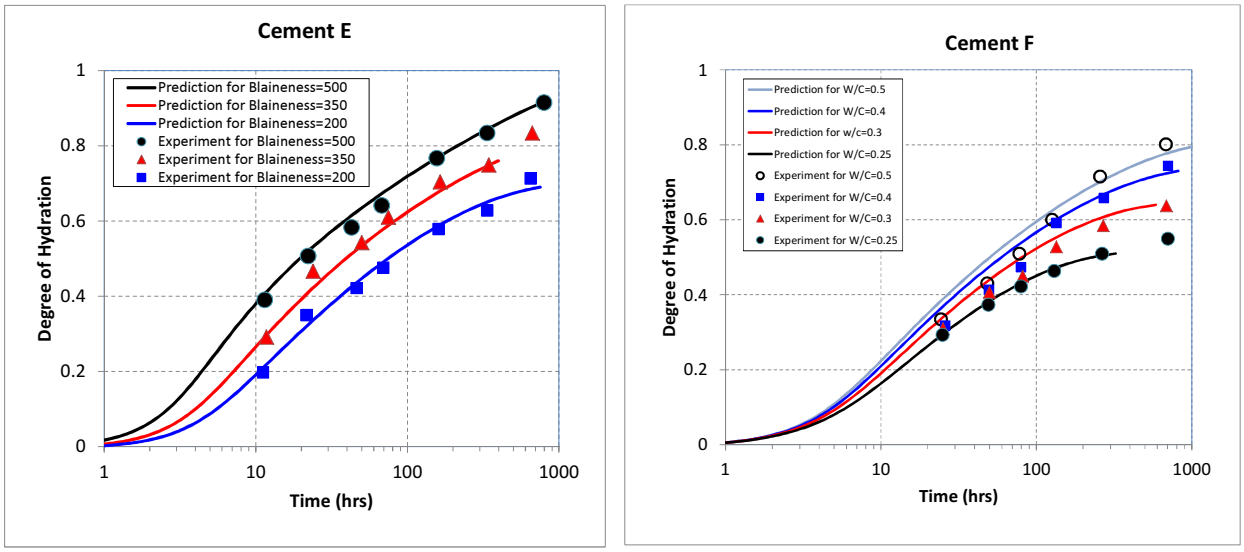

Fig. A.3 Comparison between experimental data and model predictions for cement #E and #F varying cement fineness

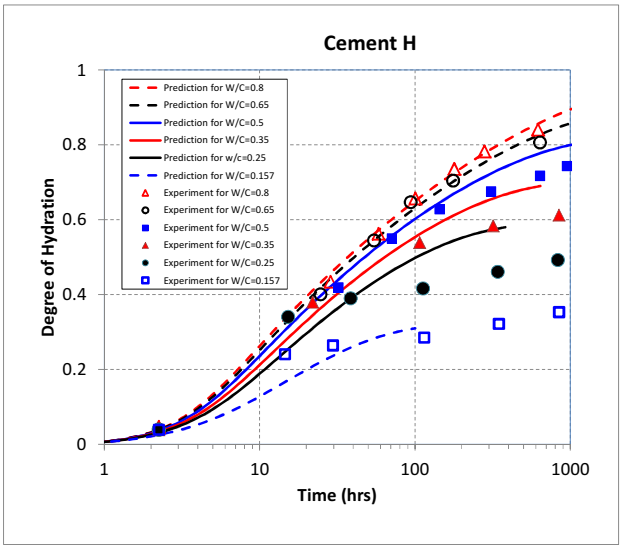

Fig. A.4 Comparison between experimental data and model predictions for cement #H at different water-cement ratios

A.1.5 Model Predictions

A.1.5.1 Initial Porosity

Using the hydration model (Lin and Meyer, 2009), degree of hydration can be obtained as a function of time for different temperatures (Fig. A.5). Degree of hydration can be used to predict the initial porosity of cement, which is important parameter in predicting the leaching rate and consequently mechanical properties and permeability of the cement. Moreover, accurate prediction of the degree of hydration is necessary to determine the appropriate curing time.

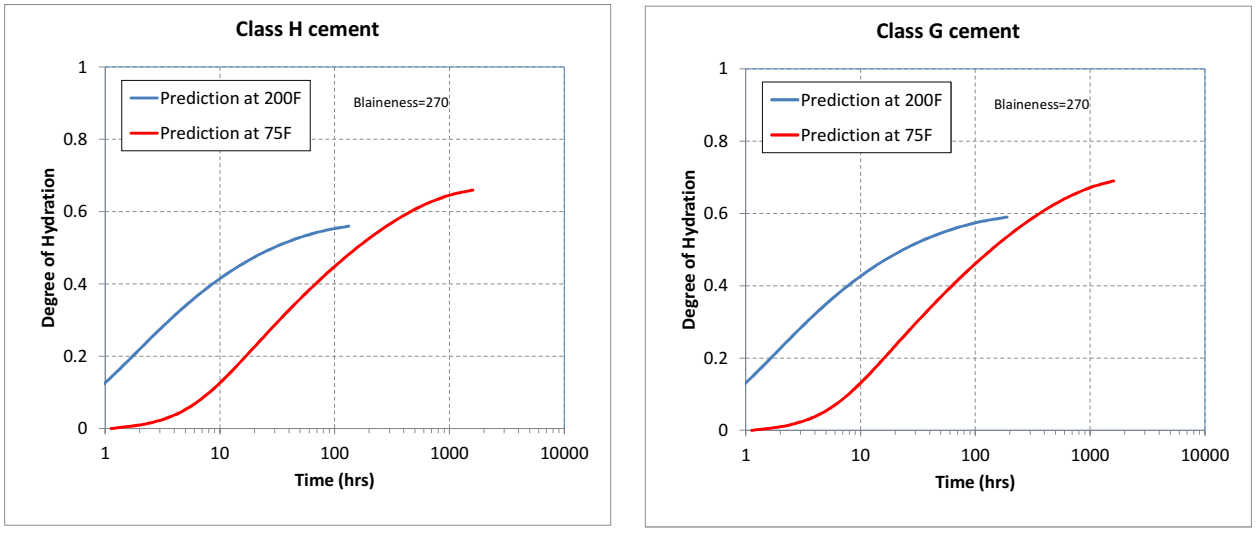

Fig. A.5 Degree of hydration versus time for cement class H and G at different temperatures

Initial porosity of cement after curing is related to the amount of free water present in the cement. The free water available in cement is a function of the degree of hydration, which is affected by cement composition, temperature, water-cement ratio, pressure, and cement fineness. For class H cement, the maximum hydration at temperature of 200^{o}F is about 60% which occurs after 100 hrs (Fig. A.5). Therefore, the amount of water needed for hydration reaction is computed assuming 60 percent cement hydration (Eqs. A.1 through A.5). The procedure for calculating the initial cement porosity is presented here. Three main assumptions of the procedure are:

i. 60% hydration
ii. No volume change while mixing of water and cement
iii. No air entrapment

First, molecular weights of different components of cement need to be determined. Table A.2 summarizes the molecular weight of different components of class H cement, and amount water needed for hydration reaction of each component based on the hydration reactions. The amount of free (unhydrated) water is then calculated by subtracting the amount of water needed for hydration reaction to total amount of water added to the cement to get the desired water-cement ratio. Therefore, total porosity can be calculated by dividing the volume of free water to the total slurry volume (Eq. A.25).

Table A.2 Molecular weight and hydration water requirement of components of class H cement

Element	Molecular Weight	Moles of element	Grams of Element (g)	Moles of water	Grams of Water (g)	Fraction in cement
C_3S	228	2	456	6	108	0.5
C_2S	172	2	344	4	72	0.3
C_4AF	516	1	516	10	180	0.12
C_3A	270	2	540	22	396	0.03

$$Porosity = \phi = \frac{Pore\ Volume}{Bulk\ Volume} = \frac{Extra\ water}{Total\ Slurry\ volume} \quad \text{.....(A.25)}$$

The porosity of class H cement predicted using this technique is approximately 26%, which shows a good agreement with experimental data obtained using different measuring techniques discussed earlier in Section 2.2. The same procedure is applied for class G cement and porosity of 31.17% is obtained. They main difference between class G and H that causes the variation is the difference in water-cement ratio.

A.1.5.2 Maximum Calcium Concentration

The hydration model not only predicts the amount of free water in the cement but also it provides the concentrations of CH and CSH and subsequently the calcium concentration, which is necessary to predict the leaching rate, mechanical properties and permeability of the cement. In order to determine the calcium concentration in the cement, first CH and CSH produced and consumed by the hydration reactions (i.e. Eqs. A.20 through A.24) have to be calculated. Tables 3 presents predicted CH and CSH concentrations for class H cement. The calcium concentrations in two different cements (H and G classes) obtained from the hydration model is shown in Table 4..

Table A.3 CH and CSH concentrations after hydration for Class H cement

Element	Grams of Element	Moles of element	Moles of CH	Moles of CSH
C_3S	1315.79	5.77	8.66	2.89
C_2S	789.47	4.59	2.29	2.29
C_4AF	315.79	0.61	-1.22	0.00
C_3A	78.95	0.29	-0.29	0.00
Total			**9.44**	**5.18**

Table A.4 Calcium concentrations in CH and CSH phases of Classes H and G cements

	Calcium Concentration (mmol/l)	
	Class H	Class G
CH	9435.1	8148.5
CSH	15541.45	13422.17
Total	24975.55	21570.67

A.1.5.3 Effects of cement additives on maximum calcium concentration

Class G and H cements are intended for use as basic cement from surface to 8000 ft depth as manufactured, or can be used with accelerators and retarders to cover a wide range of well depths and temperatures. Class G and H can be modified easily through the use of additives to meet almost any job specifications economically. The use of modified class H cement has become extremely popular. The cement additives available can be subdivided into these functional groups: i) density control additives; ii) setting time control additives: iii) lost circulation additives; iv) filteration control additives; v) viscosity control additives; and vi) special additives for unusual problems.

Silica fume, which is 100 times smaller than average cement particles, is a very effective pozzolanic material that improves compressive strength, bond strength and permeability of cement. Following is the pozzolanic reaction between silica fume and calcium hydroxide.

$$3[Ca(OH)_2] + 2[SiO_2] = [3(CaO).2(SiO_2).3(H_2O)]\ldots\ldots\ldots

Appendix B

Literature Review, Theoretical Studies on Tubular Corrosion

Summary

Literature review was conducted on fundamental aspects of CO_2 and H_2S corrosions. Electrochemistry of CO_2 and H_2S corrosion were reviewed from different literature. Comprehensive knowledge of CO_2 and H_2S corrosion electrochemistry will be helpful for corrosion modeling. Different experimental measurement techniques for CO_2 and H_2S corrosions were reviewed. The results of theoretical studies will be used for the experimental part of this project.

The effects of different parameters on CO_2 and H_2S corrosions were reviewed to better understand corrosion process and mechanisms, and develop improved models. The review will continue in the future. Fourteen CO_2 and H_2S corrosion models were reviewed from the available literature. So far, extensive research has been done by different investigators to better understand the CO_2 and H_2S corrosion mechanisms. However, many studies have emphasized on the need for improved CO_2 and H_2S corrosion models, especially for high-pressure high-temperature (HPHT) conditions. In this report, one of the mechanistic models for CO_2 corrosion has studied in details and a modified CO_2 corrosion model has been proposed for non-scale forming conditions. The proposed model will be validated with experimental data in the future. The new model can be extended for scale forming and HPHT conditions. Synergistic effect between CO_2 and H_2S corrosion will be studied on theoretical part of this research and the CO_2 and H_2S models will be coupled.

B.1 Introduction

Corrosion is known as materials degradation as a result of chemical and electrochemical reactions. Corrosion can be divided into several categories based on the mechanism of corrosion reaction including general corrosion, pitting corrosion, crevice corrosion, erosion-corrosion, galvanic corrosion, microbial corrosion, stress corrosion cracking, intergranular corrosion and other uncommon types of corrosion mechanisms. Corrosion environment can be also a good criterion for dividing into different categories based such as CO_2 corrosion, H_2S corrosion, atmospheric corrosion, acid corrosion and high temperature corrosion. In the oil and gas industry, CO_2 and H_2S corrosions are two common types of corrosion, which cause a number of problems during oil and gas production. CO_2 and H_2S are the two well known corrosive gases that are produced. Because of the diversity of corrosion related problems, CO_2 corrosion (sweet corrosion) is probably the material degradation mechanism most extensively

assessed in this industry over the last 30 years. CO_2 is also sometimes injected into oil and gas wells for production enhancement or sequestration purposes. The fundamentals of CO_2 and H_2S corrosion processes, corrosion measurement techniques, effects of different parameters on CO_2 and H_2S corrosion, and a summary of some famous CO_2 corrosion models are presented in the following sections. A modified CO_2 corrosion model for non-scale forming conditions is proposed at the end. Research is in progress on the CO_2 corrosion model to validate the model and extent the model for non-scale forming conditions.

B.2 Fundamental Concepts in CO_2 and H_2S Corrosions

The presence of CO_2 and H_2S in the gas phase enhances the internal corrosion by formation water which may occur in oil well casings and tubings. Internal corrosion control is considered as a major cost item. It is estimated (Heidersbach, 2011) that the total annual cost of corrosion in the U.S. oil and gas production industry is roughly $1.372 billion/year The annual corrosion cost for oil and gas production was estimated to be approximately eight percent of the total production and manufacturing category cost (Fig. B.1).

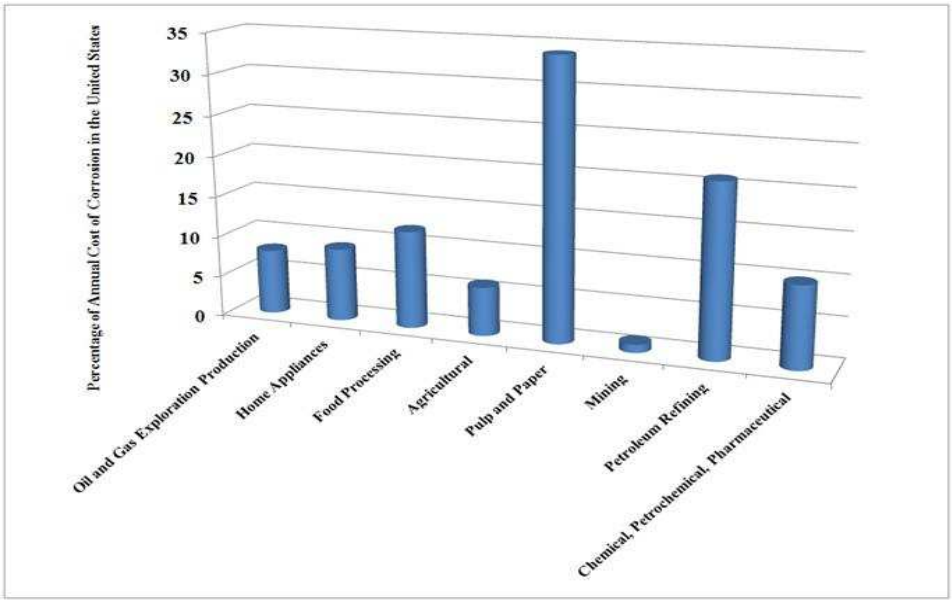

Fig. B.1 Annual cost of corrosion of oil and gas exploration industry (Heidersbach, 2011)

B.2.1 Electrochemistry of CO_2 Corrosion

The overall reaction for aqueous CO2 corrosion of carbon steel is:

$$Fe + CO_2 + H_2O \rightarrow FeCO_3 + H_2 \quad \text{.....(B.1)}$$

CO_2 corrosion of carbon steel involves anodic dissolution of iron and cathodic evolution of hydrogen. The anodic dissolution for iron in acid solutions (shown below) has been studied extensively with several multi-step mechanisms suggested to explain the various experimental results.

$$Fe \rightarrow Fe^{++} + 2e^{-} \quad \text{.....(B.2)}$$

The reaction is pH dependent in acidic solutions with a reaction order with respect to OH^- between 1 and 2, decreasing toward 1 and 0 at pH > 4 (Nesic, 2007). It has been reported (Nesic, 2007) that the anodic dissolution of iron is affected by the presence of CO_2. The carbonic species acts as a chemical ligand and catalyses the dissolution creating different kinetics of iron dissolution in CO_2 solutions compared to strong acids. It is assumed the ligand $Fe_L = Fe–CO_2$ is formed as an adsorbed species at the electrode surface. H_2CO_3 and dissolved CO_2 are the only carbonic species whose concentrations do not depend on pH. Therefore, formation of this ligand is independent of pH. Several detailed multi-step models have been presented to explain the various findings. The following corrosion mechanism has been developed by Nesic et al. (1996) to explain the experimental results for pH > 5.

$$Fe + CO_2 \Leftrightarrow Fe_L \quad \text{.....(B.3a)}$$

$$Fe_L + H_2O \Leftrightarrow Fe_LOH_{ad} + H^+ + e^- \quad \text{.....(B.3b)}$$

$$Fe_LOH_{ad} \xrightarrow{rds} Fe_LOH^+_{ad} + e^- \quad \text{.....(B.3c)}$$

$$Fe_LOH^+_{ad} + H_2O \Leftrightarrow Fe_L(OH)_{2ad} + H^+ \quad \text{.....(B.3d)}$$

$$Fe_L(OH)_{2ad} \Leftrightarrow Fe_L(OH)_{2sol} \quad \text{.....(B.3e)}$$

$$Fe_L(OH)_{2sol} + 2H^+ \Leftrightarrow Fe^{2+} + CO_2 + 2H_2O \quad \text{.....(B.3f)}$$

The presence of CO_2 increases the rate of corrosion of iron in aqueous solutions by increasing the rate of the hydrogen evolution reaction. In strong acids, which are completely dissociated, the rate of hydrogen evolution cannot exceed the rate of mass transfer at which H^+ ions can be transported to the surface from the bulk solution. In solutions with a pH > 4, the mass-transfer-controlled limiting current is small and the presence of H_2CO_3 enables hydrogen evolution at a much higher rate. Thus, at a given pH, the presence of CO_2 leads to a much

higher corrosion rate than would be found in a solution of a strong acid. Despite more than three decades of intense research, it is still not known with absolute certainty whether H_2CO_3 is reduced directly (as assumed by many workers in the field) or the final step in the reaction follows the dissociation of the H_2CO_3. Many researchers (Nesic, 2007, Gray et al., 1989; Bonis and Crolet, 1989) have assumed that the two reactions are independent and the net cathodic current is the sum of the currents for the two reactions.

$$2H^{+}+2e^{-}\rightarrow H_2 \quad \text{(B.4)}$$

$$2\ H_2CO_3+2e^{-}\rightarrow H_2+\ 2HCO_3 \quad \text{(B.5)}$$

At pH > 5 and very low partial pressures of CO_2, hydrogen evolution from the direct reduction of water which occurs at lower potentials becomes important (Schmitt and Rothmann, 1977, Nesic et al. 1995).

$$2H_2O + 2e^{-} \rightarrow H_2 +2OH^{-} \quad \text{(B.6)}$$

Gray et al. (1989) have suggested that at higher pH in CO_2 solutions, the direct reduction of the bicarbonate ion becomes important:

$$2HCO_3^{-} +2e^{-}\rightarrow H_2+\ 2CO_3^{2-} \quad \text{(B.7)}$$

Because of increasing concentrations of bicarbonate at higher pH, it is difficult to distinguish the reaction path for hydrogen evolution experimentally. It has been observed that in the range of 4 < pH < 7, the corrosion rates steadily decrease with increasing pH bringing the significance of reaction shown in Eq. (B.7) in the overall reaction while the concentration of bicarbonate ion steadily increases.

B.2.2 Electrochemistry of H_2S Corrosion

Fast and direct heterogeneous chemical corrosion reaction of H_2S with carbon steel causes the formation of mackinawite corrosion product scale on the metal surface. The overall reaction can be written as:

$$FeS(S) + H_2S \rightarrow FeS(s) + H_2 \quad \text{(B.8)}$$

This reaction can be referred as a “solid state corrosion reaction” since both the initial and final state of Fe is solid. The mackinawite formed during corrosion reaction may dissolve depending on the level of solution saturation. Oilfield brines have the typical pH range of 4 to 7, which is

usually supersaturated with respect to iron sulfide. Therefore, mackinawite scale layer does not dissolve (Brown et al., 2004). The mackinawite formed during corrosion reaction starts dissolving for pH below 4. Mackinawite dissolution increases with decreasing the pH up to the pH of 2 to 3 which all the mackinawite will dissolve in brine (Shoesmith et al. 1980).

B.3 CO_2 and H_2S Corrosion Measurement Techniques

Corrosion measurement techniques can be divided to two main categories known as non-electrochemical and electrochemical. Non-electrochemical techniques are including weight loss measurement, 3D profilometer of surface, visual observations, electrical resistance probes and ultrasonic measurement techniques. The electrochemical measurement techniques are including Linear Polarization Resistance (LPR), Electrochemical Impedance Spectroscopy (EIS), Potentiodynamic polarization, Electrochemical Frequency Modulation (EFM), Harmonics and electrochemical noise. A summary of two important electrochemical measurement techniques used in this study are discussed in the following sections. More details about electrochemical measurement techniques can be found in ASTM G3, Standard Practice for Conventions Applicable to Electrochemical Measurements in Corrosion Testing.

B.3.1 Linear Polarization Resistance

A widely used polarization method is linear polarization resistance (LPR). The polarization resistance of a material is defined as the slope of the potential–current density (*E-i*) curve (i.e. Tafel slope) at the free corrosion potential (Fig. B.2), yielding the polarization resistance *Rp,* which can be itself related to the corrosion current with the help of:

$$R_p = \frac{B}{i_{corr}} = \frac{\Delta E}{(\Delta i)_{\Delta E \to 0}} \quad \text{..... (B.9)}$$

where:

R_p = Polarization Resistance

i_{corr}= Corrosion Current

B = Empirical polarization resistance constant that can be related to the anodic (b_a) and cathodic (b_c) Tafel slopes with

$$B = \frac{b_a b_c}{2.3(b_a + b_c)} \quad \text{..... (B.10)}$$

The Tafel slopes themselves can be evaluated experimentally using real polarization plots similar to those presented in Fig. B.3 and B.4 or obtained from literature (Roberge, 1999).

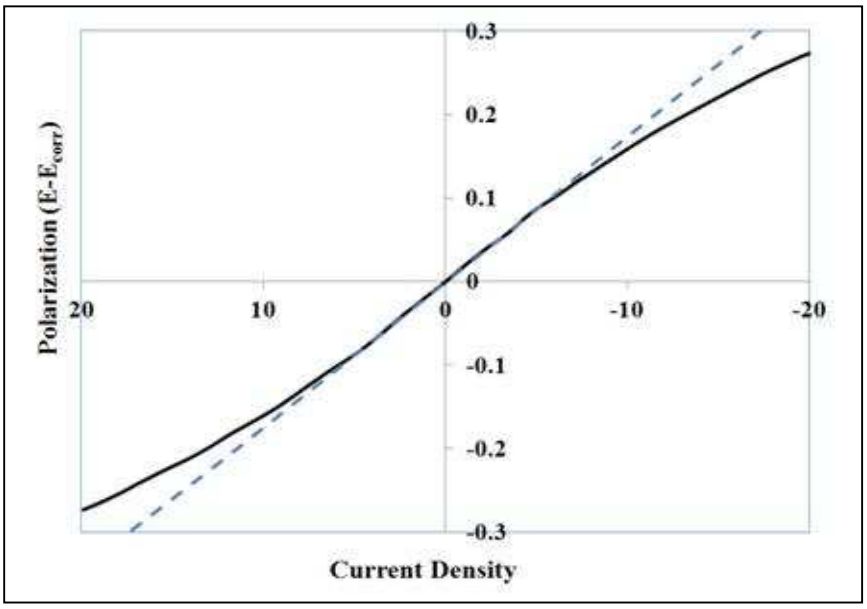

Fig. B.2 Hypothetical linear polarization plot (Roberge, 1999)

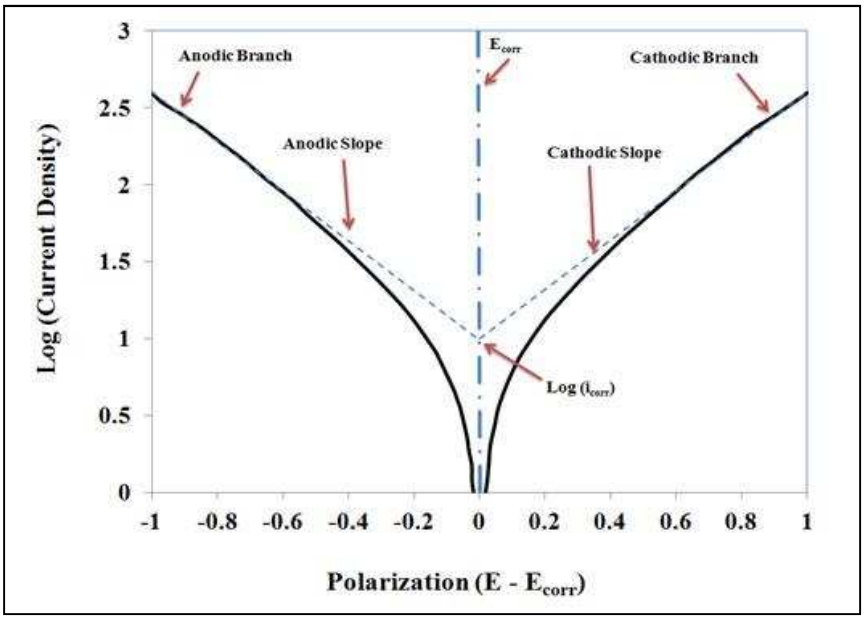

Fig. B.3 Hypothetical polarization diagram for an active system with anodic and cathodic branches (Roberge, 1999)

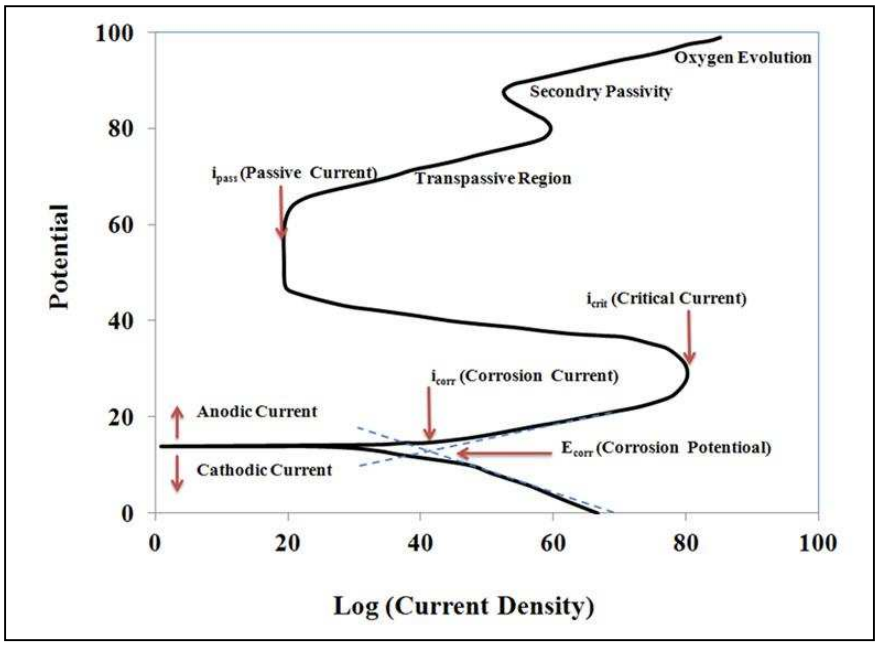

Fig. B.4 Hypothetical polarization diagram for a passivating system with anodic and cathodic branches (Roberge, 1999)

B.3.2 Electrochemical Impedance Spectroscopy

Electrochemical impedance spectroscopy (EIS) has been successfully applied to the study of corrosion systems since early seventieth; and it has been proven to be a powerful and accurate method for measuring corrosion rates. However, to determine the charge transfer resistance or polarization resistance R_p, which is proportional to the corrosion rate at the monitored interface, EIS results have to be interpreted with the help of a model of the interface. Since the early work published by Epelboin and coworkers, EIS has gained tremendous momentum and popularity in corrosion laboratories around the world (Epelboin et al. 1972). The advantage of EIS over other laboratory techniques is the possibility of using very small-amplitude signals without significantly affecting the properties being measured. To make an EIS measurement, a small-amplitude signal, usually a voltage between 5 and 50 mV, is applied to a specimen over a range of frequencies from 0.001 to 100,000 Hz.

The EIS technique monitors the real (resistance) and imaginary (capacitance) parts of the impedance response of the system. An electrical circuit model or circuit description code and initial circuit parameters are assumed depending upon the shape of the EIS spectrum. A computer program can be used to fit the best frequency response to the given EIS spectrum to calculate the EIS spectrum parameters. Depending upon how well the fitting curve overlaps the original spectrum, the quality of the fitting can be judged. It is possible to obtain a set of parameters by fitting the EIS data, which can be correlated with the corrosion of the substrate,

electrochemical reactions, and the coating condition (if a coating is present). Only a few numerous equivalent circuits really apply in the context of a freely corroding interface at or close to kinetic equilibrium to describe electrochemical interfaces. The first circuit (Fig. B.5*a*) corresponds to the simplest equivalent circuit that can describe a metal/electrolyte interface. The component *Q* describes the "leaky capacitor" behavior corresponding to the presence of a constant phase element. The admittance representation *Y** of the CPE behavior with frequency can be described by Eq. (B.10). For n = (1-β), Eq. (B.10) describes the behavior of a resistor with $R = Y_o^{-1}$ and for $n = \beta$, that of a capacitor with $C = Y_o$. For n = 0.5, Eq. (B.10) becomes the expression of a Warburg (W) component, and when $n=-\beta$, it emulates an inductance with $L = Y_o^{1.25}$ (Epelboin et al. 1972).

$$Y^*(\omega) = Y_o \omega^n \cos(n\pi/2) + jY_o \omega^n \sin(n\pi/2) \quad \text{(B.11)}$$

Figure B.6 illustrates the complex-plane presentation of EIS simulated data corresponding to the model circuit in Fig. B.5(a) when R_s =10 Ω, R_p =100 kΩ, and *Q* decomposes into C_{dl} = 40 µF and n = 0.8, and Fig. B.7 shows how the same data would appear in a Bode plot format (Epelboin et al. 1972).

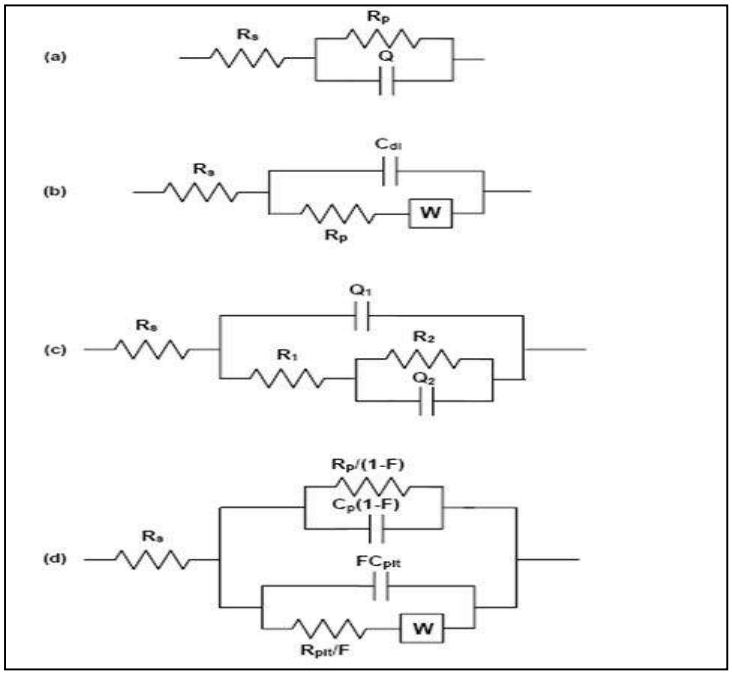

Fig. B.5 Equivalent circuit models proposed for the interpretation of EIS results measured in corroding systems: (a) simplest representation of an electrochemical interface; (b) one relaxation time constant with extended diffusion; (c) two relaxation time constants; and (d) the impedance of pitting processes of Al-based materials (Epelboin et al. 1972)

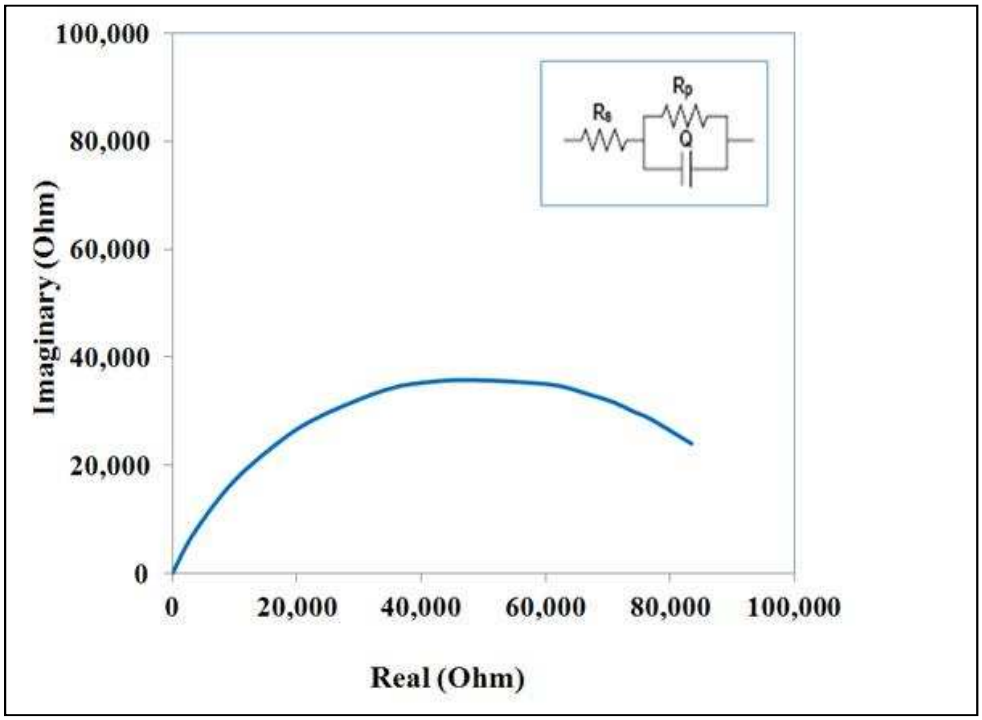

Fig. B.6 Complex-plane presentation of simulated data corresponding to the model circuit in Fig. B.5a when R_s=10 Ω, R_p= 100 KΩ, and Q decomposes into C_{dl}=40μF and n=0.8 (Epelboin et al. 1972)

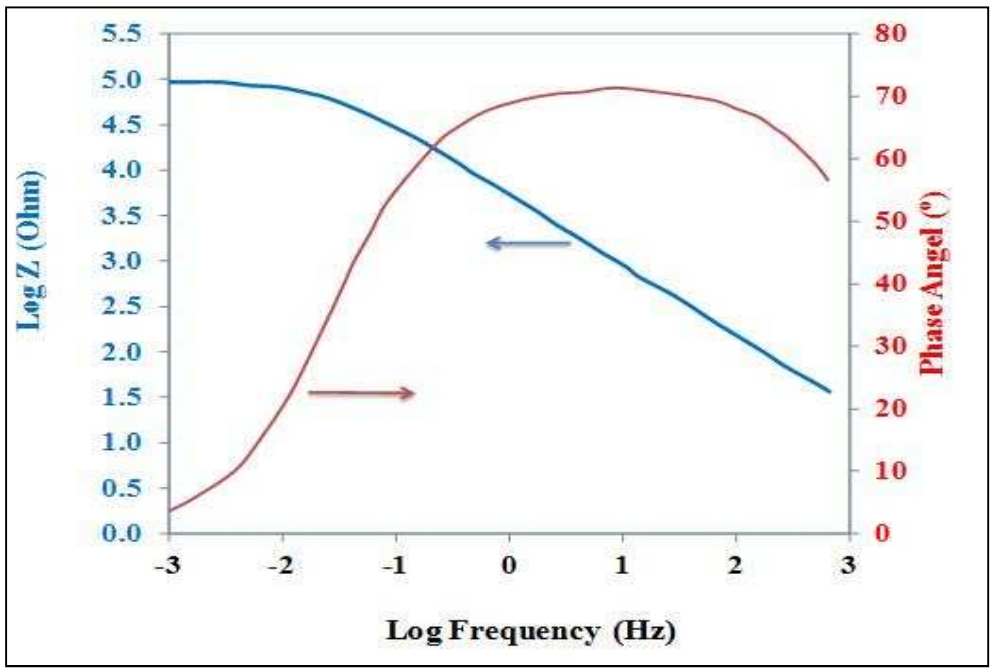

Fig. B.7 Bode representation of the same data illustrated in Fig. B.6 in complex plane format (Epelboin et al. 1972)

B.4 Effects of Different Parameter on CO_2 Corrosion

The most important parameters affecting the CO_2 corrosion behavior are NaCl concentration, pH, temperature, flow velocity, flow regime, and CO_2 pressure. More details about the effect of each parameter on CO_2 corrosion are discussed in the following sections.

B.4.1 Effect of NaCl on CO2 Corrosion

Oil and gas formations usually contain large amounts of brine (altered seawater trapped in sediment pores). Chloride concentration can vary significantly, on average, produced brine during oil and gas production contains 50,000 mg/L chloride (Hudak and Wachal, 2001), which is corrosive to metals.

Previous work by Uhlig et al. (1985) reported decreased oxygen corrosion with increased NaCl concentration in brine solutions. According to their investigation, increasing the amount of chloride in solution increases the conductivity and consequently the corrosion rate until a critical amount of NaCl (3 wt% NaCl) and, after that, increasing the chloride content will decrease the corrosion rate by decreasing the solubility of the corrosive agent (oxygen in their investigation). Hassani et al. (2011) reported a slight reduction in CO_2 corrosion rate of carbon steel by increasing the NaCl concentration from 3 to 18% (by weight). On the other hands, Fang et al. (2010) reported a considerable change in corrosion rate by increasing the NaCl concentration in brine solution. Increasing the NaCl concentration from 1 to10 wt% was reported to reduce the CO_2 corrosion rate by changing the density and viscosity, which affect the mass transfer processes, from an increase in ionic strength, which reduces the amount of dissolved CO_2, and from chloride ion adsorption onto the metal surface. At 20ºC, the corrosion mechanism gradually changes from mixed charge transfer/limiting current control to pure charge transfer control with the increase of salt concentration.

An increase in salt concentration retards the heterogeneous charge transfer reactions, as well as the homogenous chemical reactions and the mass transfer. Previous investigations on the effect of high ionic strength on CO_2 corrosion show that iron carbonate scale formation is a function of the ionic strength of the solution. In general, higher salt concentrations lead to higher values of the solubility limit for precipitation and growth of $FeCO_3$ scale (Silva et al., 2002; Sun et al., 2009). Therefore, under environmental conditions for which iron carbonate precipitation would be expected when NaCl concentration is low, if the NaCl concentration is increased, iron carbonate may no longer precipitate. Fosbøl et al. (2009) discussed the effect of high ionic strength on the diffusion process during CO_2 corrosion and the importance of including this effect in mechanistic models for CO_2 corrosion prediction.

B.4.2 Effect of pH on CO_2 Corrosion

The pH of a solution has substantial effect on CO_2 corrosion behavior. Formation of iron carbonate scale at high pH decreases the CO_2 corrosion considerably. At pH 4 or below, direct reduction of H^+ ions is important particularly at lower partial pressure of CO_2 and the pH has a direct effect on the corrosion rate. However, the most important effect of pH is indirect and relates to how pH changes conditions for formation of iron carbonate scales. High pH results in a decreased solubility of iron carbonate and leads to an increased precipitation rate and higher scaling tendency. Experimental results by Chokshi et al. (2005) indicated that at lower super-saturations obtained at pH = 6.0, the corrosion rate does not change much with time, even if some iron carbonate precipitation occurs, reflecting the fact that a relatively porous, detached and non-protective scale is formed. Higher pH (pH = 6.6) results at higher super-saturation indicated faster precipitation and formation of more protective scales, reflected by a rapid decrease in the corrosion rate with time.

pH also has some indirect effects, for example: increasing the ratio of Ac^-/HAc with pH makes the acetic acid less corrosive; high pH causes the formation of different types of corrosion products. Lower corrosion rate is usually expected at higher pH which makes the "pH stabilization" (meaning pH increase) technique an attractive way of managing CO_2 corrosion. On the other hand, it can lead to excessive scaling and can be rarely used to control corrosion caused by formation water systems (Nesic, 2007).

B.4.3 Effect of Temperature on CO_2 Corrosion

Temperature affects corrosion behavior by accelerating all the phenomena involved, including electrochemical, chemical, and transport processes. Increasing the temperature may increase or decrease the CO_2 corrosion rate depending upon the precipitation of iron carbonate scale. The corrosion rate (measured using the weight loss technique) steadily increases with temperature at low pH for which precipitation of iron carbonate or other protective type of scale does not form (Fig. B.8). The situation changes markedly when solubility of iron carbonate (or another salt) is exceeded, typically at a higher pH. In that case, increased temperature rapidly accelerates the kinetics of precipitation and protective scale formation, decreasing the corrosion rate. The peak in the corrosion rate is usually seen between 60℃ and 80℃ depending on water chemistry and flow conditions.

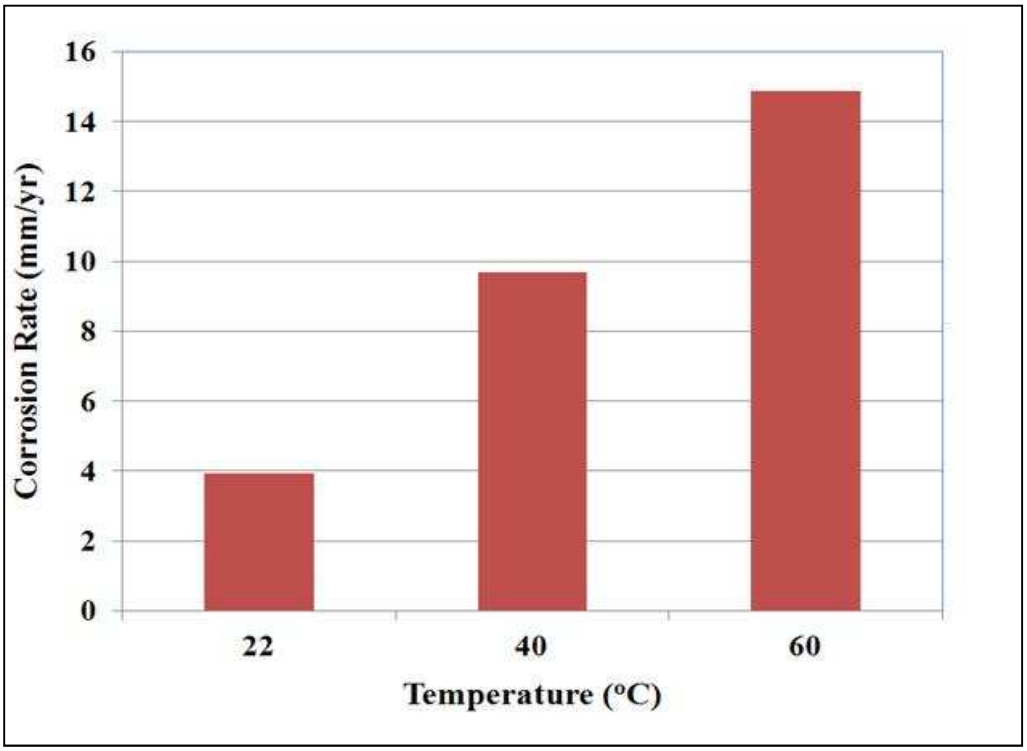

Fig. B.8 Corrosion rates vs. temperature, pH 4, P_{CO2}=1 bar, C_{Fe2+} < 5ppm, 100 ppm acetic species (HAc + Ac^-), v = 0.5 m/s (Nesic, 2007)

B.4.4 Effect of Flow Velocity and Flow Regime on CO_2 Corrosion

There are two main ways in which flow may affect CO_2 corrosion which can be distinguished based on whether or not other conditions are conducive to protective scale formation. Turbulent flow condition favors the transport of species towards and away from the metal surface when no protective scales form during corrosion which usually happens at low pH. In this case, higher corrosion rate would be expected as illustrated in Fig. B.9. The figure compares model (Nesic et al., 1995) predictions with published experimental results (Nesic, 2004).

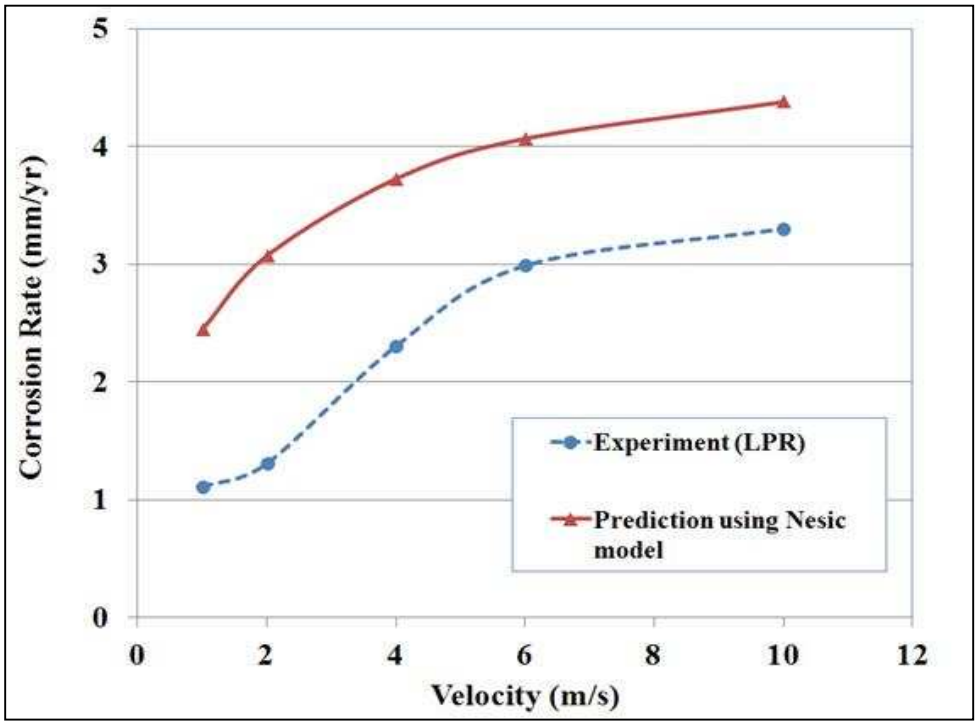

Fig. B.9 Predicted and measured corrosion rates showing the effect of fluid velocity in the absence of iron carbonate scales at 20℃, P_{CO2}=1 bar, C_{Fe}^{2+} <2 ppm.

Modification of flow distribution system such as constrictions, bends, elbows, plugged tees, valves, expansions, extractions, etc. is a usual approach for reducing the flow accelerated corrosion effects discussed earlier. Unsteady slug flow can also lead to considerable fluctuations in wall shear stress and removes the protective surface scale layer or remove the protective inhibitor films from carbon steel substrate.

Zhang and Cheng (2009) studied the effects of flow velocity and impact angle on CO_2 corrosion for direct impingement geometry using computational fluid dynamics and corrosion experiments in CO_2 saturated systems. The role of fluid hydrodynamics in the CO_2-containing solution depends on its effect on the iron-carbonate scale formation. An increasing flow velocity and shear stress could thin, degrade, or even remove completely the scale, thus increasing corrosion rate of the steel. During fluid impingement, the shearing effect in the lateral direction increases with the decreasing impact angle, accelerating the removal of the corrosion scale from the steel surface. Therefore, an oblique impact of fluid would generally result in a high corrosion rate of the steel.

The effect of impact angle on corrosion of the steel is attributed to the distribution of fluid flow field and shear stress on the electrode surface. A low flow velocity and shear stress and thus a low mass transfer rate would be generated at the centric regions at the normal impact. Therefore, a compact corrosion scale can be formed on the electrode surface to protect the steel. The high flow velocity and shear stress adjacent to the center causes higher corrosion

rate in the region. The corrosion rate decreases with the increase in radial distance due to high flow velocity and shear stress. The fluid flow velocity and shear stress, and consequently the corrosion rates are higher at the side of the impingement pattern at the oblique impact angles. The corrosion activity of a steel electrode located at the center of the sample holder generally increases with the decreasing impact angle due to the enhancing effect of shear on the corrosion scale (Zhang and Cheng, 2009).

B.4.5 Effect of CO_2 Pressure on CO_2 Corrosion

The impacts of temperature and CO_2 partial pressure on the rate of corrosion of carbon steel are shown in Fig. B.10 as presented by Ropital (2010).

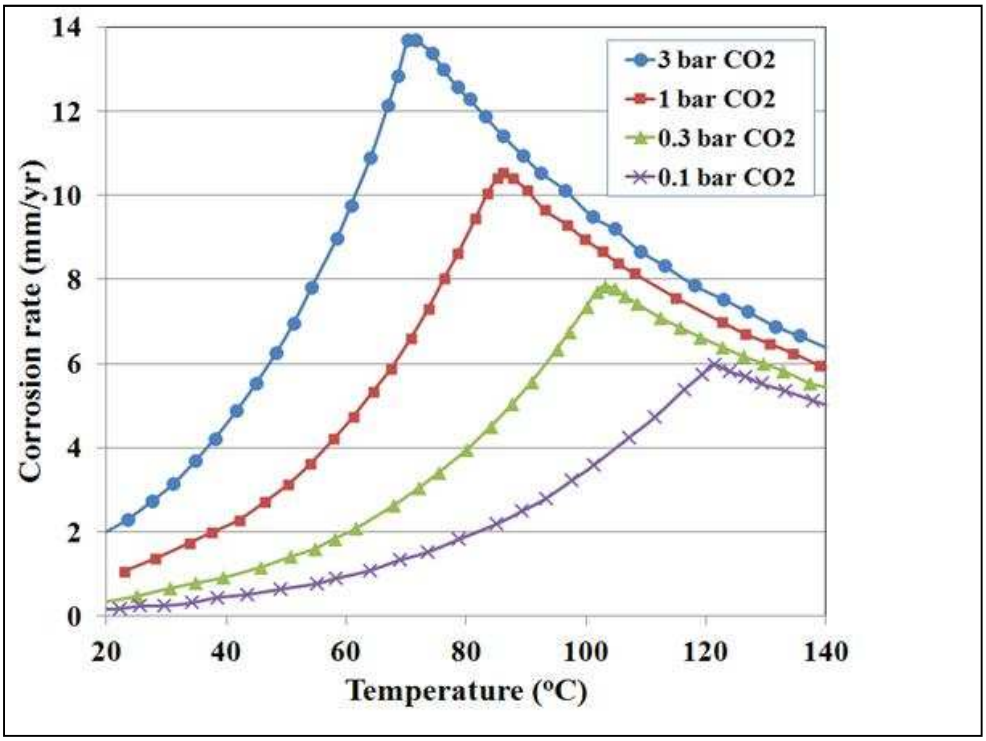

Fig. B.10 Influence of temperature and CO_2 partial pressure on the rate of corrosion of carbon steel (Ropital, 2010)

In the case of scale-free CO_2 corrosion, increase in CO_2 partial pressure (P_{CO_2}) typically leads to increased corrosion rate. The commonly accepted explanation for this observation is that with P_{CO_2} the concentration of H_2CO_3 increases and accelerates the cathodic reaction and ultimately the corrosion rate. The effect of P_{CO_2} is illustrated in Fig. B.11. The figure compares experimental data (Wang et al., 2004) with model prediction (SPPS:CO_2 1998). However, when other conditions are favorable for formation of iron carbonate scales, increased P_{CO_2} can have a beneficial effect in hindering the corrosion process. At a high pH, higher P_{CO_2} leads to an

increase in bicarbonate and carbonate ion concentration and a higher super saturation, which accelerates precipitation and scale formation.

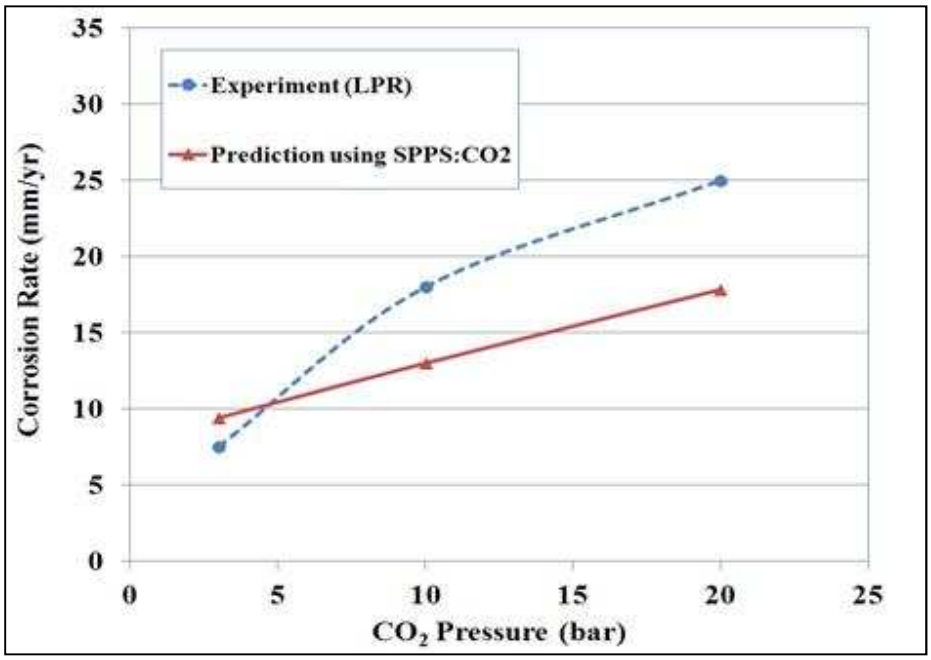

Fig. B.11 Predicted and measured corrosion rates showing the effect of CO_2 partial pressure at 60℃, pH 5, 1 m/s

B.5 Summary of Available CO_2 and H_2S Corrosion Models

There are numerous CO_2 and H_2S corrosion models available in the literature for prediction of corrosion rate and also for predicting the thickness and protective properties of corrosion products. Nyborg (2010) summarized the characteristics of fourteen CO_2/H_2S corrosion models used in the oil and gas industry and discussed the abilities and limitations of these models. Next paragraphs are the summary of these fourteen models, which were presented by Nyborg (2010). Most of these models are for pure CO_2 corrosion.

B.5.1 De Waard Model

de Waard and coworkers (hereafter denoted Model DW) developed a corrosion model which was used for several years (de Waard and Milliams, 1975: de Waard et al., 1991: de Waard et al., 1995). The effect of protective corrosion scale was not completely considered in this model.

B.5.2 Norsok M-506 Model

Norsok M-506 which hereafter denoted Model NO is an empirical model (Norsok, 1998; Halvorsen and Søntvedt, 1999). The same experimental data as DW model was used to calibrate this model plus some more experimental data at higher temperature to have a better prediction for scale forming conditions. This model is also more sensitive to pH in comparison with DW.

B.5.3 Hydrocor

Hydrocorr, which hereafter will be denoted as Model HY, is a combine corrosion and fluid flow modeling developed by Shell (Pots, 1995: Pots et al., 2002: Pots and Kapusta, 2005). A simplified H_2S corrosion model is also included in this model. The scale factor used in this model predicts a relatively low protection. This model works for multiphase flow conditions as well.

B.5.4 Corplus

Corplus is another CO_2 corrosion model which is developed by Total. This model will be denoted as Model CO hereafter (Bonis and Crolet, 1989; Crolet and Bonis, 1991; Gunaltun, 1996). This model is calibrated based on corrosion data obtained from oil and gas wells. Detailed analysis of the water chemistry is the base of this model.

B.5.5 Cassandra

Cassandra which is developed by BP will be denoted as Model CA hereafter (Hedges et al., 2005). In this model, user has the option to include or exclude the effect of protective scale layer. pH of the solution is also calculated as a function of CO_2 content, temperature, and full water chemistry.

B.5.6 KSC Model

KSC is also another CO_2 corrosion model, which will be denoted as Model KS hereafter (Nordsveen et al., 2003; Nesic et al., 2003). This model was developed by coupling the electrochemical model (Nesic et al., 1996) with species transport model. The model predicts different steps of corrosion reaction including electrochemical reactions at the steel surface, chemical reactions in the liquid phase, diffusion of species to and from the bulk phase, and diffusion through porous iron carbonate films. Effect of protective scale layer is appropriately included in this model. The model is able to predict low corrosion rates at high pH and temperature.

B.5.7 Multicorp

Ohio University also developed a CO_2 corrosion model, which will be denoted as Model MU hereafter. The basic idea of this model comes from KS model (Nordsveen et al., 2003). Multiphase flow was included in this model to extend the capabilities of this model. Effect of oil wetting and chemistry of crude oil were also included in this model. This model was verified against the experimental and field data. Effect of H_2S on CO_2 corrosion is also included in this model. Iron sulfide scale formation and iron carbonate scale formation and growth are modeled. This model is also able to handle the localized attack.

B.5.8 ECE Model

ECE is a CO_2 corrosion model developed based on DW model, which hereafter will be denoted as Model EC (de Waard et al., 2003; Smith and de Waard, 2005). This model is developed for wells and flow lines. It is able to predict the effect of small amount of H_2S. Small amount of H_2S can lead to considerable drop in corrosion rate because of formation of protective scale layer of iron sulfide. Model predictions are not very sensitive to pH.

B.5.9 Predict

Predictive model, which was developed by Honeywell, will be denoted as Model PR hereafter (Srinivasan and Kane, 1996; Sangita and Srinivasan, 2000; Srinivasan and Kane, 2003). This model is also based on DW model. Flow velocity and flow regime are incorporated in this model. Model predictions are sensitive to change in pH of solution.

B.5.10 Tulsa Model

University of Tulsa developed a CO_2 corrosion model which is called SSPS CO_2 corrosion model and hereafter will be denoted as Model TU (Dayalan et al. 1995; Dayalan et al. 1998; Adsani et al., 2006). The model is able predict the CO_2 corrosion rate in single phase and two phase flow condition. In addition, it predicts the formation of iron carbonate scale. The model considers a number phenomena that affect corrosion including chemical reaction in bulk solution, electrochemical reaction on the metal surface, mass transfer from the bulk to the metal surface, and also mass transfer from the metal surface to the bulk solution. More details of this model are provided in section B.6.

B.5.11 ULL Model

ULL which is developed at the University of Louisiana at Lafayette will be denoted as Model UL hereafter (Perkins et al., 1996; Garber et al., 1998). This model is able to predict the flow regime and the location for condensation of water and hydrocarbons in well. It is also able to predict the temperature, pressure, pH and corrosion rate profiles along the well.

B.5.12 CorPos

CorPos will be denoted as Model CP hereafter. This model is a combination of multiphase flow model, water chemistry model, and corrosion model, which is able to predict the CO_2 corrosion rate and pH of the solution along the pipe (Gartland and Salomonsen, 1999; Gartland et al., 2003). Bicarbonate produced by the corrosion reaction is also included for pH calculation. The model predicts the corrosion rate in several points along the pipe.

B.5.13 OLI Model

OLI CO_2 corrosion prediction model is denoted as Model OL hereafter. This model is a combination of thermodynamic, chemical and electrochemical reaction models. The model predicts the effect of H_2S on formation and dissociation of protective scale layers (Anderko and Young, 1999; Anderko, 2000). Parameters used in this model for scale formation has been calibrated against laboratory data.

B.5.14 SweetCor

SweetCor CO_2 corrosion model, which is developed by Shell. It is based on a large database of corrosion rate data (John et al., 1998). The model uses empirical correlations to predict corrosion rate for specific conditions.

Table B.1 by Nyborg 2010, summarizes the characteristics of these fourteen CO_2/H_2S corrosion models.

Table B.1. Important factors in CO_2/H_2S corrosion prediction models (Nyborg, 2010)

Model	DW	NO	HY	CO	CA	KS	MU	EC	PR	TU	UL	CP	OL	SW
Lab data, **F**ield data model, **M**echanistic model	L	L	M	F	L	M	M	L	L	M	F	L	M	L
Scale effect formation water*	N	M	N	W	W	M	M	W	S	S		M	W	W
Scale effect condensed water*	W	M	W	W	W	M	M	W	S	S		M	M	W
Effect of pH on corrosion rate*	W	M	W	M	W	M	M	W	S	S	S	M	W	W
Risk for localized attack				Y		Y			Y		Y			
Oil wetting effect crude oil*	S	N	M	M	N	N	S	S	S	N	S	M	N	N
Oil wetting effect condensate*	N	N	N	M	N	N	M	M	M	N	S	M	N	N
$CaCO_3$ correction for pH				Y			Y						Y	
Effect of organic acid on corrosion			Y	Y	Y		Y	Y	Y		Y			
Top of line corrosion	Y		Y				Y	Y			Y			
Effect of H_2S on corrosion rate*	N	N	W	N	N	N	M	S	S	N	W	N	S	N
Multiphase flow calculation**	N	P	M	P	N	N	P	M	P	P	M	M	N	N
Max. temperature limit °C	140	150	150	150	140	150	100	140		115		150	120	120
Max. CO_2 partial pressure bar	10	10	20	20	10	20	20	20	70	17		10	20	
Open, **C**ommercial, **P**roprietary	O	O	P	O	O	O	P	C	C	P	P	P	C	P

* S - strong effect, M - moderate effect, W - weak effect, N - no effect

** P - point calculation, M - multiphase profile calculation, N - no multiphase flow calculation

B.6 Review of Tulsa CO_2 Corrosion Model

Dalayan et al, 1995 and 1998 proposed a mechanistic model for CO_2 corrosion rate prediction. According to this model, the overall CO_2 corrosion process has four main steps (Fig. B.12). The first step in CO_2 corrosion process is the formation of reactive species in the bulk. In this step CO_2 gas dissolves in water and then hydrate to form carbonic acid. Carbonic acid can directly reduce on metal surface or it can dissociate to bicarbonate ions first and then reduce on the metal surface as a cathodic reaction. The second step in CO_2 corrosion process is the transportation of cathodic reaction species (reactants) from the bulk to the surface of metal. The driving force for transporting these species to the metal surface is consumption of these species on the surface by cathodic reaction of corrosion, which causes a concentration gradient between bulk and metal surface. The third step in CO_2 corrosion process is electrochemical corrosion reaction on the metal surface. Electrochemical corrosion reaction can be divided into two main categories as anodic and cathodic reactions. The last step in CO_2 corrosion process is the transportation of corrosion products from the metal surface to the bulk solution. The driving force for this transportation is concentration difference between metal surface and bulk solution. For the scale forming condition, mass transfer happens through the scale layer. Mass transfer through the scale layer was considered as diffusion through porous media.

Dayalan et al. (1995) based on three main hypothesizes developed their model consists of a system fifteen equations and fifteen unknowns. The model is valid for steady state CO_2 corrosion. It incorporates chemical and electrochemical reactions, and mass transport (Eqs. B.12 through B.26). CO_2 corrosion rate can be predicted for non-scale forming conditions by solving the system fifteen nonlinear equations. The main hypotheses in this model are: i) the sum of the mass transfer rates of the reactants must be equal to the sum of the electrochemical reaction rates (for both cathodic and anodic reactions); and ii) the sum of the mass transfer rates of carbonic acid and bicarbonate is equal to the mass transfer rate of carbonate ions.

According to the first hypothesis, mass transfer rate of Fe^{2+} is equal to electrochemical reaction rate of the iron dissolution. Therefore:

$$K_{mt,Fe^{2+}}([Fe^{2+}]_s - [Fe^{2+}]_b) = 2 \times 10^{-3} F . K_{Fe^{2+}} [Fe^{2+}]_s exp\left\{\frac{(2-B)F(E_{corr}-E_{Fe^{2+}})}{RT}\right\} \ldots\ldots \text{(B.12)}$$

where K_{mt} is mass transfer coefficient which can be different for different ions. $[Fe^{2+}]_s$ is iron ion concentration on the metal surface, $[Fe^{2+}]_b$ is iron ion in the bulk solution, F is Faraday constant, K_{Fe} is electrochemical reaction rate constant of iron ions, B is transfer coefficient (the value of B is 0.5 for most of the reactions), R is the universal gas constant, T is absolute temperature, E_{corr} is corrosion potential, and E^{o}_{Fe} is standard potential of iron at temperature T.

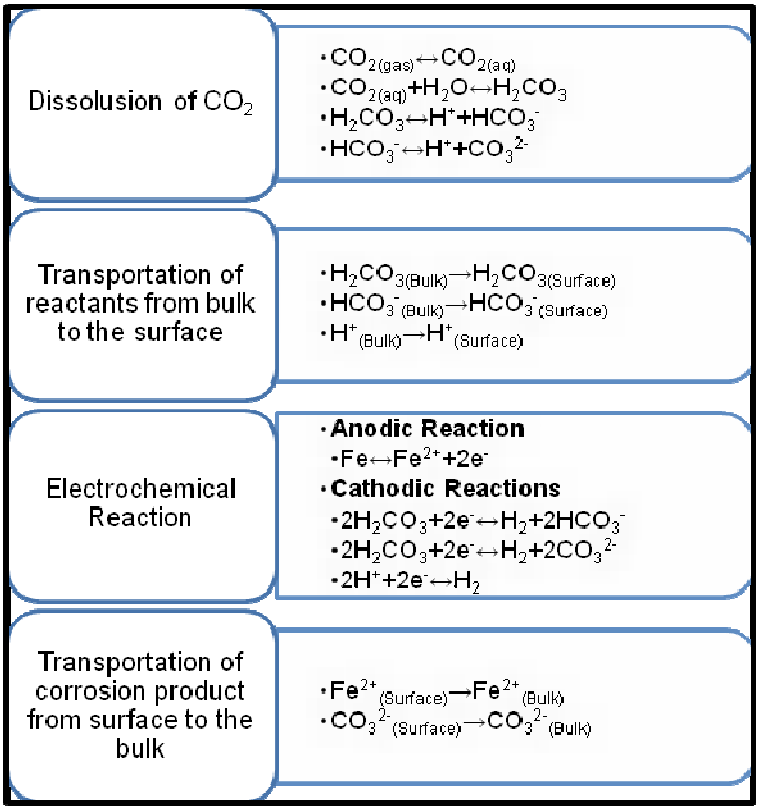

Fig.B.12 Summary of overall CO_2 corrosion process

From the second hypothesis, the sum of mass transfer rates of ($[H_2CO_3]$, $[HCO_3^-]$, $[H^+]$) are equal to the sum of electrochemical reaction rates of ($[H_2CO_3]$,$[HCO_3^-]$,$[H^+]$). Therefore:

$$K_{mt,H_2CO_3}([H_2CO_3]_b - [H_2CO_3]_s) + K_{mt,HCO_3^-}([HCO_3^-]_b - [HCO_3^-]_s) + K_{mt,H^+}([H^+]_b - [H^+]_s) = 2 \times 10^{-3} F.K_{H_2CO_3}[H_2CO_3]_s exp\left\{\frac{-BF(E_{corr}-E_{H_2CO_3})}{RT}\right\} + 2 \times 10^{-3} F.K_{HCO_3^-}[HCO_3^-]_s exp\left\{\frac{-BF(E_{corr}-E_{HCO_3^-})}{RT}\right\} + 2 \times 10^{-3} F.K_{H^+}[H^+]_s exp\left\{\frac{-BF(E_{corr}-E_{H^+})}{RT}\right\} \ldots (B.13)$$

Similarly, the sum of mass transfer rates of (H_2CO_3, HCO_3^-) is equal to the mass transfer rate of CO_3^{2-}. Therefore,

$$K_{mt,H_2CO_3}([H_2CO_3]_b - [H_2CO_3]_s) + K_{mt,HCO_3^-}([HCO_3^-]_b - [HCO_3^-]_s) = K_{mt,CO_3^{2-}}([CO_3^{2-}]_b - [CO_3^{2-}]_s) \ldots (B.14)$$

In addition, the sum of the cathodic reaction rates is equal to the sum of anodic reaction rates and it is equal to corrosion current density.

$$I_{H_2CO_3} + I_{HCO_3^-} + I_{H^+} = I_{Fe^{2+}} = 2 \times 10^{-3} F.K_{Fe^{2+}}[Fe^{2+}]_s exp\left\{\frac{(2-B)F(E_{corr}-E_{Fe^{2+}})}{RT}\right\} = 2 \times 10^{-3} F.K_{H_2CO_3}[H_2CO_3]_s exp\left\{\frac{-BF(E_{corr}-E_{H_2CO_3})}{RT}\right\} + 2 \times 10^{-3} F.K_{HCO_3^-}[HCO_3^-]_s exp\left\{\frac{-BF(E_{corr}-E_{HCO_3^-})}{RT}\right\} +$$

$$2 \times 10^{-3} F.K_{H^+}[H^+]_s exp\left\{\frac{-BF(E_{corr}-E_{H^+})}{RT}\right\}$$.....(B.15)

Electrochemical cathodic and anodic reactions are expressed as:

$$I_{H_2CO_3} = 2 \times 10^{-3} F.K_{H_2CO_3}[H_2CO_3]_s exp\left\{\frac{-BF(E_{corr}-E_{H_2CO_3})}{RT}\right\}$$.....(B.16)

$$I_{HCO_3^-} = 2 \times 10^{-3} F.K_{HCO_3^-}[HCO_3^-]_s exp\left\{\frac{-BF(E_{corr}-E_{HCO_3^-})}{RT}\right\}$$.....(B.17)

$$I_{H^+} = 2 \times 10^{-3} F.K_{H^+}[H^+]_s exp\left\{\frac{-BF(E_{corr}-E_{H^+})}{RT}\right\}$$.....(B.18)

$$I_{Fe^{2+}} = 2 \times 10^{-3} F.K_{Fe^{2+}}[Fe^{2+}]_s exp\left\{\frac{(2-B)F(E_{corr}-E_{Fe^{2+}})}{RT}\right\}$$.....(B.19)

Carbonic acid dissociation reaction has two steps. Reaction rate constants for these two steps are:

$$K_1 = First\ Dissociation\ constant = \frac{[H^+]_s[HCO_3^-]_s}{[H_2CO_3]_s}$$.....(B.20)

$$K_2 = Second\ Dissociation\ constant = \frac{[H^+]_s[CO_3^{2-}]_s}{[HCO_3^-]_s}$$.....(B.21)

H^+ ions concentration also governed by water dissociation equilibrium described below.

$$K_w = water\ Dissociation\ constant = [H^+]_s[OH^-]_s$$.....(B.22)

Equilibrium potential of all the cathodic and anodic species is a function of absolute temperature, and concentration of species based on the Nernst law.

$$E_{H_2CO_3} = E^o_{H_2CO_3} + \frac{RT}{2F} Ln\left\{\frac{[H_2CO_3]_s^{\ 2}}{[HCO_3^-]_s^{\ 2}.[H_2]}\right\}$$.....(B.23)

$$E_{HCO_3^-} = E^o_{HCO_3^-} + \frac{RT}{2F} Ln\left\{\frac{[HCO_3^-]_s^{\ 2}}{[CO_3^{2-}]_s^{\ 2}.[H_2]}\right\}$$.....(B.24)

$$E_{H^+} = E^o_{H^+} + \frac{RT}{2F} Ln\left\{\frac{[H^+]_s^{\ 2}}{[H_2]}\right\}$$.....(B.25)

$$E_{Fe^{2+}} = E^o_{Fe^{2+}} + \frac{RT}{2F} Ln\{[Fe^{2+}]_s\}$$.....(B.26)

where $E^o_{H_2CO_3}$, $E^o_{HCO_3^-}$, $E^o_{H^+}$, and $E^o_{Fe^{2+}}$ are the standard potentials for reduction and oxidation reactions.

Fifteen unknowns are the six surface concentrations ($[H^+]_s$, $[HCO_3^-]_s$, $[Fe^{2+}]_s$, $[CO_3^{2-}]_s$, $[OH^-]_s$, $[H_2CO_3]_s$), four equilibrium potentials ($E^o_{H_2CO_3}$, $E^o_{HCO_3^-}$, $E^o_{H^+}$, and $E^o_{Fe^{2+}}$), the corrosion potential (E_{corr}), and current due to four reactions (I_{H2CO3}, I_{HCO3^-}, I_{H^+}, $I_{Fe^{2+}}$).

Figure B.13 shows the comparison between the CO_2 corrosion rate prediction using the model proposed by Dayalan et al. (1995) and experimental data.

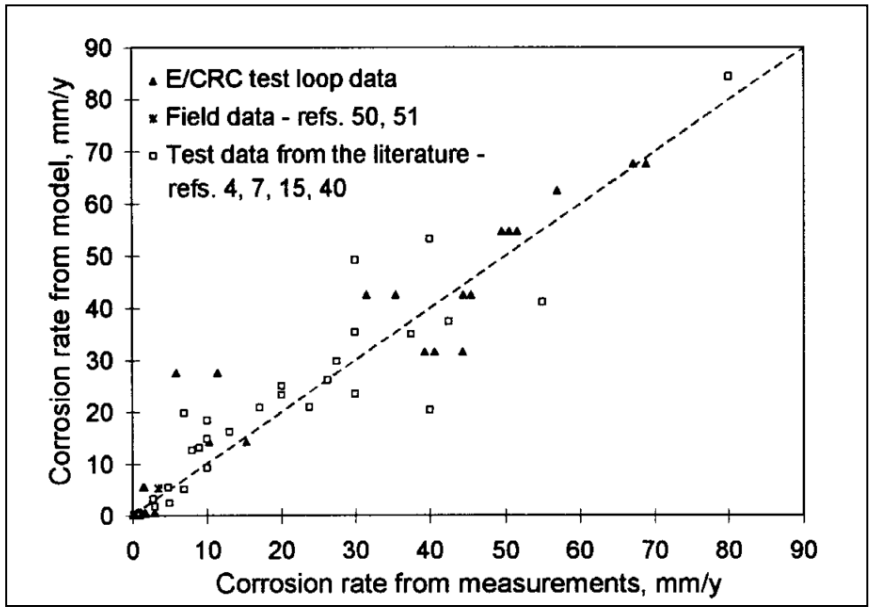

Fig.B.13 Predicted CO_2 corrosion rate vs. experimental data (Dayalan et al., 1995)

A.6 Modified Version of Tulsa CO_2 Corrosion Models for Non-Scale Forming Conditions

Based on the absolute reaction rate theory of Glasstone et al. (1939) for reactants to be converted into products, a transitory state is first reached, in which an "active complex" is formed. Formation of such a complex requires overcoming a free energy barrier of height ΔG#.

$$A + B \rightarrow [AB]^{\#} \rightarrow \text{Products} \quad \text{(B.27)}$$

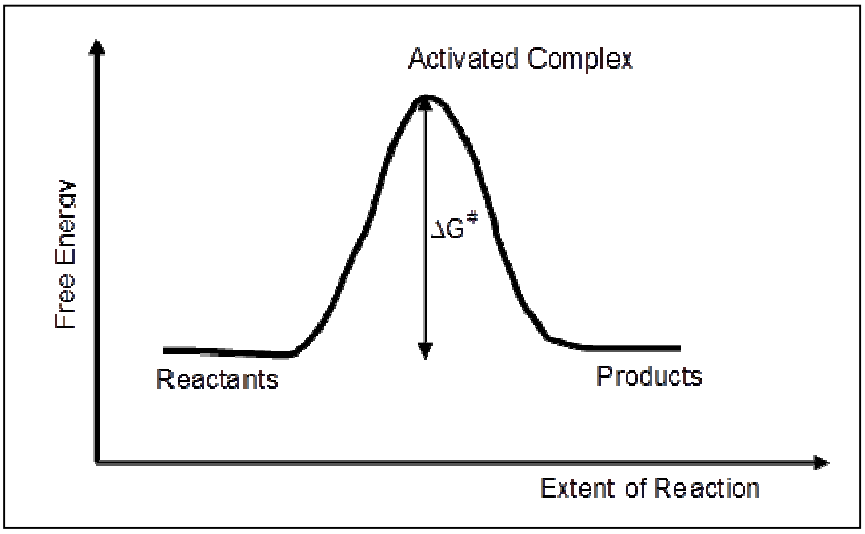

Fig.B.14 Change in free energy as a function of reaction extent

Thus, the rate of reaction (R_x) expressed as:

R_x = (Concentration of complex) × (Rate of passage over energy barrier)……(B.28)

When the activated complex is poised at the top of the energy barrier, its vibration rate (h ϑ) is just equal to the thermal energy (KT). Therefore,

h ϑ = KT ……(B.29)

where h is Plank's constant, ϑ is the frequency of vibration of complex, K is Boltzman's constant. Therefore, ϑ is the rate of passage of activated complexes over the energy barrier.

$$\vartheta = \frac{KT}{h} \text{……(B.30)}$$

Using (B.27) and (B.30):

$$R_x = [AB^{\#}]\frac{KT}{h} \text{……(B.31)}$$

Equilibrium constant for the formation of the activated complex is:

$$K^{\#} = \frac{[AB^{\#}]}{[A].[B]} \text{……(B.32)}$$

Also from thermodynamic

$\Delta G^{\#}$=-RTLn$K^{\#}$.....(B.33)

Therefore,

$$K^{\#} = exp\left\{-\frac{\Delta G^{\#}}{RT}\right\}$$.....(B.34)

Using Eqs. (B.31), (B.32), and (B.34)

$$R_x = [A][B] \underbrace{\frac{KT}{h} exp\left\{-\frac{\Delta G^{\#}}{RT}\right\}}_{Reaction\ Rate\ Const.}$$ .....(B.35)

If we change the potential from E_o to E as shown in Fig. B.15, then the change in free energy will be determined as:

$\Delta G^{\#}=\Delta G_o{}^{\#}-\alpha nF(E-E_o)$ .....(B.36)

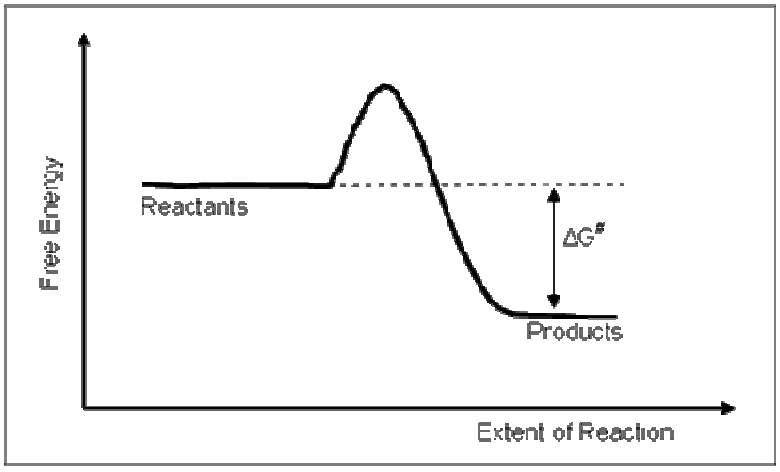

Fig. B.15 Change in free energy as a function of reaction extent

Using Eqs. (B.35) and (B.36)

$$R_x = \frac{KT}{h} exp\left\{-\frac{\Delta G_o^{\#} - \alpha nF(E-E_o)}{RT}\right\}$$.....(B.37)

where parameter α is a measure of the symmetry of the free energy barrier. When α = 0.5, the degree of decrease in the free energy barrier in the forward reaction is the same as its degree of increase in the reverse direction. (α is between 0 and 1, but usually 0.5).

Total current "I" across a surface area of A is

$$I = (Rate\ constant).\underbrace{(C_{Surf})}_{[A][B]} nFA \quad \text{.....(B.38)}$$

$$i = \frac{I}{A} = \frac{KT}{h} C_{Surf} nF exp\left\{-\frac{\Delta G_o^{\#} - \alpha nF(E-E_o)}{RT}\right\} \quad \text{.....(B.39)}$$

or

$$i = \underbrace{\frac{KT}{h} exp\left\{-\frac{\Delta G_o^{\#}}{RT}\right\} C_{Surf} nF}_{i_o} exp\left\{\frac{\alpha nF(E-E_o)}{RT}\right\} \quad \text{.....(B.40)}$$

i_o is called the exchange current density. The exchange current density represents the reaction rate in either direction at the equilibrium open circuit potential E_o. Equation (B.40) can be used in CO_2 corrosion model for modeling the current density of anodic and cathodic reaction.

Mass transfer rate of Fe^{2+} is equal to electrochemical reaction rate of the iron dissolution. Therefore:

$$K_{mt,Fe^{2+}}([Fe^{2+}]_s - [Fe^{2+}]_b) = nF\frac{KT}{h} exp\left\{-\frac{\Delta G_{Fe^{2+}}^{\#}}{RT}\right\}[Fe^{2+}]_s exp\left\{\frac{\alpha nF(E_{corr}-E_{Fe^{2+}})}{RT}\right\} \quad \text{....(B.41)}$$

Dayalan et al. (1995) assumed that the sum of mass transfer rates of ($[H_2CO_3]$, $[HCO_3^-]$, $[H^+]$) is equal to the sum of electrochemical reaction rates of ($[H_2CO_3]$, $[HCO_3^-]$, $[H^+]$) whereas cathodic reduction of carbonic acid produces bicarbonate and also cathodic reaction of bicarbonate produces carbonate ions which is not considered in this hypothesis. In this report the proposed hypothesis by Dayalan et al. (1995) was modified by assuming that mass transfer rate of each of the cathodic species is equal to the electrochemical reaction rate of that species under steady state conditions.

$$K_{mt,\,H_2CO_3}([\,H_2CO_3]_b - [\,H_2CO_3]_s) = \frac{KT}{h} exp\left\{-\frac{\Delta G_{H_2CO_3}^{\#}}{RT}\right\}[\,H_2CO_3]_s nF exp\left\{\frac{\alpha nF(E_{corr}-E_{H_2CO_3})}{RT}\right\} \quad \text{....(B.42)}$$

$$K_{mt,H^+}([H^+]_b - [H^+]_s) = \frac{KT}{h} exp\left\{-\frac{\Delta G_{H^+}^{\#}}{RT}\right\}[H^+]_s nF exp\left\{\frac{\alpha nF(E_{corr}-E_{H^+})}{RT}\right\} \quad \text{.....(B.43)}$$

Therefore, one more equation will be added to the system of fifteen equations (B.12 to B.26) and there won't be any need for the hypothesis of Eq. (B.14) in which the sum of mass transfer rates of (H_2CO_3, HCO_3^-) is equal to the mass transfer rate of CO_3^{2-}. Rest of the model formulation will be similar to that of Dayalan et al. (1995). Research is in progress to solve the system of fifteen nonlinear equations and fifteen unknowns.

A.7 Review of Ohio H_2S Corrosion Rates Prediction Model

We are currently working on better understanding of H_2S corrosion by reviewing the H_2S corrosion models proposed by Ohio University.

Project Title: Effect of H_2S and CO_2 in HPHT Wells on Tubulars and Cement

Report Type: Monthly Report

Report #: 10

Reporting Period: June 22nd, 2012 to July 21st, 2012

Authors:

Ramadan Ahmed, Principal Investigator

Subhash Shah, Co-Principal Investigator

Samuel Osisanya, Co-Principal Investigator

Shokrollah Hassani, Postdoctoral Research Associate

Rida Elgaddafi, Research Assistant

Himanshu Maheshwari, Research Assistant

Adarsh Naidu, Research Assistant

Prepared under BSEE Project # E12PC00035

by

THE UNIVERSITY OF OKLAHOMA

August 21, 2012

1. Summary of Accomplishments

This monthly report presents the progress made during the project period June 22, 2012 – July 21, 2012. Aging experiment started on cement specimens in CH_4 saturated system at temperature 350ºF and pressure of 9000 psi. However, the experiment was stopped after 6 days of aging because of brine leakage from high-pressure tube fittings. High concentration of chloride (9wt% NaCl) was used during the test, which caused pitting and crevice corrosion in some of the fittings. After repairing the damaged fittings, a new test has been started at a lower NaCl concentration (i.e. 2wt% NaCl) and lower pressure (6000 psi). During this reporting period, four different types of cement specimens were prepared including class H and class G cement with and without fly ash. Silica flour was added to control thermal retrogression. Antifoaming and viscosifying agents were used to reduce foaming tendency and minimize fluid loss, respectively. Hydroxyethylcellulose (HEC) was used as a fluid loss additive. Porosity and permeability of the dry samples were measured. Adding silica reduced the permeability of the samples.

Theoretical and modeling studies on tubular degradation are in progress. A number of corrosion models are available in the literature to predict corrosion rate in sour gas environment. Nevertheless, applications of the models are limited to low-temperature and low-pressure applications. The models require improvement to eliminate the existing limitations and extend their application range to include high-pressure and high-temperature (HPHT) conditions. A report summarizing the literature survey and modeling studies is presented in Appendix A.

Experimental data obtained at HPHT conditions is necessary to validate models develop during this investigation. Progress has been made in the development of test facility for corrosion studies. The final design the corrosion test setup has been completed. The setup will have stress corrosion cracking (SCC) and dynamic corrosion cells. The SCC cell is equipped with pneumatic power cylinder to apply axial force, and gas injection cylinders to maintain a constant differential pressure between internal and external parts of a mini-pipe specimen. At present, we are in communication with vendors to acquire autoclaves, which will be used as corrosion cells, instrumentation, and other auxiliary items needed for developing the test facility.

Our plan for the coming weeks is to continue the aging experiments. Cement cores and specimens used for evaluating cement bonding will be aged. After aging the properties of the samples will be measured. We will continue our theoretical and modeling studies on tubular corrosion as well.

2. Overall Project Progress

2.1 Theoretical Studies (Task 1)

Theoretical and modeling studies on corrosion of tubular were continued. There are numerous CO_2 and H_2S corrosion models available in the literature to predict corrosion rate and protective film thickness and properties. However, most of these models are developed for low-temperature and low-pressure applications. The validity of these models at high temperature and pressure conditions has not been verified. Mechanistic models for corrosion rate prediction in CO_2, H_2S, and CO_2/H_2S systems proposed by the University of Ohio and University of Tulsa were reviewed during the reporting period. Limitations of the models and their modeling details were investigated and some modifications have been suggested. Research is in progress to adopt the models for HPHT conditions. Details of theoretical and modeling studies on tubular CO_2 and H_2S corrosion are presented in Appendix A.

pH measurement is relevant for monitoring the corrosion behavior and explaining different phenomena occurring during corrosion experiment. However, measuring pH under HPHT conditions is extremely challenging. At present, different pH measurement techniques are emerging. Research is in progress to develop a technique to indirectly measure pH during the experiment using conductivity of the solution.

2.2 Experimental Studies on Degradation of Cement (Task 2)

As indicated in the last report, two different classes (G and H) of cement were aged under HPHT conditions (9000 psi and 350ºF). Brine concentration was 9% NaCl. The aging process was stopped after 6 days because of brine leakage from tee and cross joints (Fig. 1). The leakage is attributed to crevice corrosion, which often occurs at high concentration of NaCl in the system. This type of corrosion takes place within narrow openings and gaps such as those found under gaskets, washers, and tapered tube fittings. Large surface area becomes cathodic and the crevices will become anodic, and thus corrosion will occur in a short time. The crevices create an environment that traps pollutants and concentrates corrosion products, which in turn accelerates the rate of corrosion. Negative chloride ions diffuse into the crevice in order to balance the charge created by the positive metal ions and then act as a catalyst for the corrosion mechanism (Fig. 2). In order to manage this problem, new aging experiment has started using 2wt% NaCl solution.

Fig. 1 NaCl residual deposited on one of the Hastelloy tee joints during aging experiment 9000 psi, 350^{o}F, and 9wt% NaCl

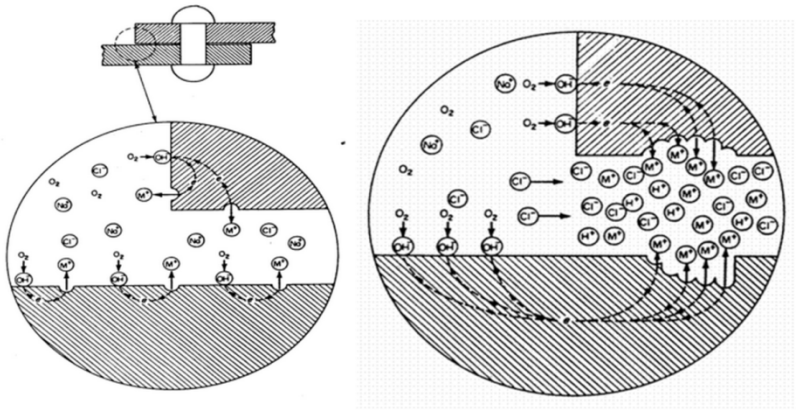

Fig. 2 Crevice corrosion of a basic metal alloy (Lister and Cook, 2010)

Microscopic examination of the cement cores showed the presence air pockets in the specimens. Although, extreme care was taken to reduce foam generation during the mixing, strong agitation of the cement slurry resulted in the formation of foam bubbles. Mixing was systematically performed to minimize the entrapment of air bubbles. In addition, the slurry was slowly agitated after pouring into the casting molds. However, examination of the samples showed the presence of air pocket. Hence, after discussing the issues with technical advisory board members, it has been decided to use antifoaming agent to reducing the foaming tendency.

Effects of fly ash and silica on physical and mechanical properties of cement will be examined in the first set of aging experiment. Silica is added to the cement to improve the high temperature resistance. As mentioned in the previous report, fly ash as a cement additive reduces slurry density and cost of cement while, improving mechanical properties and thickening time of cement. Also, fly ash can react with calcium hydroxide and forms calcium silicates.

In the second batch of aging experiment, 40 cement specimens are arranged on shelves (5 specimens per shelf) as shown in Fig. 3. Half of the first batch of the samples will be removed after 15 days and the rest will be removed after 30 days of aging. Each type of aged cement will have 5 identical specimens. Two the specimens will be used for porosity and permeability testing; they can also be used for FTIR, SEM, and cross sectioning and studying the degradation depth. Three remaining specimens will be used for compressive strength testing.

Good bonding between cement and casing is critical for effective zonal isolation and prolong the life of a well. In the second batch of experiment, in addition to the cement specimens, 12 bonding testing samples are being aged together with cement cores. Bonding test samples were prepared by casting cement into a ¾-inch seamless pipe, which has length and wall thickness of 1.75 and 0.15 inches, respectively. The pipes are coated with corrosion protective paint.

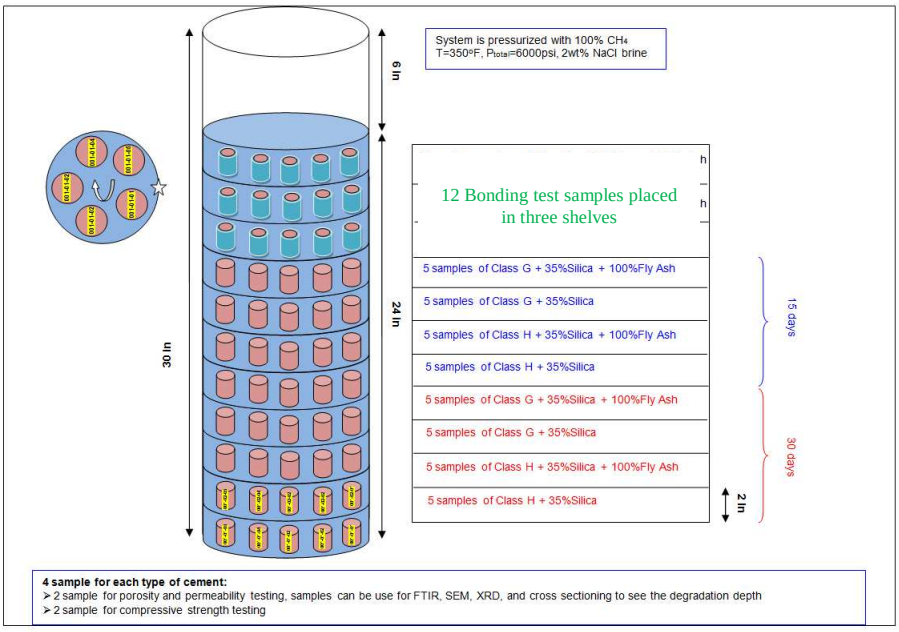

Fig. 3 Cement specimen arrangement and test condition for the second set of aging experiment

Porosity and permeability of two different classes of cement (i.e. H and G) with and without fly ash was measured after curing for five days at temperature of 200ºF (Table 1 and 2). These samples were made of cement slurry which was prepared using a high-speed API cement mixer. Porosity and permeability test results show good repeatability (Figs. 4 and 5). When compared with our previous measurements, results show one order of magnitude reduction in permeability as a result of using the API cement mixer. Class G cement with fly ash showed the minimum porosity (Fig. 4). However, class H cement with and without fly ash and class G without fly ash showed almost the same porosity of approximately 25%. Class H cement without fly ash had the maximum permeability (Fig. 5). Class G cement with and without fly ash and class H cement with fly ash exhibited comparable permeability, which is roughly 0.02 mD. In general, the measurements show a good agreement with experimental data reported in literature.

Table 1 Porosity and permeability of different cement samples in CGS units

CGS Units											
Core #	Core dimensions			Porosity					Permeability		Remarks
	Diameter	Length	Weight	V_b	V_g	V_p	Porosity	Gr. Density	K_{air}	K_{klink}	
	mm	mm	g	cc	cc	cc	%	g/cc	mD	mD	
1Go1	25.36	37.98	32.55	19.18	14.09	5.09	26.54%	2.31	0.035	0.018	Class G without Fly ash
1Go2	25.32	36.72	31.52	18.49	13.55	4.94	26.72%	2.33	0.043	0.022	
1Go3	25.34	30.27	26.24	15.27	11.29	3.98	26.06%	2.32	0.036	0.019	
1Ho1	25.26	38.30	33.53	19.19	13.83	5.36	27.93%	2.42	0.102	0.060	Class H without Fly ash
1Ho2	25.28	37.32	32.74	18.73	13.39	5.34	28.51%	2.44	0.116	0.070	
1Ho3	25.33	38.22	33.90	19.26	13.73	5.53	28.71%	2.47	0.113	0.068	
1Hf1	25.24	37.56	31.13	18.79	13.94	4.85	25.81%	2.23	0.050	0.027	Class H with Fly ash
1Hf2	25.17	37.62	31.45	18.72	14.10	4.62	24.68%	2.23	0.042	0.022	
1Hf3	25.18	36.97	30.31	18.41	13.55	4.86	26.40%	2.24	0.056	0.031	
1Gf1	25.30	33.58	29.46	16.88	13.46	3.42	20.26%	2.19	0.038	0.020	Class G with Fly ash
1Gf2	25.25	38.40	33.76	19.23	15.31	3.92	20.38%	2.20	0.036	0.018	
1Gf3	25.20	39.13	33.94	19.52	15.43	4.09	20.95%	2.20	0.040	0.021	

Table 2 Porosity and permeability results for the different cement samples in Field units

Field Units											
Core #	Core dimensions			Porosity					Permeability		Remarks
	Diameter	Length	Weight	V_b	V_g	V_p	Porosity	Gr. Density	K_{air}	K_{klink}	
	in	in	lbm	in^3	in^3	in^3	%	lbm/gal	mD	mD	
1Go1	1.00	1.50	0.07	1.17	0.86	0.31	26.54	19.29	0.035	0.018	Class G without Fly ash
1Go2	1.00	1.45	0.07	1.13	0.83	0.30	26.72	19.46	0.043	0.022	
1Go3	1.00	1.19	0.06	0.93	0.69	0.24	26.06	19.37	0.036	0.019	
1Ho1	0.99	1.51	0.07	1.17	0.84	0.33	27.93	20.21	0.102	0.060	Class H without Fly ash
1Ho2	1.00	1.47	0.07	1.14	0.82	0.33	28.51	20.37	0.116	0.070	
1Ho3	1.00	1.50	0.07	1.18	0.84	0.34	28.71	20.62	0.113	0.068	
1Hf1	0.99	1.48	0.07	1.15	0.85	0.30	25.81	18.62	0.050	0.027	Class H with Fly ash
1Hf2	0.99	1.48	0.07	1.14	0.86	0.28	24.68	18.62	0.042	0.022	
1Hf3	0.99	1.46	0.07	1.12	0.83	0.30	26.40	18.70	0.056	0.031	
1Gf1	1.00	1.32	0.06	1.03	0.82	0.21	20.26	18.29	0.038	0.020	Class G with Fly ash
1Gf2	0.99	1.51	0.07	1.17	0.93	0.24	20.38	18.37	0.036	0.018	
1Gf3	0.99	1.54	0.07	1.19	0.94	0.25	20.95	18.37	0.040	0.021	

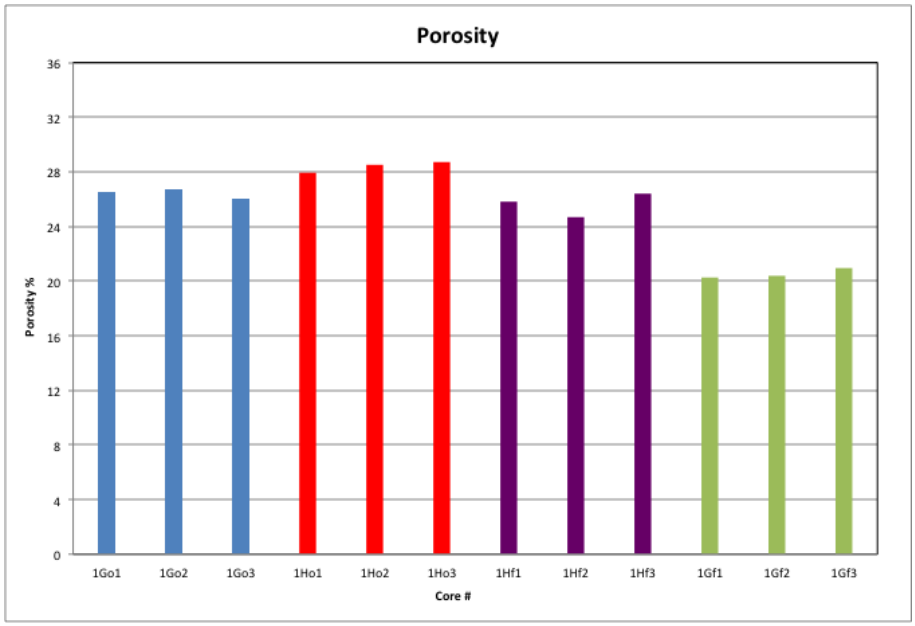

Fig. 4 Porosity measurements of different cement samples before aging

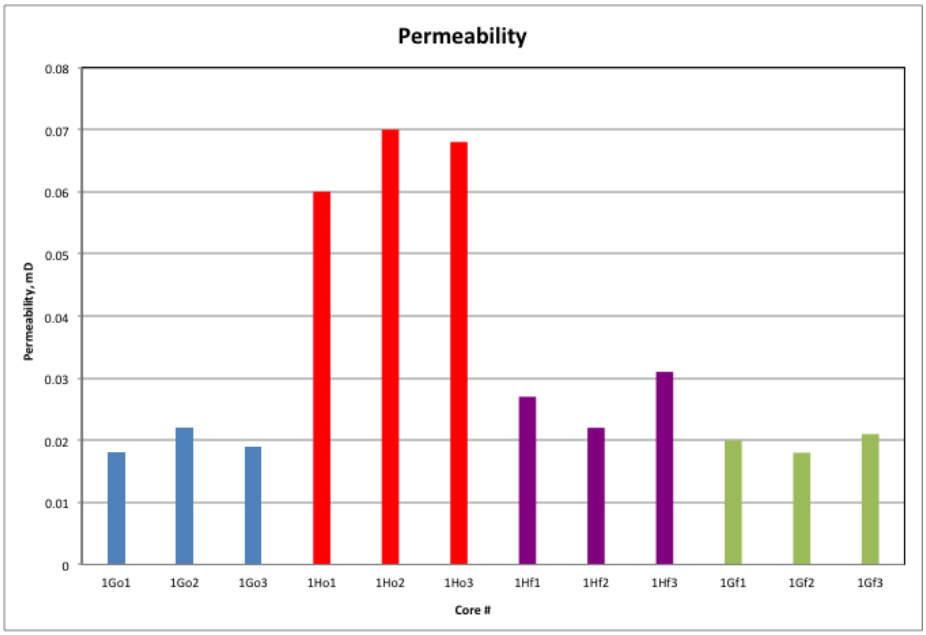

Fig. 5 Permeability measurements of different cement samples before aging

Tables 3 and 4 present the thickening time of various slurries used during the experiments and thickening time reported in different literatures, respectively. Thickening time measured during this research period shows a good agreement with previously reported values for different cement classes.

Table 3 Thickening time of four different slurries prepared during the experimental study

Cement Slurry	Density (lbm/gal)	Thickening Time, min.	Thickening Time, hrs.
Class H with fly ash	15.2	185	3:05
Class H without fly ash	16.1	170	2:50
Class G with fly ash	14.96	175	2:55
Class G without fly ash	15.65	135	2:15

Table 4 Thickening times of different slurries published in the literature

Literature Review							
Author (s)	**Title**	**Journal/Year**	**Cement Composition**	**Density (lbm/gal)**	**Thickening time (hrs:min)**	**Thickening time (min.)**	**Remarks**
Al-Dossary et al	Cementing at High Pressure Zones in KSA —Discovering Mystery behind Pipe	SPE - 142421 - PP/2011	Class G + 1.2% (Dispersant) + 0.4% (Fluid loss) + 0.22 % (Retarder)+ 0.01 gps (Defoamer)	15.8	4:00 - 5:00	240 - 300	-
			Class G + 0.6% (Dispersant) + 0.3% (Fluid loss) + 0.05gps (Retarder)+ 0.005 gps (Defoamer)	13.5	5:00 - 5:30	300 - 330	
Brandl et al	Cementing solutions for Corrosive Well Environment	SPE - 132228/2010	Class G + 35% Silica flour	15	7:00	420	-
-	Cement (Petrochem)		Class A	15.6	2:30	150	-
			Class C	14.8	1:45	105	
			Class G	15.8	2:45	105	
			Class H	16.5	2:00	120	
Crinkelmeyer et al	Improved Cementing of High Temperature Oil and Gas Wells Through Computer Applications	SPE - 5518/1975	Class H #1	15.7	2:18, 3:40	138(4% ret.), 220(5% ret.)	cement + 35% silica sand + retarder + 0.2% antifoam agent + 56%water.
			Class H #2	15.7	1:22, 1:58	82(4%), 118(5%)	
			Class H #3	15.7	3:18, 4:59	198(4%), 299(5%)	
			Class H #4	15.7	4:33, 3:26	273(4%), 306(5%)	
			Class G #1	15.7	0:59, 1:25	59(4%), 85(5%)	
			Class G #2	15.7	0:47, 0:42	47(4%), 42(5%)	
			Class G #3	15.7	0:57, 0:44	57(4%), 44(5%)	
			Class G #4	15.7	1:56, 2:50	116(4%), 170(5%)	
			Class A #1	15.7	1:02, 1:28	62(4%), 88(5%)	
			Class A #2	15.7	1:46, 2:38	106(4%), 158(5%)	
			Class A #3	15.7	1:00, 1:19	60(4%), 79(5%)	
Dubois et al	Improvement of low-permeable cement for zonal isolation at high-temperature conditions	SPE - 50782/1999	Class G clinker and silica	15.9	1:00	60	0.3% (Ret.)
					1:10	70	0.50%
					8:20	500	0.80%
					217:00:00	1302	1%
					-	-	1.50%
Garvin & Johnson	Cementing Practices - 1972	Joint Meeting MMIJ - AIME/1972	Class H (0.3% ret.)	-	4:00	240	-
			Class H (0.4% ret.)	-	4:53	293	

Figure 6 shows comparison of thickening time for different cement samples. In this graph, B_c is the consistometer reading that ranges between 0 and 10. At t = 0, when B_c = 0, the slurry has just being prepared and is least resistant to pumping. At t = t_1, when B_c = 10, the slurry becomes very thick and unpumpable. Experimental results showed that class G cement without fly ash has lowest thickening time. Adding fly ash to the cement increased the

thickening time for both class H and class G cement. However, adding silica to the cement reduced the thickening time for class H cement as it is shown in Fig. 7.

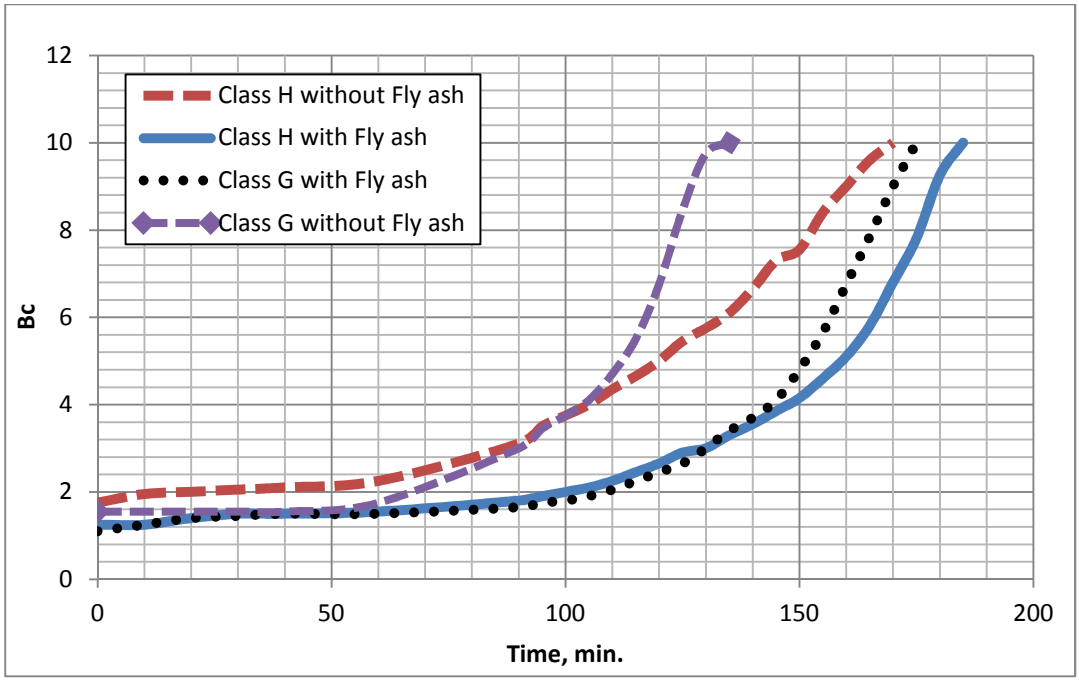

Fig. 6 Thickening time of four different cement slurries

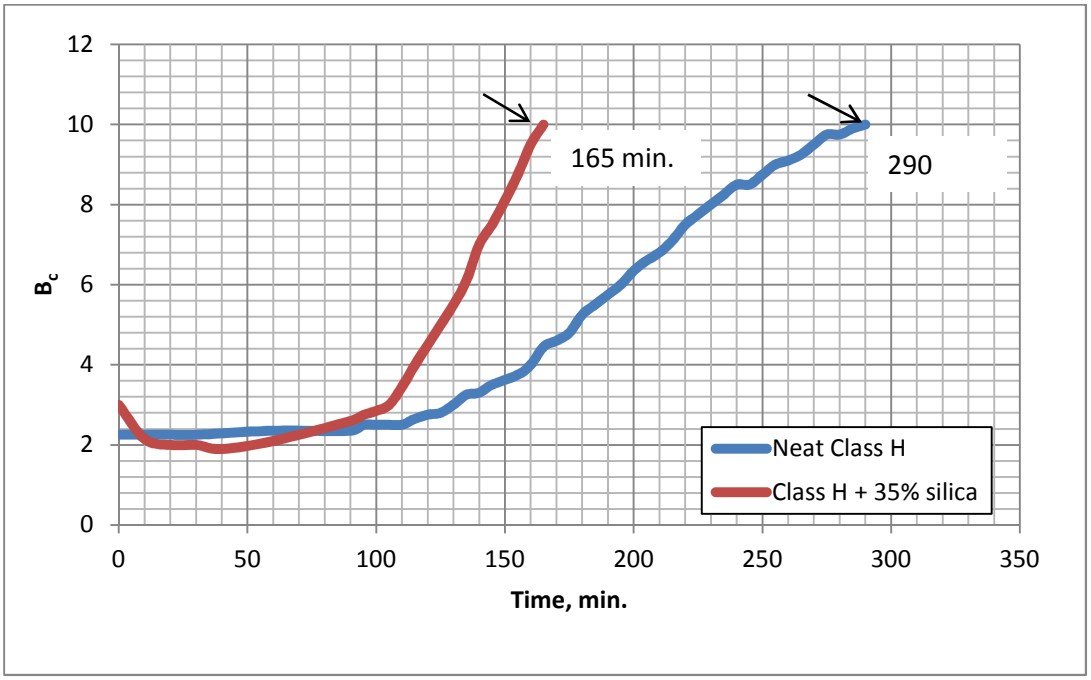

Fig. 7 Comparison of thickening time of neat Class H cement and Class H cement + 35% silica slurry

2.3 Experimental Studies on Corrosion of Tubulars (Task 3)

Different companies have been contacted for high-pressure recirculation pumps. There are two main limitations for high pressure recirculation pump including low system pressure, low flow rate and material compatibility for brine saturated with sour gases. With market available circulation pump (Micropump), the maximum pressure is 5000 psi, the maximum flow velocity that can be achieved using the pump in an 1/8 inch pipe test section is 0.3 m/s, which is really low for simulating the shear stress in the oil and gas production. On the other hand, available high pressure circulation pump with 10,000 psi system pressure (WITTE gear pump) is not designed for low viscosity liquids. Hence, it is not applicable for pumping brine solution. We have also considered using injection cylinder as a pump, acquiring a custom-made pump or syringe type pump that meets the desired specifications. However, the low flow capacity and pressure pulsation are the limiting factors for piston or syringe type pumping systems. A very different and robust approach, which is often used for elevated pressure and temperature corrosion study, is utilizing flow created by two rotating coaxial cylinders.

After considering all these alternatives, the best option left is using rotating coaxial cylinder system. The system uses a magnetic drive to rotate a cylinder placed in the HPHT autoclave. The drive rotates the cylinder at high speed creating Couette flow that can generates wall shear stress level which is experienced in real life. We have contacted different vendors to acquire the magnetic drive. Due to their air gap limitation, maximum pressure rating for magnetic drives made of Hastelloy is 5000 psi. Magnetic drives with a higher pressure rating (10,000 psi) are available in stainless steel 316 or A286 version. Corrosion studies conducted to evaluate the performance of these materials in sour gas environment show good corrosion resistance of A286 at ambient and high temperature (up to 300^{o}F) conditions. Stainless steel 316 exhibited pitting when exposed to brine saturated with sour gas.

After choosing the Couette flow type corrosion cell, the design of the HPHT corrosion test setup (Fig. 8) has been finalized. The corrosion setup has two corrosion testing cells: i) stress corrosion cracking (SCC) cell (Fig. 9a); and ii) dynamic corrosion cell (Fig. 9b). The SCC cell is equipped with gas cylinders to maintain roughly a constant differential pressure between the internal and external parts of a mini-pipe specimen Air cylinder apply axial pull force to put the specimen under tension. The SCC will allow us to study the stress corrosion cracking sensitivity of tubular under HPHT conditions. Synergistic effect of sour gas and mechanical stress will be investigated.

The dynamic corrosion cell will have a rotating cylinder inside. Specimens will be attached to a Teflon sleeve and placed in the cell. The rotation of the cylinder generates turbulence and wall shear stress needed to facilitates the removal of corrosion products and

accelerate the corrosion process. Two samples will be placed in the cell; one for weight measurement and another one to apply the linear polarization resistance (LPR) method.

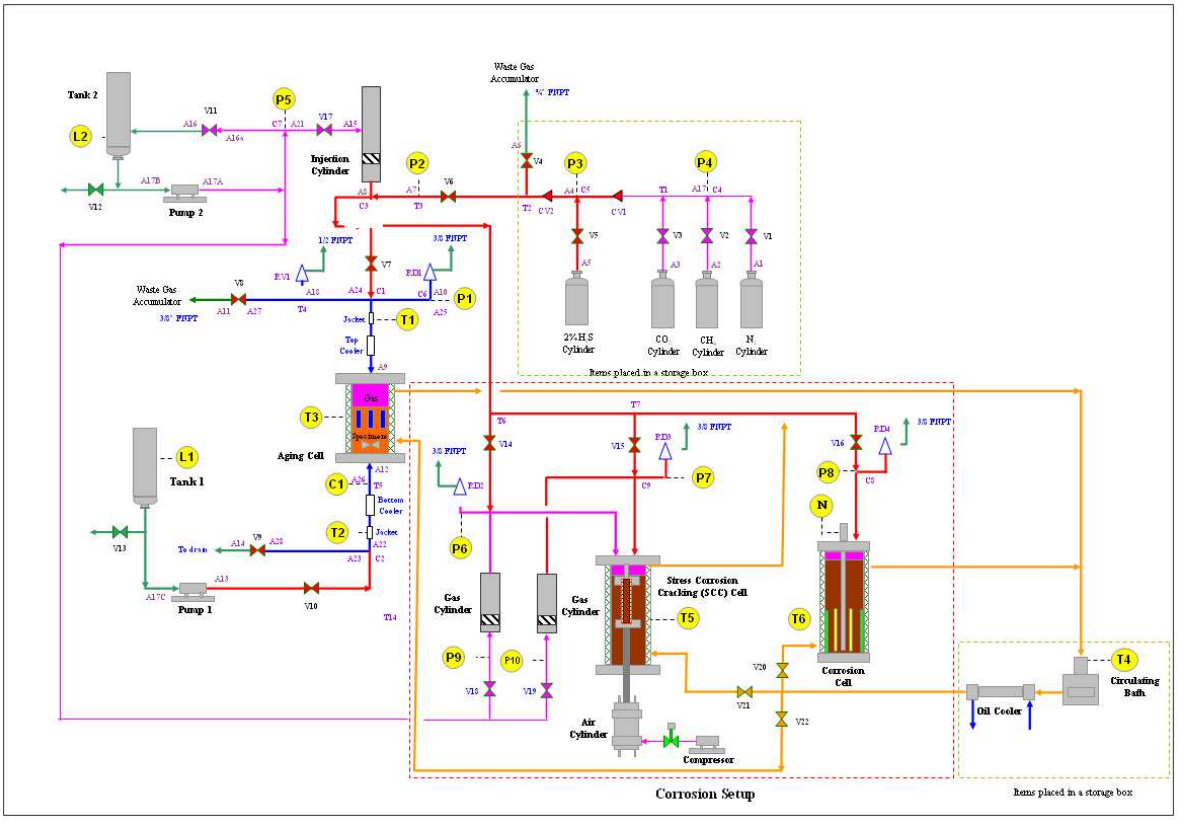

Fig. 8 Schematic of the test facility showing the corrosion setup

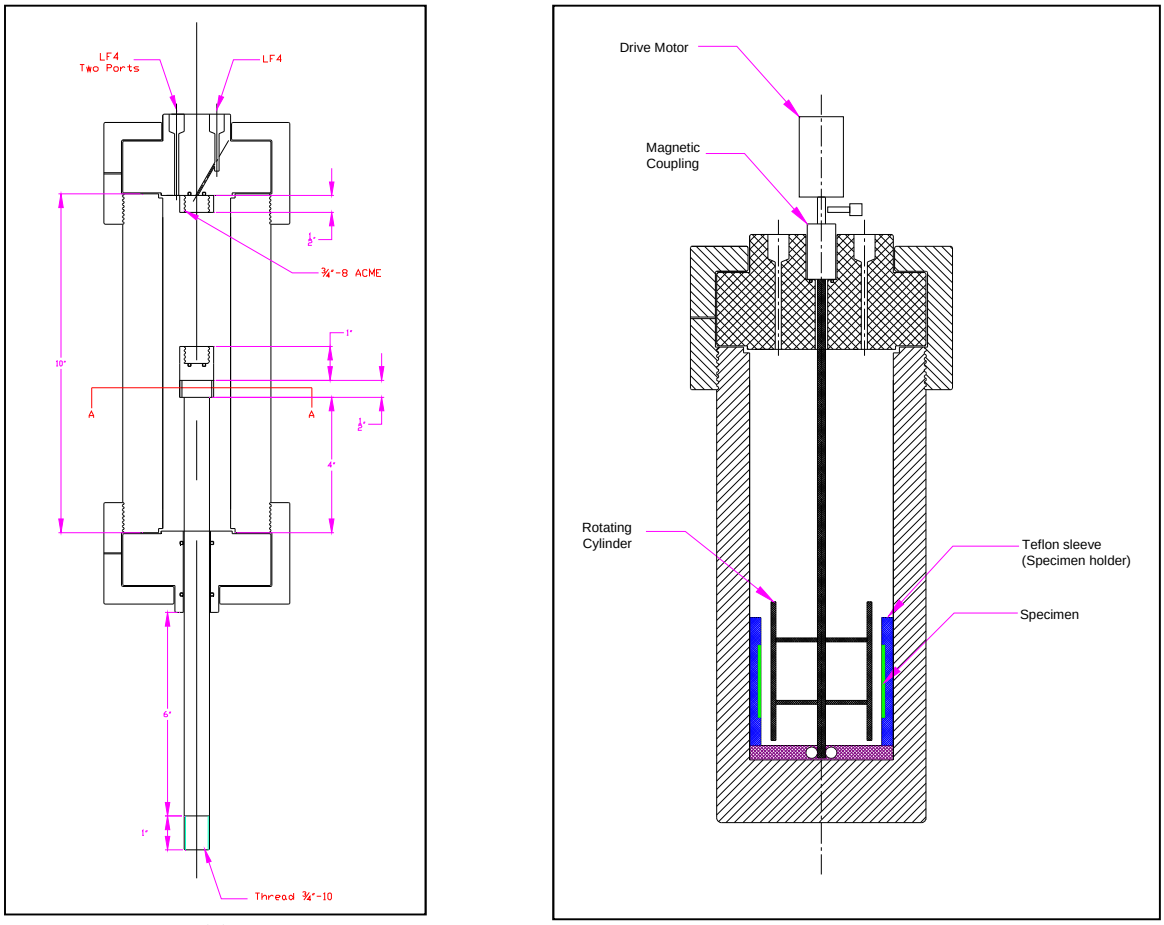

Fig. 9 Designs of corrosion test cells: a) stress corrosion cracking (SCC) cell; and b) dynamic corrosion cell

3. Problems Encountered

Major problems during this reporting period have been fluid leakage from the ageing setup and corrosion of pipe fittings. A number of control valves have been unable to completely shot off the aging cell inlets and outlets resulting in leaks that deplete system pressure with time. As result, we were unable to conducted tests at the desired pressure. Currently, the system can hold pressure up to 6000 psi. The leak becomes excessive when the system pressure increases more than 6000 psi. In order to maintain high system pressure, new heavy duty ball valves have been ordered to replace the leaking ones.

During the aging process, inlet and outlet piping in contact with brine solution experienced leakage caused by corrosion. In order to minimize corrosion and control the leakage, brine concentration has been reduced from 9% to 2%.

4. Planned Activities

- Aging experiments.
- Continue theoretical and modeling studies on cement and tubular degradation.
- Designing and ordering the parts of test setup for tubular corrosion studies.

5. Meeting and contacts

During this reporting period, we have made contacts with different companies that providing the high pressure pump, autoclave, magnetic stirrer, potentiostat, and pH meter for HPHT tubular corrosion testing. We have contacted several pump and high pressure equipment companies including Autoclave Engineers, CorrTest, Amar Equipments Pvt. Ltd., High Pressure Equipment Company, PMAC system, Micropump, and WITTE pump. We have also contacted potentiostat supplying companies including Gamry, Princeton Applied Science, Metrohm, Exova, Bio-Logic, Ivium Technologies, Digi-ivy, and ACM instrument.

Contacts also made with TAB member to get their recommendations on slurry preparation. Members suggest the use of antifoaming agent to control formation of large pores and cavities in the cores.

Furthermore, we received comments from BSEE on our last report. Our responses to the comments are presented in Appendix B.

6. Project Expenditures

This section presents the project expenses during the months of July (Table 5) and the cumulative expenditures.

Table 5 Current and cumulative expenditures, July, 2012

No.	Budget Categories	Current Expenses	Cumulative Expenses
1	Salaries & Wages	$33,686.79	$93,272.78
2	Fringe Benefits	$11,152.53	$26,198.36
3	Project Materials	$1,700.70	$36,364.44
4	Travel	$46.62	$1,123.84
5	Conference Expenses	$0.00	$0.00
6	Other Direct Costs	$0.00	$305.38
7	Equipment	$38,970.91	$141,502.67
8	Space Rental	$0.00	$0.00
9	Indirect Cost	$23,293.32	$78,632.43
10	**Total**	**$108,850.87**	**$377,399.90**

Nomenclature

R	Universal gas constant
T	Absolute temperature
R_p	Polarization Resistance
i_{corr}	Corrosion Current
B	Empirical polarization resistance constant
$[Fe^{2+}]_s$	Iron ion concentration on the metal surface
$[Fe^{2+}]_{sc}$	Iron ion concentration on the scale surface
$[Fe^{2+}]_b$	Iron ion in the bulk solution
F	Faraday constant
K_{Fe}	Electrochemical reaction rate constant of iron ions
B	Transfer coefficient (the value of B is 0.5 for most of the reactions),
E_{corr}	Corrosion potential
E^o_{Fe}	Standard potential of iron at temperature T
K_1	First dissociation constant of Carbonic Acid
K_2	Second dissociation constant of Carbonic Acid
i_o	Exchange current density
E_o	Equilibrium open circuit potential
F_{sat}	Saturation factor
T_k	Temperature in Kelvin
I	Ionic strength in molarity
C_i	Concentration of different species in the aqueous solution, all which are in mol/L
Z_i	Species' charges
CR	Corrosion rate
i_a	Anodic current density
MW_{Fe}	Atomic mass of iron
ρ_{Fe}	Density of iron
n	Number of moles of electrons involved in iron oxidation
$i_{a,Fe}$	Current density of iron oxidation, A/m^2
$i_{o,Fe}$	Exchange current density of iron oxidation, A/m^2
E_{corr}	Corrosion potential, V
$E_{rev,Fe}$	Reversible potential of iron oxidation, V
b_{Fe}	Tafel slope of iron oxidation, V
i_{corr}	Corrosion current density
i_c	Cathodic corrosion current density

i_{ct}	Exchange current density of cathodic reactions, A/m^2
i_o	Reversible potential of cathodic reactions, V
E_{rev}	Tafel slope of cathodic reactions, V
η_{FeCO3}	Scale factor due to formation of $FeCO_3$ film
η_{FeS}	Scale factor due to formation of FeS film
C_{CO_2}	Concentration of CO_2 in bulk solution, mol/m^3
$D_{H_2CO_3}$	Diffusion coefficient of H_2CO_3 in water, m^2/s
K_{hyd}	Equilibrium constant for CO_2 hydration reaction
K_{hyd}^f	Forward reaction rate constant for CO_2 hydration reaction
f	Flow factor affecting CO_2 hydration
δ_m	Mass transfer layer thickness
δ_r	Reaction layer thickness
K_{m,H_2CO_3}	Mass transfer coefficient of H_2CO_3, m/s.
$Flux_{H_2S}$	Expressed in mole/(m^{2}s)
$K_{m(H_2S)}$	Mass transfer coefficient for H_2S in the hydrodynamic boundary layer
C_{b,H_2S}	Bulk concentration of H_2S in the liquid phase (mole/m^3)
C_{O,H_2S}	Interfacial concentration of H_2S at the outer scale/solution interface (mole/m^3)
D_{H_2S}	Diffusion coefficient for dissolved H_2S in water (=$2 \times 10^{-9} m^2/s$)
ε	Outer Mackinawite scale porosity
ψ	Outer mackinawite tortuosity factor
C_{i,H_2S}	Interfacial concentration of H_2S at the inner scale/film interface (mole/m^3)
δ_{OS}	Thickness of Mackinawite scale (m)
M_{OS}	Mass of the Mackinawite scale (kg)
A	Surface area (m^2)
A_{H_2S} and B_{H_2S}	Arrhenius constants ($A_{H_2S} = 1.3 \times 10^{-4} \frac{mole}{m^2.s}$, $B_{H_2S} = 15500 \frac{Jouls}{mole}$)
C_{s,H_2S}	Concentration of H_2S on the steel surface (=10^{-7} mole/m^3)
SSR	Mackinawite retention rate
SFR	Scale formation rate
SDR	Scale damage rate
SDR_m	Mechanical scale damage rate
M_{FeS}	Molar mass of iron sulfide (kg/mole) and Δt is the time interval (sec)
$D_{H_2CO_3}$	Diffusion coefficient of carbonic acid (m^2/s)
K_{hyd}	Equilibrium constant for the CO_2 hydration reaction

K_{hyd}^{f} Forward reaction rate for the CO_2 hydration reaction

$f_{H_2CO_3}$ Flow factor

Acronyms

(HEC)	Hydroxy ethyl cellulose
(HPHT)	high-pressure high-temperature
(SCC)	stress corrosion cracking
(LPR)	linear polarization resistance
(RO)	reverse osmosis

References

Al-Dossary, A.F., Al-Majed, A., Hossain, M.E., and Rahman, M.K., 2011. Cementing at High Pressure Zones in KSA —Discovering Mystery behind Pipe‖ SPE 142421 – PP Manamah, Baharain, 20–23 March 2011.

Brandl, A., Cutler, J., Seholm, A., Sansil, M., Braun, G., Cementing solutions for corrosive well environments, SPE 132228, SPE Beijing, China, 2010

Crinkelmeyer, O.W., 1975. Improved cementing of high temperature oil and gas wells through computer applications. Society of petroleum engineers of AIME

Dayalan, E., Vani, G., Shadley, J.R., Shirazi, S.A. and Rybicki, E.F. 1995. Modeling CO_2 corrosion of carbon steel in pipe flow, Paper No. 118, presented at the NACE corrosion conference.

Dayalan, E., de Moraes, F.D., Shadley, J.R., Shirazi, S.A., Rybicki, E.F., 1998. CO2 Corrosion Prediction in Pipe Flow Under $FeCO_3$ Scale-Forming Conditions, Paper no. 51, presented at the NACE CORROSION conference, Houston, TX.

Dugstad, A., Lunde, L. and Videm, K. 1994. Parametric Study of CO_2 Corrosion of Carbon Steel, Paper No. 14, presented at the NACE CORROSION conference, Houston, TX.

Johnson, R.M, Garvin, T.R. , 1972. Cementing practice, Joint meeting

Lister and Cook, 2010, UN1001 Galvanic Corrosion [Internet]. [Cited 2010 November 28]. Available at: http://www.authorstream.com/Presentation/Cubemiddle-36438-UN1001-Galvanic-Corrosion-REACTOR-CHEMISTRY-Section-4-Eight-Forms-SERI-as-Entertainment-ppt-powerpoint/

Nesic, S., Postlethwaite, J., Olsen, S., 1996. An Electrochemical Model for Prediction of Corrosion of Mild Steel in Aqueous Carbon Dioxide Solutions. Corrosion, Vol. 52, No. 4, p. 280.

Nesic, S., Nordsveen, M., Nyborg, R., Stangeland, A., 2003. A Mechanistic Model for CO_2 Corrosion with Protective Iron Carbonate Films - Part 2: A Numerical Experiment. Corrosion, Vol. 59, No. 6, pp. 489-497.

Nesic, S., Li, H., Huang, J., Sormaz, D., 2009. An Open Source Mechanistic Model for CO_2/H_2S Corrosion of Carbon Steel, NACE corrosion conference, Paper No. 9572

Nešić, S. 2007. Key issues related to modeling of internal corrosion of oil and gas pipelines, Corrosion Science, Vol. 49, Issue 12, December 2007, Pages 4308–4338.

Nordsveen, M., Nesic, S., Nyborg, R., Stangeland, A., 2003. A Mechanistic Model for CO_2 Corrosion with Protective Iron Carbonate Films - Part 1: Theory and Verification. Corrosion, Vol. 59, No. 5, pp. 443-456.

Samaranayake C.P. and Sastry S.K., 2010. In Situ Measurement of pH Under High Pressure. J. Phys. Chem. B 2010, 114, pp. 13326–13332

Silva, C.A.R., X. Liu, and F.J. Millero, 2002. Solubility of Siderite in NaCl Solutions. Journal of Solution Chemistry, 31(2): p. 97-108.

Sun, W, 2006. PhD Dissertation. Kinetics of Iron Carbonate and Iron Sulfide Scale Formation in CO_2/H_2S Corrosion. Ohio University.

Sun, W., Nesic, S. 2007. A Mechanistic Model of H_2S Corrosion of Mild Steel, Paper No. 7655, presented at the NACE corrosion conference, March 11 - 15, Nashville, TN.

Sun, W., Nesic, S. 2008. A Mechanistic Model of Uniform Hydrogen Sulfide/Carbon Dioxide Corrosion of Mild Steel, Corrosion Journal, Vol. 65. No, 5.

Appendix A

Literature Review, Theoretical Studies on Tubular Corrosion

A.1 Review of Tulsa CO_2-Corrosion Model

Previously, a mechanistic model developed by Dayalan et al, (1995) was reviewed and modified for CO_2-corrosion rate prediction under non-scale forming conditions. During this report period, another important component has been added to the model, which is the effect of formation of iron carbonate scale on the corrosion rate. The approach, which considers seven main steps (Fig. A-1) for the overall CO_2-corrosion process under scale forming conditions was developed by Dayalan et al. (1998). The first step in CO_2-corrosion process is the rate of formation of reactive species in the bulk, which is modeled in similar manner as the CO_2-corrosion rate under non-scale forming conditions. In this step, CO_2 gas dissolves in water and then hydrates to form carbonic acid. Subsequently, the acid can directly reduce on metal surface or dissociate to bicarbonate ions first and then reduce on the metal surface as a cathodic reaction. Dayalan et al. (1998) assumed that carbonic acid reduction may also happen on the scale surface. The second and third steps in CO_2-corrosion process are the transportation of cathodic reaction species (reactants) from the bulk to the scale surface and from scale surface to the metal surface, respectively. Transportation of reaction species from scale surface to metal surface has to be through the iron-carbonate scale, which is a porous medium. The driving force for transporting these species to the metal surface is consumption of these species on the metal surface by cathodic reaction of corrosion, which causes a concentration gradient between bulk and metal surface. The forth step of corrosion process is electrochemical corrosion reaction on the scale surface and the fifth step is electrochemical corrosion reaction on the metal surface. Electrochemical corrosion reaction can be divided into two main categories as anodic and cathodic reactions. The last step in CO_2-corrosion process is the transportation of corrosion products from the metal surface to the scale surface and then from the scale surface to the bulk solution. The driving force for this transportation is concentration difference between metal surface, scale surface, and bulk solution as a result of electrochemical reactions on metal surface and scale surface

Dissolusion of CO_2	• $CO_{2(gas)} \leftrightarrow CO_{2(aq)}$ • $CO_{2(aq)} + H_2O \leftrightarrow H_2CO_3$ • $H_2CO_3 \leftrightarrow H^+ + HCO_3^-$ • $HCO_3^- \leftrightarrow H^+ + CO_3^{2-}$
Transportation of reactants from bulk to the scale surface	• $H_2CO_{3(Bulk)} \rightarrow H_2CO_{3(Scale)}$ • $HCO_3^-{}_{(Bulk)} \rightarrow HCO_3^-{}_{(Scale)}$ • $H^+{}_{(Bulk)} \rightarrow H^+{}_{(Scale)}$
Transportation of reactants from scale surface to the metal surface	• $H_2CO_{3(scale)} \rightarrow H_2CO_{3(Surface)}$ • $HCO_3^-{}_{(scale)} \rightarrow HCO_3^-{}_{(Surface)}$ • $H^+{}_{(scale)} \rightarrow H^+{}_{(Surface)}$
Electrochemical Reaction on the scale surface	• **Cathodic Reactions** • $2H_2CO_3 + 2e^- \leftrightarrow H_2 + 2HCO_3^-$ • $2H_2CO_3 + 2e^- \leftrightarrow H_2 + 2CO_3^{2-}$ • $2H^+ + 2e^- \leftrightarrow H_2$
Electrochemical Reaction on the metal surface	• **Anodic Reaction** • $Fe \leftrightarrow Fe^{2+} + 2e^-$ • **Cathodic Reactions** • $2H_2CO_3 + 2e^- \leftrightarrow H_2 + 2HCO_3^-$ • $2H_2CO_3 + 2e^- \leftrightarrow H_2 + 2CO_3^{2-}$ • $2H^+ + 2e^- \leftrightarrow H_2$
Transportation of corrosion product from the metal surface to the scale surface	• $Fe^{2+}{}_{(Surface)} \rightarrow Fe^{2+}{}_{(Scale)}$ • $CO_3^{2-}{}_{(Surface)} \rightarrow CO_3^{2-}{}_{(Scale)}$
Transportation of corrosion product from the scale surface to the bulk	• $Fe^{2+}{}_{(Scale)} \rightarrow Fe^{2+}{}_{(Surface)}$ • $CO_3^{2-}{}_{(Scale)} \rightarrow CO_3^{2-}{}_{(Surface)}$

Fig. A-1 Steps of overall CO_2-corrosion process under scale forming conditions

Based on three main hypothesizes, Dayalan et al. (1998) developed their CO_2-corrosion model consists of a system of twenty equations and twenty unknowns (Eqns. A.1 through A.20). CO_2-corrosion rate can be predicted for non-scale forming conditions by solving the system of twenty nonlinear equations. The main hypotheses in this model are: i) the sum of the mass transfer rates of the reactants must be equal to the sum of the electrochemical reaction rates (for both cathodic and anodic reactions); and ii) the sum of the mass transfer rates of carbonic acid and bicarbonate is equal to the mass transfer rate of carbonate ions. The twenty unknowns are the six metal surface concentrations ($[H^+]_s$, $[HCO_3^-]_s$, $[Fe^{2+}]_s$, $[CO_3^{2-}]_s$, $[OH^-]_s$, $[H_2CO_3]_s$), five scale surface concentrations ($[H^+]_{sc}$, $[HCO_3^-]_{sc}$, $[CO_3^{2-}]_{sc}$, $[OH^-]_{sc}$, $[H_2CO_3]_{sc}$),, the corrosion potential (E_{corr}), and current due to four reactions ($I_{H2CO3,s}$, $I_{HCO3^-,s}$, $I_{H^+,s}$, $I_{Fe^{2+},s}$, $I_{H2CO3,sc}$, $I_{HCO3^-,sc}$, $I_{H^+,sc}$). Figure A-2 shows the comparison between the Tulsa corrosion model prediction and experimental data.

$$2F \times 10^{-3} \times K_{mt,Fe^{2+},liquid}([Fe^{2+}]_{sc} - [Fe^{2+}]_b) = I_{Fe^{2+}} \quad \text{(A.1)}$$

$$2F \times 10^{-3} \times K_{mt,Fe^{2+},scale}([Fe^{2+}]_s - [Fe^{2+}]_{sc}) = I_{Fe^{2+}} \quad \text{(A.2)}$$

$$2 \times F \times K_{mt,H_2CO_3}([H_2CO_3]_{sc} - [H_2CO_3]_s) + K_{mt,HCO_3^-}([HCO_3^-]_{sc} - [HCO_3^-]_s) + K_{mt,H^+}([H^+]_{sc} - [H^+]_s) = I_{H_2CO_3,S} + I_{HCO_3^-,S} + I_{H^+,S} \quad \text{(A.3)}$$

$$K_{mt,H_2CO_3}([H_2CO_3]_b - [H_2CO_3]_s) + K_{mt,HCO_3^-}([HCO_3^-]_b - [HCO_3^-]_s) = K_{mt,CO_3^{2-}}([CO_3^{2-}]_s - [CO_3^{2-}]_b) \quad \text{(A.4)}$$

$$K_{mt,H_2CO_3}([H_2CO_3]_{sc} - [H_2CO_3]_s) + K_{mt,HCO_3^-}([HCO_3^-]_{sc} - [HCO_3^-]_s) = K_{mt,CO_3^{2-}}([CO_3^{2-}]_s - [CO_3^{2-}]_{sc}) \quad \text{(A.5)}$$

$$\left(I_{H_2CO_3,S} + I_{HCO_3^-,S} + I_{H^+,S}\right) + \left(I_{H_2CO_3,SC} + I_{HCO_3^-,SC} + I_{H^+,SC}\right) = I_{Fe^{2+}} \quad \text{(A.6)}$$

$$\left(I_{H_2CO_3,S} + I_{HCO_3^-,S} + I_{H^+,S}\right) + \left(I_{H_2CO_3,SC} + I_{HCO_3^-,SC} + I_{H^+,SC}\right) = 2 \times 10^{-3}F.K_{Fe^{2+}}[Fe^{2+}]_s exp\left\{\frac{(2-B)F(E_{corr}-E_{Fe^{2+}})}{RT}\right\} =$$
$$\left(2 \times 10^{-3}F.K_{H_2CO_3}[H_2CO_3]_s exp\left\{\frac{-BF(E_{corr}-E_{H_2CO_3})}{RT}\right\} + 2 \times 10^{-3}F.K_{HCO_3^-}[HCO_3^-]_s exp\left\{\frac{-BF(E_{corr}-E_{HCO_3^-})}{RT}\right\} + 2 \times$$
$$10{-}3F.KH{+}H{+}sexp{-}BF(Ecorr{-}EH{+})RT{+}2{\times}10{-}3F.KH2CO3H2CO3scexp{-}BF(Ecorr{-}EH2CO3)RT{+}2{\times}10{-}3F.KHCO3{-}HCO3{-}scexp{-}$$
$$BF(Ecorr{-}EHCO3{-})RT{+}2{\times}10{-}3F.KH{+}H{+}scexp{-}BF(Ecorr{-}EH{+})RT$$
(A.7)

$$I_{H_2CO_3,S} = 2 \times 10^{-3}F.K_{H_2CO_3}[H_2CO_3]_s exp\left\{\frac{-BF(E_{corr}-E_{H_2CO_3})}{RT}\right\} \quad \text{(A.8)}$$

$$I_{HCO_3^-,S} = 2 \times 10^{-3}F.K_{HCO_3^-}[HCO_3^-]_s exp\left\{\frac{-BF(E_{corr}-E_{HCO_3^-})}{RT}\right\} \quad \text{(A.9)}$$

$$I_{H^+,S} = 2 \times 10^{-3}F.K_{H^+}[H^+]_s exp\left\{\frac{-BF(E_{corr}-E_{H^+})}{RT}\right\} \quad \text{(A.10)}$$

$$I_{H_2CO_3,SC} = 2 \times 10^{-3}F.K_{H_2CO_3}[H_2CO_3]_{sc} exp\left\{\frac{-BF(E_{corr}-E_{H_2CO_3})}{RT}\right\} \quad \text{(A.11)}$$

$$I_{HCO_3^-,SC} = 2 \times 10^{-3}F.K_{HCO_3^-}[HCO_3^-]_{sc} exp\left\{\frac{-BF(E_{corr}-E_{HCO_3^-})}{RT}\right\} \quad \text{(A.12)}$$

$$I_{H^+,SC} = 2 \times 10^{-3}F.K_{H^+}[H^+]_{sc} exp\left\{\frac{-BF(E_{corr}-E_{H^+})}{RT}\right\} \quad \text{(A.13)}$$

$$I_{Fe^{2+}} = 2 \times 10^{-3}F.K_{Fe^{2+}}[Fe^{2+}]_s exp\left\{\frac{(2-B)F(E_{corr}-E_{Fe^{2+}})}{RT}\right\} \quad \text{(A.14)}$$

$$K_1 = First\ Dissociation\ constant = \frac{[H^+]_s[HCO_3^-]_s}{[H_2CO_3]_s} \quad \text{(A.15)}$$

$$K_2 = Second\ Dissociation\ constant = \frac{[H^+]_s[CO_3^{2-}]_s}{[HCO_3^-]_s} \quad \text{(A.16)}$$

$$K_w = water\ Dissociation\ constant = [H^+]_s[OH^-]_s \quad \text{(A.17)}$$

$$K_1 = First\ Dissociation\ constant = \frac{[H^+]_{sc}[HCO_3^-]_{sc}}{[H_2CO_3]_{sc}} \quad \text{(A.18)}$$

$$K_2 = Second\ Dissociation\ constant = \frac{[H^+]_{sc}[CO_3^{2-}]_{sc}}{[HCO_3^-]_{sc}} \quad \text{(A.19)}$$

$$K_w = water\ Dissociation\ constant = [H^+]_{sc}[OH^-]_{sc} \quad \text{(A.20)}$$

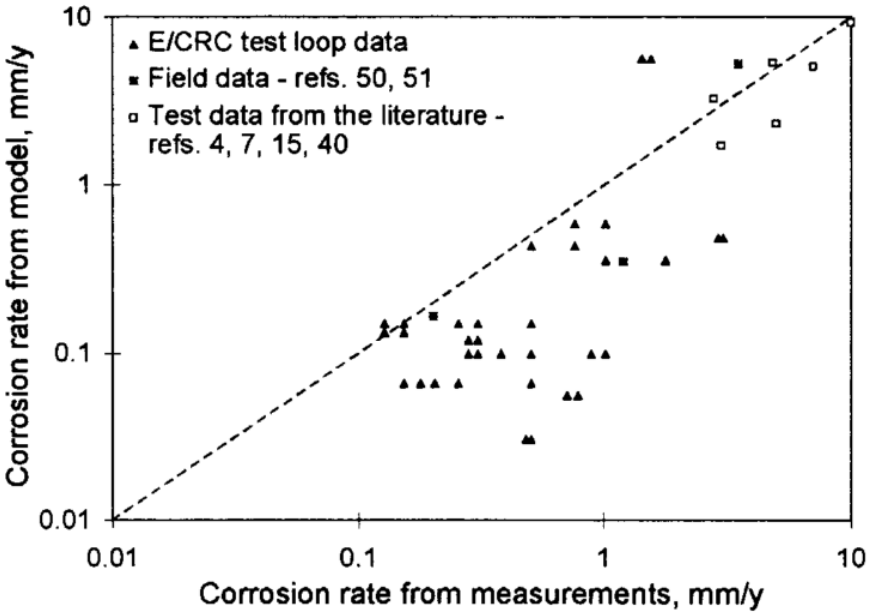

Fig. A-2 Predicted CO_2 corrosion rate vs. experimental data (Dayalan et al., 1998)

Iron-carbonate ($FeCO_3$) scale formation changes the CO_2 corrosion mechanism because it reduces the metal surface area exposed to the corrosive environment and also mass transfer of corrosion products will be through the porous layer of corrosion products, which may influence the overall mass transfer process. If the concentration of Fe^{2+} and CO_3^{2-} at the metal surface exceeds the solubility limit (K_{sp}), insoluble $FeCO_3$ scale forms at the metal surface. The thermodynamic of iron carbonate scale formation is important in corrosion study because the effect of the scale on corrosion rate and mechanisms can be substantial.

$$K_{sp} = [Fe^{2+}]_s[CO_3^{2-}]_s \quad \text{(A.21)}$$

where $[Fe^{2+}]_s$ is surface concentration of Fe^{2+}, $[CO_3^{2-}]_s$ is surface concentration of CO_3^{2-} , and K_{sp} is solubility product of $FeCO_3$ at the given temperature. The K_{sp} is a function of temperature, and ionic strength of the solution:

$$\log K_{sp} = -59.3498 - 0.041377T_k - \frac{2.1963}{T_k} + 24.5724\log T_k + 2.51I^{0.5} - 0.6571 \quad \text{(A.22)}$$

where T_k is temperature in Kelvin and I is ionic strength expressed in molarity and can be calculated as:

$$I = \tfrac{1}{2}\sum_i C_i Z_i^2 = \tfrac{1}{2}(C_1 Z_1^2 + C_2 Z_2^2 + ...) \quad \text{(A.23)}$$

where C_i are the concentrations of different species in the aqueous solution expressed in mol/L, and Z_i are the species' charges.

The entire surface of the metal is available for the anodic reaction (iron dissolution reaction to form Fe^{2+}) and for the cathodic reactions (reduction of H^+, H_2CO_3, and HCO_3^-). The surface covered by scale is not available for the anodic reaction. Also, this area is not available for cathodic reactions on the metal surface. But cathodic reactions can take place on the scale surface (the rates are considerably lower than on metal surfaces) (Dayalan et al. 1998). Corrosion continuously creates voids under scale and undermines the scale as the steel surface corrodes. On the other hands, precipitation of corrosion products also continuously fills up the voids. If the rate of precipitation of corrosion products is higher than the rate of undermining the scale by corrosion, then a dense and protective corrosion product forms on the surface. However, if the rate of undermining the scale is higher than the rate of precipitation, a thick and non-protective scale forms on the surface (Nesic 2007).

There are some limitations in the CO_2-corrosion models presented by Dayalan et al. (1995) and (1998) including temperature range (up to 250^{o}F), and some of the assumptions made in formulating the models. Dayalan et al. (1998) assumed that some of the cathodic reaction happens on the iron carbonate scale surface. This assumption is unrealistic because iron carbonate scale is a non-conductive ceramic. Research is in progress to modify some of these assumptions made in this model and increase the maximum temperature limit. We are also reviewing the models proposed by other research groups to use the current knowledge of CO_2/H_2S modeling for developing a mechanistic model for corrosion rate at HPHT conditions.

In order to adapt the model presented by Dayalan et al. (1998) for high temperature conditions, the first step is improving models used for predicting pH and concentration of corrosion species in bulk solution. The system of five equations and five unknowns for carbonic acid's first and second dissociation, water dissociation, carbon balance, and electroneutrality (Eqns. A.24 through A.28) can be solved to predict the pH of the solution. The models used for CO_2 dissolution and dissociation are applicable for HPHT conditions. Therefore, pH prediction is expected to be valid for HPHT conditions. Model predictions are compared with experimental data in Figs. A-3 and A-4. Model predictions show a good agreement with experimental data.

$$K_1 = First\ Dissociation\ constant = \frac{[H^+]_{bulk}[HCO_3^-]_{bulk}}{[H_2CO_3]_{bulk}} \quad \text{(A.24)}$$

$$K_2 = Second\ Dissociation\ constant = \frac{[H^+]_{bulk}[CO_3^{2-}]_{bulk}}{[HCO_3^-]_{bulk}} \quad \text{(A.25)}$$

$$K_w = water\ Dissociation\ constant = [H^+]_{bulk}[OH^-]_{bulk} \quad \text{.....(A.26)}$$

$$[CO_3^{2-}]_{bulk} + [HCO_3^-]_{bulk} + [H_2CO_3]_{bulk} = [CO_2]_{bulk} \quad \text{.....(A.27)}$$

$$[H^+]_{bulk} = 2[CO_3^{2-}]_{bulk} + [HCO_3^-]_{bulk} + [OH^-]_{bulk} \quad \text{..... (A.28)}$$

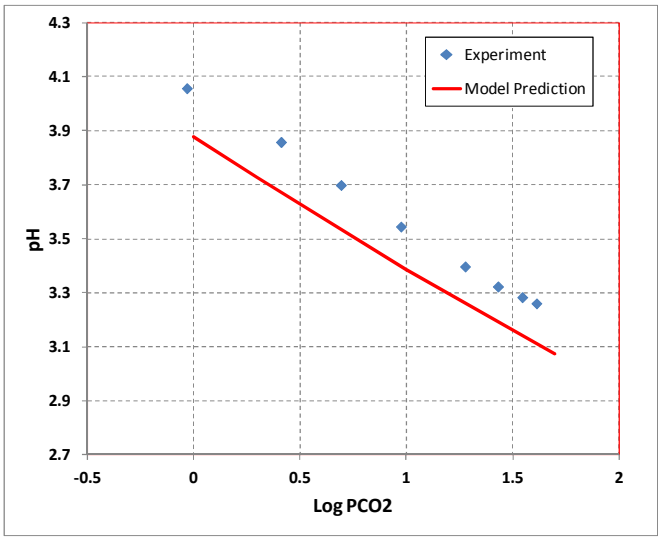

Fig. A-3 Model predictions and experimental data at 347K and 0.5 molar NaCl concentration

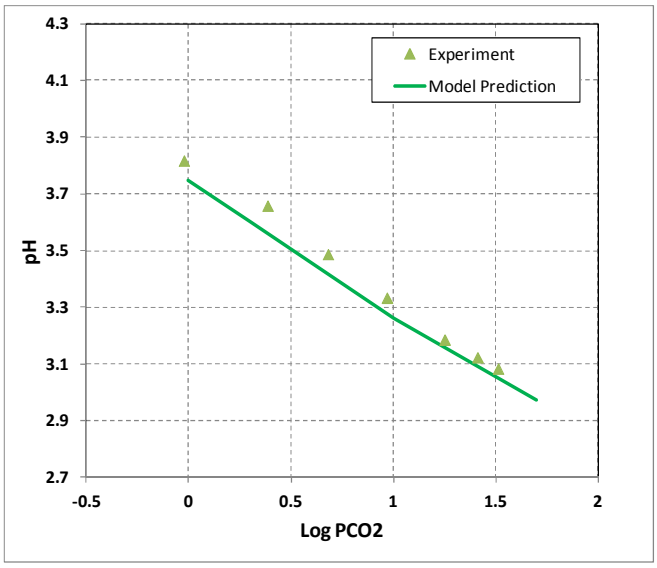

Fig. A-4 Model predictions and experimental data at 299K and 0.5 molar NaCl concentration

A.1.1 pH Measurement at HPHT Conditions

Measuring the pH is a helpful to monitor the chemistry of the solution during corrosion experiment. Besides this, simulating the pH of the solution can be used to simulate the chemistry of the solution for real oil and gas production conditions. Therefore, laboratory data can be a good representative of the real field conditions if pH can be simulated in the laboratory conditions. pH measurement under HPHT conditions is complicated since no regular pH probe works at these conditions. During this research period, we contacted different companies for purchasing a commercial available pH probe for temperature of 500^{o}F and pressure up to 10,000 psi but we were not able to find any pH probe that can handle these test conditions.

However, electrical conductivity of the solution can be used to measure the pH. Recently, Samaranayake and Sastry (2010) developed a technique for measuring pH in high pressure systems (i.e. 700 bar) but at low temperature of 25ºC. In this technique, electrical conductivity of electrolyte solution was measured and related to the pH of the solution. The electrical conductivity is created by all the ions in the solution. In order to relate the pH to the conductivity of the solution, the movement of all the ions has to be blocked but hydrogen ions. Therefore, conductivity for a given geometry and voltage would be only due to the flux of hydrogen ions. In other words, conductivity can be used to calculate the hydrogen ion concentration or pH of the solution. A Nafion membrane and two thin film reverse osmosis (RO) membranes were used to create a selective movement of hydrogen ions. The passage of hydrogen ions creates a charge separation across this membrane filter. However, the net charge of the electrolyte/test solution remains unchanged, obeying the principal of electroneutrality. During the experiments, the Nafion membrane was sandwiched between the two RO membranes and then placed between the electrodes in the test solution (Fig. A.5). With an applied voltage, the first (from either side) RO membrane rejects the passage of salt ions and suspended materials in the test solution, since they are larger than the membrane pores. Since the Nafion membrane is permeable to water and cations and is impermeable to anions, hydrogen ions (H_3O^+) become the only ionic species passing through the membranes, resulting in the passage of current through the sensor. The second RO membrane permits the application of the electric field from the other side of the test solution. It also filters the very small fraction of cations that might have passed through the first RO and the Nafion membranes. The pH sensor, consisting of this membrane filter, was made with flexible walls to permit the environmental pressure to be transmitted to the test solution. In use, the sensor was filled with the test solution and was then sealed with luer fittings. The lead wires (Chromel wires), running through the luer fittings, also served as electrodes. The high-pressure electrical lead-throughs and all electrical

connections were insulated with Teflon shrink tube and insulating epoxy. The sensor was then immersed in a pressure vessel of the hydrostatic pressure generating system.

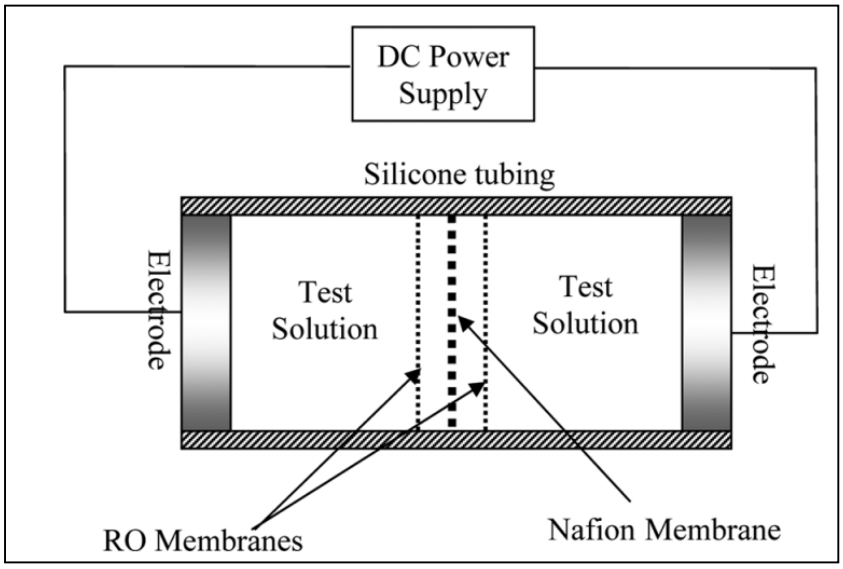

Fig. A-5 Schematic diagram of high pressure pH sensor (Samaranayake and Sastry, 2010)

According to the Nernst-Einstein equation, the electrical conductivity due to the movement of hydrogen ions (i.e., proton conductivity) can be written as:

$$\sigma_{H^+} = \frac{C_{H^+} D_{H^+} F^2}{RT} = cell\ constant \times \left(\frac{I_{H^+}}{V}\right) \quad \text{(A.29)}$$

Thus, the pH can be related to the sensor response as follows:

$$log\left(\frac{I_{H^+}}{V}\right) = pH + \log\left(constant\right) \quad \text{(A.30)}$$

A.2 Review of Ohio CO_2 Corrosion Model

Nesic et al. (2009) developed a model for prediction of CO_2-corrosion rate in the presence of organic acid and oxygen. This model is able to predict the uniform corrosion rate, and simulate the iron carbonate scale growth. Chemical reactions considered in this model are CO_2 dissolution in water, CO_2 hydration, carbonic acid dissociation, acetic acid dissociation, and iron carbonate scale formation. In addition, electrochemical reactions are considered in this model including iron dissolution, hydrogen reduction, carbonic acid reduction, oxygen reduction (Eqn. A.31), acetic acid reduction (Eqn. A.32), and direct reduction of water (Eqn. A.33).

$$O_2 + 2H_2O + 4e^- \rightarrow 4OH^-$$ ……(A.31)

$$2HAc + 2e^- \rightarrow H_2 + 2Ac^-$$ ……(A.32)

$$2H_2O + 2e^- \rightarrow H_2 + 2OH^-$$ ……(A.33)

For pH greater than 4, the dependency of CO_2-corrosion on pH tends to diminish. Nesic et al. (2009) treated this reaction as pH independent. Iron dissolution reaction can be described using Tafel's law since this reaction is under charge transfer control at the corrosion potential up to 200 mV. Direct reduction of water is very slow and often can be neglected. It also needs to be mentioned that acetic acid provides an additional source of H^+.

CO_2 corrosion rate can be calculated using the following equation

$$CR = \frac{i_a MW_{Fe}}{\rho_{Fe} nF}$$ ……(A.34)

where CR is corrosion rate, i_a is anodic current density, MW_{Fe} is atomic mass of iron, ρ_{Fe} is density of iron, n is number of moles of electrons involved in iron oxidation, and F is Faraday's law constant. Anodic current density (i_a) can be calculated using the following equation:

$$i_{a,Fe} = i_{o,Fe} \times 10^{\frac{E_{corr} - E_{rev,Fe}}{b_{Fe}}}$$ ……(A.35)

where $i_{a,Fe}$ is current density of iron oxidation, A/m^2; $i_{o,Fe}$ is exchange current density of iron oxidation, A/m^2; E_{corr} is corrosion potential, V; $E_{rev,Fe}$ is reversible potential of iron oxidation, V; b_{Fe}: Tafel slope of iron oxidation, V. The charge balance on the steel surface can be used according to Eqn. A.36 to calculate the E_{corr}. Once the corrosion potential is found, the corrosion current density and consequently corrosion rate can be calculated.

$$i_{corr} = i_c + i_{a,Fe}$$ ……(A.36)

where i_{corr} is corrosion current density and i_c is cathodic corrosion current density. The current density of individual cathodic reactions can be calculated using the following equation.

$$\frac{1}{i_c} = \frac{1}{i_{ct}} + \frac{1}{i_{lim}}$$ ……(A.37)

where i_c is current density of any cathodic reaction; i_{ct} is component of charge transfer current density; i_{lim} is component of limiting current density. All the current densities are expressed in A/m^2. The charge transfer current density of cathodic reaction can be calculated as:

$$i_{ct} = i_o \times 10^{\frac{E_{rev}-E_{corr}}{b}}.\eta_{FeCO_3}.\eta_{FeS} \quad \text{(A.38)}$$

where, i_{ct} is exchange current density of cathodic reactions in A/m^2; i_o is reversible potential of cathodic reactions in V; E_{rev} is Tafel slope of cathodic reactions expressed in V; η_{FeCO3} and η_{FeS} are scale factors due to formation of $FeCO_3$ scale and FeS film, respectively. The limiting current density of cathodic reaction can be determined as:

$$i_{lim}^{d} = \eta_{FeCO_3}.\eta_{FeS}.K_m.F.C_j \quad \text{(A.39)}$$

where K_m is mass transfer coefficient of corrosive species in m/s; C_j is bulk concentration of corrosive species in mol/m^3. Carbonic acid reduction is limited by slow reaction rate of CO_2 hydration. The limiting current density of carbonic acid reduction is:

$$i_{lim,H_2CO_3}^{d} = F.C_{CO_2}.\left(\eta_{FeCO_3}.\eta_{FeS}.D_{H_2CO_3}.K_{hyd}.K_{hyd}^{f}\right)^{0.5}.f \quad \text{(A.40)}$$

where, C_{CO_2} is concentration of CO_2 in bulk solution in mol/m^3; $D_{H_2CO_3}$ is diffusion coefficient of H_2CO_3 in water in m^2/s; K_{hyd} is equilibrium constant for CO_2 hydration reaction; K_{hyd}^{f} is forward reaction rate constant for CO_2 hydration reaction; and f is flow factor affecting CO_2 hydration, which is given by:

$$f = \frac{1+e^{-\frac{2\delta_m}{\delta_r}}}{1-e^{-\frac{2\delta_m}{\delta_r}}} \quad \text{(A.41)}$$

where δ_m is mass transfer layer thickness and δ_r is reaction layer thickness.

$$\delta_m = \frac{D_{H_2CO_3}}{K_{m,H_2CO_3}} \quad \text{(A.42)}$$

$$\delta_r = \sqrt{\frac{D_{H_2CO_3}.K_{hyd}}{K_{hyd}^{f}}} \quad \text{(A.43)}$$

where K_{m,H_2CO_3} is mass transfer coefficient of H_2CO_3, m/s.

Nesic et al. (2009) compared the proposed model with some experimental data (Figs. A-6 and A-7). Results have shown good agreement between model predictions and experimental measurements. However, the model is applicable for limited temperature range (i.e. from ambient to 250ºF). Research is in progress to extend the applicability of the current model for high temperature conditions.

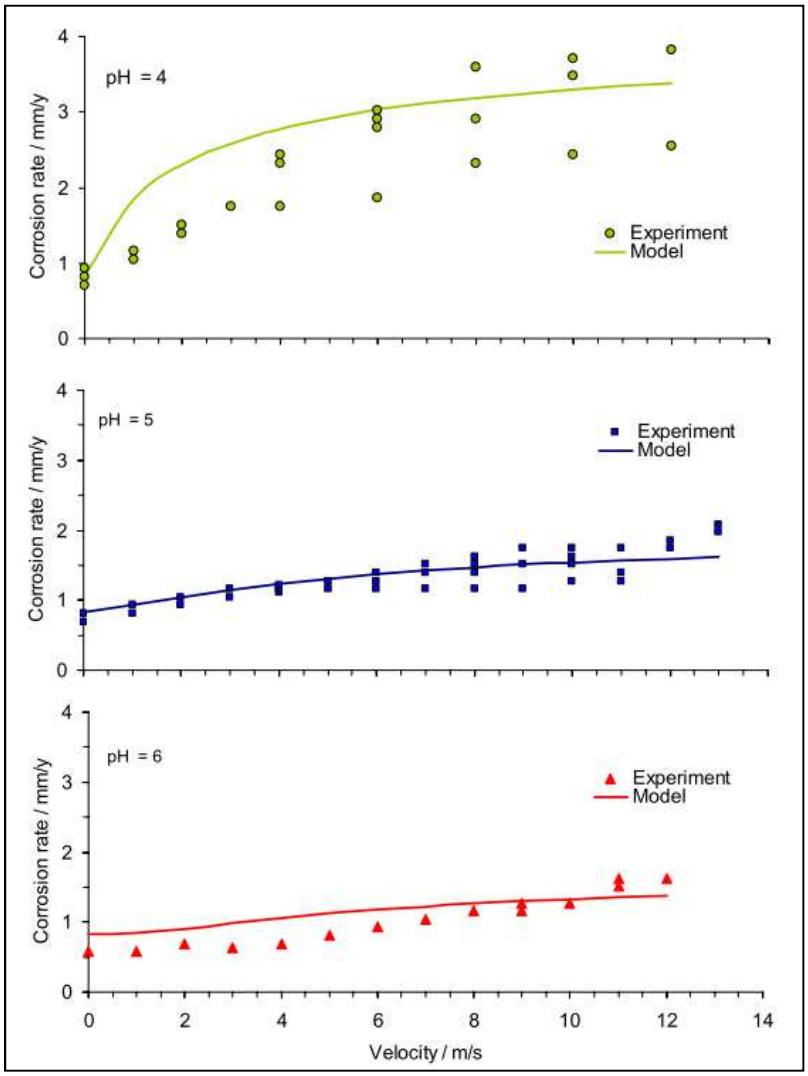

Fig. A-6 Predicted and measured corrosion rates at different flow velocities at 20°C, 1 bar partial pressure of CO_2, and pipe diameter 15 mm (Nesic et al. 2009)

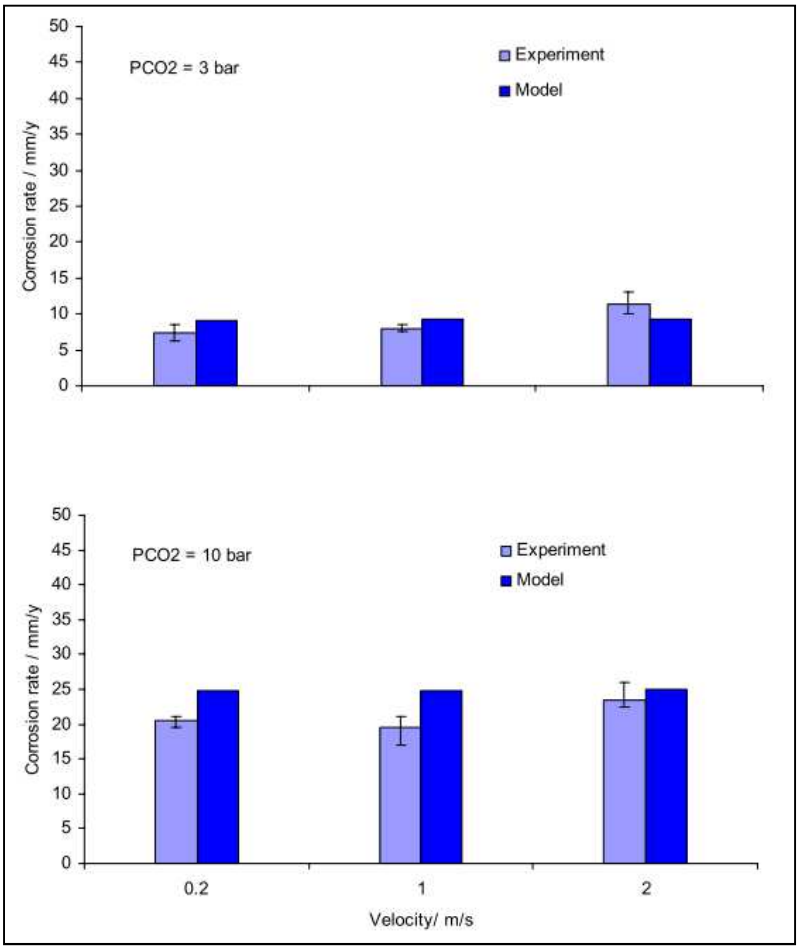

Fig. A-7 Model predictions and measurements for different partial pressure of CO_2 at 60℃, pH of 5, pipe diameter of 100 mm (Nesic et al. 2009)

At high pressures, predictions of the existing model proposed by university of Tulsa and University of Ohio show substantial discrepancies with measurements (Fig. A-8). Experimental data available in the literature is only limited to pressures up to 70 bar and temperature up to 100ºC. Research is in progress to find experimental data for high pressure high temperature CO_2/H_2S corrosion and also adopt available CO_2/H_2S corrosion model for high pressure high temperature conditions.

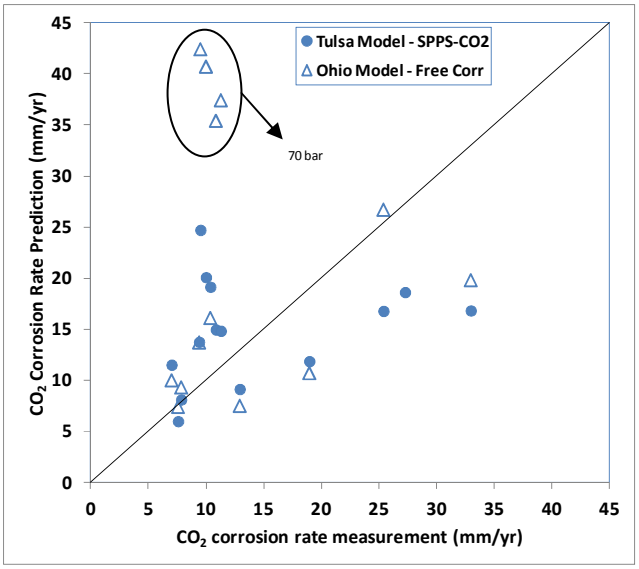

Fig. A-8 Comparison between two CO_2 corrosion models and experimental results for different partial pressures of CO_2 (3 to 70 bar), temperature (25 to 50°C), velocity (0 to 1 m/s), and pH (3 to 5)

A.3 Review of Ohio H_2S Corrosion Model

Hydrogen sulfide corrosion of mild steel is considered to be solid state reaction which means the initial and final form of iron is solid.

$$Fe + H_2S \leftrightarrow FeS_{(s)} + H_2 \quad \text{.....(A.44)}$$

Sun et al. (2007) proposed a model for H_2S corrosion. Based on this model, adsorption of H_2S onto the carbon steel metal surface immediately forms a protective non-stoichiometric layer of iron with thickness significantly less 1µm. The protective layer is known as Mackinawite. The formation of Mackinawite reduces the corrosion rate by producing a compact diffusion barrier. Corrosion undermines the scale layer and forms a new mackinawite later. New layer of Mackinawite builds up internal stress, which causes cracking and consequently delamination of scale layer. The process of scale build-up and cracking creates a thick and porous layer of scale on the surface. Sun et al. (2007) assumed the formation of two different layers of Mackinawite during H_2S corrosion process including porous outer layer and compact inner layer. They also assumed that H_2S corrosion is controlled only by mass transfer of ions through the scale layer and liquid boundary layer. Figure A-9 shows the mechanism of H_2S corrosion process.

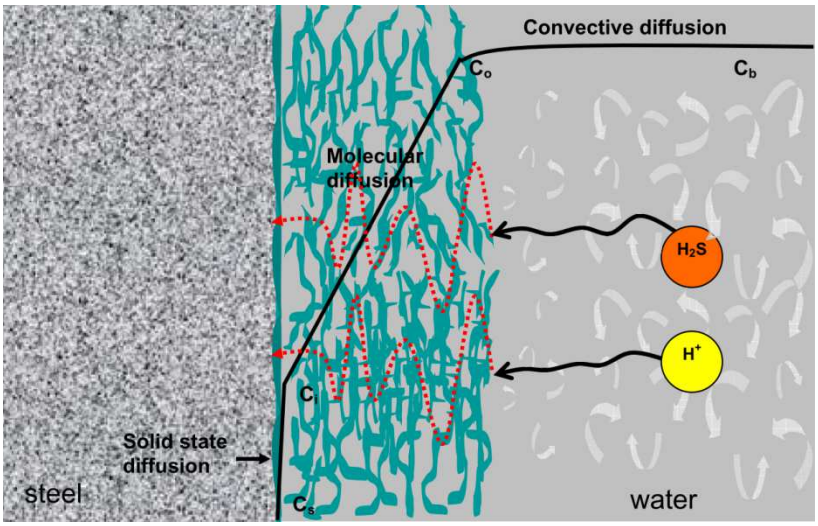

Fig. A-9 A schematic of the H_2S corrosion process (Sun et al. 2007)

Equations (A.45) through (A.47) show the flux of H_2S through the boundary layer, porous outer mackinawite, and inner mackinawite layer, respectively.

$$Flux_{H_2S} = K_{m(H_2S)}\left[C_{b,H_2S} - C_{O,H_2S}\right] \quad \text{.....(A.45)}$$

$$Flux_{H_2S} = \frac{D_{H_2S}\varepsilon\psi}{\delta_{OS}}\left[C_{O,H_2S} - C_{i,H_2S}\right] \quad \text{.....(A.46)}$$

$$Flux_{H_2S} = A_{H_2S} Ln\left(\frac{C_{i,H_2S}}{C_{s,H_2S}}\right) e^{\frac{-B_{H_2S}}{RT_K}} \quad \text{.....(A.47)}$$

where $Flux_{H_2S}$ is expressed in mole/(m^{2}s), $K_{m(H_2S)}$ is the mass transfer coefficient for H_2S in the hydrodynamic boundary layer. Under nearly stagnant condition, $K_{m(H_2S)} = 10^{-4} m/s$ in nearly stagnant condition. C_{b,H_2S} is bulk concentration of H_2S in the liquid phase in mole/m^3. C_{O,H_2S} is interfacial concentration of H_2S at the outer scale/solution interface in mole/m^3. D_{H_2S} is the diffusion coefficient for dissolved H_2S in water, which is $2 \times 10^{-9} m^2/s$. ε is the outer Mackinawite scale porosity, ψ is the outer mackinawite tortuosity factor, C_{i,H_2S} is the interfacial concentration of H_2S at the inner scale/film interface in mole/m^3. δ_{OS} is the thickness of Mackinawite scale in m.

$$\delta_{OS} = \frac{m_{OS}}{(\rho_{FeS} A)} \quad \text{.....(A.48)}$$

M_{OS} is mass of the Mackinawite scale in kg, A is surface area (m^2), A_{H_2S} and B_{H_2S} are Arrhenius constants ($A_{H_2S} = 1.3 \times 10^{-4} \frac{mole}{m^2.s}$, $B_{H_2S} = 15500 \frac{Jouls}{mole}$). T_K is temperature (in Kelvin), C_{s,H_2S} is the concentration of H_2S on the steel surface, which is typically 10^{-7} mole/m^3. Under steady state situation, three fluxes are equal to each other and are equal to the rate of H_2S consumption due to corrosion. Based on this analysis, the H_2S corrosion rate can be expressed as:

$$CR_{H_2S} = \left(A_{H_2S}\right) e^{\frac{-B_{H_2S}}{RT_K}} Ln\left(\frac{C_{b,H_2S} - CR_{H_2S}\left[\frac{\delta_{0.5}}{D_{H_2S}\varepsilon\psi} + \frac{1}{K_{m(H_2S)}}\right]}{C_{s,H_2S}}\right) \quad \text{.....(A.49)}$$

The unknown properties of the outer Mackinawite, which changes with time, were calculated separately. Mackinawite retention rate (SSR) is equal to the difference of scale formation (SFR) and scale damage rate (SDR). Experimental results by Sun et al. (2007) showed that even in stagnant conditions, about half of the sulfide scale layer removed by spalling. For corrosion occurring under flowing condition, the scale removal rate can be written as:

$$SDR_m = 0.5(1 + C.V^a)CR_{H_2S} \quad \text{.....(A.50)}$$

where SDR_m is mechanical scale damage rate. The constants c and a are determined experimentally. For flow between rotating cylinders, the values of "c" and "a" are approximately 0.55 and 0.2, respectively. The change in mass of the outer scale is:

$$\Delta m_{os} = (SRR) M_{FeS} A \Delta t \quad \text{.....(A.51)}$$

where M_{FeS} is molar mass of iron sulfide (kg/mole) and Δt is the time interval (s).

Sun et al. (2007) found that the porosity of the outer Mackinawite scale is very high (0.9). However, due to its layered structure, the tortuosity factor was found to be very low ψ = 0.003. They suggested the following steps to predict H_2S corrosion rate under scale forming conditions:

a) The corrosion rate without scale (assuming $\delta_{OS} = 0$) is calculated using Eqn. A.49.
b) Δm_{os} is computed using Eqn. A.51 in Δt time interval
c) δ_{OS} is determined from Δm_{os} and new corrosion rate can be predicted using Eqn. A.49
d) Step 2 and 3 are repeated for a new time interval

It was found that a small complication arises from the fact that at very low H_2S gas concentrations (ppm_w range), iron sulfide still forms and controls the corrosion rate. In addition, the corrosion process is substantially affected by the reduction of protons. Following the procedure suggested by Sun et al. (2007), corrosion rate equation presented below can be developed for corrosion driven by protons and controlled by the presence of the iron sulfide scale.

$$CR_{H^+} = (A_{H^+})e^{\frac{-B_{H^+}}{RT_K}} Ln\left(\frac{C_{b,H^+} - CR_{H^+}\left[\frac{\delta_{0.5}}{D_{H^+}\varepsilon\psi} + \frac{1}{K_{m(H^+)}}\right]}{C_{s,H^+}}\right) \quad \text{.....(A.52)}$$

where $K_{m(H^+)} = 3 \times 10^{-4}$ for nearly stagnant condition, $D_{H^+} = 2.8 \times 10^{-8}\, m^2/s$, $A_{H^+} = 3.9 \times 10^{-4}\, mole/(m^2.s)$, $B_{H^+} = 15500\, Joules/Mole$, C_{s,H^+} is set to $10^{-7}\, mole/(m^3)$.

Therefore, total corrosion rate is equal to sum of corrosion rates resulting from scale removal and reduction of protons.

$$CR = CR_{H^+} + CR_{H_2S} \quad \text{.....(A.53)}$$

Sun et al. (2007) compared experimental data and model predicted corrosion and scale-retention rates at different H_2S concentrations (Figs. A-10 through A-12).

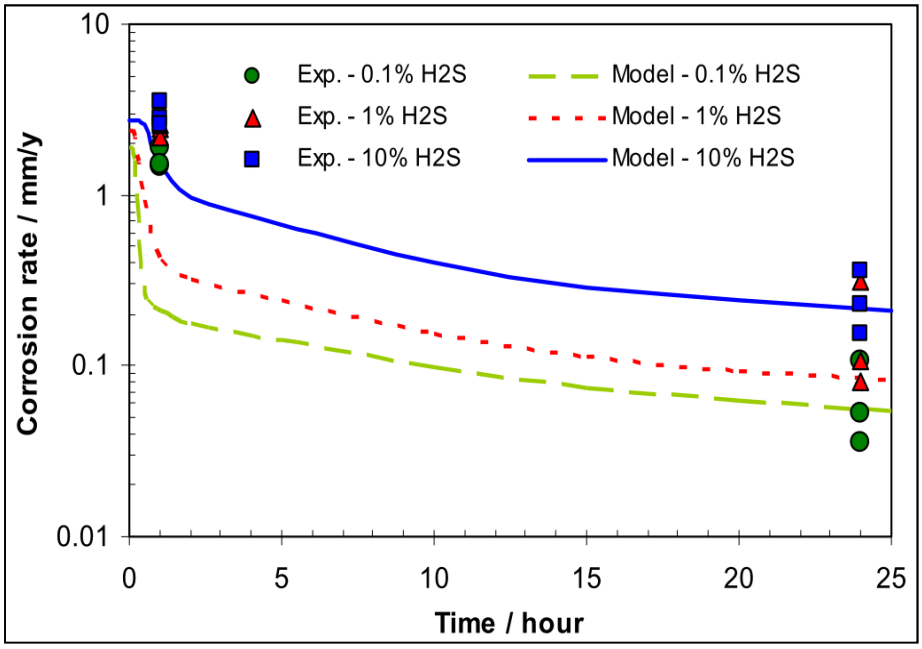

Fig. A-10 Measured and prediction corrosion rate vs. time for different H_2S gas concentrations under stagnant conditions (p = 1 bar, T = 80°C, and pH 5.0-5.5) reaction times of 1 and 24 hours (Sun et al. 2007)

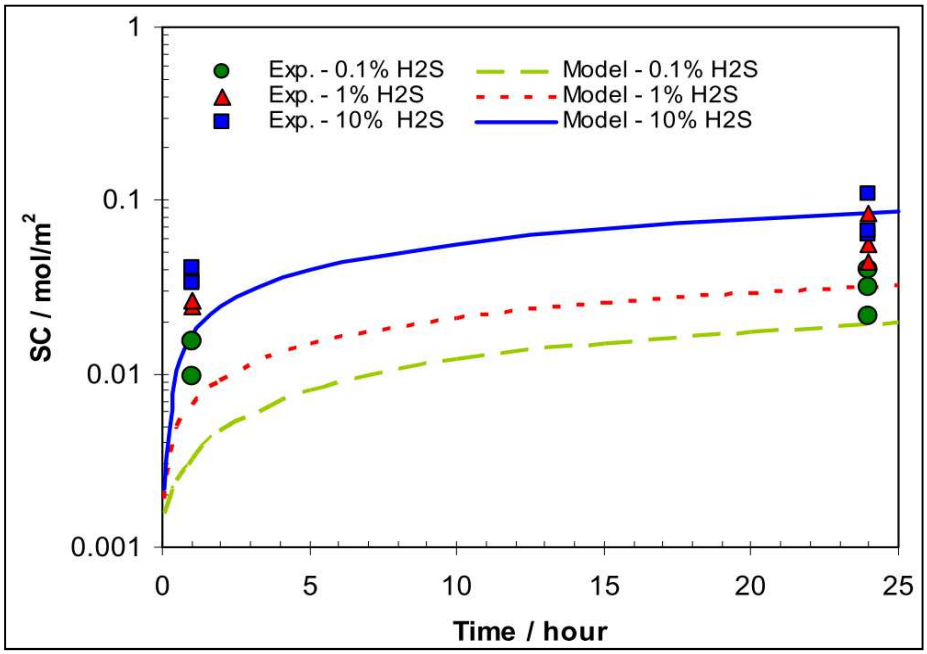

Fig. A-11 Measured and predicted scale retention vs. time for different H_2S gas concentrations under stagnant conditions (p = 1 bar, T = 80ºC, and pH 5.0-5.5) reaction time of 1 and 24 hours (Sun et al. 2007).

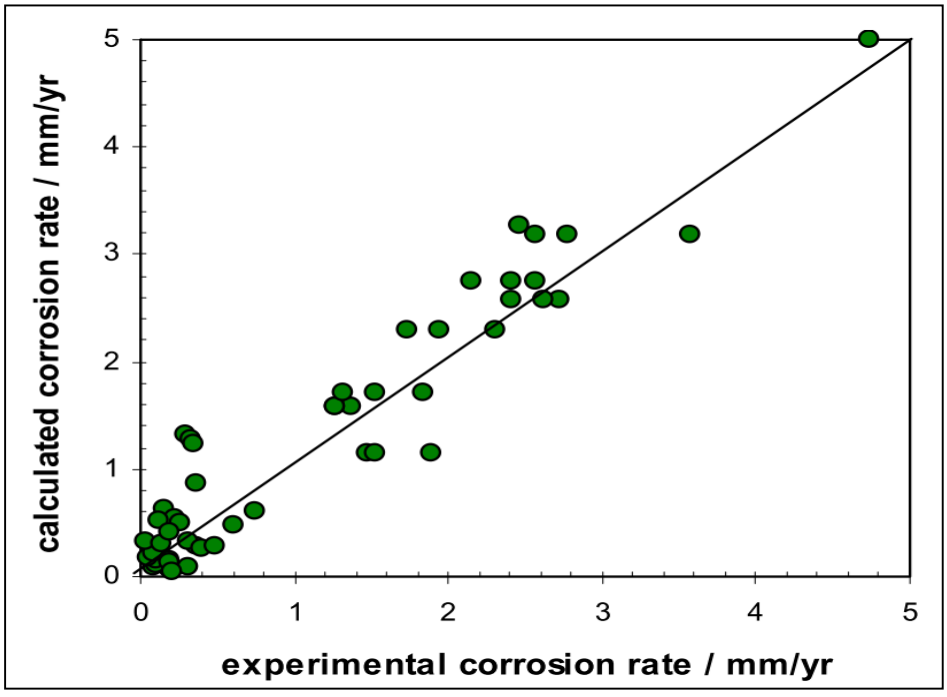

Fig. A-12 Predicted vs. measured corrosion rate (p = 1 bar, H_2S concentration ranging from 0.0075% to 10%, temperature 25°C, 60°C, and 80°C, reaction time of 1 hour and 24 hours, pH from 5.0 to 5.5, and velocity from 0 to 8000 rpm) (Sun et al. 2007).

A.4 Review of Ohio CO_2/H_2S Corrosion Model

Partial pressures of CO_2 and H_2S in the system are the determining factors of corrosion mechanism under CO_2/H_2S system. Competitive reactions of H_2S and CO_2 with iron are important phenomena affecting the composition of corrosion scale layer. Besides this, chemistry of the solution and solubility of iron carbonate and iron sulfide are also affecting the corrosion rate and formation and characteristics of scale layer.

Based on experimental results, Sun (2006) concluded that Mackinawite scale formation is the dominant process in most cases of CO_2/H_2S corrosion. Mackinawite scale forms extremely fast. Therefore, it always forms the first layer of scale on the steel surface. Iron carbonate scale may form as a second scale layer and affects the overall corrosion process. Sun (2006) proposed the following equation to predict corrosion rate in the presence of CO_2 and H_2S.

$$CR_{CO_2/H_2S} = CR_{H_2S} + CR_{CO_2} + CR_{H^+} \quad \text{.....(A.54)}$$

CR_{H_2S} and CR_{H^+} were discussed earlier in the previous section. The same analogy is applied for CO_2 corrosion prediction (i.e. convective diffusion of CO_2 through the mass transfer boundary layer is equal to the molecular diffusion of CO_2 through the liquid in the porous outer scale layer and it is also equal to solid state diffusion through the inner Mackinawite film.), Eqns. (A.55) through (A.57) represent these three fluxes, respectively.

$$Flux_{CO_2} = K_{m,CO_2}\left[C_{b,CO_2} - C_{O,CO_2}\right] \quad \text{.....(A.55)}$$

$$Flux_{CO_2} = \frac{D_{CO_2}\varepsilon\psi}{\delta_{os}}\left[C_{O,CO_2} - C_{i,CO_2}\right] \quad \text{.....(A.56)}$$

$$Flux_{CO_2} = A_{CO_2} Ln\left(\frac{C_{i,CO_2}}{C_{s,CO_2}}\right) e^{\frac{-B_{CO_2}}{RT}} \quad \text{.....(A.57)}$$

The fluxes are equal to the rate of CO_2 consumption by the corrosion process in the presence of CO_2, where $Flux_{CO_2}$ is expressed in mole/(m^{2}s), $K_{m(CO_2)}$ is the mass transfer coefficient of CO_2 in the hydrodynamic boundary layer. Under nearly stagnant conditions, $K_{m(CO_2)} = 10^{-4} m/s$. C_{b,CO_2} is bulk concentration of CO_2 in the liquid phase (mole/m^3). C_{O,CO_2} is interfacial concentration of CO_2 at the outer scale/solution interface (mole/m^3). D_{CO_2} is the diffusion coefficient for dissolved CO_2 in water $C_{O,CO_2} = 1.96 \times 10^{-9} m^2/s$), ε is the outer Mackinawite scale porosity, ψ is the outer mackinawite tortuosity factor, $C_{i,CO_2}$is the interfacial concentration

of CO_2 at the inner scale/film interface (mole/m^3). δ_{OS} is the thickness of Mackinawite scale (m) expressed as:

$$\delta_{OS} = \frac{m_{OS}}{(\rho_{FeS} A)} \quad \text{.....(A.58)}$$

M_{OS} is mass of the Mackinawite scale (kg), A is surface area (m^2), A_{CO2} and B_{CO2} are Arrhenius constants ($A_{CO_2} = 2.6 \times 10^{-5} \frac{mole}{m^2.s}$, $B_{CO_2} = 15500 \frac{Jouls}{mole}$). Combining Eqns. A.55, A.56, and A.57, CO_2 corrosion rate in the presence of the iron sulfide scale can be predicted using the following equation.

$$CR_{CO_2} = \left(A_{CO_2}\right) e^{\frac{-B_{CO_2}}{RT}} Ln\left(\frac{C_{b,CO_2} - CR_{CO_2}\left[\frac{\delta_{os}}{D_{CO_2}\varepsilon\psi} + \frac{1}{K_{m(CO_2)}}\right]}{C_{s,CO_2}}\right) \quad \text{.....(A.59)}$$

Sun (2006) assumed CO_2 hydration to be the rate controlling process since carbonic acid is the corrosive agent in CO_2 corrosion. Therefore, the CO_2 corrosion rate was expressed in terms of the limiting rate of carbonic acid hydration.

$$CR_{CO_2} = C_{S,CO_2}\left(D_{H_2CO_3} K_{hyd}^{f} K_{hyd}\right)^{0.5} f_{H_2CO_3} \quad \text{.....(A.60)}$$

where $D_{H_2CO_3}$ is the diffusion coefficient of carbonic acid (m^2/s), K_{hyd} is the equilibrium constant for the CO_2 hydration reaction, K_{hyd}^{f} is the forward reaction rate for the CO_2 hydration reaction, $f_{H_2CO_3}$is the flow factor, including the effect of the reaction diffusion layer on the limiting current, set to unity. C_{S,CO_2} can be obtained from Eqn. A.60 and replaced in Eqn. A.59 to calculated the CO_2 corrosion rate in the presence of iron sulfide scale layer.

$$CR_{CO_2} = \left(A_{CO_2}\right) e^{\frac{-B_{CO_2}}{RT}} Ln\left(\frac{C_{b,CO_2} - CR_{CO_2}\left[\frac{\delta_{os}}{D_{CO_2}\varepsilon\psi} + \frac{1}{K_{m(CO_2)}}\right]}{\frac{CR_{CO_2}}{\left(D_{H_2CO_3} K_{hyd}^{f} K_{hyd}\right)^{0.5} f_{H_2CO_3}}}\right) \quad \text{.....(A.61)}$$

Comparison made by Sun (2006) showed good agreement between model predictions and experimentally measured corrosion and scale retention rates (Figs. A-13 through A-15) in CO_2/H_2S system.

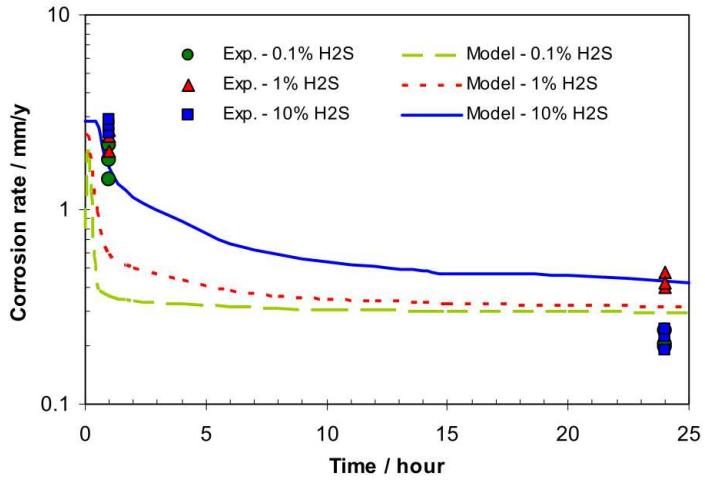

Fig. A-13 Experimental and predicted corrosion rates vs. time in CO_2/H_2S solutions under the conditions of total pressure of 1bar, H_2S gas concentration from 0.1 to 10%, T=80°C, reaction time of 1 and 24 hours, pH of 5.0-5.5, and static solution (Sun, 2006)

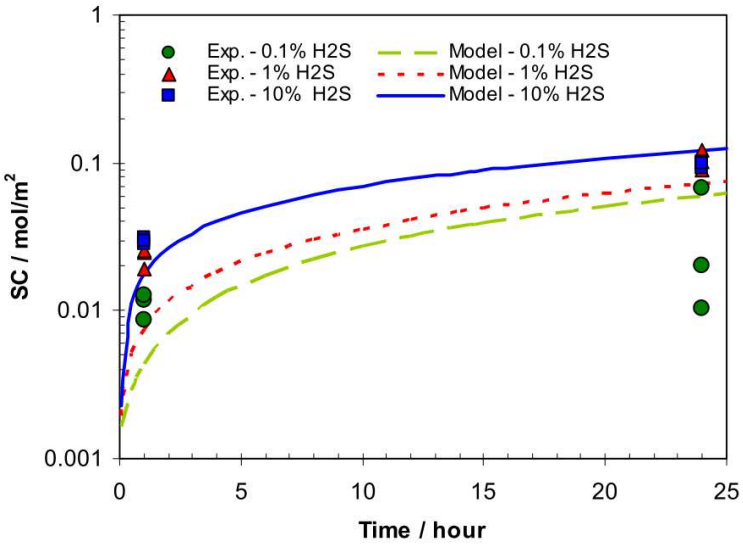

Fig. A-14 Experimental and predicted scale retention vs. time in CO_2/H_2S solutions under the conditions of total pressure p=1 bar, H_2S gas concentration from 0.1% to 10%, T=80°C, reaction time of 1 hour and 24 hours, pH 5.0-5.5, and static solution (Sun, 2006)

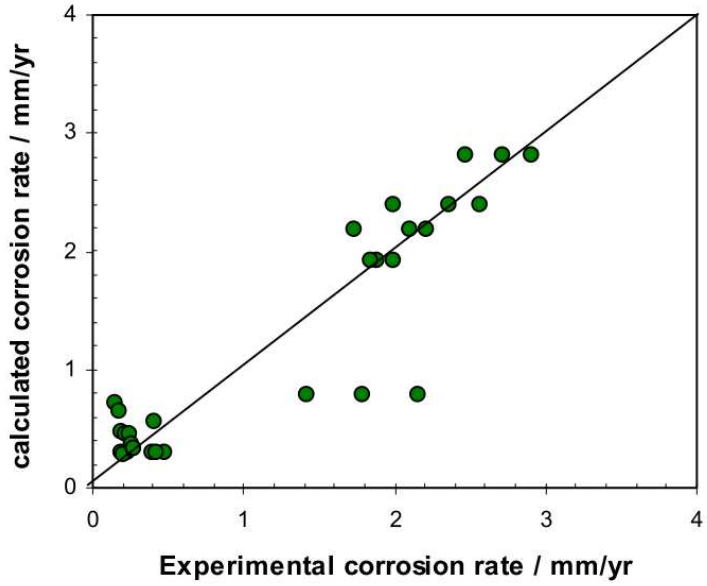

Fig. A-15 Comparison of the experimental corrosion rate and the calculated corrosion rate in CO_2/H_2S solutions under the conditions of total pressure p=1 bar, H_2S gas concentration from 0.01% to 10%, T 25°C, 60°C, and 80°C, reaction time of 1 hour and 24 hours, pH 5.0-5.5, and static conditions (Sun, 2006)

Appendix B: Response to Comments Made By Candi Hudson

2.2 Experimental Studies – Degradation of Cement (Task 2)

- The experimental test conditions are/were at pressure - 9000 psi and temperature-350F. What was the temperature ramp rate and a hold time at each temperature increment (if any)? If there was, what was the specific ramp rate and hold time at each temperature increment?
- Response: The average temperature increasing rate was about 20°F/hour. The maximum was approximately 40°F/hour .This depends on the surrounding and circulation bath temperatures. Figure B-1 displays aging cell temperature as a function of time. Heating was started at 90°F.

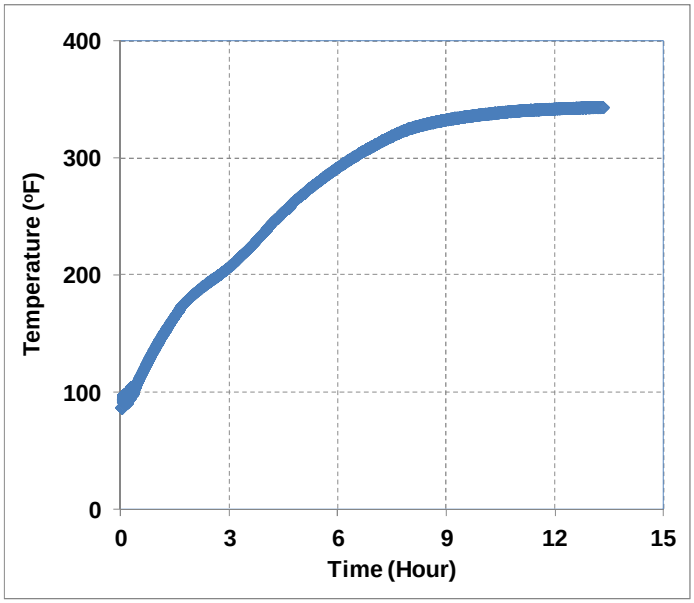

Fig. B-1 Aging cell temperature vs. time

2.2 Permeability Measurements Figure 3, Page 6

- Any reason why a measurement was not obtained for Core #35?
- Response: The instrument used to measure porosity and permeability ran out of nitrogen. These are preliminary tests conducted to develop sample preparation procedure. Actual tests will be carried out in the future.

- Any reasons why the permeability measured value for Core #32 was significantly low?
- Response: Low permeability could be attributed to the inconsistency in cement slurry. These samples were prepared using a standard laboratory agitator. However, API requires high speed cement mixers to prepare slurries that have sufficient consistency and homogeneity. New experimental data after preparing the samples using a new high speed API mixer (presented in this report) shows consistent and repeatable permeability measurements.
-

2.2 General SEM/XRF Characterization Questions

- What location of the sample was the taken for the SEM image?
    - Was a cross-sectioned sample taken from the center, or near the top or bottom of the sample?
- Response: Sample was not cut. Only top of the sample was polished for SEM analysis. In the future selected samples will be cut both horizontally and vertically.

- What were the amounts, i.e. weight & or atomic% for the XRF spectra for the identified elements (e.g. Ca, Fe, Si, etc.) in Figures 6-8?
-
- Response: Weight and atomic percentage for the XRF spectra are presented in Tables B-1 to B-4

Table B-1 Weight and atomic percentage for the XRF spectra in Figure 6 (Left)

Element	App	Intensity	Weight%	Weight%	Atomic%	
	Conc.	Corrn.		Sigma		
C K	1.64	0.4699	6.66	0.33	11.57	
O K	10.84	0.4348	47.58	0.33	62.07	
Na K	0.10	0.6888	0.28	0.05	0.26	
Mg K	0.15	0.6690	0.44	0.04	0.38	
Al K	0.50	0.7863	1.20	0.04	0.93	
Si K	4.20	0.8727	9.17	0.09	6.82	
S K	0.62	0.9063	1.30	0.04	0.85	
Cl K	0.58	0.8094	1.36	0.04	0.80	
Ca K	15.71	1.0054	29.81	0.21	15.52	
Fe K	0.93	0.8090	2.20	0.07	0.82	
Totals			100.00			

Table B-2 Weight and atomic percentage for the XRF spectra in Figure 6 (right)

Element	App	Intensity	Weight%	Weight%	Atomic%	
	Conc.	Corrn.		Sigma		
C K	1.03	0.4828	3.83	0.28	7.10	
O K	10.14	0.4104	44.37	0.36	61.73	
Na K	0.09	0.6723	0.25	0.05	0.24	
Mg K	0.22	0.6563	0.61	0.04	0.56	
Al K	1.45	0.7732	3.37	0.06	2.78	
Si K	2.92	0.8411	6.23	0.07	4.94	
S K	1.23	0.9163	2.41	0.05	1.67	
Cl K	0.21	0.8125	0.46	0.03	0.29	
Ca K	19.34	1.0174	34.13	0.24	18.95	
Ti K	0.08	0.7584	0.19	0.04	0.09	
Fe K	1.88	0.8140	4.14	0.09	1.65	
Totals			100.00			

Table B-3 Weight and atomic percentage for the XRF spectra in Figure 7 (left)

Element	App	Intensity	Weight%	Weight%	Atomic%	
	Conc.	Corrn.		Sigma		
C K	0.74	0.4411	2.24	0.32	4.16	
O K	13.40	0.4001	44.80	0.35	62.56	
Mg K	0.33	0.6850	0.65	0.04	0.60	
Al K	0.57	0.8001	0.95	0.04	0.79	
Si K	9.36	0.8874	14.11	0.12	11.23	
S K	0.11	0.8811	0.17	0.03	0.12	
Cl K	0.48	0.8029	0.80	0.04	0.50	
Ca K	26.45	1.0081	35.10	0.25	19.57	
Fe K	0.71	0.8102	1.17	0.06	0.47	
Totals			100.00			

Table B-4 Weight and atomic percentage for the XRF spectra in Figure 7 (right)

Element	App	Intensity	Weight%	Weight%	Atomic%	
	Conc.	Corrn.		Sigma		
C K	-0.53	0.4522	-1.63	0.78	-3.15	
O K	13.07	0.3919	45.90	0.50	66.85	
Mg K	0.18	0.6796	0.36	0.04	0.34	
Al K	0.45	0.7995	0.78	0.04	0.68	
Si K	9.61	0.8896	14.88	0.17	12.34	
S K	0.24	0.8801	0.38	0.03	0.27	
K K	0.11	1.1297	0.14	0.03	0.08	
Ca K	27.89	1.0120	37.94	0.39	22.05	
Ti K	0.09	0.7476	0.17	0.04	0.08	
Fe K	0.64	0.8106	1.09	0.06	0.46	
Totals			100.00			

Table B-5 Weight and atomic percentage for the XRF spectra in Figure 8 (left)

Element	App	Intensity	Weight%	Weight%	Atomic%	
	Conc.	Corrn.		Sigma		
C K	0.62	0.3632	1.87	1.23	3.10	
O K	35.72	0.6704	58.54	0.77	72.61	
Na K	0.59	0.7176	0.90	0.05	0.78	
Mg K	0.29	0.6846	0.47	0.04	0.38	
Al K	1.25	0.7995	1.72	0.05	1.26	
Si K	14.71	0.8715	18.55	0.26	13.11	
S K	0.33	0.8267	0.44	0.03	0.27	
Cl K	0.22	0.7546	0.32	0.03	0.18	
K K	0.43	1.0444	0.45	0.03	0.23	
Ca K	13.53	0.9758	15.24	0.22	7.54	
Ti K	0.08	0.7810	0.12	0.03	0.05	
Fe K	1.02	0.8121	1.39	0.06	0.49	
Totals			100.00			

Table B-6 Weight and atomic percentage for the XRF spectra in Figure 8 (right)

Element	App	Intensity	Weight%	Weight%	Atomic%	
	Conc.	Corrn.		Sigma		
C K	0.11	0.6159	0.95	0.24	3.08	
O K	0.30	0.2878	5.33	0.29	12.99	
Mg K	0.01	0.5404	0.07	0.02	0.12	
Al K	0.05	0.6721	0.36	0.02	0.52	
Si K	0.24	0.7977	1.58	0.04	2.19	
S K	0.06	0.9639	0.34	0.03	0.42	
Cl K	0.07	0.8844	0.39	0.04	0.43	
K K	0.08	1.2739	0.31	0.05	0.31	
Ca K	13.00	1.1058	60.65	0.30	58.99	
Fe K	4.99	0.8585	30.02	0.22	20.96	
Totals			100.00			

- Any idea what was the overall distribution, the amount of each phases present for unhydrated cement, hydrated cement, hydrated cement w/o ashing (CH, CSH and unhydrated cement)?
    - Is there a larger concentration amount of a particular phase? E.g. was the dominant phase CSH or CH?

- Response: We are planning to carry out the XRD analysis on samples to determine the amount of each phase present in the cement. The dominant phase based on the model prediction and SEM image is CSH. However, more accurate measurements can be done by XRD.

2.2 SEM Analysis Figure 5 – Class H Cement

- Was the sample in SEM image in Figure 5 cored or as-casted?
- Response: Casted
- Was the observed microcrack present through the entire sample?
- Response: The micro-crack was only observed on one of the samples. The crack was shown only in the polished area of the sample.

2.2 Core 28 SEM/XRF Analyses

Figure 7

- Is the magnification for Figure 7 (page 10) 1000X?
- Response: 3200X
- Fundamental question, is the white coloration on the right side of the sample (in one image and on the left side in the other image) in Figure 7 (page 10 and shown again below for reference) due to charging of the sample in the SEM and not unhydrated cement?
- Response: White spots in Figure 7 are due to charging.
- Are the pores a result of sample preparation?
- Response: It seems to be more like hydrated cement which grows in all the directions and looks like a sphere.

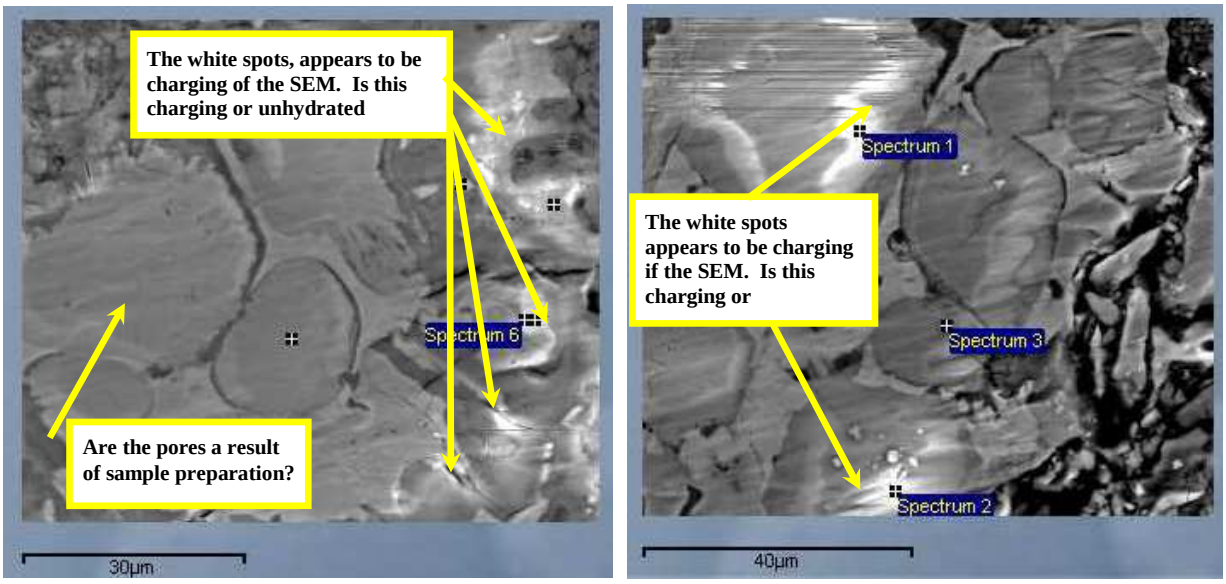

Figure 7 SEM images page 10 of Progress Report

Figure 8

- Was the magnification 800X or 1000X for Figure 8 (page 10, and shown again below for reference)?
- Response: 1400X
- Is there a microcrack in the SEM image in Figure 8 (page 10) of Core 28 sample? Appears to be a microcrack. If it is a microcrack, were any length measurements made?
- Response: It is a microcrack. Length was not measured.

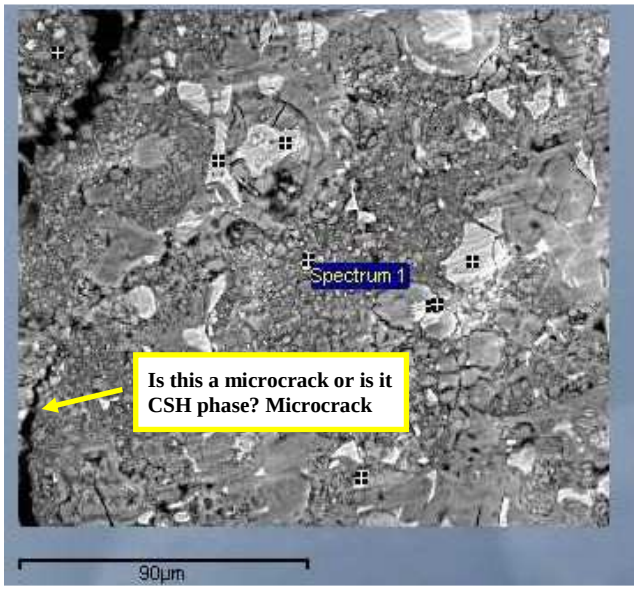

Figure 8 SEM Image Core 28 (Page 10 of Progress Report)

2.2 FTIR Characterization of Hydration Process

- Were any FTIR plots made with all three spectra (Hydrated cement, hydrated cement without ashing, unhydrated cement-Class H) on the same plot? (The plots were on separate, i.e. figures 9-11, it may be clearer to view that there was minimal difference in the absorbance of the vibrational wavelength peaks with the plots on the same graphs.)

- Response: The plots are presented in Fig. B-2 in overlapped form to compare the absorbance of the vibrational wavelength peaks. We found the overlapped plots very helpful in identifying some of the changes that took place after hydration.

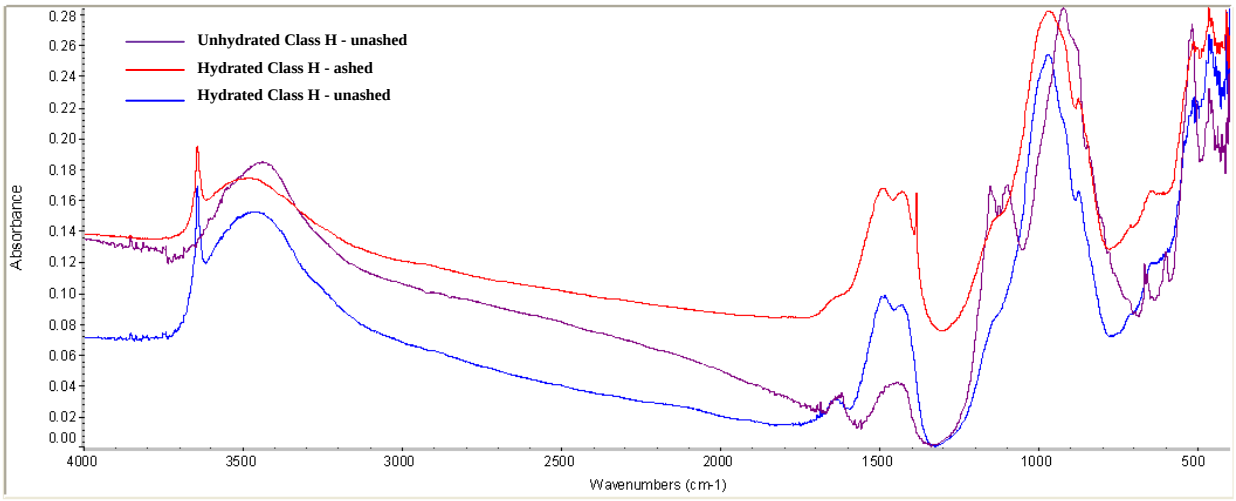

Fig. B-2 FTIR spectra of Class H cement

- The peaks on the FTIR spectra Figures 9-11 were not labeled. For clarification, it appears that some of the compounds present on the FTIR spectra are the following vibrational wavelength peaks in Figures 9-11 below?
  - CH_3 – ~1400 cm^{-1}
  - CH – ~3000 cm^{-1}

- CH_2 – ~1450 cm^{-1}
- $CaCO_3$ – ~890 cm^{-1}, ~1300-1500 cm^{-1}, ~1800 cm^{-1}
- OH^{-1} (hydroxyl group stretching) - ~3350 cm^{-1}
- CO (stretching) - ~1065 cm^{-1} and 1700 cm^{-1}

Response: In the future, FTIR spectra peaks will be labeled and interpreted.

Alternative Cement Property Compound Identification Characterization Methods

- Are there any considerations to using X-ray Photoelectron Spectroscopy (XPS) as a possible alternative method for identification of the different composition phases in addition to XRD since there were minimal differences in the FTIR spectra measurements?
  - XPS may possibly provide further insight to the elemental composition of the different phases in the cement; it can also provide the type of bonds present, e.g. double, single bond, CaO, etc.

- Response: There is an XPS available at Nanotube research center at the University of Oklahoma but it is expensive test. Therefore, we preferred to use XRD.

Compressive Strength

- Any thoughts why the compressive strength for the 2" long core samples were higher? Any considerations that may be possibly be due the longer sample size?

- Response: The compressive strength of the 2-inch sample is expected to be lower than the average. However, discrepancies are still in the acceptable error range based on the ASTM standard. Compressive strength data available in the literature are also showing significant scattering. In addition, these are preliminary tests and we are still improving our measurement technique.

- What was the stress vs. strain measurement values for cement cores #40, 42, 43?
- Response: Stress vs. strain plots shown in Fig. B-3 present preliminary results. These tests were carried primarily for testing the equipment. Data file for Sample 43 has been corrupted.

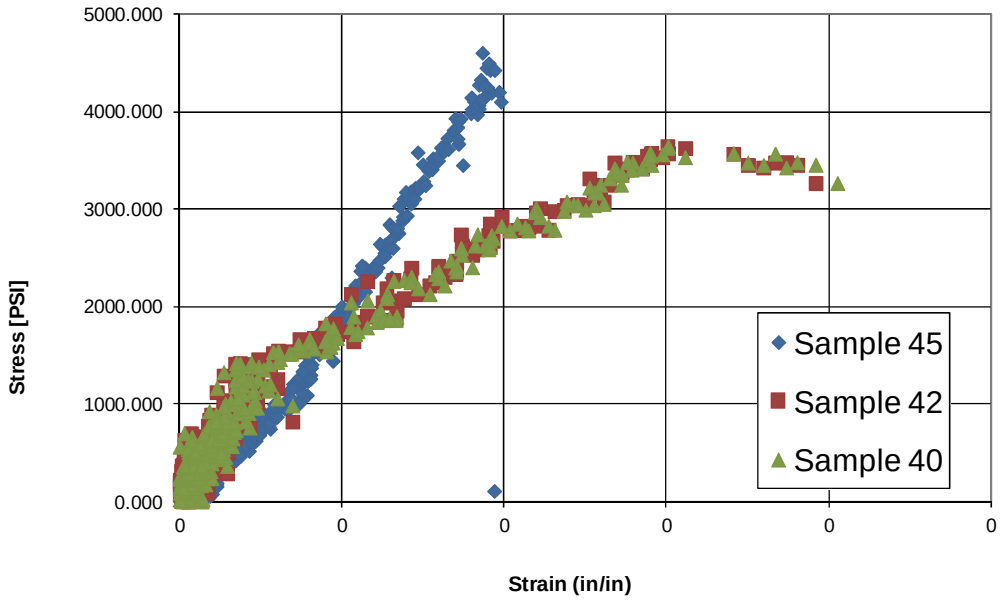

Fig. B-3 Stress versus strain plots for different cement cores

- Any considerations to performing compressive strength measurements on cement samples at different test temperatures?
- Response: With the current setup, we are unable to measure the compressive strength at elevated temperature.

Project Title: Effect of H_2S and CO_2 in HPHT Wells on Tubulars and Cement

Report Type: Monthly Report

Report #: 11

Reporting Period: July 22nd, 2012 to August 21st, 2012

Authors:

Ramadan Ahmed, Principal Investigator

Subhash Shah, Co-Principal Investigator

Samuel Osisanya, Co-Principal Investigator

Shokrollah Hassani, Postdoctoral Research Associate

Rida Elgaddafi, Research Assistant

Omosebi, Omotayo A., Research Assistant

Himanshu Maheshwari, Research Assistant

Adarsh Naidu, Research Assistant

Aman Srivastvava, Research Assistant

Prepared under BSEE Project # E12PC00035

by

THE UNIVERSITY OF OKLAHOMA

Sep 24, 2012

1. Summary of Accomplishments

This monthly report presents the progress made during the project period July 22, 2012 to August 21, 2012. Cement specimens (i.e. class H and G with and without fly ash) and bonding samples were aged in CH_4 saturated brine solution (i.e. 2wt% NaCl) for fourteen days at temperature 350ºF and pressure about 6,000 psi. Silica flour, fly ash, antifoaming agent and Hydroxyethylcellulose (HEC) were added to the cement as additives. Porosity, permeability, compressive strength, and bonding strength of the samples were measured before and after aging. Dry samples were used to carry out porosity, permeability, and bonding measurements. Compressive strength was measured using wet cores.

Confining compressive strength test results before and after aging in CH_4-brine system showed that aging slightly improves the mechanical properties of Class H cement with and without fly ash and Class G cement with fly ash. Generally, adding fly ash slightly increased the compressive strength of the samples. Nonetheless, most of fly ash containing samples were broken after aging indicating brittleness and susceptible to cracking, which occurs due to change in temperature and/or pressure. Porosity and permeability of the samples predominately reduced after aging. This observation can be attributed to additional hydration that occurs during the aging process or the formation of more stable binding components in the cement at high temperature.

Theoretical and modeling studies on tubular degradation are in progress. Different high pressure high temperature (HPHT) models for solubility of CO_2, H_2S, and CH_4 were reviewed. Three different models were studied and evaluated. A report summarizing the literature survey and modeling studies is presented in Appendix A. Model predictions are compared with published data. Predictions show a good agreement with the data for wide ranges of pressure, temperature and salinity levels. Mixed gas solubility is also predicted for HPHT conditions and compared with available measurements. Results show moderate discrepancies that require model improvement. Research is in progress to better understand the mutual interactions of different gases and their effects on solubility.

Our plan for the coming weeks is to continue the aging experiments. After aging, the properties of the samples will be measured. Beside this, we will continue theoretical and modeling studies on tubular corrosion. Also, the ongoing corrosion setup developmental activities will continue. Designs of some the components will be finalized in the coming weeks.

2. Overall Project Progress

2.1 Theoretical Studies (Task 1)

Theoretical and modeling studies on corrosion of tubular were continued. Different high pressure high temperature models for solubility of CO_2, H_2S, and CH_4 were reviewed. Three different models (Duan et al. 2003, 2006, and 2007) were used to predict the solubility of CO_2, H_2S, and CH_4 in brine solution for different temperatures, pressures, and ionic strengths. Model predictions are compared with different experimental data. Good agreement is observed between experimental data and model predictions. CO_2, H_2S, and CH_4 solubility in brine solution were also predicted under HPHT condition (i.e. 2% NaCl, 350ºF, and different pressures up to 10,000 psi). H_2S showed the maximum solubility when compared with CO_2 and CH_4 at similar pressure. CH_4 showed the minimum amount of solubility in comparison with CO_2 and H_2S. Studies are in progress to model the mutual interactions of different gases and their impacts on solubility. A report summarizing literature survey and results of modeling studies is presented in Appendix A.

At present, theoretical and modeling studies on corrosion of tubular are in progress to develop models for predicting the CO_2 and H_2S corrosion rates under high pressure high temperature conditions.

2.2 Experimental Studies on Degradation of Cement (Task 2)

Two aging experiments (Experiments 1 and 2) have been conducted so far. Four different types of cement samples (i.e. Class H and G with Silica, Class H and G with silica and fly ash) were aged under different test conditions. Experiment 1 was performed at 9,000 psi and 350ºF. The plan was to age the samples for 4 weeks to observe measurable change in physical and chemical properties. However, it was stopped after six days of aging because of severe brine leakage from the system. Substantial amount of the brine was leaked out during the test causing some of the samples to dry. Brine concentration was 9% NaCl. The leakage is attributed to crevice corrosion, which often occurs at high concentration of NaCl.

In order to control corrosion and eliminate leakage, the second test (Experiment 2) was carried out at lower NaCl concentration (2% by weight). The first two weeks of Experiment 2 was completed successfully. Half the aged samples were taken out and replaced by fresh un-aged samples. Then, the experiment is continued for another 2 weeks. Porosity, permeability, compressive strength, and bonding strength of the aged samples were measured.

2.2.1 Compressive and Bonding Strength Measurement Techniques

Mechanical properties such as compressive and bonding strengths are very important characteristics of oil well cement. Figure 1 shows schematic of experimental setup developed to measure bonding and confining compressive strengths of cement. The setup consists of : i) confining cell; ii) power cylinders to apply compression force on the specimens; iii) air-operating pump to develop the confining pressure; iv) syringe pump to supply hydraulic power to the cylinders; v) supporting frame to hold the bonding test samples in place; and vi) instrumentation and data acquisition (DAQ) system.

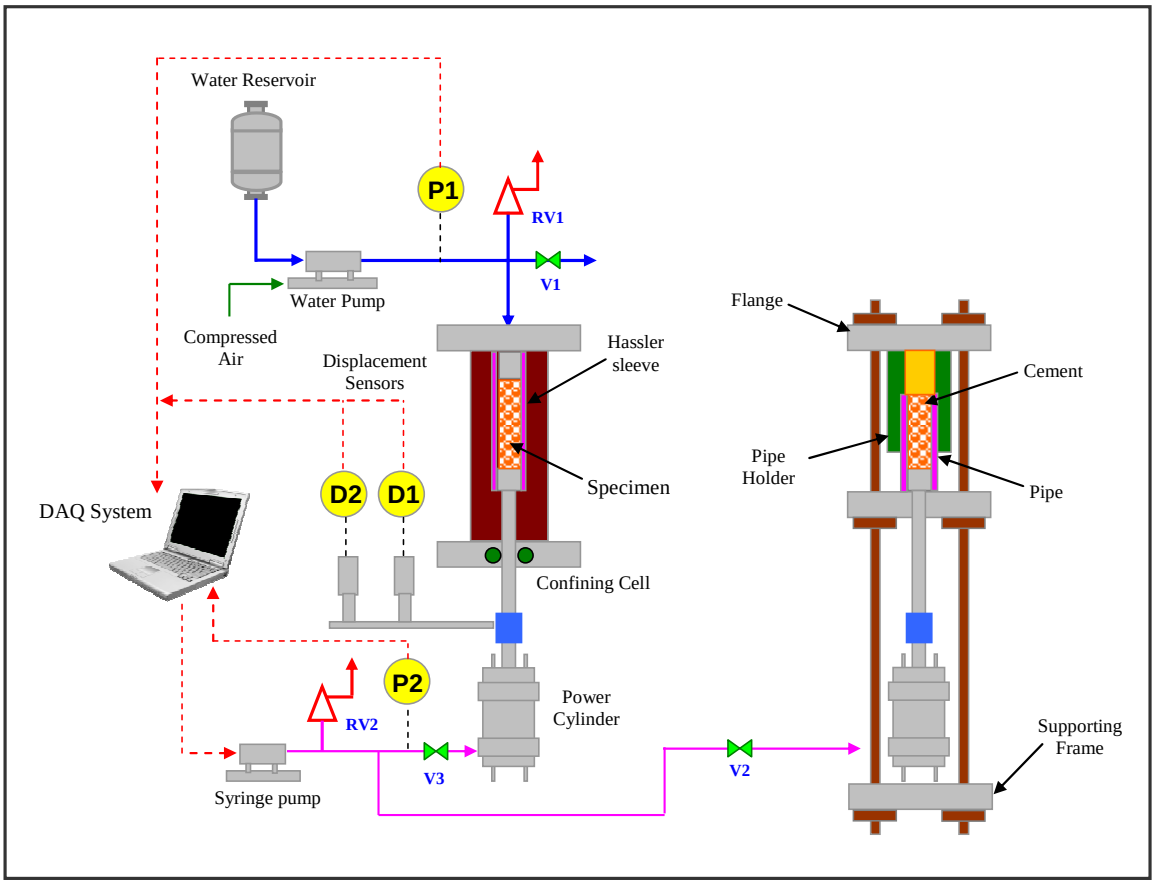

Fig. 1 Test setup for measuring compressive and bonding strength of cement samples

The confining cylinder has a shaft with a specimen holder that is connected to the power cylinder. High accuracy displacement sensors that are attached to the shaft measures the level of strain developed in the specimen. During the test, the cement sample is placed in the Hassler sleeve and mounted on the plunger attached to the cylinder shaft. Then, the plunger on cylinder lid is inserted into the Hassler sleeve and the lid is pressed to completely seal the

cylinder. After screwing and tightening the lid holder on the cylinder, the confining pressure is increased using the water injection pump. Subsequently, the syringe pump is started to apply compression force on the sample. As the sample compresses, the displacement sensors measure the movement of the plunger or piston rod at the shaft coupling. As a constant pump rate, the compressive force developed in the sample (i.e. stress load) increases with time. The DAQ system controls the speed of the syringe pump to maintain a constant stress loading rate. The sample is compressed and deformed until a complete mechanical failure occurs. During the test, the DAQ system display and records all the measurements.

For compressive strength tests, the confining pressure was maintained at 1000 psi. Stress loading rate in the final stage of the test was kept in the range of 28 to 42 psi/second as required by ASTM standard C39-C39M-12. Speed of motor was adjusted based on the measured stress loading rate using the DAQ system. Figures 2 and 3 show examples of loading rates and compressive and bonding stresses monitored during the test for Class G and Class H cement samples containing 35% silica.

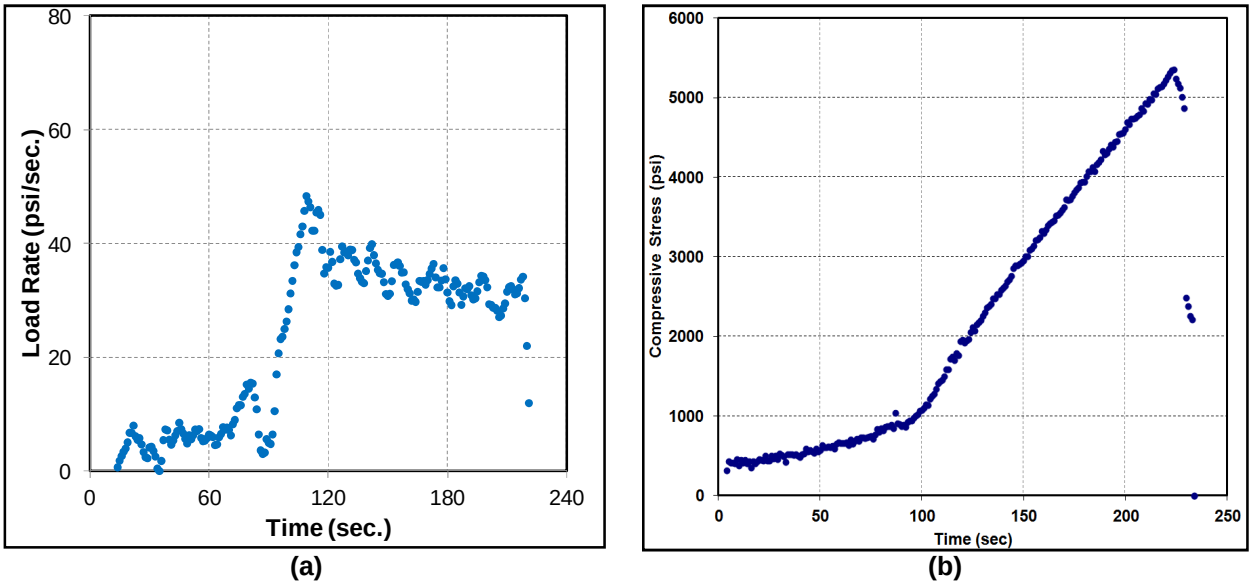

Fig. 2 Compressive strength test for unaged Class G cement containing 35% silica: a) stress rate vs. time; and b) stress vs. time

The bonding strengths of cement samples were measured using the setup developed for measuring compressive strength (Fig. 1). The setup has supporting frame with a power cylinder and sliding flanges to hold the sample. The power cylinder is attached to the supporting frame that keeps a bonding sample and its holder in place. To perform the test, the sample (short pipe

together with hardened cement) is placed on a plunger coupled with the piston rod. Then, the sample holder (pipe holder) and the supporting flange are placed on the top of the sample and secured using four bolts. The test begins when the syringe pump is turned on to apply the force on the sample using the plunger. At a constant pump rate (i.e. plunger velocity), the applied force increases with time. The DAQ system is set to control the speed of the syringe pump to maintain roughly a constant bonding shear stress loading rate of 35 psi/second (Fig. 3a). The test is stopped when abrupt reduction in the shear stress is observed (Fig. 3b).

The shear bond strength of cement indicates the force required to break the bond between cement and casing. Bonding performance of conventional cement was evaluated. Test specimens were prepared by casting cement slurry into a 1-inch diameter carbon steel pipe (Fig. 3c) that has a length of 1.5". One piece of a long 1-inch diameter seamless steel pipe was cut to small pieces (1.5" length) to have an identical pipe surface roughness in all the bonding samples. Once the slurry was set in the pipe, the specimen were cured and then placed in the aging cell. The maximum pressure developed by the syringe pump during the test was used to determine the shear bond strength. Figure 3a shows shear bonding strength as a function of time for Class H cement with silica and fly ash after aging.

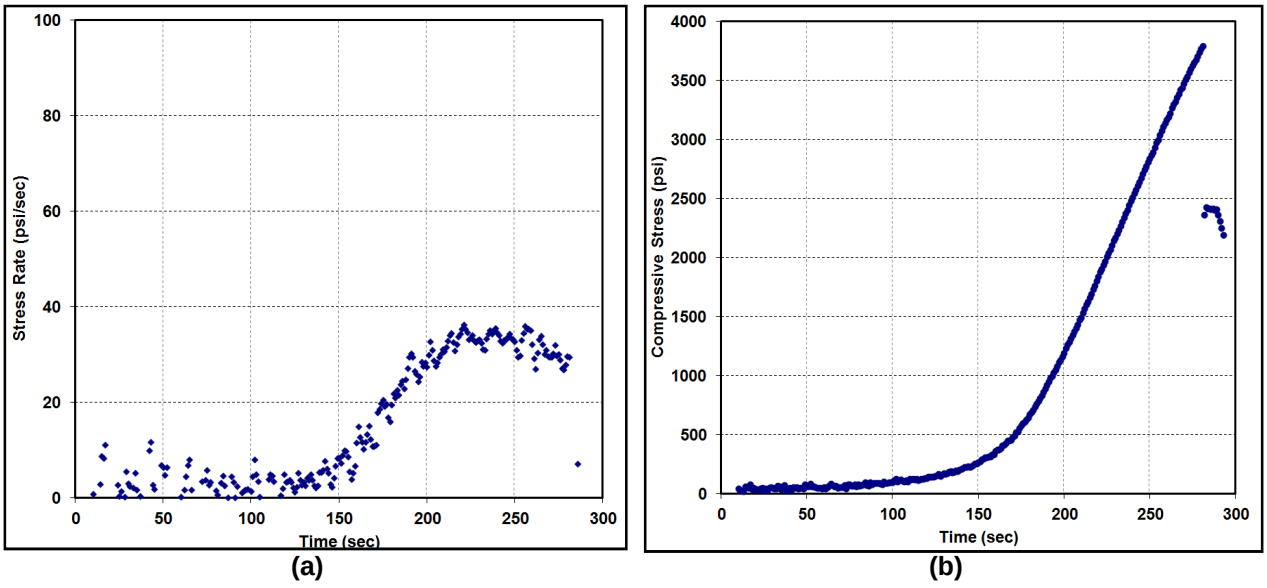

Fig. 3 Shear bonding strength measurement of Class H cement with silica and fly ash after aging (Experiment 2): a) Stress rate vs. time; and b) Stress vs. time

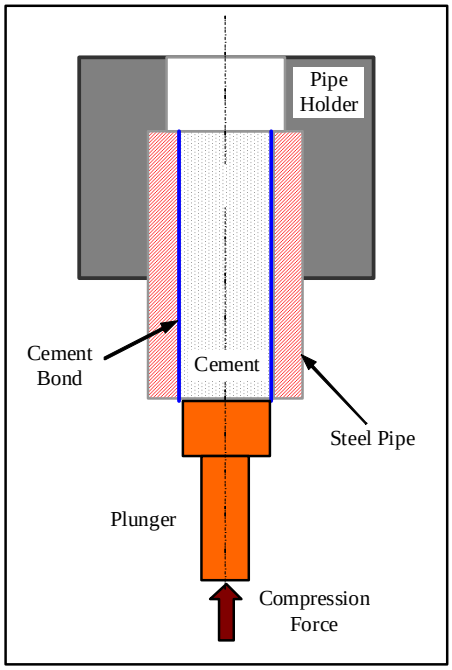

Fig. 3c Shear bonding test sample and pipe holder

2.2.2 Results for Experiment 1

Figures 4 and 5 present the measured confined compressive strength of different aged and unaged samples. The core # of the samples contains numbers and acronym separated by hyphens. The first number shows the batch number. The second acronym indicates the type of cement (GS = Class G with silica; GSF = Class G with silica and fly ash; HS = Class H with silica; HSF = Class H with silica and fly ash). The third number shows the shelf number in the aging cell that the sample was aged. The last number is the order number, which indicates the angular location of the sample in the aging cell. Although measurements exhibit scattering in some cases, they are predominately consistent.

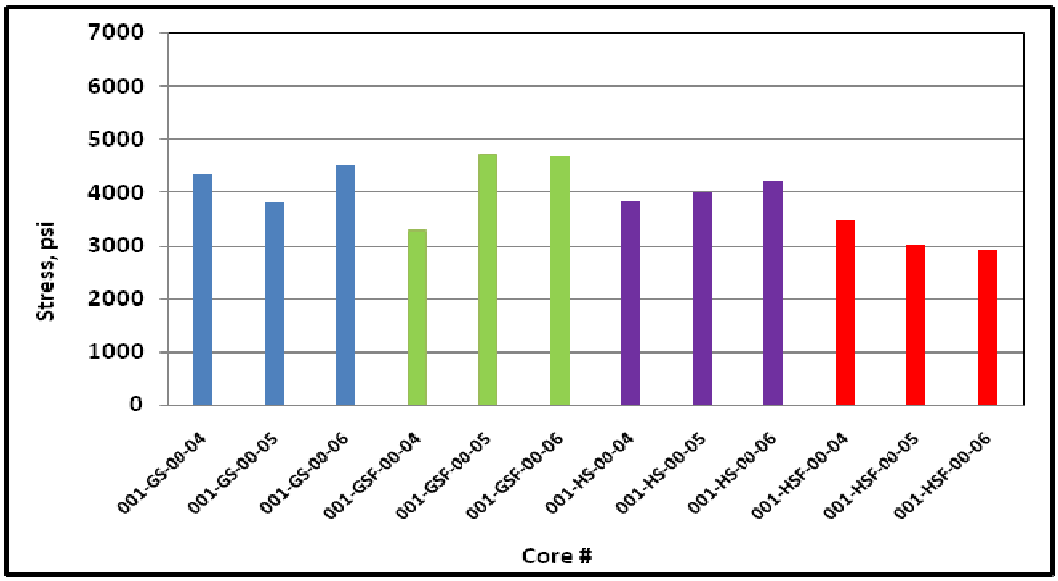

Fig. 4 Compressive strengths of cement samples (Unaged, Experiment 1)

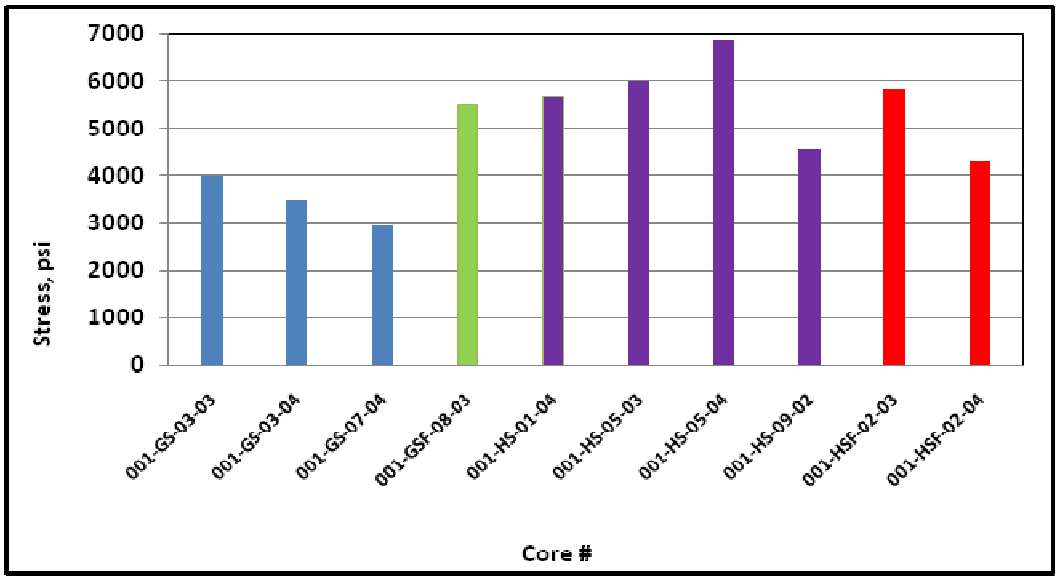

Fig. 5 Compressive strengths of cement samples (after 6 days of aging at temperature of 350^{o}F and pressure of 9,000 psi in CH_4-brine solution, Experiment 1)

Confining compressive strength test results before and after aging in CH_4-brine system showed slight improvement in the mechanical properties of Class H cement with and without fly ash and Class G with fly ash (Fig. 6). The improvement can be attributed to additional hydration of cement at high pressure high temperature conditions and/or temperature induced transformation of CSH to a more strong binding materials such as xonotlite ($Ca_6Si_6O_{17}(OH)_2$) and/or gyrolite ($NaCa_{16}Si_{23}AlO_{60}(OH)_8.64(H_2O)$), which may cause decreased permeability and

improved compressive strength. Beside this, the CH_4-Brine system does not have any destructive effect on cement performance since CH_4 has a non-polar molecular structure and it doesn't react with cement or produce acidic environment. Moreover, the thermal retrogression is minimized by adding 35% silica sand in the cement.

Furthermore, Fig. 6 shows the effect of fly ash on compressive strength of cement. Adding fly ash slightly increased the compressive strength in most of the samples. This is consistent with results presented in Figs. 7 and 8, which indicate reduction in porosity and permeability of cement with the addition of fly ash. Lower porosity caused by the addition of fly ash is attributed to the increase in compressive strength of the cement. However, most of the samples with fly ash were broken after aging which means that fly ash makes the cement more brittle and susceptible to temperature and pressure induced cracking. Although aging temperature and pressure were gradually varied, cracking occurred in most of samples containing fly ash. In addition, samples placed on top shelves exhibited more cracking than the ones placed close to the bottom of the aging cell.

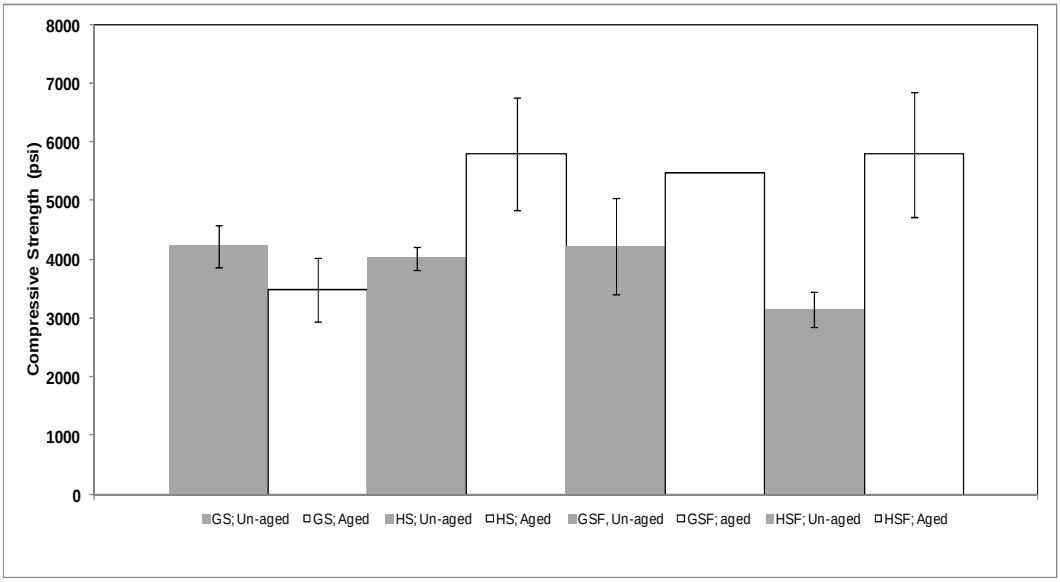

Fig. 6 Summary of compressive strengths of cement samples (before and after 6 days of aging at temperature of 350^{o}F and pressure of 9,000 psi in CH_4-brine solution, Experiment 1)

Porosity and permeability measurements before and after six days of aging in CH_4-brine system at temperature of 350ºF and pressure of 9,000 psi are shown in Figs. 7 and 8. It can be seen that porosity and permeability of the samples predominately reduced after aging. More hydration can occur during aging process reducing porosity as the water reacts with the cement causing matrix swelling, which results in pore shrinkage. Methane is non-acidic gas and it does

not have any destructive effect on cement. High temperature facilitates the curing process and reduces the porosity and permeability, and consequently improves the mechanical properties of the cement. Moreover, increased temperature creates suitable condition for thermal induced transformation of CSH to more stronger binding materials.

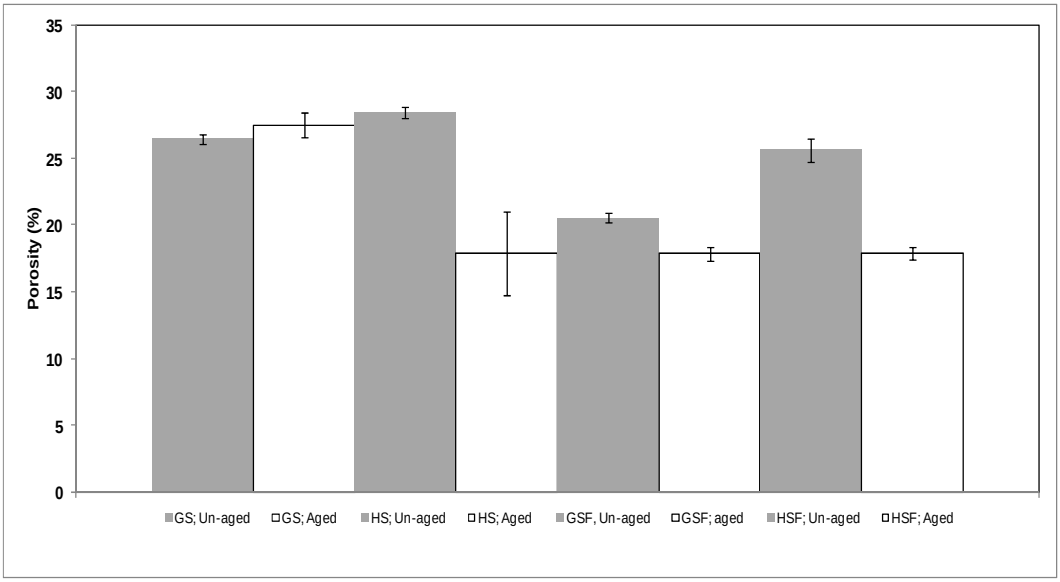

Fig. 7 Summary of porosity data before and after 6 days of aging at temperature of 350^{o}F and pressure of 9,000 psi in CH_4-brine solution (Experiment 1)

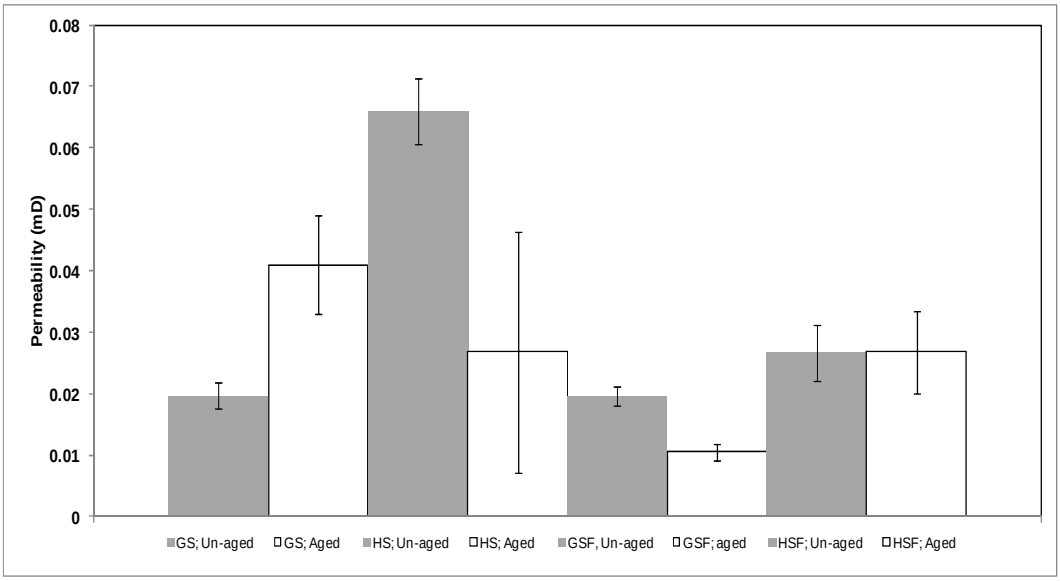

Fig. 8 Summary of permeability data before and after 6 days of aging at temperature of 350^{o}F and pressure of 9,000 psi in CH_4-brine solution (Experiment 1)

2.2.3 Results for Experiment 2

The first phase of the second aging experiment (Experiment 2) was completed successfully after 14 days of aging cement and bonding samples at temperature of 350ºF and 6,000 psi pressure of CH_4 in 2% brine solution. Half of the samples were taken out of the cell for testing compressive strength, porosity, permeability and bonding strength. The rest of the samples were kept in the aging cell for additional 14 days of aging. Rate of temperature increase at the beginning of the experiment was roughly 40ºF/hour. The arrangements of cement and bonding specimen in the cell are showed in Fig. 9.

Most of the cement samples containing fly ash were cracked during the aging. In the field, fly ash added as a cement additive to reduce slurry density and cost of cement. It reacts with calcium hydroxide and forms calcium silicates and increases cement strength and thickening time. Experimental results (i.e. Experiment 1 and 2) showed that fly ash makes the cement brittle and sensitive to temperature and pressure changes that initiate cracking even without the presence of any corrosive gas (i.e. CO_2 and H_2S). However, cracks were not developed in bonding samples containing fly ash.

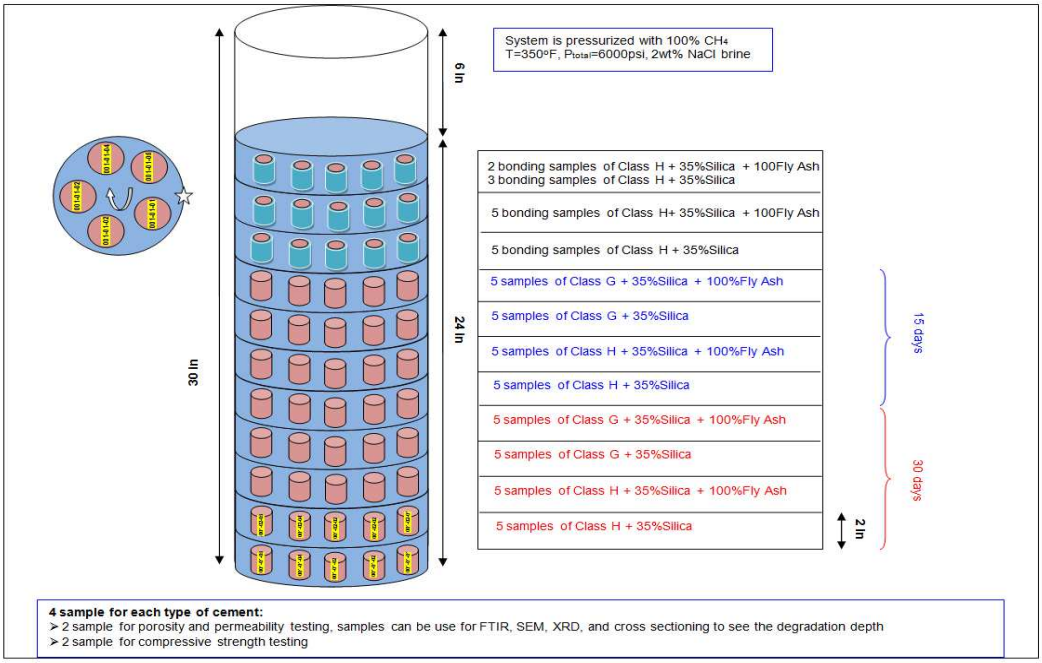

Fig. 9 Cement specimen arrangement in Phase 1 of Experiment 2

Confining compressive strength test results for class H and class G cement with and without fly ash before and after aging are presented in Figs. 10 and 11. The measurements

were obtained at confining pressure of 1000 psi and stress loading rate of 35 psi/second. All Class H cement cores with fly ash were broken after aging and we were not able to measure their compressive strength. Figure 11 shows a summary of confining compressive strength test results. Two week of aging at temperature of 350ºF and pressure of 6,000 psi in CH_4-brine system didn't considerably change the compressive strength of the samples. However, cement cores with fly ash were sensitive to the testing conditions.

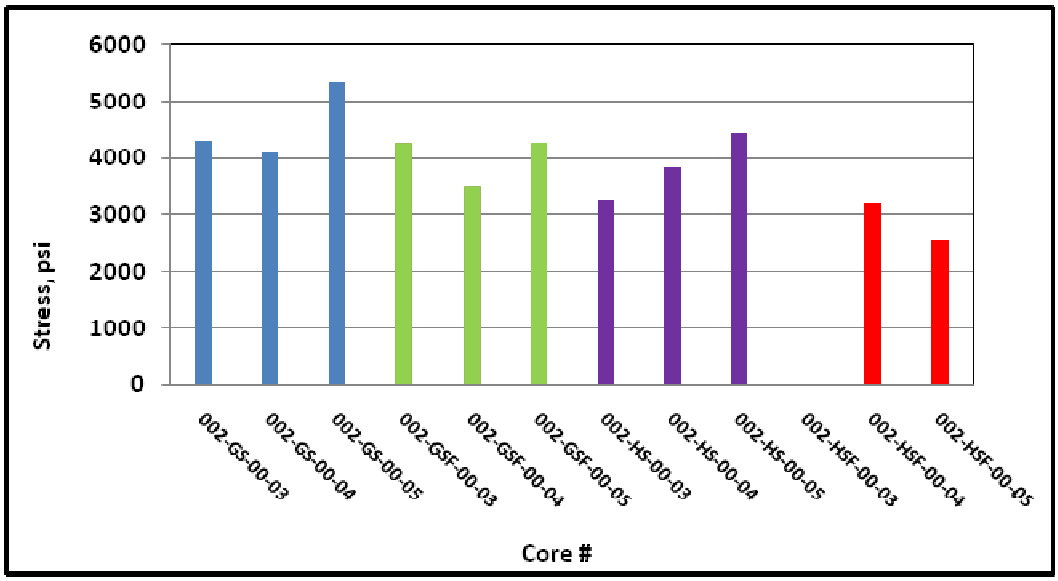

Fig. 10 Compressive strengths of wet cement samples (Unaged, Batch 2)

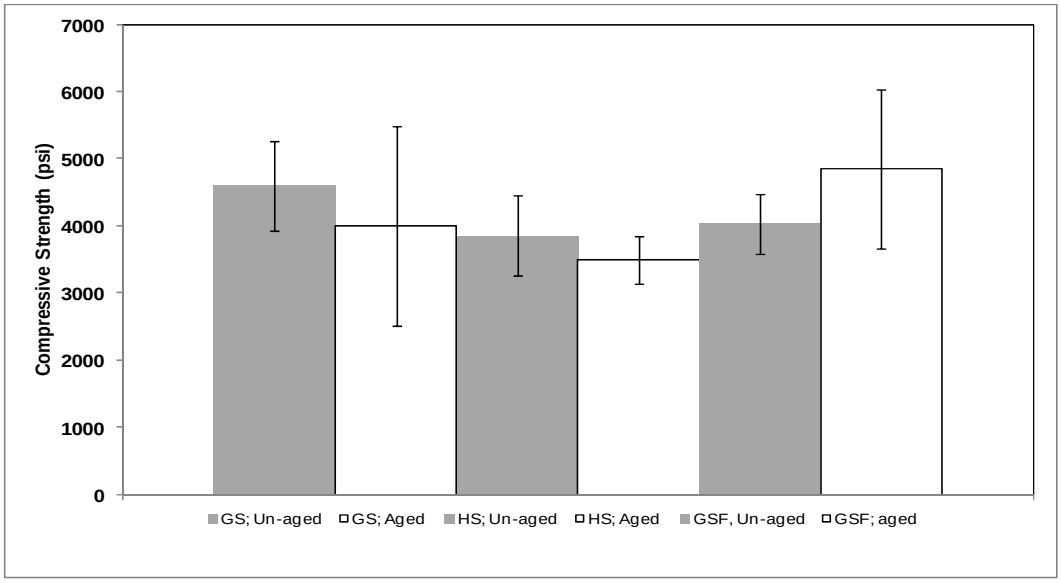

Fig. 11 Compressive strengths of wet cement samples (before and after 14 days of aging at temperature of 350ºF and pressure of 6,000 psi in CH_4-brine solution, Experiment 2)

In addition to compressive strength, shear bonding strengths of bonding samples were measured after 14 days of aging at temperature of 350ºF and pressure of 6,000 psi in CH_4-brine system. Experimental results (Fig. 12) indicate that adding fly ash to the class H cement with silica improved the bonding strength of the cement to carbon steel pipe.

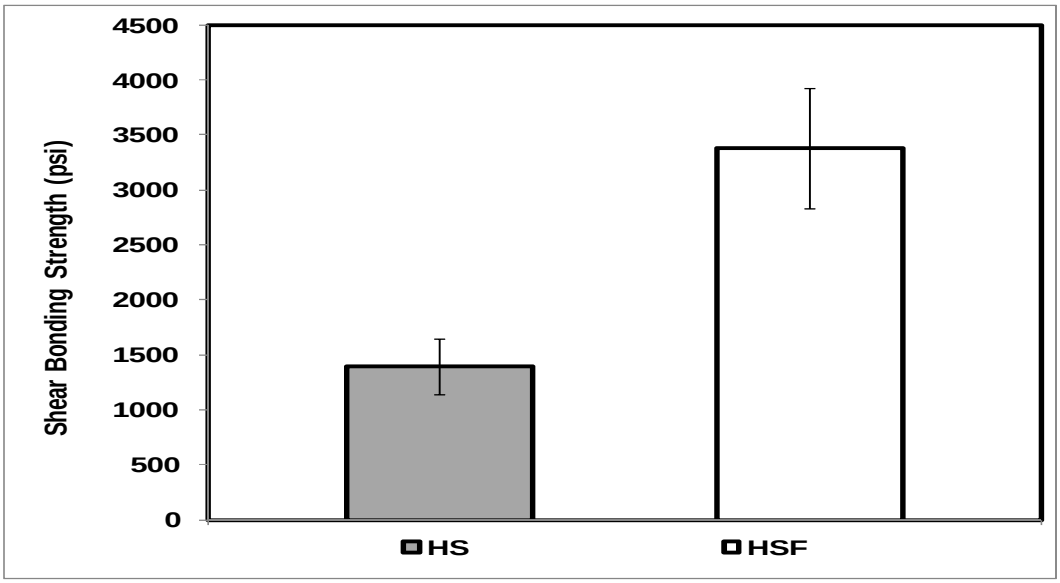

Fig. 12 Effect of fly ash on shear bonding strength of Class H cement with silica after 14 days of aging at temperature of 350ºF and pressure of 6000 psi in CH_4-brine solution (Experiment 2)

A summary of porosity and permeability experimental data before and after 14 days of aging at temperature of 350ºF and pressure of 6,000 psi in CH_4-brine solution are presented in Figs. 13 and 14, respectively. Measurements show good repeatability with small standard deviation. Aging in CH_4-brine solution slightly reduced the cement porosity for most of the cement cores (Fig. 13). One possible explanation for the porosity reduction could be additional cement hydration that occurs at high temperatures (350ºF), which may diminish free unhydrated water content and consequently reduces the porosity. Slight increase in compressive strength of the cement samples after aging in CH_4-brine solution can be also related to the reduced porosity after aging. Permeability of Class H and G samples without fly ash and Class G samples with fly ash reduced after aging. More cement hydration may be a good explanation for this behavior. However, permeability of Class H cement with fly ash slightly increased after aging.

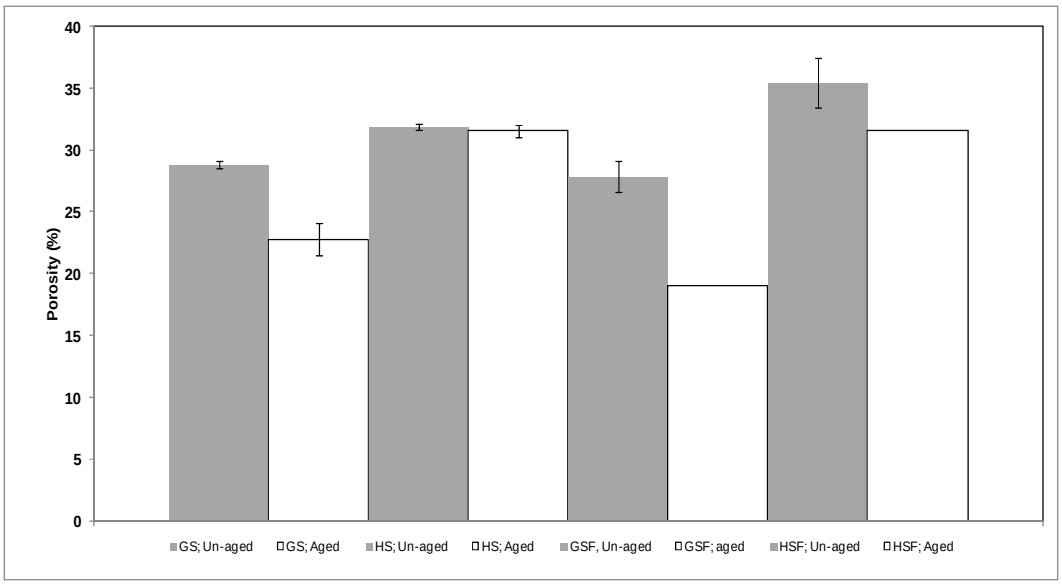

Fig. 13 Porosity of cement samples (before and after 14 days of aging at temperature of 350ºF and pressure of 6000 psi in CH_4-brine solution, Experiment 2)

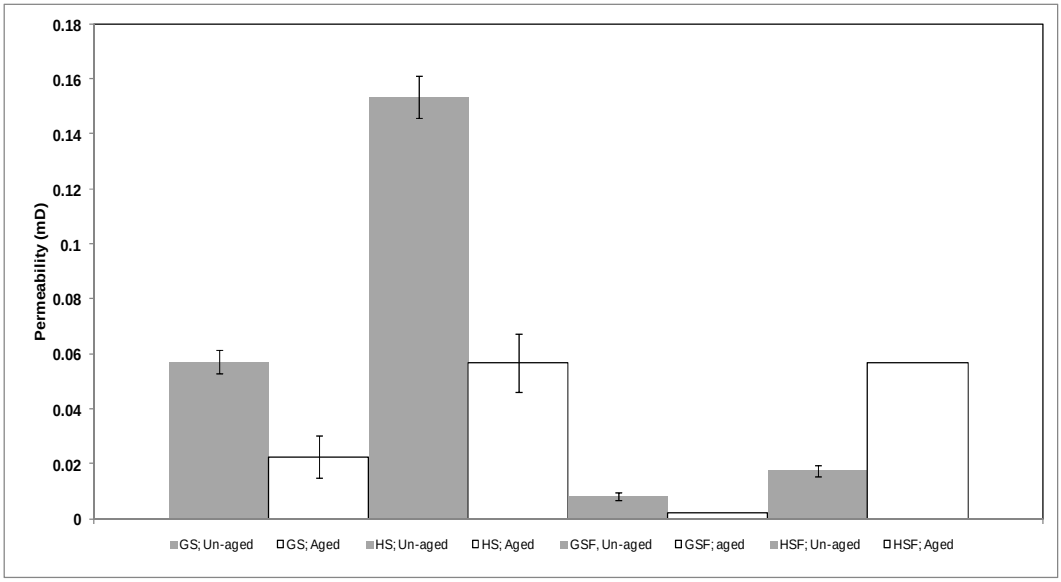

Fig. 14 Permeability of cement samples (before and after 14 days of aging at temperature of 350ºF and pressure of 6,000 psi in CH_4-brine solution, Experiment 2)

Sample arrangement for the second phase of Experiment 2 is shown in Fig.15. Aging is continued for additional 2 weeks at temperature of 350℉ and pressure of 6,000 psi in CH_4-brine solution. Forty cement cores and ten bonding samples were loaded to the aging cell. Half of the samples were previously aged for 2 weeks and the others are new samples. ASTM standard (C39-C39M-12) compressive strength test specimens have length to diameter ratio of

two. Therefore, two inch long and one inch diameter cement cores were prepared for the new set of experiments.

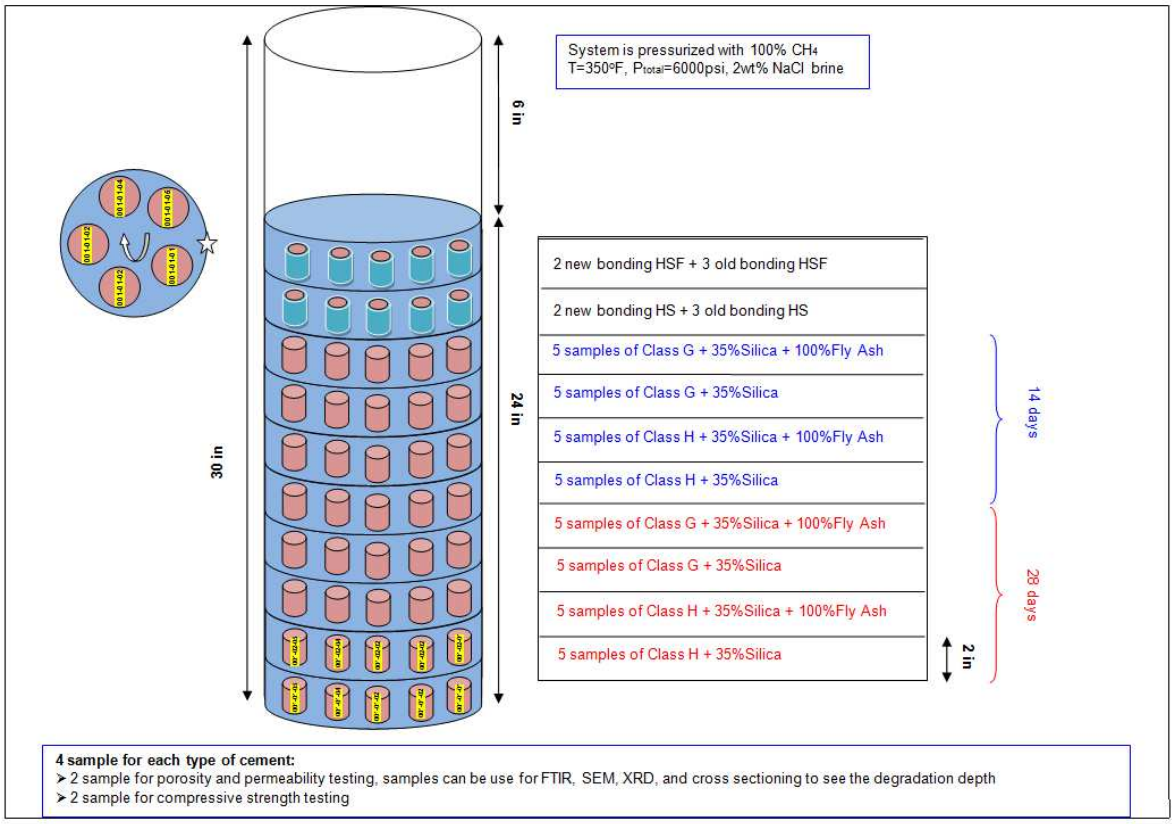

Fig. 15 Sample arrangement for the second phase of Experiment 2

2.3 Experimental Studies on Corrosion of Tubulars (Task 3)

Designing and selection of major components of corrosion test set up (stress cracking corrosion testing cell, injection cylinders, potentiostat, and magnetic drive required for corrosion cell) have been finalized. Purchase orders of these items have been completed. There are some remaining designs of components, which need to be finalized. Preliminary corrosion experiments will be started when the development of the experimental setups is completed.

3. Problems Encountered

Major problem during this reporting period was gas and liquid leakage from the aging setup. Liquid leakage was stopped by disconnecting and plugging the liquid injection line, which was installed at the bottom of the aging cell. In addition to the liquid leakage, severe CH_4 gas leakage occurred after starting the second aging phase of Experiment 2. As a result, the tested

was stopped and leaking gas tubing was repaired. Furthermore, some of the valves are still unable to completely shot off the aging cell gas inlets resulting leaks, which deplete system pressure with time. As result, we were unable to conducted tests at the maximum system pressure. Currently, the system can hold pressure up to 6,000 psi. The leak becomes excessive as the system pressure increases. In order to maintain high system pressure, heavy duty shutoff valves (ball valves) have been ordered to replace the leaking ones.

4. Planned Activities

- Aging experiments with brine-CO_2-CH_4 system.
- Continue theoretical and modeling studies on tubular degradation.
- Continue designing and acquisition of components of tubular corrosion testing setups.

5. Project Expenditures

This section presents the project expenses during the months of August (Table 6) and the cumulative expenditures.

Table 6 Current and cumulative expenditures, August, 2012

No.	Budget Categories	Current Expenses	Cumulative Expenses
1	Salaries & Wages	$11,987.95	$105,260.73
2	Fringe Benefits	$2,601.40	$28,799.76
3	Project Materials	$4,320.79	$40,685.23
4	Travel	$85.48	$1,209.32
5	Conference Expenses	$0.00	$0.00
6	Other Direct Costs	$0.00	$305.38
7	Equipment	$0.00	$141,502.67
8	Space Rental	$0.00	$0.00
9	Indirect Cost	$9,497.81	$88,130.24
10	**Total**	**$28,493.43**	**$405,893.33**

Nomenclature

HPHT	High pressure high temperature
HS	Class H with Silica
HSF	Class H with Silica and Fly ash
GS	Class G with Silica
GSF	Class G with Silica and Fly ash
R	Universal gas constant
T	Absolute temperature
P	pressure in bar
m_{CO_2}	CO_2 solubility in mole/kg
$\frac{\mu_{CO_2}^{1(0)}}{RT}$	dimensionless standard chemical potential
φ_{CO_2}	CO_2 fugacity coefficient
P_c	critical pressure
T_c	critical temperature
Z	compressibility factor
P_r	reduced pressure
T_r	reduced temperature
V_r	reduced volume

References

ASTM Standard C39/C39M – 12. 2012. Standard Test Method for Compressive Strength of Cylindrical Concrete Specimens.

Blount, C.W. and Price, L.C., 1982. Solubility of methane in water under natural conditions: A laboratory study; DOE Contract No. DE-A50878ET12145, Final Report.

Duan, Z., Sun, R., Liu, R., and Zhu, C. 2007. Accurate Thermodynamic Model for the Calculation of H2S Solubility in Pure Water and Brines, Energy & Fuels, 21, pp.2056-2065.

Duan, Z. and Sun, R. 2003. An improved model calculating CO_2 solubility in pure water and aqueous NaCl solutions from 273 to 533 K and from 0 to 2000 bar, Chemical Geology 193, pp. 257–271.

Duan Z. and Mao, S., 2006. A thermodynamic model for calculating methane solubility, density and gas phase composition of methane-bearing aqueous fluids from 273 to 523K and from 1 to 2000bar. Geochimica et Cosmochimica Acta 70 3369–3386.

Huang, S.S.S., Leu, A.D., Ng, H.J. and Robinson, D.B. 1985. The Phase Behavior Of Two Mixtures Of Methane, Carbon Dioxide, Hydrogen Sulfide, And Water, Fluid Phase Equilibr. 19, pp. 21–32.

Li, Z. and Firoozabadi, A. 2009. Cubic-Plus-Association Equation of State for Water-Containing Mixtures: Is ‘‘Cross Association’’ Necessary?. AIChE J. 55 (7) pp. 1803–1813.

Rumpf, B., Nicolaisen, H., Ocal, C. and Maurer G., 1994. Solubility of carbon dioxide in aqueous solutions of sodium chloride: experimental results and correlation. J. Solution Chem. 23 (3), 431–448.

Selleck, F.T.; Carmichael, L.T. and Sage, B.H. 1952. Phase Behavior in the Hydrogen Sulfide-Water System. Ind. Eng. Chem., 44 (9), pp 2219–2226.

Takenouchi, S. and Kennedy, G.C. 1965. The solubility of carbon dioxide in NaCl solutions at high temperatures and pressures. Am. J. Sci. 263, 445–454.

Todheide, K. and Franck, E.U. 1963. Das Zweiphasengebiet und die kritische Kurve im System Kohlendioxid-Wasser bis zu Drucken von 3500 bar. Z. Phys. Chem. 37, 387–401.

Zirrahi, M., Azin, R., Hassanzadeh, H. and Moshfeghian, M., 2012 Mutual solubility of CH_4, CO_2, H_2S, and their mixtures in brine under subsurface disposal conditions. Fluid Phase Equilibria 324 80– 93.

Appendix A

Literature Review and Theoretical Studies on Tubular Corrosion

Summary

Tubular corrosion and cement degradation modeling at HPHT conditions containing sour gases needs accurate prediction of solubility of CO_2, H_2S, and CH_4 in brine solution. In this study three different models (Duan, 2003, 2006, and 2007) were used to predict CO_2, H_2S, and CH_4 solubility in brine solution at different temperatures and pressures. Model predictions were compared with experimental data. The models were also used to predict the solubility of these gases in brine solutions under HPHT conditions (i.e. 2wt% NaCl, 350ºF, and different pressures up to 10,000 psi).

A.1. CO_2 Solubility Model

Duan and Sun (2003) developed an accurate model for CO_2 solubility prediction in pure water and brine solutions. This model is applicable for temperatures ranging from 273 to 533 K, for pressures ranging from 0 to 2,000 bar, and for ionic strength from 0 to 4.3 m. They calculated the CO_2 solubility in aqueous phase, maintaining the balance between its chemical potential in the liquid phase and that in the gas phase. The potential can be written in terms of fugacity in the vapor phase and activity in the liquid phase. They proposed the following model (Eq. A.1) for predicting the solubility of CO_2 in pure water and brine solutions.

$$ln\frac{y_{CO_2}P}{m_{CO_2}} = \frac{\mu^{1(0)}_{CO_2}}{RT} + ln\varphi_{CO_2} + \sum_c 2\lambda_{CO_2-c}m_c + \sum_a 2\lambda_{CO_2-a}m_a + \sum_c\sum_a \xi_{CO_2-c-a}m_c\, m_a \quad \text{(A.1)}$$

where y_{CO_2} is concentration of CO_2 in the gas phase, which is calculated as:

$$y_{CO_2} = \frac{P-P_{H_2O}}{P} \quad \text{(A.2)}$$

P is pressure in bar and m_{CO_2} is CO_2 solubility in mole/kg. The term $\frac{\mu^{1(0)}_{CO_2}}{RT}$, ξ and λ are dimensionless parameters, Par(T,P), determined using Eq. (A.3) and Table A.1.

$$Par(T,P) = C_1 + C_2T + \frac{C_3}{T} + C_4T^2 + \frac{C_5}{630-T} + C_6P + C_7PlnT + \frac{C_8P}{T} + \frac{C_9P}{630-T} + \frac{C_{10}P^2}{(630-T)^2} + C_{11}TlnP \quad \text{(A.3)}$$

where C_1 through C_{11} are for CO_2 solubility constants presented in Table A.1.

Table A.1 Interaction parameters for CO_2 solubility in brine and pure water

T-P Coefficients	$\frac{\mu_{CO_2}^{1(0)}}{RT}$	λ_{CO_2-Na}	$\xi_{CO_2-Na-Cl}$
C_1	2.89E+01	-4.11E-01	3.36E-04
C_2	-3.55E-02	6.08E-04	-1.98E-05
C_3	-4.77E+03	9.75E+01	
C_4	1.03E-05		
C_5	3.38E+01		
C_6	9.04E-03		
C_7	-1.15E-03		
C_8	-3.10E-01	-2.38E-02	2.12E-03
C_9	-9.10E-02	1.71E-02	-5.25E-03
C_{10}	9.30E-04		
C_{11}		1.41E-05	

P_{H_2O} in Eq. (A.2) is the vapor pressure of water. The vapor pressure is determined as:

$$P_{H_2O} = \frac{P_{C,H2O}T}{T_{C,H2O}}[1 + C_1(-t)^{1.9} + C_2t + C_3t^2 + C_4t^3 + C_5t^4] \quad \text{..... (A.4)}$$

where $P_{c,H2O}$ and $T_{c,H2O}$ are critical pressure and temperature of water (i.e. 220.9 bar and 647.3 K), $t = (T-T_c)/T_c$ and constants C_1 through C_5 are presented in Table A.2.

Table A.2 Parameters used in Eq. (A.4)

C_1	-3.86E+01
C_2	5.89E+00
C_3	5.99E+01
C_4	2.67E+01
C_5	1.06E+01

Carbon dioxide fugacity coefficient (φ_{CO_2}) is obtained from the following equation:

$$ln\varphi(T,P) = Z - 1 - lnZ + \frac{a_1+\frac{a_2}{T_r^2}+\frac{a_3}{T_r^3}}{V_r} + \frac{a_4+\frac{a_5}{T_r^2}+\frac{a_6}{T_r^3}}{2V_r^2} + \frac{a_7+\frac{a_8}{T_r^2}+\frac{a_9}{T_r^3}}{4V_r^4} + + \frac{a_{10}+\frac{a_{11}}{T_r^2}+\frac{a_{12}}{T_r^3}}{5V_r^5} + \frac{a_{13}}{2T_r^3a_{15}}\left[a_{14} + 1 - \left(a_{14} + 1 + \frac{a_{15}}{V_r^2}\right)\left(exp\left(-\frac{a_{15}}{V_r^2}\right)\right)\right] \quad \text{.....(A.5)}$$

where Z is compressibility factor, which is computed using Eq. (A.6).

$$Z = \frac{P_r V_r}{T_r} = 1 + \frac{a_1 + \frac{a_2}{T_r^2} + \frac{a_3}{T_r^3}}{V_r} + \frac{a_4 + \frac{a_5}{T_r^2} + \frac{a_6}{T_r^3}}{V_r^2} + \frac{a_7 + \frac{a_8}{T_r^2} + \frac{a_9}{T_r^3}}{V_r^4} + + \frac{a_{10} + \frac{a_{11}}{T_r^2} + \frac{a_{12}}{T_r^3}}{V_r^5} + \frac{a_{13}}{T_r^3 V_r^2}\left(a_{14} + \frac{a_{15}}{V_r^2}\right)\left(exp\left(-\frac{a_{15}}{V_r^2}\right)\right) \quad \ldots\ldots\ldots \quad (A.6)$$

The values of constants a_1 through a_{15} are presented in Table A.3.

Table A.3. Parameters used in Eqs. (A.5) and (A.6) for CO_2 solubility

a_1	8.99E-02
a_2	-4.95E-01
a_3	4.78E-02
a_4	1.04E-02
a_5	-2.83E-02
a_6	9.50E-02
a_7	5.21E-04
a_8	-2.94E-04
a_9	-1.18E-03
a_{10}	-2.51E-05
a_{11}	8.93E-05
a_{12}	7.89E-05
a_{13}	-1.67E-02
a_{14}	1.40E+00
a_{15}	2.96E-02

In Eq. (A.6), P_r, T_r and V_r are reduced pressure, reduced temperature and reduced volume, respectively. They are defined as:

$$P_r = \frac{P}{P_c} \quad \ldots\ldots\ldots\

predictions. In this project, the model will be validated using measured data obtained under HPHT conditions.

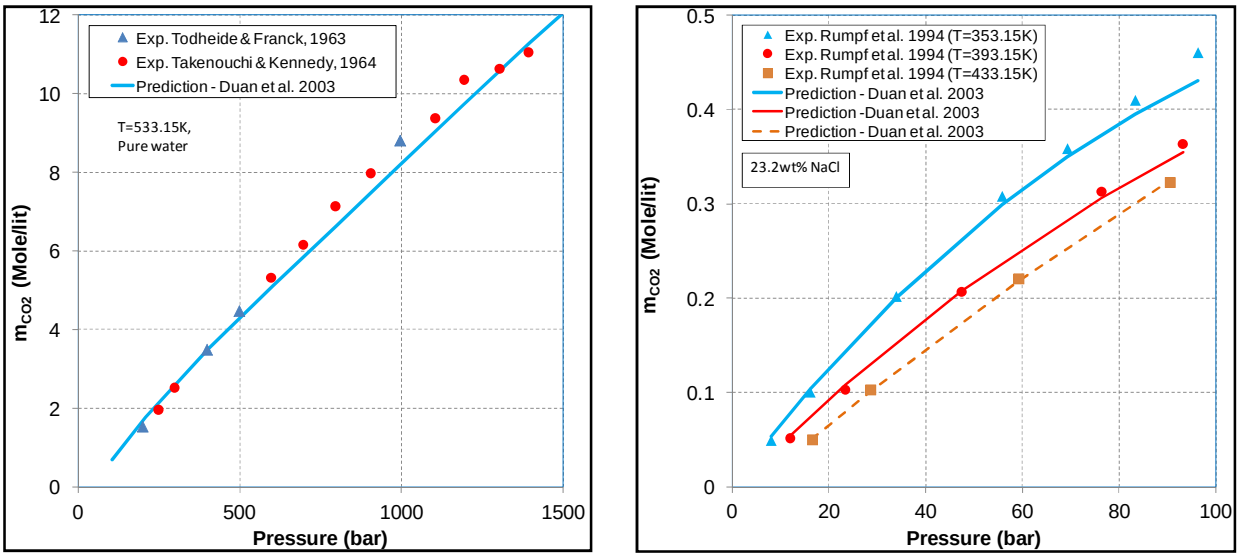

(a) (b)

Fig. A.1 Measured and prediction solubility of CO_2: a) Pure water at T=533.15 K; and b) Brine containing 23.2% NaCl at different temperatures

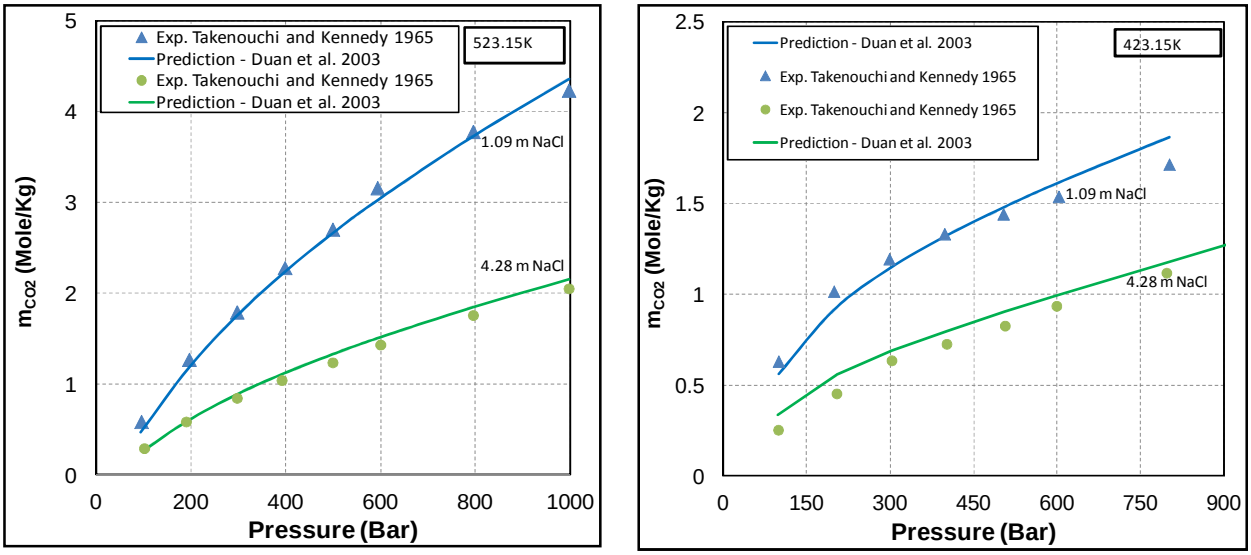

(a) (b)

Fig. A.2 Measured and prediction solubility of CO_2 at different brine concentrations: a) T=523.15K; and b) T=423.15K

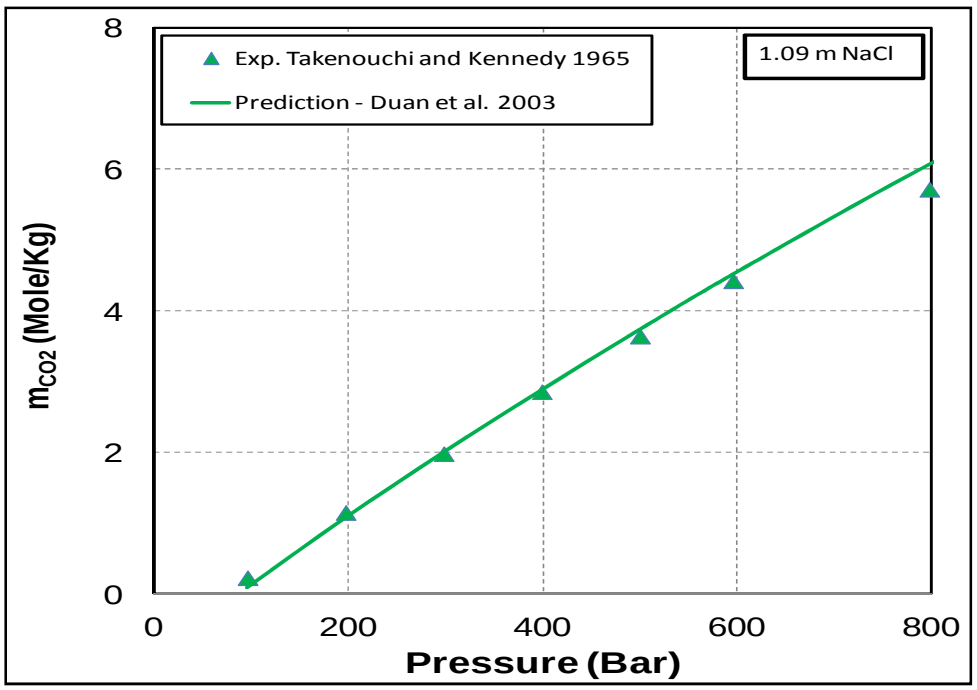

Fig. A.3 Comparison of experimental data and Duan's model predictions (T=573.15K)

A.2. Hydrogen Sulfide Solubility Model

Adopting the solubility model of CO_2, Duan et al. (2007) developed the following model for H_2S solubility prediction in pure water and brine solutions. The model is applicable for temperatures, pressures, and ionic strength ranging from 273 to 500 K, 0 to 200 bar and 0 to 6 m, respectively. The model is based on balancing CO_2 chemical potential in the liquid and gas phases. The potential can be written in terms of fugacity in the vapor phase and activity in the liquid phase.

$$ln\frac{y_{\mathrm{H2S}}P}{m_{\mathrm{H2S}}} = \frac{\mu^{1(0)}_{\mathrm{H2S}}}{RT} + ln\varphi_{\mathrm{H2S}} + \sum_c 2\lambda_{\mathrm{H2S}-c}m_c + \sum_a 2\lambda_{\mathrm{H2S}-a}m_a + \sum_c\sum_a \xi_{\mathrm{H2S}-c-a}m_c\, m_a \quad \text{.....(A.11)}$$

where y_{H2S} can be obtained using Eq. (A.2) and following the y_{CO2} calculation procedure, P is pressure in bar, m_{H2S} is H_2S solubility in mole/kg. $\frac{\mu^{1(0)}_{\mathrm{H2S}}}{RT}$, ξ and λ are dimensionless parameters determined as:

$$Par(T,P) = C_1 + C_2T + \frac{C_3}{T} + C_4T^2 + \frac{C_5}{680-T} + C_6P + \frac{C_7P}{680-T} + \frac{C_8P^2}{T^2} \quad \text{.....(A.12)}$$

φ_{H2S} is H_2S fugacity coefficient that can be obtained using Eq. (A.5) and Table A.5. The values of constants used in Eq. (A.4) are presented in Table A.4. In order to apply Eq. (A.5) for H_2S, values of the constants (a_1, a_2, a_3, …, and a_{15}) presented in Table A.5 should be used.

Table A.4 Interaction parameters for H_2S solubility in brine and pure water

T-P Coefficients	$\frac{\mu_{H_2S}^{1(0)}}{RT}$	λ_{H_2S-Na}	$\xi_{H_2S-Na-Cl}$
C_1	4.26E+01	8.50E-02	-1.08E-02
C_2	-8.63E-02	3.53E-05	
C_3	-6.08E+03	-1.59E+00	
C_4	6.87E-05		
C_5	-1.03E+02		
C_6	8.45E-04	1.19E-05	
C_7	-1.06E+00		
C_8	3.57E-03		0.00E+00

Table A.5. Parameters used in Eqs. (A.5) and (A.6) for H_2S solubility

a_1	5.24E-02
a_2	-2.75E-01
a_3	-9.68E-02
a_4	1.36E-02
a_5	-8.87E-02
a_6	4.11E-02
a_7	3.64E-04
a_8	2.27E-03
a_9	-7.70E-04
a_{10}	-2.20E-05
a_{11}	-1.17E-04
a_{12}	4.08E-05
a_{13}	5.76E-02
a_{14}	1.00E+00
a_{15}	6.00E-02

H_2S solubility data and Duan's model predictions are presented in Fig. A.4. Results show a satisfactory agreement between the experimental data and model predictions for different sets of temperature and pressure. Corrosion prediction performance of this model will be tested in this project using experimental data obtained under HPHT conditions.

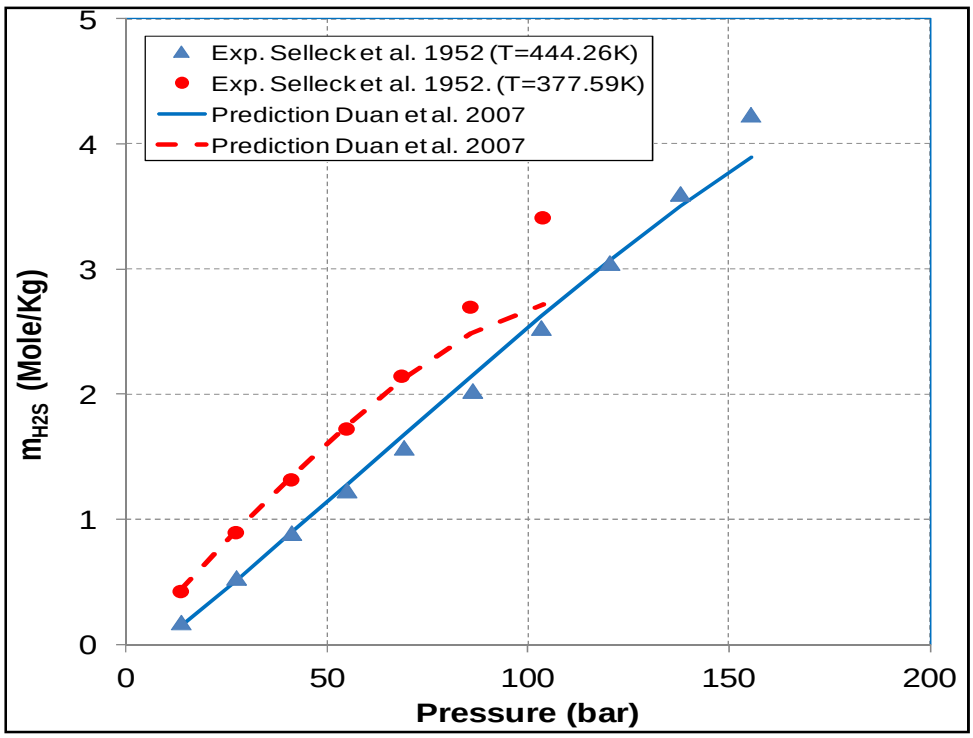

Fig. A.4 Measured and predicted solubility of H_2S

A.3. Methane Solubility Model

Methane has very limited solubility in water and brine solutions. A solubility model for CH_4 in pure water and brine solution was developed by Duan et al. (2007). The model is valid for wide range of temperature (273 to 573 K), pressure (0 to 2000 bar) and ionic strength (0 to 6 m). The model predicts the CH_4 solubility in aqueous solution establishing the balance between its chemical potential in the liquid phase and that in the gas phase. The potential can be written in terms of fugacity in the vapor phase and activity in the liquid phase.

$$ln\frac{y_{CH_4}P}{m_{CH_4}} = \frac{\mu^{1(0)}_{CH_4}}{RT} + ln\varphi_{CH_4} + \sum_c 2\lambda_{CH4-c}m_c + \sum_a 2\lambda_{CH4-a}m_a + \sum_c\sum_a \xi_{CH4-c-a}m_c\, m_a \quad \text{.....(A.13)}$$

where y_{CH_4} is methane concentration in the gas phase determined using Eq. (A.2). P is pressure in bar, m_{CH_4} is H_2S solubility in mole/kg. $\frac{\mu^{1(0)}_{CH_4}}{RT}$, ξ and λ are dimensionless parameters calculated as:

$$Par(T,P) = C_1 + C_2T + \frac{C_3}{T} + C_4T^2 + \frac{C_5}{T^2} + C_6P + C_7PT + \frac{C_8P}{T} + \frac{C_9P}{T^2} + C_{10}P^2T \quad \text{.....(A.14)}$$

The fugacity coefficient of methane φ_{CH4} is calculated using Eq. A.5 and Table A.3. The values of the solubility constants from C_1 through C_{10} are presented in Table A.6.

Table A.6 Interaction parameters for CH_4 solubility in brine and pure water

T-P Coefficients	$\frac{\mu_{CH_4}^{1(0)}}{RT}$	λ_{CH_4-Na}	$\xi_{CH_4-Na-Cl}$
C_1	8.31E+00	-8.12E-01	-2.99E-03
C_2	-7.28E-04	1.06E-03	
C_3	2.15E+03	1.89E+02	
C_4	-1.40E-05		
C_5	-6.67E+05		
C_6	7.70E-03	4.41E-05	
C_7	-5.03E-06		
C_8	-3.01E+00		
C_9	4.85E+02		
C_{10}		-4.68E-11	

The performance of the model is evaluated using published measurements. Experimental data presented in Fig. A.5 shows good agreement with model predictions. Further model validation will be carried out in the future when additional measurements are available.

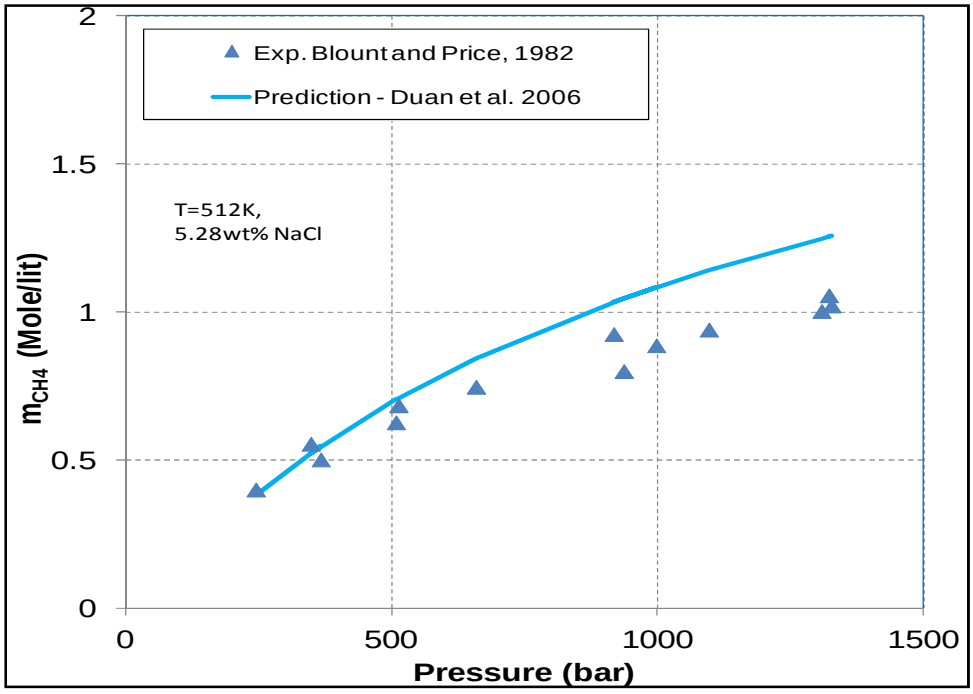

Fig. A.5 Comparison between experimental data and Duan's model

The solubility models of CO_2, H_2S, and CH_4 presented in previous sections were used to predict the amount dissolved gases under anticipated experimental conditions. Figure A.6

shows the solubility of major components of sour gas (CO_2, H_2S, and CH_4) in 2% NaCl at temperature of 350ºF and different pressures. Hydrogen sulfide has the highest solubility.

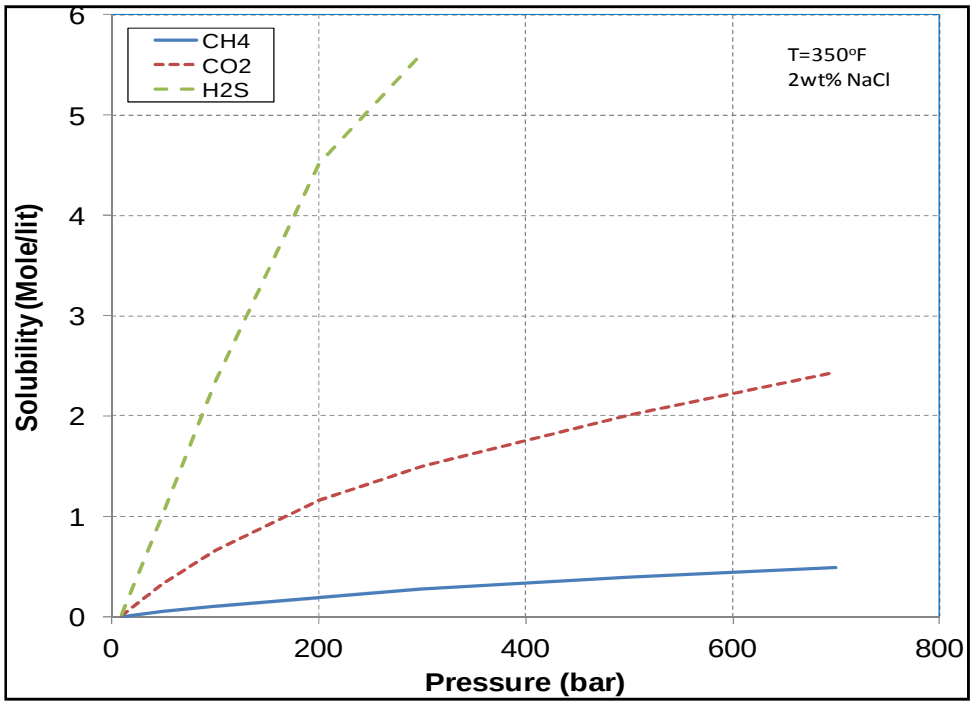

Fig. A.6 CO_2, H_2S, and CH_4 solubility prediction at temperature of 350ºF, 2wt% NaCl and different pressures

A.4. Mutual Interactions of Different Gases and Their Effects on Solubility

Solubility of mixed gas is affected by mutual interactions of the components. Figures from A.7 through A.9 show the comparison between experimental data of mixed system (i.e. CO_2, H_2S, and CH_4) and predicted solubility of pure CO_2, H_2S, and CH_4 gases. Solubility measurements are smaller than the predictions, which mean that mutual interactions tend to reduce the solubility of highly soluble components. Therefore, a separate model is needed to predict solubility of mixed gases.

Li and Firoozabadi (2009) and Zirrahi et al. (2012) proposed two different models for predicting mutual solubility of mixed gas. Research is in progress to utilize one of these models for predicting mutual solubility of mixed gas and subsequently corrosion rate in sour gas saturated brine systems under HPHT conditions.

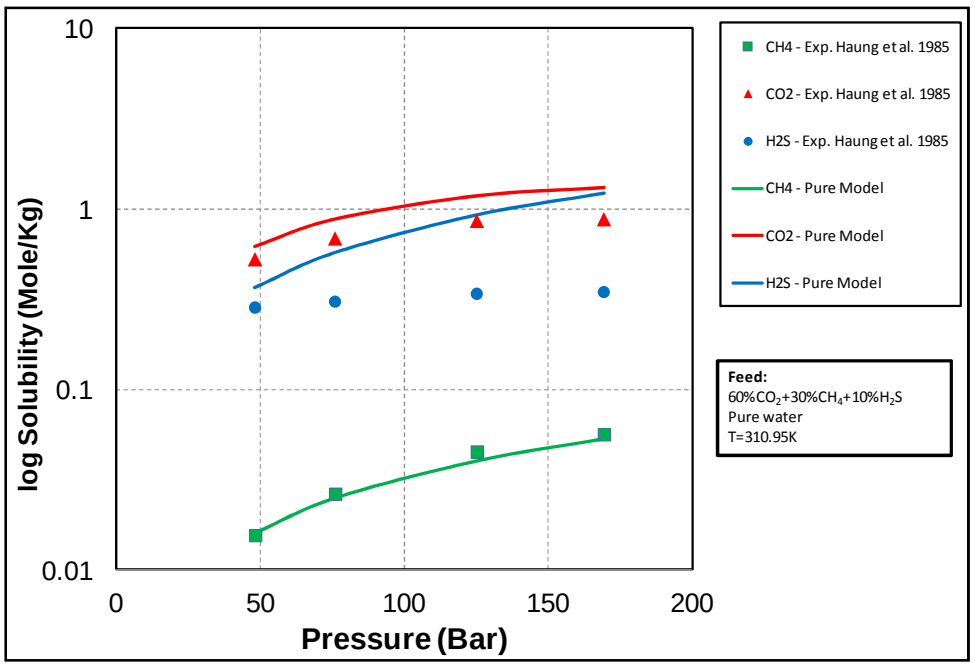

Fig. A.7 Measured and predicted solubility of mixed gas (60%CO_2, 10%H_2S, and 30%CH_4) at 310 K

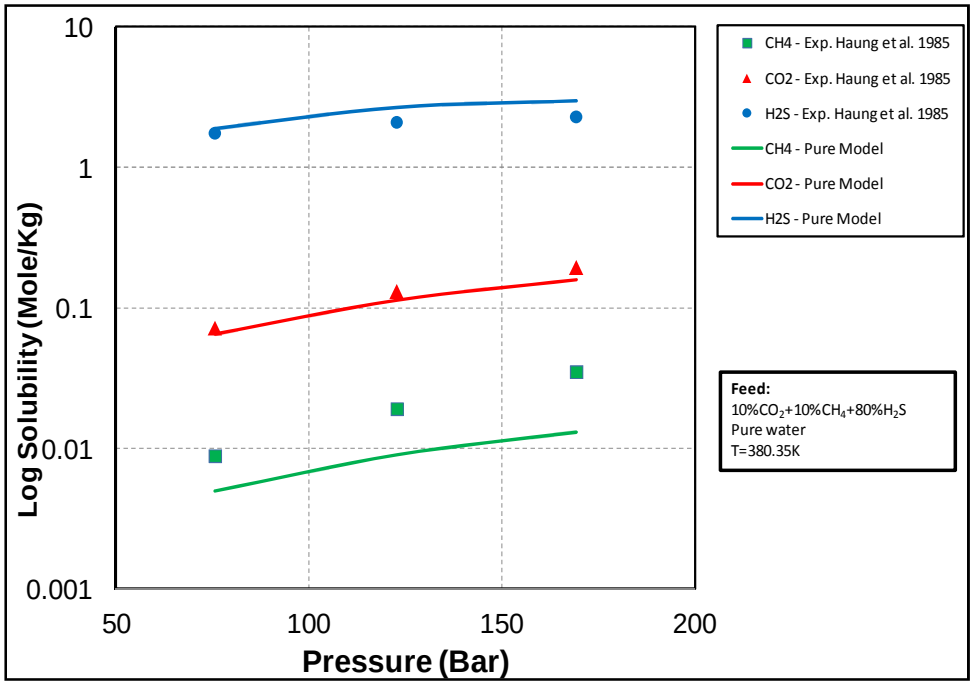

Fig. A.8 Measured and predicted solubility of mixed gas (10%CO_2, 80%H_2S, and 10%CH_4) at 380 K

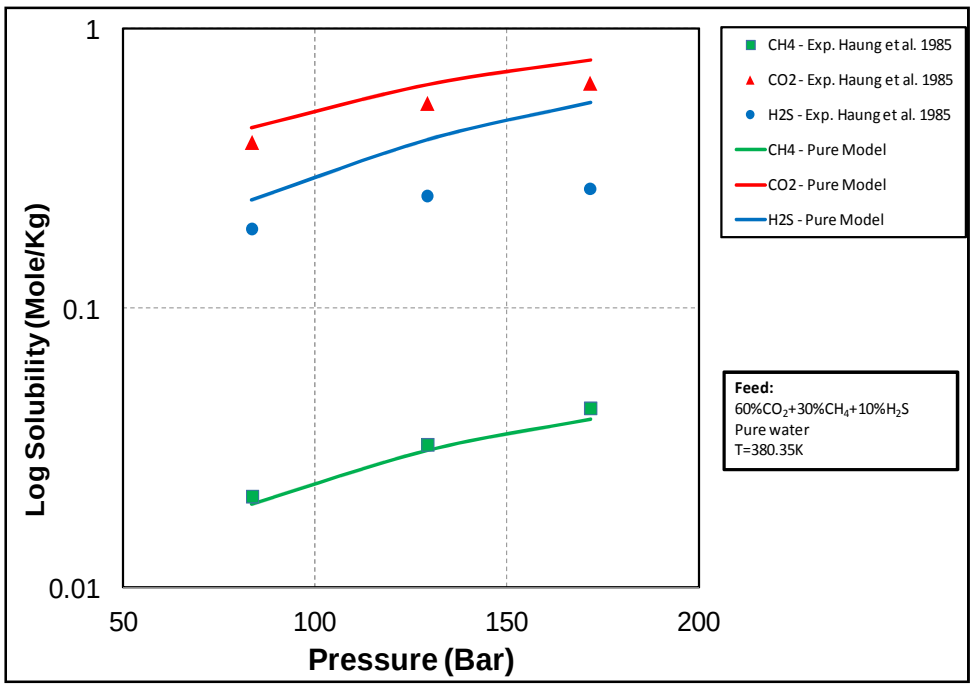

Fig. A.9 Measured and predicted solubility of mixed gas (60%CO_2, 10%H_2S, and 30%CH_4) at 380 K

Project Title: Effect of H_2S and CO_2 in HPHT Wells on Tubulars and Cement

Report Type: Monthly Report

Report #: 12

Reporting Period: August 22nd, 2012 to September 21st, 2012

Authors:

Ramadan Ahmed, Principal Investigator

Subhash Shah, Co-Principal Investigator

Samuel Osisanya, Co-Principal Investigator

Shokrollah Hassani, Postdoctoral Research Associate

Rida Elgaddafi, Research Assistant

Omosebi, Omotayo A., Research Assistant

Himanshu Maheshwari, Research Assistant

Adarsh Naidu, Research Assistant

Aman Srivastvava, Research Assistant

Prepared under BSEE Project # E12PC00035

by

THE UNIVERSITY OF OKLAHOMA

Oct. 22, 2012

1. Summary of Accomplishments

This monthly report presents the progress made during the project period August 22, 2012 – September 21, 2012. An aging experiment conducted in CH_4 saturated 2% brine was completed. Cement cores and bonding specimens made of Class H and G with and without fly ash were aged for 14 and 28 days at temperature of 350ºF and pressure of about 6000 psi. Porosity, permeability, compressive strength, and bonding strength of the samples were measured before and after aging. Beside this, a new aging experiment in 2% brine solution saturated with acidic gas (90%CH_4-10%CO_2) has been started.

Effects of different additives on cement properties has been reviewed during this research period and new cement formulations have been prepared for preliminary testing of slurry characteristics. Components for these new cement formulations will be acquired in coming weeks and we begin the preliminary experiments to evaluate physical properties of the cements. New cement samples, which fulfill the required rheological and mechanical properties for oil and gas well applications will be selected for aging experiments. More details are presented in Appendix A.

Theoretical and modeling studies on tubular degradation are in progress. A new mixture gas solubility model for CO_2, H_2S, and CH_4 is utilized to predict the gas solubility. Mixture gas solubility predictions are compared with experimental data and predictions of pure gas solubility models. In continuation of our previous work on theoretical and modeling studies on tubular degradation, corrosion models are classified into two main categories: CO_2 and H_2S/CO_2 corrosion models. When partial pressure of H_2S is higher than a critical limit, a layer of iron sulfide forms on the surface and corrosion reaction is controlled by diffusion of ions through the layer. A report summarizing the literature survey and modeling study results is presented in Appendix B.

Our plan for the coming weeks is continuing the aging experiments in 90%CH_4-10%CO_2 saturated brine solution. After aging, physical properties of the cores will be measured. Beside this, theoretical and modeling studies on tubular corrosion will be continued. In addition, the ongoing corrosion setup development activities will be continued. Designs of some of the components will be finalized in the coming weeks. We are also continuing our investigation on new cement formulations.

2. Overall Project Progress

2.1 Theoretical Studies (Task 1)

As a part of this project, different cement additives will be added to the class H and G cement to improve the acid resistance under high-pressure high-temperature (HPHT) conditions. Therefore, in this research period, effects of different additives on cement properties have been reviewed. Based on the review, certain additives have been chosen to be used in the study. Subsequently, new cement formulations have been developed for high temperature high pressure CO_2/H_2S saturated brine environments. Based on their method of protection, the additives, which have been chosen, are categorized as:

i. Nonreactive components: These additives react chemically with CO_2 and H_2S to protect the cement
ii. Sealing components: These additives lower the porosity and permeability of the cement thereby reducing the penetration of the CO_2 and H_2S

The above classification helps in identifying the key features of the additive and cement. More details are presented in Appendix A.

Rheological (viscosity and thickening time), fluid loss and mechanical properties (i.e. compressive strength and shear bonding strength) of the cement will be measured prior to aging the cores of the new cements. After testing, samples, with the desired rheological and mechanical properties will be selected and aged under high-pressure high-temperature acidic environment.

Theoretical and modeling studies on tubular degradation are in progress. Previously, different HPHT models for solubility of CO_2, H_2S, and CH_4 were reviewed. However, pure gas solubility models over-predict the solubility due to molecular interactions of different gases. During this reporting period, a new mixture gas solubility model for CO_2, H_2S, and CH_4 has been studied and used to predict the gas solubility. Model predictions are compared with lab measurements and predictions of pure gas solubility models.

In continuation of our previous investigations on corrosion modeling, two (pure CO_2 corrosion and H_2S/CO_2 corrosion) corrosion modeling approaches have been considered. When partial pressure of H_2S is higher than a critical limit, a layer of iron sulfide forms on the surface and corrosion reaction is controlled by diffusion of ions through the layer. Otherwise,

the corrosion is controlled by CO_2 and a pure CO_2 model should be applied to determine the corrosion rate. At present, theoretical and modeling studies on corrosion of tubular are in progress to develop models for predicting the CO_2 and H_2S corrosion rates under HPHT conditions.

2.2 Experimental Studies on Degradation of Cement (Task 2)

Aging experiments were continued. Aging Experiment # 2 was completed after 28 days. The test was conducted at 6,000 psi, 350ºF, and 2% NaCl solution saturated with methane. Results of the first part of this test (14 days aging test) were reported earlier in progress Report # 11. In this report, porosity, permeability, compressive strength, and density of four different types of cement samples (i.e. Class H and G with Silica, Class H and G with silica and fly ash) without aging and after 14 and 28 days of aging were compared. All the cement samples with fly ash were broken after 28 days of aging. Fly ash reduces the porosity and permeability of cement while increasing the bonding strength. However, it makes the cement more susceptible for pressure and temperature induced cracking which occurs under mechanically unconfined conditions. Aging for 14 days at 6,000 psi and 350ºF in 2% brine saturated with methane reduced the porosity and permeability of the cement due to additional hydration. No chemical degradation was expected because there was no corrosive gas in the system. The only expected degradation was thermal retrogression, which made the fly ash containing cement samples to crack. The 28-day aging didn't make a considerable change in porosity and permeability in comparison with the 14-day aging since the samples were fully hydrated and no additional hydration was possible.

2.2.1 Results of Experiment # 2

Experiment # 2 was completed after 28 days of aging at 6,000 psi and 350ºF in 2% NaCl solution saturated with methane. All the cement samples with fly ash were cracked and broken after 28 days of aging. Fly ash reduces the porosity, permeability, and increases the bonding strength of the cement samples but it makes the cement more susceptible to cracking.

2.2.1.1 Confining Compressive Strength Measurements

Comparison of compressive strength of four different types of cement samples (i.e. GS, HS, GSF, and HSF) shows (Fig. 1) aging for 14 and 28 days didn't have a considerable effect. The change in compressive strength resulting from the aging was in the range of the experimental error.

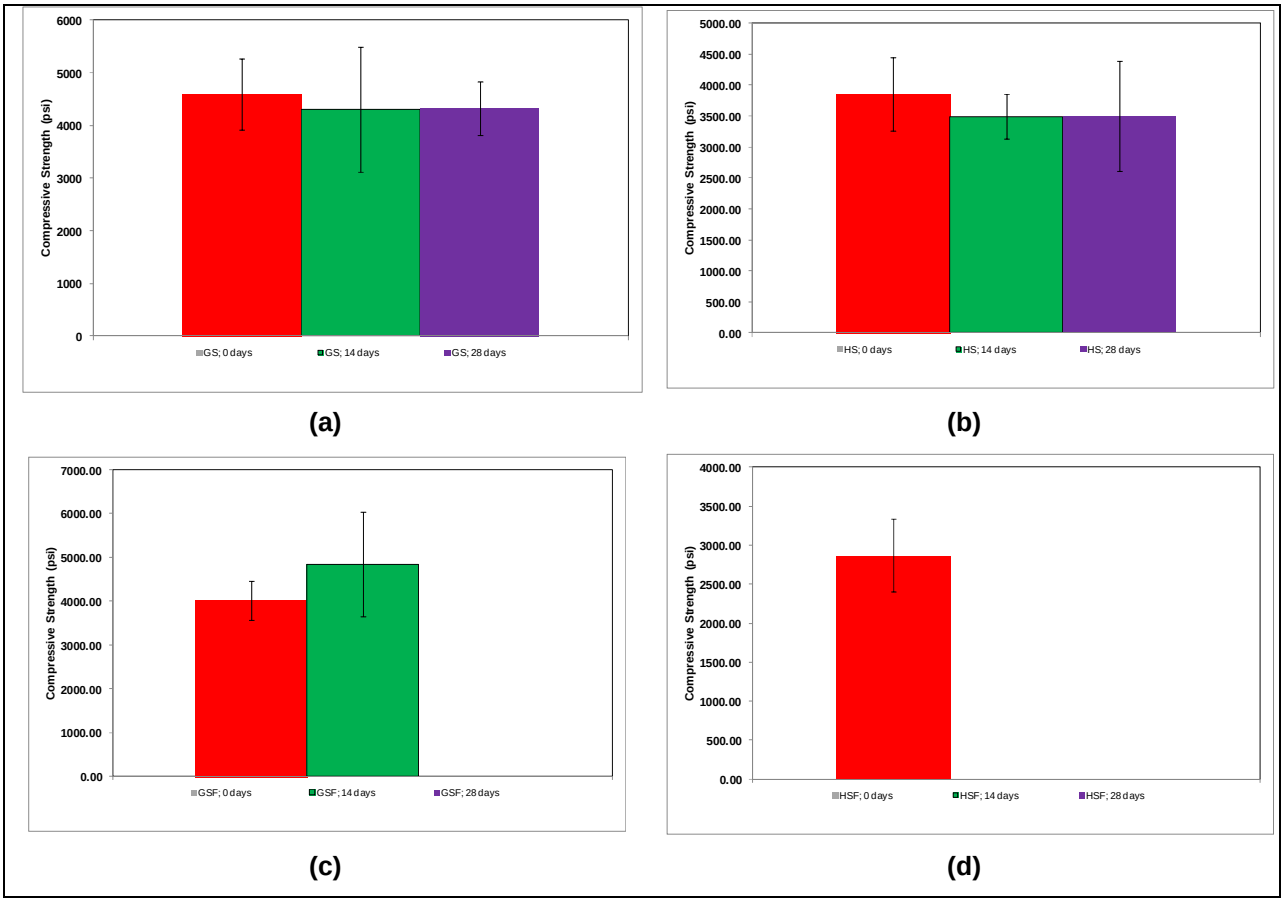

Fig. 1 Comparison of compressive strength of four different types of cement samples: a) GS; b) HS; c) GSF; and d) HSF unaged

2.2.1.2 Porosity and Permeability Measurements

Porosity measurements of the four different types of aged and unaged cement cores are presented in Fig. 2. Permeability measurements obtained from the samples are shown in Fig. 3. Fourteen-days aging reduced the porosity and permeability of the cores. One possible explanation for the porosity reduction could be additional cement hydration that occurs at high temperatures (350ºF), which may diminish free unhydrated water content and consequently reduces the porosity and permeability. Aging was carried out under non-acidic environment and no measurable degradation was observed. However, porosity and permeability of the class G cement with silica (GS) first slightly decreased after 14 days of aging and then increased (Figs. 2a and 3a).

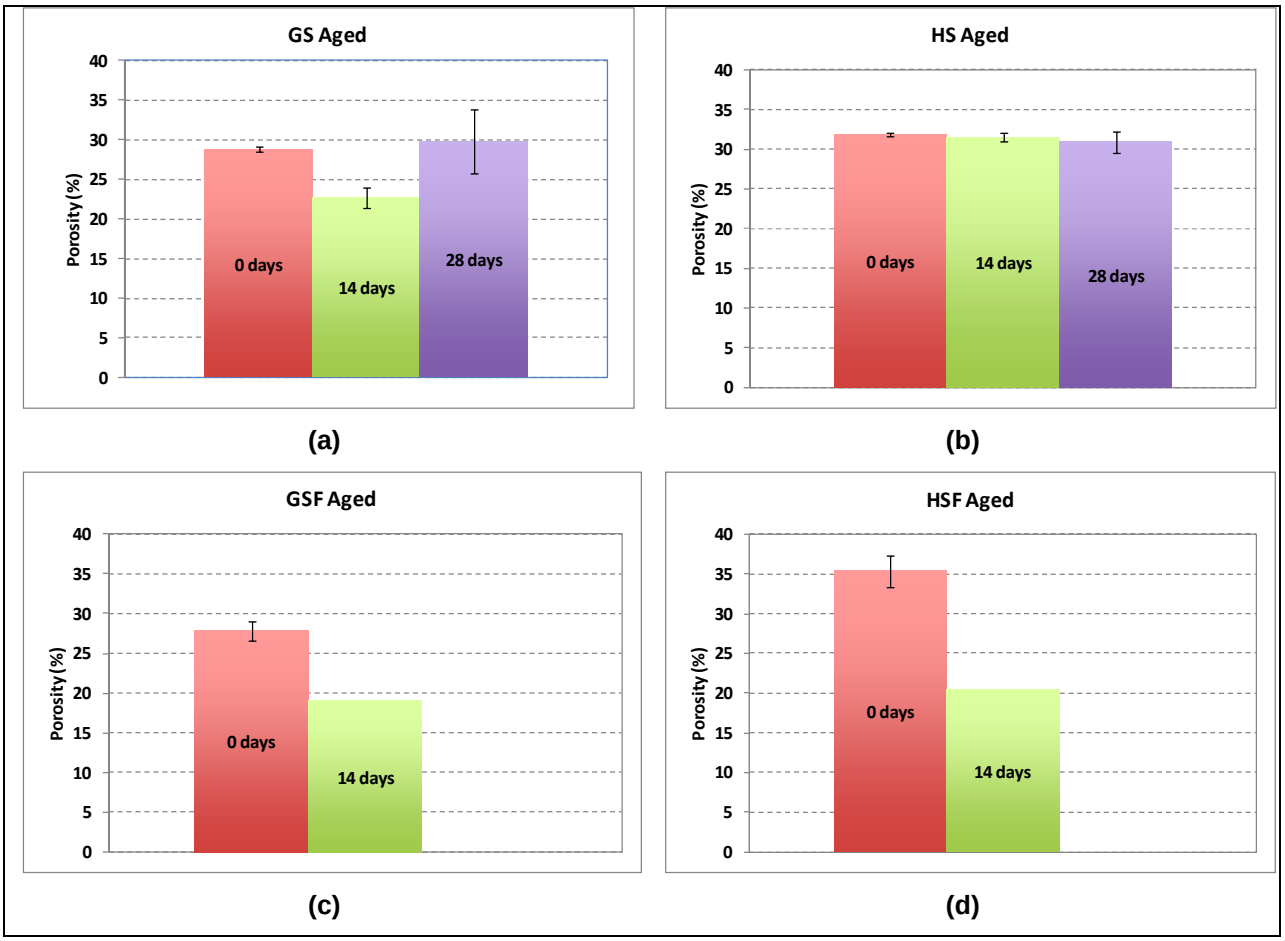

Fig. 2 Comparison of porosity of four different types of cement cores (i.e. (a) GS, (b) HS, (c) GSF, and (d) HSF) unaged and aged at 6,000 psi and 350ºF in 2% brine saturated with methane

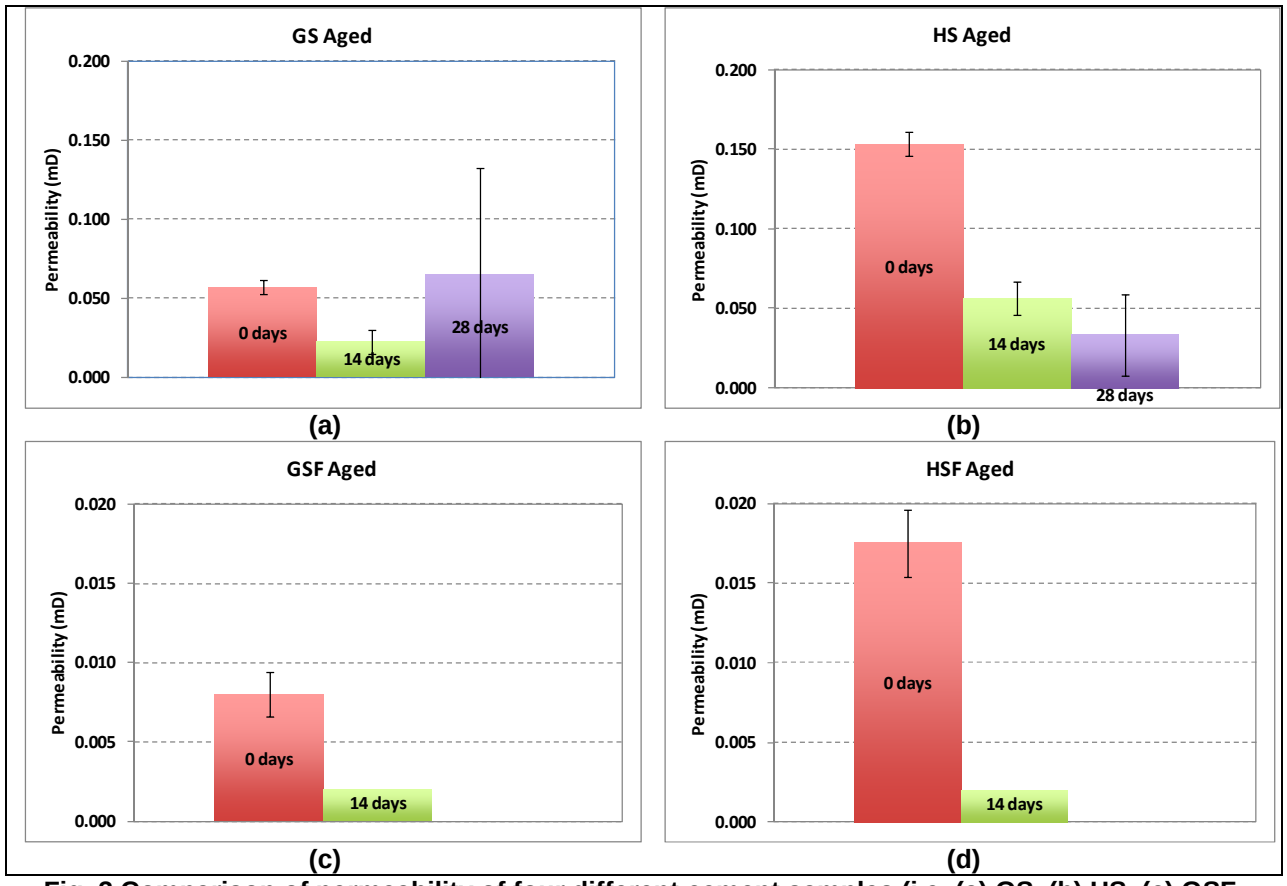

Fig. 3 Comparison of permeability of four different cement samples (i.e. (a) GS, (b) HS, (c) GSF, and (d) HSF) unaged and aged at 6,000 psi and 350ºF in 2% brine saturated with methane

2.2.1.3 Matrix Density

Matrix density of aged and unaged cement cores were determined using porosity, volume, and weight measurements. Results are presented in Fig. 4. The matrix density represents the density of cement structure without the pores. Aging for 14 and 28 days slightly reduced Class H and Class G cement matrix density. This trend can be explained by more hydration happening at high temperature condition (350ºF). Hydrated cement has lower density in compare with unhydrated cement because specific density of water is lower than cement. For cement samples with fly ash, change in cement matrix density after aging is minimal (the range of experimental error). However, they show a different trend.

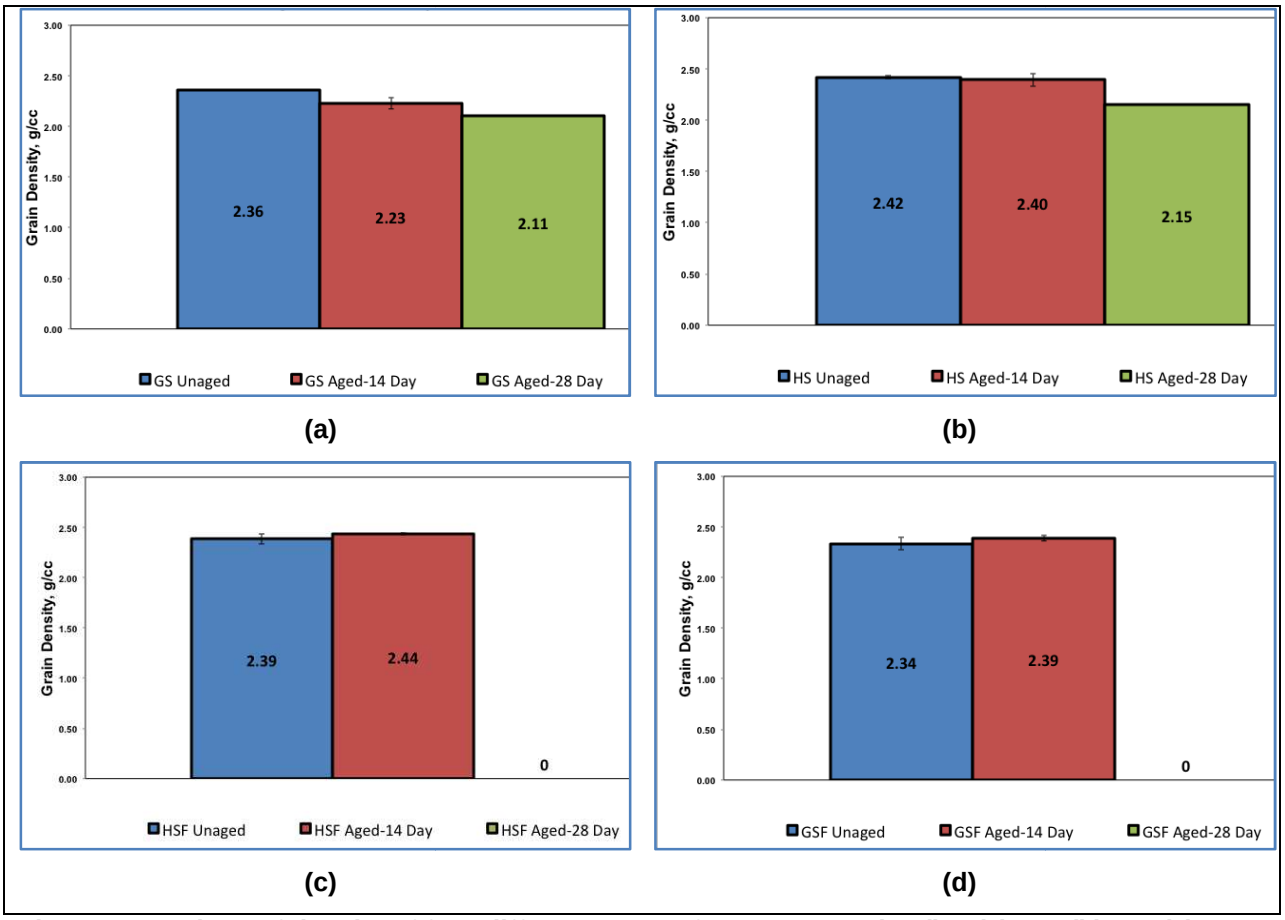

Fig. 4 Comparison of density of four different types of cement samples (i.e. (a) GS, (b) HS, (c) GSF, and (d) HSF) unaged and aged at 6,000 psi and 350ºF in 2% brine saturated with methane

2.2.2 Experiment # 2 – Repeating the 14-day Aging

Half of the cement cores in Experiment # 2 were removed after 14 days of aging and replaced by new cores. However, the new cores were 2-inch long instead of 1½-inch. Porosity, permeability, compressive strength, and density of the cores were measured and the results are presented here.

2.2.2.1 Confining Compressive Strength Measurements

Confined compressive strength of the cores after 14 days of aging in CH_4-Brine system at temperature of 350^{o}F and pressure of 6,000 psi are shown in Fig. 5. Class H cement samples with fly ash were cracked after 14 days of aging; however, class G cement samples did not show visible cracks. For Class G cement, the addition of fly ash increased the compressive strength. Previous experimental data also showed that fly ash improves the compressive strength of cement samples. Class H cement showed lower compressive strength than Class G

cement. These experimental results are not compared with previous experimental data because the new specimens were prepared following slightly different procedure.

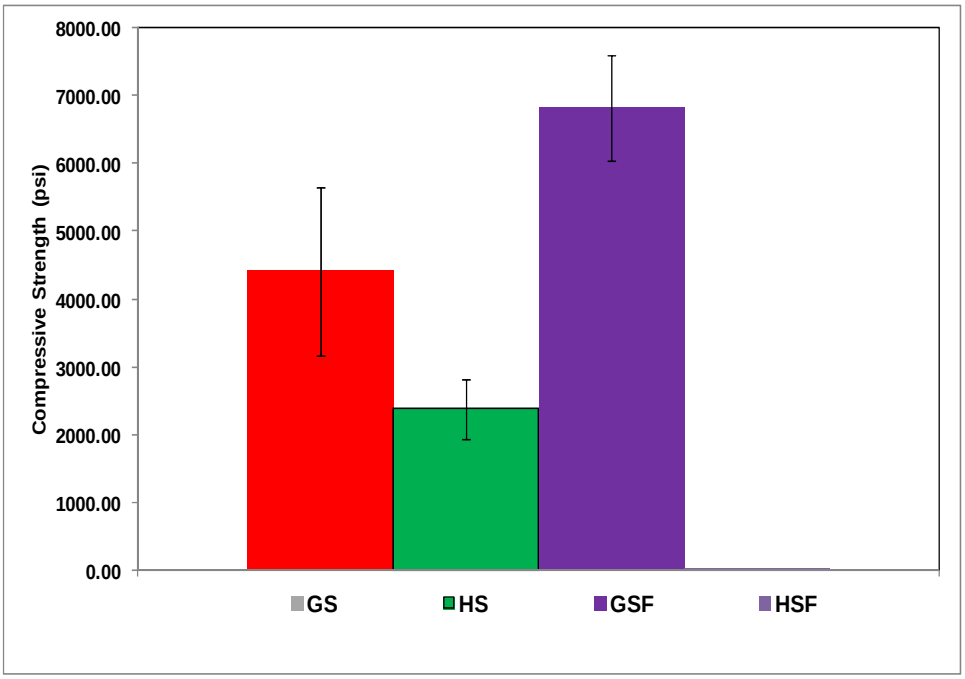

Fig. 5 Compressive strength measurements data after 14 days of aging in CH_4-Brine system at temperature of 350^{o}F and pressure of 6000 psi

2.2.2.2 Porosity and Permeability Measurements

Porosity and permeability of cement cores after 14 days of aging are shown in Figs. 6 and 7. As it mentioned earlier, the new cores were longer than the original cores. As a result, sample preparation needed slightly higher slurry volume. This minor change in slurry volume affected the agitation performance of the mixer and resulted in higher cement core permeability. Cores with 1.5 inch length will be used in the future to have identical cement sample preparation procedure. The results of this aging experiment will not be compared with the previous or future measurements. Samples with fly ash showed lower porosity and permeability compared with samples without fly ash.

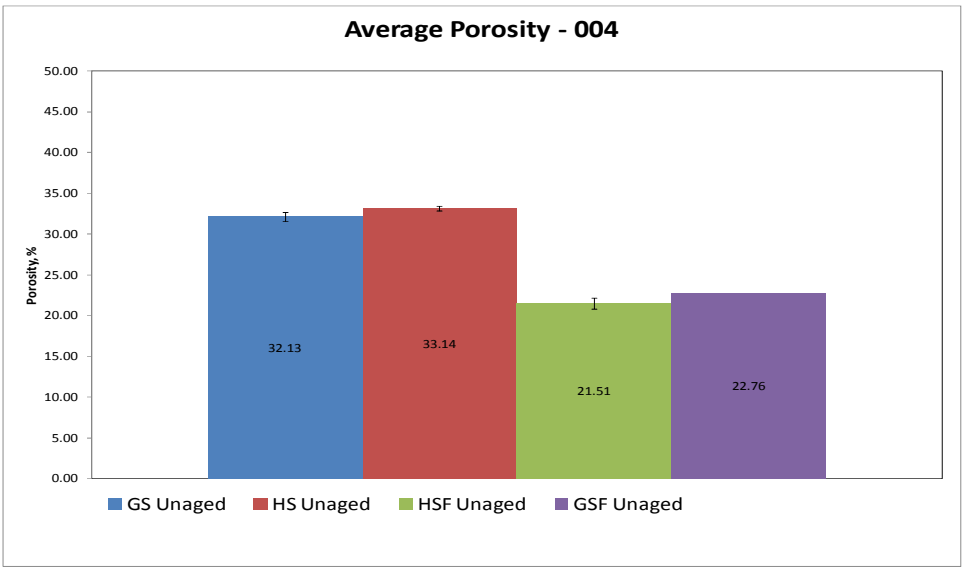

Fig. 6 Porosity measurements data after 14 days of aging in CH_4-Brine system at temperature of 350^{o}F and pressure of 6000 psi

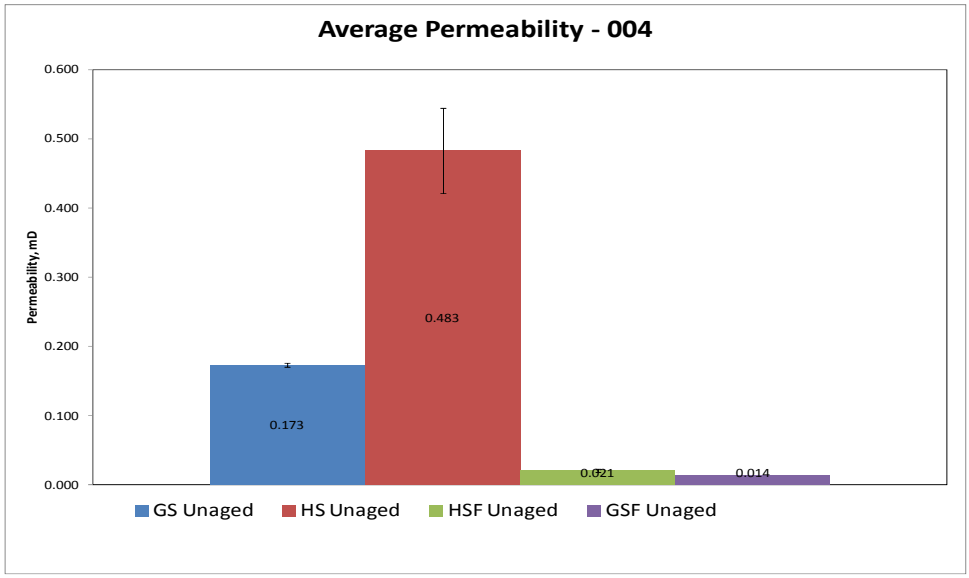

Fig. 7 Permeability measurements data after 14 days of aging in CH_4-Brine system at temperature of 350^{o}F and pressure of 6000 psi

2.3 Experimental Studies on Corrosion of Tubulars (Task 3)

Design and selection of major components of corrosion test set up (stress cracking corrosion testing cell, injection cylinders, potentiostat, and magnetic drive required for corrosion cell) have been finalized. Purchase orders of these items have been completed. There are some

remaining designs, which need to be finalized. Preliminary corrosion experiments will be started when the development of the experimental setups is completed.

3. Problems Encountered

Major problem encountered during this reporting period was sample preparation technique. The intention of having 2-inch long cores was to maintain identical core geometry with most of the previous studies. However, the new 2-inch cement cores showed higher permeability than previously tested 1.5-inch cores. This difference in permeability was related to the amount of slurry used in the preparation of the cores. Slightly larger volume of slurry was mixed to prepare 2-inch cores, which caused to lower the performance of the cement mixer and consequently increased the permeability of the cores. Hence, future tests will be carried out with 1.5-inch cores.

4. Planned Activities

- Continue aging experiments with brine-CO_2-CH_4 system.
- Continue theoretical and modeling studies on tubular degradation.
- Continue designing and acquisition of components of tubular corrosion testing setups.

5. Project Expenditures

This section presents the project expenses during the months of September (Table 1) and the cumulative expenditures.

Table 1 Current and cumulative expenditures, September, 2012

No.	Budget Categories	Current Expenses	Cumulative Expenses
1	Salaries & Wages	$9,032.61	$114,293.34
2	Fringe Benefits	$1,003.39	$29,803.15
3	Project Materials	$1,472.33	$42,157.56
4	Travel	$123.77	$1,333.09
5	Conference Expenses	$0.00	$0.00
6	Other Direct Costs	$0.00	$305.38
7	Equipment	$0.00	$141,502.67
8	Space Rental	$0.00	$0.00
9	Indirect Cost	$5,816.06	$93,946.30
10	**Total**	**$17,448.16**	**$423,341.49**

Nomenclature

a	intermolecular attraction
$a_{H2S,vap}$	activity of H_2S in gas phase
$a_{ij}{}^{P}$	interaction parameter
a^c	conventional mixing rule
a^p	intermolecular interaction term due to the polarity of the molecules
a_{H2O}	activity of water
$a_{CO2,\ vap}$	activity of CO_2 in gas phase
b	intermolecular repulsion
H_i	Henry's constant
P	total pressure
P_c	critical pressure
P^r	reference pressure
Y_i	mole fraction of component i in the gas phase
γ_i	activity coefficient in mole fraction scale
x_i	mole fraction of component I in the aqueous phase
V_i^{∞}	partial molar volume of component i
R	universal gas constant
T	absolute temperature
T_c	critical temperature
K_{ij}	binary parameter
Z	compressibility factor
$K_{FeS/FeCO3}$	equilibrium constant between FeS and $FeCO_3$
$K_{CO2,aq/CO2,vap}$	equilibrium constant between CO_2 in liquid and gas phase
$K_{H2CO3,aq}$	equilibrium constant for carbonic acid formation
$K_{H2S,aq/H2S,vap}$	equilibrium constant between H_2S in liquid and gas phase
$K_{H2S,aq/H2S,vap}$	reaction rate constant for H_2S dissolution reaction
ppH_2S_{vap}	partial pressure of H_2S
γ_{H2S} I	fugacity coefficient of H_2S

Greek Letters

φ	Fugacity coefficient
ω	Acentric factor

Acronyms

HOAP	Hydroxyapatite additive sample
HSHO	Slurry with H Class Cement, Silica Flour and HOAP
HSFHO	Slurry with H Class Cement with Silica Flour, Fly Ash and HOAP
HS	Class H Cement with silica flour
HSF	Class H Cement with silica flour and fly ash
GSF	Class G Cement with silica flour and fly ash
GS	Class G Cement with silica flour
GSFHO	Slurry with G Class Cement with Silica Flour, Fly Ash and HOAP
GSHO	Slurry with G Class Cement, Silica Flour and HOAP

References

Anjuman S. 2011, “Investigation on Rheology of Oil Well Cement Slurries”; PhD Thesis, University of Western Ontario, Canada.

Benge, G., 2009, “Improving well bore seal integrity in CO2 injection wells”, Energy Procedia 1, 3253-3529.

Berard, B., Hernández, R., and Nguyen, H., 2009, “Foamed Calcium Aluminate Cement Phosphate Cement Enables Drilling and Cementation of California Geothermal Wells”, SPE 120845.

Buntoro, A., Rubiandini, R. (2001); “The Effect of Neat Magnesium Oxide (MgO) as Expanding Additive With Burning Temperature 1200^{o}C and 1300^{o}C on Cement Shear Bond Strength at High Pressure and Temperature”; Proceeding of the 5th Inaga Annual Scientific Conference & Exhibitions, Yogyakarta, March 7 – 10.

Duan, Z., Sun, R., Liu, R., and Zhu, C., 2007. “Accurate Thermodynamic Model for the Calculation of H_2S Solubility in Pure Water and Brines”, Energy & Fuels, 21, pp.2056-2065.

Duan, Z., Sun, R., 2003. “An improved model calculating CO_2 solubility in pure water and aqueous NaCl solutions from 273 to 533 K and from 0 to 2000 bar”, Chemical Geology 193, pp. 257–271.

Duan Z., and Mao, S., 2006. “A thermodynamic model for calculating methane solubility, density and gas phase composition of methane-bearing aqueous fluids from 273 to 523K and from 1 to 2000 bar”. Geochimica et Cosmochimica Acta 70 3369–3386.

Daou, F., and Plot, B., 2009, “Cement Slurry Performance and Set-Cement Properties vs. Mircosilica Densification”, SPE Drilling & Completion.

Duguid A., 2009. “An estimate of the time to degrade the cement sheath in a well exposed to carbonate brine”, Energy Procedia 1, 3181-3188.

Dunlop, A.K., Hassell, H.L., and Rhodes, P.R., 1983. “Fundamental Considerations in Sweet Gas Well Corrosion”, Corrosion/83, Anaheim, California, Paper 46.

Ghofrani, R. and Plack, H., 1993, “CaO- and/ or MgO- Swelling Cements: A Key for Providing a Better Annular Sealing?”, SPE/ IADC 25697.

Gouédard, V.B., Rimmelé, G., Goffé, B., and Porcherie, O., 2006, “Mitigation Strategies for the risk of CO2 migration through wellbores”, IADC/ SPE – 98924.

Gray, M. L., Soong, Y., Champagne, K. J., Baltrus, J., Stevens, R. W. Toochinda, P., and Chuang, S. S. C. 2004, “CO_2 capture by amine-enriched fly ash carbon sorbents”, Separation and Purification Technology 35, 31-36.

Hashimoto, H., Komaki, E., Hayashi, F. and Uematsu, T. 1980, “Partial Decomposition of Dolomite in CO_2”, Journal of Solid State Chemistry 33, 181-188.

Hawthorne, S.B., Miller, D.J., Holubnyak, Y., Harju, J.A., Barbara, Kutchko, B., Strazisar, B.R., 2011, “Experimental investigations of the effects of acid gas (H_2S/CO_2) exposure under geological sequestration conditions”; Energy Procedia 4 5259–5266.

Huang, S.S.S., Leu, A.D., Ng, H.J., Robinson, D.B., 1985. “The Phase Behavior of Two Mixtures of Methane, Carbon Dioxide, Hydrogen Sulfide, and Water”, Fluid Phase Equilibr. 19, pp. 21–32.

Jacquemet, N., Pironon, J., and Caroli, E. 2005, “A New Experiment Procedure for Simulation of H_2S +CO_2 Geological Survey”, Oil & Gas Science Technology- Rev. IFP, Vol. 60, No. 1, pp. 193-206.

Jones, R.R. and Carpenter, A.B. 1991, “New Latex, Expanding Thixotropic Cement Systems Improve Job Performance and Reduce Costs”, SPE 21010.

Kirlov, Z., Loncaric, B., and Miksa, Z. 2000, “Investigation of a Long-Term Cement Deterioration Under a High-Temperature, Sour Gas Downhole Environment”, SPE 58771.

Kutchko, B., Strazisar, B., Dzombak, D., and Lowry, G. 2007, “Degradation of Well Cement by CO_2 under Geologic Sequestration Conditions”, Environ. Sci. Technol., 41, 4787-4792

Lecolier, E., Rivereau, A., Ferrer, N., Audibert, A., and Longaygue, X., 2006, “Durability of Oilwell Cement Formulations Aged in H_2S Containing Fluids”, IADC/ SPE 99105.

Lecolier, E., Rivereau, A., Ferrer, N., Audibert, A. and Longaygue, X. 2008, “Study of New Solutions for Acid-Resistant Cements”, IADC/ SPE 116066.

Lewis, S., Morgan, R., Gordon, C., and Santra, A., 2009. (Halliburton Energy Services Inc.); “Salt Water Stable Latex Cement Slurries”; US Patent 7576042.

Mueller, D.T. and Dillenbeck, R.L., 1991, “The Versatility of Silica Fume as an Oilwell Cement Admixture”, SPE 21688.

Rahman, R.A., and Chong, A., 1997, “Cementing Multilateral Well With Latex Cement”, SPE/ IADC 37623.

Reddy, B. R., Brothers, L.E., and Palmer, A.V., 2004. (Halliburton Energy Services Inc.); “Methods of cementing high temperature wells and cement compositions”; US Patent 6796378.

Reddy, B. R., Lewis, S. J., Santra, A., Palmer, A. V., 2010. (Halliburton Energy Services Inc.); “Wellbore Sealant Compositions Containing Cationic Latexes”, US Patent 7687440.

Rubiandini, R., Siregar, S., Suhascaryo, N., and Efrial, D., 2005, “The Effect of CaO and MgO as Expanding Additives to Improve Cement Isolation Strength under HPHT Exposure”, PROC. ITB Eng. Science Vol. 37 B, No. 1, 29-48.

Santra, A., Reddy, B. R., Liang F., and Fitzgerald, R., 2009. “Reaction of Portland cement at Downhole Conditions and the role of Pozzolanic Supplements”, SPE 121103.

Santra A., and Sweatman, R., 2010, “Understanding the Long-Term Chemical and Mechanical Integrity of Cement in a CCS Environment”, Energy Procedia, Volume 4, 2011, Pages 5243–5250.

Sasaoka, E., 1994, “Characterization of Reaction between Zinc Oxide and Hydrogen Sulfide”, Energy & Fuels, 8, 1100-1105.

Sayyadnejad, M. A., Ghaffarian, H. R., and Saeidi, M. 2008, “Removal of hydrogen sulfide by zinc oxide nanoparticles in drilling fluid”, Int. J. Environ. Sci. Tech., 5 (4), 565-569.

Shadizadeh, S. R., Kholghi, M., and Salehi Kassaei, M. H. 2010, “Experimental Investigation of Silica Fume as a Cement Extender for Liner Cementing in Iranian Oil/Gas Wells”, Iranian Journal of Chemical Engineering, Vol. 7, No. 1 (Winter), IAChE.

Smith, S., and Wright, E.J., 1994. Prediction of minimum H_2S levels required for slightly sour corrosion systems, NACE International corrosion conference, Paper 11, Baltimore, MD.

Smith, S., and Pacheco, 2002. Prediction of Corrosion in Slightly Sour systems, NACE International Corrosion conference, Paper No. 02241.

Smith, S., Brown, B., Sun, W., 2011. Corrosion at higher H_2S concentrations and moderate temperatures, NACE International Corrosion conference, Paper No. 11081.

Strazisar, B., Kutchko, B., and Huerta, N., 2009, "Chemical Reactions of Wellbore Cement Under CO_2 Storage Conditions: Effects of Cement Additives", Energy Procedia 1, 3603-3607.

Sugama, T., 2006, "Advance Cement for Geothermal Wells"; BNL-77901-2007-IR.

Wan, R., 2011. "Advanced Well Completion Engineering", Third Edition, Gulf Professional Publishing, ISBN: 0123858682.

Zirrahi, M., Azin, R., Hassanzadeh, H., Moshfeghian, M., 2012. "Mutual solubility of CH_4, CO_2, H_2S, and their mixtures in brine under subsurface disposal conditions". Fluid Phase Equilibria, 324, 80– 93.

Živica, V. 1997, "Hardening and properties of cement based materials incorporating heavy metal oxides", Bull. Mater. Sci., Vol. 20, No. 5, pp. 677-683.

Appendix A

Theoretical Development of New Cements and Effect of Different Additives

Summary

As a part of this project, new additives will be added to the Class H and G cement to improve their acid resistance. Therefore, effect of different additives on cement properties has been reviewed in this research period and preliminary cement formulations have been developed for initial screening tests involving rheology, fluid loss and consistency measurements.. The additives that have been chosen are categorized into the following two groups:

i. Additives which react chemically with CO_2 and H_2S and protect the cement.
ii. Additives which lower the porosity and permeability of the cement matrix thereby reducing the penetration of the CO_2 and H_2S.

Physical properties (i.e. density, funnel viscosity, Fann Viscometer readings, filtration loss, consistency, compressive strength and shear bond strength) of the new cements will be measured prior to aging. New cement samples with acceptable physical properties will be selected for aging experiments.

A.1. Introduction

The effects of sour gas (composition of H_2S and CO_2) on the cement matrix are extremely detrimental. These gases have the tendency to form acid with water that creates a low pH environment, which accelerates cement degradation. Acidic environment causes rapid increase in the leaching of the calcium ions from the cement matrix. The matrix mainly consists of calcium hydroxide ($Ca(OH)_2$ or CH or Portlandite) and Calcium Silicate Hydrate (C-S-H). Although both have calcium in them, the later is the main component in the cement matrix and the former is more vulnerable to acid attack (Benge, 2009). As the effect of CO_2 and H_2S are being considered together, the reactivity of each gas should be studied.

A.2. Reaction of CO_2

The following reactions have been presented to describe the effect of CO_2-saturated water on the cement:

$CO_2 + H_2O \rightarrow H_2CO_3$……(A.1)

$Ca(OH)_2 + H_2CO_3 \rightarrow CaCO_3$……(A.2)

C-S-H + $H_2CO_3 \rightarrow CaCO_3$ + amorphous silica……..…(A.3)

The formation of $CaCO_3$ by carbonation in the initial stage helps in increasing the mechanical strength of the cement and decreases the porosity/permeability. However, excessive carbonation causes cracks in the cement sheath and creates favorable condition for the carbonic acid (H_2CO_3) to react as follows;

$CaCO_3 + H_2CO_3 \rightarrow Ca(HCO_3)_2$……..……(A.4)

$Ca(HCO_3)_2 + Ca(OH)_2 \rightarrow 2CaCO_3 + H_2O$…….....(A.5)

In the reaction Eq. (A.5), the formation of H_2O and leaching of CH (with reaction from calcium bi-carbonate) can be seen. Hence, in the presence of more CO_2, the reaction shown in Eq. (A.1) reoccurs causing the reactions (A.1) to (A.5) to behave as a chain reaction. Thus, slowly the leaching of Ca^{+2} ions from the cement matrix can be observed and formation of $CaCO_3$ can be seen. Excessive $CaCO_3$ formation can cause brittleness of the cement and may result in cracking. Also as calcium bicarbonate ($Ca(HCO_3)_2$) is soluble in water, its formation as a product of the reaction (A.4) causes dissolution of calcium ions in the brine that presents in the pore space (Benge, 2009).

Some of the previous studies (Kutchko et al. 2006, 2007, Carey et al. 2006 and Gouedard et al. 2006 & 2007) have considered the reaction of CO_2 with the cement matrix as a slow process that occurs over decades. However, for CO_2 sequestration applications, it is necessary to consider more than 100 years of service life. The degrading tendency of CO_2 has been highlighted in the work of Santra & Swetaman (2010), Santra et al. (2009) and Benge (2009). Further, methods to improve the resistance of cement against CO_2 attack are (Benge, 2009)

I. Increase the system density (i.e. decease porosity) to lower the permeability. The density increase can be achieved by increasing the cement content in the mixture.

Using dispersants, increase in the viscosity can be controlled. However, it is not possible for every well.

II. Addition of special materials to fill the pore spaces in cement, such as latex.

III. Addition of special additives to reduce the reaction of CO_2 with reactive species in the cement.

IV. Use of non-Portland cement can be effective in providing a seal for the well. However, the components required for preparation of non-Portland cements are less abundant. The calcium aluminate cement is seen to have good resistance against CO_2 attack. Although non-Portland cements are commercially available, their use puts forth several challenges such as special additives, no contamination with Portland cement and narrower density window. Argonne National Laboratory has identified ceramic based cements to show good performance in wellbore applications as they can provide effective sealing against nuclear wastes.

V. Swelling technologies:

   a. Self-healing cements have special additives which react to the flowing gases or fluids and consequently swell and block the developed cracks. However, the primary focus was on hydrocarbons and effect of CO_2 has not been taken into consideration. Using flexible materials is also put into research so as to increase the Young's modulus of the set cement. This technique aided with use of expanding agents can create better swelling cement.

   b. Swell packers are used outside the casing and tend to swell in the presence of gases or fluids. They provide a complete seal in the annulus by swelling and can withstand a differential pressure up to 5000 psi. However, such packers are also made to react to hydrocarbons rather than CO_2.

VI. The various stresses along the life of a cement such as hydraulic stresses initially, setting and hardening, pressure and temperature variations, tensile sheath stresses are analyzed using simulation models and the stress modeling is performed. However, the varying Young's modulus is not considered in the models, which forces the design to be made only on the worst case scenarios.

Among the methods mentioned above for mitigating the effect of CO_2 on the cement matrix, the most effective methods have been addition of another additive to the cement (either to lower the permeability/porosity or to increase chemical resistance against CO_2) or use of non-portlandite cement.

Santra et al. (2009) compared the use of pozzolanic materials, silica fume and fly ash, against the CO_2 attack due to their tendency to react with CH and form $CaCO_3$. Santra & Sweatman (2010) have tested a cement sample 'A' against CO_2 which proved to be effective.

Barlet-Gouédard et al. (US Patent 8091642-2012) mentioned new Portland type cement with additives such as hollow elements having micro-spherical sodium-calcium-borosilicate glass, cenosphere or silica-alumina microsphere or a combination, metakolin and blast furnace slag. The slurry was foamed with either air or nitrogen forming the hollow elements. The hollow elements in the shape of quasi spherical or spherical or both, trap the carbonates formed after reaction of pozzlonas with CH and restrict further reaction with H_2CO_3.

Sugama (2006) mentioned non-portlandite type CAP (Calcium Aluminate Phosphate) cement, which is formed with calcium aluminate cement. The cement has a basic structure comprised of hydroxyapatite ($Ca_5(PO_4)_3(OH)$) and bohemite (γ-ALOOH). Hydroxyapatite (HOAP) has a unique tendency to react with CO_2 and incorporate it in as CO_3^{-2} without altering its structure. Bohemite on the other hand is completely non-reactive to CO_2. This causes the cement to be highly tolerant towards CO_2 attack. The acceptability of these materials for oil well cement application should be based on the following key properties:

1. Pumpability – can be achieved by adding citric acid as retarder and a mild dispersant
2. Low density slurry – air foaming and addition of styrene acrylic emulsion (SAE) as high-temperature anti-corrosive additive.
3. Toughness – milled carbon micro fibers and ceramic fibers (αAl_2O_3 and αAl_2O_3/ Mullite)
4. Bond durability with casing pipe's surface – self possess hybrid structure to withhold the casing pipes
5. Cost – based on above factors the cost is expected to be low and the addition of Class F fly ash further reduces the price

Another type of cement known as sodium silicate activated slag (SSAS) cement is also mentioned in Sugama (2006). This type of cement has a self-healing tendency towards acidic environments. Deposition of bassanite ($CaSO_4$) scales over the cement surface, which is formed by the reaction between H_2SO_4 with Ca, increases the tendency to retard the rate of acid attack because cement is now deprived of Ca and reacts with Mg from the slag to form lizardite phase that not only retards acid attack but also increases the cement strength.

A.3. Reaction of H_2S

H_2S has a tendency to dissolve and react with water and produce a mild acid that lowers the pH of the solution. The formation of H_3O^+ ions causes reaction with the cement and degradation. In some cases, H_2S also causes expansion of the cement sample that generates micro-cracks; thus, increases the porosity and permeability of the cement. Lecoiler et al. (2006) studied the effects of H_2S on silica containing cements and conventional cements. As with addition of silica, permeability of the cement was reduced, the damage to the sample was diminished.

Lecoiler et al. (2008) also discussed the addition of two metallic oxides such as. Hematite (Fe_2O_3) and Hausmanite (Mn_3O_4). Although Hematite addition (30% bwoc) showed damaging effect on cement sample, Hausmanite addition (15% bwoc) showed moderately encouraging results. Further investigation has been suggested by Lecolier et al. (2010) in regard to amount of Hausmanite or any other type of metal oxide which can be used.

A.4. Additives to be Considered for Testing

Based on the papers reviewed, certain additives have been considered to be used in the cement samples. The additives that have been chosen are categorized in two forms, similar to the approaches mentioned previously. The additives suggested after literature review of several papers are presented in Table A.1

Table A.1 Chemically Reactive Cement Additives

Additives which react chemically with CO_2 and H_2S							
S.N.	**Additive**	**erence**	**Property**	**Side Effect**	**Amount to be added**	**Extra Water Required**	**Justification**
1	Hydroxyapatite ($Ca_5(PO_4)_3OH$)	Sugama (2006)	Ability to react with CO_2 without altering its structure	Might help in increasing the matrix strength	30% bwoc	23% by weight of HOAP	As the hydroxyapatite is a costly additive, the amount to be added should be less so as to only provide the required property. The water content required for the Thermalock cement for Halliburton (which comprises mainly of Hydroxyapatite) utilizes approx. 23% bwoc (US Patent 7687440-2010)
2	Zinc Oxide (ZnO)	Sasaoka (1994), Sayyadnejad et al. (2008)	Ability to react with H_2S in a thermally stable reaction. Ability to absorb/ adsorb H_2S from drilling mud system	May act as a retarder	20% bwoc	Dry blended	Fe_2O_3 and Mn_3O_4 were used by Lecolier et al. (2010). Fe_2O_3 (30% bwoc) had crumbled completely after ageing. Mn_3O_4 (15% bwoc) had provided average results with the ageing. ZnO being the heaviest among Zn, Fe and Mn can also lead to crumbling of cement hence only 20% is being added.
3	Hausmanite or Mn_3O_4	Lecolier et al. (2008)	Reacts with H_2S with a thermally stable reaction	Doubles the rheology of	20% bwoc (15% bwoc	Dry Blended	The sample shall not be tested as of now as it has some

				the cement when added as 30% bwoc	already tested by Lecolier et al. (2008) with satisfactory results		proven results.
4	Dolomite or $MgCO_3$	H. Hashimoto et al. (1980)	Thermally decomposes into $CaCO_3$, MgO under CO_2 presence.	Growing formation of MgO crystals.	Not to be tested as the growing crystals of MgO may cause cracks in the cement matrix.		
5	Amine Based sorbents such as monoethanolamine (MEA), diethanolamine (DEA), methyldiethanolamine (MDEA), diisopropanolamine (DIPA)	Stratzisar et al. (2001)	Degradation of monoethanolamine Used in Carbon Dioxide Capture from Flue Gas of a Coal-fired Electric Power Generating Station	Not predictable	The additive shall not be tested as it is effective in liquid phase against sour gas. The mechanism of action of MEA against sour gas involves the process as performed in natural gas refineries. Such conditions may not be possible to replicate in downhole conditions.		

Table A.2: Porosity and Permeability Reducing Cement Additives

Additives which reduce porosity/ permeability of cement matrix							
S.N.	**Additive**	**Reference**	**Property**	**Side Effect**	**Amount to be added**	**Extra Water Required**	**Justification**
1	Catioinc Latex	US Patent 7687440-2010, Rahman & Chong, 1997, Jones and Carpenter, 1991	Reduces permeability of the cement matrix	Increases mechanical strength and reduces leaching in water medium	2.45gal/ sack	None- To be added in water	The amount of latex proved to provide a higher compressive strength, lower the permeability, improve fluid loss and reduce leaching in presence of water. Although these results were obtained for non-portland type cement as per the reference similar results can be expected from portland

							cement also. The latex is also being used in industry commercially to reduce the permeability and increase the strength of the cement (Rahman & Chong, 1997, Jones and Carpenter, 1991)
2	Microsilica	Santra et al. (2009), Shadizadeh et al. (2010), Mueller and Dillenbeck (1991- SPE 21688)	Decreases the porosity and permeability of the cement matrix and increase bonding strength	Pozzolanic substance. Amount higher than 50% bwoc makes the slurry non-flowable (Santra et al., 2009)	20% bwoc	4.47cc/ gm of Microsilica (Mueller and Dillenbeck 1991- SPE 21688)	As microsilica is itself pozzolanic material, it can provide a protection against CO_2 attack. Hence 3 different samples can be made, viz. only microsilica (20% bwoc), microsilica (20% bwoc) + latex, only latex.
3	Magnesium Oxide	Rudi Rubiandini et al., 2005, Anjuman Sarihar, PhD thesis, Uni. Of Western Ontario, 2011	Decreases the porosity and permeability of the cement matrix by expansion of the cement	Compressive strength decreases and shear bond strength increases with MgO.	5% bwoc	Dry blended	The amount has been recommended by Rubiandini et al., 2005 to obtain an optimum expanding cement. (Anjuman Sarihar, PhD thesis, 2011, Rudi Rubiandini et al., 2001). MgO increases the shear bond strength of the cement even with presence of mud film on the casing.
4	Calcium Oxide	Rudi Rubiandini et al., 2005, Anjuman Sarihar, PhD thesis, Uni. Of Western Ontario, 2011	Decreases the porosity and permeability of the cement matrix and increase bonding strength	A very rapid expansion is observed and more suitable in wells with temperature not more 70^0C (158^0F)	The additive shall not be tested as of now because MgO is more suitable for HPHT wells.		

The additives mentioned (Hausmanite, Zinc Oxide, Latex, Micro-Silica and Magnesium Oxide) need to be purchased and prepared in the batches to test their effectiveness. The additives should act as per their applications and references mentioned.

A.5. Testing of the Additives Samples

The samples which are prepared need to be tested against the neat cement slurries (the batches mentioned in Table A.1). The samples need to qualify on three different levels of testing before they are kept in the ageing cell. The tests will be conducted in the following order:

1. Testing of Slurry Properties:
    a. Density: The theoretical density of the slurry can be obtained using calculations for ideal mixing. With this the amount of each slurry ingredient required can be formulated and hence the required density slurry can be obtained. The density of the slurry should be in the range of the neat slurry. Excessive high density slurry or low density slurry need to be corrected accordingly. The actual density measurement has to be done using a mud balance immediately after the slurry is prepared.
    b. Viscosity: Viscometeric readings help in comparing the rheology of the slurry with respect to the neat cement slurries. The values obtained for 3RPM, 6RPM, 100RPM, 200RPM, 300RPM and 600RPM can be plotted on a graph and compared. The readings should be taken immediately after the slurry is prepared.
    c. Filtration Loss: The filtration loss of the slurry can be tested using the standard filtration loss test apparatus. An excessive filtration loss with respect to the neat slurry should not be accepted as it can lead to problem during cementation. The filtration loss test needs to be done immediately after the slurry is prepared.
    d. Thickening Time: The thickening time of the slurry needs to be measured using a consist-o-meter and compared with that of the neat cement slurry. An excessively long or short thickening time shall be compensated with use of accelerators or retarders. The consist-o-meter test needs to be done immediately after the slurry is prepared.

Once the slurry samples with additives are able to provide good results with the rheological tests, fluid loss and thickening time, the slurry can be taken towards curing. The samples for

shear bond strength also need to be prepared for testing after being cured. The curing shall be done in similar conditions as neat slurries, i.e. 200ºF and immersed in 2% brine for 5 days.

2. Testing of Cement Cores:
    a. Visual Test: The samples after curing at 200ºF and immersed in 2% brine solution for 5 days should be free from any sort of crack or damage.
    b. Compressive Strength Test: The samples after curing should be subjected to wet confined compressive loading condition to measure their strength. The samples should be able to withstand compressive loading condition expected in the field.
    c. Shear Bond Test: The samples should be able to withstand the level shear force loading experienced in the field.
    d. Porosity/Permeability: Porosity and permeability of the samples will be measured after 1-day drying in an oven. The samples of interest are the LT, LM, MS and MG.

A.6. Future Work

1. Generating step by step procedure and check list for preparation of new cement samples and testing them.
2. Begin the preparation of samples and recording of data in set format.
3. Keeping the data record for all the samples and tests and comparing them with neat slurry samples.
4. Analyzing the results.

Appendix B

Literature Review, Theoretical Studies on Tubular Corrosion

Summary

Tubular corrosion and cement degradation modeling at high temperature high pressure conditions needs accurate prediction of CO_2, H_2S, and CH_4 solubility in brine solutions. In previous report, pure solubility models for CO_2, H_2S, and CH_4 were presented. Pure gas solubility model predictions were previously compared with experimental data for gas mixture system. For mixed gas system, experimental data from the literature showed that the mutual interaction of dissolved gases reduces the solubility. In this report, a mixed-gas solubility model is presented which shows a better agreement with experimental data in compare with pure solubility models.

Theoretical and modeling study of CO_2/H_2S corrosion of tubular is in progress. Two main corrosion modeling approaches (pure CO_2 and H_2S/CO_2 corrosion modeling) are considered. When partial pressure of H_2S is higher than the critical limits, a layer of iron sulfide forms on the surface and corrosion reaction is controlled by diffusion of ions through the layer. An approach for calculating the critical H_2S limits is presented in Section B.2. When partial pressure of H_2S is lower than a certain limits, corrosion is controlled by CO_2 and a pure CO_2 model is applied for calculating the corrosion rate. In the second part of this appendix, critical H_2S partial pressure for CO_2 control and H_2S control corrosion reaction will be presented.

B.1 CO_2-H_2S-CH_4 Solubility Model

Zirrahi et al. (2012) developed a model for predicting mutual solubility a mixture of CH_4, CO_2, and H_2S, in brine solution at temperatures up to 370K. Zirrahi et al. (2012) used the equality of fugacity for all the components in the aqueous and gas phase at thermodynamic equilibrium.

$$f_i^v = f_i^{aq} \quad \text{(B.1)}$$

Fugacity of species in the gas phase f_i^v can be calculated as:

$$f_i^v = \rho \varphi_i Y_i \quad \text{(B.2)}$$

where P is total pressure, φ is fugacity coefficient, and Y_i is mole fraction of component i in the gas phase.

Fugacity of species in aqueous phase (f_i^{aq}) can be obtained by:

$$f_i^{aq} = \gamma_i H_i x_i \quad \text{(B.3)}$$

where H_i is Henry's constant, γ_i is activity coefficient in mole fraction scale, and x_i is mole fraction of component i in the aqueous phase. The model neglects the ionization of CO_2, CH_4, and H_2S in the aqueous phase because of the low solubility of these compounds. Prausnitz et al. (1986) developed a correlation for Henry's constant at high pressures.

$$H_i(T,P) = H_i(T,P^r) exp\left(\frac{V_i^{\infty}(P-P^r)}{RT}\right) \quad \text{(B.4)}$$

where P^r is reference pressure, V_i^{∞} is partial molar volume of component i, R is universal gas constant, and T is absolute temperature. Zirrahi et al. (2012) assumed 1 bar as the reference pressure. By combining Eqs. (B.2), (B.3), and (B.4), x_i can be calculated as:

$$x_i = \frac{Y_i \varphi_i P}{\gamma_i H_i(T,1)} exp\left(-\frac{V_i^{\infty}(P-1)}{RT}\right) \quad \text{(B.5)}$$

For carbon dioxide, $V_{CO_2(g)}^{\infty} = 32.6$ and $V_{CO_2(g)}^{\infty} = 32$ cm^3/mole; and Henry's constant for gaseous and liquid CO_2 (in bar molality scale) are obtained from the following equations:

$$Log\ H_{CO_2(g)}(T,1) = 1.189 + 1.304 \times 10^{-2} T - 5.446 \times 10^{-5} T^2 \quad \text{(B.6)}$$

$$Log\ H_{CO_2(liq)}(T,1) = 1.169 + 1.368 \times 10^{-2} T - 5.38 \times 10^{-5} T^2 \quad \text{(B.7)}$$

Zirrahi et al. (2012) modified the equation proposed by Suleimenov and Krupp (1994) for calculating Henry's constant for H_2S.

$$Log\ H_{H_2S(g)}(T,1) = a_1 + a_2 T + a_3 T^3 + \frac{a_4}{T} + a_5 \log(T) \quad \text{(B.8)}$$

$$Ln\ H_{H_2S(liq)}(T,1) = a_1 + \frac{a_2}{T} + a_3 T + a_4 \ln(T) \quad \text{(B.9)}$$

where $H_{H_2S(g)}$ is in bar molality scale, T is in Kelvin, and $H_{H_2S(liq)}$is in the molality scale in MPa.

For hydrogen sulfide, $V_{H_2S(g)}^{\infty} = 38.15$ cm^3/mole and for CH_4

$$Ln\ V_{CH_4}^{\infty} = 3.541 + 1.23 \times 10^{-3} T \quad \text{(B.10)}$$

$$Ln\ H_{CH_4}(T,1) = a_1 + \frac{a_2}{\tau} + a_3 \ln(\tau) + a_4 \tau \quad \text{(B.11)}$$

where $\tau = 0.01T$, and H_{CH_4} is on the molality scale in MPa. The mole fraction of water in the gas phase is calculated using a model similar to that of Spycher et al. (2003). The values of equilibrium constants, from a_1 through a_5 are presented in Table B.1 below.

Table B.1 Parameters needed for implementation of the equilibrium constant of H_2S and CH_4

Parameter	H_2S (gas)	H_2S (liquid)	CH_4
a_1	640.1901754766855	358.0300140642526	127.173804
a_2	0.27643029942021946	-12604.13776911219	-155.575631
a_3	0.11099712781812077	0.07327349335024513	-65.2552591
a_4	0.1646266738977218	-59.26961904310672	6.16975729
a_5	0.26532569337900316	----	----

$$Y_{H_2O} = \frac{K^o_{H_2O}\left(1-x_{H_2S}-x_{CO_2}-x_{CH_4}-x_{Salt}\right)}{\varphi_{H_2O}P} exp\left(\frac{V^{\infty}_{H_2O}(P-1)}{RT}\right) \quad \text{(B.12)}$$

$V^{\infty}_{H_2O} = 18.18$ cm^3/mole and

$$logK^o_{H_2O} = -2.209 + 3.097 \times 10^{-2}T - 1.098 \times 10^{-4}T^2 + 2.048 \times 10^{-7}T^3 \quad \text{(B.13)}$$

where T is in degree centigrade and $K^o_{H_2O}$ is on the molality scale in bar. Fugacity coefficient of all the components can be calculated using the Peng-Robinson equation as explained in the following.

$$P = \frac{RT}{V-b} + \frac{a}{V(V+b)+b(V-b)} \quad \text{(B.14)}$$

where a and b are intermolecular attraction and repulsion, respectively. For pure components, a and b are calculated by

$$b = 0.0778\frac{RT_c}{P_c} \quad \text{(B.15)}$$

$$a = a(T_c)\alpha(T) \quad \text{(B.16)}$$

$$a(T_c) = 0.45724\frac{(RT_c)^2}{P_c} \quad \text{(B.17)}$$

$$\alpha(T) = \left[1 + \beta\left(1 - \sqrt{\frac{T}{T_c}}\right)\right]^2 \quad \text{(B.18)}$$

$\beta = 0.37464 + 1.54226\omega - 0.26992\omega^2$……..(B.19)

where T_c is critical temperature, P_c is critical pressure, and ω is acentric factor for each component. Zirrahi et al. (2012) used non-random mixing rule for mixtures.

$a_{mix} = a^c_{mix} + a^p_{mix}$……..(B.20)

$a^c_{mix} = \sum_i \sum_j x_i\, x_j \left(a_i a_j\right)^{0.5} \left(1 - K_{ij}\right)$……..(B.21)

$a^p_{mix} = \sum_i \sum_j x_i\, x_j {a_{ij}}^P$……..(B.22)

$b_{mix} = \sum_i x_i\, b_i$……..(B.23)

where K_{ij} is binary parameter and ${a_{ij}}^P$ is interaction parameter (Table B.2).

Table B.2 Parameters needed for implementation of the equilibrium constant of H_2S and CH_4

Parameter	Gas Phase	Liquid Phase
$\boldsymbol{K_{CH_4-CO_2}}$	0.15196821446633	-0.140162837
$\boldsymbol{K_{CH_4-H_2S}}$	1.5716638150922	0.2235455
$\boldsymbol{K_{H_2S-CO_2}}$	-0.03784931397306	-0.11666
$\boldsymbol{a^P_{CH_4-CO_2}}$	3480693.2119225934	3.14150463×10^7
$\boldsymbol{a^P_{CH_4-H_2S}}$	4957015.77622836	4096127.203055
$\boldsymbol{a^P_{H_2S-CO_2}}$	-2728833.9654826	-5388373.22848
$\boldsymbol{a^P_{CO_2-H_2S}}$	1413558.630746885	-4274425.50189
$\boldsymbol{a_{H_2O-CO_2}}$	1.665891551×10^7-35955.73T	7722804.44-8958.79769T
$\boldsymbol{a_{H_2O-H_2S}}$	2160707.9119	7478118.844-4143.3037T
$\boldsymbol{a_{H_2O-CH_4}}$	-1863733.873895	1.101259×10^7
$\boldsymbol{a_{H_2O-CO_2-CH_4}}$	-2702471.307888	-1.235748×10^7
$\boldsymbol{a_{H_2O-H_2S-CH_4}}$	1.952427×10^7-64566.0129989T	1071705.33248
$\boldsymbol{a_{H_2O-H_2S-CO_2}}$	145169.970708P	-3.2996×10^8-1.45647×10^7P

Fugacity coefficient can be calculated as:

$ln\varphi_k = \frac{b_k}{b}(Z-1) - \ln(Z-B) - \frac{A}{2\sqrt{2}B}\left(\frac{2\sum_{i=1}^{N} Y_i a_{ik}}{a} - \frac{b_k}{b}\right) ln\left(\frac{Z+(1+\sqrt{2})B}{Z+(1-\sqrt{2})B}\right)$ ……..(B.24)

where Z is compressibility factor. The minimum real root of the following equation used as the compressibility factor of the liquid phase and the maximum real root as the compressibility factor of the gas phase.

$$Z^3 - (1-B)Z^2 + (A - 2B - 3B^2)Z - (AB - B^2 - B^3) = 0 \quad \text{(B.25)}$$

where

$$A = \frac{aP}{(RT)^2} \quad \text{(B.26)}$$

$$B = \frac{bP}{RT} \quad \text{(B.27)}$$

Spycher et al (2003), assumed that the mole fraction of water in the gas phase to be zero ($Y_{H_2O} = 0$) to apply the mixing rule.

$$a_{H_2O-acidgas} = Y_{CO_2}a_{H_2O-CO_2} + Y_{CH_4}a_{H_2O-CH_4} + Y_{H_2S}a_{H_2O-H_2S} + Y_{CO_2}Y_{CH_4}a_{H_2O-CO_2-CH_4} + Y_{CO_2}Y_{H_2S}a_{H_2O-CO_2-H_2S} + Y_{CH_4}Y_{H_2S}a_{H_2O-CH_4-H_2S} + Y_{CO_2}Y_{CH_4}Y_{H_2S}a_{H_2O-CH_4-H_2S-CO_2} \quad \text{(B.28)}$$

Zirrahi et al. (2012) simplified Eq. (B.28) by assuming tertiary interaction parameters to be zero. They used a non-random mixing rule given by,

$$a = a^c + a^p \quad \text{(B.29)}$$

$$a_{ij}^c = \sum_i \sum_j x_i\, x_j \left(a_i a_j\right)^{0.5} \left(1 - K_{ij}\right) \quad \text{(B.30)}$$

where a^c is conventional mixing rule and a^p is intermolecular interaction term due to the polarity of the molecules. CH_4 has a non-polar molecular structure. Therefore, all $a_{i-CH_4}^p$ are assumed to be zero. Spycher et al. (2003) proposed the following equation for calculation of pure CH_4, CO_2, H_2S mutual solubility in equilibrium with pure water and brine. Mole fraction of water in gas phase can be calculated using the following equation.

$$Y_{H_2O} = \frac{1 - \sum Y_i B_i}{\left(\frac{1}{A}\right) - \sum Y_i B_i} \quad \text{(B.31)}$$

where A and Bi can be calculated using following equations

$$A = \frac{K_{H_2O}^0}{\varphi_{H_2O} P} exp\left(\frac{V_{H_2O}^{\infty}(P-1)}{RT}\right) \quad \text{(B.32)}$$

$$B_i = \frac{\varphi_i P}{\gamma_i H_i(T,1)} exp\left(-\frac{V_i^{\infty}(P-1)}{RT}\right) \quad \text{(B.33)}$$

The new gas phase mole fraction can be used to calculate the solubility of components

$$x_i = Y_i B_i \quad \text{(B.34)}$$

Comparison between experimental data and model prediction for CH_4, CO_2, and H_2S solubility in pure water at temperature of 310.95K is shown in Figure B.1. Prediction for CH_4, CO_2, and H_2S solubility using mixture model shows better agreement with experimental data in compare with pure models. Mutual interaction of H_2S and CO_2 reduces the solubility of these gases. However, CH_4 solubility is not affected by mutual interaction of other gases because of non-polar molecular structure of CH_4. Solubility models are helpful tools for prediction of effect of corrosive gases on casing and cement degradation.

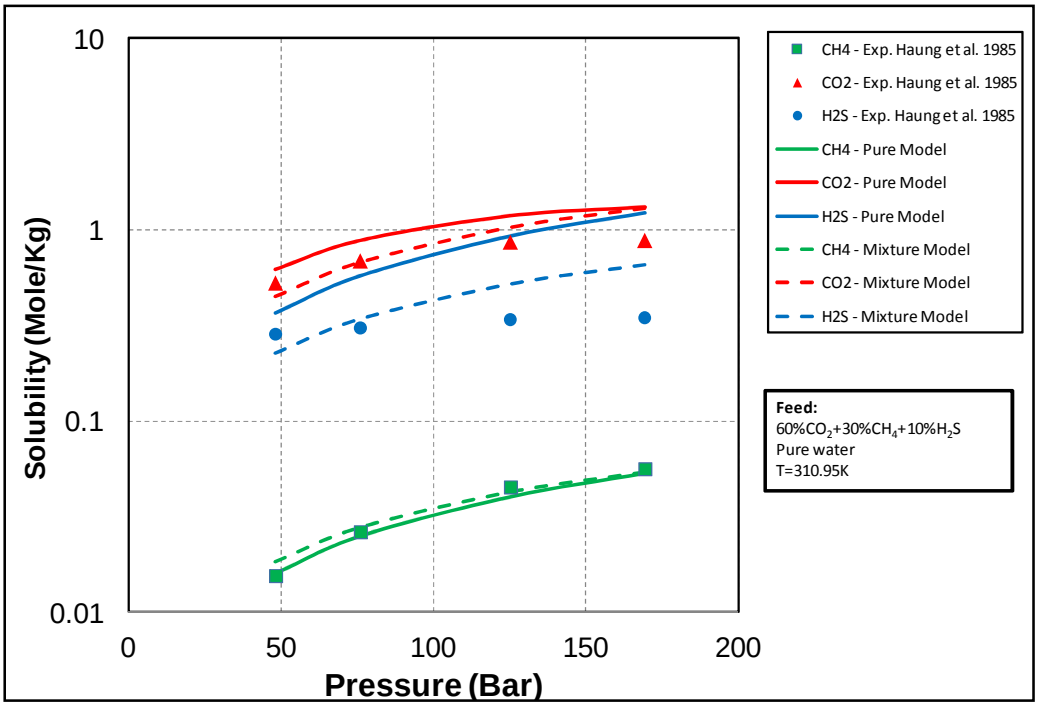

Fig. B.1 Comparison between experimental data and model prediction for CH_4, CO_2, and H_2S solubility in pure water at temperature of 310.95K

B.2 Critical H_2S Concentration for H_2S or CO_2 Controlled Corrosion Reaction

Prediction of corrosion rate in oil and gas industry is a key factor in determining the life time of oil field tubulars. Formation of corrosion products on the metal surface (porous layer) is usually a determining factor in corrosion reaction since corrosive species have to diffuse through the layer. In oil and gas production, corrosion layer formed during corrosion is usually iron

carbonate, iron sulfide or iron oxide. Type of corrosion layer forming on the carbon steel surface depends on partial pressure of H_2S and CO_2. Dunlop et al. (1983) found out that if the ratio of CO_2 partial pressure to H_2S partial pressure is smaller than 500, iron sulfide forms on the surface and if the ratio of CO_2 partial pressure to H_2S partial pressure is larger than 500, iron carbonate forms on the surface. Therefore, Dunlop et al. (1983) developed a simple way for determining the iron carbonate/iron sulfide boundary at conditions where both iron carbonate and iron sulfide are stable. The method is applicable for ideal gas at room temperature (25^{o}C). Smith (1993) proposed a more detailed version of iron carbonate/iron sulfide equilibrium as:

$$K_{FeS/FeCO3} = \frac{a_{H2O} \times K_{CO2,aq/CO2,vap} \times a_{CO2,vap}}{K_{H2CO3,aq} \times K_{H2S,aq/H2S,vap} \times a_{H2S,vap}} \quad \text{(B.35)}$$

where $K_{FeS/FeCO3}$ is equilibrium constant between FeS and $FeCO_3$, a_{H2O} is activity of water, $K_{CO2,aq/CO2,vap}$ is equilibrium constant between CO_2 in liquid and gas phase, $a_{CO2,vap}$ is activity of CO_2 in gas phase, $K_{H2CO3,aq}$ is equilibrium constant for carbonic acid formation, $K_{H2S,aq/H2S,vap}$ is equilibrium constant between H_2S in liquid and gas phase, and $a_{H2S,vap}$ is activity of H_2S in gas phase. Assuming that activity of water is equal to one and combining all the equilibrium constants in one constant, Eq. B.35 can be written as:

$$K_{FeS/FeCO3} = C \times \frac{a_{CO2,vap}}{a_{H2S,vap}} \quad \text{(B.36)}$$

"C" can be found for any temperature and non-ideal gas conditions.

Smith and Pacheco (2002) used the Fig. B.2 to explain the conceptual corrosion product stability regions of carbon steel in H_2S/CO_2 saturated environments. Iron carbonate scale is the most well known corrosion product in CO_2 saturated systems. Mackinawite, Pyrrhotite, Pyrite, and cubic FeS are common H_2S corrosion products occurring in oil and gas applications. Mackinawite is a corrosion product of carbon steel in slightly sour system. Mackinawite exists as an iron excess form ($Fe_{1+x}S$). Mackinawite can be commonly found in oilfield corrosion. It is a thermodynamically semi-stable form of FeS and it forms when the concentration of Fe^{2+} and H_2S are still below the saturation point. Mackinawite is ferromagnetic and it is a tarnish layer on the surface which reacts with oxygen immediately when it is exposed to air as it is shown in the following equation.

$$3FeS + 2O_2 \rightarrow Fe_3O_4 + 3S \quad \text{(B.37)}$$

Pyrite scale formation is possible only when elemental sulfur presents in the system. Pyrrhotite will form at high H_2S concentration environment and it is a stable form of H_2S corrosion product. Finally, Cubic FeS forms at high temperature and slightly sour system. Critical temperature for the formation of cubic FeS not only depends on the thermodynamic but also the kinetics of the reaction. Different authors have reported different temperatures as critical temperature for the cubic FeS formation in the range of 110-200^oC.

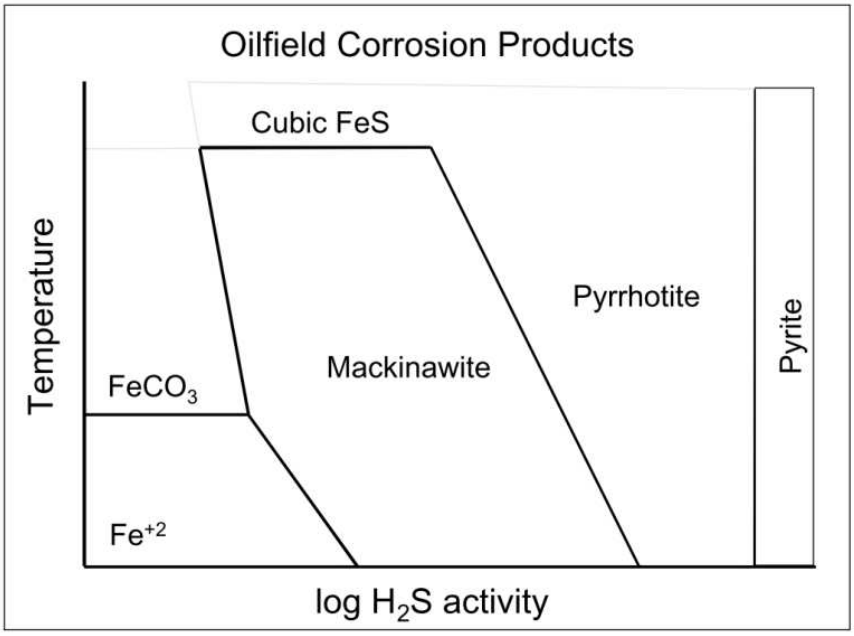

Fig. B.2 Conceptual Corrosion product diagram for CO_2/H_2S environment (Smith, 1993)

Smith and Pacheo (2002), developed a correlation for prediction of minimum H_2S required for iron sulfide corrosion product formation based on the stoichiometric FeS formation reaction;

$Fe^{2+}+H_2S \rightarrow FeS+2H^+$ ……..(B.38)

Reaction rate constant for Eq. (B.38) can be written as follow

$$K_{FeS/Fe^{2+}} = \frac{[H^+]^2}{[Fe^{2+}][H_2S]} \text{……(B.39)}$$

where $[H_2S]$ can be calculated using the following equation

$$[H_2S] = \left(K_{H2S,aq/H2S,vap}\right).\left(ppH_2S_{vap}\right).(\gamma_{H2S}) \text{……..(B.40)}$$

where $K_{H2S,aq/H2S,vap}$ is reaction rate constant for H_2S dissolution reaction, ppH_2S_{vap} is partial pressure of H_2S, γ_{H2S} is fugacity coefficient of H_2S. Critical partial pressure of H_2S can be calculated by combining and rearranging the eq. B.39 and B.40.

$$\left(ppH_2S_{vap}\right) = \frac{[H^+]^2}{K_{FeS/Fe^{2+}}[Fe^{2+}]\left(K_{H2S,aq/H2S,vap}\right).(\gamma_{H2S})} \quad \text{(B.41)}$$

Smith and Pacheco, 2002, assumed that iron ion concentration is one and also the activity of H_2S is in equilibrium between the gas and liquid phase. Hydrogen concentration is simply related to log of pH, therefore, Eq. B.41 can be written in a simpler form as;

$$\left(ppH_2S_{vap}\right) = \frac{10^{-pH}}{K_{FeS/Fe^{2+}}\left(K_{H2S,aq/H2S,vap}\right).(\gamma_{H2S})} \quad \text{(B.42)}$$

Reaction rate constant is a function of Gibbs free energy. For the iron sulfide scale formation, change of Gibbs free energy for this reaction can be written as follow

$$\Delta G_{reaction} = \Delta G_{FeS} + 2\Delta G_{H^+} - \Delta G_{Fe^{2+}} - \Delta G_{H_2S} \quad \text{(B.43)}$$

Smith and Pacheco 2002, suggested the following equation for predicting the partial pressure of critical H_2S for the formation of iron sulfide. This equation was derived from Eq. (B.42) by calculating the Gibbs free energy and it is only a function of total pressure, temperature, pH, and fugacity coefficient of H_2S. Following equation shows the boundary between Fe^{2+} ions and Mackinawite scale.

$$\left(ppH_2S_{vap}\right) = \frac{P.10^{\frac{\Delta G}{4.757T}-2pH}}{(\gamma_{H2S})} \quad \text{(B.44)}$$

where ΔG can be calculated using the following equation

$$\Delta G = 961.1 + 93.473T - 11.297TlnT - 0.135T^2 - \frac{4.196\times10^5}{T} + \frac{2.147\times10^7}{T^2} + 0.0196T^2lnT + 7.2 \times 10^4\frac{lnT}{T} \quad \text{(B.45)}$$

Smith et al. (2011) showed the effect of pH on the Mackinawite stability region (Fig. B.3). Mackinawite is more stable at lower pH.

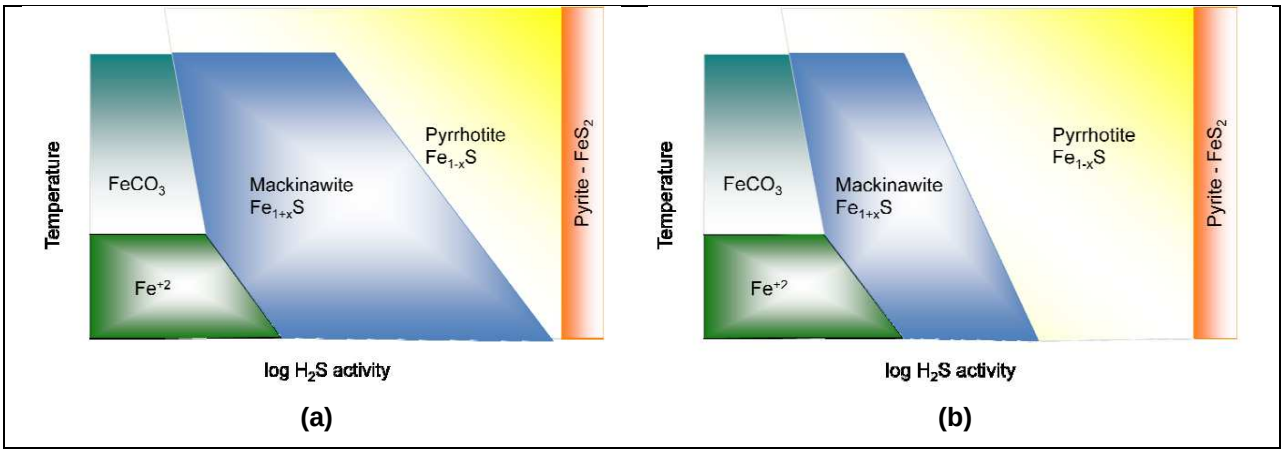

Fig. B.3 Conceptual Corrosion product diagram for CO_2/H_2S environment (a) pH=4 and (b) pH=7 (Smith et al. 2011)

Project Title: Effect of H_2S and CO_2 in HPHT Wells on Tubulars and Cement

Report Type: Monthly Report

Report #: 13

Reporting Period: September 22nd, 2012 to October 21st, 2012

Authors:

Ramadan Ahmed, Principal Investigator

Subhash Shah, Co-Principal Investigator

Samuel Osisanya, Co-Principal Investigator

Shokrollah Hassani, Postdoctoral Research Associate

Rida Elgaddafi, Research Assistant

Omosebi, Omotayo A., Research Assistant

Himanshu Maheshwari, Research Assistant

Adarsh Naidu, Research Assistant

Aman Srivastvava, Research Assistant

Prepared under BSEE Project # E12PC00035

by

THE UNIVERSITY OF OKLAHOMA

Nov. 27, 2012

1. Summary of Accomplishments

This monthly report presents the progress made during the project period September 22, 2012 to October 21, 2012. A new aging experiment was started during this research period. Silica flour, fly ash, antifoaming agent and Hydroxyethylcellulose (HEC) were added to Class H and G cement slurries as additives during slurry preparation. Cement cores and bonding samples were aged in 90%CH_4-10%CO_2 saturated 2% brine solution for fourteen days at temperature 350ºF and pressure of 6,000 psi. However, the aging was stopped after 6 days because of technical problems with the heating system.

Aged cement samples were recovered from the aging cell and physical (porosity, permeability and density) and mechanical properties (compressive strength and bonding strength) were measured. Visual observation showed that cement cores with fly ash are considerably attacked by the carbonic acid. Fly ash tends to reduce the resistance of both Class H and Class G cements against carbonic acid. Shear bonding and compressive strength of fly ash containing samples were also reduced after aging. Porosity and permeability measurements are in agreement with mechanical test results for the cement samples with fly ash.

For the class H and G cement without fly ash, 6 days of aging in CO2 saturated brine solution slightly reduced the porosity and permeability, and increased the compressive and shear bonding strength. Different explanations can be given for these observations. One of the possible explanations could be slight carbonation of the cores, which forms calcium carbonate and consequently causes expansion of cement. The carbonation can reduce porosity and permeability and improve compressive and shear bonding strength. Another explanation could be slight hydration, which occurs during early time of aging and improves the physical properties of the cores.

Theoretical and modeling studies on tubular degradation are in progress. Details of two main corrosion models (i.e. CO2 corrosion and H2S/CO2 corrosion models) are presented in Appendix A. Flowcharts outlining different calculation steps are presented to show the modeling algorithms.

Our plan for the coming weeks is to continue the aging experiments. After aging, physical properties of the samples will be evaluated. Beside this, we will continue theoretical and modeling studies on tubular corrosion. Also, the ongoing corrosion setup developmental activities will continue.

2. Overall Project Progress

2.1 Theoretical Studies (Task 1)

Research on CO_2/H_2S corrosion modeling at HPHT conditions is in progress. As it is mentioned in the previous report, uniform corrosion models for these conditions can be divided in two main categories: i) CO_2 corrosion model; and ii) H_2S/CO_2 corrosion model. Iron sulfide is one of the most important corrosion products, which is formed in the presence of small amount of H_2S in the system. Iron sulfide usually acts as a barrier and protects the carbon steel substrate from further corrosion. When the concentration of H_2S is higher than the critical concentration (the minimum H_2S concentration in which iron sulfide scale forms on the surface steel) the corrosion process is under H_2S control. However, below critical H_2S concentration, the corrosion process is under CO_2 control. Therefore, one of these two corrosion models will be applied to predict corrosion rate. A new CO_2 corrosion model has been formulated to predict corrosion rate in pure CO_2 saturated brine. Research is in progress to solve the system of equations and predict the corrosion rate. One of the best available CO_2/H_2S corrosion models from the literature has been reviewed and modified for the application of this research. Details of these studies are presented in Appendix A.

2.2 Experimental Studies on Degradation of Cement (Task 2)

A new aging experiment (Experiments # 3) was conducted during this reporting period. Four different types of cement cores (i.e. Class H and G with Silica, Class H and G with silica and fly ash) and bonding samples were aged in 2% brine saturated with gas mixture containing 90%CH_4 and 10%CO_2 at 6,000 psi and 350ºF for 6 days. For this experiment, the original plan was 14 days of aging. Silicone oil used in circulating bath as a heat transfer media was degraded after two months of operation at high temperature (i.e. 382^{o}F). The fluid became very viscous and the circulation pump was unable to circulate it in the system. Therefore, the experiment was stopped after 6 days of aging to clean the system and replace the heating fluid. After proper clean-up, the silicone oil has been replaced with synthetic oil, which is expected to last longer.

Visual observation of the cement cores showed that cores with fly ash are considerably attacked by carbonic acid that forms as a result of CO_2 dissolution. Figure 1 shows the digital pictures of the Class H cement with and without fly ash after 6 days aging. Degradation depths for Class H and G samples with fly ash were about 2 mm. Phenolphthalein indicator was also applied to the samples to determine the degradation depth. Since $Ca(OH)_2$ content in the

degraded zone is lower than the original content, the pH in degraded zone is expected to be lower than that of un-degraded part of the core. With Phenolphthalein indicator, pink color indicates higher pH values (more than 8.3). Figure 2 shows the Class H cement with fly ash after aging in CO_2 saturated brine. Pink color at the center shows the sound zone of cement which exhibit higher pH (high alkalinity) due high concentration of calcium hydroxide. Degraded zone is separated from the sound zone by a carbonation layer, which doesn't show a pink color because of low pH resulting from carbonation of calcium hydroxide.

(a) **(b)**

Fig. 1 Class H cement after 6 days aging (Experiments # 3): a) with fly ash; and b) without fly ash

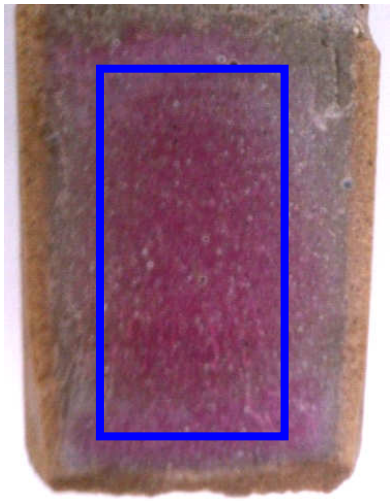

Fig. 2 Aged fly ash containing Class H cement after application of Phenolphthalein

2.2.1.1 Compressive Strength

Six HS[1] and GS cores, and three HSF and GSF specimens were used to measure compressive strength of the cores. Figure 3 presents a summary of confined compressive strength measurements of aged cores. Class H cement cores showed higher compressive strength than Class G cores. Addition of fly ash to the cement also improved the compressive strength of Class G cement. However, in some cases, fly ash made the cores brittle and prone to cracking at low compressive loads. This resulted in unexpected failure of aged cores during the test and even during core handling. The cracking tendency can be related to internal weakening of cores due to high thermal stresses and/or quick expansion of dissolved gas in the pore during depressurization of the aging cell.

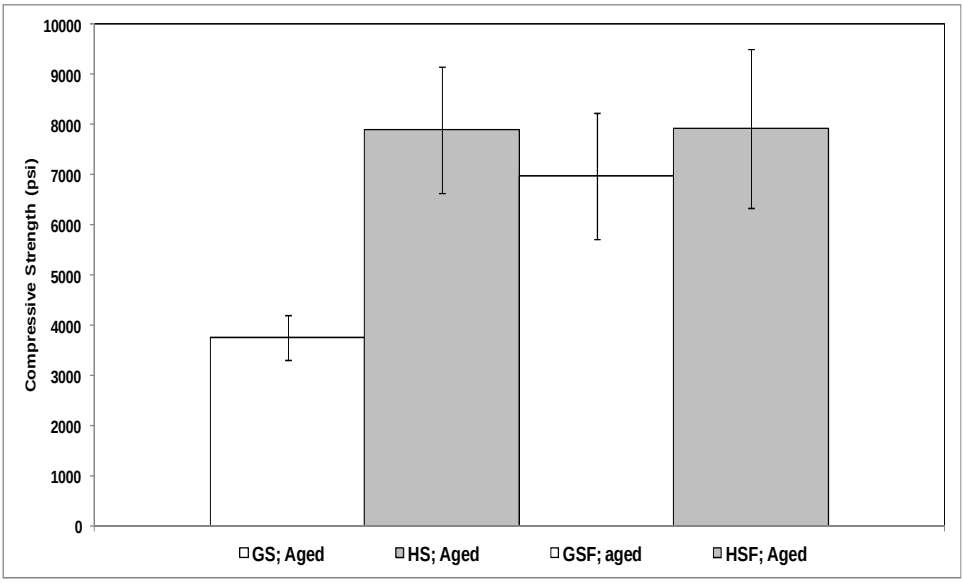

Fig. 3 Compressive strengths of aged cement cores (after 6 days of aging at temperature of 350°F and pressure of 6,000 psi in 90%CH_4-10%CO_2-brine solution, Experiment # 3)

2.2.1.2 Shear Bonding Strength

Shear bonding strength of Class H cement samples with and without fly ash were measured before and after 6 days. Before aging, samples with fly ash showed higher shear bonding strength (Fig. 4). However, after aging, the shear bonding strength of the samples with fly ash were considerably reduced due to acid attack. This behavior can be explained by low acid resistance of fly ash containing cement. As mentioned earlier, degradation depth of cement

[1] GS = Class G with silica; GSF = Class G with silica and fly ash; HS = Class H with silica; HSF = Class H with silica and fly ash.

cores with fly ash was considerably higher than that of regular cores without fly ash (Figure 1). Figure 5 presents shear bonding strength of Class H cement with and without fly ash before and after 14 and 28 days of aging at 6000 psi of 100%CH_4 and 350ºF. In this case, the aging increased the shear bonding strength of samples with fly ash. Therefore, acid attack is the key factor in reducing the shear bonding strength of fly ash containing samples.

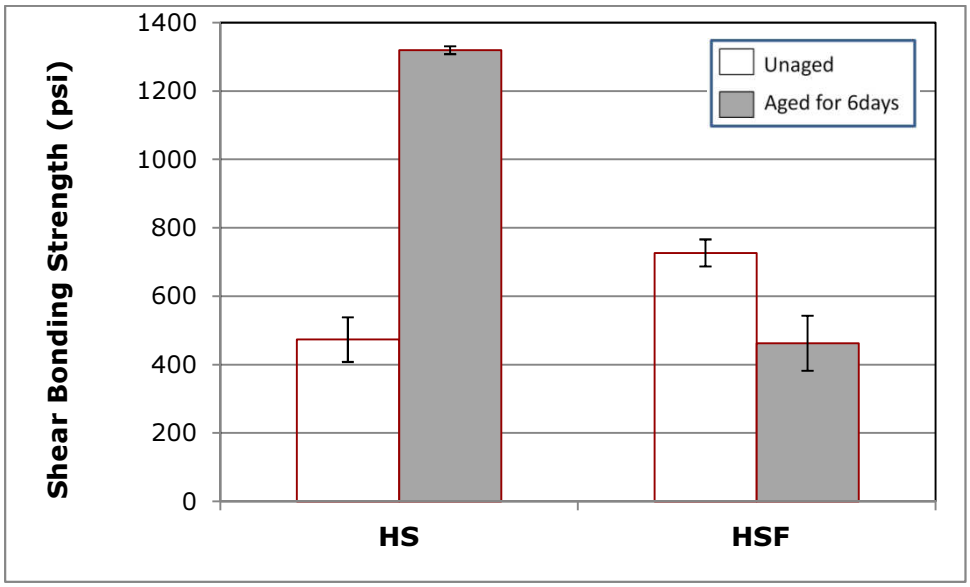

Fig. 4 Shear bonding strengths of samples before and after 6 days of aging (Experiment # 3)

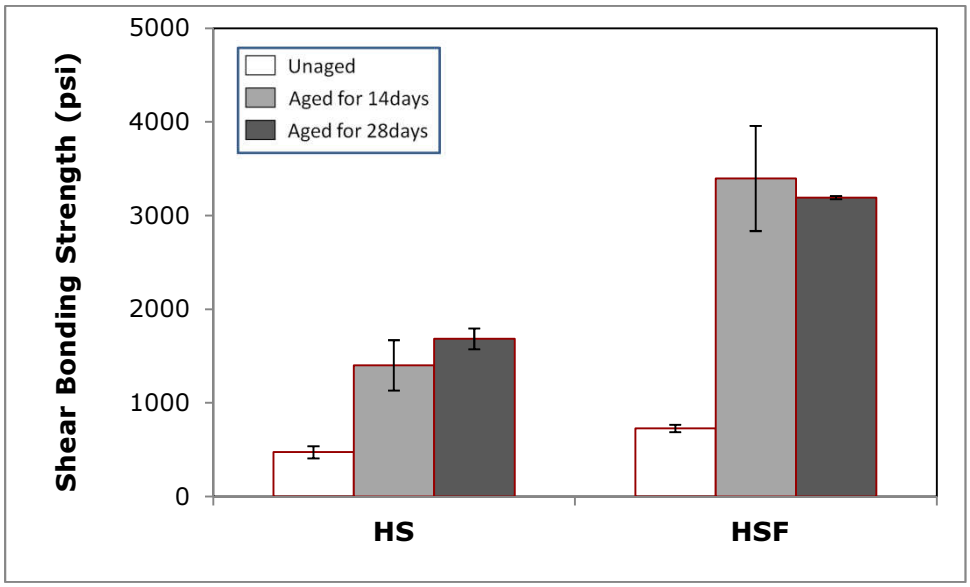

Fig. 5 Shear bonding strengths of cement samples before and after 14 and 28 days of aging (Experiment # 2)

2.2.1.3 Porosity and Permeability

Porosity and permeability of cement cores aged for six days in 90%CH_4-10%CO_2-brine system at temperature of 350ºF and pressure of 6,000 psi are shown in Figs. 6 and 7. The aging reduced porosity and permeability of cores without fly ash. Similar behavior was observed after aging Class H cement cores (with and without fly ash) in 100% CH_4 saturated brine at temperature of 350ºF and pressure of 6,000 psi. The reduction in porosity and permeability could be attributed to carbonation (i.e. the formation of calcium carbonate in CO_2 saturated system) and additional hydration during early stage of aging. However, for cores with fly ash, porosity increased after 6 days of aging in 10% CO_2 containing environment. Visual observation of the cores after aging showed that degradation depth for cores with fly ash was considerably higher than that of cores without fly ash. One of the main observations of the aging experiment in 10% CO_2 saturated brine system is that poor acid resistance of cores with fly ash in comparison with regular cores. Fly ash containing cement cores exhibited thick degraded zone, which explains the increase in porosity of the cores after aging. Previous measurements obtained after aging cores containing fly ash in 100% CH_4-brine system showed reduction in porosity.

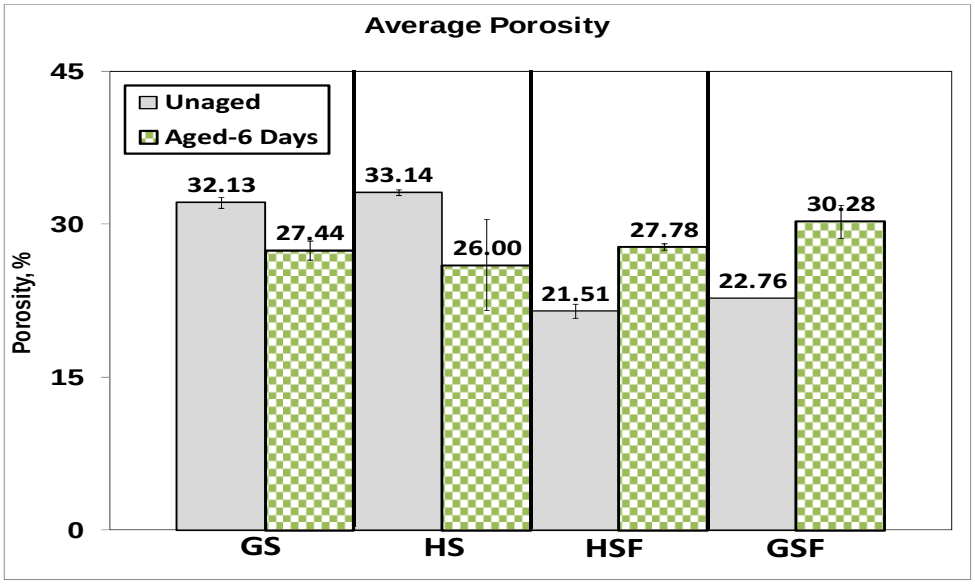

Fig. 6 Summary of porosity data before and after 6 days of aging at temperature of 350°F and pressure of 6,000 psi in 90%CH_4-10%CO_2-brine solution (Experiment # 3)

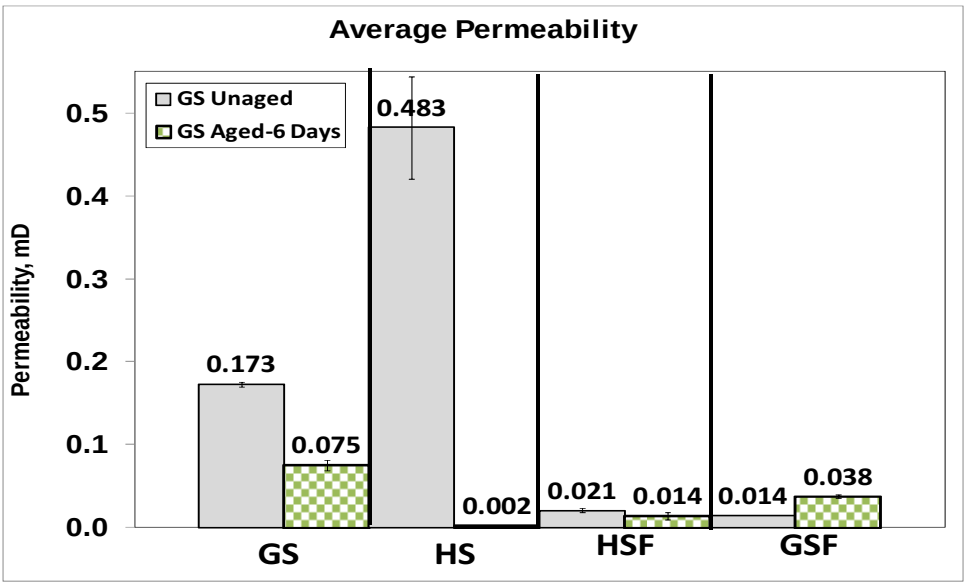

Fig. 7 Summary of permeability data before and after 6 days of aging at temperature of 350°F and pressure of 6,000 psi in 90%CH_4-10%CO_2-brine solution (Experiment # 3)

2.3 Experimental Studies on Corrosion of Tubulars (Task 3)

Considerable progress has been made in designing and selection of major components of the corrosion test setup. There are some remaining designs of components, which need to be finalized. Preliminary corrosion experiments will be started when the development of the experimental setups is completed.

3. Planned Activities

- Continuing aging experiments with brine-CO_2-CH_4 system for 14 and 28 days.
- Continue theoretical and modeling studies on tubular degradation.
- Continue designing and acquisition of components of tubular corrosion testing setups.
- TAB meeting which will be held in Houston on May 7, 2012.

4. Project Expenditures

This section presents the project expenses during the months of October (Table 1) and the cumulative expenditures.

Table 1 Current and cumulative expenditures, October, 2012

No.	Budget Categories	Current Expenses	Cumulative Expenses
1	Salaries & Wages	$8,817.39	$123,110.73
2	Fringe Benefits	$989.41	$30,792.56
3	Project Materials	$6,129.34	$48,286.90
4	Travel	$0.00	$1,333.09
5	Conference Expenses	$0.00	$0.00
6	Other Direct Costs	$0.00	$305.38
7	Equipment	$0.00	$141,502.67
8	Space Rental	$0.00	$0.00
9	Indirect Cost	$7,968.07	$101,914.37
10	Total	$23,904.21	$447,245.70

Nomenclature

HPHT	High pressure high temperature
HS	Class H with Silica
HSF	Class H with Silica and Fly ash
GS	Class G with Silica
GSF	Class G with Silica and Fly ash
R	Universal gas constant
T	Absolute temperature
P	pressure in bar
m_{CO_2}	CO_2 solubility in mole/kg
$\frac{\mu_{CO_2}^{1(0)}}{RT}$	dimensionless standard chemical potential
φ_{CO_2}	CO_2 fugacity coefficient
P_c	critical pressure
T_c	critical temperature
Z	compressibility factor
P_r	reduced pressure
T_r	reduced temperature
V_r	reduced volume
n_i^{tot}	total number of mole
P	Total pressure, bar
n_G	number of mole in gas phase
K_w	equilibrium constant of water
m_H	hydrogen ion concentration
K_1	first dissociation constant
K_2	second dissociation constant
K_H	solubility constant
$K_{m,H2S}$	Mass transfer coefficient for H_2S in the hydrodynamic boundary layer
$C_{b,H2S}$	Bulk concentration of H_2S in the liquid phase in mol/m^3
$C_{O,H2S}$	Interfacial concentration of H_2S at the outer scale/solution interface
D_{H2S}	Diffusion coefficient for dissolved H_2S in water, D_{H2S} = 2.00× 10^{-9}, in m^2/s
ε	Outer mackinawite layer porosity
Ψ	Outer mackinawite layer tortuosity factor

$C_{i,H2S}$	Interfacial concentration of H2S at the inner scale/film interface in mol/m3
δ_{os}	Thickness of the mackinawite scale $\delta_{os} = m_{os} /(\rho_{FeS} A)$ in m
m_{os}	Mass of the mackinawite scale in kg
A	Surface area of the steel in m^2
A_{H2S}, B_{H2S}	Arrhenius constants, A_{H2S} = 1.30 ×10^{-4}mol/ (m^2s) and B_{H2S} = 15500 J/mol
T_K	Temperature in Kelvin
$C_{c,H2S}$	Concentration of H_2S on the steel surface and is set to 1.00×10^{-7} in mol/m^3
$Flux_{H}^{+}$	Expressed in mol/ (m^2s)
$k_{m,H}^{+}$	Mass transfer coefficient for protons in the hydrodynamic boundary layer
$C_{b,H}^{+}$	Bulk concentration of H^+ in the liquid phase in mol/m^3
$C_{o,H}^{+}$	Interfacial concentration of H^+ at the outer scale/solution interface in mol/m^3
D_{H}^{+}	Diffusion coefficient for dissolved H^+ in water, D_{H}^{+} = 2.80×10^{-8}, in m^2/s
$C_{i,H}^{+}$	Interfacial concentration of H^+ at the inner scale/film interface in mol/m^3
$Flux_{CO2}$	Flux of CO_2 expressed in mol/ (m^2s)
$k_{m,CO2}$	Mass transfer coefficient for CO_2 in the hydrodynamic boundary layer
$C_{b,CO2}$	Bulk concentration of CO_2 in the liquid phase in mol/m^3
$C_{o,CO2}$	Interfacial concentration of CO_2 at the outer scale/solution interface
D_{CO2}	Diffusion coefficient for dissolved CO_2 in water, D_{H}^{+} = 1.96×10^{-9}, in m^2/s
$C_{i,CO2}$	Interfacial concentration of CO_2 at the inner scale/film interface in mol/m^3
D_{H2CO3}	Diffusion coefficient of H_2CO_3 in m^2/s
K_{hyd}	Equilibrium constant for CO_2 hydration reaction.
K^{f}_{hyd}	Forward reaction rate for the CO_2 hydration reaction

References

ASTM Standard C39/C39M – 12. 2012. Standard Test Method for Compressive Strength of Cylindrical Concrete Specimens.

Blount, C.W. and Price, L.C., 1982. Solubility of methane in water under natural conditions: A laboratory study; DOE Contract No. DE-A50878ET12145, Final Report.

Duan, Z. and Sun, R., Liu, R., and Zhu, C. 2007. Accurate Thermodynamic Model for the Calculation of H2S Solubility in Pure Water and Brines, Energy & Fuels, 21, pp.2056-2065.

Duan, Z.and Sun, R. 2003. An improved model calculating CO_2 solubility in pure water and aqueous NaCl solutions from 273 to 533 K and from 0 to 2000 bar, Chemical Geology 193, pp. 257–271.

Duan Z., and Mao, S., 2006. A thermodynamic model for calculating methane solubility, density and gas phase composition of methane-bearing aqueous fluids from 273 to 523K and from 1 to 2000bar. Geochimica et Cosmochimica Acta 70 3369–3386.

Huang, S.S.S., Leu, A.D., Ng, H.J. and Robinson, D.B. 1985. The Phase Behavior of Two Mixtures Of Methane, Carbon Dioxide, Hydrogen Sulfide, And Water, Fluid Phase Equilibr. 19, pp. 21–32.

Li, Z. and Firoozabadi, A. 2009. Cubic-Plus-Association Equation of State for Water-Containing Mixtures: Is ‘‘Cross Association’’ Necessary? AIChE J. 55 (7) pp. 1803–1813.

Rumpf, B., Nicolaisen, H., Ocal, C. and Maurer G., 1994. Solubility of carbon dioxide in aqueous solutions of sodium chloride: experimental results and correlation. J. Solution Chem. 23 (3), 431–448.

Selleck, F.T.; Carmichael, L.T. and Sage, B.H. 1952. Phase Behavior in the Hydrogen Sulfide-Water System. Ind. Eng. Chem., 44 (9), pp 2219–2226.

Takenouchi, S. and Kennedy, G.C. 1965. The solubility of carbon dioxide in NaCl solutions at high temperatures and pressures. Am. J. Sci. 263, 445–454.

Todheide, K. and Franck, E.U. 1963. Das Zweiphasengebiet und die kritische Kurve im System Kohlendioxid-Wasser bis zu Drucken von 3500 bar. Z. Phys. Chem. 37, 387–401.

Zirrahi, M., Azin, R., Hassanzadeh, H. and Moshfeghian, M., 2012 Mutual solubility of CH_4, CO_2, H_2S, and their mixtures in brine under subsurface disposal conditions. Fluid Phase Equilibria 324 80– 93.

Kaasa, B. and Ostvold, T. 1998. Prediction of pH and Mineral Scaling in Waters with Varying Ionic Strength Containing CO_2 and H_2S for $0<T(^oC)<200$ and $1< P$ (bar) <200, Norwegian University of Science and Technology.

Oddo, J and Tomson, M. 1982. Simplified Calculation of $CaCO_3$ Saturation at high Temperatures and Pressures in Brine Solution. SPE of AIME, P.1583-1590.

Millero, F., Huang, F., Graham, T. and Pierrot D. 2006. The Dissociation of Carbone Acid in NaCl Solutions as a Function of Concentration and Temperature. Geochimica Cosmochimica Acta 71 (2007) 46-55, Rosenstiel School of Marine and Atmospheric Science, University of Miami, miam Fl 33149, USA.

Sun, W., Nesic, S. and Young, D. 2008. Equilibrium Expressions Related to the Solubility of the Sour Corrosion Product Mackinawite. Institute for corrosion and multiphase technology, Department of chemical and bimolecular engineering, Ohio University.

Hershey, P.J., Plese, T. and Millero, F.J. 1988. The pK^{*1} for the Dissociation of H_2S in various Ionic Media. Rosenstiel School of Marine and Atmospheric Science, University of Miami.

Sun, W. and Nesic, S. 2009. A Mechanistic Model of Uniform Hydrogen Sulfide/Carbon Dioxide Corrosion of Mild Steel. NACE international.

Appendix A

Literature Review, Theoretical Studies on Tubular Corrosion

A.1. CO_2 Corrosion Model

Two different modeling approaches are considered to describe mathematically CO_2 corrosion for both scale and non-scale forming conditions. Corrosion rate under non-scale forming conditions is controlled by mass transfer in the solution and electrochemical reaction rate on the metal surface. However, under scale forming conditions, corrosion rate is controlled by mass transfer through porous media of the scale layer. During this reporting period, a new CO_2 corrosion model has been formulated, which makes rate predictions for both scale and non-scale forming conditions. This model predicts the corrosion rate based on the following assumptions:

a. Mass transfer rate of all the hydrogen ions is equal to electrochemical reaction rate of hydrogen on metal surface. The following equation can be written based on this assumption.

$$K_{mt,H^+}([H^+]_b - [H^+]_s) = 2F.K_{H^+}[H^+]_s exp\left\{\frac{-BF(E_{corr}-E_{H^+})}{RT}\right\} \quad \text{.....(A.1)}$$

b. Total cathodic reaction rate is equal to the total anodic reaction rate. Cathodic reactions are bicarbonate and hydrogen ions reduction on the metal surface. Anodic reaction is only iron ion oxidation. All the electrons produced by oxidation reaction have to be consumed by the reduction reactions. Therefore, the rate of oxidation is equal to the rate of reduction. It is assumed that all the anodic and cathodic reactions are taking place on the metal surface and no anodic or cathodic reaction takes place on scale surface since iron carbonate scale is not conductive. The following equation can be written using these assumptions.

$$\left(2F.K_{HCO_3^-}[HCO_3^-]_s exp\left\{\frac{-BF(E_{corr}-E_{HCO_3^-})}{RT}\right\} + 2F.K_{H^+}[H^+]_s exp\left\{\frac{-BF(E_{corr}-E_{H^+})}{RT}\right\}\right) = A \text{..... (A.2a)}$$

$$A = 2F.K_{Fe^{2+}}[Fe^{2+}]_s exp\left\{\frac{(2-B)F(E_{corr}-E_{Fe^{2+}})}{RT}\right\} \text{ ..... (A.2.b)}$$

c. Mass transfer rate of all the anodic species is equal to electrochemical reaction rate of all the anodic species. Hence:

$$K_{mt,Fe^{2+}}([Fe^{2+}]_s - [Fe^{2+}]_b) = 2F.K_{Fe^{2+}}[Fe^{2+}]_s exp\left\{\frac{(2-B)F(E_{corr}-E_{Fe^{2+}})}{RT}\right\} \text{ ……..(A.3)}$$

Dissociation reactions on metal surface can be used to include the effect of chemical reaction rate at the metal surface. The first and the second dissociation equations of carbonic acid and dissociation equation of water are presented below.

$$K_1 = First\ Dissociation\ constant = \frac{[H^+]_s[HCO_3^-]_s}{[CO2]_{aq}} \text{……..(A.4)}$$

$$K_2 = Second\ Dissociation\ constant = \frac{[H^+]_s[CO_3^{2-}]_s}{[HCO_3^-]_s} \text{……..(A.5)}$$

$$K_w = water\ Dissociation\ constant = [H^+]_s[OH^-]_s \text{……..(A.6)}$$

Finally, a system of equations can be established that includes 6 equations (Eqs. A.1-A.6) and 6 unknowns. The model predicts the corrosion rate under steady state condition. The unknowns are the corrosion potential and surface concentration of five different species. Constants in model equations are defined as follows:

K_{mt,HCO_3^-} is mass transfer coefficient of HCO_3^- (for scale forming conditions, through the scale layer and for non scale forming conditions through the solution)

K_{mt,H^+} is mass transfer coefficient of CO_3^{2-} (for scale forming conditions, through the scale layer and for non scale forming conditions through the solution)

$K_{mt,Fe^{2+}}$ is mass transfer coefficient of Fe^{2+} (for scale forming conditions, through the scale layer and for non scale forming conditions through the solution)

$K_{HCO_3^-}$ is electrochemical reaction rate constant of HCO_3^- ($k_2 = k_1$)

K_{H^+} is electrochemical reaction rate constant of CO_3^{2-} ($10^{(-147.9692/Tk-3.3952)/1000}$)

$K_{Fe^{2+}}$ is electrochemical reaction rate constant of Fe^{2+} ($2\times10^{(-4461.397/Tk+16.4953)/1000}$)

$E_{HCO_3^-}$ is electrochemical potential of HCO_3^- ($-0.6104+((-0.001535)\times(T_c-25))$)

E_{H^+} is electrochemical potential of CO_3^{2-} (0)

$E_{Fe^{2+}}$ is electrochemical potential of Fe^{2+} ($-0.44+((0.0000518)\times(T_c-25))$)

B=0.5

F = 96500

R = 8.314

T_c is temperature in degree C

T_K is temperature in degree K

After solving the system of equations, the corrosion potential (E_{corr}) is used to calculate corrosion current density (i_{corr}) and consequently corrosion rate.

$$i_{corr.} = i_{Fe} = 2F.K_{Fe^{2+}}[Fe^{2+}]_s exp\left\{\frac{(2-B)F(E_{corr}-E_{Fe^{2+}})}{RT}\right\} \quad \text{(A.7)}$$

$$C.R.(mpy) = 0.129 \times 10^6 \left(\frac{Mw.i_{corr.}}{n.\rho}\right) \quad \text{(A.8)}$$

where $Mw = 55.85$ is molecular weight in gr, n=2 is the number of electrons, and $\rho = 7.86$ is density in g/cm^3.

Figure A.1 shows a flowchart that shows the calculation steps involved in CO_2 corrosion rate model. The main inputs for corrosion mode are temperature, pressure, water chemistry, and flow conditions. CO_2 solubility in brine solution can be predicted as a function of temperature, pressure, and water chemistry. Bulk concentration of different species and pH of the solution can be predicted as a function of temperature, pressure, and water chemistry by knowing the CO_2 solubility. A system of 4 equations and 4 unknown was solved to predict the bulk chemistry and pH of the solution. Mass transfer coefficient of different species can be also predicted by knowing the flow characteristics. In order to calculate the corrosion potential and concentration of different species at the metal surface, system of 6 equations and 6 unknowns (Eq. A.1 - A.6) has to be solved. Super saturation at the metal surface can be calculated by determining the surface concentration of different species. If the super saturation factor is larger than one, then iron carbonate scale forms at the metal surface. Scale formation rate helps to determine the scale thickness. The formation of scale on the metal surface affects the diffusion of different species to the metal surface. Therefore, in order to account for the scale, the calculation needs to be repeated applying the system of 6 equations. Mass transfer coefficients have to be replaced by diffusion coefficients in porous media. New corrosion potential can be used to compute the corrosion rate. If super saturation factor is smaller than one, then iron

carbonate scale doesn't form on the metal surface and corrosion rate can be determined using corrosion potential calculated for non-scale forming conditions.

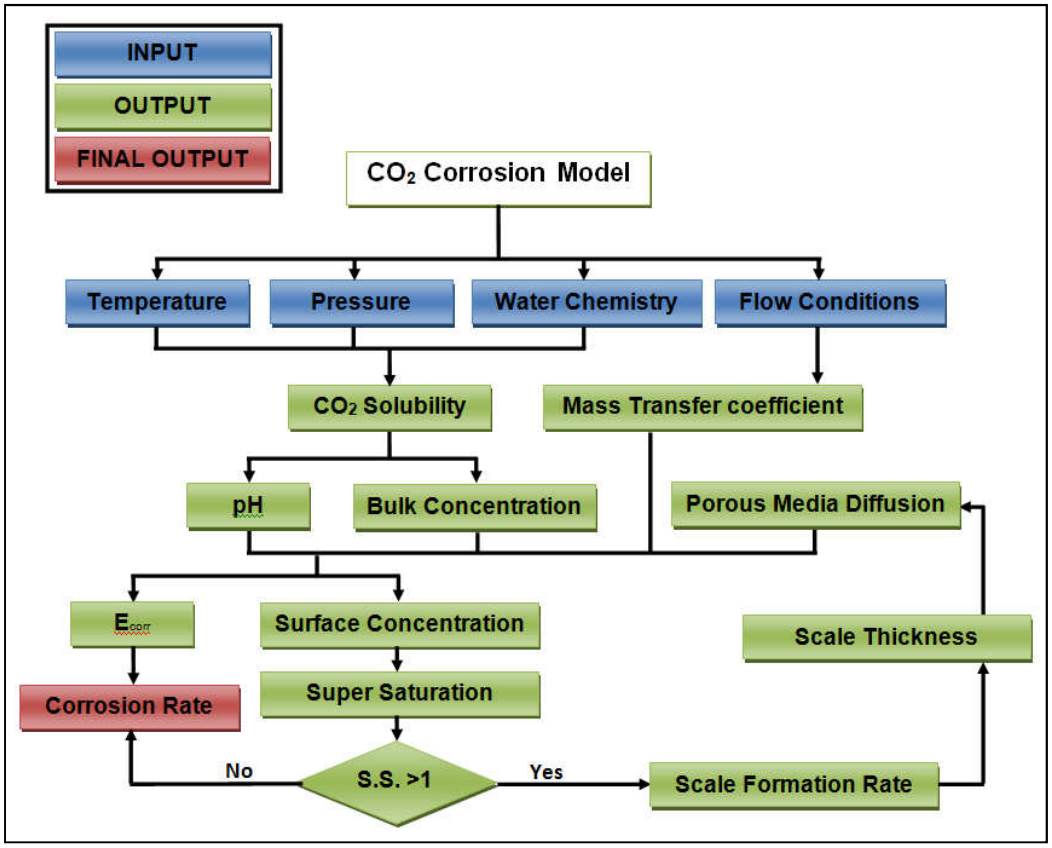

Fig. A.1 CO_2 corrosion rate prediction model

A.2 H_2S/CO_2 Corrosion Model

The presence of carbon dioxide with or without hydrogen sulfide represents the actual condition in the oil field. The internal CO_2 corrosion of mild steel in the presence of H_2S along with formation water causes corrosion problem in the oil and gas industry. CO_2/H_2S corrosion process is often controlled by the H_2S concentration due to different types of scales that are formed on steel surface. Several studies demonstrated the existence of a critical H_2S concentration, which indicates the corrosive gas or mechanism that controls the corrosion rate.

Sun and Nesic (2007) investigated the mechanism and kinetics of mild steel corrosion in H_2S environment. They developed model to predict the corrosion rate of H_2S in the presence of iron sulfide scale formation. Figure A.2 shows a schematic of H_2S corrosion process. Earlier, Nesic et al. (2006) conducted an experimental study to investigate the protective scale that forms due H_2S corrosion process. Based on the experimental results, 'mackinawite' was found as the predominant type of the iron sulfide scale. It is formed due to the direct reaction of H_2S

with the underlying steel. The model shows that the H_2S corrosion of mild steel is a function of H_2S gas concentration, temperature, velocity and the protectiveness of the scale. More recently, Sun and Nesic (2009) developed a model to predict CO_2/H_2S corrosion rate by adding CO_2 term to the H_2S model. The model assumes that mackinawite layer still protects the steel surface from corrosion in mixed CO_2/H_2S system. With the formation of mackinawite layer, the presence of CO_2 in the system has a little effect on corrosion rate.

Furthermore, in CO_2/H_2S corrosion of mild steel, there is a possibility for both iron carbonate and iron sulfide to be formed on the steel surface. A number of studies (Smith and Joosten, 2006; Lee, 2004) were conducted on the kinetic of layer formation and its effect on the corrosion kinetics. The studies demonstrated that protective layer formation is one of the key factors governing the corrosion rate. Smith and Joosten (2006) published a review article that described the research work done in the area of CO_2/H_2S corrosion in harsh oil field environment. It was concluded that the mechanism of CO_2/H_2S corrosion remains unclear. In the case of H_2S, an extensive review on the mechanism of iron sulfide formation is conducted by Lee (2004). The study indicated the existence of many types of iron sulfide layers that may form as a product of H_2S corrosion. It was found that mackinawite is the most prevalent iron sulfide that is formed on the steel surface. Mackinawite can be converted to another form of iron sulfide depending on H_2S activity, temperature and time of exposed.

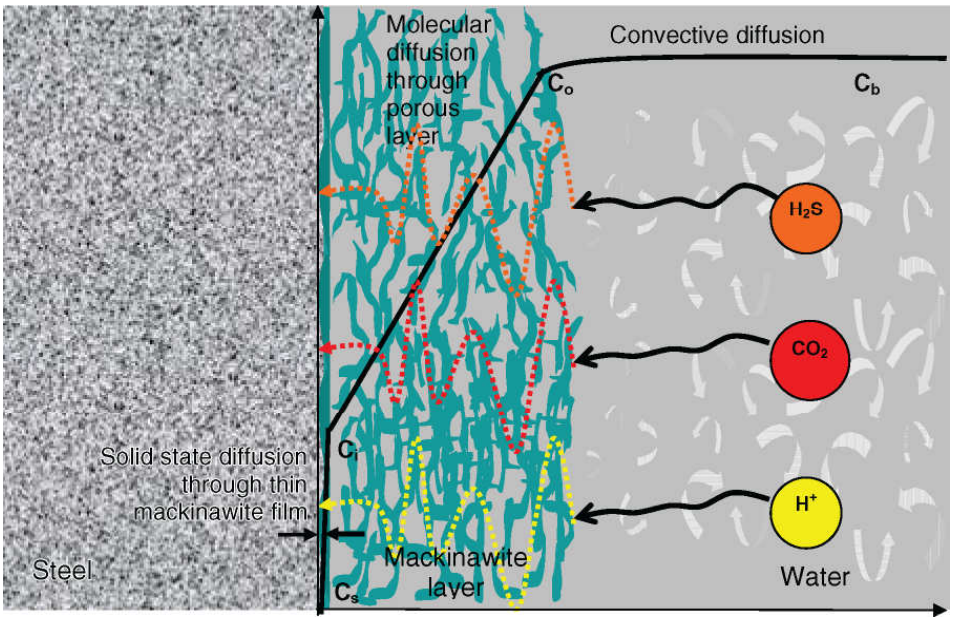

Fig. A.2 Schematic of the CO_2/H_2S corrosion process

A.2.1 Physio-Chemical Model

Based on the experimental work that has been conducted by Nesic (2006) on the H_2S corrosion, a mathematical model was constructed. The experimental results demonstrate the formation of a Mackinawite layer on the steel surface as a product of H_2S corrosion. In their earlier study, Sun and Nesic (2008) concluded that mackinawite can be the predominant iron sulfide species. However, other types of iron sulfide may form on the steel surface when attacked by H_2S, especially if the exposure is for a long duration. In general, the protective layer forms due to fast, direct and homogenous reaction of H_2S solution with steel surface. Two types of Mackinawite layers can be formed on the steel surface:

- Very thin (<< 1µm) and tight inner film
- Thick (>> 1µm) outer layer, which is loose and very porous

The outer layer can be intermixed with any type of iron sulfide or iron carbonate that may have precipitated. In brine saturated with CO_2, both iron sulfide and iron carbonate may form on the steel surface depending on water chemistry, H_2S concentration and competitiveness of iron carbonate and iron sulfide. Sun and Nesic (2008) found that mackinawite layer formation is the dominant process in the most cases of mixed CO_2/H_2S corrosion. In other cases, iron carbonate crystals may form intermixed with the mackinawite.

A.2.2 Mathematical Model

Due to the presence of the inner mackinawite film and porous outer layer, it is assumed that the corrosion rate of steel in H_2S solution is always affected by mass-transfer rather than electrochemical process. The corrosion is also influenced by the direct reaction of H_2S and CO_2 with steel surface as well as the reduction of protons (H^+). Therefore, a model can be established based on the mass transfer flux of the three elements as a result of: i) convective mass transfer through the boundary layer, ii) molecular diffusion through the liquid in pores in the outer layer, and iii) solid-state diffusion through the inner mackinawite layer. In the steady state condition, the three fluxes of each element are equal and equivalent to the corrosion rate. The fluxes can be expressed as:

i. Effect of H_2S

$$Flux_{H2S} = A_{H2S}.e^{-\frac{B_{H2S}}{RT_K}}.\ln\frac{C_{b,H2S} - Flux_{H_2S}\left(\frac{\delta_{0.5}}{D_{H_2S}.\varepsilon\psi} + \frac{1}{K_{m,H_2S}}\right)}{C_{s,H_2S}} \quad \text{..... (A.9)}$$

H_2S corrosion rate is given as: $CR_{H2S} = Flux_{H2S}.M_{Fe}/\rho_{Fe}$. The amount of Mackinawite retained on the steel surface changes with time and depends on the layer formation rate and the sulfide layer mechanical damage rate. It is expressed as:

$$SRR = SFR - SDR \quad \text{..... (A.10)}$$

where SRR is sulfide layer retention rate, SFR is the sulfide layer formation rate, which is equivalent to the corrosion rate and SDR is the sulfide layer mechanical damage rate which is 0.5CR. By knowing the layer retention rate, SRR, the change in mass of the outer sulfide layer can be calculated as:

$$\Delta m_{os} = SRR.M_{FeS}.A.\Delta t \quad \text{..... (A.11)}$$

where M_{Fes} is the molar mass of iron sulfide in kg/mol and Δt is the time interval in seconds. Then thickness of the formation is calculated as:

$$\delta_{0.5} = \Delta m_{os}/(\rho_{FeS}.A) \quad \text{..... (A.11)}$$

ii. Effect of pH

$$Flux_{H^+} = A_{H^+}.e^{-\frac{B_{H+}}{RT_K}}.\ln\frac{C_{b,H^+} - Flux_{H^+}\left(\frac{\delta_{0.5}}{D_{H^+}.\varepsilon\psi} + \frac{1}{K_{m,H^+}}\right)}{C_{s,H^+}} \quad \text{..... (A.12)}$$

The flux is equivalent to the corrosion rate by protons:

$$CR_{H^+} = \frac{Flux_{H^+}}{2}.\frac{M_{Fe}}{\rho_{Fe}} \quad \text{..... (A.13)}$$

iii. Effect of CO_2

$$Flux_{CO2} = A_{CO2}.e^{-\frac{B_{CO2}}{RT_K}}.\ln\frac{C_{b,CO2} - Flux_{CO2}\left(\frac{\delta_{0.5}}{D_{CO2}.\varepsilon\psi} + \frac{1}{K_{m,CO2}}\right)}{C_{s,CO2}} \quad \text{..... (A.14)}$$

In case of H_2S, the pure mass transfer is assumed and $C_{s,H2S}$ and $C_{s,H}^{+}$ are set to be in very small quantity, which is 1×10^{-7} mol/m^3. In CO_2 corrosion, CO_2 hydrates and forms H_2CO_3 at the steel surface which slows and controls the process. Therefore, the flux of CO_2 can be expressed as:

$$Flux_{CO2} = C_{s,CO2}\left(D_{H2CO3}.\varepsilon\psi.K_{hyd}^{f}.K_{hyd}\right)^{0.5} \quad \text{.....(A.15)}$$

By combining Eqns. (A.14) and (A.15), the flux of CO_2 can be given as:

$$Flux_{CO2} = A_{CO2}.e^{-\frac{B_{CO2}}{RT_K}}.\ln\frac{C_{b,CO2} - Flux_{CO2}\left(\frac{\delta_{0.5}}{D_{CO2}.\varepsilon\psi} + \frac{1}{K_{m,CO2}}\right)}{\frac{Flux_{CO2}}{\left(D_{H2CO3}.\varepsilon.\psi.K_{hyd}^{f}.K_{hyd}\right)^{0.5}}} \quad \text{..... (A.16)}$$

The bulk concentration of CO_2 in the solution, $C_{b,CO2}$ (mol/bar) can be estimated via Henry's constant as:

$$C_{b,CO2} = P_{CO2} \times K_{sol} \quad \text{..... (A.17)}$$

where P_{CO2} is the partial pressure of carbon dioxide in bar, K_{sol} is a Henry's constant which is a function of temperature (℉) and ionic strength (mo l/L).

$$K_{sol} = \frac{14.5}{1.00258} \times 10^{-(2.27+5.65\times10^{-3}T_f - 8.06\times10^{-6}T_f^2 + 0.075\times I)} \quad \text{(A.18)}$$

Other parameters are acquired to be obtained in order to estimate flux of CO_2 such as diffusion coefficient of H_2CO_3, equilibrium constant for the CO_2 hydration reaction and forward reaction rate for the CO_2 hydration reaction. These parameters are presented in Table A.1.

Table A.1 Parameters of Flux equations

Parameter identification	Constant	Source
Equilibrium constant of CO_2 hydration	$K_{hyd} = 2.58\times10^{-3}$	Palmer and Van Eldik(1983)
Forward reaction rate for CO_2 hydration reaction	$K_{f\,hyd} = 10^{329.85-110.54\times\log T_K - \frac{17265.4}{T_K}}$	Palmer and Van Eldik(1983)
Diffusion constant of H_2CO_3 at 20℃, (m^2/s)	$D_{ref} = 2.00\times10^{-9}$	KvareKval (1997)
Diffusion constant of H^+ at 20℃, (m^2/s)	$D_{ref} = 9.312\times10^{-9}$	Newman (1991)
Diffusion constant of CO_2 at 20℃, (m^2/s)	$D_{ref} = 1.96\times10^{-9}$	Perry (1984)
Diffusion constant of HS^- at 20℃, (m^2/s)	$D_{ref} = 2.00\times10^{-9}$	Nordsveen et al. (2001)

The influence of temperature on diffusion coefficient can be obtained from the Stokes-Einstein equation:

$$D = D_{ref} \times \frac{T}{T_{ref}} \times \frac{\mu_{ref}}{\mu} \quad \text{(A.19)}$$

where T_{ref} is a reference temperature = 20℃, the dynamic vis cosity of water is μ_{ref} = 1.002 Kg/(m.s) and the diffusion coefficient can be obtained from Table A.1. Dynamic water viscosity as a function of temperature is given as:

$$\mu = \mu_{ref} \times 10^{\frac{1.3272.(20-T)-0.001053.(20-T)^2}{T+105}} \quad \text{(A.20)}$$

Then, total corrosion rate in mixed CO_2/H_2S saturated brine environment is given as:

$$CR_T = CR_{H_2S} + CR_{H^+} + CR_{CO2} \quad \text{.....(A.21)}$$

A.2.3 Calculation Process

The following flow chart demonstrates CO_2/H_2S corrosion rate model procedure that can be summarized as:

I. Determine the bulk concentration of CO_2, H_2S and H^+ in the solution at desirable conditions.

II. Calculate H_2S corrosion rate in the absence of formation layer using Eqn. (A.9).

III. Estimate the amount of the formation scale that formed over time using Eqn. (A.12).

IV. Calculate H_2S corrosion rate in the presence of formation scale using Eqn. (A.9).

V. Calculate H^+ and CO_2 corrosion rate using Eqns. (A.13) & (A.14), and then the total corrosion rate is simply defined as the summation of the corrosion rate that is caused by H_2S, CO_2 and H^+.

VI. Steps from 3 to 5 are repeated to estimate the total corrosion rate over new time interval.

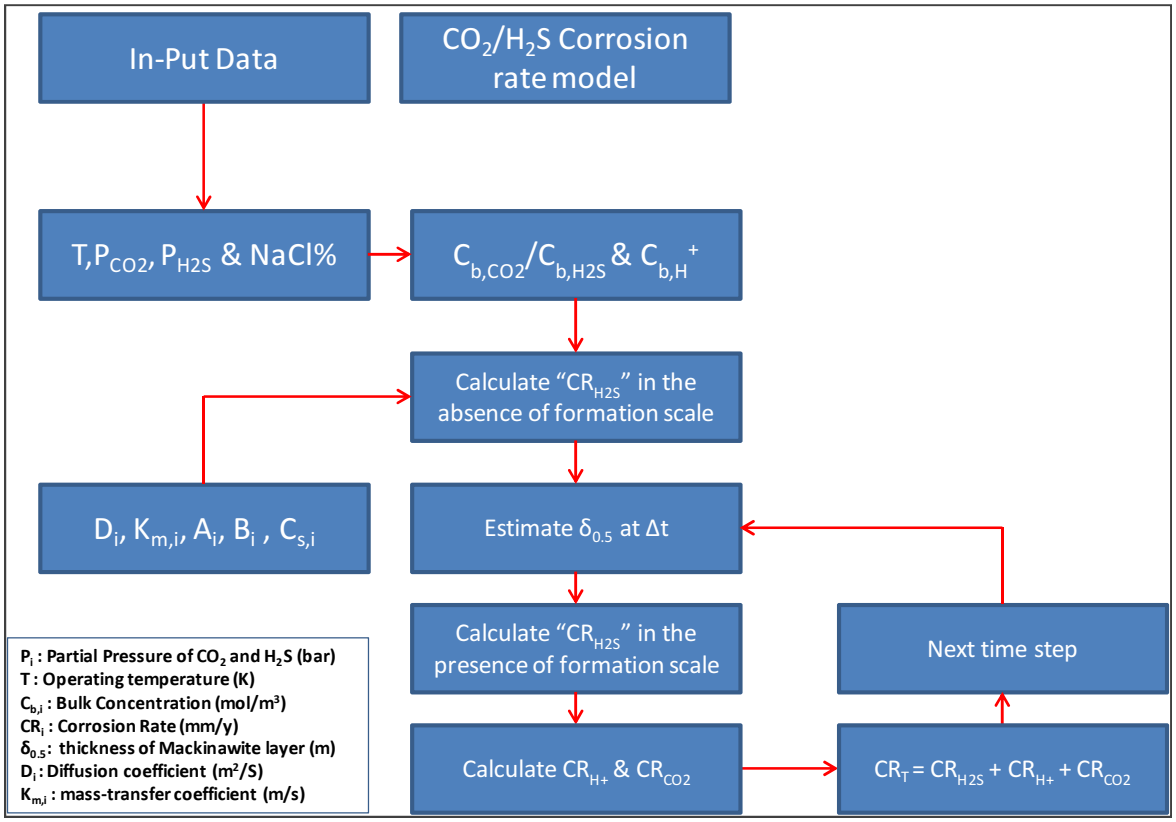

Fig. A.3 Schematic of CO_2/H_2S model calculation process

A.2.4 Model Limitations

Research is in progress to eliminate some of the limitations of CO_2/H_2S corrosion models. The following limitations are the most common ones:

i. The model assumes uniform H_2S and CO_2/H_2S corrosion. It cannot be used to predict localized corrosion in either environment.

ii. The model is applicable in the range of partial pressure of 0.01-10 bar for both hydrogen sulfide and carbon dioxide.

iii. The model does not account for any precipitation of iron sulfide, iron carbonate, or any other scale.

iv. The model also does not account for various transformation of sulfide from one type to another that depends on H_2S concentration, temperature and period of exposed time.

v. The model is valid for pH range of 3-7, because it does not account for dissolution of iron sulfide layer that may occur at very low pH.

A.2.5 Model Modification

In order to modify this model to be valid for high pressure and temperature applications, the following model formulations need to be improved;

i. The bulk concentrations of CO_2, H_2S and H^+ should be estimated at high temperature conditions.
ii. The influence of H_2S concentration and temperature on formation of iron sulfide layer should be estimated.

A.2.6 Model Verification

Model proposed by Sun and Nesic (2009) calculates the H_2S solubility in the brine to predict the corrosion rate. The model is improved in this study. Model predictions for CO_2/H_2S system are compared with experimental data obtained at P_{CO2} = 29 bar, P_{H2S} = 0.0441 – 1 psi, T = 158℃, pH = 4.2 – 4.9, and liquid velocity = 0.3 m/s (Fig. A.4). Comparison of the improved model predictions with measurements showed significant enhancement in corrosion rate prediction after 300 hours. The model is more accurate in predicting corrosion rate for longer time periods.

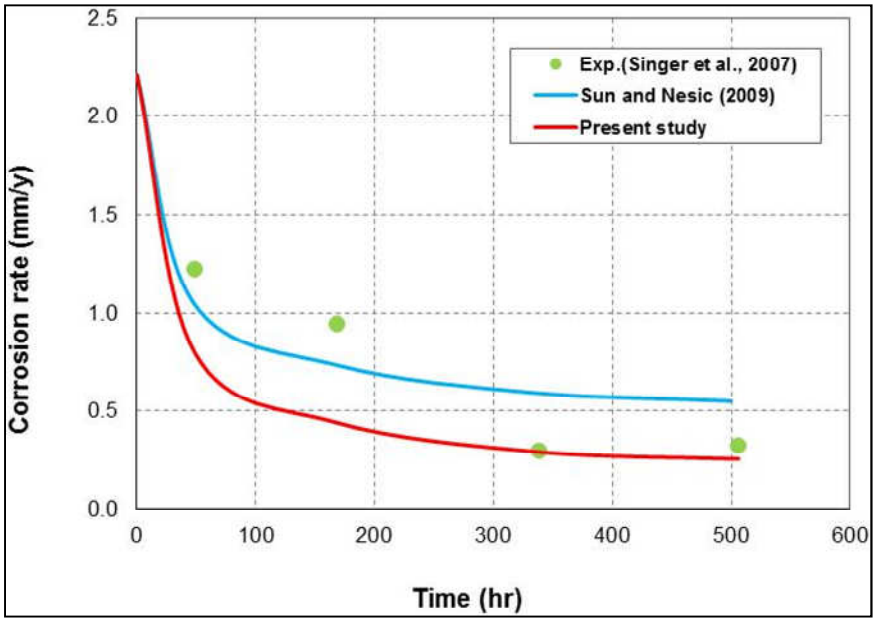

Fig. A.4 Comparison between experimental data (Singer et al. 2007), Sun and Nesic model (2009), and prediction using modified model presented in this report

Modified CO_2/H_2S corrosion model is also compared with experimental data by Kvarekval (2003) at P_{CO2}=101 psi, P_{H2S} = 20 - 62 psi, T = 248℉, pH = 3.95 – 4.6, and liquid

velocity = 10 m/s (Figure A.5). Modified CO_2/H_2S corrosion model showed better agreement with experimental data in comparison with the existing model (Sun and Nesic, 2009).

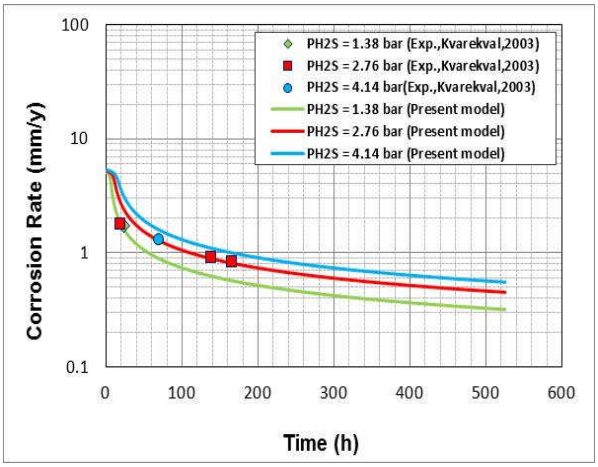

(a)

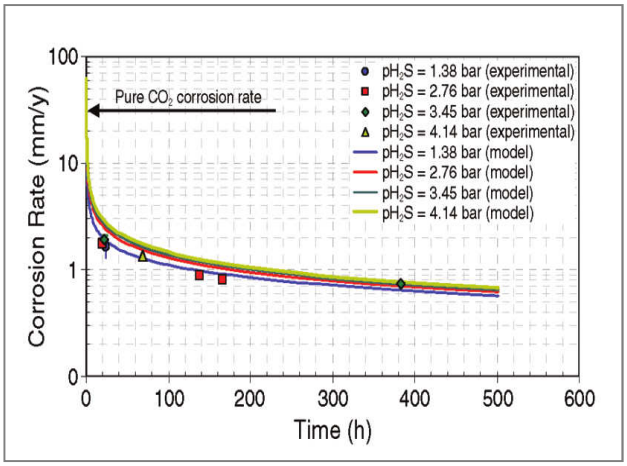

(b)

Fig. A.5 Comparison between predictions and measurements: a) data (Kvarekval, 2003); and b) data (Kvarekval, 2003; Sun and Nesic model, 2009)

Project Title: Effect of H_2S and CO_2 in HPHT Wells on Tubulars and Cement

Report Type: Monthly Report

Report #: 14

Reporting Period: October 22nd, 2012 to November 21st, 2012

Authors:

Ramadan Ahmed, Principal Investigator

Subhash Shah, Co-Principal Investigator

Samuel Osisanya, Co-Principal Investigator

Rida Elgaddafi, Research Assistant

Omosebi, Omotayo A., Research Assistant

Himanshu Maheshwari, Research Assistant

Adarsh Naidu, Research Assistant

Aman Srivastvava, Research Assistant

Prepared under BSEE Project # E12PC00035

by

THE UNIVERSITY OF OKLAHOMA

January 5, 2013

1. Summary of Accomplishments

This monthly report presents the progress made during the project period October 22, 2012 to November 21, 2012. As indicated in the previous report, sample aging was stopped after 6 days due to the degradation of heating bath oil (silicone based heating medium). After replacing the degraded silicone oil with synthetic fluid, a new aging experiment was performed with cement cores and bonding samples, which were prepared from Class H and G cement slurries. Silica flour, fly ash, antifoaming agent and Hydroxyethylcellulose (HEC) were added as additives during slurry preparation. The samples were aged in 90%CH_4-10%CO_2 saturated 2% brine solution for 14 and 28 days at high-pressure high-temperature (HPHT) condition (350ºF and 6,000 psi). O-ring seals on the heating jacket failed after operating for 21 days with the new synthetic fluid. The experiment was stopped for one week to replace the o-rings. Samples were kept in 2% brine under ambient condition during the repair process.

After successful completion of the aging process, samples were recovered from the cell. Physical and mechanical properties (porosity, permeability, density, and compressive and bonding strength) will be measured and presented in the next monthly report.

Preliminary additive screening study has been started. Results are predominately encouraging. The feasibility of various additives proposed in the previous monthly report, is going to be tested in a sequential manner, in order to assess their effectiveness. The tests involve measuring of the slurry properties such as viscosity, API fluid loss, density and thickening time. In addition, the effects of additives on properties of bonding and cored samples such as porosity, permeability, and compressive and shear bond strength will be investigated.

Theoretical and modeling studies on tubular corrosion were continued. Corrosion mechanisms are strongly related to the type of protective film formed on the surface of the metal. Published experimental studies showed the formation of two layers of mackinawite on the steel surface. In this project, corrosion mechanism prediction models will be adopted for high-pressure and high- temperature (HPHT) applications.

The third Technical Advisory Board (TAB) meeting was held on November 2, 2012. The minutes of the meeting are presented in Appendix A. Furthermore, we received feedback from BSEE on our previous reports. Our response is presented in Appendix B.

Our plan for the coming weeks is to continue the aging tests at different temperatures. After aging, physical properties of the samples will be evaluated. Beside this, we will continue theoretical and modeling studies on tubular corrosion. The corrosion setup developmental activities will also continue. Additive screen studies will be continued in the coming months.

2. Overall Project Progress

2.1 Theoretical Studies (Task 1)

Investigation on cement additives was continued during this reporting period. Based on literature review, certain additives have been selected to be used in the cement samples. The additives that have been chosen are classified (Table 1) into two categories:

Category 1. The additives, which react chemically against CO_2 and H_2S and prevent the degradation of cement.

Category 2. The additives, which lower the porosity and permeability of the cement matrix thereby reducing the transport of ionic species that cause the carbonation and leaching of cement.

Table 1: Additives considered in the research

S.N.	Category	Additive (Sample Name)	Nomenclature	Extra Water
1	Category 1 (Against CO_2)	Hydroxyapatite (HOAP)	HSHO GSHO	23% by weight of HOAP
2	Category 1 (Against H_2S)	Zinc Oxide (ZNO)	HSZN GSZN	None
3	Category 2	Magnesium Oxide (MGO)	HSMG GSMG	None
4	Category 2	SBR Latex (LT)	HSLT GSLT	None
5	Category 2	Micro Silica (MS)	HSMS GSMS	4.47 ml/gm of Micro Silica
6	Category 2	Micro Silica + SBR Latex (MSLT)	HSLM GSLM	4.47 ml/gm of Micro Silica

Studies on CO_2/H_2S corrosion modeling are in progress. As previously reported, a mechanistic model has been developed to predict corrosion rate as function of time. The model was originally formulated by Sun et al. (2008) to predict CO_2/H_2S corrosion rate at low-pressure and low-temperature conditions. Their experimental results (Sun and Nesic, 2009), showed the formation of two layers of mackinawite on the steel surface. In this investigation, their model has been extended to make predictions for high-pressure and high- temperature (HPHT) conditions by accounting the change in bulk concentration of carbon dioxide, hydrogen ion and hydrogen sulfide on the corrosion rate. Experimental measurements obtained under HPHT conditions are necessary to validate the model. Literature review indicates that the mackniwaite scale often forms on the steel surface as the initial layer. Therefore, the mackinawite stability limit models have been reviewed. Details of the models will be presented in the coming monthly reports.

2.2 Experimental Studies on Degradation of Cement (Task 2)

A new aging experiment (Experiments # 4) has been successfully completed. Four different types of cement cores (i.e. Class H and G with Silica, Class H and G with silica and fly ash) and bonding samples were aged in 2% brine saturated with gas mixture containing 90%CH_4 and 10%CO_2 at 6,000 psi and 350ºF for 14 and 28 days. O-ring seals (silicone based) used in the heating jacket failed after 21 days of aging the samples. The seals were replaced with PTFE seals that are resistant to hydrocarbons. After replacing the seal, the aging was continued for additional 7 days. The samples were recovered after 2 and 4 weeks of aging. The physical properties of the samples will be measured in the coming weeks.

To conduct additive screening study, physical properties of slurries containing different additives will be compared to that of neat Class H and Class G cement. Additive continuing samples need to qualify on three different levels of testing before they are kept in the ageing cell. The tests which need to be conducted are in the following order:

I. Slurry Properties

Slurry Density: The theoretical density of the slurries can be obtained applying ideal mixing rules. Using the mixing rule, slurry with the desired properties can be prepared by estimating the required amount of each component of the slurry. The density of the slurry should be in the range of the neat slurry. Excessive high-density or low-density slurry need to be adjusted accordingly. The actual density measurement has to be done with the mud balance immediately after the slurry is prepared.

Slurry Viscosity: Rheological properties of the slurries will be measured and compared with that of conventional cement slurry. Standard oil field viscometer (OFITE Model 900 Viscometer) will be used to measure slurry viscosity. The stress values obtained at different speeds (3RPM, 6RPM, 100RPM, 200RPM, 300RPM and 600RPM) will be plotted on a graph and compared. The viscosity measurements should be taken immediately after the slurry is prepared.

Filtration Loss: The filtration loss of cement slurry can be tested using a standard filtration press. Excessive filtration loss with respect to the neat cement slurry should not be accepted as it can lead to problem during well cementing. The filtration loss test needs to be done immediately after the slurry is prepared.

Slurry Consistency: The thickening time of the slurry needs to be measured with the consist-o-meter and compared to the neat slurry. A very long or short thickening time shall be compensated with use of accelerators or retarders. The consist-o-meter test needs to be done immediately after the slurry is prepared.

Once the additive slurry sample is able to provide acceptable density, viscosity, fluid loss and consistency, it can be taken towards curing. The samples for shear bond strength test also need to be prepared. Sample curing shall be done in similar conditions as neat cement slurries, i.e. 200ºF and immersed in 2% brine for 5 days in a pressure cooker.

II. Physical & Mechanical Properties of Cured Cement Cores

Visual Test: The cores after curing and coring should be free from any sort of crack or damage.

Compressive Strength: The cores should be subjected to wet confined compressive strength test. They should be able to withstand force at least equivalent to the un-aged conventional cement cores.

Shear Bonding: The samples should be able to withstand at least the shear force equivalent to the un-aged conventional cement cores.

Porosity/Permeability: The samples should be subjected to the porosity/permeability measurement after drying to a constant weight in an oven.

III. Ageing Experiments

Cement cores and bonding samples will be kept in the ageing cell for 14 days to observe the change in physical and mechanical properties. After aging, compressive and shear bonding strength, porosity and permeability of the samples will be measured and compared with that of conventional cement.

2.3 Experimental Studies on Corrosion of Tubulars (Task 3)

Considerable progress has been made in designing and selection of major components of the corrosion test setup. There are some remaining designs of components, which need to be

finalized. We have received injection cylinders needed for developing the corrosion setup. We are waiting for other two key items to arrive. Preliminary corrosion experiments will be started when the development of the experimental setups is completed.

3. Planned Activities

- Continuing aging experiments with brine-CO_2-CH_4 system for 14 days varying the aging temperature.
- Continue theoretical and modeling studies on tubular degradation.
- Continue cement additive screen study.
- Continue designing and acquisition of components of tubular corrosion testing setups.

4. Project Expenditures

This section presents the project expenses during the months of November (Table 2) and the cumulative expenditures.

Table 2 Current and cumulative expenditures, November, 2012

No.	Budget Categories	Current Expenses	Cumulative Expenses
1	Salaries & Wages	$7,985.60	$131,096.33
2	Fringe Benefits	$2,118.39	$32,910.95
3	Project Materials	$9,108.97	$57,395.87
4	Travel	$0.00	$1,333.09
5	Conference Expenses	$0.00	$0.00
6	Other Direct Costs	$0.00	$305.38
7	Equipment	$0.00	$141,502.67
8	Space Rental	$0.00	$0.00
9	Indirect Cost	$9,606.48	$111,520.85
10	**Total**	**$28,819.44**	**$476,065.14**

References

Sun, W., Nesic, S., Woollam, R., Young, D. 2008. Equilibrium Expressions related to the Solubility of the Sour Corrosion Product Mackinawite, Ind. Eng. Chem. Res., 47, pp 1738-1742.

Sun, W. and Nesic, S. 2009. A Mechanistic Model of Uniform Hydrogen Sulfide/Carbon Dioxide Corrosion of Mild Steel. NACE international.

Appendix A

MINUTES

3rd Technical Advisory Board Meeting

Project # M11PC00030

Project Title: Effect of H_2S and CO_2 in HPHT Wells on Tubulars and Cement

Meeting Date: November 2, 2012
Time: 8:30 AM – 3:30 PM Central Time
Meeting Location: Courtyard Hotel, Houston, TX

Attendees: Timothy Steffek (BSEE), Candi Hudson (BSEE), Christy Lan (BSEE), Arild Saasen (Det Norske), Ashok Santra (Weatherford International), Marco May (Vallourec), Benjamin Iverson (Halliburton), Scott Bray (Baker Hughes), Mark Vorderbruggen (Baker Hughes), Ramadan Ahmed (OU), Samuel Osisanya (OU), Shokrallah Hassani OU), Himanshu Maheshwari (OU), Adarsh Naidu (OU), Omotayo Omosebi (OU), Aman Srivastava (OU) and Rida Mohamed (OU).

This was the 3rd Technical Advisory Board meeting of the Project # M11PC00030 titled "Effects of Hydrogen Sulfide (H_2S) and Carbon Dioxide (CO_2) in HPHT Wells on Tubulars and Cement."

Dr. Ahmed started the meeting at 9:00 AM on Friday November 2, 2012 by welcoming the BSEE program personnel Timothy Steffek of (COR), Candi Hudson, Christy Lan and other participating Technical Advisory Board Members (TAB) to the meeting. He then made a presentation on the overall project overview to date. He presented the objectives, scope, project schedule, project deliverables to date, and challenges.

Major objectives are divided into three main tasks: one theoretical and two experimental tasks. The first task is theoretical and deals with understanding of the degradation of tubulars and cement in the presence of sour gases (H_2S and CO_2) under HPHT conditions. The second task is the experimental work to investigate the degradation of cement in the presence of sour gases under HPHT conditions. The third task is the experimental work to investigate the degradation of tubulars in the presence of sour gases under HPHT conditions.

Eight presentations were made which addressed the objectives and tasks stated in the contract. Five presentations including Dr. Ahmed opening presentation were made during the morning session and three were made during the afternoon session. The first presentation was made by Dr. Ahmed on overall project overview. Four other presentations were on the effects of sour gases on porosity, permeability, and mechanical properties of cement as well as new cement formulations to prevent cement degradation in the presence of sour gases at HPHT. The last three presentations were on the effects of sour gases on corrosion of tubulars. Below are the summary of the various presentations.

Morning Session

First Presentation

Dr. Ahmed presented the status of the project as at this time. He enumerated the challenges faced in achieving the objectives. Major challenges were:

- Tube fitting leaks due to high brine concentration. The problem was resolved by reducing brine concentration.
- Unable to maintain aging pressure of more than 6000 psi due to inlet valve leaks – Heavy duty gas tight ball valves have been ordered to replace the leaking globe valves.
- Quick degradation of heating oil (silicone oil). Problem solved by replacing silicone oil with synthetic oil.
- Excessive vaporization of synthetic oil. Problem is being solved by building a closed loop heating system – heat exchange system in which there is no contact with the oil. Then, Dr. Ahmed invited research assistants (graduate students) and postdoctoral associate to present their accomplishments of the project.

2nd Presentation by Himanshu Maheshwari (MS Graduate Student)

Mr. Maheshwari presented the results of theoretical studies of the effects of sour gases exposure on the permeability and porosity of oil well cements. He also presented the results of series of experiments on cement degradation in the presence of sour gases. He presented the mechanisms for CO_2-H_2S attack on cement under harsh high pressure and high temperature borehole conditions. The mechanisms include alteration of porosity and permeability, carbonation and leaching process, and thermodynamics & kinetics of chemical reaction. Complex cement degradation model fragmented into sub-models: Carbonation and Leaching Models, Porosity Model, and Permeability Model.

Experimental results show that porosity is a function of free water in cement slurry. At 100% CH_4 there is decrease in Φ and k due to more hydration under HPHT conditions. Cement has a property of pore shrinking after hydration process. At 10% CO_2 there is decrease in Φ and k of samples without fly ash due to accommodation of $CaCO_3$ in the void space, while there is Increase in Φ and k of samples with fly ash due to unaccommodating structure of the cement. TAB members suggested measuring the shrinkage of cement after aging. Also, one of the TAB members suggested performing aging experiments for long durations up six months. The PIs pointed out that running a long term aging test is very difficult to conduct due to limited aging facility. However, the experiment can be considered if additional aging facilities such as corrosion testing cells will be available in the future. BSEE experts stressed the need of X-Ray Diffraction Analysis (XRD) to investigate the degradation of cement.

3rd Presentation by Aman Srivastava (new MS Graduate Student)

Mr. Srivastava presentation focused on the development of new cement formulation for lowering the degradation rate due to acid attack. He presented the outcomes of an extensive literature survey of various additives for cement slurry in sour gas environment. He identified the major parameters that affect cement degradation as cement composition/structure, temperature, pressure, pH and composition of the surrounding liquid. He categorized several additives for their advantages and disadvantages (screening). Additives that are more appropriate for cement slurry have been selected for cement slurry formulation. The following tests are planned for the evaluation of the formulated cement slurries: rheology, filtration loss, physical and mechanical properties, and aging.

4th Presentation by Omotayo Omosebi (new PhD Graduate Student)

Mr. Omosebi presentation focused on the durability testing of set cement: compressive and shear bond strength tests as well as elasticity tests of set cement exposed to sour gases environment. Tests were performed on un-aged and aged set cement in CO_2 environment. The following conclusions were highlighted:

- Hydration of samples at high temperature and pressure accounts for increase in compressive strength since no acidic gas is present
- Excess water that is not used for hydration caused the reduction in compressive strength after 14 days of aging

- Inconsistencies in compressive strength of measurements of samples with fly ash occurred because the cores are susceptible to temperature and pressure variations.
- Increase in shear bonding strength is attributed to more hydration at high temperature and pressure with the cement swelling against the steel pipe.
- The dominant effect of cement hydration accounts for less degradation in the presence of CO_2.

During the discussion, TAB members suggested the use of other instrumentation that can provide strain measurements with low noise level. We are in communication with members to obtain detailed specifications of the instrumentation.

5th Presentation by Dr. Shokrollah Hassani (Post-Doctoral Fellow)

Dr. Hassani presented a new model for cement degradation under HPHT acidic environment. The model combined three mechanisms: hydration, CO_2 solubility/pH, and cement leaching. The model assumed that calcium leaching as the main mechanism for cement degradation. The leaching model predicts the amount of leached calcium ion resulting from exposure of cement to acidic solutions. It relates the calcium ion concentration in the liquid phase to that in the solid phase. Proposed model was compared to experimental data from literature.

Afternoon Session

6th Presentation by Dr. Shokrollah Hassani (Post-Doctoral Fellow)

Dr. Hassani presented CO_2/H_2S corrosion of tubulars at HPHT conditions. Corrosion of tubular depends on pH, temperature, pressure, and water chemistry. He reviewed in details the major types of corrosion of tubulars: pitting corrosion, sulfide stress cracking, and stress cracking corrosion reviewed. He presented the design and construction of experimental facility for corrosion testing that is in progress. He also presented literature review of fourteen (14) different CO_2/H_2S corrosion. Based on the review a new mechanistic model for CO_2 corrosion is developed and a modified mechanistic model for CO_2/H_2S corrosion is being proposed. Critical H_2S concentration for CO_2 and H2S corrosion control region was determined.

7th Presentation by Rida Elgaddafi (PhD Graduate Student)

The presentation here also focused on modeling of corrosion behavior of tubulars under sour gases environment. The major goal is to develop a mechanistic model for CO_2/H_2S corrosion rate prediction at HPHT. The model is used to predict pH of the fluid saturated with CH_4, CO_2 and H_2S; bulk concentration of CO_2 and H2S in the brine solution at HPHT, and to have better understanding of the kinetics of scale formation in CO_2/H_2S environment. HPHT pH model that has been developed in this study provides satisfied results when compared with the available experimental data at normal temperature and pressure. Corrosion rate model has been established to be applicable at HPHT and it shows acceptable prediction comparing to the experimental data. Literature reviews showed that H_2S concentration, temperature and solution pH have significant influence on composition and structure of corrosion scale formation. The corrosion rate decreases with time until it reaches a steady state condition after which it remains constant. This occurs due to scale formation on the steel surface, which acts as a protective layer. Modeling corrosion rate requires better understanding of the natural of scale formation that formed due to CO_2/H_2S corrosion.

8th Presentation by Adarish Naidu (Graduate Student)

Mr. Naidu presentation also focused on corrosion of tubulars exposed to CO2 containing fluids. The goal is to better understand corrosion mechanism of tubulars at HPHT and in CO2 environments. Understanding and modeling is used to predict the CO2 corrosion rate for HPHT conditions. The following results were presented:

- CO2 solubility model was used to predict the CO2 concentration in the brine solution. Model prediction was verified by experimental data from the literature.
- Bulk concentration of different species for CO2 saturated brine solution was predicted by developing and solving a system of five equations and five unknowns.
- Solution pH was predicted by knowing the chemistry of the solution. Model prediction was verified by comparing with experimental data from literature.
- A new mechanistic model was proposed for prediction of CO_2 corrosion rate.

Future Plans

Several future plans are discussed; notable among them are the following:

- The study of the effect of pressure, temperature; gas composition on mechanical properties of set cement will continue. That is, measurement of Φ, k, and alteration fronts, FTIR Mineralogy and SEM for un-aged and aged of set cement samples.

- Validation of cement degradation model with experimental data
- Development and testing of new cement formulations - durability tests will be performed for un-aged and aged samples at HPHT conditions in sour gases environment.
- Effect of temperature, pressure and gas composition on mechanical properties degradation of conventional cement
- Continuing the theoretical and modeling study of CO_2/H_2S corrosion of tubulars under HPHT conditions
- Experimental investigation of CO_2/H_2S corrosion behavior and also stress corrosion cracking of the tubulars under HPHT conditions
- Validating model prediction as well as calibrating same with experimental data at HPHT conditions

Date for Next 2 Year first Annual Meeting

The date for the next Technical Advisory Board meeting was set for Tuesday May 7, 2013 to be held in Houston. This was selected and agreed on because it coincides with Offshore Technology Conference (OTC) in Houston which is very convenient for the members.

Appendix B: Response to Comments Made by BSEE

Progress Report #12

2.2.1.1 Confining Compressive Strength Measurements

- Figures 1 a-d – Comparison of Compressive Strength of four different types of cement samples (a) GS, (b) HS, (c) GSF, (d) HSF un-aged – what were the values for the error bars in the graphs?

Response: Values of error bars are shown in Table B-1.

  - Why was there such a large error value in particular for:
    - Figure 1a – GS 14 days?
    - Figure 1b – HS 28 days?
    - Figure 1c – GSF 14 days?
    - Figure 1d – HSF 0 days?

Response: Data available in the literature indicate significant scattering (10 to 15%) of compressive strength measurements. In addition to the normal variation in compressive strength, due to the development of micro-cracks during coring and aging processes some of the samples show unexpectedly low compressive strength. Thermally induced stresses and expansion of dissolved gas in the pores can cause cracks during heating and depressurization of the aging cell.

- Figure 1c – where is the plot for GSF 28 days? *Response: All the GSF samples were broken after 28 days.*
- Figure 1d – where are the plots for HSF 14 days and HSF 28 days? *Response: All the HSF samples were broken after 14 days.*

Table B-1 Values of error bars

Core #	Aging Duration (days)	Average Strength (psi)	Error Bar (psi)
GS	0	4588	669
GSF	0	4023	446
HS	0	3854	591
HSF	0	2872	467
GS	14	4309	1185
GSF	14	4846	1190
HS	14	3489	359
GS	28	4322	510
HS	28	3500	887

2.2.1.2 Porosity and Permeability Measurements

- Why was there an initial decrease after 14 days and then an increase for the porosity and permeability measurement for class G cement with silica? *Response: Initial decrease in porosity and permeability is related to more hydration in the early stage of aging. However, the increase in porosity and permeability after 4 weeks of aging is attributed to leaching process.*
  - After what time was there an increase? *Response: Usually after 28 days, porosity and permeability starts to increase in CH4 system.*
- Figure 2 (a) GS Aged– what was the percent error for the three plots *Response: 2% for 0 days, 5% for 14 days, and 12% for 28 days*
  - Any reason why there was a large percent error for the 28 days plot? *Response: Aged samples show slightly larger error because samples are aged in different shelves which may be slightly different in terms of CO2 concentration in solution and temperature.*

    - Is the large error possibly due to the initial decrease and then increase in the permeability and porosity? *Response: We suspect it might be one of the factors.*
- Figure 2 (c) GSF aged– why wasn't there any error bars for the 14 days plot? *Response: There is an error bar but it is really small.*
- Figure 2 (d) HSF Aged – why wasn't there any error bars for the 4 days plot? *Response: There is no error bar since there was only one sample left. The rest of the samples were broken.*
- Figure 3 a-d – what was the percent error for all graphs? *Response: Error percentage was in the range of 2-50%.*
- Figure 3a GS Aged and Figure 3b HS aged – for the 28 days, why is the error range so large? (note it begins from 0) *Response: Permeability of a cement core is very sensitive to porosity change. Samples aged for 28 days show maximum error in porosity and as a result they also display higher scattering in permeability measurements.*
- Figure 4 a – where are the error bars for the GS un-aged (density 3.6) and GS aged 28 day (density 2.11)? *Response: There was only one sample left. The rest of the samples were broken.*
- What was the error value for GS aged 14 day (Figure 4a)? *Response: It is less than 2%.*
- What was the error value for HS un-aged and HS aged 14 day (Figure 4a)? *Response: It is less than 2%.*
- Figure 4c – what are the error values for HSF un-aged (density 2.39) and HSF Aged 14 day (density 2.44)? *Response: They are less than 2%.*
- Figure 4c – where is the plot for HSF Aged 28 day? Why is there a single point? *Response: Fly ash containing HSF samples were broken after 28 days of aging.*
- Figure 4d – what are the error values for GSF un-aged (density 2.34) and GHSF Aged 14 day (density 2.39)? *Response: They are less than 2%.*
- Figure 4d – where is the plot for GSF Aged 28 day? Why is there a single point? *Response: Other samples were broken after 28 days.*

2.2.2.1 Confining Compressive Strength Measurements

- What was the different cement preparation procedure for these experiments?

Response: Slightly larger volume of slurry was prepared since different molds were used to prepare 2-inch samples instead of 1.5 samples. The change in the volume of slurry affected the mixing condition and the 2-inch cement samples were more porous than the 1.5-inch samples.

Appendix A – Theoretical Development of New Cements and Effect of Different Additives

A.2 - Reaction of CO2

- What type of dispersants can increase the viscosity?

Response: Dispersants are used for lowering (i.e. controlling excessive thickening of cement slurry resulting from increased cement content) the viscosity of the cement slurry. The sentence should read: "- Increase the system density (i.e. decrease porosity) to lower the permeability. The density increase can be achieved by increasing the cement content in the slurry. However, higher concentration of cement results in excessive thickening of the slurry and a dispersant should be added to offset the increase in viscosity."

- What type of additives can reduce the reaction of CO_2 with the reactive species in the cement?
    - Are these additives the sodium-calcium-borosilicate glass, cenosphere, silica alumina microscophere, hydroxyapatite mentioned ?

Response:

- *Hydroxyapatite is a reactive component against CO_2 in the cement (Sugama 2006). The presence of Hydroxyapatite in the cement minimizes the CO_2 attack on the other binding components (CSH and Portlandite) because Hydroxyapatite consumes most of the CO_2 available in the pore space. The*

Hydroxyapatite reacts with CO_3^{-2} ions without any destruction of the cement structure.

- *The sodium-calcium-borosilicate glass or cenospheres or silica alumina microspheres are incorporated in the cement slurry system so as to trap the calcium carbonates in their spaces. This helps in reducing the further reactions involved in leaching of calcium carbonates and deterioration of desired cement properties. However, they do not participate in direct control of the reaction of CO_2 (US patent # 8091642).*

- Which group at Argonne National Laboratory identified ceramic based cements to show good performance in wellbore applications that can provide effective sealing against nuclear wastes?
    - Would this be the Engineering Development and Applications Dept. of the Nuclear Engineering Division under the direction of Chris Grandy at Argonne National Laboratory (Argonne, IL)?

Response: The reference for the ceramic based cement from Argonne National Laboratory has been taken from Benge (2009). The reference to the particular paper has been sighted in Benge (2009) as "Ross, E., Squeeze Play. Ceramic Cement Offers Cost Effective Solution for Zonal Isolation (2007) New Technology Magazine, November 2007, pp. 27."

- Did Sugama mention how SSAS increase the cement strength?

Response: According to Sugama, the combination of two crystalline phases, calcium silicate hydrate ($CaO.SiO_2.xH_2O$, CSH) and tobermorite ($5CaO.6SiO_2.xH_2O$) phases are responsible for maintaining the strength SSAS cements. Although these two phases are susceptible to acid attack, the CSH phase plays an important role in retarding the rate of acid attack and leaching. After leaching of Ca by the acid, Ca-deficient CSH preferentially reacted with the Mg from slag to form magnesium silicate hydrate ($Mg_2Si_2O_5(OH)_4$, the lizardite phase) that not only retarded the rate of acid attack, but also retained the integrity of the cemenetitious structure. Thus, after undergoing acid attack, the SSAS cement exhibits a self-healing characteristic.

- To what degree? Was it measured?

Response: A modified SSAS cement with Class F fly ash showed improved acid resistance. It was measured as weight loss after leaching the cement in acid environment. It showed 7% reduction in weight loss after acid attack.

- Any thoughts to how will obtain hydroxyapatite for additives to cement?
    - Will hydroxyapatite be synthesized in the lab or purchased commercially?
    - What grade? Medical grade as hydroxyapatite is the ceramic material of bone.

Response: The additive hydroxyapatite is purchased from the Spectrum Chemicals as 40 mesh powder. The properties are slightly different from the actual natural hydroxyapatite found in the bones as its factory made.

Table A.2 Porosity and Permeability Reducing Cement Additives

- What's the chemical composition of the suggested cationic latex?

Response: The cationic latex, which has the reference of the US patent# 7687440, refers to the cationic latex JG6082 from Dow Reichhold Inc. This particular latex is now no longer available in the USA. The composition of the latex was also not mentioned in the patent. However, styrene butadiene latex with combination of emulsifiers shall be able to provide stable cement-latex slurry with reduced porosity and permeability (Funquan et al. 2006, Hou et al. 2010).

References:

1. Benge G. (2009); “Improving well bore seal integrity in CO2 injection wells”; Energy Procedia 1 (2009), 3253-3529
2. Fuquan Sun, Lv Guangming and Jin Jianzhou (2006); “Application and research of latex tenacity cement slurry system”; SPE 104434
3. Hou Wei, Funquan Sun, Yonghui Gao, Jianguo Zeng, Mingjiang Huo, Jiandong Wang (2010); “ Research Of High Temperature Tolerance Latex Slurry System”; Twentieth (2010) International Offshore and Polar Engineering Conference Beijing, China, June 20-25, 2010, ISOPE
4. Sugama T. (2006); “Advance Cement for Geothermal Wells”; BNL-77901-2007-IR

Progress Report #11

2.2.1 Compressive and Bonding Strength Measurement Techniques

Figure 2a- Compressive strength tests for unaged Class G cement containing 35% silica-stress rate vs. time, have the following questions:

- Any considerations why the data points are nonlinear and scattered from 20 – 70 seconds and from ~110 – 220 seconds?

Response: In time interval of 20-70 seconds, there was no load applied to the samples yet and piston was moving at a constant speed to touch the sample. In time interval of 70-110 seconds, loading rate sharply increased as the sample resisted a constant rate of deformation caused by the piston moving a constant speed. When the loading rate reaches 35 psi/s, the computer is programmed to slow down the piston speed to maintain a constant loading rate of 35 psi/s. However, during the process, the piston speed may become too low and loading rate drops below the desired rate. As a result, the computer continuously adjusts the piston speed to maintain a loading rate of approximately 35 psi/s. This causes loading rate fluctuations which are shown in the figure between 110 and 220 seconds.

- Also, any considerations why there are a few data points which drop off at the end of the graph at ~220 seconds? Is this possible due to unloading at the end of testing?

Response: At the end of experiment, the sample fails and doesn't exhibit strong resistance against deformation and consequently the loading rate dropped immediately.

- Figure 2b- Compressive strength tests for unaged Class G cement containing 35% silica-stress vs. time, any considerations why there are a few data points which drop off at the end of the graph at ~240 seconds? Is this possible due to unloading at the end of testing?

Response: At the end of experiment, the sample fails and doesn't exhibit strong resistance against deformation and consequently the compressive load dropped immediately.

- Figure 3a – Shear bonding strength measurement of Class H cement with silica and fly ash after aging (Experiment 2) stress rate vs. time – there are a set of data points followed by a gap and then a single data point at about 280 seconds, is the single data point due to unloading?

Response: At the end of experiment, the bond between the cement and the pipe fails and doesn't exhibit strong resistance against sliding and as a result the loading rate dropped immediately.

- Figure 3b – Shear bonding strength measurement of Class H cement with silica and fly ash after aging (Experiment 2) stress vs. time – there is a gap between the set of data points that progresses linearly and another set of data points at about 280 seconds, is this due to unloading?

Response: At the end of experiment, the bond between the cement and the pipe fails and doesn't exhibit strong resistance against sliding and as a result the loading dropped immediately.

2.2.3 Results for Experiment 2

- What is the rate limiting step for the mixture, reaction of fly ash addition to cement, i.e. in second paragraph of this section, it's mentioned that the addition of fly ash to cement as an additive reacts with calcium hydroxide ($Ca(OH)_2$) and forms calcium silicates and increases cement strength and thickening time. Interested in knowing what is the rate limiting step for this reaction?

Response: The rate limiting step is either the reaction of calcium hydroxide with silica component of fly ash or the diffusion of reacting species in the cement pore (Biernacki et al., 2001).

- Any idea at what time cracking occurred during aging of the cement samples containing the fly ash?

Response: Cracking doesn't occur with specific time duration. It is happening at random with fly ash containing cement cores. We have seen sample cracking after 6, 14 and 28 days.

- Was there a particular orientation (angle) location where the cracks occurred in the samples?

Response: Usually cracking occurs in slightly inclined orientation from the cylindrical core axis.

- On page 12 it's mentioned that aging at 350^{o}F, pressure of 6,000 psi in CH_4-brine system for two weeks did not change the compressive strength; however, the cement cores with fly ash were sensitive to the testing conditions. How were the cement cores with fly ash sensitive to testing conditions?

Response: Because some of the fly ash samples were cracked during aging process and failed easily when compressive strength tests were performed.

- On Figure 11 – Compressive strengths of wet cement samples (before and after 14 days of aging at temperature of 350^{o}F and pressure of 6,000 psi in CH_4-brine solution, Experiment 2) – what were the values of the error bars for each plot?

Response: Approximately 20, 45, 20, 10, 15, and 35%, respectively.

- Why was there such large error bars for Class G aged and Class G with Fly ash aged?

Response: Often fly ash containing samples show large error due to micro-cracks, which significantly reduce compressive strength of some of the samples. There is no good reason for large error bars for Class G cement. This may be just a coincidence.

- On Figure 12 – Effect of fly ash on shear bonding strength of Class H cement with silica after 14 days of aging at temperature of 350^{o}F and pressure of 6000 psi in CH_4 bring solution (Experiment 2) – what were the values of the error bars for each plot in this figure?

Response: The error bars are approximately 30 and 25%.

- Why was there such a large error bar for Class H with fly ash?

Response: The absolute error is high for samples with fly ash. However, the percentage error is comparable. The addition of fly ash improved the bonding strength of the cement.

- Note: understand that there is an impact on the cement behavior with the addition of fly ash to the mixture.

Appendix A – Literature Review and Theoretical Studies on Tubular Corrosion

A.1 CO2 Solubility Model

- Duan's model will be validated using the measured data under HPHT conditions, for which alloy?

Response: Duan's model is used to predict CO_2 solubility in brine solution. There is no direct relationship between the solubility and corroded material.

- Since there were challenges due to the leakage and corrosion, can this model be validated at the lower concentration and pressure for the experiments?

Response: CO_2 solubility model is already validated with different authors. In this project corrosion models, which utilize the solubility model will be developed and validated using experimental measurements.

A.2 Hydrogen Sulfide Solubility Model

- For further understanding in Table A.4 – Interaction parameters for H2S solubility in brine and pure water, why is the T-P C8 coefficient for the Zeta parameter for H2S-Na-Cl ($z_{H2S\text{-}Na\text{-}Cl}$) 0?

Response: Because it shows the best match with experimental data of different authors. These coefficients are purely empirical.

Progress Report #10

Comments, Questions on Properties Evaluation/Characterization & Testing

2.2 Experimental Studies on Degradation of Cement (Task 2)

- In Figure 1 on p. 4 – In addition to the NaCl deposited on one of the Hastelloy tee joints during aging experiment 9000 psi, 350oF and 9wt% NaCl, was any oxidation/oxide scaling detected?

Response: There was very thin oxide scale formed on the surface of tube fittings. Oxide scaling is known to form on high temperature alloys like Hastelloy at high temperatures and pressures.

- Page 5 – What type of corrosion protective paint was (or will be) coated on the pipes?

Response: The pipes are coated with Rust-Oleum high heat primer (first coat) and enamel (second coat).

- Page 5 – What alloy was the ¾" seamless pipe?

Response: Carbon steel, ASTM A-106.

- For future characterization – what would be the experimental procedure to determine/verify that there is good adhesion/bonding between the cement and the tubular?

Response: Shear bonding strength combine with cement core shrinkage/expansion after aging.

- Curing of the cement – what was the gas environment for the curing? N2 (at what purity?)? Atmosphere?

Response: Cement samples were cured in pressure cookers at 200 deg F. The initial gas environment was atmospheric.

- Understand this was mentioned previously, what was the weight percent of fly ash and Si added to the samples again?

Response: The weight percent of fly ash and Si were 100 and 35%, respectively.

2.3 Experimental Studies on Corrosion of Tubulars (Task 3)

- For future characterization – what would be the experimental procedure to determine/verify that there is good adhesion/bonding between the cement and the tubular?

Response: Shear bonding strength combine with cement core shrinkage/expansion after aging.

- Will this involve destructive evaluation of cross-sectioning characterization?

Response: We will explore destructive characterization techniques.

- Page 10, last paragraph, second sentence, unclear to visualize. How will the specimens be "attached to a Teflon sleeve?" (It's challenging to bond to Teflon.)

Response: Teflon sleeve will be machined to hold the sample in place.

- For future studies – how will pH be measured/monitored?

Response: There is no commercial pH meter available for high pressure high temperature conditions. The pH of the solution will be predicted using available models.

Appendix A – A.1.1 pH Measurement at HPHT Conditions

- Clarify what is the cell constant in the equation A29 on page 25 of Appendix A below? Is it a constant value or determined?

Response: The cell constant depends on the design of the cell and it is determined based on the design.

$$\sigma_{H+} = \frac{C^{H+} D_{H+} F^2}{RT} = cell\ constant\ x \left(\frac{l_{H+}}{V}\right)$$

- Clarify for the following equation A30 of page 25 of Appendix A the log(constant) is the log of "cell constant" of equation A29 above?

Response: No, it is the cell constant divided by some other constants on the left hand side of the equation.

$$log\left(\frac{l_{H+}}{V}\right) = pH + log(constant)$$

CO2 Corrosion Model

- The corrosion model is based on what type of tubular alloy? (Iron Fe based?)

Response: The corrosion model is based on carbon steel.

- Any considerations, will CO2 model be developed for Nickel based-high temperature alloys in the future?

Response: The model can be adopted for Nickel based-high temperature alloys.

References:

Biernacki, J. J., Williams P.J. and Stutzman, P.E. 2001. Kinetics of Reaction of Calcium Hydroxide and Fly Ash, ACI materials Journal, No. 98-M37, July-August.

Project Title: Effect of H_2S and CO_2 in HPHT Wells on Tubulars and Cement

Report Type: Monthly Report

Report #: 15

Reporting Period: November 22nd, 2012 to December 21st, 2012

Authors:

Ramadan Ahmed, Principal Investigator

Subhash Shah, Co-Principal Investigator

Samuel Osisanya, Co-Principal Investigator

Rida Elgaddafi, Research Assistant

Omotayo Omosebi, Research Assistant

Himanshu Maheshwari, Research Assistant

Adarsh Naidu, Research Assistant

Aman Srivastvava, Research Assistant

Jueun Hwang, Research Assistant

Prepared under BSEE Project # E12PC00035

by

THE UNIVERSITY OF OKLAHOMA

January 31, 2013

1. Summary of Accomplishments

This monthly report presents the progress made during the project period November 22, 2012 to December 21, 2012. During this reporting period, aging experiments were continued using cement cores and bonding samples. Mechanical and physical properties of the cores and samples were measured before and after aging. In addition, the effects of different cement additives on properties of cement slurries and cores are being investigated.

According to our monthly plan, aging experiments were conducted at different temperatures while maintaining other test parameters (pressure, gas composition and brine concentration) constant. Three bottom shelves in aging cell were not used during the experiments; because samples previously aged in these shelves showed different properties when compared with the same samples aged in other shelves. Tests were conducted with cores made of Class H and Class G cement slurries. Fly ash containing samples showed excessive cracking in previous aging experiments. As a result, they were excluded from the experiment.

Permeability and porosity measurements obtained from Class G and Class H cores aged for 2 and 4 weeks in acidic brine show a mixed trend. After 2 weeks, core permeability and porosity reduced, and then increased. The reversal of the trend shows degradation of cement resulting from calcium leaching. Initial reduction in permeability and porosity could be due to an additional hydration and carbonation of portlandite and CSH. Aging experiments conducted at different temperatures with Class G cement show decline in core porosity and permeability as temperature increases. For Class H cement, the trend is mixed. At low temperatures (100 to 225°F), a slight reduction in porosity and permeability was observed with the increase in temperature. However, this trend was reversed at higher temperatures.

Additive screening study was continued. Zinc oxide is found to be a strong cement retarder. Magnesium oxide provided expected results in terms of improving cement properties such as porosity, permeability, and compressive and bonding strengths. Hydroxyapatite containing cement formulations have been tested for their slurry properties. Physical properties of unaged cores containing hydroxyapatite will be tested next.

Theoretical and modeling studies on tubular corrosion were continued. Corrosion mechanisms are strongly related to the type of protective film formed on the surface of the metal. Published experimental studies showed the formation of two layers of mackinawite on the steel surface. In this project, corrosion mechanism prediction models will be adopted for high-pressure and high- temperature (HPHT) applications.

Our plan for the upcoming weeks is to continue: i) the aging tests at different CO_2 concentrations; ii) theoretical and modeling studies on tubular corrosion; and iii) additive screening studies.

2. Overall Project Progress

2.1 Theoretical Studies (Task 1)

The studies by Lecolier et al. (2008 and 2010) suggested the use of metal oxides such as Fe_2O_3 and Mn_3O_4 as additives to control cement degradation in H_2S containing environment. Experiments performed with Mn_3O_4 showed improvement of cement resistance against H_2S attack. Zinc oxide is a similar material that can also be as effective against H_2S attack.

Sasaoka et al. (1994) conducted an experimental study on the reaction between ZnO and H_2S under various conditions. The paper focused on use of ZnO as a sorbent for H_2S in solid state fuel cells. One of the objectives was to examine the reaction in presence of H_2O or CO_2. In absence of H_2O or CO_2, formation of elemental sulfur was observed, which confirmed the catalytic decomposition of H_2S in presence of the sorbent ZnO. The chemical reactions can be given as:

$$ZnO + H_2S \rightarrow ZnS + H_2O \quad \text{..... (1)}$$

$$H_2S \rightarrow (1/n)Sn + H_2 \quad \text{..... (2)}$$

With inclusion of H_2O in the system, the formation of elemental sulfur was reduced. This was explained using two possible reasons. First, the active elemental surface sulfur is reacting with H_2O to form H_2S as shown below.

$$Zn^*S^* + H_2O \rightarrow Zn^*O + H_2S \quad \text{..... (3)}$$

The active surface sulfur is present due to mild deposition of sulfur from H_2S on the reactor tubes. As show in Eqn. (2), it acts as a precursor to the elemental sulfur reduction reaction shown in Eqn. (1). With removal of this active surface sulfur, the overall deposition of sulfur is reduced. Another reason presented is, as H_2O is a similar molecule to H_2S, a competitive adsorption of H_2O can inhibit the reaction with H_2S as shown below.

$$Zn^*O + H_2O \rightarrow Zn^*(OH)_2 \quad \text{..... (4)}$$

Zn* and S* represent the active surface zinc and sulfur species under experimental conditions. Introducing CO_2 in the system, an accelerated reaction was observed except in the initial stages. COS was observed in the produced gas and elemental sulfur was not found. This suggests that COS is formed in the following manner:

$$Zn^*S^* + CO_2 \rightarrow ZnO + COS \quad (5)$$

As the surface zinc and sulfur are being eliminated with formation of COS, it can be concluded that the formation of COS results in the consumption of H_2S as per Eqns. (1) and (2). Surface Zn*S* also reacts with water to form ZnO and H_2S; however, the formation of COS acts as a catalyst and accelerates the overall reaction.

Sayyadnejad et al. (2008) presented the use of ZnO nanoparticles in removing H_2S from the water-based drilling mud. The performance of nanoparticles was found to be remarkably better than bulk ZnO. The reaction between ZnO and H_2S was proposed to be the same as in Eqn. (1). However, due to presence of ZnO in nanoparticle form, the contact area for the reaction increases several folds, providing sufficiently large area for the reaction to occur.

Studies on CO_2/H_2S corrosion modeling are in progress. Literature review indicates that in the presence of H_2S, the mackniwaite scale often forms on the steel surface as the initial corrosion protective layer. Therefore, the mackinawite stability limit models have been reviewed. Details of the models are presented in Appendix A.

2.2 Experimental Studies on Degradation of Cement (Task 2)

As previously reported, aging Experiment # 4 has been successfully completed. Test parameters for aging experiments are summarized in **Table 1**. The samples were recovered after 2 and 4 weeks of aging. Besides this, two new aging experiments (Experiments # 5 and 6) were conducted at different temperatures. The samples were aged for 2 weeks and their physical properties were measured. **Figure 1** shows porosity and permeability of the samples before and after aging. The trends for HS and GS samples are similar. Both porosity and permeability for these samples at the beginning show reduction, and then the trend reverses. A number of phenomena occur during aging including hydration of cement components, carbonation of portlandite and CSH, and leaching of binding components of the cement. Hydration and carbonation tend to reduce permeability and porosity of cement cores. Hence, the initial reduction in permeability and porosity can be caused by the hydration and carbonation processes. Leaching has adverse effect on the properties of the cement. It increases the porosity and permeability of cement and reduces sealing performance. The increase in porosity and permeability observed after 2 weeks can be due to leaching.

Table 1 Test parameters for aging experiments

Batch #	Temp. (ºF)	Pressure (psi)	Partial Pressure %			Brine Conc. (%)	Aging Period (days)	Experiment #
			CH_4	CO_2	H_2S			
001	350	9000	100	0	0	9	6	1
002	350	6000	100	0	0	2	14 & 28	2
003	350	6000	100	0	0	2	14	
004	350	6000	90	10	0	2	6	3
005	350	6000	90	10	0	2	14 & 28	4
006	350	6000	90	10	0	2	14	
007	225	6000	90	10	0	2	14	5
008	100	6000	90	10	0	2	14	6

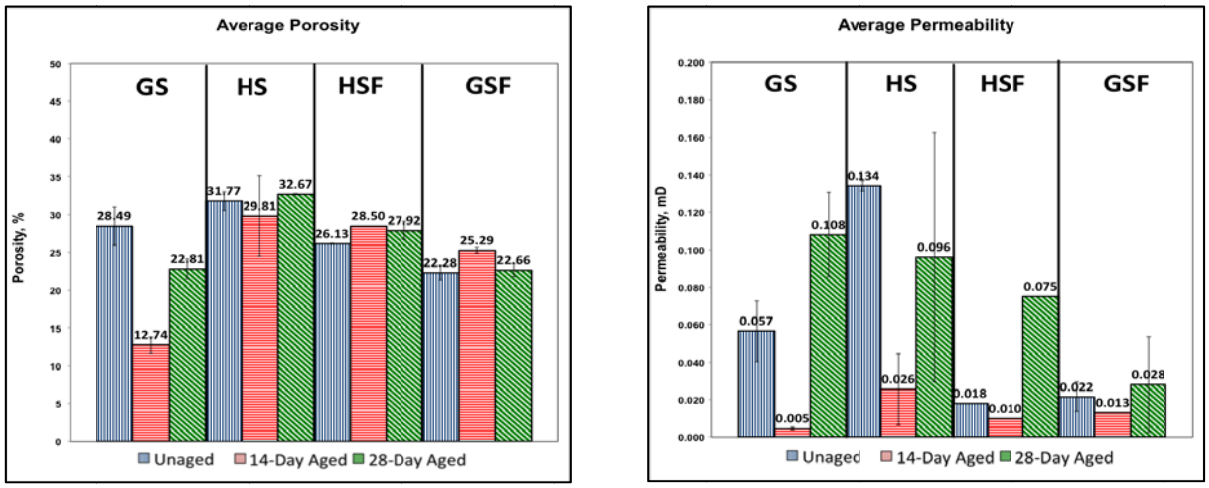

Fig. 1: Porosity and permeability of cement cores aged at 350ºF (Experiment 4, Batch 005)

New aging experiments conducted at lower temperatures showed reduction in permeability and porosity after 2 weeks of aging (**Figs. 2** and **3**). A similar reduction in these properties was observed at 350ºF.

In order to examine the effects of temperature, tests were conducting varying the aging temperature while maintaining 6000 psi pressure. Porosity and permeability of cores aged at different temperatures in brine saturated with mixed gas containing 10% CO_2 and 90% CH_4 are presented in **Fig. 4**. For Class G cement, increasing temperature facilitates the carbonation and hydration processes. As a result, porosity and permeability of the sample decreased when the aging temperature was raised. For Class H cement, the trend is mixed. Increased temperature is expected to exacerbate the leaching process, which tends to degrade the cement and increase its porosity and permeability. Despite this, the result shows a slight reduction in porosity and permeability as temperature increases from 100 to 225ºF.

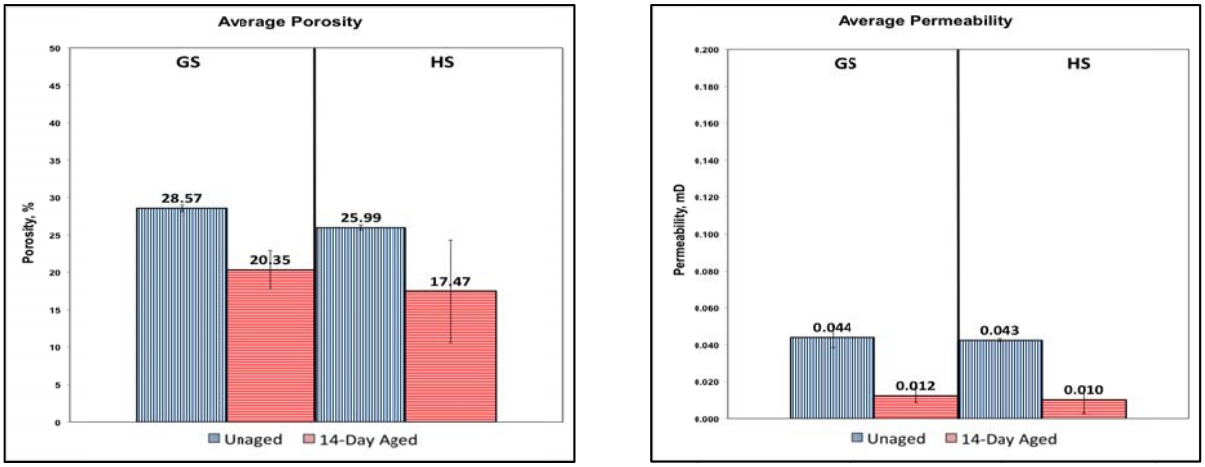

Fig. 2: Porosity and permeability of cores aged at 225ºF (Experiment # 5)

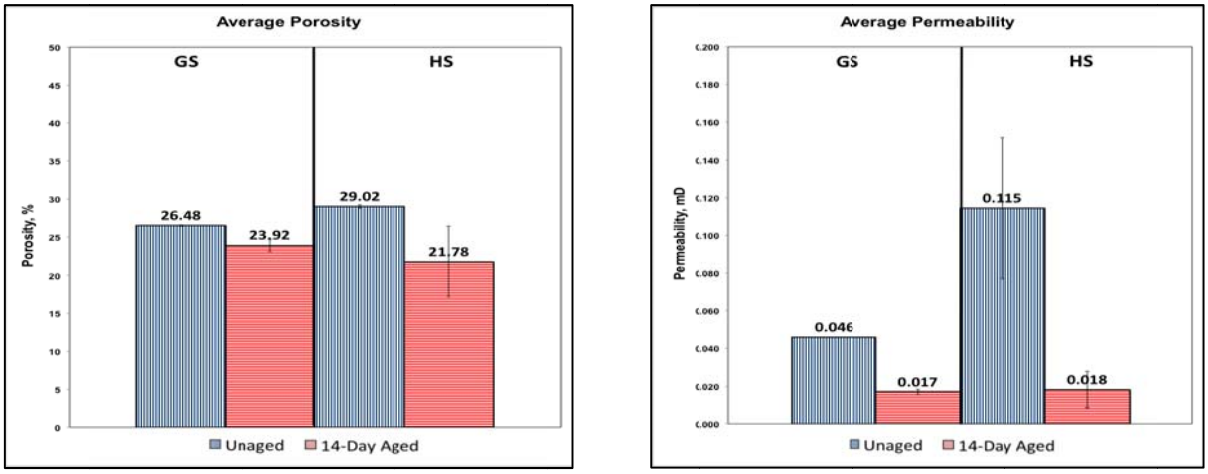

Fig. 3: Porosity and permeability of cores aged at 100ºF (Experiment # 6)

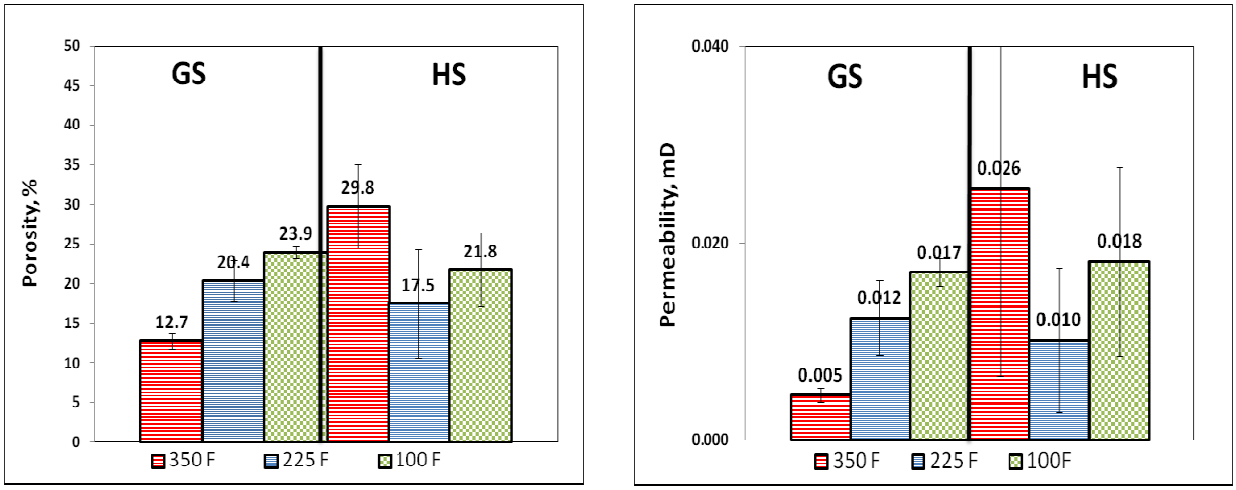

Fig. 4: Porosity and permeability of cores aged at different temperatures (P = 6000 psi, gas composition 90% CH4 and 10% CO_2)

Figure 5 summarizes compressive strength of samples aged in brine saturated with pure methane (100%) and mixed gas (10% CO_2 and 90% methane). Only limited number of cement cores containing fly ash was tested after aging since many of the samples were cracked and broken in the aging cell. Sample aged in brine saturated with pure methane are expected to hydrate and leach with time. The effects of hydration and leaching on mechanical strength offset each other. The change in mechanical strength is minimal for cores aged in brine saturated with pure methane. Class G samples showed significant reduction in strength when exposed to CO_2 containing fluid system. The strength reduction is mainly attributed to the leaching of cement by the carbonic acid. Nevertheless, fly ash containing Class G cement exhibited improved strength after exposure to CO_2 containing environment.

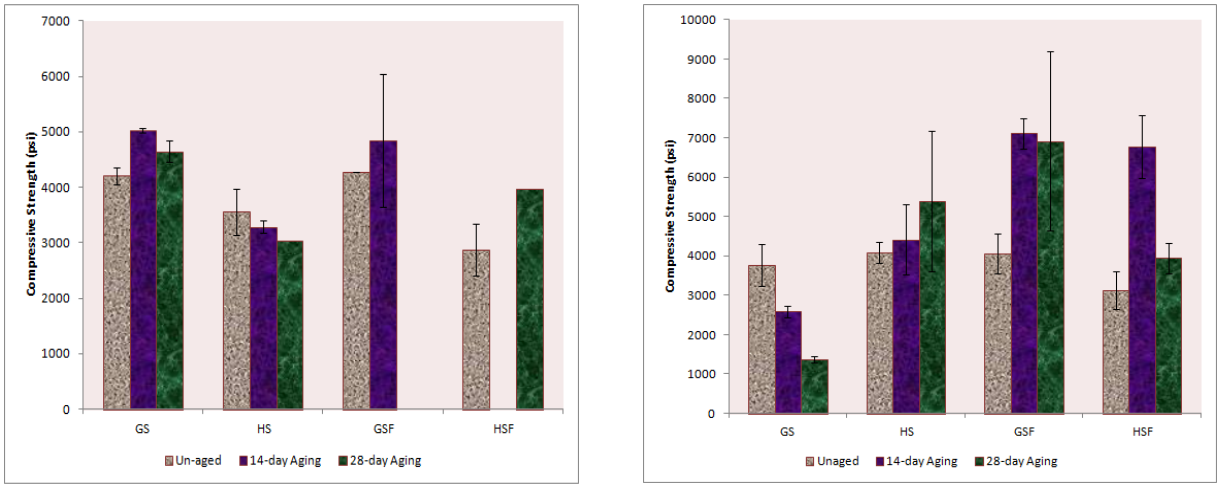

(a) **(b)**

Fig. 5: Compressive strength of aged cement cores aged at 350ºF: a) pure methane gas (Experiment 2, Batch 2); and b) mixed gas (Experiment 4, Batch 5)

Figure 6 presents compressive strength measurements of cores aged at different temperatures. GS samples show slight reduction in strength as the aging temperature increases. This could be due to cement leaching, which is more pronounced with increasing temperature. Nonetheless, this observation is contradicting with the trend of porosity variation shown in Fig. 4. During leaching, the interaction between pore fluid and cement matrix leads to dissolution of hydrated products (i.e. portlandite and calcium silicate hydrates), thus decreasing its mechanical strength while increasing the porosity and permeability.

For Class H cement with silica flour, compressive strength first increased and then decreased due to the carbonation, which is usually followed by leaching. The mechanical strength variation with temperature is consistent with porosity and permeability measurements shown in Fig. 4.

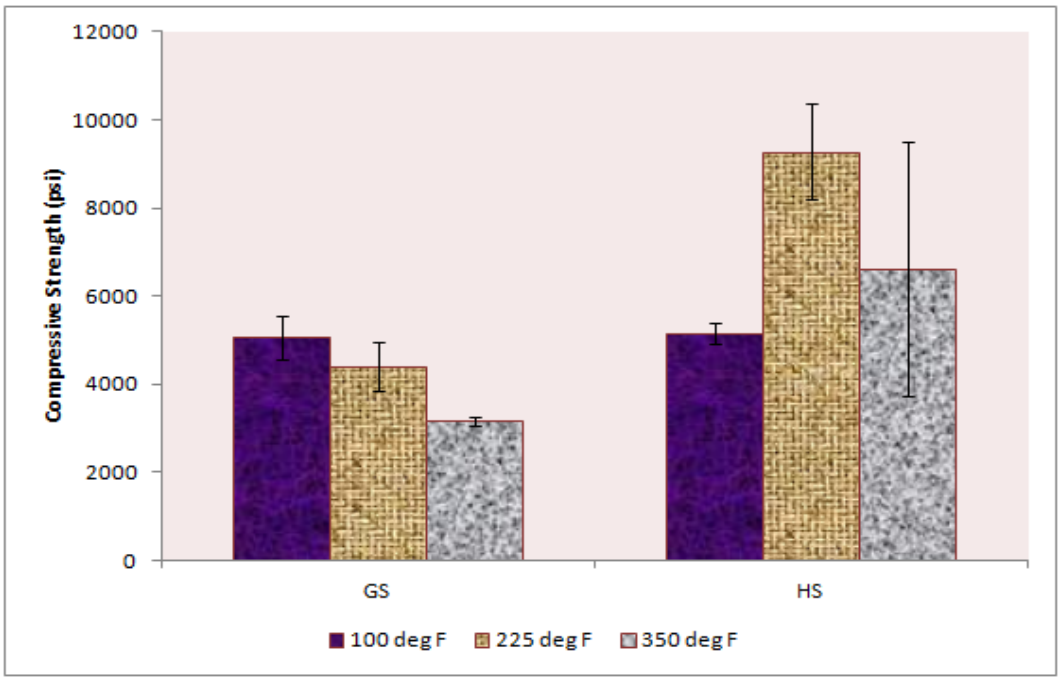

Fig. 6: Effect of temperature on compressive test for samples aged in 2% brine saturated with mixed gas (10% CO2 and 90% CH4) at 6000 psi

Cement additives screening study was continued. Zinc oxide is proved to be a very heavy retarder for the cement even after the addition of a common accelerator, NaCl. Magnesium oxide provided expected results in terms of improving cement properties such as porosity, permeability, and compressive and bonding strength. Hydroxyapatite containing cement formulations have been tested for their slurry properties. Physical properties of unaged cores containing hydroxyapatite will be tested next.

Following the chemistry of ZnO presented in Section 2.1, the ZnO has been selected as one of the potential cement additives for improving acid resistance. However, before subjecting the cement slurry sample to the H_2S environment, the slurry properties need to be optimized in order to develop field applicable cement formulations. The addition of ZnO as a retarder has been studied previously by a number of investigators (Olmo et al., 2001; Arliguie and Grandet, 1985). As per Arliguie and Grandet (1985), the retardation effect of ZnO arises from its ability to create an amorphous layer of $Zn(OH)_2$, which in combination with $Ca(OH)_2$ creates calcium-zinc hydrate:

$$2ZnO + Ca(OH)_2 + 4H_2O \rightarrow Ca[Zn(OH)3H_2O]_2 \quad \ldots\ldots\ldots\

The retardation of ZnO can be offset with the use of accelerators such as NaCl or $CaCl_2$ (Ludwig, 1951). The C_3A (Tri Calcium Alumintae) component of the cement, which is the quickest setting component, also has a tendency to develop double salts in contact with common salts. The most easily available salt for C_3A in the cement is gypsum ($CaSO_4$).

$$3CaO.Al_2O_3 + CaSO_4 + 31H_2O \rightarrow 3CaO.Al_2O_3.3CaSO_4.31H_2O \quad \text{..... (7)}$$

The solubility of gypsum is extremely low in water. Hence, a very small amount of the sulfate salt is formed and the reaction continues until all the water is saturated with the sulfate salt. With addition of chloride ions from NaCl or $CaCl_2$, the water is already saturated to an extent. Thus, the time required to reach saturation for sulfate reduces. Thus, the C_3A component becomes available for hydration rather than forming salts.

The retardation mechanism of ZnO is different. The reaction process presented in Eqn. (6) shall continue as long as Ca^{+2} ions are present in the system. As calcium is the largest component of the current cement system, even a small amount of ZnO can retard the slurry to a great extent.

In order to examine the retardation effect of ZnO, the consistency of cement slurry samples containing ZnO and brine were studied (**Fig. 7**). Consist-o-meter readings are compared to those of the baseline slurry (Class H cement containing silica). The value of 10 indicates 100 Bc, which corresponds to the API thickening time for the baseline. Cement slurry samples with different concentrations of salt were prepared to offset the retardation effect of ZnO. Regardless of the salt concentration, ZnO containing slurries were unable to thicken during the test period. For all ZnO containing samples, the consist-o-meter readings showed a significant retardation. Therefore, ZnO might not be an effective additive in the cement due to its heavy retardation. With the addition of minute quantity of ZnO (0.4% BWOC), the slurry hydration (thickening) was effectively delayed for more than 5 hours. Chloride ions of NaCl were unable to accelerator the thickening. We are considering testing the effectiveness of $CaCl_2$ as an accelerator for preparing the ZnO containing slurry.

Cement slurries containing magnesium oxide are also considered in the additive screening study. Slurry properties of Class H and Class G cements containing magnesium oxide (HSMG and GSMG) were investigated. The magnesium oxide was able to provide acceptable slurry with 5% BWOC as per the recommendation of Rubiandini et al. (2005). After testing the slurry properties, seven cement cores of GSMG and HSMG, and three bonding samples of HSMG were prepared and tested. The samples were cured for 5 days at 200ºF in 2% brine. The porosity and permeability measurements show expected results (**Fig. 8**). As MgO helps make cement expand, the permeability of HSMG and GSMG samples were significantly less than that of HS and GS cores.

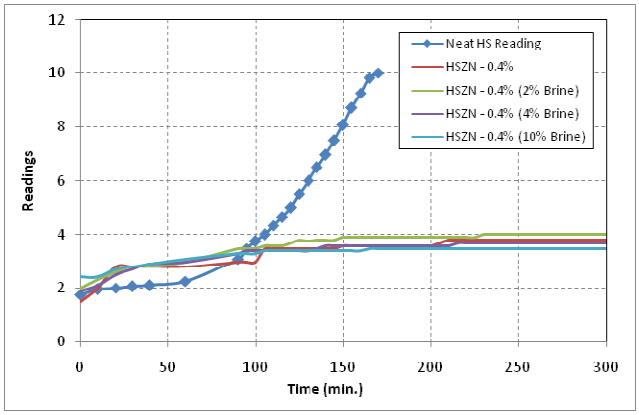

Fig. 7 Consistency of cement slurry samples containing ZnO

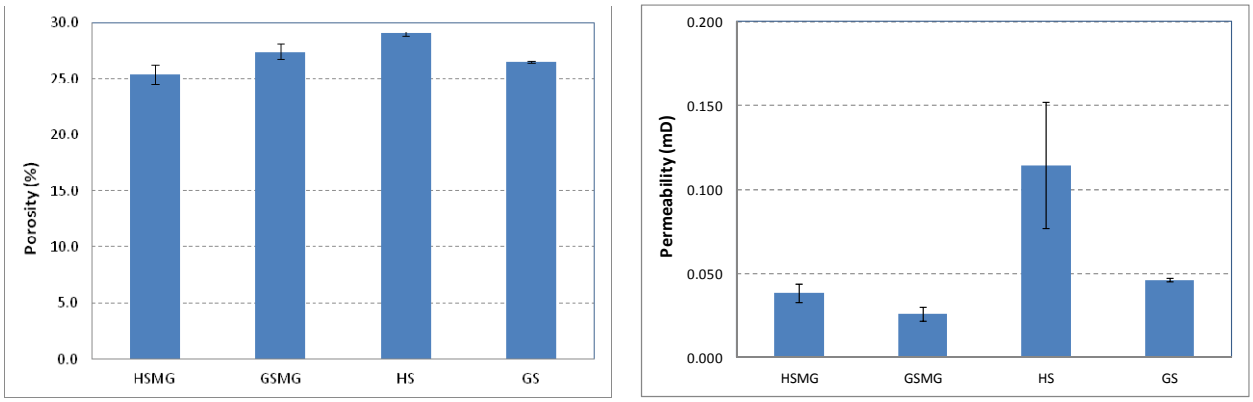

(a) **(b)**

Fig. 8 Comparison of porosity and permeability of MgO containing cores with GS and HS samples

In addition to the porosity and permeability studies, core samples containing MgO were tested for their compressive and bonding strength. The compressive strength of the HSMG samples was higher than that of HS samples (**Fig. 9a**). However, for GSMG samples, the compressive strength was slightly lower than that of the GS samples. Shear bond strength (**Fig. 9b**) obtained for the HSMG samples were higher than the bond strength of the neat HS samples.

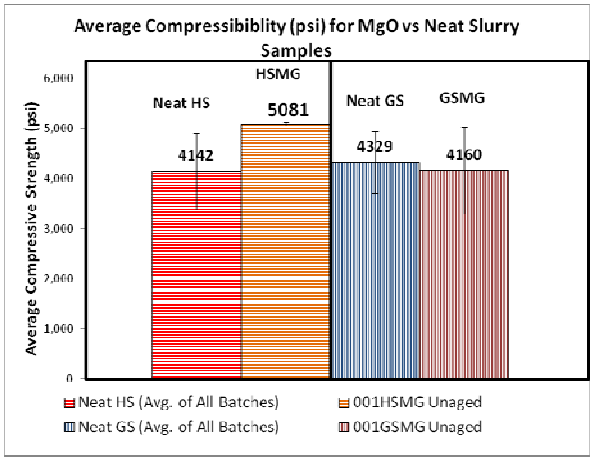

(a)

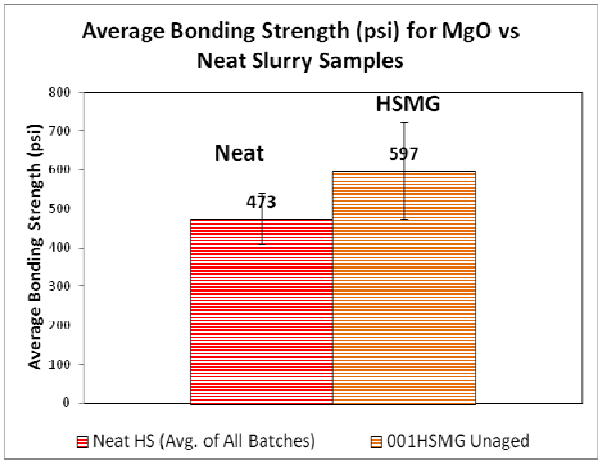

(b)

Fig. 9: Compressive and shear bonding strength of unaged samples

The slurry and core properties of the MgO cement formulations are found to be acceptable (i.e. slurry properties within the range of baseline cement slurries); therefore, they will be tested in the aging cell. The addition of magnesium oxide is expected to expand the cement and reduce porosity and permeability. This would help in reducing penetration of the sour gas in the cement matrix. In the upcoming weeks, the plan is to prepare cores and bonding samples using MgO containing slurries. Fifty percent of the samples will be kept in aging cell for 14 days.

Hydroxyapatite is one of the additives considered during the investigation. Different concentrations of hydroxyapatite (5%, 15% and 30%) containing cement slurries were prepared and tested. These concentrations yielded extremely viscous slurries, which were non-pourable. In order to obtain acceptable slurry properties, the silica flour and hydroxyethylcellulose (HEC) were not included in the slurry formulation. The purpose of silica flour is to inhibit strength retrogression at elevated temperatures. HEC acts as a water retention agent and controls fluid loss. Hydroxyapatite (HOAP) has cementitious property to sustain higher temperatures and addition of silica flour may not be necessary. The GHO and HHO slurries indicate Class G and Class H cements mixed with only hydroxyapatite along with antifoaming agent. Tests showed both slurries can have higher viscosities. However, they were pourable during the test. The API filtrate losses were also in acceptable range. The thickening time was within 1.5 hours for both the slurries. This is less than that of the base slurry and can be adjusted by the addition of retarders such as citric acid, if necessary. The HHO and GHO slurries were prepared and cured for 5 days in an oven at 200ºF in 2% brine. The physical and mechanical properties of un-aged cores will be tested.

Micro-silica acts as a filler material and also helps maintain the calcium-silicone ratio in the cement. It is required for providing strength at elevated temperatures. During slurry formulation, the

amount of micro-silica was selected so that the Ca/Si ratio does not change (35% BWOC of silica). Hence, if 20% BWOC of micro-silica is used, then 15% BWOC of silica flour should be added. The extra water added is 2.09 ml/gram of micro-silica, which is recommended by Dillenbeck et al. (1990) for better performance of micro-silica at elevated temperatures.

Preliminary testing shows that with the addition of 20% BWOC of micro-silica, the slurry can be extremely thin (**Table 2**). Therefore, the amount of micro-silica can be increased to reduce porosity and permeability further. With an addition of 35% micro-silica, the silica flour can be reduced to zero (in order to maintain the silica content of 35% BWOC). Test results presented in **Fig. 10** show acceptable range of viscometer readings. The use of dispersants such as anhydrous citric acid has been recommended by Grabowski and Gillott (1989), Dillenbeck et al. (1990) and Mueller and Dillenbeck (1991) to allow proper mixing of micro-silica. A 0.2% BWOC of anhydrous citric acid was added to act as a dispersant for proper mixing of the slurry. As presented in Table 2, HMS and GMS slurries took longer time to reach 100 Bc. The retardation is due to the addition of anhydrous citric acid. Cement particles are cationic in nature. Anionic additive such as anhydrous citric acid adheres to these particles and slows down the hydration reaction causing retardation. This retardation can be controlled with the addition of an accelerator such as NaCl. However, the use of other additives could alter the properties of cement. Furthermore, as the objective of this study is to test the effectiveness of micro-silica at HPHT sour gas environment in the lab, such retarded slurry can be conveniently monitored and controlled. If proven effective, additional tests with accelerators can be considered. Next, unaged HMS and GMS samples will be prepared and tested.

Table 2: Properties of micro-silica containing cement slurries

Slurry	HSMS	HMS	GMS
Amount	20% bwoc – MicroSilica 15% bwoc – Silica Flour 1.5% bwoc – Anhyd. Citric Acid	35% bwoc – MicroSilica 0% bwoc – Silica Flour 2.0% bwoc – Anhyd. Citric Acid	35% bwoc – MicroSilica 0% bwoc – Silica Flour 2.0% bwoc – Anhyd. Citric Acid
Remarks	Extremely Thin Slurry	None	None
Density (ppg)	13.80	12.80	12.60
Viscosity	Acceptable (Fig. 10)	Acceptable (Fig. 10)	Acceptable (Fig. 10)
API Fluid Loss	70 ml	60 ml	54 ml
Thickening Time	Not Tested	5hr. 20 min.	3hr. 20 min.

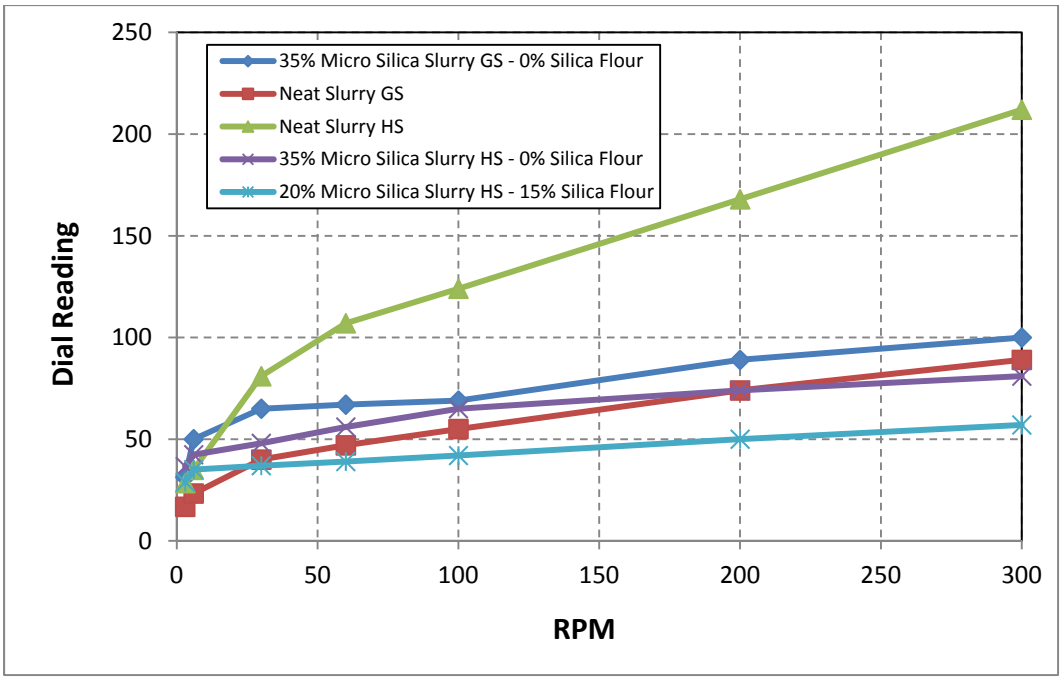

Fig. 10: Rheology of micro-silica containing cement slurries

Latex is often added to improve sealing properties of cement. The latex forms an emulsion with the cement. With constant agitation during mixing and pumping, and increased bottom-hole temperature, the latex particles tend to aggregate and flocculate. A similar experimental observation has been reported by Funquan et al. (2006). The authors suggest the use of strong hydrophilic carboxyl group, such as formic acid or acetic acid, in order to stabilize the latex containing cement system at 200ºF or above. The amount of latex suggested is 10% BWOC and amount of acetic acid to be used is 0.43% BWOC. Next, latex containing cement slurries and core samples will be prepared and tested for their physical and mechanical properties.

2.3 Experimental Studies on Corrosion of Tubulars (Task 3)

Progress has been made in designing and selection of major components of the corrosion test setup. The design of some components needs to be finalized. Potentiostat (Gamry Series G 300 Potentiostat/Galvanostat/ZRA) and magnetic drive have been received and the design of the corrosion test cell will be finalized. It is expected to conduct preliminary corrosion experiments soon.

3. Problems Encountered

Aging experiments are taking longer than initially anticipated. In order to observe measurable degradation of cement, at least 2 weeks aging is required. Each aging test requires minimum of 2 days for pressurization and heating, and additional 2 days for depressurization and cooling. Including equipment down time, an average of 3-weeks is needed for a single aging test. This may delay the completion of some of the tasks. Therefore, we are considering a no-cost extension of 6 months.

4. Planned Activities

- Continue aging experiments with brine-CO_2-CH_4 system for 14 days varying CO_2 concentration.
- Continue theoretical and modeling studies on tubular degradation.
- Continue cement additive screen study.
- Continue designing of tubular corrosion testing setups and acquisition of components.

5. Project Expenditures

This section presents the project expenses during the month of December (**Table 3**) and the cumulative expenditures.

Table 3 Current and cumulative expenditures, December, 2012

No.	Budget Categories	Current Expenses	Cumulative Expenses
1	Salaries & Wages	$8,633.33	$139,729.66
2	Fringe Benefits	$2,065.89	$34,976.84
3	Project Materials	$6,935.23	$64,331.10
4	Travel	$2,536.46	$3,869.55
5	Conference Expenses	$0.00	$0.00
6	Other Direct Costs	$280.39	$585.77
7	Equipment	$1,070.00	$142,572.67
8	Space Rental	$0.00	$0.00
9	Indirect Cost	$10,225.65	$121,746.50
10	**Total**	**$31,746.95**	**$507,812.09**

References

Arliguie, G. and Grandet, J. 1985. Etude par calorimetrie de l'hydratation du ciment Portland en presence de zinc, Cement and Concrete Research, Volume 15, Issue 5, September, Pages 825–832.

Benning, L. G., Wilkin, R. T. and Barnes, H. L. 2000. Reaction pathways in the Fe-S below 100 °C, Chem. Geol., 167, 25-51.

Clark A.H. 1966. Stability Field of Monoclinic Pyrrhotite, Transactions of the Institute of Mining and Metallurgy, Vol. 75, pp. B232-235.

Dillenbeck III R. L., Mueller D. T., Orr B. R. 1990. The Effect of Micro Silica on the Thermal Stability of Lightweight Cement Systems, paper SPE-21597, presented at the International Technical Meeting, Petroleum Society of CIM and SPE, June 10 - 13.

Funquan, S., Guangming, Lv and Jianzhou, J. 2006. Application and Research of Latex Tenacity Cement Slurry System, paper SPE-104434, presented at the SPE International Oil & Gas Conference and Exhibition, Beijing, China.

Grabowski, E. and Gillott, J. E. 1989. Effect of Replacement of Silica Flour with Silica Fume on Engineering Properties of Oil Well Cements at Normal and Elevated Temperatures and Pressures, Cement and Concrete Research, Vol. 19, pp 333-344.

Hamilton, I.E. and Sammes, N.M. 1999. Encapsulation of steel foundary bag house dusts in cement mortar, Cement Concrete Research 29, 55-61.

Lecolier E., Rivereau A., Ferrer N., Audibert A. and Longaygue X. 2010. Durability of Oilwell Cement Formulations Aged in H2S Containing Fluids, paper SPE 9910-PA, SPE Drilling & Completion, Volume 25, Number 1, March, pp. 90-95.

Lecolier E., Rivereau A., Ferrer N., Audibert A. and Longaygue X. (2008); “Study of New Solutions for Acid-Resistant Cements”; Paper SPE 116066, presented at the SPE Annual Technical Conference and Exhibition, 21-24 September, Denver, Colorado.

Ludwig, N.C. 1951. Effect of Sodium Chloride on Setting Properties of Oil-Well Cements, Spring meeting of the Mid-Continent District, Division of Production, Amarillo, Texas.

Mueller, D. T. and Dillenbeck, R. L. 1991. The Versatility of Silica Fume as an Oil well Cement Admixture, paper SPE 21688, presented at the SPE Production Operations Symposium, 7-9 April, Oklahoma City.

Naumov, G.B., Ryzhenko B. N. and Khodakovsky I. L.1974. Handbook of Thermodynamic Data, U.S.G.S. Report WRD-74-00 1, January.

Olmo, F., Chacon, E. and Irabien, A. 2001. Influence of lead, zinc, iron (III) and chromium (III) oxides on the setting time and strength development of Portland cement, Cement and Concrete Research, Volume 31, Number 8, August, pp. 1213-1219.

Rubiandini R., Siregar S., Suhascaryo N. & Efrial D. 2005. The Effect of CaO and MgO as Expanding Additives to Improve Cement Isolation Strength under HPHT Exposure, PROC. ITB Eng. Science Vol. 37 B, No. 1, 29-48.

Sasaoka E. 1994. Characterization of Reaction between Zinc Oxide and Hydrogen Sulfide, Energy & Fuels 1994, 8, 1100-1105.

Sayyadnejad, M. A., Ghaffarian, H. R., Saeidi, M. 2008. Removal of hydrogen sulfide by zinc oxide nanoparticles in drilling fluid, Int. J. Environ. Sci. Tech., 5 (4), 565-569.

Smith, S.N. and Pacheco, J.L. 2002. Prediction of Corrosion in Slightly Sour Environments, paper NACE No. 241, Houston, Texas.

Smith, S. N. and Wright E. J. 1994. Prediction of Minimum H_2S Levels Required for Slightly Sour Corrosion, Paper NACE International no. 11.Houston, Texas.

Smith, S. N. 1993. A Proposed Mechanism for Corrosion in Slightly Sour Oil and Gas Production, paper NACE No. 385,Twelfth International Corrosion Congress, Houston, Texas, Sep. 19 – 24.

Sun W.; Nesic, S.; Woollam, R , and Young D. 2008. Equilibrium Expressions related to the Solubility of the Sour Corrosion Product Mackinawite, Ind. Eng. Chem. Res., 47, pp 1738-1742 presented ExxonMobil Upstream Research Company, Feb.12.

Sun, W. and Nesic, S. 2009. A Mechanistic Model of Uniform Hydrogen Sulfide/Carbon Dioxide Corrosion of Mild Steel, paper NACE international.

Sun, W., Nesic, S., Papavinasam, S. 2006. Kinetics of Iron Sulfide and Mixed Iron Sulfide/Carbonate Scale Precipitation in CO2/H2S Corrosion, paper NACE No. 06644, Houston, Texas.

Suleimenov, O. M. and Seward, T. M. 1997. A spectrophotometric study of hydrogen sulfide ionization in aqueous solutions to 350 °C. Geochim. Cosmochim. Acta, 61, 5187-5198.

Takeno S., Zoka, H. and Niihara T. 1970. Metastable Cubic Iron Sulfide with Special Reference to Mackinawite, American Mineralogist, Vol. 55, pp. 1639-1649.

Taylor P. 1980. The stereochemistry of iron sulfides - a structural rationale for the crystallization of some metastable phases from aqueous solution, American Mineralogist, 65, pp 1026-1030.

Woollam, R.; Tummala, K.; Vera, J. and Hernandez, S. 2011. Thermodynamic Prediction of FeCO3/FeS Corrosion Product Films, paper NACE No.076, Houston, Texas.

Appendix A: Mackinawite Stability Limit Models

A number of corrosion models (Smith & Wright, 1994; Smith & Pacheco, 2002) have been developed to predict the stability limit of makinawite. The boundary limits of makinawite phase are defined based on the chemical reactions of FeS with other corrosion products, as shown in **Fig. A-1**. Makinawite is a thermodynamically semi-stable form of iron sulfide (FeS) that forms on the steel surface under conditions where iron sulfide is still soluble in the bulk solution; i.e., the concentrations of Fe^{2+} and H_2S are still less than saturation concentration. Figure A-1 demonstrates the effect of temperature and H_2S partial pressure on the stability limits of mackinawite and its transition to pyrrhotite. Although several studies have been conducted to investigate the stability limits of mackinawite; the upper temperature stability limit, in which conversion of mackinawite to cubic FeS occurs, is subject to degree of uncertainty. For instance, Taylor (1989) reported that the upper limit of thermal stability is 130°C based on thermodynamic model. It is also found that mackinawite can transform to pyrrhotite at temperatures between 170 and 200°C by exposing samples for 30 days (Takeno et al., 1970). Clark (1966) estimated the upper stability limit of mackinawite to be around 135°C. There is also the upper H_2S concentration limit to the mackinawite stability region, which is shown in Fig. A-1 using line (16). Beyond this line, pyrrhotite forms on the steel surface as a corrosion product.

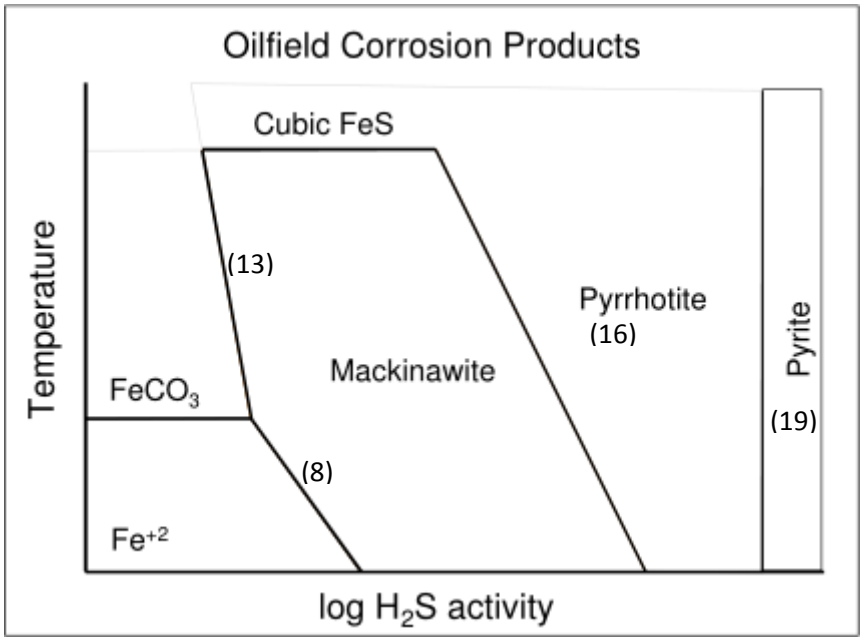

Fig. A-1 Stability limits of mackinawite phase (Smith & Pacheco, 2002)

1. Fe^{2+} and Mackinawite Boundary

The boundary between Fe^{2+} and mackinawite regions in Fig. A-1 is described using the following reaction equation:

$$Fe^{2+} + H_2S \rightarrow FeS + 2H^+ \quad \text{(A-1)}$$

The equilibrium constant of the reaction, $K_{FeS/Fe^{2+}}$, is a function of temperature and change in Gibbs free energy. Assuming one molal activity of all reactants and products, the Gibbs free energy change can be expressed as a function of temperature:

$$\Delta G^T_{reaction} = \left(G^T_{FeS} + 2 * G^T_{H^+}\right) - \left(G^T_{Fe^{2+}} + G^T_{H2S}\right) + RT \ln\left(\frac{\prod\left(activity_{products}\right)}{\prod\left(activity_{reactants}\right)}\right) \quad \text{(A-2)}$$

The equilibrium constant is expressed as:

$$\ln K_{FeS/Fe^{2+}} = \frac{\Delta G^T_{reaction}}{-RT} \quad \text{(A-3)}$$

Using unit activities of the reacts and products, the equilibrium constant can be computed as:

$$K_{FeS/Fe^{2+}} = \frac{\left(a_{FeS} * a_{H^+}\right)^2}{\left(a_{Fe^{2+}} * a_{H2Saq}\right)} \quad \text{(A-4)}$$

The H_2S activity in aqueous solution can be determined using the dissolution reaction equation: $H_2S_{vap} \rightarrow H_2S_{aq}$. Hence:

$$K_{H2Saq/H2Svap} = \frac{a_{H2Saq}}{a_{H2Svap}} \quad \text{(A-5)}$$

where the fugacity of H_2S in the vapor phase is defined as: $a_{H2Svap} = \gamma_{H2S} p_{H2S} / P$. Since the activity of solid phase is one, $a_{H^+} = 10^{-pH}$ and $a_{Fe^{2+}}$ is assumed to approach 1.0 on the steel surface. After applying these assumptions, Eqns. (A-4) & (A-5) can be combined to yield the following expression for the partial pressure of H_2S in the gas phase (i.e. the minimum partial pressure of H_2S required for the formation of makinawite).

$$p_{H2S} = \frac{(10^{-pH})^2}{K_{H2Saq/H2Svap} * \gamma_{H2S} * K_{FeS/Fe^{2+}}} \quad \text{(A-6)}$$

where:

$K_{H2Saq/H2Svap}$ is the solubility constant for H_2S in aqueous solution.

K_{FeS/Fe^2} is the activity adjusted equilibrium constant for the reaction described in Eqn. (A-1)

γ_{H2S} is the H_2S fugacity coefficient in the gas phase.

Equation (A-6) is used to calculate the minimum partial pressure of H_2S (p_{H2S}) required to form mackinawite layer on the steel surface. The minimum partial pressure depends on four parameters namely: pH of the solution, equilibrium constants for solubilities of H_2S and FeS, and fugacity for H_2S. All these parameters are functions of other process parameters such as pressure, temperature, and ionic strength. However, problems exist in the determination of Gibbs free energy of the reaction because equilibrium constants for solubility of H_2S and FeS have predictive models, which are only valid for standard conditions (25°C and 1 atm). Smith and Pacheco (2002) used Naumov's procedure to account for the effect of temperature on the Gibbs free energy. The change in Gibbs free energy during the formation of mackinawite layer is given by:

$$\Delta G^T_{reaction} = 961.1 + 93.473 * T - 11.297 * \ln(T) - 0.135 * T^2 - \frac{4.196 * 10^5}{T} + \frac{2.147 * 10^7}{T^2} + 0.0196 * T^2$$
$$* \ln(T) + 7.2 * 10^4 * \frac{\ln(T)}{T} + RT \ln\left(\frac{a_{FeS}.a^2_{H+}}{a_{Fe^{2+}}.a_{H2Saq}}\right) \quad (A-7)$$

The activity of the solid phase is considered as one, $a_{FeS} = 1$ and the activity of ferrous ions near or on the steel surface approaches a value of 1.0. Under equilibrium condition, the change in free energy is zero (i.e. $\Delta G^T_{reaction} = 0$). Applying these assumptions, Eqn. (7) can be simplified and rearranged to form:

$$\log(a_{H2Saq}) = \frac{\Delta G^0_T}{2.303 * R * T} - 2 * pH \quad \text{(A-8a)}$$

where

$$\Delta G^0_T = 961.1 + 93.473 * T - 11.297 ** \ln(T) - 0.135 * T^2 - \frac{4.196 * 10^5}{T} + \frac{2.147 * 10^7}{T^2} + 0.0196 * T^2$$
$$* \ln(T) + 7.2 * 10^4 * \frac{\ln(T)}{T} \quad (A-8b)$$

As suggested by Smith (2002), assuming equal activity for H_2S in the gas and liquid phases, we can relate the H_2S activity in the aqueous phase to its partial pressure: $a_{H2Svap} = a_{H2Saq} = \gamma_{H2S} p_{H2S} / P$. Hence, Eqn. (A-8a) can be simplified to yield.

$$p_{H2S} = \frac{10^{\frac{\Delta G_T^\circ}{4.575*T} - 2*pH}}{\gamma_{H2S}} * P \quad \text{..... (A-9)}$$

where P is total system pressure.

2. $FeCO_3$ and Makinawite Boundary

Iron carbonate ($FeCO_3$) is a common corrosion product that forms at elevated temperature when steel is exposed to acidic aqueous solutions containing dissolved CO_2. However, in the presence of small amount of H_2S, mackinawite phase could form when the corrosion product would normally be Fe^{2+} and $FeCO_3$. This occurs due to the very rapid kinetics of mackinawite formation and the fact that the mackinawite consumes most of the Fe^{2+} ions produced by the corrosion reaction. The consumption of Fe^{2+} ions keeps the ferrous iron concentration low and thereby retards $FeCO_3$ precipitation. The boundary between the $FeCO_3$ and the mackinawite regions can be defined by the following reaction equation:

$$FeCO_3 + H_2S_{aq} \rightarrow FeS_{mackinawite} + H_2CO_3 \quad \text{..... (A-10)}$$

The equilibrium constant, $K_{FeS/FeCO3}$ for this iron carbonate conversion reaction is determined as:

$$K_{FeS/FeCO3} = \frac{a_{mackinawite} * a_{H2CO3}}{a_{FeCO3} * a_{H2S_{aq}}} \quad \text{..... (A-11)}$$

The activities of solids are considered to be one (a_{soild}=1) and the activities of H_2CO_3 and H_2S_{aq} are determined as follows:

The equilibrium constant for the decomposition of carbonic acid ($H_2CO_3 \rightarrow H_2O + CO_{2aq}$) is defined as:

$$K_{H2CO3/CO2aq} = \frac{\left(a_{H2O}.a_{CO2aq}\right)}{a_{H2CO3}} \quad \text{..... (A-12)}$$

The equilibrium constant for vaporization of carbonic dioxide ($CO_{2aq} \rightarrow CO_{2vap}$) from water is expressed as:

$$K_{CO2aq/CO2vap} = \frac{a_{CO2vap}}{a_{CO2aq}} \quad \text{(A-13)}$$

After substituting Eqns. (A-5), (A-12) and (A-13) into Eqn. (A-11), the following equation for the equilibrium for the formation of iron carbonate can be obtained.

$$K_{FeS/FeCO3} = \frac{(a_{H2O} * K_{CO2aq/CO2vap} * a_{CO2vap})}{(K_{H2CO3/CO2aq} * K_{H2Saq/H2Svap} * a_{H2Svap})} \quad \text{(A-14)}$$

Assuming water activity of 1, Eqn. (A-14) can be further simplified by combining the equilibrium constants into a single parameter called Dunlop's value (C). Thus:

$$K_{FeS/FeCO3} = C * \frac{a_{CO2vap}}{a_{H2Svap}} \quad \text{(A-15)}$$

For ideal gases, the Dunlop's value under ambient temperature condition is 500 for iron carbonate conversion reaction shown in Eqn. (A-5). Using thermodynamic procedures, it is possible to estimate Dunlop's value of iron carbonate conversion reaction at higher temperatures and for real gases.

In addition to the conversion reaction, the formation of corrosion protective scale is strongly affected by the solubility of solid corrosion products in the liquid phase. Woollam et al. (2011) considered this phenomenon to estimate the equilibrium constant for iron carbonate conversion reaction using the solubility of FeS and $FeCO_3$ in water. They defined the equilibrium constant, $K_{FeS/FeCO3}$ as the ratio of the solubility limit of iron sulfide (FeS) to the solubility limit of iron carbonate ($FeCO_3$):

$$K_{FeS/FeCO3} = \frac{K_{sp,FeS}}{K_{sp,FeCO3}} \quad \text{(A-16)}$$

where

$$\log K_{sp,FeCO3} = -59.35 - 0.041377T_k - \frac{2.196}{T_K} + 24.57 * \log(T_k) \quad \text{(A-17)}$$

$$\log K_{sp,FeS} = \frac{2848.779}{T_K} - 6.347 + \log(K_{1,H2S}) \quad \text{(A-18)}$$

The first dissociation constant of H_2S ($K_{1,H2S}$) is defined by Suleimenov and Seward (1997) as:

$$\log K_{1,H2S} = 782.43945 + 0.36126T_K - (1.6722\times10^{-4}T_K^2) - (20565.7315/T_K) - (142.741722\ln(T_K)) \quad \text{(A-19)}$$

3. Boundary between FeS and Pyrrhotite

The boundary between mackinawite and pyrrhotite regions is defined by the solubility of FeS in the bulk solution. When FeS concentration is below the saturation limit in the bulk solution and H_2S activity level is greater than the required for mackinawite scale formation, mackinawite forms as a corrosion product. However, when the FeS levels in the bulk solution exceed the saturation level, pyrrhotite forms as a corrosion product. The same series of equations that were used to define the boundary between Fe^{2+} and FeS are used to determine the boundary between FeS/pyrrhotite. The only difference is that the ferrous ion concentration in the bulk solution is taken into consideration in this case. The resulting equation therefore takes the form:

$$p_{H2S} * a_{Fe^{+2}} = \frac{10^{-pH*2}}{K_{H2Saq/H2Svap} * \gamma_{H2S} * K_{FeS/Fe^{2+}}} \quad \text{(A-20)}$$

where

$a_{Fe^{+2}} = \gamma_{Fe^{2+}} * m_{Fe^{2+}}$

$\gamma_{Fe^{2+}}$: Activity coefficient of Fe^{2+} in the solution

m_{Fe2+} : Molar concentration of Fe^{2+} in the solution

Examining the similarity between Eqn. (A-20) and (A-9), Eqn. (9), which is developed to predict the boundary between ferrous ion and mackinawite can be adapted with the addition of the ferrous ion activity term to predict the boundary between mackinawite and pyrrhotite. The equation can be expressed as:

$$p_{H_2S} = \frac{10^{\frac{\Delta G_T^\circ}{4.575*T} - 2*pH} * P}{a_{Fe}^{2+} * \gamma_{H_2S}} \quad \text{(A-21)}$$

The boundary between mackinawite and pyrrhotite can be described by the following solubility reaction equation:

$$FeS_{(s)} + H_2S_{(aq)} \xrightarrow{Ksp,a_{H2S}} Fe^{2+}_{(aq)} + 2HS^-_{(aq)} \quad \text{(A-22)}$$

where the equilibrium constant for this reaction, $K_{sp,a,H2S}$ is expressed as:

$$K_{sp,a,H_2S} = \frac{\left[Fe^{2+}\right]\left[HS^-\right]^2}{\left[H_2S\right]} \quad \text{(A-23a)}$$

or

$$K_{sp,a,H_2S} = K_{sp,a}(K_{1,H_2S})^2 \quad \text{(A-23b)}$$

where $K_{sp,a}$ is the solubility limit of mackinawite in acidic solutions. The solubility process is described by the following reaction equation:

$$FeS_{(s)} + 2H^+ \xleftrightarrow{Ksp,a} Fe^{2+}_{(aq)} + H_2S_{(aq)} \quad \text{(A-24)}$$

The value of $K_{sp,a}$ is computed from the following correlation, whichis valid up to 212°F, (Benning et al., 2000):

$$K_{sp,a} = 10^{(2848.779/Tk)-6.347} \quad \text{(A-25)}$$

4. Summary

The minimum partial pressure of H_2S that is required to form the makinawite scale is dependent on the solution pH, temperature and fugacity coefficient as well as ferrous ions concentration in the solution. Mackinawite formation region boundaries are mainly controlled by operating temperature, pH, ferrous ions activity and the activity of H_2S in the solution. However, $FeCO_3$-FeS boundary is influenced by temperature, partial pressure of H_2S and CO_2 but independent of Fe^{2+} ion concentration and pH.

Makinawite limitation model (Stephen and Pacheco; 2002) is used with super-saturation of species in the solution to predict the conditions that are required to form makinawite and other corrosion products on the steel surface. However, identifying the corrosion products requires an experimental study and using different techniques such as Scanning Electron Microscopy (SEM), X-ray Diffraction methodology (XRD) and X-ray Photoelectron Spectroscopy (XPS).

Project Title: Effect of H_2S and CO_2 in HPHT Wells on Tubulars and Cement

Report Type: Monthly Report

Report #: 16

Reporting Period: December 22nd, 2012 to January 21st, 2013

Authors:

Ramadan Ahmed, Principal Investigator

Subhash Shah, Co-Principal Investigator

Samuel Osisanya, Co-Principal Investigator

Rida Elgaddafi, Research Assistant

Omotayo Omosebi, Research Assistant

Himanshu Maheshwari, Research Assistant

Adarsh Naidu, Research Assistant

Aman Srivastvava, Research Assistant

Jueun Hwang, Research Assistant

Prepared under BSEE Project # E12PC00035

by

THE UNIVERSITY OF OKLAHOMA

February 26, 2013

1. Summary of Accomplishments

This monthly report presents the progress made during the project period December 22, 2012 to January 21, 2013. During this reporting period, aging experiments were continued using cement cores and bonding samples. Properties of the cores and samples were measured before and after aging. The effects of different cement additives on properties of cement slurries and cores are being investigated. Furthermore, we received feedback from BSEE on previous monthly reports. Our response is presented in the appendix.

As planned, aging experiments were conducted varying the concentration of CO_2 in the gas phase while maintaining other test parameters constant. Permeability and porosity measurements obtained from Class G cores aged for 2 weeks in acidic brine show consistent trend. Aging in brine saturated with 10% CO_2 gas reduced the porosity and permeability of the cores due to carbonation. However, when the CO_2 concentration was increased, both cement permeability and porosity increased indicating the dominating effect of leaching. For Class H cement, the porosity trend is not consistent with that of the permeability.

Furthermore, the effects of temperature and CO_2 concentration on mechanical properties of Class G and H cements were investigated. Compressive strength of Class G cement increased when the CO_2 concentration was increased. Results of Class H cement show a different trend. In addition, increasing temperature improved the bond strength at lower temperatures (100 to 225°F). Nonetheless, when the aging temperature was increased from 225 to 350°F, bond strength reduced indicating the increase of cement leaching and bond weakening as temperature increases.

Cement additives screening study was continued. The effects of different additives on cement slurry and core properties were investigated. Magnesium oxide and hydroxyapatite provided expected results in terms of improving cement properties such as porosity, permeability, and compressive and bonding strength.

Theoretical and modeling studies on tubular corrosion were continued. Previously, a mechanistic model was considered to study uniform CO_2/H_2S corrosion. However, the model neglects the effect of electrochemical process. During this reporting period, a comprehensive corrosion model has been investigated.

Progress has been made in designing and selection of major components of the corrosion test setup. After receiving the magnetic drive, the design of the corrosion test cell has been finalized. We have also received test cell for stress cracking experiments. The cell requires a heating jacket. The design of the jacket will be prepared in the coming weeks.

Our plan for the upcoming weeks is to continue: i) the aging tests at different CO_2 concentrations; ii) theoretical and modeling studies on tubular corrosion; iii) additive screening studies; and iv) development of corrosion test setup.

2. Overall Project Progress

2.1 Theoretical Studies (Task 1)

When hardened cement sample is in contact with water, a difference in concentration between the water wetting the sample and the interstitial pore solution causes diffusion of ions toward the water. The diffusion decreases of calcium concentration in the cement. This decrease is mainly due to the diffusion of calcium ions out of the cement (resulting from the chemical potential gradient between the pore solution and the surrounding fluid) and the dissolution of the calcium-bearing hydrated products such as portlandite ($Ca(OH)_2$) and tobermorite (C-S-H). A dissolution of $Ca(OH)_2$ tends to re-establish equilibrium. Modeling this leaching process requires a thorough description of time-dependent changes in the calcium ion concentration in the liquid phase. The equations presented in Appendix A are commonly used in modeling of degredation process of cement.

The main purpose of primary cementing is to create a good zonal isolation between producing zones, so oil and gas can be produced safely for many years without having problems such as liquid and gas movement between the casing and cement (i.e. micro channeling). According to Parcevaux et al. (1984), shear-bonding strength is affected by parameters such as volumetric shrinkage development, stress-strain relationships, permeability, and compressive strength. Cured cement goes through stages where the cement reacts with carbon dioxide saturated brine. $Ca(OH)_2$ and C-S-H (calcium silicate hydrate) in the cement react with carbonic acid creating $CaCO_3$. At a fast rate, densification process occurs where $CaCO_3$ increases hardness of the cement and decrease its permeability. As a result, the cement volume can increase up to 6 percent (Santra et al, 2009). However, following the carbonation process (i.e. formation of calcium carbonate), loss of overall mechanical integrity begins because of the leaching process. Calcium carbonate reacts with carbonic acid creating $Ca(HCO_3)_2$ which is water-soluble. When the cement is surrounded by CO_2 saturated water, leaching occurs and therefore, the loss of zonal isolation can happen. According to Santra et al. (2009), several methods are found effective to prevent the loss of zonal isolation including: i) using cement substitutes such as silica flour or fly ash; ii) reducing porosity and permeability of the cement; and iii) adding supplementary material to reduce $Ca(OH)_2$ or change the composition of C-S-H to a more CO_2 resistant cement.

The corrosion process of steel is controlled by two mechanisms: mass transfer and electrochemical process. The slowest process has the most influential effect on the corrosion rate. In previous reports, a mechanistic model developed by Sun and Nesic (2008) was used to study uniform CO_2/H_2S corrosion. The model is based on the assumption that the mass transfer process, which is considered the slowest process, controls the corrosion rate. The effect of electrochemical process is neglected. During this reporting period, a comprehensive corrosion model, which was

developed by Anderko and Young (1999), has been studied. Details of the model are presented in Appendix B. The model performance will be investigated in the coming months.

2.2 Experimental Studies on Degradation of Cement (Task 2)

As previously planned, aging experiments (Experiment 7 and 8) were conducted varying CO_2 concentration. Test parameters for all the aging experiments are summarized in **Table 1**. The samples were aged for 2 weeks. After completion of each experiment, physical properties of aged and unaged samples were measured.

Table 1 Test parameters for aging experiments

Batch #	Temp. (ºF)	Pressure (psi)	Partial Pressure %			Brine Conc. (%)	Aging Period (days)	Experiment #
			CH_4	CO_2	H_2S			
001	350	9000	100	0	0	9	6	1
002	350	6000	100	0	0	2	14 & 28	2
003	350	6000	100	0	0	2	14	
004	350	6000	90	10	0	2	6	3
005	350	6000	90	10	0	2	14 & 28	4
006	350	6000	90	10	0	2	14	
007	225	6000	90	10	0	2	14	5
008	100	6000	90	10	0	2	14	6
009	225	6000	60	40	0	2	14	7
010	225	6000	0	100	0	2	14	8

Figure 1 compares porosity and permeability of unaged cement cores with those aged under different CO_2 concentrations at 6000 psi and 225ºF. When the aging was conducted in brine saturated with 10% CO_2 gas, first reduction in porosity and permeability were observed indicating the carbonation of portlandite and C-S-H. However, when the CO_2 concentration increased (from 10 to 40%), porosity and permeability of Class G cement increased indicating the presence of dominate leaching process resulting from high CO_2 concentration.

For Class H cement, the permeability trend is the same as the G cement. Nevertheless, the porosity does not follow a similar trend. Slight reduction in porosity was observed when the concentration was increased from 10 to 40%. Porosity of Class H cement aged in 10% CO_2 showed high-level of scattering. This could be one of the reasons for the unexpected porosity trend.

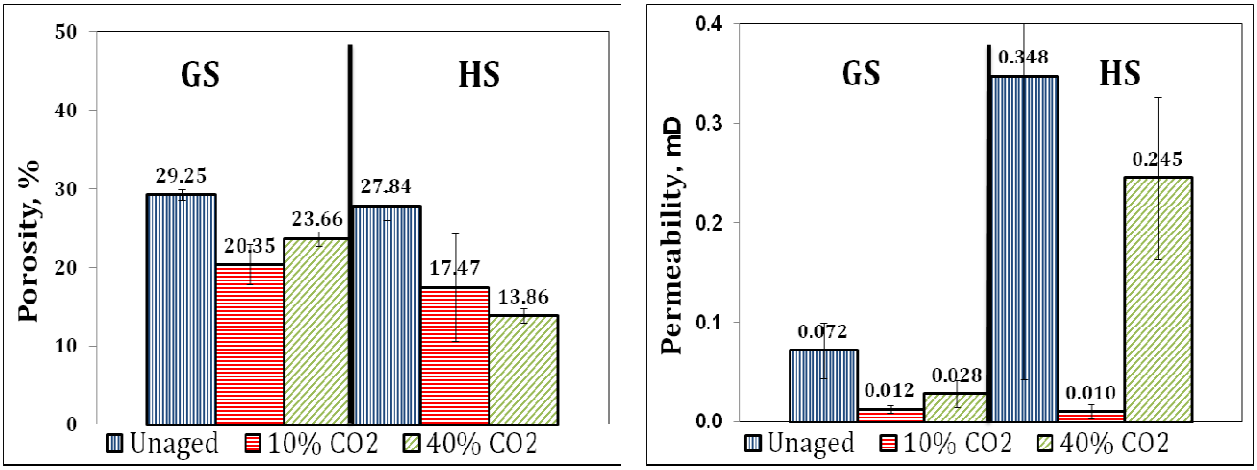

Fig. 1: Properties of unaged cores and cores aged at 6000 psi and 225°F varying CO_2 concentration: a) porosity; and b) permeability

In addition to porosity and permeability, the increase in CO_2 concentration has some effects on mechanical properties of the cement. **Figure 2** presents compressive strength of aged and unaged cement cores. This comparison is made because both Batch 7 and Batch 9 cores were aged for 14 days at the same temperature, pressure and brine concentration 2%. The only parameter varied in these experiments was the partial pressure of CO_2 in the aging cell. A progressive increase in compressive strength of Class G cement occurred as the CO_2 concentration increased in the aging cell at 225°F, 6000 psi and 2% salt concentration. This could be mainly due to carbonation that took place in the hydrated cement. Once formed, calcium carbonate fills the pore spaces in the cement thereby reducing the porosity and possibly permeability. This makes the cement stronger. However, in Class H cement, compressive strength initially increased with 10% CO_2 concentration and then decreased after the CO_2 concentration in the aging cell was increased from 10 % to 40%. The increase observed at 10% CO_2 can be attributed to carbonation in the hydrated cement while the reduction in compressive strength occurred at 40% CO_2 could be attributed to leaching of the cement by carbonic acid.

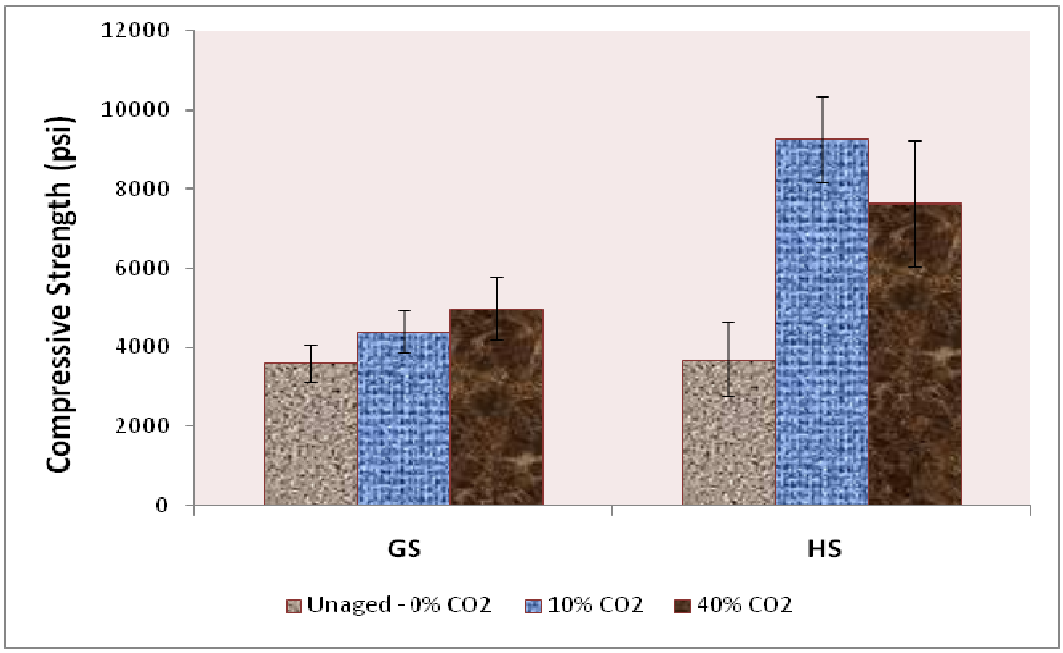

Fig. 2: Compressive strength of unaged cores and cores aged at 6000 psi and 225°F varying CO_2 concentration

The effect of temperature on the bonding strength was investigated. Bonding samples made of Class H cement were aged for 14 days at 6000 psi in 2% brine saturated with a mixture of methane and carbon dioxide (90% CH_4 and 10% CO_2). Temperature was varied from 100 to 350°F. Results show (**Fig. 3**) that increased temperature improved the bond strength at lower temperatures (100 to 225°F). However, when the aging temperature was increased further (from 225 to 350°F), bond strength reduced. The weakening of the bond could be due to cement leaching as aging temperature increases. Krilov et al. (2000) reported the exacerbation of CO_2 caused cement degradation at elevated temperature. Since additional silica was added in the slurry formulation, the contribution of strength retrogression because of increased temperature is expected to be minimal. Without the addition of silica, all Portland cements show strength retrogression at about 240°F (Yetunde et al., 2011). According to Young and Hansen (1987), tobermorite (calcium silicate hydrate) transforms into a weak porous structure at approximately 240°F, which causes strength retrogression.

Furthermore, temperature can have other effects on the bonding strength. Steel has slightly higher thermal expansion coefficient than cement. During drilling or production operations, oil and gas well cement temperature can vary due fluid circulation in the wellbore. As temperature changes, different levels of thermally induced strains will be developed at the interface between the steel and cement. This can generates additional stresses, which affect the bond performance. As a result, bond weakening can occur as temperature varies with time.

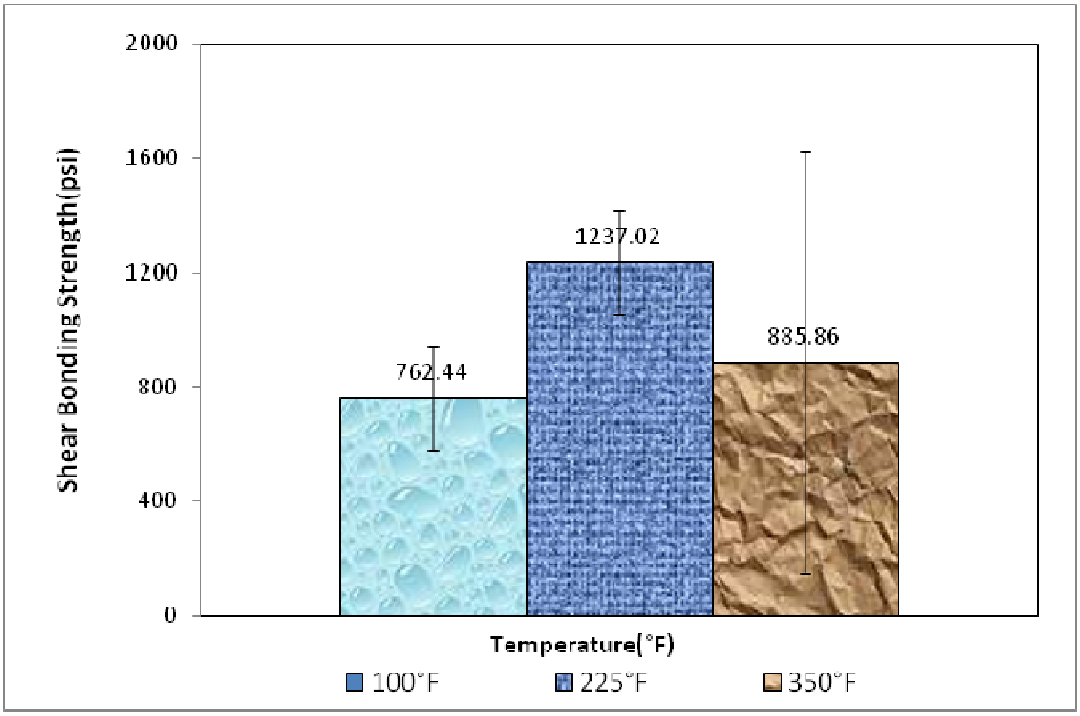

Fig. 3: Bonding strength of Class H samples aged at 6000 psi varying the temperature (Gas composition: 10% CO_2 and 90% CH_4)

Cement additives screening study was continued. The effects of different additives (magnesium oxide, hydroxyapatite, micro-silica and latex) on cement slurry and core properties were investigated. Magnesium oxide and hydroxyapatite provided expected results in terms of improving cement properties such as porosity, permeability, and compressive and bonding strength. Subsequently, aging experiments will be carried out to study the performances of the additives in acidic environment.

Despite acceptable slurry properties, micro silica containing Class G and Class H cement cores were found to be very brittle. Moreover, cement cores containing latex (latex cement) exhibited higher porosity than the baseline GS and HS cores. Tests with latex cement will be repeated to verify the consistency of the results and observations. If necessary, slurry formulations may be revised to improve properties of the cores.

For magnesium oxide containing cement (MGO), slurry and core properties presented in **Table 2** and **Table 3** were found to be comparable with properties of baseline HS and GS cements. Mechanical properties were also very similar. Slurry

Table 2 Properties of MGO cement slurries

Additive	HSMG	GSMG
Amount	5%bwoc	5%bwoc
Remarks	None	None
Density (ppg)	16.3	15.75
Rheology	Presented in **Fig. 4a**	Presented in **Fig. 4a**
API Fluid Loss	116 ml	124 ml
Thickening Time	160 min.	130 min.

properties of baseline cements are presented in **Table 4**. In order to investigate the degradation behavior of MGO cements, core samples were prepared and placed in the aging cell along with baseline cement cores. The properties of the cores will be measured after 14 days of aging at 6000 psi and 225°F.

In addition to MGO cement, hydroxyapatite (HOAP) containing cement formulations were tested for their slurry and core properties. Slurry and unaged core properties (**Table 5**) of the HOAP samples were comparable to those of the baseline cement. Therefore, HOAP cement cores have been prepared to test their degradation behavior in acidic gas environment. Next, the cores will be placed in the ageing cell for 14 days and results will be presented in the coming reports.

Table 3 Properties of unaged MGO cores

Sample	Porosity	Permeability	Compressive Strength (psi)
Class H cores	29.96 %	0.159 mD	4142
HSMG cores	25.38 %	0.039 mD	5081
Class G cores	28.32 %	0.061 mD	4329
GSMG cores	27.43 %	0.026 mD	4160

Table 4 Properties of HS and GS cement slurries

	HS	GS
Density	16.20ppg	15.45ppg
Rheology	Presented in **Fig. 4**	Presented in **Fig. 4**
API Fluid Loss	100 ml	120 ml
Thickening Time	170 min.	135 min.

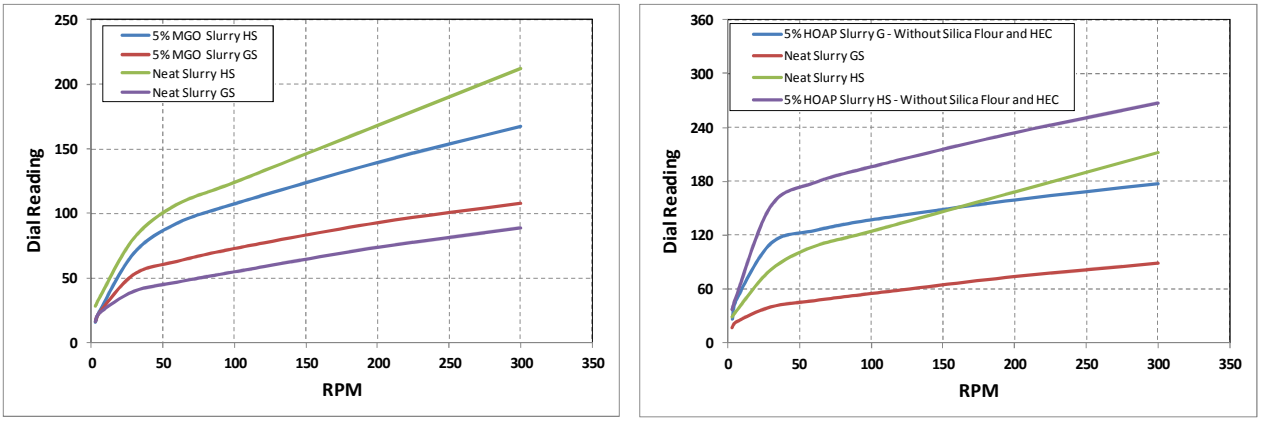

(a) (b)

Fig. 4: Rheology of Class H and G cement slurries with additives: a) MGO; and b) HOAP

Table 5 Properties of hydroxyapatite containing cement slurries

Slurry	HSHO	HSHO	HSHO	GHO	HHO
Amount	30% bwoc	15% bwoc	5% bwoc	5% bwoc	5% bwoc
Remarks	Silica Flour and HEC	Silica Flour and HEC	Silica Flour and HEC	No Silica Flour and HEC	No Silica Flour and HEC
Density (ppg)	Extremely thick slurry	Extremely thick slurry	Extremely thick slurry	15.80 ppg	16.65 ppg
Rheology				Presented in Fig. 4b	Presented in Fig. 4b
API Fluid Loss				82 ml	88 ml
Thickening Time	Not Tested			60 min.	90 min.

As mentioned in the previous report, micro-silica based cement slurry showed acceptable properties (**Table 6**), which were very similar to those of the baseline cements. Subsequently, another batch of the slurry was prepared and cured for 5 days in 2% brine at 200ºF. The cement block prepared was then taken for coring, cutting and grinding in order to prepare the core samples. However, the cured Class G and Class H cement samples were found to be very brittle. The result was unexpected since several studies (Grabowski and Gillott, 1989: Dillenbeck et al., 1990; Mueller & Dillenbeck, 1991) indicated the application of micro silica for controlling degradation. Another batch of the micro silica based slurry will be prepared in order to see if the results can be replicated. In addition, literatures will be reviewed to modify the formulation of the slurries to minimize brittleness tendency of the cores.

Table 6 Properties of micro silica containing cement slurries

Additive	**HSMS**	**HMS**	**GMS**
Amount	20% bwoc – MicroSilica 15% bwoc – Silica Flour 1.5% bwoc – Anhyd. Citric Acid	35% bwoc – MicroSilica 0% bwoc – Silica Flour 2.0% bwoc – Anhyd. Citric Acid	35% bwoc – MicroSilica 0% bwoc – Silica Flour 2.0% bwoc – Anhyd. Citric Acid
Remarks	Extremely Thin Slurry	None	None
Density (ppg)	13.80	12.80	12.60
Rheology	Presented in **Fig. 5a**	Presented in Fig. 5a	Presented in Fig. 5a
API Fluid Loss	70 ml	60 ml	54 ml
Thickening Time	Not Tested	5 hr. 20 min.	3 hr. 20 min.

Addition of latex into cement is expected to reduce its porosity and permeability. To study the effects of latex on slurry properties, latex containing samples were prepared and tested. Diluted acetic acid (50% v/v solution) was included in the formulation to acts as an emulsifier at elevated temperatures (Fuquan et al., 2006). Additionally, it acts as a dispersant and retarder because of its anionic nature. The API fluid loss for latex containing Class H cement (HSLT) was not measured to due instrument failure. The experiment will be repeated in the coming weeks. The slurry was less viscous as compared to the neat Class G and Class H slurries (Fig. 5b). This is attributed to the addition of acetic acid. The dispersed nature of the slurry also causes retardation. However, the slurry is still manageable in lab conditions and further addition of extenders might not be needed as it introduces additional test variable. Currently, we are using 0.43% BWOC acetic acid; if necessary, reducing the amount of acetic acid may be considered.

Furthermore, consistency and thickening behavior of latex cement slurries were also examined (**Fig. 6**). Their thickening times were higher than those of the baseline cements; however, still in acceptable range.

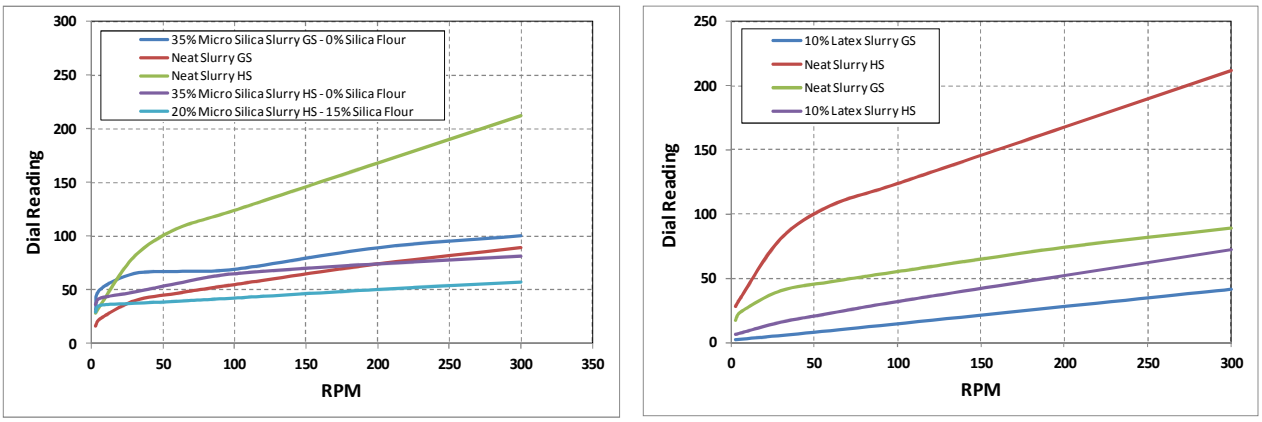

Fig. 5: Rheology of Class H and G cement slurries with additives: a) micro silica; and b) latex

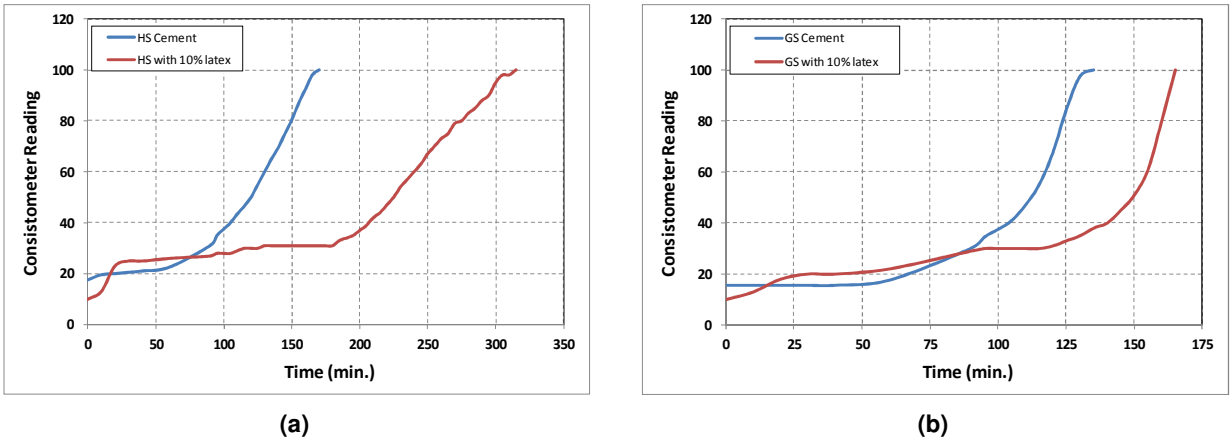

Fig. 6: Consistency of Class H and G cement slurries with latex: a) Class H; and b) Class G

After obtaining encouraging results from the slurry property tests, latex containing Class G and Class H cement cores were prepared. Cement curing conditions were identical with those of the baseline cement samples. After 5 days of curing in 2% brine at 200ºF, porosity, permeability and compressive strength of the cores were measured. Porosity and permeability of unaged latex cores were compared to those of the baseline cement (**Fig. 7**). Cores with latex were more porous than the class G and H cores. For Class H cement, the addition of latex didn't produce significant change in permeability. However, considerable increase in permeability was observed when latex was added into Class G cement. These results were contradicting to what was reported in the literature. The porosity and permeability of a latex-cement system is anticipated to be lower than the conventional system. Mehta & Monteiro (2006) attributed this unexpected behavior to the entrapment of air in the latex. Approximately, 50% (by weight) of latex is made of spherical polymeric particles (0.01 to 1 μm in diameter) held in suspension in water by surface-active agents.

The surface-active agents in the latex tend to incorporate large amount of entrained air. The entrapped air results in increased porosity and permeability. Defoaming agent (surfactant) may be needed to reduce the foaming tendency and minimize air entrapment in the latex system.

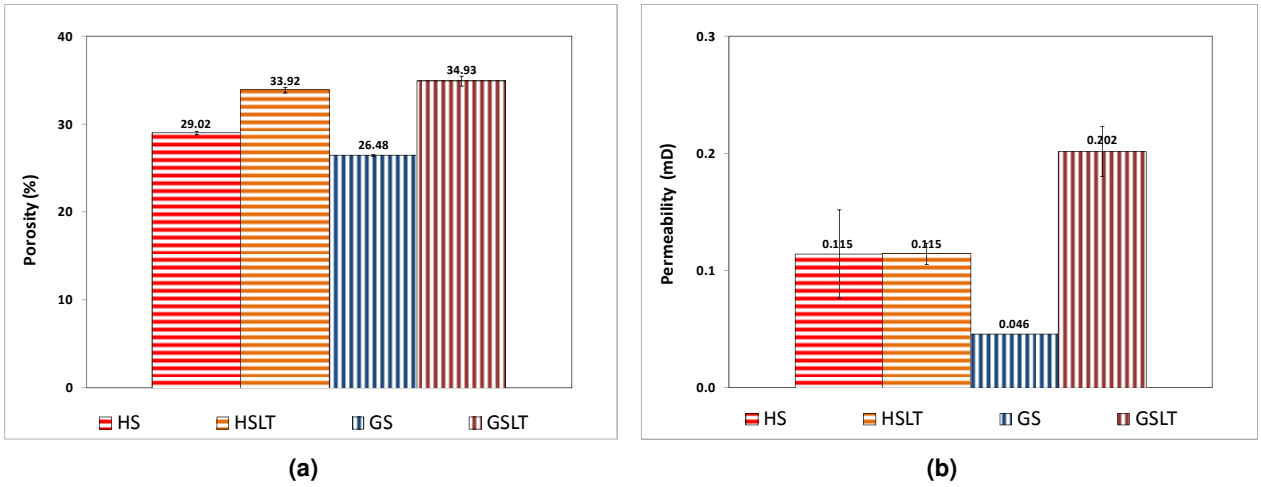

Fig. 7: Comparison of properties of unaged latex cores with baseline cement: a) porosity; and b) permeability

In the coming weeks, compressive and shear bond strength tests will be carried out with latex containing cores. Moreover, another batch of latex cement slurry will be prepared, and porosity and permeability of the cores will be measured. If the results again show increased porosity and permeability, then adding defoaming agent or formulation adjustment will be considered.

2.3 Experimental Studies on Corrosion of Tubulars (Task 3)

Progress has been made in designing and selection of major components of the corrosion test setup. Potentiostat (Gamry Series G 300 Potentiostat/Galvanostat/ZRA) and magnetic drive have been received and the design of the corrosion test cell has been finalized. Purchase order for the cell has been completed and final design drawings (**Fig. 8**) have been approved. Manufacturing will take 2 to 3 months. It is expected to conduct preliminary corrosion experiments at ambient conditions soon. Beside this, we have received tested cell for stress cracking experiments. We will be designing a heating jacket for cell.

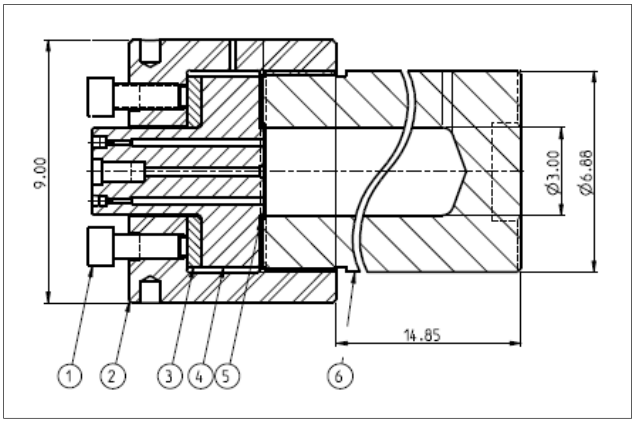

Fig. 8: Final design of the corrosion cell

3. Problems Encountered

We are using helium for measuring porosity and permeability of the cement cores. Due to the global helium shortage, the availability of helium has been significantly reduced recently. As a result, we are facing a shortage of helium to obtain these measurements. Currently, we have very limited quantity of helium in our lab. We are exploring different options such as using nitrogen. Hence, experiments were conducted to evaluate measurements obtained using nitrogen as test fluid. Comparison of results (**Fig. 9**) shows that measurements obtained using different test gases can be significantly different because of non-Darcy effects. Two of the reasons for non-Darcy effects are:

I. Gas Slippage: If pore throat of a membrane approaches the size of mean free path of molecules, then there is an increase in the velocity of the molecules or the molecules 'slip'. This results in increased flow rate and permeability.

II. Inertial Flow: Increase in velocity results in turbulent flow conditions and causes non–Darcy effects.

Knudsen number is used to quantify the level of slippage. If the Knudsen number is closer to one, then the mean free path of molecule is comparable to the pore throat; hence, higher slippage is expected. The Knudsen numbers for He and N_2 are 0.8 and 0.6, respectively. Helium shows higher slippage than N_2, hence the permeability value measured by He is expected to be more than that measured by N_2.

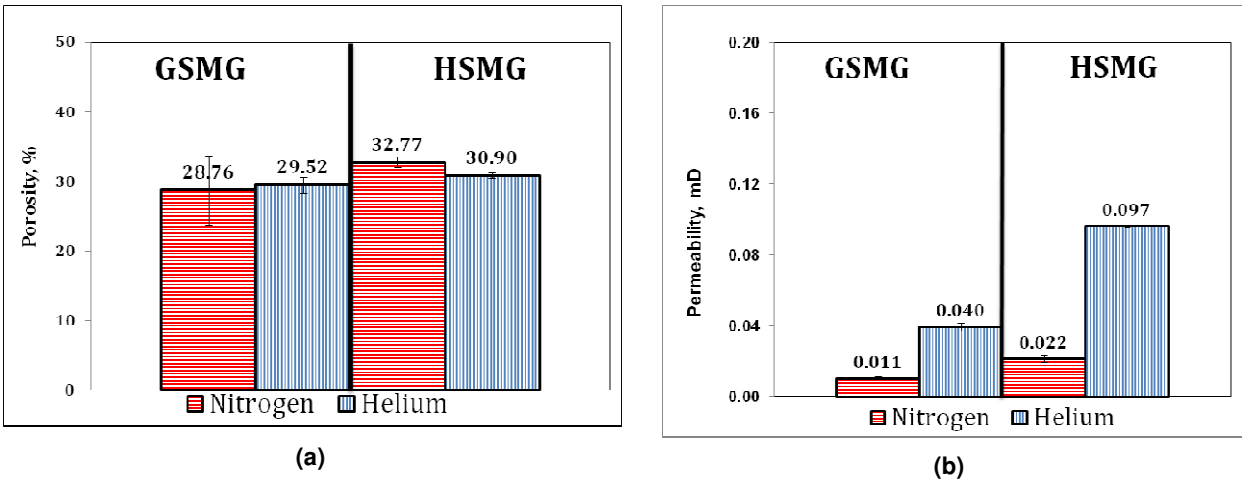

Fig. 9: Comparison of measurements obtained using nitrogen and helium: a) porosity; and b) permeability

4. Planned Activities

- Continue aging experiments with brine-CO_2-CH_4 system for 14 days varying CO_2 concentration at 225ºF.
- Continue theoretical and modeling studies on tubular degradation.
- Continue cement additive screen study.
- Continue development of tubular corrosion testing setups and acquisition of components.

5. Project Expenditures

This section presents the project expenses during the month of January (**Table 6**) and the cumulative expenditures.

Table 6 Current and cumulative expenditures, January, 2013

No.	Budget Categories	Current Expenses	Cumulative Expenses
1	Salaries & Wages	$4,725.00	$144,454.66
2	Fringe Benefits	$307.13	$35,283.97
3	Project Materials	$1,583.97	$65,915.07
4	Travel	$0.00	$3,869.55
5	Conference Expenses	$0.00	$0.00
6	Other Direct Costs	$0.00	$585.77
7	Equipment	$11,453.15	$154,025.82
8	Space Rental	$0.00	$0.00
9	Indirect Cost	$3,308.05	$125,054.55
10	**Total**	**$21,377.30**	**$529,189.39**

Nomenclature

C-S-H	Calcium silicate hydrate
GHO	Class G Cement with hydroxyapatite
GS	Class G cement with silica flour
GMS	Class G Cement with micro silica
GSHO	Class G Cement with silica flour and hydroxyapatite
GSLT	Class G Cement with silica flour and latex
GSMG	Class G Cement with silica flour and magnesium oxide
HHO	Class H Cement with hydroxyapatite
HMS	Class H Cement with micro silica
HOAP	Hydroxyapatite additive sample
HS	Class H cement with silica flour
HSHO	Class H Cement with silica flour and hydroxyapatite
HSLT	Class H Cement with silica flour and latex
HSMG	Class H Cement with silica flour and magnesium oxide
HSMS	Class H Cement with silica flour and micro silica
MGO	Magnesium oxide containing cement

References

Anderko, A. and Young, R.D., 1999. Simulation of CO_2/H_2S Corrosion using Thermodynamic and Electrochemical Models, paper NACE No. 31, conference division, Houston, Texas.

Berger, F.P. K. and Hau, F. F.L., 1977.Mass Transfer in Turbulent Pipe Flow Measured by the Electrochemical Method, Int. J. Heat Mass Transfer, Vol. 20; pp. 1,185-1194.

Bockris, J.O'M., Drazic, D. and Despic, A.R., 1961. The Electrode Kinetics of the Deposition and Dissolution of Iron, ElectrochimicaActa, Vol. 4, pp. 325 to 361.

DeWaard, C. and Milliams, D. E.1975. Carbonic Acid Corrosion of Steel, Corrosion, Vol. 31, p.131.

Dillenbeck, R. L., Mueller, D.T. and Orr B. R. 1990. The Effect of MicroSilica on the Thermal Stability of Lightweight Cement Systems, paper SPE-21597-MS, presented at the International Technical Meeting, Petroleum Society of CIM and SPE, June 10 to 13.

Eisenberg, M., Tobias, C.W. and Wilke, C.R. 1954. Ionic Mass Transfer and Concentration Polarization at Rotating Electrodes, J. Electrochem., Soc. 101: p. 306, Stanford Research Institute, Stanford, California.

Fuquan, S., Guangming, L. and Jianzhou, J. 2006. Application and Research of Latex Tenacity Cement Slurry System, paper SPE 104434, presented at the SPE International Oil & Gas Conference and Exhibition, Beijing, China.

Gerard, B., Le Bellego, C., and Bernard, O. 2002. Simplified Modelling of Calcium Leaching of Concrete in Various Environments. Materials & Structures 35: 632-640.

Grabowski, E. and Gillott, J. E. 1989. Effect of Replacement of Silica Flour with Silica Fume on Engineering Properties of Oil Well Cements at Normal and Elevated Temperatures and Pressures, Cement and Concrete Research, Vol. 19, pp 333-344.

Gray, L.G.S., Anderson, B.G., Danysh, M.J. and Tremaine, P.G., 1989. Mechanism of Carbon Steel Corrosion in Brines Containing Dissolved Carbon Dioxide at pH 4, NACE paper No.464, Houston, Texas.

Krilov, Z. B., Loncaric, I. and Miksa, Z. 2000. Investigation of a Long-Term Cement Deterioration Under a High-Temperature, Sour Gas Downhole Environment, paper 58771-MS, presented at the SPE International Symposium on Formation Damage Control, 23-24 February, Lafayette, Louisiana.

Manguy, M., and Coussy, O. 2000. Propagation Fronts during Calcium Leaching and Chloride Penetration. J. Eng. Mech. 126 (3): 250-257.

Mehta, P.K. and Moneiro, P.J.M. 2006. Concrete: Microstructure, Properties and Materials, Third Edition, Tata McGraw Hill.

Mueller D.T. and Dillenbeck, R.L. 1991. The Versatility of Silica Fume as an Oil well Cement Admixture, paper SPE-21688-MS, presented at the SPE Production Operations Symposium, 7-9 April, Oklahoma City, Oklahoma.

Nakarai, M., and Coussy, O. 2006. Modelling of Calcium Leaching from Cement Hydrates Coupled with Micro-Pore Formation. J. Adv. Concr. Tech. 4 (3): 395-407.

Nesic, S., Postlethwaite, J. and Olsen, S. 1996. An Electrochemical Model for Prediction of Corrosion of Mild Steel in Aqueous Carbon Dioxide Solutions, NACE international, April.

Oddo, J.E. and Tomson, M.B. 1982. Simplified Calculation of CaCO3 Saturation at High Temperatures and Pressures in Brine Solutions, SPE of AIME, Society of Petroleum Engineers, p. 1,583, Richardson, Texas.

Palmer D. A., van Eldik R. 1983. The chemistry of metal carbonate and carbon dioxide complexes, Chem. Rev. 83, p. 651.

Parcevaux, P.A. and Sault, P.H. 1984. Cement Shrinkage and Elasticity: A New Approach for a Good Zonal Isolation, paper 13176-MS, presented at the SPE Annual Technical Conference and Exhibition, 16-19 September, Houston, Texas.

Santra, A., Reddy, B.R. Liang, F. and Fitzgerald, R. 2009. Reaction of CO2 With Portland Cement at Downhole Conditions and the Role of Pozzolanic Supplements, paper SPE 121103-MS, presented at the SPE International Symposium on Oilfield Chemistry, 20-22 April, The Woodlands, Texas.

Sun, W. and Nesic, S., 2009. Mechanistic Model of Uniform Hydrogen Sulfide/Carbon Dioxide Corrosion of Mild steel, NACE international.

Videm, K. 1993. Fundamental Studies Aimed at Improving Models for Prediction of CO_2 Corrosion, in Progress in the Understanding and Prevention of Corrosion, Proc. 10th Europ. Corros. Cong., vol. 1, pp. 513, London, England.

Yetunde, S. and Ogbonna, J. 2011. Challenges and Remedy for Cementing of HPHT Wells in Nigerian Operation, Nigeria Annual International Conference and Exhibition, 30 July - 3 August, Abuja, Nigeria.

Young, J.F and Hansen, W. 1987. Volume relationship for C-S-H formation based on hydration stoichiometry Microstructural Development during Hydration of Cement, Res. Soc. Symp. Proc. Boston, MA.

Appendix A: Summary of models for degradation of oil well cement

Variable to Predict	Predictive Model	Required variable
Compressive Strength, σ_c	Depends on calcium concentration in the solid phase of cement, Ca_{solid}, and the leached depth, X_d	• Calcium concentration in the solid phase of cement, Ca_{solid} • Leached depth, X_d
• Concentration of calcium in the solid phase of cement, Ca_{solid}	**Model 1: Gerard et. al. (2002)** $Ca_{solid} = a - b(Ca_{liquid})^2 + cCa_{liquid} - \left[\frac{e}{\left\{1+\left(\frac{Ca_{liquid}}{x_2}\right)^n\right\}} + \frac{f}{\left\{1+\left(\frac{Ca_{liquid}}{x_1}\right)^m\right\}}\right]$ $e = C_{CH}$ $f = 0.565(C_{Total} - C_{CH})$ $b = \frac{C_{Total} - C_{CH} - f}{400}$ $c = \frac{C_{Total} - C_{CH} - f}{20} + 20b$ $a = C_{CH} + f$ **Model 2: Nakarai et. al. (2006)** $Ca_{solid} = f(Ca_{liquid}) = A\left[C_{CSH}\left(\frac{Ca_{liquid}}{Ca_{satu}}\right)^{\frac{1}{3}}\right] + B$ $A = \begin{cases} -\left(\frac{2}{x_1^3}\right)(Ca_{liquid})^3 + \left(\frac{3}{x_1^2}\right)(Ca_{liquid})^2 & (0.0 \le Ca_{liquid} \le x_1) \\ 1 & (x_1 < Ca_{liquid}) \end{cases}$ $B = \begin{cases} 0 & (0.0 \le Ca_{liquid} \le x_2) \\ \frac{C_{CH}}{(Ca_{satu} - x_2)^3}(Ca_{liquid} - x_2)^3 & (x_2 < Ca_{liquid}) \end{cases}$	• Calcium concentration in the liquid phase, Ca_{liquid} • Amount of calcium in the solid phase of the calcium hydroxide, C_{CH} • Amount of calcium in the solid phase of the C-S-H (Tobermorite) component of the cement, C_{CSH} • Total amount of solid phase calcium, C_{Total} Note: $C_{Total} = C_{CSH} + C_{CH}$ • Liquid phase calcium ion concentration when the rapid transition of C-S-H gel into silica gel begins, x_1 • Liquid phase calcium ion concentration when the calcium hydroxide has completely dissolved and the dissolution of C-S-H begins, x_2

Leached depth, X_d	**Generalized Diffusion Model** $\frac{\partial}{\partial t}(\emptyset * Ca_{liquid}) + \frac{\partial Ca_{solid}}{\partial t} - \nabla\{\emptyset D \nabla(Ca_{liquid})\} = 0$ **Simplified 1D Diffusion Model: Manguy et. al. (2000)** $\frac{\partial(\emptyset * Ca_{liquid})}{\partial t} - \frac{\partial}{\partial x}\left(\emptyset D \frac{\partial Ca_{liquid}}{\partial x}\right) = 0$ **Analytic solution of 1D Diffusion Model: Manguy et. al. (2000)** $\varepsilon \exp(-\xi_d^2) = \sqrt{\pi}\xi_d \mathrm{erf}(\xi_d)$ $X_d = 2\xi_d\sqrt{Dt}$ $\varepsilon = \frac{\emptyset C_{satu}}{C_{Total}}$	• Calcium concentration in the solid phase of cement, Ca_{solid} • Calcium concentration in the liquid phase, Ca_{liquid} • Diffusion coefficient, D • Time-dependent cement porosity, $\emptyset$ • Saturated liquid phase calcium ion concentration , C_{satu} • Total amount of solid phase calcium, C_{Total}
Diffusion coefficient, D	**Nakarai et. al. (2006)** $D = D_o * \exp\{9.95\emptyset\}, \quad D_o = 2.25 * 10^{-13} m^2/s$	• Time-dependent cement porosity, $\emptyset$
Time-dependent cement porosity, $\emptyset$	$\emptyset(Ca_{solid}) = \emptyset_o + (1 - \emptyset_o) * (C_{Total} - Ca_{solid})$	• Initial cement porosity, $\emptyset_o$ • Total amount of solid phase calcium, C_{Total} • Concentration of calcium in the solid phase of cement, Ca_{solid}
Initial cement porosity, $\emptyset_o$	$\emptyset_o = 40.18 * \ln\left\{\frac{W}{C}\right\} + 59.15$	• Water/cement ratio for the cement
Saturated liquid phase calcium ion concentration , C_{satu}	**Nakarai et. al. (2006)** $C_{satu} = \frac{1}{2}\sqrt[3]{2K_{sp}}$ $K_{sp} = \Delta K_{sp}^{Cl} + K_{sp}^{T}$ $\Delta K_{sp}^{Cl} = A(5 * 10^4 \sqrt[3]{Cl})$ $A = \begin{cases} -2Cl^3 + 3Cl^2 & (0.0 \le Cl \le 1.0) \\ 1 & (1.0 < Cl) \end{cases}$ $K_{sp}^{T} = 0.0125 * 10^9 * e^{-0.019T}$	• Solubility product of calcium hydroxide, K_{sp} • Concentration of sodium chloride in pore solution, Cl

Nomenclature

x_1 = Liquid phase calcium ion concentration when the rapid transition of C-S-H gel into silica gel begins, mmol/L

x_2 = Liquid phase calcium ion concentration when the calcium hydroxide has completely dissolved and the dissolution of C-S-H gel begins, mmol/L

C_{CSH} = Amount of calcium in the solid phase of the C-S-H gel, mmol/m^3

C_{CH} = Amount of calcium in the solid phase of the calcium hydroxide, mmol/m^3

C_{satu} = Saturated liquid phase calcium ion concentration, mmol/L

K_{sp} = Solubility product of calcium hydroxide , $mmol^3/L^3$

ΔK_{sp}^{Cl} = Effect of sodium chloride on the solubility product of calcium hydroxide, $mmol^3/L^3$

Cl = Concentration of sodium chloride (% by mass) in the pore solution

K_{sp}^{T} = Effect of temperature on the solubility product of calcium hydroxide, $mmol^3/L^3$

T = Absolute Temperature, K

$\frac{W}{C}$ = Cement/Water ratio

Appendix B: Corrosion Behavior of Tubulars under Sour Gas Environment

Anderko and Young (1998) model combines thermodynamic and electrochemical modeling approaches to describe the partial cathodic and anodic processes on the steel surface. It predicts uniform corrosion rates of carbon steels in the presence of carbon dioxide and hydrogen sulfide. It also provides the expected corrosion scale (iron carbonate and iron sulfide) using the corrosion rate. The model can be subdivided into three parts based on the influence of three parameters (CO_2, H_2S and corrosion scale) as it is shown in Fig. A-1.

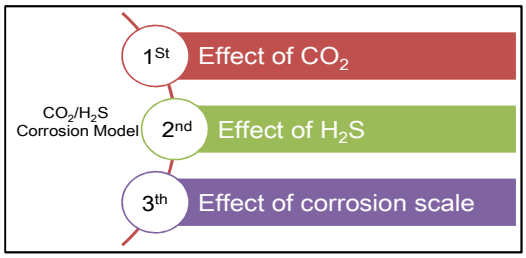

Fig. A-1 Parts of corrosion model

B.1 Effect of CO_2 on Corrosion Rate

To have better understanding the effects of CO_2 on the corrosion rate, the physical and mathematical aspects of the electrochemical process were reviewed and analyzed (Nesic et al., 1996). A model for a uniform corrosion was formulated based on the individual electrochemical reactions occurring in a water-CO_2 system in the absence of protective scale. The model takes into consideration the electrochemical reactions such as reduction of hydrogen ion (H^+), carbonic acid (H_2CO_3) and oxygen and anodic dissolution of iron. Nesic et al. (1996) conducted an experimental study to determine the electrochemical parameters (e.g. exchange current densities and Tafel slopes) of different reactions and investigate the effects of test conditions (CO_2 partial pressure, pH, temperature and flow rate) on the total cathodic and anodic curves as well as the electrochemical parameters. The influence of test conditions is summarized in Table A-1 The approach developed by Nesic et al. (1996) is slightly different from Anderko and Young's model (1996), since the corrosion mechanism is not only determined by the electrochemical processes but also by other phenomena involved in the corrosion process.

Table A-1: Effects of test conditions on CO_2 corrosion rate

Test parameters	Effects on the corrosion rate
CO_2 partial pressure	• The solution containing CO_2 produces an additional cathodic reaction because of direct reduction of H_2CO_3.
Temperature	• Increase in the controlled mass transfer, which resulted from the increase in the diffusion coefficient for H^+ and a decrease in viscosity at high temperature. • The total cathodic reaction increases with increasing temperature. However, the anodic reaction is not accelerated significantly at higher temperatures (20-50℃). • For higher temperature (greater than 50℃), the rate of anodic dissolution of iron decreases.

pH	• pH has minor influence on the limit current density in the presence of CO_2 which reduces substantially (threefold) when pH changed from 4 to 5. However, in the free CO_2 solution, the limit current density can decrease by tenfold when pH increased from 3 to 4. • The pH has no clear effect on anodic dissolution of iron in CO_2 environments over the pH range of practical interest (4 < pH < 6).
Fluid velocity	• In both cases (i.e. with and without the presence of CO_2), the anodic dissolution of iron is not affected by the flow. • The i_{lim} value for the reduction of H_2CO_3 is chemical reaction-controlled and insensitive to flow.

B.2 Thermodynamic Properties of Carbon Dioxide in Brine

The chemistry of CO_2 saturated aqueous solutions and equilibrium considerations are very important for determining the behavior of mild steel corrosion. When CO_2 is in contact with water, first carbon dioxide gas dissolves in water.

$$CO_{2(g)} \overset{K_{Sol}}{\Leftrightarrow} CO_{2(aq)} \tag{A-1}$$

For the ideal gas and ideal solutions in equilibrium, the aqueous concentration of dissolved CO_2 can be determined using the Henry's law with a known CO_2 concentration (partial pressure of CO_2) in the gas phase.

$$H_{sol(CO2)} = \frac{1}{K_{sol(CO2)}} = \frac{P_{CO2}}{C_{Co2}} \tag{A-2}$$

where K_{sol} is the solubility constant expressed as a function of temperature (Oddo and Tomson, 1982).

$$K_{sol(CO2)} = \frac{14.5}{1.00258} \times 10^{-(2.27+5.65\times10^{-3}T_f - 8.06\times10^{-6}T_f^2 + 0.0751I)} \tag{A-3}$$

where I is the ionic strength calculated as:

$$I = \frac{1}{2}\sum_i c_i.z_i^2 = \frac{1}{2}\left(c_1.z_1^2 + c_2.z_2^2 + ...\right) \tag{A-4}$$

Only small fraction of the dissolved CO_2 molecules dissociates to produce weak carbonic acid. The process is described as the hydration process of aqueous CO_2.

$$CO_{2(aq)} + H_2O \overset{K_{hyd}}{\Leftrightarrow} H_2CO_3 \tag{A-5}$$

As reported by Palmer and Van Eldik (1983), the value of equilibrium constant (K_{hyd}) is 2.58 x 10^{-3} and it remains approximately constant in the temperature range from 20 to 80ºC. For the forward reaction, the CO_2 hydration reaction constant (K_{hyd}^{f}) is expressed as a function of temperature as:

$$K_{hyd}^{f} = 10^{162.2-53.0*\log T_f - \frac{11715}{T_f}} \tag{A-6}$$

B.3 Electrochemistry of Mild Steel Corrosion in CO_2 Saturated Aqueous Solutions

For modeling purpose, the electrochemical reactions in CO_2 system are categorized into cathodic and anodic reactions.

B.3.1 Cathodic Reactions

The presence of carbon dioxide in the solution has a tendency of increasing the rate of hydrogen evolution resulting in increased corrosion rate of mild steel. It is well known that aqueous CO_2 forms weak carbonic acid (H_2CO_3) that dissociates as follows:

$$H_2CO_3 \leftrightarrow H^+ + HCO_3^- \tag{A-7}$$

$$HCO_3^- \leftrightarrow H^+ + CO_3^{2-} \tag{A-8}$$

The reduction of hydrogen:

$$2H^+ + 2e^- \rightarrow H_2 \tag{A-9}$$

At low pH (less than 4), the hydrogen reduction is considered as the most dominating cathodic reaction in acidic solutions of carbon dioxide. As it has been reported and verified by Nesic et al. (1996), the current density increases the resistance to the mass transfer of H^+, which causes a drop in the concentration at the metal surface, resulting in a deviation from Tafel behavior. Then, the limiting current density (ilim) is attained. However, in the intermediate pH range (4 < pH < 6), the direct reduction of H_2CO_3 becomes relevant cathodic reaction in addition to the H^+ reduction. The reduction of H_2CO_3 is expressed as:

$$H_2CO_3 + e^- \rightarrow H + HCO_3^- \quad \text{(A-10)}$$

The additional cathodic reaction due to direct H_2CO_3 reduction has a tendency of producing more corrosive solution than a completely dissociated acid at the same pH. The direct H_2CO_3 reduction has a limiting current that is controlled by the slowest chemical step (hydration of CO_2). At the current higher than ilim for H^+ or H_2CO_3 reduction, the direct water reduction becomes the dominant cathodic reaction and it is expressed as:

$$H_2O + e^- \rightarrow H + OH^- \quad \text{(A-11)}$$

B.3.2 Anodic Reactions

Mechanisms of anodic dissolution of iron in acidic solutions have been extensively studied (Dewaard and Milliams, 1975; Gray et al., 1989). A number of different models were proposed to describe the dissolution of iron. Generally, the dependency of the dissolution rate on the activity of hydroxide ions is the most acceptable modeling approach (Bockris et al. 1961).

$$Fe + OH^- \rightarrow FeOH + e^- \quad \text{(A-12)}$$

$$FeOH \overset{RD}{\rightarrow} FeOH^+ + e^- \quad \text{(A-13)}$$

$$FeOH^+ \rightarrow Fe^+ + OH^- \quad \text{(A-14)}$$

The assumptions of this iron dissolution model may not be valid at pH greater than 4 (Nesic et al., 1996; Videm, 1993). In addition to the influence of OH^- ions, it is assumed that the iron dissolution reaction in CO_2-contaning solution occurs without significant influence of pH.

B.4 Mathematical Model

A mathematical model has been developed by quantifying all the electrochemical reactions that have been presented in the previous section (Section B.3). This section presents the equations that are used to determine the final current-density-versus-voltage relationship for each reaction.

B.4.1 Reduction of Hydrogen Ion

The H^+ ion reduction that is described in Eqn. (A-9) can be controlled by mass transfer or charge transfer, therefore the final relationship between the current-density and voltage for H^+ reduction can be written as:

$$\frac{1}{i_{(H+)}} = \frac{1}{i_{\alpha(H+)}} + \frac{1}{i^{d}_{\lim(H+)}} \tag{A-15}$$

The charge transfer current density for H+ can be calculated as:

$$i_{\alpha(H^+)} = i_{0(H^+)} \times 10^{-\frac{E-E_{rev(H+)}}{b_{c(H+)}}} \tag{A-16}$$

The cathodic Tafel slope for the hydrogen reduction ($b_{c(H^+)}$), which is shown in Eqn. (A-16) can be obtained using the following formula.

$$b_{c(H^+)} = \frac{2.303RT}{\alpha_c F} \tag{A-17}$$

According to early studies (Bockris et al., 1961; Nesic et al., 1996), Tafel slope of H^+ reduction is b_c = 0.118 V at 25℃ and $\alpha_c = 0.5$. The exchange current density ($i_{0(H^+)}$) is a function of temperature and pH. When pH is 4, the exchange current density (ECD) at standard conditions ($i^{ref}_{0(H+)}$) is 5.0×10^{-2} A/m^2. The ECD can be corrected for pH change using the formula developed by Bockris et al. (1961).

$$\frac{\partial \log i_{0(H^+)}}{\partial pH} = -0.5 \tag{A-18}$$

The temperature dependence of the exchange current density can be calculated using an Arrhenius-type relation with activation enthalpy of H^+, which is 30 KJ/mol ($\Delta H_{(H^+)} = 30 KJ/mol$).

$$\frac{i_{0(H^+)}}{i^{ref}_{0(H^+)}} = Exp\left(-\frac{\Delta H_{(H^+)}}{R}\left[\frac{1}{T} + \frac{1}{T_{ref}}\right]\right) \tag{A-19}$$

The reversible potential for H^+ reduction ($E_{rev(H^+)}$) is also a function of pH and temperature. It can be obtained using the following equation:

$$E_{rev(H^+)} = -\frac{2.303RT}{F} pH \tag{A-20}$$

The second component of the H^+ reduction is diffusion limiting current density ($i^{d}_{\lim(H+)}$):

$$i^{d}_{\lim(H+)} = K_{m(H^+)}.F.C_{H^+} \quad \text{(A-21)}$$

where $K_{m(H^+)}$ is the mass transfer coefficient for hydrogen ions, which can be obtained from a correlation. The coefficient is a function of three dimensionless numbers (Sherwood, Reynolds and Schmidt numbers) and flow geometry. For the straight pipe, the mass transfer coefficient is computed from the following equation (Berger and Hau, 1977).

$$Sh_p = \frac{K_{m(H^+)} d_p}{D} = 0.0165 \times \mathrm{Re}^{0.86} \times Sc^{0.33} \quad \text{(A-22)}$$

For rotating cylinder (Eisenberg et al, 1954), the mass transfer coefficient is obtained from the following equation.

$$Sh_r = \frac{K_{m(H^+)} d_c}{D} = 0.0791 \times \mathrm{Re}^{0.7} \times Sc^{0.356} \quad \text{(A-23)}$$

where Schmidt number (Sc) is defined as: $Sc = \mu / \rho D$. The effect of temperature on the diffusion coefficient (D) can be obtained from the Stokes-Einstein equation as:

$$D = D_{ref} \times \frac{T}{T_{ref}} \times \frac{\mu_{ref}}{\mu} \quad \text{(A-24a)}$$

At standard temperature (t_{ref}), the diffusion coefficient (D_{ref}) for H^+ ions is 9.31×10^{-9} m^2/s. μ_{ref} is dynamic viscosity of water at standard conditions. At higher temperatures, the dynamic viscosity can be determined using the following equation.

$$\mu = \mu_{ref} \times 10^{\left(\frac{1.3272(20-T) - 0.001053(20-T)^2}{T+105} \right)} \quad \text{(A-24b)}$$

B.4.2 Reduction of Carbonic Acid

Carbonic acid reduction occurs as shown in Eqn. (A-10). The reduction process is controlled by charge-transfer and limited by slow of hydration reaction of carbon dioxide. The reduction rate of H_2CO_3 can be expressed as:

$$\frac{1}{i_{(H2CO3)}} = \frac{1}{i_{\alpha(H2CO3)}} + \frac{1}{i^{r}_{\lim(H2CO3)}} \quad \text{(A-25)}$$

The charge-transfer current density for H_2CO_3 can be determined as:

$$i_{\alpha(H2CO3)} = i_{0(H2CO3)} \times 10^{-\frac{E-E_{rev(H2CO3)}}{b_{c(H2CO3)}}} \quad \text{(A-26a)}$$

The exchange current density ($i_{0(H2CO3)}$) is a function of pH, temperature and H_2CO_3 concentration. Equation (A-19) can be used to correct the exchange current density (ECD) of H_2CO_3, which is temperature dependent with activation enthalpy ($\Delta H_{(H2CO3)}$) of $30 KJ/mol$. The ECD at the reference temperature ($i^{ref}_{0(H2CO3)}$) is approximately 6×10^{-2} A/m^2 (Nesic et al., 1996). In order to account for the effects of pH and H_2CO_3 concentration, the ECD should be corrected using the following expressions.

$$\frac{\partial \log i_{0(H2CO3)}}{\partial pH} = 0.5 \quad \text{(A-26b)}$$

and

$$\frac{\partial \log i_{0(H2CO3)}}{\partial C_{H2CO3}} = 1 \quad \text{(A-26c)}$$

Since the reduction of H_2CO_3 and H^+ are equivalent to each other, thermodynamically the reverse potential and Tafel slope of the H_2CO_3 can be obtained using Eqns. (A-17) and (A-20), respectively. The limited current density ($i^r_{\lim(H2CO3)}$) of the chemical reaction can be calculated as:

$$i^r_{\lim(H2CO3)} = F \times C_{CO_2} \times \left(D_{H2CO3}.K_{hyd}.K^f_{hyd}\right)^{0.5} \quad \text{(A-27)}$$

The bulk concentration and thermodynamic properties of carbon dioxide that appears in Eqn. (A-27) are presented earlier (Section B.2). The diffusion coefficient for H_2CO_3 in water at the reference temperature is 1.3×10^{-9} m^2/s and it can be corrected for the higher temperature using Eqn. (A-24a).

B.4.3 Reduction of Water

The reduction of water is controlled by the charge transfer process. The final current density-versus-voltage relationship for H_2O reduction can be written as:

$$i_{(H_2O)} = i_{0(H_2O)} \times 10^{-\frac{E-E_{rev(H2O)}}{b_{c(H2O)}}} \quad \text{(A-28)}$$

The ECD for water at the reference temperature ($i^{ref}_{0(H_2O)}$) is approximately 3×10^{-5} A/m^2. The ECD can be corrected for higher temperature applying Eqn. (A-19) using the activation enthalpy of water ($\Delta H_{(H2O)} = 30 KJ/mol$). The ECD is moderately influenced by temperature between pH values of 3 and 6. The reversible potential ($E_{rev(H2O)}$) and Tafel slope of the H_2O can be obtained using Eqns. (A-17) & (A-20), respectively.

B.4.3 Oxidation of Iron

The dissolution of iron as described by equations from (A-12) to (A-14) is considered as the dominant anodic reaction in corrosion of mild steel. The oxidation process is under control of charge transfer and it can be mathematically expressed as:

$$i_{(Fe)} = i_{0(Fe)} \times 10^{\frac{E-E_{rev(Fe)}}{b_{a(Fe)}}} \quad \text{(A-29)}$$

The Tafel slope of the iron dissolution reaction shown in Eqn. (A-29) can be obtained from:

$$b_{a(Fe)} = \frac{2.303RT}{\alpha_a.F} \quad \text{(A-30)}$$

Bockris et al. (1961) reported Tafel slope at standard temperature, b_a = 40 mV and the value of $\alpha_a = 1.5$. The concentration of ferrous in the solution has no influence on the dissolution kinetics of iron in the absence of corrosion scale. Moreover, it has no effect on the Tafel slope. The type of steel has large effect on anodic dissolution. Different values were found for the ECD of different types of steels (Nesic et al., 1996). At reversible potential of iron dissolution ($E_{rev(Fe)} = -0.488$), the ECD of X-65 steel ($i_{0(Fe)}$) is approximately 1.0 A/m^2, while for St52 steel, it is roughly 0.1 A/m^2. The ECD can be corrected for higher temperature using Eqn. (A-19) using the activation enthalpy of iron (40 KJ/mol), which is valid for temperatures ranging from 20 to 50℃.

B. 4.4 Implementation of the Model

The model requires inputs such as temperature, pH, partial pressure of CO_2, oxygen concentration, type of steel and the flow geometry (pipe flow or a rotating cylinder flow). Once the input data is provided, the model generates the individual and total cathodic and anodic curves. The intersection of the total cathodic curve with the anodic curve gives the corrosion potential (E_{corr}) by solving:

$$i_{(H+)} + i_{(H2CO3)} + i_{(H2O)} + i_{(O2)} = i_{(Fe)} \quad \text{(A-31)}$$

i_{corr} is computed using Eqn. (A-29) by knowing the corrosion potential. Then, the corrosion rate can be obtained as follows.

$$CR(mm/year) = \frac{0.00327 \times i_{corr} \times Ew}{\rho_{Fe}} \quad \text{(A-32)}$$

Nomenclature

$b_{a(Fe)}$	Anodic Tafel slope for Fe oxidation in V
$b_{c(H+)}$	Cathodic Tafel slope for H+ ion reduction in V
$b_{c(H2CO3)}$	Cathodic Tafel slope for H_2CO_3 reduction in V
$b_{c(H2O)}$	Cathodic Tafel slope for H_2O reduction in V
C_{CO2}	Bulk aqueous concentration of CO_2 in mol/m^3
C_{H+}	Bulk aqueous concentration of H^+ ions in mol/m^3
C_{H2CO3}	Bulk aqueous concentration of H_2CO_3 in mol/m^3
C_R	Corrosion rate in mm/y
d_p	Diameter of a pipe in m
d_c	Diameter of a rotating cylinder in m
D	Diffusion coefficient of a given species in m^2/s
D_{H+}	Aqueous diffusion coefficient for H^+ in m^2/s
$D_{ref(H+)}$	Reference aqueous diffusion coefficient for H^+
D_{H2CO3}	Aqueous diffusion coefficient of H_2CO_3 in m^2/s
$D_{ref\ (H2CO3)}$	Reference aqueous diffusion coefficient of H_2CO_3
E_w	Equivalent weight, gm
E	Potential in V
ECD	Exchange current density, A/m^2
E_{corr}	Corrosion (open circuit) potential in V
$E_{rev(Fe)}$	Reversible potential of Fe oxidation, $E_{rev(Fe\ )}$ = - 0.488 V
$E_{rev(H+)}$	Reversible potential for H^+ ion reduction in V
$E_{rev(H2CO3)}$	Reversible potential for H_2CO_3 reduction in V
$E_{rev(H2O)}$	Reversible potential for H_2O reduction in V
F	Faraday constant: F =96,485 C/mole
$H_{sol(CO2)}$	Henry's constant for dissolution of CO_2 in bar/(mol/m^3)
$\Delta H_{(Fe)}$	Activation enthalpy for Fe oxidation, $\Delta H_{(Fe)}$ = 40 kJ/mol
$\Delta H_{(H+)}$	Activation enthalpy for H+ ion reduction, $\Delta H_{(H+)}$ = 30 kJ/mol
$\Delta H_{(H2CO3)}$	Activation enthalpy for H_2CO_3 reduction, $\Delta H_{(H2CO3)}$ = 30 kJ/mol
$\Delta H_{(H2O)}$	Activation enthalpy for H_2O reduction, $\Delta H_{(H2O)}$ = 30 kJ/mol

i	Current density in A/m^2
i_{corr}	Corrosion current density in A/m^2
$i_{(Fe)}$	Anodic current density of iron oxidation in A/m^2
$i_{(H+)}$	Cathodic current density for H+ ion reduction in A/m^2
$i_{(H2CO3)}$	Cathodic current density for H_2CO_3 reduction in A/m^2
$i_{(H2O)}$	Cathodic current density for H_2O reduction in A/m^2
$i^{d}_{\lim(H+)}$	Mass transfer (diffusion) limiting current density for H+ ion reduction in A/m^2
$i^{r}_{\lim(H2CO3)}$	Chemical reaction limiting current density for H_2CO_3 reduction in A/m^2
$i_{\alpha(H+)}$	Charge transfer current density for H^+ ion reduction in A/m^2
$i_{\alpha(H2CO3)}$	Charge transfer current density for H_2CO_3 reduction in A/m^2
$i_{o(Fe)}$	Exchange current density of iron oxidation in A/m^2
$i_{o(H+)}$	Exchange current density for H^+ ion reduction in A/m^2
$i_{o(H2CO3)}$	Exchange current density for H_2CO_3 reduction in A/m^2
$i_{o(H2O)}$	Exchange current density for water reduction in A/m^2
$i^{ref}_{0(Fe)}$	Reference exchange current density of Fe oxidation in A/m^2
$i^{ref}_{0(H+)}$	Reference exchange current density of H+ reduction in A/m^2
$i^{ref}_{0(H2CO3)}$	Reference exchange current density of H_2CO_3 reduction in A/m^2
$i^{ref}_{0(H2O)}$	Reference exchange current density of H_2O reduction in A/m^2
i	ionic strength in kmol/m^3
K^{f}_{hyd}	Forward reaction rate for the CO_2 hydration reaction in 1/s
K_{hyd}	Equilibrium hydration/dehydration constant of CO_2
$k_{m(H+)}$	Aqueous mass transfer coefficient for H^+ in m/s
$k_{m(H2CO3)}$	Aqueous mass transfer coefficient for H_2CO_3 in m/s
P_{CO2}	partial pressure of CO_2 in bar
R	universal gas constant, R = 8.314 J/(mol K)
Re	Reynolds number
Sc	Schmidt number of a given species
Sh_p	Sherwood number of a given species for a straight pipe flow geometry
Sh_r	Sherwood number of a given species for a rotating cylinder flow geometry
t	temperature in ℃
T_{ref}	reference temperature in K
T	temperature in K

Tf	temperature in °F
v	water characteristic velocity in m/s

Greek characters

μ_{H2O}	Water dynamic viscosity in Kg/(m.s)
ρ_{H2O}	Density of water in kg/m^3
ρ_{Fe}	Density of iron in g/m^3
α_c	Apparent transfer coefficient
α_a	Apparent transfer coefficient

Appendix C: Response to BSEE Review Comments on Report # 13 and 14

Progress Report #13

2.1 Theoretical Studies (Task 1) (Overall Project Progress)

- For the Iron sulfide formation thickness barrier formation, has there been any observation of pattern of thickness formation with respect to environment conditions and cement type?

Response: Environment conditions such as pressure, temperature, gas and liquid composition, fluid movement are very critical for the formation of corrosion scale including the type and thickness of the scale. Cement type has also indirect effect. As a sealant, it can limit the transport of ions to the corrosion sites. This can have strong impact on the type and thickness of corrosion scale.

- Fifth sentence (copied) below is unclear, see questions following the sentence:
    - *When the concentration of H_2S is higher than the critical concentration (the minimum H_2S concentration in which iron sulfide scale forms on the surface steel) the corrosion process is under H_2S control.*

Response: This means that if the H2S concentration in the wellbore greater than the critical H2S concentration, and then the effect of CO2 on the corrosion process is minimal. However, if the concentration in the wellbore lower than the critical H2S concentration, then the effect of H2S on the corrosion process is negligible.

- What is that critical concentration H_2S value? Is this critical concentration H_2S value related to the environment conditions and alloy chemical composition?

Response: There is no unique value of the critical H_2S concentration. It depends on both the exposure condition and alloy composition.

- Given the following sentence, the dominance of H_2S would be for in the presence of H_2S and CO_2?

Response: Above the critical H2S concentration, the H2S would be dominant. Otherwise, the CO2 would be dominant.

2.2 Experimental Studies on Degradation of Cement (Task 2) (Overall Project Progress)

2.2.1.1 Compressive Strength

- Why is there such a large error for all four plots (GS Aged, HS Aged, GSF Aged, HSF Aged) of the Compressive Strength of Aged Cement Cores (Figure 3)?

Response: Compressive strength measurements of regular concrete generally show some data scattering in the order of ±20%. Aging process also causes additional sample variations and data scattering. In order to ensure accurate representation of the cement, we have increased the number of core samples for each data point from three to five.

- What are the error values for all four plots?

Response: Approximately 25%, 31%, 36% and 40%, respectively.

2.2 Experimental Studies on Degradation of Cement (Task 2) (Overall Project Progress)

2.2.1.2 Shear Bonding Strength

- Figure 4 – what are the error values for all four plots?

Response: Approximately 26%, 2%, 14% and 36%, respectively.

- Figure 5 (Shear Bonding Strength of cement samples after 14 and 28 days) – Why is there such a larger error range for the HSF 14 day sample?

Response: For all our measurements (porosity, permeability, compressive strength and bonding strength), aged samples predominately show higher data scattering. Like the compressive strength measurements, the number of samples used in each experiment has been increased from three to five.

- What are the error values for all four plots?

Response: Error values for the plot from left to right approximately 31%, 36%, 12%, 14%, 31%, and 1%, respectively.

2.2 Experimental Studies on Degradation of Cement (Task 2) (Overall Project Progress)

2.2.1.3 – Porosity & Permeability

- Were any measurements made on the degradation depths of the cement samples? This is of interest as it was indicated that visual observations were made and notices that the degradation depth for the fly ash cement cores was higher than for the cement cores without fly ash? What was the difference?

Response: Core samples are collected and preserved to measure degradation depth. Results will be presented in the coming reports.

- What was the measured thickness value of the degraded zone observed in the fly ash cement cores?

Response: 1 to 3 mm degraded zones were observed.

Appendix A – Literature Review – Theoretical Studies on Tubular Corrosion

A.1 – CO2 Corrosion Model

- For equation a (e.g. mass transfer rate of hydrogen ions equal to the electrochemical reaction rate of hydrogen on metal surface), what is "$2F.K_{H+}[H+]$?" Understand that $KH+[H^{+}]$ is electrochemical reaction rate constant of CO_3^{2-} and the solubility constant for H+, however, what is the F. term? Free energy?

  Response: F is Faraday's constant.

- For equation b (e.g. cathodic reaction rate equal to the total anodic reaction rate) what is "$2F.K_{HCO3-}[HCO_3^{-}]$?" Understand that $KHCO_3$-$[HCO_3^{-}]$ is the electrochemical reaction for HCO_3^{-} and solubility constant for HCO_3^{-}, however, what is the F term? Free energy?

Response: F is Faraday's constant.

Progress Report #14

- Recall the discussion on Hydroxyapatite during the October Houston TAB meeting. Reminder/question will the additive hydroxyapatite be purchased commercially? Or will the hydroxyapatite be synthesized in-house in the lab?
- If commercial, are there specific vendors and grades identified? Which one? What is the diameter and micro-structural properties of this hydroxyapatite grade?

Response: The additive hydroxyapatite is purchased from the Spectrum Chemicals as 40 mesh (840 microns) powder. The properties are slightly different from the actual natural hydroxyapatite found in the bones as its factory made. Its chemical specifications are as follows:

Activity (Calcium) Min. 30% Ash Min. 65% TYPICAL NUTRIENT CONTENT Protein 5.5% Fat 4.0% Phosphorus (P) 15% MAXIMUM LIMITS Moisture 5% Arsenic (As) 3 ppm Lead (Pb) 10 ppm Fluoride (F) 500 ppm

- For the filtration loss measurements of the slurry properties, what values will be considered to be excessive loss? >10% > 20%?

Response: Fluid loss more than 50% of the baseline slurries is considered as excessive loss.

- Good responses to questions on previous progress reports.

Response: We appreciate for your valuable inputs and suggestions.

Project Title: Effect of H_2S and CO_2 in HPHT Wells on Tubulars and Cement

Report Type: Monthly Report

Report #: 17

Reporting Period: January 22nd, 2013 to February 21st, 2013

Authors:

Ramadan Ahmed, Principal Investigator

Subhash Shah, Co-Principal Investigator

Samuel Osisanya, Co-Principal Investigator

Rida Elgaddafi, Research Assistant

Omotayo Omosebi, Research Assistant

Himanshu Maheshwari, Research Assistant

Adarsh Naidu, Research Assistant

Aman Srivastvava, Research Assistant

Jueun Hwang, Research Assistant

Prepared under BSEE Project # E12PC00035

by

THE UNIVERSITY OF OKLAHOMA

April 12, 2013

1. Summary of Accomplishments

This monthly report presents the progress made during the project period January 22, 2013 to February 21, 2013. During this reporting period, cement degradation and additive screening studies were continued. Properties of cement cores and bonding samples were measured before and after aging. The effects of different cement additives on properties of cement slurries and cores were investigated. Furthermore, we received feedback from BSEE on previous monthly reports. Our response is presented in Appendix A.

Aging experiments were continued using cores of baseline and specially formulated cements. Tests were performed varying the concentration of CO_2 in the gas phase while maintaining other test parameters constant. Permeability and porosity measurements demonstrate the dominating effect of leaching at high CO_2 concentrations. In addition, as the concentration of CO_2 is increased from 10% and 100%, the degradation depth also increased due to the increase in acidity of the aging solution. The degradation depth was negligible at low CO_2 concentrations; however, it became substantial at high concentrations. Increased CO_2 concentration is expected to facilitate the carbonation and leaching processes.

Compressive strengths of baseline cement cores increased after aging. The strength improvement is attributed to carbonation, which forms precipitates of calcium carbonate that fill the pore spaces, thereby creating additional support to the cement matrix. In addition to compressive strength, the change in elastic stiffness of the cement was examined. The stiffness decreased with time when cement cores were aged in brine saturated with 10% CO_2 containing gas. This observation is consistent with results of a previous study on the elastic stiffness of cement. Furthermore, the influence of CO_2 concentration on shear bonding strength of cement has been investigated. For aged sample, the bond strength improved with the increase in CO_2 concentration.

Cement additives screening study was continued. The effects of different additives on cement slurry and core properties were investigated. After aging, porosities of magnesium oxide containing (MGO) cores and baseline cement samples decreased. The compressive strengths of unaged MGO cores were found to be higher than those of the baseline cements. After aging, the compressive strength of all the cores increased.

Theoretical and modeling studies on tubular corrosion were continued. In addition, progress has been made in the development of corrosion test setup. After receiving stress corrosion cracking cell, a design of a heating jacket has been prepared and sent to a local manufacturing shop.

Our plan for the upcoming weeks is to continue: i) the aging tests at different CO_2 concentrations and temperatures; ii) theoretical and modeling studies on tubular corrosion; iii) additive screening studies; and iv) development of corrosion test setup.

2. Overall Project Progress

2.1 Theoretical Studies (Task 1)

2.1.1 Cement Bonding

Gas migration in the annular space between the casing and cement (gas channeling), resulting from cement bonding failure, has been a common problem in primary cementing (Seidel et al. 1985). Strength and sealing performances of a cement bond are affected by number factors including cement expansive properties, elasticity of the cement, wellbore temperature and pressure, and the quality of physiochemical bonding between the casing and cement.

Cement formulations with expanding tendency prevent gas channeling because of the expansion of the cement after it sets. The expanding tendency of cement originates from the formation of hydration products with large crystal structures such as ettringite phase. Ettringite is formed when sulfates react with the tri-calcium aluminate in Portland cement (Seidel et al 1985). The size of ettringite crystals is bigger than the size of tri-calcium aluminate; as a result, the cement tends to expand causing increased internal stresses when ettringite replaces the tri-calcium aluminate under confined/constrained condition (Jones 1991). The range of cement expansion varies based on the cement type, additives and the environment. Class H cement contains 4.5 to 5% of tri-calcium aluminate to create ettringite. Exposure time or life of the cement has also an impact on degree of expansion. Seidel et al. (1985) conducted experiments with Class A cement mixed with cement additives that promote expansion. Results show the effectiveness of the additive in controlling the gas migration resulting from gas channeling.

Wellbore temperature can have major impact on the bond performance of cement. Carter (1966) studied expansion behavior of cements used for primary cementing. Strain gauges were used to measure the volumetric expansion at elevated temperature. Sodium Sulfate was added to the cement to promote expansion. The cement samples were aged for 7,14,28,19,180 and 270 days at different temperatures to examine the effects of time and temperature on cement expansion. With increasing temperature, more expansion was observed for the most of the samples; however, expansion was low in samples having rapid hydration.

Carbonation occurs when cement exposed to CO_2 environment. The conversion of calcium silicate hydrate (C-S-H) and $Ca(OH)_2$ to $CaCO_3$ during carbonation process involves an expansion of cement (Ceukelaire and Van Nieuwenburg, 1993). The expansion is expected to have a positive impact on the bond strength and performance. However, with increased exposure time and acidity of the solution surrounding the cement, the carbonation product ($CaCO_3$) reacts with carbonic acid to form soluble product ($Ca(HCO_3)_2$) that can be leached out by the acid from the cement matrix.

Calcium silicate hydrate (C-S-H) is a hydration product, which is primarily responsible for the bond strength of cement. Temperature and cement composition strongly influence the crystal structure of C-S-H phase. As carbonation occurs, the pores of the cement are filled with reaction products, there are also structural changes occurring in C-S-H phase. The C-S-H changes to Alpha di-calcium silicate hydrate (α-C2SH) phase at elevated temperature. The α-C2SH is weak and porous material. This phase transformation normally happens at about 247ºF. However, by adding 35% of silica flour, it can be prevented. Silica flour promotes the formation of tobermorite phase. Tobermorite is strong, impermeable, and stable form of C-S-H up to 302ºF. Based on temperature and composition of the cement, four different crystalline phases of C-S-H can be formed at higher temperatures (**Fig. 1**).

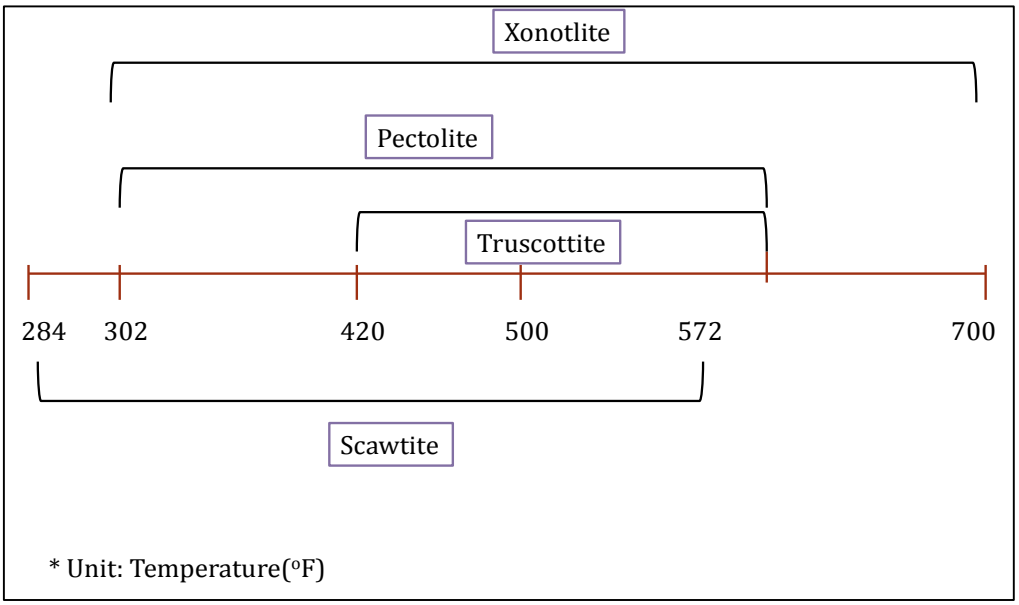

Fig. 1 Crystalline phases of C-S-H at high temperatures

As temperature increases, first tobermorite changes to xonolite and a trace of gyrolite at the range of 302 to 700ºF. Xonotlite is lower in strength than tobermorite and its permeability is approximately 5 times higher than tobermorite. As a result, it is susceptible to acidic fluid penetration at high temperature conditions. This can cause bond strength loss due to the phase transformation (Eilers 1983). Secondly, weak truscottite phase is formed in the temperature range of 420 to 600ºF with higher silica contents. The strength of truscottite is 10 to 20% of xonotlite.

Pectolite is the third structure, which is strong and very stable. It is formed in the temperature range of 302 to 600°F by adding a soluble sodium silicate into the cement. It is resistant to brine. Pectolite has the same strength as xonotlite; however, it exhibits higher

permeability than xonotlite. Scawtite is another phase that has stable structure for temperature ranging from 284 to 572°F. When CO_2 enters into cement pores, it produces scawtite by replacing silica. Although scawtite is rarely occurring phase, when it is formed, the cement becomes brittle. Among all of the four crystalline phases of C-S-H, the combinations of pectolite and truscottite have a lower permeability than xonotlite.

Elasticity is one of the most important properties of cement that need to be considered in bonding investigation. Elastic cement provides better bonding at high-temperature and high-pressure wells. Wary et al (2009) provided the stress analysis comparison of conventional and elastic cement for different types of damages. **Figure 2** shows the remaining strength capacity of cement for different damage types. The analysis suggests that elastic cement sheath maintains more than 80% of its capacity for the life of the well. This is dramatically better than the performance expected from conventional cement. According to this analysis, the elastic cement is expected to perform better and last longer for the same well-stress conditions (Wary et al 2009).

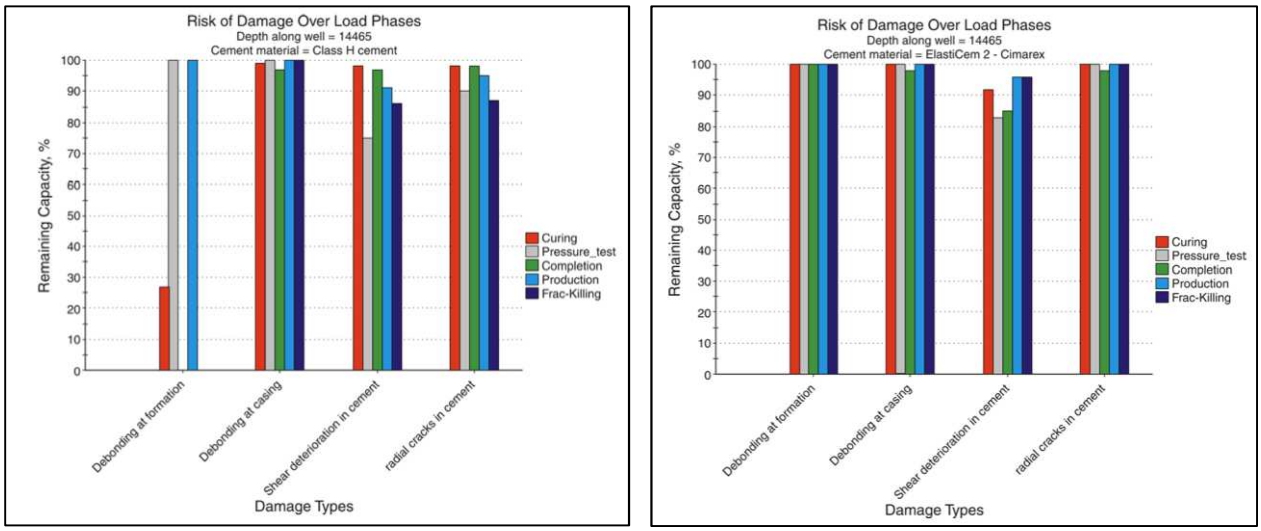

(a) **(b)**

Fig. 2 Stress analysis for cement: a) conventional; and b) elastic (Wary et al. 2009)

The elasticity of cement significantly varies during the hydration phase. According to Constantinides (2000), there are two sources for the development of elastic behavior during cement hydration. The formation of low elasticity tobermorite gel (C-S-H_a) takes place at the early stages of hydration in water-saturated conditions. At later stages of hydration in which the process is driven by complex diffusion, high-density high-elasticity tobermorite gel (C-S-H_b) forms. The elastic properties of the two types of C-S-H are independent of the mix proportions, which affect only the volumetric proportions of the two types of C-S-H (Constantinides 2000).

2.1.2 Tubular Corrosion

Previously, a mechanistic model (Nesic et al. 1996), which is developed to predict the carbon dioxide corrosion in carbon steel, was presented as the preliminary step of improving our understanding for CO_2/H_2S corrosion behavior. A number of CO_2 corrosion related phenomena such as electrochemical process, transport process, and corrosion thermodynamic and kinetics were discussed and presented in the last report. It is well known that corrosion rate is affected by environmental conditions including chemistry of the liquid in contact with the metal, gas composition, operating temperature, fluid velocity, pH, and properties of corrosion scale. The model developed by Nesic et al. (1996) does not account for the effects of protective corrosion scale and solubility of carbon dioxide. In study, the model is improved by accounting for the solubility of carbon dioxide in brine solution at HPHT conditions.

2.1.2.1 Model Improvement

It was reported (Nordsveen et al. 2003) previously that the electrochemical parameters (current exchange densities and Tafle slope) for particular electrochemical reaction depend on the temperature and concentration of species involved in the reaction at the metal surface. The current exchange density is expressed as:

$$i_0 = i_{0ref} \times \left(\frac{C_{H+}}{C_{H+(ref)}} \right)^{a1} \times \left(\frac{C_{CO_2}}{C_{CO_{2(ref)}}} \right)^{a2} \times \left(\frac{C_{H_2CO_3}}{C_{H_2CO_{3(ref)}}} \right)^{a3} \times e^{-\frac{\Delta H}{R}\left(\frac{1}{T}-\frac{1}{Tref}\right)} \quad (1)$$

The variables that appear in Eqn. (1) are specified in **Table 1**.

Table 1 Electrochemical parameters used to determine current exchange density

Reaction	$i_{0(ref)}$	a_1	$C_{H+(ref)}$	a_2	$C_{CO2(ref)}$	a_3	$C_{H2CO3(ref)}$	ΔH	T_{ref}
	$\frac{A}{m^2}$		molar		molar		molar	$\frac{KJ}{mol}$	°C
$2H^+ + 2e^- \rightarrow H_2$	0.05	0.5	10^{-4}	0	N/A	0	N/A	30	25
$2H_2CO_3 + 2e^- \rightarrow H_2 + 2HCO_3^-$	0.06	-0.5	10^{-5}	0	N/A	1	10^{-4}	50	20
$Fe \rightarrow Fe^{2+} + 2e^-$	1	0 for P_{CO2} = 1bar 0 for P_{CO2}< 1bar	10^{-4}	2 for pH<4 1for 4<pH<5 0 for pH>5	0.0366	0	N/A	37.5	25

2.1.2.2 CO_2 Corrosion Rate Model

Once the concentrations of the hydrogen ions, carbonic acid (H_2CO_3) and CO_2 solubility are predicted, using the thermodynamic of the corrosion process (present in the last report), the individual and total anodic and cathodic curves can be developed based on the electrochemical theory. The anodic and cathodic curves are presented in **Fig. 3** obtained considering the base case as P_{CO2} = 1 bar, T = 20°C, pH of 4 for the surrounding liquid, and fluid velocity of 1 m/s. The intersection between the total curves gives the corrosion potential, E_{corr} and corrosion current density, i_{corr}.

Based on the current (charge) balance, anodic current density of iron oxidation can be expressed:

$$i_{(Fe)} = i_{(H+)} + i_{(H2CO3)} + i_{(H2O)} \qquad (2)$$

Once the value of E_{corr} is obtained graphically, the corrosion current density of iron can be calculated by substituting the value E_{corr} into the iron dissolution equation.

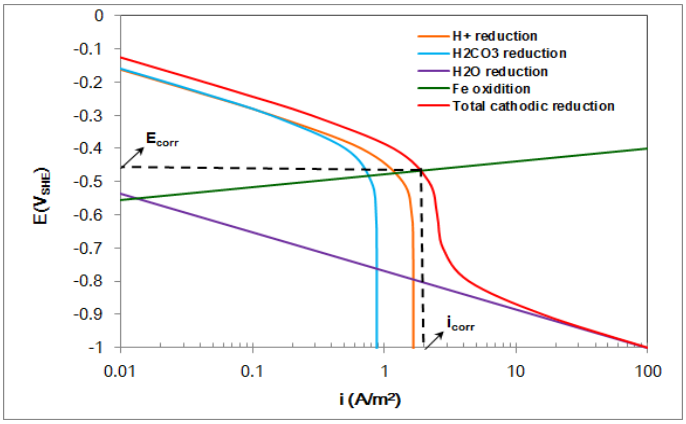

Fig. 3 Individual anodic and cathodic curves obtained considering P_{CO2} = 1 bar, T = 20°C, pH = 4, liquid 1.5% NaCl solution, V = 1 m/s and pipe diameter = 25 mm

$$i_{(Fe)} = i_{corr} = i_{0(Fe)} \times 10^{\frac{E_{corr} - E_{rev\,(Fe)}}{b_{a(Fe)}}} \qquad (3)$$

Subsequently, after determining the corrosion current density, i_{corr}, from Eqn. (3) or graphically from Fig. 3, CO_2 corrosion rate can be calculated using the Faraday law.

$$CR(mm/year) = \frac{0.00327 \times i_{corr} \times Ew}{\rho_{Fe}} \qquad (4)$$

where i_{corr} is the corrosion current density in μA/cm^2, Ew is the equivalent weight, which is described as gram molecular weight of a metal divided by the number of electrons in anodic half reaction of the metal. ρ_{Fe} is iron density in g/cm^3.

2.1.2.3 Factors Affecting CO_2 Corrosion Rate

The pH of solution surrounding a metal strongly affects the corrosion rate. After modifying the original model (Nesic et al. 1996), predictions were made to examine the influence pH on the CO_2 corrosion rate. For this analysis, the base case is considered as 0.5% brine solution at 1 bar CO_2 partial pressure, 20°C temperature, 4 to 6 pH range, 25 mm pipe diameter and 1 m/s fluid velocity. **Figure 4** compares predictions of the new model with that of the original one at different pH values. At low pH values (pH < 5), the new model predicts higher CO_2 corrosion rate than the original one. However, at high pH (pH > 5), the original model predicts a constant CO_2 corrosion rate while the new model predictions show reduction in the corrosion rate. At pH of 5, both models predict approximately the same corrosion rate.

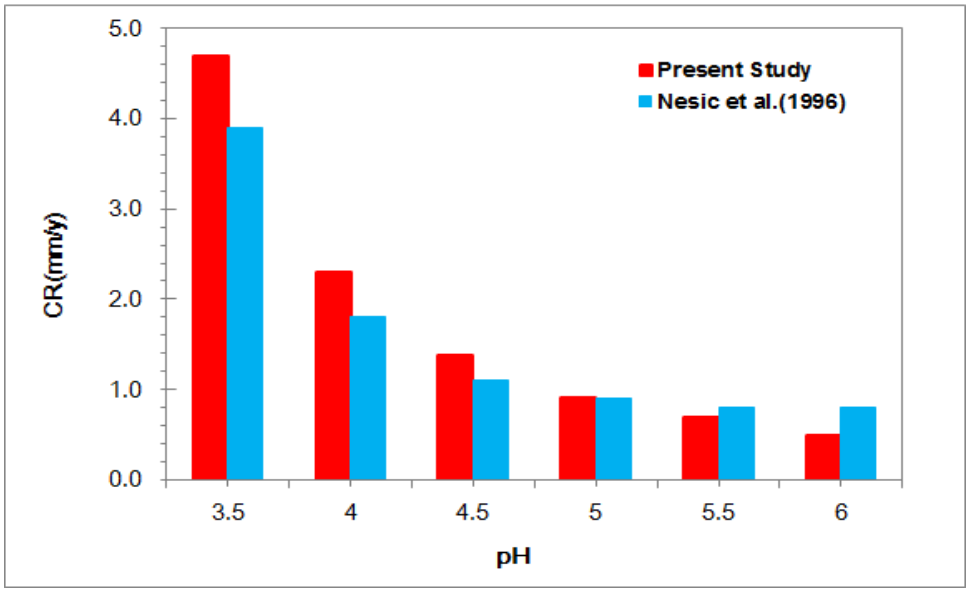

Fig. 4 Comparison of model predictions at different pH values

Gas composition is one of the key factors that influence the corrosion rate. **Figure 5** presents the predictions of the new model and the existing one. The analysis is conducted for the base case considering pH value of 4. As depicted from the figure, in the absence of the corrosion scale, both model predictions show typical behavior of the corrosion rate in the presence of the CO_2. Increasing the partial pressure of CO_2 leads to substantial increase in the corrosion rate. Commonly accepted reason for this behavior is that with increase in the partial pressure of CO_2, the concentration of H_2CO_3 increases and accelerates the cathodic reaction, resulting in higher corrosion rate. However, different forms of CO_2 corrosion can take place in the presence of corrosion scale.

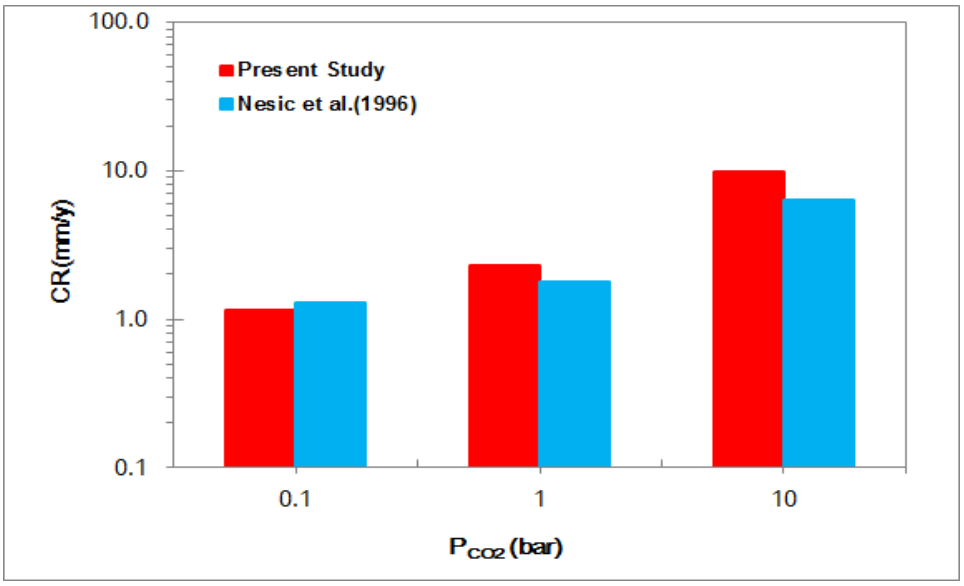

Fig. 5 Predicted corrosion rate versus partial pressure of CO_2

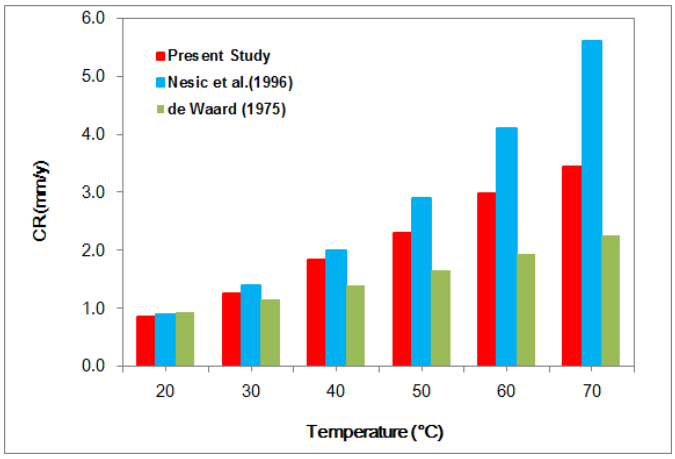

Fig. 6 Comparison of predicted temperature effect on corrosion rate

Corrosion is sensitive to temperature. As presented in **Fig. 6**, the influence of temperature on steel corrosion is predicted using the new model and compared with the predictions of previous models (Nesic et al.; 1996 and de Waard; 1973) for the base case varying the temperature from 20 to 70°C. At low solution pH and in the absence of protective scale, temperature steadily increases corrosion rate by accelerating the chemical, electrochemical, and transport processes involved in corrosion. At low temperatures (T < 35°C), model predictions are in the same range. For temperatures greater than 40°C, de Waard model predicts lower corrosion rates than the other two models due to the consideration of the corrosion scale.

In addition to temperature, high fluid velocity and turbulence facilitate the corrosion process. In the case of corrosion in which the protective scale does not form, typically at low pH, the turbulent flow can enhance the transport of species from the bulk fluid to the metal surface or vise versa. This phenomenon may lead to an increase in the corrosion rate. To study the effect of fluid velocity on corrosion rate, model predictions (**Fig. 7**) are obtained for the base case varying the fluid velocity from 1 to 20 m/s. As the velocity increases, the discrepancy between the models also increases. At

high fluid velocities (v > 5 m/s), the effect of velocity on the rate of corrosion becomes negligible. This is because the process is controlled by other phenomena such as electrochemical process rather than species transport.

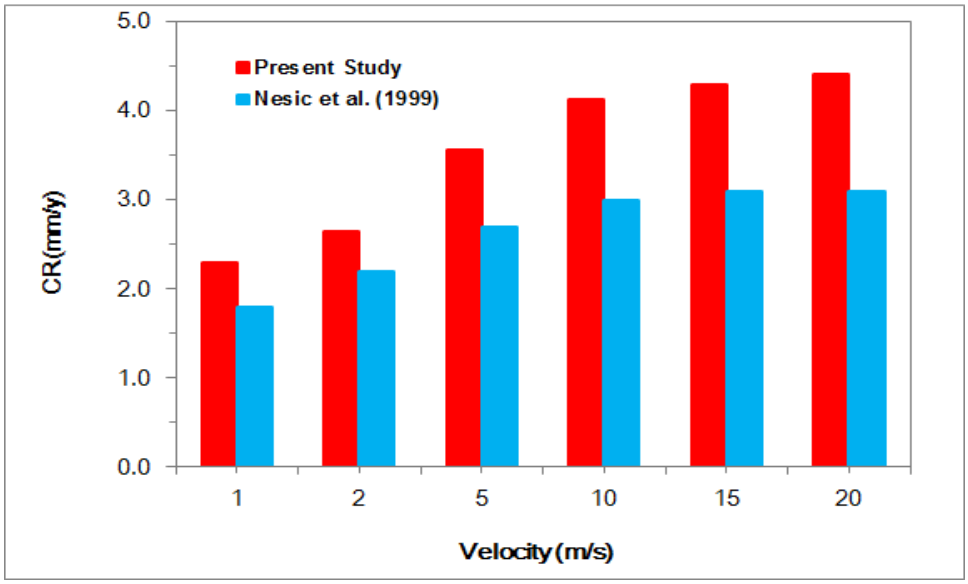

Fig. 7 Effect of fluid velocity on corrosion rate

2.2 Experimental Studies on Degradation of Cement (Task 2)

As previously planned, aging experiments (Experiment 9 and 10) were conducted varying CO_2 concentration. The samples were aged for 2 weeks at 225ºF and 6000 psi in 2% brine saturated with 10%, 40% and 100% CO_2. After completion of each experiment, physical properties of aged and unaged samples were measured. Analysis of result is continued for different measurements including core elasticity and expansion.

2.2.1 Porosities and Permeabilities of Baseline Cements

The rate of cement degradation in borehole environment is strongly affected by concentrations of acidic gases. Degradation often changes sealing performance of cement by increasing its porosity and permeability. **Figure 8** illustrates the effect of CO_2 concentration on porosity and permeability of baseline cement aged for 14 days at 225ºF and 6000 psi in 2% brine saturated with 10%, 40% and 100% CO_2. As CO_2 concentration increased from 10 to 100%, both the porosity and permeability increased for Class G cement. Different processes are expected to take place during aging. Hydration and carbonation lead to decrease in porosity and permeability; whereas, leaching causes the porosity and permeability to increase. Results shown in Fig. 8 demonstrate the dominating effect of leaching; with the increase in CO_2 concentration, porosity and permeability of the aged samples increased. However, for Class H cement, the trend of permeability is different and some

measurements show very high scattering. This is mainly due to unusually high permeability of Class H cement cores (both aged and unaged) prepared in Batch 009 (40% CO_2). Hence, this test will be repeated in the future.

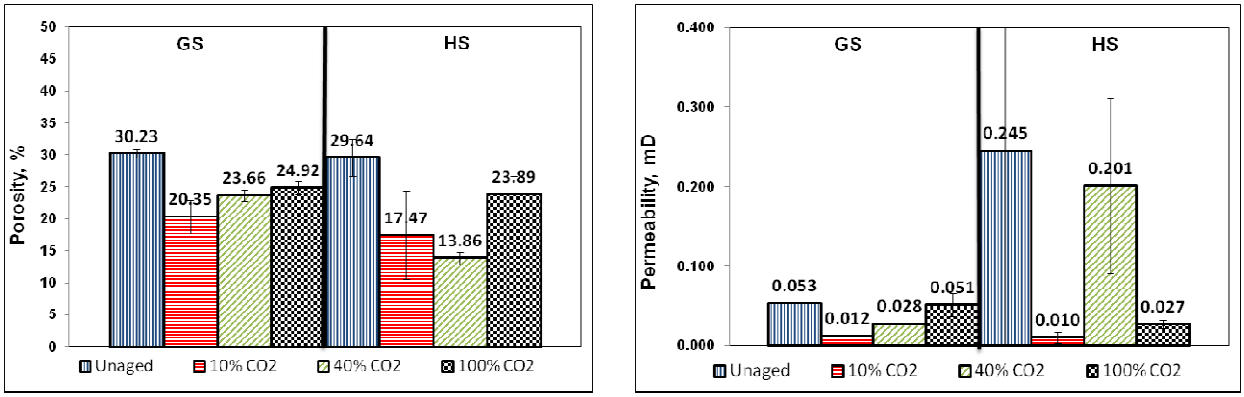

(a) (b)

Fig. 8 Properties of unaged and aged cores (aged 14 days at 225ºF and 6000 psi in 2% brine saturated with 10%, 40% and 100% CO_2): a) porosity; and b) permeability

2.2.2 Degradation Depths of Baseline Cements

Degradation depth measurements are often used to quantify the level of acid attack. Hence, dried cores were cut in the middle transversely as shown in **Fig 9**. Then, degraded depths were determined by averaging four depth measurements obtained at 90-degree angle apart from each other. The averaging is necessary because in some cases, the degraded depth is not uniform. The depth measurements are based on only color change. Hence, additional tests such as FTIR (Fourier Transform Infrared Spectroscopy), SEM (Scanning Electron Microscope) and XRD (X Ray Diffraction technique) are required to verify the expected compositional change occurring in the discolored zone.

Figure 10 demonstrates the variation in the degradation depth due to the effect of gas composition. As CO_2 concentration increases from 10% and 100%, the degradation depth deepens due to the increase in acidity of the solution. The degradation depth for 10% CO_2 concentration was negligible. Aging duration of 14 days is not sufficient for low-concentration CO_2 environment to develop noticeable degraded zone. At high concentrations of CO_2, the brine solution becomes more acidic, which facilitates the carbonation and leaching process leading to higher depth of penetration and deterioration of cement properties.

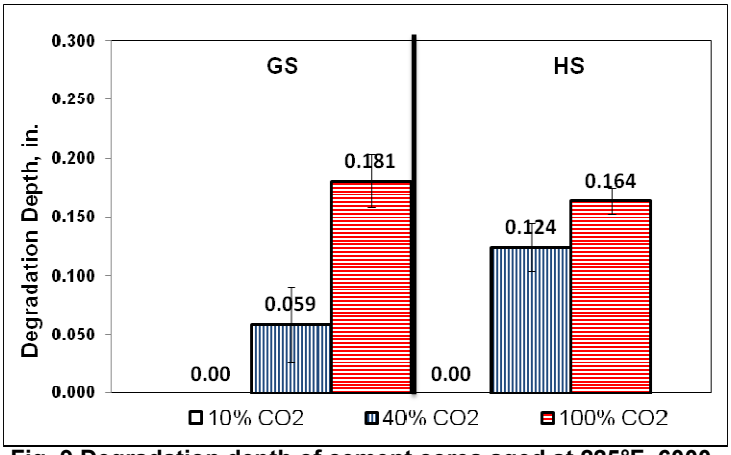

Fig. 9 Degradation depth of cement cores aged at 225°F, 6000 psi for 14 days in 2% brine saturated with mixed gas containing CH_4 and different concentrations of CO_2

Fig. 10 Degradation depth of aged cement core

2.2.3 Compressive Strengths of Baseline Cements

Compressive strengths of baseline cement cores increased after aging due to carbonation, which dominates the leaching process in the initial phase of CO_2 attack. **Figure 11** compares compressive strengths and porosities of aged and unaged baseline cement cores. Aging was conducted for 14 days in 2% brine saturated with 100% CO_2 at 225ºF and 6000 psi. Compressive strength improvement is attributed to carbonation because the calcium carbonate, formed during the process, fills the pore spaces, thereby creating additional support to the cement matrix. The filling of pore spaces can be confirmed by the decrease in porosity of the cores after aging (Fig. 11b).

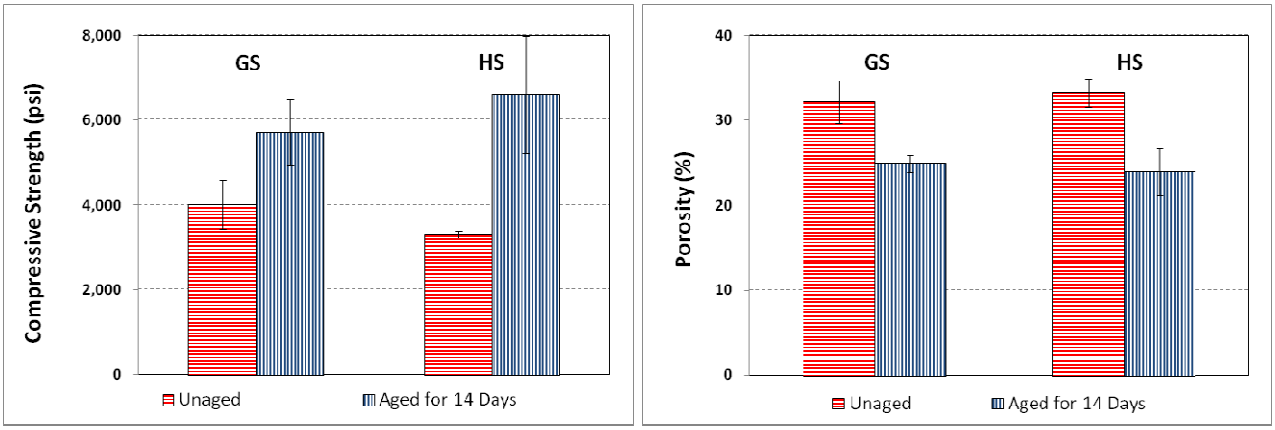

(a) **(b)**

Fig. 11 Properties of aged and unaged cement cores: a) compressive strength; and b) porosity

Figure 12 compares recent compressive strength measurements with those of previously tested cores, which were aged under the same conditions (14 days in 2% brine saturated with CO_2 containing gas at 225ºF and 6000 psi), but at different concentrations of CO_2. Although permeability and porosity trends shown in Fig. 12 indicate the presence of carbonation and leaching, results show a consistent increase in the strength of Class G cement. This could be due to structural change in addition to porosity reduction caused by carbonation, which makes the cores to preserve their gained strength due to carbonation even after exhibiting reduction in porosity and permeability. Similarly, the strength of Class H cement increased at low concentrations (10%) of CO_2 as the carbonation dominates the leaching process. However, consistent reduction in strength was observed at high CO_2 concentrations (more than 40%) due to intensive leaching of the carbonated cement. Even if the trend suggests leaching of the carbonated cement, the compressive strengths of aged cores were still higher than that of the unaged cement cores.

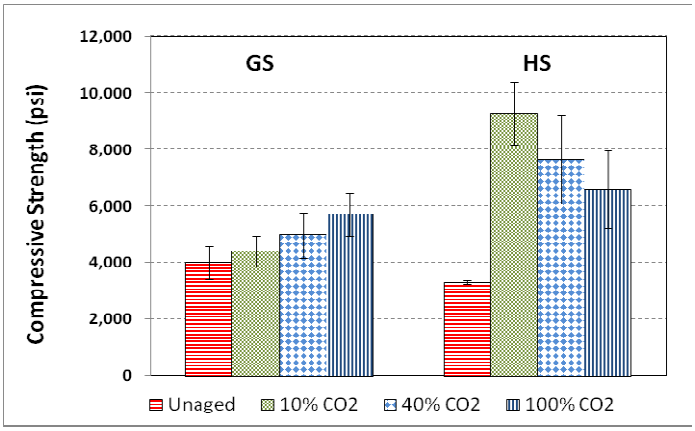

Fig. 12 Compressive strengths of 14-day aged and unaged cores (aging condition: 2% brine saturated with CO_2 containing gas at 225ºF and 6000 psi)

2.2.4 Shear Bond Strengths of Baseline Cements

The influence of CO_2 concentration on shear bonding of cement has been investigated. **Figure 13** indicates shear bond strength improvement with increased CO_2 concentration. The cement cores were aged at 225°F for 14 days under 6000 psi total pressure. The unaged cores were kept at ambient temperature in 2% brine. It can be concluded that increasing CO_2 concentration accelerates carbonation process, which makes the cement expansive. The expansion tendency of the cement creates stress condition that can improve bonding strength. After aging in brine saturated with 100% CO_2, the shear bonding strength of the samples were increased by four-fold. Results do not indicate the presence of major leaching process with increased CO_2 concentration. The leaching process may be retarded because of the pipe that partially covers the cement and reduces the contact area between the cement and the aging fluid. Therefore, to observe the bond strength reduction, the exposure time (aging duration) must be higher than 14 days to reach the leaching phase.

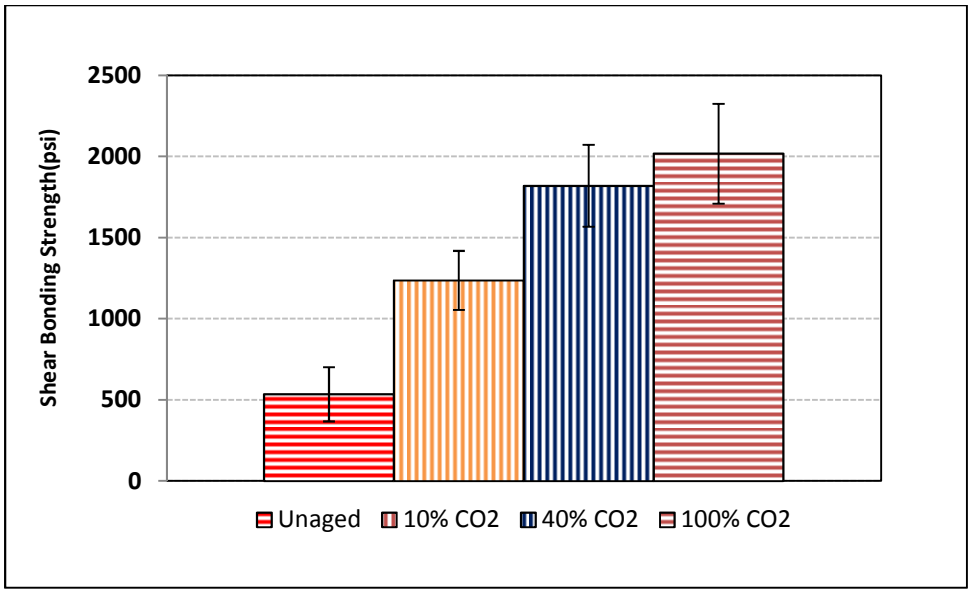

Fig. 13 Effect of CO_2 concentration on shear bond strength

Figure 14 show the relationship between the elastic stiffness and shear bond strength of the cement. The stiffness of the cement decreased with time when aged in brine saturated with 10% CO_2 containing gas. We found this trend consistent with results of a previous study (Constantinides, 2000) on the stiffness of the cement. Constantinides (2000) showed the effect of CO_2 concentration on mechanical properties of cement and the origin of macroscopic degradation of the elastic stiffness of cement material. The reduction in the stiffness is attributed to the structural change occurring in C-S-H due to carbonation.

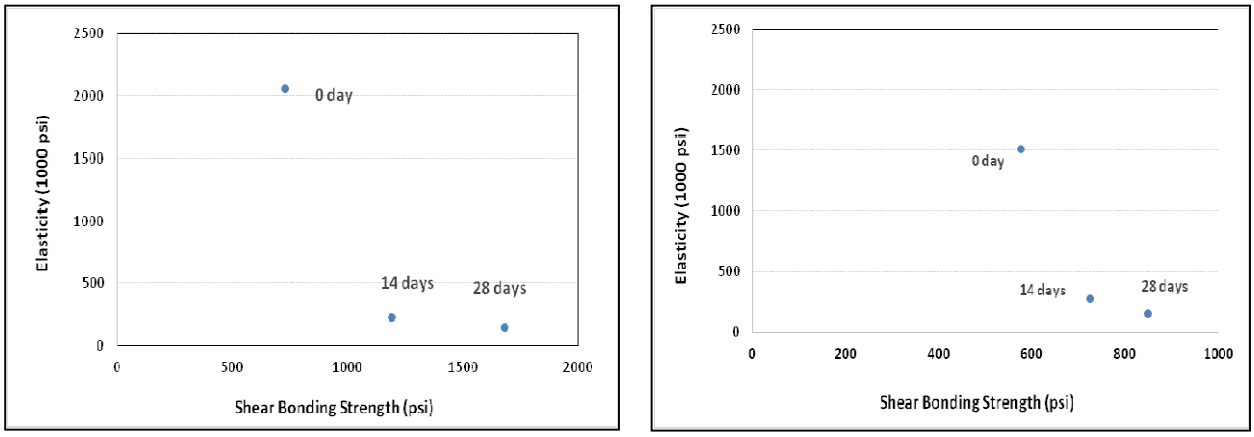

(a) **(b)**

Fig. 14 Relationship between the shear bonding strength and elasticity cement aged at 350ºF, 10% CO_2 and different aging periods: a) HS samples; and b) HSF samples

Figure 15 presents the bonding strength and elastic stiffness of samples aged at 225ºF for 14 days varying CO_2 concentration in the gas phase. Because of leaching process, which is occurring at high CO_2 concentrations, the stiffness reduction trend may change. The stiffness reduced as the concentration increases until 40%. At high CO_2 concentrations (above 40%), the influence of leaching on the mechanical properties of the cement become significant causing the stiffness to increase with increased CO_2 concentration. As the same time, the carbonation effects such as the level of improvement in bonding strength tend to diminish as shown in **Fig. 16**. At low concentrations, carbonation becomes the dominate process and makes the cement more expansive (Fig. 16) and elastic. However, for concentrations more than 40%, leaching offsets the effect of carbonation causing the stiffness to increase as the concentration increases. The diameter expansion of the cores presented in Fig. 16 is in agreement with this observation. The leaching of calcium makes the cement to become less expansive.

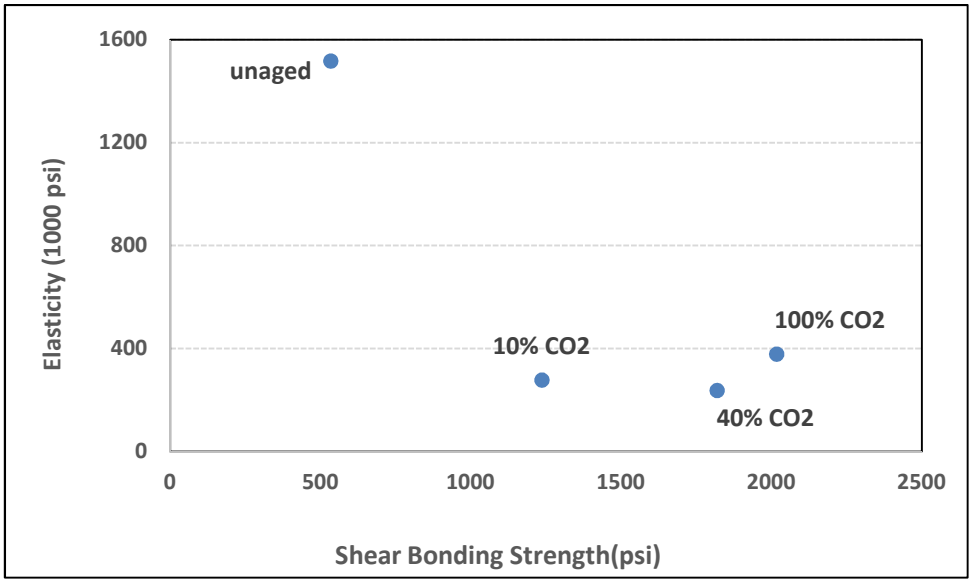

Fig. 15 Relationship between shear bonding strength and elasticity at different CO_2 concentrations for samples aged at 225ºF for 14 days

Furthermore, for unaged cement cores (Fig. 16), shrinkage of diameter was observed. While going through the hydration phase, cement particles combine to form hydrates, which in turn reduce the volume of the cores. The matrix shrinkage creates extra porosity and increases the permeability. However, using the expansive cements or adding additives that have expansion tendency to Portland cement can compensate for the shrinkage occurring during hydration. Parcevaux (1964) stated that the lowest shrinkage and highest elasticity provides the best sealing effect. In addition, it was indicated (Parcevaux 1964) that shrinkage is more related to shear bonding strength while elasticity is more related to hydraulic damage. Therefore, further investigation is needed to relate

shrinkage/expansion and elastic behavior of cement with shear bonding strength and other mechanical properties.

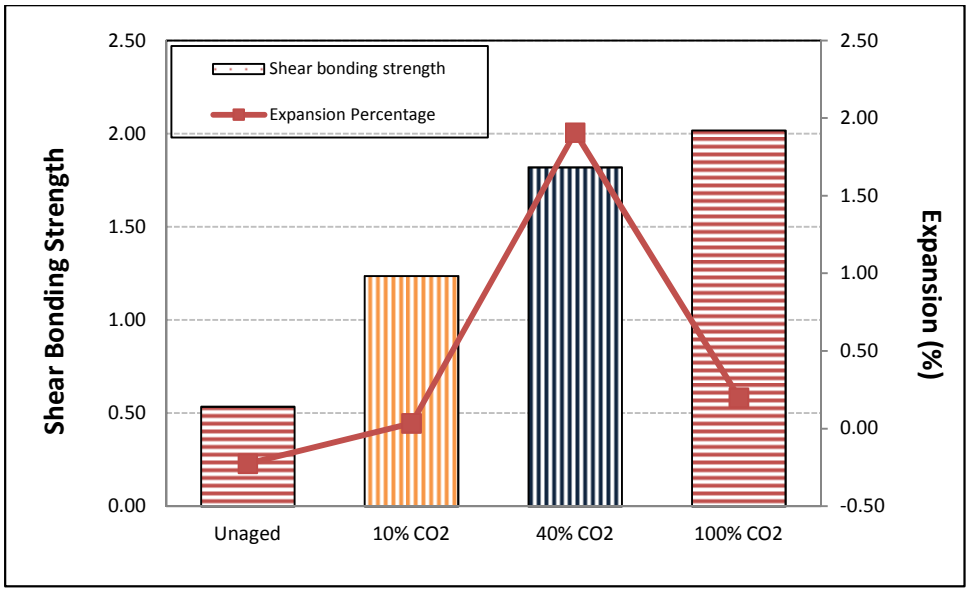

Fig. 16 Shear bonding and linear expansion of HS samples aged at 225ºF for 14 days at different CO_2 concentrations

Temperature is one of the key factors that control the degradation of cement. A number of temperature dependent phenomena such as carbonation, dissolution of CO_2, diffusion of ions in the porous cement, and leaching of calcium from the cement matrix are involved in the degradation process that leads to bond strength and elastic behavior changes. Aging tests conducted under different temperatures indicated the effect of temperature on bond strength and elastic stiffness of the cement (**Fig. 17**). Increasing the aging temperature from 100 to 225ºF resulted in increased bonding strength while maintaining the elastic behavior. The strength increase is attributed to the carbonation of cement, which is facilitated by temperature increase (Shen and Pye, 1989). However, a reduction in strength was observed, as the aging temperature was increased from 225 to 350ºF. The reversal of the trend is due to the effects of other factors such as leaching and ionic diffusion and gas solubility, which may have adverse consequence on the bond strength. The reduction in CO_2 solubility at high temperature limits the carbonation process. In addition, high temperature enhances the leaching of calcium from the cement matrix and ionic transport in the porous cement. Overall effect of these phenomena is to promote the leaching process to offset the impact of carbonation.

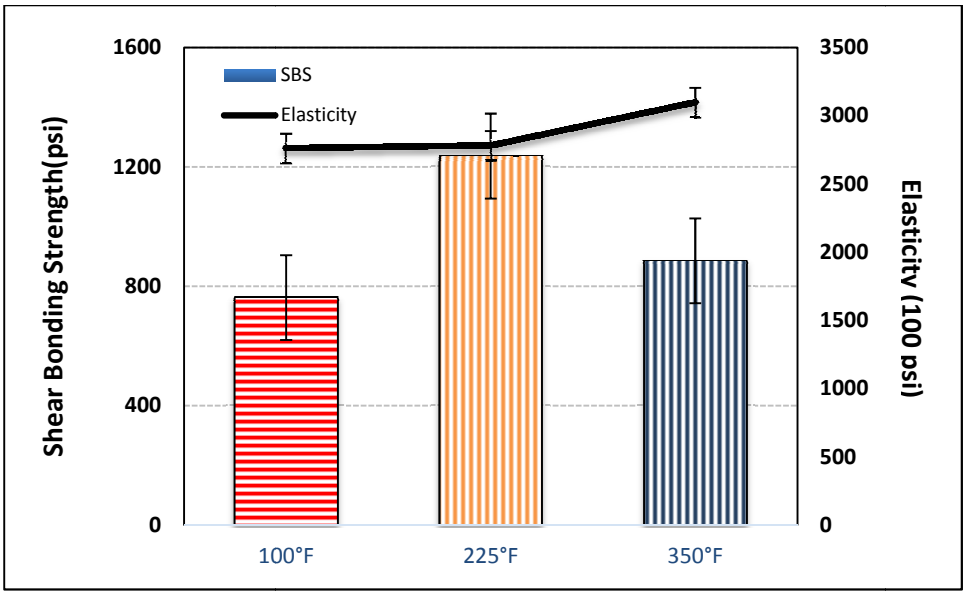

Fig. 17 Effects of aging temperature on shear bonding strength and elasticity of HS cement aged with 10% CO_2 for 14 days

2.2.5 Additive Screening Study

The testing of cement additives was continued as planned. Magnesium oxide, latex, micro-silica and hydroxyapatite containing cement cores were prepared and tested for their suitability for field applications. The results for the aged hydroxyapatite cores will be presented in the next monthly report. After aging for 14 days in acidic environment, properties of magnesium oxide based cement cores were measured. Furthermore, latex-containing cores were prepared and their porosity and permeability were measured to compare with our previous measurements. In addition, a new formulation of latex and micro-silica based slurry was prepared and its flow properties were examined. Furthermore, previously prepared micro-silica based samples were brittle; thus, reduced amounts of micro-silica containing slurries were prepared and their flow behaviors were studied.

The second batch of magnesium oxide containing (MGO) cores and samples were aged and tested for suitability of their physical and mechanical properties. Their properties are compared with those of baseline (HS and GS) cement cores aged together. The MGO cores and samples were kept on the upper shelves of the aging cell as depicted in **Table 2**. The aging was conducted for two week at 6000 psi and 225°F in 2% brine saturated with 100% CO_2 gas.

Table 2: Schematic showing the arrangement of the samples in the aging cell

Shelf	Sample
11	Additive Bonding Samples – Class H
10	Additive Cement Core Samples – Class G
9	Additive Cement Core Samples – Class H
8	Bonding Samples – Class H
7	GS Cement Core Sample
6	HS Cement Core Sample
5	GS Cement Core Sample
4	HS Cement Core Sample
3	Empty
2	Empty
1	Empty

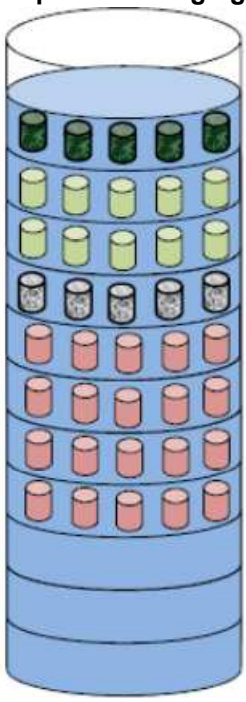

Legend

Additive Bonding Sample (Class H)

Additive Cement Core Sample (Class G/ Class H)

Bonding Sample (Class H)

Cement Core Sample (Class G/ Class H)

It can be observed from **Fig. 18** that the porosities of unaged MGO and baseline cement (HS and GS) are comparatively the same. On the other hand, the permeability was found to be higher for MGO samples. This contradicts the expectation that magnesium oxide acts as an expanding agent and makes the cement less porous/permeable. To investigate the degradation behavior of magnesium oxide containing cements, MGO cores were prepared and exposed to the aging conditions as presented in Table 2.

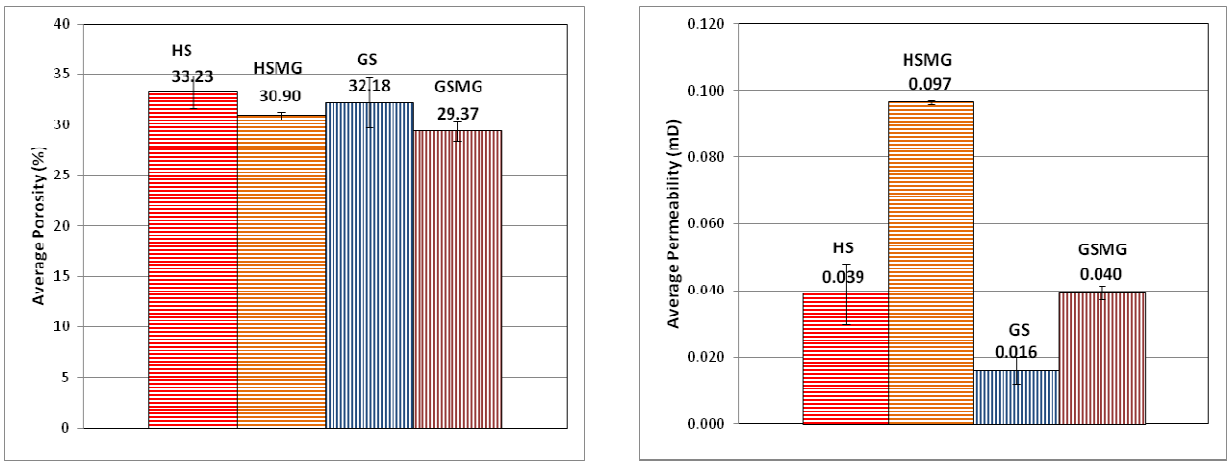

(a) (b)

Fig. 18 Properties of unaged MGO cores: a) porosity; and b) permeability

As shown in **Fig 19**, after aging, porosities of all the MGO and baseline cement cores decreased. Although the initial permeabilities of the MGO samples were higher than those of baseline cement samples, permeabilities of HSMG samples were decreased after aging. The decrease in porosity and permeability values observed in the HSMG samples can be attributed to the formation of $CaCO_3$ in presence of CO_2, whereas in case of GSMG and GS samples the increase in permeability can be attributed to leaching of the cement promoted by the formation of water-soluble calcium bicarbonate.

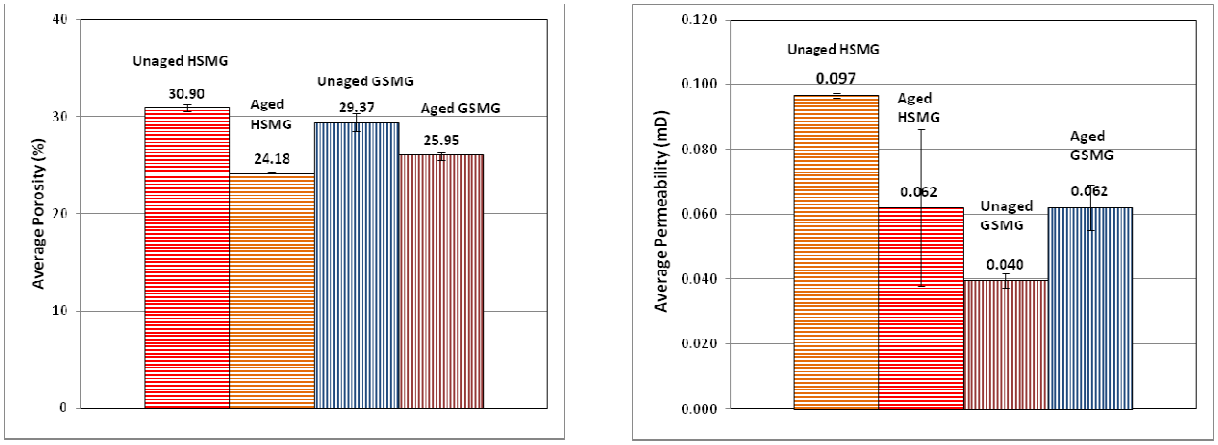

(a) (b)

Fig. 19 Properties of unaged and aged MGO cores: a) porosity; and b) permeability

Table 3 presents degradation depth of MGO and baseline cores. MGO cores exhibited higher degradation depth than the baseline cement. This is consistent with permeability measurements that show increased permeability with the addition of magnesium oxide.

Table 3: Degradation depths of aged MGO and baseline cores

Core #	Diameter (in.)	Average Diameter (in.)	Std. Dev.	Carbonated Depth (in.)	Average Carbonated Depth (in.)	Std. Dev.
HSMG	1.000	1.004	0.005	0.314	0.300	0.019
				0.318		
	1.007			0.278		
				0.290		
HS	1.007	1.003	0.006	0.153	0.164	0.011
				0.168		
	0.999			0.178		
				0.157		
GSMG	0.997	1.001	0.005	0.290	0.289	0.016
				0.266		
	1.004			0.302		
				0.296		
GS	0.997	0.999	0.003	0.160	0.181	0.022
				0.212		
	1.001			0.169		
				0.181		

In addition to porosity and permeability, the mechanical properties of magnesium oxide based cement cores were investigated. The compressive strengths of unaged MGO cores were found to be higher than those of baseline cements (**Fig. 20**). The improvement in compressive strength is attributed the expanding behavior of magnesium oxide in the cement system. After aging, the compressive strength of all the cores increased due to the formation of $CaCO_3$. The percentage increase in compressive strength after aging for MGO cores is less than those of baseline cores. As a result, the difference in compressive strength of MGO and baseline cement cores diminished after aging. MGO cores exhibited less carbonation compared with the baseline cores. This indicates better performance of magnesium oxide additive in hindering the carbonation process.

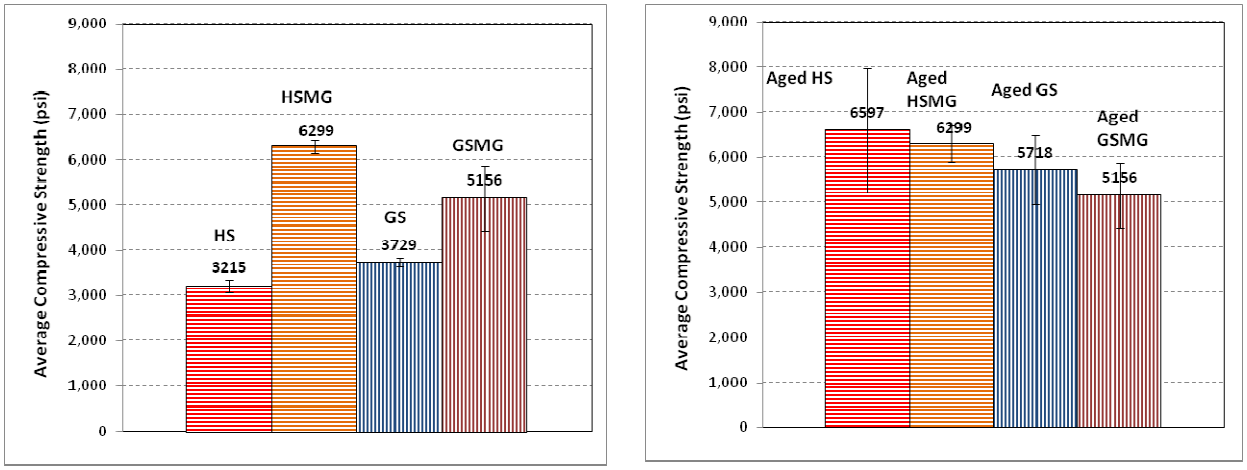

(a) (b)

Fig. 20 Compressive strength of MGO and baseline cement cores: a) unaged; and b) aged at 6000 psi, 225°F and 100% CO_2 concentration

The shear bond strengths of aged and unaged MGO samples were measured to study the impact of acid attack. Like the baseline cement, shear bond strength improved after aging due to the carbonation process that makes the cement expansive (**Fig. 21**). Since the cement is radially under confined condition, the expansion tendency elevates the stress level and increases the friction at the bonding interface. This condition eventually leads to improved bond strength. The level of strength improvement is higher for baseline samples than the MGO samples. This indicates that MGO samples experience less carbonation than the baseline. The result is encouraging in terms of limiting the acid attack by hindering conversion of binding components of the cement (C-S-H and portlandite) to $CaCO_3$, which can be easily leached out by acidic solutions.

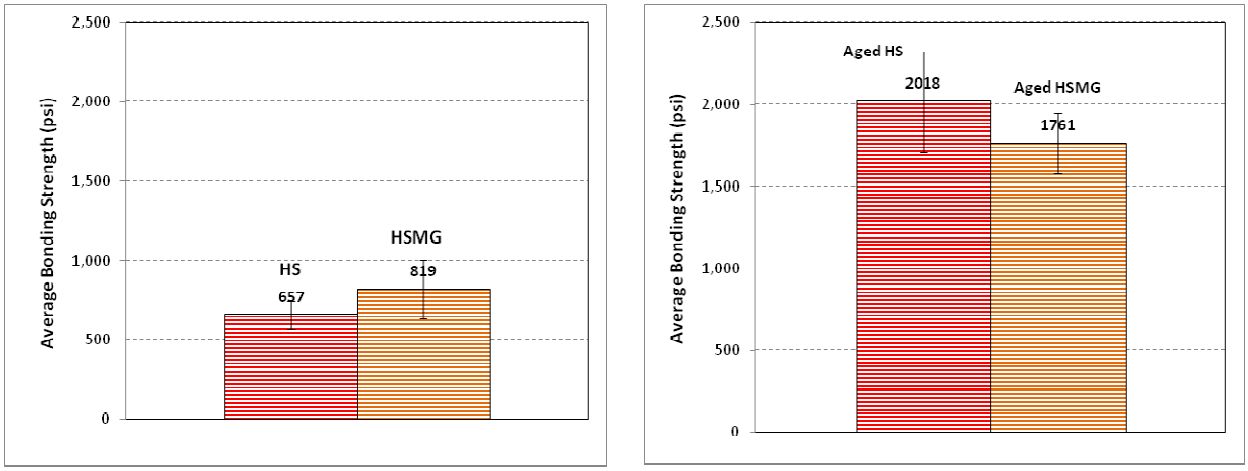

(a) (b)

Fig. 21 Shear bond strength of MGO and baseline cement cores: a) unaged; and b) aged at 6000 psi, 225°F and 100% CO_2 concentration

Latex is one of the cement additives, which is considered in this study. As previously reported, the latex containing cores prepared earlier showed an increased porosity and permeability. This result was contradicting to the general believe that adding latex reduces porosity and permeability of cement. The compressive and shear bond strengths were also less than those of the baseline samples. To verify repeatability the measurements, another batch was prepared using the same cement composition and mixing technique. Shear bond samples were not prepared for the second batch. A similar result with porosity and permeability was observed. Compressive strength measurements were almost in the range as the baseline cores. In the effort to minimize the increase in porosity and permeability, another batch of slurry was prepared with similar composition but with a different mixing method. The mixing of the components was done at a reduced agitation speed in order to avoid formation of vortex, which may introduce more air bubbles in the slurry. However, even after using reduced RPM, similar results were obtained for porosity and permeability measurements. The compressive strength tests on the third batch cores will be carried out in the coming weeks.

The latex cement formulation was adopted from Fuquan et al. (2006). The paper describes the use of carboxylic acids to act as emulsifier. The amount of anti-foaming agent added during the slurry preparation was also double to minimize air entrapment. The authors of the paper could not be reached. One of the members of the Technical Advisory Board (TAB), has provided some suggestions to improve the latex-cement slurry formulation.

Degradation studies on hydroxyapatite containing cores were continued. After obtaining encouraging results from preliminary evaluation of cement cores containing hydroxyapatite, we have started testing their degradation behavior in acidic environment. Results will be presented in the up-coming report.

As reported by Mueller et al. (1991), cements containing more than 20% BWOC of micro-silica have a tendency to be brittle. A similar result was obtained when 35% BWOC of micro-silica containing cement system was tested. Hence, the micro-silica content has been reduced to 15% BWOC and 20% BWOC of silica flour added to maintain a constant calcium-silica ratio. Citric acid amount was also reduced to 0.15% BWOC. The slurry properties were measured. Rheology of the slurry was found to be satisfactory. The filter press and consist-o-meter thickening time tests will be carried out in the coming weeks.

Adding silica and latex has been recommended by Mueller et al. (1991) and other studies to provide extra strength to the cement. A new cement formulation with 10% BWOC of latex and 15% BWOC of mirco-silica was prepared and its slurry properties were tested. Twenty percent BWOC of silica flour was added to maintain a constant calcium-silica ratio. Acetic acid was used to prevent the flocculation of latex at elevated temperatures and act as a dispersant in the cement. Hence, instead of citric acid an increased amount of acetic acid, 2.41% BWOC, was added to act as an

emulsifier for latex and a dispersant for micro-silica. The slurry properties were measured. Flow properties of the slurry are within acceptable range. The filter press readings and consist-o-meter thickening time will be presented in next monthly report.

2.3 Experimental Studies on Corrosion of Tubulars (Task 3)

The development of corrosion test setup has been start. Preliminary corrosion experiments with Potentiostat (Gamry Series G 300 Potentiostat/Galvanostat/ZRA) are in progress. The test are being carried out under atmospheric conditions using an electrochemical cell (**Fig. 22**) designed for flat corrosion coupons. The coupons are exposed to 2% brine solution. The objectives of the preliminary experiments are to develop test procedure for high-pressure corrosion experiments that will be carried out under acidic gas containing environment.

Fig. 22 Electrochemical cell (Gamry Paracell Kit)

After receiving test cell for stress cracking corrosion (SCC) experiments, a design of a heating jacket (**Fig. 23**) for the cell has been prepared. The jacket allows circulation of the heating medium around the cell to provide the required heat to conduct high temperature tests. Purchase order for the jacket has been completed and the item will be manufactured in the coming weeks. The cell will be attached to a pneumatic cylinder to apply tension force on a test specimen (mini-pipe specimen). The cylinder has 3000 lbf loading capacity at 250-psi air pressure. It is expected to create high stress level in the test specimen. The stress level can reach the yield values of common carbon steels used in oil field applications such as well casing and production tubing.

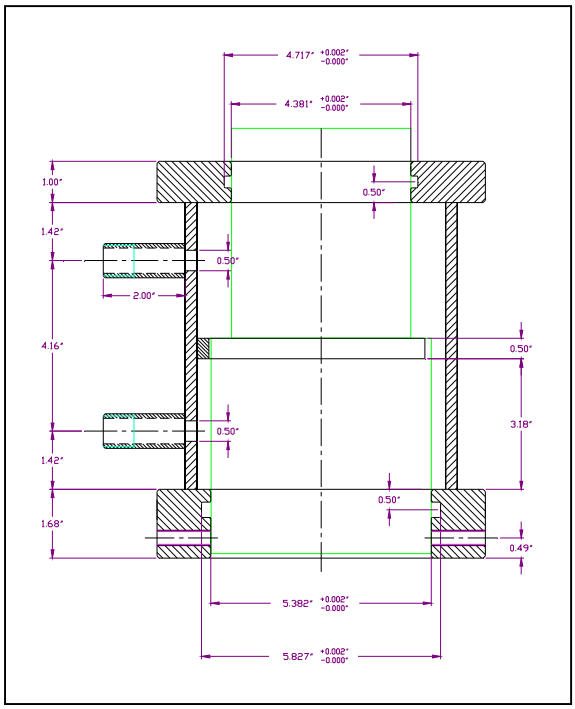

Fig. 23 Heating jacket for SCC test cell

3. Planned Activities

- Continue aging experiments with brine-CO_2-CH_4 system for 14 days varying CO_2 concentration at 100ºF.
- Continue theoretical and modeling studies on tubular degradation.
- Continue cement additive screen study.
- Continue development of tubular corrosion testing setups and acquisition of components.

4. Project Expenditures

This section presents the project expenses during the month of February (**Table 4**) and the cumulative expenditures.

Table 4 Current and cumulative expenditures, February, 2013

No.	Budget Categories	Current Expenses	Cumulative Expenses
1	Salaries & Wages	$4,725.00	$149,179.66
2	Fringe Benefits	$307.13	$35,591.10
3	Project Materials	$1,698.43	$67,613.50
4	Travel	$70.00	$3,939.55
5	Conference Expenses	$0.00	$0.00
6	Other Direct Costs	$0.00	$585.77
7	Equipment	$10,059.65	$164,085.47
8	Space Rental	$0.00	$0.00
9	Indirect Cost	$3,434.12	$128,488.67
10	**Total**	**$20,294.33**	**$549,483.72**

Nomenclature

Acronyms

C-S-H	Calcium silicate hydrate
GHO	Class G Cement with hydroxyapatite
GS	Class G cement with silica flour
GMS	Class G Cement with micro silica
GSHO	Class G Cement with silica flour and hydroxyapatite
GSLT	Class G Cement with silica flour and latex
GSMG	Class G Cement with silica flour and magnesium oxide
HHO	Class H Cement with hydroxyapatite

HMS	Class H Cement with micro silica
HOAP	Hydroxyapatite additive sample
HS	Class H cement with silica flour
HSHO	Class H Cement with silica flour and hydroxyapatite
HSLT	Class H Cement with silica flour and latex
HSMG	Class H Cement with silica flour and magnesium oxide
HSMS	Class H Cement with silica flour and micro silica
MGO	Magnesium oxide containing cement

Symbols

a_1, a_2, a_3	constants
C_{CO2}	bulk aqueous concentration of CO_2 in mol/m^3
C_{H+}	bulk aqueous concentration of H+ ions in mol/m^3
C_{H2CO3}	bulk aqueous concentration of H_2CO_3 in mol/m^3
$C_{CO2(ref)}$	bulk aqueous concentration of CO_2 at reference condition in mol/m^3
$C_{H+(ref)}$	bulk aqueous concentration of H^+ ions at reference condition in mol/m^3
$C_{H2CO3(ref)}$	bulk aqueous concentration of H_2CO_3 at reference condition in mol/m^3
ΔH	activation enthalpy in kJ/mol
io	exchange current density in A/m^2
i_{0ref}	reference exchange current density in A/m^2
i_{corr}	corrosion current density in A/m^2
$i_{(Fe)}$	anodic current density of iron oxidation in A/m^2
$i_{(H+)}$	cathodic current density for H+ ion reduction in A/m^2
$i_{(H2CO3)}$	cathodic current density for H_2CO_3 reduction in A/m^2
$i_{(H2O)}$	cathodic current density for H_2O reduction in A/m^2
R	universal gas constant, R = 8.314 J/ (mol. K)
T_{ref}	reference temperature in K
T	temperature in K

References

Carter, L.G., Waggoner, H.F. and George C. 1966. Expanding Cements for Primary Cementing, JPT. 18 (5), pp. 551-558.

Ceukelaire, D.L. and Van Nieuwenburg, D. 1993. Accelerated Carbonated of a Blast Furnace Cement Concrete, Cement and Concrete Research, Vol. 23, pp. 442-452.

Constantinides, G. 2001. The Elastic Properties of Calcium Leached Cement Pastes and Mortars: A Multi-Scale Investigation, MS thesis, MIT, Cambridge, Massachusetts.

de Waard, C. and Milliams, D. E. 1975. Carbonic Acid Corrosion of Steel, Corrosion, Vol. 31, pp. 177-181.

Eilers, L.H, Nelson, E.B and Moran, L.K. 1983. High temperature cement compositions pectolite, scawtite, truscotite or xonotlite: which do you want? J. Pet Tech. 35 (7), pp. 1373-1377.

Fuquan S., Guangming Lv and Jianzhou J. 2006. Application and Research of Latex Tenacity Cement Slurry System, paper SPE 104434 presented at the SPE International Oil & Gas Conference and Exhibition, Beijing, China.

Jones, R.R., Carpenter, R.B, New Latex, 1991. Expanding Thixotropic Cement Systems Improve Job Performance and Reduce Costs. Paper SPE 21010 presented at the SPE International Symposium on Oilfield Chemistry, 20-22 February, Anaheim, California.

Mueller D. T. and Dillenbeck III R. L. (1991); “The Versatility of Silica Fume as an Oil well Cement Admixture”; SPE 21688.

Nesic, S., Postlethwaite, J. and Olsen, S., 1996. An Electrochemical Model for Prediction of Corrosion of Mild Steel in Aqueous Carbon Dioxide Solutions, Corrosion, April, Vol. 52, No. 4, pp. 280-294.

Nordsveen, M., Nesic, S., Nyborg, R., Stangeland, A., 2003. A Mechanistic Model for CO2 Corrosion with Protective Iron Carbonate Films - Part 1: Theory and Verification. Corrosion, Vol. 59, No. 5, pp. 443-456.

Parcevaux, P.A and Sault, P.H. 1984. Cement Shrinkage and Elasticity: A New Approach for a Good Zonal Isolation. Paper SPE 13176 presented at the SPE Annual Technical Conference and Exhibition, 16-19 September, Houston, Texas.

Shen, J.C. and Pye, D.S. 1989. Effects of CO2 Attack on Cement in High-Temperature Applications, paper SPE-18618-MS, presented at the SPE/IADC Drilling Conference, 28 February-3 March, New Orleans, Louisiana.

Seidel, F.A. 1985. Use of Expanding Cement Improves Bonding and Aids in Eliminating Annular Gas Migration in Hobbs Grayburg-San Andres Wells. Paper SPE 14434 presented at the PE Annual Technical Conference and Exhibition, 22-26 September 1985, Las Vegas, Nevada.

Wray, B., Bedford D., Leotaud,L., Hunter,B., 2009. The Application of High-Density Elastic Cements To Solve HP/HT Challenges in South Texas: The Success Story. Paper SPE 122762 presented at the SPE Annual Technical Conference and Exhibition, 4-7 October 2009, New Orleans, Louisiana.

Appendix A: Response to BSEE Review Comments on Report # 15 and 16

Progress Report #15

Page 3

- For reaction equation (2) relisted below, should it be S_n instead of Sn?

$$H_2S \rightarrow (1/n)\ Sn + H_2 \qquad (2)$$

Response: Yes, n must be a subscript.

Page 7 (Based on Figure 5 – summary of compressive strength of aged samples in brine saturated with pure methane (100%), mixed gas (10% CO2 and 90% methane)

- What are possible thoughts/reasons for the improved strength for Class G with fly ash from exposure to CO_2 (sweet gas)?

Response: After exposure to CO_2 saturated brine, all the samples show first reduction and then increase in permeability (Fig. 1). The trend indicates the presence of two offsetting phenomena (carbonation and leaching) that affect the permeability of cement after degradation. Carbonation takes place first and makes the cement less permeability. Then, the acid begins to leach the carbonated cement increasing its permeability. Moreover, the leaching process reduces the amount binding material present in the cement and causes reduction in mechanical strength. GSF samples exhibit the smallest increase in permeability; hence, we expect less leaching and lower degradation.

Comment: Considering the request for 6 month no additional cost extension due to required additional time for gaining experiments (2 weeks - given the 2 days for pressure and heat, 2 days for de-pressure and cooling), appears to be reasonable.

Response: 6-month no cost extension may be request in the future.

Appendix A – Page 20

- Why was the assumption for the activity value for FeS – 1 and the activity of ferrous ions near or on the steel surface approaches 1.0 made?

Response: The activity of ferrous ions near or on the surface is close to 1.0 because the ions are homogenously distributed near to the surface and the concentration of the ions is approximately uniform. Moreover, the difference between the chemical potentials in Eqn. (A-1) approaches zero and the activity approaches 1.0 at standard state (i.e. 1 bar and 25°C).

Appendix A – Page 21

- Why the assumption for the activity for solid to be 1, i.e. $a_{solid} = 1$

Response: The activity of a species i, denoted by a_i, is defined as:

$$a_i = \exp\left(\frac{\mu_i - \mu_i^0}{RT}\right) \qquad \text{(A-1)}$$

where μ_i is the chemical potential of the species under the conditions of interest, μ_i^0 is the chemical potential of that species in the chosen standard state, R is the gas constant and T is the thermodynamic temperature.

For a solid body, a uniform and single species solid at one bar has an activity of unity. The same applies for a pure liquid.

In the pure composition of solid and liquid, the concentration of components is homogeneously distributed all over the controlled volume. Therefore, no driving force is required for the single component to transport from one side to

the other. In this case, the difference between the chemical potential in Eqn. (1) goes to zero and the activity is equal to 1 at 1 bar and any temperature.

Progress Report #16

Page 8 – Table 5 – Properties of Hydroxyapatite Containing Cement Slurries

- Was the measurement instrument also inoperable to measure the thickening time for the different Hydroxyapatite Class H cement?

Response: Yes. The slurries were extremely thick as a result, we were unable to measure their rheology and thickening time.

Page 11

- Will the possible addition of the defoaming agent to the cement slurries adverse impact the resulting data? If so, any thoughts as to how?

Response: After discussing the issue with one our technical advisory board members, we have decided to test other types of latex instead of using a deformer.

Page 12 (3-Problems Encountered)

- What Nitrogen purity grade in place of helium (due to limited supply)?

Response: The purity grade for our laboratory nitrogen is 99.9%.

Appendix A – Table A-1 Effects of test conditions on CO2 Corrosion Rate Page 20-21

- pH of what? Drilling mud? Corrosion inhibitors?

Response: This is pH of the aqueous solution in contact with corroded material (steel).

Appendix A – Equation A-6 Page 22

- Is there a temperature limitation or specific temperature range for this equation?

Response: The equation is valid up to 80°C (176°F).

Appendix A – Anodic Equations A-12-A-14 Page 23

- Why is the dissolution rate on the activity of hydroxide ions the most acceptable modeling approach?

Response: The rate of deposition and dissolution of Fe in a solution is a function of pH. A number different reaction paths and mechanisms for the iron deposition/dissolution reaction were proposed and their kinetic consequences were evaluated by Bockris et al. (1961). The mechanism that is consistent with his results and other experimental measurements is the method that considers the dissolution rate on the activity of hydroxide ions. The method presents the reaction mechanism as:

$$Fe^{+} + OH^{-} \Leftrightarrow FeOH + e^{-}$$

$$FeOH \rightarrow FeOH^{+} + e^{-}$$

$$FeOH^{+} \Leftrightarrow Fe^{2+} + OH^{-}$$

Appendix A – Equation A-19 Page 24

- Need clarification/explanation – would taking the log-log of the plot and the resulting slope yield the activation enthalpy ΔH+ value?

Response: Yes, this is possible. If the temperature dependence of the exchange current density is known and the data is presented as:

$$Log\left[\frac{i_{0(H^+)}}{i^{ref}_{0(H^+)}}\right] \text{ versus } \frac{1}{T}$$

Then, all data points lay on a single straight line and the slope of the line will provide the activation enthalpy.

Project Title: Effect of H_2S and CO_2 in HPHT Wells on Tubulars and Cement

Report Type: Monthly Report

Report #: 18

Reporting Period: February 22nd, 2013 to March 21st, 2013

Authors:

Ramadan Ahmed, Principal Investigator

Subhash Shah, Co-Principal Investigator

Samuel Osisanya, Co-Principal Investigator

Rida Elgaddafi, Research Assistant

Omotayo Omosebi, Research Assistant

Himanshu Maheshwari, Research Assistant

Adarsh Naidu, Research Assistant

Aman Srivastvava, Research Assistant

Jueun Hwang, Research Assistant

Mounraj Sharma, Research Assistant

Sagar Tale, Research Assistant

Prepared under BSEE Project # E12PC00035

by

THE UNIVERSITY OF OKLAHOMA

May 13, 2013

1. Summary of Accomplishments

This monthly report presents the progress made during the project period February 22, 2013 to March 21, 2013. During this reporting period, cement degradation studies were continued. To examine the level of degradation occurring under acidic environment, properties of cement cores and bonding samples were measured before and after aging. In addition, cement additive screening studies were conducted. The effects of different cement additives on properties of cement slurries and cores, and bonding samples were investigated.

Two aging experiments (Experiment 11 and 12) were conducted varying CO_2 concentration at 100°F and 6000 psi. The samples were aged for 2 weeks in 2% brine saturated with 40% and 100% CO_2. Physical properties of aged and unaged samples were measured after completion of each experiment

Permeability and porosity measurements obtained from aged and unaged cores demonstrate the dominating effect of leaching at 100% CO_2 concentration. Results show slight change in compressive strength as the concentration increases. At low CO_2 concentrations (up to 40%), due to carbonation process, both Class G and Class H cement strengths slightly improved as the concentration increased. In addition, shear bond strength (SBS) measurements show improvement in SBS with increased CO_2 concentration that promotes carbonation. However, results also indicate the presence of leaching process at 100% CO_2 concentration.

Different cement additives were tested for their performance and effectiveness. The effects of magnesium oxide on cement slurry and core properties were investigated. The porosity, permeability and compressive strength measurements indicate reduced carbonation in the MgO containing samples. It is also observed from the FTIR data that MgO is able to reduce calcium carbonate formation in the cement. This indicates suitability of MgO as cement additive for sour gas applications. Further degradation study will be carried out under different aging conditions.

Theoretical and modeling studies on tubular corrosion were continued. An existing corrosion model has been improved to predict uniform corrosion of carbon steel in CO_2 containing environment. The model accounts for different phenomena involved in corrosion, including electrochemical and transport processes, and corrosion thermodynamic and kinetics. In addition, progress has been made in the development of corrosion test setup. After receiving major setup components, the construction of the facility has been started.

Our plan for the upcoming weeks is to continue: i) the aging tests at different CO_2 concentrations and temperatures; ii) theoretical and modeling studies on tubular corrosion; iii) additive screening studies; and iv) development of corrosion test setup.

2. Overall Project Progress

2.1 Theoretical Studies (Task 1)

2.1.1 Tubular Corrosion

Theoretical and modeling studies on tubular corrosion were continued. Previously developed mechanistic model (Nesic et al. 1996) has been improved to predict uniform corrosion of carbon steel in carbon dioxide containing environment. The model considers a number of CO_2 corrosion related phenomena such as electrochemical process, transport process, and corrosion thermodynamic and kinetics. The original model is improved by accounting for the solubility of carbon dioxide in brine solution at HPHT conditions. The model will be evaluated in the future using laboratory measurements.

Sulfide stress cracking (SSC) is hydrogen embrittlement phenomenon caused by combine effect of stress and atomic hydrogen penetration into the metal lattice following corrosion by wet H_2S. Conditions that favor sulfide stress cracking include: i) tensile stress loading imposed by either applied forces or residual stresses; ii) susceptible material; and iii) adsorption of atomic hydrogen via exposure to an environment containing a sufficient quantity of hydrogen sulfide.

Often sulfide stress cracking leads to cathodic cracking. Metals react with H_2S forming atomic hydrogen and metallic sulfides at the surface. During SSC corrosion, free H+ ions in the aqueous solution take away electron from the metal. Those H+ ions, which take away electrons form H_2 molecule. If the concentration of H_2 at surface is sufficiently high, then hydrogen atoms diffuse through the metal leading to embrittlement. The cracking occurs, when critical concentration of H_2 diffusion is reached and the tensile stress level is above the threshold value for SSC to occur.

2.2 Experimental Studies on Degradation of Cement (Task 2)

2.2.1 Porosities and Permeabilities of Baseline Cements

During this reporting period, experimental studies on the effects of CO_2 concentration and temperature on properties of baseline cement have been completed. **Figures 1** and **2** illustrate the effect of CO_2 concentration on porosity and permeability of cement cores. The cores were aged for 14 days in 2% brine at 100°F and 6000 psi, varying CO_2 concentration in the gas phase. During aging, different processes can take place including hydration, carbonation and leaching. Hydration and carbonation lead to decrease in porosity and permeability, whereas leaching is responsible for increase in porosity and permeability. As carbon-dioxide concentration in the gas phase increased, the porosity of the cores slightly decreased due to the domination of the carbonation process. This trend is not consistent for Class H cement. Slight porosity increase was observed between 10 and 40% CO_2 concentrations. However, this increase is within measurement error. At high CO_2

concentrations, the reduction in porosity becomes negligible because of leaching, which offsets the effect of carbonation. Similarly, permeability measurements showed pronounced effect of leaching at high CO_2 concentrations. Permeability reduction trend observed at low CO_2 concentrations was reversed at high concentrations due to leaching. In spite of this, porosity and permeability of aged cores are still lower than those of unaged core samples.

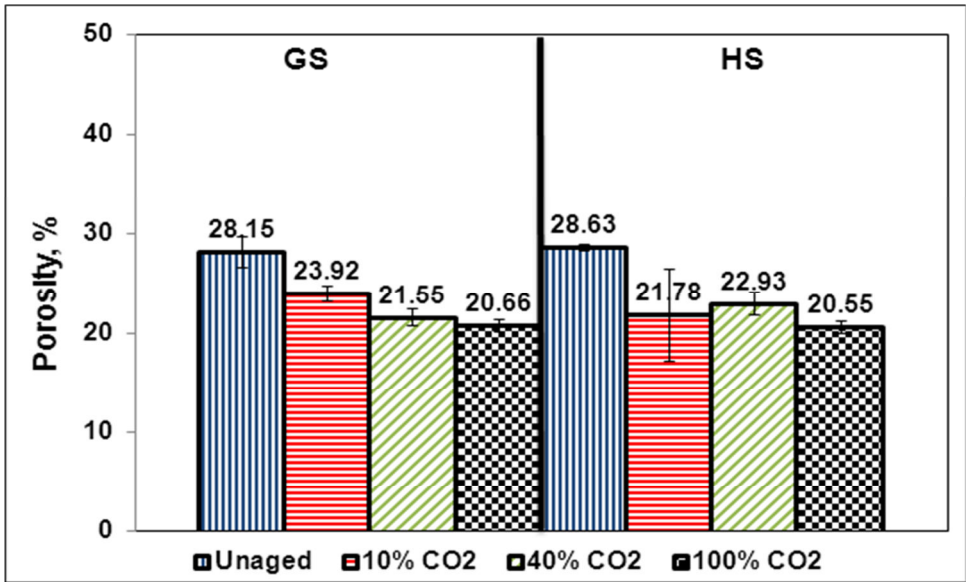

Fig. 1: Porosity of cement cores aged in 2% brine at 100°F and 6000 psi, varying CO_2 concentration in the gas phase

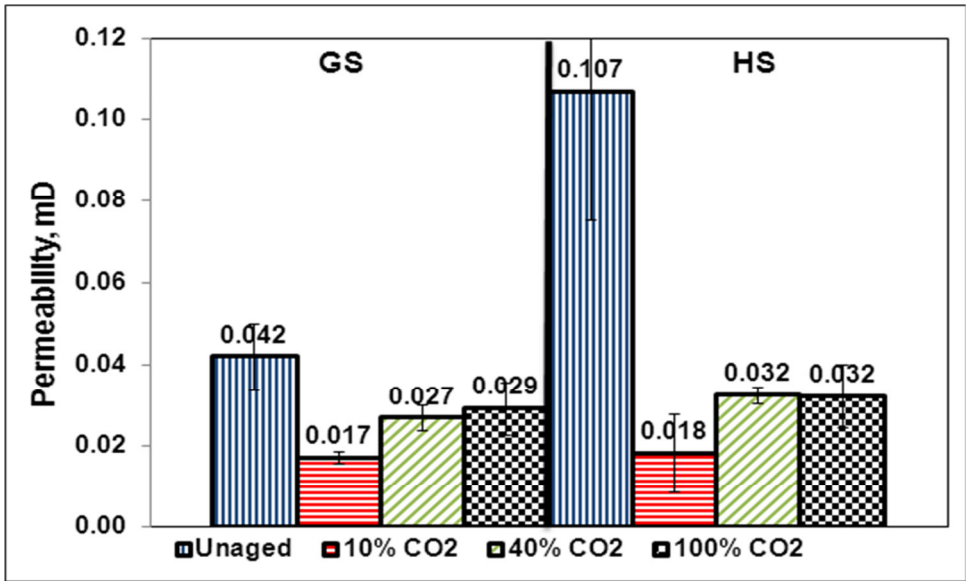

Fig. 2: Permeability of cement cores aged in 2% brine at 100°F and 6000 psi, varying CO_2 concentration in the gas phase

2.2.2 Compressive Strengths of Baseline Cements

Compressive strengths of Class G and Class H cements were measure after aging in 2% brine for 14 days at 100ºF and 6000 psi. Carbon dioxide concentration in the gas phase was increased from 40 to 100%. Results show slight change in compressive strength as the concentration increases. **Figure 3** shows results of compressive strength and porosity tests. After aging in 40% CO_2 gas containing environment, compressive strength of Class G increased due to carbonation while compressive strength of Class H slightly decreased resulting from leaching of calcium. Figure 3b shows the porosity measurements of the dry samples from this batch. Porosity decreased in both Class G and Class H cement cores because of calcium carbonate formation in pore spaces thereby reducing the porosity of the cement samples and increasing the compressive strength. The calcium carbonate formed in the pore provides additional support when the sample is compressed. As a result, the compressive strength of the cement improves after carbonation. Although carbonation occurred in Class H cement cores, an onset of leaching resulted in slight decrease in compressive strength.

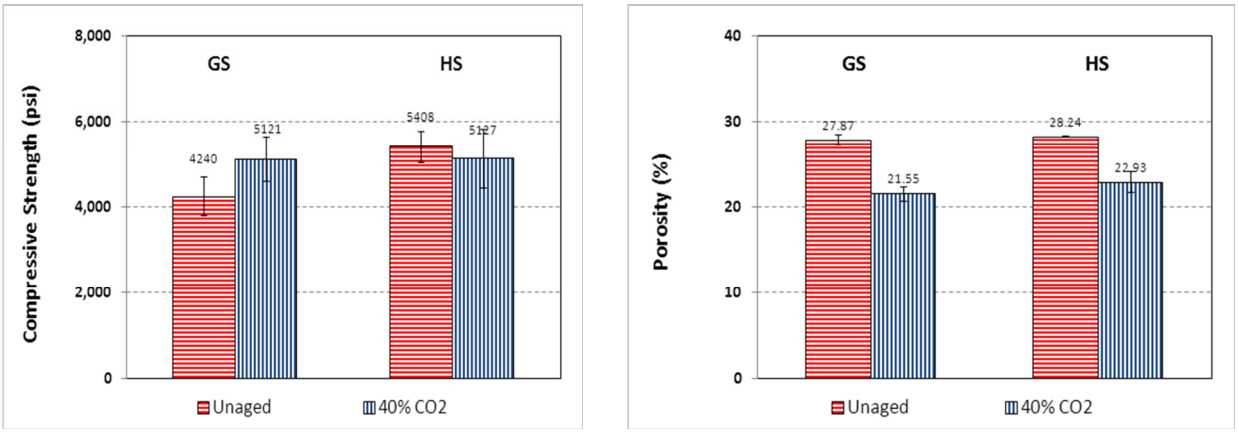

(a) **(b)**

Fig. 3: Properties of aged and unaged cement cores: a) compressive strength; and b) porosity

Figure 4 shows compressive strength of cores aged for 14 days in 2% brine at 100℉, 6000 psi and 100% CO_2. After aging, the strength increased for both Class G and Class H because of carbonation. Figure 4b shows the porosity measurements of the dry cores from this batch. Consistent with the compressive strength measurements, porosity decreased in both Class G and Class H cement because of carbonation, which increases the compressive strength.

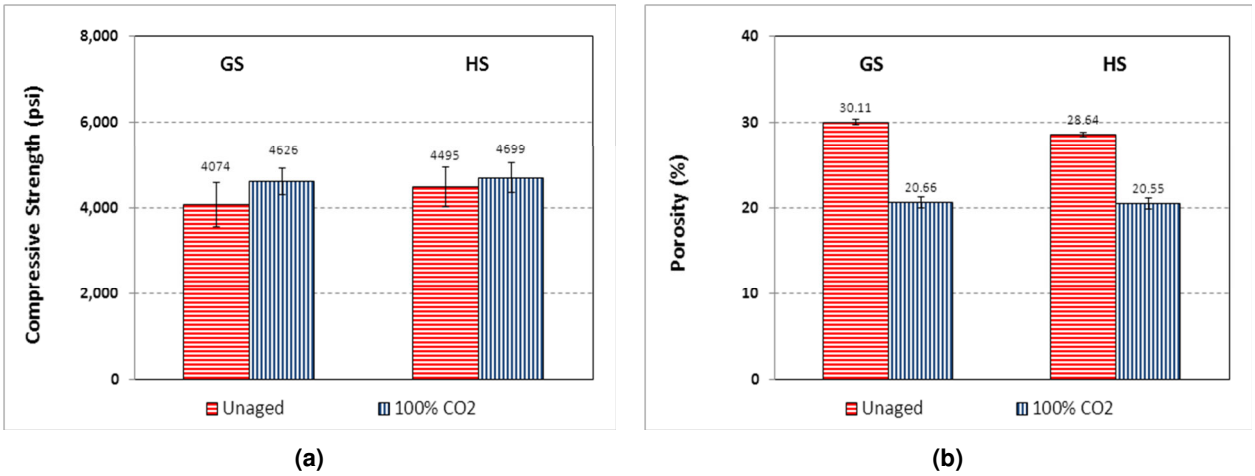

Fig. 4: Properties of aged and unaged cement cores: a) compressive strength; and b) porosity

Further analysis is made combining previous measurements obtained after aging the cores at lower CO_2 concentrations. **Figure 5** shows the impact of CO_2 exposure on the compressive strength of aged cement. At low CO_2 concentrations (up to 40%), compressive strength increased with the increase in concentration. However, because of leaching, the level of strength improvement diminished as the concentration increases. At high CO_2 concentrations (i.e. above 40%), reduction in strength was observed as the leaching intensified and dominated the carbonation process.

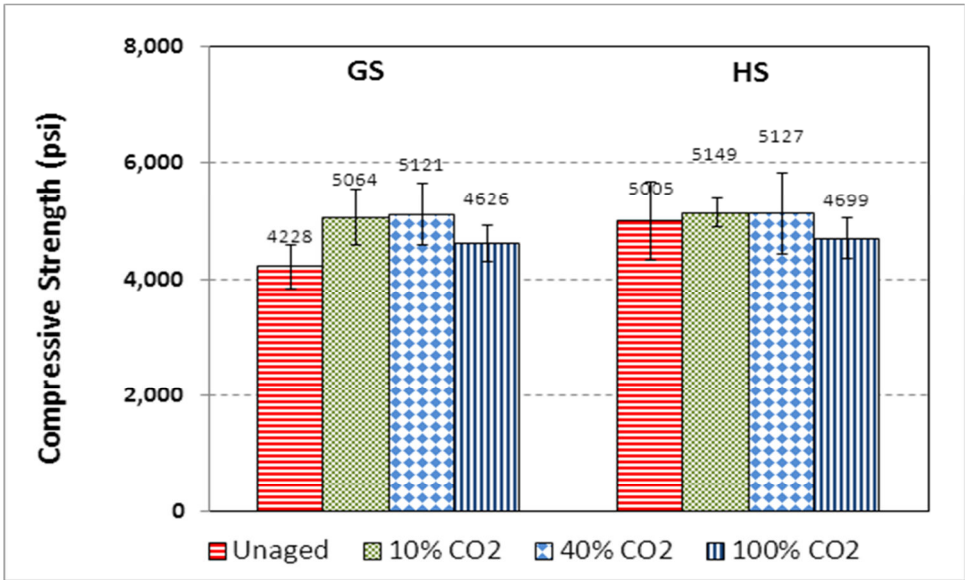

Fig. 5: Compressive strengths of unaged and aged baseline cement cores (aging condition: 2% brine saturated with CO_2 containing gas at 100ºF and 6000 psi)

2.2.3 Shear Bond Strengths of Baseline Cements

Investigation on shear bonding strength (SBS) of cement has been continued. The influence of CO_2 concentration on SBS has been investigated. Like the cement cores, the SBS samples were aged at 100℉ for 14 days under 6000 psi total pressure. **Figure 6** presents shear bond strength of the sample as a function of CO_2 concentration. The unaged samples (0% samples) were kept at ambient temperature in 2% brine. At low CO_2 concentrations (0 to 40%), increasing CO_2 content facilitated carbonation process, which makes the cement expansive resulting in improved bonding strength. However, results indicate the presence of a dominant leaching process at 100% CO_2 concentration. As the CO_2 concentration increases above 40%, the leaching process begins to offset the effect of carbonation causing significant reduction in bonding strength at 100% CO_2 concentration. This is because the solubility of CO_2 increases as its gas content increases resulting in more acidic environment, which favors calcium leaching.

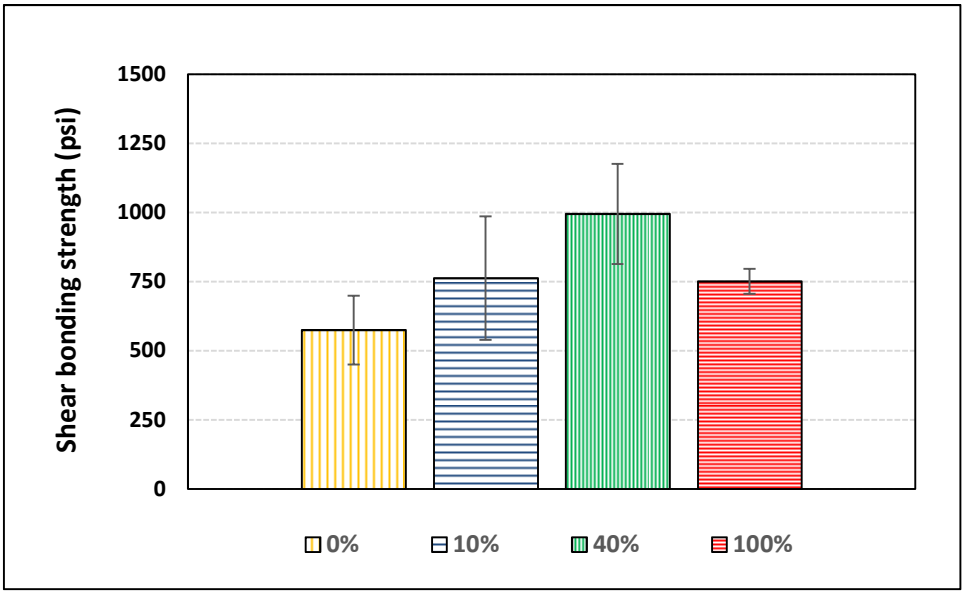

Fig. 6: Effect of CO_2 concentration on shear bond strength at 100℉

2.2.4 Additive Screening Study

The testing of cement additives was continued as mentioned in the previous report. The results obtained from a new batch of MgO are presented in this report. It can be concluded that MgO can be effective against HPHT sour gas conditions. Due to brittle nature of the previous micro-silica samples, a new formulation of micro-silica containing cement slurry was prepared and its slurry properties were tested. The results for the hydroxyapatite containing samples will be presented in the next monthly report.

To date, two batches of MgO containing cores have been subjected to the aging conditions presented in **Table 1**. The measurements obtained from Batch 2 cores were presented in previous reports. The results obtained from Batch 3 cores are presented here.

Table 1: Ageing conditions for the MgO samples

MGO	Temp. (°F)	Pressure (psi)	CO_2 Conc. (%)	Brine Conc. (%)	Days
Batch 002	225	6000	100	2	14
Batch 003	100	6000	100	2	14

Length and Diameter Measurements:

The lengths and diameters of the samples were measured before and after aging process. The unaged samples were also kept in the brine for 14 days in ambient room conditions to observe any change in dimensions due to hydration at room temperature. Change in diameter is of the main concern in oil and gas well cementing. **Table 2** presents a summary of the results. It has been observed that the magnesium oxide samples show similar levels of expansion as the baseline cement (HS and GS) cores. Despite its expansion-promoting actions, MgO did not cause any significant increase in bulk dimensions. These results are consistence with measurements obtained from Batch 002.

Table 2: Expansion of baseline and MgO containing cement cores

Sample	Un-aged Diameter (in.)	Aged Diameter (in.)	% Change	Remark
Batch 003 HSMG Un-aged	0.997	0.999	0.002	Expansion
Batch 003 HSMG Aged	0.999	0.998	-0.118%	Shrinkage
Batch 012 HS Un-aged	0.998	0.998	0.001	Expansion
Batch 012 HS Aged	0.999	1.003	0.353%	Expansion
Batch 003 GSMG Un-aged	0.998	0.998	0.000	Expansion
Batch 003 GSMG Aged	0.999	0.997	-0.195%	Shrinkage
Batch 012 GS Un-aged	0.998	0.999	0.002	Expansion
Batch 012 GS Aged	0.998	0.997	-0.013%	Shrinkage

Porosity and Permeability Measurements:

Porosity and permeability of both aged and unaged MgO containing cores are presented in **Fig. 7**. After aging, porosity and permeability of the cores reduced due to carbonation. The comparison between unaged cores of MgO and baseline cement (**Fig. 8**) shows that porosity and permeability of unaged MgO samples were found to be less than those of unaged baseline cores.

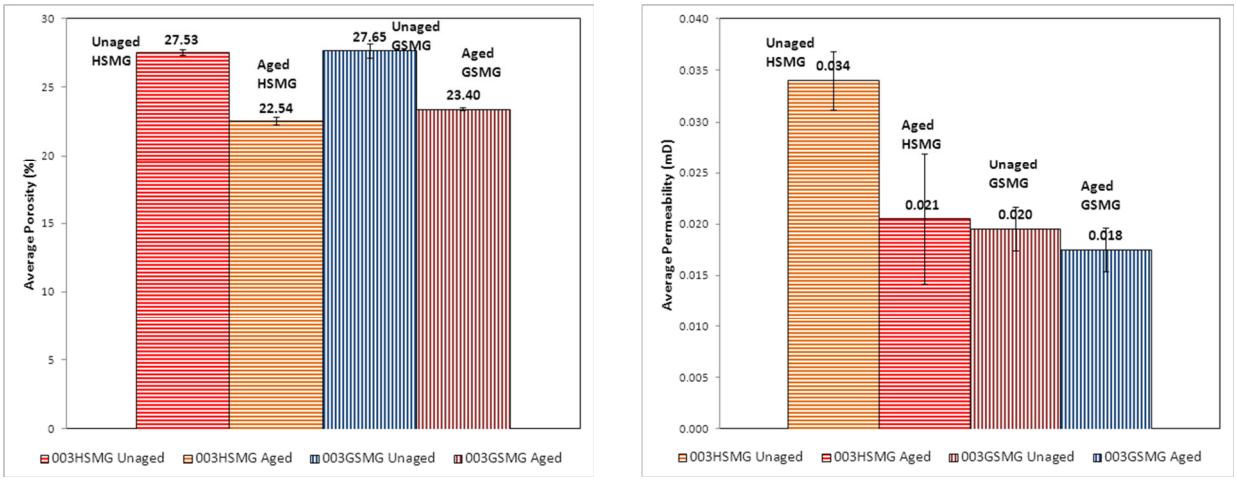

(a) **(b)**

Fig. 7: Properties of unaged and aged MgO containing cores (aging condition: 100°F and 6000 psi with 100% CO_2 gas): a) Porosity; and b) permeability

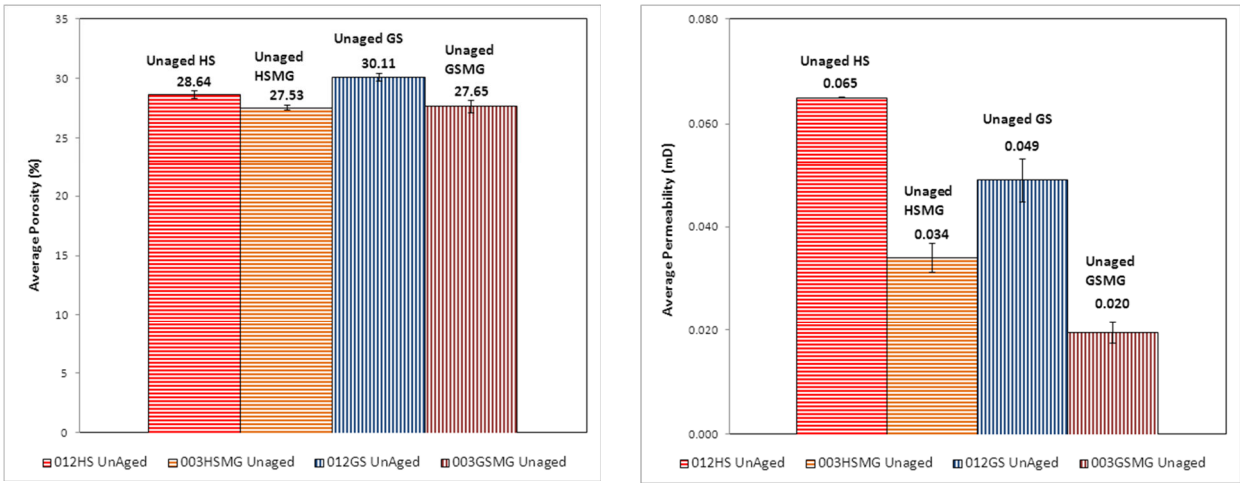

(a) **(b)**

Fig. 8: Properties of unaged cores: a) Porosity; and b) permeability

The results obtained from aged samples (**Fig. 9**) show a decrease in porosity and permeability for all the MgO and baseline samples. This decrease can be attributed to the formation of $CaCO_3$ in presence of CO_2. As it was seen in the Batch 002 results, the percentage reductions in the porosity and permeability of HSMG and GSMG samples are less than those of HS and GS samples, respectively. This trend may indicate that the level of carbonation takes place in the MgO samples is less than that occurring in baseline cement cores. The result is highly encouraging; as the additive MgO introduced in the cement system, it seems to lower the carbonation reaction occurring between CO_2 and binding components (calcium hydroxide and calcium silicon hydrate) of cement.

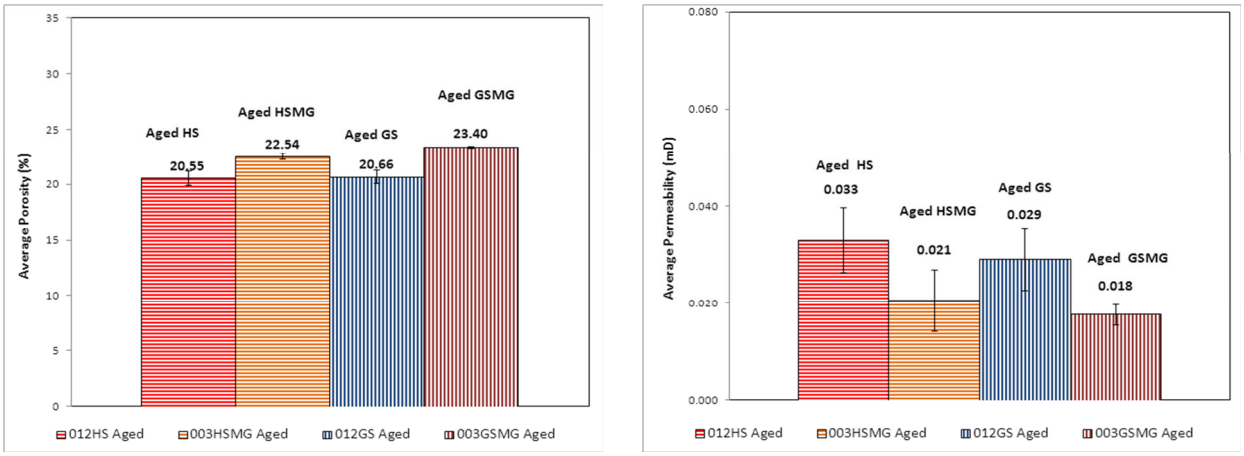

(a) **(b)**

Fig. 9: Properties of cores aged at 100°F and 6000 psi with 100% CO_2 gas: a) Porosity; and b) permeability

Shear Bond and Compressive Strength Measurements:

The compressive strengths of unaged MgO samples were found to be almost in the same range as those of unaged baseline samples (**Fig 10a**). Even after being subjected to aging conditions, the increase in compressive strength of MgO samples is not as high as the baseline samples (Fig. 10). The aging consistently increased the strength of baseline cement cores. This signifies overall lesser amount of carbonation in MgO cores as compared to baseline samples and indicates better performance of MgO additive in hindering the carbonation process. Another inference can be drawn based on the reduced compressive strength of HSMG that indicates the presence of strong leaching, which can be attributed to the increase solubility of calcium because of low-temperature. Other samples (GSMG, HS and GS) might also experienced some leaching; however, the final strength of a sample depends on the dominate process.

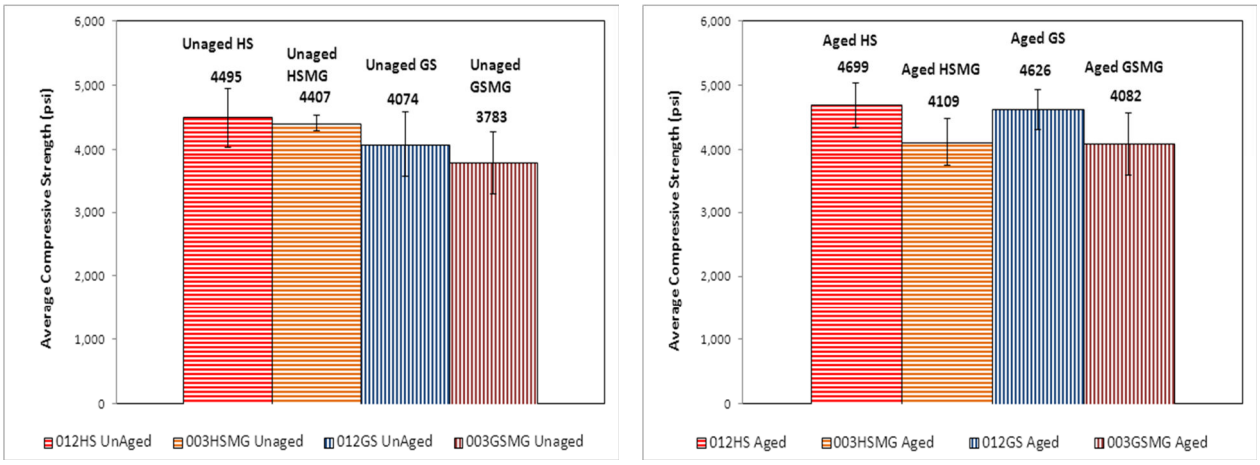

(a) **(b)**

Fig. 10: Compressive strengths of cores: a) unaged; and b) aged at 100°F and 6000 psi with 100% CO_2 gas

The shear bond strength (SBS) tests show expected results (**Fig. 11**). Unaged MgO samples exhibited higher shear bond strength than baseline cores. Both MgO and baseline samples show increase in shear bond strength due to the formation of $CaCO_3$ during aging. However, the increase in SBS of the MgO samples is higher than those of HS samples. This indicates expansive tendency of MgO samples. Expansion of the cement increases the radial stress in the samples, which has a direct impact on the bond strength. Even with lower level of carbonation, the MgO samples show higher SBS than the baseline cement samples.

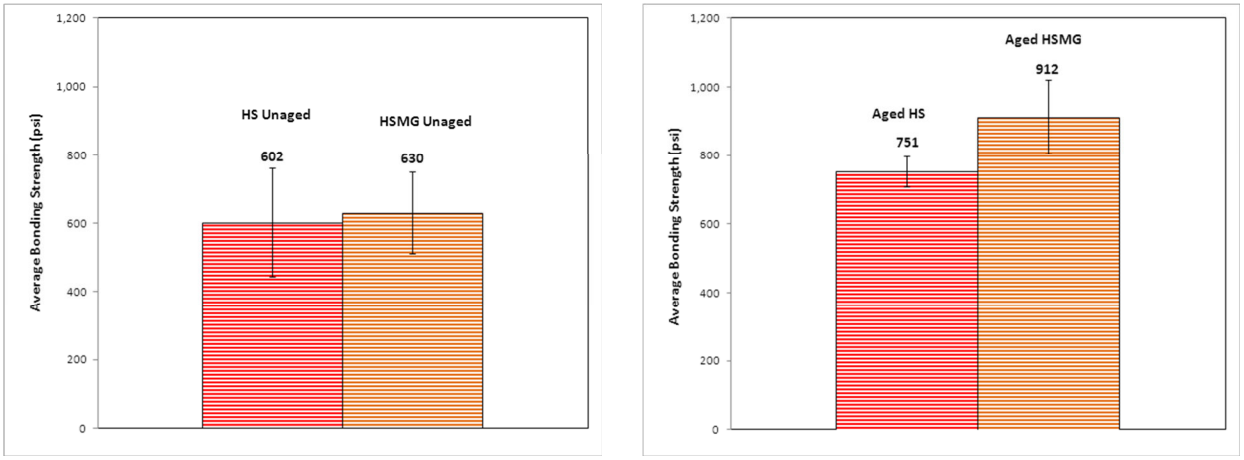

(a) **(b)**

Fig. 11: Compressive strengths of cores: a) unaged; and b) aged at 100°F and 6000 psi with 100% CO_2 gas

Results of FTIR Analysis:

The Fourier Transform Infrared Spectroscopy (FTIR) tests were conducted using MgO and baseline samples. The FTIR equipment requires small amount of powder sample. The test provides qualitative analysis of minerals present in the samples. It shows separate and distinct spectrum peaks for different molecular bonds present in the sample. The machine being used is only calibrated for shales and sandstones; hence, quantitative analysis could not be made for cement samples. However, the tests enable us to identify the level of carbonation occurring in the samples.

To perform the FTIR tests, MgO and baseline cores was first dried and then cut transversely. Three zones in the cylindrical cement core were identified as outermost, middle and innermost zones (**Fig. 12**). Small amount of representative cement core was cut from each zone and finely grinded. The amounts of calcium carbonate and calcium hydroxide oxide (CH) found in these zones indicate the level of carbonation occurring in each zone.

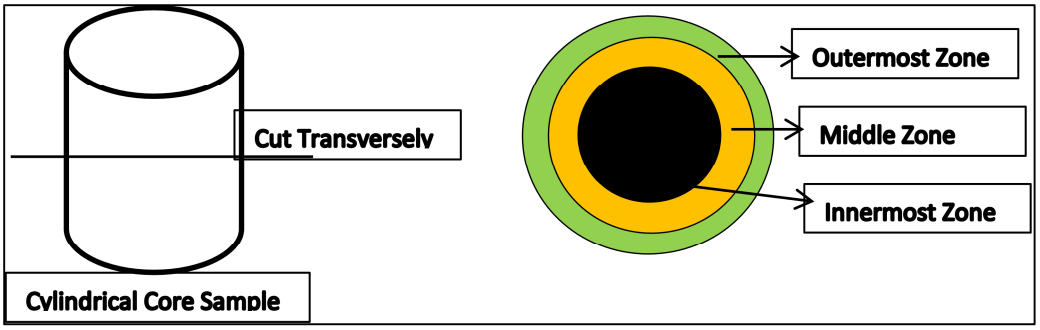

Fig. 12: Schematic of a cylindrical samples and zones selected in the cross section

Figures from **13** through **15** compare FTIR spectra of aged MgO cores (HSMG) with baseline cement (HS) samples. The spectra obtained from the outermost zones (Fig. 13) do not show the OH-bond picks that indicate the presence of calcium hydroxide (CH). Hence, CH presented in the outermost zones was completely consumed by the carbonation process during aging. In addition, the presence of strong $CaCO_3$ formation picks (1480 cm^{-1}) in both samples indicted high level of carbonation. In the innermost zone, both samples show the same and lowest degree of carbonation. However, in the middle zone, the MgO sample shows lesser $CaCO_3$ formation than the baseline samples indicating the impact of MgO in hindering the carbonation process.

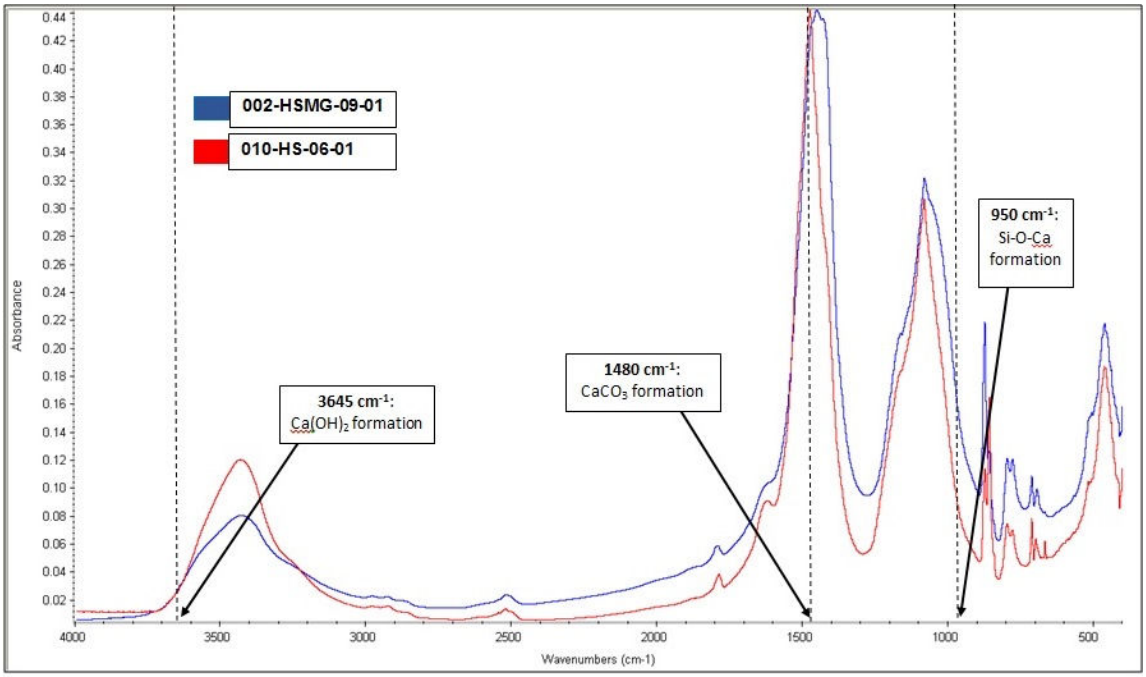

Fig. 13: FTIR spectra of aged HSMG and HS cores (outermost zones)

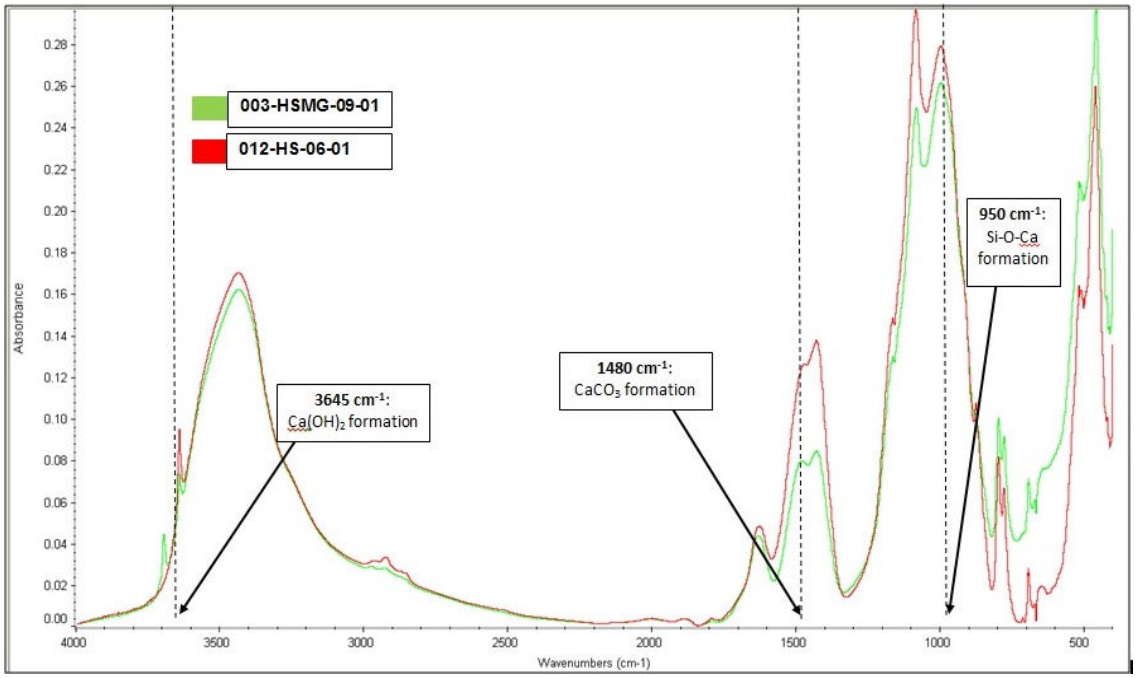

Fig. 14: FTIR spectra of aged HSMG and HS cores (middle zones)

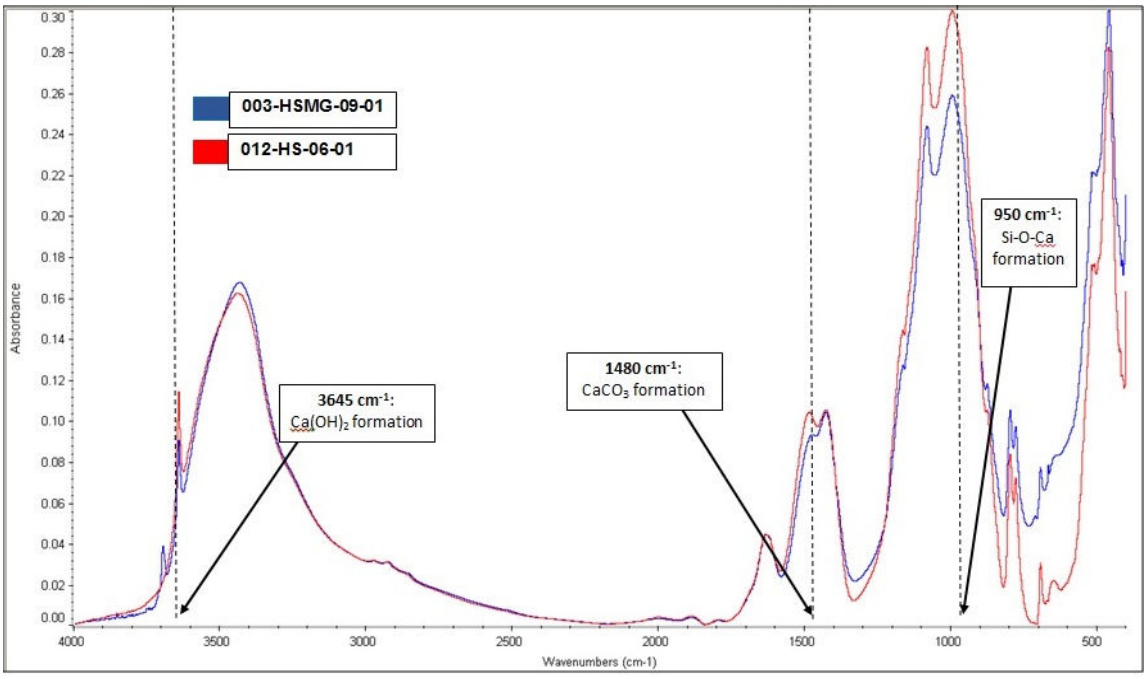

Fig. 15: FTIR spectra of aged HSMG and HS cores (innermost zones)

2.3 Experimental Studies on Corrosion of Tubulars (Task 3)

The development of corrosion test setup was continued. Preliminary corrosion experiments are in progress using a Potentiostat. The instrument is designed to carry out linear polarization resistance (LPR) test that is an established technique in corrosion measurement. The tests were condcuted under atmospheric conditions using flat corrosion coupons. The coupons were exposed to 2% brine solution. The result (**Fig. 16**) showed intermittent decrease and increase in corrosion rate with time, which indicates the formation and breakdown of corrosion scale as a function of time.

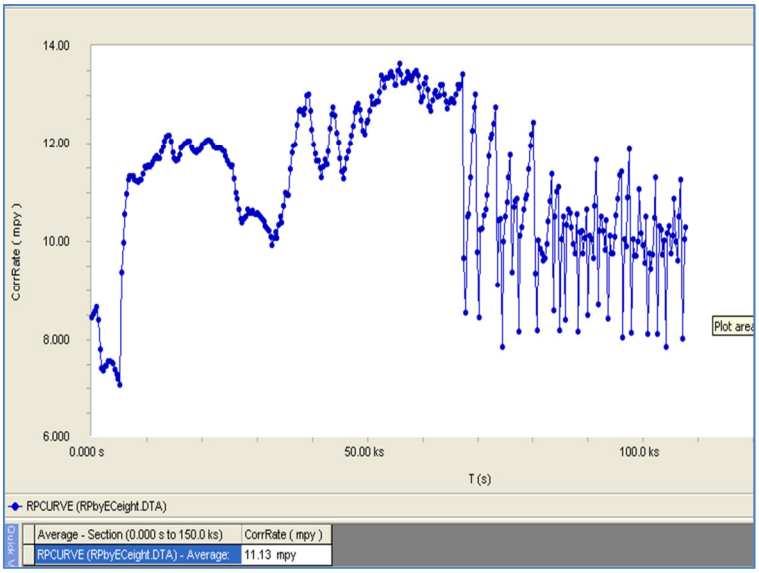

Fig. 16: Corrosion rate of carbon steel measured using LPR technique

The objectives of the preliminary experiments are to develop test procedure for high-pressure corrosion experiments that will be carried out under acidic gas containing environment.

Major items for corrosion setup have been delivered including test cells, heating jackets, injection cylinders, values and high-pressure tube fittings. The construction of the setup has been started. The stress-cracking corrosion cell has been assembled and installed on a mobile frame structure (**Fig. 17**). The cell is equipped with a rod that holds the bottom of the sample and applies tension force using a pneumatic cylinder that has 3000 lbf loading capacity. In addition to the cylinder force, the pressure inside the cell produces tension on the specimen.

Fig. 17 Corrosion Setup

3. Planned Activities

- Continue aging experiments with brine-CO_2-CH_4 system for 14 days varying CO_2 concentration at 350ºF.
- Continue theoretical and modeling studies on tubular degradation.
- Continue cement additive screen study.
- Continue the development of tubular corrosion testing setup.

4. Project Expenditures

This section presents the project expenses during the month of March (**Table 3**) and the cumulative expenditures.

Table 3 Current and cumulative expenditures, March, 2013

No.	Budget Categories	Current Expenses	Cumulative Expenses
1	Salaries & Wages	$4,500.00	$153,679.66
2	Fringe Benefits	$292.50	$35,883.60
3	Project Materials	$1,416.28	$69,029.78
4	Travel	$155.75	$4,095.30
5	Conference Expenses	$0.00	$0.00
6	Other Direct Costs	$264.46	$850.23
7	Equipment	$6,979.93	$171,065.40
8	Space Rental	$0.00	$0.00
9	Indirect Cost	$3,314.50	$131,803.17
10	**Total**	**$16,923.42**	**$566,407.14**

Nomenclature

GS	Class G cement with silica flour
GSMG	Class G Cement with silica flour and magnesium oxide
HS	Class H cement with silica flour
HSMG	Class H Cement with silica flour and magnesium oxide
MGO	Magnesium oxide containing cement
SBS	Shear bonding strength
SSC	Sulfide stress cracking
HPHT	High-pressure high-temperature

References

Nesic, S., Postlethwaite, J. and Olsen, S., 1996. An Electrochemical Model for Prediction of Corrosion of Mild Steel in Aqueous Carbon Dioxide Solutions, Corrosion, April, Vol. 52, No. 4, pp. 280-294.

Project Title: Effect of H_2S and CO_2 in HPHT Wells on Tubulars and Cement

Report Type: Monthly Report

Report #: 19

Reporting Period: March 22nd, 2013 to April 21st, 2013

Authors:

Ramadan Ahmed, Principal Investigator

Subhash Shah, Co-Principal Investigator

Samuel Osisanya, Co-Principal Investigator

Rida Elgaddafi, Research Assistant

Omotayo Omosebi, Research Assistant

Himanshu Maheshwari, Research Assistant

Adarsh Naidu, Research Assistant

Aman Srivastvava, Research Assistant

Jueun Hwang, Research Assistant

Mounraj Sharma, Research Assistant

Sagar Tale, Research Assistant

Prepared under BSEE Project # E12PC00035

by

THE UNIVERSITY OF OKLAHOMA

June 3, 2013

1. Summary of Accomplishments

This monthly report presents the progress made during the project period March 22, 2013 to April 21, 2013. During this reporting period, cement and tubular degradation studies were continued. Cement cores and bonding samples of different cement formulations were prepared and aged in acidic environment to study their degradation characteristics. Properties of the samples were measured before and after aging. Besides this, cement additive screening studies were continued. The effects of different additives on properties of cement cores were investigated.

Two aging experiments (Experiments 13 and 14) were completed during the month. The aging tests were performed varying CO_2 concentration at 350°F and 6000 psi. The samples were aged for 2 weeks in 2% brine saturated with 40% and 100% CO_2. After completion of each experiment, physical properties of aged and unaged samples were measured.

Results of porosity measurement obtained at different CO_2 concentrations displayed different trends for GS and HS samples. For aged HS cement cores, the porosity data is consistent with permeability measurements. FTIR mineralogy tests provided a strong proof of carbonation during aging in acidic environment. Compressive and bonding strengths of HS samples significantly increased after aging in acidic environment.

Different cement additives were tested for their performance and effectiveness. The effects of hydroaxipitate and styrene-butadiene (SBR) latex on degradation properties of cement were investigated. Results indicated that addition of hydroaxipitate prevents carbonation of the cement under HPHT conditions. However, excess silica flour may be needed to control thermal retrogression, which adversely affects hydroaxipitate-containing cement compressive strength. Testing of latex-based cores before and after aging showed the latex does not improve acid resistance of the cement; rather, it promotes acid attack. In the coming weeks, carboxylated-styrene-butadiene latex will be tested in place of regular SBR latex. The carboxylate latex is expected to enable a better bonding with cement, which might help in reducing the permeability of the cement and prevent acid attack.

Theoretical and modeling studies on tubular corrosion were continued. Preliminary LPR experiments were conducted. The tests were conducted to establish experimental procedure. The construction of corrosion test facility was continued.

Our plan for the upcoming weeks is to continue: i) the aging tests at different pressures; ii) theoretical and modeling studies on tubular corrosion; iii) additive screening studies; and iv) development of corrosion test setup.

2. Overall Project Progress

2.1 Experimental Studies on Degradation of Cement (Task 2)

2.1.1 Porosities and Permeabilities of Baseline Cements

During this reporting period, two aging tests were carried out. Samples were aged at 350°F and 6000 psi varying the concentration CO_2 in the gas phase. **Figures** 1 and 2 show the effect of gas composition on porosity and permeability of baseline cores aged at 350°F. Porosity results display different trends for GS and HS samples. For GS cores, increasing CO_2 concentration from 0 to 10%, resulted in significant porosity and permeability reductions. The trend suggests the dominancy of carbonation process at low CO_2 concentrations. However, as the concentration increased from 10 to 100 percent, the acidity of the brine solution increased causing the leaching process to intensify. As a result, permeability of the cores increased as the concentration increases. However, porosity of GS cores at 40% CO_2 does not follow this trend.

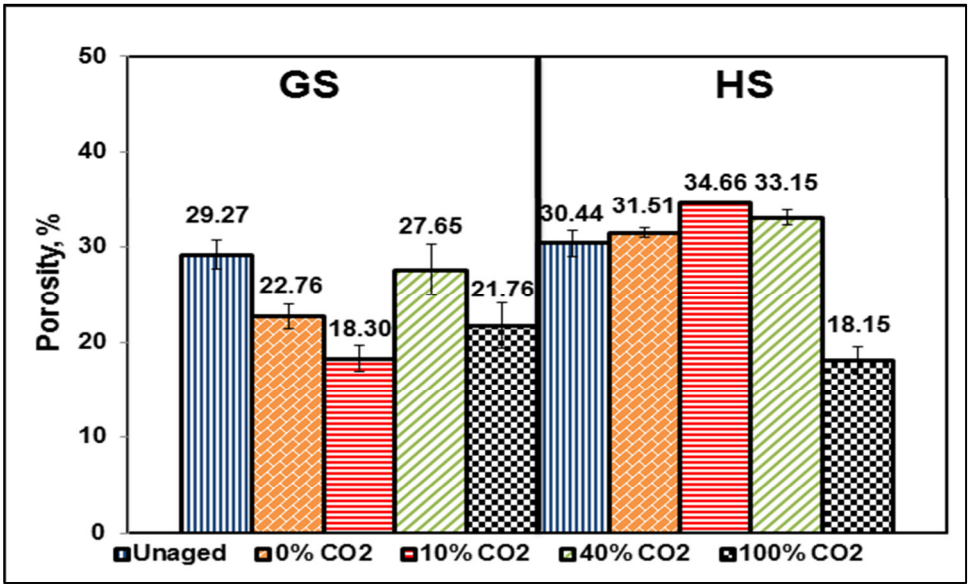

Fig. 1: Porosity of cement cores aged in 2% brine at 350°F and 6000 psi, varying CO_2 concentration in the gas phase

For aged HS cement cores, the porosity data is consistent with permeability measurements. Leaching dominates the carbonation process at lower CO_2 concentrations (up to 10% CO_2). However, when the concentration was increased above 10%, porosity and permeability of the cores decreased indicating the enhancement of carbonation process. Permeability of unaged cores was extremely high and inconsistent with porosity measurements. This abnormality could be because of micro cracks occurring in the sample or formation of highly leached outer zone with high permeability. Theoretically, porosity and permeability of aged samples are affected by the

degradation depth, and porosities and permeabilities of degraded and virgin zones. Porosity measurement obtained from a core sample represents volumetric average porosity value, while core permeability measurement shows the overall permeability of the core. This may be one of the reasons for trend variations between permeability and porosity measurements. Detailed analysis on degraded core porosity and permeability will be presented in the next report.

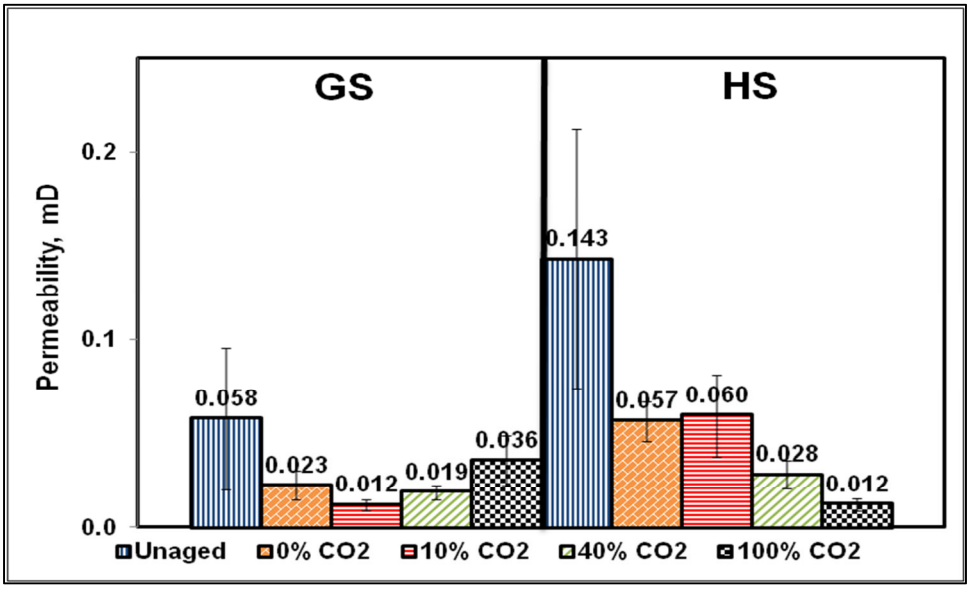

Fig. 2: Permeability of cement cores aged in 2% brine at 350°F and 6000 psi, varying CO_2 concentration in the gas phase

2.1.2 FTIR Spectroscopy

Fourier Transform Infra-Red (FTIR) mineralogy was performed to measure the degree of carbonation in different zones of cement core. Porosity and permeability measurements indirectly indicate the level of carbonation or leaching occurring in the samples whereas FTIR shows direct mineralogical change taking place during aging. **Figure 3** illustrates the different zones in an aged cement core that the samples for FTIR tests were collected.

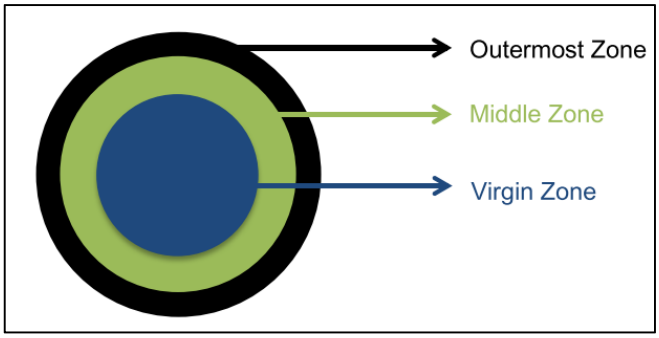

Fig. 3: Cement core zones for FTIR samples

In the FTIR spectrum (**Fig. 4**), every peak of absorbance at a certain wavenumber refers to a particular molecular bond in the substance. For instance, $CaCO_3$ shows peak is at 1480 cm^{-1} (Matsuda and Tsukada 2006). Similarly, $Ca(OH)_2$ and calcium silicate hydrate (CSH) display pick at 3645 and 950 cm^{-1}, respectively (Zaki et al. 2006; Baciu and Simitzis 2007). **Figure 4** compares FTIR spectra of samples obtained from different zones (virgin zone, middle zone, and outermost zone) of a degraded

HS cement core and unaged HS cement core. The mineralogy provides a strong proof of carbonation. At wavenumber 3645 cm^{-1}, there is a peak shown only by the unaged core. This means that calcium hydroxide (CH) is only present in the unaged cement. None of the zones of the aged cement exhibited the presence of CH. The 950 cm^{-1} peak is seen in the unaged and virgin zone only. This indicates CSH is preserved only in the unaged sample and virgin zone of aged sample. The virgin zone was partial degraded, completely losing its CH component. This indicates that calcium hydroxide is more prone to carbonation than CSH. In the middle and outermost zones, both CH and CSH are completely carbonated. The $CaCO_3$ peak (i.e. 1480 cm^{-1}) is high in middle and outermost zones whereas in the unaged and the virgin zone it is relatively low. This explicitly proves that carbonation was completed in the outermost and middle zones.

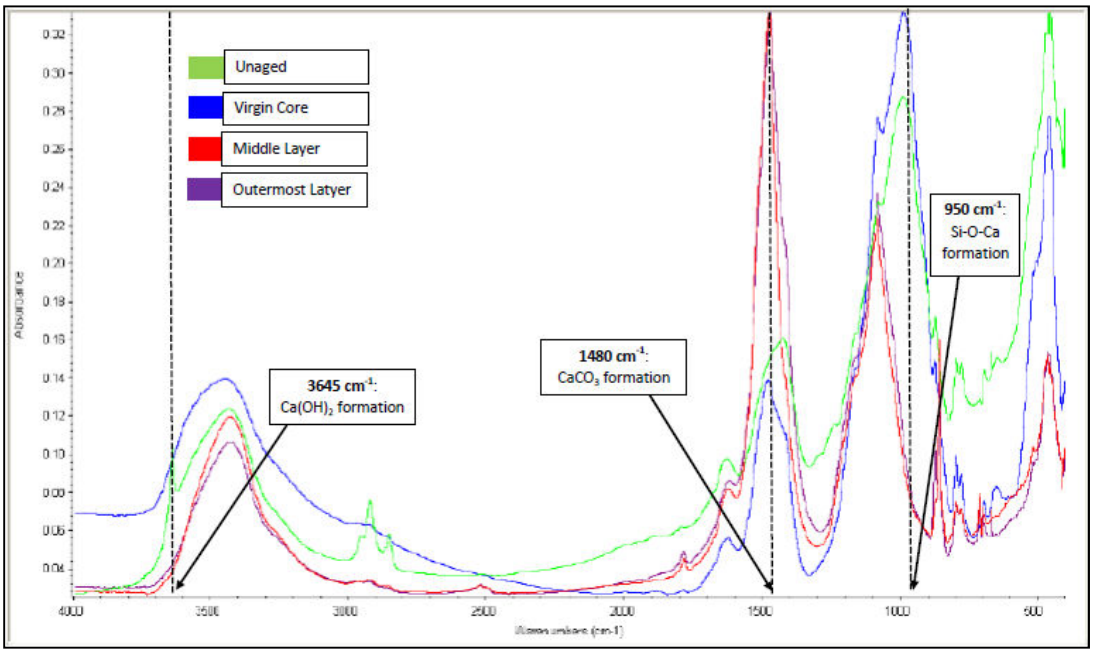

Fig. 4: FTIR spectra of sample aged for 14 days in 100% CO_2, 225°F, 6000 psi and 2% brine solution

Figures 5 through 7 summarize FTIR spectra of samples obtained from different zones of HS cement cores exposed to different aging conditions varying the CO_2 content of the gas phase and aging temperature. The figure only compares the most relevant peaks (i.e. the CH, CSH and $CaCO_3$ peaks) needed for the degradation study. Comparing the FTIR of different zones at different temperatures, we see that CH was more consumed at 225°F than other temperatures. At 225°F, CH is completely consumed in all zones of the core. The reason for this can be attributed to the effects of temperature on the solubility of CO_2 and ionic diffusion. At low temperatures (100°F), CO_2 solubility is high but the ionic diffusion in the pore space is low resulting in a lower rate of carbonation. However, at high temperature (350°F), the ionic diffusion is high but CO_2 solubility is low limiting the rate of carbonation.

As expected, the outermost zone was completely carbonated (Fig. 7) regardless of the aging temperature and CO_2 gas content. The virgin zone showed the least carbonation. The middle zone displayed intermediate carbonation. Increasing the CO_2 content of the gas phase facilitated the carbonation process.

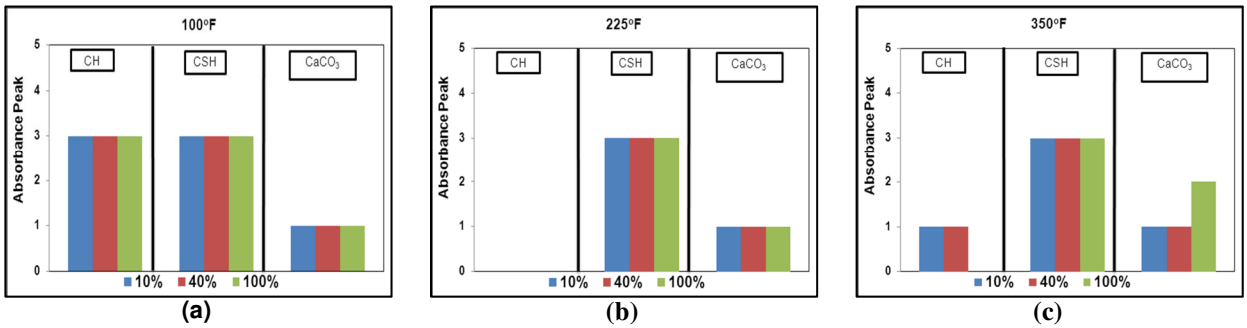

Fig. 5: FTIR peaks of samples from the virgin zone of a core aged at 350°F, 6000 psi, different CO_2 concentrations and temperatures: a) 100°F; b) 225°F; and c) 350°F

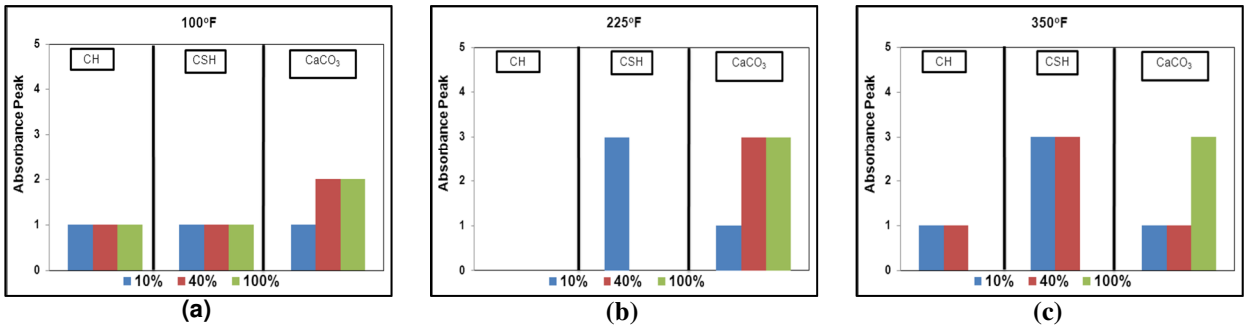

Fig. 6: FTIR peaks of samples from the middle zone of a core aged at 350°F, 6000 psi, different CO_2 concentrations and temperatures: a) 100°F; b) 225°F; and c) 350°F

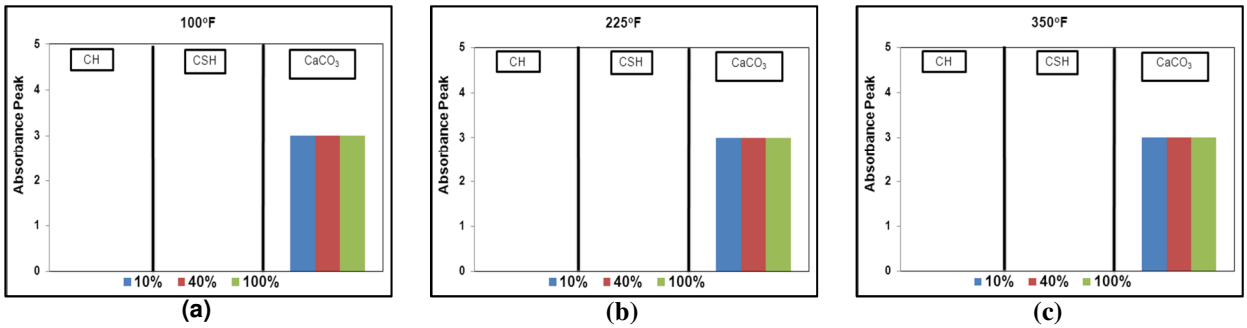

Fig. 7: FTIR peaks of samples from the outermost zone of a core aged at 350°F, 6000 psi, different CO_2 concentrations and temperatures: a) 100°F; b) 225°F; and c) 350°F

2.1.3 Microscopic Examination

Figure 8 presents scanning electron microscope (SEM) images of aged baseline cores (GS and HS cores). It shows the interface between the carbonated and uncarbonated zones. Both the cement samples were aged under the same conditions. The images display three regions: white, light grey and dark grey regions. As labeled in the images, the white region refers to the unhydrated calcium in the cement. The light grey region in the uncarbonated zone refers to CH, and the dark grey in the same zone refers to CSH. The corresponding regions in the carbonated front refer to the precipitated $CaCO_3$ (i.e. light grey refers to $CaCO_3$ formation from CH and dark grey refers to $CaCO_3$ formation from CSH).

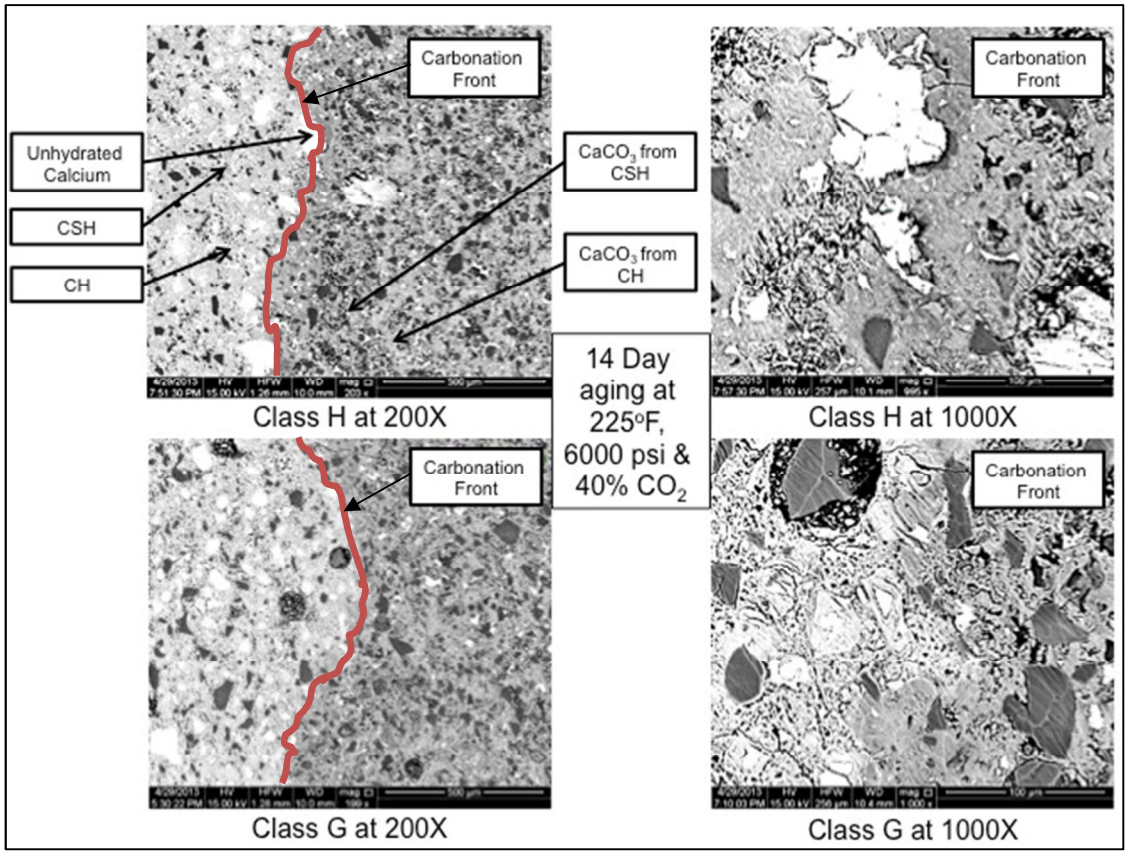

Fig. 8: SEM images of aged baseline cement cores showing the carbonation front

2.1.4 Compressive Strengths of Baseline Cements

Compressive strengths of baseline cement cores were measured after aging in 2% brine for 14 days at 350ºF and 6000 psi. Tests were conducted varying carbon dioxide concentration in the gas phase (40 and 100%). Compressive strength of HS core samples significantly increased after carbonation (**Fig. 9**). A slight change in compressive strength of GS cores was observed after CO_2 gas exposure. At reduced CO_2 gas concentration (i.e. 40%), the cores showed slight reduction in

compressive strength. Further analysis is made combining previous measurements obtained after aging the cores at lower CO_2 concentrations (**Fig. 10**). After aging in the absence of CO_2, compressive strength of Class G cement initially increased because of pore-shrinkage in the hydrated cement. The presence of low concentration of CO_2 results in compressive strength evolution dominated by leaching. At high CO_2 concentrations (i.e. greater than 10%) however, the rate of carbonation (rate of $CaCO_3$ precipitation) is faster than the rate at which water-soluble calcium bicarbonate is formed. Calcium bicarbonate is formed from further reaction of the precipitated $CaCO_3$ with CO_2-saturated brine. Due to the domination of carbonation process, the compressive strengths of the core were preserved after CO_2 exposure.

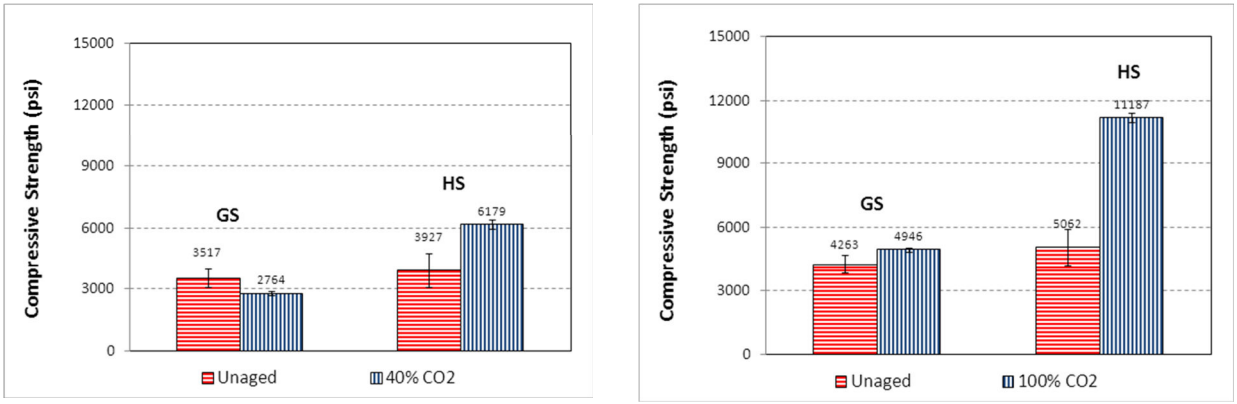

Fig. 9: Compressive strength of cement cores unaged and aged in 2% brine for 14 days at 350ºF and 6000 psi: a) 40% CO_2 concentration; and b) 100% CO_2 concentration

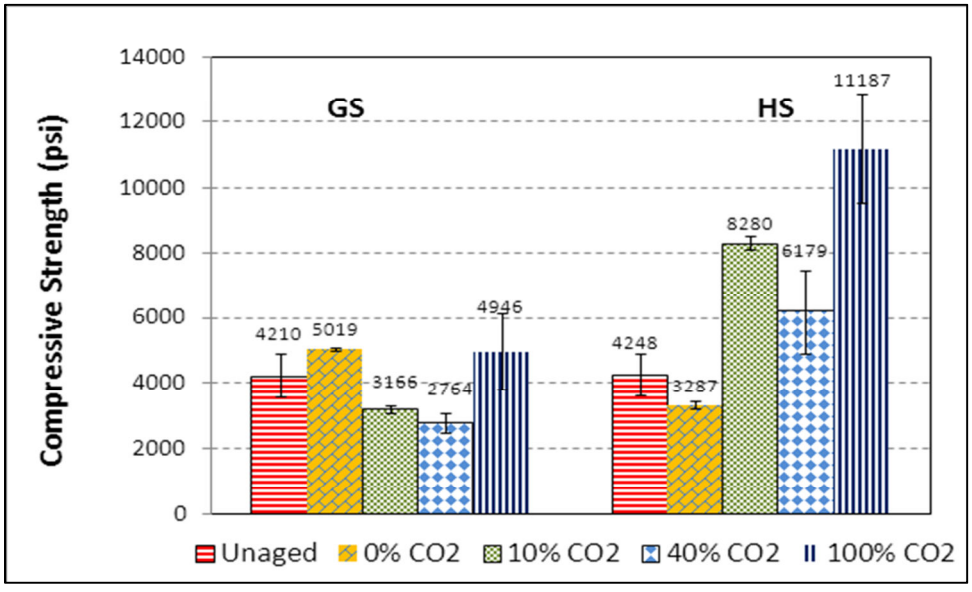

Fig. 10: Compressive strengths of unaged and aged baseline cement cores (aging condition: 2% brine saturated with CO_2 containing gas at 350ºF and 6000 psi)

For Class H cement, the first decrease could be attributed to leaching, although CO_2 was absent. When a cement sample is in contact with brine, the difference in concentration between the interstitial pore fluid and cement matrix causes the dissolution of ions into the pore fluid. This leads to diffusion of ions from the pore fluid to the bulk fluid causing reduction in calcium ion concentration in the cement sample, resulting in weaker cement matrix primarily because of dissolution of calcium-bearing binding components of cement (portlandite and tobermorite gel). In the presence of CO_2, the precipitated $CaCO_3$ fills pore spaces in the cement causing an overall increase in compressive strength. It is important to note that the above discussions are limited to 14 days of aging experiment. With further aging time, effect of leaching may become more pronounced on compressive strength progression.

2.1.5 Shear Bond Strengths of Baseline Cements

Investigation on shear bonding strength (SBS) of cement was continued. Studies on the influence of temperature and CO_2 concentration on SBS have been completed. During this reporting period, two batches of SBS samples were aged for 14 days at 350°F and 6000 psi. **Figure 11** summarizes shear bond strength measurements obtained from samples aged at different temperatures and gas phase CO_2 concentrations. Samples aged at 350°F with 100% CO_2, are expected to show significantly increased shear-bonding strength considering high aging temperature and CO_2 concentration. Measured average bonding strength of the samples was approximately 2200 psi, which is about three-fold of the unaged sample. Thus, it can be concluded that increased temperature and CO_2 concentration predominantly enhance carbonation process resulting in cement expansion and improve compressive strength and elasticity, which tend to increase the force required to break the bond between the cement and pipe. However, with increased exposure time, leaching may intensify causing reduction in bond strength.

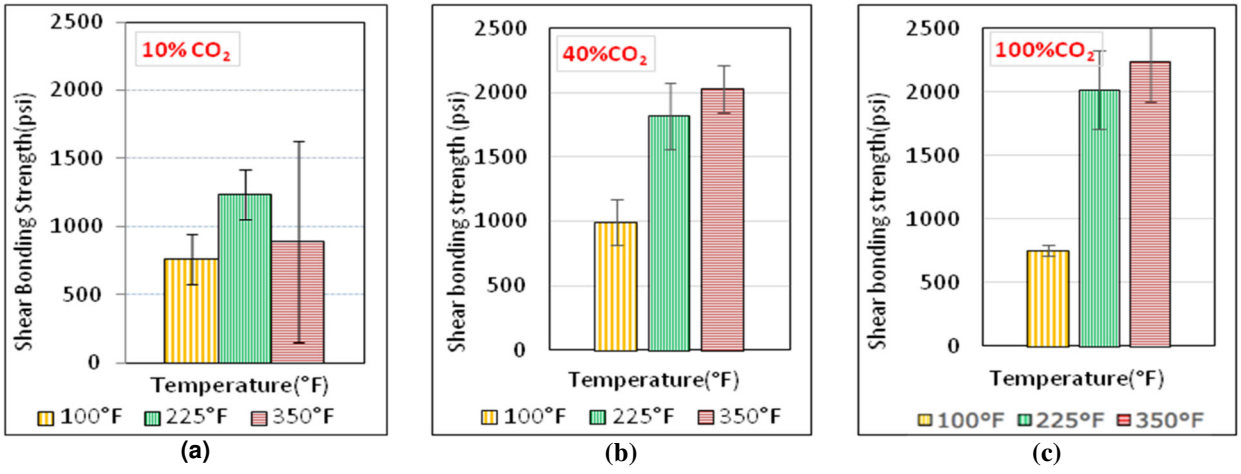

Fig. 11: Effects of temperature and CO_2 concentration on shear-bond strength of baseline (HS) cement aged at 6000 psi in 2% brine

2.2.4 Additive Screening Study

The testing of cement additives was continued as mentioned in the previous report. The results of hydroxyapatite (HOAP) and latex containing cement cores are presented in this report. The HOAP samples exhibited good resistance against CO_2 environment. The FTIR results confirm the presence of $Ca(OH)_2$ in the inner and the middle zone of the sample indicating lesser carbonation. On the other hand, unaged latex-containing samples showed high permeability; and when exposed to the acidic environment, the depth of penetration obtained was higher than that of the baseline samples.

2.2.4.1 Hydroxyapatite Containing Cement

Two batches of HOAP samples were prepared to conduct aging experiments. Samples were subjected to different aging conditions (**Table 1**). For both batches, slurry compositions were maintained the same (**Table 2**).

Table 1: Ageing conditions for the HOAP samples

HOAP	Temp. (°F)	Pressure (psi)	CO_2 Conc. (%)	Brine Conc. (%)	Days	Parallel HS/GS Batch
Batch 002	100	6000	40	2	14	Batch 011
Batch 003	350	6000	100	2	14	Batch 014

Table 2: Composition of the HOAP slurry

Component	Percentage Amount
Cement	100%
Hydroxyapatite	5% bwoc
Antifoam Agent	0.1 gal/sack of cement
Water for Cement	38% bwoc – Class H 44% bwoc – Class G
Water for HOAP	23% bwoc
bwoc = by weight of cement	

Length and Diameter Measurements

The length and diameter measurements were taken for all the samples before and after aging. Average diameters of the core before and after aging are presented in **Table 3**. The samples predominantly displayed slight expansion after aging. Batch 2 of HOAP sample showed a slight shrinkage, which could be a measurement error. The expansion is because of calcium carbonate formation in the pore (carbonation) causing increase in bulk volume. The HOAP samples also exhibited expansion, which can be attributed to the formation of carbonated-hydroxyapatite ($Ca_5(PO_4)_3CO_3$), according to the following reaction:

$$2Ca_5(PO_4)_3(OH) + CO_3^{-2} \rightarrow 2Ca_5(PO_4)_3(CO_3) + OH^{-2}$$

The formation of carbonated-hydroxyapatite layer around the core prevents the cement from further acid attack. The hexagonal structure of the hydroxyapatite is not disrupted due to the formation of carbonated-hydroxyapatite (Sugama 2006). However, a slight expansion is still observed in the samples, which can be due to the carbonation of the $Ca(OH)_2$ and CSH present in the cement matrix on the outer rim of the sample.

Table 3: Diameters of HOAP and baseline cores before and after aging

Sample	Unaged Diameter (in.)	Aged Diameter (in.)	% Change	Remark
Batch 002 HHO Aged	0.995	0.994	-0.053%	Shrinkage
Batch 011 HS Aged	0.984	0.997	1.285%	Expansion
Batch 002 GHO Aged	0.994	0.994	0.034%	Expansion
Batch 011 GS Aged	0.985	0.993	0.727%	Expansion
Batch 003 HHO Aged	0.993	0.996	0.295%	Expansion
Batch 014 HS Aged	0.995	0.997	0.182%	Expansion
Batch 003 GHO Aged	0.994	0.995	0.090%	Expansion
Batch 014 GS Aged	0.995	0.997	0.201%	Expansion

Porosity and Permeability Measurements

The porosity and permeability measurements obtained from Batch 002 and 003 samples are presented in **Figs.** 12 and 13. For both batches of samples, the porosity data indicates reduction in the pore volume, which indicates carbonation of the cement. In general, permeability reduction was observed except for GHO samples, which exhibited slight permeability increase. The reduction in permeability can be also attributed to the carbonation process. However, the slight increase can be due to two reasons. First, the formation of thin carbonation zone creating a protective layer, which limits further carbonation and reduction in permeability of the cores. Second reason can be attributed to simultaneous carbonation and leaching of the cement.

It is also important to note that Class H cement showed a higher reduction in permeability than the Class G cement. This indicates that either Class H has been subjected to more carbonation than Class G or Class G also went through leaching of the matrix.

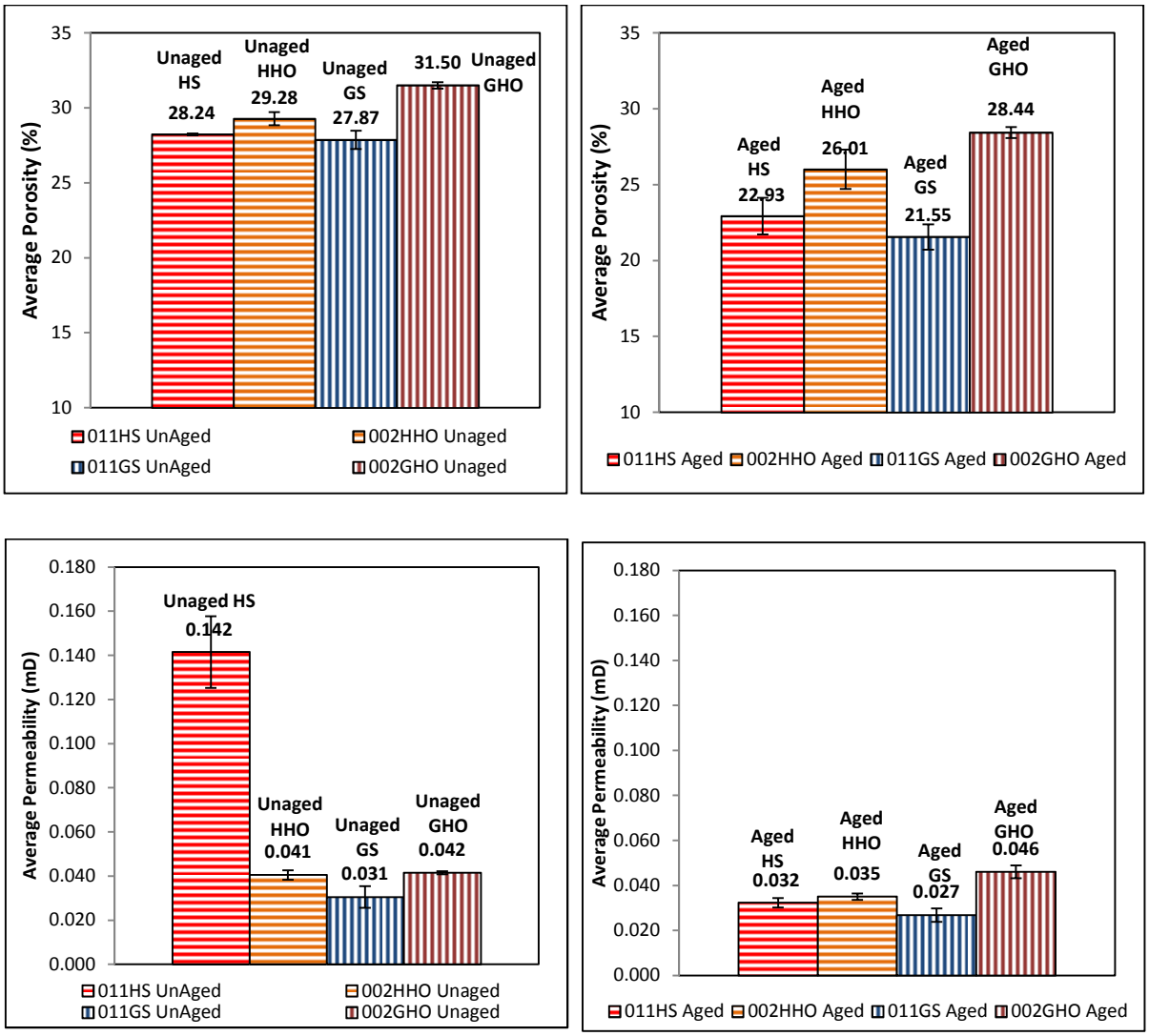

Fig. 12: Porosity and permeability of HOAP and baseline samples (aging condition: 100℉, 6000 psi and 40 % CO_2)

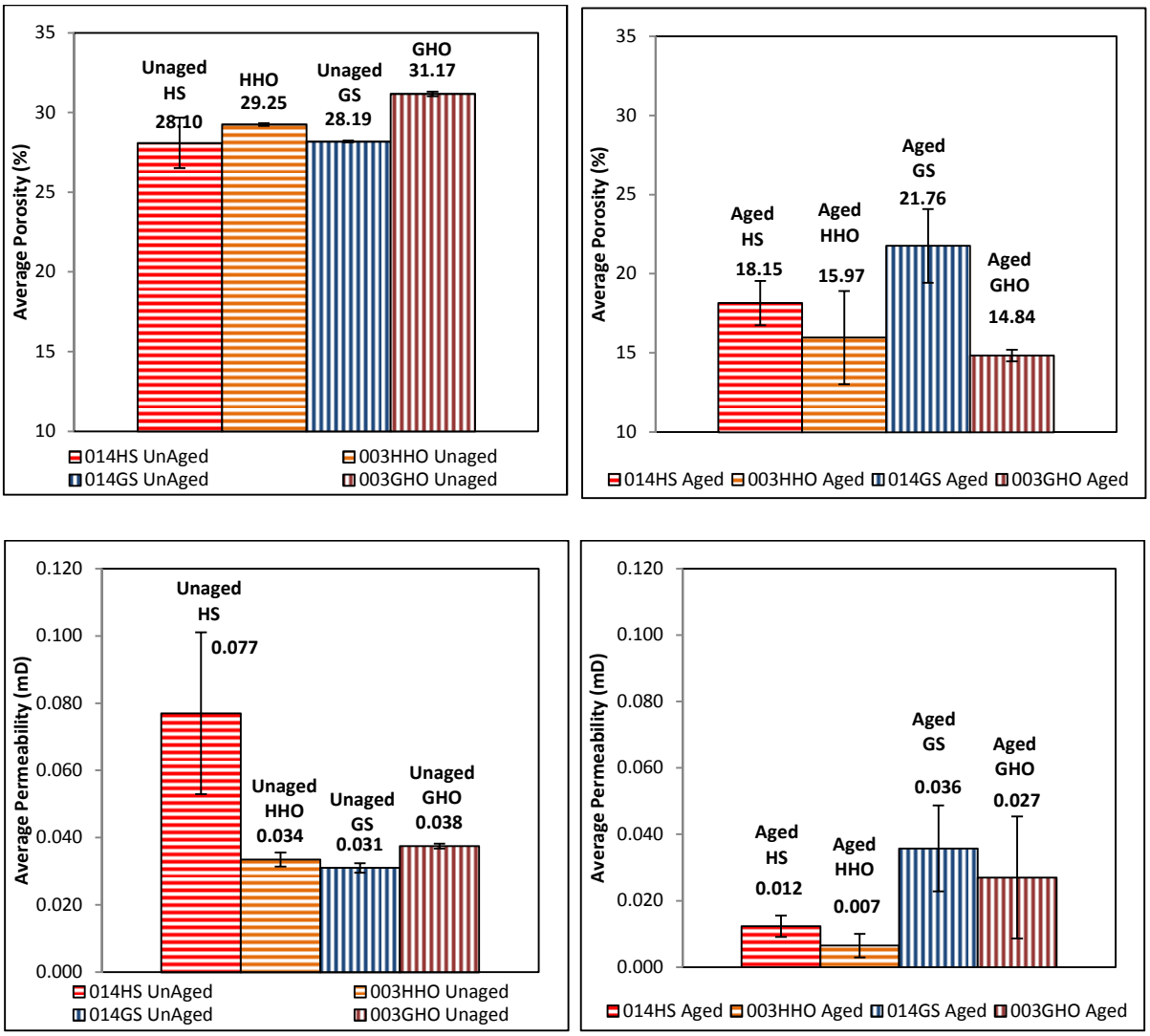

Fig. 13: Porosity and permeability of HOAP and baseline samples (aging condition: 350°F, 6000 psi and 100 % CO_2)

Degradation Depth

Batch 002 samples were aged at 100°F using 40% CO_2 gas. After aging, the samples were cut in the middle to examine the level of degradation. These samples did not exhibit feasible discoloration. However, reduction in porosity and permeability were observed while compressive and shear bond strengths were improved. The results suggest the presence of mild carbonation without discoloration of the cores.

When aged at high temperature (350°F) and high CO_2 concentration (100% CO_2 gas), both the HOAP and baseline cement samples showed (**Fig. 14**) a clear discoloration indicating the degradation depth. It can be clearly observed that HOAP samples experienced very less degradation as compared to the baseline cement samples. The discoloration front, which can be related to the depth of penetration of CO_2, is seen only as a very small outer rim in the HOAP

samples. Due to the non-uniformity of the degradation depth, an average degradation depth is calculated and used to compare the samples. The result is presented in **Table 4**. Results indicate substantial difference in degradation depth between the baseline cement and HOAP samples. The introduction of hydroxyapatite into the cement system considerably improved the resistance of the cement against carbonic acid attack.

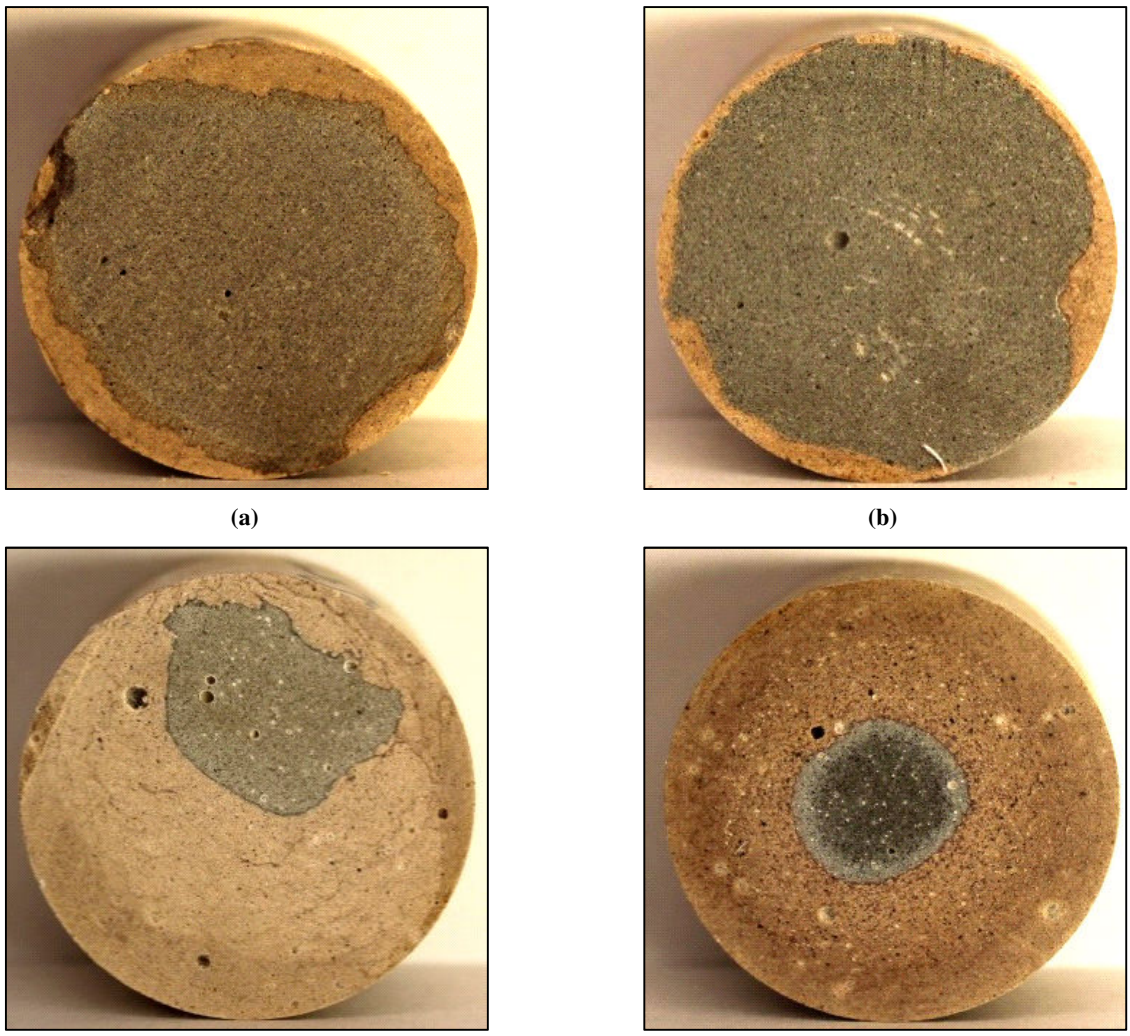

(a) **(b)** **(c)** **(d)**

Fig. 14: Middle cross section of core samples after aging at 350°F with 100% CO2 gas: a) GHO; b) HHO; c) GS; and d) HS

Table 4: Degradation depth of HOAP and baseline samples aged at 350F

Core #	Average carbonated depth (in.)	Std. Dev.
HHO	0.046	0.022
HS	0.353	0.018
GHO	0.063	0.051
GS	0.351	0.203

Compressive Strength Measurements

For samples aged at 100°F and 40% CO_2, their compressive strengths before and after aging were almost the same (**Fig. 15**). Only small variations within the range of measurement discrepancy were observed. The trend of compressive strength measurements are similar to those obtained for permeability tests. The reason can be attributed to the formation of thin carbonated layer on the outer rim that prevents further penetration of CO_2 or occurrence of comparable levels of carbonation and leaching that maintains the strength of the cores more or less the same.

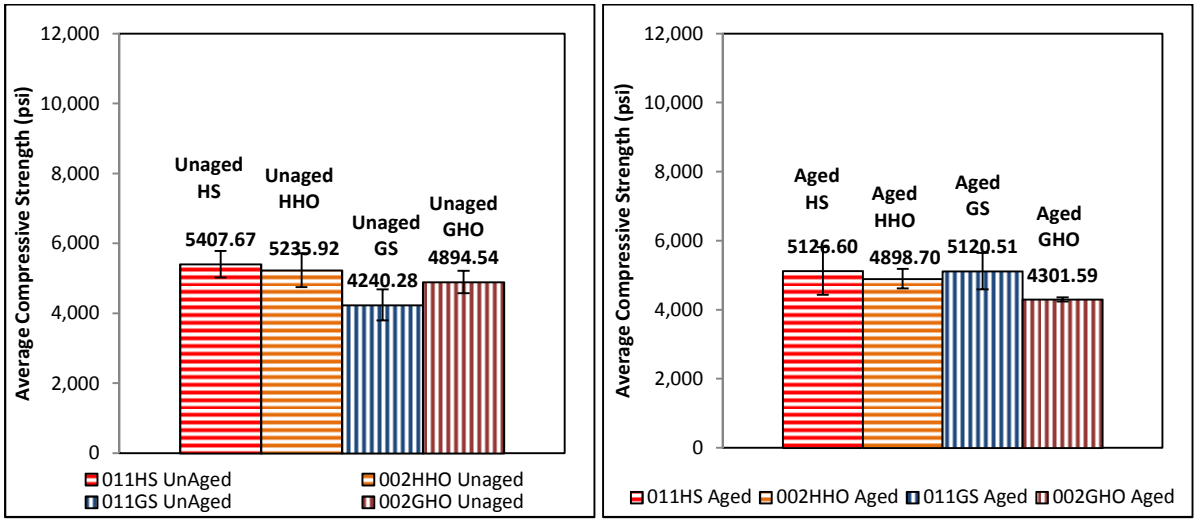

Fig. 15: Compressive strengths of baseline and HOAP cements (aging condition: 100°F, 6000 psi and 40 % CO_2)

At high temperature (350°F), HOAP samples showed reduction in compressive strength while the baseline samples displayed improvement in strength (**Fig. 16**). The increase in strength of baseline cement samples is due to precipitation of $CaCO_3$ in the pore space. The improvement in the strength is consistent with the degradation measurements obtained from baseline samples. The precipitated $CaCO_3$ in the pore provides reinforcement to the cement matrix during loading, resulting in improvement of the compressive strength. Studies on HOAP containing cement are very limited. It is not clear why the strength of HOAP samples significantly reduced after aging. Possible explanations could be leaching and/or thermal retrogression. HOAP samples did not exhibit substantial carbonation as presented in the degradation depth measurements. In addition, when it is carbonate, it does not precipitate in the pore space. However, it becomes a part of the matrix without increasing the compressive strength. As a result, leaching can dominate the aging process causing reduction in strength. Another reason is that silica flour, which is needed to prevent thermal retrogression, was not added in the HOAP slurries to maintain slurry properties within acceptable

range. The lack of excess silica in the cement system can result in thermal retrogression, when the cement is exposed to high temperatures (i.e. greater than 230°F).

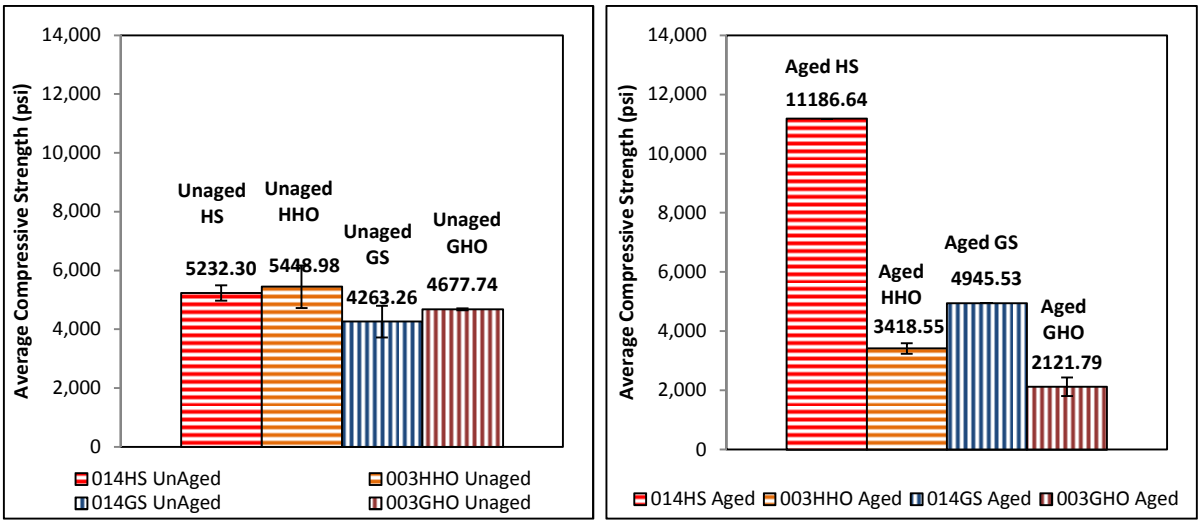

Fig. 16: Compressive strengths of baseline and HOAP cements (aging condition: 350°F, 6000 psi and 100 % CO_2)

Shear-Bond Strength Measurements

The shear-bond strength of baseline and HOAP cores were measured before and after aging. After aging at 100°F, the bond strength of baseline and HOAP cement samples increased substantially (**Fig. 17**). This is mainly due to expansion of the cement resulting from carbonation. Two experiments conducted at different temperatures and gas compositions showed increase in bond strength (Figs. 17 and 18); however, the level of increase is different. After aging at 100°F and 40% CO_2, the HOAP samples displayed more increase in SBS than HS samples. More carbonation is expected in HS samples than HOAP cores resulting in high tendency of expansion and increased bonding strength. However, at 100°F, leaching may be higher for HS samples. Leaching counterbalances the effects of carbonation and adversely affects SBS improvement.

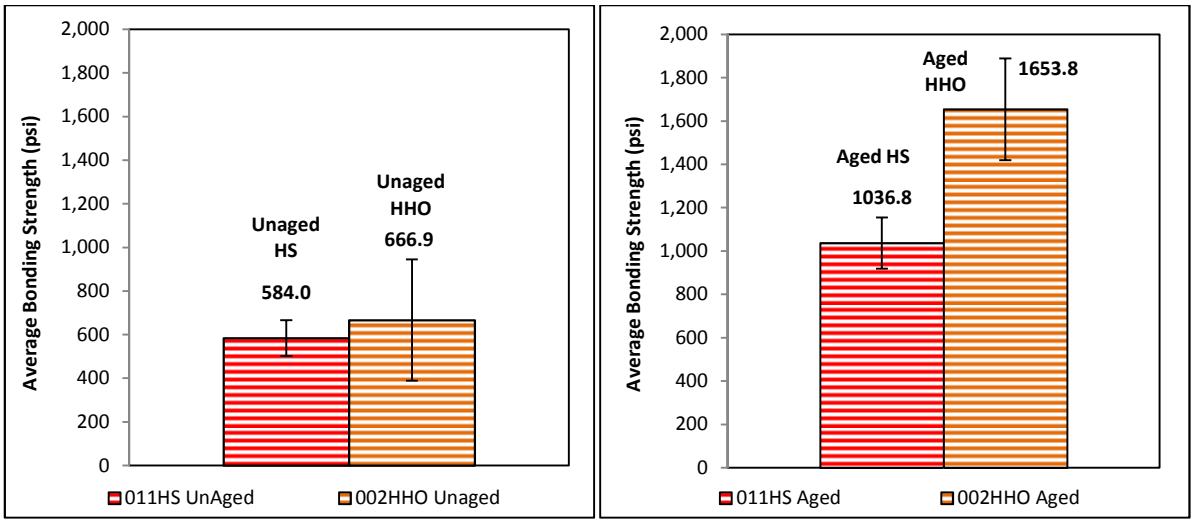

Fig. 17: Shear bond strength of baseline and HOAP samples (aging condition: 100℉, 6000 psi and 40 % CO_2)

For samples aged at 350℉ and 100% CO_2, the HOAP samples showed a lower increase in SBS than the HS samples (Fig. 18). This could be attributed to temperature retrogression resulting from lack of excess silica to prevent the formation of weak CSH phase (α-CSH). This observation is consistent with compressive strength measurements.

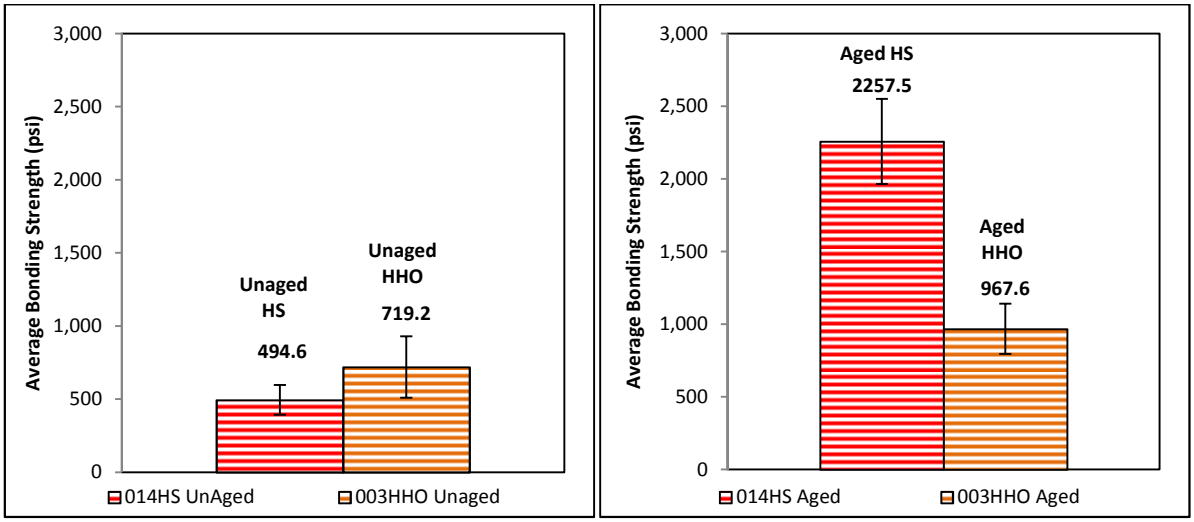

Fig. 18: Shear bond strength of baseline and HOAP samples (aging condition: 350℉, 6000 psi and 100 % CO_2)

FTIR Measurements

The porosity, permeability, degradation depth, compressive strength and shear bond strength measurements indicate a lesser amount of calcium carbonate formation in the HOAP samples. The

Fourier Transform Infrared Spectroscopy (FTIR) tests were carried by taking samples from the outermost, middle and innermost zones of a transversely cut cement cores. Spectrum peaks of relevant molecular bonds that indicate the level of CH, CSH and $CaCO_3$ in each zone are summarized and presented in **Figs.** 19 through 21.

In the inner most zone of the sample (Fig. 19), the amounts of CH and CSH are almost the same in both HS and HOAP samples after aging at 100°F and 40% CO_2. However, the amount of carbonate is higher in HOAP than HS samples. The source of this carbonate bond can be calcium carbonate and/or carbonated-hydroxyapatite ($Ca_5(PO_4)_3.CO_3$) formed from the HOAP. The type of carbonate is not distinguishable from FTIR result. On the other hand, after aging at 350°F and 100% CO_2, the CH present in the HS samples was fully carbonated while abundant amount of CH was found in the HOAP sample. In all zones, the level of carbonation is higher in the HS sample than in HOAP samples when aged at 350°F. This means that the amount of carbonate, including $CaCO_3$ and $Ca_5(PO_4)_3.CO_3$, formed in HOAP samples is lesser than calcium carbonate formed in HS samples.

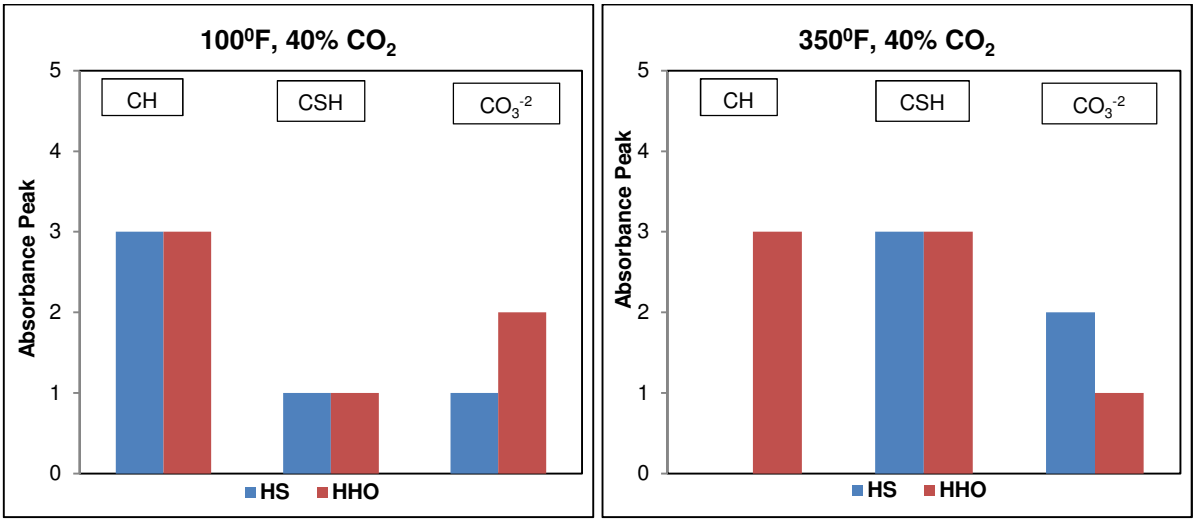

Fig. 19: Summarized FTIR data for HOAP and baseline samples (innermost Zone)

FTIR results from the middle zone also displayed (Fig. 20) good carbonation resistance of HOAP samples. After aging, CH was completely absent in the HS sample; however, it was still present in abundant amount in HOAP samples. After aging at 100°F, the amount of CSH and $CaCO_3$ was almost same in both HS and HOAP samples. However, after aging at high temperature (350°F) the CSH was not found in the HS samples indicating complete carbonation of the matrix, while abundant amount of CSH was present in HOAP samples. In addition, the amount of carbonate formed in HOAP samples was less than that formed in HS cores. The outer zone showed a complete carbonation of the matrix in both cases (Fig. 21). This result was expected as the outer rim is most vulnerably exposed to the harsh environment.

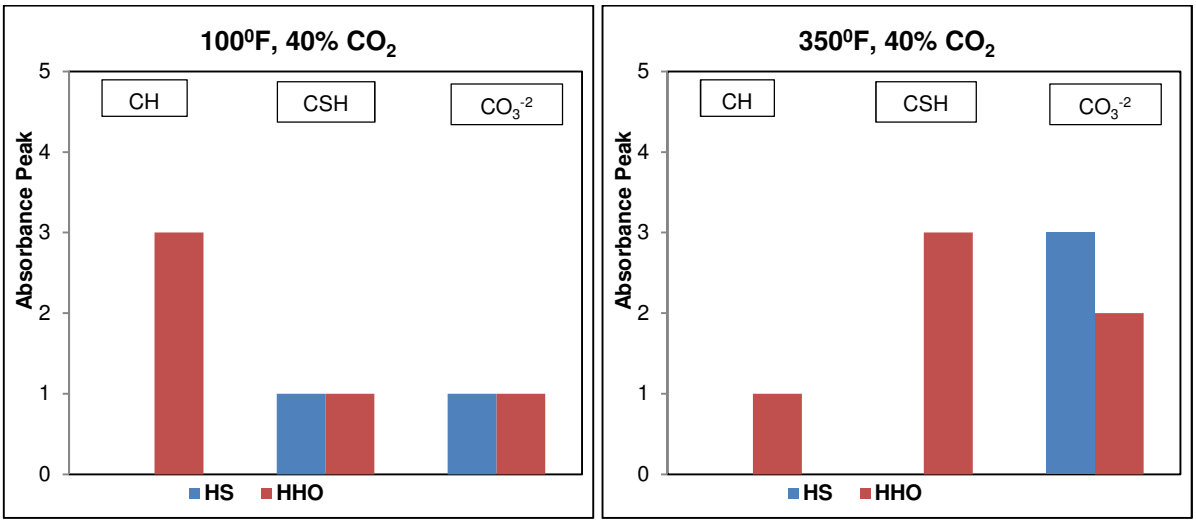

Fig. 20: Summarized FTIR data for HOAP and baseline samples (middle zone)

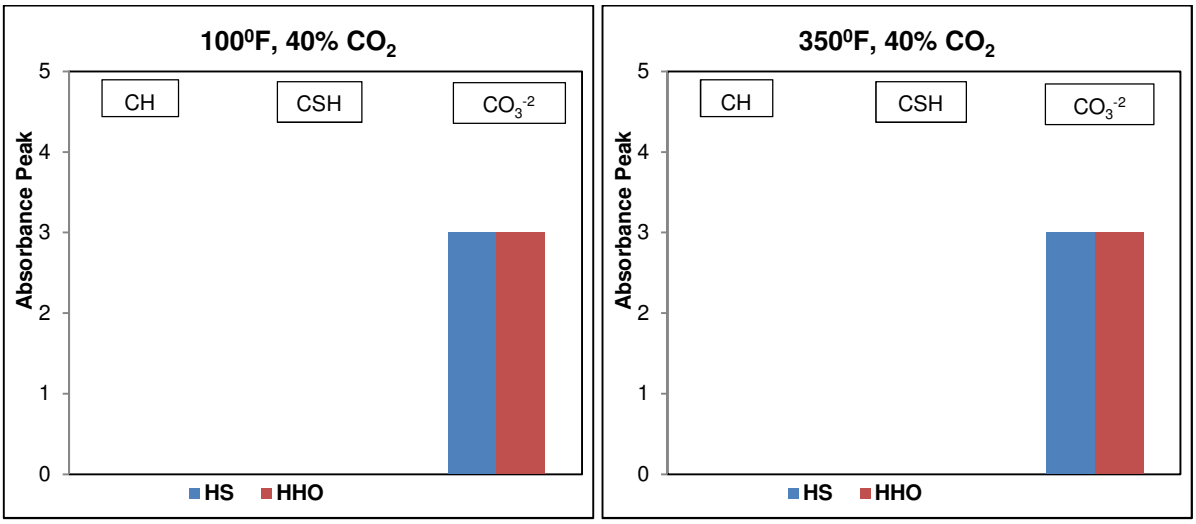

Fig. 21: Summarized FTIR data for HOAP and baseline samples (outermost zone)

2.2.4.1 Latex Cement

As was observed in the previous three unaged experiments with latex cement, the permeabilities of SBR latex samples (HSLT and GSLT) were higher than those of baseline samples. The reason for increased permeability could be either entrapment of air bubbles in the latex or improper bonding of small size latex particles with cement. In order to test if the high permeability latex cement withstands acid attack, core samples with SBR latex were prepared and aged in 2% brine at 350°F and 6000 psi using 40% CO_2 gas. The composition of the slurry is presented in **Table 5**.

Table 5: Composition of the latex slurry

Component	Percentage Amount
Cement	100%
Silica Flour	35% bwoc
SBR Latex	10% bwoc
Acetic Acid (Emulsifier)	0.43% bwoc
HEC	0.1% of water for fillers
Antifoam Agent	0.1 gal/sack of cement
Water for Cement	38% bwoc – Class H 44% bwoc – Class G
Water for Silica Flour	38.5% of silica flour
bwoc = by weight of cement	

Length and Diameter Measurements of Latex Cement

The lengths and diameters of all the samples were measured before and after the aging. Most of the cores expanded after aging due to carbonation. The average diametrical expansions of the samples were determined (**Table 6**). The HSLT samples exhibited shrinkage, which could be due to leaching of calcium during aging. The HS samples, which were kept in ambient conditions, also showed slight shrinkage. This could be due to minor leaching or measurement discrepancy. The expansion data did not provide consistent measurements to quantify the level of carbonation occurring in the samples.

Table 6: Average diametric expansions of aged and unaged samples of baseline and latex based cement

Sample	Unaged Diameter (in.)	Aged Diameter (in.)	% Change	Remark
Batch 004 HSLT Un-Aged	0.997	0.998	0.163%	Expansion
Batch 004 HSLT Aged	0.997	0.997	-0.058%	*Shrinkage*
Batch 004 GSLT Un-Aged	0.996	0.997	0.095%	Expansion
Batch 004 GSLT Aged	0.996	0.997	0.058%	Expansion
Batch 013 HS Un-Aged	0.997	0.997	-0.013%	*Shrinkage*
Batch 013 HS Aged	0.997	1.000	0.223%	Expansion
Batch 013 GSLT Un-Aged	0.997	0.997	0.034%	Expansion
Batch 013 GSLT Aged	0.996	1.000	0.404%	Expansion

Porosity and Permeability Measurements of Latex Cement

The porosity and permeability measurements obtained from latex-based and baseline cement samples are presented in **Fig. 22**. Porosity and permeability of unaged samples of latex-based cement were almost comparable with those of baseline samples. Except HS samples, all other samples showed slight reduction in porosity after aging. This result is expected, since carbonation

reduces the pore space causing reduction in porosity and permeability. Consistent with this observation, the permeability of all the samples reduced after aging due to carbonation. The reduction observed in the GSLT sample was the least but still significant.

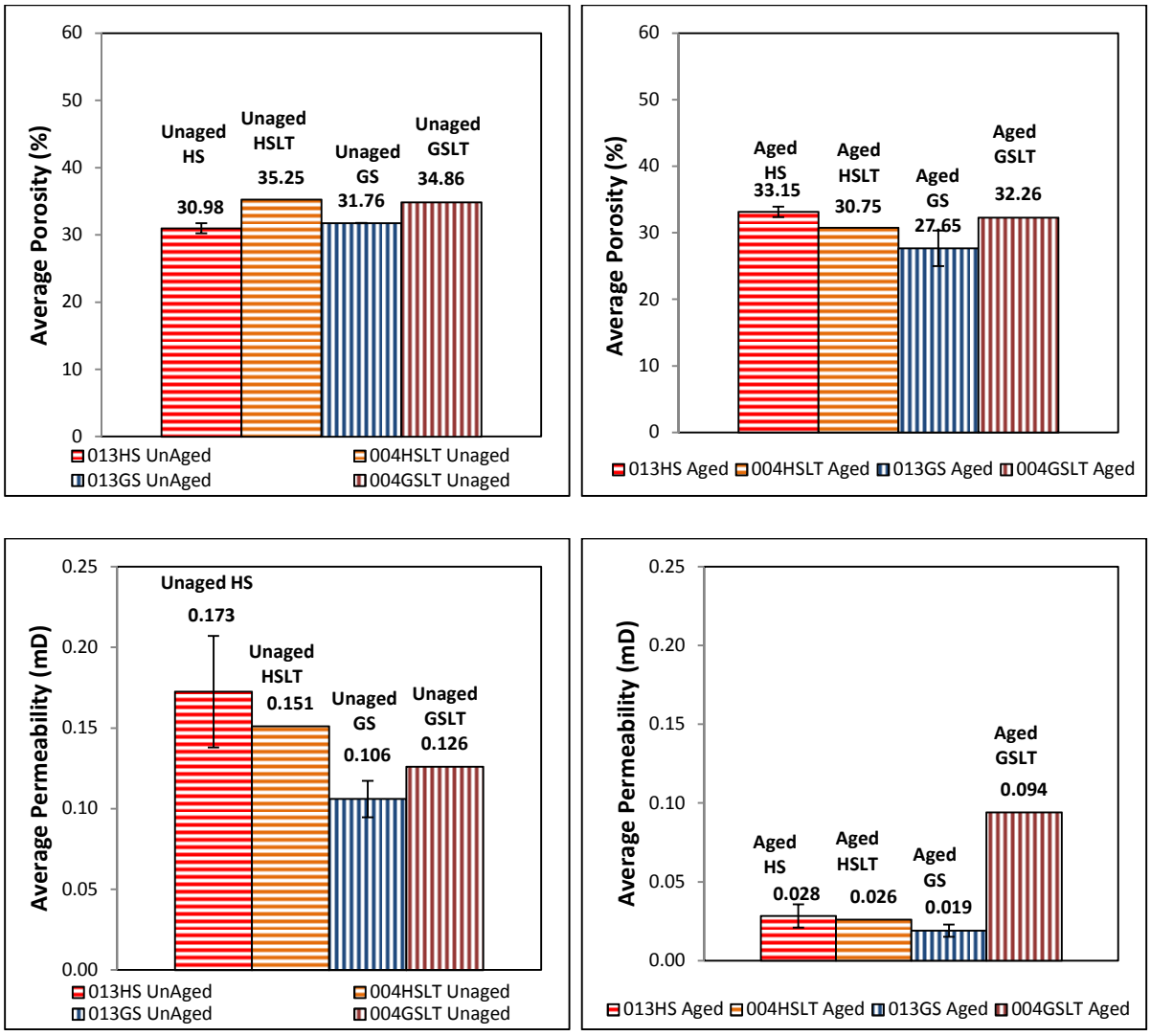

Fig. 22: Porosity and permeability of latex and baseline cement cores (aging condition at 350°F with 40% CO_2)

Degradation Depth of Latex Cement

Latex-based cement samples displayed a clear degraded zone (**Fig. 23**) when the samples were transversely cut. It was evidently observed that the degraded depth for latex samples was higher than those of the baseline samples. This confirms that even though the measured permeability was almost same for the latex and HS samples, the latex samples exhibited deeper penetration and

degradation. The average degraded depth values are calculated and presented in **Table 7**. The increased values of latex samples indicate vulnerability towards carbonation.

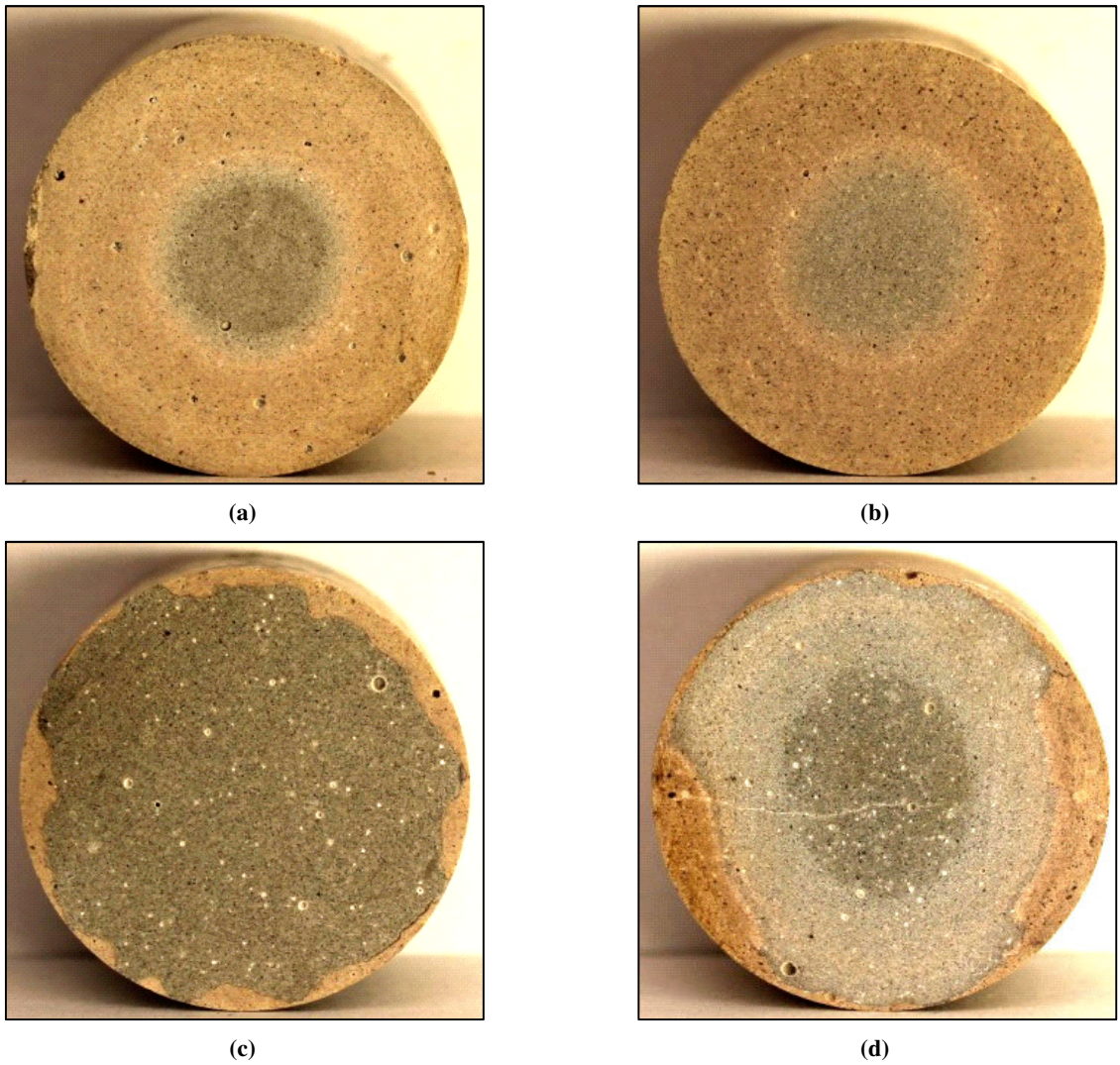

Fig. 23: Middle cross section of core samples after aging at 350°F with 40% CO2 gas: a) GSLT; b) HSLT; c) GS; and d) HS

Table 7: Degradation depth of baseline and latex-based cements

Core #	Carbonated Depth Average (in.)	Std. Dev.
004HSLT	0.310	0.006
004GSLT	0.342	0.017
013HS	0.280	0.031
013GS	0.053	0.019

Compressive Strength Measurement of Latex Cement

Compressive strength of latex containing and baseline cement samples are presented in **Fig. 24** for both aged and unaged samples. Compressive strength of the latex samples (HSLT and GSLT) increased more than the baseline samples. This is due to higher level of carbonation in the latex samples as compared to the baseline samples. The large amount of carbonation confirms poor performance of latex as a cement additive for acid attack reduction. **Table 8** presents the change in compressive strength samples after aging.

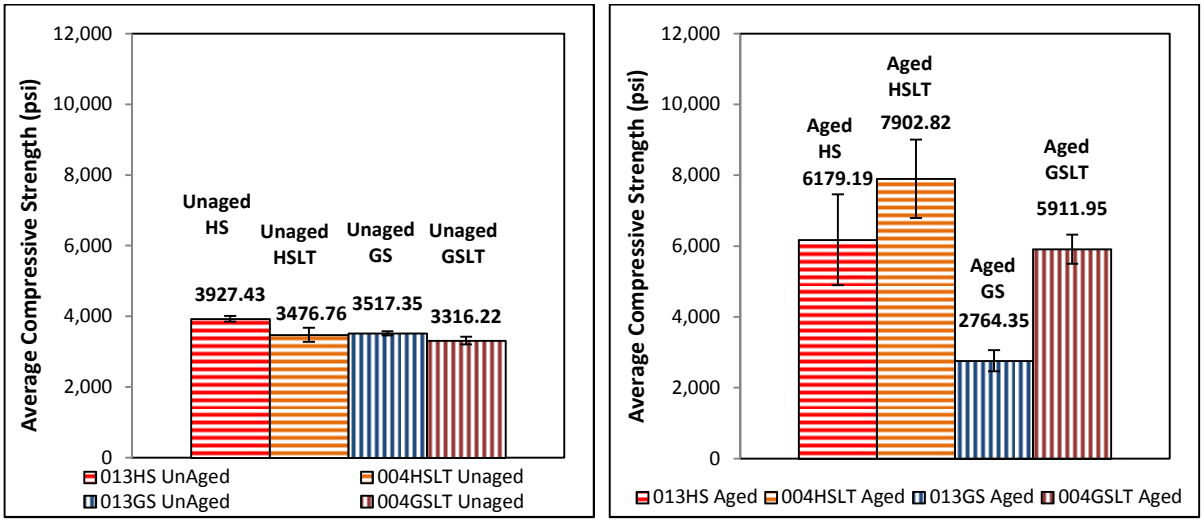

Fig. 24: Compressive strength of baseline and latex-based cements (aging condition at 350°F with 40% CO_2)

Table 8: Change in Compressive Strength of baseline and latex-based cements

Sample Name	% Change in Comp. Str.
004HSLT	127.3
004GSLT	78.3
013HS	57.3
013GS	-21.4

Shear Bond Strength Measurement of Latex Cement

The shear bond strength of latex-based cement is presented in **Fig. 25**. Both the latex and baseline samples show similar shear bond strength before and after aging. Although the addition of latex is expected to improve shear-bonding strength of the cement, results indicate minimal effect of latex on the bond strength. Moreover, the latex samples exhibited the same level of bond strength improvement that indicates similar levels of carbonation.

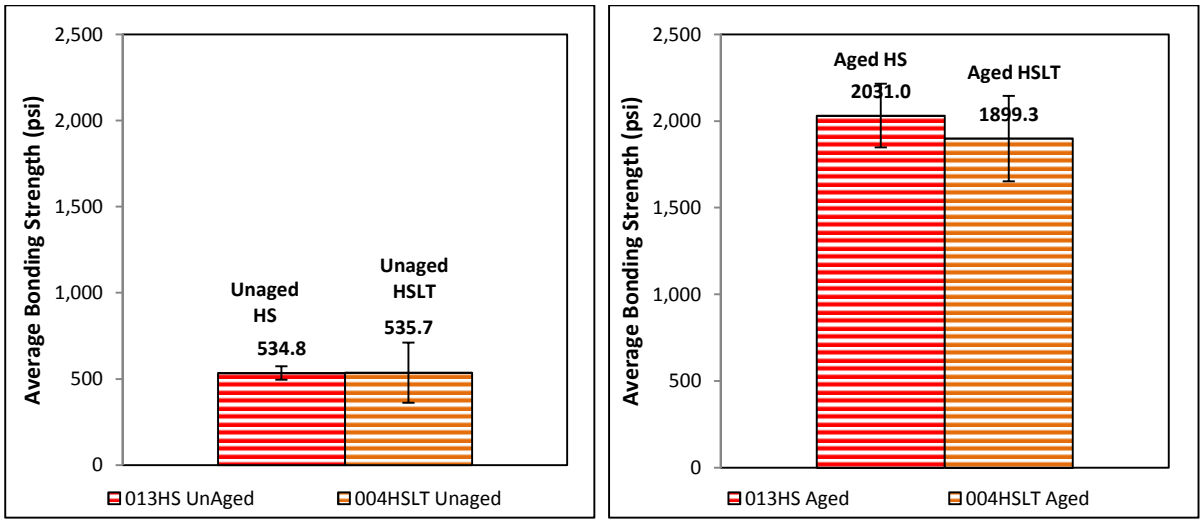

Fig. 25: Shear Bond strength latex and baseline cements (aging condition at 350°F with 40% CO_2)

FTIR Analysis of Latex Cement

In order to evaluate the carbonation level in the latex samples, the FTIR tests were conducted on samples taken from the inner, middle and outer zones of the latex and baseline cement cores. The results (**Fig. 26**) indicate poor performance of the latex cement in resisting the acid attack. In the latex cores, carbonation was occurred in outermost and middle zones while in the baseline cement it occurred only in the outermost zone. In the middle zone, aged latex samples had no traces of CH or CSH. Nevertheless, they displayed high content of CO_3^{-2} as compared to baseline samples. This confirms that latex did not prevent acid penetration. Instead, it reduced the capability of the cement to withstand acidic environment. Results of the outermost zone showed the same level of degradation in both cases. In addition, the FTIR obtained from the inner most zone of the matrix indicates that the amount of uncarbonated CH and CSH is same in both latex and HS samples. Hence, CO_2 was not able to penetrate completely inside both the samples within two weeks of aging.

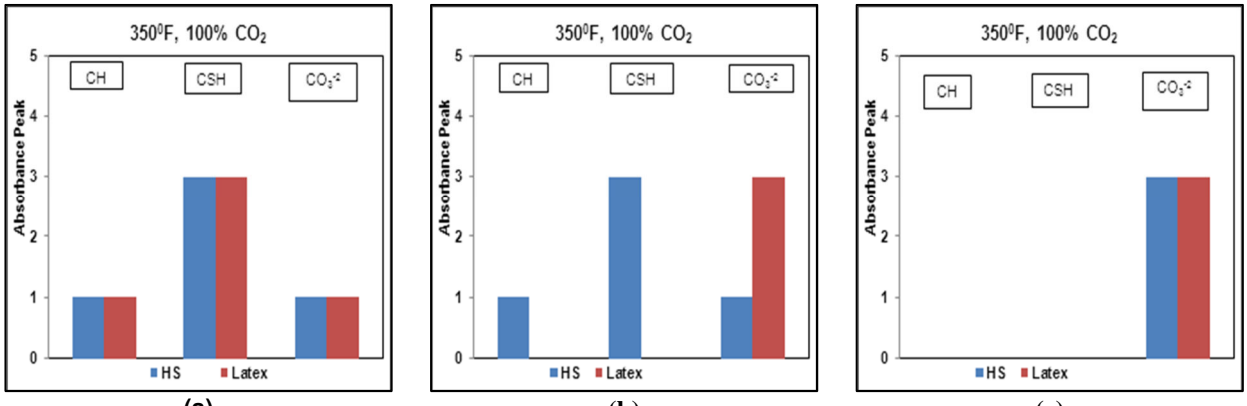

Fig. 26: Summarized FTIR of latex and baseline cements: a) innermost; b) middle; and c) outermost zones

2.3 Experimental Studies on Corrosion of Tubulars (Task 3)

Preliminary corrosion experiments were continued using a potentiostat. The first corrosion experiment on carbon steel sample (plate coupon) was conducted at atmospheric temperature and pressure with 2% NaCl solution using GAMRY instruments Para Cell Kit and Series G-750 potentiostat for linear polarization resistance (LPR) measurements. The results obtained from this experiment (**Fig. 27**) are very satisfactory because the trend of the corrosion rate is as expected. Carbon dioxide was not injected during this experiment, as the test was only to establish a procedure for the LPR method and develop data analysis techniques. After completion of the test, the sample was taken out and examined. Microscopic camera pictures of the sample (**Fig. 28**) showed the formation of corrosion product.

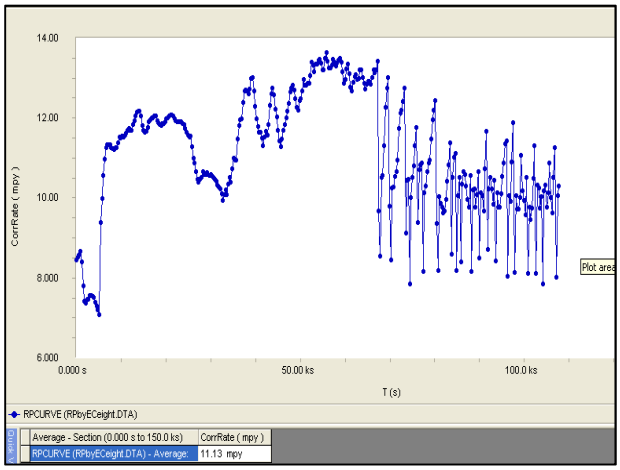

Fig.27: Corrosion rate vs. time (LPR measurement)

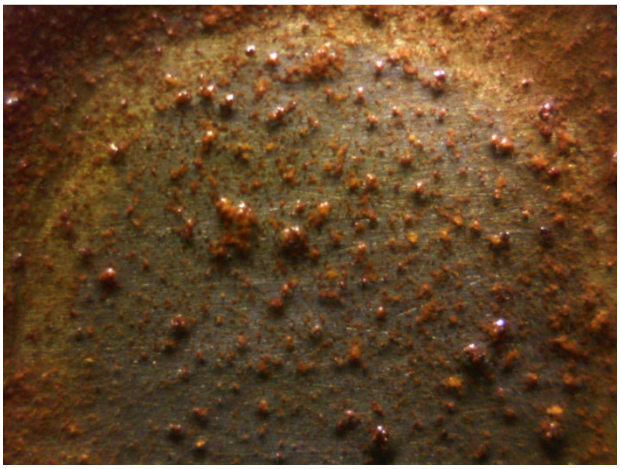

Fig. 28 Microscopic picture of corrosion test sample

During the test, the corrosion coupon was partially masked by laminating a protective film that had small circular hole at the center. The laminated mask limits the exposed area of the sample. The accumulation of the corrosion product/scale was more where the local concentration of the brine solution increased due to the formation of a narrow gap between the sample and the masking film.

The LPR test will continue in the coming months. At present, a medium-temperature experimental setup is being developed to carry out LPR test under pressurized conditions. The setup includes pressure vessel with flange at the top. The flange has connections for gas injection and installation of cable seal gland and thermocouple. The sample to be used is a carbon steel rod. A graphite counter electrode and high-temperature Ag/AgCl reference electrode will be used during the test.

The construction of corrosion setup was continued. The corrosion cell used for dynamic test has been assembled and installed on a mobile frame structure. The cell is equipped with a magnetic coupling that rotates a cylinder, which is placed in the cell to create viscometeric type of flow.

3. Planned Activities

- Continue aging experiments with brine-CO_2-CH_4 system for 14 days varying aging pressure (3,000, 6000, and 9000 psi) at 350ºF and 40% CO_2 concentration.
- Continue theoretical and modeling studies on tubular degradation.
- Continue cement additive screen study.
- Continue the development of tubular corrosion testing setup.

4. Project Expenditures

This section presents the project expenses during the month of April (**Table 9**) and the cumulative expenditures.

Table 9 Current and cumulative expenditures, April, 2013

No.	Budget Categories	Current Expenses	Cumulative Expenses
1	Salaries & Wages	($20.56)	$153,659.10
2	Fringe Benefits	($1,407.25)	$34,476.35
3	Project Materials	($15,920.34)	$53,109.44
4	Travel	$0.00	$4,095.30
5	Conference Expenses	$0.00	$0.00
6	Other Direct Costs	($6.63)	$843.60
7	Equipment	$35,072.93	$206,138.33
8	Space Rental	$0.00	$0.00
9	Indirect Cost	($8,711.32)	$123,091.85
10	**Total**	**$9,006.83**	**$575,413.97**

Nomenclature

CH	Calcium hydroxide
CSH	Calcium silicate hydrate
FTIR	Fourier Transform Infra-Red
GS	Class G cement with silica flour
GSMG	Class G Cement with silica flour and magnesium oxide
GSLT	Class G Cement with latex
HOAP	Class H cement with hydroxyapatite
HS	Class H cement with silica flour
HSMG	Class H Cement with silica flour and magnesium oxide
HSLT	Class H Cement with latex
LPR	Linear polarization resistance
SBR	styrene-butadiene
SBS	Shear bonding strength
HPHT	High-pressure high-temperature

References

Baciu D. and Simitzis J. 2007. Synthesis and characterization of a calcium silicate bioactive glass, Journal of Optoelectronics and Advanced Materials Vol. 9, No. 11, November 2007, pp. 3320 – 3324.

Matsuda, Y. and Tsukada, M. 1998. Identification of calcium carbonate contained as body in modern paints by FTIR spectroscopy, Postprints, pp. 25-33.

Sugama, T. 2006. Advance Cement for Geothermal Wells, BNL-77901-2007-IR.

Zaki, M.I., Knozinger, H., Tesche, B. and Mekhemer, G.A.H. 2006. Influence of Phosphonation and Phosphation on Surface Acid-Base and Morphological Properties of CaO as Investigated by in situ FTIR Spectroscopy and Electron Microscopy, Journal of Colloid and Interface Science, Vol. 303, pp. 9-17.

Project Title: Effect of H_2S and CO_2 in HPHT Wells on Tubulars and Cement

Report Type: Monthly Report

Report #: 20

Reporting Period: April 22nd, 2013 to May 21st, 2013

Authors:

Ramadan Ahmed, Principal Investigator

Subhash Shah, Co-Principal Investigator

Samuel Osisanya, Co-Principal Investigator

Rida Elgaddafi, Research Assistant

Omotayo Omosebi, Research Assistant

Himanshu Maheshwari, Research Assistant

Adarsh Naidu, Research Assistant

Aman Srivastvava, Research Assistant

Jueun Hwang, Research Assistant

Mounraj Sharma, Research Assistant

Sagar Tale, Research Assistant

Prepared under BSEE Project # E12PC00035

by

THE UNIVERSITY OF OKLAHOMA

July 10, 2013

1. Summary of Accomplishments

This monthly report presents the progress made during the project period April 22, 2013 to May 21, 2013. Cement and tubular degradation studies were continued during this reporting period. Cement cores and bonding samples of different cement formulations were prepared and aged in acidic environment to study their degradation characteristics. Properties of the samples were measured before and after aging. Moreover, cement additive screening studies were continued. The effects of different additives on properties of cement slurries and cores were investigated.

Two aging experiments (Experiments 7A and 13) were performed during the month. The samples were aged for 2 weeks in 2% brine saturated with 40% CO_2. After completion of each experiment, physical properties of aged and unaged samples were measured. Unaged sample refers to part of cement cores or bonding samples kept at ambient lab conditions in 2% brine for 14 days after curing.

Experiment 7A (Batch 015) is a repetition of Experiment 7 (Batch 009). Repeating the experiment was needed to check unexpected permeability measurements obtained during previous tests. Porosity of the cores did not significantly change after aging. Batch 009 showed very high permeability. Other measurements did not display considerable differences between these two batches. The reason for high permeability in Batch 009 samples could be due to the formation of cracks during sample preparation. Cracks can substantially increase the permeability of core samples.

Aging tests conducted at different pressures (3,000 and 6,000 psi) showed consistent porosity and permeability trends. As samples are aged at reduced pressure (3,000 psi), porosity and permeability both decreased as compared to the unaged ones. The reduction in porosity and permeability could be because of incomplete carbonation of CSH, which produces scawtite. For Class G cement, compressive strength measurements displayed reduction with increase in pressure while Class H cement showed a revered trend. The observed behavior of Class G is consistent with the results of a previously published study.

Experimental investigations on cement additives were continued. The effects of different additives (hydroaxipitate, magnesium oxide, and micro-silica) on acid resisting performance of cement have been tested. As previously reported, addition of hydroaxipitate prevents carbonation of the cement under HPHT conditions; however, excess silica flour is needed to control strength retrogression. A new formulation of hydroaxipitate cement that contains extra silica has been developed. Using the new formulation, cores were prepared for testing. During preparation, the cores exhibited brittleness, which may be caused by the addition of excess water for silica flour.

Studies on magnesium oxide cement have shown promising results in preventing the penetration of carbonic acid in the cement matrix. To optimize the carbonation resistance of the

cement, different slurries were prepared and tested. The slurries showed acceptable properties. Hence, the slurries were prepared and cured. Then, cored samples were prepared for aging. The results for these tests will be presented in the coming reports.

Micro-silica containing cements have been found to be very brittle. As discussed during the Technical Advisory Board (TAB) meeting, the densities of the slurries were increased by reducing the amount of water to control the brittleness.

Theoretical and experimental studies on tubular corrosion are in progress. A recent corrosion rate model developed by Sina et at. (2012) has been investigated (Appendixes A and B). Moreover, preliminary LPR experiments were continued. A corrosion experiment was performed for 292 hours. Weight-loss and LPR measurements were obtained. The average corrosion rate from the weight-loss was found to be 39.26 mpy. The LPR method showed slightly higher corrosion rate (approximately 52 mpy).

Our plan for the upcoming weeks is to continue: i) the aging tests at different pressures; ii) theoretical and modeling studies on tubular corrosion; iii) additive screening studies; and iv) development of corrosion test setup.

The forth TAB meeting was held on May 7, 2013. The minutes of the meeting are presented in Appendix C. Furthermore, we received feedback from BSEE on our previous reports. Our response is presented in Appendix D.

2. Overall Project Progress

2.1 Theoretical Studies (Task 1)

2.1.1 Tubular Corrosion

Theoretical and modeling studies on tubular corrosion are in progress. A new model developed by Sina et at. (2012) has been investigated. The model predict uniform corrosion rate in CO_2/H_2S containing corrosive environment. It takes into consideration of transient chemical reactions and species (ion) transport. The model accounts for the formation of corrosion scale on the corrosion rate predictions. However, due to the complexity of corrosion scale modeling, Sina et al. (2012) proposed a method that decouples scale growth calculation from corrosion-rate computation. Details of this model are presented in Appendix A.

2.2 Experimental Studies on Degradation of Cement (Task 2)

2.2.1 Porosities and Permeabilities of Baseline Cements

In this month, two batches of cement cores (Batches 015 and 016) were kept in the aging cell (i.e. Experiments 7A and 13). **Table 1** summarizes test parameters of aging experiments conducted to date. Experiment 7A was performed at 225°F, 40% CO_2, and 6,000 psi for 14 days. This

experiment was a repetition of Experiment 7. The repetition was needed since permeability measurements of samples tested in Experiment 7 were out of the regular trend observed from other tests. This monthly report will present the comparison of results of these two repeated experiments (i.e. Batches 009 and 015 samples), which were performed under the same aging conditions. In addition, porosity and permeability of samples aged at different aging pressures (Experiments 11 and 13) are compared to study the effect of aging pressure on cement degradation process.

Table 1 Test parameters for aging experiments

Batch #	Temp. (ºF)	Pressure (psi)	Partial Pressure %			Brine Conc. (%)	Aging Period (days)	Experiment #
			CH_4	CO_2	H_2S			
001	350	9000	100	0	0	9	6	1
002	350	6000	100	0	0	2	14 & 28	2
003	350	6000	100	0	0	2	14	
004	350	6000	90	10	0	2	6	3
005	350	6000	90	10	0	2	14 & 28	4
006	350	6000	90	10	0	2	14	
007	225	6000	90	10	0	2	14	5
008	100	6000	90	10	0	2	14	6
009	**225**	**6000**	**60**	**40**	**0**	**2**	**14**	**7**
010	225	6000	0	100	0	2	14	8
011	100	6000	60	40	0	2	14	9
012	100	6000	0	100	0	2	14	10
013	**350**	**6000**	**60**	**40**	**0**	**2**	**14**	**11**
014	350	6000	0	100	0	2	14	12
015	**225**	**6000**	**60**	**40**	**0**	**2**	**14**	**7A**
016	**350**	**3000**	**60**	**40**	**0**	**2**	**14**	**13**

Figure 1 compares porosity and permeability of Batch 009 samples with those of Batch 015 samples. The porosity measurements before aging were roughly the same as measurements obtained after aging. Permeabilities of aged Class G cements were also in the same range. However, the rest of permeability measurements showed significant differences. Batch 009 exhibited very high permeability. The reason for high permeability in Batch 009 samples could be unusual entrapment of air during the slurry preparation or formation of cracks in the cement samples during coring and drying. Porosity and other measurements (compressive and bonding strengths) from these two batches do not show significant variations; hence, air entrapment cannot be the reason for the abnormality. To investigate these observations, FTIR tests were performed on the samples. **Figure 2** compares FTIR measurements of Batches 009 and 015. As seen from the figure, the mineralogical compositions of the batches come out to be very similar. Therefore, the permeability variations are most likely due to formation of cracks during sample preparation for the permeability tests.

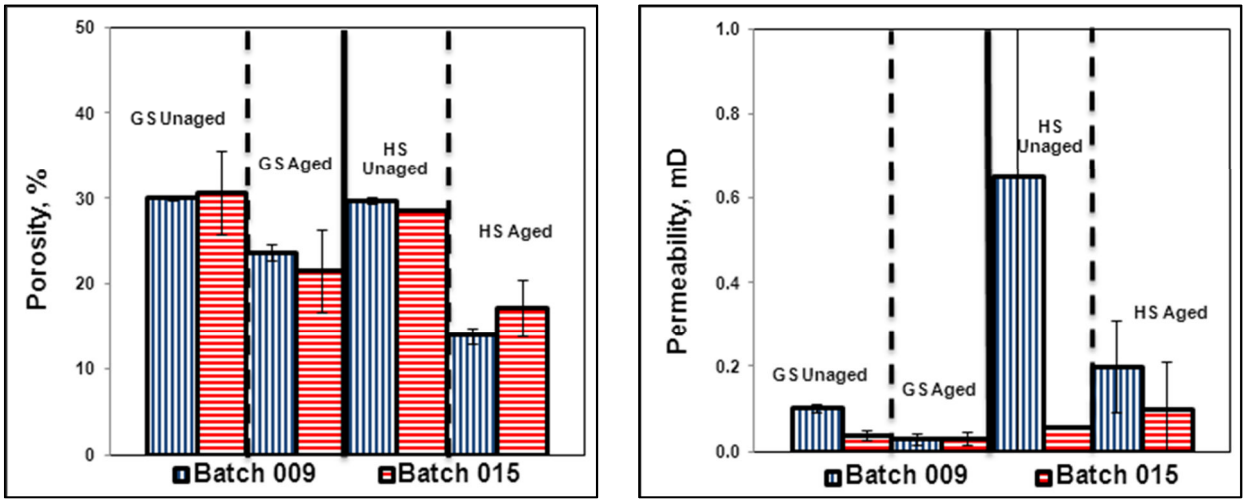

(a) (b)

Fig. 1: Comparison of Batch 009 and 015 samples: a) porosity; and b) permeability

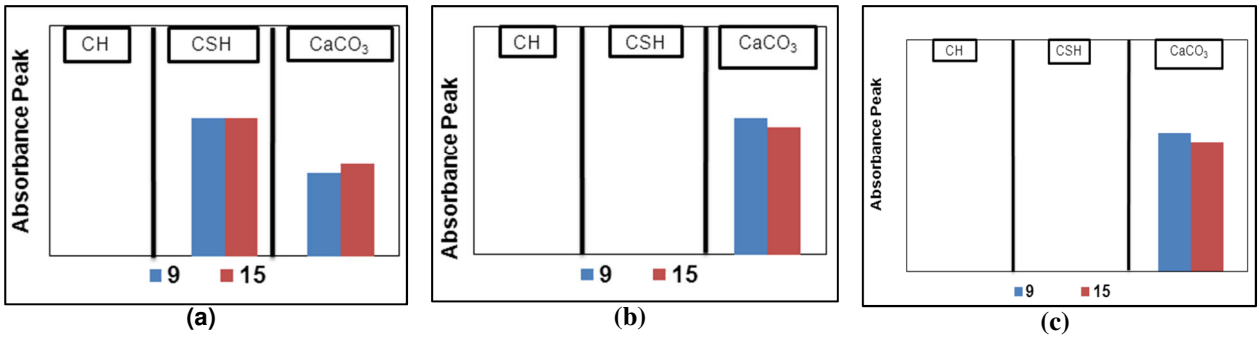

(a) (b) (c)

Fig. 2: Comparison of FTIR peaks of Batch 009 and 015 cores: a) inner (virgin) zone; b) middle zone; and c) outer zone of the cores

During this reporting period, one aging test was carried out at reduced pressure (3,000 psi). Samples were aged at 350°F in 2% brine saturated with mixed gas containing 40% CO_2 and 60% methane. A similar test was conducted previously but at 6,000 psi (Experiment 11). **Figure 3** presents porosities and permeabilities of samples aged at different pressures. The trends of porosity and permeability are consistent. As samples are aged at reduced pressure (3,000 psi), both porosity and permeability showed reduction as compared to the unaged ones. Increasing the pressure from 3,000 to 6,000 psi increased porosity and permeability of the cores. This trend is seen in both Class H and Class G cements. The carbonation process of CSH includes the formation of an intermediate product (scawtite) as shown below.

, ... (1)

When more CO_2 reacts with scawtite, it forms $CaCO_3$ thereby completing the carbonation process. At low pressures (i.e. 3000 psi), the solubility of CO_2 in brine is low; hence, less carbonic acid is available to completely carbonate the CSH phase. The reduction in porosity and permeability could be due to incomplete carbonation of CSH, which produces scawtite. Incomplete carbonation prevents the formation of $CaCO_3$ and subsequently the formation of soluble bicarbonate that can be leached out by the acid. The precipitation of scawtite in the cement pore and decrease of leaching might caused the reduction in porosity and permeability at lower pressure. Core samples are sent out for XRD analysis to substantiate the formation scawtite.

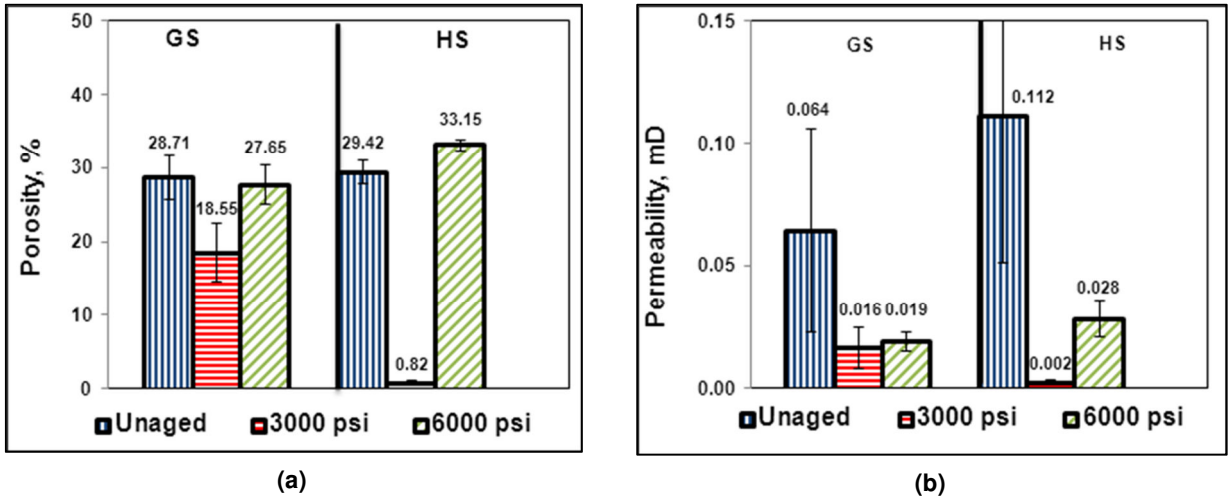

Fig. 3: Effect of pressure on properties of samples aged for 14 days at 350°F in 40% CO_2 gas saturated brine solution: a) porosity; and b) permeability

2.2.2 Comparison between FTIR and XRD Results

Fourier Transform Infrared Spectroscopy (FTIR) and X-Ray Diffraction (XRD) techniques are commonly used in cement degradation studies. XRD provides more detailed and accurate mineralogical composition of cement than FTIR. In other word, FTIR provides a qualitative analysis whereas XRD provides both qualitative and quantitative analysis of the sample mineralogy. In order to validated our FTIR results, limited number of XRD tests were conducted on both aged and unaged samples. **Figure 4** presents FTIR and XRD results of the same samples, which were aged at 225°F and 6000 psi for 14 days in 2% brine saturated with 100% CO_2. The amounts of carbonated ($CaCO_3$) and uncarbonated (CH and CSH) binding components of the cement present in the samples are displayed. Similar composition trends are observed in both measurement techniques. However, some anomalies can be explained by describing the working principles of FTIR and XRD techniques. In FTIR, the entire -CO_3 bonds are shown at wavenumber 1480 cm^{-1}. Hence, it does not specifically indicate the amount of $CaCO_3$ present in the sample. The CO_3 bonds can be from scawtite, which is partially carbonated CSH that exhibits CO_3 bonds. XRD results demonstrate the presence of more CSH phase. This is because it is able to distinguish between

CSH and scawtite. However, FTIR shows the scawtite as the CO_3 bond. Consequently, FTIR measurements displayed strong $CaCO_3$ peak. CSH peaks shown in XRD of middle and outermost zones are mostly from scawtite, as a result, CSH peaks are absent in the FTIR graphs of middle and outermost zones. In addition, the $CaCO_3$ peaks of unaged and virgin zone are very high in FTIR as compared to XRD. This is also due to scawtite, which is seen as $-CO_3$ bond by FTIR but XRD identifies it as CSH (Carbonated CSH).

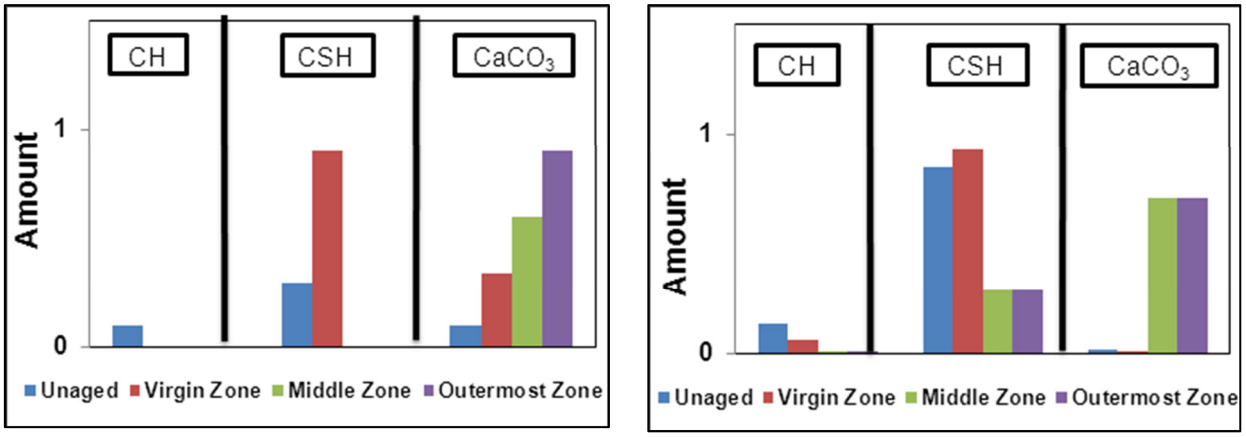

Fig. 4: Mineralogy comparison for samples aged at 100% CO_2, 225°F, 6000 psi and 2% brine solution for 14 days: a) FTIR; and b) XRD

2.2.3 Compressive Strengths of Baseline Cements

In this reporting period, compressive strength measurements were obtained by testing Batches 15 and 16 of Class G and Class H cement cores. Aging conditions are presented in **Table 1**. Most of Batch 015 measurements are consistent with previous experiment conducted using Batch 009 samples under the same aging conditions (**Fig. 5**). Compressive strength of Class G and Class H increased due to carbonation after aging at 225°F and 6000 psi for 14 days in 2% brine saturated with 40% CO_2 and 60% methane. This demonstrates the repeatability of the measurement. However, aged HS samples of Batch 009 showed increased compressive strength when compared with Batch 015 samples. Furthermore, when the results from these two batches are compared with other test results obtained at the same temperature but varying the CO_2 concentration (**Fig. 6**), compressive strength from Batch 009 samples gives more consistent and reasonable trend.

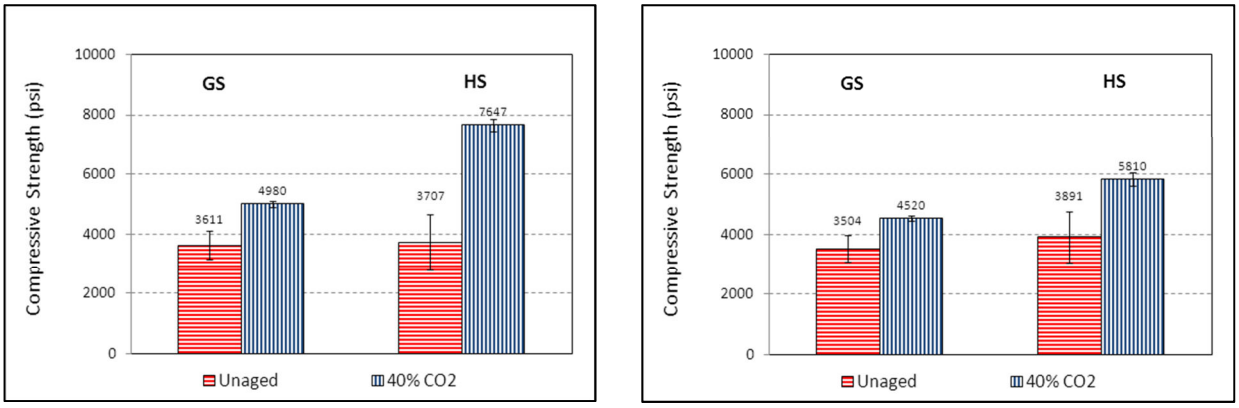

(a) (b)

Fig. 5: Compressive strength of cement cores unaged and aged in 2% brine for 14 days at 225ºF and 6000 psi: a) Batch 009; and b) Batch 015

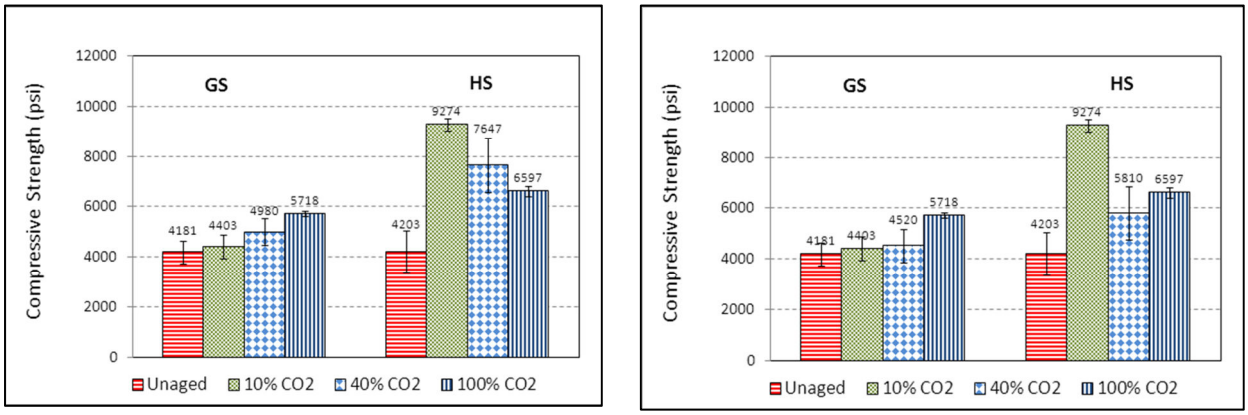

(a) (b)

Fig. 6: Effect of CO_2 on compressive strength at 225°F and 6000 psi using different-batch measurements for 40% CO_2 data points: a) Batch 009; and b) Batch 015

In order to study the effect of aging pressure on compressive strength, Batch 16 samples were aged at a reduced pressure (3,000 psi). **Figure 7** shows the comparison of the results obtained under the same aging condition but varying the pressure. Compared with results from Batch 13, increase in pressure leads to further leaching in Class G cement and more carbonation in Class H cement. Although the observed behavior of Class G is consistent with result published by Arina and Sonny (2010), it should be noted that aging temperature is high; hence, contrary to the trend observed in Class G, leaching is expected to occur at slower rate than carbonation in Class H cement. To better understand the effect of pressure on cement degradation, the next batch of experiment will be conducted at aging pressure of 9,000 psi.

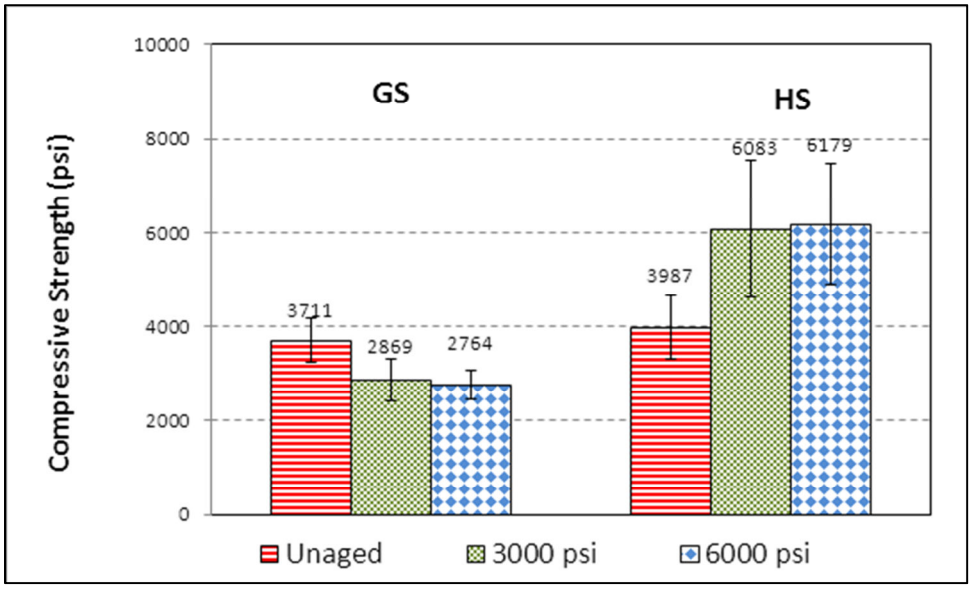

Fig. 7: Effect of aging pressure on compressive strength aged at 350°F and 40% CO_2

2.2.4 Shear Bond Strengths of Baseline Cements

Investigation on shear bonding strength (SBS) of cement was continued. SBS of samples aged at different pressures were investigated. Carbonation depths of the SBS samples were measured to correlate the depth with the bond strength. In addition, literature survey was conducted to collect published SBS data and compare with our measurements.

Comparison of Measurements

Casing roughness is one of the key factors that affect the shear and hydraulic bonding strengths of cement. Evans et al. (1964) performed SBS experiments to study the bond strengths of cement with steel using samples made of Class A cement hardened in a concentric annulus formed by two pipes (**Fig. 8**). The impact of pipe surface roughness and finish were studied during the experiments. They defined shear bond as the bond that mechanically supports pipe in the hole and determined SBS by measuring the force required to initiate pipe movement in a cement sheath. This force, when divided by the failed-bond contact area (i.e. contact area in which the bond failure occurs) yields the shear bond strength. **Table 2** presents measured shear and hydraulic bond strengths of the cement. Bond surface roughness tends to improve shear and hydraulic bonding strengths. Resin-Sand-Coated pipe showed the highest bond strength.

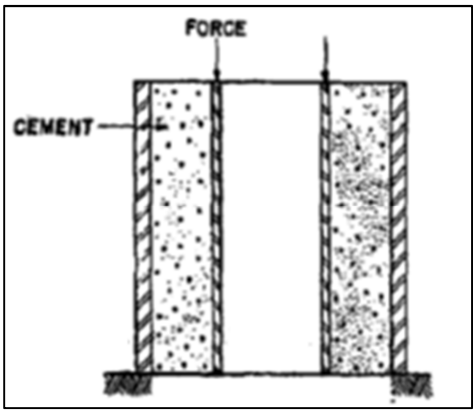

Fig. 8: Shear bond sample (Evans et al. (1964)

Table 2 Shear bonding strength of various pipe finishes (Evans et al. 1964)

Type of finish		Bond strength		
Steel		Shear(psi)	Hydraulic(psig)	Gas(psig)
New	Mill vanish	74	200-250	15
New	Varnish Chemically Removed	104	300-400	70
New	Sandblasted	123	500-700	150
Used	Rusty	141	500-700	150
New	Sandblasted-Resin-Sand Coated	2400	1100-1200	400

In addition to the surface roughness, the sample design may affect the measured bond strength. TAB members suggest comparing our measurements with data obtained from annulus based samples. They indicated annulus based SBS measurements provide higher bond strength values. At present, SBS measurements with Class H cement are not available in the literature. Therefore, as preliminary indication, we compared our measurements with data presented by Evans and Carter (1964). In our investigation, the average measured SBS of unaged sample is 550 psi. The maximum shear bond strength reported by Evans and Carter (1964) for a regular annulus was from rusty pipes, which is 141 psi (Table 2). Our measurement technique provides realistic bonding strength. To make a reasonable comparison, we will continue our research for SBS measurements from annulus-based samples for Class H cement.

The work done by Muhammad and Fathaddin (2005) was reviewed to compare our shear bonding strength measurements. Their experiments were conducted using Class G mixed with 10% to 40% silica flour. Samples were aged at 300°F and 2,000 psi in the presence of 90%CO_2 gas. **Figure 9** shows the change in shear bonding strength occurred after aging. Even though the aging environment in our experiment was slightly different (i.e. 350°F, 3,000 psi and 100% CO_2) and the type of cement used was different, the results display a similar trend. In both cases, the SBS increased with aging time. For unaged samples, the shear bonding strengths are comparable.

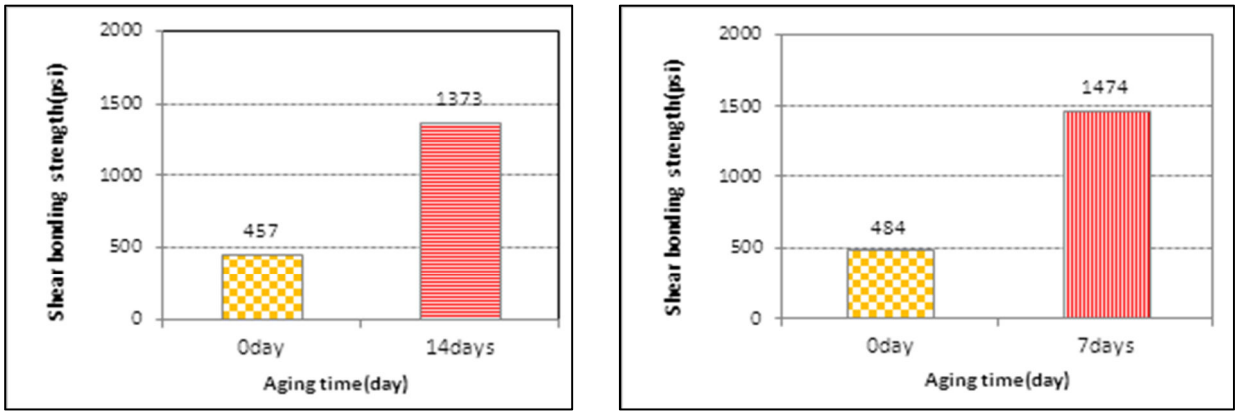

(a) **(b)**

Fig. 9: Sliced cement samples obtained from SBS samples

Carbonation Depth

Phenolphthalein solution test is often used to determine the depth of degradation after CO_2 attack in carbonated cement. Shear bonding test samples were used to study degradation depth. As these samples are kept in brine solution after the SBS test, they are suitable for phenolphthalein solution test. Moreover, the carbonation is uniaxial (**Fig. 10**) and preferable for degradation-depth model validation. To measure the degradation depth, the hardened cement was taken out from the samples and sliced into halves along the length (**Fig. 11**). According to Santra et al. (2009), areas containing free $Ca(OH)_2$ changes the color to deep purple when the set cement is exposed to phenolphthalein solution. Areas containing less or no $Ca(OH)_2$ would be stained to light color. However, cement compositions containing large amounts of pozzolan material such as high levels of silica fume would not be suitable for this test since pozzolan cement cores have dark color.

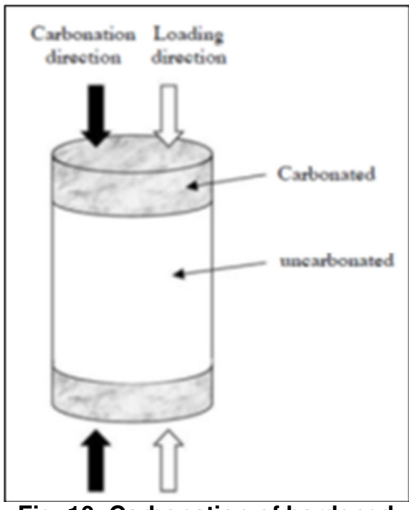

Fig. 10: Carbonation of hardened cement in SBS sample

In bonding samples, since only top and bottom parts of the cement are exposed to carbonation during the aging, the middle part remains intact (undegraded) as presented in **Fig. 11**. In the carbonated zone, which is shown as orange layers in the figure, light pinkish color was observed. As Santra et al. (2009) pointed out, it is difficult to differentiate between zero-penetration and full-penetration of CO_2 by visual examination of the dye-treated samples.

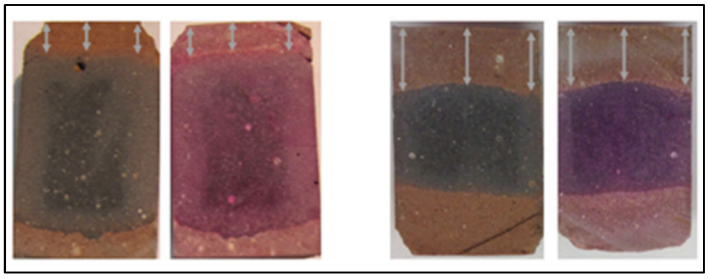

Fig. 11: Sliced cement samples obtained from SBS samples

Carbonation depth was measured by analyzing pictures of sliced cement samples. The average carbonation depth for samples aged at 350℉ and 6000 psi is presented in **Fig. 12**. As expected, carbonation depths increased with the increase in CO_2 concentration. More carbonation depth data will be obtained to correlate measurements with shear bonding strength.

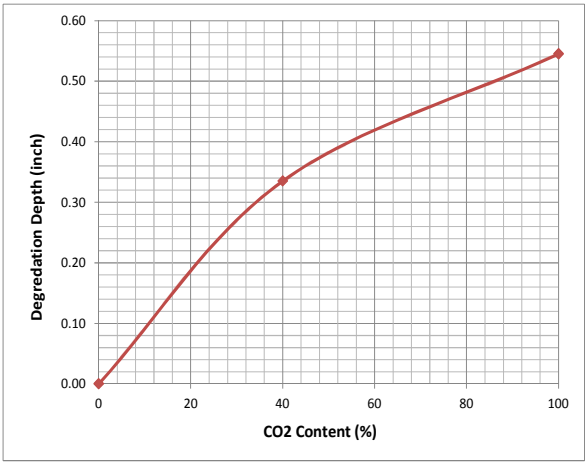

Fig. 12: Degradation depth vs. CO_2 content in the gas phase of aging fluid

Effect of Aging Pressure on Shear Bonding Strength

As outlined by Bertos et al. (2004), several factors influence cement carbonation and leaching (**Fig. 13**). Previously, the effects of aging temperature, CO_2 concentration, and composition of cement cores on SBS were investigated. Currently, we are focusing on the effect of aging pressure on SBS. **Figure 14** shows the shear bonding strengths of SBS samples (unaged and aged at different pressures). The rest of the aging conditions are kept the same (i.e. 350℉, 40% CO_2 for 14 days). The result of 9,000 psi will be included in the next month report as the samples are currently being aged in the oven.

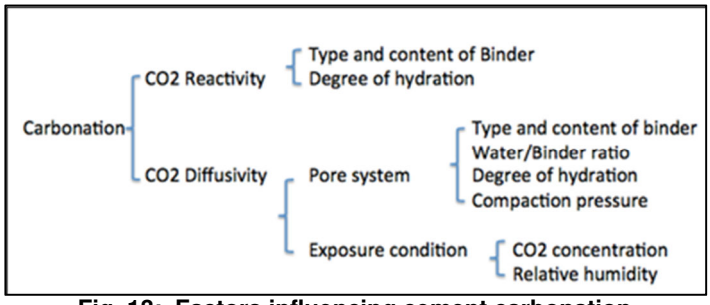

Fig. 13: Factors influencing cement carbonation

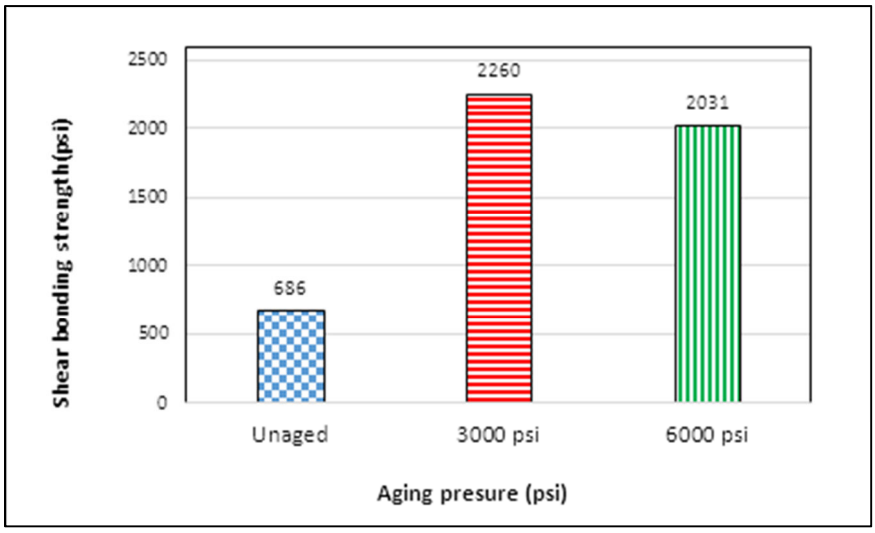

Fig. 14: Influence of aging pressure on SBS of samples aged at 350℉ for 14 days in 2% brine saturated with 40% CO_2 gas

Samples aged at lower aging pressure (3,000 psi) display higher shear bonding strength. Samples aged at 6000 psi are exposed to higher CO_2 concentration in the brine, resulting from higher solubility at higher pressure. According to Bertos et al (2004), the higher the amount of CO_2 in the gas phase, the higher is the rate of carbonation. However, excessive CO_2 pressure does not lead to increased strength in carbonated product. That is because the slower reaction would allow dissipation of heat and reduce thermally induced stresses that may weaken the final product. Bertos et al (2004) pointed out that, by varying the partial pressure of CO_2, the rate of carbonation could be controlled.

2.2.5 Additive Screening and Cement Formulation Studies

Additive screening and cement formulation studies were continued. During this month, magnesium oxide (MgO) and hydroxyapatite (HOAP) containing cements were investigated. HOAP samples showed reduced compressive strengths after aging at 350°F due to strength retrogression resulting from the lack of sufficient amount of silica in the samples. MgO sample exhibited better resistance against carbonic acid environment as seen in previous experiments. New micro-silica and HOAP slurries were also prepared and tested as discussed in the TAB meeting. Slurry with increased amount of MgO (10% BWOC) was also tested.

2.2.5.1 Hydroxyapatite Cement

It was observed from previous experiments that HOAP samples were able to reduce the carbonation of cement and preserve the binding components (portlandite and CSH) of the cement matrix. However, the addition of hydroxyapatite reduced compressive strengths of the samples. The percentage increase in the shear bond strength after aging was also found to be less than that of the baseline cement. A new aging experiment with similar slurry composition was conducted on another batch of HOAP samples (Batch 004 HOAP). Samples were aged at 350°F and 3,000 psi for 14 days in 2% brine saturated with mixed gas containing 40% CO_2 and 60% methane. After aging, properties of the samples were measured.

Porosity – Permeability Measurements

The porosity and permeability measurements are presented in **Figs. 15** and **16**, respectively. The initial porosity of all the samples, except GHO, is in the same range. The baseline HS samples show a drastic decrease in the porosity after aging. However, for all the samples the trend of permeability is consistent with that of porosity. The porosity of HHO sample remained almost the same even after aging. For baseline GS and GHO samples, the level of decrease in porosity after aging is in the same range. Furthermore, for all the samples except HS, the reduction in permeability after aging is consistent. Due to pressure reduction, the amount of dissolved CO_2 is less; hence, carbonation occurring under reduced pressure can be different.

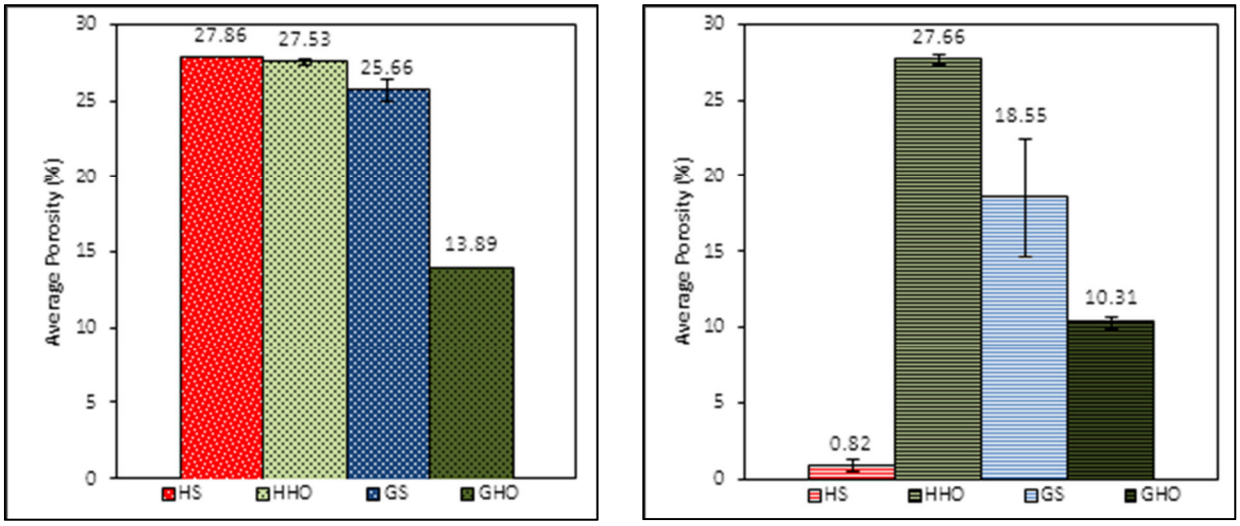

Fig. 15: Porosity of HOAP and baseline cement: a) Unaged; and b) aged at 350°F, 3000 psi, 40% CO_2 for 14 days

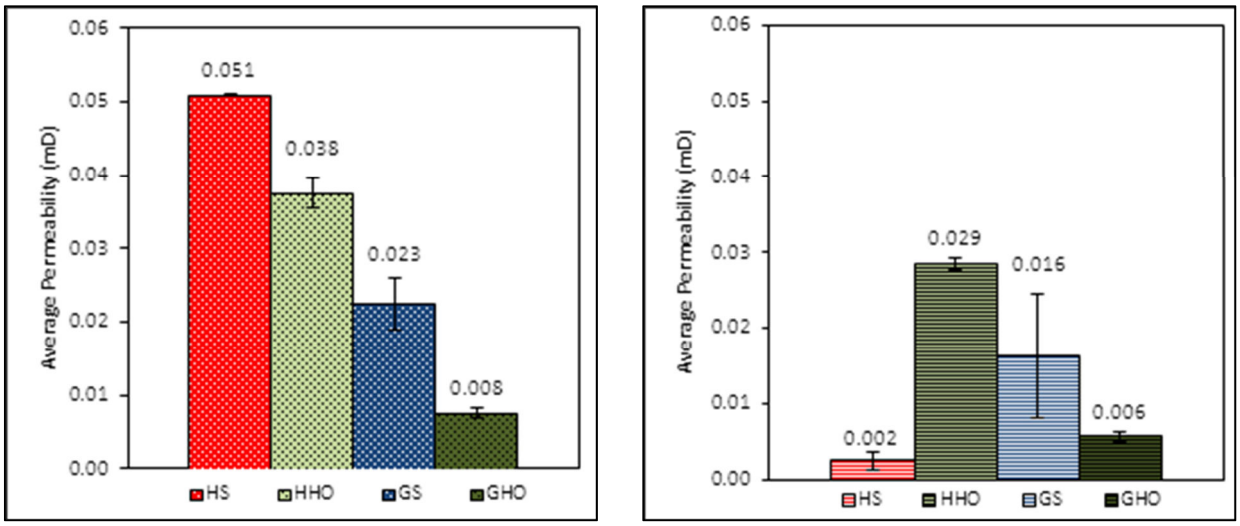

Fig. 16: Permeability of HOAP and baseline cement: a) Unaged; and b) aged at 350°F, 3000 psi, 40% CO_2 for 14 days

Compressive Strength Measurements

The compressive strengths of HOAP and baseline samples are presented in **Fig. 17**. Unaged samples showed almost similar compressive strength. After aging, compressive strength of HS sample increased due to carbonation. However, both HOAP and baseline GS samples exhibited decreased compressive strength after aging. A similar decrease in compressive strength of HOAP samples was also observed in previous experiment conducted at 350°F. This consistent reduction in the strength of HOAP samples can be due to strength retrogression commonly observed in cements when it is exposed to temperature greater than 250°F (Eilers and Root 1976; Lea 1971).

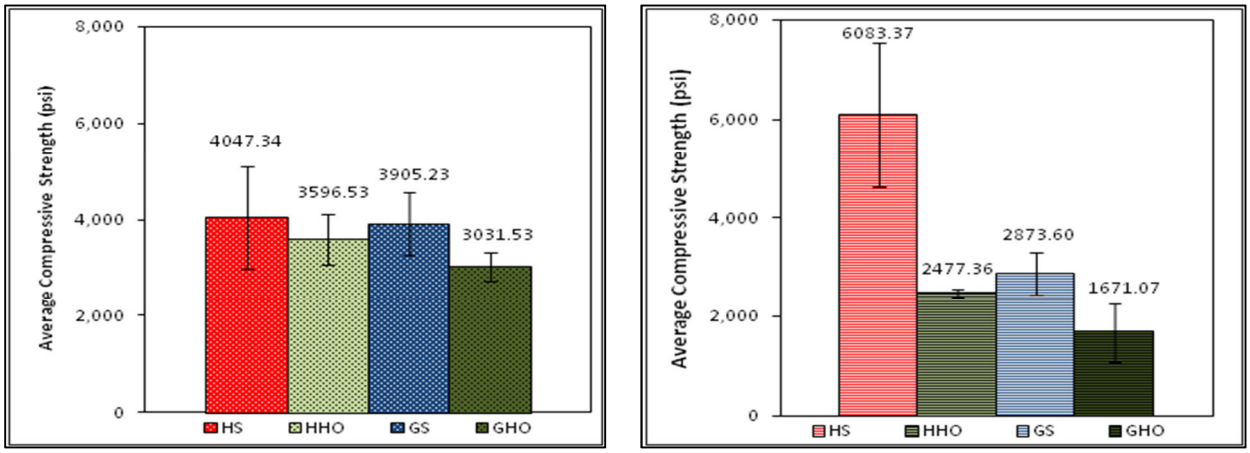

(a) **(b)**

Fig. 17: Compressive strengths of HOAP and baseline cements: a) Unaged; and b) aged at 350°F, 3000 psi, 40% CO_2 for 14 days

Shear Bond Strength Measurements

The shear bond strengths (SBS) of HOAP and baseline samples are presented in **Fig. 18**. Similar to the results obtained for compressive strength tests, the HOAP samples showed a slight decrease (-8.3%) in SBS. On the other hand, the baseline HS samples exhibited a significant increase (231.7%) in SBS. According to porosity and permeability measurements, the HOAP samples displayed moderate carbonation that could have improved SBS; however, due to the thermal retrogression, the samples displayed considerable SBS reduction. In a previous aging experiment conducted at 350°F, small increase (34.5%) in the SBS was observed as compared to baseline HS samples (356.4%). This again indicates the impact of strength retrogression on SBS, which tends to offset the effect of carbonation.

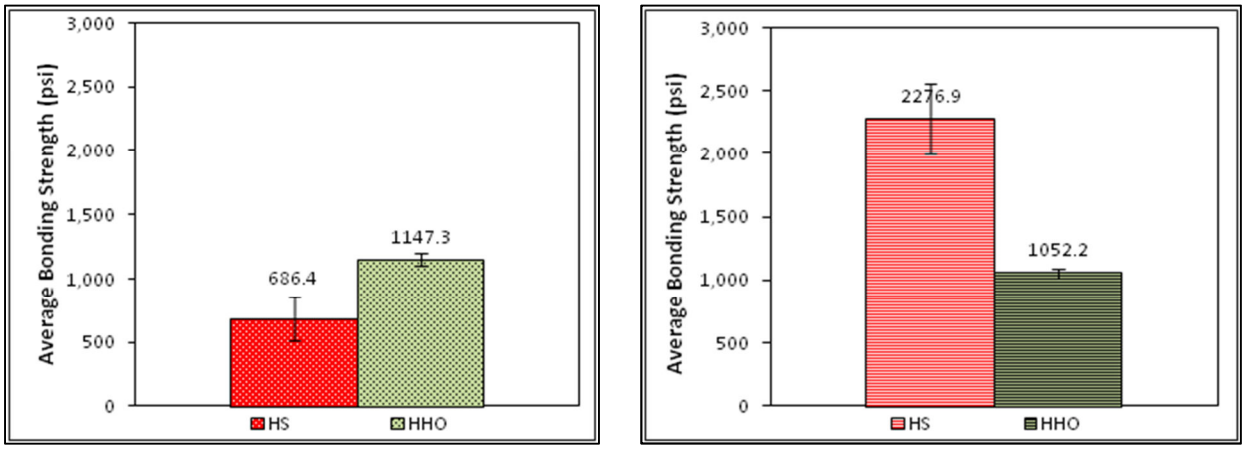

(a) **(b)**

Fig. 18: SBS of HOAP and baseline cement: a) Unaged; and b) aged at 350°F, 3000 psi, 40% CO_2 for 14 days

Controlling Strength Retrogression in HOAP Samples

Although HOAP cements exhibit good resistance against carbonation, the strength retrogression at temperature above 250°F is a major concern, which should be controlled by reducing the calcium-silicate ratio (Eilers and Root, 1976; Lea 1971). This is accomplished by the addition of silica flour or silica fume during slurry preparation. The baseline cements contain silica flour and they are resistant against thermal retrogression. The silica flour was removed from HOAP slurry formulation because of excessive thickening of the slurry with the addition of silica. In addition, as noted by Sugama (2005), HOAP cement was expected to resist thermal retrogression. However, our experiments show the presence of strength retrogression in the samples, which indicates that silica flour is required in the formulation. Therefore, new HOAP slurry formulations have been developed that include silica flour and citric acid as additives. Citric acid is used as a dispersant and retarder to ease excessive thickening of the slurries. Compositions of the new slurry formulations are presented in **Table 3**. The slurries were prepared and their properties were measured (**Table 4**). The measured slurry properties are in the range of those of the baseline cement slurries. API fluid-loss tests were not completed. Approx. 50 ml of fluid was collected in 2 minutes, which then resulted in thickening of the slurry in the testing cell. The fluid loss can be considered as only 50 ml after which no fluid-loss was observed at 100 psi and ambient temperature.

Table: 3 New HOAP slurry formulations

Component	Percentage Amount
Cement	100%
Silica Flour	35% BWOC
HOAP	5% BWOC
HEC	0.1% of water for fillers
Antifoam Agent	0.1 gal/sack of cement
Water for Cement	38% BWOC for Class H and 44% BWOC for Class G
Water for Silica Flour	38.5% BWOC
Water for HOAP	40% of HOAP
Citric Acid	0.5% BWOC
BWOC = by weight of cement	

Table 4: Slurry properties of the new formulations

	HSHO	GSHO
Density	15.40 ppg	16.10 ppg
Viscosity	Acceptable range	Acceptable range
Thickening Time	215 min.	160 min.

The amount of citric acid added to the cement slurry was optimized to 0.5% BWOC after testing different concentrations (0.25%, 0.50% and 0.75%). At 0.25% BWOC, even though the rheological readings were below the baseline HS slurry, the slurry was very thick as observed during pouring out from the mixing jar. At 0.75% BWOC, the viscosity was almost similar to base GS slurry;

however, the thickening time for the slurry came out to be more than 5 hours. As compared to base HS slurry, this was extremely high. Hence, 0.5% BWOC was considered the optimum amount of citric acid. As the slurry samples were cured (5 days, 200°F, 2% brine) and cored for unaged sample testing, the set cement was found to be somewhat brittle. The porosity, permeability, compressive strength, and shear bond strength test results will be presented in the coming monthly reports; however, as observed during preparation of the cores, the set cement was weak in nature. This can be due to excess water added to the slurry for silica flour. We will continue adjusting the formulation.

Conclusions and Future Work

All the experiments confirmed that HOAP is able to prevent carbonation of the cement under HPHT CO_2 conditions. The FTIR of previous experiments showed the presence of portlandite and CSH in the matrix, which indicates non-carbonation of cement. FTIR analysis for Batch 004 HOAP will be presented in the next report. The testing of basic HOAP slurry (without silica flour) will be continued to improve understanding of the degradation behavior of HOAP. However, strength retrogression was observed in the HOAP samples, which can be controlled by addition of silica flour. Optimization of the slurry properties will be carried out in order to formulate retrogression resistant HOAP cement. In order to increase the strength of the set cement, the amount of water in the slurry will be optimized.

2.2.5.2 Magnesium Oxide Cement

The testing of MGO cement was continued. MGO (Batch 004 MGO) and baseline cement (Batch 015) cores were aged at 225°F and 6000 psi for 14 days in 2% brine saturated with 40% CO_2 gas. The composition of the slurry was presented in previous report.

Porosity and Permeability Measurements

The porosity and permeability of MGO samples are presented in **Figs. 19** and **20**, respectively. The porosities of unaged baseline samples are in the same range. For unaged samples, the permeability of HS is lower than GS. After aging, porosity and permeability of most of the samples decreased. The reductions in porosity and permeability indicate carbonation and expansion that shrink pore volume. For GSMG samples, porosity and permeability trends after aging is unexpected. This result contradicts the general notion of increased porosity improves permeability. One of the reasons for this observation could be the phenomena of pore plugging without considerable pore volume shrinkage. Porosity is the amount of empty space available in the matrix. Hence, deposition of $CaCO_3$ or $Mg(OH)_2$ crystals (formed by hydration of MgO) in the pore space causes reduction in porosity. However, the permeability measures the connectivity of the pore space. Hence, deposition of $CaCO_3$ or $Mg(OH)_2$ crystals in the pore throat can cause substantial reduction in permeability without significant reduction in porosity.

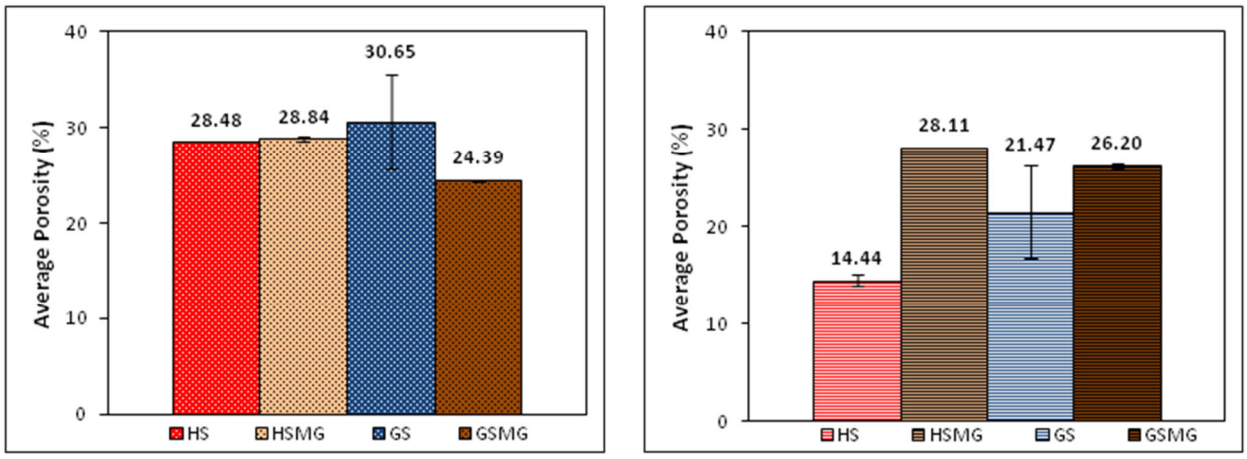

(a) **(b)**

Fig. 19: Porosity of MGO and baseline samples: a) Unaged; and b) aged at 225°F, 6000 psi, 40% CO_2 for 14 days

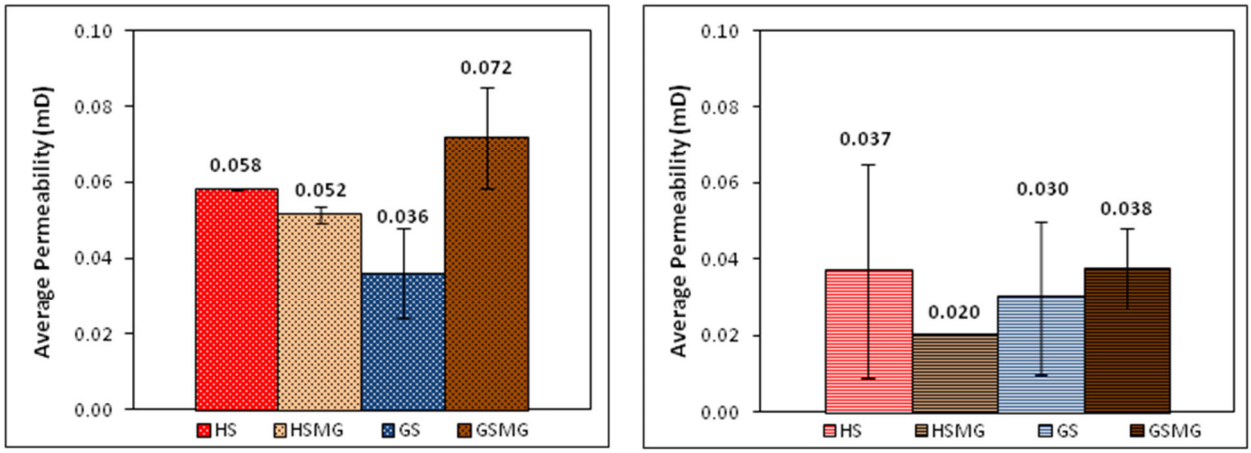

(a) **(b)**

Fig. 20: Permeability of MGO and baseline samples: a) Unaged; and b) aged at 225°F, 6000 psi, 40% CO_2 for 14 days

Compressive Strength Measurements

The compressive strength of MGO and baseline cores are presented in **Fig. 21**. Compressive strengths of unaged samples vary slightly. After aging, the strengths of the cores increased. This strength improvement is due to carbonation of the matrix and deposition of $CaCO_3$ crystals in the pore space. For MgO samples this increment is also due to matrix expansion resulting from the formation of $Mg(OH)_2$ crystals from hydration of MgO.

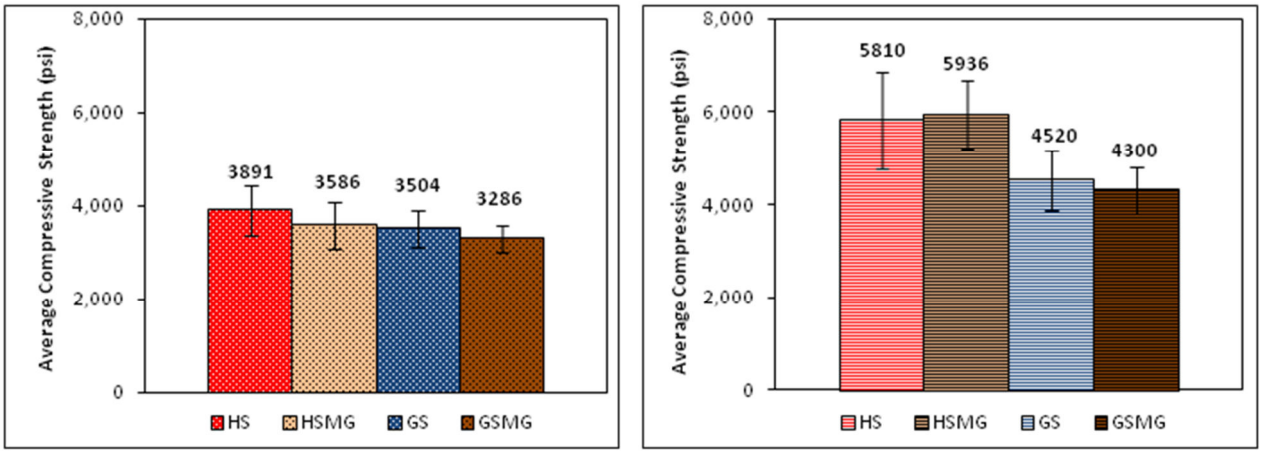

(a) (b)

Fig. 21: Compressive strength of MGO and baseline samples: a) Unaged; and b) aged at 225°F, 6000 psi, 40% CO_2 for 14 days

Shear Bond Strength Measurements

Shear bond strengths of MGO and baseline samples are presented in **Fig. 22**. SBSs of unaged samples slightly vary. However, a substantial increase in SBS was observed after aging due to carbonation and expansion. HSMG samples showed higher improvement in SBS than HS samples because of expansion.

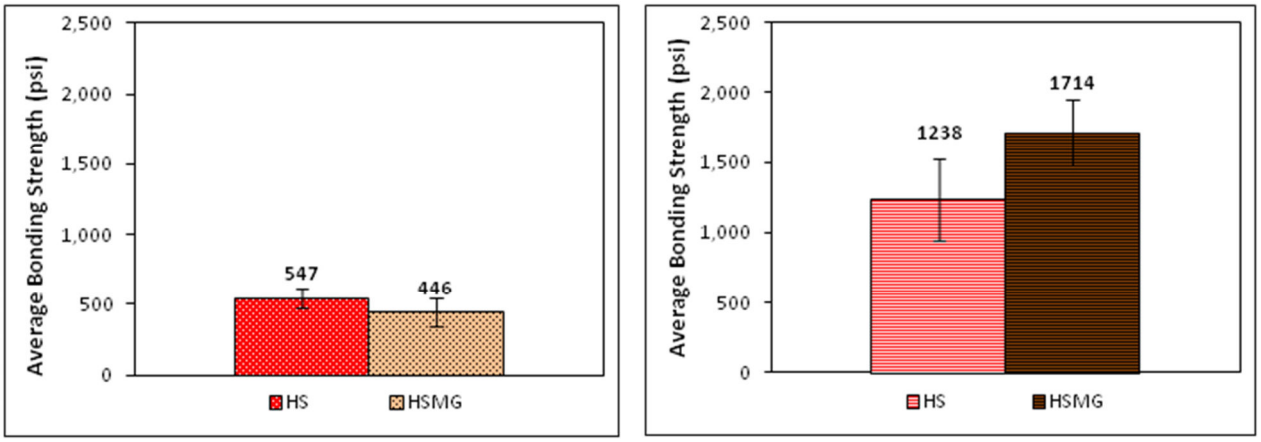

(a) (b)

Fig. 22: SBS of MGO and baseline samples: a) Unaged; and b) aged at 225°F, 6000 psi, 40% CO_2 for 14 days

FTIR Results

In order to verify the penetration of CO_2 in the MgO samples, FTIR experiments were carried out by taking samples from the inner, middle and outer most zones of aged MGO and baseline cores. The results are summarized in **Fig. 23**. The charts present peaks of $Ca(OH)_2$, CSH, $CaCO_3$, MgO, $Mg(OH)_2$ and $MgCO_3$. Area under the peak identifies the amount of the mineral present. Hence, higher peak strength indicates higher amount of respective mineral.

The main binding material of the cement, CSH is only preserved in the innermost zone. The CSH peak at 950cm^{-1} is higher in HSMG samples than the baseline samples. This means that MGO cement (HSMG) preserved CSH more than the baseline. As expected, complete carbonation was occurred in outermost and middle zones. In the innermost zone, $Mg(OH)_2$ was found in HSMG samples; however, it was fully carbonated to form $MgCO_3$ in HS samples. This confirms that HSMG is able to preserve more amount of CSH from carbonation as compared to base HS sample.

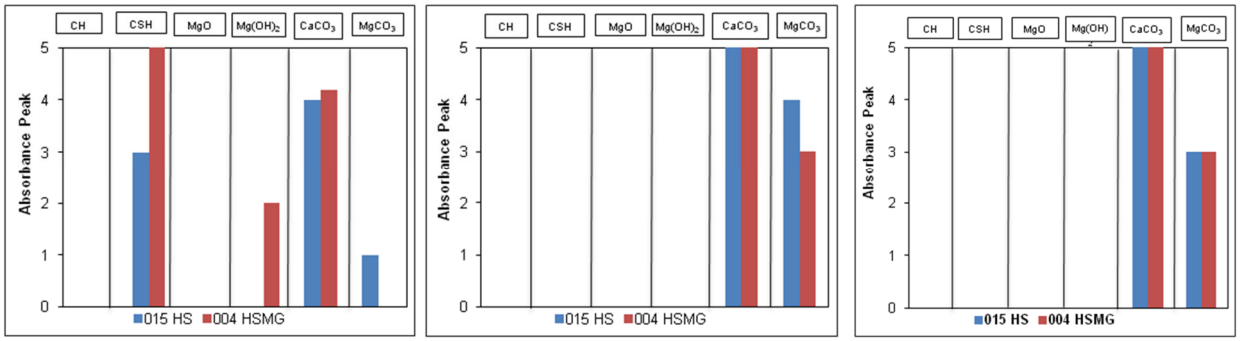

Fig. 23: FTIR peaks of MGO and baseline samples aged at 225℉ and 6000 psi for 14 days in 2% brine saturated with 40% CO_2: a) inner most zone; b) middle zone; and c) outer most zone

Adding 5% BWOC concentration of MgO into baseline cement has shown promising results in preventing the penetration of carbonic acid in the cement matrix. The presence of CH, $Mg(OH)_2$ and CSH in the FTIR spectrum corroborates the notion that expansion of $Mg(OH)_2$ crystals can lower the porosity and permeability and help increase the compressive and shear bond strength. To optimize the carbonation resistance of the cement, different cement slurries (HSMG-10 and GSMG-10) were prepared with 10% MgO BWOC and tested. The slurries exhibited acceptable properties (**Table 5**). The rheological properties of the slurry were found to be between those of the base HS and GS slurries. The thickening time was also close to those of the baseline slurries. Hence, 10% MgO slurries were prepared and cured in similar conditions as baseline samples (5 days, 200℉, and 2% brine). The cured cement samples have been cored and prepared for testing. The results will be presented in the next report.

Table 5: Slurry properties for 10% MGO Cements

	HSMG-10	**GSMG-10**
Density	15.95 ppg	15.40 ppg
Viscosity	Acceptable	Acceptable
API Fluid Loss	112 ml	120 ml
Thickening Time	180 min.	135 min.

2.2.5.3 Micro-Silica-Based Cement

Micro-silica containing cement slurries were previously tested and found to be extremely brittle. As discussed in the TAB meeting, the densities (14.25 ppg for class H and 13.85 ppg for class G) of the slurries were lower than commonly used cement slurries. Hence, to increase the densities, the amount of water was reduced and a dispersant, Sodium Poly-naphthalene Formaldehyde Sulfonate (NSF) was added to control viscosity of the slurries. The amount of NSF had to be optimized in the slurry. As suggested by Cowan and Eoff (1993), 0.5% BWOC NSF was used in order to test its effectiveness. The concentration of NSF was increased steadily (in step of 0.25% BWOC) to obtain rheologically acceptable slurries. Finally, 1.75% BWOC of NSF was selected and used in the slurry formulation. The final compositions of the slurries are presented in **Table 6**.

Table 6: Compositions of micro-silica-based slurries

Component	Percentage Amount
Cement: Class H or G	100%
Silica Flour	15% BWOC
Silica Fume	20% BWOC
HEC	0.1% of water for fillers
Antifoam Agent	0.1 gal/sack of cement
Water for Cement	38% BWOC for Class H and 44% BWOC for Class G
Water for Silica Flour	38.5% BWOC
Water for Silica Fume	0.13cc/gm of Silica Fume
Dispersant (NSF)	1.75% BWOC
BWOC = by weight of cement	

2.3 Experimental Studies on Corrosion of Tubulars (Task 3)

Preliminary corrosion experiments were continued using both weight loss and electrical measurement techniques. The experimental setup has been developed to perform moderate pressure corrosion tests. The setup consists of a 2-liter autoclave (corrosion cell, D = 3.5" and L = 13") and potentiostat (GAMRY G-series 750). Schematic of the corrosion cell is presented in **Fig. 24**. The cell is rated for maximum pressure of 3,000 psi. It is mounted on uni-strut frame. To test the integrity of the setup and piping connections, the cell was hydro tested at 1,100 psi for 60 minutes. The cell is equipped with a flanged lid (**Fig. 25**) that is used for pressurization, and mounting sensors and cable-seal gland. An electrically safe cable seal gland is utilized to pass signal leads from all the electrodes running from the inside of the autoclave to the potentiostat to measure corrosion rate using linear polarization resistance (LPR) technique. Connections for future input of CO_2 gas were made along with the installation of pressure gauge and pressure relief valve (PRV). The measurements were recorded using a software package (GAMRY DC-105) developed for corrosion rate measurement and analysis.

A high carbon steel, Grade 1045 rod (D = 0.25" x L = 3"), graphite rod and high-temperature Ag/AgCl electrode were used as working, counter, and reference electrodes, respectively. A cylindrical Teflon rod (a cylindrical PTFE block of 3.3" diameter and 1.5" height with drilled holes) is used as an electrode holder.

A preliminary experiment was conducted at atmospheric pressure and temperature in 1000 ml of 2% brine. The experiment was executed for 292 hours and the initial weight of the test specimen (i.e. working electrode) was 18.4504 gm. When the test was completed, the specimen was mechanically cleaned using soft brush and detergent, then its final weight was measured. The weight reduced by 39.2 mg. With exposed area of 1.5 cm^2 and the weight loss, the corrosion rate was determined. The average corrosion rate was found to be 39.26 mpy.

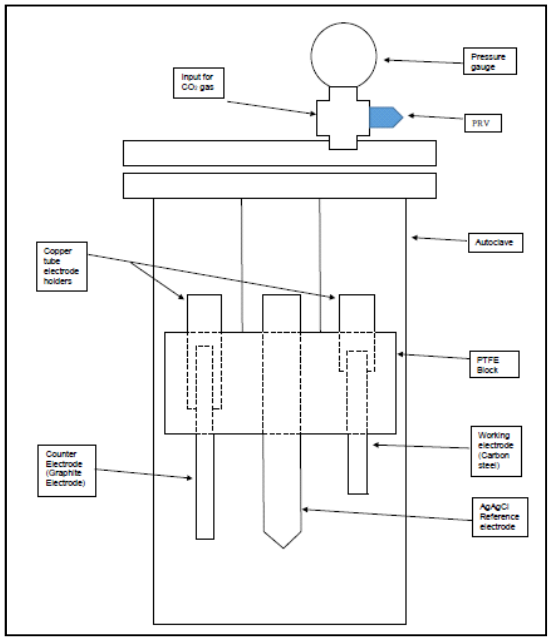

Fig. 24: Schematic of corrosion cell setup

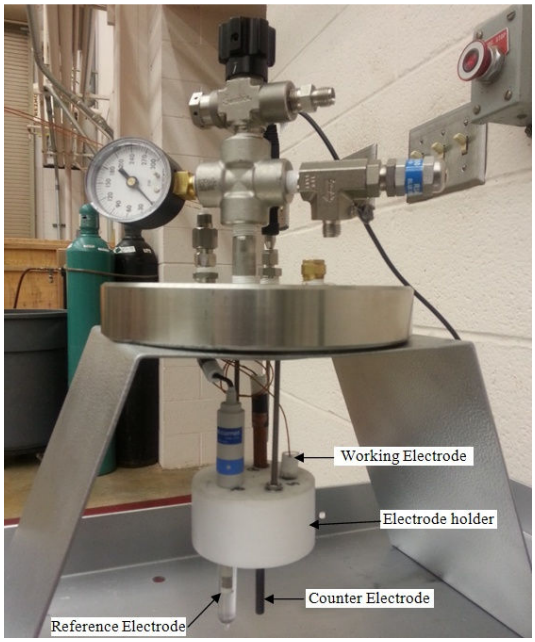

Fig. 25: Flange head for autoclave

Polarization resistance method (ASTM G 59) is a convenient technique used for measuring corrosion rate in both research and practical applications. The method involves measuring potentiostatic voltage-current curve in the immediate vicinity of the open-circuit potential, E_{oc}. The corrosion rate is then determined from the slope of voltage-current curve.

The Gamry potentiostat measures the cell current and adjusts it to the appropriate current range. **Figure 26** presents the LPR plot of the first day of the preliminary test. The initial corrosion rate obtained from the plot is 249.9 mpy. This rate was recorded at zero time (i.e. immediately after the experiment was started). The initial rate of corrosion was extremely high because bubbles were forming in the brine around the working electrode since nitrogen purging was not done. **Figure 27** displays the corrosion rate measured using LPR technique as a function of time. As expected, the

rate dropped to a constant rate in a few days as a protective scale on the working electrode (i.e. the corrosion testing specimen) was formed. After the first day, the rate of corrosion stabilized for three days. However, in the fourth day, the measurements showed sudden increase in the rate of corrosion. The reason for the increase can be the breaking of the corrosion scale resulting in more exposed area for fresh corrosion to take place and generate larger corrosion currents.

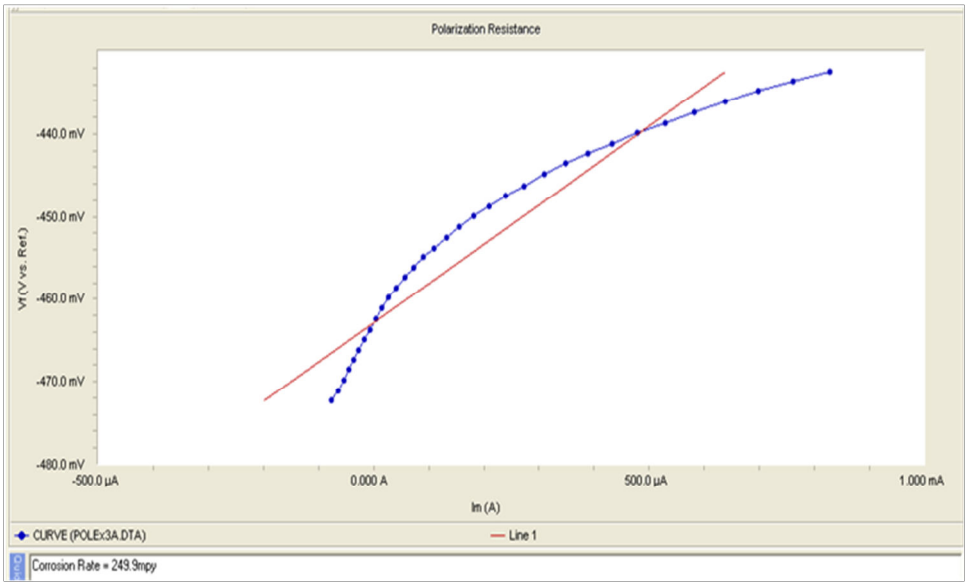

Fig. 26: Polarization resistance measurement of Day 1

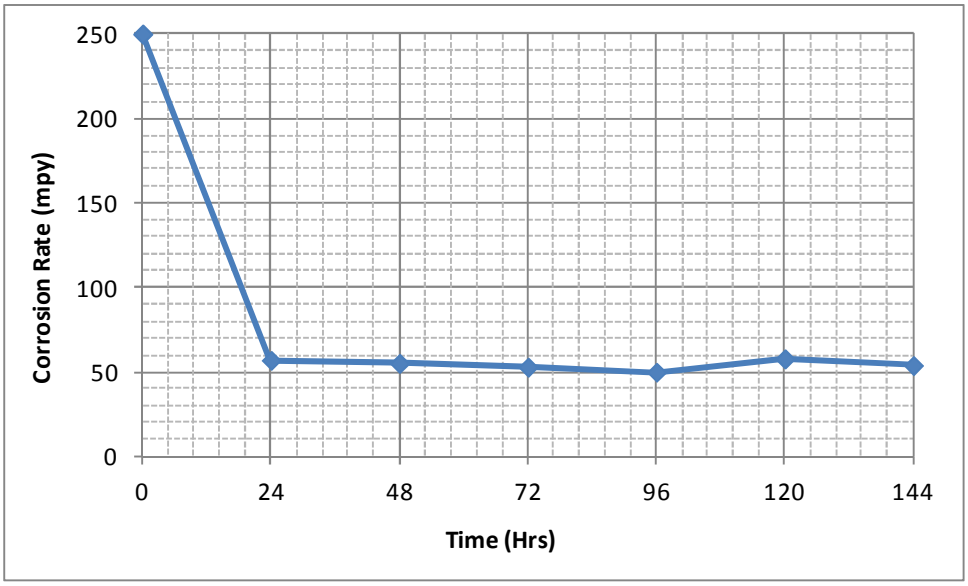

Fig. 27: Corrosion rate from LPR vs. time

A sudden increase in the rate of corrosion (from roughly 50 to 60 mpy within a span of 30 minutes) on the 5th day of the experiment was observed (**Fig. 28**). Breakdown of corrosion protective films are widely known for generating current transients, which can be detected by LPR devices as fluctuations of corrosion rate. Two types of current transients have been reported in the literature. i) a slow rise followed by a sudden decay, which indicates the characteristics of chemically induced corrosion such as pitting corrosion occurring in iron and iron base alloys; and ii) a sudden rise followed by a very slow decrease, which is possibly a characteristic of non-chemically induced localized corrosion for example abrasion, scratching and breaking. Since the experiment was conducted under static condition, breaking of the scales could be the main reason for this observation.

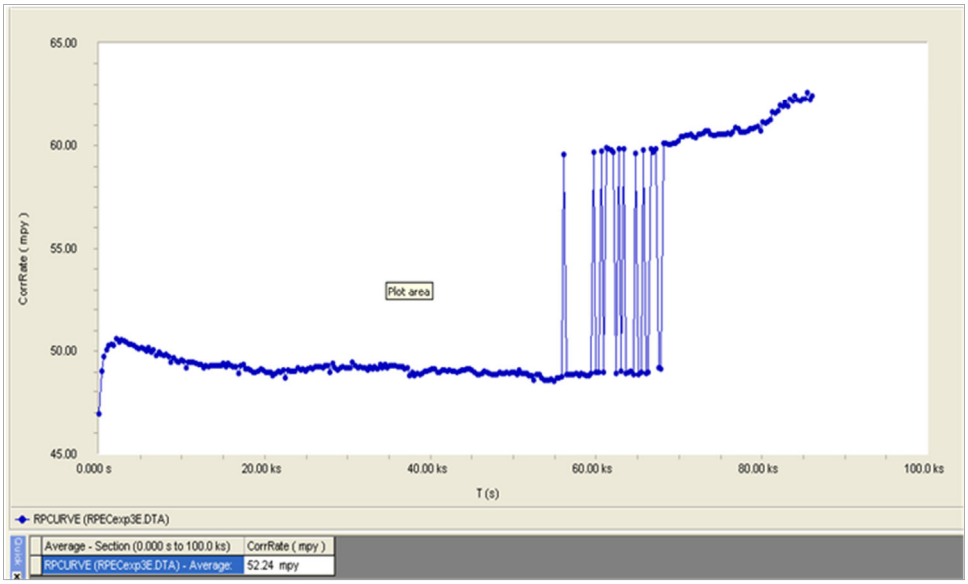

Fig. 28: Corrosion rate from LPR vs. time

The construction of corrosion setup was continued. The corrosion cell used for dynamic test and stress cracking corrosion-testing cells have been assembled and hydraulically tested for leaks.

3. Planned Activities

- Continue aging experiments with brine-CO_2-CH_4 system for 14 days varying aging pressure (3,000, 6000, and 9000 psi) at 350ºF and 100% CO_2 concentration.
- Continue theoretical and modeling studies on tubular degradation.
- Continue cement additive screen study.
- Continue the development of tubular corrosion testing setup.

4. Project Expenditures

This section presents the project expenses during the month of May (**Table 7**) and the cumulative expenditures.

Table 7 Current and cumulative expenditures, May, 2013

No.	Budget Categories	Current Expenses	Cumulative Expenses
1	Salaries & Wages	$7,933.35	$161,592.45
2	Fringe Benefits	$1,096.66	$35,573.01
3	Project Materials	$2,050.65	$55,160.09
4	Travel	$38.42	$4,133.72
5	Conference Expenses	$0.00	$0.00
6	Other Direct Costs	$0.00	$843.60
7	Equipment	$23,519.96	$229,658.29
8	Space Rental	$0.00	$0.00
9	Indirect Cost	$5,559.54	$128,651.39
10	**Total**	**$40,198.58**	**$615,612.55**

Nomenclatures

Acronyms

BWOC	By weight of cement
CH	Calcium hydroxide
CSH	Calcium silicate hydrate
FTIR	Fourier Transform Infra-Red
GHO	Class G cement with hydroxyapatite
GS	Class G cement with silica flour
GSHO	Class G Cement with silica flour and hydroxyapatite
GSMG	Class G Cement with silica flour and magnesium oxide
GSLT	Class G Cement with latex
HHO	Class H cement with hydroxyapatite
HOAP	Hydroxyapatite containing cement
HPHT	High-pressure high-temperature
HS	Class H cement with silica flour
HSHO	Class H Cement with silica flour and hydroxyapatite
HSMG	Class H Cement with silica flour and magnesium oxide

HSLT	Class H Cement with latex
LPR	Linear polarization resistance
PRV	Pressure relief valve
SBR	styrene-butadiene
SBS	Shear bonding strength
SCC	stress corrosion cracking
SEM	scanning electron microscope
XRD	X-Ray diffraction

Symbols

A_1, A_2	Dimensionless constants,
b	Tafel slope of the anodic and cathodic reaction, V
b_c	Tafel slope of the cathodic reaction, V
b_a	Tafel slope of the anodic reaction, V
C_{Scale}	Concentration of corrosion scale in the solid state
$C_{H_2CO_3}$	Bulk concentration of carbonic acid, mol/m^3
C_{CO2}	Bulk concentration in aqueous phase, mol/m^3
Δt	Time step
E	Surface potential, V
E_{rev}	Reversible potential for different species, V
$E_{rev\,H^+}$	Reversible potential of hydrogen ion, V
$E_{rev\,H2CO3}$	Reversible potential of carbonic acid, V
$E_{rev\,H2O}$	Reversible potential of water, V
$E_{rev\,Fe^{2+}}$	Reversible potential of iron ion, V
F	Faraday's constant, F = 96,485 C/mol
i	Current density for different species, A/m^2
i_0	Reference exchange current density for different species , A/m^2
$i_{0\,H^+}$	Reference exchange current density of hydrogen ion reduction, A/m^2
$i_{0\,H_2CO_3}$	Reference exchange current density of carbonic acid reduction, A/m^2
$i_{0\,H2O}$	Reference exchange current density of water reduction, A/m^2

$i_{0_{Fe^{2+}}}$	Reference exchange current density of iron ion oxidation, A/m^2
I	Ionic strength, mol/L
k	Permeability of corrosion scale
$\mathrm{K_{CO2}}$	Equilibrium constant of CO_2 hydration reaction, dimensionless
$\mathrm{K_{H2CO3:}}$	First dissociation constant of carbon dioxide, mol/L
$\mathrm{K_{HCO_3^-}}$	Second dissociation constant of carbon dioxide, mol/L
$\mathrm{K_{H_2S}}$	First dissociation constant of hydrogen sulfide , mol/L
$\mathrm{K_{H_2O}}$	Water dissociation constant, (mol/L)^2
$\mathrm{K_f}, \mathrm{K_b}$	Forward and backward kinetics constant for the carbon dioxide hydration reaction, respectively.
$\mathrm{P_{H_2S}}$	H_2S partial pressure in Pa
P	Total pressure, Psi
pH	Solution pH
PR	Scale precipitation rate
R	Universal gas constant, R =8.314 J/mol.K
RR	Reaction rate of the CO_2 hydration reaction
t	time, s
th	The thickness of the corrosion scale, m
T	Temperature in Kelvin
$\mathrm{T_f}$	Temperature in Fahrenheit
ϕ	Volumetric porosity

References

Bertos, M.F., Simons, S.J.R., Hills, C.D. and Carey, P.J. 2004. A review of accelerated carbonation technology in the treatment of cement-based materials and sequestration of CO_2. Journal of Hazardous Materials, Vol. 112, Issue 3, 30 August 2004, Pages 193–205.

Cowan, K. M. and Eoff, L. 1993. Surfactants: Additives to Improve the Performance Properties of Cements, paper SPE 25181 presented at the SPE International Symposium on Oilfield Chemistry, March 2-3, New Orleans, LA.

Dunlop, A.K., Hassell, H.L. and Rhodes, P.R., 1983. Fundamental Considerations in Sweet Gas Well Corrosion, paper No. 46, NACE International Annual Conference.

Eilers, L.H. and Root, R. L. 1976. Long-Term Effects of High Temperature on Strength Retrogression of Cements, paper SPE 5871 presented at SPE California Regional Meeting, 7-9 April, Long Beach, California.

Evans, G.W. and Carter, L.G. 1964. A study of cement-pipe bonding, Journal of Petroleum Technology, Vol. 16, Num. 2, Pages 157-160.

Fardisi, S., Tajallipour, N. and Teevens, P., 2012. Predicting General Corrosion Rates in Sour Environments with the Growth of a Protective Iron Sulphide Film, paper No.1471, NACE international annual conference, Houston, Texas.

Harker, R.I. 1965. Scawtite and its Synthesis, Mineral Magazine, Vol. 34, Num. 268, 232-236.

Lea, F.M. 1971. The Chemistry of Cement and Concrete, 3rd Edition, Chemical Publishing Co., New York City, 177-202.

Muhammad, H. and Fathaddin, T. 2005. Effects of Additives and Conditioning Time on Compressive and Shear Bond Strengths of Geothermal Well Cement, paper presented at the World Geothermal Congress 2005, Antalya, Turkey, 24-29 April.

Santra, A., Reddy, B.R., Liang, F. and Fitzerald, R. 2009. Reaction of CO_2 with Portland cement at Downhole Conditions and the Role of Pozzolanic Supplements, paper SPE 121103 presented at SPE International Symposium on Oilfield Chemistry, 20-22 April, The Woodlands, Texas.

Woollam, R., Tummala, K., Vera, J. and Hernandez, S., 2011. Thermodynamic Prediction of FeCO3/FeS Corrosion Product Films, paper No. 76, NACE international annual conference, Houston, Texas.

Song, F.M. 2010. A Comprehensive Model for Predicting CO2 Corrosion Rate in Oil and Gas Production and Transportation Systems, ElectroChimica Acta 55, p. 689.

Sun, W. and Nesic, S., 2009. A Mechanistic Model of Uniform Hydrogen Sulphide/ Carbon Dioxide Corrosion of Mild Steel, paper No. 5, pp. 291-307, NACE International Annual Conference.

Appendix A: Corrosion Behavior of Tubulars under Sour Gas Environment

Theoretical and modeling studies on tubular corrosion were continued. A new model developed by Sina et at. (2012) has been investigated. The model has been formulated to predict uniform corrosion rate in CO_2/H_2S containing corrosive environment. The model accounts for the transit chemical reactions that take place in the bulk solution, the transport of active species towards and away from the metallic surface and the electrochemical reactions at the steel surface. In addition, the model considers the formation of corrosion scale and its effect on the corrosion rate.

The rate of corrosion-scale formation (scale precipitation rate) in sour environments has been described as:

$$PR = \frac{\partial C_{Scale}}{\partial t}, \quad \text{.....} \quad \text{(A-1)}$$

where t denotes time, C_{Scale} is the concentration of corrosion scale in the solid state, and PR is the scale precipitation rate that is predicted by a semi-empirical correlation. This approach has been applied to predict $FeCO_3$ and FeS formation in sour environment. However, it has been concluded (Sun and Nesic, 2009) that Eq. (A-1) provides reasonable predictions when it is applied to $FeCO_3$ formation rather than FeS precipitation. The inaccuracy of the model for FeS precipitation rate prediction is because various mechanisms are involved in the formation the corrosion scale. For instance, iron sulfide (FeS) is formed due to direct reaction of $H_2S_{(aq)}$ with the metallic surface meanwhile the iron carbonate scale is formed on the steel surface by precipitation when the localized concentration of $FeCO_3$ in the solution reaches above the saturation limit.

Due to the complexity of corrosion scale modeling, Sina et al. (2012) proposed a method that decouples scale growth calculation from corrosion-rate computation. In the model, scale growth calculation is preformed first. After determining the thickness and porosity of the corrosion scale, the corrosion rate is computed. However, this modeling approach accounts only for the formation of iron sulfide scale and assumes minimal precipitation of $FeCO_3$. This assumption is in agreement with the available data in the literature that shows limited occurrence of iron carbonate formation in sour environment. Iron carbonate scale forms when the partial pressure ratio of CO_2 and H_2S is greater than 500 (Dunlop et al. 1983). The limiting value of the partial pressure ratio increases as the environmental temperature increases (Woollam et al. 2011). In another words, the carbon dioxide causes steel corrosion and has negligible effect on corrosion scale formation except when CO_2 concentration is very high (more than 99.8%). On the contrary, H_2S has little contribution to the corrosion reaction, since it forms very weak acid and its cathodic reaction is negligible.

A.1. Model Formulation

The new model is developed based on the assumption that electrochemical reaction is the dominant process that controls the corrosion process in CO_2/H_2S environment. The model neglects the variation in species concentration parallel to the metallic surface. Figure A-1 presents a simplified schematic of the corrosion process, which shows all the reactions involved in the corrosion process. The schematic also presents the corrosion scale with thickness δ_S that is varied with time and thin layer of electrolyte with thickness δ_E = 1 cm has been recommended by Song (2010). Beyond these two layers, the turbulent diffusion is assumed to be strong enough to keep all the bulk concentrations uniform and in equilibrium state.

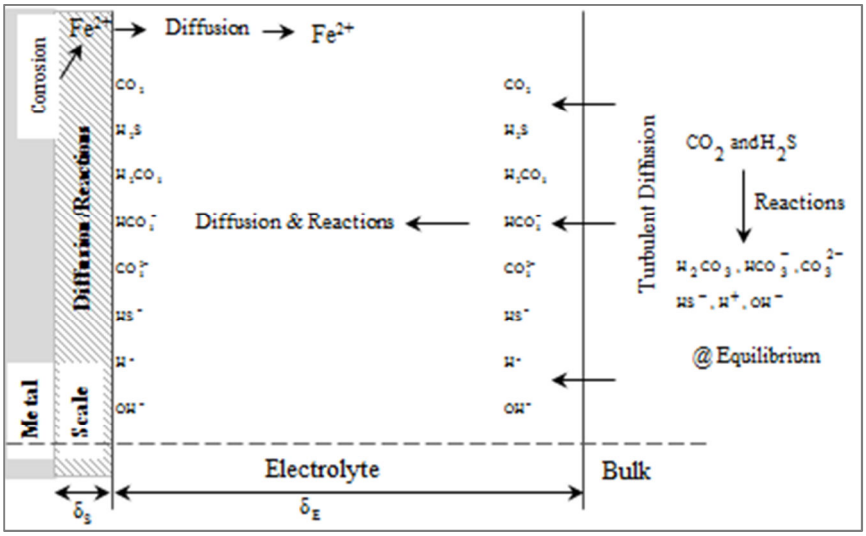

Fig. A-1 Schematic presentation of corrosion process

A.1.1 Chemical Reactions

The corrosion processes of both gases (CO_2 and H_2S) are demonstrated in Fig. A-1. The major reactions that occur in the bulk solution include CO_2 hydration, two steps of H_2CO_3 dissociation, the first step of H_2S dissociation and water dissociation. These reactions along with their equilibrium constants are presented here:

$$CO_2 + H_2O \Leftrightarrow H_2CO_3 \qquad K_{CO2} = \frac{C_{H2CO3}}{C_{CO2}}, \quad \ldots\ldots\ldots\ldots\ldots\ldots\ldots\ldots\ldots\ldots \text{ (A-2)}$$

$$H_2CO_3 \Leftrightarrow H^+ + HCO_3^- \qquad K_{H2CO3} = \frac{C_{HCO_3^-}.C_{H+}}{C_{H2CO3}}, \quad \ldots\ldots\ldots\ldots\ldots\ldots\ldots\ldots \text{ (A-3)}$$

$$HCO_3^- \Leftrightarrow H^+ + CO_3^- \qquad K_{HCO_3^-} = \frac{C_{CO_3^-}.C_{H+}}{C_{HCO_3^-}}, \quad \text{..... (A-4)}$$

$$H_2S \Leftrightarrow H^+ + HS^- \qquad K_{H2S} = \frac{C_{HS^-}.C_{H+}}{C_{H2S}}, \quad \text{.....(A-5)}$$

$$H_2O \Leftrightarrow H^+ + OH^- \qquad K_{H2O} = C_{H+}.C_{OH^-}, \quad \text{..... (A-6)}$$

Correlations for equilibrium constants of hydration and dissociation processes are provided in the Appendix B. These processes create an acidic environment and generate hydrogen, carbonate and sulfide ions. Subsequently, the diffusion process begins when the ions move from high-concentration to low-concentration zones through the electrolyte layer and corrosion scale toward the steel surface. At same moment, the iron dissolves into the solution forming Fe^{2+} ions that can also diffuse from the metal surface to the bulk solution.

A.1.2 Electrochemical Reactions

The electrochemical process involves anodic and cathodic reactions that occur at the same time at the steel surface. The anodic reaction is represented by the dissolution of the iron to ferrous ions.

$$Fe \rightarrow Fe^{2+} + 2e^-, \quad \text{..... (A-7)}$$

Due to the iron dissolution, valence electrons will be created on the metal surface resulting in negative charge. These electrons will be consumed by the cathodic reactions such as the reduction of hydrogen ions, carbonic acid and water. The cathodic reactions are expressed as:

$$2H^+ + 2e^- \rightarrow H_2, \quad \text{..... (A-8)}$$

$$2H_2CO_3 + 2e^- \rightarrow H_2 + 2HCO_3^-, \quad \text{..... (A-9)}$$

$$2H_2O + 2e^- \rightarrow H_2 + 2OH^-, \quad \text{..... (A-10)}$$

Electrochemical reaction rates are expressed in terms of current density, i, that can be obtained using Nernst equation:

$$i = \pm i_o \times 10^{\pm\frac{E-E_{rev}}{b}}, \quad \text{..... (A-11)}$$

The positive/negative sign represents the anodic/cathodic reactions. All parameters in Eq. (A-11) are defined in Appendix B including i_0 (reference exchange current density), E_{ref} (the reversible potential), b (the Tafel slope) and E denotes the surface potential. For spontaneous corrosion process, the unknown electrical potential at the metal surface (called corrosion potential and open-circuit potential) can be obtained from the charge balance equation at the metal surface:

$$\sum_{1}^{n_a} i_a = \sum_{1}^{n_c} i_c \ , \quad \text{..... (A-12)}$$

where, n_a and n_c are the total number of anodic and cathodic reactions, respectively. The exact solution for the surface potential is given as:

$$\mathrm{E} = \mathrm{b_c}.\log \mathrm{P}, \quad \text{..... (A-13)}$$

where:

$$\mathrm{P} = \left[\left(\mathrm{i_{oH+}} \times 10^{\frac{\mathrm{E_{revH}}}{\mathrm{b_c}}} + \mathrm{i_{oH2CO3}} \times 10^{\frac{\mathrm{E_{rev}}}{\mathrm{b_c}}} + \mathrm{i_{oH2O}} \times 10^{\frac{\mathrm{E_{rev}}}{\mathrm{b_c}}} \right) \frac{10^{\frac{\mathrm{E_{ref}}}{\mathrm{b_a}}}}{\mathrm{i_{oFe}}} \right]^{\frac{1}{\mathrm{m+1}}}, \text{ where } \quad m = \frac{b_c}{b_a}, \text{ ..... (A-14)}$$

A.1.3 Corrosion Scale

The protective corrosion scale results in reduction of the uniform corrosion rate due to the following reasons: i) creating a diffusion barrier resulting in reduced species (ion) transport; and ii) covering a portion of the metal surface resulting in reduced electrochemical reaction rate. The effects of the scale on corrosion rate can range from being insignificant (non-protective scale) to the most dominant controlling factor. The level of influence dependents on the properties of the corrosion scale, most importantly its type, thickness and porosity. The available experimental data in the literature showed that makinawite (FeS) is the main product of sour gas corrosion with partial pressure ratio (P_{CO2}/P_{H2S}) of less than 500. The possible mechanism for the formation of mackinawite is the solid-state growth, which is defined as the diffusion of a species into the metal leading to the direct reaction resulting in solid scale. The diffusion process could also occur in both directions, either Fe ions diffuse outward through the makinawite layer and react with the sulfide species (H_2S, HS^-, or S^{2-}) or sulfide species diffuse inward to react with Fe ions. It has been reported (Sun and Nesic, 2009) that the inward diffusion is more consistent than the outward. Amri and Varekval (2011) investigated these two diffusion scenarios by studying the characteristics and the probability of the lattice diffusion of iron and sulfide species in the mackniwaite layer. They found

that: i) the diffusion of H_2S through the mackinwaite layer is impossible at the room temperature; and ii) the lattice diffusion of iron is faster than the sulfide species in a rigid structure of pyrrhotite layer.

After investigating the formation of mackniawite layer, Sina et al. (2012) developed the following correlation to predict the Mackniawite layer thickness as a function of exposure time.

$$\mathrm{th} = 1.17\times10^{-11}\left(1+\frac{\mathrm{T}-293}{90}\right)\left(\mathrm{P_{H2S}}\times\mathrm{t}\right)^{0.5}\left(\mathrm{pH}^2-6\mathrm{pH}+9.5\right), \quad \text{(A-15)}$$

where th is thickness of scale in meter, T is temperature in Kelvin, P_{H2S} is partial pressure of H_2S in Pa, t is time in second. The initial thickness is assumed to be 1 µm. Numerically, the growth in the scale thickness is predicted as a function of P_{H2S}, temperature, time and pH of the solution.

$$\mathrm{th}(\mathrm{t}+\Delta\mathrm{t}) = \mathrm{th}(\mathrm{t}) + \frac{\partial \mathrm{th}}{\partial \mathrm{t}}\Delta\mathrm{t}, \quad \text{(A-16)}$$

where Δt is the time step, $\frac{\partial th}{\partial t}$ is obtained by differentiating Eqn. (A-15) with respect to time. In addition to the thickness of the mackinawite layer, other properties are required to simulate the corrosion process such as porosity of the layer. To simulate the corrosion process, a constant porosity value 0.9 is often assumed (Song 2010).

A.1.4 Transport Process

The electrochemical reactions that occur on the steel surface can consume and/or produce chemical species resulting in concentration gradient normal to the surface. The surface reactions will induce a flux of chemicals towards or away from the surface in the case that corrosive species diffuse to the surface and produced species (Fe^{2+}) diffuse through the corrosion scale to the bulk solution. Mass transfer can be one of the key processes that affect the corrosion rate. The impact of the scale layer on the corrosion is hindering the mass transfer process by forming a diffusion barrier.

As mentioned earlier, the bulk solution is in equilibrium state due turbulent diffusion. This equilibrium will be disturbed due the corrosion process. During the corrosion process, the chemical reactions (Eqns. from A-2 to A-6) occur in the bulk solution and produce species $(CO_3^{2-}, H^+, HS^-, S^-)$ that diffuse through the electrolyte layer. It is important to determine the contribution of these reactions to the corrosion process. The reactions from Eqn. (A-3) to (A-6) are assumed to be in equilibrium state while the hydration reaction of the carbon dioxide is considered as the slowest one that controls the rate. The rate of forward hydration reaction (A-2) is expressed as:

$$\mathrm{RR} = \mathrm{K_f}.\mathrm{C_{CO2}} - \mathrm{K_b}.\mathrm{C_{H2CO3}}, \quad \text{(A-17)}$$

where RR is the reaction rate, K_f and K_b are the forward and backward kinetics constants for the carbon dioxide hydration reaction. Because of chemical reaction in the bulk solution and electrochemical reaction at the steel surface, nine species will be created into the electrolyte layer. The nine species are $CO_2, H_2CO_3, HCO_3^-, CO_3^{2-}, H_2S, HS^-, H^+, OH^-$ and Fe^{2+}. Species conservation equation (mass balance) is used to describe the transport of all species in the solution, irrespective of whether the species are involved in the electrochemical reaction or the chemical reaction. The equation that describes the transport of species (i) in the presence of the chemical reactions can be expressed as:

$$\phi \frac{\partial C_i}{\partial t} = kD \frac{\partial^2 C_i}{\partial X^2} + \phi . RR \quad \text{..... (A-18)}$$

where C_i is the concentration of species (i), ϕ and k are the volumetric porosity and surface permeability of the corrosion scale, respectively. RR is the reaction rate, t is time and x is the spatial coordinate. It is required to solve nine transport equations in order to find all the species concentrations. Model implementation and calculation procedure will be presented in the coming report.

Appendix B: Parameters Used to Predict Corrosion Rate

All the parameters (constants of the hydration and dissociation process and electrochemical calculation) that can be used to predict the corrosion rate are provided here. The correlations were adopted from the literature (Song 2010).

B.1 Hydration and dissociation constant

$$K_{CO2} = 2.5\times10^{-3},\ K_f = 10^{329.85-110.541\log T-\frac{17,295.4}{T}}\ \text{(1/S)},\ K_b = \frac{K_f}{K_{CO2}}\ \text{(1/S)}$$

$$K_{H2CO3} = 387.6\times10^{-\left(6.41-0.001594\times Tf+8.52\times10^{-6}\times T_f^2-3.07\times10^{-5}\times P-0.4772\times\sqrt{I}+0.1180\times I\right)}\ \text{(mol/L)}$$

$$K_{HCO_3^-} = 10^{-\left(10.61-0.00497\times Tf+1.331\times10^{-6}\times T_f^2-2.624\times10^{-5}\times P-1.166\times\sqrt{I}+0.3466\times I\right)}\text{(mol/L)}$$

$$K_{H2S} = 10^{-\left(15.345-0.045676\times T+5.9666\times10^{-5}T^2\right)}\ \text{(mol/L)}$$

$$K_{H2O} = 10^{-\left(29.3868-0.0737549\times T+7.4781\times10^{-5}T^2\right)}\ \text{(mol/L)}^2$$

B.2 Value of the parameters involved in the electrochemical calculations hydrogen reduction

$$i_{H^+} = -i_{0H^+}\times10^{-\left(\frac{E-E_{revH^+}}{b_c}\right)}\ \text{(A/m}^2\text{)},\quad i_{0H^+} = 0.05\left(\frac{C_{H^+}}{1\times10^{-4}}\right)^{0.5}\times e^{\frac{-30,000}{R}\left(\frac{1}{T}-\frac{1}{298}\right)}\ \text{(A/m}^2\text{)}$$

$$E_{revH^+} = \frac{-2.303RT}{F}pH\ \ \text{(V)}\qquad ,\ b_C = \frac{2.303RT}{2F}\qquad \text{(V)}$$

Carbonic acid reduction

$$i_{H_2CO_3} = -i_{0H2CO3}\times10^{-\left(\frac{E-E_{revH_2CO_3}}{b_c}\right)}\text{(A/m}^2\text{)}$$

$$i_{0H2CO3} = 0.06\left(\frac{C_{H^+}}{1\times10^{-5}}\right)^{-0.5}\times\left(\frac{C_{H2CO3}}{1\times10^{-4}}\right)\times e^{\frac{-50,000}{R}\left(\frac{1}{T}-\frac{1}{298}\right)}\ \text{(A/m}^2\text{)}$$

$$E_{revH_2CO_3} = \frac{-2.303RT}{F}pH\ \ \text{(V)},\ \ b_C = \frac{2.303RT}{2F}\qquad \text{(V)}$$

Water reduction

$$i_{H_2O} = -i_{0H2O} \times 10^{-\left(\frac{E-E_{refH_2O}}{b_c}\right)} (A/m^2), \quad i_{0H2O} = 0.002 \times e^{\frac{-35{,}000}{R}\left(\frac{1}{T}-\frac{1}{298}\right)} (A/m^2)$$

$$E_{refH_2O} = -0.275 \ (V), \quad b_C = \frac{2.303RT}{2F} \qquad (V)$$

Iron oxidation

$$i_{Fe^{2+}} = -i_{0Fe^{2+}} \times 10^{-\left(\frac{E-E_{revFe}}{b_a}\right)} (A/m^2)$$

$$i_{0Fe^{2+}} = 0.06\left(\frac{C_{H^+}}{1\times10^{-4}}\right)^{A_1} \times \left(\frac{C_{CO2}}{0.0366}\right)^{A_2} \times e^{\frac{-37{,}500}{R}\left(\frac{1}{T}-\frac{1}{298}\right)} (A/m^2)$$

$$E_{revFe} = -0.488 \ (V), \quad b_a = \begin{cases} 0.03V.....pH < 4 \\ 0.08V.....4 < pH < 5 \\ 0.12V.....pH > 5 \end{cases}$$

$$A_1 = \begin{cases} 1.....P_{CO2} < 1bar \\ 0.....P_{CO2} > 1bar \end{cases}, \qquad A_2 = \begin{cases} 2.....pH < 4 \\ 1.....4 < pH < 5 \\ 0.....pH > 5 \end{cases}$$

Appendix C

MINUTES

4th Technical Advisory Board Meeting

E12PC00035

Project Title: Effect of H_2S and CO_2 in HPHT Wells on Tubulars and Cement

Meeting Date: May 7, 2013
Time: 8:30 AM – 3:30 PM Central Time
Meeting Location: Schlumberger Client Support Lab (CSL), 16115 Park Row, Suite 190, Houston, TX, 77084

Attendees: Andreas Brandl (Baker Hughes), Arild Saasen (Det Norske), Ashok Santra (Weatherford International), Marco May (Vallourec), Sam Lewis (Halliburton) , Ramadan Ahmed (OU), Samuel Osisanya (OU), Omotayo Omosebi (OU), Rida Elgaddafi (OU), Adarsh Naidu (OU), Aman Srivastava (OU), Himanshu Maheshwari (OU), Jueng Hwang (OU), Munraj Sharma (OU), Sagar Tale (OU)

Online Attendees: Candi Hudson (BSEE COR)

This was the 4th Technical Advisory Board meeting of the Project # E12PC00035 titled "Effects of Hydrogen Sulfide (H_2S) and Carbon Dioxide (CO_2) in HPHT Wells on Tubulars and Cement."

Dr. Ahmed started the meeting at 9:00 AM on Tuesday May 7, 2013 by welcoming Candi Hudson and other participating Technical Advisory Board (TAB) Members to the meeting. Then, he gave an overview of the project status to date. Dr. Ahmed enumerated the objectives, scope, project schedule, project deliverables to date, and challenges. The major challenges are equipment deliverability, high-pressure gas leaks, problems with heating system. These are due to the nature of the project. Now, we use synthetic oil to heat the aging cell in a closed loop system instead of an open circulating bath.

Major objectives are divided into three main tasks: one theoretical and two experimental tasks. The first task is theoretical and deals with understanding of the degradation of tubulars and cement in the presence of sour gases (H_2S and CO_2) under HPHT conditions. The second task is the experimental work to investigate the degradation of cement in the presence of sour gases under

HPHT conditions. The third task is also experimental study on the degradation of tubulars in the presence of sour gases under HPHT conditions.

Eight technical presentations were made, which addressed the objectives and tasks stated in the contract. Five presentations on the effects of sour gases on porosity, permeability, and mechanical properties of cement as well as new cement formulations to prevent cement degradation in the presence of sour gases at HPHT. Three presentations were on the effects of sour gases on corrosion of tubulars. Below are the summary of the various presentations.

1st Presentation - Himanshu Maheshwari (MS Graduate Student) – Effects of CO_2 Gas Exposure on Permeability and Porosity of Cements

Mr. Maheshwari presented the results of experimental studies of the effects of sour gases exposure on the permeability and porosity of oil well cements under various conditions of pressure, temperature, and CO_2 concentrations. The results are as follows:

Gas Composition Effect: At 10% CO_2, carbonation and hydration are dominating phenomena whereas as gas composition is increased, leaching starts to dominate. Carbonation increases with increase in CO_2 concentration.

Temperature Effect: At low CO_2 concentrations, as temperature is increased, there is more carbonation and hydration domination; hence porosity (ξ) and permeability (k) decrease.

Fourier Transformation Infrared (FTIR) and x-ray diffraction (XRD) present the direct measurement of carbonation and leaching thereby complimenting the porosity-permeability data. FTIR is qualitative while XRD is qualitative and quantitative. Results from FTIR and XRD complemented each other qualitatively. Scanning electron microscope (SEM) images showed carbonation front.

Future Plan:

- Study the effects of pressure, temperature, and gas composition on porosity and permeability of set cement.
- Validate cement degradation model with experimental data

Suggestion from Advisory Board:

- Members suggested running porosity and permeability tests on unaged sample for long time.
- Air content in cement slurry - To consult one of the articles by Hodne, N.N. and Saasen, Cement & Concrete Research.

2nd Presentation - Omotayo Omosebi (PhD Graduate Student) – Compressive Strength of Cement in CO_2 Environment

Mr. Omosebi presentation focused on the effect of cement degradation on compressive strength elasticity of set cement aged under sour gases environment. Tests were performed on un-aged and aged cement cores. Aging was carried out varying temperature and CO_2 concentration.

The following conclusions were highlighted:

- Generally, presence CO_2 produces stronger cement due to combined effect of carbonation and hydration.
- At high temperature, carbonation is more dominant, hence a stronger cement.
- At low temperature, rate of carbonation is offset by leaching which leads to net effect on compressive strength development.
- For unaged cement samples, leaching is due to formation of $CaCO_3$.

These results explained the mechanisms for cement degradation due to carbonation, leaching, and hydration. The degradation phenomenon is higher in aggressive environment such as HPHT, CO_2, and H_2S. C_3S plays major role on the initial compressive strength development. In summary, leaching, carbonation, and hydration compete under different temperature conditions. Carbonation dominates at high temperature.

Future Plan: To develop fully couple cement degradation model.

Suggestions from Advisory Members:

- To acquire cement samples from different manufacturers.
- Look at FTIR and XRD under HPHT in order to come up with strong conclusions on compressive strength of cement.

3rd - Presentation – Jueun Hwang (MS graduate student) – Shear Bonding Strength (SBS) of Cements in CO_2 Environment

Ms. Hwang presented the objectives for shear bonding strength (SBS) of cement. Results show the following:

- SBS increased with temperature up to 350oF but level of increase reduces as leaching intensified at high temperature. SBS of HS and HSF improved during the aging period up to 28 days.
- Carbonation improved the SBS at high temperature but insignificant at low temperature.
- There was a reverse trend between elastic stiffness and SBS for cement samples aged in CO_2 environment.

Suggestions from Advisory Members: One advisory board member suggested changing the bonding test-sample design. In the suggested design, the cement will be placed outside the pipe rather than inside the pipe.

Future Plans:

- Focus on SBS modeling
- Study the effects of H2S and CO_2 on SBS under HPHT.

4th Presentation - Aman Srivastava (MS Graduate Student) – Effects of Various Additives on Degradation Resistance of Oil Well Cements

Mr. Srivastava presentation focused on the development of new cement formulation for lowering the degradation rate of set cement due to acid attack. One of the major objectives of the research is to develop special cement formulation, which can resist the HPHT sour gas environment. Five additives, Zinc Oxide, Micro Silica and Latex, Magnesium Oxide (MgO) and Hydroxyapatite (HOAP) were considered in the investigation. MgO and HOAP proved to be effective additives against the carbonation process. HOAP was observed to reduce the carbonation and leaching of cement. This was confirmed by FTIR, which indicated presence of higher amount of $Ca(OH)_2$ in the middle zone of HOAP cores than the baseline samples. HOAP forms $Ca5.(PO_4)_3.CO_3$ which in turn formed a protective layer thus preventing further cement carbonation.

Future Plan:

- Perform additional experiments in order to test the effectiveness of all these additives varying compositions and aging conditions.

5th Presentation – Mounraj Sharma (MS Graduate Student) – Effects of H2S on Degradation Behavior of Cement

Mr. Sharma presented the outcomes of four papers reviewed on the effect of H_2S on cement degradation. The major outcomes are: (i) H_2S cause sulfidation of cement; (ii) H2S penetrates the cement matrix faster than CO_2; and (iii) At low pH cement leaching is accelerated.

Future Plans:

- Conduct experiments with H2S (max. 1%) to study its effect on cement degradation
- Investigate the effect of sulfidation on the properties of cement and low pH on cement leaching due to H2S dissolution.

6th Presentation by Rida Elgaddafi (PhD Graduate Student) – Corrosion Behavior of Tubulars in Sour Gases Environment

Mr. Elgaddafi discussed the factors affecting corrosion rate of tubulars as well as the corrosion mechanisms. The major factors are the environment, material types, and formation of corrosion scale. Emphasis is given for formation of corrosion scale. Corrosion rate is a function of pH, T, flow velocity, and corrosion scale. Based on these factors two models for CO_2/H_2S corrosion rates were developed for mass transfer and electrochemical process dominated conditions.

Future Plans:

- Start the experimental investigation of CO_2/H_2S corrosion behavior on tubulars under HPHT conditions. Experimental methods planned are linear polarization resistance (LPR) and weight loss technique. Use the experimental data to verify and calibrate models.
- Submit papers based on present outcomes with the aim of getting feedbacks in order to improve the research.

7th Presentation by Adarish Naidu (MS Graduate Student) – Corrosions of Tubulars Exposed to Fluids Containing CO_2

Mr. Naidu presented the fundamentals of CO_2 corrosion mechanism for tubulars. Corrosion process involves: (i) dissolution of CO_2; (ii) transportation of reactants from bulk to the metal surface; (iii) electrochemical reaction on the metal surface; and (iv) transportation of corrosion products from the scale surface to the bulk solution. Based on these four phenomena, a mechanistic model was developed to predict CO_2 corrosion rate. Modeling results were compared with experimental data from the literature. Predictions show good agreement with the measurements

Future Plans:

- Start the experimental studies of corrosion of tubulars. The experiments are divided into several parts as follows:
    I. Preliminary corrosion experiments using para-cell kit and electrochemical corrosion using autoclave both in presence of 2% brine solution
    II. Weight loss technique
    III. Linear polarization resistance technique
    IV. Validate model with experimental data

8th Presentation – Sagar Tale (MS Graduate Student) – Stress Corrosion Cracking (SCC) of Tubulars in H_2S Environments

Mr. Tale discussed the approach and scope of the research on stress corrosion cracking of tubulars in the presence of H_2S. He reviewed four papers on the subject. The outcomes of the papers are as follows:

- SCC rate depends on concentration of H_2S.
- Local hard zones formed during welding of casing act as nucleation site for H_2S corrosion
- Cementite precipitation and inter-lath constituents act as nucleation sites for SCC crack.

Future Plans:

- Continue with literature review
- Test various grades of casing in H_2S environment under tensile loading conditions
- Develop mathematical model to predict time to failure of various materials under different loading conditions

Date for Next Advisory Board Meeting

The time for the next advisory board meeting has not be set. Once done, it will be communicated to the BSEE COR and advisory board members.

Appendix D: Response to Comments on Progress Reports #18 & 19

Progress Report #18

2.2.4 Additive Screening Study

- What's the composition of the new micro-silica cement slurry formulation? E.g. what's the composition amount of silica, etc.?

Response: Old and new formulations of micro-silica cement are presented here.

Table D-1: Slurry Composition for Micro Silica (Old formulation)

Component	HSMS	GSMS
Cement	100%	100%
Silica Flour	15% bwoc	15% bwoc
Micro Silica	20% bwoc	20% bwoc
HEC	0.1% of water for fillers	0.1% of water for fillers
Antifoam Agent	0.1 gal/sack of cement	0.1 gal/sack of cement
Water for Cement	38% bwoc	44% bwoc
Water for Silica Flour	38.5% bwoc	38.5% bwoc
Water for Micro Silica	0.13cc/ gm of Micro Silica	0.13cc/ gm of Micro Silica
Dispersant (NSF)	1.75% bwoc	1.75% bwoc
bwoc = by weight of cement		

Table D-2: Slurry Composition for Micro Silica (New formulation)

Component	HSMS	GSMS
Cement	100%	100%
Silica Flour	15% bwoc	15% bwoc
Micro Silica	20% bwoc	20% bwoc
HEC	0.1% of water for fillers	0.1% of water for fillers
Antifoam Agent	0.1 gal/sack of cement	0.1 gal/sack of cement
Water for Cement	38% bwoc	44% bwoc
Water for Silica Flour	38.5% bwoc	38.5% bwoc
Water for Micro Silica	0.13cc/ gm of Micro Silica	0.13cc/ gm of Micro Silica
Dispersant (NSF)	1.75% bwoc	1.75% bwoc
Retarder (Citric Acid)	0.03% bwoc	0.06% bwoc
bwoc = by weight of cement		

3. Planned Activities

- What specifically will be performed regarding the continued theoretical and modeling studies on tubular degradation?

Response: A recent corrosion rate model developed by Sina et at. (2012) has been investigated and the detail is presented in this report. The model has been implemented in Matlab to perform corrosion predictions. Model predictions will be presented in the coming reports. In addition, we are studying the corrosion mechanisms of sulfide stress cracking. We are developing experimental database from published literature for uniform corrosion and sulfide stress cracking.

Progress Report #19

2.1.2 FTIR Spectroscopy

- Page 5 – Need clarification on the following statements: "At 225°F, CH is completely consumed in all zones of the core. The reason for this can be attributed to the effects of temperature on the solubility of CO_2 and ionic diffusion."
    - Ionic diffusion of what? Ca^{2+}? CO_2?

Response: Ionic diffusion of HCO_3^- and CO_3^{2-}.

- Page 5 – Need clarification on the following statements: "At low temperatures (100°F), CO_2 solubility is high but the ionic diffusion on the pore space is low resulting in a lower rate of carbonation. However, at high temperature (350°F), the ionic diffusion is high but CO_2 solubility is low limiting the rate of carbonation."
    - Does this mean CO2 is the rate-limiting step at 350°F?

Response: The concentration dissolved CO_2 at the reaction site (in the pore space) is one of the factors that control the rate of carbonation.

2.2.4.1 Hydroxyapatite Containing Cement

- Page 11- Should the following equation below:
    - $2Ca_5(PO_4)_3(OH)+CO_3^{-2} \rightarrow 2Ca_5(PO_4)3(CO_3)+OH^{-2}$, …… (D-1)
    - Actually be:
      $2Ca_5(PO_4)_3(OH)+CO_3^{-2} \rightarrow 2Ca_5(PO_4)_3(CO_3)+2(OH^-)$, …… (D-2)

Response: Yes, Eqn (D-2) the correct form.

2.3 Experimental Studies on Corrosion of Tubulars (Task 3)

- Need clarification – what's the actual temperature value for the medium temperature set up?

Response: The set-up is only for preliminary tests with maximum temperature of 150ºF.

- What pressure(s) will these test be performed?

Response: maximum pressure of 300 psi.

3. Planned Activities

- What specifically will be performed regarding the continued theoretical and modeling studies on tubular degradation?

Response: A recent corrosion rate model developed by Sina et at. (2012) has been investigated and the detail is presented in this report. The model has been implemented in Matlab to perform corrosion predictions. Model predictions will be presented in the coming reports. In addition, we are studying the corrosion mechanisms of sulfide stress cracking. We are developing experimental database from published literature for uniform corrosion and sulfide stress cracking.

Project Title: Effect of H_2S and CO_2 in HPHT Wells on Tubulars and Cement

Report Type: Monthly Report

Report #: 21

Reporting Period: May 22nd, 2013 to June 21st, 2013

Authors:

Ramadan Ahmed, Principal Investigator

Subhash Shah, Co-Principal Investigator

Samuel Osisanya, Co-Principal Investigator

Rida Elgaddafi, Research Assistant

Omotayo Omosebi, Research Assistant

Himanshu Maheshwari, Research Assistant

Adarsh Naidu, Research Assistant

Aman Srivastava, Research Assistant

Jueun Hwang, Research Assistant

Mounraj Sharma, Research Assistant

Sagar Tale, Research Assistant

Prepared under BSEE Project # E12PC00035

by

THE UNIVERSITY OF OKLAHOMA

August 1, 2013

1. Summary of Accomplishments

This monthly report presents the progress made during the project period May 22, 2013 to June 21, 2013. Investigations on cement and tubular degradation were continued during this reporting period. Cement cores and bonding samples of different cement formulations were prepared and aged in acidic environment to study their degradation characteristics. Properties of the samples were measured before and after aging. New cement formulation studies were continued. The effects of different additives on properties of cement slurries and cores were investigated.

Two aging experiments (Experiments 14 and 15) were performed during this month. The samples were aged for 2 weeks in 2% brine saturated with CO_2 containing methane gas. After aging, physical properties of aged and unaged samples were measured. In addition, mineralogical properties of the samples were analyzed using Fourier Transform Infrared Spectroscopy (FTIR).

Aging tests conducted at different pressures showed consistent porosity and permeability trends at different CO_2 concentrations. Compressive strength measurements indicate increased carbonation of Class G and Class H samples at high aging pressure. This is consistent with previous results obtained at a different CO_2 concentration. Shear-bonding strength of the samples did show significant change when the pressure was varied.

Experimental investigations on cement additives were continued. The effects of different additives (hydroaxipitate, magnesium oxide, micro-silica and latex) on performance of Class H and Class G cements have been examined. Although the addition of hydroxyapatite (HOAP) is able to prevent the carbonation of the samples, the reduction in compressive strength above 300℉ limits its application for HPHT wells. With addition of silica flour, the basic strength of the cement reduced significantly. Further studies will be carried out to determine the quantity of silica flour needed to control the thermal retrogression while maintaining the basic strength.

According to the experimental results, adding MgO to the cement has been an effective method in preventing acid attack. However, GSMG samples aged at 9000 psi and 350℉ showed poor performance. Additional tests will be conducted to improve the performance of GSMG cement.

Although the preliminary results obtained from micro-silica cements are encouraging, the brittleness of the cores needs to be controlled. Testing with conventional SBR latex was continued. Cement slurries with carboxylated SBR latex exhibited excessive thickening.

Theoretical and modeling studies on uniform corrosion of tubular are in progress. A recent model has been utilized to compare with experimentally measured corrosion rate. The model predictions showed reasonable agreement with experimental measurements under high H_2S partial pressure and high-temperature condition.

A new corrosion experiment was performed using a carbon steel sample. Corrosion rate measurements obtained using weight-loss and LPR methods showed consistent results. Moreover, comparison of the measurements with model predictions shows satisfactory agreement.

Our plan for the upcoming weeks is to continue: i) aging tests at different pressures; ii) theoretical and modeling studies on tubular corrosion; iii) additive screening studies; iv) low pressure corrosion experiments at different CO_2 concentrations; and v) development of corrosion test setup.

2. Overall Project Progress

2.1 Theoretical Studies (Task 1)

2.1.1 Uniform Tubular Corrosion

Theoretical and modeling studies on uniform corrosion of tubular are in progress. A model developed by Fardisi et al. (2012) has been improved and utilized to predict experimentally measured corrosion rate. Model details are presented in the previous report (Report # 20).

Model Implementation

The improved corrosion model has been formulated and implemented in MATLAB as a program, which has a subprogram that performs electrochemical calculations and solves the transport equations to find the potential surface and species concentration distributions. The concentrations of species (CO_2 and H_2S) in the solution are predicted using solubility model developed in this study. The remaining species concentrations are computed using the equilibrium constants presented in Report # 20. The model requires the following parameters as input: temperature, CO_2 and H_2S partial pressures, initial concentrations of species, and the surface potential. The current densities of all cathodic and anodic reactions are calculated using electrochemical equations presented in Report # 20. Therefore, it is possible to calculate the net consumption/production of each species at the steel surface at any given time (t). These values are used to calculate the boundary conditions, which are required to solve the transport equations that provide new concentration of species at the next time step ($t+\Delta t$). **Figure 1** shows a simplified calculation procedure.

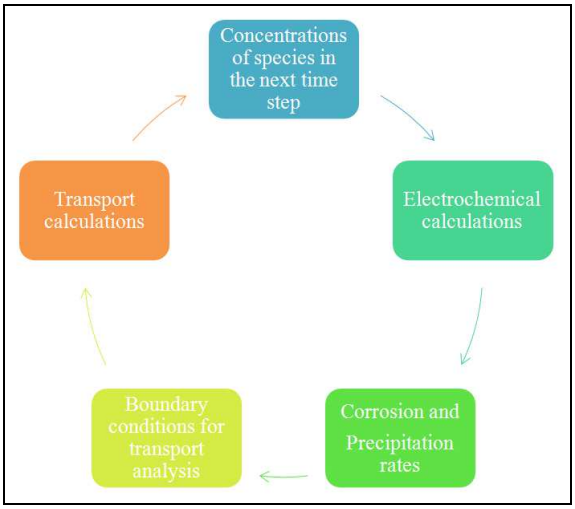

Fig. 1: Corrosion calculation procedure

Initial and Boundary Conditions

The initial condition for each species is defined as its concentration profile in the bulk solution under chemical equilibrium state. The initial concentration value is also considered as the boundary condition for the container wall, which is opposite to the metal surface. However, at the steel surface, the flux of species that are not involved in the electrochemical reactions is assumed negligible (zero). For those involved in the electrochemical reactions, the flux of species j at the metal surface can be determined using the Fickian diffusion model.

$$N_j = \frac{i_j}{n_j.F}, \quad \text{..... (1)}$$

Growth of Corrosion Scale

Corrosion scale mechanisms in sweet and sour environments have been extensively investigated (Kvarekval et al. 2003; John Lee, 2004; Sun et al. 2006; Svenningsen et al. 2009; Amri et al. 2011) applying both experimental and theoretical approaches. Different mechanisms are involved in the formation of corrosion scale such as nucleation, crystallization, agglomeration, and solid-state growth. Each mechanism has its own unique characteristics in terms of product layer (i.e. corrosion scale) morphology and growth rate. For instance, the precipitation of iron carbonate results in ordered crystal structure. Beside this, the precipitation process is slower than other mechanisms; and it is highly affected by the level of super-saturation.

The other possible mechanism for the formation of corrosion scale is solid-state growth such as the development of iron sulfide scale on steel surface in sour environment, which is caused by the diffusion of species into the metal leading to a direct chemical reaction. One of the characteristics of this mechanism is that the formation of corrosion scale is not strongly affected by the level of super-saturation; and it occurs faster than other mechanisms.

Due to the presence of different scale growth mechanisms, it is quite difficult to develop a universal approach for modeling corrosion scale. The model developed by Fardisi et al. (2012) has been proposed to distinguish between the scale-growth and uniform corrosion processes. They presented the following correlation to predict the thickness of Mackniawite layer as a function of time:

$$\delta_S = 1.17\times10^{-11}\left(1+\frac{T-293}{90}\right)\left(P_{H2S}\times t\right)^{0.5}\left(pH^2-6pH+9.5\right), \quad \text{..... (2)}$$

where δ_S is the thickness of corrosion scale in meter, T is temperature in Kelvin, P_{H2S} is partial pressure of H_2S in Pa and t is time in second. The initial scale-thickness is assumed to be 1 µm. The growth in the scale thickness is predicted as a function of P_{H2S}, temperature, time and pH of the solution. Thus:

$$\delta_S(\mathrm{t}+\mathrm{dt}) = \delta_S(\mathrm{t}) + \frac{\partial \delta_S}{\partial \mathrm{t}}\mathrm{dt}\,, \quad \ldots\ldots\ldots\

concentration profiles of the fictitious species are independent of the chemical reactions; as a result, the source terms are not shown in the model equations (Eqs. 7, 8 and 9). The remaining transport equations of iron and carbon dioxide are written as:

$$\phi \frac{\partial C_{Fe^{2+}}}{\partial t} = D_{Fe^{2+}} k \frac{\partial^2 C_{Fe^{2+}}}{\partial X^2}, \quad \text{..... (10)}$$

$$\phi \frac{\partial C_{CO2}}{\partial t} = D_{CO2} k \frac{\partial^2 C_{CO2}}{\partial X^2} + \phi RR_{CO2}, \quad \text{..... (11)}$$

where $D_{Fe2+} = 0.72 \times 10^{-9}$ m^2/s; $D_{CO2} = 2 \times 10^{-9}$ m^2/s; and RR is the rate of hydration of carbon dioxide. The source term is not included in the transport equation (Eqn. 10) due to the FeS precipitation in the scale layer. This is because the source of iron that forms iron sulfide scale is the metal itself and not the iron ions in the electrolyte.

In order to obtain numerical solutions, differential forms of the transport equations are discretized using finite difference method. An implicit approach is used to solve a system of equations (Eqs. 7 through 11). Two layers of computational grids (meshes) are constructed to represent the scale and electrolyte layers. As depicted in **Fig. 2**, the thickness of the scale layer is increased in each computational time step. The increment in the scale thickness is obtained from Eq. (3). The grids in scale layer are maintained uniform, but their size changes with computational time. In addition, the sizes of the grids in the electrolyte layer are increased by a factor of two in the direction normal to the steel surface. Based on this grid design, 20 nodes are used to mesh the whole geometry. Five nodes are used to discretize the scale layer.

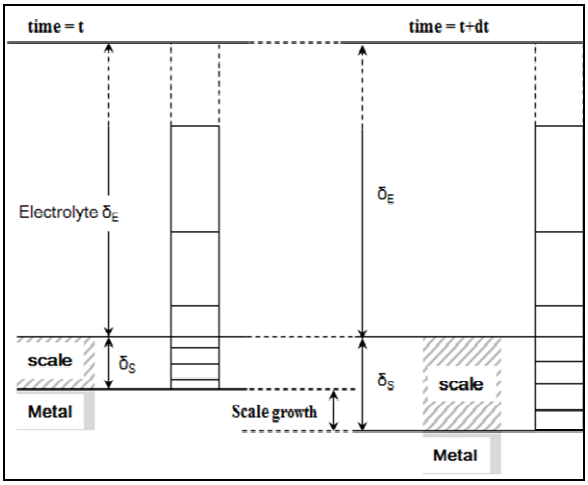

Fig. 2: Schematic of the grids structure

In order to obtain the numerical solutions, first all partial differential equations used in the model are transformed into a system of algebraic equations using the first order Eulerian approach for time and the third order discretization method for space. The algebraic system of equation is solved numerically to obtain the concentrations of the fictitious species (φ_1, φ_2, φ_3), Fe^{2+} and C_{CO2}. The concentrations of the remaining chemical species are computed using the equilibrium constants and Eqs. (4–6). Subsequently, electrochemical and precipitation calculations are performed using the new species concentrations and the boundary conditions for the model equations are updated.

The numerical computations need to be repeated, increasing the time step to obtain the concentration of each species as a function time.

Model Validation

The model predictions are validated with available experimental data (Bich and Goerz 1996) obtained under two different test conditions (**Table 1**). Due to an extensive computational time, only two cases are presented in this monthly report. As depicted in **Fig. 3a**, the model result demonstrates a reasonable agreement with experimental measurements under high H_2S partial pressure and high temperature condition. However, as the H_2S partial pressure is reduced (i.e. CO_2 partial pressure is increased), there is a considerable discrepancy between model prediction and measurement (**Fig. 3b**). In both cases, the model under-predicts the corrosion rate. The modeling study will be continued to reduce the computational time and improve model performance.

Table 1: Test conditions for corrosion experiments (Bich and Goerz 1996)

Case No.	Time (hr)	T (°C)	P_{total} (bar)	P_{CO2} (bar)	P_{H2S} (bar)	C_{CO2} (mol/m^3)	C_{H2S} (mol/m^3)
Case I	40	65	15.7	3.5	12.2	39.73	456.45
Case II	71	60	8.3	5.3	3	65.71	115.44

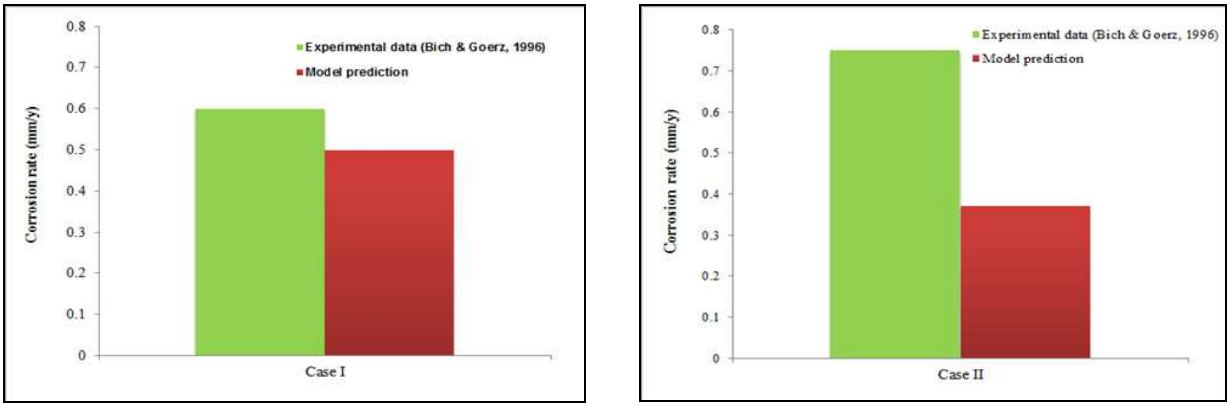

(a) **(b)**

Fig. 3: Comparison of model prediction with experimental data: a) Case I; and b) Case II

2.1.2 Sulfide Stress Cracking

Tubulars are extensively used in oil and gas resource-development and production. In some cases, reservoir fluids (oil and gas) contain H_2S, which leads to hydrogen embrittlement. This phenomenon is commonly known as Sulfide Stress Cracking (SSC). Studies on sulfide stress cracking on tubulars are limited. SSC is hydrogen embrittlement phenomenon caused by combined effect of stress and atomic hydrogen diffusion through the metal following corrosion by wet H_2S. SSC causes failure at much lower stress than ultimate tensile strength. A number of studies indicated that

microstructure, hardness, applied stress and H_2S concentration are main factors, which affect susceptibility of an alloy to the SSC.

In order to evaluate SSC resistance of metals, different methods have been developed including: i) tensile test; ii) Double Cantilever Beam (DCB) test; iii) Four Point bend test; and Hydrogen Induced Cracking (HIC) test. These tests are most commonly used method for the SSC resistance evaluation.

Tensile test has been used by Kim et al. (2010), Kimura et al. (1996) and Tsay et al. (2005) for evaluation of SSC resistance of different alloys. According NACE TM0177, during tensile testing, the specimen is exposed to corrosive environment while subjected to tensile stress. The standard corrosive environment is defined as standard solution saturated with H_2S gas. **Figure 4** shows a setup for typical SSC test. During experiment, H_2S gas is continuously bubbled into the test solution. Standard experimental duration is 720 hours or until the sample fails. Sample failure time and stress at failure point are recorded as SSC results. The lesser the duration of failure, the lesser the resistance to sulfide stress cracking.

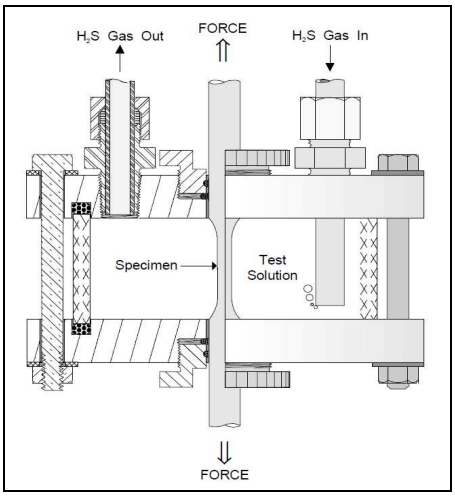

Fig. 4: Tensile test specimen in an environmental chamber

Kimura et al. (1996) used DCB test to determine the SSC resistance of steel alloys. As per NACE TM0177, DCB test gives critical stress intensity factor (i.e. KISSC). DCB test is similar to the tensile test. It is done in vessel containing standard solution saturated with H_2S. A groove is made on the specimen and then it is fatigue pricked. Initial arm displacement is measured, which is the distance between the holes of two arms. A wedge is inserted into the groove and is flushed with end of specimen until desired arm displacement is achieved. For each material, standard arm displacements are given in NACE TM0177. Wedge dimensions are based on arm displacement. Crack length and pressure required for specified displacement are measured. Based on these parameters, KISSC is calculated.

C-ring test is also one of commonly used SSC measuring techniques (Muraki et al. 2006). NACE TM0177 provides a detailed procedure for standard C-ring test. As the name suggest, specimen is C-shaped. **Fig 5** shows typical specimen for C-ring test. Holes are drilled at 180° on the specimen. During the C-ring test, a bolt is inserted into the ring holes and tightened to increase the stress level. The ring and bolt assembly is kept in vessel containing standard solution saturated with H_2S. Experimental duration is 720 hours or until the sample exhibit failure. Sample failure time and stress at failure is noted down as result.

SSC is affected by microstructure and hardness of the material. In addition, some alloys are more resistant to SSC than steel (Kimura et al. 1996), which makes chemical composition analysis important factor for SSC resistance evaluation.

Several studies (Masouri and Zafar 2004; 2005) performed microstructural analysis using Scanning Electron Microscope (SEM). The SEM technique gives information about grain structure of the material. As mentioned in previous report, inter lath layer constituents deposited on grain boundaries can act as nucleation site for cracks. Hence, microstructure examination is essential.

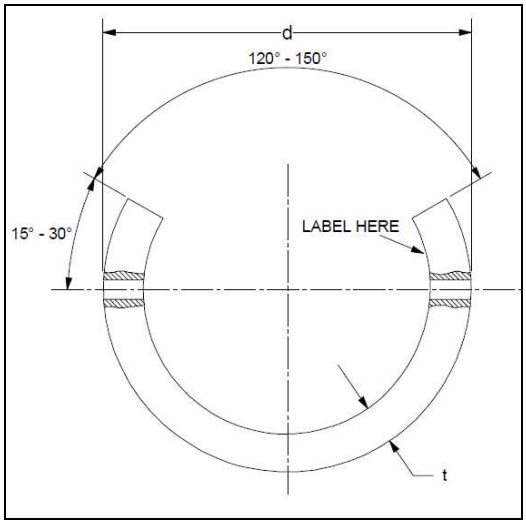

Fig. 5: C-ring test specimen (NACE TM0177)

A number of studies (Kimura et al. 1996; Masouri and Zafar 2004; 2005) were conducted to relate hardness of steel and SSC resistance. Hardness has adverse effect on the SSC resistance of metals. This means that the higher the strength, the lower is the SSC resistance. NACE MR0175 specified the upper limit of steel hardness for sour gas application as 23 HRC (i.e. Hardness on Rockwell scale C).

SSC is the phenomenon caused by hydrogen embrittlement. Thus, diffusion of hydrogen in material is important parameter for SSC resistance. Tsay et al. (2005) and Kimura et al. (1996) evaluated hydrogen permeation rate of materials using Devanathan and Starchuski cell. The more hydrogen permeation rate, the lesser is the SSC resistance of the material. Chromium steel was found to be resistant to sour environment (Kimura et al. 1996), even though Cr content did not increase threshold tensile stress of steel, which is required to initiate SSC. However, hydrogen permeation rate was significantly lower for Cr steel than Cr free steel.

Inappropriate material selection led to premature failure of metals in sour environment. Masouri and Zafar (2005) conducted a case study on failure of V150 and L80 materials. They measured the hardness values of V150, which was found to be unsuitable for sour gas applications as per NACE MR0175 standards.

Grain structure is one of the factors that determine SSC resistance of a metal. Austenite structure is known for hindering hydrogen embrittlement. Tsay et al. (2005) studied martensitic stainless steel (PH 13-8 Mo) to evaluate SSC resistance of the material. Four different samples were prepared by varying the aging conditions. Samples were aged at 800, 900, 1000, 1100℉. Tensile and hydrogen-permeation rate tests were performed on each sample. For material aged at 1100℉, elongation was the highest and hydrogen per meation rate was the least. This indicates that the material has the highest SSC resistance. Further analysis showed that material aged at 1100℉

had significant amount of austenite present in it. Austenite forms irreversible hydrogen traps, which impede hydrogen permeation inside the metal. In addition, the study showed the least hardness value for material aged at 1100℉.

Expanded tubulars show change in SSC resistance after the expansion. Muraki et al. (2006) studied the effect of expansion on SSC resistance of API L80 material. C-ring and tensile tests were performed on as received and post expanded tubular materials. Results demonstrated the reduction of SSC resistance and strength improvement with the expansion. This reduction in SSC measurements was observed when the specimens were exposed to a sour environment with partial pressure of H_2S reaching 0.1 Mpa. At low H_2S concentrations (partial pressure of H_2S less than 0.01 Mpa), SSC resistance was not affected by the expansion.

2.2 Experimental Studies on Degradation of Cement (Task 2)

2.2.1 Porosities and Permeabilities of Baseline Cements

During this reporting period, two batches of baseline cements (i.e. Batches 017 and 018) were kept in the aging cell to investigate their degradation behavior under different aging conditions. The aging conditions for all batches of cement degradation experiments are summarized in **Table 2**. Our recent tests are focused on examining the effects of pressure on the degradation behavior of baseline cement. **Table 3** presents the planned test matrix for studying the impact of pressure.

Table 2 Test parameters for aging experiments conducted to date

Batch #	Temp. (ºF)	Pressure (psi)	Partial Pressure %			Brine Conc. (%)	Aging Period (days)	Experiment #
			CH_4	CO_2	H_2S			
001	350	9000	100	0	0	9	6	1
002	350	6000	100	0	0	2	14 & 28	2
003	350	6000	100	0	0	2	14	
004	350	6000	90	10	0	2	6	3
005	350	6000	90	10	0	2	14 & 28	4
006	350	6000	90	10	0	2	14	
007	225	6000	90	10	0	2	14	5
008	100	6000	90	10	0	2	14	6
009	225	6000	60	40	0	2	14	7
010	225	6000	0	100	0	2	14	8
011	100	6000	60	40	0	2	14	9
012	100	6000	0	100	0	2	14	10
013	350	6000	60	40	0	2	14	11
014	350	6000	0	100	0	2	14	12
015	225	6000	60	40	0	2	14	7A
016	350	3000	60	40	0	2	14	13
017	**350**	**9000**	**60**	**40**	**0**	**2**	**14**	**14**
018	**350**	**3000**	**0**	**100**	**0**	**2**	**14**	**15**

Table 3 Test matrix to study the effects of pressure at 350℉ and varying CO_2 concentration

All 350°F	10% CO_2	40% CO_2	100% CO_2
3000 psi	Batch 020	Batch 016	Batch 018
6000 psi	Batch 006	Batch 013	Batch 014
9000 psi	Batch 021	Batch 017	Batch 019

Figure 6 demonstrates porosity and permeability of samples aged at 350℉ and different pressures (3000, 6000 and 9000 psi) for 14 days in 2% brine saturated with 40% CO_2 gas. Similarly, **Fig. 7** presents porosity and permeability of samples aged at 350℉ and different pressures (3000 and 6000 psi) for 14 days in brine saturated with 100% CO_2. The porosity and permeability vary with aging pressure. The trends of porosity and permeability are very similar at different CO_2 gas concentrations (40% and 100%). There is a decrease in both porosity and permeability from unaged to 3000 psi, then an increase from 3000 to 6000 psi and then again a decrease from 6000 to 9000 psi pressure. However, the decrease observed at 3000 psi is much more prominent as compared to the one at 9000 psi.

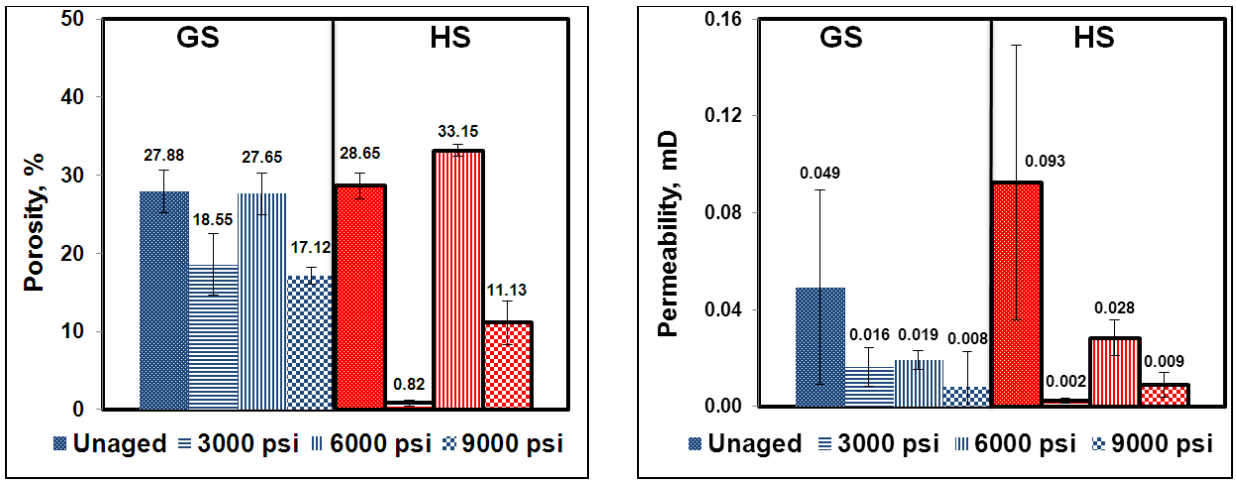

(a) **(b)**

Fig. 6: Effect of pressure on properties of samples aged for 14 days at 350℉ in 40% CO_2 gas saturated brine solution: a) porosity; and b) permeability

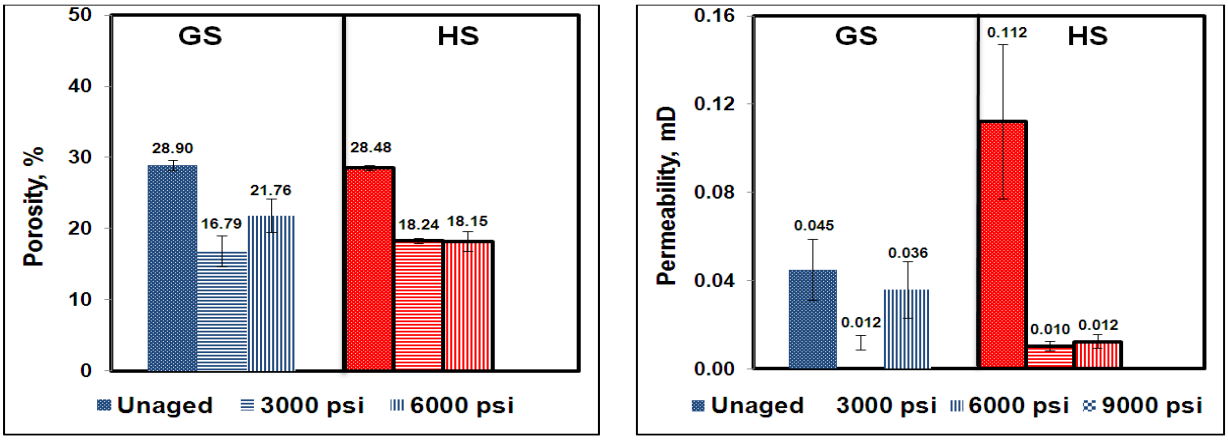

(a) (b)

Fig. 7: Effect of pressure on properties of samples aged for 14 days at 350℉ in 100% CO_2 gas saturated brine solution: a) porosity; and b) permeability

When the pressure is as low as 3000 psi, the condition favors incomplete carbonation, which leads to the formation of scawtite phase (Harker 1965; Lea 1971). When more CO_2 reacts with scawtite it forms $CaCO_3$ thereby completing the carbonation process. At low pressures, solubility of CO_2 in brine is low; hence, less carbonic acid is present in the brine to degrade the cement. At 3000 psi, the reduction in porosity and permeability could be due to the incomplete carbonation of CSH (i.e. formation of scawtite). This incomplete carbonation prevents formation of $CaCO_3$, and subsequently, the formation of soluble bicarbonate. As a result, leaching process that tends to increase porosity and permeability of the cores does not occur. Therefore, the precipitation of scawtite becomes the predominant process causing the reduction in porosity and permeability at lower pressure. However, at 6000 psi, gas solubility is higher than low-pressure leading to complete carbonation and bicarbonate formation, which is proceeded by leaching, thereby increasing the porosity and permeability of the cement.

At 9000 psi, there is again decrease in porosity-permeability. According to Roger (1996), when portlandite ($Ca(OH)_2$) reacts with super critical CO_2 (**Fig. 8**) at high pressures, it forms dense, rounded and closely packed crystals thereby plugging the pores and capillaries, which decreases the porosity and permeability while increasing the strength of the cement.

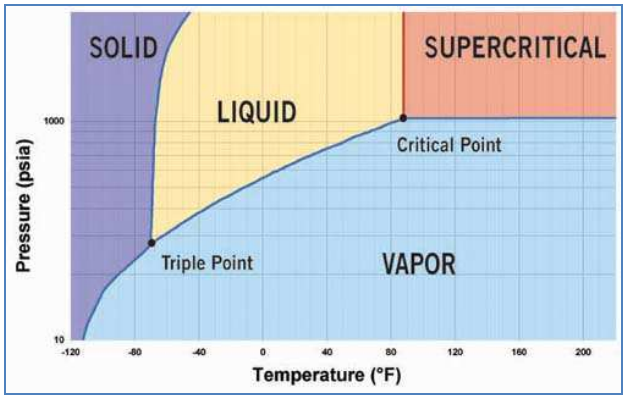

Fig. 8: Phase diagram of CO_2 (Vestergaard and Robinson 2003)

Future Work:

1. Completion of the planned experiments, associated tests, and FTIR analysis.
2. Comparison of XRD results with FTIR data to verify scawtite formation.

2.2.2 Compressive Strengths of Baseline Cements

In this period, compressive strength measurements were obtained from Batches 17 and 18 core samples. These measurements are a further step in investigating the effect of pressure on compressive strength of aged cement. The compressive strength measurements for Batch 17 are presented in **Fig. 9a**. After aging at 350℉ and 9000 psi for 14 days in 2% brine saturated with 40% CO_2, compressive strength of Class G decreased slightly due to leaching effect while Class H increased in strength because of carbonation. **Figure 9b** compares results of Batch 17 with measurements of previous experiments conducted at different aging pressures. The results show that the leaching process dominated carbonation in Class G cement. At low and intermediate pressures (less than 6000 psi), the leaching process dominates with increasing the aging pressure. However, at high aging pressures (above 6000 psi), carbonation process offsets the action of leaching, as a result, the dominance of leaching diminished.

Increasing pressure helps to dissolve more CO_2 in the brine solution. This may results in improving the carbonation process. The results of Class H cement show unexpected trend. At low and intermediate pressure range (less 6000 psi), increasing aging pressure improved compressive strength of the cores due to the dominance of carbonation. Nevertheless, the strength reached its peak value at around 6000 psi and further increase in aging pressure reduced the strength due to the formation of water-soluble calcium bicarbonate, which can be easily leach out from the cement.

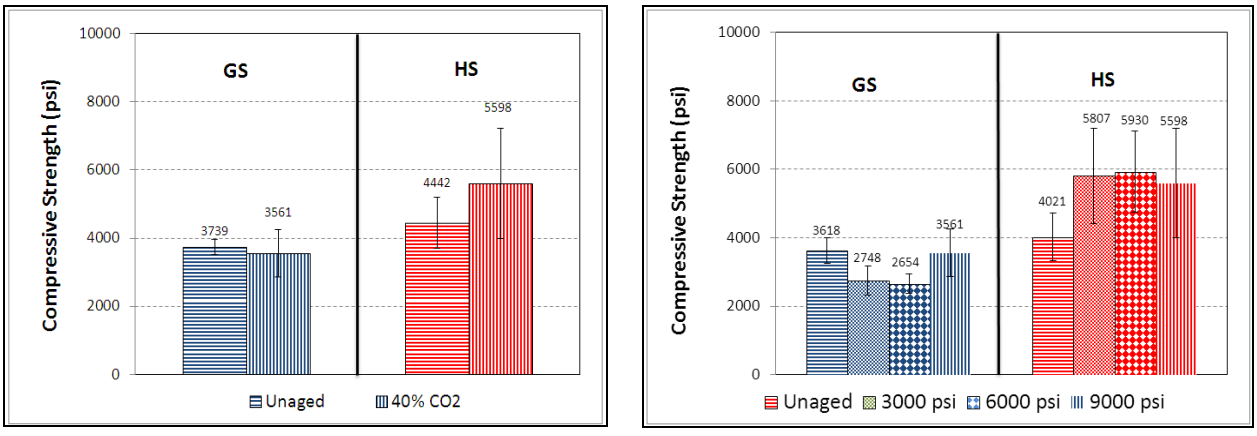

(a) **(b)**

Fig. 9: Compressive strength of cement cores unaged and aged at 350℉ for 14 days in 2% brine saturate d with 40% CO_2: a) Batch 017; and b) combined with other test batches conducted at different pressures

The compressive strength measurements for Batch 18 samples are presented in **Fig. 10a**. After aging for 14 days at 350ºF and 3000 psi in 2% brine saturated with 100% CO_2, compressive strength of Class G decreased slightly due to dominant nature of leaching while the strength of Class H cement increased because of intense carbonation. These results are consistent with measurements obtained after aging cores at 40% CO_2. In order to study the effect of aging pressure on compressive strength, Batch 18 data is presented in **Fig. 10b** together with previous experimental results. Both Class G and Class H samples show more carbonation at high aging pressure, although Class H demonstrates increased rate of carbonation, which is consistent with previous samples aged in brine saturated with 40% CO_2.

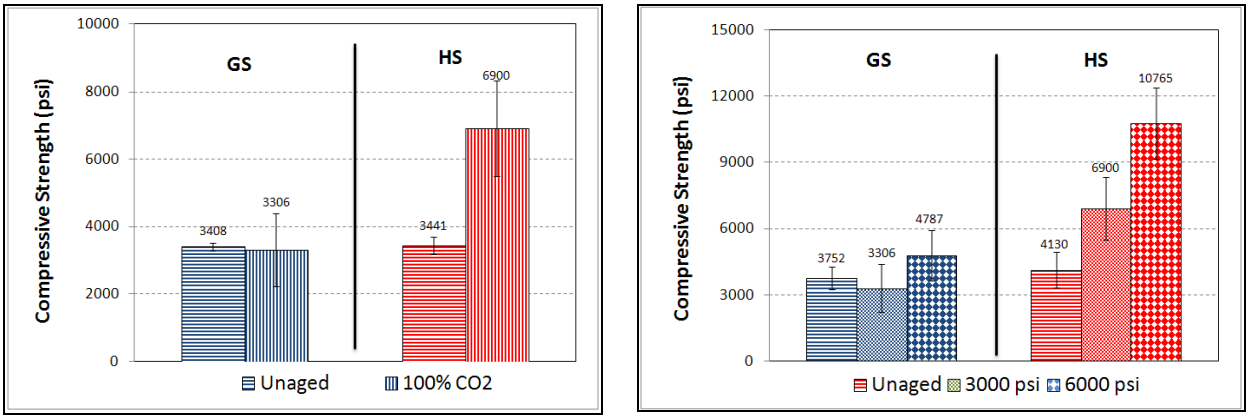

(a) **(b)**

Fig. 10: Compressive strength of cement cores unaged and aged at 350ºF for 14 days in 2% brine saturated with 100% CO_2: a) Batch 018; and b) combined with other test batches conducted at different pressures

Furthermore, the new data is combined with previous measurements (**Fig. 11**) to investigate the effect of CO_2 concentration on cement degradation at 350ºF and 3000 psi. Evidently, high CO_2 concentration results in more carbonation in both API cements although Class G shows slight leaching at low CO_2 concentration. In addition, the rate of carbonation is more pronounced in Class H, which again is consistent with previous experimental results. However, the strength improvement slows down at high CO_2 concentration because of calcium carbonates formation resulting from carbonation and subsequently bicarbonation of CSH and CH to water-soluble calcium bicarbonate, which can be leached out in the presence of high concentration of carbonic acid. Therefore, within 14 days of aging, both CO_2 and aging pressure have contributory effects on strength evolution of API oil well cements, especially in Class H.

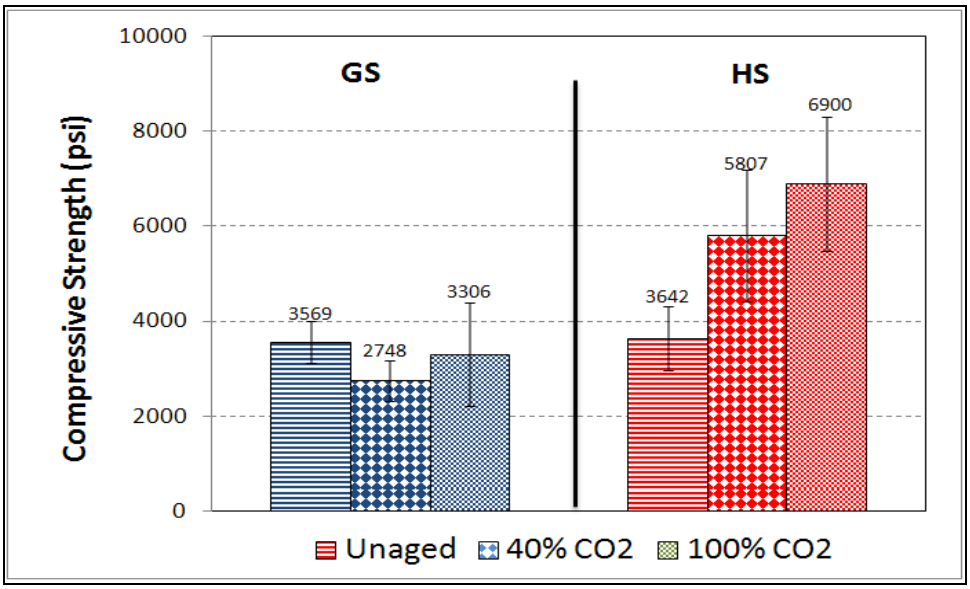

Fig. 11: Effect of CO_2 concentration on compressive strength at 350ºF and 3000 psi

2.2.3 Shear Bond Strengths of Baseline Cements

Study on shear bonding strength (SBS) of Class H cement was continued. A displacement sensor has been installed to measure strain during bonding test. The strain measurements were used to investigate stress-strain relationship. In addition, carbonation depths of the SBS samples were measured to correlate the depth with the bond strength.

Effects of Aging Pressure on SBS

In the last month report, the influence of pressure on the SBS of aged samples was presented varying it from 3000 to 6000 psi. During this month, additional aging test was conducted at 9000 psi. The new measurement is combined with previous data and presented in **Fig. 12**. For samples aged in brine saturated with 40% CO_2, shear-bonding strength remained in similar range regardless of aging pressure (Fig. 12a). There is no consistent trend. Unaged samples were not exposed to CO_2 environment; hence, they exhibited significantly lower SBS than aged samples. The reason for substantial SBS improvement is due to carbonation. Carbon dioxide becomes supercritical fluid above 88℉ and 1070 psi (Fig. 8). Supercritical CO_2 does not exhibit surface tension; thus, it can easily penetrate into very fine pores of set cement (Bertos et al. 2004). Supercritical CO_2 increases the reactive inner surface of the cementitious solid microstructure, by dissolving in the pore water and replacing the structurally bonded water with CO_2 in the hydrated components of cement (CH and CSH). The solubility of CO_2 in brine solution increases with pressure (Duan et al. 2003). Model predictions show that the solubility of CO_2 increases from 1.0 to 1.8 mol/kg when the pressure is elevated from 3000 to 9000 psi. As a result, the carbonated cement displayed enhanced SBS.

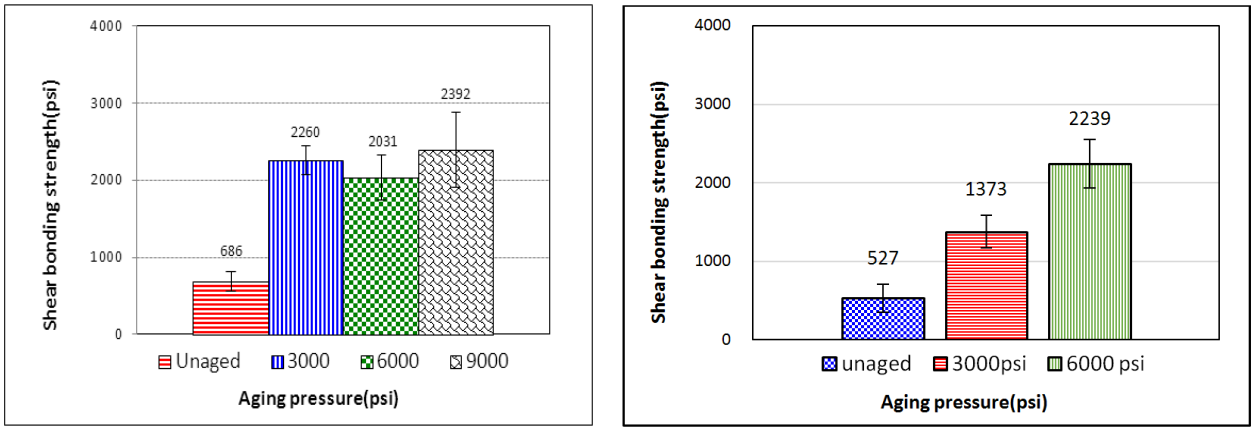

Fig. 12: Effect of aging pressure on SBS of samples aged at 350℉ for 14 days in brine saturated with different CO2 concentrations: a) 40%; and b) 100%

For samples aged in brine saturated with 100% CO_2, the SBS improved as the aging pressure was increased from 3000 to 6000 psi (Fig. 12b). Additional aging test was carried out at 9000 psi. The result will be presented in the next month report.

Carbonation Depth

Phenolphthalein solution test is common way of determining the depth of degradation after CO_2 attack in carbonated cement. As indicated in the last month report, carbonation depth measurements were obtained from shear bonding test samples using phenolphthalein solution. Areas on cement sample containing free $Ca(OH)_2$ changes to deep purple when it is exposed to phenolphthalein solution. Applying this technique, the carbonation depths were measured from the top and bottom sides of the sample; and the average value was computed and used for the investigation. At low CO_2 concentrations (less 40%), the SBS increased as the depth increases (**Fig. 13**). This observation is in agreement with the hypothesis of volume expansion because of carbonation, which results in SBS improvement. However, at high CO_2 concentration (greater than 40%), the increase in the SBS diminished as the depth increases. This could be due to the leaching of the carbonated zone, which weakens the bond strength. The formation of highly concentrated carbonic acid facilitate the conversion of $CaCO_3$ to $Ca(HCO_3)_2$, which is susceptible for leaching.

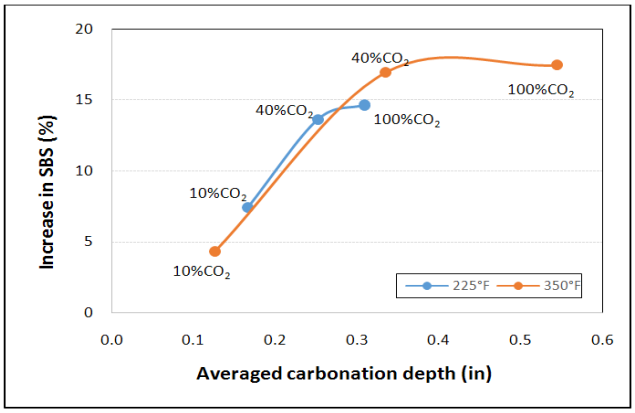

Fig. 13: SBS versus carbonation depth for samples aged at 6000 psi

Shear Modulus Measurements

A displacement transducer has been installed on the shear bonding strength-measuring apparatus (**Fig. 14**) in order to determine the relationship between bond shear stress and bond strain, and bond shear moduli. This sensor is connected to the bottom plunger and therefore, it measures plunger displacement as it pushes and breaks the bond between cement and pipe.

Fig. 14: Displacement sensor on SBS apparatus

The strain developed at the bond (ε) was determined from the displacement data as: $\varepsilon = \Delta s/L$, where Δs and L are displacement occurred at the bond during the test and bond length, respectively. The result approximately shows a linear stress-strain relationship before the bond failure (**Fig. 15**). The maximum bond shear stress was 860 psi, which is the SBS of the sample. The slope of the graph indicates the bond stiffness, which is approximately 40,000 psi in this particular case. When the bonding between cement and pipe fails, adhesion forces vanish and frictional forces remain but their magnitude reduces as the set cement is pushed out of the pipe. After bond failure, reduced stress exists due to mechanical interlocking of the cement with pipe (Chang et al. 2003).

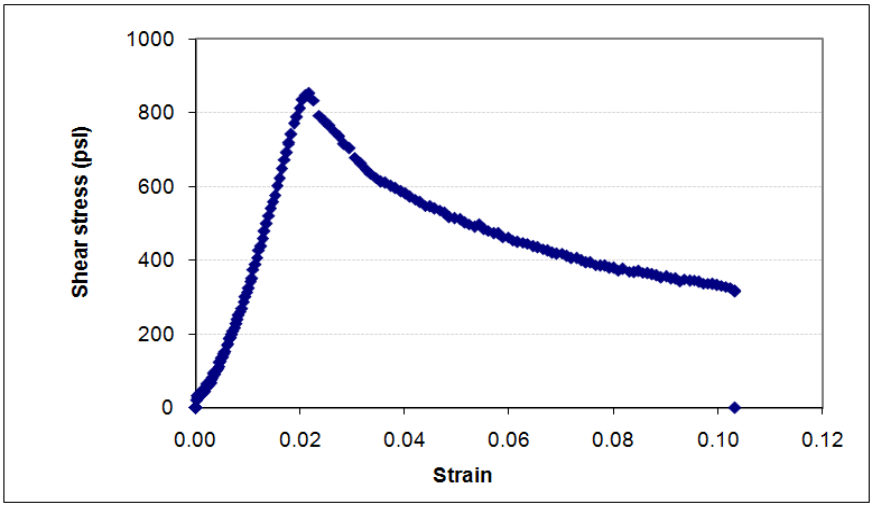

Fig. 15: Effect of CO_2 concentration on compressive strength at 350ºF and 3000 psi

2.2.4 Additive Screening and Cement Formulation Studies

Additive screening and cement formulation studies were continued during this month. Hydroxyapatite (HOAP), magnesium oxide, micro silica and latex containing cements were investigated. As noted in previous reports, HOAP samples showed reduced compressive strengths after aging at 350℉ due to strength retrogression resulting from the lack of sufficient amount of silica in the cement system. Magnesium oxide (MGO) sample also exhibited better resistance against carbonic acid environment as seen in previous experiments.

2.2.4.1 Hydroxyapatite Cement without Silica Flour

Aging experiments with the HOAP samples were continued. After aging at 100℉, the samples exhibited lesser penetration of CO_2 in the matrix and preserved the CH and CSH components. However, at 350℉, although CH and CSH components were preserved (as observed in FTIR analysis), the compressive strengths of the samples were less than those of the unaged samples.

The most recent aging experiment was conducted at 350℉ with aging conditions presented in **Table 4**. The conditions are similar to the previous hydroxyapatite experiment; nevertheless, this time 100% CO_2 was used. The composition of the slurry was similar to the previous batch.

Table 4: Aging conditions for the HOAP samples

HOAP	Temp. (℉)	Pressure (psi)	CO_2 Conc.	Brine Conc.	Days	HS/GS Batch	Exp. #.
Batch 005	350	3000	100%	2%	14	Batch 018	15

Porosity and Permeability Measurements

The porosity and permeability measurements obtained from the new samples are presented in **Figs. 16** and **17**, respectively. The initial porosity of all the samples, except GHO, was found to be similar. The baseline HS and GS samples displayed a significant reduction in porosity after aging, indicating carbonation of the matrix. On the other hand, the porosity of GHO and HHO samples increased. The increase in porosity is found to be more prominent in GHO than HHO samples. The permeability of the baseline samples (HS and GS) decreased after aging while HHO and GHO samples displayed increased permeability.

Unlike previous tests, increase in porosity and permeability was observed in this experiment. It is discussed in later sections of this report that the compressive strengths of this batch of hydroxyapatite samples were also reduced. A number of studies (Eilers et al. 1976 and 1983; Dillenbeck III et al. 1990; Grabowski and Gillott 1989; Lea 1971) indicated the transformation of Tobermorite gel to xonolite at temperature above 300℉. Tobermorite gel is a form of CSH gel having high-compressive strength and low-permeability and is formed above 247℉. It is stable up to 300℉, above which it can transform to xonolite, which is lesser in compressive strength and higher in permeability. This conversion can be prevented by lowering the calcium-silica ratio (CaO/SiO_2)

below one, which is achieved by addition of 35% – 40% silica flour (or silica fume) by weight of cement (Grabowski and Gillott, 1989). In the HHO and GHO samples, no silica flour was added; hence, the transformation of tobermorite gel to xonolite lowered the compressive strength and increased the permeability of the cement.

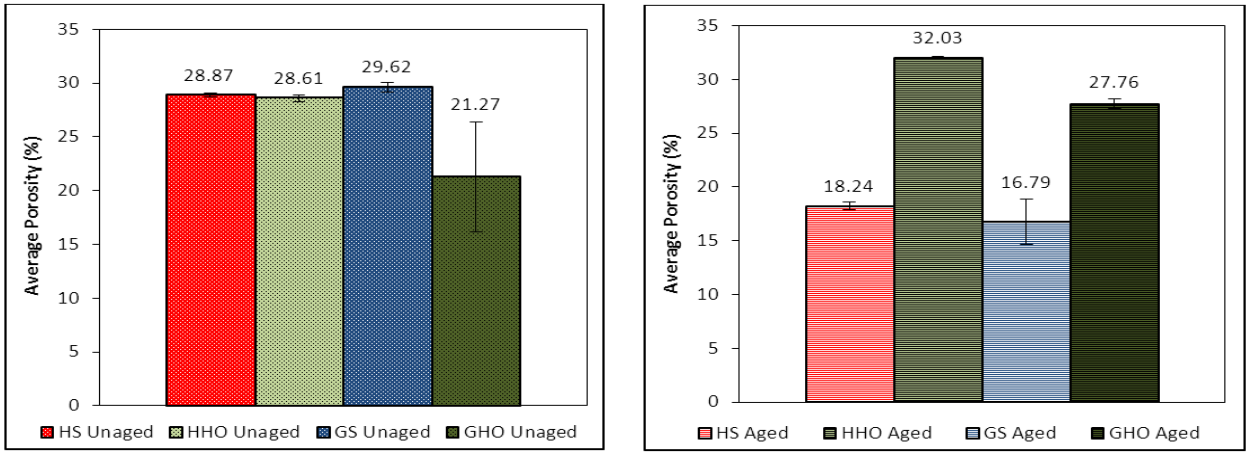

(a) **(b)**

Fig. 16: Porosities of HOAP and baseline cements: a) Unaged; and b) aged at 350℉, 3000 psi, 100% CO_2 for 14 days

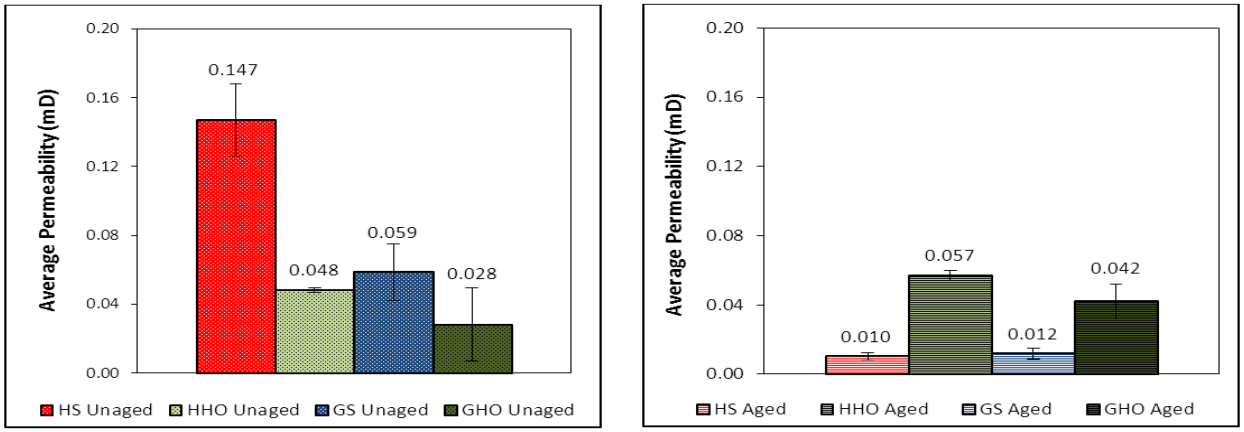

(a) **(b)**

Fig. 17: Permeabilities of HOAP and baseline cements: a) Unaged; and b) aged at 350℉, 3000 psi, 100% CO_2 for 14 days

Compressive Strength Measurements

Measured compressive strengths of baseline and HOAP samples are presented in **Fig 18**. The unaged compressive strengths of all the samples were very close to each other. After aging, compressive strength of HS samples increased due to carbonation. Nonetheless, HOAP samples showed considerable reduction in compressive strength, which can be attributed to the strength retrogression as discussed earlier. The GS samples exhibited almost the same compressive

strength after aging. The preservation of the compressive strength can be due to low carbonation or a balance between carbonation and leaching process. A similar behavior was observed when the samples were aged at 100℉ maintaining other test parameters the same. When simultaneous carbonation and leaching occurs, strength gained by carbonation process can be lost due to leaching of the soluble component ($Ca(HCO_3)_2$).

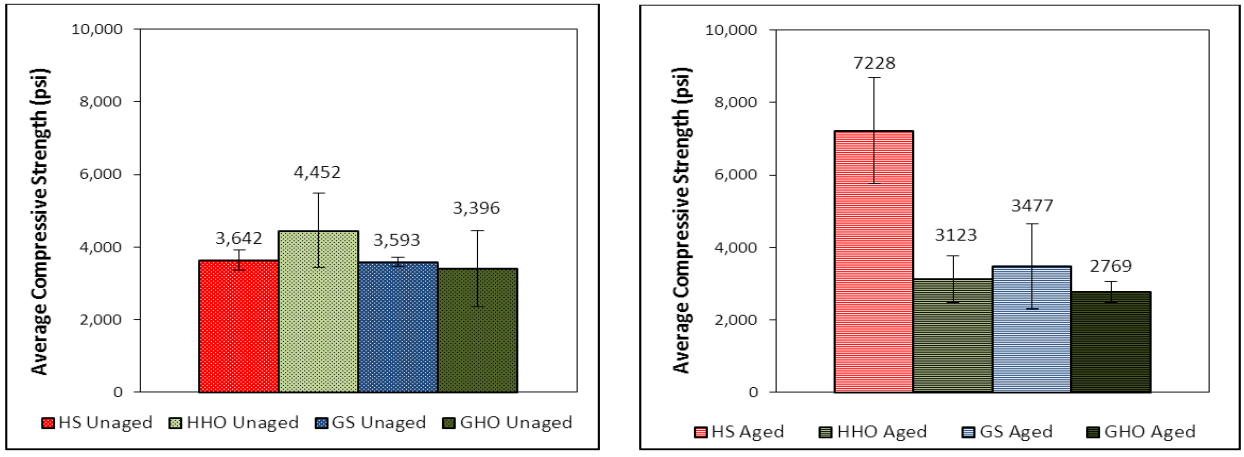

(a) **(b)**

Fig. 18: Compressive strengths of HOAP and baseline cements: a) Unaged; and b) aged at 350℉, 3000 psi , 100% CO_2 for 14 days

Shear Bond Strength Measurements

The shear bond strengths (SBS) of HOAP and baseline samples are presented in **Fig. 19**. Consistent with the compressive strength measurements, the HOAP samples showed slight reduction in SBS. The baseline HS samples on the other hand displayed a significant increase in the SBS due to carbonation.

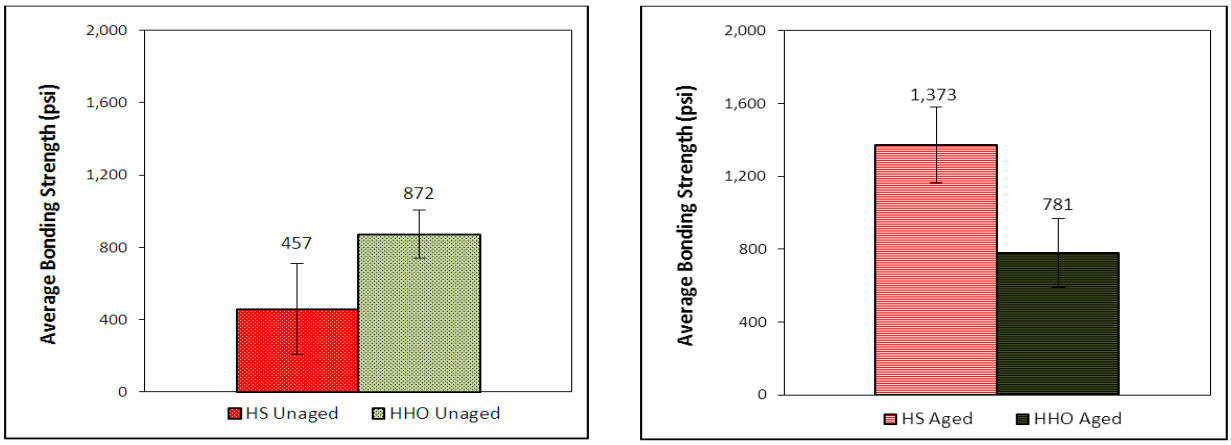

(a) **(b)**

Fig. 19: SBS of HOAP and baseline cement: a) Unaged; and b) aged at 350℉, 3000 psi, 100% CO_2 for 14 days

FTIR Results

FTIR results of previous and the latest experiment of hydroxyapatite samples are presented in **Figs. 20** and **21**, respectively. The spectra shown in the figures are presented in a simplified (bar charts) form for easy interpretation. The samples were aged at 350℉ and 3000 psi. For both experiments conducted at different concentrations of CO_2, the CH group is retained in the HOAP samples. This indicates the effectiveness of hydroxyapatite in preventing the carbonation CH. The preserved CSH group found in the HOAP samples was lower than in the baseline samples. For samples aged at 100% CO_2 concentration, the $CaCO_3$ peak found in the HOAP sample was also higher than in the baseline cement. The results of CSH and $CaCO_3$ may indicate the deeper penetration of carbonic acid in the HOAP matrix carbonizing the CSH group. However, it should be noted that FTIR analysis does not identify between $CaCO_3$ and carbonated form of HOAP ($Ca_{10}(PO_4)_6CO_3$), which is beneficial to the matrix. Both materials exhibit the -CO_3 bond peaks. In addition, the thermal retrogression of the matrix can increase the permeability and allow deeper penetration. Complete FTIR spectrum charts of samples from the recent aging experiment (100% CO_2) are presented in Appendix A.

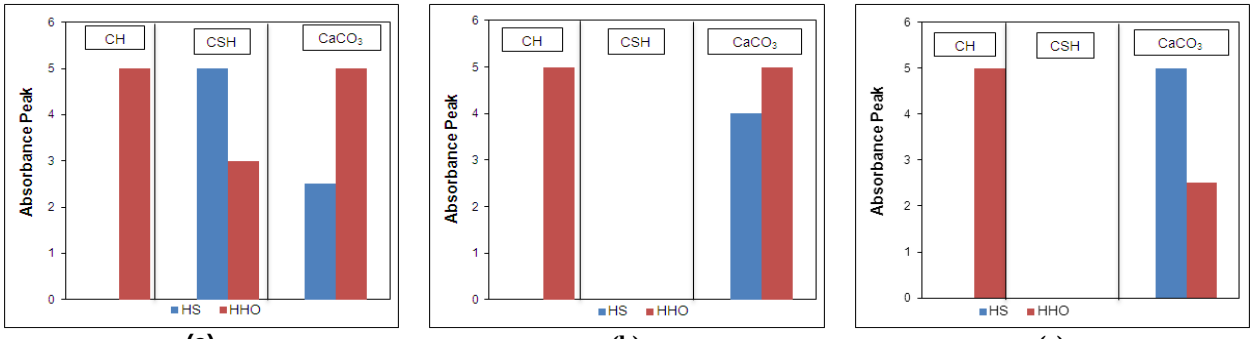

Fig. 20: FTIR peaks of HHO and baseline cores aged at 350℉ and 3000 psi for 14 days in brine saturate d with 40% CO_2 gas: a) inner zone; b) middle zone; and c) outer zone

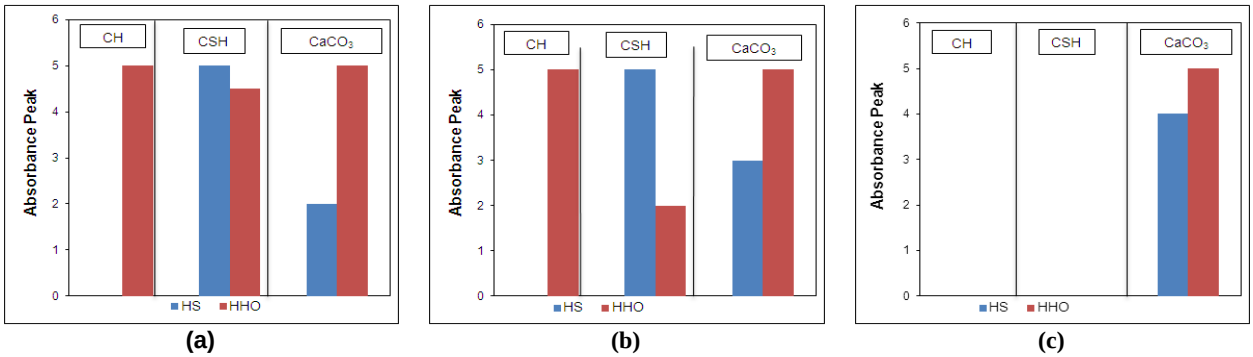

Fig. 21: FTIR peaks of HHO and baseline cores aged at 350℉ and 3000 psi for 14 days in brine saturate d with 100% CO_2 gas: a) inner zone; b) middle zone; and c) outer zone

2.2.4.2 Hydroxyapatite Cement with Silica Flour

As discussed earlier, in order to prevent the strength retrogression of the hydroxyapatite cement, silica flour was added to the HOAP slurry. The slurry properties were optimized and one batch of Class G and Class H samples was prepared. However, the HOAP samples (containing 35% silica flour, 5% hydroxyapatite and 40% water for hydroxyapatite) showed brittleness during coring. Porosity and permeability of unaged samples are shown in **Fig. 22** and their compressive and shear bond strengths are presented in **Fig. 23**. The porosity and permeability of the HOAP samples were higher than those of the baseline samples. In addition, compressive and bond strengths of the HOAP samples were found to be very low. This reduction in the strength was not observed in the cement when only silica flour was added or when only HOAP was added. Hence, this reduction in strength could be due to the presence of adverse interaction between silica flour and hydroxyapatite.

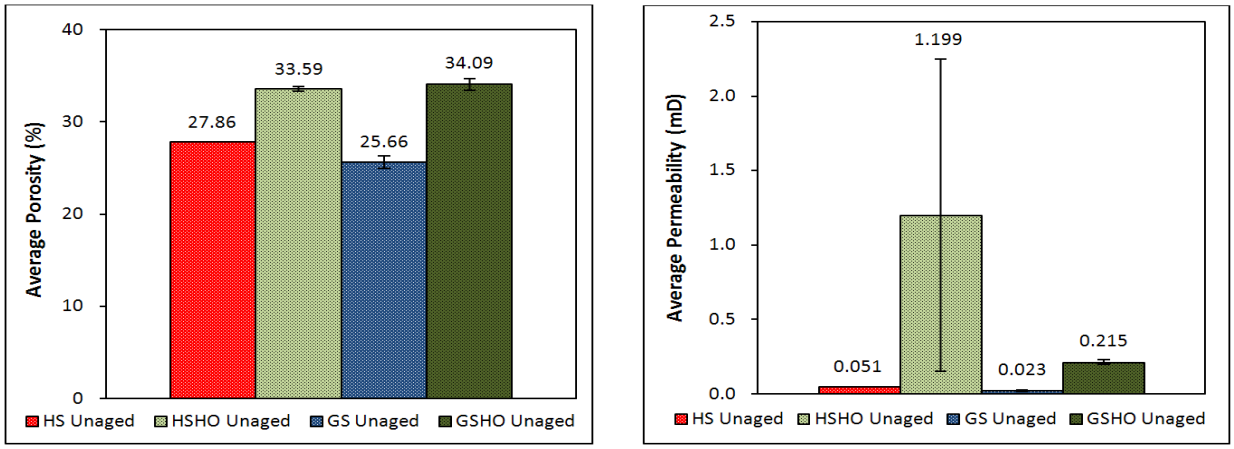

(a) **(b)**

Fig. 22: Porosity and permeability of unaged HOAP and baseline samples

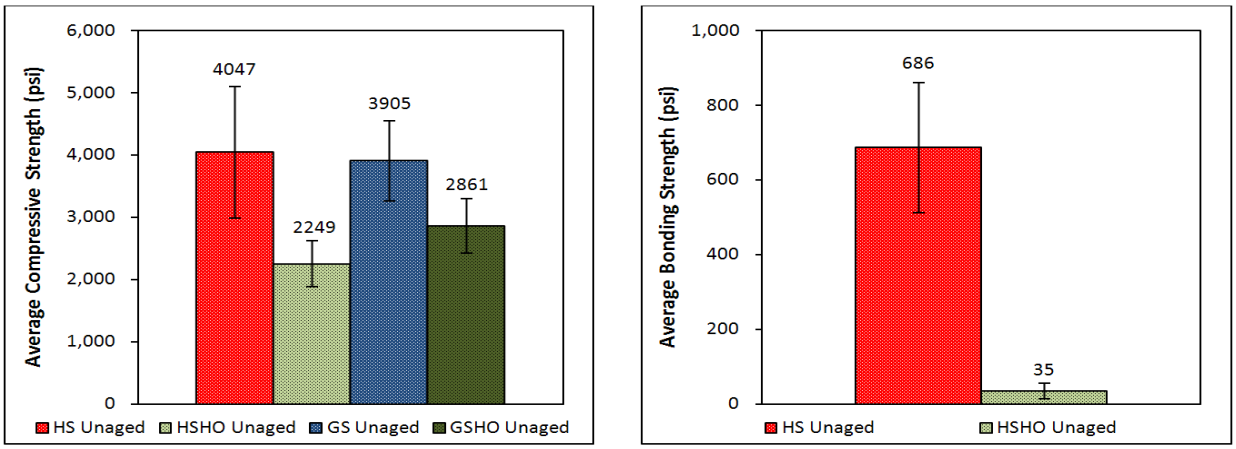

(a) **(b)**

Fig. 23: Compressive and shear bond strengths of unaged HOAP and baseline samples

In order to control the brittleness nature of silica containing HOAP cement, a new formulation with reduced water content was prepared. The slurry properties (**Table 5**) were in acceptable range. It is well known that reduction in compressive strength can be due to the presence of excess water in the system, which creates porous space in the set cement. The original slurry prepared had additional water (40% by weight of hydroxyapatite) for hydroxyapatite. Hence, the water content was reduced to 23% by weight of hydroxyapatite in the new formulation (**Table 6**).

Table 5: Property of HOAP slurry with silica flour

	HSHO	**GSHO**
Density	16.01 ppg	16.10 ppg
Viscosity	Acceptable	Acceptable
Thickening Time	225 min.	155 min.

Table 6: Slurry composition for HOAP slurry with silica flour

Component	**Percentage Amount**
Cement	100%
Silica Flour	35% BWOC
HOAP	5% BWOC
HEC	0.1% of water for fillers
Antifoam Agent	0.1 gal/sack of cement
Water for Cement	38% BWOC for Class H & 44% BWOC for Class G
Water for Silica Flour	38.5% of Silica Flour
Water for HOAP	23% of HOAP
Citric Acid	0.5% BWOC
BWOC = by weight of cement	

After the samples with the new formulation were cured (5 days, 200℉, 2% brine) and prepared for unaged testing, hardened Class H cement with HOAP (i.e. HSHO) displayed brittleness. As a result, we were not able to prepare HSHO cores. However, 8 Class G based HOAP samples (GSHO) were prepared and tested. Porosity and permeability of the samples are presented in **Fig. 24** and their compressive strength is shown in **Fig. 25**. The GSHO samples exhibited higher porosity and permeability, and lower compressive strength than the baseline cement cores.

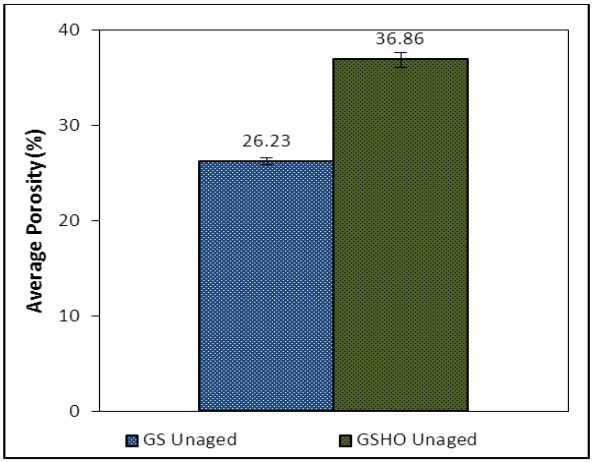

(a)

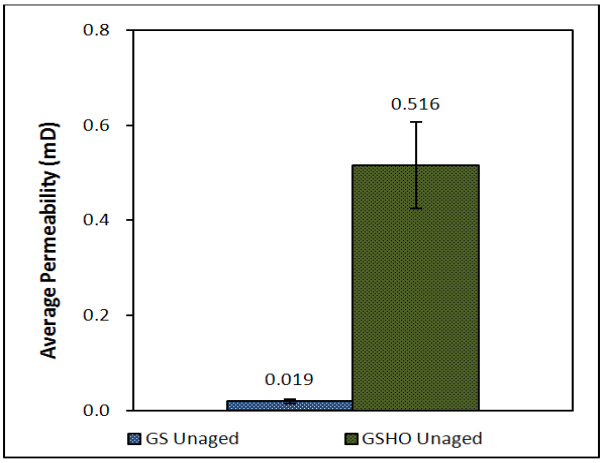

(b)

Fig. 24: Porosity and permeability of unaged GSHO (with silica flour and 23% water for HOAP) and baseline samples

Shear bond strength test was conducted on only HSHO samples (**Fig. 26**). The SBSs of HSHO samples were comparable to the baseline samples. With reduced water content, it was observed that, although the matrix strength was reduced due to the addition of silica, the shear bond strength was retained. However, as the project focuses on performance of Class H cement, low compressive strength of HSHO (Class H cement with silica flour and hydroxyapatite) requires improvement, hence reformulation of the slurry is needed.

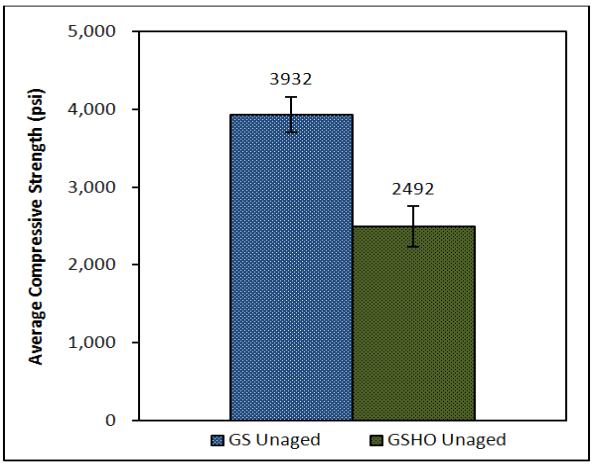

Fig. 25: Compressive strength of unaged GSHO (with silica flour and 23% water for HOAP) and baseline samples

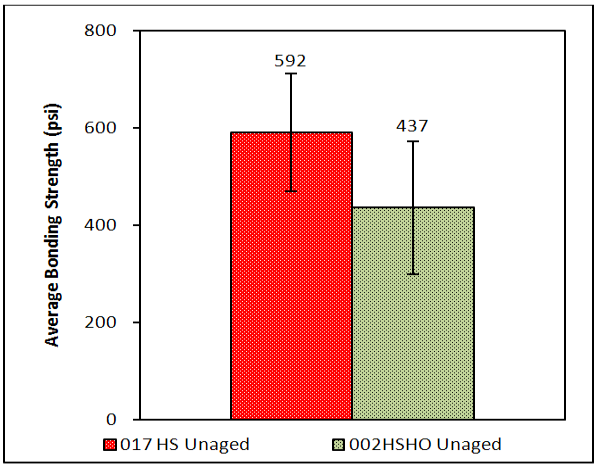

Fig. 26: Shear bond strength of unaged GSHO (with silica flour and 23% water for HOAP) and baseline samples

Although hydroxyapatite is able to prevent the carbonation of the samples, the reduction in strength above 300℉ limits its application for HPHT wells. With addition of silica flour, the basic strength of the cement is reduced significantly. Literature survey is being conducted in order to

identify the reaction between HOAP and silica flour; and for later experiments, the silica flour will be reduced to minimize the adverse interaction among silica flour, water and hydroxyapatite.

2.2.4.3 Magnesium Oxide Cement

The magnesium oxide slurry with 10% MgO BWOC was tested for suitability of slurry properties. Test results were presented in the last month report. The purpose of preparing 10% BWOC MgO slurry (MGO-10) was to test the level of expansion in the cement when the concentration of MgO is increased. This will help in determining the optimum amount of MgO, as extreme expansion can cause cracks in the cement and increase the penetration of carbonic acid. Hence, unaged MGO-10 cores were prepared and tested for their performance. In addition, testing with the original MGO samples (MGO-5) was continued.

Porosity and Permeability Measurements

MGO-10 Samples: Measured properties of unaged MGO-10 and baseline samples are presented in **Figs. 27** and **28**. Porosity and permeability of the samples were slightly higher than those of the baseline cores. MGO-10 and baseline samples showed approximately the same compressive and shear-bond strengths. Hence, the samples were aged to evaluate their degradation behavior. Aging was conducted at 9000 psi and 350℉ for 14 days in 2% brine saturated with 100% CO_2. The results will be presented in the next month report.

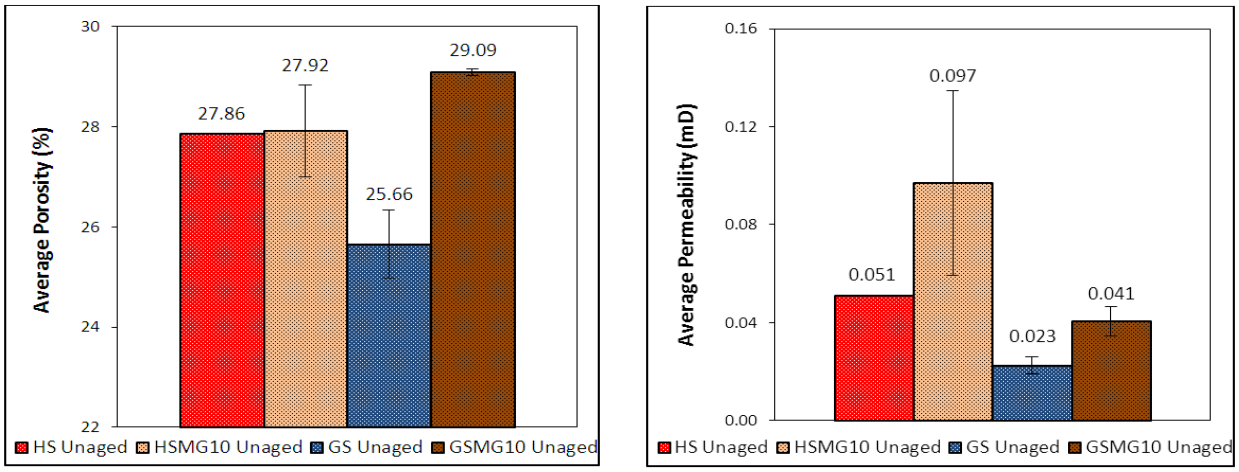

(a) **(b)**

Fig. 27: Porosity and permeability of unaged MGO-10 and baseline samples

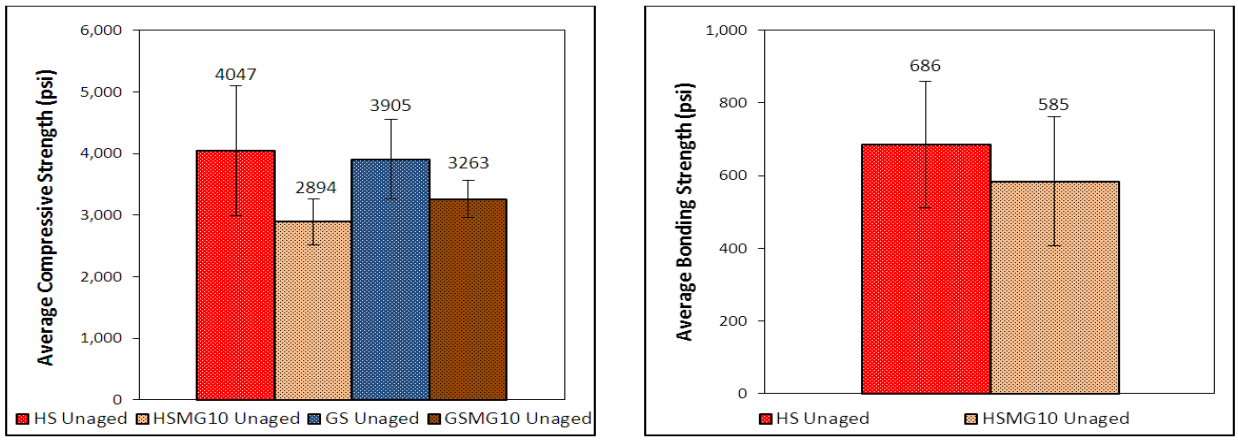

(a) **(b)**

Fig. 28: Compressive and shear bond strengths of unaged MGO-10 and baseline samples

MGO-5 Samples: Testing with the original MGO-5 samples (MgO – 5% BWOC) was also performed. New batches of cores were prepared and aged under the condition presented in **Table 7**. Porosity and permeability of MGO-5 samples are presented in **Figs. 29** and **30**, respectively. The unaged porosities of all the samples are in the same range except for GSMG, which showed lower porosity than the baseline samples. On the other hand, the permeabilities of the unaged samples vary significantly. The permeability of MGO-5 samples seems to be higher than their respective baseline cements. As this measurements were taken just after curing of the samples; the difference is mainly due to variation in composition and hydration process of the cements.

Table 7: Aging conditions for the original MgO (MGO-5) samples

HOAP	Temp. (°F)	Pressure (psi)	CO_2 Conc.	Brine Conc.	Days	Parallel HS/GS Batch	Experiment No.
Batch 005	350	9000	40%	2%	14	Batch 017	15

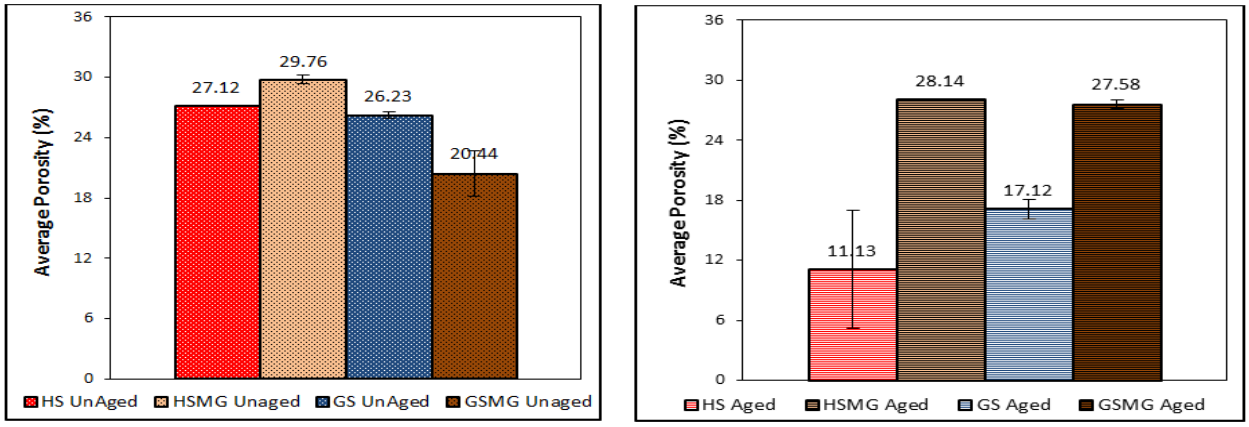

(a) **(b)**

Fig. 29: Porosities of MGO-5 and baseline samples: a) Unaged; and b) aged at 350℉, 9000 psi, 40% CO_2 for 14 days

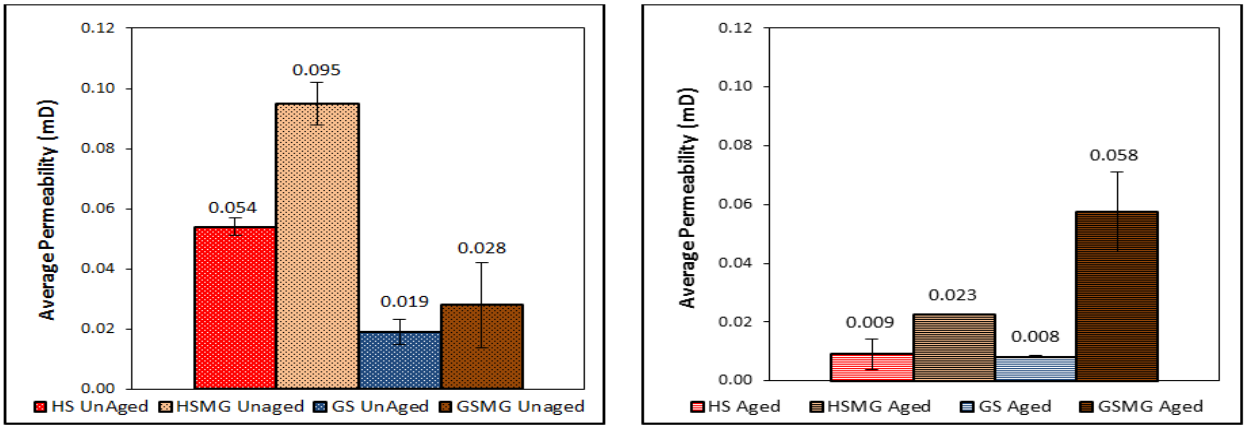

(a) **(b)**

Fig. 30: Permeabilities of MGO-5 and baseline samples: a) Unaged; and b) aged at 350℉, 9000 psi, 40% CO_2 for 14 days

After aging, decrease in the porosity was predominately observed, except in the case of GSMG samples, which displayed a considerable increase in porosity. This increase can be attributed to leaching of the calcium bicarbonate formed after complete carbonation of $Ca(OH)_2$ and CSH. Class H based MgO samples (HSMG) exhibited substantial reduction in permeability after aging. This reduction can be attributed to the expansion of $Mg(OH)_2$ crystals in the matrix, which prevents the carbonation. However, as noted in previous experimental observations, this needs to be verified using FTIR analysis.

FTIR Results

In order to verify the penetration of CO_2 in the MGO-5 samples, FTIR experiments were carried out by taking samples from inner, middle and outer zones of aged HS and HSMG samples. Summarized FTIR spectrum charts are presented in **Fig. 31**. The charts present spectrum peaks of $Ca(OH)_2$, CSH, $CaCO_3$, MgO, $Mg(OH)_2$ and $MgCO_3$ at different locations (inner, middle and outer most zones) in the samples. The actual FTIR spectrum charts are provided in the Appendix B. FTIR results obtained from the inner most zone indicates complete carbonation of $Ca(OH)_2$ and CSH in both the samples. The result from outer and middle zones showed complete conversion of MgO to $MgCO_3$ and $Mg(OH)_2$. No $MgCO_3$ was found in the inner most zones of the samples. In HSMG samples, $Mg(OH)_2$, which precipitates in the pore space was present in inner and middle zones. The $Mg(OH)_2$ crystals help in decreasing porosity and permeability, and improve compressive and shear bond strength of the cement. The amount of $CaCO_3$ in HSMG samples is less than the baseline samples in the inner zone, indicating lesser carbonation of the matrix. It should be noted that, although peak for $MgCO_3$ can be identified at $880cm^{-1}$, all carbonates provided major peak around $1480cm^{-1}$. Hence, $CaCO_3$ and $MgCO_3$ cannot be clearly distinguished using the peaks at $1480cm^{-1}$. The middle and outer zones show higher content of $CaCO_3$ along with presence of $MgCO_3$.

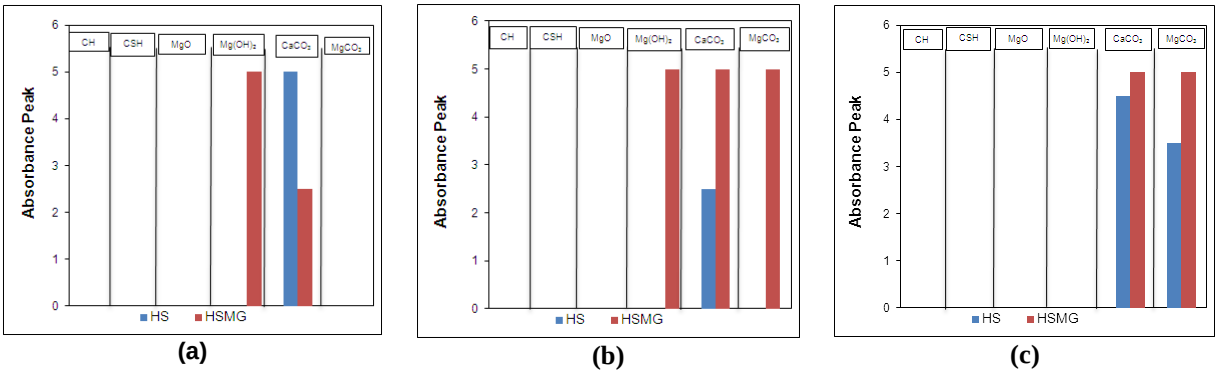

Fig. 31: FTIR peaks of MGO and baseline samples aged at 350℉ and 9000 psi for 14 days in 2% brine saturated with 40% CO_2: a) inner most zone; b) middle zone; and c) outer most zone

Addition of 5% BWOC of MgO to the cement has been effective in preventing acid attack according to the experimental results. The last aging data at 9000 psi and 350℉ gave positive results for Class H cement; however, Class G cement samples performed very poor. Such result with Class G cement was only observed at 9000 psi in which the MGO samples were aged for the first time at high-pressure condition. High-pressure may have caused breaking of the $Mg(OH)_2$ crystals or the matrix. Additional literature survey needs to be undertaken in order to investigate this observation.

Compressive Strength Measurements

The compressive strengths of MGO-5 and baseline cement samples are presented in **Fig. 32**. The strengths of all unaged samples were in the same range. After aging, increase in the compressive strength was observed for Class H based cores (HS and HSMG). The strength improvement is attributed to carbonation of the matrix and deposition of $CaCO_3$ crystals in the pore space. For MGO samples, this improvement is also due to matrix expansion by the formation of $Mg(OH)_2$ crystals from hydration of MgO. The matrix expansion results in pore shrinkage and strength improvement. On the other hand, the aging made Class G based cores (GS and GSMG) weaker. The reduction in the strength of GS and GSMG samples is mainly attributable to leaching of the soluble products such as $Ca(HCO_3)_2$ and $Mg(HCO_3)_2$, which are formed after carbonation process. The GSMG cores exhibited more strength reduction than the baseline GS samples. This could be because of more leaching tendency of the GSMG samples as they contain higher MgO content than the baseline cement. As observed in the porosity and permeability results of GSMG, the increase in the respective values may lead to this decrease in the compressive strength. Hence, adding MgO did not provide positive results with Class G cement.

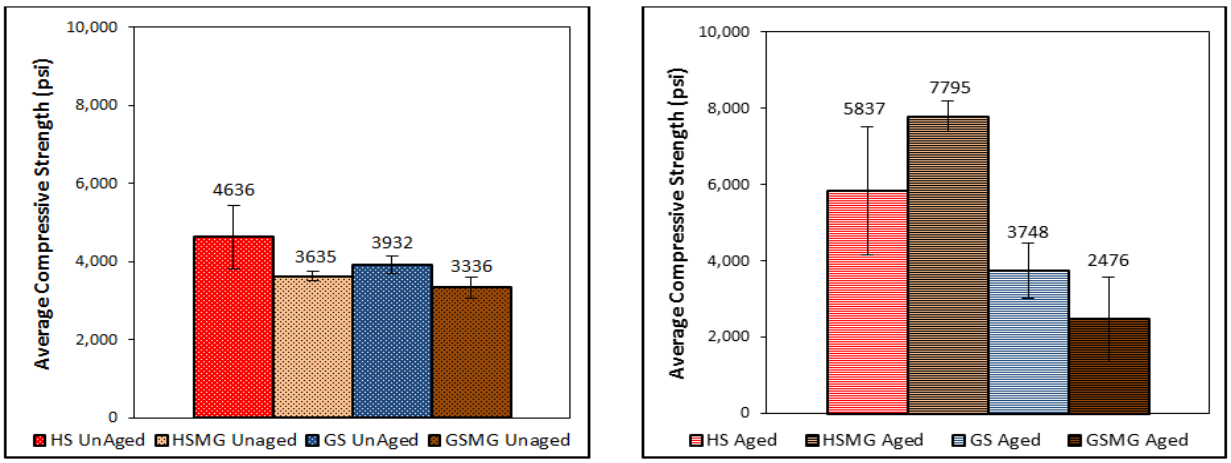

(a) **(b)**

Fig. 32: Compressive strength of MGO-5 and baseline samples: a) Unaged; and b) aged at 350℉, 9000 psi , 40% CO_2 for 14 days

Shear Bond Strength Measurements

Shear bond strengths of HSMG and baseline HS samples are presented in **Fig. 33**. For both aged and unaged cases, the SBS values do not vary significantly with the types (i.e. HS or HSMG) of cement samples. However, substantial (four to five folds) increase in SBS is observed due to carbonation after aging the samples under CO_2 containing environment. More importantly, the aged HSMG samples showed slightly higher SBS than the baseline samples, even though their unaged SBS values were lower than those of the baseline samples. The result is encouraging. It shows the benefit of expansive tendency of MgO in improving SBS.

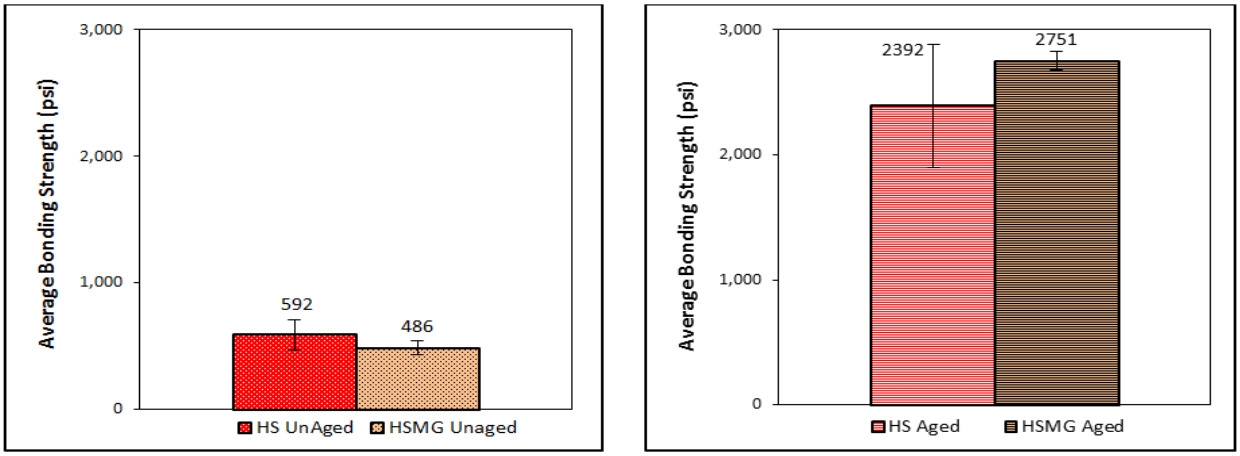

(a) **(b)**

Fig. 33: SBS of MGO-5 and baseline samples: a) Unaged; and b) aged at 350℉, 9000 psi, 40% CO_2 for 14 days

2.2.4.4 Micro-Silica-Based Cement

Micro-silica containing cement (MS) slurries were previously tested and found to be brittle. As discussed at the TAB meeting, the densities of the slurries were increased to control the brittleness. In addition, the slurries were reformulated with citric acid to delay the setting time. In preparation of the slurries, 20% BWOC micro silica (MS-20) was added together with citric acid. Slurry compositions and properties of MS-20 are presented in **Tables 8** and **9**. The slurries were prepared to examine properties of unaged core samples. During coring of the hardened cement samples, the GSMG cores were weaker than HSMS cores. The porosity and permeability of the samples are presented in **Fig. 34**. The porosities of MS-20 samples were lower than those of the baseline samples. This indicates filling of the pores with micro-silica. On the other hand, the permeabilities of the MS samples were very high. This could be due to micro cracks present in the cores.

Table 8: Formulations of MS-20 slurries

Component	HSMS	GSMS
Cement	100%	100%
Silica flour	15% BWOC	15% BWOC
Micro silica	20% BWOC	20% BWOC
HEC	0.1% of water for fillers	0.1% of water for fillers
Antifoam agent	0.1 gal/sack of cement	0.1 gal/sack of cement
Water for cement	38% BWOC	44% BWOC
Water for silica flour	38.5% of Silica Flour	38.5% of Silica Flour
Water for micro silica	0.13cc/ gm of Micro Silica	0.13cc/ gm of Micro Silica
Dispersant (NSF)	1.75% BWOC	1.75% BWOC
Retarder (citric acid)	0.03% BWOC	0.06% BWOC
BWOC = by weight of cement		

Table 9: Property of MS-20 slurry

	HSMS	**GSMS**	**Base HS**	**Base GS**
Density	16.01 ppg	16.10 ppg	16.20 ppg	15.45 ppg
Viscosity	Acceptable	Acceptable	Acceptable	Acceptable
API Filter Loss at 100 psi	40 ml	50 ml	100 ml	120 ml
Thickening Time	165 min.	160 min.	170 min.	135 min.

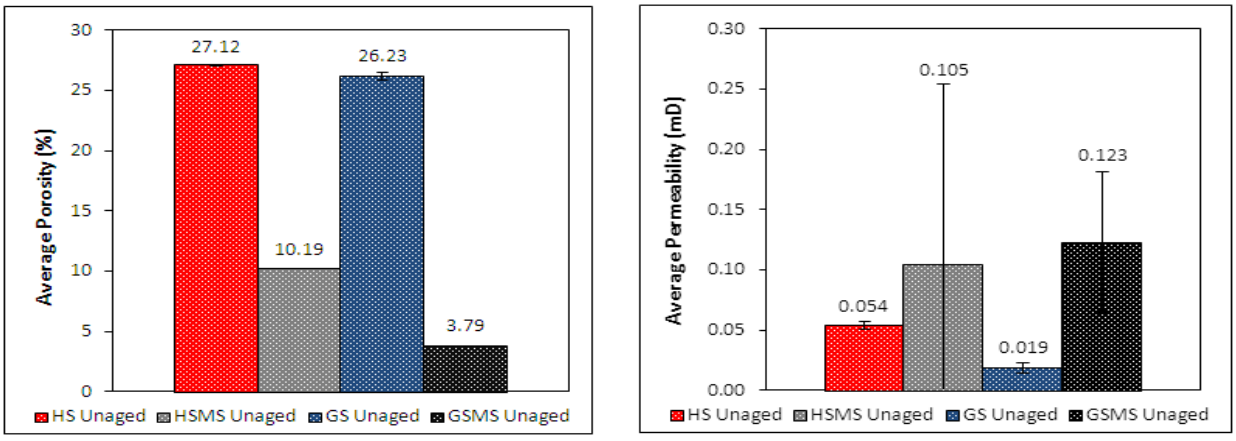

(a) **(b)**

Fig. 34: Porosity and permeability of unaged MS-20 and baseline samples

Compressive and shear bond strengths of unaged MS-20 and baseline cement cores are shown in **Fig. 35**. The HSMS samples displayed higher compressive strength than the base samples; whereas, the GSMS showed lower strength than the baseline samples. In contrary to the compressive strength measurements, the HSMS samples exhibited lower shear bond strength than the baseline samples. After examining these results, it was decided to lower the micro-silica content to 15% BWOC in the slurry. To provide the filler property of micro-silica as well as prevent the brittleness of the cement matrix, the slurry with reduced micro-silica content (MS-15) was prepared and tested. The properties of the slurry were acceptable (**Table 10**). The slurry compositions are presented **Table 11**. The samples were prepared and cured for aging experiment. However, after curing, the hardened cement blocks developed several cracks. The cracks were developed during the curing phase (without any physical movement or disturbance). One possible reason could be improper mixing of the slurry, which causes the micro-silica not to blend in the cement thoroughly. As per Grabowski and Gillott (1989), the slurry with micro-silica required longer mixing time than 35 seconds, which is recommended by API. Only six HSMS samples were prepared for the aging test. The samples are being aged at 350℉ and 3000 psi in brine saturated with 10% CO_2. Although the preliminary results from micro-silica cements are encouraging, the brittleness of the cores needs to be controlled. The next batch of MS-15 slurry will be prepared with extended mixing time (2 minutes) and the results will be compared with previous measured data obtained from samples prepared according to the API slurry mixing procedure.

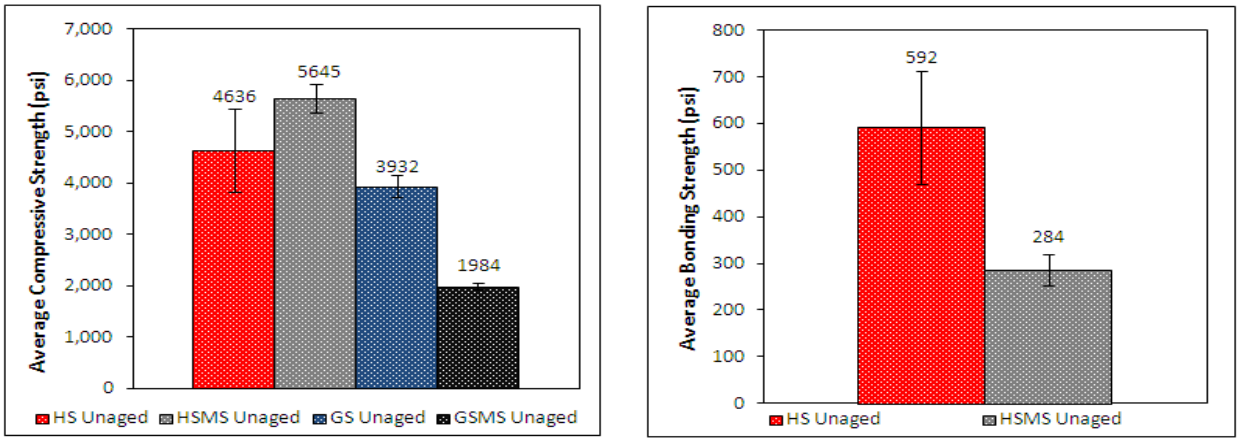

(a) **(b)**

Fig. 35: Compressive and bonding strength of unaged MS-20 and baseline samples

Table 10: Property of MS-15 slurry

	HSMS	GSMS	Base HS	Base GS
Density	16.10 ppg	15.60 ppg	16.20 ppg	15.45 ppg
Viscosity	Acceptable	Acceptable	Acceptable	Acceptable
API Filter Loss at 100 psi	72 ml	94 ml	100 ml	120 ml
Thickening Time	155 min.	115 min.	170 min.	135 min.

Table 11: Formulations of MS-15 slurries

Component	HSMS	GSMS
Cement	100%	100%
Silica Flour	20% bwoc	20% bwoc
Micro Silica	15% bwoc	15% bwoc
HEC	0.1% of water for fillers	0.1% of water for fillers
Antifoam Agent	0.1 gal/sack of cement	0.1 gal/sack of cement
Water for Cement	38% bwoc	44% bwoc
Water for Silica Flour	38.5% of Silica Flour	38.5% of Silica Flour
Water for Micro Silica	0.05cc/ gm of Micro Silica	0.05cc/ gm of Micro Silica
Dispersant (NSF)	1.25% bwoc	1.25% bwoc
Retarder (Citric Acid)	0.0015% bwoc	0.03% bwoc
bwoc = by weight of cement		

2.2.4.5 Latex-Based Cement

The carboxylated Styrene Butadiene Rubber (SBR) latex has been selected over the conventional SBR latex due to its small particle size and proper bonding with cement. The carboxylate group of the carboxylated SBR latex can improve bonding and reduce porosity and permeability of the cement. During this reporting period, tests were performed on carboxylated latex (Latex 1). The slurry composition is presented in **Table 12**. When the slurry was prepared, extremely thick paste was instantly formed in the blender. This created a serious concern.

Table 12: Composition Latex 1 cement slurry

Material	**Specific Gravity**	**Quantity**	**Mass**		**Volume**
Water for cement	0.99	38% of cement	256.34 gm	305.24 gm	308.33 cc
Water for Silica		35.0% of silica	82.63 gm		
Antifoam Agent	1.1	0.1 gal/sk	6.59 gm		5.99 cc
Dispersant (NSF)	0.7	1.25% of cement	8.43 gm		12.05 cc
50% Acetic Acid + Water	1	0.43% of cement	2.90 gm		2.90 cc
Carboxylate Latex	1.02	10.00% of cement	67.46 gm		66.13 cc
HEC		0.1% of water for fillers	0.08 gm		
Cement	3.14	100% of cement	674.57 gm		214.83 cc
Silica Flour	2.63	35% of cement	236.10 gm		89.77 cc
TOTAL			1335.10 gm		700.00 cc
Theoretical Density (ppg)	15.92 ppg (1335.10gm / 700.00 cc) (HS-15.96ppg)				
Liquid to Solid Ratio	1.002 (HS - 1.171)				
NSF = Sodium Poly – Naphthalene Formaldehyde Sulfonate HEC = Hydroxy-Ethyl Cellulose					

Diluted acetic acid (i.e. 50% water) was added as an emulsifier (**Table 13**) to control excessive thickening. Hence, 50% of the mass of the acid was reduced from the total required amount of water. One percent citric acid BWOC was also added to the slurry to act as a retarder and dispersant. Then, the slurry (Latex 2) was prepared and tested. Again, it showed rapid thickening in the blender.

Table 13: Composition Latex 2 cement slurry

Material	Specific Gravity	Percent	Mass		Volume
Water for cement	0.99	38% of cement	255.39 gm	302.67 gm	305.73 cc
Water for Silica		35.0% of silica	82.33 gm		
Antifoam Agent	1.1	0.1 gal/sk	6.56 gm		5.97 cc
Dispersant (NSF)	0.7	1.25% of cement	8.40 gm		12.00 cc
50% Acetic Acid + Water	1	0.43% of cement	2.89 gm		2.89 cc
Carboxylate Latex	1.02	10.00% of cement	67.21 gm		65.89 cc
Retarder (Citric Acid)	1.665	1.0% of cement	6.72 gm		4.04 cc
HEC		0.1% of water for fillers	0.08 gm		
Cement – Class H	3.14	100% of cement	672.09 gm		214.04 cc
Silica Flour	2.63	35% of cement	235.23 gm		89.44 cc
TOTAL			1336.91 gm		700.00 cc
Theoretical Density (ppg)	15.94 ppg (1336.91gm / 700.00cc) (HS-15.96 ppg)				
Liquid to Solid Ratio	0.986 (HS - 1.171)				

In order to control the thickening, the mixing order was adjusted. As suggested by Allan (1997), the latex was added to the slurry at end of mixing. This was expected to reduce the entrapment of air in the slurry and improve its properties. However, the slurry again displayed excessive thickening while mixing.

Ray and Gupta (1994) recommend use of 18% more water in the slurry if NSF is used as a dispersant with carboxylate polymers. Hence, slurry was prepared without citric acid but with 18% more water than required. Concentrated acetic acid was used this time. The slurry was prepared; however, very thick paste was formed within 30 seconds after blending. Subsequently, the amount of dispersant (NSF) was increased to 5% BWOC and the extra 18% water was removed. Even with 5% NSF, the slurry became very thick when it was prepared. Other attempts were also made to improve slurry properties; however, we were unable to control the rapid thickening. To find a solution, literature survey was conducted to examine thickening behavior of latex cement. Larbi and Bijen (1989) provide an explanation for the formation of thick paste like slurry. The –COO– bond, which is presented in the latex monomer, is able to react with any sodium ion present in water to form soap (saponification) as shown in below.

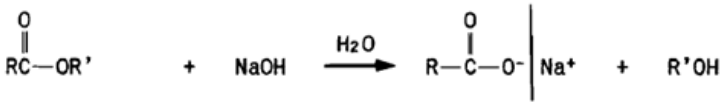

Saponification leads to the next reaction of capturing the Ca^{+2} ions available in the system. The reaction is similar to the reaction of soap in hard water, where the soap forms a scum by replacing the sodium ions with Ca^{+2} ions.

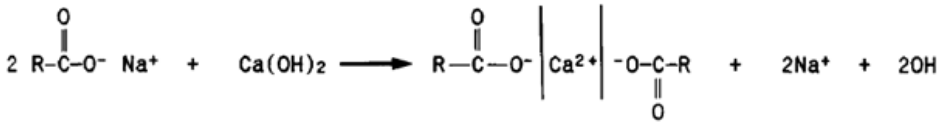

The formation of scum cannot be avoided in the reaction and hence scum like thick paste was formed in the blender during the test. Due to these set of reactions, carboxylate latex do not seem to be an effective additive for oil well cement, although its rapid setting tendency makes it ideal for road and bridge construction where such properties are required.

Testing with conventional SBR latex was continued. The lead author of the paper on Latex Cement (Fuquan et al. 2006) has been contacted to get details of their experiments. Permeability measurements published by the authors are significantly less than our measurements. The author replied that their permeability measurements were obtained using water as test fluid, while the current research is using helium gas. Moreover, the mixing procedure followed by authors was not as per the API standards and lower mixing speeds were used to avoid entrapment of air. In addition, pressurized curing conditions were used to squeeze out the air bubbles. The author has indicated that the anti-foaming agent used in the current research might be less effective than the agent used in their research. Hence, the conventional SBR latex will be tested with increased concentration of anti-foaming agent and the mixing procedure will be adjusted to avoid air entrapment.

2.3 Experimental Studies on Corrosion of Tubulars (Task 3)

Low-pressure corrosion experiments were continued using both weight loss (WL) and electrical measurement techniques. During this month, corrosion experiment was conducted with nitrogen purged nickel-plated autoclave. The description of the experimental setup was presented in the last month report. A high carbon steel sample (Grade 1045) was used as the working electrode. A graphite rod and high-temperature Ag/AgCl were used as counter and reference electrodes, respectively. To reduce the impact of atmospheric oxygen on the measurement, the autoclave was first purged with nitrogen gas and then maintained at a constant nitrogen pressure of 15 psi during the test. Inside the autoclave, the specimen (working electrode) was inserted into 2% NaCl brine solution. A potentiostat was used to measure corrosion rate using linear polarization resistance (LPR) technique. The test duration was 187 hours as required by the LPR method. Initial weight of the specimen was 24.6822 grams.

After the experiment was completed, the steel sample was taken out and standard mechanical cleaning procedure was performed. After cleaning, the sample was weighed to determine the corrosion rate by WL method. Based on weight loss, the average corrosion rate was found to be 1.639 mpy, whereas the LPR measurements showed average corrosion rate of 1.303 mpy. The corrosion rates from both LPR and WL methods are in good agreement. To test the reliability of our developed corrosion rate prediction model, comparison is made between measurement and prediction. The model predicts corrosion rate of 1.45 mpy for the exact condition

in which the experiment was carried out. Model prediction shows a very close agreement with measurements. Even though this is preliminary validation of the model, the result is encouraging.

During the experiment, instantaneous corrosion rate was measured using the LPR method. Plots of corrosion potential and corrosion rate generated by the LPR instrument are shown in **Fig. 36**. The Rp/Ec trend in the figure shows the initial corrosion rate of approximately 7 mpy. The rate decreased gradually because of formation of protective scales until the rate reach approximately 1 mpy (i.e. approximately 12 hours from time zero) and remained roughly at a constant corrosion rate until the end of the experiment. A very important observation from this experiment is that the measurement was very stable compared with results of previous tests. This shows the absence of chemically induced corrosion such as pitting. The result predominately indicates uniform corrosion. Previous experiments were conducted in a corrosion cell, which was open to the atmosphere. The presence of oxygen often leads to pitting corrosion.

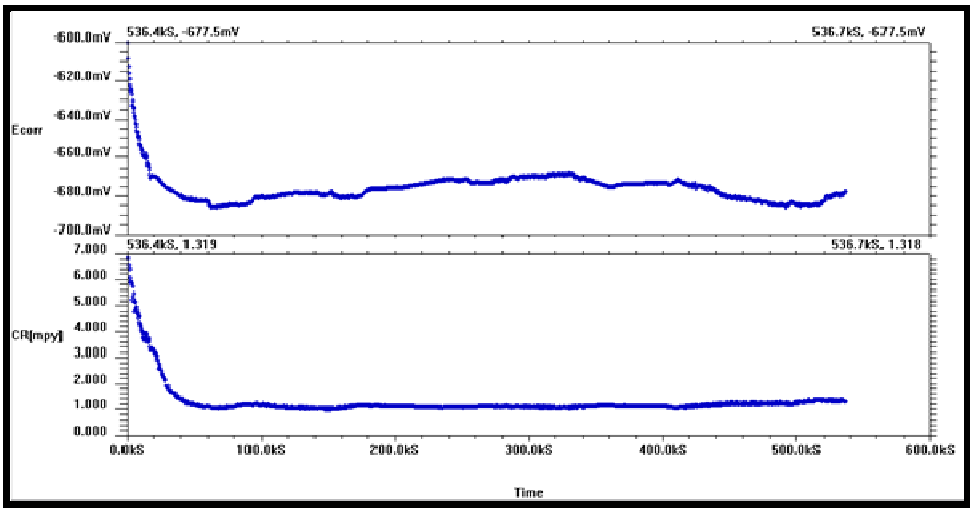

Fig. 36: Instantaneous corrosion rate vs. time (LPR data)

The construction of corrosion setup was continued. Assembling of high-pressure tubing, tube fittings and measuring instrumentation has been initiated. High-pressure fittings provided by equipment supplier are found to be incompatible with sour gas application. Hence, they have been returned to the manufacturer for special heat treatment (annealing) to meet NACE MR0175 specifications for sour gas applications.

3. Planned Activities

- Continue aging experiments with brine-CO_2-CH_4 system for 14 days varying aging pressure (3,000, 6000, and 9000 psi) at 350ºF and 10% CO_2 concentration.
- Continue theoretical and modeling studies on tubular degradation.

- Continue cement additive screen study.
- Continue the development of tubular corrosion testing setup.

4. Project Expenditures

This section presents the project expenses during the month of June (**Table 14**) and the cumulative expenditures.

Table 14 Current and cumulative expenditures, June, 2013

No.	Budget Categories	Current Expenses	Cumulative Expenses
1	Salaries & Wages	$18,744.78	$180,337.23
2	Fringe Benefits	$5,031.25	$40,604.26
3	Project Materials	$723.56	$55,883.65
4	Travel	$1,876.56	$6,010.28
5	Conference Expenses	$0.00	$0.00
6	Other Direct Costs	$150.00	$993.60
7	Equipment	$5,189.04	$234,847.33
8	Space Rental	$0.00	$0.00
9	Indirect Cost	$13,263.08	$141,914.47
10	**Total**	**$44,978.27**	**$660,590.82**

Nomenclatures

Acronyms

BWOC	By weight of cement
CH	Calcium hydroxide
CSH	Calcium silicate hydrate
DCB	Double Cantilever Beam test
FTIR	Fourier Transform Infra-Red
GHO	Class G cement with hydroxyapatite
GS	Class G cement with silica flour
GSHO	Class G Cement with silica flour and hydroxyapatite
GSMG	Class G Cement with silica flour and magnesium oxide
GSLT	Class G Cement with latex
HHO	Class H cement with hydroxyapatite
HIC	Hydrogen Induced Cracking
HOAP	Hydroxyapatite containing cement
HPHT	High-pressure high-temperature
HS	Class H cement with silica flour
HSHO	Class H Cement with silica flour and hydroxyapatite
HSMG	Class H Cement with silica flour and magnesium oxide
HSLT	Class H Cement with latex
KISSC	Stress Intensity factor
LPR	Linear polarization resistance
MGO	Magnesium oxide containing cement
MGO-5	Cement containing 5% BWOC MgO as additive
MGO-10	Cement containing 10% BWOC MgO as additive
MS	Micro silica containing cement
MS-15	Cement containing 15% BWOC micro silica as additive
MS-20	Cement containing 20% BWOC micro silica as additive
NACE	National Association of Corrosion Engineers
PRV	Pressure relief valve

SBR	styrene-butadiene
SBS	Shear bonding strength
SCC	stress corrosion cracking
SEM	Scanning Electron Microscope
SMYS	Specified Minimum Yield Strength
SOHIC	Stress Oriented Hydrogen Induced Cracking
SSC	Sulfide Stress Cracking
TCL	Total Crack Length
XRD	X-Ray diffraction

Symbols

$C_{\varphi 1}, C_{\varphi 2}, C_{\varphi 3}$	Concentrations fictitious species, mol/m^3
C_{CO2}	Bulk concentration of carbon dioxide in aqueous phase, mol/m^3
$C_{H_2CO_3}$	Bulk concentration of carbonic acid, mol/m^3
$C_{HCO_3^-}$	Bulk concentration of bicarbonate ion, mol/m^3
$C_{CO_3^{2-}}$	Bulk concentration of carbonate ion, mol/m^3
C_{H^+}	Bulk concentration of hydrogen ions, mol/m^3
$C_{Fe^{2+}}$	Bulk concentration of iron ion, mol/m^3
C_{H_2S}	Bulk concentration of hydrogen sulfide in aqueous phase, mol/m^3
C_{HS^-}	Bulk concentration of hydrogen sulfide ion, mol/m^3
C_{OH^-}	Bulk concentration of hydroxide ion, mol/m^3
$D_{\varphi 1}, D_{\varphi 2}, D_{\varphi 3}$	Average diffusion coefficients of fictitious species, m^2/s
D_{CO_2}	Diffusion coefficients of carbon dioxide, m^2/s
$D_{Fe^{2+}}$	Diffusion coefficients of iron ion, m^2/s
dt	Time step
F	Faraday's constant, F = 96,485 C/mol
i_j	Exchange current density of species j, A/m^2

N_j	Flux of species j, mol/m2.s
n_j	Number of moles of electrons exchanged per mol of species j
pH	Solution pH
P_{H_2S}	H_2S partial pressure, Pa
RR_{CO_2}	Reaction rate for carbon dioxide hydration, $mol/m^3.s$
t	Time, s
T	Temperature, Kelvin
X	Distance from the metal surface in the normal direction, m
δ_E	Thickness of electrolyte layer, m
δ_S	Thickness of corrosion scale, m
ϕ	Volumetric porosity of the corrosion scale
k	Permeability of the corrosion scale

References

Allan, M. L. 1997. Rheology of Latex Modified Grouts, Cement and Concrete Research, Vol. 27, No. 12, pp 1875 – 1884.

Amri, J., Kvarekval, J. and Malki, B. 2011. Simulation of Solid-State Growth of Iron Sulfides in Sour Corrosion Conditions, paper No. 78, March 13 - 17, Houston, Texas.

Bertos, M.F., Simonsa, S.J.R., Hillsb, C.D. and Carey, P.J. 2004. A review of accelerated carbonation technology in the treatment of cement-based materials and sequestration of CO_2, Journal of Hazardous Materials, Vol. 112, Issue 3, pp 193–205.

Bich, N. N. and Goerz, K. 1996. Caroline Pipeline Failure: Findings on Corrosion Mechanisms in Wet Sour Gas Systems Containing Significant CO_2, paper No. 26, March 24 - 29, Denver, Co.

Chang, J. J., Yeih, W., Huang, R. and Chi, J.M. 2003. Mechanical Properties Of Carbonated Concrete, Journal of the Chinese Institute of Engineers, Vol. 26, No. 4, pp. 513-522.

Duan, Z. and Sun, R. 2003. An improved model calculating CO_2 solubility in pure water and aqueous NaCl solutions from 273 to 533 K and from 0 to 2000 bar, Chemical Geology, Vol. 193, 257–271.

Dillenbeck III, R. L., Mueller, D.T. and Orr, B.R. 1990. The Effect of Micro Silica on the Thermal Stability of Lightweight Cement Systems, paper SPE 21597 presented at the CIM/SPE International Technical Meeting, 10-13 June, Calgary, Alberta, Canada.

Eilers, L.H., Nelson, E.B. and Moran, L.K. 1983. High Temperature Cement Compositions – Pectolite, Scawtite, Truscotite or Xonoloite: Which Do You Want?, JPT, Vol. 35, Num. 7, pp 1373-1377.

Eilers, L.H. and Root, R.L. 1976. Long-Term Effects of High Temperature on Strength Retrogression of Cements, paper SPE 5871 presented at the SPE California Regional Meeting, 7-9 April, Long Beach, California.

Fabbri, N., Jacquemet, D. and Seyedi, M. 2012. A chemo-poromechanical model of oil well cement carbonation under CO2 geological storage conditions, Cement and Concrete Research, Vol. 42, pp 8-19.

Fardisi, S., Tajallipour, N. and Teevens, P. 2012. Predicting General Corrosion Rates in Sour Environments with the Growth of a Protective Iron Sulphide Film, paper No.1471, March 11 - 15, Salt Lake City, Utah.

Fuquan, S., Guangming, L. and Jianzhou, J. 2006. Application and research of latex tenacity cement slurry system, paper SPE 104434 presented at the SPE International O&G Conference and Exhibition, Beijing, 5-7 December.

Grabowski, E. and Gillott, J.E. 1989. Effect of Replacement of Silica Flour with Silica Fume on Engineering Porperties of Oil Well Cements at Normal and Elevated Temperatures and Pressures, Cement and Concrete Research, Vol. 19, pp 333-344.

Harker, R.I. 1965. Scawtite and its Synthesis, Mineral Magazine, Vol. 34, 232.

John Lee, K.L. 2004. A Mechanistic Modeling of CO_2 Corrosion of Mild Steel in the Presence of H_2S, PhD dissertation, Ohio University.

Kim, W.K., Park G., Koh, S.U. and Jung, G.H. 2010. Determination of Critical Factors Affecting on Hydrogen Induced Cracking and Type I Sulfide Stress Cracking of High Strength Line pipe Steel, paper presented at the 20th International Offshore and Polar Engineering Conference, 20-25 April, Beijing, China.

Kimura, M., Kataoka, Y. and Nakano, Y. 1996. Sulfide Stress Corrosion Cracking Resistance of Low Cr Steel, paper No. 60 presented at CORROSION 96 meeting, NACE International, March 24 - 29, Denver, Colorado.

Kvarekval, J. and Nyborg, R. and Choi, H. 2003. Formation of Multilayer Iron Sulfide Films during High Temperature CO_2/H_2S Corrosion of Carbon Steel, paper No. 339, March, San Diego Ca.

Larbi, J.A. and Bijen, J.M. 1990. Interaction of Polymers with Portland Cement During Hydration: A Study of the Chemistry of the Pore Solution of Polymer Modified Cement Systems, Cement and Concrete Research, Vol. 20, pp 139-147.

Lea, F.M. 1971. The Chemistry of Cement and Concrete, 3rd Edition, Chemical Publishing Co., New York City, pp 177-202.

Masouri, D. and Zafar, M. 2004. Sulfide Stress Cracking of stainless steel 410 in sour crude oil, paper No. 4121, NACE International Annual Conference, March 28 - April 1, 2004, New Orleans, LA.

Masouri, D. and Zafar, M. 2005, Sulfide Stress Cracking of Tubular product-case histories, paper No. 5460, NACE International Annual Conference, April 3 - 7, Houston, TX.

Muraki, T., Tsuru, S. and Asahi, H. 2006, Sulfide Stress Cracking resistance of post expanded low alloy steel tubular, paper No. 6153, presented at the NACE 61st Annual Conference and Exposition, March 12 - 16, 2006 , San Diego CA.

NACE. 2001. Materials for Use in H_2S containing Environments in Oil and Gas Production, NACE Standard MR0175/ISO15156, NACE International, Houston, Texas.

NACE. 2005. Laboratory Testing of Metals for Resistance to Sulfide Stress Cracking and Stress Corrosion Cracking in H2S Environments, NACE Standard TM0177, NACE International, Houston, Texas.

Ray, I. and Gupta, A.P. 1994. Effect of Latex and Superplasticiser on Portland Cement Mortar in the Fresh State, Cement and Concrete Research, Vol. 16, pp 309-316.

Roger, J. 1996. Cements treated with high-pressure CO_2. US Patent 5,518,540, 21 May.

Sun, W., Nesic, S. and Papavinasam, S. 2006. Kinetics of Iron Sulfide and Mixed Iron Sulfide/Carbonate Sale Precipitation in CO_2/H_2S Corrosion, paper No. 644, Houston, Texas.

Svenningsen, G., Palencsar, A. and Kvarekval, J. 2009. Investigation of Iron Sulfide Surface Layer Growth in Aqueous H_2S/CO_2 Environments, paper No. 359, March 22 - 26, Atlanta, GA Vestergaard, B. and Robinson, T. 2003. CO_2 in Refrigeration Applications, Air Conditioning, Heating and Refrigeration News, October 2, available at: http://www.achrnews.com, Last accessed 06/11/2013.

Tsay, L.W. , Chi, M.Y., Chen H.R. and Chen, C. 2005. Investigation of Hydrogen sulfide stress corrosion cracking of PH 13-8 Mo stainless steel, Materials and Science Engineering A, Vol. 416, 155-160.

Appendix A: FTIR (Fourier Transform Infrared Spectroscopy) Charts

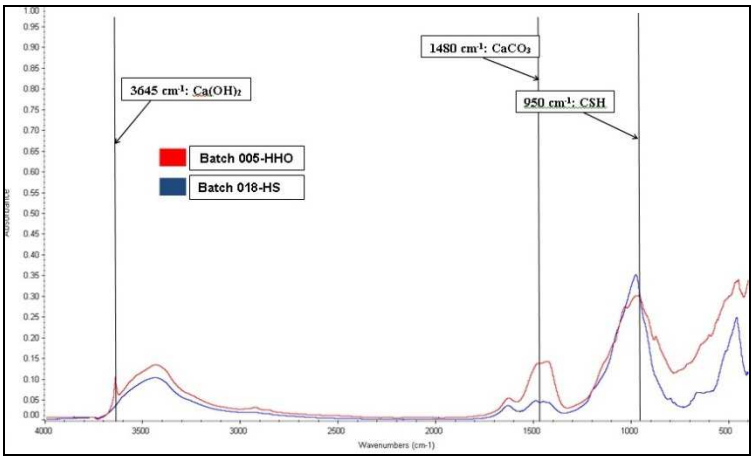

Fig. A-1: FTIR spectra of HHO and HS for inner zone aged at 350℉, 3000 psi with 100% CO_2, 14 days

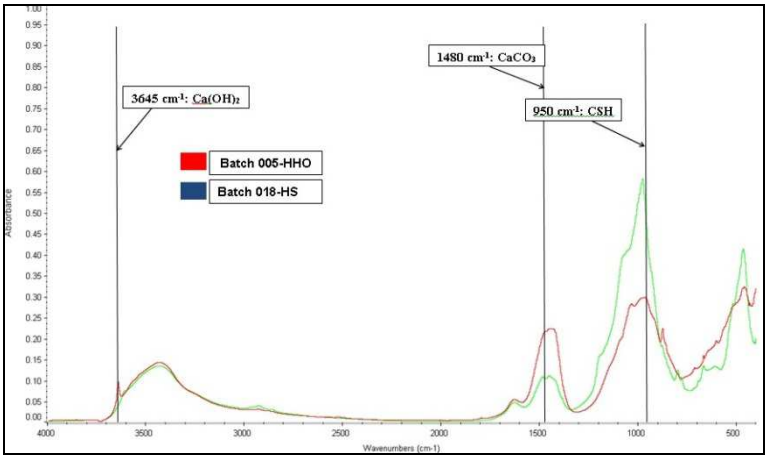

Fig. A-2: FTIR spectra of HHO and HS for middle zone aged at 350℉, 3000 psi with 100% CO_2, 14 days

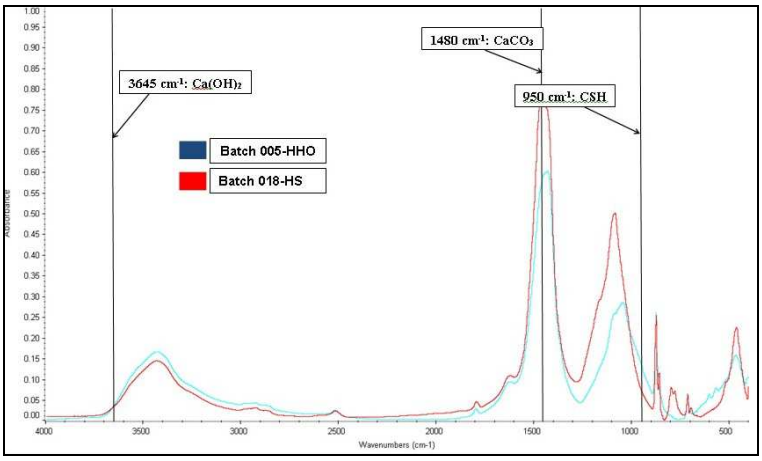

Fig. A-3: FTIR spectra of HHO and HS for outer zone aged at 350℉, 3000 psi with 100% CO_2, 14 days

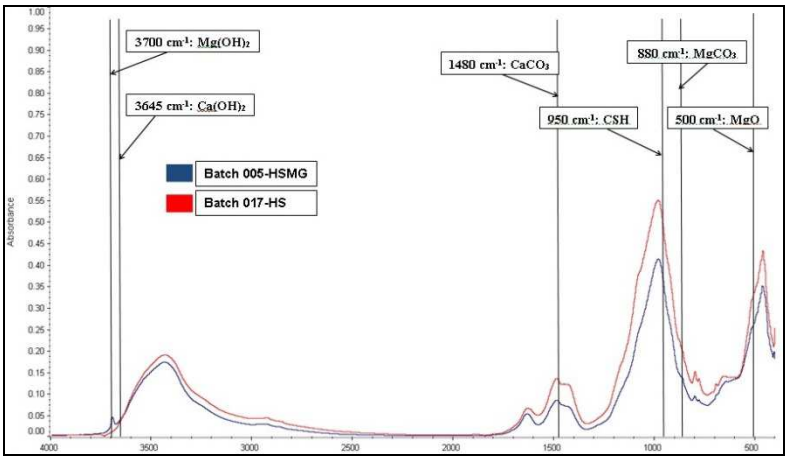

Fig. A-4: FTIR spectra of HSMG and HS for inner zone aged at 350℉, 9000 psi with 40% CO_2, 14 days

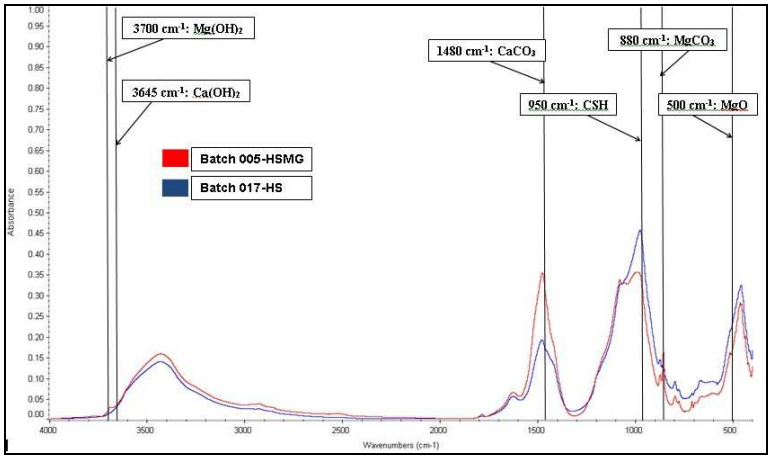

Fig. A-5: FTIR spectra of HSMG and HS for middle zone aged at 350℉, 9000 psi with 40% CO_2, 14 days

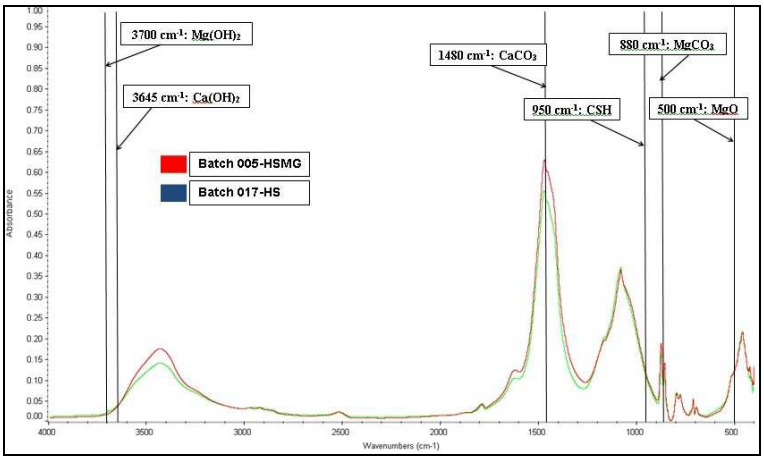

Fig. A-6: FTIR spectra of HSMG and HS for outer zone aged at 350℉, 9000 psi with 40% CO_2, 14 days

Project Title: Effect of H_2S and CO_2 in HPHT Wells on Tubulars and Cement

Report Type: Monthly Report

Report #: 22

Reporting Period: June 22nd, 2013 to July 21st, 2013

Authors:

Ramadan Ahmed, Principal Investigator

Subhash Shah, Co-Principal Investigator

Samuel Osisanya, Co-Principal Investigator

Rida Elgaddafi, Research Assistant

Omotayo Omosebi, Research Assistant

Himanshu Maheshwari, Research Assistant

Adarsh Naidu, Research Assistant

Aman Srivastava, Research Assistant

Jueun Hwang, Research Assistant

Mounraj Sharma, Research Assistant

Sagar Tale, Research Assistant

Prepared under BSEE Project # E12PC00035

by

THE UNIVERSITY OF OKLAHOMA

September 12, 2013

1. Summary of Accomplishments

This monthly report presents the progress made during the project period June 22, 2013 to July 21, 2013. During this reporting period, studies on cement and tubular degradation were continued. Cement cores and bonding samples of different cement formulations were prepared and aged in acidic environment to examine their degradation characteristics. Tests with acid resistant cement formulations were continued. The effects of different additives on properties of cement slurries and cores were investigated.

Two aging experiments (Experiments 16 and 17) were performed during this month. The samples were aged for 2 weeks in 2% brine saturated with CO_2 containing methane gas. Porosity, permeability, and compressive and bond strengths of unaged and aged samples were measured. In addition, mineralogical properties of the samples were analyzed using Fourier Transform Infrared Spectroscopy (FTIR).

At low pressures of 3000 psi, the solubility of CO_2 diminishes the carbonation of cement samples and favors the formation of scawtite that significantly reduces porosity and permeability of the cement. In addition, test results show that compressive strength of Class G aged at different pressures varies slightly. For Class H cement, high aging pressure significantly improved strength because of carbonation. Furthermore, shear bond strength (SBS) measurements showed that, for aged samples, the trends of SBS with pressure remained similar. The SBS of samples aged at 6000 psi were lower than those aged at other pressures.

Experimental investigation on cement additives continued. The effects of different additives (hydroaxipitate, magnesium oxide, micro silica, and latex) on performance of Class H and Class G cements under HPHT conditions have been examined during this reporting period. Even though the addition of hydroxyapatite (HOAP) was able to prevent the carbonation of the samples, the reduction in compressive strength was observed after aging. With the addition of silica flour, the basic strength of the cement reduced significantly. A further study was carried out to determine the quantity of silica flour needed to control the strength retrogression without reducing the basic strength. Porosity and permeability of unaged HOAP samples containing silica were higher than those of the baseline samples. The addition of HOAP with silica flour caused a drastic increase in permeability.

Magnesium oxide cement cores with 10% BWOC MgO (MGO-10) were prepared and tested for their performance. Previously, tests with MGO-5 cement showed encouraging results. The MGO-10 samples showed almost similar positive result. The baseline HS samples exhibited increased permeability after aging while the MGO-10 samples displayed reduction in permeability.

Theoretical and modeling studies on uniform corrosion of tubular are in progress. Additional focus has been given to improve the computational performance of a computer code developed using the theoretical model. Although reasonable model predictions were obtained as presented in the last month report, two major issues were observed: i) long computational time; and ii) inconsistency in model predictions due to computational instability.

Corrosion study under moderate pressure and temperature is in progress. Corrosion rate measurements were obtained at 50% CO_2 concentration. For the first two tests, the corrosion rates were fluctuating resulting from gas injection during the experiment in order to account for leakage from the vent valve. The system was repaired and the third test was performed without leakage. The result shows smooth corrosion rate trend. Moreover, both weight-loss and LPR methods showed consistent results.

Our plan for the upcoming weeks is to continue: i) aging tests at different pressures and temperatures; ii) theoretical and modeling studies on tubular corrosion; iii) additive screening and acid resistant cement development studies; iv) low pressure corrosion experiments at different CO_2 concentrations; and v) development of corrosion test setup.

2. Overall Project Progress

2.1 Theoretical Studies (Task 1)

2.1.1 Uniform Tubular Corrosion

Theoretical and modeling studies on uniform corrosion of tubular are in progress. A model developed by Fardisi et al. (2012) was improved. Experimentally measured corrosion rates were utilized to validate the model predictions. Model formulation and numerical schemes were presented in previous reports (Report # 20 and 21). All model equations were implemented into a Matlab code to obtain numerical solutions. During this reporting period, more focus has been given to improve the computational performance of the code. Although reasonable model prediction were obtained as presented in the last month report, making predictions using the code requires very long computational time. In addition, due to instability, some of the predictions obtained from code have shown inconsistency. Therefore, a considerable effort has been devoted to minimize the computational time and improve stability of the code by adjusting the grid size, and computational time step. Currently, the program requires 5 days of computational time to simulate corrosion process of 72 hours. In the coming weeks, the following steps will be implemented to reduce the computational time: i) debug the entire code to find programming issues that can cause these problems; ii) optimize computational parameters such as grid size and computational time step; and iii) utilize high-speed computers to run the code.

2.1.2 Sulfide Stress Cracking (SSC)

Last month report presented various studies conducted to understand factors that affect the SSC resistance. This report summarizes studies (Mack et al. 2000; Gaugh 1982; Kane et al. 1977; Baldy et al. 1981) performed to examine steel grades that are resistant to SSC. It presents a review of previous studies conducted to evaluate SSC resistance of various API and non-API grade steels including nitrogen strengthened steels and expandable tubulars.

Sulfide stress cracking is a problem in oil and gas industry since high-strength steels are susceptible to SSC in sour environment. In general, high-strength steels have lower SSC resistance. Some studies have underlined importance of Molybdenum (Mo) content for environmental corrosion resistance.

Expandable casing technique has been recently developed in the oil industry. In this technique, diameter of the casing is increased after reaching bottom hole. However, the change in diameter occurring under wellbore conditions leads to change in mechanical properties of the casing and hence alteration of SSC resistance. Mack et al. (2000) studied the effects of expansion on SSC resistance of various alloys used in manufacturing expandable tubulars. It is known fact that cold work changes mechanical properties of metals. An early experimental study (Baldy et al.1981) showed effects of cold work on mechanical properties of N-80 grade steel and C-Mn-Mo-V alloy.

Austenite steels have good resistance to SSC. Studies (Tsay 2005; Hashizume et al. 2000) showed improvement with SSC resistance with increase in austenite content. Austenitic stainless steels exhibit lower strength than martensitic steels.

Studies (Hashizume et al. 2000; Chauveau et al. 2012) showed that the SSC resistant of metals in sour environment is strongly related to depassivation pH, Mo content, austenite content and level of cold work. Depassivation pH (i.e. a critical pH value for the onset of intensive corrosion) is also a measure of performance of material in sour environment. Hashizume et al. (2000) and Chauveau et al. (2012) performed experiment to determine depassivation pH of steels. If surrounding pH is below depassivation pH, material undergoes severe corrosion. Figure 1 shows result of experiment performed by Hashizume et al. (2000) using carbon steel (Steel A). For pH value of less than 3.8, corrosion rate sharply increases; however, for pH value greater than 4.0,

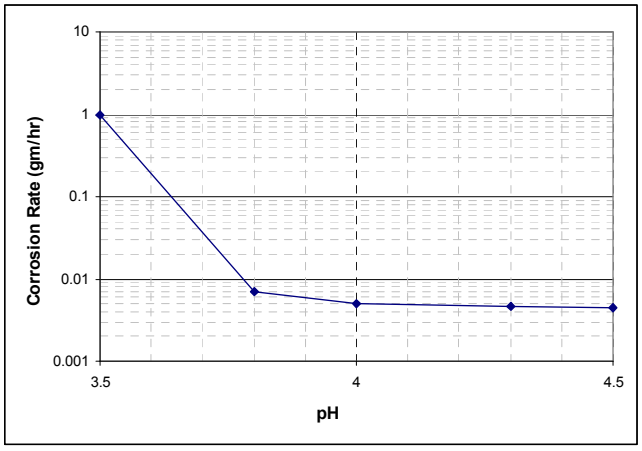

Fig. 1: Corrosion rate vs. pH for carbon steel (Hashizume et al. 2000)

the material showed a constant corrosion rate while the pH was varied. Thus, the depassivation pH is in between 3.8 and 4.0.

A study (Hashizume et al. 2000) performed on steels with different Mo content showed that depassivation pH reduces with increase in Mo content. This suggests steel with higher Mo content to be used in sour conditions. Sour conditions results in low pH; however, this pH can be still higher than depassivation pH of material containing Mo. Hence, Mo alloys may have good resistance to SSC. Another study (Baldy et al. 1981) conducted on N-80 and special N-80 material (N-80-Mo) containing a higher Mo content is in agreement with the findings of Hashizume et al. (2000). Tensile strength tests performed on N-80 and N-90-Mo showed the improvement of threshold stress (i.e. critical stress for initiation of SSC) with Mo content.

Cold work tends to reduce SSC resistance of metals. Muraki et al. (2006) showed the effect of expansion on SSC resistance of API L-80 material. The SSC resistance decreased after expansion. Mack et al. (2000) performed similar experiments on P-110 and L-80 specimens. The experiments were performed in two different environments: 2.5% H_2S and 100% H_2S. Results showed reduction in SSC resistance of L-80 in 100% H_2S environment after expansion but not in 2.5% H_2S. However, for P-110, SSC resistance reduction occurred both in 100% and 2.5% H_2S environments. Thus, reduction in SSC resistance after expansion depends on material type and concentration of H_2S in surroundings.

Nitrogen strengthened steels exhibit better SSC resistance than S17400 alloy, which is approved by NACE for sour environment (Gaugh 1982). Experiments performed on several nitrogen-strengthened steels with different Mn content showed reduction in SSC resistance as the Mn content increased.

2.2 Experimental Studies on Degradation of Cement (Task 2)

2.2.1 Porosities and Permeabilities of Baseline Cements

Experimental results were presented in previous report (Report # 21) showing the effects of CO_2 concentration on porosity and permeability of aged cores at different pressures. It was observed that at lower pressures there was decrease in porosity and permeability due to formation of scawtite (Calcium Silicate Carbonate). This was confirmed from the XRD mineralogy analysis. When the aging pressure is low, incomplete carbonation occurs, leading to the formation of scawtite (Harker 1965, Lea 1971). At high pressure (6000 psi), more CO_2 reacts with scawtite, forming $CaCO_3$ thereby completes the carbonation process. Further reaction between carbonic acid and calcium carbonate results in the formation of soluble product ($Ca(HCO_3)_2$) that can be leached out by the acid. Leaching leads to the increase in porosity and permeability. At 9000 psi, porosity and permeability decreased. This is attributed to the formation of crystals as the cement interacts with supercritical CO_2 (Roger 1996).

Test matrix is shown in **Table 1** where the highlighted batches indicate experiments completed during the month of July. The aging conditions for all batches of cement degradation experiments are summarized in **Table 2**. Our recent tests are focused on examining the effects of pressure on the degradation behavior of cement cores at 350°F and different CO_2 concentrations.

Table 1: Test matrix for aging experiments at 350°F

Pressure (psi)	10% CO_2	40% CO_2	100% CO_2
3000	**Batch 020**	Batch 016	Batch 018
6000	Batch 006	Batch 013	Batch 014
9000	Batch 021	Batch 017	**Batch 019**

Table 2 Test parameters for aging experiments conducted to date

Batch #	Temp. (ºF)	Pressure (psi)	Partial Pressure %			Brine Conc. (%)	Aging Period (days)	Experiment #
			CH_4	CO_2	H_2S			
001	350	9000	100	0	0	9	6	1
002	350	6000	100	0	0	2	14 & 28	2
003	350	6000	100	0	0	2	14	
004	350	6000	90	10	0	2	6	3
005	350	6000	90	10	0	2	14 & 28	4
006	350	6000	90	10	0	2	14	
007	225	6000	90	10	0	2	14	5
008	100	6000	90	10	0	2	14	6
009	225	6000	60	40	0	2	14	7
010	225	6000	0	100	0	2	14	8
011	100	6000	60	40	0	2	14	9
012	100	6000	0	100	0	2	14	10
013	350	6000	60	40	0	2	14	11
014	350	6000	0	100	0	2	14	12
015	225	6000	60	40	0	2	14	7A
016	350	3000	60	40	0	2	14	13
017	350	9000	60	40	0	2	14	14
018	350	3000	0	100	0	2	14	15
019	**350**	**9000**	**0**	**100**	**0**	**2**	**14**	**16**
020	**350**	**3000**	**90**	**10**	**0**	**2**	**14**	**17**

Figure 2 presents porosities and permeabilities of samples aged at two different pressures (3000 and 6000 psi). The aging was performed for 14 days at 350ºF in brine saturated with 10% CO_2. Measurements obtained after aging the cores at 9000 psi will be presented in the next report. Evidently, the trends of porosity and permeability match with each other for both Class H and Class G. For Class G cement, as pressure increases, both porosity and permeability decreased. However, in case of Class H cement, porosity and permeability increased with pressure.

Unaged samples exhibited higher porosity and permeability than samples aged at 3000 psi. This could be attributed to the formation of scawtite that reduces the pore porosity and permeability of the cement. However, as the pressure increased from 3000 to 6000 psi, the condition favored the formation of $CaCO_3$, and subsequently $Ca(HCO_3)_2$ which can be easily leached out by the acid.

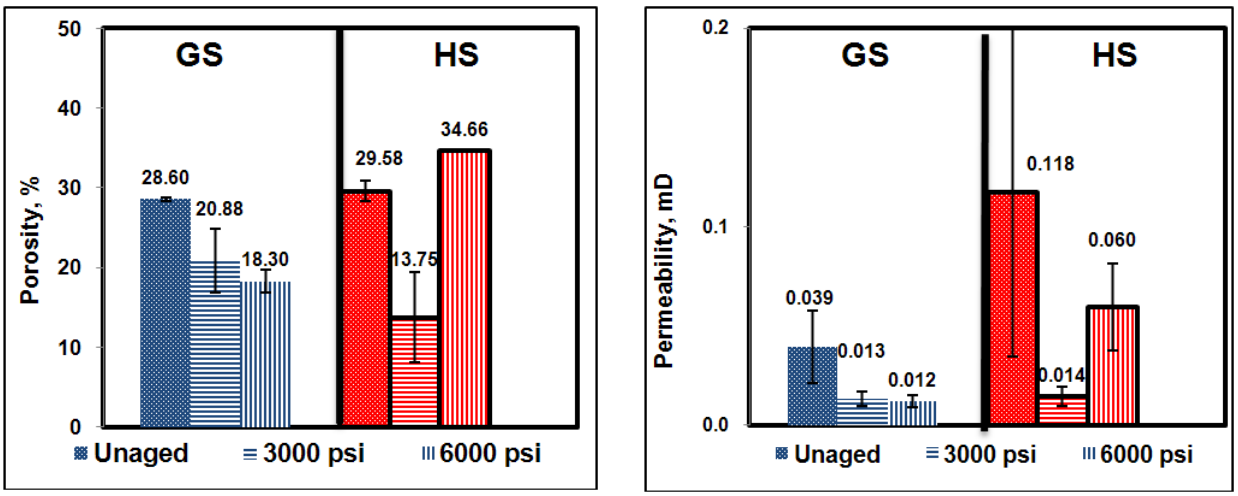

(a) (b)

Fig. 2: Effect of pressure on properties of unaged cores and samples aged for 14 days at 350°F in 10% CO_2 gas saturated brine solution: a) porosity; and b) permeability

Figure 3 illustrates the porosity and permeability of samples aged at 350ºF and different pressures (3000, 6000 and 9000 psi) for 14 days in brine saturated with 40% CO_2. For both Class H and Class G cement, porosity trends are consistent with that of permeability. At 3000 psi, incomplete carbonation occurred leading to formation of scawtite, which resulted in significant reduction in porosity and permeability of the samples. At 6000 psi, there was adequate CO_2 in the brine to form calcium carbonate and calcium bicarbonate thereby increasing the porosity and permeability of the cement due to leaching. At 9000 psi, reduction in porosity and permeability was observed due to the formation closely packed crystals when cement reacts with super critical CO_2 thereby plugging the pores and creating capillaries (Roger 1996). When similar experimental investigation was conducted at 100% CO_2 concentration, slightly different porosity and permeability trends were observed (**Fig. 4**). Significant reduction in porosity and permeability that was noticed when Class H cement was aged at 3000 psi and low CO_2 concentrations (10% and 40%) was not observed when the concentration was increased to 100%. At high CO_2 concentration the conditions favors the formation of $CaCO_3$ rather than scawtite, which is responsible for significant reduction of porosity and permeability of the cement. When aged at 100% CO_2, regardless of the pressure, porosity and permeability of all the samples decreased due to carbonation, which dominates the leaching process.

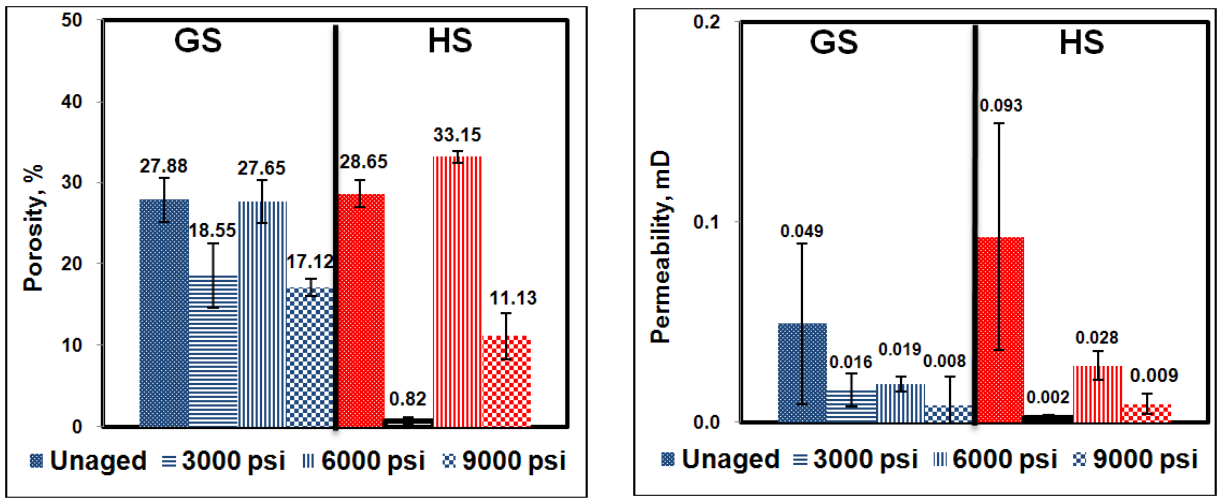

(a) (b)

Fig. 3: Effect of pressure on properties of unaged cores and samples aged for 14 days at 350°F in 40% CO_2 gas saturated brine solution: a) porosity; and b) permeability

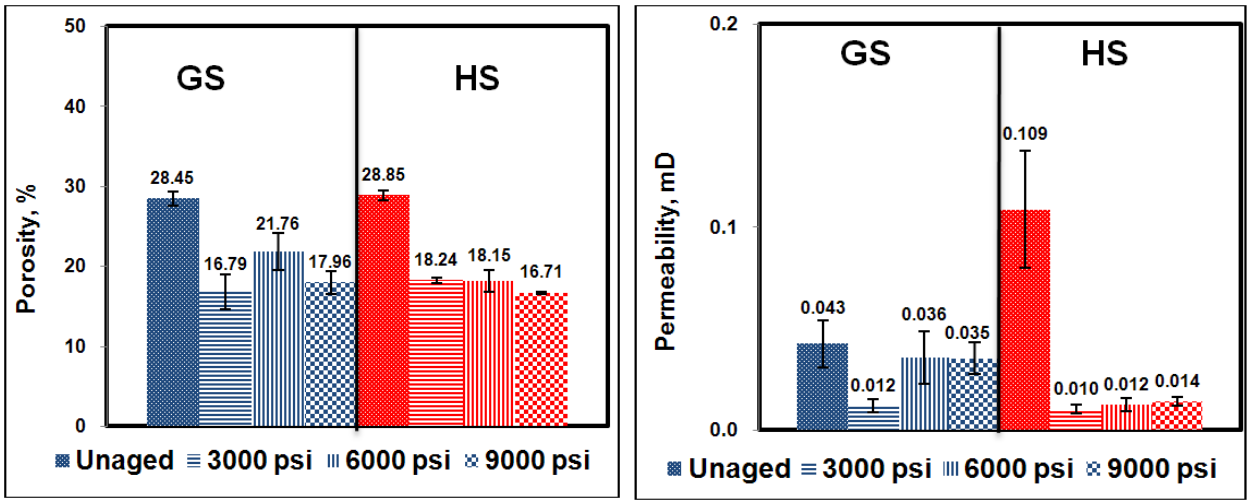

(a) (b)

Fig. 4: Effect of pressure on properties of unaged cores and samples aged for 14 days at 350°F in 100% CO_2 gas saturated brine solution: a) porosity; and b) permeability

2.2.2 Compressive Strengths of Baseline Cements

Cement degradation in the presence of carbonic acid has continued to be a major subject of investigation, especially in deep-water applications where extreme down-hole conditions exist. These environments pose serious well integrity issues that affect safety oil and gas operations and the environment. Carbonation and leaching of cementitious phases are major mechanisms governing compressive strength evolution and degradation when oil well cement is exposed to CO_2 attack. The strength is altered in a manner that accounts for all chemo-mechanical processes depending on down-hole temperature, pressure and concentration of CO_2.

This part of the report presents compressive strength result of experimental study conducted on Class G and Class H cements, which were exposed to harsh aging conditions as specified in Table 1. Compressive strengths of two batches (Batch 19 and Batch 20) of unaged and aged baseline cement samples were measured. These measurements are a further step in investigating pressure effect on compressive strength of baseline cements. Batch 19 completes series of experiments conducted to study pressure effect at 350ºF and 100% CO_2 while Batch 20 commences investigation of pressure effect at 350ºF and 10% CO_2. Aging conditions for each of this batch are summarized in Table 2.

Recent measurements are combined with previous data (Batch 14 and Batch 18) obtained after aging at different pressures. The results (**Fig. 5**) show that compressive strength of Class G cement varies slightly with pressure. However, the trend is mixed; it showed first a moderate increase in strength followed by slight decrease with pressure. This is consistent with measurements obtained from previous experiments, which suggest the domination of leaching on carbonation at low pressure. At high pressure, carbonation is faster than leaching. In Class H cement, high aging pressure favored strength gain because of increased rate of carbonation. In addition, since Class H cement is more coarsely ground than Class G (Lea 1971), it was more permeable than the G cement. As a result, greater proportion of the cement was exposed to the acid attack and carbonation, which led to strength improvement as pressure was increased.

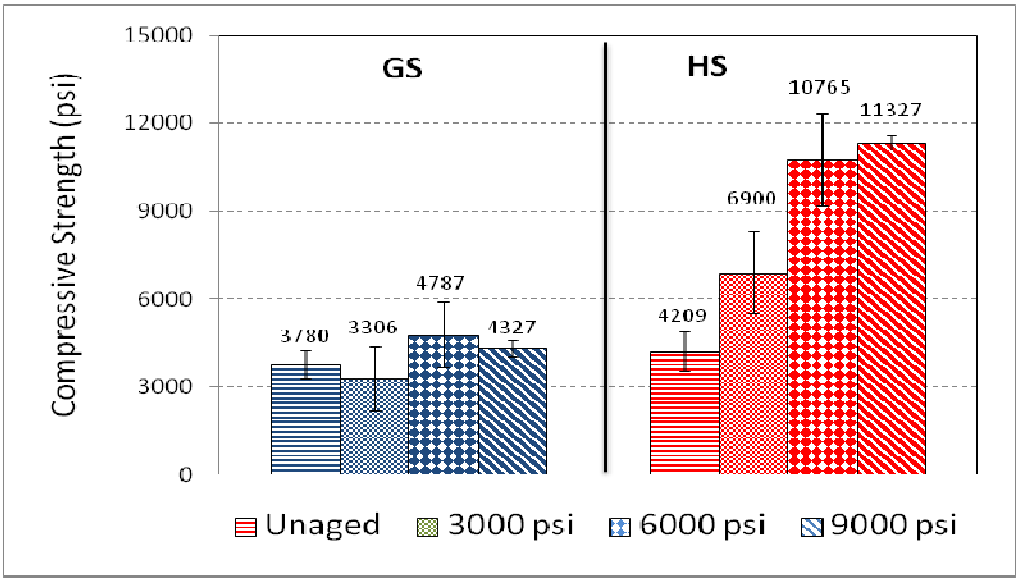

Fig. 5: Effect of pressure on compressive strength of baseline cements at 350ºF and 100% CO_2 concentration

Previous data from Batch 6 is compared with the recent measurements (**Fig. 6**). Both Batches were aged for 14 days at 350ºF in 2% brine saturated with 10% CO_2 gas. However, the aging were conducted at different pressures. Class G cement showed reduction in strength after

aging, which can be attributed to scawtite formation and/or leaching of calcium bicarbonate. The formation of scawtite resulted in strength reduction at 3000 psi. Nevertheless, as the aging pressure was increased, the scawtite phase carbonated resulting in slight strength enhancement. The compressive strength of the cement did not increase substantially as normally expected with intense carbonation. This suggests the presence of leaching. XRD analysis will be performed in the future to support this observation.

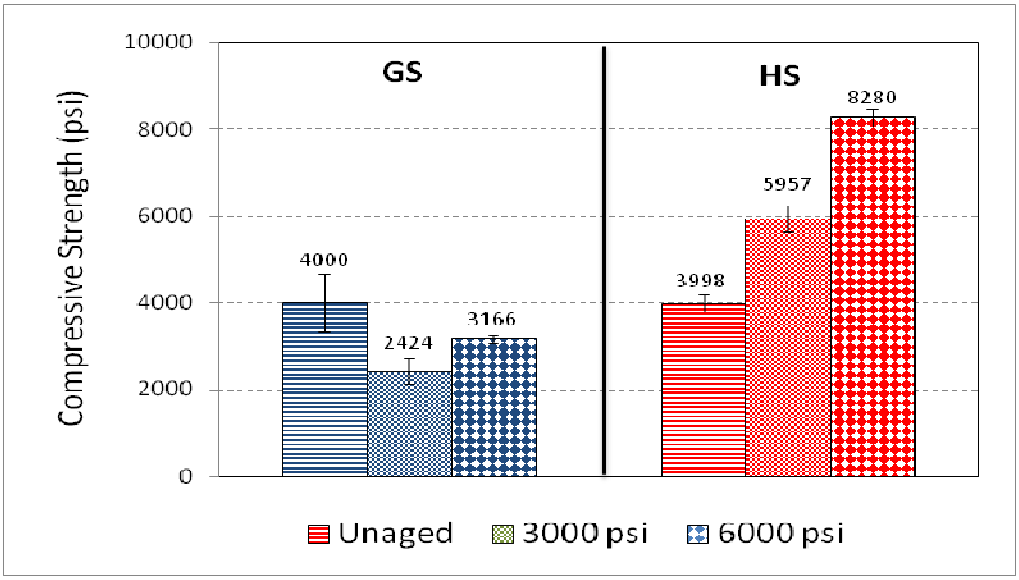

Fig. 6: Effect of pressure on compressive strength of baseline cements at 350ºF and 10% CO2 concentration

2.2.3 Shear Bond Strengths of Baseline Cements

Study on shear bonding strength (SBS) of Class H cement was continued. The effect of aging pressure on SBS is being investigated varying the concentration of CO_2. Additionally, carbonation depths of the SBS samples were measured. The relationship between SBS and carbonation depth has been examined varying temperature and pressure.

Effects of Aging Pressure on SBS

In the last month report, the influence of pressure on the SBS of aged samples was presented varying it from 3000 to 9000 psi at different CO_2 concentrations (40% and 100%). During this month, additional aging tests were conducted maintaining CO_2 concentration at 10%. The new measurements are combined with previous data and presented in **Fig. 7**. Unaged samples were not exposed to CO_2 environment; hence, they exhibited significantly lower SBS than aged samples.

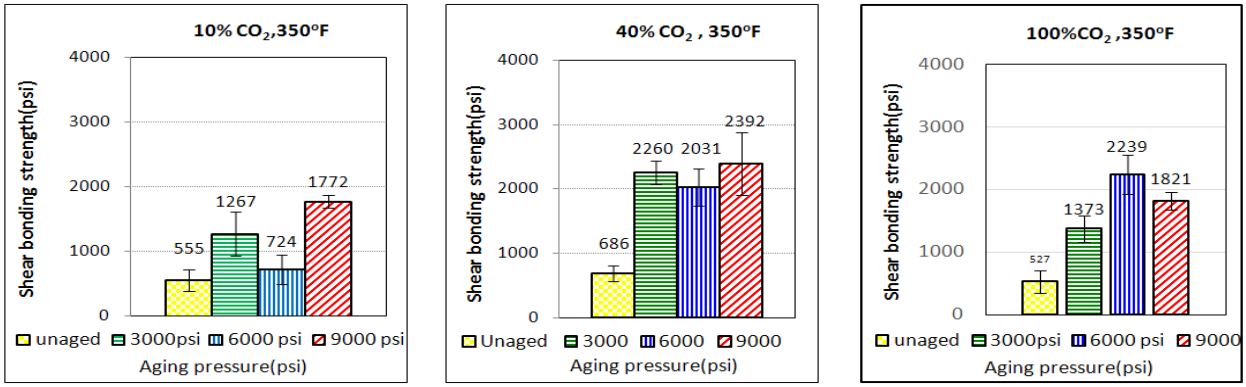

(a) (b) (c)

Fig. 7: Effect of aging pressure on SBS of samples aged at 350°F for 14 days in brine saturated with different CO2 concentrations: a) 10%; b) 40%; and c) 100%

For samples aged in brine saturated with 10% and 40% CO2, the trends of shear-bonding strength are similar (Fig. 7a and 7b); the SBS at 6000 psi is lower than those measured at other aging pressures. However, when the carbon dioxide concentration was increased to 100%, the maximum SBS was obtained by aging the samples at 6000 psi.

Carbonation Depth

As indicated in the recent reports, carbonation depth measurements were obtained from shear bonding test samples using phenolphthalein solution. Areas on cement sample containing free $Ca(OH)_2$ changes to deep purple when it is exposed to phenolphthalein solution. Applying this technique, the carbonation depths were measured from the top and bottom sides of the sample; and the average value was computed and used for the investigation. The results show the existence of a positive relationship between SBS improvement after aging (percentage increase in SBS) and the averaged carbonation depth (**Fig. 8**). An outlying data point in the figure could be due to the irregularity of some of the SBS samples. Regularly, SBS of unaged samples are expected to be in the same range since all of them were prepared following the same procedure. The SBS of unaged samples often range from 400 to 650 psi. However, the outlaying data shows unusually low (i.e. 252 psi) SBS.

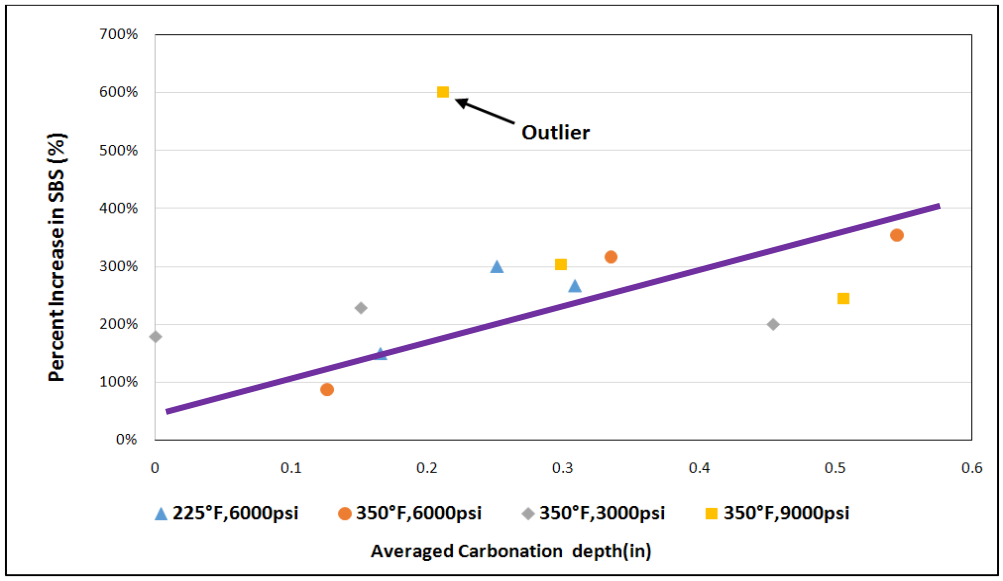

Fig. 8: Effect of carbonation depth on SBS improvement after aging

Our previous depth measurements (**Fig. 9**) obtained from samples aged at 6000 psi showed that the SBS improvement after aging is related to the carbonation depth. At constant pressure (6000 psi), the effect of temperature on the relationship between the SBS improvement and carbonation depth was minimal. The data points approximately follow a curve indicating strong relationship between SBS and carbonation depth regardless of temperature and CO_2 concentration. Further investigation will be carried out to see if similar trends emerge at other aging pressure conditions (3000 and 9000 psi).

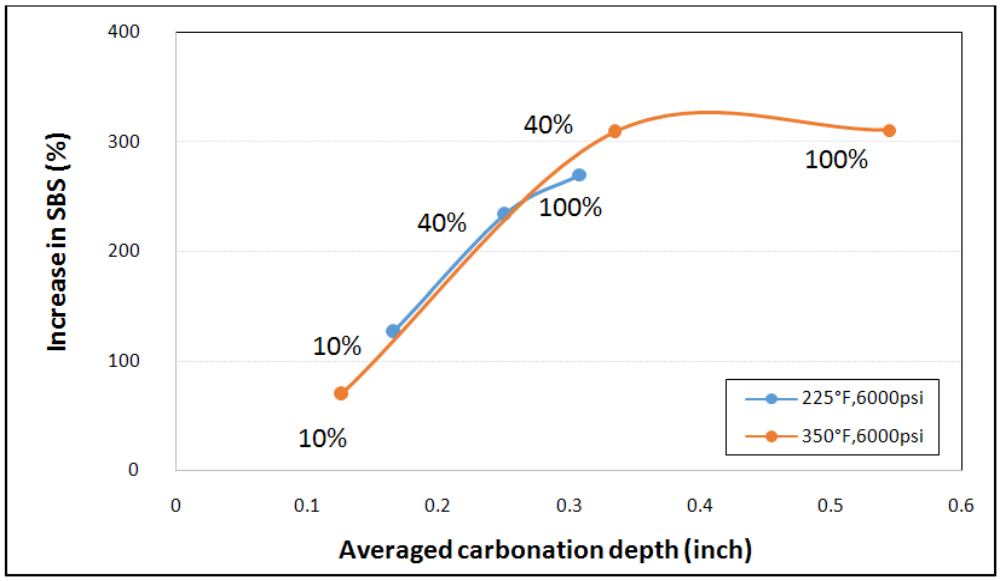

Fig. 9: SBS improvement vs. carbonation depth for samples aged at 6000 psi and different temperatures

Furthermore, tests were conducted varying the aging pressure (3000 and 9000 psi) while maintaining a constant temperature. The results of these experiments (**Fig. 10**) show the SBS first enhanced with carbonation depth and reached to its maximum level, and subsequently decreased with the depth. The reduction observed in SBS improvement is not in agreement with the hypothesis of volume expansion, which is based on the fact that cement expansion due to carbonation tends to augment the SBS. This suggests the presence of other phenomena such as leaching or scawtite formation that influence the bonding strength.

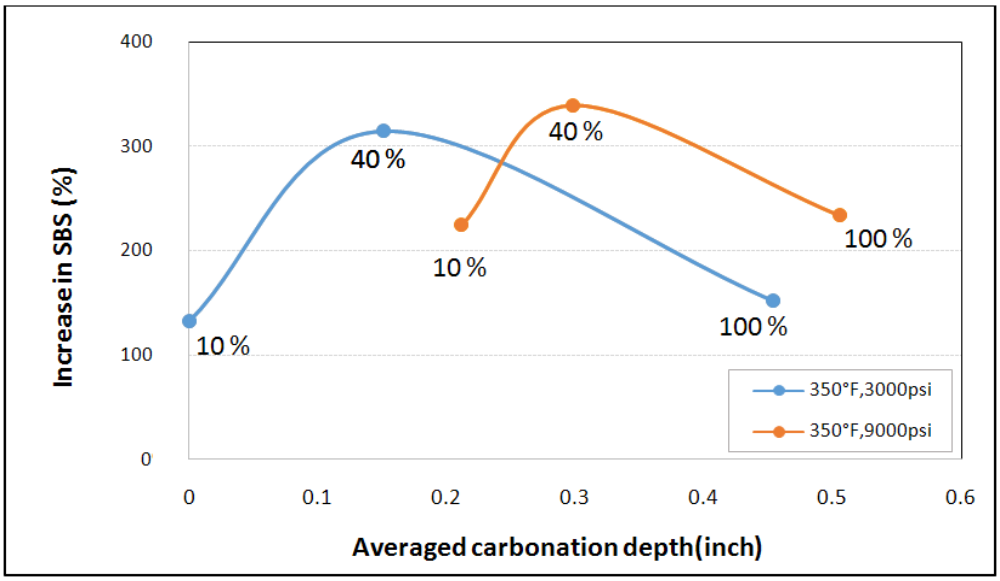

Fig. 10: SBS improvement vs. carbonation depth for samples aged at 350ºF and different temperatures

Unlike the temperature effect presented in Fig. 9, the impact of pressure on the relationship between SBS improvement and depth of carbonation is significant. For tests performed at different pressures (3000 and 9000 psi), the SBS improvement trend remained the same; however, a shift in the two curves was observed as the pressure change. The trend was slightly different for tests conducted at 6000 psi (Fig. 9); with increasing the depth of carbonation, the improvement in SBS first increased and reached to its maximum value, and leveled out.

2.2.4 Additive Screening and Cement Formulation Studies

Additive screening and cement formulation studies were continued. Hydroxyapatite (HOAP), magnesium oxide, micro silica and latex containing cements were investigated. Core samples with 10% MgO (HSMG and GSMG) were aged under CO_2 containing environment. Class H based samples (HSMG) were able to withstand the HPHT CO_2 environment, while Class G based samples displayed degradation. Samples containing 15% micro-silica were also aged under acidic

conditions. However, the hydration and pozzolanic reactions made the samples brittle and easy to break apart along clean fractures.

Cores samples containing hydroxyapatite and silica flour were prepared and aged under harsh acidic conditions. Silica flour was added to the slurry to prevent strength retrogression at elevated temperature. After aging, the sample was very weak and highly porous. Tests were also conducted with SBR latex cement slurries prepared using reduced mixer speed.

2.2.4.1 Hydroxyapatite Cement with Silica Flour

Our previous tests showed strength reduction in hydroxyapatite containing cement aged at 350°F. As the hydroxyapatite cement formulation does not include silica flour, the reduction can be due to the conversion of CSH to α-C_2SH phase, which is highly porous and permeable and very weak (Eilers et al. 1976 and 1983; Dillinbeck III et al. 1990; Grabowski and Gillott 1989; Lea 1971). The CSH (i.e. tobermorite gel) phase has higher strength and low porosity and permeability. However, at high temperature (above 240ºF), it becomes unstable phase without the presence of silica flour and the phase transformation occurs. As a result, although hydroxyapatite is effective additive in controlling cement carbonation and degradation, the lack of silica flour in its formulation may be causing thermal retrogression at higher temperatures. According to our previous aging tests conducted at 100ºF, hydroxyapatite containing cement (HOAP) samples were able to preserve the CH and CSH component of the cement after aging in acidic environment.

As reported previously, attempts were made to incorporate 35% BWOC of silica flour in the formulation of HOAP cement. However, core samples were found to be very weak and brittle after curing and hardening. During this reporting period, two slurries with different concentrations of silica flour were tested in order to examine the effectiveness of adding silica flour in preventing the strength retrogression after aging. The compositions of the slurries are presented in **Table 3**. Slurry 1 contained reduced content of silica flour than Slurry 2. The objective was to study if the reduction in strength after curing is associated with the addition of silica flour or water, which is needed to control thickening. Both slurry formulations were based on Class H cement as strength reduction was observed previously with this type of cement. The contents of other additives (NSF and citric acid) were optimized after performing several tests to obtain slurry with acceptable rheological properties and thickening time. The API fluid loss could not be measured for the slurries as they became very viscous in the filter press.

Table 3: Compositions of slurries containing HOAP and silica flour

Component	Slurry 1	Slurry 2
Cement	100%	100%
Silica Flour	17.5% bwoc	35% bwoc
HOAP	5% bwoc	5% bwoc
HEC	0.1% of water for SF	0.1% of water for SF
Antifoam Agent	0.1 gal/ sk of cement	0.1 gal/ sk of cement
Water for Cement	38% bwoc - Class H	38% bwoc - Class H
Water for Silica Flour	38.5% of Silica Flour	38.5% of Silica Flour
Water for HOAP	23% of HOAP	0% of HOAP
Dispersant (NSF)	1% bwoc	1% bwoc
Retarder (Citric Acid)	0.5% bwoc	0.25% bwoc
bwoc = by weight of cement		

After developing the HOAP slurry formulations with silica flour, slurry samples were prepared, cured, and hardened in an oven at 200°F for 5 days immersed in 2% NaCl brine. After setting, the samples were cored, cut and ground. The samples were not as brittle as the previous samples. All the samples were successfully prepared to obtain measurements of porosity, permeability, and compressive and shear bond strengths before aging.

Porosity and Permeability Measurements

The porosity and permeability measurements obtained from unaged HOAP samples are presented in **Fig. 11**. Porosity and permeability of the HOAP cores were higher than those of the baseline samples. This indicates that with similar composition as base samples, the addition of HOAP with silica flour causes a drastic increase in permeability. As hydroxyapatite exhibit hexagonal structure, crystallization of the cement matrix along with silica flour might be causing micro fractures.

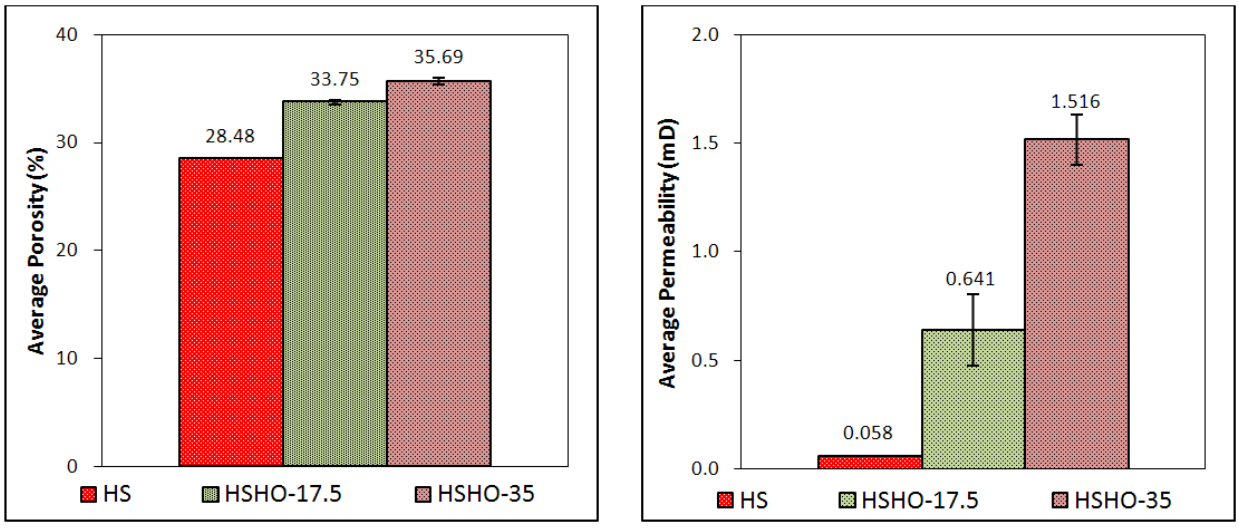

(a) (b)

Fig. 11: Porosities and permeabilities of unaged HOAP and baseline cements

Compressive and Bond Strength Measurements

Measured compressive and shear bond strengths of the samples are presented in **Fig. 12**. It shows substantial reduction in compressive strength with addition of HOAP with silica flour. This reduction in strength corresponds to the increase in porosity and permeability as shown in Fig 11b. On the other hand, shear bond strength remains almost similar to the baseline samples (Fig. 12b). HOAP sample with 17.5% silica flour had slightly higher shear bond strength but other measurements (porosity, permeability and compressive strength) poor performance of the cement with this formulation.

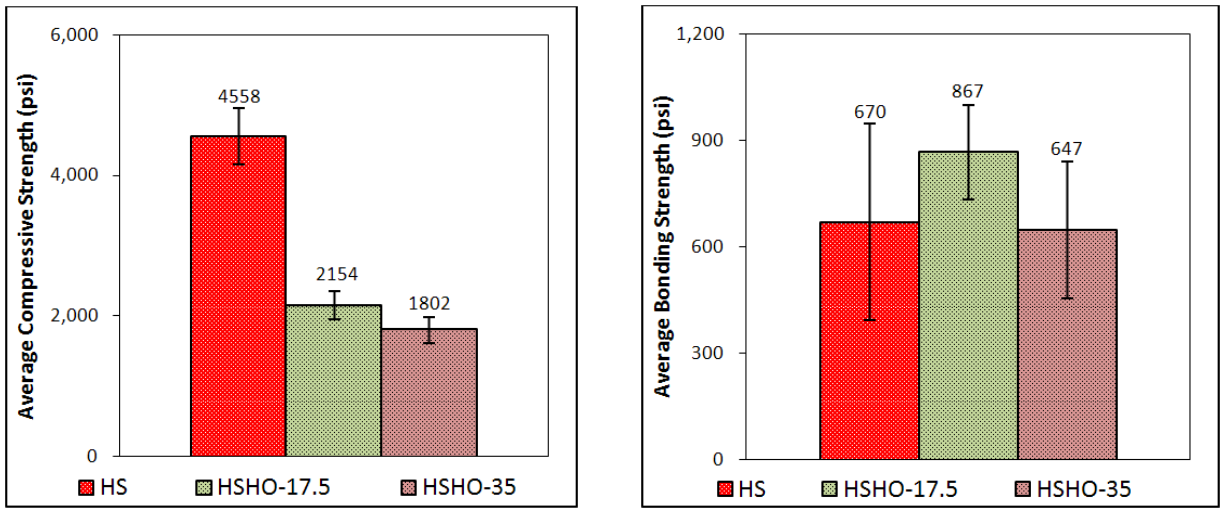

(a) **(b)**

Fig. 12: Compressive and bond strengths of unaged HOAP and baseline cements

The addition of HOAP with silica flour may be causing densification and crystallization of cement matrix, which create micro fractures that do not affect the shear bond strength but increase the porosity and permeability of the matrix and make the cement very weak. Further lowering of the silica content may cause the cement to exhibit greater reduction in strength after aging.

Future Work

Aging tests were conducted previously with base HOAP cement (i.e. HOAP cements that do not contain silica flour). The tests were performed at 100°F and 350°F but not at 225°F. Results showed significant strength reduction at 350ºF (Report # 19). During this reporting period, base HOAP cores were prepared for aging experiment. The cores will be aged at 225°F and 3000 psi in 2% brine saturated with 40% CO_2 gas. The results of this experiment will be discussed in the next month report.

In order to improve the performance of HOAP cements containing silicate flour, a new HOAP cement formulation that contains 5% HOAP + 10% silica flour + 25% micro-silica is proposed. The new cement will be tested in the coming weeks. The addition of very fine micro-silica particles is expected to improve the performance of HOAP cement.

2.2.4.2 Magnesium Oxide Cement

Magnesium oxide cement cores with 10% BWOC MgO (MGO-10) were prepared and tested for their performance. The slurry formulation was presented in previous reports. The cores were aged at 350ºF and 9000 psi. The purpose of testing MGO-10 cement was to examine the level of performance improvement occurring when the concentration of MgO was increased. MGO-5 cement was tested previously and showed encouraging results.

Porosity and Permeability Measurements

Porosity and permeability of MGO-10 cements are presented in **Figs. 13** and **14**. Before aging, the permeabilities of MGO-10 and baseline samples were comparable. After aging, baseline samples showed more reduction in porosity than MGO-10 samples. Previously, similar results were obtained with MGO–5 samples. Comparing their permeability, the MGO-10 and MGO-5 samples showed similar results, which indicate good performance. After aging, the permeability of baseline HS samples increased but the HSMG samples displayed permeability reduction. It can be deduced that while baseline HS samples suffered leaching of the matrix, the HSMG samples went through only carbonation and expansion of the matrix. On the other hand, GSMG–10 samples show slight increase in permeability. Similar trend was observed when GSMG-5 samples were aged at 350°F and 9000 psi. To further investigate the consistency of the trend, additional tests will be conducted at 225°F and 9000 psi.

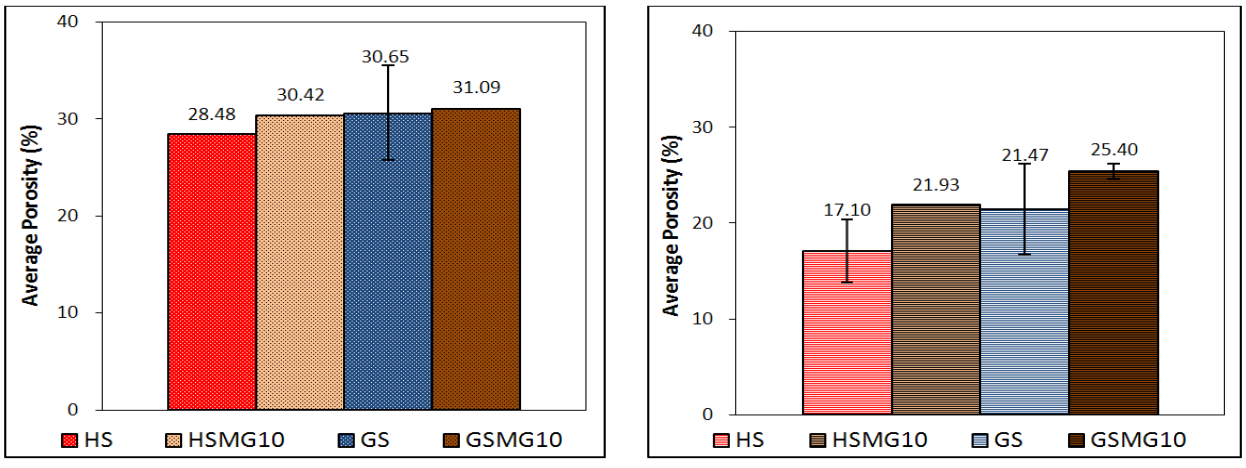

Fig. 13: Porosity of MGO-10 and baseline cores: a) unaged; and b) aged at 350°F and 9,000 psi in brine saturated 100% CO_2 for 14 days

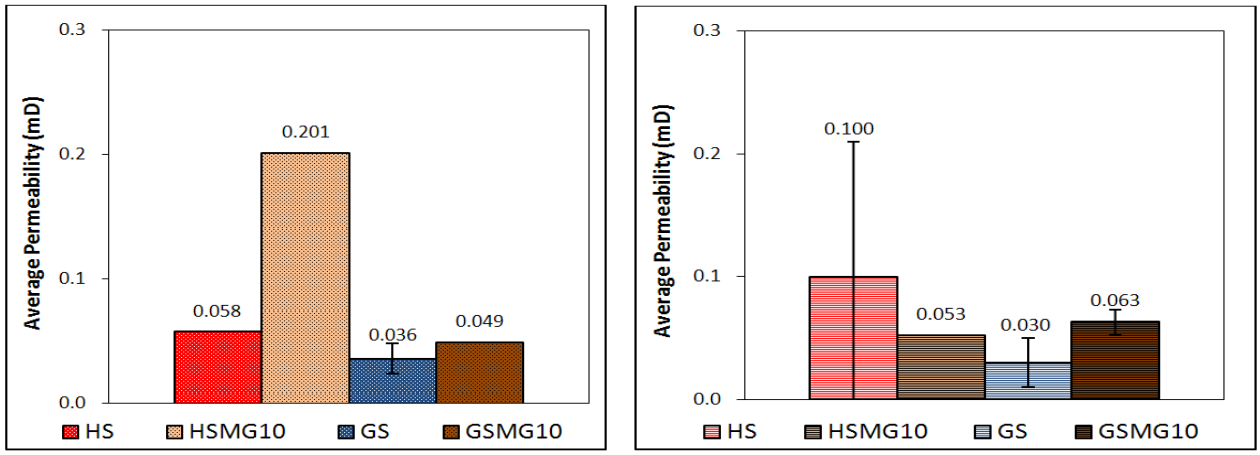

Fig. 14: Permeabilities of MGO-10 and baseline samples: a) unaged; and b) aged at 350°F and 9,000 psi in brine saturated 100% CO_2 for 14 days

Compressive Strength Measurements

Compressive strength measurements obtained from MGO-10 and baseline samples are presented in **Fig. 15**. The measurements are consistent with porosity and permeability trends observed after aging the samples. A substantial increase in strengths of HSMG-10 and baseline HS samples was seen after aging. This indicates carbonation and expansion in the matrix. On the other hand, the GSMG-10 samples displayed reduction in compressive strength, which is in agreement with the increase in permeability shown after aging. The result indicates the degradation of the GSMG-10 matrix when exposed to HPHT acidic environment.

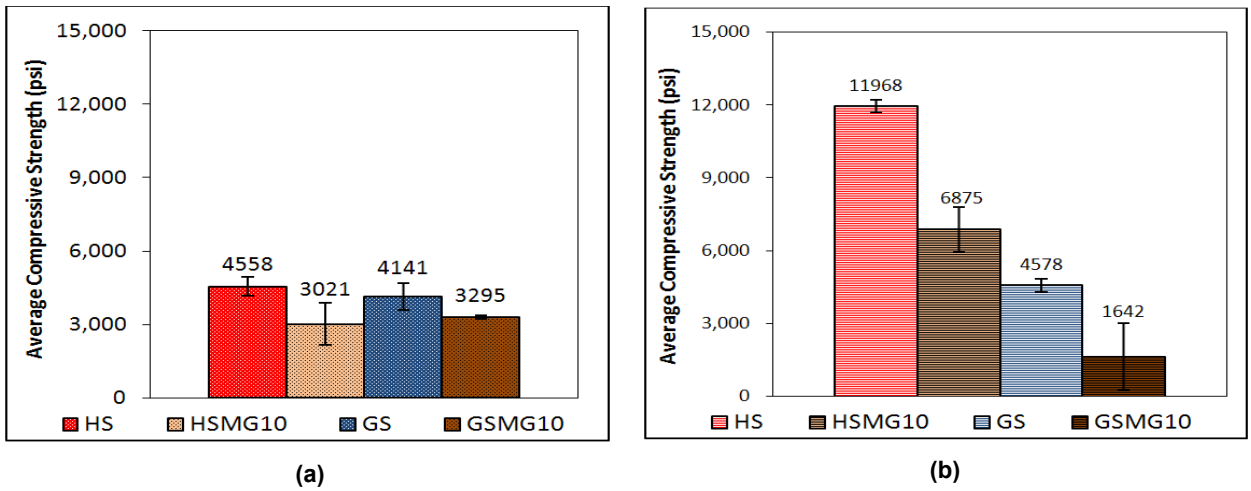

Fig. 15: Compressive strengths of MGO-10 and baseline samples: a) Unaged; and b) aged at 350°F and 9,000 psi in brine saturated 100% CO_2 for 14 days

Shear Bond Strength Measurements

Improvements in bond strength shown in both MGO-10 and baseline samples (**Fig. 16**) suggest the expansion of the matrix after aging. This expansion is due to carbonation and formation of $Mg(OH)_2$. The MGO-10 samples show slightly higher increase in bonding than the baseline samples indicating increased level of expansion because of the presence of MgO. Very similar observations were made when MgO–5 samples were aged to 350°F and 9000 psi in brine saturated with 40% CO_2 gas. This indicates that MgO can be added in 5% and 10% BWOC amounts with similar results. The impacts of MgO addition are similar in both concentrations in improving the performance of the cement.

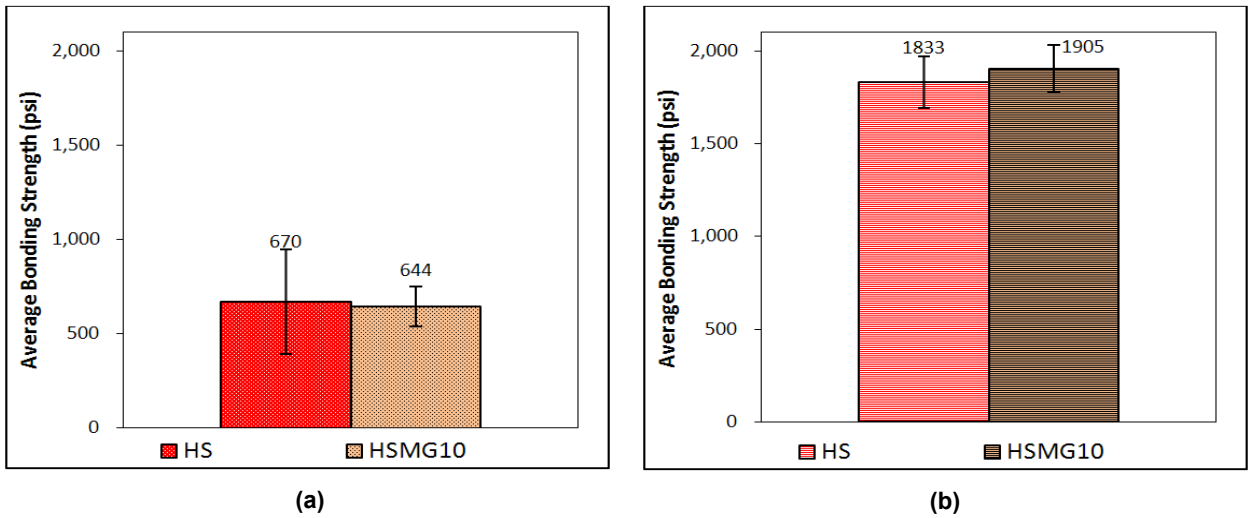

Fig. 16: Shear bond strengths of MGO-10 and baseline samples: a) Unaged; and b) aged at 350°F and 9,000 psi in brine saturated 100% CO_2 for 14 days

FTIR Results

Summarized FTIR results of MGO-10 and baseline samples are presented in **Fig. 17**. The samples were aged at 350°F and 9000 psi in 2% brine saturated with 100% CO_2. Results show that under the extreme aging conditions, all the CH and CSH groups of both samples were carbonated in the middle and outer zones. The presence of $MgCO_3$ can be seen in the outer zone of HSMG-10 samples. Results from the middle zones also show the presence of higher levels of $MgCO_3$ and $CaCO_3$. The CSH group and $Mg(OH)_2$ were preserved the inner zone of HSMG-10. This indicates the effectiveness of MgO in preserving the binding components of cement. It should be noted that the amount of $CaCO_3$ is seen to be higher in the HSMG-10 samples in the inner zone. The peak for calcium carbonate is frequently around 1500 cm^{-1}. $MgCO_3$ identified by two peaks, one at 880 cm^{-1} and another one around 1500 cm^{-1}. Hence, the peak shown at 1500 cm^{-1} cannot accurately quantify the amount $CaCO_3$ present in the MGO-10 samples.

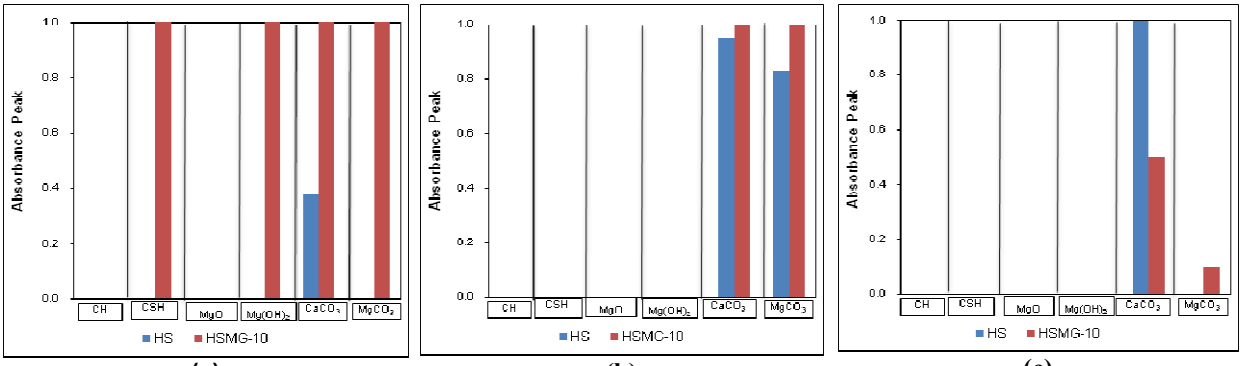

Fig. 17: FTIR peaks of MGO-10 and baseline samples aged at 350°F and 9000 psi for 14 days in 2% brine saturated with 100% CO_2: a) inner most zone; b) middle zone; and c) outer most zone

Future Work

Results show the benefits of adding magnesium oxide as additive to control cement degradation under HPHT acidic environment. MgO effectively reduces cement carbonation by forming $Mg(OH)_2$ crystals in the pores and limiting acid penetration. In addition, the crystallization improves compressive strength and makes the cement expansive resulting in increased shear bond strength. Class H cement displayed better resistance against acid attack with the addition of MgO than Class G cement that experienced increased permeability and reduced strength after aging in HPHT acidic environment. Additional aging tests need to be conducted at 225°F and 9000 psi in order to test the suitability of MgO in Class G cement under intermediate temperature conditions.

2.2.4.3 Micro-Silica-Based Cement

As discussed in previous report, due to brittle nature of micro silica cement, a new formulation with reduced micro silica content (15% BWOC) was prepared. Fine micro silica particle are expected to extend the API standard mixing time (Grabowski and Gillott 1989) of 35 seconds to 2 minutes. Slurry with 15% micro silica (MS-15) was prepared using the formulation presented in Report # 21. To test the formulation, MS-15 slurry was prepared and cured. After curing and hardening, the cement block developed several cracks, which parted the block into large pieces. Limited quantity of core samples were cut and prepared from the blocks to perform aging test. Then, the samples were aged at 350ºF and 3000 psi in 2% brine saturated with 10% CO_2 gas. After aging, all the samples were cracked and broken (**Fig. 18**). Hence, performance of the cement was not measured. However, properties of unaged samples were measured.

(a) (b)

Fig. 18: Damaged MS-15 samples after aging at 350°F and 3000psi

Porosity and Permeability Measurements

Porosity and permeability of MS-15 samples (**Fig. 19**) were significantly less than those of the baseline samples. Fine micro silica particles acted as filler materials and reduced the porosity and permeability of MS-15 samples.

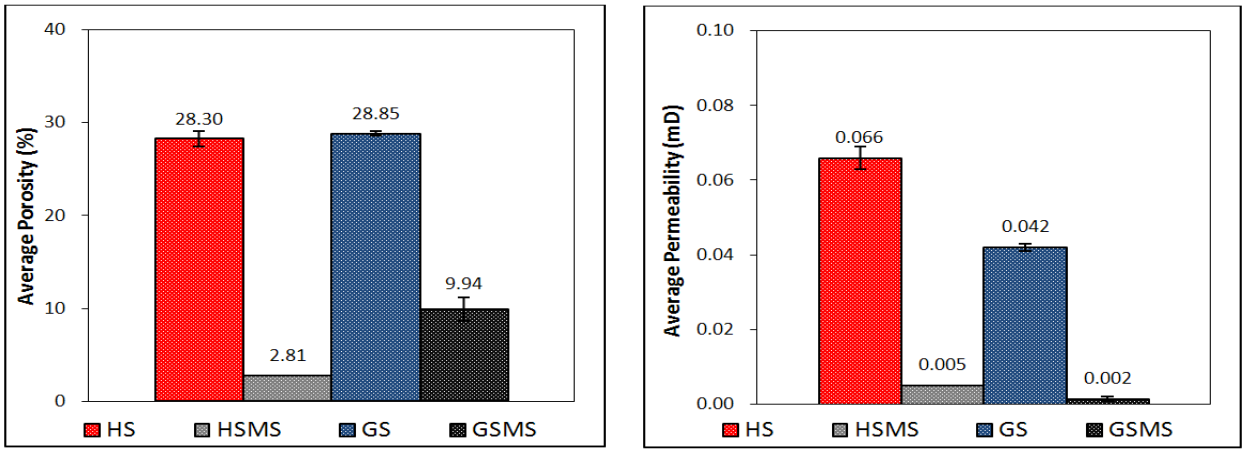

(a) (b)

Fig. 19: Porosities and permeabilities of unaged MS-15 and baseline samples

Compressive Strength Measurements

Although the samples were breaking during the preparation of cylindrical cores, the compressive strengths of the MS-15 samples were comparable with those of the baseline samples (**Fig. 20**). This suggests that compressive strength of MS-15 is high, although the samples break apart in segments under HPHT acidic environment.

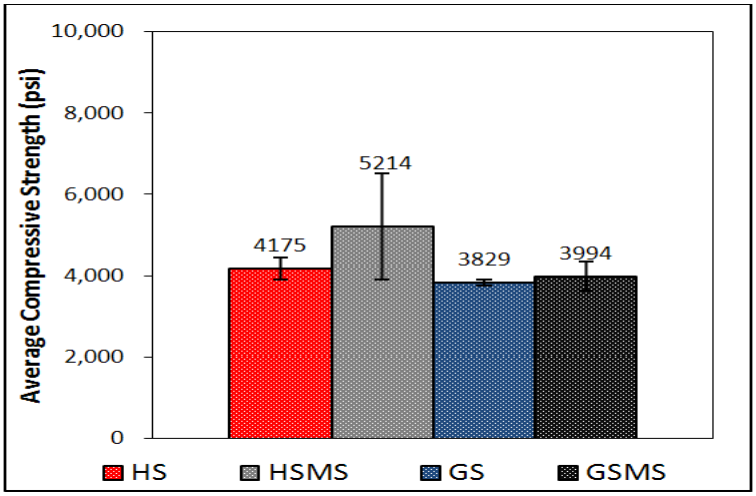

Fig. 20: Compressive strength of unaged MS-15 and baseline samples

Shear Bond Strength Measurements

Figure 21 presents shear bond strengths (SBS) of unaged and aged (at 350°F, 3000 psi, 10% CO_2 for 14 days) MS-15 and baseline samples. Results show only 41% increase in SBS was recorded for MS-15 samples, while the baseline samples displayed 183.8% increase due to carbonation and expansion. Because of low porosity and permeability, the MS-15 samples had limited carbonation, which was accompanied by only moderate improvement of the SBS.

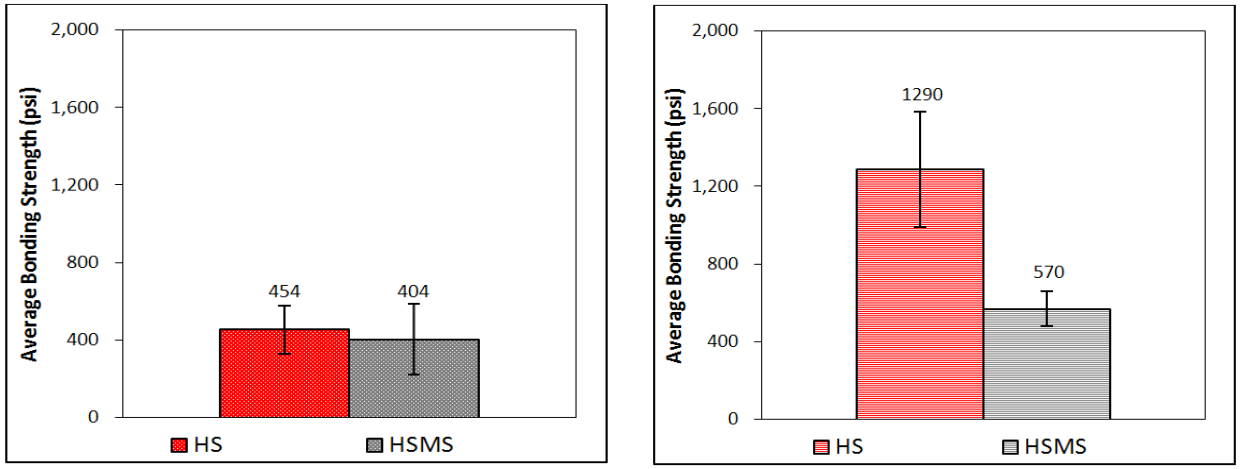

Fig. 21: Shear bond strength of MS-15 and baseline samples: a) unaged; and b) aged

It was observed that MS-15 samples form large fractures. In addition, adding dispersants did not improve the integrity of the block. Hence, micro silica content of the cement has been reduced

to 10% and new slurry (MS-10) was formulated (**Table 4**). After testing various combinations of NSF, the following slurry formulation is proposed for the next test.

Table 4: Slurry composition of MS-10

Component	HSMS	GSMS
Cement	100%	100%
Silica Flour	25% bwoc	25% bwoc
Micro Silica	10% bwoc	10% bwoc
HEC	0.1% of water for fillers	0.1% of water for fillers
Antifoam Agent	0.1 gal/sack of cement	0.1 gal/sack of cement
Water for Cement	38% bwoc	44% bwoc
Water for Silica Flour	38.5% of Silica Flour	38.5% of Silica Flour
Water for Micro Silica	0.05cc/ gm of Micro Silica	0.05cc/ gm of Micro Silica
Dispersant (NSF)	1.25% bwoc	1.25% bwoc
Retarder (Citric Acid)	0.0015% bwoc	0.02% bwoc
bwoc = by weight of cement		

2.2.4.4 Latex-Based Cement

Testing with conventional SBR latex was continued. As discussed in the previous report, the conventional SBR latex was tested with increased concentration (three-fold higher) of anti-foaming agent. In addition, the mixing procedure was adjusted to avoid air entrapment. Then, cement slurries with the desired properties were prepared and cured for testing.

Porosity and Permeability Measurements

Porosities and permeabilities of baseline and latex samples were measured to evaluate the benefits of using the latex additive. Unaged HSLT samples exhibited slightly lower porosity than the baseline samples. However, the GSLT samples showed slightly higher porosity than the baseline (**Fig. 22a**). Even though, latex-containing cements (HSLT and GSLT) showed comparable porosity, their permeabilities were significantly different from the baseline cement. This strongly suggests the presence of phenomena such as bubble entrapment and cracking that have greater impact on permeability of the samples than its porosity (**Fig. 22b**).

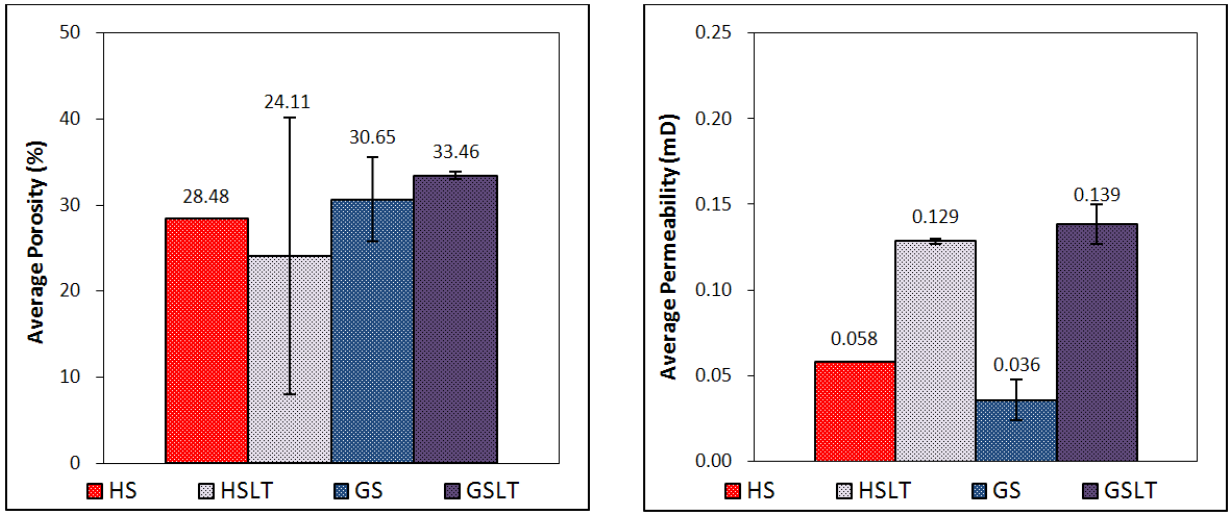

(a) (b)

Fig. 22: Porosity and Permeability of un-aged Latex Samples and Base HS/ GS samples

Compressive and Bond Strength Measurements

The compressive and bond strengths of unaged latex cement cores were also measured. Latex samples (HSLT and GSLT) showed lower compressive and bond strengths than the baseline samples (**Fig. 23**). The increase in permeability and reduction in compressive and bond strengths indicate the presence of entrapped air.

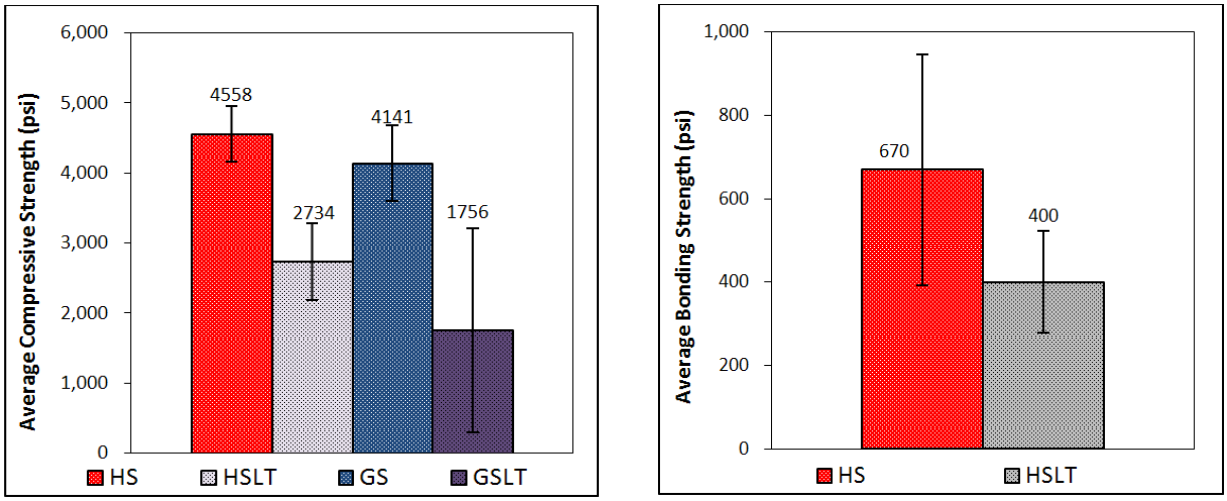

(a) (b)

Fig. 23: Porosity and permeability of unaged latex samples and baseline samples

Air bubbles in the slurry created empty voids in the set cement matrix. Hence, it was decided to prepare similar slurry at a reduced mixing speed to avoid the formation of vortex and

entrapment of air. Subsequently, the slurry was prepared with similar composition as previous test but at reduced RPM for Class H. However, it was observed that the slurry had density lower than theoretically calculated density (16.01 ppg). Similar low-density slurry was formed in the previous test. Although mixing at lower RPM does incorporate less air in the slurry, the mixing speed is still high enough to introduce air into the cement and lower the density of the slurry by 0.31 ppg. Such large difference between actual and theoretical densities was not observed with other slurry formulations such as micro silica, HOAP, MgO or even baseline slurry. Reducing the speed was found to be ineffective.

Future Work

The SBR latex cement entrapped large amount of air, which resulted in increased permeability and reduced strength. In order to create stronger cement with lower porosity and permeability, combination of latex and micro silica can be used as additives. The micro silica is expected to reduce porosity and permeability of the system while the latex improves its bond strength. The use of a mixture of latex and micro-silica additive has been recommended by previous studies (Wan 2011; Mueller & Dillinbeck 1991) to improve the strength and integrity of the cement.

2.3 Experimental Studies on Corrosion of Tubulars (Task 3)

Low-pressure corrosion experiments were continued using both weight loss (WL) and electrical measurement techniques. In the last month report, we discussed results of corrosion experiments on carbon steel sample aged in 2% brine saturated with 100% CO_2 gas. In this report, results of three similar experiments are presented. All the tests were conducted in 2% brine saturated with 50% CO_2 and 50% nitrogen. At the end of each experiment, the weight loss was measured and the resulting corrosion rate is compared with the rate obtained from the linear polarization resistance (LPR) measurement. Experiments were carried out for 187 hours at 120 psi and 78ºF. In the first experiment, after placing the corrosion coupon into the brine, CO_2 and nitrogen were injected to the test cell (autoclave). From the LPR measurement, the trend of the corrosion rate with respect to time was monitored. However, it was learned during the course of the first experiment (Exp. 1) that there was continuous pressure loss in the autoclave. The pressure loss initially was attributed to dissolution of CO_2 in the brine. Nevertheless, during the second experiment (Exp. 2), a leaky valve was found on the gas injection line, which was depleting the cell pressure. After replacing the leaking, the experiment was continued. **Figures 24** and **25** present corrosion rate measurements based on LPR method obtained during the first and the second experiments. Even though the results of these tests were somewhat influenced by the pressure loss due to the leaky valve, the experiments were continued. Mixed gas (mixture of CO_2 and N_2) was injected into the autoclave intermittently to maintain the pressure between 100 and 120 psi. After completing the tests, weight

loss measurements were performed to determine the corrosion rate. Because of pressure variation during these tests, the corrosion rate measurements (Figs. 24 and 25) showed spikes since solubility of CO_2 increase with pressure causing the corrosion rate to increase sharply. Moreover, some of these spikes can be due to breaking of protective scales, which enhances the rate of corrosion.

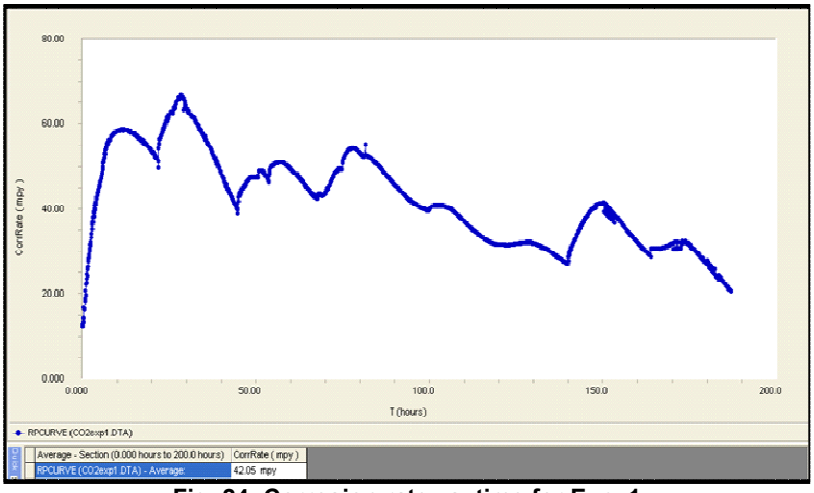

Fig. 24: Corrosion rate vs. time for Exp. 1

Fig. 25: Corrosion rate vs. time for Exp. 2

Figure 26 presents results obtained from the third experiment (Exp. 3). During this experiment, the autoclave pressure was stable and more or less constant at 120 psi. However, during the first 24 hour, the pressure reduced to 98 psi due to dissolution of CO_2 in NaCl brine solution. Then, the autoclave pressure was constant throughout the test duration. Figure 26 shows an increase in the rate of corrosion between 12 and 24 hrs which is due to the increase in the concentration of bicarbonate ions and hence formation of $FeCO_3$.

Fig. 26: Corrosion rate vs. time for Exp. 3

On further analysis of the corrosion rate trend, we observe that after the first peak the corrosion rate went all the way down gradually except for the instances where there were a few sudden spikes. These increases in the corrosion rate were attributed to the breaking of the protective scales and not resulting from pitting corrosion. With visual examining of the corrosion sample after completion of the experiment, it was observed that the only corrosion present was uniform corrosion and not pitting. In order to check repeatability of the experimental results, another similar test will be carried out and result will be presented in the next month report.

After Exp. 3 was completed, the steel sample was taken out and cleaned following the standard mechanical cleaning procedure. Then, the sample was weighed to determine the corrosion rate by weight loss (WL) method. Based on WL method, the average corrosion rate was 43.3 mpy, whereas the LPR measurements showed average rate of 48.9 mpy. The corrosion rates from both LPR and WL methods are in good agreement. Our next plan is to study the corrosion of steel at different concentrations of CO_2.

The construction of corrosion setup was continued. Assembling of high-pressure tubing, tube fittings and measuring instrumentation has been initiated. High-pressure fittings provided by equipment supplier are found to be incompatible with sour gas application. Hence, they have been returned to the manufacturer for special heat treatment (annealing) to meet NACE MR0175 specifications for sour gas applications.

3. Planned Activities

- Continue aging experiments with brine-CO_2-CH_4 system for 14 days varying aging pressure (3,000, 6000, and 9000 psi) at 350ºF/225ºF and 10% CO_2 concentration.
- Continue theoretical and modeling studies on tubular degradation.
- Continue cement additive screen and acid resistant cement formulation studies.

- Continue the development of tubular corrosion testing setup.

4. Project Expenditures

This section presents the project expenses during the month of July (**Table 5**) and the cumulative expenditures.

Table 5 Current and cumulative expenditures, July, 2013

No.	Budget Categories	Current Expenses	Cumulative Expenses
1	Salaries & Wages	$31,251.23	$211,588.46
2	Fringe Benefits	$9,840.99	$50,445.25
3	Project Materials	$905.78	$56,789.43
4	Travel	$0.00	$6,010.28
5	Conference Expenses	$0.00	$0.00
6	Other Direct Costs	$0.00	$993.60
7	Equipment	$798.00	$235,645.33
8	Space Rental	$0.00	$0.00
9	Indirect Cost	$20,999.00	$162,913.47
10	**Total**	**$63,795.00**	**$724,385.82**

Nomenclatures

BWOC	By weight of cement
CH	Calcium hydroxide
CSH	Calcium silicate hydrate
FTIR	Fourier Transform Infra-Red
GS	Class G cement with silica flour
GSHO	Class G Cement with silica flour and hydroxyapatite
GSMG	Class G Cement with silica flour and magnesium oxide
GSLT	Class G Cement with latex
HOAP	Hydroxyapatite containing cement
HPHT	High-pressure high-temperature
HS	Class H cement with silica flour
HSHO	Class H Cement with silica flour and hydroxyapatite
HSMG	Class H Cement with silica flour and magnesium oxide
HSLT	Class H Cement with latex
LPR	Linear polarization resistance
mpy	mils per year
MGO	Magnesium oxide containing cement
MGO-5	Cement containing 5% BWOC MgO as additive
MGO-10	Cement containing 10% BWOC MgO as additive
MS	Micro silica containing cement
MS-10	Cement containing 10% BWOC micro silica as additive
MS-15	Cement containing 15% BWOC micro silica as additive
NACE	National Association of Corrosion Engineers
SBR	styrene-butadiene
SBS	Shear bonding strength
SCC	stress corrosion cracking
SSC	Sulfide Stress Cracking
TCL	Total Crack Length
XRD	X-Ray diffraction

References

Baldy, M.F., Tuttle, R.N. and Kane, R.D. 1981. H_2S corrosion in Oil and Gas production- A compilation of classic papers, National Association of Corrosion Engineers, pp 614-618, Houston, Texas.

Chauveau, E., Koschel, D., Bouvier, N. and Mesquita, T.J. 2012. Influence of Metallurgy and Chemical Composition on the Sulphide Stress Cracking Resistance of Two Supermartensitics Stainless Steels, paper No. C2012-0001284, presented at NACE International Conference and Exposition, March 01, .

Dillenbeck III, R. L., Mueller, D.T. and Orr, B.R. 1990. The Effect of Micro Silica on the Thermal Stability of Lightweight Cement Systems, paper SPE 21597 presented at the CIM/SPE International Technical Meeting, 10-13 June, Calgary, Alberta, Canada.

Eilers, L.H., Nelson, E.B. and Moran, L.K. 1983. High Temperature Cement Compositions – Pectolite, Scawtite, Truscotite or Xonoloite: Which Do You Want?, JPT, Vol. 35, Num. 7, pp 1373-1377.

Eilers, L.H. and Root, R.L. 1976. Long-Term Effects of High Temperature on Strength Retrogression of Cements, paper SPE 5871 presented at the SPE California Regional Meeting, 7-9 April, Long Beach, California.

Fardisi, S., Tajallipour, N. and Teevens, P. 2012. Predicting General Corrosion Rates in Sour Environments with the Growth of a Protective Iron Sulphide Film, paper No.1471, March 11 - 15, Salt Lake City, Utah.

Fuquan, S., Guangming, L. and Jianzhou, J. 2006. Application and research of latex tenacity cement slurry system, paper SPE 104434 presented at the SPE International O&G Conference and Exhibition, Beijing, 5-7 December.

Gaugh, R.R., 1982. Sulfide Stress-Cracking Resistance of Nitrogen-Strengthened Stainless Steels, Journal of Petroleum Technology, Vol. 34, Num. 3, pp 482-486.

Grabowski, E. and Gillott, J.E. 1989. Effect of Replacement of Silica Flour with Silica Fume on Engineering Properties of Oil Well Cements at Normal and Elevated Temperatures and Pressures, Cement and Concrete Research, Vol. 19, pp 333-344.

Harker, R.I. 1965. Scawtite and its Synthesis, Mineral Magazine, Vol. 34, 232.

Hashizume, S., Inohara, Y. and Masamura, K. 2000. Effects of pH and PH2S on SSC Resistance of Martensitic Stainless Steels, paper No.130, NACE International Annual Conference, March 26 - 31, Orlando, Fl.

Hou W., Sun F., Gao Y., Zeng J., Huo M., Wang J. 2010. Research of High Temperature Tolerance Latex Slurry System, paper presented at the Proceedings of the Twentieth International Offshore and Polar Engineering Conference, June 20-25, Beijing, China.

Kane, R.D. and Greer, B.J. 1977. Sulfide Stress Cracking of High-Strength Steels In Laboratory and Oilfield Environments, Journal of Petroleum Technology, Vol. 29, Num. 11, pp 1483-1488.

Lea, F.M. 1971. The Chemistry of Cement and Concrete, 3rd Edition, Chemical Publishing Co., New York City, pp 177-202.

Mack, R., Filippov, A. and Kendziora, L. 2000. In-Situ Expansion of Casing and Tubing-Effect on Mechanical Properties and Resistance to Sulfide Stress Cracking, paper No. 164, NACE International Annual Conference, March 26 - 31, Orlando, Fl.

Mueller D. T. and Dillenbeck III R. L. 1991. The Versatility of Silica Fume as an Oil well Cement Admixture, paper SPE 21688 presented at the SPE Production Operations Symposium, April 7-9, Oklahoma City, USA.

Roger, J. 1996. Cements treated with high-pressure CO2. US Patent 5,518,540, 21 May.

Tsay, L.W. Chi, M.Y., Chen H.R. and Chen, C. 2005. Investigation of Hydrogen sulfide stress corrosion cracking of PH 13-8 Mo stainless steel, Materials and Science Engineering: A, Vol. 416, Issues 1–2, pp. 155-160.

Wan, R. 2011. Advanced Well Completion Engineering, Third Edition, Gulf Professional Publishing, New York.

Project Title: Effect of H_2S and CO_2 in HPHT Wells on Tubulars and Cement

Report Type: Monthly Report

Report #: 23

Reporting Period: July 22nd, 2013 to August 21st, 2013

Authors:

Ramadan Ahmed, Principal Investigator

Subhash Shah, Co-Principal Investigator

Samuel Osisanya, Co-Principal Investigator

Rida Elgaddafi, Research Assistant

Omotayo Omosebi, Research Assistant

Himanshu Maheshwari, Research Assistant

Adarsh Naidu, Research Assistant

Aman Srivastava, Research Assistant

Jueun Hwang, Research Assistant

Mounraj Sharma, Research Assistant

Sagar Tale, Research Assistant

Prepared under BSEE Project # E12PC00035

by

THE UNIVERSITY OF OKLAHOMA

October 24, 2013

1. Summary of Accomplishments

This monthly report presents the progress made during the project period July 22, 2013 to August 21, 2013. During this reporting period, studies on cement and tubular degradation were continued. Cement cores and bonding samples of different cement formulations were prepared and aged in acidic environment to examine their degradation characteristics. Tests with acid resistant cement formulations were continued. The effects of different additives on properties of cement slurries and cores were investigated.

During this month, two aging experiments (Experiments 18 and 19) were conducted. The samples were aged for 2 weeks in 2% brine saturated with CO_2 containing methane gas. Porosity, permeability, and compressive and bond strengths of unaged and aged samples were measured. In addition, mineralogical properties of the samples were analyzed using Fourier Transform Infrared Spectroscopy (FTIR). Results from FTIR analysis show the effect of acid attack on concentration profiles of the binding components of cement.

Porosity and permeability decreased after aging at 3000 psi due to scawtite formation then they increased at 6000 psi due to carbonation. However, further increase in pressure to 9000 psi resulted in reduction of porosity and permeability due to formation of dense crystals in the pores. Furthermore, results show that, at high temperatures and low CO_2 concentrations, the increase in aging pressure has mixed effect on compressive strength of baseline cements. Beside this, shear bond strength (SBS) measurements indicate improvement of SBS with aging temperature. Increase in temperature facilitates the carbonation process of the cement, which causes expansion that leads to superior bond strength.

Experimental investigations on cement additives were continued. The effects of hydroaxipitate, micro silica, and latex on performance of Class H and Class G cements under HPHT conditions have been studied.

Corrosion study under low-pressure and ambient temperature is in progress. Both linear polarization (LPR) and weight-loss corrosion measurement techniques were utilized. In the presence of CO_2, the corrosion rate declined with time after the maximum rate was reached. The initial increase in the rate of corrosion is attributed to the dissolution of CO_2 that results in the formation of bicarbonates and carbonates, which accelerates the corrosion process.

Our plan for the upcoming weeks is to continue: i) aging tests at different pressures and temperatures; ii) theoretical and modeling studies on tubular corrosion; iii) additive screening and acid resistant cement development studies; iv) low-pressure corrosion experiments at different CO_2 concentrations; and v) pressure testing of corrosion test setup.

2. Overall Project Progress

2.1 Theoretical Studies (Task 1)

2.1.1 Sulfide Stress Cracking (SSC)

Last month report presented various factors affecting SSC resistance. The current report presents various carbon steel grades, which are currently being used in oil field applications and newly developed grades, which have higher strength and resistance to SSC. Some of the new grades have not been yet approved by API.

The SSC test normally requires a long duration. An accelerated SSC test developed by Lee (1985) provides reproducible results at much faster rate than the NACE standard tensile test. Slight modifications have been introduced in the standard test set up to perform the accelerated experiment.

Sulfide stress cracking mechanisms vary for high-strength and low-strength steels. In addition to the strength, the hardness of the materials determines the SSC resistance. Craig (2005) reported the existence of different mechanisms that affect the SSC resistance of steel under different corrosive environments. API has set up hardness limit of 23 HRC and NACE has recommended limit of 22 HRC for casing and tubing used in sour environments. Various experiments performed by Ciaraldi (1985) showed the effects of hardness on SSC resistance of common steels. Historical development of steel grades (Bruce and Urband 1999; Waid and Stiglitz 1979) presented below demonstrates the direction of the industry toward the use of high strength steels.

1. Grade L80: It was approved by API in 1975, along with L-80 grade. J-55 and K-55 were standard API grades.
2. Grade C-90: It was developed in 1979. This grade was approved by API in 1985 for sour environment.
3. Grade T-95: It was standardized by API in 1989 for sour services.
4. C-100, C105 and C-110 are recently developed grades for sour services.

L-80, J-55 and K-55 do not have any minimum temperature limitation for operation in sour environment. These grades have good SSC resistance; however, they have lower yield strength, which limits their application in HPHT wells. C-90 and T-95 have better yield strength than L-80. According to API, for sour application tubulars must be produced as seamless pipe. In addition, C-95 has been approved by API for sour applications. It has high yield strength; nevertheless, it is difficult to produce the tubulars with controlled hardness. Furthermore, it cannot be used at lower temperature environment.

C110 is recently developed steel grade. Tubular Corporation of America (TCA) performed several tests on C110 steel. Grain size testing proved that C110 have very fine grain size (ASTM 5 or finer) which is good for SSC resistance. TCA specified hardness of 25-26 for final tempered C110 tubulars (Bruce and Urband 1999). Moreover, C-90 grade has been developed using special internal and external quenching process. Previously, it was difficult to form a heavy walled material and still

maintain uniform mechanical properties. However, the new internal external quenching system proved successful in maintaining uniform properties for casing and coupling stocks with wall thickness up to 1.5 inches (Waid and Stiglitz 1979).

2.2 Experimental Studies on Degradation of Cement (Task 2)

2.2.1 Porosities and Permeabilities of Baseline Cements

During this reporting period, two batches (Batches 21 and 22) of baseline cement cores were aged. The aging conditions for these tests are shown in **Table 1**. Test matrix (**Table 2**) developed to examine the effects of pressure on the degradation behavior of cement cores at 350°F and different CO_2 concentrations has been completed. A new test matrix (**Table 3**) will be completed in the coming weeks to study the effects of pressure on cement degradation at 225°F.

Table 1: Test parameters for aging experiments conducted to date

Batch #	Temp. (ºF)	Pressure (psi)	Partial Pressure %			Brine Conc. (%)	Aging Period (days)	Experiment #
			CH_4	CO_2	H_2S			
001	350	9000	100	0	0	9	6	1
002	350	6000	100	0	0	2	14 & 28	2
003	350	6000	100	0	0	2	14	
004	350	6000	90	10	0	2	6	3
005	350	6000	90	10	0	2	14 & 28	4
006	350	6000	90	10	0	2	14	
007	225	6000	90	10	0	2	14	5
008	100	6000	90	10	0	2	14	6
009	225	6000	60	40	0	2	14	7
010	225	6000	0	100	0	2	14	8
011	100	6000	60	40	0	2	14	9
012	100	6000	0	100	0	2	14	10
013	350	6000	60	40	0	2	14	11
014	350	6000	0	100	0	2	14	12
015	225	6000	60	40	0	2	14	7A
016	350	3000	60	40	0	2	14	13
017	350	9000	60	40	0	2	14	14
018	350	3000	0	100	0	2	14	15
019	350	9000	0	100	0	2	14	16
020	350	3000	90	10	0	2	14	17
021	**350**	**9000**	**90**	**10**	**0**	**2**	**14**	**18**
022	**225**	**3000**	**60**	**40**	**0**	**2**	**14**	**19**

Table 2: Test matrix for aging experiments at 350℉

Pressure (psi)	10% CO_2	40% CO_2	100% CO_2
3000	Batch 020	Batch 016	Batch 018
6000	Batch 006	Batch 013	Batch 014
9000	**Batch 021**	Batch 017	Batch 019

Table 3: Test matrix for aging experiments at 225℉

Pressure (psi)	10% CO_2	40% CO_2	100% CO_2
3000 psi	Batch 026	**Batch 022**	Batch 024
6000 psi	Batch 007	Batch 015	Batch 010
9000 psi	Batch 027	Batch 023	Batch 025

Figure 1 shows the effects of pressure on porosities and permeabilities of baseline cores aged for 14 days at 350°F in brine saturated with 10% CO_2. The trends of porosity and permeability match with each other for both Class H and Class G cement samples. For Class G cement, as pressure increases, both porosity and permeability decrease but increase at 9000 psi. However, in case of Class H, porosity and permeability first decrease, then increase and then again decrease. The results of Class H cement indicate the occurrence of leaching at high pressure (6000 psi), whereas in Class G cement, the degradation is still in the carbonation stage, which lowers porosity and permeability of the cores. At 9000 psi, Class G undergoes excessive leaching as compared to Class H, which showed reduction in porosity and permeability that can be attributed to the combination of excessive precipitation of salt from brine and formation crystals due to the interaction of cement components and supercritical CO_2.

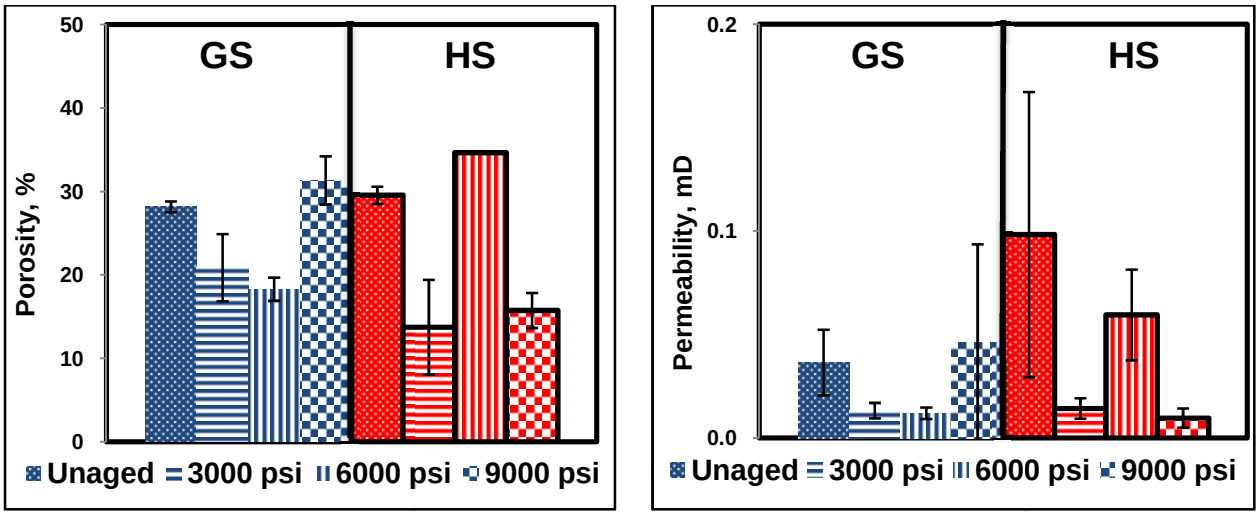

Fig. 1: Effects of aging pressure on porosity and permeability of baseline cores aged at 350°F and 10% CO_2

Figure 2 illustrates the effects of pressure on porosity and permeability of baseline samples aged at 350°F in brine saturated with 40% CO_2. Porosity and permeability trends are consistent and similar for both Class H and Class G cements. At low pressure (3000 psi), Class H cement showed extremely low porosity and permeability due to incomplete carbonation that resulted in the formation of scawtite. In addition, Class G cement showed reduction in porosity and permeability after aging at 3000 psi. At intermediate pressure (6000 psi), there was higher carbonation proceeded by leaching, thereby increasing the porosity and permeability of the cement. At high pressure (9000 psi), porosity and permeability were reduced due to the formation of dense crystals, which plug the pores and capillaries (Roger 1996).

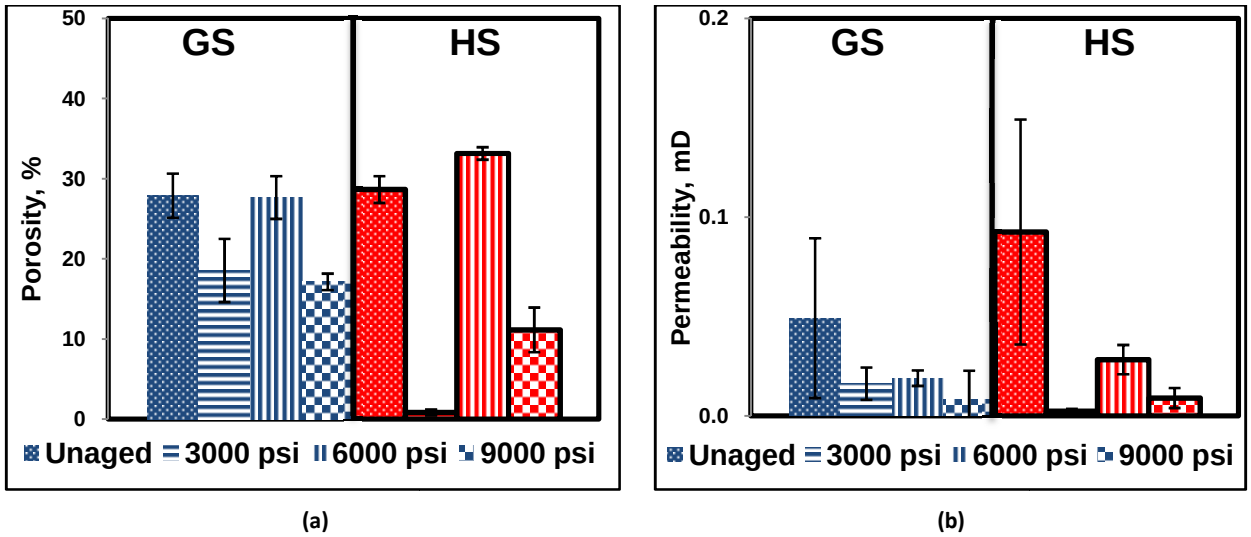

Fig. 2: Effects of aging pressure on porosity and permeability of baseline cores aged at 350F and 40% CO_2

Figure 3 demonstrates the effects of pressure on porosity and permeability of aged samples at 350°F and 100% CO_2. For Class G cement, porosity and permeability trends are consistent and similar to the ones shown with 40% CO_2. For Class H cement, these trends are not consistent. However, variations of porosity and permeability with pressure are minimal. At 100% CO_2, both porosity and permeability decreased at 3000 psi and did not change substantially with pressure was increased above 3000 psi.

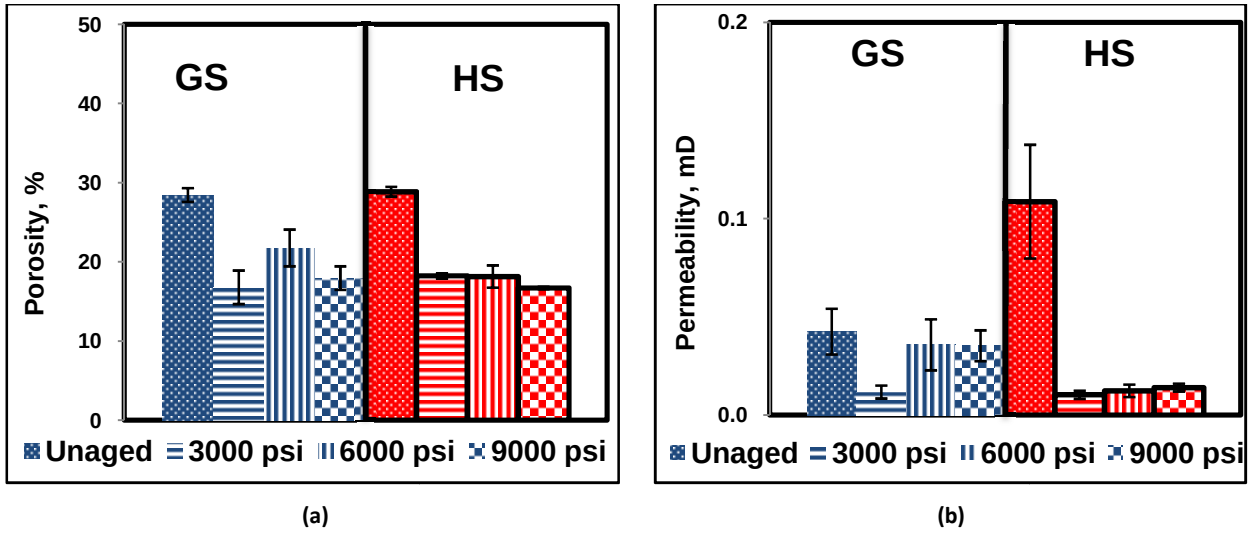

Fig. 3: Effects of aging pressure on porosity and permeability of baseline cores aged at 350°F and 100% CO_2

2.2.2 FTIR Results

Figures 4 through **17** present FTIR peaks of CH, CSH and $CaCO_3$ as a function of distance from center of a cement core and photos of the core taken after sliding at the middle. FTIR samples were taken from different batches of cement core. The samples were collected from the middle of the cores. The figures show the photo of a sample sliced from the middle. The FTIR results reduction of CH and CSH content

from the center to the edge and the increase in $CaCO_3$ concentration with radial distance from the center. A few exceptions do not follow this trend due to leaching and phase transformation.

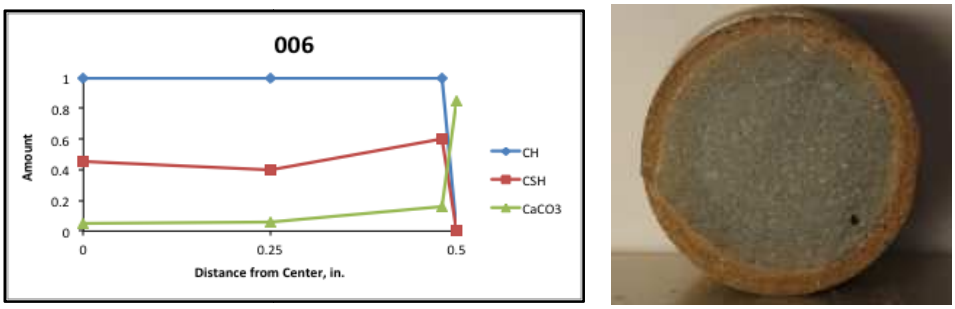

(a) (b)

Fig. 4: Variation of CH, CSH and $CaCO_3$ content of Batch 006 core: a) FTIR peak strength; and b) photo

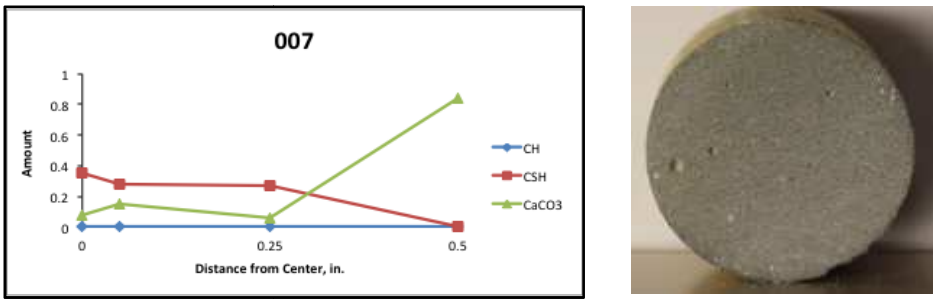

(a) (b)

Fig. 5: Variation of CH, CSH and $CaCO_3$ content in Batch 007 core: a) FTIR peak strength; and b) photo

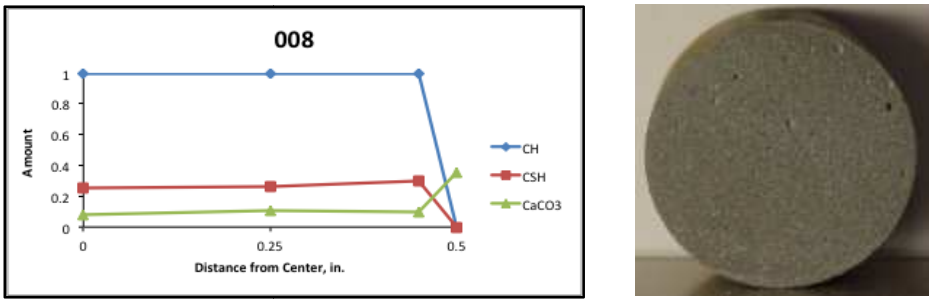

(a) (b)

Fig. 6: Variation of CH, CSH and $CaCO_3$ content in Batch 008 core: a) FTIR peak strength; and b) photo

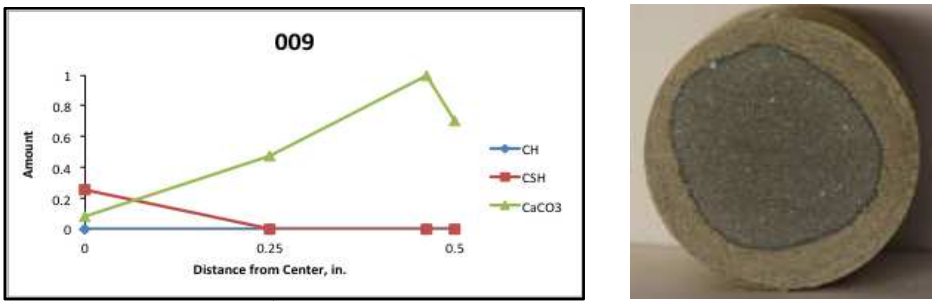

(a) (b)

Fig. 7: Variation of CH, CSH and $CaCO_3$ content in Batch 009 core: a) FTIR peak strength; and b) photo

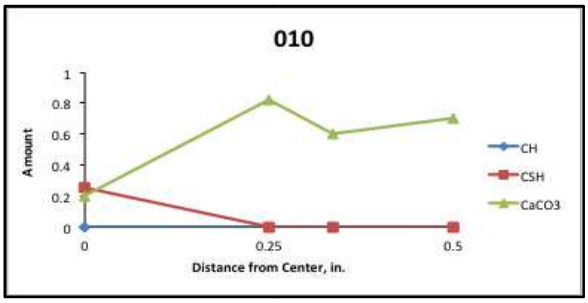

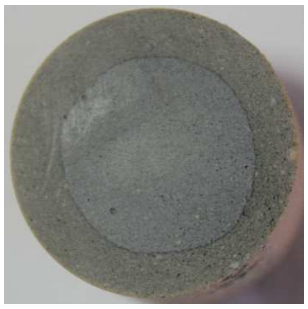

(a) (b)

Fig. 8: Variation of CH, CSH and $CaCO_3$ content in Batch 010 core: a) FTIR peak strength; and b) photo

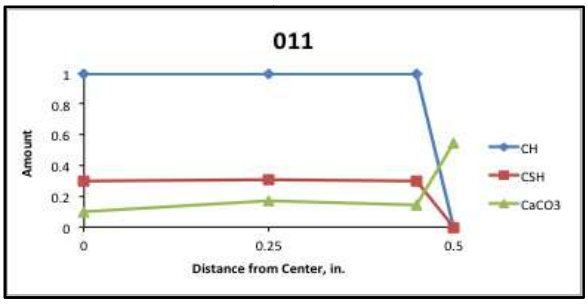

(a) (b)

Fig. 9: Variation of CH, CSH and $CaCO_3$ content in Batch 011 core: a) FTIR peak strength; and b) photo

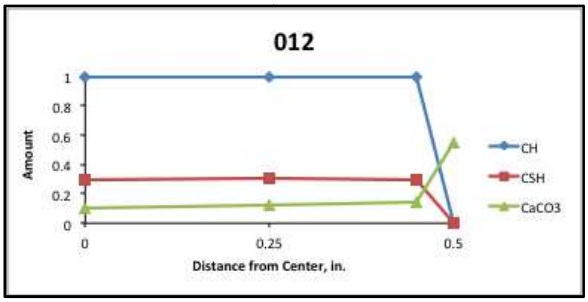

(a) (b)

Fig. 10: Variation of CH, CSH and $CaCO_3$ content in Batch 012 core: a) FTIR peak strength; and b) photo

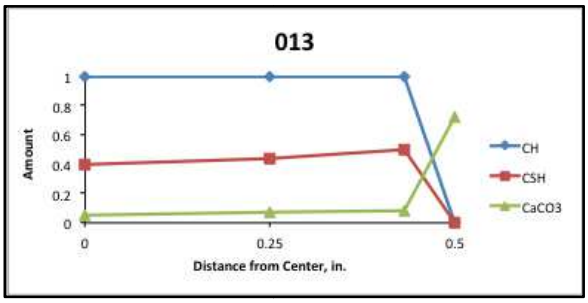

(a) (b)

Fig. 11: Variation of CH, CSH and $CaCO_3$ content in Batch 013 core: a) FTIR peak strength; and b) photo

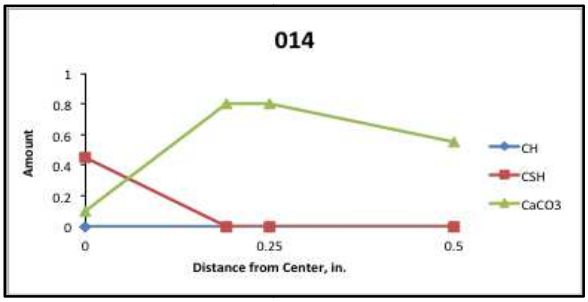

(a) (b)

Fig. 12: Variation of CH, CSH and $CaCO_3$ content in Batch 014 core: a) FTIR peak strength; and b) photo

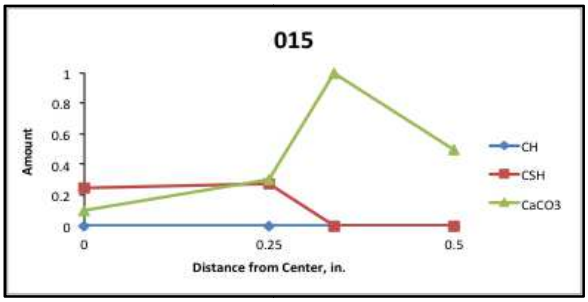

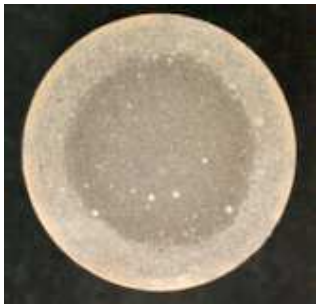

(a) (b)

Fig. 13: Variation of CH, CSH and $CaCO_3$ content in Batch 015 core: a) FTIR peak strength; and b) photo

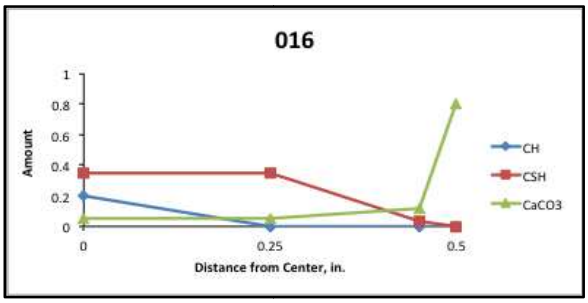

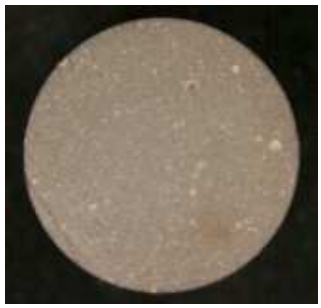

(a) (b)

Fig. 14: Variation of CH, CSH and $CaCO_3$ content in Batch 016 core: a) FTIR peak strength; and b) photo

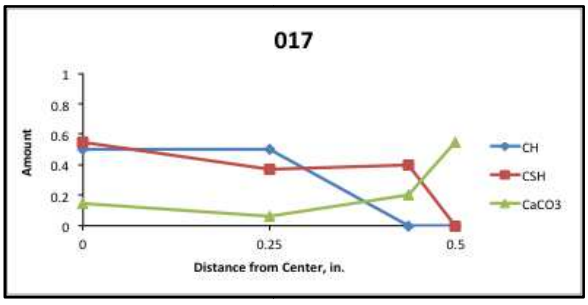

(a) (b)

Fig. 15: Variation of CH, CSH and $CaCO_3$ content in Batch 017 core: a) FTIR peak strength; and b) photo

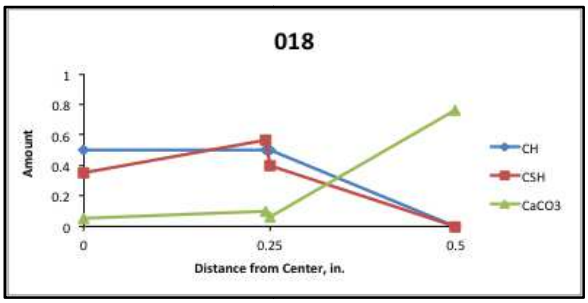

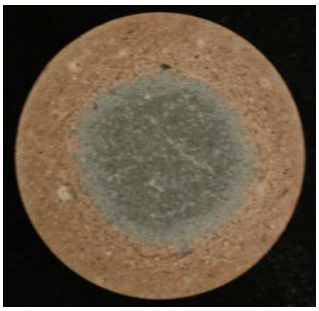

(a) (b)

Fig. 16: Variation of CH, CSH and $CaCO_3$ content in Batch 018 core: a) FTIR peak strength; and b) photo

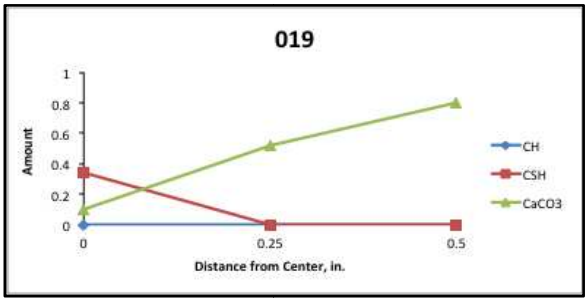

(a) (b)

Fig. 17: Variation of CH, CSH and $CaCO_3$ content in Batch 019 core: a) FTIR peak strength; and b) photo

2.2.3 Compressive Strengths of Baseline Cements

In previous report, the effects of pressure on compressive strength of Class G and Class H cements were presented for Batch 19 (aged at 350°F, 9000 psi, 100% CO_2 and 2% Brine for 14 days) and Batch 20 (aged at 350°F, 3000 psi, 10% CO_2 and 2% Brine for 14 days). Results showed that Class G cement is subjected to more carbonation at high aging pressure while this condition favors additional strength gain in Class H cement. Furthermore, the presence of scawtite at low aging pressures significantly affects strength development. If present in low quantity, scawtite makes cement stronger but this trend changes as amount of scawtite increases.

Results of two recent aging experiments (Batch 21 and 22) show that at high temperature (350°F) and low CO_2 concentration (10%), increase in aging pressure have mixed effect on compressive strength of baseline cements (**Fig. 18**). In Class G cement, strength reduction results from formation of scawtite in large quantity while complete carbonation leads to strength improvement in Class H cement. In addition, increasing CO_2 concentration resulted in more carbonation in both API oil well cements, especially Class H cement (**Fig. 19**). At intermediate temperature (225°F) and slightly high CO_2 concentration (40%), increase in aging pressure caused initial strength gain (due to presence of traces of scawtite) followed by strength loss due to leaching (**Fig. 20**).

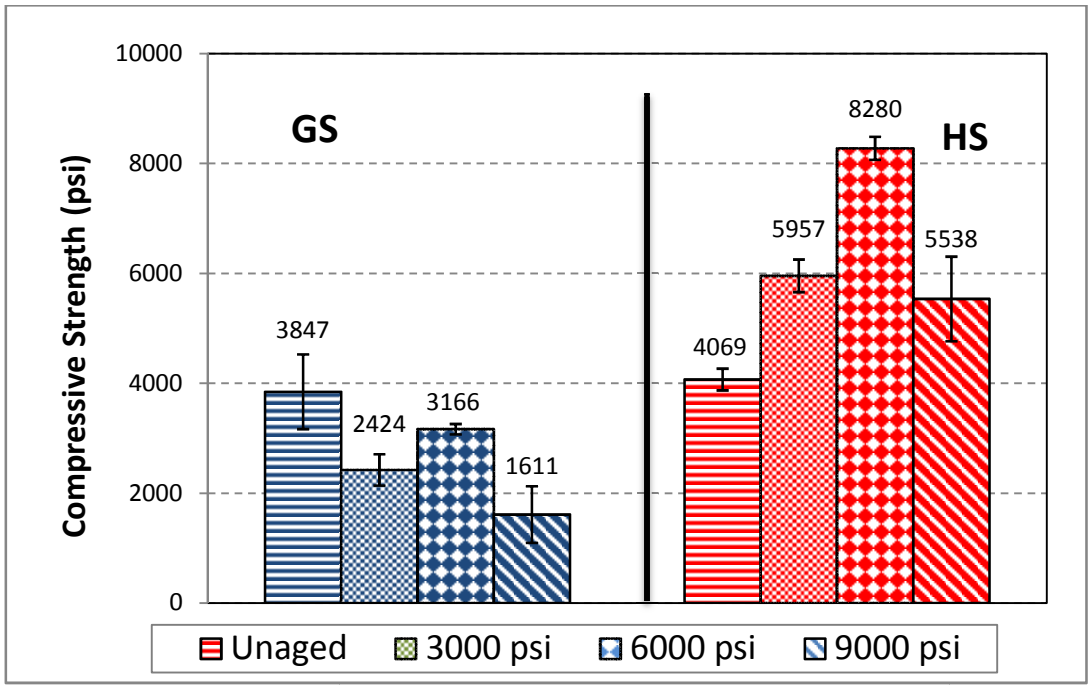

Fig. 18: Effect of aging pressure on compressive strength at 350°F and 10% CO_2

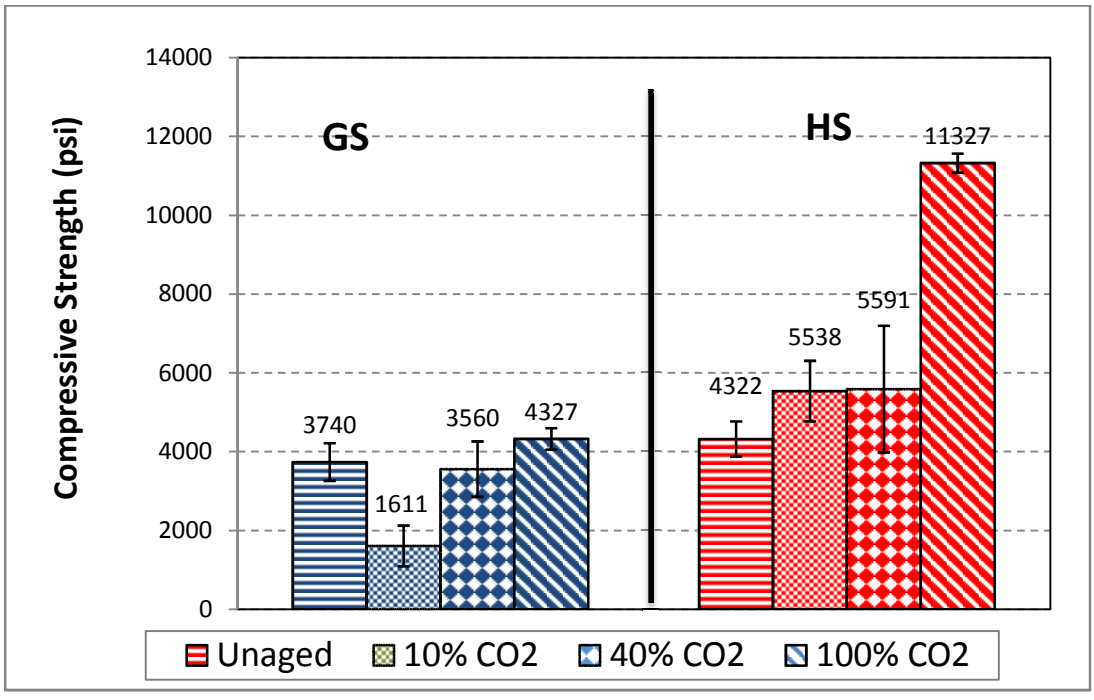

Fig. 19: Effect of CO_2 concentration on compressive strength at 350°F and 9000 psi

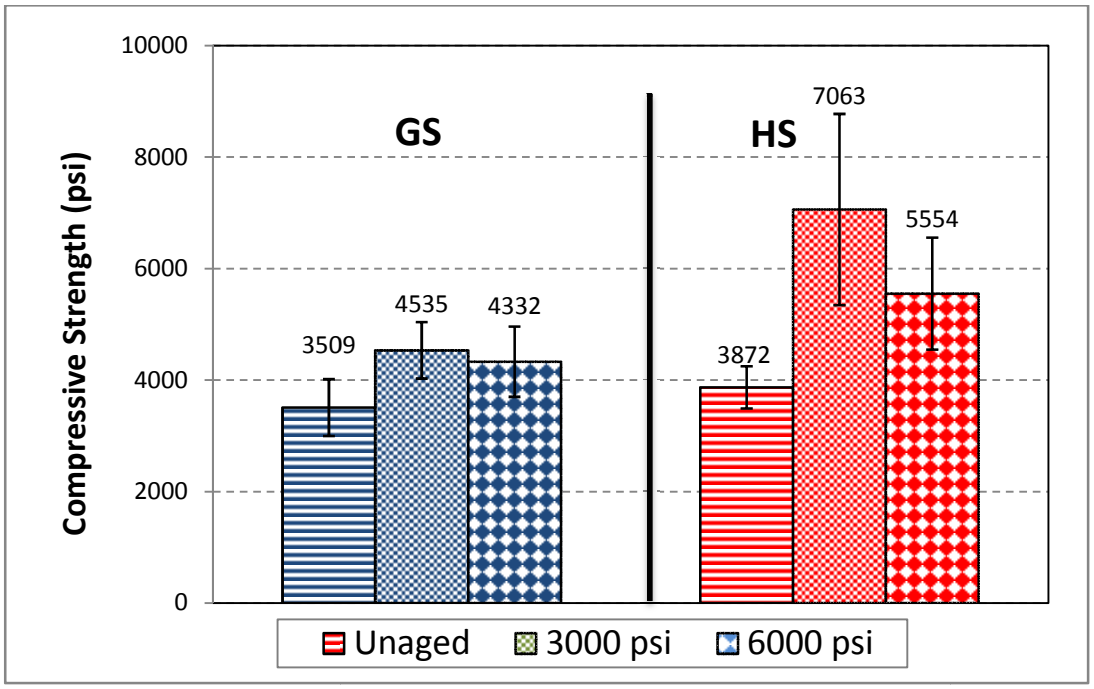

Fig. 20: Effects of aging pressure on compressive strength at 225°F and 40% CO_2 concentration

2.2.4 Shear Bond Strengths of Baseline Cements

Study on shear bonding strength (SBS) of Class H cement was continued. In this report, the influence of aging pressure on shear bond strength at 225°F is presented. Relevant literatures were reviewed to compare our experimental results with published data. Furthermore, statistical analysis was performed to determine factors that influence shear bond strength. Principal Component Analysis (PCA) and Factor Analysis (FA) were utilized and preliminary results were obtained. The FA method looks for the phenomena underlying the observed variance and covariance in a set of variables. The goal of this analysis is to find the most influential factor affecting the SBS. The analysis will continue in the coming weeks.

As the aging temperature increased, shear bond strength increased (**Fig. 21**). The increase observed at 3000 psi more pronounced than the ones recorded at other pressures. Increase in temperature promotes the carbonation of the cement, which causes expansion of the samples leading to improved bond strength. Even though higher temperature reduces the solubility of CO_2 in brine, the improvements in diffusion and carbonation reaction rates facilitate the overall carbonation process. As reported previously, depth of penetration measurements showed deepening with temperature and CO_2 concentration (**Fig. 22**). Accordingly, the penetrated depth is closely related to the SBS improvement shown after aging the samples for 14 day in brine saturated with CO_2 containing gas. However, reduction in bond strength and zonal isolation can happen after a long-term exposure to the acidic environment resulting in increased penetration depth and leaching of the carbonated zone.

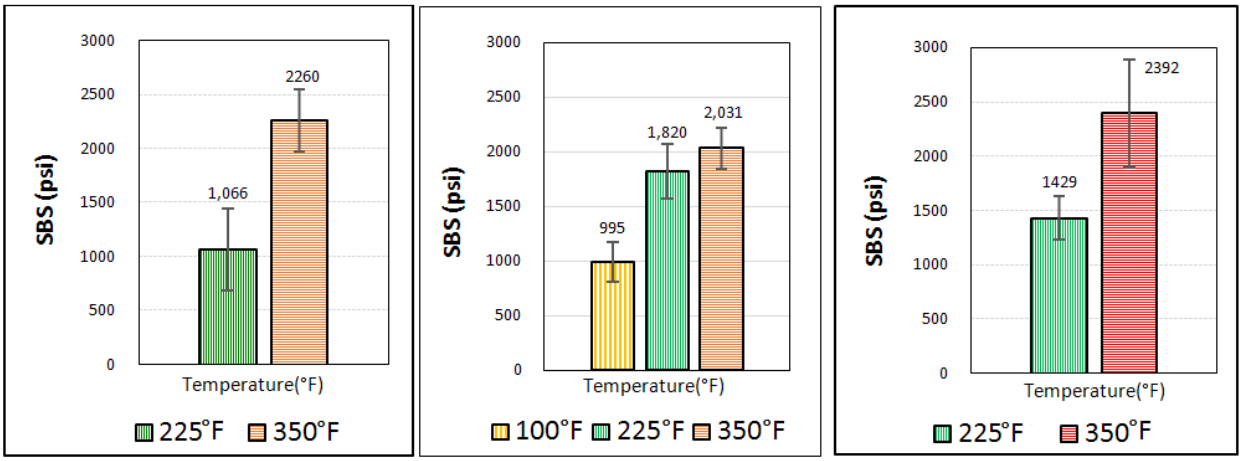

(a) (b) (c)

Fig. 21: The influence of aging temperature on SBS at 40% CO_2 concentration and different pressures: a) 3000 psi; b) 6000 psi; and c) 9000 psi

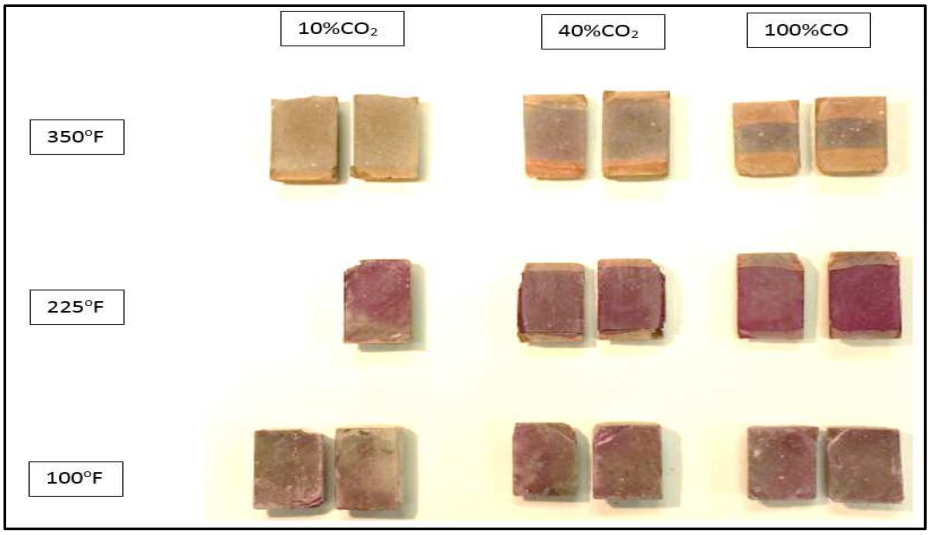

Fig. 22: Phenolphthalein test results for samples aged at 6000 psi and different temperatures and CO_2 concentrations

At higher aging pressures, CO_2 penetration into cement increases (Sauki et al. 2010). **Figure 23** shows the influence of aging pressure on SBS at different temperatures (225°F, and 350°F). Bond strength increased with pressure due to improvement in carbonation rate resulting from increased pressure that causes more gas to dissolve in the brine. The formation of $CaCO_3$ tends to increase the volume of the cement within the limited pipe space, creating very tight condition, which improves the bond. Penetrated depth measurements are in agreement with the SBS measurements (**Fig. 24**).

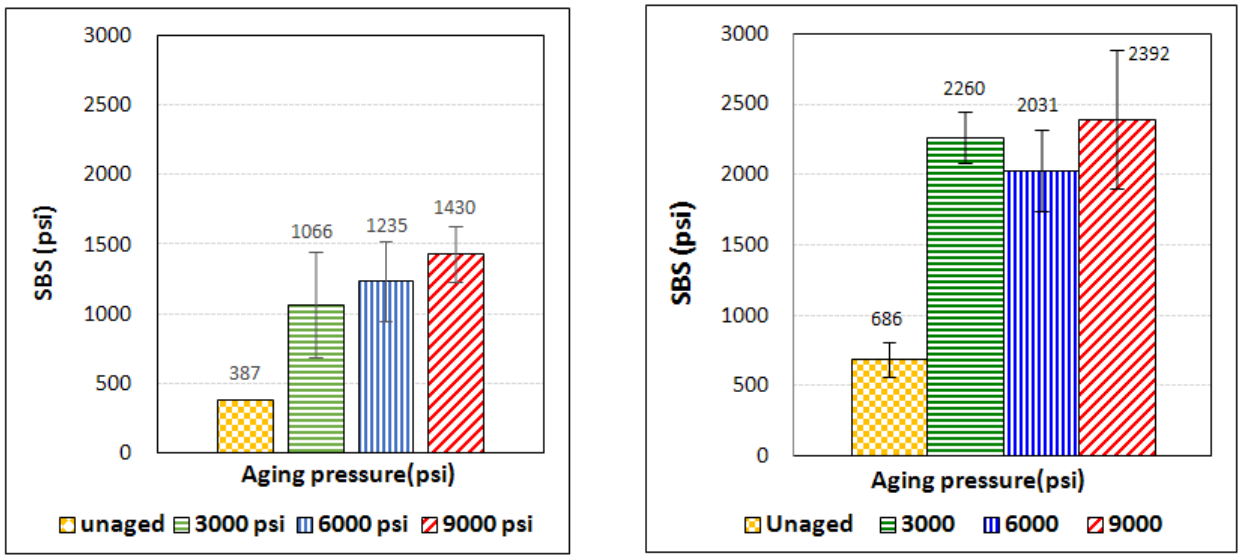

Fig. 23: Influence of aging pressure on shear bond strength at 40% CO_2 concentration and different temperature: a) 225°F; and b) 350°F

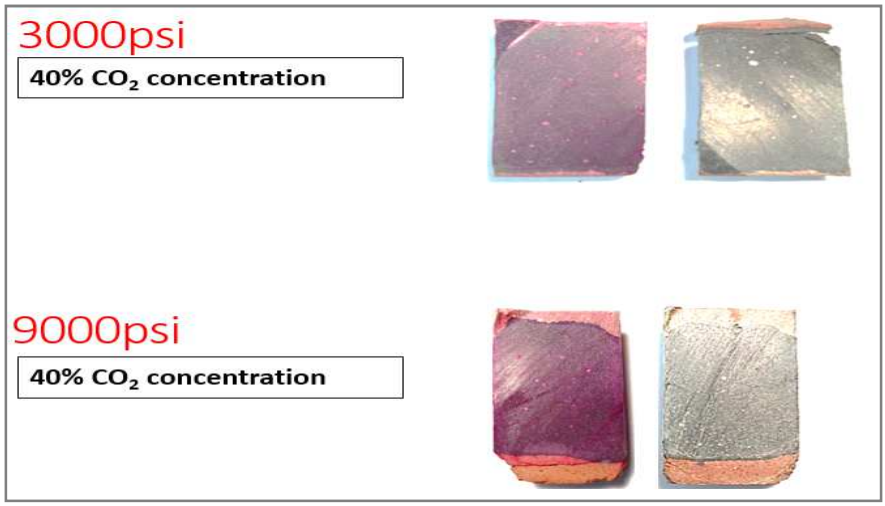

Fig. 24 Penetration depths at 225°F and different aging pressures

2.2.5 Additive Screening and Cement Formulation Studies

Additive screening and cement formulation studies were continued. Hydroxyapatite (HOAP), micro silica and latex containing cements were investigated during this reporting period. Core samples with hydroxyapatite were aged under CO_2 containing environment along with baseline samples.

2.2.5.1 Hydroxyapatite Cement without Silica Flour

Previous tests with baseline HOAP samples (HOAP samples that don't have silica flour) were conducted mostly at 350°F (except the first test which was conducted at 100°F). In all the tests, it was observed that the samples went through strength retrogression. For tests performed at 100°F, the strength reduction can be attributed to the leaching of $Ca(OH)_2$ by the pore fluid. At lower temperature, the

leaching is expected to intensify due to increased solubility of calcium hydroxide in water and the conversion $CaCO_3$ to $CaHCO_3$ resulting from increased concentration of carbonic acid in the pore fluid. At 350°F the strength retrogression is anticipated due to the transformation of CSH to α-C_2SH, which causes the cement to have high porosity and permeability and low compressive and bond strengths (Eilers et al., 1976 and 1983; Dillinbeck III et al., 1990; Grabowski and Gillott, 1989; Lea, 1971). This transformation is because of lack of sufficient amount of silica in the cement. Another aging test with baseline HOAP samples was conducted at 225°F in order to examine the impact of temperature on HOAP cement properties. Details of the aging conditions are presented in **Table 4**.

Table 4: Aging conditions for the HOAP samples

HOAP	Temp. (°F)	Pressure (psi)	CO_2 (%)	NaCl (%)	Days	Baseline	Exp. No.
Batch 006	225	3000	40	2	14	Batch 022	19

After aging, the properties of the cores were measured. The results are presented in **Figs. 25** and **26**. The data presented as unaged refers to groups of core samples kept at ambient lab conditions for 14 days while other samples were aged in the aging cell elevated temperature and pressure.

Porosity and Permeability Measurements

The porosity and permeability measurements are presented in Figs. 25 and 26. Before aging, the HOAP samples had lower porosity and permeability than the corresponding baseline samples. After aging, the porosity of the baseline samples decrease and the HOAP sample porosities slightly increased. The reduction in porosity can be attributed to the carbonation of the matrix which causes plugging of the pores. On the other hand, the slight porosity increase of HOAP samples indicates the absence of major carbonation. The small increment in porosity can be measurement disparity or due to minor leaching of $Ca(OH)_2$ from the matrix, mostly from the outer part of the core sample. For baseline samples, the permeability decreased after aging. The results of HOAP samples showed mixed trend. For the HHO samples, the permeability reduced. In the case of GHO samples, slight increase in permeability was observed after aging. The permeability of cement is strongly affected by the pore throat size, which restricts the flow of fluid from one pore to the other. Hence, the decrease in permeability can be due to carbonation of the matrix and/or plugging of pore throats caused by the precipitation of $CaCO_3$. An increase in porosity of GHO samples suggests that the samples were not substantial carbonated. Hence the plugging of pore throats can be due to the precipitation of diffusing ions of $Ca(OH)_2$.

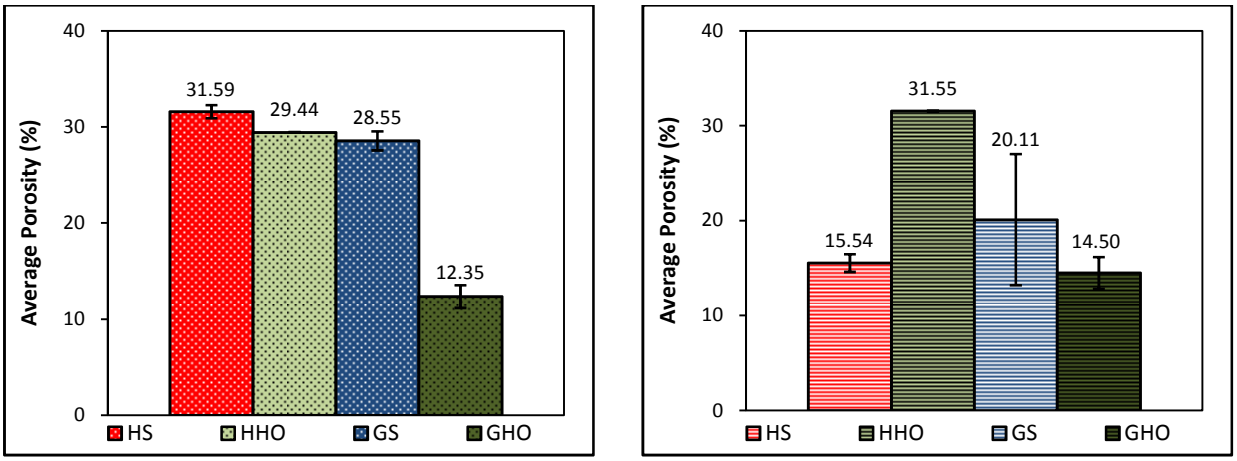

Fig. 25: Porosities of HOAP and baseline cements: a) unaged; and b) aged for 14 days at 225°F and 3000 psi in brine saturated with 40% CO_2 gas

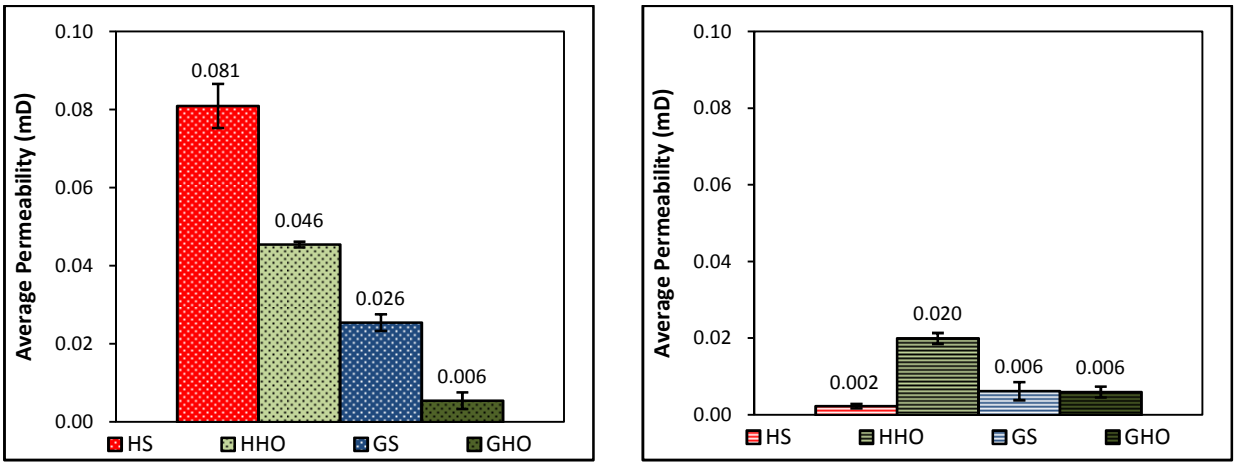

Fig. 26: Permeabilities of HOAP and baseline cements: a) unaged; and b) aged for 14 days at 225°F and 3000 psi in brine saturated with 40% CO_2 gas

Compressive Strength Measurements

Compressive strengths of HOAP and baseline cements are presented in **Fig. 27**. Before aging, the strengths of HOAP samples were slightly higher than those of the respective baseline samples. After aging, baseline samples strength increased due to carbonation of the matrix. The HOAP samples on the other hand showed reduction in the strength. The aging temperature was below 225°F, even then the strength retrogression was observed. It is widely mentioned among several literatures (Eilers et al., 1976 and 1983; Dillinbeck III et al., 1990; Grabowski and Gillott, 1989; Lea 1971) that the strength retrogression due to formation of α-C_2SH happens above 230°F. Hence, this lowering in strength may not be caused by the conversion of CSH to α-C_2SH. The strength reduction can be as a result of leaching of $Ca(OH)_2$ from the matrix or carbonation of HOAP. The carbonated HOAP can be weaker than the

actual HOAP. It is interesting to note that the strength reduction of HOAP samples is occurring irrespective of the aging temperature.

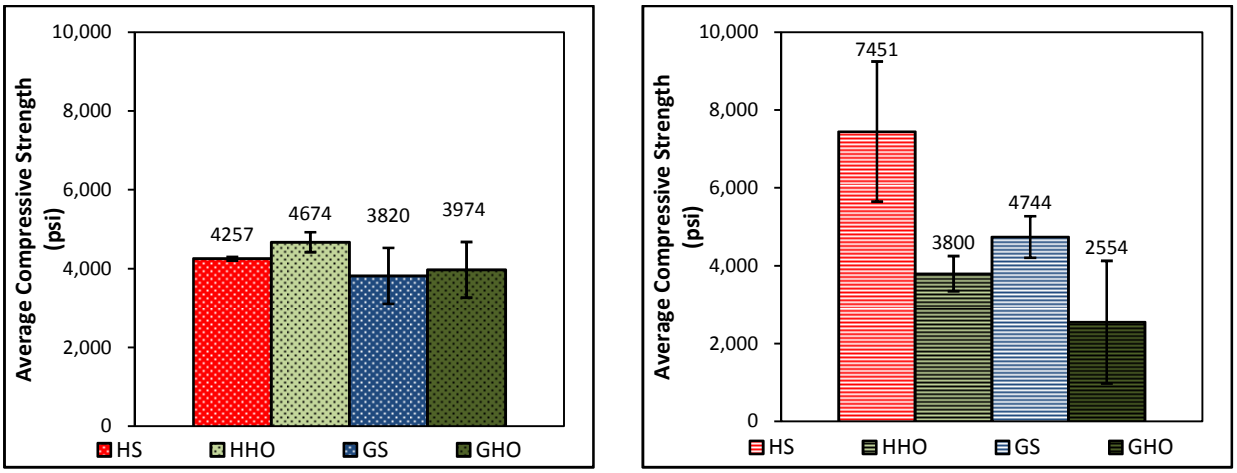

Fig. 27: Compressive strength of HOAP and baseline cements: a) unaged; and b) aged for 14 days at 225°F and 3000 psi in brine saturated with 40% CO_2 gas

Shear Bond Strength Measurements

Shear bond strength (SBS) measurements are presented in **Fig. 28**. Increase in SBS was observed in the baseline HS samples which is attributed to the carbonation of the samples. On the other hand, the HOAP samples exhibited a slight reduction in SBS after aging. The slight decrease can be due to leaching of $Ca(OH)_2$ from the matrix or carbonation of HOAP which might have lesser bonding strength with steel or weakening of the HOAP after carbonation as manifested with the compressive strength reduction.

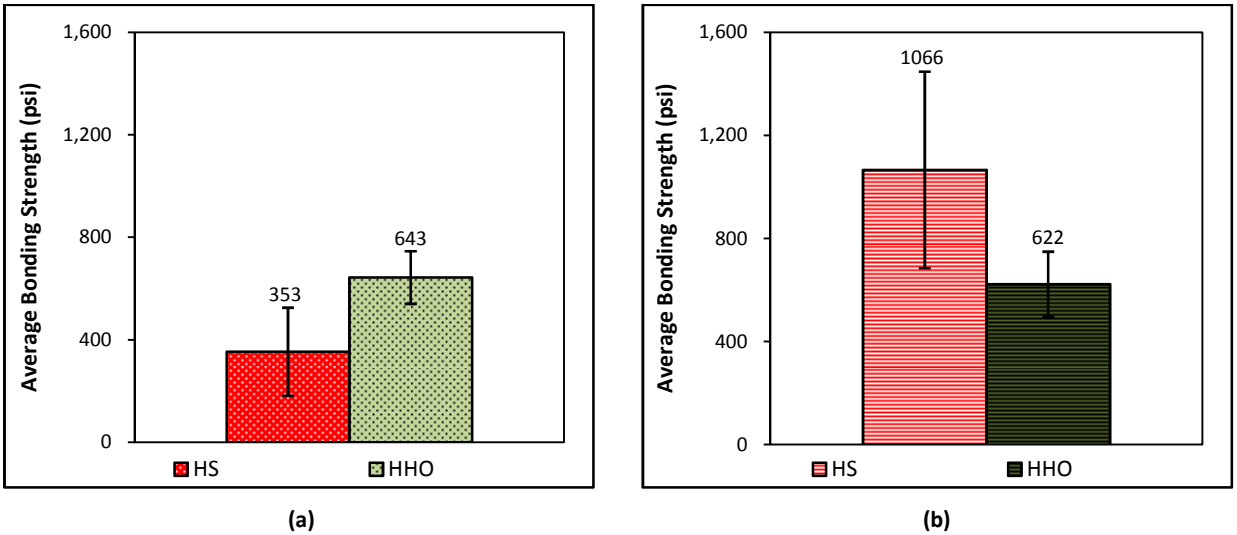

Fig. 28: Shear bond strength of HOAP and baseline cements: a) unaged; and b) aged for 14 days at 225°F and 3000 psi in brine saturated with 40% CO_2 gas

HOAP test results suggest substantial reduce of cement carbonation. Reduction in strength was observed in all the samples, which can be attributed to dissolution of $Ca(OH)_2$ in the solution brine or carbonation of HOAP (the weakening of HOAP due carbonation needs to be confirmed from the available literature). This retrogression appears to be unavoidable at any temperature. It can be inherent property of the HOAP cement. Nevertheless, the compressive strength of the matrix is still significantly above the required norms of the industry (i.e. 500 psi). Beside this, the shear bond strength showed reduction after aging at 3000 psi but it was comparable to the unaged base samples. Hence, the additive HOAP can be used to prevent the degradation of cement; however, it slightly lowers the compressive strength. Our future tests with HOAP will be conducted at different temperatures in order to confirm the conclusions discussed above. Since the absence of additional silica flour does not affect the performance of the HOAP cement at high temperatures (above 300°F), the addition of silica flour will not be considered in future experiments.

2.2.5.2 Micro-Silica-Based Cement

Aging experiments were carried out with 15% BWOC micro silica cement (MS-15). Class H samples were broken during the samples preparation procedure. Only class G samples were aged. The compressive strength tests for the aged samples will be performed in the coming weeks. The results will be reported in the next monthly report.

Porosity and Permeability Measurements

As it was mentioned in the previous monthly report, 10% BWOC micro silica cement (MS-10) was prepared and tested. The unaged porosity and permeability of MS-10 samples were substantially less than the base samples (**Fig. 29**). The reduction in porosity is attributed to the filling up of the pores with fine micro-silica particles. The low porosity and permeability may help in reducing the penetration of the CO_2 in the matrix.

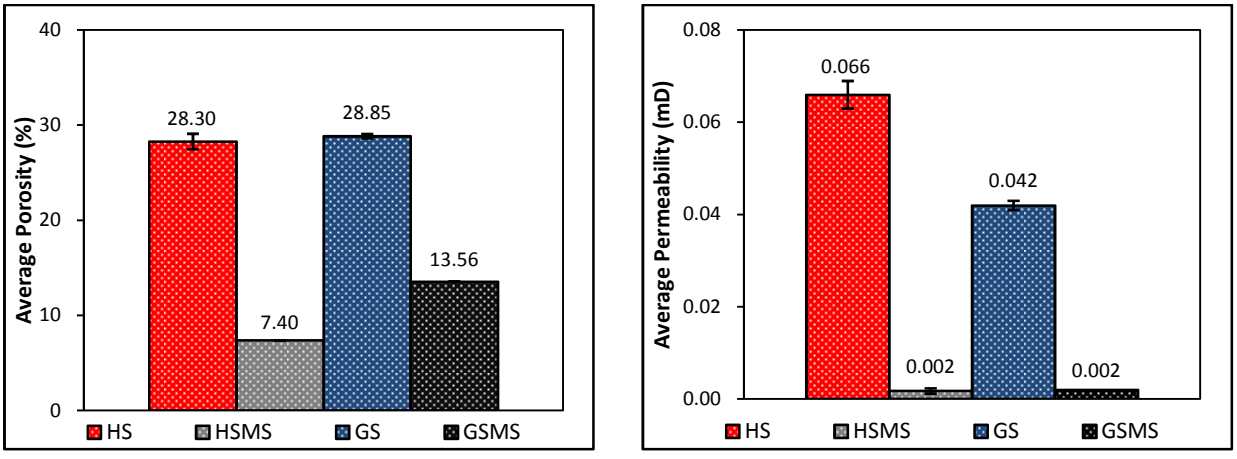

Fig. 29: Porosity and permeability of unaged baseline and micro silica (MS-10) cement samples: a) porosity; and b) permeability

Compressive and Shear Bond Strength Measurements

Compressive and shear bond strengths of micro-silica cement were found to be higher than those of the baseline samples (**Fig. 30**). The increases in compressive and shear bond strengths are in the same order. The reduction in porosity results in improvement of cement properties such as permeability, compressive and shear bond strengths. The result is encouraging but further investigation is needed to evaluate the performance of the new formulation under acidic environment.

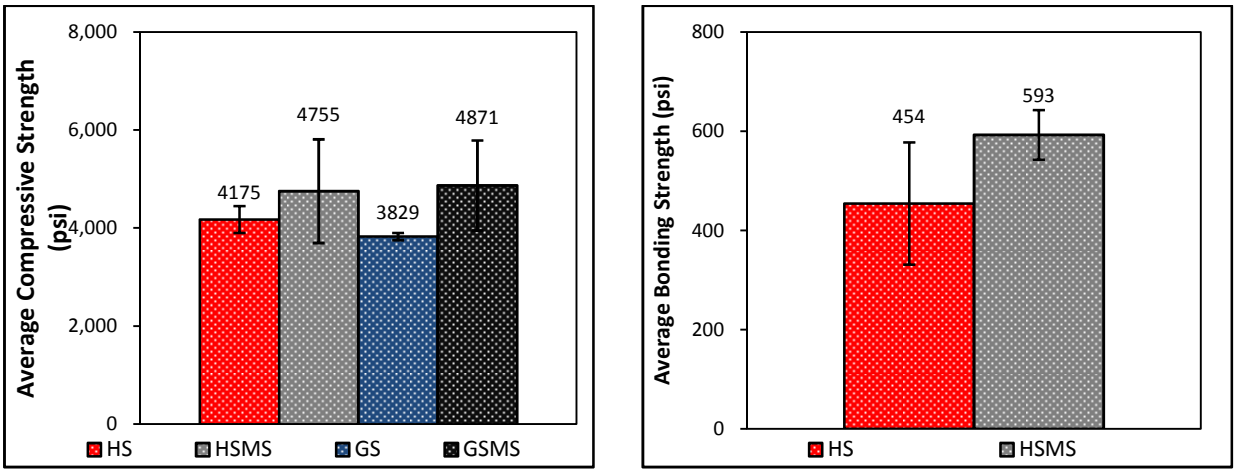

Fig. 30: compressive and shear bond strength of unaged baseline and micro silica (MS-10) samples: a) compressive strength; and b) shear bond strength

2.2.5.3 Latex-Based Cement

Testing with conventional SBR latex was continued. When latex was added as an additive, it caused entrapment of air and increase in porosity and permeability of the matrix. In order to reduce the porosity and permeability, micro silica was introduced to the latex cement. The slurry compositions are presented in **Table 5**. The slurry properties were measured and found to be comparable with the baseline slurries. Subsequently, samples were prepared for unaged testing. The properties of unaged cores will be measured in the coming weeks.

Table 5: Compositions for latex micro-silica slurries

Component	HSLM	GSLM
Cement	100%	100%
Silica Flour	25% bwoc	25% bwoc
Micro Silica	10% bwoc	10% bwoc
HEC	0.1% of water for fillers	0.1% of water for fillers
Antifoam Agent	0.1 gal/sack of cement	0.1 gal/sack of cement
Water for Cement	38% bwoc	44% bwoc
Water for Silica Flour	38.5% of Silica Flour	38.5% of Silica Flour
Dispersant (NSF)	0.75% bwoc	0.75% bwoc
Retarder (Citric Acid)	0.0015% bwoc	0.02% bwoc
Latex	10% bwoc	10% bwoc
Cement	100%	100%
Silica Flour	25% bwoc	25% bwoc

2.3 Experimental Studies on Corrosion of Tubulars (Task 3)

Low-pressure corrosion experiments were continued using both weight loss (WL) and electrical measurement techniques. During this reporting period, three experiments (Experiments 12, 13 and 14) were conducted varying CO_2 concentration in the gas phase. Tests were conducted at 120 psi and ambient temperature of 78°F for 187 hours. Brine concentration was 2% in the liquid. Experiment 13 was performed without CO_2 (i.e. 100% N_2). Experiment 12 and 14 were performed with 50% and 75% CO_2 concentrations, respectively. **Figures 31** through **33** present the LPR measurement of corrosion rates during the experiments.

When the test was conducted with 50% CO_2 gas, the average corrosion rate obtained using LPR method was 31.95 mpy (Fig. 31). The rate measured using the weight loss method was 27.57 mpy, which indicates very close agreement between the two techniques.

The general trend of the corrosion rate was declining with time after the peak rate of corrosion was reached. Initially the rate of corrosion increased and it was high for a few hours due to dissolution of CO_2 that resulted in the formation of bicarbonates and carbonates, which accelerated the corrosion. Then, the increase in rate of corrosion facilitated the formation of protective carbonate layer on the surface of the sample, which hindered the corrosion process and reduced the rate. Spikes observed in the corrosion rate plots represent the breaking of poorly formed protective layer, which resulted in sporadic spikes in the rate, and gradual decline as the layer begins to form slowly. A similar corrosion rate trend was observed when the test was conducted with 75% CO_2 gas (Fig. 33). However, the corrosion rate trend for the experiment with 0% CO_2 was different. There was no initial increase in corrosion rate because without the presence of CO_2 in the system, bicarbonates and carbonates that facilitate the corrosion process do not form at the beginning of the test and the protective carbonate layers do not develop.

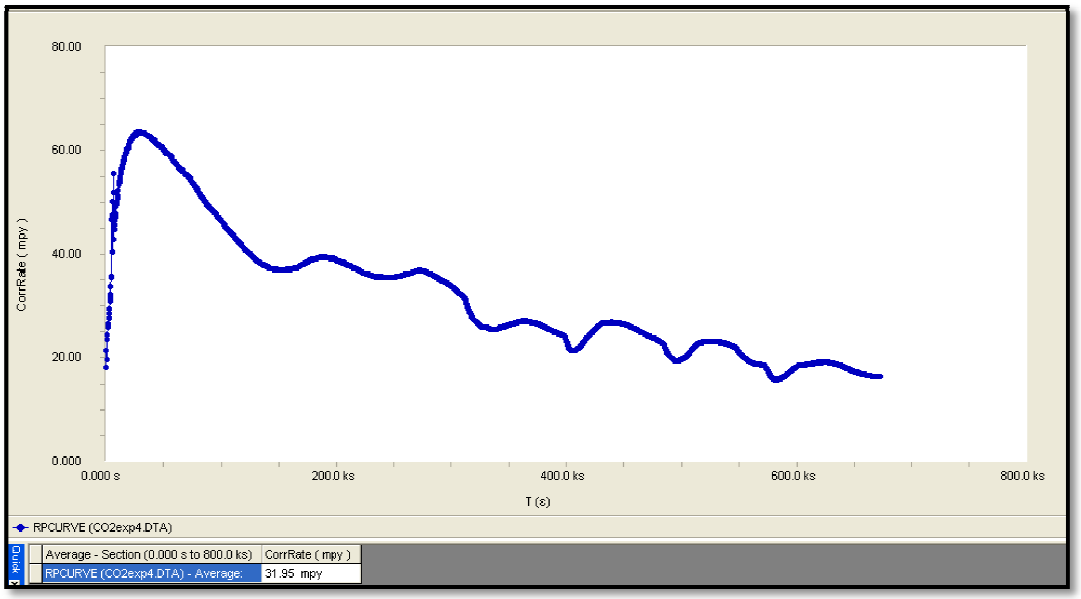

Fig. 31: Corrosion rate vs. time for Exp. 12 (50% CO_2 gas)

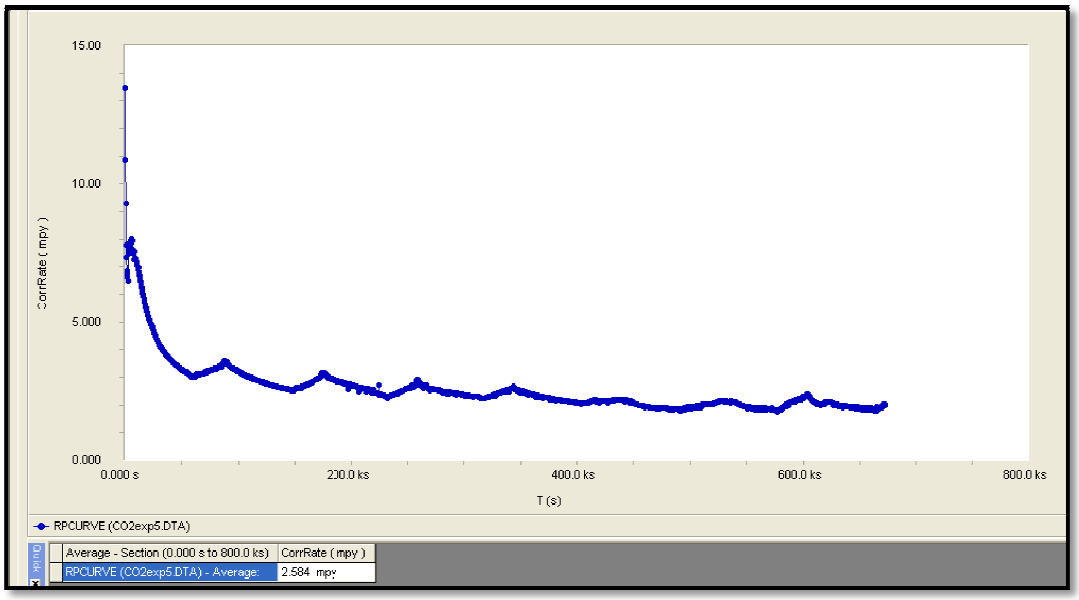

Fig. 32: Corrosion rate vs. time for Exp. 13 (0% CO_2 gas)

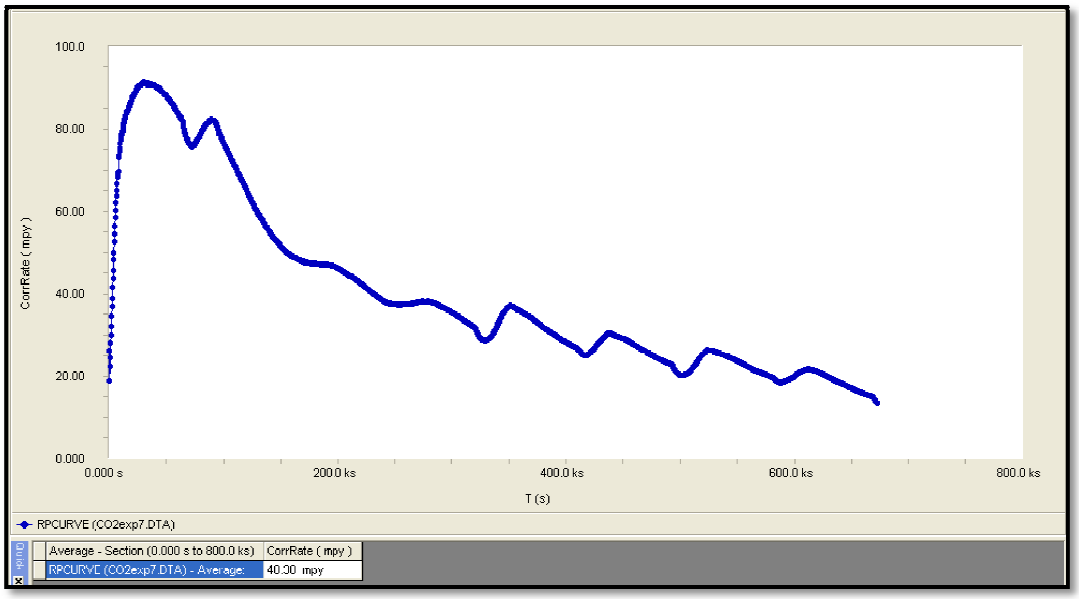

Fig. 33: Corrosion rate vs. time for Exp. 14 (75% CO_2 gas)

Corrosion rate measurements obtained from three experiments (**Table 6**) show the effects of CO_2 concentration on the corrosion process. As expected, the corrosion rate substantially increased with CO_2 content. In addition, the weight loss and LPR measurements show very good agreement when CO_2 was present in the aging fluid.

Table 6: Corrosion rate measurements obtained from weight loss method and LPR technique

	0% CO_2	50% CO_2	75% CO_2
LPR method	2.58 mpy	31.95 mpy	40.30 mpy
Weight loss method	4.11 mpy	27.57 mpy	48.10 mpy

The construction of corrosion test setup was continued. Assembling of high-pressure tubing, tube fittings and measuring instrumentation has been completed (**Fig. 34**). As reported previously, this task was delayed due to the incompatible of high-pressure fittings provided by equipment supplier for sour gas application. In the coming weeks the apparatus will be installed in the lab and instrumentation and electrical wiring works will be performed. Then, the setup will be pressure tested at maximum allowable operating temperature.

Fig. 34 Corrosion experiment setup showing test cells for uniform corrosion and sulfide stress cracking

Fig. 35 Uniform corrosion cell with magnetic coupling to simulate dynamic conditions

The corrosion setup consists of two test cells, which will be used to investigate uniform corrosion under static and dynamic condition and perform studies on sulfide stress cracking (SSC). The cells are equipped with the required devices and instrumentations. Magnetic coupling with an air motor is installed on the uniform corrosion test cell (**Fig. 35**) to simulate dynamic condition in the cell. The speed of the motor is controlled by the air supply pressure, which is controlled by a pressure regulator. The SSC cell is equipped with a pneumatic cylinder to apply tension on the test specimen (mini-pipe). The cylinder is designed to handle 250-psi pressure. Nitrogen is supplied to actuate the cylinder in both sides (forward and backward). To prevent the cylinder from over-pressurization, two relief valves are installed at inlet ports of the cylinder. The valve will prevent the cylinder from pressurization above the allowable limit due to high-pressure inlet gas supply or compression of gas trapped in the cylinder when the cylinder is retracted due to the development of high pressure in the cell without the presence of a mini-pipe or a complete failure of the mini-pipe.

3. Planned Activities

- Continue aging experiments with brine-CO_2-CH4 system for 14 days varying aging pressure (3,000, 6000, and 9000 psi) and CO_2 concentration (10%, 40% and 100%) at 350°F and 225°F.
- Continue theoretical and modeling studies on tubular degradation.
- Continue cement additive screen and acid resistant cement formulation studies.
- Begin testing of the corrosion experiment setup.

4. Project Expenditures

This section presents the project expenses during the month of August (**Table 7**) and the cumulative expenditures.

Table 7: Current and cumulative expenditures, August 2013

No.	Budget Categories	Current Expenses	Cumulative Expenses
1	Salaries & Wages	$9,826.92	$221,415.38
2	Fringe Benefits	$1,396.64	$51,841.89
3	Project Materials	$1,282.76	$58,072.19
4	Travel	$41.25	$6,051.53
5	Conference Expenses	$0.00	$0.00
6	Other Direct Costs	$0.00	$993.60
7	Equipment	$833.16	$236,478.49
8	Space Rental	$0.00	$0.00
9	Indirect Cost	$6,273.79	$169,187.26
10	**Total**	**$19,654.52**	**$744,040.34**

Nomenclatures

BWOC	By weight of cement
CH	Calcium hydroxide
CSH	Calcium silicate hydrate
FA	Factor Analysis
FTIR	Fourier Transform Infra-Red
GS	Class G cement with silica flour
GSHO	Class G Cement with silica flour and hydroxyapatite
GSMG	Class G Cement with silica flour and magnesium oxide
GSLT	Class G Cement with latex
HOAP	Hydroxyapatite containing cement
HPHT	High-pressure high-temperature
HS	Class H cement with silica flour
HSHO	Class H Cement with silica flour and hydroxyapatite
HSMG	Class H Cement with silica flour and magnesium oxide
HSLT	Class H Cement with latex
LPR	Linear polarization resistance
mpy	mils per year
MGO	Magnesium oxide containing cement
MGO-5	Cement containing 5% BWOC MgO as additive
MGO-10	Cement containing 10% BWOC MgO as additive
MS	Micro silica containing cement
MS-10	Cement containing 10% BWOC micro silica as additive
MS-15	Cement containing 15% BWOC micro silica as additive
NACE	National Association of Corrosion Engineers
PCA	Principal Component Analysis
SBR	styrene-butadiene
SBS	Shear bonding strength
SCC	stress corrosion cracking
SSC	Sulfide Stress Cracking
TCL	Total Crack Length
XRD	X-Ray diffraction

References

Bruce, E. and Urband, P.E. 1999. High Strength Sour Service C110 casing, paper SPE/IADC 52843 presented at the SPE/IADCE Drilling Conference, 9-11 March, Amsterdam, Holland.

Ciaraldi, S.W. 1986. Some factors that affect sour service performance of Carbon Steel Oil Country tubulars, SPE Drilling Engineering, Vol. 1, Num. 3, Pages 233-241.

Craig B. 2005. Metallurgical limits to increase tubular strength while maintaining the SSC resistance, paper SPE 97580 presented at the SPE HPHT Applied Technology Workshop, 17-19 May, Woodlands, Texas.

Dillenbeck III, R. L., Mueller, D.T. and Orr, B.R. 1990. The Effect of Micro Silica on the Thermal Stability of Lightweight Cement Systems, paper SPE 21597 presented at the CIM/SPE International Technical Meeting, 10-13 June, Calgary, Alberta, Canada.

Eilers, L.H., Nelson, E.B. and Moran, L.K. 1983. High Temperature Cement Compositions – Pectolite, Scawtite, Truscotite or Xonoloite: Which Do You Want?, JPT, Vol. 35, Num. 7, pp 1373-1377.

Eilers, L.H. and Root, R.L. 1976. Long-Term Effects of High Temperature on Strength Retrogression of Cements, paper SPE 5871 presented at the SPE California Regional Meeting, 7-9 April, Long Beach, California.

Grabowski, E. and Gillott, J.E. 1989. Effect of Replacement of Silica Flour with Silica Fume on Engineering Properties of Oil Well Cements at Normal and Elevated Temperatures and Pressures, Cement and Concrete Research, Vol. 19, pp 333-344.

Lea, F.M. 1971. The Chemistry of Cement and Concrete, 3rd Edition, Chemical Publishing Co., New York City, pp 177-202.

Mueller D. T. and Dillenbeck III R. L. 1991. The Versatility of Silica Fume as an Oil well Cement Admixture, paper SPE 21688 presented at the SPE Production Operations Symposium, April 7-9, Oklahoma City, USA.

Roger, J. 1996. Cements treated with high-pressure CO2. US Patent 5,518,540, 21 May.

Sauki, A. and Irawan, S. 2010. Effects of Pressure and Temperature on Well Cement Degradation by Supercritical CO2. International Journal of Engineering & Technology, Vol.10, No.04, pp. 53-61.

Waid, G.M and Stiglitz, R.J. 1979. The Development of High Strength Casing Steels with Improved H2S cracking resistance for Sour Service, paper OTC 3509, presented at the 11th Annual OTC, April 30 – May 3, Houston, Texas.

Wan, R. 2011. Advanced Well Completion Engineering, Third Edition, Gulf Professional Publishing, New York.

Project Title: Effect of H_2S and CO_2 in HPHT Wells on Tubulars and Cement

Report Type: Monthly Report

Report #: 24

Reporting Period: August 22nd, 2013 to September 21st, 2013

Authors:

Ramadan Ahmed, Principal Investigator

Subhash Shah, Co-Principal Investigator

Samuel Osisanya, Co-Principal Investigator

Rida Elgaddafi, Research Assistant

Omotayo Omosebi, Research Assistant

Himanshu Maheshwari, Research Assistant

Adarsh Naidu, Research Assistant

Aman Srivastava, Research Assistant

Jueun Hwang, Research Assistant

Mounraj Sharma, Research Assistant

Sagar Tale, Research Assistant

Prepared under BSEE Project # E12PC00035

by

THE UNIVERSITY OF OKLAHOMA

December 6, 2013

1. Summary of Accomplishments

This monthly report presents the progress made during the project period August 22, 2013 to September 21, 2013. Investigations on cement and tubular degradation were continued. Cement cores and bonding samples of different cement formulations were prepared and aged in acidic environment to examine their degradation characteristics. Tests with acid resistant cement formulations were continued. The effects of different additives on properties of cement slurries and cores were investigated.

Two aging experiments (Experiments 20 and 21) were completed during this month. The samples were aged for 2 weeks in 2% brine saturated with CO_2 containing methane gas. Porosity, permeability, and compressive and bond strengths of unaged and aged samples were measured.

In general, the porosity and permeability trends are consistent. Tests conducted at 100% CO_2 concentration show that carbonation and hydration reactions dominate the degradation process at lower pressures. However, as the pressure increases, leaching process dominates offsetting the effect of carbonation leading to increased porosity and permeability. Furthermore, compressive strength measurements show consistent strength gain due to formation of scawtite in trace amount at low pressures and complete carbonation at high pressures. In Class G cement, onset of leaching occurs at 9000 psi while strength is sustained in Class H cement at this pressure. Besides this, shear bond strength (SBS) measurements show improvement in SBS with CO_2 concentration, which intensifies carbonation of cement components causing matrix expansion. Tests conducted at different pressures, showed similar SBS trends. As anticipated, increased pressure resulted in more carbonation and hence higher bond strength.

Experimental investigations on cement additives were continued. The effects of magnesium oxide, hydroxyapatite, micro silica, and latex on performance of Class H and Class G cements under HPHT conditions were investigated. In addition, mineralogical properties of the samples were analyzed using Fourier Transform Infrared Spectroscopy (FTIR) to evaluate the effectiveness of the additives in preventing the carbonation of binding component of the cement (CSH and CH).

Corrosion study under low-pressure and ambient temperature is in progress. Both linear polarization (LPR) and weight-loss corrosion measurement techniques were utilized. In the presence of CO_2, as earlier tests, the instantaneous corrosion rate declined with time after reaching its maximum value during the first day of the experiment. The initial increase in the rate of corrosion is attributed to the dissolution of CO_2 that results in the formation of bicarbonates and carbonates, which accelerates the corrosion process.

Our plan for the upcoming weeks is to continue: i) aging tests at different pressures and temperatures; ii) theoretical and modeling studies on tubular corrosion; iii) additive screening and acid resistant cement development studies; iv) low-pressure corrosion experiments at different CO_2 concentrations; and v) pressure testing of corrosion test setup.

2. Overall Project Progress

2.1 Theoretical Studies (Task 1)

2.1.1 Sulfide Stress Cracking (SSC)

Sulfide stress cracking mechanisms vary for high-strength and low-strength steels. Last month report presented SSC resistance of common steels. This month report focuses on the effects of temperature and H_2S content on SSC resistance of common tubulars. A number of SSC corrosion studied (Veera and Castro 1997; Morana and Nice 2009; Cane and Cayard 1998; Hashizume et al. 2000) were performed at room and elevated temperature using different steel grades, including Q-125, and P-110. In these studies, test specimens were subjected high stress (90% of yield strength) and harsh corrosive conditions. Results (**Table 1**) showed good performance of Q-125 under corrosive environment when partial pressure of H_2S was maintained below 0.005 bars. P-110 performed slightly better than Q-125. With increasing pH, the stress intensity factor reduced. This means that, as the pH increases, lesser stress is required for crack propagation in the material. Temperature effect has been studied by Cane and Cayard (1998). **Figure 1** shows temperature versus time to failure trend. High temperatures (greater than 25°C), improve the life of the material. However, this trend changes at low temperatures (less than 25°C).

Table 1: Comparison of P-110and Q-125 performance

	P110			Q125		
p_{H2S} in bars	pH			pH		
	3.5	4.5	5.5	3.5	4.5	5.5
0.001	-	-	-	NF	NF	
0.005	NF	-	-	-	NF	-
0.010	452	627	NF	-	575	NF
0.100	-	21-38	NF	-	-	72
0.500	-	-	25	-	-	-

NF = no failure in 720 hours

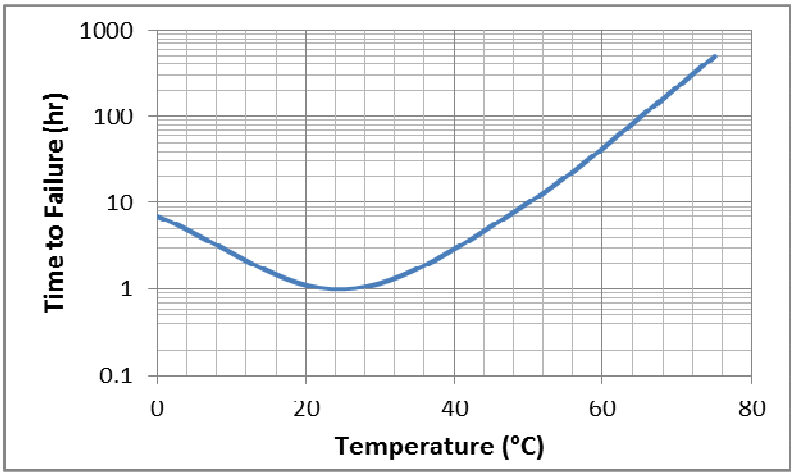

Fig. 1: Temperature effect on time to failure

2.2 Experimental Studies on Degradation of Cement (Task 2)

2.2.1 Porosities and Permeabilities of Baseline Cements

During this reporting period, two batches (Batches 23 and 24) of baseline cement cores were aged. The aging conditions for these tests are shown in **Table 2**. Test matrix (**Table 3**) is developed to examine the effects of pressure on the degradation behavior of cement cores at 225°F and CO_2 concentration. The test matrix will be completed in the coming weeks.

Table 2: Test parameters for aging experiments conducted to date

Batch #	Temp. (ºF)	Pressure (psi)	Partial Pressure %			Brine Conc. (%)	Aging Period (days)	Experiment #
			CH_4	CO_2	H_2S			
001	350	9000	100	0	0	9	6	1
002	350	6000	100	0	0	2	14 & 28	2
003	350	6000	100	0	0	2	14	
004	350	6000	90	10	0	2	6	3
005	350	6000	90	10	0	2	14 & 28	4
006	350	6000	90	10	0	2	14	
007	225	6000	90	10	0	2	14	5
008	100	6000	90	10	0	2	14	6
009	225	6000	60	40	0	2	14	7
010	225	6000	0	100	0	2	14	8
011	100	6000	60	40	0	2	14	9
012	100	6000	0	100	0	2	14	10
013	350	6000	60	40	0	2	14	11
014	350	6000	0	100	0	2	14	12
015	225	6000	60	40	0	2	14	7A
016	350	3000	60	40	0	2	14	13
017	350	9000	60	40	0	2	14	14
018	350	3000	0	100	0	2	14	15
019	350	9000	0	100	0	2	14	16
020	350	3000	90	10	0	2	14	17
021	350	9000	90	10	0	2	14	18
022	225	3000	60	40	0	2	14	19
023	**225**	**9000**	**60**	**40**	**0**	**2**	**14**	**20**
024	**225**	**3000**	**0**	**100**	**0**	**2**	**14**	**21**

Table 3: Test matrix for aging experiments at 225°F

Pressure (psi)	10% CO_2	40% CO_2	100% CO_2
3000 psi	Batch 026	Batch 022	**Batch 024**
6000 psi	Batch 007	Batch 015	Batch 010
9000 psi	Batch 027	**Batch 023**	Batch 025

Figure 2 demonstrates the porosity-permeability for samples aged for 14 days at 3000 and 6000 psi, 100% CO_2 at 225°F. The porosity trends are consistent with the trends of permeability for both Class H and Class G cement samples. With increasing pressure, porosity and permeability first decreased and then increased. At lower pressure, carbonation and hydration reactions dominate the degradation process; however, leaching becomes the dominant process offsetting the effect of carbonation leading to porosity and permeability increases as the pressure increases.

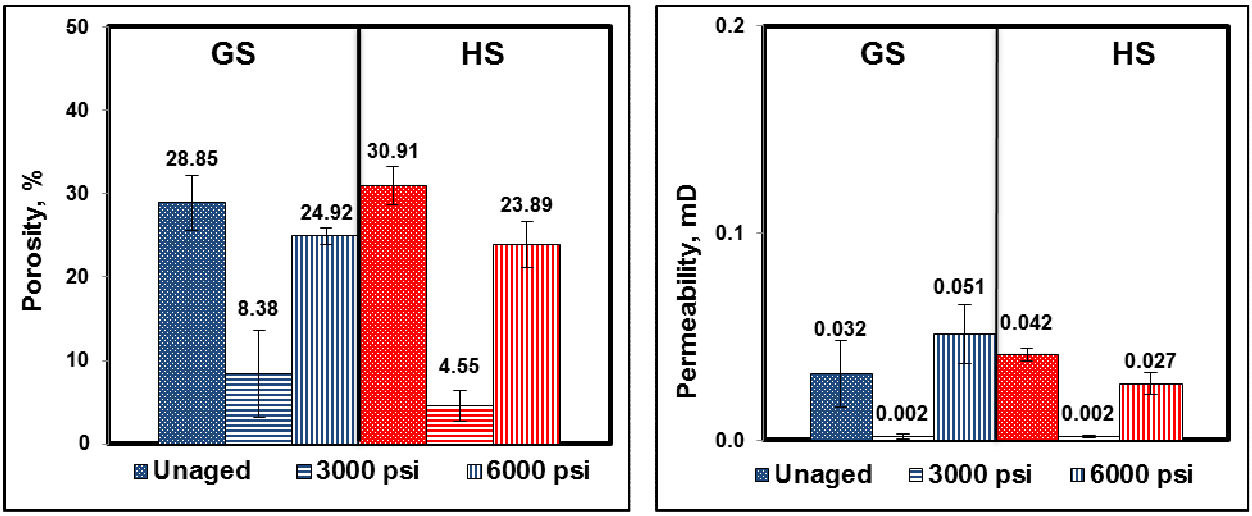

(a) (b)

Fig. 2: Effects of aging pressure on porosity and permeability of baseline cores aged at 225˚F and 100% CO_2

Figure 3 illustrates porosity and permeability of samples aged for 14 days in brine saturated with 100% CO_2 gas at 350°F and different pressures (3000 and 6000 psi). The trends of porosity and permeability are consistent for both Class G and Class H cements. Moreover, the porosity and permeability results follow similar patterns observed at 225°F.

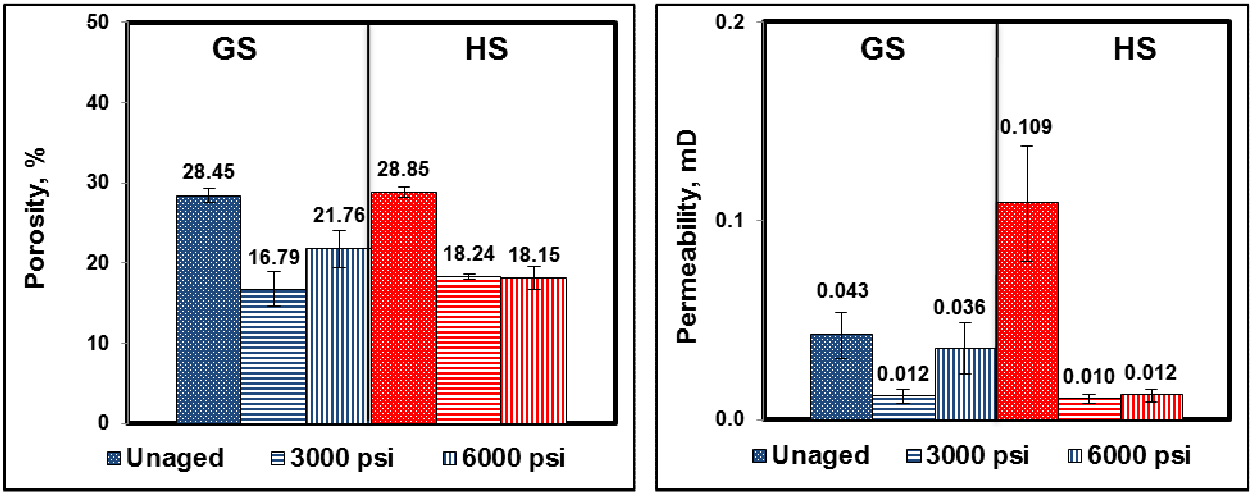

(a) (b)

Fig. 3: Effects of aging pressure on porosity and permeability of baseline cores aged at 350F and 100% CO_2

Figures 4 and **5** demonstrate the effects of CO_2 concentration on porosity and permeability of aged samples at 3000 psi and different temperatures (225°F and 350°F). For both class of cements, the porosity and permeability trends are consistent. At low temperature (225°F), increase in CO_2 concentration reduced porosity and permeability of the samples. At high temperature (350°F), Class G cement showed a similar trend. However, Class H cement exhibited reduction in porosity and

permeability at 40% CO_2 and increase at 100% CO_2. This could be attributed to the leaching of the carbonated binding components such as CSH and portlandite.

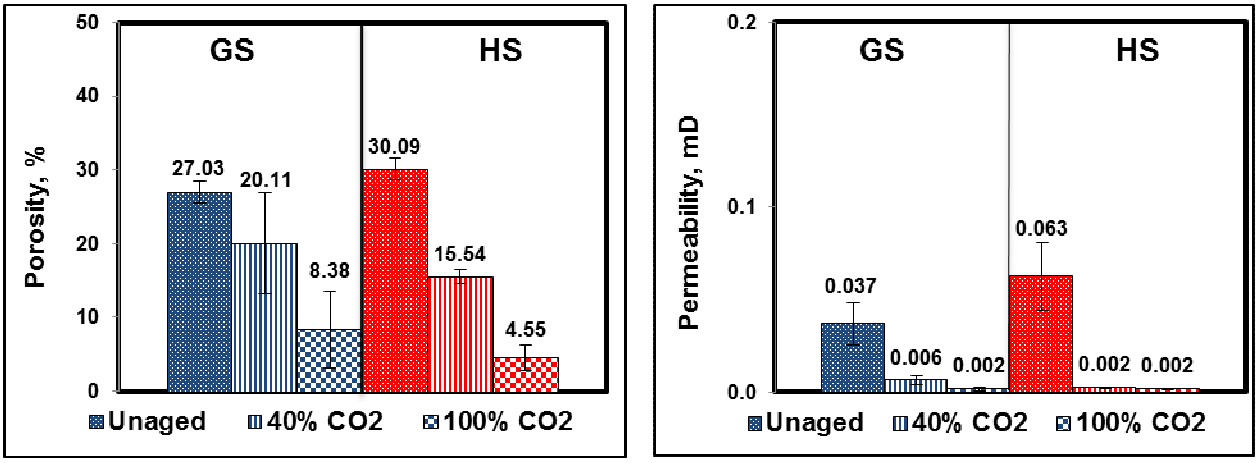

(a) (b)

Fig. 4: Effects of CO_2 concentration on porosity and permeability of baseline cores aged at 225°F and 3000 psi

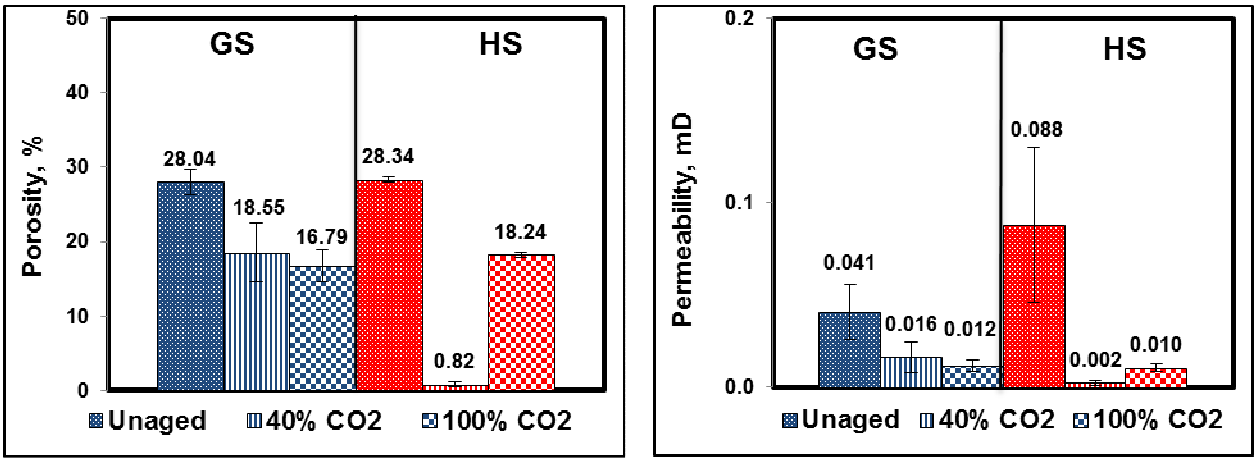

(a) (b)

Fig. 5: Effects of CO_2 concentration on porosity and permeability of baseline cores aged at 350°F and 3000 psi

Figures 6 and **7** show the effects of CO_2 concentration on porosity and permeability of aged samples at 6000 psi and different temperatures (225°F and 350°F). There is no specific trend that can be observed from the results. For Class H cement, the porosity and permeability trends are inconsistent. Porosity and permeability trends of Class G cement are consistent at 225°F.

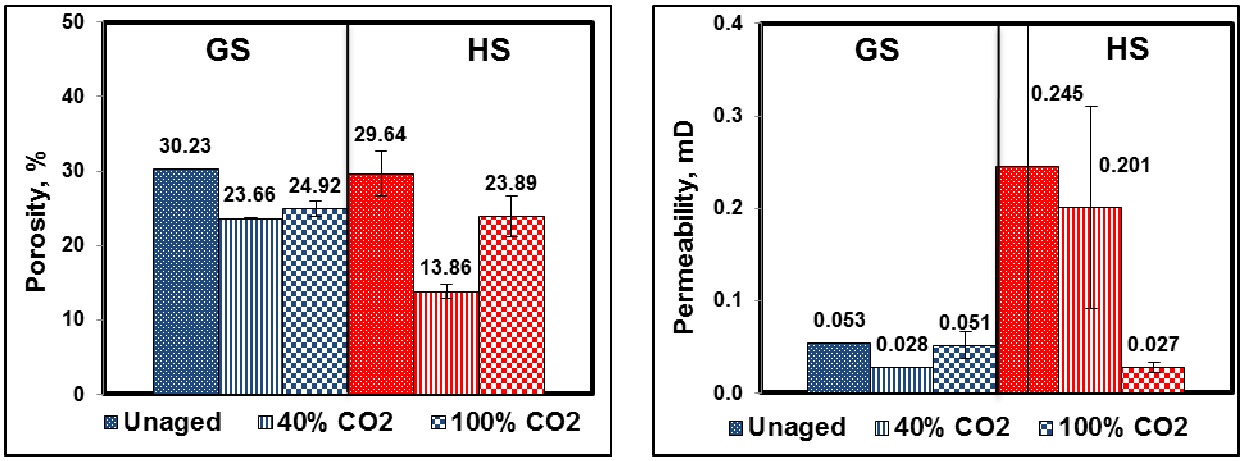

(a) (b)

Fig. 6: Effects of CO2 concentration on porosity and permeability of baseline cores aged at 225°F and 6000 psi

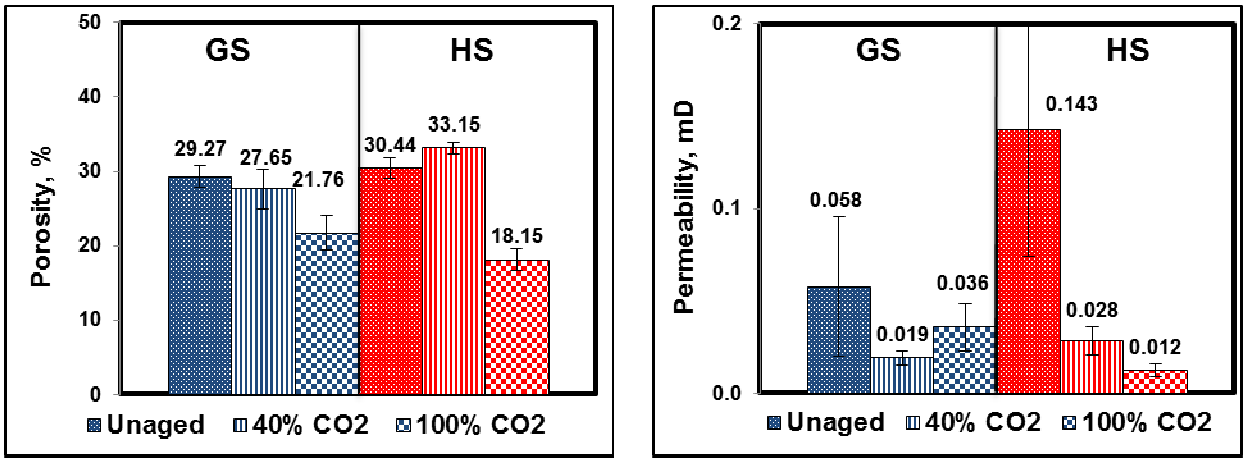

(a) (b)

Fig. 7: Effects of CO_2 concentration on porosity and permeability of baseline cores aged at 350°F and 6000 psi

2.2.2 Compressive Strengths of Baseline Cements

Compressive strength measurements of conventional cement samples are presented in this section. These measurements (Batch 23 are 24) are a further step in investigating the effect of pressure, temperature and CO_2 concentration on compressive strength of aged cement samples. Conditions in the aging cell for each of this batch are summarized in Table 2.

Figure 8 presents the compressive strength measurements for Batch 23. After aging for 14 days in saturated brine with 40% CO_2 gas at 225°F and 9000 psi, compressive strength of both cements increased due to carbonation. High aging pressure and temperature accelerate the rate at which low concentration carbonic acidic reacts with portlandite and calcium silicate hydrate present in the cement matrix. Usually, most of the portlandite is consumed first and while this occurs, cement integrity is

protected by calcium silicate hydrate. In addition, further phase transformation of calcium silicate hydrate at elevated temperature may also contribute to strength evolution or retrogression.

The new measurements are compared with previous results (Batch 9 and Batch 22). Batches 9, 22 and 23 were all aged at temperature of 225°F, 40% CO_2 concentration and 2% brine concentration for 14 days; however, the aging pressure was varied. The results show (**Fig. 9**) consistent strength gain in both cement partly due to formation of scawtite in trace amount (incomplete carbonation at low aging pressure) and complete carbonation at high aging pressure. In Class G cement, onset of leaching occurs at extremely high pressure (9000 psi) while strength is sustained in Class H cement at this pressure due to its CO_2-resistant nature. The porosity data presented in **Fig. 10** supports the compressive strength results.

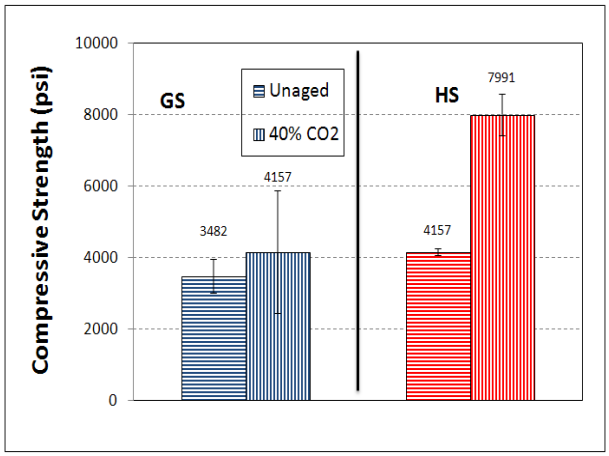

Fig. 8: Compressive strength of Batch 23 samples

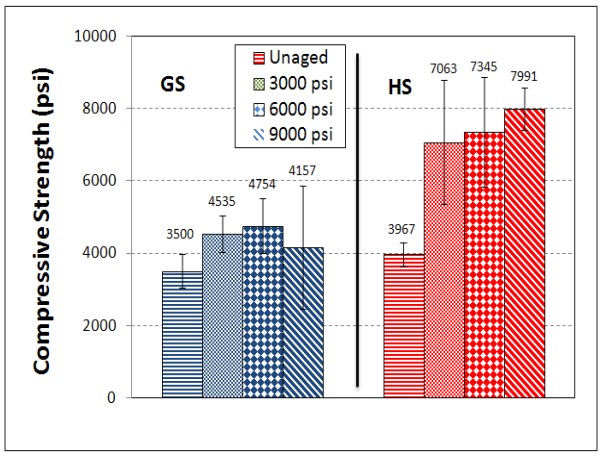

Fig. 9: Effect of pressure on compressive strength at 225°F and 40% CO_2 concentration

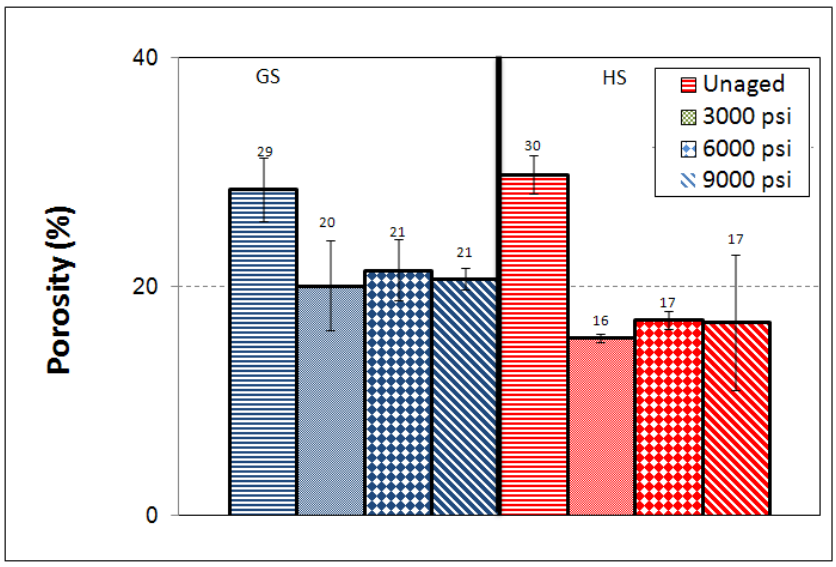

Fig. 10: Effect of pressure on porosity at 225°F and 40% CO_2

Effect of temperature on compressive strength is examined by comparing results of Batch 23 with Batch 17. Both batches were aged at 40% CO_2 and 9000 psi in 2% brine for 14 days. Temperature was the only variable. The results are presented in **Fig. 11**. In both cements, strength development persists up to 225°F due to carbonation, beyond which leaching becomes dominant at higher temperature (350°F).

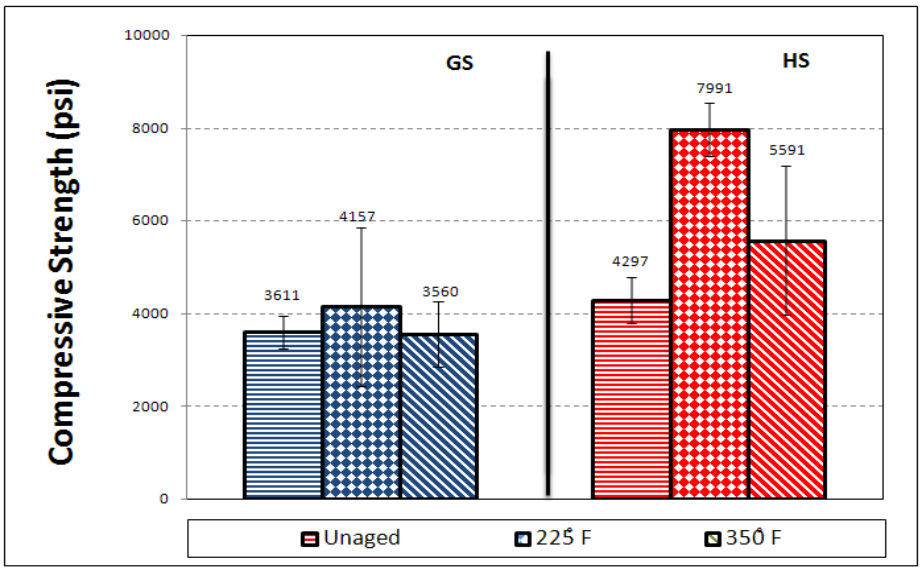

Fig. 11: Effect of temperature on compressive strength at 100% CO_2 and 3000 psi

Previous experimental data from other batches are compared with Batch 24 measurements (**Fig. 12**). All the batches were aged at 225°F, 100% CO_2 concentration and 2% brine concentration for 14 days. Only aging pressure was varied. At low aging pressure (3000 psi), strength initially increased in both cements due to the presence of traces of scawtite. However, when the pressure increased to 6000 psi, most of the scawtite was fully carbonated; hence, the formation of calcite resulted in increased strength. In Class G cement, consistent strength gain was observed with aging pressure. This is because of increased solubility of carbon dioxide at high pressure, thereby favoring precipitation of calcium carbonate. Similar trend can be observed for Class H cement at all pressures, except at 6000 psi. Generally, Class H cement showed better performance than Class G cement under high-pressure high-temperature conditions.

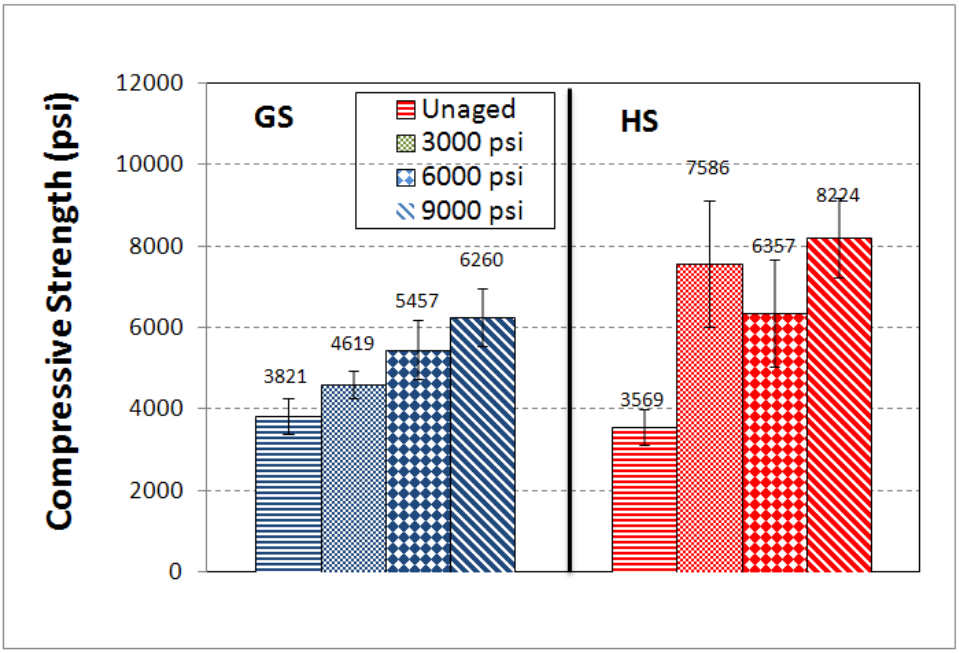

Fig. 12: Effect of pressure on compressive strength at 225°F and 100% CO_2 concentration

2.2.3 Shear Bond Strengths of Baseline Cements

Study on shear bonding strength (SBS) of Class H cement was continued. In this report, the effects of CO_2 concentration on shear bond strength at 225°F and 350°F are presented. **Figure 13** shows influence of CO_2 concentration on bond strength at 225°F for two different pressures (3000 and 9000 psi). The SBS increased with CO_2 concentration because of carbonation, which causes the cement to expand. Tests conducted at different pressures, showed similar SBS trends. As expected, increased pressure results in additional carbonation and hence higher bond strength.

Tests conducted at 350°F show a different trend (**Fig. 14**). The SBS increased as the concentration of CO_2 was increased from zero to 40 percent. However, when the concentration increased to 100%, a reduction in bond strength was observed. At low concentrations (< 40%), carbonation of the cement dominated the leaching process leading to improved strength. As the CO_2 concentration increases, additional CO_2 dissolves in brine resulting in high carbonic acid concentration in solution. This condition facilitates the leaching process causing the SBS to reduce. Tests conducted at high pressure (9000 psi), showed similar SBS trend that indicates maximum SBS at 40% CO_2 concentration. Increased pressure slightly increased the SBS.

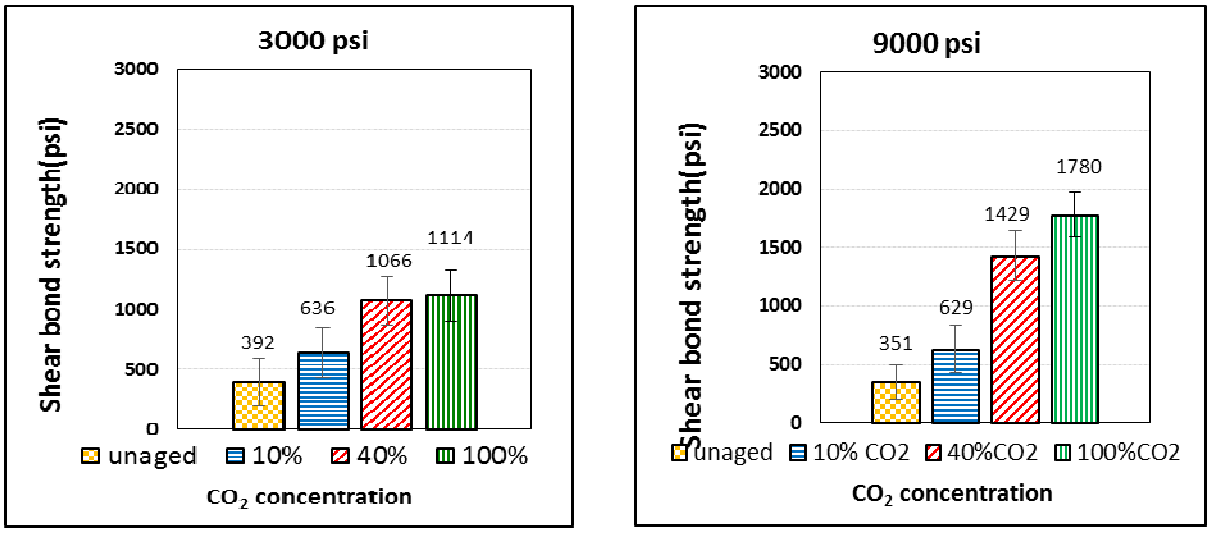

Fig. 13: Influence of CO_2 concentration on shear bond strength at 225°F

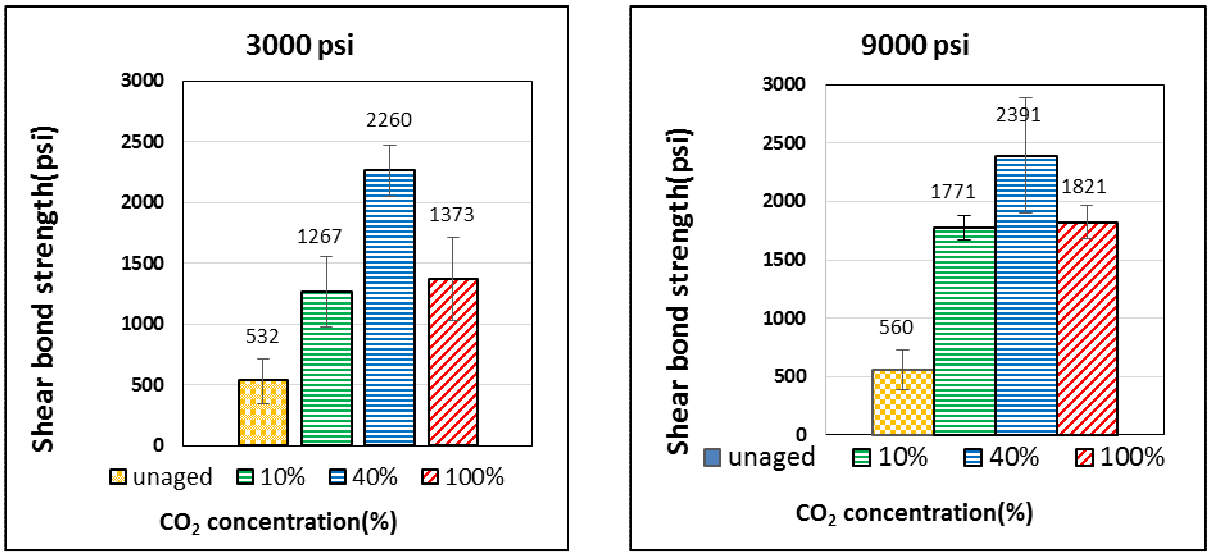

Fig. 14: Influence of CO_2 concentration on shear bond strength at 350°F

2.2.4 Additive Screening and Cement Formulation Studies

The testing of the additives was continued. Experimental results, which were not presented in the previous report, are included here. During this reporting period, MgO samples (MGO-5) were prepared with 5% BWOC of cement and tested at 9000 psi and 225°F. The CO_2 concentrations were 40% and 100% for the experiments. Although Class H cement was able prevent carbonation of the matrix, the compressive strength of Class G cement was reduced and its porosity increased. These results indicate that Class G is not able to perform better with MgO as an additive.

The aging experiment with micro-silica containing samples was performed and the properties of the cores were measured. Despite showing increased porosity and permeability, micro-silica samples

exhibited presence of CSH in the inner most zone of the matrix, which confirms non-carbonation of the CSH group. Moreover, hydroxyapatite based cement samples were also aged and results were found to be consistent with our previous measurements. The first batch of latex and micro silica based cement slurry was tested in aging cell and the results are presented henceforth. The samples showed the presence of CSH component in the matrix indicating lesser carbonation.

2.2.5.1 Magnesium Based Oxide Cement

Tests with MGO-5 samples were continued. The samples were subjected to aging conditions as shown in **Table 4**. The composition of the slurry was similar to the previous experiments. It should be noted that the MgO content has been reduced to 5%, unlike the composition mentioned in Report # 22. The 10% MgO cement (MGO-10) was tested only to observe the amount of expansion with increase in concentration. After aging, the properties of the cores were measured. The results are presented in **Figs. 15** and **16**. The data presented as "unaged" refers to groups of core samples maintained at ambient lab conditions for 14 days while other samples were aged at elevated temperature and pressure.

Table 4: Aging conditions for the MGO-5 samples

MGO-5	Temp. (°F)	Pressure (psi)	CO_2 (%)	NaCl (%)	Days	Baseline	Exp. No.
Batch 006	225	9000	40	2	14	Batch 023	20

Porosity and Permeability Measurements

For unaged samples, the porosity and permeability of the MGO-5 samples are lower than those of the baseline samples (Fig. 15a). The aging process caused the porosity and permeability of baseline samples to reduce due to carbonation. However, MgO samples showed almost similar porosity after aging. This can be attributed to the presence of MgO which results in the formation of $Mg(OH)_2$ in the matrix and reduces porosity and permeability even at unaged condition. The reduced porosity leads to lesser penetration of carbonic acid in the matrix and hence minor porosity change. All samples, except GSMG showed reduction in permeability after aging. The reverse permeability trend is mainly due to high sensitivity of permeability towards the physical phenomenon. The porosity and permeability trends are consistent.

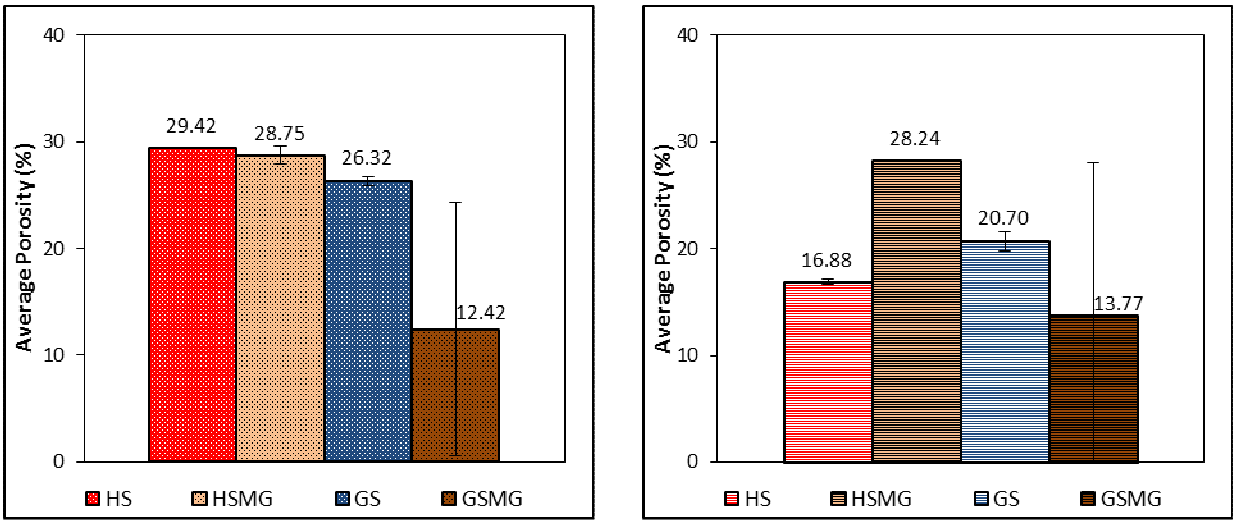

Fig. 15: Porosities of MGO-5 and baseline cements: a) unaged; and b) aged for 14 days at 225°F and 9000 psi in brine saturated with 40% CO_2 gas

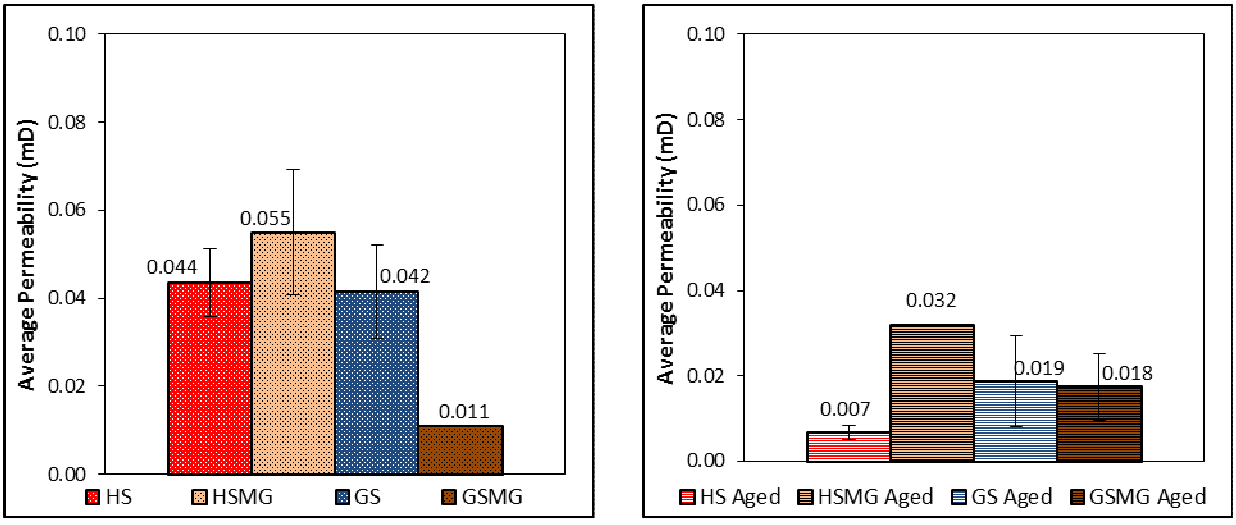

Fig. 16: Permeabilities of MGO-5 and baseline cements: a) unaged; and b) aged for 14 days at 225°F and 9000 psi in brine saturated with 40% CO_2 gas

Compressive Strength Measurements

Compressive strengths of MGO-5 and baseline cements are presented in **Fig. 17**. The compressive strength of unaged HSMG samples was significantly lower than those of baseline cores. However, GSMG samples exhibited more or less the same compressive strengths as the baseline samples. Hence, the formation of $Mg(OH)_2$ did not increase the initial compressive strength after hydration.

After aging, all samples showed increased strength. Compressive strengths of MGO-5 samples were substantially increased due to further hydration of MgO, and carbonation of $Mg(OH)_2$ and $Ca(OH)_2$. The baseline samples displayed a lesser amount of compressive strength improvement (i.e. percentage

increase) than the MGO-5 samples. This can be due to the carbonation process, which is limited to $Ca(OH)_2$. However it was observed that the porosity of MGO-5 samples did not change significantly after aging, which indicate lesser penetration of carbonic acid due to formation of $Mg(OH)_2$ crystals. Hence, it can be concluded that MGO-5 samples showed lesser acid penetration and consequently, lower carbonation, though they exhibited increased compressive strength due to the formation of $Mg(OH)_2$ crystals in the pore space.

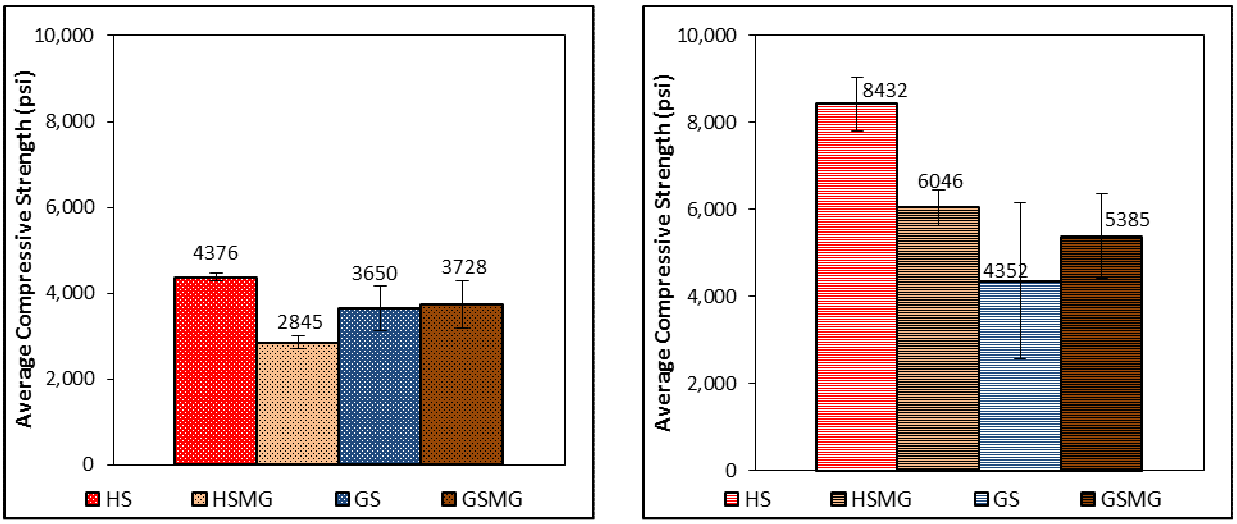

Fig. 17: Compressive strength of MGO-5 and baseline cements: a) unaged; and b) aged for 14 days at 225°F and 9000 psi in brine saturated with 40% CO_2 gas

Shear Bond Strength Measurements

The shear bond strength (SBS) measurements are presented in **Fig. 18**. The baseline HS samples showed increased SBS after aging due to carbonation and expansion of the matrix. On the other hand, HSMG samples exhibited increased SBS due to formation of $Mg(OH)_2$ crystals. It is difficult to compare the level of carbonation in the samples using the SBS data alone. Hence, FTIR tests were performed to examine the mineralogical changes occurred after aging. The FTIR spectrum is simplified in the form of bar charts for easy interpretation (**Fig. 19**). The outer and middle zones show presence of $CaCO_3$ and $MgCO_3$ only. The inner zone, however, shows presence of CSH and $Mg(OH)_2$ in the HSMG samples, indicating that the matrix has not been carbonated completely. This is good for the expansion tendency of MgO cement and helps to justify the use of MgO with Class H cement under HPHT conditions.

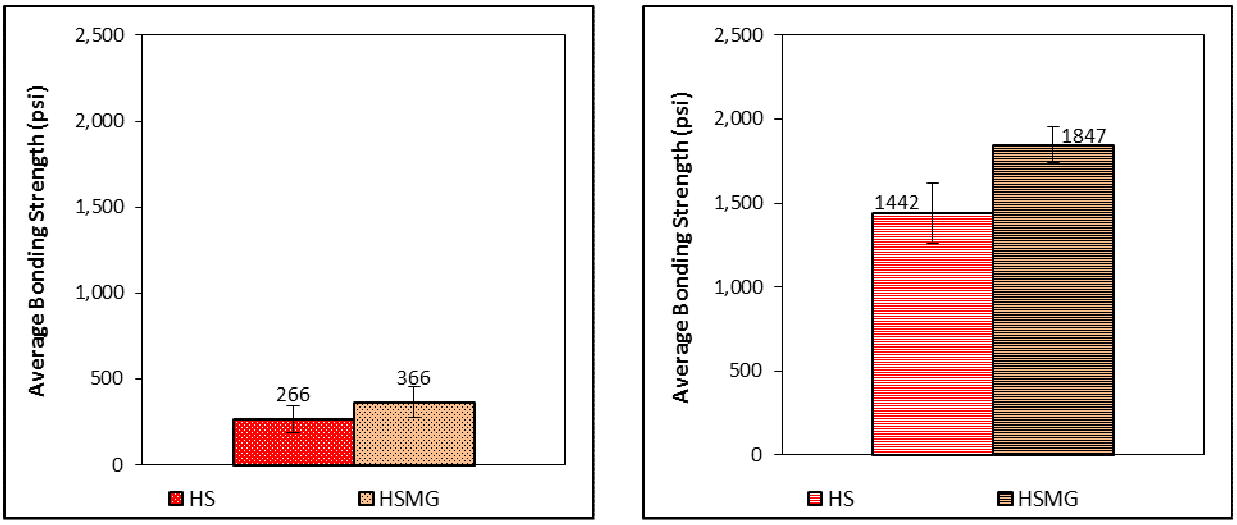

Fig. 18: Shear bond strength of MGO-5 and baseline cements: a) unaged; and b) aged for 14 days at 225°F and 9000 psi in brine saturated with 40% CO_2 gas

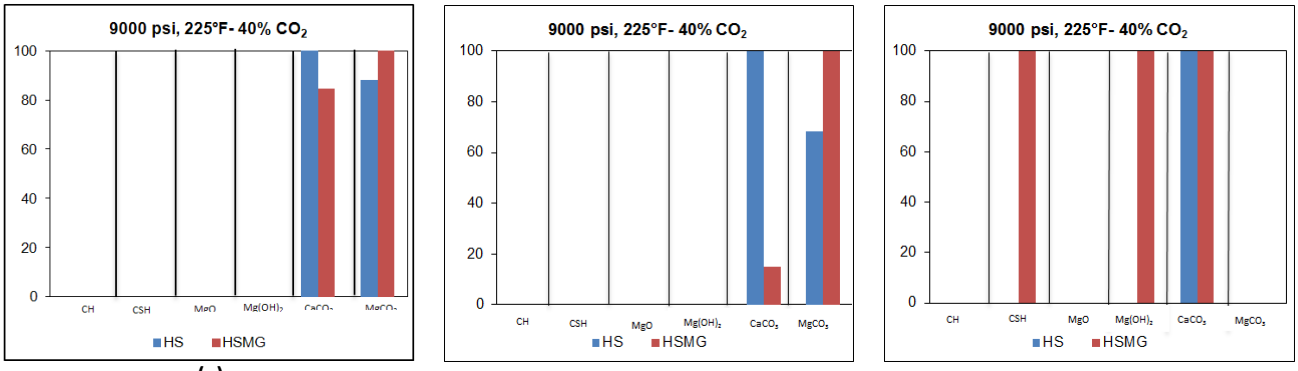

Fig. 18: Summarized FTIR data of HSMG and baseline HS samples aged at 225°F, 9000 psi, 40% CO_2 for 14 days: a) Outermost zone; b) Middle zone; and c) Innermost zone

2.2.5.2 Micro-Silica-Based Cement

Aging experiments were carried out with 10% BWOC micro silica cement (MS-10). Aging was conducted for 14 days in 2% brine saturated with 100% CO_2 gas at 225F and 3000 psi. The composition of the slurry was similar to the one presented in Report # 22.

Porosity and Permeability Measurements

The porosity and permeability measurements are presented in **Figs. 19** and **20**. Porosity and permeability of un-aged MS-10 samples were significantly lower than those of the baseline samples. This indicates the effect of micro silica as filler additive for plugging the pore spaces of the cement matrix. After aging, the porosity and permeability of the baseline samples decreased due to carbonation. It is interesting to note that the porosity of MS-10 samples increased after aging. The porosity increase confirms that the samples have not been subjected to carbonation, which would have

led to porosity reduction. However, the leaching of the matrix can cause an excessive penetration of carbonic acid. The permeability of MS-10 samples decreased after aging, indicating minimal leaching effect. This can be confirmed with FTIR analysis if the matrix still contains CSH group.

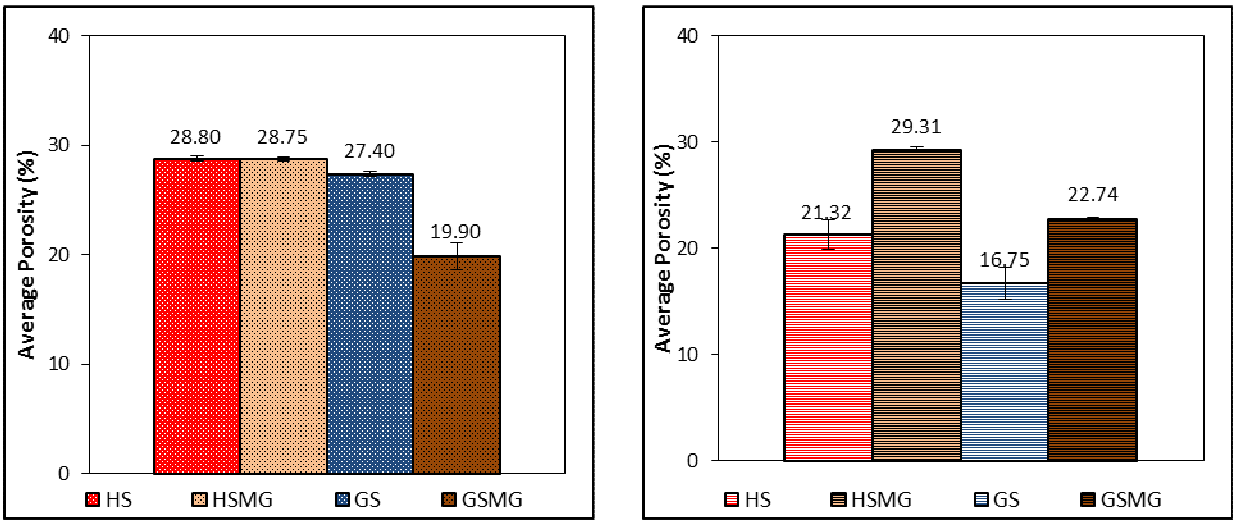

Fig. 19: Porosities of baseline and MS-10 cements: a) Un-aged; and b) Aged at 225°F, 9000 psi, 2% brine saturated with 100% CO_2 for 14 days

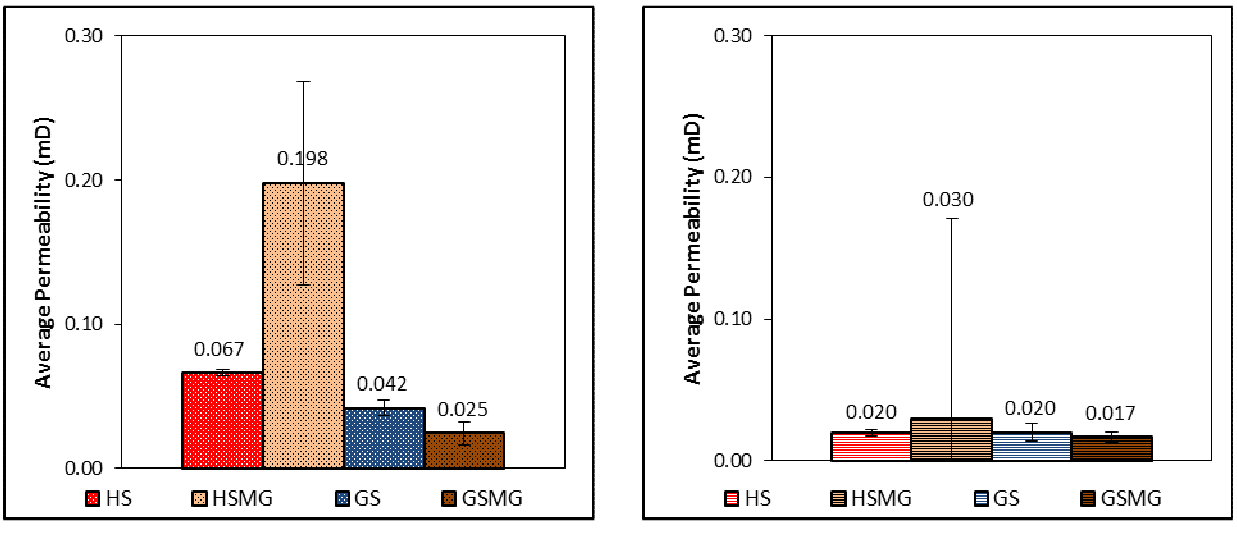

Fig. 20: Permeabilities of baseline and MS-10 cements: a) Un-aged; and b) Aged at 225°F, 9000 psi, 2% brine saturated with 100% CO_2 for 14 days

FTIR spectra of MS-10 and baseline samples are summarized in **Fig. 21**. FTIR results of micro silica samples show no peak for CH group and hence it shall not be used to compare the results with baseline samples. The outermost zone shows presence of only $CaCO_3$ as it is the most exposed part. The middle and innermost zones show presence of CSH and $CaCO_3$ in both baseline and MS-10 samples.

It can be observed that CSH is present in both HS and HSMS samples. However, an interesting observation can be made that, even with increased porosity of MS-10 samples, CSH was preserved in the middle and inner zone of the samples. Hence, micro silica was able to prevent complete carbonation of the cement even after exhibiting increased porosity and permeability.

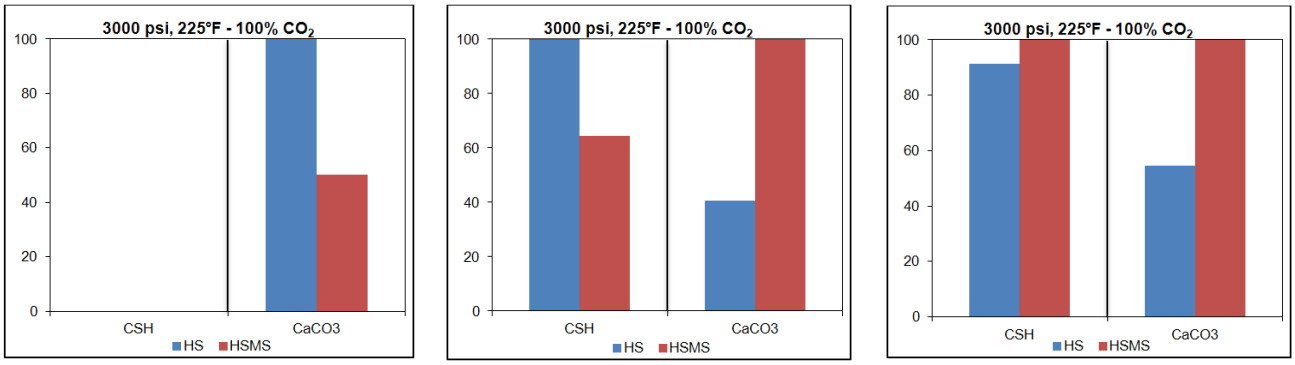

Fig. 21: Summarized FTIR data of MS-10 and baseline HS samples aged at 225°F, 9000 psi, 100% CO_2 for 14 days: a) Outermost zone; b) Middle zone; and c) Innermost zone

Compressive and Shear Bond Strength Measurements

The compressive strength tests were not conducted due to problems with lab equipment. The results will be presented in the next month report. The shear bond strength measurements are presented in **Fig. 22**. An increase in bond strength is observed for both baseline and MS-10 samples. However, less bond strength was observed with MS-10 samples because of lesser expansion. Hence, it can be interpreted that micro silica samples have been subjected to lesser carbonation.

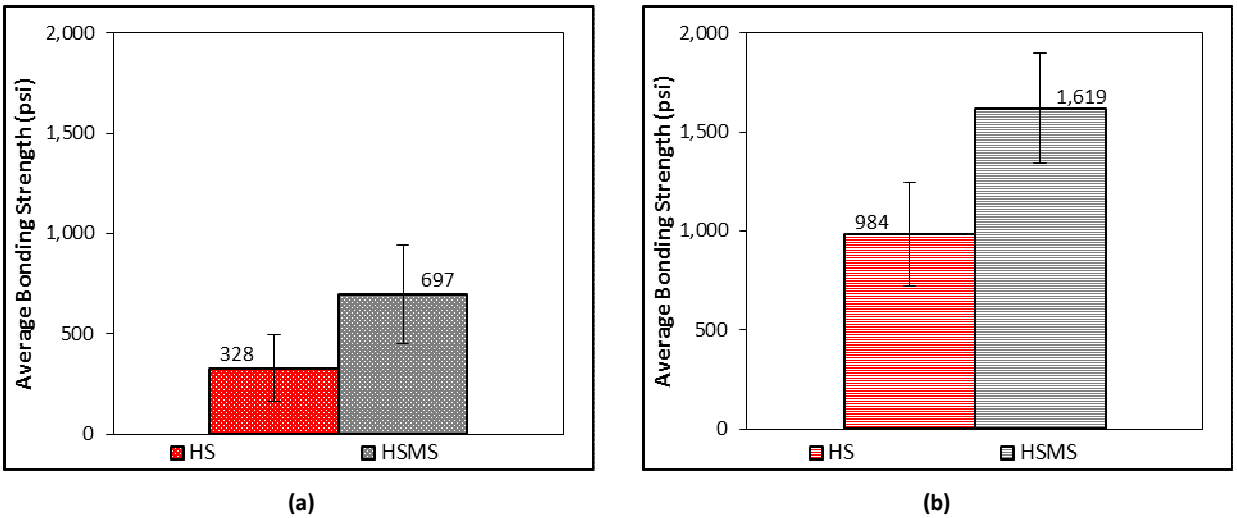

Fig. 22: Shear bond strength of baseline and MS-10 samples: a) un-aged; and b) aged for 14 days in 2% brine saturated with 100% CO_2 gas at 225°F and 3000psi

2.2.5.3 Latex-Based Cement

Testing with conventional SBR latex was continued. The slurry properties of 10% latex + 10% micro silica (LTMS) were discussed in previous monthly report. The unaged properties of the hardened cement are presented here. The porosities of LTMS and baseline samples are almost similar; however, their permeabilities differ significantly (**Fig. 23**). Having low porosity and permeability is beneficial to the cement as it lowers the penetration of carbonic acid into the matrix. The compressive strengths of the LTMS samples were seen to be lower than those of the baseline samples; however, still higher than accepted industry standards. The shear bond strengths of the LTMS samples were also higher than baseline samples (**Fig. 24**). These results show that the physical and mechanical properties of the samples are in the accepted range when compared with the properties of baseline samples. Hence, LTMS samples will be prepared and aged under high pressure and high temperature acidic environment.

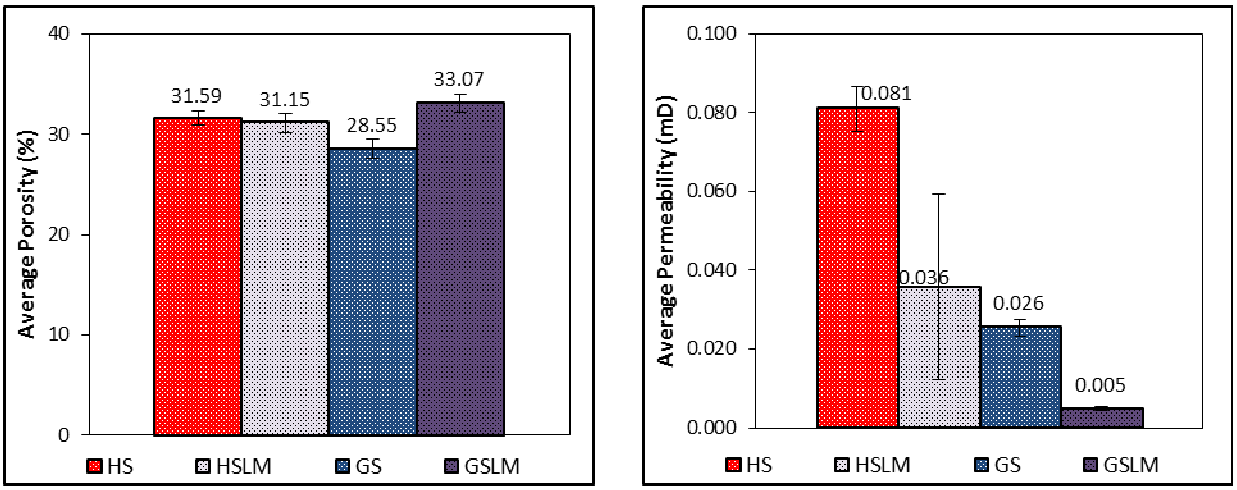

(a) (b)

Fig. 23: Porosity and permeability of un-aged LTMS and baseline samples (Batch 022)

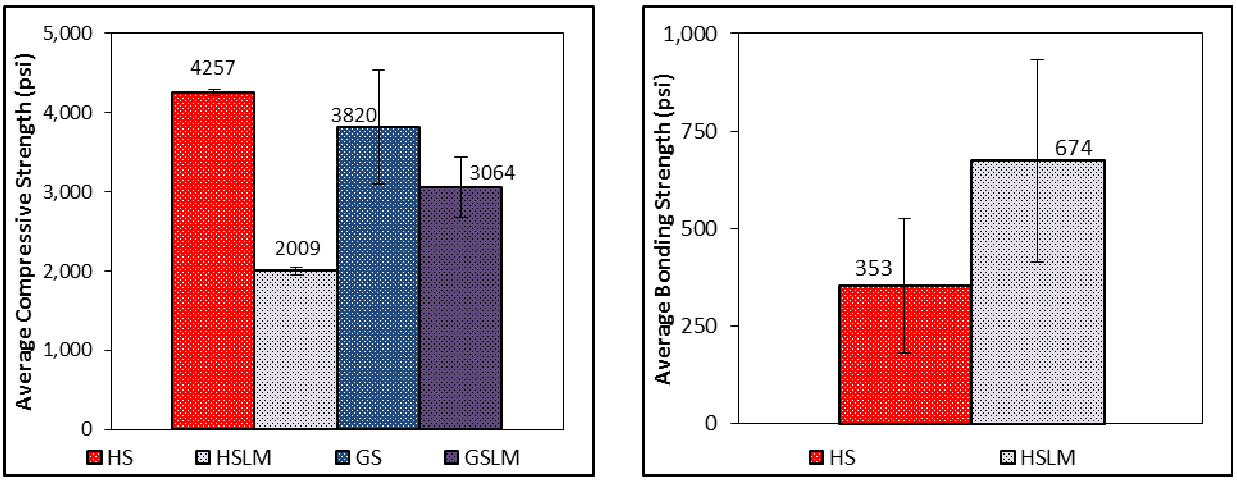

(a) (b)

Fig. 24: Compressive and bond strengths of un-aged LTMS and baseline samples (Batch 022)

2.3 Experimental Studies on Corrosion of Tubulars (Task 3)

In the last monthly report, we have presented the results for three corrosion experiments (Exp. 12, 13, and 14) conducted using high carbon steel (1045) samples. The samples were aged in 2% brine and presence of CO_2 gas. This report presents results and analysis of three similar experiments (Exp. 15, 16, and 17). Like the previous experiments, all tests presented in this report were carried out for 187 hours varying partial pressure of CO_2 and N_2. Tests were performed at 120 and 240 psi, and ambient temperature of 78°F. Test parameters and results of these experiments are summarized in **Table 5**. Experiment 17 was not completed due to leakage of CO_2 from the autoclave. Hence, the results of this experiment will not be presented.

Table 5: Test parameters and results of low-pressure corrosion experiments

Exp. #	Temp. (ºF)	Pressure (psi)	Partial Pressure %		Brine Conc. (%)	Test Period (days)	Results (mpy)	
			N_2	CO_2			LPR	WL
15	78	120	25	75	2	187	40.30	31.91
16	78	120	0	100	2	187	39.18	32.18
17	78	240	0	100	2	187	NA	NA

Figure 25 presents instantaneous corrosion rate measured using LPR method during Exp. 15 (test with 75% CO_2). The trend did not show any anomaly. The average corrosion rate was 40.30 mpy. Corrosion rate based on weight loss (WL) method was 31.91 mpy, indicating good agreement with the LPR method. Furthermore, corrosion rate of 38.31 mpy is obtained using a model developed in this study. A similar result (**Fig. 26**) was obtained when the CO_2 concentration was increased to 100% in Experiment 16. The average corrosion rate was 39.18 mpy; and using the WL method and the model it was 32.18 mpy and 35.09 mpy, respectively. Measurements and model prediction show a very close agreement. Future tests will be carried out varying the total pressure, temperature, and CO_2 concentration.

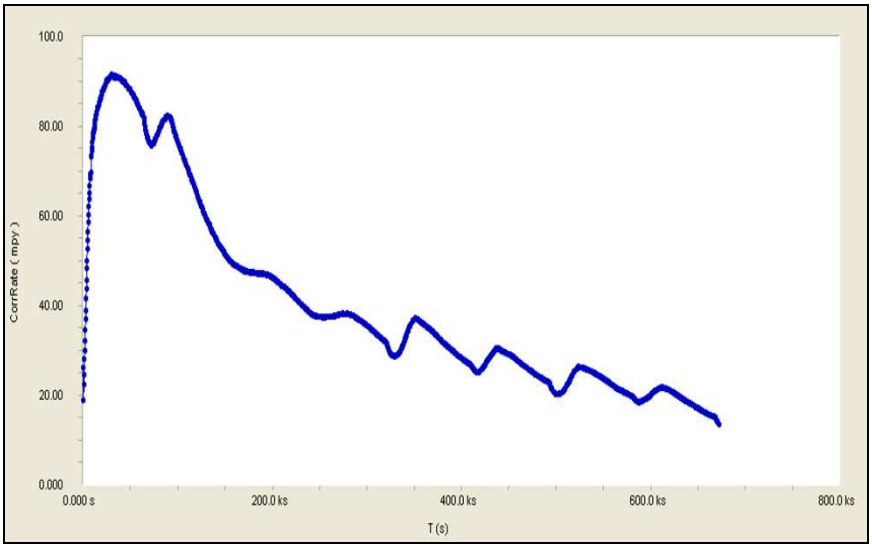

Fig. 25: Corrosion rate vs. time for Exp. 15 (75% CO_2 gas, 120 psi)

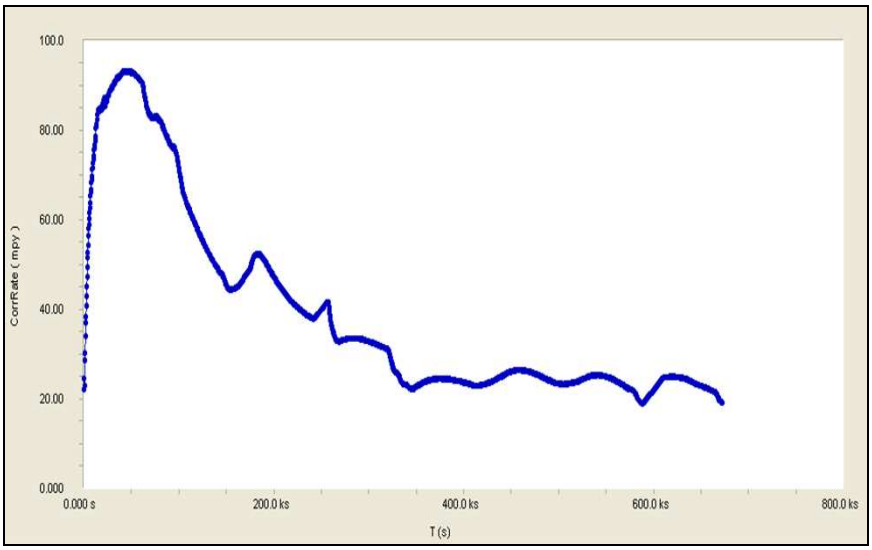

Fig. 26: Corrosion rate vs. time for Exp. 16 (100% CO2 gas, 120 psi)

3. Problems Encountered

Mini-pipe specimens are needed for stress cracking corrosion experiments. According to our original plan, ¾" diameter specimens (**Fig. 27a**) were considered for the experiments. However, we were unable to obtain very thick-walled, high strength casing pipe samples to manufacture the specimens. Therefore, the mini-pipe design had to be revised and the diameter was reduced to ½" (**Fig. 27b**). However, the local machining shops indicated that they cannot provide a quotation for manufacturing the ½" mini-pipe due to its small size. Shops are worried about maintaining uniform wall thickness, which is critical for the measurement. We are negotiating with one of the shops to perform pre-manufacturing tests to produce the mini-pipe.

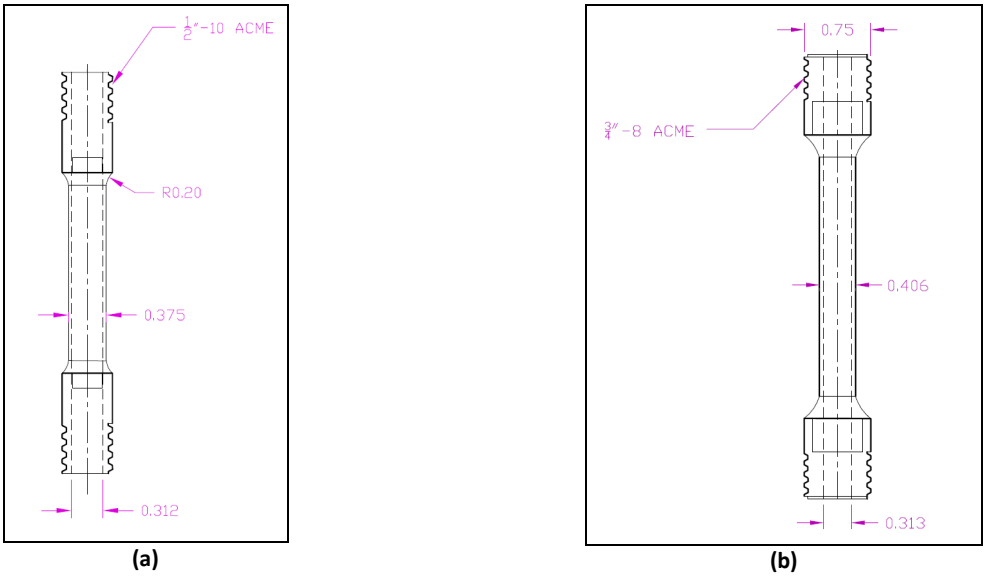

Fig. 27: Mini-pipe designs: a) ½" size; and b) ¾" size

4. Planned Activities

- Continue aging experiments with brine-CO_2-CH4 system for 14 days varying aging pressure (3,000, 6000, and 9000 psi) and CO_2 concentration (10%, 40% and 100%) at 350°F and 225°F.
- Continue theoretical and modeling studies on tubular degradation.
- Continue cement additive screen and acid resistant cement formulation studies.
- Begin testing of the corrosion experiment setup.

5. Project Expenditures

This section presents the project expenses during the month of September (**Table 6**) and the cumulative expenditures.

Table 6: Current and cumulative expenditures, September 2013

No.	Budget Categories	Current Expenses	Cumulative Expenses
1	Salaries & Wages	$7,576.92	$228,992.30
2	Fringe Benefits	$1,293.14	$53,135.03
3	Project Materials	$219.30	$58,291.49
4	Travel	$41.25	$6,092.78
5	Conference Expenses	$0.00	$0.00
6	Other Direct Costs	$0.00	$993.60
7	Equipment	$788.84	$237,267.33
8	Space Rental	$0.00	$0.00
9	Indirect Cost	$4,565.31	$173,752.57
10	**Total**	**$14,484.76**	**$758,525.10**

Nomenclatures

BWOC	By weight of cement
CH	Calcium hydroxide
CSH	Calcium silicate hydrate
FTIR	Fourier Transform Infra-Red
GS	Class G cement with silica flour
GSMG	Class G Cement with silica flour and magnesium oxide
GSLM	Class G Cement with silica flour, latex and micro silica
GSLT	Class G Cement with latex
HPHT	High-pressure high-temperature
HS	Class H cement with silica flour
HSHO	Class H Cement with silica flour and hydroxyapatite

HSMG	Class H Cement with silica flour and magnesium oxide
HSLM	Class H Cement with silica flour, latex and micro silica
HSLT	Class H Cement with latex
LPR	Linear polarization resistance
LTMS	Cement with latex and micro silica additives
mpy	mils per year
MGO	Magnesium oxide containing cement
MGO-5	Cement containing 5% BWOC MgO as additive
MGO-10	Cement containing 10% BWOC MgO as additive
MS	Micro silica containing cement
MS-10	Cement containing 10% BWOC micro silica as additive
NACE	National Association of Corrosion Engineers
SBS	Shear bonding strength
SCC	stress corrosion cracking
SSC	Sulfide Stress Cracking
XRD	X-Ray diffraction

References

Cane R.D. and Cayard M.S. 1998. Roles of H_2S in Behavior of engineering alloys: A review of literature and experience, Paper no. 274, NACE International Annual Conference, March 22 - 27, 1998 , San Diego, CA.

Hashizume, S., Inohara, Y. and Masamura, K. 2000. Effects of pH and P_{H2S} on SSC Resistance of Martensitic Stainless Steels, Paper No.130, NACE International Annual Conference, March 26 - 31, Orlando, FL.

Morana R. and Nice P.I. 2009. Corrosion assessment of High Strength Carbon Steel Grades P-110, Q-125,140 and 150 for H2S containing producing well environments, Paper No. 9093, NACE International Conference and Expo, March 22 - 26, Atlanta, GA.

Vera, J.R and Castro, J. 1997. The Relationship between Hydrogen permeation and Sulfide Stress cracking Susceptibility of OCTG materials at different temperatures and pH Values, Paper No. 47, NACE International Conference, Houston, TX.

Project Title: Effect of H_2S and CO_2 in HPHT Wells on Tubulars and Cement

Report Type: Monthly Report

Report #: 25

Reporting Period: September 22nd, 2013 to October 21st, 2013

Authors:

Ramadan Ahmed, Principal Investigator

Subhash Shah, Co-Principal Investigator

Samuel Osisanya, Co-Principal Investigator

Rida Elgaddafi, Research Assistant

Omotayo Omosebi, Research Assistant

Himanshu Maheshwari, Research Assistant

Adarsh Naidu, Research Assistant

Aman Srivastava, Research Assistant

Jueun Hwang, Research Assistant

Mounraj Sharma, Research Assistant

Sagar Tale, Research Assistant

Prepared under BSEE Project # E12PC00035

by

THE UNIVERSITY OF OKLAHOMA

January 3, 2014

1. Summary of Accomplishments

This monthly report presents the progress made during the project period September 22, 2013 to October 21, 2013. Degradation studies on cement and tubular were continued. Cement cores and bonding samples of different cement formulations were prepared and aged in acidic environment to examine their degradation characteristics. Different acid resistant cement slurries and cores were papered and tested under different aging conditions.

Two aging experiments (Experiments 21 and 22) were completed during this month. The samples were aged for 2 weeks in 2% brine saturated with CO_2 containing methane gas. Porosity, permeability, and compressive and bond strengths of unaged and aged samples were measured. Recent measurements were combined with previously obtained results. For most of the cement cores tested, the porosity and permeability trends were consistent.

For tests conducted at high CO_2 concentration (100% CO_2), with increasing pressure, porosity and permeability first decreased and then increased. This shows that, at lower pressure, carbonation and hydration reactions dominate the degradation processes. As the pressure increases, leaching intensifies due to increased CO_2 solubility, which offsets the effect of carbonation leading to porosity and permeability increases. However, at very high pressure (9000 psi), formation of dense crystals plugs the pores and capillaries leading to reduced porosity and permeability. Furthermore, measurements show the effects of pressure, temperature and CO_2 concentration on compressive strength of baseline cement. Increasing pressure tend to increase the carbonation leading to higher strength.

For Class G cement, temperature increase resulted in minor strength improvement at low temperature (225°F). However, the trend changes as the temperature was increased to 350°F. Class H cement showed strength improvement with increasing temperature. Additionally, increasing CO_2 concentration results in more strength development in both API oil well cements. Class H cement exhibited more strength gain than Class G possibly due to phase transformation at elevated aging temperature.

Experimental investigations on cement additives were continued. The effects of magnesium oxide and hydroxyapatite on performance of Class H and Class G cements under HPHT conditions were investigated. Fourier Transform Infrared Spectroscopy (FTIR) method is used to evaluate the effectiveness of the additives in preventing the carbonation of binding component of the cement (CSH and CH).

Corrosion study under low-pressure condition is in progress. The experimental setup has been improved to carry out test under controlled and increased temperature condition. Precise temperature control helped to eliminate periodic fluctuations in corrosion rate observed in previous tests. Both linear polarization (LPR) and weight-loss corrosion measurement techniques are being utilized in the study.

Our plan for the upcoming weeks is to continue: i) aging tests at different pressures and temperatures; ii) theoretical and modeling studies on tubular corrosion; iii) additive screening and acid

resistant cement development studies; iv) low-pressure corrosion experiments at different CO_2 concentrations; and v) pressure testing of corrosion test setup.

2. Overall Project Progress

2.1 Theoretical Studies (Task 1)

2.1.1 Effect of H_2S on Cement Degradation

When in contact with acidic fluid containing H_2S and CO_2, Portland cement degrades over a period of time, which results in loss of well integrity and zonal isolation. It is required to ensure long term integrity of cementing materials and safe continuation of operations. One can find abundant literature dealing with deterioration of cement pastes because of CO_2 environment. However, published data on the degradation mechanism due to H_2S and H_2S + CO_2 are scarce.

2.1.1.1 Effects of H_2S on Oil Well Cement

When in contact with acidic aqueous solutions, H3O+ ions penetrate within cement matrix and dissolve solid hydration products. Experimental works have shown that the rate of acid attack depends on chemical composition of cement as well as pH of the acid solution. Dissolution of ferrite and aluminate phases and induced leaching of Fe^{3+} and Al^{3+} is slower and occurs at lower pH values than the carbonation and leaching of Ca^{2+} from the cement matrix. As pH decreases, portlandite with stability pH of 12.6, CSH with stability pH of 10 to 11, calcium aluminate and ferrite hydrates are successively dissolved (Lecoiler et al. 2006).

A number of investigations (Benge 2009, Krilov et al. 2000, Kutchko et al. 2011) have been conducted to study the effect of CO_2 on oil well cement. It is well-established fact that CO_2 reacts with calcium from CH and CSH to form $CaCO_3$. Although less documented, the mechanism of cement degradation by H_2S containing fluids results in considerable increase in cement matrix porosity and weakening of cement (Lecoiler et al. 2008). Lecoiler et al. (2006) demonstrated that aging of Portland cement based materials in H_2S saturated brine results in weakening of cement due to calcium leaching (dissolution of Portlandite and decalcification of CSH. However, in presence of CO_2, H_2S reacts only with iron containing compounds (C_4AF) in cements to form pyrite and ettringite while the formation of carbonates is due to the reaction of CH and CSH with CO_2 only (Jacquemet et al. 2011).

Prasad et al. (2006) have studied the effects of sulfate on cement and concrete at ambient temperatures. They observed three modes of deterioration of cement and concrete:

I. Eating away of the hydrated cement paste. This mode of deterioration is known as acidic type and attributed mainly to the formation of gypsum.
II. Reaction of sulfate to hydrated aluminates phase, forming tricalcium-sulfo-aluminate-hydrate, also called ettringite. This mode of deterioration is expansion type and attributed mainly to formation of ettringite

III. The third type of deterioration is the “onion-peeling” type.

Of these modes of deterioration, the first two are important for studying the degradation of oil well cement. They suggested that the sulfate ions SO_4^{-2} react with calcium hydroxide to form gypsum (Eqn. 1), which further reacts with calcium-aluminate-hydrate to form secondary ettringite (Eqn. 2), which is expansive in nature.

$$SO_4^{-2} + Ca^{2+} + 2H_2O \longrightarrow CaSO_4.2H_2O \quad \ldots\ldots (1)$$

$$3CaO.Al_2O_3.12H_2O + 3(CaSO_4.2H_2O) + 13H_2O \longrightarrow 3CaO.Al_2O_3.3CaSO_4.31H_2O \quad \ldots\ldots (2)$$

The sulfate ions, SO_4^{-2} may also react with calcium-silicate-hydrate to form secondary ettringite. Since sulfate ions react mainly with C_3A, cement that has low C_3A has good sulfate resistance. However, Morales et al. (2003) suggests that Calcium-monosulfo-aluminate-hydrate and calcium hydroxide react with sulfate ions in Class A cement to form secondary or delayed ettringite. They proposed that C_3A reacts with gypsum in hydrated cement to form primary ettringite as per Eqn (3).

$$3CaO.Al_2O_3 + 3(CaSO_4.2H_2O) \longrightarrow Ca_6[Al(OH)_6]_2.(SO_4)_3.26H_2O \quad \ldots\ldots (3)$$

Rasheeduzzafar et al. (1990) reported that, in addition to the C_3A content, the C_3S/ C_2S ratio of cement has a significant effect on the sulfate resistance of cement (**Fig. 1**).

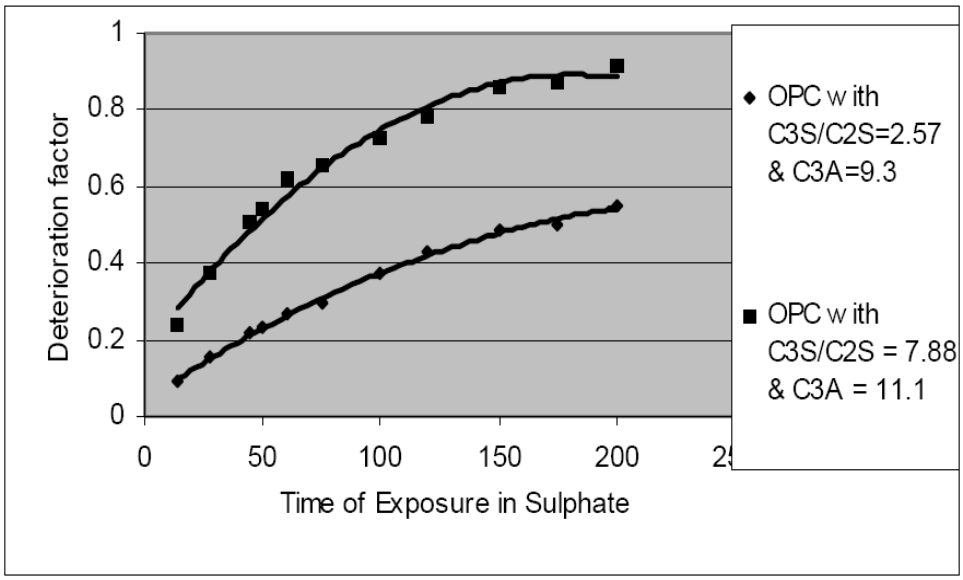

Fig. 1: Effect of C_3S/C_2S ratio on sulfate resistance of cement (Rasheeduzzafar et al. 1990)

Experiments conducted on sulfate resistant cement have also suggested that the presence of chloride ions decreases the rate of sulfate attack on cement (**Fig. 2**). Increase in sulfate resistance of the cement in presence of chlorides is attributed to:

- Increased solubility of calcium-aluminate-hydrate phase leading to calcium-sulfo-aluminate crystallization. This means ettringite forms in a non-expansive form.
- Transformation of aluminate hydrate phase into chloro aluminate phase, thereby reducing the quantity of ettringite formed.
- The rate of diffusion of chloride ions being much higher than that of the sulfate ions, allows the chloride to react with C_3A to form calcium-chloro-aluminate-hydrate, as a result, the quantity of C_3A available for sulfate ions to react and form ettringite is reduced.

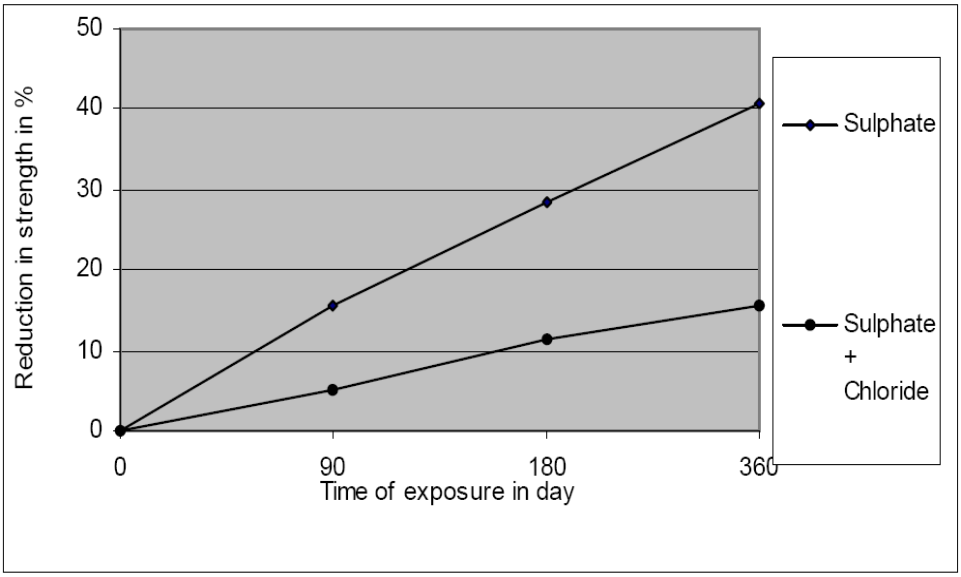

Fig. 2: Effect of chloride ions on sulfate resistance of cement (Al-Amoudi et al. 1995)

2.1.1.2 Products of H_2S Reaction with Oil Well Cement

In presence of CO_2, the major products of reaction of H_2S with oil well cement are pyrite, ettringite and gypsum. The formation of these minerals may lead to degradation of cement by expansion and development of cracks.

Under ambient conditions, oxidation of pyrite may lead to the formation of sulfuric acid and cement deterioration. In the presence of oxygen and moisture, pyrite may potentially oxidize to ferrous sulfate and sulfuric acid. The free sulfuric acid reacts with calcite and produces gypsum, which can potentially increase overall molecular volume and lead to expansion induced cracks. Secondary ettringite formation requires a supply of calcium (abundant within the cement system), aluminum (supplied by the hydrated ferrite), sulfate, and H_2O. The high pH conditions combined with H_2S as an abundant sulfur source are conducive to the formation of ettringite. The process of secondary ettringite

formation subsequent to the hardening of cement can lead to cracking, spalling, strength loss, and degradation (Kuthcko et al. 2011).

2.2 Experimental Studies on Degradation of Cement (Task 2)

2.2.1 Porosities and Permeabilities of Baseline Cements

Two batches (Batches 25 and 26) of baseline cement cores were aged along with special additives containing samples. The aging conditions for these tests are presented in **Table 1**. A test matrix (**Table 2**) developed to examine the effects of pressure on the degradation behavior of cement cores at 225°F and different CO_2 concentrations has been completed. Results of Batch 27 will be presented in the next month report.

Table 1: Test parameters for aging experiments conducted to date

Batch #	Temp. (ºF)	Pressure (psi)	Partial Pressure %			Brine Conc. (%)	Aging Period (days)	Experiment #
			CH_4	CO_2	H_2S			
001	350	9000	100	0	0	9	6	1
002	350	6000	100	0	0	2	14 & 28	2
003	350	6000	100	0	0	2	14	
004	350	6000	90	10	0	2	6	3
005	350	6000	90	10	0	2	14 & 28	4
006	350	6000	90	10	0	2	14	
007	225	6000	90	10	0	2	14	5
008	100	6000	90	10	0	2	14	6
009	225	6000	60	40	0	2	14	7
010	225	6000	0	100	0	2	14	8
011	100	6000	60	40	0	2	14	9
012	100	6000	0	100	0	2	14	10
013	350	6000	60	40	0	2	14	11
014	350	6000	0	100	0	2	14	12
015	225	6000	60	40	0	2	14	7A
016	350	3000	60	40	0	2	14	13
017	350	9000	60	40	0	2	14	14
018	350	3000	0	100	0	2	14	15
019	350	9000	0	100	0	2	14	16
020	350	3000	90	10	0	2	14	17
021	350	9000	90	10	0	2	14	18
022	225	3000	60	40	0	2	14	19
023	225	9000	60	40	0	2	14	20
024	225	3000	0	100	0	2	14	21
025	225	9000	0	100	0	2	14	22
026	225	3000	90	10	0	2	14	23

Table 2: Test matrix for aging experiments at 225°F

Pressure (psi)	10% CO_2	40% CO_2	100% CO_2
3000 psi	**Batch 026**	Batch 022	Batch 024
6000 psi	Batch 007	Batch 015	Batch 010
9000 psi	Batch 027	Batch 023	**Batch 025**

Figures 3 through **6** summarize results obtained from experiments performed varying aging temperature, pressure, CO_2 concentration. These figures are updated from the last month report comprising our recent measurements of Batches 25 and 26. Figure 3 demonstrates the porosity and permeability of samples aged for 14 days in 2% brine saturated with 100% CO_2 at 225°F. The porosity trends are consistent with permeability for both Class H and Class G cement samples. With increasing pressure, porosity and permeability first decreased and then increased. At lower pressure, carbonation and hydration reactions dominate the degradation process. As pressure increases, leaching becomes dominant offsetting the effect of carbonation leading to increases in porosity and permeability. However, at very high pressure (9000 psi), formation of dense and closely packed crystals plugs the pores and capillaries (Jones 1996) leading to decrease in porosity and permeability.

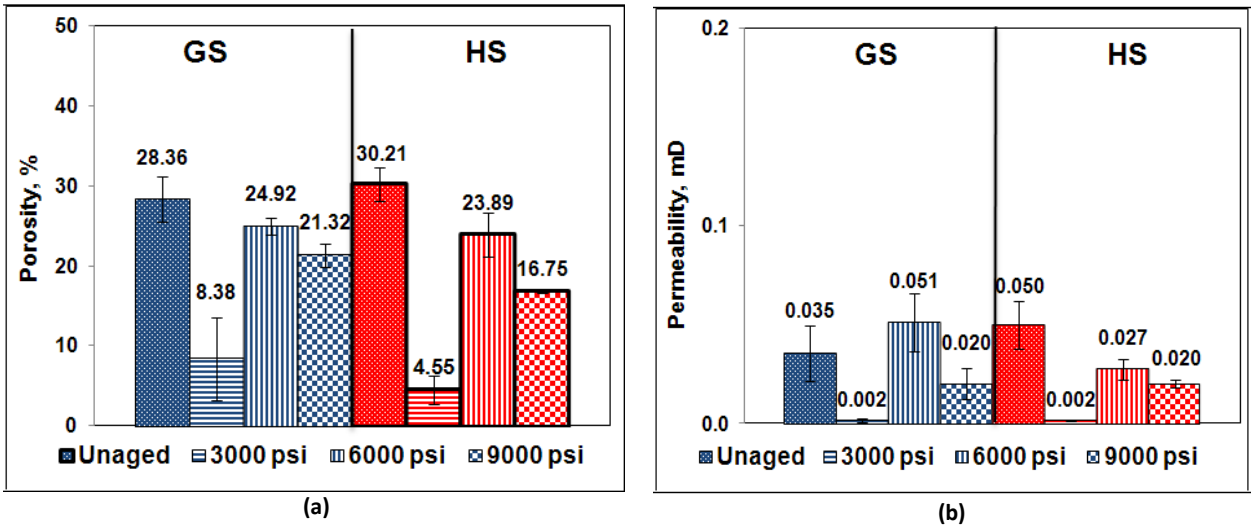

Fig. 3: Effects of aging pressure on porosity and permeability of baseline cores aged at 225°F and 100% CO_2

Figure 4 presents porosity and permeability of samples aged for 14 days in 2% brine saturated with 100% CO_2 gas at 350°F and different pressures (3000, 6000 and 9000 psi). The trends of porosity and permeability are consistent for Class G; however, Class H cement showed slight inconsistency at high pressure. Moreover, for Class G, the porosity and permeability results follow similar patterns observed at 225°F.

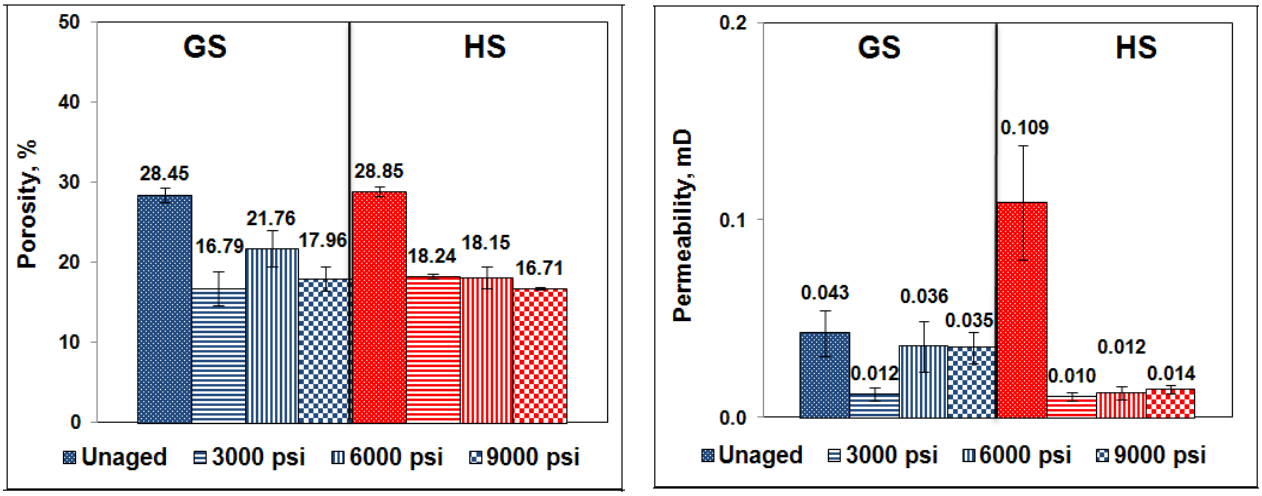

Fig. 4: Effects of aging pressure on porosity and permeability of baseline cores aged at 350F and 100% CO_2

Figures 5 and 6 demonstrate the effects of CO_2 concentration on porosity and permeability of aged samples at 3000 psi and different temperatures (225°F and 350°F). For both classes of cement, the general trends of porosity and permeability are consistent. At low temperature (225°F), increase in CO_2 concentration reduced porosity and permeability of the samples. At high temperature (350°F), Class G cement showed a similar trend. However, Class H cement exhibited reduction in porosity and permeability at 40% CO_2 and increase at 100% CO_2. This could be attributed to the leaching of the carbonated binding components such as CSH and portlandite.

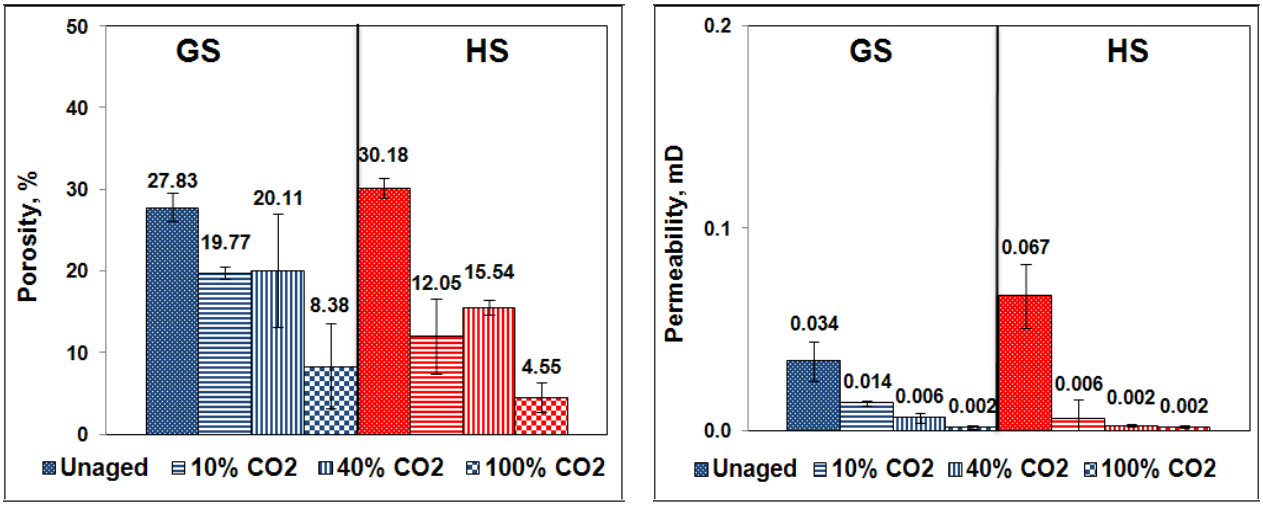

Fig. 5: Effects of CO_2 concentration on porosity and permeability of baseline cores aged at 225°F and 3000 psi

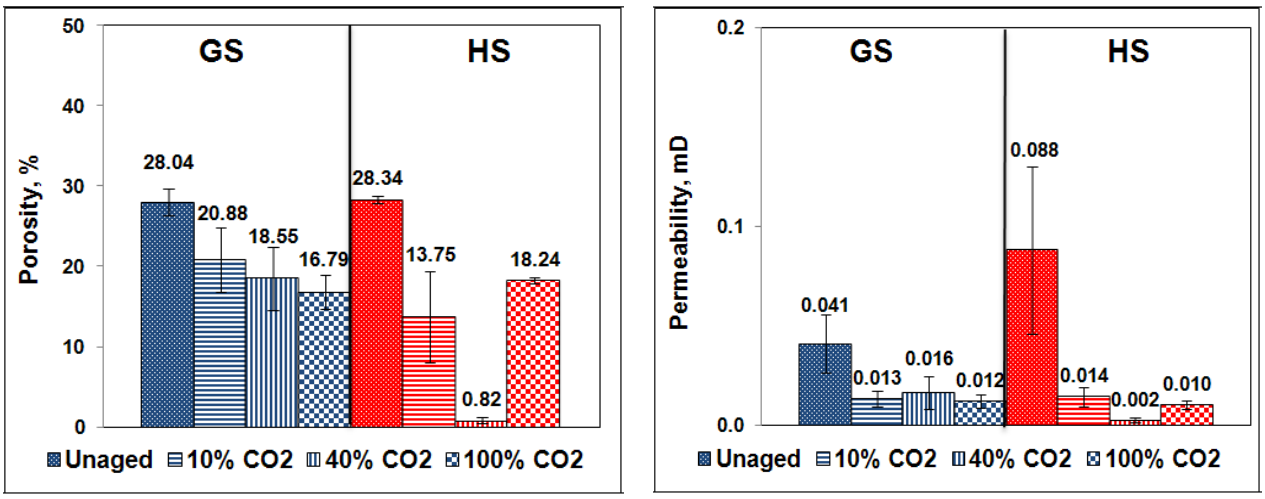

(a) (b)

Fig. 6: Effects of CO_2 concentration on porosity and permeability of baseline cores aged at 350°F and 3000 psi

Figures 7 and 8 illustrate the effects of CO_2 concentration on porosity and permeability of aged samples at 6000 psi and different temperatures (225°F and 350°F). There is no common trend, which can be observed from the results of Class G and Class H cements. In some cases, the porosity and permeability trends of Class H cement are inconsistent. Moreover, at higher temperature (350°F), the porosity trends of Class H cement reversed. On the other hand, Class G cement showed almost similar trends at different temperatures. Except for one outlier (porosity at 350°F and 40% CO_2 concentration), porosity and permeability data trends of Class G cement are consistent.

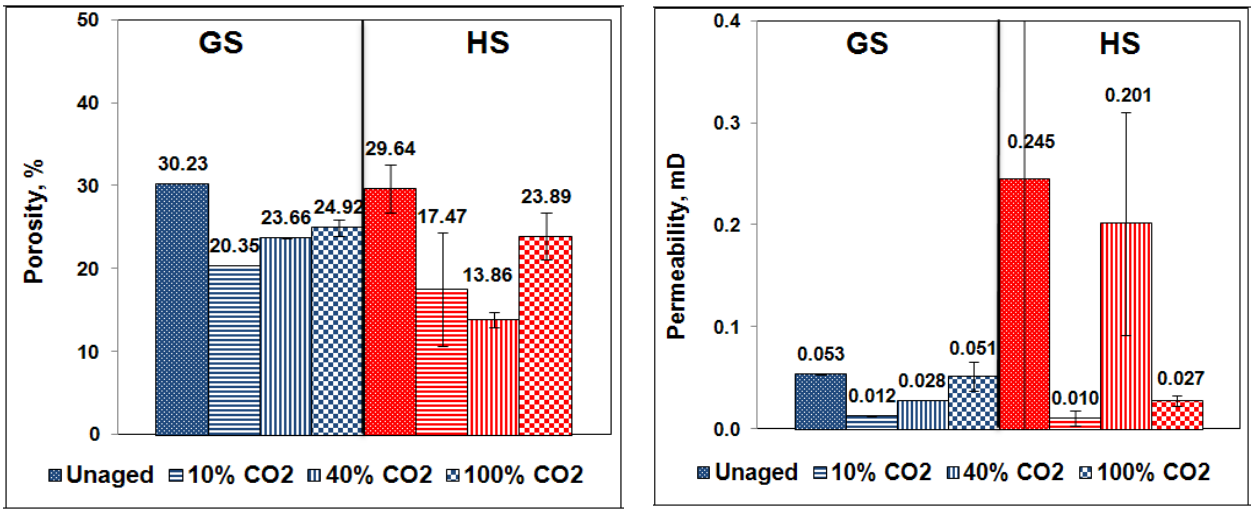

(a) (b)

Fig. 7: Effects of CO_2 concentration on porosity and permeability of baseline cores aged at 225°F and 6000 psi

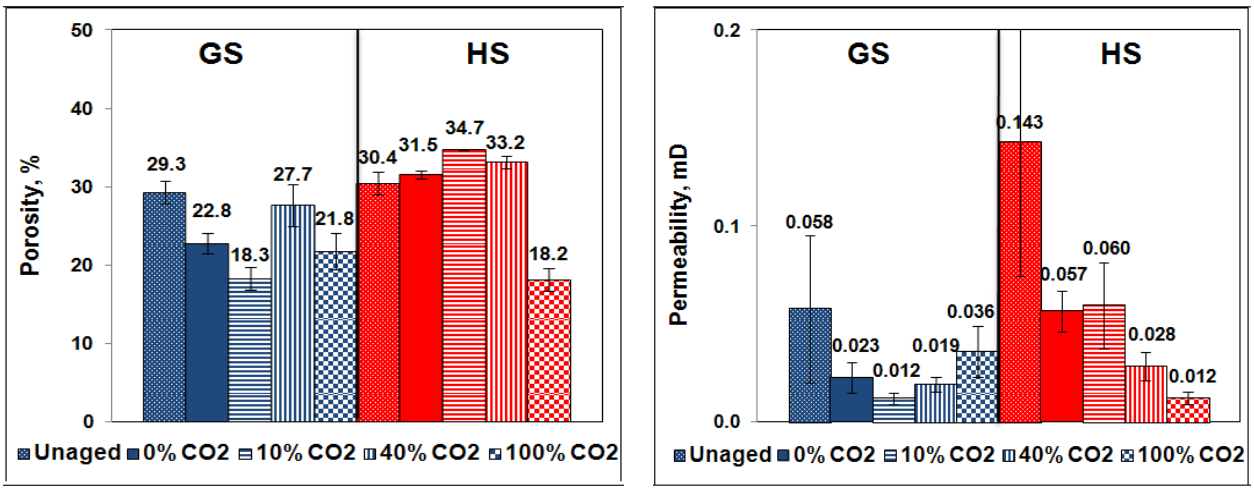

(a) (b)

Fig. 8: Effects of CO_2 concentration on porosity and permeability of baseline cores aged at 350°F and 6000 psi

2.2.2 Compressive Strengths of Baseline Cements

Study on compressive strength of conventional cement was continued. Measurements from Batches 25 and 26 are incorporated into our previous measurements and presented here. The results show the effects of pressure, temperature and CO_2 concentration on compressive strength of aged cement samples. Conditions in the aging cell for each of this batch are summarized in Table 1.

Effects of Aging Pressure

The new compressive strength data from Batch 25 is combined with previous results and presented in **Fig. 9**. At low aging pressure, strength initially increased in both cement due to the presence of traces of scawtite. As the pressure was increased to 6000 psi, most of the scawtite was fully carbonated resulting in the formation of calcite, which improved strength. In Class G cement, consistent strength gain was observed with increasing the pressure.

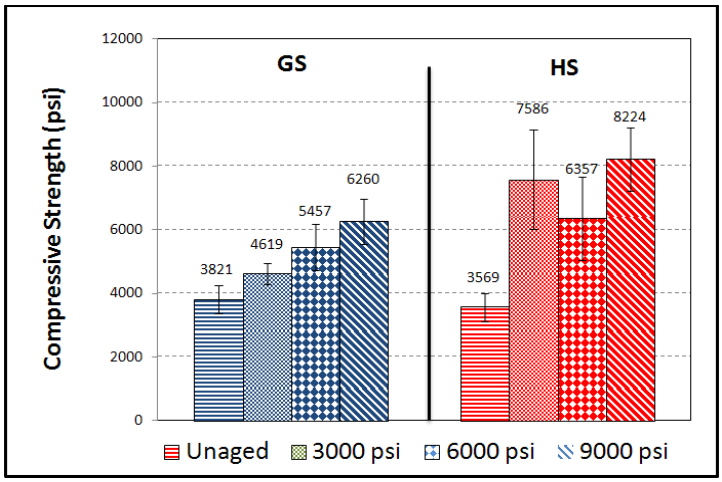

Fig. 9: Effects of pressure on compressive strength of cement cores at 225°F and 100% CO_2 concentration

The strength gain is due to increased solubility of carbon dioxide at high pressure, thereby favoring precipitation of calcium carbonate. Similar trend can be observed in Class H cement, except at 6000 psi, which may be due to thermally induced fractures in the cement. Overall, Class H cement outperformed Class G cement in high-pressure high-temperature environment.

Effects of Temperature

To study temperature effect on compressive strength, results from Batch 25 and Batch 19 are compared in **Fig. 10.** Both batches were aged at 9000 psi, 100% CO_2 concentration and 2% brine concentration for 14 days; however, the aging temperature was varied. As shown in the figure, Class G cement shows initial strength development up to 225°F due to carbonation and then strength loss due to increased rate of leaching. This trend is consistent with previous temperature effect study. Up to 225°F, Class H cement showed similar trend as Class G; however, the strength improvement continued above of 225°F indicating the absence of a dominant leaching process. Further study at temperature greater than 350°F may provide more insight into the trend of compressive strength of Class H cement at higher temperatures. In the coming weeks, high temperature (430°F) experiments will be carried out to determine the performance of the cements at high temperature conditions.

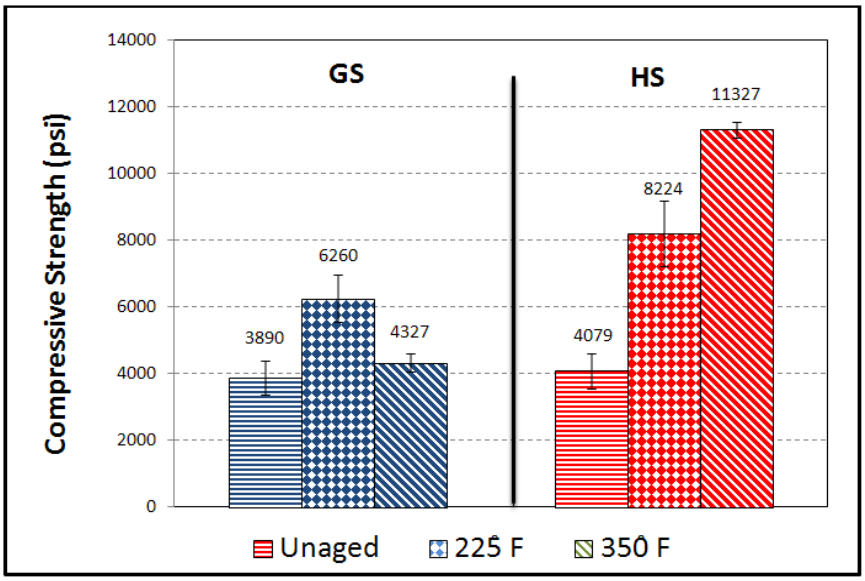

Fig. 10: Effects of temperature on compressive strength cement cores at 9000 psi and 100% CO_2

Furthermore, the effects of temperature on compressive strength of baseline (Class G and Class H) cement have been investigated at low pressure (3000 psi) and low CO_2 concentration (10% CO_2). As shown in **Fig. 11**, Class G cement showed initially minor strength improvement as the temperature was increased to 225°F. This could be due to precipitation of low trace of scawtite resulting from incomplete carbonation. The strength gain was followed by strength loss due to increased rate of leaching which is aided by high temperature. However, in Class H cement, leaching is hindered due to better resistance of the cement to acid penetration. Phase transformation of hydrated products may have also accounted for strength evolution in Class H cement at elevated temperature (350°F). It important to note that, for tests conducted at different aging conditions (Figs. 10 and 11), the compressive strength trends observed by varying temperature are very similar.

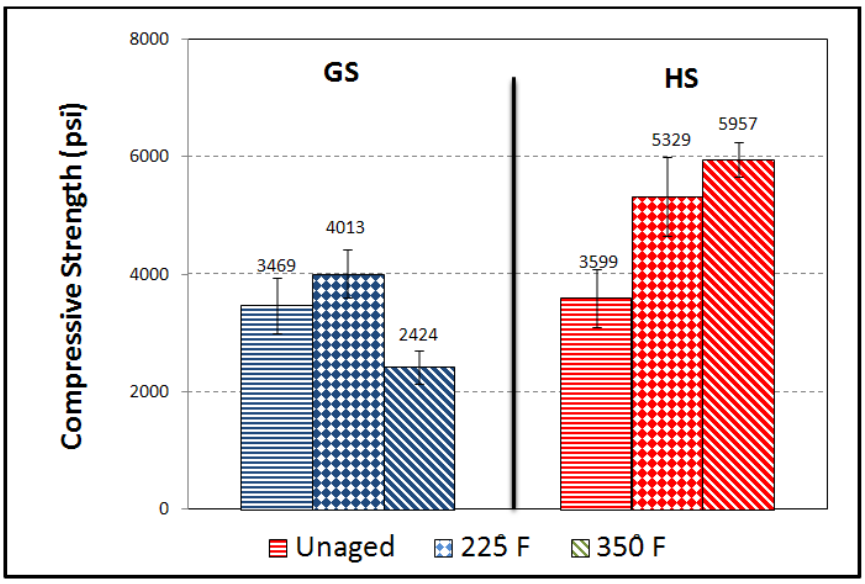

Fig. 11: Effects of temperature on compressive strength cement cores at 3000 psi and 10% CO_2 concentration

Effects of CO_2 Concentration

The effects of CO_2 concentration on compressive strengths of conventional (Class G and H) cement aged at 225°F and 3000 psi in 2% saturated-brine for 14 days were investigated (**Fig. 12**). Evidently, high CO_2 concentration results in more strength development in both API oil well cements, although it is more obvious in Class H cement. Again, further hydration and phase transformation at elevated aging temperature may have contributed to additional compressive strength development in Class H cement since it showed higher level of strength improvement at 225°F than Class G cement (Fig. 11).

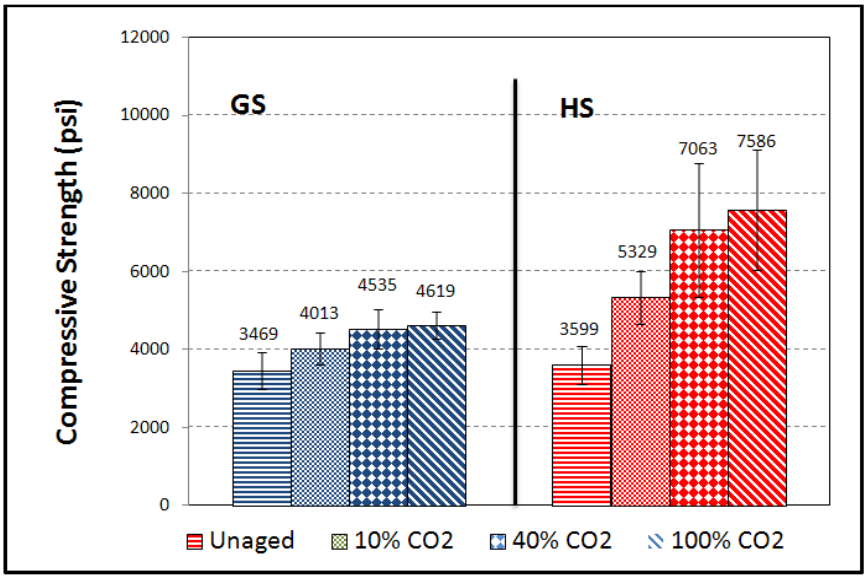

Fig. 12: Effects of CO_2 concentration on compressive strength of cement cores at 225°F and 3000 psi

2.2.3 Additive Screening and Cement Formulation Studies

The testing of additive containing cement was continued. During this reporting period, MgO samples (MGO-5) were prepared with 5% BWOC of cement and aged at HPHT conditions. The aging experiment with hydroxyapatite containing samples was performed and the properties of the cores were measured. Results show the benefit of hydroxyapatite in reducing acid attack. The cores showed the presence of CH component in the matrix indicating lesser carbonation.

2.2.3.1 Magnesium Based Oxide Cement

Tests with MGO-5 samples were continued. The samples were aged under high-pressure conditions presented in **Table 3**. The composition of the slurry was similar to the previous experiments. After aging, the properties of the cores were measured. The results are presented in **Figs. 13** and **14**. The data presented as "unaged" refers to groups of core samples maintained at ambient lab conditions for 14 days while other samples were aged at elevated temperature and pressure.

Table 3: Aging conditions for the MGO-5 samples

MGO-5	Temp. (°F)	Pressure (psi)	CO_2 (%)	NaCl (%)	Days	Baseline	Exp. No.
Batch 006	225	9000	100	2	14	Batch 025	22

Porosity and Permeability Measurements

For unaged samples, the porosity and permeability of the MGO-5 samples are lower than those of the baseline samples (Fig. 13a). Porosities of unaged samples are quite similar except for Class G, which showed comparatively lower porosity. After aging, baseline samples went through carbonation due to acid penetration. As a result, their porosities were reduced. On the other hand, the MGO-5 samples did not show significant porosity change indicating the effectiveness of MgO in limiting the penetration of carbonic acid and carbonation of cement matrix. Except for one measurement, the permeabilities of all the samples were reduced after aging.

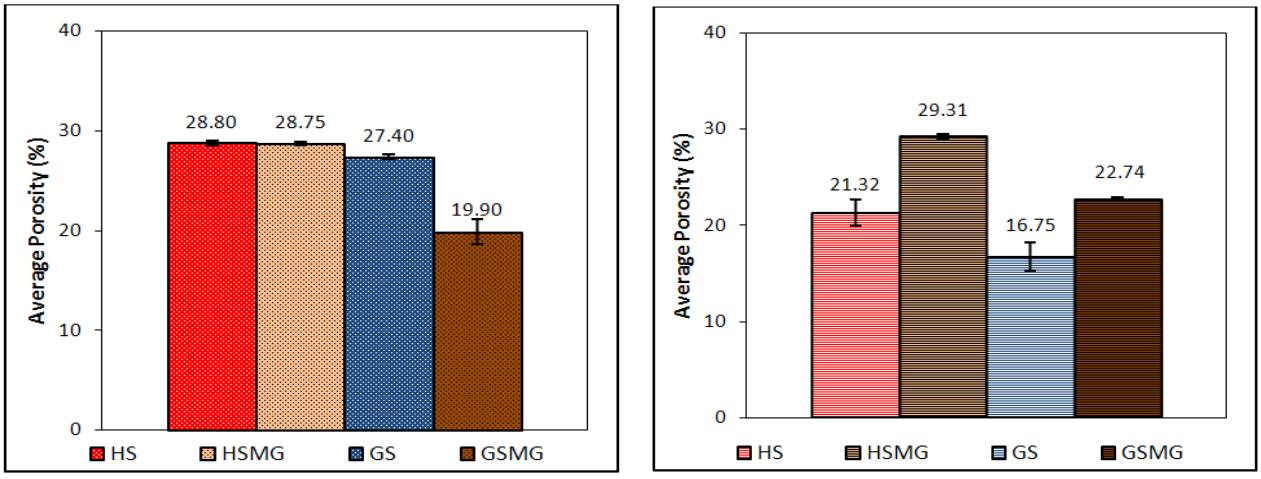

Fig. 13: Porosities of MGO-5 and baseline cements: a) unaged; and b) aged for 14 days at 225°F and 9000 psi in brine saturated with 100% CO_2 gas

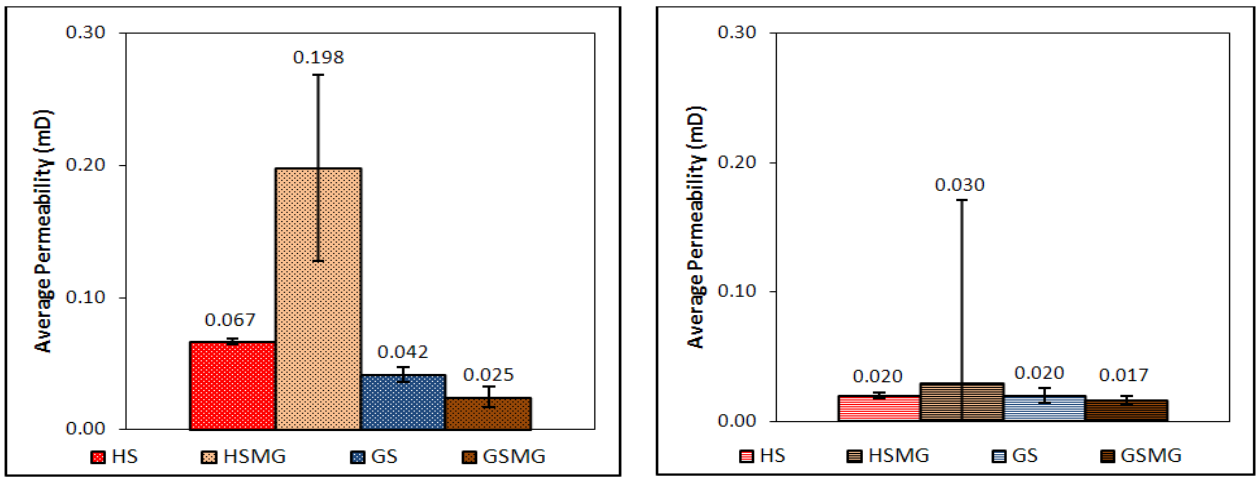

Fig. 14: Permeabilities of MGO-5 and baseline cements: a) unaged; and b) aged for 14 days at 225°F and 9000 psi in brine saturated with 100% CO_2 gas

Shear Bond Strength Measurements

The shear bond strength (SBS) measurements are presented in **Fig. 15**. Both baseline and MGO-5 samples showed increased SBS after aging due to carbonation and expansion of the matrix. It is difficult to compare the level of carbonation in the samples using the SBS data alone. Hence, FTIR tests were performed to examine the mineralogical changes occurred after aging.

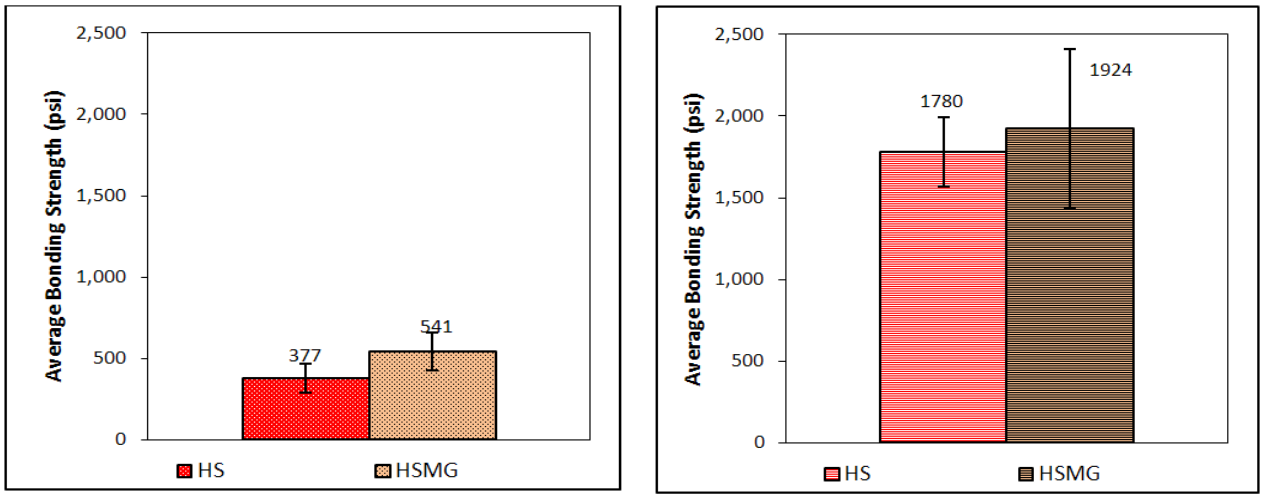

Fig. 15: Shear bond strength of MGO-5 and baseline cements: a) unaged; and b) aged for 14 days at 225°F and 9000 psi in brine saturated with 100% CO_2 gas

The FTIR spectrum is simplified in the form of bar charts for easy interpretation (**Fig. 16**). The outer, middle and inner zones of HS and HSMG samples show mostly similar spectra; and hence, they exhibit similar compositions. However, the inner and middle zones of HSMG sample show presence of $Mg(OH)_2$ which means that the inner parts of the core still contain un-carbonated components.

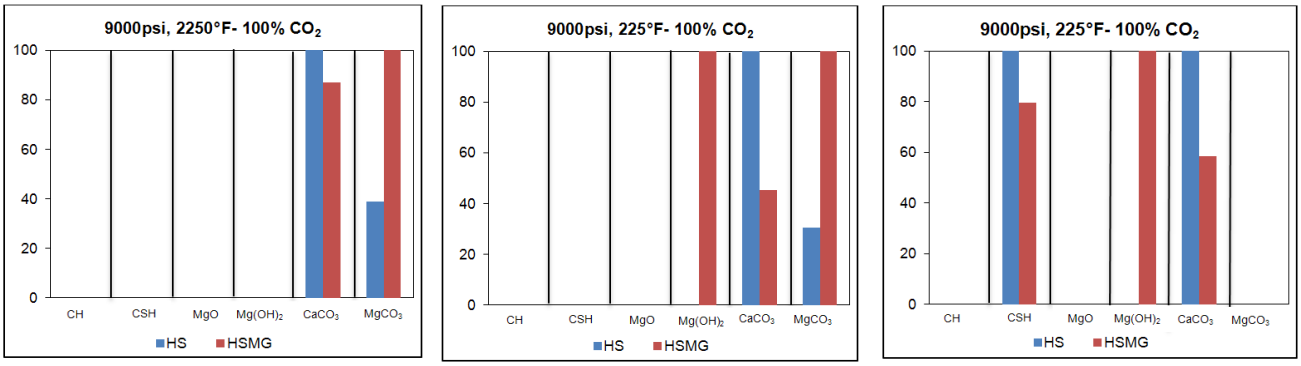

(a) (b) (c)

Fig. 16: Summarized FTIR data of HSMG and baseline HS samples aged at 225°F, 9000 psi, 100% CO_2 for 14 days: a) Outermost zone; b) Middle zone; and c) Innermost zone

In summary, the experimental results suggest that the addition of MgO reduces acid attack against cement. Moreover, due to its expansive tendency, it improves compressive and shear bond strengths of the cement. Porosity of MgO containing samples did not show significant change after aging indicating plugging of the pores by $Mg(OH)_2$ crystals and restricting CO_2 penetration. Furthermore, the FTIR results confirm the presence of $Mg(OH)_2$ in the inner matrix, which indicates lesser carbonation.

2.2.3.2 Hydroxyapatite-Based Cement

The previous tests with hydroxyapatite (HOAP) based cement indicated better performance against acidic environment as compared to baseline samples. The results of last batch of HOAP (Batch 006) aged at 225°F, 3000 psi and 40% CO_2 were presented in the previous monthly report (Report # 23). The FTIR results of the same batch are presented in **Fig. 17**. The spectra are simplified in the form of bar charts for easy interpretation. The baseline samples show presence of CSH only in the middle and inner zones and it does not show the presence of CH. On the other hand, HOAP samples indicate presence of CSH in all zones and CH in the middle and inner zones. The HOAP samples resisted the acid attack (carbonation) better than the baseline samples. The presence of carbonates is from $CaCO_3$ and $2Ca_5(PO_4)_3.CO_3$ and is not distinguishable from the FTIR.

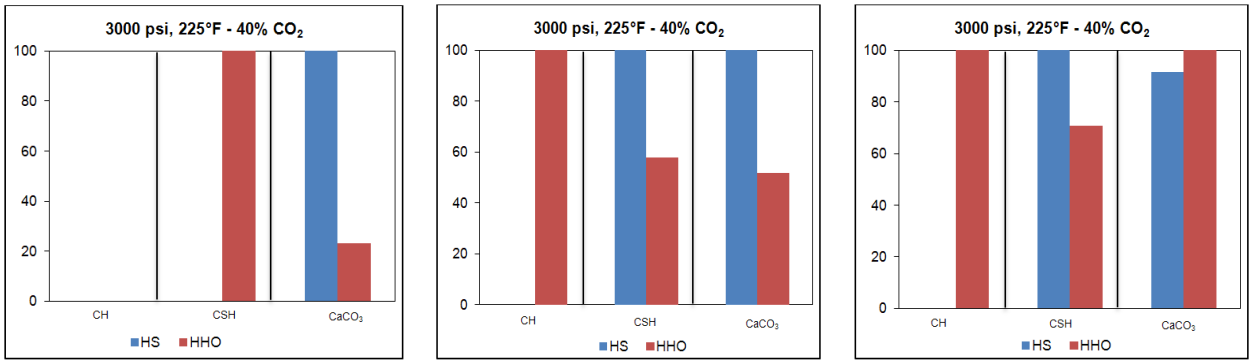

(a) (b) (c)

Fig. 17: Summarized FTIR data of HHO and baseline HS samples aged at 225°F, 3000 psi, 40% CO_2 for 14 days: a) Outermost zone; b) Middle zone; and c) Innermost zone

The FTIR results from Batch 006 confirm better performance of HOAP samples as compared to baseline cement. Another experiment was conducted at a different aging condition to evaluate the performance of HOAP samples further. The composition of the slurry is presented in previous report (Report # 19). The description of the aging condition is presented in **Table 4**.

Table 4: Aging conditions for the HOAP samples

HOAP	Temp. (°F)	Pressure (psi)	CO_2 (%)	NaCl (%)	Days	Baseline	Exp. No.
Batch 007	225	3000	10	2	14	Batch 026	23

Porosity and Permeability Measurements

The porosity and permeability measurements are presented in **Figs. 18** and **19**. Porosities unaged baseline and HOAP samples are in the same range. The permeability of the HHO sample is less than that of the base sample; however, the permeability of GHO samples is almost similar to that of baseline GS sample. After aging, although all the samples undergo a reduction in porosity, the HOAP samples show a lesser reduction over the baseline samples. This indicates reduction in the level of carbonation occurring in the samples during aging. The permeability of baseline samples reduced after aging; however, permeability of HHO samples showed minor change. Only the GHO samples exhibited an increase in permeability, which can be due to leaching of the cement matrix. The data from compressive strength, shear bond strength and FTIR also need to be verified in order to confirm the performance of the additive.

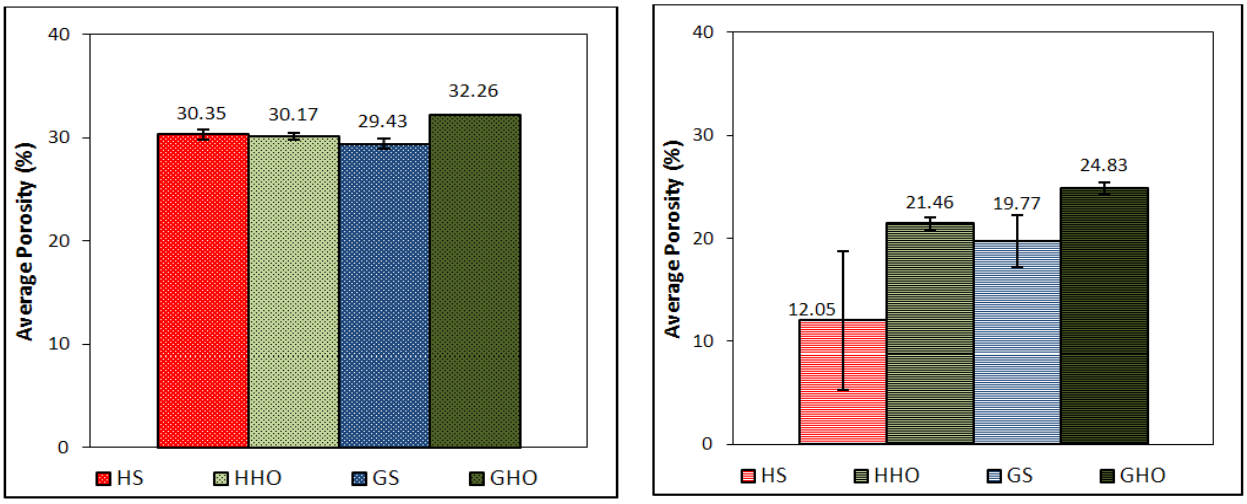

Fig. 18: Porosities of HOAP and baseline cements: a) unaged; and b) aged for 14 days at 225°F and 3000 psi in brine saturated with 10% CO_2 gas

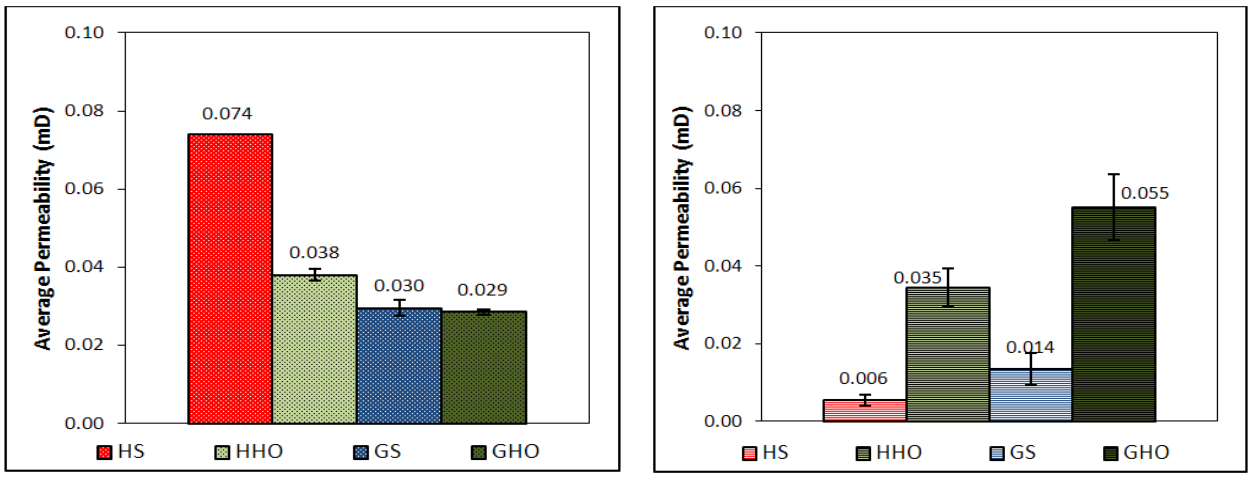

Fig. 19: Permeabilities of HOAP and baseline cements: a) unaged; and b) aged for 14 days at 225°F and 3000 psi in brine saturated with 10% CO_2 gas

The physical and mechanical properties of HOAP samples along with the FTIR results indicate the technical benefits of using hydroxyapatite as a cement additive. The addition of hydroxyapatite prevents carbonation and leaching of the matrix against acid attack. More experiments will be conducted in order to evaluate the performance of HOAP at other aging conditions.

Shear Bond Strength Measurements

The shear bond strength (SBS) measurements are presented in **Fig. 20**. The baseline and HHO samples indicate minor changes in SBS after aging. These changes do not clearly indicate the dominant process (leaching or carbonation) occurring during aging. Hence, FTIR analysis was conducted to examine compositional changes that may occur in the samples after aging.

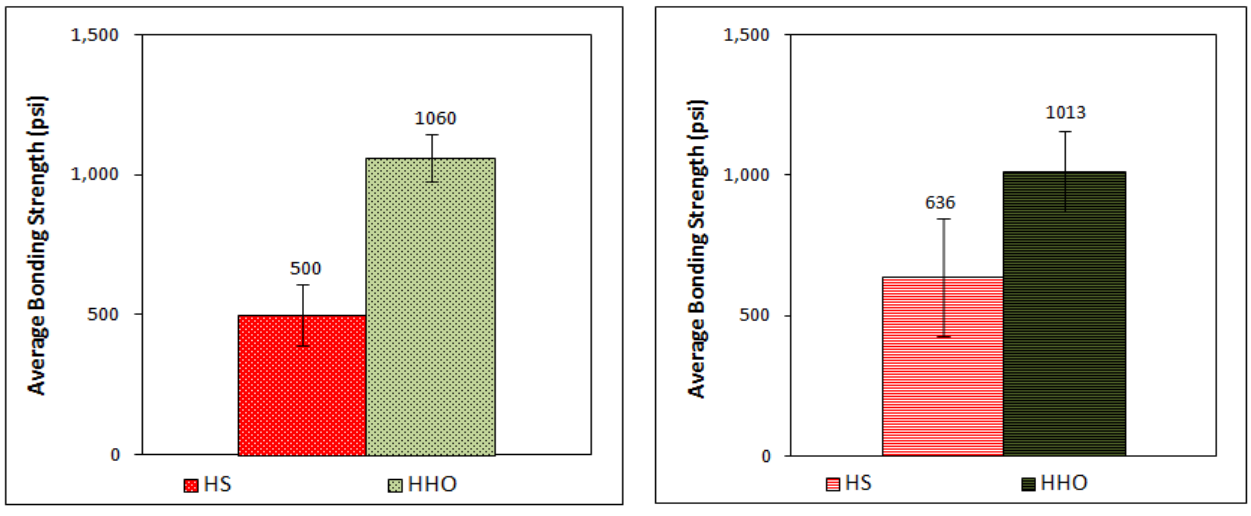

Fig. 20: Shear bond strength of HHO and baseline cements: a) unaged; and b) aged for 14 days at 225°F and 3000 psi in brine saturated with 10% CO_2 gas

The FTIR spectra of HHO and baseline cement samples are presented in **Fig. 21**. The outer most zones of both samples indicate presence of $CaCO_3$ and CSH. As the CSH is also present in the outer zone of baseline samples, it cannot be used to compare the acid resistance of the samples. However, the middle and inner zones of HOAP samples indicate the presence of CH group, indicating lesser carbonation as compared to baseline samples.

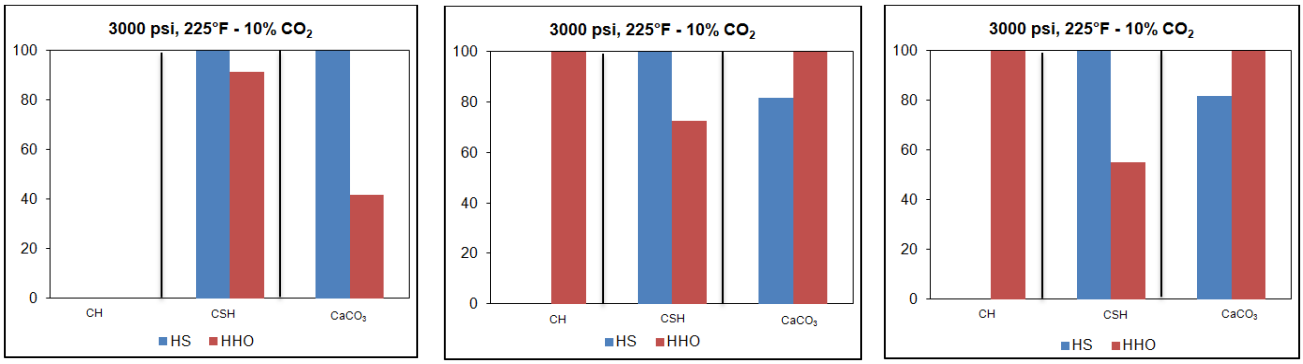

Fig. 21: Summarized FTIR data of HHO and baseline HS samples aged at 225°F, 3000 psi, 10% CO_2 for 14 days: a) Outermost zone; b) Middle zone; and c) Innermost zone

2.3 Experimental Studies on Corrosion of Tubulars (Task 3)

This section of the report presents results of recent corrosion experiments conducted after incorporating improvements suggested by the technical advisory board members to maintain precisely a constant temperature condition in the autoclave. In order to control temperature, the autoclave is placed in a heating jacket made of PVC. The jacket is connected to a circulating bath equipped with temperature controller. Hot water is circulated through the jacket to maintain temperature constant in the autoclave. The temperature control system, which includes the circulating bath, heating jacket and circulation tubes, is assembled as shown in **Fig. 22**.

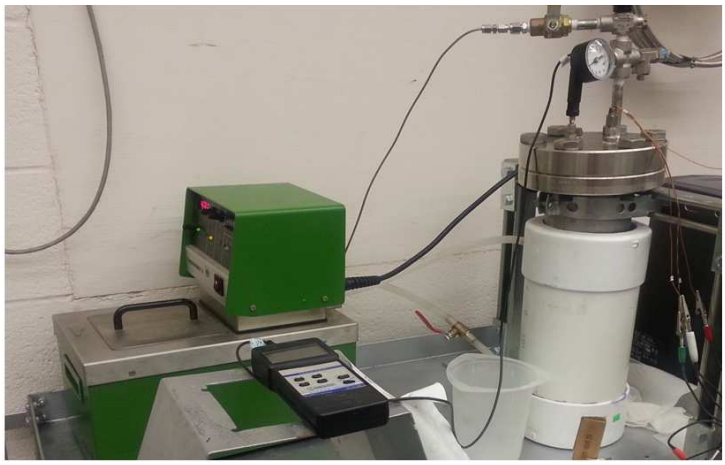

Fig. 22: Modified test setup for LPR-based corrosion study

Precise temperature control was suggested to eliminate anomalies (spikes in corrosion rate shown in **Fig. 23**), which were observed during corrosion rate measurements. Previously, these anomalies were considered to be due to breakage of the protective scale. However, small temperature variation in the lab may also cause periodic fluctuations in the corrosion measurements. In order to evaluate the effect of the surrounding temperature on the measurements, one corrosion experiments

was conducted after installing the temperature control system. The measurement from this test showed that the spikes in the corrosion rate are associated with minor temperature variation in the lab environment. Therefore, all future tests will be conducted using the temperature control system.

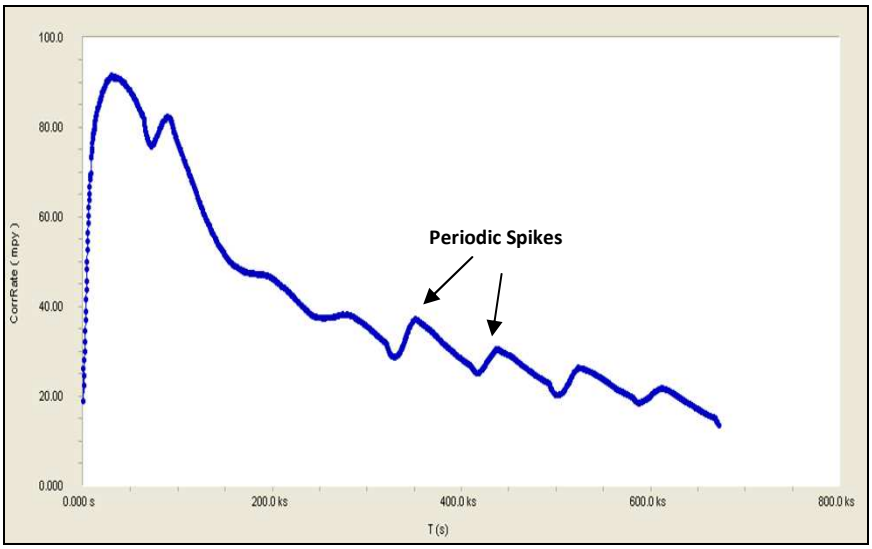

Fig. 23: Corrosion rate vs. time obtained before installing a heating jacket

3. Planned Activities

- Continue aging experiments with brine-CO_2-CH4 system for 14 days varying aging pressure (3,000, 6000, and 9000 psi) and CO_2 concentration (10%, 40% and 100%) at 225°F and 430°F.
- Continue theoretical and modeling studies on tubular degradation.
- Continue cement additive screening and acid resistant cement formulation studies.
- Begin testing of the corrosion experiment setup.

4. Project Expenditures

This section presents the project expenses during the month of October (**Table 5**) and the cumulative expenditures.

Table 5: Current and cumulative expenditures, October 2013

No.	Budget Categories	Current Expenses	Cumulative Expenses
1	Salaries & Wages	$7,576.92	$236,569.22
2	Fringe Benefits	$1,293.18	$54,428.21
3	Project Materials	$1,212.99	$59,504.48
4	Travel	$139.55	$6,232.33
5	Conference Expenses	$0.00	$0.00
6	Other Direct Costs	$0.00	$993.60
7	Equipment	$4,132.57	$241,399.90
8	Space Rental	$0.00	$0.00
9	Indirect Cost	$5,111.32	$178,863.89
10	**Total**	**$19,466.53**	**$777,991.63**

Nomenclatures

A	Aluminum
BWOC	By weight of cement
C_3A	Tri Calcium aluminate
C_3S	Tri-calcium Silicate
C_4AF	Tetra Calcium Alumino Ferrite
CH	Calcium hydroxide
CSH	Calcium silicate hydrate
F	Ferrite
FTIR	Fourier Transform Infra-Red
GHO	Class G Cement with hydroxyapatite
GS	Class G cement with silica flour
GSMG	Class G Cement with silica flour and magnesium oxide
GSLM	Class G Cement with silica flour, latex and micro silica
GSLT	Class G Cement with latex
HHO	Class H Cement with hydroxyapatite
HPHT	High-pressure high-temperature
HS	Class H cement with silica flour

HSHO	Class H Cement with silica flour and hydroxyapatite
HSMG	Class H Cement with silica flour and magnesium oxide
HSLM	Class H Cement with silica flour, latex and micro silica
HSLT	Class H Cement with latex
LPR	Linear polarization resistance
LTMS	Cement with latex and micro silica additives
mpy	mils per year
MGO	Magnesium oxide containing cement
MGO-5	Cement containing 5% BWOC MgO as additive
MGO-10	Cement containing 10% BWOC MgO as additive
MS	Micro silica containing cement
MS-10	Cement containing 10% BWOC micro silica as additive
NACE	National Association of Corrosion Engineers
SBS	Shear bonding strength
SEM	Scanning Electron Microscope
SCC	stress corrosion cracking
SSC	Sulfide Stress Cracking
XRD	X-Ray diffraction

References

Al-Amoudi, O.S.B., Maslehuddin, M., and Saadi, M.M. 1995. Effect of magnesium sulphate and sodium sulphate on the durability performance of plain and blended cements, ACI Materials Journal, No. 1, 92, Pages 15-24.

Benge, G. 2009. Improving well bore seal integrity in CO2 injection wells, Energy Procedia, Vol. 1, Issue 1, Pages 3523–3529.

Fakhreldin Y., Al-Sharji, H., Ruwehy, A.M., Saadi, K., Salim, T. and Al-Kalbani, S. 2010. Advanced systems for acid gas injection wells, paper SPE 132345, presented at the Asia Pacific Oil and Gas Conference, Brisban Australia, 18-20 October.

Jacquemet, N., Pironon, J., Lagneau, V. and Saint-Marc, J. 2011. Armouring of well cement in H2S–CO2 saturated brine by calcite coating, Applied Geochemistry, Vol. 27, Issue 3, Pages 782–795.

Jones, R. H. 1996 .Cements treated with high-pressure CO_2. US Patent 5,518,540, 21 May.

Krilov, Z., and Loncaric, B., and Miksa, Z. 2000. Investigation of a Long-Term Cement Deterioration Under a High-Temperature, Sour Gas Downhole Environment, paper SPE 58771, presented at the SPE International Symposium on Formation Damage Control, Louisiana 23–24 February.

Kutchko, B.G., Strazisar, B.R., Hawthorne, S.B., Lopano, C.L., Miller, D.J., Hakala, A. and Guthrie, G.D. 2011. H2S–CO2 reaction with hydrated Class H well cement: Acid-gas injection and CO2 Co-sequestration, International Journal of Greenhouse Gas Control, Vol. 5, Issue 4, Pages 880–888.

Lecolier, E., Rivereau, A., Ferrer, N., Audibert, A. and Longaygue, X. 2006. Durability of Oil Well cement formulations aged in H_2S containing fluids, paper SPE 99105-MS, presented at the SPE/IADC Drilling Conference, 21-23 February 2006, Miami, Florida.

Lecolier, E., Rivereau, A., Ferrer, N., Audibert, A. and Longaygue, X. 2008. Study of New solutions for Acid Resistant cement, paper SPE 116066, presented at the SPE Annual Technical Conference and Exhibition, 21-24 September 2008, Denver, Colorado.

Morales, M., Morris, W., Marcelo, A. C., Robles, J., and Bianchi, G. 2003. Improving the Sulfate Resistance Performance of API cement Class A upon Appropriate Slurry Design, paper SPE 81000, presented at the SPE Latin American and Caribbean Petroleum Engineering Conference, 27-30 April, Port-of-Spain, Trinidad and Tobago.

Prasad, J., Jain, D.K, and Ahuja, A.K. 2006. Factors influencing the sulfate resistance of cement concrete and mortar, Asian Journal of Civil engineering, Vol. 7, No. 3, Pages 259-268.

Rasheeduzzafar, D.F.H., Al-Gahtani, A.S., Al-Saadoun, S. S., and Bader, M. A. 1990. Influence of cement composition on the corrosion of reinforcement and sulphate resistance of concrete, ACI Materials Journal, Vol. 87, No. 2, Pages 114-122.

Appendix A: Amendments to Report # 24 Figs. 19 and 20

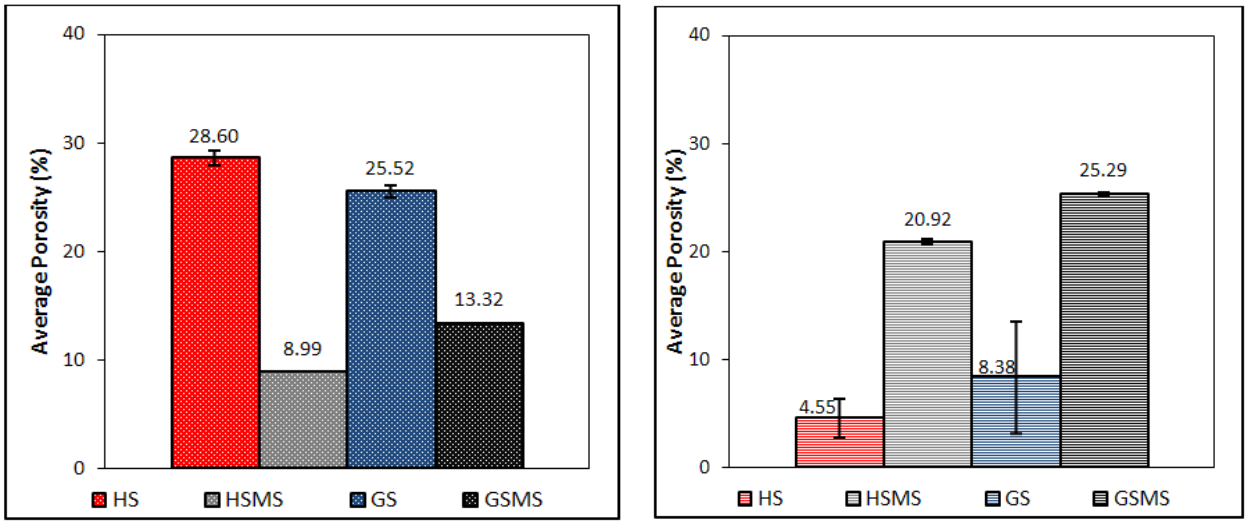

Fig. 19: Porosities of baseline and MS-10 cements: a) Un-aged; and b) Aged at 225°F, 9000 psi, 2% brine saturated with 100% CO_2 for 14 days

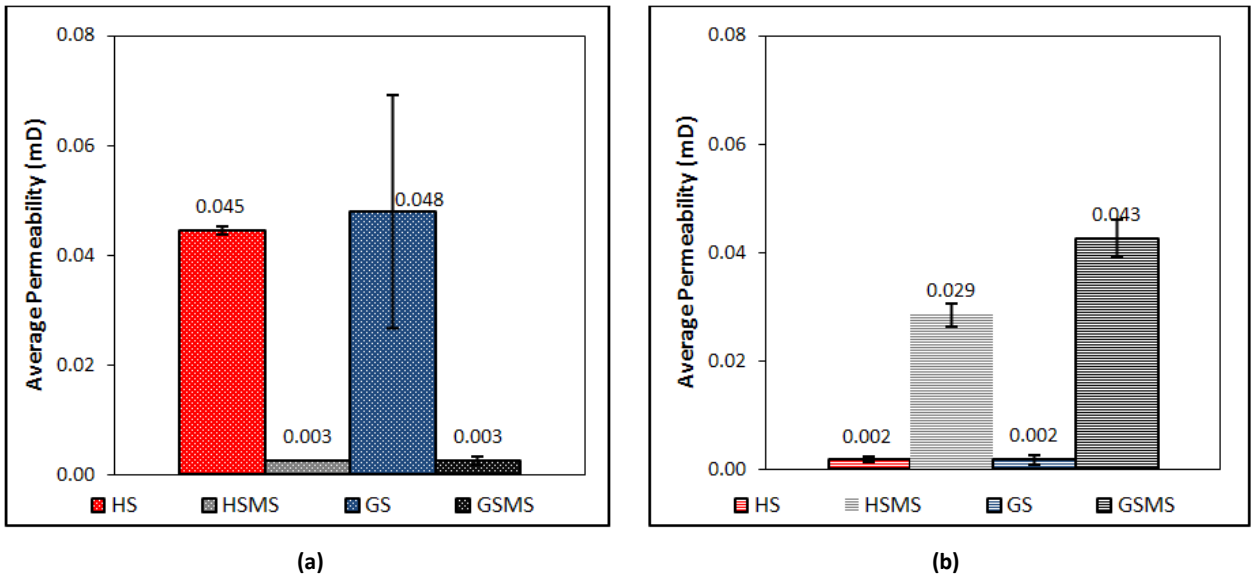

Fig. 20: Permeabilities of baseline and MS-10 cements: a) Un-aged; and b) Aged at 225°F, 9000 psi, 2% brine saturated with 100% CO_2 for 14 days

Project Title: Effect of H_2S and CO_2 in HPHT Wells on Tubulars and Cement

Report Type: Monthly Report

Report #: 26

Reporting Period: October 22nd, 2013 to November 21st, 2013

Authors:

Ramadan Ahmed, Principal Investigator

Subhash Shah, Co-Principal Investigator

Samuel Osisanya, Co-Principal Investigator

Rida Elgaddafi, Research Assistant

Omotayo Omosebi, Research Assistant

Himanshu Maheshwari, Research Assistant

Adarsh Naidu, Research Assistant

Aman Srivastava, Research Assistant

Jueun Hwang, Research Assistant

Mounraj Sharma, Research Assistant

Sagar Tale, Research Assistant

Prepared under BSEE Project # E12PC00035

by

THE UNIVERSITY OF OKLAHOMA

January 20, 2014

1. Summary of Accomplishments

This monthly report presents the progress made during the project period October 22, 2013 to November 21, 2013. Cement and tubular degradation studies were continued during this reporting period. Cement cores and bonding samples were prepared and aged in acidic environment to examine their degradation characteristics. Various acid resistant cement slurries and cores were papered and tested under different aging conditions. Moreover, the fifth TAB meeting was held on Nov. 7, 2013. The minutes of the meeting are presented in Appendix A.

Two aging experiments (Experiments 23 and 24) were completed during this month. The samples were aged for 2 weeks in 2% brine saturated with CO_2 containing methane gas. Porosity, permeability, and compressive and bond strengths of unaged and aged samples were measured. Recent measurements were combined with previously obtained results. For most of the cement cores tested, the porosity and permeability trends were consistent.

For tests conducted at high pressure (9000 psi), increase in CO_2 concentration reduced porosity and permeability of baseline samples at low CO_2 concentration (10%), and then the trend reversed due to leaching. Compressive strengths of baseline cement progressively increased as additional CO_2 gas was injected into the aging system.

Experimental investigation on cement additives was continued. The effects of micro-silica and latex on performance of Class H and Class G cements under HPHT conditions were investigated. Fourier Transform Infrared Spectroscopy (FTIR) method was used to evaluate the effectiveness of the additives in preventing the carbonation of binding component of the cement (CSH and CH). Permeability, shear bond strength and FTIR measurements indicate that latex and micro-silica containing cement samples resist carbonation better than the baseline samples. In the coming weeks, additional experiments will be carried out under different aging conditions in order to test the effectiveness of the additives (latex and micro-silica) against acid attack. Furthermore, tests were carried out using only micro-silica as a cement additive for acid resistance. Results showed substantial increase in porosity and permeability of the samples after aging. However, they were able to preserve the CSH component of the cement. It is observed from the two experiments that the effectiveness of micro-silica is limited in preventing acid attack because it tends to increase the pore space. Although the CSH component is preserved for a two-week period, prolonged exposure may lead to excessive damage to the matrix. The experiments with micro-silica will be continued to study its behavior.

Corrosion study under low-pressure is in progress. After improving the experimental setup, tests carried out under controlled temperature condition. Both linear polarization (LPR) and weight-loss corrosion measurement techniques were utilized in the study.

Our plan for the upcoming weeks is to continue: i) aging tests at different pressures and temperatures; ii) theoretical and modeling studies on tubular corrosion; iii) additive screening and acid resistant cement development studies; iv) low-pressure corrosion experiments at different CO_2 concentrations; and v) pressure testing of corrosion test setup.

2. Overall Project Progress

2.1 Theoretical Studies (Task 1)

2.1.1 Sulfide Stress Cracking

Sulfide Stress Cracking (SSC) in one of the major issues encountered in sour gas field. Casing and tubings often fail well below their maximum anticipated load capacity due to SSC. NACE Method A, NACE Method D and full size casing tests are established procedure used to determine performance of metals in sour environment. However, each of these methods has some limitations. Mini-pipe testing simulates the well condition by using tri-axial stresses instead of one-dimensional stress. Moreover, it allows both side (internal and external) exposures to the sour environment. This report mainly focuses on experimental studies used for studying SSC in the past.

NACE Method D provides threshold crack intensity, which is the minimum stress intensity required at the tip of preexisting crack for its propagation (NACE 2005). A pre-cracked mini-pipe specimen can provide the threshold crack intensity to evaluate accuracy of fracture mechanics models. An experimental setup developed by Cernocky et al. (2005) was used to perform mini-pipe tests to evaluate performance of material in sour environment. Combined effects of principal stresses (axial, hoop and radial stresses) on crack initiation and its propagation in presence of H_2S were determined. Results showed significant data scatter due to bending moment, which is generated from the force imbalance. As a result, bending moments were measured and monitored during experiment to examine their effect on the SSC measurements.

The setup developed by Cernocky et al. (2005) uses a frame with four springs (**Fig. 1**) for applying the axial load required for the test. These springs with carbon steel are needed for loading process. The carbon steel rod when loaded beyond proportional limit may show presence of creep strain. This strain is often small but if rods have high stiffness, even small strain can unload specimen significantly. This leads to erroneous results. During the test, H_2S exposure was on the outside of the mini-pipe under low-pressure condition. H_2S exposure direction can be on one side or both the sides of a mini-pipe specimen. Tests showed failure pattern can vary with the exposure direction. This is useful to understand mechanism of H_2S corrosion. Cernocky et al. pressured the internal part of the mini-pipe using water and NACE test solution. Mini-pipe internal pressure was monitored continuously using pressure sensor placed inside the specimen. In addition, temperature in the room was monitored.

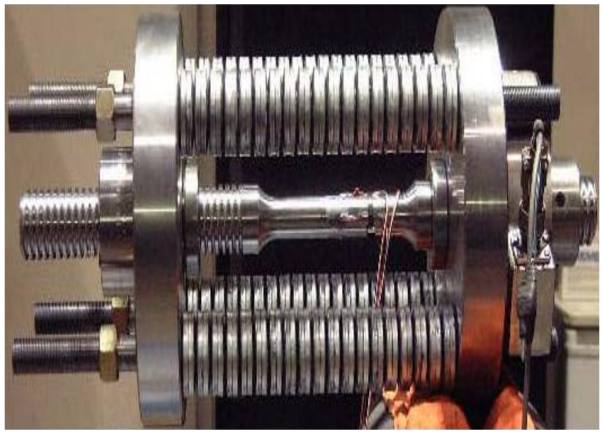

Fig. 1: Mini-pipe without sleeve in frame (Cernocky et al. 2005)

Recently conducted SSC study (Been and Crozier 2014) used axial force, which is applied using a motor (**Fig. 2**). Mini-pipe specimens were exposed to H_2S on their outside. Experiments were performed using specimens made of API casing (L-80), placed in NACE solution B saturated H_2S containing gas at 25 psi. Solution pH was ranging from 3.4 to 3.6. The specimens were subjected to stress level of 90% yield strength. H_2S concentration in the gas phase and temperature were varied during the course of the study.

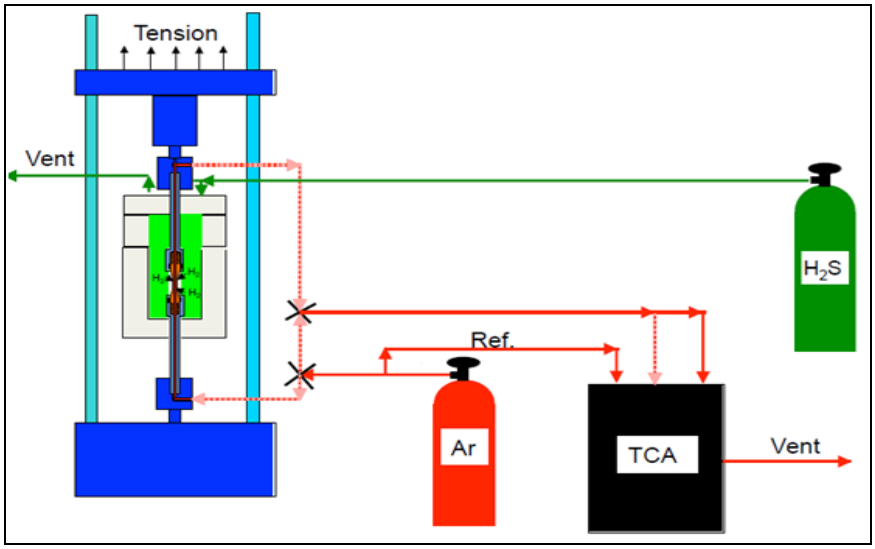

Fig. 2: Experimental set up for testing mini-pipe specimens (Been and Crozier 2014)

Results showed that the rate of hydrogen permeation (**Fig. 3**) increases with time, specimen stress loading level and H_2S pressure. Higher hydrogen permeation rate means higher susceptibility to SSC. Increase in temperature, initially resulted in rapid increase in hydrogen permeation, followed by a more gradual decrease. Similar observations were reported by other studies (Morana and Nice 2009; Hashizume et al. (2000). The studies found that increase in H_2S concentration increases susceptibility towards SSC.

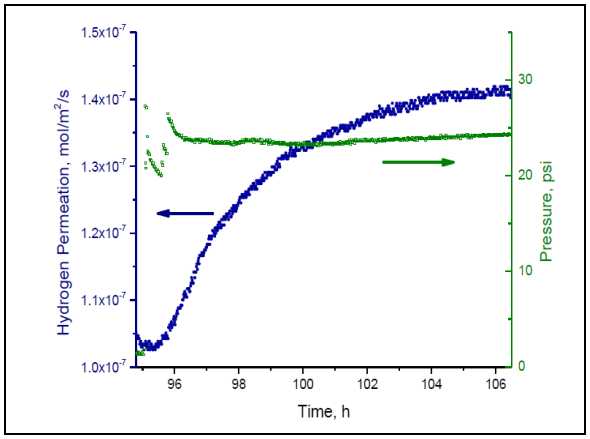

Fig. 3: Hydrogen permeation vs time (Been and Crozier 2014)

Cane and Cayard (1998) studied the effect of temperature on SSC. They found that SSC susceptibility is the highest near room temperature and as temperature increases susceptibility decreases. Moreover, results from mini-pipe tests were similar with those obtained from standard NACE tests that use a cylindrical rod specimen.

2.2 Experimental Studies on Degradation of Cement (Task 2)

2.2.1 Porosities and Permeabilities of Baseline Cements

During this reporting period, two batches (Batches 27 and 28) of baseline cement cores were aged along with special additives containing samples. The aging conditions for these tests are presented in **Table 1**. A test matrix (**Table 2**) developed to examine the effects of pressure on the degradation behavior of cement cores at 225°F and different CO_2 concentrations has been completed and results of Batch 27 are presented in this report. A new test matrix (**Table 3**) has been developed to examine the effects of CO_2 concentrations on the degradation behavior of cement cores at 430°F and 6000 psi.

Table 1: Test parameters for aging experiments conducted to date

Batch #	Temp. (ºF)	Pressure (psi)	Partial Pressure %			Brine Conc. (%)	Aging Period (days)	Experiment #
			CH_4	CO_2	H_2S			
001	350	9000	100	0	0	9	6	1
002	350	6000	100	0	0	2	14 & 28	2
003	350	6000	100	0	0	2	14	
004	350	6000	90	10	0	2	6	3
005	350	6000	90	10	0	2	14 & 28	4
006	350	6000	90	10	0	2	14	
007	225	6000	90	10	0	2	14	5
008	100	6000	90	10	0	2	14	6
009	225	6000	60	40	0	2	14	7
010	225	6000	0	100	0	2	14	8
011	100	6000	60	40	0	2	14	9
012	100	6000	0	100	0	2	14	10
013	350	6000	60	40	0	2	14	11
014	350	6000	0	100	0	2	14	12
015	225	6000	60	40	0	2	14	7A
016	350	3000	60	40	0	2	14	13
017	350	9000	60	40	0	2	14	14
018	350	3000	0	100	0	2	14	15
019	350	9000	0	100	0	2	14	16
020	350	3000	90	10	0	2	14	17
021	350	9000	90	10	0	2	14	18
022	225	3000	60	40	0	2	14	19
023	225	9000	60	40	0	2	14	20
024	225	3000	0	100	0	2	14	21
025	225	9000	0	100	0	2	14	22
026	225	3000	90	10	0	2	14	23
027	225	9000	90	10	0	2	14	24
028	430	6000	90	10	0	2	14	25

Table 2: Test matrix for aging experiments at 225°F

Pressure (psi)	10% CO_2	40% CO_2	100% CO_2
3000 psi	Batch 026	Batch 022	Batch 024
6000 psi	Batch 007	Batch 015	Batch 010
9000 psi	**Batch 027**	Batch 023	Batch 025

Table 3: Test matrix for aging experiments at 430°F

Pressure (psi)	10% CO_2	40% CO_2	100% CO_2
6000 psi	Batch 028	Batch 029	Batch 030

Effects of Aging Pressure

Figures 4 through **7** present results obtained from experiments performed varying aging temperature, pressure, CO_2 concentration. These figures are updated from previous reports comprising our recent measurements of Batches 27 and 28. For both cement classes, the porosity trends are consistent with permeability. Figures 4 and 5 demonstrate the porosity and permeability of samples aged for 14 days in 2% brine saturated with 10% CO_2 at 225°F and 350°F, respectively. For Class H, with increasing pressure, porosity and permeability first decreased then increased and again decreased. At lower pressure, carbonation and hydration reactions dominate the degradation process. As pressure increases, leaching becomes dominant offsetting the effect of carbonation leading to increases in porosity and permeability. However, at very high pressure (9000 psi), formation of dense and closely packed crystals plugs the pores and capillaries (Jones 1996) leading to decrease in porosity and permeability. Class G cement showed different trends with temperature. At 225°F, it followed the trend of Class H cement. However, at 350°F, increasing pressure, porosity and permeability first decreased and then increased.

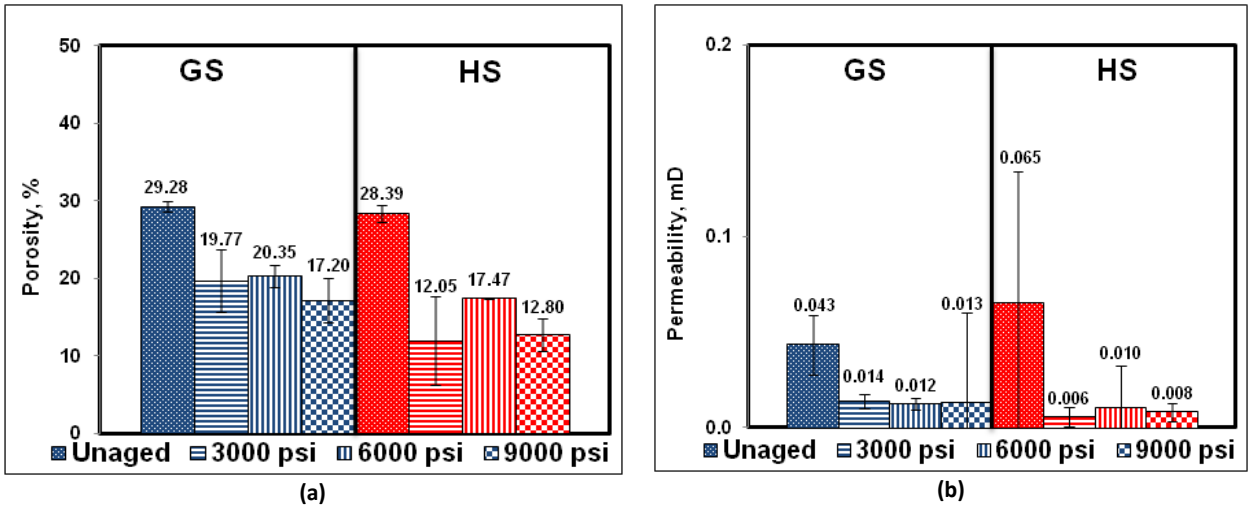

Fig. 4: Effects of aging pressure on porosity and permeability of baseline cores aged at 225°F and 10% CO_2

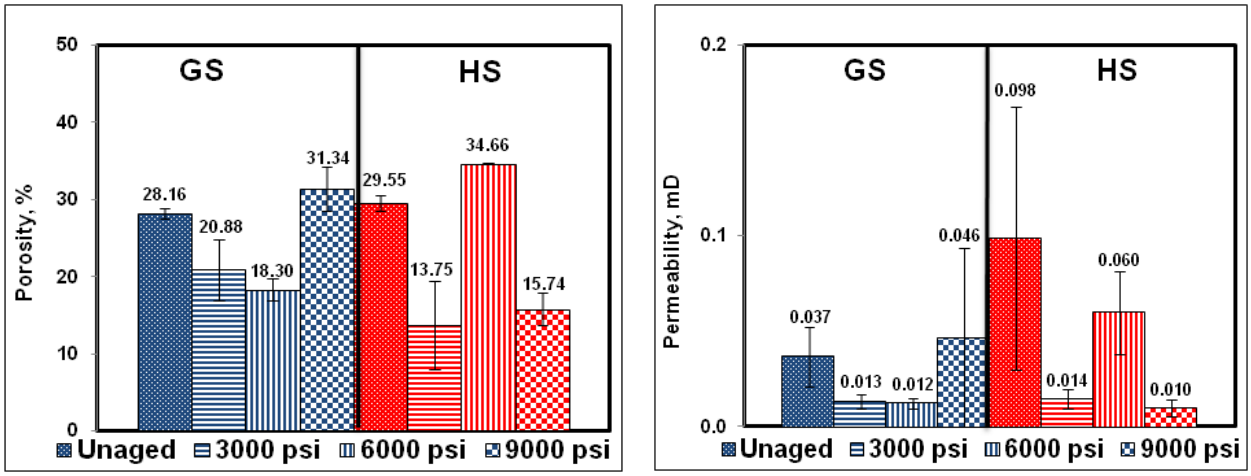

Fig. 5: Effects of aging pressure on porosity and permeability of baseline cores aged at 350˚F and 10% CO_2

Figures 6 and 7 show the porosity and permeability of samples aged for 14 days in 2% brine saturated with 40% CO_2 at 225°F and 350°F, respectively. For both cement classes, with increasing pressure, porosity and permeability first decreased then increased and again decreased. It followed the trend of Class H cement observed at 10% CO_2 concentration.

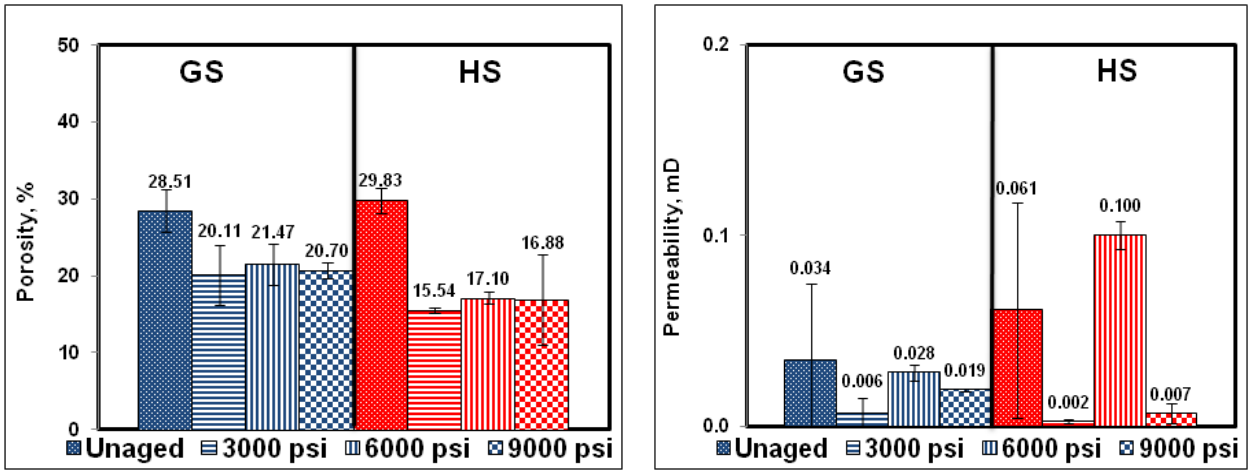

Fig. 6: Effects of aging pressure on porosity and permeability of baseline cores aged at 225˚F and 40% CO_2

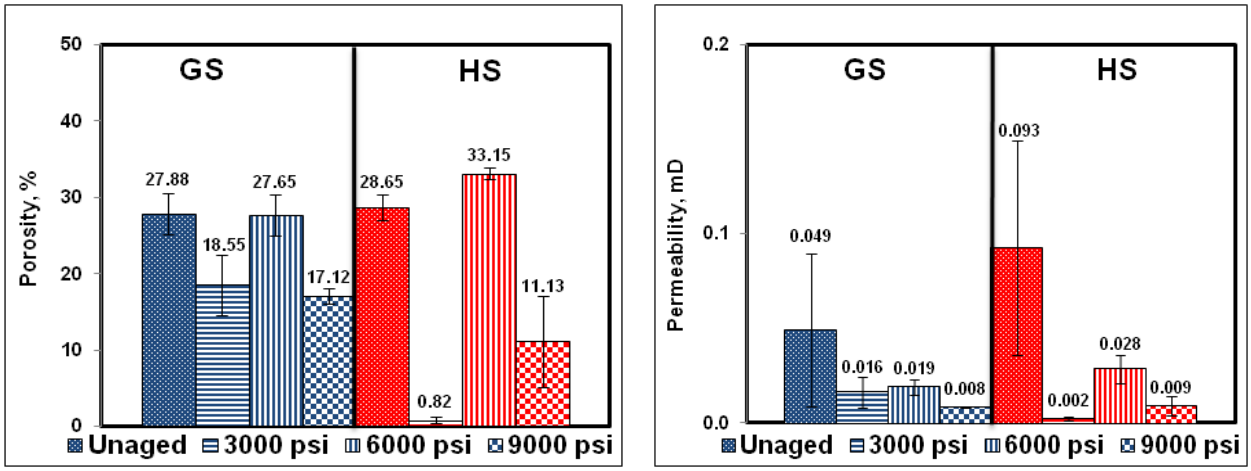

Fig. 7: Effects of aging pressure on porosity and permeability of baseline cores aged at 350°F and 40% CO_2

Effects of CO_2 Concentration

The effects of CO_2 concentration on porosity and permeability of baseline samples at low and intermediate pressures (3000 and 6000 psi) have been presented in the last month report. **Figures 8** and **9** demonstrate the effects of CO_2 concentration on porosity and permeability of aged samples at 9000 psi and various temperatures (225°F and 350°F).

For Class G cement, the general trends of porosity and permeability are consistent. However, the porosity and permeability trends vary with temperature. At 225°F, increase in CO_2 concentration reduced porosity and permeability of the samples at low CO_2 concentration (10%), then the trend reversed and the porosity and permeability increased with concentration due to intense leaching resulting from the high acid concentration in the brine. At high temperature (350°F), except 10% data point, measurements showed a similar trend.

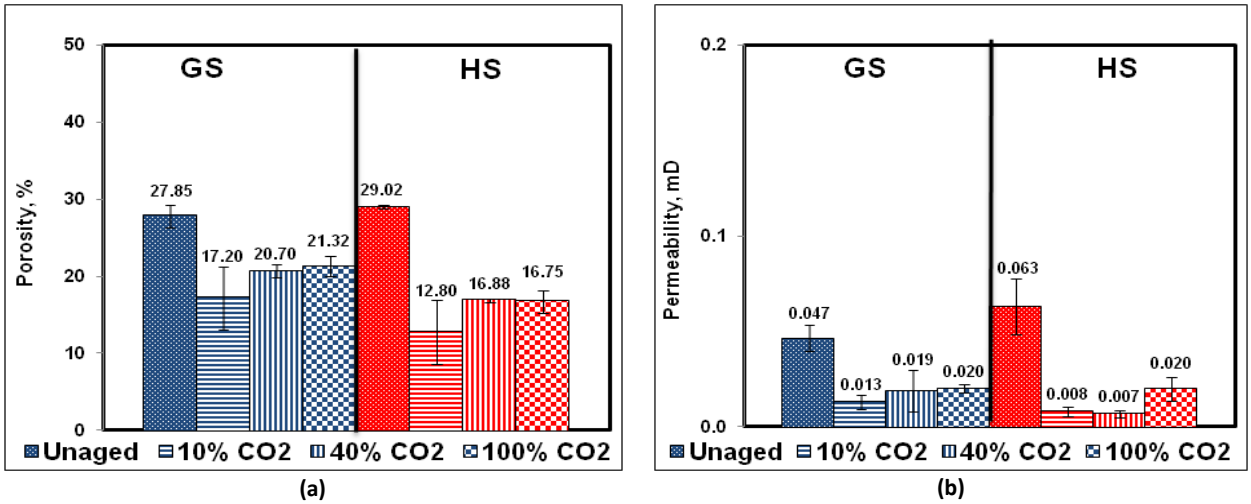

Fig. 8: Effects of CO_2 concentration on porosity and permeability of baseline cores aged at 225°F and 9000 psi

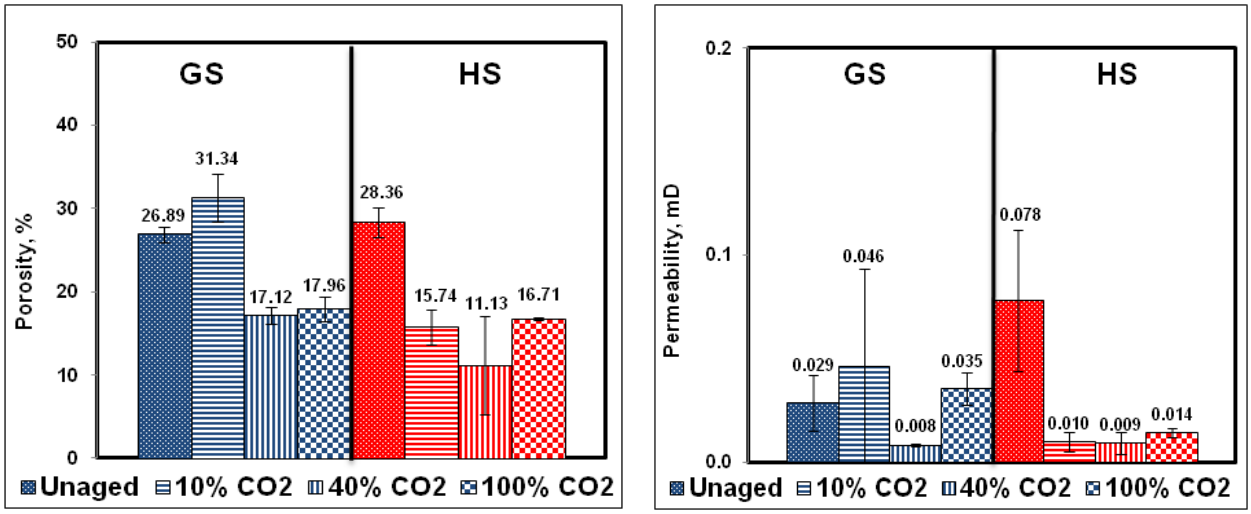

Fig. 9: Effects of CO_2 concentration on porosity and permeability of baseline cores aged at 350°F and 9000 psi

Similar to Class G, the general trends of porosity and permeability are consistent for Class G cement. Additionally, the trends with temperature remain the same. As the concentration of CO_2 increased, porosity and permeability of the samples decreased due to carbonation. However, at high concentration (100%), porosity and permeability of the samples increased because of leaching.

2.2.2 Compressive Strengths of Baseline Cements

Study on compressive strength of conventional cement was continued. Measurements from Batches 27 and 28 are incorporated into our previous measurements and presented here. Conditions in the aging cell for each of this batch are summarized in Table 1. The results show the effects of pressure, temperature and CO_2 concentration on compressive strength of aged cement samples.

Effects of Aging Pressure

The new compressive strength data from Batch 27 is combined with previous results and presented in **Fig. 10**. At low aging pressure (3000 psi), initial strength increase was observed in both cements due to the presence of scawtite. At 6000 psi, most of the scawtite is fully carbonated, resulting in the formation of calcite, which causes the strength to increase. Calcite formation peaks at 6000 psi and more CO_2 is dissolved with further increase in pressure resulting in

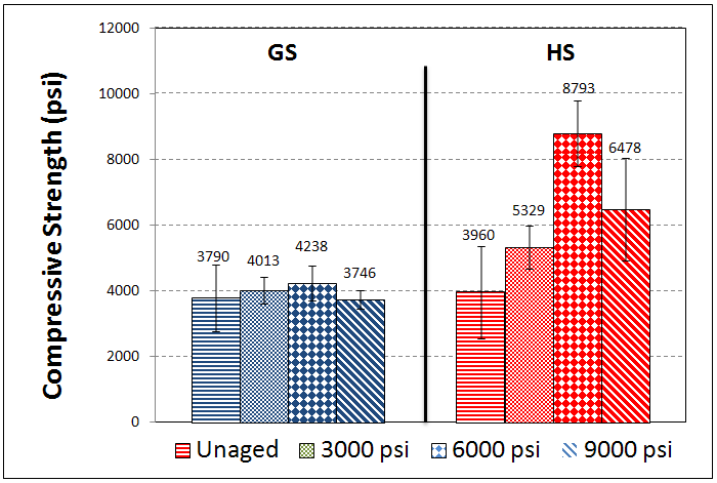

Fig. 10: Effects of pressure on compressive strength of cement cores at 225°F and 10% CO_2 concentration

leaching of the fully carbonated phases and strength reduction. Consistent with previous data, Class H cement exhibited higher strength than Class G cement after aging under HPHT conditions.

Effects of Temperature

The effects of temperature on compressive strength of baseline (Class G and Class H) cement have been investigated at intermediate pressure (6000 psi) and low CO_2 concentration (10% CO_2). As shown in **Fig. 11**, compressive strength of Class G cement showed slight variation with temperature. Temperature has impact on a number physio-chemical process involved during cement aging including carbonation, CO_2 solubility, ionic transport, leaching and solubility of solids. For Glass G cement, most of these processes offset each other leading to limited overall change in strength. As temperature increased beyond 100°F, Class H cement showed significant strength gain due to carbonation, which was followed by a progressive reduction. The reduction in strength is due to cement leaching, which is the interaction between pore fluid and cement matrix. This leads to dissolution of hydrated binding components (portlandite and calcium silicate hydrates), thus decreasing its mechanical strength.

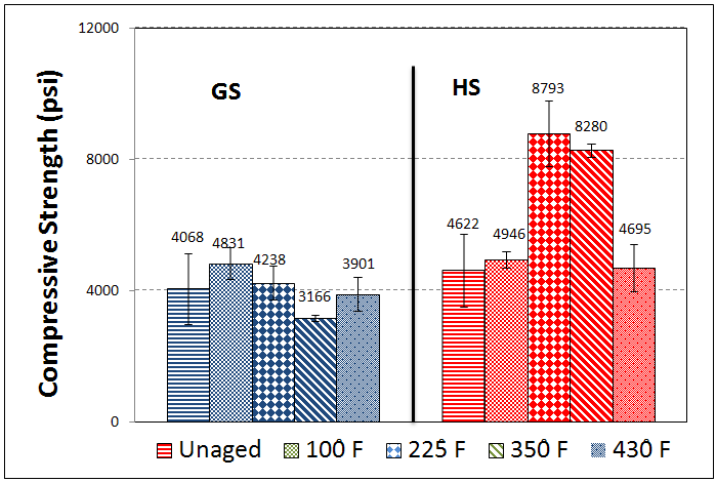

Fig. 11: Effects of temperature on compressive strength cement cores at 6000 psi and 10% CO_2

Effects of CO_2 Concentration

The effects of CO_2 concentration on compressive strengths of conventional (Class G and H) cement aged at 225°F and 9000 psi is presented in **Fig. 12**. Both Class G and Class H cements showed similar compressive strength trends. After aging, the samples progressively became stronger as more CO_2 gas was injected into the aging system. This occurs because of high pressure, which allows more CO_2 to dissolve in brine, resulting in increased rate of carbonation. Since solubility of portlandite is low at high temperature, major leaching has not occurred. Slight strength loss that may have occurred due to leaching is superseded by increased rate of carbonation.

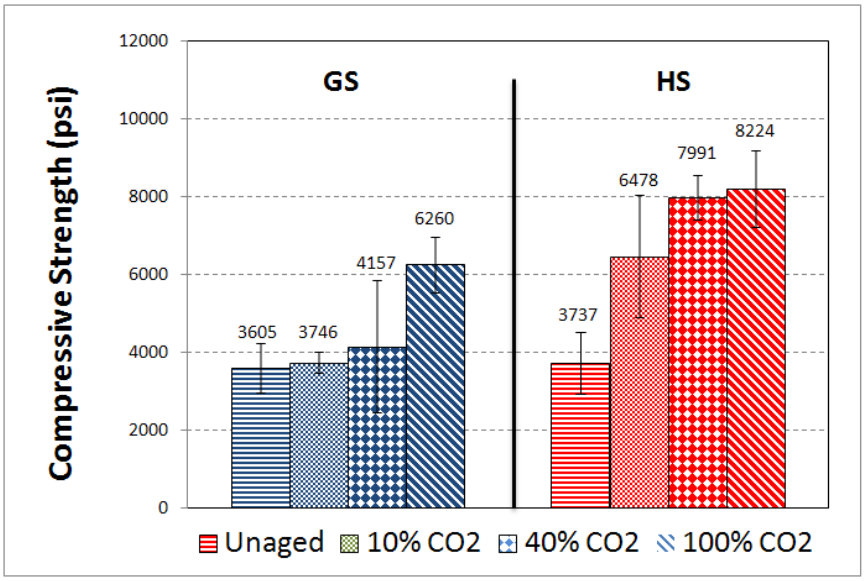

Fig. 12: Effects of CO_2 concentration on compressive strength of cement cores at 225°F and 9000 psi

2.2.3 Additive Screening and Cement Formulation Studies

The testing of additive containing cement was continued. During this reporting period, latex and micro-silica containing cement cores were aged at HPHT conditions. Results show the benefit of additives in reducing acid attack. The cores showed the presence of CSH component in the matrix after aging, indicating lesser carbonation. The second batch of micro-silica cement cores were aged and tested. Results were found to be similar to those obtained from first batch experiment. After aging, the samples showed significant increase in porosity and permeability; however, they indicated the presence of CSH component.

2.2.3.1 Latex and Micro-silica Based Cement

The slurry properties of 10% latex + 10% micro-silica (LTMS) were presented in previous report. The first batch of latex and micro-silica containing cement cores were aged under HPHT conditions and tested. The samples exhibited the presence of CSH component after aging, indicating their resistance against acid attack.

Porosity and Permeability Unaged Cores

For unaged samples, the porosity of the LTMS samples is almost similar to those of baseline samples (**Fig. 13a**); however, their permeability is significantly lower than those of baseline samples (**Fig. 13b**). Permeability reduction is beneficial to the cement as it can lower the penetration of carbonic acid between pores. In addition, compressive strengths of the samples were lower than those of baseline samples (**Fig. 14a**); however, they were above the accepted industry standards. LTMS samples exhibited higher shear bond strength than baseline samples (**Fig. 14b**).

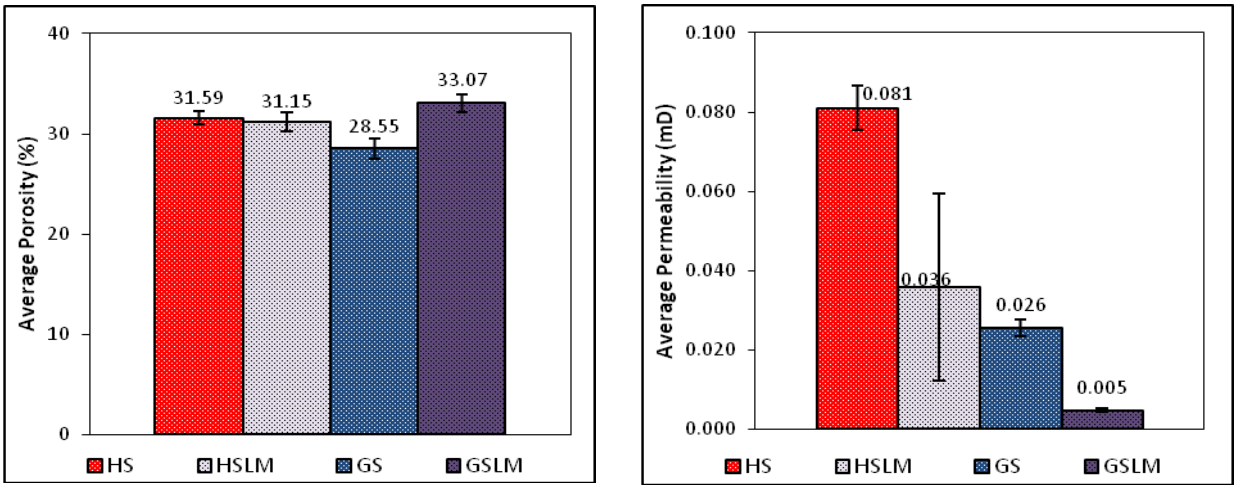

(a) (b)

Fig. 13: Porosity and permeability of unaged LTMS and baseline samples (Batch 022)

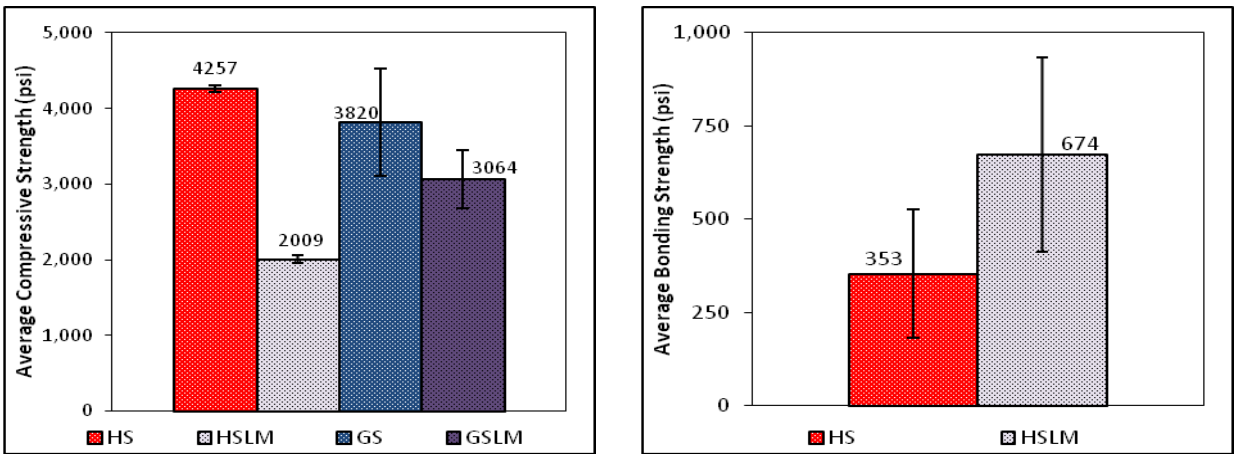

(a) (b)

Fig. 14: Compressive and shear bond strength of unaged LTMS and baseline samples (Batch 022)

Physical and mechanical properties of the unaged LTMS samples were under the accepted range with respect to the baseline samples. Hence, the cores were aged under high-pressure conditions (see **Table 4)**. After aging, the properties of the cores were measured.

Table 4: Aging conditions for the LTMS samples

LTMS	Temp. (°F)	Pressure (psi)	CO_2 (%)	NaCl (%)	Days	Baseline	Exp. No.
Batch 002	225	9000	10	2	14	Batch 027	24

Porosity and Permeability

Porosity and permeability measurements are presented in **Figs. 15** and **16**. The porosity and permeability of unaged samples are much lower than those of baseline samples due to the presence of micro-silica as filler additive. After aging, reduction in porosity and permeability of the baseline samples was observed due to carbonation. Porosities of LTMS samples were slightly reduced while their

permeabilities showed slight increase. These results are consistent with the fact that the LTMS samples have been subjected to lesser carbonation.

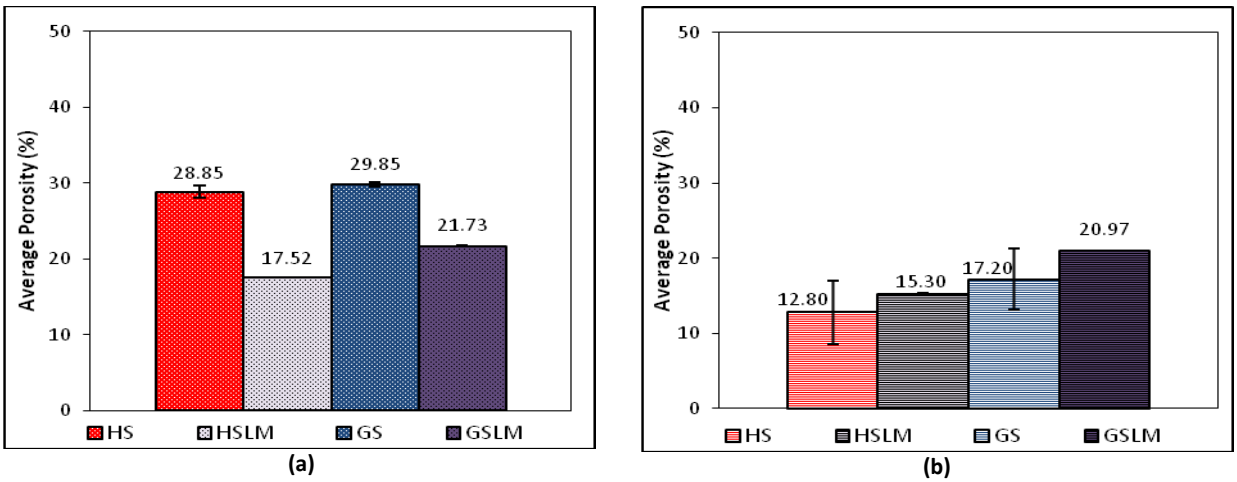

Fig. 15: Porosities of LTMS and baseline cements: a) unaged; and b) aged for 14 days at 225°F and 9000 psi in brine saturated with 10% CO_2 gas

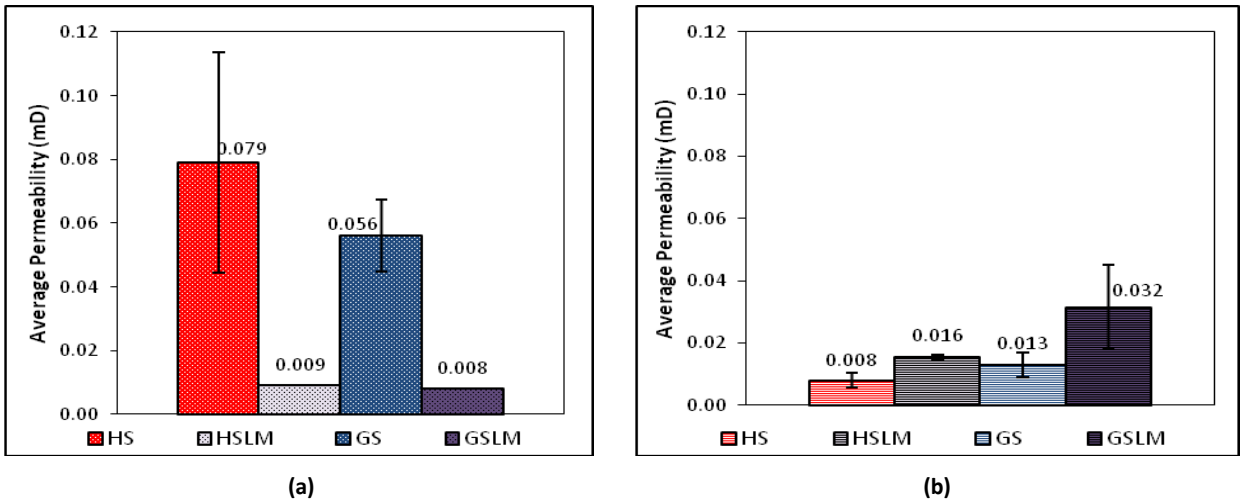

Fig. 16: Permeabilities of LTMS and baseline cements: a) unaged; and b) aged for 14 days at 225°F and 9000 psi in brine saturated with 10% CO_2 gas

Shear Bond Strength

Shear bond strength (SBS) measurements are presented in **Fig. 17**. The shear bond strengths of both unaged and aged LTMS samples were higher than those of the baseline samples. After aging, the SBS of LTMS samples was reduced. The reduction in bond strength indicates limited expansion of the matrix and hence, indicates lesser carbonation. The baseline samples on the other hand showed increase in SBS resulting from expansion of the matrix.

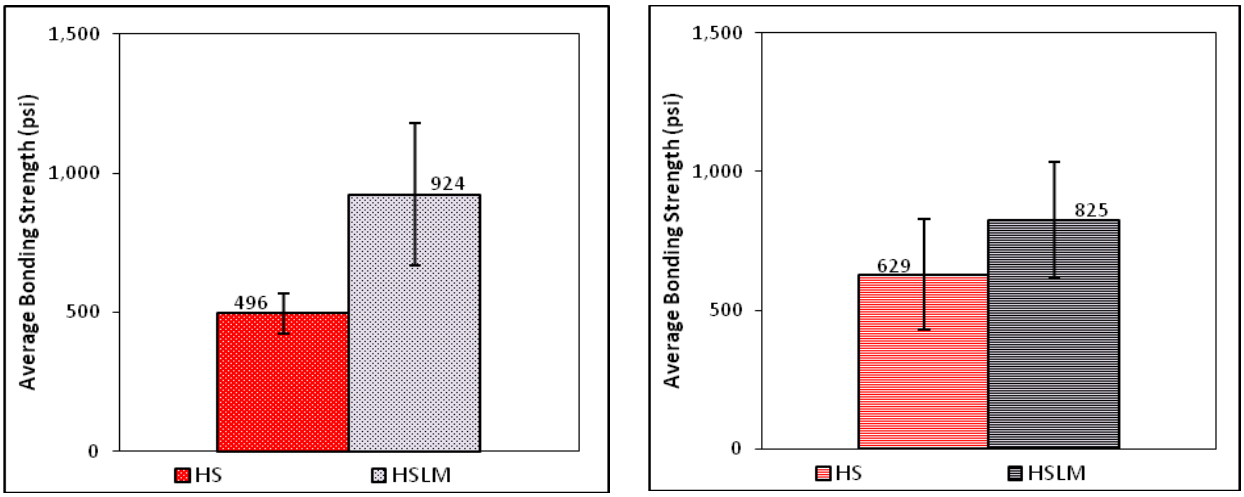

Fig. 17: Shear bond strength of LTMS and baseline cements: a) unaged; and b) aged for 14 days at 225°F and 9000 psi in brine saturated with 10% CO_2 gas

FTIR Analysis

The FTIR spectrum is simplified in the form of bar charts for easy interpretation (**Fig. 18**). It should be noted that as micro-silica is a pozzolanic material (material that can react with CH); hence, the CH content of LTMS samples is minimal. As a result, the FTIR results show no peak for CH group for the LTMS samples; and hence, it cannot be used to compare LTMS samples with the baseline. The outer most zone being the most exposed part it has the maximum $CaCO_3$. The middle and inner zone show presence of $CaCO_3$ in both samples. However, the middle and inner zone of LTMS samples show presence CSH in the matrix, which indicates less carbonation as compared to the baseline samples.

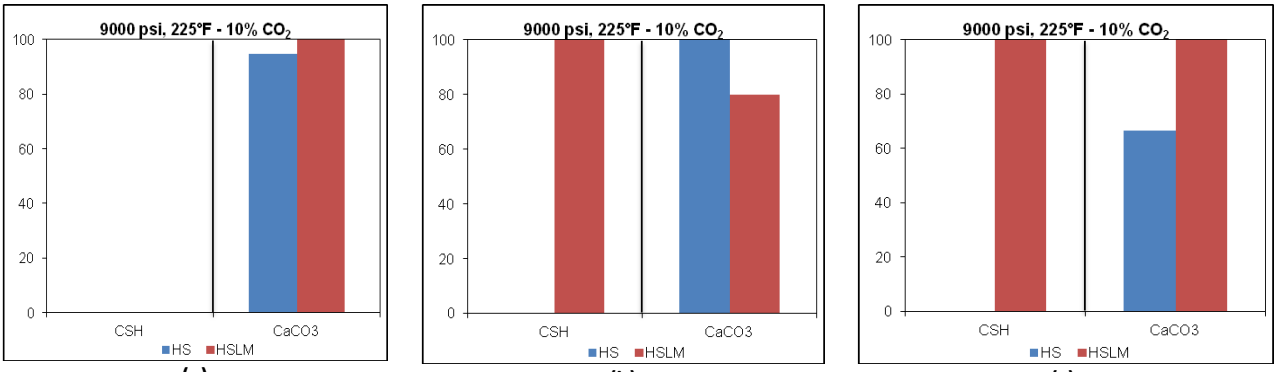

Fig. 18: Summarized FTIR data of LTMS and baseline HS samples aged at 225°F, 9000 psi, 10% CO_2 for 14 days: a) Outermost zone; b) Middle zone; and c) Innermost zone

In summary, porosity, permeability, shear bond strength and FTIR measurements indicate less carbonation of the LTMS samples. In the coming weeks, additional experiments will be carried out under different aging conditions in order to test the effectiveness of the LTMS against acid attack.

2.2.3.2 Micro-Silica Based Cement

Aging experiments with 10% BWOC micro-silica cement (MS-10) were continued. The composition of the slurry is presented in Report # 22. Previously, aging was conducted in 2% brine saturated with 100% CO_2 gas at 225°F and 3000 psi. The recent test was performed under a different aging condition (see **Table 5)**. After aging, the properties of the cores were measured.

Table 5: Aging conditions for the MS-10 samples

MS-10	Temp. (°F)	Pressure (psi)	CO_2 (%)	NaCl (%)	Days	Baseline	Exp. No.
Batch 009	430	9000	10	2	14	Batch 028	25

Porosity and Permeability

Porosities and permeabilities of MS-10 and baseline cores are presented in **Figs. 19** and **20**, respectively. Unaged MS-10 samples show lower porosity and permeability than the baseline samples. This is attributed to the fineness of micro-silica particle. After aging, porosity and permeability of all the samples increased. This was the first experiment conducted at 430°F. Such high temperature causes very rapid dissolution of ions from the matrix (leaching), resulting in substantial increase in porosity and permeability. The leaching was prominent in MS-10 samples than the baseline cores. A previous experiment (Exp. 21, Batch 024) also showed similar results; however, porosity and permeability changes occurred after aging were not as significant as in this experiment. The FTIR results of previous experiment showed presence of CSH in the inner most zone of MS-10 sample, which suggests lesser carbonation. Hence, FTIR study for this batch of cores will be necessary to confirm the effectiveness of micro-silica.

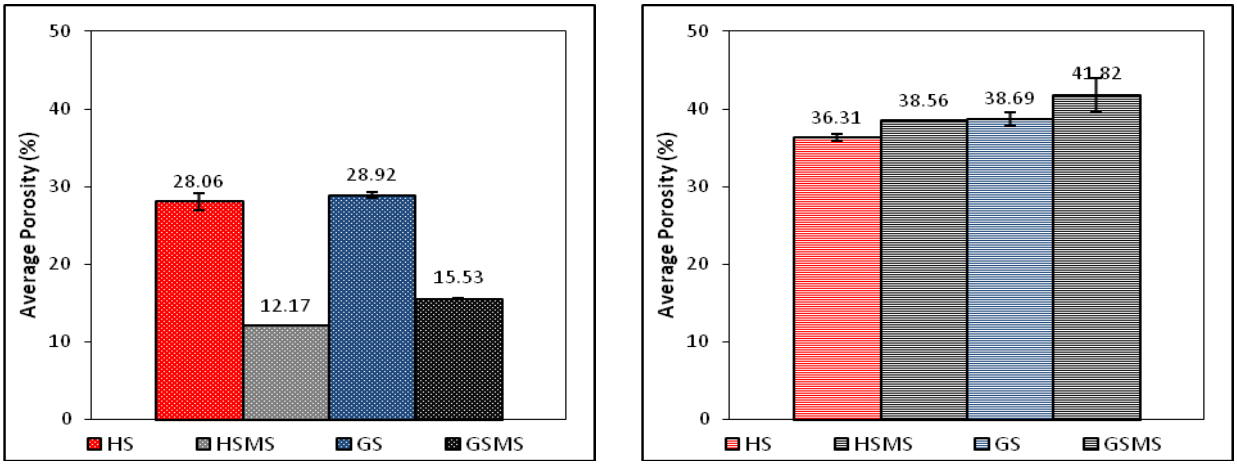

Fig. 19: Porosities of MS-10 and baseline cements: a) unaged; and b) aged for 14 days at 430°F and 6000 psi in brine saturated with 10% CO_2 gas

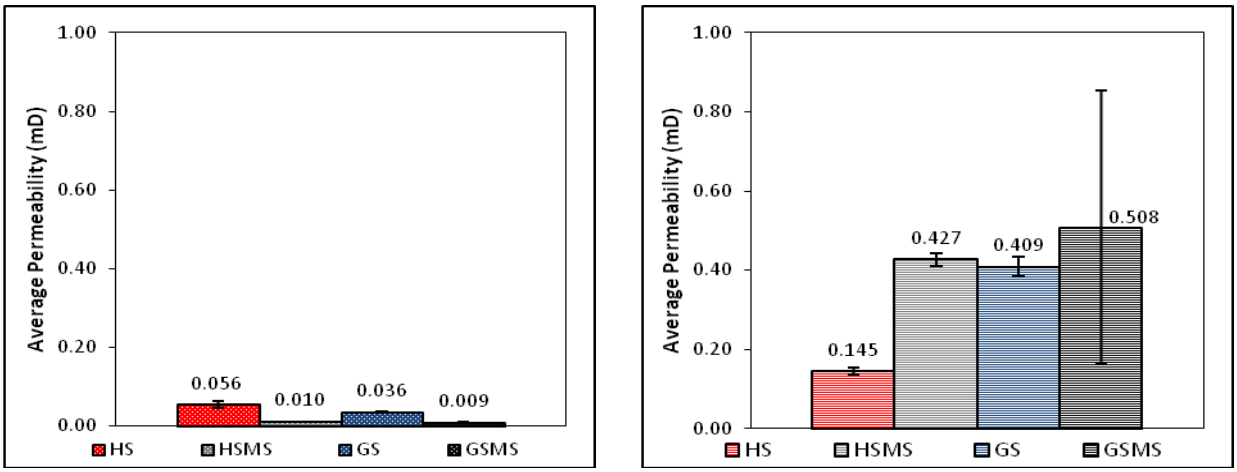

Fig. 20: Permeabilities of MS-10 and baseline cements: a) unaged; and b) aged for 14 days at 430°F and 6000 psi in brine saturated with 10% CO_2 gas

Shear Bond Strength

The shear bond strength (SBS) of MS-10 and baseline samples are presented in **Fig. 22**. The shear bond strength of unaged MS-10 samples was higher than that of the baseline samples. This is consistent with our previous experiment. After aging, an increase in SBS of base samples was observed due to expansion of the matrix resulting from carbonation. The MS-10 samples, on the other hand, showed almost the same shear bond strength after aging. This can be interpreted in two ways. First, the MS-10 samples experienced less carbonation and hence did not expand significantly to increase the bond strength. Second, the matrix underwent the same level of leaching and carbonation, which offset each other, causing the SBS to remain the same after aging. The results from FTIR need to be analyzed for a valid interpretation.

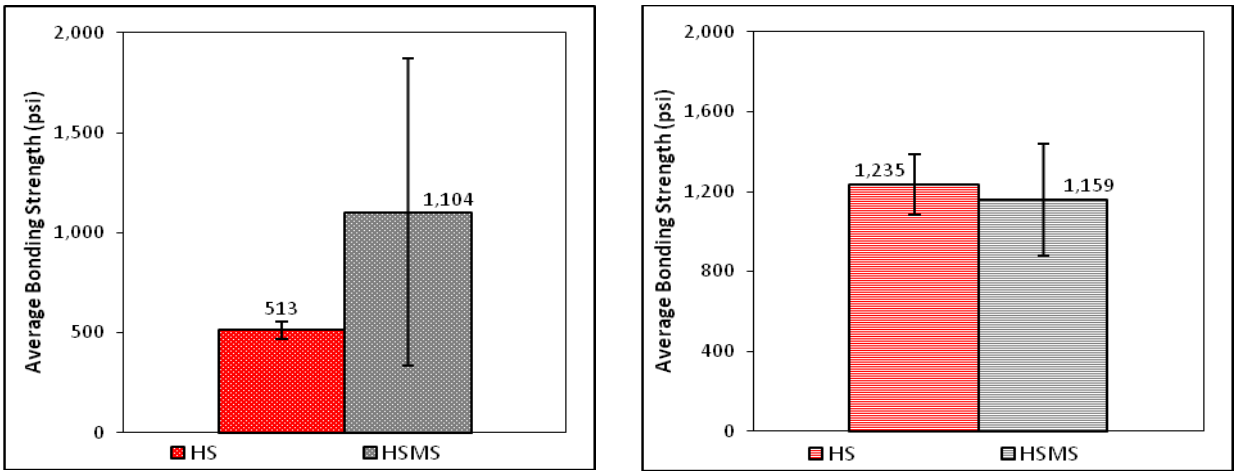

Fig. 22: Shear bond strength of HHO and baseline cements: a) unaged; and b) aged for 14 days at 225°F and 3000 psi in brine saturated with 10% CO_2 gas

FTIR Analysis

FTIR spectra of MS-10 and baseline samples are simplified in the form of bar charts for easy interpretation (**Fig. 21**). As discussed previously, micro-silica is a pozzolanic material. As a result, FTIR spectrum of MS-10 sample did not display a CH peak. Hence, CH content cannot be used to compare the levels of degradation in MS-10 and baseline samples. However, comparison can be made in terms of CSH content. The outer most zones of the samples did not show the presence of CSH group due to complete carbonation; they only contained large amount of $CaCO_3$. The middle and inner zones depicted the presence of both CSH and $CaCO_3$ in both the samples. The MS-10 samples even after going through the excessive leaching, they were able to preserve the CSH, which is the major binding component of the cement matrix.

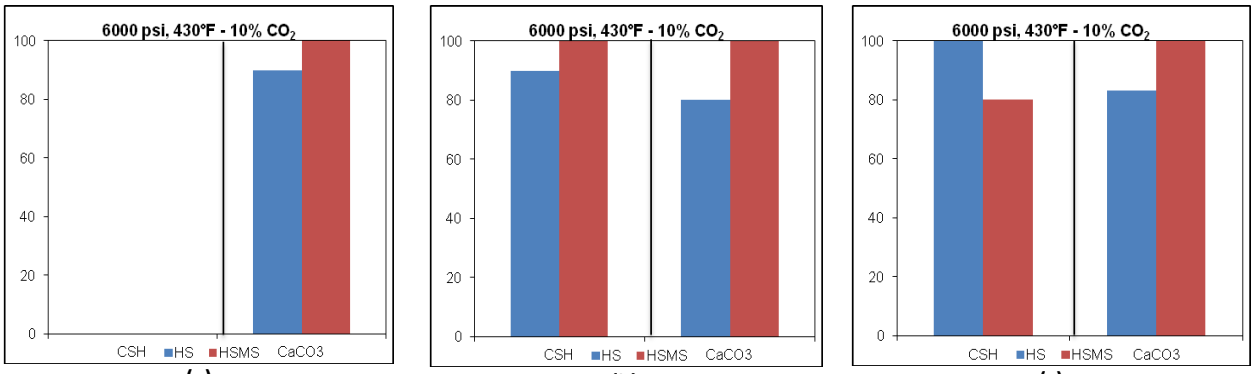

Fig. 21: Summarized FTIR data of HSMS and baseline HS samples aged at 430°F, 6000 psi, 10% CO_2 for 14 days: a) Outermost zone; b) Middle zone; and c) Innermost zone

In summary, the MS-10 samples showed a very large increase in porosity and permeability after aging. However, they were able to preserve the CSH component of the matrix. The presence of CSH is also observed in the base samples. It is observed from the two experiments that the micro-silica is working against the acid attack only to certain extent and causing an excessive increase in the pore space. Although the CSH components of the samples were preserved for two-week period, prolonged exposure may lead to excessive damage to the matrix. The experiments with micro-silica will be continued to study its behavior.

2.3 Experimental Studies on Corrosion of Tubulars (Task 3)

As indicated in last month report, the corrosion test facility has been modified to carry out tests at elevated temperature. After the modification, three tests were carriedout. The samples were aged in 2% brine and presence of CO_2 gas. Similar to the previous experiments, all tests were carried out for 187 hours varying partial pressure of CO_2 and N_2. Tests were performed at 78 and 120 F. Test parameters and results of these experiments are summarized in **Table 6**. **Figures 23 to 25** present instantaneous corrosion rates measured using LPR method during experiments. Abrupt increase in corrosion rate shown in Figs. 24 and 25 is due to injection of gas to maintain the test pressure of 120 psi.

Table 6: Test parameters and results of low-pressure corrosion experiments

Exp. #	Temp. (ºF)	Pressure (psi)	Partial Pressure %		Brine Conc. (%)	Test Period (days)	Results (mpy)	
			N_2	CO_2			LPR	WL
18	78	120	75	25	2	187	22.92	21.83
19	110	120	75	25	2	187	31.78	23.78
20	110	120	25	75	2	187	53.16	43.22

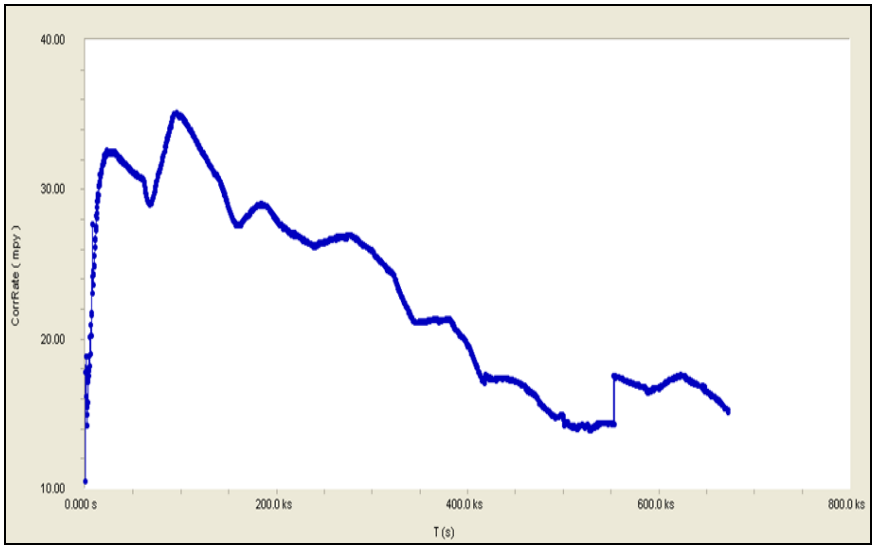

Fig. 23: Corrosion rate vs. time for Exp. 18 (25% CO_2 gas, 120 psi, 78°F)

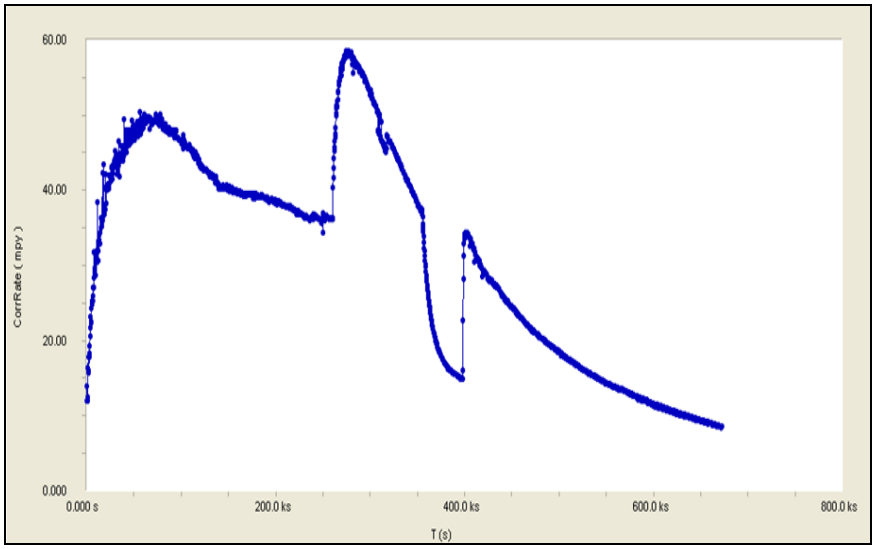

Fig. 24: Corrosion rate vs. time for Exp. 19 (25% CO_2 gas, 120 psi, 110°F)

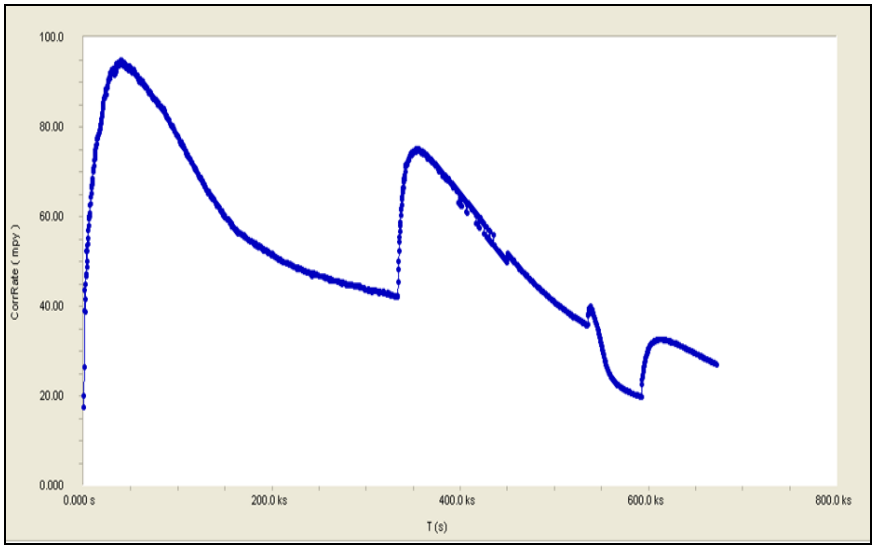

Fig. 25: Corrosion rate vs. time for Exp. 20 (75% CO_2 gas, 120 psi, 110°F)

3. Planned Activities

- Continue aging experiments with brine-CO_2-CH4 system for 14 days varying CO_2 concentration (10, 40 and 100%) at 430°F and 6000 psi.
- Continue theoretical and modeling studies on tubular degradation.
- Continue cement additive screening and acid resistant cement formulation studies.
- Begin testing of the corrosion experiment setup.

4. Project Expenditures

This section presents the project expenses during the month of November (**Table 7**) and the cumulative expenditures.

Table 7: Current and cumulative expenditures, November 2013

No.	Budget Categories	Current Expenses	Cumulative Expenses
1	Salaries & Wages	$9,115.38	$245,684.60
2	Fringe Benefits	$1,836.20	$56,264.41
3	Project Materials	$1,138.48	$60,642.96
4	Travel	$0.00	$6,232.33
5	Conference Expenses	$0.00	$0.00
6	Other Direct Costs	$0.00	$993.60
7	Equipment	$0.00	$241,399.90
8	Space Rental	$0.00	$0.00
9	Indirect Cost	$4,991.13	$183,855.02
10	**Total**	**$17,081.19**	**$795,072.82**

Nomenclatures

BWOC	By weight of cement
CH	Calcium hydroxide
CSH	Calcium silicate hydrate
FTIR	Fourier Transform Infra-Red
GHO	Class G Cement with hydroxyapatite
GS	Class G cement with silica flour
GSMG	Class G Cement with silica flour and magnesium oxide
GSLM	Class G Cement with silica flour, latex and micro-silica
GSLT	Class G Cement with latex
HHO	Class H Cement with hydroxyapatite
HPHT	High-pressure high-temperature
HS	Class H cement with silica flour
HSHO	Class H Cement with silica flour and hydroxyapatite
HSMG	Class H Cement with silica flour and magnesium oxide
HSLM	Class H Cement with silica flour, latex and micro-silica
HSLT	Class H Cement with latex
LPR	Linear polarization resistance
LTMS	Cement with latex and micro-silica additives
mpy	mils per year
MGO	Magnesium oxide containing cement
MGO-5	Cement containing 5% BWOC MgO as additive
MGO-10	Cement containing 10% BWOC MgO as additive
MS	Micro-silica containing cement
MS-10	Cement containing 10% BWOC micro-silica as additive
NACE	National Association of Corrosion Engineers
SBS	Shear bonding strength
SEM	Scanning Electron Microscope
SCC	stress corrosion cracking
SSC	Sulfide Stress Cracking
XRD	X-Ray diffraction

References

Been, J. and Crozier, B. 2014. Thermal Well Casing Corrosion Evaluation Using Hydrogen Permeation in Mini-Pipe Specimens, Alberta Innovates Technology Futures, AITF, Calgary, Alberta http://www.atimetals.com/news/corrosion-conference/Documents/CSC11-pdfs/presentation_5b_been.pdf, last accessed on 01-18-2014.

Cane, R.D. and Cayard, M.S. 1998. Roles of H2S in Behavior of engineering alloys: A review of literature and experience, paper No. 274, presented at the NACE International Annual Conference, 22-27 March, San Diego, California.

Cernocky, E.P., Aaron, V.D., Paslay, P.R. and Wink, R.E. 2005. Combined Axial Tension/Compression and Internal pressure testing of Mini-pipe in H_2S environment to determine three-dimensional (Triaxial) stress states, which produce crack initiation failure: Explanation of New test fixture, Mini-pipe specimen and preliminary test results, paper SPE 97577 presented at SPE High Pressure/High Temperature Sour Well Design Applied Technology Workshop, 17-19 May, Woodland, Texas.

Hashizume, S., Inohara, Y. and Masamura, K. 2000. Effects of pH and P_{H2S} on SSC Resistance of Martensitic Stainless Steels, paper No.130, NACE International Annual Conference.

Jones, R. H. 1996 .Cements treated with high-pressure CO_2. US Patent 5,518,540, 21 May.

Morana R. and Nice P.I. 2009. Corrosion assessment of High Strength Carbon Steel Grades P-110, Q-125,140 and 150 for H2S containing producing well environments, paper No. 9093, presented at the NACE International Conference and Expo, 22-26 March, Atlanta, Georgia.

NACE Standard TM0177, 2005. Laboratory Testing of Metals for Resistance to Sulfide Stress Cracking and Stress Corrosion Cracking in H2S Environments.

Appendix A

MINUTES

5th Technical Advisory Board Meeting

E12PC00035

Project Title: Effect of H_2S and CO_2 in HPHT Wells on Tubulars and Cement

Meeting Date: Nov. 7, 2013
Time: 8:30 AM – 3:00 PM Central Time
Meeting Location: Courtyard Houston by The Galleria, 2900 Sage Road, Houston, TX 77056 USA

Attendees: Joe Levine (BSEE), Greg Cellos (BSEE), Julian Hwang (BSEE), Arild Saasen (Det Norske), Ashok Santra (Weatherford International), Gil Go (Baker Hughes), Gunnar DeBruijn (Schlumberger), Li Li (Baker Hughes), Kyris Agapiou (Halliburton), Olav-Manguar Nes (Det Norske), Ramadan Ahmed (OU), Subhash Shah (OU), Omotayo Omosebi (OU), Adarsh Naidu (OU), Aman Srivastava (OU), Himanshu Maheshwari (OU), Jueng Hwang (OU)

Dr. Ahmed opened the meeting by welcoming the Technical Advisory Board members and all other participants. All TAB members were present, except Vellorac. He introduced the project objectives, tasks, and provided the project status. He mentioned that the project is on scheduled and currently the baseline data on Class G and H cements are being gathered. In addition, special cement is being formulated and it looks promising. However, it needs further study.

Equipment has been developed for the corrosion testing and experiments will start soon. The project has been delayed couple of months because of problems in obtaining casing pipe samples and not finding the manufacturer for the machining of samples. However, the project will finish on schedule.

1st Presentation by Himanshu Maheshwari (MS Graduate Student)

The first presentation was by Himanshu Maheshwari on the effects of sour gas on the permeability and porosity of oil well cement. He defined the objectives and described the mechanisms of CO_2 attack on cement under HPHT. He also described the aging cell and associated experimental setup. He provided the background data and discussed the results and modeling of permeability and porosity data. The following questions were asked by TAB members.

Mr. DeBruijn: What are the densities of Class G and H cements? Class G – 15.5 ppg with 44% water and Class H – 15.9 ppg with 38 % water.

Dr. Santra: Do we have XRD data before exposing sample to pressure? Yes, results from previous presentation were shown.

Mr. DeBruijn: Do we have data past 28 days? Since there is very slow degradation past 28 days, there is no need to gather data beyond it. There is not much difference between 14 and 28 day data.

Mr. Kyrish: Do you have a plan to vary silica content? No, we used only 35%.

Dr. Saasen: You should consider publishing some of the findings. Dr. Ahmed said yes we are in the process of preparing 3 manuscripts.

Mr. Gil: Are you adding more CO_2 during the process? Initially, we have 40% and yes 40% CO_2 gas is injected to maintain constant pressure.

2nd Presentation by Omotayo Omosebi (new PhD Graduate Student)

Omotayo made the next presentation and discussed the mechanical properties of oil well cement in sour gas environment. He pointed out the need for having data at 10,000 psi and 500°F, particularly in the presence of sour gas. The following were the Q& A.

Mr. Olave: Did you do deformation test on cement? No.

Dr. Santra: How do you depressurize the cell? Dr. Ahmed – we cool it down first and vent it slowly. That way there is no abrupt expansion.

Mr. Gil: How does your stress-loading rate (ASTM C39) compare to API procedure because it will influence the results. We will look into it. Mr. DeBruijn: It is very similar to API.

Mr. Omotayo: Class H is higher strength and more CO_2 resistant than Class G because Class H is denser.

Dr. Saasen: Class G is much smaller in size – finer than Class H. We should use the same amount of water for both and compare 20 day aging results.

Mr. Gil: To produce 11 B_C for Class G and H, it is recommended to use 44% water for Class G and 38% water for Class H cement.

Dr. Ahmed: If we change the water requirement, the results would not match with the baseline data.

Omotayo: Future tests will be conducted at 430°F with prolonged exposure (28 days and greater). Also the cement degradation model will be developed.

Dr. Santra: XRD test should be conducted with the actual cores used and compare the composition.

Mr. Gil: Is curing done under pressure? No, atmospheric.

3rd Presentation by Jueun Hwang (MS Graduate Student)

The next presentation on the effect of sour gas on shear bond strength of oil well cements was made by Jueun Hwang. The samples were cured in 2% brine at 200 F for 5 days. She showed the data and discussed the effect of aging (temperature, pressure, CO_2 concentration) on the shear bond strength of cements. The Q&A was as follows:

Dr. Santra: You showed data of only Class H cement samples. Gulf of Mexico and Southern states use Class H while North Sea and Northwest use Class G. We should look at couple of Class G samples also because the expansion will be different. Also, curing at 200°F and testing at 350°F can deteriorate the shear bond.

4th Presentation by Aman Srivastava (MS Graduate Student)

Aman Srivastava made presentation on the effect of additives on cement properties under acidic environment. He showed compressive strength results of mixing micro-silica, MgO, and HOAP with cement. He found 10% bwoc micro-silica was the optimum concentration to produce desirable cement in terms of the strength. Adding 20% bwoc produced brittle cement. Q&A was as follows:

Dr. Saasen: What is the density of micro-silica? 300 Kg/m3. You should use micro-silica from various manufacturers since they are so different.

Aman noted that the amount of carbonation occurring in MgO samples was less than the base samples. Class H was more carbonation resistant with MgO than Class G cement. Compressive strength increases with MgO.

Dr. Saasen: Consider increasing exposure time. Are both Class G and H sulfate resistant? Yes.

Mr. Kyris: What is the source for HOAP? We purchased from the market.

Dr. Santra: What grade MgO did you use? Lab grade.

5th Presentation by Adarish Naidu (Graduate Student)

The last presentation was on corrosion of tubulars exposed to CO_2 containing fluids and was made by Adarsh Naidu. Adarsh discussed various corrosion mechanisms and model for estimating corrosion rates. He also described various corrosion measurement techniques, particularly the weight loss method and Linear Polarization Resistant method (LPR). He mentioned that the weight loss method is the preferred method. He concluded the presentation with the future plan. There were no major questions.

Next, Dr. Subhash Shah (Co-PI) summarized all the presentations and thanked the TAB for their support, service, and participation at the meeting. He also thanked all students for conducting the difficult experiments, generating quality data, and for doing a very professional job.

The next meeting is planned for May 9, 2014 and will be held at The University of Oklahoma, Norman. Dr. Ahmed thanked all TAB members and students. The meeting was then adjourned.

Project Title: Effect of H_2S and CO_2 in HPHT Wells on Tubulars and Cement

Report Type: Monthly Report

Report #: 27

Reporting Period: November 22nd, 2013 to December 21st, 2013

Authors:

Ramadan Ahmed, Principal Investigator

Subhash Shah, Co-Principal Investigator

Samuel Osisanya, Co-Principal Investigator

Rida Elgaddafi, Research Assistant

Omotayo Omosebi, Research Assistant

Himanshu Maheshwari, Research Assistant

Adarsh Naidu, Research Assistant

Aman Srivastava, Research Assistant

Jueun Hwang, Research Assistant

Mounraj Sharma, Research Assistant

Sagar Tale, Research Assistant

Prepared under BSEE Project # E12PC00035

by

THE UNIVERSITY OF OKLAHOMA

February 10, 2014

1. Summary of Accomplishments

This monthly report presents the progress made during the project period November 22, 2013 to December 21, 2013. Investigations on cement and tubular degradation were continued during this reporting period. Due to equipment failure, cement cores and bonding samples were not aged for this period. However, compressive strength, carbonation depth and FTIR mineralogy of previously aged samples were measured. Furthermore, theoretical studies on cement degradation and tubular corrosion were continued.

FTIR analysis of baseline cement showed complete carbonation of the outer zone of the samples regardless of aging conditions. In some cases, results from the outer zone showed reduction in $CaCO_3$ content with increasing CO_2 content of the gas, which can be attributed to the conversion of calcium carbon to calcium bi-carbonate, and subsequently leaching out of the cement. CH is more susceptible to acid attack than CSH. Except in the virgin zones of cores aged at 6000 psi and 350°F, it was not fully carbonated after aging. Increased pressure tends to promote the carbonation of CSH. At high pressures (6000 and 9000 psi) and high concentration of CO_2, CSH was completely carbonated.

Solubility of carbon dioxide plays a great role in the degradation process of cement. At low pressures, solubility of CO_2 is low and precipitation of scawtite is likely to occur. Complete carbonation and leaching often take place at high pressures. As the pressure changes at constant temperature, compressive strength trend can be mixed because of complex nature of cement degradation, which involves two offsetting processes (carbonation and leaching). Despite mixed trends, generally more carbonation occurs at high pressure due to increased CO_2 solubility.

Experimental investigation on cement additives was continued. The effects of micro-silica, latex magnesium oxide and hydroaxipitate on performance of Class H and Class G cements under HPHT conditions were investigated. Fourier Transform Infrared Spectroscopy (FTIR) method was used to evaluate the effectiveness of the additives in preventing the carbonation of binding component of the cement (CSH and CH). Permeability, shear bond strength, FTIR and compressive strength measurements indicate that magnesium oxide, hydroaxipitate and latex with micro-silica containing cement samples resist carbonation better than the baseline samples. In the coming weeks, additional experiments will be carried out under different aging conditions in order to test the effectiveness of additives against acid attack.

Corrosion test setup has been installed in the lab. Testing of instrumentation and heating oil lines have been completed. Due to equipment failure, corrosion experiments under low-pressure conditions were not conducted. The equipment was repaired and tests will begin in the coming days.

Our plan for the upcoming weeks is to continue: i) aging tests at different pressures and temperatures; ii) theoretical and modeling studies on tubular corrosion; iii) additive screening and acid resistant cement development studies; iv) low-pressure corrosion experiments at different CO_2 concentrations; and v) pressure testing of corrosion test setup.

2. Overall Project Progress

2.1 Theoretical Studies (Task 1)

2.1.1 Sulfide Stress Cracking

In underbalanced drilling (UBD), formation fluids are intentionally allowed to enter the well bore. Underbalanced drilling has several advantages over the conventional method. However, due to the influx of formation fluid, tubulars are subjected to extremely corrosive environment that can lead to unexpected material failure. Catastrophic failure during sour underbalanced can lead to sour gas blow out. As mentioned in the previous reports, pH of surrounding environment is important factor for SSC resistance of tubulars (Hashizume et al. 2000). In traditional drilling, pH and chemistry of drilling fluid can be controlled. In UBD, pH of drilling fluid may change due to the entry of formation fluid in wellbore. If inert gases are used as drilling fluid, drilling string experiences variable flow rate, which changes the stress level. In addition to the stress level, temperature, composition of the material and the presence of corrosion inhibitors affect the SCC resistance of metals.

Effects of Temperature and Material Composition

Szklarz (1998) studied SSC resistance of tubulars in underbalanced drilling using Double Cantilever Beam (DCB) test. SSC resistance of L-80A, L-80B, X95, C105 and S135 materials were evaluated. Composition of each alloy is given in **Table 1**. Experiments were performed under simulated downhole conditions and standard conditions as recommended by NACE. Simulated conditions consist of an autoclave pressurized at 27.6 Mpa with different test temperatures. The pH of test solution was set to 3. Corrosion coupons were completely submerged into test solution and solution was stirred at 500 rpm.

Table 1: Compositions of materials in corrosion studies (Dezhi et al. 2012, Tucroni et al. 2001 and Szklarz 1988)

	L80-A	L80-B	X95	C105	S135	C110	HSLA
C	0.27	0.27	0.28	0.34	0.39	0.26	0.22-0.28
Si	0.27	0.2	0.27	0.23	0.22	0.22	0.16-0.3
Mn	1.36	1.34	0.45	0.65	0.62	0.46	0.36-0.5
P	0.011	0.011	0.01	0.016	0.013	0.011	50-100 ppm
S	0.01	0.003	0.005	0.003	0.006	0.002	10-30 ppm
Cr	0.79	0.003	1	1.02	1.09	0.45	0.9-1
Ni	0.02	0.003	-	-	1.12	0.04	
Mo	0.18	-	0.3	0.16	0.22	0.72	0.6-0.7
Al	0.028	0.027	-	0.006	0.017	0.016	
Cu	0.01	0.003	-	-	-	0.1	
Ti	-	-	-	-	-	0.01	0.01-0.025
V	-	-	-	-	-	0.08	
Nb	-	-	-	-	-	0.015	0.02-0.035

Results of experiments show that the critical stress intensity factor (K_{ISSC}) increases with temperature (Fig. 1). Increase in K_{ISSC} implies that more stress will be required for crack to propagate through coupons as the temperature increases. Thus, increase in temperature leads to increase in SSC resistance. Not all grades were tested at all temperatures. In addition, the figure compares performance of different alloys. It can be deduced that L-80A and L-80B showed best performance in sour environment. S135 exhibited poor SSC resistance. X95 performed better than S135 but not as good as L-80 alloy.

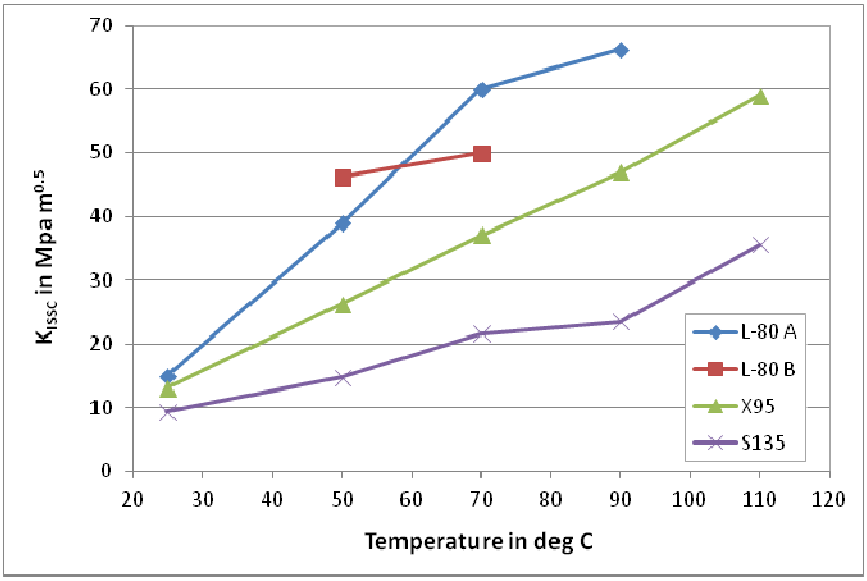

Fig 1: Effect of temperature on critical stress intensity factor for different materials (Szklarz, 1998)

Effect of Inhibitors

Deeper drilling makes the use of high strength steel tubulars mandatory. Various factors, which affect the SSC resistance, were listed in previous monthly reports. Apart from metallurgical and environmental factors, some researchers have studied the impact of corrosion inhibitors against SSC. Inhibitors are often added into drilling fluid. The function of the inhibitors is to reduce the concentration of hydrogen at the metal surface. Zeng et al. (2012) and Szklarz (1998) have observed effects of inhibitors on SSC resistance of steels. DCB tests were performed by Zeng at al. (2012) using C110 material to study the impact of inhibitors on the SSC resistance of C110. Results showed significant increase in the value of K_{ISSC} when inhibitors were used. Thus, more stress is required for crack propagation in presence of inhibitor. Szklarz (1988) observed effect of amine inhibitor on SSC resistance L-80A, L-80B, X95, C105 and S135 materials. Composition of each alloy is given in Table 1. Different concentrations of amine inhibitor were used in the study. **Figure 2** depicts the effect of amine inhibitor concentration on K_{ISSC}. As the inhibitor concentration increased, the K_{ISSC} values increased indicating improvement of SSC resistance. Similar trends were observed for all the materials considered in the study. Thus, it can be concluded that addition of amine inhibitor will help against sulfide stress cracking.

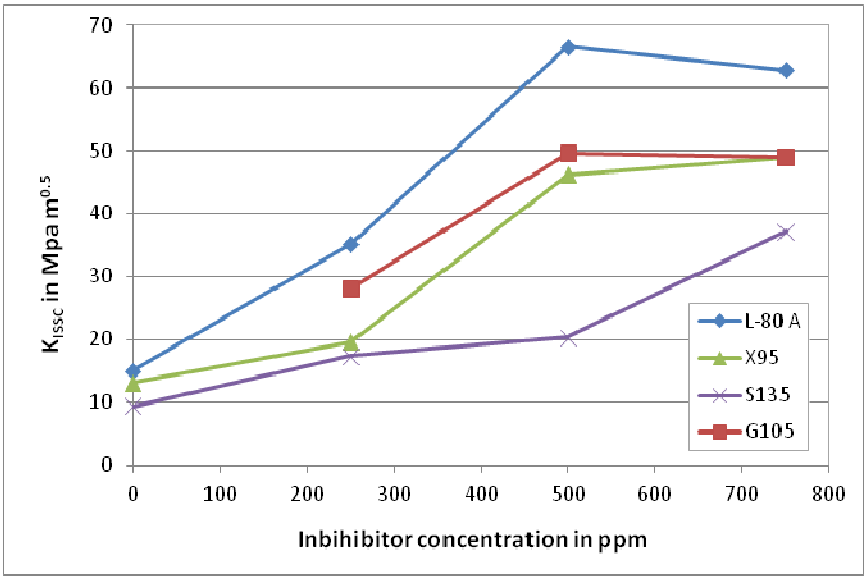

Fig 2: Effect of inhibitor concentration on K_{issc} for different materials at 250°C (Szklarz, 1998)

Effects of Microstructure and Nonmetallic Inclusions

One of the many factors, which control SSC resistance of material, is microstructure. Crack initiation and crack propagation are two most important steps in SSC. Microstructure controls crack propagation while non-metallic inclusions affect crack initiations. Various researchers (Chauveau et al. 2012; Craig 2005; Ciaraldi 1986; Tucroni et al. 2001; Ciaraldi 1986; Cane and Cayard 1998) have studied the effect of microstructures on SSC resistance and concluded that following processes are beneficial for improving SSC resistance:

- Forming fine sized grain of prior austenite
- Obtaining fully martensitic structure during quenching process
- Tempering after quenching or cold work at suitable temperature
- Reduce hardness of the material

2.1.2 Modeling Corrosion of Steel in CO_2-H_2S Saturated Brine

In previous report (Report # 21), details of mechanistic CO_2-H_2S corrosion model was presented. The model utilizes the Fickian diffusion law to describe the ionic transport process in aqueous fluid system. Model equations involve concentrations of several species. As a result, numerical solutions were obtained using a computer code implemented in MathLab. In the current form, the model does not account for the influence of flow velocity on the corrosion rate. Additionally, thickness of corrosion scale is assumed to be 10 µm with porosity of 0.9. For model validation, the predicated value was calculated by taking the average corrosion rate over the exposure time and then comparing it with weight loss measurement. The model predictions are validated (**Fig. 3**) with available experimental data in the literature (Bich and Goerz 1996; Kvarekval and Nyborg, 2003). Reasonable agreement is found

between model predictions and experimental measurements obtained under various test conditions (**Tables 2 and 3**).

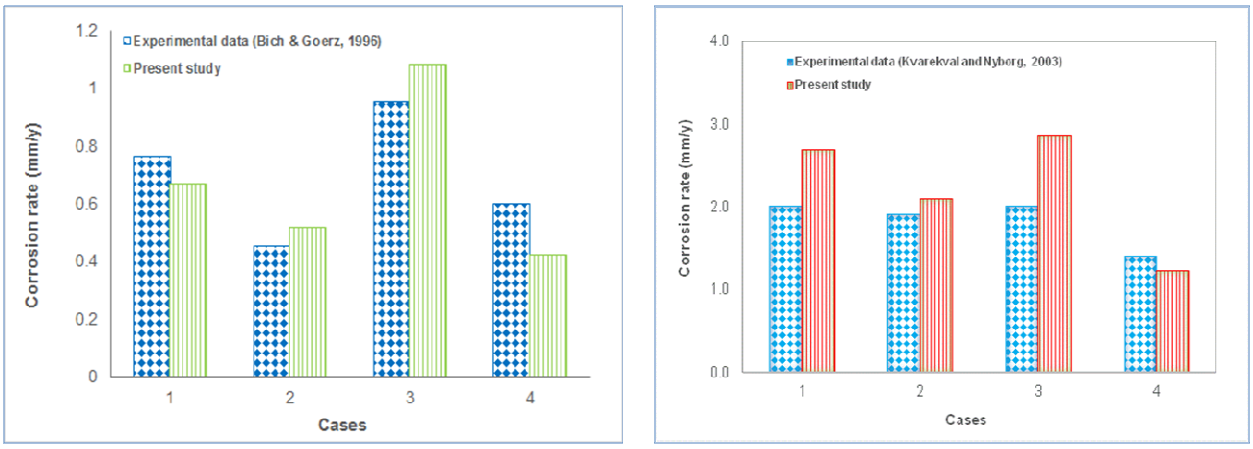

(a) **(b)**

Fig. 3: Comparison model predictions with experimental measurements of: a) Bich and Goerz (1996); and b) Kvarekval and Nyborg (2003)

Table 2: Test conditions and results of corrosion tests conducted by Bich and Goerz (1996)

Case No.	Time (hr)	T(°C)	P_{CO2} (bar)	P_{H2S} (bar)	MCR* (mm/y)	PCR+ (mm/y)
1	71	60	5.3	3	0.764	0.666
2	91	60	5.3	3	0.454	0.516
3	91	65	12.8	8	0.954	1.081
4	100	65	3.5	12.2	0.600	0.421

* Measured Corrosion Rate = MCR + Predicted Corrosion Rate = PCR

Table 3: Test conditions and results of corrosion tests conducted by Kvarekval and Nyborg (2003)

Case No.	Temperature (°C)	P_{H2S}/P_{CO2} ratio	Exposure time hr)	MCR (mm/y)	PCR(mm/y)
1	120	0.2	24.0	2.00	3.56
2	120	0.4	20.0	1.90	2.10
3	120	0.5	21.5	2.00	2.86
4	120	0.6	68.5	1.40	1.22

2.1.3 Modeling Cement Degradation

Cement degradation in the presence of carbonic acid has been a major subject of investigation, especially in deep-water application where extreme down-hole conditions exist. Accurate prediction of the mechanical degradation in sour gas environment involves development of models that account for most important mechanisms. In this respect, comprehensive model for mechanical properties degradation of oil well cement in sour gas environment under high-pressure, high-temperature (HPHT) condition must be developed. For Portland cement, principal mechanisms that lead to strength degradation are:

1. Hydration

$$2(3CaO.SiO_2) + 6H_2O \rightarrow 3CaO.2SiO_2.3H_2O + 3Ca(OH)_2$$

$$2(2CaO.SiO_2) + 4H2O \rightarrow (slow)\ 3CaO.2SiO_2.3H_2O + Ca(OH)_2$$

2. Carbonation

$$Ca(OH)_2 + H+ + HCO_3^- \rightarrow CaCO_3 + 2H_2O$$

$$C\text{-}S\text{-}H + H+ + HCO_3^- \rightarrow CaCO_3 + SiO_2$$

3. Leaching

$$CO_2 + H_2O + CaCO_3 \rightarrow Ca(HCO_3)_2$$

$$Ca(HCO_3)_2 + Ca(OH)2 \rightarrow 2CaCO_3 + 2H_2O$$

Tobermorite gel (CSH) is predominantly formed at elevated pressure, temperature below 230°F and C/S ratio of approximately one. CSH has good binding properties, high compressive strength and low permeability. An optimum curing temperature of 230°F has been recommended to prevent strength retrogression during early curing stage. Above 302°F, a moderately permeable but strong CSH phase, called Xonotlite (C6S6H), is formed. In addition, Truscottite, Pectolite, and Scawtite can be produced. A model that accounts for these phase transformations must predict degree of hydration before beginning of the CO_2 aging experiment. In the present study, the hydration mechanism will be investigated.

In the presence of brine solution, carbonation is the major reaction that occurs in addition to cement hydration. Although carbonic acid is weak (pH = 5.00 – 7.00), high temperature and pressure enhance the rate of attack thereby favoring the formation of calcite (i.e. carbonation) and subsequent formation and dissolution of calcium bicarbonate (i.e. leaching), in which the penetrated portion of the cement matrix reduced to amorphous and porous silica (i.e. strength retrogression). Initially, diffusion and carbonation controlled degradation process plays the dominant role in compressive strength development through sealing of porous and plugging conductive paths; however, strength degradation occurs after prolonged exposure due to calcium leaching. The rate, at which, the hydrated products (i.e. CH and CSH phases) get carbonated, bi-carbonated or leached, is dictated by several parameters such as temperature, cement formulation, CO_2 concentration and brine composition. Aging pressure mainly affect CO_2 solubility in brine solution; hence, carbonation is least affected by it. However, temperature strongly affects both CO_2 solubility in brine and subsequent rate of attack of cement matrix. Therefore, the following models are presently being developed to account for hydration/phase transformation, carbonation and leaching:

i. Hydration model
ii. CO_2 solubility model for bulk fluid
iii. pH model for bulk fluid
iv. Diffusion models for calcium ion concentrations in pore fluid and cement matrix

v. Heat transfer model
vi. Calcite precipitation (i.e. carbonation) model
vii. Dissolution (i.e. leaching) model
viii. Porosity and permeability models
ix. Compressive strength degradation model

2.2 Experimental Studies on Degradation of Cement (Task 2)

2.2.1 FTIR Analysis of Baseline Cement

In the previous month, a complete analysis of porosity and permeability, which includes the effect of pressure, CO_2 concentration and temperature, is presented. During this reporting period, aging experiments were not conducted due to equipment failure that occurred during the first high-temperature (430°F) test. While waiting for equipment repair, Fourier transform infrared spectroscopy (FTIR) tests were performed with previously aged samples. FTIR analysis was conducted on Class H cement. Results from various batches of cement cores are presented varying concentration and pressure at different temperatures as shown in **Tables 4, 5** and **6**.

Table 4: Test matrix for aging experiments conducted at 100°F and 6000 psi

10% CO2	40% CO2	100% CO2
Batch 008	Batch 011	Batch 012

Table 5: Test matrix for aging experiments conducted at 225°F

Pressure (psi)	10% CO_2	40% CO_2	100% CO_2
3000 psi	Batch 026	Batch 022	Batch 024
6000 psi	Batch 007	Batch 015	Batch 010
9000 psi	Batch 027	Batch 023	Batch 025

Table 6: Test matrix for aging experiments conducted at 350°F

Pressure (psi)	10% CO_2	40% CO_2	100% CO_2
3000 psi	Batch 020	Batch 016	Batch 018
6000 psi	Batch 006	Batch 013	Batch 014
9000 psi	Batch 021	Batch 017	Batch 019

Figures 4 to **9** illustrate the effect of CO_2 concentration in the gas phase on the composition of aged cement at different temperatures (225°F and 350°F). Interpretation of the results is summarized in **Table 7**. In all cases, the outer zone is fully carbonated. This is expected, as the outer zone is the most exposed zone for the acid attack. In some cases, results from the outer zone show reduction in $CaCO_3$ content with increasing CO_2 content of the gas. This could be attributed to the conversion of $CaCO_3$ to $Ca(HCO_3)_2$ and eventually leaching out of the cement matrix. CH is more reactive than CSH. It is only preserved in the virgin zone of a core aged at 6000 psi and 350°F. However, at high CO_2 concentration (100%), CH was completely carbonated. Increased pressure tends to facilitate the carbonation of CSH.

At high pressures (6000 and 9000 psi) and high concentration of CO_2, CSH was completely consumed by the acid. FTIR results that show the effects of pressure and temperature on baseline cement degradation are presented in Appendix A.

Table 7: Interpretations of FTIR results presented in Figs. 4 to 9

Figures	Zone	Discussion
Figs. 4 & 5	Virgin	CH was absent while CSH was present. Limited carbonation occurred.
	Middle	CH was absent. However, CSH was present. Slightly higher carbonation than the virgin zone.
	Outermost	CH and CSH were absent. Carbonation was considerable. Test with 100% CO_2 showed slight leaching.
Figs. 6 & 7	Virgin	CH was absent at 225°F in all zones.
	Middle	More CSH was present at 350°F than 225°F.
	Outermost	More carbonation occurred when CO_2 content of the gas was increased.
Figs. 8 & 9	Virgin	No major difference between 225°F and 350°F results.
	Middle	No major difference between 225°F and 350°F results.
	Outermost	CH and CSH were fully carbonated. As CO_2 concentration increased, leaching became dominate at 225°F.

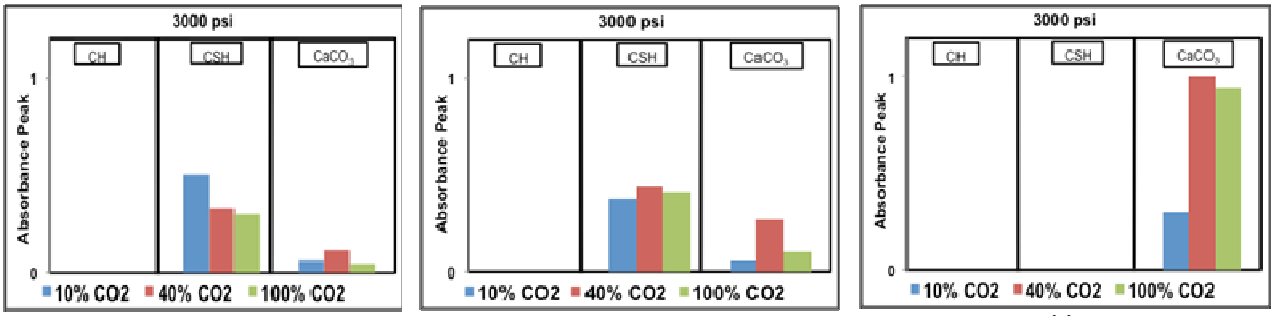

(a) (b) (c)

Fig. 4: Summarized FTIR data of baseline Class H cement samples aged at 225°F, 3000 psi for 14 days: a) Virgin zone; b) Middle zone; and c) Outermost zone

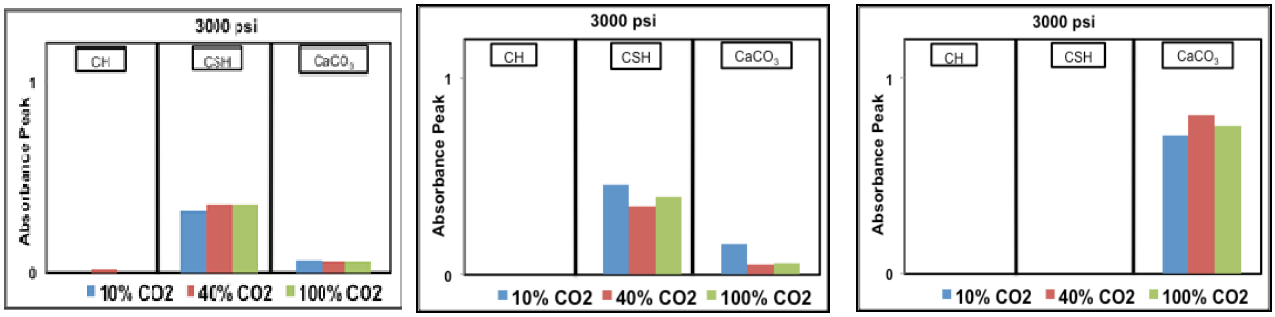

(a) (b) (c)

Fig. 5: Summarized FTIR data of baseline Class H cement samples aged at 350°F, 3000 psi for 14 days: a) Virgin zone; b) Middle zone; and c) Outermost zone

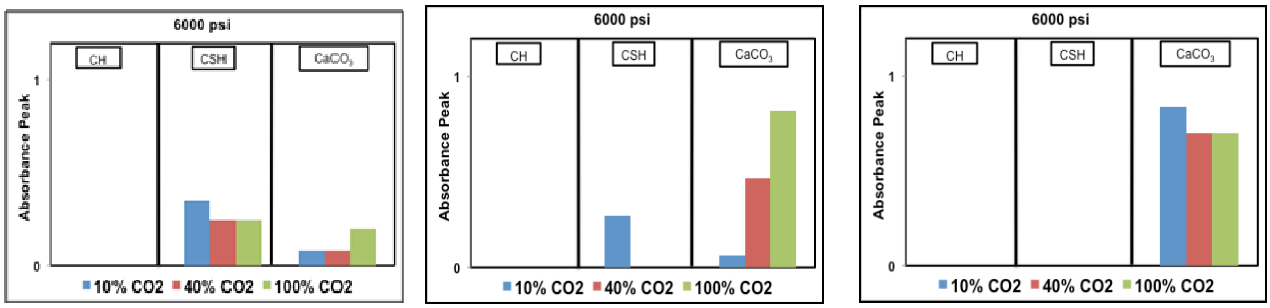

(a) (b) (c)

Fig. 6: Summarized FTIR data of baseline Class H cement samples aged at 225°F, 6000 psi for 14 days: a) Virgin zone; b) Middle zone; and c) Outermost zone

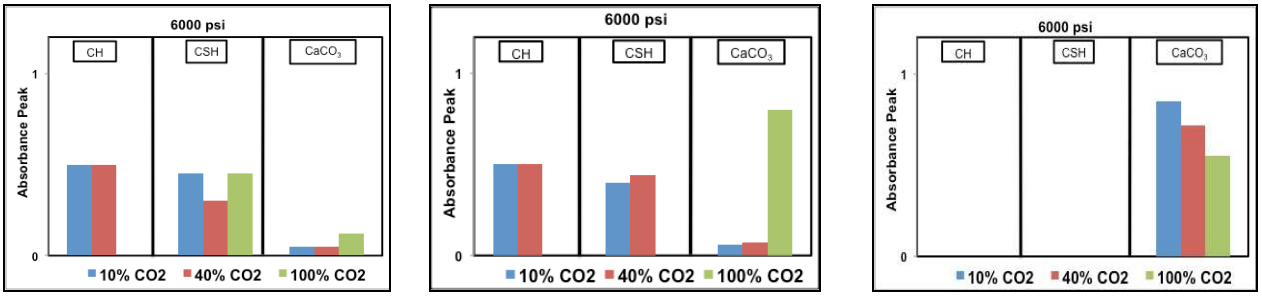

(a) (b) (c)

Fig. 7: Summarized FTIR data of baseline Class H cement samples aged at 350°F, 6000 psi for 14 days: a) Virgin zone; b) Middle zone; and c) Outermost zone

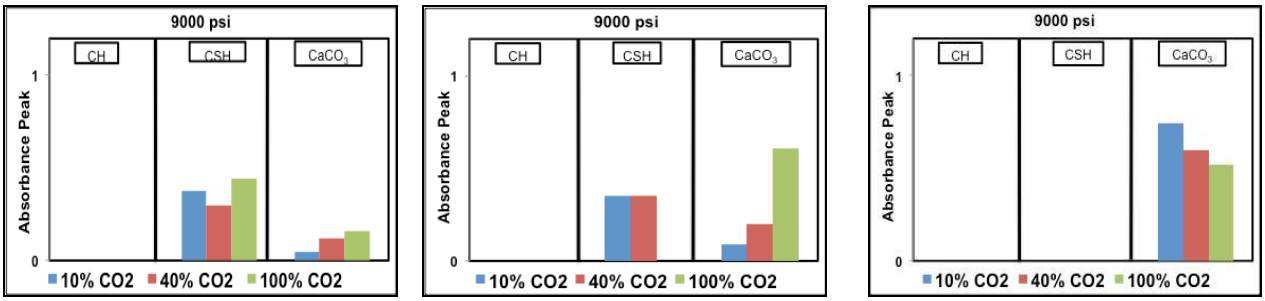

(a) (b) (c)

Fig. 8: Summarized FTIR data of baseline Class H cement samples aged at 225°F, 9000 psi for 14 days: a) Virgin zone; b) Middle zone; and c) Outermost zone

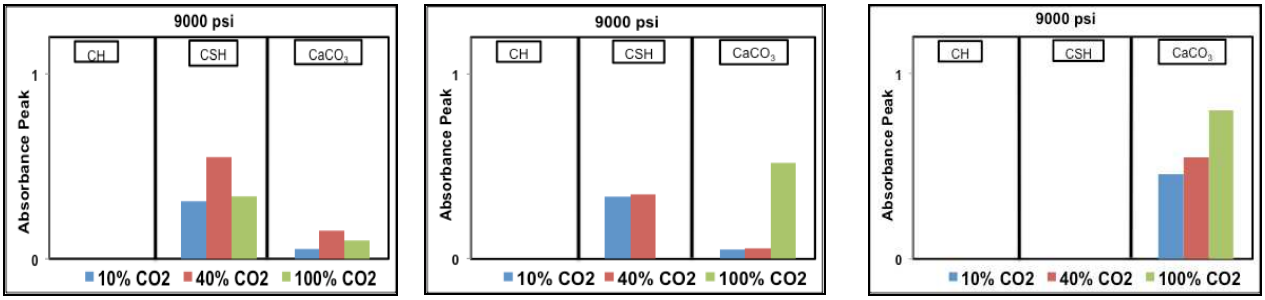

(a) (b) (c)

Fig. 9: Summarized FTIR data of baseline Class H cement samples aged at 350°F, 9000 psi for 14 days: a) Virgin zone; b) Middle zone; and c) Outermost zone

2.2.2 Compressive Strengths of Baseline Cements

Effect of Pressure on Compressive Strength

Figure 10 shows compressive strength of baseline cements after aging in 2% brine saturated with 100% CO°. At 225°F, CO_2 solubility increases with aging pressure and precipitation of scawtite is likely at low aging pressure while full carbonation and leaching are possible occurrences at high aging pressures. Mixed trend in Class H cement at 225°F may have occurred because of complex nature of cement degradation, which involves two offsetting processes (carbonation and leaching). Similar mixed trend is observed with Class G cement at 350°F. Despite mixed trends, in general result show that both Classes of cements were subjected to more carbonation at high pressure due to increased CO_2 solubility. **Figure 11** combines simulated data that show the impact of high temperature on solubility of CO_2. Although the onset of leaching starts at extremely high pressure in Class G cement, this shows that CO_2 solubility decreases with increasing temperature up to a critical temperature at which this trend changes and the solubility increases with temperature increase.

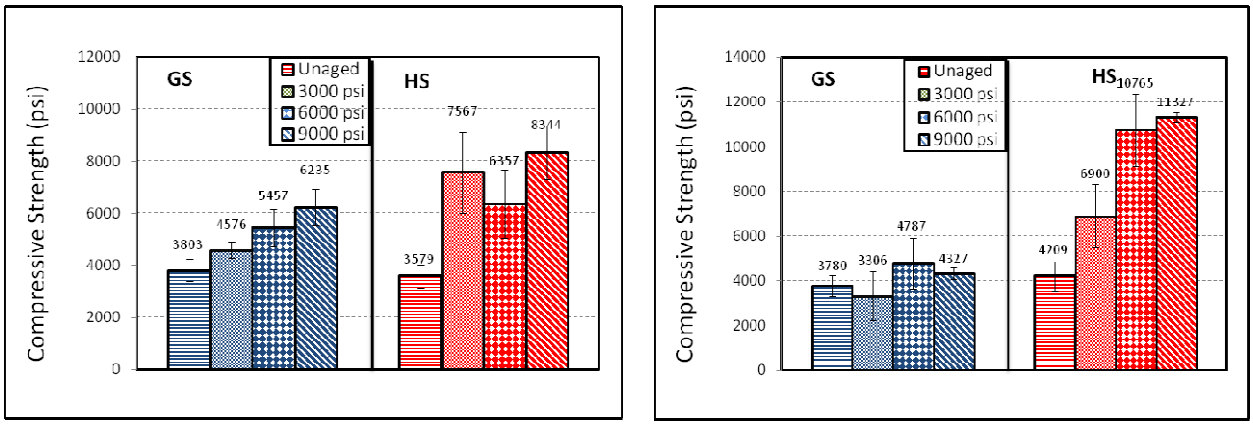

Fig. 10: Compressive strengths of cements after aging in brine saturated with 100% CO_2 at: a) 225°F, and b) 350°F

Effects of Temperature on Compressive Strength

Compressive strengths of baseline cements aged in 2% brine saturated with 100% CO_2 are shown in **Fig. 12**. At 3000 psi, although CO_2 solubility decreases with temperature (Fig. 11, 200 Bar), temperature favors carbonation reaction of the carbonic acid with hydrated cement products (CSH and CH). Carbonation results in precipitation of calcite that fills the pores of the cement, thereby increasing compressive strength. However, at higher temperatures, the

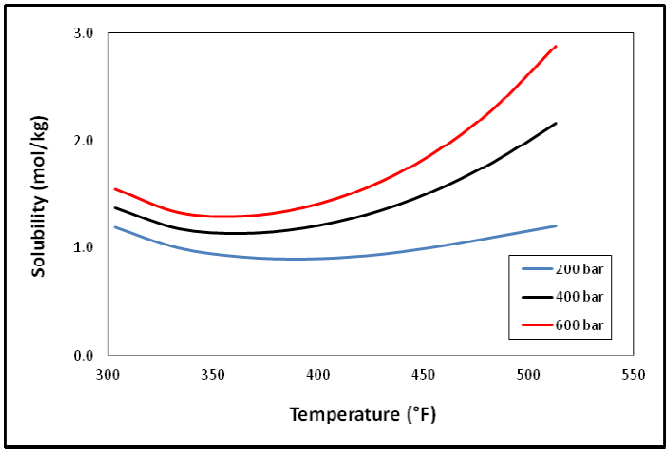

Fig. 11: Effect of temperature on CO_2 solubility in 1M NaCl solution

precipitated calcium carbonate is further attacked by carbonic acid resulting in calcium bi-carbonate, which can be easily leached out of the cement matrix causing strength retrogression. In Class H cement, less CO_2 penetration is possible; hence, occurrence of leaching requires higher temperature than Class G cement.

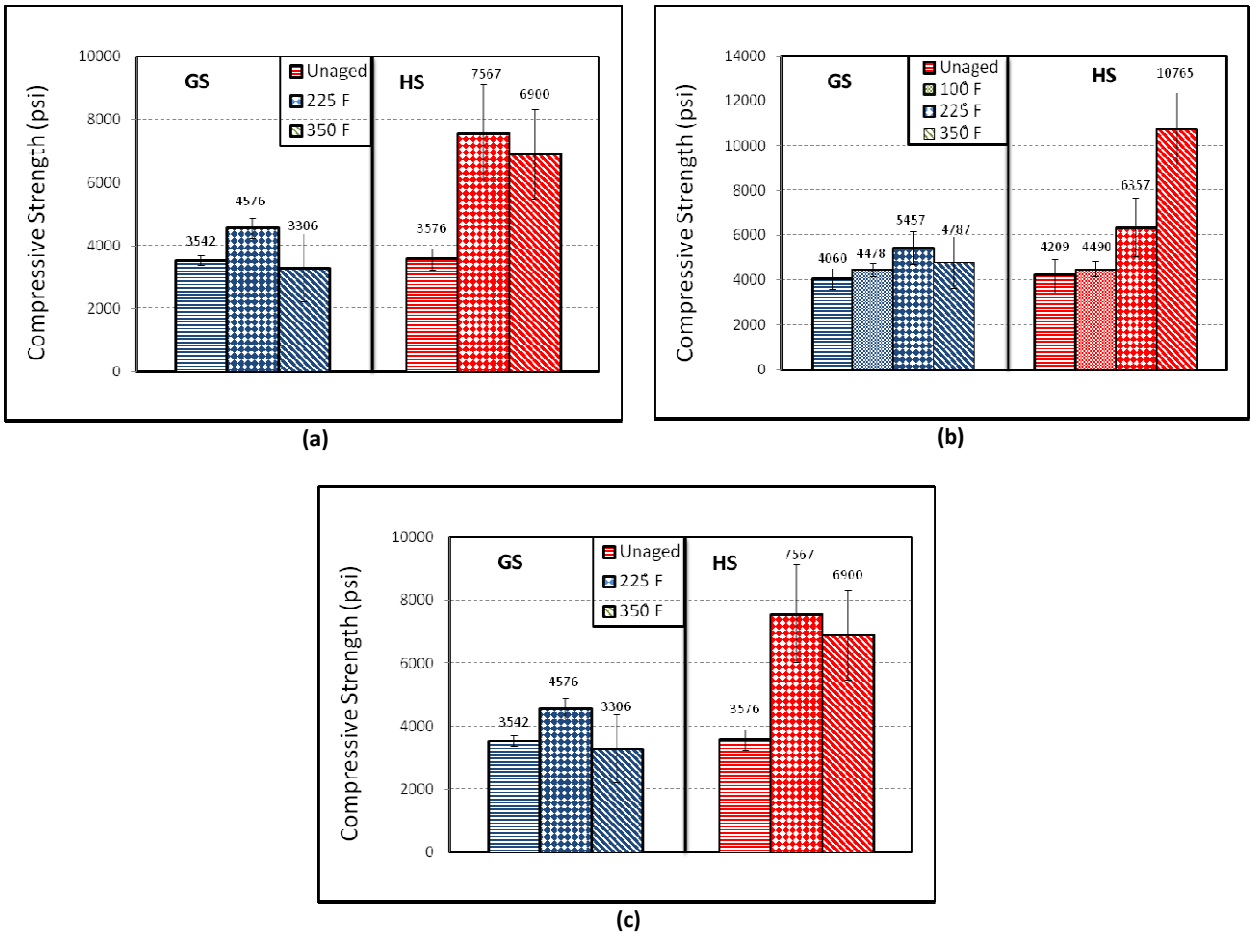

Fig. 12: Compressive strengths of baseline cements after aging in brine saturated with 100% CO_2 gas at: a) 3000 psi, b) 6000 psi, and c) 9000 psi

2.2.3 Shear Bond Strength of Baseline Cement

In this report, the results of phenolphthalein tests (i.e. carbonation depth measurements) are presented along with shear bond strength (SBS) measurements to examine the relationship between carbonation depth and increase in SBS after aging. To determine the penetrated depth, SBS samples were axially bisected into two pieces and phenolphthalein reagent was applied on the flat side of one of them. Photographs of bisected bonding samples are shown in **Fig. 13**. The region with purple color indicate uncarbonated zone containing CH. For samples aged at 10% CO_2, the coloration was mostly dark purple. For samples aged at 100% CO_2, CH was preserved only in the middle zone of the samples. For most of the samples, carbonation depth increased with the CO_2 content (**Tables 8** and **9**). However, results of samples aged at 225°F and 9000 psi do not follow this trend.

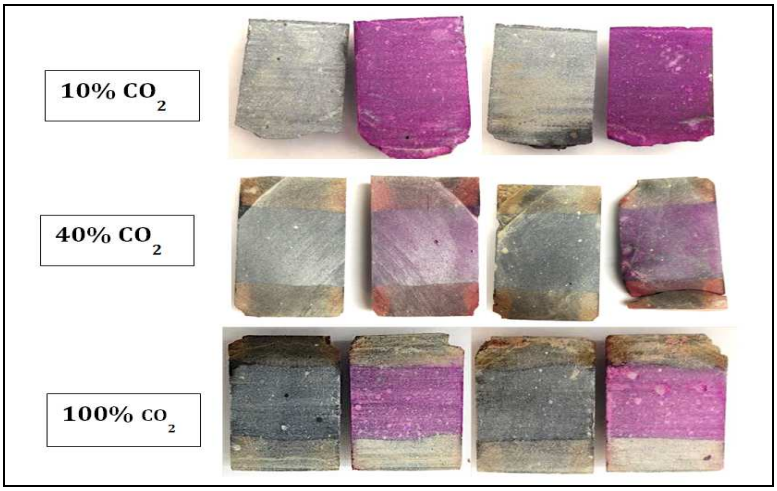

Fig. 13: Bisected bonding samples aged at 9000 psi and 225°F: before applying the reagent (Left); and after applying reagent (Right)

Table 8: Carbonated depth and SBS increases for samples aged at 225°F

225°F	3000 psi		9000 psi	
CO_2	Depth (in)	SBS Increase (%)	Depth (in)	SBS Increase (%)
10%	0.15	28	0.00	27
40%	0.35	205	0.48	437
100%	0.47	155	0.35	372

Table 9: Carbonated depth and SBS increases for samples aged at 350°F

350°F	3000 psi		9000 psi	
CO_2	Depth (in)	SBS Increase (%)	Depth (in)	SBS Increase (%)
10%	0.00	132	0.21	225
40%	0.15	315	0.30	339
100%	0.45	152	0.51	234

2.2.4 Additive Screening and Cement Formulation Studies

Due to equipment failure, new aging experiments were conducted during this month. Hence, there is no data from new aging experiment to report; however, compressive strength measurements from previous experiments that were not reported are presented in this report. This report presents compressive strengths of micro silica, micro silica plus latex, magnesium oxide and hydroxyapatite based cements.

2.2.4.1 Micro Silica Based Cement

Aging experiments with 10% BWOC micro-silica cement (MS-10) were continued. The composition of the slurry is presented in Report # 22. After aging, the properties of the cores were measured. Porosity, permeability, FTIR mineralogy and shear bond strength of the samples were presented in previous reports. The compressive strengths of MS-10 and baseline cements are presented in **Fig. 14**. As

anticipated, the baseline samples show increase in compressive strength due to carbonation of the matrix. Micro silica samples did not show significant increase in strength. Class H micro silica samples rather show a slight decrease in the strength. This can be attributed to the occurrence of limited carbonation in micro silica samples. However, it is imperative to consider other properties (porosity, permeability, shear bond strength, and mineralogical composition) to identify the dominant degradation process. Even though porosity and permeability of the samples (presented in previous reports) increased, the matrix still preserved the CSH component. Moreover, shear bond strength of the samples increased by almost 130%, indicating strong carbonation while FTIR shows a protected matrix. Due to these conflicting results obtained for various measurements, it is difficult to come up with a reasonable conclusion. Hence, additional experiments were carried out.

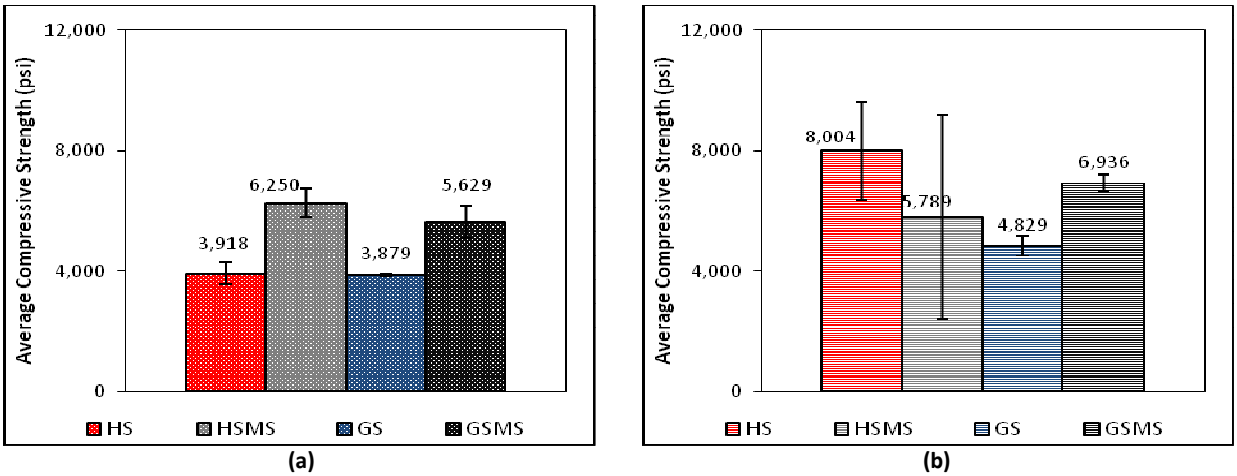

Fig. 14: Compressive strengths of MS-10 and baseline cements: a) unaged; and b) aged for 14 days at 225°F and 3000 psi in brine saturated with 100% CO_2 gas

Another batch of MS-10 samples was aged under different condition (6000 psi, 10% CO_2 and 430°F). The increment in compressive strength after aging for HSMS samples is similar to those of the baseline samples while GSMS samples showed approximately 25%reduction in the strength (**Fig. 15**). The SBSs of the MS-10 samples were almost similar after aging and FTIR results indicated the presence of CSH component in their matrix. Hence, HSMS seem to undergo similar level of carbonation as baseline samples. However, their porosity and permeability were significantly increased after aging. This increment in porosity always results in reduction of compressive strength. Such an increment in porosity after CO_2 exposure is undesirable. Although FTIR results indicate presence of CSH in the matrix, a highly porous matrix can lead to further channeling of formation fluids and gases. One more aging experiment has been conducted recently using MS-10 samples. Results of the experiment will be presented in the coming reports.

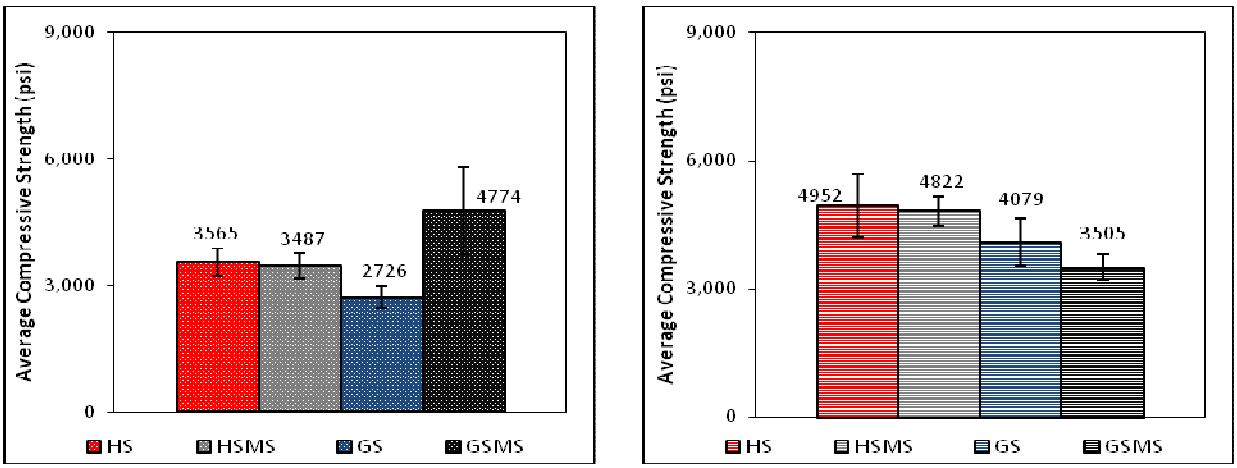

Fig. 15: Compressive strengths of MS-10 and baseline cements: a) unaged; and b) aged for 14 days at 430°F and 6000 psi in brine saturated with 10% CO_2 gas

2.2.4.2 Latex and Micro-silica Based Cement

The first batch of latex and micro-silica (10% latex + 10% micro-silica) containing cement cores (LTMS) were aged under HPHT conditions (225°F, 9000 psi and 10% CO_2). Porosity, permeability, FTIR mineralogy and shear bond strength of the samples were presented in Report # 26. The samples exhibited the presence of CSH component after aging, indicating their resistance against acid attack. Compressive strength for the samples is presented in **Fig. 16**. The strength for LTMS samples was almost similar after aging. The strength for baseline HS samples increased after aging due to carbonation while for baseline GS samples was almost the same.

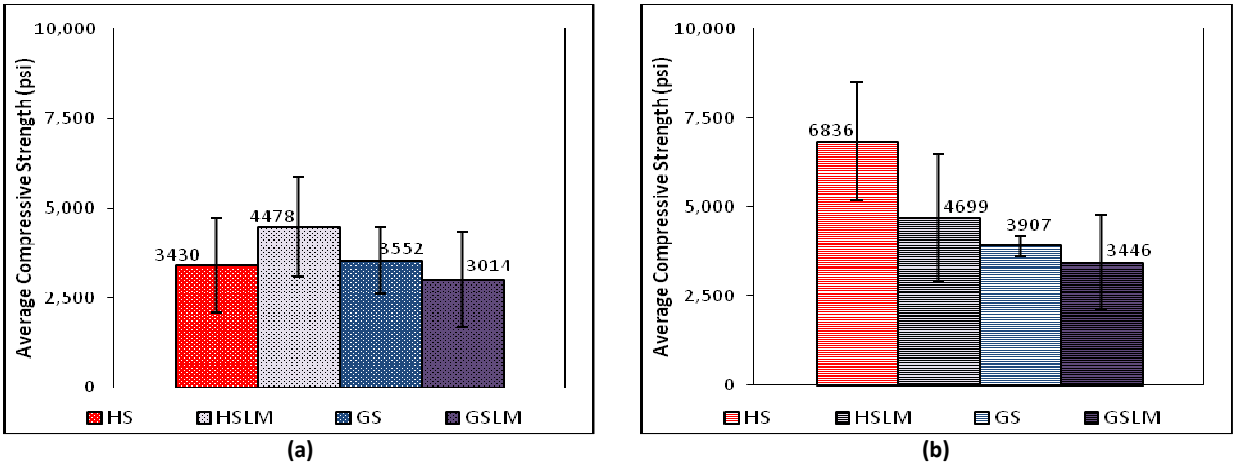

Fig. 16: Compressive strengths of LTMS and baseline cements: a) unaged; and b) aged for 14 days at 225°F and 9000 psi in brine saturated with 10% CO_2 gas

The porosity data of LTMS samples slightly decreased while the shear bond strength remained the same. The FTIR results showed presence of CSH in the matrix. Hence, the compressive strength measurements, which suggest almost similar level of carbonation, are in agreement with the other test results. Further tests with LTMS samples will help in yielding better conclusive results.

2.2.4.3 Magnesium Oxide Based Cement

Tests with MGO-5 samples were continued. Porosity, permeability, FTIR mineralogy and shear bond strength of the samples were presented in Report # 25. Compressive strengths of MGO-5 and baseline samples are presented in **Fig. 17**. MGO-5 samples showed lesser increase in compressive strength as compared to the baseline samples. Even with the presence of an expanding agent, compressive strength MGO-5 samples did not increase substantially. Measurements presented in Report # 25 indicated slight increase in porosity and significant improvement in shear bond strength. FTIR results displayed the presence of CH and CSH groups in the aged MGO-5 samples.

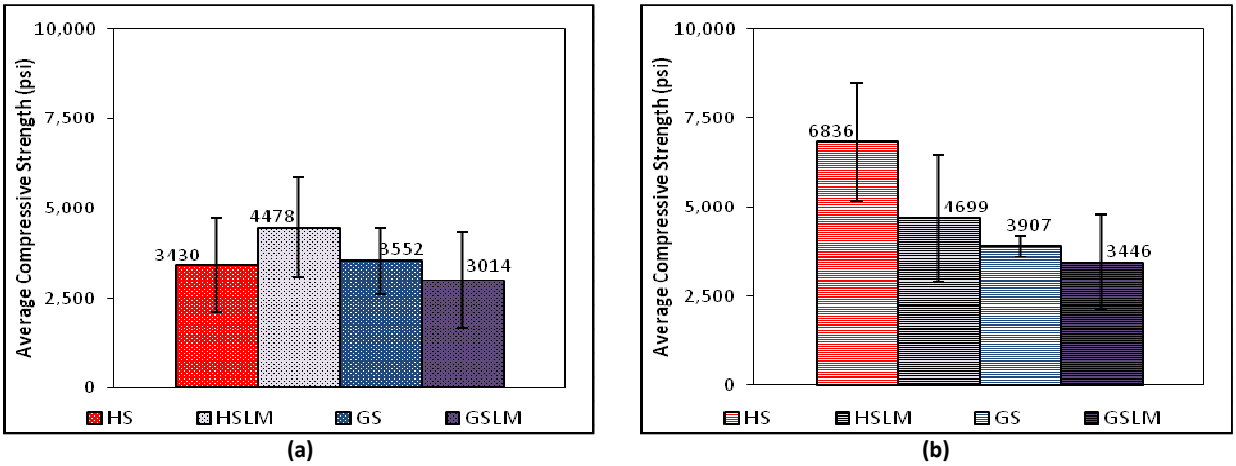

Fig. 17: Compressive strengths of MGO-5 and baseline cement samples: a) unaged; and b) aged for 14 days at 225°F and 9000 psi in brine saturated with 100% CO_2 gas

2.2.4.4 Hydroxyapatite Based Cement

Tests with hydroxyapatite-based cement (HOAP) were continued. Porosity, permeability, FTIR mineralogy and shear bond strength of the samples were presented in Report # 25. Aging condition for this batch samples is presented in **Table 10**. Compressive strengths of HOAP and baseline samples are presented in **Fig. 18**. After aging, baseline samples showed increase in strength due to carbonation; however, the strength of HOAP samples decreased due to reduced carbonation of HOAP. Porosity, permeability, SBS and FTIR mineralogy results have already demonstrated that the addition of hydroxyapatite can protect the CH and CSH components of the cement from carbonic acid attack.

Table 10: Aging conditions for HOAP samples

HOAP	Temp. (°F)	Pressure (psi)	CO_2 Conc. (%)	Salt Conc. (%)	Days	Parallel Batch	Exp. No.
Batch 007	225	3000	10	2	14	Batch 026	23

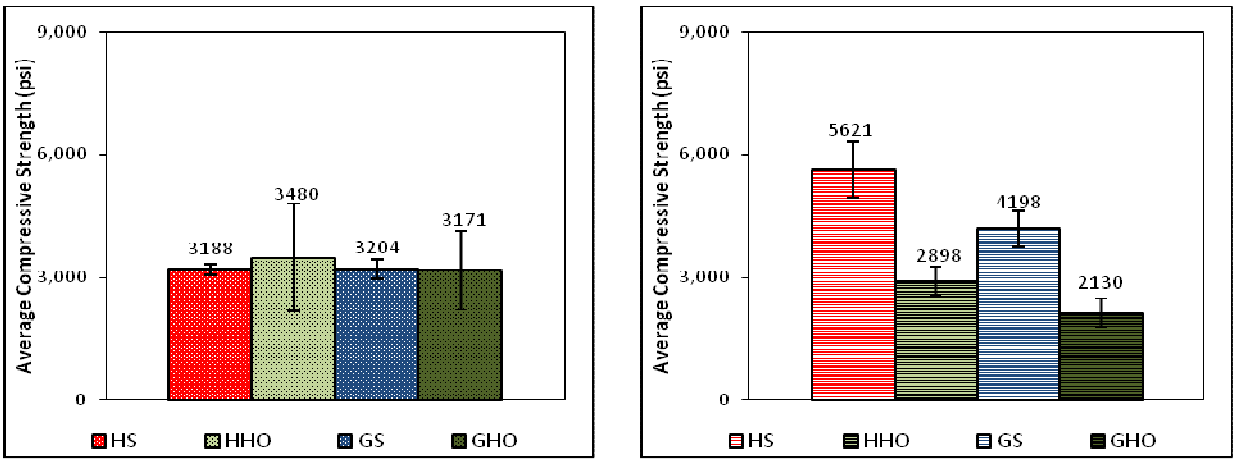

Fig. 18: Compressive strengths of HOAP and baseline cement samples: a) unaged; and b) aged for 14 days at 225°F and 3000 psi in brine saturated with 10% CO_2 gas

2.3 Experimental Studies on Corrosion of Tubulars (Task 3)

The development of corrosion test setup (**Fig. 19**) was continued. Installation and testing of instrumentation and heating oil lines have been completed. In the coming weeks, the setup will be pressure tested at maximum allowable operating temperature. The setup consists of two test cells, which will be used to investigate uniform corrosion under static and dynamic condition and perform studies on sulfide stress cracking (SSC). The cells are equipped with the required devices and instrumentation. Magnetic coupling with an air motor is installed on the uniform corrosion test cell to simulate dynamic condition in the cell. The speed of the motor is controlled by the air supply pressure, which is controlled by a pressure regulator. The SSC cell is equipped with a pneumatic cylinder to apply tension on the test specimen (mini-pipe). The cylinder is designed to handle 250-psi pressure. Nitrogen is supplied to actuate the cylinder in both sides (forward and backward).

Fig. 19: Corrosion test setup

3. Planned Activities

- Continue aging experiments with brine-CO_2-CH4 system for 14 days varying CO_2 concentration (3000, 6000 and 9000 psi) at 430°F and 100% CO_2.
- Continue theoretical and modeling studies on tubular degradation.
- Continue cement additive screening and acid resistant cement formulation studies.
- Begin testing of the corrosion experiment setup.

4. Project Expenditures

This section presents the project expenses during the month of December (**Table 11**) and the cumulative expenditures.

Table 11: Current and cumulative expenditures, December 2014

No.	Budget Categories	Current Expenses	Cumulative Expenses
1	Salaries & Wages	$7,576.92	$253,261.52
2	Fringe Benefits	$1,293.12	$57,557.53
3	Project Materials	$269.53	$60,912.49
4	Travel	$0.00	$6,232.33
5	Conference Expenses	$0.00	$0.00
6	Other Direct Costs	$0.00	$993.60
7	Equipment	$688.32	$242,088.22
8	Space Rental	$0.00	$0.00
9	Indirect Cost	$4,569.79	$188,424.81
10	**Total**	**$14,397.68**	**$809,470.50**

Nomenclatures

BWOC	By weight of cement
CH	Calcium hydroxide
CSH	Calcium silicate hydrate
FTIR	Fourier Transform Infra-Red
GHO	Class G Cement with hydroxyapatite
GS	Class G cement with silica flour
GSMG	Class G Cement with silica flour and magnesium oxide
GSLM	Class G Cement with silica flour, latex and micro-silica
GSLT	Class G Cement with latex
HHO	Class H Cement with hydroxyapatite
HPHT	High-pressure high-temperature
HS	Class H cement with silica flour
HSHO	Class H Cement with silica flour and hydroxyapatite
HSMG	Class H Cement with silica flour and magnesium oxide
HSLM	Class H Cement with silica flour, latex and micro-silica
HSLT	Class H Cement with latex
K_{ISSC}	Critical stress intensity factor
LPR	Linear polarization resistance
LTMS	Cement with latex and micro-silica additives
mpy	mils per year
MGO	Magnesium oxide containing cement
MGO-5	Cement containing 5% BWOC MgO as additive
MGO-10	Cement containing 10% BWOC MgO as additive
MS	Micro-silica containing cement
MS-10	Cement containing 10% BWOC micro-silica as additive
NACE	National Association of Corrosion Engineers
SBS	Shear bonding strength
SCC	stress corrosion cracking
SSC	Sulfide Stress Cracking
XRD	X-Ray diffraction

References

Bich, N.N. and Goerz, K. 1996. Caroline Pipeline Failure: Finding on Corrosion Mechanism in Wet Sour Gas Systems Containing Significant CO2, paper No. 26, March 24 - 29, Denver, Co.

Kvarekval, J. and Nyborg, R. 2003. Formation of Multilayer Iron Sulfide Films during High Temperature CO2/H2S Corrosion of Carbon Steel, paper No.339, Houston, Texas.

Cane, R.D. and Cayard, M.S. 1998. Roles of H_2S in Behavior of engineering alloys: A review of literature and experience, paper no. 274, NACE International Annual Conference Paper SPE 97577 presented at SPE High Pressure/High Temperature Sour Well Design Applied Technology Workshop, Woodland, 17-19 May

Chauveau, E., Koschel, D., Bouvier, N. and Mesquita, T.J. 2012. Influence of Metallurgy and Chemical Composition on the Sulphide Stress Cracking Resistance of Two Supermartensitics Stainless Steels, paper No. C2012-0001284, presented at NACE International Conference and Exposition.

Ciaraldi, S.W. 1986. Some factors that affect sour service performance of Carbon Steel Oil Country tubulars, SPE Drilling Engineering, Vol. 1, Num. 3, Pages 233-241.

Craig B. 2005. Metallurgical limits to increase tubular strength while maintaining the SSC resistance, paper SPE 97580 presented at the SPE HPHT Applied Technology Workshop, 17-19 May, Woodlands, Texas

Dezhi, Z., Chen, Z., Zhang, Z., Shao, L., Li, G., Tian,G. and She, T., 2012. Research on Stress Corrosion Sensitivity of C110 Casing in Wellbore Protection Fluid,

Hashizume, S., Inohara, Y. and Masamura, K. 2000. Effects of pH and PH_2S on SSC Resistance of Martensitic Stainless Steels, paper No.130, NACE International Annual Conference.

NACE Standard TM0177, 2005. Laboratory Testing of Metals for Resistance to Sulfide Stress Cracking and Stress Corrosion Cracking in H_2S Environments.

Szklarz K.E. 1988. SSC resistance of drilling material in a simulated underbalanced drilling, paper no. 104, NACE International Annual Conference

Tucroni, G.L., Cumino, G., Echaniz, G. , Anneli, E., Scoppio, L. and Perez,T., 2001. Improvement of Resistance to SSC Initiation and Propagation of High Strength OCTG through Microstructure and Precipitation Control, paper no. 1077, NACE International Annual Conference.

Appendix A: Results of FTIR Analysis

A.1 Effects of Pressure on Degradation of Baseline Cement

Figures A-1 to **A-6** show how the pressure affects the degradation of cement at different temperatures (225°F and 350°F). Result interpretations are summarized in **Table A-1**. As expected, the outer zone is fully carbonated. At 225°F, CSH was less preserved at 6000 psi than other test pressures (3000 and 9000 psi). However, CH component of the cement was only preserved at high temperature (350°F). This could be due to reduction in solubility of CO_2 as the temperature increases.

Table A-1: Interpretations of FTIR results presented in Figs. A-1 to A-6

Figures	Zone	Discussion
Figs. A-1, A-2 & A-3	Virgin	CH was not preserved throughout and carbonation increased with increasing CO_2 concentration
	Middle	The highest carbonation of CSH was occurred at 6000 psi.
	Outermost	Leaching tends to dominate with increasing pressure.
Figs. A-4, A-5 & A-6	Virgin	CH was maximum preserved at 40% CO_2.
	Middle	Maximum degradation occurred at 100% CO_2 where it gradually increased with increasing pressure.
	Outermost	At 10% CO_2, increasing pressure promoted carbonation up to 6000 psi, then leaching became dominant. At 40% CO_2, increasing pressure promoted leaching. At 100% CO_2, the trend is unexpected.

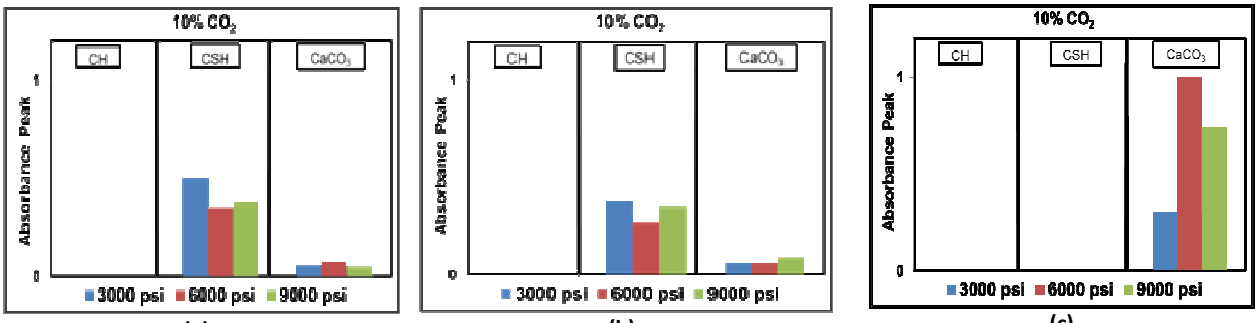

(a) (b) (c)

Fig. A-1: Summarized FTIR data of baseline Class H cement samples aged at 225°F, 10% CO_2 for 14 days: a) Virgin zone; b) Middle zone; and c) Outermost zone

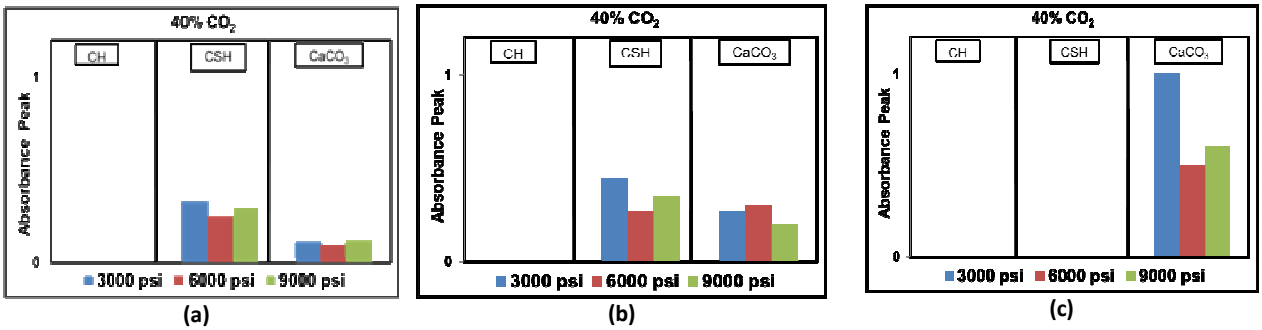

(a) (b) (c)

Fig. A-2: Summarized FTIR data of baseline Class H cement samples aged at 225°F, 40% CO2 for 14 days: a) Virgin zone; b) Middle zone; and c) Outermost zone

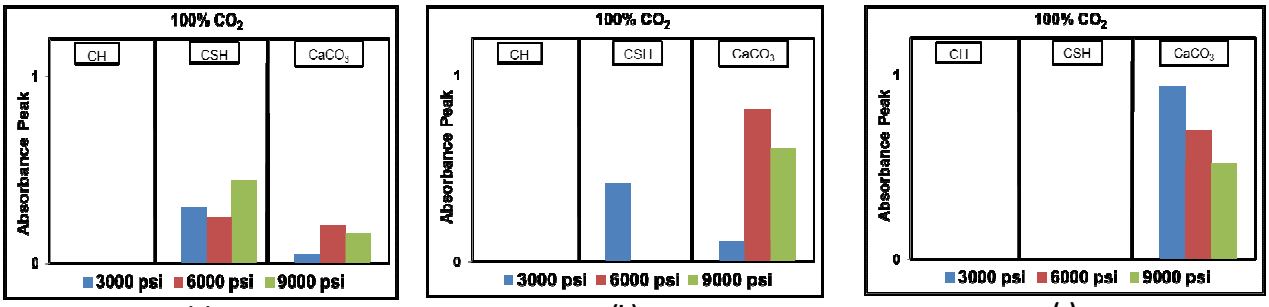

(a) (b) (c)

Fig. A-3: Summarized FTIR data of baseline Class H cement samples aged at 225°F, 100% CO2 for 14 days: a) Virgin zone; b) Middle zone; and c) Outermost zone

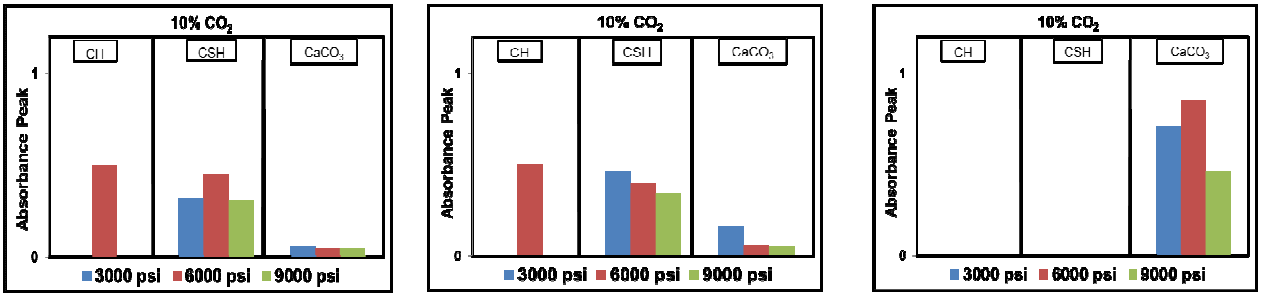

(a) (b) (c)

Fig. A-4: Summarized FTIR data of baseline Class H cement samples aged at 350°F, 10% CO2 for 14 days: a) Virgin zone; b) Middle zone; and c) Outermost zone

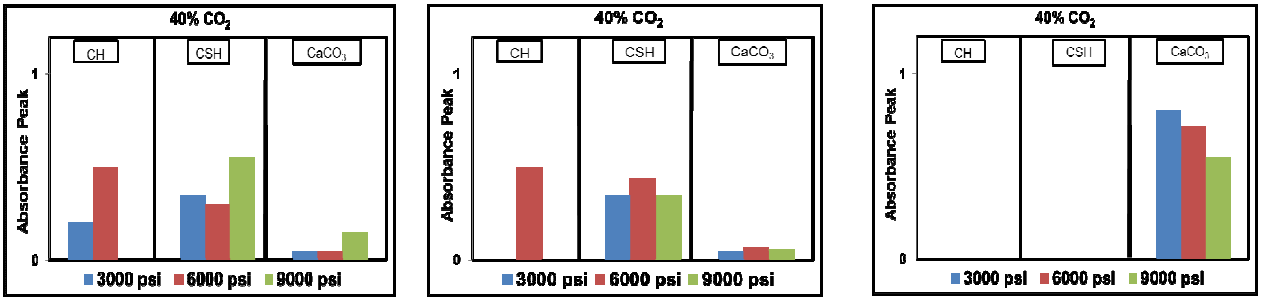

(a) (b) (c)

Fig. A-5: Summarized FTIR data of baseline Class H cement samples aged at 350°F, 40% CO2 for 14 days: a) Virgin zone; b) Middle zone; and c) Outermost zone

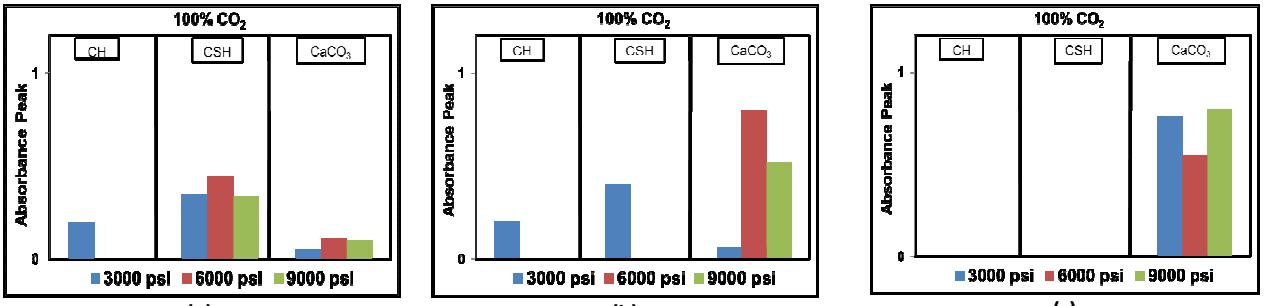

(a) (b) (c)

Fig. A-6: Summarized FTIR data of baseline Class H cement samples aged at 350°F, 100% CO2 for 14 days: a) Virgin zone; b) Middle zone; and c) Outermost zone

A.2 Effect of Temperature on Degradation of Baseline Cement

Figures A-7 to **A-15** show how the pressure affects the degradation of baseline cement at different temperatures (100, 225 and 350°F). Result interpretations are summarized in **Table A-2**.

Table A-2: Interpretations of FTIR results presented in Figs. A-7 to A-15

Figure	Zone	Discussion
Figs. A-7, A-8 & A-9	Virgin	CH was completely carbonated. Some amount of CSH was preserved
	Middle	Ditto
	Outermost	Both CH and CSH were completely carbonated.
Figs. A-10, A-11 & A-12	Virgin	Some amount of CH was preserved at 100 and 350 ^{o}F. Some amount of CSH was preserved.
	Middle	Ditto
	Outermost	Both CH and CSH were completely carbonated.
Figs. A-13, A-14 & A-15	Virgin	CH was completely carbonated. Some amount of CSH was preserved
	Middle	CSH was completely carbonated at 100% CO_2.
	Outermost	Both CH and CSH were completely carbonated.

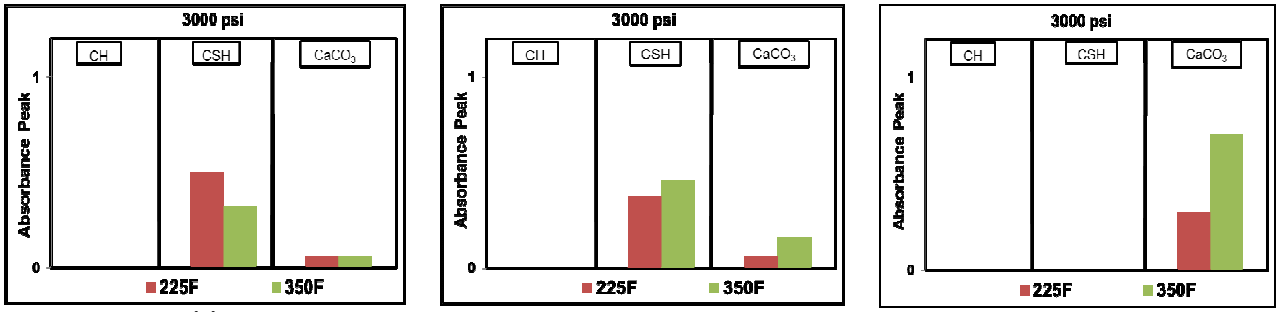

Fig. A-7: Summarized FTIR data of baseline Class H cement samples aged at 3000 psi, and 10% CO2 for 14 days: a) Virgin zone; b) Middle zone; and c) Outermost zone

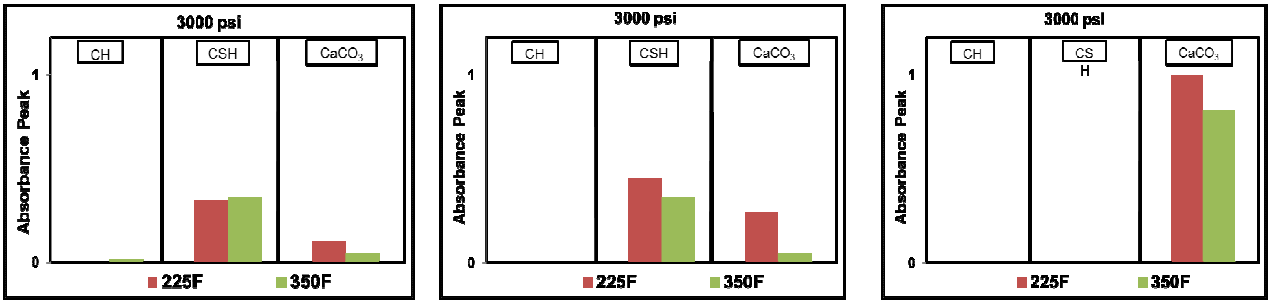

Fig. A-8: Summarized FTIR data of baseline Class H cement samples aged at 3000 psi, and 40% CO2 for 14 days: a) Virgin zone; b) Middle zone; and c) Outermost zone

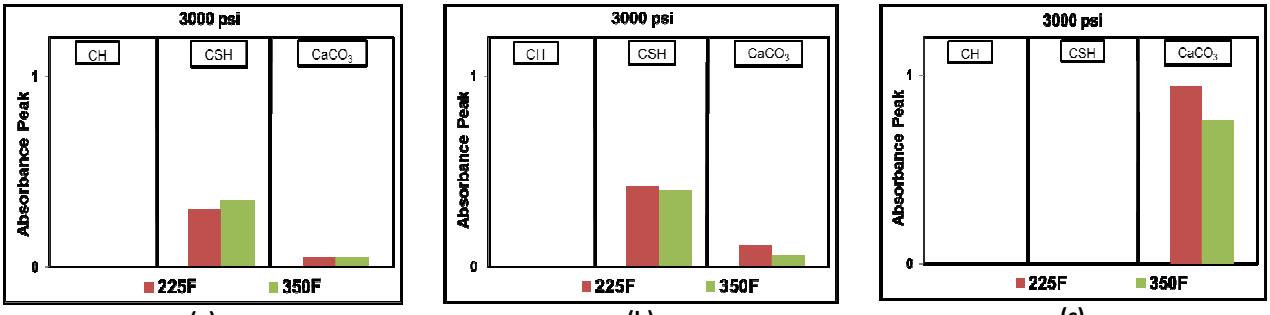

Fig. A-9: Summarized FTIR data of baseline Class H cement samples aged at 3000 psi, and 100% CO2 for 14 days: a) Virgin zone; b) Middle zone; and c) Outermost zone

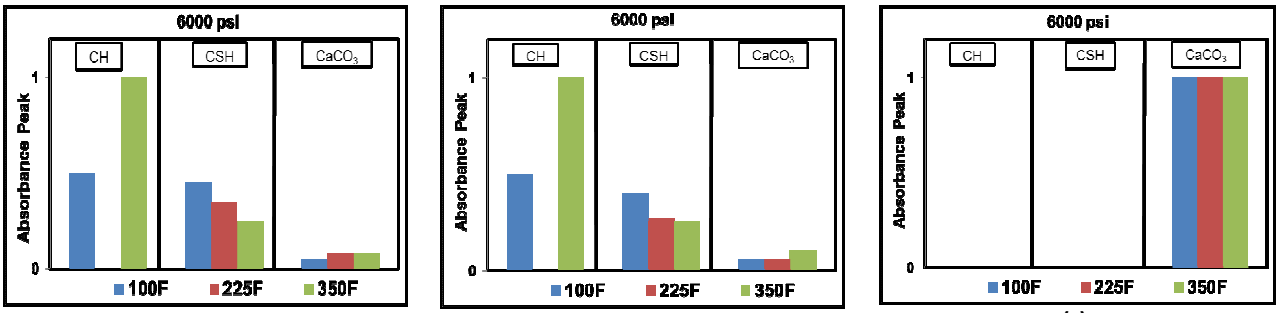

Fig. A-10: Summarized FTIR data of baseline Class H cement samples aged at 6000 psi, and 10% CO2 for 14 days: a) Virgin zone; b) Middle zone; and c) Outermost zone

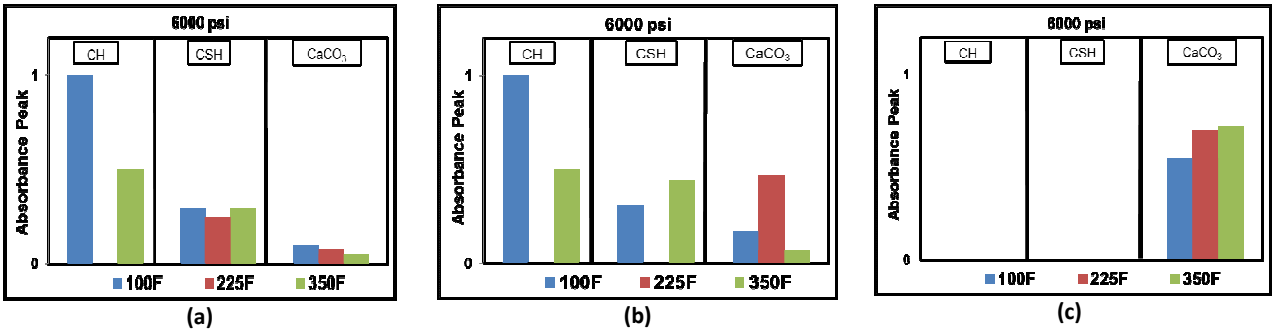

Fig. A-11: Summarized FTIR data of baseline Class H cement samples aged at 6000 psi, and 40% CO2 for 14 days: a) Virgin zone; b) Middle zone; and c) Outermost zone

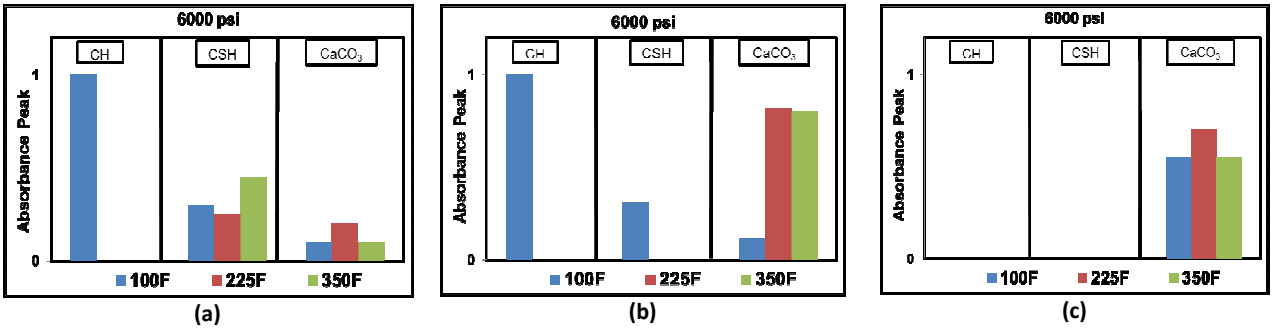

Fig. A-12: Summarized FTIR data of baseline Class H cement samples aged at 6000 psi, and 100% CO2 for 14 days: a) Virgin zone; b) Middle zone; and c) Outermost zone

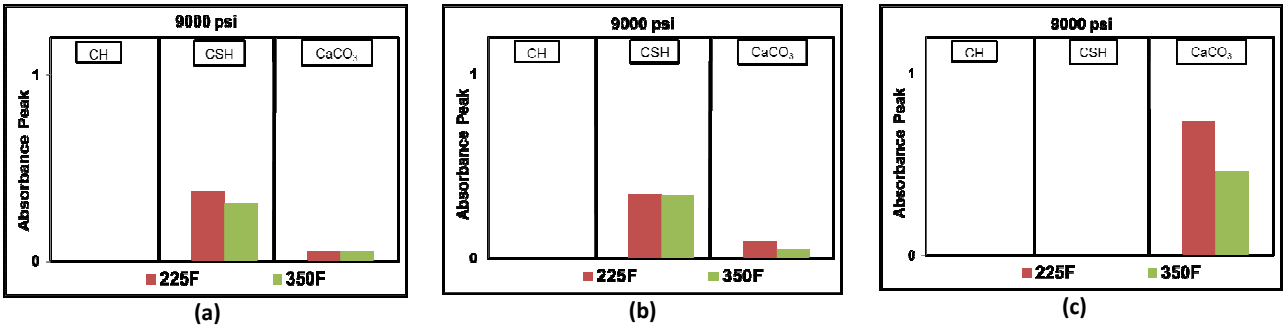

Fig. A-13: Summarized FTIR data of baseline Class H cement samples aged at 9000 psi, and 10% CO2 for 14 days: a) Virgin zone; b) Middle zone; and c) Outermost zone

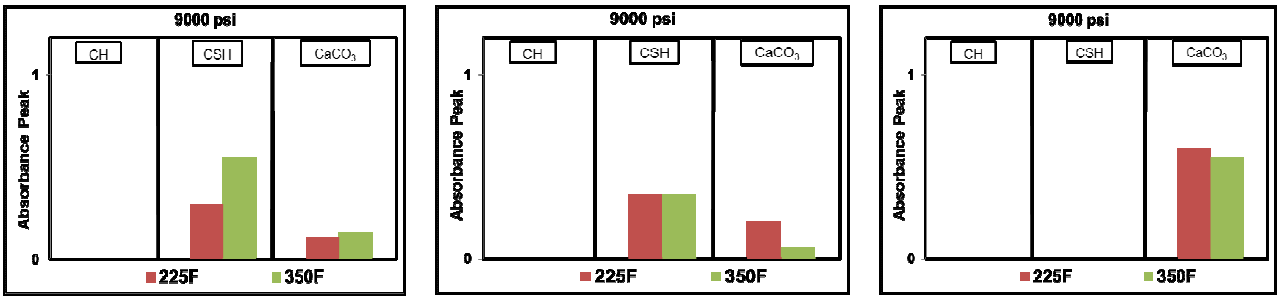

(a) (b) (c)

Fig. A-14: Summarized FTIR data of baseline Class H cement samples aged at 9000 psi, and 40% CO2 for 14 days: a) Virgin zone; b) Middle zone; and c) Outermost zone

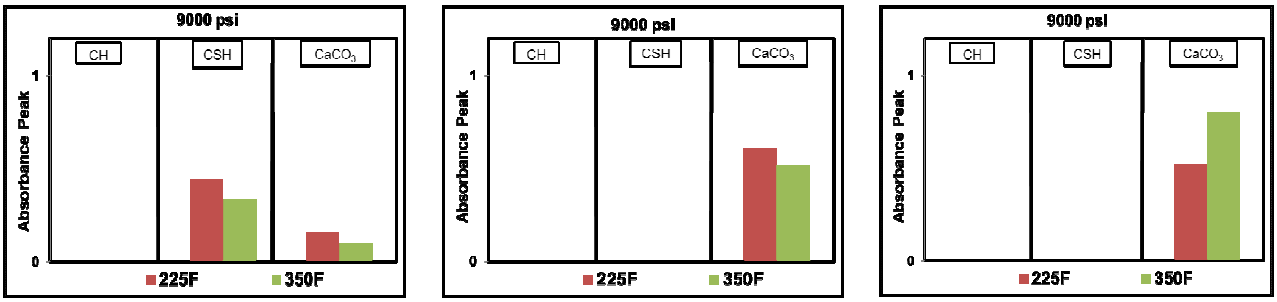

(a) (b) (c)

Fig. A-15: Summarized FTIR data of baseline Class H cement samples aged at 9000 psi, and 100% CO2 for 14 days: a) Virgin zone; b) Middle zone; and c) Outermost zone

Project Title: Effect of H_2S and CO_2 in HPHT Wells on Tubulars and Cement

Report Type: Monthly Report

Report #: 28

Reporting Period: December 22nd, 2013 to January 21st, 2014

Authors:

Ramadan Ahmed, Principal Investigator

Subhash Shah, Co-Principal Investigator

Rida Elgaddafi, Research Assistant

Omotayo Omosebi, Research Assistant

Himanshu Maheshwari, Research Assistant

Adarsh Naidu, Research Assistant

Aman Srivastava, Research Assistant

Jueun Hwang, Research Assistant

Mounraj Sharma, Research Assistant

Sagar Tale, Research Assistant

Prepared under BSEE Project # E12PC00035

by

THE UNIVERSITY OF OKLAHOMA

February 27, 2014

1. Summary of Accomplishments

This monthly report presents the progress made during the project period December 22, 2013 to January 21, 2014. The aging cell became operational after repair and experiments resumed. Cement and tubular degradation studies were continued during this period. Cement cores and bonding samples were prepared and aged in HPHT acidic environment to examine their degradation characteristics. Micro-silica based acid resistant cement slurries and cores were prepared and tested under different aging conditions.

Two aging experiments (Experiments 26 and 27) were completed during this month. The samples were aged for 2 weeks in 2% brine saturated with CO_2 containing methane gas. Porosity, permeability, and compressive and bond strengths of unaged and aged samples were measured. Recent measurements were combined with previously obtained results.

For tests conducted at high-pressure high-temperature conditions (6000 psi and 430°F), with increasing CO_2 concentration porosity and permeability initially increased and then decreased. Initial increases in these properties are attributed to reduction in CO_2 solubility at high temperature, which limits carbonation. However, as the concentration increased, more CO_2 dissolved in the brine favoring carbonation, which resulted in porosity and permeability reduction.

Temperature has strong impact on a number of physio-chemical processes involved during cement degradation. At high CO_2 concentration (100%), Class G cement strength showed consistent trend with temperature change; first increase in strength due to carbonation occurring at low temperature, which is followed by progressive strength reduction because of leaching, which is promoted by increased temperature. Class H cement showed a similar trend, at different CO_2 concentrations (10, 40 and 100% CO_2).

Experimental investigation on cement additives was continued. The effects of micro-silica on performance of Class H and Class G cements under HPHT acidic conditions were investigated. Porosity, permeability and compressive strength measurements indicate that micro-silica containing cement samples do not resist acid attack better than the baseline samples. In the coming weeks, additional experiments will be carried out under different aging conditions in order to test the effectiveness of other additives against acid attack.

Corrosion study under low-pressure is in progress. After improving the experimental setup, tests will be carried out at constant temperature. Both linear polarization (LPR) and weight-loss corrosion measurement techniques were utilized in the study. Results of new experiment will be presented in the next month report.

Our plan for the upcoming weeks is to continue: i) aging tests at 430°F and different pressures; ii) theoretical and modeling studies on tubular corrosion; iii) additive screening and acid resistant cement development studies; iv) low-pressure corrosion experiments at different CO_2 concentrations; and v) pressure testing of corrosion test setup.

2. Overall Project Progress

2.1 Theoretical Studies (Task 1)

2.1.1 Sulfide Stress Cracking

Sulfide stress cracking (SSC) is one the major issues in the oil and gas Industry limiting the applications of high strength steels. Various methods can be developed to test SSC resistance of metals. This report focuses on: i) Four Point Bend (FPB) test to determine SSC resistance of material; ii) stress distribution in minipipe; and iii) effects of water flooding on SSC resistance of existing casing.

Four Point Bend Test

Sulfide Stress Cracking is phenomenon, which leads to failure of materials at the stress below their yield strength. Steel alloys with high strength are more susceptible to SSC. Failure of pipeline/casing due to SSC can be harmful to the environment as well as personnel since it will lead to leak of H_2S. Previous month reports presented various methods such as NACE method A and Double Cantilever Beam (DCB) techniques to test the SSC resistance of material. FPB test is another approach to determine SSC resistance of material. The FPB approach facilitates testing of small area because of its compact size (NACE TM0177 2005). **Figure 1** shows experimental setup for FPB test. A pusher block applies the push force from the top. The force is applied using action bolts and measured using a load cell. Four blocks are placed above and below the specimen as shown in the figure. Lower part of the figure shows bending stress distribution. The maximum stress is constant between the inner two points. Stress outside these inner points linearly reduces to zero.

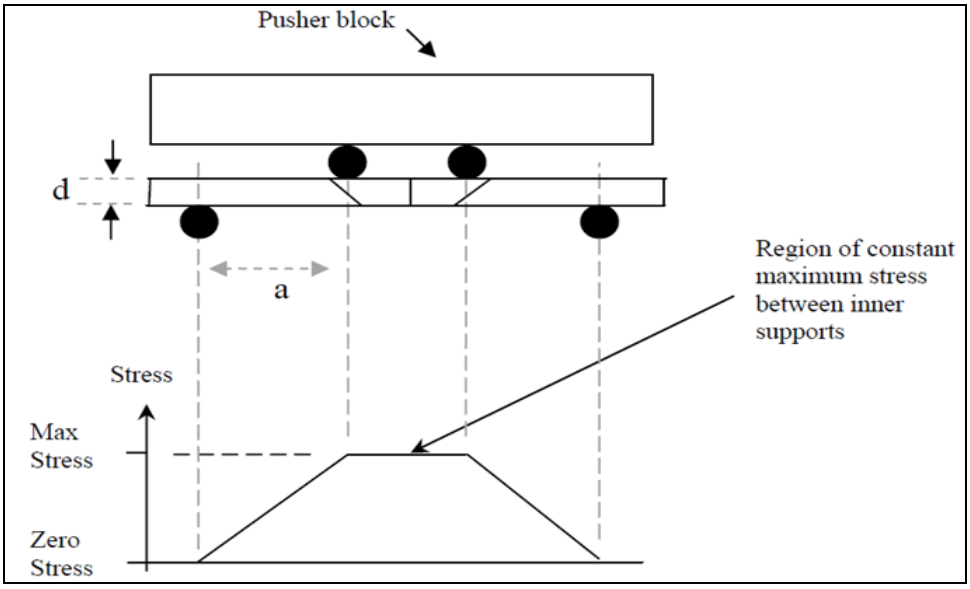

Fig. 1: FPB test experimental set up (Skogsberg et al. 2001)

During the experiment, the entire test assembly is immersed for 720 hours in NACE solution, which is saturated with H_2S at a desired pH. The test is often conducted at room temperature since the SSC rate is the highest. Test results are presented as failure or no failure case. The maximum stress developed during four point bending stress test is given by:

$$S = 3aF/(bd^2), \quad \text{..... (1)}$$

Where, S is tensile stress on bottom of tensile stress (psi); a is distance between outer support and nearest inner support (in); F is applied force (lbf); and b is testing sample width (in).

Stress Distribution in Minipipe

Cernocky et al. (2005) performed minipipe tests for find out SSC resistance. Similar experiments will be performed in this project. Minipipes are subjected to tri-axial stress unlike NACE method, in which the specimen is under a uniaxial stress load.

For stress distribution purpose, minipipe can be treated as pressure vessel. In the past, a closed minipipe specimen was used by Cernocky et al. (2005). When ends of mini pipe are closed, internal pressure of fluid also contributes to overall axial tension. As a result, the following stresses will develop in the minipipe: i) axial stress; ii) hoop stress; and c) radial stress. Thus, minipipe is under tri-axial stress state similar to field loading conditions. All the above stresses can be combined to get von Mises stress. Cernocky et al. (2005) used von Mises stress criteria for minipipe failure. Stress levels are different for inside and outside part of mini pipe. Pressure inside closed mini pipe creates axial tension. Thus, total axial tension is given by:

$$Total\ Tension = Pi * \frac{\pi {D_i}^2}{4} + \text{Frame tension} \quad \text{..... (2)}$$

Axial stress is same across the thickness and given by:

$$\sigma_a = \frac{Total\ Tension}{\frac{\pi({D_o}^2 - {D_i}^2)}{4}} \quad \text{..... (3)}$$

Hoop stress varies across the thickness of a minipipe. It is dependent on radial distance from centre. The generalized equation for hoop stress is given by:

$$\sigma_h = \frac{\left({P_i}^2{r_i}^2 - {P_i}^2{r_o}^2\right) * r^2 - {r_i}^2 * {r_o}^2 * (P_o - P_i)}{({r_o}^2 - {r_i}^2) * r^2} \quad \text{..... (4)}$$

The above equation can be simplified for inside of pipe by substituting $r = r_i$. Thus, hoop stress acting on inside of the minipipe is:

$$\sigma_{hi} = \frac{(r_i^2 + r_o^2) * P_i^2 - 2 * r_o^2 * P_o}{(r_o^2 - r_i^2)} \quad \text{..... (5)}$$

Similarly, the hoop stress acting on outside of the minipipe can be calculated as:

$$\sigma_{ho} = \frac{2 * r_i^2 * P_i - (r_i^2 + r_o^2) * P_o^2}{(r_o^2 - r_i^2)} \quad \text{..... (6)}$$

Radial stress also varies in the minipipe. Generalized equation for radial stress is expressed as:

$$\sigma_r = \frac{(P_i^2 r_i^2 - P_i^2 r_o^2) * r^2 - r_i^2 * r_o^2 * (P_o - P_i)}{(r_o^2 - r_i^2) * r^2} \quad \text{..... (7)}$$

Hence, radial stresses acting inside and outside of the minipipe are: $\sigma_{ri} = -P_i$ and $\sigma_{ro} = -P_o$, respectively. All the above stress equations can be combined to determine the van Mises stress as:

$$\sigma_{von\,Mises} = \frac{1}{\sqrt{2}} * \sqrt{(\sigma_h - \sigma_r)^2 + (\sigma_h - \sigma_a)^2 + (\sigma_a - \sigma_r)^2} \quad \text{..... (8)}$$

Cernocky et al. (2005) theoretically studied the distribution of stresses on minipipe with ID of 0.687" and OD of 0.9". They considered outside and inside pressures of 0 and 19,000 psig, respectively. **Figure 2** shows theoretically calculated stress distribution in the minipipe wall. Results show that the von Mises stress (combined stress) is maximum in the inner part and greater than the axial stress.

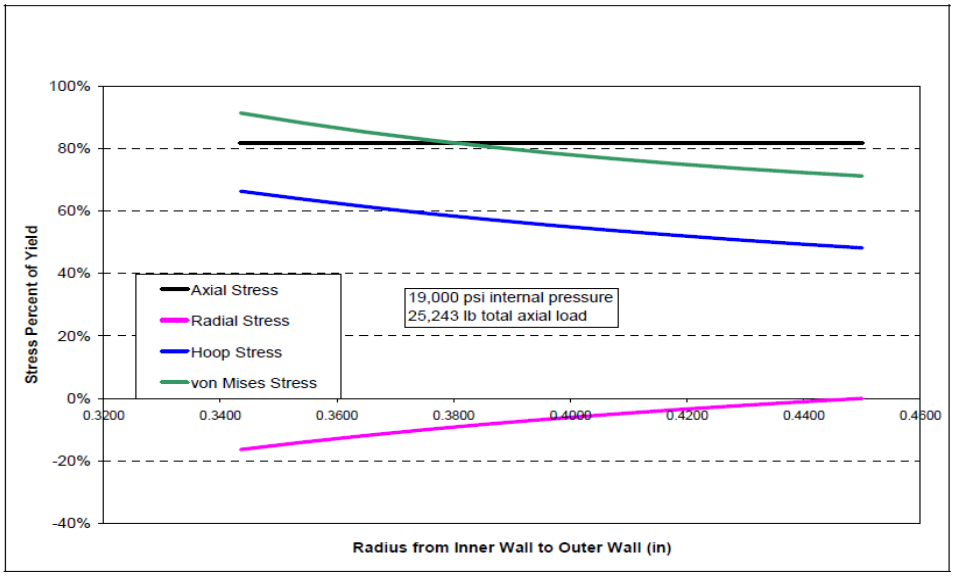

Fig. 2: Stress distribution in minipipe wall (Cernocky et al. 2005)

Water Flooding Impact on SSC Resistance

Water flooding is a method of secondary recovery in which water is injected into a reservoir to displace residual oil. Water flooding may change SSC resistance of casing. Water flooding can affect strain levels, pH and H_2S concentration in well. These factors have strong impact on SSC resistance of well tubulars. Skosgsberg et al. (2001) examined the effect of water flooding on SSC resistance of existing casing. This was part of case study in Gulf of Mexico. Existing casing were made of P110 material and hence P110 was tested for its SSC resistance. Water flooding may result in straining the casing. Thus, to simulate actual field condition, it was desired to have load levels, which will strain the samples to the predetermined values (2%, 4% and 6%). However, the required stresses (to achieve desired strain) could not be attained using standard tensile test equipment. Hence, the samples were pre-strained using computerized servo-hydraulic equipment that precisely controls the strain level. The specimens were pre-strained to the values slightly less than target strain using this equipment. Rest of the straining occurred during the actual experiment. **Figure 3** shows stress strain curve for a specimen. **Figure 4** shows stress-strain curve of one of the specimen which was strained to 4% of its original length. Testing conditions were kept similar to the conditions during actual water flooding operation. Seawater (pH = 7.4) was used as test solution at 130°F and 5000 psi. H_2S concentration (partial pressure) varied between 0.03 to 3 psi. Solution pH was measured at the start and end of the experiment but no attempts were made to keep pH constant. Test duration was for 720 hours.

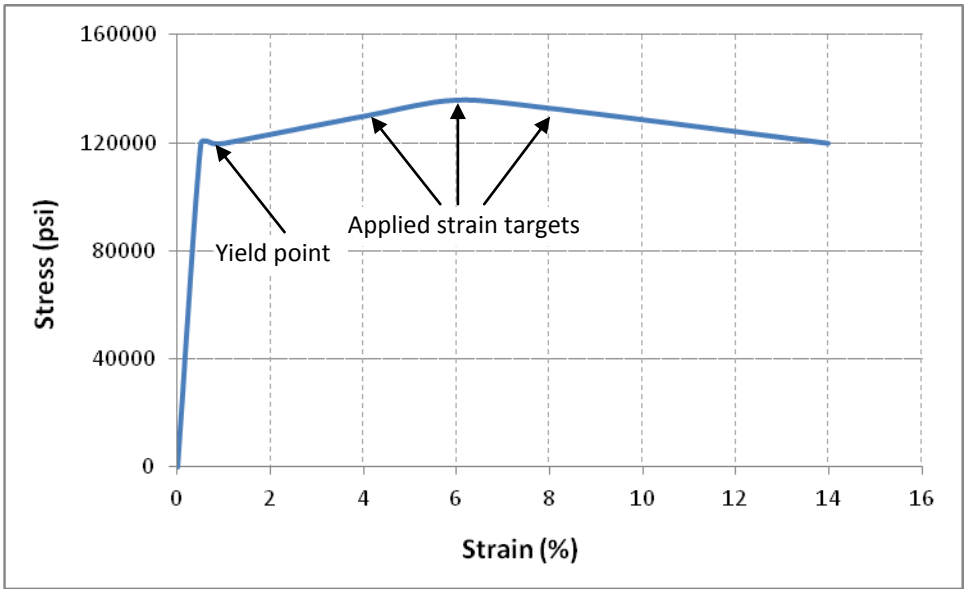

Fig. 3: Stress Strain curve for P110 material (Skogsberg et al. 2001)

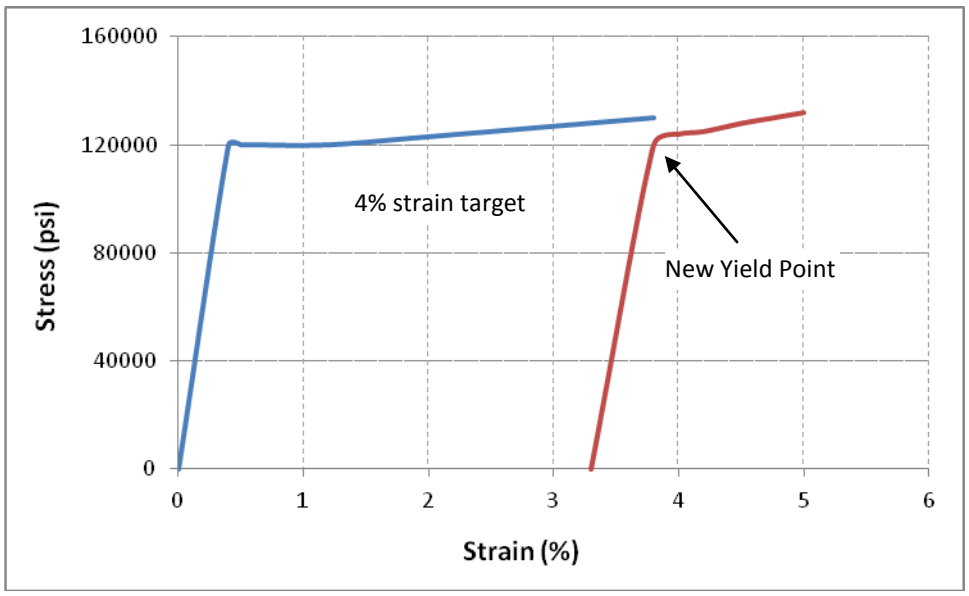

Fig. 4: Specimen strained to 4% (Skogsberg et al. 2001)

Metallographic examination revealed slight pitting corrosion when specimens were exposed to high H_2S concentration environment ($p_{H2S} \geq 0.3$ psi). **Figure 5** shows pitting corrosion observed in samples strained to 6%. Although pitting was observed, none of sample showed presence of crack during the experiment. High pH had resulted in increase in performance of material.

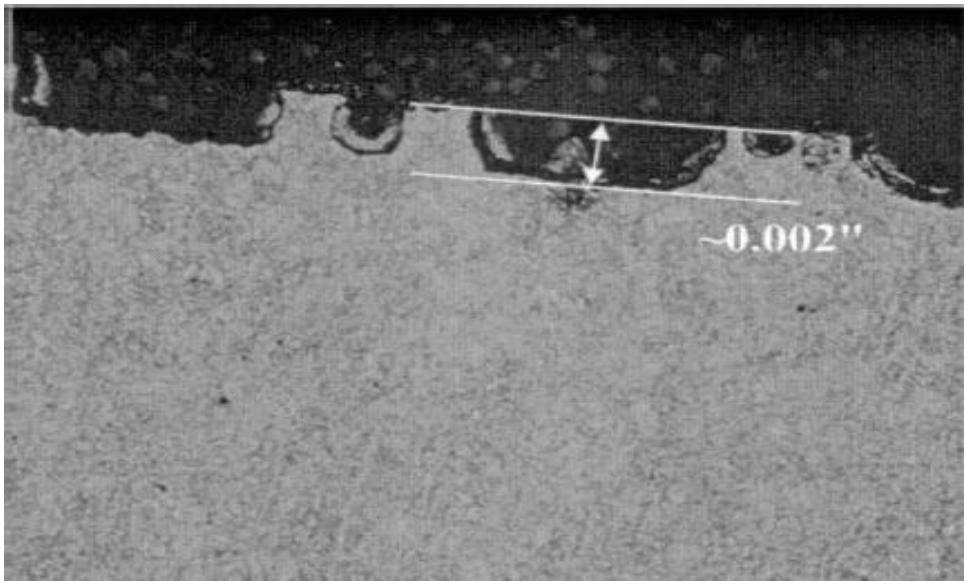

Fig 5: Metallographic examination of 6% strained specimen aged in 0.3 psi H_2S (Skogsberg et al. 2001)

Morana & Nice (2009) also reported improvement in SSC resistance with increase in pH. In addition, other studies (Ciaraldi 1986 and Baldy et al. 1981) have demonstrated that pre-straining on cold work drastically affects the SSC performance of a material. In these studies, the impact of

increased pH seemed to have compensated the loss of resistance against SSC due to pre-straining on cold work. Thus, it can be deduced that water flooding may not significantly affect the SSC resistance of tubulars.

2.2 Experimental Studies on Degradation of Cement (Task 2)

2.2.1 Porosities and Permeabilities of Baseline Cements

During this reporting period, two batches (Batches 29 and 30) of baseline cement cores were aged along with special additives containing samples. The aging conditions for these tests are presented in **Table 1**.

Table 1: Test parameters for aging experiments conducted to date

Batch #	Temp. (ºF)	Pressure (psi)	Partial Pressure %			Brine Conc. (%)	Aging Period (days)	Experiment #
			CH_4	CO_2	H_2S			
001	350	9000	100	0	0	9	6	1
002	350	6000	100	0	0	2	14 & 28	2
003	350	6000	100	0	0	2	14	
004	350	6000	90	10	0	2	6	3
005	350	6000	90	10	0	2	14 & 28	4
006	350	6000	90	10	0	2	14	
007	225	6000	90	10	0	2	14	5
008	100	6000	90	10	0	2	14	6
009	225	6000	60	40	0	2	14	7
010	225	6000	0	100	0	2	14	8
011	100	6000	60	40	0	2	14	9
012	100	6000	0	100	0	2	14	10
013	350	6000	60	40	0	2	14	11
014	350	6000	0	100	0	2	14	12
015	225	6000	60	40	0	2	14	7A
016	350	3000	60	40	0	2	14	13
017	350	9000	60	40	0	2	14	14
018	350	3000	0	100	0	2	14	15
019	350	9000	0	100	0	2	14	16
020	350	3000	90	10	0	2	14	17
021	350	9000	90	10	0	2	14	18
022	225	3000	60	40	0	2	14	19
023	225	9000	60	40	0	2	14	20
024	225	3000	0	100	0	2	14	21
025	225	9000	0	100	0	2	14	22
026	225	3000	90	10	0	2	14	23
027	225	9000	90	10	0	2	14	24
028	430	6000	90	10	0	2	14	25
029	430	6000	60	40	0	2	14	26
030	430	6000	100	0	0	2	14	27

A test matrix developed to examine the effects of pressure and CO_2 concentrations on the degradation behavior of cement cores at 430°F is shown in **Table 2**. Three of the tests that show the effects of CO_2 concentration have been completed.

Table 2: Test matrix for aging experiments at 430°F

Pressure (psi)	10% CO_2	40% CO_2	100% CO_2
3000	-	-	Batch 031
6000	Batch 028	**Batch 029**	**Batch 030**
9000	-	-	Batch 032

Effects of CO_2 Concentration

As presented in previous reports, at low temperatures (100, 225 and 350°F), the overall trends of porosity and permeability demonstrated that initially both porosity and permeability decrease at 10% CO_2 and then they start to increase with increase in CO_2 composition. This is due to formation of scawtite resulting from incomplete carbonation. Formation of scawtite decreases porosity and permeability of cement due to its inability to form bicarbonate that can be leachable by the acid. As CO_2 concentration is increased, complete carbonation occurs, leading to formation leachable bicarbonate and increased porosity and permeability. At very high temperature (430°F), the trend is completely opposite (**Fig. 6**) of that was observed at lower temperatures. As CO_2 concentration increased, porosity and permeability initially increased and then decreased. High temperature reduces solubility; as a result, carbonation is dominated by leaching at low CO_2 concentrations. However, as the concentration increases, more CO_2 dissolves in the brine favoring carbonation, which results is porosity and permeability reduction. Permeability of Class H cement is not consistent with porosity measurements at high CO_2 concentrations (40 and 100% CO_2).

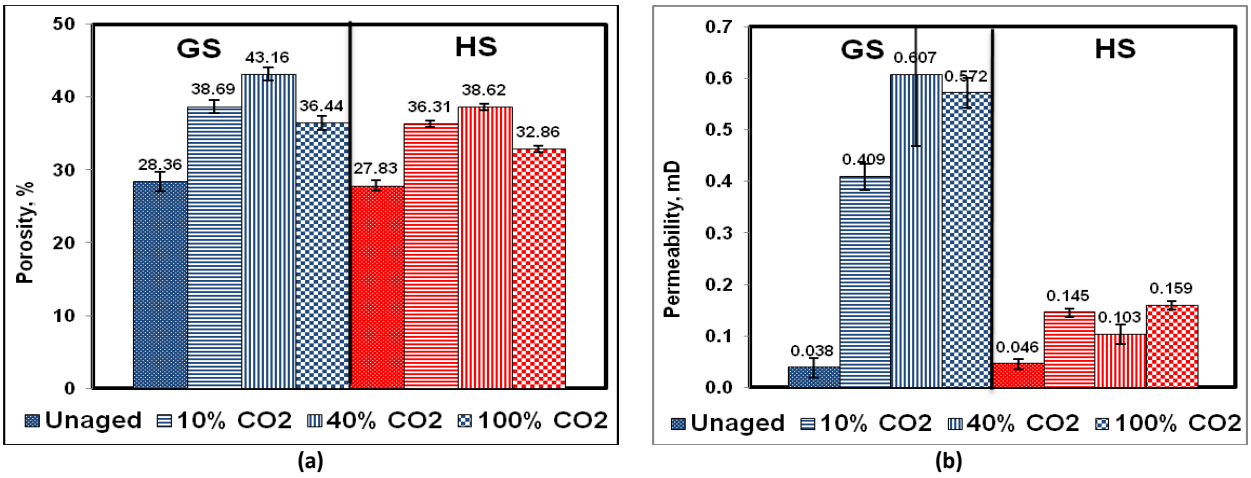

Fig. 6: Effects of CO_2 concentration on porosity and permeability of baseline cores aged at 430°F and 6000 psi

Effects of Temperature

Figures 7 to **9** demonstrate the effects of temperature on degradation of aged baseline cements. The general trend that is observed here is that at lower temperatures (less than 225°F) incomplete carbonation forms scawtite thereby decreasing the porosity and permeability. Nevertheless, as the temperature increases above 225°F, both porosity and permeability increase due to carbonation and leaching of bicarbonate from the cement matrix.

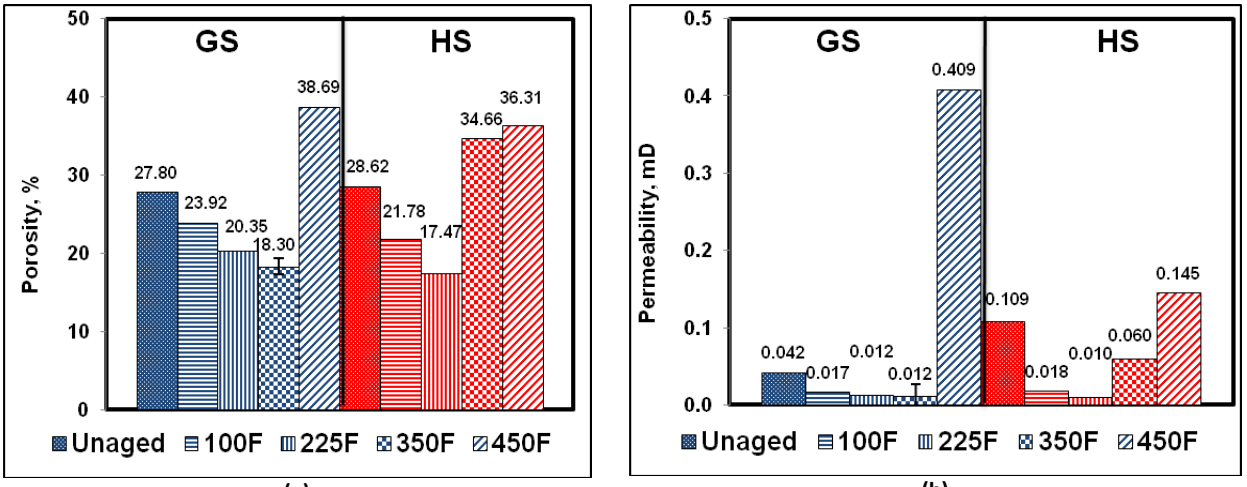

(a) (b)

Fig. 7: Effects of temperature on porosity and permeability of baseline cores aged at 6000 psi and 10% CO_2

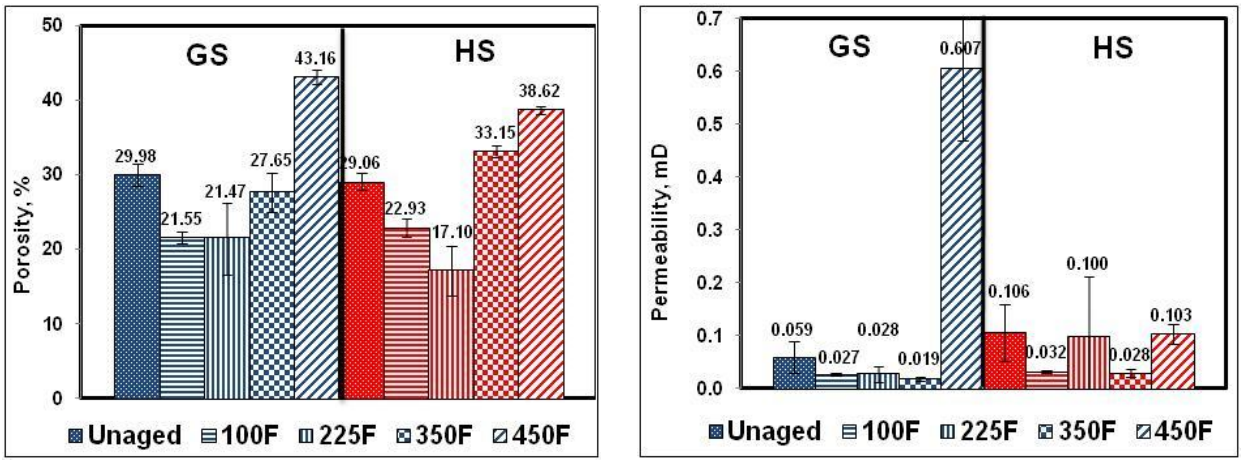

(a) (b)

Fig. 8: Effects of temperature on porosity and permeability of baseline cores aged at 6000 psi and 40% CO_2

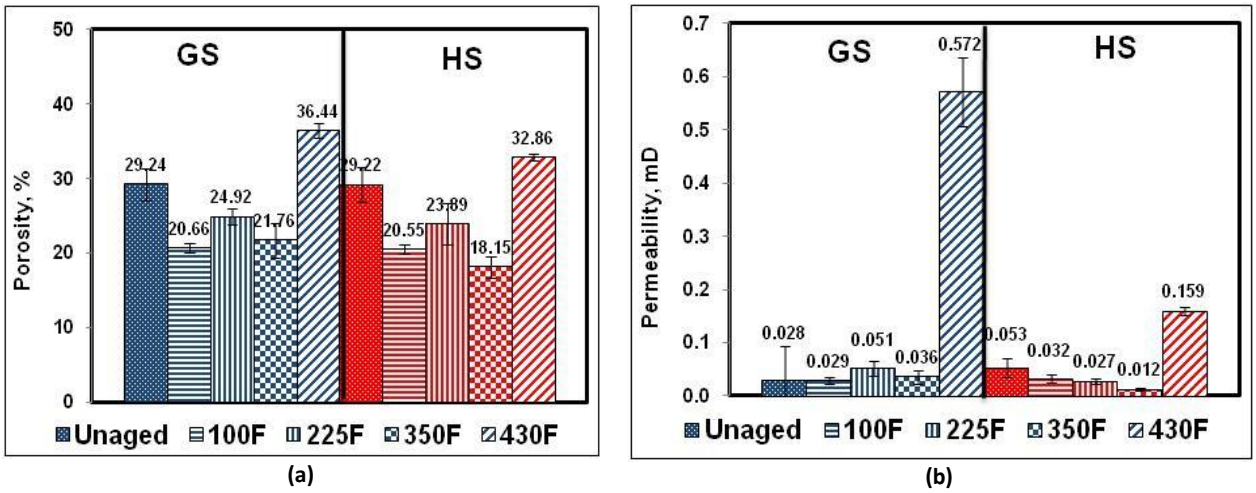

Fig. 9: Effects of temperature on porosity and permeability of baseline cores aged at 6000 psi and 100% CO_2

2.2.2 Compressive Strengths of Baseline Cements

Study on compressive strength of conventional cement was continued. Measurements from Batches 29 and 30 are incorporated into our previous measurements and presented here. The results show the effects of temperature and CO_2 concentration on compressive strength of aged cement samples.

The effects of temperature and CO_2 concentration on compressive strength of baseline (Class G and Class H) cement have been investigated (**Figs. 10 to 12**) at intermediate pressure (6000 psi). Temperature has impact on a number of physio-chemical process involved during cement aging including carbonation, CO_2 solubility, ionic transport, leaching and solubility of solids. For Class G cement, most of these processes offset each other leading to mixed trend in compressive strength at low CO_2 concentrations (10 and 40% CO_2). At high CO_2 concentration (100%), Class G cement strength showed consistent trend with temperature change; first increase in strength at low temperature, which is followed by progressive strength reduction. Class H cement showed a similar trend at different concentrations. As the temperature increases, significant strength gain was observed due to carbonation, then progressive strength reduction due to cement leaching. At extreme high temperature (430°F), the interaction between pore fluid and cement matrix intensifies, leading to dissolution of hydrated binding materials (portlandite and calcium silicate hydrates), which results in substantial reduction in cement mechanical strength. Furthermore, the results presented in the figures, show the effect of CO_2 concentration on the strength. Increase in CO_2 concentration from 10 to 40% had minimal effect on compressive strength of Class G cement; only slight increase or decrease in strength was observed as concentration changes. Class H cement strength predominately improved with increase in CO_2 content of the gas. This is mainly due to carbonation occurring at higher CO_2 concentration. However, as the temperature increases, CO_2 gas solubility reduces resulting in diminished carbonation that can be dominated by leaching, which is intensified by increased temperature.

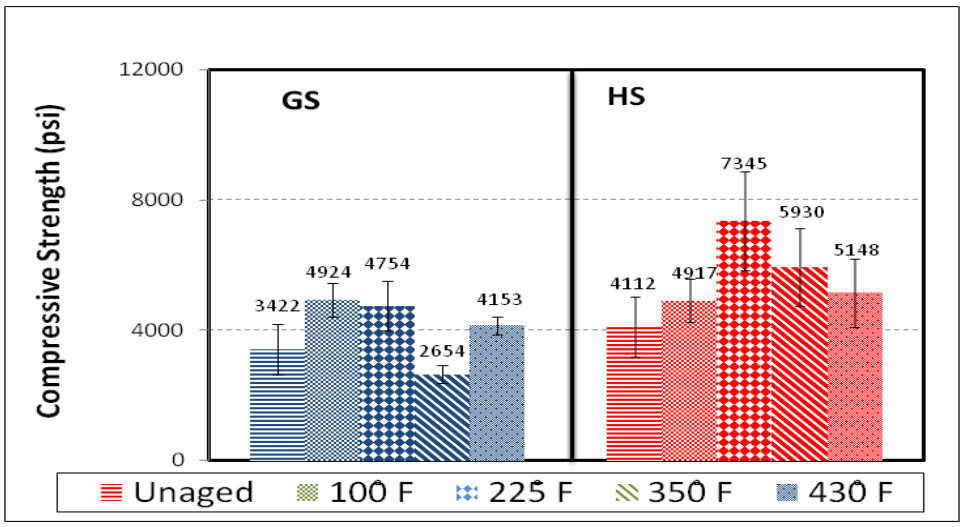

Fig. 10: Effects of temperature on compressive strength of baseline cores aged at 6000 psi and 10% CO_2

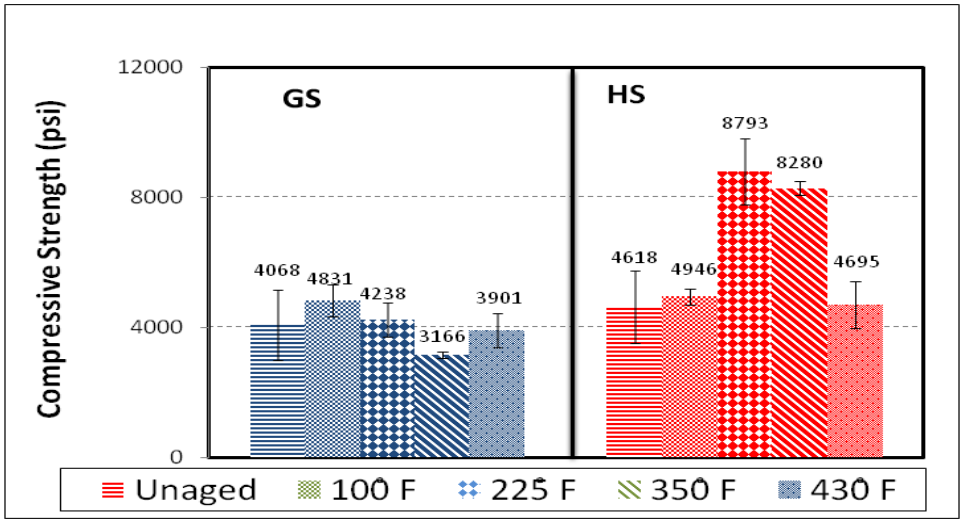

Fig. 11: Effects of temperature on compressive strength of baseline cores aged at 6000 psi and 40% CO_2

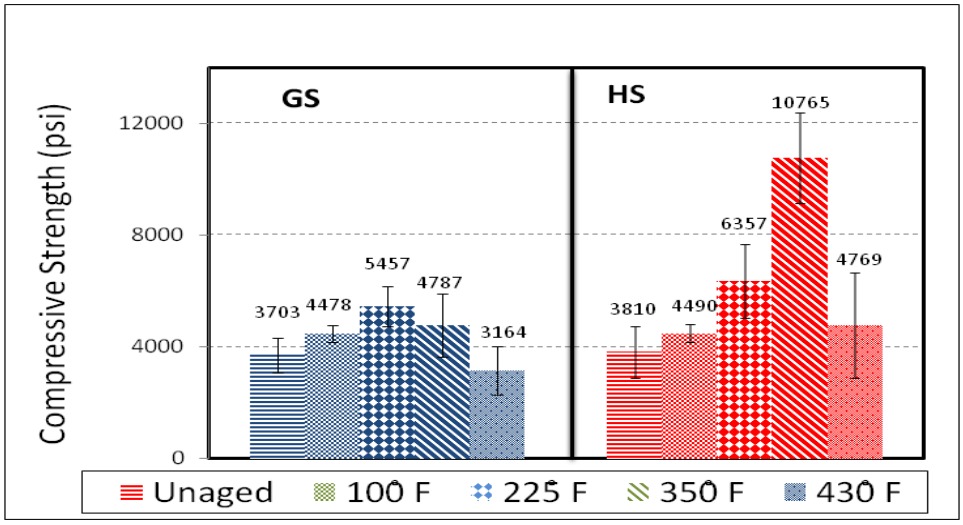

Fig. 12: Effects of temperature on compressive strength of baseline cores aged at 6000 psi and 100% CO_2

2.2.3 Additive Screening and Cement Formulation Studies

The testing of additive containing cement was continued. This report presents results of the third experiment carried out with micro-silica (MS-10) samples and the combined results of all the three experiments. The micro-silica samples showed an extremely high increase in permeability after the aging experiment. Although the compressive and shear bond strengths did not show significant carbonation, the increment in permeability may lead to invasion of acidic gases into the cement matrix.

2.2.3.1 Micro-Silica Based Cement

The third experiment with MS-10 samples was conducted to test their durability against HPHT acid environment. The composition of the slurry is presented in Report # 22. **Table 3** summarizes the aging condition for the recent experiment. After aging, the properties of the cores were measured.

Table 3: Aging conditions for the MS-10 samples

MS-10	Temp. (°F)	Pressure (psi)	CO_2 (%)	NaCl (%)	Days	Baseline	Exp. No.
Batch 010	430	6000	40	2	14	Batch 029	26

Porosity and Permeability

Porosities and permeabilities of MS-10 and baseline cores are presented in **Figs. 13** and **14**, respectively. Both aged and unaged MS-10 samples show slightly lower porosity than the baseline samples. This is attributed to the fineness of micro-silica particle. Before aging, permeabilities of MS-10 samples were significantly lower than those of the baseline samples. However, after aging, the permeabilities of the MS-10 samples increased substantially and became comparable with those of the baseline cement samples. It is important to note that similar increases in permeability were observed in MS-10 samples in previous tests (Experiment 21 and 26). During these tests, the base samples showed better performance in preserving permeability. Results suggest that MS-10 samples are not able to sustain HPHT acidic environment better than the baseline samples.

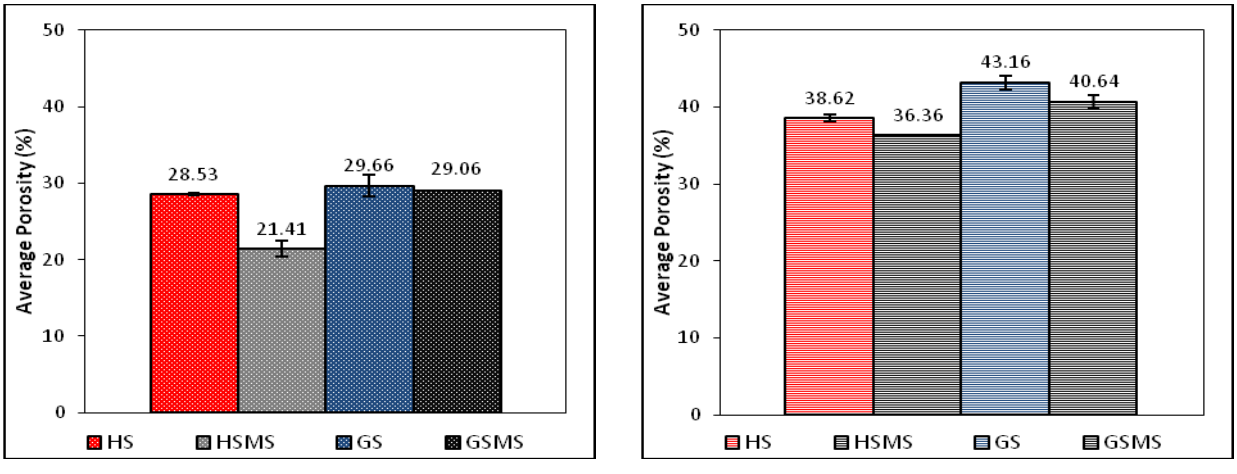

Fig. 13: Porosities of MS-10 and baseline cements: a) unaged; and b) aged for 14 days at 430°F and 6000 psi in brine saturated with 40% CO_2 gas

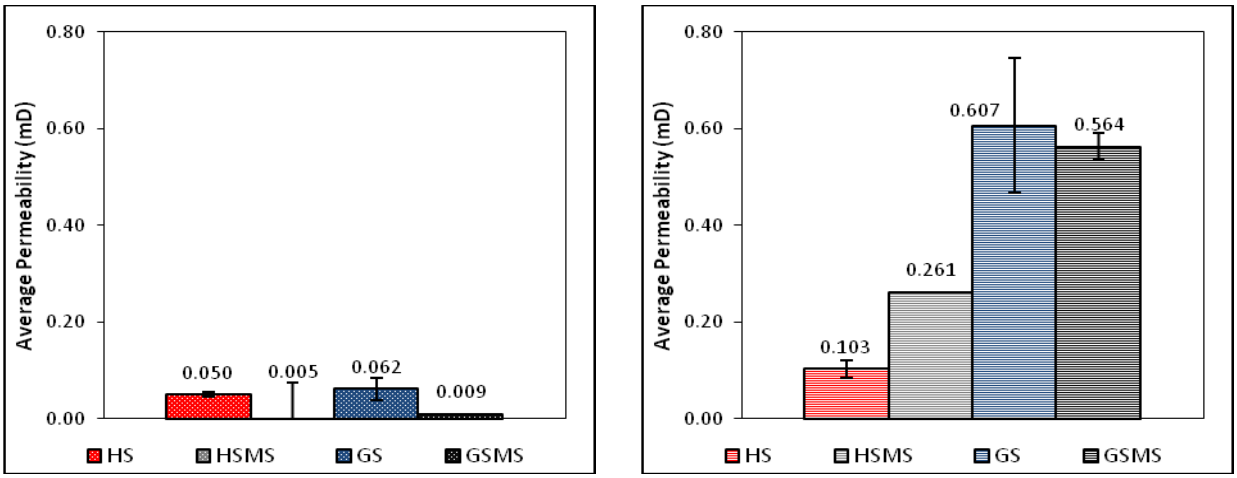

Fig. 14: Permeabilities of MS-10 and baseline cements: a) unaged; and b) aged for 14 days at 430°F and 6000 psi in brine saturated with 40% CO_2 gas

Compressive Strength

The compressive strength of MS-10 and baseline samples is presented in **Fig. 15**. After aging, baseline samples show expected increase in strength due to carbonation of the matrix. Although considerable increase in permeability, which was observed, signifies leaching, the strengths of the samples were increased indicating carbonation of the matrix as well. On the other hand, Class H micro-silica samples show substantial reduction in the strength and Class G micro-silica samples demonstrated minimal strength increment after aging. When visually examined after aging, three of Class H samples were badly damaged and their compressive strengths were not measured. One of the unaged sample was also found to be cracked and damaged and hence could not be used in strength test.

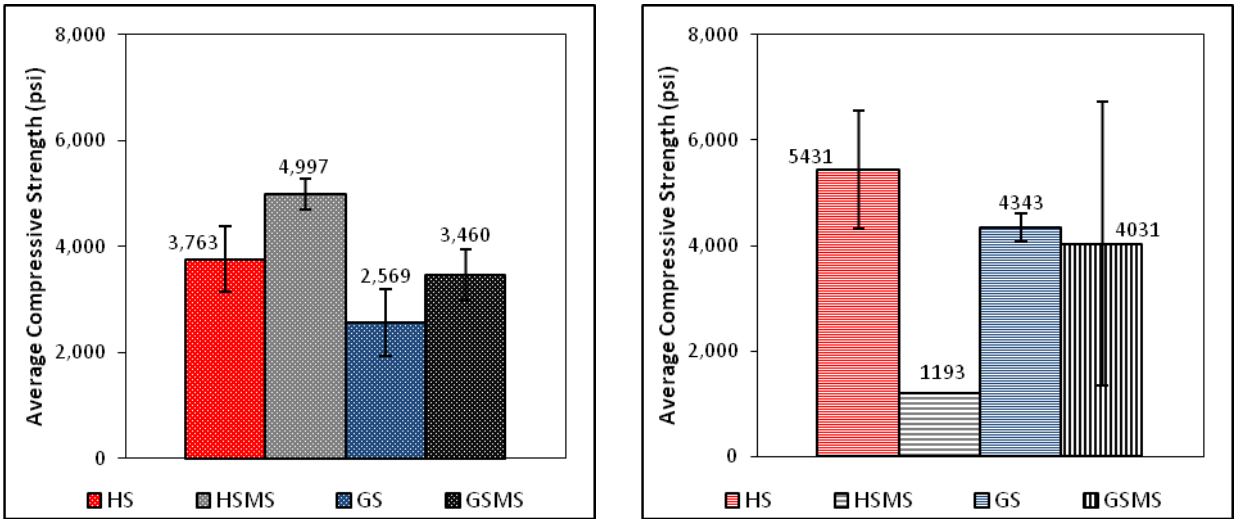

Fig. 15: Compressive Strength of MS-10 and baseline cements: a) unaged; and b) aged for 14 days at 430°F and 6000 psi in brine saturated with 40% CO_2 gas

Shear Bond Strength

The shear bond strength (SBS) of MS-10 and baseline samples are presented in **Fig. 16**. The shear bond strength of unaged MS-10 samples was higher than that of the baseline samples. This is consistent with our previous experiment. After aging, increase in SBS was observed in MS-10 and baseline samples. The increase in permeability and reduction in the compressive strength did not affect the increase in shear bond strength for micro-silica. The result cannot be considered to be in favor of the additive as it shows similar results as those of baseline samples.

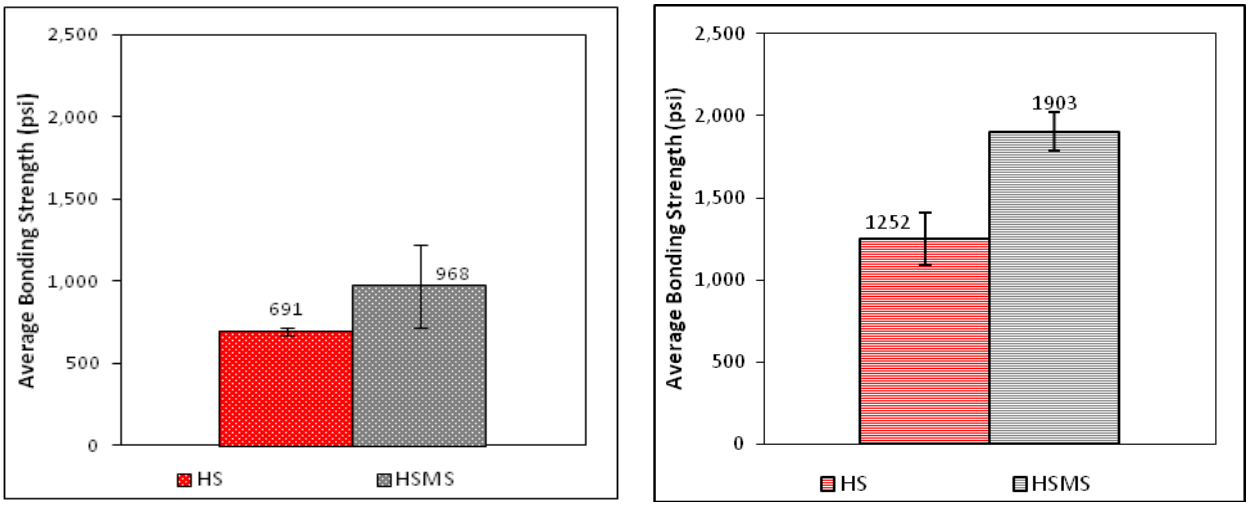

Fig. 16: Shear bond strength of MS-10 and baseline cements: a) unaged; and b) aged for 14 days at 430°F and 6000 psi in brine saturated with 40% CO_2 gas

Summary of Three MS-10 Experiments

The results of all three MS-10 experiments are compared in order to evaluate the performance of micro-silica as a cement additive for acidic environment. The aging conditions for the experiments are summarized in **Table 4**. **Figure 17** depicts the porosity of Class H cements (MS-10 and baseline) for the three batches. It can be observed that MS-10 samples show increase in porosity irrespective of the aging conditions. However, baseline samples indicate reduction in porosity for the first aging experiment and a slight increase for the other tests. Permeability results also show similar trend (**Fig. 18**). The micro-silica samples exhibited several folds of permeability increase while baseline samples permeability showed mixed results, which indicate moderate increases in two cases and significantly reduction in on case.

Table 4: Aging conditions for different batch of MS-10 samples

MS-10	Temp. (°F)	Pressure (psi)	CO_2 (%)	NaCl (%)	Days	Baseline	Exp. No.
Batch 008	225	3000	100	2	14	Batch 024	21
Batch 009	430	6000	10	2	14	Batch 028	25
Batch 010	430	6000	40	2	14	Batch 029	26

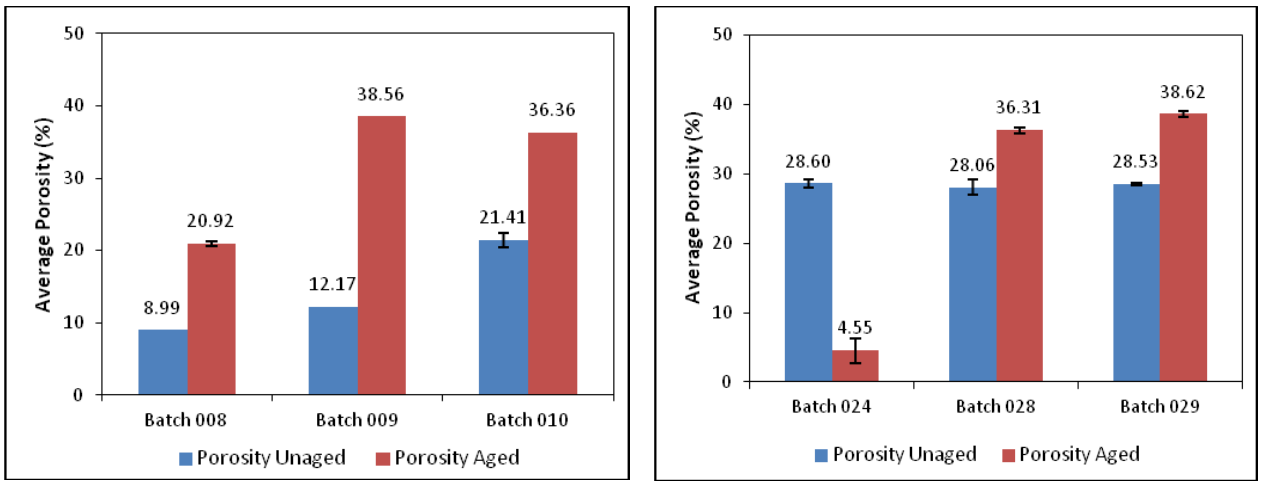

(a) **(b)**

Fig. 17: Porosity of aged and unaged samples: a) MS-10; and b) baseline Class H samples

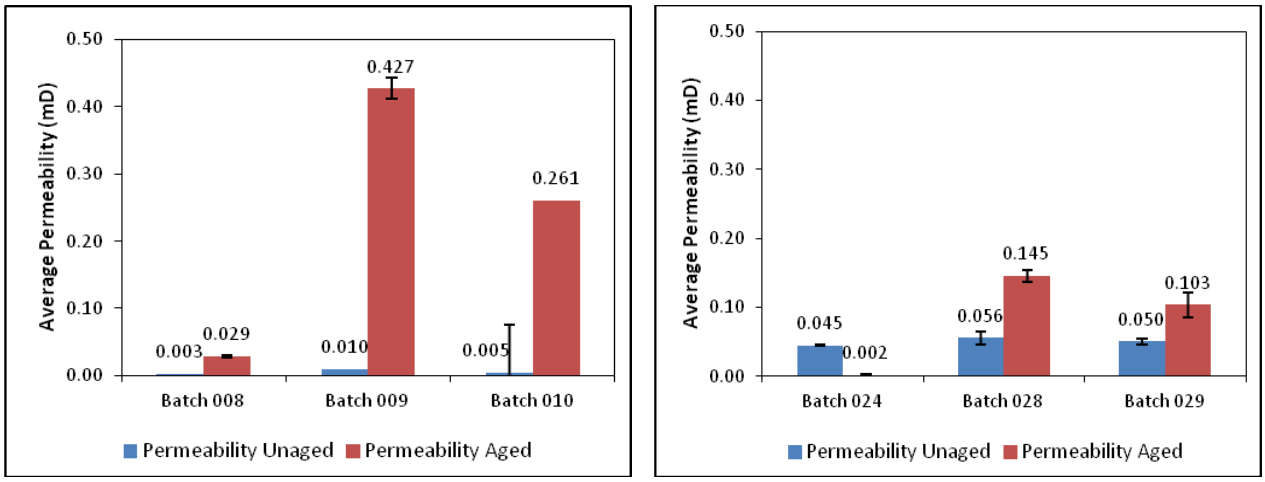

(a) **(b)**

Fig. 18: Permeability of aged and unaged samples: a) MS-10; and b) baseline Class H samples

The compressive strengths of the MS-10 and baseline line samples are summarized in **Fig. 19**. Consistent with the porosity and permeability results, two MS-10 experiments indicated reduction in compressive strength while one test showed improvement. Baseline samples predominately show increase in strength due to carbonation. Again, results do suggest ineffectiveness of micro-silica as an additive for formulating acidic resistant cement.

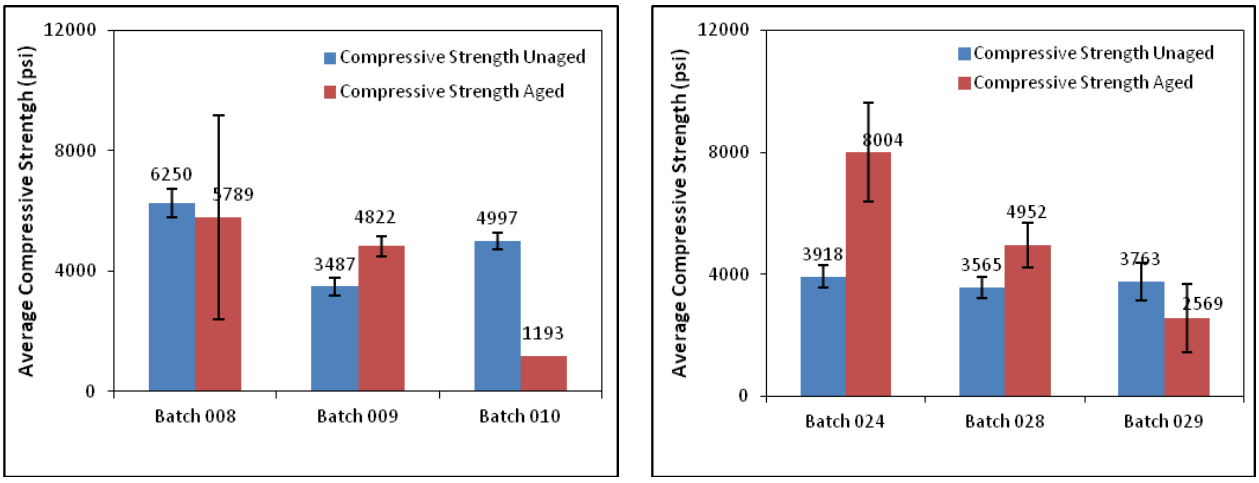

(a) **(b)**

Fig. 19: Compressive strength of aged and unaged samples: a) MS-10; and b) baseline Class H samples

The shear bond strength (SBS) is one of the cement properties that can be used to compare performances of the MS-10 and baseline samples. Results indicate increase in SBS after aging for MS-10 and baseline samples. Predominately, MS-10 samples showed higher SBS than baseline samples. In general, the results suggest improved performance of MS-10 samples in preserving their SBS.

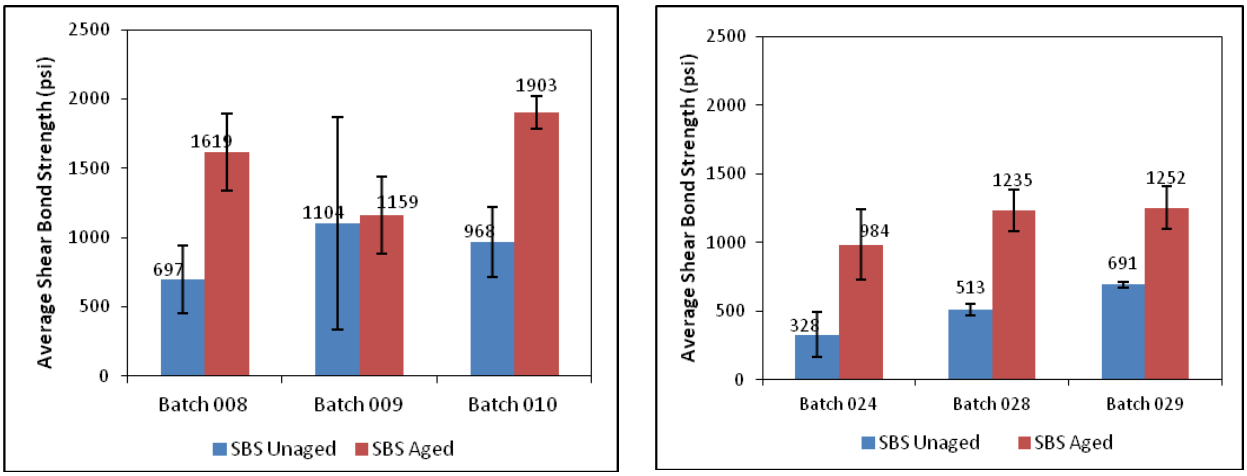

(a) **(b)**

Fig. 19: Shear bond strength of aged and unaged samples: a) MS-10; and b) baseline Class H samples

Similar comparison between MS-10 and baseline samples were conducted for Class G based cements. The comparison show almost similar results as the Class H based cements. Predominately, micro-silica samples showed higher increase in the porosity and permeability after aging than the baseline samples. Like the Class H based samples, reduction in their compressive strength after aging was higher than that of the baseline samples.

2.3 Experimental Studies on Corrosion of Tubulars (Task 3)

After the modification low-pressure corrosion setup, CO_2 corrosion tests were conducted. The samples were aged in 2% brine and presence of CO_2 gas. Tests were carried out for 187 hours varying partial pressure of CO_2 and N_2. Test results will be analyzed and presented in the next month report.

The development of corrosion test setup was continued. Installation and testing of nitrogen and gas venting lines have been completed. The venting lines that are connected to depressurization lines and pressure relief devices such as rupture disks and relief valves. The gas collected from the venting lines will be collected in waste-gas accumulation tank where H_2S containing gas will mixed with air and vented to the atmosphere at allowable concentration. The accumulation tank and its accessories have been tested during this reporting period. The experimental setup is ready to perform tests with H_2S containing gas.

As previously reported, obtaining a manufacturing shop for mini-pipe specimens has been very difficult. Several manufacturing shops declined our invitation to bid due to difficulties in machining small minipipe specimens with acceptable degree of precision. However, we have found recently, a shop that can manufacture the mini-pipe specimens. In the coming days, a manufacturing order will be issued and the shop will begin manufacturing of the specimens. The manufacturer will deliver the items (mini-pipes, flat coupons, and adaptors/attachments for the specimens) within six weeks after receiving the order.

3. Planned Activities

- Continue cement core aging experiments with brine-CO_2-CH4 system for 14 days varying pressure (3000, 6000 and 9000 psi) at 430°F and 100%.
- Continue theoretical and modeling studies on tubular degradation.
- Continue cement additive screening and acid resistant cement formulation studies.
- Continue testing of the corrosion experiment setup.

4. Project Expenditures

This section presents the project expenses during the month of January (**Table 5**) and the cumulative expenditures.

Table 5: Current and cumulative expenditures, January 2014

No.	Budget Categories	Current Expenses	Cumulative Expenses
1	Salaries & Wages	$8,446.92	$261,708.44
2	Fringe Benefits	$1,305.35	$58,862.88
3	Project Materials	$544.32	$61,456.81
4	Travel	$2,171.48	$8,403.81
5	Conference Expenses	$0.00	$0.00
6	Other Direct Costs	$1,771.25	$2,764.85
7	Equipment	$0.00	$242,088.22
8	Space Rental	$0.00	$0.00
9	Indirect Cost	$7,119.66	$195,544.47
10	**Total**	**$21,358.98**	**$830,829.48**

Nomenclatures

BWOC	By weight of cement
CH	Calcium hydroxide
CSH	Calcium silicate hydrate
DCB	Double Cantilever Beam
FPB	Four Point Bend
FTIR	Fourier Transform Infra-Red
GHO	Class G Cement with hydroxyapatite
GS	Class G cement with silica flour
GSMG	Class G Cement with silica flour and magnesium oxide
GSLM	Class G Cement with silica flour, latex and micro-silica
GSLT	Class G Cement with latex
HHO	Class H Cement with hydroxyapatite
HPHT	High-pressure high-temperature
HS	Class H cement with silica flour
HSHO	Class H Cement with silica flour and hydroxyapatite
HSMG	Class H Cement with silica flour and magnesium oxide
HSLM	Class H Cement with silica flour, latex and micro-silica

HSLT	Class H Cement with latex
LPR	Linear polarization resistance
LTMS	Cement with latex and micro-silica additives
mpy	mils per year
MGO	Magnesium oxide containing cement
MGO-5	Cement containing 5% BWOC MgO as additive
MGO-10	Cement containing 10% BWOC MgO as additive
MS	Micro-silica containing cement
MS-10	Cement containing 10% BWOC micro-silica as additive
NACE	National Association of Corrosion Engineers
SBS	Shear bonding strength
SEM	Scanning Electron Microscope
SCC	stress corrosion cracking
SSC	Sulfide Stress Cracking
XRD	X-Ray diffraction

References

Baldy, M.F., Tuttle, R.N. and Kane, R.D. 1981. H2S corrosion in Oil and Gas production- A compilation of classic papers, National Association of Corrosion Engineers, pp 614-618, Houston, Texas.

Cernocky, E.P., Aaron, V.D., Paslay, P.R. and Wink, R.E. 2005. Combined Axial Tension/Compression and Internal pressure testing of Mini-pipe in H_2S environment to determine three-dimensional (Triaxial) stress states, which produce crack initiation failure: Explanation of New test fixture, Mini-pipe specimen and preliminary test results, paper SPE 97577 presented at SPE High Pressure/High Temperature Sour Well Design Applied Technology Workshop, 17-19 May, Woodland, Texas.

Ciaraldi, S.W. 1986. Some factors that affect sour service performance of Carbon Steel Oil Country tubulars, SPE Drilling Engineering, Vol. 1, Num. 3, Pages 233-241.

Morana R. and Nice P.I. 2009. Corrosion assessment of High Strength Carbon Steel Grades P-110, Q-125,140 and 150 for H2S containing producing well environments, paper No. 9093, presented at the NACE International Conference and Expo, 22-26 March, Atlanta, Georgia.

NACE Standard TM0177, 2005. Laboratory Testing of Metals for Resistance to Sulfide Stress Cracking and Stress Corrosion Cracking in H2S Environments.

Skogsberg, L.A.,Stockman, J.A. and Thomson, M.J. 2001. The effect of plastic strain on sulfide stress cracking, Paper No. 1073, presented at the NACE International Conference and Expo, Houston, Texas, 11-16 March.

Project Title: Effect of H_2S and CO_2 in HPHT Wells on Tubulars and Cement

Report Type: Monthly Report

Report #: 29

Reporting Period: January 22nd, 2014 to February 21st, 2014

Authors:

Ramadan Ahmed, Principal Investigator

Subhash Shah, Co-Principal Investigator

Rida Elgaddafi, Research Assistant

Omotayo Omosebi, Research Assistant

Himanshu Maheshwari, Research Assistant

Adarsh Naidu, Research Assistant

Aman Srivastava, Research Assistant

Jueun Hwang, Research Assistant

Mounraj Sharma, Research Assistant

Sagar Tale, Research Assistant

Prepared under BSEE Project # E12PC00035

by

THE UNIVERSITY OF OKLAHOMA

April 15, 2014

1. Summary of Accomplishments

This monthly report presents the progress made during the project period January 22, 2014 to February 21, 2014. Cement and tubular degradation studies were continued during this period. Cement cores and bonding samples were prepared and aged in HPHT acidic environment to examine their degradation characteristics. Latex micro-silica based acid resistant cement slurries and cores were prepared and tested under different aging conditions.

Two aging experiments (Experiments 28 and 29) were completed. The samples were aged for 2 weeks in 2% brine saturated with CO_2 containing methane gas. Porosity, permeability, and compressive and bond strengths of unaged and aged samples were measured. Recent measurements were combined with previously obtained results to examine the effects of different aging parameters on the degradation behaviors of oil well cements.

Temperature has significant effect on degradation process of cement. Cement core porosity and permeability after aging vary considerably with temperature. The trends of porosity and permeability with temperature at 100% CO_2 are very similar to the ones observed at lower CO_2 concentrations (10 and 40% CO_2). At lower temperatures incomplete carbonation forms scawtite reducing porosity and permeability the cores. Nevertheless, both porosity and permeability increased with temperature due to leaching of bicarbonate from the cement matrix.

Experimental investigation on cement additives was continued. The effects of latex micro-silica on performance of Class H and Class G cements under HPHT acidic conditions were investigated. Porosity, permeability and shear-bond strength measurements indicate that latex micro-silica containing cement samples do not resist acid better than the baseline samples. In the coming weeks, additional experiments will be carried out under different aging conditions in order to test the effectiveness of other additives against acid attack.

Corrosion study under low-pressure is in progress. Both weight loss and LPR corrosion measurement techniques were utilized in the study. Five tests were conducted during this month at 110°F and 120 psi. Partial pressure of CO_2 was varied from 0 to 100%. Results showed that at low CO_2 partial pressures (<60%), the corrosion rate increases with the CO_2 content. However, the trend reverses at high CO_2 concentrations.

The development of corrosion test setup has been completed. The experimental setup is ready to perform corrosion tests at high pressure and temperature. A manufacturing shop that can produce mini-pipe and flat corrosion specimens has been found. We are waiting for manufacturing order that will be issued when the necessary documentation submitted by the shop.

Our plan for the upcoming weeks is to continue: i) aging tests at 6000 psi, 10% CO_2, 300 ppm H_2S and different temperatures; ii) theoretical and modeling studies on tubular corrosion; iii) additive screening and acid resistant cement development studies; and iv) low-pressure corrosion experiments at different CO_2 concentration.

2. Overall Project Progress

2.1 Theoretical Studies (Task 1)

2.1.1 Modeling Sulfide Stress Cracking

Sulfide stress cracking (SSC) is one the major issues in the oil and gas Industry limiting the application of high strength steels and steel alloys. During this reporting period, modeling of SSC has been initiated. Sulfide stress cracking involves complex corrosion mechanism. The following chemical reactions show initiation of SSC at the steel surface:

Step 1: H_2S dissociation in water

$$H_2S \rightarrow 2H^+ + S^{-2} \quad \text{..... (1)}$$

Step 2: Oxidation of steel in presence of water

$$Fe \rightarrow Fe^{+2} + 2e^- \quad \text{..... (2)}$$

Step 3: Reduction of Hydrogen ion

$$H^+ + 2e \rightarrow 2H \quad \text{..... (3)}$$

Step 4: Ferrous ion and sulfide ions combine to form H_2S

$$Fe^{2+} + S^{-2} \rightarrow FeS \quad \text{..... (4)}$$

Overall reaction is given by:

$$H_2S + Fe \rightarrow 2H + FeS \quad \text{..... (5)}$$

Furthermore, the first four reactions represent mechanism for localized corrosion attack. Hydrogen ions reduce to hydrogen atoms. Some of the atoms combine to form hydrogen molecule while others remain as free hydrogen atoms and enter into crystalline structure of steel and its alloys, resulting in the embrittlement of the metal, which leads to SSC. Thus, the modeling of SSC must consider all these reaction steps and ionic transport processes. The modeling of SSC is currently in progress. Details of model will be presented in the coming reports.

2.2 Experimental Studies on Degradation of Cement (Task 2)

2.2.1 Porosities and Permeabilities of Baseline Cements

During this reporting period, two batches (Batches 31 and 32) of baseline cement cores were aged along with special additive containing samples. The aging conditions for these tests are presented in **Table 1**.

Table 1: Test parameters for aging experiments conducted to date

Batch #	Temp. (ºF)	Pressure (psi)	Partial Pressure %			Brine Conc. (%)	Aging Period (days)	Experiment #
			CH_4	CO_2	H_2S			
001	350	9000	100	0	0	9	6	1
002	350	6000	100	0	0	2	14 & 28	2
003	350	6000	100	0	0	2	14	
004	350	6000	90	10	0	2	6	3
005	350	6000	90	10	0	2	14 & 28	4
006	350	6000	90	10	0	2	14	
007	225	6000	90	10	0	2	14	5
008	100	6000	90	10	0	2	14	6
009	225	6000	60	40	0	2	14	7
010	225	6000	0	100	0	2	14	8
011	100	6000	60	40	0	2	14	9
012	100	6000	0	100	0	2	14	10
013	350	6000	60	40	0	2	14	11
014	350	6000	0	100	0	2	14	12
015	225	6000	60	40	0	2	14	7A
016	350	3000	60	40	0	2	14	13
017	350	9000	60	40	0	2	14	14
018	350	3000	0	100	0	2	14	15
019	350	9000	0	100	0	2	14	16
020	350	3000	90	10	0	2	14	17
021	350	9000	90	10	0	2	14	18
022	225	3000	60	40	0	2	14	19
023	225	9000	60	40	0	2	14	20
024	225	3000	0	100	0	2	14	21
025	225	9000	0	100	0	2	14	22
026	225	3000	90	10	0	2	14	23
027	225	9000	90	10	0	2	14	24
028	430	6000	90	10	0	2	14	25
029	430	6000	60	40	0	2	14	26
030	430	6000	100	0	0	2	14	27
031	430	3000	100	0	0	2	14	28
032	430	9000	100	0	0	2	14	29

A test matrix developed to examine the effects of pressure and CO_2 concentration on the degradation behavior of cement cores at 430°F is shown in **Table 2**. Tests results show the effects of CO_2 concentration and pressure on degradation of cement. The planned test matrix has been completed.

Table 2: Test matrix for aging experiments at 430°F

Pressure (psi)	10% CO_2	40% CO_2	100% CO_2
3000	-	-	**Batch 031**
6000	Batch 028	Batch 029	Batch 030
9000	-	-	**Batch 032**

Effects of Temperature

Figures 1 to **3** demonstrate the effects of temperature on porosity and permeability of baseline cements. The porosity and permeability trends with temperature for samples aged at high CO_2 concentration (100% CO_2) are similar to the ones observed (Report # 28) at lower CO_2 concentrations (10 and 40% CO_2). At lower aging temperature, incomplete carbonation resulted in scawtite formation thereby decreasing the porosity and permeability. However, as the temperature is increased, porosity and permeability of the cores increase due to carbonation and subsequently, leaching of bicarbonate from the cement matrix.

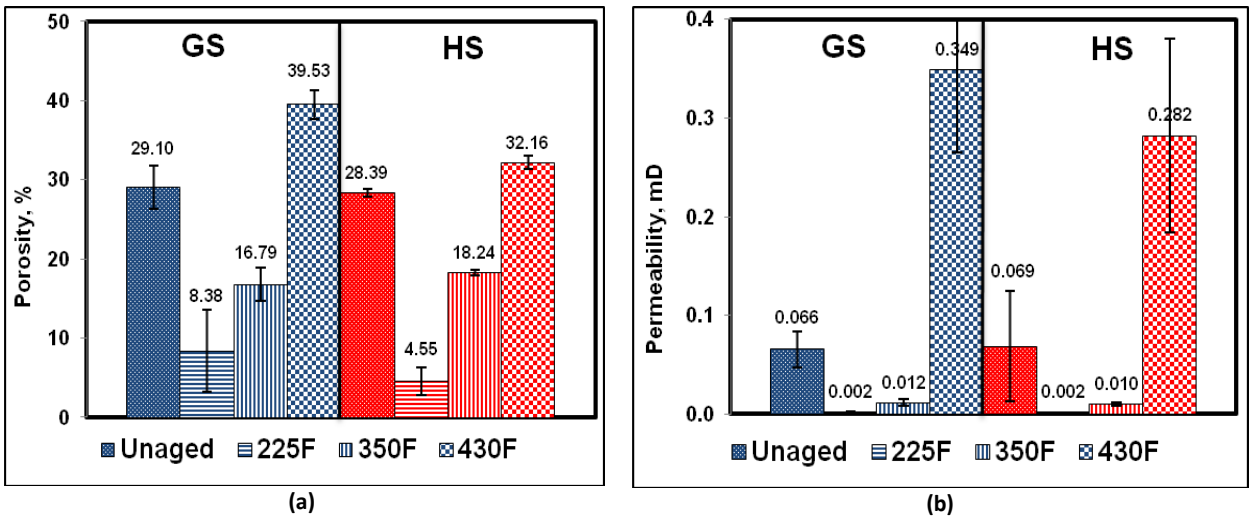

(a) (b)

Fig. 1: Effects of temperature on porosity and permeability of baseline cores aged at 3000 psi and 100% CO_2

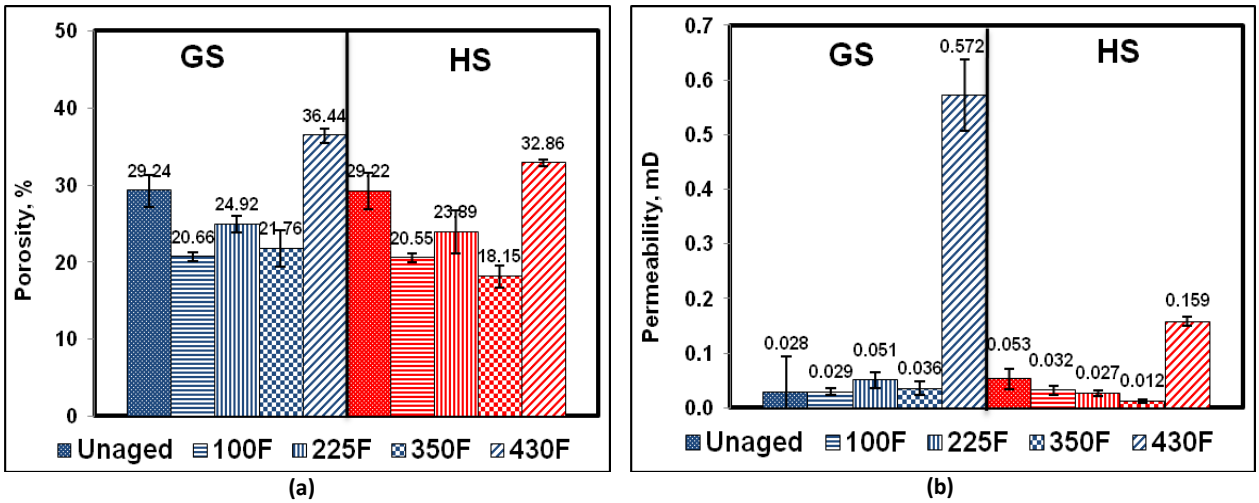

(a) (b)

Fig. 2: Effects of temperature on porosity and permeability of baseline cores aged at 6000 psi and 100% CO_2

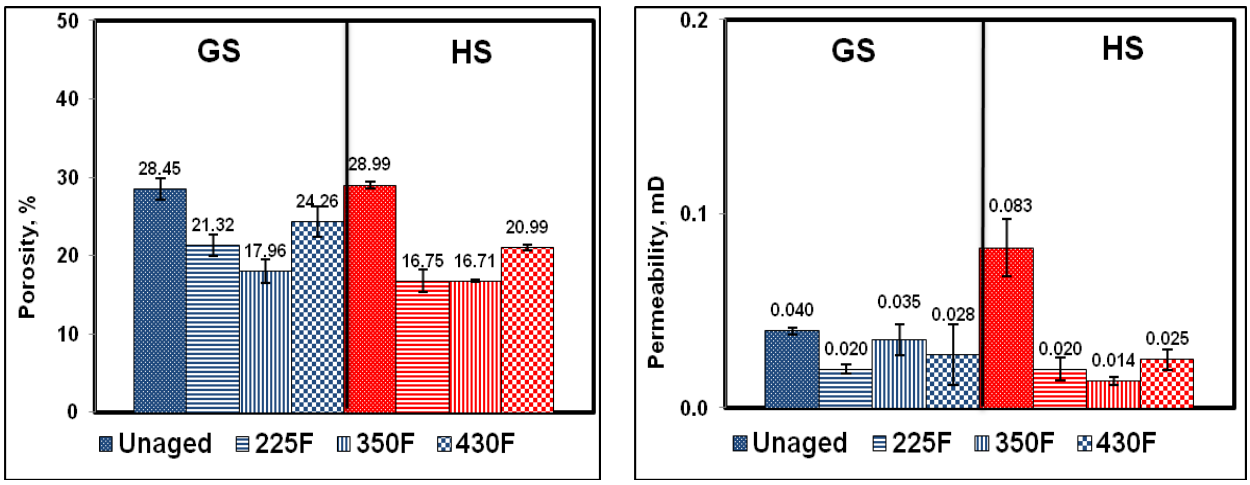

Fig. 3: Effects of temperature on porosity and permeability of baseline cores aged at 9000 psi and 100% CO_2

2.2.3 Additive Screening and Cement Formulation Studies

The testing of additive containing cement was continued. This report presents results of the recent experiments (second and third experiments) carried out with latex and micro-silica containing (LTMS) samples along with results of previous experiments. The latex micro-silica cement samples showed substantial increase in permeability after aging. The compressive strength will be measured in the coming weeks. The shear bond strength did not show significant change after aging.

2.2.3.1 Latex Micro-Silica Based Cement

Experiments with LTMS samples were conducted to test their durability against HPHT acid environment. The composition of the slurry is presented in previous report. **Table 3** summarizes the aging condition for all LTMS experiments. After aging, the properties of the cores were measured.

Table 3: Aging conditions for the LTMS samples

LTMS	Temp. (°F)	Pressure (psi)	CO_2 (%)	NaCl (%)	Days	Baseline	Exp. No.
Batch 002	225	9000	10	2	14	Batch 027	24
Batch 003	430	6000	100	2	14	Batch 030	27
Batch 004	430	3000	100	2	14	Batch 031	28

Porosity and Permeability

Figures 4 and **5** present the porosities and permeability of Class H cement (with and without additives) for the three batches. The porosities of baseline and LTMS samples exhibit very similar trend. However, permeability data shows slightly different trend. In the first experiment (Experiment 24), the permeability of baseline samples decreased after aging while that of LTMS samples showed substantial increase. The increase in permeability can be detrimental to the cement because it allows penetration of acidic into the matrix structure.

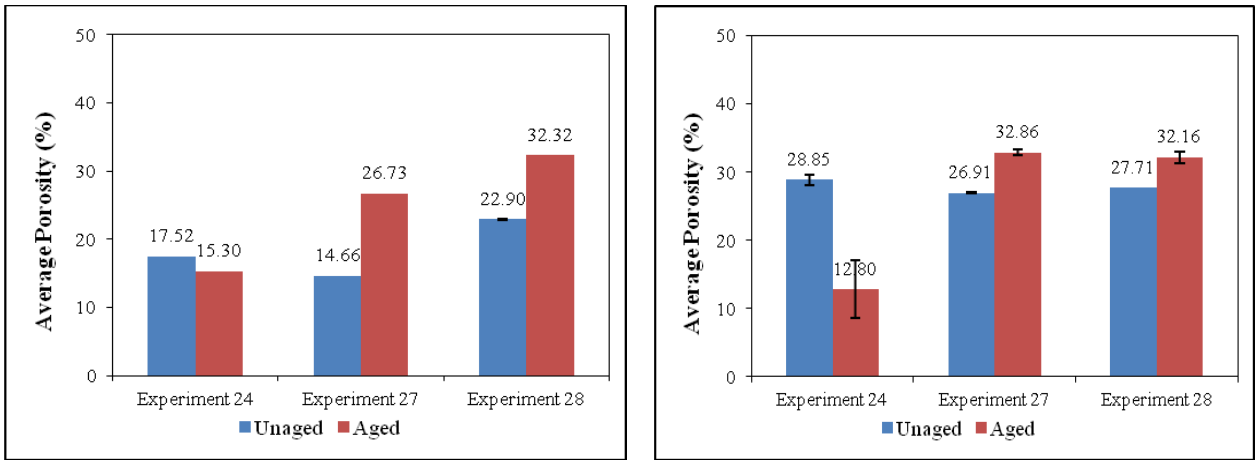

(a) (b)

Fig. 4: Porosities of aged and unaged Class H cement cores: a) LTMS; and b) baseline

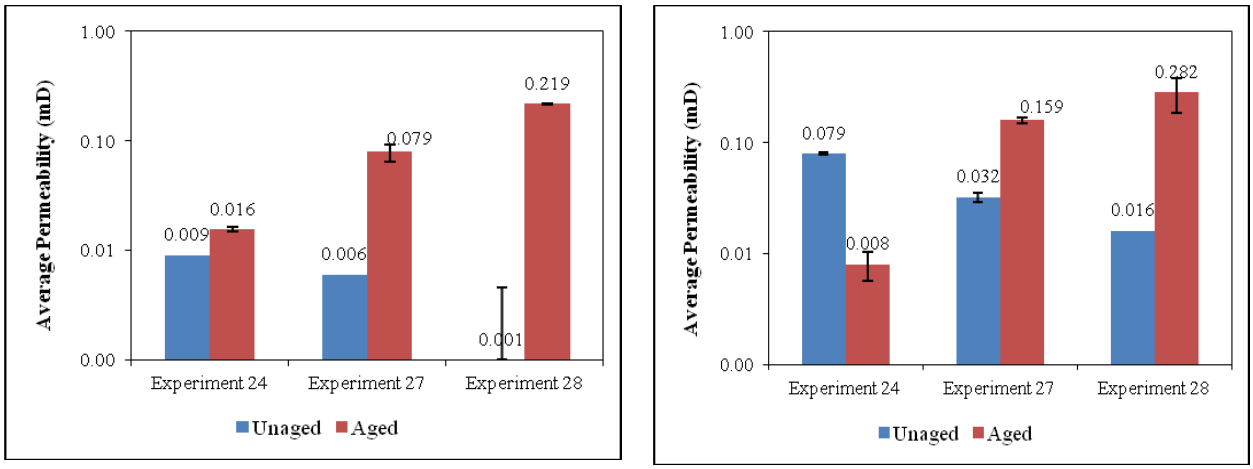

(a) (b)

Fig. 5: Permeabilities of aged and unaged Class H cement cores: a) LTMS; and b) baseline

Similar tests were performed with Class G based cement samples. Porosities and permeability of Class G cement (with and without additives) for the three batches are presented in **Figs. 6** and **7**. Porosity and permeability of Class G based LTMS and baseline samples also show trends, which are consistent with those of Class H samples. However, the increase in permeability observed after aging was more severe than that observed with Class H based LTMS samples. The increase in permeability limits the application LTMS cement in harsh acidic environment.

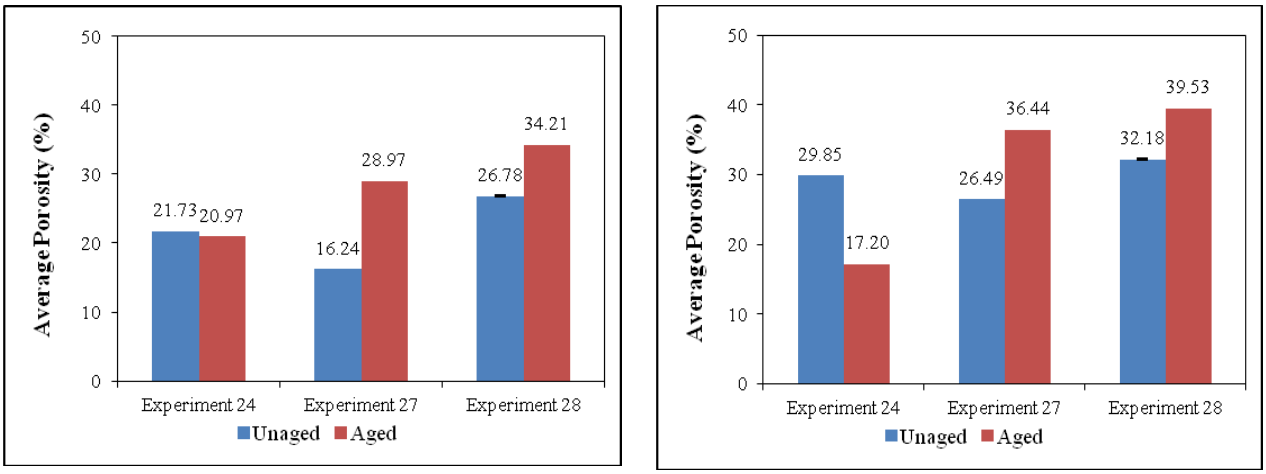

(a) (b)

Fig. 6: Porosities of aged and unaged Class G cement cores: a) LTMS; and b) baseline

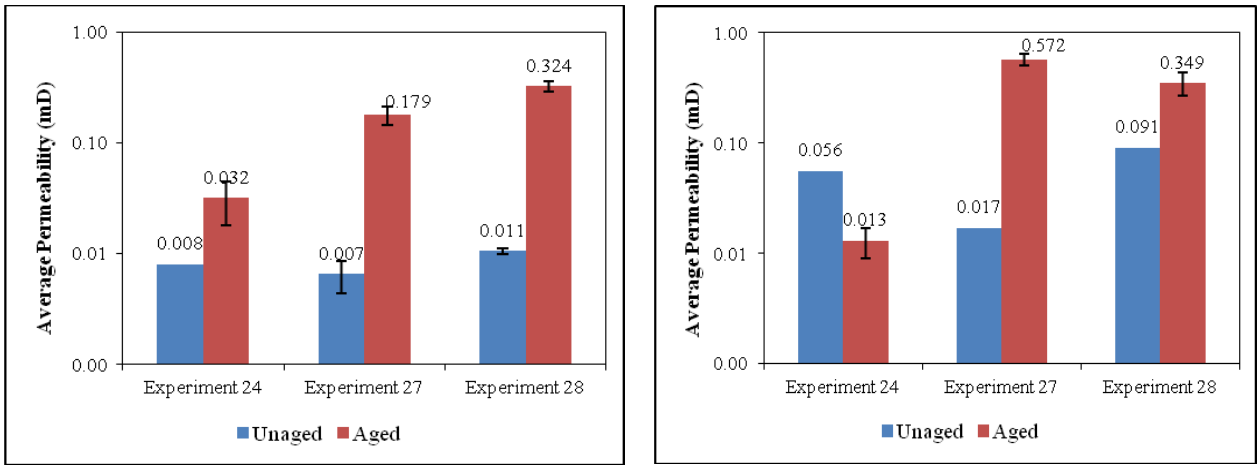

(a) (b)

Fig. 7: Permeabilities of aged and unaged Class G cement cores: a) LTMS; and b) baseline

Shear Bond Strength

The data presented in **Fig. 8** depicts the change in shear bond strength (SBS) of Class H cements, after aging. SBS of unaged LTMS samples show substantial scattering. For tests conducted at high temperature (430°F), baseline and LTMS samples show consistent change in SBS after aging. Results of Experiment # 24 exhibit opposite SBS trend like the permeability measurements. However, the difference in SBS between the LTMS and baseline sample is not significant. The addition of latex and micro-silica does not seem to have a significant effect on shear bond strength after aging.

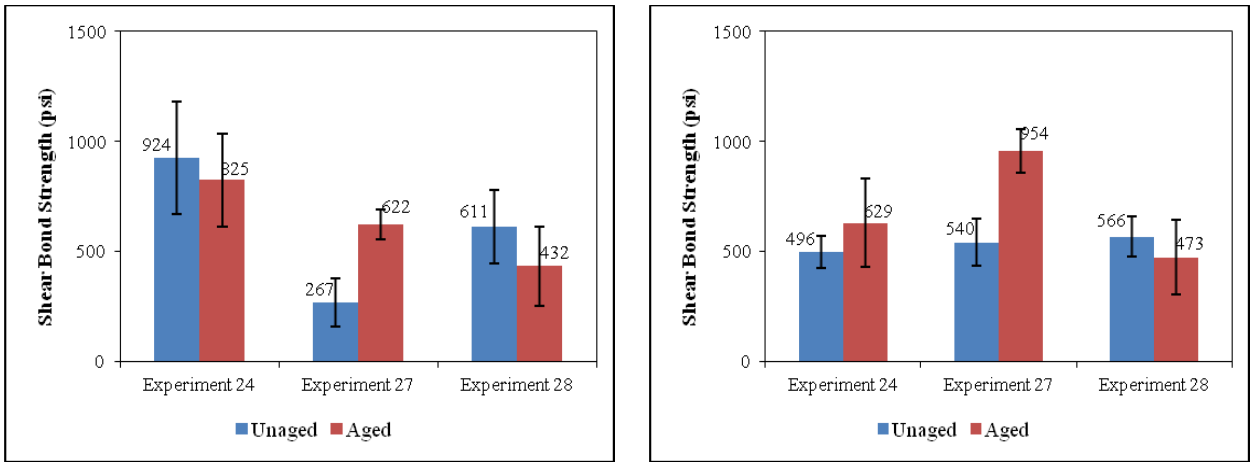

Fig. 8: Permeabilities of aged and unaged Class G cement cores: a) LTMS; and b) baseline

2.3 Experimental Studies on Corrosion of Tubulars (Task 3)

After the modification and improvement of the low-pressure corrosion setup, tests were performed. The samples were aged in 2% brine and presence of CO_2 gas for 187 hours varying partial pressures of CO_2 and N_2. The experiments were performed at 110°F. Test parameters and results of these experiments are summarized in **Table 4**. Two measurement techniques (LPR and WL) were used. Both techniques provided comparable measurements of corrosion rate. The trend of corrosion rate with CO_2 partial pressure obtained in these experiments is consistent with available experimental data in the literature.

Table 4: Test parameters and results of low-pressure corrosion experiments

Exp. #	Temp. (ºF)	Pressure (psi)	Partial Pressure %		Brine Conc. (%)	Test Period (hrs)	Results (mpy)	
			N_2	CO_2			LPR	WL
15	78	120	25	75	2	187	40.30	31.91
16	78	120	0	100	2	187	39.18	32.18
17	78	240	0	100	2	187	NA	NA
18	78	120	75	25	2	187	22.92	21.83
19	110	120	75	25	2	187	31.78	23.78
20	110	120	25	75	2	187	53.16	43.22
21	110	120	100	0	2	187	12.37	15.40
22	110	120	75	25	2	187	31.07	23.78
23	110	120	50	50	2	187	70.35	43.39
24	110	120	25	75	2	187	53.16	43.22
25	110	120	0	100	2	187	44.92	32.49

The corrosion rates measured at a pressure of 120 psi in the presence of CO_2 are presented in **Fig. 9** along with published data by Seiersten (2001). The average corrosion rate increased as the CO_2 partial pressure increased from 0 to 60 psi. Above 60 psi, the rate decreased as the partial pressure was increased from 60 psi to 120 psi (Fig.9a). The increase in the corrosion rate at lower partial pressures could be due to reduction of the pH and increasing rate of the carbonic acid reduction in the presence of

non-protective corrosion scale (Schmitt and Horstemeier, 2006). The reduction in the corrosion rate corresponding to the pressure interval 60-120 psi is not fully understood; however, declining trend in corrosion rate was reported by Seiersten (2001) at 40°C (Fig. 9b). The presence of this unique CO_2 corrosion behavior at higher temperature will be investigated in the future.

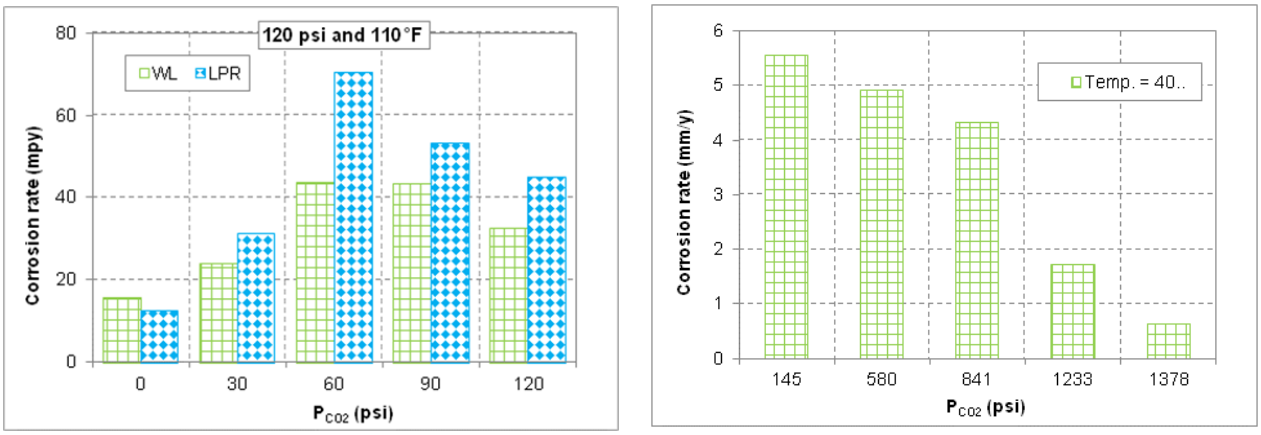

(a) (b)

Fig. 9: Corrosion rate measurements vs. CO_2 partial pressure: a) current study; and b) Seiersten (2001)

To investigate the influence of the temperature on CO_2 corrosion, the recent data is presented together with our previous experimental measurements. **Figure 10** shows the corrosion rate measurements obtained from the weight loss technique at two different temperatures (78°F and 110°F) and various CO_2 partial pressures. As depicted in the figure, the temperature has a significant influence on the corrosion rate representing acceleration of all processes involved in the corrosion such as chemical, electrochemical reaction and transport process (Nesic et al., 1996). As temperature increases from 78 to 110°F, the corrosion rate predominately increased. At high CO_2 partial pressure (120 psi), temperature effect on corrosion rate was insignificant.

The development of corrosion test setup has been completed. The experimental setup is ready to perform corrosion tests at high pressure and temperature conditions. As previously reported, we have found a shop that can manufacture mini-pipe and flat corrosion specimens. We are waiting for manufacturing order to be issued. Then, the shop will begin manufacturing of the specimens and it is anticipated that it will take 6 to 8 weeks.

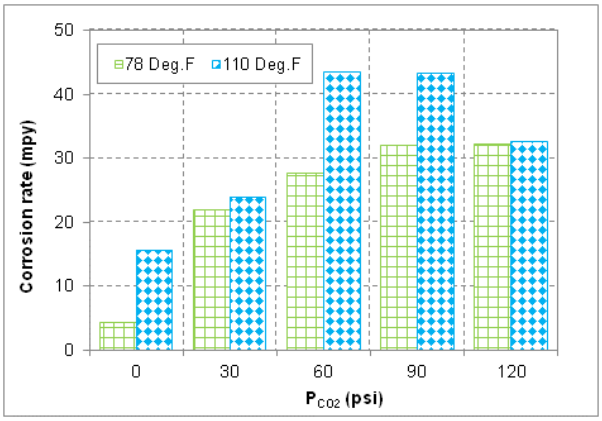

Fig. 10: Corrosion rate measurements vs. CO_2 partial pressure at different temperatures

3. Planned Activities

- Continue cement core aging experiments with brine-CO_2-CH_4 system for 14 days varying temperature, 6000 psi, 10% and 300 ppm H_2S.
- Continue theoretical and modeling studies on tubular degradation.
- Continue cement additive screening and acid resistant cement formulation studies.

4. Project Expenditures

This section presents the project expenses during the month of February (**Table 5**) and the cumulative expenditures.

Table 5: Current and cumulative expenditures, February 2014

No.	Budget Categories	Current Expenses	Cumulative Expenses
1	Salaries & Wages	$8,446.60	$270,155.04
2	Fringe Benefits	$1,409.88	$60,272.76
3	Project Materials	$298.71	$61,755.52
4	Travel	$2,351.09	$10,754.90
5	Conference Expenses	$0.00	$0.00
6	Other Direct Costs	$0.00	$2,764.85
7	Equipment	$894.75	$242,982.97
8	Space Rental	$0.00	$0.00
9	Indirect Cost	$6,262.17	$201,806.64
10	**Total**	**$19,663.20**	**$850,492.68**

Nomenclatures

BWOC	By weight of cement
CH	Calcium hydroxide
CSH	Calcium silicate hydrate
DCB	Double Cantilever Beam
FPB	Four Point Bend
FTIR	Fourier Transform Infra-Red
GHO	Class G Cement with hydroxyapatite
GS	Class G cement with silica flour
GSMG	Class G Cement with silica flour and magnesium oxide
GSLM	Class G Cement with silica flour, latex and micro-silica
GSLT	Class G Cement with latex

HHO	Class H Cement with hydroxyapatite
HPHT	High-pressure high-temperature
HS	Class H cement with silica flour
HSHO	Class H Cement with silica flour and hydroxyapatite
HSMG	Class H Cement with silica flour and magnesium oxide
HSLM	Class H Cement with silica flour, latex and micro-silica
HSLT	Class H Cement with latex
LPR	Linear polarization resistance
LTMS	Cement with latex and micro-silica additives
mpy	mils per year
MGO	Magnesium oxide containing cement
MGO-5	Cement containing 5% BWOC MgO as additive
MGO-10	Cement containing 10% BWOC MgO as additive
MS	Micro-silica containing cement
MS-10	Cement containing 10% BWOC micro-silica as additive
NACE	National Association of Corrosion Engineers
SBS	Shear bonding strength
SEM	Scanning Electron Microscope
SCC	stress corrosion cracking
SSC	Sulfide Stress Cracking
XRD	X-Ray diffraction

References

Nesic, S., Postlethwaite, J. and Olsen, S. 1996. An Electrochemical Model for Prediction of Corrosion of Mild Steel in Aqueous Carbon Dioxide Solutions, paper No.0010-9312, corrosion.

Schmitt, G. and Hörstemeier, M. 2006. Fundamental aspects of CO2 metal loss corrosion - Part II: Influence of different parameters on CO2 corrosion mechanisms, paper No.112, 12-16 March, San Diego, California.

Seiersten, M. 2001. Materials Selection for Separation, Transportation and Disposal of CO2, paper No. 042, 11-16 March, Houston, Texas.

Project Title: Effect of H_2S and CO_2 in HPHT Wells on Tubulars and Cement

Report Type: Monthly Report

Report #: 31

Reporting Period: March 22nd, 2014 to April 21st, 2014

Authors:

Ramadan Ahmed, Principal Investigator

Subhash Shah, Co-Principal Investigator

Rida Elgaddafi, Research Assistant

Omotayo Omosebi, Research Assistant

Himanshu Maheshwari, Research Assistant

Aman Srivastava, Research Assistant

Jueun Hwang, Research Assistant

Mounraj Sharma, Research Assistant

Sagar Tale, Research Assistant

Prepared under BSEE Project # E12PC00035

by

THE UNIVERSITY OF OKLAHOMA

July 11, 2014

1. Summary of Accomplishments

This monthly report presents the progress made during the project period March 22, 2014 to April 21, 2014. During this reporting period, cement and tubular degradation studies were continued. Cement cores and bonding samples were prepared and aged in HPHT acidic environment to examine their degradation characteristics. Acid resistant cement slurries and cores were prepared and tested.

Two aging experiments (Experiments 31 and 32) were completed during this month. The samples were aged for 2 weeks in 2% brine saturated with methane gas containing CO_2 and H_2S. Porosity, permeability, and compressive and bond strengths of unaged and aged samples were measured. Recent measurements were combined with previously obtained results to examine the effects of H_2S and temperature on the degradation behavior of conventional (i.e. baseline) and new cement (i.e. special additive containing cement) formulations.

Results show substantial effects of temperature and H_2S presence in the gas phase on degradation behavior of cement under high pressure and high temperature (HPHT) conditions. At low-temperature (100°F), porosity and permeability of Class H samples aged in fluid system without H_2S reduced after aging. The reduction is attributed to the formation of $CaCO_3$ due to carbonation of calcium hydroxide (CH) and calcium silicate hydrate (CSH). However, when the samples aged in fluid system with H_2S, their porosity and permeability increased due to secondary ettringite formation and/or reduced carbonation. Above 190°F, ettringite does not form. As a result, tests conducted at 225 and 350°F did not show noticeable difference between aging in fluid system with and without H_2S.

At low temperature (100°F), the trend shown by Class G cement is similar to that of Class H cement. At 225°F, porosity and permeability of Class G samples aged with and without H_2S are less than those of unaged samples. This can be due to increased carbonation as a result of optimum combination of CO_2 dissolution and ionic diffusion at this temperature.

FTIR results of samples aged at 225°F showed lower carbonate formation in samples aged in fluid system with H_2S than without H_2S. Reduction in carbonation enhances porosity and permeability since leaching becomes the dominate process as less precipitate occupies the pores.

Extensive additive screening and cement formulation study indicated that hydroxyapatite and magnesium oxide containing cement (HOAP and MGO-5) are the most viable formulations that can withstand acid attack under HPHT conditions. Performance testing of these new formulations was continued. The recent experiments were carried out with hydroxyapatite (HOAP) and magnesium oxide based cement samples aged in fluid system containing H_2S. The results are similar to previous measurements. MgO acts as an expanding additive and prevents degradation of MGO-5 cement. Substantial increase in compressive and shear bond strengths was observed due to expansion of cement. Although HOAP samples degraded somewhat due to exposure at high temperature, they showed limited carbonation by preserving their CH content and compressive strength.

Corrosion study under low-pressure was continued. Two tests at 140°F and 120 psi were conducted during this month. Testing was interrupted for two weeks, due to reference electrode failure. A new electrode was purchased and installed, and then the testing was resumed.

Our plan for the upcoming weeks is to continue: i) aging tests at 6000 psi, 100°F, 300 ppm H_2S and different CO_2 concentrations; ii) theoretical and modeling studies on tubular corrosion; iii) testing of performance of new acid resistant cement formulations; and iv) low-pressure corrosion experiments at various CO_2 concentration.

2. Overall Project Progress

2.1 Theoretical Studies (Task 1)

2.1.1 Mechanism of Sulfide Stress Cracking

Work is continued towards starting the SSC (Sulfide Stress Cracking) mini-pipe experiments. Apart from experimental study, a mathematical model is being developed to predict the SSC. The model utilizes published experimental measurements, which show approximate hydrogen diffusion rate and critical values of hydrogen concentration for different metals (Asahi et al. 1994). The critical values represent the concentration of hydrogen below which no SSC occurs for that metal at a given temperature and pressure. Once the critical value of hydrogen concentration is known, it can be used to determine the corresponding H_2S concentration in liquid (Kumar et al. 2014). The H_2S concentration in liquid is related to the partial pressure of H_2S. For this purpose, a solubility model is being developed based on published studies (Zirrahi et al. 2012, Duan et al. 2007). Thus, based on solubility model and critical hydrogen concentration, environmental conditions can be predicted for each metal in which it won't undergo SSC. These predictions will be used to develop the test matrix.

2.2 Experimental Studies on Degradation of Cement (Task 2)

2.2.1 Porosities and Permeabilities of Baseline Cements

Two aging experiments were completed during this month. Cement cores and samples aged under HPHT conditions in brine (2% NaCl) saturated with methane gas containing 10% CO_2 and and 300 ppm H_2S. The aging conditions for the new tests (Batches 034 and 035) are presented in **Table 1** along with those of previous experiments. The new tests are highlighted. After aging cement cores and bonding samples at 6000 psi and different temperatures (225 and 350°F), their mechanical and physical properties including porosity, permeability, compressive and bond strengths were measured. In addition, FTIR mineralogy of the samples was analyzed and SEM (Scanning Electron Microscopy) examination was performed on selected samples.

Table 1: Test parameters for aging experiments conducted to date

Batch #	Temp. (ºF)	Pressure (psi)	Partial Pressure %			Brine Conc. (%)	Aging Period (days)	Experiment #
			CH_4	CO_2	H_2S (ppm)			
001	350	9000	100	0	0	9	6	1
002	350	6000	100	0	0	2	14 & 28	2
003	350	6000	100	0	0	2	14	
004	350	6000	90	10	0	2	6	3
005	350	6000	90	10	0	2	14 & 28	4
006	350	6000	90	10	0	2	14	
007	225	6000	90	10	0	2	14	5
008	100	6000	90	10	0	2	14	6
009	225	6000	60	40	0	2	14	7
010	225	6000	0	100	0	2	14	8
011	100	6000	60	40	0	2	14	9
012	100	6000	0	100	0	2	14	10
013	350	6000	60	40	0	2	14	11
014	350	6000	0	100	0	2	14	12
015	225	6000	60	40	0	2	14	7A
016	350	3000	60	40	0	2	14	13
017	350	9000	60	40	0	2	14	14
018	350	3000	0	100	0	2	14	15
019	350	9000	0	100	0	2	14	16
020	350	3000	90	10	0	2	14	17
021	350	9000	90	10	0	2	14	18
022	225	3000	60	40	0	2	14	19
023	225	9000	60	40	0	2	14	20
024	225	3000	0	100	0	2	14	21
025	225	9000	0	100	0	2	14	22
026	225	3000	90	10	0	2	14	23
027	225	9000	90	10	0	2	14	24
028	430	6000	90	10	0	2	14	25
029	430	6000	60	40	0	2	14	26
030	430	6000	100	0	0	2	14	27
031	430	3000	100	0	0	2	14	28
032	430	9000	100	0	0	2	14	29
033	100	6000	90	10	300	2	14	30
034	225	6000	90	10	300	2	14	31
035	350	6000	90	10	300	2	14	32

A test matrix developed to examine the effects of temperature and H_2S on the degradation behavior of cements at 6000 psi is presented in **Table 2**. Test results show noticeable effects of H_2S and temperature on cement degradation. Specifically, the presence H_2S in the system substantially affects cement degradation at low temperature (100°F); hence, future tests will be carried out varying carbon dioxide concentration at 100°F. The planned test matrix will be completed in coming months.

Table 2: Test matrix for aging experiments examining the effect of H_2S on cement degradation

Temperature (°F)	0% CO_2	10% CO_2	40% CO_2
100	Batch 036	**Batch 033**	Batch 037
225		**Batch 034**	
350		**Batch 035**	

Figures 1 and **2** demonstrate porosity and permeability of Class H samples aged in fluid systems with and without H_2S at 6000 psi and various temperatures (100, 225 and 350°F). At 100°F, results of samples aged in fluid system without H_2S indicate reduction in porosity and permeability after aging. The reduction can be attributed to the formation of $CaCO_3$ due to carbonation of CH and CSH. However, samples aged in fluid system with H_2S showed increase in porosity and permeability. Possible reasons for the increase could be the formation of secondary ettringite (i.e. ettringite formed after hardening of the cement) and/or leaching-dominated carbonation because of reduction in solubility of CO_2 as the H_2S dissolves in the brine. Reaction of H_2S with ferrites and aluminates at temperature less than 190°F forms ettringite (Kutchko et al. 2011 and Jacquemet et al. 2005). The formation of ettringite could result in expansion and micro cracks. The presence of ettringite was confirmed using SEM images and EDX analysis (Report # 30). Above 190°F, ettringite does not form. As a result, tests conducted at 225 and 350°F did not show noticeable difference between aging in fluid system with and without H_2S. At 225°F, porosity and permeability of Class H samples aged with and without H_2S are less than those of unaged samples. This might have caused by increased carbonation as a result of optimum dissolution of CO_2 and ionic diffusion at this temperature.

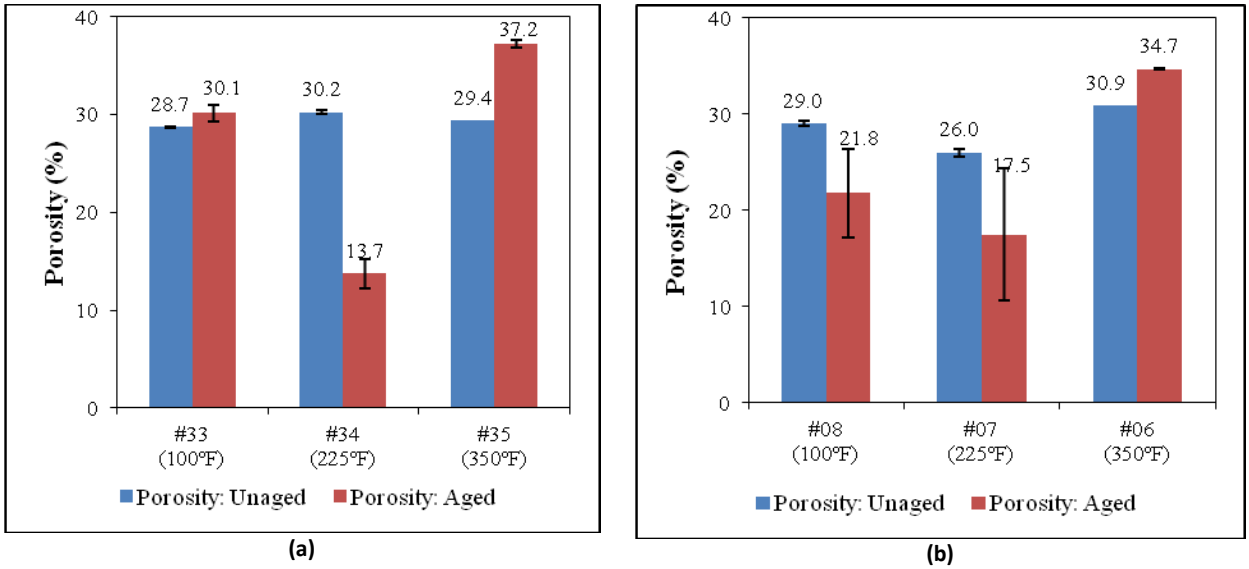

Fig. 1: Porosity of Class H cores aged for 14 days in brine saturated with methane containing 10% CO_2 at 6000 psi in fluid system: a) with H_2S; b) without H_2S

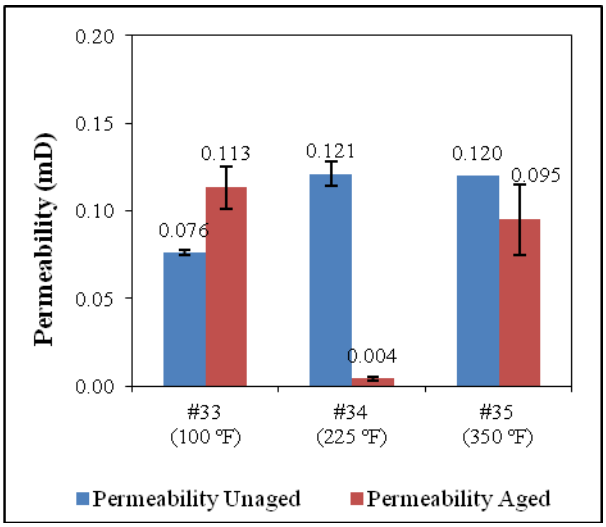

(a)

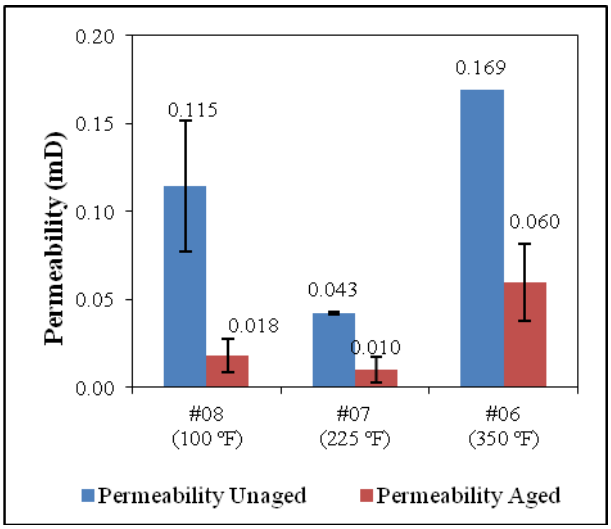

(b)

Fig. 2: Permeability of Class H cores aged for 14 days in brine saturated with methane containing 10% CO_2 at 6000 psi in fluid system: a) with H_2S; b) without H_2S

The porosity and permeability of Class G cement samples aged in fluid systems with and without H_2S is presented in **Figs. 3** and **4**, respectively. At temperature of 100°F, the trend is similar to that of Class H cement. At high temperature (350°F), samples aged without H_2S showed decrease in porosity and permeability because of carbonation. However, in case of aging in system with H_2S, porosity and permeability increased. In the presence of H_2S, ferrites in cement react with dissolved H_2S to form pyrite (Kutchko et al. 2011; Jacquemet et al. 2005). Furthermore, with exposure to oxygen and moisture, pyrite may potentially oxidize to ferrous sulfate and sulfuric acid. The free sulfuric acid may react with the calcite present to produce gypsum that can potentially increase molecular volume and lead to expansion and micro cracks (Kutchko et al. 2011; Lea and Hewlett 1998).

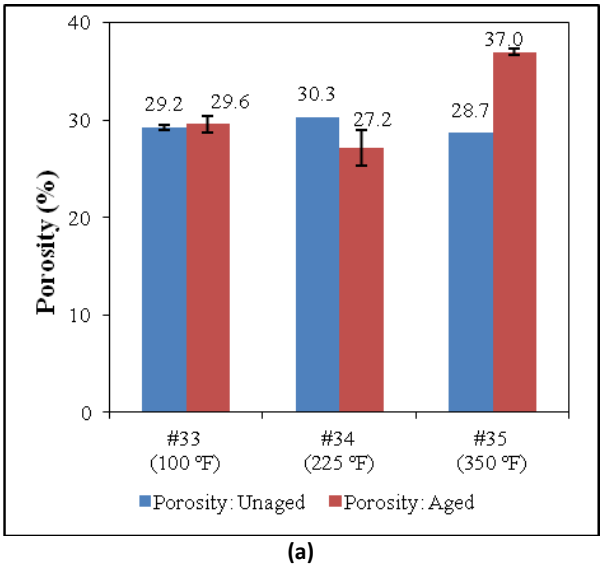

(a)

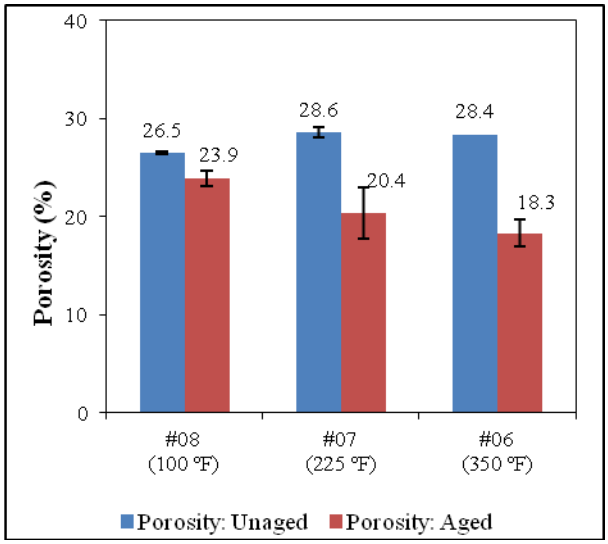

(b)

Fig. 3: Porosity of of Class G cores aged for 14 days in brine saturated with methane containing 10% CO_2 at 6000 psi in fluid system: a) with H_2S; b) without H_2S

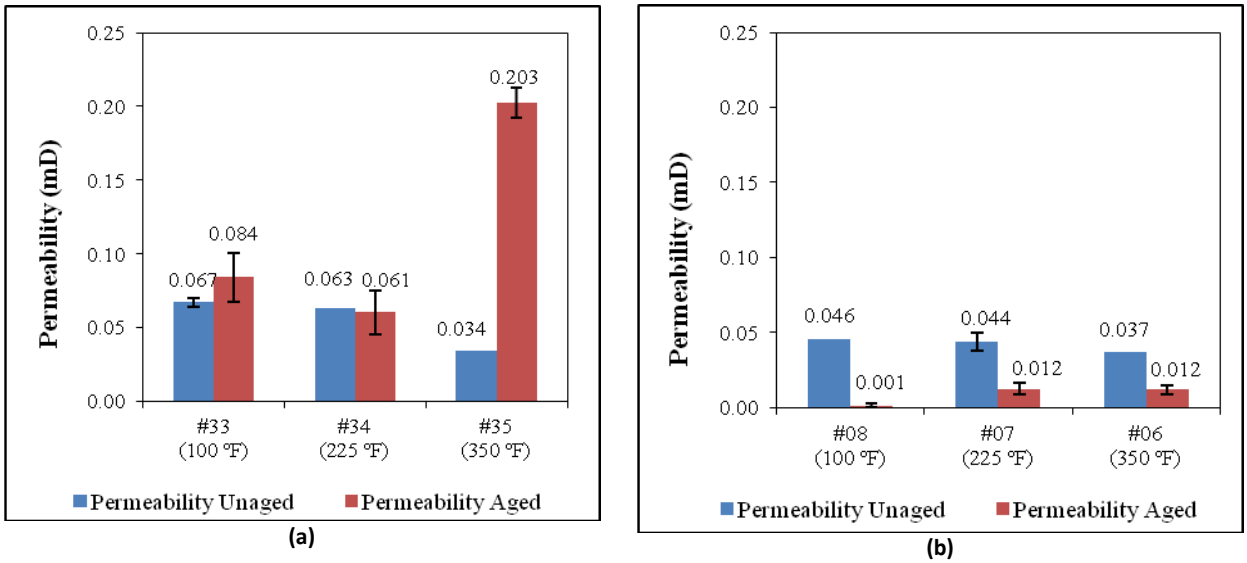

Fig. 4: Permeability of Class G cores aged for 14 days in brine saturated with methane containing 10% CO_2 at 6000 psi in fluid system: a) with H_2S; b) without H_2S

Figure 5 presents FTIR results of samples aged at 225°F in fluid system with and without H_2S. Carbonate formation was lower in fluid system with H_2S than without H_2S. Reduction in carbonation leads to leaching dominated situation causing porosity and permeability to increase as a result of strong dissolution and ionic transport of calcium-bearing components of the cement. In addition, reduction in carbonation limits the formation of precipitates in the pores leaving more void spaces unfilled.

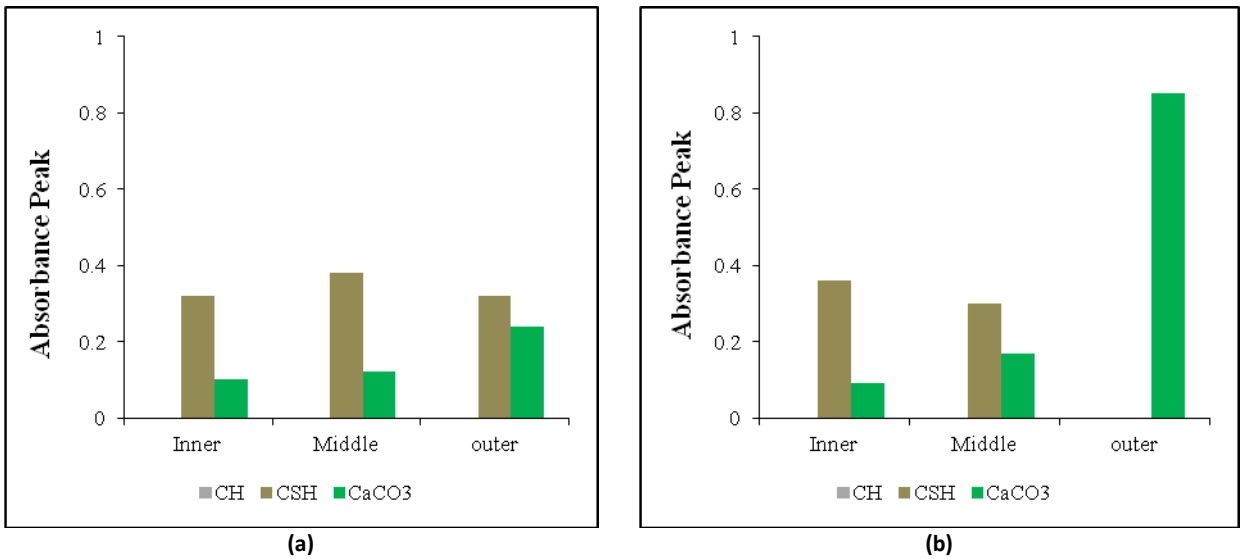

Fig. 5: FTIR results of different zones of Class H sample aged for 14 days in brine saturated with methane containing 10% CO_2 at 225°F and 6000 psi in fluid system: a) with H_2S; b) without H_2S

FTIR results of samples aged at 350°F with and without H_2S are shown in **Fig. 6**. The results demonstrate a trend, which is similar to that observed at 225°F, indicating more favorable condition for carbonation in fluid system without H_2S than with H_2S.

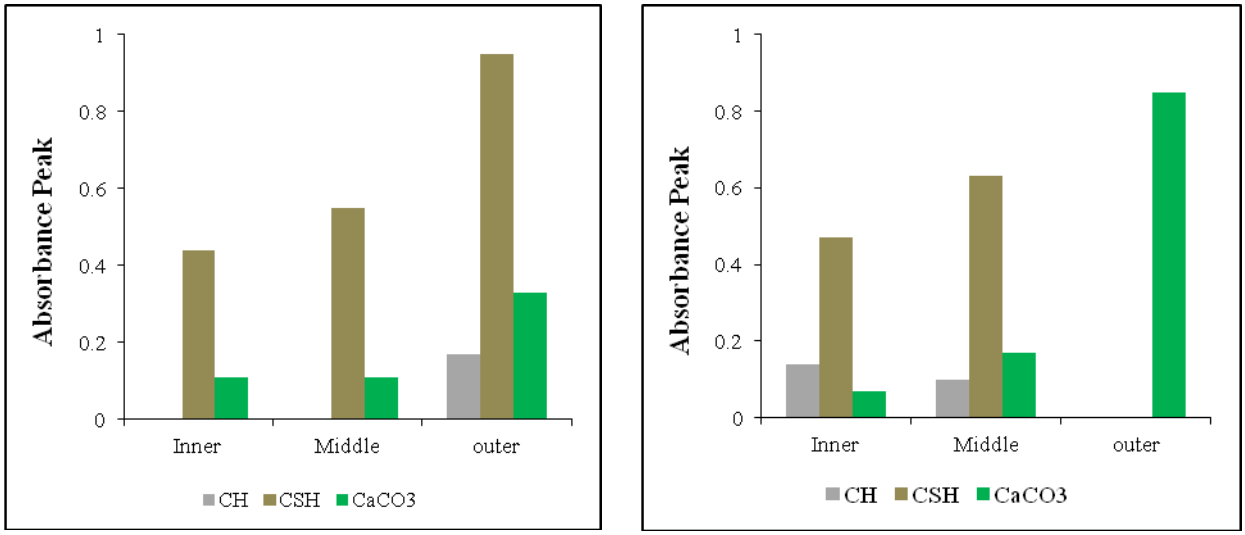

Fig. 6: FTIR results of different zones of Class H sample aged for 14 days in brine saturated with methane containing 10% CO_2 at 350°F and 6000 psi in fluid system: a) with H_2S; b) without H_2S

2.2.2 Compressive Strength of Baseline Cements

In previous report, results of tests conducted on Batch 33 samples were presented. Measurements show strength gain after aging in the absence of H_2S gas due to intense carbonation. However, when the samples were aged in fluid system with H_2S, reduction or slight increase in compressive strength was observed due to limited carbonation, which is counteracted by the leaching process. The presence of H_2S substantially reduces the solubility of CO_2 in brine. Since H_2S is more solubility than CO_2 in brine at low temperatures (approximately less than 150°F).

During this month, compressive strength measurements were conducted on samples from Batch 34 and 35, which were both exposed to fluid system containing H_2S. Effect of H_2S on compressive strength is investigated by comparing the new measurement with Batch 7 samples, which were aged in similar condition without the presence of H_2S. At moderately high temperature (225°F), additional strength gain was observed when samples were aged in fluid system without H_2S than with H_2S (**Fig. 7**). Higher strength again is attributed to enhanced carbonation in the absence of H_2S. At this temperature, the presence of H_2S can substantially reduce solubility of CO_2 in the brine reducing the potential for carbonation of CH and CSH. Class H cement has a tendency to be carbonated when exposed to pure CO_2 gas than Class G cement. Hence, Class H cement is more susceptible to loss of mechanical strength in the event of sulfate attack than Class G cement. This observation is consistent with previous measurements (Report # 30) obtained at 100°F.

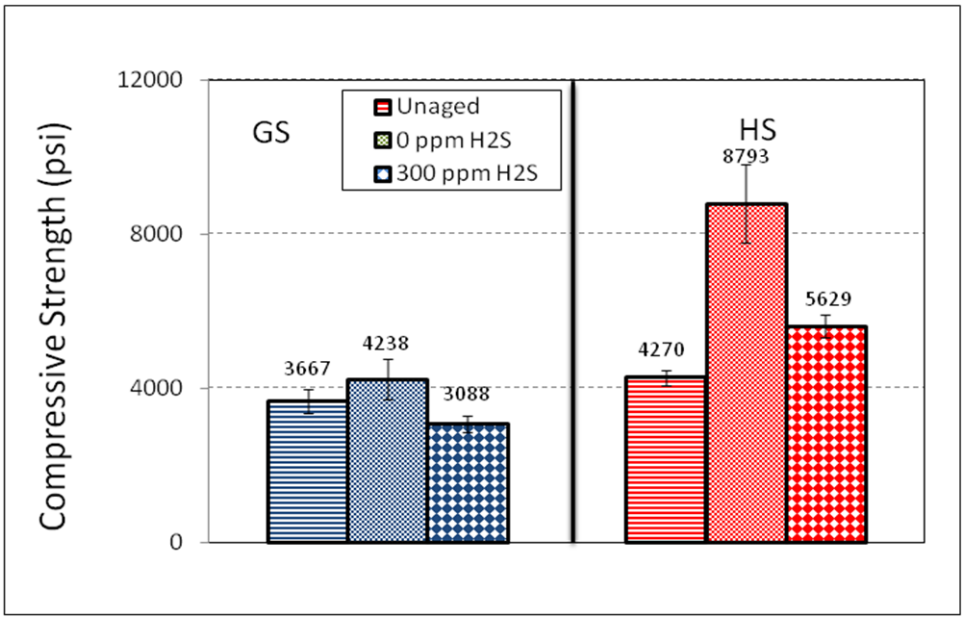

Fig. 7: Effect of H_2S on compressive strength at 225°F, 10% CO_2, CH_4 and 6000 psi

At high temperature (350°F), both classes of cements gained strength after aging in fluid system without H_2S (**Fig. 8**). However, when aged in fluid system containing H_2S, Class G cement showed reduction in strength while Class H cement displayed improvement in strength. Strength improvement is due to carbonation and strength reduction is attributed to reduction in CO_2 solubility, which tends to reduce carbonation resulting in leaching domination and/or development of micro cracks due to sulfate attack.

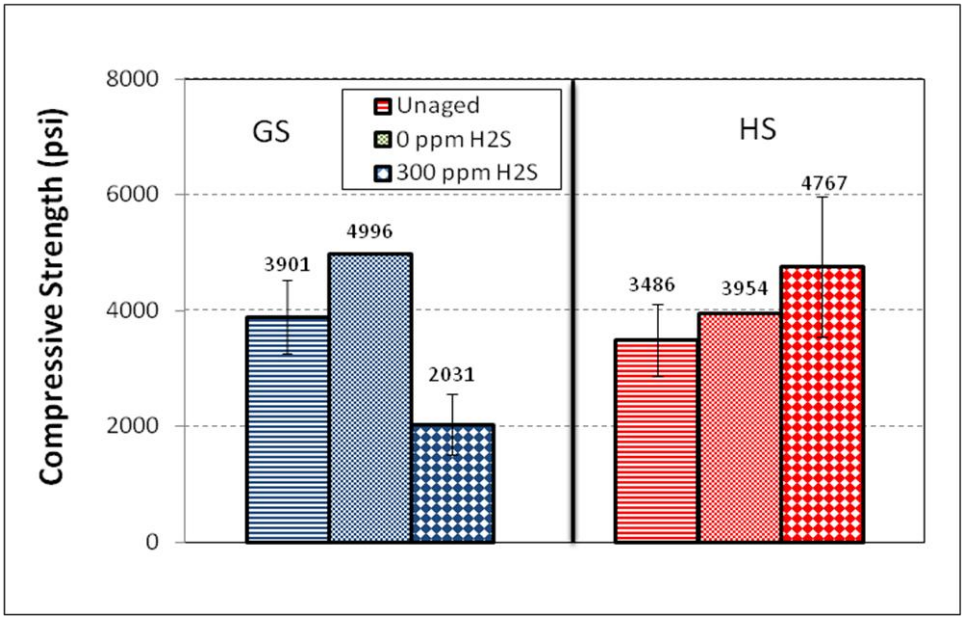

Fig. 8: Effect of H_2S on compressive strength at 350°F, 10% CO_2, 90% CH_4 and 6000 psi

2.2.3 Shear Bond Strength of Baseline Cement

Study on shear bond strength (SBS) of Class H cement was continued. In this report, the effect of H_2S on SBS is presented. **Figure 9** shows the effect of H_2S gas on SBS at 6000 psi and different temperatures. When samples aged in fluid system without H_2S, SBS increased due to carbonation up to 350°F (Fig. 9b). Carbonation fills the pore space by precipitated $CaCO_3$ thereby reducing porosity and permeability, and increasing compressive and bond strengths of the cement. When the samples were aged in fluid system containing H_2S, SBS was not improved with temperature up to 225°F. At low temperature, H_2S solubility in brine is higher than that of CO_2. As a result, the presence of dissolved H_2S substantially reduces the solubility of CO_2 and formation of carbonic acid. With limited carbonic acid attack, minimal cement carbonation occurs. At 350°F, enormous increase in SBS was observed after aging in fluid system with H_2S. This is due to the combined effect of cement carbonation and formation of gypsum at high temperatures. At high temperature (350°F), solubility of CO_2 increases while that of H_2S reduces. The condition favors the carbonation of cement to some extent and SBS development. At the same time, limited H_2S can dissolve to form ferrites, which has the potential to produce gypsum that increases molecular volume and leads to expansion and SBS improvement. The SBS measurements are in agreement with other cement property measurements such porosity, permeability and compressive strength.

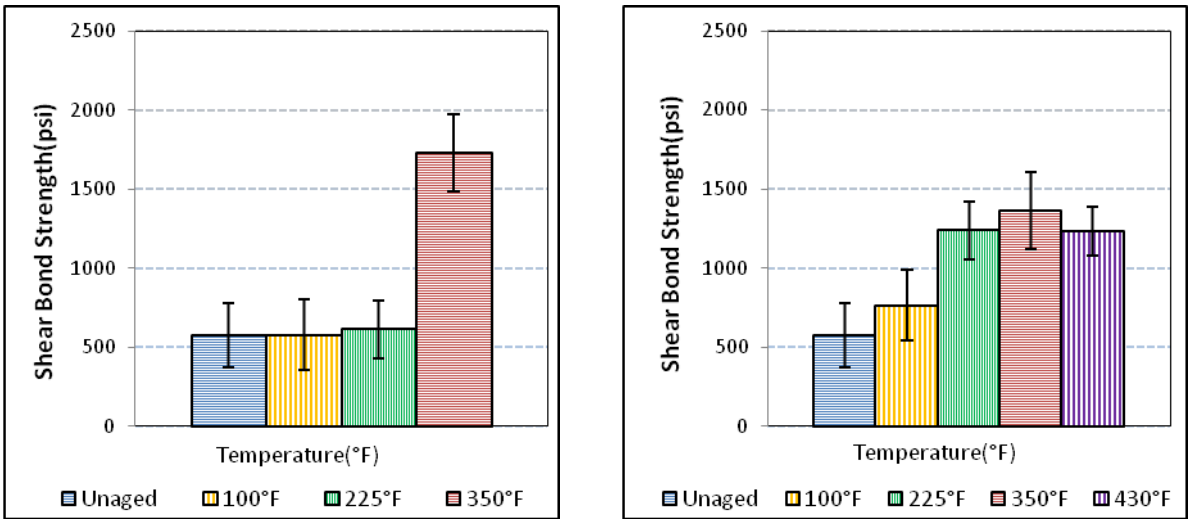

Fig. 9: SBS of Class H sample aged for 14 days in brine saturated with methane containing 10% CO_2 at 6000 psi and different temperatures in fluid system: a) with H_2S; b) without H_2S

2.2.4 Testing the Performance of New Cement Formulations

Extensive additive screening and cement formulation study indicated that hydroxyapatite and magnesium oxide containing cement (HOAP and MGO-5) are the most viable formulations that can withstand acid attack under HPHT conditions. In the temperature range of 100 – 350°F, hydroxyapatite based cement was able to protect the CH and CSH components of the cement matrix, along with

maintaining physical characteristics of cement including porosity, permeability, and compressive and shear bond strengths.

Testing of new cement formulations containing special additives was continued. This report presents results of recent aging experiments carried out with hydroxyapatite (HOAP) and magnesium oxide (MGO-5) cement samples aged in fluid system containing H_2S. Two experiments at 225°F and 350°F were conducted using MGO-5 and HOAP samples, respectively. The results are similar to the measurements obtained from previous experiments. Magnesium oxide behaved as an expanding additive and prevented degradation of MGO-5 cement. Increases in compressive and shear bond strength were also observed due to the expansion of the cement.

The HOAP samples showed some degradation when exposed to high temperature. However, they showed limited carbonation by preserving their CH content and compressive strength.

2.2.4.1 Magnesium Oxide Cement (MGO-5)

Tests with MGO-5 samples were continued. The samples were aged under HPHT conditions presented in **Table 3**. The composition of the slurry was provided in previous report. After aging, the properties of the cores were measured.

Table 3: Aging conditions for the MGO-5 samples

MGO-5	Temp. (°F)	Pressure (psi)	CO_2 (%)	CH4 (%)	H2S (ppm)	NaCl (%)	Days	Baseline	Exp. No.
Batch 008	225	6000	90	10	300	2	14	Batch 034	31

Porosity and Permeability

After aging, porosity of baseline cements showed reduction due to carbonation in the matrix (**Fig. 10**). The MGO-5 samples also exhibited reduction in porosity and permeability (**Fig. 11**), which is attributed to the simultaneous effects of carbonation and matrix expansion (i.e. pore shrinkage) due to $Mg(OH)_2$ formation. The reduction in porosity and permeability of MGO-5 samples and Class H baseline samples were approximately similar; however, wide variation was observed in Class G based cement. Class G based MGO-5 sample showed substantially higher reduction in porosity and permeability than baseline Class G cement.

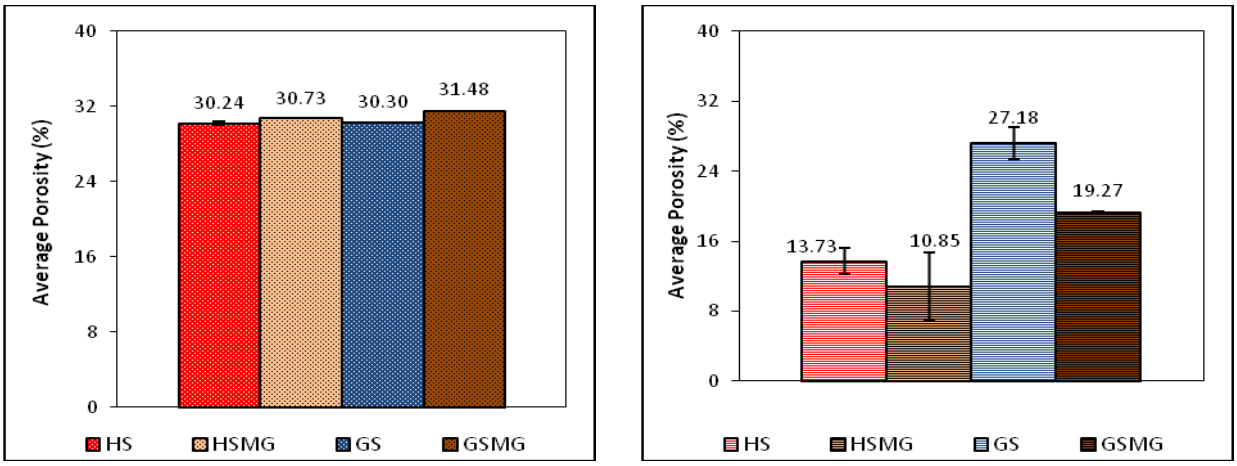

Fig. 10: Porosities of baseline and MGO-5 cores: a) unaged; and b) aged for 14 days in brine saturated with methane containing 10% CO_2 and 300 ppm H_2S at 225°F and 6000 psi

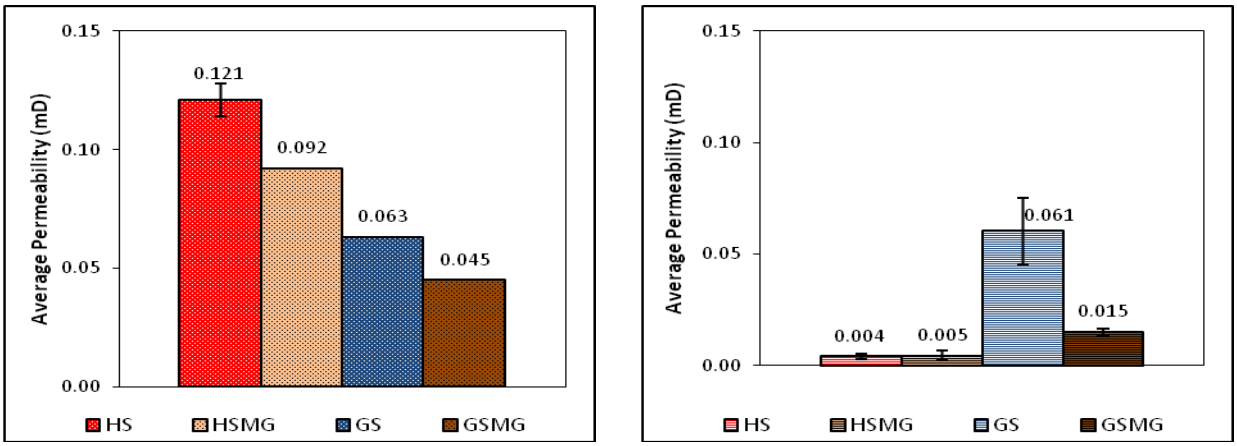

Fig. 11: Permeabilities of baseline and MGO-5 cores: a) unaged; and b) aged for 14 days in brine saturated with methane containing 10% CO_2 and 300 ppm H_2S at 225°F and 6000 psi

Compressive Strength Measurements

Compressive strengths of MGO-5 and baseline samples are presented in **Fig. 12**. After aging, baseline and MGO-5 samples showed similar increase in strength due to carbonation. Consistent with the porosity and permeability measurements, compressive strength measurements of Class H and Class G cements indicate similar performance between baseline and MGO-5 cement.

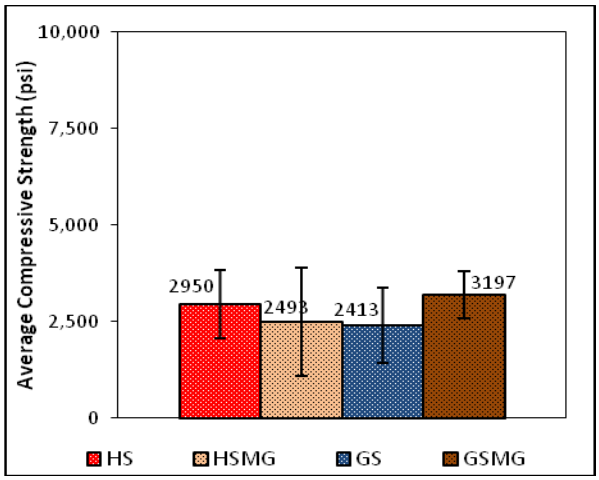

(a)

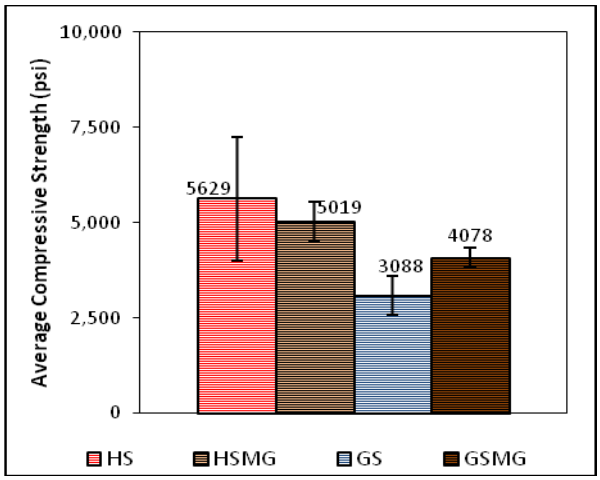

(b)

Fig. 12: Compressive strength of baseline and MGO-5 cores: a) unaged; and b) aged for 14 days in brine saturated with methane containing 10% CO_2 and 300 ppm H_2S at 225°F and 6000 psi

Shear Bond Strength

The shear bond strength (SBS) measurements are presented in **Fig. 13**. Both baseline and MGO-5 samples showed increase in SBS after aging due to carbonation and expansion of the matrix. It is difficult to compare the level of carbonation in the samples using the SBS data alone because MGO-5 samples can undergo expansion, which causes excessive increase in SBS without carbonation.

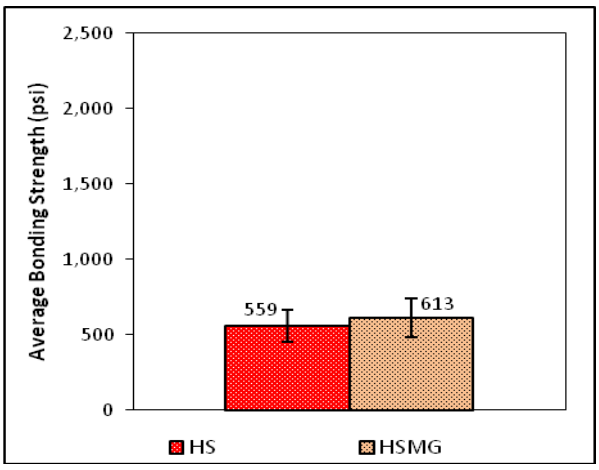

(a)

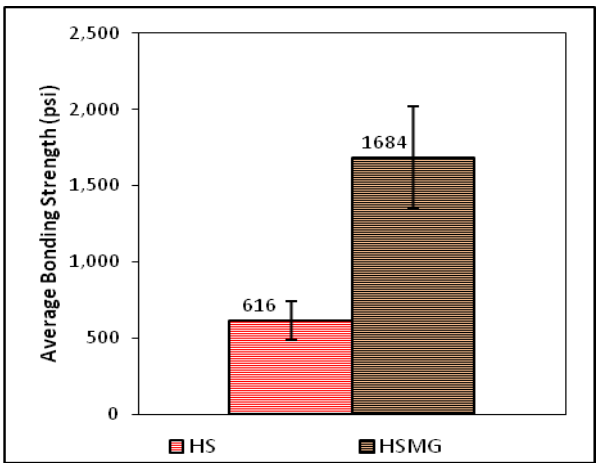

(b)

Fig. 13: SBS of baseline and MGO-5 cores: a) unaged; and b) aged for 14 days in brine saturated with methane containing 10% CO_2 and 300 ppm H_2S at 225°F and 6000 psi

FTIR

Summarized FTIR results of Class H based MGO-5 (HSMG) and baseline (HS) cement are presented in **Fig. 14**. The spectra are simplified in the form of bar charts for easy interpretation. The MGO-5 samples showed presence of $Mg(OH)_2$ in all the layers of the sample, which indicates the expansion tendency of the matrix and reduced acid penetration. The amount of CSH was almost similar for the MGO-5 and

baseline samples in all the sections; however, the $CaCO_3$ content in the MGO samples was lower than that in baseline sample. This indicates reduced carbonation in the MGO-5 samples. For the same level of carbonation, MGO-5 cement is expected to show stronger $CaCO_3$ peak than the baseline. The FTIR results confirm better performance of MGO-5/HSMG cement as compared to baseline cement.

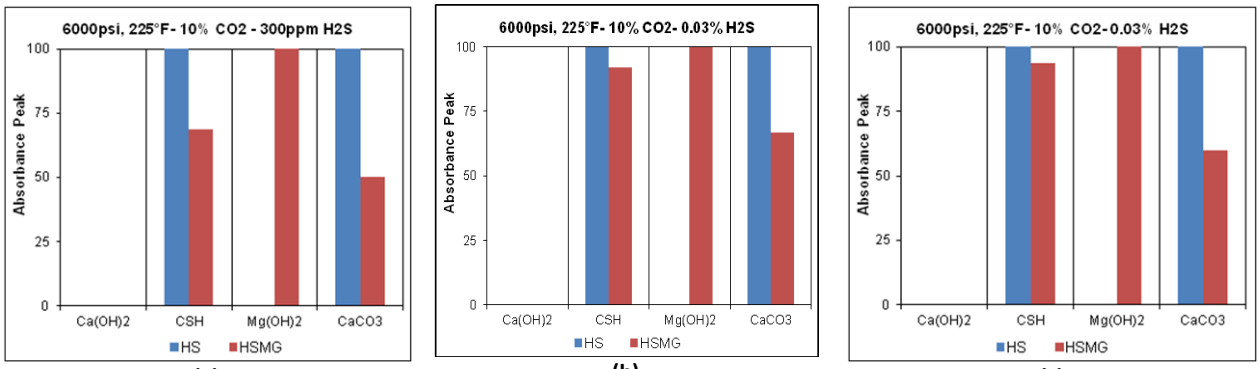

Fig. 14: Summarized FTIR data of Class H based MGO-5 (HSMG) and baseline HS samples aged for 14 days brine saturated with methane containing 10% CO_2 and 300 ppm H_2S at 6000 psi and 225°F: a) Outermost zone; b) Middle zone; and c) Innermost zone

2.2.4.2 Hydroxyapatite-Based Cement

The previous tests with hydroxyapatite (HOAP) based cement indicated better performance against acidic environment as compared to baseline samples. Another experiment was conducted at a different aging condition to evaluate the performance of HOAP samples further. In recent experiment, HOAP samples were aged for 14 days at 225°F, 6000 psi, 10% CO_2, and 300 ppm H_2S.

Porosity and Permeability Measurements

The porosity and permeability measurements are presented in **Figs. 15** and **16**. Porosities of unaged baseline and HOAP samples were in the same range. The permeabilities of the HHO and baseline samples were very similar; however, the permeabilities of GHO samples were significantly higher than that of baseline GS samples. After aging, although all the samples showed increased porosity, the HOAP samples displayed a lesser increase over the baseline samples. This indicates reduction in the level of carbonation occurring in the samples during aging. The permeability of baseline Class H samples slightly reduced after aging; however, permeability of other samples (HHO, GS and GHO) showed substantial increase. This suggests that HOAP samples prevent carbonation. Nonetheless, due to high temperature and the absence of silica flour, leaching occurred causing the porosity and permeability to increase. Compressive strength, shear bond strength and FTIR measurements need to be examined in order to evaluate the overall performance of the HOAP cement.

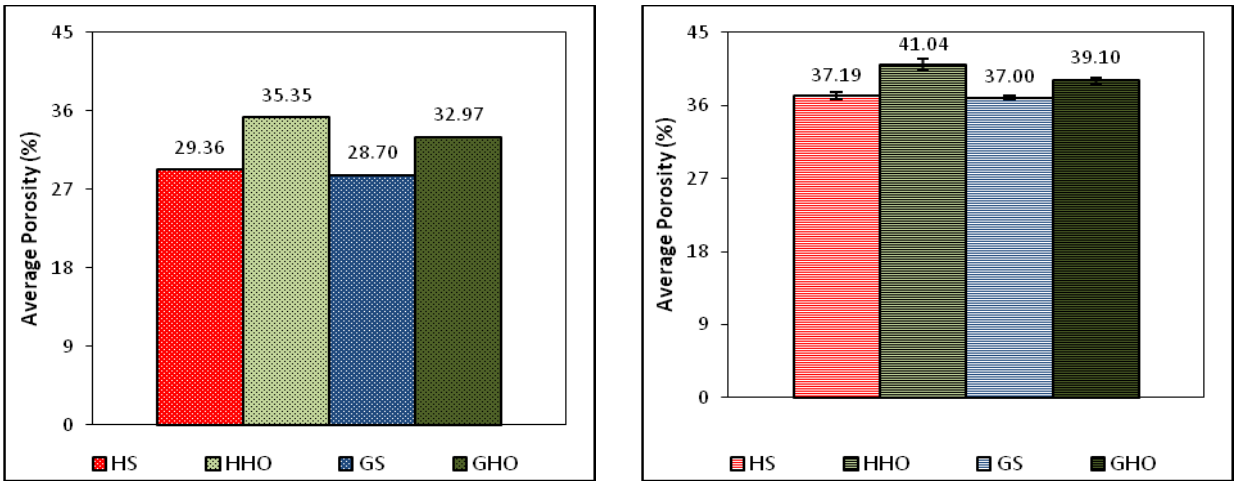

Fig. 15: Porosities of HOAP and baseline cements: a) unaged; and b) aged for 14 days at 350°F and 6000 psi in brine saturated with methane containing 10% CO_2 and 300 ppm H_2S

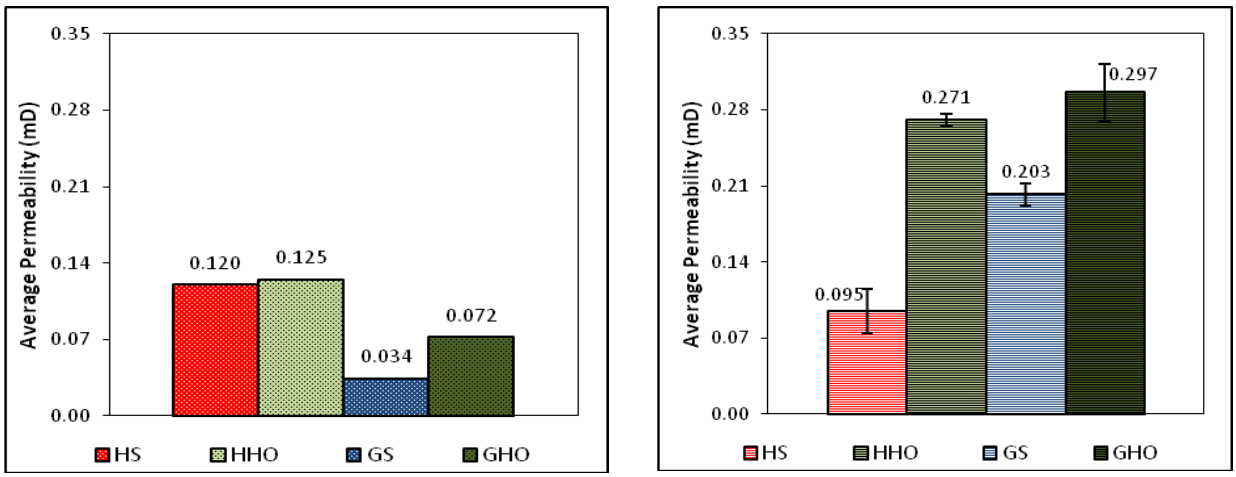

Fig. 16: Permeabilities of HOAP and baseline cements: a) unaged; and b) aged for 14 days at 350°F and 6000 psi in brine saturated with methane containing 10% CO_2 and 300 ppm H_2S

Compressive Strength Measurements

Compressive strengths of HOAP and baseline samples are presented in **Fig. 17**. Unaged HOAP showed equivalent or better compressive strength to those of baseline samples. After aging, all the samples except baseline Class H (HS) exhibited reduction in strength due to leaching and thermal retrogression in the case of HOAP samples.

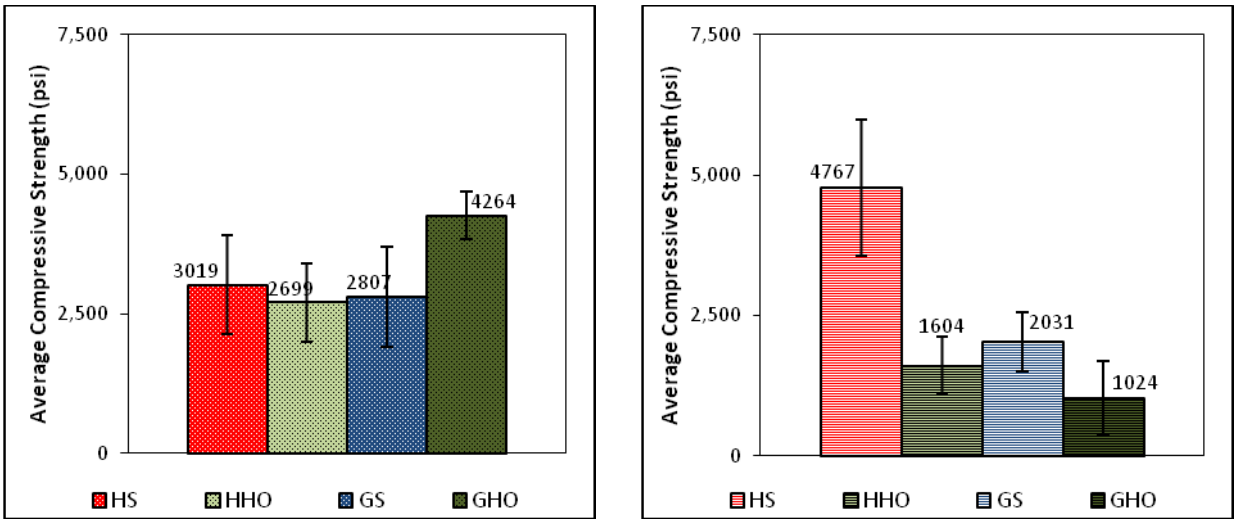

Fig. 17: Compressive strength of HOAP and baseline cements: a) unaged; and b) aged for 14 days at 350°F and 6000 psi in brine saturated with methane containing 10% CO_2 and 300 ppm H_2S

Shear Bond Strength Measurements

The shear bond strength (SBS) measurements are presented in **Fig. 18**. SBS of unaged HOAP cement demonstrated higher strength than the baseline cement. After aging, the baseline showed substantial increase (approximately 70%) in strength resulting from carbonation. HOAP samples exhibited minor reduction (roughly 10%) in SBS after aging. The minor reduction in strength suggests limited carbonation of HOAP samples during aging.

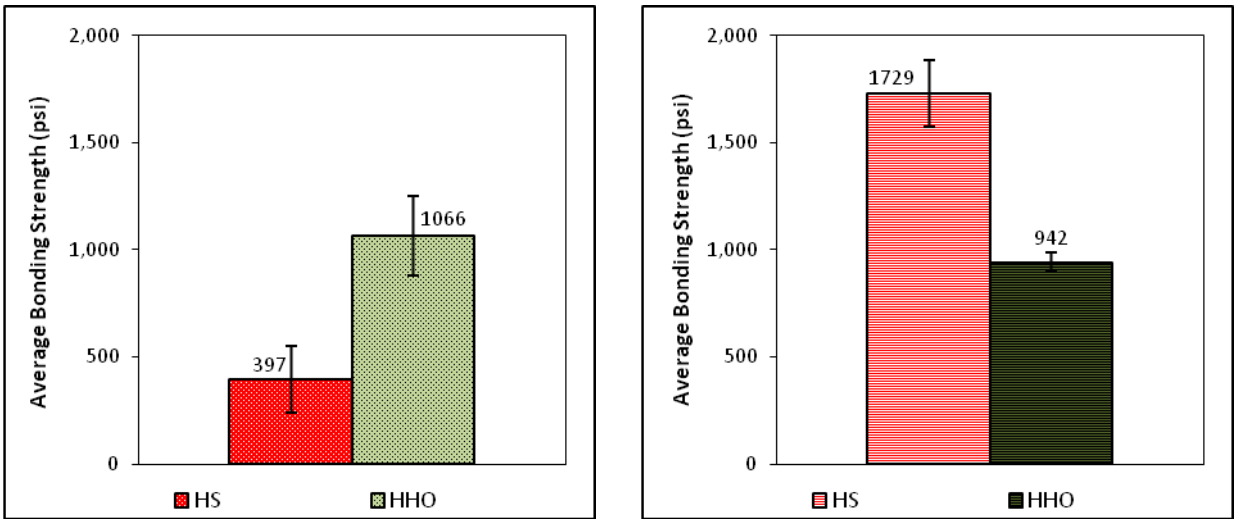

Fig. 18: Shear bond strength of HOAP and baseline cements: a) unaged; and b) aged for 14 days at 350°F and 6000 psi in brine saturated with methane containing 10% CO_2 and 300 ppm H_2S

FTIR

FTIR results of Class H based HOAP and baseline samples are presented in **Fig. 19**. The outer zone being the most vulnerable zone, it is expected to have the least amount of CH and CSH. However, the baseline samples displayed unexpectedly higher amount of CH in the outermost zone than the other zones. This could be a false FTIR peak detection. As expected, the middle and inner zones of HOAP samples indicate higher presence of CH in the matrix than in the baseline samples. This indicates better preservation of CH in HOAP than the baseline sample.

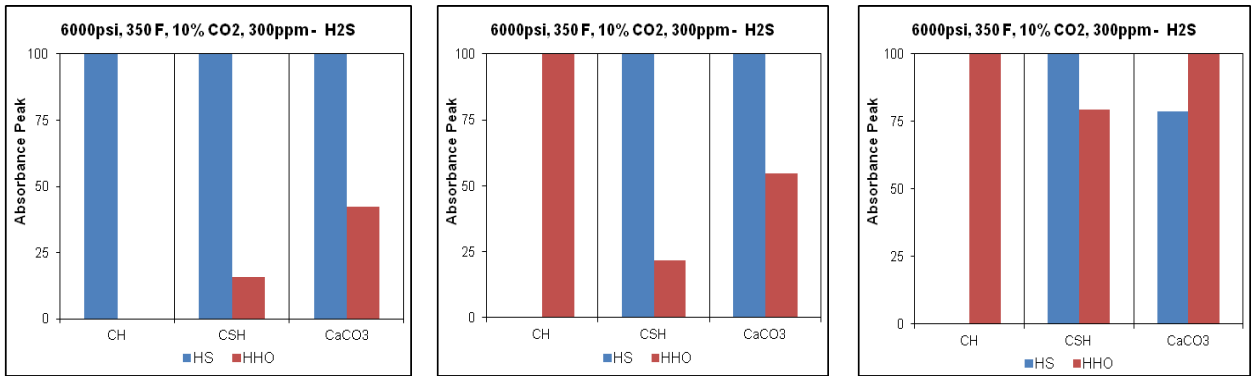

(a) **(b)** **(c)**

Fig. 19: Summarized FTIR data of HHO and baseline HS samples aged for 14 days in brine saturated with methane containing 10% CO_2 and 300 ppm H_2S at 350°F, 6000 psi: a) Outermost zone; b) Middle zone; and c) Innermost zone

The physical and mechanical properties of HOAP samples along with the FTIR results indicate the technical benefits of using hydroxyapatite as a cement additive. The addition of hydroxyapatite prevents carbonation and leaching of the matrix against acid attack.

2.3 Experimental Studies on Corrosion of Tubulars (Task 3)

Low-pressure corrosion tests were continued. Corrosion experiments were conducted using a moderate pressure autoclave (maximum pressure of 3000 psi) and cylindrical carbon steel (1045) specimens. The average corrosion rate was measured using linear polarization resistance (LPR) and weight loss technique. These experiments were conducted at 120 psi (total pressure) varying temperature (78, 110, 140 and 176°F) and CO_2 concentration (0, 25, 50, 75 and 100%).

The test results demonstrate consistent trend, which indicate corrosion occurring when samples are exposed to corrosive environment. Initially, three temperatures (78, 110, 140 and 176°F) were considered to investigation the effect of temperature on corrosion rate. However, considerable change in the corrosion rate was observed between 110 and 176°F; therefore, in order to accurately describe the corrosion behavior as a function of temperature, additional tests were performed at 140°F. During the reporting period, two corrosion experiments were conducted at 140°F and different CO_2 concentrations (50 and 100%). Testing was interrupted for two weeks, due to reference electrode failure. A new electrode was purchased and installed, and then the testing was resumed.

Instantaneous corrosion rate, which was measured using LPR technique at 140°F and 50% CO_2 is presented in **Fig. 20**. Due to computer failure, the instantaneous corrosion rate at 100% CO_2 concentration was not recorded. The test will be repeated in the future to obtain LPR data. Experimental parameters and results of these tests are summarized in **Table 4**. Corrosion rate measured using weight loss (WL) method is lower than that of LPR.

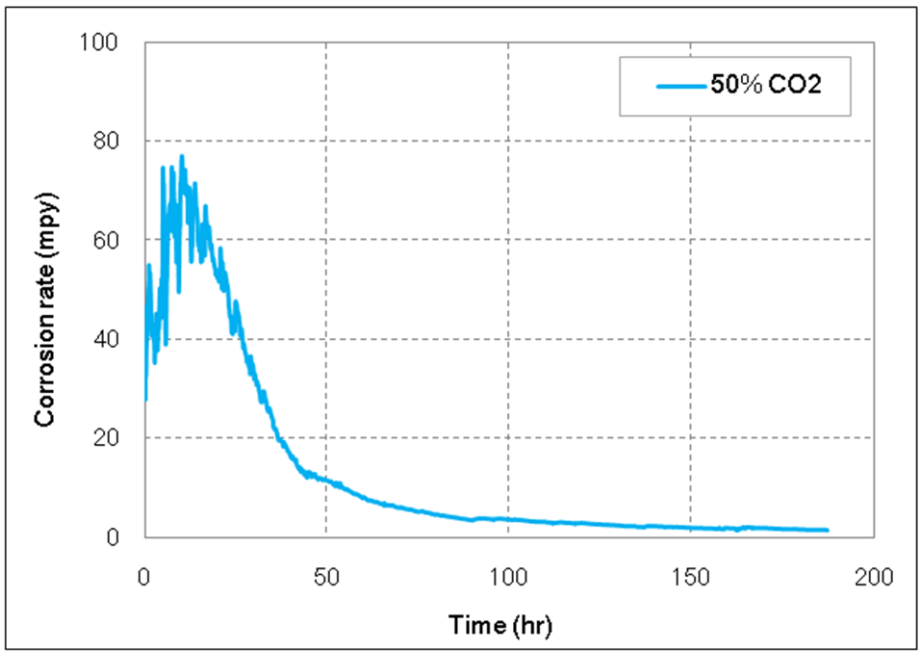

Fig. 20: Instantaneous corrosion rate vs. time at 140°F, 50% CO_2 concentration and 120 psi (LPR measurement)

Table 4: Test parameters and results of low-pressure corrosion experiments

Exp. #	Temp. (°F)	Pressure (psi)	Partial Pressure %		Brine Conc. (%)	Test Period (days)	Results (mpy)	
			N_2	CO_2			LPR	WL
15	78	120	25	75	2	187	40.30	31.91
16	78	120	0	100	2	187	39.18	32.18
17	78	240	0	100	2	187	NA	NA
18	78	120	75	25	2	187	22.92	21.83
19	110	120	75	25	2	187	31.78	23.78
20	110	120	25	75	2	187	53.16	43.22
21	110	120	100	0	2	187	12.37	15.40
22	110	120	75	25	2	187	31.07	23.78
23	110	120	50	50	2	187	70.35	43.39
24	110	120	25	75	2	187	53.16	43.22
25	110	120	0	100	2	187	44.92	32.49
26	176	120	100	0	2	187	4.04	3.10
27	176	120	75	25	2	187	16.53	11.77
28	176	120	50	50	2	187	24.23	12.71
29	176	120	25	75	2	187	17.39	10.87
30	176	120	0	100	2	187	22.56	12.04
31	**140**	**120**	**50**	**50**	**2**	**187**	**13.33**	**9.63**
32	**140**	**120**	**100**	**0**	**2**	**187**	**NA**	**17.6**

Figure 21 shows average corrosion rate from weight loss measurement as a function of CO_2 partial pressure (concentration in the gas phase) for various temperatures. The measurements are presented together with previous measurements to investigate the trend of corrosion rate curves. Due to lack of measured data at low CO_2 concentration, the influence of CO_2 partial pressure on corrosion rate at 140°F cannot be fully understood. Even though there are some outlying data points, results show a general trend of corrosion rate increasing with partial pressure of CO_2. Thus, at low partial pressures (0 to 60 psi), the corrosion rate increased with the partial pressure. However, above 60 psi, the rate decreased with the partial pressure. At 100% CO_2 (partial pressure of 120 psi), corrosion rate sharply decreased as the temperature increased from 110 to 140°F. In general, corrosion rate is expected to decrease with reduction in CO_2 solubility. For temperature less than 230°F, the solubility of CO_2 in brine (NaCl) solution decreased with increasing temperature.

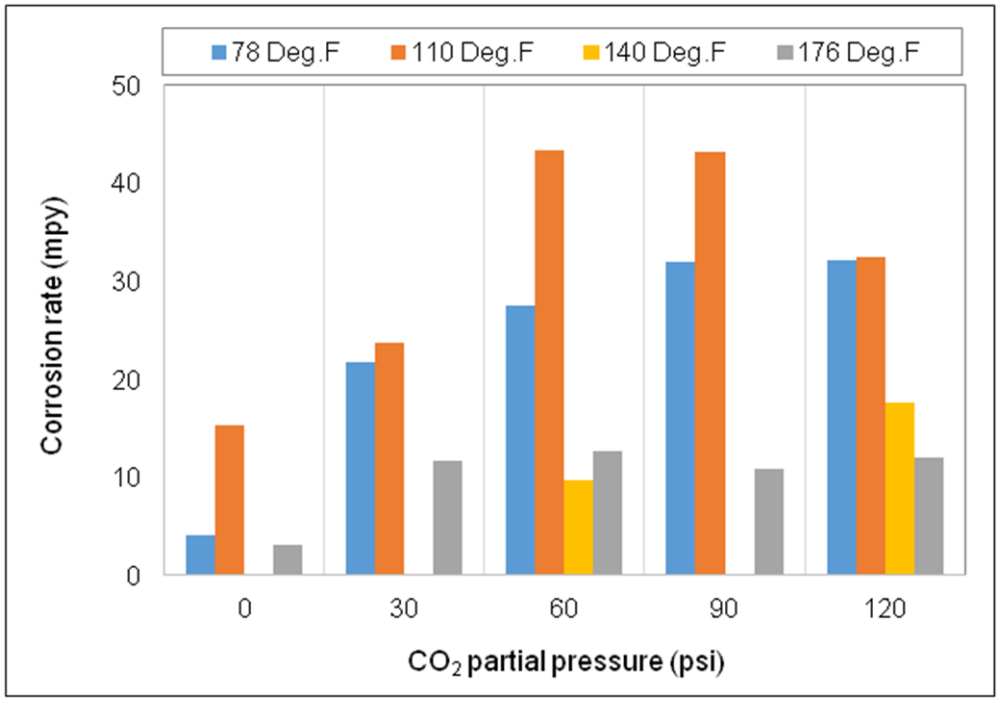

Fig. 21: Average corrosion rate measured WL method vs. partial pressures for different temperature

As previously reported, we have found a shop that can manufacture mini-pipe and flat corrosion specimens. A manufacturing order has been issued. The shop will soon begin production of the specimens. Manufacturing of the specimens is expected to take 6 to 8 weeks.

3. Planned Activities

- Continue testing baseline and new cement formulations for their performance by aging them in brine saturated with methane gas containing 300 ppm H_2S at 6000 psi and 100°F varying CO_2 concentration.
- Continue theoretical and modeling studies on tubular degradation.
- Continue experimental studies on tubular degradation under low-pressure and moderate-temperature conditions.

4. Project Expenditures

This section presents the project expenses during the month of April (**Table 5**) and the cumulative expenditures.

Table 5: Current and cumulative expenditures, April 2014

No.	Budget Categories	Current Expenses	Cumulative Expenses
1	Salaries & Wages	$8,464.60	$283,822.71
2	Fringe Benefits	$1,409.93	$61,941.23
3	Project Materials	$2,795.01	$64,732.18
4	Travel	$0.00	$10,878.07
5	Conference Expenses	$0.00	$0.00
6	Other Direct Costs	$0.00	$3,545.35
7	Equipment	$496.57	$243,630.43
8	Space Rental	$0.00	$0.00
9	Indirect Cost	$6,334.77	$211,414.88
10	**Total**	**$19,500.88**	**$879,964.85**

Nomenclatures

BWOC	By weight of cement
CH	Calcium hydroxide
CSH	Calcium silicate hydrate
EDX	Energy-dispersive X-ray spectroscopy
FTIR	Fourier Transform Infra-Red
GHO	Class G Cement with hydroxyapatite
GS	Class G cement with silica flour
GSMG	Class G Cement with silica flour and magnesium oxide
HHO	Class H Cement with hydroxyapatite
HPHT	High-pressure high-temperature

HS	Class H cement with silica flour
LPR	Linear polarization resistance
mpy	mils per year
MGO	Magnesium oxide containing cement
MGO-5	Cement containing 5% BWOC MgO as additive
NACE	National Association of Corrosion Engineers
SBS	Shear bonding strength
SEM	Scanning Electron Microscope
SCC	stress corrosion cracking
SSC	Sulfide Stress Cracking
XRD	X-Ray diffraction

References

Asahi, H., Ueno, M. and Yonezawa, T. 1994. Prediction of Sulfide Stress Cracking in High-Strength Tubulars. Corrosion, Vol 50, 537-545.

Duan, Z., Sun, R., Liu, R. and Zhu, C. 2007. Accurate Thermodynamics Model for calculation of H2S solubility in pure water and brines, Energy and Fuels, Vol 21, 2056-2065.

Jacquemet, N., Pironon, J. and Caroli, E. 2005. A New Experimental Procedure for Simulation of H2S + CO2 Geological Storage. Oil & Gas Science Technology- Rev. IFP, 60 (1): 193-206.

Kumar, A., Huang, W., Pacheco, J. L., Reddy, R. V., and Sun, W. 2014. Selecting Representative Laboratory Test Conditions for Mildly Sour Sulfide Stress Corrosion, paper no 4243, NACE international, Houston.

Kutchko, B. G., Strazisar, B. R., Hawthorne, S. B., et al. 2011. H2S–CO2 reaction with hydrated Class H well cement: Acid-gas injection and CO2 Co-sequestration. International Journal of Greenhouse Gas Control, 5: 880-888.

Lea, F. M. and Hewlett, P.C. 1998. Lea's Chemistry of Cement and Concrete, Arnold Publishing, London.

Zirrahi, M., Azin, R., Hassanzadeh, H. and Moshfeghian,M. 2012. Mutual solubility of CH4, CO2, H2S, and their mixtures in brine under subsurface disposal conditions, Fluid Phase Equilibria, Vol 324, 80-93.

Project Title: Effect of H_2S and CO_2 in HPHT Wells on Tubulars and Cement

Report Type: Monthly Report

Report #: 32

Reporting Period: April 22nd, 2014 to May 21st, 2014

Authors:

Ramadan Ahmed, Principal Investigator

Subhash Shah, Co-Principal Investigator

Rida Elgaddafi, Research Assistant

Omotayo Omosebi, Research Assistant

Himanshu Maheshwari, Research Assistant

Aman Srivastava, Research Assistant

Jueun Hwang, Research Assistant

Mounraj Sharma, Research Assistant

Sagar Tale, Research Assistant

Prepared under BSEE Project # E12PC00035

by

THE UNIVERSITY OF OKLAHOMA

July 30, 2014

1. Summary of Accomplishments

This monthly report presents the progress made during the project period April 22, 2014 to May 21, 2014. During this period, studies on degradation of cement and tubular were continued. New aging experiments were not conducted due to equipment failure. A high-pressure rod seal on stress cracking corrosion (SCC) autoclave failed. The seal was repaired and the autoclave was put into operation. In addition, modeling studies and data analysis on previous measurements were continued. The sixth TAB meeting was also held on May 9, 2014 as planned. The minutes of the meeting are presented in Appendix A. In addition, a report (Appendix B) has been prepared on completion of Milestones 6 and 7.

To carry out exploratory data analysis, recent measurements (porosity, permeability, and FTIR results of baseline cements) are combined with previously obtained results. The analysis has been conducted using ANOVA and SOM techniques. According to ANOVA analysis, the impacts of temperature and pressure on porosity and permeability (ϕ-k) of degraded cement are stronger than the effect of CO_2 concentration. Results of SOM analysis have indicated the relevancy of CH and CSH contents in evaluating the level of degradation using the FTIR data from the virgin and middle zones. In addition, the SOM analysis has revealed that the $CaCO_3$ content of the outer zone could provide useful information regarding the degree of degradation.

Further analysis has been performed using compressive strength of baseline cements from previous aging experiments. The effect of CO_2 concentration on compressive strength is investigated considering two different temperatures (225 and 350°F). Results show that strength of both well cements increases while porosity and permeability decreases with increase in CO_2 concentration. The governing mechanisms being diffusion and carbonation of CH and CSH and subsequent leaching (i.e. dissolution), both of which occur simultaneously and evolution of properties is direct consequence of interrelated processes. In most cases, CH and CSH formed carbonates faster than subsequent conversion to bicarbonate, which suggests the establishment of carbonation dominated degradation process. Overall, Class H cement demonstrates better integrity for zonal isolation than Class G cement.

Corrosion experiments under low-pressure was performed due to equipment repair. The autoclave used to conduct the experiment was re-coated (inside) with nickel lining to prevent corrosion of the vessel, which may interfere with the measurement. Modeling studies on tubular corrosion are in progress. Sulfide stress cracking (SSC) corrosion model requires accurate prediction of H_2S solubility in brine saturated with mixed gas. A new H_2S solubility calculation procedure has been formulated to predict the solubility of H_2S in water and NaCl solutions. The predictions of the new method showed satisfactory agreement with published experimental measurements.

Our plan for the upcoming weeks is to continue: i) aging tests at 6000 psi, 100°F, 300 ppm H_2S and different CO_2 concentrations; ii) theoretical and modeling studies on tubular corrosion; iii) testing of performance of new acid resistant cement formulations; and iv) low-pressure corrosion experiments at various CO_2 concentration.

2. Overall Project Progress

2.1 Theoretical Studies (Task 1)

2.1.1 Mechanism of Sulfide Stress Cracking

A corrosion model is being developed to predict sulfide stress cracking (SSC) of tubulars. The model requires a method to accurately predict H_2S concentration, which is one of the most important factors in SSC corrosion. Hydrogen sulfide concentration in liquid, which is in equilibrium with H_2S gas, is proportional to its partial pressure. This means that, to predict H_2S concentration in liquid, vapor-liquid equilibrium calculations are needed. A number of H_2S solubility calculation procedures have been presented in the literature. A new method has been formulated to predict the solubility of H_2S in water and NaCl solutions. The method is based on the Peng-Robinson equation of state and procedure developed by Duan and Sun (2003). The predictions of the new method, when compared with available experimental data, showed a good agreement.

2.1.1.1 Solubility of H_2S

For a gas that is in equilibrium with liquid, the following conditions are valid: i) temperature of the phases is equal; ii) pressure of the phases is same; iii) chemical potentials of each component in both phases are equal; and iv) the Gibbs free energy is at its global minimum. The first and the second conditions represent thermal and mechanical equilibrium criteria. The third condition can also be expressed in terms of fugacity for non-ideal gases.

$$f_i^l = f_i^v \quad \text{..... (1)}$$

where i represents the components.

For ideal gas-liquid mixtures, Raoult's or Henry's law can be used to determine the solubility of the gas. However, H_2S under high-pressure does not behave like an ideal gas. In addition, H_2S and water do not form an ideal mixture. Thus, these laws are not adequate to determine the solubility of H_2S in brine solutions. These laws either over-predict (Henry's law) or under-predict (Raoult's law) the gas solubility in case of real gases. Some modification should be made to these laws in order to account for non-ideality of real gases.

Solubility models for real gases are commonly develop based on either Henry's law (Zirrahi et al. 2012) or Raoult's law (Duan et al. 2007). The model developed by Duan et al. (2007) accounts for chemical potential and it is considered more accurate than the other model. As mentioned earlier, the chemical potential of the phases are the same for each component at equilibrium. Thus:

$$\mu_i^l = \mu_i^v \quad \text{..... (2)}$$

The chemical potential of dissolved gas is a function of temperature, pressure and its activity. Therefore, the chemical potential of hydrogen sulfide in the liquid is expressed as:

$$\mu^{l}_{H_2S}\ T,P,x\ = \mu^{lstd}_{H_2S}\ T,P\ + RT\ln a_{H_2S}(T,P,x) \quad \text{..... (3)}$$

where the activity of H_2S is defined as:

$$a_{H_2S} = x_{H_2S} * \Upsilon_{H_2S} \quad \text{..... (4)}$$

Combining Eqs. (3) and (4) yields the following expression to determine the chemical potential of hydrogen sulfide in the liquid phase.

$$\mu^{l}_{H_2S}\ T,P,x\ = \mu^{lstd}_{H_2S}\ T,P\ + RT\ln x_{H_2S}(T,P,x) + RT\ln \Upsilon_{H_2S}(T,P,x) \quad \text{..... (5)}$$

The first term in the right side of Eq. (5) represents the standard chemical potential of H_2S in ideal solution in unit of molality. γ_{H2S} is activity coefficient of H_2S. Similarly, the chemical potential of H_2S in the vapor phase is given by:

$$\mu^{v}_{H_2S}(T,P,y) = \mu^{vstd}_{H_2S}(T,P) + RT\ln f_{H_2S}(T,P,y) \quad \text{..... (6)}$$

where f_{H2S} is fugacity of H_2S, which is a function of pressure and mole fraction. Hence:

$$f_{H_2S} = P * y_{H_2S} * \Phi_{H_2S} \quad \text{..... (7)}$$

Inserting Eq. (7) into (6), the chemical potential of H_2S can be expressed as a function of mole fraction.

$$\mu^{v}_{H_2S}(T,P,y) = \mu^{vstd}_{H_2S}(T,P) + RT\ln P * y_{H_2S} + RT\ln \Phi_{H_2S}(T,P,y) \quad \text{..... (8)}$$

Since the chemical potential of H_2S in the liquid and gas phases must be the same at equilibrium condition, Eqs. (5) and (8) can be equated and rearranged to yield the following expression:

$$ln\left(P * \frac{y_{H_2S}}{x_{H_2S}}\right) = \frac{\left\{\mu^{lstd}_{H_2S}(T,P) - \mu^{vstd}_{H_2S}(T,P)\right\}}{RT} - \ln \Phi_{H_2S}(T,P,y) + RT\ln \Upsilon_{H_2S}(T,P,x) \quad \text{..... (9)}$$

Equation (9) can be used to predict solubility of H_2S at any pressure and temperature, if its fugacity, activity coefficient, and chemical potential are known at standard conditions. $\mu^{vstd}_{H2S}(T,P)$ is the chemical potential of H_2S at 1 bar, which can be estimated from the ideal gas equation.

2.1.1.2 Fugacity Coefficient of H_2S

According to Duan et al. (2007), for temperature range of 273 to 500 K, fugacity coefficient of water-H_2S mixture is approximately the same as that of pure H_2S. Consequently, pure H_2S fugacity coefficient, which is a function of the Z-factor, can be used to estimate the fugacity of the mixture.

In the model developed by Duan et al. (2007), iterative z-factor calculation procedure is required with initial guess value of reduced volume. The initial value should be close to the solution otherwise the procedure generates multiple and unrealistic solutions. However, only limited data is available in the literature regarding the values of reduced volume. Hence, the Peng-Robinson equation is used to compute the Z-factor.

$$Z^3 - (1 - B)Z^3 + (A - 2B - 3B^2)Z - (AB - B^2 - B^3) = 0 \quad \text{..... (10)}$$

where A and B are intermolecular attraction and repulsion factors, which are function of critical pressure and temperature. These factors are calculated as (Zirrahi et al. 2012):

$$A = \frac{aP}{RT^2} \quad \text{..... (11)}$$

$$B = \frac{bP}{RT} \quad \text{..... (12)}$$

where a and b are parameters that are calculated from critical pressure and temperature.

$$a = \frac{0.45724 * (RT_c)^2}{P_c}\left\{1 + \beta(1 - \sqrt{\frac{T}{T_c}}\right\}^2 \quad \text{..... (13)}$$

$$b = \frac{0.0778RT_c}{P_c} \quad \text{..... (14)}$$

where b is a parameter determined using the following correlation:

$$\beta = 0.37464 + 1.54226 * \omega - 0.26992 * \omega^2 \quad \text{..... (15)}$$

where β is a parameter used in Eq. (13) and ω denotes the acentric factor of the gas, which is 0.081 for H_2S.

The solution for the Peng-Robinson equation (Eq. 10) is numerically obtained applying the Newton-Raphson method. An initial guess of Z-factor is needed for this method. To initialize the Z-factor, Aspen software is used to generate Z-factor values at different pressures and temperatures. The results obtained from the software have been utilized to create a correlation to initialize the Z-factor. After developing a reliable method to predict the Z-factor, the model developed by Duan et al. (2007) is applied to determine the fugacity coefficient. Thus:

$$\ln \Phi(\mathrm{T},\mathrm{P}) = \mathrm{Z} - 1 - \ln Z + \frac{a_1 + a_2/T_r^2 + a_3/T_r^3}{V_r} + \frac{a_4 + a_5/T_r^2 + a_6/T_r^3}{2{V_r}^2} + \frac{a_7 + a_8/T_r^2 + a_9/T_r^3}{4{V_r}^4} + \frac{a_{10} + a_{11}/T_r^2 + a_{12}/T_r^3}{5{V_r}^5} + \frac{a_{13}}{2{T_r}^3 a_{15}}\{a_{14} + 1 - (a_{14} + 1 + a_{15}/V_r^2) * \exp(-a_{15}/V_r^2)\} \quad \text{..... (16)}$$

where reduced temperature, pressure and volume are defined as:

$$T_r = \frac{T}{T_c} \;;\quad P_r = \frac{P}{P_c} \;;\quad V_r = \frac{T_r Z}{P_r} \quad \text{..... (17)}$$

Values of the correlation parameters from a1 through a15 are calculated using saturation data of the gas (presented in Report # 8).

2.1.1.3 Solubility Model Validation

Figures 1 and **2** compare solubility of H_2S in pure water and brine solution predicted by the model with experimental measurements of Selleck et al. (1952) and Xia et al. (2000), respectively. Figure 2 also presents a comparison of solubility data at various temperatures (313, 353 and 393 K).

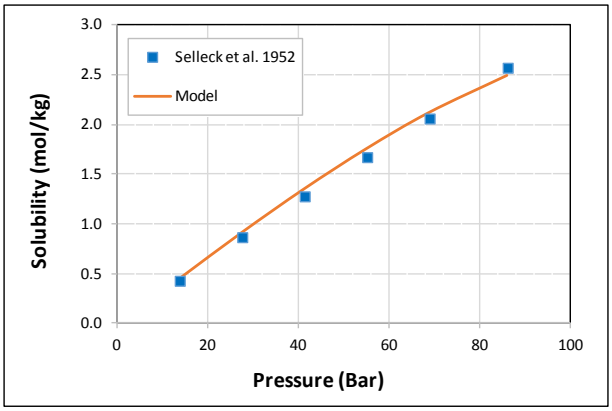

Fig. 1: Predicted and measured solubility vs. pressure for water at 366 K (data from Selleck et al. 1952)

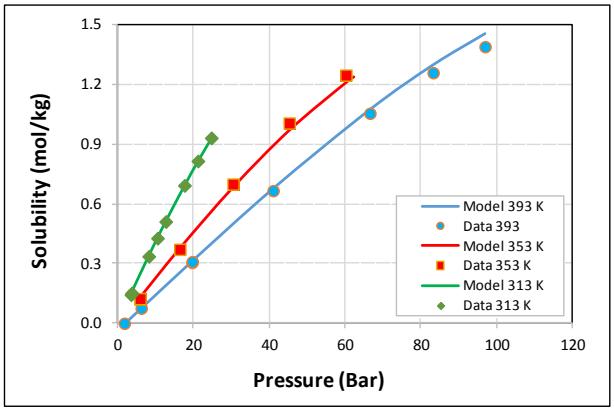

Fig. 2: Predicted and measured solubility vs. pressure for 4 m NaCl solutions (data from Xia et. al.(2000)

Model predictions show very good agreement with the measurements. Discrepancies between the measurements and predictions increase with pressure. Possible reason for the discrepancies could be some of the assumptions used in the development of the model might not be valid at high pressures.

For instance, fugacity coefficient of water-H_2S mixture is considered approximately the same as that of pure H_2S. This assumption is valid under low-pressure conditions. At high pressures, molecular distance diminishes causing the attraction and repulsion forces to increase. This can significantly change the behavior of water-H_2S mixtures. Hence, this validation is limited to moderate pressure (0 to 100 bar). High-pressure data is not available for comparison. As anticipated, both model predictions and experimental data show reduction in solubility of H_2S with temperature.

Figure 3 presents the solubility of H_2S as a function of pressure for different salt concentrations and temperatures. NaCl has salting out effect on H_2S solubility, meaning increase in salt concentration reduces the solubility. Salting out effect occurs at both temperatures. However, its impact increases with temperature, and more prominent at high pressures. For instance at 200 bar, solubility ratio of H_2S in pure water to 6 M NaCl solution is 2.04 at 418 K, while it reduces to 2.00 at 388 K. Drummond (1981) reported the increase in salting out effect with temperature.

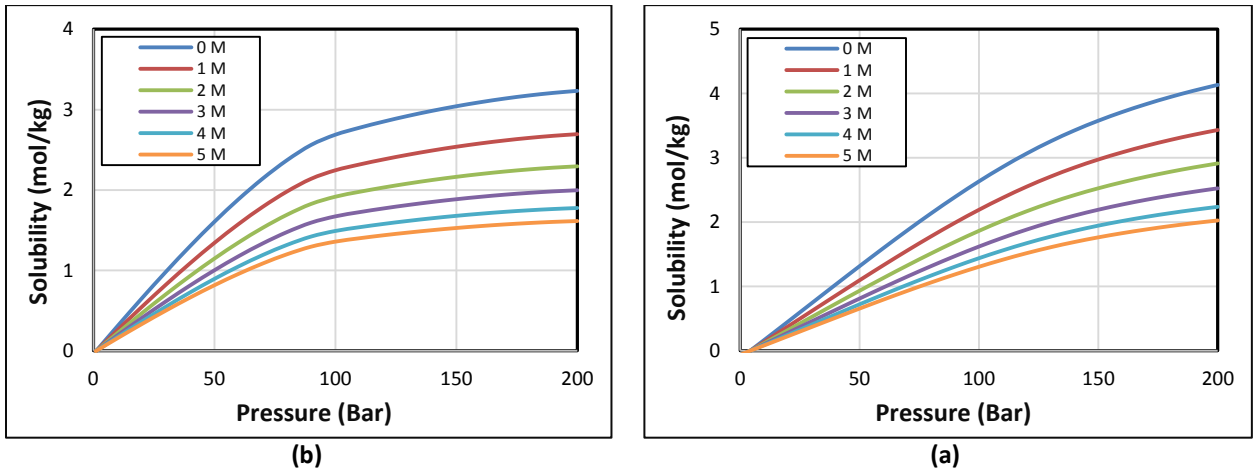

Fig 3: Solubility of H_2S vs. pressure at different NaCl concentrations: a) T= 378 K (220°F); and b) T= 418 K (293°F)

2.1.2 Modeling Mutual Solubility of CO_2 and H_2S

Published studies in the area of mutual solubility were investigated in the effort to develop uniform corrosion model. The investigation was focused on different multi-component gas systems (CO_2-H_2O, H_2S-H_2O, and CH_4-H_2O) and their combinations. The theoretical solubility models in the aqueous solutions are based on the balanced between the chemical potentials of a given component in the gas and liquid phases. In brine-gas mixture system, the gas phase contains some water vapor. Since the amount of water vapor in the gas phase is unknown, an iterative calculation is often needed to determine the composition of the gas phase. In this study, a simplified semi-empirical equation has been developed to estimate the mole fraction of water vapor in gas phase. The model is based on the work of Duan and Mao (2006), which is widely accepted by experts in this field. The equation predicts mutual solubility in the moderate range of pressure and temperature.

In order to evaluate the accuracy of the model, its predications are compared with published data and predictions of an existing model (Duan and Sun 2003). Wide range of pressure (0 to 2000 bar)

is considered for the model validation. Temperature and ionic strength are also varied. The new model has demonstrated better accuracy than existing one in predicting experimental measurements (**Figs. 4** and **5**).

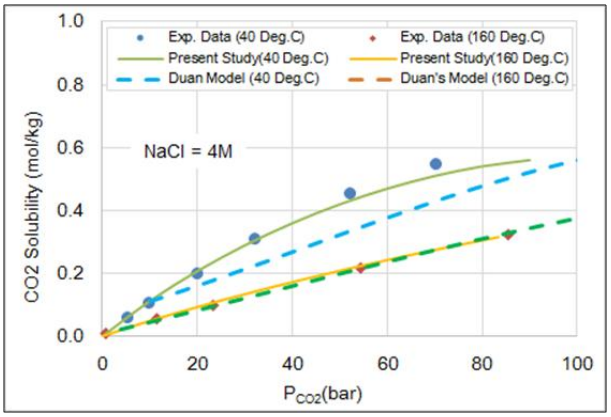

Fig.4: Comparison of prediction with measurements at various temperatures and 4 M NaCl solution (Data from Rumpf et al. 1994)

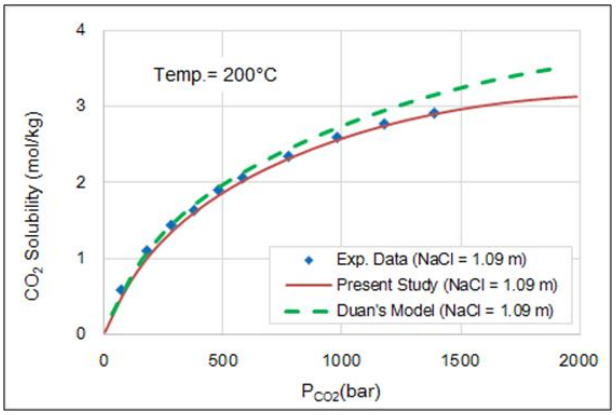

Fig.5: Comparison of prediction with measurements at 200°C and 1.09 M NaCl solution (Data from Takenouchi and Kennedy 1965)

Furthermore, the model has the capability to predict ionic concentration and pH of the solution. The predictions of model are validated by comparing them with the measurements available in the literature (**Fig. 6**). The model shows good performance. Slight discrepancy (approximately 4% maximum) exists at the intermediate pressures (150 to 300 psi). At low pressures (less than 100 psi), the pH decreases sharply. Then, it stabilizes and remains approximately the same with pressure.

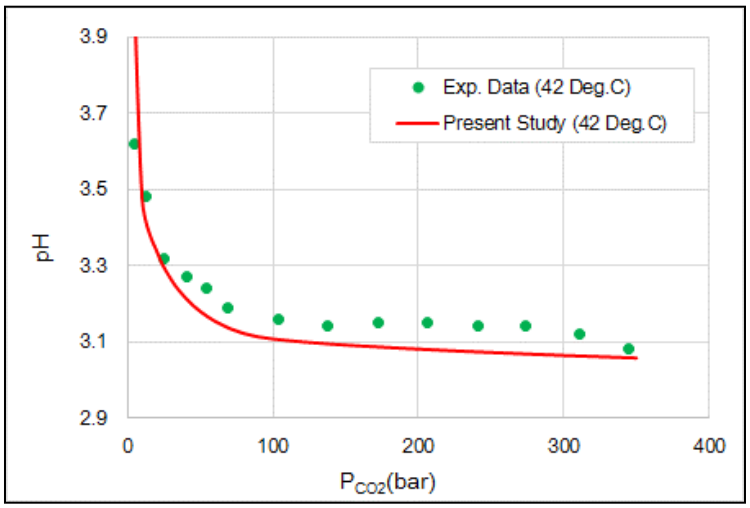

Fig. 6: pH vs. CO_2 partial pressure, comparision of model predictions with measurments (Meyssami et al. 1965)

2.2 Experimental Studies on Degradation of Cement (Task 2)

2.2.1 Porosities and Permeabilities of Baseline Cements

New aging experiments were not conducted during this month due to equipment failure and maintenance. Exploratory data analysis was performed applying two data analysis methods: i) Analysis of Variance (ANOVA); and ii) Self Organizing Maps (SOM). Porosity, permeability and FTIR mineralogy measurements are considered in the analysis. Results of ϕ-k were analyzed using the ANOVA method whileTIR mineralogy measurements were analyzed using the SOM approach.

2.2.1.1 Analysis of Variance (ANOVA)

The main objective of the ANOVA technique is to identify the most relevant test variables that influence the experimental measurements. The technique systematically quantifies the effect of every test variable on the measurements (Roy 2001). The details of the ANOVA calculation procedure are available in the literature (Roy 2001; Sagheer 2009). Applying this method, the impact of each test variable on the ϕ-k of degraded cement is determined. For this investigation, the dependent variables (measurements) are porosity and permeability. Temperature, pressure, and CO_2 concentration are the independent variables (factors). **Figures 7** and **8** present the influence of the independent variables on porosity and permeability of Class H and Class G cement samples, respectively.

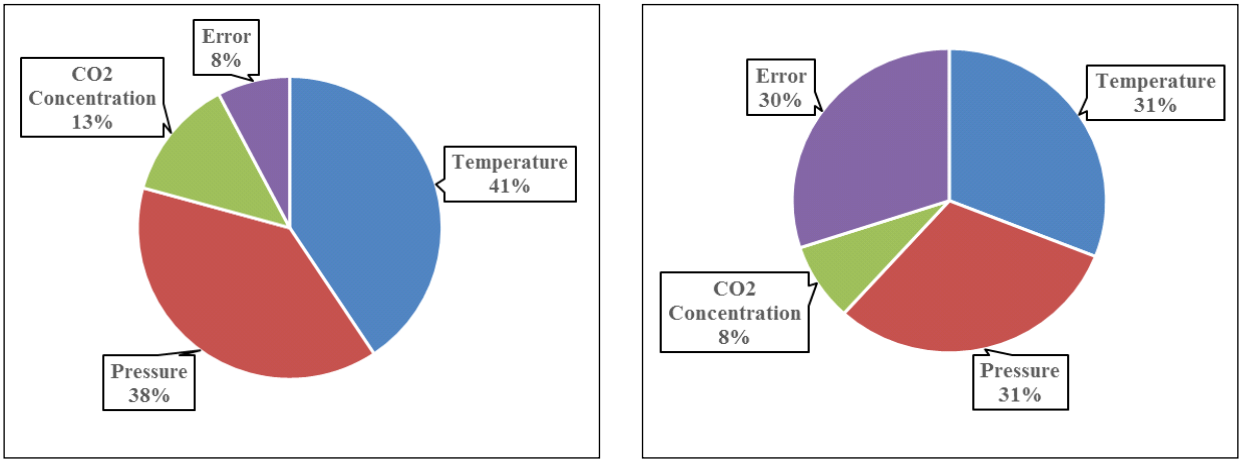

(a) **(b)**

Fig. 7: Results of ANOVA analysis for Class H cement showing the effects of pressure, temperature, and CO_2 concentration on: a) porosity; and b) permeability

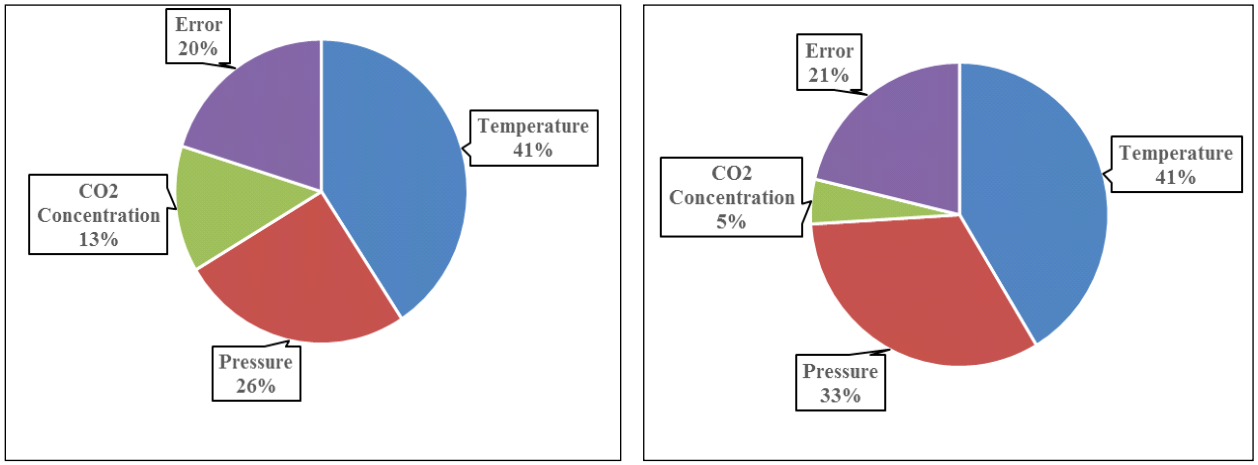

(a) **(b)**

Fig. 8: Results of ANOVA analysis for Class G cement showing the effects of pressure, temperature, and CO_2 concentration on: a) porosity; and b) permeability

The error term in these graphs represents the combined effects of experimental and test-unrepeatability errors (Roy 2001). As seen from the figures, Class H cement, the error term for porosity measurements is significantly lower than that of permeability. This is anticipated because the porosity measurements are more consistent and repeatable than permeability measurements. The results of the analysis have demonstrated that temperature and pressure have stronger impact on ϕ-k of degraded cement than CO_2 concentration. This analysis considered CO_2 concentration ranging from 10 to 100%. However, the effect of CO_2 concentration on ϕ-k at low concentrations (0 to 10%) could be stronger than at high concentrations.

2.2.1.2 Self Organizing Maps (SOM)

Another method used for statistical analysis is the SOM technique. The method is based on neural-network algorithms. The SOM approach presents the variables in color-coded maps for the purpose of visualization and interpretation. The color-coded mapping requires placing a vector from data space into the map (Kohonen 1995).

The SOM analysis was performed on FTIR data using MATLAB. Applying SOM method, FTIR data points were clustered into different classes, which had similar properties or values. More color variation or contrast suggests more importance of that specific variable in a given data classification. The SOM for the FTIR of Class H cement is shown in **Fig. 9**. The variables (columns) are FTIR peak strength of CH, CSH and $CaCO_3$, and the classifications (rows) are based on the origins (virgin, middle, or outmost zone) of the FTIR samples. The FTIR peak strength is related to the amount of the component associate to the peak.

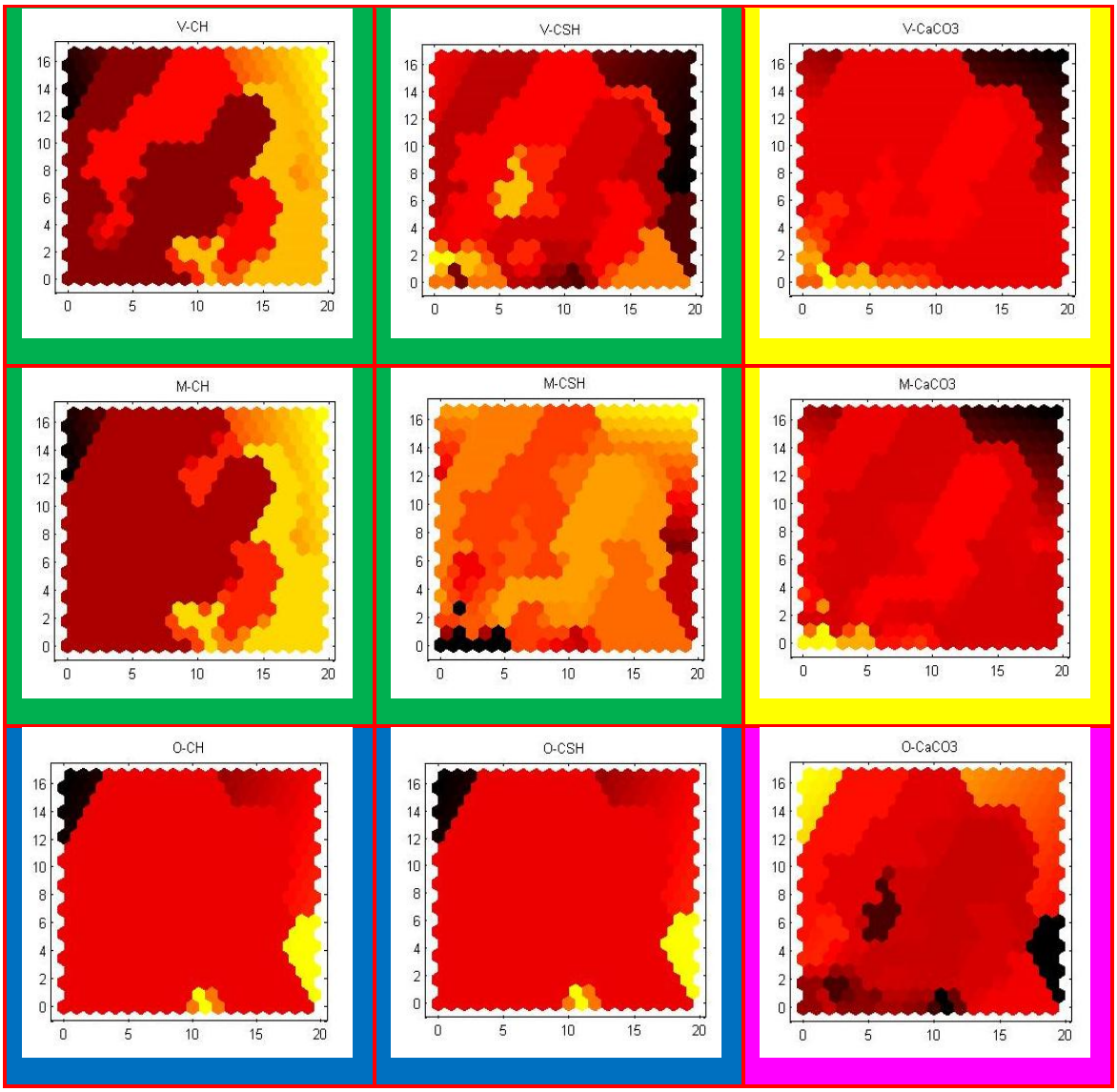

Fig. 9: SOM generated using FTIR data of Class H cement

As shown in the figures, maps that are presented in the green background area display high-contrast indicating the relevancy of CH and CSH contents in assessing the level of degradation using the data from the virgin and middle zones. Similarly, a map that is shown in the pink background area displays high-contrast. This demonstrates the importance of $CaCO_3$ content in evaluating the level of degradation in outermost zone.

Maps that are shown in blue background area do not exhibit high-contrast. This means, the FTIR measurements of CH and CSH from the outer-zone do not show substantial variations, and they cannot be utilized for quantifying the degree of degradation. As expected, the outer zones of the samples were highly degraded. As a result, CH and CSH variations are not seen. Likewise, maps presented in the yellow-background area display low-contrast. Again, this implies that the FTIR measurements of $CaCO_3$ from the virgin and middle zones do not indicate considerable variations, and they cannot be used for

evaluating the degree of degradation. This is anticipated, since virgin and middle zones were partially degraded; substantial variation in $CaCO_3$ content was not observed in the samples.

2.2.2 Compressive Strength of Baseline Cements

During this month, further analysis was performed using measurements from previous aging experiments (**Table 1)**. The effect of CO_2 concentration on compressive strength is investigated considering two different temperatures (225 and 350°F).

Table 1: Aging conditions of samples for different batches

Batch #	Temp. (°F)	Pressure (psi)	Partial Pressure %			Brine Conc. (%)	Aging Period (days)	Experiment #
			CH_4	CO_2	H_2S (ppm)			
16	350	3000	60	40	0	2	14	13
18	350	3000	0	100	0	2	14	15
20	350	3000	90	10	0	2	14	17
22	225	3000	60	40	0	2	14	19
24	225	3000	0	100	0	2	14	21
26	225	3000	90	10	0	2	14	23

2.2.2.1 Effect of CO_2 Concentration at 225°F

Figures 10 and **11** show mechanical and physical properties of Class H and Glass G cements a function of CO_2 concentration at 225°F and 3000 psi. Lines in Fig. 11 represent permeability data. As CO_2 concentration increases, compressive strength of both well cements increases while porosity and permeability decreases. The principal mechanisms that lead to cement degradation in carbonic acid environment are carbonation and leaching. Of these mechanisms, the rate controlling process is carbonation and subsequent leaching, both processes being affected by diffusion, dissolution, and reaction kinetics.

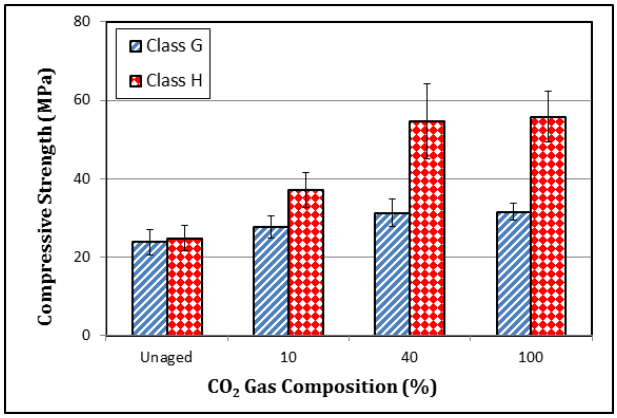

Fig. 10: Compressive strength vs. CO_2 concentration for cements aged at 225°F and 3000 psi

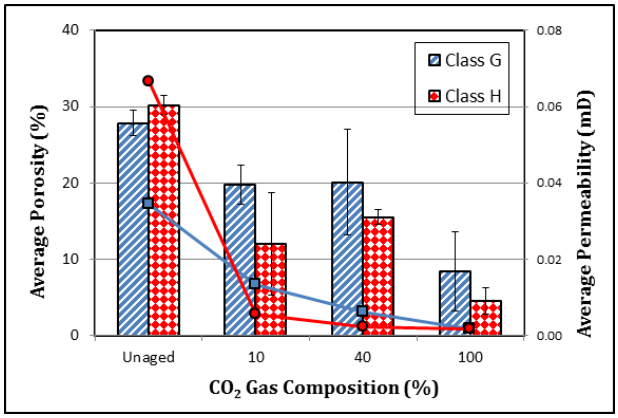

Fig. 11: Porosity and permeability vs. CO_2 concentration for cements aged at 225°F and 3000 psi

When carbonic acid attacks cement, the hydrates (CSH and CH) dissolve into the pore fluid and react with the acid to form calcium carbonate (calcite). Due to its low solubility, calcium carbonate

precipitates, and fills the pores of the cement, thereby resulting in reduction in ϕ-k. However, carbonate precipitation improves mechanical strength. With continuous supply of CO_2, the precipitated calcite is converted to water-soluble calcium bicarbonate, which is subsequently leached out further, leading to increased porosity and permeability, and reduced strength. Both carbonation and leaching processes take place simultaneously during acid exposure. Thus, the physical and mechanical properties are dictated by the dominant process.

As CO_2 concentration increases, additional CO_2 dissolves in brine. This increases carbonic acid and reduces the pH of the solution. Subsequently, solubility of calcite increases since low pH facilitates dissolution. At low temperature and pressure, the hydrates are carbonated faster than subsequent conversion to bicarbonate. However, in some cases, the rate of carbonation may be low and carbonation becomes the rate controlling mechanism. While these results hold for 14 days of exposure adopted in this study, effect of leaching may become more pronounced with prolonged exposure.

Furthermore, phase transformation of partially carbonated (calcium silicate carbonate) and un-carbonated CSH may have contributed to the trend observed in experimental data. Although the effect of pressure on CSH and calcium silicate carbonate (CSC aka scawtite) phase transformation is not well understood, the effect of temperature is well-documented (Taylor 1964; Eilers et al. 1980; Nelson et al. 1981; Richardson 2008). Transformation of CSH to tobermorite ($5CaO.6SiO_2.5H_2O$) or clinotobermorite is likely to occur at approximately 225°F and C/S ≈ 1. Of the CSH phases, tobermorite is the strongest and the least permeable (Meller et al. 2007; Sanders and Smothers 1957).

To explain the compressive strength and ϕ-k measurements further, FTIR results are presented in **Fig. 12**. The FTIR spectrum peaks of calcium hydroxide, CSH and calcium carbonate extracted from FTIR spectra of different zones for the cores. In virgin and middle zones, only CSH was preserved while all the portlandite was consumed regardless of the CO_2 concentration. This is due to high reactivity and quick dissolution of portlandite in carbonic acid environment, which resulted in the formation of $CaCO_3$ in all zones.

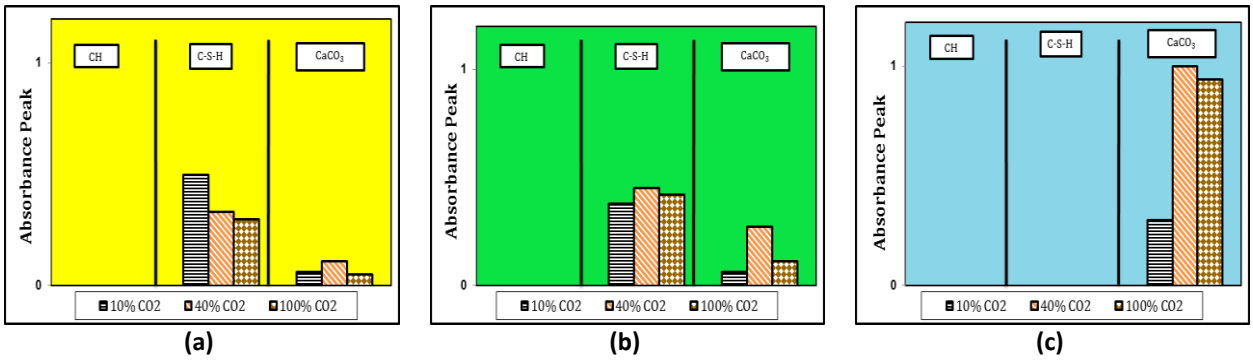

Fig. 12: FTIR of Class H cement aged at 225°F and 3000 psi: a) virgin zone; b) middle zone; and c) outermost zone

Overall, Class H cement demonstrated better integrity for zonal isolation than Class G cement because it is stronger, less porous, and less permeable after exposure. This observation is in agreement with experimental studies conducted by Bruckdorfer (1986) in which Class H cement was found to be more CO_2-resistant. This justifies its suitability as the standard cement used for oil and gas well cementing in the US Gulf coast, the Midcontinent, and the Permian basin while Class G is used primarily in the western US, Canada, and most other parts of the world (Smith 1991).

2.2.2.2 Effect of CO_2 Content at 350°F

In this section, the effects of CO_2 concentration on compressive strength (**Fig. 13**) as well as ϕ-k of Class G and Class H cements (**Fig. 14**) are investigated. Lines in Fig. 14 represent permeability data. For Class H cement, the trend is similar to the results obtained from tests conducted at 225°F: strength increased while ϕ-k decreased as CO_2 concentration was increased. However, close examination of the experimental data reveals that elevated temperature accelerated the rate of leaching at high CO_2 concentrations (40% and above). However, carbonation was still dominating. As result, strength improved and ϕ-k decreased compared to the unaged sample.

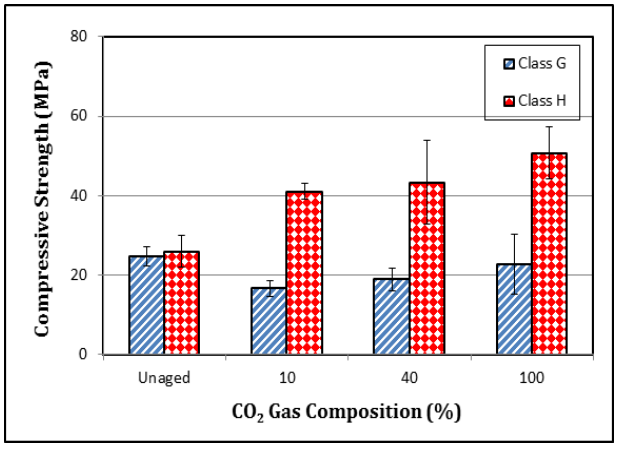

Fig. 13: Compressive strength vs. CO_2 concentration for cements aged at 350°F and 3000 psi

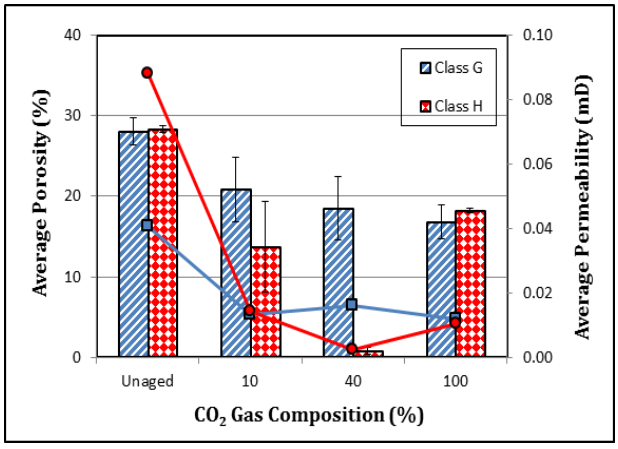

Fig. 14: Porosity and permeability vs. CO_2 concentration for cements aged at 350°F and 3000 psi

FTIR data (**Fig. 15**) reveals the preservation of CSH in virgin and middle zones of the samples at any CO_2 concentration. However, CH was almost completely consumed indicating its high solubility and reactivity toward carbonic acid. Due to limited ionic diffusion in the cement matrix, the acid concentrations in the outer and inner zones vary greatly. CSH was not significantly consumed in virgin and middle zones, even though the acid was able to reach all the zones. The preservation of CSH maintained the mechanical strength. In the outer zone, acid concentration is high, pH is low, and ionic transport is very high. This condition intensifies dissolution and carbonation of CH and CSH, resulting in complete consumption of CH and CSH.

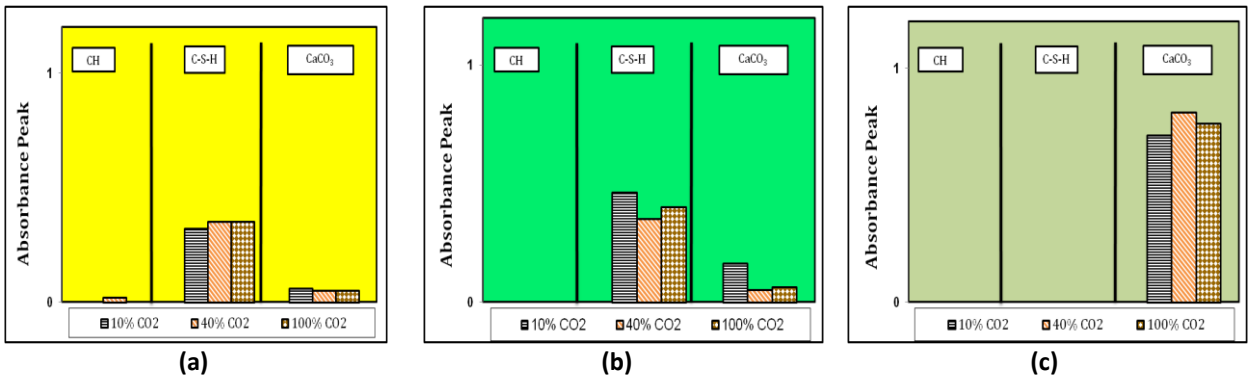

Fig. 15: FTIR results of Class H cement sample aged at 350°F and 3000 psi: a) virgin zone; b) middle zone; and c) outermost zone

2.2.3 Shear Bond Strength of Baseline Cement

Study on shear bond strength (SBS) of Class H cement was continued. As reported previously (Report # 20), shear bond test samples were used to study degradation depth. To measure the degradation depth, the hardened cement was taken out from tested SBS samples and sliced into halves along the length. Subsequently, phenolphthalein solution was applied and the degraded depth was measured. During this month, statistical analysis for the penetrated depth was performed using ANOVA method. Statistical software, Qualitek-4 (QT4) and Minitab, were used to conduct the analysis.

Figure 16 shows the results of ANOVA technique using QT4. The bar graph shows the percent influence of each test variable. Temperature has the highest (58%) influence, and pressure has the least (13%) effect on penetrated depth of SBS cement cores. The error bar is only 9%.

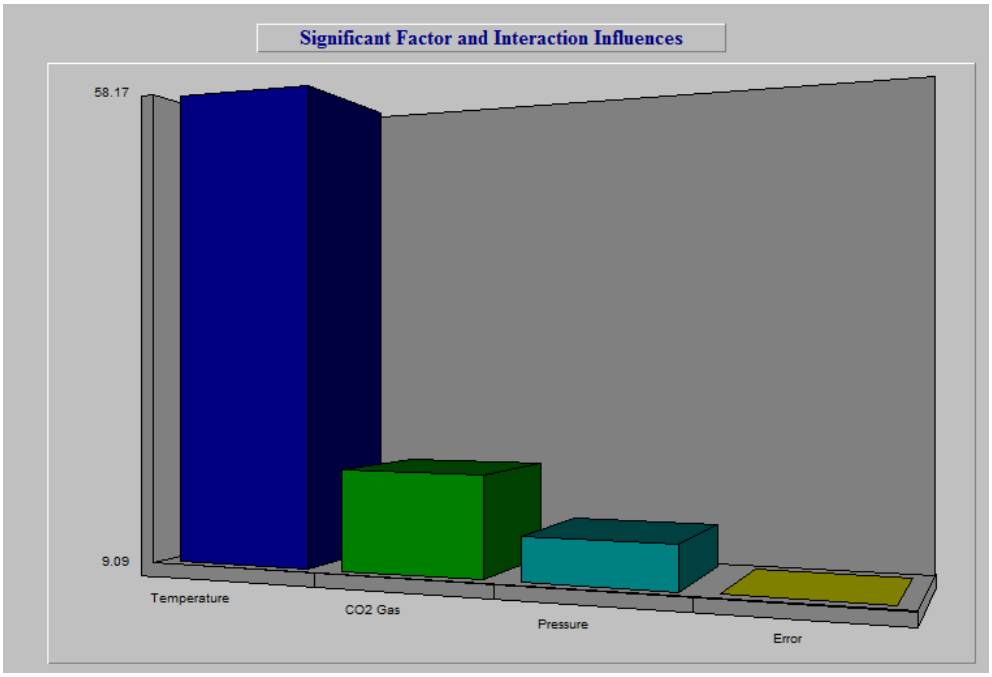

Fig. 16: Degradation depth analysis result using ANOVA method for Class H sample

2.3 Experimental Studies on Corrosion of Tubulars (Task 3)

Low-pressure corrosion tests facility was down for repair. Corrosion protective lining (nickel coating) of the autoclave used to conducted experiments showed localized corrosion damage (pitting). The autoclave has been sent for a repair. Experiments will resume next month.

Preliminary testing was started using high-pressure corrosion setup. However, during HPHT testing, high-pressure rod seal (**Fig. 17**) used to contain the pressure in the stress cracking corrosion (SCC) cell failed. The cell was disassembled and the seal was recovered and replaced with a new one. Then, cell was reinstalled and tested at HPHT condition. During the test, the seal was able to hold pressure up 10,000 psi while allowing free rod movement. We are waiting for mini-pipe and flat specimens to start the actual test. Manufacturing of the specimens will be completed in the coming weeks.

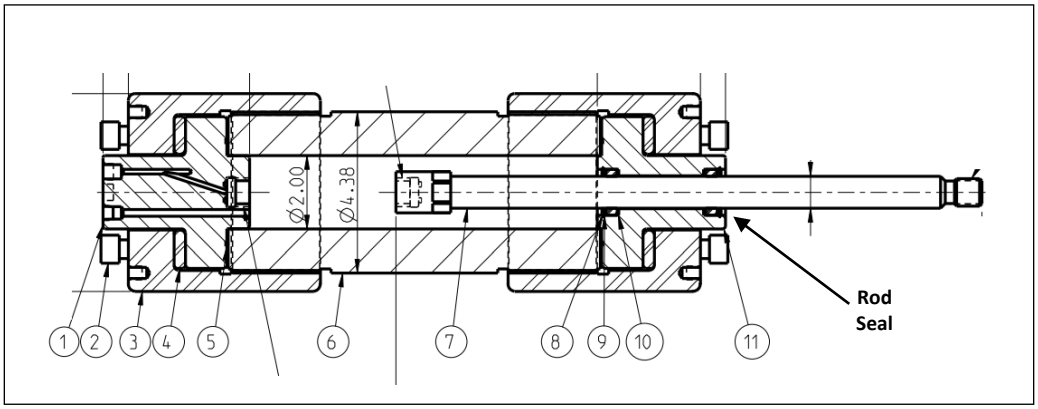

Fig. 17: Design of SCC cell

3. Planned Activities

- Continue testing baseline and new cement formulations for their performance by aging them in brine saturated with methane gas containing 300 ppm H_2S at 6000 psi and 100°F varying CO_2 concentration.
- Continue theoretical and modeling studies on tubular degradation.
- Continue experimental studies on tubular degradation under low-pressure and moderate-temperature conditions.

4. Project Expenditures

This section presents the project expenses during the month of May (**Table 2**) and the cumulative expenditures.

Table 2: Current and cumulative expenditures, May 2014

No.	Budget Categories	Current Expenses	Cumulative Expenses
1	Salaries & Wages	$10,446.90	$294,269.61
2	Fringe Benefits	$2,011.35	$63,952.58
3	Project Materials	$820.53	$65,552.71
4	Travel	$134.96	$11,013.03
5	Conference Expenses	$0.00	$0.00
6	Other Direct Costs	$448.00	$3,993.35
7	Equipment	$602.38	$244,232.81
8	Space Rental	$0.00	$0.00
9	Indirect Cost	$6,930.87	$218,345.75
10	**Total**	**$21,394.99**	**$901,359.84**

Nomenclatures

Acronyms

ANOVA	Analysis of Variance
BWOC	By weight of cement
CH	Calcium hydroxide
CSH	Calcium silicate hydrate
FTIR	Fourier Transform Infra-Red Spectroscopy
GS	Class G cement with silica flour
HPHT	High-pressure high-temperature
HS	Class H cement with silica flour
SBS	Shear bonding strength
SCC	stress corrosion cracking
SOM	Self Organizing Maps
SSC	Sulfide Stress Cracking
XRD	X-Ray diffraction

Symbols

a	Activity
f	Fugacity
m	molality
P	Pressure in bar
ϕ-k	Porosity and permeability
Pc	Critical Pressure
Pr	Reduced Pressure
R	Gas constant in cm3*bar/K/kg-mol
T	Temperature in Kelvin
Tc	Critical Temperature
Tr	Reduced Temperature
Vr	Reduced Volume
x	Mole fraction in liquid phase (solubility of gas)
y	Mole fraction in vapor phase
Z	Compressibility factor

Creek Letters

ε	Third order interaction parameter
Φ	Fugacity coefficient
Υ	Activity coefficient
λ	Second order interaction parameter
μ	Chemical Potential

Subscripts

a	anion
c	cation

Superscript

l	liquid phase
v	vapor phase
aq	aqueous
std	standard

References

Bruckdorfer, R. A. 1986. Carbon Dioxide Corrosion In Oil Well Cements, SPE 15176 Billings, MT, May 19 – 21.

Duan, Z. and Mao, S., 2006. A Thermodynamic Model for Calculating Methane Solubility, Density and Gas Phase Composition of Methane-Bearing Aqueous Fluids from 273 to 523 K and from 1 to 2000 bar, Geochimica et Cosmochimica Acta, V.70, Issue 13, pp. 3369–3386, 1 July.

Drummond, S. E. Jr. 1981. Boiling and Mixing of Hydrothermal fluids: Chemical Effects on mineral precipitation, PhD dissertation, The Pennsylvania State University, State College, Pennsylvania (March 1981).

Duan, Z. and Sun, R. 2003. An improved model calculating CO2 solubility in pure water and aqueous NaCl solutions from 273 to 533 K and from 0 to 2000 bar, Chemical Geology, Vol. 193, 257-271.

Duan, Z., Sun, R., Liu, R. and Zhu, C. 2007. An accurate thermodynamic model for the calculations of H2S solubility in pure water and brines, Energy & Fuels, Vol. 21, 2056-2065.

Eilers, L. H., Nelson, E. B. and Moran, L. K. 1980. High Temperature Cement Compositions – Pectolite, Scawtite, Truscottite or Xonotlite: Which Do You Want?, Paper SPE 9286 presented at SPE Annual Technical Conference and Exhibition, Dallas, Texas, 21 – 24 September.

Meller, N., Hall, C., Kyritsis, K., Giriat, G., Jakobsen, H. J. and Skibsted, J. 2007. Incorporation of Aluminium Guest-ions in Nominally Alumina-free Calcium Silicate Hydrates: Effects on Crystal Structure and Thermal Stability, In 12th International Congress on the Chemistry of Cement.

Meyssami, B. Balaban, M.O., and Teixeira, A.A., 1992. Prediction of pH in Model Systems Pressurized with Carbon-Dioxide, Biotechnol. Progr. 8,pp.149–154.

Nelson, E. B., Eilers, L. H. and Kalousek, G. L. 1981. Formation and Behavior of Calcium Silicate Hydrates in a Geothermal Environment, Cem. Concr. Res. 11, 371 – 381.

Richardson, I. G. 2008. The Calcium Silicate Hydrates, Cem. Concr. Res. 38, 137 – 158.

Roy. R. K. 2001. Design of experiments using the Taguchi approach 16 steps to product and process improvement", John Wiley & Sons, Inc.

Rumpf, B., Nicolaisen, H., Ocal, C., and Maurer, G.,1994. Solubility of Carbon-Dioxide in Aqueous-Solutions of Sodium-Chloride – Experimental Results and Correlation, J. Solution Chem. 23, pp.431–448.

Sagheer, M. 2009. Study of Effect of Down-Hole Mechanical Cleaning Devices (Mcds) On Cuttings Transport. MS Thesis, University of Tulsa. 2009.

Sanders, L. D. and Smothers, W. J. 1957. Effect of Tobermorite on the Mechanical Strength of Autoclaves Portland Cement-Silica Mixtures, J. Am. Conc. Inst. 28, 127-134.

Selleck, F. T., Carmichael, L. T. and Sage, B. H. 1952. Phase behavior in the Hydrogen Sulfide-water system, Industrial and Engineering Chemistry, Vol. 44, 2219-2226.

Shibue, Y. 2003. Vapor pressures of aqueous NaCl and CaCl2 solutions at elevated temperatures, Fluid Phase Equilibria, Vol. 213, 39-51.

Smith, D. K. 1991. Worldwide Cementing Practices, First Ed., American Petroleum Institute, January, p. 11.

Takenouchi, S., and Kennedy, G.C., 1965. The Solubility of Carbon Dioxide in NaCl Solutions at High Temperatures and Pressures, Am. J. Sci. 263, pp.445–454.

Taylor, H. F. W. 1964. The Chemistry of Cements. London: Academic Press, Ltd., 106-122.

Xia, J., Kamps, A.P., Rumpf, B. and Maurer, G. 2000. Solubility of Hydrogen Sulfide in Aqueous Solutions of the Single Salts Sodium Sulfate, Ammonium Sulfate, Sodium Chloride, and Ammonium Chloride at Temperatures from 313 to 393 K and Total Pressures up to 10 MPa, Industrial & Engineering Chemistry Research, Vol. 39, 1064-1073.

Zirrahi, M., Azin, R., Hassanzadeh, H. and Moshfeghian, M. 2012. Mutual solubility of CH4, CO2 and H2S and their mixtures in brine under subsurface disposal conditions, Fluid Phase Equilibria, Vol. 324, 80-93.

Appendix A

MINUTES

6th Technical Advisory Board Meeting

E12PC00035

Project Title: Effect of H_2S and CO_2 in HPHT Wells on Tubulars and Cement

Meeting Date: May. 9, 2014
Time: 8:30 AM – 2:00 PM Central Time
Meeting Location: Sarkeys Energy Center, Room # 350, 100 E. Boyd St., Norman, OK 73019-1003

Attendees: Arild Saasen (Det Norske), Ashok Santra (Weatherford International), Gunnar DeBruijn (Schlumberger), Kyris Agapiou (Halliburton), Matt George (Weatherford International), Stuart Cole (Vallourec), Ramadan Ahmed (OU), Subhash Shah (OU), Omotayo Omosebi (OU), Rida Elgaddafi (OU), Aman Srivastava (OU), Himanshu Maheshwari (OU), Jueng Hwang (OU); Mounraj Sharma (OU), Sagar Tale (OU)

All Technical Advisory board (TAB) members were present, except member from Baker Hughes.

Dr. Ahmed opened the meeting by welcoming the Technical Advisory Board members and all other participants. He introduced the project objectives, task descriptions, and provided the project status. He mentioned that the project is in preparation to start corrosion test with mini-pipes and corrosion coupons. He discussed the design change in mini-pipe and its implications on manufacturing.

The following questions were asked by TAB members.

Dr. Santra: Do you have a plan for publishing your findings? Dr. Ahmed: Currently, 1st drafts of four papers have been prepared. We will be reviewing and revising the articles in the coming months.

Mr. George: What type of materials will be used for making the corrosion specimens? Dr. Ahmed: Specimens are cut from T95, C110 and Q125 grade casings.

Mr. George: How many specimens will be made? Dr. Ahmed: 60 mini-pipes and 120 flat coupons will be made. He briefly discussed size limitations and manufacturing issues associated with mini-pipes. In addition, he mentioned that a workshop has been found that has the capability to manufacture the specimens with the required accuracy.

1st Presentation by Himanshu Maheshwari (MS Graduate Student)

The first presentation was by Himanshu Maheshwari on the effects of sour gas on the permeability and porosity of oil well cement. He defined the objectives, scope of work and methodology used in investigation. He presented the effects of CO_2 on porosity and permeability of baseline cement at HPHT conditions. He discussed FTIR and SEM measurements, and results of statistical analysis. His study shows that pressure and temperature have more impact on degradation of cement than CO_2 concentration. The following questions were asked by TAB members.

Dr. Saasen; There are three new articles on cement degradation that might be useful for your investigation. Dr. Ahmed: We will continue updating our literature survey.

Mr. DeBruijn: Do you have information on reactions of cement component with acid under high temperature? Himanshu: Information in this area is limited. However, FTIR and XRD analyses may provide some information on details of the reaction occurring at high temperature. Dr. Ahmed: EDX on SEM may also provide additional information to better understand the degradation at high temperature.

2nd Presentation by Omotayo Omosebi (PhD Graduate Student)

Omotayo made the next presentation and discussed the mechanical properties of oil well cement in acid environment. He presented experimental data that shows the effect of carbon dioxide on cement strength under HPHT conditions. He discussed the mechanisms of degradation including diffusion, dissolution, carbonation and leaching. He presented a cement degradation model that can predict the change in cement strength with exposure time. He pointed out the need for an improved degradation model to predict accurately the lifespan of oil and gas well cement. He also noted that, at high temperatures, cement strength is maintained due to decrease in solubility of portlandite. The following were the Q& A.

Dr. Santra: Does you model accounts for carbonation of cement? Tayo: With its current formulation, it does not account for carbonation. In the future, carbonation will be included.

Mr. DeBruijn: Does your model accounts for phase transformation occurring at high temperatures? Tayo: No. It considers only CSH phase.

3rd Presentation by Jueun Hwang (MS Graduate Student)

The third technical presentation was made by Jueun Hwang on the effect of sour gas on shear bond strength (SBS) of oil well cement. She briefly discussed study objectives, approach, sample preparation technique, test equipment description, and experimental procedure. Then, she showed SBS measurements and discussed the effects of temperature, pressure, CO_2 concentration on SBS of Class H cement. She presented SBS and bond elastic stiffness as a function of CO_2

concentration. These two properties of the cement bond showed opposite trend. The Q&A was as follows:

Dr. Saasen: Do you have a plan to test foam cement? Jueun: No.

Dr. Saasen: Does the CO_2 become 100% soluble? Dr. Ahmed: CO_2 solubility decreases with temperature at low temperatures (approximately less 350°F) and then it increases with temperature.

Dr. Santra: Can you have supercritical CO_2? Dr. Ahmed: During 100% CO_2 test, we expect supercritical conditions in the aging cell.

Dr. Santra: Curing at low temperature and testing at high temperature may produce uneven expansion, which breaks or weakens the bond.

Mr. DeBruijn: Measure the strains for shear bond and compressive strength tests.

4th Presentation by Aman Srivastava (MS Graduate Student)

Aman Srivastava presented results of experimental study on the effects of additives on cement properties under acidic environment. He presented formulations of different additive cements (microsilica, latex, latex-microsilica, MgO, and hydroxyapatite) and showed their porosity, permeability, compressive and bond strength after aging under various conditions in the presence of CO_2. He found 5% bwoc MgO and 5% bwoc hydroxyapatite based cement have better acid resistant than the baseline (Class H and Class G) cements. The Q&A was as follows:

Mr. DeBruijn: No aluminates in oil well cement. Gypsum up to 100°F. How much gypsum or anhydride?

Mr. DeBruijn: No industry standard for testing permeability of cement, therefore the phase “extreme permeability” may not have clear meaning.

Dr. Santra: 10% microsilica creates very viscous cement slurry. Aman: We used 1.25% bwoc Sodium Poly-naphthalene Formaldehyde Sulfonate (NSF). The dispersant made the slurry less viscous and flowable.

Dr. Agapiou: With hydroxyapatite, consider using aluminum containing additives, they may create cement that is more acid resistant.

5th Presentation by Mounraj Sharma (MS Graduate Student)

Mounraj’s presentation was focused on the effect of H_2S on cement properties under HPHT Conditions. He discussed mechanisms of CO_2-H_2S attack, physical processes and chemical reactions involved during cement degradation. He showed experimental results (porosity,

permeability, SBS and shear bond strength) that indicate the impacts of H_2S on cement degradation. In addition, to support his findings and conclusions, he presented results of FTIR analysis and SEM images that show the formation of different mineral in pores. The Q&A was as follows:

Dr. Agapiou: Use of XRD helps to support your conclusions.

Mr. DeBruijn: What was the concentration of H_2S? Mounraj: 300 ppm.

Mr. DeBruijn: Good Study with H_2S, consider higher concentration to get more degradation.

Dr. Santra: For high temperature, cement use high density (16.4 ppg), then MgO will have significant effect.

6th Presentation by Rida Elgaddafi (PhD Graduate Student)

Rida Elgaddafi presented progress made in studying uniform corrosion of tubulars under sour gas environment. He discussed factors affecting uniform corrosion, corrosion mechanisms in brine saturated with mixed (CO_2 and H_2S) gas, theoretical modeling, and results of experimental study conducted at elevated pressure and temperature conditions. He presented experimental setup, test procedure, and results of weight loss and LPR measurements. He found a consistent trend of corrosion rate that shows maximum rate in the range of 50 to 75% CO_2 concentration. The trend varies with temperature. However, the general trend does not change significantly. The Q&A was as follows:

Mr. Cole: Are you going to apply tension on the flat coupons?

Dr. Ahmed: The coupons are used for uniform corrosion study. They will not be subjected to mechanical loads. However, we measure elastic properties of the coupons before and after the test to assess the changes occurring in strength of the material.

Mr. Cole: What types of protective scales are expected?

Dr. Ahmed: With the presence of H_2S, mackinawite layer is expected to form. Other protective scales such as iron sulfide can also form depending on pressure, temperature and gas compositions.

Mr. Cole: What type of technique you will be using to identify the type of the protective scale?

Dr. Ahmed: We will be using FTIR, SEM, and EDX to determine the type of scale.

7th Presentation by Sagar Tale (MS Graduate Student)

The last presentation was given by Sagar Tale on Sulfide Stress Cracking (SSC) in tubulars. Sagar discussed the approach and scope of the research, mechanism of sulfide stress cracking, types of test (tensile Test A and constant extension rate) used to evaluate SSC resistance, and experiment plan. He mentioned that the mini-pipe specimens are exposed to corrosive environment for 200 hours. Then, the samples are taken out and subjected to constant extension rate test to evaluate the change in ductility occurring after the exposure. The Q&A was as follows:

Dr. Saasen: What is the level of tension that will be applied to the mini-pipe? Sagar: 80% of the minimum yield strength

Mr. Cole: C110 and Q125 are now API standard grades.

Next, Dr. Subhash Shah (Co-PI) summarized all the presentations and thanked the TAB for their support, service, and participation at the meeting. He also thanked all students for conducting the difficult experiments, generating quality data, and for doing a very professional job.

Appendix B: Milestones 6 and 7 Completion Report

Cement Additive Screening Studies and Development of Test Setups to Study Sour Gas Corrosion of Tubulars

EXECUTIVE SUMMARY

This report presents accomplishments of the project in completing cement additive screening studies and developmental work to build test setups to investigate sour gas corrosion of tubulars. Extensive literature review and laboratory experiments were conducted to perform the additive screening study and to develop the corrosion test setups.

The additive screening studies were conducted in three stages: i) literature survey; ii) initial screening study; and iii) final screening and formulation studies. Extensive literature review was performed to identify different potential additives, investigate their characteristics and impact on the properties of cement, and determine their suitability for well cementing applications. To accomplish this, the additives were classified into two categories based on the mechanism in which they reduce acid attack and improve degradation resistance of the cement. The first category includes additives that react chemically with the acid and reduce the acid concentration in the pore. The second category consists of additives, which reduce porosity and permeability of the set cement thereby minimizing ionic diffusion in the pores and limit acid penetration. The literature review resulted in the development of a list of potential additives that were considered for the initial screening study.

In the initial screening stage, additive containing baseline cement (additive cement) slurries were prepared and rigorously tested for their suitability. The slurry screening tests were performed to check if the additive cement formulations meet the required slurry properties such as: pumpability, thickening time, fluid loss, and rheological properties. Properties of additive cements were compared with baseline cements (Class H and Glass B). Several adjustments were made in the formulations of the slurries to bring their properties within acceptable range (i.e. comparable with baseline cements). Slurries that behaved very similar to the baseline cements were selected for further investigation. Cement slurries with selected additives were prepared and cured at 200°F and ambient pressure. Small portion of each slurry was used to prepare shear bond samples. After hardening and coring, porosity, permeability, compressive and bond strength of the samples were measured and compared with those of the baseline samples. Additive formulations that produce samples with similar characteristics as the baseline cement were chosen for final screening and formulation studies.

In the final screening and formulation stage, both baseline and additive cement cores and bonding samples were aged under high-pressure high-temperature (HPHT) sour gas conditions. Six additive based cement formulations (microsilica, latex, latex-microsilica, magnesium oxide, calcium hydroxyapatite and fly ash) were considered. After aging under various conditions, porosity, permeability compressive and bond strength of the samples were measured to eliminate unfit formulations or adjust the ones that needed improvement. In addition, the changes occurring in the mineralogical composition of the sample were investigated using Fourier transform infrared spectroscopy (FTIR). Results indicated that hydroxyapatite and magnesium oxide containing cement are the most viable formulations that can withstand acid attack under HPHT conditions. Performance testing of these new formulations is in progress.

Laboratory investigations on sour gas corrosion of oil field tubulars require experimental setups that can reasonably simulate actual field conditions. To replicate these harsh well conditions, two new experimental setups were developed. They are used to study stress-cracking corrosion (SCC) and static and dynamic (SD) corrosion under HPHT conditions. Stress cracking setup has the capability to control pressures inside and outside of a test specimen (mini-pipe) while applying a constant tensile load on the specimen. Both inside and outside of the specimen can be exposed to harsh condition. Before and after the test, the elastic properties of the specimens are measured to quantify the level of brittleness after exposure to harsh sour environment. In addition, the specimens are examined using a microscope to identify crack development. The setup allows continuous measurement and recording of the test parameters to identify crack initiation time and condition.

The SD corrosion setup is equipped with a rotary system that has a magnetic coupling to transfer torque under HPHT conditions. The dynamic flow condition is established with the rotation of a cylinder inside a pressure vessel (autoclave) design and built for this particular setup. Corrosion coupons (specimen) are mounted on the inside of a sleeve (coupon holder). For testing, the sleeve with coupons is inserted into the vessel. Then, the rotating cylinder is place inside the sleeve for creating the dynamic flow condition.

The SCC and SD test setups are capable to perform experiments under HPHT conditions (10,000 psi and 400°F). At present, both setups are operational and preliminary tests are underway.

TABLE OF CONTENTS

EXECUTIVE SUMMARY 2
TABLE OF CONTENTS 4
LIST OF FIGURES 7
LIST OF TABLES 11
B1. Cement Additive Screening Study 12
B1.1 Objectives 12
B1.2 Scope and Methodology 12
B1.3 Literature Review 12
B1.3.1 Microsilica 13
B1.3.2 Latex 14
B1.3.3 Latex-Microsilica 14
B1.3.4 Magnesium Oxide 14
B1.3.5 Calcium Hydroxyapatite 15
B1.3.6 Dolomite 16
B1.3.7 Amine Based Sorbents 16
B1.3.8 Zinc Oxide 16
B1.3.9 Fly Ash 16
B1.4 Initial Screening Study 17
B1.4.1 Methods Used 17
B1.4.2 Results 18
B1.4.2.1 Microsilica 18
B1.4.2.2 Latex 21
B1.4.2.3 Latex with Microsilica 23
B1.4.2.4 Magnesium Oxide 25
B1.4.2.5 Calcium Hydroxyapatite (HOAP) 28
B1.4.2.6 Zinc Oxide 30
B1.4.2.7 Fly Bsh 31
B1.5 Final Screening and Formulation Study 33
B1.5.1 Microsilica Cement 33
B1.5.1.1 Porosity and Permeability 34

B1.5.1.2 Compressive Strength 35
B1.5.1.3 Shear Bond Strength 36
B1.5.1.4 FTIR Analysis 37
B1.5.1.5 Summary 39
B1.5.2 Latex Cement 39
B1.5.2.1 Porosity and Permeability 40
B1.5.2.2 Degradation Depth 40
B1.5.2.3 Compressive Strength 41
B1.5.2.4 Shear Bond Strength 42
B1.5.2.5 FTIR Analysis 42
B1.5.2.6 Summary 43
B1.5.3 Latex-Microsilica Cement 43
B1.5.3.1 Porosity and Permeability 44
B1.5.3.2 Compressive Strength 45
B1.5.3.3 Shear Bond Strength 46
B1.5.3.4 FTIR Analysis 46
B1.5.3.5 Summary 48
B1.5.4 Magnesium Oxide Cement 48
B1.5.4.1 Porosity and Permeability 49
B1.5.4.2 Compressive Strength 50
B1.5.4.3 Shear Bond Strength 51
B1.5.4.4 FTIR Analysis 52
B1.5.4.5 Summary 54
B1.5.5 Calcium Hydroxyapatite Cement 55
B1.5.5.1 Porosity and Permeability 55
B1.5.5.2 Compressive Strength 58
B1.5.5.3 Shear Bond Strength 58
B1.5.5.4 FTIR Analysis 59
B1.5.5.5 Summary 62
B1.5.6 Cement with Fly Ash 62
B1.5.6.1 Porosity and Permeability 63
B1.5.6.2 Compressive Strength 64

B1.5.6.3 Shear Bond Strength 64
B1.5.6.4 Summary 66
B1.5.7 Conclusions 66
B2. Development of Test Setups to Study Sour Gas Corrosion of Tubulars 68
B2.1 Stress Cracking Corrosion (SCC) Setup 69
B2.2 Stress Analysis in the Mini-Pipe 71
B2.3 SCC Test Procedure 71
B2.4 Static and Dynamic Corrosion Test Setup 73
B2.5 Static and Dynamic Corrosion Test Procedure 74
B2.6 Determination of Wall Shear Stress at the Coupon Surface 75
Nomenclatures 77
References 79

LIST OF FIGURES

Figure B.1: Rheological data of MS-10 and baseline slurries 20

Figure B.2: Porosity and permeability of unaged MS-10 and baseline samples 20

Figure B.3: Compressive and shear bond strengths of unaged MS-10 and baseline samples 21

Figure B.4: Porosity and permeability of unaged latex and baseline samples 22

Figure B.5: Compressive and bond strength measurements of unaged latex and baseline samples 22

Figure B.6: Rheological data of LTMS and baseline slurries 24

Figure B.7: Porosity and permeability of unaged LTMS and baseline cements 25

Figure B.8: Compressive and shear bond strengths of unaged LTMS and baseline cements 25

Figure B.9: Viscometeric readings of MGO-5 and baseline slurries 26

Figure B.10: Porosity and permeability of unaged MGO-5 and baseline samples 27

Figure B.11: Compressive and shear bond strengths of unaged MGO-5 and baseline samples 27

Figure B.12: Viscometeric readings of HOAP and baseline slurries 29

Figure B.13: Porosity and permeability of unaged HOAP and baseline samples 29

Figure B.14: Compressive and shear bond strengths of unaged HOAP and baseline samples 30

Figure B.15: Consistency of cement slurry containing ZnO 30

Figure B.16 Thickening time of fly ash and baseline cements 32

Figure B.17: Porosity and permeability of unaged fly ash and baseline samples 33

Figure B.18: Porosity of aged (orange) and unaged (blue) Class H based cores: a) HSMS; and b) HS 34

Figure B.19: Permeability of aged (orange) and unaged (blue) Class H based cores: a) HSMS; and b) HS 34

Figure B.20: Porosity of aged (orange) and unaged (blue) Class G based cores: a) GSMS; and b) GS 35

Figure B.21: Permeability of aged (orange) and unaged (blue) Class G based cores: a) GSMS; and b) GS 35

Figure B.22: Compressive strength of aged (orange) and unaged (blue) Class H based cores: a) HSMS; and b) HS 36

Figure B.23: Compressive strength of aged (orange) and unaged (blue) Class G based cores: a) GSMS; and b) GS 36

Figure B.24: SBS of aged (orange) and unaged (blue) Class H based cores: a) HSMS; and b) HS 37

Figure B.25: Schematic of a cylindrical samples and zones selected in the cross section 37

Figure B.26: FTIR results of inner zones of HSMS and HS samples aged at different conditions: a) Exp. 21; b) Exp. 25; and c) Exp. 26 38

Figure B.27: FTIR results of middle zones of HSMS and HS samples aged at different conditions: a) Exp. 21; b) Exp. 25; and c) Exp. 26 38

Figure B.28: FTIR results of middle zones of HSMS and HS samples aged at different conditions: a) Exp. 21; b) Exp. 25; and c) Exp. 26 39

Figure B.29: Porosity and permeability of latex and baseline cores (aged at 350°F with 40% CO_2) 40

Figure B.30: Middle cross sections of cores aged at 350°F with 40% CO2 gas: a) GSLT; b) HSLT; c) GS; and d) HS 41

Figure B.31: Compressive strength of baseline and latex-based cements aged at 350°F with 40% CO_2 ... 41

Figure B.32: Shear bond strength of latex and baseline cements aged at 350°F with 40% CO_2 42

Figure B.33: Summarized FTIR of latex and baseline cements: a) innermost; b) middle; and c) outermost zones 43

Figure B.34: Porosity of aged (orange) and unaged (blue) samples: a) HSLM; and b) HS 44

Figure B.35: Permeability of aged (orange) and unaged (blue) samples: a) HSLM; and b) HS 44

Figure B.36: Porosity of aged (orange) and unaged (blue) samples: a) GSLM; and b) GS 45

Figure B.37: Permeability of aged (orange) and unaged (blue) samples: a) GSLM; and b) GS 45

Figure B.38: Compressive strength of aged (orange) and unaged (blue) samples: a) HSLM; and b) HS 45

Figure B.39: Compressive strength of aged (orange) and unaged (blue) samples: a) GSLM; and b) GS 46

Figure B.40: Average shear bond strength of aged (orange) and unaged (blue) samples: a) HSLM; and b) HS 46

Figure B.41: FTIR results of inner zones of LTMS and baseline HS samples aged at different conditions: a) Exp. 24; b) Exp. 27; and c) Exp. 28 47

Figure B.42: FTIR results (middle zone) of LTMS and baseline HS samples aged at different conditions: a) Exp. 24; b) Exp. 27; and c) Exp. 28 47

Figure B.43: FTIR results (outer zone) of LTMS and baseline HS samples aged at different conditions: a) Exp. 24; b) Exp. 27; and c) Exp. 28 48

Figure B.44: Porosity of aged (orange) and unaged (blue) samples: a) HSMG; and b) HS 49

Figure B.45: Permeability of aged (orange) and unaged (blue) samples: a) HSMG; and b) HS 49

Figure B.46: Porosity of aged (orange) and unaged (blue) samples: a) GSMG; and b) GS 50

Figure B.47: Permeability of aged (orange) and unaged (blue) samples: a) GSMG; and b) GS 50

Figure B.48: Compressive strength of aged (orange) and unaged (blue) samples: a) HSMG; and b) HS ... 51

Figure B.49: Compressive strength of aged (orange) and unaged (blue) samples: a) GSMG; and b) GS ... 51

Figure B.50: Average shear bond strength of aged and unaged samples: a) HSMG; and b) HS..... 52

Figure B.51: FTIR results of inner zone of MGO-5 and baseline HS samples aged at different conditions: a) Exp. 8; b) Exp. 10; c) Exp. 7A; d) Exp. 14; e) Exp. 20; and f) Exp. 22 53

Figure B.52: FTIR results of middle zone of MgO and baseline HS samples aged at different conditions: a) Exp. 8; b) Exp. 10; c) Exp. 7A; d) Exp. 14; e) Exp. 20; and f) Exp. 22 54

Figure B.53: FTIR results of outer zone of MgO and baseline HS samples aged at different conditions: a) Exp. 8; b) Exp. 10; c) Exp. 7A; d) Exp. 14; e) Exp. 20; and f) Exp. 22 54

Figure B.54: Porosity of aged (orange) and unaged (blue) samples: a) HHO; and b) HS 56

Figure B.55: Permeability of aged (orange) and unaged (blue) samples: a) HHO; and b) HS..... 56

Figure B.56: Porosity of aged (orange) and unaged (blue) samples: a) GHO; and b) GS 57

Figure B.57: Permeability of aged (orange) and unaged (blue) samples: a) GHO; and b) GS..... 57

Figure B.58: Average compressive strength of aged and unaged samples: a) HHO; and b) HS 58

Figure B.59: Compressive strength of aged (orange) and unaged (blue) samples: a) GHO; and b) GS..... 58

Figure B.60: Shear bond strength of aged (orange) and unaged (blue) samples: a) HHO; and b) HS 59

Figure B.61: FTIR results in inner zone of HOAP and baseline HS samples aged at different conditions: a) Exp. 9; b) Exp. 12; c) Exp. 13; d) Exp. 15; e) Exp. 19; f) Exp. 23; and g) Exp. 29 60

Figure B.62: FTIR results (middle zone) of HOAP and baseline HS samples aged at different conditions: a) Exp. 9; b) Exp. 12; c) Exp. 13; d) Exp. 15; e) Exp. 19; f) Exp. 23; and g) Exp. 29 61

Figure B.63: FTIR results (outer zone) of HOAP and baseline HS samples aged at different conditions: a) Exp. 9; b) Exp. 12; c) Exp. 13; d) Exp. 15; e) Exp. 19; f) Exp. 23; and g) Exp. 29 62

Figure B.64: Porosity and permeability of cement cores aged at 350°F (Experiment 4, Batch 005)..... 63

Figure B.65: Compressive strength of unaged and aged baseline and fly ash cement cores aged at 350ºF 64

(Experiment 4, Batch 5) 64
Figure B.66: Shear bond strengths of samples before and after 6 days of aging (Experiment # 3) 65
Figure B.67: Class H cement after 6 days aging (Experiments # 3): a) with fly ash; and b) without fly ash 65
Figure B.69: Schematics of cement degradation and tubular corrosion facilities 68
Figure B.70: Corrosion test setup 69
Figure B.71: Schematic of tubular corrosion test facility 69
Figure B.72: Design of SCC cell 70
Figure B.73: Assembly of SCC cell with heating jacket and hydraulic cylinder 70
Figure B.74: Control volume for mini-pipe, adapter and pulling rod assembly 71
Figure B.76; Teflon coated specimen holder (sleeve) 74
Figure B.77 Coupon used for static and dynamic corrosion test 74
Figure B.78: Base of the specimen holder 75
Figure B.79 Rotating cylinder 75
Figure B.80 Flow between parallel plates 76

LIST OF TABLES

Table B.1: Potential cement additives considered in the literature survey 13

Table B.2: Compositions of microsilica based slurries (MS-10) 19

Table B.3: Properties of MS-10 and baseline slurries 19

Table B.4: Summary of latex cement slurry testing results (Reports 17 to 24) 22

Table B.5: Composition of latex slurry 23

Table B.6: Compositions of LTMS slurries 23

Table B.7: Properties of LTMS slurries 24

Table B.8: Formulations of MgO based cement (MGO-5) slurries 26

Table B.9: Properties of MGO-5 and baseline cement slurries 26

Table B.10: Formulations of HOAP based cement slurries 28

Table B.11: Properties of HOAP and baseline slurries 28

Table B.12: Formulation of Class H cement with fly ash (HSF) 31

Table B.13: Formulation of Class G cement with fly ash (GSF) 31

Table B.14: Porosity and permeability of fly ash and baseline samples 32

Table B.15: Aging conditions for MS-10 samples 33

Table B.16: Degradation depth of baseline and latex-based cements 41

Table B.17: Aging conditions for LTMS samples 43

Table B.18: Aging conditions for MGO samples 48

Table B.19: Aging conditions for HOAP samples 55

Table B.20; Test parameters for aging experiments 63

B1. Cement Additive Screening Study

B1.1 Objectives

A number of earlier cement degradation studies (Moroni et al. 2008; Moroni et al. 2009a, 2009b; Brandl et al. 2010) indicated that systematically designed cement formulations can resist sour gas attack under HPHT conditions. In this part of the project, focus has been given on testing and evaluation of different cement formulations that have potential for HPHT well applications. The principal objective of cement additive screening study is to develop new acid resistant cement formulations.

B1.2 Scope and Methodology

The goal of the additive screening study has been accomplished through a systematic literature survey, consultation with Technical Advisory Board (TAB) members, theoretical analysis, and testing of different cement formulations that contain various special cement additives. As stated in the objective, the effects of various additives on acid resistance of oil well cements (Class H and Class G) were tested. In order to select effective additives, potential cement additives were grouped into two categories (Category 1 and Category 2) based on the mechanism in which they improve the degradation resistance of the base cement.

> **Category 1:** These additives can react chemically with the acid and reduce the acid concentration in the pore. The additives behave as sacrificial elements to the cement. Moreover, the product formed by some reactive additives may reduce the porosity and permeability of the set cement.
>
> **Category 2:** These types of additives decrease initial porosity and permeability of the set cement; consequently, they reduce the penetration of carbonic acid by limiting the diffusion of ions in the cement.

The above approaches helped to develop six new cement formulations, which were finally tested by aging the hardened cement samples under HPHT acidic environment. In every aging experiment, baseline and special additive containing samples were exposed to similar aging conditions. After aging, their physical properties such as compressive strength, porosity, permeability and shear bond strength were measured. Various experiments were performed at different aging conditions. The samples were aged for 2 weeks. They were immersed in 2% brine solution saturated with sour gas (Methane, CO_2 and H_2S). Tests were performed varying temperature (100 to 430°F), pressure (3000 to 9000 psi) and CO_2 concentration (0 to 100%). Sample preparation, aging test and cement property measurement procedures were properly recorded and maintained the same to obtain consistent data.

B1.3 Literature Review

An extensive literature survey was conducted in order to develop methods to reduce cement degradation during acid attack through addition of special additives that can hinder the physiochemical

processes involved in the degradation process. Several additives that are compatible with Portland cement were studied for their influence on the degradation process under HPHT conditions. A summary of the cement additive considered in the investigation is presented in **Table B.1**.

Table B.1: Potential cement additives considered in the literature survey

Additive	Property	Studies	Its Effects on cement
Microsilica	Ultrafine pozzolanic substance which can fill up the pore space	Group 1	The micro-silica has been widely studied due to its pozzolanic reaction with CH group, it has the potential to protect the cement against carbonation.
Latex	Reduces the porosity and permeability of the set cement.	Group 2	It improves expansion tendency of the cement.
MgO and/ or Cao	Act as expanding additives	Group 3	Improve sealing performance. They are effective up to 392°F. The optimum concentration is 3-5%.
Calcium Hydroxyapatite or $Ca_5(OH)(PO_4)_3$	Incorporates CO_2 without altering the structure	Group 4	The addition of calcium hydroxyapatite can improve strength of the cement and CO_2 absorbing property.
Dolomite or $MgCO_3$	Thermally decomposes into $CaCO_3$ and MgO in the presence of CO_2.	Group 5	It helps in improving cement strength and reducing its porosity and permeability. However, with time it can cause cracking problems.
Amine Based Sorbent	$2RNH_2 + CO_2 + H_2O \leftrightarrow (RHN_3)_2CO_3$	Group 6	It is used as a sorbent for H_2S and CO_2 in oil refineries.
Zinc Oxide, ZnO	Cement retarder	Group 7	Reacts with H_2S
Fly ash	Cement filler	Group 8	Reduces portlandite and C-S-H contents of the cement

Group 1: Daou and Piot (2009); Grabowski and Gillott (1989); Sasaki et al. (1985); Shadizadeh et al. (2010); Shahriar (2011); Eilers and Root (1976); Eilers et al. (1983); Santra et al. (2009); Mueller and Dillinbeck (1991); Dillinbeck et al. (1990);
Group 2: Abdul Rahman et al. (1997); Jones and Carpenter (1991); Fuquan et al. (2006); Ray and Gupta (1994); Hou et al. (2010);
Group 3: Rubiandini et al. (2005); Zhang et al. (2011 and 2012); Nokken (2010); Ali and Mullick (1998); Ghofrani and Plack (1993); Agzamov et al. (2012), Buntoro and Rubiandini (2001); Cheung (1999); Mehta and Monteiro (2006);
Group 4: Sugama et al. (2006); Teraoka et al. (1998); Sugama and Carciello (1992 and 1993); Martin and Brown (1995);
Group 5: Hashimoto et al. (1980);
Group 6: Strazisar et al. (2001);
Group 7: Lecolier et al. (2008); and
Group 8: Santra et al., 2009.

The additives presented in Table B.1 were selected for further consideration based on their special properties in reducing acid attack as outlined here.

B1.3.1 Microsilica

Microsilica is a pozzolanic and non-crystalline material that has extremely fine particle size (less than 1 micron). Its chemical composition is similar to silica flour (SiO_2); however, it has smaller particle size than silica flour. Being a pozzolanic material, it has limited cementitious property unless mixed with water in presence of calcium hydroxide. Because of its fine particle size and large surface area, extra water for hydration is required. The addition of microsilica to Portland cements has been previously

studied (Eilers and Root 1976; Dillinbeck III et al. 1990; Eilers et al. 1983; Grabowski and Gillott 1989; Mueller and Dillinbeck 1991). Although it is able to fulfill the silica content requirement, the integrity and strength of the cement is a major issue in acidic environment. The studies revealed that microsilica can prevent carbonation of cement by reacting chemically in the system as well as reducing the initial porosity and permeability. Hence, microsilica has been included in the initial screening study.

B1.3.2 Latex

Latexes used as cement additives are colloidal solutions usually consisting of 50% by weight of small - spherical particles of polymer (0.01 to 1 μm) and 50% water. In order to obtain a stable colloidal mix, surface acting agents are added, which may lead to entrapment of air. Anti-foaming agents are usually added to the commercial latex to avoid this problem. The use of latex in well cements has been studied (Abdul-Rahman and Chong 1997; Fuquan et al. 2006; Hou et al. 2010; Zeng et al. 2012; Reddy et al. 2010; Jones and Carpenter 1991; Pavlock et al. 2012; Jennings et al. 2003) since early 90's. The prime advantage identified with the additive is that it controls the fluid loss from the cement and prevents gas seepage. The studies suggested the use of latex in closely spaced reservoirs to prevent gas seepage between various zones (Jones and Carpenter 1991).

Among various kinds of latex available in the market, styrene butadiene is the most common latex used for construction and well cementing applications. It can be either anionic or neutral depending on the type of surfactant used. The latex is known to be highly sensitive towards temperature and mechanical effects (Abdul-Rahman and Chong 1997). With temperatures above 212°F, it is possible for the latex to flocculate and settle down (Fuquan et al. 2006). This limits the addition of latex in the oil well cement as an additive. By introducing a strong hydrophilic carboxyl ion (such as acetic acid, citric acid) the flocculation can be reduced inducing chemical stability (Hou et al. 2010). The mechanical stability needs to be taken care with respect to the mixing procedure. Large shear rates may lead to damage of the polymer and may cause entrapment of air bubbles. Due to its ability to prevent gas seepage and minimize fluid invasion, the latex cement has been selected for the initial screening study.

B1.3.3 Latex-Microsilica

Another technique to utilize latex is to use it with microsilica. Although it has not been proposed for use in well cement, extensive studies (Rossignolo et al. 2003, Rossignolo and Agnesini 2002 and 2004, Rossignolo 2009), which were conducted on latex-microsilica, recommended it for construction purpose. Wan (2011) noted the use of latex and microsilica together in order to obtain a stronger matrix. Because of its ability to reduce gas migration and provide better cement bond, latex-microsilica cement formulation has been considered for the initial screening study.

B1.3.4 Magnesium Oxide

Magnesium oxide is an expanding cement additive. Its expanding property has been studied (Zhang et al. 2012 and 2011; Nokken 2010; Ali and Mullick 1998; Ghofrani and Plack 1993; Agzamov et al. 2013;

Rubiandini et al. 2005; Buntoro and Rubiandini 2001; Cheung 1999) extensively. As reported by Rubiandini et al. (2005), the use of magnesium oxide as an expanding additive in cement was proposed by Danjuschewskij (1983).

Magnesium oxide is industrially produced by calcining dolomite ($CaMg(CO_3)_2$). The temperature at which the calcination is performed defines the reactivity of magnesium oxide formed. Calcination above 1652°F tends to lower the reactivity and causes MgO to hydrate very slowly. MgO calcined at temperatures below 1652°F hydrate faster, causing expansion of cement in early stages. The calcination temperature for the magnesium oxide used in this investigation is approximately 2282°F.

The hydration of MgO basically involves formation of $Mg(OH)_2$ crystals, which occupy the pore space and provide swelling of the cement matrix (Rubiandini et al. 2005). Swelling or expansion is required to take place at the precise point of time during setting of the cement in the well and reduce its porosity and permeability. Expansion that occurs in the liquid slurry phase does affect the cement properties. Expansion after the complete setting causes cracking of the cement, which is highly undesirable. Hence, expansion needs to occur during the gelling or setting phase of the cement so that the porous space of the cement is effectively reduced (Ghofrani and Plack 1993).

Experimental results (Rubiandini et al. 2005) showed the expansion property of MgO and compressive and shear bond strength improvements obtained after its addition. The additives showed more expansion with increased calcination temperature. It was also observed that 3 – 5% bwoc MgO content was optimal to provide high compressive and shear bond strengths at temperatures above 482°F (Buntoro and Rubiandini 2001). Ghofrani and Plack (1993) also observed similar results with MgO when subjected to hydration.

Extensively documented properties of MgO are: i) the formation of $Mg(OH)_2$ crystals; ii) swelling of cement that helps in reducing porosity and permeability; and iii) improvement in compressive and shear bond strengths. Although $Mg(OH)_2$ undergoes carbonation to form $MgCO_3$, these crystals are insoluble in water. Hence, they do not easily leach out like calcium bicarbonate (Cheremisinoff 1995). These properties made MgO a suitable cement additive for HPHT applications. Despite a number of studies have been conducted on magnesium oxide, the full extent of its benefit is not well realized. This is because the level of expansion is highly dependent on number of factors including temperature, pressure, composition and properties of surrounding fluid, and composition of the cement sample. Hence, magnesium oxide, with calcination temperature of 2282°F, has been considered in initial screening study.

B1.3.5 Calcium Hydroxyapatite

Calcium hydroxyapatite (aka hydroxyapatite) is a natural occurring mineral form of calcium apatite. The human bone structure is 50% composed of hydroxyapatite and it is often used for dental and orthopedic prostheses because of its biocompatibility (Teraoka et al. 1998). The use of hydroxyapatite-based cements in oil well was brought forward by the work performed at Brookhaven National Laboratory (Sugama 2006) through their CAP (calcium aluminate phosphate) cement project.

Limited studies were conducted to evaluate the performance of hydroxyapatite as a cement additive. It has been observed that after acid attack, the strength of hydroxyapatite-based (HOAP) cement reduces (Sugama and Carciello 1992, 1993; Martin and Brown 1995). Further, investigation is needed to study the performance of this additive. Hence, hydroxyapatite has been selected as potential additives in initial screen study.

B1.3.6 Dolomite

Dolomite has the property to thermally decompose into $CaCO_3$ and MgO crystals when it is in contact with carbonic acid. Such reaction towards carbonic acid can help in protecting the cement against the acid attack. However, MgO and $CaCO_3$ crystals continue to grow with the reaction (Hashimoto et al. 1980). The growth of crystals results in cement expansion and cracks leading to a serious acid attack. Therefore, dolomite has not been considered in the initial screening study.

B1.3.7 Amine Based Sorbents

Amine-based sorbents such as monoethanolamine (MEA), diethanolamine (DEA), methyldiethanolamine (MDEA), diisopropanolamine (DIPA) are used in refineries as sorbents to sweeten sour gases, (i.e. absorb CO_2 and H_2S). However, the procedure requires the sorbent in liquid form, and it is performed under highly controlled conditions in the refinery towers. Such level of precision is difficult to achieve under downhole conditions. Consequently, even though amine-based sorbents have capability to react with H_2S and CO_2, they might be difficult to incorporate in the well cements as additive and hence they have not been considered for the initial screening study.

B1.3.8 Zinc Oxide

Sasaoka et al. (1994) conducted an experimental study on the reaction between ZnO and H_2S under various conditions. The paper focused on use of ZnO as a sorbent for H_2S in solid state fuel cells. One of the objectives was to examine the reaction in presence of water or carbon dioxide. In absence of water or carbon dioxide, formation of elemental sulfur was observed, which confirmed the catalytic decomposition of H_2S in presence of the sorbent ZnO. With inclusion of water in the system, the formation of elemental-sulfur was reduced. This was explained using two possible reasons. First, the active elemental-sulfur is reacting with water to form H_2S. Second, as water is a similar molecule to H_2S, a competitive adsorption of water could inhibit the reaction with H_2S. Hence, zinc oxide has been selected for the initial screening study.

B1.3.9 Fly Ash

Incorporating pozzolanic fillers such as fly ash effectively decreases portlandite and C-S-H contents of cement thereby reducing the potential for the formation of calcium carbonate, which further reacts with the acid to form water soluble calcium bicarbonate that can be easily leached out. To study the effects of filler materials on the carbonation process, Santra et al. (2009) conducted experiments with samples-containing different quantities of silica and fly ash. After aging for 15 days at 2000 psi and 200ºF in the

presence of fresh water saturated with CO_2, the samples were cut in half to examine visually the degree of penetration. The penetration depth was determined by examining different colors formed on carbonated and uncarbonated portions of the sample when phenolphthalein indicator was applied. The results showed that the addition of fly ash did improve the resistance of the cement against acid attack as reported by earlier studies (Garev et al. 2007 and Black et al. 2007). Due to these conflicting results, fly ash has been considered for the initial screening study.

B1.4 Initial Screening Study

Additive containing cement (additive cement) samples were rigorously tested before they were kept in the aging cell. Performance evaluation method was established for selecting additive cement formulations that meet basic characteristics of conventional oil well cement (baseline cement) in unaged condition.

B1.4.1 Methods Used

In order to conduct the additive screening study, initial cement formulations were developed for each selected additives. The formulations were based on the findings of literature review, inputs from TAB members, and studying the behavior of the additives. Subsequently, physical properties of the formulated slurries were measured and compared with those of the baseline cement slurries. The following pre-aging tests were performed to select suitable additives:

I. Slurry Properties

Slurry Density: Applying ideal mixing rules, the theoretical density of the additive cement slurry was determined based on its formulation. The density of the slurry was adjusted to be in the range of that of the baseline slurry by slightly modifying its formulation. The actual density of the slurry was measured immediately after its preparation. Conventional oil field mud balance was used to measured slurry density.

Slurry Viscosity: Rheological properties of the slurries were measured and compared with that of baseline cement slurry. Standard oil field viscometer (OFITE Model 900 Viscometer) was used to measure slurry viscosity. The viscosity measurements were taken immediately after the slurry was prepared.

Filtration Loss: The filtration loss of cement slurry was tested using a standard filter press. The test was performed using freshly prepared slurry. Measurements of the additive cement slurry were compared with that of the baseline.

Slurry Consistency: The thickening time of the slurry was measured with the consist-o-meter and compared with that of the baseline cement slurry. A very long or short thickening time was compensated with use of accelerators or retarders. The consist-o-meter test was conducted immediately after the slurry was prepared.

II. Hardened Cement Properties

Additive slurries that provided acceptable density, viscosity, fluid loss and consistency were further investigated for their suitability. Additive slurries were prepared and cured with baseline cement slurries. After preparation, the slurries were poured into rubber molds, immersed into 2% brine (NaCl) solution and placed in an oven for 5 days. Oven temperature was maintained at 200°F. In addition, parts of the slurries were poured into one-end plugged steel pipes to prepare shear bond strength (SBS) samples. SBS samples were also immersed in brine and cured in the oven together with other samples. After curing, hardened slurry samples were taken out of the rubber molds and 1-inch diameter cores were cut from the hardened cement. Subsequently, the following tests were performed to check if the additive cement meets the required physical properties.

Visual Test: After curing and coring, the cement cores and SBS samples were examined for any irregularity such as micro cracks or other types of physical damages.

Compressive Strength: Confined compressive strength of the cores were measured and compared with that of the baseline cement. Cores with compressive strength similar or better than the unaged conventional cement were selected for further testing. The confined compressive strengths of the cement samples were measured using a special setup developed in this project (Report # 11). The confining pressure was 1000 psi for all the tests. The tests were conducted as per the ASTM-C39/C39M-12 standard.

Shear Bonding: Selected samples were able to show shear bond strength (SBS), which was comparable with that of the unaged conventional cements. SBS of the samples were measured using a setup developed during the investigation (Report # 11). The contact length of the cement column with the pipe wall was measured to compute the bond area between cement and the pipe. During the test, a hydraulic piston was used to push the cement from the bottom side to break the bond. The shear bond strength of the cement was determined using the contact surface area and the pressure required to break the bond.

Porosity and Permeability: Porosity and permeability of the samples were measured using an automated porosity and permeability testing device (Coretest Model AP-608). Confining pressure of 500 psi and differential pressure of 200 psi were used during the tests (Report # 6). The samples were dried for 24 hours in an oven at 100°F to avoid presence of any moisture in the pore spaces prior to the measurement. Helium gas was used as test fluid.

B1.4.2 Results

B1.4.2.1 Microsilica

Light microsilica with bulk density of 288 – 352 kg/m^3 and particle size of less than a micron was used as a cement additive. Several preliminary tests were performed using different cement formulations (Reports # 15 to 24) before the hardened slurry was tested. These tests were required to formulate the

slurry that has similar or comparable properties as the corresponding baseline cement slurries and hardened cores. The changes in the compositions were required to optimize the concentration of microsilica and secondary additives such as anhydrous citric acid, Sodium Poly-naphthalene Formaldehyde Sulfonate (NSF) and silica flour. The final microsilica based slurry formulations are presented in **Table B.2**.

Table B.2: Compositions of microsilica based slurries (MS-10)

Component	Class G	Class H
Water for cement	44% bwoc	38 % bwoc
Water for Silica Flour	38.5% bwoc	38.5% bwoc
Anti-Foaming Agent	0.1 gal/sk of cement	0.1 gal/sk of cement
Citric Acid	0.02% bwoc	0% bwoc
NSF	1.25% bwoc	1.25% bwoc
HEC	0.1% of water for Silica	0.1% of water for Silica
Cement	100% bwoc	100% bwoc
Silica Flour	25% bwoc	25% bwoc
Microsilica	10% bwoc	10% bwoc

Slurry properties obtained as per the procedure presented in Section B1.4.1 are shown in **Table B.3.** Properties of MS-10 and baseline slurries were comparable. It is important to note that microsilica based slurry formulations were mixed for 2 minutes at 12000 RPM, whereas the baseline cement formulations were prepared according to the API standard (mixing the slurry at 4,000 RPM for 15 seconds, followed by a 35-second mixing at 12,000 RPM). The special mixing procedure for microsilica based slurry was suggested by Grabowski and Gillott (1989) to ensure homogenous mixing and consistent slurry properties.

Table B.3: Properties of MS-10 and baseline slurries

Property	HSMS	HS	GSMS	GS
Theoretical Density	16.01 ppg	15.96 ppg	15.55 ppg	15.51 ppg
Measured Density	16.20 ppg	16.20 ppg	15.50 ppg	15.45 ppg
Filtration Loss at 7.5 min.	44 ml	50 ml	54 ml	60 ml
Rheological Properties	Bingham PV = 33.52 cP YP = 8.7 lbf/100ft^2	Power Law n = 0.44 K = 14.4 lbf.s$^{0.44}$/100ft^2	Bingham PV = 23.94 cP YP = 9.57 lbf/100ft^2	Power Law n = 0.35 K = 10.5 lbf.s$^{0.35}$/100ft^2
Thickening Time	220 min.	170 min.	145 min.	135 min.

Figure B.1 shows viscometer measurements of MS-10 and baseline slurries. The dial readings of microsilica slurries were less than that of the baseline slurries, which means that microsilica slurries

were less viscous. As a result, they are expected to have better flowability, which is the basic requirement for cement slurry.

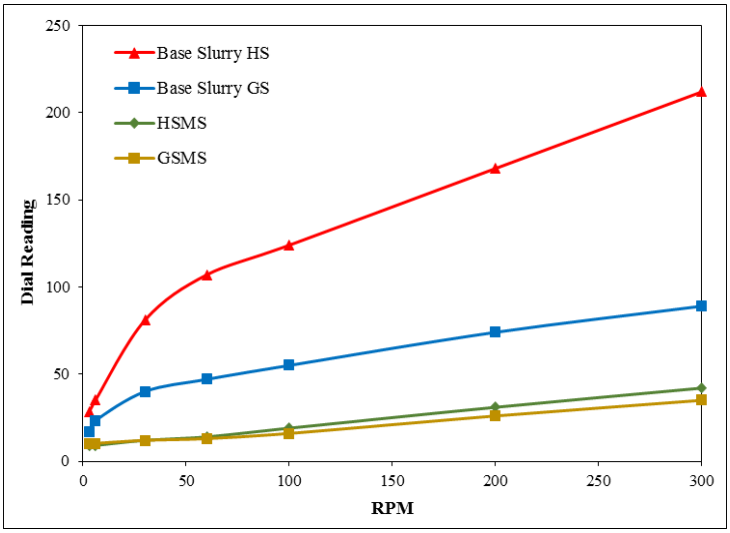

Figure B.1: Rheological data of MS-10 and baseline slurries

After hardening, the slurry samples were cored and cement properties such as porosity, permeability, and compressive and shear bond strengths were measured. The unaged porosity and permeability of MS-10 samples were significantly less than that of the baseline samples (**Fig. B.2**). The values presented in the figure are average values obtained from four samples. The smaller particle size of microsilica was able to fill up the pore space in the matrix and reduce the pore volume as anticipated. The low porosity and permeability is beneficial in reducing the penetration of the acidic in the matrix.

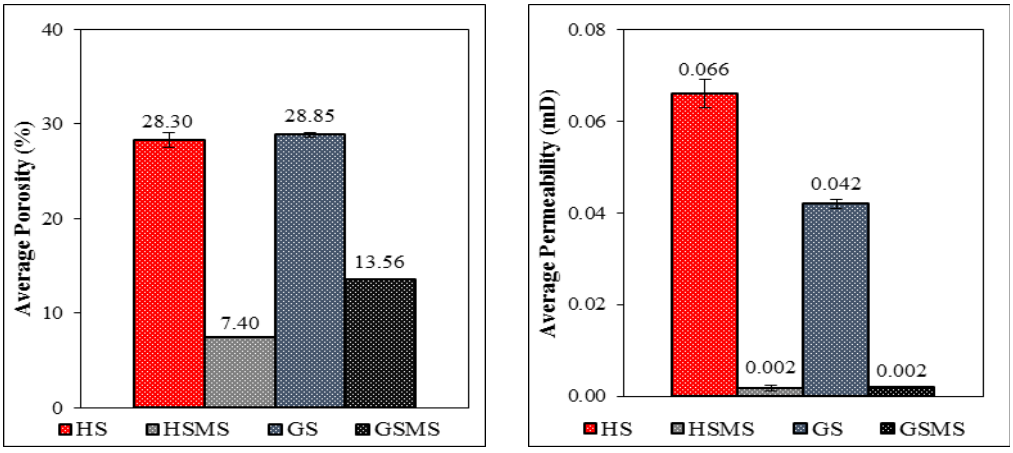

(a) Porosity **(b) Permeability**

Figure B.2: Porosity and permeability of unaged MS-10 and baseline samples

The average compressive and shear bond strengths of MS-10 samples (**Fig. B.3**) were slightly higher than that of the baseline samples. This suggests that the matrix properties of the cement system

containing microsilica are better than those of the baseline samples. After obtaining encouraging results, microsilica samples were selected for further testing under HPHT acidic environment.

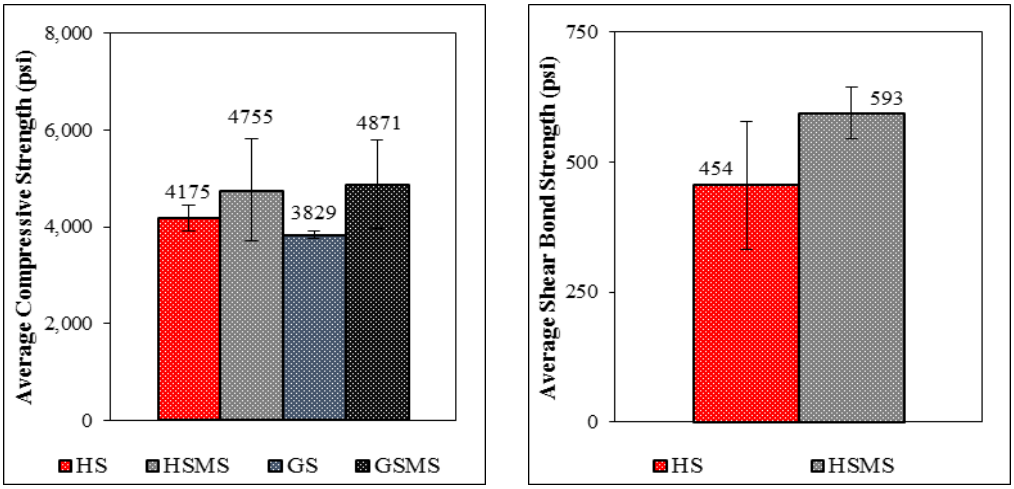

(a) Compressive strength **(b) Shear bond strength**

Figure B.3: Compressive and shear bond strengths of unaged MS-10 and baseline samples

B1.4.2.2 Latex

Latex based cement was selected as a candidate for preliminary screening study as per the literature review. For the testing, styrene butadiene latex (Styrofan 1186) was used as recommended by the Technical Advisory Board (TAB) members. The latex was in liquid form, containing approximately 50% active polymer components. In order to cure the slurry at 200° F, cationic agent was required to prevent thermal degradation and flocculation (Hou et al. 2010). For this purpose, concentrated acetic acid (0.43% bwoc) was added as recommended by Fuquan et al. (2006).

The latex based cement was prepared with latex concentration of 10% bwoc. This concentration has been recommended by previous studies (Hou et al. 2010). However, during slurry preparation, large amount of air bubbles were formed. The rheology and filtrate loss of latex slurry were found to be better than baseline slurry, even though the density of the slurry was substantially less than that of the baseline cement (Reports 17 to 24).

Consistent with the density reduction, porosity and permeability of unaged latex samples were more than those of baseline samples (**Fig. B.4**). In addition, latex samples exhibited higher compressive and shear bond strengths than the baseline samples (**Fig. B.5**). The entrapment of air in latex slurry can be the reasons behind the increase in porosity and reduction in compressive strength. Class G cement was more susceptible towards increase in the porosity. Several different formulations of latex based cement were prepared and tested yielding similar problem of high porosity and permeability. The outcomes of the tests are summarized in **Table B.4**. In reference to the list of solution methods presented in Table B.4, the last option was to use a filler material such as microsilica along with latex.

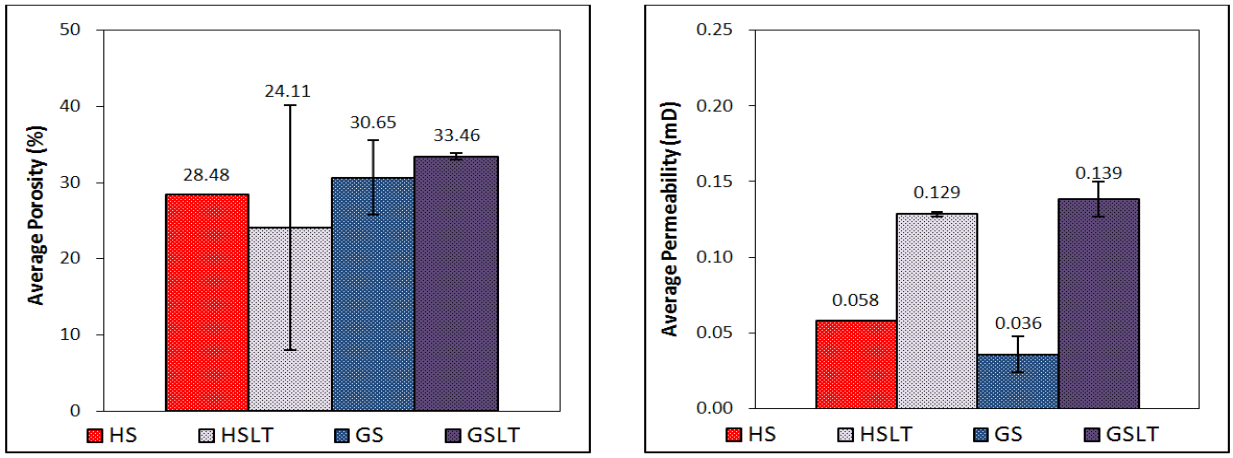

(a) (b)

Figure B.4: Porosity and permeability of unaged latex and baseline samples

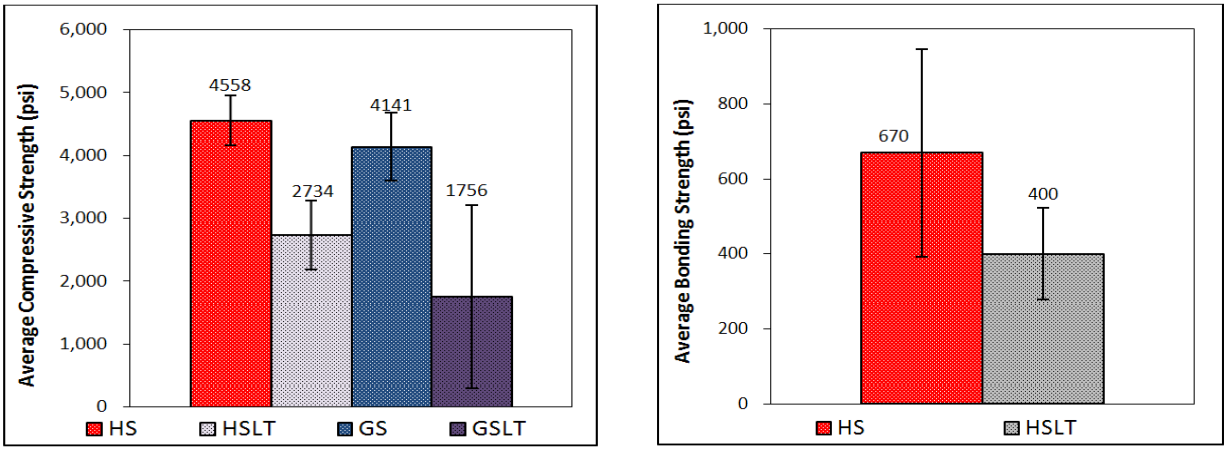

(a) (b)

Figure B.5: Compressive and bond strength measurements of unaged latex and baseline samples

Table B.4: Summary of latex cement slurry testing results (Reports 17 to 24)

Possible Reasons for Porosity Increased	Measures Taken	Remarks/Outcomes
Property of latex to entrap air	Reduce mixing speed	Not recommended by API
	Use larger amount of surfactant	Not highly effective as tests revealed
	Use pressurized curing	Not applicable for the current research as baseline slurries were cured at atmospheric pressure
Small particle size of latex, which is not able to bond with cement and hence creates gaps which may act as micro-cracks.	Improve bonding between latex and cement using a carboxylate – SBR latex	Tested for several compositions, carboxylate group results in thick slurry.
	Use filler material such as microsilica to fill in the pore space and cracks	LTMS slurry was tested. Its porosity was extremely low.

As it was observed in a number of unaged sample tests, the permeabilities of latex samples (HSLT and GSLT) were higher than those of baseline samples. The reason for increased permeability could be entrapment of air bubbles in the latex. The composition of the latex slurry is presented in **Table B.5**. Even though latex showed higher unaged core permeability than the baseline, other properties were comparable. As a result, it has been selected for further testing under HPHT acidic environment.

Table B.5: Composition of latex slurry

Component	Percentage Amount
Cement	100%
Silica Flour	35% bwoc
SBR Latex	10% bwoc
Acetic Acid (Emulsifier)	0.43% bwoc
HEC	0.1% of water for fillers
Antifoam Agent	0.1 gal/sack of cement
Water for Cement	38% bwoc – Class H
Water for Silica Flour	38.5% of silica flour
bwoc = by weight of cement	

B1.4.2.3 Latex with Microsilica

To prepare latex-microsilica based slurry, 10% latex and 10% microsilica were added to the baseline cement. This formulation was adopted from a similar study (Hou et al. 2010) conducted on latex cement. Several tests were performed with different LTMS slurry formulations to obtain optimized dispersant concentration to be used (Reports 23 and 24). The final compositions of the slurries are presented in **Table B.6**.

Table B.6: Compositions of LTMS slurries

Component	Class G	Class H
Water for cement	44% bwoc	38% bwoc
Water for Silica Flour	38.5% bwoc	38.5% bwoc
Anti-Foaming Agent	0.1 gal/sk of cement	0.1 gal/sk of cement
Citric Acid	0.02% bwoc	0.002% bwoc
NSF	0.75% bwoc	0.75% bwoc
HEC	0.1% of water for Silica	0.1% of water for Silica
Cement	100% bwoc	100% bwoc
Silica Flour	25% bwoc	25% bwoc
Micro-silica	10% bwoc	10% bwoc
SB Latex	10% bwoc	10% bwoc

As suggested by Allan (1997), latex was added in the cement system after the addition of all solids to minimize the entrapment of air. The LTMS slurry properties (**Table B.7**) were close to that of the baseline slurry. The density of Class H based LTMS slurry was slightly (about 1 ppg) less than that of baseline Class H. Filtration loss and thickening time were in acceptable range.

Table B.7: Properties of LTMS slurries

Property	HSLM	HS	GSLM	GS
Theoretical Density	15.38 ppg	15.96 ppg	14.99 ppg	15.51 ppg
Measured Density	15.30 ppg	16.20 ppg	14.80 ppg	15.45 ppg
Filtration Loss at 7.5 min.	27 ml	50 ml	30 ml	60 ml
Rheological Properties	Bingham PV = 28.73 cP YP = 5.39 lbf/100ft^2	Power Law n = 0.44 K = 14.4 lbf.s$^{0.44}$/100ft^2	Bingham PV = 23.94 cP YP = 7.07 lbf/100ft^2	Power Law n = 0.35 K = 10.5 lbf.s$^{0.35}$/100ft^2
Thickening Time	230 min.	170 min.	160 min.	135 min.

Figure B.6 presents viscometeric readings of LTMS and baseline slurries. The additive slurries were less viscous than the baseline slurries. This means they are more flowable than the baseline. Porosities of unaged LTMS and baseline samples were similar (**Fig. B.7a**). However, the permeabilities of LTMS samples were significantly less than those of the baseline samples (**Fig. B.7b**).

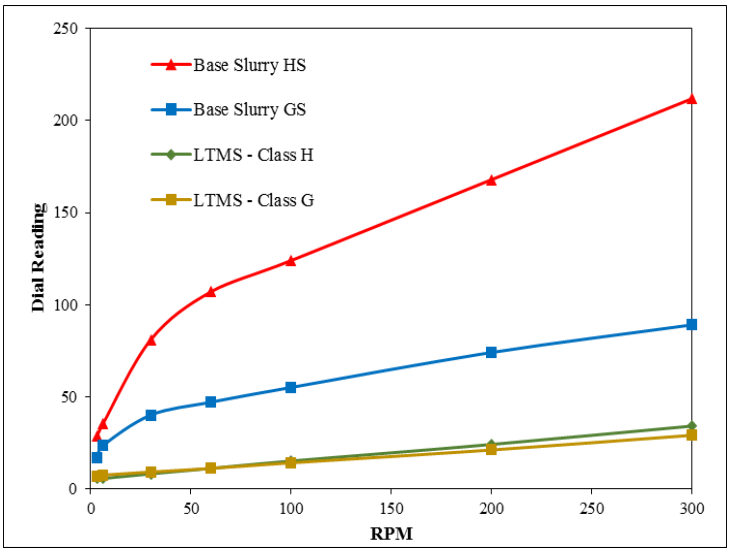

Figure B.6: Rheological data of LTMS and baseline slurries

Compressive strengths of HSLM samples were considerably less than that of the baseline samples. This observation was a major setback because the strength reduction could be due to entrapment of air in the system as observed in latex cement previously. Despite this, GSLM samples

exhibited almost comparable compressive strength. Moreover, the shear bond strengths of latex-microsilica samples were higher than that of the baseline samples (**Fig. B.8**).

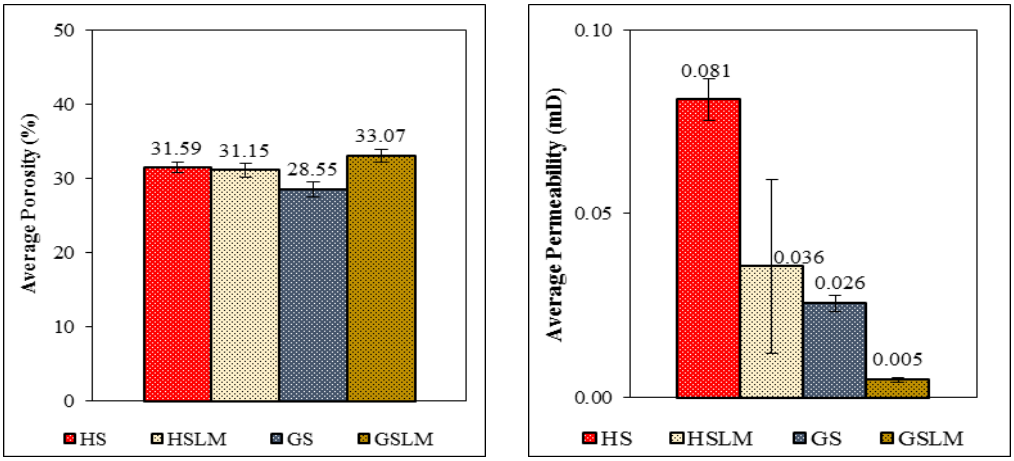

(a) Porosity **(b) Permeability**

Figure B.7: Porosity and permeability of unaged LTMS and baseline cements

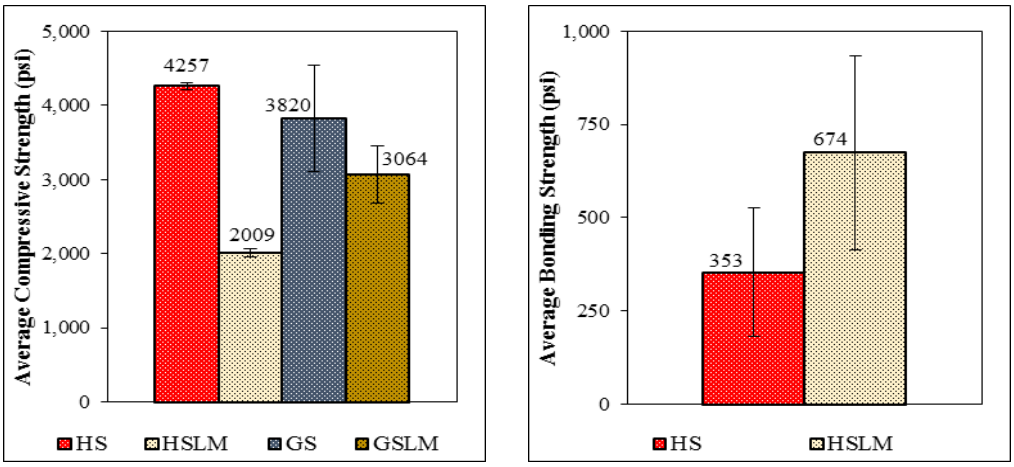

(a) Compressive strength **(b) Shear bond strength**

Figure B.8: Compressive and shear bond strengths of unaged LTMS and baseline cements

Although the results obtained from unaged samples were mixed (some show property improvements while other indicate poor performance), the LTMS slurry has been selected for final screening test. Hence, slurries and core samples were prepared and aged at three different conditions to evaluate their degradation behavior.

B1.4.2.4 Magnesium Oxide

Cement slurries containing magnesium oxide were also considered in the additive screening study. Slurry properties of Class H and Class G cements containing magnesium oxide (HSMG and GSMG) were investigated. Magnesium oxide was able to provide acceptable slurry with 5% BWOC as per the

recommendation of Rubiandini et al. (2005). **Table B.8** presents the compositions of magnesium oxide based cement slurries. Properties of the slurries were measured and found to be very similar to those of the baseline slurries (**Table B.9**).

Table B.8: Formulations of MgO based cement (MGO-5) slurries

Component	Class G	Class H
Water for cement	44% bwoc	38% bwoc
Water for Silica Flour	38.5% bwoc	38.5% bwoc
Anti-Foaming Agent	0.1 gal/sk of cement	0.1 gal/sk of cement
HEC	0.1% of water for Silica	0.1% of water for Silica
Cement	100% bwoc	100% bwoc
Silica Flour	35% bwoc	35% bwoc
MgO	5% bwoc	5% bwoc

Table B.9: Properties of MGO-5 and baseline cement slurries

Property	HSMG	HS	GSMG	GS
Theoretical Density	16.15 ppg	15.96 ppg	14.99 ppg	15.51 ppg
Measured Density	16.30 ppg	16.20 ppg	14.80 ppg	15.45 ppg
Filtration Loss at 7.5 min.	58 ml	50 ml	62 ml	60 ml
Rheological Properties	Power Law n = 0.52 K = 7.9 $lbf.s^{0.52}/100ft^2$	Power Law n = 0.44 K = 14.4 $lbf.s^{0.44}/100ft^2$	Power Law n = 0.40 K = 9.9 $lbf.s^{0.40}/100ft^2$	Power Law n = 0.35 K = 10.5 $lbf.s^{0.35}/100ft^2$
Thickening Time	160 min.	170 min.	130 min.	135 min.

Figure B.9 shows the viscometer readings of MGO and baseline slurries. For practical range of shear rate, the MgO slurries were less viscous than the baseline slurries. After testing the slurry properties, seven cement cores of GSMG and HSMG, and three bonding samples of HSMG were prepared and tested. The samples were cured for 5 days at 200ºF in 2% brine. The porosity and permeability measurements showed expected results (**Fig. B.10**). The permeability of MGO-5 (HSMG and GSMG) samples were significantly less than that of the baseline (HS and GS) cores due to MgO addition, which makes the cement matrix to expand and shrink the pores.

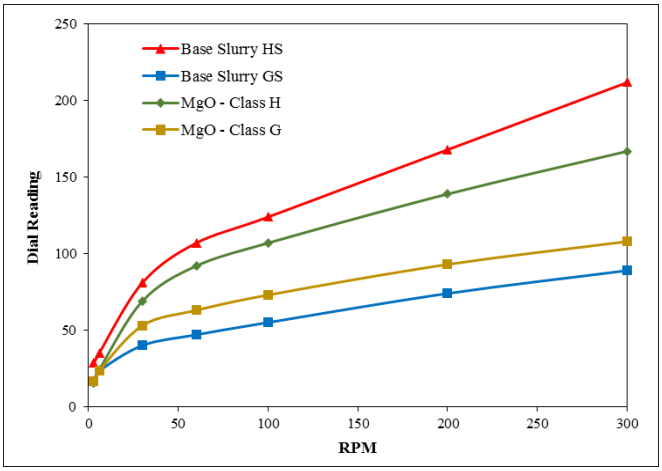

Figure B.9: Viscometeric readings of MGO-5 and baseline slurries

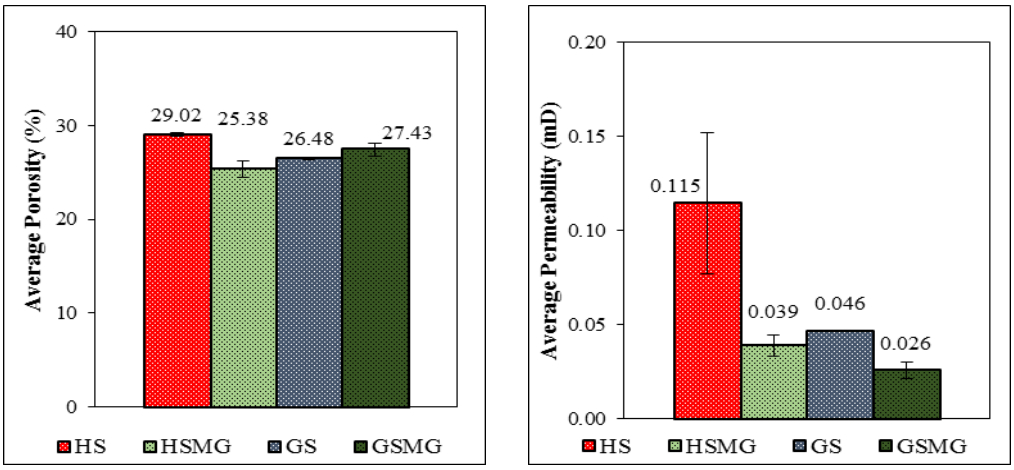

(a) Porosity **(b) Permeability**

Figure B.10: Porosity and permeability of unaged MGO-5 and baseline samples

In addition to their porosity and permeability, MGO-5 cores were tested for their compressive and bonding strengths. MGO-5 and baseline samples displayed very similar compressive and shear bond strengths. Increase in compressive and shear bond strengths of MGO-5 samples were anticipated; however, incomplete hydration of MgO to Mg(OH)2 crystals, due to curing at 200°F, resulted in properties that were similar to those of the baseline samples (**Fig. B.11**). Shear bond strength (Fig. B.11b) obtained for the HSMG samples were slightly lower than that of the baseline HS samples.

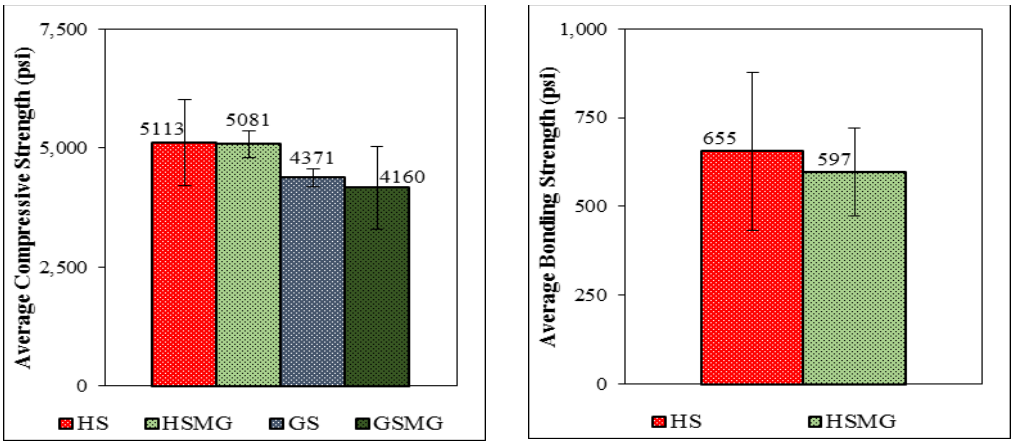

(a) Compressive strength **(b) Shear bond strength**

Figure B.11: Compressive and shear bond strengths of unaged MGO-5 and baseline samples

Extensive testing of slurry and core properties of the MGO-5 showed suitability of the slurry for the intended applications. MgO based cements were found to be acceptable (i.e. slurry properties within the range of baseline cement slurries); therefore, they have been selected for final screening study.

B1.4.2.5 Calcium Hydroxyapatite (HOAP)

Different concentrations (5%, 15% and 30%) of hydroxyapatite containing cement slurries were prepared and tested. It was observed that with addition of hydroxyethylcellulose (HEC) and silica flour, the slurries were very thick. HEC is added to reduce fluid loss. Based on the literature survey, HOAP is expected to reduce the filter loss by forming a structured matrix. Considering this hypothesis, addition of HEC was abandoned, even though present in very small quantities. Silica flour is added to the cement to prevent conversion of tobermorite (CSH) to α-CSH at higher temperature to avoid strength retrogression. Calcium hydroxyapatite based cements are resistant to high temperature and they do not require silica flour to prevent strength retrogression (Sugama 2006). This property of calcium hydroxyapatite was considered and the silica flour was excluded in the formulation of HOAP cement.

To test the hypothesis of not using HEC and silica flour on the matrix properties, it was essential to prepare the HOAP slurries. The water requirement for HOAP is 23% by weight of HOAP (Reddy et al. 2010). Even without HEC and silica flour, the slurries were still very thick. Hence, citric acid (0.125% bwoc) was added in order to disperse and retard the slurries (**Table B.10**). Then, the slurry properties were measured and found to be very similar to those of the baseline cement (**Table B.11**).

Table B.10: Formulations of HOAP based cement slurries

Component	**Class G**	**Class H**
Water for cement	44% bwoc	38% bwoc
Water for HOAP	23% by weight of HOAP	23% by weight of HOAP
Anti-Foaming Agent	0.1 gal/sk of cement	0.1 gal/sk of cement
Citric Acid	0.125% bwoc	0.125% bwoc
Cement	100% bwoc	100% bwoc
HOAP	5% bwoc	5% bwoc

Table B.11: Properties of HOAP and baseline slurries

Property	**HHO**	**HS**	**GHO**	**GS**
Theoretical Density	16.39 ppg	15.96 ppg	15.77 ppg	15.51 ppg
Measured Density	16.40 ppg	16.20 ppg	15.70 ppg	15.45 ppg
Filtration Loss at 7.5 min.	67 ml	50 ml	65 ml	60 ml
Rheological Properties	Power Law n = 0.31 K = 21.6 $lbf.s^{0.31}/100ft^2$	Power Law n = 0.44 K = 14.4 $lbf.s^{0.44}/100ft^2$	Power Law n = 0.34 K = 20.3 $lbf.s^{0.34}/100ft^2$	Power Law n = 0.35 K = 10.5 $lbf.s^{0.35}/100ft^2$
Thickening Time	165 min.	170 min.	130 min.	135 min.

Figure B.12 shows viscometeric readings of HOAP and baseline slurries. The readings of HOAP slurries were between those of baselines (Class H and Class G) slurries, which indicate acceptable fluidity.

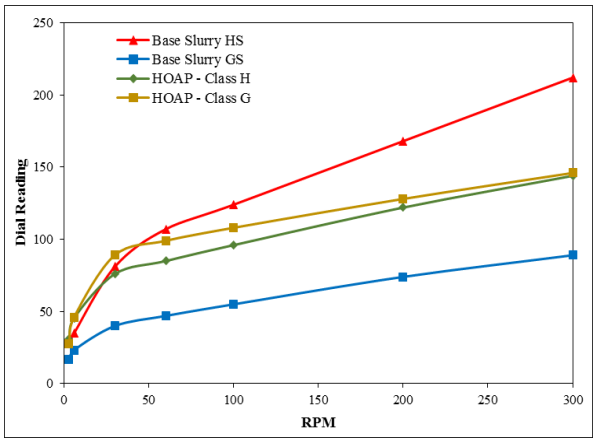

Figure B.12: Viscometeric readings of HOAP and baseline slurries

Based on these encouraging results, HOAP core were prepared and their properties were measured. Porosities of unaged HOAP cores were almost similar to those of the baseline samples; however, their permeabilities were lower than those of the corresponding baseline samples (**Fig. B.13**). Reduction in permeability due to the addition of calcium hydroxyapatite may help in limiting the extent of acid penetration under downhole conditions.

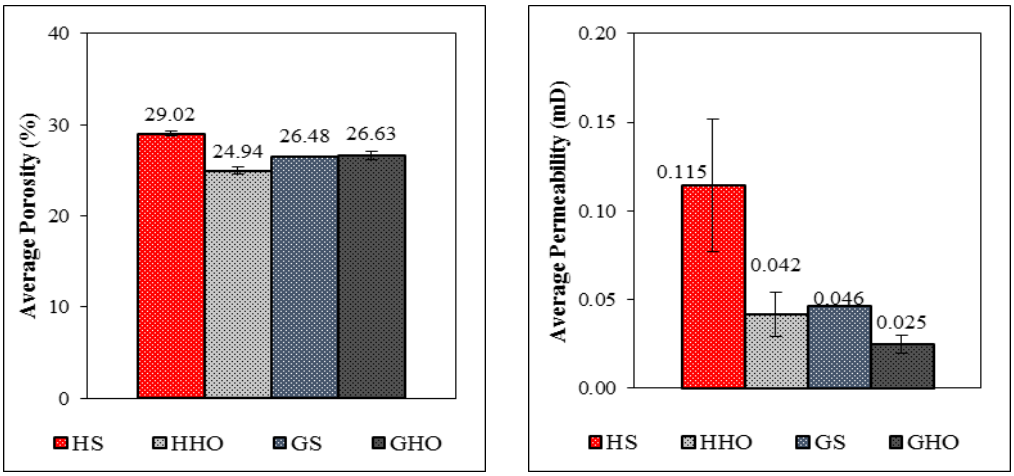

(a) Porosity **(b) Permeability**

Figure B.13: Porosity and permeability of unaged HOAP and baseline samples

HOAP and baseline cement samples exhibited comparable compressive and shear bond strengths (**Fig. B.14**). Similar properties for unaged samples indicate analogous matrix structures for the baseline and additive cement cores. The most useful characteristic of hydroxyapatite is to prevent the carbonation through chemical interaction; hence, the actual performance of HOAP against carbonic acid attack can only be observed after aging samples under simulated harsh downhole conditions. Therefore, HOAP cement slurries have been selected for final screening study.

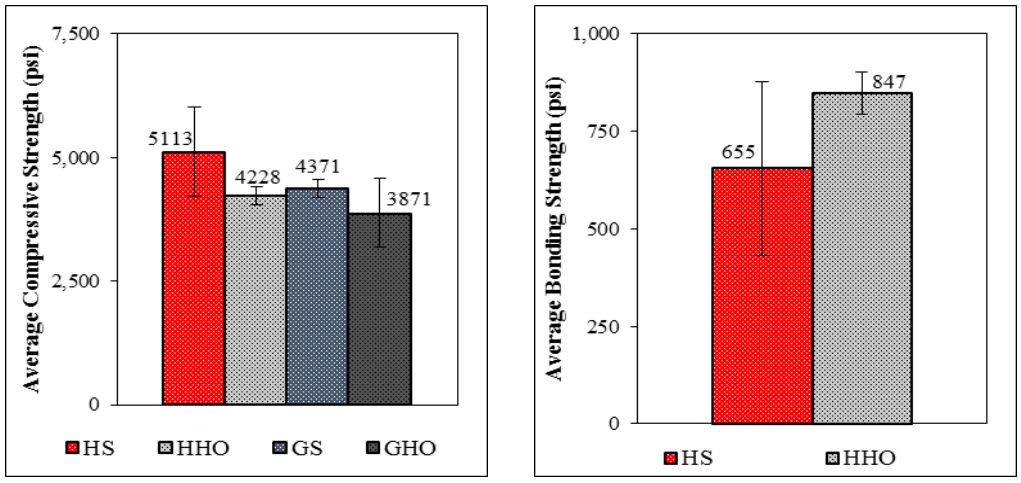

(a) Compressive strength **(b) Shear bond strength**

Figure B.14: Compressive and shear bond strengths of unaged HOAP and baseline samples

B1.4.2.6 Zinc Oxide

An experimental study (Sasaoka et al. 1994) conducted on the reaction between ZnO and H_2S under various conditions showed encouraging results that indicate the potential of ZnO in hindering cement degradation. Based on this, ZnO has been selected as one of the potential cement additives for improving acid resistance. However, Zinc oxide is known to be a very heavy cement retarder even after the addition of common accelerators such as NaCl.

Before aging ZnO cement samples in H_2S containing environment, the slurry properties had to be tested for their suitability by comparing them with that of baseline cements. A number of studies (Olmo et al. 2001; Arliguie and Grandet 1985) investigated the retardation property of ZnO. The retardation effect of ZnO arises from its ability to create an amorphous layer of $Zn(OH)_2$, which in combination with $Ca(OH)_2$ creates calcium-zinc-hydrate. The calcium-zinc-hydrate seems to form a protective layer that inhibits the normal hydration of cement grains by hindering the transport of hydration water to C_3S (Tri-Calcium Silicate) phase (Hammilton and Sammes, 1999), thereby retarding the overall hydration reaction.

In order to examine the retardation effect of ZnO, the consistency of cement slurry samples containing ZnO and NaCl were studied (**Fig. B.15**). Consist-o-meter readings are compared to those of the baseline slurry (Class H cement containing silica). The value of 10 indicates 100 Bc, which corresponds to the API thickening time for the baseline. Cement slurry samples with different concentrations of salt were prepared to offset the retardation effect

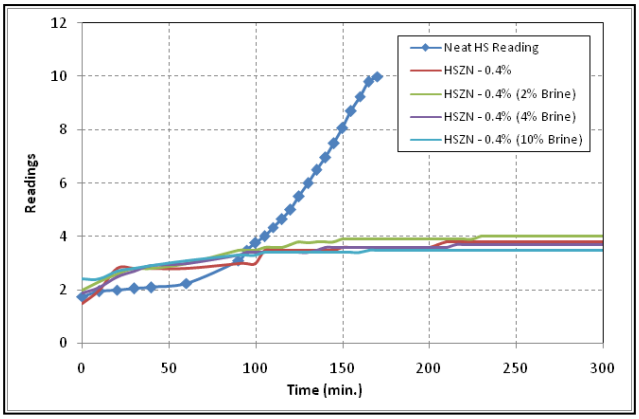

Figure B.15: Consistency of cement slurry containing ZnO

of ZnO. Regardless of the salt concentration, ZnO containing slurries were unable to thicken during the test period. For all ZnO containing samples, the consist-o-meter readings showed a significant retardation. With the addition of small quantity of ZnO (0.4% BWOC), the slurry hydration (thickening) was effectively delayed for more than 5 hours. Chloride ions of NaCl were unable to accelerator the thickening. When tested with other accelerator, similar results were obtained. Therefore, ZnO might not be an effective additive in the cement due to its heavy retardation property. As a result, it has not been selected for further study.

B1.4.2.7 Fly Bsh

There is a general belief that incorporating pozzolanic fillers such as silica fumes and fly ash effectively decreases portlandite and C-S-H contents of the cement thereby reducing the formation of calcium carbonate, which further reacts with the acid to form water soluble calcium bicarbonate that can be easily leached out (Santra et al. 2009). Before aging the fly ash cements under acidic environment, their slurry and core properties were tested and compared with that of baseline cements. Fly ash class F was used in this research because it has lower sulfate content. The amount of fly ash added to the cement was 100% by weight (**Tables B.12** and **B.13**).

Table B.12: Formulation of Class H cement with fly ash (HSF)

Material	Percent	Mass (g)	Specific Gravity	Volume (cc)
HEC	0.1% of water of filler	0.45	-	-
Cement	100%	860	3.14	273.9
Silica Fume	35% of cement	301	2.63	114.4
Fly Ash	100% of cement	860	2.63	327.0
Water for cement	38% cement	327	1.00	326.8
Water for Silica	38.5% silica	116	1.00	115.8
Water for Fly ash	38.5% fly ash	331	1.00	330.9
Total		**2795**		**1488.9**
Density (g/cc)	**1.88**			
Density (lbm/gal)	**15.66**			

Table B.13: Formulation of Class G cement with fly ash (GSF)

Material	Percent	Mass (g)	Specific Gravity	Volume (cc)
HEC	0.1% of water of filler	0.45	-	-
Cement	100%	860	3.14	273.9
Silica Fume	35% of cement	301	2.63	114.4
Fly Ash	100% of cement	860	2.63	327.0
Water for cement	44% cement	378	1.00	378.4
Water for Silica	38.5% silica	116	1.00	115.8
Water for Fly ash	38.5% fly ash	331	1.00	330.9
Total		**2846**		**1540.5**
Density (g/cc)	**1.85**			
Density (lbm/gal)	**15.42**			

Figure B.16 shows comparison of thickening time for fly ash and baseline cement samples. In this graph, Bc is the consistometer reading that ranges between 0 and 10. At t = 0, when Bc = 0, the slurry has just being prepared and is least resistant to pumping. At t = t1, when Bc = 10, the slurry becomes very thick and unpumpable. Experimental results showed that Class G cement without fly ash has lowest thickening time. Adding fly ash to the cement increased the thickening time for both Class H and Class G cements.

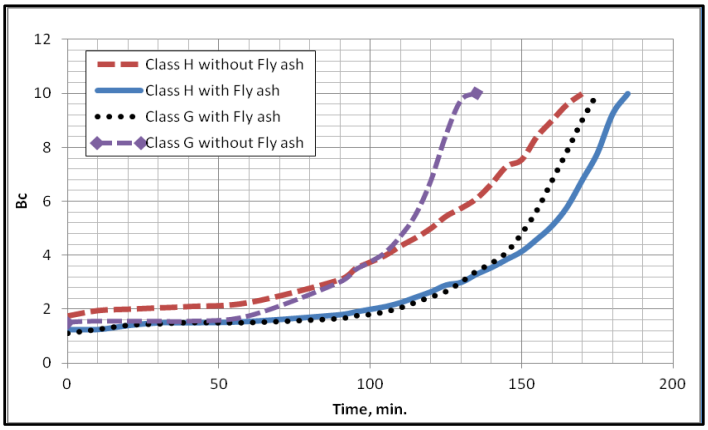

Figure B.16 Thickening time of fly ash and baseline cements

Porosity and permeability of fly ash and baseline cements were measured after curing for five days at temperature of 200°F (**Table B.14**). Class G cement with fly ash showed the minimum porosity while other samples showed almost the same porosity of approximately 25%. Class H cement without fly ash had the maximum permeability (**Fig. B.17**). Class G cement with and without fly ash and class H cement with fly ash exhibited comparable permeability, which is roughly 0.02 mD.

Table B.14: Porosity and permeability of fly ash and baseline samples

CGS Units											
Core #	Core dimensions			Porosity					Permeability		Remarks
	Diameter	Length	Weight	V_b	V_g	V_p	Porosity	Gr. Density	K_{air}	K_{klink}	
	mm	mm	g	cc	cc	cc	%	g/cc	mD	mD	
1Go1	25.36	37.98	32.55	19.18	14.09	5.09	26.54%	2.31	0.035	0.018	Class G without Fly ash
1Go2	25.32	36.72	31.52	18.49	13.55	4.94	26.72%	2.33	0.043	0.022	
1Go3	25.34	30.27	26.24	15.27	11.29	3.98	26.06%	2.32	0.036	0.019	
1Ho1	25.26	38.30	33.53	19.19	13.83	5.36	27.93%	2.42	0.102	0.060	Class H without Fly ash
1Ho2	25.28	37.32	32.74	18.73	13.39	5.34	28.51%	2.44	0.116	0.070	
1Ho3	25.33	38.22	33.90	19.26	13.73	5.53	28.71%	2.47	0.113	0.068	
1Hf1	25.24	37.56	31.13	18.79	13.94	4.85	25.81%	2.23	0.050	0.027	Class H with Fly ash
1Hf2	25.17	37.62	31.45	18.72	14.10	4.62	24.68%	2.23	0.042	0.022	
1Hf3	25.18	36.97	30.31	18.41	13.55	4.86	26.40%	2.24	0.056	0.031	
1Gf1	25.30	33.58	29.46	16.88	13.46	3.42	20.26%	2.19	0.038	0.020	Class G with Fly ash
1Gf2	25.25	38.40	33.76	19.23	15.31	3.92	20.38%	2.20	0.036	0.018	
1Gf3	25.20	39.13	33.94	19.52	15.43	4.09	20.95%	2.20	0.040	0.021	

Slurry and core properties of fly ash cements (GSF and HSF) were tested and compared with properties of baseline cements. Fly ash based cements showed acceptable (i.e. slurry properties within the range of baseline cement slurries) property suitable for cementing applications; therefore, they have been selected for testing in the aging cell under HPHT conditions.

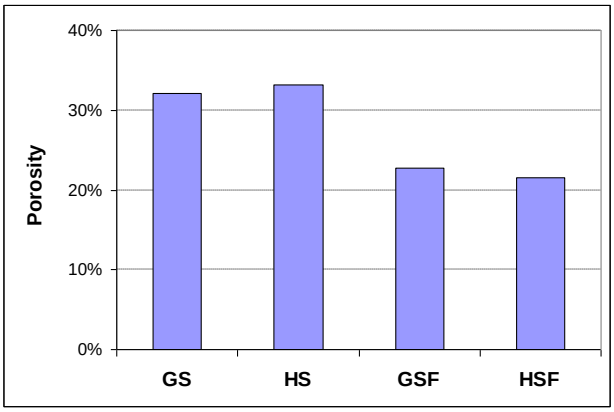

(a) Porosity

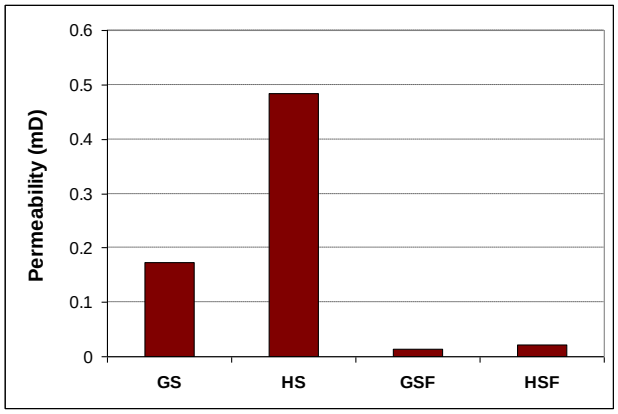

(b) Permeability

Figure B.17: Porosity and permeability of unaged fly ash and baseline samples

B1.5 Final Screening and Formulation Study

Additive cement formulations that were selected from the initial screening were tested again for their performance in HPHT acidic environment. The cores were prepared and aged in a high-pressure autoclave. During experiment, all the aged cores were completely immersed in 2% NaCl solution (brine) saturated with methane gas containing CO_2 and H_2S. After aging, physical properties (porosity, permeability, compressive and bond strengths were measured) of the cores were measured and compared with properties of unaged cores to quantify the degree of degradation. In addition, FTIR mineralogy, SEM, EDX and XRD analyses were performed to assess the degradation of additive cements.

B1.5.1 Microsilica Cement

Three HPHt experiments were conducted with microsilica based cements (MS-10). The aging conditions of these experiments are presented in **Table B.15**. Baseline samples were also aged simultaneously under similar conditions; hence, the parallel HS and GS batches mentioned for each condition in the table refers to the baseline samples, which were in the aging cell along with corresponding additive samples.

Table B.15: Aging conditions for MS-10 samples

Experiment No.	Microsilica Batches	Temp. (°F)	Pressure (psi)	CO2 Conc. (%)	Baseline Batch
21	Batch 008	225	3000	100	Batch 024
25	Batch 009	430	6000	10	Batch 028
26	Batch 010	430	6000	40	Batch 029

After aging, porosity, permeability, compressive and shear bond strengths tests test were performed. In addition, FTIR analysis was conducted to assess the level of degradation occurring in the samples.

B1.5.1.1 Porosity and Permeability

Figures B.18 and **B.19** depict unaged and aged porosity and permeability (ϕ-k) of Class H based microsilica and baseline cements. The decrease in ϕ-k indicates carbonation in the matrix and the increase demonstrates leaching. At temperature 225°F and 100% CO_2 concentration, ϕ-k of baseline samples increased due to carbonation (Experiment 21). At higher temperature (430°F), significant leaching occurred and ϕ-k of the samples increased. It can be deduced that excessive temperature (430°F) leads to rapid diffusion of ions form the matrix, causing major leaching.

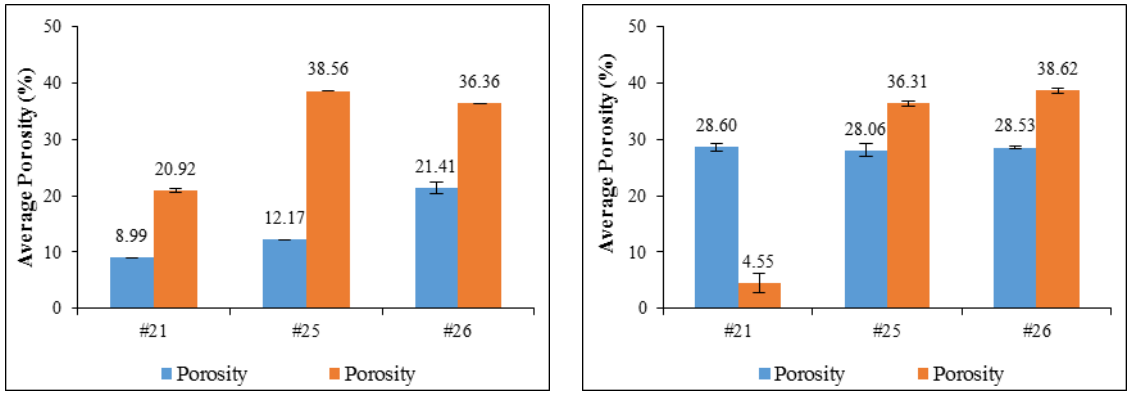

Figure B.18: Porosity of aged (orange) and unaged (blue) Class H based cores: a) HSMS; and b) HS

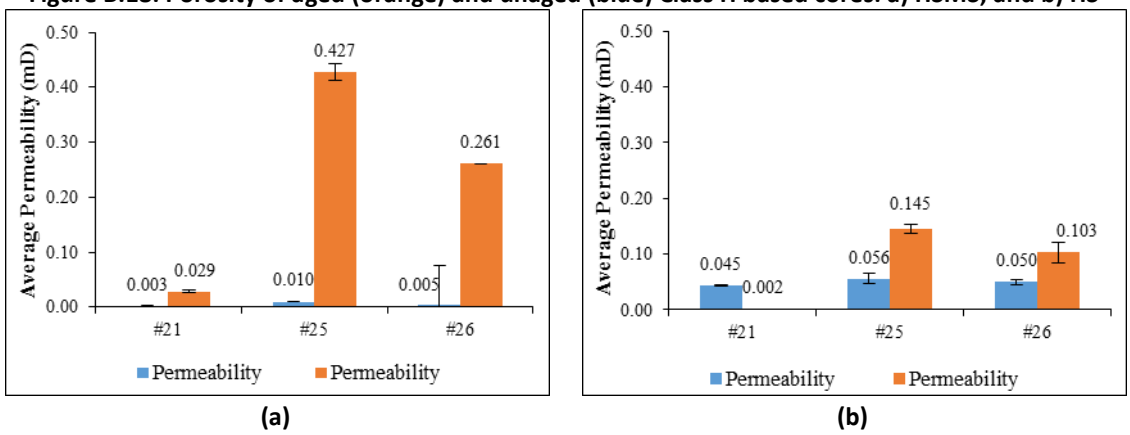

Figure B.19: Permeability of aged (orange) and unaged (blue) Class H based cores: a) HSMS; and b) HS

The microsilica samples indicated a consistent increase in ϕ-k irrespective of the temperature. The level of increase was significantly higher for microsilica samples than the baseline. Such high ϕ-k increase is detrimental to the integrity of the cement matrix. One possible reason for the huge increment in the ϕ-k of microsilica could be incomplete pozzolanic reaction occurring at higher temperature. Pozzolanic reactions are exothermic; and hence, they tend to slow down at higher temperatures (Siddique and Khan 2011). The incomplete pozzolanic reaction results in poor unconsolidated CSH, which is formed resulting from the interaction of microsilica and CH. Due to continuous carbonation and leaching, the matrix resulted in the partially carbonated and weaker matrix.

Results of Class G based microsilica and baseline samples indicate almost similar trends as the Class H. Increases in the ϕ-k values of microsilica samples were observed in all the three experiments (**Figs. B.20** and **B.21**). Large permeability increment, which makes the cement susceptible for acid penetration, was considerably higher for microsilica samples as compared to baseline cement.

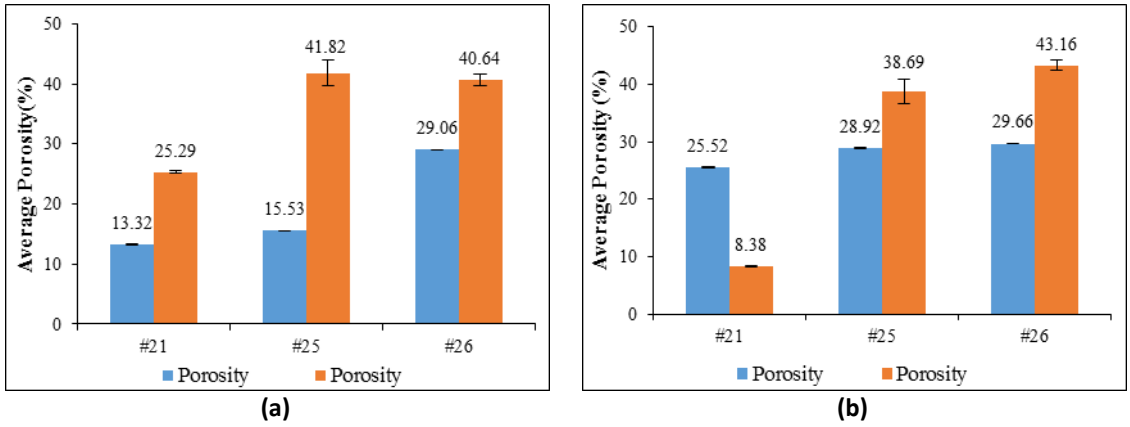

Figure B.20: Porosity of aged (orange) and unaged (blue) Class G based cores: a) GSMS; and b) GS

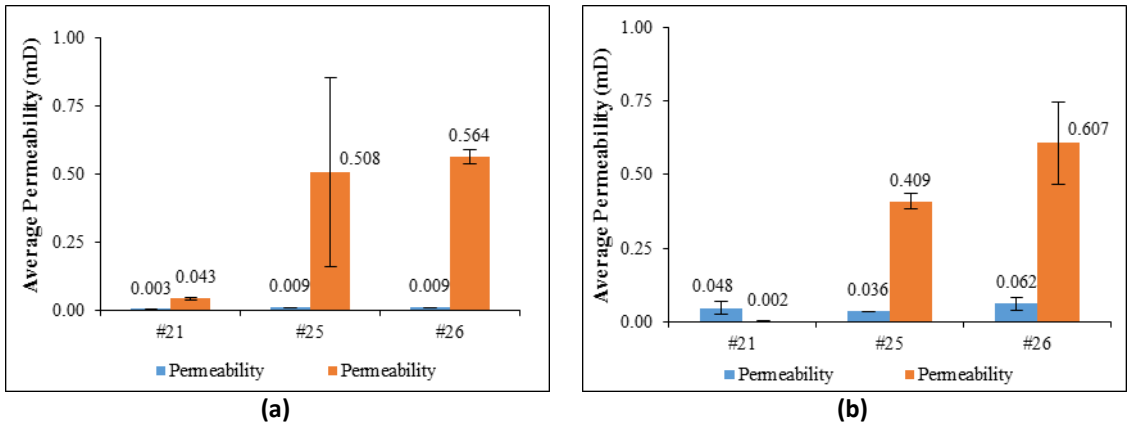

Figure B.21: Permeability of aged (orange) and unaged (blue) Class G based cores: a) GSMS; and b) GS

B1.5.1.2 Compressive Strength

Figures B.22 and **B.23** present compressive strength of microsilica and baseline samples (aged and unaged) for Class H and Class G, respectively. Baseline samples consistently showed increased strength after aging, which suggest carbonation of the matrix. At 225°F and 100% CO_2 (Experiment 21), microsilica samples indicated slight carbonation. At 430°F with 10% CO_2 (Experiment 25), HSMS samples exhibited a slight increase in the strength, while the GSMS cores showed a small decrease. Unaged microsilica samples displayed significant variation in strength. This indicates that compressive strength of microsilica samples are very sensitive to other factors that have minor influence on mechanical properties of conventional cements (baseline).

With increase in the CO_2 concentration to 40% at 430°F (Experiment 26), the matrix of HSMS became extremely weak. Compressive strength measurements of aged GSMS samples demonstrated

considerable scattering, which can indicate inconsistency in the integrity of the matrix due to severe degradation. Few microsilica samples also showed cracks after aging and were eliminated from the test. This suggests formation of highly permeable and weak matrix of microsilica cement when aged at high temperature (430°F) and increased CO_2 concentration (40%).

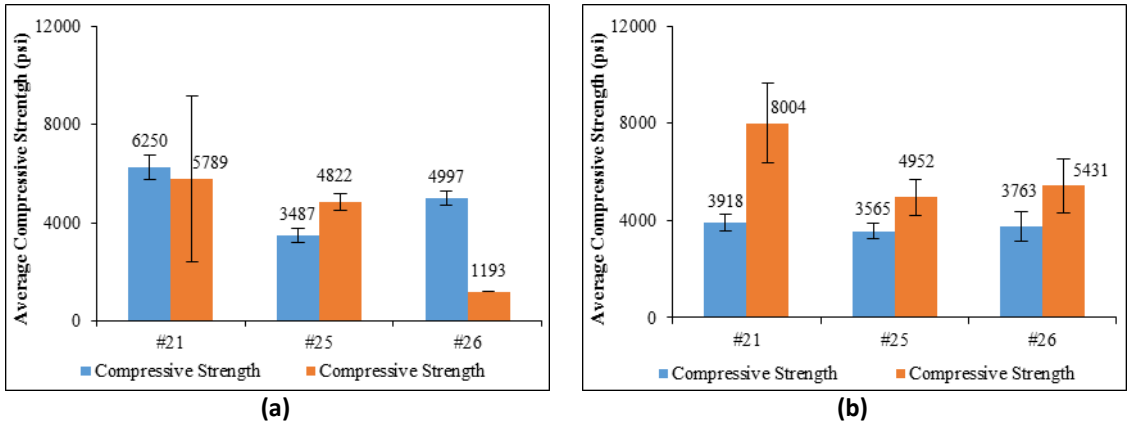

Figure B.22: Compressive strength of aged (orange) and unaged (blue) Class H based cores: a) HSMS; and b) HS

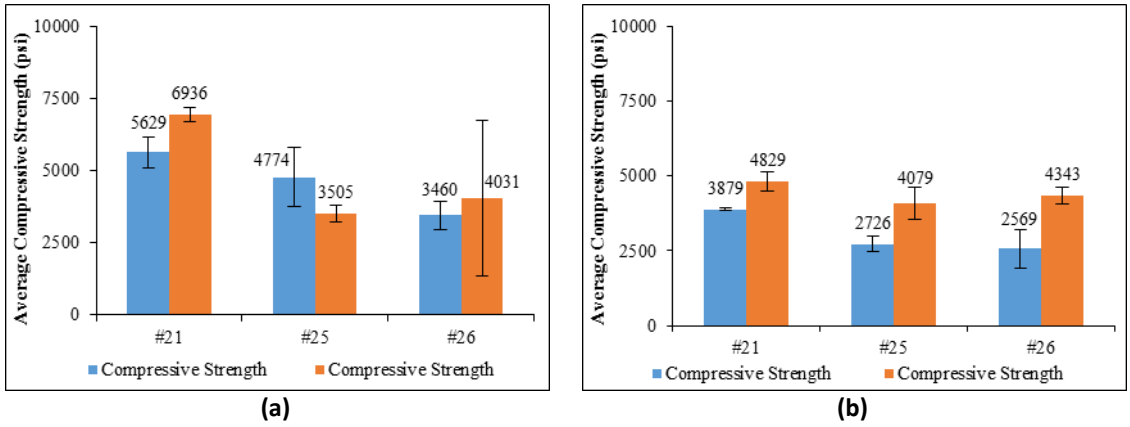

Figure B.23: Compressive strength of aged (orange) and unaged (blue) Class G based cores: a) GSMS; and b) GS

B1.5.1.3 Shear Bond Strength

The shear bond strength (SBS) of microsilica and baseline samples (**Fig. B.24**) increased after aging. For microsilica samples, the increase was minimal at 430°F and 10% CO_2 (Experiment 25). However, this particular test showed the highest measurement scattering for unaged microsilica samples. In addition, the SBS of aged microsilica samples was the lowest one, which may indicate leaching of carbonated zone of the samples. In other words, the samples might have carbonated and leached out at the same time, maintaining SBS value approximately constant. This can be attributed towards incomplete pozzolanic reactions as mentioned previously. In general, the microsilica samples displayed similar performance as the baseline samples.

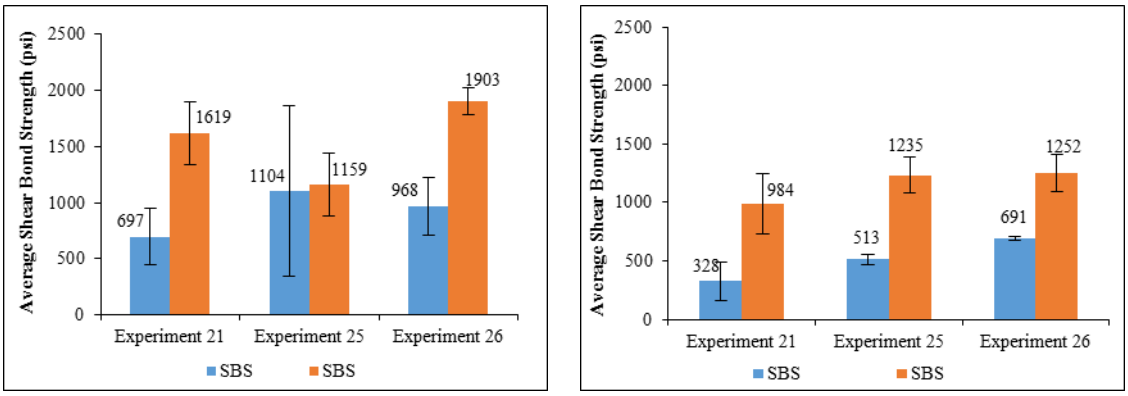

Figure B.24: SBS of aged (orange) and unaged (blue) Class H based cores: a) HSMS; and b) HS

B1.5.1.4 FTIR Analysis

In order to further investigate the level of degradation, FTIR analysis was conducted on samples used to measure ϕ-k. The level of degradation was evaluated by monitoring major binding components of the cement (CH and CSH) and the main product of the carbonation process ($CaCO_3$). To perform the FTIR tests, microsilica and baseline cores were first dried and then cut transversely. Three zones in the cylindrical cement cores were identified as outermost, middle and innermost zones (**Fig. B.25**). Small amount of representative cement sample was cut from each zone and finely grinded. The amounts of calcium carbonate and calcium hydroxide oxide (CH) found in these zones indicate the level of carbonation occurring in each zone.

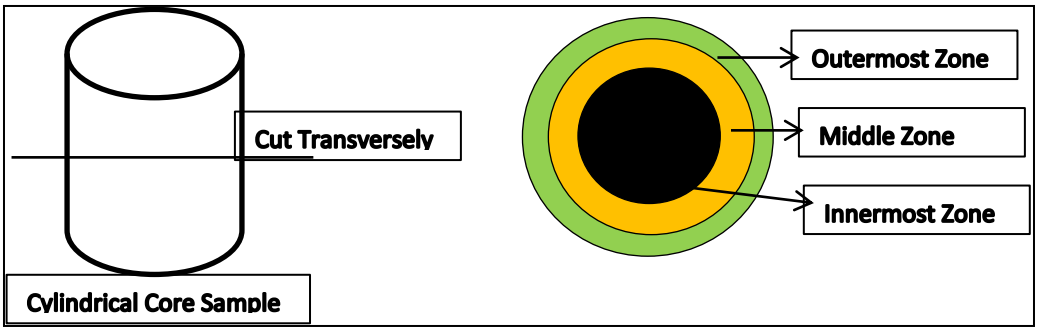

Figure B.25: Schematic of a cylindrical samples and zones selected in the cross section

Inner Zone

The inner zone is expected to be the least degraded zone, as it is at the center of the core and farthest away from the bulk fluid. Microsilica (HSMS) and baseline (HS) samples exhibited (**Fig. B.26**) similar mineralogy after aging in Experiments 21 and 25. Results of the FTIR analysis show the presence of substantial amount of CSH which may indicate preserved matrix. However in Experiment 26, which was conducted at 430°F and 40% CO_2, the HSMS samples were found to be highly degraded according to permeability and compressive strength measurements. The presence of CH and CSH in the matrix could

be attributed to incomplete pozzolanic reaction. Moreover, higher $CaCO_3$ content as compared to HS signifies a highly carbonated matrix. Even though, the contents of CH and CSH in microsilica cement were higher than those of the baseline HS samples, microsilica cement samples were more carbonated than the baseline samples.

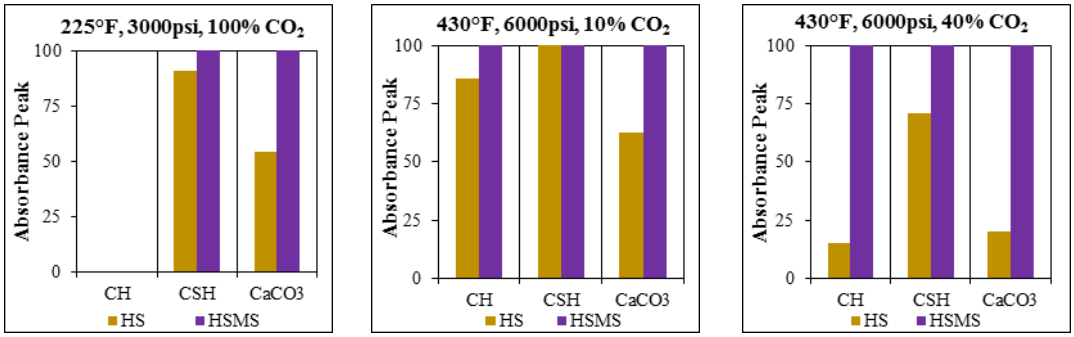

Figure B.26: FTIR results of inner zones of HSMS and HS samples aged at different conditions: a) Exp. 21; b) Exp. 25; and c) Exp. 26

Middle Zone

The middle zone showed greater amount of carbonation being closer to the bulk fluid. Microsilica samples displayed higher or similar content of $CaCO_3$ as compared to the baseline samples in all the experiments (**Figure B.27**). On the other hand, their CH and CSH contents were almost similar or less than those of the baseline samples. The microsilica did show better resistance against acid attack than the baseline samples.

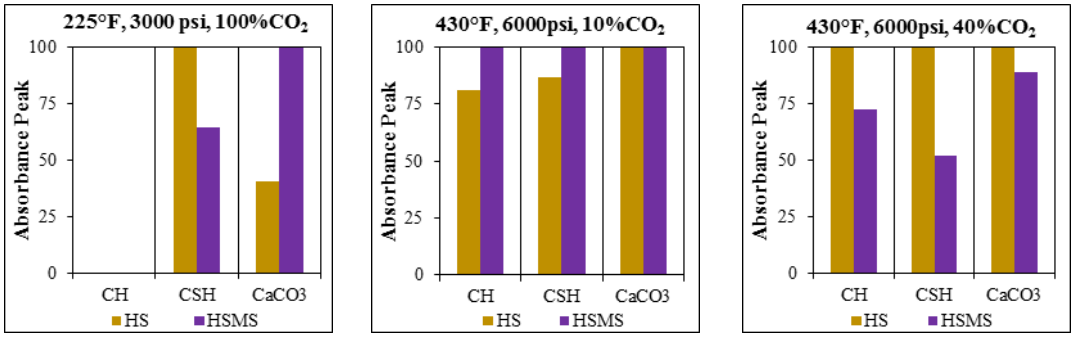

Figure B.27: FTIR results of middle zones of HSMS and HS samples aged at different conditions: a) Exp. 21; b) Exp. 25; and c) Exp. 26

The outer zone is the most exposed part of the sample. The zone is selected for evaluation since usually it shows substantial degradation. The outer zones of both microsilica and baseline samples demonstrated significant carbonation of the binding materials after aging **Fig. B.28**. However, when subjected to 430°F and 40% CO_2 (Experiment 26) the baseline samples showed unanticipated result by

preserving CH and CSH in the matrix. Although $CaCO_3$ was present in the samples, the presence of CH and CSH in the baseline HS samples indicates more degradation of microsilica samples than the baseline samples.

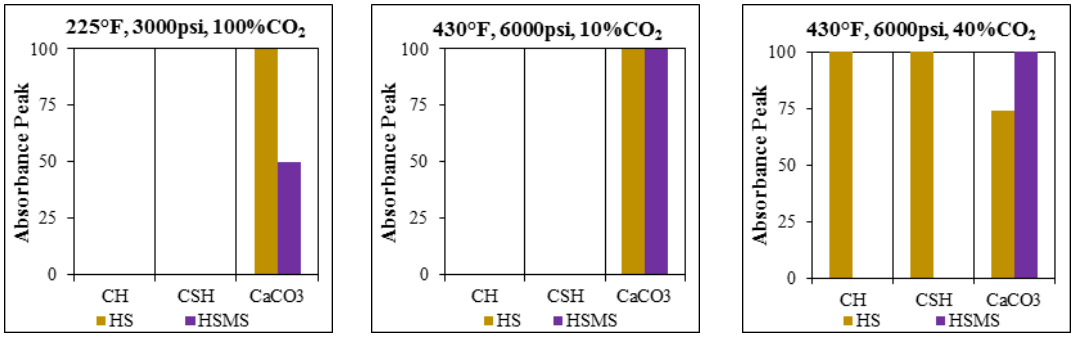

(a) (b) (c)

Figure B.28: FTIR results of middle zones of HSMS and HS samples aged at different conditions: a) Exp. 21; b) Exp. 25; and c) Exp. 26

B1.5.1.5 Summary

The results of these three experiments show that the addition of microsilica does not improve the performance of the baseline cement. As result, porosity and permeability of microsilica samples were predominately increased after aging. This is an indication of severe leaching of the matrix that reduces the compressive strength. In agreement with this, compressive strength for Class H based microsilica (HSMS) samples cement showed significant reduction with increase in temperature. Class G based microsilica cement was stronger than the HSMS. Cracking of core samples inside the aging cell in Experiment 26, which was conducted at 430°F and 40% CO_2, indicated weakening of the microsilica samples. The shear bond strength measurements of the additive cement exhibited almost similar performance as the baseline samples. Possible explanation of these results is attributed to partial pozzolanic reactions at 430°F.

The FTIR results showed slightly lower amount of CH and CSH components in the matrix of microsilica than the baseline samples. Evidently, the performance of microsilica cement against acid attack and carbonation is not better than the baseline samples. Moreover, the matrix damage through increased porosity and permeability renders the additive unsuitable for HPHT sour gas environment.

B1.5.2 Latex Cement

Latex is often added to improve sealing properties of cement. The latex forms an emulsion with the cement. A similar experimental observation has been reported by Funquan et al. (2006). The authors suggest the use of strong hydrophilic carboxyl group, such as formic acid or acetic acid, in order to stabilize the latex containing cement system at 200ºF or above.

Unaged latex cores exhibited higher permeability than the baseline samples (B1.4.2.2). In order to improve the performance of the cement styrene butadiene latex was substituted by SBR latex. However, the permeabilities of the SBR latex samples (HSLT and GSLT) were higher than those of

baseline samples. In order to test if high permeability latex cement withstands acid attack, core samples with SBR latex were prepared and aged in 2% brine at 350°F and 6000 psi using 40% CO_2 gas. The composition of the slurry is presented in Table B.5.

B1.5.2.1 Porosity and Permeability

The porosity and permeability measurements obtained from latex and baseline cement samples are presented in **Fig. B.29**. Porosity and permeability of unaged samples of latex cement were almost comparable with those of baseline samples. Except HS samples, all other samples showed slight reduction in porosity after aging. This result is expected, since carbonation reduces the pore space causing reduction in porosity and permeability. Consistent with this observation, the permeability of all the samples reduced after aging due to carbonation. The reduction observed in the GSLT sample was the least but still significant.

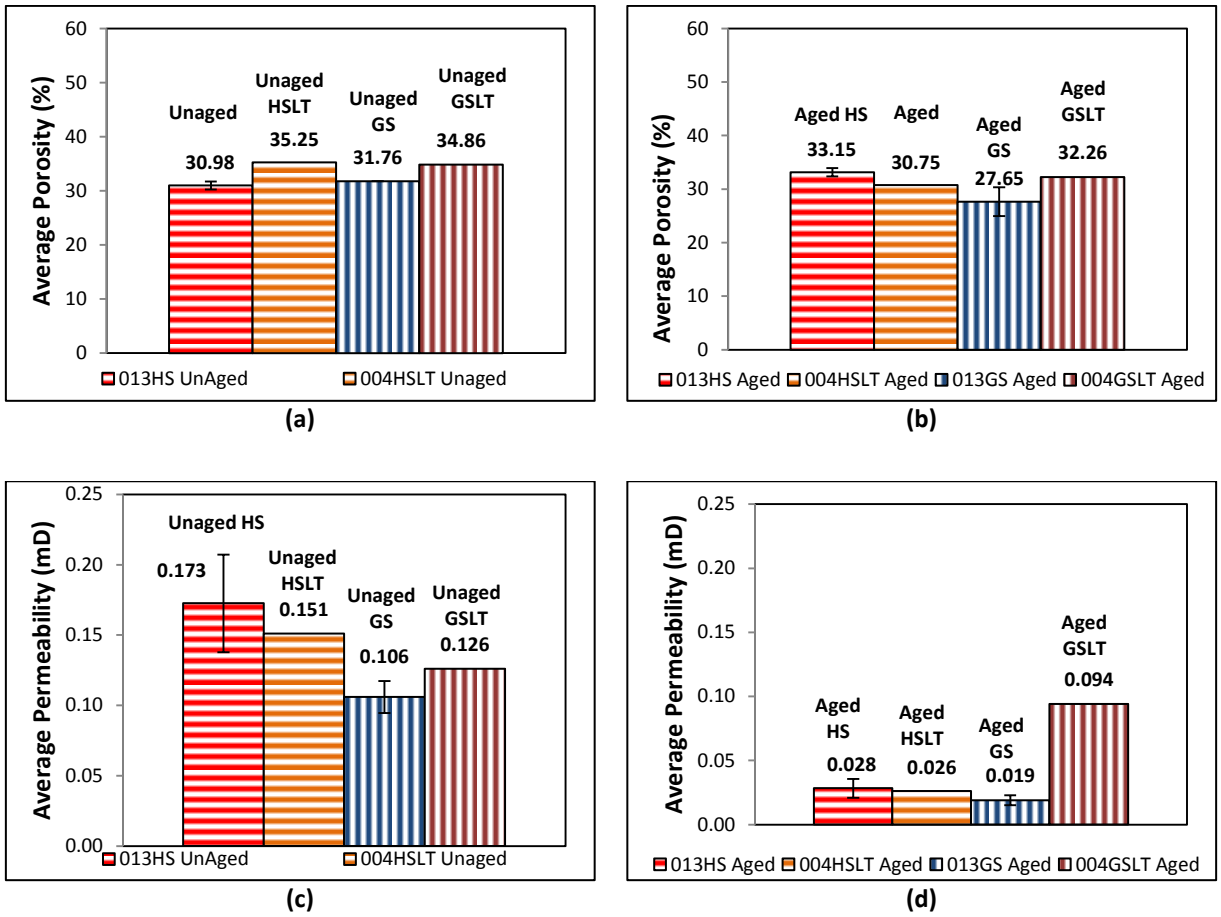

Figure B.29: Porosity and permeability of latex and baseline cores (aged at 350°F with 40% CO_2)

B1.5.2.2 Degradation Depth

Aged latex cement samples displayed a clear degraded zone (**Fig. B.30**) when they were transversely cut. It was evidently observed that the degraded depths of latex cements were higher than those of the baseline samples. This confirms that even though the measured permeability was almost same for the

latex and HS samples, the latex samples exhibited deeper penetration and degradation. The average degraded depth measurements are presented in **Table B.16**. The increased depth values of latex samples indicate vulnerability towards carbonation.

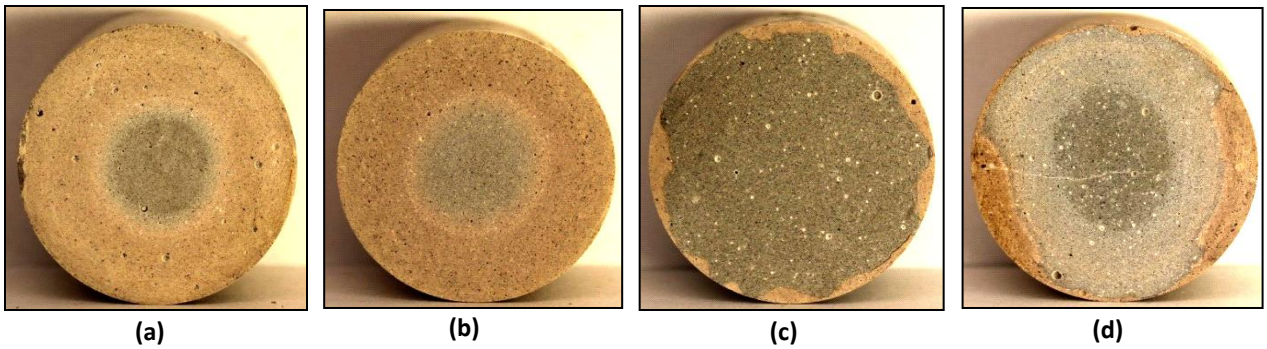

Figure B.30: Middle cross sections of cores aged at 350°F with 40% CO2 gas: a) GSLT; b) HSLT; c) GS; and d) HS

Table B.16: Degradation depth of baseline and latex-based cements

Core #	Carbonated Depth Average (in.)	Std. Dev.
004HSLT	0.310	0.006
004GSLT	0.342	0.017
013HS	0.280	0.031
013GS	0.053	0.019

B1.5.2.3 Compressive Strength

Compressive strengths of aged and unaged latex and baseline cement samples are presented in **Fig. B.31**. Compressive strength of the latex samples increased more than the baseline samples. This is due to higher level of carbonation in the latex samples as compared to the baseline. High level of carbonation confirms poor performance of latex as a cement additive for acid attack reduction.

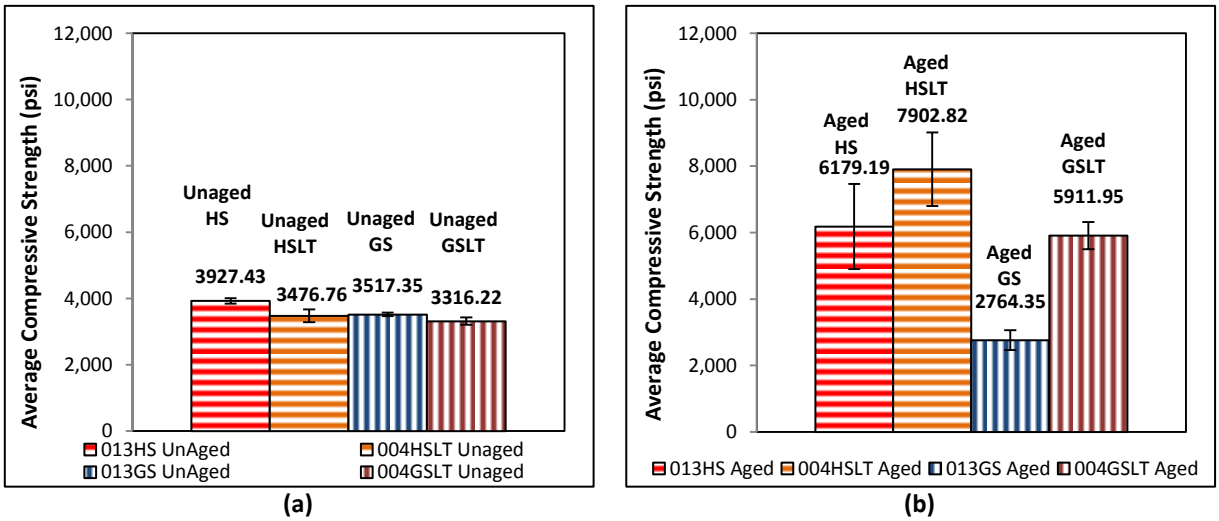

Figure B.31: Compressive strength of baseline and latex-based cements aged at 350°F with 40% CO_2

B1.5.2.4 Shear Bond Strength

Shear bond strengths of latex and baseline cements are presented in **Fig. B.32**. Both samples show similar shear bond strength before and after aging. Although the addition of latex is expected to improve shear-bonding strength of the cement, results indicate minimal effect of latex on the bond strength. Moreover, the latex samples demonstrated the same level of bond strength improvement that suggests similar level of carbonation.

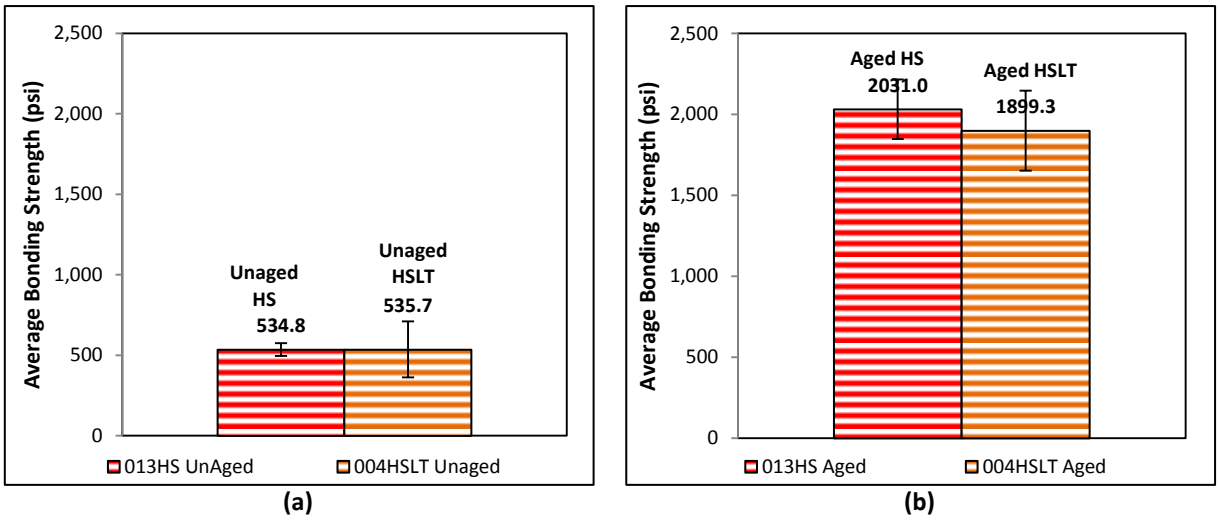

Figure B.32: Shear bond strength of latex and baseline cements aged at 350°F with 40% CO_2

B1.5.2.5 FTIR Analysis

In order to evaluate the carbonation level in the latex samples, the FTIR tests were conducted on samples taken from the inner, middle and outer zones of the latex and baseline cement cores. The results (**Fig. B.33**) indicate poor performance of the latex cement in resisting the acid attack. In the latex cement core, carbonation was occurred in outermost and middle zones while in the baseline cement, it occurred only in the outermost zone. Middle zone of aged latex samples had no traces of CH or CSH. Nevertheless, they displayed high content of CO_3^{-2} bond as compared to baseline samples. This confirms that latex did not prevent acid penetration. Instead, it reduced the capability of the cement to withstand acidic environment. Results of the outermost zone showed the same level of degradation in both cases. In addition, the FTIR obtained from the inner most zone of the matrix indicates that the amount of uncarbonated CH and CSH is same in both latex and HS samples. Hence, CO_2 was not able to penetrate completely inside both the samples within two weeks of aging.

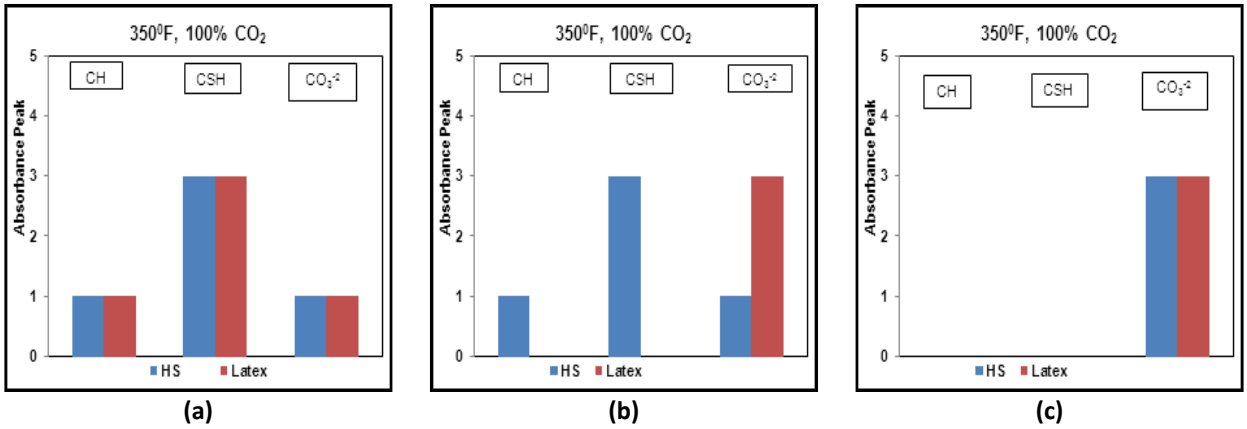

Figure B.33: Summarized FTIR of latex and baseline cements: a) innermost; b) middle; and c) outermost zones

B1.5.2.6 Summary

Latex and baseline cores did not show significant porosity change after aging; however, their permeability deceased considerably except for GSLT, which exhibited minimal reduction. Moreover, latex had higher degradation depth compared to the baseline cement. Particularly, GSLT was severely penetrated as compared to GS. Furthermore, latex cores showed higher compressive strength than the baseline cement, which suggests incidence of intense carbonation. SBS of both samples were very similar. FTIR analysis results suggest the preservation of CH and CSH in the middle zone of the baseline core while the additive sample completely lost its CH and CSH content. In general, the performance of baseline cement is better than the latex cement under HPHT acidic environment. Latex is not suitable cement additive for controlling acid attack.

B1.5.3 Latex-Microsilica Cement

The slurry compositions and properties of latex-microsilica cement (LTMS) are presented in Section B1.2.2.3. The aging conditions for LTMS samples are presented in **Table B.17**. The first batch of latex-microsilica cement cores were aged in 2% brine for 14 days under HPHT conditions and tested. The samples exhibited the presence of CSH component after aging, indicating their resistance against acid attack.

Table B.17: Aging conditions for LTMS samples

Exp. No.	LTMS Batch	Temp. (°F)	Pressure (psi)	CO_2 Conc. (%)	Baseline Batch
24	Batch 002	225	9000	10	Batch 027
27	Batch 003	430	6000	100	Batch 030
28	Batch 004	430	3000	100	Batch 031

The core property measurements (porosity, permeability, compressive strength and shear bond strength, and FTIR analysis) were conducted and the results are presented here.

B1.5.3.1 Porosity and Permeability

Figure B.34 depicts porosity of Class H cement based LTMS and baseline samples. The porosity of the baseline samples reduced 43% due to carbonation at 225°F. The LTMS samples on the other hand retained their original porosity, which indicates better performance. The permeability for baseline samples at similar conditions also showed almost 90% reduction while that of HSLM samples increased 77% (**Fig. B.35**). This increment in permeability contradicts the consistent porosity measurements. When subjected to 430°F and 100% CO_2 (Experiment 27 and 28) at varying pressures, a significant increases in the porosity and permeability were observed with LTMS and baseline samples again. Such a porous and permeable matrix may be detrimental for the integrity of the cement. It is important to be noted that even with addition of latex and microsilica, the additive samples were not performing better than baseline samples.

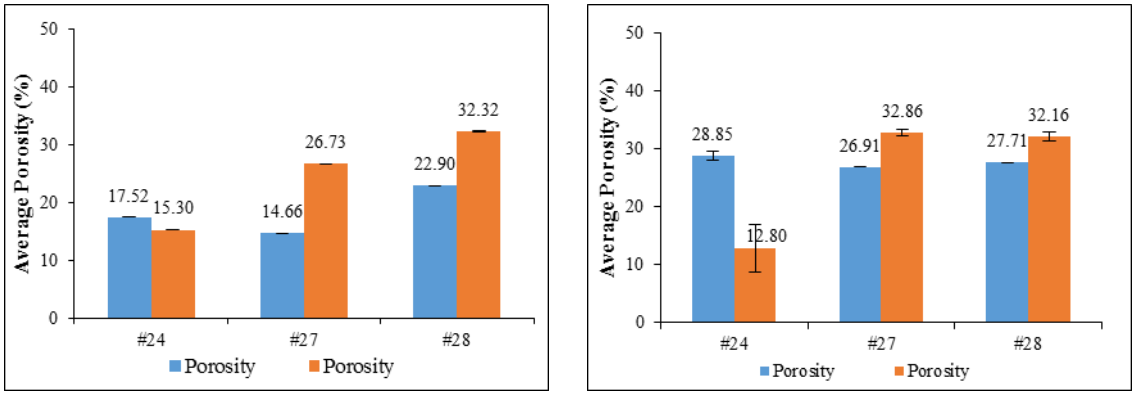

(a) **(b)**

Figure B.34: Porosity of aged (orange) and unaged (blue) samples: a) HSLM; and b) HS

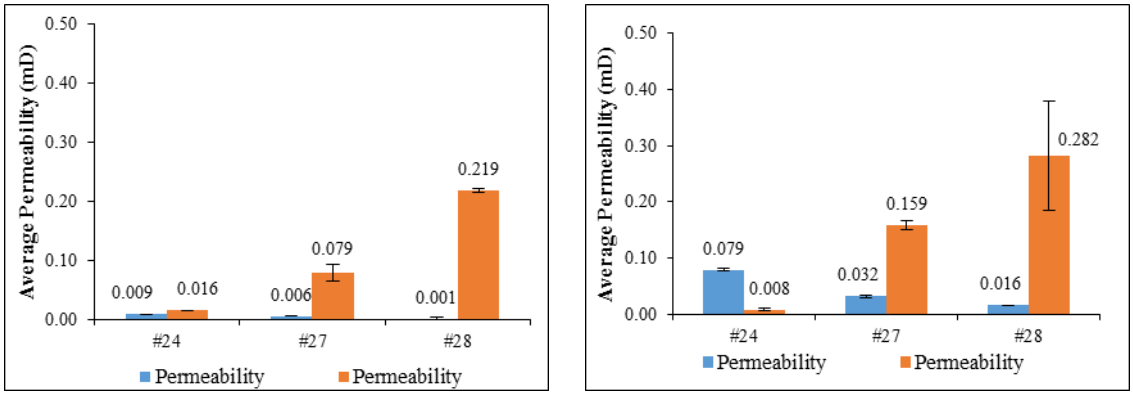

(a) **(b)**

Figure B.35: Permeability of aged (orange) and unaged (blue) samples: a) HSLM; and b) HS

Class G cement also showed similar trends of porosity and permeability changes as Class H samples (**Figs. B.36** and **B.37**). The increment in permeability of GSLM samples, although significantly high, was not as excessive as that of HSLM samples.

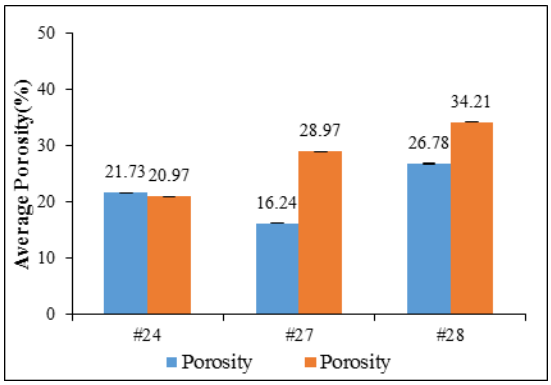

(a)

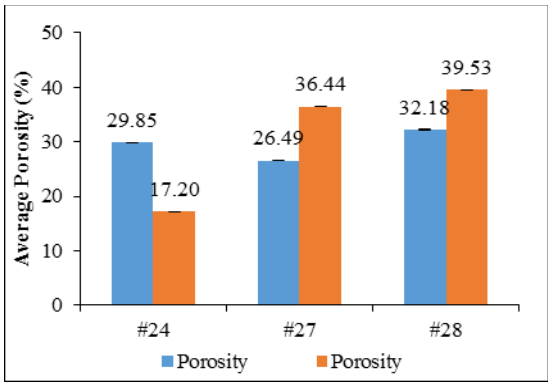

(b)

Figure B.36: Porosity of aged (orange) and unaged (blue) samples: a) GSLM; and b) GS

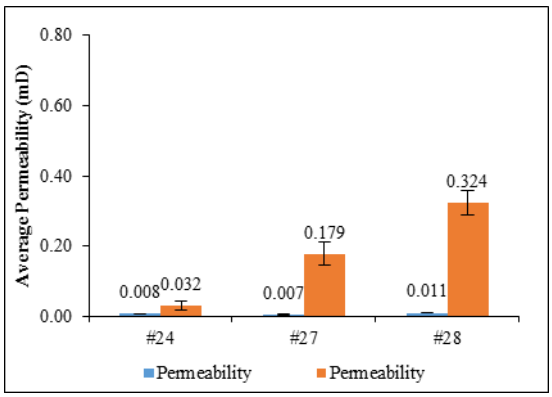

(a)

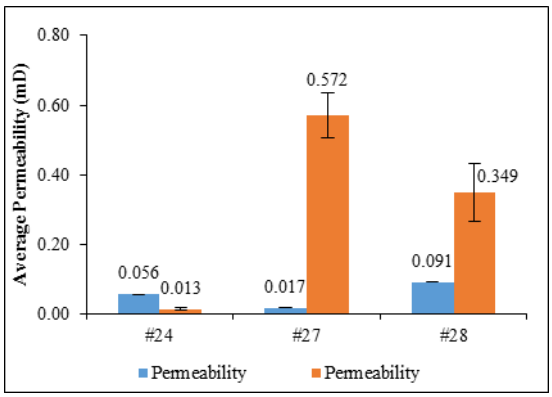

(b)

Figure B.37: Permeability of aged (orange) and unaged (blue) samples: a) GSLM; and b) GS

B1.5.3.2 Compressive Strength

For high temperature tests (Experiments 27 and 28), compressive strength of all the samples (additive and baseline) were consistent with porosity and permeability (ϕ-k) results (**Figs. B.38** and **B.39**). Compressive strength increased after aging. However, at 225°F, all the samples show a different trend between compressive strength and ϕ-k. Results do not demonstrate the benefits of the additive in reducing degradation. The latex-microsilica samples behave in similar way as the baseline samples.

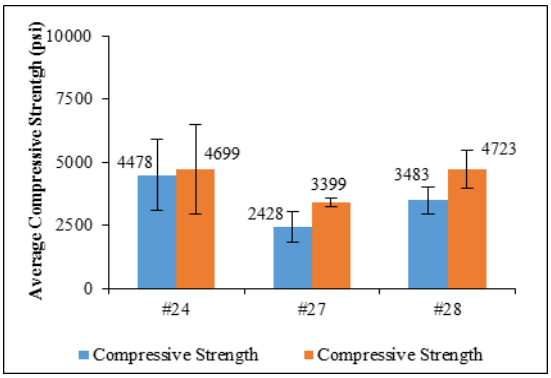

(a)

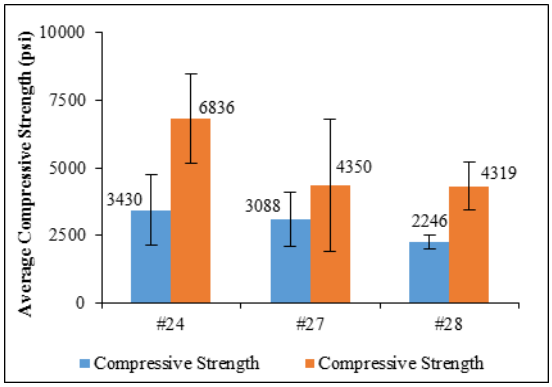

(b)

Figure B.38: Compressive strength of aged (orange) and unaged (blue) samples: a) HSLM; and b) HS

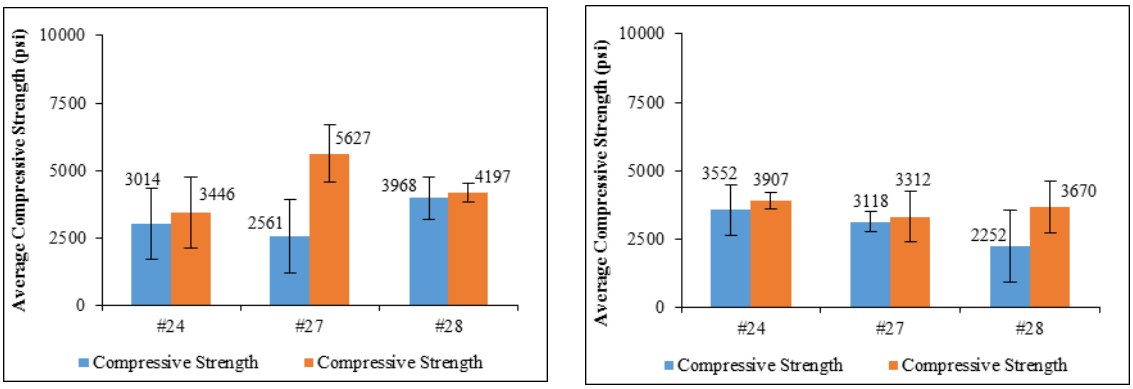

Figure B.39: Compressive strength of aged (orange) and unaged (blue) samples: a) GSLM; and b) GS

B1.5.3.3 Shear Bond Strength

Shear bond strength trends of LTMS and baseline samples are similar (**Fig. B.40**), except for Experiment 24, which was conducted at 225°F. Shear bond strength of LTMS samples predominately reduced after aging. Increase in SBS was observed in Experiment 27. This conveys that the additive slurry did not have better bonding or sealing performance than the baseline cement.

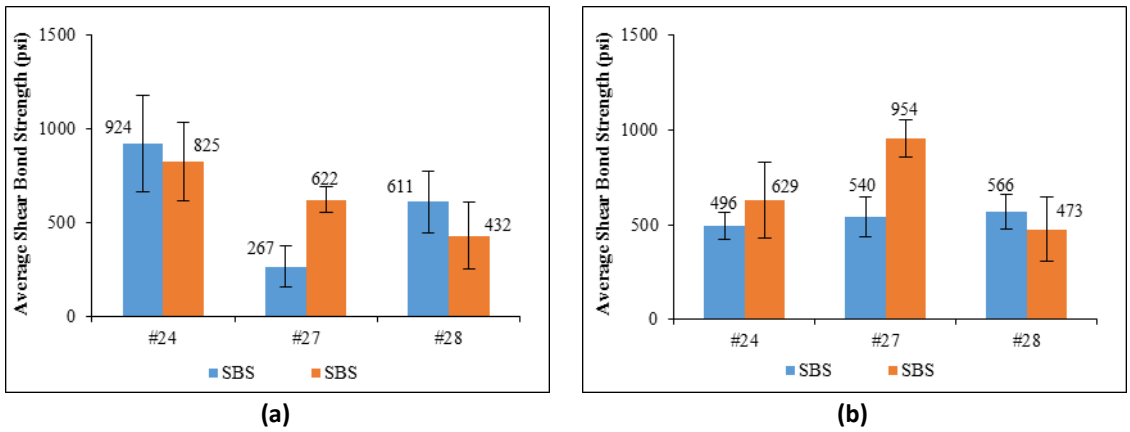

Figure B.40: Average shear bond strength of aged (orange) and unaged (blue) samples: a) HSLM; and b) HS

B1.5.3.4 FTIR Analysis

FTIR results of latex-microsilica and baseline samples are presented here. The minerals under focus are CH, CSH and $CaCO_3$. Similar to FTIR analysis of microsilica (Section B1.5.1.4), three zones (inner, middle, and outmost zones) on the LTMS and baseline cores were considered for the analysis.

Inner Zone

FTIR results of the samples from the inner zones of LTMS and baseline cores are depicted in **Fig. B.41.** Aging at lower temperature (225°F) led to heavy leaching of baseline samples (Experiment 24). Although CH was completely carbonated in both LTMS and baseline samples, the former have still retained certain amount of CSH in the matrix. The level of $CaCO_3$ was also higher for the LTMS samples indicating substantial carbonation. When aged at high temperature (430°F), the baseline samples were

able to preserve the CH and CSH components. At higher pressure (6000 psi), the LTMS matrix showed complete loss of CH and CSH components (Experiment 27) while at low pressure (3000 psi), the least damage to the matrix was observed (Experiment 28). This observation is not consistent with permeability of LTMS samples that show huge increase after aging. The inconsistent could be as a result of partial pozzolanic reactions occurring at higher temperature (430°F). Other zones of the samples also need to be analyzed in order to better understand the degradation process.

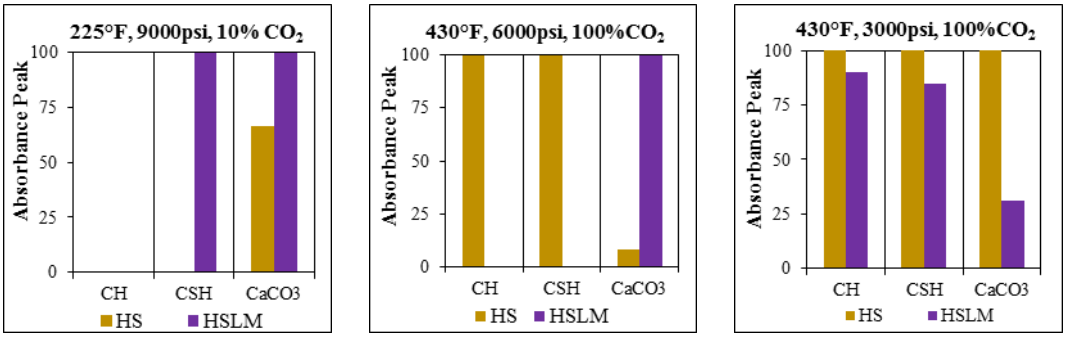

(a) (b) (c)

Figure B.41: FTIR results of inner zones of LTMS and baseline HS samples aged at different conditions: a) Exp. 24; b) Exp. 27; and c) Exp. 28

Middle Zone

FTIR results of the middle zones of LTMS and baseline cores are displayed in **Fig. B.42**. The baseline cores preserved CH and CSH components after aging at 430°F while LTMS was unable to protect these components. However, at 225°F, LTMS cores were able to preserve the CSH component in the inner zone. This suggests that although LTMS samples performed better at lower temperature (225°F), they did not resist acid attack at high temperature (430°F) because increased temperature enhances CO_2 dissolution and carbonation of CH and CSH.

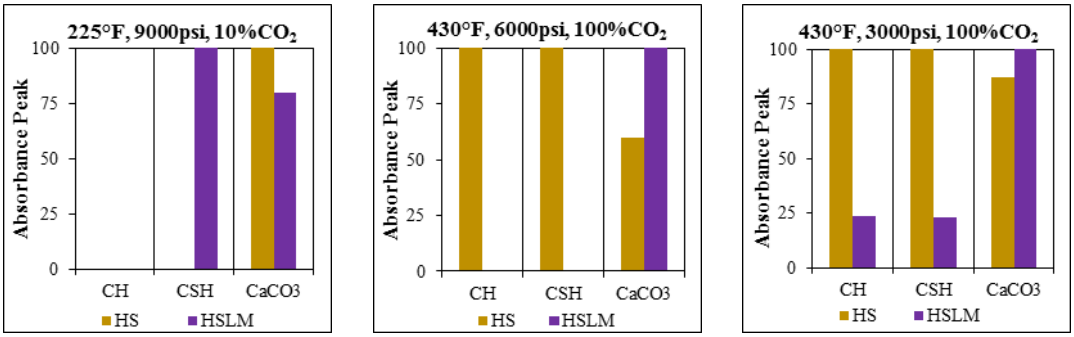

(a) (b) (c)

Figure B.42: FTIR results (middle zone) of LTMS and baseline HS samples aged at different conditions: a) Exp. 24; b) Exp. 27; and c) Exp. 28

Outer Zone

FTIR results of the outer zones of LTMS and baseline cores are shown in **Fig. B.43**. Since this zone is the most exposed part of the cores, severe degradation is expected. In two aging experiments (Experiments

24 and 28), the binding components (CH and CSH) were completely consumed by the carbonation process. However, in Experiments 27, the baseline samples preserved their CH and CSH components at 6000 psi, 430°F and 100% CO_2 while LTMS completely lost these components. This indicates poor performance of the additive as compared to the baseline samples.

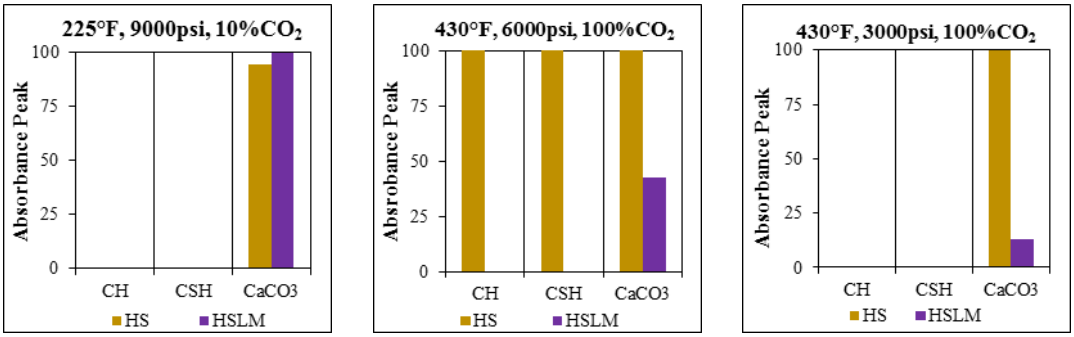

Figure B.43: FTIR results (outer zone) of LTMS and baseline HS samples aged at different conditions: a) Exp. 24; b) Exp. 27; and c) Exp. 28

B1.5.3.5 Summary

Similar to the baseline cement, the LTMS cores showed substantial increase in the permeability and porosity after aging. For all the tests, the increase in permeability of LTMS cores was more than 72%, which shows major degradation in the matrix properties. The compressive strength of the additive cores indicated similar performance as the baseline cores or indicated greater degree of carbonation. Although the FTIR results reveal presence of CH and CSH components in the inner most zone for HSLM cores, results from other zone show contradictory findings. In general, there is no noticeable difference between the performance of LTMS and baseline cement under HPHT acidic environment. The LTMS cores did not show better acid resistant than the baseline cores.

B1.5.4 Magnesium Oxide Cement

Magnesium oxide is one of the additives selected for final screening study. To test their performance, MGO-5 and baseline samples were aged under six different conditions presented in **Table B.18**. Aged and unaged sample properties (porosity, permeability, compressive and shear bond strengths and FTIR mineralogy) were obtained.

Table B.18: Aging conditions for MGO samples

Experiment No.	MGO Batch	Temp. (°F)	Pressure (psi)	CO_2 Conc. (%)	Baseline Batch
8	Batch 002	225	6000	100	Batch 010
10	Batch 003	100	6000	100	Batch 012
7A	Batch 004	225	6000	40	Batch 015
14	Batch 005	350	9000	40	Batch 017
20	Batch 006	225	9000	40	Batch 023
22	Batch 007	225	9000	100	Batch 055

B1.5.4.1 Porosity and Permeability

Figure B.44 depicts aged and unaged MGO-5 and baseline sample porosities for Class H based cements. All baseline samples showed substantial reduction in the porosity, which is attributed to carbonation. However, MGO-5 samples showed limited reduction in porosity resulting from expansion of the matrix (through formation of $Mg(OH)_2$) and partial carbonation that occurred simultaneously. The formation of $Mg(OH)_2$ crystals is beneficial because it can reduce the pore space and penetration of the acid into the matrix thereby limiting the carbonation process.

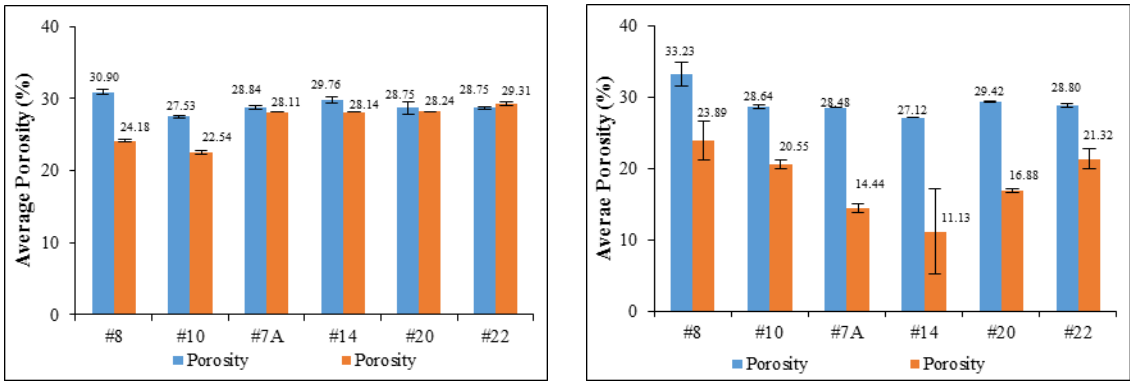

(a) **(b)**

Figure B.44: Porosity of aged (orange) and unaged (blue) samples: a) HSMG; and b) HS

Consistent with the porosity data, permeability of Class H based MGO-5 and baseline cements showed substantial reduction (**Fig. B.45**). However, permeability alone cannot be used to compare the performance of the MGO-5 samples, as it tends to be highly sensitive to experimental errors and development of micro-cracks resulting from abrupt change in test parameters such as pressure and temperature. It is important to note that porosity and permeability reductions of MGO-5 samples were less than those of the baseline samples. The $Mg(OH)_2$ crystallization in the MGO-5 samples led to blocking of the pore space; and hence, further decrease in porosity due to carbonation was limited. Examining the change in porosity and permeability of HSMG samples, it can be concluded that addition of magnesium oxide helps in reducing the penetration of carbonic acid.

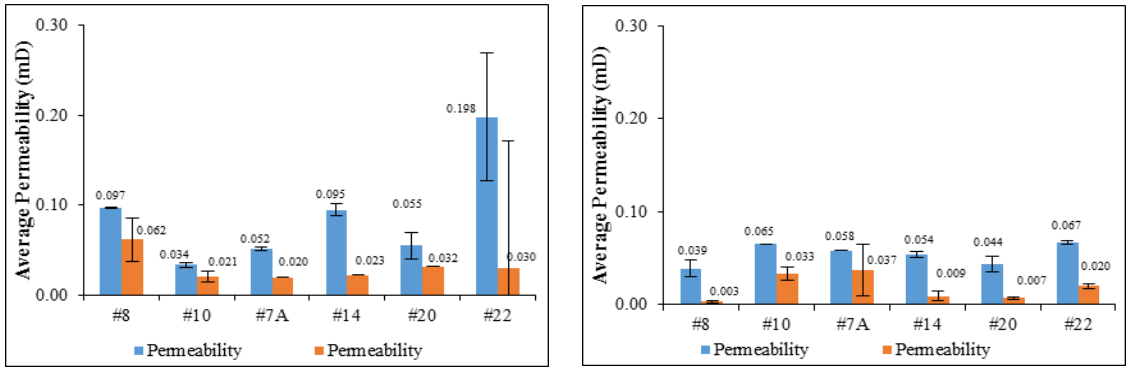

(a) **(b)**

Figure B.45: Permeability of aged (orange) and unaged (blue) samples: a) HSMG; and b) HS

The Class G based MGO-5 samples did not show a consistent decrease in the porosity or permeability (**Figs. B.46** and **B.47**). Even though baseline samples displayed consistent decrease in porosity resulting from carbonation, measurements from GSMG samples were mixed. In addition, some of MGO-5 samples (Experiments 8 and 14) permeability measurements demonstrated excessive increase, which indicates poor performance. Such increase in permeability is attributed to severe leaching or development of micro cracks. There is inconsistency in the performance of Class G based MGO-5.

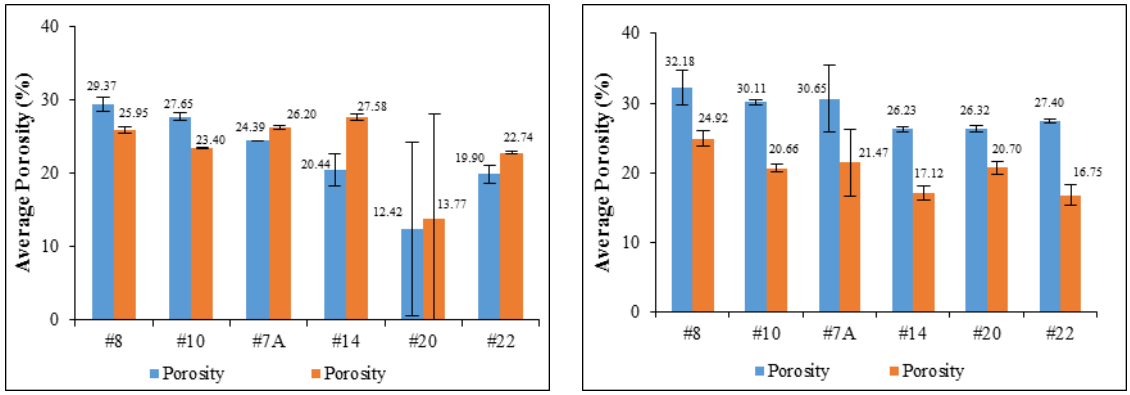

(a) **(b)**

Figure B.46: Porosity of aged (orange) and unaged (blue) samples: a) GSMG; and b) GS

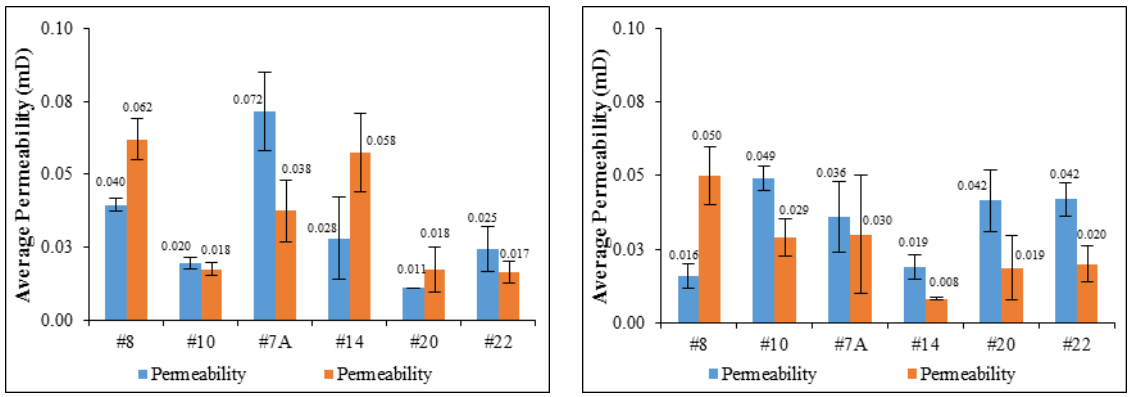

(a) **(b)**

Figure B.47: Permeability of aged (orange) and unaged (blue) samples: a) GSMG; and b) GS

B1.5.4.2 Compressive Strength

The compressive strength for all baseline samples increased after aging due to carbonation of the matrix (**Fig. B.48**). The improvement in strength is due to deposition of carbonate crystals in the pore space reinforcing the structure. The MGO-5 samples demonstrated a similar increase in the strength, which may be attributed to matrix expansion and carbonation. Results of Experiment 10 show minimal change in compressive strength of the baseline and MGO-5 samples. This could be due to aging at low temperature and high CO_2 concentration (100°F, 6000 psi and 100% CO2) condition, which accelerates

the dissolution and leaching of CH and CSH from the matrix (Nakarai et al. 2006). The strength gained by the carbonation can be offset by the leaching of the CH and CSH in the presence of excess carbonic acid.

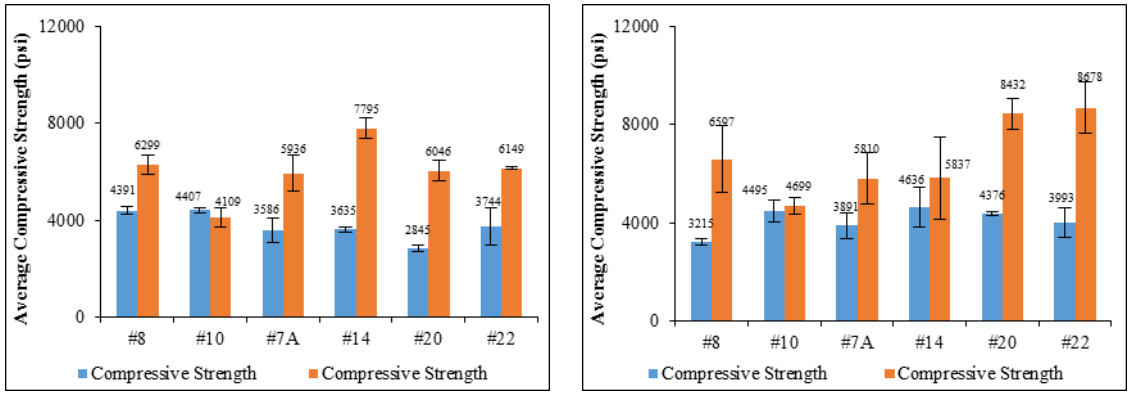

Figure B.48: Compressive strength of aged (orange) and unaged (blue) samples: a) HSMG; and b) HS

The compressive strengths of MGO-5 and baseline Class G cements were predominately increased after aging (**Fig. B.49**). However, the average strength improvement for MGO-5 samples was slightly lower than that of the baseline samples. Moreover, like the porosity results, MGO-5 samples displayed inconsistent increase and decrease in their compressive strength. Baseline samples showed better consistence than the additive samples.

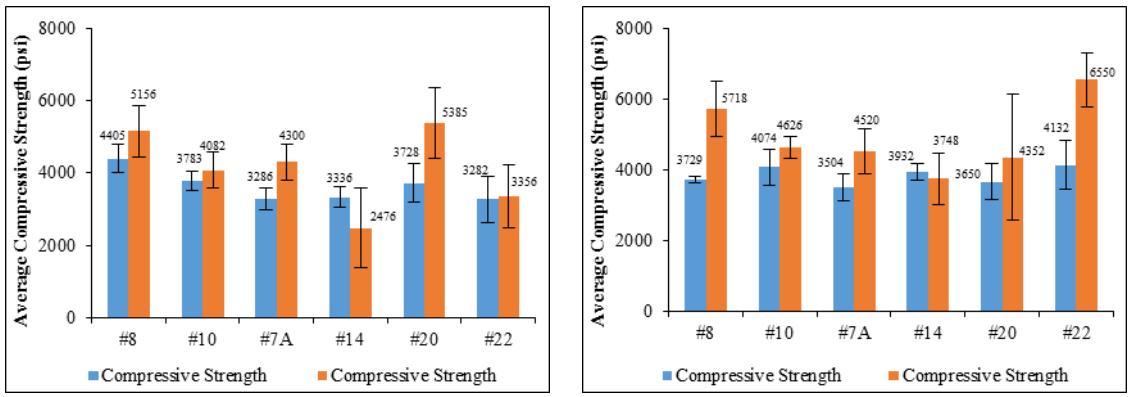

Figure B.49: Compressive strength of aged (orange) and unaged (blue) samples: a) GSMG; and b) GS

B1.5.4.3 Shear Bond Strength

As the cement matrix expands, the shear bond strength is expected to increase. The MGO-5 and baseline samples showed steady increase in the shear bond strength (**Fig. B.50**). Baseline samples expand due to carbonation. The expansion of MgO takes place due to hydration occurring inside the matrix, while carbonation caused by acid attack is happening as the same time. However, it is difficult to measure the extent of hydration of MgO and carbonation of CH and CSH in the matrix to quantify the level expansion. Results of Experiment 10 indicate the lowest increment in the shear bond strength in

both the samples due to leaching of CH component as a result of low temperature combined with high CO_2 concentration (100°F, 6000 psi, 100% CO_2).

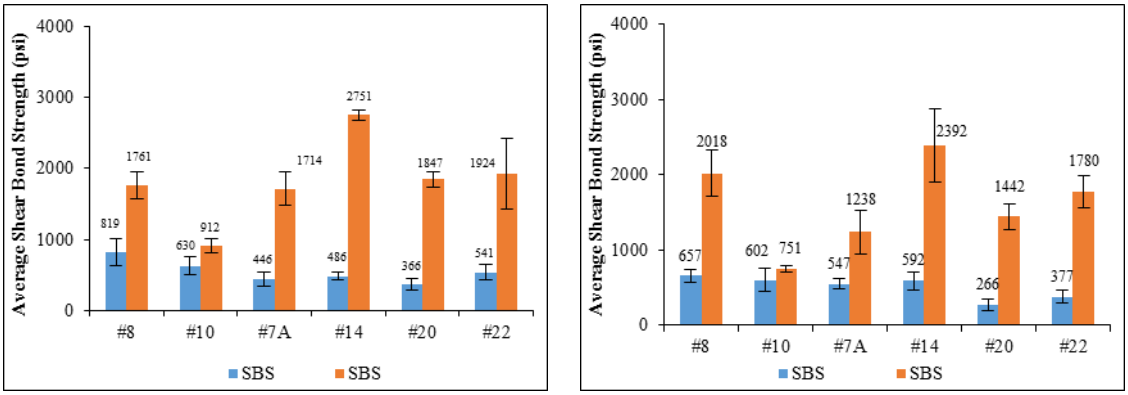

Figure B.50: Average shear bond strength of aged and unaged samples: a) HSMG; and b) HS

B1.5.4.4 FTIR Analysis

FTIR results of Class H based MGO-5 and baseline samples are presented in this section. The minerals under focus for the FTIR analysis are CH, CSH, $CaCO_3$ (denoted by CCO3) and $Mg(OH)_2$ (denoted by MH). MgO and $MgCO_3$ can also be identified at wave lengths of 500 cm^{-1} and 880/1480 cm^{-1}, respectively. However, the noise in the FTIR spectrum is in the order of hundreds (0 – 500 1/cm); hence, very low measurements like that of MgO may not provide reliable information.

Inner Zone

The results of the inner zone (**Fig. B.51**) indicate the presence of CH and CSH components along with $Mg(OH)_2$ in the matrix. All experiments except the one conducted at 350°F (Experiment 14), demonstrated the presence of CH and/or CSH. The presence of $Mg(OH)_2$ in the cement demonstrate the reduction of carbonic acid penetration. $Mg(OH)_2$ crystals also undergo carbonation forming $MgCO_3$, which is insoluble compound that precipitates in the matrix. Unlike $CaCO_3$, $MgCO_3$ does not react with carbonic acid to form a soluble product (Cheremisinoff, 1995) that can be leached out by the surrounding fluid. Hence, carbonation of $Mg(OH)_2$ to $MgCO_3$ is beneficial in limiting acid attack.

The $CaCO_3$ bars in the FTIR spectrum shown in the charts include both $MgCO_3$ and $CaCO_3$. Hence, it can be misleading to assess the performance of MGO-5 by comparing $CaCO_3$ peaks alone; other peaks can be used to evaluate its performance. According to the results, the performance of MGO-5 in Class H cement seems to be effective to a certain extent. MGO-5 cement expected to resist acid attack by generating $Mg(OH)_2$ crystals during carbonation. The formation the crystals in the pore space reduces porosity and permeability of the cement and limits the penetration of the acid.

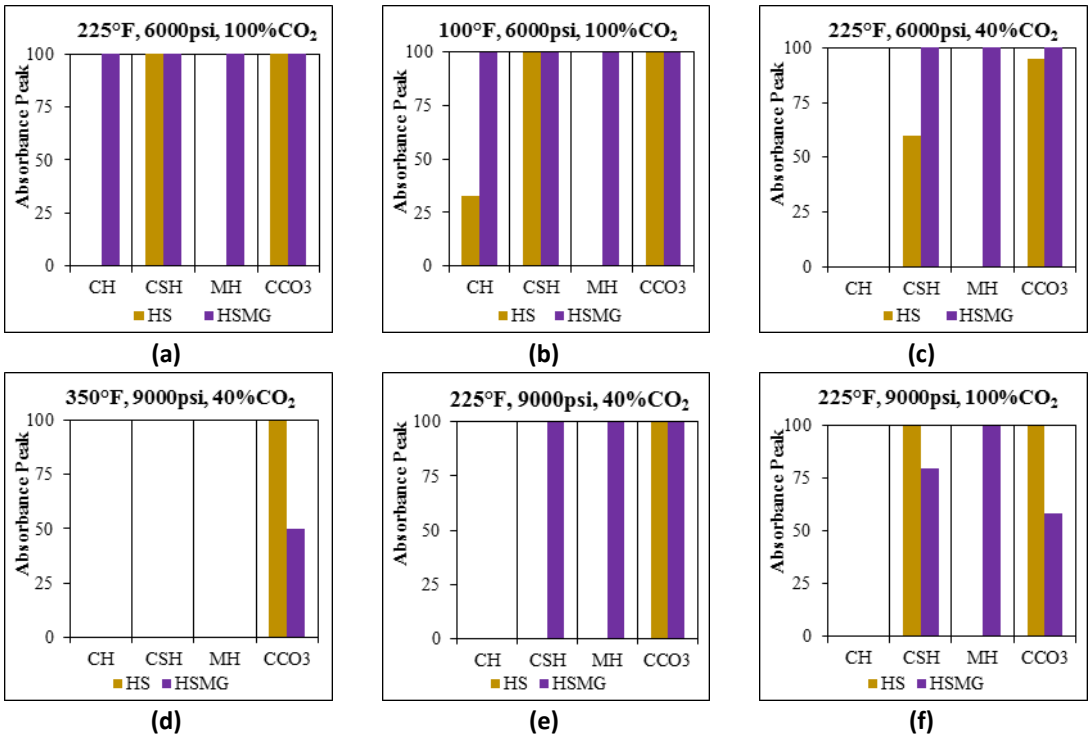

Figure B.51: FTIR results of inner zone of MGO-5 and baseline HS samples aged at different conditions: a) Exp. 8; b) Exp. 10; c) Exp. 7A; d) Exp. 14; e) Exp. 20; and f) Exp. 22

Middle Zone

The middle zone is expected to show more carbonation that the inner zone (**Fig. B.52**). The CH and CSH were only preserved when aged at 100°F and 100% CO_2 (Exp. 10). Results are consistent with the inner zone measurements. $Mg(OH)_2$ was preserved in 3 experiments. The CSH, which was preserved in the inner zone during Experiment 8 and 22 was completely carbonated in the middle zone.

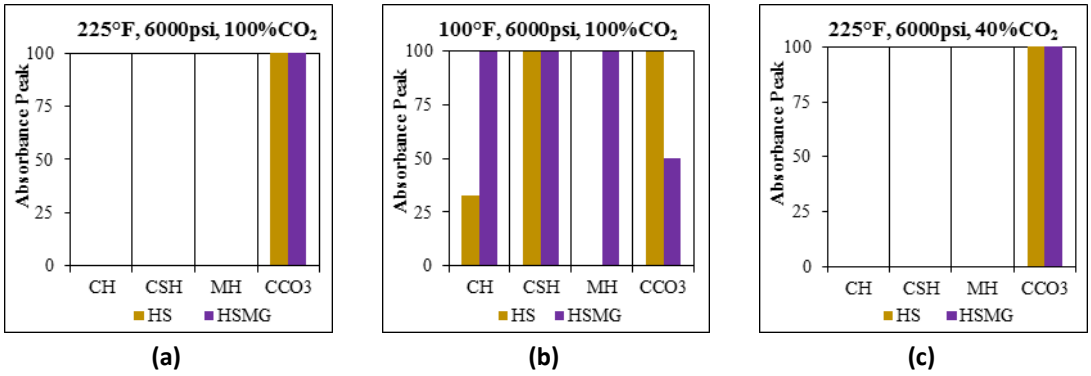

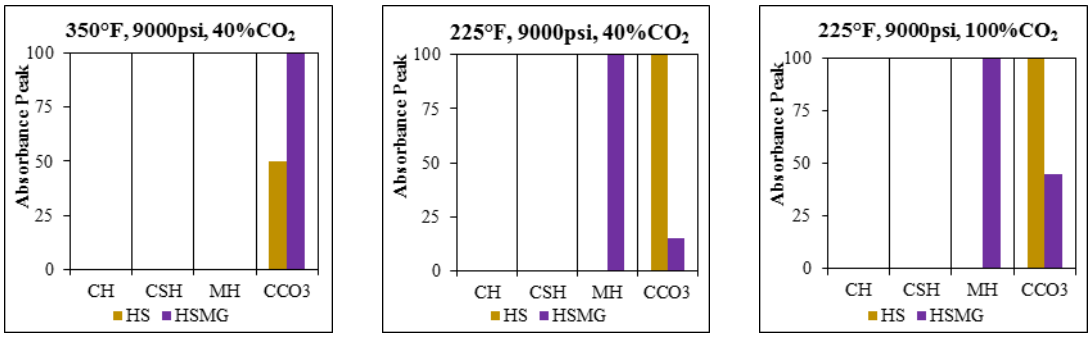

(d) (e) (f)

Figure B.52: FTIR results of middle zone of MgO and baseline HS samples aged at different conditions: a) Exp. 8; b) Exp. 10; c) Exp. 7A; d) Exp. 14; e) Exp. 20; and f) Exp. 22

Outermost Zone

The outermost zone is the most degraded zone due to direct exposure. Only $CaCO_3$ was found to be present in all the samples. It should be noted that the $CaCO_3$ peaks also comprise $MgCO_3$ content (**Fig. B.53**).

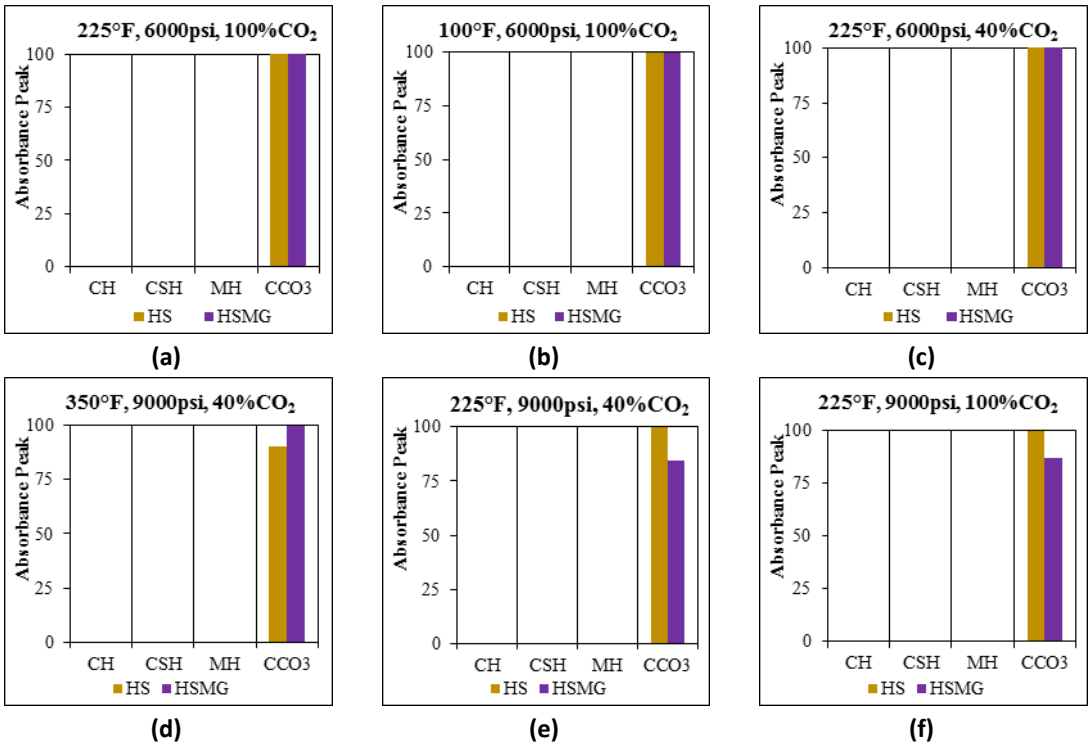

(a) (b) (c)

(d) (e) (f)

Figure B.53: FTIR results of outer zone of MgO and baseline HS samples aged at different conditions: a) Exp. 8; b) Exp. 10; c) Exp. 7A; d) Exp. 14; e) Exp. 20; and f) Exp. 22

B1.5.4.5 Summary

Examining the results of six experiments, it can be concluded that MGO-5 was able to act as an expanding agent in the cement. The formation of $Mg(OH)_2$ leads to expansion of matrix, which is highly dependent on temperature. Although the $Mg(OH)_2$ crystals were able to reduce porosity, they were susceptible to carbonation to form $MgCO_3$. The advantage of the formation of $MgCO_3$ over $CaCO_3$ is

that, it does not form soluble product that can be easily leached out when it reacts with the acid. The presence of CH and CSH component in the inner zone confirm a protected MGO-5 matrix, even though the middle and outer zone indicate a leached zone.

B1.5.5 Calcium Hydroxyapatite Cement

The hydroxyapatite containing cement (HOAP) is one of the new formulation that showed promising results in the initial screening study. To investigate the performance of this formulation, HOAP and baseline samples were prepared and aged under different conditions (**Table B.19**). During aging, samples were immersed for 14 days in 2% brine saturated with CO_2 and H_2S containing methane gas.

Table B.19: Aging conditions for HOAP samples

Experiment No.	HOAP Batch	Temp. (°F)	Pressure (psi)	CO_2 Conc. (%)	Baseline Batch
9	Batch 002	100	6000	40	011
12	Batch 003	350	6000	100	014
13	Batch 004	350	3000	40	016
15	Batch 005	350	3000	100	018
19	Batch 006	225	3000	40	022
23	Batch 007	225	3000	10	026
29	Batch 008	430	9000	100	032

The matrix properties (porosity, permeability, compressive strength and shear bond strength, FTIR analysis) of aged and unaged samples were measured to quantify the level of degradation occurring during aging and compare the performance of HOAP with the baseline cement.

B1.5.5.1 Porosity and Permeability

Figure B.54 presents porosity for Class H based HOAP and baseline samples. In all the experiments, porosity of baseline decreased after aging due to carbonation. On the other hand, only three of HOAP samples (Experiments 12, 23 and 29) showed porosity reduction after aging. The reduction occurred in these samples could be due to partial carbonation of the matrix; and hence, the results from compressive strength, shear bond strength and FTIR measurements need to be analyzed to better understand the impacts of different test parameters. For Experiment 23, the reduction for HOAP samples was 29%, which considerably less than that of the baseline samples (60%). Measurements from Experiments 12 and 29 showed substantial decrease in porosity of the samples when aged at 350 and 430°F, respectively. The high temperature enhances ionic diffusion through the cement, resulting in rapid acid penetration and carbonation. Moreover, above 350°F, increasing temperature tends to increase CO_2 solubility, which facilitates the carbonation process.

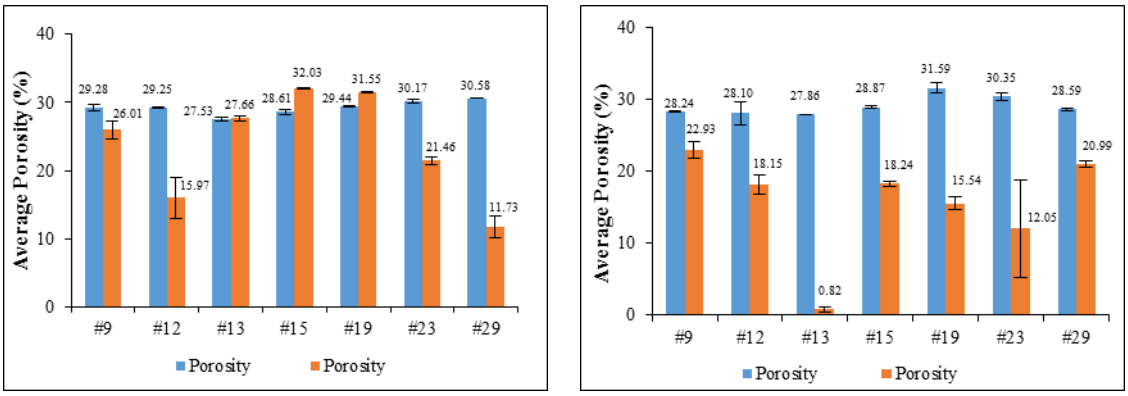

(a) **(b)**

Figure B.54: Porosity of aged (orange) and unaged (blue) samples: a) HHO; and b) HS

One of the baseline samples (Experiment #13), displayed very low porosity after aging (0.82%). This reduction is not realistic with respect to carbonation process. The possible reason for this reduction could be deposition of salt on the outer surface of the slurry resulting in blocking of pores on the outer zone.

Most of the HOAP samples showed slight change in porosity after aging, which suggests minimal carbonation and preservation of CH and CSH components of the cement. In addition, permeabilities of HOAP and baseline samples indicate different trends (**Fig. B.55**). The scale of the permeability chart has been modified to logarithmic for better visualization. The drastic reduction in permeability of baseline samples demonstrated severe carbonation resulting in blocking of the pore throats. On the other hand, HOAP samples remain predominately immune against carbonation. Permeability reductions observed in Experiments 12 and 19 were less significant than that of the baseline samples.

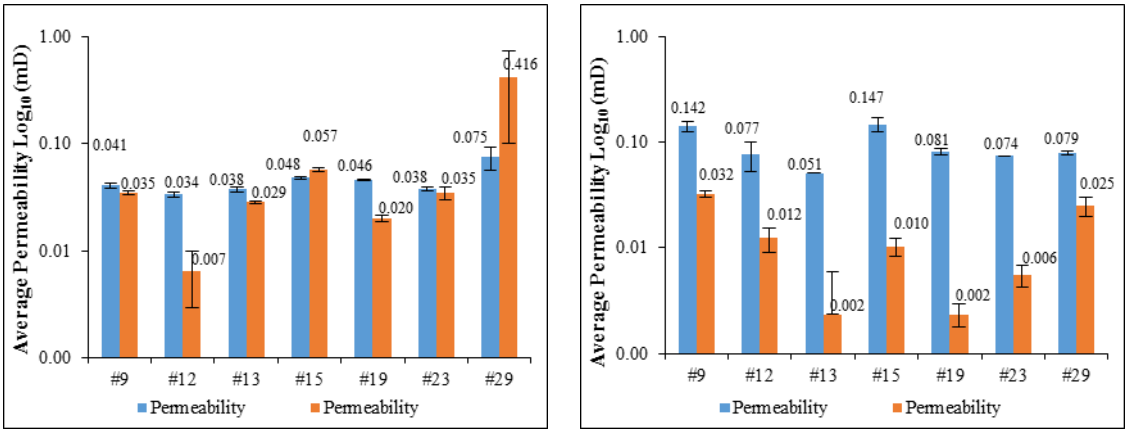

(a) **(b)**

Figure B.55: Permeability of aged (orange) and unaged (blue) samples: a) HHO; and b) HS

Substantial permeability increase was observed in Experiment 29 that can be attributed to high temperature (430°F), which causes rapid ionic diffusion in the cement leading to harsh leaching

condition. However, this abnormal increase is contradictory to the reduction in porosity observed. It needs to be verified for its consistency with compressive strength and FTIR results.

Class G based HOAP (GHO) and baseline samples demonstrated (**Fig. B.56**) reduction in porosity after aging, except for tests (Experiments 15 and 19). The porosity increases in Experiments 15 and 19 can be due to combine effects increased temperature (350°F) and CO_2 concentration (100% CO_2) leading to heavy leaching rather than carbonation. The baseline samples on the other hand demonstrated a consistent porosity decline due to carbonation.

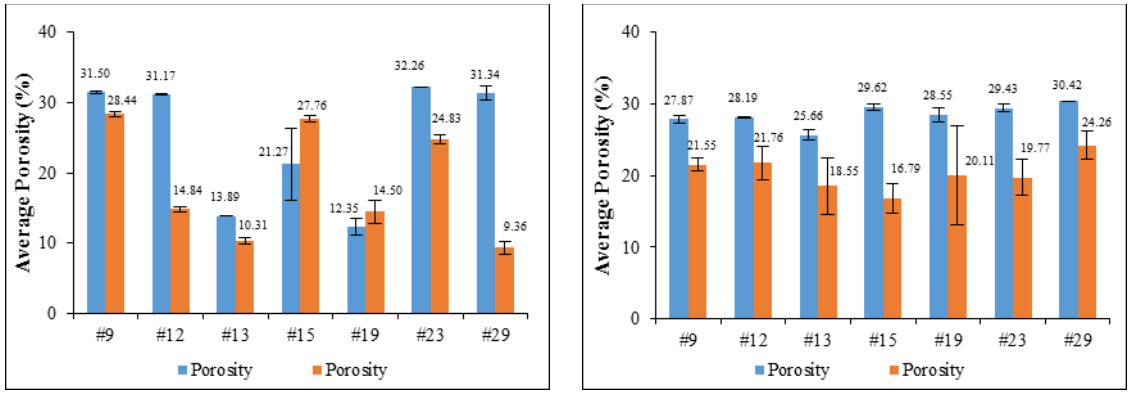

(a) **(b)**

Figure B.56: Porosity of aged (orange) and unaged (blue) samples: a) GHO; and b) GS

Permeability of Class G baseline samples predominantly decreased after aging (**Fig. B.57**). Some samples showed minor increase in permeability, which is in the order of the margin of error. However, the corresponding HOAP sample displayed mixed results. In general, the performance of Class G based HOAP cement is as good as the baseline cement. In Experiments 29, porosity of GHO samples diminished significantly while permeability increased dramatically. Similar inconsistency between permeability and porosity measurements were observed in HHO samples. Possible reason for the inconsistency could be carbonation of the matrix at high temperature (430°F), when HOAP fail to act as an additive against acid attack.

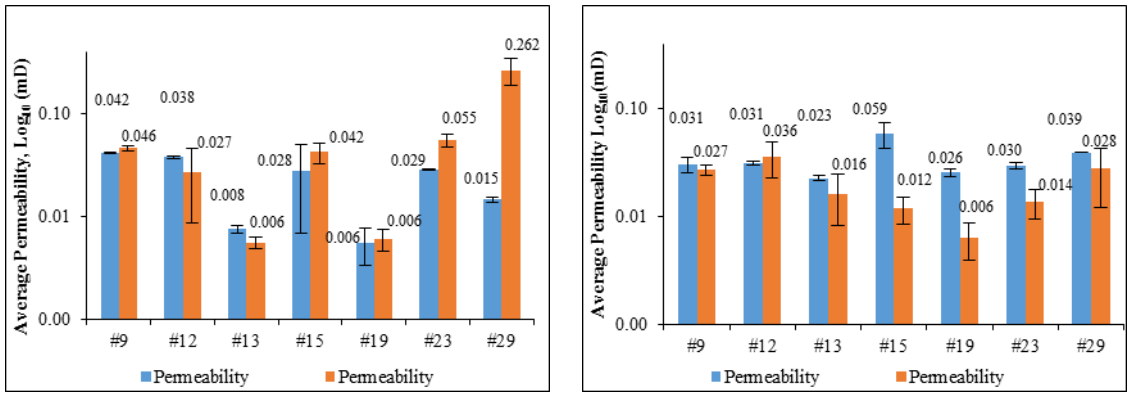

(a) **(b)**

Figure B.57: Permeability of aged (orange) and unaged (blue) samples: a) GHO; and b) GS

B1.5.5.2 Compressive Strength

HOAP samples displayed consistent decrease in compressive strength after aging (**Figs. B.58** and **B.59**). In spite of this, the baseline samples showed a prominent increase except in some cases (Experiments 9, 13 and 15). The increase is attributed to carbonation of the cement binding components to form $CaCO_3$. Interestingly, the moderate reduction in the strength of HOAP could be due to carbonation of calcium hydroxyapatite. Carbonated hydroxyapatite has inferior compressive strength than uncarbonated hydroxyapatite (Sugama and Carciello 1992 and 1993; Martin and Brown 1995). This also indicates that HOAP was able to act as a reactive additive (Category 1 as shown in Section B1.1) against carbonic acid attack. For Experiment 29, conducted at 430°F, there is a substantial decrease in the strength which suggests thermal retrogression of the samples at higher temperature. Although the decrease in the strength is a major concern in using the HOAP for high temperature applications (above 430°F), the strength obtained after the aging was still above the accepted industry standards (500 psi).

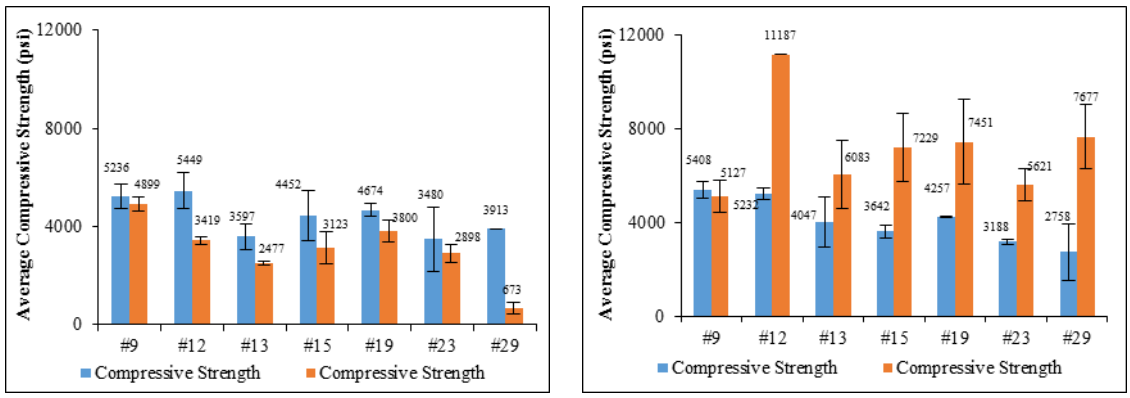

Figure B.58: Average compressive strength of aged and unaged samples: a) HHO; and b) HS

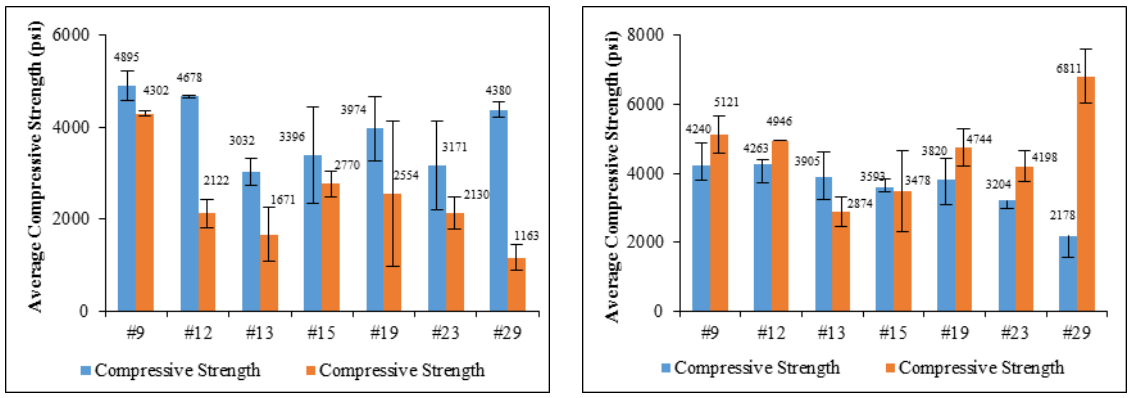

Figure B.59: Compressive strength of aged (orange) and unaged (blue) samples: a) GHO; and b) GS

B1.5.5.3 Shear Bond Strength

The shear bond strength (SBS) of HOAP samples mostly remained the same after aging (**Fig. B.60**). This implies that HOAP cement is not susceptible towards carbonation and expansion. Samples in Experiment

9 conducted at 100°F, showed the largest increase in the SBS. This can be due to increased solubility of CO_2 at low temperature causing carbonation of hydroxyapatite, which may lead to expansion and increase in the SBS. Consistent with compressive strength data, results of Experiment 29 conducted at 430°F indicated extreme reduction in the shear bond strength. This is attributed to thermal retrogression that makes the hydroxyapatite cement very weak.

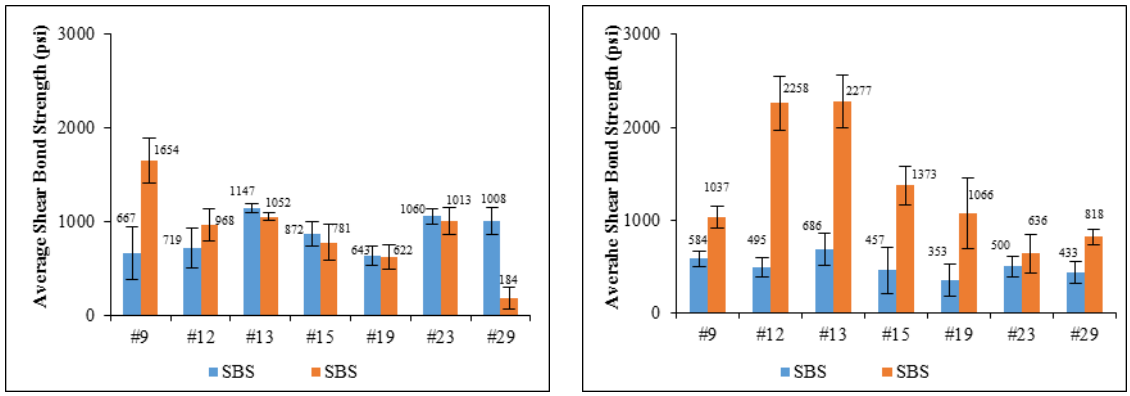

(a) (b)

Figure B.60: Shear bond strength of aged (orange) and unaged (blue) samples: a) HHO; and b) HS

B1.5.5.4 FTIR Analysis

The minerals under focus for the FTIR analysis are CH, CSH and $CaCO_3$. The carbonated form of HOAP also shares similar wavelength as $CaCO_3$ and hence is not distinguishable in the spectrum. The CO_3^{-2} bond peak shows the presence of $CaCO_3$ carbonated calcium hydroxyapatite the samples.

Inner Zone

FTIR mineralogy results of inner zones of HOAP and baseline cores are displayed in **Fig. B.61**. Except for Experiment 9, which was conducted at 100°F, CH was not preserved in all the baseline samples. However, CH and CSH were preserved in HOAP samples noticeably indicating the performance of hydroxyapatite. CSH component of the matrix varied for each experiment. In some experiments the baseline samples preserved higher level of CSH in the inner most zone. The HOAP samples showed varying amount of CSH. HOAP may have been able to intercalate CSH in the matrix distorting the structure. Interestingly the CH and CSH components in Experiment 29 (430°F) are more in HOAP samples, indicating a preserved state even after thermal retrogression which resulted in high-permeability and low compressive and bond strengths.

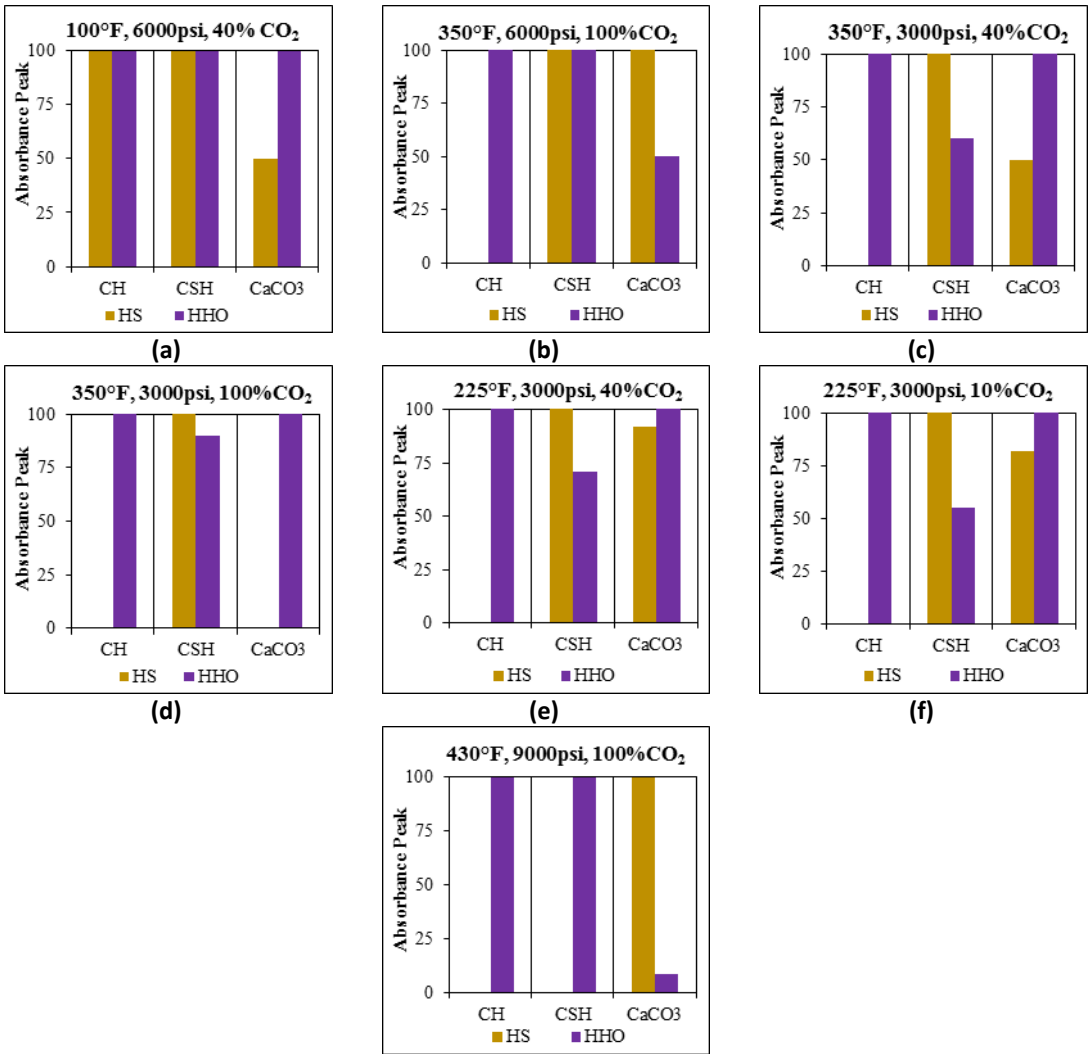

Figure B.61: FTIR results in inner zone of HOAP and baseline HS samples aged at different conditions: a) Exp. 9; b) Exp. 12; c) Exp. 13; d) Exp. 15; e) Exp. 19; f) Exp. 23; and g) Exp. 29

Middle Zone

The FTIR results obtained from the middle zones of HOAP and baseline samples are presented in **Fig. B.62**. Being exposed to the harsh condition more than the inner zone, the middle zone is expected to show a reduced presence of CH and CSH. The HOAP samples were able to prevent degradation of CH while it was completely carbonated from baseline samples. In addition, HOAP samples mostly preserved CSH, although the amount varying from experiment to experiment. Experiment 13 is the only test that CSH was completely carbonated form HOAP samples. The CSH was completely carbonated in the baseline samples during Experiment 12, 13 and 15.

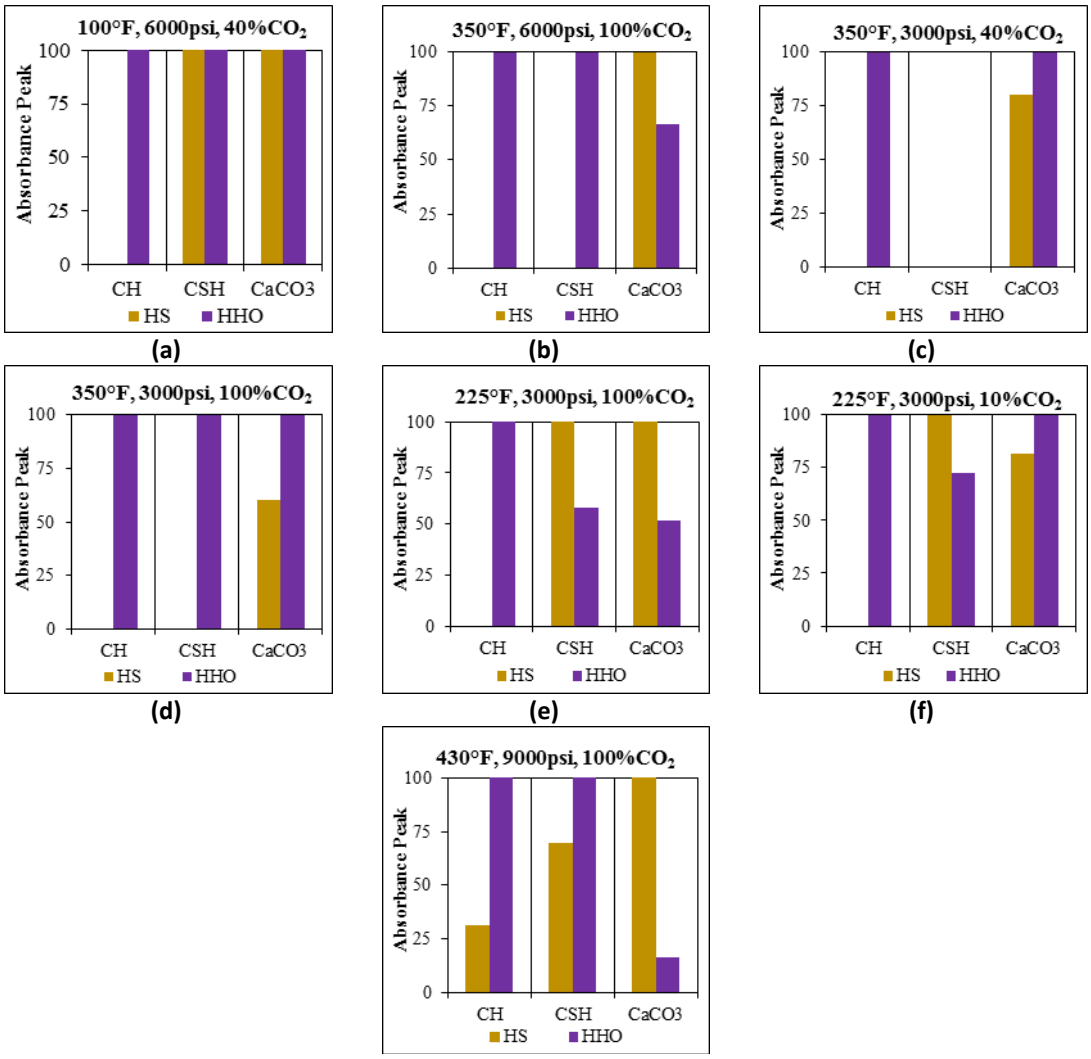

Figure B.62: FTIR results (middle zone) of HOAP and baseline HS samples aged at different conditions: a) Exp. 9; b) Exp. 12; c) Exp. 13; d) Exp. 15; e) Exp. 19; f) Exp. 23; and g) Exp. 29

Outer Zone

The outer layer is highly exposed to the acid attack. Therefore, it is expected to have maximum amount of $CaCO_3$ and minimum levels of CH and CSH content. The FTIR results obtained from the outer zones of HOAP and baseline samples are presented in **Fig. B.63**. In most cases, the CH and CSH components were completely consumed. The baseline samples mostly display strong $CaCO_3$ peaks and limited peaks of CH (one case) and CSH (two cases) implying strong acid attack and carbonation. The HOAP samples showed slightly better performance than baseline samples. They showed one peak of CH and three peaks of CSH. The HOAP sample also preserved the essential component (CSH) in their outer most zone even under extreme condition (430°F, 9000 psi and 100% CO_2), which resulted in dramatic permeability increase (Experiment 29).

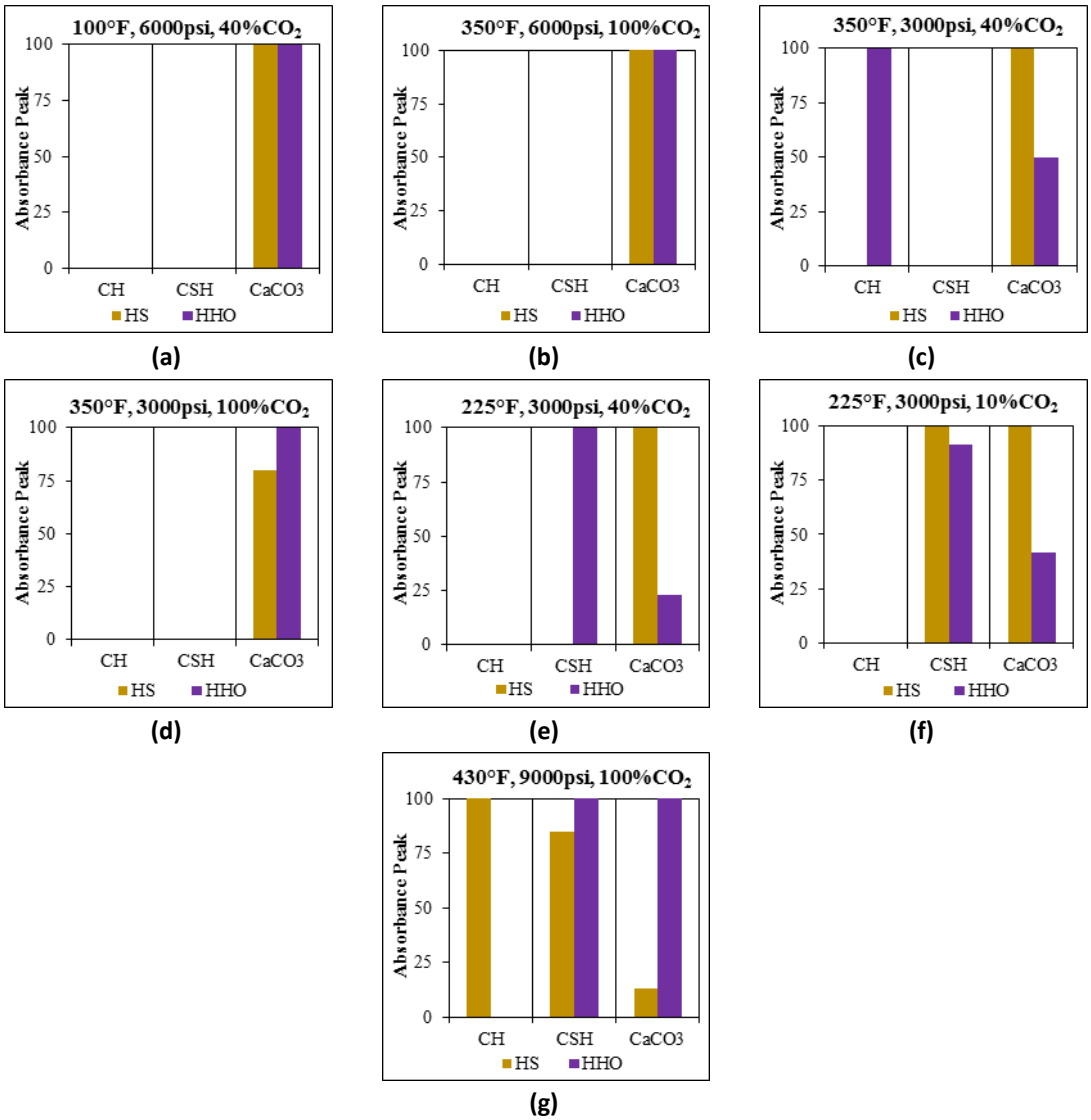

Figure B.63: FTIR results (outer zone) of HOAP and baseline HS samples aged at different conditions: a) Exp. 9; b) Exp. 12; c) Exp. 13; d) Exp. 15; e) Exp. 19; f) Exp. 23; and g) Exp. 29

B1.5.5.5 Summary

Consistent porosity, permeability and shear bond strength of HOAP samples after aging, along with a slight reduction in the compressive strength due to limited carbonation indicate the protection of the main binding components of the cement (CH and CSH) from carbonic acid attack. In addition, the FTIR mineralogy results evidently demonstrated the presence of CSH and CH in the matrix of HOAP samples while they were completely carbonated in baseline samples. This proves that HOAP is able to react with CO_2 and protect the matrix from carbonation. However, at higher temperature (430°F), the samples exhibited severe thermal retrogression in the strength.

B1.5.6 Cement with Fly Ash

Fly ash is commonly used additive in cementing application. It provides both economic and technical benefits. Class H fly ash was used in this investigation. The slurry properties and formulations are

presented in Section B1.2.2.7. This was the first additive tested during the investigation. Experiments were performed varying aging duration, brine concentration and pressure. Test parameters for aging experiments of fly ash cement are summarized in **Table B.20**. Six batch of fly ash samples were prepared and tested in brine (NaCl) saturated with 10% CO_2 containing method gas. Experiments were also conducted using 100% methane.

Table B.20; Test parameters for aging experiments

Batch #	Temp. (°F)	Pressure (psi)	Partial Pressure %			Brine Conc. (%)	Aging Period (days)	Experiment #
			CH_4	CO_2	H_2S			
001	350	9000	100	0	0	9	6	1
002	350	6000	100	0	0	2	14 & 28	2
003	350	6000	100	0	0	2	14	
004	350	6000	90	10	0	2	6	3
005	350	6000	90	10	0	2	14 & 28	4
006	350	6000	90	10	0	2	14	

B1.5.6.1 Porosity and Permeability

Figure B.64 shows porosity and permeability of the samples before and after aging (2 and 4 weeks). The trends for baseline (HS and GS) samples are similar. Both porosity and permeability for these samples showed consistent trend. At the beginning, they displayed reduction, and then the trend reversed. Fly ash cement sample (HSF and GSF) displayed a different trend. Porosity and permeability trends did not have consistent trend. However, the variation in porosity was minimal. After aging for two weeks their permeability decreased, and then it increased when the samples were aged for additional 2 weeks. In both GSF and HSF samples, porosity slightly reduced when the samples were aged for additional 2 weeks. The reason for this inconsistency between porosity and permeability trend could be the formation of micro cracks that do not increase the pore volume but increase the permeability by creating additional path for the fluid to flow and increase the connectivity of the pores.

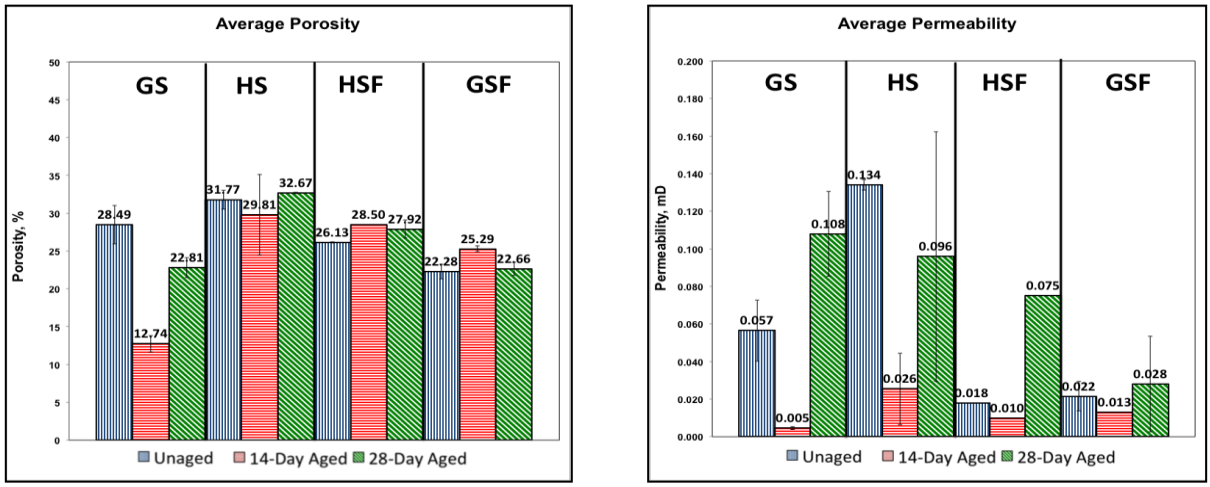

Figure B.64: Porosity and permeability of cement cores aged at 350°F (Experiment 4, Batch 005)

During the test, some of the fly ash cement cores exhibited brittleness and they were prone to cracking at low compressive loads. This resulted in unexpected failure of aged cores during the test and even during core handling. The cracking tendency can be related to internal weakening of cores due to high thermal stresses generated at high temperature (350°F).

B1.5.6.2 Compressive Strength

Figure B.65 summarizes compressive strength of samples aged in brine saturated with 10% CO_2 and 90% methane gas. Only limited numbers of cement cores containing fly ash were tested after aging since many of the samples were cracked and broken in the aging cell. Fly ash cement samples displayed considerable strength gain after aging for 2 weeks, and then reduction in strength was observed. The addition of fly ash did not limit the carbonation of the cement. The baseline samples demonstrated both improvement (Class H) and reduction (Class G) in strength with aging time. The strength reduction observed with Class G samples is mainly attributed to the leaching of cement by the carbonic acid. The compressive strength data indicated that the performance of baseline HS is better than the fly ash based cement samples. Compressive strength of HS samples was less affected by the acid attack.

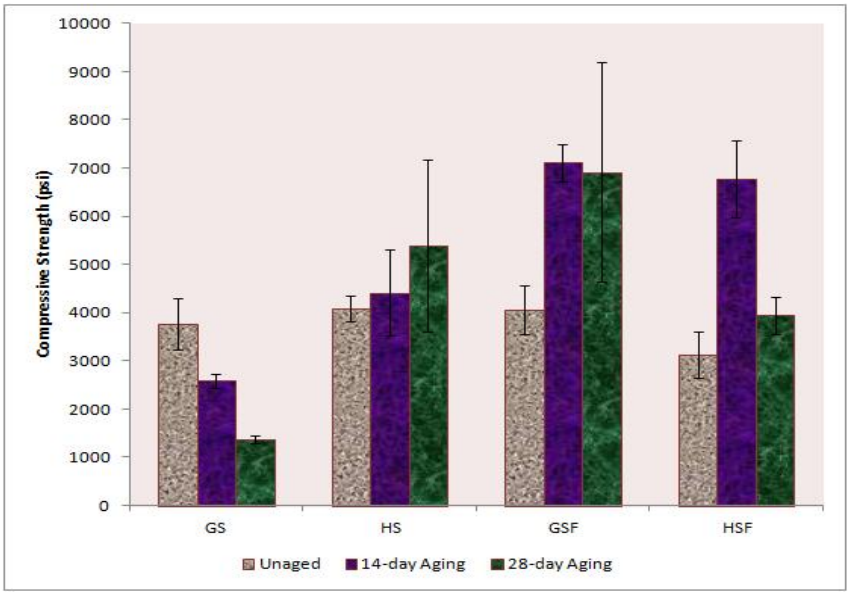

Figure B.65: Compressive strength of unaged and aged baseline and fly ash cement cores aged at 350ºF (Experiment 4, Batch 5)

B1.5.6.3 Shear Bond Strength

Shear bonding strength of unaged and aged Class H cement samples with and without fly ash were measured. Before aging, samples with fly ash showed higher shear bonding strength (**Fig. B.66**). However, after aging, the SBS of the samples with fly ash were considerably reduced due to acid attack. This behavior can be explained by low acid resistance of fly ash containing cement.

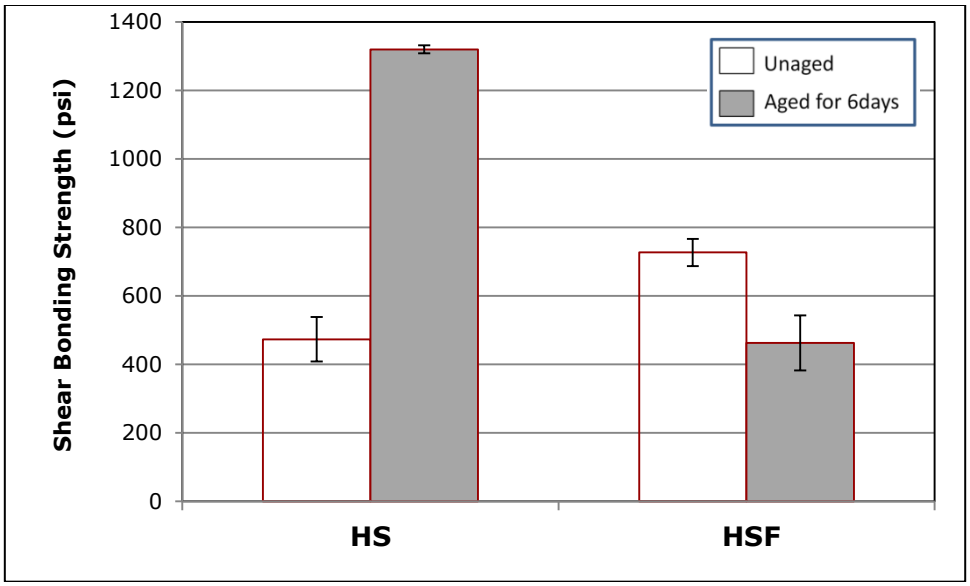

Figure B.66: Shear bond strengths of samples before and after 6 days of aging (Experiment # 3)

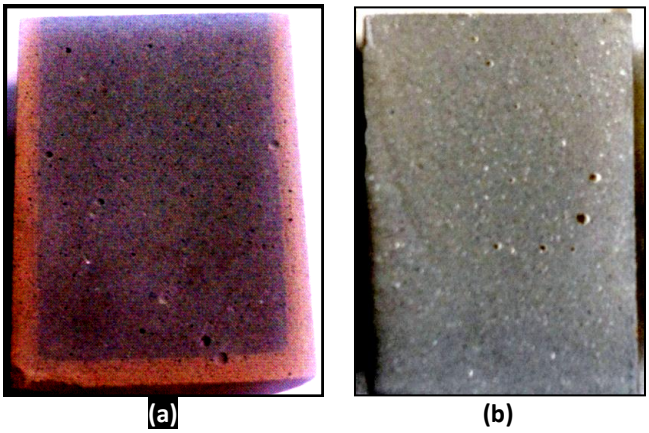

Figure B.67: Class H cement after 6 days aging (Experiments # 3): a) with fly ash; and b) without fly ash

Visual observation of the cement cores revealed that cores with fly ash were considerably attacked by carbonic acid. **Figure B.67** shows the digital pictures of Class H cement with and without fly ash after 6 days of aging. Degradation depths for Class H and G samples with fly ash were approximately 2 mm. Phenolphthalein indicator was also applied to the samples to determine the degradation depth. Since $Ca(OH)_2$ content in the degraded zone is lower than the original content, the pH in degraded zone is expected to be lower than that of un-degraded part (sound zone) of the core. With Phenolphthalein indicator, pink color indicates higher pH values (more than 8.3). Figure B.67a shows the Class H cement with fly ash after aging in brine saturated with methane gas containing 10% CO_2. Pink color at the center shows the sound zone of cement, which indicates higher pH (high alkalinity) due high concentration of calcium hydroxide. Degraded zone doesn't show a pink color because of low pH resulting from carbonation of calcium hydroxide.

When fly ash samples were aged without the presence of CO_2 in the fluid system, their SBS increased. **Figure B.68** presents shear bond strength of Class H cement with and without fly ash before and after 14 and 28 days of aging at 6000 psi of 100% CH_4 and 350°F. In this case, the aging increased the SBS of samples with fly ash. Therefore, acid attack is the key factor in reducing the shear bonding strength of fly ash containing samples (Fig. B.66).

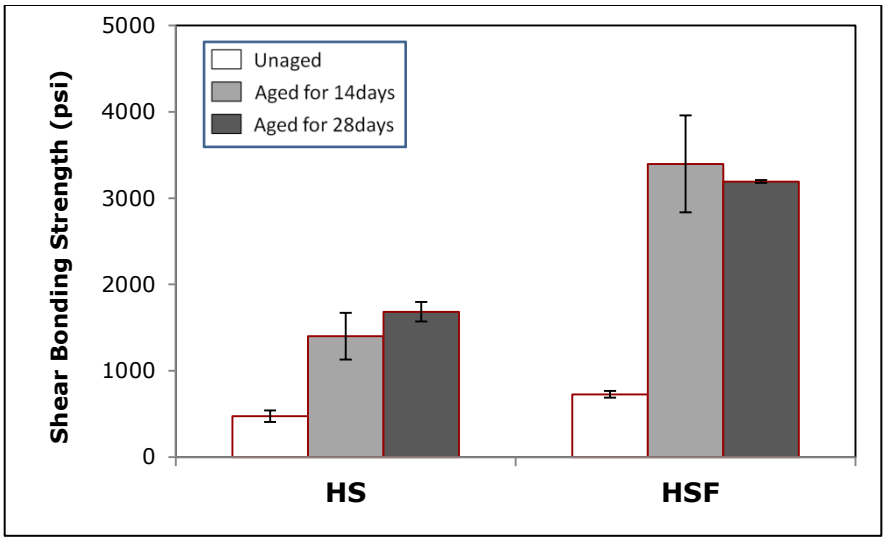

Figure B.68: Shear bond strength of unaged and aged samples (Experiment # 2)

B1.5.6.4 Summary

All the measurements (porosity, permeability, compressive strength and SBS) of fly ash cement indicate its susceptibility to carbonic acid attack. Without carbonic acid, the SBS of fly ash cement increased after aging. However, when aged in acid environment, SBS substantially decreased.

Fly ash cement because of its low CH and CSH content, it is expected to have limited carbonation. Despite this, the compressive strength of fly ash cement increased more than the baseline cement, indicating greater carbonation of the matrix. Porosity and permeability measurements exhibited inconsistency that can be explained by crack formation in the cement during aging as the temperature increases. Even some samples were cracked and disintegrated during coring and after aging. In addition, degraded depth of fly ash samples was significantly higher than the baseline cement. Therefore, fly ash cement is not suitable for cementing HPHT wells producing carbon dioxide.

B1.5.7 Conclusions

After exposure to harsh simulated downhole conditions for 14 days, the cement matrix of baseline samples mostly depicted carbonation. This was observed as increase in compressive and shear bond strength and reduction in porosity and permeability of the baseline samples. In addition, FTIR examinations confirm the conversion of CH and CSH into $CaCO_3$ in carbonated cement. Four of the additive cements (microsilica cement, latex cement, microsilica-latex cement and fly ash based cement) did not show better performance than the baseline cement. These cement formulations were not able to prevent acid penetration into their pores or carbonation of CH and CSH better than the baseline.

Class H based MGO-5 cement was able to resist acid attack under different test conditions. Leaching and carbonation of MGO-5 cement was prevented under HPHT carbonic acid environment by the addition of 5% MgO. However, Class G based MGO-5 cement displayed mixed performance; and hence, it is reliability is quite questionable.

Addition of hydroxyapatite has been very effective in controlling acid attack under HPHT carbonic acid environment. In the range of 100 to 350°F, the matrix was able to protect the CH and CSH components of the matrix, along with maintaining the porosity and permeability and shear bond strength to similar levels. At high temperature (430°F), major strength retrogression was observed. Hence, hydroxyapatite cement formulation is suitable and performs better than the baseline cement in the temperature range of 100 to 350°F.

B2. Development of Test Setups to Study Sour Gas Corrosion of Tubulars

The construction of corrosion test facility has been completed. The new setups use the existing auxiliary facilities such as heating system, gas supply and injection system, instrumentation system, and data acquisition (DAQ) system. **Figure B.69** shows the schematics of cement degradation and tubular corrosion testing facilities. The experimental setups reasonably simulate actual field conditions varying pressure, temperate, and aging/test fluid composition.

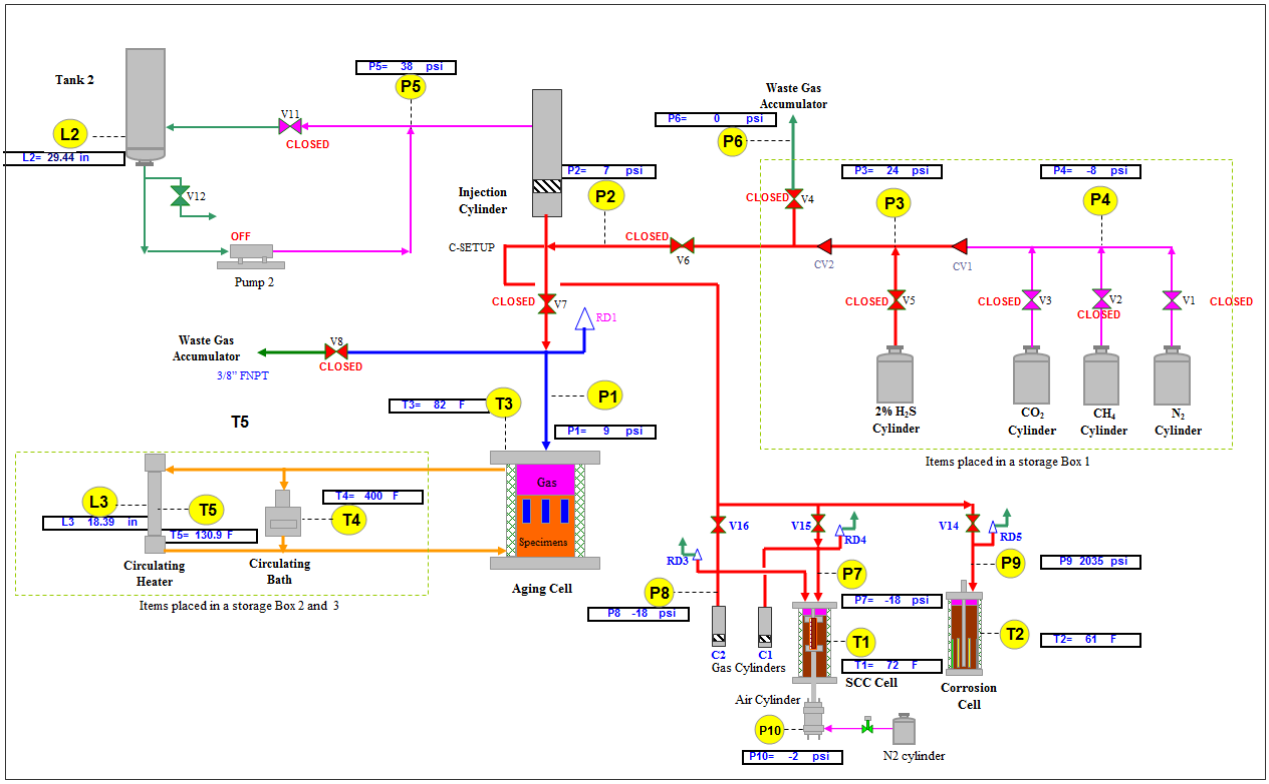

Figure B.69: Schematics of cement degradation and tubular corrosion facilities

The new test facility (**Fig. B.70**) consists of two experimental setups for studying: i) stress cracking corrosion; and ii) uniform corrosion under static and dynamic conditions. The setups (**Fig. B.71**) consist of: two corrosion test cells, two gas accumulators, a pneumatic cylinder with regulator and nitrogen supply cylinder, and magnetic drive system with air motor. Both test setups have capabilities to operate under HPHT sour gas environments. Specimens used for corrosion experiments have the same material (T95, C110 and Q125) as conventional well casings and tubulars. The setups are connected to the existing DAQ system to display and record all the experimental parameters. Critical test parameters are automatically controlled from the DAQ system.

B2.1 Stress Cracking Corrosion (SCC) Setup

Mini-pipe specimens are used for stress-cracking tests. One end (the bottom end when assembled) of the mini-pipe is plugged. During the experiment, both ends of a mini-pipe are attached to a pulling rod (7/8 inch diameter) installed at the bottom of the cell (**Fig. B.72**). The rod is connected to a power cylinder (**Fig. B.73**) to apply the force required to generate the desired stress level in the specimen. A double acting pneumatic cylinder with 4½ inches bore diameter and 1 inch rod diameter, and maximum force of 3780 lbf (at 250 psi) is used to provide the force. The cylinder applies a pull force to put the specimen under a constant tensile stress. Nitrogen from a supply cylinder (maximum 2500 psi) is used as a pneumatic fluid to actuate the cylinder. A pressure regulator is installed to reduce the output pressure (P10) and maintain between 0 to 250 psi. To prevent the cylinder from over-pressurization, two pressure relief valves (set at 275 psi) are installed on the inlets of the cylinder. Over-pressurization can occur due to high nitrogen supply pressure or axial force acting on the rod resulting from hydraulic pressure inside the pressure cell. It is important to note that, in addition to the cylinder, the hydraulic pressure acting on the pipe bottom and pulling rod create a considerable tensile force on the specimen.

Figure B.70: Corrosion test setup

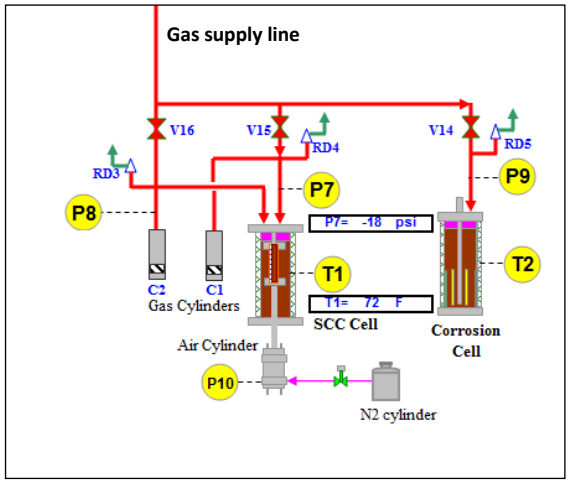

Figure B.71: Schematic of tubular corrosion test facility

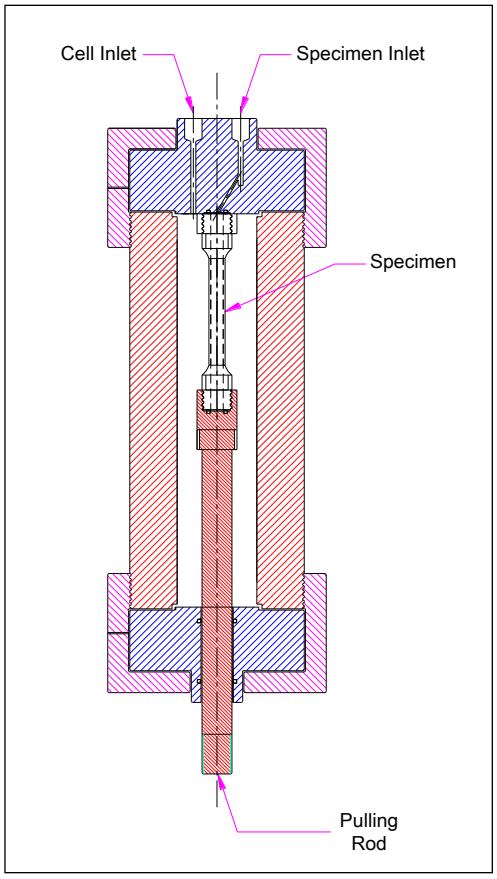

Figure B.72: Design of SCC cell

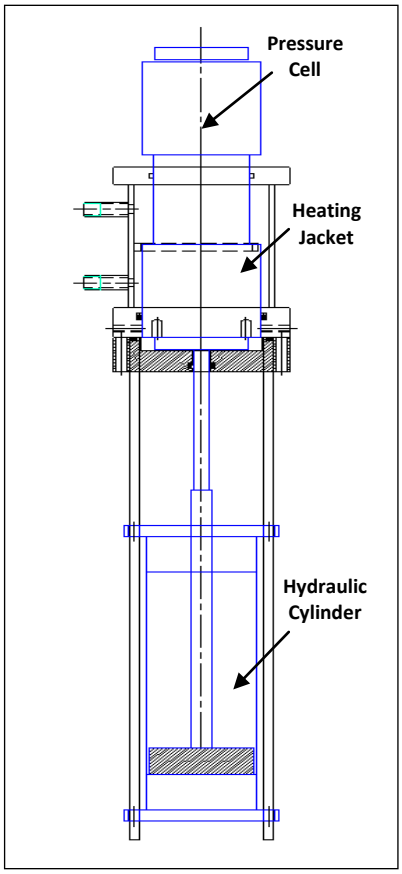

Figure B.73: Assembly of SCC cell with heating jacket and hydraulic cylinder

During the test, the internal (P7) and external (P8) sides of the specimen are pressurized and maintained at different pressure levels. This helps to simulate the underbalanced and overbalanced wellbore conditions between the wellbore and formation fluid pressures. Moreover, the pressure differential helps to reliably detect the stress cracking point as pressure begins to communicate between interior and exterior parts of the specimen. Both internal and external sides of the specimen are exposed to brine solution (2% NaCl) saturated with sour gases. Inner parts of the specimen and the pressure cell (SCC cell in which the specimen placed) are approximately 90% filled with the brine to maximize the exposure area for corrosion. Moreover, the interface between the brine solution and the gas should be in the specimen and the cell to facilitate the dissolution of gas in the liquid. Because of limited volume in the specimen and the SCC cell, two gas accumulators (C1 and C2), with volume capacity 250 ml, are directly connected to the inside of the specimen and SCC cell (Fig. B.71). The gas accumulators are filled with test gas using the injection cylinder. Two rapture disks (RD3 and RD4 with burst pressure of 10,500 psi) are installed on both accumulator inlet lines to prevent over pressurization. The gas inlet to the accumulators is regulated using remotely controlled valves (V15 and V16).

The SCC cell is placed in a heating jacket to control test temperature. The jacket completely covers the cell except the top lid part. The bottom part of the cell, including the cylinder rod inlet, is covered with the jacked. The maximum pressure rating of the jacket is 100 psi. In the case of high pressure fluid leak form the rod seal of the cell, there is a possibility of over-pressurization of the jacket and the entire heating system. In order to avoid this situation, a relief valve is installed in the inlet line of the jacket. The existing heating system provides the heating medium for controlling the temperature. Temperature in the cell is measured using a thermocouple sensor placed in the cell.

B2.2 Stress Analysis in the Mini-Pipe

The axial stress developed in the mini-pipe specimen is a function of cell pressure, specimen internal pressure, and the force applied by the cylinder (Fcyd). Considering a control volume shown in **Fig. B.74**, the force balance in the vertical axis for equilibrium condition yields the following equation:

$$T + P_o * \frac{\Pi}{4} * \left(D_c^2 - D_{rod}^2 \right) = P_o * \frac{\Pi}{4} * \left(D_c^2 - D_o^2 \right) + P_i * \frac{\Pi}{4} * D_{in}^2 + P_{cyd} * \frac{\Pi}{4} * \left(D_{cyl}^2 - D_{p,Rod}^2 \right) \quad \text{..... (A-1)}$$

where T is the tension in the mini-pipe. The second term on the left side of Eq. (1) is upward pressure force at Point 2 acting on the bottom of the adapter; the first term on the right side of the equation is the downward pressure force acting on the top of the adapter at Point 1; the second term on the right side of the equation represents the downward pressure force acting on the bottom of the mini-pipe; and the last term in the equation is the cylinder force acting downward. D_{cyl} and D_{in} denote the cylinder bore diameter and inner diameter of the mini-pipe. The buoyancy force, friction force and weight of the assembly are negligible compared to the pressure forces. Then, the axial stress is given by:

$$\sigma_{axial} = T / \frac{\Pi}{4} * \left(D_o^2 - D_{in}^2 \right) \quad \text{..... (A-2)}$$

The force balance in lateral direction yields an expression for the circumferential stress.

$$\sigma_{\text{circumferential}} = (P_i - P_o) * \frac{D_{in}}{2t} \quad \text{..... (A-3)}$$

where t denotes the wall thickness of the mini-pipe at the mid section.

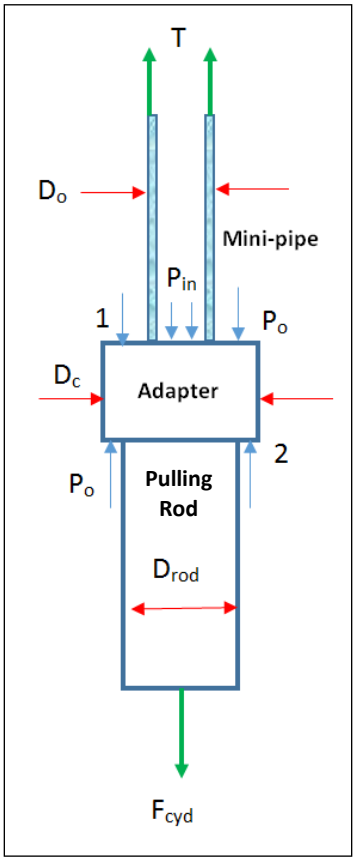

Figure B.74: Control volume for mini-pipe, adapter and pulling rod assembly

B2.3 SCC Test Procedure

When the experiments are carried out, a specimen is assembled in the SCC cell. First, the hydraulic cylinder rod is raised to attach the specimen, and then the specimen is mounted on the rod by screwing.

Subsequently, the SCC cell lid is assembled on the top of the specimen, after placing appropriate hydraulic seals to isolate the inner and outer parts of the specimen. The seals prevent pressure communication between the inner and outer parts. The assembly of pulling rod, mini-pipe specimen and SCC cell lid is slowly lowered and the cell lid cover is mounted.

The SSC lid has two inlets, one for the inside of the specimen and the other one for the outside (i.e. inside of the SCC cell). After mounting the lid cover, the two inlets are used to fill the specimen and SCC cell with brine. Then, the inlets are connected to the gas accumulators and heating begins. When the temperature of the cell reaches slightly above the critical temperature of CO_2, the gas is injected into the accumulators to pressurize the cell and the inside of the specimen as the same time. This is performed by opening V15 and V16 simultaneously, and injecting the gas phase through the supply line (Fig. B.71). This is conducted while heating the cell to test temperature. When the desired temperature and cell pressure are established, the pressure inside the specimen is increased separately by closing V16 and continuing the gas injection through V15 until the required pressure is reached. The supply gas pressure is limited to 2500 psi (maximum). The injection system is used in order to pressurize the cell and the mini-pipe to a higher pressure, which is greater than the supply pressure. The procedure of gas metering and injection involves: i) filling the cylinder with the supply gas by opening V6, V11 and one of the supply gas cylinder valves; ii) pressurization by closing V6 and V11, and pumping oil into the top side of the injection cylinder; and iii) gas injection by opening V15 and V16 simultaneously while pumping the hydraulic oil into the injection cylinder until it reaches a full stroke. Subsequently, V15 and V16 are closed and V11 and V6 are opened for charging the cylinder with the gas. These steps are repeated until the desired pressure is established in the cell.

To increase the stress level in the specimen, nitrogen is supplied to the hydraulic cylinder. The pressure at the inlet of the cylinder (P10) is regulated so that the stress level in the specimen is 85% of the minimum yield stress.

The SCC test is performed in 8 days. After completion of the SCC test, the pressures inside the specimen and SCC cell are equalized by opening V15 and V16. Then, the heating system is shut down to cool the cell and depressurization begins by opening V15, V16, V6 and V4. The gas in the cell is sent to waste gas accumulator, in which it is slowly vented to the atmosphere after being mixed with air to maintain H_2S emission concentration of less than 10 ppm. After completion of the test, the specimen is examined using a microscope to study the crack pattern and structure. Each specimen should be photographed and all of the relevant information about that specimen is properly documented.

B2.4 Static and Dynamic Corrosion Test Setup

The static and dynamic (SD) corrosion test setup is a facility developed to carry out uniform corrosion studies under HPHT conditions in the presence of acidic gases. During the development of the setup, two different methods (fluid circulating in a pipe section or fluid shearing between two rotating co-axial cylinders) were considered for creating the dynamic flow under HPHT conditions.

To develop a facility with fluid recirculation, different companies were contacted to provide price quotes for high-pressure recirculation pump. There were two main limitations for a high-pressure recirculation pump including low system pressure, and low flow rate and material compatibility for brine saturated with sour gases. With market available circulation pump (Micropump), the maximum pressure is 5000 psi, the maximum average fluid velocity that can be achieved using the pump in an 1/8 inch pipe test section is 0.3 m/s, which is very low for simulating the shear stress occurring in the oil and gas drilling and production systems. On the other hand, available high-pressure circulation pump with 10,000 psi system pressure (WITTE gear pump) is not designed for low viscosity liquids. Hence, it is not suitable for pumping brine solution. We also considered using injection cylinder as a pump, acquiring a custom-made pump or syringe type pump that meets the desired specifications. However, the low flow capacity and pressure pulsation are the limiting factors for piston or syringe type pumping systems.

After considering all these alternatives, the best option left was using rotating coaxial cylinder system. The system uses a magnetic drive to rotate a cylinder placed in the HPHT autoclave. The drive rotates the cylinder at high-speed creating Couette flow that can generate wall shear stress level, which is often experienced in real life. Different vendors were contacted to supply the magnetic drive. Due to their air gap limitation, maximum pressure rating for magnetic drives made of Hastelloy is 5000 psi. Magnetic drives with a higher pressure rating (10,000 psi) are available in stainless steel 316 or A286 version. Corrosion studies conducted to evaluate the performance of these materials in sour gas environment show good corrosion resistance of A286 at ambient and high temperature (up to 300°F) conditions. Stainless steel 316 exhibited pitting when exposed to brine saturated with sour gas.

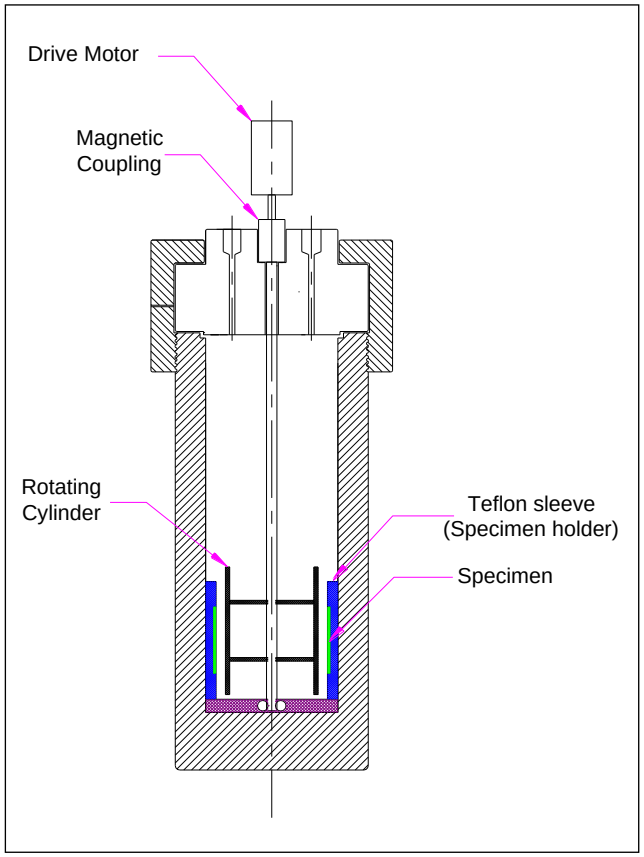

Figure B.75: Dynamic corrosion cell

After choosing the Couette flow type corrosion cell, the design of the HPHT corrosion test setup (**Fig. B.75**) has been finalized. The dynamic corrosion cell has a rotating cylinder inside. Three specimens are attached to a Teflon coated specimen holder (**Fig. B.76**) and placed in the cell. The clearance between the cylinder and the holder is 3.4 mm. The rotation of the cylinder generates turbulence and wall shear stress needed to facilitate the removal of corrosion products and accelerate the corrosion process. As shown in Fig. B.75, magnetic coupling with an air motor is installed on the top of the cell to simulate dynamic condition. The speed of the motor is controlled by the air supply pressure and flow rate, which are controlled by a pressure regulator and air inlet valve, respectively.

The SD corrosion cell is placed in a heating jacket to control the temperature. The jacket completely covers the side and bottom parts of the cell. The jacket is rated for 100 psi. Hydraulic pressure acting on the bottom creates a force that can lift the vessel. In order to prevent the lifting, the jacket is clapped to the vessel and the hydraulic pressure is limited to 15 psi using a rupture disk. The rupture disk is installed at the inlet of the jacket. The heating medium is circulated through the jacket to control the temperature. Temperature is measured using a thermocouple sensor placed in the cell.

B2.5 Static and Dynamic Corrosion Test Procedure

To perform the static and dynamic corrosion experiment, three corrosion coupons (**Fig. B.77**) are cleaned with appropriate solvent. The coupons have two heads and a test section. The heads are used to hold the coupons during tensile strength test, which is carried out after the corrosion experiment is completed. After cleaning the coupons, the weight of each coupon is measured. The rear-side and two heads of the coupons are coated with high-temperature anti-corrosion paint. Only the front part of the test section is exposed to the test fluid during the test. Then, the coupons are inserted into specimen slots of the holder. High temperature sealant is used to attach the coupon with the specimen holder.

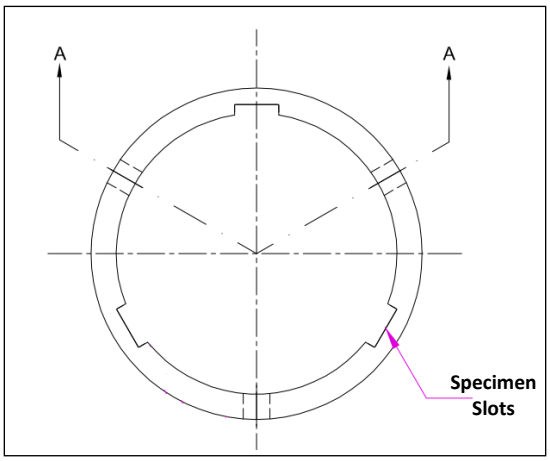

Figure B.76; Teflon coated specimen holder (sleeve)

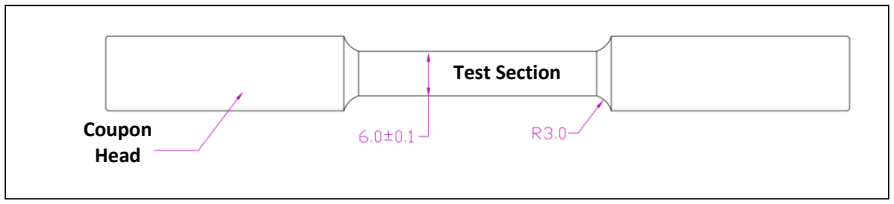

Figure B.77 Coupon used for static and dynamic corrosion test

Once the coupons are attached to the holder, the base (**Fig. B.78**) of the specimen holder is installed. The base acts as a bearing for the cylinder (**Fig. B.79**). It is equipped with trust bearing to reduce the mechanical friction between the holder base and cylinder base. Subsequently, the base and the rotating cylinder is assembled and attached to the drive shaft. The vessel is filled (proximately 70%) with brine solution and the specimen assembled is slow lowered until its touch the bottom of the vessel. Then, the bolts on the lid of the vessel are tightened.

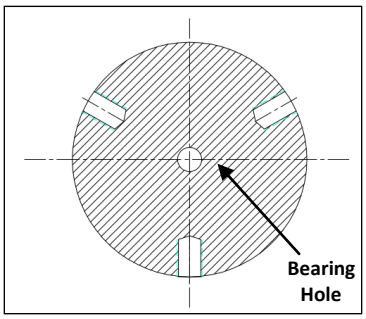

Figure B.78: Base of the specimen holder

Once the vessel is ready for gas injection, the heater is turned on to bring the cell temperature to the desired level. After that, gas from one of the supply tanks is allowed to fill the vessel by opening V14. Injection cylinder is needed to increase the vessel pressure above the supply pressure. The operation of the injection cylinder is similar to the one described in Section B2.3. When the desired pressure and temperature condition is established, the air is supplied to the drive motor to rotate the inner cylinder. The speed of the motor is controlled using inlet air valve and supply pressure.

One SD corrosion test is completed in one week. After completion of the test, the air supply to the motor is cut-off and the heater is shut down to cool the cell. The corrosion cell is depressurized opening V14, V6 and V4. The gas from the vessel is sent to the waste gas accumulator for gradual venting. After completion of the test, the coupons are examined using a microscope to study the corrosion scale characteristics. Each specimen is photographed and all of the relevant information is documented. The corrosion scale is carefully removed and preserved for further studies. After cleaning the corrosion scale, the final weight of the coupon is measured. Subsequently, the tensile strength of the couple is measured.

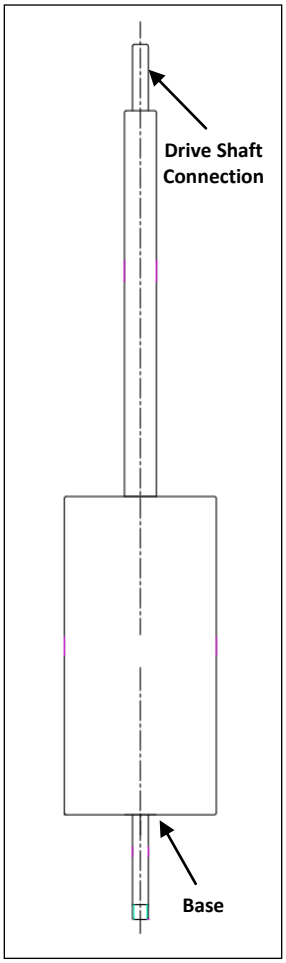

Figure B.79 Rotating cylinder

B2.6 Determination of Wall Shear Stress at the Coupon Surface

Dynamic flow condition strongly affects some types of corrosion by preventing scale development on the surface of the corroded metal surface. The disruption of the scale formation process is related to a number of factors including fluid properties (viscosity and density) and flow parameters such as rotation speed of the cylinder and annular clearance between the rotating cylinder and coupon holder. Studies show that the corrosion rate under dynamic conditions is strongly related to the wall shear stress. Due to low fluid viscosity and high rotational speed of the rotating cylinder, the flow during the corrosion test is predominately under turbulent flow condition. For turbulent flow, the wall shear stress is related

to the fluid viscosity and density, annular clearance and rotational speed of the cylinder. For the sake of simplicity, narrow annular flows are often approximated using parallel plate flows (**Fig. B.80**).

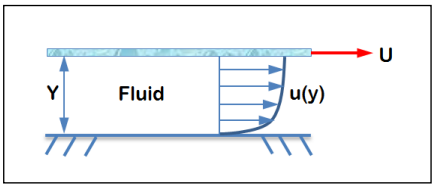

Figure B.80 Flow between parallel plates

The velocity distribution developed between two parallel plates (moving and stationary plates) under turbulent flow condition follow a logarithmic profile. Near wall velocity profiles of simple turbulent flows are modeled using the wall equations. Spalding (94) developed a generalized formulation of the law of the wall that is valid for the whole turbulent boundary layer including the viscous sublayer. Spalding equation is expressed in simplified form as:

$$y^+ = \frac{w}{\kappa} + A(e^w - 1 - w - 0.5w^2 - 0.33w^3 - 0.0417w^4) \quad \text{..... (A-4)}$$

where the parameter $w = u^+\kappa$, constant $A = 0.1108$, and $\kappa = 0.4$. u^+ and y^+ are dimensionless local velocity and dimensionless distance from the wall, respectively. Dimensionless flow parameters (u^+ and y^+) are defined as: $u^+ = u/u^*$; and $y^+ = yu^+\rho/\mu$. The friction velocity is determined from the wall shear stress as: $u^* = (\tau_w/\rho)^{0.5}$. The moving plate velocity is approximately, $U = \omega R_{cyl}$, where R_{cyl} and ω are the radius and rotation speed of the rotating cylinder. Hence, the wall shear is numerical determine from the above equation knowing the values of U, Y, ρ and μ.

Nomenclatures

Acronyms

BWOC	By weight of cement
CH	Calcium hydroxide
CSH	Calcium silicate hydrate
FTIR	Fourier Transform Infra-Red
GHO	Class G Cement with hydroxyapatite
GS	Class G cement with silica flour
GSMG	Class G Cement with silica flour and magnesium oxide
GSLM	Class G Cement with silica flour, latex and micro-silica
GSLT	Class G Cement with latex
HHO	Class H Cement with hydroxyapatite
HPHT	High-pressure high-temperature
HS	Class H cement with silica flour
HSHO	Class H Cement with silica flour and hydroxyapatite
HSMG	Class H Cement with silica flour and magnesium oxide
HSLM	Class H Cement with silica flour, latex and micro-silica
HSLT	Class H Cement with latex
LPR	Linear polarization resistance
LTMS	Cement with latex and micro-silica additives
mpy	mils per year
MGO	Magnesium oxide containing cement
MGO-5	Cement containing 5% BWOC MgO as additive
MGO-10	Cement containing 10% BWOC MgO as additive
MS	Micro-silica containing cement
MS-10	Cement containing 10% BWOC micro-silica as additive
NACE	National Association of Corrosion Engineers
SBS	Shear bonding strength
SD	Static and dynamic
SEM	Scanning Electron Microscope
SCC	stress corrosion cracking

XRD	X-Ray diffraction

Symbols

D_c	Diameter of mini-pipe adapter
D_{in}	Inner diameter of a mini-pipe
D_o	outer diameter a mini-pipe
D_{rod}	Diameter of the pulling rod
$D_{p,rod}$	Diameter of the piston rod
P_{cyl}	Pressure is pneumatic cylinder
P_{in}	Pressure inside the mini-pipe
P_o	Pressure in the SCC vessel
t	Annular clearance between rotating cylinder and corrosion coupon holder
T	Tension at the middle of a mini-pipe
u	Local fluid velocity in narrow slot
u+	Dimensionless velocity at the moving plate
u*	Friction velocity
U	Mean fluid velocity in narrow slot
y	Distance of any arbitrary point from the stationary plate
Y+	Dimensionless distance between the moving and stationary plates
Y	Distance between the moving and stationary plates

Greek Symbols

κ	Von Karman constant
μ	Fluid viscosity
ρ	Fluid density
τ_w	Wall shear stress acting on a corrosion coupon
σ_{axial}	Axial stress in a mini-pipe
$\sigma_{circumferential}$	Circumferential stress in a mini-pipe

References

Abdul Rahman, R. and Chong, A. 1997. Cementing Multilateral Well With Latex Cement. Paper SPE 37623 presented at SPE/IADC Drilling Conference, Amsterdam, Netherlands, 4-6 March.

Agzamov, F., Karimov, N.and Akchurin, K. 2013. Preparation of expanding oil well cements. Oil and Gas Business Journal (published online December 11, 2001).

Ali, M.M. and Mullick, A.K. 1998. Volume Stabilization of High MgO Cement: Effect of Curing Conditions and Fly Ash Addition, Cement and Concrete Research 28 (11): 1585-1594.

Allan, M.L. 1997. Rheology of Latex Modified Grouts, Cement and Concrete Research 27 (12): 1875 – 1884.

Arliguie, G. and Grandet, J. 1985. Etude par calorimetrie de l'hydratation du ciment Portland en presence de zinc, Cement and Concrete Research, Volume 15, Issue 5, September, Pages 825–832.

Black, L., Breen, C., Yarwood, J., Grave, K., and Stemmermann, P. 2007. Structural Features of CSH(I) and its Carbonation in air - A Raman Spectroscopic Study - Part II: Carbonated Phases, J. of American Ceramic Society, Soc. 90: 908 - 917.

Brandl, A., Cutler, J., Seholm, A., Sansil, M. and Braun, G. 2010. Cementing Solutions for Corrosive Well Environments. Paper SPE 132228-MS presented at International Oil & Gas Conference and Exhibition, China, 8-10 June.

Buntoro, A. and Rubiandini, R.S. 2001. The Effect of Neat Magnesium Oxide (MgO) as Expanding Additive With Burning Temperature 1200°C and 1300°C on Cement Shear Bond Strength at High Pressure and Temperature. Proceedings of the 5th INAGA Annual Scientific Conference and Exhibitions, Yogyakarta, Indonesia, 7-10 March.

Cheremisinoff, P. N. 1995. Handbook of Water and Wastewater Treatment Technology. New York: Marcel Decker Inc.

Cheung, P. 1999. Expanding Additive for Cement Composition. US Patent No. 5942031.

Danjuschewskij, V.S. 1983. Gefuege und Eigenshaften hydraulicer Bindemitel nach dem Erhaerten Bei Boheren Temperaturen und Laengeren Zeiten, ITE-Fachberiche 107 (10).

Daou, F. and Piot, B. 2009. Cement Slurry Performance and Set-Cement Properties vs. Micro-silica Densification. SPE Drilling & Completion 24 (4): 590-598. SPE 112701-PA.

Dillenbeck III, R.L., Mueller, D.T. and Orr, B.R. 1990. The Effect of Micro-Silica on the Thermal Stability of Lightweight Cement Systems. Paper SPE 21597 presented at International Technical Meeting, Petroleum Society of CIM and SPE, Calgary, 10-13 June.

Eilers, L.H. and Root, R.L. 1976. Long-Term Effects of High Temperature on Strength Retrogression of Cements. Paper SPE 5871 presented at SPE California Regional Meeting, Long Beach, California, 7-9 April.

Eilers, L.H., Nelson, E.B. and Moran, L.K. 1983. High Temperature Cement Compositions – Pectolite, Scawtite, Truscotite or Xonoloite: Which Do You Want? Journal of Petroleum Technology 35 (7): 1373-1377.

Fuquan, S., Guangming, Lv and Jianzhou, J. 2006. Application and Research of Latex Tenacity Cement Slurry System. Paper SPE 104434 presented at SPE International Oil & Gas Conference and Exhibition, Beijing, China, 5-7 December.

Garev, K., Stemmermann, P., Black, L. and Yarwood, J. 2007. Structural Features of CSH(I) and its Carbonation in air - A Raman Spectroscopic Study - Part I: Fresh Phases, J. of American Ceramic Society, Soc. 90: 900 - 908.

Ghofrani, R. and Plack, H. 1993. CaO- and/ or MgO- Swelling Cements: A Key for Providing a Better Annular Sealing? Paper SPE 25697 presented at SPE/IADC Drilling Conference, Amsterdam, 22-25 February.

Grabowski, E. and Gillott, J.E. 1989. Effect of Replacement of Silica Flour with Silica Fume on Engineering Properties of Oil-Well Cements at Normal and Elevated Temperatures and Pressures. Cement and Concrete Research 19: 333-344.

Hashimoto, H., Komaki, E., Hayashi, F. and Uematsu, T. 1980, Partial Decomposition of Dolomite in CO2, Journal of Solid State Chemistry 33, 181-188.

Hamilton, I.W. and Sammes. N.M. 1999. Encapsulation of steel foundry dusts in cement mortar. Cement and Concrete Research, Vol. 29, 55-61.

Hou, W., Fuquan, S., Gao, Y., Zeng, J., Huo, M. and Wang, J. 2010. Research of High Temperature Tolerance Latex Slurry System. In Twentieth International Offshore and Polar Engineering Conference, Beijing, China, 20-25 June.

Jones, R.R. and Carpenter, A.B. 1991. New Latex, Expanding Thixotropic Cement Systems Improve Job Performance and Reduce Costs. Paper SPE 21010 presented at SPE International Symposium on Oilfield Chemistry, Anaheim, California, 20-22 February.

Lecolier E., Rivereau A., Ferrer N., Audibert A. and Longaygue X. 2008. Study of New Solutions for Acid-Resistant Cements, Paper SPE 116066, presented at the SPE Annual Technical Conference and Exhibition, 21-24 September, Denver, Colorado.

Martin, R. I. and Brown, P. W. 1995. Mechanical properties of Hydroxyapatite formed at physiological temperature. Journal of Material Science: Materials in Medicine, 6: 138-143.

Mehta, P.K. and Monteiro, P.J.M. 2006. Concrete: Microstructure, Properties and Materials. Third Edition, Tata McGraw Hill.

Moroni, N., Repetto, E., and Ravi, K. 2008. Zonal Isolation in Reservoir Containing CO2 and H2S. Paper SPE 112703 presented at the IADC/SPE Drilling Conference, Orlando, Florida, 4–6 March. DOI: 10.2118/112703-MS.

Moroni, N. Santra, A. Ravi, K., and W. Hunter 2009a. Holistic Design of Cement Systems to Survive CO2 Envioenment, Paper SPE 124733 presented at the Annual Technical Conference and Exhibition, New Orleans, Louisiana, 4–7 October. DOI: 10.2118/124733-MS.

Moroni, N., Repetto, C., Dettori, N., Ravi, K. 2009b. Zonal Isolation Achieved in Kashagan Field through Integrated Approach, paper SPE-119296-MS, presented at the SPE/IADC Drilling Conference and Exhibition, 17-19 March, Amsterdam, The Netherlands.

Paper SPE/IADC 119296 presented at Drilling Conference and Exhibition, Amsterdam, The Netherlands, 17–19 March, DOI: 10.2118/119296-MS.

Mueller, D.T. and Dillenbeck III, R.L. 1991. The Versatility of Silica Fume as an Oilwell Cement Admixture. Paper SPE 21688 presented at SPE Production Operations Symposium, Oklahoma City, Oklahoma, 7-9 April.

Nakarai, K., Ishida, T., Maekawa, K. 2006. Modeling of Calcium Leaching from Cement Hydrates Coupled with Micro-Pore Formation. Journal of Advanced Concrete Technology, 4 (3): 395-407.

Nokken, M.R. 2010. Expansion of MgO in Cement Pastes Measured by Different Methods. ACI Materials Journal, 107 (1): 80-84.

Olmo, F., Chacon, E. and Irabien, A. 2001. Influence of lead, zinc, iron (III) and chromium (III) oxides on the setting time and strength development of Portland cement, Cement and Concrete Research, Volume 31, Number 8, August, pp. 1213-1219.

Ray, I. and Gupta, A.P. 1994. Effect of Latex and Super-plasticiser on Portland Cement Mortar in the Fresh State. Cement and Concrete Composites 16: 309-316.

Reddy, B.R., Lewis, S.J., Santra, A. and Palmer, A.V. 2010. Wellbore Sealant Compositions Containing Cationic Latexes. US Patent 7687440.

Rossignolo, J.A. and Agnesini, M.V.C. 2002. Mechanical properties of polymer-modified lightweight aggregate concrete. Cement and Concrete Research 32: 329-334.

Rossignolo, J.A., Agnesini, M.V.C. and Morais, J.A. 2003. Properties of high-performance LWAC for precast structures with Brazilian lightweight aggregates. Cement and Concrete Research 25: 77-82.

Rossignolo, J.A. and Agnesini, M.V.C. 2004. Durability of polymer-modified lightweight aggregate concrete. Cement and Concrete Research 26: 375-380.

Rubiandini R., Siregar S., Suhascaryo N. & Efrial D. 2005. The Effect of CaO and MgO as Expanding Additives to Improve Cement Isolation Strength under HPHT Exposure, PROC. ITB Eng. Science Vol. 37 B, No. 1, 29-48.

Santra, A., Reddy, B.R., Liang, F. and Fitzgerald, R. 2009. Reaction of CO2 with Portland cement at Down-hole Conditions and the role of Pozzolanic Supplements. Paper SPE 121103 presented at SPE International Symposium on Oilfield Chemistry, Woodlands, Texas, USA, 20-22 April.

Sasaki, S., Kobayashi, W. and Okabayashi, S. 1985. Effects of various Factors on Thickening time and Strength of Silica Cement under High Temperature. SPE Publication 015335.

Shadizadeh, S.R., Kholghi, M. and Salehi Kassaei, M.H. 2010. Experimental Investigation of Silica Fume as a Cement Extender for Liner Cementing in Iranian Oil/Gas Wells. Iranian Journal of Chemical Engineering 7 (1 – Winter).

Shahriar, A. 2011. Investigation on Rheology of Oil Well Cement Slurries, PhD Dissertation, The University of Western Ontario, School of Graduate and Postdoctoral Studies, London, Ontario.

Siddique, R. and Khan, M. I. 2011. Supplementary Cementing Materials. Springer- Verlag, Berlin-Heidelberg.

Spaldings, D. 1961. A single formula for the law of the wall, ASME C: J. Appl. Mech. Vol. 28, Issue 3, 455-458.

Strazisar, B., Kutchko, B., and Huerta, N., 2009, "Chemical Reactions of Wellbore Cement Under CO2 Storage Conditions: Effects of Cement Additives", Energy Procedia 1, 3603-3607.

Sugama, T. and Carciello, N.R. 1992. Carbonation of Hydrothermally Treated Phosphate-Bonded Calcium Aluminate Cements. Cement and Concrete Research 22: 783-792.

Sugama, T. and Carciello, N.R. 1993. Carbonation of Calcium Phosphate Cements after Long Term Exposure to Na2CO3-Laden Water at 250°C. Cement and Concrete Research 23: 1409-1417.

Sugama, T. 2006. Advanced Cements for Geothermal Wells. BNL-77901-2007-IR. Technische Universität München, Research Focus, http://www.bauchemie-tum.de/master-framework/?p=Tief&i=13&m=1&lang=en (accessed on 03/15/2014).

Teraoka, K., Ito, A., Maekawa, K., Onuma, K., Tateishi, T. and Tsutsumi, S. 1998. Mechanical Properties of Hydroxyapatite and OH-Carbonated Hydroxyapatite Single Crystals. Journal of Dental Research 77 (7): 1560-1568.

Wan, R. 2011. Production Casing and Cementing. In Advanced Well Completion Engineering, Chapter 5, 221-294, Third Edition, Waltham, Massachusetts: Gulf Professional Publishing.

Zhang, Z., Xu, L. and Tang, M. 2011. Effect of Particle Size on Expansive Behavior of MgO-Based Expansive Agent in Cement Paste. Advanced Materials Research 194-196: 1143-1146.

Zhang, Z., Xu, L., Liu, F. and Tang, M. 2012. Effect of Amount on Expansion Property of MgO- type Expansive Agent Used in Cement- based Materials. Advanced Materials Research 391-392: 803-806.

Project Title: Effect of H_2S and CO_2 in HPHT Wells on Tubulars and Cement

Report Type: Monthly Report

Report #: 33

Reporting Period: May 22nd, 2014 to June 21st, 2014

Authors:

Ramadan Ahmed, Principal Investigator

Subhash Shah, Co-Principal Investigator

Rida Elgaddafi, Research Assistant

Omotayo Omosebi, Research Assistant

Jueun Hwang, Research Assistant

Sagar Tale, Research Assistant

Prepared under BSEE Project # E12PC00035

by

THE UNIVERSITY OF OKLAHOMA

August 12, 2014

1. Summary of Accomplishments

This monthly report presents the progress made during the project period May 22, 2014 to June 21, 2014. During this period, studies on degradation of cement and tubular were continued. New aging experiments were not conducted due to equipment maintenance. Remote control valves and gas injection lines of the aging cell setup were repaired and tested. Modeling studies and data analysis on previous cement property measurements were continued. In addition, mechanical properties of unaged baseline (Class G and Class H) cements were investigated.

During this month, unaged baseline cores were prepared and their confined compressive strengths (CCS) were measured to perform failure analysis, which provides additional mechanical properties of cement such as failure angle and cohesion constant. Using CCS measurements, failure envelopes have been generated for baseline cements based on Mohr-Coulomb failure criteria. The failure envelopes are useful to determine the maximum sustainable fluid injection or drawdown pressure to avoid cement failure.

Modeling of sulfide stress cracking corrosion was continued. The model requires accurate prediction of H_2S and CO_2 concentration in the surrounding brine solution. H_2S solubility calculation procedure, which is based the Peng-Robinson equation of state was presented in the last monthly report. During this month, an analogous model has been developed to predict solubility of CO_2 in water and brine following a similar approach. Model predictions are validated using published measurements.

Five new corrosion experiments under low-pressure condition were performed at 140°F. Carbon dioxide concentration was varied from 0 to 100%. New measurements were compared with previously reported. When corrosion rate curves are presented as a function of CO_2 concentration, they show very similar trends. At low concentrations, the corrosion rate increased with the concentration. The trend reversed at high concentrations. Results indicate strong impact of CO_2 concentration (partial pressure) and temperature. These parameters greatly influence the solubilities of CO_2 and iron carbonate (corrosion product) in the solution, which are highly prominent in controlling the corrosion rate and formation of protective scale.

Corrosion test specimens (mini-pipe and flat coupon) are needed for performing HPHT tubular degradation studies. Manufacturing of the specimens has been completed. The required specimens and their accessories have been delivered. The specimens are made of high-strength API grade carbon steels. To prevent atmospheric corrosion before the test, specimens are placed in vacuum storage containers. Elastic properties of the specimens will be measured before and after the corrosion test to assess the level of embitterment occurring after exposure to sour gas environment.

Our plan for the upcoming weeks is to continue: i) aging tests at 6000 psi, 100°F, 300 ppm H_2S and different CO_2 concentrations; ii) theoretical and modeling studies on tubular corrosion; iii) testing of new acid-resistant cement formulations; iv) low-pressure corrosion experiments at various CO_2

concentrations; and v) corrosion experiments under HPHT conditions varying CO_2 concentration with and without the presence of H_2S.

2. Overall Project Progress

2.1 Theoretical Studies (Task 1)

2.1.1 Mechanism of Sulfide Stress Cracking

A corrosion model is being developed to predict sulfide stress cracking (SSC) of tubulars. The model requires a method to accurately predict H_2S concentration. The last monthly report presented a H_2S solubility model based the Peng- Robinson and Duan et al. (2003) equations.

A model to predict solubility of CO_2 in water and brine has been developed following the H_2S solubility model formulation. For validation purpose, the predictions of the model are compared (**Fig. 1**) with previously published measurements (Wiebe and Gaddy 1939). Predictions show a good agreement with the measurements. Nevertheless, the discrepancy between predictions and measurements increase slightly with pressure. At higher pressures, vapor phase mixtures of gas-water become highly non-ideal. The assumption made for fugacity coefficient calculation may not be valid at high pressures and results in discrepancy.

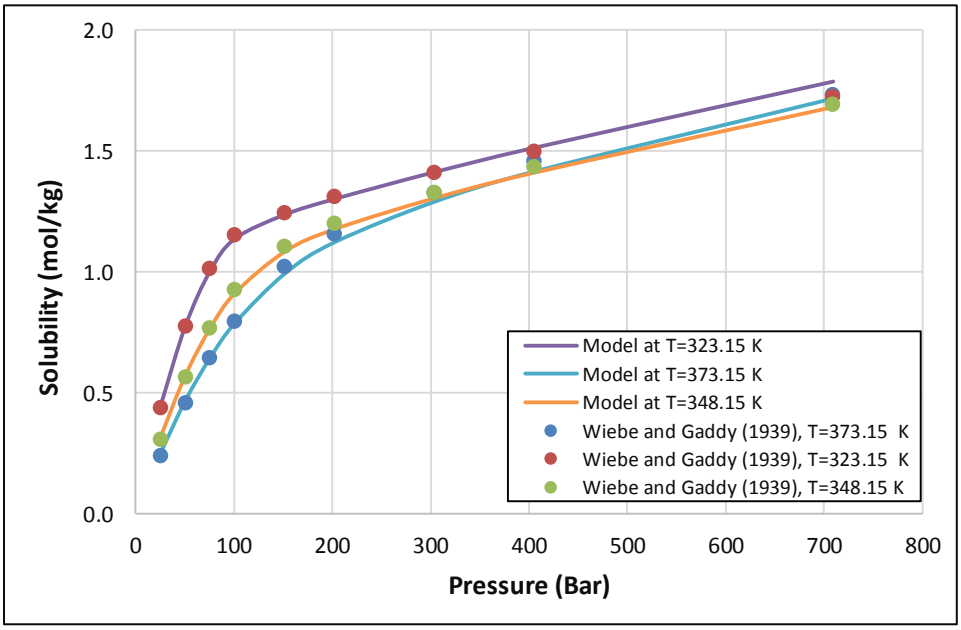

Fig. 1: Measured and predicted solubility of CO_2 in pure water at different temperatures (data from Wiebe and Gaddy, 1939)

The solubility curves presented in Fig. 1 indicate the presence of different regimes. At low-pressures (below 100 bar), the solubility is very sensitive to pressure change. As pressure increases, the solution tends to saturate with CO_2. This causes the solubility to increase gradually with pressure.

Moreover, above 400 bar, reversal of solubility trend was observed. As a result, solubility at 373.15 K is slightly higher than that at 348.15 K. **Figure 2** validates model predictions against experimental data (Takenouchi and Kennedy 1964) obtained at higher pressures (100 to 800 psi). The measurements show very good match with model predictions for a wide range of pressure. To further validate the performance of model, its predictions have been compared (**Table 1**) with other available measurements (Drummond 1981; GehRig 1980). A satisfactory agreement with a maximum error of 6.4% has been observed.

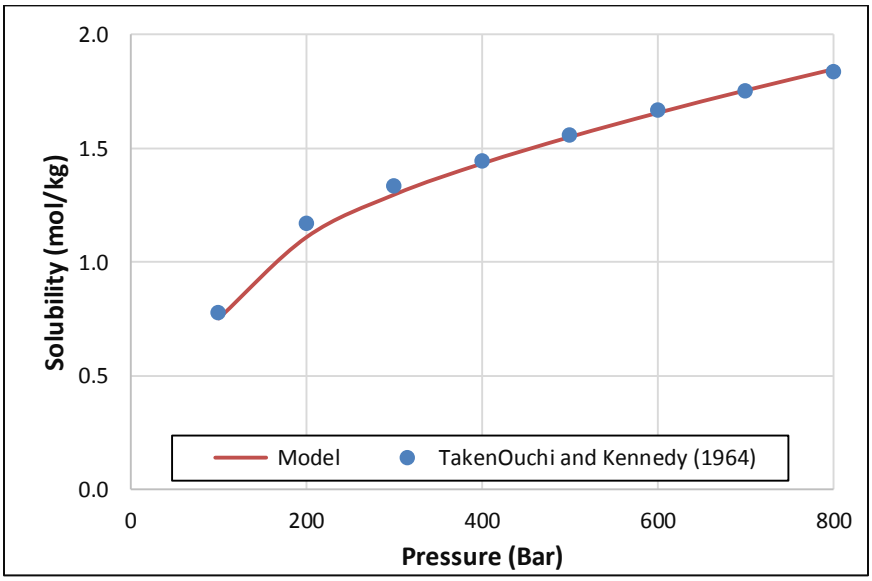

Fig. 2: Comparison of CO_2 solubility model with experimental data in pure water at 383 K (TakenOuchi and Kennedy, 1964)

Table 1: Predicted and measured solubility of CO_2 in pure water and brine

Temperature K	P in Bar	Solubility (mole/kg)		Deviation,%	Liquid	Data Source
		Data	Model			
311	40	0.83	0.80	3.6	Water	Drummond (1981)
352	52	0.52	0.55	5.8	Water	Drummond (1981)
373	58	0.50	0.52	4.0	Water	Drummond (1981)
388	62	0.50	0.51	2.0	Water	Drummond (1981)
403	67	0.50	0.52	4.0	Water	Drummond (1981)
416	71	0.54	0.53	1.9	Water	Drummond (1981)
423	1458	2.36	2.24	5.1	1 M NaCl	GehRig (1980)
413	1965	2.36	2.51	6.4	1 M NaCl	GehRig (1980)
573	887	6.07	6.14	1.2	1 M NaCl	GehRig (1980)
528	1670	6.07	6.08	0.2	1 M NaCl	GehRig (1980)

After extensive validation, a parametric study (**Figs. 3** and **4**) was conducted to assess the effects of temperature, pressure and salt concentration on the solubility of CO_2. Figure 3 shows the solubility as

a function of temperature at various pressures. At low pressures (below 200 bar), CO_2 solubility gradually reduces with temperature. However, this trend changes at high-pressures (above 200 bar). The solubility slightly reduces with temperature, at lower temperatures (approximately 360 to 400 K) and increases at high temperatures (above 400 K). The temperature at which lowest solubility is observed for a particular pressure slightly reduces with pressure. For example at 200 bar, the lowest solubility is around 393 K while for 400 bar it is 363 K. Literature is still being explored in order to find the reason behind this abnormal solubility behavior. Moreover, at high-temperature and high-pressure conditions (above 400 K and 200 Bar), the solubility becomes very sensitive to the temperature change.

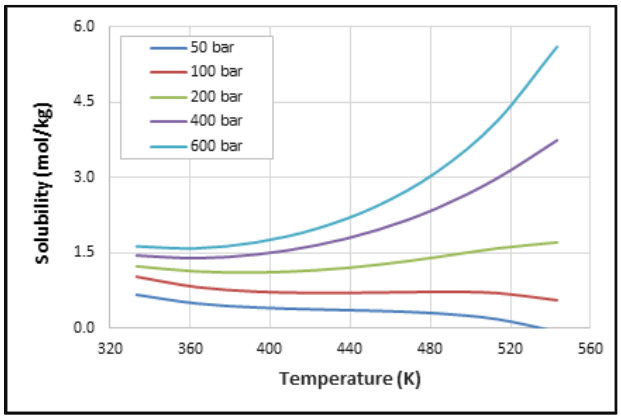

Fig. 3: Predicted solubility vs. temperature for different pressures

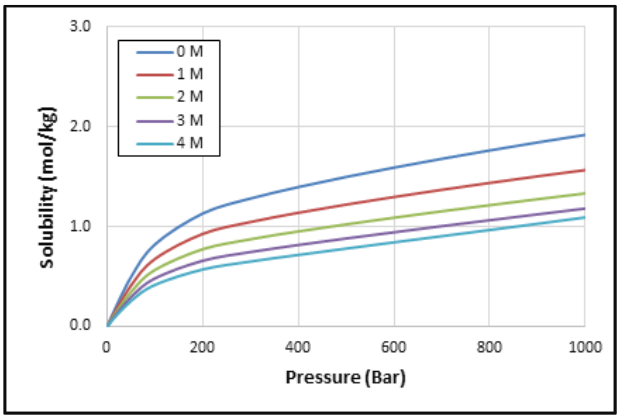

Fig. 4: Predicted solubility vs. pressure for different NaCl solutions

Reduction in solubility of gases in liquids due to dissolve salt (i.e. salting-out) is a common phenomenon in gas-liquid systems. Aqueous solutions saturated with CO_2 exhibit salting-out effect, which increases with temperature (Fig. 4). For instance, at 1000 bar pressure, the ratio of CO_2 solubility in pure water to 4M NaCl is 1.75 at 363 K while it increases to 2.23 at 453 K.

The CO_2 solubility model is mainly based the Peng- Robinson and Duan's equations. The model utilizes interaction parameters that are strictly valid for temperature and pressure ranges shown in **Table 2**. Therefore, care must be taken in the use of this model out of these ranges.

Table 2: CO_2 solubility model validity range

Model	Temperature range in K	Pressure range in bar	Molality of NaCl range
CO_2 solubility	273-533	0-2000	0-4.3

2.2 Experimental Studies on Degradation of Cement (Task 2)

2.2.1 Compressive Strength of Baseline Cements

During this month, new aging experiments were not conducted due to equipment failure and maintenance. However, unaged baseline cores were prepared and their compressive strengths were measured to perform failure analysis, which provides the failure angle and cohesion constant. The

effect of confining pressure (**Table 3**) on mechanical strength measurement was investigated. Similar to rock behavior, results show mechanical strength increasing consistently with confining pressure. Furthermore, linear regression was performed to obtain mechanical properties (cohesion constant, friction angle and unconfined compressive strength). Subsequently, failure envelopes were generated for baseline (Class G and Class H) cements based on Mohr Coulomb failure criteria. The envelopes can be used to predict the maximum sustainable fluid injection or drawdown pressure to avoid cement failure.

Table 3: Confining pressure of compressive strength test

Test #	Confining Pressure (psi)	
	Class G	Class H
1	-	250
2	500	500
3	-	750
4	1000	1000
5	-	1250
6	1500	1500
7	-	1750
8	2000	2000

2.2.1.1 Effect of Confining Pressure on Compressive Strength Measurements

Compressive strength of solids measured under restrained condition depends on the magnitude of horizontal stresses or in the case of a cylindrical core surrounded by pressured fluid, the confining pressure. **Figure 5** shows results of compressive strength tests conducted at different confining pressures.

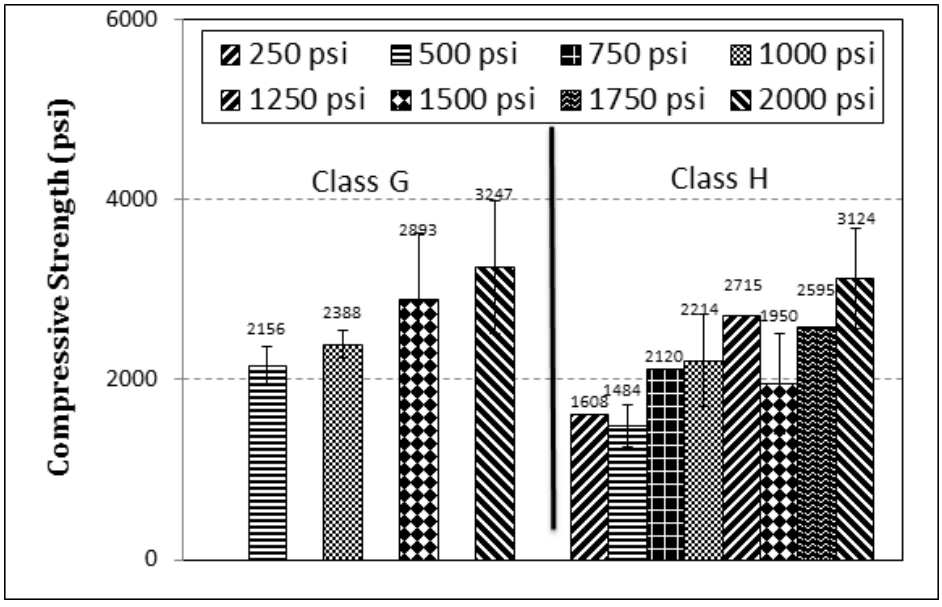

Fig. 5: Effect confining pressure on compressive strength measurements

As expected, the compressive strength of baseline cement increases consistently with confining pressure. This is a similar behavior exhibited by porous solids such as rocks (Brady and Brown 2006). Like rock samples, when the specimen is initially loaded, it compresses but commencement of dilation (i.e. increase in volume due to internal fracturing) is expected before the peak stress is reached and this may continue in the post-peak range. Class H cement data points displayed scattering. Tests conducted at confining pressures of 1500 psi showed unexpectedly low values. This is likely due to the condition of Class H cement when the samples were prepared. Prior to mixing, Class H cement powder exhibited minor lump formation indicating entrapment of moisture, which may have led to pre-hydration and unexpectedly low compressive strength.

2.2.1.2 Data Analysis and Interpretation of Results

Figure 6 shows schematic diagram of shear failure on an arbitrary plane "ab" during tri-axial compression test. The maximum stress, σ_1, corresponds to the confined compressive strength of the sample while σ_3 is the confining pressure. Both of these stresses are principal stresses since the shear stress component is zero on their planes of action. Coulomb's failure criterion, presented in Appendix A, is applied to develop the following linear relationship between σ_1 and σ_3:

$$\sigma_1 = \frac{2c\cos\varphi}{1-\sin\varphi} + \frac{1+\sin\varphi}{1-\sin\varphi}\sigma_3 \quad \text{..... (1)}$$

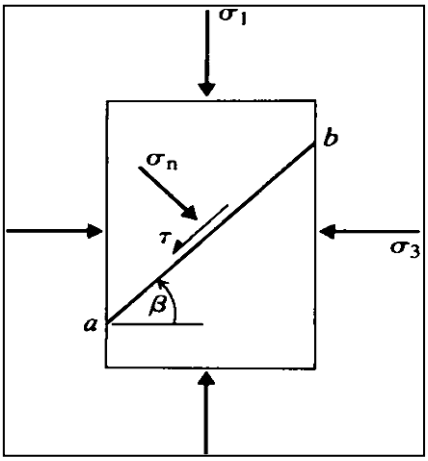

Fig. 6: Schematic of shear failure on an arbitrary plane ab

where c is the cohesion constant and φ is the friction angle. Therefore, a plot of the maximum stress versus confining pressure produces straight line on Cartesian graph with constant slope and intercept to determine the friction angle and cohesion constant, respectively.

Figure 7 shows the plots of the maximum stress versus confining pressure (i.e. Coulomb strength envelope in terms of principal stresses) for Class G and Class H samples cured at 200°F for 5 days in 2% brine solution. As expected, the linear relationships are indicated on these plots. For Class G cement, the r-square value for the data points is close to 1, which indicates good match to the fitted regression line. Although Class H cement data shows scattering and low r-square value, the slope and intercept values are very similar to that of Class G cement.

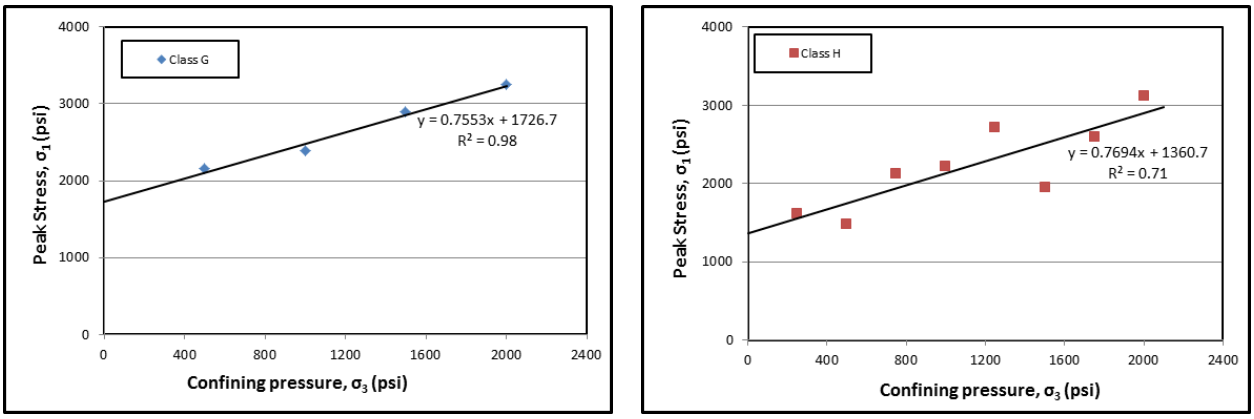

(a) (b)

Fig. 7: Coulomb strength envelopes of: a) Class G; and b) Class H cement

Analysis of compressive strength measurements (**Table 4**) suggests that the grains of Class G cement are held together by stronger cohesive force than those of Class H cement. However, this contradicts our previous observations (Report # 32) that Class H cement offers better cement integrity than Class G. Additional tests are being conducted to verify these results.

Table 4: Mechanical properties of baseline cements

Cement Type	Cohesion, c (psi)	Friction angle, φ (°)	Plane of Failure angle, β (°)	Unconfined Compressive Strength, σ_c (psi)
Class G	993	352	127	1727
Class H	775	353	128	1361

2.2.1.3 Failure Behavior of Well Cement after Curing

Failure envelopes based on the Mohr-Coulomb failure criteria have been generated for baseline cements and the results are presented in **Fig. 8**. Unlike natural rocks, these preliminary results indicate a negative slope for the straight line relationship between shear and normal stresses. Usually, in-situ wellbore stress states prior to depletion or injection are represented by the Mohr circle. As fluids are injected or produced through the wellbore, the level of wellbore stress concentrations is altered. This results in shift of the Mohr circle to the left or right, as well as decreases or increases in its size, respectively. As long as the circle remains within the failure envelope, integrity of well cement is preserved but shear failure occurs as soon as the stress state lies outside the failure line. Therefore, maximum sustainable fluid injection or drawdown pressure to avoid cement failure can be estimated using the failure envelopes presented in Fig. 8.

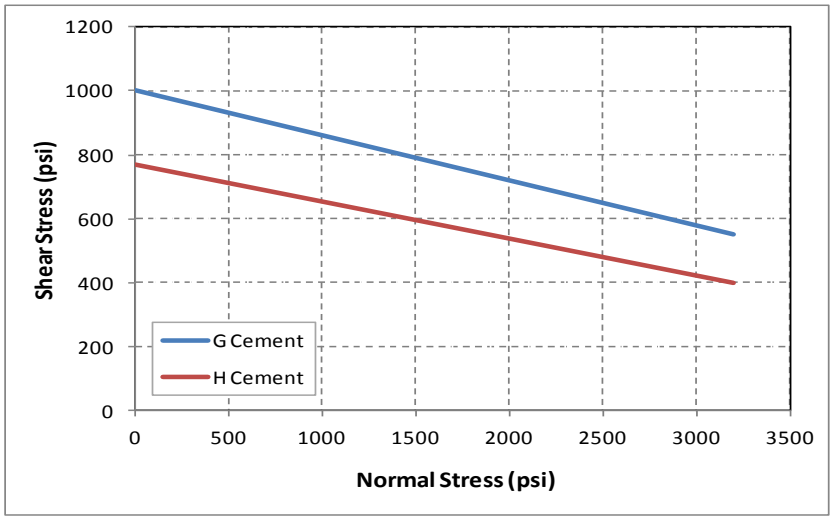

Fig. 8: Failure behavior of Class G and Class H cements after Curing

2.2.2 Shear Bond Strength of Baseline Cement

As reported previously, shear bond test samples were used to study degradation depth. Statistical analysis was performed using penetrated depth measurements (**Table 5**). Experimental data points were fitted to a regression model that describes the relationship between shear bond strength increase and penetrated depth (**Fig. 9**). The SBS increased with the depth up to certain level and then started to decrease as the acid penetrated deeper into the cement core. The regression model that relates the increase in SBS to the penetration depth is expressed as:

$$\Delta(\mathrm{SBS})\,(\%) = 30.36 + 3350 d_p - 12903 d_p^2 + 13943 d_p^3 \quad \text{..... (2)}$$

where d_p is average penetration depth (inch). Equation (2) predicts approximately 30% increase in SBS after aging even without penetration. This can be attributed to the expansion occurring due to hydration of the cement in the aging cell. Even though considerable cement hydration occurs in first couple of days of curing, the process continues for a longer period of time.

Table 5: Measured penetrated depth

Batch #	Temperature	Pressure	CO2 Gas	Depth 1	Depth 2	Depth 3	Depth 4	Depth 5	Depth 6	Depth 7
	1 = 100F	1 = 3000psi	1 = 10%							
	2 = 225F	2 = 6000psi	2 = 40%							
	3 = 350F	3 = 9000psi	3 = 100%							
N/A	1	1	1	0.00000001	0.00000001	0.00000001	0.00000001	0.00000001	0.00000001	0.00000001
Batch 11	1	2	2	0.00000001	0.00000001	0.00000001	0.00000001	0.00000001	0.00000001	0.00000001
Batch 12	1	3	3	0.00000001	0.00000001	0.00000001	0.00000001	0.00000001	0.00000001	0.00000001
Batch 22	2	1	2	0.3524	0.26590201	0.18606731	0.29178698	0.36899483	0.38254298	0.47706966
Batch 10	2	2	3	0.4705	0.27450712	0.38193462	0.36743168	0.29395557	0.37290277	0.2912456
Batch 27	2	3	1	0.00000001	0.00000001	0.00000001	0.00000001	0.00000001	0.00000001	0.00000001
Batch 18	3	1	3	0.454129	0.3858614	0.51855263	0.43294572	0.47729237	0.43540236	0.47472041
Batch 6	3	2	1	0.13	0.27006127	0.26935513	0.24759742	0.23541663	0.25152528	0.24084502
Batch 17	3	3	2	0.298023	0.26020749	0.37345375	0.24752476	0.31760404	0.24027835	0.34906728

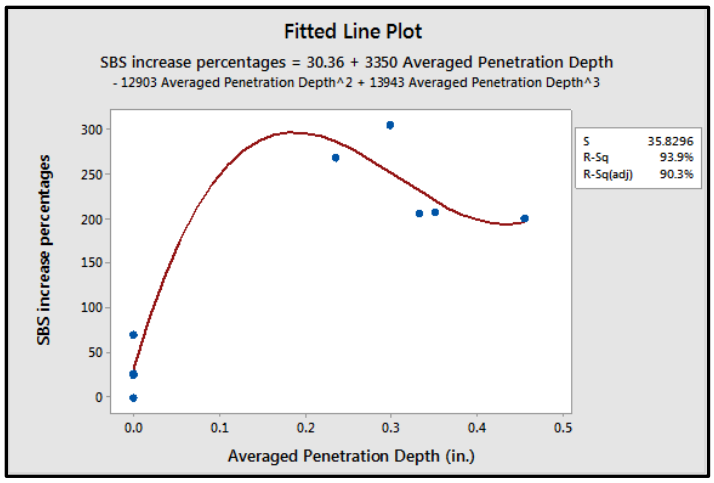

Fig. 9: SBS vs. penetration depth (MINITAB multiple regression analysis)

In addition to the regression equation, the MINITAB software was used to determine the discrepancy and level of uncertainty associated with the correlation (**Fig. 10**). In the probability plot (Fig. 10a), most of the data points are clustered around the red line indicating reasonable match between the measured data and correlation prediction. The residual plot (Fig. 10b) shows the deviation as function of fitted values. Maximum discrepancy of 50% was observed.

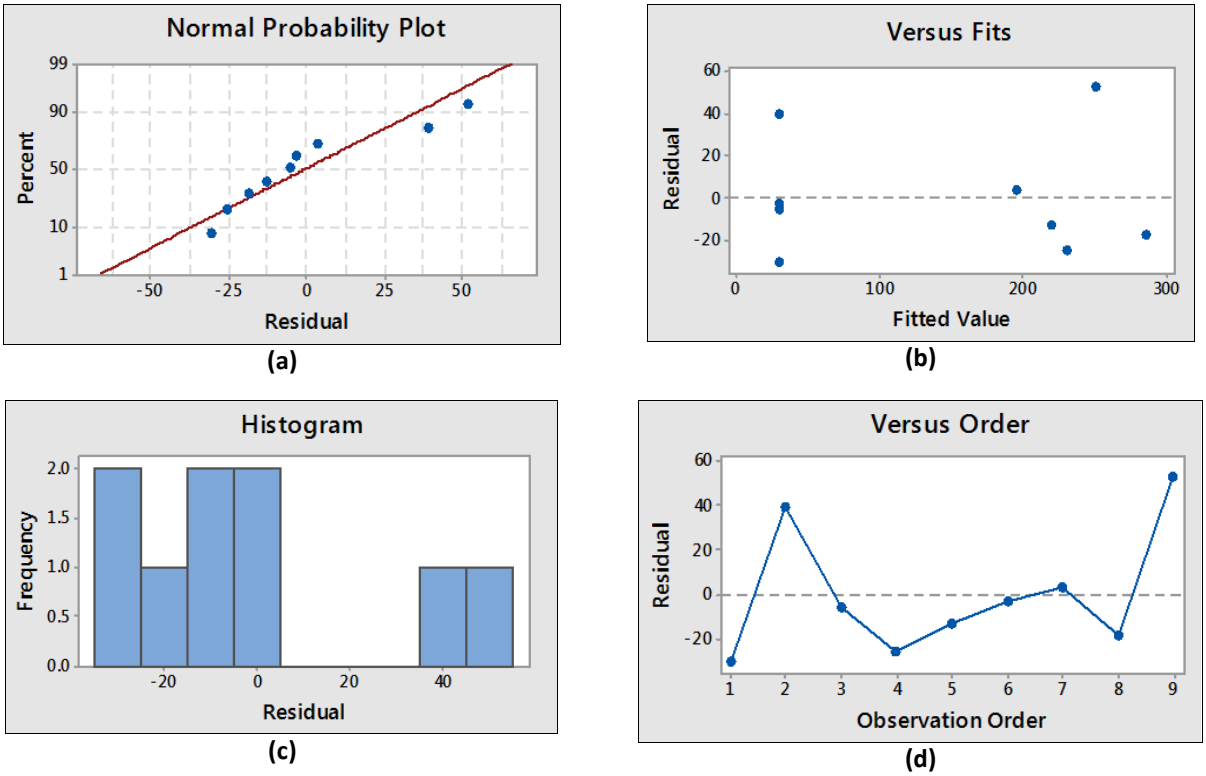

Fig. 10: Residual plots for SBS increase

2.3 Experimental Studies on Corrosion of Tubulars (Task 3)

After repairing the autoclave (testing cell), low-pressure corrosion experiments were continued. Five CO_2 corrosion tests were performed at 120 psi and 140°F. Corrosion coupons were placed in 2% NaCl solution saturated with CO_2 containing gas. Carbon dioxide concentration in the gas phase was varied from 0 to 100%. Both LPR and weight loss methods were used to measure corrosion rate. The LPR measurements show instantaneous corrosion rate during the test. Experimental parameters and results of these tests are summarized in **Table 6**. Predominantly, the LPR data shows good agreement with weight loss measurement.

Table 6: Test parameters and results of low-pressure corrosion experiments

Exp. #	Temp. (ºF)	Pressure (psi)	Partial Pressure %		Brine Conc. (%)	Test Period (days)	Results (mpy)	
			N_2	CO_2			LPR	WL
15	78	120	25	75	2	187	40.30	31.91
16	78	120	0	100	2	187	39.18	32.18
17	78	240	0	100	2	187	NA	NA
18	78	120	75	25	2	187	22.92	21.83
19	110	120	75	25	2	187	31.78	23.78
20	110	120	25	75	2	187	53.16	43.22
21	110	120	100	0	2	187	12.37	15.40
22	110	120	75	25	2	187	31.07	23.78
23	110	120	50	50	2	187	70.35	43.39
24	110	120	25	75	2	187	53.16	43.22
25	110	120	0	100	2	187	44.92	32.49
26	176	120	100	0	2	187	4.04	3.10
27	176	120	75	25	2	187	16.53	11.77
28	176	120	50	50	2	187	24.23	12.71
29	176	120	25	75	2	187	17.39	10.87
30	176	120	0	100	2	187	22.56	12.04
31	**140**	**120**	**100**	**0**	**2**	**187**	**2.58**	**2.72**
32	**140**	**120**	**75**	**25**	**2**	**187**	**11.00**	**6.33**
33	**140**	**120**	**50**	**50**	**2**	**187**	**13.33**	**14.30**
34	**140**	**120**	**25**	**75**	**2**	**187**	**38.48**	**26.76**
35	**140**	**120**	**0**	**100**	**2**	**187**	**24.40**	**24.23**

To investigate the influence of temperature on corrosion rate, the new data points are presented (**Fig. 11**) together with previously reported measurements. For temperature below 110°F, the corrosion rate increased with temperature. Above 110°F, it showed slight reduction or remained unchanged as the temperature was increased. The corrosion rate trend depends on the CO_2 partial pressure. The maximum corrosion rate was observed at 110°F regardless of the CO_2 concentration. The reduction in corrosion rate above 110°F is attributed to the decrease in iron carbonate solubility, which promotes the formation of protective scale that can limit further corrosion of the material. In addition, the increase in temperature has a negative impact on the solubility of CO_2. The reduction in the solubility of CO_2 tends to increase the pH of the solution thereby slowing the corrosion process.

Furthermore, in addition to temperature, concentration (partial pressure) of CO_2 is expected to affect the corrosion rate. The increase in CO_2 concentration enhances the dissolution of CO_2 and the formation of carbonic acid, which reduces the pH. The reduction in pH results in increase in iron

carbonate solubility, which facilitates the corrosion process by preventing the formation of protective scale. However, as the CO_2 concentration approaches 100%, the pH reduction with the CO_2 concentration diminishes, causing the corrosion rate to stabilize or reduce.

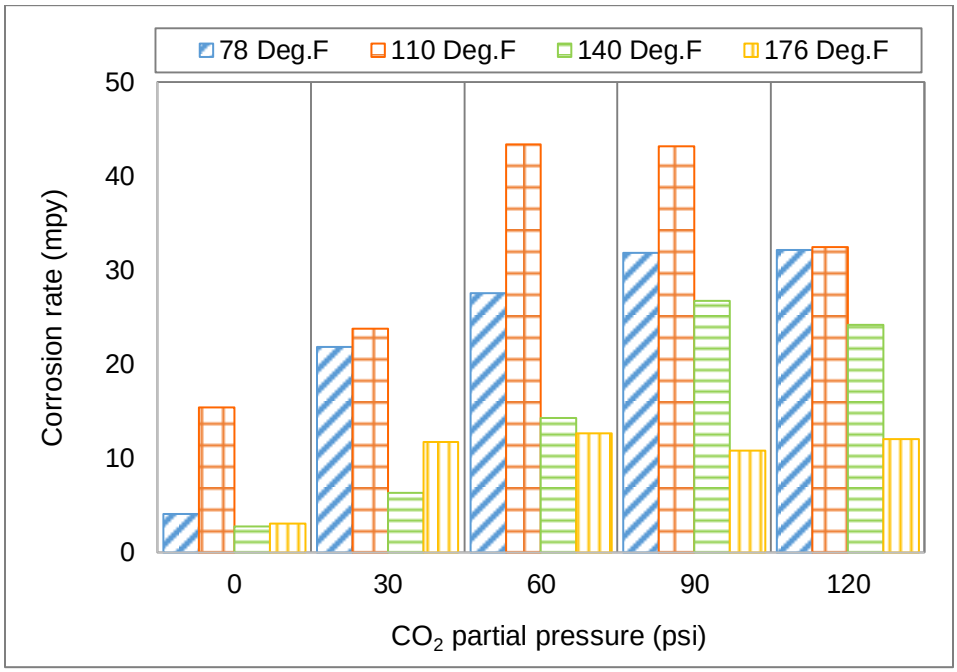

Fig. 11: Effect of temperature on corrosion rate at various CO_2 partial pressures

Corrosion test specimens are needed to conducted tubular corrosion investigation under HPHT sour gas environment. Sixty mini-pipe specimens (**Fig. 12**) and one hundred twenty corrosion coupons (**Fig. 13**) have been manufactured and delivered during this month. The specimens are made of T95, C110 and Q125 API grade carbon steels. To prevent atmospheric corrosion occurring before the test, specimens are placed in vacuum storage containers, which contain silica gel adsorbent.

Fig. 12: Mini-pipe speciemen

Fig. 13: Flat corrosion coupone

Mini-pipe specimens are stretched during the test to induce stress cracking corrosion. Along with the specimens, we have received holders (**Fig. 14**), which are used for applying tension force on the mini-pipe during the test. The holders are made of Hastelloy (HC-276) to withstand the corrosive environment in the test cell. They are screwed to the mini-pipe on both ends. The bottom of the mini-pipe is plugged. Holder placed on the top of the mini pipe has a sealing mechanism to prevent pressure communication between the outside and inside of the mini pipe.

Mechanical properties of mini-pipes and flat coupons are measured before and after the corrosion experiment. The changes occurring in the yield stress and elastic modulus after the test are used to investigate the corrosion process and determine the corrosion mechanisms. In order to perform mechanical property tests, special grips (**Fig. 15**) are designed and manufactured.

Fig. 14: Mini-pipe holders

Fig. 15: Grips for flat coupons

3. Planned Activities

- Continue testing baseline and new cement formulations for their performance by aging them in brine saturated with methane gas containing 300 ppm H_2S at 6000 psi and 100°F varying CO_2 concentration.
- Continue theoretical and modeling studies on tubular degradation.
- Continue experimental studies on tubular degradation under low-pressure and moderate-temperature conditions.
- Start HPHT corrosion experiments with mini-pipes.

4. Project Expenditures

This section presents the project expenses during the month of June (**Table 7**) and the cumulative expenditures.

Table 7: Current and cumulative expenditures, June 2014

No.	Budget Categories	Current Expenses	Cumulative Expenses
1	Salaries & Wages	$16,441.32	$310,710.93
2	Fringe Benefits	$5,123.91	$69,076.49
3	Project Materials	$58.82	$65,611.53
4	Travel	$52.64	$11,065.67
5	Conference Expenses	$0.00	$0.00
6	Other Direct Costs	($3,461.54)	$531.81
7	Equipment	$3,904.98	$248,137.79
8	Space Rental	$0.00	$0.00
9	Indirect Cost	$9,107.58	$227,453.33
10	**Total**	**$31,227.71**	**$932,587.55**

Nomenclatures

BWOC	By weight of cement
c	Cohesion constant
CH	Calcium hydroxide
CSH	Calcium silicate hydrate
d_p	Average penetration depth
FTIR	Fourier Transform Infra-Red Spectroscopy
GS	Class G cement with silica flour
HPHT	High-pressure high-temperature
HS	Class H cement with silica flour
SBS	Shear bonding strength
SCC	stress corrosion cracking
SSC	Sulfide Stress Cracking
XRD	X-Ray diffraction
β	Orientation of angle of the critical plane
ΔSBS	Increase in SBS
φ	Friction angle
τ	Shear stress
σ_n	Normal stress

References

Brady, B. H. G. and Brown, E. T. 2006. Rock Mechanics for Underground Mining, Third Edition, Kluwer Academic Publishers, New York, 20052.

Drummond, S. E. Jr. 1981. Boiling and Mixing of Hydrothermal fluids: Chemical Effects on mineral precipitation, PhD dissertation, The Pennsylvania State University, State College, Pennsylvania (March 1981).

Duan, Z. and Sun, R. 2003. An improved model calculating CO_2 solubility in pure water and aqueous NaCl solutions from 273 to 533 K and from 0 to 2000 bar, Chemical Geology, Vol. 193, 257-271.

Takenouchi, S. and Kennedy, G.C. 1964. The binary system H_2O–CO_2 at high temperatures and pressures, American Journal of Science, Vol. 262, 1055– 1074.

Wiebe, R. and Gaddy, V.N. 1939. The solubility in water of Carbon dioxide at 500, 750 and 1000 at pressures to 700 atm, Journal of American Chemical Society, Vol. 61, 315-318.

Appendix A: Coulomb's Failure Criterion

From Coulomb failure criterion,

$$\tau = c + \sigma_n \tan\varphi \quad \text{..... (A-1)}$$

where c is the cohesion constant and φ is the friction angle. τ and σ_n are shear and normal stresses.

The normal and shear stress equations for the solid element shown in Fig. 6 are:

$$\sigma_n = \frac{\sigma_1+\sigma_3}{2} + \frac{\sigma_1-\sigma_3}{2}\cos 2\beta \quad \text{..... (A-2)}$$

$$\tau = \frac{\sigma_1-\sigma_3}{2}\sin 2\beta \quad \text{..... (A-3)}$$

Substituting Eqs. (A-2) and (A-3) into (A-1), the limiting stress condition can be derived for any plane defined by angle, β.

$$\frac{\sigma_1-\sigma_3}{2}\sin 2\beta = c + \left(\frac{\sigma_1+\sigma_3}{2} + \frac{\sigma_1-\sigma_3}{2}\cos 2\beta\right)\tan\varphi$$

Simplifying further,

$$\sigma_1 = \frac{2c+\sigma_3\,(\sin 2\beta+\tan\varphi\,(1-\cos 2\beta)}{\sin 2\beta-\tan\varphi\,(1+\cos 2\beta)} \quad \text{..... (A-4)}$$

Geometrically, the orientation of the critical plane has been obtained (from Mohr circle construction) as:

$$\beta = \frac{\pi}{4} + \frac{\varphi}{2} \quad \text{..... (A-5)}$$

Therefore, for the critical plane:

$$\sin 2\beta = \sin(\varphi + \tfrac{\pi}{2}) = \cos\varphi, \quad \text{..... (A-6)}$$

$$\cos 2\beta = \cos(\varphi + \tfrac{\pi}{2}) = -\sin\varphi \quad \text{..... (A-7)}$$

Hence, Eq. (A-4) becomes:

$$\sigma_1 = \frac{2c\cos\varphi}{1-\sin\varphi} + \frac{\sigma_3\,(1+\sin\varphi}{1-\sin\varphi} \quad \text{..... (A-8)}$$

Project Title: Effect of H_2S and CO_2 in HPHT Wells on Tubulars and Cement

Report Type: Monthly Report

Report #: 34

Reporting Period: June 22nd, 2014 to July 21st, 2014

Authors:

Ramadan Ahmed, Principal Investigator

Subhash Shah, Co-Principal Investigator

Rida Elgaddafi, Research Assistant

Omotayo Omosebi, Research Assistant

Jueun Hwang, Research Assistant

Sagar Tale, Research Assistant

Prepared under BSEE Project # E12PC00035

by

THE UNIVERSITY OF OKLAHOMA

August 28, 2014

1. Summary of Accomplishments

This monthly report presents the progress made during the project period June 22, 2014 to July 21, 2014. During this reporting period, cement and tubular degradation studies were continued. Baseline and acid-resistant cement cores and bonding samples were prepared and aged in HPHT acidic environment to examine their degradation characteristics. Additionally, the first corrosion experiment with mini-pipe specimen was conducted under HPHT condition. Mechanical properties of the mini-pipe were measured before and after exposure to corrosive environment.

One aging experiment (Experiments 33) was completed during this month. Cement cores and bonding samples were aged for 2 weeks in 2% brine saturated with methane gas containing H_2S. Porosity, permeability, and compressive and bond strengths of unaged and aged samples will be measured and presented in the next monthly report.

Two new corrosion experiments under low-pressure conditions were performed at 140°F. The tests were carried out at a reduced brine concentration (1% NaCl). Carbon dioxide content of the gas phase was varied from 0 to 25%. New measurements are compared with previously reported ones. Corrosion of carbon steel is significantly affected by brine concentration. In the absence of CO_2, the average corrosion rates increased with salt concentration. However, when CO_2 was present, the corrosion rate trend was reversed. These observations are consistent with the findings of previously published studies.

A new tensile strength testing setup has been developed to measure mechanical properties of mini-pipes and flat coupons, before and after the corrosion test. These tests are aimed to assess the level of embrittlement and uniform corrosion occurring after exposure to sour gas environment.

Our plan for the upcoming weeks is to continue: i) aging tests at 9000 psi, 100°F, 300 ppm H_2S and different CO_2 concentrations; ii) theoretical and modeling studies on tubular corrosion; iii) testing of new acid-resistant cement formulations; iv) low-pressure corrosion experiments at various CO_2 concentrations and 1% NaCl solution; and v) corrosion experiments under HPHT conditions varying CO_2 content of the gas phase with and without the presence of H_2S.

2. Overall Project Progress

2.1 Theoretical Studies (Task 1)

2.1.1 Sulfide Stress Cracking

Previous monthly reports presented solubility models for H_2S and CO_2 in water and brine. These models were validated by comparing their predictions with published experimental measurements. This report presents the application of H_2S solubility model to predict the susceptibility of material for sulfide stress cracking (SSC) in a sour environment. Using the available SSC model, safe operating conditions for different casing materials have been predicted. The SSC process involves entry of hydrogen into the

metal crystalline structure. This leads to embrittlement of the metal. Hydrogen concentration in the metal structure is most important factor in assessing SSC. Establishing a relationship between hydrogen content of the steel and concentration of dissolved H_2S in brine solution is useful to predict SSC.

2.1.1.1 SSC Model

Asahi et al. (1994) developed a model to predict SSC based hydrogen content of metals. To develop the model two types of experiments were conducted. First, an electrochemical cell was used to determine hydrogen content in steel based on pH and concentration (partial pressure of hydrogen sulfide) of surrounding solution. Secondly, Four Point Bent Beam (FPBB) tests were performed to determine critical hydrogen content of steel. Then, susceptibility of steel towards SSC was established by comparing the actual hydrogen content to the critical hydrogen content.

In the electrochemical experiments, steel plate of known thickness was placed between two chambers. One chamber contained corrosive solution saturated with H_2S while other chamber contained NaOH solution. The steel specimen was set to 0.2 V saturated calomel electrode (SCE). Experiments were performed at 25, 50 and 80°C. Permeation current, which can be converted to permeation rate of hydrogen, was measured with time. Initially, the current increased with time and later decreased and attained a steady state value. The maximum permeation rate is taken into account while developing the model, since it gives the highest hydrogen content. Diffusion constant was calculated by comparing the theoretical permeation curve with the actual. Increase in temperature resulted in increases in the permeation rate and diffusion coefficient. According to this model, under steady state condition, hydrogen content in steel is expressed as:

$$\mathrm{H_{Fe}} = \mathrm{J} * \mathrm{L}/\mathrm{D} \quad \ldots\ldots (1)$$

where H_{Fe} is hydrogen content, D is diffusion constant, J is permeation rate and L is steel plate thickness. J and D are determined experimentally.

Using Eq. (1), Asahi et al. (1994) calculated the hydrogen content[1]. Similar experiments were performed at different pH and H_2S concentrations. Lower pH resulted in higher hydrogen content, which caused more hydrogen to permeate into the steel. Hydrogen content was correlated to the product of concentrations of hydrogen and hydrogen sulfide ($\mathrm{H^+} * \mathrm{H_2S}$). Applying regression analysis, the following relation has been developed to estimate hydrogen content:

$$\mathrm{H_{Fe}} = \mathrm{A} * (\mathrm{H^+} * \mathrm{H_2S})^{0.26} \quad \ldots\ldots (2)$$

where A is the regression coefficient. During the test, the value of A was found to be 13 from the tested specimens[2]. The regression coefficient in Eq. (2) varies with the type of steel due to difference in

[1] The unit of hydrogen content in Eq. (1) is not defined in the article.

[2] It was not 13 for each specimen but average from all.

trapping sites present in steel matrix. The H_{Fe} is used to assess susceptibility of steel for SSC in sour environment. Equation (2), which forms the first part of SSC model provides conservative estimate of hydrogen content for other materials.

The second part of model formulation involved SSC experiments to determine the critical hydrogen content of steel. In these tests, FPBB specimens were subjected to different stress conditions in corrosive solution. Hydrogen sulfide concentration and pH of corrosive solution were predetermined. The tests were performed at 25, 50 and 80°C. Failure stress was determined in each case. According to NACE, if the material withstands SSC under highly stressed condition (i.e. 85% of its yield strength), then it is safe to use in sour environment. Results of the SSC tests are shown in **Fig 1**. Using pH and P_{H2S}, hydrogen content in the steel was determined. It can be concluded that as hydrogen content in the steel increases, failure stress of steel decreases. Moreover, it shows that steel is highly susceptible for SSC at lower temperature.

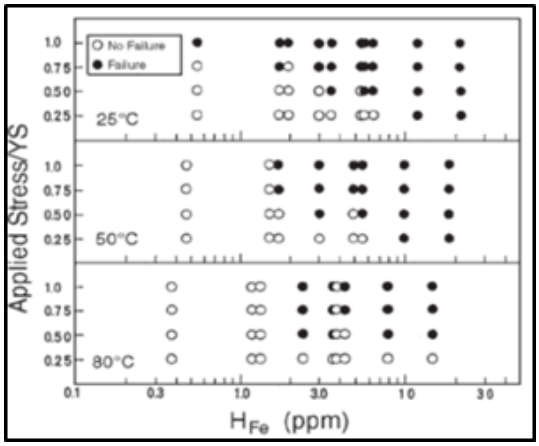

Fig 1: Results of FPBB test as function of hydrogen content in steel (Asahi et al. 1994)

Using FPBB test results, the values of critical hydrogen content (i.e. hydrogen content below which material resists SSC at stress level of 85% of yield stress) were determined under different conditions. The critical hydrogen content (H_C) is function of temperature and yield strength. By plotting the H_C against the maximum yield strengths, the following relationships have been developed. These relationships can be used for typical API grade tubulars.

$$\log H_c = -4.05 * 10^{-3} * MYS + 4.01 \; at \; 25^0C \quad \text{..... (3a)}$$

$$\log H_c = -3.45 * 10^{-3} * MYS + 3.89 \; at \; 50^0C \quad \text{..... (3b)}$$

$$\log H_c = -3.14 * 10^{-3} * MYS + 3.91 \; at \; 80^0C \quad \text{..... (3c)}$$

where MYS is maximum yield strength in MPa. If maximum yield strength is known, the H_C can be determined. For computing H_2S concentration, Asahi et al. (1994) used Henry's law to predict H_2S solubility; however, this law is valid at low pressures. In this project, the solubility model developed previously (Report # 32) can be utilized to predict H_2S solubility at higher pressures. Thus, for different environmental conditions (known pH and gas phase H_2S concentration), liquid phase H_2S concentration can be calculated using the solubility model, H^+ ion concentration can be estimated from pH {pH = -log $[H^+]$} and the hydrogen content in the steel can be determined using Eq. (2).

For a given material with known maximum yield strength, critical hydrogen content can be computed using Eq. (3). Comparing the critical hydrogen content with the expected hydrogen content, the susceptibility of steel towards SSC can be determined. Asahi et al. (1994) provided critical hydrogen content values for some of common tubular materials. Based on these values, safe operating conditions have been obtained for different materials. **Tables 1** and **2** show safe operating regime for N-80 steel under different environments. The tables present H_2S concentration (mole/kg) in the solution at various H_2S partial pressures and temperatures. Red highlighted cells in the tables indicate favorable conditions for the occurrence of SSC. That means the H_2S concentration in solution is expected to be higher than the critical H_2S concentration, which implies that the material is likely to experience SSC.

Table 1: SSC susceptibility of N-80 material at pH =4

H_2S partial Pressure(Bar)	pH=4					
	T= 25 ^{0}C	T= 40 ^{0}C	T= 50 ^{0}C	T= 60 ^{0}C	T= 70 ^{0}C	T=80 ^{0}C
0.001	1.00E-04	7.05E-05	5.80E-05	4.91E-05	4.25E-05	3.77E-05
0.01	1.00E-03	7.05E-04	5.80E-04	4.91E-04	4.25E-04	3.77E-04
0.1	1.00E-02	7.05E-03	5.80E-03	4.91E-03	4.25E-03	3.77E-03
1	9.86E-02	6.98E-02	5.59E-02	4.42E-02	3.35E-02	2.30E-02
10	9.58E-01	7.15E-01	6.07E-01	5.24E-01	4.60E-01	4.08E-01
20	1.78E+00	1.36E+00	1.17E+00	1.02E+00	9.06E-01	8.16E-01
30			1.66E+00	1.47E+00	1.32E+00	1.20E+00
40				1.86E+00	1.69E+00	1.55E+00
50					2.02E+00	1.87E+00
60						2.15E+00

Table 2: SSC susceptibility of N-80 material at pH =5

H_2S partial Pressure(Bar)	pH=5					
	T= 25 ^{0} C	T= 40 ^{0} C	T= 50 ^{0} C	T= 60 ^{0} C	T= 70 ^{0} C	T=80 ^{0} C
0.001	1.00E-04	7.05E-05	5.80E-05	4.91E-05	4.25E-05	3.77E-05
0.01	1.00E-03	7.05E-04	5.80E-04	4.91E-04	4.25E-04	3.77E-04
0.1	1.00E-02	7.05E-03	5.80E-03	4.91E-03	4.25E-03	3.77E-03
1	9.86E-02	6.98E-02	5.59E-02	4.42E-02	3.35E-02	2.30E-02
10	9.58E-01	7.15E-01	6.07E-01	5.24E-01	4.60E-01	4.08E-01
20	1.78E+00	1.36E+00	1.17E+00	1.02E+00	9.06E-01	8.16E-01
30			1.66E+00	1.47E+00	1.32E+00	1.20E+00
40				1.86E+00	1.69E+00	1.55E+00
50					2.02E+00	1.87E+00
60						2.15E+00

2.2 Experimental Studies on Degradation of Cement (Task 2)

2.2.1 Compressive Strength of Baseline Cements

One aging experiment was completed during this month. Cement cores and bonding samples were aged under HPHT conditions in brine (2% NaCl) saturated with methane gas containing 300 ppm H_2S. The aging conditions for the new test (Batches 036) are presented in **Table 3** along with those of previous experiments. The mechanical and physical properties including porosity, permeability, compressive and bond strengths of the samples will be measured and presented in the next monthly report.

Table 3: Test parameters for aging experiments conducted to date

Batch #	Temp. (ºF)	Pressure (psi)	Partial Pressure %			Brine Conc. (%)	Aging Period (days)	Experiment #
			CH_4	CO_2	H_2S (ppm)			
001	350	9000	100	0	0	9	6	1
002	350	6000	100	0	0	2	14 & 28	2
003	350	6000	100	0	0	2	14	
004	350	6000	90	10	0	2	6	3
005	350	6000	90	10	0	2	14 & 28	4
006	350	6000	90	10	0	2	14	
007	225	6000	90	10	0	2	14	5
008	100	6000	90	10	0	2	14	6
009	225	6000	60	40	0	2	14	7
010	225	6000	0	100	0	2	14	8
011	100	6000	60	40	0	2	14	9
012	100	6000	0	100	0	2	14	10
013	350	6000	60	40	0	2	14	11
014	350	6000	0	100	0	2	14	12
015	225	6000	60	40	0	2	14	7A
016	350	3000	60	40	0	2	14	13
017	350	9000	60	40	0	2	14	14
018	350	3000	0	100	0	2	14	15
019	350	9000	0	100	0	2	14	16
020	350	3000	90	10	0	2	14	17
021	350	9000	90	10	0	2	14	18
022	225	3000	60	40	0	2	14	19
023	225	9000	60	40	0	2	14	20
024	225	3000	0	100	0	2	14	21
025	225	9000	0	100	0	2	14	22
026	225	3000	90	10	0	2	14	23
027	225	9000	90	10	0	2	14	24
028	430	6000	90	10	0	2	14	25
029	430	6000	60	40	0	2	14	26
030	430	6000	100	0	0	2	14	27
031	430	3000	100	0	0	2	14	28
032	430	9000	100	0	0	2	14	29
033	100	6000	90	10	300	2	14	30
034	225	6000	90	10	300	2	14	31
035	350	6000	90	10	300	2	14	32
036	100	6000	100	0	300	2	14	33

2.3 Experimental Studies on Corrosion of Tubulars (Task 3)

In the previous report, the influence of the carbon dioxide concentration and temperature on the corrosion of the carbon steel in solution containing 2% NaCl was summarized. Recent measurements are consistent with previous data, showing the influence of CO_2 concentration and temperature on corrosion rate of carbon steel.

In order to investigate the effect of water chemistry on corrosion rate, new experiments were conducted at reduced salt concentration (1% NaCl). Two new corrosion experiments were performed at 140°F and different CO_2 concentrations (0 and 25%). LPR and weight loss (WL) measurement techniques were utilized during the tests. In **Table 4,** experimental parameters and results of these tests (Experiments 36 and 37) are presented along with those of previous measurements. Results showed disagreement between LPR and WL measurements. Hence, in order to examine the effect of salt concentration on the CO_2 corrosion rate, only the corrosion rate measurements from weight loss method were compared with previous data obtained at 2% NaCl.

Table 4: Test parameters and results of low-pressure corrosion experiments conducted to date

Exp. #	Temp. (ºF)	Pressure (psi)	Partial Pressure %		Brine Conc. (%)	Test Period (days)	Results (mpy)	
			N_2	CO_2			LPR	WL
15	78	120	25	75	2	187	40.30	31.91
16	78	120	0	100	2	187	39.18	32.18
17	78	240	0	100	2	187	NA	NA
18	78	120	75	25	2	187	22.92	21.83
19	110	120	75	25	2	187	31.78	23.78
20	110	120	25	75	2	187	53.16	43.22
21	110	120	100	0	2	187	12.37	15.40
22	110	120	75	25	2	187	31.07	23.78
23	110	120	50	50	2	187	70.35	43.39
24	110	120	25	75	2	187	53.16	43.22
25	110	120	0	100	2	187	44.92	32.49
26	176	120	100	0	2	187	4.04	3.10
27	176	120	75	25	2	187	16.53	11.77
28	176	120	50	50	2	187	24.23	12.71
29	176	120	25	75	2	187	17.39	10.87
30	176	120	0	100	2	187	22.56	12.04
31	140	120	100	0	2	187	2.58	2.72
32	140	120	75	25	2	187	11.00	6.33
33	140	120	50	50	2	187	13.33	14.30
34	140	120	25	75	2	187	38.48	26.76
35	140	120	0	100	2	187	24.40	24.23
36	140	120	100	0	1	187	3.69	1.23
37	140	120	75	25	1	187	5.16	20.97

In general, corrosion rate is strongly affected by the salt concentration with or without the presence of carbon dioxide. **Figure 2** shows the corrosion rate measured using the weight loss method at different salt concentrations and CO_2 partial pressures. For pure nitrogen case (i.e. in the absence of the carbon dioxide), the average corrosion rates increased with the increase in salt concentration. According to Fang (2006), the activity coefficient of H^+ ion increases with increase in the salt concentration, which leads to pH reduction and subsequently increased corrosion rate. However, in the presence of carbon dioxide, a reverse trend was observed when the salt concentration was increased from 1 to 2 wt%. The corrosion rate decreased (by 70%) with the salt concentration. These observations have been found consistent with previously published results (Fang 2006; Fang et al. 2010). The presence of salt retards both the anodic and cathodic reactions, which predominately determine the rate of CO_2 corrosion (Fang et al. 2010). Hence, CO_2 corrosion rates decreased with the increase in the salt concentration.

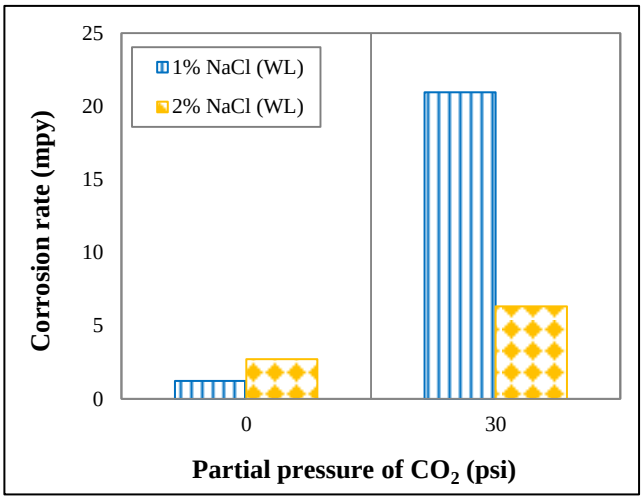

Fig. 2: The effect of salt concentration on corrosion rate at 140°F and various CO_2 concentrations

During this month, the tensile strength testing facility has been developed to evaluate the change occurring in mechanical properties of flat and mini-pipe specimens after acid attack. Tensile strength tests were performed on specimens, according to the ASTM E8M specification. **Figure 3** shows the geometry of a flat coupon, which is 32 mm in length, 6 mm in width and 2 mm in thickness at the reduced investigation section.

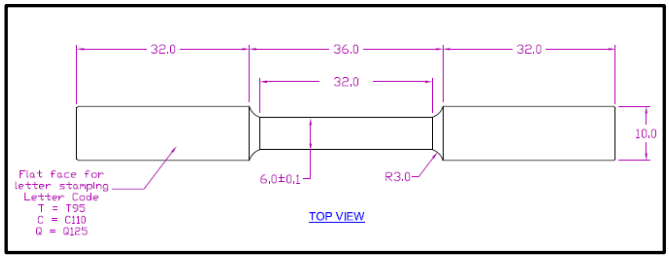

Fig. 3: Design of flat coupone

A hydraulic cylinder (3.25-inch cylinder and 1.375 inch rod) is used to apply the tensile load. The cylinder is connected a computer controlled syringe pump to vary the stress at a contact rate of approximately 100,000 psi/min. The tensile strength tests were conducted by applying the tension load on the specimen and record corresponding elongation or change in length (**Fig. 4**). The main objective of performing the test is to assess change occurring in mechanical properties (Young's modulus, yield strength, tensile strength, and elongation to failure) of the specimens after exposure to corrosive environment. The result clearly shows the elastic and plastic deformation regimes.

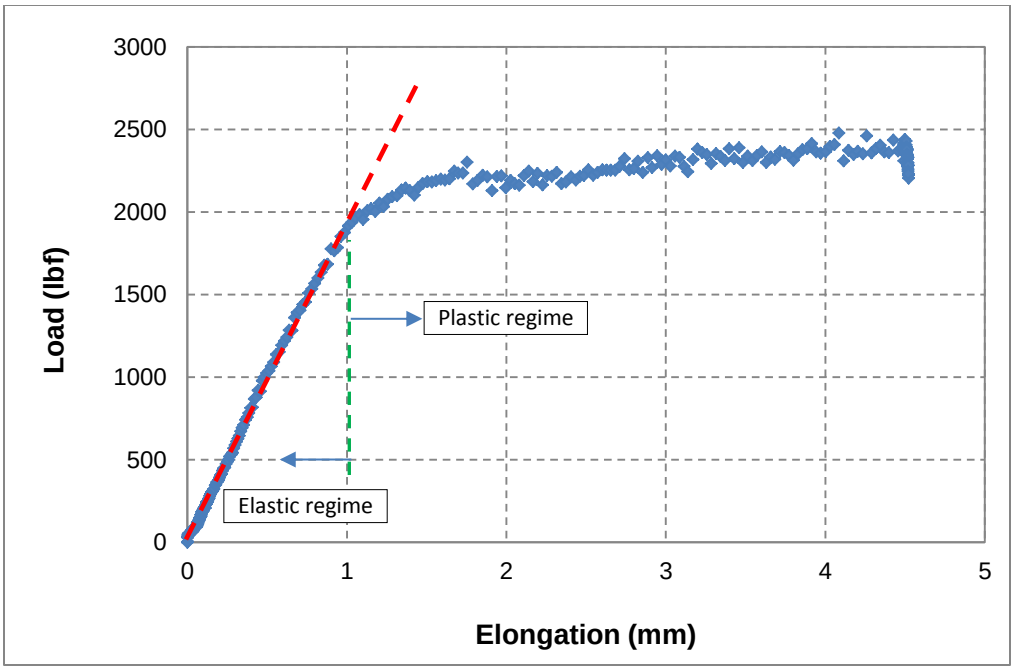

Fig. 4; Applied instantaneous load versus elongation for C110 coupon

During this reporting period, the first corrosion experiment with mini-pipe (C110 material) was conducted. The tested was performed in inert environment (methane only) maintaining 6000 and 4000 psi inside (P7) and outside (P8) pressures, respectively (**Fig. 5**). During the experiment, one end of the mini-pipe is attached to a pulling rod (7/8 inch diameter) installed at the bottom of the cell while the other end is connected to the lid of the corrosion testing vessel (**Fig. 6**). Due to internal pressurization of the pulling rod, the mini-pipe is subjected to a tensile load. In addition, the pulling rod is connected to a pneumatic cylinder to apply additional tension force required to generate the desired stress level (85% of the minimum yield stress) in the specimen. During the test, 50 psi pressure was maintained in the cylinder. The mini-pipe was completely immersed in 2% NaCl solution during the experiment. The outer surface of the mini-pipe was cleaned using organic solvent to remove oil and grease used during its installation. The corrosion test was completed in eight days. The specimen was recovered after the test and showed substantial damage. In the final days of the experiment, the pressure differential between inside and outside of the mini-pipe reduced from 2000 psi to 1000 psi. The Teflon seal used to isolate the inside of the mini-pipe from its outside lost its sealing ability. A seal material with more sealing ability (i.e. elasticity) such as fluoroelastomer (Viton) will be used in the next test. In the coming weeks, mechanical properties of the corroded mini-pipe will be tested.

3. Planned Activities

- Continue testing baseline and new cement formulations for their performance by aging them in brine saturated with methane gas containing 300 ppm H_2S at 6000 psi and 100°F varying CO_2 concentration.
- Continue theoretical and modeling studies on tubular degradation.
- Continue experimental studies on tubular degradation under low-pressure and moderate-temperature conditions.
- Continue HPHT corrosion experiments with mini-pipes and start HPHT corrosion tests with flat coupon.

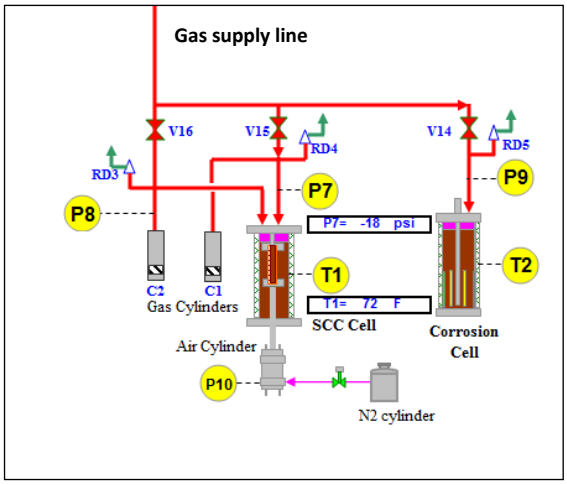

Fig. 5: Schematic of tubular corrosion test facility

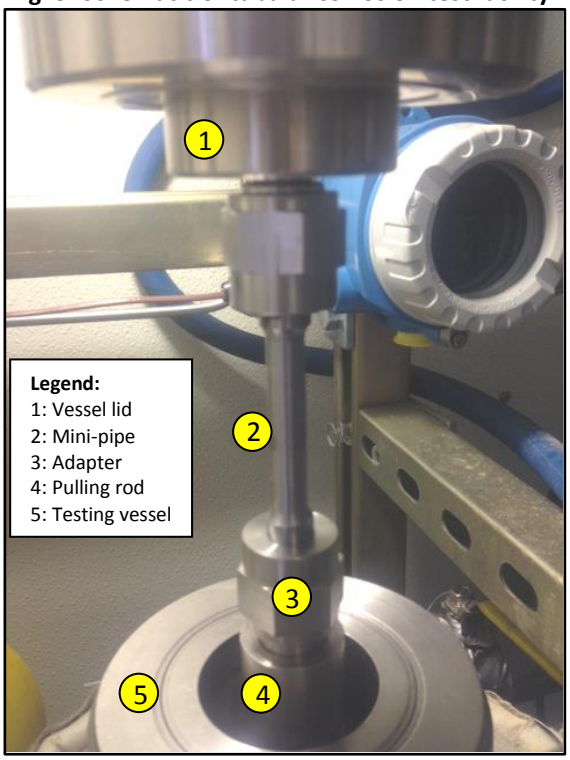

Fig. 6: Assembly of mini-pipe, adapters, pulling rod and vessel lid

4. Project Expenditures

This section presents the project expenses during the month of July (**Table 5**) and the cumulative expenditures.

Table 5: Current and cumulative expenditures, July 2014

No.	Budget Categories	Current Expenses	Cumulative Expenses
1	Salaries & Wages	$27,149.10	$337,860.03
2	Fringe Benefits	$8,414.08	$77,490.57
3	Project Materials	$31,685.56	$97,297.09
4	Travel	$0.00	$11,065.67
5	Conference Expenses	$0.00	$0.00
6	Other Direct Costs	$23.21	$555.02
7	Equipment	$1,501.45	$249,639.24
8	Space Rental	$0.00	$0.00
9	Indirect Cost	$33,635.98	$261,089.31
10	**Total**	**$102,409.38**	**$1,034,996.93**

Nomenclatures

API	American Petroleum Institute
ASTM	American Society for Testing and Materials
D	Diffusion constant
FPBB	Four Point Bent Beam
HPHT	High-pressure high-temperature
H_C	Critical hydrogen content
H_{Fe}	Hydrogen content
J	Permeation rate
L	plate thickness
MYS	maximum yield strength in
NACE	National Association of Corrosion Engineers
SSC	Sulfide stress cracking
SCE	Saturated calomel electrode

References

Asahi, H., Ueno, M. and Yonezawa, T. 1994. Prediction of Sulfide Stress Cracking in High Strength tubulars, Corrosion, Vol. 50, 537-545.

Fang, H., Brown B., and Nesic, S. 2010. High Salt Concentration Effects on CO2 Corrosion and H2S Corrosion, paper No. 276, 14-18 March, San Antonio, Texas.

Fang, H. 2006. Low Temperature and High Salt Concentration Effects on General CO2 Corrosion for Carbon Steel, thesis, November, Ohio University.

Project Title: Effect of H_2S and CO_2 in HPHT Wells on Tubulars and Cement

Report Type: Monthly Report

Report #: 35

Reporting Period: July 22nd, 2014 to August 21st, 2014

Authors:

Ramadan Ahmed, Principal Investigator

Subhash Shah, Co-Principal Investigator

Rida Elgaddafi, Research Assistant

Omotayo Omosebi, Research Assistant

Jueun Hwang, Research Assistant

Sagar Tale, Research Assistant

Prepared under BSEE Project # E12PC00035

by

THE UNIVERSITY OF OKLAHOMA

October 31, 2014

1. Summary of Accomplishments

This monthly report presents the progress made during the project period July 22, 2014 to August 21, 2014. Investigations on cement and tubular degradation were continued during this reporting period. Baseline and acid-resistant cement cores and bonding samples were prepared and aged in HPHT acidic environment to examine their degradation characteristics. In addition, corrosion experiments with mini-pipes and flat coupons were conducted under HPHT conditions. Mechanical properties of the coupons and mini-pipes were measured.

One batch of cement aging experiment (Experiments 37) was completed during this month. Cement cores and bonding samples (baseline and additive cement) were aged for 2 weeks in 2% brine saturated with methane gas containing CO_2 and H_2S. Compressive and shear bond strengths (SBS) of unaged and aged samples were measured. After aging, the SBS of baseline samples increased while that of magnesium oxide containing cement (MGO) remained unchanged. Hydroxyapatite based cement (HHO) samples showed higher SBS than the baseline samples. Aging improved the SBS in HHO and baseline samples.

Three low-pressure corrosion experiments were performed at 140°F. The tests were carried out at a reduced brine concentration (1% NaCl). Carbon dioxide content of the gas phase was varied from 25 to 75%. Corrosion rate measurements are compared with previously reported ones. At low CO_2 concentrations (less 50%), considerable increase in the corrosion rates was observed as the salt concentration was reduced from 2 to 1%. This observation is consistent with the findings of previous studies.

Stress cracking and uniform corrosion experiments were conducted under HPHT conditions. Three mini-pipe and flat specimens were tested. Mechanical properties of the specimens were measured before and after the test. The measurements are compared to identify the presence of embrittlement. As expected, hydrogen embrittlement was not observed in a specimen tested without the presence of sour gas. In addition, stress-strain data was obtained for a baseline specimen. The data is consistent with the API specifications of the tubular material.

Three identical flat coupons were tested in each batch of uniform corrosion experiment. Minor differences were observed in the corrosion rate of the coupons. Surfaces of the corroded coupons were examined using a microscope to study the corrosion product and determine the type of corrosion. The examination shows the formation of non-protective layer on the coupon surface, which is consistent with previous studies.

Our plan for the upcoming weeks is to continue: i) aging tests at 9000 psi, 100°F, 300 ppm H_2S and different CO_2 concentrations; ii) theoretical and modeling studies on tubular corrosion; iii) testing of new acid-resistant cement formulations; iv) low-pressure corrosion experiments at various CO_2 concentrations and 1% NaCl solution; and v) stress cracking and uniform corrosion experiments under HPHT conditions varying CO_2 content of the gas phase with and without the presence of H_2S.

2. Overall Project Progress

2.1 Experimental Studies on Degradation of Cement (Task 2)

2.2.1 Aging Experiment and Degradation

Degradation study on baseline and new cement formulations (i.e. additive cement formulations) was continued. One aging experiment was completed during this month. Cement cores and bonding samples were aged under HPHT conditions in brine (2% NaCl) saturated with methane gas containing 300 ppm H_2S. The aging conditions for the new test (Batch 37) are presented in **Table 1** along with those of previous experiments. The mechanical properties including compressive and bond strengths of recent samples (Batches 36 and 37) are measured.

Table 1: Test parameters for aging experiments conducted to date

Batch #	Temp. (ºF)	Pressure (psi)	Partial Pressure %			Brine Conc. (%)	Aging Period (days)	Experiment #
			CH_4	CO_2	H_2S (ppm)			
001	350	9000	100	0	0	9	6	1
002	350	6000	100	0	0	2	14 & 28	2
003	350	6000	100	0	0	2	14	
004	350	6000	90	10	0	2	6	3
005	350	6000	90	10	0	2	14 & 28	4
006	350	6000	90	10	0	2	14	
007	225	6000	90	10	0	2	14	5
008	100	6000	90	10	0	2	14	6
009	225	6000	60	40	0	2	14	7
010	225	6000	0	100	0	2	14	8
011	100	6000	60	40	0	2	14	9
012	100	6000	0	100	0	2	14	10
013	350	6000	60	40	0	2	14	11
014	350	6000	0	100	0	2	14	12
015	225	6000	60	40	0	2	14	7A
016	350	3000	60	40	0	2	14	13
017	350	9000	60	40	0	2	14	14
018	350	3000	0	100	0	2	14	15
019	350	9000	0	100	0	2	14	16
020	350	3000	90	10	0	2	14	17
021	350	9000	90	10	0	2	14	18
022	225	3000	60	40	0	2	14	19
023	225	9000	60	40	0	2	14	20
024	225	3000	0	100	0	2	14	21
025	225	9000	0	100	0	2	14	22
026	225	3000	90	10	0	2	14	23
027	225	9000	90	10	0	2	14	24
028	430	6000	90	10	0	2	14	25
029	430	6000	60	40	0	2	14	26
030	430	6000	100	0	0	2	14	27
031	430	3000	100	0	0	2	14	28
032	430	9000	100	0	0	2	14	29
033	100	6000	90	10	300	2	14	30

Batch #	Temp. (ºF)	Pressure (psi)	Partial Pressure %			Brine Conc. (%)	Aging Period (days)	Experiment #
			CH_4	CO_2	H_2S (ppm)			
034	225	6000	90	10	300	2	14	31
035	350	6000	90	10	300	2	14	32
036	100	6000	100	0	300	2	14	33
037	100	6000	60	40	300	2	14	34

2.2.2 Shear Bond Strength of Baseline and Additive Cements

The shear bond strengths (SBS) of baseline and additive (MGO and HHO) samples are presented in **Tables 2** and **3,** respectively. The shear bond strength of unaged magnesium oxide based cement (MGO) samples was greater than that of the baseline samples. After aging, increase in SBS was observed in baseline samples while that of the MGO (i.e. HSMG) samples remained approximately the same. The HHO samples show higher SBS than the baseline samples. In general, aging improved the SBS in HHO and baseline samples.

Table 2: Shear bond strength of baseline samples

Batch	Core #	Temperature (F)	Pressure (psi)	CH4 (%)	CO2 (%)	H2S (%)	Brine (%)	Days Aged	SBS(PSI)	Average	stdev
036	036-HS-00-01	unaged	unaged	0	0	0	2	0	749.4	750.4	228.5
	036-HS-00-02	unaged	unaged	0	0	0	2	0	539.4		
	036-HS-00-03	unaged	unaged	0	0	0	2	0	1133.9		
	036-HS-00-04	unaged	unaged	0	0	0	2	0	628.3		
	036-HS-00-05	unaged	unaged	0	0	0	2	0	700.9		
	036-HS-08-01	100	6000	100	0	0.03	2	14	904.9	829.0	63.0
	036-HS-08-02	100	6000	100	0	0.03	2	14	746.2		
	036-HS-08-03	100	6000	100	0	0.03	2	14	806.8		
	036-HS-08-04	100	6000	100	0	0.03	2	14	877.9		
	036-HS-08-05	100	6000	100	0	0.03	2	14	809.0		
037	037-HS-00-01	unaged	unaged	0	0	0	2	0	422.8	493.3	76.5
	037-HS-00-02	unaged	unaged	0	0	0	2	0	472.5		
	037-HS-00-03	unaged	unaged	0	0	0	2	0	475.6		
	037-HS-00-04	unaged	unaged	0	0	0	2	0	602.2		
	037-HS-00-05	unaged	unaged	0	0	0	2	0	-		
	037-HS-08-01	100	6000	60	40	0.03	2	14	748.9	737.6	49.1
	037-HS-08-02	100	6000	60	40	0.03	2	14	720.6		
	037-HS-08-03	100	6000	60	40	0.03	2	14	794.1		
	037-HS-08-04	100	6000	60	40	0.03	2	14	761.0		
	037-HS-08-05	100	6000	60	40	0.03	2	14	663.6		

Table 3: Shear bond strength of additive samples

Batch	Core #	Temperature (F)	Pressure (psi)	Natural Gas (%)	CO2 (%)	H2S (%)	Brine (%)	Days Aged	SBS(PSI)	Average SBS, uncorrected	stdev, uncorrected
36	011-HHO-00-01	unaged	unaged	0	0	0	2	0	838.3	894.3	43
	011-HHO-00-02	unaged	unaged	0	0	0	2	0	949.4		
	011-HHO-00-03	unaged	unaged	0	0	0	2	0	921.8		
	011-HHO-00-04	unaged	unaged	0	0	0	2	0	887.6		
	011-HHO-00-05	unaged	unaged	0	0	0	2	0	874.3		
	011-HHO-11-01	100	6000	60	40	0.03	2	14	1270.8	1117.3	89
	011-HHO-11-02	100	6000	60	40	0.03	2	14	1063.7		
	011-HHO-11-03	100	6000	60	40	0.03	2	14	1074.2		
	011-HHO-11-04	100	6000	60	40	0.03	2	14	1059.5		
	011-HHO-11-05	100	6000	60	40	0.03	2	14	1118.6		
37	010-HSMG-00-01	unaged	unaged	0	0	0	2	0	517.1	608.6	95
	010-HSMG-00-02	unaged	unaged	0	0	0	2	0	767.2		
	010-HSMG-00-03	unaged	unaged	0	0	0	2	0	614.1		
	010-HSMG-00-04	unaged	unaged	0	0	0	2	0	561.1		
	010-HSMG-00-05	unaged	unaged	0	0	0	2	0	583.5		
	010-HSMG-11-01	100	6000	100	0	0.03	2	14	546.2	612.8	76
	010-HSMG-11-02	100	6000	100	0	0.03	2	14	559.1		
	010-HSMG-11-03	100	6000	100	0	0.03	2	14	703.5		
	010-HSMG-11-04	100	6000	100	0	0.03	2	14	686.2		
	010-HSMG-11-05	100	6000	100	0	0.03	2	14	568.9		

2.2.3 Compressive Strength of Baseline and Additive Cements

Tables 4 and **5** present compressive strengths of baseline and hydroxyapatite based cement (HHO) samples, respectively. Unaged HHO and baseline samples showed approximately the same compressive strengths. After aging, HHO samples displayed moderate reduction in strength; however, Class H baseline sample (HS) exhibited significant increase. This observation is in agreement with our previous results from similar experiments. The presence of hydroxyapatite limits carbonation of calcium silicate hydrate (CSH) and calcium hydroxide (CH) and as a result, calcium leaching becomes dominant causing the reduction in strength.

Table 4: Compressive strength of baseline samples (Batch 36)

Unaged Samples						
Core #	**Confine Pressure**	**Pressure (psi)**	**Experimental Stress (psi)**	**Strain**	**Average Stress**	**Standard Deviation**
036-GS-00-03	1000	296	2571	0.0082	2520	49
036-GS-00-04	1000	303	2630	0.0296		
036-GS-00-05	1000	313	2713	0.0082		
036-HS-00-03	1000	365	3166	0.0124	2747	251
036-HS-00-04	1000	301	2611	0.0174		
036-HS-00-05	1000	338	2935	0.0106		
Aged Samples						
Core #	**Confine Pressure**	**Pressure (psi)**	**Experimental Stress (psi)**	**Strain**	**Average Stress**	**Standard Deviation**
036-GS-05-03	1000	269	2331	0.0259	2456	328
036-GS-05-04	1000	319	2767	0.0112		
036-GS-05-05	1000	219	1902	0.0134		
036-GS-07-03	1000	272	2361	0.0120		
036-GS-07-04	1000	354	3069	0.0147		
036-GS-07-05	1000	267	2316	0.0218		
036-HS-04-03	1000	284	2461	0.0042	3216	729
036-HS-04-04	1000	190	1644	0.0009		
036-HS-04-05	1000	479	4156	0.0001		
036-HS-06-03	1000	360	3123	0.0002		
036-HS-06-04	1000	485	4208	0.0006		
036-HS-06-05	1000	346	2999	0.0001		

Table 5: Compressive strength of HHO samples (Batch 36)

Unaged Samples						
Core #	**Confine Pressure**	**Pressure (psi)**	**Experimental Stress (psi)**	**Strain**	**Average Stress**	**Standard Deviation**
011-GHO-00-03	1000	289	2509	0.0005	2675	358
011-GHO-00-04	1000	280	2430	0.0001		
011-GHO-00-05	1000	356	3086	0.0002		
011-HHO-00-03	1000	301	2614	0.0001	2768	147
011-HHO-00-04	1000	335	2907	0.0002		
011-HHO-00-05	1000	321	2782	0.0001		
Aged Samples						
Core #	**Confine Pressure**	**Pressure (psi)**	**Experimental Stress (psi)**	**Strain**	**Average Stress**	**Standard Deviation**
011-GHO-10-03	1000	237	2061	0.0004	1933	289
011-GHO-10-04	1000	185	1602	0.0004		
011-GHO-10-05	1000	246	2135	0.0002		
011-HHO-09-03	1000	254	2207	0.0001	2308	95
011-HHO-09-04	1000	276	2395	0.0003		
011-HHO-09-05	1000	268	2322	0.0001		

Batch 37 baseline aging test was conducted with magnesium oxide based cement (MGO). Compressive strengths of baseline and MGO samples are presented in **Tables 6** and **7,** respectively. Unaged MGO and baseline samples showed slightly different compressive strengths. Their compressive

strengths were not significantly affected by aging. Nevertheless, Class G based additive sample (GSMG) displayed slight increase in compressive.

Table 6: Compressive strength of baseline samples (Batch 37)

Unaged Samples						
Core #	**Confine Pressure**	**Pressure (psi)**	**Experimental Stress (psi)**	**Strain**	**Average Stress**	**Standard Deviation**
037-GS-00-03	1000	270	2340	0.0123		
037-GS-00-04	1000	344	2985	0.0062		
037-GS-00-05	1000	311	2699	0.0099	2555	298
037-HS-00-03	1000	355	3082	0.0135		
037-HS-00-04	1000	304	2641	0.0055		
037-HS-00-05	1000	313	2718	0.0157	2661	214
Aged Samples						
Core #	**Confine Pressure**	**Pressure (psi)**	**Experimental Stress (psi)**	**Strain**	**Average Stress**	**Standard Deviation**
037-GS-05-03	1000	277	2401	0.0147		
037-GS-05-04	1000	377	3271	0.0120		
037-GS-05-05	1000	291	2525	0.0209	2516	304
037-GS-07-03	1000	291	2528	0.0125		
037-GS-07-04	1000	285	2476	0.0095		
037-GS-07-05	1000	298	2586	0.0154		
037-HS-04-03	1000	391	3390	0.0156		
037-HS-04-04	1000	247	2139	0.0213		
037-HS-04-05	1000	339	2938	0.0150	2589	451
037-HS-06-03	1000	345	2995	0.0129		
037-HS-06-04	1000	300	2600	0.0044		
037-HS-06-05	1000	267	2321	0.0114		

Table 7: Compressive strength of unaged MGO samples (Batch 36)

Unaged Samples						
Core #	**Confine Pressure**	**Pressure (psi)**	**Experimental Stress (psi)**	**Strain**	**Average Stress**	**Standard Deviation**
010-GSMG-00-03	1000	173	1504	0.0254		
010-GSMG-00-04	1000	288	2495	0.0102	2290	706
010-GSMG-00-05	1000	331	2870	0.0117		
010-HSMG-00-03	1000	391	3391	0.0117		
010-HSMG-00-04	1000	258	2241	0.0260	2766	581
010-HSMG-00-05	1000	307	2667	0.0094		
Aged Samples						
Core #	**Confine Pressure**	**Pressure (psi)**	**Experimental Stress (psi)**	**Strain**	**Average Stress**	**Standard Deviation**
010-GSMG-10-03	1000	304	2638	0.0113		
010-GSMG-10-04	1000	274	2380	0.0164	2545	143
010-GSMG-10-05	1000	302	2616	0.0137		
010-HSMG-09-03	1000	268	2324	0.0202		
010-HSMG-09-04	1000	273	2366	0.0105	2447	177
010-HSMG-09-05	1000	305	2650	0.0119		

2.2 Experimental Studies on Corrosion of Tubulars (Task 3)

2.2.1 Sulfide Stress Cracking

Our previous monthly report presented model used for predicting susceptibility of material in different sour environments. Experimental investigation on tubular materials for sulfide stress cracking (SSC) has been started during this month. This report presents experimental setup and procedure the investigation. In order to quantify the level of SSC or embrittlement occurring after exposure to corrosive environment, stress-strain data of uncorroded and corroded sample were obtained. Specimen exposed to sour environment in SSC cell failed after 7 days of testing. Crack initiation and development patterns at the failure point indicate hydrogen embrittlement.

2.2.1.1 Introduction

A new SSC testing procedure developed in this investigation involves the application of a constant tensile load (i.e. tensile stress) during exposure to corrosive environment. The method combines the standard NACE Method A and Constant Extension Rate Test (CERT) procedures. The Standard NACE Method A procedure is commonly used for SSC testing; however, this method requires 1 month (NACE TM0177) to obtain the results while the new method provides results in 7 days. Literatures that are related to CERT (Horstemeier et al. 2010, Kermani and MacGuish, 1990) procedure were presented in previous monthly report. Mini-pipe specimens are used in this project instead of solid cylindrical ones that are used in NACE Method A. This is because mini-pipe can simulate the wellbore conditions better than the cylindrical ones. The new SSC testing method involves the following three steps:

Step 1: The specimen is stretched to 80% of elastic limit in air using tensile strength testing (TST) machine

Step 2: The specimen is stretched (85% of MYS) and kept in corrosive solution for 7 days

Step 3: The specimen is taken out of the solution and stretched to failure in air using the TST machine

Step 1 involves stretching the sample until the stress level reaches 80% of its yield stress limit and recording the stress-strain data. This step is repeated 3 times to get an average measurement. One un-corroded (baseline) specimen of each material is stretched to failure in order to measure the yield stress and ultimate tensile strength. The measurements confirmed the material properties provided by the manufacture. They are used as reference values for evaluating embrittlement. The stress-strain curves of uncorroded specimens showed ductile failure. Step 2 is performed in SSC cell where the specimen is exposed to corrosive environment.

2.2.1.2 TST Setup and Procedure

Tensile strength testing was performed on TST setup, which is shown in **Fig 1**. The setup is consists of: i) hydraulic cylinder, which applies the tensile load that increases at a controlled rate; ii) syringe pump with a variable speed drive; iii) data acquisition (DAQ) system; iv) mini-pipe holders and adapters; and v) support frame. In order to perform the test, top side of a mini-pipe specimen is first screwed into a holder, which is attached to the support frame. On the bottom side, the specimen is connected to piston rod of the hydraulic cylinder using an adapter and coupler. The cylinder pressure increases with time as the specimen is being stretched. The pressure is precisely controlled by the syringe pump using the variable speed drive, which controlled by the DAQ computer. The stress rate is maintained at approximately 55,000 psi/min according

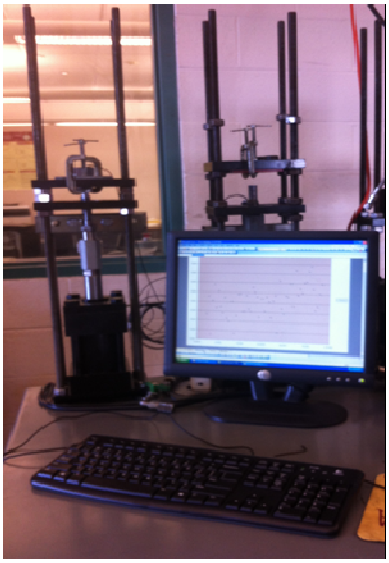

Fig. 1: TST machine

to the ASTM recommendations (ASTM E8/E8M – 09). A displacement sensor is connected to the coupler to measure the elevation change during the test. Changes in elevation readings are converted into strain values using the effective specimen length (i.e. length of the narrow zone). The cylinder pressure is measured using pressure transmitter and recorded by the DAQ system. Pressure readings are converted to stress values using cross-section area of the specimen (i.e. measured in the narrow zone) and area of the cylinder.

2.2.1.3 SSC Test Setup and Procedure

Mini-pipes are hollow specimens with open end at the top and sealed end at the bottom. Adapters of the mini-pipe screw into the header of the cell and pulling rod (**Fig. 2**). An O-ring is used to seal the top joint. Mini-pipe has threads at top and bottom. 340 ml of 2% brine (sodium chloride) was injected into the cell while inside of the mini-pipe was filled with 4.5 ml of brine. Both inside and outside of the mini-pipe were purged twice with 1800 psi of Nitrogen for 15 minutes. Subsequently, the cell and mini-pipe were pressurized simultaneously to 4,000 psi by injecting methane gas containing H_2S and CO_2 gas. The injection of carbon dioxide reduces the pH of the solution. When the pressure stabilized, the gas supply line to the cell was closed. Pressurization of the inner side was continued until the pressure reached 6000 psi. During the test duration, a pressure differential of approximately 2000 psi was kept between inside and outside of mini-pipe. The two pressures would equalize when the mini-pipe fails. After pressurization, steady values of pressure and temperature were maintained on both sides of the mini-pipe.

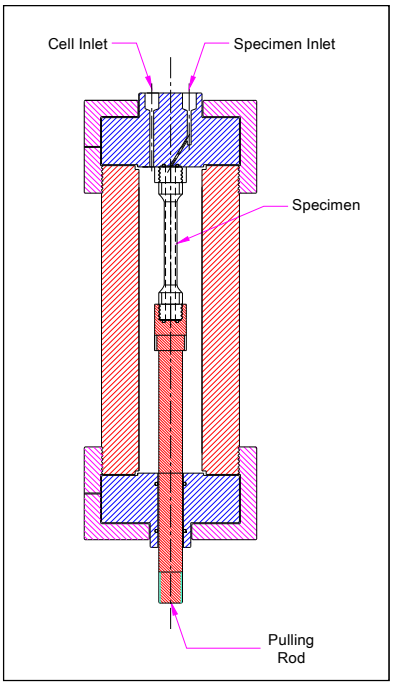

Fig. 2: TST machine

Materials which are susceptible to SSC develop cracks in the first 200 hours of exposure (Kermani and MacGuish, 1990). Hence, test duration of 7 days is selected. After exposure to H_2S environment, hydrogen atoms penetrate into the steel surface and occupy positions in steel matrix (crystal structure) leading to embrittlement. A TST experiment is carried out if a specimen doesn't fail after seven days of exposure. Material, which is susceptible to SSC shows brittle failure. In addition, mechanical properties (Young's modulus, plastic strain to failure and ultimate tensile strength) of SSC susceptible specimen are expected to change after the exposure.

2.2.1.4 Results

During this reporting period, C110 material was tested for its SSC susceptibility. Four specimens were tested. **Table 8** shows the experimental conditions in which specimens were exposed. The label of each specimen involves four different parts. First number designates the specimen number, the second number shows the material type, the third number indicates the date on which specimen is kept in the corrosion cell and the last number shows the date on which the specimen is removed from the cell. The

first mini-pipe (Mini-pipe 1) test was conducted at 6000 and 4000 psi inside and outside pressures, respectively. The test was performed for 15 days without H_2S and CO_2 to measure any embrittlement occurring due to brine solution. After the test, the specimen did not fail. The specimen was later tested with the TST machine. Stress-strain data for this specimen is shown in **Fig. 3**. The data shows ductile behavior of the specimen indicating absence of hydrogen embrittlement. Uncorroded sample (Mini-pipe 2) was stretched to failure in the TST machine to measure the ultimate and yield strengths, plastic strain to failure and Young's modulus. The specimen serve as a reference, hence it was not exposed to corrosive environment. Stress-strain data (**Fig. 4**) of the specimen was obtained. The material displayed expected yield strength. Mini-pipe 3 was stretched to 80% of its yield stress in tensile machine for three times to determine its elastic properties. One set of stress-strain measurement is shown in **Fig. 5**. For initial stress values, very small strain was observed, later strain increased linearly with stress. Young's modulus is slope of this linear portion of stress-strain data. Average of three measurements is obtained (**Table 9)**.

Table 8: Specimen corrosion testing conditions

Mini-pipe No.	Label	Temp. (°F)	Pressure (psi)		Gas Composition			Time Duration (Days)
			Inside	Outside	H2S (ppm)	CH4 (%)	CO2 (%)	
1	01-C110-07/25-08/06	100	6000	4000	0	100	0	15
2	02-C110-08/25-08/25	0	0	0	0	100	0	0
3	03-C110-08/27-09/03	100	6000	4000	300	90	10	7
4	04-C110-09/05-09/12	100	6000	4000	300	100	0	7

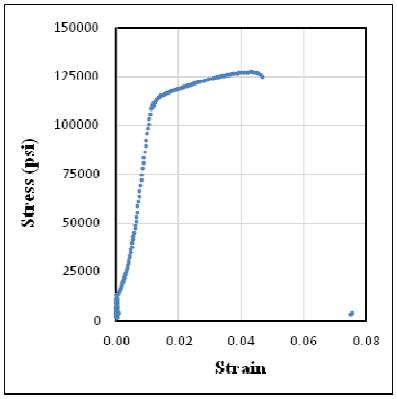

Fig. 3: Stress vs. strain for corroded sample (Mini-pipe 1)

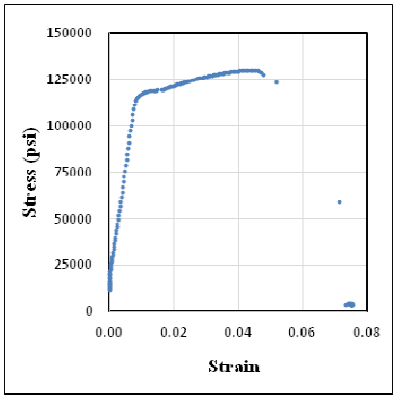

Fig. 4: Stress vs. strain for un-corroded sample (Mini-pipe 2)

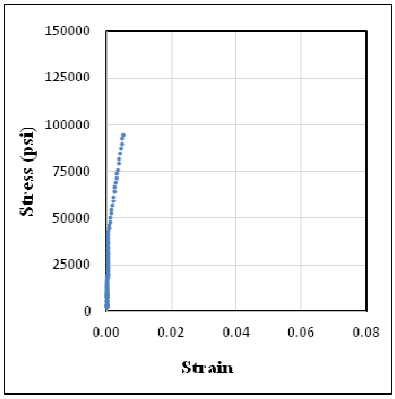

Fig. 5: Stress vs. strain for un-corroded sample (Mini-pipe 3)

Table 9: Mechanical properties of samples before and after corrosion test

Mini-pipe No.	Before Exposure				After Exposure			
	YS (psi)	UTS (psi)	PS	E (psi)	YS (psi)	UTS (psi)	PS	E (psi)
1	-	-	-	-	109,855	127,619	0.03	11,785,921
2	111,529	130,156	0.04	11,842,002	-	-	-	-
3	-	-	-	11,704,810	-	-	-	-
4	-	-	-	12,594,080	-	-	-	-

UTS = Ultimate tensile Strength, PS = Plastic strain to failure, YS = Yield strength, E = Young's modulus

Mini-pipe 3 was the first specimen to be exposed to sour environment in the SSC cell. The specimen was subjected to a stress equal to 85% of its yield strength. It was failed in the cell on the 7th day of the test indicating the susceptible of the material to SSC. Magnified image of broken edge of the specimen was compared (**Fig. 6**) with images of other specimens which were not exposed to sour environment (unbrittled) but stretched to failure using the TST machine. The unbrittled specimens (Mini-pipes 1 and 2) show fibrous region around the crack. Furthermore, they show noticeable elongation around the failure region indicating ductility of the material. For Mini-pipe 3, crack seems to develop instantaneously without elongating the specimen. The failure line was almost perpendicular to direction of stress.

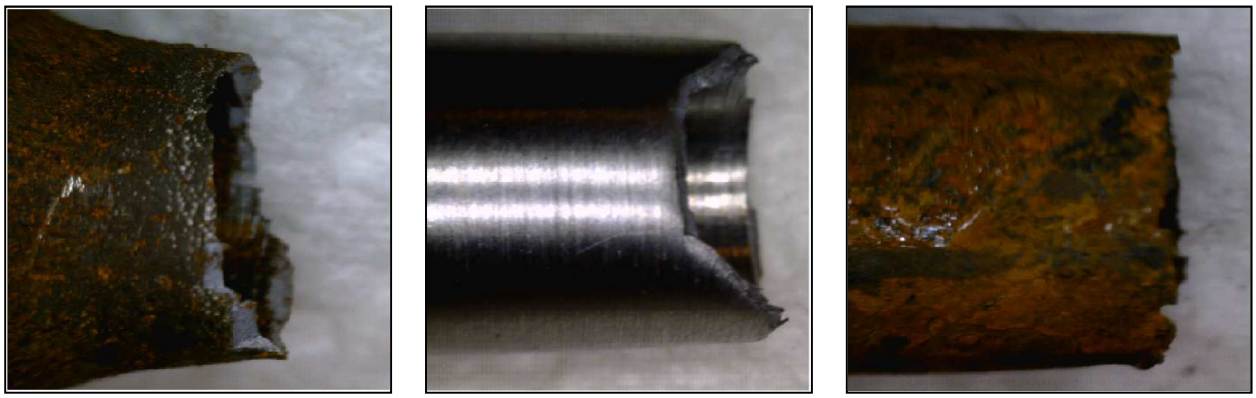

Mini-pipe 1 **Mini-pipe 2** **Mini-pipe 3**

Fig 6: Crack characteristics of broken mini-pipe specimens

2.2.2 Uniform Corrosion in Sour Gas Environment

During this reporting period, corrosion experiments were conducted to evaluate corrosion of carbon steel in the CO_2 environment under low and high pressure conditions. Results from low-pressure corrosion tests indicate strong influence of CO_2 concentration and minor effect of salt concentration (i.e. in the range of 1 to 2% NaCl) on corrosion rate. Furthermore, during this reporting period, the first batch of HPHT test was conducted. The average corrosion rate obtained from three specimens was approximately 276 mpy. A non-protective corrosion layer was formed on the specimen surface partially covering the area in contact with corrosive fluid system (exposure area).

2.2.2.1 Low-Pressure Experiments

The experimental investigation on the effect of salt concentration on the corrosion rate was continued. Due to the discrepancy between the LPR and WL measurements, the corrosion test at 25% CO_2 concentration and 140°F was repeated to verify the accuracy of the results. Furthermore, two more corrosion experiments were conducted during the last month under the same pressure and temperature varying CO_2 concentration. In **Table 10,** experimental parameters and results of these tests (Experiments 38, 39 and 40) are presented along with those of previous measurements. Results showed disagreement between LPR and WL measurements.

Table 10: Test parameters and results of low-pressure corrosion experiments conducted to date

Exp. #	Temp. (ºF)	Pressure (psi)	Partial Pressure %		Brine Conc. (%)	Test Period (days)	Results (mpy)	
			N_2	CO_2			LPR	WL
15	78	120	25	75	2	187	40.30	31.91
16	78	120	0	100	2	187	39.18	32.18
17	78	240	0	100	2	187	NA	NA
18	78	120	75	25	2	187	22.92	21.83
19	110	120	75	25	2	187	31.78	23.78
20	110	120	25	75	2	187	53.16	43.22
21	110	120	100	0	2	187	12.37	15.40
22	110	120	75	25	2	187	31.07	23.78
23	110	120	50	50	2	187	70.35	43.39
24	110	120	25	75	2	187	53.16	43.22
25	110	120	0	100	2	187	44.92	32.49
26	176	120	100	0	2	187	4.04	3.10
27	176	120	75	25	2	187	16.53	11.77
28	176	120	50	50	2	187	24.23	12.71
29	176	120	25	75	2	187	17.39	10.87
30	176	120	0	100	2	187	22.56	12.04
31	140	120	100	0	2	187	2.58	2.72
32	140	120	75	25	2	187	11.00	6.33
33	140	120	50	50	2	187	13.33	14.30
34	140	120	25	75	2	187	38.48	26.76
35	140	120	0	100	2	187	24.40	24.23
36	140	120	100	0	1	187	3.69	1.23
37	140	120	75	25	1	187	5.16	20.97
38	**140**	**120**	**75**	**25**	**1**	**187**	**9.86**	**25.13**
39	**140**	**120**	**50**	**50**	**1**	**187**	**6.40**	**21.24**
40	**140**	**120**	**25**	**75**	**1**	**187**	**6.50**	**23.78**

Figure 7 shows the effect of NaCl concentration on corrosion rate at different CO_2 concentrations. At low CO_2 concentrations (less 50%), considerable reduction occurred in the corrosion rates as the salt concentration slightly increased from 1 to 2%. These results are consistent with previous studies (Fang et al., 2010, Fang, et al., 2006) which reported reduction in cathodic and anodic reactions due to increased salt concentration. The adsorption of chloride ions is expected to be the reason for this behavior. At high CO_2 concentrations (greater than 50%), the increase in salt concentration has negligible impact on the corrosion rate. In the coming weeks, experiments will be carried out at 100% CO_2 to obtain a complete trend of corrosion rate.

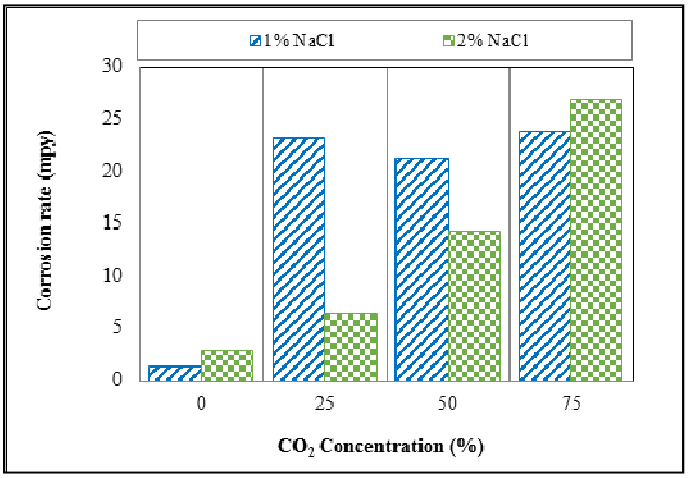

Fig. 7: The effect of salt concentration on corrosion rate at 140°F and various CO_2 concentrations

2.2.2.2 High-Pressure Experiments

The first corrosion experiment on C110 carbon steel alloy was performed under HPHT condition to simulate oil and gas field environment. The test was carried out using HPHT autoclave (corrosion cell). Tensile strengths of the samples (corrosion coupons) were measured before and after the experiment to assess the effect of the corrosion process on their mechanical properties. The major objective of HPHT test is to determine the influence of pressure and temperature on the corrosion rate of common oil field tubulars.

During the HPHT corrosion experiment, coupons were covered with protective coating except the exposure area (i.e. one-side of the narrow investigation section shown in **Fig. 8)**. The weights of the samples were measured and recorded before applying the coating. The exposure area has 192 mm^2 surface. Before the experiment, the test section of each specimen was rinsed with solvent and dried. Three specimens were mounted on the inside of a sleeve using high-temperature silicone seal. After setting, the sleeve together with the coupons was inserted into the autoclave and a cylindrical rotor was inserted in the middle of the sleeve. The autoclave was filled with 950 mL of brine solution, which was prepared with deionized water and 2 wt% of NaCl. The solution was deoxygenated by purging the cell with pure nitrogen for 30 minutes. Then, the test cell was heated to 100°F (±5°F) and pressurized by injecting CH_4 and CO_2 up to the desired pressure. The corrosion test was lasted for 168 hrs (7 days). The testing conditions are shown in **Table 11**.

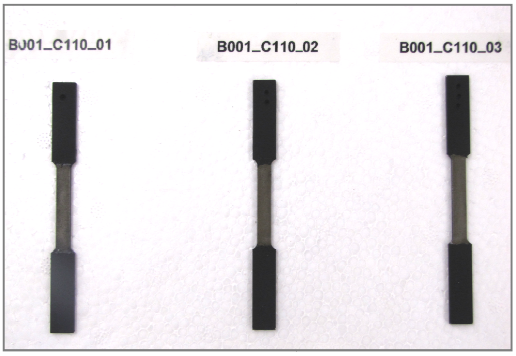

Fig. 8: Corrosion coupon covered with protective coating

When the test was completed, the system was gradually depressurized and the immerged specimens were removed from the autoclave and kept in separate vials. A sample of test solution was collected and stored in sealed vials for future analysis, if it is needed. Prior to the weight measurement, surface analysis of the corroded specimens was carried out using a digital microscope. Then, the corroded specimens were soaked in a solution that removes the coating and rinsed with alcohol and water, and dried in the air. After removing the coating and cleaning, the final weight of the coupons were measured using an electronic balance with precise of ±0.1 mg. The average corrosion rate was calculated as:

Table 11: Test Parameters

Test Parameters	Value
Total pressure (psi)	6000
CO_2 Concentration (%)	100
H_2S Concentration (%)	0
CH_4 Concentration (%)	0
Temperature (°F)	100
NaCl %	2
Exposure time (hrs)	168
Flow velocity (m/s)	0
Steel grade	C110 alloy

$$CR = \frac{438.78 \times (w_1 - w_2)}{t \times A} \quad (1)$$

where CR is average corrosion rate in mpy; w_1 and w_2 are initial and final specimen weight in milligrams, respectively; t is the test duration in hours; and A is the exposed surface area in cm^2. The weight losses

and corresponding corrosion rates are presented in **Table 12**. In addition, tensile loading tests were conducted on the specimens before and after corrosion experiments to measure the initial and final modulus of elasticity of the coupon materials.

Table 12 Mass loss data and calculated corrosion rate

Coupon No.	Initial weight (gm)	Final weight (gm)	Corrosion rate (mpy)	Initial Young's modulus (psi)
C110-1	13.3848	13.2129	2.34E+02	5.79E+06
C110-2	13.4397	13.2212	2.97E+02	6.02E+06
C110-3	13.4478	13.2323	2.93E+02	7.71E+06

Figure 9 shows average corrosion rates of the three specimen of C110 alloy in 2% NaCl solution saturated with 100% CO_2 at 6000 psi and 100°F. Minor differences were observed in the corrosion rate measurements of the specimens. The surface of the corroded specimen was examined using a microscope to study the corrosion protective layer developed during the test. **Figure 10** presents the images of C110-1 coupon before and after corrosion test. Comparison of the images shows the formation of non-protective layer on the steel surface (Fig. 10b). This result is consistent with previous studies (Dugstad, 1997 and Yin et al., 2008), in which non-protective layer was formed at low temperature (below 140°F) due to strong solubility of iron carbonate in brine solution. Cabrini et al. (2014) concluded that the test specimen was partially covered by corrosion film that is mainly consisting of cementite at 77°F and 2000 psi of the CO_2 partial pressure.

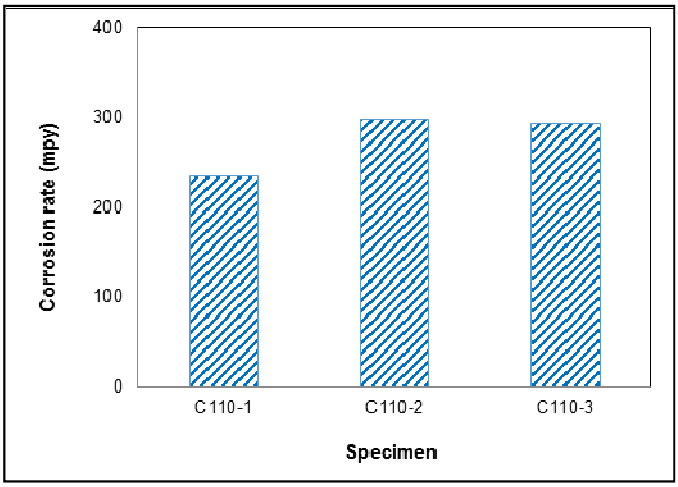

Fig. 9 Average corrosion rate of C110 specimens at 6000 psi and 100°F

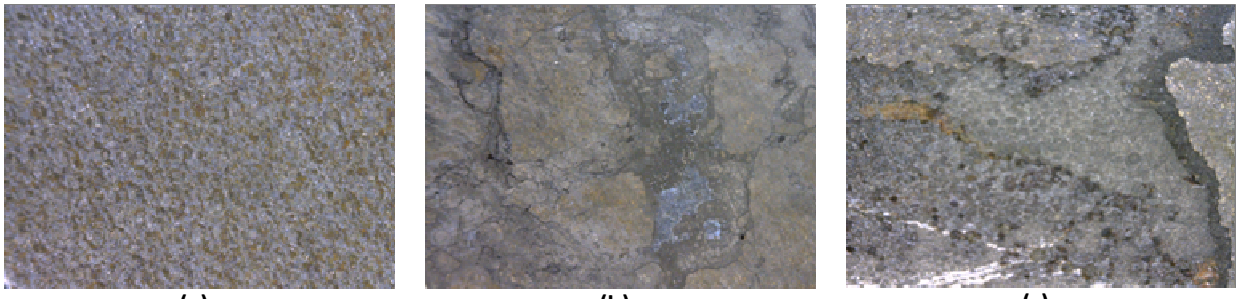

(a) **(b)** **(c)**

Fig 10: Optical micrographs of C110-1 specimens: a) pre-corroded; b) corroded; and c) de-scaled and cleaned

After cleaning and de-scaling, the corroded surface was inspected to assess the occurrences of the localized corrosion. As displayed in Fig. 10c, pitting corrosion occurred on the exposed surface in addition to the significant reduction in the thickness of the investigation section. The existence of pitting corrosion requires further examination using scanning electron microscopy (SEM). After microscopic examination, a complete tensile strength test was performed on the corroded specimens.

3. Planned Activities

- Continue testing baseline and new cement formulations for their performance by aging them in brine saturated with methane gas containing 300 ppm H_2S at 9000 psi and 100°F varying CO_2 concentration.
- Continue theoretical and modeling studies on tubular degradation.
- Continue experimental studies on tubular degradation under low-pressure and moderate-temperature conditions.
- Continue HPHT corrosion experiments with mini-pipes and flat coupons.

4. Project Expenditures

This section presents the project expenses during the month of August (**Table 13**) and the cumulative expenditures.

Table 13: Current and cumulative expenditures, August 2014

No.	Budget Categories	Current Expenses	Cumulative Expenses
1	Salaries & Wages	$7,170.31	$345,030.34
2	Fringe Benefits	$1,240.25	$78,730.82
3	Project Materials	$1,828.25	$99,125.34
4	Travel	($608.60)	$10,457.07
5	Conference Expenses	$0.00	$0.00
6	Other Direct Costs	$0.00	$555.02
7	Equipment	$773.71	$250,412.95
8	Space Rental	$0.00	$0.00
9	Indirect Cost	$4,815.11	$265,904.42
10	**Total**	**$15,219.03**	**$1,050,215.96**

Nomenclatures

A	Exposed surface area in cm^2
API	American Petroleum Institute
CERT	Constant Extension Rate Test
CR	Average corrosion rate in mpy
ASTM	American Society for Testing and Materials
FTIR	Fourier Transform Infra-Red
GHO	Class G Cement with hydroxyapatite
GS	Class G cement with silica flour
GSMG	Class G Cement with silica flour and magnesium oxide
HHO	Class H Cement with hydroxyapatite
HPHT	High-pressure high-temperature
HS	Class H cement with silica flour
HSHO	Class H Cement with silica flour and hydroxyapatite
HSMG	Class H Cement with silica flour and magnesium oxide
LPR	Linear polarization resistance
mpy	mils per year
MGO	Magnesium oxide containing cement
MYS	maximum yield strength in
NACE	National Association of Corrosion Engineers
SBS	Shear bond strength
SCC	Stress corrosion cracking
SEM	Scanning Electron Microscope
SSC	Sulfide stress cracking
t	Test duration in hr
w_1	Initial specimen weight
w_2	Final specimen weight

References

Cabrini, M., Lorenzi, S., Pastore, T., and Radaelli, M. 2014. Corrosion Rate of High CO2 Pressure Pipeline Steel for Carbon Capture Transport and Storage, La Metallurgia Italiana.

Dugstad, A. 1997. Formation of Protective Corrosion Films Formation during CO2 Corrosion of Carbon Steel, Norway, Trondheim.

Fang, H. 2006. Low Temperature and High Salt Concentration Effects on General CO2 Corrosion for Carbon Steel, thesis, November, Ohio University.

Horstemeier, M., Bosch, C., Orlans, B. and Delattre, L. 2010. Validation of the Constant Extension Rate Test (CERT) for high strength OCTG steels as a ranking tool for SSC resistance, NACE paper no. 10309, presented at NACE corrosion conference and expo, Houston.

Kermani, M.B. and MacCuish, R.G., 1990. Materials Assessment for Sour Service Applications, SPE paper no. 20457, 65th Annual Technical Conference and Exhibition, New Orleans.

NACE Standard TM0177, 2005, Laboratory Testing of Metals for Resistance to Sulfide Stress Cracking and Stress Corrosion Cracking in H2S Environments.

Yin, Z. F., Feng, Y. R., Zhao, W. Z., Bai, Z. Q., and Lin, G. F., 2009. Effect of Temperature on CO2 Corrosion of Carbon Steel, Surf. Interface Anal., 41, 517–523, 18 March.

Project Title: Effect of H_2S and CO_2 in HPHT Wells on Tubulars and Cement

Report Type: Monthly Report

Report #: 36

Reporting Period: August 22nd, 2014 to Spetmber21st, 2014

Authors:

Ramadan Ahmed, Principal Investigator

Subhash Shah, Co-Principal Investigator

Rida Elgaddafi, Research Assistant

Omotayo Omosebi, Research Assistant

Jueun Hwang, Research Assistant

Sagar Tale, Research Assistant

Prepared under BSEE Project # E12PC00035

by

THE UNIVERSITY OF OKLAHOMA

December 3, 2014

1. Summary of Accomplishments

This monthly report presents the progress made during the project period August 22, 2014 to September 21, 2014. Experimental and theoretical investigations on cement and tubular degradation were continued during this reporting period. In order to examine degradation characteristics of baseline and acid-resistant (hydroxyapatite based) cements, cores and bonding samples were prepared and aged in high-pressure and high-temperature (HPHT) acidic environment. In addition to cement degradation tests, uniform and stress-cracking corrosion experiments were conducted under HPHT conditions using minipipes and flat coupons. Mechanical properties of the coupons and minipipes were measured to evaluate the level of corrosion.

One batch of cement aging experiment (Experiments 38) was completed during this month. Cement cores and bonding samples (baseline and hydroxyapatite cements) were aged for 2 weeks in 2% brine saturated with methane gas containing H_2S. Porosity, permeability, and compressive and shear bond strengths (SBS) of unaged and aged samples were measured. After aging, porosity and permeability of this hydroxyapatite (HOAP) samples decreased after aging. Porosity and permeability measurements show reasonable consistency; as expected, predominately permeability increased with porosity. SBS of baseline sample improved after aging while that of the HOAP sample showed slight reduction. HOAP and baseline samples showed approximately the same compressive strengths before aging. After aging, the samples showed different trends; Class G based samples displayed reduction in strengths while Class H based samples exhibited slight strength improvement.

Uniform corrosion experiments were continued. Two types of tests (low-pressure and high-pressure) were performed. Low-pressure (120 psi) tests were carried out at a reduced brine concentration (1% NaCl) and two different temperatures (140 and 176°F). Carbon dioxide content of the gas phase was varied. As the CO_2 concentration increased at constant temperature and pressure, the corrosion rate increased at low CO_2 concentrations (less than 25%). In the intermediate concentration range (between 25 and 75%), the rate did not show significant change. However, at high CO_2 concentrations (greater than 75%), the rate exhibited considerable reduction. Similar corrosion rate variations with CO_2 concentration was observed when similar tests were conducted under high-pressure (6000 psi) conditions. Moreover, these measurements are in agreement with previously published data from other studies.

Two stress-cracking corrosion experiments were conducted under HPHT conditions. Mechanical properties of the specimens were measured before and after the test. The measurements are compared to identify the presence of embrittlement. Ultimate Tensile Strength (UTS) and Plastic strain to failure (PSF) of minipipes reduced due to embrittlement and other related phenomena.

Our plan for the upcoming weeks is to continue: i) aging tests at 9000 psi, 100°F, 300 ppm H_2S and different CO_2 concentrations; ii) theoretical and modeling studies on tubular corrosion; iii) testing of new acid-resistant cement formulations; iv) low-pressure corrosion experiments at various CO_2 concentrations and 1% NaCl solution; and v) stress cracking and uniform corrosion experiments under HPHT conditions varying CO_2 content of the gas phase with and without the presence of H_2S.

2. Overall Project Progress

2.1 Experimental Studies on Degradation of Cement (Task 2)

2.2.1 Aging Experiment and Degradation

Degradation study on baseline and new cement formulations (i.e. additive cement formulations) was continued. One cement-aging experiment was completed during this month. Cement cores and bonding samples were aged under HPHT conditions in brine (2% NaCl) saturated with methane gas containing 300 ppm H_2S. The aging conditions for the new test (Batch 38) are presented in **Table 1** along with those of previous experiments. Mechanical and physical properties of the samples including porosity, permeability, and compressive and bond strengths were measured.

Table 1: Test parameters for aging experiments conducted to date

Batch #	Temp. (ºF)	Pressure (psi)	Partial Pressure %			Brine (%)	Aging Period (days)	Exp. #	Additive Batch #
			CH_4	CO_2	H_2S (ppm)				
001	350	9000	100	0	0	9	6	1	
002	350	6000	100	0	0	2	14 & 28	2	
003	350	6000	100	0	0	2	14		
004	350	6000	90	10	0	2	6	3	
005	350	6000	90	10	0	2	14 & 28	4	
006	350	6000	90	10	0	2	14		
007	225	6000	90	10	0	2	14	5	
008	100	6000	90	10	0	2	14	6	
009	225	6000	60	40	0	2	14	7	
010	225	6000	0	100	0	2	14	8	
011	100	6000	60	40	0	2	14	9	
012	100	6000	0	100	0	2	14	10	
013	350	6000	60	40	0	2	14	11	
014	350	6000	0	100	0	2	14	12	
015	225	6000	60	40	0	2	14	7A	
016	350	3000	60	40	0	2	14	13	
017	350	9000	60	40	0	2	14	14	
018	350	3000	0	100	0	2	14	15	
019	350	9000	0	100	0	2	14	16	
020	350	3000	90	10	0	2	14	17	
021	350	9000	90	10	0	2	14	18	
022	225	3000	60	40	0	2	14	19	
023	225	9000	60	40	0	2	14	20	
024	225	3000	0	100	0	2	14	21	
025	225	9000	0	100	0	2	14	22	
026	225	3000	90	10	0	2	14	23	
027	225	9000	90	10	0	2	14	24	
028	430	6000	90	10	0	2	14	25	009 - MS
029	430	6000	60	40	0	2	14	26	010 - MS
030	430	6000	100	0	0	2	14	27	003 - LTMS
031	430	3000	100	0	0	2	14	28	004 - LTMS
032	430	9000	100	0	0	2	14	29	008 - HOAP
033	100	6000	90	10	300	2	14	30	009 - HOAP

Batch #	Temp. (ºF)	Pressure (psi)	Partial Pressure %			Brine (%)	Aging Period (days)	Exp. #	Additive Batch #
			CH_4	CO_2	H_2S (ppm)				
034	225	6000	90	10	300	2	14	31	009 - MGO
035	350	6000	90	10	300	2	14	32	010 - HOAP
036	100	6000	100	0	300	2	14	33	011 - HOAP
037	100	6000	60	40	300	2	14	34	010 - MGO
038	**100**	**9000**	**100**	**0**	**300**	**2**	**14**	**35**	**012 - HOAP**

2.2.2 Porosity and Permeability of Baseline and Additive Cements

Tables 2 and **3** present porosity and permeability of baseline and additive (HOAP) samples, respectively. After aging, porosity and permeability of additive samples increased. However, an experiment conducted in the presence of CO_2 and at lower pressure (Batch 30) showed a different trend. Porosity and permeability of the additive samples decreased after aging. In addition, porosity and permeability measurements show reasonable consistency. As theoretically expected, the permeability predominately increased with porosity.

Table 2: Porosity and permeability of baseline samples (Batch 38)

Core #	Core dimensions			Porosity and Permeability Measurements					
	Dia. mm)	L (mm)	W (g)	ϕ (%)	Ave. ϕ (%)	Std. Dev. (%)	K (mD)	Ave. K (mD)	Std. Dev. (mD)
038 HS 00 01	25.36	35.42	31.3	23.627	20.71	4.13	0.04	0.050	0.014
038 HS 00 02	29.28	39.85	35.2	17.791			0.06		
038 GS 00 01	25.31	37.91	33.6	21.495	21.18	0.44	0.012	0.012	0.000
038 GS 00 02	25.26	38.2	33.9	20.874			0.012		

Table 3: Porosity and permeability of additives (HOAP) samples (Batch 12/38)

Core #	Core dimensions			Porosity and Permeability Measurements					
	Dia. mm)	L (mm)	W (g)	ϕ (%)	Ave. ϕ (%)	Std. Dev. (%)	K (mD)	Ave. K (mD)	Std. Dev. (mD)
012 HHO 00 01	35.16	38.6	34.0	11.338	17.51	8.72	0.011	0.023	0.016
012 HHO 00 02	25.03	36.94	32.4	23.677			0.034		
012 GHO 00 01	25.03	26.84	21.4	28.814	23.35	7.73	0.04	0.046	0.008
012 GHO 00 02	25.11	55.32	31.3	17.882			0.051		
012 HHO 09 01	25.2	39.4	34.2	23.205	23.52	0.45	0.059	0.102	0.060
012 HHO 09 02	25.18	34.39	29.7	23.841			0.144		
012 GHO 10 01	25.19	32.6	26.2	27.063	26.76	0.43	0.173	0.185	0.016
012 GHO 10 02	25.13	35.49	28.5	26.458			0.196		

2.2.2 Shear Bond Strength of Baseline and Additive Cements

The shear bond strengths (SBS) of baseline and additive (HHO) samples are presented in **Tables 4** and **5,** respectively. The SBSs of baseline sample (both aged and unaged cases) were less than that of HHO sample. After aging, baseline sample SBS increased while that of the HHO sample showed slight reduction. However, in previous aging experiment (conducted at 6000 psi and 10% CO_2), HHO sample displayed slight improvement in SBS. This can be attributed to the carbonation of CH and CSH phases in the presence of carbonic acid.

Table 4: Shear bond strength of baseline samples

Batch	Core #	Temp. (F)	Pressure (psi)	CH4 (%)	CO2 (%)	H2S (%)	Brine (%)	Days Aged	SBS (psi)	Ave. SBS	Stdev
038	038-HS-00-01	Unaged	Atmospheric	0	0	0	2	0	318.8	548.8	356
	038-HS-00-02	Unaged	Atmospheric	0	0	0	2	0	475.3		
	038-HS-00-03	Unaged	Atmospheric	0	0	0	2	0	1177.5		
	038-HS-00-04	Unaged	Atmospheric	0	0	0	2	0	384.1		
	038-HS-00-05	Unaged	Atmospheric	0	0	0	2	0	388.3		
	038-HS-08-01	100	9000	100	0	0.03	2	14	288.2	764.9	515
	038-HS-08-02	100	9000	100	0	0.03	2	14	753.4		
	038-HS-08-03	100	9000	100	0	0.03	2	14	817.1		
	038-HS-08-04	100	9000	100	0	0.03	2	14	1589.4		
	038-HS-08-05	100	9000	100	0	0.03	2	14	376.3		

Table 5: Shear bond strength of additive (HHO) samples

Batch	Core #	Temp. (F)	Pressure (psi)	CH4 (%)	CO2 (%)	H2S (%)	Brine (%)	Days Aged	SBS (psi)	Ave. SBS	Stdev
012/038	012-HHO-00-01	Unaged	Atmospheric	0	0	0	2	0	1232	1149.8	83
	012-HHO-00-02	Unaged	Atmospheric	0	0	0	2	0	1095		
	012-HHO-00-03	Unaged	Atmospheric	0	0	0	2	0	1203		
	012-HHO-00-04	Unaged	Atmospheric	0	0	0	2	0	1032		
	012-HHO-00-05	Unaged	Atmospheric	0	0	0	2	0	1187		
	012-HHO-11-01	100	9000	100	0	0.03	2	14	1193	980.5	413
	012-HHO-11-02	100	9000	100	0	0.03	2	14	988		
	012-HHO-11-03	100	9000	100	0	0.03	2	14	270		
	012-HHO-11-04	100	9000	100	0	0.03	2	14	1305		
	012-HHO-11-05	100	9000	100	0	0.03	2	14	1146		

2.2.3 Compressive Strength of Baseline and Additive Cements

Tables 6 and **7** present compressive strengths of hydroxyapatite based cement (HOAP) baseline and samples, respectively. Unaged HOAP and baseline samples showed approximately the same compressive strengths. The addition of 5% hydroxyapatite did not affect the unaged compressive strength of the cement. Measurements from previous batches (Batches 36 and 37) showed similar observations. After aging, baseline samples exhibited different trends; Class G samples showed reduction in strengths while Class H samples displayed slight strength improvement. Similarly, HHO samples displayed mixed trend. The strengths of Class G based additive sample (GHO) decreased after aging while Class H base additive sample (HHO) displayed strength improvements.

Table 6: Compressive strength of additive (HOAP) samples (Batch 12/38)

Unaged Samples						
Core #	Confine Pressure	Pressure (psi)	Experimental Stress (psi)	Strain	Average Stress	Standard Deviation
012-GHO-00-03	1000	535	4642	0.0000		
012-GHO-00-04	1000	390	3380	0.0000		
012-GHO-00-05	1000	317	2752	0.0001	3591	963
012-HHO-00-03	1000	415	3598	0.0000		
012-HHO-00-04	1000	269	2331	0.0001		
012-HHO-00-05	1000	375	3250	0.0000	3060	655
Aged Samples						
Core #	Confine Pressure	Pressure (psi)	Experimental Stress (psi)	Strain	Average Stress	Standard Deviation
012-GHO-10-03	1000	425	3687	0.0002		
012-GHO-10-04	1000	271	2351	0.0000		
012-GHO-10-05	1000	348	3019	0.0001	3019	668
012-HHO-09-03	1000	511	4437	0.0000		
012-HHO-09-04	1000	278	2411	0.0001		
012-HHO-09-05	1000	441	3825	0.0000	3557	1039

Table 7: Compressive strength of baseline samples (Batch 38)

Unaged Samples						
Core #	Confine Pressure	Pressure (psi)	Experimental Stress (psi)	Strain	Average Stress	Standard Deviation
038-GS-00-03	1000	483	4190	0.0012		
038-GS-00-04	1000	456	3956	0.0007		
038-GS-00-05	1000	352	3058	0.0001	3734	597
038-HS-00-03	1000	352	3053	0.0556		
038-HS-00-04	1000	284	2464	0.0019		
038-HS-00-05	1000	415	3597	0.0028	3038	567
Aged Samples						
Core #	Confine Pressure	Pressure (psi)	Experimental Stress (psi)	Strain	Average Stress	Standard Deviation
038-GS-05-01	1000	480	4168	0.0154		
038-GS-05-02	1000	327	2834	0.0088		
038-GS-05-03	1000	384	3329	0.0001		
038-GS-05-04	1000	344	2987	0.0078		
038-GS-05-05	1000	436	3780	0.0000		
038-GS-07-01	1000	512	4443	0.0004		
038-GS-07-02	1000	266	2309	0.0013		
038-GS-07-03	1000	388	3368	0.0000		
038-GS-07-04	1000	382	3316	0.0227		
038-GS-07-05	1000	372	3229	0.0152	3376	627
038-HS-04-01	1000	307	2661	0.0481		
038-HS-04-02	1000	513	4447	0.0197		
038-HS-04-03	1000	334	2898	0.0385		
038-HS-04-04	1000	324	2810	0.0001		
038-HS-04-05	1000	253	2192	0.0001		
038-HS-06-01	1000	408	3540	0.0000		
038-HS-06-02	1000	405	3516	0.0882		
038-HS-06-03	1000	361	3134	0.0001		
038-HS-06-04	1000	352	3054	0.0000		
038-HS-06-05	1000	334	2896	0.0001	3115	611

2.2 Experimental Studies on Corrosion of Tubulars (Task 3)

2.2.1 Sulfide Stress Cracking

Sulfide Stress cracking experiments were continued. C110 material was tested for its SSC susceptibility. During this reporting period, two specimens (Minipipes 5 and 6) were tested. **Table 8** summarizes the SSC tests completed up to now. The table also shows the experimental conditions in which specimens were exposed. Internal and external pressures of the specimen were maintained at 4000 and 6000 psi, respectively.

Table 8: Specimen corrosion testing conditions

No.	Label	Temp. (°F)	Pressure (psi)		Gas Composition			Time Duration (Days)	Remarks
			Inside	Outside	H2S (ppm)	CH4 (%)	CO2 (%)		
1	01-C110-07/25-08/06	100	6000	4000	0	100	0	15	
2	02-C110-08/25-08/25	-	-	-	-	-	-	-	Baseline
3	03-C110-08/27-09/03	100	6000	4000	270	90	10	7	Sample failed after 7 days of exposure
4	04-C110-09/05-09/12	100	6000	4000	300	100	0	7	
5	**05-C110-09/05-09/13**	**100**	**6000**	**4000**	**285**	**95**	**5**	**7**	
6	**06-C110-09/05-09/14**	**100**	**6000**	**4000**	**270**	**10**	**10**	**7**	**Brine completely leaked from the cell**

When Minipipe 6 was tested, brine in the cell, in which the minipipe was immersed, was leaked out of the cell. The leak was caused due to severe damage on the pulling rod, which is used to apply the tensile load on the specimen. Hence, the cell was disassembled and a new pulling rod made of beryllium cupper was installed and the leaking seal was replaced. The new rod has a ball joint that prevents damage when the specimen is attached to the rod before the experiment. Then, the cell was tested for leaks and put in operation. In the coming weeks, the failed experiment will be repeated.

Ultimate Tensile Strength (UTS) of Minipipe 5 was 114,424 psi while the unexposed minipipe (baseline) displayed UTS of 130,156 psi. Thus, there is a significant reduction in UTS. Plastic strain to failure (PSF) for baseline specimen (Minipipe 2) was 0.037 while that of exposed (Minipipe 5) was reduced to 0.023 (**Fig. 1**). In addition, Young's modulus of Minipipe 5 increased from 1.09 x 10^7 to 1.14 x 10^7 psi after sour environment exposure. Embrittlement is one of the reasons behind reduction in plastic strain to failure and increase in the Young's modulus.

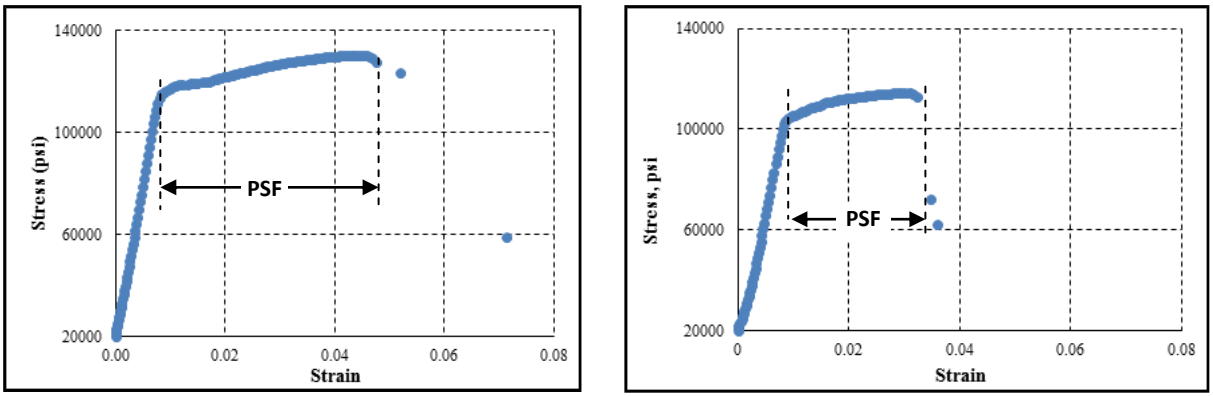

Fig. 1: Stress vs. strain of mini-pipes: a) Mini-pipe 2 (baseline); and b) Mini-pipe 5 (exposed)

Minipipe 6 was exposed to the same experimental conditions as that of Minipipe 3. This was performed to check the reproducibility of experimental measurement. However, during the test, the corrosion-cell seal failed and brine present outside of the specimen was completely leaked out. As a result, external part of the sample was not exposed to the test fluid during the experiment. Thus, the results of this test can be different from that of Minipipe 3. After removing the specimen from SSC cell, it was stretched to failure. It did not show signs of embrittlement (**Fig. 2**). Mechanical properties shown in **Table 9** support this conclusion. The PSF and UTS values of Minipipe 6 were very comparable to that of the baseline (Minipipe 2). Moreover, no significant difference was observed between the elastic modulus of the baseline and the Minipipe 6.

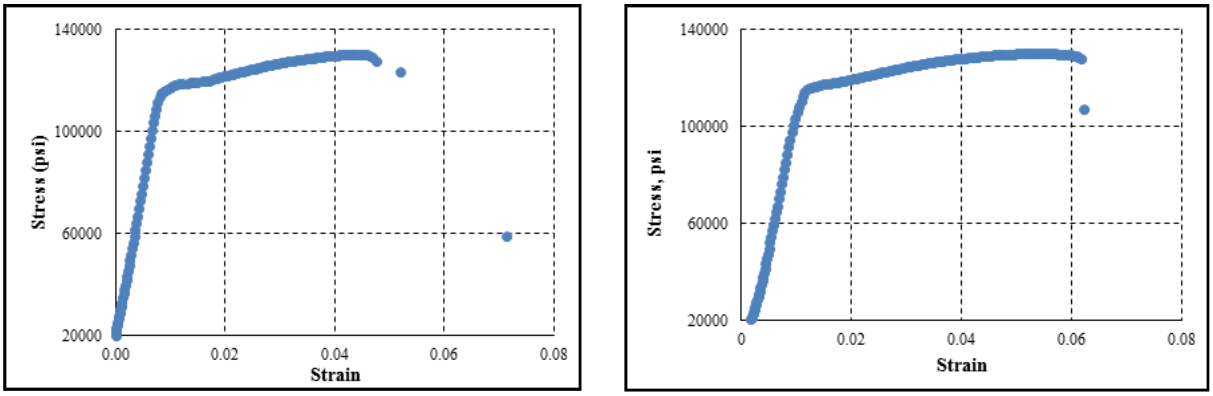

(a) (b)

Fig. 2: Stress vs. strain of mini-pipes: a) Mini-pipe 2; and b) Mini-pipe 6

Table 9: Mechanical properties of samples before and after corrosion test

Mini-pipe No.	Before Exposure				After Exposure			
	YS (psi)	UTS (psi)	PSF	E (psi)	YS (psi)	UTS (psi)	PSF	E (psi)
1	-	-	-	-	109,855	127,619	0.030	11,785,921
2	111,529	130,156	0.040	11,842,002	-	-	-	-
3	-	-	-	11,704,810	-	-	-	-
4	-	-	-	12,594,080	112768	134981	0.043	12078823
5				10,911,219	102217	114424	0.023	11368960
6				11,599,401	110686	130118	0.049	11444081

UTS = Ultimate tensile Strength, PSF = Plastic strain to failure, YS = Yield strength, E = Young's modulus

Figure 3 shows microscopic pictures of Minipipes 5 and 6 when they were strained to failure after exposure to sour conditions. The figure also displays picture for Minipipe 2, which was strained to failure without exposure to corrosive environment. Minipipe 5 showed minor shear deformation near the crack region while Minipipe 6 exhibited substantial shear deformation. Moreover, Minipipe 5 displayed highest fibrous region near the crack. None of specimens were completely embrittled; however, signs of partial embrittlement were observed in Minipipe 5. Observations obtained from microscopic examination of the specimens are in agreement with mechanical property measurements.

Mini-pipe 2 **Mini-pipe 5** **Mini-pipe 6**

Fig. 3: Crack characteristics of broken mini-pipe specimens

2.2.2 Uniform Corrosion in Sour Gas Environment

Uniform corrosion experiments were continued during this reporting period. Tests were conducted to evaluate corrosion of carbon steel in the CO_2 environment under low and high pressure conditions.

2.2.2.1 Low-Pressure Experiments

The experimental investigation is in progress to study the effect of salt concentration on the corrosion rate carbon steel under low pressure conditions. Test parameters and results of new corrosion experiments are presented in **Table 10** along with those of previous measurements. Corrosion rates obtained from the LPR method are substantially lower than the weight loss measurements. This is consistent with previous measurements obtained from experiments conducted at 1% NaCl concentration.

Table 10: Test parameters and results of low-pressure corrosion experiments conducted to date

Exp. #	Temp. (°F)	Pressure (psi)	Partial Pressure %		Brine Conc. (%)	Test Period (days)	Results (mpy)	
			N_2	CO_2			LPR	WL
15	78	120	25	75	2	187	40.30	31.91
16	78	120	0	100	2	187	39.18	32.18
17	78	240	0	100	2	187	NA	NA
18	78	120	75	25	2	187	22.92	21.83
19	110	120	75	25	2	187	31.78	23.78
20	110	120	25	75	2	187	53.16	43.22
21	110	120	100	0	2	187	12.37	15.40
22	110	120	75	25	2	187	31.07	23.78
23	110	120	50	50	2	187	70.35	43.39
24	110	120	25	75	2	187	53.16	43.22
25	110	120	0	100	2	187	44.92	32.49
26	176	120	100	0	2	187	4.04	3.10
27	176	120	75	25	2	187	16.53	11.77
28	176	120	50	50	2	187	24.23	12.71
29	176	120	25	75	2	187	17.39	10.87
30	176	120	0	100	2	187	22.56	12.04
31	140	120	100	0	2	187	2.58	2.72
32	140	120	75	25	2	187	11.00	6.33
33	140	120	50	50	2	187	13.33	14.30
34	140	120	25	75	2	187	38.48	26.76
35	140	120	0	100	2	187	24.40	24.23
36	140	120	100	0	1	187	3.69	1.23
37	140	120	75	25	1	187	5.16	20.97
38	140	120	75	25	1	187	9.86	25.13
39	140	120	50	50	1	187	6.40	21.24
40	140	120	25	75	1	187	6.50	23.78
41	**140**	**120**	**0**	**100**	**1**	**187**	**4.31**	**14.77**
42	**176**	**120**	**0**	**100**	**1**	**187**	**1.76**	**4.63**

Figures 4 compares corrosion rate measurements obtained from electrochemical (LPR) and weight loss (WL) methods at various CO_2 concentrations and different temperatures (140°F and 176°F). At low CO_2 concentrations (less than 25%), the corrosion rate measured using both techniques significantly increased as more carbon dioxide gas was injected into the system. However, at high CO_2 concentrations (greater than 75%), the rate showed considerable reduction. Similar corrosion rate trend with variation of CO_2 concentration has been reported (Choi and Nesic 2011; Choi et al. 2013).

The corrosion rate reduction at high CO_2 concentration occurs due to the formation of the non-protective corrosion scale that minimizes the exposure area for cathodic reaction. The difference between LPR and WL measurements could be the attributed to instrument calibration problem (β value of 30 mV) resulting from reduced brine concentration.

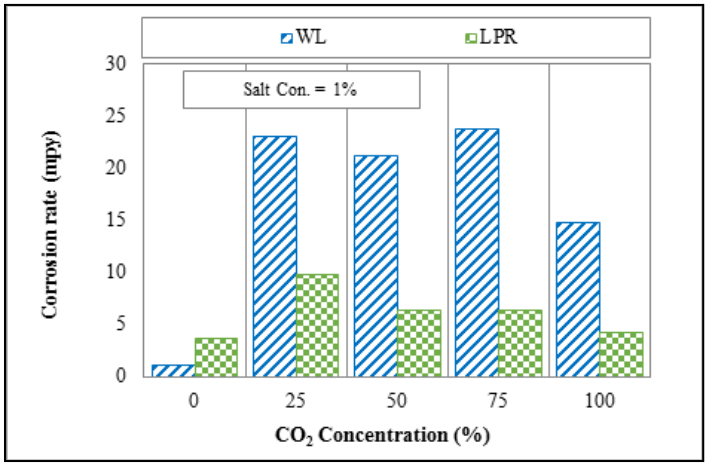

Fig. 4: Corrosion rate versus CO_2 concentration at 140°F and 120 psi

2.2.2.2 High-Pressure Experiments

The corrosion experiments on C110 carbon steel alloy were conducted during this reporting period. Four new batches of experiments were carried out varying CO_2 concentrations (0, 25, 50 and 75%). Test pressure, temperature and NaCl concentration were maintained at 6000 psi, 100°F and 2% NaCl, respectively. Three coupons were used for each batch of experiment in order to obtain average corrosion rate and mechanical property measurements. The same sample-preparation and test procedures were followed to carry out these experiments. Test conditions for different batches experiments are presented in **Table 11**.

Table 11: Test conditions for HPHT uniform corrosion tests

Batch No.	Pressure (psi)	Temperature (F)	Test Duration (hr)	CO_2 Conc. (%)	CH_4 Conc. (%)	H_2S Conc. (%)
001	6000	100	187	100	0	0
002	6000	100	187	50	50	0
003	6000	100	187	0	100	0
004	6000	100	187	25	75	0
005	6000	100	187	75	25	0

Tensile strengths of the specimens were measured before and after the corrosion experiments to assess the impact of the corrosion on mechanical properties of C110 alloy. Prior to the test, each coupon was stretched three times by applying force equivalent to 75% of its yield strength in order to measure the initial modulus of elasticity. Corrosion rates of the specimens in each batch are presented in **Fig 5**. The corresponding weight loss measurements are presented in **Table 12**. As displayed from the figure, moderate differences were observed between identical measurements indicating the level of uncertainty. Hence, three specimens were used in each batch of experiment and the average corrosion rate was determined based on three measurements.

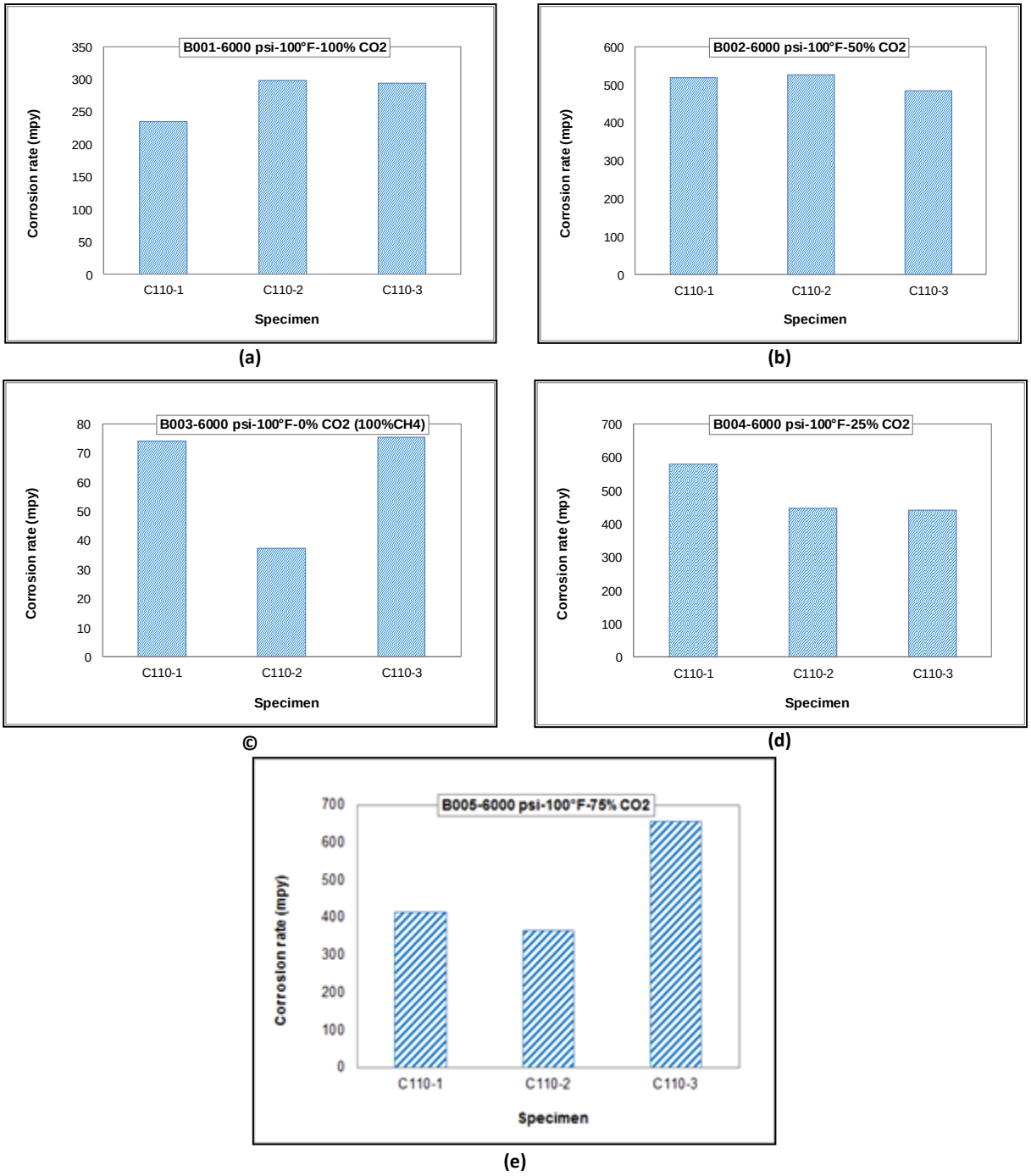

Fig. 5: Average corrosion rate of specimens at 6000 psi and 100°F and various CO_2 concentrations: a) 100% CO_2; b) 50% CO_2; c) 0% CO_2; d) 25% CO_2; and e) 75% CO_2

Table 12: Corrosion rate and mechanical properties of C110 specimens before and after corrosion test

Batch No.	Specimen No.	CO_2 Con.%	Initial weight gm	Final weight gm	CR (mpy)	E (psi)	E* (psi)	Yield strength (psi)	Tensile Strength (psi)
001	C110-1	100	13.3848	13.2129	234	5.79E+06	9.91E+06	107,560	123,600
	C110-2		13.4397	13.2212	297	6.02E+06	8.62E+06	105,950	119,933
	C110-3		13.4478	13.2323	293	7.71E+06	9.44E+06	108,140	120,673
002	C110-1	50	13.4875	13.1076	517	1.07E+07	8.57E+06	104,960	117,283
	C110-2		13.3884	13.0029	524	5.10E+06	9.01E+06	97,180	116,388
	C110-3		13.3376	12.9835	482	5.54E+06	8.25E+06	95,140	116,198
003	C110-1	0	13.4459	13.3916	74	1.00E+07	7.76E+06	93,250	130,891
	C110-2		13.4196	13.3924	37	1.15E+07	8.43E+06	96,780	131,917
	C110-3		13.3234	13.2680	75	1.07E+07	8.25E+06	96,940	129,187
004	C110-1	25	13.3739	12.949	578	8.75E+06	8.13E+06	91,000	113,833
	C110-2		13.3092	12.9818	445	8.48E+06	6.99E+06	95,510	116,450
	C110-3		13.4018	13.0782	440	8.15E+06	8.44E+06	94,880	117,009
005	C110-1	75	13.4127	13.1079	415	8.71E+06	8.09E+06	103,240	111,286
	C110-2		13.4881	13.2212	363	1.10E+07	6.52E+06	101,290	112,891
	C110-3		13.4635	12.9808	657	8.43E+06	6.01E+06	101,000	111,062

E and E* are Young's modulus measured before and after corrosion test, respectively.

Average corrosion rate obtained using three coupons is presented in **Fig. 6** as a function of CO_2 concentration. Like the low-pressure experiments (Fig. 5), at low CO_2 concentrations (less than 25%), the corrosion rate significantly increased as carbon dioxide concentration was increased. This is attributed to accelerated cathodic reaction (Nesic 2007), which facilitates the corrosion process considerably. This is in agreement with the finding of Wang et al. (2004) who reported strong increase in cathodic limiting current density due to dominant effect of increased H_2CO_3 concentration while the anodic reaction is unaffected. Similar results have been reported by Choi and Nesic (2011) and Zhang et al. (2013). In the intermediate concentrations (between 25% and 75%), the effect of CO_2 concentration on the corrosion rate was minimal. However at high CO_2 concentrations (greater than 75%), the corrosion rate was decreased by 46% due to the formation of corrosion protect film which was confirmed by examining the corroded surface of the coupons. It is important to note that the trend of corrosion rate curves obtained from high-pressure tests is very similar to the one obtained from low-pressure tests (Fig. 5). However, the level of corrosion is very intense at high pressures. The corrosion rate increased approximately by a factor of 20.

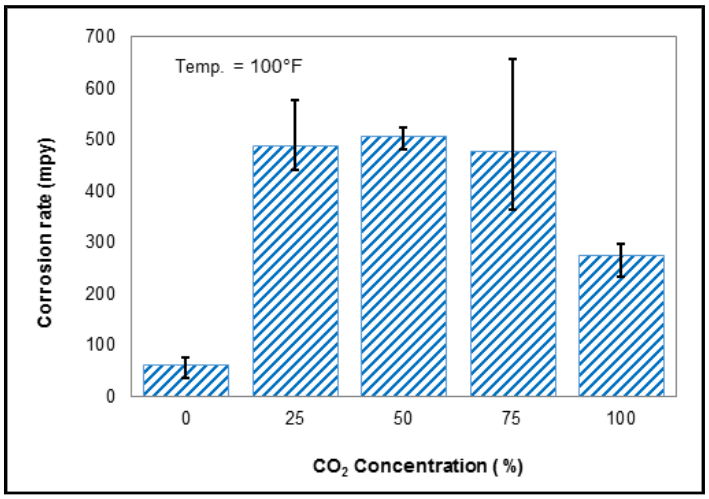

Fig. 6: Average corrosion rate as function CO_2 concentration at 6000 psi and 100°F

Although the mechanical properties of grade C110 steel are available from the manufacturer, a complete tensile strength test was performed to determine the change occurring in specimen load-carry capacity due to corrosion. As a result of corrosion, material loss from the exposed surface (i.e. reduction in specimen thickness) is expected. Material property changes are not anticipated, as the specimens are free of stress load during the test. Young's modulus, yield strength and ultimate tensile strength of pre-corroded specimen (C110) were 3.370×10^6, 0.105×10^6, and 0.133×10^6 psi, respectively. These values are considered as baselines to evaluate the embrittlement effect. Mechanical properties were obtained based on the loading-displacement curve data obtained from tensile strength test. The measured mechanical properties were also compared to the other obtained for pre-corroded specimen and presented in **Table 13**.

Table 13: Corrosion rate and mechanical properties of C110 specimens before and after corrosion test

Batch No.	Specimen No.	CO_2 Con.%	Initial weight gm	Final weight gm	CR (mpy)	Young's Modulus (psi)*	Young's Modulus (psi)**	Yield strength (psi)**	Tensile Strength (psi)**
001	C110-1	100	13.3848	13.2129	234	5.79E+06	9.91E+06	107,560	123,600
	C110-2		13.4397	13.2212	297	6.02E+06	8.62E+06	105,950	119,933
	C110-3		13.4478	13.2323	293	7.71E+06	9.44E+06	108,140	120,673
002	C110-1	50	13.4875	13.1076	517	1.07E+07	8.57E+06	104,960	117,283
	C110-2		13.3884	13.0029	524	5.10E+06	9.01E+06	97,180	116,388
	C110-3		13.3376	12.9835	482	5.54E+06	8.25E+06	95,140	116,198
003	C110-1	0	13.4459	13.3916	74	1.00E+07	7.76E+06	93,250	130,891
	C110-2		13.4196	13.3924	37	1.15E+07	8.43E+06	96,780	131,917
	C110-3		13.3234	13.2680	75	1.07E+07	8.25E+06	96,940	129,187
004	C110-1	25	13.3739	12.9490	578	8.75E+06	8.13E+06	91,000	113,833
	C110-2		13.3092	12.9818	445	8.48E+06	6.99E+06	95,510	116,450
	C110-3		13.4018	13.0782	440	8.15E+06	8.44E+06	94,880	117,009
005	C110-1	75	13.4127	13.1079	415	8.71E+06	8.09E+06	103,240	111,286
	C110-2		13.4881	13.2212	363	1.10E+07	6.52E+06	101,290	112,891
	C110-3		13.4635	12.9808	657	8.43E+06	6.01E+06	101,000	111,062

*Measured before corrosion test and **Measured after corrosion test

According to measurements presented in Table 13, it is apparent that the corrosion process has considerable impact on load-capacity of the specimens. This is mainly due to reduction in specimen thickness which decreases load handling capacity; and hence, ultimate tensile strength (UTS), if the thickness reduction is not considered in the calculation of UTS. **Figure 7** presents UTS (determined without considering thickness change) of corroded specimen as a function of CO_2 concentration.

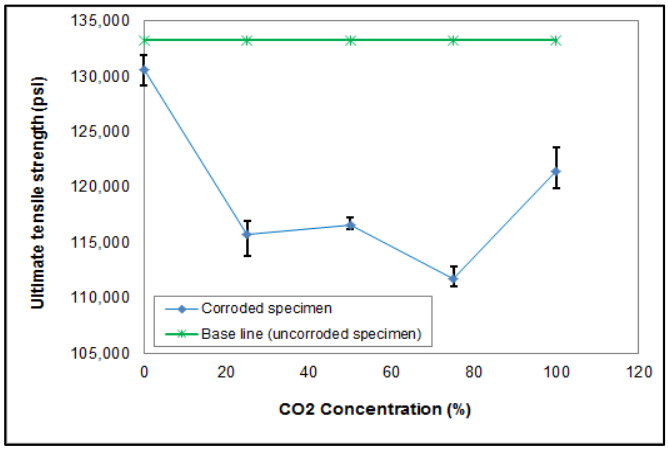

Fig. 7: UTS of specimens as a function of CO_2 concentrations

Highly corroded specimens which were exposed to acidic environment showed significant reduction in the UTS while the specimen corroded without the presence of CO2 showed the least reduction in UTS.

The UTS trend is consistent with the corrosion rate trend shown in Fig. 6. As the CO_2 concentration was increased, corrosion rate increased at low CO_2 concentrations (less than 25%), remained unchanged in the intermediate concentration range (between 25 and 75%), and reduced at high concentrations (greater than 75%).

Figure 8 shows the surface morphologies of the corroded specimens in the brine saturated with methane containing various concentrations of CO_2 at 6000 psi and 100°F. The surfaces of the specimens were examined via digital microscope to investigate corrosion protective (scale) layers formed during the test. It can be seen that the morphologies of corrosion scale is different and depended upon CO_2 concentration. For instance, the corrosion scales ware compact, dense and adherent to metal surface when the specimens were tested at 100% CO_2 concentration (Fig. 8b). In addition, at low CO_2 concentrations (less than 25%), scales were formed which hindered the corrosion process resulting in reduction in corrosion rate. No corrosion scale was detected (Fig. 8d) when tested in the absence of carbon dioxide (100% CH_4). Except for samples tested at 100% CO_2, the specimen surfaces exposed to the corrosive environment were not fully covered with scale.

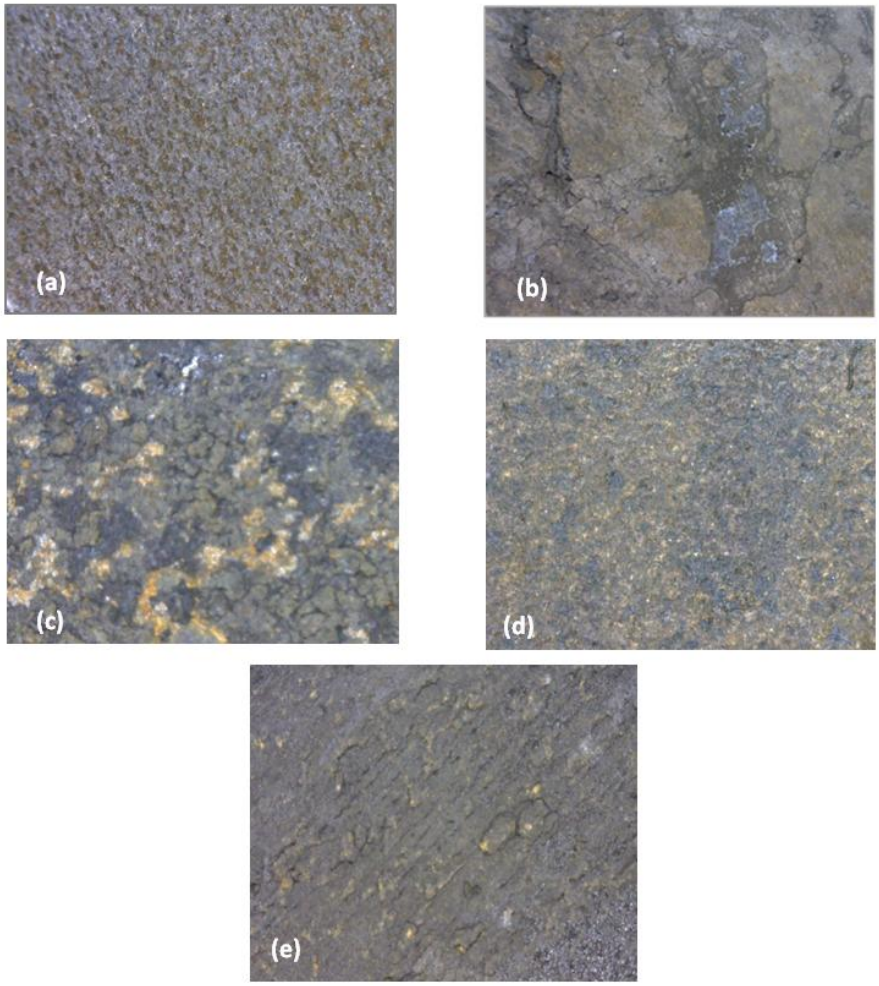

Fig. 8: Optical micrographs of specimens: a) un-corroded; b) corroded with 100% CO_2; c) corroded with 50% CO_2; d) corroded with 0% CO_2; and e) corroded with 25% CO_2

3. Planned Activities

- Continue testing baseline and new cement formulations for their performance by aging them in brine saturated with methane gas containing 300 ppm H_2S at 9000 psi and 100°F varying CO_2 concentration.
- Continue theoretical and modeling studies on tubular degradation.
- Continue experimental studies on tubular degradation under low-pressure and moderate-temperature conditions.
- Continue HPHT corrosion experiments with mini-pipes and flat coupons.

4. Project Expenditures

This section presents the project expenses during the month of September (**Table 14**) and the cumulative expenditures.

Table 14: Current and cumulative expenditures, September 2014

No.	Budget Categories	Current Expenses	Cumulative Expenses
1	Salaries & Wages	$6,704.60	$351,734.94
2	Fringe Benefits	$1,219.70	$79,950.52
3	Project Materials	$661.53	$99,786.87
4	Travel	$0.00	$10,457.07
5	Conference Expenses	$0.00	$0.00
6	Other Direct Costs	$718.86	$1,273.88
7	Equipment	($706.50)	$249,706.45
8	Space Rental	$0.00	$0.00
9	Indirect Cost	$4,652.34	$270,556.76
10	**Total**	**$13,250.53**	**$1,063,466.49**

Nomenclatures

A	Exposed surface area in cm^2
API	American Petroleum Institute
CR	Average corrosion rate in mpy
ASTM	American Society for Testing and Materials
GHO	Class G Cement with hydroxyapatite
GS	Class G cement with silica flour
GSMG	Class G Cement with silica flour and magnesium oxide
HHO	Class H Cement with hydroxyapatite
HPHT	High-pressure high-temperature

HS	Class H cement with silica flour
HSHO	Class H Cement with silica flour and hydroxyapatite
HSMG	Class H Cement with silica flour and magnesium oxide
K	Permeability of cement cores
LPR	Linear polarization resistance
mpy	mils per year
MGO	Magnesium oxide containing cement
MYS	maximum yield strength in
NACE	National Association of Corrosion Engineers
SBS	Shear bond strength
SCC	Stress corrosion cracking
SEM	Scanning Electron Microscope
SSC	Sulfide stress cracking
t	Test duration in hr
w_1	Initial specimen weight
w_2	Final specimen weight

Greek Letters

ϕ	Porosity of cement cores

References

Choi, Y.S., Farelas, F., Nešic, S., Magalhães, A. O. A., and Andrade, C. D. 2013. Corrosion Behavior of Deep Water Oil Production Tubing Material under Supercritical CO2 Environment: Part 1—Effect of Pressure and Temperature. Paper NACE No.2380, 17-21 March, Orlando, Florida.

Choi, Y. S. and Nesic, S. 2011. Determining the Corrosive Potential of CO2 Transport Pipeline in High PCO2–Water Environments. International Journal of Greenhouse Gas Control, 5 (2011) 788–797, 13 December.

Nesic, S. 2007. Key Issues Related to Modeling of Internal Corrosion of Oil and Gas Pipelines – a Review. Corrosion Science 49, 4308–4338.

Wang, S., George, K., Nesic, S. 2004. High Pressure CO_2 Corrosion Electrochemistry and the Effect of Acetic Acid. Paper NACE No.375, Houston, TX.

Project Title: Effect of H_2S and CO_2 in HPHT Wells on Tubulars and Cement

Report Type: Monthly Report

Report #: 37

Reporting Period: September 22nd, 2014 to October 21st, 2014

Authors:

Ramadan Ahmed, Principal Investigator

Subhash Shah, Co-Principal Investigator

Rida Elgaddafi, Research Assistant

Omotayo Omosebi, Research Assistant

Jueun Hwang, Research Assistant

Sagar Tale, Research Assistant

Prepared under BSEE Project # E12PC00035

by

THE UNIVERSITY OF OKLAHOMA

January 10, 2015

1. Summary of Accomplishments

This monthly report presents the progress made during the project period September 22, 2014 to October 21, 2014. Experimental investigations on cement and tubular degradation were continued during this reporting period. Uniform and stress-cracking corrosion experiments were performed under HPHT conditions using minipipes and flat coupons. Weight loss and LPR techniques were utilized to measure uniform corrosion rate. In addition, mechanical properties of the specimen were measured to assess the level of corrosion. Furthermore, in order to examine degradation characteristics of acid-resistant (magnesium oxide based) cements, cores and samples for bonding tests were prepared and aged in high-pressure and high-temperature (HPHT) acidic environment.

One batch of cement aging experiment was completed during this month. Cement cores and bonding samples made of baseline and magnesium oxide cements were aged for 2 weeks in 2% brine saturated with methane gas containing CO_2 and H_2S. Porosity, permeability, and compressive and shear bond strengths (SBS) of unaged and aged samples were measured.

After aging, the porosity of all samples decreased while their permeability showed unusual increase. This abnormality may indicate the development of micro-cracks that can increase permeability without significant increase in porosity. The presence of H_2S in fluid system promotes the formation of secondary ettringite in the set cement, leading to the development of micro-cracks.

Compressive and shear bond strengths are important properties of oil well cement. SBSs of baseline and MGO samples (aged and unaged) were comparable. However, previous tests demonstrated slightly higher SBS for MGO than baseline samples, which can be attributed to expansive property of magnesium oxide. After aging, the SBSs of baseline and additive showed minor improvement. Compressive strengths of unaged MGO samples were approximately the same regardless of the cement class used in their formulation. After aging, baseline and additive cements displayed minor alteration in compressive strength.

Uniform corrosion experiments were continued. Low-pressure and high-pressure tests were performed. Low-pressure corrosion experiments were carried out at 120 psi and 176°F in 1% NaCl solution. Carbon dioxide content of the gas phase was varied. At constant temperature and pressure, the corrosion rate reduced with CO_2 concentration. Similar corrosion rate trend has been reported in the literature. In addition, tests conducted at different temperature showed reduction in corrosion rate with increasing temperature regardless of CO_2 concentration. This is consistent with our earlier measurements.

Two stress-cracking corrosion experiments were conducted under HPHT conditions. Mechanical properties of the specimens were measured before and after the test. A corroded specimen showed significant embrittlement as indicated by reduction in plastic strain to failure (PSF) and ultimate tensile strength (UTS) after the test. Moreover, Young's modulus of the corroded sample increased slightly after exposure.

Our plan for the upcoming weeks is to continue: i) aging tests at 9000 psi, 100°F, 300 ppm H_2S and varying CO_2 concentration; ii) testing of new acid-resistant cement formulations; iii) low-pressure

corrosion experiments using 1% NaCl solution and varying CO_2 concentration; and iv) stress cracking and uniform corrosion experiments under HPHT condition varying CO_2 content of the gas phase.

2. Overall Project Progress

2.1 Experimental Studies on Degradation of Cement (Task 2)

2.2.1 Aging Experiment and Degradation

Degradation study on new cement formulation was continued. During this month, one cement-aging experiment was completed. Baseline and MGO cement cores and bonding samples were aged in brine (2% NaCl) saturated with methane gas containing 300 ppm H_2S under HPHT condition. Test parameters of the new experiment (Batch 39) are presented in **Table 1** along with those of previous tests. Mechanical and physical properties of samples including porosity, permeability, and compressive and bond strengths were measured.

Table 1: Test parameters for aging experiments conducted to date

Batch #	Temp. (°F)	Pressure (psi)	Partial Pressure %			Brine (%)	Aging Period (days)	Exp. #	Additive Batch #
			CH_4	CO_2	H_2S (ppm)				
001	350	9000	100	0	0	9	6	1	
002	350	6000	100	0	0	2	14 & 28	2	
003	350	6000	100	0	0	2	14		
004	350	6000	90	10	0	2	6	3	
005	350	6000	90	10	0	2	14 & 28	4	
006	350	6000	90	10	0	2	14		
007	225	6000	90	10	0	2	14	5	
008	100	6000	90	10	0	2	14	6	
009	225	6000	60	40	0	2	14	7	
010	225	6000	0	100	0	2	14	8	
011	100	6000	60	40	0	2	14	9	
012	100	6000	0	100	0	2	14	10	
013	350	6000	60	40	0	2	14	11	
014	350	6000	0	100	0	2	14	12	
015	225	6000	60	40	0	2	14	7A	
016	350	3000	60	40	0	2	14	13	
017	350	9000	60	40	0	2	14	14	
018	350	3000	0	100	0	2	14	15	
019	350	9000	0	100	0	2	14	16	
020	350	3000	90	10	0	2	14	17	
021	350	9000	90	10	0	2	14	18	
022	225	3000	60	40	0	2	14	19	
023	225	9000	60	40	0	2	14	20	
024	225	3000	0	100	0	2	14	21	
025	225	9000	0	100	0	2	14	22	
026	225	3000	90	10	0	2	14	23	
027	225	9000	90	10	0	2	14	24	
028	430	6000	90	10	0	2	14	25	009 - MS

Batch #	Temp. (°F)	Pressure (psi)	Partial Pressure %			Brine (%)	Aging Period (days)	Exp. #	Additive Batch #
			CH_4	CO_2	H_2S (ppm)				
029	430	6000	60	40	0	2	14	26	010 - MS
030	430	6000	100	0	0	2	14	27	003 - LTMS
031	430	3000	100	0	0	2	14	28	004 - LTMS
032	430	9000	100	0	0	2	14	29	008 - HOAP
033	100	6000	90	10	300	2	14	30	009 - HOAP
034	225	6000	90	10	300	2	14	31	009 - MGO
035	350	6000	90	10	300	2	14	32	010 - HOAP
036	100	6000	100	0	300	2	14	33	011 - HOAP
037	100	6000	60	40	300	2	14	34	010 - MGO
038	100	9000	100	0	300	2	14	35	012 - HOAP
039	**100**	**9000**	**90**	**10**	**300**	**2**	**14**	**35**	**011 - MGO**

2.2.2 Porosity and Permeability of Baseline and Additive Cements

Tables 2 and **3** present porosity and permeability of baseline and MGO samples, respectively. After aging, porosity of all samples decreased while their permeability showed substantial increase (**Fig. 1a**). Normally, permeability predominately decreases with reduction in porosity. The abnormal trend can be attributed to the development of micro-cracks that can increase permeability without significant increase in porosity. In the presence of H_2S, secondary ettringite can form in the set cement, leading to the development of micro-cracks.

Table 2: Porosity and permeability of baseline samples (Batch 39)

Core #	Core Type	Core dimensions			Porosity and Permeability Measurements					
		Dia. mm)	L (mm)	W (g)	ϕ (%)	Ave. ϕ (%)	Std. Dev. (%)	K (mD)	Ave. K (mD)	Std. Dev. (mD)
039 GS 00 01	Unaged	25.2	34.2	29.3	28.6	27.58	1.39	0.011	0.023	0.016
039 GS 00 02		25.1	33.5	28.7	26.6			0.034		
039 GS 05 01	Aged	25.2	26.6	25.1	9.4	12.10	3.87	0.04	0.046	0.008
039 GS 05 02		25.1	32.8	30.1	14.8			0.051		
039 HS 00 01	Unaged	25.1	35.2	31.6	27.8	27.46	0.51	0.059	0.102	0.060
039 HS 00 04		25.2	33.4	30.0	27.1			0.144		
039 HS 04 01	Aged	25.1	35.2	31.6	9.4	7.07	3.31	0.173	0.185	0.016
039 HS 04 02		25.2	33.3	34.3	4.7			0.196		

Table 3: Porosity and permeability of additives (MGO) samples (Batch MGO-11/39)

Core #	Core Type	Core dimensions			Porosity and Permeability Measurements					
		Dia. mm)	L (mm)	W (g)	ϕ (%)	Ave. ϕ (%)	Std. Dev. (%)	K (mD)	Ave. K (mD)	Std. Dev. (mD)
011 GSMG 00 01	Unaged	32.1	32.0	27.1	18.6	23.22	6.59	0.011	0.023	0.016
011 GSMG 00 02		25.1	32.6	27.8	27.9			0.034		
011 GSMG 10 01	Aged	25.2	31.4	30.3	6.2	6.21	0.04	0.04	0.046	0.008
011 GSMG 10 02		25.2	33.1	31.7	6.2			0.051		
011 HSMG 00 01	Unaged	25.1	31.0	27.2	28.5	28.04	0.62	0.059	0.102	0.060
011 HSMG 00 02		25.2	32.2	28.7	27.6			0.144		
011 HSMG 09 01	Aged	25.2	38.3	35.5	16.2	16.40	0.28	0.173	0.185	0.016
011 HSMG 09 02		25.2	30.9	28.9	16.6			0.196		

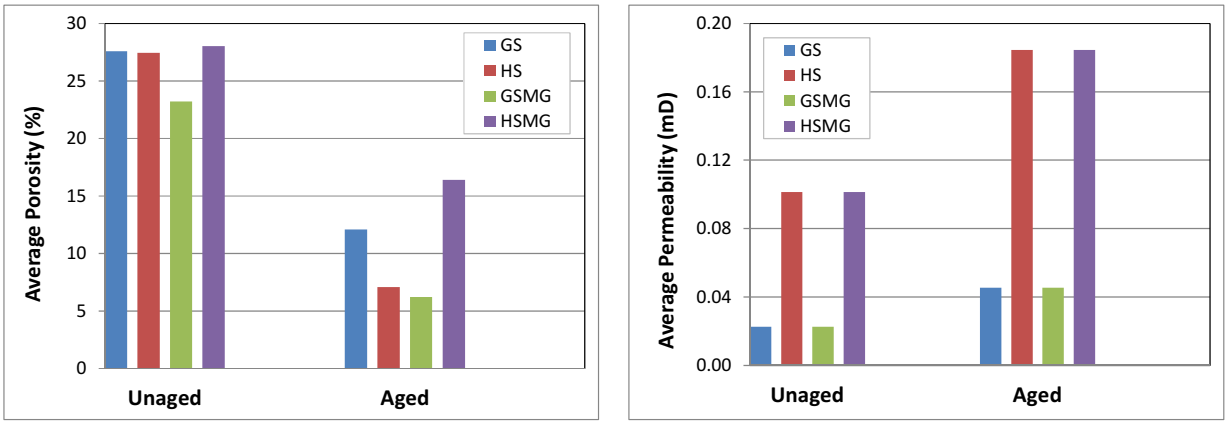

Fig. 1: Average porosity and permeability of baseline and additive samples: a) porosity; and b) permeability

2.2.3 Shear Bond Strength of Baseline and Additive Cements

The shear bond strengths of baseline and MGO samples are presented in **Tables 4** and **5,** respectively. The SBSs of baseline and MGO samples (both aged and unaged cases) were approximately the same (**Fig. 2**). However, in previous aging experiment (Batch 37), MGO samples displayed slightly higher SBS than baseline samples. The improvement in SBS can be attributed to expansive property of magnesium oxide, which enhances bond performance by creating very tight interface between cement and steel pipe. After aging, the SBSs of baseline and additive samples increased, indicating moderate carbonation.

Table 4: Shear bond strength of baseline samples

Batch	Core #	Temp. (F)	Pressure (psi)	CH4 (%)	CO2 (%)	H2S (%)	Brine (%)	Days Aged	SBS (psi)	Ave. SBS	Stdev
039	039-HS-00-01	Ambient	Atmospheric	0	0	0	2	0	983.8	1084.6	158
	039-HS-00-02	Ambient	Atmospheric	0	0	0	2	0	1038.6		
	039-HS-00-03	Ambient	Atmospheric	0	0	0	2	0	1090.9		
	039-HS-00-04	Ambient	Atmospheric	0	0	0	2	0	1351.9		
	039-HS-00-05	Ambient	Atmospheric	0	0	0	2	0	957.8		
	039-HS-08-01	100	9000	90	10	0.03	2	14	1312.8	1432.9	423
	039-HS-08-02	100	9000	90	10	0.03	2	14	1607.0		
	039-HS-08-03	100	9000	90	10	0.03	2	14	1115.1		
	039-HS-08-04	100	9000	90	10	0.03	2	14	1047.1		
	039-HS-08-05	100	9000	90	10	0.03	2	14	2082.4		

Table 5: Shear bond strength of additive (MGO) samples

Batch	Core #	Temp. (F)	Pressure (psi)	CH4 (%)	CO2 (%)	H2S (%)	Brine (%)	Days Aged	SBS (psi)	Ave. SBS	Stdev
MGO-011/039	011-HSMG-00-01	Ambient	Atmospheric	0	0	0	2	0	1370	1058.9	367
	011-HSMG-00-02	Ambient	Atmospheric	0	0	0	2	0	607		
	011-HSMG-00-03	Ambient	Atmospheric	0	0	0	2	0	1491		
	011-HSMG-00-04	Ambient	Atmospheric	0	0	0	2	0	976		
	011-HSMG-00-05	Ambient	Atmospheric	0	0	0	2	0	851		
	011-HSMG-11-01	100	9000	100	0	0.03	2	14	844	1405.6	355
	011-HSMG-11-02	100	9000	100	0	0.03	2	14	1752		
	011-HSMG-11-03	100	9000	100	0	0.03	2	14	1302		
	011-HSMG-11-04	100	9000	100	0	0.03	2	14	1502		
	011-HSMG-11-05	100	9000	100	0	0.03	2	14	1628		

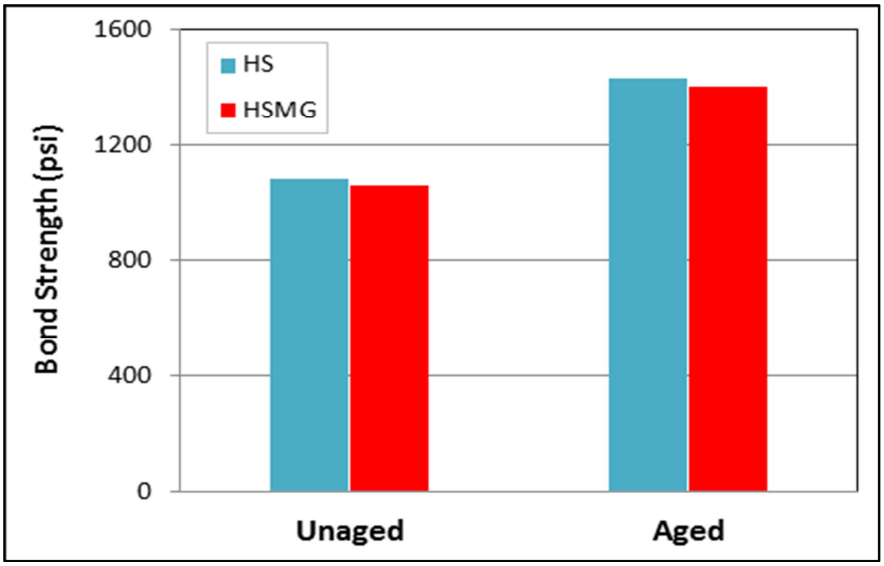

Fig. 2: Bond strength of baseline and additive samples

2.2.4 Compressive Strength of Baseline and Additive Cements

Tables 6 and **7** present compressive strengths baseline and MGO cements, respectively. Compressive strengths of unaged baseline samples were significantly different (**Fig. 3**). Class H cement exhibited substantially higher strength than Class G cement. It also demonstrated the highest data scattering and measurement error. Nonetheless, MGO samples showed approximately the same compressive strength regardless of the cement class used in their formulations. Previous measurements (Batches 36 and 37) from unaged baseline sample showed comparable compressive strength between Class H and Class G cements. After aging, all samples displayed minor variation in compressive strength.

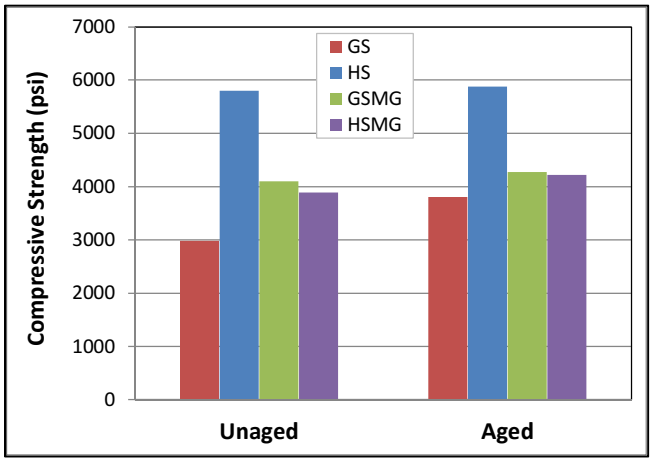

Fig. 3: Compressive strength of baseline and additive samples

Table 6: Compressive strength of baseline samples (Batch 39)

Compressive Strength Data for Batch 38 Samples						
Unaged Samples						
Core #	Confine Pressure	Pressure (psi)	Experimental Stress (psi)	Strain	Average Stress	Standard Deviation
039-GS-00-03	1000	377	3269	9.9000	2978	762
039-GS-00-04	1000	344	2113	9.9000		
039-GS-00-05	1000	409	3551	9.9000		
039-HS-00-03	1000	725	6293	9.9000	5801	1854
039-HS-00-04	1000	532	3751	9.9000		
039-HS-00-05	1000	848	7358	9.9000		
Aged Samples						
Core #	Confine Pressure	Pressure (psi)	Experimental Stress (psi)	Strain	Average Stress	Standard Deviation
039-GS-05-03	1000	412	3578	9.9000	3806	788
039-GS-05-04	1000	351	3044	9.9000		
039-GS-05-05	1000	609	5287	9.9000		
039-GS-07-03	1000	381	3308	9.9000		
039-GS-07-04	1000	453	3928	9.9000		
039-GS-07-05	1000	425	3690	9.9000		
039-HS-04-03	1000	733	6360	9.9000	5877	720
039-HS-04-04	1000	618	5364	9.9000		
039-HS-04-05	1000	754	6541	9.9000		
039-HS-06-03	1000	548	4755	9.9000		
039-HS-06-04	1000	663	5749	9.9000		
039-HS-06-05	1000	748	6493	9.9000		

Table 7: Compressive strength of additive (MGO) samples (Batch MGO-011/39)

Compressive Strength Data for Batch MGO-011/39 Samples						
Unaged Samples						
Core #	Confine Pressure	Pressure (psi)	Experimental Stress (psi)	Strain	Average Stress	Standard Deviation
011-GSMG-00-03	1000	458	3971	9.9000	4101	1101
011-GSMG-00-04	1000	606	5261	9.9000		
011-GSMG-00-05	1000	354	3071	9.9000		
011-HSMG-00-03	1000	375	3249	9.9000	3891	592
011-HSMG-00-04	1000	462	4006	9.9000		
011-HSMG-00-05	1000	509	4416	9.9000		
Aged Samples						
Core #	Confine Pressure	Pressure (psi)	Experimental Stress (psi)	Strain	Average Stress	Standard Deviation
011-GSMG-10-03	1000	583	5056	9.9000	4274	699
011-GSMG-10-04	1000	467	4055	9.9000		
011-GSMG-10-05	1000	528	3710	9.9000		
011-HSMG-09-03	1000	387	3357	9.9000	4221	1139
011-HSMG-09-04	1000	437	3795	9.9000		
011-HSMG-09-05	1000	635	5512	9.9000		

2.2 Experimental Studies on Corrosion of Tubulars (Task 3)

2.2.1 Sulfide Stress Cracking

Sulfide Stress cracking experiments were continued. C110 material was tested for its SSC susceptibility. During this reporting period, two specimens (Minipipes 7 and 8) were tested. **Table 8** summarizes the SSC tests completed to date. The table also shows the experimental conditions in which specimens were exposed. Internal and external pressures of specimen were maintained at 4000 and 6000 psi, respectively.

Table 8: Specimen corrosion testing conditions

No.	Label	Temp. (°F)	Pressure (psi)		Gas Composition			Time Duration (Days)	Remarks
			Inside	Outside	H2S (ppm)	CH4 (%)	CO2 (%)		
1	01-C110-07/25-08/06	100	6000	4000	0	100	0	15	
2	02-C110-08/25-08/25	-	-	-	-	-	-	-	Baseline
3	03-C110-08/27-09/03	100	6000	4000	270	90	10	7	Sample failed after 7 days of exposure
4	04-C110-09/05-09/12	100	6000	4000	300	100	0	7	
5	05-C110-09/05-09/13	100	6000	4000	285	95	5	7	
6	06-C110-09/05-09/14	100	6000	4000	270	10	10	7	Brine completely leaked from the cell
7	07-C110-10/17-10/24	100	6000	4000	255	85	15	7	
8	08-C110-10/28-11/04	100	6000	4000	270	90	10	7	

As indicated in the previous report (Report 36), the rod seals on sulfide stress cracking cell were severely damaged due to rod-misalignment caused during assembling of minipipe specimens. The cell was disassembled, a new pulling rod made of beryllium copper was installed, and the leaking seal was replaced. The new rod has a ball joint to allow slight rod curving that prevents damage on the seals when a specimen is attached to the rod for testing. After replacing damaged seals and repairing the rod, two experiments were successfully performed.

Specimen 7 was strained to failure after exposure to sour environment. The specimen showed significant embrittlement as indicated by reduced plastic strain to failure (PSF) compared to the baseline (**Fig. 4**). Moreover, it exhibited lower ultimate tensile strength (UTS) than the baseline (**Table 9**). Its Young's modulus also increased slightly after exposure. Specimen 8 did not show signs of embrittlement.

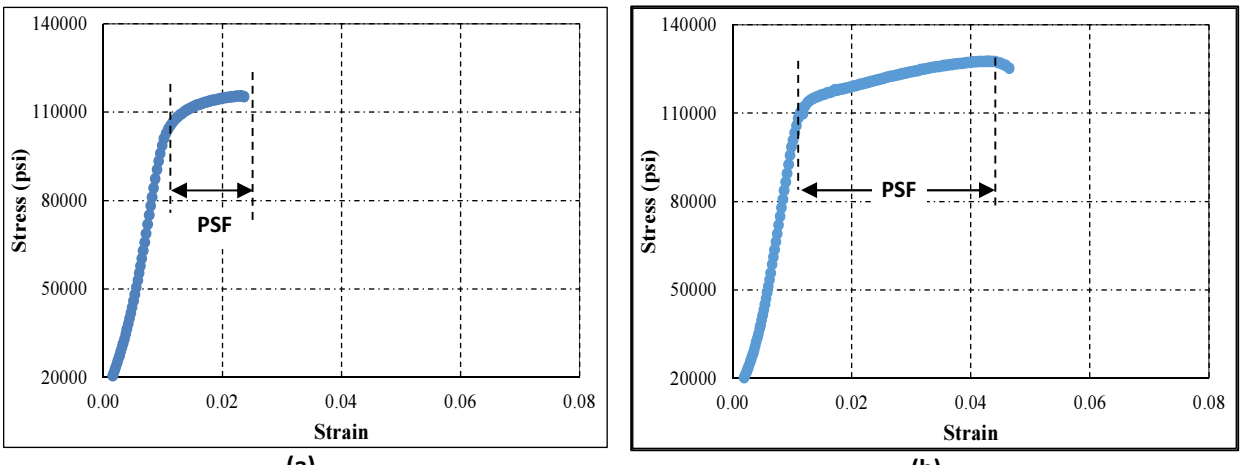

Fig. 4: Stress vs. strain of mini-pipes: a) Mini-pipe 7 (exposed); and b) Mini-pipe 2 (baseline)

Table 9: Mechanical properties of samples before and after corrosion test

Mini-pipe No.	Before Exposure				After Exposure			
	YS (psi)	UTS (psi)	PSF	E (psi)	YS (psi)	UTS (psi)	PSF	E* (psi)
1	-	-	-	-	109,855	127,619	0.030	11,785,921
2	111,529	130,156	0.040	11,842,002	-	-	-	-
3	-	-	-	11,704,810	-	-	-	-
4	-	-	-	12,594,080	112768	134981	0.043	12078823
5	-	-	-	10,911,219	102217	114424	0.023	11368960
6	-	-	-	11,599,401	110686	130118	0.049	11444081
7	-	-	-	11,221,136	-	115479	0.014	11,561,000
8	-	-	-	12,044,218	-	120026	0.069	11,441,529

UTS = Ultimate tensile Strength, PSF = Plastic strain to failure, YS = Yield strength, E = Young's modulus before exposure, E* = Young's modulus after exposure

2.2.2 Uniform Corrosion in Sour Gas Environment

During this reporting period, uniform corrosion experiments were continued. Tests were conducted to evaluate corrosion of carbon steel in CO_2 environment under low and high pressure conditions.

2.2.2.1 Low-Pressure Experiments

Experimental investigation on corrosion rate of carbon steel under low-pressure condition is in progress. To examine the effects of CO_2 and salt concentration on corrosion, series of experiments were performed at a constant pressure of 120 psi. Test parameters and results of new corrosion experiments are presented in **Table 10** along with previous measurements.

Table 10: Test parameters and results of low-pressure corrosion experiments conducted to date

Exp. #	Temp. (°F)	Pressure (psi)	Partial Pressure %		Brine Conc. (%)	Test Period (days)	Results (mpy)	
			N_2	CO_2			LPR	WL
15	78	120	25	75	2	187	40.30	31.91
16	78	120	0	100	2	187	39.18	32.18
17	78	240	0	100	2	187	NA	NA
18	78	120	75	25	2	187	22.92	21.83
19	110	120	75	25	2	187	31.78	23.78
20	110	120	25	75	2	187	53.16	43.22
21	110	120	100	0	2	187	12.37	15.40
22	110	120	75	25	2	187	31.07	23.78
23	110	120	50	50	2	187	70.35	43.39
24	110	120	25	75	2	187	53.16	43.22
25	110	120	0	100	2	187	44.92	32.49
26	176	120	100	0	2	187	4.04	3.10
27	176	120	75	25	2	187	16.53	11.77
28	176	120	50	50	2	187	24.23	12.71
29	176	120	25	75	2	187	17.39	10.87
30	176	120	0	100	2	187	22.56	12.04
31	140	120	100	0	2	187	2.58	2.72
32	140	120	75	25	2	187	11.00	6.33
33	140	120	50	50	2	187	13.33	14.30
34	140	120	25	75	2	187	38.48	26.76
35	140	120	0	100	2	187	24.40	24.23
36	140	120	100	0	1	187	3.69	1.23
37	140	120	75	25	1	187	5.16	20.97
38	140	120	75	25	1	187	9.86	25.13
39	140	120	50	50	1	187	6.40	21.24

40	140	120	25	75	1	187	6.50	23.78
41	140	120	0	100	1	187	4.31	14.77
42	176	120	0	100	1	187	1.76	4.63
43	**176**	**120**	**25**	**75**	**1**	**187**	**2.79**	**9.00**
44	**176**	**120**	**50**	**50**	**1**	**187**	**4.95**	**12.59**
45	**176**	**120**	**75**	**25**	**1**	**187**	**17.79**	**36.98**

Figures 5 compares corrosion rate measurements obtained from electrochemical (LPR) and weight loss (WL) methods at 176°F and various CO_2 concentrations. The trend of corrosion rate curve indicates rate reduction with CO_2 concentration. Both measuring techniques provided similar trends. The corrosion rate reduction with CO_2 concentration is not common. However, similar corrosion rate trend has been reported previously (Seiersten 2001). No explanation was provided for this type of corrosion rate trend. One of the possible explanations is that the concentration of Fe^{2+} increases with the increase in CO_2 concentration, resulting in reduction of corrosion rate. At 100% CO_2 concentration, the super-saturation exceeds the solubility limit of Fe^{2+} and; therefore, porous corrosion scale can be formed under these conditions, significantly diminishing the corrosion rate. The difference between LPR and WL measurements could be attributed to the use of calibration factor B (30 mV) in determining the corrosion rate from the electrochemical measurements. **Figure 6** compares the corrosion rates measured from weight-loss measurements at two different temperatures and various CO_2 concentrations. As depicted in the figure, the corrosion rate decreases with the increase of test temperature regardless of CO_2 concentration. This result is consistent with our previous finding.

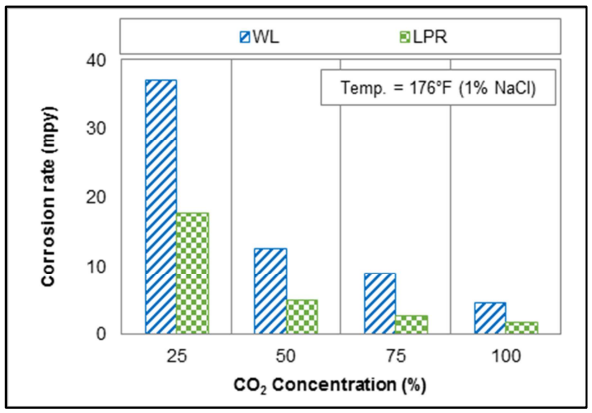

Fig. 5: Corrosion rate versus CO_2 concentration at 176°F and 120 psi

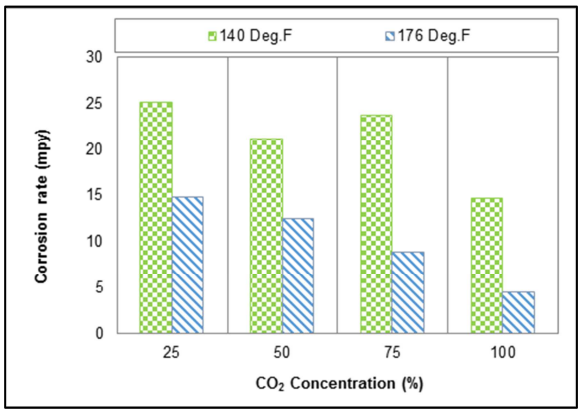

Fig. 6: Effect of temperature on corrosion rate at various CO_2 concentrations and 1% NaCl

To examine the effect of salt concentration on corrosion rate, new and previously reported weight-loss based measurements are presented in **Fig. 7**. The relationship between CO_2 concentration and corrosion rate is influenced by temperature and salt concentration. The trends of corrosion rate curves substantially vary with temperature and salt concentration. Even though discrepancies exist between measurements obtained from LPR and weight loss methods, trends of corrosion rate curves obtained using both techniques are very similar (Table 10). In two sets of experiments (176°F and 2% NaCl, and 140°F 1% NaCl), slight variations in corrosion rate were observed as the CO_2 concentration

was increased. However, in other test sets (176°F and 1% NaCl, and 140°F 2% NaCl), a considerable variation in rates was observed as the concentration was increased from 25 to 100%.

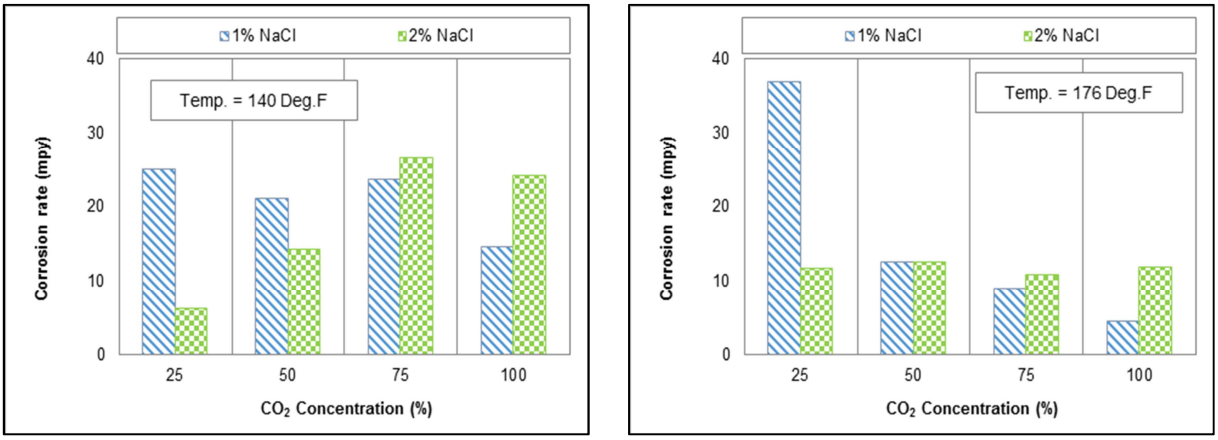

Fig. 7: Corrosion rate vs. CO_2 concentration at 120 psi and different salt concentrations: a) 140°F; and 176°F

2.2.2.2 High-Pressure Experiments

In addition to low-pressure tests, corrosion experiments on carbon steel (Grade C110) were conducted during this reporting period. Three new batches of experiments were carried out varying CO_2 concentration (0, 75 and 100%) and total pressure (3,000 and 9,000 psi). Test temperature and NaCl concentration were maintained at 100°F and 2% NaCl, respectively. Three coupons were used for each batch of experiment in order to obtain average corrosion rate and mechanical property measurements. Test parameters for different batches of experiments are presented in **Table 11**.

Table 11: Test conditions for HPHT uniform corrosion tests

Batch No.	Pressure (psi)	Temperature (F)	Test Duration (hr)	CO_2 Conc. (%)	CH_4 Conc. (%)	H_2S Conc. (%)
001	6000	100	187	100	0	0
002	6000	100	187	50	50	0
003	6000	100	187	0	100	0
004	6000	100	187	25	75	0
005	6000	100	187	75	25	0
006	**9000**	**100**	**187**	**100**	**0**	**0**
007	**3000**	**100**	**187**	**0**	**100**	**0**
008	**9000**	**100**	**187**	**75**	**25**	**0**

Corrosion rate of Grade C110 steel in the brine solution was obtained applying weight loss method. The corrosion rate and mechanical property measurements obtained from recent tests are combined with previously reported ones in **Table 12**. The Young's modulus measurements before and after exposure vary due to specimen property changes resulting from localized corrosion and reduction in specimen thickness.

Table 12: Corrosion rate and mechanical properties of C110 specimens before and after corrosion test

Batch No.	Specimen No.	CO_2 Con.%	Initial weight gm	Final weight gm	CR (mpy)	E (psi)	E* (psi)	Yield strength (psi)	Tensile Strength (psi)
001	C110-1	100	13.3848	13.2129	234	5.79E+06	9.91E+06	107,560	123,600
	C110-2		13.4397	13.2212	297	6.02E+06	8.62E+06	105,950	119,933
	C110-3		13.4478	13.2323	293	7.71E+06	9.44E+06	108,140	120,673
002	C110-1	50	13.4875	13.1076	517	1.07E+07	8.57E+06	104,960	117,283
	C110-2		13.3884	13.0029	524	5.10E+06	9.01E+06	97,180	116,388
	C110-3		13.3376	12.9835	482	5.54E+06	8.25E+06	95,140	116,198
003	C110-1	0	13.4459	13.3916	74	1.00E+07	7.76E+06	93,250	130,891
	C110-2		13.4196	13.3924	37	1.15E+07	8.43E+06	96,780	131,917
	C110-3		13.3234	13.2680	75	1.07E+07	8.25E+06	96,940	129,187
004	C110-1	25	13.3739	12.949	578	8.75E+06	8.13E+06	91,000	113,833
	C110-2		13.3092	12.9818	445	8.48E+06	6.99E+06	95,510	116,450
	C110-3		13.4018	13.0782	440	8.15E+06	8.44E+06	94,880	117,009
005	C110-1	75	13.4127	13.1079	415	8.71E+06	8.09E+06	103,240	111,286
	C110-2		13.4881	13.2212	363	1.10E+07	6.52E+06	101,290	112,891
	C110-3		13.4635	12.9808	657	8.43E+06	6.01E+06	101,000	111,062
006	**C110-1**	**100**	**13.4039**	**13.1518**	**343**	**1.14E+07**	**8.43E+06**	**100,000**	**116,283**
	C110-2		**13.3703**	**12.9598**	**558**	**1.08E+07**	**8.57E+06**	**96,410**	**113,007**
	C110-3		**13.4606**	**13.2294**	**315**	**1.10E+07**	**6.36E+06**	**95,570**	**117,066**
007	**C110-1**	**0**	**13.4169**	**13.3859**	**42**	**9.98E+06**	**6.96E+06**	**100,920**	**130,212**
	C110-2		**13.4447**	**13.4144**	**41**	**9.29E+06**	**6.94E+06**	**100,530**	**130,658**
	C110-3		**13.4041**	**13.3635**	**55**	**9.47E+06**	**7.05E+06**	**101,170**	**128,982**
008	**C110-1**	**75**	**13.3681**	**12.9327**	**592**	**7.74E+06**	**8.37E+06**	**97,530**	**110,554**
	C110-2		**13.4538**	**13.0456**	**555**	**7.97E+06**	**8.67E+06**	**99,660**	**110,922**
	C110-3		**13.3742**	**12.9952**	**516**	**8.44E+06**	**9.24E+06**	**100,480**	**112,723**

E and E* are Young's modulus measured before and after corrosion test, respectively.

Reduction in corrosion rate was observed as the CO_2 concentration was increased from 75 to 100% (**Fig. 8**). The reduction could be due to the formation of corrosion scale, which limits the exposure of the metal to corrosive environment. Increase in CO_2 concentration causes more CO_2 to dissolve and reduces the pH of surrounding solution, resulting in the formation of protective scale. In addition, pressure has significant effect on solubility of acidic gases and hence, it can affect corrosion rate of metal. **Figure 9** compares the corrosion rate measurements obtained at different pressures (6000 and 9000 psi) maintaining other test parameters constant (100°F and 100% of CO_2 concentration). The rate increased by 30% as the pressure was elevated to 9000 psi. This behavior can be attributed to increased concentration of carbonic acid in solution. As the partial pressure of CO_2 increases, the concentration of acid also increases, accelerating the cathodic reactions and therefore, increasing the corrosion rate. **Figure 10** demonstrates the influence of pressure on corrosion rate in the absence of carbon dioxide. The rate increased approximately 25% as pressure was raised to 6000 psi.

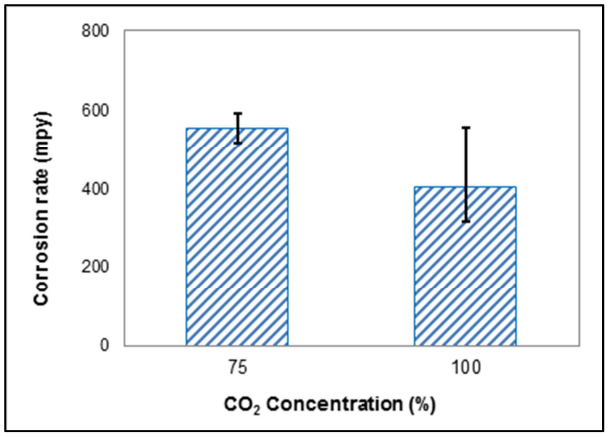

Fig. 8 Average corrosion rate at 9000 psi, 100°F and different CO_2 concentrations

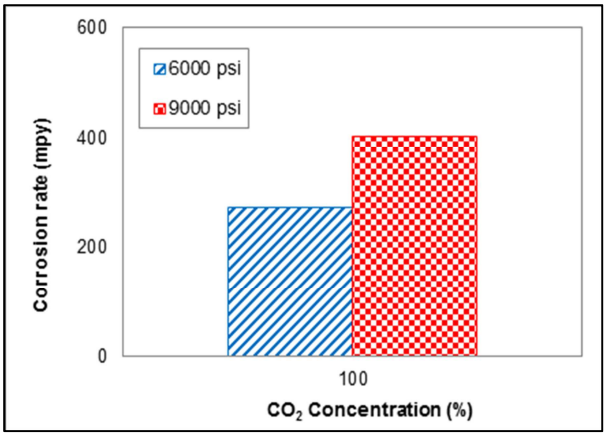

Fig. 9 Average corrosion rate at 100°F, 100% CO_2 concentration and different pressures

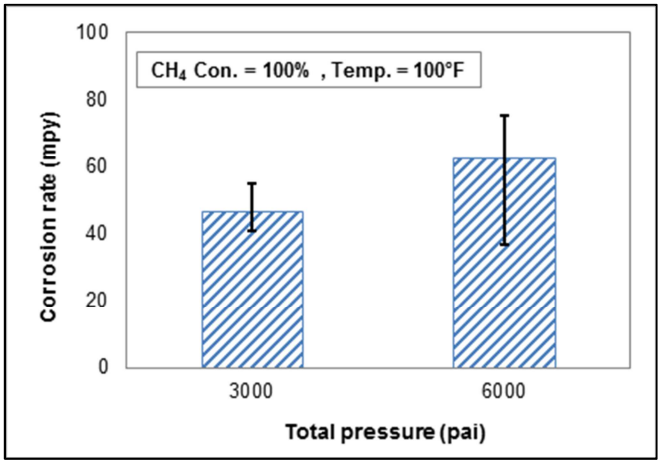

Fig. 10 Average corrosion rate at 100°F, 0% CO_2 concentration and different pressures

Figure 11 shows the surface morphologies of specimens corroded in brine saturated with CO_2 containing methane gas at 100°F and different pressures. A specimen surface was examined via digital microscope to detect the formation of corrosion protective layer during the corrosion process. Micrographs of corroded specimens were compared with that of pre-corroded ones. The examination shows that morphologies of corrosion scales vary with CO_2 concentration. For instance, at 9000 psi and 100% CO_2 concentration, the specimen were partially covered by compact and dense corrosion scale (Figs. 11b), which hinders the corrosion process, resulting in reduction in rate. Under these conditions, pitting or localized corrosion was not detected on the exposed surfaces of the specimens.

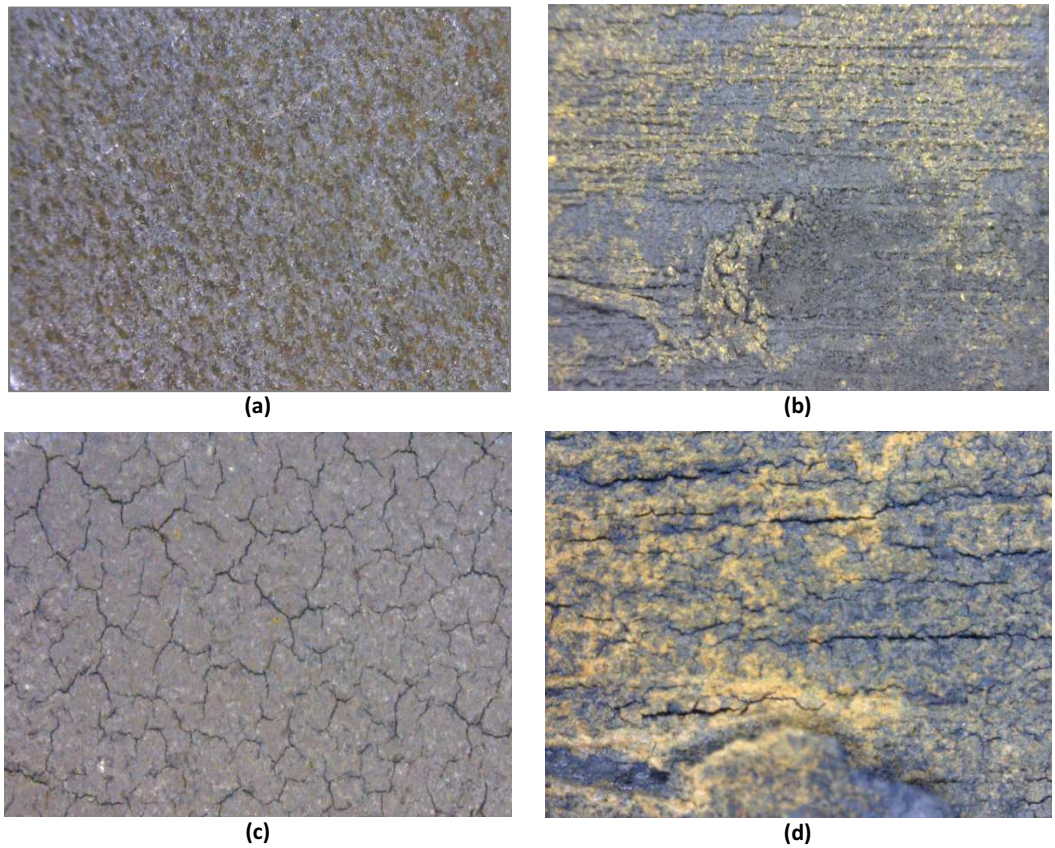

Fig. 11 Optical micrographs of C110-1 specimens: a) un-corroded; b) corroded (B006-C110-03); c) corroded (B007-C110-01); and d) corroded (B008-C110-01)

No corrosion protective film (iron carbonate) was detected in the absence of carbon dioxide (Fig. 11c). However, the specimen surface was covered with thin layer of rust (iron oxide). Figure 11d shows the micrograph of specimen exposed to harsh corrosive environment (9000 psi, 75% CO_2 concentration and 100°F). Under these conditions, the corrosion scale was less intensive than the one that was formed at 100% CO_2 concentration (Fig. 11b).

3. Planned Activities

- Continue testing baseline and new cement formulations for their performance by aging them in brine saturated with methane gas containing 300 ppm H_2S at 9000 psi and 100°F varying CO_2 concentration.
- Continue theoretical and modeling studies on tubular degradation.
- Continue experimental studies on tubular degradation under low-pressure and moderate-temperature conditions.
- Continue HPHT corrosion experiments with mini-pipes and flat coupons.

4. Project Expenditures

This section presents the project expenses during the month of October (**Table 13**) and the cumulative expenditure.

Table 13: Current and cumulative expenditures, October 2014

No.	Budget Categories	Current Expenses	Cumulative Expenses
1	Salaries & Wages	$2,930.63	$354,665.57
2	Fringe Benefits	$53.51	$80,004.03
3	Project Materials	$2,638.26	$102,425.13
4	Travel	$128.69	$10,585.76
5	Conference Expenses	$0.00	$0.00
6	Other Direct Costs	$0.00	$1,273.88
7	Equipment	$330.17	$250,036.62
8	Space Rental	$0.00	$0.00
9	Indirect Cost	$2,875.55	$273,432.31
10	**Total**	**$8,956.81**	**$1,072,423.30**

Nomenclature

A	Exposed surface area, cm^2
API	American Petroleum Institute
ASTM	American Society for Testing and Materials
CR	Average corrosion rate, mpy
E	Young's modulus measured before corrosion test
E*	Young's modulus measured after corrosion test
GHO	Class G Cement with hydroxyapatite
GS	Class G cement with silica flour
GSMG	Class G Cement with silica flour and magnesium oxide
HHO	Class H Cement with hydroxyapatite
HPHT	High-pressure high-temperature
HS	Class H cement with silica flour
HSHO	Class H Cement with silica flour and hydroxyapatite
HSMG	Class H Cement with silica flour and magnesium oxide
K	Permeability of cement cores
LPR	Linear polarization resistance
mpy	mils per year
MGO	Magnesium oxide containing cement

MYS	maximum yield strength
NACE	National Association of Corrosion Engineers
PSF	Plastic strain to failure,
SBS	Shear bond strength
SCC	Stress corrosion cracking
SEM	Scanning Electron Microscope
SSC	Sulfide stress cracking
t	Test duration, hr
UTS	Ultimate tensile Strength
w_1	Initial specimen weight
w_2	Final specimen weight
YS	Yield strength

Greek Symbols

ϕ	Porosity of cement cores

References

Seiersten, M. 2001. Material Selection for Separation, Transportation and Disposal of CO2, Paper no. 01042, NACE International, 11-16 March, Houston, Texas.

Project Title: Effect of H_2S and CO_2 in HPHT Wells on Tubulars and Cement

Report Type: Monthly Report

Report #: 38

Reporting Period: October 22nd, 2014 to November 21st, 2014

Authors:

Ramadan Ahmed, Principal Investigator

Subhash Shah, Co-Principal Investigator

Rida Elgaddafi, Research Assistant

Omotayo Omosebi, Research Assistant

Jueun Hwang, Research Assistant

Sagar Tale, Research Assistant

Prepared under BSEE Project # E12PC00035

by

THE UNIVERSITY OF OKLAHOMA

January 20, 2015

1. Summary of Accomplishments

This monthly report presents the progress made during the project period October 22, 2014 to November 21, 2014. During this reporting period, experimental studies on cement and tubular degradation were continued. Uniform and stress-cracking corrosion experiments were performed under HPHT conditions using minipipes and flat coupons. Weight loss and LPR techniques were utilized to measure uniform corrosion rate. In addition, mechanical properties of test specimens were measured to assess the level of corrosion. Furthermore, cement cores and shear bond samples were prepared and aged in high-pressure and high-temperature (HPHT) acidic environment to evaluate performance of acid-resistant hydroxyapatite-based cement (HOAP).

One batch of cement aging experiment was completed during this month. Cement cores and bonding samples of baseline and hydroxyapatite-based cements were prepared and aged for 2 weeks in 2% brine saturated with methane gas containing CO_2 and H_2S. Porosity, permeability, and compressive and shear bond strengths (SBS) of unaged and aged samples were measured.

Porosity and permeability of all samples decreased after aging. Although Class G cement-based additive samples (HHO) displayed abnormally high permeability, after aging their permeability reduced substantially. Besides this, SBS of the samples improved after aging due to carbonation. Compressive strengths of Class G based cements (baseline and GHO) decreased after aging due to bi-carbonation and leaching of binding components of the cement. However, reduction in porosity and permeability indicated the absence of major leaching.

Investigation on uniform corrosion is in progress. Tests were conducted under low-pressure and high-pressure conditions. During this month, low-pressure uniform corrosion experiments were carried out at 120 psi and 176°F in 1% NaCl solution saturated with mixed gas containing nitrogen and carbon dioxide. In order to study the effect of carbon dioxide on corrosion rate, CO_2 content of the gas was varied. Results are consistent with our previous measurements obtained from testing the material in 2% NaCl solution. At high CO_2 concentration (more than 25%), the corrosion rate gradually decreased with the concentration. At low concentration (less than 25%) however, the trend was reversed. Results of high-pressure corrosion test show similar trend. At low CO_2 concentration (less than 25%), the average corrosion rate increased with CO_2 concentration. In the intermediate concentration range (25 to 75%), the corrosion rate was approximately constant. Slight reduction in the corrosion rate was observed when the concentration was increased above 75%.

Two stress-cracking corrosion experiments were conducted under HPHT conditions. Mechanical properties of the specimens were measured before and after the test. During the test, specimens were immersed in 2% sodium chloride solution saturated with methane gas containing CO_2 and H_2S. Carbon dioxide content of the gas phase was varied from 0 to 15%. Corroded specimen showed significant embrittlement as indicated by reduction in plastic strain to failure (PSF) and ultimate tensile strength (UTS) after the test. PSF and UTS of the specimens decreased as CO_2 concentration was increased.

Our plan for the upcoming weeks is to continue: i) aging tests at 3000 psi, 100°F, 300 ppm H_2S and varying CO_2 concentration; ii) testing of new acid-resistant cement formulations; iii) low-pressure corrosion experiments using 1% NaCl solution and varying CO_2 concentration; and iv) stress cracking and uniform corrosion experiments under HPHT condition varying CO_2 content of the gas phase.

2. Overall Project Progress

2.1 Experimental Studies on Degradation of Cement (Task 2)

2.1.1 Aging Experiment and Degradation

Degradation study on new cement formulations (MGO and HOAP) was continued. During this month, one cement-degradation test was carried out. Baseline and HOAP cement cores and shear bond samples were prepared and aged in brine (2% NaCl) saturated with methane gas containing 300 ppm H_2S and CO_2 under HPHT condition. Test parameters of the new experiment (Batch 40) are presented in **Table 1** along with those of previous tests. Mechanical properties (porosity, permeability, and compressive and bond strengths) of unaged and aged samples were measured to assess the level of degradation and performance of the new formulation.

Table 1: Test parameters for aging experiments conducted to date

Batch #	Temp. (ºF)	Pressure (psi)	Partial Pressure %			Brine (%)	Aging Period (days)	Exp. #	Additive Batch #
			CH_4	CO_2	H_2S (ppm)				
001	350	9000	100	0	0	9	6	1	
002	350	6000	100	0	0	2	14 & 28	2	
003	350	6000	100	0	0	2	14		
004	350	6000	90	10	0	2	6	3	
005	350	6000	90	10	0	2	14 & 28	4	
006	350	6000	90	10	0	2	14		
007	225	6000	90	10	0	2	14	5	
008	100	6000	90	10	0	2	14	6	
009	225	6000	60	40	0	2	14	7	
010	225	6000	0	100	0	2	14	8	
011	100	6000	60	40	0	2	14	9	
012	100	6000	0	100	0	2	14	10	
013	350	6000	60	40	0	2	14	11	
014	350	6000	0	100	0	2	14	12	
015	225	6000	60	40	0	2	14	7A	
016	350	3000	60	40	0	2	14	13	
017	350	9000	60	40	0	2	14	14	
018	350	3000	0	100	0	2	14	15	
019	350	9000	0	100	0	2	14	16	
020	350	3000	90	10	0	2	14	17	
021	350	9000	90	10	0	2	14	18	
022	225	3000	60	40	0	2	14	19	
023	225	9000	60	40	0	2	14	20	
024	225	3000	0	100	0	2	14	21	
025	225	9000	0	100	0	2	14	22	
026	225	3000	90	10	0	2	14	23	
027	225	9000	90	10	0	2	14	24	
028	430	6000	90	10	0	2	14	25	009 - MS
029	430	6000	60	40	0	2	14	26	010 - MS
030	430	6000	100	0	0	2	14	27	003 - LTMS
031	430	3000	100	0	0	2	14	28	004 - LTMS

Batch #	Temp. (ºF)	Pressure (psi)	Partial Pressure %			Brine (%)	Aging Period (days)	Exp. #	Additive Batch #
			CH_4	CO_2	H_2S (ppm)				
032	430	9000	100	0	0	2	14	29	008 - HOAP
033	100	6000	90	10	300	2	14	30	009 - HOAP
034	225	6000	90	10	300	2	14	31	009 - MGO
035	350	6000	90	10	300	2	14	32	010 - HOAP
036	100	6000	100	0	300	2	14	33	011 - HOAP
037	100	6000	60	40	300	2	14	34	010 - MGO
038	100	9000	100	0	300	2	14	35	012 - HOAP
039	100	9000	90	10	300	2	14	35	011 - MGO
040	**100**	**9000**	**60**	**40**	**300**	**2**	**14**	**36**	**013 - HOAP**

2.1.2 Porosity and Permeability of Baseline and Additive Cements

Tables 2 and **3** present porosity and permeability of baseline and HOAP samples, respectively. As expected, porosity and permeability of samples decreased after aging (**Fig. 1a**) due to carbonation of calcium hydroxide (CH) and calcium silicate hydrates (CSH). Unaged HHO samples exhibited abnormally high-permeability, which is inconsistent with porosity measurements. Increase in permeability after aging can be an indication of micro-cracking resulting from the secondary ettringite formation that can increase permeability without significant increase in porosity. However, HHO samples displayed significant reduction in permeability after aging. Hence, this unusually observation can be associated with other phenomena or human error during sample preparation and testing.

Table 2: Porosity and permeability of baseline samples (Batch 40)

Core #	Core Type	Core dimensions			Porosity and Permeability Measurements					
		Dia. mm)	L (mm)	W (g)	ϕ (%)	Ave. ϕ (%)	Std. Dev. (%)	K (mD)	Ave. K (mD)	Std. Dev. (mD)
040 GS 00 01	Unaged	25.3	39.1	27.3	28.0	29.98	2.86	0.08	0.078	0.003
040 GS 00 02		25.3	34.3	27.9	32.0			0.076		
040 GS 07 01	Aged	25.3	32.4	28.6	23.8	24.45	0.85	0.038	0.039	0.001
040 GS 07 02		25.3	33.5	29.3	25.0			0.04		
040 HS 00 01	Unaged	28.6	32.9	28.2	23.2	26.30	4.39	0.091	0.088	0.004
040 HS 00 02		25.3	32.2	27.9	29.4			0.085		
040 HS 04 01	Aged	25.5	32.3	28.7	25.9	27.20	1.87	0.046	0.052	0.008
040 HS 04 02		25.3	32.3	28.2	28.5			0.058		

Table 3: Porosity and permeability of additives (HOAP) samples (Batch HHO-13/40)

Core #	Core Type	Core dimensions			Porosity and Permeability Measurements					
		Dia. mm)	L (mm)	W (g)	ϕ (%)	Ave. ϕ (%)	Std. Dev. (%)	K (mD)	Ave. K (mD)	Std. Dev. (mD)
013 GHO 00 01	Unaged	25.3	35.5	28.3	32.7	32.43	0.44	0.066	0.056	0.014
013 GHO 00 02		25.3	38.3	30.9	32.1			0.046		
013 GHO 10 01	Aged	25.4	30.1	25.5	25.8	25.20	0.88	0.037	0.031	0.009
013 GHO 10 02		25.3	35.3	30.5	24.6			0.024		
013 HHO 00 01	Aged	25.3	37.6	31.5	30.5	30.68	0.24	0.189	0.189	0.001
013 HHO 00 02		25.2	34.4	28.8	30.9			0.188		
013 HHO 09 01	Unaged	25.3	35.1	30.2	28.6	28.94	0.54	0.068	0.060	0.012
013 HHO 09 02		25.3	35.1	31.3	29.3			0.051		

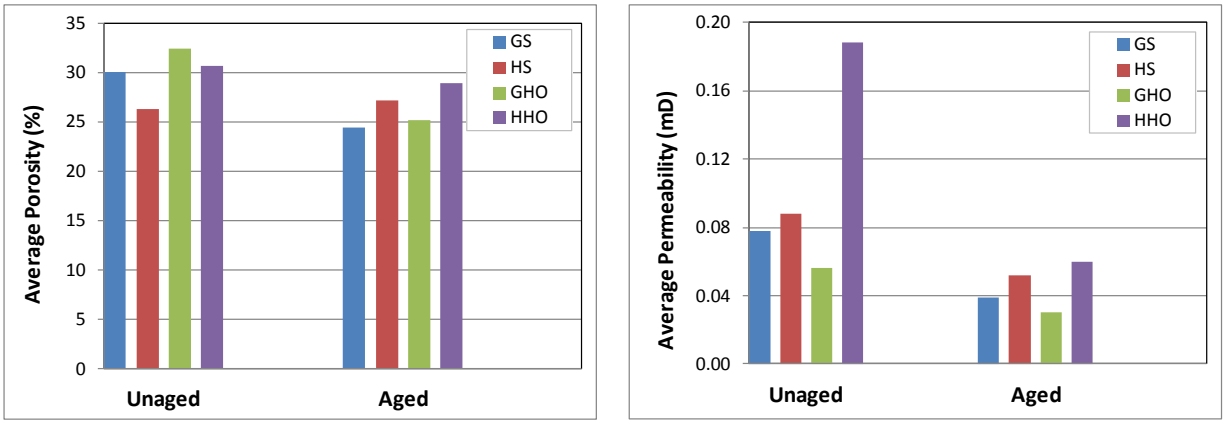

Fig. 1: Porosity and permeability of unaged and aged baseline and additive samples (aging condition 9000 psi, 40% CO_2 and 300 ppm H_2S)

2.1.3 Shear Bond Strength of Baseline and Additive Cements

The shear bond strengths of baseline and HOAP samples are presented in **Tables 4** and **5,** respectively. Due to equipment failure, measured SBS of unaged HOAP samples were significantly lower than those of the baseline and similar HOAP samples from other batches. The equipment was repaired and then the remaining samples were tested. Therefore, for comparison purpose the data from previous batch (Batch HHO-12/38) is used for unaged HOAP samples.

Table 4: Shear bond strength of baseline samples

Batch	Core #	Temp. (F)	Pressure (psi)	CH4 (%)	CO2 (%)	H2S (%)	Brine (%)	Days Aged	SBS (psi)	Ave. SBS	Stdev
040	040-HS-00-01	Ambient	Atmospheric	0	0	0	2	0	726	680.5	144
	040-HS-00-02	Ambient	Atmospheric	0	0	0	2	0	663		
	040-HS-00-03	Ambient	Atmospheric	0	0	0	2	0	562		
	040-HS-00-04	Ambient	Atmospheric	0	0	0	2	0	902		
	040-HS-00-05	Ambient	Atmospheric	0	0	0	2	0	548		
	040-HS-08-01	100	9000	0	40	60	2	14	1125	1181.6	85
	040-HS-08-02	100	9000	0	40	60	2	14	1194		
	040-HS-08-03	100	9000	0	40	60	2	14	1111		
	040-HS-08-05	100	9000	0	40	60	2	14	1297		

Table 5: Shear bond strength of additive (HOAP) samples

Batch	Core #	Temp. (F)	Pressure (psi)	CH4 (%)	CO2 (%)	H2S (%)	Brine (%)	Days Aged	SBS (psi)	Ave. SBS	Stdev
HHO-013/040	013-HHO-00-01	Ambient	Atmospheric	0	0	0	2	0	364	339	66
	013-HHO-00-02	Ambient	Atmospheric	0	0	0	2	0	354		
	013-HHO-00-03	Ambient	Atmospheric	0	0	0	2	0	283		
	013-HHO-00-04	Ambient	Atmospheric	0	0	0	2	0	266		
	013-HHO-00-05	Ambient	Atmospheric	0	0	0	2	0	429		
	013-HHO-11-01	100	9000	0	40	60	2	14	1356	1496	300
	013-HHO-11-02	100	9000	0	40	60	2	14	1905		
	013-HHO-11-03	100	9000	0	40	60	2	14	1560		
	013-HHO-11-04	100	9000	0	40	60	2	14	1569		
	013-HHO-11-05	100	9000	0	40	60	2	14	1090		

Figure 2 compares SBS of aged and unaged baseline and additive samples. Aged additive (HHO) samples displayed higher (approximately 20%) SBS than baseline samples. Aging was conducted in the presence of CO_2. Therefore, natural phenomena occurring after curing can be hydration, carbonation, leaching and secondary ettringite formation. Carbonation and formation of secondary ettringite result in expansion, which tends to improve SBS by creating very tight interface between cement and steel pipe. Hydration and leaching processes are expected to have adverse effects on SBS.

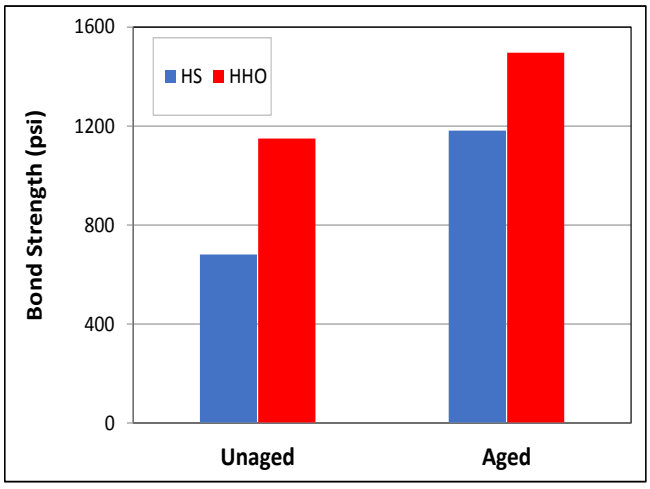

Fig. 2: Bond strength of baseline and additive samples

2.1.4 Compressive Strength of Baseline and Additive Cements

Tables 6 and **7** present compressive strengths of baseline and HOAP cements, respectively. Compressive strengths of Class G based cements (baseline and GHO) decreased after aging due to bi-carbonation and leaching him (**Fig. 3**). However, reduction in porosity and permeability of the samples indicated dominant carbonation resulting from the acid attack. The reaction between carbonic acid and binding components of set cement (calcium hydroxide and calcium silicate hydrate) forms calcium carbonate, which precipitates in the pore causing the reduction in porosity and permeability. In the presence of excess carbonic acid, bi-carbonation of occurs, resulting in highly soluble reaction products, which can be easily leached out from the cement. Without leaching, precipitated calcium carbonate provides structural support in the pore which tends to improve compressive strengths of the cement. However, in some cases, the improvement in strength can be offset by a structural degradation of the cement matrix resulting from the reaction between binding components and carbonic acid. Moreover, the presence of leaching has a negative impact on strength development as it dissolves the precipitated calcium carbonate and extracts the binding components of cement from the matrix.

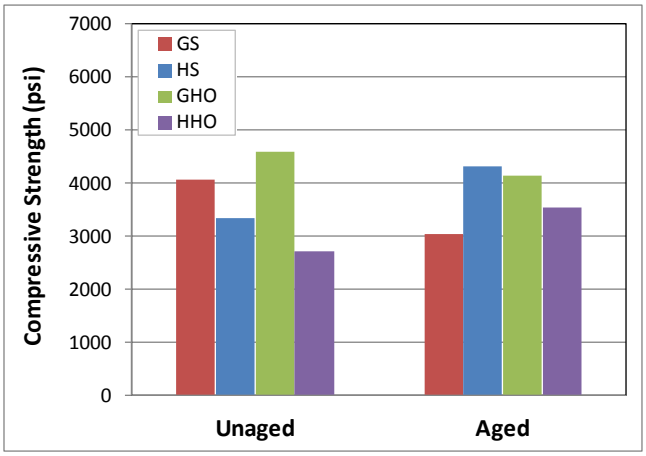

Fig. 3: Compressive strengths of baseline and HOAP samples (aging cond. 9000 psi, 40% CO_2 and 300 ppm H_2S)

Table 6: Compressive strength of baseline samples (Batch 40)

Compressive Strength Data for Batch 40 Samples					
Unaged Samples					
Core #	**Confine Pressure**	**Pressure (psi)**	**Experimental Stress (psi)**	**Average Stress**	**Standard Deviation**
040-GS-00-03	1000	497	4311	4056	361
040-GS-00-05	1000	438	3800		
040-HS-00-03	1000	168	1461	3353	1722
040-HS-00-04	1000	557	4829		
040-HS-00-05	1000	434	3769		
Aged Samples					
Core #	**Confine Pressure**	**Pressure (psi)**	**Experimental Stress (psi)**	**Average Stress**	**Standard Deviation**
040-GS-05-03	1000	348	3019	3054	782
040-GS-05-04	1000	371	3218		
040-GS-05-05	1000	242	2096		
040-GS-07-03	1000	477	4142		
040-GS-07-04	1000	414	3593		
040-GS-07-05	1000	260	2254		
040-HS-04-03	1000	611	5305	4315	1131
040-HS-04-04	1000	554	4809		
040-HS-04-05	1000	346	2135		
040-HS-06-03	1000	491	4258		
040-HS-06-04	1000	511	4436		
040-HS-06-05	1000	570	4945		

Table 7: Compressive strength of additive (HOAP) samples (Batch HOAP-13/40)

Compressive Strength Data for Batch HOAP-13/40 Samples					
Unaged Samples					
Core #	**Confine Pressure**	**Pressure (psi)**	**Experimental Stress (psi)**	**Average Stress**	**Standard Deviation**
013-GHO-00-03	1000	422	3657		
013-GHO-00-04	1000	630	5462		
013-GHO-00-05	1000	538	4670	4596	905
013-HHO-00-03	1000	281	2439		
013-HHO-00-04	1000	264	2289		
013-HHO-00-05	1000	391	3393	2707	599
Aged Samples					
Core #	**Confine Pressure**	**Pressure (psi)**	**Experimental Stress (psi)**	**Average Stress**	**Standard Deviation**
013-GHO-10-03	1000	504	4371		
013-GHO-10-04	1000	465	4039		
013-GHO-10-05	1000	567	4050	4153	189
013-HHO-09-03	1000	486	4218		
013-HHO-09-04	1000	416	3608		
013-HHO-09-05	1000	325	2816	3547	703

Improvement in compressive strength of Class H based cements (baseline and HHO) was observed after aging. This is in agreement with porosity and permeability measurements, which indicated the presence of carbonation. Besides this, Class G based additive samples (GHO) showed higher strength compared to the baseline. The samples retained their strength even after aging.

2.2 Experimental Studies on Corrosion of Tubulars (Task 3)

2.2.1 Sulfide Stress Cracking

Experimental study on sulfide stress cracking (SSC) behavior of API carbon steel (Grade C110) was continued. During this reporting period, two specimens (Minipipes 9 and 10) were tested. **Table 8** summarizes the SSC tests completed to date. It shows the experimental conditions in which specimens were exposed. Internal and external pressures of specimen were maintained at 4000 and 6000 psi, respectively. Carbon dioxide concentration was varied from 0 to 15%. Minipipe 10 was tested to repeat experiment conducted on Minipipe 3. The repeat testing was needed because this is the only test in which the specimen showed complete failure after seven days of exposure to sour environment. It has demonstrated the reliability of the SSC measurements and other experimental observations.

Table 8: Specimen corrosion testing conditions

No.	Label	Temp. (°F)	Pressure (psi)		Gas Composition			Time Duration (Days)	Remarks
			Inside	Outside	H2S (ppm)	CH4 (%)	CO2 (%)		
1	01-C110-07/25-08/06	100	6000	4000	0	100	0	15	
2	02-C110-08/25-08/25	-	-	-	-	-	-	-	Baseline
3	03-C110-08/27-09/03	100	6000	4000	270	90	10	7	Sample failed after 7 days of exposure
4	04-C110-09/05-09/12	100	6000	4000	300	100	0	7	
5	05-C110-09/05-09/13	100	6000	4000	285	95	5	7	
6	06-C110-09/05-09/14	100	6000	4000	270	90	10	7	Brine completely leaked from the cell
7	07-C110-10/17-10/24	100	6000	4000	255	85	15	7	
8	08-C110-10/28-11/04	100	6000	4000	270	90	10	7	
9	**09-C110-11/05-11/12**	**100**	**6000**	**4000**	**293**	**97.5**	**2.5**	**7**	
10	**10-C110-11/13-11/20**	**100**	**6000**	**4000**	**270**	**90**	**10**	**7**	**Sample failed after 7 days of exposure**

Specimen 9 was strained to failure after exposure to sour environment. The specimen showed lower ultimate tensile strength (UTS) and plastic strain to failure (PSF) than the baseline (Specimen 2), which indicate embrittlement (**Table 9**).

Table 9: Mechanical properties of samples before and after corrosion test

Mini-pipe No.	Before Exposure				After Exposure			
	YS (psi)	UTS (psi)	PSF	E (psi)	YS (psi)	UTS (psi)	PSF	E* (psi)
1	-	-	-	-	109,855	127,619	0.030	11,785,921
2	111,529	130,156	0.040	11,842,002	-	-	-	-
3	-	-	-	11,704,810	-	100799	0.000	-
4	-	-	-	12,594,080	112768	134981	0.043	12078823
5	-	-	-	10,911,219	102217	114424	0.023	11368960
6	-	-	-	11,599,401	110686	130118	0.049	11444081
7	-	-	-	11,221,136	-	115479	0.014	11,561,000
8	-	-	-	12,044,218	-	120026	0.069	11,441,529
9				**11,792,032**		**116742**	**0.036**	**11255892**
10	**-**	**-**	**-**	**13,377,764**	**-**	**100799**	**0.000**	**-**

UTS = Ultimate tensile Strength, PSF = Plastic strain to failure, YS = Yield strength, E = Young's modulus before exposure, E* = Young's modulus after exposure

Concentration of CO_2 was varied during the investigation to examine its effect on SSC susceptibility. UTS and PSF were used to assess the susceptibility of material towards SSC in sour conditions. **Figure 4** shows variation of UTS and PSF of specimens with CO_2 concentration. Experiment with 10% of CO_2 was carried out four times (Specimen 3, 6, 8, and 10). Specimen 3 and 10 were broken inside the SSC cell. When Specimen 6 was tested, fluid inside the reactor completely leaked out. Average UTS and PSF of Specimen 3, 8, and 10 are considered for determining UTS and PSF at 10% CO_2 concentration. At low CO_2 concentration (0 to 5%), UTS reduced with concentration and then the effect diminished. The trend indicates the embrittlement occurring in the material. However, as the concentration increased above 10%, the trend changed. UTS slightly increased when CO_2 concentration was raised from 10 to 15%. The trend reversal could be due to the change in H_2S concentration in the gas. Using supply gas with constant H_2S concentration (300 ppm), increasing CO_2 content has dilution effect that slightly reduces H_2S concentration in the gas as CO_2 concentration is increased (Table 8). Hence, in the future, experiments will be carried out with supply gas containing 500 ppm H_2S. This will ensure approximately constant H_2S concentration in the gas while increasing CO_2 content at 40%.

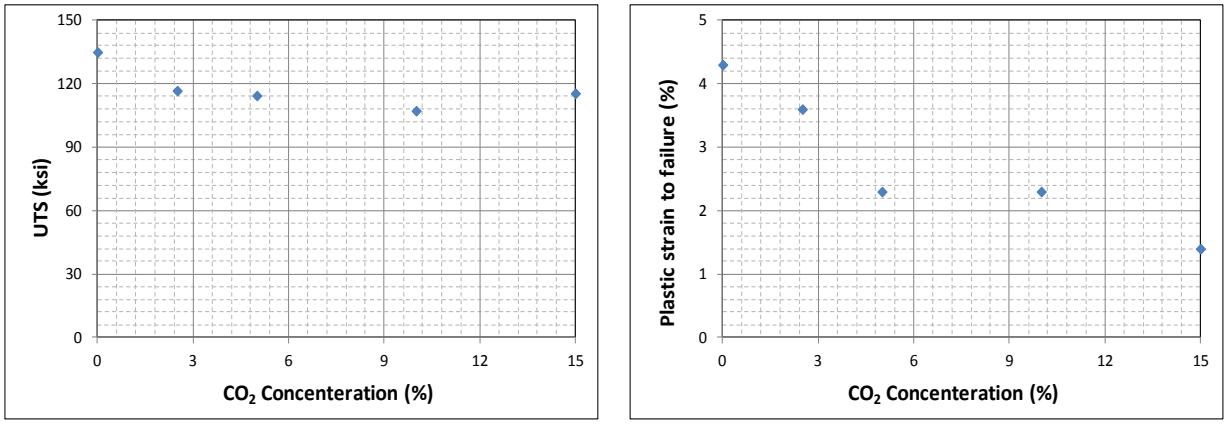

Fig. 4: Mechanical properties of specimens as a function of CO_2 concentration: a) UTS; and b) PSF

Furthermore, PSF trend shown in Fig. 4b demonstrates the embrittlement occurred in the specimens. With increasing the CO_2 content, the PSF substantially reduced indicating the level of embrittlement. Increasing the CO_2 content decreases pH of brine solution (surrounding fluid), which has significant effect on SSC. A number of studies (Morana and Nice 2009; Snape 1967; Hashizume and Inohara 2000) were conducted to investigate the effects of pH on SSC resistance of different carbon steel alloys. Results demonstrated that the reduction in pH facilitates the SSC corrosion of steels. In addition to pH, the concentration (i.e. partial pressure) of H_2S affects SSC corrosion of steels**.** **Figure 5** presents safe operating zone for Q-125 (Morana and Nice 2009). The area on left side of the green line represents zone where the metal is not vulnerable to SSC while the area on right side of the red line represents zone where it is highly susceptible to SSC. The area in between the two lines is intermediate zone where there is moderate level of vulnerability to SSC. Q-125 can be safely used in the area identified as No SSC zone.

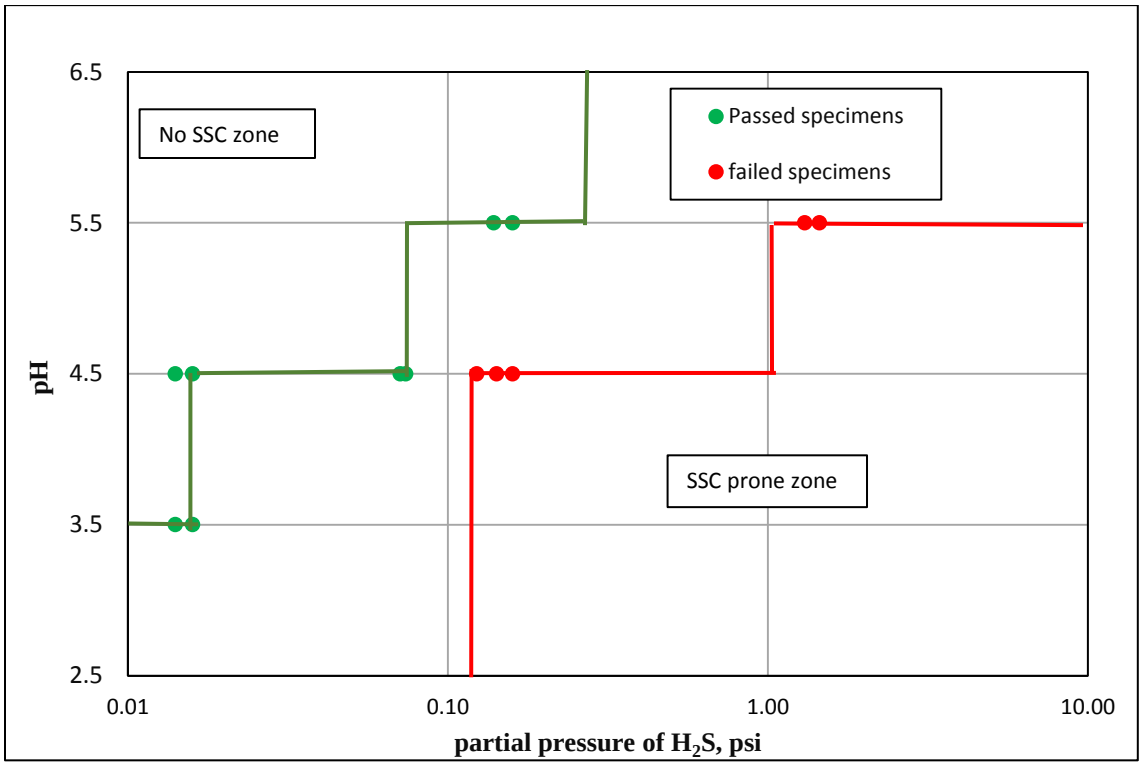

Fig. 5: Operating window of Q-125 (Redrawn from Morana and Nice 2009)

2.2.2 Uniform Corrosion in Sour Gas Environment

During this reporting period, uniform corrosion experiments were conducted to evaluate corrosion of carbon steel in CO_2 environment under low and high pressure conditions.

2.2.2.1 Low-Pressure Experiments

Experimental investigation on corrosion rate of carbon steel under low-pressure condition is in progress. To examine the effects of CO_2 and salt concentrations on corrosion, four experiments were performed at a constant pressure of 120 psi. Test parameters and results of the experiments are presented in **Table 10** along with previous measurements. Test parameters were unstable during Experiment 45 (25% CO_2 and 176°F). Hence, the test was repeated to verify its reproducibility. Results showed significant reduction (approximately 50%) in corrosion rate measurement.

Table 10: Test parameters and results of low-pressure corrosion experiments conducted to date

Exp. #	Temp. (ºF)	Pressure (psi)	Partial Pressure %		Brine Conc. (%)	Test Period (days)	Results (mpy)	
			N_2	CO_2			LPR	WL
15	78	120	25	75	2	187	40.30	31.91
16	78	120	0	100	2	187	39.18	32.18
17	78	240	0	100	2	187	NA	NA
18	78	120	75	25	2	187	22.92	21.83
19	110	120	75	25	2	187	31.78	23.78
20	110	120	25	75	2	187	53.16	43.22
21	110	120	100	0	2	187	12.37	15.40
22	110	120	75	25	2	187	31.07	23.78
23	110	120	50	50	2	187	70.35	43.39
24	110	120	25	75	2	187	53.16	43.22
25	110	120	0	100	2	187	44.92	32.49
26	176	120	100	0	2	187	4.04	3.10
27	176	120	75	25	2	187	16.53	11.77
28	176	120	50	50	2	187	24.23	12.71
29	176	120	25	75	2	187	17.39	10.87
30	176	120	0	100	2	187	22.56	12.04
31	140	120	100	0	2	187	2.58	2.72
32	140	120	75	25	2	187	11.00	6.33
33	140	120	50	50	2	187	13.33	14.30
34	140	120	25	75	2	187	38.48	26.76
35	140	120	0	100	2	187	24.40	24.23
36	140	120	100	0	1	187	3.69	1.23
37	140	120	75	25	1	187	5.16	20.97
38	140	120	75	25	1	187	9.86	25.13
39	140	120	50	50	1	187	6.40	21.24
40	140	120	25	75	1	187	6.50	23.78
41	140	120	0	100	1	187	4.31	14.77
42	176	120	0	100	1	187	1.76	4.63
43	176	120	25	75	1	187	2.79	9.00
44	176	120	50	50	1	187	4.95	12.59
45	176	120	75	25	1	187	17.79	36.98
46	**176**	**120**	**100**	**0**	**1**	**187**	**0.69**	**2.60**
47	**176**	**120**	**75**	**25**	**1**	**187**	**5.79**	**14.90**
48	**110**	**120**	**25**	**75**	**1**	**187**	**8.55**	**33.23**
49	**110**	**120**	**0**	**100**	**1**	**187**	**6.21**	**30.81**

Figures 6 compares corrosion rate measurements obtained from electrochemical (LPR) and weight loss (WL) at different temperatures (110 and 176°F). Pressure and brine composition were maintained the same. The effect of the CO_2 concentration on corrosion rate was found to be different from what has been normally observed. At high CO_2 concentration (above 25%), in both cases, the

corrosion rate gradually decreased with the concentration. Besides this, the corrosion rate substantially reduced with temperature regardless of CO_2 concentration (**Fig. 7).**

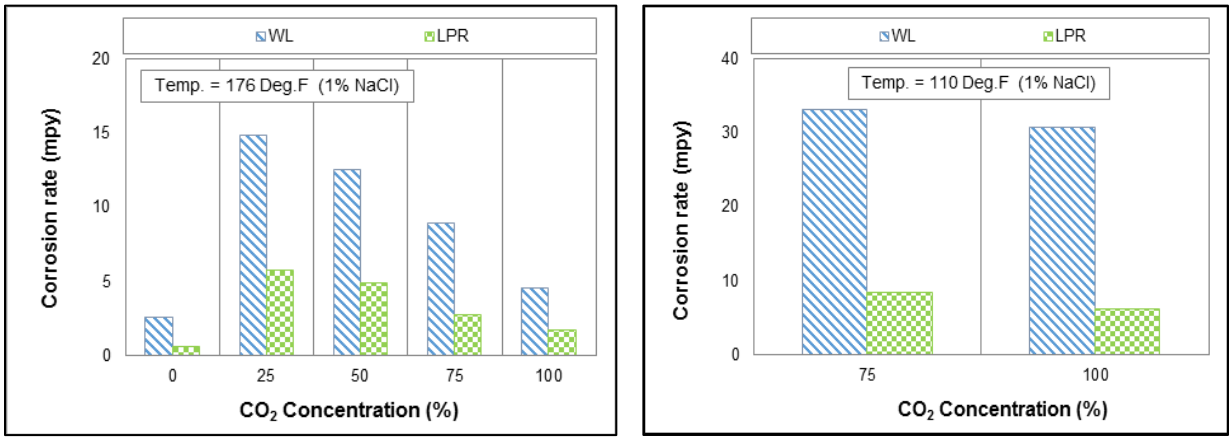

Fig. 6: Corrosion rate versus CO2 concentration at 120 psi and different temperatures: a) at 176°F; and b) 110°F

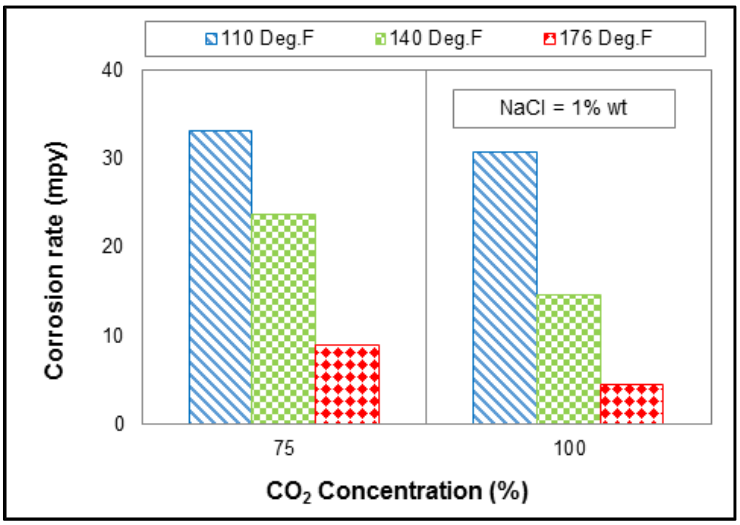

Fig. 7: Corrosion rate versus temperature at different CO_2 concentrations

Temperature has major effect on corrosion. Increase in temperature facilitates the corrosion reactions and transport of species (molecular diffusion), hence results in a higher corrosion rate. On the other hand, increase in temperature accelerates precipitation of corrosion product and formation of protective scale, resulting in reduction of corrosion rate. In pure CO_2 system, the corrosion products such as iron carbonate ($FeCO_3$), precipitate and deposit on the metal surface after their solubility limit is reached. Johnson and Tomson (1991) reported extreme sensitivity of rate of iron carbonate precipitation to temperature. Moreover, with increasing temperature, CO_2 solubility decreases causing reduction in carbonic acid concentration and increase in pH, which have negative impact on corrosion process. In general, the severity of corrosion in carbonic acid environment is higher in low-temperature than high-temperature (Valdes et al. 1998).

2.2.2.2 High-Pressure Experiments

Investigation on corrosion behavior of carbon steel (Grade C110) is in progress. During this reporting period, three new batches of experiments were carried out at 9,000 psi and varying CO_2 concentration (0, 25 and 50%). Test temperature and NaCl concentration were maintained at 100°F and 2% NaCl, respectively. Three coupons were used for each batch of experiment in order to obtain average corrosion rate and mechanical property measurements. Test parameters for different batch of experiments are presented in **Table 11**.

Table 11: Test conditions for HPHT uniform corrosion tests

Batch No.	Pressure (psi)	Temperature (F)	Test Duration (hr)	CO_2 Conc. (%)	CH_4 Conc. (%)	H_2S Conc. (%)
001	6000	100	187	100	0	0
002	6000	100	187	50	50	0
003	6000	100	187	0	100	0
004	6000	100	187	25	75	0
005	6000	100	187	75	25	0
006	9000	100	187	100	0	0
007	3000	100	187	0	100	0
008	9000	100	187	75	25	0
009	**9000**	**100**	**187**	**50**	**50**	**0**
010	**9000**	**100**	**187**	**25**	**75**	**0**
011	**9000**	**100**	**187**	**0**	**100**	**0**

Corrosion rate of API carbon steel (Grade C110) in the brine solution saturated with methane containing carbon dioxide was measured using weight loss method. In addition to the corrosion rate, mechanical properties of the specimens were measured before and after exposure to the corrosive environment. Results (**Table 12**) show significant corrosion after the exposure. Mechanical property measurements before and after exposure vary due to changes in specimen characteristics resulting from localized corrosion and reduction in specimen thickness.

Table 12: Corrosion rate and mechanical properties of C110 specimens before and after corrosion test

Batch No.	Specimen No.	CO_2 Con.%	Initial weight gm	Final weight gm	CR (mpy)	E (psi)	E* (psi)	Yield strength (psi)	Tensile Strength (psi)
001	C110-1	100	13.3848	13.2129	234	5.79E+06	9.91E+06	107,560	123,600
	C110-2		13.4397	13.2212	297	6.02E+06	8.62E+06	105,950	119,933
	C110-3		13.4478	13.2323	293	7.71E+06	9.44E+06	108,140	120,673
002	C110-1	50	13.4875	13.1076	517	1.07E+07	8.57E+06	104,960	117,283
	C110-2		13.3884	13.0029	524	5.10E+06	9.01E+06	97,180	116,388
	C110-3		13.3376	12.9835	482	5.54E+06	8.25E+06	95,140	116,198
003	C110-1	0	13.4459	13.3916	74	1.00E+07	7.76E+06	93,250	130,891
	C110-2		13.4196	13.3924	37	1.15E+07	8.43E+06	96,780	131,917
	C110-3		13.3234	13.2680	75	1.07E+07	8.25E+06	96,940	129,187
004	C110-1	25	13.3739	12.949	578	8.75E+06	8.13E+06	91,000	113,833
	C110-2		13.3092	12.9818	445	8.48E+06	6.99E+06	95,510	116,450
	C110-3		13.4018	13.0782	440	8.15E+06	8.44E+06	94,880	117,009

Batch No.	Specimen No.	CO_2 Con.%	Initial weight gm	Final weight gm	CR (mpy)	E (psi)	E* (psi)	Yield strength (psi)	Tensile Strength (psi)
005	C110-1	75	13.4127	13.1079	415	8.71E+06	8.09E+06	103,240	111,286
	C110-2		13.4881	13.2212	363	1.10E+07	6.52E+06	101,290	112,891
	C110-3		13.4635	12.9808	657	8.43E+06	6.01E+06	101,000	111,062
006	**C110-1**	**100**	**13.4039**	**13.1518**	**343**	**1.14E+07**	**8.43E+06**	**100,000**	**116,283**
	C110-2		**13.3703**	**12.9598**	**558**	**1.08E+07**	**8.57E+06**	**96,410**	**113,007**
	C110-3		**13.4606**	**13.2294**	**315**	**1.10E+07**	**6.36E+06**	**95,570**	**117,066**
007	**C110-1**	**0**	**13.4169**	**13.3859**	**42**	**9.98E+06**	**6.96E+06**	**100,920**	**130,212**
	C110-2		**13.4447**	**13.4144**	**41**	**9.29E+06**	**6.94E+06**	**100,530**	**130,658**
	C110-3		**13.4041**	**13.3635**	**55**	**9.47E+06**	**7.05E+06**	**101,170**	**128,982**
008	**C110-1**	**75**	**13.3681**	**12.9327**	**592**	**7.74E+06**	**8.37E+06**	**97,530**	**110,554**
	C110-2		**13.4538**	**13.0456**	**555**	**7.97E+06**	**8.67E+06**	**99,660**	**110,922**
	C110-3		**13.3742**	**12.9952**	**516**	**8.44E+06**	**9.24E+06**	**100,480**	**112,723**

E and E* are Young's modulus measured before and after corrosion test, respectively.

At low CO_2 concentration (less than 25%), the average corrosion rate greatly increased with CO_2 concentration (**Fig. 8**). In the intermediate concentration range (25 to 75%), the corrosion rate was approximately constant. Slight reduction in the corrosion rate was observed when the concentration was increased above 75%. Figure 8b compares the corrosion rate measurements obtained at different pressures (6000 and 9000 psi). In general, the effect of pressure on corrosion rate is minimal. However, at CO_2 concentration above 50%, a slight increase in corrosion rate was observed when the pressure was raised from 6000 to 9000 psi. The increase in corrosion rate can be attributed to the increase in carbonic acid concentration in brine. As the pressure increases, the concentration of the acid also increases to due to increased solubility. This condition accelerates the cathodic reactions and therefore increasing the corrosion rate.

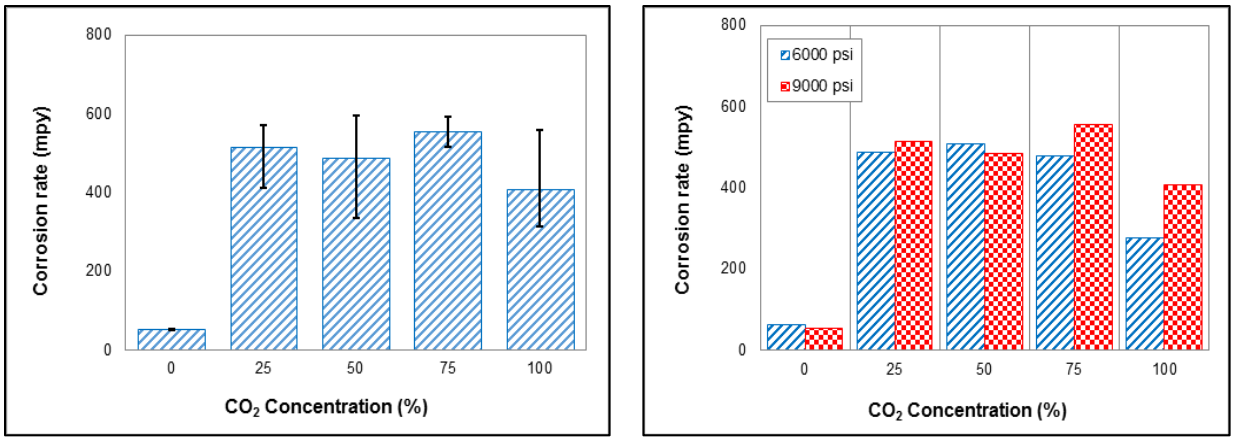

(a) (b)

Fig. 8: Corrosion rate versus CO_2 concentration at 100°F: a) 9000 psi; and b) 6000 and 9000 psi

Furthermore, increase in pressure in the absence of CO_2 slightly affected the corrosion process. Tests conducted under different pressures (**Fig. 9**) demonstrated the influence of pressure on corrosion rate of C110 in the absence of carbon dioxide (brine saturated with pure methane). Slight variation in

corrosion rate was observed as the pressure was increased from 3000 to 9000 psi. One possible explanation for this phenomenon could be the improvement in molecular diffusion in the brine as more methane is dissolved due to increased pressure.

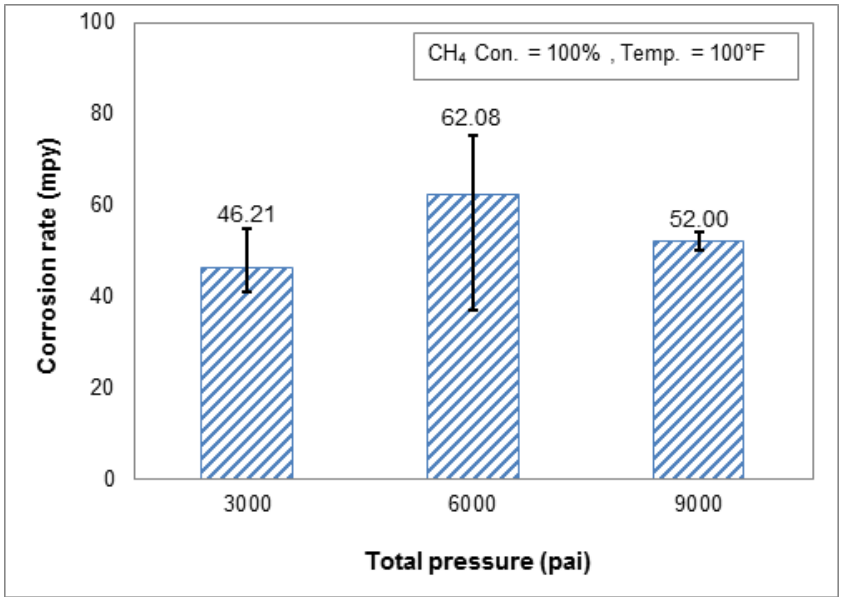

Fig. 9: Corrosion rate versus CO_2 concentration at 100°F: a) 9000 psi; and b) 6000 and 9000 psi

3. Planned Activities

- Continue testing baseline and new cement formulations for their performance by aging them in brine saturated with methane gas containing 300 ppm H_2S at 3000 psi and 100°F varying CO_2 concentration.
- Continue theoretical and modeling studies on tubular degradation.
- Continue experimental studies on tubular degradation under low-pressure and moderate-temperature conditions.
- Continue HPHT corrosion experiments with mini-pipes and flat coupons.

4. Project Expenditures

This section presents the project expenses during the month of November (**Table 13**) and the cumulative expenditure.

Table 13: Current and cumulative expenditures, November 2014

No.	Budget Categories	Current Expenses	Cumulative Expenses
1	Salaries & Wages	$2,930.63	$354,665.57
2	Fringe Benefits	$53.51	$80,004.03
3	Project Materials	$2,638.26	$102,425.13
4	Travel	$128.69	$10,585.76
5	Conference Expenses	$0.00	$0.00
6	Other Direct Costs	$0.00	$1,273.88
7	Equipment	$330.17	$250,036.62
8	Space Rental	$0.00	$0.00
9	Indirect Cost	$2,875.55	$273,432.31
10	**Total**	**$8,956.81**	**$1,072,423.30**

Nomenclature

A	Exposed surface area, cm^2
API	American Petroleum Institute
ASTM	American Society for Testing and Materials
CR	Average corrosion rate, mpy
E	Young's modulus measured before corrosion test
E*	Young's modulus measured after corrosion test
GHO	Class G Cement with hydroxyapatite
GS	Class G cement with silica flour
GSMG	Class G Cement with silica flour and magnesium oxide
HHO	Class H Cement with hydroxyapatite
HOAP	Acid-resistant hydroxyapatite-based cement
HPHT	High-pressure high-temperature
HS	Class H cement with silica flour
HSHO	Class H Cement with silica flour and hydroxyapatite
HSMG	Class H Cement with silica flour and magnesium oxide
K	Permeability of cement cores
LPR	Linear polarization resistance

mpy	mils per year
MGO	Magnesium oxide containing cement
MYS	maximum yield strength
NACE	National Association of Corrosion Engineers
PSF	Plastic strain to failure,
SBS	Shear bond strength
SCC	Stress corrosion cracking
SEM	Scanning Electron Microscope
SSC	Sulfide stress cracking
t	Test duration, hr
UTS	Ultimate tensile Strength
w_1	Initial specimen weight
w_2	Final specimen weight
YS	Yield strength

Greek Symbols

ϕ	Porosity of cement cores

References

Johnson M. L. and Tomson, M. B. 1991. Ferrous Carbonate Precipitation Kinetics and its Impact CO_2 Corrosion, paper No. 268, NACE international, Houston, Texas.

Hashizume, S. and Inohara, Y. 2000. Effects of pH and PH2S on SSC Resistance of Martensitic Stainless Steels. Paper No. 0130 presented at the Corrosion, Orlando, Florida, 26-31 March.

Morana, R. and Nice, P. I. 2009. Corrosion Assessment of High Strength Carbon Steel Grades P-110 Q-125 140 And 150 For H2S Containing Producing Well Environments. Paper No. 9093 presented at the NACE International Corrosion Conference & Expo, Atlanta, Georgia, 22-26 March.

Snape, E. 1967. Sulfide Stress Corrosion of Some Medium and Low Alloy Steels. Corrosion 23 (6): 154-172.

Valdes, A., Case, R., Ramirez, M., and Ruiz, A. 1998. The Effect of Small Amounts of H2S on CO2 Corrosion of a Carbon Steel, paper No.22, March 22 - 27, San Diego CA.

Project Title: Effect of H_2S and CO_2 in HPHT Wells on Tubulars and Cement

Report Type: Monthly Report

Report #: 39

Reporting Period: November 22nd, 2014 to December 21st, 2014

Authors:

Ramadan Ahmed, Principal Investigator

Subhash Shah, Co-Principal Investigator

Rida Elgaddafi, Research Assistant

Omotayo Omosebi, Research Assistant

Jueun Hwang, Research Assistant

Jiwon Jeon, Research Assistant

Prepared under BSEE Project # E12PC00035

by

THE UNIVERSITY OF OKLAHOMA

Feb. 24, 2015

1. Summary of Accomplishments

This monthly report presents the progress made during the project period November 22, 2014 to December 21, 2014. During this reporting period, studies on degradation behavior of baseline and acid-resistant cements have been completed. Deliverables associated with these studies have been prepared and attached as appendices to this report. Furthermore, experimental studies on tubular corrosion were continued. Uniform and stress-cracking corrosion experiments were performed under High-pressure high-temperature (HPHT) conditions using minipipes and flat coupons. Mechanical properties of test specimens were measured to assess the level of corrosion.

The last batch of cement aging experiment was completed during this month. Cement cores and bonding samples of baseline and magnesium oxide-based cements were prepared and aged for 2 weeks in 2% brine saturated with methane gas containing H_2S. Porosity, permeability, and compressive and shear bond strengths (SBS) of unaged and aged samples were measured.

After aging in the absence of carbon dioxide, porosity of baseline and additive samples did not display substantial change. Additive samples exhibited a lower SBS than baseline samples. SBS of baseline and additive samples slightly reduced after aging. Major degradation phenomenon occurring in the absence of carbon dioxide is the formation of secondary ettringite. Due to expansive nature of ettringite, SBS improvement is expected if substantial amount of this mineral is formed in the cement. However, in addition to concentration of H_2S, the formation of ettringite is affected by other factors such as pH and temperature. After aging, compressive strengths of Class G based cements increased possibly due to ettringite formation while those of Class H based cements decreased.

Investigation on uniform corrosion is in progress. Tests were conducted under low-pressure and high-pressure conditions. The low-pressure experiments were carried out at 120 psi and 110°F in 1% NaCl solution saturated with mixed gas containing nitrogen and carbon dioxide. Results of previous experiments are combined with recent measurements to analyze the effect of different test parameters on the corrosion rate. The analysis shows that, in the presence of CO_2 in the surrounding fluid system, the corrosion rate decreases with temperature. This finding is consistent with results of previous studies. In addition to low-pressure tests, a series of high-pressure corrosion experiments were conducted varying pressure (3000, 6000 and 9000 psi) and CO_2 concentrations (50, 75 and 100%). Two different grades of carbon steels (Grades C110 and Q125) were tested. The corrosion rate increased with the increasing CO_2 concentration, which causes pH reduction and increase in carbonic acid concentration (H_2CO_3). When tested under extremely corrosive conditions (50% CO_2, and 6000 and 9000 psi), Q125 grade demonstrated better corrosion resistance than C110 grade.

Four stress-cracking corrosion experiments were conducted under HPHT conditions using different steel grades (C110 and Q125). Mechanical properties of the specimens were measured before and after the test. During the test, specimens were immersed in 2% sodium chloride solution saturated with methane gas containing CO_2 and H_2S. Carbon dioxide content of the gas phase was varied from 0 to 15%. When tests conducted in the presence of CO_2, Q125 specimen showed significant embrittlement as indicated by reduction in plastic strain to failure (PSF) and ultimate tensile strength (UTS) after the test.

Our plan for the upcoming weeks is to continue: i) low-pressure corrosion experiments using 1% NaCl solution and varying CO_2 concentration; and ii) stress cracking and uniform corrosion experiments under HPHT condition varying CO_2 content of the gas phase.

2. Overall Project Progress

2.1 Experimental Studies on Degradation of Cement (Task 2)

2.1.1 Aging Experiment and Degradation

Degradation studies on new cement formulations, hydroxyapatite-based and magnesium oxide-based cements (MGO and HOAP), have been completed. During this month, one cement-degradation test was performed at 3000 psi. Baseline and MGO cement cores and shear bond samples were prepared and aged in brine (2% NaCl) saturated with methane gas containing 300 ppm H_2S under HPHT condition. Test parameters of the new experiment (Batch 41) are presented in **Table 1** along with those of previous tests. Mechanical and physical properties (porosity, permeability, and compressive and bond strengths) of unaged and aged samples were measured to assess the level of degradation and performance of the new formulation.

Table 1: Test parameters for aging experiments conducted to date

Batch #	Temp. (ºF)	Pressure (psi)	Concentration %			Brine (%)	Aging Period (days)	Exp. #	Additive Batch #
			CH_4 (%)	CO_2 (%)	H_2S (ppm)				
001	350	9000	100	0	0	9	6	1	001-FLAS
002	350	6000	100	0	0	2	14 & 28	2	002-FLAS
003	350	6000	100	0	0	2	14		003-FLAS
004	350	6000	90	10	0	2	6	3	004-FLAS
005	350	6000	90	10	0	2	14 & 28	4	005-FLAS
006	350	6000	90	10	0	2	14		006-FLAS
007	225	6000	90	10	0	2	14	5	
008	100	6000	90	10	0	2	14	6	
009	225	6000	60	40	0	2	14	7	
010	225	6000	0	100	0	2	14	8	002-MGO
011	100	6000	60	40	0	2	14	9	002-HOAP
012	100	6000	0	100	0	2	14	10	003-MGO
013	350	6000	60	40	0	2	14	11	004-LT
014	350	6000	0	100	0	2	14	12	003-HOAP
015	225	6000	60	40	0	2	14	7A	004-MGO
016	350	3000	60	40	0	2	14	13	004-HOAP
017	350	9000	60	40	0	2	14	14	005-MGO
018	350	3000	0	100	0	2	14	15	005-HOAP
019	350	9000	0	100	0	2	14	16	
020	350	3000	90	10	0	2	14	17	005-MS-10
021	350	9000	90	10	0	2	14	18	006-MS-10
022	225	3000	60	40	0	2	14	19	006-HOAP
023	225	9000	60	40	0	2	14	20	006-MGO
024	225	3000	0	100	0	2	14	21	008-MS-10
025	225	9000	0	100	0	2	14	22	007-MGO
026	225	3000	90	10	0	2	14	23	007-HOAP
027	225	9000	90	10	0	2	14	24	002-LTMS
028	430	6000	90	10	0	2	14	25	009 – MS-10
029	430	6000	60	40	0	2	14	26	010 – MS-10
030	430	6000	100	0	0	2	14	27	003 - LTMS
031	430	3000	100	0	0	2	14	28	004 - LTMS

Batch #	Temp. (ºF)	Pressure (psi)	Concentration %			Brine (%)	Aging Period (days)	Exp. #	Additive Batch #
			CH_4 (%)	CO_2 (%)	H_2S (ppm)				
032	430	9000	100	0	0	2	14	29	008 - HOAP
033	100	6000	90	10	300	2	14	30	009 - HOAP
034	225	6000	90	10	300	2	14	31	008 - MGO
035	350	6000	90	10	300	2	14	32	010 - HOAP
036	100	6000	100	0	300	2	14	33	011 - HOAP
037	100	6000	60	40	180	2	14	34	010 - MGO
038	100	9000	100	0	300	2	14	35	012 - HOAP
039	100	9000	90	10	300	2	14	36	011 - MGO
040	100	9000	60	40	180	2	14	37	013 - HOAP
041	**100**	**3000**	**100**	**0**	**300**	**2**	**14**	**38**	**012 - MGO**

2.1.2 Porosity and Permeability of Baseline and Additive Cements

Tables 2 and **3** present porosity and permeability of baseline and additive (MGO) samples, respectively. Porosity of baseline and additive samples did not show significant variation after aging (**Fig. 1a**) due to the absence of carbon dioxide, which reacts normally with calcium hydroxide (CH) and calcium silicate hydrates (CSH) to form insoluble calcium carbonate in the pore resulting in porosity reduction. Both aged and unaged baseline HS samples exhibited abnormally high porosity and permeability, which are also inconsistent with each other. The unusual high porosity and permeability can be associated with introduction of air during sample preparation.

Table 2: Porosity and permeability of baseline samples (Batch 41)

Core #	Core Type	Core dimensions			Porosity and Permeability Measurements					
		Dia. mm)	L (mm)	W (g)	ϕ (%)	Ave. ϕ (%)	Std. Dev. (%)	K (mD)	Ave. K (mD)	Std. Dev. (mD)
041 GS 00 01	Unaged	25.3	31.8	25.5	30.7	31.09	0.49	0.088	0.085	0.005
041 GS 00 02		25.3	29.9	23.9	31.4			0.081		
041 GS 05 01	Aged	25.2	25.9	24.7	37.8	34.57	4.58	0.066	0.073	0.009
041 GS 05 02		25.3	32.8	26.2	31.3			0.079		
041 HS 00 01	Unaged	25.3	29.5	22.0	38.1	38.34	0.34	0.521	0.645	0.175
041 HS 00 04		25.3	28.0	20.7	38.6			0.768		
041 HS 04 01	Aged	25.3	31.1	23.2	37.6	38.13	0.69	0.431	0.491	0.085
041 HS 04 02		25.2	33.7	24.8	38.6			0.551		

Table 3: Porosity and permeability of additives (MGO) samples (Batch MGO-12/41)

Core #	Core Type	Core dimensions			Porosity and Permeability Measurements					
		Dia. mm)	L (mm)	W (g)	ϕ (%)	Ave. ϕ (%)	Std. Dev. (%)	K (mD)	Ave. K (mD)	Std. Dev. (mD)
012 GSMG 00 01	Unaged	25.3	31.8	25.5	29.1	32.13	4.35	0.047	0.038	0.013
012 GSMG 00 02		25.3	29.9	23.9	35.2			0.029		
012 GSMG 10 01	Aged	25.3	30.0	30.3	35.6	33.51	2.90	0.023	0.024	0.001
012 GSMG 10 02		25.3	35.0	31.1	31.5			0.025		
012 HSMG 00 01	Aged	25.3	36.0	31.5	28.2	28.40	0.32	0.036	0.040	0.005
012 HSMG 00 02		25.3	35.8	31.3	28.6			0.043		
012 HSMG 09 01	Unaged	25.3	37.3	32.4	28.6	29.02	0.58	0.049	0.054	0.006
012 HSMG 09 02		25.3	39.1	33.5	29.4			0.058		

Often damaging effect of H_2S on cement is attributed to the formation secondary ettringite in the pore space. All the samples showed reduction in permeability, which is most likely related to the formation of ettringite that fills the pore space. However, as indicated by the porosity measurements, the formation of ettringite was limited; and hence, it is not expected to cause major expansion and/or formation of microcracks that can influence permeability of the cement. Formation of excessive amount of ettringite in the pore affects cement performance such as sealing ability.

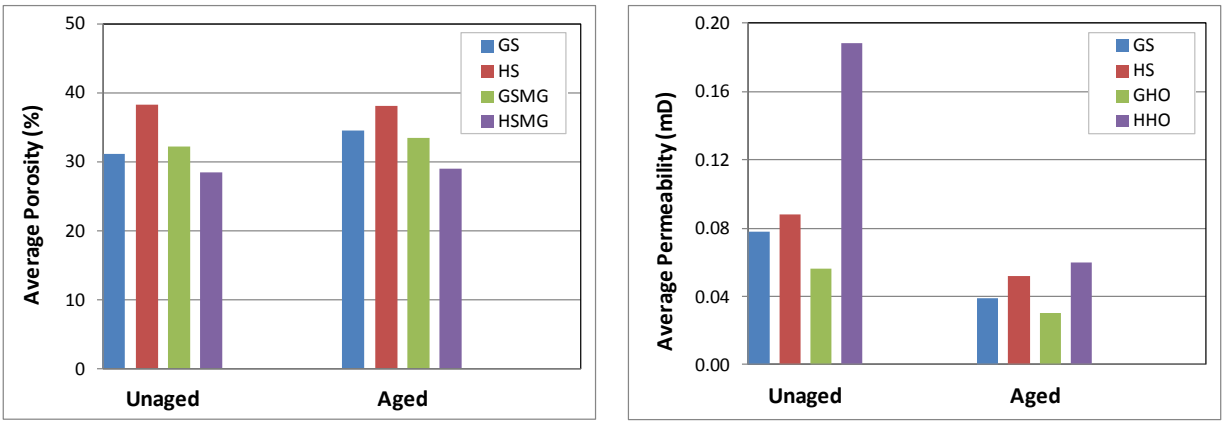

Fig. 1: Porosity and permeability of unaged and aged baseline and additive samples (aging condition 100°F, 3000 psi and 300 ppm H_2S)

2.1.3 Shear Bond Strength of Baseline and Additive Cements

The formation of ettringite not only effects the porosity and permeability of cement but also other properties such as shear bond strength (SBS). Samples for bond strength experiment were prepared for Class H based cements (baseline and additive) and tested. Results demonstrated the effect of MGO addition on cement bond strengths. SBSs of additive samples (both aged and unaged) were lower than those of the baseline samples (**Fig. 2**). After aging, SBS of the samples slightly reduced. The formation of limited amount of ettringite was not sufficient to cause SBS improvement. Due to expansive nature of ettringite, SBS improvement is expected when substantial amount of ettringite is formed in the cement. Moreover, the presence of other reactive substances such as carbonic acid synergizes expansion and cracking resulting from ettringite formation. When cement reacts with carbonic acid, calcium carbonate is formed in the pore, resulting in pore volume reduction. This condition limits the pore space and results in expansive tendency that can improve SBS. However, severe expansion induces stresses that can create micro cracks in cement, which increase the permeability of the cement without altering its porosity. **Tables 4** and **5** present a summary of SBS measurements of baseline and MGO samples.

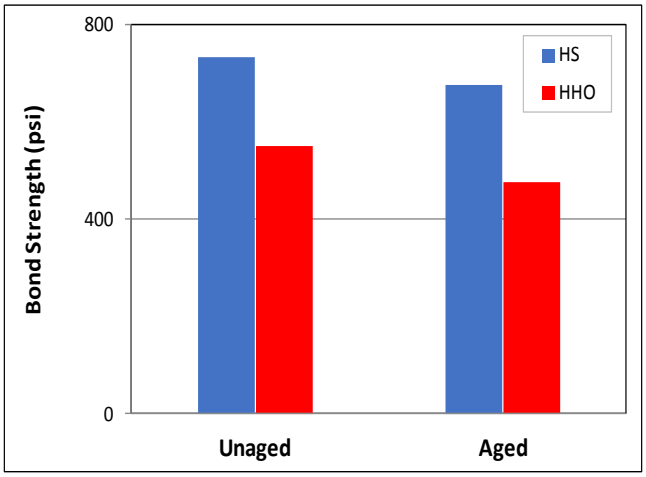

Fig. 2: Bond strength of baseline and additive samples

Table 4: Shear bond strength of baseline samples

Batch	Core #	Temp. (F)	Pressure (psi)	CH4 (%)	CO2 (%)	H2S (%)	Brine (%)	Days Aged	SBS (psi)	Ave. SBS	Stdev
041	041-HS-00-01	Ambient	Atmospheric	0	0	0	2	0	828	732.3	72
	041-HS-00-02	Ambient	Atmospheric	0	0	0	2	0	700		
	041-HS-00-03	Ambient	Atmospheric	0	0	0	2	0	642		
	041-HS-00-04	Ambient	Atmospheric	0	0	0	2	0	713		
	041-HS-00-05	Ambient	Atmospheric	0	0	0	2	0	779		
	041-HS-08-01	100	3000	100	0	300 ppm	2	14	632	675.1	81
	041-HS-08-02	100	3000	100	0	300 ppm	2	14	578		
	041-HS-08-03	100	3000	100	0	300 ppm	2	14	797		
	041-HS-08-04	100	3000	100	0	300 ppm	2	14	677		
	041-HS-08-05	100	3000	100	0	300 ppm	2	14	692		

Table 5: Shear bond strength of additive (MGO) samples

Batch	Core #	Temp. (F)	Pressure (psi)	CH4 (%)	CO2 (%)	H2S (%)	Brine (%)	Days Aged	SBS (psi)	Ave. SBS	Stdev
MGO-012/041	012-HSMG-11-01	Ambient	Atmospheric	0	0	0	2	0	655	550	79
	012-HSMG-11-02	Ambient	Atmospheric	0	0	0	2	0	520		
	012-HSMG-11-03	Ambient	Atmospheric	0	0	0	2	0	451		
	012-HSMG-11-04	Ambient	Atmospheric	0	0	0	2	0	522		
	012-HSMG-11-05	Ambient	Atmospheric	0	0	0	2	0	602		
	012-HSMG-11-01	100	3000	100	0	300 ppm	2	14	447	475	83
	012-HSMG-11-02	100	3000	100	0	300 ppm	2	14	381		
	012-HSMG-11-03	100	3000	100	0	300 ppm	2	14	605		
	012-HSMG-11-04	100	3000	100	0	300 ppm	2	14	493		
	012-HSMG-11-05	100	3000	100	0	300 ppm	2	14	451		

2.1.4 Compressive Strength of Baseline and Additive Cements

Compressive strength of Class G based cements (baseline and GSMG) increased after aging possibly due to ettringite formation (**Fig. 3**). However, for Class H based cements (baseline and HSMG) it decreased indicating the presence of other physiochemical phenomena beside ettringite formation. The formation of ettringite improves compressive strength while leaching results in reduction of strength. Class H based cements were more susceptible to leaching than Class G based cements because they exhibited higher permeability than Class G based cements. Formation and precipitation of ettringite create structural support in the pore, which tends to improve compressive strengths of the cement. However, in some cases, the improvement in strength can be offset by a structural degradation of the cement matrix resulting from the reaction between binding components of cement and hydrosulfuric acid. Moreover, the occurrence of leaching has a negative impact on strength development as it dissolves the precipitated ettringite and extracts the binding components of cement from the matrix. **Tables 6** and **7** present compressive strengths of baseline and MGO cements, respectively.

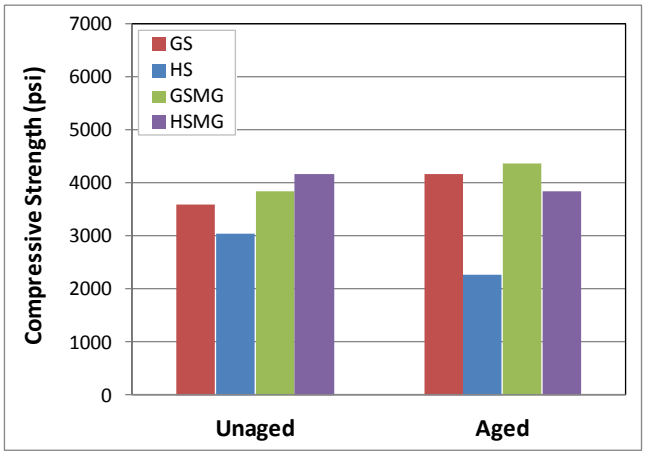

Fig. 3: Compressive strengths of baseline and MGO samples (aged at 3000 psi, 100% CH_4 and 300 ppm H_2S)

Improvement in compressive strength was observed with the addition of magnesium oxide. MGO samples retained their improved strength even after aging.

Table 6: Compressive strength of baseline samples (Batch 41)

Compressive Strength Data for Batch 41 Samples					
Unaged Samples					
Core #	**Temperature (°F)**	**Pressure (psi)**	**Experimental Stress (psi)**	**Average Stress**	**Standard Deviation**
041-GS-00-03	Ambient	Atmospheric	3976	3594	658
041-GS-00-04	Ambient	Atmospheric	3971		
041-GS-00-05	Ambient	Atmospheric	2834		
041-HS-00-03	Ambient	Atmospheric	2175	3041	1598
041-HS-00-04	Ambient	Atmospheric	4885		
041-HS-00-05	Ambient	Atmospheric	2063		
Aged Samples					
Core #	**Temperature (°F)**	**Pressure (psi)**	**Experimental Stress (psi)**	**Average Stress**	**Standard Deviation**
041-GS-05-03	100	3000	4863	4158	523
041-GS-05-04	100	3000	4777		
041-GS-05-05	100	3000	3687		
041-GS-07-03	100	3000	3998		
041-GS-07-04	100	3000	3797		
041-GS-07-05	100	3000	3828		
041-HS-04-03	100	3000	1553	2256	477
041-HS-04-04	100	3000	2802		
041-HS-04-05	100	3000	2503		
041-HS-06-03	100	3000	1886		
041-HS-06-04	100	3000	2166		
041-HS-06-05	100	3000	2627		

Table 7: Compressive strength of additive (MGO) samples (Batch MGO-12/41)

Compressive Strength Data for Batch MGO-012/41 Samples					
Unaged Samples					
Core #	**Temperature (°F)**	**Pressure (psi)**	**Experimental Stress (psi)**	**Average Stress**	**Standard Deviation**
012-GSMG-00-03	Ambient	Atmospheric	3283	3834	480
012-GSMG-00-04	Ambient	Atmospheric	4061		
012-GSMG-00-05	Ambient	Atmospheric	4158		
012-HSMG-00-03	Ambient	Atmospheric	4896	4172	628
012-HSMG-00-04	Ambient	Atmospheric	3838		
012-HSMG-00-05	Ambient	Atmospheric	3782		
Aged Samples					
Core #	**Temperature (°F)**	**Pressure (psi)**	**Experimental Stress (psi)**	**Average Stress**	**Standard Deviation**
012-GSMG-10-03	100	3000	3544	4367	721
012-GSMG-10-04	100	3000	4672		
012-GSMG-10-05	100	3000	4885		
012-HSMG-09-03	100	3000	3937	3830	171
012-HSMG-09-04	100	3000	3633		
012-HSMG-09-05	100	3000	3922		

2.2 Experimental Studies on Corrosion of Tubulars (Task 3)

2.2.1 Sulfide Stress Cracking

Experimental study on sulfide stress cracking (SSC) behavior of API carbon steels (Grades T95, C110 and Q125) is in progress. During this reporting period, four SSC experiments were conducted. **Table 8** summarizes the SSC tests completed to date. It shows the experimental conditions in which specimens were exposed. Internal and external pressures of specimen were maintained at 4000 and 6000 psi, respectively. Carbon dioxide concentration was varied from 0 to 15%. Minipipes 12 and 15 are baseline specimens, which were not corroded. Mechanical properties of the specimens were tested to establish baselines.

Table 8: Specimen corrosion testing conditions

No.	Label	Temp. (°F)	Pressure (psi)		Gas Composition			Time Duration	Remarks
			Inside	Outside	H2S (ppm)	CH4 (%)	CO2 (%)	(Days)	
1	01-C110-07/25-08/06	100	6000	4000	0	100	0	15	
2	02-C110-08/25-08/25	-	-	-	-	-	-	-	Baseline for C110
3	03-C110-08/27-09/03	100	6000	4000	270	90	10	7	Sample failed after 7 days of exposure
4	04-C110-09/05-09/12	100	6000	4000	300	100	0	7	
5	05-C110-09/05-09/13	100	6000	4000	285	95	5	7	
6	06-C110-09/05-09/14	100	6000	4000	270	90	10	7	Brine completely leaked from the cell
7	07-C110-10/17-10/24	100	6000	4000	255	85	15	7	
8	08-C110-10/28-11/04	100	6000	4000	270	90	10	7	
9	09-C110-11/05-11/12	100	6000	4000	293	97.5	2.5	7	
10	10-C110-11/13-11/20	100	6000	4000	270	90	10	7	Sample failed after 7 days of exposure
11	**11-C110-12/02-12/09**	**100**	**6000**	**4000**	**255**	**85**	**15**	**7**	
12	**12-Q125-11/24-11/24**	**-**	**-**	**-**	**-**	**-**	**-**	**-**	**Baseline for Q125**
13	**13- Q125-11/24-12/01**	**100**	**6000**	**4000**	**270**	**90**	**10**	**7**	
14	**14- Q125-12/10-12/17**	**100**	**6000**	**4000**	**0**	**100**	**0**	**7**	
15	**15- T95-12/10-12/10**	**-**	**-**	**-**	**-**	**-**	**-**	**-**	**Baseline for T95**
16	**16- Q125-12/17-12/24**	**100**	**6000**	**4000**	**300**	**100**	**0**	**7**	

Specimen 13 was strained to failure after exposure to sour environment. The specimen showed lower ultimate tensile strength (UTS) and plastic strain to failure (PSF) than those of the baseline

(Specimen 12) and specimens, which were not exposed to highly corrosive brine-H_2S-CO_2 fluid system (**Table 9**).

Table 9: Mechanical properties of samples before and after corrosion test

Minipipe No.	Before Exposure				After Exposure			
	YS (psi)	UTS (psi)	PSF	E (psi)	YS (psi)	UTS (psi)	PSF	E* (psi)
1	-	-	-	-	109,855	127,619	0.030	11,785,921
2	111,529	130,156	0.040	11,842,002	-	-	-	-
3	-	-	-	11,704,810	-	100799	0.000	-
4	-	-	-	12,594,080	112768	134981	0.043	12,078,823
5	-	-	-	10,911,219	102217	114424	0.023	11,368,960
6	-	-	-	11,599,401	110686	130118	0.049	11,444,081
7	-	-	-	11,221,136	-	115479	0.014	11,561,000
8	-	-	-	12,044,218	-	120026	0.069	11,441,529
9				11,792,032		116742	0.036	11,255,892
10	-	-	-	13,377,764	-	100799	0.000	-
11	**-**	**-**	**-**	**13,377,764**		**118484**	**0.035**	**13,527,372**
12	**150,072**	**169,282**	**0.051**	**13,580,537**	**-**	**-**	**-**	**-**
13	**-**	**-**	**-**	**13,594,795**	**132,903**	**152,493**	**0.028**	**11,757,738**
14	**-**	**-**	**-**	**13,890,878**	**144,533**	**165,460**	**0.080**	**7,321,033**
15	**95,399**	**121,115**	**0.058**	**12,125,404**	**-**	**-**	**-**	**-**
16	**-**	**-**	**-**	**10,613,970**	**144,528**	**164,641**	**0.084**	**10,642,228**

UTS = Ultimate tensile strength, PSF = Plastic strain to failure, YS = Yield strength, E = Young's modulus before exposure, E* = Young's modulus after exposure

2.2.2 Uniform Corrosion in Sour Gas Environment

During this reporting period, low-pressure and high-pressure uniform corrosion experiments were performed to assess corrosion behaviors of carbon steels in CO_2 environment.

2.2.2.1 Low-Pressure Experiments

Low-pressure corrosion study was continued. Corrosion rate of common carbon steel was measured under different experimental conditions. To examine the effects of CO_2 and salt concentrations on corrosion rate, three tests were performed at a constant pressure of 120 psi. Test parameters and results of the experiments are presented in **Table 10** along with previous measurements.

Table 10: Test parameters and results of low-pressure corrosion experiments conducted to date

Exp. #	Temp. (ºF)	Pressure (psi)	Partial Pressure %		Brine Conc. (%)	Test Period (days)	Results (mpy)	
			N_2	CO_2			LPR	WL
15	78	120	25	75	2	187	40.30	31.91
16	78	120	0	100	2	187	39.18	32.18
17	78	240	0	100	2	187	N/A	N/A
18	78	120	75	25	2	187	22.92	21.83
19	110	120	75	25	2	187	31.78	23.78
20	110	120	25	75	2	187	53.16	43.22
21	110	120	100	0	2	187	12.37	15.40
22	110	120	75	25	2	187	31.07	23.78
23	110	120	50	50	2	187	70.35	43.39
24	110	120	25	75	2	187	53.16	43.22

Exp. #	Temp. (ºF)	Pressure (psi)	Partial Pressure %		Brine Conc. (%)	Test Period (days)	Results (mpy)	
			N_2	CO_2			LPR	WL
25	110	120	0	100	2	187	44.92	32.49
26	176	120	100	0	2	187	4.04	3.10
27	176	120	75	25	2	187	16.53	11.77
28	176	120	50	50	2	187	24.23	12.71
29	176	120	25	75	2	187	17.39	10.87
30	176	120	0	100	2	187	22.56	12.04
31	140	120	100	0	2	187	2.58	2.72
32	140	120	75	25	2	187	11.00	6.33
33	140	120	50	50	2	187	13.33	14.30
34	140	120	25	75	2	187	38.48	26.76
35	140	120	0	100	2	187	24.40	24.23
36	140	120	100	0	1	187	3.69	1.23
37	140	120	75	25	1	187	5.16	20.97
38	140	120	75	25	1	187	9.86	25.13
39	140	120	50	50	1	187	6.40	21.24
40	140	120	25	75	1	187	6.50	23.78
41	140	120	0	100	1	187	4.31	14.77
42	176	120	0	100	1	187	1.76	4.63
43	176	120	25	75	1	187	2.79	9.00
44	176	120	50	50	1	187	4.95	12.59
45	176	120	75	25	1	187	17.79	36.98
46	176	120	100	0	1	187	0.69	2.60
47	176	120	75	25	1	187	5.79	14.90
48	110	120	25	75	1	187	8.55	33.23
49	110	120	0	100	1	187	6.21	30.81
50	**110**	**120**	**50**	**50**	**1**	**187**	**22.23**	**46.88**
51	**110**	**120**	**100**	**0**	**1**	**187**	**6.57**	**6.51**
52	**110**	**120**	**75**	**25**	**1**	**187**	**78.62**	**101.78**

Comparison of the corrosion rate measurements obtained from electrochemical (LPR) and weight loss (WL) methods (**Fig. 4**) at different CO_2 concentration and temperature showed significant variation. Even though discrepancies exist between these two methods of measurements, the trend of corrosion rate obtained from the methods is very similar. As previously reported, the difference between LPR and WL measurements is attributed to calibration challenge with LPR instrument, as salt concentration was reduced 2% to 1%. When salt concentration was 2%, LPR instrument reference voltage of 30 mV (B = 30 mV) was used for determining the corrosion rate from the electrochemical measurements. This reference value was obtained after performing calibration tests using the two-point method. During this month, similar tests were conducted at salt concentration of 1% and a new B value of 120 mV was obtained. After calibration, both techniques showed comparable corrosion rate measurements presented in **Table 10** (Exps. 51 and 52).

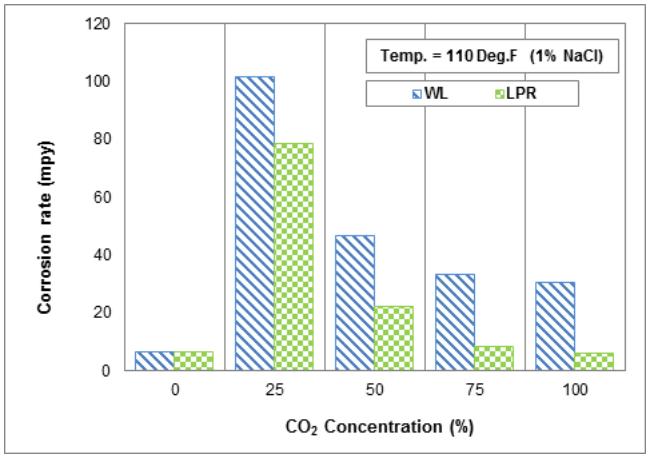

Fig. 4: Comparison of corrosion rate measurements at different CO_2 concentrations

Temperature is one of the key factors that influences the corrosion rate of carbon steel. **Figure 5** compares the corrosion rates obtained from weight-loss technique at three different temperatures and various CO_2 concentrations. As depicted from the figure, in the presence of CO_2, the corrosion rate decreases with temperature regardless of CO_2 concentration. This finding is consistent with results of a previous study (Seiersten, 2001). In the absence of CO_2, the corrosion rate was remarkably low and the trend was varying with temperature. The minimum corrosion rate was observed at 140°F.

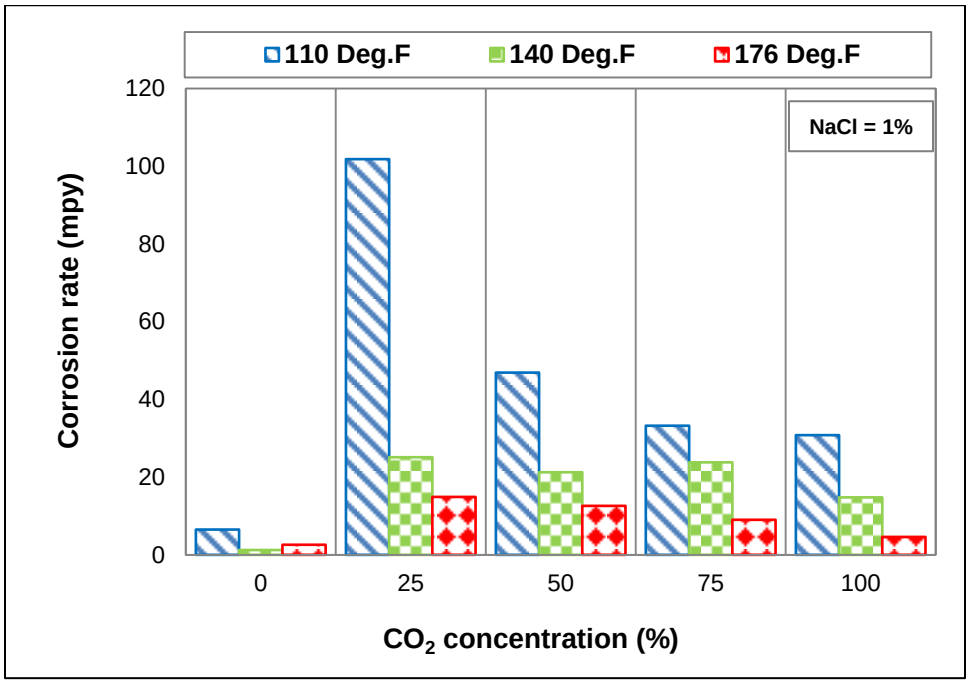

Fig. 5: Comparison of corrosion rate measurements at different CO_2 concentrations

Figure 6 demonstrates the effect of NaCl concentration on corrosion rate at various CO_2 concentrations. At low and high CO_2 concentrations (less 25% and greater than 75%), increase in salt concentration from 1 to 2% increased corrosion rate. In the intermediate concentration range (25 to 75%), reduction in the corrosion rate was observed with increase in salt concentration. This observation is consistent with results of a previous study (Fang, 2006), which has reported retardation of corrosion related reaction processes (heterogeneous charge

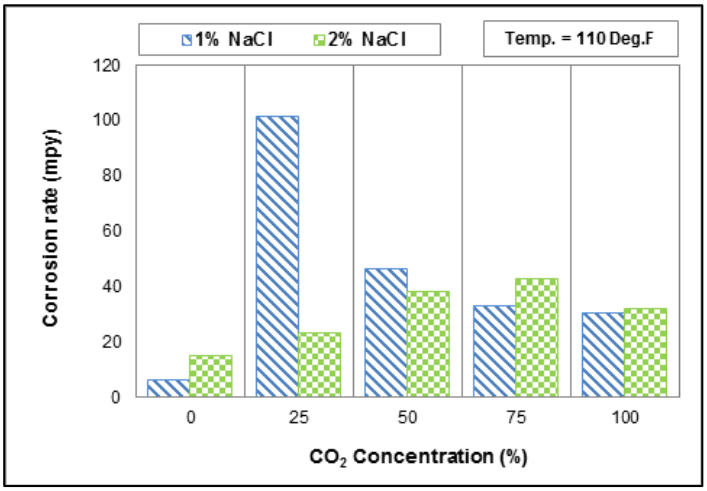

Fig. 6: Effect of salt concentration on corrosion rate at various CO_2 concentrations (120 psi, 110°F)

transfer reactions and homogenous chemical reactions) and reduction of mass transfer rate with increasing salt concentration. The effect of salt concentration on corrosion rate was minimal at high CO_2 concentration (greater than 50%).

2.2.2.2 High-Pressure Experiments

During this reporting period, four high-pressure corrosion experiments (highlighted in **Table 11**) were conducted varying pressure (3000, 6000 and 9000 psi) and CO_2 concentrations. Two different grades of carbon steels (Grades C110 and Q125) were tested. Test temperature and NaCl concentration were maintained at 100°F and 2% NaCl, respectively. Two coupons were used for each batch of experiment in order to obtain average corrosion rate and mechanical property measurements. Test parameters for different batch of experiments are presented in Table 11. Batches 12 and 13 were performed at 3000 psi and CO_2 concentrations of 75 and 100% using C110 specimens in order to examine the impact of CO_2 on the corrosion rate under these conditions. According to our previous corrosion experiments, highly corrosive test conditions at 100°F were found to be in intermediate CO_2 concentration range (approximately 50%) and high pressures (6000 and 9000 psi). Therefore, to compare corrosion resistance of different steel grades under extreme corrosion conditions, tests were performed at 50% CO_2 concentration and pressure of 6000 and 9000 psi.

Table 11: Test conditions for HPHT uniform corrosion tests

Batch No.	Material	Pressure (psi)	Temp. (°F)	Duration (Days)	CO_2 Conc. (%)	CH_4 Conc. (%)	H_2S Conc. (ppm)
001	C110	6000	100	7	100	0	0
002	C110	6000	100	7	50	50	0
003	C110	6000	100	7	0	100	0
004	C110	6000	100	7	25	75	0
005	C110	6000	100	7	75	25	0
006	C110	9000	100	7	100	0	0
007	C110	3000	100	7	0	100	0
008	C110	9000	100	7	75	25	0
009	C110	9000	100	7	50	50	0
010	C110	9000	100	7	25	75	0
011	C110	9000	100	7	0	100	0
012	**C110**	**3000**	**100**	**7**	**75**	**25**	**0**
013	**C110**	**3000**	**100**	**7**	**100**	**0**	**0**
014	**Q125**	**6000**	**100**	**7**	**50**	**50**	**0**
015	**Q125**	**9000**	**100**	**7**	**50**	**50**	**0**

Figure 7 presents corrosion rate of C110 alloy as a function of CO_2 concentration at 3000 psi. The corrosion rate increased with the CO_2 concentration due to increase in carbonic acid concentration (H_2CO_3) in the brine. As the partial pressure of CO_2 increases, the acid concentration also increases, accelerating the cathodic reactions and therefore increasing the corrosion rate. This corrosion rate trend is consistent with previous measurements available in the literature (Choi et al., 2014; Huang et al., 2014; Schmitt and Horstemeier, 2006). However, the corrosion rate trend at 3000 psi was found to be different from our previous observations at 6000 and 9000 psi, in which the corrosion rate increased at low and intermediate CO_2 concentrations and decreased as the concentration approached 100%.

In order to evaluate corrosion resistance of different steel grades, which are used in the oil field, corrosion rates of C110 and Q125 measured under harsh downhole conditions (HPHT) are compared in **Fig. 8**. Under these conditions, Q125 grade showed better corrosion resistance than C110 grade. Pressure effects are minimal. Corrosion rates of studied materials slightly decreased when the pressure was increased from 6000 to 9000 psi.

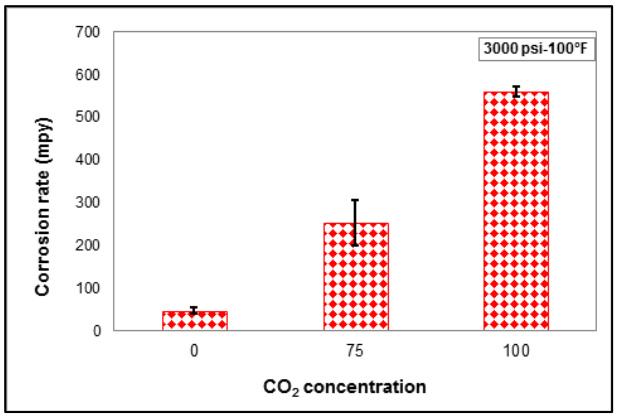

Fig. 7: Corrosion rate of C110 as a function CO_2 concentration (3000 psi and 100°F)

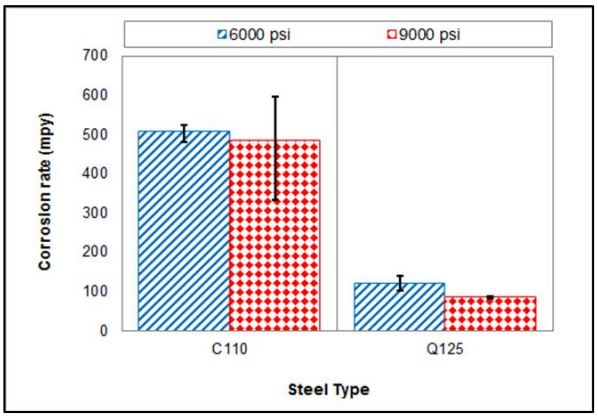

Fig. 8: Corrosion rates of C110 and Q125 measured under harsh downhole conditions (50% CO_2 and 100°F)

Figure 9 presents the influence of pressure on the corrosion rate of C110 at 100% CO_2 and 100°F. The highest corrosion rate was recorded at 3000 psi. In addition to electrochemical reaction and ionic diffusion and the transport, the formation of protective scale on the surface of a metal determines the corrosion rate. When tested at low-pressure (3000 psi), only loose protective corrosion scale was formed on the specimen surface whereas at 6000 psi, more compact and dense scale was formed resulting in the lowest corrosion rate.

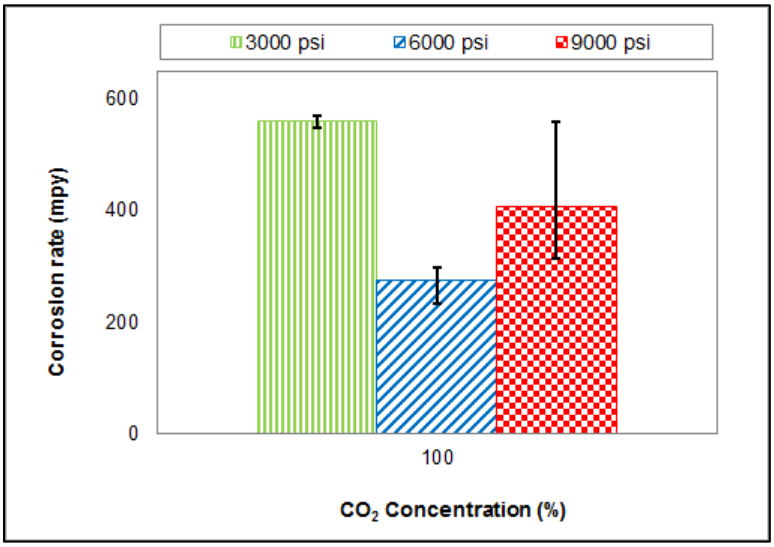

Fig. 9: Corrosion rate of C110 at different pressures (100% CO_2 and 100°F)

In addition to the corrosion rate, mechanical properties of the specimens were measured before and after exposure to the corrosive environment. Results (**Table 12**) show the occurrence of significant corrosion after the exposure. Results of new experiments are highlighted in Table 12. Mechanical property measurements before and after exposure vary due to changes in specimen characteristics resulting from localized corrosion and reduction in specimen thickness.

Table 12: Corrosion rate and mechanical properties of C110 specimens before and after corrosion test

Batch No.	Specimen No.	CO_2 Con.%	Initial weight gm	Final weight gm	CR (mpy)	E (psi)	E* (psi)	Yield strength (psi)	Tensile Strength (psi)
001	C110-1	100	13.3848	13.2129	234	5.79E+06	9.91E+06	107,560	123,600
	C110-2		13.4397	13.2212	297	6.02E+06	8.62E+06	105,950	119,933
	C110-3		13.4478	13.2323	293	7.71E+06	9.44E+06	108,140	120,673
002	C110-1	50	13.4875	13.1076	517	1.07E+07	8.57E+06	104,960	117,283
	C110-2		13.3884	13.0029	524	5.10E+06	9.01E+06	97,180	116,388
	C110-3		13.3376	12.9835	482	5.54E+06	8.25E+06	95,140	116,198
003	C110-1	0	13.4459	13.3916	74	1.00E+07	7.76E+06	93,250	130,891
	C110-2		13.4196	13.3924	37	1.15E+07	8.43E+06	96,780	131,917
	C110-3		13.3234	13.2680	75	1.07E+07	8.25E+06	96,940	129,187
004	C110-1	25	13.3739	12.949	578	8.75E+06	8.13E+06	91,000	113,833
	C110-2		13.3092	12.9818	445	8.48E+06	6.99E+06	95,510	116,450
	C110-3		13.4018	13.0782	440	8.15E+06	8.44E+06	94,880	117,009
005	C110-1	75	13.4127	13.1079	415	8.71E+06	8.09E+06	103,240	111,286
	C110-2		13.4881	13.2212	363	1.10E+07	6.52E+06	101,290	112,891
	C110-3		13.4635	12.9808	657	8.43E+06	6.01E+06	101,000	111,062
006	C110-1	100	13.4039	13.1518	343	1.14E+07	8.43E+06	100,000	116,283
	C110-2		13.3703	12.9598	558	1.08E+07	8.57E+06	96,410	113,007
	C110-3		13.4606	13.2294	315	1.10E+07	6.36E+06	95,570	117,066
007	C110-1	0	13.4169	13.3859	42	9.98E+06	6.96E+06	100,920	130,212
	C110-2		13.4447	13.4144	41	9.29E+06	6.94E+06	100,530	130,658
	C110-3		13.4041	13.3635	55	9.47E+06	7.05E+06	101,170	128,982
008	C110-1	75	13.3681	12.9327	592	7.74E+06	8.37E+06	97,530	110,554
	C110-2		13.4538	13.0456	555	7.97E+06	8.67E+06	99,660	110,922
	C110-3		13.3742	12.9952	516	8.44E+06	9.24E+06	100,480	112,723
009	C110-1	50	13.4238	12.9867	595	1.14E+07	8.15E+06	97,480	111,270
	C110-2		13.2956	13.0504	334	8.45E+06	8.55E+06	98,740	118,488
	C110-3		13.4920	13.1036	528	8.47E+06	8.35E+06	102,700	113,291
010	C110-1	25	13.3937	13.092	410	9.30E+06	8.33E+06	99,250	119,451
	C110-2		13.3812	12.9699	559	1.23E+07	7.15E+06	101,270	114,472
	C110-3		13.3518	12.9320	571	1.25E+07	7.36E+06	100,120	112,456
011	C110-1	0	13.4399	13.4033	50	8.81E+06	5.89E+06	107,870	129,910
	C110-2		13.3882	13.3497	52	9.25E+06	7.43E+06	110,000	128,725
	C110-3		13.4730	13.4332	54	1.10E+07	8.06E+06	106,890	127,023
012	**C110-1**	**100**	**13.3637**	**12.9442**	**571**	**1.20E+07**	**7.52E+06**	**99,760**	**110,045**
	C110-2		**13.3376**	**12.9346**	**548**	**1.19E+07**	**5.62E+06**	**100,570**	**111,029**
013	**C110-1**	**75**	**13.3668**	**13.2191**	**201**	**1.10E+07**	**6.20E+06**	**101,540**	**121,867**
	C110-2		**13.3789**	**13.1548**	**305**	**1.01E+07**	**6.31E+06**	**101,200**	**120,463**
014	**Q125 -1**	**50**	**13.2108**	**13.1086**	**139**	**1.07E+07**	**8.20E+06**	**117,600**	**155,273**
	Q125-2		**12.9513**	**12.8756**	**103**	**9.03E+06**	**7.88E+06**	**116,830**	**151,903**

Batch No.	Specimen No.	CO_2 Con.%	Initial weight gm	Final weight gm	CR (mpy)	E (psi)	E* (psi)	Yield strength (psi)	Tensile Strength (psi)
015	Q125-1	50	13.0443	12.9842	82	1.18E+07	8.28E+06	117,070	151,036
	Q125-2		13.2890	13.2249	87	9.03E+06	9.19E+06	120,140	157,005

E and E* are Young's modulus measured before and after corrosion test, respectively.

3. Planned Activities

- Continue experimental studies on tubular degradation under low-pressure and moderate-temperature conditions.
- Continue HPHT corrosion experiments with minipipes and flat coupons.

4. Project Expenditures

This section presents the project expenses during the month of December (**Table 13**) and the cumulative expenditure.

Table 13: Current and cumulative expenditures, December 2014

No.	Budget Categories	Current Expenses	Cumulative Expenses
1	Salaries & Wages	$570.71	$358,136.28
2	Fringe Benefits	($11.71)	$80,045.76
3	Project Materials	$105.00	$106,393.19
4	Travel	$0.00	$10,719.04
5	Conference Expenses	$0.00	$0.00
6	Other Direct Costs	$54.53	$1,433.39
7	Equipment	$626.51	$252,045.41
8	Space Rental	$0.00	$0.00
9	Indirect Cost	$359.27	$277,328.96
10	**Total**	**$1,704.31**	**$1,086,102.03**

Nomenclature

A	Exposed surface area, cm^2
API	American Petroleum Institute
ASTM	American Society for Testing and Materials
CR	Average corrosion rate, mpy
E	Young's modulus measured before corrosion test
E*	Young's modulus measured after corrosion test
GHO	Class G Cement with hydroxyapatite
GS	Class G cement with silica flour
GSMG	Class G Cement with silica flour and magnesium oxide
HHO	Class H Cement with hydroxyapatite
HOAP	Acid-resistant hydroxyapatite-based cement
HPHT	High-pressure high-temperature

HS	Class H cement with silica flour
HSMG	Class H cement with silica flour and magnesium oxide
K	Permeability of cement cores
LPR	Linear polarization resistance
mpy	mils per year
MGO	Magnesium oxide containing cement
MYS	maximum yield strength
NACE	National Association of Corrosion Engineers
PSF	Plastic strain to failure,
SBS	Shear bond strength
SCC	Stress corrosion cracking
SSC	Sulfide stress cracking
t	Test duration, hr
UTS	Ultimate tensile strength
w_1	Initial specimen weight
w_2	Final specimen weight
YS	Yield strength

Greek Symbols

ϕ	Porosity of cement cores

References

Choi, Y.S., Farelas, F., Nesic S., Magalhães, A. A. O., and Andrade C. D. 2014. Corrosion Behavior of Deep Water Oil Production Tubing Material under Supercritical CO_2 Environment: Part I. Effect of Pressure and Temperature, paper No. 2380, NACE International, 17-21 March, Orlando, Florida.

Fang, H. 2006. Low Temperature and High Salt Concentration Effects on General CO_2 Corrosion for Carbon Steel, thesis, November, Ohio University.

Huang, J., Guraieb, P., Yan, C., Contreras, E., Tomson, M. B., and Tomson, R. 2014. Corrosion Testing of Deepwater Tubing Materials under Extreme Pressure and Temperature Conditions, SPE paper OTC-25193-MS, 05-08 May, Houston, Texas.

Seiersten, M. 2001. Material Selection for Separation, Transportation and Disposal of CO_2, paper no. 01042, NACE International, 11-16 March, Houston, Texas.

Schmitt, G. and Horstemeier, M. 2006. Fundamental Aspects of CO_2 Metal Loss Corrosion - Part II: Influence of Different Parameters on CO_2 Corrosion Mechanisms, paper No.06112, NACE International, 12-16 March, San Diego, California.

Appendices

Deliverables of Cement Degradation Studies

EXECUTIVE SUMMARY

This document presents deliverables associated with cement degradation studies including: i) Predictive performance model for cement based on resulting data (Appendices A, D, E and F); ii) Detailed analysis of resulting experimental acid resistance of cement formulations (Appendix B); iii) Experimental results showing acid resistance of new cement formulations (Appendix B); and iv) Electronic Experimental Database (Appendix C).

Appendices A, D, E and F present cement degradation model that predicts degree of hydration, cement porosity, degradation depth and compressive strength. The major challenge in modeling cement degradation is the involvement of different natural phenomena such as hydration, carbonation and leaching, which affect key cement properties such as porosity, permeability and strength. As the cement properties (such as porosity and permeability) are continuously changing with time, the degradation process intensifies through further penetration of the aggressive fluid into the undamaged zone of the cement. As a result, cement degradation modeling is highly complex and involves a number of simplifying assumptions. The model developed in this project is based on the following assumptions: i) Hydration, carbonation and leaching are major cement degradation mechanisms; ii) Bulk fluid is under static condition; iii) Degradation process is governed by chemical reaction and mass transfer (diffusion in porous cement); and iv) Calcium leaching is solely responsible for the loss of cement mechanical integrity.

Appendix B presents two project deliverables: i) Detailed analysis of resulting experimental acid resistance of cement formulations; and ii) Experimental results showing acid resistance of new cement formulations. After performing extensive cement additive screening and formulation studies, two cement formulations, which are based on hydroxyapatite and magnesium oxide, have been developed for Class H and Class G cements. After aging under various conditions, porosity, permeability compressive and bond strengths of the samples were measured to evaluate acid resistance of the new formulations. In addition, the changes occurring in the mineralogical composition of the samples were investigated using Fourier Transform Infrared Spectroscopy (FTIR). The results indicated that Class H based hydroxyapatite and magnesium oxide containing cements are the most viable formulations that can withstand acid attack under High-Pressure High-Temperature (HPHT) conditions.

Appendix C shows the experimental database developed during the project. The database summarizes all useful measurements collected during cement degradation studies. It shows new additive-based cement formulations, which were considered in the investigation and their performance (i.e. in terms of change in key cement performance indicators such as porosity, permeability, shear bond and compressive strengths) under HPHT acidic environments. In addition, the database presents performance of conventional baseline (Class G and Class H) cements under simulated borehole conditions. The database is expected to serve as the foundation for the development of acid resistant cement formulations for different applications.

TABLE CONTENT

EXECUTIVE SUMMARY **2**

TABLE CONTENT **3**

LIST OF FIGURES **5**

LIST OF TABLES **8**

APPENDIX A: CEMENT DEGRADATION MODEL **9**

A.1 Overview *9*

A.2 Model Assumptions *9*

A.3 Model Formulation *9*

A.3.1 Hydration Model 10

A.3.1.1 Numerical Procedure 12

A.3.1.2 Results 14

A.3.2 Porosity Model 15

A.3.3 Degradation Model 16

A.3.4 Mechanical Strength Degradation Model 22

A.3.4.1 Ultimate Strength before Curing 22

A.3.4.2 Mechanical Strength after Curing 23

A.3.4.3 Mechanical Strength after CO_2 Aging 24

APPENDIX B: PERFORMANCE OF NEW CEMENT FORMULATIONS **27**

B.1 Detailed Analysis of Acid Resistance of New Cement Formulations *27*

B.1.1 Calcium Hydroxyapatite 27

B.1.1.1 Porosity and Permeability 28

B.1.1.2 Compressive Strength 32

B.1.1.3 Shear Bond Strength 34

B.1.1.4 FTIR Analysis 35

B.1.1.5 Summary 38

B.1.2 Magnesium Oxide 39

B.1.2.1 Porosity and Permeability 40

B.1.2.2 Compressive Strength 43

B.1.2.3 Shear Bond Strength 45

B.1.2.4 FTIR Analysis 46

B.1.2.5 Summary 48

B.2 Experimental Results Showing Acid Resistance of New Cement Formulations *49*

B.2.1 Acid Resistance of Hydroxyapatite Cement 49

B.2.1.1 Performance under Low Temperature Conditions 50

B.2.1.2 Performance under High Temperature Conditions 51

B.2.1.3 Performance Comparison using FTIR Measurements....54
B.2.2 Acid Resistance Magnesium Oxide Cement....56
B.2.2.1 Performance under Intermediate Temperature Conditions....56
B.2.2.2 Performance under High Temperature Conditions....59

APPENDIX C: EXPERIMENTAL DATABASE: PROPERTIES OF CEMENTS....63

C.1 Additive Cement....63
C.1.1 Properties of Fly Ash Based Cement (FLAS)....63
C.1.2 Properties of Hydroxyapatite Based Cement (HOAP)....68
C.1.3 Properties of Magnesium Oxide Based Cement (MGO-5)....79
C.1.4 Properties of Latex Based Cement (LT)....89
C.1.5 Properties of Latex Microsilica Based Cement (LTMS)....93
C.1.6 Properties of Microsilica Based Cement (MS-10)....97

C.2 Baseline Cements....103
C.2.1 Porosity and Permeability....103
C.2.2 Shear Bond Strength....113
C.2.3 Compressive Strength....123

APPENDIX D: SOLUBILITY MODEL....142

APPENDIX E: NUMERICAL SCHEME FOR DEGRADATION DEPTH MODEL....146

APPENDIX F: MECHANICAL STRENGTH DEGRADATION MODEL....147

NOMENCLATURES....151

REFERENCES....154

LIST OF FIGURES

Fig. A.1: Simplified block diagram of cement degradation model....10
Fig. A.2: Model prediction of degree of hydration for Class H and Class G cements....14
Fig. A.3: Model validation for degree of hydration while curing oil well cement....15
Fig. A.4: Temperature effect on degree of hydration of Class G cement....15
Fig. A.5: Pressure effect on degree of hydration of Class H cement....15
Fig. A.6: Comparison of predicted initial porosity with experimental data....16
Fig. A.7: Predicted degradation depth for Class G and Class H at T=350^{o}F, P_{CO2} = 600 psi, NaCl = 2%wt....21
Fig. A.8: Predicted degradation depth for Class H cement at T=350^{o}F, NaCl = 2%wt, P = 6000 psi....21
Fig. A.9: Effect of salt concentration on solid-phase calcium profile of Class H cement at P=6000 psi, T=350°F, CO_2 = 10%, t = 14 days....21
Fig. A.10: Comparison of solid-phase calcium profile different cement classes at P = 6000 psi, T = 350°F, CO_2 =10%, t = 14 days....21
Fig. A.11: CO_2 concentration effect on solid-phase calcium profile of Class G cement P = 6000 psi, T=350°F, NaCl = 2 wt%, t = 14 days....22
Fig. A.12: Temperature effect on solid-phase calcium profile of Class G cement P = 6000 psi, T = 350°F, ...22
NaCl = 2 wt%, t = 14 days....22
Fig. A.13: Comparison of strength predictions during curing with experimental data (Akkaya et al. 2003)....23
Fig. A.14: Comparison of after curing strength predictions with experimental data....23
Fig. A.15: Strength predictions during curing Class G and Class H cement....24
Fig. A.16: Comparison of chemical shrinkage in class G and class H during curing....24
Fig. A.17: Stress distribution in a degraded cylindrical cement sample....24
Fig. A.18: Comparison of compressive strength predictions with experimental data at different pressures for Class G cement (10% CO_2 and 350°F)....26
Fig. A.19: Comparison of compressive strength predictions with experimental data at different CO_2 concentration for Class G cement (6000 psi and 350°F)....26
Fig. B.2: Porosity of aged (orange) and unaged (blue) samples: a) HHO; and b) HS....28
Fig. B.3: Porosity of unaged and aged (in the presence of H_2S) samples: a) HHO; and b) HS....29
Fig. B.4: Permeability of aged (orange) and unaged (blue) samples: a) HHO; and b) HS....29
Fig. B.5: Permeability of unaged and aged (in the presence of H_2S) samples: a) HHO; and b) HS....30
Fig. B.6: Porosity of aged (orange) and unaged (blue) samples: a) GHO; and b) GS....30
Fig. B.7: Porosity of unaged and aged (in the presence of H_2S) samples: a) GHO; and b) GS....31
Fig. B.8: Permeability of aged (orange) and unaged (blue) samples: a) GHO; and b) GS....31
Fig. B.9: Permeability of unaged and aged (in the presence of H_2S) samples: a) GHO; and b) GS....32
Fig. B.10: Compressive strength of aged and unaged samples: a) HHO; and b) HS....33
Fig. B.11: Compressive strength of aged (orange) and unaged (blue) samples: a) GHO; and b) GS....33

Fig. B.12: Compressive strength of unaged and aged (in the presence of H_2S) samples: a) HHO; and b) HS.....33
Fig. B.13: Compressive strength of unaged and aged (in the presence of H_2S) samples: a) GHO; and b) GS 34
Fig. B.14: Shear bond strength of aged (orange) and unaged (blue) samples: a) HHO; and b) HS.....35
Fig. B.15: Shear bond strength of unaged and aged (in the presence of H_2S) samples: a) HHO; and b) HS.....35
Fig. B.16: FTIR results in inner zone of HOAP and baseline HS samples aged at different conditions: a) Exp. 9; b) Exp. 12; c) Exp. 13; d) Exp. 15; e) Exp. 19; f) Exp. 23; and g) Exp. 29.....36
Fig. B.17: FTIR results (middle zone) of HOAP and baseline HS samples aged at different conditions: a) Exp. 9; b) Exp. 12; c) Exp. 13; d) Exp. 15; e) Exp. 19; f) Exp. 23; and g) Exp. 29 37
Fig. B.18: FTIR results (outer zone) of HOAP and baseline HS samples aged at different conditions: a) Exp. 9; b) Exp. 12; c) Exp. 13; d) Exp. 15; e) Exp. 19; f) Exp. 23; and g) Exp. 29.....38
Fig. B.20: Porosity of aged (orange) and unaged (blue) samples: a) HSMG; and b) HS.....40
Fig. B.21: Porosity of unaged and aged (in the presence of H_2S) samples: a) HSMG; and b) HS.....41
Fig. B.22: Permeability of aged (orange) and unaged (blue) samples: a) HSMG; and b) HS.....41
Fig. B.23: Permeability of unaged and aged (in the presence of H_2S) samples: a) HSMG; and b) HS.....42
Fig. B.24: Porosity of aged (orange) and unaged (blue) samples: a) GSMG; and b) GS.....42
Fig. B.25: Permeability of aged (orange) and unaged (blue) samples: a) GSMG; and b) GS 42
Fig. B.26: Porosity of unaged and aged (in the presence of H_2S) samples: a) GSMG; and b) GS.....43
Fig. B.27: Permeability of unaged and aged (in the presence of H_2S) samples: a) GSMG; and b) GS.....43
Fig. B.28: Compressive strength of aged (orange) and unaged (blue) samples: a) HSMG; and b) HS.....44
Fig. B.29: Compressive strength of unaged and aged (in the presence of H_2S) samples: a) HSMG; and b) HS.....44
Fig. B.30: Compressive strength of aged (orange) and unaged (blue) samples: a) GSMG; and b) GS.....44
Fig. B.31: Compressive strength of unaged and aged (in the presence of H_2S) samples: a) GSMG; and b) GS.....45
Fig. B.32: Shear bond strength of aged and unaged samples: a) HSMG; and b) HS 45
Fig. B.33: Shear bond strength of unaged and aged (in the presence of H_2S) samples: a) HSMG; and b) HS 46
Fig. B.34: FTIR results of inner zone of MGO-5 and baseline HS samples aged at different conditions: a) Exp. 8; b) Exp. 10; c) Exp. 7A; d) Exp. 14; e) Exp. 20; and f) Exp. 22 47
Fig. B.35: FTIR results of middle zone of MgO and baseline HS samples aged at different conditions: a) Exp. 8; b) Exp. 10; c) Exp. 7A; d) Exp. 14; e) Exp. 20; and f) Exp. 22 48
Fig. B.36: FTIR results of outer zone of MgO and baseline HS samples aged at different conditions: a) Exp. 8; b) Exp. 10; c) Exp. 7A; d) Exp. 14; e) Exp. 20; and f) Exp. 22 48
Fig. B.37: Porosity and permeability of HOAP and baseline samples (aging at 100°F, 6000 psi and 40 % CO_2).....50
Fig. B.38: Shear bond strength of baseline and HOAP samples.....51
(aging condition: 100°F, 6000 psi and 40 % CO_2).....51
Fig. B.39: Compressive strengths of baseline and HOAP cements (aging at 100°F, 6000 psi and 40 % CO_2) 51
Fig. B.40: Middle cross-section of cores after aging at 350°F with 100% CO_2 gas: a) GHO; b) HHO; c) GS; and d) HS 52
Fig. B.41: Compressive strengths of baseline and HOAP cements (aging at 350°F, 6000 psi and 100 % CO_2) 53

Fig. B.42: Shear bond strength of baseline and HOAP samples (aged at 350°F, 6000 psi and 100 % CO_2) 54
Fig. B.43: Summarized FTIR data for HOAP and baseline samples (innermost Zone) 54
Fig. B.44: Summarized FTIR data for HOAP and baseline samples (middle zone) 55
Fig. B.45: Summarized FTIR data for HOAP and baseline samples (outermost zone) 55
Fig. B.47: Porosities of MGO-5 and baseline cements: a) unaged; and b) aged 57
Fig. B.48: Permeabilities of MGO-5 and baseline cements: a) unaged; and b) aged 57
Fig. B.49 Compressive strength of MGO-5 and baseline cements: a) unaged; and b) aged 58
Fig. B.50 Shear bond strength of MGO-5 and baseline cements: a) unaged; and b) aged 58
Fig. B.51: Summarized FTIR data of HSMG and baseline HS samples aged at 225°F, 9000 psi, 40% CO_2 for 14 days: a) Outermost zone; b) Middle zone; and c) Innermost zone 59
Fig. B.52: Porosities of MGO-5 and baseline samples: a) Unaged; and b) aged at 350°F, 9000 psi and 40% CO_2.....60
Fig. B.53: Permeabilities of MGO-5 and baseline samples: a) Unaged; and b) aged at 350°F, 9000 psi and 40% $CO_2$60
Fig. B.54: FTIR peaks of MGO and baseline samples aged at 350°F and 9000 psi for 14 days in 2% brine saturated with 40% CO_2: a) inner most zone; b) middle zone; and c) outer most zone 61
Fig. B.55: Compressive strength of MGO-5 and baseline samples: a) Unaged; and b) aged at 350°F, 9000 psi, 40% CO_2 for 14 days 62
Fig. B.56: SBS of MGO-5 and baseline samples: a) Unaged; and b) aged at 350°F, 9000 psi, 40% CO_2 for 14 days 62
Fig. D.1: Measured and prediction solubility of CO_2: a) Pure water at T=533.15 K; and b) Brine containing 23.2% NaCl at different temperatures 144
Fig. D.2: Measured and prediction solubility of CO_2 at different brine concentrations: a) T=523.15K; and b) T=423.15K 144
Fig. D.3: Comparison of experimental data and Duan's model predictions (T=573.15K).....145
Fig. F.1: Degraded zones of cement core: a) stress distribution during failure; and b) degradation depth.....147

LIST OF TABLES

Table B.1: Aging conditions for HOAP samples 27
Table B.2: Aging conditions for MGO samples 40
Table B.3: Composition of the HOAP slurries 49
Table B.4 Properties of hydroxyapatite containing cement slurries 49
Table B.5: Degradation depth of HOAP and baseline samples aged at 350°F 52
Table B.6: Formulations of MgO based cement (MGO-5) slurries 56
Table B.7: Properties of MGO-5 and baseline cement slurries 56
Table B.8: Aging conditions for the MGO-5 samples 56
Table B.9: Aging conditions for the MGO-5 samples 59
Table C.1: Porosity and permeability of fly ash based cement (FLAS) 63
Table C.2: Shear bond strength of fly ash based cement (FLAS) 65
Table C.3: Compressive strength of fly ash based cement (FLAS) 66
Table C.4: Porosity and permeability of hydroxyapatite-based cement (HOAP) 68
Table C.5: Shear bond strength of hydroxyapatite based cement (HOAP) 71
Table C.6: Compressive strength of hydroxyapatite-based cement (HOAP) 75
Table C.7: Porosity and permeability of magnesium oxide based cement (MGO-5) 79
Table C.8: Shear bond strength of magnesium oxide based cement (MGO-5) 82
Table C.9: Compressive strength of magnesium oxide based cement (MGO-5) 85
Table C.10: Porosity and permeability of latex based cement (LT) 89
Table C.11: Shear bond strength of latex based cement (LT) 90
Table C.12: Compressive strength of latex based cement (LT) 91
Table C.13: Porosity and permeability of latex microsilica based cement (LTMS) 93
Table C.14: Shear bond strength of latex microsilica based cement (LTMS) 94
Table C.15: Compressive strength of latex microsilica based cement (LTMS) 95
Table C.16: Porosity and permeability of micro silica based cement (MS-10) 97
Table C.17: Shear bond strength of micro silica based cement (MS-10) 99
Table C.18: Compressive strength of micro silica based cement (MS-10) 101
Table C.19: Porosity and permeability of baseline cements 103
Table C.20: Shear bond strength of micro silica based cements 113
Table C.21: Compressive Strength of baseline cements 123
Table D.1: Interaction parameters for CO_2 solubility in brine and pure water 142
Table D.2: Parameters used in Eq. (D-4) 143
Table D.3: Parameters used in Eqs. (D-5) and (D-6) for CO_2 solubility 143

APPENDIX A: CEMENT DEGRADATION MODEL

A.1 Overview

The major challenge in modeling cement degradation occurring in acidic environment is the involvement of different natural phenomena such as hydration, carbonation and leaching, which lead to change in important cement properties (porosity, permeability and strength). As the alteration in physical and mechanical properties takes place, the degradation process intensifies through further penetration of the aggressive fluid into the undamaged zone of the cement.

A.2 Model Assumptions

Modeling cement deterioration process is highly complex due to several controlling parameters and driving mechanisms. As a result, modeling assumptions are required to reasonably simplify the model to have adequate representation of cement degradation process. In this study, the following assumptions are made for the development of cement degradation model:

i. Hydration, carbonation and leaching are considered as major cement degradation mechanisms
ii. Bulk fluid is under static condition, hence no advective transport
iii. Degradation process is governed by reaction and diffusion
iv. Calcium leaching is solely responsible for the loss of cement integrity

A.3 Model Formulation

Figure 5.1 shows a simplified block diagram of cement degradation model. The key parameters to be predicted are degree of cement hydration, initial porosity of cured cement, saturated calcium concentration, penetration depth, new porosity, permeability and compressive strength. Cement hydration degree is a function of cement composition, water/cement ratio, temperature and pressure. Once the degree of hydration is determined, initial porosity can be predicted from the extra water in hydrated cement. Most commonly, the degradation process is governed by diffusion process; therefore, loss in mechanical integrity due to dissolution of CH and C-S-H are predicted using Fick's law. Temperature, CO_2 pressure and NaCl concentration are used as initial conditions to predict the pH of the fluid system and consequently the saturated calcium concentration in cement. Applying Mainguy's analytical model, predicted initial porosity and saturated calcium concentration are used in the diffusion model to calculate the depth of penetration. Next, solid-phase calcium profile in the penetrated zone is predicted by first calculating total calcium, CH and CSH concentrations from cement hydration equations and hydration model. New porosity of the penetrated zone is computed from the degraded depth and calcium concentration in solid phase. The molecular diffusion coefficient in the degraded zone is then recalculated using the newly computed cement properties. This iterative procedure is repeated at each time step for the entire period of exposure. By using the penetrated depth and sample dimensions, new compressive strength model is developed by adopting the methodology proposed by Corde et al. (1996).

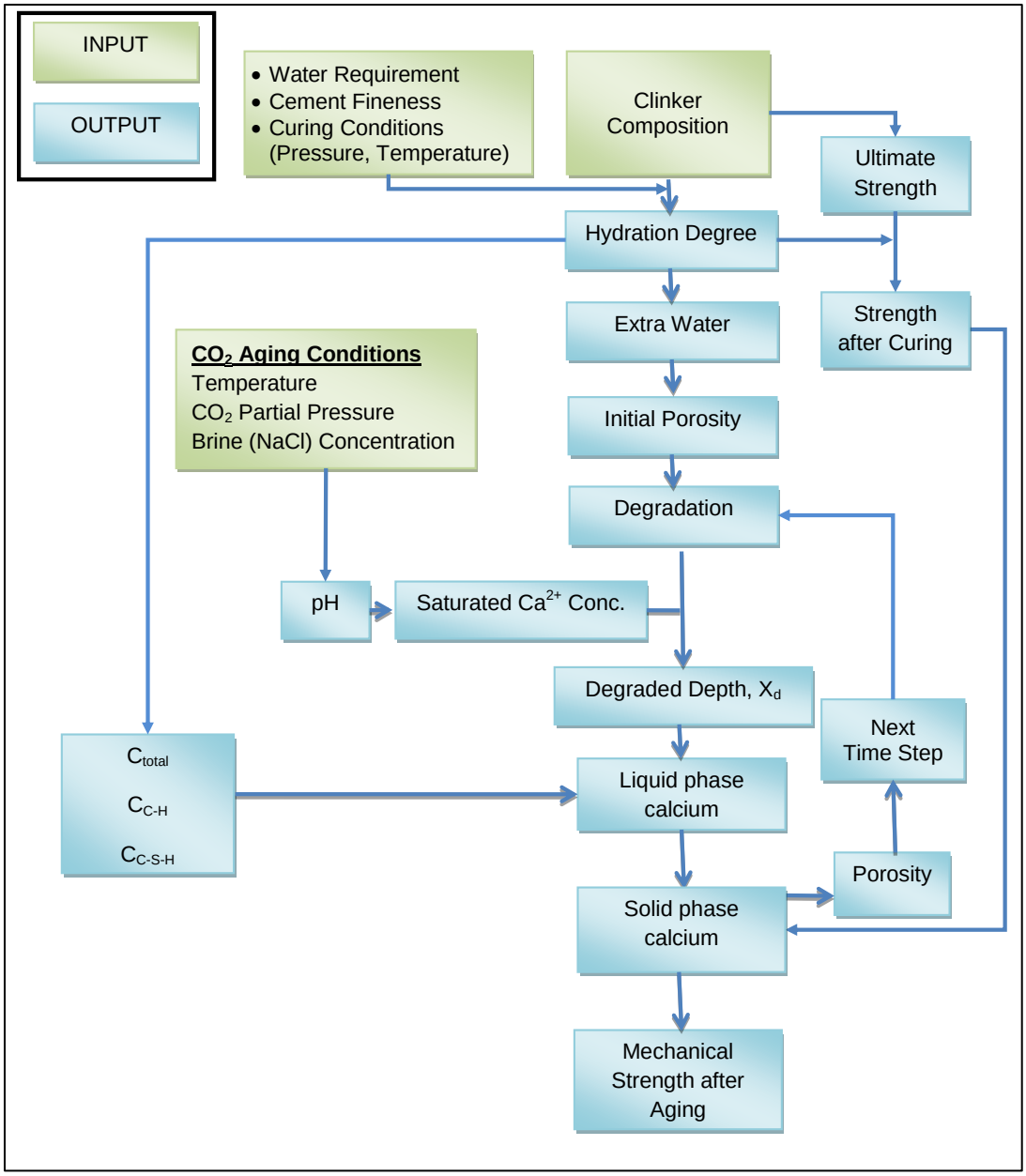

Fig. A.1: Simplified block diagram of cement degradation model

A.3.1 Hydration Model

The first step in cement degradation modeling is to predict the degree of hydration. This is crucial for initial porosity and strength estimation after curing before the exposure to carbonic acid environment. In addition, the initial amount of portlandite and calcium silicate hydrate can be predicted from the degree of hydration. In this study, the model proposed by Lin and Meyer (2009) is applied to predict the degree of hydration at the time when curing process is completed. Calculation procedure of this model is explained below:

Step 1: Compositions of C_3S, C_2S, C_3A and C_4AF are predicted using the following API – recommended oxide analysis.

$$C_3S = 4.07CaO - 7.6SiO_2 - 6.72Al_2O_3 - 1.43Fe_2O_3 - 2.85SO_3 \quad \text{(A-1)}$$

$$C_2S = 2.87SiO_2 - 0.754C_3S \quad \text{(A-2)}$$

$$C_3A = 2.65Al_2O_3 - 1.69Fe_2O_3 \quad \text{(A-3)}$$

$$C_4AF = 3.04Fe_2O_3 \quad \text{(A-4)}$$

These equations are valid only when $Al_2O_3 / Fe_2O_3 > 0.64$.

Step 2: Using above compositions, cement fineness and water-to-cement ratio, the following parameters can be determined:

$$A_o^{'} = -0.0767C_4AF + 0.0184 \quad \text{(A-5)}$$

$$A_o = A_o^{'}\left(\frac{\text{Blaine}}{350}\right) \quad \text{(A-6)}$$

$$k = 0.56(C_3S)^{-0.206}(C_2S)^{-0.128}(C_3A)^{0.161} \quad \text{(A-7)}$$

$$n_o = 10.945C_3S + 11.25C_2S - 4.10C_3A - 0.892 \quad \text{(A-8)}$$

$$E_a = 22100(C_3A)^{0.30}(C_4AF)^{0.25}(\text{Blaine})^{0.35} \quad \text{(A-9)}$$

$$\beta_1 = \frac{1}{9.33\left(\frac{\text{Blaine}}{100}\right)^{2.82} + 0.38} \quad \text{(A-10)}$$

$$\beta_{\text{hundred 2}} = \frac{\text{Blaine} - 220}{147.78 + 1.656(\text{Blaine} - 220)} \quad \text{(A-11)}$$

where, 'Blaine' represents cement fineness, which varies from 270 to 420 m^2/kg. Large value means finer cement particles (Lin and Meyer 2009).

Step 3: The ultimate degree of hydration, at a particular temperature, is computed using the following equations:

$$\alpha_{u,293} = \frac{\beta_1 * \frac{w}{c}}{\beta_2 + \frac{w}{c}} \quad \text{(A-12a)}$$

$$\alpha_{u,T} = \alpha_{u,293} * \text{Exp}[-0.00003(T - 293)^2 * \text{SGN}(T - 293)] \quad \text{(A-12b)}$$

where

$$\text{SGN}(T - 293) = \begin{cases} 1, & \text{when } T \geq 293K \\ -1, & \text{when } T < 293K \end{cases} \quad \text{(A-13)}$$

$$\mathrm{SGN(T-293)} = \begin{cases} 1, & \text{when T} \geq 293\text{K} \\ -1, & \text{when T} < 293\text{K} \end{cases}$$

Theoretical ultimate degree of hydration is computed using:

$$\alpha_{u,T} = \frac{\frac{w}{c}}{0.4} \quad \text{..... (A-14)}$$

If the estimated ultimate degree of hydration exceeds the theoretical value, the theoretical value is selected.

Step 4: Rate of hydration, at a particular curing temperature and pressure, is computed from:

$$\dot{\alpha} = \frac{d\alpha}{dt} = A_\alpha n_\alpha * e^{-\frac{E_a}{RT}} * e^{\frac{E_a}{293R}} \quad \text{..... (A-15)}$$

where,

$$A_\alpha = k\left(\frac{A_o}{k\alpha_u} + \alpha\right)(\alpha_u - \alpha) * e^{\left[0.02*\left(\frac{p}{p_{atm}}-1\right)^{0.07}\left\{\frac{\alpha}{\alpha_u}-1.5*\left(\frac{\alpha}{\alpha_u}\right)^2+0.4\right\}\right]} \quad \text{..... (A-16)}$$

$$n_\alpha = e^{\left[-n_o\left\{1+(1-\alpha)^2\ln\left(\frac{350}{Blaine}\right)\right\}\left\{e^{28*10^{-6}(T-293)^2}\right\}^{10\alpha^4}\alpha\right]} \quad \text{..... (A-17)}$$

Equation (A-15) is a non-linear ordinary differential equation and requires numerical procedure to obtain the solution.

A.3.1.1 Numerical Procedure

Applying forward finite difference approximation to find the solution of ordinary differential equation (A-15), the following expression can be obtained:

$$\frac{\alpha^{s+1}-\alpha^s}{\Delta t} = A_\alpha n_\alpha e^{-\frac{E_a}{RT}} e^{\frac{E_a}{293R}}) \quad \text{..... (A-18)}$$

Rearranging the above equation yields:

$$\alpha^{s+1} = \alpha^s + \Delta t A_\alpha n_\alpha e^{-\frac{E_a}{RT}} e^{\frac{E_a}{293R}} \quad \text{..... (A-19)}$$

A function that compares the left side and right side of equation (A-19) can be defined as:

$$f(\alpha) = \alpha^{s+1} - \alpha^s - \Delta t A_\alpha n_\alpha e^{-\frac{E_a}{RT}} e^{\frac{E_a}{293R}} \quad \text{..... (A-20)}$$

The Newton-Raphson iterative scheme can be used to solve numerically the above equation as:

$$\alpha^{n+1} = \alpha^n - \frac{f(\alpha)}{f'(\alpha)} \quad \text{..... (A-21)}$$

The following representations are made in Eqs. (A-16) and (A-17) for ease of derivations:

$$Y_{\alpha} = \alpha \left\{1 + (1 - \alpha)^2 \ln\left(\frac{350}{\text{Blaine}}\right)\right\} \quad \text{(A-22)}$$

$$Z_{\alpha} = \left\{e^{28*10^{-6}(T-293)^2}\right\}^{10\alpha^4} \quad \text{(A-23)}$$

$$X = -n_o YZ \quad \text{(A-24)}$$

$$s_{\alpha} = e^{\left[0.02\left(\frac{p}{p_{atm}}-1\right)^{0.07}\left\{\frac{\alpha}{\alpha_u}-1.5\left(\frac{\alpha}{\alpha_u}\right)^2+0.4\right\}\right]} \quad \text{(A-25)}$$

$$T_{\alpha} = k\left(\frac{A_o}{k\alpha_u} + \alpha\right)(\alpha_u - \alpha) \quad \text{(A-26)}$$

$$B_{\alpha} = A_{\alpha} n_{\alpha} * e^{-\frac{E_a}{RT}} * e^{\frac{E_a}{293R}} \quad \text{(A-27)}$$

Therefore:

$$n_{\alpha} = e^{X} \quad \text{(A-28)}$$

$$A_{\alpha} = T_{\alpha} s_{\alpha} \quad \text{(A-29)}$$

$$f(\alpha) = \alpha^{s+1} - \alpha^{s} - \Delta t B_{\alpha} \quad \text{(A-30)}$$

Differentiating the above equations (Eqs. 22 to 30), the following expressions can be obtained:

$$f'(\alpha) = 1 - \Delta t B'_{\alpha} \quad \text{(A-31)}$$

$$A'_{\alpha} = T_{\alpha} s'_{\alpha} + T'_{\alpha} s_{\alpha} \quad \text{(A-32)}$$

$$n'_{\alpha} = X' e^{X} \quad \text{(A-33)}$$

$$B'_{\alpha} = e^{-\frac{E_a}{RT}} * e^{\frac{E_a}{293R}} * (A_{\alpha} n'_{\alpha} + A'_{\alpha} n_{\alpha}) \quad \text{(A-34)}$$

$$T'_{\alpha} = k\left[-\left(\frac{A_o}{k\alpha_u} + \alpha\right) + (\alpha_u - \alpha)\right] \quad \text{(A-35)}$$

$$s'_{\alpha} = 0.02\left(\frac{p}{p_{atm}} - 1\right)^{0.07}\left[\frac{1}{\alpha_u} - \frac{3\alpha}{\alpha_u^2}\right] * e^{\left[0.02\left(\frac{p}{p_{atm}}-1\right)^{0.07}\left\{\frac{\alpha}{\alpha_u}-1.5\left(\frac{\alpha}{\alpha_u}\right)^2+0.4\right\}\right]} \quad \text{(A-36)}$$

$$X' = -n_o(Y'Z + Z'Y) \quad \text{(A-37)}$$

$$Z'_{\alpha} = 10\alpha^4\left\{e^{28*10^{-6}(T-293)^2}\right\}^{10\alpha^4-1} \quad \text{(A-38)}$$

$$Y'_{\alpha} = -2\alpha(1-\alpha)\ln\left(\frac{350}{\text{Blaine}}\right) + \left[1 + (1-\alpha)^2 \ln\left(\frac{350}{\text{Blaine}}\right)\right] \quad \text{(A-39)}$$

Equations (A-30) – (A-39) are substituted into equation (A-21) and a MATLAB program has been developed to compute the degree of hydration subject to convergence error of 0.00001.

A.3.1.2 Results

Figure A.2 shows model prediction from the hydration model using the input data summarized in **Table A.1.** Three stages of hydration can be observed from these plots; slow induction period, acceleration period and final slow reaction period. The induction period is characterized with low heat evolution and gradual nucleation of hydration products (i.e. CH and CSH). The cement begins to set during the acceleration period and early compressive strength development begins with accelerating growth of principal product of hydration (i.e. CSH). In the late stage of cement to degradation, gradual densification of microstructure around residual unhydrated C_3S and CH re-crystallization occur (Bensted and Barnes 2002). Since less water is available to facilitate hydration of chemical compounds in Class H cement, only 58% of these compounds were hydrated compared to 60% in Class G. Both API oil well cements attained ultimate degree of hydration at approximately 100 hours; hence the 5 days curing time reported in chapter 4 of this report.

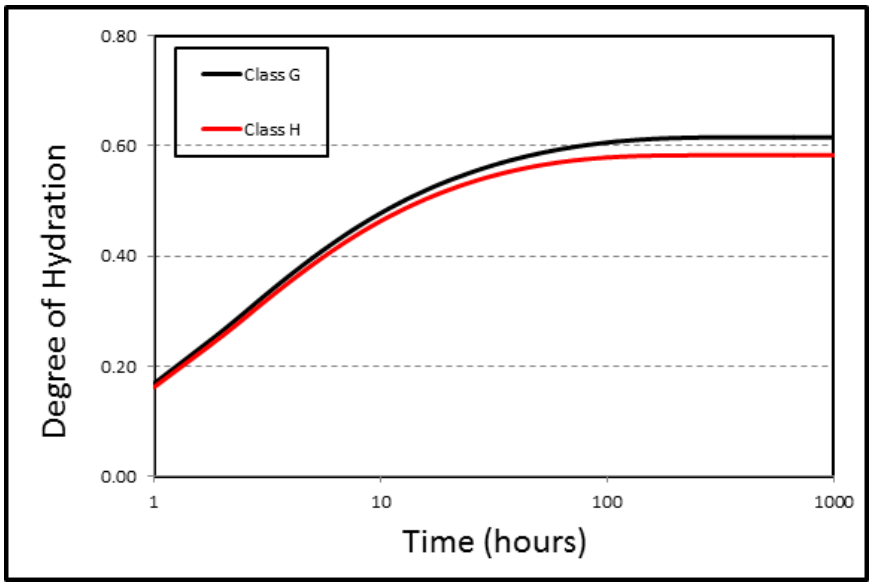

Fig. A.2: Model prediction of degree of hydration for Class H and Class G cements

Table A.1: Cement clinker composition, water requirement and curing conditions

Cement Class	W/C Ratio	C_3S	C_2S	C_3A	C_4AF	Blaine (m^2/kg)	Curing Temperature (^oF)	Curing Pressure (psi)
G	0.44	0.502	0.244	0.03	0.18	280	200	14.7
H	0.38	0.502	0.244	0.03	0.18	280	200	14.7

Remark: API recommends the following standard chemical composition: Maximum/Minimum C3S composition = 0.58/0.48; Maximum C3A composition = 0.03; Maximum C4AF + 2*C3A composition = 0.24.

Model validation was conducted using experimental data originally published by Lerch and Ford (1948) and reported by Lin and Meyer (2009). The model appears to match reasonably with the experimental data (**Fig. A.3**). While increase in curing temperature minimizes curing time, less degree of hydration is achieved since cement hydration is exothermic and pore water is rapidly consumed (**Fig. A.4**). The model also shows that variation of curing pressure does not show significant effect on degree of hydration (**Fig. A.5**).

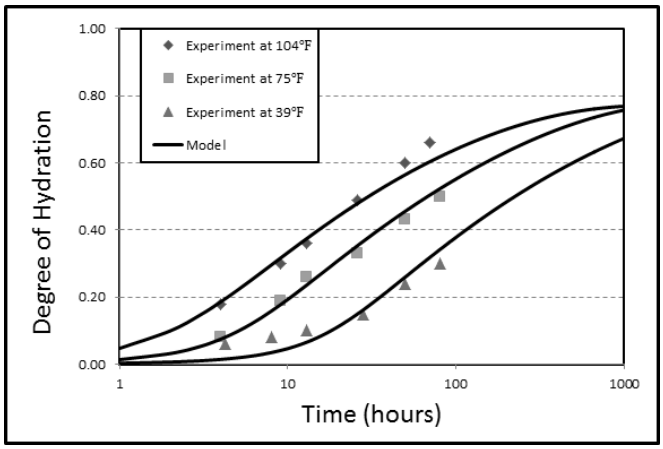

Fig. A.3: Model validation for degree of hydration while curing oil well cement

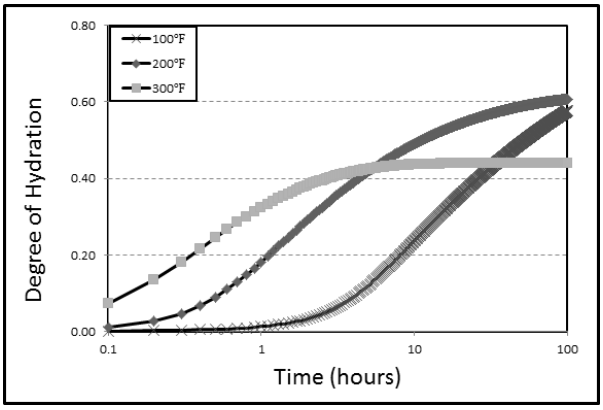

Fig. A.4: Temperature effect on degree of hydration of Class G cement

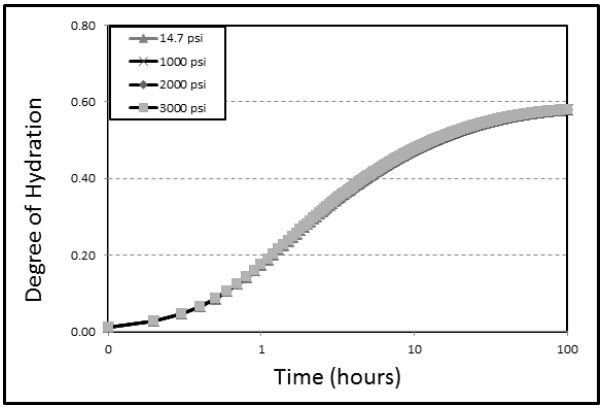

Fig. A.5: Pressure effect on degree of hydration of Class H cement

A.3.2 Porosity Model

One major use of the degree of hydration is predicting initial porosity of the hydrated cement before exposure to CO_2-brine system, which alters this initial state after calcite precipitation and subsequent dissolution. Assuming no volumetric change during mixing and no air entrapment, extra (free) water after hydration is computed from hydration reaction kinetics and material balance. Then, the following relation can be used to compute porosity of the set slurry.

$$\text{Porosity} = \phi = \frac{\text{Pore Volume}}{\text{Bulk Volume}} = \frac{\text{Extra water}}{\text{Total Slurry volume}} \quad \text{..... (A-40)}$$

Estimated initial porosities of Class G and Class H are approximately 30 and 24%, respectively. **Figure A.6** shows comparison of the model prediction and experimentally measured porosity data with acceptable match.

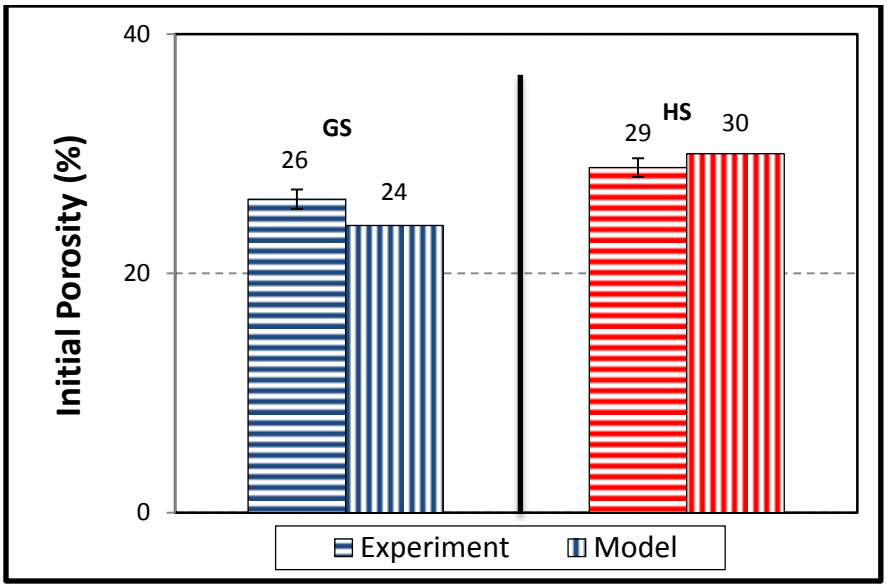

Fig. A.6: Comparison of predicted initial porosity with experimental data

A.3.3 Degradation Model

Cement degradation models generally represent the dissolution process of calcium hydroxide and progressive gradual decalcification of calcium silicate hydrate. Ionic transfer (a diffusion process) between bulk fluid and pore solution are integrated with interaction between pore fluid and cement matrix, chemical species transport in the cement pores and mechanical strength models. This integrated model predicts degraded depth and relative compressive strength, considering temperature, CO2 partial pressure, brine concentration and water-to-cement ratio as input parameters. Figure A.1 shows the formulation and simplified numerical algorithm of the model.

In this section, procedure is outlined for application of Mainguy and Coussy (2000) analytical model to predict degraded depth. Further, the model is improved to predict degradation process in CO_2-brine environment.

Step 1: Determination of Saturation Concentration of Calcium Ions: $\mathrm{C_{satu}}$ is saturation concentration of calcium ions, which depends on temperature, brine concentration and concentration of CO_2. In pure brine solution ($\mathrm{pH}\sim 7$), the following model has been proposed by Nakarai et al. (2006):

$$\mathrm{C_{satu}} = \frac{1}{2}\sqrt[3]{2\mathrm{K_{sp}}} \quad \text{(A-41)}$$

$\mathrm{K_{sp}}$ is the solubility product of calcium hydroxide, which depends on temperature and brine concentration. Effects of these variables are modeled in the following equation:

$$\mathrm{K_{sp}} = 0.0125 * 10^{9}\mathrm{e}^{-0.019\mathrm{T}} + \mathrm{A}\left(5 * 10^{4}\sqrt[3]{\mathrm{C_{NaCl}}}\right) \quad \text{(A-42)}$$

where,

$$A = \begin{cases} -2C_{NaCl}^3 + 3C_{NaCl}^2, & \text{when } 0.0 \le C_{NaCl} \le 1.0 \\ 1, & \text{when } C_{NaCl} > 1.0 \end{cases} \quad \text{..... (A-43)}$$

In CO_2-saturated brine solution where $pH < 7$ (i.e. acidic environment), C_{satu} corresponds to the maximum amount of calcite that is soluble in the pore solution. This requires analyzing ionic speciation of each component in pore solution. The chemical equilibrium reactions and associated dissociation constants involved in CO_2-corrosion of oil well cement can be summarized as:

Dissolution and dissociation of calcium carbonate in pore fluid occurs due to calcium concentration difference between the matrix and pore fluid:

$$CaCO_{3\,(s)} \rightleftharpoons Ca^{2+}{}_{(aq.)} + CO_3{}^{2-}{}_{(aq.)} \quad \text{..... (A-44)}$$

The dissociation constant for this process is defined as:

$$K_{sp} = [Ca^{2+}_{(aq)}][CO^{2-}_{3(aq)}] \quad \text{..... (A-45)}$$

Dissolved CO_2 exists in equilibrium with CO_2 gas above the brine solution:

$$CO_{2\,(g)} \rightleftharpoons CO_{2\,(aq.)} \quad \text{..... (A-46)}$$

Applying Henry's law, the relationship between CO_2 gas pressure and concentration of dissolved CO_2 in the brine solution can be expressed as:

$$K_H = \frac{P_{CO_2}}{[CO_{2(aq)}]} \quad \text{..... (A-47)}$$

Dissolved CO_2 exists in equilibrium with aqueous carbonic acid, Hence:

$$CO_{2\,(aq.)} + H_2O_{\,(l)} \rightleftharpoons H_2CO_{3\,(aq.)} \quad \text{..... (A-48)}$$

The overall equilibrium constant for the dissociation of carbonic acid is expressed as:

$$K_h = \frac{[H_2CO_{3(aq)}]}{[CO_{2(aq)}]} \quad \text{..... (A-49)}$$

The first dissociation equilibrium between H_2CO_3 (aq.) and HCO_3^-(aq.) is:

$$H_2CO_{3\,(aq.)} \rightleftharpoons H^+{}_{(aq.)} + HCO_3{}^-{}_{(aq.)} \quad \text{..... (A-50)}$$

The first dissociation constant of carbonic acid is expressed as:

$$K_{a1} = \frac{\left[H^{+}_{(aq)}\right]\left[HCO^{-}_{3(aq)}\right]}{\left[H_2CO_{3(aq)}\right]} \quad \text{(A-51)}$$

The second dissociation equilibrium between $HCO_3^{-}{}_{(aq.)}$ and $CO_3^{2-}{}_{(aq.)}$ is:

$$HCO_3^{-}{}_{(aq.)} \rightleftharpoons H^{+}{}_{(aq.)} + CO_3^{2-}{}_{(aq.)} \quad \text{(A-52)}$$

The second dissociation constant of carbonic acid is defined as:

$$K_{a2} = \frac{\left[H^{+}_{(aq)}\right]\left[CO^{2-}_{3(aq)}\right]}{\left[HCO^{-}_{3(aq)}\right]} \quad \text{(A-53)}$$

Dissociation of water:

$$HO_{2(l)} \rightleftharpoons H^{+}{}_{(aq.)} + OH^{-}{}_{(aq.)} \quad \text{(A-54)}$$

Dissociation constant of water is:

$$K_w = \left[H^{+}_{(aq)}\right]\left[OH^{-}_{(aq)}\right] \quad \text{(A-55)}$$

Electrical neutrality (charge balance) equation for the process is described as:

$$2[Ca^{2+}] + \left[H^{+}_{(aq)}\right] = \left[HCO^{-}_{3(aq)}\right] + 2\left[CO^{2-}_{3(aq)}\right] + \left[OH^{-}_{(aq)}\right] \quad \text{(A-56)}$$

Equilibrium concentrations of $[Ca^{2+}]$, $\left[H^{+}_{(aq)}\right]$, $\left[HCO^{-}_{3(aq)}\right]$, $\left[CO^{2-}_{3(aq)}\right]$, $\left[OH^{-}_{(aq)}\right]$, $\left[H_2CO_{3(aq)}\right]$ and $\left[CO_{2(aq)}\right]$ can now be obtained by solving the seven equations above (Eqs. A-45, A-47, A-49, A-51, A-53, A-55 and A-56). Combining these equations yields the equilibrium calcium ion concentration (i.e. $[Ca^{2+}]$), which represents the maximum amount of calcium carbonate that can dissolve in pore fluid.

$$C_{Satu} = [Ca^{2+}]_{max} = \frac{K_{sp}K_H}{K_h K_{a1} K_{a2}} \frac{[H^{+}]^2}{P_{CO_2}} \quad \text{(A-57)}$$

K_{sp} is determined from Eq. (A-41). K_H is dissolution/solubility constant of CO_2 in brine solution and obtained using solubility model (Duan and Sun 2003) presented in Appendix D. To account for the effect of temperature and brine concentration, the first and second dissociation constants of carbonic acid in brine solution are estimated using Millero et al. (2007) model in which the following expression has been obtained:

$$K_h K_{a1} = K_1 = \frac{\left[H^{+}_{(aq)}\right]\left[HCO^{-}_{3(aq)}\right]}{\left[CO_{2(aq)}\right]} \quad \text{(A-58)}$$

Step 2: Determination of Dimensionless Degraded Depth: Degradation depth of cement can be determined using the analytical solution (model) of the governing equation (Eq. A-59) presented by Mainguy and Coussy (2000). Using this model, the degradation depth for 1D diffusion-dissolution problem can be obtained by solving the mass balance equation, diffusion equation (i.e. transport law of the solute through the porous medium), equilibrium equation (law governing the kinetics of dissolution), and initial condition at the time of exposure. To determine the degradation depth, first, Dimensionless depth, ξ_d, is determined by solving the following analytical solution:

$$\varepsilon \exp\left(-\xi_d^2\right) = \sqrt{\pi}\xi_d \mathrm{erf}(\xi_d) \quad \text{..... (A-59)}$$

where dimensionless quantities in the previous equations are defined as:

$$\varepsilon = \frac{\emptyset C_{satu}}{C_{total}} \quad \text{..... (A-60a)}$$

$$\xi 0 \frac{x}{2\sqrt{Dt}} \quad \text{..... (A-60b)}$$

$$\mathrm{er\,f}(\xi_d) = \frac{2}{\sqrt{\pi}} \int_0^{\xi_d} e^{-t^2} \, dt \quad \text{..... (A-61)}$$

where $\emptyset$ is porosity at any time and location and C_{total} is the solid-phase total calcium concentration. Numerical procedure for solving Eq. (A-59) is detailed in Appendix E.

Step 3: Determination of Degradation Depth: Degraded depth, x_d, is estimated using:

$$x_d = 2\xi_d\sqrt{Dt} \quad \text{..... (A-62)}$$

where diffusivity, $D\,(m^2/s) = 2.35 \times 10^{-13} \exp(9.95\,\emptyset)$. During degradation, porosity of the cement balance was time and location. Thus:

$$\emptyset = \emptyset_o + (1 - \emptyset_o)\left(C_{s,o} - C_s(x,t)\right)\frac{M_w}{\rho_s} \quad \text{..... (A-63)}$$

where $\emptyset_o$ and $C_{s,o}$ are initial porosity and solid-phase calcium concentration (mol/L), respectively. M_w is the molecular weight of calcium (40.0 g/mol), and ρ_s is cement density. $C_s(x,t)$ is calcium concentration at any time and location (mol/L). $\emptyset_o$ is the initial porosity obtained from hydration model. $C_{s,o}$ is equal to the total calcium concentration associated with the amount of C-H and C-S-H present in the cement.

Step 4: Determination of Liquid-Phase Calcium Ion Concentration: In the degraded zone, liquid-phase calcium ion concentrations are predicted using the following model:

$$\bar{C}_l = \begin{cases} \frac{C_l}{C_{satu}} = \frac{erf(\xi)}{erf(\xi_d)} & \text{when } 0.0 \leq \xi \leq \xi_d \\ 1 & \text{when } 0.0 \leq \xi \leq \xi_d \end{cases} \quad \text{..... (A-64)}$$

Step 5: Determination of Solid-Phase Calcium Ion Concentration: Solid-phase calcium ion concentrations are then predicted using Nakarai et al. (2006) model.

$$C_s = f(C_l) = A\left[C_{CSH}\left(\frac{C_l}{C_{satu}}\right)^{\frac{1}{3}}\right] + B \quad \text{..... (A-65)}$$

where,

$$A = \begin{cases} -\left(\frac{2}{x_1^3}\right)(C_l)^3 + \left(\frac{3}{x_1^2}\right)(C_l)^2 & (0.0 \leq C_l \leq x_1) \\ 1 & (x_1 < C_l) \end{cases} \quad \text{..... (A-66a)}$$

$$B = \begin{cases} 0 & (0.0 \leq C_l \leq x_2) \\ \frac{C_{CH}}{(C_{satu} - x_2)^3}(C_l - x_2)^3 & (x_2 < C_l) \end{cases} \quad \text{..... (A-66b)}$$

where x_1 is the liquid-phase calcium ion concentration when rapid transition of C-S-H gel into silica gel begins (mmol/L). x_2 is the liquid-phase calcium ion concentration when the calcium hydroxide has completely dissolved and dissolution of C-S-H gel begins (mmol/L). C_{CSH} is amount of calcium in the solid-phase of the C-S-H gel (mmol/m^3). C_{CH} is amount of calcium in the solid-phase of the calcium hydroxide (mmol/m^3) and C_{satu} is saturated liquid-phase calcium ion concentration (mmol/L). In this study, 2 mmol/L liquid-phase calcium ion concentration is assumed as the commencement of rapid transition of C-S-H gel into silica gel as recommended by a similar study (Nakarai, 2006). Furthermore, as suggested by the same author, x_2 is assumed as $C_{satu} - 2.99$. C_{CSH} and C_{CH} for each cement classes are obtained from hydration chemistry and degree of hydration. **Table A.2** shows the values of C_{CSH} and C_{CH} for this study. Once the solid-phase calcium concentration after exposure has been determined, mechanical strength model can then be applied.

Table A.2: Amount of calcium in hydrated oil well cements

Cement Type	Portlandite	Calcium Silicate Hydrate	Total Solid-Phase Calcium before Exposure
Class G (mmol/m^3)	8149	13422	21571
Class H (mmol/m^3)	9435	15541	24976

Degradation depth obtained from the model is plotted in **Fig. A.7** as a function of square root of time. The result shows that Class G cement is more penetrated than Class H cement after for 14 days of exposure to 2% brine solution saturated with methane containing CO_2 at 350^{o}F. A study of CO_2 composition effect on degradation behavior of class H cement is presented in **Fig. A.8**. As more CO_2 is injected, deeper penetration is achieved due to increased production of carbonic acid, which alters the

state of equilibrium and leads to dissolution of calcite. Furthermore, the rate of degradation (i.e. slope of the plot) mainly is a function of cement composition and CO_2 partial pressure. This observation was compiled by previous studies (Matteo et al. 2011; Matteo and Scherer 2012) in which temperature and solution pH (a function of CO_2 partial pressure) were reported as effective variables on degradation rate. Since solution pH is a function of CO_2 partial pressure, therefore, decreasing pH of the liquid phase (i.e. acidic environment) leads to high saturation concentration of calcium ion, which consequently results in depth of degradation increasing.

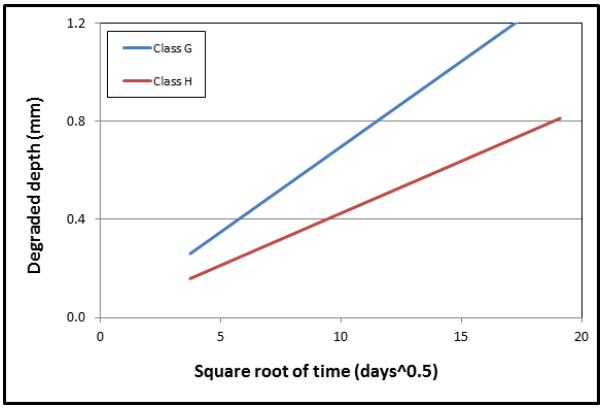

Fig. A.7: Predicted degradation depth for Class G and Class H at T=350°F, P_{CO2} = 600 psi, NaCl = 2%wt

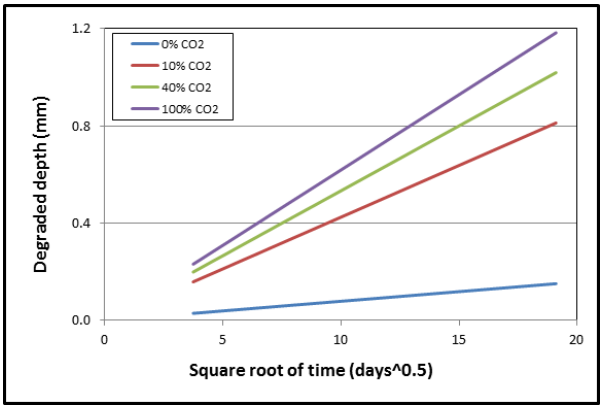

Fig. A.8: Predicted degradation depth for Class H cement at T=350°F, NaCl = 2%wt, P = 6000 psi

Predicted solid-phase calcium concentration profile as a function of salt concentration in the bulk fluid is shown in **Fig. A.9**. Increasing salinity of brine up to 5 wt% leads to slight decrease in degradation depth. Mechanical behavior of cement is affected by NaCl in different ways depending on temperature and concentration. Some experimental studies conducted at lower temperature and pressure (Barlèt-Gouédard et al., 2006; Duguid et al. 2004 2006) have shown that sodium chloride (NaCl) increases dissolution rate during leaching. Furthermore, effect of water-to-cement ratio on solid-phase calcium is presented in **Fig. A.10**. With less water requirement, Class H is more CO_2 resistant than Class G. This agrees with our experimental observations and results of other studies (Bruckdorfer 1986).

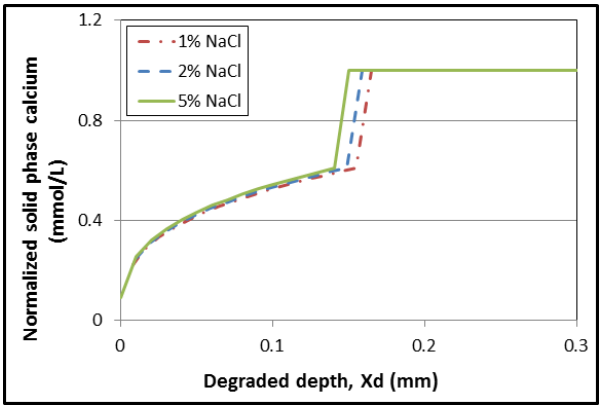

Fig. A.9: Effect of salt concentration on solid-phase calcium profile of Class H cement at P=6000 psi, T=350°F, CO_2 = 10%, t = 14 days

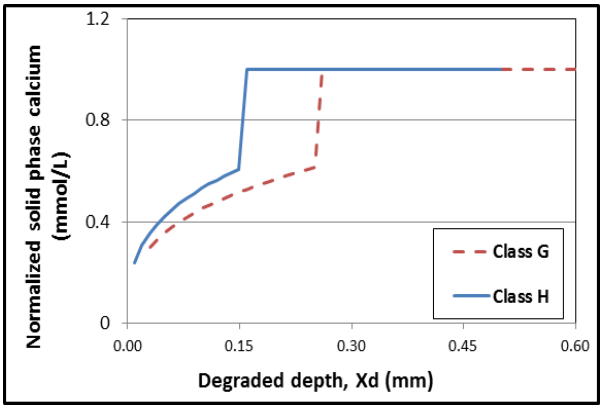

Fig. A.10: Comparison of solid-phase calcium profile different cement classes at P = 6000 psi, T = 350°F, CO_2 =10%, t = 14 days

Results of simulation study conducted on CO_2 concentration show that loss of integrity is faster with increase in CO_2 partial pressure (**Fig. A.11**). This is because of the shift in equilibrium position in response to increased production of carbonic acid and this result in dissolution of precipitated calcite. In addition, temperature effect was also studied (**Fig. A.12**). Although more calcite precipitation is likely at temperature below approximately 250°F, calcium hydroxide (a key component of cement integrity) has been reported to be highly leached at low temperature (Nakarai, 2006). Similarly, reduction in dissolution of portlandite protects further penetration of carbonic acid at higher temperature. Although dissolution of calcite is more likely to occur at high temperature due to shift in equilibrium, our experimental measurements show mixed trend.

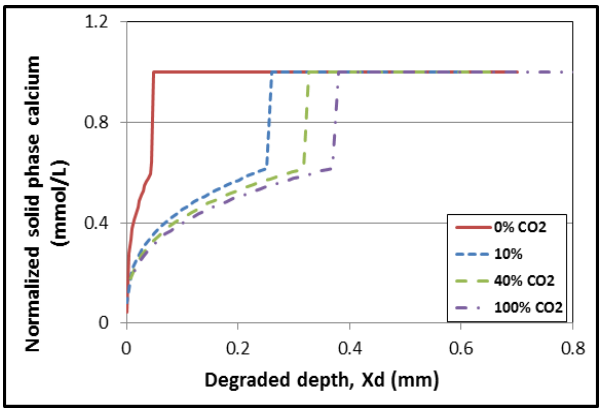

Fig. A.11: CO_2 concentration effect on solid-phase calcium profile of Class G cement P = 6000 psi, T=350°F, NaCl = 2 wt%, t = 14 days

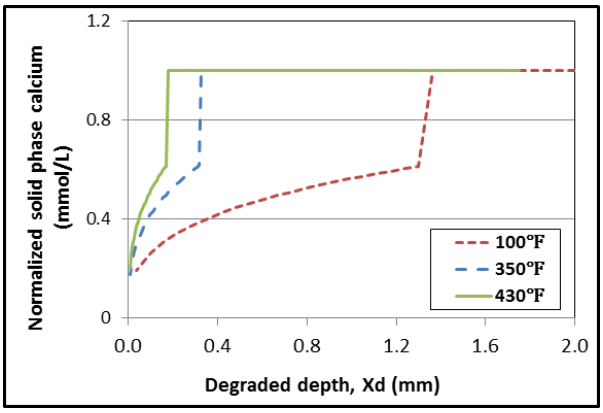

Fig. A.12: Temperature effect on solid-phase calcium profile of Class G cement P = 6000 psi, T = 350°F, NaCl = 2 wt%, t = 14 days

A.3.4 Mechanical Strength Degradation Model

Compressive strength predictions are evaluated at three stages of the degradation process, which include ultimate strength before curing, strength after curing, and mechanical strength after CO_2 exposure.

A.3.4.1 Ultimate Strength before Curing

Major components of cement (C_3S and C_2S) are considered as main contributors to strength development. In the hydration reaction, the volume fraction of CSH to CH in hydrated sediments is higher in C_2S than in C_3S; hence, for the same reacted amounts, C_2S contributes more to strength development than C_3S, since CSH contributes more to strength development than CH. To prevent strength retrogression at elevated temperature, 35% BWOC silica flour is usually mixed with the base slurry and its contribution is also included in ultimate strength computation. For cement with known volume fraction of C_3S and C_2S, Maekawa et al. (2009) presented the following equation for ultimate strength estimation.

$$\sigma_\infty = \frac{Ax_{C_3S}+Bx_{C_2S}}{x_{C_3S}+x_{C_2S}} x_c + Cx_{SF} \quad \text{(A-67)}$$

where A, B and C are material constants with values, 215, 250 and 300 MPa, respectively. x_c and x_{SF} are weight fractions of Portland cement and silica flour, respectively. Thus: $x_c + x_{SF} = 1$. x_{C_2S} and x_{C_3S} are volume fractions of C_2S and C_3S, respectively.

A.3.4.2 Mechanical Strength after Curing

Compressive strength development during cement curing is mostly affected by the degree of hydration. In this study, strength model proposed by Powers (1958) is used with slight modification in the value of empirical parameter K.

$$\sigma_c = \sigma_\infty \left[\frac{0.71n}{0.32ng\frac{w}{c}}\right]^k \quad \text{(A-68)}$$

where σ_∞ is strength, α is degree of hydration, $\frac{w}{c}$ is water to cement ratio. k is empirical parameter, which is defined as:

$$k = f\left(\frac{w}{C}\right) \approx 13 - 16 * \left(\frac{w}{c}\right) \quad \text{(A-69)}$$

The above strength models were used to predict mechanical strength development while curing proceeds. **Figure A.13** illustrates model prediction comparing with literature data (Akkaya et al. 2003). Moreover, compressive strength predicted from the present model predominantly matched our compressive strength measurements for Class G and Class H cement samples cured at 200°F, 14.7 psi for 5 days (**Fig. A.14**). Applying this model, comparison is made between strength estimated for Class G and Class H (**Fig. A.15**).

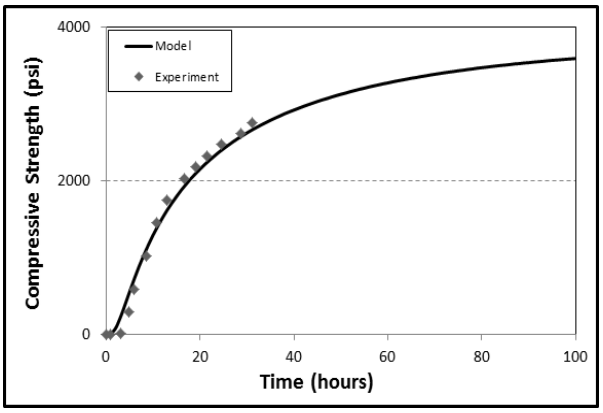

Fig. A.13: Comparison of strength predictions during curing with experimental data (Akkaya et al. 2003)

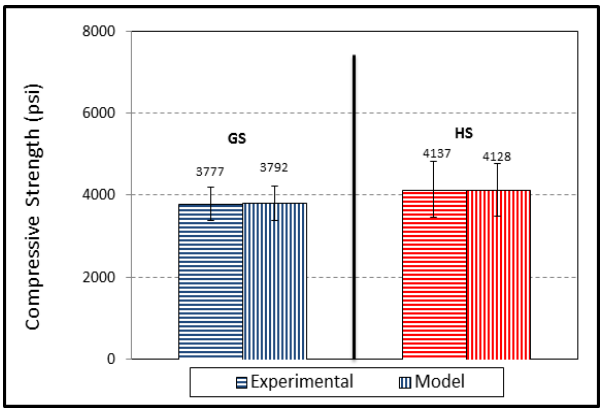

Fig. A.14: Comparison of after curing strength predictions with experimental data

The result clearly shows that Class H cement exhibits better strength performance than Class G cement, although less degree of hydration was achieved. Several authors have noted that hydrated compounds are susceptible to chemical shrinkage, which leads to pore volume reduction. Lin and Meyer (2009) also presented the following model for estimate chemical shrinkage of cement during hydration and application of this model shows that more shrinkage is possible in Class H cement than Class G cement (**Fig. A.16**).

$$v_{chsh} = \frac{0.0625\alpha}{0.32+\frac{w}{c}} \quad \text{(A-70)}$$

where v_{chsh} is chemical shrinkage volume.

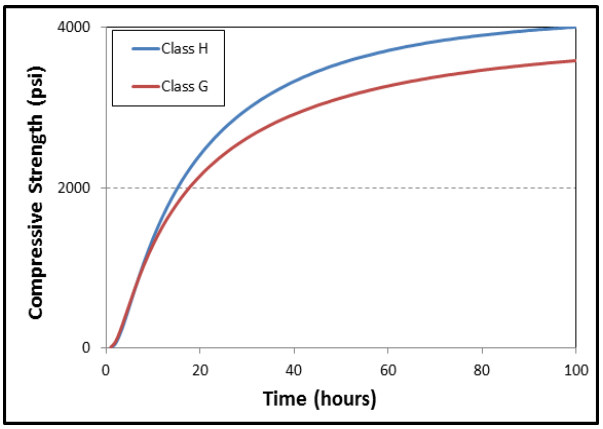

Fig. A.15: Strength predictions during curing Class G and Class H cement

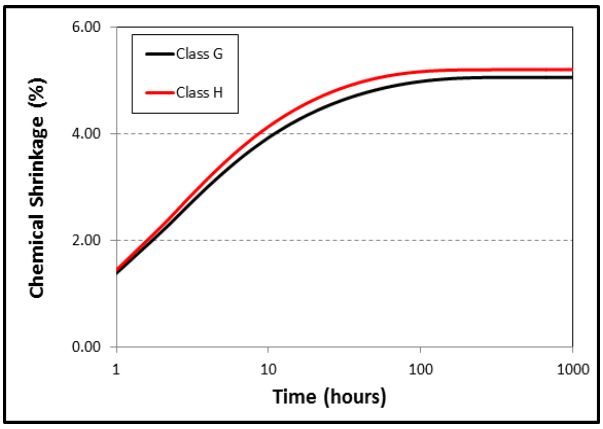

Fig. A.16: Comparison of chemical shrinkage in class G and class H during curing

A.3.4.3 Mechanical Strength after CO_2 Aging

The next step in model formulation is to predict alteration in mechanical strength after curing due to acidic attack. After exposure to carbonic acid, cement is subjected to several interacting mechanisms, which include diffusion, carbonation and leaching. The deterioration in mechanical strength arises from loss of calcium in portlandite and calcium silicate hydrates. Therefore, the distribution of calcium in the invaded zone is an indication of loss of strength. Applying elasto-plasticity theory, Carde et al. (1996) presented a methodology for formulating compressive strength models from solid-phase calcium profile in leached zone of cement materials. This methodology is adopted in developing a new mechanical strength model for cement that has been exposed to acidic environment under HPHT conditions.

Predicted solid-phase calcium profiles (Figs. A.9 to A.12) in cement after 14 days of acid attack show the effect of salt concentration, cement Class, CO_2 concentration, and temperature on cement degradation. Application of Carde's hypothesis implies the similar shape (**Fig. A.17)** can be assumed for stress distribution in degraded cement.

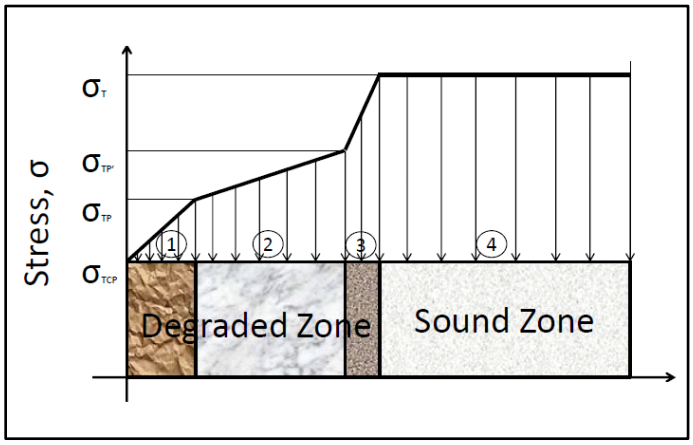

Fig. A.17: Stress distribution in a degraded cement sample

Based on the approach developed by Carde et al. (1996), reduction in compressive strength occurring after CO_2 exposure can be determined using the following analytical equations:

$$\frac{\Delta F}{F} = 1 - \frac{1}{\pi r^2}\left[\frac{F_1}{\sigma_T} + \frac{F_2}{\sigma_T} + \frac{F_3}{\sigma_T} + \frac{F_4}{\sigma_T}\right] \quad \text{(A-71)}$$

where the terms in the parenthesis are expressed as:

$$\frac{F_1}{\sigma_T} = 2\pi\left[\frac{R_P - R_{CP}}{R_1}\left\{\frac{r}{2}[r^2 - (r - R_1)^2] - \frac{1}{3}[r^3 - (r - R_1)^3]\right\} + R_P\left\{rR_1 - \frac{1}{2}[r^2 - (r - R_1)^2]\right\}\right] \quad \text{(A-72)}$$

$$\frac{F_2}{\sigma_T} = \frac{2\pi}{R_2 - R_1}\left[\begin{array}{c}\left(R_P' - R_P\right)\left\{\frac{r}{2}[(r - R_1)^2 - (r - R_2)^2] - \frac{1}{3}[(r - R_1)^3 - (r - R_2)^3]\right\} \\ +\left(R_P R_2 - R_P' R_1\right)\left\{r(R_2 - R_1) - \frac{1}{2}[(r - R_1)^2 - (r - R_2)^2]\right\}\end{array}\right] \quad \text{(A-73)}$$

$$\frac{F_3}{\sigma_T} = \frac{2\pi}{x_d - R_2}\left[\begin{array}{c}\left(1 - R_P'\right)\left\{\frac{r}{2}[(r - R_2)^2 - (r - x_d)^2] - \frac{1}{3}[(r - R_2)^3 - (r - x_d)^3]\right\} \\ +\left(R_P' x_d - R_2\right)\left\{r(x_d - R_2) - \frac{1}{2}[(r - R_2)^2 - (r - x_d)^2]\right\}\end{array}\right] \quad \text{(A-74)}$$

$$\frac{F_4}{\sigma_T} = \pi x_d(2r - x_d) \quad \text{(A-75)}$$

Detailed derivations of the above equations are presented in Appendix F.

The terms in the above model are defined in the nomenclature. Mechanical strength after CO_2 attack has been predicted using the model. To validate the model, lab measurements are compared with predictions considering the effects of pressure and CO_2 concentration on cement degradation. For the pressure effect, trend predicted by the current model for Class G cement shows acceptable agreement with the general trend of experimental measurements (**Fig. 5.18**). As the pressure increases, consistent reduction of compressive strengths is predicted using the model while experimental data shows slight improvement in strength when the pressure is increased from 3,000 to 6,000 psi. These discrepancies could be attributed to data scattering, which is inherent in compressive strength measurements of degraded cement. The trend of model predictions shows the effect of leaching process on cement strengths and its dominance over carbonation. As a result, the overall effect of pressure increase causes considerable reduction in strengths, resulting from increased acid concentration. In the CO_2 effect case study, similarly, model predictions present acceptable match with experimental data up to 40% CO_2 concentration (**Fig. A.19**). However, carbonation trend was not well captured at 100% CO_2 concentration, rather progressive decalcification ensued.

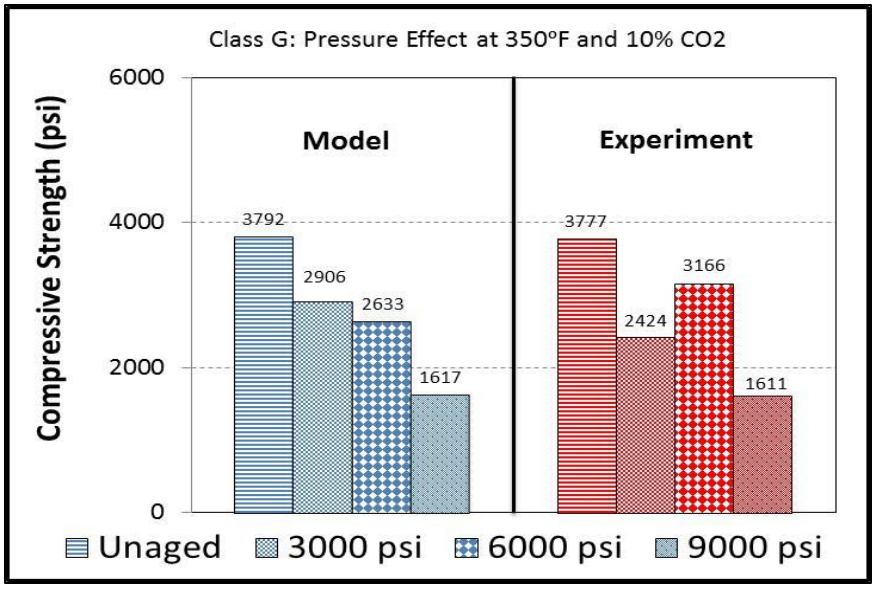

Fig. A.18: Comparison of compressive strength predictions with experimental data at different pressures for Class G cement (10% CO_2 and 350°F)

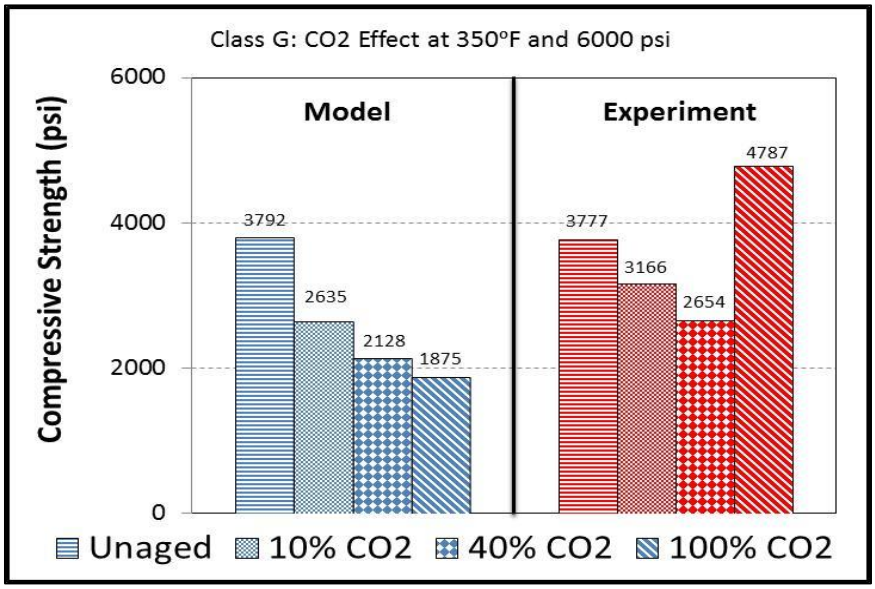

Fig. A.19: Comparison of compressive strength predictions with experimental data at different CO_2 concentration for Class G cement (6000 psi and 350°F)

APPENDIX B: PERFORMANCE OF NEW CEMENT FORMULATIONS

B.1 Detailed Analysis of Acid Resistance of New Cement Formulations

Extensive additive screening and cement formulation study indicated that hydroxyapatite and magnesium oxide containing cement (HOAP and MGO-5) are the most viable formulations that can withstand acid attack under HPHT conditions.

B.1.1 Calcium Hydroxyapatite

Calcium hydroxyapatite (aka hydroxyapatite) is a natural occurring mineral form of calcium apatite. The human bone structure is 50% composed of hydroxyapatite and it is often used for dental and orthopedic prostheses because of its biocompatibility (Teraoka et al. 1998). The use of hydroxyapatite-based cements in oil well was brought forward by the work performed at Brookhaven National Laboratory (Sugama 2006) through their CAP (calcium aluminate phosphate) cement project.

Limited studies were conducted to evaluate the performance of hydroxyapatite as a cement additive. It has been observed that after acid attack, the strength of hydroxyapatite-based (HOAP) cement reduces (Sugama and Carciello 1992, 1993; Martin and Brown 1995). Further, investigation is needed to study the performance of this additive. Hence, hydroxyapatite has been selected as potential additives in this study.

The hydroxyapatite containing cement (HOAP) is one of the new formulations that showed promising results in the initial screening study. To investigate the performance of this formulation, HOAP and baseline samples were prepared and aged under different conditions (**Table B.1**). During aging, samples were immersed for 14 days in 2% brine saturated with CO_2 and H_2S containing methane gas.

Table B.1: Aging conditions for HOAP samples

HOAP Batch #	Exp. #	Baseline Batch #	Temp. (ºF)	Pressure (psi)	Concentration		
					CH_4 (%)	CO_2 (%)	H_2S (ppm)
002	9	11	100	6000	60	40	0
003	12	14	350	6000	0	100	0
004	13	16	350	3000	60	40	0
005	15	18	350	3000	0	100	0
006	19	22	225	3000	60	40	0
007	23	26	225	3000	90	10	0
008	29	32	430	9000	100	0	0
009	30	33	100	6000	90	10	300
010	32	35	350	6000	90	10	300
011	33	36	100	6000	100	0	300
012	35	38	100	9000	100	0	300
013	37	40	100	9000	60	40	180

The matrix properties (porosity, permeability, compressive strength and shear bond strength, FTIR analysis) of aged and unaged samples were measured to quantify the level of degradation occurring during aging and compare the performance of HOAP with the baseline cement.

B.1.1.1 Porosity and Permeability

Figure B.2 illustrates the porosity for Class H based HOAP and baseline samples. In all the experiments, porosity of baseline decreased after aging due to carbonation. On the other hand, only three of HHO samples (Experiments # 12, 23 and 29) showed porosity reduction after aging. The reduction occurred in these samples could be due to partial carbonation of the matrix; and hence, the results from compressive strength, shear bond strength and FTIR measurements need to be analyzed to better understand the impacts of different test parameters. For Experiment # 23, the reduction for HHO samples was 29%, which is considerably less than that of the baseline samples (60%). Measurements from Experiments # 12 and 29 showed substantial decrease in porosity of the samples when aged at 350 and 430°F, respectively. The high temperature enhances ionic diffusion through the cement, resulting in rapid acid penetration and carbonation. Moreover, above 350°F, increasing temperature tends to increase CO_2 solubility, which facilitates the carbonation process.

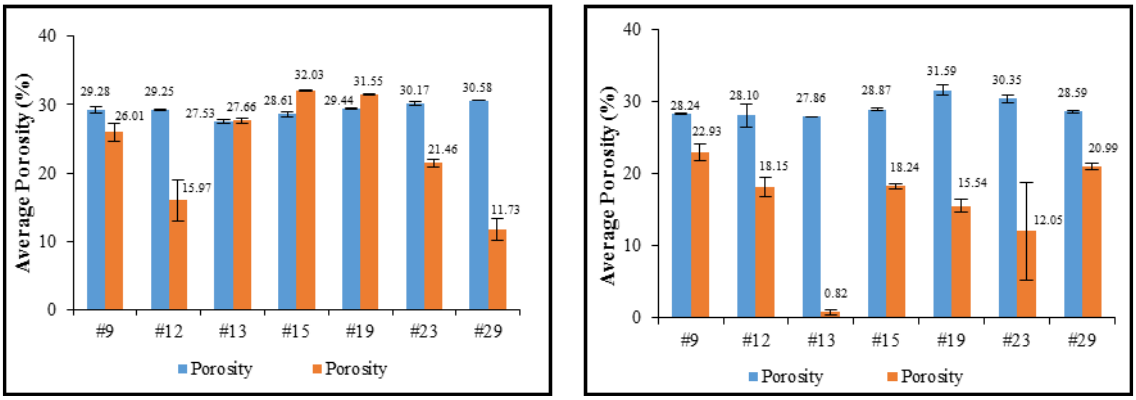

(a) **(b)**

Fig. B.2: Porosity of aged (orange) and unaged (blue) samples: a) HHO; and b) HS

One of the baseline samples (Experiment #13), displayed very low porosity after aging (0.82%). This reduction is not realistic with respect to carbonation process. The possible reason for this reduction could be because of deposition of salt on the outer surface of the slurry resulting in blocking of pores on the outer zone.

Recent aging tests (Experiments # 30, 32, and 37) were conducted in the presence of H_2S. Results presented in **Fig. B.3** shows the performance of HHO cement. After aging, the change in HHO cement porosity was negligible. While the baseline cement showed increase in porosity in two experiments (Experiments # 30 and 32). These experiments were conducted under low CO_2 concentration conditions. Hence, leaching is expected to dominate the degradation process. As a result, baseline samples showed increase in porosity while the additive samples exhibited a slight reduction. These results are consistent with our previous observations when tests were conducted without the presence of H_2S, HHO cement preserved its original property after exposure to acidic environment.

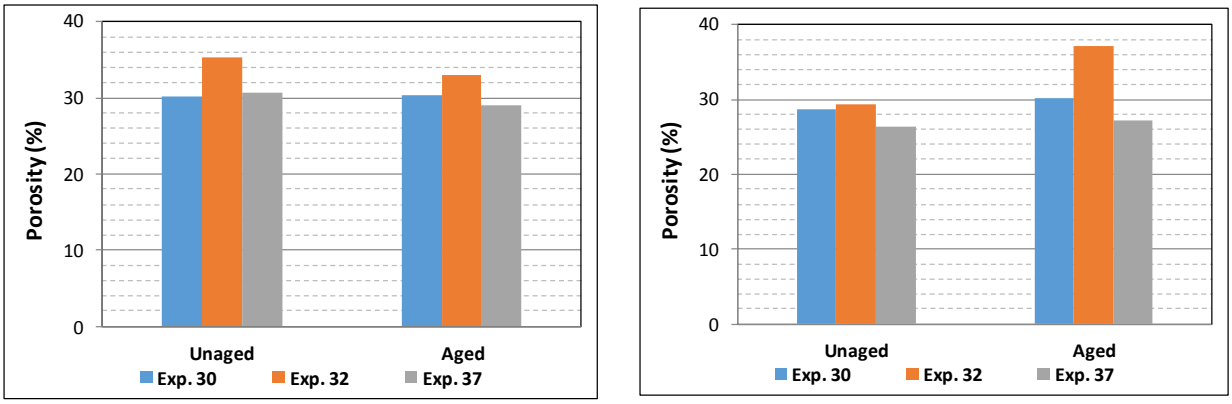

Fig. B.3: Porosity of unaged and aged (in the presence of H_2S) samples: a) HHO; and b) HS

Most of the HOAP samples showed slight change in porosity after aging, which suggests minimal carbonation and preservation of CH and CSH components of the cement. In addition, permeability of HOAP and baseline samples indicate different trends (**Fig. B.4**). The scale of the permeability chart has been modified to logarithmic for better visualization. The drastic reduction in permeability of baseline samples demonstrated severe carbonation resulting in blocking of the pore throats. On the other hand, HOAP samples remain predominately immune against carbonation. Permeability reductions observed in Experiments # 12 and 19 were less significant than that of the baseline samples.

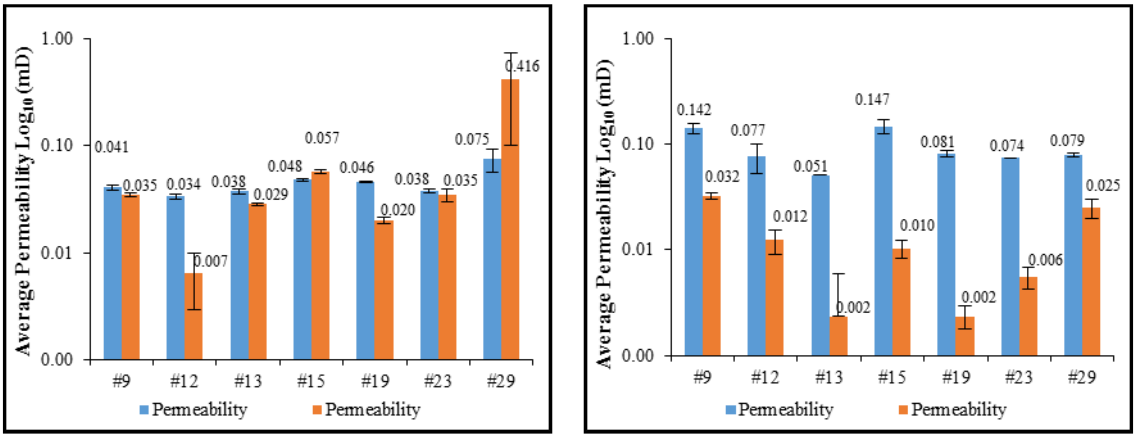

Fig. B.4: Permeability of aged (orange) and unaged (blue) samples: a) HHO; and b) HS

Substantial permeability increase was observed in Experiment # 29 that can be attributed to high temperature (430°F), which causes rapid ionic diffusion in the cement leading to harsh leaching condition.

In addition to CO_2, the presence of H_2S also affects the degradation behavior of oil well cement. Tests conducted in the presence of H_2S demonstrated the effectiveness of hydroxyapatite in minimizing carbonation and leaching processes. Permeability of HHO samples decreased (**Fig. B.5**) when aged under different conditions due to the formation of ettringite, which reduces the pore space and subsequently porosity and permeability. However, in the presence of leaching, the reduction in permeability resulting

from the formation of ettringite can be offset by the leaching process and this causes increase in permeability as indicated in baseline (HS) samples. For both types of samples (additives and baseline), the maximum reduction in permeability was observed in Experiment # 37, in which the samples were aged in fluid containing high concentration of CO_2 (40%). This means that, in addition to the formation of ettringite, considerable amount of calcium carbonate was formed as the cement reacts with carbonic acid. The precipitation of calcium carbonate in the pore resulted in the reduction in porosity and permeability of the cement samples.

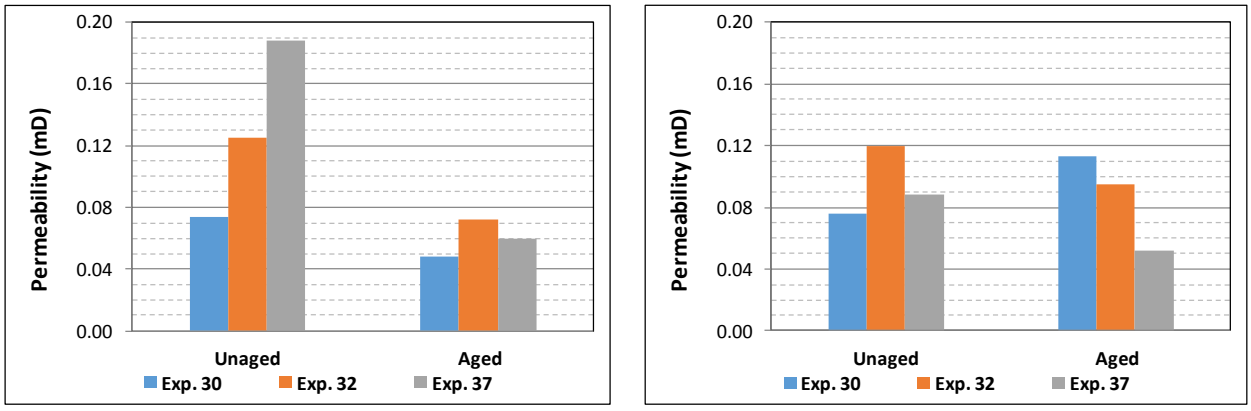

Fig. B.5: Permeability of unaged and aged (in the presence of H_2S) samples: a) HHO; and b) HS

Class G based HOAP (GHO) and baseline samples demonstrated (**Fig. B.6**) reduction in porosity after aging, except for two tests (Experiments # 15 and 19). Increases in porosity in Experiments # 15 and 19 could be due to combine effects of high temperature (350°F) and high CO_2 concentration (100% CO_2) leading to heavy leaching rather than carbonation. The baseline samples on the other hand demonstrated a consistent porosity decline due to carbonation.

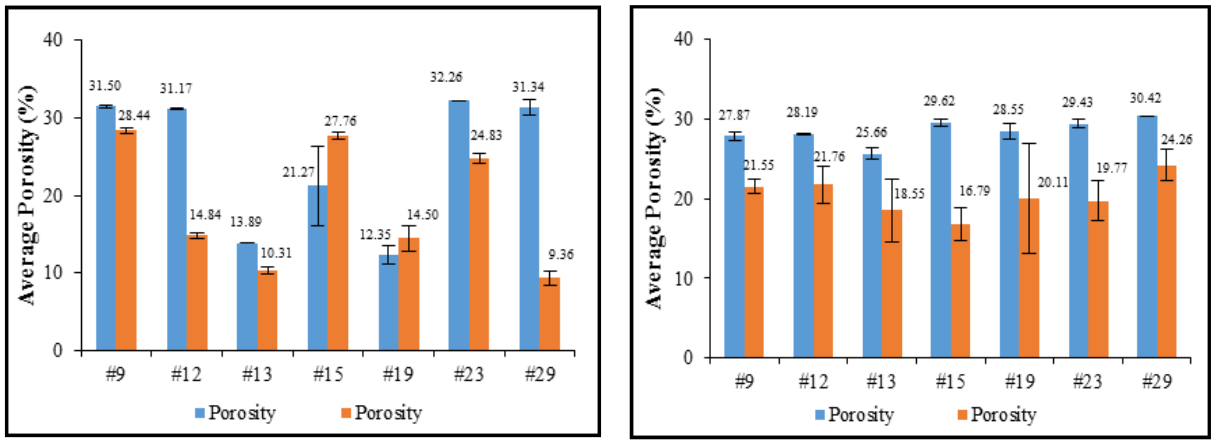

Fig. B.6: Porosity of aged (orange) and unaged (blue) samples: a) GHO; and b) GS

Results of aging tests conducted in the presence of H_2S (**Fig. B.7**) demonstrated acid resistance of the GHO cement. After aging, the porosity of GHO cement slightly reduced. This is attributed to the formation of ettringite as hydrosulfuric acid reacts with the binding components of cement (CH and CSH). On the other hand, baseline cement exhibited mixed trend indicating the presence of leaching, which offsets the impact of ettringite formation on porosity. These measurements are consistent with results obtained from Class H based additive cement (HHO).

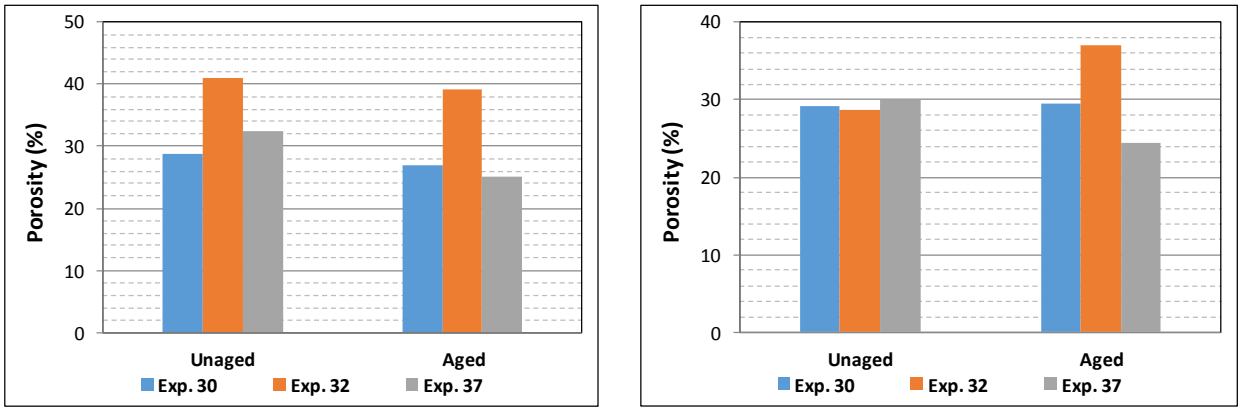

Fig. B.7: Porosity of unaged and aged (in the presence of H_2S) samples: a) GHO; and b) GS

Permeability of Class G baseline samples predominantly decreased after aging (**Fig. B.8**). Some samples showed minor increase in permeability, which is in the order of the margin of error. However, the corresponding HOAP sample (GHO) displayed mixed results. In general, the performance of GHO cement is as good as the baseline cement. In Experiments # 29, porosity of GHO samples diminished significantly while permeability increased dramatically. Similar inconsistency between permeability and porosity measurements were observed in HHO samples. Possible reason for the inconsistency could be carbonation of the matrix at high temperature (430°F), when hydroxyapatite fails to act as an additive against acid attack.

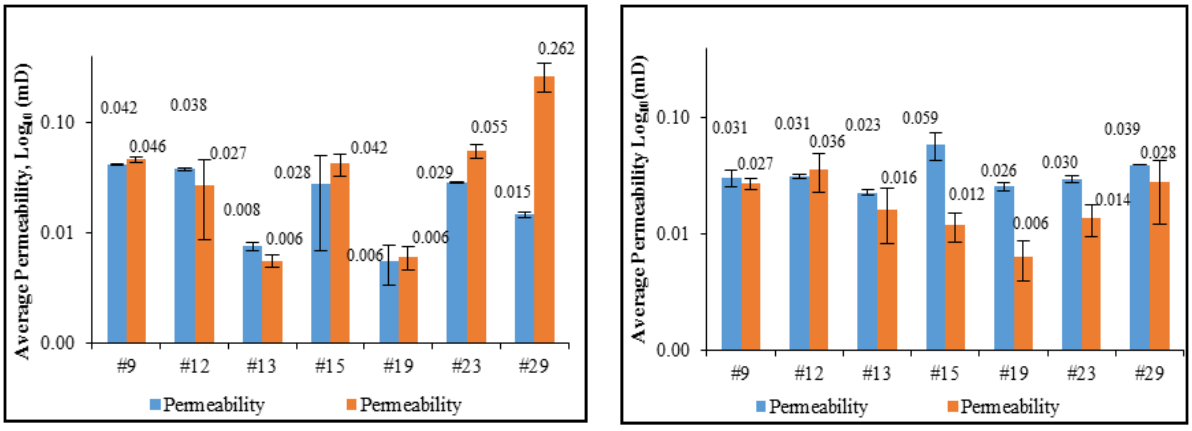

Fig. B.8: Permeability of aged (orange) and unaged (blue) samples: a) GHO; and b) GS

Permeability measurements obtained from samples aged in an environment containing H_2S showed (**Fig. B.9**) the effectiveness of hydroxyapatite in limiting leaching of the cement. Except for high-temperature experiment (Experiment # 32), permeability of GHO samples slightly decreased when aged under different conditions due to the formation of ettringite in the pore space, which reduces porosity and permeability of cement. When aged at high temperature (350°F), permeability of GHO samples slightly increased. Since GHO cement formulation does not include silica, it is prone to structural transformation occurring at high temperatures (greater than 230°F). This transformation can facilitate the leaching process leading to increase in permeability. Moreover, ettringite solubility increases with temperature, resulting in increased porosity and permeability. Consistent with the porosity measurements, baseline cement exhibited increase in permeability in two experiments (Experiments # 30 and 32) demonstrating the presence of leaching, which offsets the carbonation process. However, at high CO_2 concentration (Experiment # 37), carbonation dominated the leaching process leading to reduction in permeability, which is consistent with the porosity measurement.

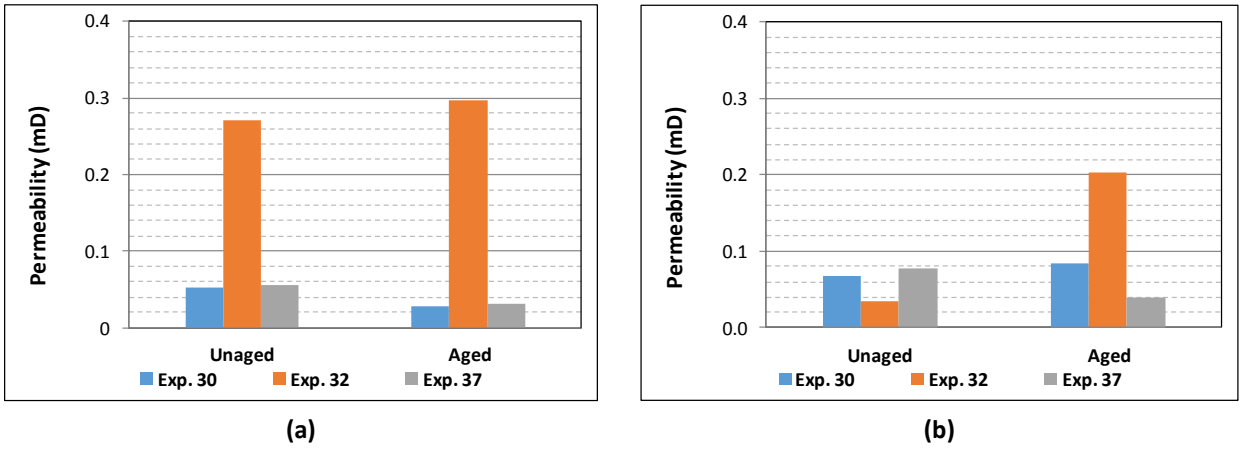

Fig. B.9: Permeability of unaged and aged (in the presence of H_2S) samples: a) GHO; and b) GS

B.1.1.2 Compressive Strength

HOAP samples displayed consistent decrease in compressive strength after aging (**Figs. B.10** and **B.11**). In spite of this, the baseline samples showed a prominent increase except in some cases (Experiments # 9, 13 and 15). The increase is attributed to carbonation of the cement binding components to form $CaCO_3$. Interestingly, the moderate reduction in the strength of HOAP could be due to carbonation of calcium hydroxyapatite. Carbonated hydroxyapatite has lower compressive strength than uncarbonated hydroxyapatite (Sugama and Carciello 1992 and 1993; Martin and Brown 1995). This also indicates that HOAP is able to act as a reactive additive against carbonic acid attack. At high temperature (430°F, Experiment # 29), there was a substantial decrease in the strength, which demonstrated the presence of thermal retrogression. Although the decrease in the strength is a major concern in using the HOAP for high temperature applications (above 430°F), the obtained strength after the aging was still above the accepted industry standards (500 psi).

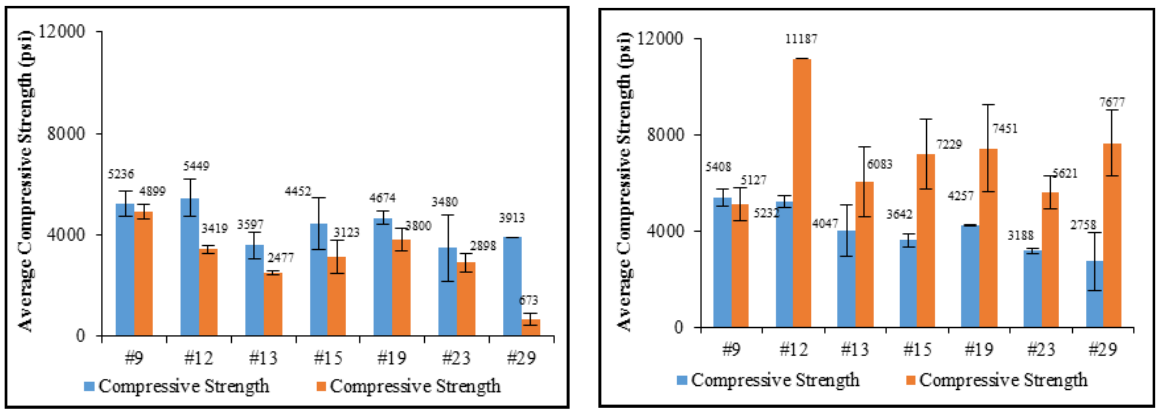

(a) **(b)**

Fig. B.10: Compressive strength of aged and unaged samples: a) HHO; and b) HS

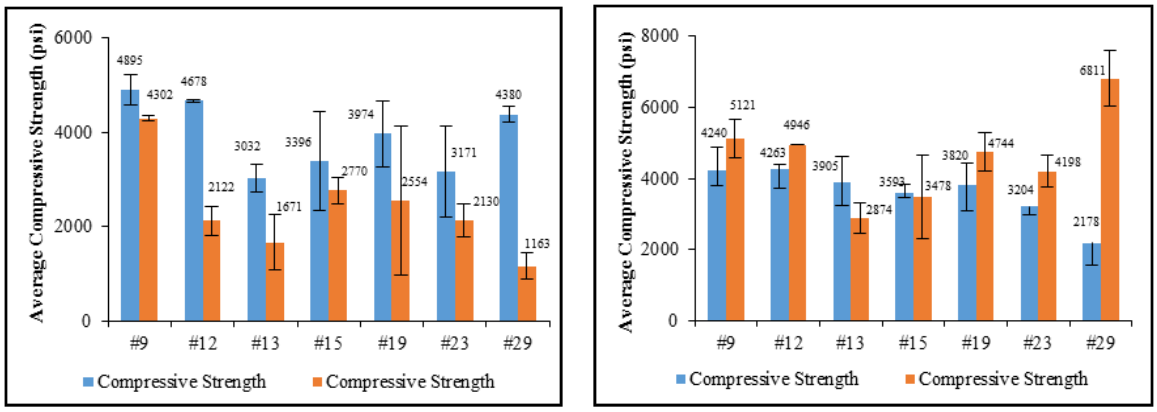

(a) **(b)**

Fig. B.11: Compressive strength of aged (orange) and unaged (blue) samples: a) GHO; and b) GS

Before aging, compressive strength of additive and baseline cements were in the same range. After aging, compressive strength of HHO samples aged in environment containing H_2S showed mostly improvement in strength after the exposure (**Figs. B.12)**.

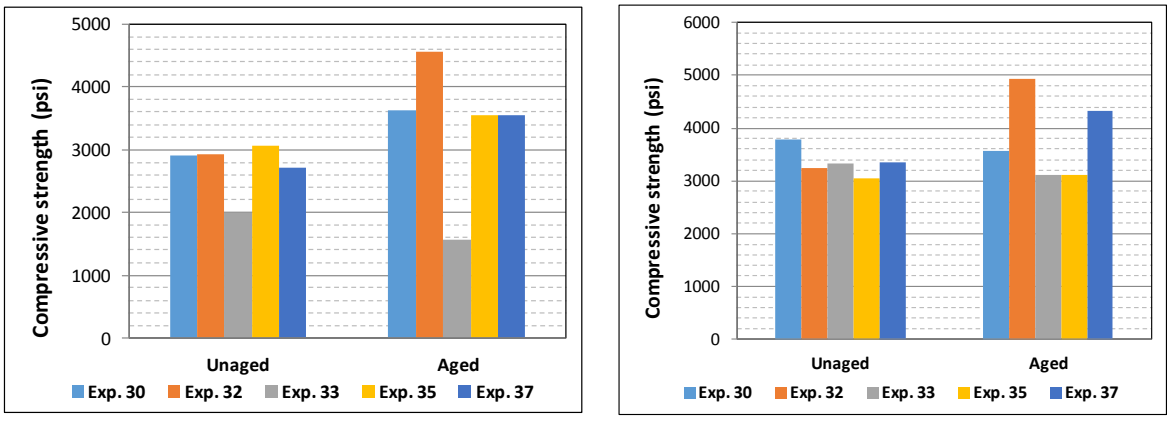

(a) **(b)**

Fig. B.12: Compressive strength of unaged and aged (in the presence of H_2S) samples: a) HHO; and b) HS

The improvement in strength can be attributed to the formation of ettringite. Both reduction and improvement in strength was observed when samples were tested without the presence of CO_2 (Experiments # 33 and 35). These variations are in the order of measurement error. Baseline samples did not display consistent improvement in strength. Carbonation was mostly prominent in the presence of CO_2 in the aging fluid system.

Unaged compressive strength of GHO samples vary significantly. This could be the result of small variation in the mixing procedure of the cement. Although efforts were made to replicate the mixing procedure, similar strength measurements were not obtained for GHO samples. Aging experiments conducted in environment containing H_2S showed mostly reduction in strength of GHO samples after the exposure (**Figs. B.13)**. The improvement in strength can be attributed to the formation of ettringite. Unaged baseline samples from different batches display similar compressive strength. After aging, baseline samples showed slight and inconsistent changes in compressive strengths. In the presence of carbon dioxide (Experiments 30 and 37), slight improvement in strength was observed.

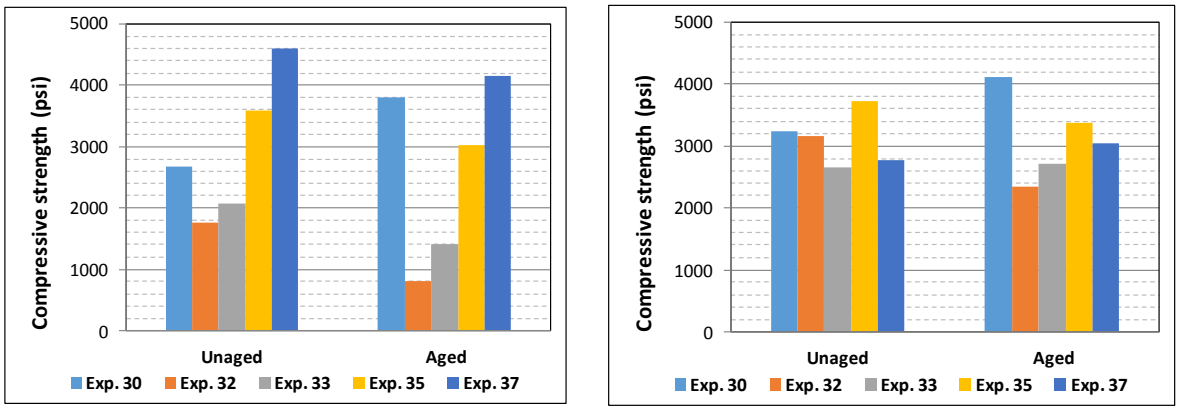

Fig. B.13: Compressive strength of unaged and aged (in the presence of H_2S) samples: a) GHO; and b) GS

B.1.1.3 Shear Bond Strength

The shear bond strength (SBS) of HOAP samples mostly remained the same after aging (**Fig. B.14**). This implies that HOAP cement is not susceptible towards carbonation and expansion. Samples in Experiment # 9 conducted at 100°F, showed the largest increase in the SBS. This can be due to increased solubility of CO_2 at low temperature causing carbonation of hydroxyapatite, which may lead to expansion and increasing of the SBS. Consistent with compressive strength data, results of Experiment # 29 conducted at 430°F indicated extreme reduction in the shear bond strength. This is attributed to thermal retrogression that makes the hydroxyapatite cement very weak.

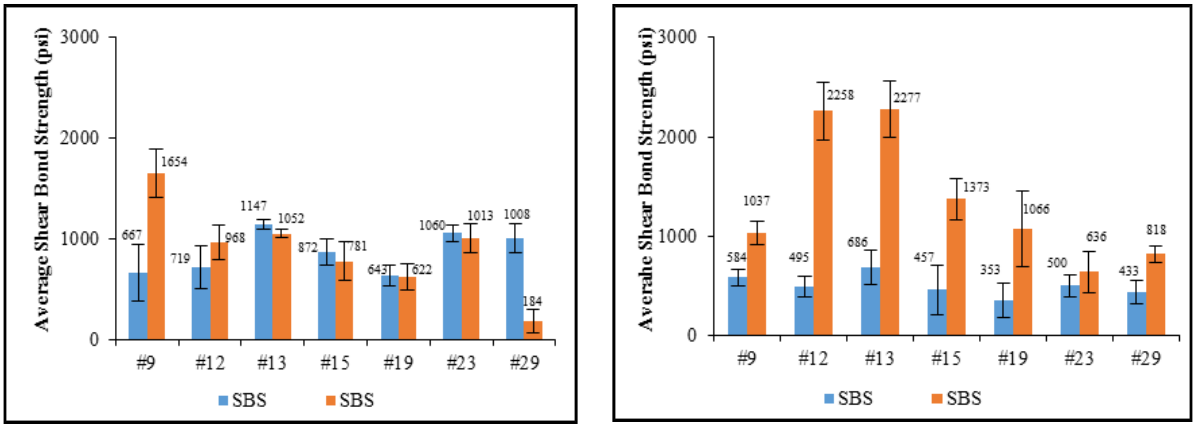

(a) (b)

Fig. B.14: Shear bond strength of aged (orange) and unaged (blue) samples: a) HHO; and b) HS

In the presence of H_2S, HHO samples mostly exhibited slight change in SBS (**Fig. B.15**). Experiment # 37 is an exceptional case in which the unaged sample SBS was considerably low. In general, the additive samples displayed higher SBS than baseline samples. After aging, SBS of baseline samples consistently increase. Three of these experiments (Experiments # 30, 32, and 37) were conducted in the presence of CO_2 and therefore it is expected that carbonation caused the SBS improvement. However, the rest of the experiments (Experiments # 33 and 35) were performance on the absence of CO_2. Hence, only the formation of ettringite is expected to improve the SBS.

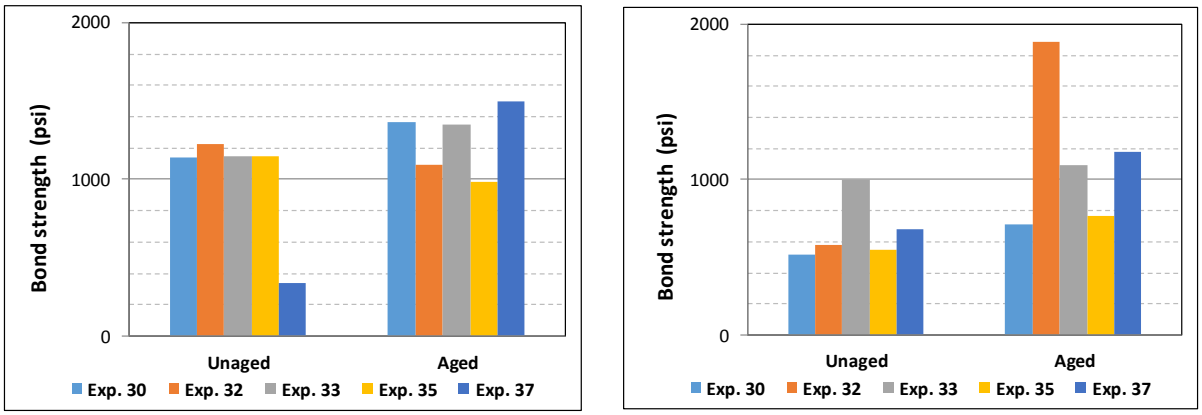

(a) (b)

Fig. B.15: Shear bond strength of unaged and aged (in the presence of H_2S) samples: a) HHO; and b) HS

B.1.1.4 FTIR Analysis

The minerals under focus for the FTIR analysis are CH, CSH and CaCO3. The carbonated form of HOAP also shares similar wavelength as CaCO3 and hence is not distinguishable in the spectrum. The CO3-2 bond peak shows the presence of CaCO3 carbonated calcium hydroxyapatite the samples.). To perform the FTIR tests, additive and baseline cores (with radius R) were first dried and then cut transversely. Three zones in the cylindrical cement cores were identified as outermost (r = R), middle (r = R/2) and innermost (r = 0) zones. Small amount of representative cement sample was cut from each zone and

finely grinded. The amounts of CH, CSH and CaCO3 found in these zones indicate the level of carbonation occurring in each zone.

Inner Zone

FTIR mineralogy results of inner zones of HOAP and baseline cores are displayed in **Fig. B.16**. Except for Experiment # 9, which was conducted at 100°F, CH was not preserved in all the baseline samples. However, CH and CSH were preserved in HOAP samples noticeably indicating the performance of hydroxyapatite. CSH component of the matrix varied for each experiment. In some experiments, the baseline samples preserved higher level of CSH in the inner zone. The HOAP samples showed varying amount of CSH. HOAP may have been able to intercalate CSH in the matrix distorting the structure. Interestingly the CH and CSH components in Experiment # 29 (430°F) are more in HOAP samples, indicating a preserved state even after thermal retrogression, which resulted in high-permeability and low compressive and bond strengths.

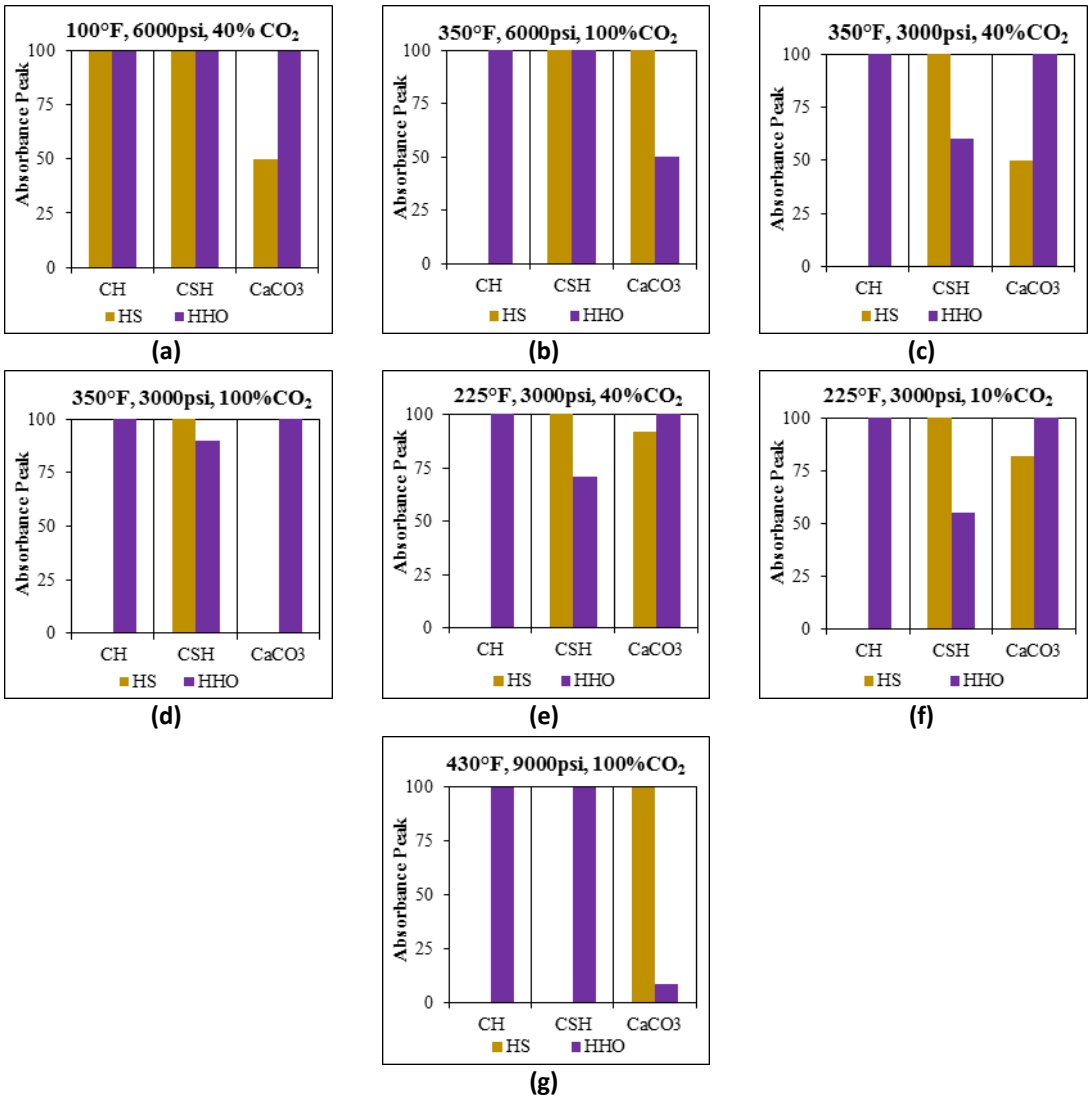

Fig. B.16: FTIR results in inner zone of HOAP and baseline HS samples aged at different conditions: a) Exp. 9; b) Exp. 12; c) Exp. 13; d) Exp. 15; e) Exp. 19; f) Exp. 23; and g) Exp. 29

Middle Zone

The FTIR results obtained from the middle zones of HOAP and baseline samples are presented in **Fig. B.17**. Being exposed to the harsh condition more than the inner zone, the middle zone is expected to show a reduced presence of CH and CSH. The HOAP samples were able to prevent degradation of CH while it was completely carbonated from baseline samples. In addition, HOAP samples mostly preserved CSH, although the amount varying from experiment to experiment. Experiment # 13 is the only test that CSH was completely carbonated form HOAP samples. The CSH was completely carbonated in the baseline samples during Experiments # 12, 13 and 15.

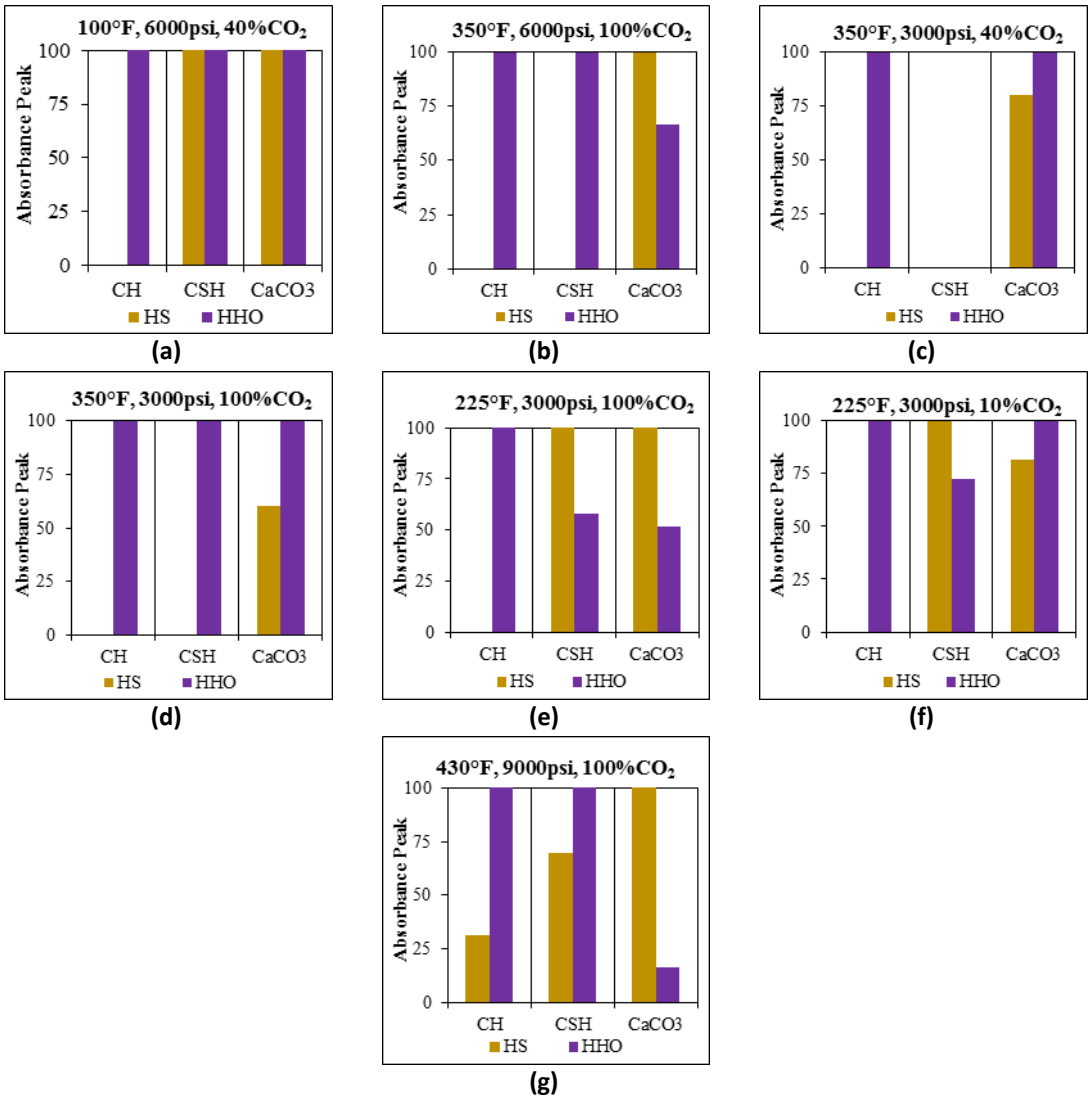

Fig. B.17: FTIR results (middle zone) of HOAP and baseline HS samples aged at different conditions: a) Exp. 9; b) Exp. 12; c) Exp. 13; d) Exp. 15; e) Exp. 19; f) Exp. 23; and g) Exp. 29

Outer Zone

The outer layer is highly exposed to the acid attack. Therefore, it is expected to have maximum amount of $CaCO_3$ and minimum levels of CH and CSH content. The FTIR results obtained from the outer zones of HOAP and baseline samples are presented in **Fig. B.18**. In most cases, the CH and CSH components were

completely consumed. The baseline samples mostly display strong $CaCO_3$ peaks and limited peaks of CH (one case) and CSH (two cases) implying strong acid attack and carbonation. The HOAP samples showed slightly better performance than baseline samples. They showed one peak of CH and three peaks of CSH. The HOAP samples also preserved the essential component (CSH) in their outer most zone even under extreme condition (430°F, 9000 psi and 100% CO_2), which resulted in dramatic permeability increase (Experiment # 29).

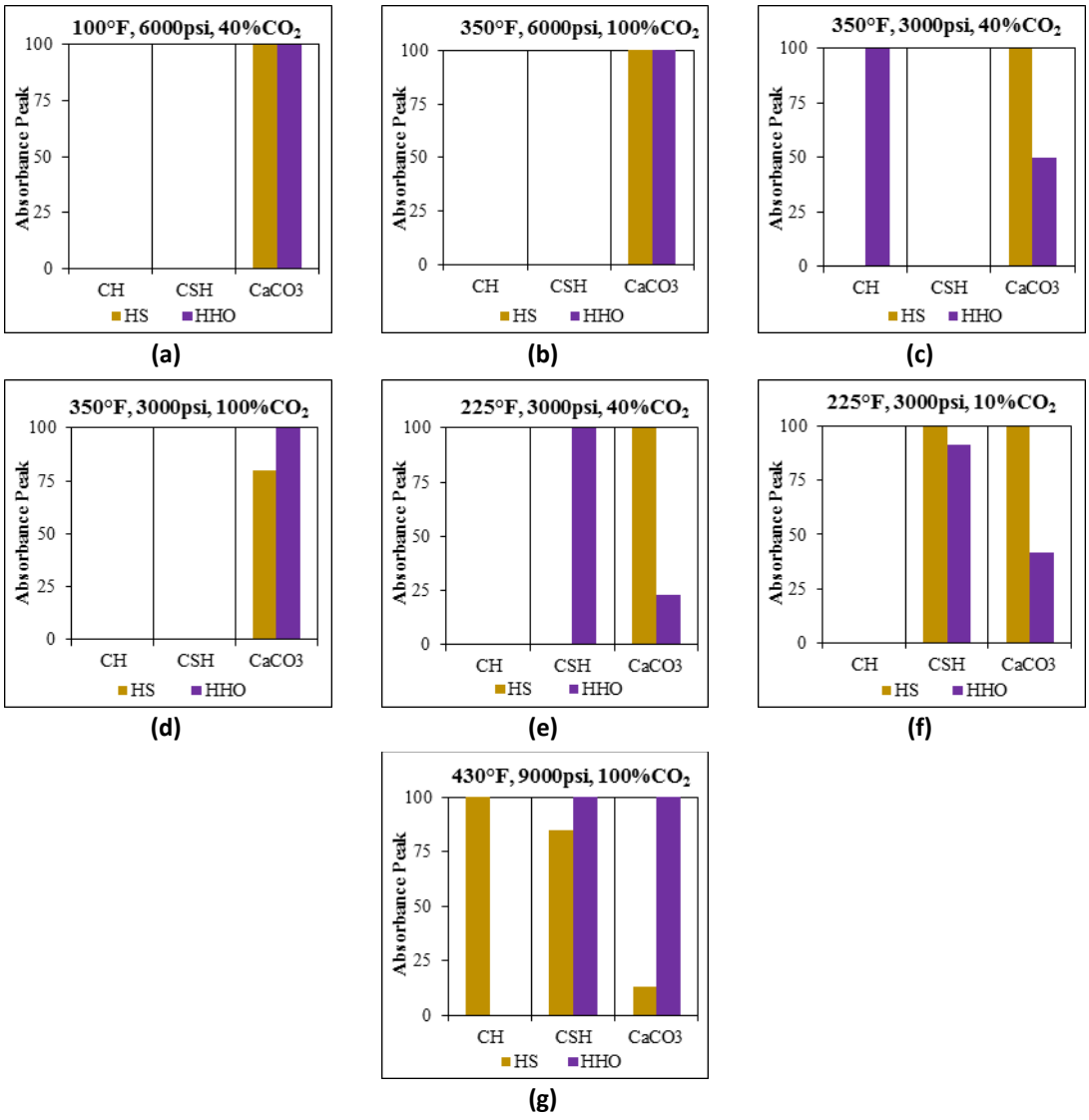

Fig. B.18: FTIR results (outer zone) of HOAP and baseline HS samples aged at different conditions: a) Exp. 9; b) Exp. 12; c) Exp. 13; d) Exp. 15; e) Exp. 19; f) Exp. 23; and g) Exp. 29

B.1.1.5 Summary

Consistent porosity, permeability and shear bond strength of HOAP samples after aging, along with a slight reduction in the compressive strength due to limited carbonation indicate the protection of the main binding components of the cement (CH and CSH) from carbonic acid attack. In addition, the FTIR mineralogy results evidently demonstrated the presence of CSH and CH in the matrix of HOAP samples while they were completely carbonated in baseline samples. This proves that HOAP is able to react with

CO_2 and protect the matrix from carbonation. However, at higher temperature (430°F), the samples exhibited severe thermal retrogression in the strength.

B.1.2 Magnesium Oxide

Magnesium oxide is an expanding additive for cement. The expanding property has been studied (Zhang et al. 2012 and 2011; Nokken 2010; Ali and Mullick 1998; Ghofrani and Plack 1993; Agzamov et al. 2013; Rubiandini et al. 2005; Buntoro and Rubiandini 2001; Cheung 1999) extensively. As reported by Rubiandini et al. (2005), the use of magnesium oxide as an expanding additive in cement was proposed by Danjuschewskij (1983).

Magnesium oxide is industrially produced by calcinating dolomite ($CaMg(CO_3)_2$). The temperature at which the calcination is performed defines the reactivity of magnesium oxide. Calcination above 1652°F tends to lower the reactivity and causes MgO to hydrate very slowly. MgO calcinated at temperatures below 1652°F hydrate faster, causing expansion of cement in early stages. Calcination temperature of magnesium oxide used in this investigation is approximately 2282°F.

The hydration of MgO involves formation of $Mg(OH)_2$ crystals, which occupy the pore space and result in expansion of the cement matrix (Rubiandini et al. 2005). The expansion is required to take place at the precise point of time during setting of the cement in the well, and to reduce cement porosity and permeability. Expansion that occurs in the liquid slurry phase does affect the cement properties. Expansion after the complete setting causes cracking of the cement, which is highly undesirable. Hence, expansion has to occur during the setting phase of the cement so that the porous space of the cement is effectively reduced (Ghofrani and Plack 1993).

Experimental results (Rubiandini et al. 2005) showed the expansion property of MgO, and improvement of compressive and shear bond strength after its addition. Moreover, the results indicated that expansion tendency of MgO increases with calcination temperature. It was also observed that addition of 3 – 5% BWOC MgO into the cement was optimal to provide high compressive and shear bond strengths at temperatures above 482°F (Buntoro and Rubiandini 2001). Ghofrani and Plack (1993) also report similar results with MgO when subjected to hydration. In summary, extensively documented properties of MgO are: i) the formation of $Mg(OH)_2$ crystals; ii) swelling and expansion of cement that reduce porosity and permeability; and iii) improvement in compressive and shear bond strengths.

Although $Mg(OH)_2$ undergoes carbonation to form $MgCO_3$, these crystals are insoluble in water. Hence, they do not easily leach out like calcium bicarbonate (Cheremisinoff 1995). These properties made MgO a suitable cement additive for HPHT applications. Despite a number of studies have been conducted on magnesium oxide, the full extent of its benefit is not well investigated. This is because the level of expansion is highly dependent on number of factors including temperature, pressure, composition and properties of surrounding fluid, and composition of the cement sample.

In this project, magnesium oxide is one of the additives selected for developing acid resistance cement formulations. To test the performance the new formulations, 5% magnesium oxide cements (MGO-5) and baseline samples were aged under different conditions presented in **Table B.2**. Aged and unaged sample properties (porosity, permeability, compressive and shear bond strengths and FTIR mineralogy) were measured and analyzed.

Table B.2: Aging conditions for MGO samples

MGO Batch #	Exp. #	Baseline Batch #	Temp. (ºF)	Pressure (psi)	Concentration		
					CH_4 (%)	CO_2 (%)	H_2S (ppm)
2	8	10	225	6000	0	100	0
3	10	12	100	6000	0	100	0
4	7A	15	225	6000	60	40	0
5	14	17	350	9000	60	40	0
6	20	23	225	9000	60	40	0
7	22	25	225	9000	0	100	0
8	31	34	225	6000	90	10	300
10	34	37	100	6000	60	40	180
11	36	39	100	9000	90	10	300
12	38	41	100	3000	100	0	300

B.1.2.1 Porosity and Permeability

Figure B.20 depicts porosities of aged and unaged Class H based MGO-5 (HSMG) and baseline (HS) samples. Aging was conducted predominantly in brine (2% NaCl) saturated with methane gas containing CO_2. All baseline samples showed substantial reduction in the porosity, which is attributed to carbonation. However, MGO-5 samples showed limited reduction in porosity resulting from expansion of the matrix (through formation of $Mg(OH)_2$) and partial carbonation that occurred simultaneously. The formation of $Mg(OH)_2$ crystals is beneficial because it can reduce the pore space and prevent penetration of the acid into the matrix thereby limiting the carbonation process.

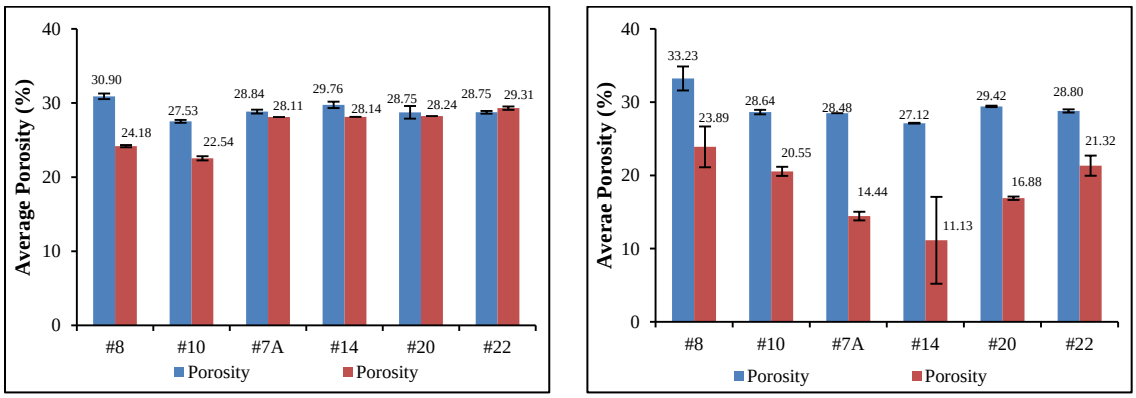

(a) **(b)**

Fig. B.20: Porosity of aged (orange) and unaged (blue) samples: a) HSMG; and b) HS

Furthermore, the performances of the new formulations were tested in the presence of H_2S **Figure B.21** present porosities of aged and unaged HSMG and baseline samples. Baseline samples aged in CO_2-H_2S containing environment (Experiments # 31 and 36) showed substantial reduction in the porosity, which is attributed to carbonation. However, HSMG samples showed mixed results (i.e. slight porosity increase in Experiment # 31 and moderate porosity reduction in Experiment # 36). The reduction in porosity is attributed to expansion of the matrix. The formation of $Mg(OH)_2$ crystals is expected to reduce the pore space and prevent acid penetration and subsequently the carbonation process.

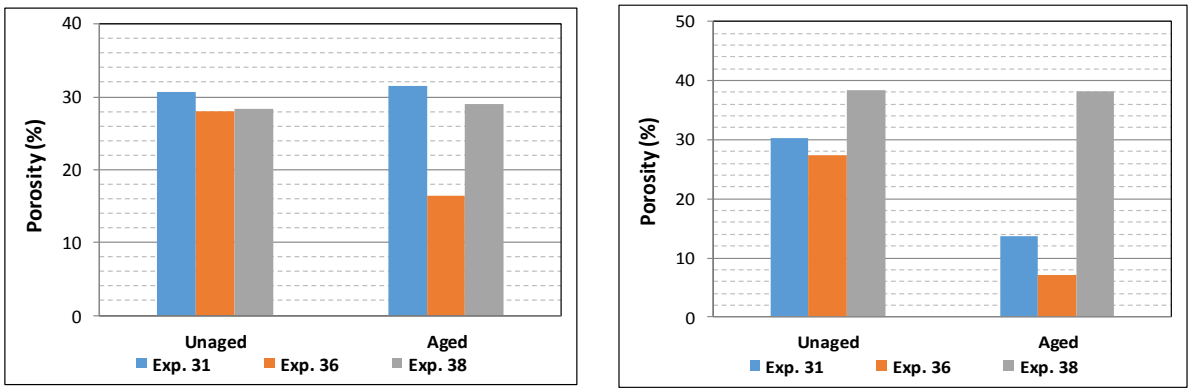

Fig. B.21: Porosity of unaged and aged (in the presence of H_2S) samples: a) HSMG; and b) HS

Consistent with the porosity data, permeability of HSMG and baseline samples showed substantial reduction after aging (**Fig. B.22**). However, permeability alone cannot be used to compare the performance of the MGO-5 samples, as it tends to be highly sensitive to experimental errors and development of micro-cracks resulting from abrupt change in test parameters such as pressure and temperature. It is important to note that porosity and permeability reductions of HSMG samples were less than those of the baseline samples. The $Mg(OH)_2$ crystallization blocks the pore space and limits further decrease in porosity due to carbonation.

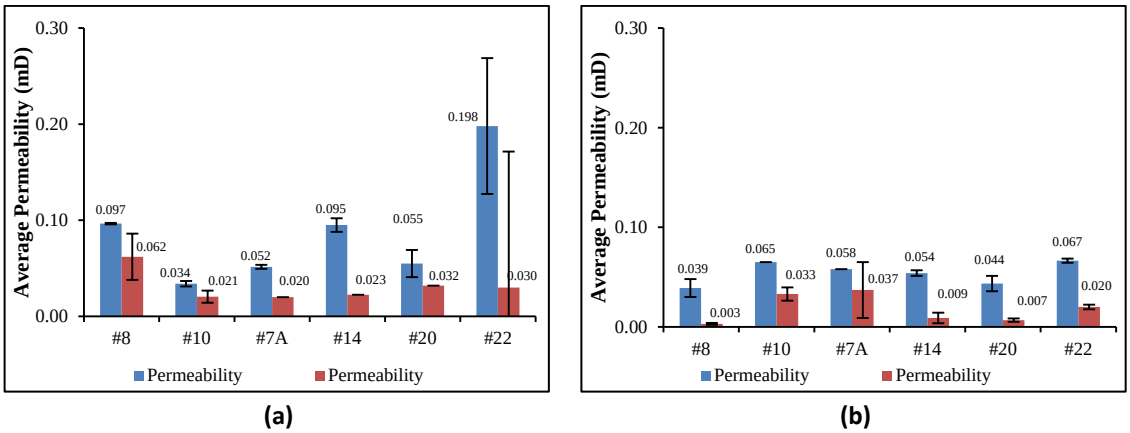

Fig. B.22: Permeability of aged (orange) and unaged (blue) samples: a) HSMG; and b) HS

In the presence of H_2S, permeability of baseline samples showed (**Fig. B.23**) substantial reduction after aging, while HSMG samples displayed reduction in only one of the experiments (Experiment # 31). The reduction in permeability was more pronounced when aging was carried about in CO_2 containing environment (Experiments # 31 and 36). Hence, examining the change in porosity and permeability of HSMG samples, it can be concluded that the addition of magnesium oxide reduces the penetration of carbonic acid and consequently limits the reduction in porosity and permeability resulting from carbonation.

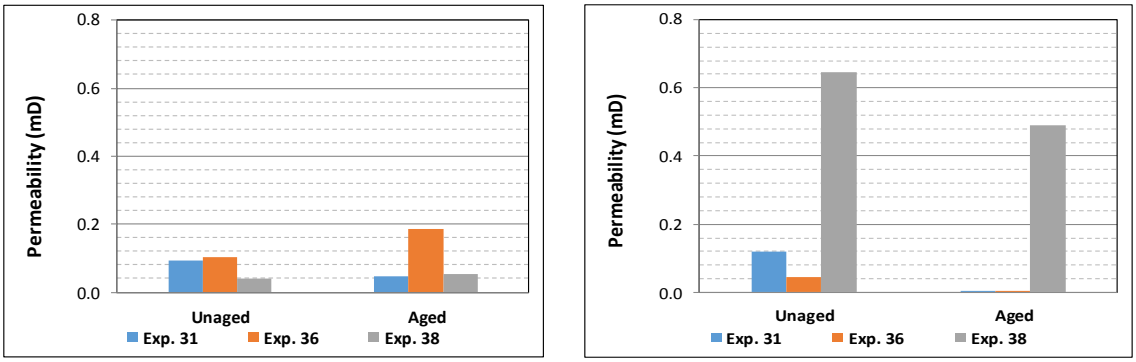

Fig. B.23: Permeability of unaged and aged (in the presence of H_2S) samples: a) HSMG; and b) HS

Class G based MGO-5 (GSMG) samples did not show a consistent decrease in the porosity or permeability (**Figs. B.24** and **B.25**). Even though baseline samples displayed consistent decrease in porosity resulting from carbonation, measurements from GSMG samples were mixed. In addition, permeability measurements of some of GSMG samples (Experiments # 8 and 14) demonstrated excessive increase, which indicates poor performance. Such an increase in permeability is attributed to severe leaching or development of micro cracks. There is inconsistency in the performance of GSMG.

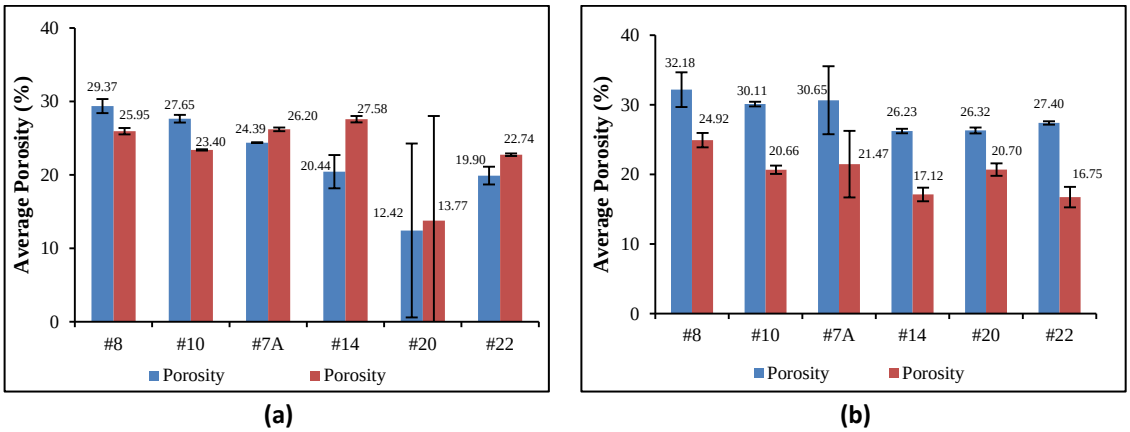

Fig. B.24: Porosity of aged (orange) and unaged (blue) samples: a) GSMG; and b) GS

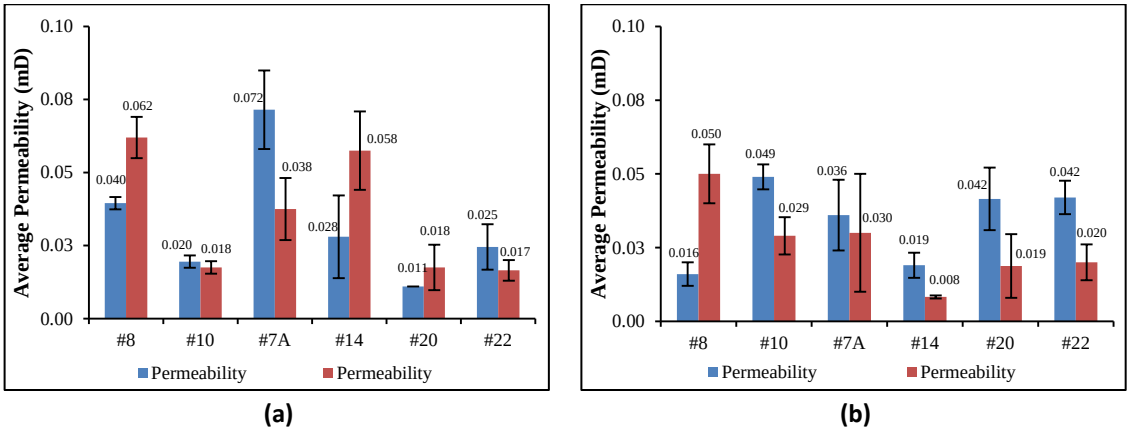

Fig. B.25: Permeability of aged (orange) and unaged (blue) samples: a) GSMG; and b) GS

Aging tests conducted in the presence of H_2S showed very similar results. GSMG samples porosity or permeability predominately increased after aging while baseline samples displayed mostly decrease in porosity and permeability due to carbonation (**Figs. B.26** and **B.27**). Measurements from GSMG samples indicate poor performance resulting from severe leaching and formation of micro cracks.

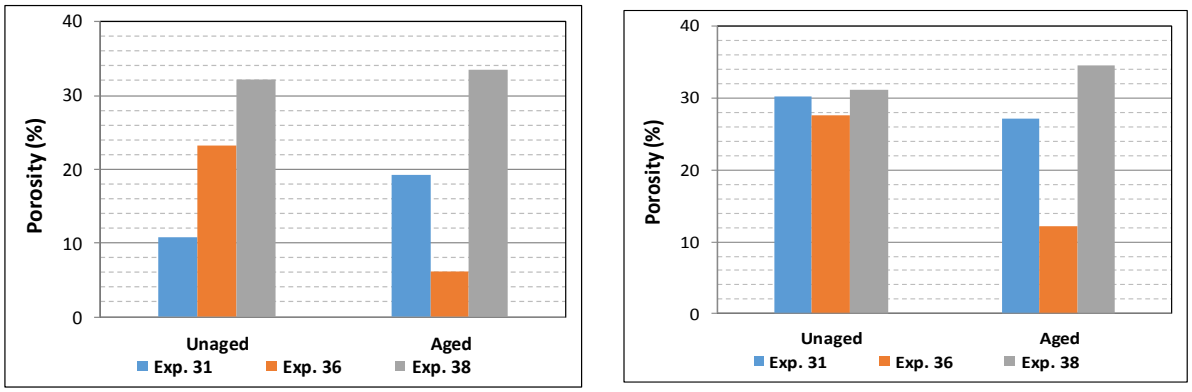

Fig. B.26: Porosity of unaged and aged (in the presence of H_2S) samples: a) GSMG; and b) GS

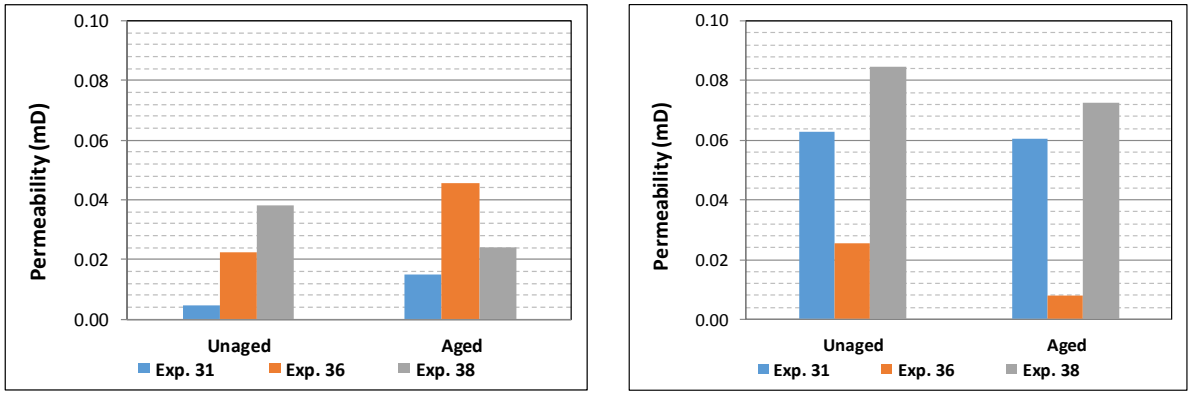

Fig. B.27: Permeability of unaged and aged (in the presence of H_2S) samples: a) GSMG; and b) GS

B.1.2.2 Compressive Strength

The compressive strength for all baseline samples increased after aging due to carbonation of the matrix (**Fig. B.28**). The improvement in strength is due to deposition of carbonate crystals in the pore space reinforcing the structure. The HSMG samples demonstrated a similar increase in the strength, which may be attributed to matrix expansion and carbonation. Results of Experiment # 10 show minimal change in compressive strength of the baseline and HSMG samples. This could be due to aging at low temperature (100°F) and high CO_2 concentration (100% CO_2), which accelerates the dissolution and leaching of CH and CSH from the matrix (Nakarai et al. 2006). The strength gained by the carbonation can be offset by the leaching of the CH and CSH in the presence of excess carbonic acid. Similar results were obtained when the samples were aged in H_2S containing environment (**Fig. B.29**).

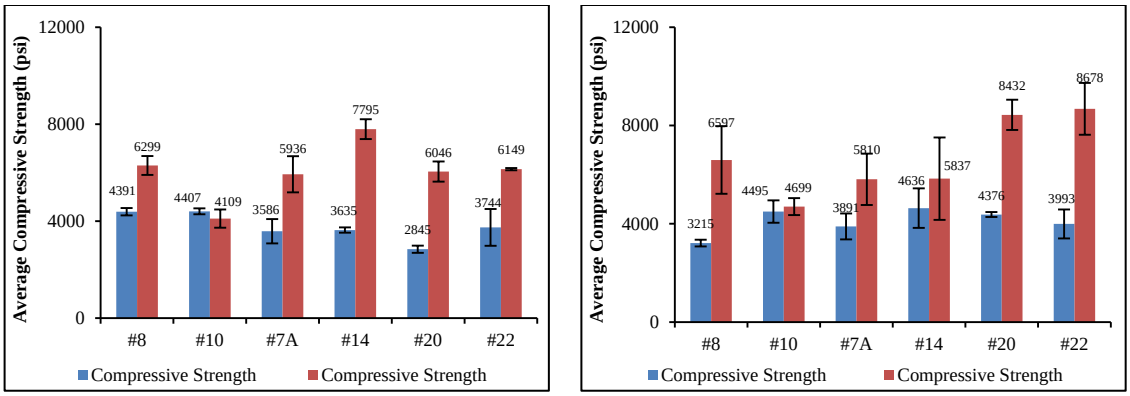

Fig. B.28: Compressive strength of aged (orange) and unaged (blue) samples: a) HSMG; and b) HS

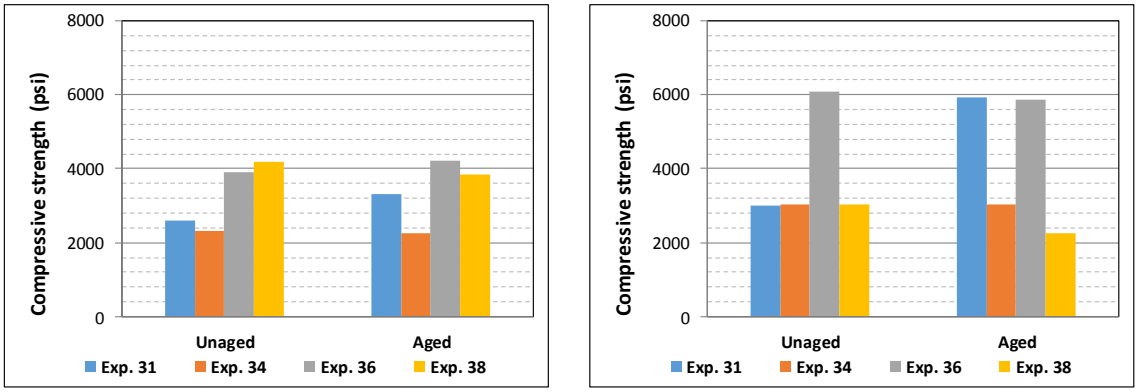

Fig. B.29: Compressive strength of unaged and aged (in the presence of H_2S) samples: a) HSMG; and b) HS

Compressive strengths of GSMG and baseline cements were predominately increased after aging (**Fig. B.30**). However, the average strength improvement for GSMG samples was slightly lower than that of the baseline samples. Moreover, like the porosity results, GSMG samples displayed inconsistent increase and decrease in their compressive strength. Baseline samples showed better consistence than the additive samples. Very similar results were obtained when the samples were tested in H_2S containing environment (**Fig. B.31**).

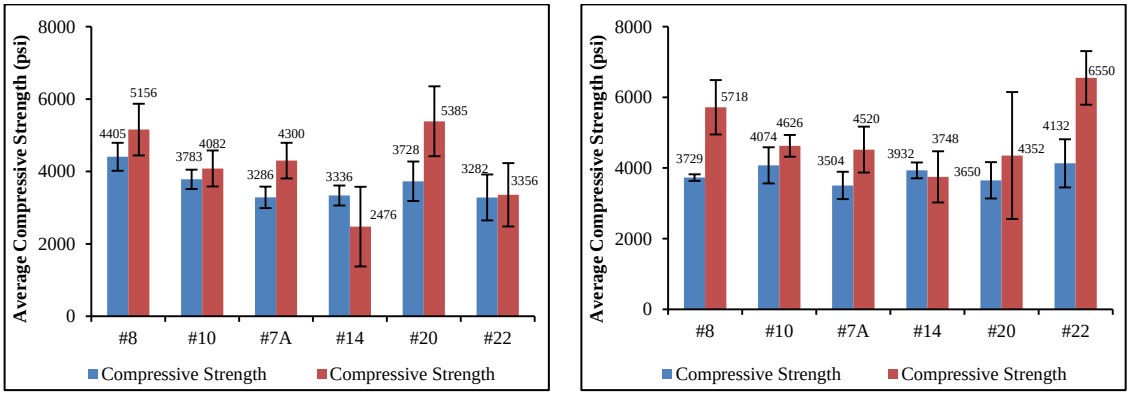

Fig. B.30: Compressive strength of aged (orange) and unaged (blue) samples: a) GSMG; and b) GS

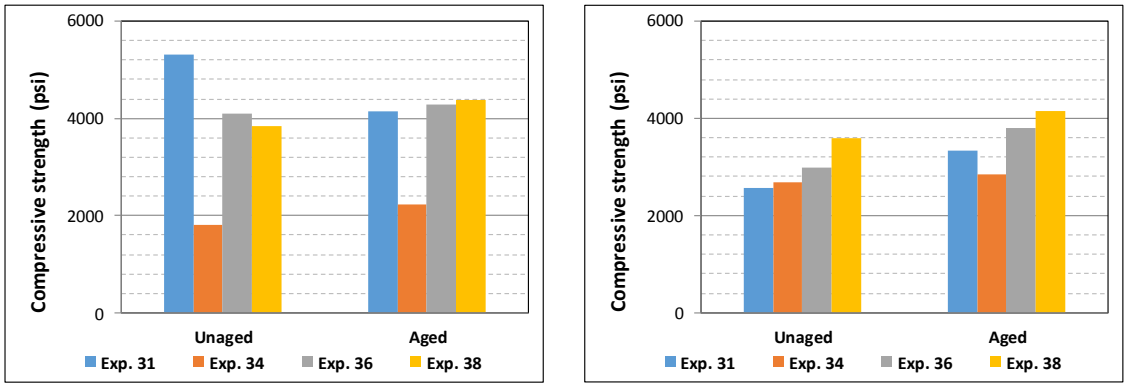

Fig. B.31: Compressive strength of unaged and aged (in the presence of H_2S) samples: a) GSMG; and b) GS

B.1.2.3 Shear Bond Strength

As the cement matrix expands, the shear bond strength is expected to increase. The MGO-5 and baseline samples showed steady increase in the shear bond strength (**Fig. B.32**). In the presence of CO_2, baseline samples are expected to expand due to carbonation. The expansion of MgO takes place due to hydration occurring inside the matrix, while carbonation caused by acid attack is happening as the same time. However, measuring the extent of hydration of MgO and carbonation of CH and CSH in the matrix to quantify the expansion level is challenging. Results of Experiment # 10 indicate the lowest increment in the shear bond strength in both the samples due to leaching of CH component because of low temperature (100°F) and high CO_2 concentration (100% CO_2). When experiments conducted in the presence of H_2S, similar results were obtained (**Fig. B.33**).

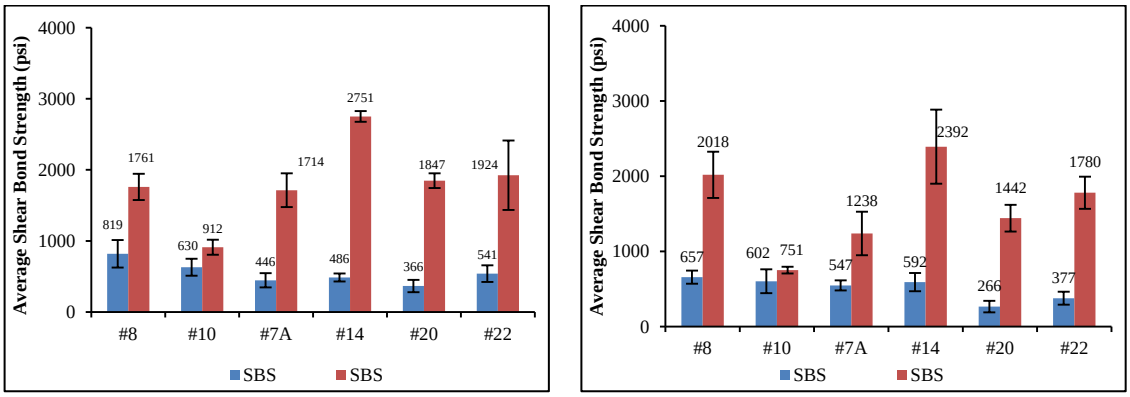

Fig. B.32: Shear bond strength of aged and unaged samples: a) HSMG; and b) HS

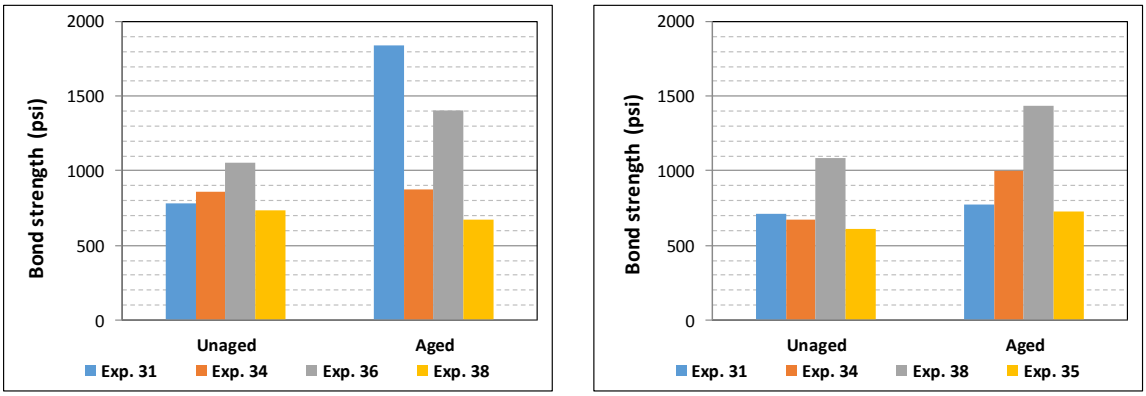

Fig. B.33: Shear bond strength of unaged and aged (in the presence of H_2S) samples: a) HSMG; and b) HS

B.1.2.4 FTIR Analysis

FTIR results of Class H based MGO-5 and baseline samples are presented in this section. The minerals under focus for the FTIR analysis are CH, CSH, $CaCO_3$ (denoted by CCO3) and $Mg(OH)_2$ (denoted by MH). MgO and $MgCO_3$ can also be identified at wave lengths of 500 cm^{-1} and 880/1480 cm^{-1}, respectively. However, the noise in the FTIR spectrum is in the order of hundreds (0 – 500 1/cm); hence, very low measurements like that of MgO may not provide reliable information.

Inner Zone

The results of the inner zone (**Fig. B.34**) indicate the presence of CH and CSH components along with $Mg(OH)_2$ in the matrix. All experiments except the one conducted at 350°F (Experiment 14), demonstrated the presence of CH and/or CSH. The presence of $Mg(OH)_2$ in the cement demonstrate the reduction of carbonic acid penetration. $Mg(OH)_2$ crystals also undergo carbonation forming $MgCO_3$, which is insoluble compound that precipitates in the matrix. Unlike $CaCO_3$, $MgCO_3$ does not react readily with carbonic acid to form a soluble product (Cheremisinoff, 1995) that can be leached out by the surrounding fluid. Hence, carbonation of $Mg(OH)_2$ to $MgCO_3$ is beneficial in limiting acid attack.

The $CaCO_3$ bars in the FTIR spectrum shown in the charts include both $MgCO_3$ and $CaCO_3$. Hence, it can be misleading to assess the performance of MGO-5 by comparing $CaCO_3$ peaks alone; other peaks can be used to evaluate its performance. According to the results, the performance of MGO-5 in Class H cement seems to be effective to a certain extent. MGO-5 cement expected to resist acid attack by generating $Mg(OH)_2$ crystals during carbonation. The formation the crystals in the pore space reduce porosity and permeability of the cement and limit the penetration of the acid.

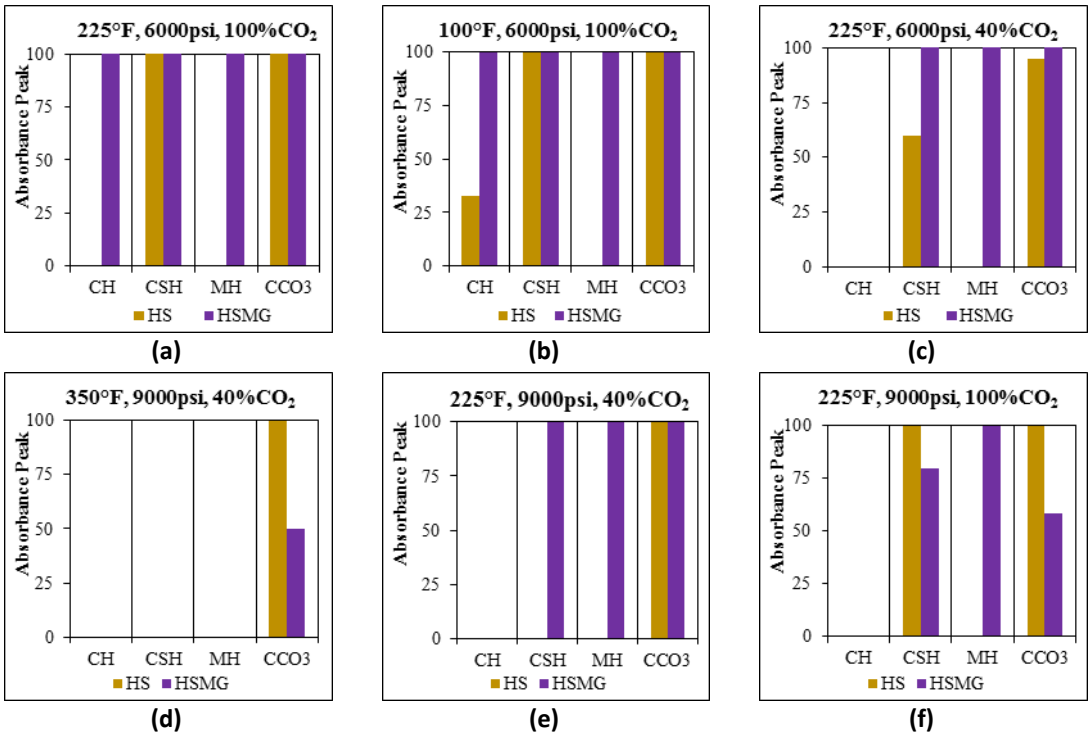

Fig. B.34: FTIR results of inner zone of MGO-5 and baseline HS samples aged at different conditions: a) Exp. 8; b) Exp. 10; c) Exp. 7A; d) Exp. 14; e) Exp. 20; and f) Exp. 22

Middle Zone

The middle zone is expected to show more carbonation than the inner zone (**Fig. B.35**). The CH and CSH were only preserved when aged at 100°F and 100% CO_2 (Experiment # 10). Results are consistent with the inner zone measurements. $Mg(OH)_2$ was preserved in three experiments. The CSH, which was preserved in the inner zone during Experiments # 8 and 22 was completely carbonated in the middle zone.

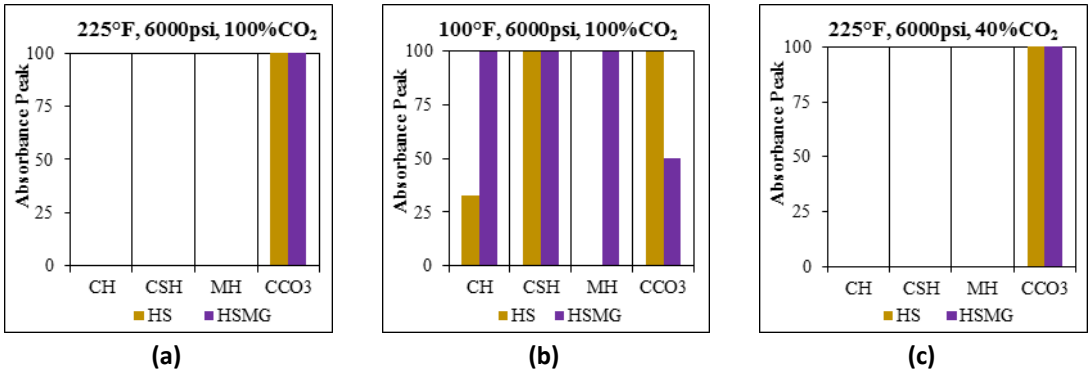

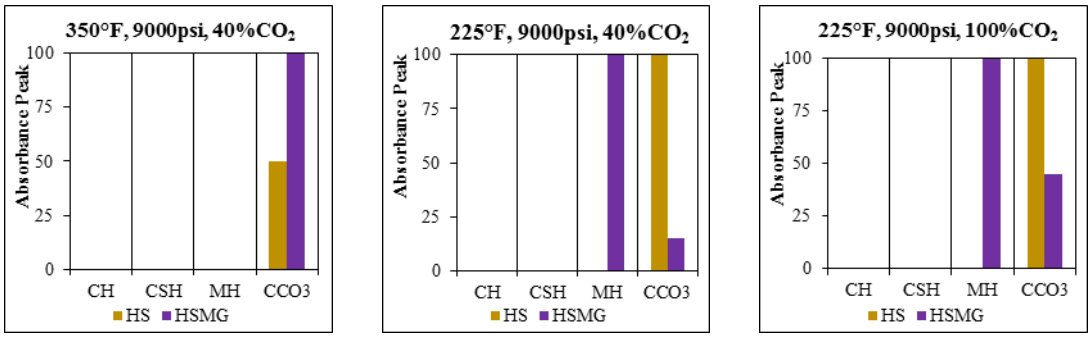

(d) (e) (f)

Fig. B.35: FTIR results of middle zone of MgO and baseline HS samples aged at different conditions: a) Exp. 8; b) Exp. 10; c) Exp. 7A; d) Exp. 14; e) Exp. 20; and f) Exp. 22

Outermost Zone

The outermost zone is the most degraded zone due to direct exposure. Only $CaCO_3$ was found to be present in all the samples. It should be noted that the $CaCO_3$ peaks also comprise $MgCO_3$ content (**Fig. B.36**).

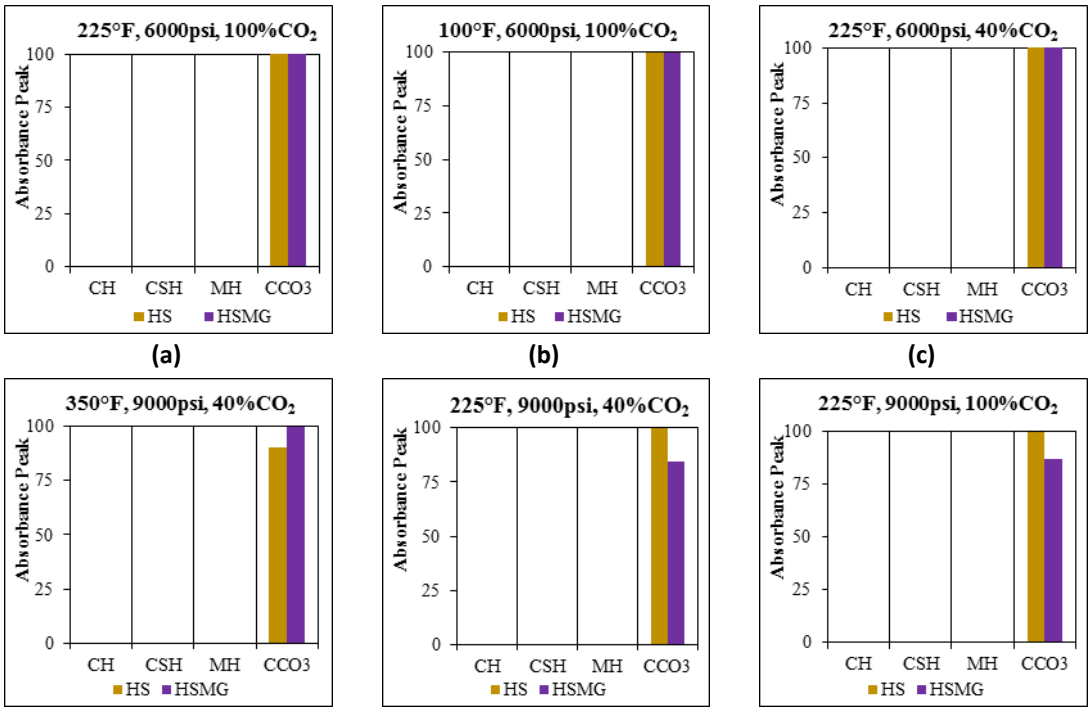

(a) (b) (c)

(d) (e) (f)

Fig. B.36: FTIR results of outer zone of MgO and baseline HS samples aged at different conditions: a) Exp. 8; b) Exp. 10; c) Exp. 7A; d) Exp. 14; e) Exp. 20; and f) Exp. 22

B.1.2.5 Summary

Examining the results of ten experiments, it can be concluded that MGO-5 was able to act as an expanding agent in the cement. The formation of $Mg(OH)_2$ leads to expansion of matrix, which is highly dependent on temperature. Although the $Mg(OH)_2$ crystals were able to reduce porosity, they were susceptible to carbonation to form $MgCO_3$. The advantage of the formation of $MgCO_3$ over $CaCO_3$ is

that, it does not form soluble product that can be easily leached out when it reacts with the acid. According to FTIR study, the presence of CH and CSH component in the inner zone confirms a protected MGO-5 matrix, even though the middle and outer zone indicate a leached zone.

B.2 Experimental Results Showing Acid Resistance of New Cement Formulations

Addition of magnesium oxide or hydroxyapatite is expected to preserve cement properties such as porosity, permeability, and compressive and bonding strength after exposure to acidic environment.

B.2.1 Acid Resistance of Hydroxyapatite Cement

Twelve aging experiments were performed to evaluate performance of hydroxyapatite-based cement (HOAP). Samples were subjected to different aging conditions (Table B.1). For all batches of aging experiments, slurry compositions (**Table B.3**) and properties were maintained the same. Properties of the slurries are presented in **Table B.4**.

Table B.3: Composition of the HOAP slurries

Component	Unit	GHO	HHO
Cement	%	100	100
Hydroxyapatite	% BWOC	5	5
Antifoam Agent	gal/sack of cement	0.1	0.1
Water for Cement	% BWOC	44	38
Water for HOAP	% BWOC	23	23

BWOC = by weight of cement

Table B.4 Properties of hydroxyapatite containing cement slurries

Slurry	GHO	HHO
Amount	5% bwoc	5% bwoc
Remarks	No Silica Flour and HEC	No Silica Flour and HEC
Density (ppg)	15.80 ppg	16.65 ppg
API Fluid Loss	82 ml	88 ml
Thickening Time	60 minutes	90 minutes

Hydroxyapatite cement samples are expected to react with the acid, and form carbonated-hydroxyapatite ($Ca_5(PO_4)_3CO_3$), according to the following reaction:

$$2Ca_5(PO_4)_3(OH) + CO_3^{-2} \rightarrow 2Ca_5(PO_4)_3(CO_3) + OH^{-2} \quad \text{..... (B-1)}$$

The formation of carbonated-hydroxyapatite layer around the core prevents the cement from further acid attack. The hexagonal structure of the hydroxyapatite remains intact without disruption due to the formation of carbonated-hydroxyapatite (Sugama 2006). However, after aging, a slight expansion is still observed in the samples, which can be as a result of carbonation of $Ca(OH)_2$ and CSH present in the cement matrix.

B.2.1.1 Performance under Low Temperature Conditions

Batch 002 samples were aged at 100°F using 40% CO_2 gas. After aging, the samples were cut in the middle to examine the depth of degradation. The samples did not exhibit feasible discoloration that indicates changes in property. However, reduction in porosity and permeability (**Fig. B.37**) were observed while their shear bond strengths were improved substantially (**Figs. B.38**) due to expansion of the cement resulting from carbonation. More carbonation is expected in HS samples than HOAP cores resulting in high tendency of expansion and increased bonding strength. However, at 100°F, leaching may be higher for HS samples. Leaching counterbalances the effects of carbonation and adversely affects SBS improvement.

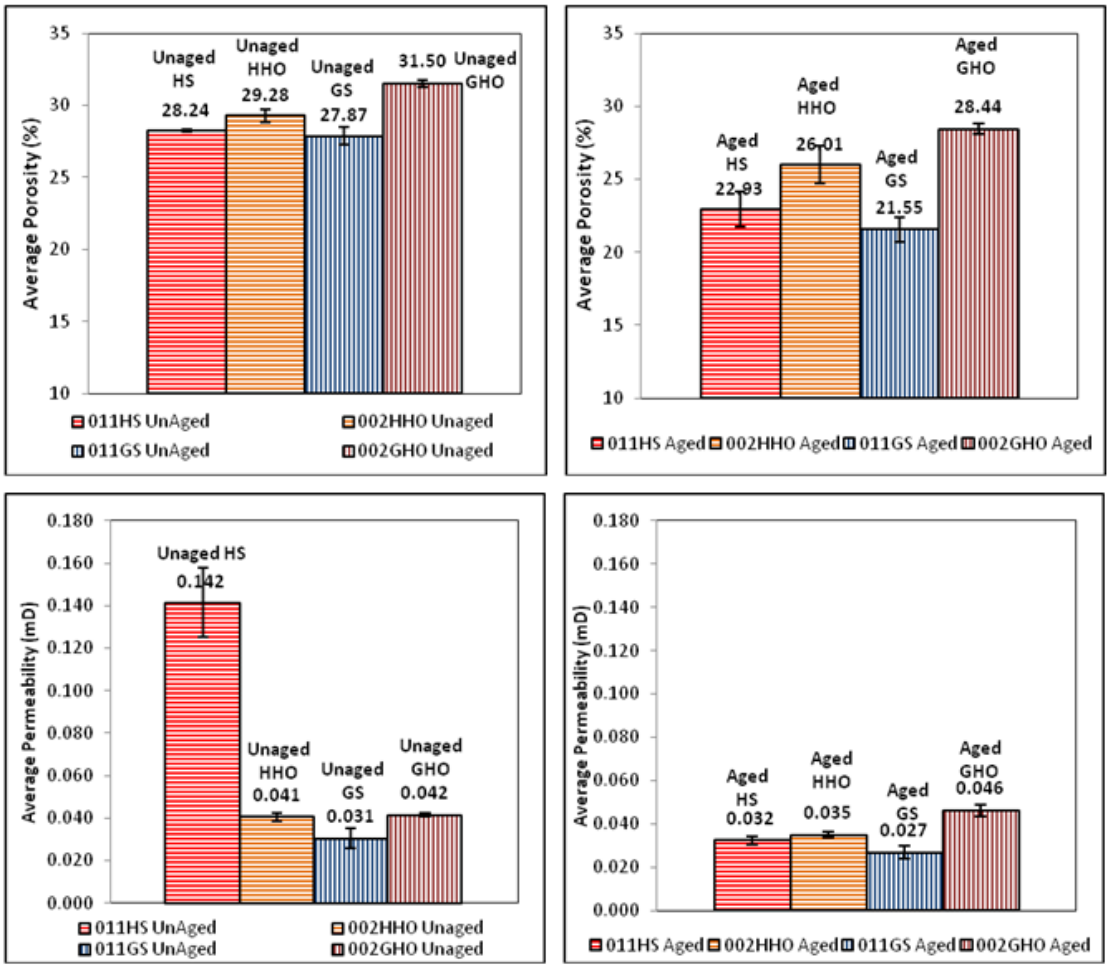

Fig. B.37: Porosity and permeability of HOAP and baseline samples (aging at 100°F, 6000 psi and 40 % CO_2)

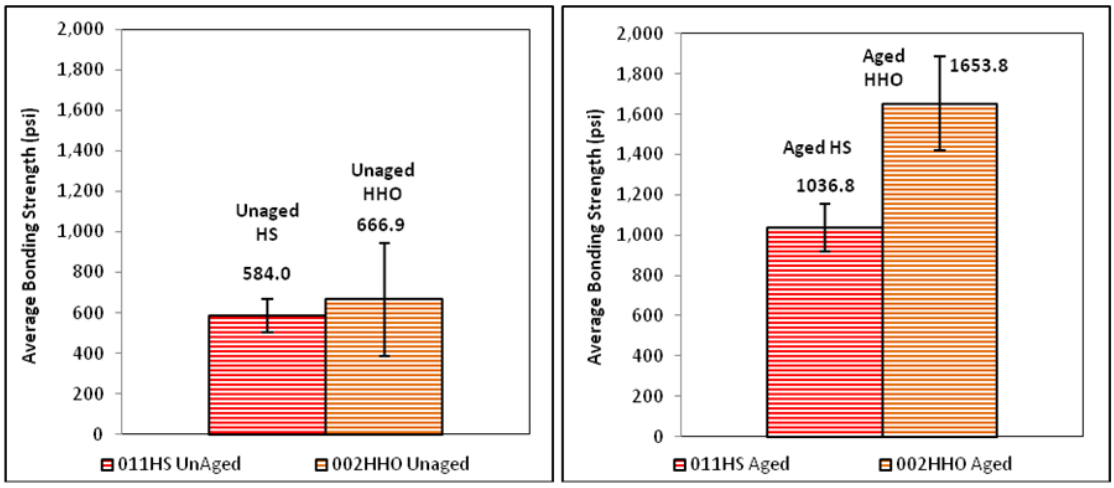

Fig. B.38: Shear bond strength of baseline and HOAP samples (aging condition: 100°F, 6000 psi and 40 % CO_2)

Compressive strength of aged and unaged samples were approximately the same (**Fig. B.39)** This suggests the presence of mild carbonation without discoloration of the cores. Only small variations within the range of measurement discrepancy were observed. The trend of compressive strength measurements are similar to those obtained for permeability tests. The reason can be attributed to the formation of thin carbonated layer on the outer rim of HOAP samples that prevents further penetration of CO_2 or occurrence of comparable levels of carbonation and leaching that maintains the strength of the cores more or less the same.

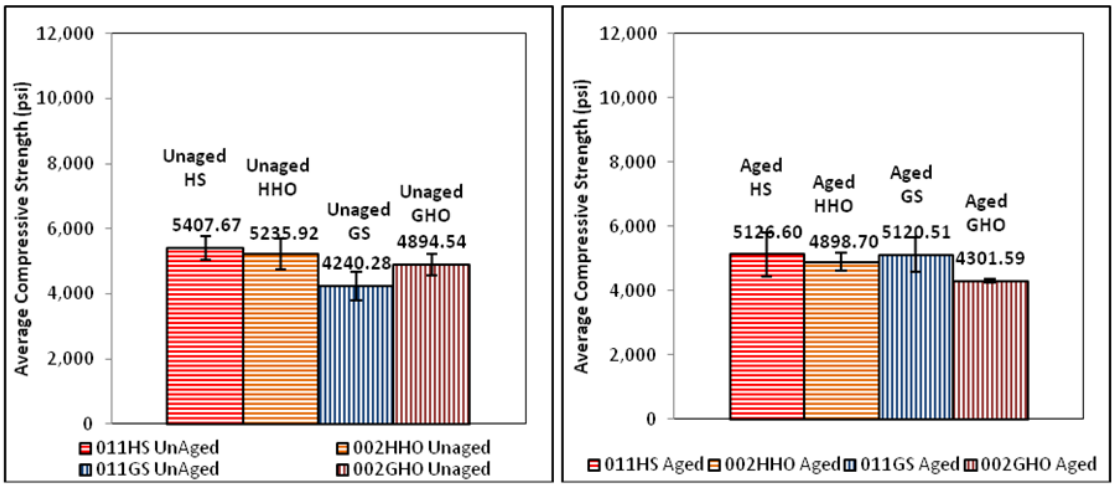

Fig. B.39: Compressive strengths of baseline and HOAP cements (aging at 100°F, 6000 psi and 40 % CO_2)

B.2.1.2 Performance under High Temperature Conditions

When aged at high temperature (350°F) and high CO_2 concentration (100% CO_2 gas), both the HOAP and baseline cement samples showed (**Fig. B.40**) a clear discoloration indicating the degradation depth. It can be clearly observed that HOAP samples experienced very less degradation as compared to the baseline cement samples. The discoloration front, which can be related to the depth of penetration of CO_2, is observed only as a very small outer rim in the HOAP samples. Due to the non-uniformity of the degradation depth, an average degradation depth is calculated and used to compare the samples.

Results (**Table B.5)** indicate substantial difference in degradation depth between the baseline cement and HOAP samples. The introduction of hydroxyapatite into the cement system considerably improved the resistance of the cement against carbonic acid attack.

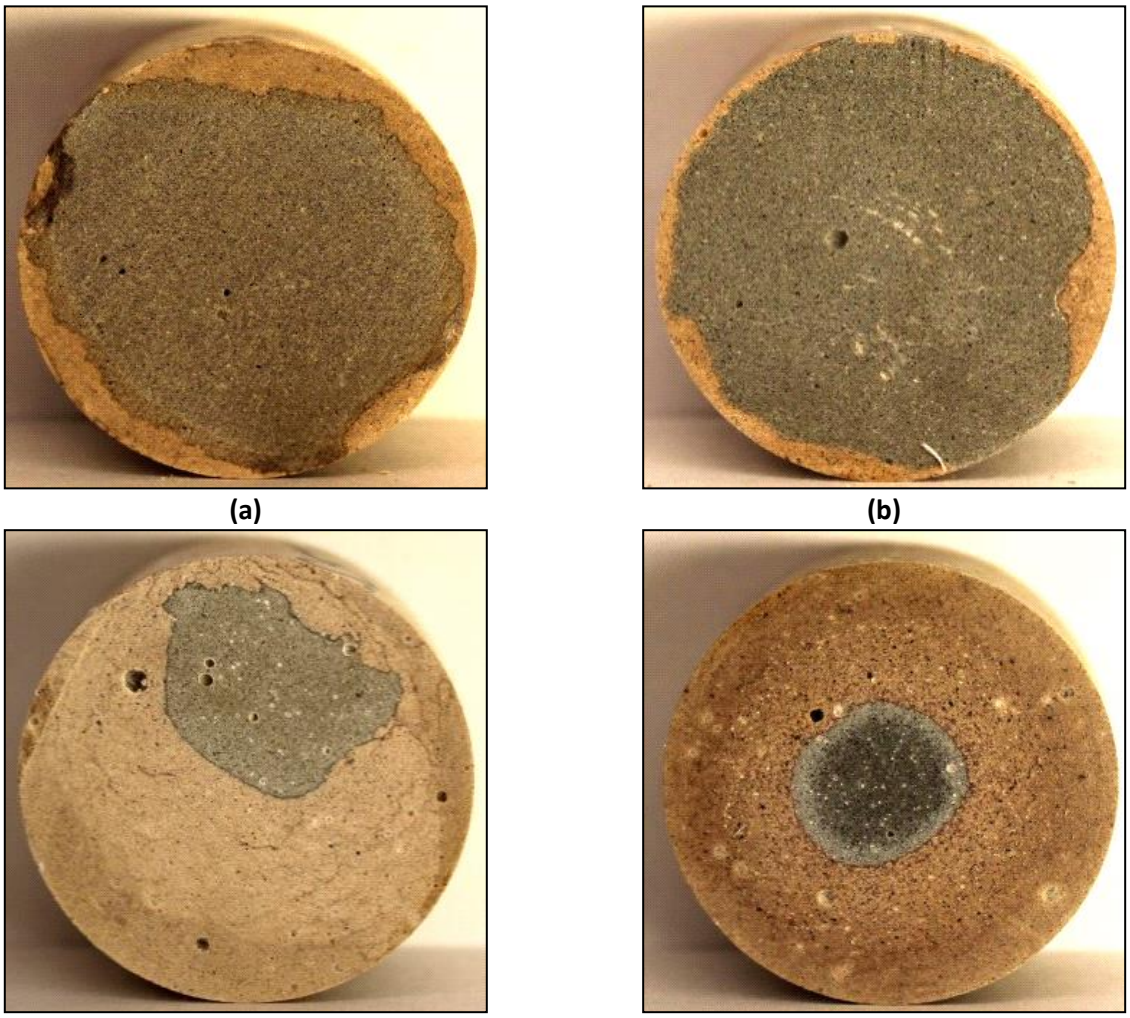

Fig. B.40: Middle cross-section of cores after aging at 350°F with 100% CO_2 gas: a) GHO; b) HHO; c) GS; and d) HS

Table B.5: Degradation depth of HOAP and baseline samples aged at 350°F

Core #	Average carbonated depth (in.)	Std. Dev.
HHO	0.046	0.022
HS	0.353	0.018
GHO	0.063	0.051
GS	0.351	0.203

At high temperature (350°F), HOAP samples showed reduction in compressive strength while the baseline samples displayed improvement (**Fig. B.41**). The increase in strength of baseline cement is

due to carbonation which results in precipitation of $CaCO_3$ in the pore space. The strength improvement is consistent with the degradation measurements obtained from baseline samples. The precipitated $CaCO_3$ in the pore provides reinforcement to the cement matrix, resulting in improvement of the compressive strength. Studies on HOAP containing cement are very limited. It is not clear why the strength of HOAP samples reduced after aging. Possible explanations could be leaching and/or thermal retrogression. HOAP samples did not exhibit substantial carbonation as presented in the degradation depth measurements. In addition, when it is carbonate, it does not precipitate in the pore space. However, it becomes a part of the matrix without increasing the compressive strength. As a result, leaching can dominate the aging process causing reduction in strength. Another reason is that silica flour, which is needed to prevent thermal retrogression, was not added in the HOAP slurries to maintain slurry properties within acceptable range. The lack of excess silica in the cement system can result in thermal retrogression, when the cement is exposed to high temperatures (i.e. greater than 230°F).

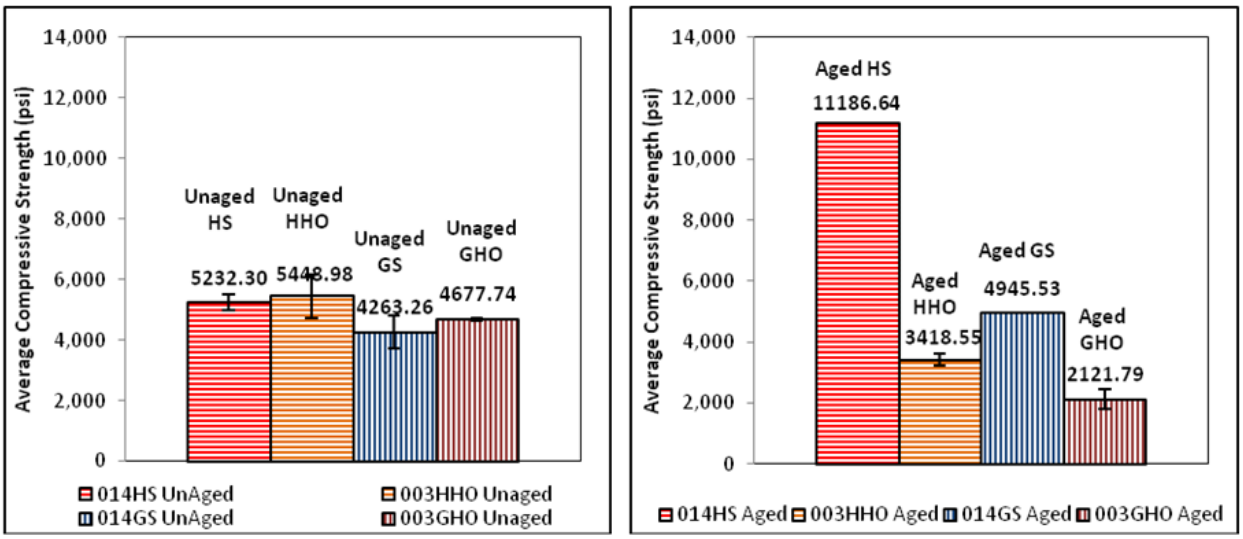

Fig. B.41: Compressive strengths of baseline and HOAP cements (aging at 350°F, 6000 psi and 100 % CO_2)

For samples aged at 350°F and 100% CO_2, the HOAP samples showed a lower increase in SBS than the HS samples (**Fig. B.42**). This could be attributed to temperature retrogression resulting from lack of excess silica to prevent the formation of weak CSH phase (α-CSH). This observation is consistent with compressive strength measurements.

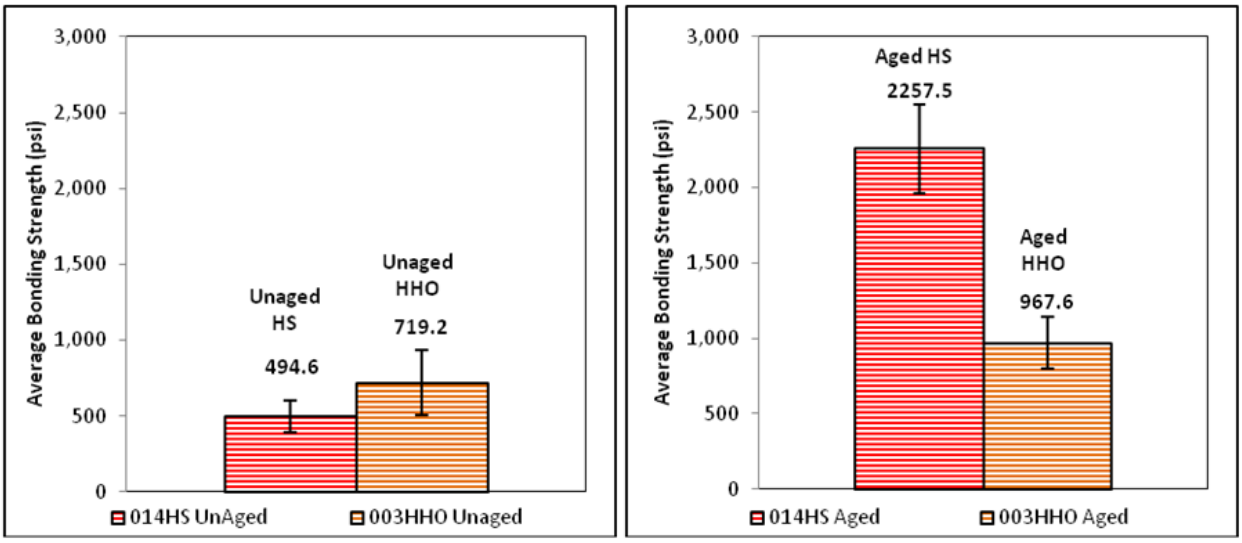

Fig. B.42: Shear bond strength of baseline and HOAP samples (aged at 350°F, 6000 psi and 100 % CO_2)

B.2.1.3 Performance Comparison using FTIR Measurements

The porosity, permeability, degradation depth, compressive strength and shear bond strength measurements indicate a lesser amount of calcium carbonate formation in the HOAP samples. The Fourier Transform Infrared Spectroscopy (FTIR) tests were carried by taking samples from the outermost, middle and innermost zones of a transversely cut cement cores. Spectrum peaks of relevant molecular bonds that indicate the level of CH, CSH and $CaCO_3$ in each zone are summarized and presented from **Figs. B.43** to **B.45**.

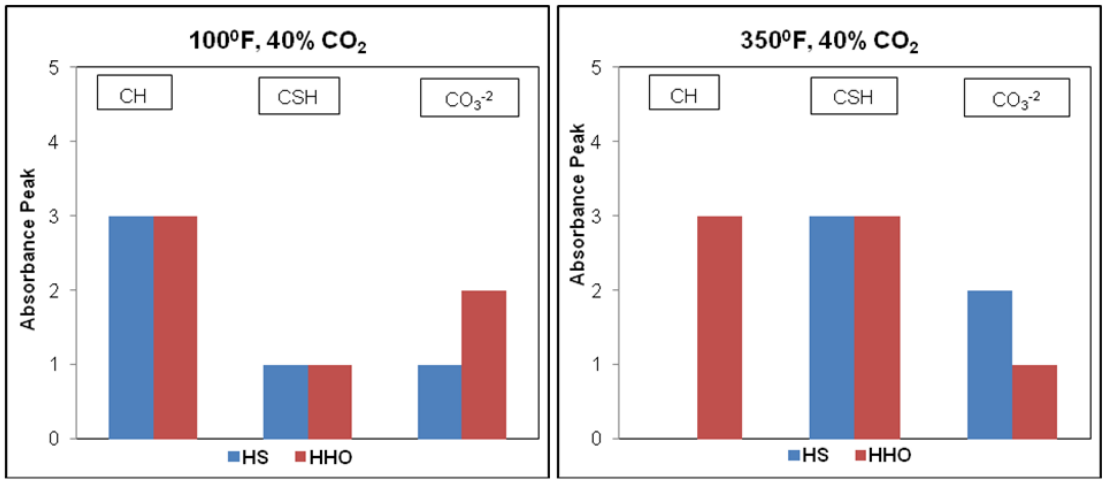

Fig. B.43: Summarized FTIR data for HOAP and baseline samples (innermost Zone)

In the inner zone of the sample (Fig. B.43), the amounts of CH and CSH were almost the same in both HS and HOAP samples after aging at 100°F and 40% CO_2. However, the amount of carbonate was higher in HOAP than HS samples. The source of this carbonate bond can be calcium carbonate and/or carbonated-hydroxyapatite ($Ca_5(PO_4)_3.CO_3$) formed from the HOAP. The type of carbonate is not distinguishable from FTIR result. On the other hand, after aging at 350°F and 100% CO_2, the CH present in the HS samples was fully carbonated while abundant amount of CH was found in the HOAP sample. In

all zones, the level of carbonation is higher in the HS sample than in HOAP samples when aged at 350°F. This means that the amount of carbonate, including $CaCO_3$ and $Ca_5(PO_4)_3.CO_3$, formed in HOAP samples is lesser than calcium carbonate formed in HS samples.

FTIR results from the middle zone also displayed (**Fig. B.44**) acceptable carbonation resistance of HOAP samples. After aging, CH was completely absent in the HS sample; however, it was still present in abundant amount in HOAP samples. After aging at 100°F, the amount of CSH and $CaCO_3$ was almost same in both HS and HOAP samples. However, after aging at high temperature (350°F) the CSH was not found in the HS samples indicating complete carbonation of the matrix, while abundant amount of CSH was present in HOAP samples. In addition, the amount of carbonate formed in HOAP samples was less than that formed in HS cores. The outer zone showed a complete carbonation of the matrix in both cases (**Fig. B.45**). This result was expected as the outer rim is most vulnerably exposed to the harsh environment.

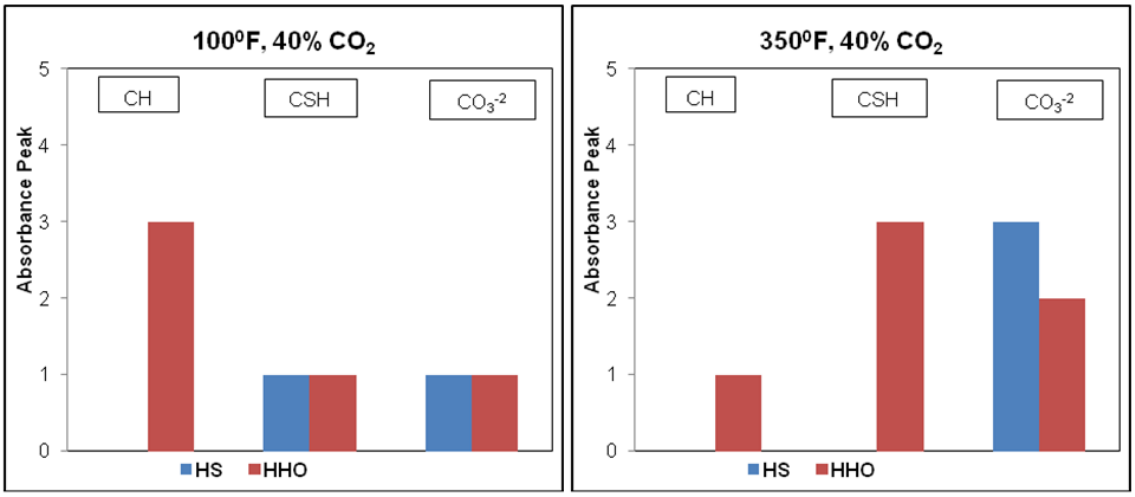

Fig. B.44: Summarized FTIR data for HOAP and baseline samples (middle zone)

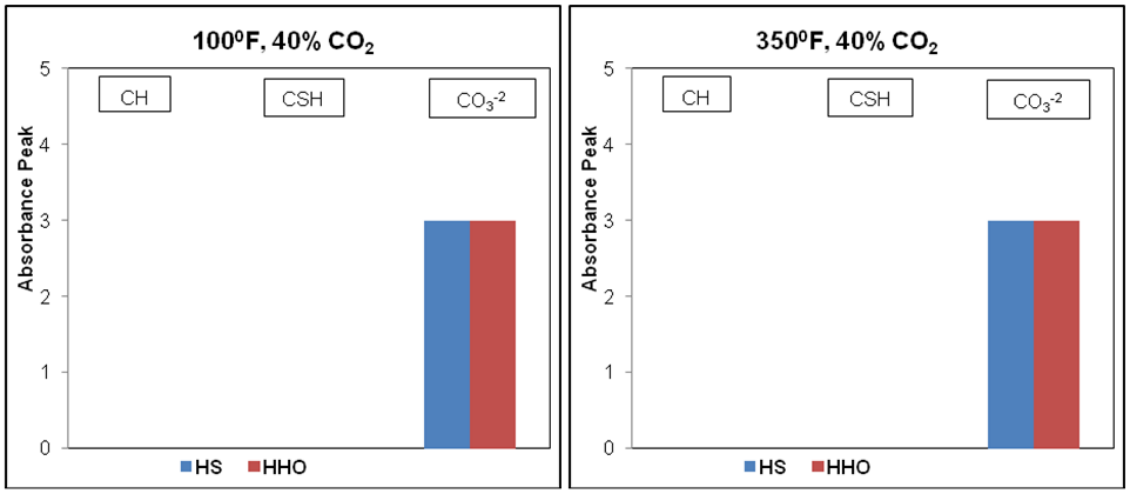

Fig. B.45: Summarized FTIR data for HOAP and baseline samples (outermost zone)

B.2.2 Acid Resistance Magnesium Oxide Cement

Additive screening and cement formulation study indicated that magnesium oxide containing cement (MGO-5) is viable formulations that can withstand acid attack under HPHT conditions. During the investigation, ten aging experiments were performed to evaluate performance of magnesium oxide-based cements. Samples were exposed to different aging conditions (Table B.2). During the investigation, slurry compositions (**Table B.6**) and properties (**Table B.7)** were maintained approximately the same.

Table B.6: Formulations of MgO based cement (MGO-5) slurries

Component	Class G	Class H
Water for Cement	44% BWOC	38% BWOC
Water for Silica Flour	38.5% BWOC c	38.5% BWOC c
Anti-Foaming Agent	0.1 gal/sk of Cement	0.1 gal/sk of Cement
HEC	0.1% of Water for Silica	0.1% of Water for Silica
Cement	100% BWOC	100% BWOC
Silica Flour	35% BWOC	35% BWOC c
MgO	5% BWOC	5% BWOC

Table B.7: Properties of MGO-5 and baseline cement slurries

Property	HSMG	HS	GSMG	GS
Theoretical Density	16.15 ppg	15.96 ppg	14.99 ppg	15.51 ppg
Measured Density	16.30 ppg	16.20 ppg	14.80 ppg	15.45 ppg
Filtration Loss at 7.5 min.	58 ml	50 ml	62 ml	60 ml
Rheological Properties	Power Law n = 0.52 K = 7.9 $lbf.s^{0.52}/100ft^2$	Power Law n = 0.44 K = 14.4 $lbf.s^{0.44}/100ft^2$	Power Law n = 0.40 K = 9.9 $lbf.s^{0.40}/100ft^2$	Power Law n = 0.35 K = 10.5 $lbf.s^{0.35}/100ft^2$
Thickening Time	160 min.	170 min.	130 min.	135 min.

B.2.2.1 Performance under Intermediate Temperature Conditions

In Batch 006, tests with MGO-5 samples were conducted under HPHT conditions presented in **Table B.8**. After aging, the properties (porosity, permeability, compressive strength and shear bond strength) of aged and unaged cores were measured.

Table B.8: Aging conditions for the MGO-5 samples

MGO-5	Temp. (°F)	Pressure (psi)	CO_2 (%)	CH_4 (%)	NaCl (%)	Days	Baseline	Exp. No.
Batch 006	225	9000	40	60	2	14	Batch 023	20

After aging, porosity of baseline cements showed considerable reduction due to carbonation in the matrix , which occurred as a result of acid penetration (**Fig. B.46**). Most of MGO-5 samples exhibited slight reduction in porosity and permeability (**Fig. B.47**), which is attributed to the simultaneous effects of carbonation and matrix expansion (i.e. pore shrinkage) due to $Mg(OH)_2$ formation. Class G based MGO-5 samples showed increase in permeability. The reversal of permeability trend is mainly due to high sensitivity of permeability towards the physo-chemical phenomena occurring during aging. For

aged samples, porosity and permeability trends are consistent. However, it was inconsistent for unaged samples. Limited porosity and permeability changes occurred in MGO samples after aging indicate the effectiveness of magnesium oxide in preventing the penetration of carbonic acid and carbonation of cement matrix.

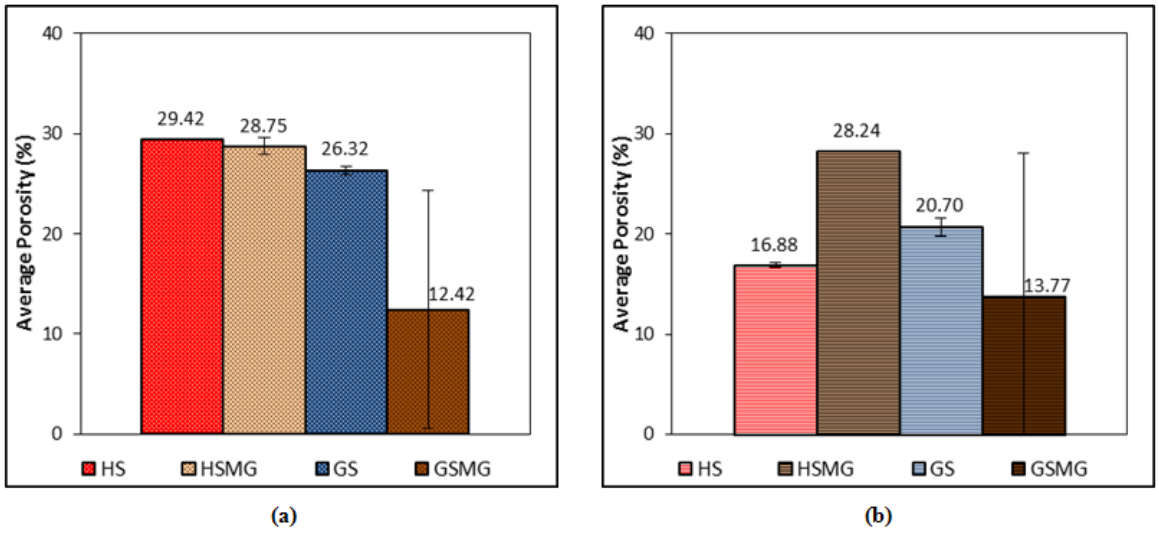

Fig. B.47: Porosities of MGO-5 and baseline cements: a) unaged; and b) aged

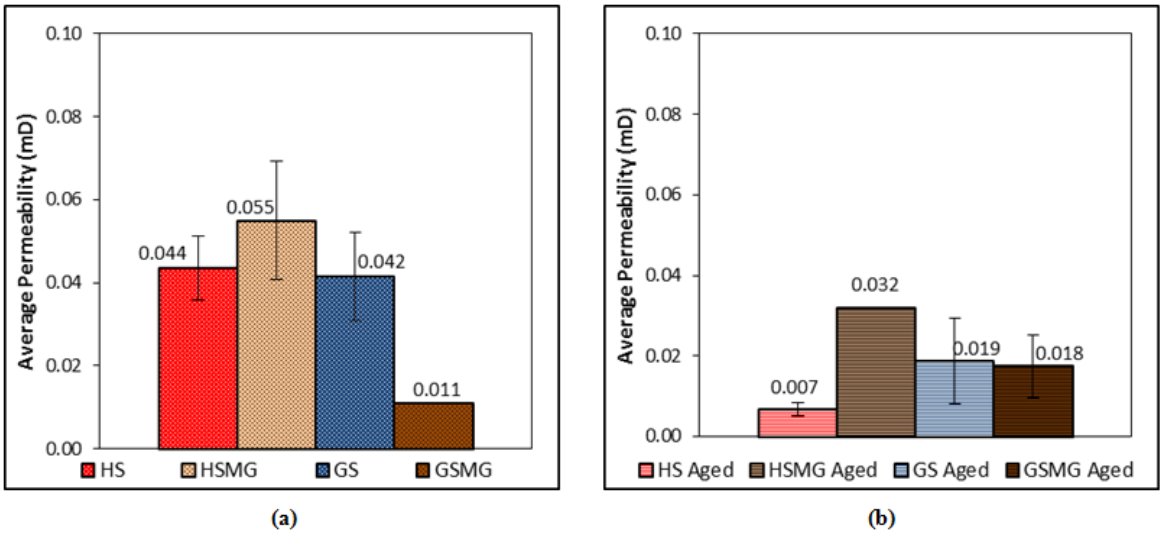

Fig. B.48: Permeabilities of MGO-5 and baseline cements: a) unaged; and b) aged

Compressive strengths of MGO-5 and baseline cements are presented in **Fig. B.49**. Compressive strength of unaged HSMG samples was significantly lower than that of baseline cores. However, GSMG samples exhibited more or less the same compressive strengths as the baseline samples. Hence, the formation of $Mg(OH)_2$ did not increase the initial compressive strength after hydration. After aging, all samples showed improvement in strength. Compressive strengths of MGO-5 samples were substantially increased due to further hydration of MgO, and carbonation of $Mg(OH)_2$ and $Ca(OH)_2$. The baseline samples displayed a lesser amount of compressive strength improvement (i.e. percentage increase) than the MGO-5 samples. This can be due to the carbonation process, which is limited to $Ca(OH)_2$. However

it was observed that the porosity of MGO-5 samples did not change significantly after aging, which indicate lesser penetration of carbonic acid due to formation of $Mg(OH)_2$ crystals. Hence, it can be concluded that MGO-5 samples showed lesser acid penetration and consequently, lower carbonation, though they exhibited increased compressive strength due to the formation of $Mg(OH)_2$ crystals in the pore space.

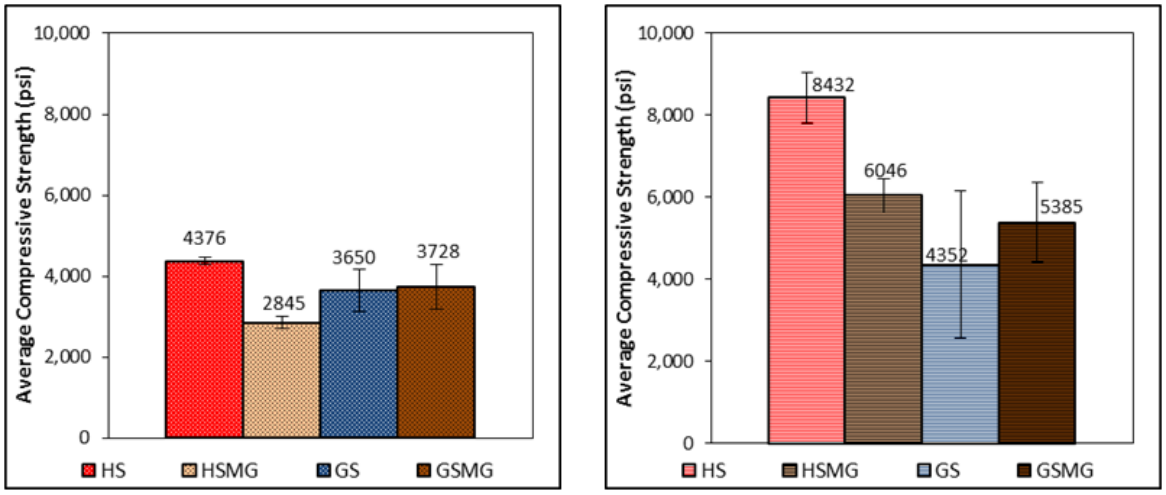

Fig. B.49 Compressive strength of MGO-5 and baseline cements: a) unaged; and b) aged

The shear bond strength (SBS) measurements are presented in **Fig. B.50**. Baseline HS samples showed increased SBS after aging due to carbonation and expansion of the matrix. At the same time, HSMG samples exhibited increased SBS due to a carbonation and formation of $Mg(OH)_2$ crystals. It is challenging to compare the level of carbonation upcoming in the HSMG samples using the SBS data alone. Hence, FTIR tests were in the performed to examine the mineralogical changes occurred after aging.

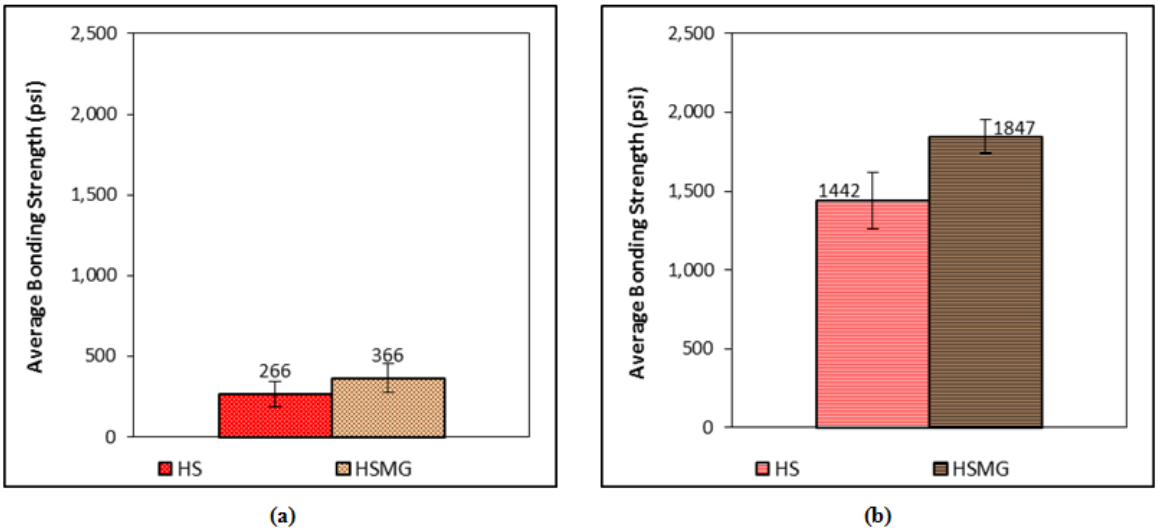

Fig. B.50 Shear bond strength of MGO-5 and baseline cements: a) unaged; and b) aged

FTIR spectrum is simplified in the form of bar charts for easy interpretation (**Fig. B.51**). The outer and middle zones show presence of $CaCO_3$ and $MgCO_3$ only. The inner zone, however, shows presence of CSH and $Mg(OH)_2$ in the HSMG samples, indicating that the matrix has not been carbonated completely. This is promising indication of performance single MGO cement, which justifies its application in HPHT acidic environment.

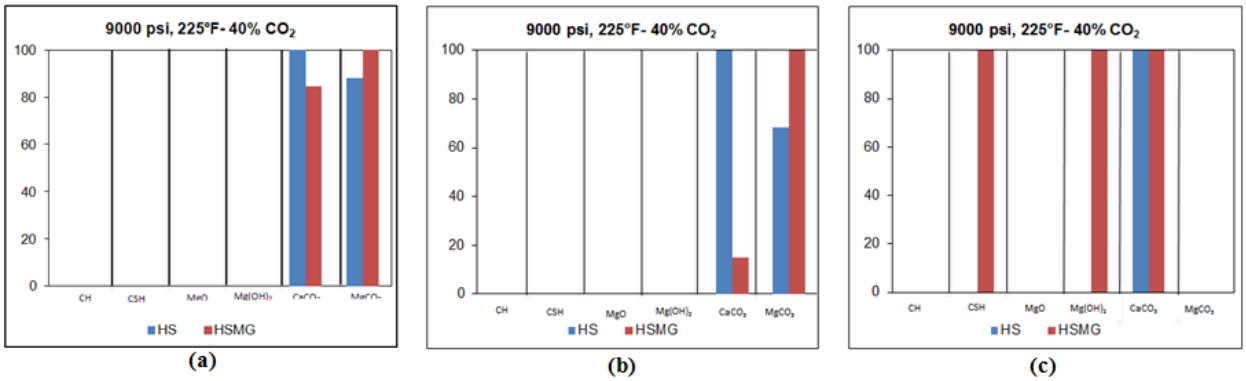

Fig. B.51: Summarized FTIR data of HSMG and baseline HS samples aged at 225°F, 9000 psi, 40% CO_2 for 14 days: a) Outermost zone; b) Middle zone; and c) Innermost zone

B.2.2.2 Performance under High Temperature Conditions

An aging experiment (Batch 005) conducted with MGO-5 and baseline samples under high temperature condition (**Table B.9**) demonstrated the performance of the new cement formulations. After aging, the properties (porosity, permeability, compressive strength and shear bond strength) of aged and unaged cores were measured.

Table B.9: Aging conditions for the MGO-5 samples

MGO-5	Temp. (°F)	Pressure (psi)	CO_2 (%)	CH_4 (%)	NaCl (%)	Days	Baseline	Exp. No.
Batch 005	350	9000	40	60	2	14	Batch 017	15

Porosity and permeability of MGO-5 and baseline samples are presented in **Figs. B.52** and **B.53**, respectively. The unaged porosities of all the samples are in the same range except for GSMG, which showed lower porosity than the baseline samples. On the other hand, the permeability of the unaged samples varies significantly. The permeability of MGO-5 samples is higher than their respective baseline cement samples. As these measurements were taken just after curing of the samples; the difference is mainly due to variation in composition and hydration process of the cements. After aging, decrease in the porosity was predominately observed, except in the case of GSMG samples, which displayed a considerable increase in porosity. This increase can be attributed to leaching of the calcium bicarbonate formed after complete carbonation of $Ca(OH)_2$ and CSH. Class H based MgO samples (HSMG) exhibited substantial reduction in permeability after aging. This reduction can be attributed to the expansion of $Mg(OH)_2$ crystals in the matrix, which prevents the carbonation. This has been verified using FTIR analysis, which is presented next.

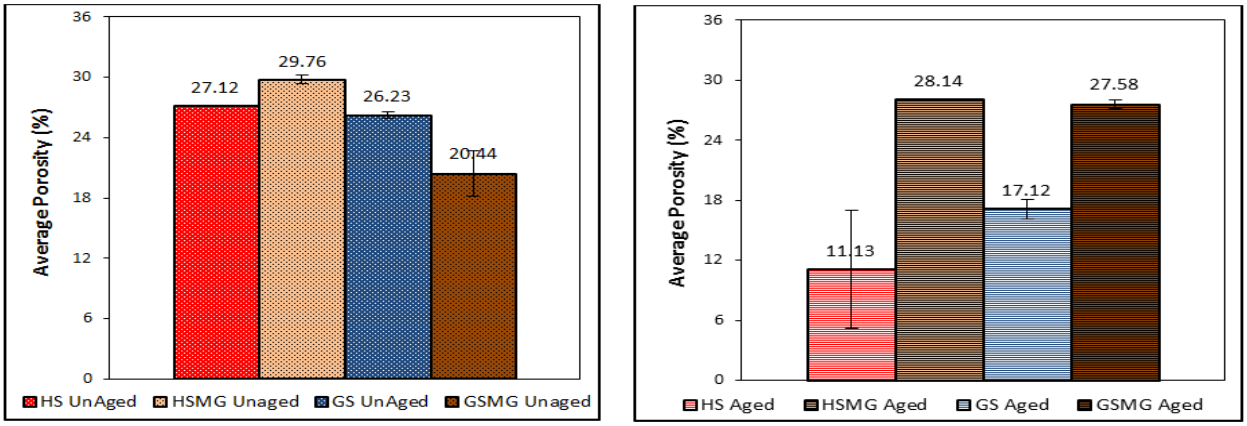

(a) **(b)**

Fig. B.52: Porosities of MGO-5 and baseline samples: a) Unaged; and b) aged at 350°F, 9000 psi and 40% CO_2

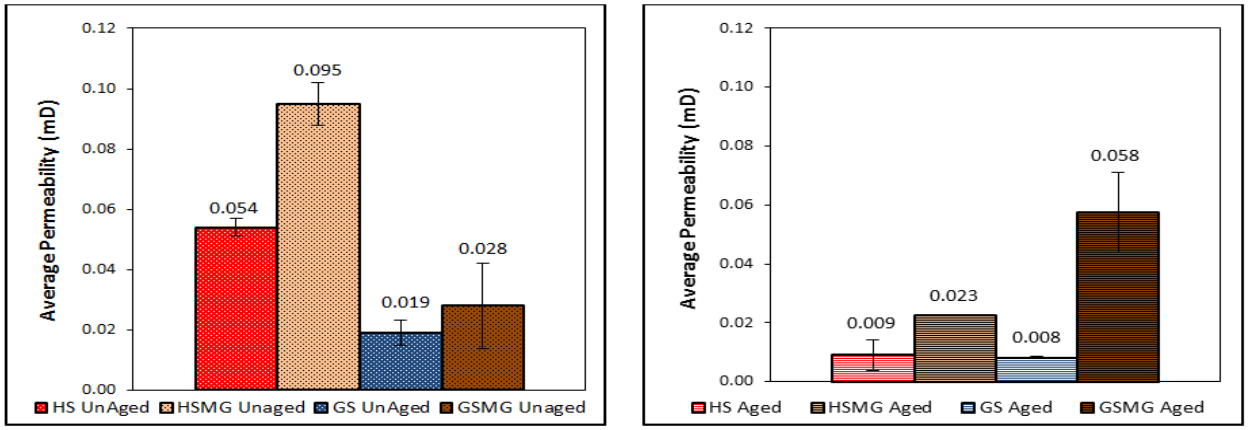

(a) **(b)**

Fig. B.53: Permeabilities of MGO-5 and baseline samples: a) Unaged; and b) aged at 350°F, 9000 psi and 40% CO_2

In order to verify the penetration of CO_2 in the MGO-5 samples, FTIR experiments were carried out by taking samples from inner, middle and outer zones of aged HS and HSMG samples. Summarized FTIR spectrum charts are presented in **Fig. B.54**. The charts present spectrum peaks of $Ca(OH)_2$, CSH, CaCO3, MgO, $Mg(OH)_2$ and $MgCO_3$ at different locations (inner, middle and outer most zones) in the samples. FTIR results obtained from the inner zone indicates complete carbonation of CH and CSH in both the samples. The result from outer and middle zones showed complete conversion of MgO to MgCO3 and Mg(OH)2. No MgCO3 was found in the inner zones of the samples. In HSMG samples, Mg(OH)2, which precipitates in the pore space was present in inner and middle zones. The $Mg(OH)_2$ crystals help in decreasing porosity and permeability, and improve compressive and shear bond strength of the cement. The amount of $CaCO_3$ in HSMG samples is less than the baseline samples in the inner zone, indicating lesser carbonation of the matrix. It should be noted that, although peak for $MgCO_3$ can be identified at 880cm^{-1}, all carbonates provided major peak around 1480cm^{-1}. Hence, $CaCO_3$ and $MgCO_3$ cannot be clearly distinguished using the peaks at 1480cm^{-1}. The middle and outer zones of MGO-5 showed higher content of $CaCO_3$ along with presence of $MgCO_3$.

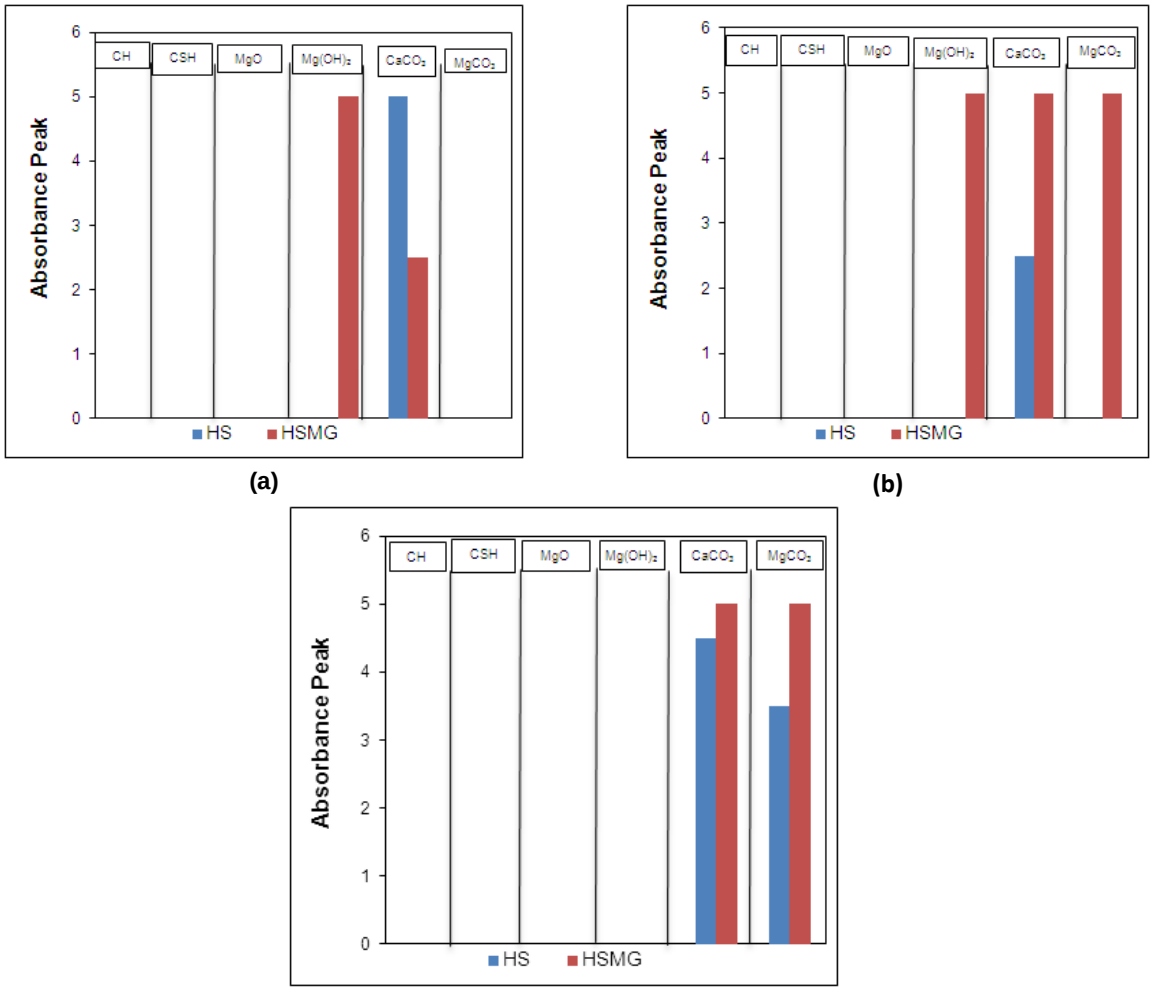

Fig. B.54: FTIR peaks of MGO and baseline samples aged at 350°F and 9000 psi for 14 days in 2% brine saturated with 40% CO_2: a) inner most zone; b) middle zone; and c) outer most zone

Compressive strengths of MGO-5 and baseline cement samples are presented in **Fig. B.55**. The strengths of all unaged samples were in the same range. After aging, increase in the compressive strength was observed for Class H based cores (HS and HSMG). The strength improvement is attributed to carbonation of the matrix and deposition of $CaCO_3$ crystals in the pore space. For MGO samples, this improvement is also due to matrix expansion by the formation of $Mg(OH)_2$ crystals from hydration of MgO. The matrix expansion results in pore shrinkage and strength improvement. In spite of this, the aging made Class G based cores (GS and GSMG) slightly weaker. The reduction in the strength of GS and GSMG samples is mainly attributable to leaching of the soluble products such as $Ca(HCO_3)_2$ and $Mg(HCO_3)_2$, which are formed after carbonation process. The GSMG cores exhibited more strength reduction than the baseline GS samples. This could be because of more leaching tendency of the GSMG samples as they contain higher MgO content than the baseline cement. As observed in the porosity and permeability results of GSMG, the increase in the respective values may lead to this decrease in the compressive strength. Hence, adding MgO did not improve performance of Class G cement under HPHT conditions.

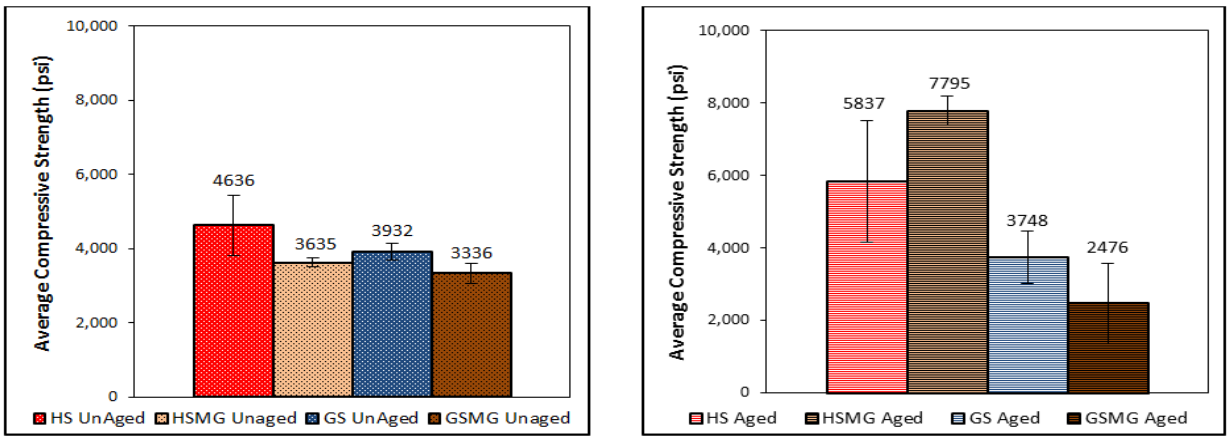

(a) **(b)**

Fig. B.55: Compressive strength of MGO-5 and baseline samples: a) Unaged; and b) aged at 350°F, 9000 psi, 40% CO_2 for 14 days

Shear bond strengths of HSMG and baseline HS samples are presented in **Fig. B.56**. For both aged and unaged cases, the SBS values do not vary significantly with the types (i.e. HS or HSMG) of cement samples. However, substantial (four to five folds) increase in SBS is observed due to carbonation after aging the samples under CO_2 containing environment. More importantly, the aged HSMG samples showed slightly higher SBS than the baseline samples, even though their unaged SBS values were lower than those of the baseline samples. The result demonstrated the benefits of adding MgO in improving performance of Class H cement.

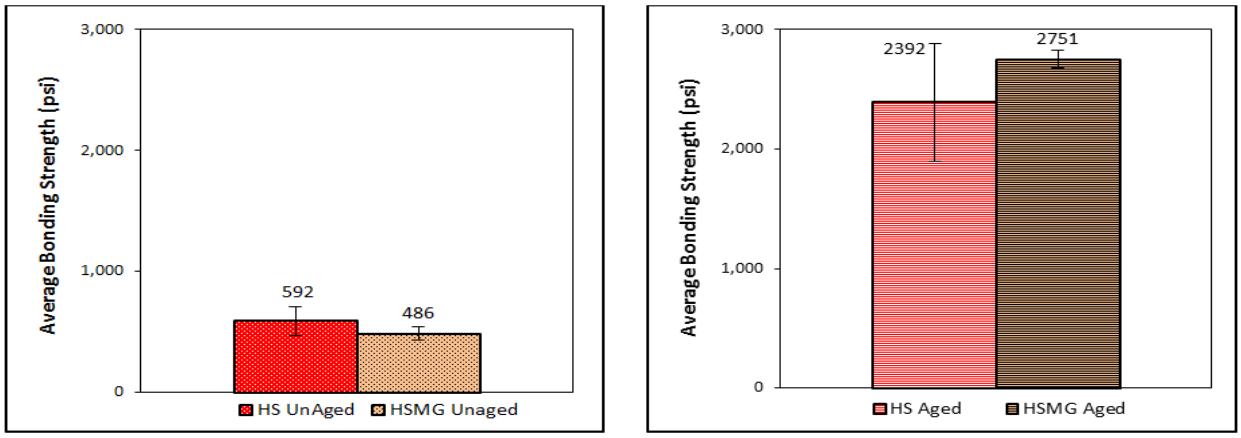

(a) **(b)**

Fig. B.56: SBS of MGO-5 and baseline samples: a) Unaged; and b) aged at 350°F, 9000 psi, 40% CO_2 for 14 days

Addition of 5% BWOC of MgO to the cement has been effective in preventing acid attack according to the experimental results. Although HSMG showed good performance at 9000 psi and 350°F, performance of Class G based MGO cement (GSMG) was comparable with the baseline cement. Such result with Class G cement was only observed at 9000 psi. High-pressure may have caused breaking of the $Mg(OH)_2$ crystals or the matrix.

APPENDIX C: EXPERIMENTAL DATABASE: PROPERTIES OF CEMENTS

C.1 Additive Cement

C.1.1 Properties of Fly Ash Based Cement (FLAS)

Table C.1: Porosity and permeability of fly ash based cement (FLAS)

Additive Batch #	Baseline Batch #	Core #	T (°F)	P (psi)	CH_4 (%)	CO_2 (%)	H_2S (ppm)	Brine (%)	Days Aged	Ø (%)	K_{klink} (mD)	Ave. Ø (%)	Stdev	Ave. K (mD)	Stdev
001	001	001 HSF-00-01	70	0	0	0	0	2	0	25.8	0.027	26	1	0.027	0.005
		001 HSF-00-02	70	0	0	0	0	2	0	24.7	0.022				
		001 HSF-00-03	70	0	0	0	0	2	0	26.4	0.031				
		001 GSF-00-01	70	0	0	0	0	2	0	20.3	0.020	21	0	0.020	0.002
		001 GSF-00-02	70	0	0	0	0	2	0	20.4	0.018				
		001-GSF-00-03	70	0	0	0	0	2	0	21.0	0.021				
		001-HSF-02-01	350	9000	100	0	0	9	6	18.6	0.014	19	1	0.016	0.007
		001-HSF-02-02	350	9000	100	0	0	9	6	19.7	0.026				
		001-HSF-06-01	350	9000	100	0	0	9	6	18.8	0.012				
		001-HSF-10-01	350	9000	100	0	0	9	6	19.3	0.012				
		001-GSF-04-01	350	9000	100	0	0	9	6	17.5	0.010	18	0	0.011	0.001
		001-GSF-04-02	350	9000	100	0	0	9	6	18.6	0.009				
		001-GSF-08-01	350	9000	100	0	0	9	6	17.7	0.011				
		001-GSF-08-02	350	9000	100	0	0	9	6	17.7	0.012				
002	002	002-HSF-00-01	70	0	0	0	0	2	0	34.0	0.016	35	2	0.018	0.002
		002-HSF-00-02	70	0	0	0	0	2	0	36.8	0.019				
		002-GSF-00-01	70	0	0	0	0	2	0	28.7	0.009	28	1	0.008	0.001
		002-GSF-00-02	70	0	0	0	0	2	0	27.0	0.007				
		002-HSF-06-04	350	6000	100	0	0	2	14	20.4	0.002	20		0.002	
		002-GSF-08-01	350	6000	100	0	0	2	14	19.0	0.002	19		0.002	
003	003	003-GSF-00-01	70	0	0	0	0	2	0	22.8	0.014	23		0.014	
		003-GSF-08-01	350	6000	100	0	0	2	14	29.2	0.002	27	3	0.002	0.001
		003-GSF-08-02	350	6000	100	0	0	2	14	25.2	0.001				
004	004	004-HSF-00-01	70	0	0	0	0	2	0	22.0	0.022	22	1	0.021	0.002
		004-HSF-00-02	70	0	0	0	0	2	0	21.0	0.019				
		004-HSF-02-01	350	6000	90	10	0	2	6	26.1	0.017	27	1	0.007	0.008
		004-HSF-02-02	350	6000	90	10	0	2	6	26.7	0.011				
		004-HSF-06-01	350	6000	90	10	0	2	6	27.6	0.000				
		004-HSF-06-02	350	6000	90	10	0	2	6	28.0	0.000				
		004-GSF-04-01	350	6000	90	10	0	2	6	30.7	0.036	30	1	0.025	0.022
		004-GSF-04-02	350	6000	90	10	0	2	6	29.1	0.000				

Additive Batch #	Baseline Batch #	Core #	T (°F)	P (psi)	CH_4 (%)	CO_2 (%)	H_2S (ppm)	Brine (%)	Days Aged	Ø (%)	K_{klink} (mD)	Ave. Ø (%)	Stdev	Ave. K (mD)	Stdev
		004-GSF-08-01	350	6000	90	10	0	2	6	31.4	0.039				
005	005	005-HSF-00-01	70	0	0	0	0	2	0	26.2	0.018	26	0	0.018	0.000
		005-HSF-00-02	70	0	0	0	0	2	0	26.1	0.018				
		005-GSF-00-01	70	0	0	0	0	2	0	21.6	0.016	22	1	0.022	0.008
		005-GSF-00-02	70	0	0	0	0	2	0	23.0	0.027				
		005-HSF-02-01	350	6000	90	10	0	2	28	-	-	28	1	4.381	7.514
		005-HSF-02-02	350	6000	90	10	0	2	28	28.5	0.010				
		005-HSF-06-01	350	6000	90	10	0	2	28	28.8	13.057				
		005-HSF-06-02	350	6000	90	10	0	2	28	27.1	0.075				
		005-GSF-04-01	350	6000	90	10	0	2	28	25.6	0.013	24	2	0.021	0.017
		005-GSF-04-02	350	6000	90	10	0	2	28	25.0	0.013				
		005-GSF-08-01	350	6000	90	10	0	2	28	22.0	0.010				
		005-GSF-08-02	350	6000	90	10	0	2	28	23.3	0.046				
006	006	006-HSF-00-01	70	0	0	0	0	2	0	28.6	0.009	29		0.009	
		006-HSF-03-01	350	6000	90	10	0	2	14	20.5	0.009	20		0.009	

Table C.2: Shear bond strength of fly ash based cement (FLAS)

Additive Batch #	Baseline Batch #	Core #	T (°F)	P (psi)	CH_4 (%)	CO_2 (%)	H_2S (ppm)	Brine (%)	Days Aged	SBS (psi)	Ave. SBS (psi)	St. dev. (psi)
001	001	002-HSF-11-01	350	6000	100	0	0	2	14	2462	2620	732
		002-HSF-11-02	350	6000	100	0	0	2	14	2179		
		002-HSF-11-03	350	6000	100	0	0	2	14	3697		
		002-HSF-11-04	350	6000	100	0	0	2	14	2142		
		002-HSF-10-03	350	6000	100	0	0	2	28	3181	3429	389
		002-HSF-10-04	350	6000	100	0	0	2	28	3230		
		002-HSF-10-05	350	6000	100	0	0	2	28	3878		
002	002	003-HSF-10-01	350	6000	100	0	0	2	14	2585	2680	135
		003-HSF-10-02	350	6000	100	0	0	2	14	2776		
003	003	004-HSF-00-01	70	0	0	0	0	2	0	731	727	40
		004-HSF-00-02	70	0	0	0	0	2	0	764		
		004-HSF-00-03	70	0	0	0	0	2	0	685		
		004-HSF-10-01	350	6000	90	10	0	2	6	456	463	81
		004-HSF-10-02	350	6000	90	10	0	2	6	447		
		004-HSF-10-03	350	6000	90	10	0	2	6	598		
		004-HSF-10-04	350	6000	90	10	0	2	6	384		
		004-HSF-10-05	350	6000	90	10	0	2	6	428		
004	004	005-HSF-10-01	350	6000	90	10	0	2	14	339	1169	1098
		005-HSF-10-02	350	6000	90	10	0	2	14	464		
		005-HSF-10-03	350	6000	90	10	0	2	28	1871		
		005-HSF-10-04	350	6000	90	10	0	2	28	404		
		005-HSF-10-05	350	6000	90	10	0	2	28	2768		
005	005	006-HSF-11-01	350	6000	90	10	0	2	14	2521	1923	846
		006-HSF-11-02	350	6000	90	10	0	2	14	1325		

Table C.3: Compressive strength of fly ash based cement (FLAS)

Additive Batch #	Baseline Batch #	Core #	T (°F)	P (psi)	CH_4 (%)	CO_2 (%)	H_2S (ppm)	Brine (%)	Days Aged	Comp. Strength (psi)	Ave. Comp. Strength (psi)	Stdev (psi)
001	001	001-GSF-00-01	70	0	0	0	0	9	0	3674	3790	753
		001-GSF-00-02	70	0	0	0	0	9	0	3425		
		001-GSF-00-03	70	0	0	0	0	9	0	2849		
		001-GSF-00-04	70	0	0	0	0	9	0	3398		
		001-GSF-00-05	70	0	0	0	0	9	0	4712		
		001-GSF-00-06	70	0	0	0	0	9	0	4682		
		001-GSF-08-03	350	9000	100	0	0	9	6	5479	5479	
		001-HSF-00-01	70	0	0	0	0	9	0	2463	2798	448
		001-HSF-00-02	70	0	0	0	0	9	0	2216		
		001-HSF-00-03	70	0	0	0	0	9	0	2676		
		001-HSF-00-04	70	0	0	0	0	9	0	3487		
		001-HSF-00-05	70	0	0	0	0	9	0	3017		
		001-HSF-00-06	70	0	0	0	0	9	0	2927		
		001-HSF-02-03	350	9000	100	0	0	9	6	5839	5083	1070
		001-HSF-02-04	350	9000	100	0	0	9	6	4326		
002	002	002-GSF-00-03	70	0	0	0	0	2	0	4280	4023	446
		002-GSF-00-04	70	0	0	0	0	2	0	3509		
		002-GSF-00-05	70	0	0	0	0	2	0	4280		
		002-GSF-08-03	350	6000	100	0	0	2	28	4004	4846	1190
		002-GSF-08-05	350	6000	100	0	0	2	28	5687		
		002-HSF-00-04	70	0	0	0	0	2	0	3202	2872	467
		002-HSF-00-05	70	0	0	0	0	2	0	2542		
		002-HSF-02-05	350	6000	100	0	0	2	28	3974	3974	
003	003	003-GSF-08-03	350	6000	100	0	0	2	14	2909	5551	2353
		003-GSF-08-04	350	6000	100	0	0	2	14	6322		
		003-GSF-08-05	350	6000	100	0	0	2	14	7421		
004	004	004-GSF-00-03	70	0	0	0	0	2	0	4144	3921	380
		004-GSF-00-04	70	0	0	0	0	2	0	4138		
		004-GSF-00-05	70	0	0	0	0	2	0	3482		
		004-GSF-04-03	350	6000	90	10	0	2	6	3713	5873	1969
		004-GSF-04-04	350	6000	90	10	0	2	6	3617		
		004-GSF-04-05	350	6000	90	10	0	2	6	6262		
		004-GSF-08-03	350	6000	90	10	0	2	6	6092		
		004-GSF-08-04	350	6000	90	10	0	2	6	6734		
		004-GSF-08-05	350	6000	90	10	0	2	6	8822		
		004-HSF-00-03	70	0	0	0	0	2	0	3339	3296	261
		004-HSF-00-04	70	0	0	0	0	2	0	3016		
		004-HSF-00-05	70	0	0	0	0	2	0	3533		
		004-HSF-02-03	350	6000	90	10	0	2	6	7610	5709	2662

Additive Batch #	Baseline Batch #	Core #	T (°F)	P (psi)	CH_4 (%)	CO_2 (%)	H_2S (ppm)	Brine (%)	Days Aged	Comp. Strength (psi)	Ave. Comp. Strength (psi)	Stdev (psi)
		004-HSF-02-04	350	6000	90	10	0	2	6	9636		
		004-HSF-02-05	350	6000	90	10	0	2	6	3902		
		004-HSF-06-03	350	6000	90	10	0	2	6	6527		
		004-HSF-06-04	350	6000	90	10	0	2	6	2672		
		004-HSF-06-05	350	6000	90	10	0	2	6	3906		
005	005	005-GSF-00-03	70	0	0	0	0	2	0	3842	4061	502
		005-GSF-00-04	70	0	0	0	0	2	0	4635		
		005-GSF-00-05	70	0	0	0	0	2	0	3705		
		005-GSF-04-03	350	6000	90	10	0	2	28	6764	7018	1463
		005-GSF-04-04	350	6000	90	10	0	2	28	7533		
		005-GSF-04-05	350	6000	90	10	0	2	28	7054		
		005-GSF-08-03	350	6000	90	10	0	2	28	4910		
		005-GSF-08-04	350	6000	90	10	0	2	28	6459		
		005-GSF-08-05	350	6000	90	10	0	2	28	9387		
		005-HSF-00-03	70	0	0	0	0	2	0	2630	3133	480
		005-HSF-00-04	70	0	0	0	0	2	0	3183		
		005-HSF-00-05	70	0	0	0	0	2	0	3587		
		005-HSF-02-03	350	6000	90	10	0	2	28	7019	4702	2739
		005-HSF-02-04	350	6000	90	10	0	2	28	7408		
		005-HSF-02-05	350	6000	90	10	0	2	28	5894		
		005-HSF-06-03	350	6000	90	10	0	2	28	0		
		005-HSF-06-04	350	6000	90	10	0	2	28	3667		
		005-HSF-06-05	350	6000	90	10	0	2	28	4222		
006	006	006-HSF-00-03	70	0	0	0	0	2	0	4642	4642	

C.1.2 Properties of Hydroxyapatite Based Cement (HOAP)

Table C.4: Porosity and permeability of hydroxyapatite-based cement (HOAP)

Additive Batch #	Baseline Batch #	Core #	T (°F)	P (psi)	CH_4 (%)	CO_2 (%)	H_2S (ppm)	Brine (%)	Days Aged	Ø (%)	K_{klink} (mD)	Ave. Ø (%)	Stdev	Ave. K (mD)	Stdev
001	Unaged batch	001-HHO-00-01	70	0	0	0	0	2	0	25	0.041	25	0	0.042	0.013
		001-HHO-00-02	70	0	0	0	0	2	0	25	0.029				
		001-HHO-00-03	70	0	0	0	0	2	0	25	0.037				
		001-HHO-00-04	70	0	0	0	0	2	0	25	0.059				
		001-GHO-00-01	70	0	0	0	0	2	0		-	27	0	0.025	0.005
		001-GHO-00-02	70	0	0	0	0	2	0	27	0.02				
		001-GHO-00-03	70	0	0	0	0	2	0	26	0.024				
		001-GHO-00-04	70	0	0	0	0	2	0	27	0.03				
		001-HHO-C-00-01	70	0	0	0	0	2	0	30	0.092	30	0	0.081	0.013
		001-HHO-C-00-02	70	0	0	0	0	2	0	30	0.085				
		001-HHO-C-00-03	70	0	0	0	0	2	0	29	0.066				
		001-HHO-C-00-04	70	0	0	0	0	2	0						
		001-GHO-C-00-01	70	0	0	0	0	2	0	30	0.044	30	1	0.042	0.006
		001-GHO-C-00-02	70	0	0	0	0	2	0	29	0.035				
		001-GHO-C-00-03	70	0	0	0	0	2	0	30	0.046				
		001-GHO-C-00-04	70	0	0	0	0	2	0						
002	011	002-HHO-00-01	70	0	0	0	0	2	0	30	0.042	29	0	0.041	0.002
		002-HHO-00-02	70	0	0	0	0	2	0	29	0.039				
		002-GHO-00-01	70	0	0	0	0	2	0	31	0.042	32	0	0.042	0.001
		002-GHO-00-02	70	0	0	0	0	2	0	32	0.041				
		002-HHO-09-01	100	6000	60	40	0	2	14	27	0.036	26	1	0.035	0.001
		002-HHO-09-02	100	6000	60	40	0	2	14	25	0.034				
		002-GHO-10-01	100	6000	60	40	0	2	14	28	0.048	28	0	0.046	0.003
		002-GHO-10-02	100	6000	60	40	0	2	14	29	0.044				
003	014	003-HHO-00-01	70	0	0	0	0	2	0	29	0.035	29	0	0.034	0.002
		003-HHO-00-02	70	0	0	0	0	2	0	29	0.032				
		003-GHO-00-01	70	0	0	0	0	2	0	14	0.004	16	3	0.007	0.004
		003-GHO-00-02	70	0	0	0	0	2	0	18	0.009				
		003-HHO-09-01	350	6000	0	100	0	2	14	31	0.038	31	0	0.038	0.001
		003-HHO-09-02	350	6000	0	100	0	2	14	31	0.037				
		003-GHO-10-01	350	6000	0	100	0	2	14	15	0.014	15	0	0.027	0.018
		003-GHO-10-02	350	6000	0	100	0	2	14	15	0.04				
004	016	004-HHO-00-01	70	0	0	0	0	2	0	28	0.039	28	0	0.038	0.002
		004-HHO-00-02	70	0	0	0	0	2	0	27	0.036				
		004-GHO-00-01	70	0	0	0	0	2	0	28	0.028	28	0	0.029	0.001
		004-GHO-00-02	70	0	0	0	0	2	0	27	0.029				
		004-HHO-09-01	350	3000	60	40	0	2	14	14	0.007	14	0	0.008	0.001
		004-HHO-09-02	350	3000	60	40	0	2	14	14	0.008				

Additive Batch #	Baseline Batch #	Core #	T (°F)	P (psi)	CH_4 (%)	CO_2 (%)	H_2S (ppm)	Brine (%)	Days Aged	Ø (%)	K_{klink} (mD)	Ave. Ø (%)	Stdev	Ave. K (mD)	Stdev
		004-GHO-10-01	350	3000	60	40	0	2	14	10	0.006	10	0	0.006	0.001
		004-GHO-10-02	350	3000	60	40	0	2	14	11	0.005				
005	018	005-HHO-00-01	70	0	0	0	0	2	0	29	0.049	29	0	0.048	0.001
		005-HHO-00-02	70	0	0	0	0	2	0	28	0.047				
		005-GHO-00-01	70	0	0	0	0	2	0	25	0.043	21	5	0.028	0.021
		005-GHO-00-02	70	0	0	0	0	2	0	18	0.013				
		005-HHO-09-01	350	3000	60	40	0	2	14	32	0.059	32	0	0.057	0.003
		005-HHO-09-02	350	3000	60	40	0	2	14	32	0.055				
		005-GHO-10-01	350	3000	60	40	0	2	14	28	0.035	28	0	0.042	0.010
		005-GHO-10-02	350	3000	60	40	0	2	14	27	0.049				
006	022	006-HHO-00-01	70	0	0	0	0	2	0	29	0.046	29	0	0.046	0.001
		006-HHO-00-02	70	0	0	0	0	2	0	29	0.045				
		006-GHO-00-01	70	0	0	0	0	2	0	32	0.021	32	0	0.020	0.001
		006-GHO-00-02	70	0	0	0	0	2	0	32	0.019				
		006-HHO-09-01	225	3000	60	40	0	2	14	12	0.004	12	1	0.006	0.002
		006-HHO-09-02	225	3000	60	40	0	2	14	13	0.007				
		006-GHO-10-01	225	3000	60	40	0	2	14	13	0.005	15	2	0.006	0.001
		006-GHO-10-02	225	3000	60	40	0	2	14	16	0.007				
007	026	007-HHO-00-01	70	0	0	0	0	2	0	30	0.037	30	0	0.038	0.001
		007-HHO-00-02	70	0	0	0	0	2	0	30	0.039				
		007-GHO-00-01	70	0	0	0	0	2	0	32	0.028	32	0	0.029	0.001
		007-GHO-00-02	70	0	0	0	0	2	0	32	0.029				
		007-HHO-09-01	225	3000	90	10	0	2	14	21	0.031	21	1	0.035	0.005
		007-HHO-09-02	225	3000	90	10	0	2	14	22	0.038				
		007-GHO-10-01	225	3000	90	10	0	2	14	25	0.049	25	1	0.055	0.008
		007-GHO-10-02	225	3000	90	10	0	2	14	24	0.061				
008	032	008-HHO-00-01	70	0	0	0	0	2	0	31	0.062	31	0	0.075	0.018
		008-HHO-00-02	70	0	0	0	0	2	0	31	0.087				
		008-GHO-00-01	70	0	0	0	0	2	0	31	0.014	31	1	0.015	0.001
		008-GHO-00-02	70	0	0	0	0	2	0	32	0.015				
		008-HHO-09-01	430	9000	0	100	0	2	14	11	0.192	12	2	0.416	0.317
		008-HHO-09-02	430	9000	0	100	0	2	14	13	0.64				
		008-GHO-10-01	430	9000	0	100	0	2	14	10	0.316	9	1	0.262	0.076
		008-GHO-10-02	430	9000	0	100	0	2	14	9	0.208				
009	033	009-HHO-00-01	70	0	0	0	0	2	0	30	0.063	30	1	0.074	0.015
		009-HHO-00-02	70	0	0	0	0	2	0	31	0.084				
		009-GHO-00-01	70	0	0	0	0	2	0	27	0.056	29	2	0.053	0.004
		009-GHO-00-02	70	0	0	0	0	2	0	30	0.05				
		009-HHO-09-01	100	6000	90	10	300	2	14	30	0.048	30		0.048	
		009-HHO-09-02	100	6000	90	10	300	2	14						
		009-GHO-10-01	100	6000	90	10	300	2	14	27	0.028	27	0	0.028	0.001

Additive Batch #	Baseline Batch #	Core #	T (°F)	P (psi)	CH_4 (%)	CO_2 (%)	H_2S (ppm)	Brine (%)	Days Aged	Ø (%)	K_{klink} (mD)	Ave. Ø (%)	Stdev	Ave. K (mD)	Stdev
		009-GHO-10-02	100	6000	90	10	300	2	14	27	0.027				
010	035	010-HHO-00-01	70	0	0	0	0	2	0			35		0.125	
		010-HHO-00-02	70	0	0	0	0	2	0	35	0.125				
		010-GHO-00-01	70	0	0	0	0	2	0	41	0.267	41	1	0.271	0.006
		010-GHO-00-02	70	0	0	0	0	2	0	42	0.275				
		010-HHO-09-01	350	6000	90	10	300	2	14			33		0.072	
		010-HHO-09-02	350	6000	90	10	300	2	14	33	0.072				
		010-GHO-10-01	350	6000	90	10	300	2	14	39	0.315	39	0	0.297	0.026
		010-GHO-10-02	350	6000	90	10	300	2	14	39	0.278				
012	038	012 HHO 09 01	100	9000	100	0	300	2	14	23	0.059		0	0.102	0.060
		012 HHO 09 02	100	9000	100	0	300	2	14	24	0.144				
		012 GHO 10 01	100	9000	100	0	300	2	14	27	0.173	27	0	0.185	0.016
		012 GHO 10 02	100	9000	100	0	300	2	14	26	0.196				
		012 HHO 00 01	70	0	0	0	0	2	0	11	0.011	18	9	0.023	0.016
		012 HHO 00 02	70	0	0	0	0	2	0	24	0.034				
		012 GHO 00 01	70	0	0	0	0	2	0	29	0.040	23	8	0.046	0.008
		012 GHO 00 02	70	0	0	0	0	2	0	18	0.051				
013	040	013 GHO 00 01	70	0	0	0	0	2	0	33	0.066	32	0	0.056	0.014
		013 GHO 00 02	70	0	0	0	0	2	0	32	0.046				
		013 HHO 00 01	70	0	0	0	0	2	0	31	0.189	31	0	0.189	0.001
		013 HHO 00 02	70	0	0	0	0	2	0	31	0.188				
		013 GHO 10 01	100	9000	60	40	180	2	14	26	0.037	25	1	0.031	0.009
		013 GHO 10 02	100	9000	60	40	180	2	14	25	0.024				
		013 HHO 09 01	100	9000	60	40	180	2	14	29	0.068	29	1	0.060	0.012
		013 HHO 09 02	100	9000	60	40	180	2	14	29	0.051				

Table C.5: Shear bond strength of hydroxyapatite based cement (HOAP)

Additive Batch #	Baseline Batch #	Core #	T (°F)	P (psi)	CH_4 (%)	CO_2 (%)	H_2S (ppm)	Brine (%)	Days Aged	SBS (psi)	Ave. SBS (psi)	Stdev (psi)
001	Unaged batch	001-HHO-00-01	70	0	0	0	0	2	0	899	883	56
		001-HHO-00-02	70	0	0	0	0	2	0	929		
		001-HHO-00-03	70	0	0	0	0	2	0	820		
		001-HHO-C-00-01	70	0	0	0	0	2	0	1195	977	226
		001-HHO-C-00-02	70	0	0	0	0	2	0	744		
		001-HHO-C-00-03	70	0	0	0	0	2	0	992		
002	011	002-HHO-00-01	70	0	0	0	0	2	0	713	690	292
		002-HHO-00-02	70	0	0	0	0	2	0	0		
		002-HHO-00-03	70	0	0	0	0	2	0	891		
		002-HHO-00-04	70	0	0	0	0	2	0	270		
		002-HHO-00-05	70	0	0	0	0	2	0	887		
		002-HHO-11-01	100	6000	60	40	0	2	14	2072	1671	234
		002-HHO-11-02	100	6000	60	40	0	2	14	1617		
		002-HHO-11-03	100	6000	60	40	0	2	14	1657		
		002-HHO-11-04	100	6000	60	40	0	2	14	1489		
		002-HHO-11-05	100	6000	60	40	0	2	14	1521		
003	014	003-HHO-00-01	70	0	0	0	0	2	0	854	719	211
		003-HHO-00-02	70	0	0	0	0	2	0	705		
		003-HHO-00-03	70	0	0	0	0	2	0	358		
		003-HHO-00-04	70	0	0	0	0	2	0	825		
		003-HHO-00-05	70	0	0	0	0	2	0	853		
		003-HHO-11-01	350	6000	0	100	0	2	14	944	968	173
		003-HHO-11-02	350	6000	0	100	0	2	14	792		
		003-HHO-11-03	350	6000	0	100	0	2	14	915		
		003-HHO-11-04	350	6000	0	100	0	2	14	929		
		003-HHO-11-05	350	6000	0	100	0	2	14	1257		
004	016	004-HHO-00-01	70	0	0	0	0	2	0	1160	1203	48
		004-HHO-00-02	70	0	0	0	0	2	0	1187		
		004-HHO-00-03	70	0	0	0	0	2	0	1254		
		004-HHO-00-04	70	0	0	0	0	2	0	1256		
		004-HHO-00-05	70	0	0	0	0	2	0	1160		
		004-HHO-11-01	350	3000	60	40	0	2	14	1080	1094	38
		004-HHO-11-02	350	3000	60	40	0	2	14	1139		
		004-HHO-11-03	350	3000	60	40	0	2	14	1129		
		004-HHO-11-04	350	3000	60	40	0	2	14	1071		
		004-HHO-11-05	350	3000	60	40	0	2	14	1052		
005	018	005-HHO-00-01	70	0	0	0	0	2	0	950	942	127
		005-HHO-00-02	70	0	0	0	0	2	0	758		
		005-HHO-00-03	70	0	0	0	0	2	0	1086		
		005-HHO-00-04	70	0	0	0	0	2	0	1027		
		005-HHO-00-05	70	0	0	0	0	2	0	887		

Additive Batch #	Baseline Batch #	Core #	T (°F)	P (psi)	CH_4 (%)	CO_2 (%)	H_2S (ppm)	Brine (%)	Days Aged	SBS (psi)	Ave. SBS (psi)	Stdev (psi)
		005-HHO-11-01	350	3000	0	100	0	2	14	860		
		005-HHO-11-02	350	3000	0	100	0	2	14	1867		
		005-HHO-11-03	350	3000	0	100	0	2	14	688	1112	454
		005-HHO-11-04	350	3000	0	100	0	2	14	1013		
		005-HHO-11-05	350	3000	0	100	0	2	14	1131		
		006-HHO-00-01	70	0	0	0	0	2	0	903		
		006-HHO-00-02	70	0	0	0	0	2	0	844		
		006-HHO-00-03	70	0	0	0	0	2	0	847	800	107
		006-HHO-00-04	70	0	0	0	0	2	0	624		
		006-HHO-00-05	70	0	0	0	0	2	0	784		
006	022	006-HHO-11-01	225	3000	0	100	0	2	14	801		
		006-HHO-11-02	225	3000	0	100	0	2	14	930		
		006-HHO-11-03	225	3000	0	100	0	2	14	582	773	131
		006-HHO-11-04	225	3000	0	100	0	2	14	717		
		006-HHO-11-05	225	3000	0	100	0	2	14	837		
		007-HHO-00-01	70	0	0	0	0	2	0	1066		
		007-HHO-00-02	70	0	0	0	0	2	0	1096		
		007-HHO-00-03	70	0	0	0	0	2	0	1161	1154	85
		007-HHO-00-04	70	0	0	0	0	2	0	1286		
		007-HHO-00-05	70	0	0	0	0	2	0	1161		
007	026	007-HHO-11-01	225	3000	90	10	0	2	14	1252		
		007-HHO-11-02	225	3000	90	10	0	2	14	1031		
		007-HHO-11-03	225	3000	90	10	0	2	14	999	1001	317
		007-HHO-11-04	225	3000	90	10	0	2	14	1248		
		007-HHO-11-05	225	3000	90	10	0	2	14	475		
		008-HHO-00-01	70	0	0	0	0	2	0	1017		
		008-HHO-00-02	70	0	0	0	0	2	0	1083		
		008-HHO-00-03	70	0	0	0	0	2	0	1345	1140	142
		008-HHO-00-04	70	0	0	0	0	2	0	1225		
		008-HHO-00-05	70	0	0	0	0	2	0	1028		
008	032	008-HHO-11-01	430	9000	0	100	0	2	14	207		
		008-HHO-11-02	430	9000	0	100	0	2	14	334		
		008-HHO-11-03	430	9000	0	100	0	2	14	317	327	96
		008-HHO-11-04	430	9000	0	100	0	2	14	475		
		008-HHO-11-05	430	9000	0	100	0	2	14	302		
		009-HHO-00-01	70	0	0	0	0	2	0	1239		
		009-HHO-00-02	70	0	0	0	0	2	0	1225		
		009-HHO-00-03	70	0	0	0	0	2	0	1060	1140	86
009	033	009-HHO-00-04	70	0	0	0	0	2	0	1072		
		009-HHO-00-05	70	0	0	0	0	2	0	1104		
		009-HHO-11-01	100	6000	90	10	300	2	14	1383	1367	31
		009-HHO-11-02	100	6000	90	10	300	2	14	1360		

Additive Batch #	Baseline Batch #	Core #	T (°F)	P (psi)	CH_4 (%)	CO_2 (%)	H_2S (ppm)	Brine (%)	Days Aged	SBS (psi)	Ave. SBS (psi)	Stdev (psi)
		009-HHO-11-03	100	6000	90	10	300	2	14	1332		
		009-HHO-11-04	100	6000	90	10	300	2	14	1411		
		009-HHO-11-05	100	6000	90	10	300	2	14	1349		
010	035	010-HHO-00-01	70	0	0	0	0	2	0	1452	1228	174
		010-HHO-00-02	70	0	0	0	0	2	0	1162		
		010-HHO-00-03	70	0	0	0	0	2	0	1129		
		010-HHO-00-04	70	0	0	0	0	2	0	1364		
		010-HHO-00-05	70	0	0	0	0	2	0	1034		
		010-HHO-11-01	100	6000	90	10	300	2	14	1142	1096	26
		010-HHO-11-02	100	6000	90	10	300	2	14	1087		
		010-HHO-11-03	100	6000	90	10	300	2	14	1087		
		010-HHO-11-04	100	6000	90	10	300	2	14	1090		
		010-HHO-11-05	100	6000	90	10	300	2	14	1074		
011	036	011-HHO-00-01	70	0	0	0	0	2	0	1111	1148	33
		011-HHO-00-02	70	0	0	0	0	2	0	1184		
		011-HHO-00-03	70	0	0	0	0	2	0	1181		
		011-HHO-00-04	70	0	0	0	0	2	0	1124		
		011-HHO-00-05	70	0	0	0	0	2	0	1140		
		011-HHO-11-01	100	6000	60	40	180	2	14	1465	1349	72
		011-HHO-11-02	100	6000	60	40	180	2	14	1300		
		011-HHO-11-03	100	6000	60	40	180	2	14	1310		
		011-HHO-11-04	100	6000	60	40	180	2	14	1296		
		011-HHO-11-05	100	6000	60	40	180	2	14	1375		
012	038	012-HHO-00-01	70	0	0	0	0	2	0	1232	1150	83
		012-HHO-00-02	70	0	0	0	0	2	0	1095		
		012-HHO-00-03	70	0	0	0	0	2	0	1203		
		012-HHO-00-04	70	0	0	0	0	2	0	1032		
		012-HHO-00-05	70	0	0	0	0	2	0	1187		
		012-HHO-11-01	100	9000	100	0	300	2	14	1193	980	413
		012-HHO-11-02	100	9000	100	0	300	2	14	988		
		012-HHO-11-03	100	9000	100	0	300	2	14	270		
		012-HHO-11-04	100	9000	100	0	300	2	14	1305		
		012-HHO-11-05	100	9000	100	0	300	2	14	1146		
013	040	013-HHO-00-01	70	0	0	0	0	2	0	364	339	66
		013-HHO-00-02	70	0	0	0	0	2	0	354		
		013-HHO-00-03	70	0	0	0	0	2	0	283		
		013-HHO-00-04	70	0	0	0	0	2	0	266		
		013-HHO-00-05	70	0	0	0	0	2	0	429		
		013-HHO-11-01	100	9000	60	40	180	2	14	1356	1496	300
		013-HHO-11-02	100	9000	60	40	180	2	14	1905		
		013-HHO-11-03	100	9000	60	40	180	2	14	1560		

Additive Batch #	Baseline Batch #	Core #	T (°F)	P (psi)	CH_4 (%)	CO_2 (%)	H_2S (ppm)	Brine (%)	Days Aged	SBS (psi)	Ave. SBS (psi)	Stdev (psi)
		013-HHO-11-04	100	9000	60	40	180	2	14	1569		
		013-HHO-11-05	100	9000	60	40	180	2	14	1090		

Table C.6: Compressive strength of hydroxyapatite-based cement (HOAP)

Additive Batch #	Baseline Batch #	Core #	T (°F)	P (psi)	CH_4 (%)	CO_2 (%)	H_2S (ppm)	Brine (%)	Days Aged	Comp. Strength (psi)	Ave. Comp. Strength (psi)	Stdev (psi)
001	Unaged Batch	001-GHO-00-05	70	0	0	0	0	2	0	3197	3871	697
		001-GHO-00-06	70	0	0	0	0	2	0	4745		
		001-GHO-00-07	70	0	0	0	0	2	0	3441		
		001-GHO-00-08	70	0	0	0	0	2	0	4102		
		001-GHO-C-00-05	70	0	0	0	0	2	0	3758	4111	426
		001-GHO-C-00-06	70	0	0	0	0	2	0	3992		
		001-GHO-C-00-07	70	0	0	0	0	2	0	4584		
		001-HHO-00-05	70	0	0	0	0	2	0	4412	4261	186
		001-HHO-00-06	70	0	0	0	0	2	0	3990		
		001-HHO-00-07	70	0	0	0	0	2	0	4304		
		001-HHO-00-08	70	0	0	0	0	2	0	4339		
		001-HHO-C-00-05	70	0	0	0	0	2	0	697	1754	1013
		001-HHO-C-00-06	70	0	0	0	0	2	0	2538		
		001-HHO-C-00-07	70	0	0	0	0	2	0	1082		
		001-HHO-C-00-08	70	0	0	0	0	2	0	2700		
002	011	002-GHO-00-03	70	0	0	0	0	2	0	4855	4895	321
		002-GHO-00-04	70	0	0	0	0	2	0	4596		
		002-GHO-00-05	70	0	0	0	0	2	0	5233		
		002-GHO-10-03	100	6000	60	40	0	2	14	4250	4302	61
		002-GHO-10-04	100	6000	60	40	0	2	14	4286		
		002-GHO-10-05	100	6000	60	40	0	2	14	4368		
		002-HHO-00-03	70	0	0	0	0	2	0	5589	5282	469
		002-HHO-00-04	70	0	0	0	0	2	0	4742		
		002-HHO-00-05	70	0	0	0	0	2	0	5514		
		002-HHO-09-03	100	6000	60	40	0	2	14	4673	4932	341
		002-HHO-09-04	100	6000	60	40	0	2	14	4804		
		002-HHO-09-05	100	6000	60	40	0	2	14	5319		
003	014	003-GHO-00-03	70	0	0	0	0	2	0	4740	4688	48
		003-GHO-00-04	70	0	0	0	0	2	0	4647		
		003-GHO-00-05	70	0	0	0	0	2	0	4676		
		003-GHO-10-03	350	6000	0	100	0	2	14	1846	2212	320
		003-GHO-10-04	350	6000	0	100	0	2	14	2349		
		003-GHO-10-05	350	6000	0	100	0	2	14	2441		
		003-HHO-00-03	70	0	0	0	0	2	0	5789	5457	734
		003-HHO-00-04	70	0	0	0	0	2	0	4616		
		003-HHO-00-05	70	0	0	0	0	2	0	5967		
		003-HHO-09-03	350	6000	0	100	0	2	14	3352	3448	204
		003-HHO-09-04	350	6000	0	100	0	2	14	3309		
		003-HHO-09-05	350	6000	0	100	0	2	14	3683		

Additive Batch #	Baseline Batch #	Core #	T (°F)	P (psi)	CH_4 (%)	CO_2 (%)	H_2S (ppm)	Brine (%)	Days Aged	Comp. Strength (psi)	Ave. Comp. Strength (psi)	Stdev (psi)
004	016	004-GHO-00-03	70	0	0	0	0	2	0	2735	2597	161
		004-GHO-00-04	70	0	0	0	0	2	0	2635		
		004-GHO-00-05	70	0	0	0	0	2	0	2419		
		004-GHO-10-03	350	3000	60	40	0	2	14	2234	1761	528
		004-GHO-10-04	350	3000	60	40	0	2	14	1192		
		004-GHO-10-05	350	3000	60	40	0	2	14	1856		
		004-HHO-00-03	70	0	0	0	0	2	0	3487	3675	557
		004-HHO-00-04	70	0	0	0	0	2	0	3235		
		004-HHO-00-05	70	0	0	0	0	2	0	4302		
		004-HHO-09-03	350	3000	60	40	0	2	14	2858	3148	319
		004-HHO-09-04	350	3000	60	40	0	2	14	3490		
		004-HHO-09-05	350	3000	60	40	0	2	14	3097		
005	018	005-GHO-00-03	70	0	0	0	0	2	0	3103	3605	1036
		005-GHO-00-04	70	0	0	0	0	2	0	4796		
		005-GHO-00-05	70	0	0	0	0	2	0	2915		
		005-GHO-10-03	350	3000	60	40	0	2	14	2939	3252	271
		005-GHO-10-04	350	3000	60	40	0	2	14	3390		
		005-GHO-10-05	350	3000	60	40	0	2	14	3426		
		005-HHO-00-03	70	0	0	0	0	2	0	5316	4751	988
		005-HHO-00-04	70	0	0	0	0	2	0	5327		
		005-HHO-00-05	70	0	0	0	0	2	0	3610		
		005-HHO-09-03	350	3000	60	40	0	2	14	3862	3535	635
		005-HHO-09-04	350	3000	60	40	0	2	14	2803		
		005-HHO-09-05	350	3000	60	40	0	2	14	3939		
006	022	006-GHO-00-03	70	0	0	0	0	2	0	4644	4114	497
		006-GHO-00-04	70	0	0	0	0	2	0	4041		
		006-GHO-00-05	70	0	0	0	0	2	0	3658		
		006-GHO-10-03	225	3000	0	100	0	2	14	3744	2642	1630
		006-GHO-10-04	225	3000	0	100	0	2	14	3412		
		006-GHO-10-05	225	3000	0	100	0	2	14	769		
		006-HHO-00-03	70	0	0	0	0	2	0	5105	4852	308
		006-HHO-00-04	70	0	0	0	0	2	0	4509		
		006-HHO-00-05	70	0	0	0	0	2	0	4942		
		006-HHO-09-03	225	3000	60	40	0	2	14	4089	3879	485
		006-HHO-09-04	225	3000	60	40	0	2	14	3324		
		006-HHO-09-05	225	3000	60	40	0	2	14	4224		
007	026	007-GHO-00-03	70	0	0	0	0	2	0	4276	3418	784
		007-GHO-00-04	70	0	0	0	0	2	0	2738		
		007-GHO-00-05	70	0	0	0	0	2	0	3241		
		007-GHO-10-03	225	3000	90	10	0	2	14	2236	2262	187

Additive Batch #	Baseline Batch #	Core #	T (°F)	P (psi)	CH_4 (%)	CO_2 (%)	H_2S (ppm)	Brine (%)	Days Aged	Comp. Strength (psi)	Ave. Comp. Strength (psi)	Stdev (psi)
		007-GHO-10-04	225	3000	90	10	0	2	14	2461		
		007-GHO-10-05	225	3000	90	10	0	2	14	2090		
		007-HHO-00-03	70	0	0	0	0	2	0	2357	3713	1314
		007-HHO-00-04	70	0	0	0	0	2	0	3802		
		007-HHO-00-05	70	0	0	0	0	2	0	4980		
		007-HHO-09-03	225	3000	90	10	0	2	14	2810	3146	316
		007-HHO-09-04	225	3000	90	10	0	2	14	3191		
		007-HHO-09-05	225	3000	90	10	0	2	14	3437		
008	032	008-GHO-00-03	70	0	0	0	0	2	0	862	766	313
		008-GHO-00-04	70	0	0	0	0	2	0	417		
		008-GHO-00-05	70	0	0	0	0	2	0	1020		
		008-GHO-10-03	430	9000	0	100	0	2	14	1647	1461	168
		008-GHO-10-04	430	9000	0	100	0	2	14	1413		
		008-GHO-10-05	430	9000	0	100	0	2	14	1322		
		008-HHO-00-03	70	0	0	0	0	2	0	3868	3806	174
		008-HHO-00-04	70	0	0	0	0	2	0	3609		
		008-HHO-00-05	70	0	0	0	0	2	0	3940		
		008-HHO-09-03	430	9000	0	100	0	2	14	4968	4569	361
		008-HHO-09-04	430	9000	0	100	0	2	14	4475		
		008-HHO-09-05	430	9000	0	100	0	2	14	4264		
009	033	009-GHO-00-03	70	0	0	0	0	2	0	3786	2679	1642
		009-GHO-00-04	70	0	0	0	0	2	0	3459		
		009-GHO-00-05	70	0	0	0	0	2	0	793		
		009-HHO-00-03	70	0	0	0	0	2	0	4616	2909	1799
		009-HHO-00-04	70	0	0	0	0	2	0	3079		
		009-HHO-00-05	70	0	0	0	0	2	0	1031		
		009-GHO-10-03	100	6000	90	10	300	2	14	4022	3797	653
		009-GHO-10-04	100	6000	90	10	300	2	14	3060		
		009-GHO-10-05	100	6000	90	10	300	2	14	4308		
		009-HHO-09-03	100	6000	90	10	300	2	14	3129	3625	611
		009-HHO-09-04	100	6000	90	10	300	2	14	4307		
		009-HHO-09-05	100	6000	90	10	300	2	14	3438		
010	035	010-GHO-00-03	70	0	0	0	0	2	0	2122	1769	599
		010-GHO-00-04	70	0	0	0	0	2	0	2107		
		010-GHO-00-05	70	0	0	0	0	2	0	1078		
		010-HHO-00-03	70	0	0	0	0	2	0	2831	2919	566
		010-HHO-00-04	70	0	0	0	0	2	0	2402		
		010-HHO-00-05	70	0	0	0	0	2	0	3524		
		010-GHO-10-03	350	6000	90	10	300	2	14	0	807	961
		010-GHO-10-04	350	6000	90	10	300	2	14	550		

Additive Batch #	Baseline Batch #	Core #	T (°F)	P (psi)	CH_4 (%)	CO_2 (%)	H_2S (ppm)	Brine (%)	Days Aged	Comp. Strength (psi)	Ave. Comp. Strength (psi)	Stdev (psi)
		010-GHO-10-05	350	6000	90	10	300	2	14	1870		
		010-HHO-09-03	350	6000	90	10	300	2	14	4929	4561	410
		010-HHO-09-04	350	6000	90	10	300	2	14	4119		
		010-HHO-09-05	350	6000	90	10	300	2	14	4634		
011	036	011-GHO-00-03	70	0	0	0	0	2	0	2026	2078	542
		011-GHO-00-04	70	0	0	0	0	2	0	1563		
		011-GHO-00-05	70	0	0	0	0	2	0	2644		
		011-HHO-00-03	70	0	0	0	0	2	0	1959	1998	107
		011-HHO-00-04	70	0	0	0	0	2	0	2118		
		011-HHO-00-05	70	0	0	0	0	2	0	1915		
		011-GHO-10-03	100	6000	100	0	300	2	14	1534	1405	297
		011-GHO-10-04	100	6000	100	0	300	2	14	1065		
		011-GHO-10-05	100	6000	100	0	300	2	14	1615		
		011-HHO-09-03	100	6000	100	0	300	2	14	1339	1574	313
		011-HHO-09-04	100	6000	100	0	300	2	14	1930		
		011-HHO-09-05	100	6000	100	0	300	2	14	1455		
012	038	012-GHO-00-03	70	0	0	0	0	2	0	4642	3591	963
		012-GHO-00-04	70	0	0	0	0	2	0	3380		
		012-GHO-00-05	70	0	0	0	0	2	0	2752		
		012-HHO-00-03	70	0	0	0	0	2	0	3598	3060	655
		012-HHO-00-04	70	0	0	0	0	2	0	2331		
		012-HHO-00-05	70	0	0	0	0	2	0	3250		
		012-GHO-10-03	100	9000	100	0	300	2	14	3678	3016	663
		012-GHO-10-04	100	9000	100	0	300	2	14	2351		
		012-GHO-10-05	100	9000	100	0	300	2	14	3019		
		012-HHO-09-03	100	9000	100	0	300	2	14	4437	3549	1036
		012-HHO-09-04	100	9000	100	0	300	2	14	2411		
		012-HHO-09-05	100	9000	100	0	300	2	14	3799		
013	040	013-GHO-00-03	70	0	0	0	0	2	0	3657	4596	905
		013-GHO-00-04	70	0	0	0	0	2	0	5462		
		013-GHO-00-05	70	0	0	0	0	2	0	4670		
		013-HHO-00-03	70	0	0	0	0	2	0	2439	2707	599
		013-HHO-00-04	70	0	0	0	0	2	0	2289		
		013-HHO-00-05	70	0	0	0	0	2	0	3393		
		013-GHO-10-03	100	9000	60	40	180	2	14	4371	4153	189
		013-GHO-10-04	100	9000	60	40	180	2	14	4039		
		013-GHO-10-05	100	9000	60	40	180	2	14	4050		
		013-HHO-09-03	100	9000	60	40	180	2	14	4218	3547	703
		013-HHO-09-04	100	9000	60	40	180	2	14	3608		
		013-HHO-09-05	100	9000	60	40	180	2	14	2816		

C.1.3 Properties of Magnesium Oxide Based Cement (MGO-5)

Table C.7: Porosity and permeability of magnesium oxide based cement (MGO-5)

Additive Batch #	Baseline Batch #	Core #	T (°F)	P (psi)	CH_4 (%)	CO_2 (%)	H_2S (ppm)	Brine (%)	Days Aged	Ø (%)	K_{klink} (mD)	Ave. Ø (%)	Stdev	Ave. K (mD)	Stdev
001	Unaged batch	001-HSMG-00-01	70	0	0	0	0	2	0	26	0.038	25	1	0.039	0.006
		001-HSMG-00-02	70	0	0	0	0	2	0	26	0.044				
		001-HSMG-00-03	70	0	0	0	0	2	0	24	0.031				
		001-HSMG-00-04	70	0	0	0	0	2	0	25	0.041				
		001-GSMG-00-01	70	0	0	0	0	2	0	28	0.024	27	1	0.026	0.004
		001-GSMG-00-02	70	0	0	0	0	2	0	27	0.024				
		001-GSMG-00-03	70	0	0	0	0	2	0	28	0.023				
		001-GSMG-00-04	70	0	0	0	0	2	0	27	0.032				
		001-HSMG10-00-01	70	0	0	0	0	2	0	28	0.13	28	1	0.097	0.038
		001-HSMG10-00-02	70	0	0	0	0	2	0	27	0.046				
		001-HSMG10-00-03	70	0	0	0	0	2	0	28	0.092				
		001-HSMG10-00-04	70	0	0	0	0	2	0	29	0.12				
		001-GSMG10-00-01	70	0	0	0	0	2	0	29	0.04	29	0	0.041	0.006
		001-GSMG10-00-02	70	0	0	0	0	2	0	29	0.037				
		001-GSMG10-00-03	70	0	0	0	0	2	0	29	0.049				
		001-GSMG10-00-04	70	0	0	0	0	2	0	29	0.036				
002	010	002-HSMG-00-01	70	0	0	0	0	2	0	31	0.097	31	0	0.097	0.001
		002-HSMG-00-02	70	0	0	0	0	2	0	31	0.096				
		002-GSMG-00-01	70	0	0	0	0	2	0	32	0.011	29	5	0.011	0.001
		002-GSMG-00-02	70	0	0	0	0	2	0	25	0.01				
		002-HSMG-09-01	225	6000	0	100	0	2	14	24	0.045	24	0	0.062	0.024
		002-HSMG-09-02	225	6000	0	100	0	2	14	24	0.079				
		002-GSMG-10-01	225	6000	0	100	0	2	14	26	0.067	26	0	0.062	0.007
		002-GSMG-10-02	350	9000	0	100	0	2	14	26	0.057				
003	012	003-HSMG-00-01	70	0	0	0	0	2	0	28	0.032	28	0	0.034	0.003
		003-HSMG-00-02	70	0	0	0	0	2	0	27	0.036				
		003-GSMG-00-01	70	0	0	0	0	2	0	22	0.016	23	0	0.021	0.006
		003-GSMG-00-02	70	0	0	0	0	2	0	23	0.025				
		003-HSMG-09-01	100	6000	0	100	0	2	14	28	0.018	28	1	0.020	0.002
		003-HSMG-09-02	100	6000	0	100	0	2	14	27	0.021				
		003-GSMG-10-01	100	6000	0	100	0	2	14	23	0.019	23	0	0.018	0.002
		003-GSMG-10-02	100	6000	0	100	0	2	14	23	0.016				
004	015	004-HSMG-00-01	70	0	0	0	0	2	0	29	0.05	29	0	0.052	0.002
		004-HSMG-00-02	70	0	0	0	0	2	0	29	0.053				
		004-GSMG-00-01	70	0	0	0	0	2	0	24	0.062	24	0	0.072	0.013
		004-GSMG-00-02	70	0	0	0	0	2	0	24	0.081				
		004-HSMG-09-01	225	6000	60	40	0	2	14	-	-	28		0.020	

Additive Batch #	Baseline Batch #	Core #	T (°F)	P (psi)	CH_4 (%)	CO_2 (%)	H_2S (ppm)	Brine (%)	Days Aged	Ø (%)	K_{klink} (mD)	Ave. Ø (%)	Stdev	Ave. K (mD)	Stdev
		004-HSMG-09-02	225	6000	60	40	0	2	14	28	0.02				
		004-GSMG-10-01	225	6000	60	40	0	2	14	26	0.045	26	0	0.038	0.011
		004-GSMG-10-02	225	6000	60	40	0	2	14	26	0.03				
005	017	005-HSMG-00-01	70	0	0	0	0	2	0	29	0.09	30	0	0.095	0.007
		005-HSMG-00-02	70	0	0	0	0	2	0	30	0.1				
		005-GSMG-00-01	70	0	0	0	0	2	0	19	0.018	20	2	0.028	0.014
		005-GSMG-00-02	70	0	0	0	0	2	0	22	0.038				
		005-HSMG-09-01	350	9000	60	40	0	2	14	28	0.022	28	0	0.023	0.001
		005-HSMG-09-02	350	9000	60	40	0	2	14	28	0.023				
		005-GSMG-10-01	350	9000	60	40	0	2	14	28	0.067	28	0	0.058	0.013
		005-GSMG-10-02	350	9000	60	40	0	2	14	27	0.048				
006	023	006-HSMG-00-01	70	0	0	0	0	2	0	29	0.065	29	1	0.055	0.014
		006-HSMG-00-02	70	0	0	0	0	2	0	28	0.045				
		006-GSMG-00-01	70	0	0	0	0	2	0	21	0.011	12	12	0.011	0.000
		006-GSMG-00-02	70	0	0	0	0	2	0	4	0.011				
		006-HSMG-09-01	225	9000	60	40	0	2	14	29	0.02	28	1	0.032	0.017
		006-HSMG-09-02	225	9000	60	40	0	2	14	27	0.044				
		006-GSMG-10-01	225	9000	60	40	0	2	14	4	0.023	14	14	0.018	0.008
		006-GSMG-10-02	225	9000	60	40	0	2	14	24	0.012				
007	025	007-HSMG-00-01	70	0	0	0	0	2	0	29	0.248	29	0	0.198	0.071
		007-HSMG-00-02	70	0	0	0	0	2	0	29	0.148				
		007-GSMG-00-01	70	0	0	0	0	2	0	21	0.03	20	1	0.025	0.008
		007-GSMG-00-02	70	0	0	0	0	2	0	19	0.019				
		007-HSMG-09-01	225	9000	0	100	0	2	14	29	0.029	29	0	0.030	0.001
		007-HSMG-09-02	225	9000	0	100	0	2	14	29	0.031				
		007-GSMG-10-01	225	9000	0	100	0	2	14	23	0.019	23	0	0.017	0.004
		007-GSMG-10-02	225	9000	0	100	0	2	14	23	0.014				
008	034	008-HSMG-00-01	70	0	0	0	0	2	0	31	0.092	31		0.092	
		008-HSMG-00-02	70	0	0	0	0	2	0						
		008-GSMG-00-01	70	0	0	0	0	2	0	8	0.003	11	4	0.005	0.002
		008-GSMG-00-02	70	0	0	0	0	2	0	14	0.006				
		008-HSMG-09-01	225	6000	90	10	300	2	14	31	0.045	31		0.045	
		008-HSMG-09-02	225	6000	90	10	300	2	14						
		008-GSMG-10-01	225	6000	90	10	300	2	14	19	0.016	19	0	0.015	0.001
		008-GSMG-10-02	225	6000	90	10	300	2	14	19	0.014				
011	039	011 GSMG 00 01	70	0	0	0	0	2	0	18.6		23	7	0.023	0.016
		011 GSMG 00 02	70	0	0	0	0	2	0	27.9					
		011 HSMG 00 01	70	0	0	0	0	2	0	28.5		28	1	0.102	0.060
		011 HSMG 00 02	70	0	0	0	0	2	0	27.6					
		011 GSMG 10 01	100	9000	90	10	300	2	14	6.24		6	0	0.046	0.008

Additive Batch #	Baseline Batch #	Core #	T (°F)	P (psi)	CH_4 (%)	CO_2 (%)	H_2S (ppm)	Brine (%)	Days Aged	Ø (%)	K_{klink} (mD)	Ave. Ø (%)	Stdev	Ave. K (mD)	Stdev
		011 GSMG 10 02	100	9000	90	10	300	2	14	6.18					
		011 HSMG 09 01	100	9000	90	10	300	2	14	16.2		16	0	0.185	0.016
		011 HSMG 09 02	100	9000	90	10	300	2	14	16.6					
012	041	012 GSMG 00 01	70	0	0	0	0	2	0	29.1		32	4	0.038	0.013
		012 GSMG 00 02	70	0	0	0	0	2	0	35.2					
		012 HSMG 00 01	70	0	0	0	0	2	0	28.2		28	0	0.040	0.005
		012 HSMG 00 02	70	0	0	0	0	2	0	28.6					
		012 GSMG 10 01	100	3000	100	0	300	2	14	35.6		34	3	0.024	0.001
		012 GSMG 10 02	100	3000	100	0	300	2	14	31.5					
		012 HSMG 09 01	100	3000	100	0	300	2	14	28.6		29	1	0.054	0.006
		012 HSMG 09 02	100	3000	100	0	300	2	14	29.4					

Table C.8: Shear bond strength of magnesium oxide based cement (MGO-5)

Additive Batch #	Baseline Batch #	Core #	T (°F)	P (psi)	CH_4 (%)	CO_2 (%)	H_2S (ppm)	Brine (%)	Days Aged	SBS (psi)	Ave. SBS (psi)	Stdev (psi)
001	Unaged batch	001-HSMG-00-01	70	0	0	0	0	2	14	691	597	125
		001-HSMG-00-02	70	0	0	0	0	2	14	455		
		001-HSMG-00-03	70	0	0	0	0	2	14	645		
		001-HSMG10-00-01	70	0	0	0	0	2	14	510	585	178
		001-HSMG10-00-02	70	0	0	0	0	2	14	788		
		001-HSMG10-00-03	70	0	0	0	0	2	14	457		
002	010	002-HSMG-00-01	70	0	0	0	0	2	0	919	838	195
		002-HSMG-00-02	70	0	0	0	0	2	0	952		
		002-HSMG-00-03	70	0	0	0	0	2	0	492		
		002-HSMG-00-04	70	0	0	0	0	2	0	896		
		002-HSMG-00-05	70	0	0	0	0	2	0	932		
		002-HSMG-11-01	225	6000	0	100	0	2	14	1840	1774	182
		002-HSMG-11-02	225	6000	0	100	0	2	14	1549		
		002-HSMG-11-03	225	6000	0	100	0	2	14	1647		
		002-HSMG-11-04	225	6000	0	100	0	2	14	1817		
		002-HSMG-11-05	225	6000	0	100	0	2	14	2017		
		002-HSMG10-00-01	70	0	0	0	0	2	0	797	753	110
		002-HSMG10-00-02	70	0	0	0	0	2	0	660		
		002-HSMG10-00-03	70	0	0	0	0	2	0	926		
		002-HSMG10-00-04	70	0	0	0	0	2	0	694		
		002-HSMG10-00-05	70	0	0	0	0	2	0	687		
		002-HSMG10-11-01	350	9000	0	100	0	2	14	1826	2004	133
		002-HSMG10-11-02	350	9000	0	100	0	2	14	1991		
		002-HSMG10-11-03	350	9000	0	100	0	2	14	1948		
		002-HSMG10-11-04	350	9000	0	100	0	2	14	2072		
		002-HSMG10-11-05	350	9000	0	100	0	2	14	2181		
003	012	003-HSMG-00-01	70	0	0	0	0	2	0	624	652	122
		003-HSMG-00-02	70	0	0	0	0	2	0	510		
		003-HSMG-00-03	70	0	0	0	0	2	0	819		
		003-HSMG-00-04	70	0	0	0	0	2	0	727		
		003-HSMG-00-05	70	0	0	0	0	2	0	582		
		003-HSMG-11-01	100	6000	0	100	0	2	14	924	929	99
		003-HSMG-11-02	100	6000	0	100	0	2	14	1021		
		003-HSMG-11-03	100	6000	0	100	0	2	14	859		
		003-HSMG-11-04	100	6000	0	100	0	2	14	808		
		003-HSMG-11-05	100	6000	0	100	0	2	14	1035		
004	015	004-HSMG-00-01	70	0	0	0	0	2	0	361	493	91
		004-HSMG-00-02	70	0	0	0	0	2	0	537		
		004-HSMG-00-03	70	0	0	0	0	2	0	549		
		004-HSMG-00-04	70	0	0	0	0	2	0	439		
		004-HSMG-00-05	70	0	0	0	0	2	0	579		

Additive Batch #	Baseline Batch #	Core #	T (°F)	P (psi)	CH_4 (%)	CO_2 (%)	H_2S (ppm)	Brine (%)	Days Aged	SBS (psi)	Ave. SBS (psi)	Stdev (psi)
		004-HSMG-11-01	225	6000	60	40	0	2	14	2076		
		004-HSMG-11-02	225	6000	60	40	0	2	14	1636		
		004-HSMG-11-03	225	6000	60	40	0	2	14	1514	1707	236
		004-HSMG-11-04	225	6000	60	40	0	2	14	1514		
		004-HSMG-11-05	225	6000	60	40	0	2	14	1793		
		005-HSMG-00-01	70	0	0	0	0	2	0	617		
		005-HSMG-00-02	70	0	0	0	0	2	0	542		
		005-HSMG-00-03	70	0	0	0	0	2	0	544	554	51
		005-HSMG-00-04	70	0	0	0	0	2	0	583		
005	017	005-HSMG-00-05	70	0	0	0	0	2	0	482		
		005-HSMG-11-01	350	9000	60	40	0	2	14	2747		
		005-HSMG-11-02	350	9000	60	40	0	2	14	2693		
		005-HSMG-11-03	350	9000	60	40	0	2	14	2888	2800	80
		005-HSMG-11-04	350	9000	60	40	0	2	14	2816		
		005-HSMG-11-05	350	9000	60	40	0	2	14	2856		
		006-HSMG-00-01	70	0	0	0	0	2	0	585		
		006-HSMG-00-02	70	0	0	0	0	2	0	585		
		006-HSMG-00-03	70	0	0	0	0	2	0	392	521	83
		006-HSMG-00-04	70	0	0	0	0	2	0	485		
		006-HSMG-00-05	70	0	0	0	0	2	0	559		
006	023	006-HSMG-11-01	225	9000	60	40	0	2	14	2140		
		006-HSMG-11-02	225	9000	60	40	0	2	14	2037		
		006-HSMG-11-03	225	9000	60	40	0	2	14	1901	1999	100
		006-HSMG-11-04	225	9000	60	40	0	2	14	2014		
		006-HSMG-11-05	225	9000	60	40	0	2	14	1904		
		007-HSMG-00-01	70	0	0	0	0	2	0	691		
		007-HSMG-00-02	70	0	0	0	0	2	0	892		
		007-HSMG-00-03	70	0	0	0	0	2	0	606	689	118
		007-HSMG-00-04	70	0	0	0	0	2	0	633		
		007-HSMG-00-05	70	0	0	0	0	2	0	626		
007	025	007-HSMG-11-01	225	9000	0	100	0	2	14	1785		
		007-HSMG-11-02	225	9000	0	100	0	2	14	1781		
		007-HSMG-11-03	225	9000	0	100	0	2	14	1741	2018	492
		007-HSMG-11-04	225	9000	0	100	0	2	14	1890		
		007-HSMG-11-05	225	9000	0	100	0	2	14	2892		
		008-HSMG-00-01	70	0	0	0	0	2	0	787		
		008-HSMG-00-02	70	0	0	0	0	2	0	603		
		008-HSMG-00-03	70	0	0	0	0	2	0	910	784	115
		008-HSMG-00-04	70	0	0	0	0	2	0	775		
008	034	008-HSMG-00-05	70	0	0	0	0	2	0	845		
		008-HSMG-11-01	225	6000	90	10	300	2	14	1554	1838	328
		008-HSMG-11-02	225	6000	90	10	300	2	14	2369		

Additive Batch #	Baseline Batch #	Core #	T (°F)	P (psi)	CH_4 (%)	CO_2 (%)	H_2S (ppm)	Brine (%)	Days Aged	SBS (psi)	Ave. SBS (psi)	Stdev (psi)
		008-HSMG-11-03	225	6000	90	10	300	2	14	1595		
		008-HSMG-11-04	225	6000	90	10	300	2	14	1766		
		008-HSMG-11-05	225	6000	90	10	300	2	14	1905		
010	037	010-HSMG-00-01	70	0	0	0	0	2	0	753	856	97
		010-HSMG-00-02	70	0	0	0	0	2	0	1010		
		010-HSMG-00-03	70	0	0	0	0	2	0	881		
		010-HSMG-00-04	70	0	0	0	0	2	0	809		
		010-HSMG-00-05	70	0	0	0	0	2	0	829		
		010-HSMG-11-01	100	6000	100	0	300	2	14	808	876	78
		010-HSMG-11-02	100	6000	100	0	300	2	14	810		
		010-HSMG-11-03	100	6000	100	0	300	2	14	967		
		010-HSMG-11-04	100	6000	100	0	300	2	14	953		
		010-HSMG-11-05	100	6000	100	0	300	2	14	842		
011	039	011-HSMG-00-01	70	0	0	0	0	2	0	1369	1058	366
		011-HSMG-00-02	70	0	0	0	0	2	0	606		
		011-HSMG-00-03	70	0	0	0	0	2	0	1489		
		011-HSMG-00-04	70	0	0	0	0	2	0	974		
		011-HSMG-00-05	70	0	0	0	0	2	0	851		
		011-HSMG-11-01	100	9000	100	0	300	2	14	844	1405	354
		011-HSMG-11-02	100	9000	100	0	300	2	14	1749		
		011-HSMG-11-03	100	9000	100	0	300	2	14	1301		
		011-HSMG-11-04	100	9000	100	0	300	2	14	1502		
		011-HSMG-11-05	100	9000	100	0	300	2	14	1627		
012	041	012-HSMG-00-01	70	0	0	0	0	2	0	828	732	72
		012-HSMG-00-02	70	0	0	0	0	2	0	700		
		012-HSMG-00-03	70	0	0	0	0	2	0	642		
		012-HSMG-00-04	70	0	0	0	0	2	0	713		
		012-HSMG-00-05	70	0	0	0	0	2	0	779		
		012-HSMG-11-01	100	3000	100	0	300	2	14	632	675	81
		012-HSMG-11-02	100	3000	100	0	300	2	14	578		
		012-HSMG-11-03	100	3000	100	0	300	2	14	797		
		012-HSMG-11-04	100	3000	100	0	300	2	14	677		
		012-HSMG-11-05	100	3000	100	0	300	2	14	692		

Table C.9: Compressive strength of magnesium oxide based cement (MGO-5)

Additive Batch #	Baseline Batch #	Core #	T (°F)	P (psi)	CH_4 (%)	CO_2 (%)	H_2S (ppm)	Brine (%)	Days Aged	Comp. Strength (psi)	Ave. Comp. Strength (psi)	Stdev (psi)
001	Unaged Batch	001-GSMG-00-05	70	0	0	0	0	2	0	4596	4160	867
		001-GSMG-00-06	70	0	0	0	0	2	0	3162		
		001-GSMG-00-07	70	0	0	0	0	2	0	4723		
		001-GSMG10-00-05	70	0	0	0	0	2	0	3261	3219	267
		001-GSMG10-00-06	70	0	0	0	0	2	0	2957		
		001-GSMG10-00-07	70	0	0	0	0	2	0	3573		
		001-GSMG10-00-08	70	0	0	0	0	2	0	3084		
		001-HSMG-00-05	70	0	0	0	0	2	0	5379	5090	300
		001-HSMG-00-06	70	0	0	0	0	2	0	5110		
		001-HSMG-00-07	70	0	0	0	0	2	0	4780		
		001-HSMG10-00-05	70	0	0	0	0	2	0	3323	2842	326
		001-HSMG10-00-06	70	0	0	0	0	2	0	2624		
		001-HSMG10-00-07	70	0	0	0	0	2	0	2766		
		001-HSMG10-00-08	70	0	0	0	0	2	0	2657		
002	010	002-GSMG-00-03	70	0	0	0	0	2	0	4002	4405	388
		002-GSMG-00-04	70	0	0	0	0	2	0	4437		
		002-GSMG-00-05	70	0	0	0	0	2	0	4776		
		002-GSMG10-00-03	70	0	0	0	0	2	0	8057	7181	922
		002-GSMG10-00-04	70	0	0	0	0	2	0	7266		
		002-GSMG10-00-05	70	0	0	0	0	2	0	6220		
		002-GSMG-10-03	225	6000	0	100	0	2	14	5733	5156	714
		002-GSMG-10-04	225	6000	0	100	0	2	14	4358		
		002-GSMG-10-05	225	6000	0	100	0	2	14	5379		
		002-GSMG10-10-03	350	9000	0	100	0	2	14	800	2088	1365
		002-GSMG10-10-04	350	9000	0	100	0	2	14	3519		
		002-GSMG10-10-05	350	9000	0	100	0	2	14	1945		
		002-HSMG-00-03	70	0	0	0	0	2	0	4568	4391	153
		002-HSMG-00-04	70	0	0	0	0	2	0	4304		
		002-HSMG-00-05	70	0	0	0	0	2	0	4302		
		002-HSMG10-00-03	70	0	0	0	0	2	0	2240	3331	955
		002-HSMG10-00-04	70	0	0	0	0	2	0	3737		
		002-HSMG10-00-05	70	0	0	0	0	2	0	4016		
		002-HSMG-09-03	225	6000	0	100	0	2	14	5947	6313	415
		002-HSMG-09-04	225	6000	0	100	0	2	14	6764		
		002-HSMG-09-05	225	6000	0	100	0	2	14	6226		
		002-HSMG10-09-03	350	9000	0	100	0	2	14	3691	3674	24
		002-HSMG10-09-04	350	9000	0	100	0	2	14	3683		
		002-HSMG10-09-05	350	9000	0	100	0	2	14	3646		
003	012	003-GSMG-00-03	70	0	0	0	0	2	0	4064	3783	268

Additive Batch #	Baseline Batch #	Core #	T (°F)	P (psi)	CH_4 (%)	CO_2 (%)	H_2S (ppm)	Brine (%)	Days Aged	Comp. Strength (psi)	Ave. Comp. Strength (psi)	Stdev (psi)
		003-GSMG-00-04	70	0	0	0	0	2	0	3754		
		003-GSMG-00-05	70	0	0	0	0	2	0	3530		
		003-HSMG-00-03	70	0	0	0	0	2	0	4309		
		003-HSMG-00-04	70	0	0	0	0	2	0	4370	4407	121
		003-HSMG-00-05	70	0	0	0	0	2	0	4542		
		003-GSMG-10-03	100	6000	0	100	0	2	14	4463		
		003-GSMG-10-04	100	6000	0	100	0	2	14	3521	4082	496
		003-GSMG-10-05	100	6000	0	100	0	2	14	4261		
		003-HSMG-09-03	100	6000	0	100	0	2	14	3896		
		003-HSMG-09-04	100	6000	0	100	0	2	14	3975	4139	354
		003-HSMG-09-05	100	6000	0	100	0	2	14	4545		
		004-GSMG-00-03	70	0	0	0	0	2	0	3023		
		004-GSMG-00-04	70	0	0	0	0	2	0	3539	3352	286
		004-GSMG-00-05	70	0	0	0	0	2	0	3495		
		004-HSMG-00-03	70	0	0	0	0	2	0	4132		
		004-HSMG-00-04	70	0	0	0	0	2	0	3151	3586	500
		004-HSMG-00-05	70	0	0	0	0	2	0	3474		
004	015	004-GSMG-10-03	225	6000	60	40	0	2	14	3969		
		004-GSMG-10-04	225	6000	60	40	0	2	14	5000	4345	570
		004-GSMG-10-05	225	6000	60	40	0	2	14	4066		
		004-HSMG-09-03	225	6000	60	40	0	2	14	5977		
		004-HSMG-09-04	225	6000	60	40	0	2	14	5215	5985	774
		004-HSMG-09-05	225	6000	60	40	0	2	14	6763		
		005-GSMG-00-03	70	0	0	0	0	2	0	3684		
		005-GSMG-00-04	70	0	0	0	0	2	0	3636	3463	343
		005-GSMG-00-05	70	0	0	0	0	2	0	3068		
		005-HSMG-00-03	70	0	0	0	0	2	0	3603		
		005-HSMG-00-04	70	0	0	0	0	2	0	3621	3727	199
		005-HSMG-00-05	70	0	0	0	0	2	0	3957		
005	017	005-GSMG-10-03	350	9000	60	40	0	2	14	3461		
		005-GSMG-10-04	350	9000	60	40	0	2	14	1365	2515	1062
		005-GSMG-10-05	350	9000	60	40	0	2	14	2720		
		005-HSMG-09-03	350	9000	60	40	0	2	14	7697		
		005-HSMG-09-04	350	9000	60	40	0	2	14	8497	7983	446
		005-HSMG-09-05	350	9000	60	40	0	2	14	7755		
		006-GSMG-00-03	70	0	0	0	0	2	0	3763		
		006-GSMG-00-04	70	0	0	0	0	2	0	4838	4177	578
006	023	006-GSMG-00-05	70	0	0	0	0	2	0	3929		
		006-HSMG-00-03	70	0	0	0	0	2	0	3398	3230	217
		006-HSMG-00-04	70	0	0	0	0	2	0	2986		

Additive Batch #	Baseline Batch #	Core #	T (°F)	P (psi)	CH_4 (%)	CO_2 (%)	H_2S (ppm)	Brine (%)	Days Aged	Comp. Strength (psi)	Ave. Comp. Strength (psi)	Stdev (psi)
		006-HSMG-00-05	70	0	0	0	0	2	0	3306		
		006-GSMG-10-03	225	9000	60	40	0	2	14	5744	5643	1054
		006-GSMG-10-04	225	9000	60	40	0	2	14	6643		
		006-GSMG-10-05	225	9000	60	40	0	2	14	4542		
		006-HSMG-09-03	225	9000	60	40	0	2	14	6706	6538	401
		006-HSMG-09-04	225	9000	60	40	0	2	14	6829		
		006-HSMG-09-05	225	9000	60	40	0	2	14	6081		
007	025	007-GSMG-00-03	70	0	0	0	0	2	0	2549	3416	772
		007-GSMG-00-04	70	0	0	0	0	2	0	3669		
		007-GSMG-00-05	70	0	0	0	0	2	0	4030		
		007-HSMG-00-03	70	0	0	0	0	2	0	3646	4086	736
		007-HSMG-00-04	70	0	0	0	0	2	0	4935		
		007-HSMG-00-05	70	0	0	0	0	2	0	3676		
		007-GSMG-10-03	225	9000	0	100	0	2	14	4664	3778	828
		007-GSMG-10-04	225	9000	0	100	0	2	14	3646		
		007-GSMG-10-05	225	9000	0	100	0	2	14	3024		
		007-HSMG-09-03	225	9000	0	100	0	2	14	6354	6362	31
		007-HSMG-09-04	225	9000	0	100	0	2	14	6396		
		007-HSMG-09-05	225	9000	0	100	0	2	14	6336		
008	027	008-GSMG-00-03	70	0	0	0	0	2	0	5883	5322	557
		008-GSMG-00-04	70	0	0	0	0	2	0	4768		
		008-GSMG-00-05	70	0	0	0	0	2	0	5314		
		008-HSMG-00-03	70	0	0	0	0	2	0	964	2594	1541
		008-HSMG-00-04	70	0	0	0	0	2	0	4027		
		008-HSMG-00-05	70	0	0	0	0	2	0	2792		
		008-GSMG-10-03	225	6000	90	10	300	2	14	3944	4134	298
		008-GSMG-10-04	225	6000	90	10	300	2	14	3980		
		008-GSMG-10-05	225	6000	90	10	300	2	14	4477		
		008-HSMG-09-03	225	6000	90	10	300	2	14	2530	3329	709
		008-HSMG-09-04	225	6000	90	10	300	2	14	3577		
		008-HSMG-09-05	225	6000	90	10	300	2	14	3882		
010	037	010-GSMG-00-03	70	0	0	0	0	2	0	637	1806	1043
		010-GSMG-00-04	70	0	0	0	0	2	0	2142		
		010-GSMG-00-05	70	0	0	0	0	2	0	2641		
		010-HSMG-00-03	70	0	0	0	0	2	0	3120	2325	884
		010-HSMG-00-04	70	0	0	0	0	2	0	1373		
		010-HSMG-00-05	70	0	0	0	0	2	0	2482		
		010-GSMG-10-03	100	6000	60	40	180	2	14	2434	2230	231
		010-GSMG-10-04	100	6000	60	40	180	2	14	1979		
		010-GSMG-10-05	100	6000	60	40	180	2	14	2277		

Additive Batch #	Baseline Batch #	Core #	T (°F)	P (psi)	CH_4 (%)	CO_2 (%)	H_2S (ppm)	Brine (%)	Days Aged	Comp. Strength (psi)	Ave. Comp. Strength (psi)	Stdev (psi)
		010-HSMG-09-03	100	6000	60	40	180	2	14	2142	2264	187
		010-HSMG-09-04	100	6000	60	40	180	2	14	2171		
		010-HSMG-09-05	100	6000	60	40	180	2	14	2479		
011	039	011-GSMG-00-03	70	0	0	0	0	2	0	3971	4101	1101
		011-GSMG-00-04	70	0	0	0	0	2	0	5261		
		011-GSMG-00-05	70	0	0	0	0	2	0	3071		
		011-HSMG-00-03	70	0	0	0	0	2	0	3249	3891	592
		011-HSMG-00-04	70	0	0	0	0	2	0	4006		
		011-HSMG-00-05	70	0	0	0	0	2	0	4416		
		011-GSMG-10-03	100	9000	90	10	300	2	14	5056	4274	699
		011-GSMG-10-04	100	9000	90	10	300	2	14	4055		
		011-GSMG-10-05	100	9000	90	10	300	2	14	3710		
		011-HSMG-09-03	100	9000	90	10	300	2	14	3357	4221	1139
		011-HSMG-09-04	100	9000	90	10	300	2	14	3795		
		011-HSMG-09-05	100	9000	90	10	300	2	14	5512		
012	041	012-GSMG-00-03	70	0	0	0	0	2	0	3283	3834	480
		012-GSMG-00-04	70	0	0	0	0	2	0	4061		
		012-GSMG-00-05	70	0	0	0	0	2	0	4158		
		012-HSMG-00-03	70	0	0	0	0	2	0	4896	4172	628
		012-HSMG-00-04	70	0	0	0	0	2	0	3838		
		012-HSMG-00-05	70	0	0	0	0	2	0	3782		
		012-GSMG-10-03	100	3000	100	0	300	2	14	3544	4367	721
		012-GSMG-10-04	100	3000	100	0	300	2	14	4672		
		012-GSMG-10-05	100	3000	100	0	300	2	14	4885		
		012-HSMG-09-03	100	3000	100	0	300	2	14	3937	3830	171
		012-HSMG-09-04	100	3000	100	0	300	2	14	3633		
		012-HSMG-09-05	100	3000	100	0	300	2	14	3922		

C.1.4 Properties of Latex Based Cement (LT)

Table C.10: Porosity and permeability of latex based cement (LT)

Additive Batch #	Baseline Batch #	Core #	T (°F)	P (psi)	CH_4 (%)	CO_2 (%)	H_2S (ppm)	Brine (%)	Days Aged	Ø (%)	K_{klink} (mD)	Ave. Ø (%)	Stdev	Ave. K (mD)	Stdev
001	Unaged batch	001-HSLT-00-01	70	0	0	0	0	2	0	34	0.125	34	0	0.121	0.006
		001-HSLT-00-02	70	0	0	0	0	2	0	34	0.116				
		001-HSLT-00-03	70	0	0	0	0	2	0	34	0.115	34	0	0.109	0.008
		001-HSLT-00-04	70	0	0	0	0	2	0	34	0.103				
		001-GSLT-00-01	70	0	0	0	0	2	0	34	0.2	35	1	0.217	0.023
		001-GSLT-00-02	70	0	0	0	0	2	0	35	0.233				
		001-GSLT-00-03	70	0	0	0	0	2	0	35	0.187	35	0	0.188	0.001
		001-GSLT-00-04	70	0	0	0	0	2	0	35	0.188				
002	Unaged batch	002-HSLT-00-01	70	0	0	0	0	2	0	33	0.076	33	0	0.080	0.005
		002-HSLT-00-02	70	0	0	0	0	2	0	33	0.083				
		002-GSLT-00-01	70	0	0	0	0	2	0	35	0.213	35	0	0.201	0.017
		002-GSLT-00-02	70	0	0	0	0	2	0	35	0.189				
003	Unaged batch	003-HSLT-00-01	70	0	0	0	0	2	0	34	0.129	34	0	0.133	0.006
		003-HSLT-00-02	70	0	0	0	0	2	0	34	0.137				
		003-GSLT-00-01	70	0	0	0	0	2	0	38	0.184	36	2	0.183	0.002
		003-GSLT-00-02	70	0	0	0	0	2	0	35	0.181				
004	013	004-HSLT-00-01	70	0	0	0	0	2	0			35		0.151	
		004-HSLT-00-02	70	0	0	0	0	2	0	35	0.151				
		004-GSLT-00-01	70	0	0	0	0	2	0			31		0.026	
		004-GSLT-00-02	70	0	0	0	0	2	0	31	0.026				
		004-HSLT-09-01	350	6000	60	40	0	2	14			35		0.126	
		004-HSLT-09-02	350	6000	60	40	0	2	14	35	0.126				
		004-GSLT-10-01	350	6000	60	40	0	2	14			32		0.094	
		004-GSLT-10-02	350	6000	60	40	0	2	14	32	0.094				
005	Unaged batch	005-HSLT-00-01	70	0	0	0	0	2	0	32	0.13	32	0	0.130	
		005-HSLT-00-02	70	0	0	0	0	2	0						
		005-HSLT-00-03	70	0	0	0	0	2	0	32	0.129	32	0	0.128	0.001
		005-HSLT-00-04	70	0	0	0	0	2	0	32	0.127				
		005-GSLT-00-01	70	0	0	0	0	2	0	33	0.122	33	1	0.131	0.013
		005-GSLT-00-02	70	0	0	0	0	2	0	34	0.14				
		005-GSLT-00-03	70	0	0	0	0	2	0	34	0.148	34	0	0.147	0.002
		005-GSLT-00-04	70	0	0	0	0	2	0	34	0.145				

Table C.11: Shear bond strength of latex based cement (LT)

Additive Batch #	Baseline Batch #	Core #	T (°F)	P (psi)	CH_4 (%)	CO_2 (%)	H_2S (ppm)	Brine (%)	Days Aged	SBS (psi)	Ave. SBS (psi)	Stdev (psi)
001	Unaged batch	001-HSLT-00-01	70	0	0	0	0	2	14	282	374	96
		001-HSLT-00-02	70	0	0	0	0	2	14	474		
		001-HSLT-00-03	70	0	0	0	0	2	14	365		
004	013	004-HSLT-00-01	70	0	0	0	0	2	14	645	547	169
		004-HSLT-00-02	70	0	0	0	0	2	14	753		
		004-HSLT-00-03	70	0	0	0	0	2	14	348		
		004-HSLT-00-04	70	0	0	0	0	2	14	590		
		004-HSLT-00-05	70	0	0	0	0	2	14	402		
		004-HSLT-11-01	350	6000	60	40	0	2	14	2001	1908	253
		004-HSLT-11-02	350	6000	60	40	0	2	14	2075		
		004-HSLT-11-03	350	6000	60	40	0	2	14	1635		
		004-HSLT-11-04	350	6000	60	40	0	2	14	1645		
		004-HSLT-11-05	350	6000	60	40	0	2	14	2185		
005	Unaged batch	005-HSLT-00-01	70	0	0	0	0	2	14	559	533	127
		005-HSLT-00-02	70	0	0	0	0	2	14	645		
		005-HSLT-00-03	70	0	0	0	0	2	14	395		

Table C.12: Compressive strength of latex based cement (LT)

Additive Batch #	Baseline Batch #	Core #	T (°F)	P (psi)	CH_4 (%)	CO_2 (%)	H_2S (ppm)	Brine (%)	Days Aged	Comp. Strength (psi)	Ave. Comp. Strength (psi)	Stdev (psi)
001	Unaged Batch	001-GSLM-00-05	70	0	0	0	0	2	0	4007	3345	593
		001-GSLM-00-06	70	0	0	0	0	2	0	2862		
		001-GSLM-00-07	70	0	0	0	0	2	0	3685		
		001-GSLM-00-08	70	0	0	0	0	2	0	2827		
		001-HSLM-00-05	70	0	0	0	0	2	0	2423	2446	64
		001-HSLM-00-06	70	0	0	0	0	2	0	2498		
		001-HSLM-00-07	70	0	0	0	0	2	0	2365		
		001-HSLM-00-08	70	0	0	0	0	2	0	2497		
002	027	002-GSLM-00-03	70	0	0	0	0	2	0	2449	3014	1327
		002-GSLM-00-04	70	0	0	0	0	2	0	4530		
		002-GSLM-00-05	70	0	0	0	0	2	0	2064		
		002-HSLM-00-03	70	0	0	0	0	2	0	5581	4746	1240
		002-HSLM-00-04	70	0	0	0	0	2	0	3321		
		002-HSLM-00-05	70	0	0	0	0	2	0	5334		
		002-GSLM-10-03	225	9000	90	10	0	2	14	3536	3543	1317
		002-GSLM-10-04	225	9000	90	10	0	2	14	2230		
		002-GSLM-10-05	225	9000	90	10	0	2	14	4864		
		002-HSLM-09-03	225	9000	90	10	0	2	14	4426	4757	1804
		002-HSLM-09-04	225	9000	90	10	0	2	14	3140		
		002-HSLM-09-05	225	9000	90	10	0	2	14	6703		
003	030	003-GSLM-00-03	70	0	0	0	0	2	0	3965	3810	135
		003-GSLM-00-04	70	0	0	0	0	2	0	3721		
		003-GSLM-00-05	70	0	0	0	0	2	0	3742		
		003-HSLM-00-03	70	0	0	0	0	2	0	3559	2785	680
		003-HSLM-00-04	70	0	0	0	0	2	0	2515		
		003-HSLM-00-05	70	0	0	0	0	2	0	2282		
		003-GSLM-10-03	430	6000	0	100	0	2	14	4783	5838	914
		003-GSLM-10-04	430	6000	0	100	0	2	14	6379		
		003-GSLM-10-05	430	6000	0	100	0	2	14	6353		
		003-HSLM-09-03	430	6000	0	100	0	2	14	2659	2859	1568
		003-HSLM-09-04	430	6000	0	100	0	2	14	4517		
		003-HSLM-09-05	430	6000	0	100	0	2	14	1401		
004	031	004-GSLM-00-03	70	0	0	0	0	2	0	3792	3582	267
		004-GSLM-00-04	70	0	0	0	0	2	0	3673		
		004-GSLM-00-05	70	0	0	0	0	2	0	3281		
		004-HSLM-00-03	70	0	0	0	0	2	0	3134	2428	617
		004-HSLM-00-04	70	0	0	0	0	2	0	1992		
		004-HSLM-00-05	70	0	0	0	0	2	0	2159		
		004-GSLM-10-03	430	3000	0	100	0	2	14	4398	5627	1073

Additive Batch #	Baseline Batch #	Core #	T (°F)	P (psi)	CH_4 (%)	CO_2 (%)	H_2S (ppm)	Brine (%)	Days Aged	Comp. Strength (psi)	Ave. Comp. Strength (psi)	Stdev (psi)
		004-GSLM-10-04	430	3000	0	100	0	2	14	6379		
		004-GSLM-10-05	430	3000	0	100	0	2	14	6104		
		004-HSLM-09-03	430	3000	0	100	0	2	14	2220	2630	1478
		004-HSLM-09-04	430	3000	0	100	0	2	14	4270		
		004-HSLM-09-05	430	3000	0	100	0	2	14	1401		

C.1.5 Properties of Latex Microsilica Based Cement (LTMS)

Table C.13: Porosity and permeability of latex microsilica based cement (LTMS)

Additive Batch #	Baseline Batch #	Core #	T (°F)	P (psi)	CH4 (%)	CO2 (%)	H2S (ppm)	Brine (%)	Days Aged	Ø (%)	Kklink (mD)	Ave. Ø (%)	Stdev	Ave. K (mD)	Stdev
001	Unaged batch	001-HSLM-00-01	70	0	0	0	0	2	0	31	0.065	31	0	0.039	0.037
		001-HSLM-00-02	70	0	0	0	0	2	0	31	0.012				
		001-HSLM-00-03	70	0	0	0	0	2	0	32	0.022	31	2	0.033	0.016
		001-HSLM-00-04	70	0	0	0	0	2	0	30	0.044				
		001-GSLM-00-01	70	0	0	0	0	2	0	32	0.004	33	1	0.005	0.001
		001-GSLM-00-02	70	0	0	0	0	2	0	34	0.005				
		001-GSLM-00-03	70	0	0	0	0	2	0	34	0.005	33	1	0.005	0.000
		001-GSLM-00-04	70	0	0	0	0	2	0	32	0.005				
002	027	002-HSLM-00-01	70	0	0	0	0	2	0	18	2.046	18	0	1.028	1.440
		002-HSLM-00-02	70	0	0	0	0	2	0	18	0.009				
		002-GSLM-00-01	70	0	0	0	0	2	0	22	0.008	22	0	0.008	0.000
		002-GSLM-00-02	70	0	0	0	0	2	0	22	0.008				
		002-HSLM-09-01	225	9000	90	10	0	2	14	16	0.015	15	2	0.016	0.001
		002-HSLM-09-02	225	9000	90	10	0	2	14	14	0.016				
		002-GSLM-10-01	225	9000	90	10	0	2	14	21	0.041	21	1	0.032	0.013
		002-GSLM-10-02	225	9000	90	10	0	2	14	21	0.022				
003	030	003-HSLM-00-01	70	0	0	0	0	2	0	14	0.004	15	0	0.005	0.001
		003-HSLM-00-02	70	0	0	0	0	2	0	15	0.006				
		003-GSLM-00-01	70	0	0	0	0	2	0	17	0.008	16	1	0.007	0.002
		003-GSLM-00-02	70	0	0	0	0	2	0	16	0.005				
		003-HSLM-09-01	430	6000	0	100	0	2	14	27	0.069	27	0	0.079	0.014
		003-HSLM-09-02	430	6000	0	100	0	2	14	27	0.089				
		003-GSLM-10-01	430	6000	0	100	0	2	14	29	0.155	29	0	0.179	0.033
		003-GSLM-10-02	430	6000	0	100	0	2	14	29	0.202				
004	031	004-HSLM-00-01	70	0	0	0	0	2	0	26	0.002	23	5	0.002	0.001
		004-HSLM-00-02	70	0	0	0	0	2	0	20	0.001				
		004-GSLM-00-01	70	0	0	0	0	2	0	32	0.01	27	8	0.011	0.001
		004-GSLM-00-02	70	0	0	0	0	2	0	21	0.011				
		004-HSLM-09-01	430	3000	0	100	0	2	14	32	0.221	32	0	0.219	0.004
		004-HSLM-09-02	430	3000	0	100	0	2	14	32	0.216				
		004-GSLM-10-01	430	3000	0	100	0	2	14	34	0.299	34	0	0.324	0.035
		004-GSLM-10-02	430	3000	0	100	0	2	14	34	0.348				

Table C.14: Shear bond strength of latex microsilica based cement (LTMS)

Additive Batch #	Baseline Batch #	Core #	T (°F)	P (psi)	CH_4 (%)	CO_2 (%)	H_2S (ppm)	Brine (%)	Days Aged	SBS (psi)	Ave. SBS (psi)	Stdev (psi)
001	Unaged batch	001-HSLM-00-01	70	0	0	0	0	2	14	696	812	266
		001-HSLM-00-02	70	0	0	0	0	2	14	1116		
		001-HSLM-00-03	70	0	0	0	0	2	14	624		
002	027	002-HSLM-00-01	70	0	0	0	0	2	14	1432	1034	254
		002-HSLM-00-02	70	0	0	0	0	2	14	954		
		002-HSLM-00-03	70	0	0	0	0	2	14	772		
		002-HSLM-00-04	70	0	0	0	0	2	14	1116		
		002-HSLM-00-05	70	0	0	0	0	2	14	898		
		002-HSLM-11-01	225	9000	90	10	0	2	14	1105	930	209
		002-HSLM-11-02	225	9000	90	10	0	2	14	1148		
		002-HSLM-11-03	225	9000	90	10	0	2	14	752		
		002-HSLM-11-04	225	9000	90	10	0	2	14	677		
		002-HSLM-11-05	225	9000	90	10	0	2	14	968		
003	030	003-HSLM-00-01	70	0	0	0	0	2	14	433	378	102
		003-HSLM-00-02	70	0	0	0	0	2	14	305		
		003-HSLM-00-03	70	0	0	0	0	2	14	441		
		003-HSLM-00-04	70	0	0	0	0	2	14	237		
		003-HSLM-00-05	70	0	0	0	0	2	14	476		
		003-HSLM-11-01	430	6000	0	100	0	2	14	768	768	71
		003-HSLM-11-02	430	6000	0	100	0	2	14	865		
		003-HSLM-11-03	430	6000	0	100	0	2	14	669		
		003-HSLM-11-04	430	6000	0	100	0	2	14	793		
		003-HSLM-11-05	430	6000	0	100	0	2	14	744		
004	031	004-HSLM-00-01	70	0	0	0	0	2	14	942	759	150
		004-HSLM-00-02	70	0	0	0	0	2	14	781		
		004-HSLM-00-03	70	0	0	0	0	2	14	747		
		004-HSLM-00-04	70	0	0	0	0	2	14	527		
		004-HSLM-00-05	70	0	0	0	0	2	14	801		
		004-HSLM-11-01	430	3000	0	100	0	2	14	866	558	174
		004-HSLM-11-02	430	3000	0	100	0	2	14	463		
		004-HSLM-11-03	430	3000	0	100	0	2	14	478		
		004-HSLM-11-04	430	3000	0	100	0	2	14	460		
		004-HSLM-11-05	430	3000	0	100	0	2	14	524		

Table C.15: Compressive strength of latex microsilica based cement (LTMS)

Additive Batch #	Baseline Batch #	Core #	T (°F)	P (psi)	CH_4 (%)	CO_2 (%)	H_2S (ppm)	Brine (%)	Days Aged	Comp. Strength (psi)	Ave. Comp. Strength (psi)	Stdev (psi)
001	Unaged Batch	001-GSLT-00-05	70	0	0	0	0	2	0	3010	3106	259
		001-GSLT-00-06	70	0	0	0	0	2	0	2820		
		001-GSLT-00-07	70	0	0	0	0	2	0	3162		
		001-GSLT-00-08	70	0	0	0	0	2	0	3434		
		001-HSLT-00-05	70	0	0	0	0	2	0	3084	3318	203
		001-HSLT-00-06	70	0	0	0	0	2	0	3580		
		001-HSLT-00-07	70	0	0	0	0	2	0	3317		
		001-HSLT-00-08	70	0	0	0	0	2	0	3289		
002	Cores weren't aged	002-GSLT-00-05	70	0	0	0	0	2	0	4246	3714	547
		002-GSLT-00-07	70	0	0	0	0	2	0	3152		
		002-GSLT-00-08	70	0	0	0	0	2	0	3745		
		002-HSLT-00-05	70	0	0	0	0	2	0	4851	4054	649
		002-HSLT-00-06	70	0	0	0	0	2	0	3753		
		002-HSLT-00-07	70	0	0	0	0	2	0	3351		
		002-HSLT-00-08	70	0	0	0	0	2	0	4260		
003	Unaged Batch	003-GSLT-00-05	70	0	0	0	0	2	0	4257	3671	445
		003-GSLT-00-06	70	0	0	0	0	2	0	3462		
		003-GSLT-00-07	70	0	0	0	0	2	0	3221		
		003-GSLT-00-08	70	0	0	0	0	2	0	3745		
		003-HSLT-00-05	70	0	0	0	0	2	0	4946	4120	661
		003-HSLT-00-06	70	0	0	0	0	2	0	3799		
		003-HSLT-00-07	70	0	0	0	0	2	0	3422		
		003-HSLT-00-08	70	0	0	0	0	2	0	4314		
004	013	004-GSLT-00-03	70	0	0	0	0	2	0	3427	3367	132
		004-GSLT-00-04	70	0	0	0	0	2	0	3459		
		004-GSLT-00-05	70	0	0	0	0	2	0	3216		
		004-HSLT-00-03	70	0	0	0	0	2	0	3325	3500	216
		004-HSLT-00-04	70	0	0	0	0	2	0	3436		
		004-HSLT-00-05	70	0	0	0	0	2	0	3741		
		004-GSLT-10-03	350	6000	60	40	0	2	14	6066	5920	419
		004-GSLT-10-04	350	6000	60	40	0	2	14	5448		
		004-GSLT-10-05	350	6000	60	40	0	2	14	6247		
		004-HSLT-09-03	350	6000	60	40	0	2	14	9178	7918	1096
		004-HSLT-09-04	350	6000	60	40	0	2	14	7388		
		004-HSLT-09-05	350	6000	60	40	0	2	14	7188		
005	Unaged Batch	005-GSLT-00-05	70	0	0	0	0	2	0	3318	2216	1473
		005-GSLT-00-06	70	0	0	0	0	2	0	3648		
		005-GSLT-00-07	70	0	0	0	0	2	0	1066		
		005-GSLT-00-08	70	0	0	0	0	2	0	831		

Additive Batch #	Baseline Batch #	Core #	T (°F)	P (psi)	CH_4 (%)	CO_2 (%)	H_2S (ppm)	Brine (%)	Days Aged	Comp. Strength (psi)	Ave. Comp. Strength (psi)	Stdev (psi)
		005-HSLT-00-05	70	0	0	0	0	2	0	3384	3214	553
		005-HSLT-00-06	70	0	0	0	0	2	0	2468		
		005-HSLT-00-07	70	0	0	0	0	2	0	3790		
		005-HSLT-00-08	70	0	0	0	0	2	0	3215		

C.1.6 Properties of Microsilica Based Cement (MS-10)

Table C.16: Porosity and permeability of micro silica based cement (MS-10)

Additive Batch #	Baseline Batch #	Core #	T (°F)	P (psi)	CH_4 (%)	CO_2 (%)	H_2S (ppm)	Brine (%)	Days Aged	Ø (%)	K_{klink} (mD)	Ave. Ø (%)	Stdev	Ave. K (mD)	Stdev
003	Unaged batch	003-HSMS-00-01	70	0	0	0	0	2	0	42	1.887	42		1.887	
		003-GSMS-00-01	70	0	0	0	0	2	0	47	5.214	47		5.214	
004	Unaged batch	004-HSMS-00-01	70	0	0	0	0	2	0	11	0.277	10	1	0.105	0.150
		004-HSMS-00-02	70	0	0	0	0	2	0	10	0.004				
		004-HSMS-00-03	70	0	0	0	0	2	0	10	0.033				
		004-GSMS-00-01	70	0	0	0	0	2	0	4	0.082	4	1	0.123	0.058
		004-GSMS-00-02	70	0	0	0	0	2	0	3	0.164				
006	Unaged batch	006-GSMS-00-01	70	0	0	0	0	2	0	11	0.01	11	0	0.009	0.001
		006-GSMS-00-02	70	0	0	0	0	2	0	11	0.008				
		006-GSMS-10-01	350	9000	90	10	0	2	14						
		006-GSMS-10-02	350	9000	90	10	0	2	14						
007	Unaged batch	007-HSMS-00-01	70	0	0	0	0	2	0	7	0.002	7	1	0.002	0.001
		007-HSMS-00-02	70	0	0	0	0	2	0	7	0.001				
		007-HSMS-00-03	70	0	0	0	0	2	0	7	0.002				
		007-HSMS-00-04	70	0	0	0	0	2	0	8	0.002				
		007-GSMS-00-01	70	0	0	0	0	2	0	14	0.002	14	0	0.002	0.000
		007-GSMS-00-02	70	0	0	0	0	2	0	14	0.002				
		007-GSMS-00-03	70	0	0	0	0	2	0	14	0.002				
		007-GSMS-00-04	70	0	0	0	0	2	0	13	0.002				
008	024	008-HSMS-00-01	70	0	0	0	0	2	0	9	0.003	9	0	0.003	0.001
		008-HSMS-00-02	70	0	0	0	0	2	0	9	0.002				
		008-GSMS-00-01	70	0	0	0	0	2	0	13	0.002	13	0	0.003	0.001
		008-GSMS-00-02	70	0	0	0	0	2	0	13	0.003				
		008-HSMS-09-01	225	3000	0	100	0	2	14	21	0.03	21	0	0.029	0.002
		008-HSMS-09-02	225	3000	0	100	0	2	14	21	0.027				
		008-GSMS-10-01	225	3000	0	100	0	2	14	25	0.045	25	0	0.043	0.004
		008-GSMS-10-02	225	3000	0	100	0	2	14	25	0.04				
009	028	009-HSMS-00-01	70	0	0	0	0	2	0	12	0.009	12	0	0.010	0.001
		009-HSMS-00-02	70	0	0	0	0	2	0	12	0.011				
		009-GSMS-00-01	70	0	0	0	0	2	0	16	0.008	16	0	0.009	0.001
		009-GSMS-00-02	70	0	0	0	0	2	0	15	0.01				
		009-HSMS-09-01	430	6000	90	10	0	2	14	39	0.416	39	0	0.427	0.016
		009-HSMS-09-02	430	6000	90	10	0	2	14	39	0.438				
		009-GSMS-10-01	430	6000	90	10	0	2	14	40	0.263	42	2	0.508	0.346
		009-GSMS-10-02	430	6000	90	10	0	2	14	43	0.752				

Additive Batch #	Baseline Batch #	Core #	T (°F)	P (psi)	CH_4 (%)	CO_2 (%)	H_2S (ppm)	Brine (%)	Days Aged	Ø (%)	K_{klink} (mD)	Ave. Ø (%)	Stdev	Ave. K (mD)	Stdev
010	029	010-HSMS-00-01	70	0	0	0	0	2	0	22	0.005	21	1	0.005	0.001
		010-HSMS-00-02	70	0	0	0	0	2	0	21	0.004				
		010-GSMS-00-01	70	0	0	0	0	2	0		0.009	29		0.009	
		010-GSMS-00-02	70	0	0	0	0	2	0	29					
		010-HSMS-09-01	430	6000	60	40	0	2	14			36		0.261	
		010-HSMS-09-02	430	6000	60	40	0	2	14	36	0.261				
		010-GSMS-10-01	430	6000	60	40	0	2	14	40	0.544	41	1	0.564	0.028
		010-GSMS-10-02	430	6000	60	40	0	2	14	41	0.583				

Table C.17: Shear bond strength of micro silica based cement (MS-10)

Additive Batch #	Baseline Batch #	Core #	T (°F)	P (psi)	CH_4 (%)	CO_2 (%)	H_2S (ppm)	Brine (%)	Days Aged	SBS (psi)	Ave. SBS (psi)	Stdev (psi)
003	Unaged batch	003-HSMS-00-01	70	0	0	0	0	2	14	282	655	331
		003-HSMS-00-02	70	0	0	0	0	2	14	916		
		003-HSMS-00-03	70	0	0	0	0	2	14	767		
004	Unaged batch	004-HSMS-00-01	70	0	0	0	0	2	14	436	345	82
		004-HSMS-00-02	70	0	0	0	0	2	14	319		
		004-HSMS-00-03	70	0	0	0	0	2	14	279		
005	020	005-HSMS-00-01	70	0	0	0	0	2	14	486	542	174
		005-HSMS-00-02	70	0	0	0	0	2	14	816		
		005-HSMS-00-03	70	0	0	0	0	2	14	417		
		005-HSMS-00-04	70	0	0	0	0	2	14	603		
		005-HSMS-00-05	70	0	0	0	0	2	14	390		
		005-HSMS-11-01	350	3000	90	10	0	2	14	858	702	97
		005-HSMS-11-02	350	3000	90	10	0	2	14	694		
		005-HSMS-11-03	350	3000	90	10	0	2	14	615		
		005-HSMS-11-04	350	3000	90	10	0	2	14	627		
		005-HSMS-11-05	350	3000	90	10	0	2	14	718		
006	021	006-HSMS-00-01	70	0	0	0	0	2	14	554	778	170
		006-HSMS-00-02	70	0	0	0	0	2	14	743		
		006-HSMS-00-03	70	0	0	0	0	2	14	733		
		006-HSMS-00-04	70	0	0	0	0	2	14	1020		
		006-HSMS-00-05	70	0	0	0	0	2	14	839		
		006-HSMS-11-01	225	3000	0	100	0	2	14	1609	1427	124
		006-HSMS-11-02	225	3000	0	100	0	2	14	1456		
		006-HSMS-11-03	225	3000	0	100	0	2	14	1363		
		006-HSMS-11-04	225	3000	0	100	0	2	14	1275		
		006-HSMS-11-05	225	3000	0	100	0	2	14	1434		
007		007-HSMS-00-01	70	0	0	0	0	2	14	746	748	47
		007-HSMS-00-02	70	0	0	0	0	2	14	795		
		007-HSMS-00-03	70	0	0	0	0	2	14	701		
008	024	008-HSMS-00-01	70	0	0	0	0	2	14	843	832	248
		008-HSMS-00-02	70	0	0	0	0	2	14	825		
		008-HSMS-00-03	70	0	0	0	0	2	14	761		
		008-HSMS-00-04	70	0	0	0	0	2	14	519		
		008-HSMS-00-05	70	0	0	0	0	2	14	1210		
		008-HSMS-11-01	225	3000	0	100	0	2	14	1425	1747	278
		008-HSMS-11-02	225	3000	0	100	0	2	14	1943		
		008-HSMS-11-03	225	3000	0	100	0	2	14	1548		
		008-HSMS-11-04	225	3000	0	100	0	2	14	1718		
		008-HSMS-11-05	225	3000	0	100	0	2	14	2103		
009	028	009-HSMS-00-01	70	0	0	0	0	2	14	1046	1254	850
		009-HSMS-00-02	70	0	0	0	0	2	14	685		

Additive Batch #	Baseline Batch #	Core #	T (°F)	P (psi)	CH_4 (%)	CO_2 (%)	H_2S (ppm)	Brine (%)	Days Aged	SBS (psi)	Ave. SBS (psi)	Stdev (psi)
		009-HSMS-00-03	70	0	0	0	0	2	14	1037		
		009-HSMS-00-04	70	0	0	0	0	2	14	2745		
		009-HSMS-00-05	70	0	0	0	0	2	14	754		
		009-HSMS-11-01	430	6000	90	10	0	2	14	1502		
		009-HSMS-11-02	430	6000	90	10	0	2	14	1328		
		009-HSMS-11-03	430	6000	90	10	0	2	14	871	1284	276
		009-HSMS-11-04	430	6000	90	10	0	2	14	1170		
		009-HSMS-11-05	430	6000	90	10	0	2	14	1551		
		010-HSMS-00-01	70	0	0	0	0	2	14	960		
		010-HSMS-00-02	70	0	0	0	0	2	14	858		
		010-HSMS-00-03	70	0	0	0	0	2	14	893	1090	261
		010-HSMS-00-04	70	0	0	0	0	2	14	1418		
		010-HSMS-00-05	70	0	0	0	0	2	14	1323		
010	029	010-HSMS-11-01	430	6000	60	40	0	2	14	1958		
		010-HSMS-11-02	430	6000	60	40	0	2	14	1951		
		010-HSMS-11-03	430	6000	60	40	0	2	14	1873	2005	126
		010-HSMS-11-04	430	6000	60	40	0	2	14	2204		
		010-HSMS-11-05	430	6000	60	40	0	2	14	2039		

Table C.18: Compressive strength of micro silica based cement (MS-10)

Additive Batch #	Baseline Batch #	Core #	T (°F)	P (psi)	CH_4 (%)	CO_2 (%)	H_2S (ppm)	Brine (%)	Days Aged	Comp. Strength (psi)	Ave. Comp. Strength (psi)	Stdev (psi)
003	Unaged Batch	003-GSMS-00-01	70	0	0	0	0	2	0	2425	2365	86
		003-GSMS-00-02	70	0	0	0	0	2	0	2304		
		003-HSMS-00-01	70	0	0	0	0	2	0	2584	2366	307
		003-HSMS-00-02	70	0	0	0	0	2	0	2149		
004	Unaged Batch	004-GSMS-00-03	70	0	0	0	0	2	0	2033	1984	69
		004-GSMS-00-04	70	0	0	0	0	2	0	1935		
		004-HSMS-00-04	70	0	0	0	0	2	0	6096	5716	351
		004-HSMS-00-05	70	0	0	0	0	2	0	5405		
		004-HSMS-00-06	70	0	0	0	0	2	0	5647		
005	020	005-GSMS-00-03	70	0	0	0	0	2	0	6578	5237	1162
		005-GSMS-00-04	70	0	0	0	0	2	0	4561		
		005-GSMS-00-05	70	0	0	0	0	2	0	4571		
		005-HSMS-00-02	70	0	0	0	0	2	0	4244	4243	3
		005-HSMS-09-03	350	3000	90	10	0	2	14	4241		
006	021	006-GSMS-00-03	70	0	0	0	0	2	0	5170	4421	798
		006-GSMS-00-04	70	0	0	0	0	2	0	4511		
		006-GSMS-00-05	70	0	0	0	0	2	0	3582		
		006-GSMS-10-03	350	9000	90	10	0	2	14	2792	2399	1477
		006-GSMS-10-04	350	9000	90	10	0	2	14	3639		
		006-GSMS-10-05	350	9000	90	10	0	2	14	766		
007	Unaged Batch	007-GSMS-00-05	70	0	0	0	0	2	0	6180	5209	716
		007-GSMS-00-06	70	0	0	0	0	2	0	4589		
		007-GSMS-00-07	70	0	0	0	0	2	0	5307		
		007-GSMS-00-08	70	0	0	0	0	2	0	4759		
		007-HSMS-00-05	70	0	0	0	0	2	0	3802	5204	1074
		007-HSMS-00-06	70	0	0	0	0	2	0	6396		
		007-HSMS-00-07	70	0	0	0	0	2	0	5150		
		007-HSMS-00-08	70	0	0	0	0	2	0	5469		
008	024	008-GSMS-00-03	70	0	0	0	0	2	0	6239	5652	532
		008-GSMS-00-04	70	0	0	0	0	2	0	5512		
		008-GSMS-00-05	70	0	0	0	0	2	0	5203		
		008-HSMS-00-03	70	0	0	0	0	2	0	6682	6257	487
		008-HSMS-00-04	70	0	0	0	0	2	0	6363		
		008-HSMS-00-05	70	0	0	0	0	2	0	5726		
		008-GSMS-10-03	225	3000	0	100	0	2	14	6759	6936	259
		008-GSMS-10-04	225	3000	0	100	0	2	14	7233		
		008-GSMS-10-05	225	3000	0	100	0	2	14	6817		
		008-HSMS-09-03	225	3000	0	100	0	2	14	8340	5837	3364
		008-HSMS-09-04	225	3000	0	100	0	2	14	7157		

Additive Batch #	Baseline Batch #	Core #	T (°F)	P (psi)	CH_4 (%)	CO_2 (%)	H_2S (ppm)	Brine (%)	Days Aged	Comp. Strength (psi)	Ave. Comp. Strength (psi)	Stdev (psi)
		008-HSMS-09-05	225	3000	0	100	0	2	14	2013		
009	028	009-GSMS-00-03	70	0	0	0	0	2	0	5950	4774	1019
		009-GSMS-00-04	70	0	0	0	0	2	0	4202		
		009-GSMS-00-05	70	0	0	0	0	2	0	4170		
		009-HSMS-00-03	70	0	0	0	0	2	0	3540	3546	277
		009-HSMS-00-04	70	0	0	0	0	2	0	3826		
		009-HSMS-00-05	70	0	0	0	0	2	0	3272		
		009-GSMS-10-03	430	6000	90	10	0	2	14	3332	3516	318
		009-GSMS-10-04	430	6000	90	10	0	2	14	3884		
		009-GSMS-10-05	430	6000	90	10	0	2	14	3333		
		009-HSMS-09-03	430	6000	90	10	0	2	14	5213	4822	339
		009-HSMS-09-04	430	6000	90	10	0	2	14	4617		
		009-HSMS-09-05	430	6000	90	10	0	2	14	4637		
010	029	010-GSMS-00-03	70	0	0	0	0	2	0	3333	3643	647
		010-GSMS-00-04	70	0	0	0	0	2	0	3209		
		010-GSMS-00-05	70	0	0	0	0	2	0	4386		
		010-HSMS-00-03	70	0	0	0	0	2	0	5275	3412	2959
		010-HSMS-00-04	70	0	0	0	0	2	0	4961		
		010-HSMS-00-05	70	0	0	0	0	2	0	0		
		010-GSMS-10-03	430	6000	60	40	0	2	14	944	4164	2843
		010-GSMS-10-04	430	6000	60	40	0	2	14	5219		
		010-GSMS-10-05	430	6000	60	40	0	2	14	6328		
		010-HSMS-09-03	430	6000	60	40	0	2	14	0	1193	
		010-HSMS-09-04	430	6000	60	40	0	2	14	0		
		010-HSMS-09-05	430	6000	60	40	0	2	14	1193		

C.2 Baseline Cements

C.2.1 Porosity and Permeability

Table C.19: Porosity and permeability of baseline cements

Batch #	Core #	T (°F)	P (psi)	CH_4 (%)	CO_2 (%)	H_2S (ppm)	Brine (%)	Days Aged	Ø (%)	K_{klink} (mD)	Ave. Ø (%)	Stdev	Ave. K (mD)	Stdev
001	01GS-00-01	70	0	0	0	0	2	0	27	0.018	26.4	0.3	0.020	0.002
	01GS-00-02	70	0	0	0	0	2	0	27	0.022				
	01GS-00-03	70	0	0	0	0	2	0	26	0.019				
	01HS-00-01	70	0	0	0	0	2	0	28	0.060	28.4	0.4	0.066	0.005
	01HS-00-02	70	0	0	0	0	2	0	29	0.070				
	01HS-00-03	70	0	0	0	0	2	0	29	0.068				
	01-GS-03-01	350	9000	100	0	0	9	6	26	0.047	27.5	1.0	0.041	0.008
	01-GS-03-02	350	9000	100	0	0	9	6	28	0.030				
	01-GS-07-01	350	9000	100	0	0	9	6	27	0.040				
	01-GS-07-02	350	9000	100	0	0	9	6	29	0.047				
	01-HS-01-01	350	9000	100	0	0	9	6	19	0.012	17.9	3.1	0.027	0.020
	01-HS-01-02	350	9000	100	0	0	9	6	19	0.019				
	01-HS-05-01	350	9000	100	0	0	9	6	15	0.008				
	01-HS-05-02	350	9000	100	0	0	9	6	22	0.052				
	01-HS-09-01	350	9000	100	0	0	9	6	15	0.043				
002	002-GS-00-01	70	0	0	0	0	2	0	29	0.054	28.8	0.3	0.057	0.004
	002-GS-00-02	70	0	0	0	0	2	0	29	0.060				
	002-HS-00-01	70	0	0	0	0	2	0	32	0.148	31.8	0.3	0.154	0.008
	002-HS-00-02	70	0	0	0	0	2	0	32	0.159				
	002-GS-07-01	350	6000	100	0	0	2	14	22	0.028	26.3	4.8	0.044	0.046
	002-GS-07-02	350	6000	100	0	0	2	14	24	0.017				
	002-GS-03-01	350	6000	100	0	0	2	14	27	0.017				
	002-GS-03-02	350	6000	100	0	0	2	14	33	0.113				
	002-HS-05-01	350	6000	100	0	0	2	14	32	0.064	31.2	0.9	0.045	0.021
	002-HS-05-02	350	6000	100	0	0	2	14	31	0.049				
	002-HS-01-01	350	6000	100	0	0	2	14	30	0.015				
	002-HS-01-02	350	6000	100	0	0	2	14	32	0.051				
003	003-GS-07-01	350	6000	100	0	0	2	14	45	0.333	44.1	1.2	0.317	0.023
	003-GS-07-02	350	6000	100	0	0	2	14	43	0.301				
	003-HS-05-01	350	6000	100	0	0	2	14	44	0.397	43.6	0.3	0.405	0.011
	003-HS-05-02	350	6000	100	0	0	2	14	43	0.413				
004	004-GS-00-01	70	0	0	0	0	2	0	33	0.171	32.1	0.5	0.173	0.003
	004-GS-00-02	70	0	0	0	0	2	0	32	0.175				
	004-HS-00-01	70	0	0	0	0	2	0	33	0.526	33.1	0.3	0.483	0.062
	004-HS-00-02	70	0	0	0	0	2	0	33	0.439				
	004-GS-03-01	350	6000	90	10	0	2	6	23	0.002	24.8	3.2	0.054	0.035
	004-GS-03-02	350	6000	90	10	0	2	6	21	0.064				
	004-GS-07-01	350	6000	90	10	0	2	6	27	0.073				

Batch #	Core #	T (°F)	P (psi)	CH_4 (%)	CO_2 (%)	H_2S (ppm)	Brine (%)	Days Aged	Ø (%)	K_{klink} (mD)	Ave. Ø (%)	Stdev	Ave. K (mD)	Stdev
	004-GS-07-02	350	6000	90	10	0	2	6	28	0.077				
	004-HS-01-01	350	6000	90	10	0	2	6	20	0.002	23.0	3.2	0.010	0.017
	004-HS-01-02	350	6000	90	10	0	2	6	23	0.002				
	004-HS-05-01	350	6000	90	10	0	2	6	-	0.000				
	004-HS-05-02	350	6000	90	10	0	2	6	26	0.036				
005	005-GS-00-01	70	0	0	0	0	2	0	30	0.068	28.5	2.5	0.057	0.016
	005-GS-00-02	70	0	0	0	0	2	0	27	0.045				
	005-HS-00-01	70	0	0	0	0	2	0	31	0.136	31.8	1.2	0.134	0.003
	005-HS-00-02	70	0	0	0	0	2	0	33	0.132				
	005-GS-03-01	350	6000	90	10	0	2	28	12	0.004	25.3	14.6	0.056	0.061
	005-GS-03-02	350	6000	90	10	0	2	28	14	0.005				
	005-GS-07-01	350	6000	90	10	0	2	28	39	0.092				
	005-GS-07-02	350	6000	90	10	0	2	28	37	0.124				
	005-HS-01-01	350	6000	90	10	0	2	28	34	0.039	31.2	3.5	0.061	0.057
	005-HS-01-02	350	6000	90	10	0	2	28	26	0.012				
	005-HS-05-01	350	6000	90	10	0	2	28	33	0.143				
	005-HS-05-02	350	6000	90	10	0	2	28	33	0.049				
006	006-GS-00-01	70	0	0	0	0	2	0	28	0.037	28.4		0.037	
	006-HS-00-01	70	0	0	0	0	2	0	31	0.169	30.9		0.169	
	006-GS-04-01	350	6000	90	10	0	2	14	19	0.014	18.3	1.4	0.012	0.003
	006-GS-04-02	350	6000	90	10	0	2	14	17	0.010				
	006-HS-09-01	350	6000	90	10	0	2	14	35	0.075	34.7	0.1	0.060	0.022
	006-HS-09-02	350	6000	90	10	0	2	14	35	0.044				
007	007-GS-00-01	70	0	0	0	0	2	0	29	0.040	28.6	0.5	0.044	0.006
	007-GS-00-02	70	0	0	0	0	2	0	28	0.048				
	007-HS-00-01	70	0	0	0	0	2	0	26	0.042	26.0	0.4	0.043	0.001
	007-HS-00-02	70	0	0	0	0	2	0	26	0.043				
	007-GS-05-01	225	6000	90	10	0	2	14	18	0.008	20.4	2.6	0.012	0.004
	007-GS-05-02	225	6000	90	10	0	2	14	19	0.014				
	007-GS-07-01	225	6000	90	10	0	2	14	22	0.017				
	007-GS-07-02	225	6000	90	10	0	2	14	23	0.011				
	007-HS-04-01	225	6000	90	10	0	2	14	19	0.006	17.5	6.9	0.010	0.007
	007-HS-04-02	225	6000	90	10	0	2	14	8	0.004				
	007-HS-06-01	225	6000	90	10	0	2	14	19	0.011				
	007-HS-06-02	225	6000	90	10	0	2	14	23	0.020				
008	008-GS-00-01	70	0	0	0	0	2	0	26	0.046	26.5	0.1	0.046	0.000
	008-GS-00-02	70	0	0	0	0	2	0	27	0.046				
	008-HS-00-01	70	0	0	0	0	2	0	29	0.141	29.0	0.2	0.115	0.037
	008-HS-00-02	70	0	0	0	0	2	0	29	0.088				
	008-GS-05-01	100	6000	90	10	0	2	14	23	0.018	23.9	0.8	0.017	0.001
	008-GS-05-02	100	6000	90	10	0	2	14	24	0.018				
	008-GS-07-01	100	6000	90	10	0	2	14	24	0.015				
	008-GS-07-02	100	6000	90	10	0	2	14	25	0.017				
	008-HS-04-01	100	6000	90	10	0	2	14	24	0.019	21.8	4.6	0.018	0.010
	008-HS-04-05	100	6000	90	10	0	2	14	15	0.009				

Batch #	Core #	T (°F)	P (psi)	CH_4 (%)	CO_2 (%)	H_2S (ppm)	Brine (%)	Days Aged	Ø (%)	K_{klink} (mD)	Ave. Ø (%)	Stdev	Ave. K (mD)	Stdev
	008-HS-06-01	100	6000	90	10	0	2	14	25	0.031				
	008-HS-06-02	100	6000	90	10	0	2	14	24	0.014				
009	009-GS-00-01	70	0	0	0	0	2	0	30	0.108	29.9	0.2	0.100	0.011
	009-GS-00-02	70	0	0	0	0	2	0	30	0.092				
	009-HS-00-01	70	0	0	0	0	2	0	29	0.121	29.7	0.4	0.653	0.752
	009-HS-00-02	70	0	0	0	0	2	0	30	1.185				
	009-GS-05-01	225	6000	60	40	0	2	14	14	0.014	21.2	4.9	0.028	0.014
	009-GS-05-02	225	6000	60	40	0	2	14	23	0.035				
	009-GS-07-01	225	6000	60	40	0	2	14	25	0.019				
	009-GS-07-02	225	6000	60	40	0	2	14	23	0.043				
	009-HS-04-01	225	6000	60	40	0	2	14	15	0.225	13.9	0.9	0.201	0.110
	009-HS-04-02	225	6000	60	40	0	2	14	13	0.334				
	009-HS-06-01	225	6000	60	40	0	2	14	14	0.175				
	009-HS-06-02	225	6000	60	40	0	2	14	13	0.070				
010	010-GS-00-01	70	0	0	0	0	2	0	34	0.019	32.2	2.5	0.016	0.004
	010-GS-00-02	70	0	0	0	0	2	0	30	0.013				
	010-HS-00-01	70	0	0	0	0	2	0	32	0.032	33.2	1.6	0.039	0.009
	010-HS-00-02	70	0	0	0	0	2	0	34	0.045				
	010-GS-05-01	225	6000	0	100	0	2	14	25	0.034	24.9	1.0	0.051	0.015
	010-GS-05-02	225	6000	0	100	0	2	14	26	0.048				
	010-GS-07-01	225	6000	0	100	0	2	14	23	0.069				
	010-GS-07-02	225	6000	0	100	0	2	14	25	0.054				
	010-HS-04-01	225	6000	0	100	0	2	14	26	0.032	23.9	2.8	0.043	0.032
	010-HS-04-02	225	6000	0	100	0	2	14	26	0.090				
	010-HS-06-01	225	6000	0	100	0	2	14	23	0.028				
	010-HS-06-02	225	6000	0	100	0	2	14	20	0.022				
011	011-GS-00-01	70	0	0	0	0	2	0	28	0.034	27.9	0.6	0.031	0.005
	011-GS-00-02	70	0	0	0	0	2	0	27	0.027				
	011-HS-00-01	70	0	0	0	0	2	0	28	0.130	28.2	0.1	0.142	0.016
	011-HS-00-02	70	0	0	0	0	2	0	28	0.153				
	011-GS-05-01	100	6000	60	40	0	2	14	22	0.031	21.6	0.8	0.027	0.003
	011-GS-05-02	100	6000	60	40	0	2	14	20	0.026				
	011-GS-07-01	100	6000	60	40	0	2	14	22	0.026				
	011-GS-07-02	100	6000	60	40	0	2	14	22	0.024				
	011-HS-04-01	100	6000	60	40	0	2	14	24	0.033	22.9	1.2	0.035	0.005
	011-HS-04-02	100	6000	60	40	0	2	14	24	0.042				
	011-HS-06-01	100	6000	60	40	0	2	14	22	0.034				
	011-HS-06-02	100	6000	60	40	0	2	14	22	0.030				
012	012-GS-00-01	70	0	0	0	0	2	0	30	0.052	30.1	0.3	0.049	0.004
	012-GS-00-02	70	0	0	0	0	2	0	30	0.046				
	012-HS-00-01	70	0	0	0	0	2	0	28	0.065	28.6	0.3	0.065	0.000
	012-HS-00-02	70	0	0	0	0	2	0	29	0.065				
	012-GS-05-01	100	6000	0	100	0	2	14	21	0.025	20.7	0.6	0.029	0.006
	012-GS-05-02	100	6000	0	100	0	2	14	21	0.023				
	012-GS-07-01	100	6000	0	100	0	2	14	20	0.037				

Batch #	Core #	T (°F)	P (psi)	CH_4 (%)	CO_2 (%)	H_2S (ppm)	Brine (%)	Days Aged	Ø (%)	K_{klink} (mD)	Ave. Ø (%)	Stdev	Ave. K (mD)	Stdev
	012-GS-07-02	100	6000	0	100	0	2	14	21	0.031				
	012-HS-04-01	100	6000	0	100	0	2	14	20	0.023				
	012-HS-04-02	100	6000	0	100	0	2	14	20	0.036	20.5	0.6	0.033	0.007
	012-HS-06-01	100	6000	0	100	0	2	14	20	0.037				
	012-HS-06-02	100	6000	0	100	0	2	14	21	0.036				
	013-GS-00-01	70	0	0	0	0	2	0	32	0.098	31.8	0.0	0.106	0.011
	013-GS-00-02	70	0	0	0	0	2	0	32	0.114				
	013-HS-00-01	70	0	0	0	0	2	0	30	0.148	31.0	0.8	0.173	0.035
	013-HS-00-02	70	0	0	0	0	2	0	32	0.197				
	013-GS-05-01	350	6000	60	40	0	2	14	27	0.015				
013	013-GS-05-02	350	6000	60	40	0	2	14	26	0.017	27.6	2.7	0.019	0.004
	013-GS-07-01	350	6000	60	40	0	2	14	27	0.024				
	013-GS-07-02	350	6000	60	40	0	2	14	32	0.020				
	013-HS-04-01	350	6000	60	40	0	2	14	33	0.031				
	013-HS-04-02	350	6000	60	40	0	2	14	34	0.034	33.1	0.8	0.030	0.007
	013-HS-06-01	350	6000	60	40	0	2	14	32	0.034				
	013-HS-06-02	350	6000	60	40	0	2	14	33	0.020				
	014-GS-00-01	70	0	0	0	0	2	0	28	0.030	28.2	0.1	0.031	0.001
	014-GS-00-02	70	0	0	0	0	2	0	28	0.032				
	014-HS-00-01	70	0	0	0	0	2	0	27	0.060	28.1	1.6	0.077	0.024
	014-HS-00-02	70	0	0	0	0	2	0	29	0.094				
	014-GS-05-01	350	6000	0	100	0	2	14	23	0.050				
014	014-GS-05-02	350	6000	0	100	0	2	14	18	0.019	21.8	2.3	0.036	0.013
	014-GS-07-01	350	6000	0	100	0	2	14	23	0.040				
	014-GS-07-02	350	6000	0	100	0	2	14	22	0.034				
	014-HS-04-01	350	6000	0	100	0	2	14	19	0.016				
	014-HS-04-02	350	6000	0	100	0	2	14	16	0.009	18.1	1.4	0.012	0.003
	014-HS-06-01	350	6000	0	100	0	2	14	19	0.011				
	014-HS-06-02	350	6000	0	100	0	2	14	19	0.010				
	015-GS-00-01	70	0	0	0	0	2	0	27	0.027	30.7	4.9	0.036	0.012
	015-GS-00-02	70	0	0	0	0	2	0	34	0.044				
	015-HS-00-01	70	0	0	0	0	2	0	-	-	28.5		0.058	
	015-HS-00-02	70	0	0	0	0	2	0	28	0.058				
	015-GS-05-01	225	6000	60	40	0	2	14	17	0.025				
015	015-GS-05-02	225	6000	60	40	0	2	14	20	0.050	21.5	4.8	0.028	0.015
	015-GS-07-01	225	6000	60	40	0	2	14	28	0.021				
	015-GS-07-02	225	6000	60	40	0	2	14	21	0.016				
	015-HS-04-01	225	6000	60	40	0	2	14	21	0.226				
	015-HS-04-02	225	6000	60	40	0	2	14	18	0.598	17.1	3.3	0.225	0.265
	015-HS-06-01	225	6000	60	40	0	2	14	14	0.017				
	015-HS-06-02	225	6000	60	40	0	2	14	15	0.057				
	016-GS-00-01	70	0	0	0	0	2	0	26	0.025	25.7	0.7	0.023	0.004
	016-GS-00-02	70	0	0	0	0	2	0	25	0.020				
	016-HS-00-01	70	0	0	0	0	2	0	28	0.055	27.9	0.3	0.051	0.006
016	016-HS-00-02	70	0	0	0	0	2	0	28	0.047				
	016-GS-05-01	350	3000	60	40	0	2	14	15	0.009				
	016-GS-05-02	350	3000	60	40	0	2	14	16	0.011	18.5	3.9	0.016	0.008
	016-GS-07-01	350	3000	60	40	0	2	14	23	0.027				

Batch #	Core #	T (°F)	P (psi)	CH_4 (%)	CO_2 (%)	H_2S (ppm)	Brine (%)	Days Aged	Ø (%)	K_{klink} (mD)	Ave. Ø (%)	Stdev	Ave. K (mD)	Stdev
	016-GS-07-02	350	3000	60	40	0	2	14	20	0.018				
	016-HS-04-01	350	3000	60	40	0	2	14	1	0.001				
	016-HS-04-02	350	3000	60	40	0	2	14	1	0.001	0.8	0.4	0.002	0.001
	016-HS-06-01	350	3000	60	40	0	2	14	1	0.003				
	016-HS-06-02	350	3000	60	40	0	2	14	0	0.003				
	017-GS-00-01	70	0	0	0	0	2	0	26	0.016	26.2	0.3	0.019	0.004
	017-GS-00-02	70	0	0	0	0	2	0	26	0.022				
	017-HS-00-01	70	0	0	0	0	2	0	27	0.056	27.1	0.1	0.054	0.003
	017-HS-00-02	70	0	0	0	0	2	0	27	0.052				
	017-GS-05-01	350	9000	60	40	0	2	14	16	0.008				
017	017-GS-05-02	350	9000	60	40	0	2	14	18	0.008	17.1	1.0	0.008	0.001
	017-GS-07-01	350	9000	60	40	0	2	14	17	0.008				
	017-GS-07-02	350	9000	60	40	0	2	14	18	0.009				
	017-HS-04-01	350	9000	60	40	0	2	14	6	0.005				
	017-HS-04-02	350	9000	60	40	0	2	14	6	0.004	11.1	5.9	0.008	0.005
	017-HS-06-01	350	9000	60	40	0	2	14	15	0.007				
	017-HS-06-02	350	9000	60	40	0	2	14	17	0.015				
	018-GS-00-01	70	0	0	0	0	2	0	29	0.047	29.6	0.5	0.059	0.016
	018-GS-00-02	70	0	0	0	0	2	0	30	0.070				
	018-HS-00-01	70	0	0	0	0	2	0	29	0.132	28.9	0.2	0.147	0.021
	018-HS-00-02	70	0	0	0	0	2	0	29	0.162				
	018-GS-05-01	350	3000	0	100	0	2	14	17	0.012				
018	018-GS-05-02	350	3000	0	100	0	2	14	16	0.011	16.8	2.1	0.012	0.003
	018-GS-07-01	350	3000	0	100	0	2	14	20	0.016				
	018-GS-07-02	350	3000	0	100	0	2	14	14	0.008				
	018-HS-04-01	350	3000	0	100	0	2	14	18	0.012				
	018-HS-04-02	350	3000	0	100	0	2	14	18	0.009	18.2	0.3	0.010	0.002
	018-HS-06-01	350	3000	0	100	0	2	14	18	0.008				
	018-HS-06-02	350	3000	0	100	0	2	14	19	0.011				
	019-GS-00-01	70	0	0	0	0	2	0	27	0.032	27.5	0.3	0.038	0.008
	019-GS-00-02	70	0	0	0	0	2	0	28	0.044				
	019-HS-00-01	70	0	0	0	0	2	0	29	0.100	29.6	0.6	0.102	0.003
	019-HS-00-02	70	0	0	0	0	2	0	30	0.104				
	019-GS-05-01	350	9000	0	100	0	2	14	17	0.032				
019	019-GS-05-02	350	9000	0	100	0	2	14	17	0.026	18.0	1.5	0.035	0.008
	019-GS-07-01	350	9000	0	100	0	2	14	20	0.044				
	019-GS-07-02	350	9000	0	100	0	2	14	18	0.039				
	019-HS-04-01	350	9000	0	100	0	2	14	17	0.014				
	019-HS-04-02	350	9000	0	100	0	2	14	17	0.013	16.7	0.1	0.014	0.002
	019-HS-06-01	350	9000	0	100	0	2	14	17	0.016				
	019-HS-06-02	350	9000	0	100	0	2	14	17	0.012				
	020-GS-00-01	70	0	0	0	0	2	0	29	0.042	28.8	0.2	0.042	0.001
	020-GS-00-02	70	0	0	0	0	2	0	29	0.041				
	020-HS-00-01	70	0	0	0	0	2	0	28	0.064	28.3	0.8	0.066	0.003
020	020-HS-00-02	70	0	0	0	0	2	0	29	0.068				
	020-GS-05-01	350	3000	90	10	0	2	14	19	0.008				
	020-GS-05-02	350	3000	90	10	0	2	14	19	0.014	20.9	4.0	0.013	0.004
	020-GS-07-01	350	3000	90	10	0	2	14	27	0.017				

Batch #	Core #	T (°F)	P (psi)	CH_4 (%)	CO_2 (%)	H_2S (ppm)	Brine (%)	Days Aged	Ø (%)	K_{klink} (mD)	Ave. Ø (%)	Stdev	Ave. K (mD)	Stdev
	020-GS-07-02	350	3000	90	10	0	2	14	18	0.014				
	020-HS-04-01	350	3000	90	10	0	2	14	21	0.020				
	020-HS-04-02	350	3000	90	10	0	2	14	8	0.012	13.7	5.7	0.014	0.004
	020-HS-06-01	350	3000	90	10	0	2	14	11	0.012				
	020-HS-06-02	350	3000	90	10	0	2	14	15	0.011				
	021-GS-00-01	70	0	0	0	0	2	0	28	0.026	27.3	0.3	0.031	0.007
	021-GS-00-02	70	0	0	0	0	2	0	27	0.036				
	021-HS-00-01	70	0	0	0	0	2	0	29	0.063	29.5	0.3	0.060	0.004
	021-HS-00-02	70	0	0	0	0	2	0	30	0.057				
	021-GS-05-01	350	9000	90	10	0	2	14	34	0.116				
021	021-GS-05-02	350	9000	90	10	0	2	14	33	0.021	31.3	2.9	0.046	0.047
	021-GS-07-01	350	9000	90	10	0	2	14	30	0.013				
	021-GS-07-02	350	9000	90	10	0	2	14	28	0.035				
	021-HS-04-01	350	9000	90	10	0	2	14	17.4	0.015				
	021-HS-04-02	350	9000	90	10	0	2	14	17.1	0.008	15.7	2.1	0.009	0.004
	021-HS-06-01	350	9000	90	10	0	2	14	12.8	0.007				
	021-HS-06-02	350	9000	90	10	0	2	14	15.7	0.007				
	022-GS-00-01	70	0	0	0	0	2	0	27.9	0.024	28.6	1.0	0.026	0.002
	022-GS-00-02	70	0	0	0	0	2	0	29.3	0.027				
	022-HS-00-01	70	0	0	0	0	2	0	32.1	0.085	31.6	0.7	0.081	0.006
	022-HS-00-02	70	0	0	0	0	2	0	31.1	0.077				
	022-GS-05-01	225	3000	60	40	0	2	14	20.5	0.006				
022	022-GS-05-02	225	3000	60	40	0	2	14	10.3	0.003	20.1	6.9	0.006	0.002
	022-GS-07-01	225	3000	60	40	0	2	14	25.6	0.008				
	022-GS-07-02	225	3000	60	40	0	2	14	24.1	0.008				
	022-HS-04-01	225	3000	60	40	0	2	14	16.7	0.003				
	022-HS-04-02	225	3000	60	40	0	2	14	15.6	0.003	15.5	0.9	0.003	0.001
	022-HS-06-01	225	3000	60	40	0	2	14	14.4	0.002				
	022-HS-06-02	225	3000	60	40	0	2	14	15.4	0.002				
	023-GS-00-01	70	0	0	0	0	2	0	26.6	0.034	26.3	0.4	0.042	0.011
	023-GS-00-02	70	0	0	0	0	2	0	26.0	0.049				
	023-HS-00-01	70	0	0	0	0	2	0	29.5	0.049	29.4	0.1	0.044	0.008
	023-HS-00-02	70	0	0	0	0	2	0	29.4	0.038				
	023-GS-05-01	225	9000	60	40	0	2	14	19.4	0.032				
023	023-GS-05-02	225	9000	60	40	0	2	14	21.0	0.009	20.7	0.9	0.019	0.011
	023-GS-07-01	225	9000	60	40	0	2	14	21.0	0.023				
	023-GS-07-02	225	9000	60	40	0	2	14	21.4	0.011				
	023-HS-04-01	225	9000	60	40	0	2	14	16.7	0.009				
	023-HS-04-02	225	9000	60	40	0	2	14	17.0	0.006	16.9	0.2	0.007	0.002
	023-HS-06-01	225	9000	60	40	0	2	14	16.7	0.005				
	023-HS-06-02	225	9000	60	40	0	2	14	17.2	0.007				
	024-GS-00-01	70	0	0	0	0	2	0	25.9	0.033	25.5	0.6	0.048	0.021
	024-GS-00-02	70	0	0	0	0	2	0	25.1	0.063				
	024-HS-00-01	70	0	0	0	0	2	0	28.1	0.044	28.6	0.7	0.045	0.001
024	024-HS-00-02	70	0	0	0	0	2	0	29.1	0.045				
	024-GS-05-01	225	3000	0	100	0	2	14	2.2	0.001				
	024-GS-05-02	225	3000	0	100	0	2	14	6.3	0.001	8.4	5.2	0.002	0.001
	024-GS-07-01	225	3000	0	100	0	2	14	13.9	0.003				

Batch #	Core #	T (°F)	P (psi)	CH_4 (%)	CO_2 (%)	H_2S (ppm)	Brine (%)	Days Aged	Ø (%)	K_{klink} (mD)	Ave. Ø (%)	Stdev	Ave. K (mD)	Stdev
	024-GS-07-02	225	3000	0	100	0	2	14	11.2	0.002				
	024-HS-04-01	225	3000	0	100	0	2	14	3.0	0.002				
	024-HS-04-02	225	3000	0	100	0	2	14	3.8	0.001	4.6	1.8	0.002	0.001
	024-HS-06-01	225	3000	0	100	0	2	14	4.4	0.002				
	024-HS-06-02	225	3000	0	100	0	2	14	7.1	0.002				
	025-GS-00-01	70	0	0	0	0	2	0	27.6	0.038	27.4	0.2	0.042	0.006
	025-GS-00-02	70	0	0	0	0	2	0	27.2	0.046				
	025-HS-00-01	70	0	0	0	0	2	0	28.6	0.065	28.8	0.2	0.067	0.002
	025-HS-00-02	70	0	0	0	0	2	0	29.0	0.068				
	025-GS-05-01	225	9000	0	100	0	2	14	20.4	0.018				
025	025-GS-05-02	225	9000	0	100	0	2	14	20.6	0.018	21.3	1.4	0.020	0.002
	025-GS-07-01	225	9000	0	100	0	2	14	23.4	0.022				
	025-GS-07-02	225	9000	0	100	0	2	14	20.9	0.022				
	025-HS-04-01	225	9000	0	100	0	2	14	17.6	0.027				
	025-HS-04-02	225	9000	0	100	0	2	14	15.1	0.016	16.7	1.5	0.020	0.006
	025-HS-06-01	225	9000	0	100	0	2	14	18.3	0.023				
	025-HS-06-02	225	9000	0	100	0	2	14	16.0	0.014				
	026-GS-00-01	70	0	0	0	0	2	0	29.8	0.031	29.4	0.5	0.030	0.002
	026-GS-00-02	70	0	0	0	0	2	0	29.1	0.028				
	026-HS-00-01	70	0	0	0	0	2	0	30.0	0.074	30.3	0.5	0.074	0.000
	026-HS-00-02	70	0	0	0	0	2	0	30.7	0.074				
	026-GS-05-01	225	3000	90	10	0	2	14	16.8	0.008				
026	026-GS-05-02	225	3000	90	10	0	2	14	22.3	0.014	19.8	2.5	0.014	0.004
	026-GS-07-01	225	3000	90	10	0	2	14	18.5	0.014				
	026-GS-07-02	225	3000	90	10	0	2	14	21.4	0.018				
	026-HS-04-01	225	3000	90	10	0	2	14	7.8	0.004				
	026-HS-04-02	225	3000	90	10	0	2	14	5.6	0.005	12.0	6.7	0.006	0.001
	026-HS-06-01	225	3000	90	10	0	2	14	20.6	0.007				
	026-HS-06-02	225	3000	90	10	0	2	14	14.2	0.006				
	027-GS-00-01	70	0	0	0	0	2	0	30.0	0.056	29.8	0.2	0.056	0.000
	027-GS-00-02	70	0	0	0	0	2	0	29.7	0.056				
	027-HS-00-01	70	0	0	0	0	2	0	28.3	0.080	28.9	0.8	0.079	0.002
	027-HS-00-02	70	0	0	0	0	2	0	29.4	0.077				
	027-GS-05-01	225	9000	90	10	0	2	14	19.6	0.016				
027	027-GS-05-02	225	9000	90	10	0	2	14	18.1	0.016	17.2	4.1	0.013	0.004
	027-GS-07-01	225	9000	90	10	0	2	14	11.2	0.008				
	027-GS-07-02	225	9000	90	10	0	2	14	20.0	0.012				
	027-HS-04-01	225	9000	90	10	0	2	14	14.3	0.010				
	027-HS-04-02	225	9000	90	10	0	2	14	18.0	0.010	12.8	4.2	0.008	0.002
	027-HS-06-01	225	9000	90	10	0	2	14	9.8	0.006				
	027-HS-06-02	225	9000	90	10	0	2	14	9.1	0.006				
	028-GS-00-01	70	0	0	0	0	2	0	29.2	0.036	28.9	0.4	0.036	0.001
	028-GS-00-02	70	0	0	0	0	2	0	28.6	0.035				
	028-HS-00-01	70	0	0	0	0	2	0	27.3	0.049	28.1	1.1	0.056	0.009
028	028-HS-00-02	70	0	0	0	0	2	0	28.8	0.062				
	028-GS-05-01	430	6000	90	10	0	2	14	39.4	0.424				
	028-GS-05-02	430	6000	90	10	0	2	14	38.8	0.378	38.7	0.9	0.409	0.026
	028-GS-07-01	430	6000	90	10	0	2	14	39.2	0.435				

Batch #	Core #	T (°F)	P (psi)	CH_4 (%)	CO_2 (%)	H_2S (ppm)	Brine (%)	Days Aged	Ø (%)	K_{klink} (mD)	Ave. Ø (%)	Stdev	Ave. K (mD)	Stdev
	028-GS-07-02	430	6000	90	10	0	2	14	37.4	0.398				
	028-HS-04-01	430	6000	90	10	0	2	14	36.4	0.154	36.3	0.4	0.145	0.009
	028-HS-04-02	430	6000	90	10	0	2	14	35.7	0.136				
	028-HS-06-01	430	6000	90	10	0	2	14	36.5	0.151				
	028-HS-06-02	430	6000	90	10	0	2	14	36.6	0.140				
029	029-GS-00-01	70	0	0	0	0	2	0	28.7	0.046	29.7	1.4	0.062	0.023
	029-GS-00-02	70	0	0	0	0	2	0	30.7	0.078				
	029-HS-00-01	70	0	0	0	0	2	0	28.4	0.047	28.5	0.2	0.050	0.004
	029-HS-00-02	70	0	0	0	0	2	0	28.7	0.053				
	029-GS-05-01	430	6000	60	40	0	2	14	44.0	0.716	43.2	0.9	0.607	0.139
	029-GS-05-02	430	6000	60	40	0	2	14	43.8	0.708				
	029-GS-07-01	430	6000	60	40	0	2	14	42.0	0.420				
	029-GS-07-02	430	6000	60	40	0	2	14	42.8	0.584				
	029-HS-04-01	430	6000	60	40	0	2	14	39.2	0.101	38.6	0.5	0.103	0.019
	029-HS-04-02	430	6000	60	40	0	2	14	38.7	0.125				
	029-HS-06-01	430	6000	60	40	0	2	14	38.6	0.080				
	029-HS-06-02	430	6000	60	40	0	2	14	38.0	0.107				
030	030-GS-00-01	70	0	0	0	0	2	0	26.7	0.017	26.5	0.2	0.017	0.000
	030-GS-00-02	70	0	0	0	0	2	0	26.3	0.017				
	030-HS-00-01	70	0	0	0	0	2	0	27.0	0.034	26.9	0.1	0.032	0.003
	030-HS-00-02	70	0	0	0	0	2	0	26.9	0.030				
	030-GS-05-01	430	6000	0	100	0	2	14	35.2	0.572	36.4	0.9	0.572	0.065
	030-GS-05-02	430	6000	0	100	0	2	14	36.1	0.480				
	030-GS-07-01	430	6000	0	100	0	2	14	37.4	0.606				
	030-GS-07-02	430	6000	0	100	0	2	14	37.0	0.628				
	030-HS-04-01	430	6000	0	100	0	2	14	32.3	0.160	32.9	0.5	0.159	0.008
	030-HS-04-02	430	6000	0	100	0	2	14	33.0	0.160				
	030-HS-06-01	430	6000	0	100	0	2	14	33.4	0.148				
	030-HS-06-02	430	6000	0	100	0	2	14	32.8	0.168				
031	031-GS-00-01	70	0	0	0	0	2	0	32.2	0.091	27.7	6.3	0.100	0.012
	031-GS-00-02	70	0	0	0	0	2	0	23.3	0.108				
	031-HS-00-01	70	0	0	0	0	2	0	27.7	0.016	29.9	3.0	0.044	0.039
	031-HS-00-02	70	0	0	0	0	2	0	32.0	0.071				
	031-GS-05-01	430	3000	0	100	0	2	14	39.1	0.368	39.5	1.8	0.349	0.084
	031-GS-05-02	430	3000	0	100	0	2	14	40.4	0.436				
	031-GS-07-01	430	3000	0	100	0	2	14	41.5	0.357				
	031-GS-07-02	430	3000	0	100	0	2	14	37.2	0.235				
	031-HS-04-01	430	3000	0	100	0	2	14	33.1	0.357	32.4	0.8	0.356	0.167
	031-HS-04-02	430	3000	0	100	0	2	14	32.0	0.171				
	031-HS-06-01	430	3000	0	100	0	2	14	33.1	0.576				
	031-HS-06-02	430	3000	0	100	0	2	14	31.5	0.319				
032	032-GS-00-01	70	0	0	0	0	2	0	-	-	30.4		0.039	
	032-GS-00-02	70	0	0	0	0	2	0	30.4	0.039				
	032-HS-00-01	70	0	0	0	0	2	0	28.5	0.082	28.6	0.2	0.079	0.004
	032-HS-00-02	70	0	0	0	0	2	0	28.7	0.076				

Batch #	Core #	T (°F)	P (psi)	CH_4 (%)	CO_2 (%)	H_2S (ppm)	Brine (%)	Days Aged	Ø (%)	K_{klink} (mD)	Ave. Ø (%)	Stdev	Ave. K (mD)	Stdev
	032-GS-05-01	430	9000	0	100	0	2	14	22.5	0.023				
	032-GS-05-02	430	9000	0	100	0	2	14	24.5	0.028	24.3	1.9	0.028	0.015
	032-GS-07-01	430	9000	0	100	0	2	14	26.9	0.048				
	032-GS-07-02	430	9000	0	100	0	2	14	23.2	0.011				
	032-HS-04-01	430	9000	0	100	0	2	14	21.3	0.024				
	032-HS-04-02	430	9000	0	100	0	2	14	20.5	0.019	21.0	0.4	0.025	0.005
	032-HS-06-01	430	9000	0	100	0	2	14	21.3	0.032				
	032-HS-06-02	430	9000	0	100	0	2	14	21.0	0.025				
033	033-GS-00-01	70	0	0	0	0	2	0			28.7	0.1	0.076	0.001
	033-GS-00-02	70	0	0	0	0	2	0			29.2	0.3	0.067	0.003
	033-HS-00-01	100	6000	90	10	300	2	14			30.1	0.8	0.113	0.012
	033-HS-00-02	100	6000	90	10	300	2	14			29.6	0.8	0.084	0.017
034	034-GS-00-01	70	0	0	0	0	2	0			30.2	0.2	0.121	0.007
	034-GS-00-02	70	0	0	0	0	2	0			30.3	0.0	0.063	0.000
	034-HS-00-01	225	6000	90	10	300	2	14			13.7	1.5	0.004	0.001
	034-HS-00-02	225	6000	90	10	300	2	14			27.2	1.8	0.061	0.015
035	035-GS-00-01	70	0	0	0	0	2	0			29.4	0.0	0.120	0.000
	035-GS-00-02	70	0	0	0	0	2	0			28.7	0.0	0.034	0.000
	035-HS-00-01	350	6000	90	10	300	2	14			37.2	0.4	0.095	0.020
	035-HS-00-02	350	6000	90	10	300	2	14			37.0	0.3	0.203	0.010
038	038-GS-00-01	70	0	0	0	0	2	0	21.5	0.012	21.2	0.4	0.012	0.000
	038-GS-00-02	70	0	0	0	0	2	0	20.9	0.012				
	038-HS-00-01	70	0	0	0	0	2	0	23.6	0.040	20.7	4.1	0.040	
	038-HS-00-02	70	0	0	0	0	2	0	17.8					
039	039-GS-00-01	70	0	0	0	0	2	0	28.6	0.028	27.6	1.4	0.026	0.004
	039-GS-00-02	70	0	0	0	0	2	0	26.6	0.023				
	039-HS-00-01	70	0	0	0	0	2	0	27.8	0.047	27.5	0.5	0.045	0.003
	039-HS-00-02	70	0	0	0	0	2	0	27.1	0.043				
	039-GS-05-01	100	9000	90	10	300	2	14	9.4	0.009	12.1	3.9	0.008	0.001
	039-GS-05-02	100	9000	90	10	300	2	14	14.8	0.007				
	039-HS-04-01	100	9000	90	10	300	2	14	9.4	0.003	7.1	3.3	0.003	0.001
	039-HS-04-02	100	9000	90	10	300	2	14	4.7	0.002				
040	040 GS 00 01	70	0	0	0	0	2	0	28.0	0.080	30.0	2.9	0.078	0.003
	040 GS 00 02	70	0	0	0	0	2	0	32.0	0.076				
	040 HS 00 01	70	0	0	0	0	2	0	23.2	0.091	26.3	4.4	0.088	0.004
	040 HS 00 02	70	0	0	0	0	2	0	29.4	0.085				
	040 GS 07 01	100	9000	60	40	180	2	14	23.8	0.038	24.4	0.8	0.039	0.001
	040 GS 07 02	100	9000	60	40	180	2	14	25.0	0.040				
	040 HS 04 01	100	9000	60	40	180	2	14	25.9	0.046	27.2	1.9	0.052	0.008
	040 HS 04 02	100	9000	60	40	180	2	14	28.5	0.058				
041	041-GS-00-01	70	0	0	0	0	2	0	30.7	0.088	31.1	0.5	0.085	0.005
	041-GS-00-02	70	0	0	0	0	2	0	31.4	0.081				
	041-HS-00-01	70	0	0	0	0	2	0	38.1	0.521	38.3	0.3	0.645	0.175
	041-HS-00-02	70	0	0	0	0	2	0	38.6	0.768				
	041-GS-05-01	100	3000	100	0	300	2	14	37.8	0.066	34.6	4.6	0.073	0.009
	041-GS-07-01	100	3000	100	0	300	2	14	31.3	0.079				
	041-HS-04-01	100	3000	100	0	300	2	14	37.6	0.431	38.1	0.7	0.491	0.085

Batch #	Core #	T (°F)	P (psi)	CH_4 (%)	CO_2 (%)	H_2S (ppm)	Brine (%)	Days Aged	Ø (%)	K_{klink} (mD)	Ave. Ø (%)	Stdev	Ave. K (mD)	Stdev
	041-HS-06-01	100	3000	100	0	300	2	14	38.6	0.551				

C.2.2 Shear Bond Strength

Table C.20: Shear bond strength of micro silica based cements

Batch #	Core #	T (°F)	P (psi)	CH_4 (%)	CO_2 (%)	H_2S (ppm)	Brine (%)	Days Aged	SBS (psi)	Ave. SBS (psi)	Stdev (psi)
002	002-HS-11-01	350	6000	100	0	0	2	14	1439	1892	577
	002-HS-11-02	350	6000	100	0	0	2	14	1695		
	002-HS-11-03	350	6000	100	0	0	2	14	2542		
	002-HS-09-03	350	6000	100	0	0	2	28	1763	1584	196
	002-HS-09-04	350	6000	100	0	0	2	28	1374		
	002-HS-09-05	350	6000	100	0	0	2	28	1614		
003	003-HS-09-01	350	6000	100	0	0	2	14	3103	2844	366
	003-HS-09-02	350	6000	100	0	0	2	14	2585		
004	004-HS-00-01	70	0	0	0	0	2	0	465	494	99
	004-HS-00-02	70	0	0	0	0	2	0	413		
	004-HS-00-03	70	0	0	0	0	2	0	604		
	004-HS-09-01	350	6000	90	10	0	2	6	1312	1365	243
	004-HS-09-02	350	6000	90	10	0	2	6	1765		
	004-HS-09-03	350	6000	90	10	0	2	6	1333		
	004-HS-09-04	350	6000	90	10	0	2	6	1314		
	004-HS-09-05	350	6000	90	10	0	2	6	1101		
005	005-HS-09-01	350	6000	90	10	0	2	14	1350	879	402
	005-HS-09-02	350	6000	90	10	0	2	14	503		
	005-HS-09-03	350	6000	90	10	0	2	28	1012		
	005-HS-09-04	350	6000	90	10	0	2	28	419		
	005-HS-09-05	350	6000	90	10	0	2	28	1113		
006	006-HS-10-01	350	6000	90	10	0	2	14	478	522	62
	006-HS-10-02	350	6000	90	10	0	2	14	566		
007	007-HS-08-01	225	6000	90	10	0	2	14	1243	1199	235
	007-HS-08-02	225	6000	90	10	0	2	14	1090		
	007-HS-08-03	225	6000	90	10	0	2	14	1052		
	007-HS-08-04	225	6000	90	10	0	2	14	1019		
	007-HS-08-05	225	6000	90	10	0	2	14	1590		
	007-HS-09-01	225	6000	90	10	0	2	14	1324	1282	124
	007-HS-09-02	225	6000	90	10	0	2	14	1219		
	007-HS-09-03	225	6000	90	10	0	2	14	1105		
	007-HS-09-04	225	6000	90	10	0	2	14	1430		
	007-HS-09-05	225	6000	90	10	0	2	14	1330		
008	008-HS-00-01	70	0	0	0	0	2	0	506	659	220
	008-HS-00-02	70	0	0	0	0	2	0	574		
	008-HS-00-03	70	0	0	0	0	2	0	617		
	008-HS-00-04	70	0	0	0	0	2	0	1046		
	008-HS-00-05	70	0	0	0	0	2	0	554		

Batch #	Core #	T (°F)	P (psi)	CH_4 (%)	CO_2 (%)	H_2S (ppm)	Brine (%)	Days Aged	SBS (psi)	Ave. SBS (psi)	Stdev (psi)
	008-HS-08-01	100	6000	90	10	0	2	14	764		
	008-HS-08-02	100	6000	90	10	0	2	14	744		
	008-HS-08-03	100	6000	90	10	0	2	14	1232	750	309
	008-HS-08-04	100	6000	90	10	0	2	14	630		
	008-HS-08-05	100	6000	90	10	0	2	14	382		
	008-HS-09-01	100	6000	90	10	0	2	14	748		
	008-HS-09-02	100	6000	90	10	0	2	14	920		
	008-HS-09-03	100	6000	90	10	0	2	14	690	783	144
	008-HS-09-04	100	6000	90	10	0	2	14	614		
	008-HS-09-05	100	6000	90	10	0	2	14	943		
	009-HS-00-01	70	0	0	0	0	2	0	348		
	009-HS-00-02	70	0	0	0	0	2	0	300		
	009-HS-00-03	70	0	0	0	0	2	0	505	455	181
	009-HS-00-04	70	0	0	0	0	2	0	371		
	009-HS-00-05	70	0	0	0	0	2	0	749		
	009-HS-08-01	225	6000	60	40	0	2	14	1905		
	009-HS-08-02	225	6000	60	40	0	2	14	1614		
009	009-HS-08-03	225	6000	60	40	0	2	14	1431	1693	226
	009-HS-08-04	225	6000	60	40	0	2	14	1953		
	009-HS-08-05	225	6000	60	40	0	2	14	1563		
	009-HS_09-01	225	6000	60	40	0	2	14	1804		
	009-HS_09-02	225	6000	60	40	0	2	14	2346		
	009-HS_09-03	225	6000	60	40	0	2	14	1923	1982	216
	009-HS_09-04	225	6000	60	40	0	2	14	1992		
	009-HS_09-05	225	6000	60	40	0	2	14	1846		
	010-HS-00-01	70	0	0	0	0	2	0	507		
	010-HS-00-02	70	0	0	0	0	2	0	689		
	010-HS-00-03	70	0	0	0	0	2	0	719	672	95
	010-HS-00-04	70	0	0	0	0	2	0	696		
	010-HS-00-05	70	0	0	0	0	2	0	751		
010	010-HS-08-01	225	6000	0	100	0	2	14	2227		
	010-HS-08-02	225	6000	0	100	0	2	14	1965		
	010-HS-08-03	225	6000	0	100	0	2	14	1582	2018	308
	010-HS-08-04	225	6000	0	100	0	2	14	2385		
	010-HS-08-05	225	6000	0	100	0	2	14	1931		
	011-HS-00-01	70	0	0	0	0	2	0	594		
	011-HS-00-02	70	0	0	0	0	2	0	513		
011	011-HS-00-03	70	0	0	0	0	2	0	632	584	82
	011-HS-00-04	70	0	0	0	0	2	0	492		
	011-HS-00-05	70	0	0	0	0	2	0	688		

Batch #	Core #	T (°F)	P (psi)	CH_4 (%)	CO_2 (%)	H_2S (ppm)	Brine (%)	Days Aged	SBS (psi)	Ave. SBS (psi)	Stdev (psi)
	011-HS-08-01	100	6000	60	40	0	2	14	732		
	011-HS-08-02	100	6000	60	40	0	2	14	1179		
	011-HS-08-03	100	6000	60	40	0	2	14	963	1001	179
	011-HS-08-04	100	6000	60	40	0	2	14	1152		
	011-HS-08-05	100	6000	60	40	0	2	14	979		
012	012-HS-00-01	70	0	0	0	0	2	0	397		
	012-HS-00-02	70	0	0	0	0	2	0	500		
	012-HS-00-03	70	0	0	0	0	2	0	619	602	159
	012-HS-00-04	70	0	0	0	0	2	0	694		
	012-HS-00-05	70	0	0	0	0	2	0	801		
	012-HS-08-01	100	6000	0	100	0	2	14	759		
	012-HS-08-02	100	6000	0	100	0	2	14	788		
	012-HS-08-03	100	6000	0	100	0	2	14	787	756	47
	012-HS-08-04	100	6000	0	100	0	2	14	676		
	012-HS-08-05	100	6000	0	100	0	2	14	772		
013	013-HS-00-01	70	0	0	0	0	2	0	555		
	013-HS-00-02	70	0	0	0	0	2	0	498		
	013-HS-00-03	70	0	0	0	0	2	0	593	535	39
	013-HS-00-04	70	0	0	0	0	2	0	505		
	013-HS-00-05	70	0	0	0	0	2	0	523		
	013-HS-08-01	350	6000	60	40	0	2	14	1861		
	013-HS-08-02	350	6000	60	40	0	2	14	1929		
	013-HS-08-03	350	6000	60	40	0	2	14	2154	2031	184
	013-HS-08-04	350	6000	60	40	0	2	14	2291		
	013-HS-08-05	350	6000	60	40	0	2	14	1919		
014	014-HS-00-01	70	0	0	0	0	2	0	643		
	014-HS-00-02	70	0	0	0	0	2	0	403		
	014-HS-00-03	70	0	0	0	0	2	0	394	493	104
	014-HS-00-04	70	0	0	0	0	2	0	477		
	014-HS-00-05	70	0	0	0	0	2	0	548		
	014-HS-11-01	350	6000	0	100	0	2	14	2352		
	014-HS-11-02	350	6000	0	100	0	2	14	2695		
	014-HS-11-03	350	6000	0	100	0	2	14	2253	2239	313
	014-HS-11-04	350	6000	0	100	0	2	14	1943		
	014-HS-11-05	350	6000	0	100	0	2	14	1953		
015	015-HS-00-01	70	0	0	0	0	2	0	672		
	015-HS-00-02	70	0	0	0	0	2	0	536		
	015-HS-00-03	70	0	0	0	0	2	0	572	605	60
	015-HS-00-04	70	0	0	0	0	2	0	580		
	015-HS-00-05	70	0	0	0	0	2	0	665		
	015-HS-08-01	225	6000	60	40	0	2	14	1148	1290	291

Batch #	Core #	T (°F)	P (psi)	CH_4 (%)	CO_2 (%)	H_2S (ppm)	Brine (%)	Days Aged	SBS (psi)	Ave. SBS (psi)	Stdev (psi)
	015-HS-08-02	225	6000	60	40	0	2	14	1805		
	015-HS-08-03	225	6000	60	40	0	2	14	1168		
	015-HS-08-04	225	6000	60	40	0	2	14	1230		
	015-HS-08-05	225	6000	60	40	0	2	14	1100		
016	016-HS-00-01	70	0	0	0	0	2	0	885		
	016-HS-00-02	70	0	0	0	0	2	0	882		
	016-HS-00-03	70	0	0	0	0	2	0	539	731	150
	016-HS-00-04	70	0	0	0	0	2	0	695		
	016-HS-00-05	70	0	0	0	0	2	0	655		
	016-HS-11-01	350	3000	60	40	0	2	14	2737		
	016-HS-11-02	350	3000	60	40	0	2	14	2151		
	016-HS-11-03	350	3000	60	40	0	2	14	2019	2272	292
	016-HS-11-04	350	3000	60	40	0	2	14	2373		
	016-HS-11-05	350	3000	60	40	0	2	14	2082		
017	017-HS-00-01	70	0	0	0	0	2	0	709		
	017-HS-00-02	70	0	0	0	0	2	0	695		
	017-HS-00-03	70	0	0	0	0	2	0	797	654	117
	017-HS-00-04	70	0	0	0	0	2	0	546		
	017-HS-00-05	70	0	0	0	0	2	0	521		
	017-HS-11-01	350	9000	60	40	0	2	14	2681		
	017-HS-11-02	350	9000	60	40	0	2	14	1688		
	017-HS-11-03	350	9000	60	40	0	2	14	3021	2445	492
	017-HS-11-04	350	9000	60	40	0	2	14	2464		
	017-HS-11-05	350	9000	60	40	0	2	14	2369		
018	018-HS-00-01	70	0	0	0	0	2	0	286		
	018-HS-00-02	70	0	0	0	0	2	0	555		
	018-HS-00-03	70	0	0	0	0	2	0	479	570	245
	018-HS-00-04	70	0	0	0	0	2	0	569		
	018-HS-00-05	70	0	0	0	0	2	0	959		
	018-HS-09-01	350	3000	0	100	0	2	14	1389		
	018-HS-09-02	350	3000	0	100	0	2	14	1788		
	018-HS-09-03	350	3000	0	100	0	2	14	1248	1461	199
	018-HS-09-04	350	3000	0	100	0	2	14	1457		
	018-HS-09-05	350	3000	0	100	0	2	14	1421		
019	019-HS-00-01	70	0	0	0	0	2	0	1246		
	019-HS-00-02	70	0	0	0	0	2	0	429		
	019-HS-00-03	70	0	0	0	0	2	0	669	701	328
	019-HS-00-04	70	0	0	0	0	2	0	460		
	019-HS-00-05	70	0	0	0	0	2	0	700		
	019HS-09-01	350	9000	0	100	0	2	14	2108	1932	146

Batch #	Core #	T (°F)	P (psi)	CH_4 (%)	CO_2 (%)	H_2S (ppm)	Brine (%)	Days Aged	SBS (psi)	Ave. SBS (psi)	Stdev (psi)
	019HS-09-02	350	9000	0	100	0	2	14	2068		
	019HS-09-03	350	9000	0	100	0	2	14	1809		
	019HS-09-04	350	9000	0	100	0	2	14	1870		
	019HS-09-05	350	9000	0	100	0	2	14	1803		
020	020-HS-00-01	70	0	0	0	0	2	0	543		
	020-HS-00-02	70	0	0	0	0	2	0	510		
	020-HS-00-03	70	0	0	0	0	2	0	795	602	132
	020-HS-00-04	70	0	0	0	0	2	0	483		
	020-HS-00-05	70	0	0	0	0	2	0	680		
	020-HS-08-01	350	3000	90	10	0	2	14	895		
	020-HS-08-02	350	3000	90	10	0	2	14	1730		
	020-HS-08-03	350	3000	90	10	0	2	14	1283	1406	329
	020-HS-08-04	350	3000	90	10	0	2	14	1604		
	020-HS-08-05	350	3000	90	10	0	2	14	1518		
021	021-HS-00-01	70	0	0	0	0	2	0	282		
	021-HS-00-02	70	0	0	0	0	2	0	394		
	021-HS-00-03	70	0	0	0	0	2	0	526	402	98
	021-HS-00-04	70	0	0	0	0	2	0	469		
	021-HS-00-05	70	0	0	0	0	2	0	338		
	021-HS-11-01	350	9000	90	10	0	2	14	2075		
	021-HS-11-02	350	9000	90	10	0	2	14	1802		
	021-HS-11-03	350	9000	90	10	0	2	14	1837	1919	107
	021-HS-11-04	350	9000	90	10	0	2	14	1956		
	021-HS-11-05	350	9000	90	10	0	2	14	1924		
022	022-HS-01-01	70	0	0	0	0	2	0	727		
	022-HS-01-02	70	0	0	0	0	2	0	617		
	022-HS-01-03	70	0	0	0	0	2	0	342	498	177
	022-HS-01-04	70	0	0	0	0	2	0	489		
	022-HS-01-05	70	0	0	0	0	2	0	313		
	022-HS-11-01	225	3000	60	40	0	2	14	1024		
	022-HS-11-02	225	3000	60	40	0	2	14	951		
	022-HS-11-03	225	3000	60	40	0	2	14	972	1208	385
	022-HS-11-04	225	3000	60	40	0	2	14	1869		
	022-HS-11-05	225	3000	60	40	0	2	14	1223		
023	023-HS-00-01	70	0	0	0	0	2	0	491		
	023-HS-00-02	70	0	0	0	0	2	0	317		
	023-HS-00-03	70	0	0	0	0	2	0	461	412	73
	023-HS-00-04	70	0	0	0	0	2	0	434		
	023-HS-00-05	70	0	0	0	0	2	0	357		
	023-HS-08-01	225	9000	60	40	0	2	14	1814	1574	175

Batch #	Core #	T (°F)	P (psi)	CH_4 (%)	CO_2 (%)	H_2S (ppm)	Brine (%)	Days Aged	SBS (psi)	Ave. SBS (psi)	Stdev (psi)
	023-HS-08-02	225	9000	60	40	0	2	14	1411		
	023-HS-08-03	225	9000	60	40	0	2	14	1395		
	023-HS-08-04	225	9000	60	40	0	2	14	1626		
	023-HS-08-05	225	9000	60	40	0	2	14	1626		
024	024-HS-00-01	70	0	0	0	0	2	0	623	558	76
	024-HS-00-02	70	0	0	0	0	2	0	589		
	024-HS-00-03	70	0	0	0	0	2	0	516		
	024-HS-00-04	70	0	0	0	0	2	0	618		
	024-HS-00-05	70	0	0	0	0	2	0	446		
	024-HS-08-01	225	3000	0	100	0	2	14	1568	1244	220
	024-HS-08-02	225	3000	0	100	0	2	14	997		
	024-HS-08-03	225	3000	0	100	0	2	14	1142		
	024-HS-08-04	225	3000	0	100	0	2	14	1168		
	024-HS-08-05	225	3000	0	100	0	2	14	1346		
025	025-HS-00-01	70	0	0	0	0	2	0	478	545	73
	025-HS-00-02	70	0	0	0	0	2	0	664		
	025-HS-00-03	70	0	0	0	0	2	0	538		
	025-HS-00-04	70	0	0	0	0	2	0	547		
	025-HS-00-05	70	0	0	0	0	2	0	497		
	025-HS-08-01	225	9000	0	100	0	2	14	1789	1905	209
	025-HS-08-02	225	9000	0	100	0	2	14	2154		
	025-HS-08-03	225	9000	0	100	0	2	14	1992		
	025-HS-08-04	225	9000	0	100	0	2	14	1980		
	025-HS-08-05	225	9000	0	100	0	2	14	1611		
026	026-HS-00-01	70	0	0	0	0	2	0	483	586	102
	026-HS-00-02	70	0	0	0	0	2	0	640		
	026-HS-00-03	70	0	0	0	0	2	0	472		
	026-HS-00-04	70	0	0	0	0	2	0	641		
	026-HS-00-05	70	0	0	0	0	2	0	695		
	026-HS-08-01	225	3000	0	10	0	2	14	836	735	213
	026-HS-08-02	225	3000	0	10	0	2	14	957		
	026-HS-08-03	225	3000	0	10	0	2	14	808		
	026-HS-08-04	225	3000	0	10	0	2	14	399		
	026-HS-08-05	225	3000	0	10	0	2	14	673		
027	027-HS-00-01	70	0	0	0	0	2	0	553	604	74
	027-HS-00-02	70	0	0	0	0	2	0	615		
	027-HS-00-03	70	0	0	0	0	2	0	521		
	027-HS-00-04	70	0	0	0	0	2	0	714		
	027-HS-00-05	70	0	0	0	0	2	0	617		
	027-HS-08-01	225	9000	90	10	0	2	14	475	738	196

Batch #	Core #	T (°F)	P (psi)	CH_4 (%)	CO_2 (%)	H_2S (ppm)	Brine (%)	Days Aged	SBS (psi)	Ave. SBS (psi)	Stdev (psi)
	027-HS-08-02	225	9000	90	10	0	2	14	957		
	027-HS-08-03	225	9000	90	10	0	2	14	905		
	027-HS-08-04	225	9000	90	10	0	2	14	687		
	027-HS-08-05	225	9000	90	10	0	2	14	666		
028	028-HS-00-01	70	0	0	0	0	2	0	601	645	41
	028-HS-00-02	70	0	0	0	0	2	0	649		
	028-HS-00-03	70	0	0	0	0	2	0	605		
	028-HS-00-04	70	0	0	0	0	2	0	681		
	028-HS-00-05	70	0	0	0	0	2	0	687		
	028-HS-08-01	430	6000	90	10	0	2	14	1431	1318	149
	028-HS-08-02	430	6000	90	10	0	2	14	1274		
	028-HS-08-03	430	6000	90	10	0	2	14	1265		
	028-HS-08-04	430	6000	90	10	0	2	14	1499		
	028-HS-08-05	430	6000	90	10	0	2	14	1121		
029	029-HS-00-01	70	0	0	0	0	2	0	750	803	36
	029-HS-00-02	70	0	0	0	0	2	0	845		
	029-HS-00-03	70	0	0	0	0	2	0	802		
	029-HS-00-04	70	0	0	0	0	2	0	791		
	029-HS-00-05	70	0	0	0	0	2	0	827		
	029-HS-08-01	430	6000	60	40	0	2	14	1437	1375	158
	029-HS-08-02	430	6000	60	40	0	2	14	1605		
	029-HS-08-03	430	6000	60	40	0	2	14	1181		
	029-HS-08-04	430	6000	60	40	0	2	14	1350		
	029-HS-08-05	430	6000	60	40	0	2	14	1303		
030	030-HS-00-01	70	0	0	0	0	2	0	516	665	109
	030-HS-00-02	70	0	0	0	0	2	0	587		
	030-HS-00-03	70	0	0	0	0	2	0	729		
	030-HS-00-04	70	0	0	0	0	2	0	778		
	030-HS-00-05	70	0	0	0	0	2	0	714		
	030-HS-08-01	430	6000	0	100	0	2	14	988	1037	91
	030-HS-08-02	430	6000	0	100	0	2	14	1138		
	030-HS-08-03	430	6000	0	100	0	2	14	1000		
	030-HS-08-04	430	6000	0	100	0	2	14	931		
	030-HS-08-05	430	6000	0	100	0	2	14	1126		
031	031-HS-00-01	70	0	0	0	0	2	0	741	699	89
	031-HS-00-02	70	0	0	0	0	2	0	588		
	031-HS-00-03	70	0	0	0	0	2	0	825		
	031-HS-00-04	70	0	0	0	0	2	0	656		
	031-HS-00-05	70	0	0	0	0	2	0	687		
	031-HS-08-01	430	3000	0	100	0	2	14	419	571	180
	031-HS-08-02	430	3000	0	100	0	2	14	572		

Batch #	Core #	T (°F)	P (psi)	CH_4 (%)	CO_2 (%)	H_2S (ppm)	Brine (%)	Days Aged	SBS (psi)	Ave. SBS (psi)	Stdev (psi)
	031-HS-08-03	430	3000	0	100	0	2	14	856		
	031-HS-08-04	430	3000	0	100	0	2	14	413		
	031-HS-08-05	430	3000	0	100	0	2	14	595		
032	032-HS-00-01	70	0	0	0	0	2	0	592	577	106
	032-HS-00-02	70	0	0	0	0	2	0	742		
	032-HS-00-03	70	0	0	0	0	2	0	585		
	032-HS-00-04	70	0	0	0	0	2	0	482		
	032-HS-00-05	70	0	0	0	0	2	0	486		
	032-HS-08-01	430	9000	0	100	0	2	14	877	930	90
	032-HS-08-02	430	9000	0	100	0	2	14	982		
	032-HS-08-03	430	9000	0	100	0	2	14	824		
	032-HS-08-04	430	9000	0	100	0	2	14	915		
	032-HS-08-05	430	9000	0	100	0	2	14	1053		
033	033-HS-00-01	70	0	0	0	0	2	0	520	520	34
	033-HS-00-02	70	0	0	0	0	2	0	515		
	033-HS-00-03	70	0	0	0	0	2	0	574		
	033-HS-00-04	70	0	0	0	0	2	0	478		
	033-HS-00-05	70	0	0	0	0	2	0	512		
	033-HS-08-01	100	6000	90	10	300	2	14	778	712	51
	033-HS-08-02	100	6000	90	10	300	2	14	718		
	033-HS-08-03	100	6000	90	10	300	2	14	679		
	033-HS-08-04	100	6000	90	10	300	2	14	648		
	033-HS-08-05	100	6000	90	10	300	2	14	738		
034	034-HS-00-01	70	0	0	0	0	2	0	906	711	113
	034-HS-00-02	70	0	0	0	0	2	0	706		
	034-HS-00-03	70	0	0	0	0	2	0	630		
	034-HS-00-04	70	0	0	0	0	2	0	638		
	034-HS-00-05	70	0	0	0	0	2	0	673		
	034-HS-08-01	225	6000	90	10	300	2	14	750	771	136
	034-HS-08-02	225	6000	90	10	300	2	14	838		
	034-HS-08-03	225	6000	90	10	300	2	14	783		
	034-HS-08-04	225	6000	90	10	300	2	14	926		
	034-HS-08-05	225	6000	90	10	300	2	14	560		
035	035-HS-00-01	70	0	0	0	0	2	0	621	578	146
	035-HS-00-02	70	0	0	0	0	2	0	708		
	035-HS-00-03	70	0	0	0	0	2	0	643		
	035-HS-00-04	70	0	0	0	0	2	0	589		
	035-HS-00-05	70	0	0	0	0	2	0	329		
	035-HS-08-01	350	6000	90	10	300	2	14	1829	1888	138
	035-HS-08-02	350	6000	90	10	300	2	14	2024		

Batch #	Core #	T (°F)	P (psi)	CH_4 (%)	CO_2 (%)	H_2S (ppm)	Brine (%)	Days Aged	SBS (psi)	Ave. SBS (psi)	Stdev (psi)
	035-HS-08-03	350	6000	90	10	300	2	14	1678		
	035-HS-08-04	350	6000	90	10	300	2	14	1940		
	035-HS-08-05	350	6000	90	10	300	2	14	1971		
036	036-HS-00-01	70	0	0	0	0	2	0	1007	997	223
	036-HS-00-02	70	0	0	0	0	2	0	809		
	036-HS-00-03	70	0	0	0	0	2	0	1372		
	036-HS-00-04	70	0	0	0	0	2	0	857		
	036-HS-00-05	70	0	0	0	0	2	0	940		
	036-HS-08-01	100	6000	100	0	300	2	14	1169	1093	57
	036-HS-08-02	100	6000	100	0	300	2	14	1026		
	036-HS-08-03	100	6000	100	0	300	2	14	1077		
	036-HS-08-04	100	6000	100	0	300	2	14	1134		
	036-HS-08-05	100	6000	100	0	300	2	14	1061		
037	037-HS-00-01	70	0	0	0	0	2	0	675	671	164
	037-HS-00-02	70	0	0	0	0	2	0	711		
	037-HS-00-03	70	0	0	0	0	2	0	720		
	037-HS-00-04	70	0	0	0	0	2	0	845		
	037-HS-00-05	70	0	0	0	0	2	0	402		
	037-HS-08-01	100	6000	60	40	180	2	14	1006	1001	64
	037-HS-08-02	100	6000	60	40	180	2	14	985		
	037-HS-08-03	100	6000	60	40	180	2	14	1076		
	037-HS-08-04	100	6000	60	40	180	2	14	1035		
	037-HS-08-05	100	6000	60	40	180	2	14	904		
038	038-HS-00-01	70	0	0	0	0	2	0	319	549	356
	038-HS-00-02	70	0	0	0	0	2	0	475		
	038-HS-00-03	70	0	0	0	0	2	0	1177		
	038-HS-00-04	70	0	0	0	0	2	0	384		
	038-HS-00-05	70	0	0	0	0	2	0	388		
	038-HS-08-01	100	9000	100	0	300	2	14	288	765	515
	038-HS-08-02	100	9000	100	0	300	2	14	753		
	038-HS-08-03	100	9000	100	0	300	2	14	817		
	038-HS-08-04	100	9000	100	0	300	2	14	1589		
	038-HS-08-05	100	9000	100	0	300	2	14	376		
039	039-HS-00-01	70	0	0	0	0	2	0	984	1085	158
	039-HS-00-02	70	0	0	0	0	2	0	1039		
	039-HS-00-03	70	0	0	0	0	2	0	1091		
	039-HS-00-04	70	0	0	0	0	2	0	1352		
	039-HS-00-05	70	0	0	0	0	2	0	958		
	039-HS-08-01	100	9000	90	10	300	2	14	1313	1433	423
	039-HS-08-02	100	9000	90	10	300	2	14	1607		

Batch #	Core #	T (°F)	P (psi)	CH_4 (%)	CO_2 (%)	H_2S (ppm)	Brine (%)	Days Aged	SBS (psi)	Ave. SBS (psi)	Stdev (psi)
	039-HS-08-03	100	9000	90	10	300	2	14	1115		
	039-HS-08-04	100	9000	90	10	300	2	14	1047		
	039-HS-08-05	100	9000	90	10	300	2	14	2082		
040	040-HS-00-01	70	0	0	0	0	2	0	726	681	144
	040-HS-00-02	70	0	0	0	0	2	0	663		
	040-HS-00-03	70	0	0	0	0	2	0	562		
	040-HS-00-04	70	0	0	0	0	2	0	902		
	040-HS-00-05	70	0	0	0	0	2	0	548		
	040-HS-08-01	100	9000	60	40	180	2	14	1125	1182	85
	040-HS-08-02	100	9000	60	40	180	2	14	1194		
	040-HS-08-03	100	9000	60	40	180	2	14	1111		
	040-HS-08-05	100	9000	60	40	180	2	14	1297		
041	041-HS-00-01	70	0	0	0	0	2	0	587	610	144
	041-HS-00-02	70	0	0	0	0	2	0	733		
	041-HS-00-03	70	0	0	0	0	2	0	415		
	041-HS-00-04	70	0	0	0	0	2	0	703		
	041-HS-08-01	100	3000	100	0	300	2	14	744	723	218
	041-HS-08-02	100	3000	100	0	300	2	14	1080		
	041-HS-08-03	100	3000	100	0	300	2	14	676		
	041-HS-08-04	100	3000	100	0	300	2	14	500		
	041-HS-08-05	100	3000	100	0	300	2	14	618		

C.2.3 Compressive Strength

Table C.21: Compressive Strength of baseline cements

Batch #	Core #	T (°F)	P (psi)	CH_4 (%)	CO_2 (%)	H_2S (ppm)	Brine (%)	Days Aged	Comp. Strength (psi)	Ave. Comp. Strength (psi)	Stdev (psi)
001	001-GS-00-01	70	0	0	0	0	9	0	3991	4072	275
	001-GS-00-02	70	0	0	0	0	9	0	3849		
	001-GS-00-03	70	0	0	0	0	9	0	3991		
	001-GS-00-04	70	0	0	0	0	9	0	4277		
	001-GS-00-05	70	0	0	0	0	9	0	3802		
	001-GS-00-06	70	0	0	0	0	9	0	4520		
	001-HS-00-01	70	0	0	0	0	9	0	3608	4244	795
	001-HS-00-02	70	0	0	0	0	9	0	3991		
	001-HS-00-03	70	0	0	0	0	9	0	5813		
	001-HS-00-04	70	0	0	0	0	9	0	3837		
	001-HS-00-05	70	0	0	0	0	9	0	3996		
	001-HS-00-06	70	0	0	0	0	9	0	4221		
	001-GS-03-03	350	9000	100	0	0	9	6	4010	3377	483
	001-GS-03-04	350	9000	100	0	0	9	6	3492		
	001-GS-07-03	350	9000	100	0	0	9	6	3060		
	001-GS-07-04	350	9000	100	0	0	9	6	2947		
	001-HS-01-04	350	9000	100	0	0	9	6	5675	5785	961
	001-HS-05-03	350	9000	100	0	0	9	6	5998		
	001-HS-05-04	350	9000	100	0	0	9	6	6897		
	001-HS-09-02	350	9000	100	0	0	9	6	4569		
002	002-GS-00-03	70	0	0	0	0	2	0	4316	4588	669
	002-GS-00-04	70	0	0	0	0	2	0	4098		
	002-GS-00-05	70	0	0	0	0	2	0	5351		
	002-HS-00-03	70	0	0	0	0	2	0	3261	3854	591
	002-HS-00-04	70	0	0	0	0	2	0	3857		
	002-HS-00-05	70	0	0	0	0	2	0	4444		
	002-GS-03-03	350	6000	100	0	0	2	28	4519	4338	831
	002-GS-03-04	350	6000	100	0	0	2	28	3747		
	002-GS-03-05	350	6000	100	0	0	2	28	4782		
	002-GS-07-03	350	6000	100	0	0	2	28	4989		
	002-GS-07-04	350	6000	100	0	0	2	28	5049		
	002-GS-07-05	350	6000	100	0	0	2	28	2943		
	002-HS-01-03	350	6000	100	0	0	2	28	3365	3520	882
	002-HS-01-04	350	6000	100	0	0	2	28	2725		
	002-HS-01-05	350	6000	100	0	0	2	28	4470		
	002-HS-05-03	350	6000	100	0	0	2	28	3205	3489	360
	002-HS-05-04	350	6000	100	0	0	2	28	3893		
	002-HS-05-05	350	6000	100	0	0	2	28	3368		
003	003-GS-07-03	350	6000	100	0	0	2	14	5132	4448	1241

Batch #	Core #	T (°F)	P (psi)	CH_4 (%)	CO_2 (%)	H_2S (ppm)	Brine (%)	Days Aged	Comp. Strength (psi)	Ave. Comp. Strength (psi)	Stdev (psi)
	003-GS-07-04	350	6000	100	0	0	2	14	5197		
	003-GS-07-05	350	6000	100	0	0	2	14	3015		
	003-HS-05-03	350	6000	100	0	0	2	14	2031		
	003-HS-05-04	350	6000	100	0	0	2	14	2904	2398	453
	003-HS-05-05	350	6000	100	0	0	2	14	2260		
004	004-GS-00-03	70	0	0	0	0	2	0	3448		
	004-GS-00-04	70	0	0	0	0	2	0	3498	3503	58
	004-GS-00-05	70	0	0	0	0	2	0	3564		
	004-HS-00-03	70	0	0	0	0	2	0	3431		
	004-HS-00-04	70	0	0	0	0	2	0	3318	3345	76
	004-HS-00-05	70	0	0	0	0	2	0	3288		
	004-GS-03-03	350	6000	90	10	0	2	6	3279		
	004-GS-03-04	350	6000	90	10	0	2	6	4181		
	004-GS-03-05	350	6000	90	10	0	2	6	3161		
	004-GS-07-03	350	6000	90	10	0	2	6	4070	3749	442
	004-GS-07-04	350	6000	90	10	0	2	6	4095		
	004-GS-07-05	350	6000	90	10	0	2	6	3706		
	004-HS-01-03	350	6000	90	10	0	2	6	8760		
	004-HS-01-04	350	6000	90	10	0	2	6	9095		
	004-HS-01-05	350	6000	90	10	0	2	6	9095		
	004-HS-05-03	350	6000	90	10	0	2	6	6208	7886	1260
	004-HS-05-04	350	6000	90	10	0	2	6	6819		
	004-HS-05-05	350	6000	90	10	0	2	6	7337		
005	005-GS-00-03	70	0	0	0	0	2	0	4388		
	005-GS-00-04	70	0	0	0	0	2	0	3495	3767	539
	005-GS-00-05	70	0	0	0	0	2	0	3418		
	005-HS-00-03	70	0	0	0	0	2	0	4399		
	005-HS-00-04	70	0	0	0	0	2	0	3974	4092	269
	005-HS-00-05	70	0	0	0	0	2	0	3902		
	005-GS-03-03	350	6000	90	10	0	2	28	2432		
	005-GS-03-04	350	6000	90	10	0	2	28	2616		
	005-GS-03-05	350	6000	90	10	0	2	28	2705		
	005-GS-07-03	350	6000	90	10	0	2	28	1281	1976	674
	005-GS-07-04	350	6000	90	10	0	2	28	1392		
	005-GS-07-05	350	6000	90	10	0	2	28	1428		
	005-HS-01-03	350	6000	90	10	0	2	28	5173		
	005-HS-01-04	350	6000	90	10	0	2	28	3449		
	005-HS-01-05	350	6000	90	10	0	2	28	4628	4903	1373
	005-HS-05-03	350	6000	90	10	0	2	28	4315		
	005-HS-05-04	350	6000	90	10	0	2	28	4394		

Batch #	Core #	T (°F)	P (psi)	CH_4 (%)	CO_2 (%)	H_2S (ppm)	Brine (%)	Days Aged	Comp. Strength (psi)	Ave. Comp. Strength (psi)	Stdev (psi)
	005-HS-05-05	350	6000	90	10	0	2	28	7463		
006	006-GS-00-03	70	0	0	0	0	2	0	4996	4996	
	006-HS-00-03	70	0	0	0	0	2	0	3954	3954	
	006-GS-04-03	350	6000	90	10	0	2	14	3272	3166	94
	006-GS-04-04	350	6000	90	10	0	2	14	3136		
	006-GS-04-05	350	6000	90	10	0	2	14	3090		
	006-HS-09-03	350	6000	90	10	0	2	14	3312	6624	2872
	006-HS-09-04	350	6000	90	10	0	2	14	8429		
	006-HS-09-05	350	6000	90	10	0	2	14	8131		
007	007-GS-00-03	70	0	0	0	0	2	0	4839	4922	518
	007-GS-00-04	70	0	0	0	0	2	0	5477		
	007-GS-00-05	70	0	0	0	0	2	0	4450		
	007-HS-00-03	70	0	0	0	0	2	0	4942	5589	583
	007-HS-00-04	70	0	0	0	0	2	0	6074		
	007-HS-00-05	70	0	0	0	0	2	0	5752		
	007-GS-05-03	225	6000	90	10	0	2	14	4799	4403	537
	007-GS-05-04	225	6000	90	10	0	2	14	4385		
	007-GS-05-05	225	6000	90	10	0	2	14	3618		
	007-GS-07-03	225	6000	90	10	0	2	14	4587		
	007-GS-07-04	225	6000	90	10	0	2	14	3962		
	007-GS-07-05	225	6000	90	10	0	2	14	5068		
	007-HS-04-03	225	6000	90	10	0	2	14	7944	9274	1090
	007-HS-04-04	225	6000	90	10	0	2	14	10653		
	007-HS-04-05	225	6000	90	10	0	2	14	8164		
	007-HS-06-03	225	6000	90	10	0	2	14	9456		
	007-HS-06-04	225	6000	90	10	0	2	14	9158		
	007-HS-06-05	225	6000	90	10	0	2	14	10269		
008	008-GS-00-03	70	0	0	0	0	2	0	4467	4371	181
	008-GS-00-04	70	0	0	0	0	2	0	4483		
	008-GS-00-05	70	0	0	0	0	2	0	4162		
	008-HS-00-03	70	0	0	0	0	2	0	5188	5113	897
	008-HS-00-04	70	0	0	0	0	2	0	5970		
	008-HS-00-05	70	0	0	0	0	2	0	4181		
	008-GS-05-03	100	6000	90	10	0	2	14	4495	5064	482
	008-GS-05-04	100	6000	90	10	0	2	14	5279		
	008-GS-05-05	100	6000	90	10	0	2	14	5103		
	008-GS-07-03	100	6000	90	10	0	2	14	5253		
	008-GS-07-04	100	6000	90	10	0	2	14	4516		
	008-GS-07-05	100	6000	90	10	0	2	14	5739		
	008-HS-04-02	100	6000	90	10	0	2	14	5061	5149	247

Batch #	Core #	T (°F)	P (psi)	CH_4 (%)	CO_2 (%)	H_2S (ppm)	Brine (%)	Days Aged	Comp. Strength (psi)	Ave. Comp. Strength (psi)	Stdev (psi)
	008-HS-04-03	100	6000	90	10	0	2	14	5080		
	008-HS-04-04	100	6000	90	10	0	2	14	4813		
	008-HS-06-03	100	6000	90	10	0	2	14	5057		
	008-HS-06-04	100	6000	90	10	0	2	14	5430		
	008-HS-06-05	100	6000	90	10	0	2	14	5453		
009	009-GS-00-03	70	0	0	0	0	2	0	3480	3611	483
	009-GS-00-04	70	0	0	0	0	2	0	4145		
	009-GS-00-05	70	0	0	0	0	2	0	3207		
	009-HS-00-03	70	0	0	0	0	2	0	2763	3707	940
	009-HS-00-04	70	0	0	0	0	2	0	4642		
	009-HS-00-05	70	0	0	0	0	2	0	3714		
	009-GS-05-03	225	6000	60	40	0	2	14	4088	4980	808
	009-GS-05-04	225	6000	60	40	0	2	14	5413		
	009-GS-05-05	225	6000	60	40	0	2	14	5142		
	009-GS-07-03	225	6000	60	40	0	2	14	3928		
	009-GS-07-04	225	6000	60	40	0	2	14	6002		
	009-GS-07-05	225	6000	60	40	0	2	14	5306		
	009-HS-04-03	225	6000	60	40	0	2	14	7966	7647	1574
	009-HS-04-04	225	6000	60	40	0	2	14	7504		
	009-HS-04-05	225	6000	60	40	0	2	14	8972		
	009-HS-06-03	225	6000	60	40	0	2	14	7340		
	009-HS-06-04	225	6000	60	40	0	2	14	9250		
	009-HS-06-05	225	6000	60	40	0	2	14	4847		
010	010-GS-00-03	70	0	0	0	0	2	0	3646	4009	573
	010-GS-00-04	70	0	0	0	0	2	0	4670		
	010-GS-00-05	70	0	0	0	0	2	0	3712		
	010-HS-00-03	70	0	0	0	0	2	0	3340	3314	68
	010-HS-00-04	70	0	0	0	0	2	0	3237		
	010-HS-00-05	70	0	0	0	0	2	0	3365		
	010-GS-05-03	225	6000	0	100	0	2	14	4828	5718	768
	010-GS-05-04	225	6000	0	100	0	2	14	6495		
	010-GS-05-05	225	6000	0	100	0	2	14	4731		
	010-GS-07-03	225	6000	0	100	0	2	14	6118		
	010-GS-07-04	225	6000	0	100	0	2	14	5773		
	010-GS-07-05	225	6000	0	100	0	2	14	6364		
	010-HS-04-03	225	6000	0	100	0	2	14	6607	6597	1375
	010-HS-04-04	225	6000	0	100	0	2	14	7316		
	010-HS-04-05	225	6000	0	100	0	2	14	4079		
	010-HS-06-03	225	6000	0	100	0	2	14	7642		
	010-HS-06-04	225	6000	0	100	0	2	14	7753		

Batch #	Core #	T (°F)	P (psi)	CH_4 (%)	CO_2 (%)	H_2S (ppm)	Brine (%)	Days Aged	Comp. Strength (psi)	Ave. Comp. Strength (psi)	Stdev (psi)
	010-HS-06-05	225	6000	0	100	0	2	14	6185		
011	011-GS-00-03	70	0	0	0	0	2	0	4743	4240	447
	011-GS-00-04	70	0	0	0	0	2	0	4089		
	011-GS-00-05	70	0	0	0	0	2	0	3889		
	011-HS-00-03	70	0	0	0	0	2	0	5825	5408	380
	011-HS-00-04	70	0	0	0	0	2	0	5318		
	011-HS-00-05	70	0	0	0	0	2	0	5080		
	011-GS-05-03	100	6000	60	40	0	2	14	5026	5121	531
	011-GS-05-04	100	6000	60	40	0	2	14	5262		
	011-GS-05-05	100	6000	60	40	0	2	14	5389		
	011-GS-07-03	100	6000	60	40	0	2	14	5099		
	011-GS-07-04	100	6000	60	40	0	2	14	5768		
	011-GS-07-05	100	6000	60	40	0	2	14	4178		
	011-HS-04-03	100	6000	60	40	0	2	14	4489	5127	691
	011-HS-04-04	100	6000	60	40	0	2	14	5500		
	011-HS-04-05	100	6000	60	40	0	2	14	5957		
	011-HS-06-03	100	6000	60	40	0	2	14	4324		
	011-HS-06-04	100	6000	60	40	0	2	14	4757		
	011-HS-06-05	100	6000	60	40	0	2	14	5732		
012	012-GS-00-03	70	0	0	0	0	2	0	3703	4074	513
	012-GS-00-04	70	0	0	0	0	2	0	4659		
	012-GS-00-05	70	0	0	0	0	2	0	3860		
	012-HS-00-03	70	0	0	0	0	2	0	4864	4495	455
	012-HS-00-04	70	0	0	0	0	2	0	3987		
	012-HS-00-05	70	0	0	0	0	2	0	4634		
	012-GS-05-03	100	6000	0	100	0	2	14	4774	4626	307
	012-GS-05-04	100	6000	0	100	0	2	14	4975		
	012-GS-05-05	100	6000	0	100	0	2	14	4563		
	012-GS-07-03	100	6000	0	100	0	2	14	4504		
	012-GS-07-04	100	6000	0	100	0	2	14	4110		
	012-GS-07-05	100	6000	0	100	0	2	14	4829		
	012-HS-04-03	100	6000	0	100	0	2	14	4352	4699	345
	012-HS-04-04	100	6000	0	100	0	2	14	4779		
	012-HS-04-05	100	6000	0	100	0	2	14	4870		
	012-HS-06-03	100	6000	0	100	0	2	14	4204		
	012-HS-06-04	100	6000	0	100	0	2	14	4892		
	012-HS-06-05	100	6000	0	100	0	2	14	5097		
013	013-GS-00-03	70	0	0	0	0	2	0	3455	3517	55
	013-GS-00-04	70	0	0	0	0	2	0	3536		
	013-GS-00-05	70	0	0	0	0	2	0	3561		

Batch #	Core #	T (°F)	P (psi)	CH_4 (%)	CO_2 (%)	H_2S (ppm)	Brine (%)	Days Aged	Comp. Strength (psi)	Ave. Comp. Strength (psi)	Stdev (psi)
	013-HS-00-03	70	0	0	0	0	2	0	3859		
	013-HS-00-04	70	0	0	0	0	2	0	3905	3927	82
	013-HS-00-05	70	0	0	0	0	2	0	4018		
	013-GS-05-03	350	6000	60	40	0	2	14	2751		
	013-GS-05-04	350	6000	60	40	0	2	14	2817		
	013-GS-05-05	350	6000	60	40	0	2	14	2557	2764	299
	013-GS-07-03	350	6000	60	40	0	2	14	2310		
	013-GS-07-04	350	6000	60	40	0	2	14	3090		
	013-GS-07-05	350	6000	60	40	0	2	14	3062		
	013-HS-04-03	350	6000	60	40	0	2	14	4283		
	013-HS-04-04	350	6000	60	40	0	2	14	6230		
	013-HS-04-05	350	6000	60	40	0	2	14	7125	6179	1282
	013-HS-06-03	350	6000	60	40	0	2	14	7368		
	013-HS-06-04	350	6000	60	40	0	2	14	7099		
	013-HS-06-05	350	6000	60	40	0	2	14	4970		
	014-GS-00-03	70	0	0	0	0	2	0	4718		
	014-GS-00-04	70	0	0	0	0	2	0	3670	4263	538
	014-GS-00-05	70	0	0	0	0	2	0	4402		
	014-HS-00-03	70	0	0	0	0	2	0	4721		
	014-HS-00-04	70	0	0	0	0	2	0	5416	5062	348
	014-HS-00-05	70	0	0	0	0	2	0	5048		
	014-GS-05-03	350	6000	0	100	0	2	14	3346		
	014-GS-05-04	350	6000	0	100	0	2	14	5713		
	014-GS-05-05	350	6000	0	100	0	2	14	3917		
014	014-GS-07-03	350	6000	0	100	0	2	14	6493	4946	1170
	014-GS-07-04	350	6000	0	100	0	2	14	4795		
	014-GS-07-05	350	6000	0	100	0	2	14	5410		
	014-HS-04-03	350	6000	0	100	0	2	14	9880		
	014-HS-04-04	350	6000	0	100	0	2	14	12301		
	014-HS-04-05	350	6000	0	100	0	2	14	9953		
	014-HS-06-03	350	6000	0	100	0	2	14	9265	11187	1665
	014-HS-06-04	350	6000	0	100	0	2	14	12648		
	014-HS-06-05	350	6000	0	100	0	2	14	13073		
	015-GS-00-03	70	0	0	0	0	2	0	3694		
	015-GS-00-04	70	0	0	0	0	2	0	3060	3504	387
	015-GS-00-05	70	0	0	0	0	2	0	3760		
015	015-HS-00-03	70	0	0	0	0	2	0	4500		
	015-HS-00-04	70	0	0	0	0	2	0	3614	3891	527
	015-HS-00-05	70	0	0	0	0	2	0	3561		
	015-GS-05-03	225	6000	60	40	0	2	14	4717	4520	651

Batch #	Core #	T (°F)	P (psi)	CH_4 (%)	CO_2 (%)	H_2S (ppm)	Brine (%)	Days Aged	Comp. Strength (psi)	Ave. Comp. Strength (psi)	Stdev (psi)
	015-GS-05-04	225	6000	60	40	0	2	14	4752		
	015-GS-05-05	225	6000	60	40	0	2	14	3388		
	015-GS-07-03	225	6000	60	40	0	2	14	4149		
	015-GS-07-04	225	6000	60	40	0	2	14	4928		
	015-GS-07-05	225	6000	60	40	0	2	14	5186		
	015-HS-04-03	225	6000	60	40	0	2	14	7625		
	015-HS-04-04	225	6000	60	40	0	2	14	5788		
	015-HS-04-05	225	6000	60	40	0	2	14	4691	5810	1047
	015-HS-06-03	225	6000	60	40	0	2	14	5775		
	015-HS-06-04	225	6000	60	40	0	2	14	4885		
	015-HS-06-05	225	6000	60	40	0	2	14	6096		
	016-GS-00-03	70	0	0	0	0	2	0	4527		
	016-GS-00-04	70	0	0	0	0	2	0	3954	3905	648
	016-GS-00-05	70	0	0	0	0	2	0	3234		
	016-HS-00-03	70	0	0	0	0	2	0	5134		
	016-HS-00-04	70	0	0	0	0	2	0	3989	4047	1059
	016-HS-00-05	70	0	0	0	0	2	0	3019		
	016-GS-05-03	350	3000	60	40	0	2	14	2360		
	016-GS-05-04	350	3000	60	40	0	2	14	2884		
	016-GS-05-05	350	3000	60	40	0	2	14	2817		
016	016-GS-07-03	350	3000	60	40	0	2	14	3669	2869	436
	016-GS-07-04	350	3000	60	40	0	2	14	2655		
	016-GS-07-05	350	3000	60	40	0	2	14	2832		
	016-HS-04-03	350	3000	60	40	0	2	14	5510		
	016-HS-04-04	350	3000	60	40	0	2	14	6591		
	016-HS-04-05	350	3000	60	40	0	2	14	5041		
	016-HS-06-03	350	3000	60	40	0	2	14	5402	6083	1460
	016-HS-06-04	350	3000	60	40	0	2	14	8838		
	016-HS-06-05	350	3000	60	40	0	2	14	5119		
	017-GS-00-03	70	0	0	0	0	2	0	4318		
	017-GS-00-04	70	0	0	0	0	2	0	3914	4092	206
	017-GS-00-05	70	0	0	0	0	2	0	4043		
	017-HS-00-03	70	0	0	0	0	2	0	5707		
	017-HS-00-04	70	0	0	0	0	2	0	4117	4712	867
017	017-HS-00-05	70	0	0	0	0	2	0	4312		
	017-GS-05-03	350	9000	60	40	0	2	14	3431		
	017-GS-05-04	350	9000	60	40	0	2	14	4064		
	017-GS-05-05	350	9000	60	40	0	2	14	4270	3846	715
	017-GS-07-03	350	9000	60	40	0	2	14	2644		
	017-GS-07-04	350	9000	60	40	0	2	14	4681		

Batch #	Core #	T (°F)	P (psi)	CH_4 (%)	CO_2 (%)	H_2S (ppm)	Brine (%)	Days Aged	Comp. Strength (psi)	Ave. Comp. Strength (psi)	Stdev (psi)
	017-GS-07-05	350	9000	60	40	0	2	14	3988		
	017-HS-04-03	350	9000	60	40	0	2	14	4013	5934	1671
	017-HS-04-04	350	9000	60	40	0	2	14	6056		
	017-HS-04-05	350	9000	60	40	0	2	14	7254		
	017-HS-06-03	350	9000	60	40	0	2	14	7470		
	017-HS-06-04	350	9000	60	40	0	2	14	3733		
	017-HS-06-05	350	9000	60	40	0	2	14	7078		
018	018-GS-00-03	70	0	0	0	0	2	0	3584	3680	169
	018-GS-00-04	70	0	0	0	0	2	0	3580		
	018-GS-00-05	70	0	0	0	0	2	0	3875		
	018-HS-00-03	70	0	0	0	0	2	0	3788	3722	250
	018-HS-00-04	70	0	0	0	0	2	0	3933		
	018-HS-00-05	70	0	0	0	0	2	0	3446		
	018-GS-05-03	350	3000	0	100	0	2	14	3520	3563	1243
	018-GS-05-04	350	3000	0	100	0	2	14	2726		
	018-GS-05-05	350	3000	0	100	0	2	14	3212		
	018-GS-07-03	350	3000	0	100	0	2	14	3218		
	018-GS-07-04	350	3000	0	100	0	2	14	2688		
	018-GS-07-05	350	3000	0	100	0	2	14	6016		
	018-HS-04-03	350	3000	0	100	0	2	14	8518	7351	1430
	018-HS-04-04	350	3000	0	100	0	2	14	6834		
	018-HS-04-05	350	3000	0	100	0	2	14	4982		
	018-HS-06-03	350	3000	0	100	0	2	14	7550		
	018-HS-06-04	350	3000	0	100	0	2	14	7168		
	018-HS-06-05	350	3000	0	100	0	2	14	9055		
019	019-GS-00-03	70	0	0	0	0	2	0	3719	4356	552
	019-GS-00-04	70	0	0	0	0	2	0	4639		
	019-GS-00-05	70	0	0	0	0	2	0	4708		
	019-HS-00-03	70	0	0	0	0	2	0	4521	4747	351
	019-HS-00-04	70	0	0	0	0	2	0	5151		
	019-HS-00-05	70	0	0	0	0	2	0	4567		
	019-GS-05-03	350	9000	0	100	0	2	14	4667	4851	233
	019-GS-05-04	350	9000	0	100	0	2	14	5024		
	019-GS-05-05	350	9000	0	100	0	2	14	4852		
	019-GS-07-03	350	9000	0	100	0	2	14	4496		
	019-GS-07-04	350	9000	0	100	0	2	14	4946		
	019-GS-07-05	350	9000	0	100	0	2	14	5119		
	019-HS-04-03	350	9000	0	100	0	2	14	12593	12298	310
	019-HS-04-04	350	9000	0	100	0	2	14	12124		
	019-HS-04-05	350	9000	0	100	0	2	14	11938		

Batch #	Core #	T (°F)	P (psi)	CH_4 (%)	CO_2 (%)	H_2S (ppm)	Brine (%)	Days Aged	Comp. Strength (psi)	Ave. Comp. Strength (psi)	Stdev (psi)
	019-HS-06-03	350	9000	0	100	0	2	14	12008		
	019-HS-06-04	350	9000	0	100	0	2	14	12634		
	019-HS-06-05	350	9000	0	100	0	2	14	12493		
020	020-GS-00-03	70	0	0	0	0	2	0	4169	4058	139
	020-GS-00-04	70	0	0	0	0	2	0	4102		
	020-GS-00-05	70	0	0	0	0	2	0	3902		
	020-HS-00-03	70	0	0	0	0	2	0	4194	4563	324
	020-HS-00-04	70	0	0	0	0	2	0	4694		
	020-HS-00-05	70	0	0	0	0	2	0	4800		
	020-GS-05-03	350	3000	90	10	0	2	14	3073	2892	330
	020-GS-05-04	350	3000	90	10	0	2	14	2773		
	020-GS-05-05	350	3000	90	10	0	2	14	2923		
	020-GS-07-03	350	3000	90	10	0	2	14	2345		
	020-GS-07-04	350	3000	90	10	0	2	14	3336		
	020-GS-07-05	350	3000	90	10	0	2	14	2904		
	020-HS-04-03	350	3000	90	10	0	2	14	6565	6502	188
	020-HS-04-04	350	3000	90	10	0	2	14	6507		
	020-HS-04-05	350	3000	90	10	0	2	14	6471		
	020-HS-06-03	350	3000	90	10	0	2	14	6270		
	020-HS-06-04	350	3000	90	10	0	2	14	6377		
	020-HS-06-05	350	3000	90	10	0	2	14	6821		
021	021-GS-00-03	70	0	0	0	0	2	0	4444	4175	804
	021-GS-00-04	70	0	0	0	0	2	0	3271		
	021-GS-00-05	70	0	0	0	0	2	0	4811		
	021-HS-00-03	70	0	0	0	0	2	0	4704	4539	342
	021-HS-00-04	70	0	0	0	0	2	0	4146		
	021-HS-00-05	70	0	0	0	0	2	0	4767		
	021-GS-05-03	350	9000	90	10	0	2	14	1956	1905	626
	021-GS-05-04	350	9000	90	10	0	2	14	1015		
	021-GS-05-05	350	9000	90	10	0	2	14	2365		
	021-GS-07-03	350	9000	90	10	0	2	14	2772		
	021-GS-07-04	350	9000	90	10	0	2	14	1457		
	021-GS-07-05	350	9000	90	10	0	2	14	1865		
	021-HS-04-03	350	9000	90	10	0	2	14	7400	6074	864
	021-HS-04-04	350	9000	90	10	0	2	14	6137		
	021-HS-04-05	350	9000	90	10	0	2	14	6005		
	021-HS-06-03	350	9000	90	10	0	2	14	6524		
	021-HS-06-04	350	9000	90	10	0	2	14	4873		
	021-HS-06-05	350	9000	90	10	0	2	14	5506		
022	022-GS-00-03	70	0	0	0	0	2	0	3441	4109	836

Batch #	Core #	T (°F)	P (psi)	CH_4 (%)	CO_2 (%)	H_2S (ppm)	Brine (%)	Days Aged	Comp. Strength (psi)	Ave. Comp. Strength (psi)	Stdev (psi)
	022-GS-00-04	70	0	0	0	0	2	0	5047		
	022-GS-00-05	70	0	0	0	0	2	0	3841		
	022-HS-00-03	70	0	0	0	0	2	0	4295		
	022-HS-00-04	70	0	0	0	0	2	0	4718	4406	274
	022-HS-00-05	70	0	0	0	0	2	0	4205		
	022-GS-05-03	225	3000	60	40	0	2	14	5362		
	022-GS-05-04	225	3000	60	40	0	2	14	5278		
	022-GS-05-05	225	3000	60	40	0	2	14	6079	5206	529
	022-GS-07-03	225	3000	60	40	0	2	14	4714		
	022-GS-07-04	225	3000	60	40	0	2	14	4600		
	022-GS-07-05	225	3000	60	40	0	2	14	5205		
	022-HS-04-03	225	3000	60	40	0	2	14	10382		
	022-HS-04-04	225	3000	60	40	0	2	14	6012		
	022-HS-04-05	225	3000	60	40	0	2	14	5774	7755	1839
	022-HS-06-03	225	3000	60	40	0	2	14	8590		
	022-HS-06-04	225	3000	60	40	0	2	14	8962		
	022-HS-06-05	225	3000	60	40	0	2	14	6810		
	023-GS-00-03	70	0	0	0	0	2	0	4503		
	023-GS-00-04	70	0	0	0	0	2	0	3902	3871	647
	023-GS-00-05	70	0	0	0	0	2	0	3209		
	023-HS-00-03	70	0	0	0	0	2	0	4615		
	023-HS-00-04	70	0	0	0	0	2	0	4687	4535	205
	023-HS-00-05	70	0	0	0	0	2	0	4302		
	023-GS-05-03	225	9000	60	40	0	2	14	5885		
	023-GS-05-04	225	9000	60	40	0	2	14	6107		
023	023-GS-05-05	225	9000	60	40	0	2	14	5865	4830	1817
	023-GS-07-03	225	9000	60	40	0	2	14	5662		
	023-GS-07-04	225	9000	60	40	0	2	14	3996		
	023-GS-07-05	225	9000	60	40	0	2	14	1466		
	023-HS-04-03	225	9000	60	40	0	2	14	9318		
	023-HS-04-04	225	9000	60	40	0	2	14	8572		
	023-HS-04-05	225	9000	60	40	0	2	14	7814	8773	567
	023-HS-06-03	225	9000	60	40	0	2	14	8609		
	023-HS-06-04	225	9000	60	40	0	2	14	9261		
	023-HS-06-05	225	9000	60	40	0	2	14	9064		
	024-GS-00-03	70	0	0	0	0	2	0	4447		
	024-GS-00-04	70	0	0	0	0	2	0	4002	4188	231
024	024-GS-00-05	70	0	0	0	0	2	0	4115		
	024-HS-00-03	70	0	0	0	0	2	0	4254	4209	375
	024-HS-00-04	70	0	0	0	0	2	0	4560		

Batch #	Core #	T (°F)	P (psi)	CH_4 (%)	CO_2 (%)	H_2S (ppm)	Brine (%)	Days Aged	Comp. Strength (psi)	Ave. Comp. Strength (psi)	Stdev (psi)
	024-HS-00-05	70	0	0	0	0	2	0	3814		
	024-GS-05-03	225	3000	0	100	0	2	14	5102	5352	361
	024-GS-05-04	225	3000	0	100	0	2	14	4829		
	024-GS-05-05	225	3000	0	100	0	2	14	5730		
	024-GS-07-03	225	3000	0	100	0	2	14	5674		
	024-GS-07-04	225	3000	0	100	0	2	14	5568		
	024-GS-07-05	225	3000	0	100	0	2	14	5206		
	024-HS-04-03	225	3000	0	100	0	2	14	7450	8257	1567
	024-HS-04-04	225	3000	0	100	0	2	14	9830		
	024-HS-04-05	225	3000	0	100	0	2	14	9493		
	024-HS-06-03	225	3000	0	100	0	2	14	5629		
	024-HS-06-04	225	3000	0	100	0	2	14	9082		
	024-HS-06-05	225	3000	0	100	0	2	14	8059		
025	025-GS-00-03	70	0	0	0	0	2	0	4871	4317	608
	025-GS-00-04	70	0	0	0	0	2	0	3666		
	025-GS-00-05	70	0	0	0	0	2	0	4412		
	025-HS-00-03	70	0	0	0	0	2	0	4203	4165	667
	025-HS-00-04	70	0	0	0	0	2	0	3479		
	025-HS-00-05	70	0	0	0	0	2	0	4812		
	025-GS-05-03	225	9000	0	100	0	2	14	7271	6718	750
	025-GS-05-04	225	9000	0	100	0	2	14	6606		
	025-GS-05-05	225	9000	0	100	0	2	14	7425		
	025-GS-07-03	225	9000	0	100	0	2	14	6455		
	025-GS-07-04	225	9000	0	100	0	2	14	5400		
	025-GS-07-05	225	9000	0	100	0	2	14	7151		
	025-HS-04-03	225	9000	0	100	0	2	14	7828	8883	1175
	025-HS-04-04	225	9000	0	100	0	2	14	8343		
	025-HS-04-05	225	9000	0	100	0	2	14	7860		
	025-HS-06-03	225	9000	0	100	0	2	14	10694		
	025-HS-06-04	225	9000	0	100	0	2	14	9936		
	025-HS-06-05	225	9000	0	100	0	2	14	8635		
026	026-GS-00-03	70	0	0	0	0	2	0	3081	3505	383
	026-GS-00-04	70	0	0	0	0	2	0	3826		
	026-GS-00-05	70	0	0	0	0	2	0	3609		
	026-HS-00-03	70	0	0	0	0	2	0	3663	3501	152
	026-HS-00-04	70	0	0	0	0	2	0	3480		
	026-HS-00-05	70	0	0	0	0	2	0	3361		
	026-GS-05-03	225	3000	90	10	0	2	14	4634	4304	444
	026-GS-05-04	225	3000	90	10	0	2	14	4824		
	026-GS-05-05	225	3000	90	10	0	2	14	3600		

Batch #	Core #	T (°F)	P (psi)	CH_4 (%)	CO_2 (%)	H_2S (ppm)	Brine (%)	Days Aged	Comp. Strength (psi)	Ave. Comp. Strength (psi)	Stdev (psi)
	026-GS-07-03	225	3000	90	10	0	2	14	4036		
	026-GS-07-04	225	3000	90	10	0	2	14	4488		
	026-GS-07-05	225	3000	90	10	0	2	14	4240		
	026-HS-04-03	225	3000	90	10	0	2	14	5374		
	026-HS-04-04	225	3000	90	10	0	2	14	5822		
	026-HS-04-05	225	3000	90	10	0	2	14	6804	5803	685
	026-HS-06-03	225	3000	90	10	0	2	14	6257		
	026-HS-06-04	225	3000	90	10	0	2	14	5732		
	026-HS-06-05	225	3000	90	10	0	2	14	4829		
	027-GS-00-03	70	0	0	0	0	2	0	2919		
	027-GS-00-04	70	0	0	0	0	2	0	4671	3613	931
	027-GS-00-05	70	0	0	0	0	2	0	3250		
	027-HS-00-03	70	0	0	0	0	2	0	4584		
	027-HS-00-04	70	0	0	0	0	2	0	3796	3459	1327
	027-HS-00-05	70	0	0	0	0	2	0	1996		
	027-GS-05-03	225	9000	90	10	0	2	14	3699		
	027-GS-05-04	225	9000	90	10	0	2	14	4198		
	027-GS-05-05	225	9000	90	10	0	2	14	3710		
027	027-GS-07-03	225	9000	90	10	0	2	14	4093	4075	335
	027-GS-07-04	225	9000	90	10	0	2	14	4587		
	027-GS-07-05	225	9000	90	10	0	2	14	4166		
	027-HS-04-03	225	9000	90	10	0	2	14	5684		
	027-HS-04-04	225	9000	90	10	0	2	14	7099		
	027-HS-04-05	225	9000	90	10	0	2	14	7308		
	027-HS-06-03	225	9000	90	10	0	2	14	9371	7056	1823
	027-HS-06-04	225	9000	90	10	0	2	14	4370		
	027-HS-06-05	225	9000	90	10	0	2	14	8506		
	028-GS-00-03	70	0	0	0	0	2	0	2448		
	028-GS-00-04	70	0	0	0	0	2	0	2827	2832	387
	028-GS-00-05	70	0	0	0	0	2	0	3221		
	028-HS-00-03	70	0	0	0	0	2	0	3321		
	028-HS-00-04	70	0	0	0	0	2	0	3940	3604	312
	028-HS-00-05	70	0	0	0	0	2	0	3551		
028	028-GS-05-03	430	6000	90	10	0	2	14	3511		
	028-GS-05-04	430	6000	90	10	0	2	14	5045		
	028-GS-05-05	430	6000	90	10	0	2	14	4878		
	028-GS-07-03	430	6000	90	10	0	2	14	4529	4320	595
	028-GS-07-04	430	6000	90	10	0	2	14	3927		
	028-GS-07-05	430	6000	90	10	0	2	14	4031		
	028-HS-04-03	430	6000	90	10	0	2	14	5039	5167	856

Batch #	Core #	T (°F)	P (psi)	CH_4 (%)	CO_2 (%)	H_2S (ppm)	Brine (%)	Days Aged	Comp. Strength (psi)	Ave. Comp. Strength (psi)	Stdev (psi)
	028-HS-04-04	430	6000	90	10	0	2	14	3664		
	028-HS-04-05	430	6000	90	10	0	2	14	5359		
	028-HS-06-03	430	6000	90	10	0	2	14	5087		
	028-HS-06-04	430	6000	90	10	0	2	14	6236		
	028-HS-06-05	430	6000	90	10	0	2	14	5618		
029	029-GS-00-03	70	0	0	0	0	2	0	2560	2637	664
	029-GS-00-04	70	0	0	0	0	2	0	2016		
	029-GS-00-05	70	0	0	0	0	2	0	3337		
	029-HS-00-03	70	0	0	0	0	2	0	3652	3785	658
	029-HS-00-04	70	0	0	0	0	2	0	3204		
	029-HS-00-05	70	0	0	0	0	2	0	4500		
	029-GS-05-03	430	6000	60	40	0	2	14	4496	4454	376
	029-GS-05-04	430	6000	60	40	0	2	14	3982		
	029-GS-05-05	430	6000	60	40	0	2	14	4128		
	029-GS-07-03	430	6000	60	40	0	2	14	4537		
	029-GS-07-04	430	6000	60	40	0	2	14	5056		
	029-GS-07-05	430	6000	60	40	0	2	14	4528		
	029-HS-04-03	430	6000	60	40	0	2	14	5036	4687	2521
	029-HS-04-04	430	6000	60	40	0	2	14	5088		
	029-HS-04-05	430	6000	60	40	0	2	14	4292		
	029-HS-06-03	430	6000	60	40	0	2	14	6853		
	029-HS-06-04	430	6000	60	40	0	2	14	6851		
	029-HS-06-05	430	6000	60	40	0	2	14	0		
030	030-GS-00-03	70	0	0	0	0	2	0	3937	3555	346
	030-GS-00-04	70	0	0	0	0	2	0	3463		
	030-GS-00-05	70	0	0	0	0	2	0	3263		
	030-HS-00-03	70	0	0	0	0	2	0	3960	3521	1002
	030-HS-00-04	70	0	0	0	0	2	0	2374		
	030-HS-00-05	70	0	0	0	0	2	0	4229		
	030-GS-05-03	430	6000	0	100	0	2	14	4555	3624	953
	030-GS-05-04	430	6000	0	100	0	2	14	4132		
	030-GS-05-05	430	6000	0	100	0	2	14	4327		
	030-GS-07-03	430	6000	0	100	0	2	14	3865		
	030-GS-07-04	430	6000	0	100	0	2	14	2311		
	030-GS-07-05	430	6000	0	100	0	2	14	2555		
	030-HS-04-03	430	6000	0	100	0	2	14	4041	4756	2456
	030-HS-04-04	430	6000	0	100	0	2	14	3647		
	030-HS-04-05	430	6000	0	100	0	2	14	1316		
	030-HS-06-03	430	6000	0	100	0	2	14	4352		
	030-HS-06-04	430	6000	0	100	0	2	14	8013		

Batch #	Core #	T (°F)	P (psi)	CH_4 (%)	CO_2 (%)	H_2S (ppm)	Brine (%)	Days Aged	Comp. Strength (psi)	Ave. Comp. Strength (psi)	Stdev (psi)
	030-HS-06-05	430	6000	0	100	0	2	14	7165		
031	031-GS-00-03	70	0	0	0	0	2	0	3459	2601	1335
	031-GS-00-04	70	0	0	0	0	2	0	3282		
	031-GS-00-05	70	0	0	0	0	2	0	1062		
	031-HS-00-03	70	0	0	0	0	2	0	2867	2627	212
	031-HS-00-04	70	0	0	0	0	2	0	2465		
	031-HS-00-05	70	0	0	0	0	2	0	2548		
	031-GS-05-03	430	3000	0	100	0	2	14	3652	4062	958
	031-GS-05-04	430	3000	0	100	0	2	14	5332		
	031-GS-05-05	430	3000	0	100	0	2	14	3924		
	031-GS-07-03	430	3000	0	100	0	2	14	5058		
	031-GS-07-04	430	3000	0	100	0	2	14	3602		
	031-GS-07-05	430	3000	0	100	0	2	14	2804		
	031-HS-04-03	430	3000	0	100	0	2	14	6533	4735	924
	031-HS-04-04	430	3000	0	100	0	2	14	4727		
	031-HS-04-05	430	3000	0	100	0	2	14	4559		
	031-HS-06-03	430	3000	0	100	0	2	14	3899		
	031-HS-06-04	430	3000	0	100	0	2	14	4334		
	031-HS-06-05	430	3000	0	100	0	2	14	4354		
032	032-GS-00-01	70	0	0	0	0	2	0	4169	3069	966
	032-GS-00-03	70	0	0	0	0	2	0	3353		
	032-GS-00-04	70	0	0	0	0	2	0	2900		
	032-GS-00-05	70	0	0	0	0	2	0	1853		
	032-HS-00-03	70	0	0	0	0	2	0	2819	2355	475
	032-HS-00-04	70	0	0	0	0	2	0	1870		
	032-HS-00-05	70	0	0	0	0	2	0	2376		
	032-GS-05-03	430	9000	0	100	0	2	14	7237	6961	819
	032-GS-05-04	430	9000	0	100	0	2	14	6435		
	032-GS-05-05	430	9000	0	100	0	2	14	7954		
	032-GS-07-03	430	9000	0	100	0	2	14	5612		
	032-GS-07-04	430	9000	0	100	0	2	14	7181		
	032-GS-07-05	430	9000	0	100	0	2	14	7345		
	032-HS-04-03	430	9000	0	100	0	2	14	9036	8086	1212
	032-HS-04-04	430	9000	0	100	0	2	14	8928		
	032-HS-04-05	430	9000	0	100	0	2	14	8858		
	032-HS-06-03	430	9000	0	100	0	2	14	5990		
	032-HS-06-04	430	9000	0	100	0	2	14	8419		
	032-HS-06-05	430	9000	0	100	0	2	14	7287		
033	033-GS-00-03	70	0	0	0	0	2	0	2834	3235	722
	033-GS-00-04	70	0	0	0	0	2	0	4069		

Batch #	Core #	T (°F)	P (psi)	CH_4 (%)	CO_2 (%)	H_2S (ppm)	Brine (%)	Days Aged	Comp. Strength (psi)	Ave. Comp. Strength (psi)	Stdev (psi)
	033-GS-00-05	70	0	0	0	0	2	0	2802		
	033-HS-00-03	70	0	0	0	0	2	0	3972	3784	431
	033-HS-00-04	70	0	0	0	0	2	0	4089		
	033-HS-00-05	70	0	0	0	0	2	0	3291		
	033-GS-05-03	100	6000	90	10	300	2	14	4536	4110	483
	033-GS-05-04	100	6000	90	10	300	2	14	3646		
	033-GS-05-05	100	6000	90	10	300	2	14	4108		
	033-GS-07-03	100	6000	90	10	300	2	14	4735		
	033-GS-07-04	100	6000	90	10	300	2	14	4139		
	033-GS-07-05	100	6000	90	10	300	2	14	3497		
	033-HS-04-03	100	6000	90	10	300	2	14	3320	3566	367
	033-HS-04-04	100	6000	90	10	300	2	14	4055		
	033-HS-04-05	100	6000	90	10	300	2	14	3320		
	033-HS-06-03	100	6000	90	10	300	2	14	4022		
	033-HS-06-04	100	6000	90	10	300	2	14	3360		
	033-HS-06-05	100	6000	90	10	300	2	14	3318		
034	034-GS-00-03	70	0	0	0	0	2	0	1288	2572	1136
	034-GS-00-04	70	0	0	0	0	2	0	2981		
	034-GS-00-05	70	0	0	0	0	2	0	3447		
	034-HS-00-03	70	0	0	0	0	2	0	2172	3018	991
	034-HS-00-04	70	0	0	0	0	2	0	4109		
	034-HS-00-05	70	0	0	0	0	2	0	2774		
	034-GS-05-03	225	6000	90	10	300	2	14	2437	3330	760
	034-GS-05-04	225	6000	90	10	300	2	14	4063		
	034-GS-05-05	225	6000	90	10	300	2	14	2920		
	034-GS-07-03	225	6000	90	10	300	2	14	3999		
	034-GS-07-04	225	6000	90	10	300	2	14	3965		
	034-GS-07-05	225	6000	90	10	300	2	14	2598		
	034-HS-04-03	225	6000	90	10	300	2	14	3880	5930	1619
	034-HS-04-04	225	6000	90	10	300	2	14	5768		
	034-HS-04-05	225	6000	90	10	300	2	14	6591		
	034-HS-06-03	225	6000	90	10	300	2	14	8124		
	034-HS-06-04	225	6000	90	10	300	2	14	4299		
	034-HS-06-05	225	6000	90	10	300	2	14	6915		
035	035-GS-00-03	70	0	0	0	0	2	0	3328	3158	884
	035-GS-00-04	70	0	0	0	0	2	0	3945		
	035-GS-00-05	70	0	0	0	0	2	0	2202		
	035-HS-00-03	70	0	0	0	0	2	0	3304	3245	890
	035-HS-00-04	70	0	0	0	0	2	0	4103		
	035-HS-00-05	70	0	0	0	0	2	0	2327		

Batch #	Core #	T (°F)	P (psi)	CH_4 (%)	CO_2 (%)	H_2S (ppm)	Brine (%)	Days Aged	Comp. Strength (psi)	Ave. Comp. Strength (psi)	Stdev (psi)
	035-GS-05-03	350	6000	90	10	300	2	14	2042	2340	456
	035-GS-05-04	350	6000	90	10	300	2	14	2409		
	035-GS-05-05	350	6000	90	10	300	2	14	2910		
	035-GS-07-03	350	6000	90	10	300	2	14	2575		
	035-GS-07-04	350	6000	90	10	300	2	14	1604		
	035-GS-07-05	350	6000	90	10	300	2	14	2499		
	035-HS-04-03	350	6000	90	10	300	2	14	6583	4926	1252
	035-HS-04-04	350	6000	90	10	300	2	14	3928		
	035-HS-04-05	350	6000	90	10	300	2	14	5123		
	035-HS-06-03	350	6000	90	10	300	2	14	6234		
	035-HS-06-04	350	6000	90	10	300	2	14	3781		
	035-HS-06-05	350	6000	90	10	300	2	14	3910		
036	036-GS-00-03	70	0	0	0	0	2	0	2571	2661	78
	036-GS-00-04	70	0	0	0	0	2	0	2698		
	036-GS-00-05	70	0	0	0	0	2	0	2713		
	036-HS-00-03	70	0	0	0	0	2	0	3531	3339	252
	036-HS-00-04	70	0	0	0	0	2	0	3054		
	036-HS-00-05	70	0	0	0	0	2	0	3433		
	036-GS-05-03	100	6000	100	0	300	2	14	2780	2723	446
	036-GS-05-04	100	6000	100	0	300	2	14	2767		
	036-GS-05-05	100	6000	100	0	300	2	14	2275		
	036-GS-07-03	100	6000	100	0	300	2	14	2692		
	036-GS-07-04	100	6000	100	0	300	2	14	3511		
	036-GS-07-05	100	6000	100	0	300	2	14	2316		
	036-HS-04-03	100	6000	100	0	300	2	14	2494	3104	984
	036-HS-04-04	100	6000	100	0	300	2	14	1644		
	036-HS-04-05	100	6000	100	0	300	2	14	4156		
	036-HS-06-03	100	6000	100	0	300	2	14	3123		
	036-HS-06-04	100	6000	100	0	300	2	14	4208		
	036-HS-06-05	100	6000	100	0	300	2	14	2999		
037	037-GS-00-03	70	0	0	0	0	2	0	2340	2675	323
	037-GS-00-04	70	0	0	0	0	2	0	2985		
	037-GS-00-05	70	0	0	0	0	2	0	2699		
	037-HS-00-03	70	0	0	0	0	2	0	3782	3047	637
	037-HS-00-04	70	0	0	0	0	2	0	2641		
	037-HS-00-05	70	0	0	0	0	2	0	2718		
	037-GS-05-03	100	6000	60	40	180	2	14	2974	2851	338
	037-GS-05-04	100	6000	60	40	180	2	14	3271		
	037-GS-05-05	100	6000	60	40	180	2	14	2615		
	037-GS-07-03	100	6000	60	40	180	2	14	3185		

Batch #	Core #	T (°F)	P (psi)	CH_4 (%)	CO_2 (%)	H_2S (ppm)	Brine (%)	Days Aged	Comp. Strength (psi)	Ave. Comp. Strength (psi)	Stdev (psi)
	037-GS-07-04	100	6000	60	40	180	2	14	2476		
	037-GS-07-05	100	6000	60	40	180	2	14	2586		
	037-HS-04-03	100	6000	60	40	180	2	14	3885		
	037-HS-04-04	100	6000	60	40	180	2	14	2496		
	037-HS-04-05	100	6000	60	40	180	2	14	3274	3048	667
	037-HS-06-03	100	6000	60	40	180	2	14	3710		
	037-HS-06-04	100	6000	60	40	180	2	14	2600		
	037-HS-06-05	100	6000	60	40	180	2	14	2321		
	038-GS-00-03	70	0	0	0	0	2	0	4190		
	038-GS-00-04	70	0	0	0	0	2	0	3929	3725	593
	038-GS-00-05	70	0	0	0	0	2	0	3058		
	038-HS-00-03	70	0	0	0	0	2	0	3053		
	038-HS-00-04	70	0	0	0	0	2	0	2464	3038	567
	038-HS-00-05	70	0	0	0	0	2	0	3597		
	038-GS-05-01	100	9000	100	0	300	2	14	4168		
	038-GS-05-02	100	9000	100	0	300	2	14	2834		
	038-GS-05-03	100	9000	100	0	300	2	14	3329		
	038-GS-05-04	100	9000	100	0	300	2	14	2987		
	038-GS-05-05	100	9000	100	0	300	2	14	3780	3375	629
	038-GS-07-01	100	9000	100	0	300	2	14	4443		
038	038-GS-07-02	100	9000	100	0	300	2	14	2297		
	038-GS-07-03	100	9000	100	0	300	2	14	3368		
	038-GS-07-04	100	9000	100	0	300	2	14	3316		
	038-GS-07-05	100	9000	100	0	300	2	14	3229		
	038-HS-04-01	100	9000	100	0	300	2	14	2661		
	038-HS-04-02	100	9000	100	0	300	2	14	4447		
	038-HS-04-03	100	9000	100	0	300	2	14	2898		
	038-HS-04-04	100	9000	100	0	300	2	14	2810		
	038-HS-04-05	100	9000	100	0	300	2	14	2192	3115	611
	038-HS-06-01	100	9000	100	0	300	2	14	3540		
	038-HS-06-02	100	9000	100	0	300	2	14	3516		
	038-HS-06-03	100	9000	100	0	300	2	14	3134		
	038-HS-06-04	100	9000	100	0	300	2	14	3054		
	038-HS-06-05	100	9000	100	0	300	2	14	2896		
	039-GS-00-03	70	0	0	0	0	2	0	3269		
	039-GS-00-04	70	0	0	0	0	2	0	2124	2981	756
	039-GS-00-05	70	0	0	0	0	2	0	3551		
039	039-HS-00-03	70	0	0	0	0	2	0	6293		
	039-HS-00-04	70	0	0	0	0	2	0	4618	6090	1381
	039-HS-00-05	70	0	0	0	0	2	0	7358		
	039-GS-05-03	100	9000	90	10	300	2	14	3578	3810	786

Batch #	Core #	T (°F)	P (psi)	CH_4 (%)	CO_2 (%)	H_2S (ppm)	Brine (%)	Days Aged	Comp. Strength (psi)	Ave. Comp. Strength (psi)	Stdev (psi)
	039-GS-05-04	100	9000	90	10	300	2	14	3044		
	039-GS-05-05	100	9000	90	10	300	2	14	5287		
	039-GS-07-03	100	9000	90	10	300	2	14	3322		
	039-GS-07-04	100	9000	90	10	300	2	14	3928		
	039-GS-07-05	100	9000	90	10	300	2	14	3700		
	039-HS-04-03	100	9000	90	10	300	2	14	6360		
	039-HS-04-04	100	9000	90	10	300	2	14	5364		
	039-HS-04-05	100	9000	90	10	300	2	14	6541	5875	720
	039-HS-06-03	100	9000	90	10	300	2	14	4755		
	039-HS-06-04	100	9000	90	10	300	2	14	5738		
	039-HS-06-05	100	9000	90	10	300	2	14	6493		
	040-GS-00-03	70	0	0	0	0	2	0	4311		
	040-GS-00-04	70	0	0	0	0	2	0	188	2766	2248
	040-GS-00-05	70	0	0	0	0	2	0	3800		
	040-HS-00-03	70	0	0	0	0	2	0	1461		
	040-HS-00-04	70	0	0	0	0	2	0	4829	3353	1722
	040-HS-00-05	70	0	0	0	0	2	0	3769		
	040-GS-05-03	100	9000	60	40	180	2	14	3019		
	040-GS-05-04	100	9000	60	40	180	2	14	3218		
	040-GS-05-05	100	9000	60	40	180	2	14	2096		
040	040-GS-07-03	100	9000	60	40	180	2	14	4142	3054	782
	040-GS-07-04	100	9000	60	40	180	2	14	3593		
	040-GS-07-05	100	9000	60	40	180	2	14	2254		
	040-HS-04-03	100	9000	0	40	180	2	14	5305		
	040-HS-04-04	100	9000	0	40	180	2	14	4809		
	040-HS-04-05	100	9000	0	40	180	2	14	2135	4315	1131
	040-HS-06-03	100	9000	0	40	180	2	14	4258		
	040-HS-06-04	100	9000	0	40	180	2	14	4436		
	040-HS-06-05	100	9000	0	40	180	2	14	4945		
	041-GS-00-03	70	0	0	0	0	2	0	3976		
	041-GS-00-04	70	0	0	0	0	2	0	3971	3594	658
	041-GS-00-05	70	0	0	0	0	2	0	2834		
	041-HS-00-03	70	0	0	0	0	2	0	2175		
	041-HS-00-04	70	0	0	0	0	2	0	4885	3041	1598
	041-HS-00-05	70	0	0	0	0	2	0	2063		
041	041-GS-05-03	100	3000	100	0	300	2	14	4863		
	041-GS-05-04	100	3000	100	0	300	2	14	4777		
	041-GS-05-05	100	3000	100	0	300	2	14	3687		
	041-GS-07-03	100	3000	100	0	300	2	14	3998	4158	523
	041-GS-07-04	100	3000	100	0	300	2	14	3797		
	041-GS-07-05	100	3000	100	0	300	2	14	3828		

Batch #	Core #	T (°F)	P (psi)	CH_4 (%)	CO_2 (%)	H_2S (ppm)	Brine (%)	Days Aged	Comp. Strength (psi)	Ave. Comp. Strength (psi)	Stdev (psi)
	041-HS-04-03	100	3000	100	0	300	2	14	1553	2256	477
	041-HS-04-04	100	3000	100	0	300	2	14	2802		
	041-HS-04-05	100	3000	100	0	300	2	14	2503		
	041-HS-06-03	100	3000	100	0	300	2	14	1886		
	041-HS-06-04	100	3000	100	0	300	2	14	2166		
	041-HS-06-05	100	3000	100	0	300	2	14	2627		

APPENDIX D: SOLUBILITY MODEL

Duan and Sun (2003) developed an accurate model for CO_2 solubility prediction in pure water and brine solutions. This model is applicable for temperatures ranging from 32 to 500°F, for pressures ranging from 0 to 30,000 psi, and for ionic strength from 0 to 4.3M. They calculated the CO_2 solubility in aqueous phase, maintaining the balance between its chemical potential in the liquid phase and that in the gas phase. The potential can be written in terms of fugacity in the vapor phase and activity in the liquid phase. They proposed the following model (Eq. D-1) for predicting the solubility of CO_2 in pure water and brine solutions.

$$\ln\frac{y_{CO_2}P}{m_{CO_2}} = \frac{\mu^{1(0)}_{CO_2}}{RT} + \ln\varphi_{CO_2} + \sum_c 2\lambda_{CO_2-c}m_c + \sum_a 2\lambda_{CO_2-a}m_a + \sum_c\sum_a \xi_{CO_2-c-a}m_c\, m_a \quad \text{(D-1)}$$

where y_{CO_2} is concentration of CO_2 in the gas phase, which is calculated as:

$$y_{CO_2} = \frac{P - P_{H_2O}}{P} \quad \text{(D-2)}$$

P is pressure in bar and m_{CO_2} is CO_2 solubility in mole/kg. The term $\frac{\mu^{1(0)}_{CO_2}}{RT}$, ξ and λ are dimensionless parameters, Par(T,P), determined using Eq. (D-3) and **Table D.1**.

$$Par(T,P) = C_1 + C_2T + \frac{C_3}{T} + C_4T^2 + \frac{C_5}{630-T} + C_6P + C_7P\ln T + \frac{C_8P}{T} + \frac{C_9P}{630-T} + \frac{C_{10}P^2}{(630-T)^2} + C_{11}T\ln P \quad \text{(D-3)}$$

where C_1 through C_{11} are for CO_2 solubility constants presented in Table D.1.

Table D.1: Interaction parameters for CO_2 solubility in brine and pure water

T-P Coefficients	$\frac{\mu^{1(0)}_{CO_2}}{RT}$	λ_{CO_2-Na}	$\xi_{CO_2-Na-Cl}$
C_1	2.89E+01	-4.11E-01	3.36E-04
C_2	-3.55E-02	6.08E-04	-1.98E-05
C_3	-4.77E+03	9.75E+01	
C_4	1.03E-05		
C_5	3.38E+01		
C_6	9.04E-03		
C_7	-1.15E-03		
C_8	-3.10E-01	-2.38E-02	2.12E-03
C_9	-9.10E-02	1.71E-02	-5.25E-03
C_{10}	9.30E-04		
C_{11}		1.41E-05	

P_{H_2O} in Eq. (D-2) is the vapor pressure of water. The vapor pressure is determined as:

$$P_{H_2O} = \frac{P_{C,H2O}T}{T_{C,H2O}}[1 + C_1(-t)^{1.9} + C_2t + C_3t^2 + C_4t^3 + C_5t^4] \quad \text{(D-4)}$$

where $P_{c,H2O}$ and $T_{c,H2O}$ are critical pressure and temperature of water (i.e. 220.9 bar and 647.3 K), t = (T-T_c)/T_c and constants C_1 through C_5 are presented in **Table D.2**.

Table D.2: Parameters used in Eq. (D-4)

C_1	C_2	C_3	C_4	C_5
-38.6	5.89	59.9	26.7	10.6

Carbon dioxide fugacity coefficient (φ_{CO_2}) is obtained from the following equation:

$$\ln\varphi(T,P) = Z - 1 - \ln Z + B(V_r, T_r) + C(V_r, T_r) \quad \text{(D-5a)}$$

where

$$B(V_r, T_r) = \frac{a_1 + \frac{a_2}{T_r^2} + \frac{a_3}{T_r^3}}{V_r} + \frac{a_4 + \frac{a_5}{T_r^2} + \frac{a_6}{T_r^3}}{2V_r^2} + \frac{a_7 + \frac{a_8}{T_r^2} + \frac{a_9}{T_r^3}}{4V_r^4} + \frac{a_{10} + \frac{a_{11}}{T_r^2} + \frac{a_{12}}{T_r^3}}{5V_r^5} \quad \text{(D-5b)}$$

$$C(V_r, T_r) = \frac{a_{13}}{2T_r^3 a_{15}}\left[a_{14} + 1 - \left(a_{14} + 1 + \frac{a_{15}}{V_r^2}\right)\left(\exp\left(-\frac{a_{15}}{V_r^2}\right)\right)\right] \quad \text{(D-5c)}$$

where Z is compressibility factor, which is computed using Eq. (D-6).

$$Z = \frac{P_r V_r}{T_r} = 1 + D(V_r, T_r) + E(V_r, T_r) \quad \text{(D-6a)}$$

where

$$D(V_r, T_r) = \frac{a_1 + \frac{a_2}{T_r^2} + \frac{a_3}{T_r^3}}{V_r} + \frac{a_4 + \frac{a_5}{T_r^2} + \frac{a_6}{T_r^3}}{V_r^2} + \frac{a_7 + \frac{a_8}{T_r^2} + \frac{a_9}{T_r^3}}{V_r^4} + \frac{a_{10} + \frac{a_{11}}{T_r^2} + \frac{a_{12}}{T_r^3}}{V_r^5} \quad \text{(D-6b)}$$

$$E(V_r, T_r) = \frac{a_{13}}{T_r^3 V_r^2}\left(a_{14} + \frac{a_{15}}{V_r^2}\right)\left(\exp\left(-\frac{a_{15}}{V_r^2}\right)\right) \quad \text{(D-6c)}$$

The values of constants a_1 through a_{15} are presented in Table D.3.

Table D.3: Parameters used in Eqs. (D-5) and (D-6) for CO_2 solubility

a1	a2	a3	a4	a5	a6	a7	a8	a9	a10	a11	a12	a13	a14	a15
0.0899	-0.495	0.0478	0.0104	-0.0283	0.095	0.00052	-0.0003	-0.0012	-0.0000251	0.0000893	0.0000789	-0.0167	1.4	0.0296

In Eq. (D-6), P_r, T_r and V_r are reduced pressure, reduced temperature and reduced volume, respectively. These parameters are defined as:

$$P_r = \frac{P}{P_c} \quad \text{(D-7)}$$

$$T_r = \frac{T}{T_c} \quad \text{(D-8)}$$

$$V_r = \frac{V}{V_c} \quad \text{(D-9)}$$

where P_c and T_c are critical pressure and temperature, respectively. V_c is mole based critical specific volume, defined as:

$$V_c = \frac{RT_c}{P_c} \quad \text{.....(D-10)}$$

R is the universal gas constant. V_r can be obtained by solving Eq. (D-6). Then, the value of V_r can be used to calculate compressibility factor, Z.

Published experimental data and Duan's model predictions are presented from **Figs. D.1** through **D.3**. Results show acceptable agreement between experimental data and model predictions.

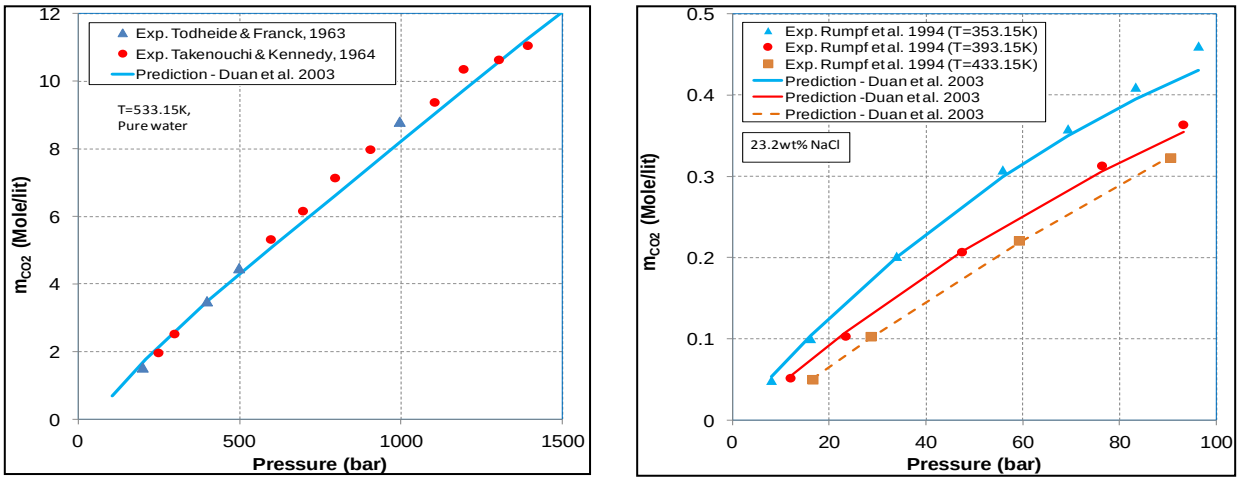

Fig. D.1: Measured and prediction solubility of CO_2: a) Pure water at T=533.15 K; and b) Brine containing 23.2% NaCl at different temperatures

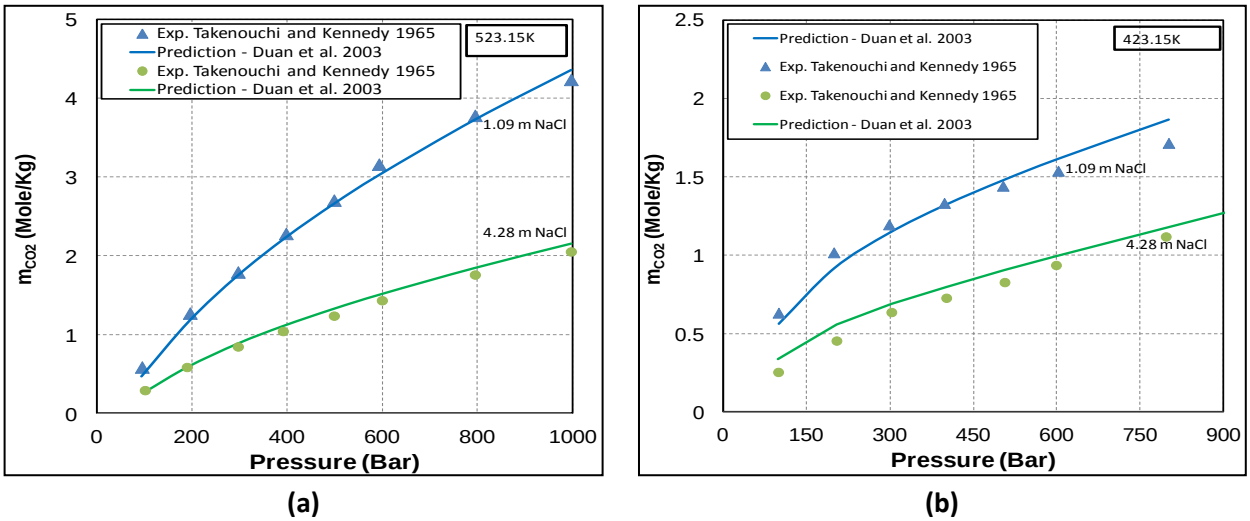

Fig. D.2: Measured and prediction solubility of CO_2 at different brine concentrations: a) T=523.15K; and b) T=423.15K

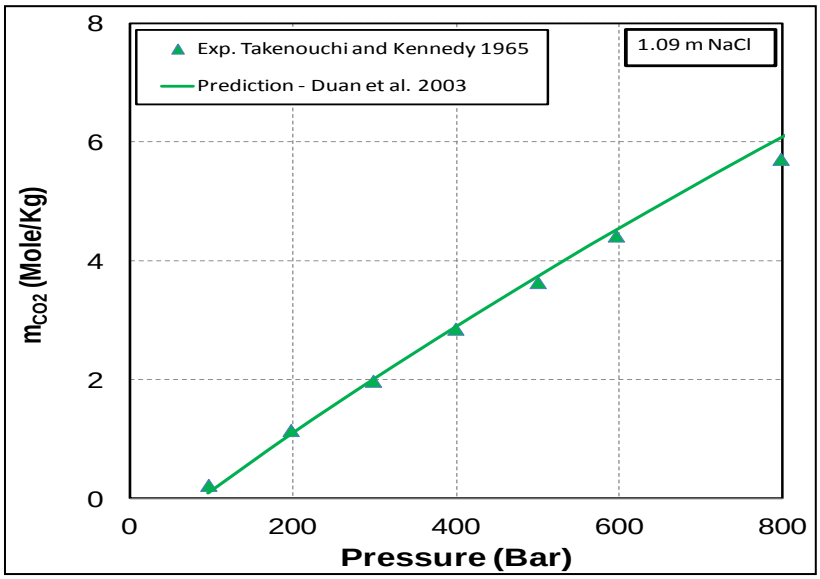

Fig. D.3: Comparison of experimental data and Duan's model predictions (T=573.15K)

APPENDIX E: NUMERICAL SCHEME FOR DEGRADATION DEPTH MODEL

Recalling Eq. (A-59), we can write an equation dimensionless degradation depth as:

$$\varepsilon \exp\left(-\xi_d^2\right) = \sqrt{\pi}\xi_d \mathrm{erf}(\xi_d) \quad \text{(E-1)}$$

Therefore, we can rewrite the relationship as a function.

$$f(\xi_d) = \varepsilon \exp\left(-\xi_d^2\right) - \sqrt{\pi}\xi_d \mathrm{erf}(\xi_d) \quad \text{(E-2)}$$

Newton – Raphson iterative scheme can also be used to obtain numerically the solution of Eq. (B.2)

$$\xi_d^{n+1} = \xi_d^{n} - \frac{f(\xi_d)}{f'(\xi_d)} \quad \text{(E-3)}$$

Differentiating Eq. (E-2) and simplifying yield:

$$f'(\xi_d) = -2\xi_d(\varepsilon + 1)\exp\left(-\xi_d^2\right) - \sqrt{\pi}\,\mathrm{er}\,f(\xi_d) \quad \text{(E-4)}$$

Substituting Eqs. (E-2) and (E-4) into (E-3), the following expression can be obtained:

$$\xi_d^{n+1} = \xi_d^{n} + \frac{\varepsilon \exp\left(-\xi_d^2\right) - \sqrt{\pi}\,\xi_d \mathrm{erf}(\xi_d)}{2\xi_d(\varepsilon + 1)\exp\left(-\xi_d^2\right) + \sqrt{\pi}\,\mathrm{er}\,f(\xi_d)} \quad \text{(E-5)}$$

A MATLAB program was also developed to compute dimensionless degraded depth subject to convergence error of 0.00001.

APPENDIX F: MECHANICAL STRENGTH DEGRADATION MODEL

Considering a thin infinitesimal strip of thickness dx, located at distance x from the sample (with radius r) surface as shown in **Fig. F.1**, the force exerted on the strip under compression loading can be expressed as:

$$dF = \sigma dA \quad \text{..... (F-1)}$$

where $dA = 2\pi(r - x)dx$

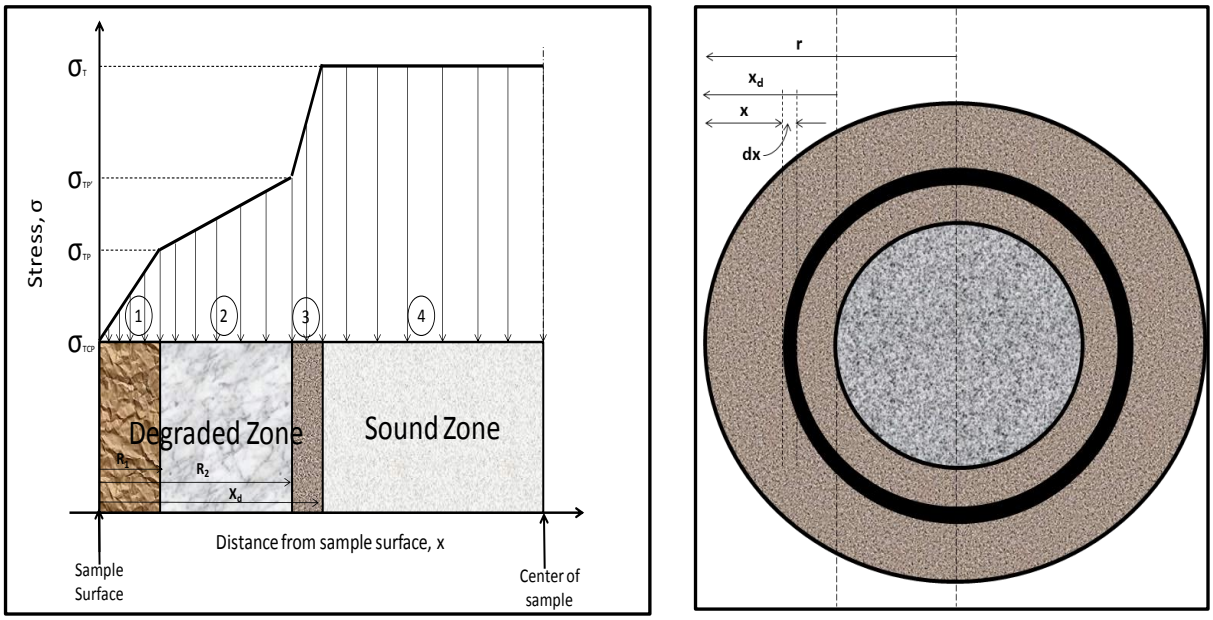

Fig. F.1: Degraded zones of cement core: a) stress distribution during failure; and b) degradation depth

Force acting on any zone can be obtained by integrating the stress distribution (σ_{di}) over the area.

$$F_k = \int_{x_{dj}}^{x_{di}} \sigma_{di} dA \quad \text{..... (F-2)}$$

For undegraded sample, stress distribution is uniform when the failure occurs. Thus: $\sigma_o = \sigma_T, o < x \leq r$. For degraded sample, the following strength ratios are first defined two relates the stress distribution to the calcium concentration profile.

$$R_P = \frac{\sigma_{T-P}}{\sigma_T} \quad \text{..... (F-3)}$$

$$R_{CP} = \frac{\sigma_{T-CP}}{\sigma_T}, \quad \text{..... (F-4)}$$

$$R'_P = \frac{\sigma_{T-P'}}{\sigma_T} \quad \text{(F-5)}$$

Since the loss of calcium is the principal mechanism that results in loss of structural integrity, strength ratios R_p, R_{cp} and R'_p are assumed identical to solid-phase calcium concentration ratios in the degraded zone. Hence, for Region 1: Ca $(HCO_3)_2$ leached zone (amorphous and porous silica), assuming linear stress distribution, the following expression can be obtained:

$$\sigma_{d1} = \frac{\sigma_{T-P}-\sigma_{T-CP}}{R_1}x + \sigma_{T-P}, r - R_1 < x \leq r \quad \text{(F-6)}$$

Therefore, the total force acting on this region can be determined by integrating the above equation.

$$F_1 = \int_{r-R_1}^{r} \sigma_{d1} dA = \int_{r-R_1}^{r} \left[\frac{\sigma_{T-P}-\sigma_{T-CP}}{R_1}x + \sigma_{T-P}\right] dA = \int_{r-R_1}^{r} \sigma_T \left[\frac{R_P-R_{CP}}{R_1}x + R_P\right] dA \quad \text{(F-7)}$$

This force is normalized by the original strengths of the material:

$$\frac{F_1}{\sigma_T} = \int_{r-R_1}^{r} \left[\frac{R_P-R_{CP}}{R_1}x + R_P\right] 2\pi(r-x)dx = \int_{r-R_1}^{r} \frac{R_P-R_{CP}}{R_1} 2\pi(r-x)xdx + \int_{r-R_1}^{r} R_P 2\pi(r-x)dx \quad \text{(F-8)}$$

$$\frac{F_1}{\sigma_T} = 2\pi \left[\frac{R_P-R_{CP}}{R_1}\left\{r\int_{r-R_1}^{r} xdx - \int_{r-R_1}^{r} x^2 dx\right\} + R_P\left\{r\int_{r-R_1}^{r} dx - \int_{r-R_1}^{r} xdx\right\}\right] \quad \text{(F-9)}$$

$$\frac{F_1}{\sigma_T} = 2\pi \left[\frac{R_P-R_{CP}}{R_1}\left\{\frac{r}{2}[r^2-(r-R_1)^2] - \frac{1}{3}[r^3-(r-R_1)^3]\right\} + R_P\left\{rR_1 - \frac{1}{2}[r^2-(r-R_1)^2]\right\}\right] \quad \text{(F-10)}$$

Applying similar procedure, the following relationship can be established for Region II (fully carbonated zone):

$$\sigma_{d2} = \frac{\sigma_{T-P'}-\sigma_{T-P}}{R_2-R_1}x + \frac{\sigma_{T-P}R_2-\sigma_{T-P'}R_1}{R_2-R_1}, r-R_2 < x \leq r-R_1 \quad \text{(F-11)}$$

Therefore,

$$F_2 = \int_{r-R_2}^{r-R_1} \sigma_{d2} dA = \int_{r-R_2}^{r-R_1} \left[\frac{\sigma_{T-P'}-\sigma_{T-P}}{R_2-R_1}x + \frac{\sigma_{T-P}R_2-\sigma_{T-P'}R_1}{R_2-R_1}\right] dA \quad \text{(F-12)}$$

$$F_2 = \sigma_T \int_{r-R_2}^{r-R_1} \left[\frac{R'_P-R_P}{R_2-R_1}x + \frac{R_PR_2-R'_PR_1}{R_2-R_1}\right] 2\pi(r-x)dx \quad \text{(F-13)}$$

$$\frac{F_2}{\sigma_T} = \frac{1}{R_2-R_1}\int_{r-R_2}^{r-R_1}[(R'_P-R_P)x + R_PR_2 - R'_PR_1]2\pi(r-x)dx \quad \text{(F-14)}$$

$$\frac{F_2}{\sigma_T} = \frac{2\pi}{R_2-R_1}\left[(R'_P-R_P)\left\{r\int_{r-R_2}^{r-R_1} xdx - \int_{r-R_2}^{r-R_1} x^2dx\right\} + (R_PR_2-R'_PR_1)\left\{r\int_{r-R_2}^{r-R_1} dx - \int_{r-R_2}^{r-R_1} xdx\right\}\right] \quad \text{(F-15)}$$

$$\frac{F_2}{\sigma_T} = \frac{2\pi}{R_2-R_1}\left[\begin{array}{c}(R'_P-R_P)\left\{\frac{r}{2}[(r-R_1)^2-(r-R_2)^2] - \frac{1}{3}[(r-R_1)^3-(r-R_2)^3]\right\} \\ +(R_PR_2-R'_PR_1)\left\{r(R_2-R_1) - \frac{1}{2}[(r-R_1)^2-(r-R_2)^2]\right\}\end{array}\right] \quad \text{(F-16)}$$

For Region III ($Ca(OH)_2$ leached zone), applying similar procedure, the following expressions for stress distribution and the normalized force can be obtained:

$$\sigma_{d3} = \frac{\sigma_T - \sigma_{T-P\prime}}{x_d - R_2} x + \frac{\sigma_{T-P\prime} x_d - \sigma_T R_2}{x_d - R_2}, x_d < x \leq r - R_2 \quad \text{(F-17)}$$

Therefore,

$$F_3 = \int_{x_d}^{r-R_2} \sigma_{d3} dA = \int_{x_d}^{r-R_2} \left[\frac{\sigma_T - \sigma_{T-P\prime}}{x_d - R_2} x + \frac{\sigma_{T-P\prime} x_d - \sigma_T R_2}{x_d - R_2}\right] dA \quad \text{(F-18)}$$

$$F_3 = \sigma_T \int_{r-x_d}^{r-R_2} \left[\frac{1 - R'_P}{x_d - R_2} x + \frac{R'_P x_d - R_2}{x_d - R_2}\right] 2\pi(r - x) dx \quad \text{(F-19)}$$

$$\frac{F_3}{\sigma_T} = \frac{1}{x_d - R_2} \int_{r-x_d}^{r-R_2} [(1 - R'_P)x + R'_P x_d - R_2] 2\pi(r - x) dx \quad \text{(F-20)}$$

$$\frac{F_3}{\sigma_T} = \frac{2\pi}{x_d - R_2} \left[(1 - R'_P)\left\{r \int_{r-x_d}^{r-R_2} x dx - \int_{r-x_d}^{r-R_2} x^2 dx\right\} + (R'_P x_d - R_2)\left\{r \int_{r-x_d}^{r-R_2} dx - \int_{r-x_d}^{r-R_2} x dx\right\}\right] \quad \text{(F-21)}$$

$$\frac{F_3}{\sigma_T} = \frac{2\pi}{x_d - R_2} \begin{bmatrix} (1 - R'_P)\left\{\frac{r}{2}[(r - R_2)^2 - (r - x_d)^2] - \frac{1}{3}[(r - R_2)^3 - (r - x_d)^3]\right\} \\ +(R'_P x_d - R_2)\left\{r(x_d - R_2) - \frac{1}{2}[(r - R_2)^2 - (r - x_d)^2]\right\} \end{bmatrix} \quad \text{(F-22)}$$

Similarly for Region 4 (Sound zone):

$$\sigma_{d4} = \sigma_T, 0 < x \leq x_d$$

Therefore,

$$F_4 = \int_0^{x_d} \sigma_{d4} dA = \int_0^{x_d} \sigma_T dA \quad \text{(F-23)}$$

$$F_4 = \sigma_T \int_0^{x_d} 2\pi(r - x) dx \quad \text{(F-24)}$$

$$\frac{F_4}{\sigma_T} = 2\pi\left[r \int_0^{x_d} dx - \int_0^{x_d} x dx\right] \quad \text{(F-25)}$$

$$\frac{F_4}{\sigma_T} = 2\pi\left(r x_d - \frac{x_d^2}{2}\right) = \pi x_d(2r - x_d) \quad \text{(F-26)}$$

Therefore,

$$\frac{F_1}{\sigma_T} = 2\pi\left[\frac{R_P - R_{CP}}{R_1}\left\{\frac{r}{2}[r^2 - (r - R_1)^2] - \frac{1}{3}[r^3 - (r - R_1)^3]\right\} + R_P\left\{r R_1 - \frac{1}{2}[r^2 - (r - R_1)^2]\right\}\right] \quad \text{(F-27)}$$

$$\frac{F_2}{\sigma_T} = \frac{2\pi}{R_2 - R_1} \begin{bmatrix} (R'_P - R_P)\left\{\frac{r}{2}[(r - R_1)^2 - (r - R_2)^2] - \frac{1}{3}[(r - R_1)^3 - (r - R_2)^3]\right\} \\ +(R_P R_2 - R'_P R_1)\left\{r(R_2 - R_1) - \frac{1}{2}[(r - R_1)^2 - (r - R_2)^2]\right\} \end{bmatrix} \quad \text{(F-28)}$$

$$\frac{F_3}{\sigma_T} = \frac{2\pi}{x_d - R_2}\left[\begin{array}{c}(1 - R'_P)\left\{\frac{r}{2}[(r - R_2)^2 - (r - x_d)^2] - \frac{1}{3}[(r - R_2)^3 - (r - x_d)^3]\right\} \\ +(R'_P x_d - R_2)\left\{r(x_d - R_2) - \frac{1}{2}[(r - R_2)^2 - (r - x_d)^2]\right\}\end{array}\right] \quad \text{(F-29)}$$

$$\frac{F_4}{\sigma_T} = \pi x_d(2r - x_d) \quad \text{(F-30)}$$

$$F_d = \left[\frac{F_1}{\sigma_T} + \frac{F_2}{\sigma_T} + \frac{F_3}{\sigma_T} + \frac{F_4}{\sigma_T}\right]\sigma_T \quad \text{(F-31)}$$

Reduction in performance due to degradation is quantified as degraded ratio:

$$\frac{\Delta F}{F} = \frac{F_o - F_d}{F_o} = \frac{\sigma_T \pi r^2 - \left[\frac{F_1}{\sigma_T} + \frac{F_2}{\sigma_T} + \frac{F_3}{\sigma_T} + \frac{F_4}{\sigma_T}\right]\sigma_T}{\sigma_T \pi r^2} = 1 - \frac{1}{\pi r^2}\left[\frac{F_1}{\sigma_T} + \frac{F_2}{\sigma_T} + \frac{F_3}{\sigma_T} + \frac{F_4}{\sigma_T}\right] \quad \text{(F-32)}$$

NOMENCLATURES

Acronyms

BWOC	By weight of cement
CH	Calcium hydroxide
CSH	Calcium silicate hydrate
FTIR	Fourier Transform Infra-Red
GHO	Class G cement with hydroxyapatite
GS	Class G cement with silica flour
GSMG	Class G cement with silica flour and magnesium oxide
GSLM	Class G cement with silica flour, latex and micro-silica
GSLT	Class G cement with latex
HHO	Class H cement with hydroxyapatite
HPHT	High-pressure high-temperature
HS	Class H cement with silica flour
HSHO	Class H cement with silica flour and hydroxyapatite
HSMG	Class H cement with silica flour and magnesium oxide
HSLM	Class H cement with silica flour, latex and micro-silica
HSLT	Class H cement with latex
LPR	Linear polarization resistance
LTMS	Cement with latex and micro-silica additives
mpy	mils per year
MGO	Magnesium oxide containing cement
MGO-5	Cement containing 5% BWOC MgO as additive
MGO-10	Cement containing 10% BWOC MgO as additive
MS	Micro-silica containing cement
MS-10	Cement containing 10% BWOC micro-silica as additive
NACE	National Association of Corrosion Engineers
SBS	Shear bonding strength
SD	Static and dynamic

Symbols

K_H	Henry's constant
K_h	Dissociation constant of CO_2
K_{a1}	First dissociation constant of H_2CO_3
K_{a2}	Second dissociation constant of H_2CO_3
$Ø_0$	Initial porosity of cement
Ø	Porosity of cement at current time step
t	Time from commencement of degradation process
D	Effective diffusion coefficient component in each direction
U	Bulk fluid velocity component in each direction
Cs	Specie concentration in solid phase
x, y, z	Distance from the edge of the sample in each direction

k	Thermal conductivity
Blaine	Cement fineness
α	Degree of hydration
E_a	Activation energy
R	Universal gas constant
W/C	Water–to-cement ratio
K_{sp}	Solubility constant of calcium hydroxide
C_{NaCl}	Concentration of sodium chloride in wt%
K_{spc}	Solubility constant of calcium carbonate
K_w	Solubility constant of water
$[Ca^{2+}]$	Concentration of Ca^{2+}
$[H^+_{(aq)}]$	Concentration of H^+
$[HCO^-_{3(aq)}]$	Concentration of HCO^-_3
$[CO^{2-}_{3(aq)}]$	Concentration of CO^{2-}_3
$[OH^-_{(aq)}]$	Concentration of OH^-
$[H_2CO_{3(aq)}]$	Concentration of H_2CO_3
$[CO_{2(aq)}]$	Concentration of CO_2
ε	Dimensionless variable
C_{total}	Solid phase total calcium concentration
ξ_d	Dimensionless degraded depth
x_d	Degradation depth
D	Effective diffusion coefficient
$C_{s,0}$	Initial solid – phase calcium concentration (mol/L)
$C_s(x,t)$	Calcium concentration at any time and location (mol/L)
C_{satu}	Saturated liquid phase calcium ion concentration (mmol/L)
$\bar{C}_l$	Dimensionless liquid phase calcium concentration
C_l	Liquid phase calcium concentration
C_{CH}	Amount of calcium in the solid phase of the calcium hydroxide (mmol/L)
C_{CSH}	Amount of calcium in the solid phase of the C-S-H gel (mmol/L)
x_1	Liquid phase Ca^{+2} concentration when C-S-H begins to convert into silica (mmol/L)
x_2	Liquid phase Ca^{+2} concentration when he dissolution of CSH gel begins (mmol/L)
X_c	Weight fraction of Portland cement
X_{SF}	Weight fraction of silica flour
X_{C2S}	Volume fraction of C_2S
X_{C3S}	volume fraction of C_3S
σ_∞	Ultimate strength
K	Empirical parameter
v_{chsh}	Chemical shrinkage
T	Absolute Temperature, K
P	Total pressure, bar
y	Mole fraction of CO_2 in vapor phase
m	Molality of brine solution

ϕ	Fugacity coefficient
μ	Chemical potential
$\frac{\mu_{CO_2}^{1(0)}}{RT}$	Interaction parameter
λ_{CO_2-Na}	Interaction parameter
$\xi_{CO_2-Na-Cl}$	Interaction parameter
C_{NaCl}	Weight percentage of NaCl
σ	Compressive strength of control sample
r	Radius of cement sample
σ_o	Initial uniform stress in sample
$\sigma_{T\text{-}P}$	First Intermediate stress achieved in leaching zone
$\sigma_{T\text{-}CP}$	Minimum stress achieved in leaching zone
$\sigma_{T\text{-}P'}$	Second Intermediate stress achieved in leaching zone
σ_T	Stress in sound zone
r_1, r_2, r_3	Distance of each leached zone from edge of the sample

REFERENCES

Agzamov, F., Karimov, N. and Akchurin, K. 2013. Preparation of expanding oil well cements. Oil and Gas Business Journal (published online December 11, 2001).

Akkaya, Y., Voigt, T., Subramaniam, K. V. and Shah, S. P. 2003. Nondestructive measurement of concrete strength gain by an ultrasonic wave reflection method. Materials and Structures, Vol. 36, No. 8, pp. 507-514.

Ali, M.M. and Mullick, A.K. 1998. Volume stabilization of high MgO cement: effect of curing conditions and fly ash addition, Cement and Concrete Research 28 (11): 1585-1594.

Barlet-Gouédard, V., Rimmelé, G., Goffé, B. and Porcherie, O., 2006. Mitigation strategies for the risk of CO_2 migration through wellbores, paper SPE 98924 presented at the IADC/SPE Drilling Conference, Miami, USA, February 2006.

Bruckdorfer, R. A. 1986. Carbon Dioxide corrosion In oil well cements. Paper SPE 15176 presented at the Rocky Mountain Regional Meeting of the Society of Petroleum Engineers, Billings, MT, 19 – 21 May.

Buntoro, A. and Rubiandini, R.S. 2001. The effect of neat Magnesium Oxide (MgO) as expanding additive with burning temperature 1200°C and 1300°C on cement shear bond strength at high pressure and temperature. Proceedings of the 5th INAGA Annual Scientific Conference and Exhibitions, Yogyakarta, Indonesia, 7-10 March.

Carde, C., Francois, R. and Torrenti, J M. 1996. Leaching of both Calcium Hydroxide and C-S-H from cement paste: modeling the mechanical behavior. Cement and Concrete Research 26 (8): 1257-1268.

Cheung, P. 1999. Expanding additive for cement composition. US Patent No. 5942031.

Cheremisinoff, P. N. 1995. Handbook of water and wastewater treatment technology. New York: Marcel Decker Inc.

Danjuschewskij, V.S. 1983. Gefuege und eigenshaften hydraulicer Bindemitel nach dem erhaerten bei boheren temperaturen und Laengeren Zeiten, ITE-Fachberiche 107 (10).

Duan, Z. and Sun, R. 2003. An improved model calculating CO_2 solubility in pure water and aqueous NaCl solutions from 273 to 533 K and from 0 to 2000 bar. Chemical Geology J. 193: 257-271.

Duguid, A., Radonjic, M., Bruant, R., et al. 2004. The Effect of CO_2 sequestration on oil well cements. Proceedings of the 7th International Conference on Greenhouse Gas Control Technologies, Vancouver, 5-9 September.

Duguid, A., Radonjic, M. and Scherer, G. 2006. The effect of carbonated brine on the interface between well cement and geologic formations under diffusion-controlled conditions. Proceedings of the 8th International Conference on Greenhouse Gas Control Technologies, Trondheim, Norway, 19-22 June.

Ghofrani, R. and Plack, H. 1993. CaO- and/ or MgO- swelling cements: a key for providing a better annular sealing. Paper SPE 25697 presented at SPE/IADC Drilling Conference, Amsterdam, 22-25 February.

Bensted, J. and Barnes, P. 2002. Structure and Performance of Cements. Second Edition, London and New York: Spon Press.

Lerch, W. and Ford, C. L. 1948. Long-term study of cement performance in concrete: chapter 3. Chemical and physical tests of the cements, ACI Journal, 19 (8), pp. 745–795.

Lin, F. and Meyer, C. 2009. Hydration kinetics modeling of Portland cement considering the effects of curing temperature and applied pressure, Cement and Concrete Research, Volume 39, Issue 4, April 2009, Pages 255-265.

Maekawa, K., Ishida, T. and Kishi, T. 2009. Multi-scale modeling of structural concrete. London and New York: Taylor and Francis Group.

Mainguy, M. and Coussy, O. 2000. Propagation fronts during calcium leaching and chloride penetration. Journal of Engineering Mechanics 126: 250 – 257.

Martin, R. I. and Brown, P. W. 1995. Mechanical properties of Hydroxyapatite formed at physiological temperature. Journal of Material Science: Materials in Medicine, 6: 138-143.

Matteo, E. N., Scherer, G. W., Huet, B., et al. 2011. Understanding boundary condition effects on the corrosion kinetics of Class H well cement. Energy Procedia??? 4: 5370–5376.

Matteo, E. N. and Scherer, G. 2012. Experimental study of the diffusion-controlled acid degradation of Class H Portland cement, International Journal of Greenhouse Gas Control 7: 181 – 191.

Millero, F., Huang, F., Graham, T., et al. 2007. The Dissociation of carbonic acid in NaCl solutions as a function of concentration and temperature. Geochimica et Cosmochimica Acta 71: 46-55.

Nakarai, K., Ishida, T. and Maekawa, K. 2006. Modeling of calcium leaching from cement hydrates coupled with micro-pore formation. Journal of Advanced Concrete 4: 395 – 407.

Nokken, M.R. 2010. Expansion of MgO in cement pastes measured by different methods. ACI Materials Journal, 107 (1): 80-84.

Powers T. C. 1958. The physical structure and engineering properties of concrete. PCA Research & Development Laboratories, Bulletin 90, Chicago.

Sugama, T. and Carciello, N.R. 1992. Carbonation of hydrothermally treated phosphate-bonded calcium aluminate cements. Cement and Concrete Research 22: 783-792.

Sugama, T. and Carciello, N.R. 1993. Carbonation of calcium phosphate cements after long term exposure to Na_2CO_3-laden water at 250°C. Cement and Concrete Research 23: 1409-1417.

Sugama, T. 2006. Advanced cements for geothermal wWells. BNL-77901-2007-IR. Technische Universität München, Research Focus, available at: http://www.bauchemie-tum.de/master-framework/?p=Tief&i=13&m=1&lang=en (accessed on 03/15/2014).

Teraoka, K., Ito, A., Maekawa, K., Onuma, K., Tateishi, T. and Tsutsumi, S. 1998. Mechanical properties of hydroxyapatite and OH-carbonated hydroxyapatite single crystals. Journal of Dental Research 77 (7): 1560-1568.

Rubiandini R., Siregar S., Suhascaryo N. and Efrial D. 2005. The Effect of CaO and MgO as expanding additives to improve cement isolation strength under HPHT exposure, PROC. ITB Eng. Science Vol. 37 B, No. 1, 29-48.

Zhang, Z., Xu, L. and Tang, M. 2011. Effect of particle size on expansive behavior of MgO-based expansive agent in cement paste. Advanced Materials Research 194-196: 1143-1146.

Zhang, Z., Xu, L., Liu, F. and Tang, M. 2012. Effect of amount on expansion property of MgO- type expansive Aagent used in cement-based materials. Advanced Materials Research 391-392: 803-806.

Project Title: Effect of H_2S and CO_2 in HPHT Wells on Tubulars and Cement

Report Type: Monthly Report

Report #: 40

Reporting Period: December 22nd, 2014 to January 21st, 2015

Authors:

Ramadan Ahmed, Principal Investigator

Subhash Shah, Co-Principal Investigator

Rida Elgaddafi, Research Assistant

Omotayo Omosebi, Research Assistant

Jueun Hwang, Research Assistant

Jiwon Jeon, Research Assistant

Prepared under BSEE Project # E12PC00035

by

THE UNIVERSITY OF OKLAHOMA

March 16, 2015

1. Summary of Accomplishments

This monthly report presents the progress made during the project period December 22, 2014 to January 21, 2015. During this reporting period, experimental studies on tubular corrosion were continued. Uniform and stress-cracking corrosion experiments were performed under high-pressure condition using minipipes and flat coupons. Mechanical properties of test specimens were measured to assess the level of corrosion. Furthermore, low-pressure uniform corrosion tests have been completed during this month. Linear polarization resistance (LPR) and weight loss (WL) techniques were utilized in measuring uniform corrosion under low-pressure condition.

The last batch of low-pressure corrosion experiments were carried out at 120 psi and 110°F in 1% NaCl solution saturated with mixed gas containing nitrogen and carbon dioxide. The experiments were performed varying CO_2 concentration. Good agreement between LPR and weight loss measurements was observed. The measurement showed maximum corrosion rate at 25% CO_2 concentration.

In addition to low-pressure tests, high-pressure uniform corrosion experiments were conducted varying CO_2 and H_2S concentrations. Three different grades of carbon steel (Grades T95, C110 and Q125) were tested. Q125 grade demonstrated the highest resistance to uniform corrosion. At low H_2S concentration (less than 10 ppm), the corrosion rate slightly increased with increasing H_2S concentration. However, this trend changed and the rate decreased with H_2S concentration above 10 ppm. These observations are consistent with results of previous corrosion studies.

During this month, four stress-cracking corrosion experiments were conducted under high-pressure condition using different steel grades (T95 and Q125). Mechanical properties of the specimens were measured before and after the test. Specimens were immersed in 2% sodium chloride solution saturated with methane gas containing CO_2 and H_2S. Carbon dioxide content of the gas phase was varied from 0 to 15%. Plastic strain to failure (PSF) and ultimate tensile strength (UTS) measurements obtained from different steel grades indicated that without the presence of CO_2, SSC susceptibility is very low. PSF measurements of Q125 and C110 at different CO_2 concentration showed similar trends. At low CO_2 concentrations (0 to 5%), PSF reduced with concentration and remained constant when the concentration was increased above 5%. The trend indicates the embrittlement occurring in the materials. Q125 exhibited higher embrittlement than C110. This means that Q125 is more susceptible to stress-cracking corrosion than C110, even though it shows superior resistance against uniform corrosion.

Our plan for the upcoming weeks is to continue stress cracking and uniform corrosion experiments under high-pressure condition varying CO_2 and H_2S contents of the gas phase.

2. Overall Project Progress

2.1 Experimental Studies on Corrosion of Tubulars (Task 3)

2.1.1 Sulfide Stress Cracking

Experimental study on sulfide stress cracking (SSC) behavior of API carbon steel (Grades T95, C110 and Q125) was continued. **Table 1** summarizes the SSC tests completed to date. It shows the experimental conditions in which specimens were exposed. Four new SSC experiments (Tests 17 to 20) were

conducted during this reporting period. Internal and external pressures of specimen were maintained at 4000 and 6000 psi, respectively. Carbon dioxide concentration was varied from 0 to 2.5%. Our previous measurements obtained at low concentrations (0 to 5%) indicated the sensitivity of SSC to CO_2 content of the gas.

Table 1: Specimen corrosion testing conditions

Test #	Label	Temp. (°F)	Pressure (psi)		Gas Composition			Time Duration	Remarks
			Inside	Outside	H2S (ppm)	CH4 (%)	CO2 (%)	(Days)	
1	01-C110-07/25-08/06	100	6000	4000	0	100	0	15	
2	02-C110-08/25-08/25	-	-	-	-	-	-	-	Baseline for C110
3	03-C110-08/27-09/03	100	6000	4000	270	90	10	7	Sample failed after 7 days of exposure
4	04-C110-09/05-09/12	100	6000	4000	300	100	0	7	
5	05-C110-09/05-09/13	100	6000	4000	285	95	5	7	
6	06-C110-09/05-09/14	100	6000	4000	270	90	10	7	Brine completely leaked from the cell
7	07-C110-10/17-10/24	100	6000	4000	255	85	15	7	
8	08-C110-10/28-11/04	100	6000	4000	270	90	10	7	
9	09-C110-11/05-11/12	100	6000	4000	293	97.5	2.5	7	
10	10-C110-11/13-11/20	100	6000	4000	270	90	10	7	Sample failed after 7 days of exposure
11	11-C110-12/02-12/09	100	6000	4000	255	85	15	7	
12	12-Q125-11/24-11/24	-	-	-	-	-	-	-	Baseline for Q125
13	13- Q125-11/24-12/01	100	6000	4000	270	90	10	7	
14	14- Q125-12/10-12/17	100	6000	4000	0	100	0	7	
15	15 - T95-12/10-12/10	-	-	-	-	-	-	-	Baseline for T95
16	16- Q125-12/17-12/24	100	6000	4000	300	100	0	7	
17	**17 - T95-01/05-01/12**	**100**	**6000**	**4000**	**0**	**100**	**0**	**7**	
18	**18 - T95-01/13-01/20**	**100**	**6000**	**4000**	**300**	**100**	**0**	**7**	
19	**19- Q125-01/20-01/27**	**100**	**6000**	**4000**	**293**	**97.5**	**2.5**	**7**	
20	**20 - T95-01/27-02/03**	**100**	**6000**	**4000**	**293**	**97.5**	**2.5**	**7**	

Specimens 17 and 18 were strained to failure after exposure to corrosive environment with and without the presence of H_2S. The specimens showed (**Table 2**) very similar ultimate tensile strength (UTS) and plastic strain to failure (PSF). This indicates that, in addition to the presence of 300 ppm H_2S, carbon dioxide or other material, which reduces pH, is needed to create favorable condition for the occurrence of SSC. A number of studies (Morana and Nice 2009; Snape 1967; Hashizume et al. 2000)

demonstrated decrease in SSC resistance of carbon steels with reduction in pH. SSC is hydrogen embrittlement phenomenon caused by combined effects of stress and hydrogen atom, which diffuses into lattice structure of a metal in the presence of acidic solution containing H_2S. Requirements for SSC to occur include high tensile stress (i.e. greater than 75% of yield strength), susceptible material with structural defect, and formation and entry of atomic hydrogen into lattice structure. In this study, specimens were exposed to stress level of up to 85% of their minimum yield strength.

Table 2: Mechanical properties of samples before and after corrosion test

Minipipe No.	Before Exposure				After Exposure			
	YS (psi)	UTS (psi)	PSF	E (psi)	YS (psi)	UTS (psi)	PSF	E* (psi)
1	-	-	-	-	109,855	127,619	0.030	11,785,921
2	111,529	130,156	0.040	11,842,002	-	-	-	-
3	-	-	-	11,704,810	-	100799	0.000	-
4	-	-	-	12,594,080	112768	134981	0.043	12,078,823
5	-	-	-	10,911,219	102217	114424	0.023	11,368,960
6	-	-	-	11,599,401	110686	130118	0.049	11,444,081
7	-	-	-	11,221,136	-	115479	0.014	11,561,000
8	-	-	-	12,044,218	-	120026	0.069	11,441,529
9				11,792,032		116742	0.036	11,255,892
10	-	-	-	13,377,764	-	100799	0.000	-
11	-	-	-	13,377,764		118484	0.035	13,527,372
12	150,072	169,282	0.051	13,580,537	-	-	-	-
13	-	-	-	13,594,795	132,903	152,493	0.028	11,757,738
14	-	-	-	13,890,878	144,533	165,460	0.080	7,321,033
15	95,399	121,115	0.058	12,125,404	-	-	-	-
16	-	-	-	10,613,970	144,528	164,641	0.084	10,642,228
17	**-**	**-**	**-**	**8,916,085**	**105,167**	**122,075**	**0.135**	**7,031,822**
18	**-**	**-**	**-**	**7,477,965**	**101,540**	**121,952**	**0.137**	**10,000,342**
19	**-**	**-**	**-**	**10,431,875**	**141,344**	**162,711**	**0.066**	**6,395,980**
20	**-**	**-**	**-**	**7,676,120**	**105,217**	**119,540**	**0.126**	**7,580,194**

UTS = Ultimate tensile strength, PSF = Plastic strain to failure, YS = Yield strength, E = Young's modulus before exposure, E* = Young's modulus after exposure

UTS and PSF measurements obtained from Specimens 17 and 18 indicated that without the presence of CO_2, SSC susceptibility is very low. Hence, concentration of CO_2 was varied from 0 to 15% during the investigation to examine the effect of CO_2 concentration on SSC susceptibility. **Figure 1** shows measured PSF of specimens as a function of CO_2 concentration for two different steel grades (Q125 and C110). At 10% of CO_2, experiment with C110 was carried out four times (Specimen 3, 6, 8, and 10). Specimen 3 and 10 were broken inside the SSC cell. When Specimen 6 was tested, fluid inside the reactor completely leaked out. Average UTS and PSF of Specimen 3, 8, and 10 are used for determining UTS and PSF at 10% CO_2 concentration. Both materials showed similar PSF trend. At low CO_2 concentration (0 to 5%), PSF of C110 reduced with concentration and remained constant between 5 to 10% CO_2 concentration. The trend indicated the embrittlement occurring in the material. However, as the concentration increased above 10%, the trend changed. The PSF slightly increased when CO_2

concentration was raised from 10 to 15%. The trend reversal could be due to the change in H_2S concentration in the gas. Using supply gas with constant H_2S concentration (300 ppm), increasing CO_2 content has dilution effect that slightly reduces H_2S concentration in the gas as CO_2 concentration is increased (Table 1).

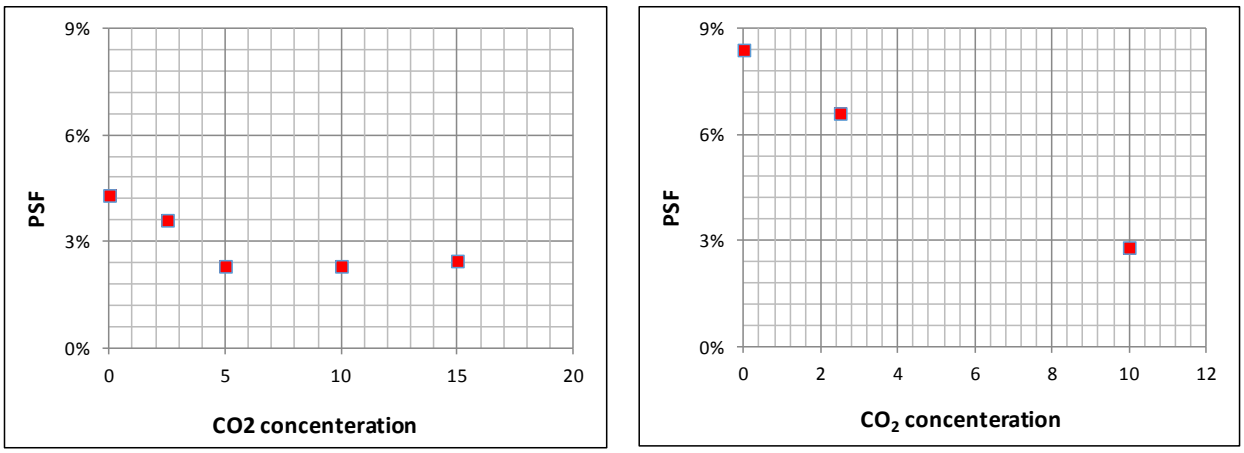

Fig. 1: Plastic strain to failure versus CO_2 concentration: a) C110; and b) Q125

Recent experiments with Q125 were carried out using supply gas containing 500 ppm H_2S. As a result, H_2S concentration was approximately maintained constant, while increasing CO_2 content. The results showed (Fig. 1b) consistent and substantial reduction in PSF of Q125 with increase in CO_2 concentration. Moreover, slight reduction in UTS was observed (**Fig. 2**) when CO_2 concentration was increased. UTS and PSF follow very similar trends.

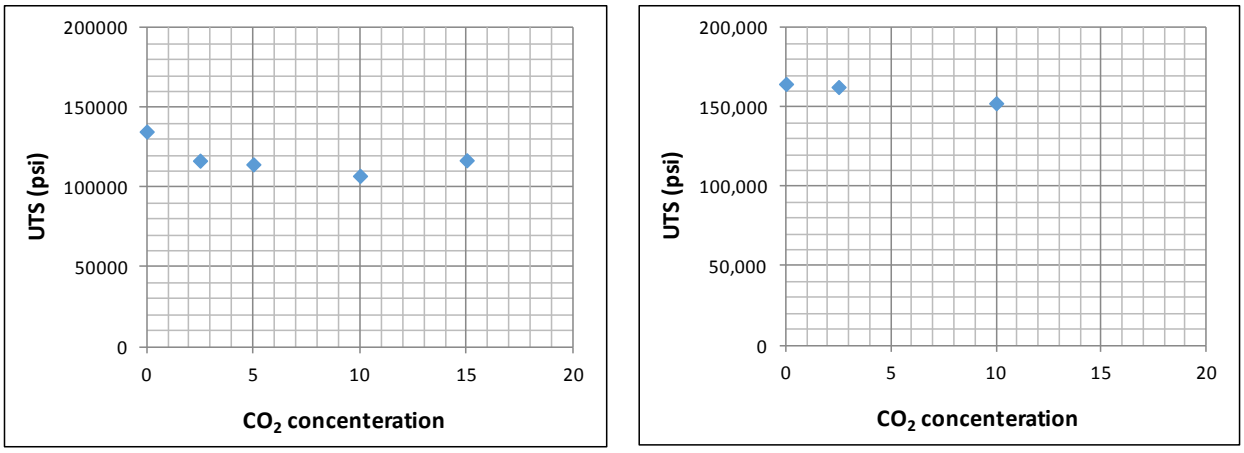

Fig. 2: Ultimate tensile strength versus CO_2 concentration: a) C110; and b) Q125

2.1.2 Uniform Corrosion in Sour Gas Environment

During this reporting period, low-pressure and high-pressure uniform corrosion experiments were performed to assess corrosion behavior of carbon steel in CO_2 environment.

2.1.2.1 Low-Pressure Experiments

Low-pressure corrosion study was continued. Corrosion rate of common carbon steel was measured under different experimental conditions. The average corrosion rate was measured using linear polarization resistance (LPR) and weight loss techniques. To examine the effects of CO_2 and salt concentrations on corrosion rate, three tests were performed at a constant pressure of 120 psi. Test parameters and results of the experiments are presented in **Table 3** along with previous measurements.

Table 3: Test parameters and results of low-pressure corrosion experiments conducted to date

Exp. #	Temp. (ºF)	Pressure (psi)	Partial Pressure %		Brine Conc. (%)	Test Period (days)	Results (mpy)	
			N_2	CO_2			LPR	WL
15	78	120	25	75	2	187	40.30	31.91
16	78	120	0	100	2	187	39.18	32.18
17	78	240	0	100	2	187	N/A	N/A
18	78	120	75	25	2	187	22.92	21.83
19	110	120	75	25	2	187	31.78	23.78
20	110	120	25	75	2	187	53.16	43.22
21	110	120	100	0	2	187	12.37	15.40
22	110	120	75	25	2	187	31.07	23.78
23	110	120	50	50	2	187	70.35	43.39
24	110	120	25	75	2	187	53.16	43.22
25	110	120	0	100	2	187	44.92	32.49
26	176	120	100	0	2	187	4.04	3.10
27	176	120	75	25	2	187	16.53	11.77
28	176	120	50	50	2	187	24.23	12.71
29	176	120	25	75	2	187	17.39	10.87
30	176	120	0	100	2	187	22.56	12.04
31	140	120	100	0	2	187	2.58	2.72
32	140	120	75	25	2	187	11.00	6.33
33	140	120	50	50	2	187	13.33	14.30
34	140	120	25	75	2	187	38.48	26.76
35	140	120	0	100	2	187	24.40	24.23
36	140	120	100	0	1	187	3.69	1.23
37	140	120	75	25	1	187	5.16	20.97
38	140	120	75	25	1	187	9.86	25.13
39	140	120	50	50	1	187	6.40	21.24
40	140	120	25	75	1	187	6.50	23.78
41	140	120	0	100	1	187	4.31	14.77
42	176	120	0	100	1	187	1.76	4.63
43	176	120	25	75	1	187	2.79	9.00
44	176	120	50	50	1	187	4.95	12.59
45	176	120	75	25	1	187	17.79	36.98
46	176	120	100	0	1	187	0.69	2.60
47	176	120	75	25	1	187	5.79	14.90
48	110	120	25	75	1	187	8.55	33.23
49	110	120	0	100	1	187	6.21	30.81
50	110	120	50	50	1	187	22.23	46.88
51	110	120	100	0	1	187	6.57	6.51
52	110	120	75	25	1	187	78.62	101.78
53	**110**	**120**	**50**	**50**	**1**	**187**	**31.86**	**34.62**
54	**110**	**120**	**25**	**75**	**1**	**187**	**20.88**	**33.18**
55	**110**	**120**	**0**	**100**	**1**	**187**	**38.82**	**41.99**

After a new LPR instrument calibration constant (B = 120 mV) was obtained (Report 39), series of uniform corrosion experiments were performed under varying CO_2 concentration at low-pressure condition. Good agreement between LPR and weight loss measurements was observed (**Fig. 3**). Both techniques showed the occurrence of maximum corrosion rate at 25% CO_2 concentration. Microscopic examination of the specimen indicated the absence of corrosion scale at concentration. Formation of corrosion protective scale is one of the phenomena that affect corrosion rate considerably.

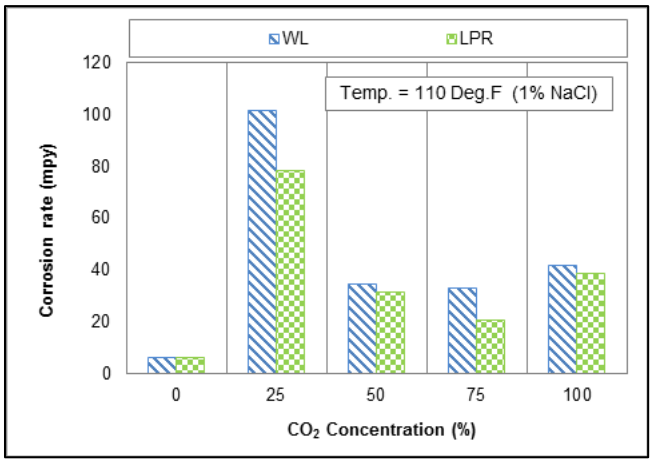

Fig. 3: Comparison of corrosion rate measurements at different CO_2 concentrations

2.1.2.2 High-Pressure Experiments

During this month, six high-pressure corrosion experiments (highlighted in **Table 4**) were conducted at 6000 and 9000 psi while varying CO_2 and H_2S concentrations. Three different grades of carbon steel (Grades T95, C110 and Q125) were tested. Test temperature and NaCl concentration were maintained at 100°F and 2% NaCl, respectively. Two coupons were used for each batch of experiment in order to obtain average corrosion rate and mechanical property measurements. Test parameters for different batch of experiments are presented in Table 4.

Table 4: Test conditions for HPHT uniform corrosion tests

Batch No.	Material	Pressure (psi)	Temp. (°F)	Duration (Days)	CO_2 Conc. (%)	CH_4 Conc. (%)	H_2S Conc. (ppm)
001	C110	6000	100	7	100	0	0
002	C110	6000	100	7	50	50	0
003	C110	6000	100	7	0	100	0
004	C110	6000	100	7	25	75	0
005	C110	6000	100	7	75	25	0
006	C110	9000	100	7	100	0	0
007	C110	3000	100	7	0	100	0
008	C110	9000	100	7	75	25	0
009	C110	9000	100	7	50	50	0
010	C110	9000	100	7	25	75	0
011	C110	9000	100	7	0	100	0
012	C110	3000	100	7	75	25	0
013	C110	3000	100	7	100	0	0
014	Q125	6000	100	7	50	50	0
015	Q125	9000	100	7	50	50	0
016	**T95**	**6000**	**100**	**7**	**50**	**50**	**0**
017	**T95**	**9000**	**100**	**7**	**50**	**50**	**0**
018	**C110**	**6000**	**100**	**7**	**50**	**-**	**10**
019	**C110**	**6000**	**100**	**7**	**50**	**-**	**50**
020	**Q125**	**6000**	**100**	**7**	**75**	**25**	**0**
021	**Q125**	**6000**	**100**	**7**	**100**	**0**	**0**

Figure 4 compares the corrosion rates of different API grade steels (T95, C110 and Q125) in 2% NaCl solution saturated with methane containing 50% CO_2 at 6000 and 9000 psi, and 100°F. Under these conditions, Q125 showed the highest corrosion resistance. Increasing pressure slightly reduced the corrosion rate in all steel grades. **Figure 5** presents the impact of H_2S concentration on the CO_2 corrosion rate of C110 grade steel. At low H_2S concentration (less than 10 ppm), the corrosion rate slightly increased with increase in H_2S concentration. However, above 10 ppm, the rate decreased with the concentration. These results are consistent with findings of a previous study (Valdes, et al. 1998) conducted on regular carbon steel, in which the maximum corrosion rate was observed at 10 ppm of H_2S concentration.

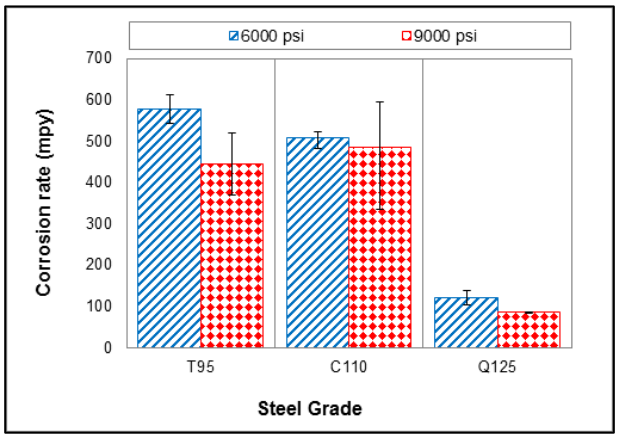

Fig. 4: Corrosion rates of API grade steels at different pressures (50% CO2 and 100°F)

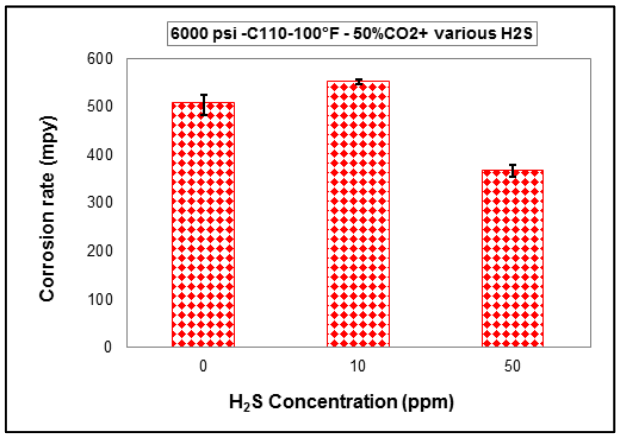

Fig. 5: Corrosion rate of C110 as a function of H_2S concentration (100°F, 50% CO_2 and 6000 psi)

Figure 6 shows the influence of CO_2 concentration on corrosion rate of Q125 grade steel. The corrosion rate increased with CO_2 concentration resulting from increased solubility of CO_2 in the brine, which reduces the pH and facilitates the corrosion process. As the CO_2 concentration increases, carbonic acid concentration in the solution increases, accelerating the cathodic reactions and therefore increasing the corrosion rate. The corrosion rate increasing-trend with CO_2 concentration has been found consistent with previous studies (Choi et al., 2014; Zhang et al., 2013; Schmitt and Horstemeier, 2006).

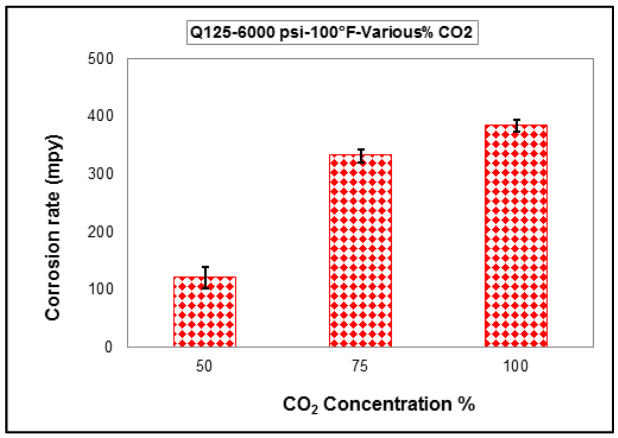

Fig. 6: Comparison of corrosion rate measurements at different CO_2 concentrations

In addition to the corrosion rate, mechanical properties of the specimens were measured before and after exposure to the corrosive environment. Results presented in **Table 5** (new experiments are highlighted) show the occurrence of significant corrosion after the exposure. Mechanical property measurements before and after exposure vary due to changes in specimen characteristics resulting from localized corrosion and reduction in specimen thickness.

Table 5: Corrosion rate and mechanical properties of C110 specimens before and after corrosion test

Batch No.	Specimen No.	CO_2 Con.%	Initial weight gm	Final weight gm	CR (mpy)	E (psi)	E* (psi)	Yield strength (psi)	Tensile Strength (psi)
001	C110-1	100	13.3848	13.2129	234	5.79E+06	9.91E+06	107,560	123,600
	C110-2		13.4397	13.2212	297	6.02E+06	8.62E+06	105,950	119,933
	C110-3		13.4478	13.2323	293	7.71E+06	9.44E+06	108,140	120,673
002	C110-1	50	13.4875	13.1076	517	1.07E+07	8.57E+06	104,960	117,283
	C110-2		13.3884	13.0029	524	5.10E+06	9.01E+06	97,180	116,388
	C110-3		13.3376	12.9835	482	5.54E+06	8.25E+06	95,140	116,198
003	C110-1	0	13.4459	13.3916	74	1.00E+07	7.76E+06	93,250	130,891
	C110-2		13.4196	13.3924	37	1.15E+07	8.43E+06	96,780	131,917
	C110-3		13.3234	13.2680	75	1.07E+07	8.25E+06	96,940	129,187
004	C110-1	25	13.3739	12.949	578	8.75E+06	8.13E+06	91,000	113,833
	C110-2		13.3092	12.9818	445	8.48E+06	6.99E+06	95,510	116,450
	C110-3		13.4018	13.0782	440	8.15E+06	8.44E+06	94,880	117,009
005	C110-1	75	13.4127	13.1079	415	8.71E+06	8.09E+06	103,240	111,286
	C110-2		13.4881	13.2212	363	1.10E+07	6.52E+06	101,290	112,891
	C110-3		13.4635	12.9808	657	8.43E+06	6.01E+06	101,000	111,062
006	C110-1	100	13.4039	13.1518	343	1.14E+07	8.43E+06	100,000	116,283
	C110-2		13.3703	12.9598	558	1.08E+07	8.57E+06	96,410	113,007
	C110-3		13.4606	13.2294	315	1.10E+07	6.36E+06	95,570	117,066
007	C110-1	0	13.4169	13.3859	42	9.98E+06	6.96E+06	100,920	130,212
	C110-2		13.4447	13.4144	41	9.29E+06	6.94E+06	100,530	130,658
	C110-3		13.4041	13.3635	55	9.47E+06	7.05E+06	101,170	128,982
008	C110-1	75	13.3681	12.9327	592	7.74E+06	8.37E+06	97,530	110,554
	C110-2		13.4538	13.0456	555	7.97E+06	8.67E+06	99,660	110,922
	C110-3		13.3742	12.9952	516	8.44E+06	9.24E+06	100,480	112,723
009	C110-1	50	13.4238	12.9867	595	1.14E+07	8.15E+06	97,480	111,270
	C110-2		13.2956	13.0504	334	8.45E+06	8.55E+06	98,740	118,488
	C110-3		13.4920	13.1036	528	8.47E+06	8.35E+06	102,700	113,291
010	C110-1	25	13.3937	13.092	410	9.30E+06	8.33E+06	99,250	119,451
	C110-2		13.3812	12.9699	559	1.23E+07	7.15E+06	101,270	114,472
	C110-3		13.3518	12.9320	571	1.25E+07	7.36E+06	100,120	112,456
011	C110-1	0	13.4399	13.4033	50	8.81E+06	5.89E+06	107,870	129,910
	C110-2		13.3882	13.3497	52	9.25E+06	7.43E+06	110,000	128,725
	C110-3		13.4730	13.4332	54	1.10E+07	8.06E+06	106,890	127,023
012	C110-1	100	13.3637	12.9442	571	1.20E+07	7.52E+06	99,760	110,045
	C110-2		13.3376	12.9346	548	1.19E+07	5.62E+06	100,570	111,029
013	C110-1	75	13.3668	13.2191	201	1.10E+07	6.20E+06	101,540	121,867
	C110-2		13.3789	13.1548	305	1.01E+07	6.31E+06	101,200	120,463
014	Q125 -1	50	13.2108	13.1086	139	1.07E+07	8.20E+06	117,600	155,273
	Q125-2		12.9513	12.8756	103	9.03E+06	7.88E+06	116,830	151,903
015	Q125-1	50	13.0443	12.9842	82	1.18E+07	8.28E+06	117,070	151,036
	Q125-2		13.2890	13.2249	87	9.03E+06	9.19E+06	120,140	157,005
016	**T95-1**	**50**	**13.5557**	**13.1052**	**613**	**8.58E+06**	**7.37E+06**	**93,240**	**103,405**
	T95-2		**13.1735**	**12.7736**	**544**	**7.35E+06**	**8.24E+06**	**90,980**	**103,170**
017	**T95-1**	**50**	**13.3376**	**13.0653**	**370**	**6.21E+06**	**7.44E+06**	**90,190**	**109,001**
	T95-2		**13.2942**	**12.9121**	**520**	**5.40E+06**	**7.33E+06**	**90,170**	**105,425**
018	**C110-1**	**50**	**13.3801**	**12.9783**	**547**	**8.60E+06**	**8.48E+06**	**100,050**	**114,088**

Batch No.	Specimen No.	CO_2 Con.%	Initial weight gm	Final weight gm	CR (mpy)	E (psi)	E* (psi)	Yield strength (psi)	Tensile Strength (psi)
	C110-2		13.4545	13.0451	557	8.06E+06	8.05E+06	102,670	114,466
019	C110-1	50	13.246	12.9677	379	8.21E+06	9.65E+06	100,300	112,331
	C110-2		13.2357	12.9752	354	8.04E+06	9.26E+06	107,350	114,472
020	Q125 -1	75	13.3003	13.0650	320	8.78E+06	9.25E+06	126,180	148,642
	Q125-2		13.2306	12.9783	343	8.07E+06	8.83E+06	125,720	145,371
021	Q125 -1	100	13.1388	12.8640	374	8.12E+06	8.85E+06	122,660	142,615
	Q125-2		12.9428	12.6524	395	8.64E+06	7.64E+06	122,990	140,851

E and E* are Young's modulus measured before and after corrosion test, respectively.

3. Planned Activities

- Continue experimental studies on tubular degradation under low-pressure and moderate-temperature conditions.
- Continue HPHT corrosion experiments with minipipes and flat coupons.

4. Project Expenditures

This section presents the project expenses during the month of January (**Table 6**) and the cumulative expenditure.

Table 6: Current and cumulative expenditures, January 2015

No.	Budget Categories	Current Expenses	Cumulative Expenses
1	Salaries & Wages	$4,503.09	$362,639.37
2	Fringe Benefits	$97.52	$80,143.28
3	Project Materials	$363.74	$106,756.93
4	Travel	$0.00	$10,719.04
5	Conference Expenses	$0.00	$0.00
6	Other Direct Costs	$177.58	$1,610.97
7	Equipment	$60.06	$252,105.47
8	Space Rental	$0.00	$0.00
9	Indirect Cost	$2,570.97	$279,899.93
10	**Total**	**$7,772.96**	**$1,093,874.99**

Nomenclature

A	Exposed surface area, cm^2
API	American Petroleum Institute
ASTM	American Society for Testing and Materials
CR	Average corrosion rate, mpy
E	Young's modulus measured before corrosion test
E*	Young's modulus measured after corrosion test
LPR	Linear polarization resistance

mpy	mils per year
MYS	maximum yield strength
NACE	National Association of Corrosion Engineers
PSF	Plastic strain to failure,
SCC	Stress corrosion cracking
SSC	Sulfide stress cracking
t	Test duration, hr
UTS	Ultimate tensile strength
w_1	Initial specimen weight
w_2	Final specimen weight
YS	Yield strength

References

Choi, Y.S., Farelas, F., Nesic S., Magalhães, A. A. O., and Andrade C. D. 2014. Corrosion Behavior of Deep Water Oil Production Tubing Material under Supercritical CO2 Environment: Part I. Effect of Pressure and Temperature, paper No. 2380, NACE International, 17-21 March, Orlando, Florida.

Hashizume, S.and Inohara, Y. 2000. Effects of pH and PH2S on SSC Resistance of Martensitic Stainless Steels. Paper No 0130 presented at the Corrosion, Orlando, Florida, 26-31 March.

Morana, R.and Nice, P. I. 2009. Corrosion Assessment Of High Strength Carbon Steel Grades P-110 Q-125 140 And 150 For H2S Containing Producing Well Environments. Paper No. 9093 presented at the NACE International Corrosion Conference & Expo, Atlanta, Georgia, 22-26 March.

Schmitt, G. and Horstemeier, M. 2006. Fundamental Aspects of CO2 Metal Loss Corrosion - Part II: Influence of Different Parameters on CO2 Corrosion Mechanisms, paper No.06112, NACE International, 12-16 March, San Diego, California.

Snape, E. 1967. Sulfide Stress Corrosion of Some Medium and Low Alloy Steels. Corrosion 23 (6): 154-172.

Valdes, A., Case, R., Ramriez, M. and Ruiz, A. 1998. The Effect of Small Amounts of H2S on CO2 Corrosion of Carbon Steel, Paper no. 98022, NACE International, 22-27 March, San Diego, California.

Zhang, H, Zevenbergen, J., and Benedictus, T. 2013. Corrosion Studies on Casing Steel in CO2 Storage Environments, Energy Procedia,Volume 37, pp. 5816–5822.

Project Title: Effect of H_2S and CO_2 in HPHT Wells on Tubulars and Cement

Report Type: Monthly Report

Report #: 41

Reporting Period: January 22nd, 2015 to February 21st, 2015

Authors:

Ramadan Ahmed, Principal Investigator

Subhash Shah, Co-Principal Investigator

Rida Elgaddafi, Research Assistant

Omotayo Omosebi, Research Assistant

Jueun Hwang, Research Assistant

Jiwon Jeon, Research Assistant

Prepared under BSEE Project # E12PC00035

by

THE UNIVERSITY OF OKLAHOMA

March 23, 2015

1. Summary of Accomplishments

This monthly report presents the progress made during the project period January 22, 2015 to February 21, 2015. Experimental studies on tubular corrosion were continued during this reporting period. Uniform and stress-cracking corrosion experiments were performed under high-pressure condition using minipipes and flat coupons. Mechanical properties of test specimens were measured to assess the level of corrosion. Moreover, we have started preparing the final project report.

During this month, cement-aging cell was modified and used to perform corrosion tests. As a result, we were able to conduct eight high-pressure uniform corrosion experiments varying CO_2 and H_2S concentrations. Tests were performed using three different grades of carbon steel (Grades T95, C110 and Q125). Q125 demonstrated the highest uniform corrosion resistance. When corrosion rate was presented as a function of CO_2 concentration, local maxima was observed at 25% concentration indicating the presence of different corrosion phenomena, which are influenced by CO_2 concentration. The relationship between CO_2 concentration and corrosion rate is very complex. CO_2 concentration determines the pH of solution, thickness and type of corrosion scale formed on the surface of a metal, and electrochemical reaction occurring at the interface between the surrounding fluid and metal. Hence, offsetting or synergizing effects between different phenomena is expected. This creates unfavorable or highly suitable condition for uniform corrosion resulting in localized minima or maxima for corrosion rate. Both high-pressure and low-pressure corrosion rate measurements displayed the local maxima at 25% CO_2 concentration.

In addition to uniform corrosion experiments, four stress-cracking corrosion (SSC) tests were performed under high-pressure using different steel grades (T95 and Q125). Specimens were exposed to 2% sodium chloride solution saturated with methane gas containing CO_2 and 300 ppm H_2S. Carbon dioxide content of the gas phase was varied from 5 to 15%. Internal and external pressures of the mini pipe were maintained at 6000 and 4000 psi, respectively. Mechanical properties of the specimens were measured before and after the test. Plastic strain to failure (PSF) and ultimate tensile strength (UTS) measurements indicated the presence of favorable condition for severe SSC to occur at approximately 10% CO_2 concentration.

Our plan for the upcoming weeks is to continue stress cracking and uniform corrosion experiments under high-pressure condition varying CO_2 and H_2S contents of the gas phase.

2. Overall Project Progress

2.1 Experimental Studies on Corrosion of Tubulars (Task 3)

2.1.1 Sulfide Stress Cracking

Experimental study on sulfide stress cracking (SSC) behavior of API carbon steel (Grades T95, C110 and Q125) was continued. **Table 1** summarizes the SSC tests completed to date. It shows the experimental conditions in which specimens were exposed. Four new SSC experiments (Tests 21 to 24) were completed during this month. Internal and external pressures of specimen were maintained at 4000 and 6000 psi, respectively. Carbon dioxide concentration was varied from 5 to 15%. Our previous measurements with C110 indicated the presence of a minimum PSF at around 10% CO_2 concentration. New tests were aimed to verify if other steel grades also exhibit minimum PSF at this concentration.

Table 1: Specimen corrosion testing conditions

Test #	Label	Temp. (°F)	Pressure (psi)		Gas Composition			Time Duration	Remarks
			Inside	Outside	H2S (ppm)	CH4 (%)	CO2 (%)	(Days)	
1	01-C110-07/25-08/06	100	6000	4000	0	100	0	15	
2	02-C110-08/25-08/25	-	-	-	-	-	-	-	Baseline for C110
3	03-C110-08/27-09/03	100	6000	4000	270	90	10	7	Sample failed after 7 days of exposure
4	04-C110-09/05-09/12	100	6000	4000	300	100	0	7	
5	05-C110-09/05-09/13	100	6000	4000	285	95	5	7	
6	06-C110-09/05-09/14	100	6000	4000	270	90	10	7	Brine completely leaked from the cell
7	07-C110-10/17-10/24	100	6000	4000	255	85	15	7	
8	08-C110-10/28-11/04	100	6000	4000	270	90	10	7	
9	09-C110-11/05-11/12	100	6000	4000	293	97.5	2.5	7	
10	10-C110-11/13-11/20	100	6000	4000	270	90	10	7	Sample failed after 7 days of exposure
11	11-C110-12/02-12/09	100	6000	4000	255	85	15	7	
12	12-Q125-11/24-11/24	-	-	-	-	-	-	-	Baseline for Q125
13	13- Q125-11/24-12/01	100	6000	4000	270	90	10	7	
14	14- Q125-12/10-12/17	100	6000	4000	0	100	0	7	
15	15 - T95-12/10-12/10	-	-	-	-	-	-	-	Baseline for T95
16	16- Q125-12/17-12/24	100	6000	4000	300	100	0	7	
17	17 - T95-01/05-01/12	100	6000	4000	0	100	0	7	
18	18 - T95-01/13-01/20	100	6000	4000	300	100	0	7	
19	19- Q125-01/20-01/27	100	6000	4000	293	97.5	2.5	7	
20	20 - T95-01/27-02/03	100	6000	4000	293	97.5	2.5	7	
21	**21-Q125-0203-0210**	**100**	**6000**	**4000**	**300**	**95**	**5**	**7**	
22	**22-Q125-0210-0217**	**100**	**6000**	**4000**	**300**	**85**	**15**	**7**	
23	**23-T95-0217-0224**	**100**	**6000**	**4000**	**300**	**95**	**5**	**7**	
24	**24-T95-0224-0303**	**100**	**6000**	**4000**	**300**	**90**	**10**	**7**	

Table 2 summarizes mechanical properties of samples measured before and after corrosion experiment. UTS and PSF were obtained from destructive test. Hence, they were only measured after exposing specimens to corrosive environment. These are key measurements and are correlated with

sulfide stress cracking phenomenon, which occurs at high tensile stress loading. In this study, all specimens were exposed to stress level of 85% of their minimum yield strength (i.e. specified by the manufacturers).

Table 2: Mechanical properties of samples before and after corrosion test

Minipipe No.	Before Exposure				After Exposure			
	YS (psi)	UTS (psi)	PSF	E (psi)	YS (psi)	UTS (psi)	PSF	E* (psi)
1	-	-	-	-	109,855	127,619	0.030	11,785,921
2	111,529	130,156	0.040	11,842,002	-	-	-	-
3	-	-	-	11,704,810	-	100799	0.000	-
4	-	-	-	12,594,080	112768	134981	0.043	12,078,823
5	-	-	-	10,911,219	102217	114424	0.023	11,368,960
6	-	-	-	11,599,401	110686	130118	0.049	11,444,081
7	-	-	-	11,221,136	-	115479	0.014	11,561,000
8	-	-	-	12,044,218	-	120026	0.069	11,441,529
9				11,792,032		116742	0.036	11,255,892
10	-	-	-	13,377,764	-	100799	0.000	-
11	-	-	-	13,377,764		118484	0.035	13,527,372
12	150,072	169,282	0.051	13,580,537	-	-	-	-
13	-	-	-	13,594,795	132,903	152,493	0.028	11,757,738
14	-	-	-	13,890,878	144,533	165,460	0.080	7,321,033
15	95,399	121,115	0.058	12,125,404	-	-	-	-
16	-	-	-	10,613,970	144,528	164,641	0.084	10,642,228
17	-	-	-	8,916,085	105,167	122,075	0.135	7,031,822
18	-	-	-	7,477,965	101,540	121,952	0.137	10,000,342
19	-	-	-	10,431,875	141,344	162,711	0.066	6,395,980
20	-	-	-	7,676,120	105,217	119,540	0.126	7,580,194
21	**-**	**-**	**-**	**6,744,550**	**136,403**	**156,584**	**0.049**	**8,431,876**
22	**-**	**-**	**-**	**9,507,949**	**134,333**	**156,737**	**0.050**	**8,740,819**
23	**-**	**-**	**-**	**8,724,446**	**103,495**	**117,293**	**0.126**	**9,335,596**
24	**-**	**-**	**-**	**8,366,828**	**101,594**	**115,885**	**0.106**	**8,796,036**

UTS = Ultimate tensile strength, PSF = Plastic strain to failure, YS = Yield strength, E = Young's modulus before exposure, E* = Young's modulus after exposure

Figure 1 presents measured PSF of different carbon steel grades (T95, C110 and Q125) as a function of CO_2 concentration. PSF represents the maximum plastic deformation strain occurring during tensile strength test. Different steel grades showed similar PSF trend. At low concentration (0 to 10% CO_2), PSF of the steels reduced with concentration. The reduction trend indicates the embrittlement occurring in the material. For C110, as CO_2 content was increased above 10%, the trend was reversed and slight improvement in PSF was observed (Fig. 1b). Initially, the trend reversal was thought to be due to dilution effect, which reduced H_2S content below 300 ppm (Table 1) in the gas as CO_2 concentration increased when supply (methane) gas containing 300 ppm H_2S was used. However, recent experiments conducted with Q125 at constant H_2S concentration (i.e. using 500 ppm H_2S supply gas) showed similar trend (Fig. 1c). Above 10% CO_2, PSF of Q125 substantially increased with concentration. Therefore, the

trend reversal could be due to corrosion related phenomena, which maximize the sulfide stress cracking corrosion around 10% CO_2 for these particular sets of experiments. Two C110 specimens were completely failed at this concentration when subjected to stress level of 85 percent of their minimum yield stress. This indicates the occurrence of severe sulfide stress cracking corrosion at approximately 10% CO_2.

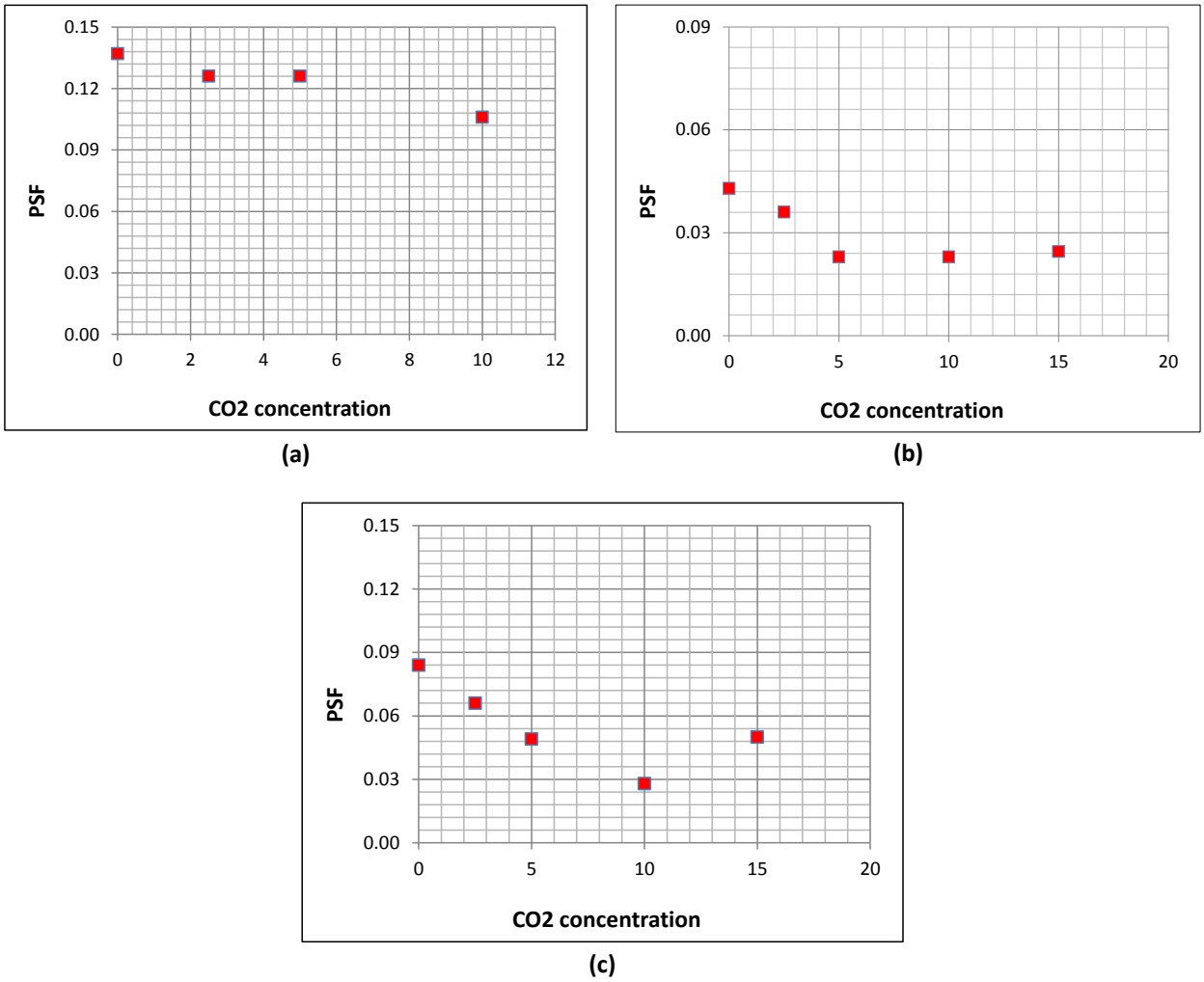

Fig. 1: Plastic strain to failure versus CO_2 concentration: a) T95; b) C110; and b) Q125

Figure 2 presents ultimate tensile strength (UTS) of corroded specimens of API grade steels as a function of CO_2 concentration. The trends of UTS and PSF with CO_2 concentration are very similar. Consistent with PSF measurements, minimum UTS values of C110 and Q125 were observed at approximately 10% CO_2. UTS of T95 gradually decreased as the concentration was increased to 10%. Currently, an experiment is in progress to obtain UTS at 15% CO_2. The results of this test will be presented in the next month report. In general, results suggest sulfide embrittlement tends to decrease the UTS of the steels. This observation is in agreement with published research results in the area of sulfide stress cracking corrosion. Moreover, it is important to note that the UTS measurements are consistent with the API grade number assignment (i.e. Q125 exhibited the highest UTS and T95 showed the lowest). However, PSF measurements did not follow API grade numbering. C110 displayed the

lowest PSF value at all concentrations. Moreover, it was the only steel grade, which showed a complete failure when tested at 10% CO_2.

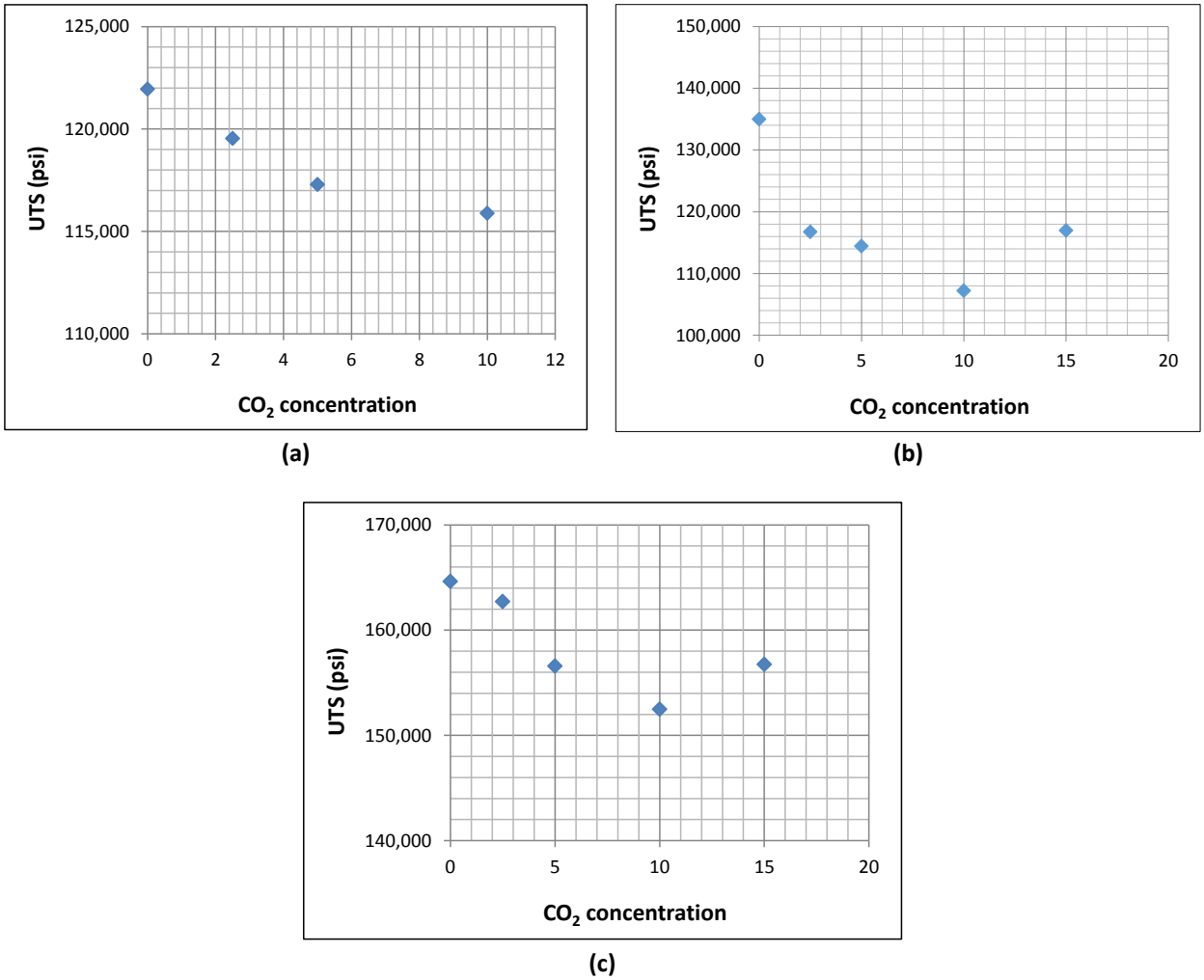

Fig. 2: Ultimate tensile strength versus CO2 concentration: a) T95; b) C110; and b) Q125

2.1.2 Uniform Corrosion in Sour Gas Environment

High-pressure uniform corrosion experiments were continued during this month. Tests were performed to assess corrosion behavior of API carbon steels in CO_2 environment. Eight corrosion experiments (highlighted in **Table 3**) were conducted at 6000 psi while varying CO_2 and H_2S concentration. In addition to the uniform corrosion-testing cell, cement-aging cell was modified and utilized to conduct uniform corrosion experiments. Two grades of carbon steel (T95 and Q125) were tested. Test temperature and salt concentration were maintained at 100°F and 2% NaCl, respectively. Two coupons were used for each batch of experiment in order to obtain average corrosion rate and mechanical property measurements. Test parameters for each batch of experiment are presented in Table 4.

Table 3: Test conditions for HPHT uniform corrosion tests

Batch No.	Material	Pressure (psi)	Temp. (°F)	Duration (Days)	CO_2 Conc. (%)	CH_4 Conc. (%)	H_2S Conc. (ppm)
001	C110	6000	100	7	100	0	0
002	C110	6000	100	7	50	50	0
003	C110	6000	100	7	0	100	0
004	C110	6000	100	7	25	75	0
005	C110	6000	100	7	75	25	0
006	C110	9000	100	7	100	0	0
007	C110	3000	100	7	0	100	0
008	C110	9000	100	7	75	25	0
009	C110	9000	100	7	50	50	0
010	C110	9000	100	7	25	75	0
011	C110	9000	100	7	0	100	0
012	C110	3000	100	7	75	25	0
013	C110	3000	100	7	100	0	0
014	Q125	6000	100	7	50	50	0
015	Q125	9000	100	7	50	50	0
016	T95	6000	100	7	50	50	0
017	T95	9000	100	7	50	50	0
018	C110	6000	100	7	50	0	10
019	C110	6000	100	7	50	0	50
020	Q125	6000	100	7	75	25	0
021	Q125	6000	100	7	100	0	0
022	**Q125**	**6000**	**100**	**7**	**0**	**100**	**0**
023	**Q125**	**6000**	**100**	**7**	**25**	**75**	**0**
024	**T95**	**6000**	**100**	**7**	**75**	**25**	**0**
025	**T95**	**6000**	**100**	**7**	**100**	**0**	**0**
026	**T95**	**6000**	**100**	**7**	**25**	**75**	**0**
027	**T95**	**6000**	**100**	**7**	**0**	**100**	**0**
028	**Q125**	**6000**	**100**	**7**	**50**	**0**	**10**
029	**Q125**	**6000**	**100**	**7**	**50**	**0**	**50**

Figure 3 presents the corrosion rates of different API grade steels (T95 and Q125) as a function of CO_2 concentration in 2% NaCl solution saturated with methane containing 50% CO_2 at 6000 psi and 100°F. Both steel grades demonstrated similar corrosion rate trend with concentration. At low concentration (less than 25% CO_2), corrosion rate increased with increasing CO_2 concentration. However, above 25% CO_2, increasing CO_2 content reduced corrosion rate. However, as the concentration increased above 50%, this trend changed and the rate increased. These results are consistent with our previous corrosion rate measurements obtained at low-pressure when high-strength carbon steel (grade 1045), which meets properties of ASTM A108, was tested in 2% NaCl solution saturated with nitrogen gas containing carbon dioxide (**Fig. 4**). Maximum corrosion rate was recorded at 25% CO_2. Grade 1045 carbon steel has minimum yield strength of 77,000 psi. Furthermore, Q125 showed consistently higher corrosion resistance than T95.

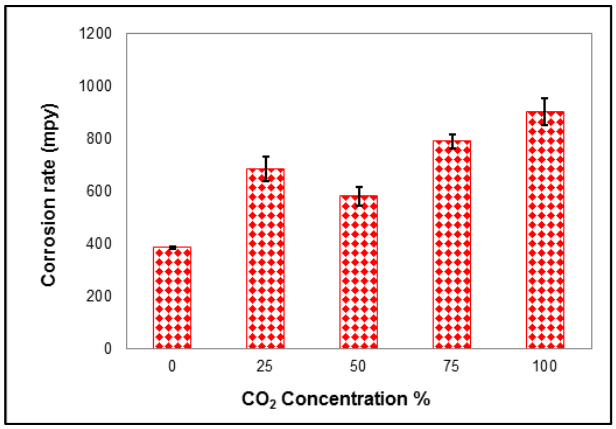

(a)

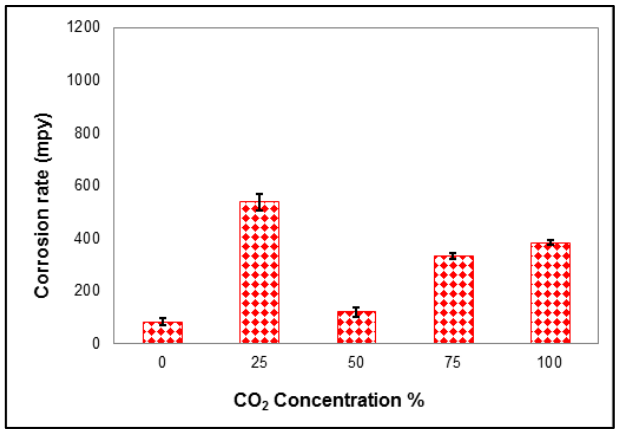

(b)

Fig. 3: Corrosion rates of API grade steels as function CO_2 concentration measured at 6000 psi and 100°F: a) T95; and b) Q125

Figure 5 presents the impact of H_2S concentration on the CO_2 corrosion rate of Q110 grade steel. At low H_2S concentration (less than 10 ppm), the corrosion rate sharply increased with increase in H_2S concentration. However, above 10 ppm, the rate displayed only slight increase with the concentration. Our previous measurements obtained from C110 (**Fig. 6**) showed reduction in corrosion rate at high CO_2 concentration. The presence of maximum corrosion rate at approximately 10 ppm H_2S concentration has been previously reported by Valdes et al. (1998).

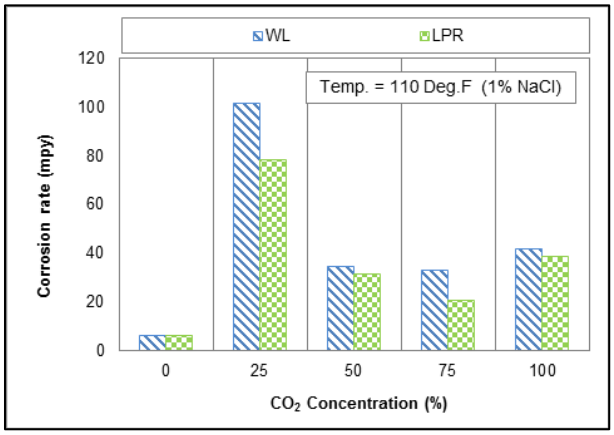

Fig. 4: Comparison of corrosion rate measurements at different CO_2 concentrations (Carbon steel 1045)

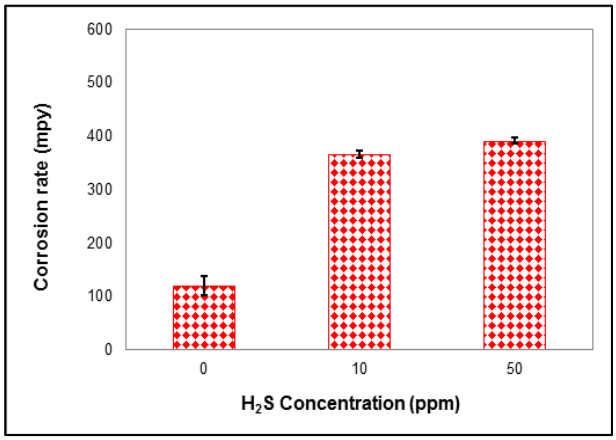

Fig. 5: Corrosion rate of Q125 as a function of H_2S concentration (100°F, 50% CO_2 and 6000 psi)

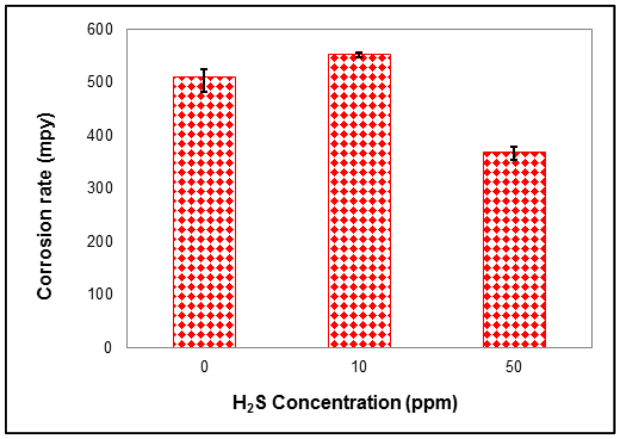

Fig. 6: Corrosion rate of C110 as a function of H_2S concentration (100°F, 50% CO_2 and 6000 psi)

In addition to the corrosion rate, mechanical properties of specimens were measured before and after exposure to the corrosive environment. Results presented in **Table 4** (new experiments are highlighted) show the occurrence of significant corrosion after the exposure. Mechanical property measurements before and after exposure are expected to vary due to changes in specimen characteristics resulting from localized corrosion and reduction in specimen thickness.

Table 4: Corrosion rate and mechanical properties of specimens before and after corrosion test

Batch No.	Specimen No.	CO_2 Con.%	Initial weight gm	Final weight gm	CR (mpy)	E (psi)	E* (psi)	Yield strength (psi)	Tensile Strength (psi)
001	C110-1	100	13.3848	13.2129	234	5.79E+06	9.91E+06	107,560	123,600
	C110-2		13.4397	13.2212	297	6.02E+06	8.62E+06	105,950	119,933
	C110-3		13.4478	13.2323	293	7.71E+06	9.44E+06	108,140	120,673
002	C110-1	50	13.4875	13.1076	517	1.07E+07	8.57E+06	104,960	117,283
	C110-2		13.3884	13.0029	524	5.10E+06	9.01E+06	97,180	116,388
	C110-3		13.3376	12.9835	482	5.54E+06	8.25E+06	95,140	116,198
003	C110-1	0	13.4459	13.3916	74	1.00E+07	7.76E+06	93,250	130,891
	C110-2		13.4196	13.3924	37	1.15E+07	8.43E+06	96,780	131,917
	C110-3		13.3234	13.2680	75	1.07E+07	8.25E+06	96,940	129,187
004	C110-1	25	13.3739	12.949	578	8.75E+06	8.13E+06	91,000	113,833
	C110-2		13.3092	12.9818	445	8.48E+06	6.99E+06	95,510	116,450
	C110-3		13.4018	13.0782	440	8.15E+06	8.44E+06	94,880	117,009
005	C110-1	75	13.4127	13.1079	415	8.71E+06	8.09E+06	103,240	111,286
	C110-2		13.4881	13.2212	363	1.10E+07	6.52E+06	101,290	112,891
	C110-3		13.4635	12.9808	657	8.43E+06	6.01E+06	101,000	111,062
006	C110-1	100	13.4039	13.1518	343	1.14E+07	8.43E+06	100,000	116,283
	C110-2		13.3703	12.9598	558	1.08E+07	8.57E+06	96,410	113,007
	C110-3		13.4606	13.2294	315	1.10E+07	6.36E+06	95,570	117,066
007	C110-1	0	13.4169	13.3859	42	9.98E+06	6.96E+06	100,920	130,212
	C110-2		13.4447	13.4144	41	9.29E+06	6.94E+06	100,530	130,658
	C110-3		13.4041	13.3635	55	9.47E+06	7.05E+06	101,170	128,982
008	C110-1	75	13.3681	12.9327	592	7.74E+06	8.37E+06	97,530	110,554
	C110-2		13.4538	13.0456	555	7.97E+06	8.67E+06	99,660	110,922
	C110-3		13.3742	12.9952	516	8.44E+06	9.24E+06	100,480	112,723
009	C110-1	50	13.4238	12.9867	595	1.14E+07	8.15E+06	97,480	111,270
	C110-2		13.2956	13.0504	334	8.45E+06	8.55E+06	98,740	118,488
	C110-3		13.4920	13.1036	528	8.47E+06	8.35E+06	102,700	113,291
010	C110-1	25	13.3937	13.092	410	9.30E+06	8.33E+06	99,250	119,451
	C110-2		13.3812	12.9699	559	1.23E+07	7.15E+06	101,270	114,472
	C110-3		13.3518	12.9320	571	1.25E+07	7.36E+06	100,120	112,456
011	C110-1	0	13.4399	13.4033	50	8.81E+06	5.89E+06	107,870	129,910
	C110-2		13.3882	13.3497	52	9.25E+06	7.43E+06	110,000	128,725
	C110-3		13.4730	13.4332	54	1.10E+07	8.06E+06	106,890	127,023
012	C110-1	100	13.3637	12.9442	571	1.20E+07	7.52E+06	99,760	110,045
	C110-2		13.3376	12.9346	548	1.19E+07	5.62E+06	100,570	111,029
013	C110-1	75	13.3668	13.2191	201	1.10E+07	6.20E+06	101,540	121,867
	C110-2		13.3789	13.1548	305	1.01E+07	6.31E+06	101,200	120,463
014	Q125 -1	50	13.2108	13.1086	139	1.07E+07	8.20E+06	117,600	155,273
	Q125-2		12.9513	12.8756	103	9.03E+06	7.88E+06	116,830	151,903

Batch No.	Specimen No.	CO_2 Con.%	Initial weight gm	Final weight gm	CR (mpy)	E (psi)	E* (psi)	Yield strength (psi)	Tensile Strength (psi)
015	Q125-1	50	13.0443	12.9842	82	1.18E+07	8.28E+06	117,070	151,036
	Q125-2		13.2890	13.2249	87	9.03E+06	9.19E+06	120,140	157,005
016	T95-1	50	13.5557	13.1052	613	8.58E+06	7.37E+06	93,240	103,405
	T95-2		13.1735	12.7736	544	7.35E+06	8.24E+06	90,980	103,170
017	T95-1	50	13.3376	13.0653	370	6.21E+06	7.44E+06	90,190	109,001
	T95-2		13.2942	12.9121	520	5.40E+06	7.33E+06	90,170	105,425
018	C110-1	50	13.3801	12.9783	547	8.60E+06	8.48E+06	100,050	114,088
	C110-2		13.4545	13.0451	557	8.06E+06	8.05E+06	102,670	114,466
019	C110-1	50	13.246	12.9677	379	8.21E+06	9.65E+06	100,300	112,331
	C110-2		13.2357	12.9752	354	8.04E+06	9.26E+06	107,350	114,472
020	Q125 -1	75	13.3003	13.0650	320	8.78E+06	9.25E+06	126,180	148,642
	Q125-2		13.2306	12.9783	343	8.07E+06	8.83E+06	125,720	145,371
021	Q125 -1	100	13.1388	12.8640	374	8.12E+06	8.85E+06	122,660	142,615
	Q125-2		12.9428	12.6524	395	8.64E+06	7.64E+06	122,990	140,851
022	**Q125 -1**	**0**	**12.9684**	**12.8976**	**96**	**8.23E+06**	7.67E+06	**130,800**	**151,123**
	Q125-2		**13.2393**	**13.1888**	**69**	**8.30E+06**	7.96E+06	**133,100**	**157,469**
023	**Q125 -1**	**25**	**13.2973**	**12.9259**	**505**	**9.45E+06**	8.80E+06	**127,700**	**141,463**
	Q125-2		**13.2585**	**12.8393**	**570**	**8.51E+06**	8.11E+06	**120,500**	**140,209**
024	**T95-1**	**75**	**13.2812**	**12.6815**	**816**	**8.59E+06**	7.83E+06	**87,500**	**96,891**
	T95-2		**13.1886**	**12.6272**	**764**	**8.59E+06**	7.18E+06	**87,830**	**98,713**
025	**T95-1**	**100**	**13.1777**	**12.4770**	**953**	**7.53E+06**	7.00E+06	**83,840**	**92,673**
	T95-2		**13.5060**	**12.8808**	**850**	**8.60E+06**	7.58E+06	**86,600**	**96,532**
026	**T95-1**	**25**	**13.1866**	**12.6496**	**730**	**9.03E+06**	8.35E+06	**89,610**	**98,581**
	T95-2		**13.2638**	**12.7952**	**637**	**8.64E+06**	7.77E+06	**91,660**	**102,082**
027	**T95-1**	**0**	**13.1711**	**12.8920**	**380**	**8.59E+06**	8.63E+06	**96,050**	**107,909**
	T95-2		**13.6589**	**13.3721**	**390**	**8.47E+06**	7.49E+06	**101,110**	**111,145**
028	**Q125 -1**	**50**	**13.0742**	**12.8092**	**360**	**7.67E+06**	8.72E+06	**125,490**	**141,986**
	Q125-2		**13.0549**	**12.7815**	**372**	**9.30E+06**	8.15E+06	**124,980**	**144,785**
029	**Q125 -1**	**50**	**13.0385**	**12.7462**	**398**	**8.79E+06**	8.06E+06	**122,070**	**142,666**
	Q125-2		**13.0300**	**12.7461**	**386**	**8.38E+06**	8.42E+06	**123,750**	**136,764**

E and E* are Young's modulus measured before and after corrosion test, respectively.

3. Planned Activities

- Continue HPHT corrosion experiments with minipipes and flat coupons.
- Continue preparation of the final project report.

4. Project Expenditures

This section presents the project expenses during the month of February (**Table 5**) and the cumulative expenditure.

Table 5: Current and cumulative expenditures, February 2015

No.	Budget Categories	Current Expenses	Cumulative Expenses
1	Salaries & Wages	$11,640.00	$378,279.37
2	Fringe Benefits	$2,971.00	$84,554.28
3	Project Materials	$1,790.00	$108,546.93
4	Travel	$119.00	$10,838.04
5	Conference Expenses	$0.00	$0.00
6	Other Direct Costs	$45.00	$1,655.97
7	Equipment	$1,933.00	$254,038.47
8	Space Rental	$0.00	$0.00
9	Indirect Cost	$8,283.00	$290,902.93
10	**Total**	**$26,781.00**	**$1,128,815.99**

Nomenclature

A	Exposed surface area, cm^2
API	American Petroleum Institute
ASTM	American Society for Testing and Materials
CR	Average corrosion rate, mpy
E	Young's modulus measured before corrosion test
E*	Young's modulus measured after corrosion test
LPR	Linear polarization resistance
mpy	mils per year
MYS	maximum yield strength
NACE	National Association of Corrosion Engineers
PSF	Plastic strain to failure,
SCC	Stress corrosion cracking
SSC	Sulfide stress cracking
t	Test duration, hr
UTS	Ultimate tensile strength
w_1	Initial specimen weight
w_2	Final specimen weight
YS	Yield strength

References

Valdes, A., Case, R., Ramriez, M. and Ruiz, A. 1998. The Effect of Small Amounts of H2S on CO2 Corrosion of Carbon Steel, Paper no. 98022, NACE International, 22-27 March, San Diego, California.

Project Title: Effect of H_2S and CO_2 in HPHT Wells on Tubulars and Cement

Report Type: Monthly Report

Report #: 42

Reporting Period: February 22nd, 2015 to March 21st, 2015

Authors:

Ramadan Ahmed, Principal Investigator

Subhash Shah, Co-Principal Investigator

Rida Elgaddafi, Research Assistant

Omotayo Omosebi, Research Assistant

Jueun Hwang, Research Assistant

Jiwon Jeon, Research Assistant

Prepared under BSEE Project # E12PC00035

by

THE UNIVERSITY OF OKLAHOMA

April 10, 2015

1. Summary of Accomplishments

This monthly report presents the progress made during the project period February 22, 2015 to March 21, 2015. Experimental studies on tubular corrosion have been completed. Uniform and stress-cracking corrosion experiments were performed under high-pressure condition using minipipes and flat coupons. Mechanical properties of test specimens were measured to assess the level of corrosion. Moreover, we are preparing the final project report and presentations. The final project presentation is scheduled for 28th of May 2015.

During this month, three uniform corrosion tests were performed using different grades of carbon steel (Grades T95, C110 and Q125). Results showed the impact of H_2S concentration on uniform corrosion of T95. The corrosion rate varied with H_2S concentration, demonstrating a trend very similar to that of C110. The experiment with Q125 was conducted under dynamic condition, rotating the inner bob (rotor) of the uniform corrosion cell at 1000 revolutions per minute (rpm). Under dynamic condition, remarkably high corrosion rate (nearly ten-fold) was observed. Ionic diffusion enhancement and prevention of protective scale formation due to turbulence and wall shear stress increased the corrosion rate significantly.

During this reporting period, two stress-cracking corrosion (SSC) tests were conducted using T95 and Q125. Internal and external pressures of specimen were maintained at 4000 and 6000 psi, respectively. Mechanical properties of the specimens were measured before and after the test. As presented in the previous report (Report # 41), plastic strain to failure (PSF) and ultimate tensile strength (UTS) measurements obtained from C110 and Q125 indicated the presence of favorable condition for severe SSC to occur at approximately 10% CO_2 concentration. In order to verify this for T95, tests were performed varying carbon dioxide concentration from 15 to 25%. H_2S concentration was maintained at 300 ppm. Results obtained from T95 experiment demonstrated similar behavior with a minimum PSF at around 10% CO_2 concentration.

2. Overall Project Progress

2.1 Experimental Studies on Corrosion of Tubulars (Task 3)

2.1.1 Sulfide Stress Cracking

Experimental study on sulfide stress cracking (SSC) behavior of API carbon steel has been completed. **Table 1** summarizes all SSC tests conducted in the project. The table provides detailed information on experimental conditions in which specimens were exposed. During this reporting period, two tests (Tests 21 to 24) were performed using T95 and Q125. Internal and external pressures of specimen were maintained at 4000 and 6000 psi, respectively. Carbon dioxide concentration was varied from 15 to 25%. Our previous measurements with C110 and Q125 indicated the presence of a minimum PSF at around 10% CO_2 concentration. T95 carbon steel was tested at 15% CO_2 to verify if it exhibits a similar PSF trend.

Table 1: Specimen corrosion testing conditions

Test #	Label	Temp. (°F)	Pressure (psi)		Gas Composition			Time Duration	Remarks
			Inside	Outside	H2S (ppm)	CH4 (%)	CO2 (%)	(Days)	
1	01-C110-07/25-08/06	100	6000	4000	0	100	0	15	
2	02-C110-08/25-08/25	-	-	-	-	-	-	-	Baseline for C110
3	03-C110-08/27-09/03	100	6000	4000	270	90	10	7	Sample failed after 7 days of exposure
4	04-C110-09/05-09/12	100	6000	4000	300	100	0	7	
5	05-C110-09/05-09/13	100	6000	4000	285	95	5	7	
6	06-C110-09/05-09/14	100	6000	4000	270	90	10	7	Brine completely leaked from the cell
7	07-C110-10/17-10/24	100	6000	4000	255	85	15	7	
8	08-C110-10/28-11/04	100	6000	4000	270	90	10	7	
9	09-C110-11/05-11/12	100	6000	4000	293	97.5	2.5	7	
10	10-C110-11/13-11/20	100	6000	4000	270	90	10	7	Sample failed after 7 days of exposure
11	11-C110-12/02-12/09	100	6000	4000	255	85	15	7	
12	12-Q125-11/24-11/24	-	-	-	-	-	-	-	Baseline for Q125
13	13- Q125-11/24-12/01	100	6000	4000	270	90	10	7	
14	14- Q125-12/10-12/17	100	6000	4000	0	100	0	7	
15	15 - T95-12/10-12/10	-	-	-	-	-	-	-	Baseline for T95
16	16- Q125-12/17-12/24	100	6000	4000	300	100	0	7	
17	17 - T95-01/05-01/12	100	6000	4000	0	100	0	7	
18	18 - T95-01/13-01/20	100	6000	4000	300	100	0	7	
19	19- Q125-01/20-01/27	100	6000	4000	293	97.5	2.5	7	
20	20 - T95-01/27-02/03	100	6000	4000	293	97.5	2.5	7	
21	21-Q125-0203-0210	100	6000	4000	300	95	5	7	
22	22-Q125-0210-0217	100	6000	4000	300	85	15	7	
23	23-T95-0217-0224	100	6000	4000	300	95	5	7	
24	24-T95-0224-0303	100	6000	4000	300	90	10	7	
25	**25-T95-0311-0318**	**100**	**6000**	**4000**	**300**	**85**	**15**	**7**	
26	**26-Q125-0325-0401**	**100**	**6000**	**4000**	**300**	**75**	**25**	**7**	**Sample failed after 7 days of exposure**

Mechanical properties of samples, measured before and after corrosion experiment, are summarized in **Table 2**. UTS and PSF were obtained from complete tensile strength test. Hence, they were only measured after exposing specimens to corrosive environment. These measurements are well correlated with sulfide stress cracking phenomenon (i.e. sulfide embrittlement) that occurs when metals are subjected to high tensile stress loading in environment containing hydrogen sulfide. In this study, specimens were exposed to stress level of 85% of their minimum yield strength specified by the manufacturers.

Table 2: Mechanical properties of samples before and after corrosion test

Minipipe No.	Before Exposure				After Exposure			
	YS (psi)	UTS (psi)	PSF	E (psi)	YS (psi)	UTS (psi)	PSF	E* (psi)
1	-	-	-	-	109,855	127,619	0.030	11,785,921
2	111,529	130,156	0.040	11,842,002	-	-	-	-
3	-	-	-	11,704,810	-	100799	0.000	-
4	-	-	-	12,594,080	112768	134981	0.043	12,078,823
5	-	-	-	10,911,219	102217	114424	0.023	11,368,960
6	-	-	-	11,599,401	110686	130118	0.049	11,444,081
7	-	-	-	11,221,136	-	115479	0.014	11,561,000
8	-	-	-	12,044,218	-	120026	0.069	11,441,529
9				11,792,032		116742	0.036	11,255,892
10	-	-	-	13,377,764	-	100799	0.000	-
11	-	-	-	13,377,764		118484	0.035	13,527,372
12	150,072	169,282	0.051	13,580,537	-	-	-	-
13	-	-	-	13,594,795	132,903	152,493	0.028	11,757,738
14	-	-	-	13,890,878	144,533	165,460	0.080	7,321,033
15	95,399	121,115	0.058	12,125,404	-	-	-	-
16	-	-	-	10,613,970	144,528	164,641	0.084	10,642,228
17	-	-	-	8,916,085	105,167	122,075	0.135	7,031,822
18	-	-	-	7,477,965	101,540	121,952	0.137	10,000,342
19	-	-	-	10,431,875	141,344	162,711	0.066	6,395,980
20	-	-	-	7,676,120	105,217	119,540	0.126	7,580,194
21	-	-	-	6,744,550	136,403	156,584	0.049	8,431,876
22	-	-	-	9,507,949	134,333	156,737	0.050	8,740,819
23	-	-	-	8,724,446	103,495	117,293	0.126	9,335,596
24	-	-	-	8,366,828	101,594	115,885	0.106	8,796,036
25	**-**	**-**	**-**	**8,562,738**	**103,133**	**117,799**	**0.116**	**9,205,450**
26	**-**	**-**	**-**	**9,052,546**	**-**	**109,037**	**0.000**	**-**

UTS = Ultimate tensile strength, PSF = Plastic strain to failure, YS = Yield strength, E = Young's modulus before exposure, E* = Young's modulus after exposure

Figure 1 presents measured PSF and UTS of T95 as a function of CO_2 concentration. At low concentration (less than 10% CO_2), PSF and UTS reduced with the concentration. The reduction trend indicates the embrittlement occurring in the material. As CO_2 content was increased above 10%, the

trend was reversed and slight enhancement in PSF and UTS was observed. As presented in Report # 41, similar PSF and UTS trends were observed when other steel grades (Q125 and C110) were tested.

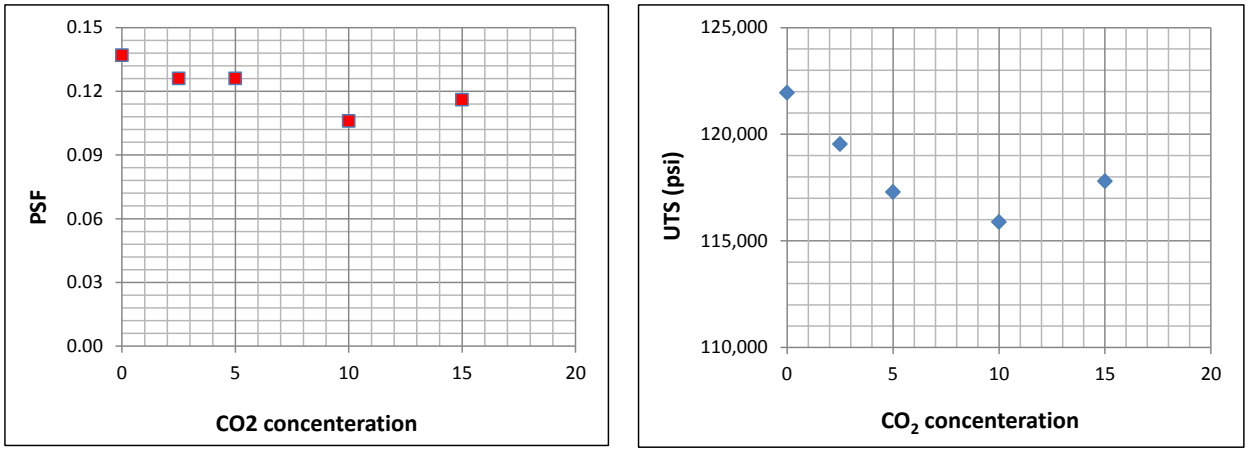

Fig. 1: PSF and UTS versus CO_2 concentration

2.1.2 Uniform Corrosion in Sour Gas Environment

High-pressure uniform corrosion experiments were completed during this month. Three corrosion tests (highlighted in **Table 3**) were conducted to assess corrosion behavior of API carbon steels in CO_2 environment. Experiments were performed at 6000 psi and 50% CO_2 and varying H_2S concentration. In addition, one batch of dynamic corrosion test was carried out. Two grades of carbon steel (T95 and Q125) were tested during this reporting period. Test temperature and salt concentration were maintained at 100°F and 2% NaCl, respectively.

Table 3: Test conditions for HPHT uniform corrosion tests

Batch No.	Material	Pressure (psi)	Temp. (°F)	Duration (Days)	CO_2 Conc. (%)	CH_4 Conc. (%)	H_2S Conc. (ppm)
001	C110	6000	100	7	100	0	0
002	C110	6000	100	7	50	50	0
003	C110	6000	100	7	0	100	0
004	C110	6000	100	7	25	75	0
005	C110	6000	100	7	75	25	0
006	C110	9000	100	7	100	0	0
007	C110	3000	100	7	0	100	0
008	C110	9000	100	7	75	25	0
009	C110	9000	100	7	50	50	0
010	C110	9000	100	7	25	75	0
011	C110	9000	100	7	0	100	0
012	C110	3000	100	7	75	25	0
013	C110	3000	100	7	100	0	0
014	Q125	6000	100	7	50	50	0
015	Q125	9000	100	7	50	50	0
016	T95	6000	100	7	50	50	0
017	T95	9000	100	7	50	50	0

018	C110	6000	100	7	50	0	10
019	C110	6000	100	7	50	0	50
020	Q125	6000	100	7	75	25	0
021	Q125	6000	100	7	100	0	0
022	**Q125**	**6000**	**100**	**7**	**0**	**100**	**0**
023	**Q125**	**6000**	**100**	**7**	**25**	**75**	**0**
024	**T95**	**6000**	**100**	**7**	**75**	**25**	**0**
025	**T95**	**6000**	**100**	**7**	**100**	**0**	**0**
026	**T95**	**6000**	**100**	**7**	**25**	**75**	**0**
027	**T95**	**6000**	**100**	**7**	**0**	**100**	**0**
028	**Q125**	**6000**	**100**	**7**	**50**	**0**	**10**
029	**Q125**	**6000**	**100**	**7**	**50**	**0**	**50**
030	**T95**	**6000**	**100**	**7**	**50**	**-**	**10**
031*	**Q125**	**6000**	**100**	**7**	**50**	**50**	**0**
032	**T95**	**6000**	**100**	**7**	**50**	**-**	**50**

* Batch 031 was conducted under dynamic condition (rotor speed of 1000 rpm)

Figures 2 presents the impact of H_2S concentration on uniform corrosion rate of T95 in 2% NaCl solution saturated with mixed gas containing 50% CO_2 and 50% methane. These measurements were obtained from tests conducted at 6000 psi and 100°F. The results demonstrate a corrosion rate trend, which is very similar to that of C110 (**Fig. 3**). At low H_2S concentration (less than 10 ppm), the rate increased with increasing concentration of hydrogen sulfide. Above 10 ppm of H_2S, the corrosion rate declined as the H_2S concentration was increased. The reduction in the corrosion rate occurs due to the formation of a protective corrosion scale. The corrosion rate trend observed in these experiments is consistent with published results obtained from tests performed at low pressure (Valdes et al. 1998).

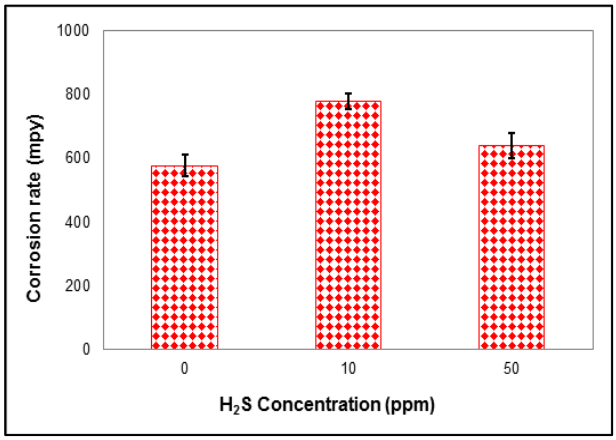

Fig. 2: Corrosion rate of T95 as a function of H_2S concentration (100°F, 50% CO_2 and 6000 psi)

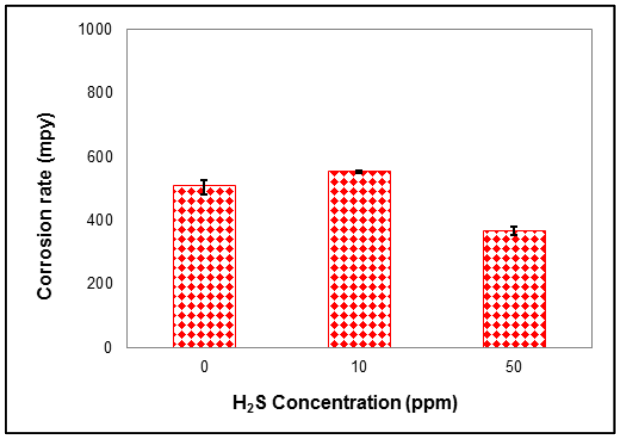

Fig. 3: Corrosion rate of C110 as a function of H_2S concentration (100°F, 50% CO_2 and 6000 psi)

Furthermore, the influence of fluid movement (i.e. wall shear stress and turbulence) on the corrosion rate of Q125 at 6000 psi and 50% CO_2 concentration was investigated (**Fig. 4**). As presented in Report # 10, the uniform corrosion cell is equipped with a rotating inner bob. Under dynamic condition, remarkably high corrosion rate (nearly ten-fold) was observed as rotor speed was increased from 0 to

1000 rpm. Possible explanation for the sharp increase in corrosion rate can be the occurrence of two natural phenomena, namely diffusion enhancement and prevention of protective scale formation. Often corrosion process is controlled by corrosive species (ions) transport rate (diffusion rate). Corrosion occurs when corrosive species reach the steel surface from the bulk (i.e. mass transfer rate). Increasing the rotational speed under turbulent flow condition increases momentum and species diffusion. Improved diffusion rate tends to increase the corrosion rate through the enhancement of the rate-controlling phenomenon. In addition, the development of higher wall shear stress at the metal surface can affect the integrity and formation of the corrosion scale. The results obtained from these experiments are consistent with published experimental studies (Nor et al., 2011; Nor et al., 2012 and Farelas et al., 2013) conducted at low pressure.

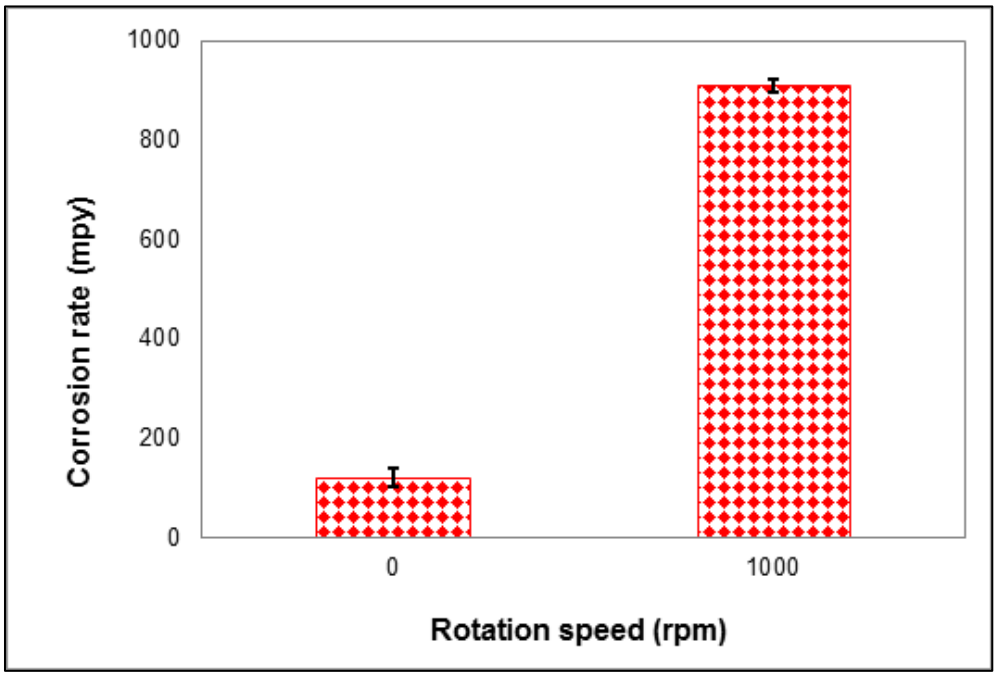

Fig. 4: Effect of rotational speed on corrosion rate of Q125 at 6000 psi, 100°F and 50% CO_2

Results presented in **Table 4** show mechanical properties of specimens measured before and after exposure to the corrosive environment. The new experiments are highlighted. Results demonstrate the occurrence of significant corrosion after the exposure as exhibited by considerable change in mechanical measurements after exposure.

Table 4: Corrosion rate and mechanical properties of specimens before and after corrosion test

Batch No.	Specimen No.	CO_2 Con.%	Initial weight gm	Final weight gm	CR (mpy)	E (psi)	E* (psi)	Yield strength (psi)	Tensile Strength (psi)
001	C110-1	100	13.3848	13.2129	234	5.79E+06	9.91E+06	107,560	123,600
	C110-2		13.4397	13.2212	297	6.02E+06	8.62E+06	105,950	119,933
	C110-3		13.4478	13.2323	293	7.71E+06	9.44E+06	108,140	120,673
002	C110-1	50	13.4875	13.1076	517	1.07E+07	8.57E+06	104,960	117,283
	C110-2		13.3884	13.0029	524	5.10E+06	9.01E+06	97,180	116,388
	C110-3		13.3376	12.9835	482	5.54E+06	8.25E+06	95,140	116,198

Batch No.	Specimen No.	CO_2 Con.%	Initial weight gm	Final weight gm	CR (mpy)	E (psi)	E* (psi)	Yield strength (psi)	Tensile Strength (psi)
003	C110-1	0	13.4459	13.3916	74	1.00E+07	7.76E+06	93,250	130,891
	C110-2		13.4196	13.3924	37	1.15E+07	8.43E+06	96,780	131,917
	C110-3		13.3234	13.2680	75	1.07E+07	8.25E+06	96,940	129,187
004	C110-1	25	13.3739	12.949	578	8.75E+06	8.13E+06	91,000	113,833
	C110-2		13.3092	12.9818	445	8.48E+06	6.99E+06	95,510	116,450
	C110-3		13.4018	13.0782	440	8.15E+06	8.44E+06	94,880	117,009
005	C110-1	75	13.4127	13.1079	415	8.71E+06	8.09E+06	103,240	111,286
	C110-2		13.4881	13.2212	363	1.10E+07	6.52E+06	101,290	112,891
	C110-3		13.4635	12.9808	657	8.43E+06	6.01E+06	101,000	111,062
006	C110-1	100	13.4039	13.1518	343	1.14E+07	8.43E+06	100,000	116,283
	C110-2		13.3703	12.9598	558	1.08E+07	8.57E+06	96,410	113,007
	C110-3		13.4606	13.2294	315	1.10E+07	6.36E+06	95,570	117,066
007	C110-1	0	13.4169	13.3859	42	9.98E+06	6.96E+06	100,920	130,212
	C110-2		13.4447	13.4144	41	9.29E+06	6.94E+06	100,530	130,658
	C110-3		13.4041	13.3635	55	9.47E+06	7.05E+06	101,170	128,982
008	C110-1	75	13.3681	12.9327	592	7.74E+06	8.37E+06	97,530	110,554
	C110-2		13.4538	13.0456	555	7.97E+06	8.67E+06	99,660	110,922
	C110-3		13.3742	12.9952	516	8.44E+06	9.24E+06	100,480	112,723
009	C110-1	50	13.4238	12.9867	595	1.14E+07	8.15E+06	97,480	111,270
	C110-2		13.2956	13.0504	334	8.45E+06	8.55E+06	98,740	118,488
	C110-3		13.4920	13.1036	528	8.47E+06	8.35E+06	102,700	113,291
010	C110-1	25	13.3937	13.092	410	9.30E+06	8.33E+06	99,250	119,451
	C110-2		13.3812	12.9699	559	1.23E+07	7.15E+06	101,270	114,472
	C110-3		13.3518	12.9320	571	1.25E+07	7.36E+06	100,120	112,456
011	C110-1	0	13.4399	13.4033	50	8.81E+06	5.89E+06	107,870	129,910
	C110-2		13.3882	13.3497	52	9.25E+06	7.43E+06	110,000	128,725
	C110-3		13.4730	13.4332	54	1.10E+07	8.06E+06	106,890	127,023
012	C110-1	100	13.3637	12.9442	571	1.20E+07	7.52E+06	99,760	110,045
	C110-2		13.3376	12.9346	548	1.19E+07	5.62E+06	100,570	111,029
013	C110-1	75	13.3668	13.2191	201	1.10E+07	6.20E+06	101,540	121,867
	C110-2		13.3789	13.1548	305	1.01E+07	6.31E+06	101,200	120,463
014	Q125 -1	50	13.2108	13.1086	139	1.07E+07	8.20E+06	117,600	155,273
	Q125-2		12.9513	12.8756	103	9.03E+06	7.88E+06	116,830	151,903
015	Q125-1	50	13.0443	12.9842	82	1.18E+07	8.28E+06	117,070	151,036
	Q125-2		13.2890	13.2249	87	9.03E+06	9.19E+06	120,140	157,005
016	T95-1	50	13.5557	13.1052	613	8.58E+06	7.37E+06	93,240	103,405
	T95-2		13.1735	12.7736	544	7.35E+06	8.24E+06	90,980	103,170
017	T95-1	50	13.3376	13.0653	370	6.21E+06	7.44E+06	90,190	109,001
	T95-2		13.2942	12.9121	520	5.40E+06	7.33E+06	90,170	105,425
018	C110-1	50	13.3801	12.9783	547	8.60E+06	8.48E+06	100,050	114,088
	C110-2		13.4545	13.0451	557	8.06E+06	8.05E+06	102,670	114,466
019	C110-1	50	13.246	12.9677	379	8.21E+06	9.65E+06	100,300	112,331
	C110-2		13.2357	12.9752	354	8.04E+06	9.26E+06	107,350	114,472
020	Q125 -1	75	13.3003	13.0650	320	8.78E+06	9.25E+06	126,180	148,642
	Q125-2		13.2306	12.9783	343	8.07E+06	8.83E+06	125,720	145,371
021	Q125 -1	100	13.1388	12.8640	374	8.12E+06	8.85E+06	122,660	142,615
	Q125-2		12.9428	12.6524	395	8.64E+06	7.64E+06	122,990	140,851

Batch No.	Specimen No.	CO_2 Con.%	Initial weight gm	Final weight gm	CR (mpy)	E (psi)	E* (psi)	Yield strength (psi)	Tensile Strength (psi)
022	Q125 -1	0	12.9684	12.8976	96	8.23E+06	7.67E+06	130,800	151,123
	Q125-2		13.2393	13.1888	69	8.30E+06	7.96E+06	133,100	157,469
023	Q125 -1	25	13.2973	12.9259	505	9.45E+06	8.80E+06	127,700	141,463
	Q125-2		13.2585	12.8393	570	8.51E+06	8.11E+06	120,500	140,209
024	T95-1	75	13.2812	12.6815	816	8.59E+06	7.83E+06	87,500	96,891
	T95-2		13.1886	12.6272	764	8.59E+06	7.18E+06	87,830	98,713
025	T95-1	100	13.1777	12.4770	953	7.53E+06	7.00E+06	83,840	92,673
	T95-2		13.5060	12.8808	850	8.60E+06	7.58E+06	86,600	96,532
026	T95-1	25	13.1866	12.6496	730	9.03E+06	8.35E+06	89,610	98,581
	T95-2		13.2638	12.7952	637	8.64E+06	7.77E+06	91,660	102,082
027	T95-1	0	13.1711	12.8920	380	8.59E+06	8.63E+06	96,050	107,909
	T95-2		13.6589	13.3721	390	8.47E+06	7.49E+06	101,110	111,145
028	Q125 -1	50	13.0742	12.8092	360	7.67E+06	8.72E+06	125,490	141,986
	Q125-2		13.0549	12.7815	372	9.30E+06	8.15E+06	124,980	144,785
029	Q125 -1	50	13.0385	12.7462	398	8.79E+06	8.06E+06	122,070	142,666
	Q125-2		13.0300	12.7461	386	8.38E+06	8.42E+06	123,750	136,764
030	**T95-1**	**50**	**13.2402**	**12.6493**	**804**	**8.64E+06**	**8.49E+06**	**88,330**	**95,708**
	T95-2		**13.2607**	**12.6008**	**898**	**9.46E+06**	**8.04E+06**	**83,600**	**92,865**
031*	**Q125 -1**	**50**	**13.2407**	**12.5630**	**922**	**8.17E+06**	**7.12E+06**	**121,600**	**134,114**
	Q125-2		**13.2171**	**12.7181**	**679**	**9.36E+06**	**8.30E+06**	**122,620**	**133,815**
032	**T95-1**	**50**	**13.2512**	**12.8109**	**599**	**8.51E+06**	**8.12E+06**	**87,290**	**97,884**
	T95-2		**13.2402**	**12.6493**	**804**	**8.40E+06**	**8.64E+06**	**91,270**	**100,457**

E and E* are Young's modulus measured before and after exposure, respectively. * Batch 031 was conducted under dynamic condition (rotor speed of 1000 rpm)

3. Project Expenditures

This section presents the project expenses during the month of March (**Table 5**) and the cumulative expenditure.

Table 5: Current and cumulative expenditures, March 2015

No.	Budget Categories	Current Expenses	Cumulative Expenses
1	Salaries & Wages	$3,867.20	$382,146.57
2	Fringe Benefits	($261.46)	$84,292.82
3	Project Materials	($429.29)	$108,117.64
4	Travel	$138.18	$10,976.22
5	Conference Expenses	$0.00	$0.00
6	Other Direct Costs	$661.49	$2,317.46
7	Equipment	($1,121.47)	$252,917.00
8	Space Rental	$0.00	$0.00
9	Indirect Cost	$3,022.43	$293,925.36
10	**Total**	**$5,877.08**	**$1,134,693.07**

Nomenclature

A	Exposed surface area, cm^2
API	American Petroleum Institute
ASTM	American Society for Testing and Materials
CR	Average corrosion rate, mpy
E	Young's modulus measured before corrosion test
E*	Young's modulus measured after corrosion test
mpy	mils per year
MYS	maximum yield strength
NACE	National Association of Corrosion Engineers
PSF	Plastic strain to failure,
SCC	Stress corrosion cracking
SSC	Sulfide stress cracking
t	Test duration, hr
UTS	Ultimate tensile strength
w_1	Initial specimen weight
w_2	Final specimen weight
YS	Yield strength

References

Farelas, F., Choi Y.-S. Nesic, S., Magalhães A. A.O., and de Azevedo Andrade C. 2013. Corrosion Behavior of Deep Water Oil Production Tubing Material under Supercritical CO_2 Environment: Part II. Effect of Crude Oil and Flow, NACE paper No. 2381, 17-21 March, Orlando, Florida.

Nor A. M., Suhor, M.F., Mohamed, M.F., Singer, M. and Nesic, S. 2011. Corrosion of Carbon Steel in High CO2 Environment: Flow Effect, NACE paper No. 11242, 13-17 March, Houston, Texas.

Nor, A. M., Suhor, M.F., Mohamed, M.F., Singer, M. and Nesic, S. 2012. Corrosion Of Carbon Steel In High CO_2 Containing Environments - The Effect Of High Flow Rate, NACE paper No. 1683, 11-15 March, Salt Lake City, Utah.

Valdes, A., Case, R., Ramriez, M. and Ruiz, A. 1998. The Effect of Small Amounts of H_2S on CO_2 Corrosion of Carbon Steel, Paper no. 98022, NACE International, 22-27 March, San Diego, California.